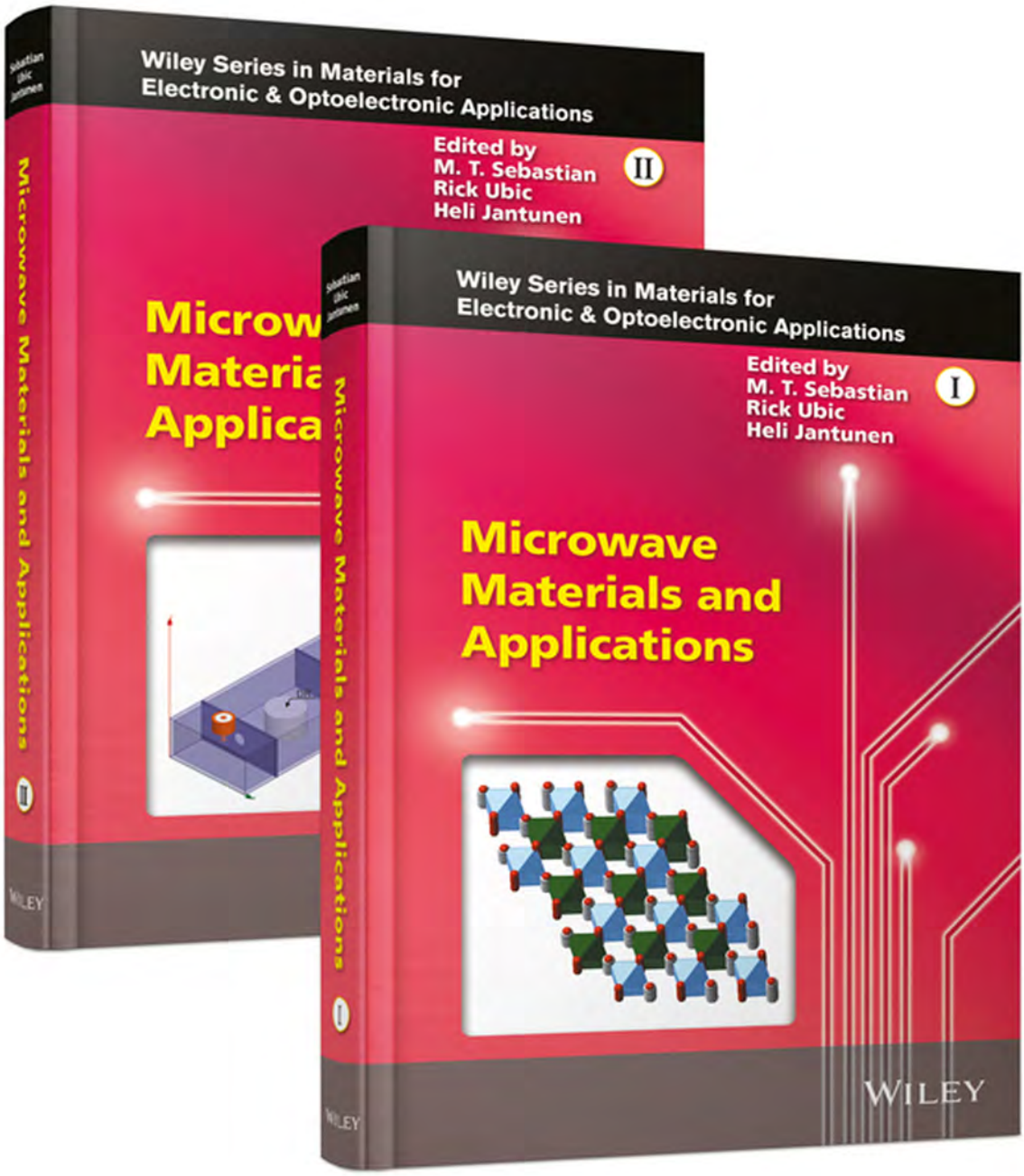
Wiley Series in Materials for
Electronic & Optoelectronic Applications
Edited by
M. T. Sebastian
Rick Ubic
Heli Jantunen
II
Microwave Materials and Applications
Wiley Series in Materials for
Electronic & Optoelectronic Applications
Edited by
M. T. Sebastian
Rick Ubic
Heli Jantunen
I
Microwave
Materials and
Applications
WILEY

Microwave Materials and Applications

Wiley Series in Materials for Electronic and Optoelectronic Applications

www.wiley.com/go/meoa

Series Editors

Professor Arthur Willoughby, *University of Southampton, Southampton, UK*

Dr Peter Capper, *SELEX Galileo Infrared Ltd, Southampton, UK*

Professor Safa Kasap, *University of Saskatchewan, Saskatoon, Canada*

Published Titles

Bulk Crystal Growth of Electronic, Optical and Optoelectronic Materials, Edited by P. Capper

Properties of Group-IV, III–V and II–VI Semiconductors, S. Adachi

Charge Transport in Disordered Solids with Applications in Electronics, Edited by S. Baranovski

Optical Properties of Condensed Matter and Applications, Edited by J. Singh

Thin Film Solar Cells: Fabrication, Characterization, and Applications, Edited by J. Poortmans and V. Arkhipov

Dielectric Films for Advanced Microelectronics, Edited by M. R. Baklanov, M. Green, and K. Maex

Liquid Phase Epitaxy of Electronic, Optical and Optoelectronic Materials, Edited by P. Capper and M. Mauk

Molecular Electronics: From Principles to Practice, M. Petty

CVD Diamond for Electronic Devices and Sensors, Edited by R. S. Sussmann

Properties of Semiconductor Alloys: Group-IV, III–V, and II–VI Semiconductors, S. Adachi

Mercury Cadmium Telluride, Edited by P. Capper and J. Garland

Zinc Oxide Materials for Electronic and Optoelectronic Device Applications, Edited by C. Litton, D. C. Reynolds, and T. C. Collins

Lead-Free Solders: Materials Reliability for Electronics, Edited by K. N. Subramanian

Silicon Photonics: Fundamentals and Devices, M. Jamal Deen and P. K. Basu

Nanostructured and Subwavelength Waveguides: Fundamentals and Applications, M. Skorobogatiy

Photovoltaic Materials: From Crystalline Silicon to Third-Generation Approaches, Edited by G. Conibeer and A. Willoughby

Glancing Angle Deposition of Thin Films: Engineering the Nanoscale, Matthew M. Hawkeye, Michael T. Taschuk, and Michael J. Brett

Microwave Materials and Applications

Volume I

Edited by

MAILADIL T. SEBASTIAN
University of Oulu, Finland

RICK UBIC
Boise State University, ID, US

HELI JANTUNEN
University of Oulu, Finland

WILEY

This edition first published 2017
© 2017 John Wiley & Sons, Ltd

All rights reserved. No part of this publication may be reproduced, stored in a retrieval system, or transmitted, in any form or by any means, electronic, mechanical, photocopying, recording or otherwise, except as permitted by law. Advice on how to obtain permission to reuse material from this title is available at http://www.wiley.com/go/permissions.

The right of Mailadil T. Sebastian, Heli Jantunen and Rick Ubic to be identified as the authors of the editorial material in this work has been asserted in accordance with law.

Registered Offices
John Wiley & Sons, Inc., 111 River Street, Hoboken, NJ 07030, USA
John Wiley & Sons Ltd, The Atrium, Southern Gate, Chichester, West Sussex, PO19 8SQ, UK

Editorial Office
The Atrium, Southern Gate, Chichester, West Sussex, PO19 8SQ, UK

For details of our global editorial offices, customer services, and more information about Wiley products visit us at www.wiley.com.

Wiley also publishes its books in a variety of electronic formats and by print-on-demand. Some content that appears in standard print versions of this book may not be available in other formats.

Limit of Liability/Disclaimer of Warranty: While the publisher and authors have used their best efforts in preparing this book, they make no representations or warranties with respect to the accuracy or completeness of the contents of this book and specifically disclaim any implied warranties of merchantability or fitness for a particular purpose. It is sold on the understanding that the publisher is not engaged in rendering professional services and neither the publisher nor the authors shall be liable for damages arising herefrom. If professional advice or other expert assistance is required, the services of a competent professional should be sought.

Library of Congress Cataloging-in-Publication Data

Names: Sebastian, M. T., 1952– editor. | Jantunen, Heli, editor. | Ubic, Rick, editor.
Title: Microwave materials and applications / edited by Dr. Mailadil T. Sebastian, Dr. Heli Jantunen, Dr. Rick Ubic.
Description: Chichester, UK ; Hoboken, NJ : John Wiley & Sons, 2017. | Includes bibliographical references and index.
Identifiers: LCCN 2016052142 | ISBN 9781119208525 (cloth) | ISBN 9781119208556 (epub)
Subjects: LCSH: Microwave devices–Materials. | Dielectrics.
Classification: LCC TK7876 .M2545 2017 | DDC 621.381/30284–dc23
LC record available at https://lccn.loc.gov/2016052142

A catalogue record for this book is available from the British Library.

ISBN: 9781119208525

Set in 10/12pt TimesLTStd by Aptara Inc., New Delhi, India

10 9 8 7 6 5 4 3 2 1

Contents

VOLUME I

List of Contributors **xv**
Series Preface **xvii**
Preface **xix**

1. Measurement of Microwave Dielectric Properties and Factors Affecting Them **1**
M.T. Sebastian, M.A.S. Silva, and A.S.B. Sombra

1.1 Introduction 1
1.2 Permittivity (ε_r) and quality factor (Q) 2
1.3 Measurement of Microwave Dielectric Properties 7
1.4 Methods of Measurement 8
1.4.1 Hakki and Coleman (Courtney) Method 8
1.4.2 $TE_{01\delta}$ Mode Dielectric Resonator Method 11
1.4.3 Measurement of the Quality Factor by a Strip Line Excited Using the Cavity Method 14
1.4.4 Whispering Gallery Mode (WGM) Resonators 17
1.4.5 Split Post Dielectric Resonator (SPDR) 18
1.4.6 Cavity Perturbation Method 20
1.4.7 TM_{0n0} Mode and Re-entrant Cavity Methods 21
1.4.8 TE_{01n} Mode Cavities 22
1.4.9 Thin Samples and Free-Space Methods 24
1.5 Measurement of EMI Shielding Effectiveness 29
1.5.1 Waveguide Method 29
1.6 Terahertz and Millimeter Wave Measurements 31
1.6.1 Backward Wave Oscillator (BWO) 31
1.6.2 Terahertz Time-Domain Spectroscopy (THz-TDS) 32
1.7 Measurement of Dielectric Properties of Powder Samples 34
1.8 Estimation of Dielectric Loss by Spectroscopic Methods 35
1.9 Factors Affecting Dielectric Loss 39
1.10 Measurement of Temperature Coefficient of Resonant Frequency 41
1.11 Tuning of the Resonant Frequency 42
References 45

2. Modeling of Microwave Dielectric Properties of Composites **53**
Marko Tuhkala, Merja Teirikangas, and Jari Juuti

2.1 Introduction 53
2.2 Connectivity 54
2.3 Electrostatic Theory 56
2.3.1 Polarizability 56
2.3.2 Scattering 56
2.3.3 Orientation 57
2.4 Mixing Equations 59
2.4.1 Clausius–Mossotti 60
2.4.2 Maxwell–Garnett 60
2.4.3 Bruggeman Symmetric 63
2.4.4 Bruggeman Non-symmetric 64
2.4.5 Sen Scala–Cohen 64
2.4.6 Coherent Potential 64
2.4.7 Looyenga 65
2.4.8 Lichtenecker 65
2.4.9 Modified Lichtenecker 66
2.4.10 Differential 66
2.4.11 General Mixing Model 67
2.4.12 Effective Medium Theory (EMT) 68
2.4.13 Jayasundere–Smith 69
2.4.14 Vo–Shi 70
2.4.15 Interphase Power Law (IPL) 71
2.5 Effect of Porosity 71
2.5.1 Permittivity 72
2.5.2 Dielectric Losses 73
2.5.3 Dielectric Properties of Powders 74
2.6 Conclusion 77
References 77

3. Perovskites **81**
K.P. Surendran and Rick Ubic

3.1 Introduction 81
3.2 Lattice Constant Prediction 83
3.3 Tolerance Factor 84
3.4 Octahedral Tilting 86
3.5 Simple Perovskites 87
3.5.1 $LnAlO_3$ Type Materials 87
3.5.2 $Ag(Nb_{1-x}Ta_x)O_3$ Type Materials 88
3.5.3 Ca-Based Perovskites 89
3.6 Cation Ordering 89
3.6.1 1:1 Ordered Perovskites 90
3.6.2 1:2 Ordering 103

3.6.3 1:3 Ordering 130
3.6.4 1:2:1 Ordering 132
3.7 Cation Deficient Perovskites 133
3.8 Summary 135
References 136

4. High Permittivity Materials 149
Rick Ubic, G. Subodh, and M.T. Sebastian

4.1 Introduction 149
4.2 The $BaO–Ln_2O_3–TiO_2$ System 149
4.2.1 Crystal Structure of $Ba_{6-3x}Ln_{8+2x}Ti_{18}O_{54}$ 151
4.2.2 Tolerance Factor and Its Effect on the Temperature Coefficient 154
4.2.3 Microwave Dielectric Properties of $BaO–Ln_2O_3–TiO_2$ System 155
4.3 The Effect of Processing Parameters on Electrical Properties 162
4.4 Titania 164
4.5 $Sr_{1-3x/2}Ce_xTiO_3$ Ceramics 166
4.5.1 Crystal Structure of $Sr_{1-3x/2}Ce_xTiO_3$ System 166
4.5.2 Microstructure and Dielectric Properties of SCT ceramics 172
4.5.3 $(Sr_{0.75-x}Pb_xCe_{0.167})TiO_3$ 173
4.6 $Pb_n(Nb_{1-x}Ta_x)O_{5+n}$ 174
4.6.1 $Pb_nNb_2O_{5+n}$ $(1.5 \leq n < 2)$ 176
4.6.2 $Pb_2Nb_2O_7$ 179
4.6.3 Pb-Rich Phases $(n > 2)$ 181
4.6.4 Doping Studies 182
4.6.5 Microwave Properties 182
4.7 $(Pb_{1-x}Ca_x)(Fe_{1/2}B_{1/2})O_3$ [B = Nb, Ta] 185
4.8 $Ag(Nb_{1-x}Ta_x)O_3$ 187
4.9 Summary 190
References 190

5. Millimeter-Wave Materials 203
Hitoshi Ohsato

5.1 Introduction: New Frontiers of Millimeter-Wave Dielectrics 203
5.2 Dielectric Properties for Millimeter Wave 207
5.2.1 Quality Factor Q 207
5.2.2 Dielectric Constant ε_2 208
5.2.3 Temperature Coefficient of Resonant Frequency τ_f 208
5.3 Candidates of Millimeter-Wave Dielectrics 209
5.4 Specialized Study 212
5.4.1 Forsterite 212
5.4.2 Willemite 222
5.4.3 Indialite/Cordierite Glass Ceramics 226
5.4.4 Other Silicates 232
5.4.5 Substituted Ge for Si 236

5.4.6 Corundum 242
5.4.7 Spinel 250
5.4.8 Borate, Phosphate, and Vanadate 255
Acknowledgments 259
References 259

6. Other Important Materials 267
M.T. Sebastian and R.C. Pullar

6.1 Spinel 267
6.1.1 $ZnAl_2O_4$ 267
6.1.2 $MgAl_2O_4$ 277
6.1.3 A_2TiO_4 (A = Mg, Zn) 280
6.2 $Li_2ATi_3O_8$ (A = Mg, Zn) Ceramics 280
6.2.1 Effect of Glass Addition in $Li_2ATi_3O_8$ (A = Mg, Zn) 284
6.3 $Li_2Zn_3Ti_4O_{12}$ 289
6.4 Apatites 290
6.4.1 $A_2RE_8(SiO_4)_6O_2$ ceramics 292
6.4.2 $(Ca, Ba)_2RE_8Si_6O_{26}$ (RE = Rare Earths) 295
6.4.3 $Ca_{2+x}RE_{8-x}(SiO_4)_{6-x}(PO_4)_xO_2$ (RE = Rare Earths) 297
6.4.4 Effect of Isovalent Substitutions in $Ca_4La_6(SiO_4)_4(PO_4)_2O_2$ 300
6.4.5 $LiRE_9(SiO_4)_6O_2$ (RE = Rare Earths) 302
6.5 Alumina 303
6.6 Zirconium Tin Titanate 306
6.7 Dielectric Materials in the $BaO–TiO_2$ System 314
6.7.1 $BaTi_4O_9$ 315
6.7.2 $BaTi_5O_{11}$ 316
6.7.3 $Ba_2Ti_9O_{20}$ 316
6.8 Columbite Niobates ($M^{2+}Nb_2O_6$) 318
6.8.1 Synthesis of Columbite Ceramics 320
6.8.2 Microwave Dielectric Properties of Columbites 322
6.8.3 Microwave Properties of Solid Solutions and Non-stoichiometric Columbites 325
Acknowledgments 327
References 328

7. Microwave Dielectric Properties of Glasses and Bulk Glass Ceramics 345
Martin Letz

7.1 Glasses 345
7.1.1 Silica Glass, a Special Glass System 346
7.1.2 Multicomponent Glasses 347
7.1.3 Solder Glasses, Sealing Glasses, Glass Joins, Passivation Glasses, and Glass Powder Additives 349
7.2 Bulk Glass Ceramics 349
7.2.1 The $BiNbO_4$ System 351
7.2.2 The $La_4Ti_9O_{24}$ and $La_2Ti_2SiO_9$ System 351

7.2.3 Properties of Glass Ceramics from the Lithium Aluminum Silicate System 352
7.2.4 Photosensitive Crystallizing Glasses 352
References 353

8. High Temperature Cofired Ceramic (HTCC), Low Temperature Cofired Ceramic (LTCC), and Ultralow Temperature Cofired Ceramic (ULTCC) Materials 355
M.T. Sebastian and Heli Jantunen

8.1 High Temperature Cofired Ceramics (HTCC) 355
8.1.1 Introduction 355
8.2 HTCC Alumina 357
8.3 Aluminium Nitride HTCC 359
8.4 $ZrSiO_4$ 361
8.5 Low Temperature Cofired Ceramics (LTCC) 366
8.5.1 Introduction 366
8.5.2 Important Characteristics of LTCC 367
8.5.3 Glass–Ceramic Composites 370
8.5.4 Microwave Dielectric Properties of Glasses 373
8.5.5 LTCC Materials and Their Properties 374
8.5.6 Constrained Sintering 390
8.6 Ultralow Temperature Cofired Ceramics (ULTCC) 395
8.6.1 Introduction 395
8.6.2 Ultralow Temperature Cofireable Ceramics (ULTCC Category II) 395
8.6.3 ULTCC Category I 406
8.7 Discussion and Conclusion 408
References 411

Index **i1**

VOLUME II

List of Contributors **xv**
Series Preface **xvii**
Preface **xix**

9. Voltage Tunable Microwave Dielectrics for Frequency and Phase Agile Devices 427
K. Sudheendran and K.C. James Raju

9.1 Introduction to Voltage Tunable Materials 427
9.2 Different Classes of Voltage Tunable Materials 428
9.2.1 Ferroelectric-Based Voltage Tunable Materials 428
9.2.2 Non-ferroelectric Voltage Tunable Materials 428
9.2.3 Multiferroic Voltage Tunable Materials 430

9.3 Importance of Voltage Tunable Materials in Frequency and Phase Agile Devices 432
9.3.1 Varactors in Frequency and Phase Agile Devices 432
9.4 Growth Techniques for Voltage Tunable Thin Films on Various Substrates 434
9.4.1 Pulsed Laser Deposition Technique 434
9.4.2 Sputter Deposition Techniques 435
9.4.3 Chemical solution deposition technique (CSD) 436
9.5 Characterization techniques 437
9.5.1 Low-Frequency Measurement of Ferroelectric Thin Films 438
9.6 High-Frequency Characterization 438
9.6.1 Modified Cavity Perturbation Technique 439
9.6.2 Calibration Comparison Technique 441
9.6.3 Extraction of the Conductor Loss 443
9.6.4 Tunability Measurement 446
9.6.5 Reflection Measurements 446
9.7 Design and Realization Aspects of Varactors Using Tunable Materials 449
9.7.1 Planar and Parallel Plate Structures 449
9.7.2 Realization and Characterization of the Varactors 451
9.8 Conclusions 454
Acknowledgment 454
References 454

10. Dielectric Inks 457
J. Varghese and M.T. Sebastian

10.1 Introduction 457
10.2 Methodology 461
10.2.1 Formulation of Printing Inks 461
10.3 Dielectric Inks and Their Properties 462
10.3.1 Preliminary Treatment of Ceramic Particles 462
10.3.2 Raw Materials Selection and Optimization for Screen Printable Ink 465
10.3.3 Rheology of Dielectric Inks 466
10.3.4 Microstructure and Surface Roughness of Printed Layers 467
10.3.5 Dielectric Properties of Printed Layers 470
10.4 Polymer-Based Dielectric Inks, Properties and Applications 473
10.5 Commercially Available Dielectric Inks, Properties and Applications 475
10.6 Conclusion 475
Acknowledgment 477
References 477

11. Polymer–Ceramic Composites for Microwave Applications 481
R. Ratheesh and M.T. Sebastian

11.1 Introduction: Microwave Substrates 481
11.2 Types of Polymer–Ceramic Composites 483

11.3 Thermoplastic Matrix and Composites 485
11.3.1 Poly(tertrafluoroethylene) 485
11.4 PTFE/Ceramic Composites 489
11.4.1 Preparation and Dielectric Properties 489
11.4.2 Temperature Variation of Relative Permittivity 496
11.4.3 Moisture Absorption Characteristics 498
11.4.4 Coefficient of Thermal Expansion 499
11.4.5 Mechanical Properties 501
11.5 Polyethylene–Ceramic Composites 502
11.6 Polystyrene–Ceramic Composites 507
11.7 Epoxy-Ceramic Composites 510
11.8 Liquid Crystal Polymer (LCP) 513
11.9 Thermal Conductivity 514
11.9.1 Geometric Mean Model 515
11.9.2 Effective Medium Theory (EMT) Model 515
11.9.3 Cheng–Vachon Model 515
11.9.4 Maxwell–Eucken Model 516
11.9.5 Nielson Model 516
11.9.6 Agari–Uno Model 516
11.10 Polymer Nanoceramic Composites 518
11.11 Ultrawideband Antenna Design Using Copper Cladded Ceramic-Filled PTFE Substrates 521
11.11.1 Antenna Configuration 522
11.12 Conclusion 526
References 527

12. Rubber–Ceramic Composites 537
M.T. Sebastian and L.K. Namitha

12.1 Introduction 537
12.2 Silicone Rubber 539
12.2.1 Introduction 539
12.2.2 Composite Preparation 541
12.2.3 Dielectric Properties 543
12.2.4 Mechanical Properties 549
12.2.5 Coefficient of Thermal Expansion (CTE) 550
12.2.6 Thermal Conductivity 550
12.2.7 Moisture Absorption of Composites 552
12.3 Butyl Rubber (BR) 553
12.3.1 Introduction 553
12.3.2 Preparation of Butyl Rubber (BR)–Ceramic Composites 554
12.3.3 Dielectric Properties 556
12.3.4 Bending 561
12.3.5 Thermal Conductivity 563
12.3.6 Mechanical Properties 564

12.3.7 Moisture Absorption of Composites 565
12.3.8 Coefficient of Thermal Expansion (CTE) 566
12.4 Fabrication of Flexible Microstrip Antenna 567
12.5 Conclusions 570
References 570

13. Designing of Materials for EMI Shielding Applications 575
Swati Varshney and S.K. Dhawan

13.1 Electromagnetic Shielding and Microwave Absorption Mechanism 577
13.2 Shielding Effectiveness (SE) 577
13.3 Measurement of Shielding Effectiveness 578
13.4 Electromagnetic Shielding Materials 581
13.5 New Insight into Designing of Materials for Microwave Shielding 583
13.6 Nanostructured Graphene/Fe_3O_4 Incorporated Polyaniline for EMI Shielding 584
13.7 Designing of Polypyrrole–γ-Fe_2O_3 Nanocomposite Wave Absorber 586
13.7.1 Magnetic Measurements 586
13.7.2 Microwave Absorption Investigations 587
13.7.3 Dielectric and Permeability Studies 588
13.8 Designing of Conducting Polymer Composite by Incorporating Ferrofluid 590
13.9 Designing of Polypyrrole–Aqueous Ferrofluid (PFF) Nanocomposite Microwave Absorber 593
13.9.1 Magnetic Measurements 593
13.9.2 Microwave Absorption Investigations 594
13.9.3 Dielectric and Permeability Studies 596
13.10 Conclusions 596
Acknowledgments 598
References 598

14. Microwave Ferrites and Applications 603
Vincent G. Harris

14.1 Introduction 603
14.2 Structure, chemistry, magnetism, and gyromagnetic properties 604
14.3 Ferrite Materials Processing for Microwave Applications 611
14.3.1 Ferrite Processing as Bulk Polycrystalline Substrates 612
14.3.2 Thin-Film Processing 612
14.3.3 Thick-Film Processing of Ferrites 617
14.4 Semiconductor Integration of Ferrite Thin and Thick Films for MIC Development 620
14.4.1 Selection of Semiconductor Substrate Materials 621
14.4.2 Ferrite Film Growth on Semiconductor Substrates 622
14.5 Ferrite–Based Microwave Device Development 628
14.5.1 Monolithic Integrated Circuits (MICs) 629
14.5.2 Microwave Materials Property Needs 630

14.5.3 Circulators and Isolators 632
14.5.4 Phase Shifters 635
14.5.5 Filters 639
14.6 Outlook 642
References 643

15. Applications of Microwave Dielectrics 653
Heike Bartsch, Alexander Schulz, Jens Müller, Alexander Ebert, Steffen Spira, Frank Wollenschläger, and Matthias Hein

15.1 General Requirements for Microwave Applications 653
15.2 LTCC Microwave Components and Materials 654
15.2.1 Conductor Patterning Technologies 654
15.2.2 Transmission Lines and Transitions 656
15.2.3 Lumped Passive Integrated Components 659
15.2.4 Integrated Functional Materials for Passives 663
15.3 LTCC Application Examples 666
15.3.1 Power Dividers 666
15.3.2 A 60 GHz Stripline Parallel Coupled Bandpass Filter 667
15.3.3 Integrated Antennas 671
15.3.4 Microwave Modules 674
References 676

16. Applications of Dielectric Resonators 683
P. Mohanan and S. Mridula

16.1 Introduction 683
16.2 Dielectric Resonator Antenna (DRA) 684
16.2.1 Excitation Techniques 686
16.2.2 Rectangular Dielectric Resonator Antenna 688
16.2.3 Resonant Modes of the DRA 693
16.2.4 Cylindrical DRA 696
16.2.5 Hemispherical DRA 696
16.3 Applications of Dielectric Resonator in Microwave Oscillators 698
16.3.1 Diode Oscillators 699
16.3.2 Transistor Oscillators 699
16.3.3 State of the Art DROs 702
16.4 Application of Dielectric Resonators in Microwave Filters 703
16.4.1 Dielectric Resonator Bandpass Filters 704
16.4.2 Tunable Dielectric Resonator Filters 706
16.4.3 State of the Art DR Filters 709
References 710

Appendix: List of Low-Loss Ceramic Dielectric Materials and Their Properties 715
M.T. Sebastian

Index **i1**

List of Contributors

Heike Bartsch, Electronics Technology Group, Department of Electrical Engineering and Information Technology, Technische Universität Ilmenau, lmenau, Germany

S.K. Dhawan, Polymeric and Soft Materials Section, National Physical Laboratory (CSIR), New Delhi, India

Alexander Ebert, RF and Microwave Research Laboratory, Department of Electrical Engineering and Information Technology, Technische Universität Ilmenau, lmenau, Germany

Vincent G. Harris, Center for Microwave Magnetic Materials and Integrated Circuits, Department of Electrical and Computer Engineering, Northeastern University, Boston, Massachusetts, USA

Matthias Hein, RF and Microwave Research Laboratory, Department of Electrical Engineering and Information Technology, Technische Universität Ilmenau, lmenau, Germany

K.C. James Raju, CASEST, School of Physics, University of Hyderabad, Hyderabad, India

Heli Jantunen, Microelectronics Research Unit, Faculty of Information Technology and Electrical Engineering, University of Oulu, Oulu, Finland

Jari Juuti, Microelectronics Research Unit, University of Oulu, Oulu, Finland

Martin Letz, SCHOTT AG, Research and Technology Development, Mainz, Germany

P. Mohanan, Department of Electronics, Cochin University of Science and Technology, Kochi, India

S. Mridula, Department of Electronics, Cochin University of Science and Technology, Kochi, India

Jens Müller, Electronics Technology Group, Department of Electrical Engineering and Information Technology, Technische Universität Ilmenau, lmenau, Germany

L.K. Namitha, Materials Science and Technology Division, CSIR-NIIST, Trivandrum, India

Hitoshi Ohsato, Nagoya Industrial Science Research Institute and Nagoya Institute of Technology, Nagoya, Japan; Microelectronics Research Unit, University of Oulu, Oulu, Finland

R.C. Pullar, Department of Materials and Ceramic Engineering/CICECO – Aveiro Institute of Materials, University of Aveiro, Campus Universitário de Santiago, Aveiro, Portugal

R. Ratheesh, Centre for Materials for Electronics Technology (CMET), Microwave Materials Division, Thrissur, India

Alexander Schulz, Electronics Technology Group, Department of Electrical Engineering and Information Technology, Technische Universität Ilmenau, lmenau, Germany

M.T. Sebastian, Microelectronics Research Unit, Faculty of Information Technology and Electrical Engineering, University of Oulu, Oulu, Finland

M.A.S. Silva, LOCEM–Laboratory of Telecommunications and Materials Science and Engineering, Physics Department, Federal University of Ceará (UFC), Ceará, Brazil

A.S.B Sombra, LOCEM–Laboratory of Telecommunications and Materials Science and Engineering, Physics Department, Federal University of Ceará (UFC), Ceará, Brazil

Steffen Spira, RF and Microwave Research Laboratory, Department of Electrical Engineering and Information Technology, Technische Universität Ilmenau, lmenau, Germany

G. Subodh, Department of Physics, Kerala Univeriversity, Trivandrum, India

K. Sudheendran, Department of Physics, Sree Kerala Varma College, University of Calicut, Thrissur, India

K.P. Surendran, Materials Science and Technology Division, CSIR NIIST, Trivandrum, India

Merja Teirikangas, Microelectronics Research Unit, University of Oulu, Oulu, Finland

Marko Tuhkala, Microelectronics Research Unit, University of Oulu, Oulu, Finland

Rick Ubic, Micron School of Materials Science and Engineering, Boise State University, Idaho, USA

J. Varghese, Microelectronics Research Unit, Faculty of Information Technology and Electrical Engineering, University of Oulu, Oulu, Finland

Swati Varshney, Polymeric and Soft Materials Section, National Physical Laboratory (CSIR), New Delhi, India; Department of Chemistry, Delhi Institute of Tool Engineering, Okhla, New Delhi, India

Frank Wollenschläger, RF and Microwave Research Laboratory, Department of Electrical Engineering and Information Technology, Technische Universität Ilmenau, lmenau, Germany

Series Preface

Wiley Series in Materials for Electronic and Optoelectronic Applications

This book series is devoted to the rapidly developing class of materials used for electronic and optoelectronic applications. It is designed to provide much-needed information on the fundamental scientific principles of these materials, together with how these are employed in technological applications. The books are aimed at (postgraduate) students, researchers, and technologists, engaged in research, development, and the study of materials in electronics and photonics, and industrial scientists developing new materials, devices, and circuits for the electronic, optoelectronic, and communications industries.

The development of new electronic and optoelectronic materials depends not only on materials engineering at a practical level but also on a clear understanding of the properties of materials and the fundamental science behind these properties. It is the properties of a material that eventually determine its usefulness in an application. The series therefore also includes such titles as electrical conduction in solids, optical properties, thermal properties, and so on, all with applications and examples of materials in electronics and optoelectronics.

The characterization of materials is also covered within the series in as much as it is impossible to develop new materials without the proper characterization of their structure and properties. Structure–property relationships have always been fundamentally and intrinsically important to materials science and engineering.

Materials science is well known for being one of the most interdisciplinary sciences. It is the interdisciplinary aspect of materials science that has led to many exciting discoveries, new materials, and new applications. It is not unusual to find scientists with a chemical engineering background working on materials projects with applications in electronics. In selecting titles for the series, we have tried to maintain the interdisciplinary aspect of the field, and hence its excitement to researchers in this field.

Arthur Willoughby
Peter Capper
Safa Kasap

Preface

A large number of papers continue to be published in the area of microwave materials and applications; however, there have hitherto been no books in the open literature that treat the different types of microwave materials, such as low-loss dielectric ceramics, glass ceramics, polymer- and elastomer-based composites, cofired ceramics, electromagnetic interference (EMI) shielding materials, tunable dielectrics, dielectric inks, or microwave ferrites. Our purpose here is to provide a comprehensive and self-consistent volume whereby the aforementioned lack of a reference book in the open literature can be remedied.

Microwave dielectric materials play a key role in global society, with a wide range of applications straddling terrestrial and satellite communications, including Internet of Things (IoT), software radio, GPS, DBS TV, environmental monitoring via satellite, etc. The mobile phone is one of the most widely spread technologies on the planet. In many countries the number of mobile subscriptions exceeds the population. The IoT is posed to make an explosive growth in the near future. In this paradigm, many everyday objects will be networked via radio-frequency identification (RFID), printed electronics, and sensor network technologies. Fifth generation (5G) mobile networks or wireless systems represent the next major phase of mobile telecommunication standards beyond the current 4G/IMT-Advanced standards. In addition to providing greater speeds, 5G networks will also need to meet the needs of new uses, such as the IoT as well as broadcast-like services and lifeline communications for times of natural disaster. According to GSMA Intelligence, the revenue for mobile network operators from interconnected devices in the segments of automotive, health, utilities, and consumer electronics will be $1.3 trillion by 2020. The worldwide data volume in mobile communication systems doubles nearly every year. To address this challenge, higher frequency bands will be used for which broadband and multiband equipment is required. The new standard Long Term Evolution (LTE-A) and the standardization process for 5G mobile communications necessitates changes in the technology of antennas and filters. In order to meet the specifications of future systems, new designs and improved or new microwave dielectric components are required. The recent progress in the IoT, microwave telecommunications, satellite broadcasting, and intelligent transport systems (ITSs) has resulted in an increasing demand for low-loss dielectric materials, tunable dielectrics, microwave ferrites, and EMI shielding materials. Low-loss dielectric oxide ceramics have revolutionized the microwave wireless communication industry by reducing the size and cost of filter, oscillator, and antenna components in applications ranging from cellular phones to the IoT. Wireless communication technology demands materials with highly specialized properties. Recently the demand for materials with low sintering temperatures has increased not only to lower the energy cost of devices but also to integrate with polymers and silver-based electrodes. Several polymer-based (polymer–ceramic) composites have also recently been developed for wireless communication technology.

A dielectric resonator is an electromagnetic component that exhibits resonance for a narrow range of frequencies. The resonance is similar to that of a circular hollow metallic waveguide except that the boundary is defined by a large change in permittivity rather than by a conductor. Dielectric resonators (DRs) generally consist of a puck of ceramic that has a high permittivity and a low dissipation factor (tan δ). The resonant frequency is determined by the overall physical dimensions of the puck, the permittivity of the material, and its immediate surroundings. The key properties required for a dielectric resonator are high quality factor ($Q \sim 1/\tan \delta$), high relative permittivity (ε_r), and near-zero temperature coefficient of resonant frequency (τ_f). The first chapter describes the different techniques for measuring the microwave properties of materials. Chapter 2 discusses the modeling of relative permittivity of composites using different mixing rules. Developing dielectric resonator materials in which these three properties are simultaneously optimized is difficult. Low-permittivity ceramics are used for millimeter-wave communications and also as substrates for microwave integrated circuits. The medium permittivity ceramics with ε_r in the range 25–50 are used for satellite communication and in cell phone base stations. High-ε_r materials are used in mobile phones where miniaturization of components is very important. For millimeter-wave applications, temperature-stable, low-permittivity, and high-Q (low-loss) substrates are required for high-speed signal transmission with minimum attenuation. Chapters 3 to 6 describes such materials.

The term dielectric resonator (DR) first appeared in 1939 when Richtmeyer showed that a suitably shaped dielectric piece can function as a microwave resonator; however, it took more than 20 years to generate further interest in DRs and to verify Richtmeyer's prediction experimentally. In the early 1960s Okaya and Barash rediscovered DRs while working on rutile single crystals. They measured the permittivity and Q of TiO_2 single crystals at room temperature down to 50 K in the microwave frequency range using the commensurate transmission line technique. In the early 1960s Cohn and his co-workers performed extensive theoretical and experimental work on DRs. Rutile ceramics that had an isotropic permittivity of about 100 were used for their experiments, but TiO_2 has a poor (+450 ppm/^{o}C) resonant frequency stability that prevented its commercial exploitation. The first microwave filter using TiO_2 ceramics was proposed by Cohen in 1968, but this filter was not useful for practical applications because of its high ε_r and frequency instability with temperature. A real breakthrough in dielectric resonator ceramic technology occurred in the early 1970s when the first temperature-stable low-loss barium tetratitanate ($BaTi_4O_9$) ceramics were developed by the Raytheon Company. Later, barium nanotitanate ($Ba_2Ti_9O_{20}$) with improved performance was reported by Bell Laboratories. The next breakthrough came from Japan when Murata Manufacturing Company produced (Zr, Sn)TiO_4 ceramics. Commercial production of dielectric resonators started in the early 1980s.

In the last two decades there has been extensive progress in the development of terahertz (THz) technology. This progress has enabled a multitude of potential applications, be it communications, biomedical, imaging, security, quality control of food and agricultural products, matter and light control, or chemical agent detection – in every application it has emerged as one of the most promising areas of interest. The terahertz region of the electromagnetic spectrum, referring roughly to the frequencies from 100 GHz or 0.1 THz to 30 THz, is the bridge between the microwave and infrared spectral bands. The promise of THz radiation resides in its unique properties and characteristics: its non-ionizing nature; its submillimeter spatial resolution; its transmission through dielectric materials that are

transparent to it; its interaction with water molecules, making it useful for certain medical diagnoses; its unique signature for molecular and rotational energy levels of many biological and chemical agents; and its potential for wireless communications. Although a large number of materials have been characterized in the microwave frequency range, relatively little attention has been paid to millimeter-wave or terahertz characterization of materials, possibly due to the relatively expensive facilities required. Chapter 5 discusses mm-wave material systems and applications of this technology.

Glasses have good thermal properties compared to polymers and better material homogeneity in comparison to ceramics, and hence they are considered for microwave applications; however, glasses in general have higher dielectric losses and a limited range of dielectric constants. Glass–ceramic composites have the advantage of an increased range of dielectric constants and reduced losses. They can be made with excellent homogeneity to produce sophisticated miniaturized microwave electronic devices. Chapter 7 discusses microwave dielectric properties of important glasses and glass–ceramics.

In the past, microwave devices have been traditionally machined from metal, and coaxial RF connections were made with metallic connectors, generally leading to expensive, heavy, and bulky packages. Moreover, today's electronic circuits for the automotive industry, entertainment electronics, and telecommunications have to handle a steadily increasing level of functionality whilst occupying the smallest volume possible. In the development of complex miniaturized circuits, flexible glass/ceramic or ceramic tapes with sintering aids made of high-temperature cofired ceramics (HTCCs), low-temperature cofired ceramics (LTCCs), and ultralow-temperature cofired ceramics (ULTCCs) play a decisive role as base materials. The choice of HTCC, LTCC, or ULTCC tapes is based on the electrode materials used and cofiring temperature. Cofired ceramics have become crucial in the development of various modules and substrates. In this technology, several thin layers of low-permittivity ceramics or glass/ceramic composites and conductors are combined, and the resulting multilayered modules are generally used in the form of a 3D wiring circuit board. These materials also enable a versatile mix of passive microwave components like microstrips, striplines, antennas, filters, resonators, capacitors, inductors, phase shifters, and dividers, making possible a whole matrix of designs that are not practical on regular alumina or any soft substrates. Thus these integrated components enable, for example, interconnection with 3D stripline circuitry. Chapter 8 describes the preparation characterization and properties of important HTCC, LTCC, and ULTCC ceramics.

Tunable microwave materials are extensively being investigated and utilized to meet the stringent requirements of modern wireless communication systems. The potential of tunable materials has been established for a variety of microwave applications such as tunable phase shifters (which introduce a controllable phase shift between the input and output of the device) and delay lines. The high power handling capabilities of ferroelectric varactors (variable capacitors) make these devices highly desirable for tunable matching networks. Tunable dielectric materials are also used in antenna beam steering as an efficient and cost-effective replacement for expensive and bulky phased array designs. Significant progress has been made in the development of more sensitive, low-loss, and versatile tunable materials. Bulk ferroelectric materials have relatively high loss tangents, limiting their applications in the microwave regime; however, thin films of ferroelectric materials have been investigated for extra-high tunability and temperature stability. The dielectric properties of thin films are significantly different from those of the bulk material of the

same composition. Moreover, very high electric fields can be applied to these thin films to achieve high tunability. Among the ferroelectric materials, barium strontium titanate (BST) is the dominant candidate for microwave tunable applications. Chapter 9 discusses the recent advances in tunable microwave dielectric materials.

Recently, there has been an increasing trend towards printing for the manufacture of low-cost consumer electronics due to the high flexibility of the printing process, providing significant advantages over conventional manufacturing processes including the possibility of low-cost flexible electronic devices. Applications for printed electronics include smart packages, flexible displays, distributed sensors, and antennas. Different types of inks based on advanced materials such as capacitor materials with a high relative permittivity, insulator layers with a low relative permittivity, and sealing glasses with a low melting point have been reported if the inorganic materials are considered. Screen printing is a simple and low-cost manufacturing method widely used for the fabrication of ceramic thick films in the range 10–100 μm. The screen printable ceramic ink consists of ceramic fillers with suitable organic solvents, dispersants, and binders. The high- and low-relative permittivity inks are extensively used in dynamic random access memory (DRAM) capacitors, photovoltaics and multilayer ceramic (MLC) circuits. Chapter 10 discusses the preparation and properties of important low-loss dielectric inks.

Materials used in microelectronic packaging have to simultaneously fulfill diverse requirements, such as low dielectric loss (tan δ), moderate relative permittivity (ε_r), low thermal dependence of permittivity (τ_ε), moisture absorption resistance, low coefficient of thermal expansion (CTE), and high dimensional stability and mechanical stiffness. Polymer–ceramic composites, especially type 0–3, are a potential material group suitable for producing demanding and functional packages that combine the electrical properties of ceramics and the mechanical flexibility, chemical stability, and processing possibilities of polymers. It is well known that the connectivity between the phases in the composite materials is very important in achieving the desired properties. The preparation of 0–3 type composite materials by combining a dielectric or a ferroelectric ceramic and a polymer for suitable properties means not only choosing the right materials, processed in a particular way, but also coupling them with the best possible design structure. This concept of connectivity describes the interspatial relationships in a multiphase material controlling the mechanical and electrical properties and thermal fluxes between the phases. Additionally, the filler particle size, interfacial properties, percolation level, and porosity effects can also play a role in the composite properties. Interfacial effects can occur between the ceramic grains and the polymer matrix, leading to large dielectric relaxations normally at low frequencies. The properties of the polymer–ceramic composites are determined by the number of phases and the way in which the phases are interconnected. The response of a ceramic–polymer composite to an external excitation (electric field, temperature, stress, etc.) depends on the response of individual phases, their interfaces as well as the connectivity concept. Chapter 11 describes the preparation, characterization, and properties of important polymer–ceramic composites with 0–3 connectivity for electronic circuits.

Flexible electronics constitute an important research area for the next generation of consumer electronics and is becoming a part of our day-to-day life. They are increasingly being used in a number of applications that benefit from their low profile, light weight, and good dielectric properties. These applications and potential applications are in various societal sectors, including healthcare, the automotive industry, human–machine interfaces, mobile

communications, and computing. Flexible circuits make portable devices more resilient. For some applications, particularly in the biomedical field, electronic circuits are conformally wrapped around curved surfaces. The dielectric materials used for flexible electronic applications must have mechanical flexibility, optimum relative permittivity, low-loss tangent, temperature stability of relative permittivity, low coefficient of thermal expansion (CTE), and high thermal conductivity. It is very difficult to identify a single material that possesses all of these properties simultaneously. Ceramics with high permittivity and low loss are available, but their high processing temperatures and brittle nature preclude their use as a single phase. At the same time low-loss elastomers with good flexibility and easy processing are available, but their high CTE, low permittivity, and low thermal conductivity limits their single-phase use; however, through the composite approach one can improve or tailor the individual properties of both elastomer and ceramics. In such systems, the circuits must not only be flexible but also stretchable. Chapter 12 describes synthesis, characterization, and properties of elastomer–ceramic composites.

The explosive growth in wireless communication systems has led to an increased use of electronic equipment, which in turn has caused a widespread problem of electromagnetic interference (EMI). EMI affects human health and reduces the lifetime and performance of electronic instruments. It also leads to malfunctioning of electronic devices used all over the planet and even in space exploration. This EMI problem can be solved by shielding electronic equipment against electromagnetic radiation. Extensive research has been done in order to develop lightweight microwave shielding materials with high efficiency and strength. Chapter 13 discusses the recent advances in EMI shielding materials.

Ferrite materials are insulating magnetic oxides with both high permeability and moderate permittivity in the range 5–20 at wavelengths from DC to the millimeter range. Due to their low eddy-current losses, there exist no other materials with such a wide range of electronic applications in terms of power generation, conditioning, and conversion. Electromagnetic waves can pass through ferrites with negligible attenuation but undergo a phase shift that can be influenced by DC magnetic fields. Ferrites are extensively used in the fabrication of microwave isolators, circulators, switches, inductors, and EMI shields. The ability to process thick-film ferrites having perpendicular magnetic anisotropy and self-bias properties allows for the redesign of conventional microwave passive components as lightweight planar constructs. Low-loss ferrites are also used in tunable microwave electronics that are small in size, profile, and weight. Microwave materials and device technologies are in a state of significant positive change with the potential to greatly impact a wide range of technologies that involve the sending, receiving, and manipulation of electromagnetic signals. Chapter 14 describes the preparation, characterization, and properties of important microwave ferrite materials.

Chapters 15 and 16 discuss briefly the different applications of microwave materials.

The topics covered in this book include microwave measurements, dielectric resonators, microwave substrates, tunable dielectrics, and EMI shielding materials. The book also has a data table (Appendix) listing the reported low-loss dielectric materials with properties and references arranged in order of increasing permittivity. Although the title of the book is microwave materials, it may be noted that the materials discussed in this book are useful for several other applications, such as capacitors and gate dielectrics. Actually, several thousand research papers are published annually on microwave materials, so the data or many very useful materials are scattered; hence, it is the purpose of this book to bring the

data and science of these useful microwave materials together for the benefit of researchers and technologists across the world.

In conclusion we thank all contributing authors for their great zeal and hard work in compiling their respective chapters. This book has been realized only due to their willingness to participate in this collaborative effort. A book project of this magnitude cannot see the light of day without a constant source of encouragement and support; hence, we express our gratitude to our families, friends, and colleagues. We also thank John Wiley & Sons Ltd for publishing this book.

M.T. Sebastian, R. Ubic, and H. Jantunen

1

Measurement of Microwave Dielectric Properties and Factors Affecting Them

M.T. Sebastian,[1] M.A.S. Silva,[2] and A.S.B. Sombra[2]
[1]Microelectronics Research Unit, Faculty of Information Technology and Electrical Engineering, University of Oulu, Oulu, Finland
[2]LOCEM–Laboratory of Telecommunications and Materials Science and Engineering, Physics Department, Federal University of Ceará (UFC), Ceará, Brazil

1.1 Introduction

Recently extensive researches have been done on microwave materials such as dielectric resonators (DR), electromagnetic interference (EMI) shielding materials, tunable dielectrics, high-temperature cofired ceramics (HTCC), low-temperature cofired ceramics (LTCC), polymer or rubber–ceramic composites, dielectric inks, microwave ferrites, etc. The number of papers published in the area of microwave materials and applications has increased considerably over the years, as shown in Figure 1.1.

In 1897, Lord Rayleigh demonstrated that an infinitely long cylindrical rod made up of dielectric material could serve as a waveguide [1]. In 1939 Richtmeyer theoretically predicted that a suitably shaped dielectric piece can function as a microwave resonator [2]. However, it took about 20 years to test Richtmeyer's prediction experimentally. In the early 1960s Okaya and Barash experimented [3, 4] with rutile single crystals and measured the relative permittivity in the microwave frequency range. In 1965 Cohn first reported [5] a dielectric resonator-based device – the filter. A dielectric resonator (DR) is a solid puck, usually ceramic, which can function as a resonator in the microwave and millimeter wave bands. The resonance is similar to that of a circular hollow metallic waveguide except for

Microwave Materials and Applications, First Edition.
Edited by Mailadil T. Sebastian, Rick Ubic and Heli Jantunen.
© 2017 John Wiley & Sons, Ltd. Published 2017 by John Wiley & Sons, Ltd.

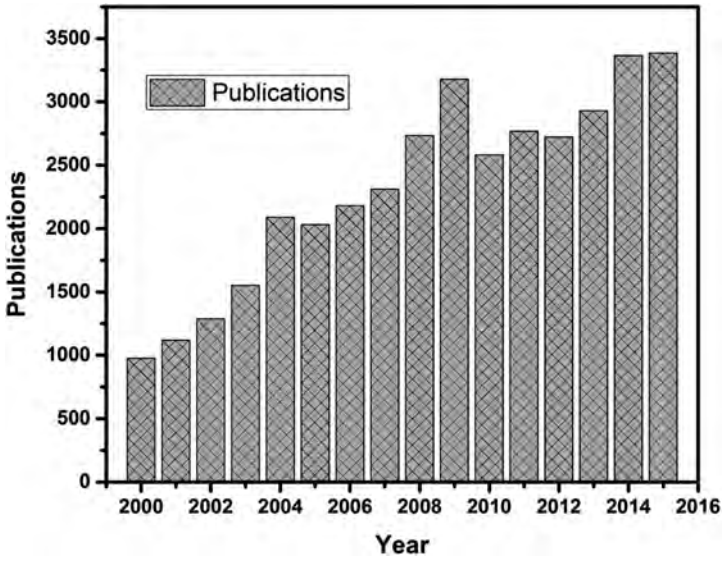

Figure 1.1 *Plot of number of papers published versus year (as per scopus.com using the keyword microwave materials).*

the boundary being defined by a large change in permittivity rather than by a conductor. The resonant frequency is determined by the overall physical dimensions of the resonator and the dielectric constant of the material. As the dielectric constant increases, the resonant frequency decreases. Dielectric resonators are extensively used in the fabrication of oscillators (DRO), bandpass and bandstop filters, dielectric resonator antenna, etc. In the microwave frequency range, the dielectric properties of materials are obtained by analyzing the behavior of electromagnetic waves that pass in the dielectric resonator (DR). Traditionally DRs are made from ceramic materials with high permittivity and high Q factor or low dielectric loss in the microwave region. These DRs are usually prepared in appropriated form by the solid-state ceramic route. They are much smaller in size compared to their metallic counterparts. The three important characteristics of an ideal DR are high relative permittivity (ε_r) for resonator applications and low ε_r for millimeter wave and substrate applications, low dielectric loss (loss tangent), and low coefficient of temperature variation of the resonant frequency (τ_f). The dielectric properties of different types of microwave materials such as DRs, HTCC/LTCC sheets, polymer–ceramic laminates, EMI shielding materials, microwave ferrites, etc., are measured by different techniques depending on their geometric shape, size, and properties [6, 7]. The present chapter elaborates the different techniques used for measuring the microwave dielectric properties.

1.2 Permittivity (ε_r) and quality factor (Q)

The relative permittivity (ε_r) is the physical property of a material that is associated with its energy storing capacity when a potential is applied across it. It is related to the macroscopic properties like polarization or capacitance. The miniaturization process of some devices or

circuits is usually made easier by employing a high ε_r material. A high ε_r facilitates circuit miniaturization because the wavelength inside the DR is inversely proportional to the square root of its permittivity, as given by

$$\lambda_d = \frac{\lambda_0}{\sqrt{\varepsilon_r}} \tag{1.1}$$

where

λ_d = wavelength in the dielectric
λ_0 = wavelength in air (actually in vacuum)
ε_r = real dielectric permittivity

The dimension of the dielectric sample must be an integral multiple of half-wavelength in the dielectric to resonate in the simplest fundamental mode [8]. If that wavelength is reduced, then the physical dimensions of the resonator must be reduced as well. The permittivity of a material determines the relative speed that an electrical signal can travel in it. A low permittivity will result in a high signal propagation speed. When microwaves enter a dielectric material, they are slowed down by a factor roughly equal to the square root of the permittivity, which implies that the wavelength decreases by the same amount and the frequency is unaffected, as shown in Figure 1.2.

The signal propagation is one of the most important aspects in electronic packaging. This is a direct function of the relative permittivity. In the case of ceramic packages, the relative permittivity of the ceramic over and within the metal lines is deposited or embedded governs the propagation delay, t_d, which is given by [9]

$$t_d = \frac{l\sqrt{\varepsilon_r}}{c} \tag{1.2}$$

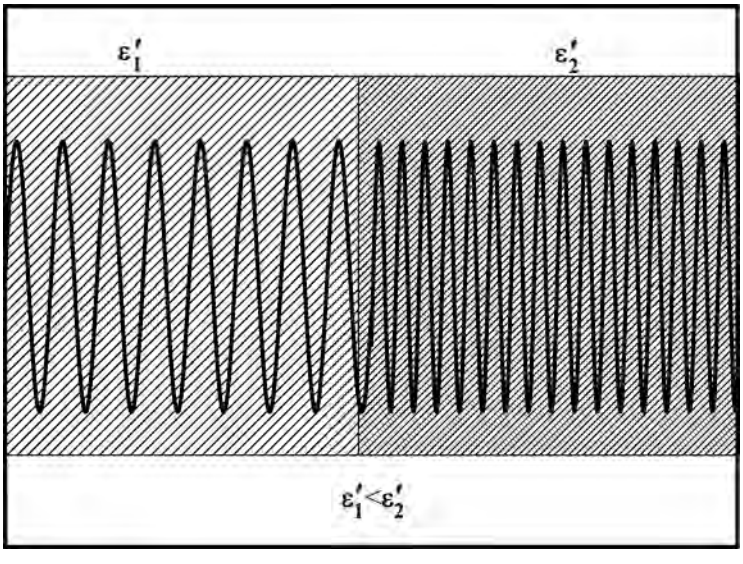

Figure 1.2 *The wavelength is reduced by a factor of $\sqrt{\varepsilon}$ when the wave enters the dielectric.*

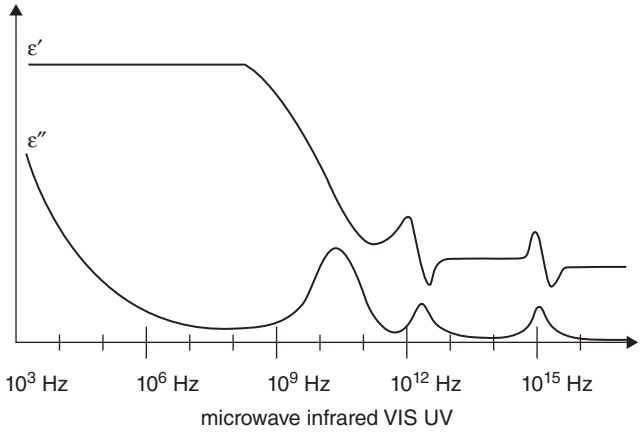

Figure 1.3 *Frequency dependence of polarization processes and peak power losses.*

where l is the line length, ε_r is the relative permittivity of the substrate, and c is the speed of light. Thus substrates with low relative permittivity are required to increase the speed of the signal [10].

By definition, the ε_r is related to the refractive index n ($\varepsilon_r = n^2$). The dielectric permittivity is frequency dependent, and it is very rare that the square of the refractive index measured at optical frequencies is the same as permittivity measured at microwaves. In some materials following this rule, like diamond ($\varepsilon_r = 5.68$, $n^2 = 5.85$) or germanium ($\varepsilon_r = 16$, $n^2 = 16.73$) [11], the same polarization processes are excited by both optical and microwave (or RF) frequencies. In other materials, this rule is not valid since dipolar polarization processes that occur at lower frequencies do not usually occur at higher optical frequencies, that is, the polarization processes are not the same in both frequency ranges. In the microwave frequency region, ionic and electronic polarization mechanisms contribute predominantly to the net dipole moments and the permittivity as depicted in Figure 1.3.

The dielectric loss tangent (tan δ) of a material is associated with dissipation of the electrical energy due to different physical processes such as electrical conduction, dielectric relaxation, dielectric resonance, and loss from non-linear processes [12, 13]. Another concept of dielectric loss is explained by the delay between the electric field and the electric displacement vectors [14]. The dielectric loss of the material is the total sum of intrinsic and extrinsic losses presented by a material. Gurevich and Tagantsev developed a complete theory of intrinsic dielectric losses and these dielectric losses are the losses in the perfect crystals that depend on the crystal structure and can be described by the interaction of the phonon system with the AC electric field [15, 16]. The equilibrium of the phonon system is changed when an AC electric field is applied and a relaxation is observed that is associated with energy dissipation [15, 17]. The dielectric relaxation occurs at low frequency and the phonon frequency is much higher than the microwave frequency. Hence the heat dissipation observed in this relaxation in the ideal lattice should be of anharmonic origin. The dielectric losses are related to the crystal symmetry, AC field frequency, and temperature (intrinsic

features) and these intrinsic losses fix the lower limit of losses in defect-free single crystals or ideal pure materials.

The imperfections in the crystal lattice such as impurities, microstructural defects, grain boundaries, porosity, microcracks, order–disorder, random crystallite orientation, dislocations, vacancies, dopant atoms, etc. (extrinsic features), can also lead to losses. These extrinsic losses can be, in principle, minimized by proper material processing. The losses due to different types of defect show different frequency and temperature dependence. The crystals belonging to different symmetry groups have very different temperature and frequency dependences of dielectric loss [15].

In the microwave frequency range, dielectric ceramics often use the term "quality factor" for the reciprocal of tan δ. The quality factor, or Q, is a measure of the power loss of a microwave system that is defined as

$$Q = 2\pi \frac{\text{Maximum energy stored per cycle}}{\text{Average energy dissipated per cycle}} \tag{1.3}$$

Some losses for a microwave resonator are described as: (a) dielectric, (b) conduction, (c) radiation, (d) external [8]. The dielectric Q_d, conduction Q_c, and radiation Q_r quality factors and these losses are given by

$$Q_d = 2\pi \frac{W_1}{P_d T} = \frac{\omega_0 W_1}{P_d}, \quad Q_c = \frac{\omega_0 W_1}{P_c}, \quad Q_r = \frac{\omega_0 W_1}{P_r}$$

where W_1 is the total stored electric energy in the resonator, ω_0 is the angular resonant frequency, P_d, P_c, and P_r represent the power dissipated in the dielectric, conductor, and radiation, respectively, and

$$T = \frac{2\pi}{\omega_0}$$

The unloaded quality factor Q_u is related as the sum of the other Q-factors by the relation

$$\frac{1}{Q_u} = \frac{1}{Q_d} + \frac{1}{Q_c} + \frac{1}{Q_r} \tag{1.4}$$

where $1/Q_d$ is dielectric loss, $1/Q_c$ is the loss due to conductivity of the metallic plates, and $1/Q_r$ is the loss due to radiation. The radiation loss can be ignored in most resonant cavities because these are completely shielded and so there is no radiation effect.

External losses ($1/Q_{ext}$) arise due to coupling between the resonator and feed. To introduce an electromagnetic field in the resonator, microwave conducting probes are brought close to it (few millimeters of separation) – the higher the ε_r of the resonator, the closer the probe must be to it. The electromagnetic fields around them induce electromagnetic fields in the dielectric ceramic, and so they are coupled. However, the presence of conducting probes in the electromagnetic field lines of the resonator leads to additional loss. The total or loaded Q-factor is defined as [8]

$$\frac{1}{Q_L} = \frac{1}{Q_d} + \frac{1}{Q_c} + \frac{1}{Q_r} + \frac{1}{Q_{ext}} \tag{1.5}$$

where $1/Q_L$ is the total loss of the system and $1/Q_{ext}$ is the loss due to external coupling.

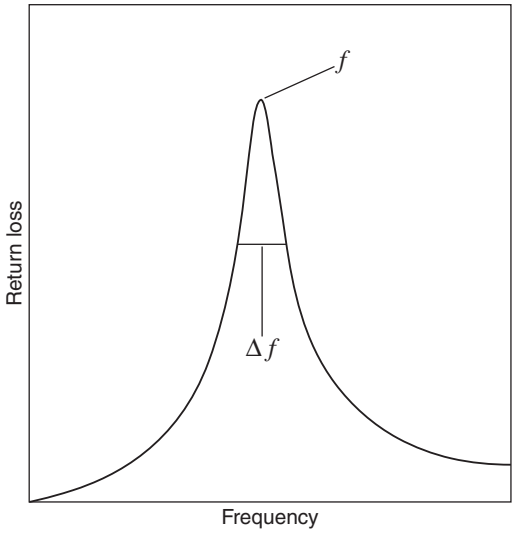

Figure 1.4 *The $TE_{01\delta}$ resonant peak and associated parameters.*

Q_L is determined experimentally from the shape of the resonance peak, as illustrated in Figure 1.4. A bandwidth (BW) is defined as the width of the resonance curve at half power points (3 dB down from the peak). The peak frequency (resonant frequency) f divided by the 3 dB width is equal to Q_L.

The loaded Q_L is obtained from the measured resonant frequency f and half power (–3 dB) bandwidth Δf of TE_{011} mode resonance:

$$Q_L = \frac{f}{\Delta f} \tag{1.6}$$

In practice, resonators are often used with adjustable couplings that allow such approximation without the need for measuring coupling coefficients. If conduction, radiation, and external losses are negligible, then $Q_L = 1/\tan\delta$. When we measure the dielectric loss, at a particular frequency, we get the total loss tangent and we cannot distinguish the contributing factors.

If all conduction, radiation, and external losses are negligible, then the loaded Q-factor depends on dielectric losses in the resonant structure. If the resonant structure contains several (N) dielectrics (one of them is the sample under test) then the Q-factor due to dielectric losses is related to the dielectric losses in particular dielectric regions by the following formula [14]:

$$\frac{1}{Q_d} = \sum_{i=1}^{N} P_{ei} \tan\delta_i \tag{1.7}$$

where P_{ei} is the electric energy filling factor for the ith dielectric region and is defined by

$$P_{ei} = \frac{\iiint_{vd} \varepsilon_i |E|^2 \mathrm{d}v}{\iiint_{vt} \varepsilon\,(v)\,|E|^2 \mathrm{d}v} \tag{1.8}$$

where V_d is the volume of the dielectric resonator, v_t is the volume of the whole resonant structure, $\varepsilon(v)$ is the spatially dependent permittivity inside the whole resonant structure, and ε_i is the permittivity of the ith dielectric region.

In most practical structures conductor losses appear and this must be accounted for in order to determine the Q-factor due to dielectric losses (Q_d) from measured values of the loaded Q-factors:

$$\frac{1}{Q_c} = \frac{R_s}{G} \tag{1.9}$$

The geometric factor G is defined as [14]

$$G = \omega \frac{\iiint_{vi} \mu_0 |H|^2 \mathrm{d}v}{\iint_S |H_t|^2 \mathrm{d}s} \tag{1.10}$$

where μ_0 is the permeability of the resonator.

The coupling losses ($1/Q_{ext}$) are usually determined experimentally and are given by

$$\frac{1}{Q_u} = \frac{1}{Q_d} + \frac{1}{Q_c} + \frac{1}{Q_r} = \frac{1/Q_L}{1 + \beta c_1 + \beta c_2} \tag{1.11}$$

where βc_1 and βc_2 are coupling coefficients for a resonator with two coupling ports. The radiation loss is negligible when the sample is kept in a closed cavity.

1.3 Measurement of Microwave Dielectric Properties

The knowledge of dielectric properties in a different frequency range is important for characterizing the dielectric materials for different practical applications. The precise measurement of the dielectric properties is essential for predicting the device performance. Several methods have been developed and employed for measuring permittivity and permeability of materials in the high-frequency region. The resonant cavity method has been used as the most accurate measurement technique. However, this method has the disadvantage that the measured results are applicable only over a narrow frequency band. Electrical properties of material over a wide range of frequencies can be measured with less accuracy using the transmission line methods. The transmission and reflection methods are used to evaluate the dielectric properties of medium- and high-loss materials as a function of frequency [14, 18].

There are various methods that enable measurement of the quality factors of low-loss dielectrics [18–25], but none of them consider the practical effects like noise, crosstalk, coupling losses, transmission line delay, and impedance mismatch. Inadequate accounting of these effects may lead to significant uncertainty in the measured Q-factor. Determination of the complex permittivity and other electromagnetic properties require precise measurements of the resonant frequencies and Q-factors. For some measurement techniques, these parameters have to be measured in the presence and absence of the test sample, but for other techniques only once in the presence of the test sample is needed. Once the resonant frequencies, Q-factors of the resonant structures, and dimensions of the test samples are measured, computations have to be performed to obtain ε_r and $\tan\delta$.

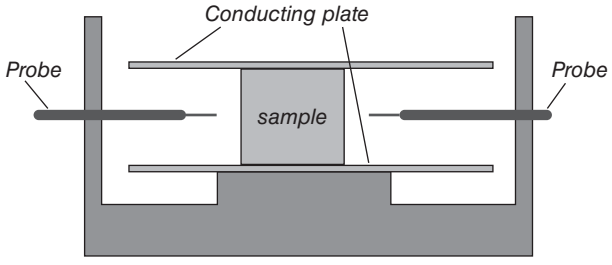

Figure 1.5 *Schematic sketch of the Courtney setup for measuring the dielectric constant under an end shorted condition.*

1.4 Methods of Measurement

1.4.1 Hakki and Coleman (Courtney) Method

1.4.1.1 Permittivity

The complex permittivity of the material of the dielectric resonator is often measured using the method developed by Hakki and Coleman [19] and modified by Courtney [20] in which a cylindrical resonator of material is inserted between two mathematically infinite conducting plates, as shown in Figure 1.5. The end plates are usually made of well-polished copper plates coated with silver or gold. Consider the cylindrical resonator with relative permittivity ε_r, length L, and diameter D placed between the end metal plates (see Figure 1.5). The diameter of the conducting plates should be much larger than that of the dielectric puck. The dielectric properties are obtained by TE_{011} mode analysis. The dielectric puck diameter to height ratio should be about 2 to get wide mode separation, so that the TE_{011} mode is not disturbed by other adjacent modes. If the dielectric material is isotropic then the characteristic equation for such a resonant structure for the TE_{0ml} mode is [19] given by

$$\alpha \frac{J_0(\alpha)}{J_1(\alpha)} = -\beta \frac{K_0(\beta)}{K_1(\beta)} \tag{1.12}$$

where $J_0(\alpha)$ and $J_1(\alpha)$ are the Bessel functions of first kind of order zero and one, respectively. $K_0(\beta)$ and $K_1(\beta)$ are the modified Bessel functions of second kind of orders zero and one, respectively. The parameters α and β depend on the geometry, the resonant wavelength inside the dielectric resonator, and dielectric properties. Thus

$$\alpha = \frac{\pi D}{\lambda_0}\left[\varepsilon_r - \left(\frac{l\lambda_0}{2L}\right)^2\right]^{1/2} \tag{1.13}$$

$$\beta = \frac{\pi D}{\lambda_0}\left[\left(\frac{l\lambda_0}{2L}\right)^2 - 1\right]^{1/2} \tag{1.14}$$

where

l = longitudinal variations of the field along the axis
L = length of the DR
D = diameter of the DR
λ_0 = free space resonant wavelength

The real part of the permittivity of the resonator can be calculated using the mode chart parameters (α_1 and β_1), the resonant frequency (f), and the dimensions of the dielectric puck using the equation

$$\varepsilon_r = 1 + \left[\frac{c}{\pi D f}\right]^2 \left(\alpha_1^2 + \beta_1^2\right) \tag{1.15}$$

Hakki and Coleman [19] used an iris coupling from a waveguide to couple a microwave to the DR. Later Courtney [20] modified the method by using two horizontally oriented E-field probes for coupling the microwave to the dielectric resonator. This enabled a wide range of frequencies to be spanned, since there is no cut-off frequency for coaxial lines. The TE_{011} mode is used for the measurements since this mode propagates inside the sample but is evanescent outside the dielectric resonator sample. Therefore a large amount of electrical energy can be stored in high Q dielectric resonators [25]. In the end shorted condition the E field becomes zero close to the metal wall and electric energy vanishes in the air gap [21]. The TE and TM modes do not contain electric and magnetic fields in the axial (z) direction. The TE_{011} mode is chosen for measurement because for this mode only azimuthal component of the electric field exists and the error due to the air gap is practically eliminated [26]. For a cylindrical resonator, TE and TM modes exist only if the azimuthal mode index $m = 0$; otherwise all other modes are hybrid; that is, they have all six electromagnetic components. Hybrid modes are usually divided into two mode families: HE and EH. They are only occasionally used in measurements of dielectrics (uniaxially anisotropic crystals).

Figure 1.6 shows the frequency response of the TE_{011} mode resonator. By knowing the diameter D and length L of the sample, β is calculated using Equation (1.14). The permittivity ε_r is calculated using Equation (1.15). To avoid the error due to surface roughness the sample should be well polished. In this method, the accuracy is limited by precision of the measurement of the resonant frequency and the dimensions of the sample. The possible error in the measurement of permittivity is of the order of 0.3%. Such an error is possible when dimensional uncertainties of the samples are of the order of 0.15%. The simple measurement setup is the advantage of this method. This is one of the fairly accurate and the most frequently used techniques for measurement of permittivity and this method is proposed as one of the international standards IEC techniques [27] for measurements of the complex permittivity of low-loss solids. In the Courtney method, the ε_r is measured only at one resonant frequency corresponding to the TE_{011} mode. By identifying other resonant TE modes such as TE_{021}, TE_{031}, TE_{041}, etc., it is possible to measure ε_r in a range of frequencies. The quasi-TM modes and TM modes are not suitable for ε_r measurements due to the fact that a minute air gap between the dielectric sample and the metal plate considerably alters the resonant frequency, which affects the accuracy of ε_r measurement [23, 28].

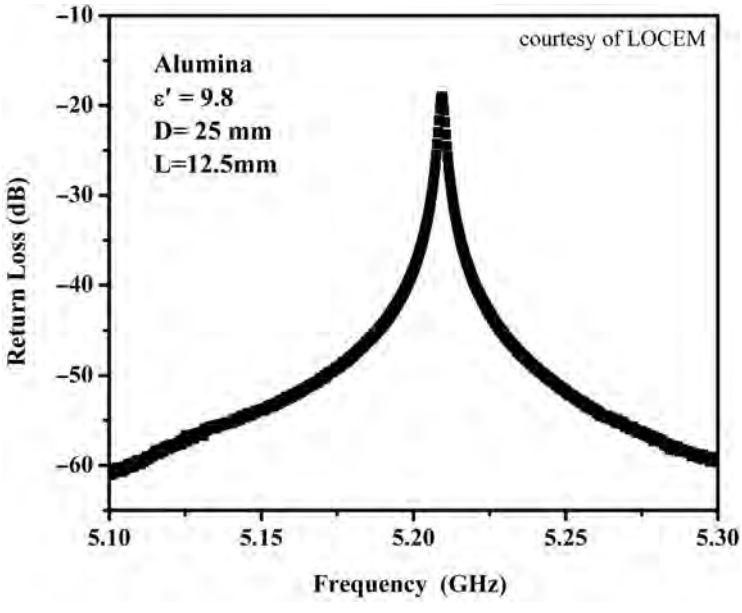

Figure 1.6 *The TE_{011} resonance of a ceramic puck with $\varepsilon_r = 9.8$ under an end shorted condition.*

1.4.1.2 Measurement of Loss Tangent

The quality factor for the TE_{011} mode can be measured using the Hakki and Coleman method [18–21, 23, 29–31]. The quality factor measured by this method will be low since loss occurs due to the conducting plates and radiation effects. However, correction to conductor losses can be applied knowing the surface resistance of the conducting plates. The unloaded Q_u is obtained from the measured resonant frequency f and half power (–3 dB) bandwidth Δf of TE_{011} mode resonance given by (1.6).

The tan δ can be calculated [18–21, 23, 29–31] from

$$\tan\delta = \frac{A}{Q_u} - BR_s \quad = A\left[\frac{1}{Q_u} - \frac{R_s}{A/B}\right] = \frac{1}{P_e}\left[\frac{1}{Q_u} - \frac{1}{Q_c}\right]$$
$$A = 1 + \frac{W}{\varepsilon_r}; B = \left(\frac{\lambda_0}{\lambda_g}\right)^3 \left(\frac{1+W}{30\pi^2\varepsilon_r l}\right); W = \frac{J_1{}^2(\alpha)}{K_1{}^2(\beta)} \frac{K_0(\beta)K_2(\beta) - K_1{}^2(\beta)}{J_1{}^2(\beta) - J_0(\alpha)J_2(\alpha)} \tag{1.16}$$

where Q_c is given by Equation (1.9) and $G = A/B$ and $P_e = 1/A$. R_s is the surface resistance of the conducting plates and is given by [29]

$$R_s = \sqrt{\frac{\pi f \mu}{\sigma}} \tag{1.17}$$

where

σ = conductivity of the conducting plates
μ = permeability for a non-magnetic metal = $4\pi \times 10^{-7}$ H/m

λ_0 = resonant wavelength
$\lambda_g = 2L/l$ ($l = 1, 2, 3,\ldots$)
λ_g = guiding wavelength of an infinitely long dielectric rod wave guide
W = ratio of electric field energy stored outside to inside the rod [22, 29]

Kobayashi and Tamura [29] has reported a method of measuring the value of R_s using two rod samples cut from a dielectric rod that have the same diameters but different lengths. One of the rods for a TE_{01p} mode resonator is p times as long as the other for a TE_{011} mode resonator where $p \geq 2$. The modes have almost the same resonant frequency but differ in observed unloaded quality factors because of different conductor loss contributions in the two cases. Since both rods have the same tan δ, the following equation can be obtained:

$$R_s = 30\pi^2[\lambda_g/\lambda_0]^3 \frac{\varepsilon_r + W}{1 + W} \frac{p}{p-1} \left[\frac{1}{Q_{ml}} - \frac{1}{Q_{mp}}\right] \tag{1.18}$$

where Q_{ml} and Q_{mp} are measured unloaded quality factors for TE_{011} and TE_{01p} modes, respectively.

1.4.2 $TE_{01\delta}$ Mode Dielectric Resonator Method

The Q-factor of a dielectric resonator sample measured by the Hakki–Coleman or Courtney method can be affected by the conductor and radiation losses. These effects can be avoided by using the cavity method in which the DR is kept on a low-loss single crystal quartz or Teflon spacer inside the cavity. The quality factor (Q), permittivity (ε_r), and τ_f of the DRs can be measured using a transmission mode cavity proposed by Krupka *et al.* [14, 32]. Figure 1.7 shows the cavity setup for the measurement of the Q-factor.

The DR is placed inside a cylindrical metallic cavity usually made of copper and the inner surfaces are finely polished and usually gold or silver coated and the cavity is closed after loading the DR sample. The cavity is fed using loop coupling. The cavity has an infinite number of modes when excited with a microwave spectrum of frequencies. Usually a D/L ratio of about 2 is maintained to get maximum mode separation and to avoid interference from other adjacent modes. For high-permittivity materials, the first mode is the $TE_{01\delta}$

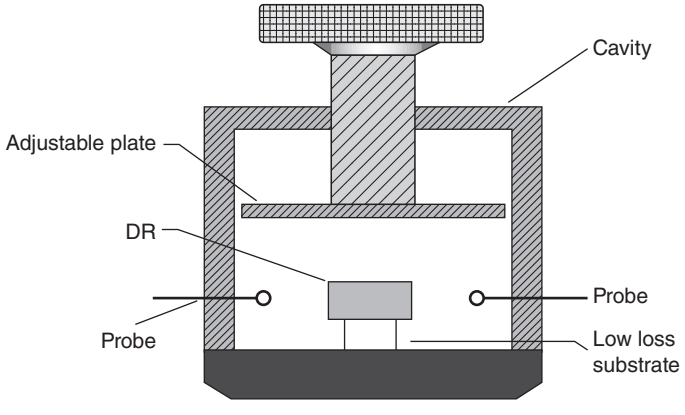

Figure 1.7 *The cavity setup for the measurement of Q-factor.*

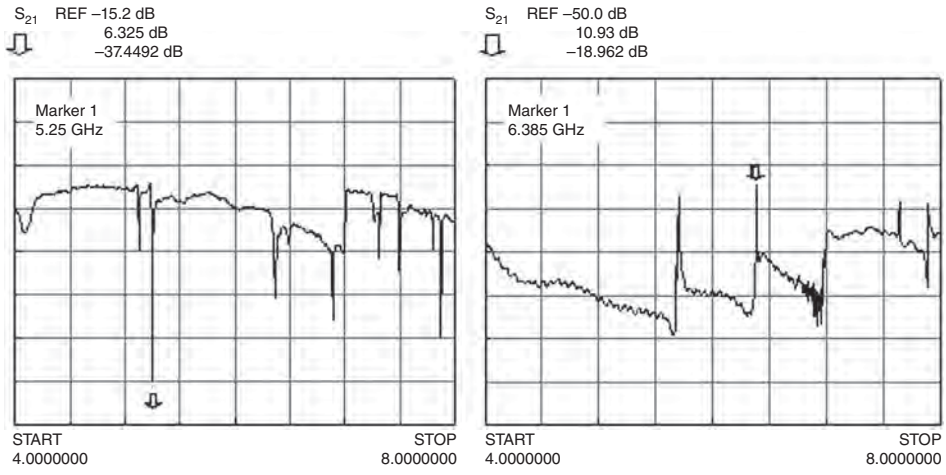

Figure 1.8 *Microwave resonance spectra of* $Ba(Mg_{1/3}Ta_{2/3})O_3$ *ceramic with* $\varepsilon_r = 24$*: (a) reflection and (b) transmission configuration.*

mode but for low-permittivity materials a few modes may appear before the $TE_{01\delta}$ mode. The resonant frequency, quality factor, and τ_f are dependent on the resonator surroundings.

The electric field is symmetric with the geometry of the sample and the cavity, which helps to reduce the sources of loss due to cavity. In the $TE_{01\delta}$ cavity method, the field confinement is not complete in the z direction and hence the TE_{011} mode is designated as $TE_{01\delta}$. As seen in Figure 1.7, the sample is isolated using low-loss substrate (a quartz or a Teflon spacer), from the effects of losses due to the finite resistivity of the metallic cavity. Figure 1.8 shows the typical resonance spectra of $Ba(Mg_{1/3}Ta_{2/3})O_3$ ceramic ($\varepsilon_r = 24$). One can assume that the unloaded Q-factor is equal to the loaded Q-factor if the coupling is weak. The $TE_{01\delta}$ mode frequency is noted and the unloaded Q-factor is measured.

After identifying the mode, the resonant frequency and 3 dB bandwidth are determined. From this, the coupling coefficient βc_1 and βc_2 for the coupling ports are determined using the relations $\beta c_1 = (1 - S_{11})/(S_{11} + S_{22})$ and $\beta c_2 = (1 - S_{22})/(S_{11} + S_{22})$, where S_{11} and S_{22} are reflection coefficients of port 1 and port 2 in magnitude [33].

From the measured Q_L, Q_u can be calculated using Equation (1.11). Sometimes, the desired mode (the $TE_{01\delta}$ one) may be close to other modes. In such cases the cavity volume can be slightly changed by rotating the top screw, which moves the top plate up or down that separates the modes. The ability to tune the frequency is very useful for the identification of the desired resonant mode and to allow it to measure samples of various dimensions. Figure 1.9 shows a typical test fixture manufactured by QWED. Rigorous electromagnetic analysis must be performed to evaluate permittivity and the dielectric loss tangent of the sample under test. The Rayleigh–Ritz method has been used in a computer program for a typical test fixture manufactured by QWED.

The $TE_{01\delta}$ mode method is one of the most accurate techniques for measuring loss tangent and permittivity of isotropic low-loss materials [32, 34]. Assuming that all parasitic losses can be neglected (that are small for $TE_{01\delta}$ mode if permittivity of the sample is large)

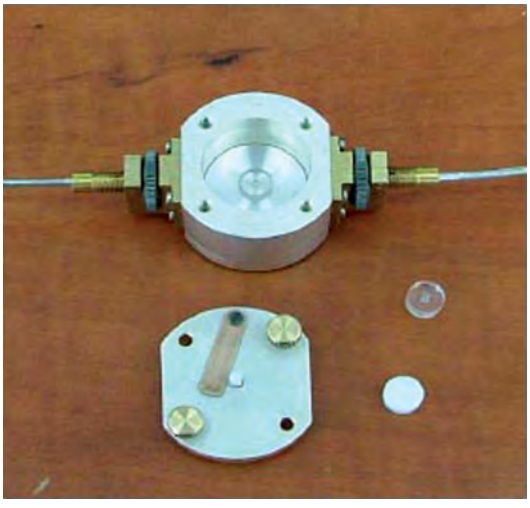

Figure 1.9 *The cavity manufactured by QWED for the quality factor measurement.*

and assuming that the electric energy filling factor is equal to unity, the inverse of the measured unloaded Q-factor is approximately equal to the dielectric loss tangent. Moreover, these assumptions are not valid for very low-loss dielectric materials (in this case conductor losses must be rigorously taken into account) and for low-permittivity materials (the electric energy filling factor in the sample is substantially smaller than 1).

The cavity method using the $TE_{01\delta}$ mode has several advantages, such as easy mode identification, small parasitic losses, and lack of mode degeneracy [14]. However, the evaluation of ε_r and tan δ requires advanced numerical computations (this can only be done by employing dedicated computer programs) because of the absence of exact solutions of Maxwell's equation. For this reason the Hakki and Coleman method is still used as it allows relatively easy determination of permittivity.

The uncertainty in dielectric loss tangent using the $TE_{01\delta}$ mode cavity method with optimized enclosure is of the order of $\pm\, 2 \times 10^{-6}$ or 0.03 tan δ (whichever is larger) and uncertainty of ε_r measurements is $\Delta\varepsilon/\varepsilon = \pm\, \Delta$ dim/dim (where dim = dimensions of the test sample). The measurement frequency depends on the size and permittivity of the test samples. Measurements at higher frequencies are possible by using smaller cavities and smaller test samples or by using several higher order quasi-TE_{0nm} modes [35].

The presence of resonator support and the coupling loop can perturb the electromagnetic field and this may lower the Q value and shift the resonant frequency [36]. In order to minimize this perturbation caused by the support and coupling loop, the test cavity should be large. However, on increasing the size of the test cavity, the resonant modes of the cavity move to lower frequencies. When ε_r of the dielectric resonator is larger than about 20, the $TE_{01\delta}$ mode of the dielectric resonator shifts to below the first test cavity mode (TM_{010}). Valant *et al.* observed that the electromagnetic field could penetrate into the conducting walls of the test cavity (skin effect) lowering the measured Q value of the dielectric resonator [36]. The test cavity size should be large in order to avoid the skin

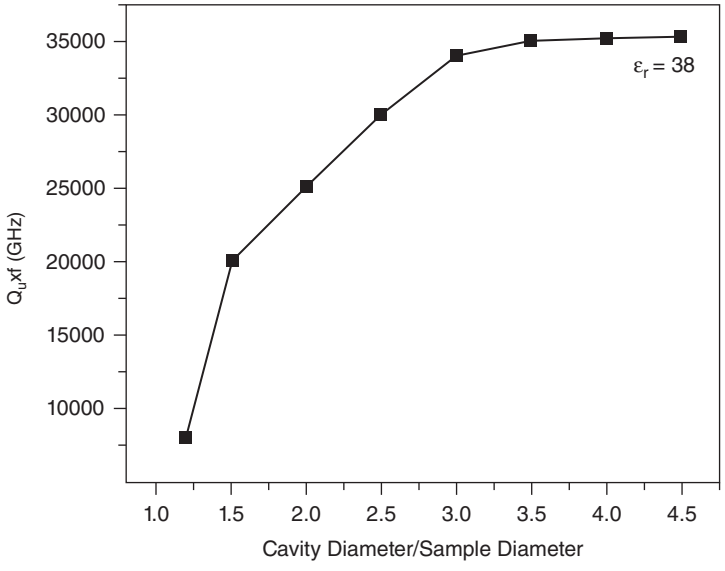

Figure 1.10 *Variation of Qf with ratio of the cavity diameter/sample diameter.*

effect. The quality factor decreases when the cavity diameter/puck diameter ratio is smaller than 3, as shown in Figure 1.10.

Normally, the size of cavity used is 3–5 times of the test sample. The contribution of the surface resistance of metals of the cavity can be calculated from the quality factor of the TE_{011} resonance of the empty cavity before calculating losses by conduction of the cavity walls. This value can be applied to correct the measured Q of the sample [8]. One can measure ε_r and tan δ at low frequencies by the parallel plate capacitor method using an LCR meter for new materials. This will give an approximate idea of ε_r and tan δ and in turn will help to calculate the approximate resonant frequency of the DR using the following equation [37]:

$$f \propto \frac{1}{v_r\sqrt{\varepsilon_r}} \tag{1.19}$$

where v_r is the volume of the DR.

Knowledge of the value of the resonant frequency will further help to find the size of the DR at a given frequency or the size of the cavity required to measure the Q-factor.

1.4.3 Measurement of the Quality Factor by a Strip Line Excited Using the Cavity Method

In the microstrip line excited cavity method, the dielectric resonator is magnetically coupled to a 50 ohm microstrip line, as shown in Figure 1.11, along with the equivalent circuit [38].

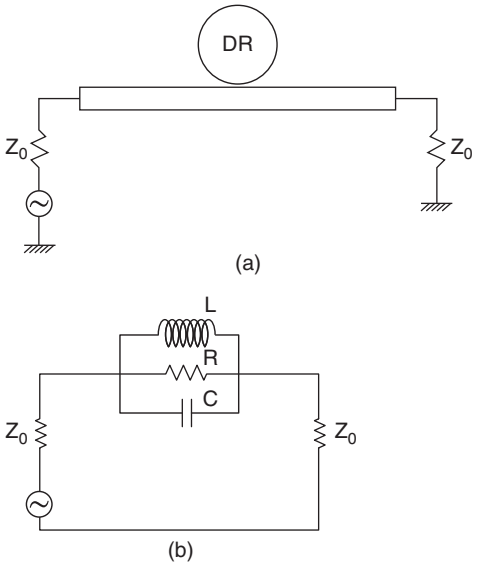

Figure 1.11 *Schematic diagram of a DR coupled to (a) a microstrip line and (b) an equivalent circuit. (After Khanna and Garault [38]).*

The ratio of the resonator coupled resistance R at the resonant frequency to the resistance external to the resonator is called the coupling factor β_c:

$$\beta_c = \frac{R}{R_{ext}} = \frac{S_{110}}{S_{210}} \tag{1.20}$$

where S_{110} and S_{210} are the real quantities representing the reflection and transmission coefficients, respectively, at the resonant frequency.

Under critical coupling ($\beta_c = 1$), the power dissipated in the external circuit is equal to the power dissipated in the resonator (P_d), which is equally divided into the power reflected to the generator ($P_r = {S_{110}}^2$) and the power transmitted to the load ($P_t = {S_{210}}^2$). In the shielded resonator configuration, from the conservation of energy, power dissipated in the resonator is given by

$$P_d = 1 - |S_{110}|^2 - |S_{210}|^2 \tag{1.21}$$

The coupling factor β_c is a function of the distance between the dielectric resonator and the microstrip line under fixed shielding conditions. The expression for the unloaded voltage transmission coefficient S_{21u} derived by Khanna and Garault is given by [38]

$$S_{21u} = S_{210}\sqrt{\frac{2}{\left(1 + {S_{210}}^2\right)}} \tag{1.22}$$

where S_{21u} corresponds to the voltage transmission coefficient of the unloaded resonator.

The frequencies f_1 and f_2 corresponding to S_{21u} given by Equation (1.22) is obtained from the network analyser (Figure 1.12). The difference in frequencies ($f_2 - f_1$) is Δf. The

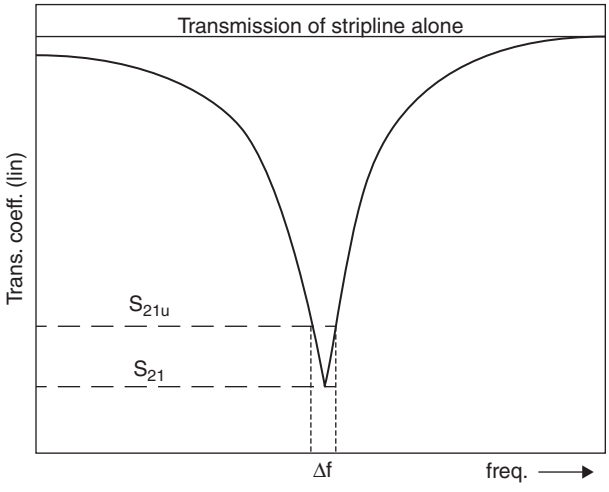

Figure 1.12 *Typical resonant curve of a DR coupled to a microstrip line used in determining the quality factor by the strip line method.*

frequency corresponds to the peak of the S_{21} curve is the resonant frequency. Knowing the resonant frequency f and Δf, the unloaded quality factor, Q_u, is calculated using Equation (1.6).

Figure 1.13 shows the experimental setup for the Q measurement by the microstrip line excited cavity method. A 50 Ω microstrip line of width 3 mm is etched on RT-Duroid 5880 ($\varepsilon_r \sim 2.2$ and thickness 1.9 mm) and kept at the bottom wall of a rectangular cavity made of copper. The cavity is excited using 3.5 mm microstrip edge connectors as shown in Figure 1.13. The dielectric resonator is placed near the microstrip line and the resonance spectra is observed on the network analyzer.

The $TE_{01\delta}$ mode is identified from among the different modes. Set the central frequency as the resonant frequency and reduce the span to enhance the frequency resolution. Then the network analyzer is calibrated for S_{21} THRU by connecting an identical microstrip

Figure 1.13 *The experimental setup for measuring the quality factor by the strip line method. The DR is coupled to the strip line.*

transmission line used in the cavity. Then connect it to the cavity with DR and measure the resonant frequency *f*. The transmission coefficient S_{210} corresponding to *f* is taken. The factor S_{21u} is calculated using Equation (1.22). From the width Δf corresponding to S_{21u} and *f*, the unloaded quality factor is calculated.

1.4.4 Whispering Gallery Mode (WGM) Resonators

The $TE_{01\delta}$, $TM_{01\delta}$, or $HE_{11\delta}$ modes are the main modes used in dielectric measurements by the Courtney, $TE_{01\delta}$, or strip line methods [19, 20, 30, 34] and the *Q* measured by these methods depends on dielectric loss of the material as well as on the radiation and conductor losses of the cavity. Hence a simple measurement of the quality factor by the Courtney, $TE_{01\delta}$, or microstrip line methods is not sufficient to determine accurately the dielectric loss of low-loss dielectric materials.

It was reported [39–45] that Whispering Gallery modes (WGMs) would confine the entire fields within the resonator, which in turn give negligible radiation and conductor losses at microwave frequencies. The quality factor of the WGM dielectric resonator is limited only by the intrinsic losses in the dielectric material. The measured WGM Q-factor is approximately equal to 1/tan δ.

In WGM resonators, most of the electromagnetic energy is confined to the dielectric near the perimeter of the air–dielectric interface, which in turn reduces the radiation and conductor losses [41, 43]. The WGM technique allows measurements of two permittivity components of uniaxially anisotropic materials (several single crystals exhibit uniaxial anisotropy). Permittivity components can be determined from measurements of resonant frequencies and Q-factors of two modes belonging to different mode families employing rigorous numerical analysis, for example, mode-matching. The electrical energy filling factors for E (quasi-TM mode) and H (quasi-TE mode) modes are given by [41, 44, 45]

$$P_{\varepsilon_\perp} = 2\frac{\partial f}{\partial \varepsilon_\perp}\frac{\varepsilon_\perp}{f}; \quad P_{\varepsilon||} = 2\frac{\partial f}{\partial \varepsilon_{||}}\frac{\varepsilon_{||}}{f} \tag{1.23}$$

The dielectric loss tangent for the dielectric can be solved [43, 44] using the equation:

$$Q_E^{-1} = \tan\delta(P_{\varepsilon\perp} + P_{\varepsilon||}) + R_s/G_E \tag{1.24}$$

$$Q_H^{-1} = \tan\delta(P_{\varepsilon\perp} + P_{\varepsilon||}) + R_s/G_H \tag{1.25}$$

where

R_s = surface resistance of the cavity enclosing the DR
εll = permittivity parallel to the anisotropic axis
$\varepsilon_\perp$ = permittivity perpendicular to it

The conductor losses decrease as the surface resistance becomes smaller and as the geometric factor (*G*) increases [45]. The geometric factor *G* is significantly large and the effect of losses due to cavity walls can be ignored when compared to the loss tangent. The energy filling factors (WGM modes) of DR for all these modes are close to unity and will have high quality factors. In effect, acting on these modes, radiation losses are negligible. The WGM method offers good suppression of spurious modes because the propagation constant along the *z* axis is very small and unwanted modes leak out axially. The WGM modes offer a high level of integration. The WGM dielectric resonators are classified as either $WGE_{n,m,l}$

in which the electric field is essentially transverse or $WGH_{n,m,l}$, for which the electric field is essentially axial. The integer n denotes the azimuthal variation, m radial variation, and l the axial ones. WGMs are periodic according to the azimuthal number, and the number of modes in a bandwidth increases with the diameter of the DR. Therefore, for a small diameter of the resonator, the frequency interval between two successive modes will be large. Dielectric resonators acting on their WGMs can be excited in different ways. In the low-frequency range, one can use an electric or magnetic dipole. However, this type of excitation is stationary and traveling WGM cannot be excited. In the millimeter wave region either dielectric image waveguides or microstrip transmission lines are used to excite traveling WGMs.

1.4.5 Split Post Dielectric Resonator (SPDR)

The split post dielectric resonator (SPDR) provides an accurate method for measuring the complex permittivity and loss tangent of substrates and thin films at a single frequency point. The sample should be in the form of a flat rectangular piece or a sheet [46–50]. The SPDR uses a particular resonant mode, which has a specific resonant frequency depending on the dimensions and the dielectric constant of this resonator. This method does not have flexibility in the measurement of frequency and dimensions as the samples need to be prepared in the form of thin sheets. In this method, flat samples of the test material are inserted through one of the open sides of the fixture. The laminar dielectric under test is placed between two low-loss dielectric rods or resonators kept in a metallic enclosure, as shown schematically in Figure 1.14. The sample must be very thin with parallel faces. The air gap between the sample and the dielectric resonator does not affect the accuracy of the measurement. The required thickness of the sample also depends on the ε_r of the material. Materials with high ε_r must have less thickness.

The setup for the SPDR method consists of a pair of dielectric resonators and a metal enclosure of relatively small height. This configuration allows formation of an evanescent electromagnetic field, not only in the air gap between the dielectric resonators but also in the

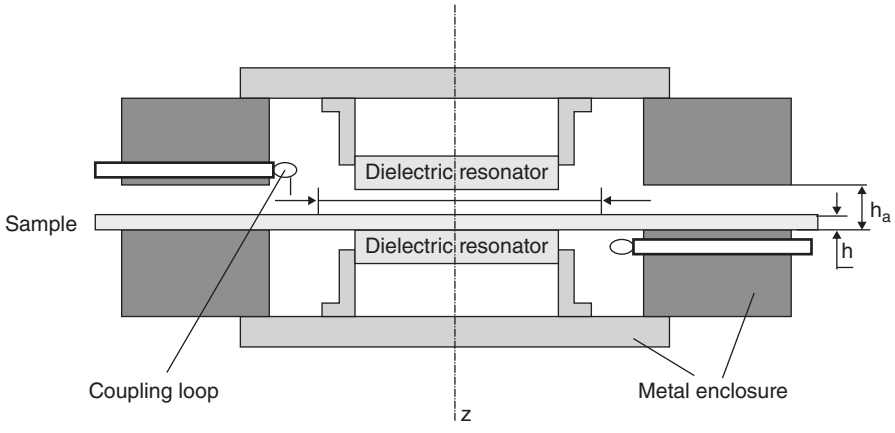

Figure 1.14 *Schematic sketch of SPDR.*

cavity region for radii greater than the radius of the dielectric resonator. This simplifies the numerical analysis and reduces possible radiation effects. Although different modes of the resonator can be identified and used for the microwave characterization, the $TE_{01\delta}$ mode is preferable since this mode is insensitive to the presence of air gaps perpendicular to the z axis of the fixture. The thickness of the sample needs to be measured and is provided as a parameter to evaluate the dielectric properties.

The complex permittivity can be calculated based on the rigorous electromagnetic modeling of the split post resonant structure using the Rayleigh–Ritz technique [47]. The real part of the complex permittivity can be computed from the measured resonant frequencies and thickness of the sample using the following equation [47]:

$$\varepsilon_r' = 1 + \frac{f_0 - f_s}{h f_0 K_\varepsilon \left(\varepsilon_r', h\right)} \tag{1.26}$$

where h is the thickness of the test sample, f_0 is the resonant frequency of the empty SPDR, f_s is the resonant frequency of the SPDR with the dielectric sample, and K_ε is a function of ε_r' and h has to be evaluated for a number of ε_r and h using the Rayleigh–Ritz technique [47]. The iterative procedure is used to evaluate subsequent values of ε_r' from Equation (1.26). The loss tangent of the test sample is calculated from the measured unloaded Q-factors of the SPDR with and without the dielectric sample based on

$$\tan\delta = \left(\frac{1}{Q_u} - \frac{1}{Q_{DR}} - \frac{1}{Q_c}\right) / P_e \tag{1.27}$$

where Q_{DR}^{-1} and Q_c^{-1} denote losses of the metallic and dielectric parts of the resonator, respectively, and P_e is the electric energy filling factor of the sample given by Equation (1.8). Uncertainty of the dielectric measurements of a sample of thickness h can be estimated as $\Delta\varepsilon/\varepsilon = \pm\,(0.0015 + \Delta h/h)$ and $\Delta \tan\delta = 2 \times 10^{-5}$ or $\pm\, 0.03 \tan\delta$ for dielectric permittivity and uncertainty in loss tangent measurements, respectively.

The dielectric properties measured by SPDR methods are obtained for only one frequency determined by dimensions and dielectric permittivity of the resonator. Thus each SPDR is designed for a particular nominal frequency and the actual measurement is taken close to the nominal frequency; this determines the requirements for the size of the sample. For example, for SPDR of nominal frequency 5–6 GHz, the minimum sample size should be 30 × 30 mm and thickness 2.1 mm. QWED manufactures SPDRs with dedicated software for the evaluation of permittivity and loss tangents. SPDR has superior accuracy as compared to the reflection-transmission methods. The method is convenient and quick to measure low-loss laminar dielectrics such as substrates or LTCC, printed circuit boards, and even thin films and is not suitable for dielectric resonators. Classically, the most precise measurements with resonators have been performed employing network analyzers. Recently QWED developed an **inexpensive computer-controlled microwave oscillator system** (microwave frequency Q meter), which enables quick and automatic measurements with a dedicated SPDR [48]. Figure 1.15 shows the general view of a microwave frequency Q meter connected to the SPDR and to the computer manufactured by QWED. The hardware part of the Q meter consists of the PLL-stabilized microwave source with DDS generated reference controlled by a fast 32-bit ARM microcontroller. A wideband logarithmic

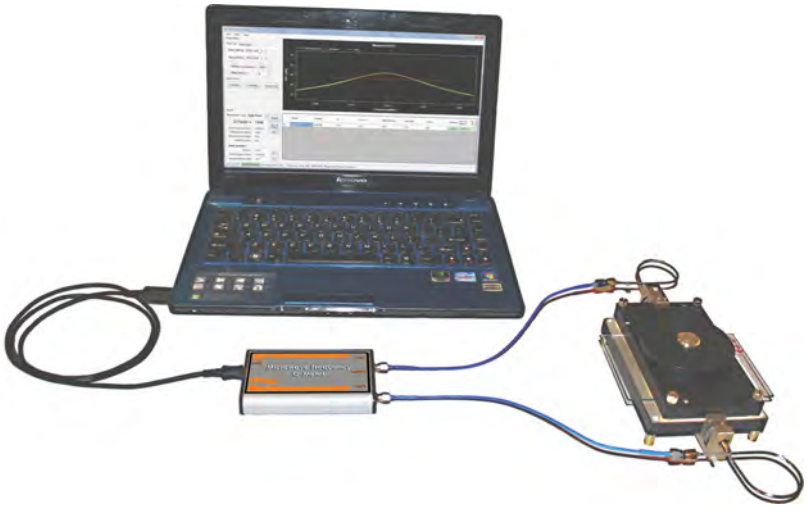

Figure 1.15 *Photographs of SPDR connected to a Q meter and computer. Source: Reproduced with permission from QWED, Poland.*

power detector is used to measure the transmitted power level through the resonator. A multipoint resonance curve-fitting algorithm enables the Q-factor to be accurately calculated. The only external information required is the thickness of the sample under test. The good hardware simplicity as well as the use of a computer screen for presentation of the results leads to a significant cost reduction to start exploration of electromagnetic properties of materials with SPDR. The microwave frequency Q meter can be connected to the computer via a USB port. The relative permittivity and dielectric loss tangent can be easily measured with dedicated SPDRs. These Q meters are available in the frequency range up to 5.2 GHz (type: 4.4 GHz ÷ 5.2 GHz; type II: 1.4 GHz ÷ 2.6 GHz; type II: 0.7 GHz ÷ 1.3 GHz).

1.4.6 Cavity Perturbation Method

The cavity perturbation technique was a method used to obtain approximate solutions but its applications were limited not only to low-permittivity samples but also to specific modes and specific samples. The cavity perturbation technique is widely used for the determination of the dielectric characteristics of thin sheet samples of low and medium dielectric loss [18, 51]. In the cavity perturbation technique, a small piece of the material, usually in the form of a disk or sheet, is placed in a metallic resonant cavity operating in a known mode. The material characteristics are estimated from the shift in the resonant frequency and change in the Q of the system [52–55].

This technique was developed by Slater [55] and is used to measure the dielectric properties of materials with permittivity less than 10. The cavity perturbation method provided frequencies determined by cavity and DR dimensions and hence it is not a swept frequency measurement. The cavity is excited with optimum iris coupling; typically the diameter of the iris is equal to the shorter dimension of the waveguide (WG)/2.2 and can be used for the measurement of dielectric properties of the samples.

The resonant frequency and quality factor of the empty cavity is determined for different cavity modes. After measuring frequency and quality factor the thin sheet sample is inserted and positioned at the E-field antinode. If the sample is purely dielectric the maximum electric field can be easily determined by simply moving the sample across the slit. The mode will shift to the low frequency side and retraces from there. The sample is kept at the retracing position where the electric field is maximum. If the sample is slightly magnetic the permittivity can be measured only for the odd modes by keeping it at the middle of the cavity. The new resonant frequency and Q of the sample is again measured. The complex dielectric constant of the sample is calculated [18, 51, 56] using the following equations:

$$\varepsilon_r' = 1 + \left[\frac{V_c(f_0 - f_s)}{2V_s f_s}\right] \tag{1.28}$$

$$\varepsilon_r'' = \frac{(\varepsilon' - 1)}{2\varepsilon'} \frac{f_s}{(f_0 - f_s)} \left[\frac{1}{Q_s} - \frac{1}{Q_0}\right] \tag{1.29}$$

$$\tan\delta = \frac{\varepsilon_r''}{\varepsilon_r'} \tag{1.30}$$

where

f_0 = resonant frequency of the empty cavity
f_s = resonant frequency of the cavity with sample
V_c = volume of the cavity
V_s = volume of the sample
Q_0 = quality factor of the empty cavity
Q_s = quality factor of the cavity with sample

The experimental error is found to be less than 2% in the case of permittivity and 1.3% in the case of dielectric loss. Here also the measured Q_s and Q_0 can be corrected by measuring S_{11} and S_{22}, as mentioned earlier, by proper calibration of the network analyser. The main advantage of this method is the easiness of determining the permittivity and loss using a simple device with moderate accuracy.

1.4.7 TM_{0n0} Mode and Re-entrant Cavity Methods

The microwave dielectric properties can also be measured in the frequency range 2–10 GHz using the TM_{0n0} mode cavities with rod dielectric samples [57, 58]. In the frequency range 50 MHz to 2 GHz a re-entrant cavity method can be employed [59, 60] to evaluate the dielectric properties. Both TM_{010} and re-entrant cavities are closed with a lid after insertion of the samples. For the TM_{010} mode cavity, a transcendental equation is known only if the height of the sample is equal to the height of the cavity. For a re-entrant cavity, the exact solution for a transcendental equation in a closed form does not exist. It can be solved using rigorous mode-matching methods [60]. Karpova [61] was the first to present a mode-matching numerical technique to solve Maxwell's equation for a re-entrant cavity. Since the electric energy filling factor in the re-entrant cavity is close to unity, resolution in the loss tangent measurement is of the order of 5×10^{-5}. A similar resolution in the loss tangent is possible for the TM_{010} mode cavities provided the test sample has a sufficiently large diameter. The uncertainty in a real permittivity measurement is about 0.5–2% for the TM_{010}

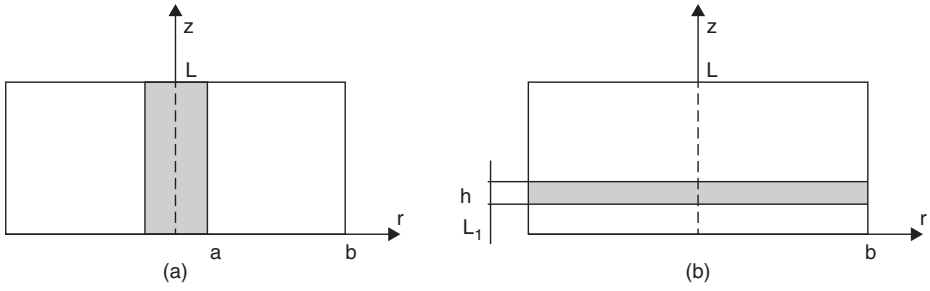

Figure 1.16 *Cylindrical cavities containing (a) a dielectric rod and (b) a dielectric disk.*

mode cavity and about 1–3% for the re-entrant cavity. The loss tangent and permittivity can be measured as a function of frequency by employing higher-order TM_{0n0} modes.

1.4.8 TE_{01n} Mode Cavities

Complex permittivity and Q-factor of low-loss disk samples (Figure 1.16) can be measured by the TE_{01n} mode method [62–64]. Normally, the operating frequency range for these cavities is in the range 8–40 GHz. The TE_{01n} mode in the cavities have a circumferential electric field distribution, which is tangential to a cylindrical sample kept symmetrically in the cavity [14]. Hence, the electric field is continuous across dielectric–air interfaces that allow an air gap omission without degradation of measurement uncertainties. The physical contact between the lateral surface and the cavity bottoms is not important since the surface currents in the metal cavity walls are circumferential.

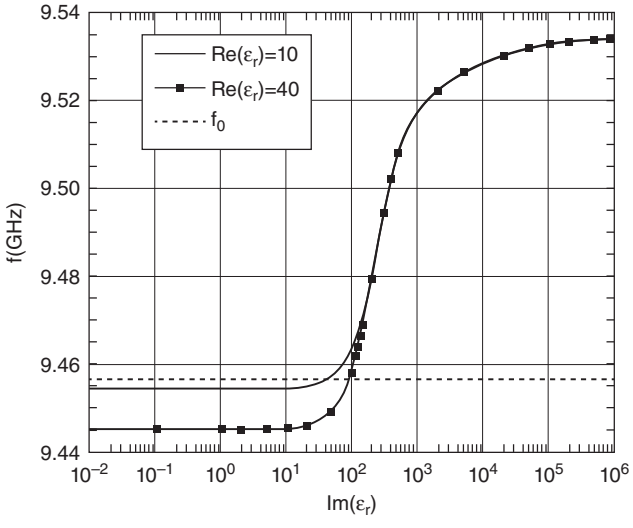

Figure 1.17 *Variation of resonant frequency with an imaginary part of permittivity for the TE_{011} mode cylindrical cavity with a dielectric disk sample. Dotted line corresponds to the TE_{011} mode frequency of the empty cavity. Source: Adapted from Krupka 2006 [14].*

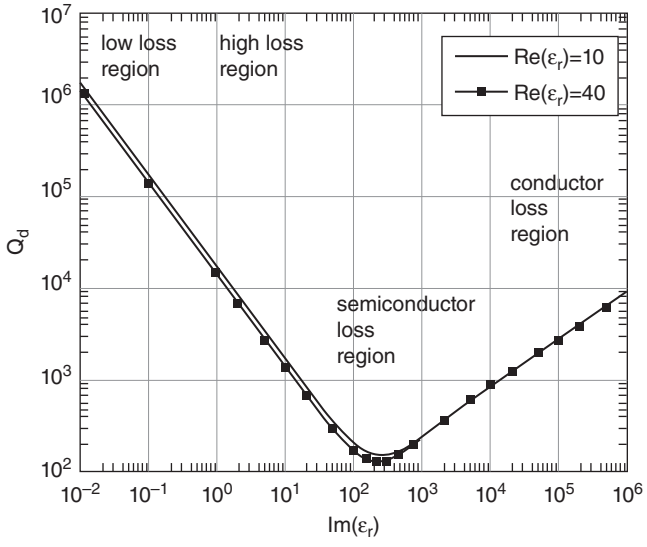

Figure 1.18 *Variation of Q-factor due to dielectric losses as a function of the imaginary part of permittivity for the TE_{011} mode cylindrical cavity containing a dielectric disk sample. Source: Adapted from Krupka 2006 [14].*

The variations of resonant frequency and Q-factor due to dielectric losses versus the imaginary part of permittivity for the TE_{011} mode cylindrical cavity containing the dielectric sample are shown in Figures 1.17 and 1.18. The resonant frequency is smaller than that for the empty cavity (Figure 1.17) in the low-loss dielectric region. The resonance frequency displacement ($f_0 - f$) depends on the real permittivity and thickness of the sample. The quality factor due to dielectric loss in this region is given by Equation (1.9) and depends linearly on the dielectric loss tangent.

The real part of the complex permittivity can be determined from the measured resonant frequency and the simplified transcendental equation in the low dielectric loss region, where both complex permittivity and complex angular frequency have imaginary parts equal to zero. The surface resistance in a closed cavity can be determined from the measured Q-factor of the empty cavity and then scaling up to the frequency of the cavity containing the sample using the formula

$$R_s(\omega) = R_s(\omega_0)\sqrt{\frac{\omega}{\omega_0}} \tag{1.31}$$

where ω_0 is the resonant angular frequency of the empty cavity.

When the imaginary part of permittivity becomes very large (see Figure 1.18), then both the resonant frequency and the Q_d depend on the imaginary part of the permittivity. In this case only the imaginary part of permittivity can be determined. For low-loss materials the TE_{01n} mode cavities method can be employed using thicker samples. The ideal thickness of the sample is a half wavelength or its multiple [14]. The electric energy filling factors in the dielectric sample become relatively large and a higher resolution loss tangent measurement

(5×10^{-5}) can be achieved. The uncertainty in the permittivity measured using TE_{01n} mode cavities is of the order of 0.5% [14]. At lower frequencies, < 8 GHz, the dimensions of the TE_{01n} mode cavities and samples become too large for practical applications.

1.4.9 Thin Samples and Free-Space Methods

The microwave dielectric properties of thin samples can be measured using the Kent [49] method, the Yu–Cullen [65] method, and the free-space method [18, 66–68]. The size of the sample should be larger than the wavelength of the electromagnetic wave. To further minimize the effects of the scatterings from the sample boundary, the sample size should be twice larger than the wavelength. The wave that is incident in the sample must be planar, for this condition the separation between antenna and sample (d) must fulfill the relation

$$d > \frac{2D^2}{\lambda}$$

where λ is the wavelength of the operating electromagnetic wave and D is the largest dimension of the antenna aperture. The measurement results may be affected by the environment [69]. At lower frequencies, the effects of the environment are more serious. To minimize these effects, it is recommended to conduct free-space measurements in an anechoic chamber. Meanwhile, one can also use time-domain gating to eliminate the unwanted signal caused by environment reflections and multireflections.

1.4.9.1 Free-Space Methods

Free-space techniques for the study of magneto-dielectric material properties measurements have several advantages. In the traditional techniques, some problems associated with interfaces (materials/air/hollow metallic waveguides), such as the inhomogeneity of dielectric material, contactless, and air gaps, can promote unwanted higher-order modes excited in the measurements, but this problem does not exist in free-space measurement.

Free-space measurements are realized by reflection methods like short-circuited reflection (Figure 1.19) and metal-backing and bistatic reflection (Figure 1.20). The basis of these methods is measuring the reflection caused by a metal plate kept close to the sample and the interference caused in this reflection due to the dielectric properties of the sample.

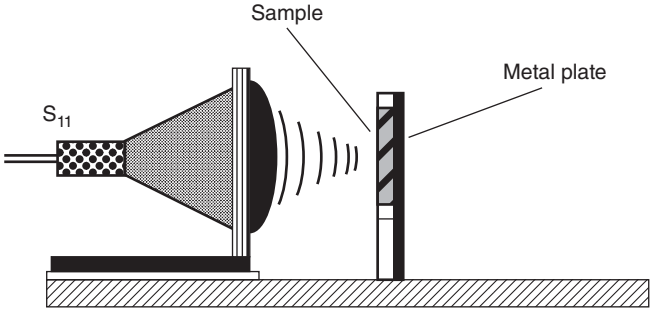

Figure 1.19 *Setup for free-space by the short-circuited reflection method.*

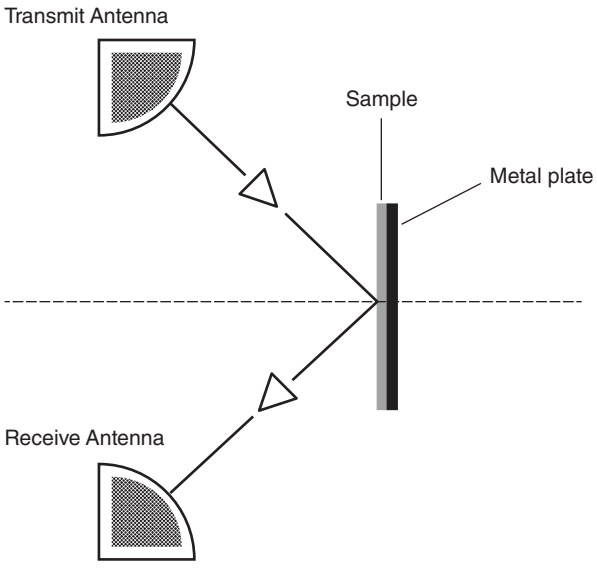

Figure 1.20 *Setup for free-space by metal-backing and bistatic reflection.*

The measurement of permittivity is given by

$$S_{11} = \frac{jz\tan(\beta d) - 1}{jz\tan(\beta d) + 1}; \quad z = \frac{1}{\sqrt{\varepsilon_r}}; \quad \beta = \frac{2\pi}{\lambda}\sqrt{\varepsilon_r} \tag{1.32}$$

where z is the wave impedance of material normalized to the wave impedance of free space and β is the phase constant of the material. However, the permittivity of the sample cannot be expressed explicitly in terms of S_{11} and d, and numerical methods are often used in the calculation of dielectric permittivity.

It is possible to make accurate free-space measurements at microwave frequencies by using precision horn lens antennas that have far-field focusing ability. The typical measurement setup consists of two antennas and a sample holder as shown in Figure 1.21. The

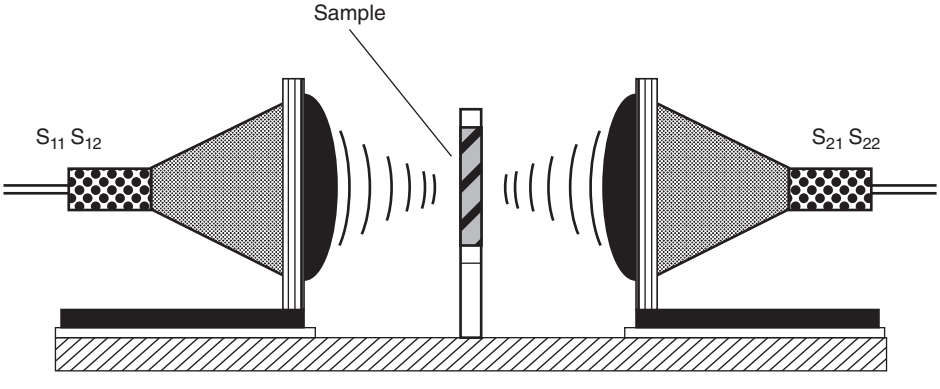

Figure 1.21 *Accurate setup for free-space measurements.*

transmission and reception antennas are spot-focusing horn lens antennas. The effects of sample boundaries and the measurement environment are minimized by using focusing antennas. A specially fabricated sample holder is placed at the common focal plane for holding planar samples. The microwave signal incident to planar samples can be taken as plane waves, and the properties of the sample under test are obtained from the reflection and transmission through the sample. The dielectric and magnetic properties are obtained by relations of S parameters obtained by reflection and transmission of horn lens antennas in a free-space setup:

$$S_{11} = \frac{\Gamma(1 - T^2)}{1 - \Gamma^2 T^2}$$
$$\varepsilon_r = \frac{\gamma}{\gamma_0}\left(\frac{1 - \Gamma}{1 + \Gamma}\right)$$
$$S_{21} = \frac{T(1 - \Gamma^2)}{1 - \Gamma^2 T^2}$$
$$\mu_r = \frac{\gamma}{\gamma_0}\left(\frac{1 + \Gamma}{1 - \Gamma}\right)$$

where

S_{11} and S_{21} are S parameters for reflection and transmission, respectively
T and Γ reflection coefficients and transmission, respectively
μ_r = relative permeability
ε_r = relative permittivity
γ and γ_0 are propagation constant of the sample and of free space, respectively

The free-space measurements are commonly accompanied by a precise mathematic algorithm; the Nicolson–Ross–Weir (NRW) algorithm, for example, is very much utilized in the measurements of free space.

1.4.9.2 Sheet Resonator or Kent method

The dielectric properties of microwave substrates can be measured by the method proposed by Kent [49]. The sheet sample is kept between the flat flanges of the two metal circular waveguides as shown in Figure 1.22. The dielectric properties of the sheet can be calculated from the resonant frequency and the quality factor of the TE modes excited in the waveguide. The transmission through the sheet sample of the TE mode reaches its maximum at a frequency below the cut-off frequency of the waveguides and above the cut-off frequency of the cylindrical portion of the sample. The frequency of these TE modes can be obtained from the waveguide radius, thickness, and the dielectric constant of the sheet sample.

For the TE_{01} mode, the reciprocal of the unloaded quality factor is given by

$$\frac{1}{Q_0} = \frac{(\varepsilon_r''/\varepsilon_r') + (\delta/a)(\theta_c/\theta_0)^2 U}{1 + U} \tag{1.33}$$

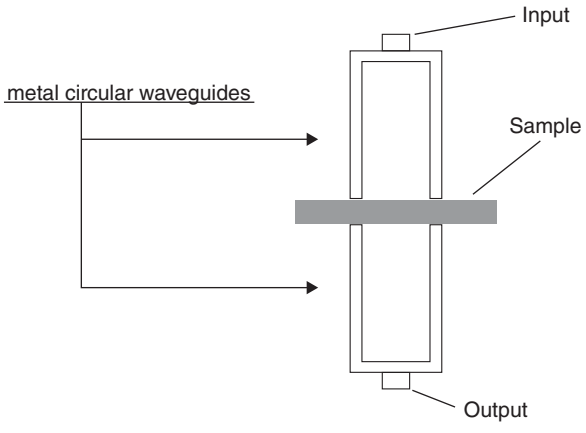

Figure 1.22 *Schematic for dielectric measurement by the Kent method.*

where δ is the skin depth of the waveguide wall, $(\varepsilon_r' - j\varepsilon_r'')$ is the relative complex permittivity of the substrate, a is radius of waveguide and [49]

$$\varepsilon_r' U = \frac{\cos^3\theta}{(\theta + \sin\theta\cos\theta)\sin\theta} \tag{1.34}$$

where the quantity U is the ratio of the electric energy in the waveguide to that in the substrate. The value of U increases when the resonant frequency f_0 approaches the cut-off frequency f_c and the dielectric constant ε_r' decreases.

1.4.9.3 Open Resonator Method (Yu–Cullen Method)

The use of the cavity resonator can be difficult in the microwave frequency range. This is due to the fact that the resonator size is directly proportional to the wavelength and the quality factor of a cavity resonator varies with the wavelength as $\lambda^{3/2}$. The decrease is rather rapid as the wavelength decreases. Hence, at high microwave frequencies the measurements in cavity resonators can be difficult [70].

This difficulty can be overcome by using the open resonators [71]. The important feature of an open resonator is that the number of modes is proportional to the length rather than the volume of the resonator. This method usually works in the frequency range of 10 to 200 GHz. Using the open resonator method, flat disk-shaped solid samples can be measured, and liquids or powders can be measured provided they are restrained within a solid annulus, which is outside the microwave beam area and covered by plates with a low dielectric constant and a low loss tangent.

Yu–Cullen [65] used a biconcave open resonator and the measurement configuration is shown in Figure 1.23. A parallel plane-sided slab of dielectric material with thickness t is placed midway between two identical spherical mirrors with radius R_0. The total length of the resonator is $L = 2d$ and the distance between the sample plane and the spherical mirror is d. There are two techniques for the measurement of materials properties. In one technique, the length of the cavity is fixed and the resonant frequency is measured with and without the sample. In the other technique, the length of the cavity is adjusted to establish resonance

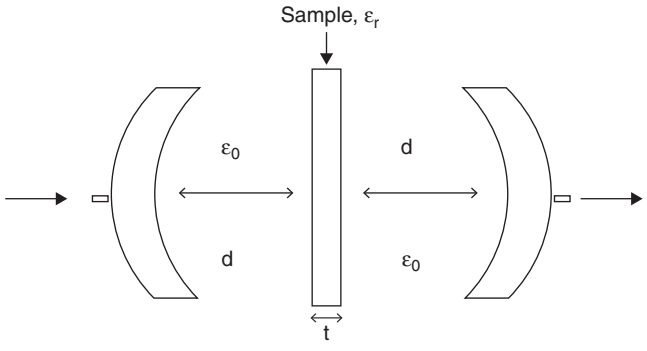

Figure 1.23 *Schematic for dielectric measurement by the Yu–Cullen method.*

with and without the sample at the same frequency. Here, we discuss the basic algorithms for these two techniques, and more detailed discussions can be found in references [65] and [70]. It should be noted that in an open resonator method for materials property characterization, usually the refractive index n is used. For a dielectric material, the relationship between the refractive index and dielectric permittivity is given by

$$n = \sqrt{\varepsilon_r'} \tag{1.35}$$

The relations for measurements of dielectric properties of a sample by the two techniques are shown below. For symmetric modes the variation of frequency is given by

$$\Delta = \frac{n^2}{n^2 \sin^2(nkt - \Phi_T) + \cos^2(nkt - \Phi_T)} \tag{1.36}$$

For assymetric modes:

$$\Delta = \frac{n^2}{n^2 \cos^2(nkt - \Phi_T) + \sin^2(nkt - \Phi_T)} \tag{1.37}$$

For the second technique the solution is

$$d + t = d_0 - p + \frac{t(n - \Delta)}{n^2 k^2 w_t^2} + \frac{3}{4k^2 R_0} \tag{1.38}$$

The rest of the calculation follows along the same lines as the frequency-variation method, solving the transcendental equation for n and iterating if necessary.

The dielectric loss is calculated by equations for symmetric and asymmetric modes:

$$\tan\delta = \frac{2nk(d + t\Delta_s)}{Q[2nkt\Delta_s + \Delta_s \sin 2(nkt - \Phi_T)} \tag{1.39}$$

$$\tan\delta = \frac{2nk(d + t\Delta_a)}{Q[2nkt\Delta_a - \Delta_a \sin 2(nkt - \Phi_T)} \tag{1.40}$$

where k is number wave; t is sample thickness; Φ is an angle of the beam with the axis of the resonator.

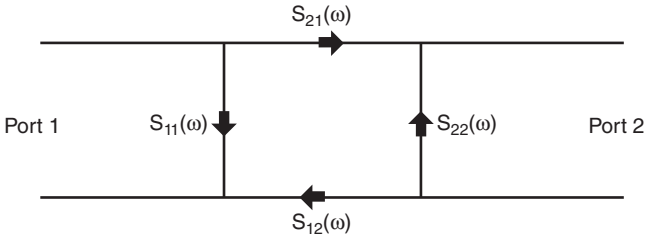

Figure 1.24 *Diagram for the S parameter in the network analyzer.*

1.5 Measurement of EMI Shielding Effectiveness

The EMI shielding measurements are performed by the waveguide method using a vector network analyzer. It is a non-resonant method in which the material under test is inserted into a segment of the transmission line and the properties of the materials are deduced on the basis of the reflection from the material and the transmission through the material.

Since the incident and reflected waves have both magnitude and direction, the *S* parameters are complex numbers. A signal flow graph of a two-port device using *S* parameter notation is shown in Figure 1.24. In the notation $S_{\text{out in}}$, the first number represents the output port and the second number represents the input port.

For a two-port network, the relation between the incident and reflected waves are expressed in terms of $S_{11}(\omega)$, $S_{22}(\omega)$, $S_{12}(\omega)$, and $S_{21}(\omega)$, where $S_{11}(\omega)$ is the response measured at port 1 with the stimulus applied at port 1, $S_{22}(\omega)$ is the response measured at port 2 with the stimulus applied at port 2, $S_{12}(\omega)$ is the response measured at port 1 with the stimulus applied at port 2, and $S_{21}(\omega)$ is the response measured at port 2 with the stimulus applied at port 1. Thus *S* parameters represent the frequency domain response characteristics.

1.5.1 Waveguide Method

In electromagnetic and communication engineering, the waveguide is any linear structure that guides the electromagnetic waves. The dimensions of the waveguide determine the frequency it can support. Waveguide transmission lines are used as a sample holder in this method. The sample is kept inside the wave-guide sample holder coupled to the network analyzer through coaxial waveguide adapters and cables, as shown in Figure 1.25.

In a waveguide, radiated waves undergo reflection, absorption, and transmission. The complex scattering parameters that correspond to the reflection (S_{11} and S_{22}) and transmission (S_{21} and S_{12}) in the samples are measured using the network analyzer. The EMI shielding effectiveness (EMI SE) as well as reflection (SE_R) and absorption (SE_A) shielding effectiveness are calculated from these scattering parameters [72]. If the power fed at port 1 is P_i, power reflected at the same port is P_r, and the output power at port 2 is P_o, then the losses by reflection and absorption is given by the equations

$$SE_R = 10 \log [P_i/(P_i - P_r)] = 10 \log [1/(1 - S_{11})] \tag{1.41}$$

$$SE_A = 10 \log [(P_i - P_r)/P_o] = 10 \log [(1 - S_{11})/(S_{12})] \tag{1.42}$$

$$\text{EMI SE} = SE_R + SE_A \tag{1.43}$$

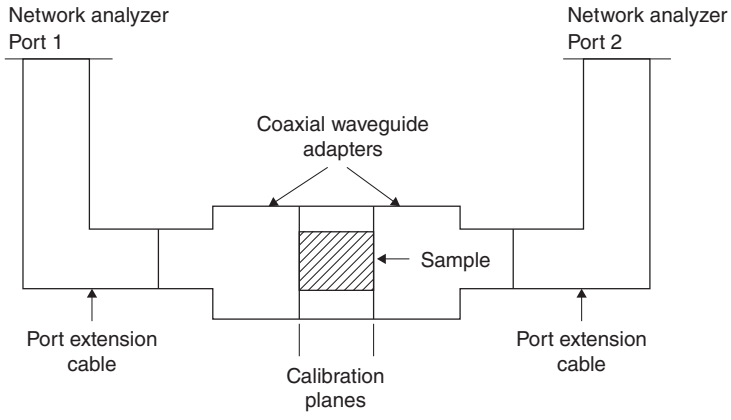

Figure 1.25 *Schematic for the waveguide method.*

Full two-port calibrations were initially done on the test setup in order to remove errors due to directivity, source match, load match, isolation, etc., in both forward and backward directions. The error associated with this measurement is less than 2%. This method has the advantages of easy sample preparation due to the rectangular shape of the sample as well as error due to the air gap can also be avoided. Figure 1.26 shows the measurement setup used in the present example.

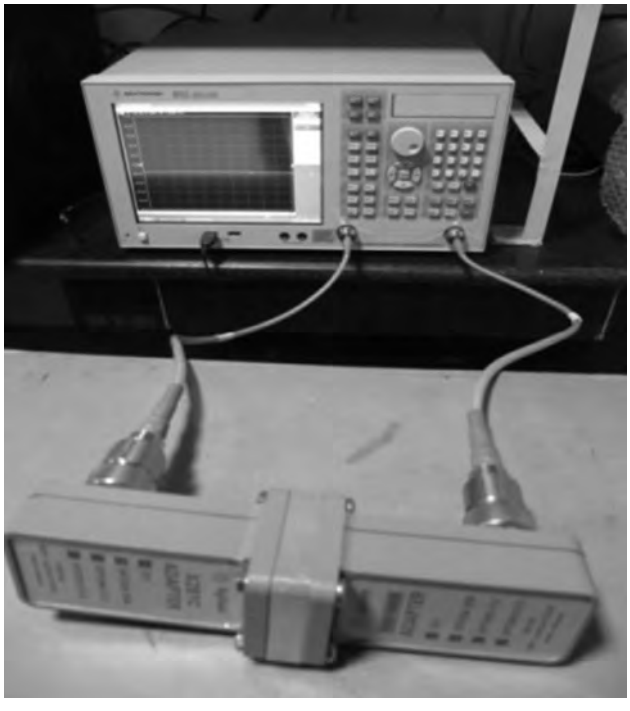

Figure 1.26 *Measurement setup used for cavity methods.*

1.6 Terahertz and Millimeter Wave Measurements

The millimeter wave spectral range is a link between the conventional radio frequency (RF) techniques that work up to approximately 300 MHz. The microwave frequency range (MW) is considered from 300 MHz up to 30 GHz. The millimeter wave range (mm) is considered in between 30 GHz up to 300 GHz. The THz range is generally considered to be 0.3–30 THz. Above 300 MHz stray capacitances and cable length effects lead to errors in the measurement of the components of the electrical impedance, because of the decreasing source intensity and problems associated with finite sample size effects. This frequency is the limit of the THz range. The availability of appropriate sources and detectors, and the development of new experimental measuring configurations lead to the increased importance of the THz range in the study of materials.

1.6.1 Backward Wave Oscillator (BWO)

A backward wave oscillator (BWO), also known as a carcinotron or backward wave tube, is a vacuum tube that is used to generate millimeter waves up to the terahertz range. It is a traveling wave tube. It is an oscillator with a wide electronic tuning range and operates in the range of $\lambda \sim 3$–0.3 mm (100 GHz–1 THz). The study of dielectric and conductive properties of crystals, ceramics, glasses and polymers, powders, composites, liquids, films, and fibers are reported in the literature. The experimental setup for studying the dielectric properties of materials is basically an optical experimental setup measuring channel. In this technique the radiation is normally incident on the sample, which is in the form of a plane-parallel plate. The experiment can either be in a transmission geometry (coefficient T) and phase shift (ϕ) of the transmitted wave or in reflection geometry (coefficient R) and phase shift (ϕ) of the reflection coefficient, which are related to the materials characteristics ε' and ε'' [73]:

$$T = \mathrm{e}^{-4\pi kd/\lambda} \frac{(1-R)^2 + 4R\sin^2\psi}{\left(1 - \mathrm{Re}^{-4\pi kd/\lambda}\right)^2 + 4\mathrm{Re}^{-4\pi kd/\lambda}\sin^2\left(\frac{2\pi\eta d}{\lambda} + \psi\right)} \tag{1.44}$$

$$\phi = \frac{2\pi nd}{\lambda} - \arctan\frac{k(n^2+k^2-1)}{(k^2+n^2)(2+n)n} + \arctan\frac{\mathrm{Re}^{-4\pi kd/\lambda}\sin^2\left(\frac{2\pi nd}{\lambda} + \psi\right)}{1 - \mathrm{Re}^{-4\pi kd/\lambda}\cos^2\left(\frac{2\pi nd}{\lambda} + \psi\right)} \tag{1.45}$$

$$R = \frac{(n-1)^2 + k^2}{(n+1)^2 + k^2}, \psi = \arctan\left(\frac{2k}{n^2+k^2-1}\right), \varepsilon' = n^2 - k^2, \varepsilon'' = 2nk \tag{1.46}$$

where d is the sample thickness, and n and k are the refractive index and extinction coefficients, respectively, that is, the optical parameters of the material. One can use T, ϕR, and ϕ to calculate ε' and ε''.

The quasi-optical BWO spectroscopy is a powerful technique to study the dielectric response of solids in the terahertz to subterahertz ranges. In reality, spectroscopic studies of a variety of materials, ranging from dielectrics to conductors and superconductors, and components like filters and polarizers to food products, are reported in the literature [74–82]. The BWO spectrometers are associated with a wide range of operation (30 GHz to nearly 1.5 THz), high-frequency resolution ($\Delta\nu/\nu \approx 10^{-5}$), and a wide dynamic range

(40–50 dB). The possibility of continuous frequency tuning and the direct measurement of dielectric response spectra are strong characteristics of this technique.

Studies of BWO spectroscopy for biological systems in the millimeter waves and terahertz range are also reported in the literature [83, 84]. In reference [85] a study of tumorous and non-tumorous breast tissues using the backward-wave oscillator-based free-space quasi-optical spectroscopy was employed to obtain transmission data from 30 to 120 GHz. This high-precision experimental technique yields dielectric data with a sensitivity of 10^{-6}, with high accuracy and resolution [86–90]. The results show different characteristics of breast tissues with tumorous and non-tumorous tissues. The technique shows good possibilities for applications for *in vivo* breast cancer detection and diagnostics [85].

1.6.2 Terahertz Time-Domain Spectroscopy (THz-TDS)

The THz range is generally considered to be 0.3–30 THz, where in the literature different definitions can be found. A high interest in this frequency region led to the development of new sources and experimental techniques have been developed to access the THz range [90]. Because of the difficulties in the availability of solid-state THz sources, the research community have focused on all optical techniques producing THz radiation, employing visible/near-IR femtosecond pulsed lasers. This development of broadband THz time-domain spectroscopy (THz-TDS) [91, 92] has led to an increase in the study of the properties of the materials in this region of the spectra. The coherent THz-TDS spectroscopy technique opens the possibility to study the electrical properties of materials, demonstrating the potential use of THz radiation for spectroscopy in a number of application areas. The solid-state THz semiconductor laser and the quantum cascade laser present an active new frontier in the THz area of research [93, 94].

Terahertz time-domain spectroscopy (THz-TDS) is a spectroscopic technique that operates with electromagnetic transients generated using optical femtosecond (1 fs = 10^{-15} s) laser pulses. These THz transients are electromagnetic pulses of duration around 1 ps duration. Their spectral bandwidth varies from frequencies below 100 GHz to 5 THz. The optical detection gives the terahertz electric field with a time resolution of a fraction of a picosecond. From the experimental results the real and imaginary parts of the dielectric function of the material can be obtained. The THz-TDS experimental setup is composed of a femtosecond laser source, a beamsplitter, a THz transmitter, focusing and collimating optics, the sample, a THz detector, and a variable delay line, as shown in Figure 1.27. A computer controls the variable delay line and displays the detector photocurrent versus path length.

The THz switch operates when a laser pulse with photon energy higher than the photoconductor's bandgap energy is focused on the gap of the transmission line. Figure 1.28 shows a photoconductive switch integrated in a microstrip transmission line. In this case, by measuring this signal as a function of the time delay between the arrival of the THz and probe pulses at the electro-optic crystal using a variable delay line, the electric field of the THz pulse in the time domain can be obtained, and the Fourier transform analysis gives the frequency spectrum of the THz radiation pulse. From this measurement, both the real and imaginary parts of the dielectric function of the medium under study may be extracted. The analysis of the transmission and reflection analysis of the THz pulses in thick samples could be done using the measurements of ε' and ε''. In general, broadband THz radiation can be generated either in an optoeletronic manner involving photogenerated transient currents in

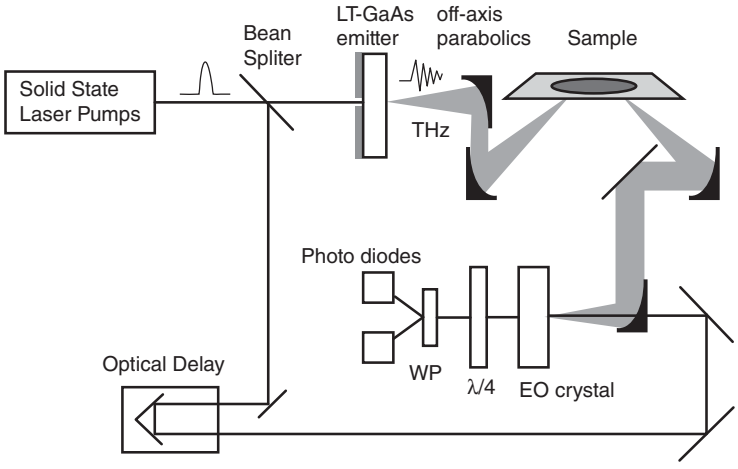

Figure 1.27 *Experimental optical arrangement of a THz system.*

photoconductive antennas [95] or in an optical manner involving optical rectification in EO materials [96].

On the other hand, many groups are looking for new materials such as amorphous electro-optic polymers (EO) that could generate and detect broadband terahertz radiation (0.3−30 THz) [97]. Recently a ∼12 THz, spectral gap-free THz system based on a polymer emitter–sensor pair has been reported in the literature [97]. The THz properties of materials were explored for sensing and identification of explosives, drugs, and controlled materials [98]. Dispersive Fourier transform spectroscopy (DFTS) is another alternative used to study dielectric data of materials in this range of 400 GHz to 1.2 THz [99]. This technique can be used in several interferometer configurations and to study liquids, powders, and gases [99]. In reference [99] the technique was used to study powders of flour, dry milk, corn starch, pesticides, baking soda, and talc.

The refractive index and the real part of the dielectric permittivity were found to be the most reliable for identification and detection purposes. Studies of liquids like ethanol, gasoline, and mixtures are reported in the literature [100], where the frequency-dependent permittivity of mixture solutions provides information concerning the relaxation process in solvent and solute molecules. In this study the dielectric properties of ethanol/gasoline mixtures in the terahertz spectral region are investigated [100]. The relaxation study of both liquids (gasoline and ethanol) are modeled using the Debye model in the THz frequency region.

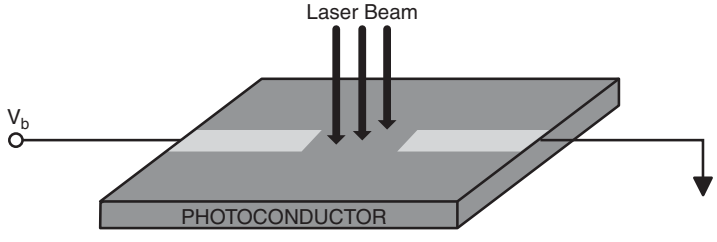

Figure 1.28 *A photoconductive switch integrated in a microstrip transmission line.*

1.7 Measurement of Dielectric Properties of Powder Samples

Dielectric ceramic powders with low loss are extensively used to improve dielectric properties of polymers. In the last 10 years interesting polymer–ceramic composites have been introduced enabling free adjustment of permittivity of devices in several wireless communication applications [101]. In addition, inks based on low-temperature curing polymers with embedded dielectric ceramic particles are used in advanced printed electronics. In these cases it is crucial to know the dielectric properties of powder particles, which can differ significantly as compared to bulk properties. The microwave dielectric properties of powder samples were measured by different techniques [102–108]. Recently Tuhkala *et al.* [106, 109, 110] reported an indirectly coupled open-ended coaxial cavity resonator method operating in TEM mode at 4 GHz to estimate the relative permittivity and loss tangents of powder samples. In this method the open-ended coaxial cavity with optimized dimensions and conductivity is first filled with powder samples. The effective dielectric constant and loss tangent are then determined by the shift in the resonant frequency and change in Q-factor between an empty resonator and a powder sample filled resonator. A schematic setup for the measurement is shown in Figure 1.29.

For a completely filled cavity, the effective dielectric constant is given by

$$\varepsilon_r = {}^{c}\!/_{(4Lf)^2}$$

where c is the speed of the light in vacuum, L is the resonator length, and f is the resonant frequency.

The dielectric constant of powder samples can be obtained from a measured resonator response, volume fractions of each phase (powder, air, and different phases), and calculating the effective dielectric constant using Bruggeman symmetric [111] and Looyenga [112] mixing rules.

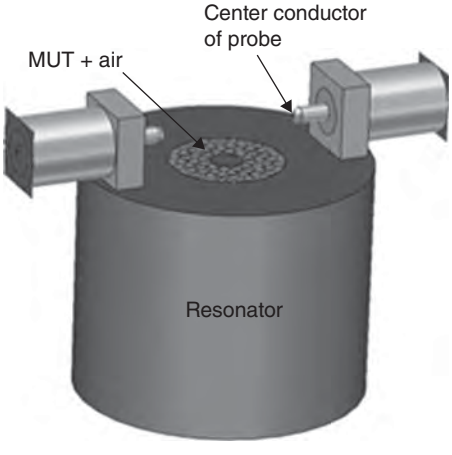

Figure 1.29 *Schematic for dielectric measurements of powder samples. Source: Tuhkala* et al. *2013 [106]. Reproduced with permission of AIP.*

In the same manner the effective loss tangent can be obtained from the following equation, which utilizes general mixing rules:

$$\tan \delta_{eff} = \frac{1}{Q_{filled}} - \frac{1}{Q_{empty}}$$

The method expects careful estimation of the volume fraction of the powder, homogeneous distribution of the powder throughout the cavity, management of the measurement environment (mainly humidity), and probe coupling, which should be loose enough not to disturb the measurement itself and to produce a symmetric resonance peak. Tuhkala *et al.* [109, 110] estimated the microwave dielectric properties of several materials with reasonable accuracy using this technique. They also reported an estimation of the humidity level of the powders [110], the effect of surfactant treatment [113], and an evaluation of the amount of two powder phases [109] using the above method [106].

1.8 Estimation of Dielectric Loss by Spectroscopic Methods

The intrinsic losses in the dielectric material can be obtained by spectroscopic methods using a combination of far-infrared and submillimeter (or THz) spectroscopy [15]. This will give an idea of the lowest possible loss in the sample. It is possible because the intrinsic microwave losses are fully determined by the multiphonon absorption of the ideal (but necessarily anharmonic) crystal and the polar lattice vibration (optic phonons).

The far-infrared reflection spectra can be analyzed by the Kramers–Kronig relation and classical dispersion theory [114–116]. The K-K relationship between r and the phase of reflected wave Θ is given by [114]

$$\begin{aligned} \Theta(\nu) &= \frac{2\nu}{\pi} \int_0^\infty \frac{\ln r(\nu')}{\nu'^2 - \nu^2} \mathrm{d}\nu' \\ r &= \sqrt{R} \\ R(\nu) &= |r(\nu) \quad \exp(i\theta(\nu))|^2 \end{aligned} \tag{1.47}$$

The K-K integration requires data from zero to infinite frequency. The accuracy of the analysis is affected by extrapolation of experimental data taken in the finite frequency range 0 and to infinite frequency. The combination of K-K and classical dispersion theory proves [117] to be a better and more reliable analysis. The optical parameters n and k can be determined from the reflected intensity R and the phase angle Θ using the following relationships [117]:

$$n = \frac{1 - R}{1 + R - 2\sqrt{R}\cos\Theta} \tag{1.48}$$

$$k = \frac{-2\sqrt{2R}\sin\Theta}{1 + R - 2\sqrt{2}R\cos\Theta} \tag{1.49}$$

$$\varepsilon' = n^2 k^2 \tag{1.50}$$

$$\varepsilon'' = 2nk \tag{1.51}$$

where

n = refractive index
ε' and ε'' = real and imaginary parts of the dielectric constant, respectively
K = extinction coefficient

The analysis involves four steps:

(a) The K-K analysis allows the phase angle $\Theta(\nu)$ spectrum to be calculated from the experimental reflectivity spectrum $R(\nu)$.
(b) Calculation of real and imaginary parts of the complex index of refraction using Equations (1.48) and (1.49).
(c) Calculation of real and imaginary parts of complex permittivity using Equations (1.50) and (1.51).
(d) Finally the complex permittivity is fitted by means of a suitable model.

The complex permittivity spectra for both components can be expressed as a sum of quasi-harmonic damped oscillators and ε' and ε'' are then given by [114]

$$\varepsilon'(\nu) = \varepsilon_\infty + \sum_j 4\pi\rho_j\nu_j^2 \frac{\nu_j^2 - \nu^2}{\left(\nu_j^2 - \nu^2\right)^2 + \gamma_j^2\nu^2} \tag{1.52}$$

$$\varepsilon''(\nu) = \sum_j 4\pi\rho_j\nu_j^2 \frac{\gamma_j\nu}{\left(\nu_j^2 - \nu^2\right)^2 + \gamma_j^2\nu^2} \tag{1.53}$$

This sum is all over j resonances (i.e., oscillators describing phonons) in the spectrum. The dispersion parameters are $4\pi\rho_j = \Delta\varepsilon_j{\nu_j}^2$ is the strength of the oscillator, where $\Delta\varepsilon_j$ marks the contribution of the jth mode to the static permittivity, γ_j = width (phonon damping), and ν_j = resonant frequency (phonon eigenfrequency). For the $\nu \ll \nu_j$ condition (microwave region) Equations (1.52) and (1.53) can be written in the form:

$$\varepsilon' = e_\infty + 4\pi\rho_j \quad \text{for } \nu \ll \nu_j \tag{1.54}$$

$$\varepsilon''(\nu) \propto V \sum_j \frac{4\pi\rho_j\gamma_j}{\nu_j^2} \tag{1.55}$$

This means that the permittivity is independent of frequency and the dielectric loss ε'' is proportional to frequency at frequencies much below the phonon frequencies ν_j, which lies in the THz range. The $\varepsilon_\infty$is the permittivity caused by electronic polarization at higher frequencies and can be obtained using the frequency independent middle-infrared reflectivity by the equation [118]

$$\varepsilon_\infty = \frac{\left(1 + \sqrt{R}\right)^2}{\left(1 - \sqrt{R}\right)^2} \tag{1.56}$$

The normal incidence of reflectivity is given by Fresnel formula:

$$R = \frac{(n-1)^2 + k^2}{(n+1)^2 + k^2} \tag{1.57}$$

The phonon parameters can be obtained by K-K analysis. Each peak in the plot ε'' versus frequency obtained by the K-K analysis corresponds to a phonon frequency ν_j and γ_j is given by the frequency half-width of the ε_j'' peak. The oscillator strength is determined by:

$$4\pi\rho_j = \frac{\gamma_j \varepsilon_j''}{\nu_j} \tag{1.58}$$

Complex permittivity can be calculated by direct fitting of the experimental reflectivity spectra using the formulas in Equations (1.53) and (1.54) and

$$R = \left(\frac{\left(\sqrt{\varepsilon} - 1\right)}{\left(\sqrt{\varepsilon} + 1\right)} \right)^2 \tag{1.59}$$

The simulation process is done in the following way:

(a) Fix ν_j and γ_j and adjust ρ_j to give the correct width of the reflection band.
(b) Fix ν_j and ρ_j and adjust γ_j to give the correct maximum reflectivity.
(c) ν_j is adjusted to align the fitted curve with the experimental.

Once the best fit is obtained, tan δ can be determined:

$$\tan\delta = \frac{\varepsilon''}{\varepsilon'} = \frac{\sum_j 4\pi\rho_j \nu_j^2 \frac{\gamma_j \nu}{\left(\nu_j^2 - \nu^2\right)^2 + \gamma_j^2 \nu^2}}{\varepsilon_\infty + \sum_j 4\pi\rho_j \nu_j^2 \frac{\nu_j^2 - \nu^2}{\left(\nu_j^2 - \nu^2\right)^2 + \gamma_j^2 \nu^2}} \tag{1.60}$$

At low frequencies $\nu \ll \nu_j$ [117] we obtain

$$\tan\delta = \frac{\sum_j 4\pi\rho_j \frac{\gamma_j \nu}{\nu_j^2}}{\varepsilon_\infty + \sum_j 4\pi\rho_j} \tag{1.61}$$

Equation (1.61) shows that tan δ is linearly frequency dependent.

The far-infrared spectroscopy (FIR) and terahertz transmission spectroscopy are useful methods used to estimate the intrinsic losses [119, 120]. It was reported as early as 1962 that experimental ε'' is proportional to the frequency well below the phonon frequencies ($f \leq 10^{12}$ Hz) [121]. The lattice absorption is the dominant loss mechanism at high frequencies [121, 122] and several authors extrapolated the data at high frequencies obtained by FIR and SMM to the microwave frequency range [120, 123]. Several authors [116, 118, 124–129] estimated the dielectric constant and dielectric loss tangent of materials by analyzing the FIR reflectivity data using the K-K analysis and classical dispersion theory. They found reasonable agreement between the ε_r obtained by the spectroscopic method with that measured by microwave methods. However, the loss tangents measured by microwave methods were found to be higher than those obtained by the far-infrared method. In the loss tangent obtained by microwave methods is the sum of intrinsic and extrinsic dielectric losses. The presence of porosity and crystal defects contribute to the loss factor and the spectroscopic methods give only the intrinsic loss factor. Thus it is possible by the far-infrared and

SMM method to find the lowest loss factor in a particular material, which in turn is helpful when optimizing the ceramic preparation to get a low-loss material and to reduce extrinsic losses. The relative influence of defects on losses decreases with increasing frequency [126]. Hence their influence cannot be measured in the optical frequency range. This enables one to estimate the order of magnitude of intrinsic microwave losses from IR reflectivity on new materials without much processing. Unlike the microwave losses, the IR reflectivity of dense ceramics is less sensitive to sample preparation (i.e., extrinsic losses contribute only slightly to IR spectra). Hence the IR spectroscopic method can be successfully and simply used for estimating the intrinsic microwave losses and dielectric constants of new materials [120, 124, 126]. Nevertheless, it should be stressed that the accuracy of the far-IR (FIR) experiment is rather limited. Therefore it is necessary to combine FIR reflectivity studies with SMM or THz measurements, which are more sensitive than FIR reflectivity on small dielectric losses below phonon frequencies.

The fundamental loss mainly corresponds to the absorption of the energy quantum of the electromagnetic field $\hbar\omega$ ($\omega = 2\pi\nu$ is the AC field frequency) in a collision process with thermal phonons, which have much higher energies [15]. Under such a situation, the absorption of $\hbar\omega$ of energy corresponds to three fundamental loss mechanisms: three quantum, four quantum, and quasi-Debye mechanisms. The three quantum process involves an $\hbar\omega$ quantum and two phonons [15, 130, 131]. The four quantum mechanism corresponds to the field quantum absorption processes involving three phonons. The application of a DC field to a centrosymmetric crystal breaks its central symmetry and therefore gives rise to a quasi-Debye mechanism [15, 130].

In centrosymmetric materials, the crystalline symmetry permits only three quantum and four quantum mechanisms. However, in non-centrosymmetric materials all the three mechanisms are allowed and the quasi-Debye mechanism is dominant for the intrinsic loss. As the ε_r increases, the dielectric loss also increases. For the intrinsic loss mechanism in cubic centrosymmetric crystals, the real ε' and imaginary ε'' are related by $\varepsilon'' \propto \varepsilon^x$, where $x = 2.5$ to 5 [130]. The role of intrinsic losses at microwave frequencies increases with increasing ε_r.

Petzelt and co-workers [120, 123–126, 129, 132, 133] made measurements on many microwave ceramic materials in the IR and SMM (submillimeter) range using FTIR and a backward wave oscillator (BWO) and/or time-resolved THz spectroscopy. The extrapolated losses from the THz to MW range (using $\varepsilon'' \propto \omega$) were compared with those measured directly by microwave methods. It was found in many cases that the extrapolated loss factors were much lower than those measured by microwave methods, indicating that the proportionality $\varepsilon'' \propto \omega$ is not satisfied. The microwave measurements are very sensitive to extrinsic loss depending on the ceramic processing, whereas the spectroscopic methods are not (i.e., extrinsic losses contribute only slightly into dielectric losses in the THz range). The difference in loss factor between those extrapolated from SMM and the microwave methods is attributed to the extrinsic loss factor.

For well-processed ceramics, the model predicts the simple proportionality for intrinsic losses $\varepsilon'' \propto \omega$ (or Qf is a constant), which is usually obeyed, due the minimization of extrinsic losses. However, is not usual to use the extrapolation of the damped harmonic oscillator models down to the microwave range, because it assumes frequency-independent phonon damping, which is not necessary. This is explained by microscopic phonon transport theory [15, 126, 134], which indicates that the simple damped oscillator model with

frequency-independent damping is valid only in the vicinity of phonon eigenfrequencies and the microwave frequencies lie 3–4 orders of magnitude below the phonon frequencies. Nevertheless, far-infrared spectroscopy was used frequently (together with THz spectroscopy) [128, 133, 134] for estimation of intrinsic microwave dielectric losses, and it was shown that the linear extrapolation from the THz to MW range works quite well, although there is no exact detailed theoretical reason for it.

The temperature dependence for dielectric losses of two phonon difference decay processes dominate at room temperature and near the Debye temperature (T_D) in the microwave range far below the eigenfrequencies and therefore $\varepsilon'' \propto \omega T^2$. At low temperatures, the ε'' temperature dependence is very strong, which differs from the classical damped oscillator model $\varepsilon'' \propto \omega T$. The difference is attributed to the presence of extrinsic sources of losses that are strongly frequency dependent [120, 126].

1.9 Factors Affecting Dielectric Loss

The presence of moisture or humidity affects the tan δ [20, 135]. The microwave measurements are usually done in an air-conditioned room in order to minimize its effects and the samples should be heated in an oven to remove the moisture before starting the experiments. The material should also contain the lowest possible concentration of dipoles and charge carriers with the lowest possible mobility to possess low loss [136]. Several technically important insulating materials are far from high purity and often contain deliberate or accidental admixtures of substances that are necessary for their processing. These impurities may cause disordered charge distributions in the crystal lattice, leading to loss [136]. Schlömann [136] reported that in ionic non-conducting crystals, the loss tangent increases when the ions are distributed in such a disorderly way that they break the periodic arrangement of atoms in the crystal. The loss tangent depends strongly on the spatial correlation between charge deviations. Further, Schlömann reported that the loss tangent is negligible if the disordered charge distribution in the crystal maintains the charge neutrality within a short range of the order of lattice constant. The intrinsic quality factor (Q_i = 1/tan δ) of any given material will vary with the frequency of measurements. For many materials, the dielectric loss tangent almost linearly increases as the frequency increases. Hence often the intrinsic quality factor (1/tan δ) is reported as ($Q_i f = f$/tan δ, in GHz) since this value is the first approximation constant. The assumption that the value of $Q_i f$ is constant is satisfied for the well-densified ceramics in a certain limited frequency range. In practice, samples measured at higher frequencies (5–12 GHz) always give higher $Q_i f$ values than the same material measured at lower frequencies of 1–3 GHz. Recently Li and Chen reported [137] that the product Qf is frequency dependent and increases with frequency. The frequency dependence of the Qf value is attributed to the presence of defects-induced extrinsic dielectric loss. It may be noted that larger samples resonating at lower frequencies statistically contain more imperfections than smaller ceramic disks resonating at higher frequencies. This difference may be related to ceramic processing. The presence of porosity decreases the quality factor due to the presence of moisture in the pores. Hence porous samples show an increase in $Q_i f$ on warming up due to the escape of moisture.

Gurevich and Tagantsev [15, 16] investigated the fundamental theory of intrinsic losses and reported that the lower limit of intrinsic losses are found in pure defect-free single

crystals. Several phonon processes contribute to intrinsic losses in a dielectric and their importance depends on the AC field frequency, temperature range. and symmetry of the crystal under consideration. The loss mechanisms are different for a crystal with and without a center of symmetry. Guvevich *et al.* [15, 16] analyzed the lattice anharmonicity for various crystal symmetries and obtained numerical estimates of tan δ of ideal crystals.

For hexagonal symmetry and $T \ll T_D$ (T_D = Debye temperature),

$$\tan\delta = \frac{\eta\omega(kT)^5}{\varepsilon_r \rho v_s^5 h^2 (kT_D)^2} \tag{1.62}$$

and for rhombohedral or cubic symmetry,

$$\tan\delta = \frac{\eta\omega^2(kT)^4}{\varepsilon_r \rho v_s^5 h (kT_D)^2} \tag{1.63}$$

where η is a dimensionless anharmonicity parameter ranging between 1 and 100, ω is the angular frequency, k = Boltzmann constant, T = absolute temperature, v_s = sound velocity, T_D = Debye temperature, and ρ is the density.

For the hexagonal symmetry, tan δ decreases rapidly with a decrease of temperature as T^5 and in centrosymmetric crystals as T^4. The decrease in tan δ as a function of temperature in the range 3.5 to 300 K was verified experimentally [17] for three hexagonal sapphire samples of different defect concentrations, as shown in Figure 1.30. The curve (a) is for a sample

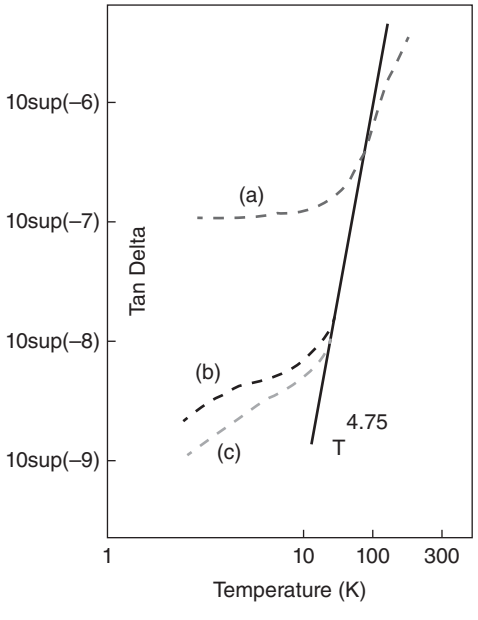

Figure 1.30 *Variation of tan δ of three different sapphire crystals as a function of temperature on cooling: (a) crystal with disorientation, (b) crystal grown at the rate of 8 mm/h, and (c) crystal grown at the rate of 4 mm/h. Source: Adapted from Braginsky* et al. *1987 [17].*

that contained a block structure with a disorientation of 1°, the curve (b) corresponds to a sample grown at the rate of 8 mm/h, and curve (c) at the rate of 4 mm/h. It is observed that curve (a) shows a higher loss due to the larger defect concentration. It is also observed in Figure 1.30 that tan δ decreased with decreasing temperature. All samples showed a linear section in the temperature range 50 to 300 K, where tan $\delta \sim T^{\alpha}$ ($\alpha = 4.75$). This value is reported as the lower limit of the dielectric losses at a given frequency, which is independent of the variation of the defect structure and is of fundamental origin [17]. At temperatures $T < 50$ K, the value of tan δ is greatly affected by the level of crystal perfection. Bragisnsky *et al.* [17] extrapolated from the experimentally obtained tan δ–temperature plot (Figure 1.30) to predict a tan $\delta \sim 5 \times 10^{-15}$ at 4 K at 10 GHz for a defect-free crystal. This corresponds to a Q value of about 2×10^{14}, which can be considered as the upper limit of the quality factor in a perfect sapphire crystal. There is no predictive theory to account for the microwave loss in dielectric ceramics. Hence the approach to find new dielectric resonator materials is largely done by the trial and error method involving preparing and testing a large number of samples.

1.10 Measurement of Temperature Coefficient of Resonant Frequency

The temperature coefficient of resonant frequency (τ_f) is the parameter that determines the thermal stability of the resonator. The τ_f indicates how much the resonant frequency drifts with a change in the temperature. The electronic devices based on microwave resonators are required to have τ_f values close to zero. Microwave circuits will normally have some low characteristics τ_f, so the resonator components that are introduced into them are required to compensate for the inherent drift. For this reason the τ_f values of resonators are typically non-zero but have some low finite values. The origin of τ_f is related to the linear expansion coefficient α_L of the resonator and its dielectric constant variation with temperature [8]. Mathematically the relationship is

$$\tau_f = -\alpha_L - \frac{\tau_\varepsilon}{2} \tag{1.64}$$

where τ_ε is the temperature coefficient of the permittivity and α_L is the linear thermal expansion coefficient of the dielectric material, which is usually positive.

In practice, the Equation (1.64) is valid for 100% electric energy storage in the sample and the thermal expansion of the metal cavity enclosing the DR is negligible. For an ideal resonator the temperature coefficient of resonant frequency (τ_f) should be near zero. Hence from Equation (1.64) for a zero τ_f, τ_ε should have twice the value of α_L and should be negative. Since resonators are used in communication systems, temperature stability is an important factor and should be close to zero. For most of the electronic ceramic materials α_L is about +10 ppm/°C, indicating the significant influence of τ_ε on τ_f.

Experimentally τ_f is measured by following the drift in the resonant peak frequency f as the temperature is slowly varied. In order to measure τ_f, the dielectric resonator is kept end-shorted between two copper plates under the Courtney setup. This is then kept inside a temperature-controlled oven. The E-field probe is kept near the DR in such a way as to get resonance. The TE_{011} mode is identified and the setup is then slowly heated (~ 1 °C/minute) in the range 25 to 80 °C. The probe of the thermocouple is kept just inside the oven so that

it does not disturb the resonant frequency. Shift of the resonant frequency as a result of heating in the reflection mode is noted using a network analyzer when the temperature is steady. The variation of resonant frequency is plotted as a function of temperature. The τ_f is calculated from the slope of the curve using

$$\tau_f = \frac{f_{80} - f_{25}}{f_{25}\,(80 - 25))} = \frac{1}{f}\frac{\Delta f}{\Delta T} \times 10^6 \tag{1.65}$$

The τ_f is expressed as parts per million per degree Celsius (ppm/°C).

The τ_f can also be measured by the cavity method used for measuring the quality factor. The thermal expansion of the cavity during heating limits the accuracy of the method. However, use of a cavity made of invar can minimize the inaccuracy. In fact, thermal expansion of the cavity is negligibly small for whispering gallery modes and also for a $TE_{01\delta}$ mode resonant structure if permittivity of the sample is large and the sample is situated away from all cavity walls. The τ_f is related to thermal expansion and relative permittivity by the relation (1.64). The temperature coefficient of the dielectric constant τ_ε is of considerable interest to users of dielectric substrates. This can be obtained by the parallel plate capacitor method using an LCR meter at low frequency (e.g., 1 MHz) and heating the sample. From the ε_r noted at different temperatures the τ_ε can be obtained. At microwave frequency, one can obtain τ_ε from the value of τ_f and α_L and using Equation (1.64). The temperature coefficient of resonance frequency and the Q-factor are quantities that characterize the resonator and depend not only on the properties of the ceramic sample but also on the properties of other parts of the resonance system.

The high dielectric loss ceramics cannot enable the measurements of τ_f due to the fact that monitoring the TE_{011} mode is not possible. Ceramics with a high dielectric loss do not have the TE_{011} mode clearly detectable, which leads to difficulties of taking the measurements of τ_f of this kind of material. For these kinds of materials another method for τ_f measurements was developed by Silva *et al.* [138]. This new procedure uses an experimental setup where the dielectric loss would not affect the mode identification. The experimental setup for a dielectric resonator antenna (DRA) showed it to be an ideal setup for this measurement, where the peaks are very well defined modes and the high dielectric loss would not affect the mode identification. The experiment setup consists of a DRA, fed laterally by an SMA probe, coupled to a ceramic oven, as shown in Figure 1.31.

The dominant mode for this DRA is the $HE_{11\delta}$ mode and the measurement of τ_f of any sample is made to accomplish the shift of the resonant frequency of $HE_{11\delta}$ mode with increasing temperature (see Figure 1.32). For samples that have a high dielectric loss, the traditional measurements for the Hakki–Coleman setup do not allow the TE_{011} mode visualization to be obtained, due to the convolution of the TE_{011} mode with adjacent modes (see Figure 1.33). In this case the τ_f could not be obtained. Figure 1.33 shows a measurements of a high dielectric loss ceramic by the SFS method [138], where the new methodology to enable measurements for this kind ceramic can be seen.

1.11 Tuning of the Resonant Frequency

The resonant frequency of a resonator depends on the resonator surroundings, relative permittivity, and the sample dimensions. It is possible to tune the frequency of a particular

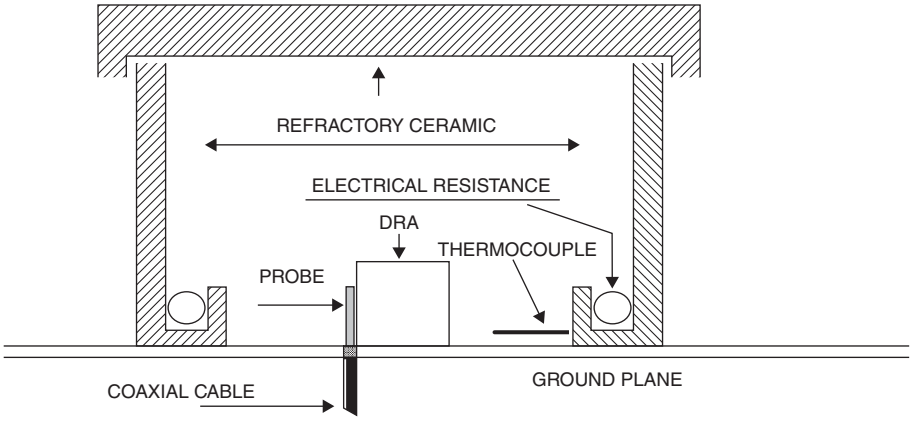

Figure 1.31 *Experimental setup for τ_f measurements by an $HE_{11\delta}$ frequency shift.*

resonator [139–142] by a tuning plate, dielectric plug, or a dielectric disk, as shown in Figure 1.34. The dielectric plug or dielectric disk tuning may decrease the quality factor only by less than 5%, whereas plate tuning leads to a considerable decrease of the Q-factor. When a metallic tuner is introduced, the resonant frequency will increase as the tuner approaches the DR, but if a dielectric tuner is used then the resonant frequency will decrease. By these methods, a change in resonant frequency up to about 15% can be achieved.

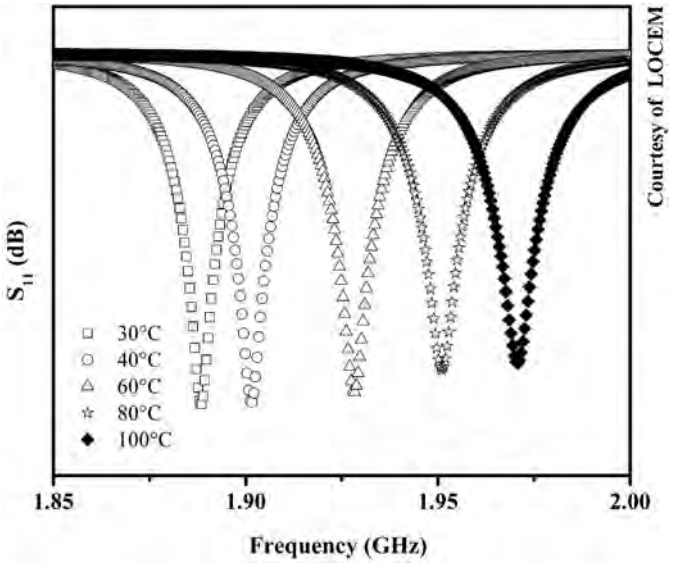

Figure 1.32 *The frequency displacement of $HE_{11\delta}$ mode frequency as a function of temperature variation.*

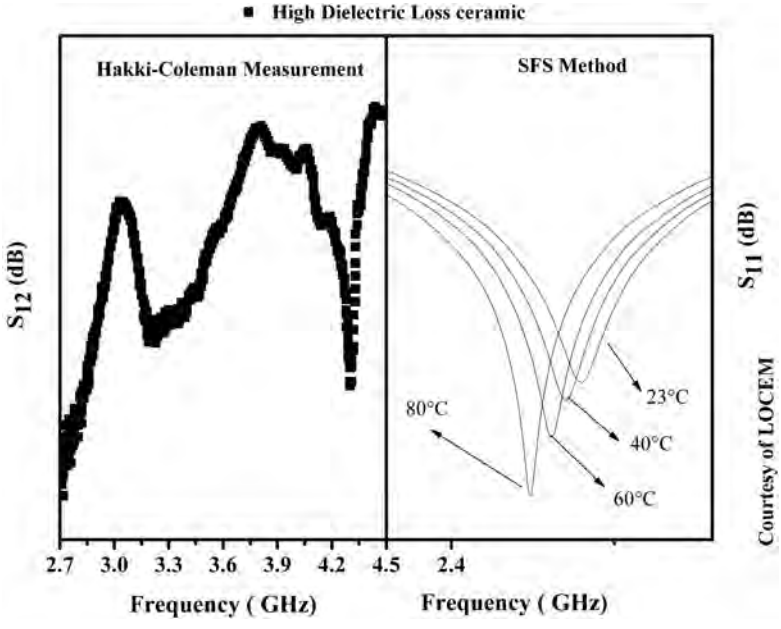

Figure 1.33 *The frequency profile of Hakki–Coleman measurements of a high dielectric loss ceramic in comparison with the measurements using the SFS method.*

However, when using a metallic plate tuner, the tuning range may be limited to only a few percent in order to avoid serious degradation of the Q-factor and τ_f. Another way to tune the frequency is by changing the physical size of the DR by machining and reducing the thickness or diameter of the DR. It is also possible to tune the frequency by increasing the size of the resonator by attaching a small piece of low-loss ceramic to the DR using low-loss glue. The resonators can be mounted to a ceramic substrate using a small drop of low-loss adhesive such as cyanoacrylic. Recently Petrov and Alford [143] reported fast resonant frequency tuning in dielectric resonators by incorporating a thick film of $Ba_{1-x}Sr_xTiO_3$.

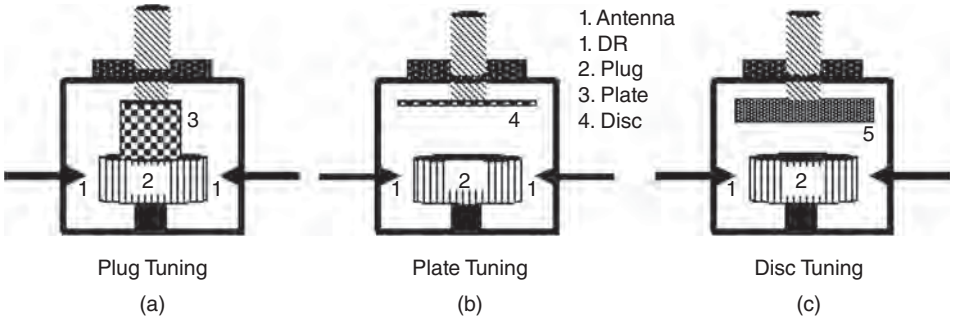

Figure 1.34 *Schematic diagrams showing tuning of the resonant frequency: (a) plug tuning, (b) plate tuning, and (c) disk tuning.*

References

1. Rayleigh, Lord (1987) On the passage of wave through tubes, or the vibration of dielectric cylinders. *Philosophical Magazine*, **43**, 125–132.
2. Richtmyer, R.D. (1939) Dielectric resonators. *Journal of Applied Physics*, **10** (6), 391.
3. Okaya, A. and Barash, L. (1962) The dielectric microwave resonator. *Proceedings of the IRE*, **50** (10), 2081–2092.
4. Okaya, A. (1962) The rutile microwave resonator. *Proceedings of the IRE*, **48**, 1921.
5. Cohn, S.B. (1965) Microwave filters containing high-Q dielectric resonators. *G-MTT Symposium Digest*, **MTT002**, 49–54.
6. Sebastian, M.T. (2010) *Dielectric Materials for Wireless Communication*, Elsevier Science, 688 pp.
7. Sebastian, M.T., Ubic, R., and Jantunen, H. (2015) Low-loss dielectric ceramic materials and their properties. *International Materials Reviews*, **60** (7), 392–412.
8. Kajfez, D. and Guillon, P. (1998) *Dielectric Resonators*, Noble Publishing Corporation, 547 pp.
9. Schwartz, B. (1984) Microwlwctronic packaging II. *American Ceramic Society Bulletin*, **63**, 577–581.
10. Tummala, R.R. (1991) Ceramic and glass–ceramic packaging in the 1990s. *Journal of the American Ceramic Society*, **74** (5), 895–908.
11. Moulson, A.J. and Herbert, J.M. (2003) *Electroceramics: Materials, Properties, Applications*, John Wiley & Sons.
12. Raghavan, V. (2004) *Materials Science and Engineering: A First Course*, PHI Learning, 430 pp.
13. Burfoot, J.C. (1967) *Ferroelectrics: An Introduction to the Physical Principles*, London: D. Van Nostrand Company, London 261 pp.
14. Krupka, J. (2006) Frequency domain complex permittivity measurements at microwave frequencies. *Measurement Science and Technology*, **17** (6), R55–R70.
15. Gurevich, V.L. and Tagantsev, A.K. (1991) Intrinsic dielectric loss in crystals. *Advances in Physics*, **40** (6), 719–767.
16. Gurevich, V.-L. and Tagantsev, A.K. (1986) Intrinsic dielectric loss in crystals: low temperature. *Soviet Physics JETP*, **64**, 10.
17. Braginsky, V.B., Ilchenko, V.S., and Bagdassarov, K.S. (1987) Experimental observation of fundamental microwave absorption in high-quality dielectric crystals. *Physics Letters A*, **120** (6), 300–305.
18. Chen, L.F., Ong, C.K., Neo, C.P., Varadan, V.V., and Varadan, V.K. (2004) *Microwave Electronics: Measurement and Materials Characterization*, John Wiley & Sons, 552 pp.
19. Hakki, B.W. and Coleman, P.D. (1960) A dielectric resonator method of measuring inductive capacities in the millimeter range. *IEEE Transactions on Microwave Theory and Techniques*, **8** (4), 402–410.
20. Courtney, W.E. (1970) Analysis and evaluation of a method of measuring the complex permittivity and permeability microwave insulators. *IEEE Transactions on Microwave Theory and Techniques*, **18** (8), 476–485.
21. Kobayashi, Y. and Katoh, M. (1985) Microwave measurement of dielectric properties of low-loss materials by the dielectric rod resonator method. *IEEE Transactions on Microwave Theory and Techniques*, **33** (7), 586–592.
22. Kobayashi, Y. and Tanaka, S. (1980) Resonant modes of a dielectric rod resonator short-circuited at both ends by parallel conducting plates. *IEEE Transactions on Microwave Theory and Techniques*, **28** (10), 1077–1085.
23. Cohn, S.B. and Kelly, K.C. (1966) Microwave measurement of high-dielectric- constant materials. *IEEE Transactions on Microwave Theory and Techniques*, **14** (9), 406–410.
24. Ginzton, E.L. (2012) *Microwave Measurements*, Literary Licensing, LLC, 534 pp.
25. Vanzura, E.J. and Rogers, J.E. (1991) Resonant circuit model evaluation using reflected S-parameter data, in *Conference Record. IEEE Instrumentation and Measurement Technology Conference*, IEEE, pp. 150–155.

26. Rebsch, D.L., Webb, D.C., Moore, R.A., and Cowlishaw, J.D. (1965) A mode chart for accurate design of cylindrical dielectric resonators (correspondence). *IEEE Transactions on Microwave Theory and Techniques*, **13** (4), 468–469.
27. International Standard IEC 61338-1–4, 1st edn (2005-11) Waveguide type dielectric resonators. Part 1–4: General information and test conditions – Measurement method of complex permittivity for dielectric resonator materials at millimetre-wave frequency. International Electrotechnical Commission, Geneva, Switzerland.
28. Wheless, P. and Kajfez, D. (1985) The use of higher resonant modes in measuring the dielectric constant of dielectric resonators. *MTT-S International Microwave Symposium Digest*, **MTT005**, 473–476.
29. Kobayashi, Y. and Tamura, H. (1994) Round Robin Test on a dielectric resonator method for measuring complex permittivity at microwave frequency (Special Issue on Measurement Techniques for Microwave/Millimeter Wave). *IEICE Transactions on Electronics, The Institute of Electronics, Information and Communication Engineers*, **77** (6), 882–887.
30. Pospieszalski, M.W. (1977) On the theory and application of the dielectric post resonator (Short Papers). *IEEE Transactions on Microwave Theory and Techniques*, **25** (3), 228–231.
31. Takagi, H., Fujinami, N., Tamura, H., and Wakino, K. (1992) Measurement accuracy of complex permittivity in the dielectric rod resonator method. *Japanese Journal of Applied Physics*, **31** (Part 1, No. 9B), 3269–3271.
32. Krupka, J., Derzakowski, K., Riddle, B., and Baker-Jarvis, J. (1998) A dielectric resonator for measurements of complex permittivity of low loss dielectric materials as a function of temperature. *Measurement Science and Technology*, **9** (10), 1751–1756.
33. Leong, K., Mazierska, J., and Krupka, J. (1997) Measurements of unloaded Q-factor of transmission mode dielectric resonators, in *IEEE MTT-S International Microwave Symposium Digest*, IEEE, pp. 1639–1642.
34. Tamura, H., Matsumoto, H., and Wakino, K. (1989) Low temperature properties of microwave dielectrics. *Japanese Journal of Applied Physics*, **28** (S2), 21.
35. Krupka, J., Huang, W.-T., and Tung, M.-J. (2005) Complex permittivity measurements of low-loss microwave ceramics employing higher order quasi TE 0 np modes excited in a cylindrical dielectric sample. *Measurement Science and Technology*, **16** (4), 1014–1020.
36. Valant, M., Suvorov, D., and Maček S. (1996) Measurement error analysis in the determination of microwave dielectric properties using cavity reflection method. *Ferroelectrics*, **176** (1), 167–177.
37. Scott, A.W. (1993) *Understanding Microwaves*, John Wiley & Sons, Inc., New York.
38. Khanna, A. and Garault, Y. (1983) Determination of loaded, unloaded, and external quality factors of a dielectric resonator coupled to a microstrip line. *IEEE Transactions on Microwave Theory and Techniques*, **31** (3), 261–264.
39. Wait, J.R. (1967) Electromagnetic whispering gallery modes in a dielectric rod. *Radio Science*, **2** (9): 1005–1017.
40. Cros, D. and Guillon, P. (1990) Whispering gallery dielectric resonator modes for W-band devices. *IEEE Transactions on Microwave Theory and Techniques*, **38** (11), 1667–1674.
41. Krupka, J., Cros, D., Aubourg, M., and Guillon, P. (1994) Study of whispering gallery modes in anisotropic single-crystal dielectric resonators. *IEEE Transactions on Microwave Theory and Techniques*, **42** (1), 56–61.
42. Blair, D.G., Woode, R.A., Tobar, M.E., and Ivanov, E.N. (1994) Measurement of dielectric loss tangent of alumina at microwave frequencies and room temperature. *Electronics Letters*, **30** (25), 2120–2122.
43. Ivanov, E.N., Blair, D.G., and Kalinichev, V.I. (1993) Approximate approach to the design of shielded dielectric disk resonators with whispering-gallery modes. *IEEE Transactions on Microwave Theory and Techniques*, **41** (4), 632–638.
44. Tobar, M.E. and Mann, A.G. (1991) Resonant frequencies of higher order modes in cylindrical anisotropic dielectric resonators. *IEEE Transactions on Microwave Theory and Techniques*, **39** (12), 2077–2082.

45. Krupka, J., Derzakowski, K., Abramowicz, A., Tobar, M.E., and Geyer, R.G. (1999) Use of whispering-gallery modes for complex permittivity determinations of ultra-low-loss dielectric materials. *IEEE Transactions on Microwave Theory and Techniques*, **47** (6), 752–759.
46. Krupka, J. (1996) Measurements of the complex permittivity of microwave circuit board substrates using split dielectric resonator and reentrant cavity techniques, in *Seventh International Conference on Dielectric Materials, Measurements and Applications*, IEEE, pp. 21–24.
47. Krupka, J., Gregory, A.P., Rochard, O.C., Clarke, R.N., Riddle, B., and Baker-Jarvis, J. (2001) Uncertainty of complex permittivity measurements by split-post dielectric resonator technique. *Journal of the European Ceramic Society*, **21** (15), 2673–2676.
48. Krupka, J. (2013) Contactless methods of conductivity and sheet resistance measurement from semiconductors, conductors and superconductors. *Measurement Science and Technology*, **24**, 062001.
49. Kent, G. (1988) An evanescent-mode tester for ceramic dielectric substrates. *IEEE Transactions on Microwave Theory and Techniques*, **36** (10), 1451–1454.
50. Krupka, J. (2003) Precise measurements of the complex permittivity of dielectric materials at microwave frequencies. *Materials Chemistry and Physics*, **79** (2–3), 195–198.
51. Parkash, A., Vaid, J.K., and Mansingh, A. (1979) Measurement of dielectric parameters at microwave frequencies by cavity-perturbation technique. *IEEE Transactions on Microwave Theory and Techniques*, **27** (9), 791–795.
52. Von Aulock, W. and Rowen, J.H. (1957) Measurement of dielectric and magnetic properties of ferromagnetic materials at microwave frequencies. *Bell System Technical Journal*, **36** (2), 427–448.
53. Spencer, E., Lecraw, R., and Reggia, F. (1956) Measurement of microwave dielectric constants and tensor permeabilities of ferrite spheres. *Proceedings of the IRE*, **44** (6), 790–800.
54. Artman, J.O. and Tannenwald, P.E. (1953) Measurement of permeability tensor in ferrites. *Physical Review*, **91** (4), 1014–1015.
55. Slater, J.C. (1946) Microwave electronics. *Reviews of Modern Physics*, **18** (4), 441–512.
56. Daiqing, Li, Free, C.E., Pitt, K.E.G., and Barnwell, P.G. (2001) A simple method for accurate loss tangent measurement of dielectrics using a microwave resonant cavity. *IEEE Microwave and Wireless Components Letters*, **11** (3), 118–120.
57. Bussey, H.E. and Steinert, L.A. (1958) Exact solution for a gyromagnetic sample and measurements on a ferrite. *IEEE Transactions on Microwave Theory and Techniques*, **6** (1), 72–76.
58. Ohlsson, P.O.R. (1975) Theory for and experiments with a TM_{02n} applicator. *Journal of Microwave Power and Electromagnetic Energy (JMPEE)*, **10** (3), 271–280.
59. Parry, J.V.L. (1951) The measurement of permitivity and power factor of dielectrics at frequencies from 300 to 600 Mc/s. *Proceedings of the IEE – Part III: Radio and Communication Engineering*, **98** (54), 303–311.
60. Kaczkowski, A. and Milewski, A. (1980) High-accuracy wide-range measurement method for determination of complex permittivity in reentrant cavity: Part A – Theoretical analysis of the method. *IEEE Transactions on Microwave Theory and Techniques*, **28** (3), 225–228.
61. Karpova, O.V. (1959) On an absolute method of measurement of dielectric properties of a solid using shaped resonator. *Sovet Physics*, **1**, 220–228.
62. Horner, F., Taylor, T.A., Dunsmuir, R., *et al.* (1946) Resonance methods of dielectric measurement at centimetre wavelengths. *Journal of the Institution of Electrical Engineers – Part III: Radio and Communication Engineering*, **93** (21), 53–68.
63. Cook, R.J., Jones, R.G., and Rosenberg, C.B. (1974) Comparison of cavity and open-resonator measurements of permittivity and loss angle at 35 GHz. *IEEE Transactions on Instrumentation and Measurement*, **23** (4), 438–442.
64. Stumper, U. (1973) A TE_{01n} cavity resonator method to determine the complex permittivity of low loss liquids at millimeter wavelengths. *Review of Scientific Instruments*, **44** (2), 165.
65. Yu, P.K. and Cullen, A.L. (1982) Measurement of permittivity by jeans of an open resonator. I. Theoretical. *Proceedings of the Royal Society of London. A. Mathematical and Physical Sciences*, **380** (1778), 49–71.

66. Ghodgaonkar, D.K., Varadan V.V., Varadan, V.K. (1989) Free-space method for measurement of dielectric constants and loss tangents at microwave frequencies. *IEEE Transactions on Instrumentation and Measurement*, **38** (3), 789–793.
67. Campbell, C.K. (1978) Free-space permittivity measurements on dielectric materials at millimeter wavelengths. *IEEE Transactions on Instrumentation and Measurement*, **27** (1), 54–58.
68. Amiet, A. and Jewsbury, P. (2000) Free space microwave permittivity and permeability measurements, in *Microwave Conference, 2000 Asia-Pacific Publication*, pp. 445–448.
69. Bartley, P.G. and Begley, S.B. (2005) Improved free-space *S*-parameter calibration. *2005 IEEE Instrumentationand Measurement Technology Conference Proceedings*, **1** (May), 17–19.
70. Cullen, A.L. (1983) Millimeter wave open resonator techniques, Chapter 4, in *Infrared and Millimeter Waves*, vol. **10**, Elsevier, p. 424.
71. Afsar, M.N., Li, X., and Chi, H. (1990) An automated 60 GHz open resonator system for precision dielectric measurements. *IEEE Transactions on Microwave Theory and Techniques*, **38**, (12), 1845–1853.
72. Das, A. and Das, S.K. (2008) *Microwave Engineering*, McGraw-Hill Higher Education, Boston, MA.
73. Born, M., Wolf, E., Bhatia, A.B., *et al.* (2000) *Principles of Optics: Electromagnetic Theory of Propagation, Interference and Diffraction of Light*, Cambridge University Press.
74. Gorshunov, B.P, Volkov, A.A., Prokhorov, A.S, and Spektor, I.E. (2008) Methods of terahertz–subterahertz BWO spectroscopy of conducting materials. *Physics of the Solid State*, **50** (11), 2001–2012.
75. Kozlov, G. and Volkov, A. (1998) Coherent source submillimeter wave spectroscopy, in *Millimeter and Submillimeter Wave Spectroscopy of Solids SE – 3* (ed. G. Grüner), Springer, Berlin and Heidelberg, pp. 51–109.
76. Gorshunov, B., Volkov, A., Spektor, I., *et al.* (2005) Terahertz BWO-Spectrosopy. *International Journal of Infrared and Millimeter Waves*, **26** (9), 1217–1240.
77. Gorshunov, B.P., Prokhorov, A.S., Spektor, I.E., and Volkov, A.A. (2005) Submillimeter spectroscopy of materials with correlated electrons. *Radiophysics and Quantum Electronics*, **48** (10–11), 825–830.
78. Arik, E., Altan, H., and Esenturk, O. (2014) Dielectric properties of ethanol and gasoline mixtures by terahertz spectroscopy and an effective method for determination of ethanol content of gasoline. *The Journal of Physical Chemistry A*, **118** (17), 3081–3089.
79. Beluze, L., Badot, J.C., Weil, R., and Lucas, V. (2006) Broadband dielectric and resistivity spectroscopy of $WO_3 \cdot H_2O$ in the range of $10^3 - 10^{10}$ Hz: particle size effect. *The Journal of Physical Chemistry B*, **110** (14), 7304–7308.
80. Afsar, M.N., Chamberlain, J., and Chantry, G.W. (1976) High-precision dielectric measurements on liquids and solids at millimeter and submillimeter wavelengths. *IEEE Transactions on Instrumentation and Measurement*, **IM-25** (4), 290–294.
81. Choi, M.K, Taylor, K., Bettermann, A., and van der Weide, D.W. (2002) Broadband 10–300 GHz stimulus-response sensing for chemical and biological entities. *Physics in Medicine and Biology*, **47** (21), 3777.
82. Quéffélec, P., Konn, A.-M., Gelin, P., and Mallégol, S. (2003) Experimental demonstration of the nonreciprocity of magnetic composite materials for microwave applications. *Journal of Applied Physics*, **93** (10), 7474.
83. Kanamadi, C.M., Das, B.K., Kim, C.W., *et al.* (2009) Dielectric and magnetic properties of $(x)CoFe_2O_4 + (1 - x)Ba_{0.8}Sr_{0.2}TiO_3$ magnetoelectric composites. *Materials Chemistry and Physics*, **116** (1), 6–10.
84. Brown, E.R., Bjarnason, J.E., Chan, T.L.J., Lee, A.W.M., and Celis, M.A. (2004) Optical attenuation signatures of *Bacillus subtillis* in the THz region. *Applied Physics Letters*, **84** (18), 3438.
85. Khan, U.A., Al-Moayed, N., Nguyen, N., *et al.* (2007) Broadband dielectric characterization of tumorous and nontumorous breast tissues. *IEEE Transactions on Microwave Theory and Techniques*, **55** (12), 2887–2893.
86. Afsar, M.N. and Khan, U. (2005) Measurement of broadband dielectric properties of 10% formalin and 1,4-dioxane using dispersive Fourier transform spectroscopy, in *2005 IEEE Instrumentationand Measurement Technology Conference Proceedings*, IEEE, pp. 925–928.

87. Afsar, M.N., Wang, Y., and Moonshiram, A. (2003) Measurement of transmittance and permittivity of dielectric materials using dispersive Fourier transform spectroscopy. *Microwave and Optical Technology Letters*, **38** (1), 27–30.
88. Kratzenberg, E., Afsar, M.N., and Wang, Y. (2003) Complex permittivity measurements of chicken blood. *Microwave and Optical Technology Letters*, **39** (1), 54–56.
89. Afsar, M.N., Moonshiram, A., and Wang, Y. (2004) Assessment of random and systematic errors in millimeter-wave dielectric measurement using open resonator and Fourier transform spectroscopy systems. *IEEE Transactions on Instrumentation and Measurement*, **53** (4), 899–906.
90. Almoayed, N.N. and Afsar, M.N. (2006) High-resolution absorption coefficient and refractive index spectra of carbon monoxide gas at millimeter and submillimeter wavelengths. *IEEE Transactions on Instrumentation and Measurement*, **55** (4), 1033–1037.
91. Nichols, E.F. and Tear, J.D. (1925) Joining the infra-red and electric-wave spectra. *Astrophysics Journal*, **61**, 17.
92. Auston, D.H., Cheung K.P., and Smith, P.R. (1984) Picosecond photoconducting Hertzian dipoles. *Applied Physics Letters*, **45** (3), 284.
93. Dahl, C., Grüner, G., Genzel, L., *et al.* (1998) *Millimeter and Submillimeter Wave Spectroscopy of Solids*, Springer, Berlin and Heidelberg, 287 pp.
94. Köhler, R., Tredicucci, A., Beltram, F., *et al.* (2002) Terahertz semiconductor-heterostructure laser. *Nature*, **417** (6885), 156–159.
95. Fattinger, C. and Grischkowsky, D. (1988) Point source terahertz optics. *Applied Physics Letters*, **53** (16), 1480.
96. Zhang, X.-C., Jin, Y., and Ma, X.F. (1992) Coherent measurement of THz optical rectification from electro-optic crystals. *Applied Physics Letters*, **61** (23), 2764.
97. Zheng, X., McLaughlin, C.V., Cunningham, P., and Hayden, L.M. (2007) Organic broadband terahertz sources and sensors. *Journal of Nanoelectronics and Optoelectronics*, **2**, 58–76.
98. Davies, A.G., Burnett, A.D., and Fan, W., *et al.* (2008) Terahertz spectroscopy of explosives and drugs. *Materials Today*, **11** (3), 18–26.
99. Khan, U.A., Nguyen, N., and Afsar, M.N. (2008) Millimeter- and submillimeter-wave dielectric measurements of household powders using Fourier transform spectroscopy. *IEEE Transactions on Instrumentation and Measurement*, **57** (2), 286–293.
100. Lowry, H.H. (1927) The significance of the dielectric constant of a mixture. *Journal of the Franklin Institute*, **203** (3), 413–439.
101. Sebastian, M.T. and Jantunen, H. (2010) Polymer–ceramic composites of 0–3 connectivity for circuits in electronics: a review. *International Journal of Applied Ceramic Technology*, **7**, 415–434.
102. Conger, N.L. (1967) Measurement of dielectric constant and loss factor of powder materials in the microwave region. *Review of Scientific Instruments*, **38** (3), 384.
103. Nelson, S.O. and Kraszewski, A.W. (1998) Sensing pulverized material mixture proportions by resonant cavity measurements. *IEEE Transactions on Instrumentation and Measurement*, **47** (5), 1201–1204.
104. Nelson, S.O. and Bartley, P.G. (1998) Open-ended coaxial-line permittivity measurements on pulverized materials. *IEEE Transactions on Instrumentation and Measurement*, **47** (1), 133–137.
105. Ebara, H., Inoue, T., and Hashimoto, O. (2006) Measurement method of complex permittivity and permeability for a powdered material using a waveguide in microwave band. *Science and Technology of Advanced Materials*, **7** (1), 77–83.
106. Tuhkala, M., Juuti, J., and Jantunen, H. (2013) Method to characterize dielectric properties of powdery substances. *Journal of Applied Physics*, **114** (1), 014108.
107. Gershon, D.L., Calame, J.P., Carmel, Y., *et al.* (1999) Open-ended coaxial probe for high-temperature and broad-band dielectric measurements. *IEEE Transactions on Microwave Theory and Techniques*, **47** (9), 1640–1648.
108. Murata, K., Hanawa, A., and Nozaki, R. (2005) Broadband complex permittivity measurement techniques of materials with thin configuration at microwave frequencies. *Journal of Applied Physics*, **98** (8), 084107.

109. Tuhkala, M., Juuti, J., and Jantunen, H. (2014) An indirectly coupled open-ended resonator applied to characterize dielectric properties of $MgTiO_3$–$CaTiO_3$ powders. *Journal of Applied Physics*, **115** (18), 184101.
110. Tuhkala, M., Juuti, J., and Jantunen, H. (2013) Use of an open-ended coaxial cavity method to characterize powdery substances exposed to humidity. *Applied Physics Letters*, **103** (14), 142907.
111. Bruggeman, D.A.G. (1935) Berechnung verschiedener physikalischer Konstanten von heterogenen Substanzen. I. Dielektrizitätskonstanten und Leitfähigkeiten der Mischkörper aus isotropen Substanzen. *Annalen der Physik*, **416** (7), 636–664.
112. Looyenga, H. (1965) Dielectric constants of heterogeneous mixtures. *Physica*, **31** (3), 401–406.
113. Tuhkala, M., Juuti, J., and Jantunen, H. (2014) Determination of complex permittivity of surfactant treated powders using an open-ended coaxial cavity resonator. *Powder Technology*, **256**, 140–145.
114. Spitzer, W.G., Miller, R.C., Kleinman, D.A., and Howarth, L.E. (1962) Far infrared dielectric dispersion in $BaTiO_3$, $SrTiO_3$ and TiO_2. *Physical Review*, **126** (5), 1710–1721.
115. Spitzer, W.G. and Kleinman, D.A. (1961) Infrared lattice bands of quartz. *Physical Review*, **121** (5), 1324–1335.
116. Perry, C.H., McCarthy, D.J., and Rupprecht, G. (1965) Dielectric dispersion of some perovskite zirconates. *Physical Review*, **138** (5A), A1537–A1538.
117. Kudesia, R., McHale, A.E, Condrate, R.A., and Snyder, R.L. (1993) Microwave characteristics and far-infrared reflection spectra of zirconium tin titanate dielectrics. *Journal of Materials Science*, **28** (20), 5569–5575.
118. Wakino, K., Sagala, D.A., and Tamura, H. (1985) Far infrared reflection spectra of $Ba(ZnTa)O_3$–$BaZrO_3$ dielectric resonator material. *Japanese Journal of Applied Physics*, **24** (S2), 1042.
119. Grischkowsky, D., Keiding, S., Exter, M. van, and Fattinger, C. (1990) Far-infrared time-domain spectroscopy with terahertz beams of dielectrics and semiconductors. *Journal of the Optical Society of America B*, **7** (10), 2006.
120. Petzelt, J., Kamba, S., Kozlov, G.V., and Volkov, A.A. (1996) Dielectric properties of microwave ceramics investigated by infrared and submillimetre spectroscopy. *Ferroelectrics*, **176** (1), 145–165.
121. Rupprecht, G. and Bell, R.O. (1962) Microwave losses in strontium titanate above the phase transition. *Physical Review*, **125** (6), 1915–1920.
122. Silverman, B.D. (1962) Microwave absorption in cubic strontium titanate. *Physical Review*, **125** (6), 1921–1930.
123. Kamba, S., Petzelt, J., Buixaderas, E., *et al.* (2001) High frequency dielectric properties of $A_5B_4O_{15}$ microwave ceramics. *Journal of Applied Physics*, **89** (7), 3900.
124. Zurmühlen, R., Petzelt, J., Kamba, S., *et al.* (1995) Dielectric spectroscopy of $Ba(B_{1/2}'B_{1/2}')O_3$ complex perovskite ceramics: correlations between ionic parameters and microwave dielectric properties. I. Infrared reflectivity study (1012–1014 Hz). *Journal of Applied Physics*, **77** (10), 5341.
125. Zurmühlen, R., Petzelt, J., Kamba, S., *et al.* (1995) Dielectric spectroscopy of $Ba(B_{1/2}'B_{1/2}')O_3$ complex perovskite ceramics: correlations between ionic parameters and microwave dielectric properties. II. Studies below the phonon eigenfrequencies (102–1012 Hz). *Journal of Applied Physics*, **77** (10), 5351.
126. Petzelt, J. and Setter, N. (1993) Far infrared spectroscopy and origin of microwave losses in low-loss ceramics far infrared spectroscopy in low loss ceramics. *Ferroelectrics*, **150** (1), 89–102.
127. Fukuda, K., Kitoh, R., and Awai, I. (1995) Microwave characteristics of mixed phases of $BaTi_4O_9$–$BaPr_2Ti_4O_{12}$ ceramics. *Journal of Materials Science*, **30** (5), 1209–1216.
128. Ferreira, V.M., Baptista, J.L., Kamba, S., and Petzelt, J. (1993) Dielectric spectroscopy of $MgTiO_3$-based ceramics in the 109–1014 Hz region. *Journal of Materials Science*, **28** (21), 5894–5900.
129. Petzelt, J., Pačesová, S., Fousek, J., *et al.* (1989) Dielectric spectra of some ceramics for microwave applications in the range of 1010–1014 Hz. *Ferroelectrics*, **93** (1), 77–85.

130. Tagantsev, A.K., Sherman, V.O., Astafiev, K.F., Venkatesh, J., and Setter, N. (2003) Ferroelectric materials for microwave tunable applications. *Journal of Electroceramics*, **11** (1/2), 5–66.
131. Subbaswamy, K.R. and Mills, D.L. (1986) Theory of microwave absorption in wide-band-gap insulators: the role of thermal phonon lifetimes. *Physical Review B*, **33** (6), 4213–4220.
132. Tagantsev, A.K., Petzelt, J., and Setter, N. (1993) Relation between intrinsic microwave and submillimeter losses and permitivity in dielectrics. *Solid State Communications*, **87**, 1117–1120.
133. Petzelt, J. and Kamba, S. (2003) Submillimetre and infrared response of microwave materials: extrapolation to microwave properties. *Materials Chemistry and Physics*, **79** (2–3), 175–180.
134. Wakino, K. (1996) Miniaturization techniques of microwave components for mobile communications systems: using low loss dielectrics. IEICE Technical Report, *Microwaves*, *The Institute of Electronics, Information and Communication Engineers*, **96** (26), 7–14.
135. Mollá, J., González, M., Vila, R., and Ibarra, A. (1999) Effect of humidity on microwave dielectric losses of porous alumina. *Journal of Applied Physics*, **85** (3), 1727.
136. Schlömann, E. (1964) Dielectric losses in ionic crystals with disordered charge distributions. *Physical Review*, **135** (2A), A413–A419.
137. Li, L. and Chen, X.M. (2014) Frequency-dependent *Qf* value of microwave dielectric ceramics. Jantunen, H. (ed.), *Journal of the American Ceramic Society*, **97** (10), 3041–3043.
138. Silva, M.A.S., Fernandes, T.S.M., and Sombra, A.S.B. (2012) An alternative method for the measurement of the microwave temperature coefficient of resonant frequency (τ_f). *Journal of Applied Physics*, **112** (7), 074106.
139. Tao, S., Zaki, K.A., and Chi, W. (2000) Tunable dielectric resonators with dielectric tuning disks. *IEEE Transactions on Microwave Theory and Techniques*, **48** (12), 2439–2445.
140. Felix, H.G. and Martinez, J.P. (1985) Analysis of dielectric resonators with tuning screw and supporting structure. *IEEE Transactions on Microwave Theory and Techniques*, **33** (12), 1453–1457.
141. Chen, S.-W., Zaki, K.A., and West, R.G. (1990) Tunable, temperature-compensated dielectric resonators and filters. *IEEE Transactions on Microwave Theory and Techniques*, **38** (8), 1046–1052.
142. Poplavko, Y.M., Prokopenko, Y.V., Molchanov, V.I., and Dogan, A. (2001) Frequency-tunable microwave dielectric resonator. *IEEE Transactions on Microwave Theory and Techniques*, **49** (6), 1020–1026.
143. Petrov, P.K. and Alford, N.M. (2001) Tunable dielectric resonator with ferroelectric element. *Electronics Letters*, **37** (17), 1066.

2

Modeling of Microwave Dielectric Properties of Composites

Marko Tuhkala, Merja Teirikangas, and Jari Juuti
Microelectronics Research Unit, University of Oulu, Oulu, Finland

2.1 Introduction

The twenty-first century is the era of ubiquitous electronics where a wide range of functionalities is integrated not only into smart machines and devices but also into objects typically considered as passive, such as walls, roofs, pavements, etc. Miniaturized electronics have been used in many fields of modern technology and especially in communication gadgets like mobile phones, palm-tops, i-pods, GPS, automobile power electronics, safety robotics, medical instruments, etc. Different types of ceramics have for long played a crucial role in electrical devices. They have acted as insulators, super-, semi-, and ionic conductors, varistors, thermistors, and magnetic materials. They have provided capacitors, resonators, filters, and substrates for different purposes, The development of electroceramics is still on-going: in particular, in recent years dimensionally small electroceramics, among other nanomaterials, have emerged into the field to expand the applicable properties even further. Very often this requires composite approaches where phases with very different properties are introduced involving polymer, ceramic, metal, graphene, and other nanomaterials as filler material.

High permittivity ceramics with low dielectric losses have gained significant attention in many important technological applications, such as in RF filters, antennas, high-energy capacitors, and IC-gate dielectrics. However, ceramics typically require high processing temperatures (above 600°C) and therefore their direct integration with widely used polymer substrates involves different post-processing steps for assembly, soldering, and

Microwave Materials and Applications, First Edition.
Edited by Mailadil T. Sebastian, Rick Ubic and Heli Jantunen.
© 2017 John Wiley & Sons, Ltd. Published 2017 by John Wiley & Sons, Ltd.

gluing, which increases the manufacturing costs. Furthermore, fabrication of complex three-dimensional structures is challenging and expensive. On the other hand, composite technology, where artificial material is fabricated by combining, for example, ceramic and polymer in an ordered or random manner, is being used widely for electronic, sonar, medical diagnostics and NDT purposes. In order to overcome some of the manufacturing issues and adjust the physical properties beyond the range of ceramics, different types of composites have been widely researched to offer new functionalities and also fabrication flexibility.

In the field of microwaves the most common approach in composites is to increase the low permittivity of the host matrix, for example, polymer, by the addition of a high permittivity ceramic or a metal. If the required permittivity and dielectric loss characteristics are met, this approach enables decreased costs compared to the fabrication of ceramic components. It also offers easily tailorable three-dimensional shapes, easier integration, and decreased energy consumption or utilization of a specific processing route like injection molding or printing. In contrast to this approach, due to the ever increasing data speed, dielectric materials with low ε_r are wanted in order to reduce the interconnect resistance–capacitance delay, signal propagation delay, and crosstalk noise between metal lines and hence the power dissipation of ICs [1, 2]. As a consequence, even low permittivity SiO_2 has become an unsuitable choice of material for certain applications and therefore composites with controlled porosity that is, with a gas filler, have been developed. In this chapter different aspects of microwave composites and especially the modeling of their dielectric properties are covered to give guidelines for their utilization.

2.2 Connectivity

In the development of different types of composites the connectivity between the different phases has a significant impact on their effective properties. The interspatial relationship in a material with two or more phases has a high importance because it controls the mechanical, electrical, magnetic, and thermal fluxes between the phases. Therefore the effective properties of the composite material may change by orders of magnitude depending on the connections between filler materials. A simple illustration can be made by imagining an electric wire in which the metallic conductor is cut into pieces and connections between the pieces are made with plastic insulation in series, rather than in parallel, thus increasing the overall resistance of the system significantly.

The connectivity concept was first introduced by Newnham *et al.* [3]. In a composite each phase can be self-connected in zero, one, two, or three dimensions. Therefore, in a two-phase composite there are 16 different combinations and 10 different types of connectivity due to symmetry. Different connectivities are 0–0, 0–1, 0–2, 0–3, 1–1, 1–2, 1–3, 2–2, 2–3, and 3–3, representing the connectivity of filler and host matrix [3]. Schematics of different connectivities are illustrated in Figure 2.1 using cube-shaped building blocks. For example, in a composite with 1–3 connectivity there is one phase self-connected in all three dimensions while another phase is self-connected only in one dimension. A composite with 0–3 connectivity is the most popular one with a randomly distributed filler phase in a host matrix because it is easy to prepare and with relatively low cost. Also, composites with 1–3 connectivity as well as 2–2 have been relatively widely studied due to their easy and well-controllable fabrication.

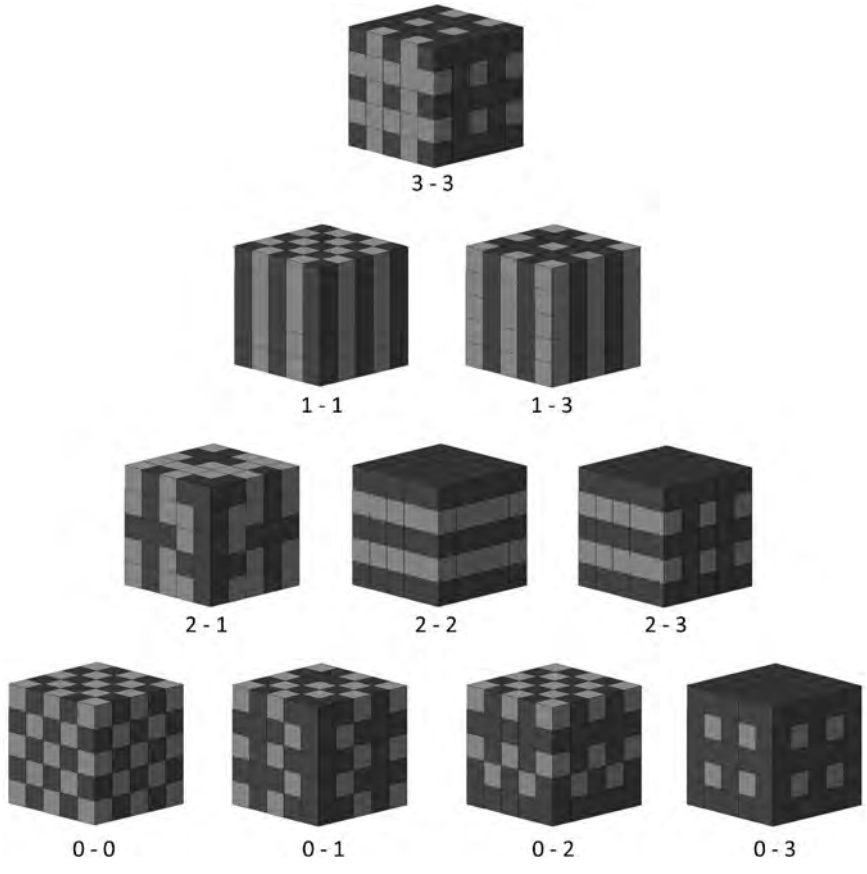

Figure 2.1 *Schematics of connectivity families with two different phases. The number of connectivities is reduced from 16 to 10 due to symmetry involved in the families.*

The different phases in Figure 2.1 cover a wide range of different materials, especially if the filler phases are considered. A typical host matrix having a higher level of connectivity consists of polymer or ceramic offering a feasible level of mechanical rigidity, processing route, and starting point for adjustment of the electrical, magnetic, and mechanical properties. Filler material can be ceramic, metal, polymer, graphene, or even gas and may take practically any shape, such as fibers, flakes, spheres, or even predefined structures. The composites are different types of ceramic–ceramic, ceramic–polymer, and metal–polymer mixtures covering a continuously expanding range of nanomaterials [4–8]. In addition to these two main phases, different types of surface engineering have been used to improve dielectric properties, dispersion, processability, properties, and/or coupling of filler and host matrix and to decrease agglomeration size and to enhance chemical bonding and physical wetting between filler and matrix [9–12]. Furthermore, as an extension of the primary filler phase, some additions of secondary phases in the form of nanoparticles have also been used to improve properties [13].

2.3 Electrostatic Theory

2.3.1 Polarizability

Polarization is one of the basic principles of dielectrics. When dielectric materials are under an external electric field they will be polarized. These materials act not only as electrical isolators but, due to their ability to be polarized, they can also act as energy stores. When an alternating electric field, for example, an electromagnetic wave that has a certain frequency, travels through the material, the electron clouds around the atoms are aligned with the direction of the incident electric field. This is called depolarization, which can be expressed with an equation of electric displacement ($D = \varepsilon_r \varepsilon_0 \times E$), where ε_r, ε_0, and E represent relative permittivity of the dielectric material, vacuum permittivity, and incident electric field, respectively [14]. Due to polarization, part of the energy is stored in the electric dipoles and is released as the direction of the electric field reverses. If the wave were analyzed during its travel through the material, it would be found to a have a lower velocity than in free space (speed of light) and thus would have a shorter wavelength. For this reason dielectric materials are frequently used in miniaturization, for example, in antenna and capacitor applications. For example, in free space, a half wavelength of a 2.4 GHz signal is approximately 62 mm, but when an antenna is made on a dielectric material having a real part of relative permittivity (ε_r') of 10, the half wavelength is only ~20 mm and thus the antenna can be shortened. However, because all real materials differ from ideal ones, there is also dissipation involved (Figure 2.2), as described by a complex value of permittivity ($\varepsilon_r^* = \varepsilon_r' - j\varepsilon''$) where the imaginary part of permittivity ε'' indicates the loss modulus. The effect of this factor, which is often expressed as a loss tangent ($\tan \delta = \varepsilon''/\varepsilon'$), can be seen as a decreased amplitude as a consequence of lost energy of the electromagnetic wave as it travels through the material.

2.3.2 Scattering

As described above, inclusions, that is, fillers in the composites, affects an incident electromagnetic wave in that part of the energy is stored (ε'') and part of the energy is lost (loss tan δ or ε'') so that the wave continues through the particles of the material with a lower energy than previously. In addition to this, there is a second factor that affects the energy of an electromagnetic wave that has penetrated the particles. This additional effect, which is also part of the overall loss mechanism, is called scattering.

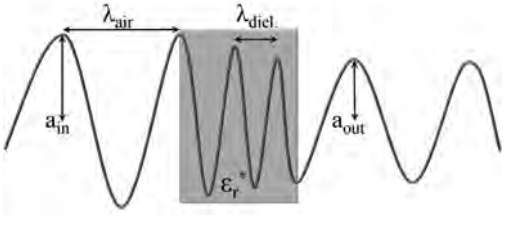

Figure 2.2 *Electromagnetic wave traveling through dielectric material (having complex permittivity ε_r^*). The effect of the higher complex permittivity of dielectric material results in a decreased wavelength in the medium (λ_{air} versus λ_{diel}) and a corresponding reduced amplitude (a_{in} versus a_{out}).*

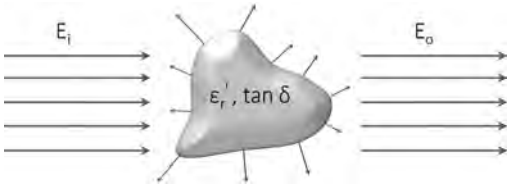

Figure 2.3 *Particle that is affected by the electromagnetic wave also causes scattering. Electric field in a certain direction before (E_i) and after (E_o) passing the particle differs as a consequence of losses in the material but also due to scattering. Either Rayleigh or Mie scattering dominates when the particle is much smaller or the same size as the wavelength, respectively.*

Scattering means that part of the energy is "released" in directions different from that of the incident electric field (Figure 2.3). This radiation is caused by the oscillating dipoles, which in turn are caused by polarization (stored energy) due to the incident electric field. The field distribution inside a small scatterer, which is also known as a Rayleigh scatterer [15], does not vary significantly due to its very small size compared to the affecting electromagnetic wave. However, it should be noted that the field distribution inside a particle is shape dependent [16], for example, it is different for a spherical particle versus a disk-shaped particle. Thus, scattering can be calculated based on a static field solution.

When a medium has multiple small particles that all act as scatterers, the electromagnetic field attenuates exponentially. When the frequency of the incident field increases, the size of the scatterer becomes larger compared to the wavelength. In this case the polarization current is not the same everywhere inside the particle. This frequency-dependent scattering is known as Mie scattering.

2.3.3 Orientation

The polarizability, α, of an inclusion is the simplest measure of its response to an incident electric field. In Figure 2.4 mixtures with spherical and needle-type inclusions with permittivity ε_i occupying random positions in the environment with permittivity ε_e are shown. In the case of spherical particles the space is occupied homogenously in all directions with respect to the incident propagating waves. However, when needle-like fillers with particular orientations are introduced, incident waves E_{iz} and E_{ix} are influenced differently by the particles.

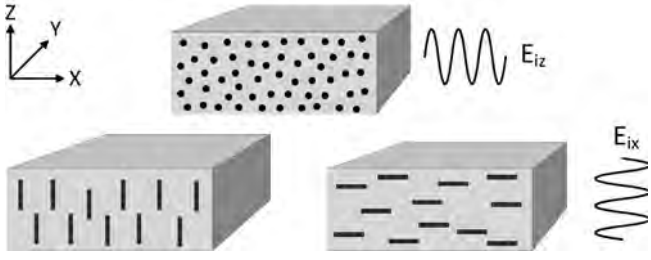

Figure 2.4 *Sphere- and needle-shaped particles orientated into two different directions with respect to the incident electromagnetic waves E_{iz} and E_{ix}.*

The relation between the volume-average field and flux density is given by

$$\langle D \rangle = \varepsilon_{eff} \langle E \rangle$$

where

$$\langle D \rangle = V_f \varepsilon_i E_i + (1 - V_f) \varepsilon_e E_m$$

and

$$\langle E \rangle = V_f E_i + (1 - V_f) E_m$$

where V_f is the volume fraction of the filler, ε_i and ε_m the permittivities of the filler inclusion and matrix, respectively, and E_i and E_m are the electric fields affecting the filler and matrix.

The polarizability of an inclusion can be used to measure its response to an electric field. The dipole moment p is proportional to the external field (E_m), $p = \alpha E_m$. For homogeneous spheres the polarizability is easy to calculate and is referred to the environment (matrix) with permittivity ε_m [16]:

$$p = \int (\varepsilon_i - \varepsilon_e) E \, \mathrm{d}V \tag{2.1}$$

As mentioned, with spherical particles there is dielectric isotropy so that the response of the medium does not depend on the direction of the electric field but only on its amplitude. When more complicated inclusions, for example, anisotropic or heterogeneous particles, are introduced the internal electric field may become non-uniform.

In order to estimate the effect of the particle shapes of the filler material, ellipsoids (Figure 2.5) allow the study of many special cases, such as disks and needles.

Depolarization factors $N_{x,y,z}$ for any ellipsoid fulfill $N_x + N_y + N_Z = 1$ and for a sphere $N_x = N_y = N_z = 1/3$. Thus

$$N_x = \frac{a_x a_y a_z}{\left(a_x^2 - a_y^2\right)\sqrt{a_x^2 - a_z^2}} [F(\phi, k) - E(\phi, k)] \tag{2.2}$$

$$N_y = 1 - N_x - N_z \tag{2.3}$$

$$N_z = \frac{a_y}{a_y^2 - a_z^2} \left[a_y - \frac{a_x a_z}{\sqrt{a_x^2 - a_z^2}} E(\phi, k) \right] \tag{2.4}$$

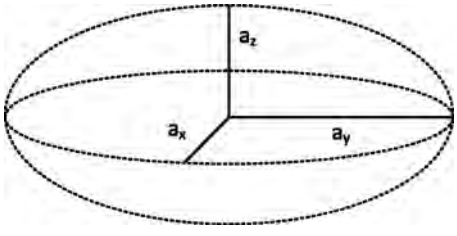

Figure 2.5 *Ellipsoid with dimensions of a_x, a_y and a_z.*

where the incomplete elliptic integrals are defined as

$$F(\phi, k) = \int_0^{\phi} \frac{\mathrm{d}\theta}{\sqrt{1 - k^2 \sin^2 \theta}} \tag{2.5}$$

$$E(\phi, k) = \int_0^{\phi} \sqrt{1 - k^2 \sin^2 \theta}\, \mathrm{d}\theta \tag{2.6}$$

where k is an elliptic module.

The dipole moment induced in an ellipsoid depends on the direction of the electric field that excites it. For example, if an ellipsoid is exposed to an external uniform electric field E in the direction of the x axis (Figure 2.4 bottom right), then the internal field E_i is also x-directed and the field ratio is [16]

$$E_i = \frac{\varepsilon_e}{\varepsilon_e + N_x(\varepsilon_i - \varepsilon_e)} E \tag{2.7}$$

Further discussion and equations about the effect of orientation and particle shapes are covered in the Maxwell–Garnett section.

2.4 Mixing Equations

Mixing equations are used to estimate the effective dielectric or magnetic properties of composites. Some are based on electrostatic theories and some have a stronger empirical background. Common to all is the fact that they estimate the total permittivity of a dielectric material based on the properties and volume fractions of the material components used. Some mixing equations even cover the effect of particle shapes with reasonable accuracy. In addition to sophisticated estimations of effective permittivity (combination of material permittivities), mixing equations can also be utilized to derive the properties of the material components when effective permittivity and volume fractions are measurable. They are applicable for DC and AC fields as far as the properties of each element, that is, inclusions and matrix, are defined for the frequencies in question. Moreover, quasistatic conditions should be met where the wavelength of the electromagnetic wave within each element in a composite is much greater than their dimensions [17]. However, it is important to note that the properties of small particles can be markedly different from the properties of the same material in bulk form [16]. This can be due to the effect of particle shapes and sizes and the previously mentioned scattering. Another factor that can cause a similar effect on different measurement results is adsorbed water, that is, bound water, which can surround the particles [18].

In material characterization the porosity is a significant factor that can in some cases give rise to an incorrect determination of filler material properties. In order to determine the correct dielectric properties of a material, the level of porosity should be taken into consideration. In addition, percolation plays an important role in composites, especially those with 0–3 connectivity. The percolation threshold describes the point, that is, filler volume fraction, where initially isolated inclusions become connected with each other, thus distorting the pure 0–3 connectivity. Below the percolation threshold certain shaped and sized particles have clearance (matrix material) between neighboring particles. At the point of

percolation, electrical properties such as permittivity and dielectric loss change dramatically and rapidly from the level obtained for isolated particles. The level of the percolation threshold depends on particle shape and size distribution. For example, Bruggeman symmetric and coherent potential formulas have percolation threshold levels approximately at volume fractions of 0.3 and 0.25, respectively, for spherical particles with singular particle size. However, in the case of coarse and fine particles or fibers and needles much lower volume fractions are needed to form a connected network due to their high aspect ratio [4, 19, 20]. Different mixing equations account for percolation differently, which can be seen in the manner in which dielectric properties evolve after the percolation threshold. Moreover, mixing equations are typically based on certain assumptions such that they work either below or above the percolation threshold. In some cases such as the differential equation both regions are taken into account [21].

2.4.1 Clausius–Mossotti

The Clausius–Mossotti formula covers microscopic quantities and relations of polarizabilities and scatterer densities, which are relevant when describing molecular dependencies of matter:

$$\frac{\varepsilon_i - 1}{\varepsilon_i + 2}\frac{M}{\rho} = \frac{4\pi N_A \alpha}{3} \tag{2.8}$$

where $\varepsilon_{i'}$, M, ρ, N_A, and α represent relative permittivity of particle (inclusion), molecular weight, density, Avogadro constant, and molecular dielectric polarization, respectively [22]. The equation is valid for cubic or isotropic materials. Shannon used the Clausius–Mossotti equation for calculating mean dielectric constants based on the ion polarizabilities of components. He found an agreement between observed and calculated total polarizabilities that implied a good predictability using the Clausius–Mossotti equation for well-behaved compounds [23]. Polarizabilities reported by Shannon are shown in Table 2.1 [23, 24] while Vineis *et al.* reported a polarizability value of 6.12 for La instead of 6.07 [25]. According to the molecular additivity rule, it is also possible to break molecular polarizabilities of complex oxide and fluoride compounds into simpler compounds, which facilitates the estimation of permittivity of different compositions. It appears from Table 2.1 that Ba, Pb, and Bi obtain relatively high polarizability while they also form compositions like $Pb_{1.5}Nb_2O_{6.5}$, $Ba_{0.6}Sr_{0.4}TiO_3$, and $Bi_6Ti_5TeO_{22}$ with relatively high ε_r of 259, 838, and 350, respectively [24].

2.4.2 Maxwell–Garnett

One of the best-known mixing rules that has been used in permittivity estimations of dielectric composites is the Maxwell–Garnett theory:

$$\varepsilon_{eff} = \varepsilon_e + 3V_f\varepsilon_e\frac{\varepsilon_i - \varepsilon_e}{\varepsilon_i + 2\varepsilon_e - V_f(\varepsilon_i - \varepsilon_e)} \tag{2.9}$$

Table 2.1 *Ion dielectric polarizabilities in units of Å³ [23, 24]*

Li 1.20	Be 0.19										B 0.05	C	N	O 2.01	F 1.62	Ne
Na 1.80	Mg 1.32										Al 0.79	Si 0.87	$P^{(V)}$ 1.22	S	Cl	Ar
K 3.83	Ca 3.16	Sc 2.81	$Ti^{(IV)}$ 2.93	$V^{(V)}$ 2.92	$Cr^{(II)}$ 1.45	$Mn^{(II)}$ 2.64	$Fe^{(II)}$ 2.23	$Co^{(II)}$ 1.65	$Ni^{(II)}$ 1.23	$Cu^{(II)}$ 2.11	Zn 2.04	Ga 1.50	Ge 1.63	$As^{(V)}$ 1.72	Se	Br	Kr
Rb 5.29	Sr 4.24	Y 3.81	Zr 3.25	Nb 3.97	Mo	Tc	Ru	Rh	Pd	Ag	Cd 3.40	In 2.62	Sn 2.83	$Sb^{(III)}$ 4.27	$Te^{(IV)}$ 5.23	I	Xe
Cs 7.43	Ba 6.40	La 6.07	Hf	Ta 4.73	W	Re	Os	Ir	Pt	Au	Hg	$Tl^{(I)}$ 7.28	$Pb^{(II)}$ 6.58	Bi 6.12	Po	At	Rn
Lanthanides		$Ce^{(III/IV)}$ 6.15 / 3.94	Pr 5.32	Nd 5.01	Pm	Sm 4.74	$Eu^{(II/III)}$ 4.83 / 4.53	Gd 4.37	Tb 4.25	Dy 4.07	Ho 3.97	Er 3.81	Tm 3.82	Yb 3.58	Lu 3.64		
Actinides		Th 4.92	Pa	$U^{(IV)}$ 4.45	Np	Pu	Am	Cm	Bk	Cf	Es	Fm	Md	No	Lr		

where ε_{eff}, ε_e, and V_f represent effective relative permittivity, permittivity of matrix, and volume fraction of the filler, respectively. Using the equation, the effective permittivity of a dielectric composite can be expressed with information of the dielectric properties of the surrounding matrix and inclusions. The model is valid for very porous media ($V_f \ll 1$) and when inclusions are homogenously dispersed.

The Maxwell–Garnett equation (2.9) is also known as the Rayleigh formula when it is written in its symmetrical form:

$$\frac{\varepsilon_{eff} - \varepsilon_e}{\varepsilon_{eff} + 2\varepsilon_e} = V_f \frac{\varepsilon_i - \varepsilon_e}{\varepsilon_i + 2\varepsilon_e} \tag{2.10}$$

The Maxwell–Garnett equation treats permittivities of matrix and inclusions ansymmetrically, which means that calculated effective permittivities are different when, for example, $\varepsilon_i = 20 \times \varepsilon_e$ or $\varepsilon_e = 20 \times \varepsilon_i$. The effect of symmetry can be seen clearly in a comparison of Bruggeman symmetric (see Equation 2.16 later) and non-symmetric equations (see Equation 2.17 later) in Figure 2.6 (see Section 2.4.4).

In composites where aligned ellipsoids (according to Figure 2.4, bottom left) with permittivity ε_i are embedded in a matrix with permittivity ε_e, the effective permittivity is anisotropic. In such a case the Maxwell–Garnet equation becomes

$$\varepsilon_{eff} = \varepsilon_e + V_f \varepsilon_e \frac{\varepsilon_i - \varepsilon_e}{\varepsilon_e + (1 - V_f) N_x (\varepsilon_i - \varepsilon_e)} \tag{2.11}$$

Random orientation in a mixture with elliptical inclusions, either needles or flakes, without any preferred direction of the particles makes the mixture isotropic and therefore its effective permittivity results as

$$\varepsilon_{eff} = \varepsilon_e + \varepsilon_e \frac{\dfrac{V_f}{3} \displaystyle\sum_{j=x,y,z} \dfrac{\varepsilon_i - \varepsilon_e}{\varepsilon_e + N_j(\varepsilon_i - \varepsilon_e)}}{1 - \dfrac{V_f}{3} \displaystyle\sum_{j=x,y,z} \dfrac{N_j(\varepsilon_i - \varepsilon_e)}{\varepsilon_e + N_j(\varepsilon_i - \varepsilon_e)}} \tag{2.12}$$

The Maxwell–Garnett equation can also be utilized in estimations of the effective permittivity of composites with randomly distributed needles (Equation 2.13) and disk-shaped (Equation 2.14) inclusions [16]:

$$\varepsilon_{eff} = \varepsilon_e + V_f(\varepsilon_i - \varepsilon_e) \frac{\varepsilon_i + 5\varepsilon_e}{(3 - 2V_f)\varepsilon_i + (3 + 2V_f)\varepsilon_e} \tag{2.13}$$

$$\varepsilon_{eff} = \varepsilon_e + V_f(\varepsilon_i - \varepsilon_e) \frac{2\varepsilon_i + \varepsilon_e}{(3 - V_f)\varepsilon_i + V_f\varepsilon_e} \tag{2.14}$$

In the case of multiphase composites, which contain two or more homogenous material constituents, the Maxwell–Garnett equation can be written as follows:

$$\frac{\varepsilon_{eff} - \varepsilon_e}{\varepsilon_{eff} + 2\varepsilon_e} = V_{f_1} \frac{\varepsilon_1 - \varepsilon_e}{\varepsilon_1 + 2\varepsilon_e} + V_{f_2} \frac{\varepsilon_2 - \varepsilon_e}{\varepsilon_2 + 2\varepsilon_e} + \cdots + V_{f_n} \frac{\varepsilon_n - \varepsilon_e}{\varepsilon_n + 2\varepsilon_e} \tag{2.15}$$

where subscripts in volume fractions, 1, 2, and n, represent the number of dielectric components.

Gong *et al.* used the Maxwell–Garnett effective medium theory (Equation 2.9) in their evaluation of the dielectric properties of composite media [26]. They found that the difference between calculated and measured permittivities were 6% and 38% for spherical and cylindrical pores of their dielectric samples, respectively. This is due to assumptions in Maxwell-Garnett that inclusions are spherical shaped and evenly dispersed inside the host material [26]. Sihvola *et al.* have proposed a scattering correction factor for the Maxwell–Garnett mixing rule [27]. This correction term takes into account the electrical size of scatterers. However, they found it suitable only for low-volume fractions of inclusions. Hsiang *et al.* found correlation with the Maxwell–Garnet equation when the porosity was below 10% when measuring dielectric properties of porous $BaTiO_3$ samples at 1 kHz frequency [28]. At the porosity of 25%, deviation between measurement results and the theoretical model was very large, that is, a theoretical permittivity value of 2800 and a measured value of 2000. Hsiang *et al.* suspected that when the porosity of $BaTiO_3$ ceramics increased above 10% there was a reduced constraining force, which resulted in a decrease of the internal stress and domain density, that is, the ceramic sample was close to the powder state. Thus, the dielectric constant of $BaTiO_3$ could not be considered a constant due to the porosity [28].

2.4.3 Bruggeman Symmetric

The Bruggeman symmetric, which is also known as the Polder–Van Santen formula or Loor formula, estimates effective permittivities based on an assumption that inclusions are spherically shaped and evenly distributed inside the surrounding matrix. As the name of the equation implies, it treats inclusions and environment symmetrically. This means that values of inclusions and environment are interchangeable and the estimated effective permittivity is the same when, for example, $\varepsilon_i = 20 \times \varepsilon_e$ or $\varepsilon_e = 20 \times \varepsilon_i$ when their volume fractions are 0–1 and dependent upon each other [16]:

$$\frac{\varepsilon_i - \varepsilon_{eff}}{\varepsilon_i + 2\varepsilon_{eff}} V_f + \frac{\varepsilon_e - \varepsilon_{eff}}{\varepsilon_e + 2\varepsilon_{eff}} (1 - V_f) = 0 \tag{2.16}$$

Polder–Van Santen, that is, Bruggeman symmetric, and several other mixing rules were used by Mätzler when measuring the dielectric properties of dry snow at 1 GHz frequency. Good correlation between measurement results and the Bruggeman symmetric mixing model (Equation 2.16) using a coaxial probe was found. Results correlated also with the Looyenga mixing model (see Equation 2.20 later) but other power-law-based mixing equations and the Maxwell–Garnett equation (2.9) gave lower correlation in this particular experiment [29]. On the other hand, Campos *et al.* found clear correlation with the Maxwell–Garnett equation in addition to the Bruggeman symmetric when estimating optical properties of porous silicon with an additional assumption of spherical pores. Results showed that the best adjusted porosities were achieved with the Bruggeman symmetric and Maxwell–Garnett equations using porosity levels of 47% and 67%, respectively. The calculated results correlated well with the samples with porosities of 44% and 67%, respectively [30].

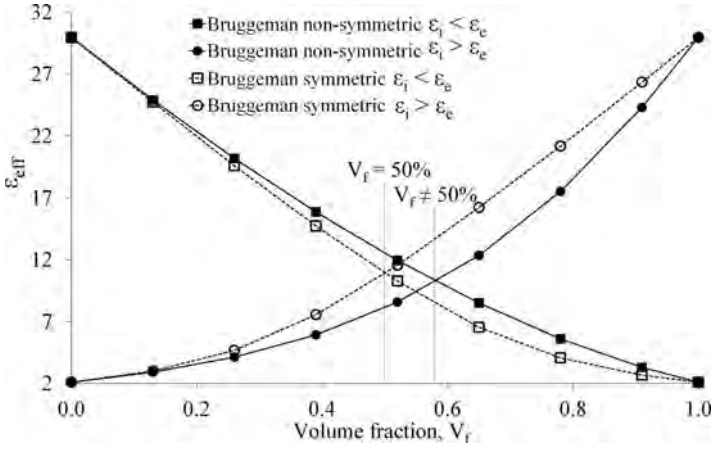

Figure 2.6 *Bruggeman symmetric and non-symmetric equations with varying inclusion and matrix permittivities of 2.1 and 30, respectively.*

2.4.4 Bruggeman Non-symmetric

The Bruggeman non-symmetric model treats the inclusion and environment permittivities asymmetrically. Thus, effective permittivities at the same volume fractions differ when the permittivities of dielectric components are interchanged [16]:

$$\frac{\varepsilon_i - \varepsilon_{eff}}{\varepsilon_i - \varepsilon_e} = (1 - V_f)\left(\frac{\varepsilon_{eff}}{\varepsilon_e}\right)^{1/3} \tag{2.17}$$

In Figure 2.6 the basic principle of symmetric and non-symmetric equations can be seen clearly. In the figure effective permittivities by symmetric and non-symmetric Bruggeman equations are drawn when matrix permittivity, ε_e, is either 2.1 or 30 and the inclusion permittivity, ε_i, is correspondingly 30 or 2.1, respectively. The symmetricity can be seen at a volume fraction of 0.5, where the asymmetric rule shows a different effective permittivity value when the permittivities of inclusion and matrix are their opposites.

2.4.5 Sen Scala–Cohen

As can be seen from the comparison between Bruggeman non-symmetric (Equation 2.17) and Sen Scala–Cohen (Equation 2.18) mixing equations, the Sen Scala–Cohen is a complement of the Bruggeman non-symmetric mixing equation [16]:

$$\frac{\varepsilon_{eff} - \varepsilon_e}{\varepsilon_i - \varepsilon_e} = V_f\left(\frac{\varepsilon_{eff}}{\varepsilon_i}\right)^{1/3} \tag{2.18}$$

2.4.6 Coherent Potential

The coherent potential mixing rule estimates the effective permittivity formed by a dielectric matrix and spherical inclusions. The main principle behind the rule is that the real values

of individual scatterers are replaced by an effective medium that has been generated using the Green function [31]:

$$\varepsilon_{eff} = \varepsilon_e + V_f(\varepsilon_i - \varepsilon_e)\frac{3\varepsilon_{eff}}{3\varepsilon_{eff} + (1 - V_f)(\varepsilon_i - \varepsilon_e)} \tag{2.19}$$

2.4.7 Looyenga

The Looyenga mixing equation, also known as Landau–Lifshitz–Looyenga, is based on a power-law approximation. This can be expressed as ${\varepsilon_{eff}}^{\beta} = (1 - V_{fi}){\varepsilon_e}^{\beta} + V_{fi}{\varepsilon_i}^{\beta}$. The equation averages effective permittivity with certain power β. In the case of the Looyenga mixing approximation the power is 1/3, which exists also in several differential analysis-based mixing equations, for example, Bruggeman non-symmetric (Equation 2.17) and Sen Scala–Cohen (Equation 2.18). As mentioned in the previous section with the Bruggeman symmetric, the Looyenga equation also treats environment and inclusions symmetrically [16]:

$$\varepsilon_{eff}^{1/3} = (1 - V_f)\varepsilon_e^{1/3} + V_f\varepsilon_i^{1/3} \tag{2.20}$$

When the power β is 1, the power law approximation represents a linear version of it, which is known as the Silberstein formula. The Silberstein mixing rule assumes that there is no depolarization affect, for example, with disk-shaped particles, as the depolarization field in the $z$direction is zero:

$$\varepsilon_{eff} = (1 - V_f)\varepsilon_e + V_f\varepsilon_i \tag{2.21}$$

Bouledjnib and Sahli compared the Maxwell–Garnett, Bruggeman symmetric, Looyenga, and Lichtenecker equations with their experiments regarding computational modeling for N-phase porous materials [32]. They found that the Looyenga and Bruggeman symmetric equations gave a good prediction of porous dielectrics where the relative error between theoretical and experimental samples was less than 6%.

2.4.8 Lichtenecker

The Lichtenecker mixing equation is also based on a power law approximation when it is written in the form $\varepsilon_{eff} = {\varepsilon_i}^{f}{\varepsilon_e}^{1\text{-}f}$. The well-known form of the equation averages logarithms of the permittivities:

$$\log \varepsilon_{eff} = V_f \log \varepsilon_i + (1 - V_f) \log \varepsilon_e \tag{2.22}$$

Although the Lichtenecker formula has been mentioned to be a semi-empirical formula it is based on effective medium theory. Zakri *et al.* showed a clear physical foundation and effective medium-based theory in their work regarding Lichtenecker's mixing equation [33].

Wu *et al.* compared several mixing equations with their measurement results of PTFE/Zr_2TiO_6 composites and found the best correlation with the Lichtenecker equation. The correlation with Lichtenecker was better than with the modified version of it when the volume fraction of filler was below 25 vol.%. Wu *et al.* concluded that decreased

correlation above that point was the result of losing 0–3 connectivity when the particles became connected [34]. Kim *et al.* reported a clear correlation with porous TiO_2/ZBS glass composites at 17 GHz and the logarithmic mixing rule for a three-phase composite [35]. In their experiments the composites were 65 to 90% of the theoretical density.

2.4.9 Modified Lichtenecker

The modified Lichtenecker equation is based on a similar power law approximation but it contains an additional factor, k. The factor is an empirical fitting factor that is justified by the nature of fillers and matrices. Very commonly a value of 0.3 has been used for k with well-dispersed particles in homogeneous composites. Sonoda *et al.* reported fitting factors in the range of 0.22–0.3 [10] while Hu *et al.* had a correlation with their BST–COC composites when using a k factor of 0.43 [36]. The effect of the fitting factor on the effective permittivity of composite is shown in Figure 2.7 and is given by

$$\log \varepsilon_{eff} = \log \varepsilon_e + V_f (1 - k) \log \left(\frac{\varepsilon_i}{\varepsilon_e} \right) \tag{2.23}$$

where factor k is an empirical fitting factor.

2.4.10 Differential

The differential equation method (Equation 2.24) is a combination of two mixing rules: Maxwell–Garnett (Equation 2.9) and Bruggeman symmetric (Equation 2.16). With low-volume fractions the equation correlates with Maxwell–Garnett and approaches

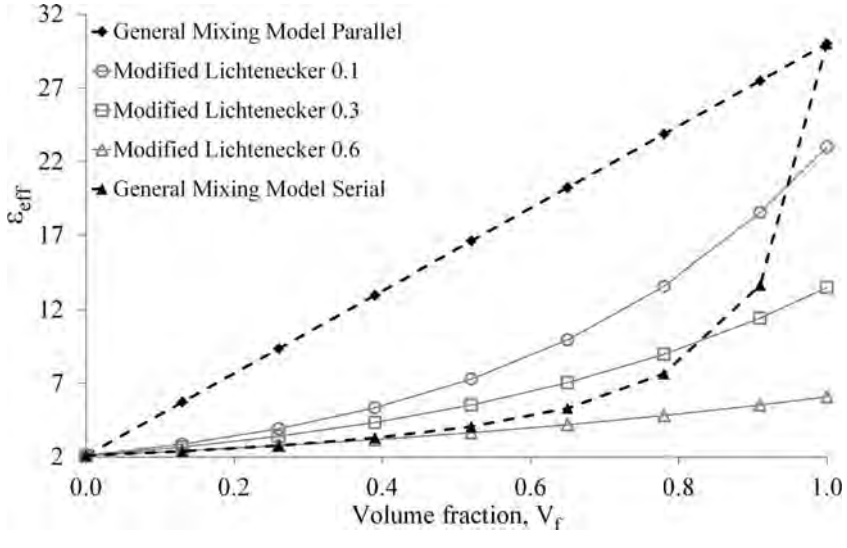

Figure 2.7 *Modified Lichtenecker equation with k-factors of 0.1, 0.3, and 0.6 and* $\varepsilon_e = 2.1$, $\varepsilon_i = 30$.

permittivity estimations of Bruggeman symmetric as the volume fractions increase, that is, above the percolation threshold where particles become connected [21]:

$$\frac{d\varepsilon_{eff}}{dV} = \frac{3\varepsilon_e(\varepsilon_i - \varepsilon_{eff})}{\varepsilon_i + 2\varepsilon_{eff} - 3V_f\varepsilon_i} \Rightarrow$$
$$V_f = 1 - \frac{1}{3}\frac{\varepsilon_i - \varepsilon_{eff}}{\varepsilon_i - \varepsilon_e}\left(2 + \left(\frac{\varepsilon_i - \varepsilon_{eff}}{\varepsilon_i - \varepsilon_e}\right)^{\varepsilon_i/\varepsilon_{e^{-1}}}\right) \tag{2.24}$$

The equation above is a derived result for spherical inclusions. However, it can be derived also for randomly oriented ellipsoids:

$$\frac{d\varepsilon_{eff}}{d\mathrm{V}} = \varepsilon_e(\varepsilon_i - \varepsilon_{eff})\frac{\sum_{j=x,y,z}(\varepsilon_{eff} + N_j(\varepsilon_i - \varepsilon_{eff}))^{-1}}{3 - V_f\varepsilon_i\sum_{j=x,y,z}(\varepsilon_{eff} + N_j(\varepsilon_i - \varepsilon_{eff}))^{-1}} \Rightarrow$$
$$V_f = 1 + (N_j - 1)\frac{\varepsilon_i - \varepsilon_{eff}}{\varepsilon_i - \varepsilon_e} - N_j\left(\frac{\varepsilon_i - \varepsilon_{eff}}{\varepsilon_i - \varepsilon_e}\right)^{\varepsilon_i/\varepsilon_e} \tag{2.25}$$

where N_j represents the depolarization factor of the ellipsoidal inclusions in three-dimensional space x, y, z. With spherical inclusions $N_x = N_y = N_z = 1/3$, Jylhä and Sihvola concluded that the suitability of the equation is good, with applications having a strong contrast between inclusions and environment and where inclusions are uniformly and randomly distributed [21].

2.4.11 General Mixing Model

Many of the equations that model the effective permittivity of composites are based on either the parallel or serial models described here. The general mixing model [37, 38] assumes that inclusions in a medium are affecting the permittivity in the same way as a dielectric material in a plate capacitor when it is either serial or parallel connected to an effective electric field (Figure 2.8):

$$\varepsilon_{eff}^{\alpha} = \sum_n V_{f_n}\varepsilon_n^{\alpha} \tag{2.26}$$

where α and n represent the mixing model and nth dielectric component of the composite.

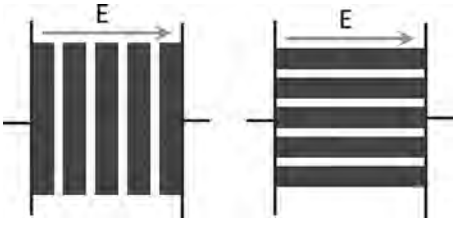

Figure 2.8 *Dielectric material under E-field in serial and parallel models.*

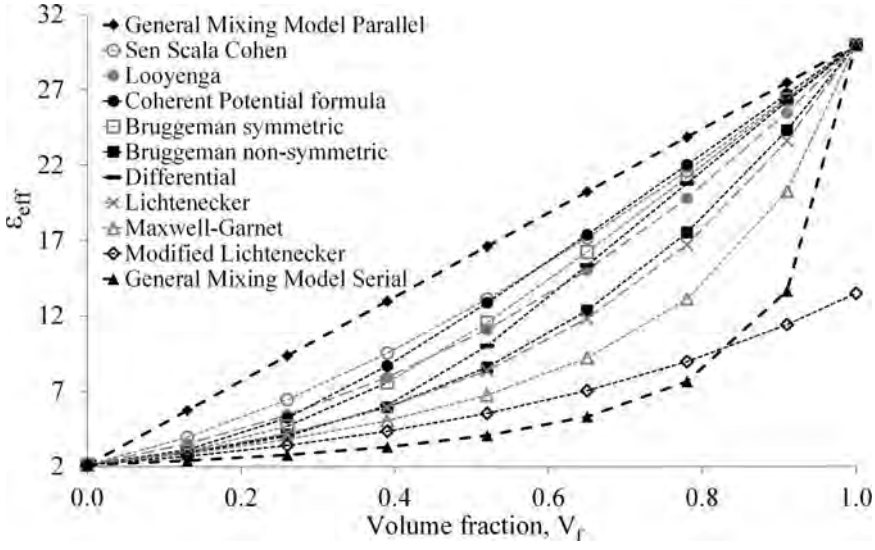

Figure 2.9 *Presented mixing equations with $\varepsilon_e = 2.1$, $\varepsilon_i = 30$, and $k = 0.3$.*

The presented models represent two extreme modes when α is either –1 (serial) or 1 (parallel). The logarithmic model ($\alpha = 0$) fits between these two modes. It is notable that all the presented mixing models, except the modified Lichtenecker due to its factor k, fit between these two extreme cases of the general mixing model, that is, $-1 \leq \alpha \leq 1$. Sun *et al.* reported on the correlation with the logarithmic version of the equation and multiphase porous composites based on the Monte Carlo method when pores are also considered as a fourth phase [39]. This can be clearly seen in Figure 2.9 where the aforementioned mixing equations are included and are within the boundaries of all general mixing models except for the modified Lichtenecker at high-volume fractions.

Loss factors are more complicated and there are far fewer mixing equations for modeling them. However, a general mixing model for losses has been shown to be successful in modeling loss tangents of dielectric composites [18, 37, 38, 40, 41]:

$$\tan \delta_{eff}^{\alpha} = \sum_{n} V_{f_n} \tan \delta_n^{\alpha}, \tag{2.27}$$

where $\tan \delta_{eff}$ and $\tan \delta_n$ represent the effective loss tangents of composite and loss tangents of the nth dielectric component.

2.4.12 Effective Medium Theory (EMT)

In composite materials the particle size of the filler may be small compared to the total dimensions of the composite and also the wavelength. Thus the dielectric properties of the composite may be treated as an effective medium in which the dielectric permittivity can

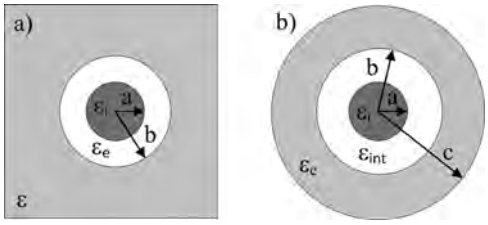

Figure 2.10 *(a) Random unit cell embedded in the effective media in the EMT model. (b) Composite schematic including filler, interphase and matrix in the Vo–Shi model where a, b, and c represent radii of different constituents.*

be obtained by averaging over the dielectric permittivity of the phases. The EMT model for an effective dielectric constant prediction of composite is [42]

$$\varepsilon = \varepsilon_e \left[1 + \frac{V_{fei}(\varepsilon_i - \varepsilon_e)}{\varepsilon_e + n(1 - V_{fei})(\varepsilon_i - \varepsilon_e)}\right] \tag{2.28}$$

where n is the shape factor, in order to account for the morphology of the filler particles, and V_{fei} is the volume ratio of the filler and matrix. In the model a random unit cell (Figure 2.10a) is considered as a core ε_i that is surrounded by a shell ε_e where their sizes are respective to their volumes. The volume ratio can be calculated from the radius of core and shell by $V_{fei} = a^3/b^3$.

The morphology factor, n, which compensates for the shape of the used filler, is determined empirically. A small value of n indicates a near-spherical shape of the filler and for non-spherical particles the value is higher. Teirikangas *et al*. have found that if the shape factor n is modified to fit the measurement results the shape factor n has a trend to decrease or increase as a function of filler loading and is also affected by the matrix material used [43]. One drawback using the EMT model is that the particle size of the filler should be very small [42, 44].

2.4.13 Jayasundere–Smith

In general, the theoretical predictions are valid only for low filler contents and deviations from prediction increase as the filler content is increased. This is due to the imperfect dispersion of filler contents at higher loadings and to the porosity enclosed but also because the theoretical predictions do not typically consider the matrix–filler interphase interactions. The Jayasundere–Smith equation (2.29) is a modification of the Kerner equation by including the interactions between neighboring spheres. It considers the composite as a bi-phase system of fillers with ε_i dispersed in a continuous medium with ε_e. The Jayasundere–Smith equation is only valid for a filler content up to 30 vol.% and when $\varepsilon_i \gg \varepsilon_e$ [44]:

$$\varepsilon_{eff} = \frac{\varepsilon_e(1 - V_f) + \varepsilon_i V_f \left[\frac{3\varepsilon_e}{\varepsilon_i + 2\varepsilon_e}\right]\left[\frac{1 + 3V_f(\varepsilon_i - \varepsilon_e)}{\varepsilon_i + 2\varepsilon_e}\right]}{1 - V_f + V_f \left[\frac{3\varepsilon_e}{\varepsilon_i + 2\varepsilon_e}\right]\left[\frac{1 + 3V_f(\varepsilon_i - \varepsilon_e)}{\varepsilon_i + 2\varepsilon_e}\right]} \tag{2.29}$$

where ε_{eff}, ε_e, and ε_i are the permittivity of the composite, matrix, and filler, respectively. V_f is the volume fraction of the filler material.

2.4.14 Vo–Shi

In contrast to the abovementioned equations, the Vo–Shi equation also takes into account the interphase region formed in the matrix materials around the particles (Figure 2.10b), which can have dielectric properties differing from those of the bulk matrix [45]:

$$\varepsilon_{eff} = \frac{h + 2l}{h - l} \tag{2.30}$$

where

$$h = \left[1 + 2\frac{(\varepsilon_e - \varepsilon_{\text{int}})(\varepsilon_{\text{int}} - \varepsilon_i)}{(2\varepsilon_e + \varepsilon_{\text{int}})(2\varepsilon_{\text{int}} + \varepsilon_i)}\left(\frac{a^3}{b^3}\right) - 2\frac{(\varepsilon_e - 1)(\varepsilon_e - \varepsilon_{\text{int}})}{(\varepsilon_e + 2)(2\varepsilon_e + \varepsilon_{\text{int}})}\left(\frac{b^3}{c^3}\right)\right.$$

$$\left. -2\frac{(\varepsilon_e - 1)(\varepsilon_e + 2\varepsilon_{\text{int}})(\varepsilon_{\text{int}} - \varepsilon_i)}{(\varepsilon_e + 2)(2\varepsilon_e + \varepsilon_{\text{int}})(2\varepsilon_{\text{int}} + \varepsilon_i)}\left(\frac{a^3}{c^3}\right)\right] \tag{2.31}$$

$$l = \left[\frac{(\varepsilon_e - 1)}{(\varepsilon_e + 2)}j - \frac{(2\varepsilon_e + 1)m}{(\varepsilon_e + 2)(2\varepsilon_e + \varepsilon_{\text{int}})}\left(\frac{b^3}{c^3}\right)\right] \tag{2.32}$$

$$j = \left[1 + 2\frac{(\varepsilon_e - \varepsilon_{\text{int}})(\varepsilon_{\text{int}} - \varepsilon_i)}{(2\varepsilon_e + \varepsilon_{\text{int}})(2\varepsilon_{\text{int}} + \varepsilon_i)}\left(\frac{a^3}{b^3}\right)\right] \tag{2.33}$$

$$m = \left[(\varepsilon_e - \varepsilon_{\text{int}}) + \frac{(\varepsilon_e + 2\varepsilon_{\text{int}})(\varepsilon_{\text{int}} - \varepsilon_i)}{(2\varepsilon_{\text{int}} + \varepsilon_i)}\left(\frac{a^3}{b^3}\right)\right] \tag{2.34}$$

$$\frac{a^3}{b^3} = \frac{(1 + xV_f)}{(1 + x)} \tag{2.35}$$

$$\frac{a^3}{c^3} = V_f \tag{2.36}$$

$$\frac{b^3}{c^3} = V_f\left[1 + x\frac{(1 - V_f)}{(1 + xV_f)}\right] \tag{2.37}$$

Here ε_{int} is the relative permittivity of the interphase region and x is the interphase volume constant reflecting the strength of the matrix–filler interaction. The value x is zero when the interaction, that is, bonding, is neglible, while a high positive value represents a strong interaction. It has been proved that an interphase region around inclusions can have a relative permittivity less than that of the bulk polymer. This result can be explained by a change in the chemical polarizability of the polymer as a consequence of chemical bonding between polymer and the surface of the inclusion. The effect of bonding can be calculated by means of chemical polarization equations [12, 45, 46]. On the other hand, Murugaraj *et al.*, utilizing the Vo–Shi model, have suggested a significantly enhanced relative permittivity of the polymer interphase obtaining $\varepsilon_{\text{int}} = 19.24$–$280$ in experiments performed with PI-alumina PI-silica composites [47].

2.4.15 Interphase Power Law (IPL)

Another model also including interphases is the interphase power law (IPL) model which is extended from a two-phase power law system into a three-component system [48]:

$$\varepsilon_{eff}^{\beta} = V_f \varepsilon_i^{\beta} + V_{f\text{int}} \varepsilon_{\text{int}}^{\beta} + V_{fe} \varepsilon_e^{\beta} \tag{2.38}$$

where $V_{f\text{int}}$ and V_{fe} represent volume fraction of interphase and matrix, respectively, and β is a dimensionless parameter describing orientation and shape of the filler.Permittivity is given in complex form, for example, $\varepsilon_i{}^* = \varepsilon_i' + j\varepsilon_i''$, containing a real part and a loss factor of permittivity and thus also enabling the calculation of losses. Equation (2.38) contains, for example, Landau, Looyenga, and Lifshitz models as special cases when $V_{f\text{int}} = 0$ and $\beta = 1/3$ (see Equation 2.20). It was shown by Todd and Shi that the IPL model gives good correspondence of effective permittivity and dielectric losses compared to measured values of $BaTiO_3$–TMPTA composite while significant discrepancies were observed with. for example, Bruggeman, Vo–Shi, Landau, Lifshitz, and Looyenga models [48].

2.5 Effect of Porosity

Porosity appears as a constituent in composites in two different ways, either as an unwanted porosity or as an engineered porosity in both inorganic and polymer based composites. In ceramics, porosity is usually aimed to be minimized and porosity correction is used to estimate what would be the permittivity and dielectric loss of ideal, fully dense ceramics. In engineered porosity, pores are deliberately introduced in order to decrease permittivity and/or losses. The initial point of porosity introduction is quite opposite to the typical starting point in polymer-based composites. Typically, filler is incrementally added into the matrix starting from 0 vol.% while in the case of porosity the starting point is 100 vol.% of matrix and this portion is incrementally decreased. It should be noted also that, quite often, in calculations based on mixing equations, bulk ceramics are taken as a reference point assuming a volume fraction of 1. However, some pores usually exist in such structures that influence the permittivity and dielectric losses and should be taken into account in estimations.

It is possible to reach required targets for lower permittivity either by using dielectric material with lower polarizability, that is, lower permittivity, or by using inclusions with lower permittivity embedded into the structures (Figure 2.11).

Thus, the measured permittivity of the sample in Figure 2.11 represents the effective permittivity in a similar fashion to that in the earlier presented cases of mixing equations. Although solid inclusions are feasible in some cases, the typical choice for inclusions for this type of composite is air, which has one of the lowest permittivity values, $\varepsilon_r \approx 1$, and extremely low losses and cost. However, the aim for ultra-low permittivities with porous dielectrics is not as straightforward as one might expect and several researchers have reported on the differences in dielectric constants even when varying only the sizes of particles and pores [49, 50].

It is known, for example, that during processing of porous silicon particles in air, impurities are trapped in the pores, which affect the dielectric properties. This effect can be decreased by using oxidation during the process [51]. Vanstreels *et al.* found that increased

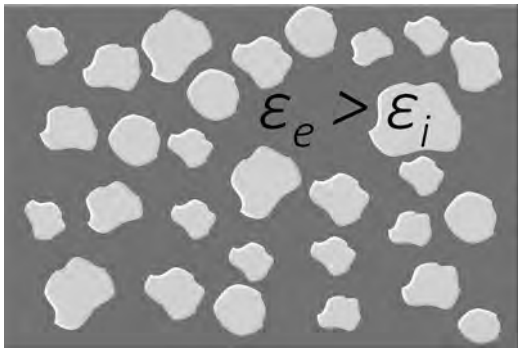

Figure 2.11 *Permittivity of the dielectric can be decreased using low permittivity fillers or increasing porousness.*

porosity reduced the breakdown voltage, which in turn could degrade the electrical reliability performance of the dielectric material but did not affect the leakage current [52]. However, Wang *et al.* demonstrated an increase in leakage current with carbon-doped silicon oxide dielectrics [53]. Similarly, less advantageous findings of increased leakage currents and decreased breakdown voltages were presented by Van Besien *et al.* with their experiment using PE-CVD dielectrics [54]. Thus, the manufacture of porous dielectrics offers challenges to be solved, but also some aspects that should be taken into account when comparing theoretical values derived from mixing equations with measured values.

However, the required dielectric constant can also be achieved by affecting the porosity of the manufactured dielectric [55]. This has been shown, for example, by utilizing silicon technology where pores of a few nanometers have been used to reduce dielectric constants. However, the increased amount of pores, especially close to the percolation threshold, is in direct contradiction to the requirements for electrical, mechanical, and thermal strength. Furthermore, the associated variations in phase stability and mechanical shrinkage can pose extra challenges to achieving the desired targets of tailored dielectrics. Liu *et al.* showed a ~30% decrease in permittivity of methylsilsesquioxane films when the porosity level was increased from 0 to 50 vol.% [56]. Gong *et al.* were able to decrease the dielectric constant from 90 to 46 by using glassy-carbon-assisted porous titania in the gigahertz range. They were also able to achieve an even lower permittivity value ($\varepsilon_r = 12.25$) with microcellular porous titania [26].

In addition to such experiments, simulations have been used to determine the effect of pores in dielectrics. Bouledjnib and Salah simulated several mixing equations and porosities with different shapes. They found that in the cases of cylindrical, hexagonal, and cubic-shaped pores the first one decreased the simulated permittivity by the greatest amount [57]. Similar findings concerning the effect of pore shape on permittivity were found by Elsner and Hermann in their simulations [58].

2.5.1 Permittivity

The significant impact of porosity in material characterization may lead to misinterpretation of the results. In order to determine dielectric properties of fully dense materials, the

porosity effect should be taken into account when measuring dielectrics which have densities significantly less than the theoretical maximum. Several equations have been developed to enable sophisticated estimations of material properties. They estimate the total permittivity of the material based on dielectric properties and volume fractions of the constituents of composites. Some of these mixing equations even cover the effect of particle shapes with reasonable accuracy. In addition to the earlier mentioned mixing equations, the following equations have been successfully used, especially in the case of porosity corrections.

For sphere-shaped porosity in a dielectric medium the following equations have been utilized [28]:

$$1 - P = \left(\frac{\varepsilon_e}{\varepsilon_{eff}}\right)^{1/3} \frac{\varepsilon_{eff} - 1}{\varepsilon_e - 1} \tag{2.39}$$

where P is the fractional porosity and the relative permittivity of pores is assumed to be the relative permittivity of air, that is, 1. Since there is no analytical solution for Equation (2.39) with respect to ε_{eff}, a linearized approximation for $\varepsilon_e - \varepsilon_{eff} \ll \varepsilon_e$ gives

$$\varepsilon_{eff} = \varepsilon_e \left(1 - \frac{3P(\varepsilon_e - 1)}{2\varepsilon_e + 1}\right) \tag{2.40}$$

This approximation showed good correlation for polycrystalline alumina with fractional porosity values from 0 to 0.45.

Alternatively, one can use the Bötcher mixing equation, which assumes a dispersion of sphere-shaped pores (or another phase) in a mixture of solid and air. This mixing equation allows the interaction of the two different phases in an approach similar to that used in the Bruggeman equation. Therefore the Bötcher equation is also accurate for high values of porosity [59]:

$$\frac{\varepsilon_{eff} - \varepsilon_2}{3\varepsilon_{eff}} = \frac{V_{f1}\left(\varepsilon_1 - \varepsilon_2\right)}{\varepsilon_1 + 2\varepsilon_{eff}} \tag{2.41}$$

where V_{f1} is the volume fraction of phase 1 and ε_1 and ε_2 are the permittivities of phases 1 and 2, respectively [59].

2.5.2 Dielectric Losses

Losses in dielectrics are affected by intrinsic and extrinsic factors. Intrinsic loss factors are due to crystal structures, that is, symmetry with the AC field frequency, and thus interaction with phonons (oscillating atoms within crystals), and temperature. The extrinsic loss factors are dependent on, for example, impurities, defects in microstructures, grain boundaries, porosity, cracks, random crystallite orientation, vacancies, and dopant atoms, which can affect the crystal lattice. These extrinsic factors can be minimized using proper manufacturing processes. At low frequencies, temperature and ion content dependent DC conductivity has a remarkable effect. When the frequencies are increased to the microwave range the effect of DC conductivity becomes neglible, as can be deduced from, for example, the Drude model [60–62].

The porosity adds an additional term to the total loss of a dielectric. Penn *et al.* have demonstrated with sintered alumina that the loss is strongly dependent on pore volume and its surface area [63]. The relationship between tan δ and the porosity P is given by

$$\tan\delta = (1-P)\tan\delta_0 + A'P\left(\frac{P}{1-P}\right)^{2/3} \tag{2.42}$$

where tan δ_0 is the loss of fully dense alumina and the value for A' given in the model was 9.277×10^{-3} [63,64].

Alumina is a strongly hydrophilic material and the adsorbed humidity can affect the observed losses, which are in the range of $\times 10^{-4}$ with alumina and $\times 10^{-1}$ with water in the gigahertz frequency range [18,64,65]. Furthermore, nano-sized pores in sintered components can absorb species and water, which is not desirable for microwave passive components [26]. On the other hand, Gong *et al.* found that samples with an increased amount of pores still had very low loss tangents ($\times 10^{-4}$) [26]. In contrast, Park *et al.* reported that their simulation results of decreased quality factors were directly proportional to the pore amount and inversely proportional to pore size in the 5 GHz frequency range [66]. Thus, from their simulation results point of view, high porosity with small pore size would be more beneficial when aiming for lower permittivity and a less degrading quality factor, that is, lower dielectric losses. Therefore, these various aspects should be taken into account when considering the losses and their calculations

2.5.3 Dielectric Properties of Powders

Powders differ from solid and sintered dielectrics or typical polymer-based composites in that particles do not form such strong bonds between neighboring particles as is the case with sintered components. However, powders can be treated as air–particle composites where the air is a matrix between fillers, that is, particles. Therefore, mixing equations have been used in the estimation of powdery materials. Many of the experiments have concentrated on easily available natural materials such as sand, snow, ice, grains, and flours. However, synthetic materials have also been under study, such as dielectric powders, that is, ceramics and polymers. Tuhkala *et al.* have utilized several mixing equations in the characterization of different modifications of powdery materials using a coaxial resonator. The best correlation in the determination of permittivity was achieved using Bruggeman symmetric (Equation 2.16) and Looyenga (Equation 2.20) equations in combination where a certain compaction level (43% of the theoretical maximum) was used to achieve accurate results [18,67–69]. A similar correlation with the same equations was also achieved earlier by Conger and Tung [70] and Nelson and Bartley [71].

2.5.3.1 Particle Coatings and Moisture Adsorption

Mixing equations have been successfully utilized in the determination of particle coating. Tuhkala *et al.* found correlation with the general mixing model in parallel mode and surfactant covered particles in their measurements [68]. In addition, they showed clear correlation with the amount of adsorbed water [18]. In both experiments the amount of either water or surfactant could be determined from the measurement results using mixing equations. In these cases the general mixing model (Equation 2.26) was covering multiple phases of the

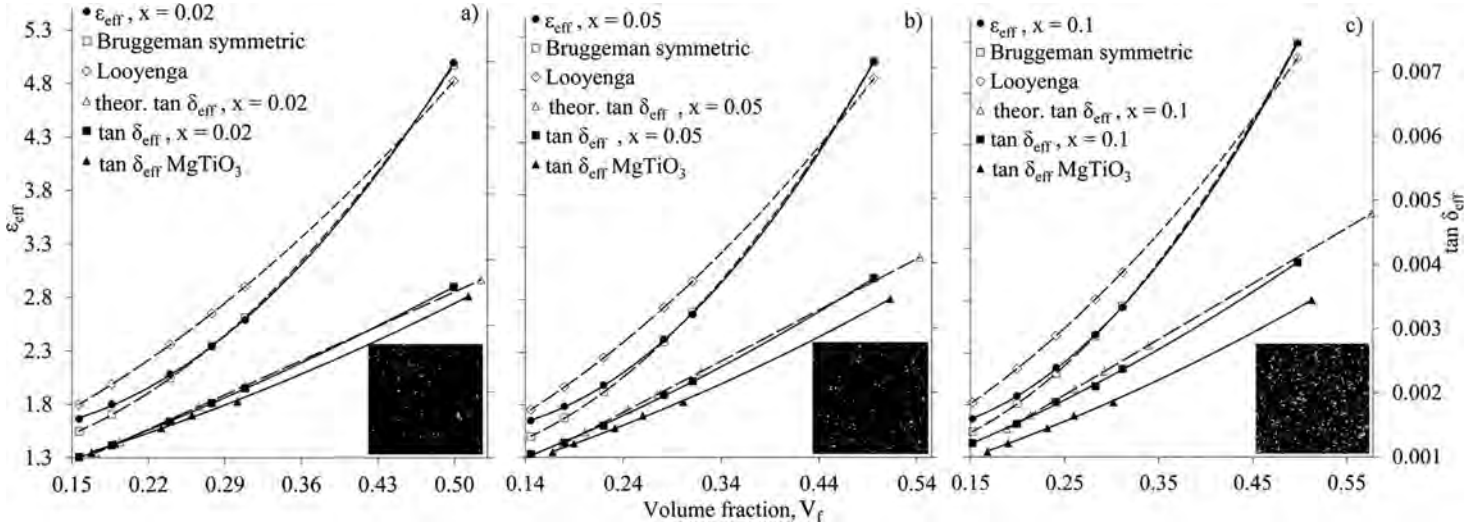

Figure 2.12 *Measured effective permittivities of (1 – x)$MgTiO_3$–x$CaTiO_3$ composite powders with $CaTiO_3$ molar ratios (x) of (a) 0.02, (b) 0.05, and (c) 0.1 and effective permittivities of Bruggeman symmetric and Looyenga mixing models with inclusion permittivities of (a) 13.5, (b) 14.0, and (c) 14.9. Measured effective loss tangents of $MgTiO_3$ and composite powders and theoretical effective loss tangents calculated by the general mixing model. The resonance frequencies of the resonator perturbed by the powder samples were within the range 2.12–3.66 GHz. EPMA figures of calcium distribution (light dots in 100 μm × 100 μm analysis areas) in composite powders as inserts. Source: Reprinted with permission from Journal of Applied Physics. Copyright 2014, AIP Publishing LLC [69].*

treated powder composites. Similar correlation with the general mixing model in parallel mode was found by Fukuda *et al.* [41] and Huang and Weng [40].

In the case of treated particles under an incident electric field, the changed interactions between particles could also be seen in some of the measurement results. These changes are not universally covered by any of the presented mixing equations but are also included when empirical fitting factors have been used. Although changed interactions between particles can occur, the presented mixing rules can be used in a sophisticated manner when determining the properties of modified particles [72, 73]. However, it should be noted that well-correlated curves as a function of volume fraction do not always guarantee the determination of the correct dielectric properties when using theoretical mixing models [66, 73]. In such cases the mixing equations could be used in combination. Furthermore, special attention should be paid to the compaction level when determining dielectric properties of powdery materials due to the percolation threshold and definitions of the mixing models [73, 74].

2.5.3.2 Powder Mixtures

Mixing equations have also been utilized to distinguish the amount of different phases in powder composites. Clear correlation with the calculated values and measurement results have been found utilizing the general mixing model equation with $MgTiO_3$–$CaTiO_3$ powder composites having different molar ratios (Figure 2.12) [69].

Moreover, correlation was also found using different-shaped and sized powder composites. Despite the fact that the used equations of Bruggeman symmetric and Looyenga are defined for spherically shaped particles, correlation was found with powders having elongated micrometer-sized $BaTiO_3$ particles (Figure 2.13) [75]. However, the correlation may differ when using larger amounts of needle-shaped particles. Nevertheless, mixing equations can also be utilized with powder mixtures formed by differently shaped particles to determine the required dielectric properties of the powder constituents. Furthermore,

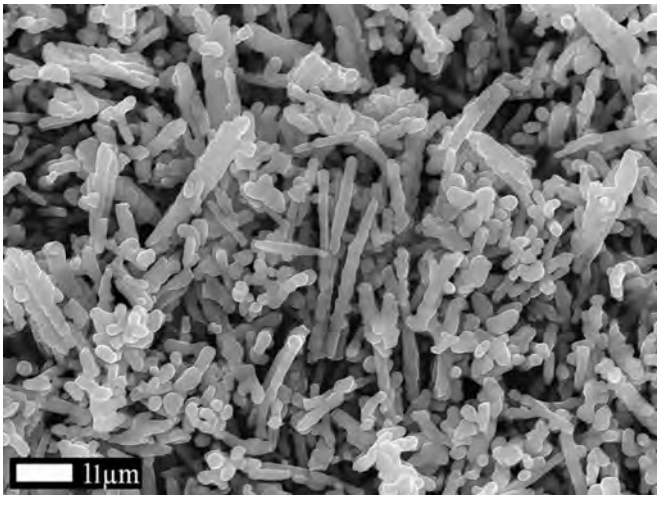

Figure 2.13 *SEM figure of elongated $BaTiO_3$ particles. Source: Adapted from Tuhkala* et al. *2015 [75].*

such data and mixing equations can be used in designing the optimum filler selection for a specified level of permittivity and to minimize dielectric losses and filler amounts [72, 73].

2.6 Conclusion

The presented mixing equations and their feasibility in certain applications are justified and applicable. Even though some of them have a deeper background regarding electrostatic theories and some are more or less empirically defined, they can give valuable information when, for example, designing dielectrics for RF and microwave applications.

As shown above, correlations have been found in numerous different cases, materials, and measurement methods, whether the samples in question were solid ceramics, composites with or without porosity, or other inclusions, or even in powder form. However, none of the presented equations have shown a general solution for all cases. This is obvious as factors arising from material physics, such as scattering, defects, impurities, changes in dispersion, varying particle size and shape, etc., often influence the obtained effective results and are hard to take into account. Despite these limitations with detailed analysis, mixing equations offer a powerful tool to a deeper understanding of the materials under research and their further design for specific applications.

References

1. Maex, K., Baklanov, M.R., Shamiryan, D., *et al.* (2003) Low dielectric constant materials for microelectronics. *Journal of Applied Physics*, **93** (11), 8793–8841.
2. Chiang, C.-C., Ko, I.-H., Chen, M.-C., *et al.* (2004) Improvement in leakage current and breakdown field of Cu-comb capacitor using a silicon oxycarbide dielectric barrier. *Journal of the Electrochemical Society*, **151** (9), G606–G611.
3. Newnham, R.E., Skinner D.P., and Cross, L.E. (1978) Connectivity and piezoelectric–pyroelectric composites. *Material Research Bulletin*, **13** (5), 525–536.
4. Kong, L.B., Li, Z.W., Liu, L., *et al.* (2013) Recent progress in some composite materials and structures for specific electromagnetic applications. *International Materials Reviews*, **58** (4), 203–259.
5. Xia, T., Zhang, C., Oyler, N.A., and Chen, X. (2013) Hydrogenated TiO_2 nanocrystals: a novel microwave absorbing material. *Advanced Materials*, **25**, 6905–6910.
6. Chen, Z., Xu, C., Ma, C., *et al.* (2013) Lightweight and flexible graphene foam composites for high-performance electromagnetic interference shielding. *Advanced Materials*, **25**, 1296–1300.
7. Sebastian, M.T. and Jantunen, H. (2010) Polymer–ceramic composites of 0–3 connectivity for circuits in electronics: a review. *International Journal of Applied Ceramic Technology*, **7** (4), 415–434.
8. Sebastian, M.T. and Jantunen, H. (2008) Low loss dielectric materials for LTCC applications: a review. *International Materials Review*, **53** (2), 57–90.
9. Caruso, F. (2001) Nanoengineering of particle surfaces. *Advanced Materials*, **13** (1), 11–22.
10. Sonoda, K., Juuti, J., Moriya Y., and Jantunen, H. (2010) Modification of the dielectric properties of 0–3 ceramic–polymer composites by introducing surface active agents onto the ceramic filler surface. *Composite Structures*, **92** (5), 1052–1058.
11. Sonoda, K., Teirikangas, M., Juuti, J., *et al.* (2011) Effect of surface modification on dielectric and magnetic properties of metal powder/polymer nanocomposites. *Journal of Magnetism and Magnetic Materials*, **323**, 2281–2286.
12. Todd, M.G. and Shi, F.G. (2003) Characterizing the interphase dielectric constant of polymer composite materials: effect of chemical coupling agents. *Journal of Applied Physics*, **94**(7), 4551–4557.

13. Teirikangas, M., Juuti J., and Jantunen, H. (2011) Organic–inorganic RF composites with enhanced permittivity by nanoparticle additions. *Progress in Electromagnetics Research*, **115**, 147–157.
14. Reitz, J.R., Milford, F.J., and Christy, R.W. (eds) (1993) *Foundations of Electromagnetic Theory*, Addison-Wesley Longman, Inc., Boston, MA.
15. Bohren, C.F. and Fraser, A.B. (1985) Colors of the sky. *The Physics Teacher*, **23**, 267–272.
16. Sihvola, A. (1999) *Electromagnetic Mixing Formulae and Applications*, The Institution of Engineering and Technology, London.
17. Nathan, L.B.S., Dobson, D.C., Eso, O., and Golden, K.M. (2011) Spatial bounds on the effective complex permittivity for time-harmonic waves in random media. *Multiscale Modeling and Simulation*, **9** (3), 1113–1143.
18. Tuhkala, M., Juuti, J., and Jantunen, H. (2013) Use of an open-ended coaxial cavity method to characterize powdery substances exposed to humidity. *Applied Physics Letters*, **103** (142907), 1–4.
19. Deepa, K.S., Sebastian, M.T., and James, J. (2007) Effect of interparticle distance and interfacial area on the properties of insulator-conductor composites. *Applied Physics Letters*, **91** (202904), 1–3.
20. Liu, Z., Bai, G., Huang, Y., *et al.* (2007) Microwave absorption of single-walled carbon nanotubes/soluble cross-linked polyurethane composites. *Journal of Physical Chemistry C*, **111**, 13696–13700.
21. Jylhä, L. and Sihvola, A. (2007) Equation for the effective permittivity of particle-filled composities for material design applications. *Journal of Physics D: Applied Physics*, **40** (16), 4966–4973.
22. Van Rysselberghe, P. (1931) Remarks concerning the Clausius–Mossotti law. *The Journal of Physical Chemistry*, **36** (4), 1152–1155.
23. Shannon, R.D. (1992) Dielectric polarizabilities of ions in oxides and fluorides. *Journal of Applied Physics*, **73** (1), 348–366.
24. Sebastian, M.T. (2008) *Dielectric Materials for Wireless Communication*, Elsevier, Amsterdam.
25. Vineis, C., Davies, P.K., Negas T., and Bell, S. (1996) Microwave dielectric properties of hexagonal perovskites. *Material Research Bulletin*, **31** (5), 431–437.
26. Gong, X., She, W.H., Hoppenjans, E.E., *et al.* (2005) Tailored and anisotropic dielectric constants through porosity in ceramic components. *IEEE Transactions on Microwave Theory and Techniques*, **53** (11), 3638–3647.
27. Sihvola, A. and Sharma, R. (1999) Scattering corrections for Maxwel Garnett mixing rule. *Microwave and Optical Technology Letters*, **22** (4), 229–231.
28. Hsiang, H.-I., Yen, F.-S., and Huang, C.-Y. (1995) Effects of porosity on dielectric properties of $BaTiO_3$ ceramics. *Japanese Journal of Applied Physics*, **34** (1), 1922–1925.
29. Mätzler, C. (1996) Microwave permittivity of dry snow. *IEEE Transactions on Geoscience and Remote Sensing*, **34** (2), 573–581.
30. Campos, A.M., Torres, J., and Giraldo, J.J. (2002) Porous silicon dielectric function modeling from effective medium theories. *Surface Review and Letters*, **9** (5 and 6), 1631–1635.
31. Wołoszyn, M., and Maksymowicz, A.Z. (2002) Coherent potential approximation technique in a simple example of resistivity calculations for binary alloys. *TASK Quarterly: Scientific Bulletin of Academic Computer Centre in Gdansk*, **6** (4), 669–680.
32. Bouledjnib, L. and Sahli, S. (2011) Dielectric constant computation model for *N*-phase porous materials. *International Review on Modelling and Simulations*, **4** (4), 2005–2011.
33. Zakri, T., Laurent, J.-P., and Vauclin, M. (1998) Theoretical evidence for 'Lichtenecker's mixure formulae' based on the effective medium theory. *Journal of Physics D: Applied Physics*, **31** (13), 1589–1594.
34. Wu, K.-T., Yuan, Y., Zhang, S.-R., *et al.* (2013) $ZrTi_2O_6$ filler PTFE composites for microwave substrate applications. *Journal of Polymer Research*, **20** (8), 1–6.
35. Kim, K.S., Shim, S.H., Kim, S., and Yoon, S.O. (2010) Low temperature and microwave dielectric properties of TiO_2/ZBS glass composites. *Ceramics International*, **36** (5), 1571–1575.
36. Hu, T., Juuti, J., Jantunen, H., and Vilkman, T. (2007) Dielectric properties of BST/polymer composite. *Journal of the European Ceramic Society*, **27** (13–15), 3997–4001.

37. Wakino, K., Okada, T., Yoshida N., and Tomono, K. (1993) A new equation for predicting the dielectric constant of a mixture. *Journal of American Ceramic Society*, **76** (10), 2588–2594.
38. Abraham, R., Gyo, R., and Bhalla, A.S. (2005) Modeling permittivity and tangent loss in dielectric materials using finite element method and Monte Carlo simulation. *Ferroelectrics*, **315** (1), 1–15.
39. Sun, Y., Han J., and Zhang, Y. (2009) Relative dielectric constant calculation model for three-phase porous composite materials. *Computational Material Science*, **4** (4), 1125–1128.
40. Huang, C.-L. and Weng, M.-H. (2001) Improved high Q value of $MgTiO_3$–$CaTiO_3$ microwave dielectric ceramics at low sintering temperature. *Materials Research Bulletin*, **36** (15), 2741–2750.
41. Fukuda, K., Kitoh R., and Awai, I. (1993) Microwave characteristics of TiO_2–Bi_2O_3 dielectric resonator. *Japanese Journal of Applied Physics*, **32** (10), 4584–4588.
42. Rao, Y., Qu, J., Marinis, T., and Wong, C.P. (2000) A precise numerical prediction of effective dielectric constant for polymer–ceramic composite based on effective-medium theory. *IEEE Transactions on Components and Packaging Technologies*, **23** (4).
43. Teirikangas, M., Juuti, J., and Jantunen, H. (2009) Extrinsic influences of the polymer matrix on electrical properties of high frequency composites. *Ferroelectrics*, **387**, 70–76.
44. Sebastian, M.T. and Jantunen, H. (2010) Polymer–ceramic composites of 0–3 connectivity for circuits in electronics: a review. *International Journal of Applied Ceramic Tecnology*, **7** (4), 415–434.
45. Vo, H.T. and Shi, F.G. (2002) Towards model-based engineering of optoelectronic packaging materials: dielectric constant modeling. *Microelectronics Journal*, **33**, 409–415.
46. Todd, M.G. and Shi, F.G. (2003) Molecular basis of the interphase dielectric properties of microelectronic and optoelectronic packaging materials. *IEEE Transactions on Components and Packaging Technologies*, **26** (3), 667–672.
47. Murugaraj, P., Mora-Huertas, N., and Mainwaring, D. (2005) Dielectric enhancement in polymer–nanoparticle composite through interphase polarizability. *Journal of Applied Physics*, **98** (054304), 1–6.
48. Todd, M.G. and Shi, F.G. (2005) Complex permittivity of composite systems: a comprehensive interphase approach. *IEEE Transactions on Dielectrics and Electrical Insulation*, **12** (3), 601–611.
49. Jones, S.B. and Friedman, S.P. (2000) Particle shape effects on the effective permittivity of anisotropic or isotropic media consisting of aligned or randomly oriented ellipsoidal particles. *Water Resources Research*, **36** (10), 2821–2833.
50. Blonquist J.M. Jr, Jones, S.B., Lebron, I., and Robinson, D.A. (2006) Microstructural and phase configurational effects determining water content: dielectric relationships of aggregated porous media. *Water Resources Research*, **42** (5), 1–13.
51. Astrova, E.V. and Tolmachev, V.A. (2000) Effective refractive index and composition of oxidized porous silicon films. *Materials Science and Engineering: B*, **69**, 142–148.
52. Vanstreels, K., Ciofi, I., Barbarin, Y., and Baklanov, M. (2013) Influence of porosity on dielectric breakdown of ultralow-*k* dielectrics. *Journal of Vacuum Science and Technology B*, **31** (050604), 1–5.
53. Wang, R.C., Chang-Liao, K.S., Wang, T.K., *et al.* (2008) Electrical conduction and TDDB reliability characterization for low-*k* SiCO dielectric in Cu interconnects. *Thin Solid Films*, **517** (3), 1230–1233.
54. Van Besien, E., Pantouvaki, M., and Zhao, L. (2012) Influence of porosity on electrical properties of low-*k* dielectrics. *Microelectronic Engineering*, **92**, 59–61.
55. Kim, E.S., Park, H.S., and Yoon, K.H. (2003) Porosity dependence of microwave dielectric properties of complex perovskite $(Pb_{0.5}Ca_{0.5})(Fe_{0.5}Ta_{0.5})O_3$ ceramics. *Materials Chemistry and Physics*, **79** (2–3), 213–217.
56. Liu, J., Gan, D., Hu, C., *et al.* (2002) Porosity effect on the dielectric constant and thermomechanical properties of organosilicate films. *Applied Physics Letters*, **81** (22), 4180–4182.
57. Bouledjnib, L. and Salah, S. (2010) Investigation of pores influence on dielectric constant value in low *k* materials using Monte Carlo method. *Moroccan Journal of Condenced Matter*, **12** (3), 199–203.

58. Elsner, A. and Hermann, H. (2007) Computer simulation and optimization of properties of porous low-*k* dieletrics. *Material Science – Poland*, **25** (4), 1193–1202.
59. Sebastian, M.T., Ubic, R., and Jantunen, H. (2015) Low-loss dielectric ceramic materials and their properties. *International Materials Reviews*, **60** (7), 392–412.
60. Nyfors, E.G. (2000) Cylindrical microwave resonator sensors for measuring materials under flow. Doctor of Science thesis, Helsinki University of Technology.
61. Allen, P.B. (2006) Electron transport, in *Conceptual Foundations of Material Properties: A Standard Model for Calculation of Ground- and Excited-State Properties* (eds S.G. Louie and M.L. Cohen), Elsevier, Amsterdam, pp. 165–218.
62. Macutkevic, J. and Banys, J. (2013) Comment on "giant dielectric permittivity of detonation-produced nanodiamond is caused by water." *Journal of Materials Chemistry C*, **1** (19), 3255–3256.
63. Penn, S.J., Alford, N.M., and Templeton, A. (1997) Effect of porosity and grain size on the microwave dielectric properties of sintered alumina. *Journal of American Ceramic Society*, **80** (7), 1885–1888.
64. Penn, S. and Alford, N. (1999) Ceramic dielectric for microwave applications, in *Handbook of Low and High Dielectric Constants and Their Applications* (ed. H.S. Nalwa), Elsevier, Amsterdam, pp. 493–530.
65. Zahn, M., Ohki, Y., Fenneman, D.B., *et al.* (1986) Dielectric properties of water and water/ethylene glycol mixtures for use in pulsed power system design. *Proceedings of the IEEE*, **74** (9), 1182–1221.
66. Park, J.-H., Park, J.-G., and Kim, Y. (2002) Computer simulation on the relations between the porosity and the microwave properties in dielectric ceramics. *Materials Research Society Symposia Proceedings*, **699**, 27–31.
67. Tuhkala, M., Juuti, J., and Jantunen, H. (2013) Method to characterize dielectric properties of powdery substances. *Journal of Applied Physics*, **114** (014108), 1–8.
68. Tuhkala, M., Juuti, J., and Jantunen, H. (2014) Determination of complex permittivity of surfactant treated powdery substances by an open-ended coaxial cavity resonator. *Powder Technology*, **256**, 140–145.
69. Tuhkala, M., Juuti, J., and Jantunen, H. (2014) An indirectly coupled open-ended resonator applied to characterize dielectric properties of $MgTiO_3$–$CaTiO_3$ powders. *Journal of Applied Physics*, **115** (184101), 1–5.
70. Conger, N.L. and Tung, S.E. (1964) Measurement of dielectric constant and loss factor of powder materials in the microwave region. *The Review of Scientific Instruments*, **38** (3), 384–386.
71. Nelson, S.O. and Bartley, P.G. (1998) Open-ended coaxial-line permittivity measurements on pulverized materials. *IEEE Transactions on Instrumentation and Measurement*, **47** (1), 133–137.
72. Tuhkala, M., Juuti, J., Teirikangas, M., *et al.* (2015) Loading efficiency equation for the estimation of dielectric properties of ceramic–polymer 0–3 composites. *Materials Today Communications*, **5**, 60–63.
73. Tuhkala, M., Juuti, J., Teirikangas, M., and Jantunen, H. (2015) Polymer–ceramic composite filler selection using mixing rules. *Journal of Applied Physics*, **117** (6), 1–5.
74. Sheen J. and Hong, Z.W. (2010) Microwave measurements of dielectric constants by exponential and logarithmic mixture equations. *Progress in Electromagnetics Research*, **100**, 13–26.
75. Tuhkala, M., Maček, M., Siponkoski, T., *et al.* (2015) The effect of $BaTiO_3$ particle shape on complex permittivity of $0.98MgTiO_3$–$0.02BaTiO_3$ composite powders at GHz frequencies. *Materials Research Bulletin*, **76**, 300–304.

3

Perovskites

K.P. Surendran[1] *and Rick Ubic*[2]
[1]*Materials Science and Technology Division, CSIR NIIST, Trivandrum, India*
[2]*Micron School of Materials Science and Engineering, Boise State University, Idaho, USA*

3.1 Introduction

Perovskites are ubiquitous in modern devices because their wide compositional range and structural variability gives rise to useful properties like piezoelectricity, pyroelectricity, ferroelectricity, superconductivity, colossal magnetoresistance, magnetodielectricity, half metallicity, proton conduction, catalysis, spin-dependent transport, and microwave resonance. They are also of interest as passive components in wireless telecommunications devices, substrates, or buffer layers for compound semiconductor heteroepitaxy, and films in tunable ferroelectric superlattice structures. The term "perovskite" is used to describe an arrangement of cations and an anion (typically oxygen), with the generic stoichiometry ABX_3, that is, isomorphous with $CaTiO_3$. Although $CaTiO_3$ is the mineral *perovskite*, its oxygen sublattice is distorted and the unit cell orthorhombic (*Pnma*). It is actually $SrTiO_3$, which has the aristotypical cubic perovskite structure ($Pm\bar{3}m$) usually pictured in basic texts. In this ideal cubic form, the A site is coordinated to 12 anions to form cuboctahedra. The A-site cations are usually large, electropositive metals. The B site is coordinated to six anions, forming octahedra, and are typically occupied by smaller, more highly charged species. Cations of the transition metals most commonly occupy the B site, although cations of p-block elements such as Al^{3+}, Si^{4+}, Ga^{3+}, Ge^{4+}, As^{5+}, Sb^{5+}, and Te^{6+} can also occupy this site. The anions are coordinated to two B-site cations, which are their nearest neighbors, and four A-site cations about 41% further away. The anion octahedra are corner-shared, which is a key feature of all perovskites. An example of the simple ABO_3 perovskite structural model is shown in Figure 3.1, and others abound in the literature [1, 2].

Microwave Materials and Applications, First Edition.
Edited by Mailadil T. Sebastian, Rick Ubic and Heli Jantunen.
© 2017 John Wiley & Sons, Ltd. Published 2017 by John Wiley & Sons, Ltd.

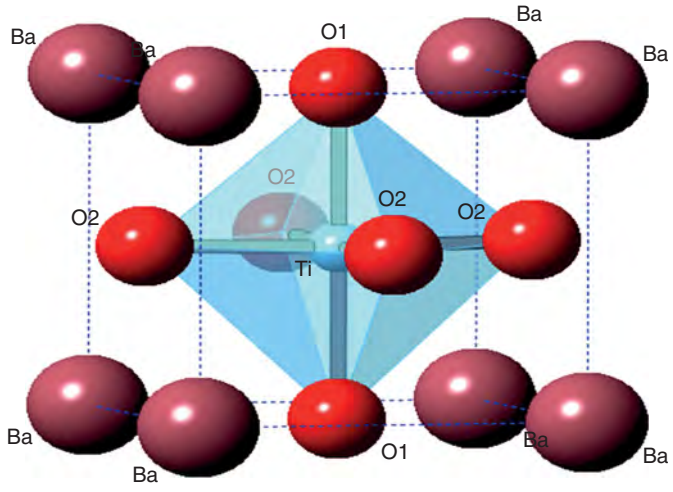

Figure 3.1 *Simple ABX_3 perovskite structure (e.g., $BaTiO_3$), where A (Ba) and B (Ti) are cations and X (O) is the anion.*

In a simple ABO_3 perovskite with only one ion at each site, possible combinations of A- and B-site charges include $A^{+1}B^{+5}O_3$ (e.g., $LiNbO_3$), $A^{+2}B^{+4}O_3$ (e.g., $CaTiO_3$), $A^{+3}B^{+3}O_3$ (e.g., $LaAlO_3$), and even the peculiar $B^{+6}O_3$ (e.g., ReO_3). Very few perovskites have the aristotypical cubic structure, rather a number of lower symmetry variants exist as a result of structural distortions due to either second-order Jahn–Teller (SOJT) effects or antiferrodistortive (AFD) instabilities. The SOJT distortions result in antiparallel (therefore polar) ionic displacements of cation and anion sublattices and typically yield piezoelectric or ferroelectric (FE) behavior, whereas AFD displacements involve rotations of rigid octahedra and influence the temperature stability of dielectric properties.

Complex perovskites of the type $(A'A'')(B'B'')O_3$ are also well-established materials for many functional applications [3]. These materials usually have divalent species on the A site, although some compositions also incorporate trivalent rare-earth cations on the A site with charge compensation conferred by the simultaneous incorporation of a trivalent species like Al^{+3} on the B site, for example, $(Ca_{1-x}Nd_x)(Ti_{1-x}Al_x)O_3$ [3]. Chemical ordering of different A or B cation species, driven by large differences in size and/or charge, can also result in a lowering of symmetry and marked changes in properties like dielectric loss. Octahedral tilting (Figure 3.2) occurs as a consequence of the mismatch in size between the A-site cation and BO_6 octahedra and can be predicted in many cases with great accuracy via the tolerance factor. Phase transitions between various ABO_3 perovskite structures with different tilt systems have been extensively studied [1]. The propensity of oxides to adopt the perovskite structures allows great latitude in chemical substitutions on both cation sites and, therefore, a great deal of control over properties.

There are hundreds of additional compositions that have either the A_3BX antiperovskite or BAX_3 inverse perovskite structures, not to mention all the perovskite-related mixed A_3O_9—$A_3A'O_6$ compounds and $A_{m-1}B_mO_{3m+1}$ layered Aurivillius, Ruddlesdden–Popper, and Dion–Jacobson structures that have ion-exchange, intercalation, ionic conduction, and luminescent properties.

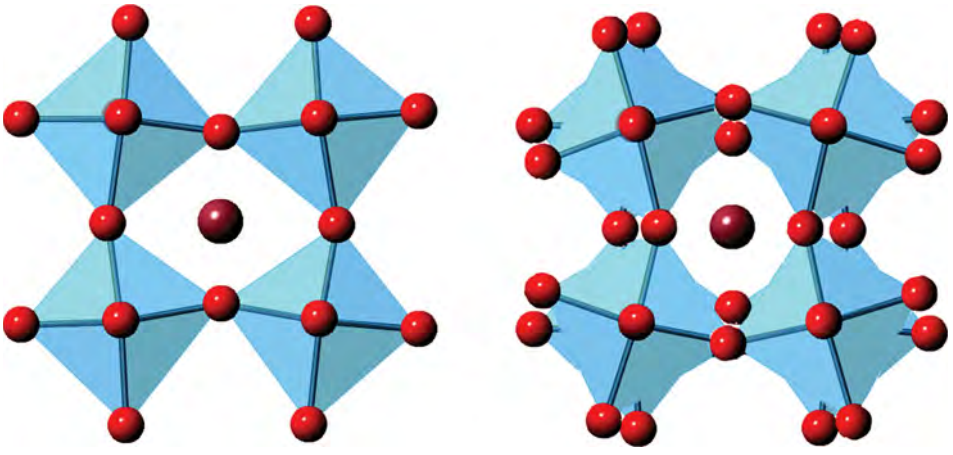

Figure 3.2 *Schematic representation of octahedral tilting in perovskites: (left) in-phase octahedral tilting about a single axis, (right) antiphase octahedral tilting about a single axis.*

3.2 Lattice Constant Prediction

In a recent study [4], an empirical model was derived which relates the ionic radii (A- and B-site cations and the X-site anion) to the pseudocubic lattice constant with an average absolute error of 0.806%:

$$a_{pc} = 0.05444 + 0.467016(r_A + r_X) + 1.30838(r_B + r_X) \tag{3.1}$$

where r_A, r_B, and r_X are the various ionic radii assuming twelvefold, sixfold, and twofold coordination, respectively.

Ubic [5] used a modified version of Equation (3.1), assuming sixfold coordination for all ionic species, which yielded results with an average absolute error of just 0.60%:

$$a_{pc} = 0.06741 + 0.49052(r_A + r_X) + 1.29212(r_B + r_X) \tag{3.2}$$

This mathematical model was derived with experimental data from 132 different perovskites, and it predicts lattice constants with accuracy even where second-order Jahn–Teller (SOJT) distortions would be expected. Its results are also slightly better than those calculated from the SPuDS program [6], which requires bond valence parameters as inputs.

Ubic and Subodh [7] later used a similar approach in modeling the lattice constants of orthorhombic perovskites in the space group *Pbnm*, which accounts for > 90% of observed orthorhombic perovskites [7]. The equations so derived, again assuming sixfold coordination for all constituents, yield results with absolute relative errors of 0.616%, 1.089%, and 0.714% for lattice constants a, b, and c, respectively:

$$a_o = 1.514921(r_A + r_X) + 1.310215(r_B + r_X) - 0.86631 \tag{3.3}$$

$$b_o = 0.082623(r_A + r_X) + 2.101275(r_B + r_X) + 1.114993 \tag{3.4}$$

$$c_o = 1.625883(r_A + r_X) + 2.470594(r_B + r_X) - 1.20754 \tag{3.5}$$

Cation displacements and ordering can further complicate the crystal structure and the presence of twinning can encumber the interpretation of electron diffraction patterns.

3.3 Tolerance Factor

Most perovskites are ionic compounds and the ions comprising them can be regarded, to a first approximation, as spheres with ionic radii *r*. Indeed, relationships between composition and structure have historically been based on the simple theory of Coulombic interactions, considering close-packing, space-filling, or symmetry arguments. Such reasoning inevitably led to radius-ratio rules. Roth [8], who studied $A^{3+}B^{3+}(O^{2-})_3$ compounds, used this approach to map structural stability fields for A—M_2O_3, B—M_2O_3, bixbyite, ilmenite, corundum, orthorhombic perovskite, rhombohedral perovskite, and three different hexagonal forms; however, the regions bordering different structural types were not well defined. Newnham [9] produced a similar map for $A^{2+}B^{4+}(O^{2-})_3$ compounds, while Giaquinta and zur Loye [10] used a combination of ionic radii and bond ionicities to improve the accuracy of the structural plot for $A^{3+}B^{3+}(O^{2-})_3$. The concept of the global instability index (*GII*) was introduced by Salinas-Sanchez *et al.* [11] to calculate the stability of the perovskite structure and the occurrence of octahedral tilting based on differences between experimental and calculated bond valence sums. The *GII* is defined as

$$GII = \left[\left\{ \sum_{i=1}^{N} \left(d_i^2 \right) \right\} \Big/ N \right]^{1/2} \tag{3.6}$$

where the discrepancy factor, d_i, is the difference between the formal valence and calculated bond valence for the *i*th ion and *N* is the number of ions in the unit cell. The *GII* is typically < 0.1 v.u. (valence units) for untilted perovskites and < 0.2 v.u. for tilted perovskites. Crystal structures for which $GII > 0.2$ are generally unstable. Woodward [12] later developed the POTATO program, which used geometrical considerations to predict the structure of tilted perovskites but required the tilt system, tilt angles, and octahedral bond distances as inputs. Lufaso and Woodward [6] later developed an algorithm, automated in the structure prediction diagnostic software (SPuDS), based on *GII* minimization to predict the structures and lattice parameters of perovskites from composition alone; however, because it relies solely on *GII*, in many cases (including $SrTiO_3$ and $CaTiO_3$) it is unable to predict the most stable perovskite structures [7] and does not currently support some species (e.g., Pm^{3+}) or *any* polyatomic ions (e.g., NH^{3+}). Zhang *et al.* [13] later attempted to use artificial neural networks in order to predict *GII* and the formability of perovskites.

The concept of the perovskite tolerance factor, *t*, was first suggested by Goldschmidt [14] and later developed by others, notably Megaw [15], to indicate the stability of various perovskite structures for a given set of ions. By assuming that the cation and anion sublattices are closely packed, the tolerance factor can be viewed as a measure of distortion of oxygen octahedra. As A—X bonds are in <110> and B—X bonds are in <001>, the lattice constant can be derived in two ways ($a' = 2(r_A + r_X)$ and $a'' = \sqrt{2}(r_B + r_X)$, respectively), the ratio of which is *t*:

$$t = \frac{a'}{a''} = \frac{r_A + r_X}{\sqrt{2}(r_B + r_X)} \tag{3.7}$$

At low values of t, a' tends to be underestimated and a'' overestimated, whereas at high values of t, the reverse is true. This discrepancy implies stretching/compressing of the A—X and B—X bonds, which has been demonstrated in bond valence (BV) calculations [5]. For a perfect regular octahedron, $a' = a''$ and $t = 1$.

One could also interpret the distortive effect of t by looking directly at octahedra. Geometrically, the ratio of edge length to half-height (the distance from the octahedral center to a vertex) in a regular octahedron is

$$\frac{\text{Edge}}{\text{Half-height}} = \frac{{}^1\!/_2 < 110 >}{{}^1\!/_2 < 001 >} = \frac{r_A + r_X}{r_B + r_X} = \frac{{}^a\!/_{\sqrt{2}}}{{}^a\!/_2} = \sqrt{2} \tag{3.8}$$

By normalizing this ratio by $\sqrt{2}$, the result is identical to the tolerance factor, t.

Lufaso and Woodward [6] later introduced the concept of a bond-valence-based tolerance factor:

$$t_{BV} = \frac{R_{0(A-X)} - B\ln(V_A/N_A)}{\sqrt{2}R_{0(B-X)} - B\ln(V_B/N_B)} \tag{3.9}$$

where $R_{0(\text{A-X})}$ and $R_{0(\text{B-X})}$ are the bond valence parameters (the length of a bond of unit valence) for A—X and B—X bonds, V_A and V_B are the ideal valence states of A and B cations, N_A and N_B are the coordinations of A ($N_\text{A} = 12$) and B ($N_\text{B} = 6$) cations, and $B = 0.37$. Because it relies on bond-valence data, this model also does not currently support some cation species or any polyatomic ions. Ye *et al.* [16] used a pattern-recognition method to find regularities in the formation and distortion of perovskites and Li *et al.* [17] used $r_\text{A} - r_\text{B}$ structure maps to study perovskite formability.

Colla *et al.* [18,19] and Reaney *et al.* [20] have shown that temperature stability in Ba- and Sr-based complex perovskites is fundamentally related to the onset and degree of octahedral tilting. Moreover, it can be tuned through ±300 ppm/°C without significantly altering Q or ε_r by manipulating the perovskite tolerance factor, t, from 1.01 to 0.93. Reducing t results in the onset of octahedral tilt transitions. The tolerance factor was first suggested by Megaw [15] to determine the stability of the perovskite phase for a given set of ions. In general, the perovskite phase is stable when the value of t is close to unity, which is true for $SrTiO_3$, for which $t = 1.00$. Reducing t results in the onset of octahedral tilt transitions and the lowering of symmetry.

The relationship between the tolerance factor and the pseudocubic perovskite lattice constant has been discussed at some length by Ubic [5], who derived an equation for tolerance factor based solely on the pseudocubic lattice constant (which can either be experimentally measured or calculated via Equation (3.4) and published values of r_B and r_X):

$$t = \frac{a_{pc} - 0.05444}{0.660460361(r_B + r_X)} - 1.981012 \tag{3.10}$$

With this equation it can be shown that, for example, the $t = 0.9729$ calculated for $CaTiO_3$ via Equation (3.9) using ionic radii published by Shannon [21] and corresponding to antiphase tilting according to Reaney *et al.* [20] would become $t = 0.9464$ or 0.9370 according to Equations (3.9) or (3.10), respectively, in either case indicating the presence of both in-phase and antiphase tilting, in agreement with the established structure [22]. An even more extreme example is that of $MgSiO_3$, the ideal tolerance factor (Equation 3.10) of

which would be $t = 1.0436$, suggesting an untilted structure. In this case, Equations (3.9) and (3.10) predict a tolerance factor of $t = 0.9391$ or 0.9462, respectively, again in keeping with the tilted *Pbnm* structure reported experimentally [23]. The large error resulting from Equation (3.10) in this case is probably due to the degree of uncertainty in the ionic radius value of Mg^{2+} in twelvefold coordination. Significantly, Equation (3.10) can also be used to derive the correct tilt structure for complex perovskites like $Ba(Sm_{1/2}Sb_{1/2})O_3$, for which Equations (3.7) and (3.9) fail.

3.4 Octahedral Tilting

Tolerances with regards to ionic size ratios within the ideal cubic structure are quite small, so values of $t < 1$ imply a distortion of the octahdera and are known to trigger various octahedral tilt transitions [20], which reduce crystal symmetry. This variation in structure gives rise to useful properties like ferroelectricity, superconductivity, colossal magnetoresistance, and spin-dependent transport.

As shown in Figure 3.2, tilting of this nature is generally categorized as either in-phase or antiphase with respect to a particular pseudocubic axis. In-phase tilts involve cooperative tilting of octahedra in the same sense about an axis whereas antiphase tilting involves successive octahedra along a given axis tilting alternately clockwise and anticlockwise. In-phase tilting in, say, a clockwise sense about one axis necessitates in-phase tilting about adjacent parallel axes in an anticlockwise sense; thus the periodicity in directions perpendicular to the tilt axis is doubled. For the same reason, antiphase tilting also results in period doubling in these directions plus the direction parallel to the tilt axis.

If $t \ll 1$, a rhombohedral sesquioxide forms instead, as in $MgTiO_3$ ($t = 0.81$), which adopts the ilmenite structure [15]. Colla *et al.* [18, 19, 24] and Steiner *et al.* [25] showed that it is the onset of tilt transitions in perovskite-based compounds that is the major factor influencing the behavior of the temperature coefficient of the dielectric constant (τ_ε) by allowing for steady thermal expansion with little modification of the octahedral volume. Continuing this theme, Reaney *et al.* [20] pooled previously published dielectric data for niobate and tantalate perovskites, correlated them with t, and analysed the tilt systems via electron diffraction to show the strong influence that t has on τ_ε by virtue of its effect to prompt tilting. They observed that perovskites with $t < \sim 0.985$ contained axes about which oxygen octahedra were tilted in an antiphase arrangement, causing cell doubling in the three pseudocubic directions. Similarly, perovskites for which $t < \sim 0.965$ undergo a further tilt transition whereby octahedra are tilted in-phase about one or more axes as well. Perovskites for which $t > \sim 0.985$ were not observed to contain a tilt superlattice; however, many researchers have reported aluminates [26], cuprates [27], nickelates [28], and ferrites [29] with tilted structures despite having $t \sim 1$. For example, $LaAlO_3$ has been reported in the $R\bar{3}c$ system [26] with octahedra tilted 5.0° about the pseudocubic [111] (tilt system $a^-a^-a^-$) yet it has a $t = 1.0166$–1.0540. According to Woodward [30], the rhombohedral $a^-a^-a^-$ tilt system is stabilized by highly charged A-site cations and small tilt angles. The tilt about the pseudocubic <111> in $Sr_{1-3x/2}Ce_xTiO_3$ ($0 \leq x \leq 0.20$) materials is reportedly [31] only $0 \leq \phi \leq 4.7°$, which is even smaller than that reported in $LaAlO_3$. At higher tilt angles, the orthorhombic $a^+b^-b^-$ tilt system should be preferred, as in the case of $La(Zn_{1/2}Ti_{1/2})O_3$, which has an in-phase tilt angle of 8.3° [32].

These tilt systems are most conveniently described using the notation scheme developed by Glazer [33]. This notation uses three letters (*a*, *b*, and *c*), each with a superscript of "0", "+", or "–". These three letters refer to the magnitude of the tilts about the three <100> crystallographic directions of the cubic (or pseudocubic) perovskite structure. If the letters are the same then the magnitude of the tilts about these axes are the same. A superscript of "0" means that there is no tilting about this axis. A "+" means that the tilting about this axis is in-phase, whereas a "–" indicates that the tilting about this axis is antiphase. For example, $a^0a^0a^0$ means there is no tilting about any axis while the notation $a^+b^-b^-$ means there is antiphase tilting of equal magnitude about the *b* and *c* axes and in-phase tilting of a different magnitude about the *a* axis.

3.5 Simple Perovskites

Several of the archetypal ABO_3 (A = Ba, Sr, Ca; B = Ti, Zr, Hf) type dielectrics have high dielectric constants, which will be discussed in Chapter 4. The simplest of them all, barium titanate ($BaTiO_3$), has the ideal cubic perovskite structure above the Curie point ($T_C \sim 130\,°C$). On cooling below T_C, the oxygen and titanium ions shift from their ideal positions, resulting in a ferroelectric tetragonal phase [34]. Tetragonal $BaTiO_3$, in spite of being ferroelectric, can be tailored into a low-loss paraelectric through suitable substitutions. For example, Feteira *et al.* [35] found that $BaTiO_3$ substituted with 8 vol.% Ga crystallized with hexagonal symmetry in space group $P6_3/mmc$.

3.5.1 $LnAlO_3$ Type Materials

A psuedocubic crystal structure, low dielectric constant, and dielectric loss qualifies $LnAlO_3$ type materials for applications as substrates in physical deposition techniques [36]. The $LnAlO_3$ (Ln = La, Pr, and Nd) compounds crystallize with rhombohedral symmetry while those with Ln = Y, Er, Ho, Dy, Nd, and Sm have an orthorhombic symmetry [37]. As shown in Figure 3.3, the dielectric constant of $LnAlO_3$ increases as a function of the tolerance factor, but the rate of increase is different in different crystal-structure regimes. In addition, the non-zero magnetic susceptibility of rare-earth aluminates has an adverse effect on their quality factor. $LaAlO_3$ is reported to possess the best dielectric properties among rare-earth aluminates. There were several attempts to compensate the high negative τ_f of $LaAlO_3$ through the addition of positive τ_f dielectrics like $SrTiO_3$, $CaTiO_3$, and TiO_2. Cho *et al.* [38] found that in the $LaAlO_3$–$SrTiO_3$ system, the dielectric properties of the intermediate mixture-phase compositions showed a non-monotonic behavior. Other groups have attempted to lower the sintering temperature of $LaAlO_3$–$SrTiO_3$ ceramics [39]. In $(1-x)LaAlO_3$–$xTiO_2$ mixtures, the thermostable composition corresponding to $x = 0.5$ showed interesting microwave dielectric properties ($\varepsilon_r = 37$, $Qf = 37\,000$ GHz, and $\tau_f = 1$ ppm/°C) [40]. On the other hand, a composition-induced structural transition was observed by Khalyavin *et al.* in the $(1-x)CaTiO_3$–$xLaAlO_3$ system [41]. They reported that with an increasing amount of $LaAlO_3$ in the mixture, the oxygen octahedra tilt accompanied by a space group change from *Pnma* to *Inma* between $x = 0.4$ and 0.5 and then from *Inma* to *R*3*c* for $0.5 \leq x \leq 0.6$.

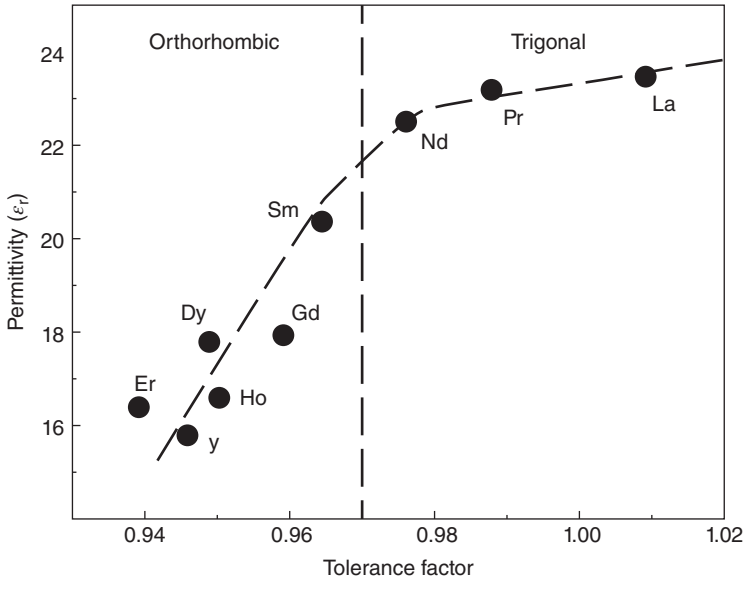

Figure 3.3 *Variation of ε_r as a function of tolerance factor t in $LnAlO_3$. Source: Cho* et al. *2012 [37]. Reproduced with permission from Cambridge University Press.*

$NdAlO_3$ is another prominent dielectric among lanthanide aluminates, with interesting microwave dielectric properties ($\varepsilon_r = 22$, $Qf = 58\,000$ GHz and $\tau_f = -35$ ppm/°C) [37]. Here also the high negative τ_f can be compensated by mixing with $CaTiO_3$, TiO_2, Nd_2O_3, etc. Jancar *et al.* [42] showed that in $(1 - x)CaTiO_3$–$xNdAlO_3$ solid solutions, owing to the similar ionic radii, Nd^{3+} can be substituted by Ca^{2+} and Al^{3+} by Ti^{4+} according to $Ca_{1-x}Nd_xTi_{1-x}Al_xO_3$. The specific composition $Ca_{0.7}Nd_{0.3}Ti_{0.7}Al_{0.3}O_3$ is temperature-stable with $Qf = 33\,000$ GHz, $\varepsilon_r = 44$, and $\tau_f = 0$ ppm/°C [43]. In this composition, the high-quality factor can only be achieved by effectively minimizing dislocations, twin or antiphase boundaries, and the formation of the parasitic $CaAl_{12}O_{19}$ phase [42].

3.5.2 $Ag(Nb_{1-x}Ta_x)O_3$ Type Materials

Dielectrics in the $Ag(Nb_{1-x}Ta_x)O_3$ system are difficult to form in phase-pure form [44]. One of the reasons for this difficulty could be the volatilization of silver at high temperatures, which can either be controlled by processing in an oxygen atmosphere [45] or by adopting wet chemical methods thereby lowering the sintering temperature [46]. The sintering temperature has been reduced to 900 °C by the addition of Cu [47]; however, copper can be detrimental to the dielectric properties [48]. Most of the compositions in this series possess high-temperature coefficients of permittivity (τ_ε). Valant *et al.* [49] found a methodology to control τ_ε by using a coarse-grained mixture of 45 wt% $Ag(Nb_{0.65}Ta_{0.35})O_3$ and 55 wt% $Ag(Nb_{0.35}Ta_{0.65})O_3$. The microwave dielectric properties of this composition were $\varepsilon_r = 430$, $Qf = 700$ GHz, and $\tau_\varepsilon = 40$ ppm/°C. A detailed description of the dielectric properties of $Ag(Nb_{1-x}Ta_x)O_3$ type perovskites is given in Chapter 4.

3.5.3 Ca-Based Perovskites

Despite possessing low dielectric loss and high permittivity, the perovskites based on $Ln_{2/3}TiO_3$ were reported to be unstable, obviously due to the formation of vacancies in the A cationic sublattice [50]. Additives such as $CaTiO_3$ [51] or $LaAlO_3$ [52] were used to stabilize the $La_{2/3}TiO_3$ phase and improve the dielectric properties. In the case of $CaTiO_3$ addition, the resultant ceramic can be stoichiometrically represented as $Ca_{1-x}La_{2x/3}\square_{x/3}TiO_3$, where $\square$ is an A-site cation vacancy. These materials showed high ε_r of about 100 and $Qf > 10\,000$ GHz, but high positive τ_f values [53]. Unlike this system, the dielectrics in the $CaTiO_3$—$Li_xLn_{1-x}TiO_3$ system are high-permittivity distorted perovskites with both positive and negative τ_f values [54]. Liu *et al.* [55] reported that a few compositions in this system could yield high permittivities, moderate Q-factors and small τ_f values. In particular, the compound $Ca_{0.4}(Li_{1/2}Nd_{1/2})_{0.6}TiO_3$ had $\varepsilon_r = 113$, $Qf = 5000$ GHz, and $\tau_f = 8$ ppm/°C. Since most of these dielectrics have high dielectric constants, a detailed discussion on their structure-property relationship is given in Chapter 4.

3.6 Cation Ordering

If either the A or B sites are occupied stoichiometrically by two ionic species, the term *complex perovskite* applies. Chemical ordering then refers to the phenomenon whereby the two A- or B-site species occupy crystallographically distinct sites, thus reducing the symmetry of the crystal and changing its properties. The ordering is generally driven by large differences in size and/or charge between the two cation species.

The A-site cation ordered perovskites are mostly ferroelectric [56] and hence excluded in this review. The B-site ordered perovskites, which comprise by far the largest preponderance of ordered perovskites in the literature, can be further categorized as follows:

1:1 Ordered perovskites: $A^{2+}(B^{3+}_{1/2}B^{5+}_{1/2})O_3$, $A^{2+}(B^{2+}_{1/2}B^{6+}_{1/2})O_3$, $(A^{1+}_{1/2}A^{3+}_{1/2})BO_3$

1:2 Ordered perovskites: $A^{2+}_{1/3}B^{5+}_{2/3}$ and $A^{6+}_{1/3}B^{3+}_{2/3})O_3$

1:3 Ordered perovskites: $A^{2+}(B^{1+}_{1/4}B^{5+}_{3/4})O_3$

1.2.1 Ordered perovskites: $A^{2+}(B^{2+}_{1/4}B^{5+}_{2/4}B^{4+}_{1/4})O_3$

Ordering of this type prefers $\{111\}$ pseudocubic planes, such that the B and B′ cations occupy sites on alternate $\{111\}$ planes repeating in a ratio consistent with the stoichiometry. Thus, ordering preserves all but one of the cubic <111> triads and reduces the symmetry to trigonal. Other structural effects can reduce the symmetry still further. If the ratio of B to B′ is 1:1, the ordering that results has the so-called rock-salt geometry.

Over the last few decades, a plethora of mainly 1:1 ordered complex perovskite materials have been discovered. Where two different ions occupy the octahedral site in approximately equal amounts, ordering driven by differences in cation charge and size is common, and the resulting $A(B_{1/2}B'_{1/2})O_3$ (or $A_2BB'O_6$) oxides are referred to as *double perovskites*. The structure of such 1:1 ordered compounds was studied by Howard *et al.* [57] using a group theoretical approach.

On the other hand, if the B site is shared by two ions in the ratio 1:2, then the resultant structure could be referred to as a *triple perovskite*, such as $A(B_{1/3}B'_{2/3})O_3$. The importance of these 1:2 B-site systems is due to their relaxor ferroelectric and piezoelectric

properties (e.g., $PbMg_{1/3}Nb_{2/3}O_3$) and their application as temperature-compensated, low-loss dielectrics in microwave communications devices (e.g., $BaZn_{1/3}Ta_{2/3}O_3$). For the Ba-based members of this family (e.g., $Ba(Zn_{1/3}Ta_{2/3})O_3$, $Ba(Mg_{1/3}Ta_{2/3})O_3$, $Ba(Mg_{1/3}Nb_{2/3})O_3$, etc.), small alterations in the degree and length scale of ordering can induce large changes in dielectric loss. The high losses of partially ordered $BaZn_{1/3}Ta_{2/3}O_3$ (BZT) are believed to arise from the formation of elastically strained ordering-induced domain boundaries. These losses can be improved by either reducing the volume of such boundaries via extended high-temperature heat treatments or the stabilization of the boundaries via the addition of small concentrations of $BaZrO_3$, leading to partial segregation of Zr^{4+} cations [58]. Additional anomalies in the loss at greater $BaZrO_3$ concentrations are associated with a cation ordering transition from 1:2 to a 1:1 double perovskite form. A very comprehensive survey of simple and complex perovskites, including their structures and properties, is given in the text by Sebastian [59].

Perovskites with appreciable 1:3 cation order are very few in number, as in most cases the occurrence of the ordered state is thermodynamically unstable [60].

One of the reasons of the less common occurrence of A-site ordered dielectrics lies in their restrictions in oxidation states. Since B-site cations are typically transition metals or fourth or fifth row *p*-block metals they have a large number of possible oxidation states, and charge differences of 3 or 4 are not uncommon. Meanwhile, the type of elements that usually occupy the A sites (alkali, alkali earth, lanthanide, Pb^{2+}, or Bi^{3+} cations) rarely differ in charge by more than 2. While A-site ordering in perovskites is most commonly reported as layering on pseudocubic $\{100\}$, the so-called layered geometry [61], A-site ordering can theoretically also occur on either $\{110\}$ (columnar) or $\{111\}$ (rock salt). For example, $NaLaMgWO_6$ orders with a layered geometry [61], whereas $CaFeTiO_6$ orders in a columnar fashion [62] and $NaBaLiNiF_6$ orders with the rock-salt geometry [63].

3.6.1 1:1 Ordered Perovskites

If the B site of the perovskite accommodates two different species in equal proportions with a charge difference of 2 (e.g., La^{3+} and Ta^{5+}) or, more usually, 3 (e.g., Mg^{2+} and Ta^{5+} or Zn^{1+} and Ti^{4+}), the resultant structure can show 1:1 ordering under suitable conditions below the order–disorder phase transition temperature. In order to accommodate this order, the crystal periodicity must be doubled; hence, these perovskites are commonly referred to as *double perovskites*. They have the general formula $AB_{1/2}B'_{1/2}O_3$ (or $ABB'O_6$), where B and B′ are the two different cations in octahedral coordination situated on distinct crystallographic sites. The cation order maximizes the separation of similar ions. With this peculiar arrangement, the intermediate O^{2-} anions can satisfy the different bond length requirements of the two cations B′ and B″ by moving towards the smaller ion [60]. This structure can be viewed in terms of an ordered alternation of B′ and B″ cation layers perpendicular to the [111] cubic direction (see Figure 3.4).

It was reported [64] that Ba, Sr, and Ca compounds of this type occur with an ordered arrangement of B and B′ cations when

$$K = \frac{|R_B - R_{B'}|}{R_B} \geq 0.09 \tag{3.11}$$

where R_B and $R_{B'}$ are the ionic radii of B and B′ cations, respectively.

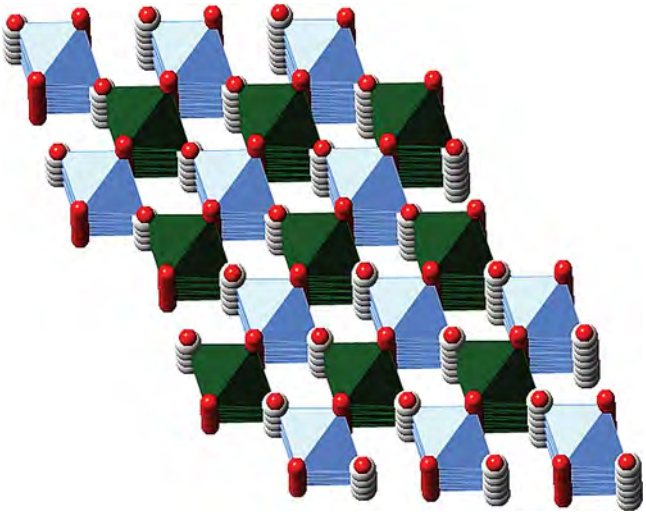

Figure 3.4 *1:1-Ordered double-perovskite $A(B'_{1/2}B''_{1/2})O_3$ structure viewed along $\langle 110\rangle_c$ to highlight the doubled $\langle 111\rangle$ repeat of the B′ and B″ cation sites. This figure is also shown in the Plate Section.*

3.6.1.1 $Ba^{2+}(Ln^{3+}_{1/2}Ta^{5+}_{1/2})O_3$

The structures of ordered perovskites based on $Ba(Ln_{1/2}Ta_{1/2})O_3$ (Ln = Y^{3+} or trivalent lanthanide cation) was the subject of some considerable debate during the time immediately following their first synthesis as single crystals by Galasso *et al.* [65]. The Ba-based ordered 1:1 tantalate double perovskites can crystallize in either cubic, tetragonal, orthorhombic, or monoclinic symmetries depending on the size of the lanthanide species [65–68].

In 2007, Saines *et al.* [66] used neutron diffraction and synchrotron X-ray diffraction analysis to demystify the crystal structures of 14 members of the Ba_2LnTaO_6 series at room temperature. As shown in Figure 3.5, the structure across the series changes symmetry from monoclinic (*I2/m*) to tetragonal (*I4/m*) to cubic ($Fm\bar{3}m$), in general agreement with previous findings; however, Ba_2LaTaO_6 was found to be an exception, consisting of a mixture of phases with *I2/m* and $R\bar{3}$ symmetries. It was found [67] that the La- and Pr-containing compounds had an intermediate rhombohedral phase whereas the other tantalates had a tetragonal intermediate. This difference in symmetry appears to be a consequence of the larger size of the La^{3+} and Pr^{3+} cations compared to the other lanthanides [67].

The microwave permittivities of the Ba_2LnTaO_6 system vary in the range 32–39, and *Qf* values can reach up to ~50 000 GHz [68, 69]. The microwave dielectric properties of this system are given in the Appendix at the end of Volume II. In a detailed investigation, Khalam [69] reported that the addition of a small amount (0.5 wt%) of additive (MgO, ZnO, or CuO) significantly improved the quality factor of $Ba(Sm, Ta)O_6$ ceramics. The temperature coefficient of resonant frequency (τ_f) changes drastically as a function of the tolerance factor, as shown in Figure 3.6. In the figure the horizontal dashed line corresponds to $\tau_f = 0$ and the vertical dashed lines indicate approximately the critical values of *t* according to Reaney

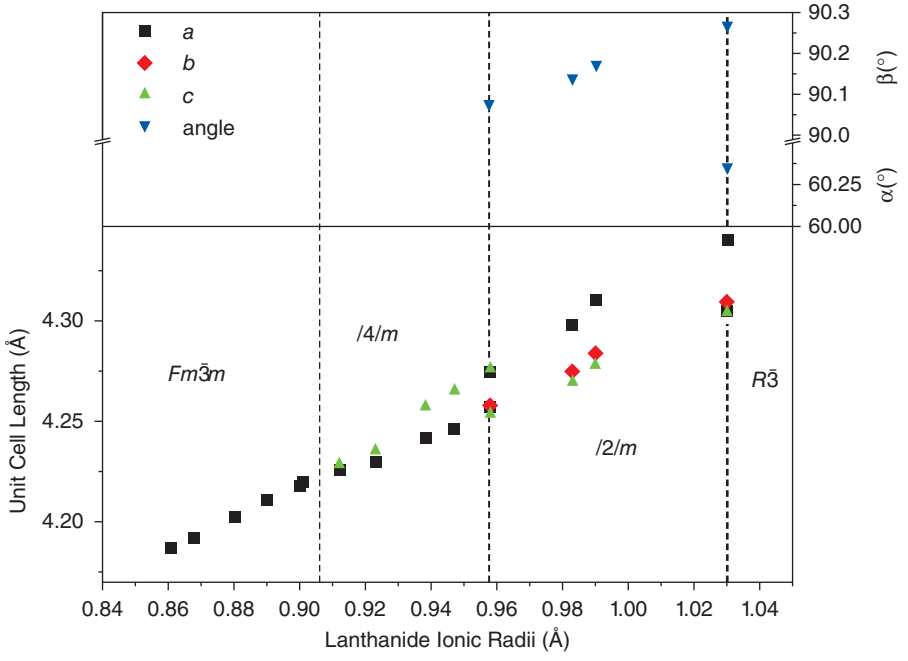

Figure 3.5 *Unit-cell parameters for Ba_2LnTaO_6 reflecting the increase in symmetry of the various members of this series with decreasing lanthanide ionic radius. Source: Saines* et al. *2007 [66] Reproduced with permission from Elsevier.*

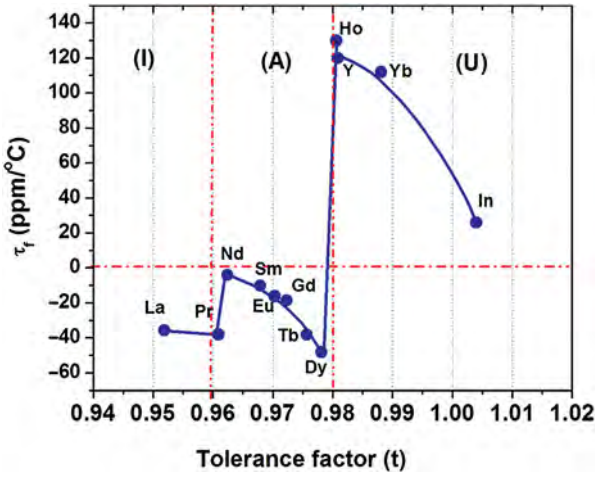

Figure 3.6 *The τ_f as a function of tolerance factor (t) for Ba_2LnTaO_6 ceramics. Source: Khalam* et al. *2008 [68]. Reproduced with permission from John Wiley & Sons.*

et al. [20], which correspond to octahedral tilt transitions. In sharp contrast to Ba_2LnNbO_6, which has smaller values of τ_f, the τ_f values of Ba_2LnTaO_6 vary from 120 ppm/°C to –48 ppm/°C, depending on the lanthanide ion and *t*. Khalam [69] also calculated the Ln—O bond lengths and bond valences of these compounds and correlated them with ionic radius and *t*. It was shown that ε_r increases linearly with increasing bond length except in the case of Ln = La. To a large extent *t* determines the tilting of an oxygen octahedral, which in turn influences the microwave dielectric properties of these compounds [69].

3.6.1.2 $Ba^{2+}(Ln^{3+}_{1/2}Nb^{5+}_{1/2})O_3$

Until the beginning of this millennium there were few reports on the crystal structure and electrical properties of complex perovskites of the form $Ba(B_{1/2}Nb_{1/2})O_3$ (Ln = Y^{3+} or trivalent lanthanide cation); however, the controversies about the structure and properties of these materials were just as alive as they were for their tantalate counterparts. This issue first surfaced in the work of Galasso [70], who reported that these compounds are face-centered cubic with the $(NH_4)_3FeF_6$ structure, but synchrotron X-ray diffraction patterns of some of the compounds showed splitting of the main reflections, indicating a non-cubic symmetry [71].

Like its tanatale analog, Ba_2NdNbO_6 undergoes phase transitions from monoclinic to tetragonal to cubic symmetry when heated above ambient temperatures [71]. Upon heating, Ba_2NdNbO_6 undergoes a first-order phase transition from *I2/m* (monoclinic) to *I4/m* (tetragonal) symmetry (Figure 3.7), with these two phases coexisting between 235 and 355 °C. Above 425 °C the structure of Ba_2NdNbO_6 was found to be cubic ($Fm\bar{3}m$) by Saines *et al.* [71],who suggested that π-bonding is the cause of the tetragonal symmetry at intermediate temperatures.

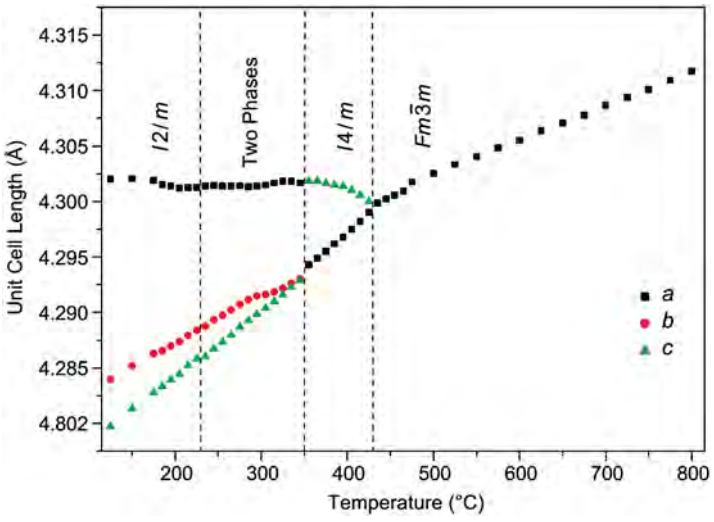

Figure 3.7 *Temperature dependence of the reduced lattice parameters for Ba_2NdNbO_6 obtained from analysis of synchrotron X-ray diffraction data. Source: Saines* et al. *2007 [71]. Reproduced with permission from Elsevier.*

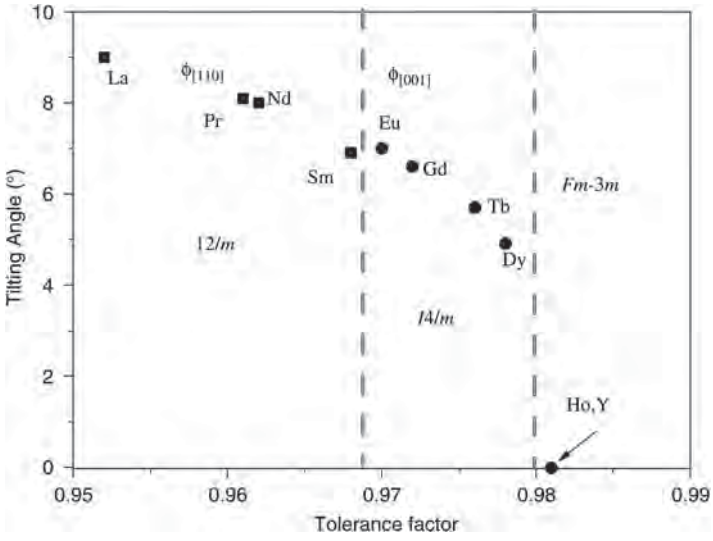

Figure 3.8 *Calculated tilting angles in Ba_2LnNbO_6 (Ln = La, Pr, Nd, Sm, Eu, Gd, Tb, Dy, Ho, and Y) as a function of the tolerance factor, t. Source: Fu and Ijdo 2006 72]. Reproduced with permission from Elsevier.*

Subsequent studies [72] revealed that the room-temperature symmetry of $Ba(Ln_{1/2}Nb_{1/2})O_3$ can be cubic, tetragonal, orthorhombic, or monoclinic, depending on the tolerance factor. The symmetry increases as the ionic radius of the lanthanide decreases, that is, substitution with higher atomic-number lanthanides. An increase in the tolerance factor indicates that the volume of the BO_6 octahedra are better matched to the size of the AO_{12} cuboctahedra, thereby reducing the need for the octahedral tilting. Since octahedral tilting is primarily responsible for lowering the symmetry, the symmetry tends to increase as the B-type cation gets smaller. This fact has been nicely illustrated by Fu and Ijdo [72], who calculated the average tilt angles and found them to increase with increasing ionic radii of the lanthanide (Figure 3.8).

The microwave dielectric properties of Ba_2LnNbO_6 have been investigated [73, 74] and are found to be correlated to bond valence and tolerance factor. The microwave dielectric properties of these compounds are given in the Appendix given at the end of Volume 2. The Ba_2LnNbO_6 dielectrics are mostly thermostable with $|\tau_f| \leq 15$ ppm/°C with the exception of Ba_2PrNbO_6. Among the Ba-based double perovskite niobates, Ba_2TbNbO_6 has the highest Q-factor ($Qf = 52\,400$ GHz) [73].

3.6.1.3 $Sr^{2+}(Ln^{3+}_{1/2}Ta^{5+}_{1/2})O_3$

In 2002, Kanaiwa *et al.* [75] studied the crystal structure of $Sr^{2+}(Ln^{3+}_{1/2}Ta^{5+}_{1/2})O_3$ using the Rietveld refinement technique and found that their crystal symmetry is monoclinic ($P2_1/n$) with a rock-salt ordering of Ln and Ta; however, in 2006, Khalam and Sebastian [76] concluded that Sr_2YTaO_6 and Sr_2LaTaO_6 have rhombohedral symmetry ($R3m$). Indeed,

the crystal structure of Sr_2YTaO_6 has also been disputed [77, 78]. A few authors [79, 80] reported Sr_2GaTaO_6 as cubic in the space group $Fm\bar{3}m$, but it was later shown to be tetragonal (*I4/m*) [81]. In short, Sr_2LnTaO_6 dielectrics are expected to have rhombohedral, monoclinic, or tetragonal structures [64, 65] depending on the ionic radii or tolerance factor.

It was reported [59] that the addition of a small amount of Nb_2O_5 could improve the densification of Sr_2LnTaO_6 ceramics. The microwave dielectric properties of Sr_2LnTaO_6 ceramics are given in the Appendix. The Sr_2YTaO_6 analog has the highest quality factor (54 300 GHz). The τ_f values decrease with decreasing Ln ionic radii.

It has long been established that engineered extrinsic cation vacancies can provide additional pathways for the interdiffusion of the B-site cations and can, consequently, enhance the kinetics of the ordering process. Khalam and Sebastian [59, 76] reported that a slight non-stoichiometry of A- or B-site ions has considerable influence on the microwave dielectric properties of Sr_2LnTaO_6 ceramics. They prepared $Sr_{1+x}(Eu_{0.5}Ta_{0.5})O_3$, $Sr(Eu_{0.5+y}Ta_{0.5})O_3$, and $Sr(Eu_{0.5}Ta_{0.5+z})O_3$, with $x = y = z = -0.02$ – 0.1 by a conventional solid-state route. The stoichiometric composition $Sr(Eu_{0.5}Ta_{0.5})O_3$ has $\varepsilon_r = 30$, $Qf = 45500$ GHz, and $\tau_f = -63$ ppm/°C. It was found that ε_r of $Sr_{1+x}(Eu_{0.5}Ta_{0.5})O_3$ and $Sr(Eu_{0.5}Ta_{0.5+z})O_3$ decreases for both positive and negative values of x and z, respectively. On the other hand, the ε_r of $Sr(Eu_{0.5+y}Ta_{0.5})O_3$ decreases with positive values of y (excess of Eu) and increases for Eu deficiency. Interestingly, the Q-factor of $Sr_{1+x}(Eu_{0.5}Ta_{0.5})O_3$ increases when x becomes negative (Sr deficient), reaching a maximum (59 500 GHz at $x = -0.005$), and decreases for positive values of x (Sr rich). The Q-factor of $Sr(Eu_{0.5+y}Ta_{0.5})O_3$ and $Sr(Eu_{0.5}Ta_{0.5+z})O_3$ increase for positive values of y and z, respectively (i.e., excess Eu and Ta). These materials showed maximum Qf values for $y = 0.015$ (67 000 GHz) and $z = 0.01$ (56 500 GHz), respectively. Khalam and Sebastian have also made solid solutions between positive and negative τ_f materials in order to tune the resultant τ_f to zero [59, 76], successfully producing $(Sr_{0.05}Ba_{0.95})(Y_{0.5}Ta_{0.5})O_3$ ($\tau_f = -0.4$ ppm/°C) and $(Sr_{0.15}Ba_{0.85})(Yb_{0.5}Ta_{0.5})O_3$ ($\tau_f = -0.8$ ppm/°C).

3.6.1.4 $Sr^{2+}(Ln^{3+}_{1/2}Nb^{5+}_{1/2})O_3$

During the late 1980s, Takata and Kageyama studied $Sr(B^{3+}_{1/2}B'^{5+}_{1/2})O_3$ ceramics due to their potential applications as microwave dielectrics and found that the microwave dielectric properties of $Sr(B^{3+}_{1/2}Nb^{5+}_{1/2})O_3$ were inferior to those of its tantalate counterpart [82]. Later, Khalam and Sebastian [83] also made a detailed investigation of strontium-based ordered double perovskite niobates. They added CeO_2 as a sintering aid to most of these ceramics, which are difficult to sinter otherwise, and found that the charge difference of 2 and the B-site cation size difference, which ranged from 0.16 to 0.39 Å, was primarily responsible for the observed B-site cation ordering. The intensity of superstructure reflections, which can be thought of as a signature of the cation ordering, decreased gradually from In to Nd in the series. The $Sr(B_{1/2}Nb_{1/2})O_3$ ceramics with B = Sm, Eu, Gd, Tb, Dy, and Ho are isostructural with $Sr(Sm_{1/2}Ta_{1/2})O_3$, which has tetragonal symmetry with space group *I4/m*, although $Sr(Y_{1/2}Nb_{1/2})O_3$, $Sr(Er_{1/2}Nb_{1/2})O_3$, $Sr(Yb_{1/2}Nb_{1/2})O_3$, and $Sr(In_{1/2}Nb_{1/2})O_3$ are reportedly isostructural with $Sr(Ni_{0.5}W_{0.5})O_3$ [84], crystallizing in the orthorhombic system with space group *Pnma*, in which ordering is forbidden.

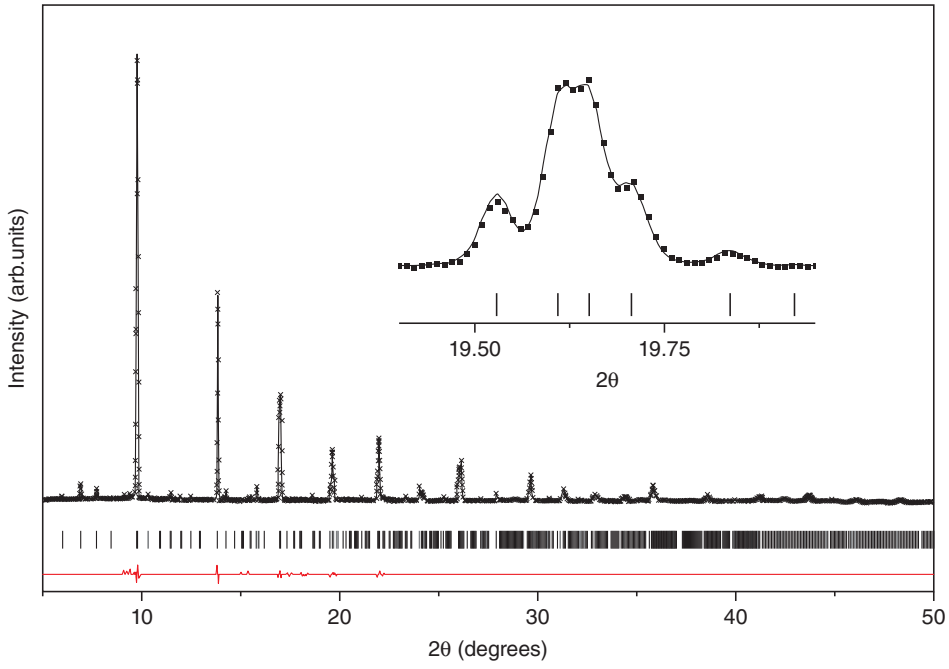

Figure 3.9 *Synchrotron X-ray diffraction pattern (crosses) recorded from Sr_2YNbO_6 powder. The X-ray wavelength was 0.4973 Å. The pattern was fitted (continuous line) assuming a monoclinic structure with $P2_1/n$ space-group symmetry. The markers below the pattern indicate the expected peak positions and the curve below these markers show the difference between the observed and calculated patterns. The inset shows detail of the fit near the group of reflections indexed as 440 in the doubled (~ 8.25 Å) pseudocubic perovskite cell. Source: Howard* et al. *2005 [78]. Reproduced with permission of the International Union of Crystallography.*

On the other hand, Howard *et al.* [78] reported monoclinic symmetry ($P2_1/n$) for $Sr(Y_{1/2}Nb_{1/2})O_3$. They synthesized the double perovskite using solid-state methods and X-ray patterns were recorded at different sample temperatures from 100 to 300 K. The 300 K pattern is shown in Figure 3.9. As shown, the pattern was well fitted using the Rietveld refinement method [78] assuming B-site ordering in $P2_1/n$, the most common space group of order perovskites derived from disordered forms in *Pnma*.

The microwave dielectric properties of $Sr(B_{1/2}Nb_{1/2})O_3$ ceramics are given in the Appendix. The ε_r is found to increase linearly with increasing B-site ionic radii, with the exception of La [83]. The $Sr(B_{1/2}Nb_{1/2})O_3$ ceramics have quality factors (Qf) in the range 3250–44 000 GHz. A few specific $Sr(B_{1/2}Nb_{1/2})O_3$ compositions with B = La, Pr, Nd, and Gd have poor ordering and show relatively poor quality factors as compared to other ceramics in the system. Among the Sr-based ordered double perovskite niobates, $Sr(Eu_{1/2}Nb_{1/2})O_3$ has the highest quality factor (44 000 GHz). The τ_f of $Sr(B_{1/2}Nb_{1/2})O_3$ ceramics varies from –20 to –73 ppm/°C. The τ_f becomes increasingly negative as the ionic radii of B-site ions decreases. Besides CeO_2, Khalam and Sebastian [83] added liquid-phase sintering promoters like B_2O_3 into $Sr(B_{1/2}Nb_{1/2})O_3$ in order to enhance their sintarability. It was found that the $|\tau_f|$ of both CeO_2- and glass-added ceramics increases linearly with

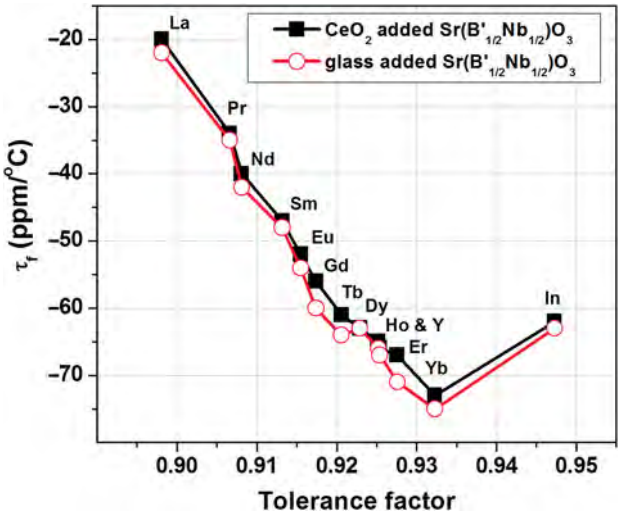

Figure 3.10 *The variation in the τ_f of CeO_2-added and B_2O_3-added $Sr(B_{1/2}Nb_{1/2})O_3$ ceramics versus the tolerance factor. Source: Khalam and Sebastian 2006 [83]. Reproduced with permission from John Wiley & Sons.*

an increase in the tolerance factor, with the exception of $Sr(In_{1/2}Nb_{1/2})O_3$, as shown in Figure 3.10.

3.6.1.5 $Ca^{2+}(Ln^{3+}_{1/2}Ta^{5+}_{1/2})O_3$

Similar to other double perovskites, $Ca(B_{1/2}Ta_{1/2})O_3$ ceramics also have an ordered structure marked by the presence of {odd, odd, odd} superlattice reflections in diffraction patterns. Several Russian researchers [85, 86] studied crystal structure of these dielectrics in a systematic way and found that $Ca(B_{1/2}Ta_{1/2})O_3$ ceramics (B = La, Pr, Nd, Sm, Eu, Gd, Tb, Dy, Ho, Y, Er, Yb, and In) have monoclinic symmetry with the space group $P2_1/n$. Both Filipev and Fesenko [64] in 1965 and Khalam *et al.* [87] in 2007 found that, unlike their Ba or Sr counterparts, $Ca(B_{1/2}Ta_{1/2})O_3$ ceramics present the possibility of intersubstitution between A- and B-site species because of their comparable ionic sizes. Interestingly, Ca^{2+} and La^{3+} have ionic radii of 1.34 Å and 1.36 Å, respectively, in twelvefold coordination [21].

The microwave dielectric properties of $Ca(B_{1/2}Ta_{1/2})O_3$ (B = La, Pr, Nd, Sm, Eu, Gd, Tb, Dy, Ho, Y, Er, Yb, and In) ceramics are given in the Appendix given at the end of Volume 2. The *Qf* value of $Ca(B_{1/2}Ta_{1/2})O_3$ ceramics varies in the range 20 600–59 200 GHz with the maximum value for $Ca(Yb_{1/2}Ta_{1/2})O_3$. Among the lanthanides in this series, Yb^{3+} has the largest ionic size difference with Ca^{2+} and has the correspondingly highest Q-factor [87]. Conversely, La^{3+} has the smallest ionic size difference with Ca^{2+} and has the lowest Q-factor. These facts again strengthen the possibility of intersubstitution between A-site and B-site ions with comparable sizes with a concomitant lowering of the Q-factor. The highest value of *Qf* was found for $Ca(Yb_{1/2}Ta_{1/2})O_3$ ceramic as 59 200 GHz [87].

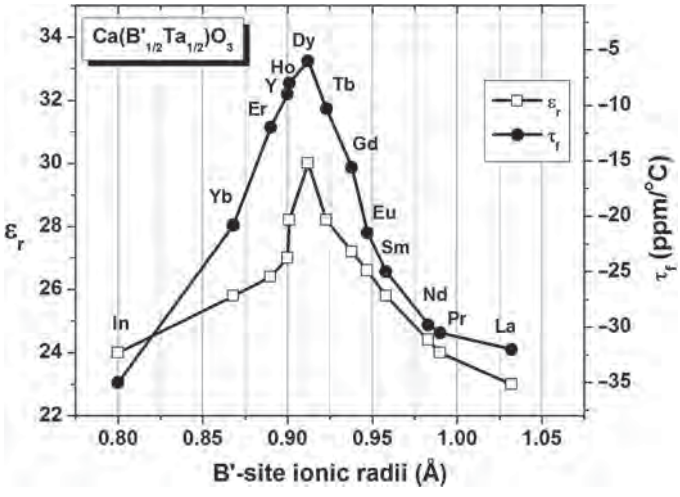

Figure 3.11 *The variation of ε_r and τ_f of $Ca(B_{1/2}Ta_{1/2})O_3$ (B = La, Pr, Nd, Sm, Eu, Gd, Tb, Dy, Ho, Y, Er, Yb, and In) ceramics versus B-site ionic radii. Source: Khalam* et al. *2007 [87], reproduced with permission from John Wiley & Sons.*

The variation of ε_r versus B-site ionic radii is shown in Figure 3.11. The ε_r of $Ca(B_{1/2}Ta_{1/2})O_3$ ceramics increases to 30 as the B-site ionic radius increases up to r_{Dy} = 0.912 Å and then decreases as the size further increases to r_{La} = 1.032 Å. The decrease in ε_r with large sized B cations ($r_B \geq 0.923$ Å) may be due to the mixing of comparably sized Ca^{2+} and B^{3+} ions. With the substitution of xCa on the B site, a maximum of $(2x/3)$B can occupy the A site whilst maintaining charge neutrality. As shown in Figure 3.11, the $|\tau_f|$ of $Ca(B_{1/2}Ta_{1/2})O_3$ ceramics decreases with B-site ionic size up to r_{Dy} = 0.912 Å and then increases with a further increase in size up to r_{La} = 1.032 Å. The tolerance factors of Ba- and Sr-based rare earth perovskites are inversely related to their B-site ionic radii. The accuracy of the tolerance factors of $Ca(B_{1/2}Ta_{1/2})O_3$ ceramics with small B-site ionic size differences ($r_B - r_{Ta}$) will be limited due to the possibility of mixing of Ca^{2+} and larger B cations; therefore, it was suggested [87] that the tolerance factor of $Ca(B_{1/2}Ta_{1/2})O_3$ compounds with large B ions (La, Pr, etc.) would be more accurately calculated according to the compositional formula $(Ca_{1-x}B_{2x/3})(B_{1/2\text{-}2x/3}Ca_xTa_{1/2})O_3$ with $x \leq 0.75$.

3.6.1.6 $Ca^{2+}(Ln^{3+}_{1/2}\ Nb^{5+}_{1/2})O_3$

Complex perovskites of the form $Ca(B_{1/2}B'_{1/2})O_3$ also have interesting structural and dielectric characteristics. In the crystal structure, B-site ions have a size difference of 0.16–0.392 Å and a charge difference of 2. For $Ca(B_{1/2}Nb_{1/2})O_3$ ceramics, the K-factor, defined by Equation (3.11), assumes values $0.25 \leq K \leq 0.6125$, suggesting an ordered B site. Several research groups have studied the structure and symmetry of $Ca(B_{1/2}B'_{1/2})O_3$, which is as controversial as some other double perovskites, and reported them as monoclinic, triclinic, orthorhombic, or rhombohedral, depending on the size of B cations and the tolerance factor. For example, Galasso [70] attributed monoclinic symmetry to $Ca(B_{1/2}Nb_{1/2})O_3$

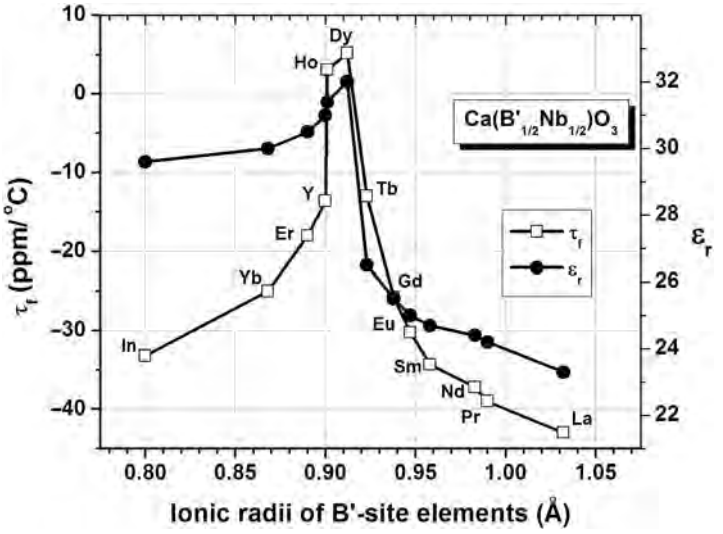

Figure 3.12 *The dielectric constant and temperature coefficient of resonant frequency of $Ca(B_{1/2}Nb_{1/2})O_3$ ceramics versus ionic radii of B-site elements. Source: Khalam and Sebastian 2007 [89]. Reproduced with permission from John Wiley & Sons.*

(B = La, Pr, Nd, Sm, Gd, Tb, Dy, Ho, Y, Er, Yb) ceramics. This conclusion was later questioned by Trunov *et al.* [88] who reported a monoclinic cell for $Ca(B_{1/2}Nb_{1/2})O_3$ with B = Pr—Tb, while for B = La—Gd they reported an orthorhombic symmetry. Filipev and Fesenko [64] asserted that the structural phase boundary (monoclinic–triclinic) should be at B = Tb in this system. During this transition, the intensities of superlattice lines become quite strong while that of the fundamental perovskite are weak. This fact was reiterated by Khalam and Sebastian [89], who saw a sharp change in intensities of superlattice lines and perovskite lines as a consequence of the structural transformation from orthorhombic to monoclinic. For the materials with B = Dy—In, the superlattice peaks are less intense while the parent perovskite peaks are strong as compared to patterns for B = La—Tb [89].

Khalam and Sebastian [89] also measured the microwave dielectric properties of these niobate double perovskites (see the Appendix). As depicted in Figure 3.12, the ε_r of $Ca(B_{1/2}Nb_{1/2})O_3$ ceramics increases linearly up to $r_B = 0.91$ Å and then it steeply decreases beyond $r_B = 0.92$ Å. This change in ε_r is believed to be a consequence of the orthorhombic-to-monoclinic structural transformation at $r_B = 0.91$–0.92 Å. It was reported [90] that in $Ca(B_{1/2}Nb_{1/2})O_3$ perovskites with $r_B \geq 0.93$ Å, a partial/full intermixing of comparable Ca and B-site ions is very likely to occur. The τ_f of these ceramics follows a similar trend as ε_r, as reported by Khalam and Sebastian [89]. The τ_f values of $Ca(B_{1/2}Nb_{1/2})O_3$ perovskite ceramics with B = Dy—In vary linearly from –33 to 5 ppm/°C while those of B = Tb—La vary from –13 to –43 ppm/°C. The sharp down-turn in τ_f between the two regimes is also believed to be due to the structural transformation. This structural change at the boundary between $Ca(Tb_{1/2}Nb_{1/2})O_3$ and $Ca(Dy_{1/2}Nb_{1/2})O_3$ is clearly seen in the powder X-ray diffraction patterns (Figure 3.12).

As a general trend, the Ca-based perovskites were reported [90] with negative τ_f values. Nevertheless, Khalam and Sebastian [89] observed small positive τ_f values (5 and 3 ppm/°C) for $Ca(Dy_{1/2}Nb_{1/2})O_3$ and $Ca(Ho_{1/2}Nb_{1/2})O_3$, which have tolerance factors of 0.89 and 0.892, respectively. In this study most of the $Ca(B_{1/2}Nb_{1/2})O_3$ ceramics except $Ca(Gd_{1/2}Nb_{1/2})O_3$ showed quality factors in the range 31 000–38 000 GHz, as given in the Appendix. However, a low quality factor (Qf = 11 000 GHz) was obtained for $Ca(Gd_{1/2}Nb_{1/2})O_3$. In order to nullify their negative τ_f values, Khalam and Sebastian have also attempted to add positive τ_f materials like TiO_2 and $CaTiO_3$ into $Ca(B_{1/2}Nb_{1/2})O_3$ perovskites, which was achieved only with the degradation of the Q-factor [89]. However, solid solutions of $Ca(Y_{1/2}Nb_{1/2})O_3$ and $Ba(Y_{1/2}Nb_{1/2})O_3$ resulted in a thermostable composition, $0.05Ca(Y_{1/2}Nb_{1/2})O_3$–$0.95Ba(Y_{1/2}Nb_{1/2})O_3$, which showed good dielectric properties, $\varepsilon_r = 35.2$, $Qf = 48\,300$ GHz, and $\tau_f = 1.2$ ppm/°C.

3.6.1.7 $Ln^{3+}[(Zn,Mg,Co)^{2+}_{1/2}\ Ti^{4+}_{1/2}]O_3$

The family of rare-earth zinc/magnesium/cobalt titanates are of interest as possible microwave resonator materials chiefly because of their negative τ_f values, although $La(Mg_{0.5}Ti_{0.5})O_3$ has also been considered as a candidate substrate material for the growth of high-Tc superconducting films [91,92], where the requirement is for low τ_r and high Q. The negative τ_f of these materials, combined with the typical ease with which perovskites accept dopants, means that solid solutions can be formulated with materials with positive values for τ_f (e.g., $CaTiO_3$, $SrTiO_3$, etc.) which, if properly synthesised, can have $\tau_f \approx 0$.

The structure of $La(Mg_{0.5}Ti_{0.5})O_3$ (LMT) was first described [93, 94] as "probably orthorhombic" and at least partly disordered on the B site. It was later reported [95] as a cubic phase with a lattice constant of $a = 7.868$ Å. Several years later, Negas *et al.* [96] found it to be orthorhombic, but Harshé *et al.* [91] failed to find any orthorhombic peak splitting and again suggested a cubic unit cell, but with a lattice constant of $a = 3.9195$ Å. Its average perovskite tolerance factor is 0.952, which, according to the work of Reaney *et al.* [20], suggests the presence of both in-phase and antiphase tilting of oxygen octahedra. Accordingly, Meden and Ceh [97] refined its structure in the orthorhombic space group *Pbnm*, which forbids B-site ordering. More recently, LMT has been reported [98–102] as an ordered perovskite in the monoclinic space group $P2_1/n$; however, it becomes disordered and orthorhombic when doped with very small amounts of either $CaTiO_3$ [103], $SrTiO_3$ [98], or $BaTiO_3$ [99]. In 2004 [102], pure $La(Mg_{0.5}Ti_{0.5})O_3$ has been ascribed lattice constants of $a = 5.5608$ Å, $b = 5.5749$ Å, $c = 7.8610$ Å, $\beta = 90.034°$ in $P2_1/n$, and the structural model published by Avdeev *et al.* [99] shows the B site to be mostly ordered, but with about 4% disorder. Other lanthanide members of the group, $Ln(Mg_{1/2}Ti_{1/2})O_3$ (Ln = Nd, Tb, Dy, Ho, Y, Er, and Yb) were reported to be monoclinic [95].

The microwave dielectric properties of LMT have been measured by various groups. Cho *et al.* [92] suggested that they were the first to measure such values ($\varepsilon_r = 29$, $Qf = 75\,500$ at 10 GHz, and $\tau_f = -65$ ppm/°C), but they were in fact beaten by both a Kyocera Corporation patent [90], which reported $\varepsilon_r = 32$ and $\tau_f = -88.3$ ppm/°C, as well as by Negas *et al.* [96], who published values ($\varepsilon_r = 33$, $Qf = 40\,000$ at 5 GHz, and $\tau_f = -100$ ppm/°C) eight years earlier. As dense samples have sometimes been difficult to prepare (e.g., the pellets in the work of Vanderah *et al.* [102] were only 90% dense), there has been some variability in the measured properties. The relative permittivity varies from 27 [103] to 33 [96] and Qf values

range from 40 000 [96] to ≈ 60 000 [98, 102] to 75 500 [92] all the way up to 114 300 [100, 104]. Similarly, τ_f measurements seem to vary between groups, with values typically ≈ –81 ppm/°C [98, 100, 102, 104, 105]; although values of −65 ppm/°C [92] and –100 ppm/°C [96] have also been reported. Commercially promising compositions were found by doping with either $CaTiO_3$ (0.44LMT–0.56CT: $\varepsilon_r = 47$, $Qf = 28\ 120$ at 3.8 GHz and $\tau_f = 0$) [96] or $BaTiO_3$ (0.5LMT–0.5BT: $\varepsilon_r \approx 60$, $Qf \approx 9600$ GHz, and $\tau_f = -2$ ppm/°C) [101]. Kyocera Corporation holds a patent [105] on compositions in the system $(1-x)La(Mg^1/_2Ti^1/_2)O_3$–$xCaTiO_3$ ($0 \leq x \leq 0.7$), including the temperature-stable composition $x = 0.55$, for which they disclose $\varepsilon_r = 47.6$, tan $\delta = 0.00028$, and $\tau_f = 0.6$ ppm/°C. Seabra *et al.* reported that the $Nd(Mg_{1/2}Ti_{1/2})O_3$ analog has a very high quality factor (Qf = 151 000 GHz) [100], and temperature-stable compositions have been made by various researchers [103, 104, 106] by creating solid solutions of $Nd(Mg_{1/2}Ti_{1/2})O_3$, with its negative τ_f, and other perovskites, with positive τ_f values.

The structure of $La(Zn_{0.5}Ti_{0.5})O_3$ (LZT) published by Kucheiko *et al.* [107] was orthorhombic, with lattice constants $a = 5.6077$ Å, $b = 7.8986$ Å, $c = 5.5641$ Å. The microwave properties they measured were $\varepsilon_r = 28.69$, $Qf = 59\ 892$, and $\tau_f = -71$ ppm/°C, but the density of their samples was only about 90% of the theoretical density (ρ_{th}). These properties were later re-measured by Cho *et al.* [108] on samples that were about 97% ρ_{th}. They reported $\varepsilon_r = 34$, $Qf = 59\ 000$, and $\tau_f = -52$ ppm/°C. Like LMT, LZT is reportedly ordered but becomes disordered upon the addition of small amounts of either $CaTiO_3$ [109] or $SrTiO_3$ (Cho *et al.* [110] dopants, although evidence of short-range order was still found by FTIR at higher doping levels [110]. In the case of $xSrTiO_3$–$(1-x)$LZT, long-range order on the B site is lost [109, 110] at $x \geq 0.4$. A-site cation displacements and in-phase octahedral tilting are lost [109, 110] at $x \geq 0.6$, and finally antiphase tilts disappear [110] at $x \geq 0.9$. As for LMT, commercially promising compositions are all doped to about the 50% level. Indeed, Yeo *et al.* [111] reported that $0.5LZT–0.5CaTiO_3$ had $\varepsilon_r = 50$, $Qf = 38\ 000$, and $\tau_f = 0$, while Cho *et al.* [110] found that $0.5LZT–0.5SrTiO_3$ had $\varepsilon_r = 55$, $Qf \approx 60\ 000$, and $\tau_f = 0$. Kyocera Corporation [112] have also developed ceramics in the system $CaTiO_3$—$La(Zn_{1-x}M_x)O_3$ (M = W, Ni, Co, Zr, Sn, Mn, and Cu).

The average tolerance factor of LZT is $t = 0.947$, which, like LMT, indicates the presence of both in-phase and antiphase tilting of oxygen octahedra. The effects of this tilting have been observed [109] via XRD in the form of $^1/_2(311)$ and $^1/_2(310)$ superlattice reflections corresponding to antiphase and in-phase tilting, respectively. Systematic cation displacement was also detected by the appearance of $^1/_2(210)$ reflections, and $^1/_2(111)$ reflections were observed and ascribed to the doubling of the unit cell caused by B-site cation ordering. Ubic *et al.* [113] made a detailed structural study of $La(Zn_{1/2}Ti_{1/2})O_3$ via electron and neutron diffraction. The selected-area electron diffraction patterns are shown in Figure 3.13. As can be seen, Figure 3.13a and 3.13d contain γ superlative reflections indicative of in-phase tilting about a single pseudocubic axis. The α reflections visible in Figure 3.13e to g show the presence of antiphase tilting about the remaining two axes. The B site is ordered on pseudocubic {111}, but the presence of the pseudocubic $^1/_2(111)$ reflection is in itself insufficient to prove the existence of such order, as some intensity is also due to antiphase tilting (it is the allowed (101) reflection in the parent *Pbnm* structure). Reitveld refinement of neutron-diffraction data showed that $La(Zn_{1/2}Ti_{1/2})O_3$ forms as an ordered perovskite in the monoclinic space group $P2_1/n$. Ubic *et al.* [113] determined the microwave dielectric properties of $Ln(Zn_{1/2}Ti_{1/2})O_3$ as $\varepsilon_r = 34$, $Qf = 36\ 090$ GHz and $\tau_f = 70$ ppm/°C.

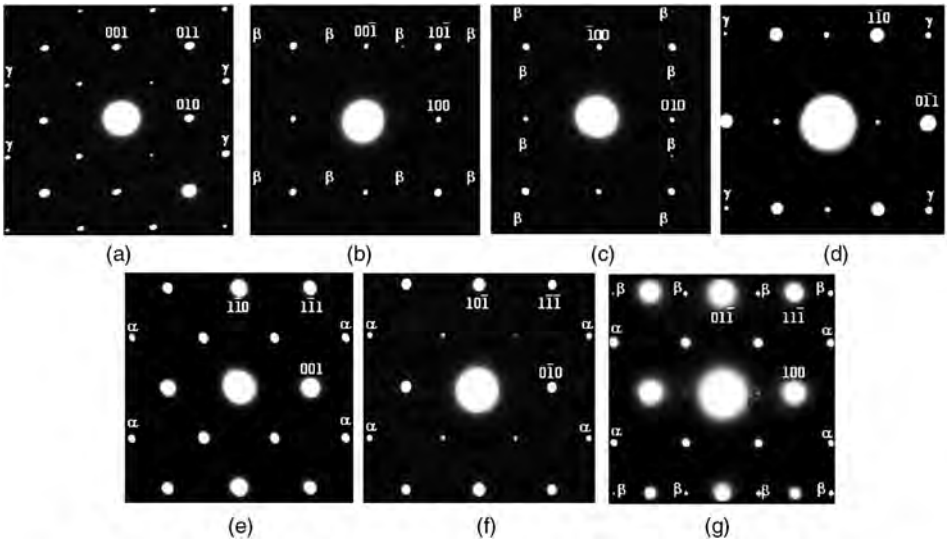

Figure 3.13 *SADPs of LZT indexed according to the simple pseudocubic perovskite unit cell (a = 3.9449 Å) corresponding to (a) [100], (b) [010], (c) [001], (d) [111], (e) [110], (f) [101], and (g) [011]. Source: Adapted from Ubic* et al. *2006 [113].*

The third prominent dielectric in the series $Ln(B_{1/2}Ti_{1/2})O_3$ is $La(Co_{1/2}Ti_{1/2})O_3$, which also belongs to the space group $P2_1/n$ and is a high-Q dielectric material with $\varepsilon_r = 30$, $Qf =$ 67 000 GHz, and $\tau_f = -64$ ppm/°C [114]. In 2005 Cairns *et al.* [115] reported the formation of single-phase $La(Co_{1/2}Ti_{1/2})O_3$ by the solid-state method. Their structural analysis using XRD and TEM showed that $La(Co_{1/2}Ti_{1/2})O_3$ has either an orthorohombic *Pbnm* structure with disordered Co/Ti ions or monoclinic $P2_1/n$ structure with Co/Ti ordering. The tilt system in either case is $a^-a^-c^+$. A subsequent investigation [116] also found partial ordering in this system. A similar lanthanide double perovskite composition, $Sm(Co_{1/2}Ti_{1/2})O_3$, with an orthorhombic crystal structure also yielded interesting microwave dielectric properties ($\varepsilon_r = 26$, $Qf = 76\,000$ GHz, and $\tau_f = -16$ ppm/°C) [117].

3.6.1.8 $A^{2+}(Mg^{2+}_{1/2}Te^{6+}_{1/2})O_3$

Several studies have been performed on double perovskites with hexavalent cations, such as Mo, Re, W, and Te [118, 119]. According to Augsburger *et al.* [120], p-elements like tellurium can successfully be stabilized on perovskite B sites. Recently, a resurged interest in Te-based compositions has emerged since they have excellent microwave properties with very low sintering temperatures (~700 °C), making them potentially useful for low-temperature co-fired ceramic (LTCC) applications [121].

Ubic *et al.* [122] investigated the structure and microstructure of such compounds using XRD, TEM, and SEM methods. In that work, $Sr_{2-x}Ca_xMgTeO_6$ ($0 \le x \le 2$) ceramics were prepared via the solid-state ceramic route. As expected, the system undergoes a transition from pseudocubic tetragonal $I4/m$ symmetry at $x = 0$ (Sr_2MgTeO_6) to pseudotetragonal

monoclinic $P2_1/n$ symmetry for $x > 0$. The dielectric properties of the ceramics were studied and it was found that the τ_f is negative throughout the series, ε_r was in the range 13.2−14.3, and *Qf* varied from 27 500 to 81 000 (5−6 GHz) [122]. In general, the low ε_r values and reasonably high *Qf* values make these ceramics potential candidates for millimeter-wave (30–300 GHz) applications, for which temperature-stable ceramics with $\varepsilon_r \sim 10$ are required.

3.6.2 1:2 Ordering

In the early 1950s, Roy [123] made extensive research on a series of barium-based complex perovskite compositions of the type $Ba(B'_{1/2}B''_{1/2})O_3$ and $Ba(B'_{1/3}B''_{2/3})O_3$ and reported them to have a psuedocubic unit cell. In 1961, Galasso *et al.* [124] studied the effect of different ions such as Sr, Ca, Zn, Co, and Ni on the B′ site in the complex perovskite composition $Ba_3B'Ta_2O_9$ using powder diffraction methods. This study was mainly carried out with $Ba_3SrTa_2O_9$, with a presumption that these compounds would crystallize in a cubic form with $a = 4.17$ Å; however, their study revealed that most of them had a small rhombohedral distortion.

In 1963, Galasso and Pyle [125] established the conditions that can lead to the formation of structural order in $Ba(B'_{1/3}Ta_{2/3})O_3$ type complex perovskites. They observed that larger differences in size and charge between B-site cations in complex perovskites give rise to a more ordered structure – a rule that is still considered conventional wisdom for 1:2 complex perovskites. In the same paper were reported the unit-cell parameters of some new compounds like $Ba(Mg_{1/3}Ta_{2/3})O_3$ ($a = 5.782$ Å, $c = 7.067$ Å) and $Ba(Zn_{1/3}Ta_{2/3})O_3$ ($a = 5.782$ Å, $c = 7.097$ Å) for the first time. The structures of the niobium counterparts of these compounds were also published [126] subsequently, and $Ba(Zn_{1/3}Nb_{2/3})O_3$ was found to crystallize only in cubic perovskite form.

Since the pioneering work of Kawashima *et al.* [127] on $Ba(Zn_{1/3}Nb_{2/3})O_3$–$Ba(Zn_{1/3}Ta_{2/3})O_3$ ceramics for applications in mobile and satellite communication systems, there started an intense search by various Japanese research groups to develop low-loss dielectric materials with complex perovskite structures. Kawashima *et al.* [127] found that one of the end members of the solid solution, $Ba(Zn_{1/3}Ta_{2/3})O_3$ (BZT), could have a dielectric constant of 30 and quality factor of 9200 at 11–12 GHz with a near-zero temperature coefficient of resonant frequency.

3.6.2.1 $Ba^{2+}(Mg^{2+}_{1/3}Ta^{5+}_{2/3})O_3$

The efforts to develop high-Q materials culminated in a major success when Nomura *et al.* [128] made the remarkable finding that a dense ceramic of $Ba(Mg_{1/3}Ta_{2/3})O_3$ (BMT) had the very high quality factor and temperature stability useful for microwave dielectric resonator applications. To enhance its sinterability, a small amount of Mn was used as a sintering aid, and the microwave dielectric properties of this complex perovskite ceramic were determined as $Q = 16\,800 \pm 300$ at 10.5 GHz, $\varepsilon_r = 25$, and $\tau_f = 2.7$ ppm/°C.

BMT is commonly used for satellite communications systems, and many pieces of this ceramic currently orbit the earth. It is commonly made via either a conventional mixed-oxide route or the columbite route; however, it is notoriously difficult to make with optimum properties and generally requires days at high temperature to promote ordering.

The emergence of $Ba(Mg_{1/3}Ta_{2/3})O_3$ as a high-Q dielectric resonator for microwave communication applications stimulated a new surge of interest among researchers working on the materials science aspects of low-loss materials [129]. Many investigators observed that the formation of additional phases such as $BaTa_2O_6$ and $Ba_5Ta_4O_{15}$ may promote extensive grain growth in $Ba(Mg_{1/3}Ta_{2/3})O_3$ to the detriment of its microwave dielectric properties. In a significant publication, Sugiyama *et al.* [130] observed that the impingement of ordered domains resulted in the formation of sub-boundaries in the parent $Ba(Mg_{1/3}Ta_{2/3})O_3$ grain. These sub-boundaries are in a strained condition, which introduces dislocations at the interface resulting in dielectric loss. The first attempt to explore the origin of the low loss of $Ba(Mg_{1/3}Ta_{2/3})O_3$ was undertaken by Wakino and Tamura [131], who studied the low-temperature dielectric properties and correlated them with the anharmonic terms in the crystal's Hamiltonian.

The efforts to improve the dielectric properties of these ceramics were carried out by many researchers in parallel with the innovations in the science of advanced materials synthesis. The main hurdles in the synthesis of $Ba(Mg_{1/3}Ta_{2/3})O_3$ ceramics include (a) the high sintering temperature (> 1600 °C) and long high-temperature anneal (> 1500 °C) required to achieve complete cation ordering; (b) volatilization of MgO and the consequent formation of Mg-free secondary phases like $BaTa_2O_6$, $Ba_5Ta_4O_{15}$, and $Ba_4Ta_2O_9$; and (c) thermal destabilization of the cation order from 1:2 to 1:1 or to disordered perovskite above the order–disorder transformation temperature [132]. It is understood that the bulk material transport mechanisms of $Ba(Mg_{1/3}Ta_{2/3})O_3$ ceramic can be enhanced through a rapid heating procedure as suggested by Matsumoto *et al.* [133]. They have succeeded in densifying the ceramic from a green density of 49% to a final sintered density above 91% of its theoretical density (7.637 g/cm^3) with excellent microwave dielectric properties (ε_r = 25, τ_f = 4 ppm/°C and Q = 20 000 at 10–22 GHz). Yet another modification in the synthesis of this ceramic was reported by Tsai *et al.* [134] who used hot isostatic pressing (HIP) to achieve better densification and dielectric constant, but the unloaded quality factor was hardly affected. Alternate synthesis techniques like solution synthesis and liquid-phase sintering have also been adopted to improve the properties of BMT [147–149].

The research and development on BMT could be categorized in two streams, viz. (i) efforts directed towards understanding the complex crystal chemistry of BMT, and thereby shed light on to the structure–property relations of ordered triple perovskites with low dielectric loss, and (ii) research giving weightage to a technological perspective where the improvement of dielectric properties and circuit performance of the solid-state component are of chief concern. A microwave circuit designer can improvise and optimize circuit performance only with a sound knowledge of the crystal chemistry of the solid-state components, which has been done using spectroscopy (IR and Raman), crystallographic refinement of X-ray and neutron diffraction data, and electron microscopy (HRTEM and electron diffraction).

The long-range cation ordering parameter (S) is defined as the occupational probability difference between two non-equivalent states [135]. In 1:1 ordered complex perovskites, the long-range ordering parameter gradually reduces to zero when the temperature increases (Figure 3.14). Therefore the 1:1 order–disorder transition is a second-order phase transition. On the other hand, the long-range ordering parameter of 1:2 type ordering suddenly drops to zero at the transition temperature, which indicates that the transition is first-order [136, 137].

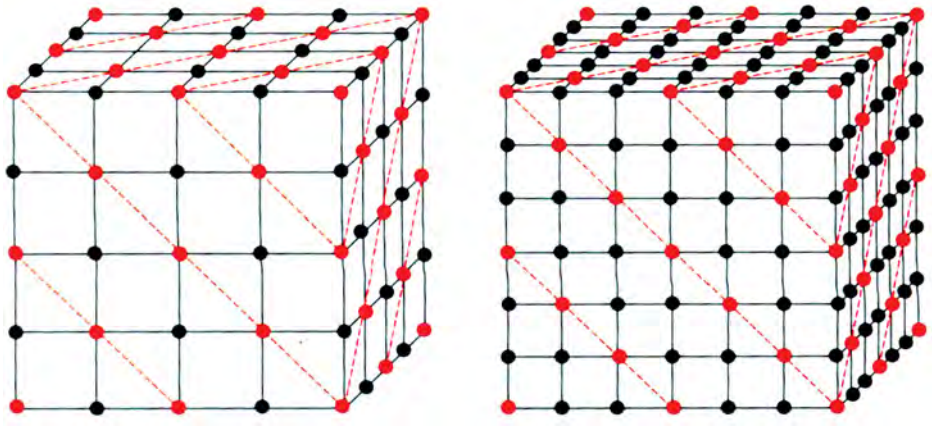

Figure 3.14 *Ordered cationic arrangement of B-site ions in complex perovskites: 1:1 arrangement (left) and 1:2 arrangement (right). Source: Sagala and Nambu 1992 [137]. Reproduced with permission from Physical Society of Japan.*

The cation ordering parameter of $Ba(Mg_{1/3}Ta_{2/3})O_3$ can be conveniently calculated by indexing powder diffraction lines according to the ordered trigonal unit cell and then comparing the intensities of the strongest powder profile line (110, 102) with that of the (100) superstructure line, as given below:

$$S = \sqrt{\frac{(I_{(100)}/I_{(110),(102)})_{\text{observed}}}{(I_{(100)}/I_{(110),(102)})_{\text{theoretical}}}} \tag{3.12}$$

Matsumoto *et al.* [133] calculated the theoretical value of this ratio as 8.3%; however, the structural analyses carried out by Janaswamy *et al.* [138] and Lufaso *et al.* [139] suggest that a more accurate value for the ratio is 8.7%.

The crystal structures of BMT refined from X-ray diffraction data showed appreciably different B-site bond lengths (Å) [Mg—O : 2.07(2) × 6, Ta—O : 2.04(2) × 3, and 2.033(6) × 3] compared to [Mg—O : 2.076(8) × 6, Ta—O : 1.967(8) × 3, and 2.089(1) × 3]. Differences in the crystal structures of BMT may be partially attributed to the difficulty in refining accurate O positions from X-ray diffraction data. It is unclear from the reported crystal structures if Ta^{5+} shifts out of the center of the octahedra to form three short Ta—O bonds or retains long Ta—O bonds [142].

Soon after the report on BZT came out, Lufaso [143] made a candid attempt to address the wide scatter of dielectric properties of isostructural compounds in $Ba(B'_{1/3}B''_{2/3})O_3$ system based on their powder/neutron diffraction characteristics. The neutron diffraction data revealed that a complete cation order was indicated for $Ba(Mg_{1/3}Ta_{2/3})O_3$ (BMT), $Ba(Mg_{1/3}Nb_{2/3})O_3$ (BMN), and $Ba(Ni_{1/3}Ta_{2/3})O_3$ (BNT), and a nearly complete cation order for $Ba(Ni_{1/3}Ta_{2/3})O_3$ (BNN) and $Ba(Zn_{1/3}Nb_{2/3})O_3$ (BZN). In contrast to many 1:1 ordered B-site cation perovskites, the crystal structures of 2:1 ordered perovskites exhibit

an out-of-center distortion of B''^{5+} in $[B''^{5+}O_6]$. The magnitude of the octahedral distortion is quantified using the octahedral distortion parameter (Δd) calculated according to

$$\Delta d = \frac{1}{6}\left[\sum_{n=1,6}\frac{[d_n - (d)]}{(d)}\right]^2 \tag{3.13}$$

where (d) is the mean M—O bond distance and d_n are the individual M—O bond distances. Lufaso obtained the values of Δd for $Ba(Mg_{1/3}Ta_{2/3})O_3$, $Ba(Mg_{1/3}Nb_{2/3})O_3$, $Ba(Ni_{1/3}Ta_{2/3})O_3$, $Ba(Ni_{1/3}Nb_{2/3})O_3$, $Ba(Zn_{1/3}Nb_{2/3})O_3$, and $Ba(Zn_{1/3}Ta_{2/3})O_3$ as 15.1(BMT), 16.9 (BMN), 12.4 (BNT), 11.8 (BNN), 13.8 (BZN), and 13.4 (BZT) [143]. A slightly larger distortion of the Nb^{5+} coordination environment for $B' = Mg, Zn$ is revealed by a larger Δd for $B'' = Nb$ than for $B'' = Ta$. Partial B-site disorder of BNN and BZN yields a slightly smaller Δd than in a fully ordered composition because of the preference of Ni^{2+} and Zn^{2+} to occupy a more symmetric octahedral coordination.

Although the out-of-center distortion primarily occurs because of the asymmetry in the bond network, the connectivity in the bond network is not the sole driving force for the distortion. In general, a distortion depends on both electronic and structural components in the nature of the bond network. The highly charged d^0 cations (Ta^{5+} or Nb^{5+}) have low-lying d orbitals that are able to mix with the filled p orbitals of the oxygen. In the extended perovskite structure this results in a number of different electronic configurations with closely spaced energies. A spontaneous distortion can remove any near degeneracy, which is known as a second-order Jahn–Teller distortion [144]. In general, second-order Jahn–Teller distortions that occur for d^0 cations (e.g., Ti^{4+}, Nb^{5+}, Ta^{5+}, W^{6+}) exhibit a tendency for multiple bond lengths [145].

The crystal structure of $Ba(Mg_{1/3}Ta_{2/3})O_3$ shown in Figure 3.15, which illustrates that the shift of Ta occurs towards the face of the $[TaO_6]$ octahedra towards a neighbouring layer of $[MgO_6]$. In a variety of similar structure types, the coordination environment distortion is typically larger for Nb^{5+} than for Ta^{5+}. Other factors being equal, the more ionic Ta^{5+} has less driving force than the more covalent Nb^{5+} to adopt a distorted coordination environment because of the reduced mixing of the O 2p and B''^{5+} d orbitals and decreased second-order Jahn–Teller distortion. The significance of the coordination differences and

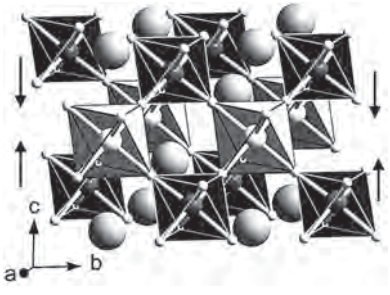

Figure 3.15 *Crystal structure of $Ba(Mg_{1/3}Ta_{2/3})O_3$. The large spheres represent Ba atoms and the small spheres oxygen atoms. Medium spheres represent Mg in pale $[MgO_6]$ octahedra and Ta in dark $[TaO_6]$ octahedra. Ta distorts out-of-center towards the octahedral face with O bonded to Mg. Source: Adapted from Lufaso 2004 [143].*

reduced second-order Jahn–Teller distortion has a significant effect on the dielectric properties of these complex perovskites [143].

With the help of TEM analysis a possible model for grain growth of BMT was also done by Liang and Green [146]. They emphasized that grains are probably growing via the merge of the adjacent grains resulting in the formation of wavy polar domain boundaries, dislocations and even the dislocation networks, which are detrimental to the microwave dielectric properties. The presence of abundant defects in large BMT grains is believed to be the prime factor degrading the microwave dielectric properties of the BMT materials sintered at a too-high temperature.

Effect of Glass Additives in BMT From a technologist's perspective the improvement of dielectric properties and hence a better performance of the solid-state component is of major concern irrespective of whatsoever happens in the chemical structure of the material. It is well documented that, as commercial dielectric resonators, complex perovskite oxide $Ba(Mg_{1/3}Ta_{2/3})O_3$ (BMT) has shown the ideal dielectric properties in the microwave frequency region and so far no other low-loss material could dwarf BMT in this regard. However, the sintering temperature of this ceramic is above 1600 °C, which poses practical difficulties since high-temperature sintering is not cost effective. The efforts to improve the dielectric properties of these ceramics were carried out by many researchers in resonance with the innovations in the science of advanced material synthesis. As outlined elsewhere, the main hurdles in the synthesis of $Ba(Mg_{1/3}Ta_{2/3})O_3$ ceramics include (a) the high sintering temperature above 1600 °C, where the evaporative escape of constituent MgO can occur; (b) formation of magnesium-free additional phases like $BaTa_2O_6$, $Ba_5Ta_4O_{15}$ and $Ba_4Ta_2O_9$; (c) and thermal destabilization of the cation order from 1:2 to 1:1 or disordered perovskite.

The efforts to improve the microwave dielectric properties can be categorized into four, namely (a) liquid-phase sintering of BMT for better densification with addition of non-wetting glass fluxes, (b) deliberate introduction of a slight cationic non-stoichiometry for enhanced material transport, involving cation ordering transformation, (c) doping with aliovalent metal oxides, and (d) substitutional solid solution with suitable cations.

As outlined elsewhere, a number of strategies have been worked out to reduce the sintering temperature of BMT ceramics, such as (a) chemical synthesis [147, 148], (b) using starting powders with smaller particle size [149], and (c) liquid-phase sintering [150] by adding low melting additive into the ceramic. After conducting a detailed investigation on the dielectric properties of glasses at ultra-high frequencies, Navias *et al.* [151] noted that the dielectric losses of borosilicate glasses are comparatively lower than alkali-containing glasses. This is due to the fact that, in the latter, alkali ions that are weakly held in the glassy network absorb energy and eventually give rise to dielectric loss. On the other hand, borosilicate glasses have continuous atomic structures, with SiO_4 and BO_3 configurations joined to form (—Si—O—B—O—) linkages, will have high electrical resistance and low dielectric loss [152]. In another study [153], the microwave dielectric properties of a few borosilicate glasses ($BaO—B_2O_3—SiO_2$, $PbO—B_2O_3—SiO_2$, and $ZnO—B_2O_3—SiO_2$) have been reported in which it was observed that the τ_f of all these glasses are negative.

As cited above, a large number of papers were published on the interaction of glasses with low-loss microwave dielectrics. However, the vitreous-phase densification and dielectric loss aspects of silicate/borate and borosilicate glasses in complex perovskites

such as $Ba(Mg_{1/3}Ta_{2/3})O_3$, which can provide useful information to research on LTCC materials, had not been revealed until Surendran *et al.* [154] on the liquid-phase sintering effects in BMT using a number of glass systems such as B_2O_3, SiO_2, B_2O_3–SiO_2, ZnO–B_2O_3, 5ZnO–$2B_2O_3$, Al_2O_3–SiO_2, Na_2O–$2B_2O_3.10H_2O$, BaO–B_2O_3–SiO_2, MgO–B_2O_3–SiO_2, PbO–B_2O_3–SiO_2, ZnO–B_2O_3–SiO_2, and 2MgO–$2Al_2O_3$–$5SiO_2$ made an effort to find out an ideal glass system that promotes liquid-phase sintering without deteriorating the microwave dielectric properties. The aims of the research work on BMT with glass addition are (a) to reduce the preparation temperature of BMT and thereby the cost of production without any deterioration in the microwave dielectric properties, (b) to probe the relation between structural order and quality factor, (c) to suppress the formation of secondary phases such as barium tantalates, which are detrimental to the microwave quality factor, and (d) to improve the microwave dielectric properties of BMT. Among the above-mentioned glasses, only four glasses, B_2O_3, ZnO–B_2O_3, 5ZnO–$2B_2O_3$, and ZnO-B_2O_3-SiO_2, have been observed to improve the densification of BMT [154].

Surendran *et al*. [154] also found that the addition of 2 wt% glasses like ZnO–B_2O_3, 5ZnO–$2B_2O_3$ and ZnO–B_2O_3–SiO_2 could bring down the sintering temperature of BMT to 1375, 1330, and 1335 respectively. The addition of glasses like B_2O_3, ZnO–B_2O_3, 5ZnO–$2B_2O_3$, and ZnO–B_2O_3–SiO_2 suppressed the formation of additional phases like $BaTa_2O_6$, $Ba_5Ta_4O_{15}$, and $Ba_4Ta_2O_9$, which could have been detrimental to the high phase of the BMT dielectric. The dielectric properties of BMT ceramics fluxed with different amounts of glasses yield interesting results. The microwave dielectric properties of undoped, unannealed $Ba(Mg_{1/3}Ta_{2/3})O_3$ prepared by sintering at 1600 °C with a densification of 93.1% of the theoretical density are $\varepsilon_r = 24.8$, $\tau_f = 8$ ppm/°C and $Qf = 80\,000$ GHz. In order to promote cation ordering in complex perovskite BMT the sintered samples were subjected to a very slow cooling rate (1 °C/minute). The dielectric constant increased from 24.8 (pure BMT) to 25.02 when the sample was added with 0.2 wt.% of boric oxide and further addition resulted in a decrease of it [154]. On adding 0.5 wt.% of 5ZnO–$2B_2O_3$ glass, the measured values of ε_r increased to 25.45 and then gradually decreased to 24.5 with 2.0 wt.% of the additive. The maximum value of ε_r for BMT doped with ZnO–B_2O_3 were 25.12 for 0.1 wt.% of the additives, which decreases on further addition due to the formation of $Zn(BO_2)_2$. For the glass system ZnO–B_2O_3–SiO_2 the dielectric constant slightly increases for small values of the glass content and then decreases as the presence of glass in the mixture increases [154]. The τ_f of BMT decreases with B_2O_3 and ZnO–B_2O_3–SiO_2 addition and approached more negative values when the doping level of the glass increased.

As shown in Figure 3.16, the quality factor of BMT increased for a small amount of B_2O_3. For 0.5 wt.% of B_2O_3 addition *Qf* reached 124 700 GHz. The unloaded quality factor decreased with further addition of B_2O_3 glass where the densification factor also followed a similar trend [154]. The unloaded quality factor of BMT increased to $Qf = 136\,500$ GHz with 0.2 wt.% of ZnO–B_2O_3 addition. It is interesting to note that the quality factor of BMT increased steadily with 5ZnO–$2B_2O_3$ content. It is believed that the formation of the low melting β-$Zn_5B_4O_{11}$ has been beneficial to the materials transport mechanism in these glass fluxed ceramics. The best microwave property among binary glass added BMT ceramic was found for 1.0 wt.% 5ZnO–$2B_2O_3$ addition where the *Qf* was 141 800 GHz. The unloaded quality factor of 0.2 wt.% ZnO–B_2O_3–SiO_2 glass added BMT was around $Qf = 152\,800$ GHz (see Figure 3.16). It must be remembered that the reduction in sintering temperature in this research report was not sufficient enough for applications in multilayer structures using the LTCC technique where the sintering temperature must be less than

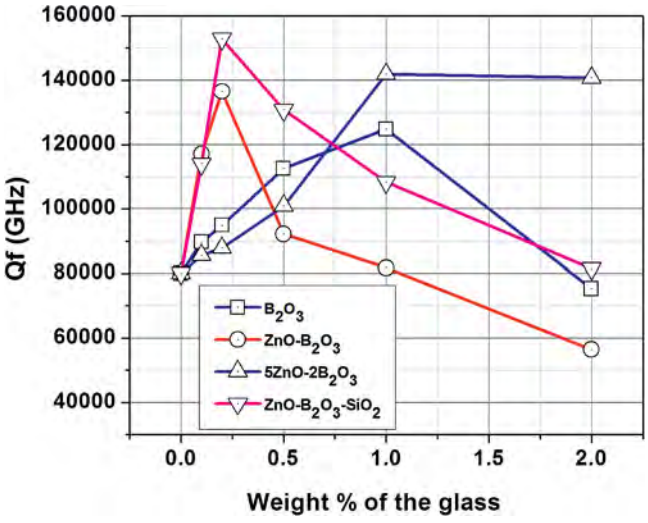

Figure 3.16 *Variation of quality factor of BMT with glass addition. Source: Adapted from Surendran* et al. *2004 [154].*

961 °C, which is the melting point of silver electrode. The effect of low melting additives such as NaF, $LiNbO_3$, and MgO—CaO—Al_2O_3—SiO_2 (MCAS) has been reported [155–157] in the literature in an effort to bring down the sintering temperature, but the *Qf* value has been considerably lowered, which cannot be afforded in industrial production.

Non-stoichiometry in BMT One method to improve the sinterability of the ceramic is to enhance the material transport processes in the dielectric by altering the material's stoichiometry. Historically, Desu and O'Bryan [158] made the first attempt in correlating microwave quality factor of a complex perovskite candidate $Ba(Zn_{1/3}Ta_{2/3})O_3$ (BZT) with B-site cation non-stoichiometry. In another significant attempt, Paik *et al.* [159] investigated the effect of Mg deficiency on the microwave dielectric properties of complex perovskite $Ba(Mg_{0.33}Nb_{0.67})O_3$. It was also reported [160] that among the three starting materials, the reactivity of MgO is inferior to $BaCO_3$ and Ta_2O_5. An improvement in the degree of 1:2 ordering and sinterability was proposed by Lu and Tsai [161] in Ba-deficient $Ba(Mg_{1/3}Ta_{2/3})O_3$ ceramics, but they did not study the effects of A-site cation deficiency on the microwave dielectric properties of BMT. The MgO evaporation at high temperature causes lattice defects, which has been addressed through burying the BMT specimen in MgO powder, as reported by some authors [162]. The effect of Mg deficiency on the microwave dielectric properties of BMT was also investigated by a Lee *et al.* [163], who found that an Mg-deficient specimen showed a faster rate of grain growth than stoichiometric BMT. However, slight non-stoichiometric samples showed lower *Q* values, which could be due to vacancy migration and resultant densification. In 2005, Surendran *et al.* [164] revisited the problem of non-stoichiometry in BMT by preparing compositions based on $Ba(Mg_{0.33-x}\ Ta_{0.67})O_3$ ($x = -0.015, -0.010, -0.005.\ 0.0, 0.005, 0.010, 0.015, 0.020, 0.025,$ and 0.030) and $Ba_{1-x}(Mg_{0.33}Ta_{0.67})O_3$ ($x = -0.015, -0.010, -0.005.\ 0.0, 0.0025, 0.005,$ 0.0075, 0.010, 0.015, 0.020, 0.025, and 0.030).

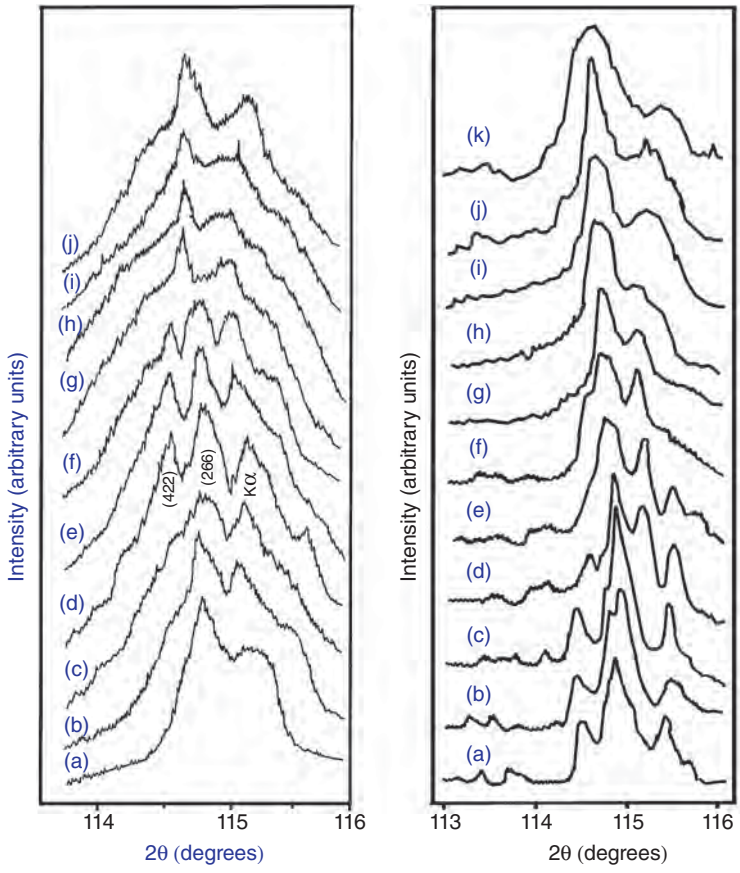

Figure 3.17 *(left) X-ray diffraction line profiles of (422) and (266) reflections for* $Ba(Mg_{0.33-x}Ta_{0.67})O_3$ *for x = (a) 0.03, (b) 0.025, (c) 0.02, (d) 0.015, (e) 0.01, (f) 0.005, (g) 0.0, (h) –0.005, (i) –0.010, and (j) –0.015. (right) X-ray diffraction line profiles of (422) and (266) reflections for* $Ba_{1-x}(Mg_{0.33}Ta_{0.67})O_3$ *for x = (a) 0.0025, (b) 0.005, (c) 0.0075, (d) 0.01, (e) 0.015, (f) 0.02, (g) 0.025, (h) 0.03, (i) –0.005, (j) –0.01, and (k) –0.015, Source: Adapted from Surendran* et al. *2005 [164].*

The non-stoichiometry generates lattice distortion. The splitting of the profiles of (422) and (266) reflections due to the lattice distortion of non-stoichiometric $Ba(Mg_{0.33-x}Ta_{0.67})O_3$ and $Ba_{1-x}(Mg_{0.33}Ta_{0.67})O_3$ for different values of x are shown in Figure 3.17 (left) and (right), respectively. The XRD patterns shown in Figure 3.17 were recorded with a slow scan of $2\theta = 1$ degree/minute. At 1600 °C, the temperature is sufficient to attain a highly ordered perovskite, but the sintering time (4 hours) is insufficient to reach equilibrium cation order conditions at that temperature. Slow cooling assists in the ordering, but does not guarantee the presence of equilibrium ordering. Changes in composition, which kinetically assists cation ordering are being followed in this experiment. As given in Figure 3.18, a larger level of Mg deficiency $x > 0.015$ will initiate the formation of additional phases like $BaTa_2O_6$ and $Ba_5Ta_4O_{15}$ [164] whose presence is reported to deteriorate

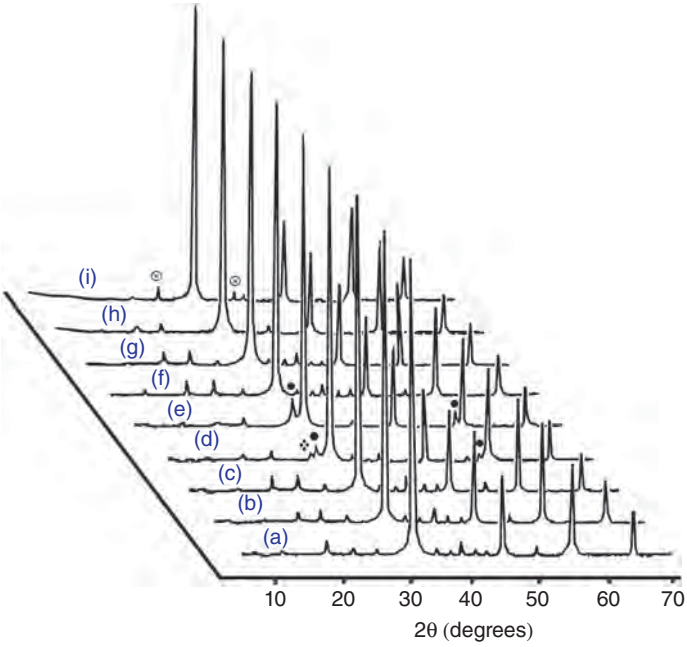

Figure 3.18 *Powder diffraction patterns of some typical non-stoichiometric compositions of BMT: (a) pure* $Ba(Mg_{0.333}Ta_{0.667})O_3$, *(b)* $Ba(Mg_{0.3233}Ta_{0.667})O_3$, *(c)* $Ba(Mg_{0.3183}Ta_{0.667})O_3$, *(d)* $Ba(Mg_{0.3133}Ta_{0.667})O_3$, *(e)* $Ba(Mg_{0.3033}Ta_{0.667})O_3$, *(f) 0.9925* $Ba(Mg_{0.3183}Ta_{0.667})O_3$, *(g) 0.99* $Ba(Mg_{0.3183}Ta_{0.667})O_3$, *(h) 0.98*$Ba(Mg_{0.3183}Ta_{0.667})O_3$, *(i) 0.97* $Ba(Mg_{0.3183}Ta_{0.667})O_3$. • *stands for* $Ba_5Ta_4O_{15}$, *for* ❖ $BaTa_2O_6$, *and* ⊗ $MgTa_2O_6$. *Source: Adapted from Surendran* et al. *2005 [164].*

the dielectric quality factor in BMT. On the other hand the X-ray diffractogram of typical Ba-deficient BMT ceramics (see Figure 3.18f to i) shows comparatively better cation ordering of B-site cations, which is evidenced by the appearance of discrete $\pm 1/3\{hkl\}$ superlattice reflections perpendicular to, for example, <111> and $<11\bar{1}>$. The samples are free of additional phases for $x \leq 0.025$. However, decreasing the barium concentration below a threshold level will result in the formation of additional phases like $MgTa_2O_6$ (see Figure 3.18i) [164].

The ordering of Mg and Ta ions results in the expansion of the original unit cell along the <111> direction so that the value of *c/a* assumes a value greater than $\sqrt{(3/2)} = 1.22474$. It is interesting to note that the value of the cell parameter *c* also increases from 7.0699 to 7.0845 Å when *x* changes from 0.0 to 0.015 and the cell parameter ratio *c/a* increases up to $x = 0.015$. On the other hand, the lattice parameter ratio is smallest for MgO-deficient samples. In Ba-deficient samples, the *c/a* ratio increases with *x* and reaches a maximum value for $x = 0.0075$. It is therefore expected that the B-site cation is fully ordered for the complex perovskite composition $Ba_{0.9925}(Mg_{0.33}Ta_{0.67})O_3$. As a general rule, the increase of deviation from the ideal stoichiometry would cause an increase in the volume of the unit cell in complex perovskites.

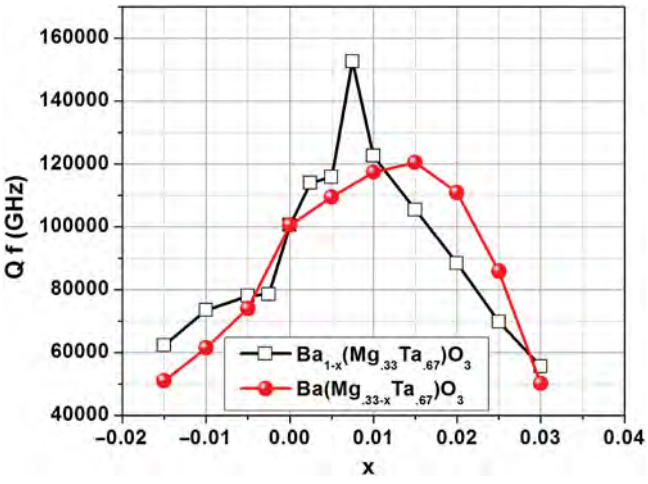

Figure 3.19 *Variation of unloaded quality factor of* $Ba(Mg_{0.33-x}Ta_{0.67})O_3$ *and* $Ba_{1-x}(Mg_{0.33}T_{0.67})O_3$ *as a function of x. Source: Adapted from Surendran* et al. *2005 [164].*

The microwave quality factors of barium and magnesium non-stoichiometric BMT samples are given in Figure 3.19. A slight non-stoichiometry may be beneficial for enhanced material transport. The extensive deviation from stoichiometry and the associated point defects in complex perovskite $Ba(Mg_{0.33}Ta_{0.67})O_3$ can give rise to additional losses in BMT. Rong *et al*. [166] emphasized that the major cause for dielectric loss in complex perovskites is the enhanced concentration of point defects. The *Qf* of pure stoichiometric BMT is 100 500 GHz. For a slight decrease of Mg concentration ($x = 0.015$ in $Ba(Mg_{0.33-x}Ta_{0.67})O_3$) the BMT ceramic observes a marginal increase in quality factor, as *Qf* reaches 120 500 GHz. The Mg deficiency and excess Mg introduce a series of lattice defects in the crystal, apart from the distortion of the octahedral skeleton of oxygen. Consequently, the quality factor decreases. On the other hand, the unloaded quality factor increases with small percentages of Ba deficiency. The quality factor of $Ba_{0.9925}(Mg_{0.33}Ta_{0.67})O_3$ is $Qf = 152\,580$ GHz. With a further increase of x the quality factor decreases. The quality factors of Ba-rich compositions are comparatively lower than Ba-deficient samples [164]. Ohsato [167] has a different interpretation on the improvement of properties when a slight amount of cation deficiency is introduced in perovskites. His interpretation is based on Kugimiya's observation [168], who got the highest *Qf* for compositions at the Ta and Ba rich side in the BMT system. He interpreted that the high *Q* cation deficient phases that Surendran *et al.* observed may be located in the eutectic region of the $BaO—MgO—TaO_{5/2}$ phase diagram, accompanied by a secondary phase, say $BaTa_{4/5}O_3$ [167]. Ohsato believes that, as the amount of the secondary phase is small, the detection may be difficult.

It is assumed that the substitution of Mg in vacant Ba sites leads to the formation of a possible composition $Ba_{1-x/3}\ Mg_{x/3}[Mg_{(1-x)/3}Ta_{2/3}]O_3$. However, this process could take place only at a very slow pace due to the difference in ionic radii between Ba^{2+} (1.35 Å for six coordination) and Mg^{2+} (0.72 Å for six coordination). The possible

representations of Mg-deficient compositions are (i) $Ba[(Mg_{1/3})_xBa_xTa_{2/3}]O_3$ and (ii) $Ba[\square_xMg_{1/3-5x/3}Ta_{2/3}+2_{x/3}]O_3$ ($\square$ = magnesium vacancy), which can be assumed to be similar to Zn-deficient $Ba(Zn_{1/3}Ta_{2/3})O_3$. The Raman spectra of the non-stoichiometric samples showed an increase in the frequency of the E_g(Ba) mode around 106 cm^{-1}, as well as the bandwidth variations observed in the E_g(O) mode around 157 cm^{-1} coinciding with the highest Q verified for the compositions $Ba_{0.9925}(Mg_{0.333}Ta_{0.667})O_3$ and $Ba(Mg_{0.318}Ta_{0.667})O_3$ [164].

Effect of Dopants in BMT Additives such as MnO, SnO_2, NiO, WO_3, ZrO_2, TiO_2, Y_2O_3, V_2O_5, etc., when doped to barium magnesium tantalates improved their microwave dielectric properties [169]. However, the exact action of these dopants are different in different dopant conditions and the role of a dopant in the parent matrix is still regarded as a matter of debate. Sometimes these doping mechanisms may initiate lattice site substitutions that can result in significant structural distortions. These structural distortions are therefore not only interesting crystallographically but they are also important since the distortions can have a critical influence on the dielectric properties of the perovskite material.

A galaxy of papers were available in the literature dealing with the role of additives on the densification, cation ordering, and microwave dielectric properties of $Ba(Mg_{1/3}Ta_{2/3})O_3$ ceramics. Additives such as MnO, SnO_2, NiO, WO_3, ZrO_2, TiO_2, Y_2O_3, Nd_2O_3, V_2O_5, CuO, La_2O_3 [170–180], etc., when doped to barium magnesium tantalates, drastically influenced their microwave dielectric properties. However, the action of these dopants are different in dopants with different doping conditions of $Ba(Mg_{1/3}Ta_{2/3})O_3$ and the exact role of a dopant in the parent matrix is still regarded as a matter of debate. In addition to that the reason behind the low-loss nature of BMT is also an active area of interest, which can throw light into the structure–property relationship of low-loss complex perovskite dielectrics.

The first reported study on the effect of dopants on $Ba(Mg_{1/3}Ta_{2/3})O_3$ was made by Nomura [128] who found that doping with Mn (1 mol%) not only promotes sinterability by lowering the sintering temperature but also increases the unloaded Q value appreciably. A number of parameters starting from the synthesizing stage, up to the final high-temperature densification have to be controlled to achieve a high Q phase in BMT ceramics [181]. The origin and purity of the initial raw materials also have a considerable influence on the sinterability. Moreover, the particle size of the starting materials, sintering temperature, sintering duration, and annealing, etc., have a substantial influence on the long-range cation ordering and microwave quality factor of BMT when it is prepared through the solid-state reaction technique.

In order to investigate the effect of property modifications with dopants, Surendran *et al.* [182] doped BMT precursor with different mole % of additives with different ionic radius and valencies. Dopants such as $MnCO_3$, ZnO, ZrO_2, SnO_2, Sb_2O_3, and WO_3 yielded interesting results when they are sintered at a temperature range at 1625 °C for 4 hours. The order parameter for pure BMT is 0.853, which increased with dopants except tetravalent ZrO_2. On the other hand, doping with ZrO_2 decreases the cation ordering. The dielectric constants of Mn- and Zn-doped samples increase to 26.7 and 25.9 from 24.4 (for pure BMT), respectively, when BMT is doped with 0.5 mole % of the additives. With higher concentrations of the dopant ions, the measured dielectric constant decreases, which may be due to high-temperature phenomena like abnormal grain growth. The temperature

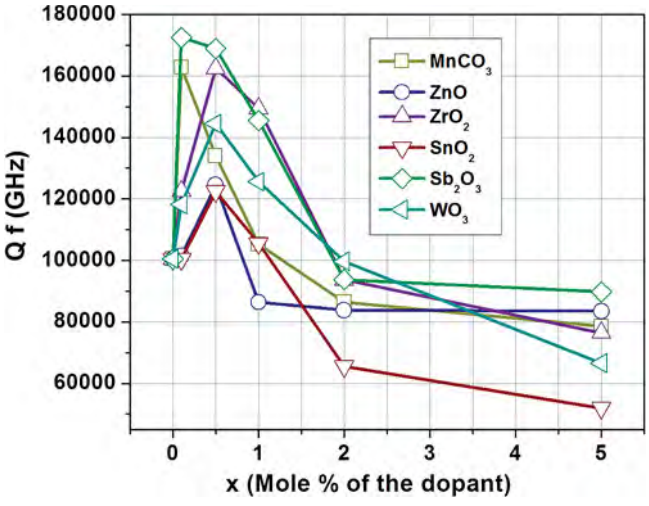

Figure 3.20 *Variation of the quality factor of BMT with concentration of the dopant. Source: Adapted from Surendran* et al. *2005 [182].*

coefficient of resonant frequency (τ_f) for pure BMT is 8 ppm/°C. With the exception of SnO_2, the τ_f of most of the doped specimens increases when the dopant level is higher (5 mol%), which is attributed to the possible lattice distortion caused by the partial substitution of the dopant ion at the lattice site of BMT. The addition of SnO_2 on BMT decreases the τ_f to negative values.

The microwave dielectric properties of pure as well as doped ones improve with long-time annealing. On annealing the BMT samples at 1450 °C for 40 hours (which has been the optimized condition for annealing), the dielectric quality factor increases from Qf = 80 000 to 100 500 GHz. The quality factor of BMT doped with 0.1 mole % of Sb_2O_3 is found to be best (Qf = 172 500) among all the additives we studied in this investigation (see Figure 3.20). The Mn-doped BMT samples are showing a high quality factor of Qf = 162 800 GHz for 0.1 mol% of the additive, which is consistent with the report of Nomura [128]. The quality factor is decreased with a further increase of the dopant. When tetravalent additives are added to BMT, the Qf reaches its maximum value (162 500 GHz) for 0.5 mol% of ZrO_2 dopant where the ordering parameter is 0.501. The ionic radii of W^{6+}, Ta^{5+}, and Mg^{2+} with a coordination number 6 are 0.58, 0.64, and 0.72 Å respectively. A partial substitution of W^{6+} at the Ta^{5+} site not only brings about a charge difference of 4 between B- and B-site cations but the ionic radius difference also increases from 0.08 to 0.14 Å. This promotes better cation ordering in the BMT lattice. The quality factor frequency product of 0.5 mol% WO_3-doped BMT is 144 500 GHz, which has a comparably good cation ordering (0.892) [182]. The ZnO doped samples also have a quality factor of Qf = 124 550 GHz for 0.5 mol% of the dopant.

The average ionic radius of B-site cation of BMT (i.e., $Mg_{1/3}Ta_{2/3}$) is calculated as 0.653 Å. A plot of the unloaded quality factor of BMT ceramic doped with 0.1 mol% of the dopants as a function of the ionic radius of the dopants is given in Figure 3.21. From these

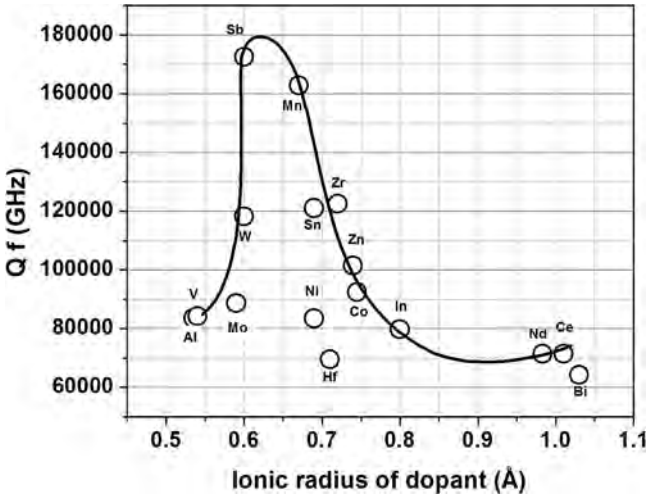

Figure 3.21 *Plot of ionic radius of the dopant versus quality factor of BMT ceramic. Source: Adapted from Suendran* et al. *2005 [182].*

results, Surendran *et al.* concluded that, when the ionic radii of the dopants are between 0.6 and 0.7 Å (i.e., close to the average ionic radii of the B-site ion in BMT), the quality factor touches maximum values [182].

Dielectric loss, which comes from the dynamics of mechanisms responsible for the lattice vibrations, depends on the number of degeneracies in the phonon spectrum. It is well documented that the crystallographic symmetry lowering induced by ordering reduces the number of degeneracies and thus lowers the dielectric loss in ordered structures. In this mechanism, because the most important contribution comes from optical phonons, the imaginary part of the dielectric constant (i.e., loss) can be expressed as

$$\varepsilon'' \infty \left(\frac{h\omega}{kT}\right)\left[\sinh\left(\frac{h\omega_0}{kT}\right)\right]^{-2} \tag{3.14}$$

where ω_0 is the average frequency of the optical phonon and ω is the measurement frequency. This expression implies three fundamental points: (i) dielectric loss varies linearly with frequency, (ii) at high temperatures ($kT > h\omega$), the variation of dielectric loss with temperature is also linear, and (iii) in the low-temperature range the dielectric loss tends towards zero.

It is worth mentioning that a linear decrease of dielectric loss at subzero measurement temperatures was observed by Alford *et al.* [183] in well-sintered dense BMT, which is expected to be free of oxygen vacancies, prepared from high pure raw materials. Understandably, these contradictions demanded a more meticulous design of experiments on the cryogenic behavior of BMT. This work was undertaken by Surendran *et al.* [182] who investigated the cryogenic behaviour of pure, annealed, and doped BMT systematically. In their study, the dielectric loss properties of high pure BMT are studied over a range of temperatures 20–300 K where they observed non-linear behaviour in both cases, that is, as sintered and after annealed at 1450 °C for 48 hours (see Figure 3.22). However, the quality

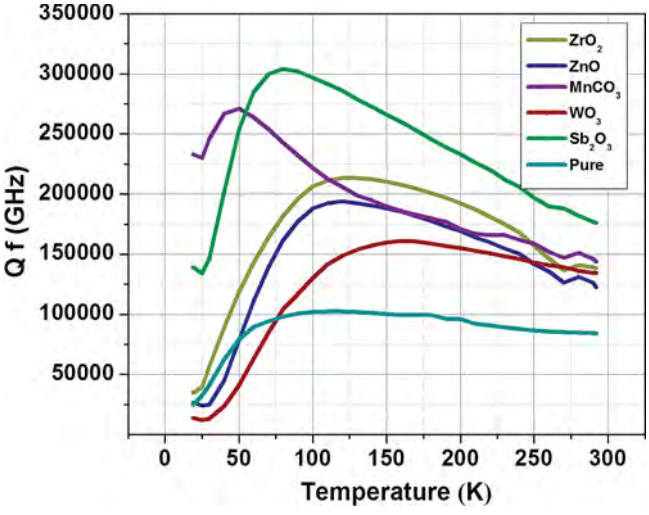

Figure 3.22 *Variation of unloaded quality factor of pure and doped BMT at cryogenic temperature. Source: Adapted from Surendran 2005 [182].*

factor increased in annealed samples and there occurs a "bumpy" behavior, which is not commonly observed in low-loss single crystals [184] like alumina. Comparing theoretical predictions of loss [185–187] with Q-factor measurements is not straightforward because theories assume defect-free single crystals, whereas the measurements are performed on polycrystalline dielectrics, which are never defect free. Intrinsic losses are dependent on crystal structure and can be described by the interaction of the phonon system with the AC electric field. The AC electric field alters the equilibrium of the phonon system and the subsequent relaxation is essentially possible owing to extrinsic factors like impurity ions, thick grain boundaries, etc. This could be the reasons behind the non-linear behaviour of the dielectric loss below the ice point. It is interesting to note that in doped samples (see Figure 3.22), the presence of paramagnetic impurities at grain boundaries play a significant role even in controlling the order–disorder phase transition, which is intimately related to its loss factor.

It is a well-appreciated fact that most substitutions of the cations in BMT could generate no better dielectric properties compared to the starting material BMT. For example, the efforts to replace Ta in $Ba(Mg_{1/3}Ta_{2/3})O_3$ with Ti and W collectively based on $Ba(Mg_{1/3}Ta_{(2-2x)/3}W_{x/3}Ti_{x/3})O_3$ could result in inferior dielectric characteristics [188]. The effect of different tetravalent octahedral site substitutions on the cation ordering in $Ba(Mg_{1/3}Ta_{2/3})O_3$ perovskites were explored by Chai *et al.* [189] through their landmark investigation on the phase stabilities and structures of their solid solutions with $BaTiO_3$, $BaSnO_3$, $BaeO_3$, and $BaZrO_3$. Chai *et al.* proved that the size M^{4+} cation in $(1 - x)Ba(Mg_{1/3}Ta_{2/3})O_3{-}xBaM^{4+}O_3$ (cation with an oxidation state 4) plays a critical role in the formation of the 1:1 ordered structure. The introduction of a larger dopant such as Ce (0.87 Å) or Zr (0.72 Å) removes the 1:2 order in BMT and stabilizes a region of 1:1 order that is up to 25 mol% substitution. For example, in the cerate system, the 1:2 ordered form of $Ba(Mg_{1/3}Ta_{2/3})O_3$ has very limited stability and transforms to a cubic, 1:1

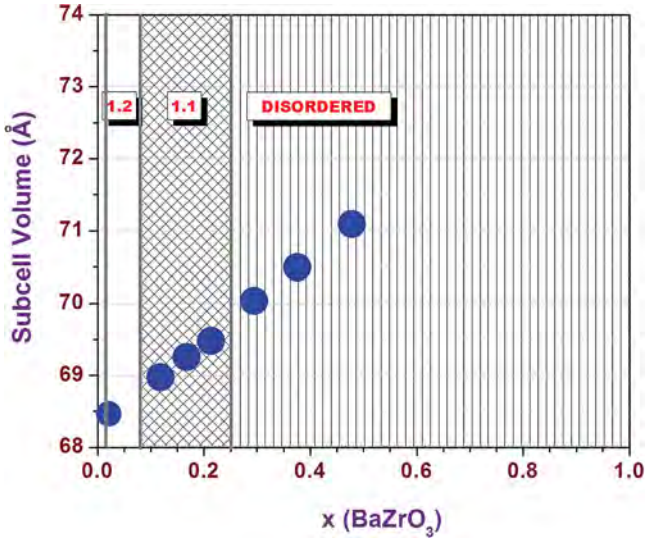

Figure 3.23 *Volume of the subcell versus concentration of $BaZrO_3$ in BMT. Source: Chai* et al. *1997 [189]. Reproduced with permission from Elsevier.*

ordered structure with a doubled perovskite repeat between 7 and 25 mol% $BaCeO_3$. In this report the authors pointed out that bigger tetravalent cations like Zr^{4+} or Sn^{4+} induce a 1:1 ordering in the crystal lattice while undersized cations like Ti^{4+} promote a disordered structure [189]. The cerium oxide that bears multiple oxidation states of 3 and 4 can form possible configurations $Ba[(Mg_{1-x}Ce_x)_{1/3}Ta_{2/3}]O_{3-\delta}$ or $Ba(Mg_{1/3}Ta_{2/3})_{1-x}\,Ce_xO_3$ if it reacts with the BMT matrix. A similar picture is viewed in $Ba(Mg_{1/3}Ta_{2/3})O_3$—$BaZrO_3$, where the crystal structure transforms from 1:2 ordered to a 1:1 ordered cubic $Fm\bar{3}m$ for substitution levels between 10 to 25 mol% of $BaZrO_3$, as shown in Figure 3.23. Based on these observations, Chai *et al.* [189] proposed a new random site model for cationic ordering. In this model, the B′ positions are occupied by Ta and B′ sites containing a random distribution of the remaining cations. With this model the 1:1 ordered phase can be represented by $Ba\{[Mg_{(2-y)/3}Ta_{(1-2y)/3}Zr_y]_{12}[Ta]_{1/2}\}O_3$, where the predicted range of y (= $2x$), $0.0 < y \leq 0.5$ is in excellent agreement with the range of homogeneity determined in the phase stability studies. In 2006, Surendran *et al.* [190] found that the quality factor of the solid solution phases between BMT and $BaTiO_3$ can be correlated to their tolerance factor. The resonance vanishes when the tolerance factor of the solid solution phases are greater than 1.045. In other words, the upper limit of tolerance factor for a partial substitution of a tetravalent Ti^{4+} ion at the B site of BMT is 1.045. For a higher level of Ti^{4+} ion occupation will increase the tolerance factor and destabilize the basic perovskite structure into a disordered one.

In the case of A-site substitution, however, a lot of noteworthy contributions have been made by Japanese investigators [191, 192], especially in $Ba_{1-x}Sr_x(Mg_{1/3}Ta_{2/3})O_3$ poly crystals. The structural change due to the phase transformation has been connected with the tilting of the oxygen octahedra in the perovskite unit cell. The $Sr(Mg_{1/3}Ta_{2/3})O_3$ has

a lower symmetry. According to these reports, it was revealed that during the process of phase transformation $Ba(Mg_{1/3}Ta_{2/3})O_3 \rightarrow Sr(Mg_{1/3}Ta_{2/3})O_3$, some additional lines are observed in the X-ray diffraction patterns, which suggests a monoclinic crystal structure fitting for the proposed region. However, these phase transitions are useful for a technological perspective as the dielectric properties deteriorate with increasing value of x in $Ba_{1-x}Sr_x(Mg_{1/3}Ta_{2/3})O_3$ [192].

3.6.2.2 $Ba^{2+}(Zn^{2+}_{1/3}Ta^{5+}_{2/3})O_3$

As seen in the previous section 3.6.2, Kawshima and coworkers [127] in 1977 were the first to report the usefulness of microwave dielectric resonator materials in the $Ba(B'_{1/3}B''_{2/3})O_3$ system. Along with structurally similar other complex perovskites, they reported $Ba(Zn'_{1/3}Ta_{2/3})O_3$ (BZT) with promising dielectric properties $\varepsilon_r = 30$, $\tau_f = 0 \pm 0.5$ ppm/°C, and $Q = 6500$. Ever since BZT was investigated commercially and academically it has become one of the most useful candidates for microwave dielectric applications. It has been reported that 1:2 ordering in the B site for compounds of general formula $Ba(B'_{1/3}B''_{2/3})O_3$ is a strong function of radius mismatch between B and B′′ ions. As early as 1963, Galasso and Pyle [125] observed that the ordering increased with increasing difference between the radius of B and B′ ions. Several years later, Jacobson *et al.* [193] studied the long-range order in BZT by X-ray diffraction and refined the structure by neutron diffraction data. The ordering in BZT produces superstructure reflections originating from the B-site cation ordering and deviation of the *c*/*a* ratio from $\sqrt{(3/2)}$ (~1.2247), the ideal value for a hexagonal structure [194, 195]. As in the case of $Ba(Mg_{1/3}Ta_{2/3})O_3$, here, also, the ordering of the Ta and Zn cations on the B sites leads to a trigonal distortion of the cubic perovskite unit cell (see Figure 3.24), and the appearance of superstructure peaks in

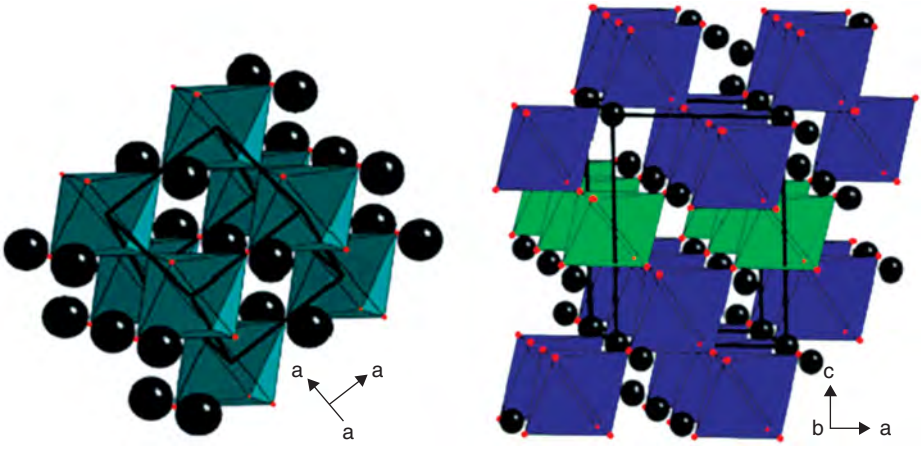

Figure 3.24 *Illustration of the crystal structure of the disordered cubic perovskite subcell (left, <111> direction vertical) and the ordered trigonal supercell (P3hm1) (right, c-axis vertical) of $Ba_3ZnTa_2O_9$ showing layers of TaO_6 and ZnO_6 octahedral. Source: Mallinson* et al. *2007 [196]. Reprinted with permission from American Chemical Society, © 2016.*

the X-ray diffraction pattern, the strongest of these being the (001) and (100) reflections of the trigonal cell [196]. In BZT, the perfectly ordered structure is formed by the following process:

1. A perovskite-type structure is formed, but Zn and Ta are in disorder.
2. Zn and Ta are partially in order.
3. Zn and Ta are completely in order and the lattice is distorted.

As a widely accepted protocol, high-quality BZT could be prepared by calcination in the range 1100–1200 °C and sintering at temperatures in the range 1500–1550 °C [158, 197]. Nevertheless, the high-volatilization issue of ZnO is a practical problem to be addressed, to achieve a high Q phase of BZT [140]. It should be noted that the ordering in $Ba(Zn_{1/3}Ta_{2/3})O_3$ could be calculated using superstructure reflections as described above; however, it is inaccurate to quantify the extent of order based on the intensities of one or two superlattice reflections due to the occurrence of Zn vacancies. The superstructure reflection intensities and widths depend in a complex manner on the thermal history, as the ordering is a kinetic process that is accelerated at higher temperatures yet is opposed thermodynamically by a decrease in the order parameter on approaching the transition temperature [141].

In this connection, Bieringer *et al*. [142] made a meticulous comparative study on the crystallographic structure of as-received (pre-sintered) powder and sintered (pellet) BZT samples. The two crystal structures of BZT have significantly different B-site bond lengths (Å) [Zn—O: 1.977(4) × 6, Ta—O: 2.023(7) × 3 and 2.141(10) × 3] compared to [Zn—O: 2.1246(22) × 6, Ta—O: 1.9355(23) × 3 and 2.0827(13) × 3]. The considerable differences in the phase assemblage within the two samples and the atomic-level structures of these phases indicate the extreme sensitivity of the BZT system to processing, presumably due to the difficulty in ensuring homogeneous ZnO partial pressure throughout the annealing environment. The Rietveld refinements indicate, via the cell volume comparison between the two BZT phases in each sample, that the well-ordered phases in both cases are not the Zn-deficient ones, suggesting a complex ordering mechanism in which a Zn-deficient less-ordered phase assists the growth of well-ordered domains in a second phase that is microscopically almost identical in both pellet and powder samples. The presence of the highly Zn-deficient impurity phase together with the more highly ordered and larger domain BZT phases in the powder sample is consistent with the importance of Zn loss in driving cation ordering in pure BZT. The BZT structure is only capable of tolerating a low level of Zn B-site vacancies before a related structure with face- as well as corner-sharing octahedra is stabilized; these octahedral vacancies may be sufficiently mobile to enhance the cation diffusion processes responsible for ordering within trigonal BZT, leading to both enhanced trigonal domain sizes and greater Zn/Ta differentiation within the domains. The refinement converged but yielded an anomalously large negative displacement parameter for Zn. The results indicated that subsequent to the ZnO loss, there occurs appearance of a $Ba_8ZnTa_6O_{24}$ impurity to accommodate the Zn deficiency and the sharpening of the superstructure reflections due to an increase in the ordered domain size [142].

Earlier reports also suggest that sintering at temperatures above 1500 °C or prolonged heat treatment leads to volatilization of ZnO [158, 198], leading to poor densification near the surface of the samples. However, homogeneous densification can be achieved when BZT pellets were muffled in ZnO powder [199]. Alternatively, ZnO loss can be avoided

during heat treatment by a double pre-calcination procedure [200]. The surface of the prolonged sintered samples showed that the as-sintered surface is depleted of Zn ions and enriched in Ta concentration [158]. Eventually this can lead to formation of new zinc-deficient phases such as $Ba_8ZnTa_6O_{24}$ [201], $Ba_3Ta_2O_8$, and $BaTa_2O_6$ [198, 202, 203]. Excessive Zn evaporation in turn affects the cation order and causes the microwave dielectric properties to deteriorate. Having said that, several researchers believed that a minor amount of ZnO loss can also be beneficial since it can generate enhancement of the cation diffusion and domain growth, a higher extent of cation order, and a supplementary distortion [201, 204]. When Zn^{2+} ions on the B′ site were depleted, they are partially replaced by Ba^{2+}, which have a much larger ionic size (1.61 Å) comparatively to 0.74 Å for Zn. This substitution creates a supplementary unit cell distortion, even when the long-range order is saturated and leads to an increase of Q.

As a sintered BZT specimen is likely to be disordered or partially ordered, its order can be improved by annealing at about 1400 °C for various time lengths up to 120 hours, as demonstrated by Desu and O'Bryan [158]. Kawashima *et al.* [195, 198] also made a similar observation of marginal improvement in the cation order and hence Q-factor through long-time annealing. These investigators noticed that the intensity of the $hkl = 100$ reflection increased with increase in sintering time, showing a resultant increase in Zn—Ta ordering, and reached a saturation value at about 60 hours of sintering. Later on, Reaney *et al.* [205] thoroughly investigated the order–disorder transition in BZT using XRD and HRTEM. Their principal strategy to achieve high order was to anneal and quench the sintered sample from 1600 °C. It should be noted that samples quenched from 1625 °C did not show any superlattice reflections, indicating that order–disorder transitions occur between these two temperatures. This is clearly visible in Figure 3.25, which depicts the electron diffraction patterns recorded from samples quenched from 1600 and 1625 °C. The samples quenched at 1600 °C showed the presence of 1:2 B-site cation ordering as superlattice reflections at $h \pm 1/3, k \pm 1/3$, and $l \pm 1/3$ positions (Figure 3.25a). However, the BZT specimen quenched from 1625 °C did not show superlattice reflections resulting from (see Figure 3.25b) the 1:2 ordering, other than some diffuse spots corresponding to 1:1 ordering. This can be an intermediate metastable structure frozen in during quenching [141, 205]. In 1997, Barber

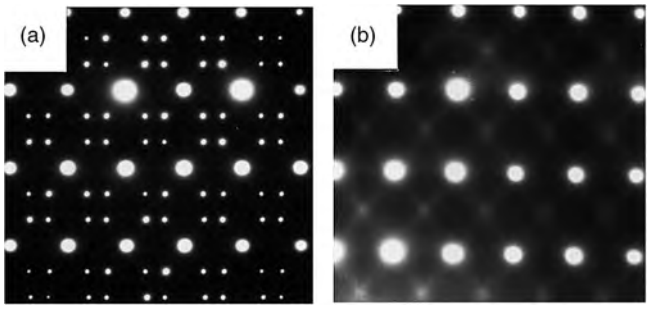

Figure 3.25 *Electron diffraction patterns recorded from BZT with the beam perpendicular to a pseudocubic {110} direction obtained from the center of a grain in a sample quenched from (a) 1600 °C and (b) 1625 °C. Source: Qazi* et al. *2001 [141]. Reproduced with permission from Elsevier.*

et al. [206] also observed a similar metastable 1:1 B-site ordering in the early stages of ordering in BZT.

BZT, being one of the highest Q materials ever, was the reason several investigators invested their efforts on improving their microwave dielectric properties through doping, annealing, ZnO muffling, and solid solution with suitable other low-loss materials. The effect of various dopants on the Q-factor of BZT was reviewed and tabulated by Sebastian in his book entitled *Dielectric Materials for Wireless Communications* and in a recent review [59, 207]. However, it is still unclear as to which is the right strategy or the suitable dopant that can generate the high-Q phase in this complex perovskite. For example, though there were several reports on the arresting of ZnO loss and thereby improving the quality factor, there were a few examples where ZnO muffling deteriorates properties [208]. The same report suggests that addition of 0.5–1.5 mol% $BaWO_4$ improved the sinterability of BZT and increased *Qf* to 160 000–200 000 GHz when sintered at 1570–1580 °C. Oxides such as Al_2O_3, SnO_2, ZrO_2, Ga_2O_3, Ta_2O_5, $Sr(Ga_{1/2}Ta_{1/2})O_3$, etc., were some of the additives that yielded good improvement in the dielectric properties of BZT [59, 199]. Of all the additives, the highest *Qf* reported (~210 000 GHz) was with the addition of $Ba_{0.75}Sr_{0.25}(Ga_{1/2}Ta_{1/2})O_3$ and $BaWO_4$. After doping a series of additives to BZT, Varma *et al.* [209] made an interesting observation that the quality factor increased when the ionic radii of the additive is close to either of the B-site ions (Zn or Ta). Figure 3.26 shows the variation of the *Qf* in BZT as a function of the ionic radii of the additive cations [209]. Interestingly, the Q-factor was found to be increased when the ionic radii of the dopant was close to that of Zn (0.74 Å) or to that of Ta (0.64 Å). This investigation revealed that an

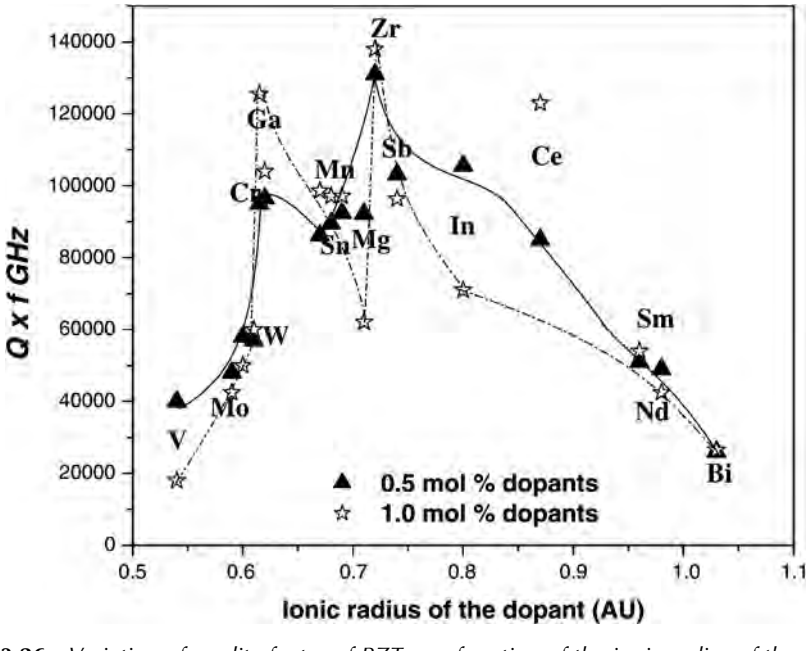

Figure 3.26 *Variation of quality factor of BZT as a function of the ionic radius of the additive cation. Source: Varma* et al. *2005 [209]. © The Japan Society of Applied Physics.*

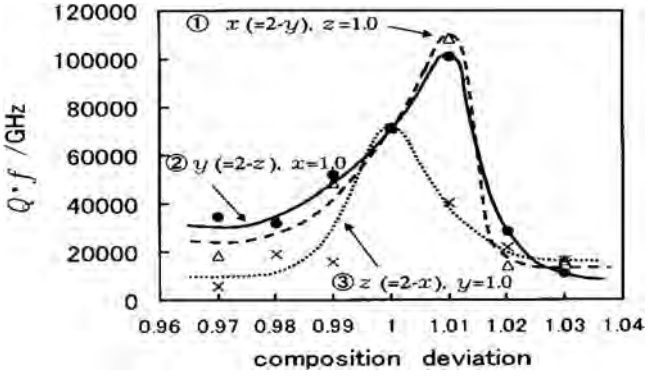

Figure 3.27 *The dependence of microwave quality factor of $Ba(Zn_{1/3}Ta_{2/3})O_3$ on the compositional deviation around $xBaO—y_{1/3}ZnO—z_{2/3}TaO_{5/2}$ system ($x + y + z = 3$). Source: Adapted from Ohsato 2016 [272].*

amount of 0.5 mol% of Mg, Ni, Cr, In, Ga, Sn, Zr, Ce, Mn, and Sb improved the quality factor of BZT. The highest *Qf* was found for those samples added with Zr, Cr, and Ce. Contrary to expectations, in a few of the doped samples the quality factor was very much improved although the order parameter was decreased. The exact reason for this discrepancy is unclear. Nonetheless, it can be hypothesized that those cation additives having ionic radii close to that of the B-site ions, by improving the *Qf* indirectly implies that they are substituting for Zn or Ta in BZT [209].

In 2005, Ohsato and coworkers [210, 272] investigated the effect of non-stoichiometry on the cation order and microwave dielectric properties of BZT. They have synthesized compositional deviations based on the formula $xBaO—y_{1/3}ZnO—z_{2/3}TaO_{5/2}$ system ($x + y + z = 3$). They observed that the superlattice ordering ratio was found to be dependent on slight compositional deviations. As shown in Figure 3.27, a cation ordered structure with perovskite single phase was obtained as the composition approached the stoichiometric form of $Ba(Zn_{1/3}Ta_{2/3})O_3$, where a significant high Q-factor ($Qf = 110\,000$ GHz) was observed [272]. In Figure 3.27, the first area (I) is composed of a single phase of BZT with an ordering structure and high *Qf*. Compositions E and K have about 50% higher *Qf* than pure BZT composition A. The composition K is located on the boundary area (I) as has a minor secondary phase. The ordering ratio on the E is lower than A and the density of the composition E is the same as A. The second one (II) is ordered BZT with a secondary phase $BaTa_2O_6$ with a certain amount of Zn. The ordering ratio of compounds located in this area is high – about 70 to 80%. As the composition was deviated from stoichiometry, the Q-factor decreased, which was believed to be due to the presence of a disordered phase with poor densification and the presence of the secondary phase. This observation contradicts a few of the previous assumptions that the presence of a slight non-stoichiometry may improve the densification and hence the Q-factor through stabilization of the ordered phase [158]. Based on these observations, Ohsato and coworkers [210, 272] constructed a ternary phase diagram for BZT as shown in Figure 3.28. According to this phase diagram, ordered compositions of BZT compounds are located on the Ta_2O_5-rich side (region II), which is precipitated with secondary phase $BaTa_2O_6$ as a eutectic phase diagram system.

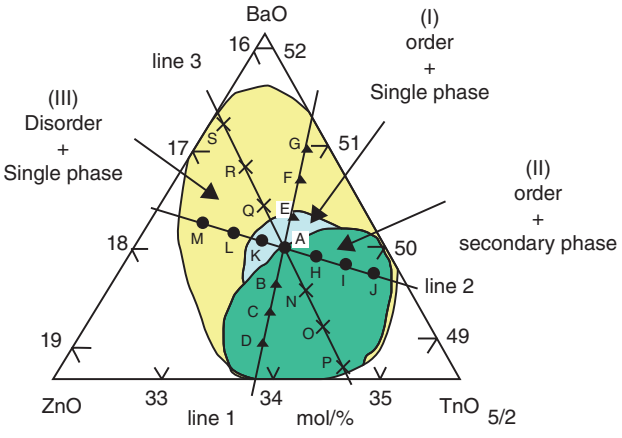

Figure 3.28 *BaO—ZnO—$TaO_{5/2}$ partial ternary system in the vicinity of BZT. Synthesized compositions are shown by alphabets A to S. A point is pure BZT. Three areas are shown as (I) for order/single phase, (II) for order/secondary phase, and (III) for disorder/single phase. Source: Adapted from Ohsato 2016 [272].*

Since a few of the dopants improved the quality factor in BZT, mainly through improved densification, and in some cases with an improvement in the 1:2 long-range order of the B-site cation. Now the important question is, do we really need a cation order in order to achieve a high Q-factor in complex perovskites? As seen in the discussions on BMT in the previous subsections, the cation order favors the stabilization of the high Q phase. In BZT research, this issue was curiously raised after Tamura *et al.* [211] examined the microwave characteristics and cell geometries of BZT—$x$$BaZrO_3$. In the case of $BaZrO_3$ substitution, the high Qf value was maintained for additions up to approximately 4 mol% and was then gradually degraded at higher additive levels. In their opinion, short duration annealing (4 hours at 1500 °C) only required stabilizing a high Q phase [211]. More importantly, addition of a small amount of $BaZrO_3$ decreased the ordering in BZT while improving the Qf factor. This material has $\varepsilon_r = 29$, $Qf > 120\,000$ GHz, and τ_f close to zero. Ever since, $BaZrO_3$ additives are currently used to produce high Q commercial BZT resonators. Later on, Yang *et al.* [212] also studied the effect of ZrO_2 addition on the chemical order and microwave dielectric properties of BZT. They found that addition of a small amount of ZrO_2 destabilized the 1:2 cation ordering, but improved the Qf up to 164 000 GHz when 2 mol% ZrO_2 was added. In both of the above-mentioned researches, as the ZrO_2 or $BaZrO_3$ content increased, the superstructure reflections consequent to 1:2 ordering disappeared and the ceramic transformed to a 1:1 ordered structure. The controversial observation of disordered (or otherwise 1:1 ordered) phase yielding a high Q-factor has been revisited by Davies *et al.* in 1997 [213]. Using HRTEM, they investigated the crucial issues of sensitivity of the Q-factor to the ordering of the Zn and Ta cations in $BaZrO_3$ with added BZT and also the possible reasons behind low levels of $BaZrO_3$ addition that reduce the time required to process these systems to a high Q state.

It was found that in $(1-x)Ba(Zn_{1/3}Ta_{2/3})O_3$—$xBaZrO_3$, during annealing, the unit cell undergoes a hexagonal distortion domain with a hexagonal structure. They subsequently

were nucleated and domain growth followed. The formation of such a domain structure implies that disordered or partially ordered samples contain high levels of unstable domain boundaries. For the trigonal 1:2 structure two different types of boundaries are possible: (i) twin boundary separating domains in which the nucleation and growth of the ordered structure has propagated along different <111> orientations, where four discrete variants are possible, and (ii) an antiphase boundary (APB) associated with each set of ordering orientations. From an energetic and structural perspective, the domain boundaries are highly unfavorable as they produce a region with local cation disorder and associated elastic strain. This investigation emphasized that the importance of dielectric losses associated with the formation of the domain boundaries has to be understood. It is understood that the lowering of the losses at these regions is directly related to the reduction in the degree of strain at the interface, which arises from the preferential segregation of the Zr ions to the boundary regions. Davies and coworkers suggested that Zr is effective in stabilizing the boundaries, which may be due to the preferential segregation of Zr to the boundary regions [213]. Using a detailed electron diffraction analysis of BZT doped with different amounts of $BaZrO_3$ recorded along [110], they concluded that the superstructure reflections at $h \pm 1/2$, $k \pm 1/2$, $l \pm 1/2$ are presumably due to chemical ordering and not due to octahedral tilting, which is temperature sensitive [19]. The structure of the 1:1 phase was interpreted using a "random layer" model in which the ordering arises from an alternation of a Ta layer with a second layer that contains a random distribution of the Zn, Zr, and residual Ta cations. Ceramics in this compositional range also exhibit very low losses. Davies and coworkers [213] concluded that the homogeneity range of the 1:1 phase extends from $x = 0.04$ to approximately $x = 0.25$; substitutions beyond this range stabilize a disordered perovskite.

In 1997, Chai and Davies further investigated the phase stabilities across the entire pseudobinary of $(1-x)Ba(Zn_{1/3}Ta_{2/3})O_3$–$xBaZrO_3$ ($x = 0.075$, 0.15, 0.25, 0.35, 0.4, and 0.5) solid solution [214] system using Rietveld techniques. As expected, the substitution of Zr^{4+} destabilizes the 1:2 cation ordering in BZT and promotes the formation of a cubic, 1:1 ordered structure with a doubled perovskite repeat. The homogeneity range of the 1:1 phase extends from $x = 0.04$ to approximately $x = 0.25$ and any substitutions beyond this range stabilize a disordered perovskite. From these observations, Chai and Davies suggested a "random layer" model for the 1:1 ordered $Ba\{B'_{1/2}B''_{1/2}\}O_3$ model, where the B′ positions were assumed to be occupied exclusively by Ta^{5+} and the B′ sites by a random distribution of Zn^{2+}, Zr^{4+}, and the remaining Ta^{5+} cations. A convenient way to represent this ordered solid solution can be represented by $Ba\{[Zn_{(2-y)/3}Ta_{(1-2y)/3}Zr_y]_{1/2}[Ta]_{1/2}\}O_3$ ($y = 2x$) [214]. As shown in Figure 3.29, the possible simplest arrangements of B-site ions in such a configuration is $Ba\{[Zn,Ta,Zr]_{1/2}Ta_{1/2}\}O_3$ [215]. Here the combination of Zr, Zn, and Ta ions in the B′ plane has the average charge 3^+ and the crystal transformed to a 1:1 ordered structure. In this model, the B′ positions are believed to be occupied exclusively by Ta^{5+} while B′ sites by a random distribution of Zn, Zr, and the remaining Ta cations.

3.6.2.3 $Ba^{2+}(Mg^{2+}_{1/3}Nb^{5+}_{2/3})O_3$

Barium magnesium niobate [$Ba(Mg_{1/3}Nb_{2/3})O_3$ or BMN] is a complex perovskite, which has been of interest as a candidate microwave dielectric material because BMN has a high dielectric permittivity of 32 and a high Q-factor ($Q = 5600$ at 10 GHz) at room temperature

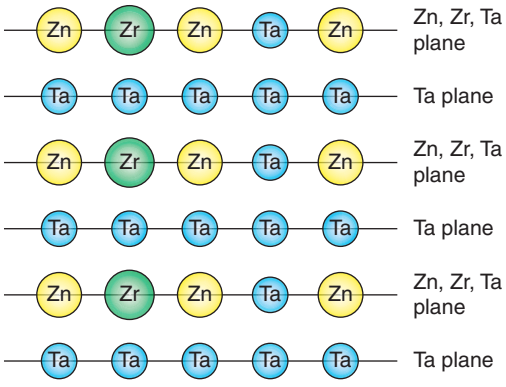

Figure 3.29 *Representation of 1:1 B-site ordering in Ba(Zr, Zn, Ta)O_3 crystal. Source: Tamura 2006 [215]. Reprinted with permission from Elsevier.*

[216]. This complex perovskite has a trigonal structure (P3m1, No. 164) with 1:2 ordering at the B site. In 2001, Moreira *et al.* [216] studied the influence of processing conditions on long-range order and microwave properties of $Ba(Mg_{1/3}Nb_{2/3})O_3$ ceramics. They obtained highly ordered materials using hydrothermal synthesis, followed by sintering above 1350 °C. Employing this route, they could generate relative densities of 99% of the theoretical value and long-range order (S) of 0.98. Based on these results, Moreira and coworkers [216] asserted that the hydrothermal processing route is the most adequate and cost-effective method to produce highly ordered BMN powders, leading to ideal ceramics for microwave applications at lower sintering temperatures than those usually used.

Ma *et al.* recently found that isovalent substitution with cations of comparable ionic radius may also result in a 1:2 ordered structure in BMN [217]. They have investigated a B′-site doped composition, $Ba((Co, Zn, Mg)_{1/3}Nb_{2/3})O_3$, using transmission electron microscopy from different projections ($<110>_c$, $<111>_c$, and $<112>_c$). For the $<110>_c$ and $<111>_c$ zone axes, the occurrence of 1/3{111}-type superlattice reflections in their corresponding selected area electron diffraction images directly revealed the 1:2 ordered structure (see Figure 3.30). The most informative $<110>_c$ zone gave two sets of$<112>_c$ ordering variants, providing a convenient way to detect the twin boundaries. The $<112>_c$ zone axis variant with only one set of $<111>_c$ axes could be used to detect single antiphase boundaries. In addition, the $<111>_c$ zone axis, which is parallel to the ordering direction, clearly showed the hexagonal symmetry of a 1:2 ordered structure in the corresponding high-resolution transmission electron microscopy image (see Figure 3.30). As clearly visible in the figure, the brighter B′ columns connected by red dotted lines form an outside hexagon, inside which there is a smaller hexagon with yellow dotted lines connecting the less bright B′ columns. Thus the 1:2 ordered structure with hexagonal symmetry is clearly confirmed. For a completely ordered sample, there is always a certain proportion of areas without a super period lattice.

The effect of various additives on BMN were mainly aimed in improving the cation order in these materials. Noteworthy is the effort by Tian *et al.* [218], who investigated the effect of addition of $BaWO_4$ on the microstructure, phase formation, 1:2 ordering, and microwave dielectric properties of BMN. They could see the secondary phases of $Ba_5Nb_4O_{15}$ and

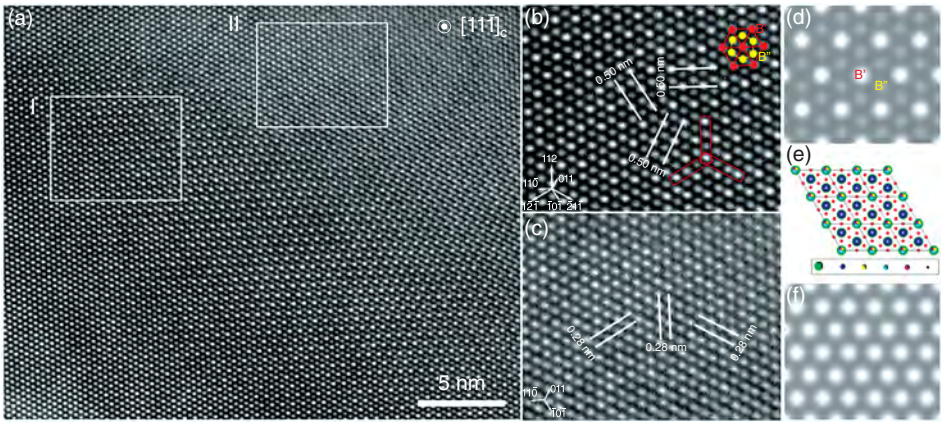

Figure 3.30 *HRTEM image viewed along the [11$\bar{1}$]$_c$ zone axis. Higher amplification lattice images of the labeled areas: (b) area I and (c) area II. Simulated unfocused HRTEM images for (d) 1:2 ordered and (f) disordered Ba($B'_{1/3}B''_{2/3}$)O_3 perovskites; d = 110 nm and thickness t = 4.3 nm along the [11$\bar{1}$]$_c$ zone axis. (e) Schematic diagram of [11$\bar{1}$]$_c$ projection for ordered Ba((Co, Zn, Mg)$_{1/3}$Nb$_{2/3}$)O_3 ceramics. Source: Ma* et al. *2015 [217] Reprinted with permission from Royal Society of Chemistry.*

$BaWO_4$ found in all $BaWO_4$-added samples. This report claimed that addition of 3 mol% $BaWO_4$ gave the highest Qf = 82 300 GHz with ε_r = 31 and τ_f = 32 ppm/°C. It should be noted that the melting point of $BaWO_4$ is at 1430 °C and addition of $BaWO_4$ may lead to liquid-phase sintering. The increase in the quality factor in $BaWO_4$-added BMN is attributed to increase in density and order parameter. Any addition above the level of 3 mol% $BaWO_4$ to BMN degraded its quality factor [218].

3.6.2.4 $Ba^{2+}(Zn^{2+}_{1/3}Nb^{5+}_{2/3})O_3$

The 1:2 ordered perovskite $Ba(Zn_{1/3}Ta_{2/3})O_3$, or BZN, is a widely studied candidate among complex perovskites since it is a material where order–disorder transition takes place at a lower temperature (1350 °C), compared to BMT or BZT, which have higher transition temperatures [219]. Since chemical ordering brings low symmetry and disordering brings high symmetry, Ohsato and coworkers [219] demonstrated that the disordered BZN samples sintered at 1400 °C showed a drastic increase of *Qf*, density, and grain size compared with ordered samples sintered at 1200 and 1300 °C. Interestingly, even with annealing for duration up to 100 h, the structure transformed into an ordered one, but the *Qf* did not improve at all. Therefore, they concluded that the crystal-structural ordering in some complex perovskite systems like BZN has no significant effect on the Q-factor improvement. Ohsato and coworkers asserted that the microwave quality factor strongly depends on the density and grain size but not on the crystal-structure order. Their observation of decreasing *Qf* through annealing might be aided by the low symmetry accompanied with ordering [219].

Ohsato and coworkers' observation of a lower order–disorder transition at a lower temperature in BZN was re-examined by Lee *et al.* [220] in 2007. They investigated the effect of calcination on the evolution of ordered structure and on the quality factor with Raman

spectroscopy, X-ray diffractometry, and transmission electron microscopy. This investigation indicated that in BZN, single calcination at a lower temperature inhibited the growth of the ordered domain during sintering. In contrast, the 1:2-ordered domain in double-calcined BZN powder grew significantly with a higher sintering temperature and a longer soaking time. The best way to achieve a higher degree of 1:2 ordering and better homogeneity to perform double calcination (the first calcination at 1000 °C followed by a second calcination at 1250 °C for 12 h). This is because avoiding the second calcination at 1250 °C could promote the formation of the 1:1 ordered $Ba(Zn_{1/2}Nb_{1/2})O_3$ phase and a disordered phase. The disordered phase is an Nb^{5+} rich phase that was formed in order to maintain the electroneutrality in the structure.

There is a widespread belief that ZnO muffling can be an effective strategy to tackle the Zn volatization from the surface of Ba(Zn, $B''O_3$ ($B'' =$ Ta, Nb)-type materials. However, the research by Wu and Davies [221] found that *Qf* values of stoichiometric BZN pellets heated in ZnO-rich environments were severely degraded compared with the samples muffled in their own powder, even though the ZnO-rich environments improve the density and grain size. As shown in Figure 3.31, the highest *Qf* (~85 000 GHz) was observed in the samples of BZN that were muffled in their own powder during sintering and annealing. On the other hand, sintered and annealed BZN samples with a ZnO powder or in a ZnO vapour had slightly higher densities and larger grain sizes, but the *Qf* values decreased to values as low as 15 000 GHz. It should be noted that the reduction in *Qf* coincides with a large decrease in the cation order. However, even after the partial reaction with ZnO vapor, the composition remains in the high *Q* region (*Qf* = 110 000 at 8 GHz). Wu and Davies believed that the ZnO vapor lowers the sintering temperature of these non-stoichiometric compositions to a value that lies in the stability field of the cation ordered structure [221].

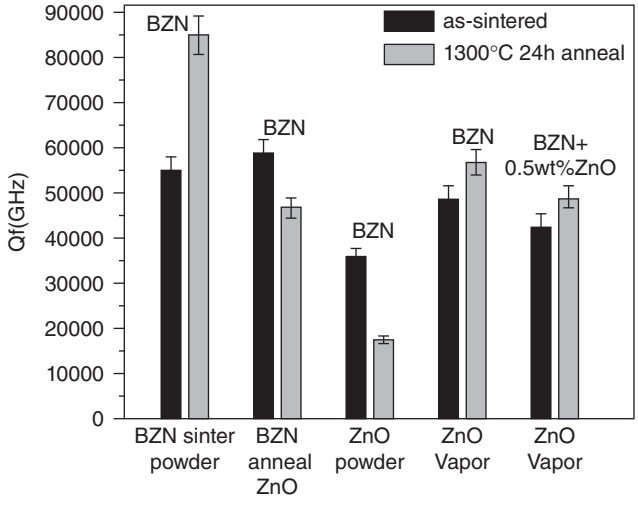

Figure 3.31 *Qf values of stoichiometric $Ba(Zn_{1/3}Nb_{2/3})O_3$ (BZN) after heat treatments in different ZnO loss-protective environments. Source: Wu and Davies 2006 [221]. Reprinted with permission from John Wiley & Sons.*

The effect of various dopants on the order–disorder transition and microwave dielectric properties of $Ba(Zn_{1/2}Nb_{1/2})O_3$ were tabulated in detail by Sebastian [59]. Additives such as $BaSnO_3$, $BaZrO_3$, V_2O_5, $Ba(Co_{1/3}Nb_{2/3})O_3$, $Ba(Ga_{1/2}Ta_{1/2})O_3$, CeO_2, and $Ba_3W_2O_9$ improve the quality factor of BZN. Since BZN has a relatively high τ_f of about 30 ppm/°C, this delimits its use in practical applications. Several attempts were made in the direction of lowering the τ_f of BZN by adding dopants such as B_2O_3, Sb_2O_3—B_2O_3, and by forming solid solution with $Ba(Mg_{1/3}Nb_{2/3})O_3$ (BMN), $Ba(Co_{1/3}Nb_{2/3})O_3$ (BCN), $BaSnO_3$, $Ba(Ni_{1/3}Nb_{2/3})O_3$ (BNN), $Ca(Zn_{1/3}Nb_{2/3})O_3$ (CZN), $Sr(Zn_{1/3}Nb_{2/3})O_3$ (SZN), and $Ba(Ga_{1/2}Ta_{1/2})O_3$ (BGT) [222–226]. Interesting dielectric properties are observed in the solid solution of $Ba(Zn_{1/2}Nb_{1/2})O_3$ with $Sr(Zn_{1/3}Nb_{2/3})O_3$, which is a hexagonally ordered perovskite with $\varepsilon_r = 40$, $Qf = 20\,000$ GHz, and $\tau_f = 38$ ppm/°C. Several authors tailored the τ_f of BZN by forming a solid solution with SZN and obtained a nearly temperature-compensated ceramic, although the quality factor was reduced [227, 228]. In 2007, Varma and Sebastian [229] made a detailed investigation on the effect of dopants (0.5–2.0 mol%) of varying valencies and ionic radii on BZN and reported that dopants with ionic radii close to that of Zn or Nb improve the quality factor of BZN. Figure 3.32 shows the variation of quality factor of BZN as a function of the dopant ionic radii. Earlier, Colla *et al.* [18] found a strong correlation between tolerance factor and the temperature coefficient of permittivity (τ_ε) of these complex perovskites. It is likely that the octahedral tilt resulting from structural phase transitions leads to doubling of the unit cell and appearance of superstructure reflections [18].

Wu and Davies [230] investigated substitution of a small amount of $Ba_3W_2O_9$ (BW) in BZN within a very limited range $0 \leq x \leq 0.02$ in the $(1-x)$BZN—(x)BW system, and found that the additive accelerates the kinetics of cation ordering increases the stability of order and improves the sinterability, resulting in a high Qf of 118 500 GHz, the highest reported for a niobate perovskite. The sintered $(1-x)$BZN—(x)BW ceramics were subjected to several durations of annealing (6—24 h) at 1300 °C to develop ordering. The addition of

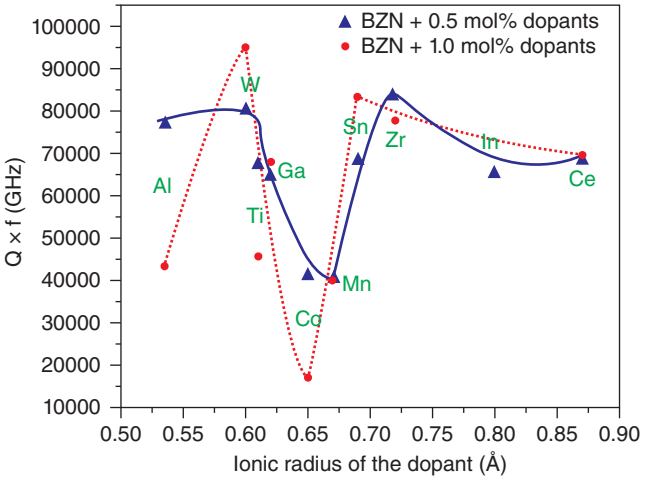

Figure 3.32 *Variation of Qf with ionic radius of dopant for 1 and 0.5 mol% dopant addition in BZN. Source: Varma and Sebastian 2007 [229]. Reprinted with permission from Elsevier.*

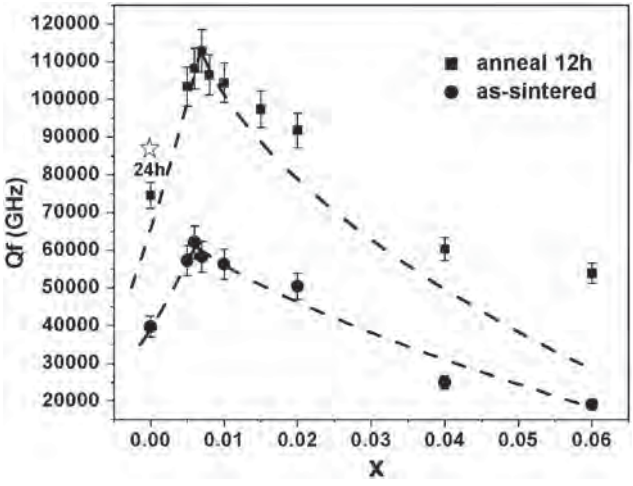

Figure 3.33 *Change in the Qf of (1 – x)BZN—(x)BW with x after sintering (square data points) and annealing (circles). The highest reported Qf value for pure BZN is indicated by a star. Source: Wu and Davies 2006 [230]. Reprinted with permission from John Wiley & Sons.*

more than 2 mol% $Ba_3W_2O_9$ led to the formation of secondary phases, mainly $BaWO_4$. It was found that the *Qf* increased dramatically with *x*, as shown in Figure 3.33. They also found that the variation of *Q* is in accordance with the change in intensity of the (100) order superlattice reflection and the *c*/*a* ratio [230]. Obviously, the substitution of hexavalent W at the B site creates a vacancy, resulting in a possible ordered structure with a stoichiometry, $Ba(Zn_{1-x}\square_x)_{1/3}(Nb_{1-x}W_x)_{2/3}O_3$. In other words, the substitution of W^{6+} for Nb^{5+} in BZN is stabilized by charge compensation through the introduction of vacancies on the Zn sites. The stabilization of the order was ascribed to the instability of the local bonding of oxygen in vacancy-containing Zn—O—Zn "clusters." It is believed that the Zn vacancies also increase the kinetics of the ordering and coarsening process thereby allowing the *c*/*a* distortion of dense ceramic samples to approach their maximum equilibrium value.

Besides the effect of dopants, the contribution of defects associated with impure starting materials and non-stoichiometry can also have a profound effect on the mixing, reactivity, properties, and the degree of order in BZN. With this objective, Kim *et al.* [231] investigated the defect concentration in the two typical niobate triple perovskite compounds [$Ba(Zn_{1/3}Nb_{2/3})O_3$ and $Ba(Ni_{1/3}Nb_{2/3})O_3$], and found that the chemical inhomogeneity in the calcined powder was responsible for the formation of a liquid phase in the non-equilibrium state. These compounds are postulated to melt incongruently above temperatures at which the 1:2 ordered phase forms. The secondary phase formed in BZN was a pyrochlore-like compound of which the composition was Ba:Nb = 1:1 with a small amount of zinc [231].

Wu and Davies' [232] efforts gave a comprehensive explanation to the age-old question in BZN as to whether the quality factor improvement in BZN are primarily associated with changes in density and grain size rather than the cation order. They prepared several pseudobinary systems in BaO—ZnO—Nb_2O_5 with excess and deficient BaO, ZnO, and Nb_2O_5 to examine the extent of any non-stoichiometry in $Ba(Zn_{1/3}Nb_{2/3})O_3$. BZN was found to

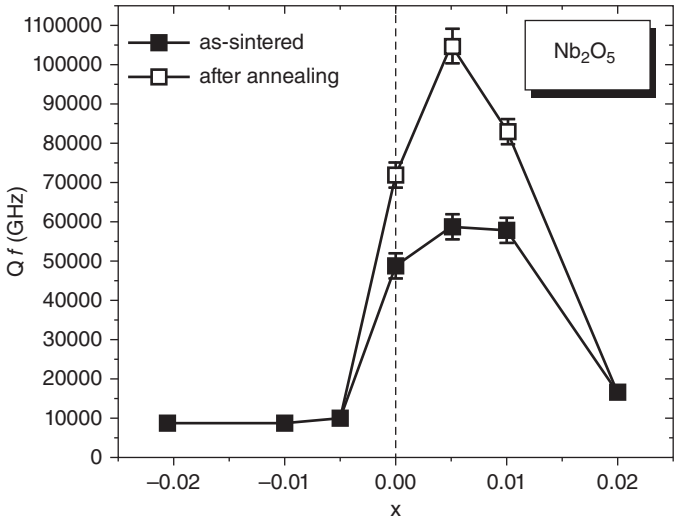

Figure 3.34 *Qf values of $Ba(Zn_{1/3}Nb_{2/3})O_3$ (BZN) with an excess and deficiency of Nb_2O_5. As-sintered samples are indicated by solid squares and annealed samples by open squares. Source: Wu and Davies 2006 [232]. Reprinted with permission from John Wiley & Sons.*

support a limited range of non-stoichiometry in several directions, though a map of the *Qf* values for the non-stoichiometric compositions shows that the highest quality factors do not coincide with a stoichiometric bulk chemistry with Ba:Zn:Nb = 3:1:2. Wu and Davies found that the introduction of a deficiency of ZnO did not significantly affect Q_u while with excess ZnO the *Qf* was significantly degraded due to the large decrease in the degree of order [232]. At higher levels of BaO deficiency, the *Qf* decreased abruptly to 15 000 GHz, but excess BaO also result in disordered perovskite. As shown in Figure 3.34, samples with Nb_2O_5-excess ($x = 0.005$) gave an excellent dielectric response with $Qf = 108\,000$ at 8 GHz. It was found that this sample had well-developed order and a highly dense microstructure. The reduction in *Qf* for $x \geq 0.01$ coincided with the formation of secondary phases. Interestingly enough, the highest *Qf* values (110 000 at 8 GHz) are located in two regions near the $Ba_5Nb_4O_{15}$ and $BaNb_2O_6$ lines. These results concluded that the changes in the dielectric loss properties in high-density ceramics are dominated mainly by the alterations in the cation order, rather than changes in density and grain structure [232].

3.6.3 1:3 Ordering

In complex perovskites, alterations in the degree of order can induce substantial changes in magnetic behavior, dielectric/ferroelectric response, and electronic or ionic conductivity. The commonly seen combinations include mixed-metal cation order on the A- and B-site positions and vacancy/mixed anion order on the oxygen sublattice. In any crystal structure, an ordered arrangement is stabilized when two cationic species occupying the same site differ sufficiently in their coordination preference, valence, or size. As a general trend, examples of A-site ordering are quite rare and often involve vacancies as the alternate cation

species, whereas B-site-ordered perovskites are quite common owing to the increased covalent character of the corner-shared BO_3 framework.

As already shown, 1:1 and 1:2 B-site ordered complex perovskites are numerous and can have impressive microwave dielectric properties. Several attempts have been made to stabilize cation order in complex perovskites with other stoichiometric cation ratios, for example, 1:3 [233]; however, a few typical 1:3 $A(B'_{1/4}B''_{3/4}$ type compositions such as $Ba(Na_{1/4}Ta_{3/4})O_3$and $Sr(Na_{1/4}Ta_{3/4})O_3$ [234] were reported to be disordered. Thus only a couple of perovskites like $Ba(Li_{1/4}Nb_{3/4})O_3$ [235, 236] and $Ba(Re_{1/4}Cr_{3/4})O_3$ [237] with hexagonal stacking sequences were believed to be the sole examples for which the ordering involved a more complex stoichiometry. Nevertheless, the first example of 1:3 order in a cubic perovskite was observed in $Ba(B'_{0.25}B''_{0.75})O_3$ ($B' = Li^+$, Na^+, $B'' = Sb^{5+}$, Bi^{5+}) [238, 239], which forms a cubic body-centered superstructure. The composition $Sr(Li_{0.25}Sb_{0.75})O_3$ also has a distorted monoclinic version of the same structure [240]. In 2001, 1:3 order was identified in a metastable polymorph of $Ca_4Nb_2O_9$ that crystallizes in a monoclinic base-centered supercell [241]. A similar pseudomonoclinic supercell with 1:3 order between Ca and Nb had also been reported for a calcium niobate [242].

Recently Davies *et al.* [60] reported three new families with 1:3 order; $A(B'_{1/4}B''_{3/4}$ were successfully synthesized and their properties were investigated. For example, in the case of $Sr(Li_{1/4}Nb_{3/4})O_3$ and $Sr(Li_{1/4}Ta_{3/4})O_3$, which were believed to have a random B-site distribution, were proved to form structures with the help of transmission electron microscopy. On the other hand, compositions such as $Ca(Li_{1/4}Nb_{3/4})O_3$ and $Ca(Li_{1/4}Ta_{3/4})O_3$ could not be synthesized in single-phase form using the conventional solid-state route. However, Davies and coworkers could generate a single-phase perovskite through the use of $CaC_2O_4{\cdot}H_2O$, $LiTaO_3$, and Nb_2O_5 as precursors [60]. Levin *et al.* found that the X-ray diffraction pattern of $Ca(Li_{1/4}Ta_{3/4})O_3$ was analogous to the 1:3-ordered polymorph of $Ca_4Nb_2O_9$ [243] and could be indexed in the same 1:3-ordered, tilted, P1 triclinic cell. Another composition with 1:3 order, $Sr(Na_{1/4}Nb_{3/4})O_3$, could also be stabilized, but only after extended annealing at ~1000 °C. It was revealed that the deliberate removal of an integer charge on the A site leads to many new potential classes of 1:3-ordered perovskites. For example, 1:3 distribution of B^{2+} and B^{5+} yields a fractional charge (1.67^+) that can be balanced by a mixture of monovalent and divalent cations on the A site, that is, $(A^{1+}_{1/3}A^{2+}_{2/3})(B^{2+}_{1/4}B^{5+}_{3/4})O_3$. Compositions such as $(Na_{1/3}Ba_{2/3})(Ca_{1/4}Nb_{3/4})O_3$, $(Na_{1/3}Sr_{2/3})(Ca_{1/4}Nb_{3/4})O_3$, and $(Na_{1/3}Ca_{2/3})(Ca_{1/4}Nb_{3/4})O_3$ can be synthesized and were demonstrated to be forming from 1:3 <111> cation order [60].

Davies and coworkers gave a possible explanation for the <111> layering in this kind of perovskite that lies in the different local formal charges on the A-site sublattice that result from the 1:3 B-site order. Figure 3.35 shows a schematic representation of the 1:3-ordered $A(B'_{1/4}B''_{3/4})O_3$ structure that highlights the different B-site arrangements in the constituent perovskite subcells. In this case, the 1:3 (…$B'B''B''B''$…) layering yields a monoclinic base-centered supercell with $a_{ord} = a\sqrt{6}$, $b_{ord} = a\sqrt{2}$, $c_{ord} = a2\sqrt{2}$, $\beta = 125.3^o$. The B-site order produces two different A-site environments: one, A(1), has $1B'$ and $7B''$ nearest neighbors while the second, A(2), has $3B'$ and $5B''$ neighbors [60].

After conducting an extensive research to develop new 1:3 ordered perovskites, Davies *et al.* mapped the stability of the 1:3-ordered perovskites as a function of the charge and size differences of the β-sites and delineates phases with and without cation order [60]. It

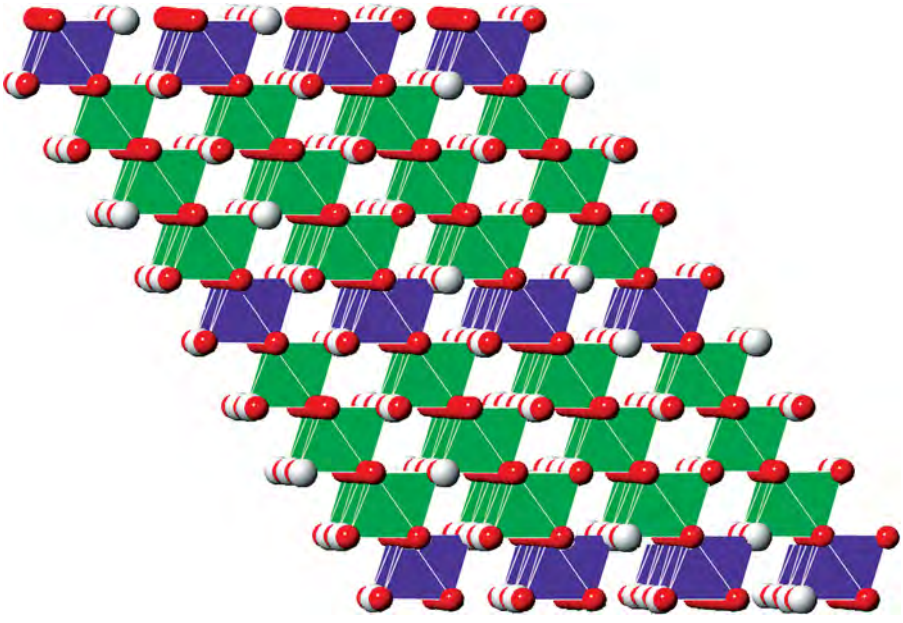

Figure 3.35 *Schematic illustration of the perovskite subcells in the 1:3-ordered* $A(B'_{1/4}B''_{3/4})O_3$ *structure highlighting the different B′ and B″ sites.*

is important to note that for a given charge difference, the formation of 1:3 order requires a larger size difference compared with the 1:2-ordered systems. For a given family, the 1:3 order is further stabilized by a reduced tolerance factor. Davies and coworkers emphasized that the lower tolerance factor reflects a decrease in the stability of their disordered counterparts, which in turn provides a more negative free energy (ΔG) for the ordering reaction [60].

The microwave dielectric properties of these materials are given in the Appendix given at the end of Volume 2. The quality factors of 1:3-ordered materials are very inferior to their 1:2 -ordered counterparts. Therefore, one of their practical utilities may be as additives to the known high Q systems to enhance the stability of the cation order and reduce the sintering temperature. Nevertheless, the new systems also have a broad range of negative and positive τ_f values that may be useful in providing alternate ways to tune the temperature coefficient.

3.6.4 1:2:1 Ordering

As demonstrated in the previous sections, the cation ordering is highly important for understanding and tailoring the properties of complex perovskites. Besides 1:1, 1:2, and 1:3 ordered perovskites, an unusual variant that can exist in a complex perovskite structure was reported by Cava *et al.* [244–246] in the $Ca(Ca_{1/4}B_{2/4}Ti_{1/4})O_3$ (B = Nb, Ta) system, where mixing of three aliovalent cations occurs at the B site, forming a unique 1:2:1 ordering. This material is believed to be a variant derived from $CaTiO_3$—$Ca_4B_2O_9$ (B = Nb, Ta) polymorphs. The low-temperature phase of $Ca(Ca_{1/4}\ Ta_{2/4}Ti_{1/4})O_3$ exhibits 1:2-type ordering

while that of $Ca(Ca_{1/4}Nb_{2/4}Ti_{1/4})O_3$ shows a mixing of 1:1 + 1:3 ordering. In 1977, Hervieu *et al.* [247] found that $Ca_4Nb_2O_9$ possesses an orthorhombic phase at high temperature but a monoclinic phase at low temperature. They proposed a peculiar perovskite-like structure for $Ca_4Nb_2O_9$ polymorphs where one-fourth of Ca ions occupy the B site when represented in $Ca(Ca_{1/3}Nb_{2/3})O_3$ form. Later, Levin *et al.* [248] studied the octahedral tilting and cation ordering of Ca/Nb ions at the B site of $Ca(Ca_{1/3}Nb_{2/3})O_3$ polymorphs. According to them, there can be four temperature-dependent polymorphs, including two high-temperature phases, which exhibit disordering or 1:1 ordering, and two low-temperature phases, which have 1:2 ordering of Ca/Nb ions in the octahedral site.

$Ca_5Nb_2TiO_{12}$ is an interesting composition derived from the solid solution, $xCaTiO_3$—$(1-x)Ca_4Nb_2O_9$ ceramics [249]. This compound can be conveniently represented in the usual complex perovskite form as $Ca(Ca_{1/4}Nb_{2/4}Ti_{1/4})O_3$ with the A site occupied by Ca while the B site is partly occupied by Ca, Nb, and Ti in 1:2:1 ordering. Structural studies revealed that both $Ca_5Nb_2TiO_{12}$ and $Ca_5Ta_2TiO_{12}$ are found to possess different types of ordering between (111) planes, namely, 1:1, 1:2, and 1:3, besides distortions by octahedral tilting. For example, $Ca_5Nb_2TiO_{12}$ was found to possess 1:3 microdomains while 1:2 was noticed for $Ca_5Ta_2TiO_{12}$. Furthermore, it was also revealed that both tantalates and niobates undergo a tilting phase transition from the disordered *Pm*3*m* to distorted *Pnma* (with the $a^-b^+a^-$ tilt of octahedra) symmetries at high temperatures [249]. It was Bijumon *et al.* [250–252] who first suggested the usefulness of these compounds for microwave resonator applications. They reported that $Ca_5Nb_2TiO_{12}$ has $\varepsilon_r = 48$, $Qf > 26\,000$ GHz, and $\tau_f = 40$ ppm/°C, while its tantalum counterpart has $\varepsilon_r = 38$, $Qf > 33\,000$ GHz, and $\tau_f = 10$ ppm/°C.

With the objective of improving the dielectric properties, Bijumon and Sebastian added a series of divalent, trivalent, tetravalent, and pentavalant dopants into both $Ca_5Nb_2TiO_{12}$ and $Ca_5Ta_2TiO_{12}$ [253]. It was found that the addition of small amounts of (0.5–1 mol %) MgO, ZnO, NiO, CuO, Cr_2O_3, SnO_2, Sb_2O_5, and Co_3O_4 into both $Ca_5Nb_2TiO_{12}$ and $Ca_5Ta_2TiO_{12}$ improved the quality factors with a marginal decrease in ε_r. The quality factor of $Ca_5Ta_2TiO_{12}$ reached a maximum of more than 38 000–40 000 GHz with the addition of liquid-phase sintering promoters like MgO and CuO [253]. After analysing the doping results, Bijumon and Sebastian made a correlation between the quality factor and the cationic radii of the dopants in $Ca_5Nb_2TiO_{12}$ and $Ca_5Ta_2TiO_{12}$ (see Figure 3.36). As shown, the average B-site ionic radii of both $Ca(Ca_{1/4}Nb_{2/4}Ti_{1/4})O_3$ and $Ca(Ca_{1/4}Ta_{2/4}Ti_{1/4})O_3$ are the same (0.7213 Å) for a coordination of 6. As shown in Figure 3.36, when the ionic radii of the dopants fall between 0.65 and 0.75 Å (i.e., close to the average ionic radii of the B-site ion in $Ca_5B_2TiO_{12}$ (B = Nb, Ta) ceramics), the quality factor reaches maximum, with the exception of Mn^{2+} and Hf^{4+}[253]. This research group has also developed a few interesting thermostable dielectric resonators in this system. For example, the compositions $Ca_5Nb_2Ti_{0.4}Hf_{0.6}O_{12}$ ($\varepsilon_r = 32$, $Qf = 22\,000$ GHz) and $Ca_5Ta_2Ti_{0.6}Hf_{0.4}O_{12}$ ($\varepsilon_r = 34$, $Qf = 26\,000$ GHz) were found to possess zero τ_f [254, 255].

3.7 Cation Deficient Perovskites

Besides the ordered perovskites described in Sections 3.2 to 3.6, a plethora of anion- or cation-deficient perovskites also exist in nature. What is more attractive is that these

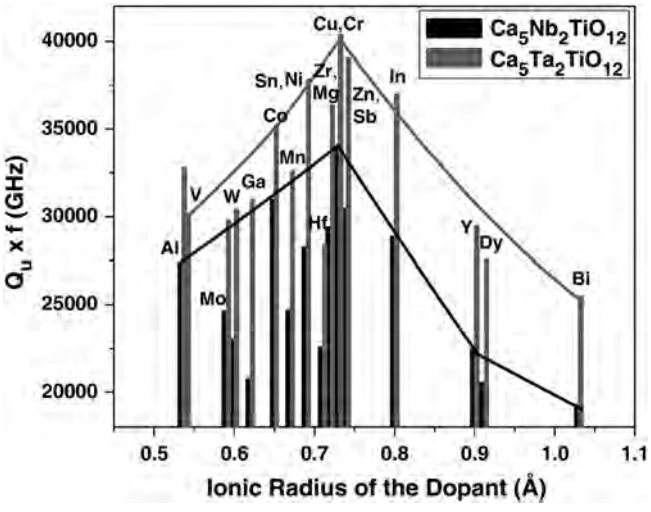

Figure 3.36 *Plot of ionic radius of dopant versus quality factor of 1 mol%-doped $Ca_5Nb_2TiO_{12}$ and $Ca_5Ta_2TiO_{12}$ ceramics. Source: Bijumon and Sebastian 2007 [253]. Reproduced with permission from John Wiley & Sons.*

vacancies are often found to be ordered, forming superstructures that bring about interesting dielectric properties. This kind of perovskite can be conveniently described based on the general formula $A_nB_{n-1}O_{3n}$, where blocks of $(n - 1)$ corner-sharing octahedra were separated by vacant octahedral layers [256]. Their structure is distinctly different from the cubic close-packing sequence of a conventional ABO_3 structure, since the former have mixed cubic and hexagonal AO_3 stacking sequences. These trigonal structured oxides can accommodate a variety of cations at A and B sites, based on A = Ba^{2+}, Sr^{2+}, Ca^{2+}, and La^{3+} and B = Mg^{2+}, Al^{3+}, Ti^{3+}, Ti^{4+}, Nb^{5+}, and Ta^{5+} [257]. In a perovskite configuration, the B cations occupy a quarter of the available octahedral positions in such a way that the BO_6 octahedron forms a three-dimensional network of corner-sharing octahedra. This close packing is usually denoted by *h* (hexagonal) or *c* (cubic) depending on whether neighboring layers are alike or different [258].

$A_5B_4O_{15}$ is the most popular among cation-deficient $A_nB_{n-1}O_{3n}$ perovskites, which came into the limelight after Galasso and Katz reported the earliest member of this family, $Ba_5Ta_4O_{15}$, in 1961 [256]. The $A_5B_4O_{15}$ (A = Ba, Sr, Ca; B = Ta, Nb) compounds were reported to have hexagonal symmetry and crystallize in the space group with one formula per unit cell. In principle, these compounds can be represented as $AB_{0.8}O_3$, giving rise to a vacancy of 0.2B cation per 1A cation to accommodate the charge neutrality. The crystal structure of these materials has been largely controversial. For example, Whiston and Smith [259] reported $Sr_5Nb_4O_{15}$ as hexagonal whereas Weiden *et al.* resolved its structure based on a monoclinic symmetry [260]. However, after a series of Raman scattering, IR, and single-crystal X-ray diffraction studies, the most accepted structure suggested for pentastrontium tetraniobate is hexagonal [261]. Hutchinson and Jacobson found that the ordering of cation vacancies occurs in this kind of 5H material [262]. The microwave dielectric applications of the cation-deficient perovskites were revealed only after Sebastian and

coworkers determined the microwave dielectric properties $A_5B_4O_{15}$ type materials [263–265]. The typical cation deficient perovskite, $Ba_5Nb_4O_{15}$, has promising dielectric properties (ε_r = 40, Qf = 53 000 GHz) despite their τ_f being +80 ppm/°C, which can be tailored to zero through solid solution with isostructural dielectric materials [264]. The microwave dielectric properties of prominent $A_5B_4O_{15}$ type materials are given in the Appendix.

An interesting class of hexagonal perovskites of the general formula $Ba_nLa_4Ti_{3+n}O_{12+3n}$ with n = 1 and 2 was reported by Vineis *et al.*, which have promising microwave dielectric properties [266]. $BaLa_4Ti_4O_{15}$, with the $P\bar{3}c1$ space group, has a high Q-factor (Qf = 47 000 GHz) and dielectric constant (ε_r = 46). Interestingly, this compound belongs to the cation-deficient hexagonal perovskite family $A_nB_{n-1}O_{3n}$ (n = 5), where (Ba, La) occupy the A sites and Ti at the B site [266]. Several other researchers also have investigated the structure-property relationship of this family of materials [267, 268]. The compound, $CaLa_4Ti_4O_{15}$ with ε_r of 41 and τ_f = –26 ppm/°C, shows the highest quality factor (Qf = 50 200 GHz) in this family, probably due to the smallest internal strain at the A site because of the comparable ionic radius of Ca with La ions [269].

$Ba_8ZnTa_6O_{24}$ belongs to another class of cation deficient perovskites in the group $A_8B_7O_{24}$ that is commonly formed as a secondary phase during the evaporation of Zn^{2+} in $Ba(Zn_{1/3}Ta_{2/3})O_3$ [270]. It crystallizes in the hexagonal perovskite structure with ε_r = 30.5, Qf = 62 300 GHz, and τ_f = 36 ppm/°C. Interestingly, a specific composition $Ba_8(Ni_{0.25}Zn_{0.75})\ Ta_6O_{24}$ shows a high quality factor (Qf = 90 000 GHz), which has the potential to be used for practical microwave applications, after tailoring its τ_f [271].

3.8 Summary

Despite being one of the most common and structurally simple minerals, perovskites allow for a huge amount of compositional and structural variation, giving rise to a multitude of interesting dielectric properties. Simple perovskites like $LaAlO_3$, $NdAlO_3$, $LaGaO_3$, and $CaTiO_3$ possess high Q-factors, but most of them are far from being thermostable. Solid solutions of positive- and negative-τ_f materials can be a convenient way to engineer temperature-stable dielectrics, like $CaTiO_3$—$NdAlO_3$. Slight distortions of the perovskite structure can result in several with lower symmetry. When multiple cations substitute on the B site of a perovskite, ordering among themselves can occur, depending on the size and charge difference between the species. Some of the 1:2-ordered complex perovskite oxides are of great importance in mobile and satellite telecommunication systems, where cheap, temperature-stable, and high Q materials can effectively reduce the size and cost of filter and oscillator components. Among them, $Ba(Mg_{1/3}Ta_{2/3})O_3$ (BMT) was reported to possess the highest Q-factor ($Qf \geq$ 200 000 GHz), which renders it a common choice for satellite communication systems, and many pieces of this ceramic are currently orbiting the earth. Interestingly, B-site cation order favors the stabilization of the high-Q phase in BMT. On the other hand, the high Q phase of $Ba(Zn_{1/3}Ta_{2/3})O_3$ (BZT) has been controversial, in that even partly disordered or 1:1-ordered samples also yielded high Q-factors. Besides BMT and BZT, which both have huge markets at high microwave frequency (>10 GHz) applications, $Ba[(Zn,Co)_{1/3}Nb_{2/3}]O_3$ is another complex perovskite that is commercially produced for low microwave frequencies (2—5 GHz). For still lower

frequency applications (< 2 GHz), ceramics with $\varepsilon_r \geq 70$ can provide greater miniaturization due to the requirements for narrow bandwidth and extremely low insertion loss (< 0.3 dB). Hexagonal perovskites like $ALa_4Ti_4O_{15}$ (A = Ca, Sr, Ba) are ideal for such high-ε_r applications.

References

1. Glazer, A.M. (2011) A brief history of tilts. *Phase Transitions*, **84**, 405–420.
2. Hazen, R.M. (1988) Perovskites. *Scientific American*, **258**, 74–81.
3. Pawlak, D.A., Ito, M., Dobrzycki, L., Wozniak, K., Oku, M., Shimamura, K., and Fukuda, T. (2005) Structure and spectroscopic properties of $(AA')(BB')O_3$ mixed-perovskite crystals. *Journal of Materials Research*, **20**, 3329–3337.
4. Ubic, R., Subodh, G., Sebastian, M.T., Gout, D., and Proffen, T. (2009) Effective size of vacancies in the $Sr_{1-3x/2}Ce_xTiO_3$ superstructure. *Ceramic Transactions*, **204**, 177–186.
5. Ubic, R. (2007) Revised method for the prediction of lattice constants in cubic and pseudocubic perovskites. *Journal of American Ceramic Society*, **90**, 3326–3330.
6. Lufaso, M.W. and Woodward, P.M. (2001) Prediction of the crystal structures of perovskites using the software program SPuDS. *Acta Crystallographica Section B*, **57**, 725–738.
7. Ubic, R. and Subodh, G. (2009) Prediction of lattice constants in orthorhombic perovskites. *Journal of Alloys and Compounds*, **488**, 374–379.
8. Roth, R.S. (1957) Classification of perovskite and other ABO_3-type compounds. *Journal of Research of the National Bureau of Standards*, **58**, 75–88.
9. Newnham, R.E. (1983) Structure–property relations in ceramic capacitors. *Journal of Materials Education*, **5**, 947–982.
10. Giaquinta, D.M. and zur Loye, H.-C. (1994) Structural prediction in the ABO_3 phase diagram *Chemistry of Materials*, **6**, 365–372.
11. Salinas-Sanchez, A., García-Muñoz, J.L., Rodriguez-Carvajal, J., Saez-Puche, R., and Martinez, J.L. (1992) Structural characterization of R_2BaCuO_5 (R = Y, Lu, Yb, Tm, Er, Ho, Dy, Gd, Eu and Sm) oxides by X-ray and neutron diffraction. *Journal of Solid State Chemistry*, **100**, 201–211.
12. Woodward, P.M. (1997) POTATO – a program for generating perovskite structures distorted by tilting of rigid octahedral. *Journal of Applied Crystallography*, **30**, 206–207.
13. Zhang, Y., Ubic, R., Xue, D.F., and Yang, S. (2012) Predicting the structural stability and formability of ABO_3-type perovskite compounds using artificial neural networks. *Materials Focus*, **1**, 57–64.
14. Goldschmidt, B.M. (1926) Die Gesetze der Krystallochemie. *Naturwissenschaften*, **14**, 477–485.
15. Megaw, H.D. (1946) Crystal structure of double oxides of the perovskite type. *Proceedings of the Physical Society of London*, **58**, 133–152.
16. Ye, C.Z., Yang, J., Yao, L.X., and Chen, N.Y. (2002) Regularities of formation and lattice distortion of perovskite-type compounds. *Chinese Science Bulletin*, **47**, 458–460.
17. Li, C., Soh, K.C.K., and Wu, P. (2004) Formability of ABO_3 perovskites. *Journal of Alloys and Compounds*, **372**, 40–48.
18. Colla, E.L., Reaney, I.M., and Setter, N. (1992) The temperature-coefficient of the relative permittivity of complex perovskites and its relation to structural transformations. *Ferroelectrics*, **133**, 217–222.
19. Colla, E.L., Reaney, I.M., and Setter, N. (1993) Effect of structural changes in complex perovskites on the temperature coefficient of the relative permittivity. *Journal of Applied Physics*, **74**, 3414–3425.
20. Reaney, I.M., Colla, E.L., and Setter, N. (1994) Dielectric and structural characteristics of Ba-based and Sr-based complex perovskites as a function of tolerance factor. *Japanese Journal of Applied Physics*, **33**, 3984–3990.

21. Shannon, R.D. (1976) Revised effective ionic radii and systematic study of inter atomic distances in halides and chalcogenides. *Acta Crystallographica*, **A32**, 751–757.
22. Ali, R. and Yashima, M. (2005) Space group and crystal structure of the perovskite $CaTiO_3$ from 296 to 1720 K. *Journal of Solid State Chemistry*, **178**, 2867–2872.
23. Dobson, D.P. and Jacobsen, S.D. (2004) The flux growth of magnesium silicate perovskite single crystals. *American Mineralogist*, **89**, 807–811.
24. Colla, E.L., Reaney, I.M., and Setter, N. (1994) A microscopic model for the temperature coefficient of the resonant frequency (τ_f) in complex perovskites used for microwave filter. *Ferroelectrics*, **154**, 35–40.
25. Steiner, O., Colla, E.L., Reaney, I.M., and Setter, N. (1993) Dielectric behaviour as a function of temperature and structure of complex perovskites $Ba_xSr_{1-x}(Mg_{0.33}Ta_{0.67})O_3$ and $A(B'_{1/3}B''_{2/3})O_3$ complex ierovskites $Ba_xSr_{1-x}(In_{0.5}Nb_{0.5})O_3$ in *Euroceramics* (eds P. Duran and J.F. Fernandez), 3rd edn, vol. 2, Faenza Editrice, Iberia, Spain, pp. 223–228.
26. Howard, C.J., Kennedy, B.J., and Chakoumakos, B.C. (2000) Neutron powder diffraction study of rhombohedral rare-earth aluminates and the rhombohedral to cubic phase transition. *Journal of Physics: Condensed Matter*, **12**, 349–365.
27. Demazeau, G., Parent, C., Pouchard, M., and Hagenmuller, P. (1972) Sur deux nouvelles phases oxygenees du cuivre trivalent: $LaCuO_3$ et $La_2Li_{0.50}Cu_{0.50}O_4$. *Materials Research Bulletin*, **7**, 913–920.
28. García-Muñoz, J.L., Rodriguez-Carvajal, J., Lacorre, P., and Torrance, J.B. (1992) Neutron-diffraction study of $RNiO_3$ (R = La, Pr, Nd, Sm): electronically induced structural changes across the metal–insulator transition. *Physical Review B: Condensed Matter*, **46**, 4414–4425.
29. Battle, P.D., Gibb, T.C., and Lightfoot, P. (1990) The structural consequences of charge disproportionation in mixed-valence iron oxides. I. The crystal structure of $Sr_2LaFe_3O_{8.94}$ at room temperature and 50 K. *Journal of Solid State Chemistry*, **84**, 271–279.
30. Woodward, P.M. (1997) Octahedral tilting in perovskites. II. Structure stabilizing forces. *Acta Crystallographica Section B*, **53**, 44–66.
31. Ubic, R., Subodh, G., Sebastian, M.T., Gout, D., and Proffen, T. (2008) Structure of compounds in the $Sr_{1-3x/2}Ce_xTiO_3$ homologous series. *Chemistry of Materials*, **20**, 3127–33.
32. Ubic, R., Hu, Y., and Abrahams, I. (2006) Neutron and electron diffraction studies of $La(Zn_{1/2}Ti_{1/2})O_3$ perovskite. *Acta Crystallographica Section B: Structural Science*, **62**, 521–529.
33. Glazer, A.M. (1972) Classification of tilted octahedra in perovskites. *Acta Crystallogrraphica*, **B28**, 3384–3392.
34. Vijatović, M.M., Bobić, J.D., and Stojanović, B.D. (2008) History and challenges of barium titanate: Part II. *Science of Sintering*, **40**, 235–244.
35. Feteira, A., Sinclair, D.C., Reaney, I.M., and Lanagan, M.T. (2005) Structure property relationship of $BaTi_{1-2y}Ga_yNb_yO_3$ ($0 \leq y \leq 0.3$) ceramics. *Journal of American Ceramic Society*, **88**, 3055–3062.
36. Sánchez, F., Ocal, C., and Fontcuberta, J. (2014) Tailored surfaces of perovskite oxide substrates for conducted growth of thin films. *Chemical Society Reviews*, **43**, 2272–2285.
37. Cho, S.-Y., Kim, I.-T., and Hong, K.S. (1999) Microwave dielectric properties and applications of rare earth aluminates. *Journal of Materials Research*, **14**, 114–119.
38. Cho, S.-Y., Hong, K.S., and Ko, K.H. (1999) Mixture like behaviour in the microwave dielectric properties of the $(1 - x)LaAlO_3$–$xSrTiO_3$ system. *Materials Research Bulletin*, **34**, 511–516.
39. Huang, C.-L. and Chiang, K.-H. (2002) Dielectric properties of B_2O_3 doped $(1 - x)LaAlO_3$–$xSrTiO_3$ ceramic system at microwave frequency range. *Materials Research Bulletin*, **37**, 1941–1948.
40. Lim, D.G., Kim, B.H., Kim, T.-G., and Jung, H.J. (1999) Microwave dielectric properties of $(1 - x)LaAlO_3$–$xTiO_2$ system. *Materials Research Bulletin*, **34**, 1577–1582.
41. Khalyavin, D., Salak, A.N., Senos, A.M.R., Mantas, P.Q., and Ferreira, V.M. (2006) Structure sequence in the $CaTiO_3$–$LaAlO_3$ microwave ceramics – Revised. *Journal of American Ceramic Society*, **89**, 1721–1723.

42. Jancar, B., Valant, M., and Suvorov, D. (2004) Solid state reactions occurring during the synthesis of $CaTiO_3$–$NdAlO_3$ perovskite solid solutions. *Chemistry of Materials*, **16**, 1075–1082
43. Jancar B., Suvorov, D., Valant, M., and Drazic, D. (2003) Characterisation of $CaTiO_3$–$NdAlO_3$ dielectric ceramics. *Journal of the European Ceramic Society*, **3**, 1391–1400.
44. Valant, M. and Suvorov, D. (1999) A new high permittivity $AgNb_{1-x}Ta_xO_3$ microwave ceramics. Part-1. Crystal structures and phase composition relations. *Journal of American Ceramic Society*, **82**, 81–87.
45. Valant, M. and Suvorov, D. (1999) New high permittivity $AgNb_{1-x}Ta_xO_3$ microwave ceramics. Part II: Dielectric characteristics. *Journal of American Ceramic Society*, **82**, 88–93.
46. Telli, M.B. (2005) Chemical solution deposition of silver tantalate niobate $Ag(Ta_xNb_{1-x})O_3$ thin films. Doctoral Thesis, Pennsylvania State University, USA.
47. Kim, H.T., Shrout, T., Rindall, C. and Lanagan, M. (2002) Low temperature sintering and dielectric properties of $Ag(Nb.Ta)O_3$ composite ceramics. *Journal of American Ceramic Society*, **85**, 2738–2744.
48. Duguey, S., Leburgeois, R., Grattepain, C., Haintz, J.M., and Ganne, J.P. (2007) Study of copper substitution in $Ag(Nb_xTa_{1-x})O_3$. *Journal of European Ceramic Society*, **27**, 1171–1175.
49. Valant, M., Suvorov, D., Hoffmann, C., and Sommaria, H. (2001) $Ag(Nb,Ta)O_3$ based ceramics with suppressed temperature dependence of permittivity. *Journal of European Ceramic Society*, **21**, 2647–2651.
50. Yokohama, M., Ota, T., Yamai, I., and Takahashi, J. (1989) Flux growth of perovskite type $La_{2/3}TiO_{3-x}$ crystals. *Journal of Crystal Growth*, **96**, 490–496.
51. Yoshida, M., Hara, N., Takada, T., and Seki, A. (1997) Structure and dielectric properties of $(Ca_{1-x}Nd_{2x/3})TiO_3$. *Japanese Journal of Applied Physics*, **36**, 6818–6823.
52. Moon, J.H., Park, H.S., Lee, K.T., Choi, J.H., Yeo, D.H., and Kim, H.J. (1997) Microwave dielectric properties of the $(1-x)La_{2/3}TiO_3$–$LnAlO_3$ system. *Japanese Journal of Applied Physics*, **36**, 6814–6817.
53. Kim, I.-S., Jung, W H., Inaguma, Y., Nakamura, T., and Itoh, M. (1995) Dielectric properties of A site deficient perovskite type lanthanum–calcium–titanium oxide solid solution system $(1-x)La_{2/3}TiO_3$–$xCaTiO_3$ ($0.1 \leq x \leq 0.96$). *Materials Research Bulletin*, **30**, 307–316.
54. Takahashi, H., Baba, Y., Ezaki, K., and Shibata, K. (1996) Microwave dielectric properties and crystal structure of CaO–Li_2O–$(1-x)Sm_2O_3$–xLn_2O_3–TiO_2 (Ln = lanthanide) ceramic system. *Japanese Journal of Applied Physics*, **35**, 5069–5073.
55. Liu, T., Zhao, X.-Z., and Chen, W. (2006) A/B site modified $CaTiO_3$ dielectric ceramics for microwave applications. *Journal of American Ceramic Society*, **89**, 1153–1155.
56. Young, J. and Rondinelli, J.M. (2014) Improper ferroelectricity and piezoelectric responses in rhombohedral (A, A)B_2O_6 perovskite oxides. *Physical Review B*, **89**, 174110.
57. Howard, C.J., Kennedy, B.J., and Woodward, P.M. (2003) Structures of ordered double perovskites – A group theoretical analysis. *Acta Crystallographica B*, **59**, 463–471.
58. Davies, P. (1999) Cation ordering in complex oxides. *Current Opinion in Solid State and Materials Science*, **4**, 467–471.
59. Sebastian, M.T. (2008) *Dielectric Materials for Wireless Communication*, Elsevier Science Publishers, Amsterdam.
60. Davies, P.K., Wu, H., Borisevich, A.Y., Molodetsky, I.E., and Farber, L. (2008) Crystal chemistry of complex perovskites: new cation-ordered dielectric oxides. *Annual Review of Materials Research*, **38**, 369–401.
61. Sekiya, T., Yamamoto, T., and Torii, Y. (1984) Cation ordering in (Na, La)(Mg, W)O_6 with the perovskite structure. *Bulletin of the Chemical Society of Japan*, **57**, 1859–1862.
62. Leinenweber, K. and Parise, J. (1995) High-pressure synthesis and crystal structure of $CaFeTi_2O_6$, a new perovskite structure type. *Journal of Solid State Chemistry*, **114**, 277–281.
63. Ducau, M., Suh, K.S., Senegas, J., and Darriet, J. (1992) Crystal structure and NMR studies of a cubic perovskite: the fluoride $NaBaLiNiF_6$. *Materials Research Bulletin*, **27**, 1115–1123.
64. Filipev, V.S. and Fesenko, E.G. (1965) Unit cells of some compounds of $A_2B'B''O_6$ types. *Soviet Physics – Crystallography*, **10**, 243–247.
65. Galasso, F., Layden, G., and Flichbagh, D. (1966) $Ba(B_{0.5}Ta_{0.5})O_3$ ordered perovskite-type compounds, possible new laser host materials. *Journal of Chemical Physics*, **44**, 2703–2707.

66. Saines, P.J., Spencer, J.R., Kennedy, B.J., and Avdeev, M. (2007) Structures and crystal chemistry of the double perovskites $Ba_2LnB'O_6$ (Ln = lanthanide B′ = Nb^{5+} and Ta^{5+}): Part I. Investigation of Ba_2LnTaO_6 using synchrotron X-ray and neutron powder diffraction. *Journal of Solid State Chemistry*, **180**, 2991–3000.
67. Saines, P.J., Spencer, J.R., Kennedy, B.J., Kubota, Y., Minakata, C., Hano, H., Kato, K., and Takata, M. (2007) Structures and crystal chemistry of the double perovskites $Ba_2LnB'O_6$ (Ln = lanthanide and B′ = Nb, Ta): Part II – Temperature dependence of the structures of $Ba_2LnB'O_6$. *Journal of Solid State Chemistry*, **180**, 3001–3007.
68. Khalam, L.A, Anjana, P.S., and Sebastian, M.T. (2009) The effect of dopants on the dielectric properties of $Ba(B'_{1/2}Ta_{1/2})O_3$ (B′ = La, Pr, Nd, Sm, Eu, Gd, Tb, Dy, Ho, Y, Yb, and In) microwave ceramics. *International Journal of Applied Ceramic Technology*, **6**, 571–580.
69. Khalam, L.A. (2007) $A(B'_{1/2}B''_{1/2})O_3$ [A = Ba, Sr, Ca, Mg; B′ = rare earths, B″ = Nb, Ta] microwave ceramics for wireless communications. PhD Thesis, Kerala University.
70. Galasso, F.S. (1970) *Structure and Properties of Inorganic Solids*, Pergamon Press, Hedington Hill, Oxford.
71. Saines, P.J., Kennedy, B.J., and Elcombe, M.M. (2007) Structural phase transitions and crystal chemistry of the series $Ba_2LnB'O_6$ (Ln = lanthanide and B′ = Nb^{5+} or Sb^{5+}). *Journal of Solid State Chemistry*, **180**, 401–409.
72. Fu, W.T. and Ijdo, D.J.W. (2006) New insight into the symmetry and the structure of the double perovskites Ba_2LnNbO_6 (Ln = lanthanides and Y). *Journal of Solid State Chemistry*, **179**, 1022–1028.
73. Khalam, L.A., Sreemoolanathan, H., Ratheesh, R., Mohanan, P., and Sebastian, M.T. (2004) Preparation characterisation and microwave dielectric properties of $Ba(B_{1/2}Nb_{1/2})O_3$ [B′ = La, Pr, Nd, Sm, Eu, Gd, Tb, Dy, Ho, Y, Yb, In] ceramics. *Materials Science and Engineering B*, **107**, 264–270.
74. Sreemoolanathan, H., Ratheesh, R., Sebastian, M.T., and Mohanan, P. (1997) $Ba(Tb_{1/2}Nb_{1/2})O_3$: a new ceramic microwave dielectric resonator. *Materials Letters*, **33**, 161–165.
75. Kanaiwa, Y., Wakeshima, M., and Hinatsu, Y. (2002) Synthesis, crystal structure, and magnetic properties of ordered perovskites Sr_2LnTaO_6 (Ln = lanthanides). *Materials Research Bulletin*, **37**, 1825–1836.
76. Khalam, L.A. and Sebastian, M.T. (2006) Effect of cation substitution and non-stoichiometry on the microwave dielectric properties of $Sr(B'_{0.5}Ta_{0.5})O_3$ [B′ = lanthanide] perovskites. *Journal of American Ceramic Society*, **89**, 3689–3695.
77. Woodward, P.M. (1997) Structural distortions, phase transitions, and cation ordering in the perovskite and tungsten trioxide structures. PhD Thesis, Oregon State University, USA.
78. Howard, C.J., Barnes, P.W., Kennedy, B.J., and Woodward, P.M. (2005) Structures of the ordered double perovskites Sr_2YTaO_6 and Sr_2YNbO_6. *Acta Crystallographica*, **B61**, 258–262.
79. Takahashi, S.J., Kageyama, K., Fuji, T., Yamada, Y., and Kodaira, K. (1997) Formation and microwave dielectric properties of $Sr(Ga_{0.5}Ta_{0.5})O_3$ based complex perovskites. *Journal of Materials Science: Materials in Electronics*, **8**, 79–84.
80. Woodward, P., Hoffmann, R.D., and Sleight, A.W. (1994) Order–disorder in $A_2M^{3+}M^{5+}O_6$ perovskite. *Journal of Materials Research*, **9**, 2118–2127.
81. Barnes, P.W., Lufaso, M.W., and Woodward, P.M. (2006) Structure determination of $A_2M^{3+}TaO_6$ and $A_2M^{3+}NbO_6$ ordered perovskites: octahedral tilting and pseudosymmetry. *Acta Crystallographica*, **B62**, 384–396.
82. Takata, M. and Kageyama, K. (1989) Microwave characteristics of $A(B^{3+}_{1/2}B^{5+}_{1/2})O_3$. *Journal of American Ceramic Society*, **72**, 1955–1959.
83. Khalam, L.A. and Sebastian, M.T. (2006) Microwave dielectric properties of $Sr(B'_{1/2}Nb_{1/2})O_3$ [B′ = La, Pr, Nd, Sm, Eu, Gd, Tb, Dy, Ho, Y, Er, Yb and In] ceramics. *International Journal of Applied Ceramic Technology*, **3**, 364–374.
84. Fuji, T., Sato, H., Ito, S., and Messing, G. (2004) Crystal structure and dielectric properties of complex perovskite (Sr, Ba, Ca)$(Ni_{0.5}W_{0.5})O_3$. *Solid State Ionics*, **172**, 425–429.
85. Trunov, V.K., Konstatinova, L.I., Velikodnaji, Y.A., Evdokinov, A.A., and Frotov, A.M. (1981) The compounds of Ca_2MNbO_6. *Russian Journal of Inorganic Chemistry*, **26**, 1738–1741.

86. Trunov, V.K., Konstatinova, L.I., and Evdokimov, A.A. (1983) An X-ray diffraction study of the compounds Ca_2LnTaO_6. *Russian Journal of Inorganic Chemistry*, **28**, 807–810.
87. Khalam, L.A., Thomas, S., and Sebastian, M.T. (2007) Temperature stable and low loss dielectrics in the $Ca(B'_{1/2}Ta_{1/2})O_3$ [B′ = lanthanides, Y and In] system. *Journal of American Ceramic Society*, **90**, 2476–2483.
88. Trunov, V.K., Sirotkin, V.P., and Evdokimov, A.A. (1983) An X-ray diffraction study of the compounds Sr_2LnEO_6 [E = Nb, Ta], *Russian Journal of Inorganic Chemistry*, **28**, 349–350.
89. Khalam, L.A. and Sebastian, M.T. (2007) Low loss dielectrics in the $Ca(B'_{1/2}Nb_{1/2})O_3$ [B′ = lanthanides, Y] system. *Journal of American Ceramic Society*, **90**, 1467–1474.
90. Ikawa, H. and Takamoto, M. (2003) Products and microwave dielectric properties of ceramics with nominal compositions $(Ba_{1-x}Ca_x)(B'_{1/2}B''_{1/2})O_3$ [$B' = Y^{3+}$, Nd^{3+}, Gd^{3+}, $B'' = Nb^{5+}$, Ta^{5+}]. *Materials Chemistry and Physics*, **79**, 222–225.
91. Harshé, G., Bhalla, A.S., and Cross, L.E. (1994) Synthesis and dielectric properties of cubic perovskite $La(Mg_{1/2}Ti_{1/2})O_3$. *Materials Letters*, **18**, 173–175.
92. Cho, S.Y., Kim, C.H., Kim, D.W., Hong, K.S., and Kim, J.H. (1999) Dielectric properties of $Ln(Mg_{1/2}Ti_{1/2})O_3$ as substrates for high-T_c superconductor thin films. *Journal of Materials Research*, **14**, 2484–2487.
93. Macke, A.J.H. and Blasse, G. (1976) Vibrational spectra of oxidic stannates in relation to order-disorder phenomena. *Journal of Inorganic and Nuclear Chemistry*, **38**, 1407–1409.
94. Macke, A.J.H. (1977) Luminescence and energy transfer in the ordered perovskite system $La_2MgSn_{1-x}Ti_xO_6$. *Physica Status Solidi A: Applied Research*, **39**, 117–123.
95. German, M. and Kovba, L.M. (1983) New ternary oxides with a perovskite structure. *Russian Journal of Inorganic Chemistry*, **28**, 586–587.
96. Negas, T., Yeager, G., Bell, S., and Amren, R. (1991) *Chemistry of Electronic Ceramic Materials* (eds P.K. Davies and R.S. Roth), Technomic Publishing Co. Inc., Lancaster, PA, USA, pp. 21–34.
97. Meden, A. and Ceh, M. (1998) Structure determination and Rietveld refinement of $La(Mg_{0.5}Ti_{0.5})O_3$. *Materials Science Forum*, **278–281**, 773–778.
98. Lee, D.Y., Yoon, S.J., Yeo, J.H., Nahm, S., Paik, J.H., Whang, K.C., and Ahn, B.G. (2000) Crystal structure and microwave dielectric properties of $La(Mg_{1/2}Ti_{1/2})O_3$ ceramics. *Journal of Materials Science Letters*, **19**, 131–134.
99. Avdeev, M., Seabra, M.P., and Ferreira, V.M. (2002) Crystal structure of dielectric ceramics in the $La(Mg_{0.5}Ti_{0.5})O_3$–$BaTiO_3$ system. *Journal of Materials Research*, **17**, 1112–1117.
100. Seabra, M.P., Salak, A.N., Avdeev, M., and Ferreira, V.M. (2003) Structure and dielectric characterisation of the $La(Mg_{1/2}Ti_{1/2})O_3$–$Nd(Mg_{1/2}Ti_{1/2})O_3$ system. *Journal of Physics: Condensed Matter*, **15**, 4229–4238.
101. Seabra, M.P., Avdeev, M., Ferreira, V.M., Pullar, R.C., Alford, N. McN., and Reaney, I.M. (2004) Structure property relations in $x BaTiO_3$–$(1-x)La(Mg_{1/2}Ti_{1/2})O_3$ solid solutions. *Journal of American Ceramic Society*, **87**, 584–590.
102. Vanderah, T.A., Miller, V.L., Levin, I., Bell, S.,M., and Negas, T. (2004) Phase relations, crystal chemistry, and dielectric properties in sections of the La_2O_3–CaO–MgO–TiO_2 system. *Journal of Solid State Chemistry*, **177**, 2023–2038.
103. Salak, A.N., Seabra, M.P. and Ferreira, V.M. (2003) $La(Mg_{1/2}Ti_{1/2})O_3$–$La_{2/3}TiO_3$ microwave dielectric ceramics. *Journal of European Ceramic Society*, **23**, 2409–2412.
104. Seabra, M.P., Avdeev, M., Ferreira, V.M., Pullar, R.C. and Alford, N.M. (2003) Structure and microwave dielectric properties of $La(Mg_{0.5}Ti_{0.5})O_3$–$CaTiO_3$ system. *Journal of European Ceramic Society*, **23**, 2403–2408.
105. Kyocera Corporation (1987) Dielectric ceramic material, US Patent No. 4670409.
106. Santha, N., Jawahar, I.N., Mohanan, P., and Sebastian, M.T. (2002) Microwave dielectric properties of $(1-x)CaTiO_3$–$xSm(Mg_{1/2}Ti_{1/2})O_3$ [$0.1 \leq x \leq 1$] ceramics *Materials Letters*, **54**, 318–322.
107. Kucheiko, S., Kim, H.J., Yeo, D.H., and Jung, H.J. (1996) Microwave dielectric properties of $LaZn_{0.5}Ti_{0.5}O_3$ ceramics prepared by sol–gel process. *Japanese Journal of Applied Physics*, **35**, 668–672.

108. Cho, S.Y., Seo, M.K., Hong, K.S., Park, S.J., and Kim, I.T. (1997) Influence of ZnO evaporation on the microwave dielectric properties of $La(Zn_{1/2}Ti_{1/2})O_3$. *Materials Research Bulletin*, **32**, 725–735.
109. Cho, S.Y., Youn, H.J., Lee, H.J. and Hong, K.S. (2001) Contribution of structure to temperature dependence of resonant frequency in the $(1 - x)La(Zn_{1/2}Ti_{1/2})O_3 \cdot xATiO_3$ (A = Ca, Sr) system. *Journal of American Ceramic Society*, **84**, 753–758.
110. Cho, S.Y., Kim, I.T., and Hong, K.S. (1998) Crystal structure and microwave dielectric properties of $(1 - x)La(Zn_{1/2}Ti_{1/2})O_3$–$xSrTiO_3$ system. *Japanese Journal of Applied Physics*, **37**, 593–596.
111. Yeo, D.H., Kim, J.B., Moon, J.H., Yoon, S.J., and Kim, H.J. (1996) Dielectric properties of $(1 - x)CaTiO_3$–$xLa(Zn_{1/2}Ti_{1/2})O_3$ ceramics at microwave frequencies. *Japanese Journal of Applied Physics*, **35**, 663–667.
112. Kyocera Corporation (2000) Dielectric ceramic composition, preparation method therefore, and dielectric resonator, US Patent No. 6143680.
113. Ubic, R., Hu, Y., and Abrahams, I. (2006) Neutron and electron diffraction studies of $La(Zn_{1/2}Ti_{1/2})O_3$ perovskite. *Acta Crystallographica*, **B62**, 521–529.
114. Huang, C.-L. and Tseng, J.F. (2004) Dielectric characteristics of $La(Co_{1/2}Ti_{1/2})O_3$ ceramics at microwave frequencies. *Materials Letters*, **58**, 3732–3736.
115. Cairns, D.L., Reaney, I.M., Zheng, H., Iddles, D., and Price, T. (2005) Synthesis and characterization of $La(Co_{1/2}Ti_{1/2})O_3$. *Journal of European Ceramic Society*, **25**, 433–439.
116. Rodriguez, E., Lopez, M.L., Campa, J., Viera, M.L., and Pico, L.C. (2002) Crystal and magnetic structure of perovskite La_2MTiO_6 [M = Co, Ni]. *Journal of Materials Chemistry*, **12**, 2798–2802.
117. Song, H.-T., Hsu, C.-S., Kuo, M.-T., and Huang, C.-L. (2004) Microwave characteristics of $Sm(Co_{1/2}Ti_{1/2})O_3$ dielectric resonators. *Materials Letters*, **58**, 2829–2833.
118. Ortega-San Martın, L., Chapman, J.P., Cuello, G., Gonzalez-Calbet, J., Arriortua, M.I., and Rojo, T. (2005) Crystal structure of the ordered double perovskite, Sr_2NiTeO_6. *Zeitschrift für Anorganische und Allgemeine Chemie*, **631**, 2127–2130.
119. Patwe, S.J., Achary, S.N., Mathews, M.D., and Tyagi, A.K. (2006) Crystal structure and thermal expansion behavior of Ca_2MgWO_6. *Materials Chemistry and Physics*, **98**, 486–493.
120. Augsburger, M.S., Viola, M.C., Pedregosa, J.C., Carbonio, R.E., and Alonso, J.A. (2006) Crystal structure and magnetism of the double perovskites $Sr_3Fe_2TeO_9$ and $Ba_3Fe_2TeO_9$: a neutron diffraction study. *Journal of Materials Chemistry*, **16**, 4235–4242.
121. Kwon, D.K., Lanagan, M.T., and Shrout, T.R. (2007) Microwave dielectric. Properties of BaO–TeO2 binary compounds. *Materials Letters*, **61**, 1827–1831.
122. Ubic, R., Letourneau, S., Thomas, S., Subodh, G., and Sebastian, M.T. (2010) Structure, microstructure, and microwave dielectric properties of $(Sr_{2-x}Ca_x)(Mg, Te)O_6$ double perovskites. *Chemistry of Materials*, **22**, 4572–4578.
123. Roy, R. (1954) Multiple ion substitution in the perovskite lattice. *Journal of American Ceramic Society*, **37**, 581–588.
124. Galasso, F.S., Barrante, J.R., and Katz, L. (1961) Alkaline earth tantalum oxygen phases including the crystal structure of an ordered perovskite compound $Ba_3SrTa_2O_9$. *Journal of American Chemical Society*, **83**, 2830–2832.
125. Galasso, F.S. and Pyle, J. (1963) Ordering in compounds of the $A(B'_{0.33}Ta_{0.67})O_3$ type. *Inorganic Chemistry*, **23**, 482–484.
126. Galasso, F.S. and Pyle, J. (1963) Preparation and study of ordering in $A(B'_{0.33}Nb_{0.67})O_3$ perovskite type compounds. *Journal of Physical Chemistry*, **67**, 1561–1562.
127. Kawashima, S., Nishida, M., Ueda, I., Ouchi, H., and Hayakawa, S. (1977) Dielectric properties of $Ba(Zn_{1/3}Nb_{2/3})O_3$–$Ba(Zn_{1/3}Ta_{2/3})O_3$ ceramics, in *Proceedings of the 1st Meeting of Ferroelectric Materials and Their Applications* (eds O. Omoto and A. Kumada), Keihin Printing Co., Ltd, Kyoto, Tokyo, pp. 293–296.
128. Nomura, S., Toyoma, K., and Kaneta, K. (1982) $Ba(Mg_{1/3}Ta_{2/3})O_3$ ceramics with temperature stable high dielectric constant and low microwave loss. *Japanese Journal of Appled Physics*, **21**, L624–L626.

129. Nomura, S. (1983) Ceramics for microwave dielectric resonator. *Ferroelectrics*, **49**, 61–70.
130. Sugiyama, M., Inuzuka, T., and Kubo, H. (1990) Effects of processing on microstructure and dielectric properties in $Ba(Mg_{1/3}Ta_{2/3})O_3$ ceramics. *Ceramic Transactions*, **15**, 153–166.
131. Wakino, K. and Tamura, H. (1990) Microwave dielectric materials. *Ceramic Transactions*, **15**, 305–314.
132. Yoon, K.H., Yoo, S.J., Kim, W.S., Kim, J.B., and Kim, E.S. (1999) Effect of BaO/WO_3 on the microwave loss quality of $Ba(Mg_{1/3}Ta_{2/3})O_3$. *Japanese Journal of Appled Physics*, **38**, 5616–5626.
133. Matsumoto, K., Hiuga, T., Takada, K., and Ichimura, H. (1986) $Ba(Mg_{1/3}Ta_{2/3})O_3$ ceramics with ultra-low loss at microwave frequencies, in *Proceedings of Sixth IEEE International Symposium on Application of Ferroelectrics*, Institute of Electrical and Electronic Engineers, Bethlehem, PA, pp. 118–121.
134. Tsai, T.R., Liang, M.-H., Hu, C.T., Chi, C.C., and Lin, I.-N. (2001) Terahertz spectroscopic technique for characterizing the microwave dielectric properties of $Ba(Mg_{1/3}Ta_{2/3})O_3$ materials. *Journal of European Ceramic Society*, **21**, 2787–2790.
135. DuPont, L., Chai, L., and Davies, P.K. (1999) A- and B-site order in $(Na_{1/2}La_{1/2})(Mg_{1/3}Ta_{2/3})O_3$ perovskites. *Proceedings Materials Research Society, Solid State Chemistry of Inorganic Materials II*, **547**, 93–98.
136. Liu, Z.-R., Liu, J.-S., Su, B.-L., and Zhang, X.-W. (2000) Cluster-variation-method studies on the atomic ordering in complex perovskite alloys. *Physical Review B*, **61**, 11918.
137. Sagala, D.A. and Nambu, S. (1992) Lattice energy calculation for ordered and disordered $Ba(Zn_{1/2}Ta_{2/3})O_3$. *Journal of the Physical Society of Japan*, **61**, 1791–1797.
138. Janaswamy, S., Murthy, G.S., Dias, E.D. and Murthy, V.R.K. (2002) Structural analysis of $Ba(Mg_{1/3}Ta_{2/3})O_3$ ceramics. *Materials Letters*, **55**, 414–419.
139. Lufaso, M.W., Hopkins, E., Bell, S.M., and Llobet, A. (2005) Crystal chemistry and microwave dielectric properties of $Ba_3MNb_{2-x}Sb_xO_9$ (M = Mg, Ni, Zn). *Chemistry of Materials*, **17**, 4250–4255.
140. Moussa, S.M., Ibberson, R.M., Bieringer, M., Fitch A.N., and Rosseinsky, M.J. (2003) In situ measurement of cation order and domain growth in an electroceramic. *Chemistry of Materials*, **15**, 2527–2533.
141. Qazi, I., Reaney, I.M., and Lee, W.E. (2001) Order–disorder phase transition in $Ba(Zn_{1/3}Ta_{2/3})O_3$. *Journal of European Ceramic Society*, **21**, 2613–2616.
142. Bieringer, M., Moussa, S.M., Noailles, L.D., Burrows, A., Kiely, C.J., Rossiensky, M.J., and Ibberson, R.M. (2003) Cation ordering, domain growth and zinc loss in the microwave dielectric oxide $Ba_3ZnTa_2O_9$. *Chemistry of Materials*, **15**, 586–597.
143. Lufaso, M.W. (2004) Crystal structures, modeling, and dielectric property relationships of 2:1 ordered $Ba_3MM'_2O_9$ (M = Mg, Ni, Zn; M′ = Nb, Ta) perovskites. *Chemistry of Materials*, **16**, 2148–2156.
144. Wheeler, R.A., Whangbo, M.H., Hughbanks, T., Hoffmann, R., Burdett, J.K., and Albright, T.A. (1986) Symmetric vs. asymmetric linear M–X–M linkages in molecules, polymers, and extended networks. *Journal of American Chemical Society*, **108**, 2222–2236.
145. Kunz, M. and Brown, I.D. (1995) Out-of-center distortions around octahedrally coordinated d^0 transition metals. *Journal of Solid State Chemistry*, **115**, 395–406.
146. Liang, M.-H., Hu, C.-T., Cheng, H.-F., Lin, I.-N., and Steeds, J. (2001) Effect of sintering process on microstructure characteristics of $Ba(Mg_{1/3}Ta_{2/3})O_3$ ceramics and their microwave dielectric properties. *Journal of European Ceramic Society*, **21**, 2759–2763.
147. Ravichandran, D., Meyer Jr, R., Roy, R., Guo, R., Bhalla, A.S., and Cross, L.E. (1996) Sol–gel synthesis of $Ba(Mg_{1/3}Ta_{2/3})O_3$: phase pure powder and thin films. *Materials Research Bulletin*, **31**, 817–825.
148. Renoult, O., Boilot, J-P., Chaput, F., Papiernik, R., Hubert-Pfalzgraf, L.G., and Lejeune, M. (1992) Sol–gel processing and microwave characteristics of $Ba(Mg_{1/3}Ta_{2/3})O_3$ dielectrics. *Journal of American Ceramic Society*, **75**, 3337–3340.
149. Liang, M.-H., Wu, S.-Y., Hu, C.-T., and Lin, I.-N. (2003) Enhancing the sinterability of $Ba(Mg_{1/3}Ta_{2/3})O_3$ dielectrics by using chemically-derived powders. *Materials Chemistry and Physics*, **79**, 276–281.

150. Shirey, H.M. (2002) Low Temperature synthesis of the microwave dielectric material barium magnesium tantalate (BMT), MS Thesis, University of Pittsburgh, USA.
151. Navias, L. and Green, R.L. (1946) Dielectric properties of glasses at ultrahigh frequencies and their relation to composition. *Journal of American Ceramic Society*, **29**, 267–276.
152. Salama, S.N., Salman, S.M., and Darwish, H. (1995) Crystallization characteristics of some lithia calcia magnesia borosilicate glasses. *Ceramic International*, **21**, 159–167.
153. Wu, J.-M. and Huang, H.-L. (1999) Microwave properties of zinc, barium and lead borosilicate glasses. *Journal of Non-Crystalline Solids*, **260**, 116–124.
154. Surendran, K.P., Mohanan, P., and Sebastian, M.T. (2004) The effect of glass additives on the microwave dielectric properties of $Ba(Mg_{1/3}Ta_{2/3})O_3$ ceramics. *Journal of Solid State Chemistry*, **177**, 4031–4046.
155. Chen, X.M. and Wu, Y.J. (1996) Dielectric characteristics of $Ba(Mg_{1/3}Ta_{2/3})O_3$ ceramics sintered at low temperatures. *Journal of Materials Science: Materials in Electronics*, **7**, 427–431.
156. Pollet, M., Marinel, S., Roulland, F., and Allainmat, G. (2003) Low temperature sintering of B_2O_3/$LiNbO_3$ added $BaMg_{1/3}Ta_{2/3}O_3$ ceramics. *Materials Science and Engineering B*, **10**4, 58–62.
157. Cheng, C.-M., Hsieh, Y.-T. and Yang, C.-F. (2003) The sintering and microwave dielectric characteristics of MgO–CaO–Al_2O_3–SiO_2 glass fluxed $Ba(Mg_{1/3}Ta_{2/3})O_3$ ceramics. *Materials Letters*, **57**, 1471–1476.
158. Desu, S.B. and O'Bryan, H.M. (1985) Microwave loss quality of $Ba(Zn_{1/3}Ta_{2/3})O_3$ ceramics. *Journal of American Ceramic Society*, **68**, 546–551.
159. Paik, J.H., Nahm, S., Byun, J.D., Kim, M.H., and Lee, H.J. (1998) The effect of Mg deficiency on the microwave dielectric properties of $Ba(Mg_{1/3}Nb_{2/3})O_3$ ceramics. *Journal of Materials Science Letters*, **17**, 1777–1780.
160. Kusumoto, K. and Sekiya, T. (1998) Processing and properties of $(1 - x)Pb(Mg_{1/3}Nb_{2/3})O_3$–$xPbTiO_3$ solid solutions from PbO- and MgO-excess compositions, *Materials Research Bulletin*, **33**, 1367–1375.
161. Lu C.-H. and Tsai, C.C. (1996) Reaction kinetics, sintering characteristics and ordering behaviour of microwave dielectrics: barium magnesium tantalates. *Journal of Materials Research*, **11**, 1219–1227.
162. Chen, H., Yang, C., Fu, C., and Zhou, D. (2005) Study on BMT millimeter wave dielectric resonators. *International Journal of Infrared and Millimeter Waves*, **26**, 307–313.
163. Lee, J.-A., Kim, J.-J., Lee, H.-Y., Kim, T.-H., and Choy, T.-G. (1994) Effect of MgO content on microstructural evolution and microwave dielectric properties of $Ba(Mg_{1/3}Ta_{2/3})O_3$ ceramics. *Journal of Korean Ceramic Society*, **31**, 1299–1306.
164. Surendran, K.P., Sebastian, M.T., Mohanan, P., Moreira, R.L., and Dias, A. (2005) Effect of nonstoichiometry on the structure and microwave dielectric properties of $Ba(Mg_{0.33}Ta_{0.67})O_3$. *Chemistry of Materials*, **17**, 141–151.
165. Liang, M.H., Hu, C.-T., Chiou, C.-G., Tsai, Y.-N., and Lin, I.-N. (1999) Effect of $Ba_5Ta_4O_{15}$ incorporation on sintering behaviour and microwave dielectric properties of $Ba(Mg_{1/3}Ta_{2/3})O_3$ materials, *Japanese Journal of Applied Physics*, **38**, 5621–5624.
166. Rong, G., Newman, N., Shaw, B., and Cronin, D. (1999) Role of Ni and Zr doping on the electrical, optical, magnetic and structural properties of barium zinc tantalate ceramics. *Journal of Materials Research*, **14**, 4011–4019.
167. Ohsato, H., Koga, E., Kgomiya, I., and Kakimoto, K. (2009) Phase relationship and microwave dielectric properties in the vicinity of $Ba(Zn_{1/3}Ta_{2/3})O_3$, Book chapter in *Advances in Electronic Ceramics II* (eds S. Priya, A. Weidenkaff, D.P. Norton, D. Singh, and J. Salem), John Wiley & Sons, Inc., Hoboken, NJ, USA.
168. Kugimiya, K. (2004) Crystallographic study on the Q of $Ba(Mg_{1/3}Ta_{2/3})O_3$ dielectrics, in Abstract for *Meeting of Microwave/Millimeterwave Dielectrics and Related Materials on the Ceramic Society*, Nagoya Institute of Technology, Nagoya, Japan.
169. Surendran, K.P. and Sebastian, M.T. (2004) Talking with $Ba(Mg_{1/3}Ta_{2/3})O_3$ ceramics, in *Proceedings of the National Symposium on Advances in Microwave and Lightwaves*, October 13–14, University of Delhi South Campus, New Delhi, India.

170. Tien, L.-C., Chou, C.-C., and Tsai, D.-S. (2000) Microstructure of $Ba(Mg_{1/3}Ta_{2/3})O_3$–$BaSnO_3$ microwave dielectrics. *Ceramic International*, **26**, 57–62.
171. Kim, E.-S., Kim, J.-B., and Jo, K.-H. (1993) Microwave dielectric properties of $Ba(Mg_{1/3}Ta_{2/3})O_3$ ceramics with partial substitution of Mg by Ca or Ni. *Ceramic Transactions*, **2**, 231–240.
172. Yoon, K.H., Kim, D.P., and Kim, E.S. (1994) Effect of $BaWO_4$ on the microwave dielectric properties of $Ba(Mg_{1/3}Ta_{2/3})O_3$. *Journal of American Ceramic Society*, **77**, 1062–1066.
173. Ra, S.H. and Phule, P.P. (1999) Processing and microwave dielectric properties of barium magnesium tantalates ceramics for high quality personnel communication service filters. *Journal of Materials Research*, **14**, 4259–4265.
174. Lan, W.A., Liang, M.-H., Hu, C.-T., Liu, K.-S., and Lin, I.-N. (2003) Influence of Zr doping on the microstructure and microwave dielectric properties of $Ba(Mg_{1/3}Ta_{2/3})O_3$ materials. *Materials Chemistry and Physics*, **79**, 266–269.
175. Choi, C.H., Nahm, S., Song, Y.W., Byun, J.D., Kim, Y.S., Lee, H.J., and Park, H.M. (1999) Effect of TiO_2 and SnO_2 on the microwave dielectric properties of $Ba(Mg_{1/3}Ta_{2/3})O_3$ ceramics. *Journal of Korean Physical Society*, **35**, S410–S414.
176. Liang, M.-H., Hu, C.-T., Chiou, C.-G., Chang, H.-Y., and Lin, I.-N. (1999) Enhancing the densification process on Ba(Mg1/3Ta2/3)O3 microwave dielectrics by Y_2O_3 incorporation. *Ferroelectrics*, **231**, 103–108.
177. Hu, X., Chen, X.M., and Wu, Y.J. (2002) Nd substituted $Ba(Mg_{1/3}Ta_{2/3})O_3$ microwave dielectric ceramics. *Materials Letters*, **54**, 279–283.
178. Huang, C.-L., Chiang, K.-H., and Chuang, S.-C. (2004) Influence of V_2O_5 additions to $Ba(Mg_{1/3}Ta_{2/3})O_3$ ceramics on sintering behaviour and microwave dielectric properties. *Materials Research Bulletin*, **39**, 629–636.
179. Huang, C.-L. and Lin, R.-J. (2002) Liquid phase sintering and microwave dielectric properties of $Ba(Mg_{1/3}Ta_{2/3})O_3$ ceramics. *Japanese Journal of Applied Physics*, **41**, 712–716.
180. Yoon, H.-K., Hong, K.S., and Kim, H. (1997) Co-existence of 1:2 and 1:1 long range ordering types in La modified $Ba(Mg_{0.33}Ta_{0.67})O_3$ ceramics. *Journal of Materials Research*, **12**, 589–592.
181. Kolodiazhnyi, T.V., Petrice, A., Johari, G.P., and Belous, A.G. (2002) Effect of preparation conditions on cation ordering and dielectric properties of $Ba(Mg_{1/3}Ta_{2/3})O_3$ ceramics. *Journal of European Ceramic Society*, **22**, 2013–2014.
182. Surendran, K.P., Mohanan, P., Jacob, M.V., and Sebastian, M.T. (2005) The effect of dopants on the microwave dielectric properties of $Ba(Mg_{1/3}Ta_{2/3})O_3$ ceramics. *Journal of Applied Physics*, **98**, 094114.
183. Alford, N.M, Penn, S.J., Templeton, A., Wang, X., and Webb, S. (1998) Materials and processing developments in microwave ceramics, in *Proceedings of the World Ceramics Congress, Part of 9th CIMTEC* (ed. P. Vincenzini), World Ceramic Congress and Forum on New Materials, 14-19 June, Florence, Italy, pp. 3–14.
184. Braginsky, V.B., Ilchenko, V.S., and Bagdassarov, S.K. (1987) Experimental observation of fundamental microwave absorption in high quality dielectric crystals. *Physics Letters*, **120**, 300–305.
185. Gurevich, V.L. and Tagantsev, A.K. (1986) Intrinsic dielectric loss in crystals: low temperature. *Soviet Physics – Journal of Experimental and Theoretical Physics*, **64**, 142–151.
186. Bilz, H. and Kress, W. (1979) *Phonon Dispersion Relations in Insulators*, Springer, New York.
187. Gurevich, G.L. and Tagantsev, A.K. (1991) Intrinsic dielectric loss in crystals. *Advances in Physics*, **40**, 719–767.
188. Surendran, K.P., Mohanan, P., and Sebastian, M.T. (2006) Low loss dielectric $Ba[(Mg_{1/3}Ta_{2/3})_{1-x}(Ti_{x/3}W_{x/3})]O_3$ systems. *Materials Research Bulletin*, **41**, 784–779.
189. Chai, L., Akbas, M.A., Davies, P.K., and Parise, J.B. (1997) Cation ordering transformations in Ba(Mg1/3Ta2/3)O3–BaZrO3 perovskite solid solutions. *Materials Research Bulletin*, **32**, 1261–1269.
190. Surendran, K.P., Mohanan, P., and Sebastian, M.T. (2006) Low loss dielectrics in $Ba[(Mg_{1/3}Ta_{2/3})_{1-x}Ti_x]O_3$ and $Ba[(Mg_{1-x}Zn_x)_{1/3}Ta_{2/3}]O_3$ systems. *Journal of Materials Research*, **20**, 2919–2926.

191. Nagai, T., Inuzuka, T., and Sugiyama, M. (1992) Contribution of dielectric constant to change in temperature coefficient of resonant frequency in $Ba_{1-x}Sr_x(Mg_{1/3}Ta_{2/3})O_3$ compounds. *Japanese Journal of Applied Physics*, **31**, 3132–3135.
192. Sugiyama, M. and Nagai, T. (1993) Anomaly in dielectric constant of $Ba_{1-x}Sr_x(Mg_{1/3}Ta_{2/3})O_3$ solid solution and its relation to structural change, *Japanese Journal of Applied Physics*, **32**, 4360–4363.
193. Jacobson, A.J., Collins, B.M., and Fender, B.E.F. (1976) A powder neutron and X-ray diffraction determination of the structure of $Ba_3Ta_2ZnO_9$: an investigation of perovskite phases in the system Ba–Ta–Zn–O and the preparation of $Ba_2TaCdO_{5.5}$ and $Ba_2CeInO_{5.5}$. *Acta Crystallographica*, **B 32**, 1083–1087.
194. Kawashima, S., Nishida, N., Ueda, I., and Ouchi, H. (1983) $Ba(Zn_{1/3}Ta_{2/3})O_3$ ceramics with low dielectric loss at microwave frequencies. *Journal of American Ceramic Society*, **66**, 421–423.
195. Wakino, K., Nishigaki, T., Tamura, S., and Tamura, H. (1984) An X-band GaAs oscillator using a dielectric resonator, in *Proceedings of the 37th Annual Frequency Control Symposium*, Systematics General, Sterling, VA, USA, pp. 481–484.
196. Mallinson, P.M., Claridge, J.B., Rosseinsky, M.J., Ibberson, R.M., Wright, J.P., and Fitch, A.N. (2007) High-temperature processing of $Ba_3ZnTa_2O_9$: an in situ study using synchrotron X-ray powder diffraction. *Chemistry of Materials*, **19**, 4731–4740.
197. Sagala, D.A. and Nambu, S. (1992) Microscopic calculation of dielectric loss at microwave frequencies for complex perovskite $Ba(Zn_{1/3}Ta_{2/3})O_3$. *Journal of American Ceramic Society*, **75**, 2573–2575.
198. Kawashima, S. (1993) Influence of ZnO evaporation on microwave dielectric loss and sinterability of $Ba(Zn_{1/3}Ta_{2/3})O_3$ ceramics. *American Ceramic Society Bulletin*, **72**, 120–126.
199. Kim, J.S., Kim, J.-W., Cheon, C.I., Kim, Y.-S., Nahm, S., and Byun, J.D. (2001) Effect of chemical element doping and sintering atmosphere on the microwave dielectric properties of barium zinc tantalates. *Journal of European Ceramic Society*, **21**, 2599–2604.
200. Davies, P.K. (1995) Influence of structural defects on the dielectric properties of ceramic microwave resonators, in *Materials and Processes for Wireless Communication* (eds T. Negas and H. Ling), *Ceramic Transactions*, vol. 53, American Ceramic Society, Westerville, USA, pp. 183–197.
201. Ioachim, A., Toascan, M.I., Nedelcu, L., and Mihut, L. (2008) *Proceedings of 6th WSEAS International Conference on Applied Electromagnetics*, Wireless and Optical Communications (ELECTROSCIENCE '08), July 2–4, Trondheim, Norway.
202. Tolmer, V. and Desgardin, G. (1997) Low temperature sintering and influence of the process on the dielectric properties of $Ba(Zn_{1/3}Ta_{2/3})O_3$. *Journal of American Ceramic Society*, **80**, 1981–1991.
203. Roulland, F., Terras, R., and Marinel, S. (2003) Influence of both milling conditions and lithium salt addition on the sinterability of $Ba(Zn_{1/3}Ta_{2/3})O_3$. *Materials Science and Engineering B*, **104**, 156–162.
204. Nalwa, H.S. (1999) *Handbook of Low and High Dielectric Constant Materials and Their Applications*, Academic Press, London.
205. Reaney, I.M., Qazi, I., and Lee, W.E. (2000) Order–disorder behaviour in $Ba(Zn_{1/3}Ta_{2/3})O_3$. *Journal of Applied Physics*, **88**, 6708–6714.
206. Barber, D.J., Moulding, K.M., Zhou, J., and Li, M. (1997) Structural order in $Ba(Zn_{1/3}Ta_{2/3})O_3$, $Ba(Zn_{1/3}Nb_{2/3})O_3$, $Ba(Mg_{1/3}Ta_{2/3})O_3$ microwave dielectric ceramics. *Journal of Materials Science*, **32**, 1531–1544.
207. Sebastian M.T., Ubic, R., and Jantunen, H. (2015) Low loss dielectric materials for LTCC applications: a review. *International Materials Review*, **60**, 392–412 (Supplementary file).
208. Kim, J.S., Kim, J.-W., Cheon, C.I., Kim, Y.-S., Nahm, S., and Byun, J.D. (2001) Effect of chemical element doping and sintering atmosphere on the microwave dielectric properties of barium zinc tantalates. *Journal of European Ceramic Society*, **21**, 2599–2604.
209. Varma, M.R., Reghunathan, R., and Sebastian, M.T. (2005) Effect of dopants on the microwave dielectric properties of $Ba(Zn_{1/3}Ta_{2/3})O_3$ ceramics. *Japanese Journal of Applied Physics*, **44**, 298–303.

210. Koga, E., Moriwake, H., Kakimoto, K., and Ohsato, H. (2005) Influence of composition deviation from stoichiometric $Ba(Zn_{1/3}Ta_{2/3})O_3$ on superlattice ordering and microwave quality factor Q. *Journal of Ceramic Society of Japan*, **113**, 171–178.
211. Tamura, H., Konoike, T., Sakabe, Y., and Wakino, K. (1984) Improved high Q dielectric resonators with complex perovskite structure. *Journal of American Ceramic Society*, **67**, C59–C61.
212. Yang, J.-I., Nahm, S., Choi, C.-H., Lee, H.-J., and Park, H.-M. (2002) Microstructure and microwave dielectric properties of $Ba(Zn_{1/3}Ta_{2/3})O_3$ with ZrO_2 addition. *Journal of American Ceramic Society*, **85**, 165–168.
213. Davies, P.K., Tong, J., and Negas, T. (1997) Effect of ordering induced domain boundaries of low loss $Ba(Zn_{1/3}Ta_{2/3})O_3$–$BaZrO_3$ perovskite microwave dielectrics. *Journal of American Ceramic Society*, **80**, 1727–1740.
214. Chai, L. and Davies, P.K. (1997) Formation and structural characterization of 1:1 ordered perovskites in the $Ba(Zn_{1/3}Ta_{2/3})O_3$–$BaZrO_3$ system. *Journal of American Ceramic Society*, **80**, 3193–3198.
215. Tamura, H. (2006) Microwave dielectric losses caused by lattice defects. *Journal of European Ceramic Society*, **26**, 1775–1780.
216. Moreira, R.L., Matinaga, F.M., and Dias, A. (2001) Raman-spectroscopic evaluation of the long-range order in $Ba(B'_{1/3}B''_{2/3})O_3$ ceramics. *Applied Physics Letters*, **78**, 428–430.
217. Ma, P.P., Gu, H., and Chen, X.M. (2015) Evaluation of the 1:2 ordered structure of $Ba(B'_{1/3}B''_{2/3})O_3$ perovskites along various zone axes using transmission electron microscopy. *Journal of Materials Chemistry C*, **3**, 10755–10760.
218. Tian, Z.-Q., Liu, H.-X., Yu, H.-T., and Ouyang, S.-X. (2004) Effect of $BaWO_4$ on microstructure and microwave dielectric properties of $Ba(Mg_{1/3}Nb_{2/3})O_3$. *Materials Chemistry and Physics*, **86**, 228–232.
219. Koga, E., Yamagishi, Y., Moriwake, H., Kakimoto, K., and Ohsato, H. (2006) Order–disorder transition and its effect on microwave quality factor Q in $Ba(Zn_{1/3}Nb_{2/3})O_3$ system. *Journal of Electroceramics*, **17**, 375–379.
220. Lee, C.-T., Lin, Y.-C., Huang, C.-Y., Su, C.-Y., and Hu, C.-L. (2007) Cation ordering and dielectric characteristics in barium zinc niobate. *Journal of American Ceramic Society*, **90**, 483–489.
221. Wu, H. and Davies, P.K. (2006) Influence of non-stoichiometry on the structure and properties of $Ba(Zn_{1/3}Nb_{2/3})O_3$ microwave dielectrics: III. Effect of the muffling environment. *Journal of American Ceramic Society*, **89**, 2264–2270.
222. Lee, J.-H., Jang, Y.I., Youn, H.J., Jang, J.W., and Kim, B.K. (1999) Low firing and microwave dielectric properties of $Ba[(Ni_{0.6}Zn_{0.4})_{0.33}Nb_{0.64}]O_3$ ceramics doped with Sb_2O_5 and B_2O_3. *Journal of Materials Science*, **34**, 625–628.
223. Wang, J.-L., Hsu, C.-H., Huang, C.-L., and Lin, R.-J. (2005) Effect of CuO additives on sintering and microwave dielectric properties of 0.95 $Ba(Zn_{1/3}Nb_{2/3})O_3$–0.05 $BaZrO_3$ ceramics. *Japanese Journal of Applied Physics*, **44**, 8039–8042.
224. Sun, J.-S., Yu, J.-J., You, J.-C., and Wei, C.C. (1995) Microwave dielectric properties of $Ba(Sn_xZn_{(1-x)/3}Nb_{(1-x)2/3})O_3$ ($0 \leq x \leq 0.32$) ceramics. *Journal of Materials Science*, **28**, 2163–2168.
225. Hughes, H., Iddles, D.M., and Reaney, I.M. (2001) Niobate based dielectrics suitable for third generation mobile phone base stations. *Applied Physics Letters*, **79**, 2952–2954.
226. Wu, H. and Davies, P.K. (2006) Influence of non-stoichiometry on the structure and properties of $Ba(Zn_{1/3}Nb_{2/3})O_3$ microwave dielectrics. IV. Tuning τ_f and the part size dependence of Qf. *Journal of American Ceramic Society*, **89**, 2271–2278.
227. Kim, J.S., Lee, J.H., Lim, Y.-S., Jang, J.W., and Kim, I.-T. (1997) Revisit to the anomaly in dielectric properties of $Ba_{1-x}Sr_x(Zn_{1/3}Nb_{2/3})O_3$ solid solution systems. *Japanese Journal of Applied Physics*, **36**, 5558–5581.
228. Onoda, M., Kuwata, J., Kaneta, K., Toyoma, K., and Nomura, S. (1982) $Ba(Zn_{1/3}Nb_{2/3})O_3$–$Sr(Zn_{1/3}Nb_{2/3})O_3$ solid solution ceramics with temperature stable high dielectric constant and microwave loss. *Japanese Journal of Applied Physics*, **21**, 1710.
229. Varma, M.R. and Sebastian, M.T. (2007) Effects of dopant addition on the microwave dielectric properties of $Ba(Zn_{1/3}Nb_{2/3})O_3$ ceramics. *Journal of European Ceramic Society*, **27**, 2827–2833.

230. Wu, H. and Davies, P.K. (2006) Influence of non-stoichiometry on the structure and properties of $Ba(Zn_{1/3}Nb_{2/3})O_3$ microwave dielectrics. I. Substitution of $Ba_3W_2O_9$. *Journal of American Ceramic Society*, **89**, 2239–2249.
231. Kim, I.-T., Hong, K.S., and Yoon, S.-J. (1995) Effects of non-stoichiometry and chemical inhomogeneity on the order–disorder phase formation in the complex perovskite compounds, $Ba(Ni_{1/3}Nb_{2/3})O_3$ and $Ba(Zn_{1/3}Nb_{2/3})O_3$. *Journal of Materials Science*, **30**, 514–521.
232. Wu, H. and Davies, P.K. (2006) Influence of non-stoichiometry on the structure and properties of $Ba(Zn_{1/3}Nb_{2/3})O_3$ microwave dielectrics. II. Compositional variations in pure BZN. *Journal of American Ceramic Society*, **89**, 2250–2263.
233. Galasso, F. and Pinto, J. (1965) Preparation of $Ba(Na_{0.25}Ta_{0.75})O_3$ and $Sr(Na_{0.25}Ta_{0.75})O_3$ with the perovskite structure. *Inorganic Chemistry*, **4**, 235–236.
234. Hikichi, Y., Chen, Z., Newnham, R.E. and Cross, L.E. (1982) Preparation, thermal change and dielectric properties of cubic perovskites $A(B_{1/4}Nb_{3/4})O_3$ (A = Ba or Sr, B = Na or Li). *Materials Research Bulletin*, **17**, 1371–1377.
235. Negas, T., Roth, R.S., Parker, H.S., and Brower, W.S. (1973) Crystal chemistry of lithium in octahedrally coordinated structures. I. Synthesis of $Ba_8(Me_6Li_2)O_{24}$ (Me = Nb or Ta) and $Ba_{10}(W_6Li_4)O_{30}$. *Journal of Solid State Chemistry*, **8**, 1–13.
236. Collins, B.M., Jacobson, A.J., and Fender, B.E.F. (1974) Preparation of the ordered perovskite-like compounds barium tantalum or niobium lithium oxide ($Ba_4M_3LiO_{12}$). Powder neutron diffraction determination of the structure of barium tantalum lithium oxide ($Ba_4Ta_3LiO_{12}$). *Journal of Solid State Chemistry*, **10**, 29–35.
237. Baud, G., Picaud, B., and Besse, J.P. (1975) New series of rhenium perovskite compounds of $Ba_4M_3ReO_{12}$ type. *Journal of American Ceramic Society*, **58**, 259.
238. Alonso, A., Mzayek, E., and Rasines, I. (1987) A new kind of 1:3 ordering in cubic perovskites: the oxides $BaM_{0.25}Sb_{0.75}O_3$ (M = Li, Na). *Materials Research Bulletin*, **22**, 69–74.
239. Subramanian, M.A. (1994) Ordered perovskites containing pentavalent bismuth: $Ba(Bi_{0.75}M_{0.25})O_3$ and $Ba(Bi_{0.67}M_{0.33})O_3$. *Journal of Solid State Chemistry*, **111**, 134–140.
240. Alonso, J.A., Mzayek, E., and Rasines, I. (1990) The distorted perovskite $Sr(Na_{1/4}Sb_{1/4})O_3$: a novel example of 1:3 B-cation ordering. *Journal of Solid State Chemistry*, **84**, 16–22.
241. Levin, I., Chan, J.Y., Geyer, R.G., Maslar, J.E., and Vanderah, T.A. (2001) Cation ordering types and dielectric properties in the complex perovskite $Ca(Ca_{1/3}Nb_{2/3})O_3$. *Journal of Solid State Chemistry*, **156**, 122–134.
242. Hervieu, M., Studer, F., and Raveau, B. (1977) Perovskite oxides in the Ca–Nb–O system. *Journal of Solid State Chemistry*, **22**, 273–289.
243. Levin, I., Bendersky, L.A., Cline, J.P., Roth, R.S., and Vanderah, T.A. (2000) Octahedral tilting and cation ordering in perovskite-like $Ca_4Nb_2O_9 = Ca(Ca_{1/3}\ Nb_{2/3})O_3$ polymorphs. *Journal of Solid State Chemistry*, **150**, 43–61.
244. Cava, R.J., Krajewski, J.J., and Roth, R.S. (1999) $Ca_5Nb_2TiO_{12}$ and $Ca_5Ta_2O_{12}$: low temperature coefficient and low loss dielectric materials. *Materials Research Bulletin*, **34**, 355–362.
245. Cava, R.J. (2001) Dielectric materials for applications in microwave communications. *Journal of Materials Chemistry*, **11**, 54–62.
246. Bendersky, L.A., Krajewski, J.J., and Cava, R.J. (2001) Dielectric properties and microstructure of $Ca_5Nb_2TiO_{12}$ and $Ca_5Ta_2O_{12}$. *Journal of European Ceramic Society*, **21**, 2653–2658.
247. Hervieu, M., Studer, F., and Raveu, B. (1977) Oxydes de type perovskite du systeme Ca–Nb–O. *Journal of Solid State Chemistry*, **22**, 273–289.
248. Levin, I., Bendersky, L.A., Cline, J.P., Roth, R.S., and Vanderah, T.A. (2000) Octahedral tilting and cation ordering in perovskite like $Ca_4Nb_2O_9$:$Ca(Ca_{1/3}Nb_{2/3})O_3$ polymorphs. *Journal of Solid State Chemistry*, **150**, 43–61.
249. Bendersky, L.A., Levin, I., Roth, R.S., and Shapiro, A.J. (2001) $Ca_4Nb_2O_9$–$CaTiO_3$: phase equilibria and microstructures. *Journal of Solid State Chemistry*, **160**, 257–271.
250. Bijumon, P.V. (2006) Novel low loss $A(A_{1/4}B_{2/4}C_{1/4})O_3$ dielectrics and their applications in broadband antennas. PhD Thesis, Cochin University of Science and Technology, India.
251. Bijumon, P.V., Mohanan, P., and Sebastian, M.T. (2002) Synthesis, characterization and properties of $Ca_5A_2TiO_{12}$ (A = Nb, Ta) ceramic dielectric materials for applications in microwave communication systems. *Japanese Journal of Applied Physics*, **41**, 3834–3835.

252. Dias, A., Bijumon, P.V., Sebastian, M.T., and Moreira, R.L. (2005) Vibrational spectroscopy and microwave dielectric properties of $Ca_{5-x}Ba_xNb_2TiO_{12}$ and $Ca_{5-x}Ba_xTa_2TiO_{12}$ ceramics. *Journal of Applied Physics*, **98**, 084105.
253. Bijumon, P.V. and Sebastian, M.T. (2007) Doped $Ca(Ca_{1/4}A_{2/4}Ti_{1/4})O_3$ (A = Nb, Ta) dielectrics for microwave telecommunication applications. *International Journal of Applied Ceramic Technology*, **4**, 60–74.
254. Bijumon, P.V. and Sebastian, M.T. (2004) Temperature stable microwave dielectric ceramics in the $Ca_5A_2Ti_{1-x}Zr_xO_{12}$ (A = Nb, Ta) system. *Journal of Materials Research*, **19**, 2922–2928.
255. Bijumon, P.V. and Sebastian, M.T. (2006) Microwave dielectric properties of temperature stable $Ca_5A_2Ti_{1-x}Hf_xO_{12}$ (A = Nb, Ta) ceramics. *Journal of Electroceramics*, **16**, 239–245.
256. Galasso, F. and Katz, L. (1961) Preparation and structure of $Ba_5Ta_4O_{15}$. *Acta Crystallographica*, **14**, 647–650.
257. Trolliard, G., Tenezee, N., Boullay, Ph., Manier, M., and Mercurio, D. (2003) HRTEM study of cation deficient perovskite related $A_nB_{n-1}O_{3n}$ ($n \geq 4\delta$) microphases in $Ba_5Nb_4O_{15}$–$BaTiO_3$ system. *Journal of Solid State Chemistry*, **173**, 91–100.
258. Sebastian, M.T. and Krishna, P. (1994) *Random, Non-random and Periodic Faulting in Crystals*, Gordon & Breach Science Publishers, Reading, UK.
259. Whiston, C.D. and Smith, A.J. (1967) Double oxide containing niobium and or tantalum. II. Systems involving strontium or barium. *Acta Crystallographica*, **23**, 82–84.
260. Weiden, M., Grauel, A., Norwig, J., Horn, S., and Steglich, F. (1995) Crystalline structure of the strontium niobates $Sr_4Nb_2O_9$ and $Sr_5Nb_4O_{15}$. *Journal of Alloys and Compounds*, **218**, 13–16.
261. Tenezee, N., Mercurio, D., Trolliard, G., and Mesjard, J.C.C. (2000) Reinvestigation of the crystal structure of pentastrontium tetraniobate $Sr_5Nb_4O_{15}$. *Zeitschrift für Kristallographie*, **215**, 11–12.
262. Hutchinson, J.L. and Jacobson, A.J. (1977) Electron microscopy of the perovskite-related phases 4H $Ba_{0.1}Sr_{0.9}MnO_{2.96}$, 5H $Ba_5Nb_4O_{15}$ and 6H $BaFeO_{2.79}$. *Journal of Solid State Chemistry*, **20**, 417–422.
263. Sreemoolanathan, H., Sebastian, M.T., and Mohanan, P. (1995) High permittivity and low loss ceramics in the BaO–SrO–Nb_2O_5-system. *Materials Research Bulletin*, **30**, 653–658.
264. Jawahar, I.N., Mohanan, P., and Sebastian, M.T. (2003) $A_5B_4O_{15}$ [A = Ba, Sr, Ca, Zn, B = Nb, Ta] microwave dielectric ceramics. *Materials Letters*, **57**, 4043–4048.
265. Ratheesh, R., Sreemoolanathan, H., and Sebastian, M.T. (1997) Vibrational analysis of $Ba_{5-x}Sr_xNb_4O_{15}$ microwave dielectric ceramic resonators. *Journal of Solid State Chemistry*, **131**, 2–8.
266. Vineis, C., Davies, P.K., Negas, T., and Bell, S. (1996) Microwave dielectric properties of hexagonal perovskites. *Materials Research Bulletin*, **31**, 431–437.
267. Jawahar, I.N., Santha, N.I. and Sebastian, M.T. (2002) Microwave dielectric properties of MO–La_2O_3–TiO_2 (M = Ca, Sr, Ba) ceramics. *Journal of Materials Research*, **17**, 3084–3089.
268. Wada, K., Fukami, Y., Kakimoto, K., and Ohsato, H. (2005) Microwave dielectric properties of textured $BaLa_4Ti_4O_{15}$ ceramics with layered perovskite structure. *Japanese Journal of Applied Physics*, **44**, 7094–7097.
269. Tohodo, Y., Okawa, T., Okabe, H., Kakimoto, K., and Ohsato, H. (2004) Microwave dielectric homologous materials $ALa_4Ti_4O_{15}$ (A = Ba, Ca, Sr) with high Q, high dielectric constant for base station. *Key Engineering Materials*, **269**, 203–206.
270. Thirumal, M. and Davies, P.K. (2005) $Ba_8ZnTa_6O_{24}$: a new high Q dielectric perovskite. *Journal of American Ceramic Society*, **88**, 2126–2128.
271. Kawaguchi, S., Ogawa, H., Kan, A., and Ishihara, S. (2006) Microwave dielectric properties of $Ba_8Ta_6(Ni_{1-x}M_x)O_{24}$ (M = Zn and Mg) ceramics. *Journal of European Ceramic Society*, **26**, 2045–2049.
272. Ohsato, H. (2016) Microwave dielectrics with perovskite-type structure, Book chapter in *Perovskite Materials – Synthesis, Characterisation, Properties, and Applications* (eds L. Pan and G. Zhu), Intech Publishers, Croatia.

4

High Permittivity Materials

Rick Ubic,[1] G. Subodh,[2] and M.T. Sebastian[3]
[1]Micron School of Materials Science and Engineering, Boise State University, Idaho, USA
[2]Department of Physics Kerala University, Trivandrum, India
[3]Microelectronics Research Unit, Faculty of Information Technology and Electrical Engineering,University of Oulu, Oulu, Finland

4.1 Introduction

The desirable properties of high-performance microwave ceramics include a high dielectric constant, a high quality factor, and a low temperature coefficient of resonant frequency. Among the reported few thousands of microwave dielectric materials, the number of compounds with a high dielectric constant (>100), with a good quality factor, and a low temperature coefficient of resonant frequency are limited. The microwave dielectric properties of high ε_r materials are given in the Appendix at the end of Volume II. High dielectric constant ceramics (>100) have attracted intensive attention for the miniaturization dielectric resonators and microwave devices [1]. In the present chapter we review the microwave dielectric properties of materials having a high ε_r.

4.2 The $BaO–Ln_2O_3–TiO_2$ System

It was in the mid- to late-1970s and early 1980s that many of the discoveries in the $BaO–Nd_2O_3–TiO_2$ system were made, mostly in Eastern Europe and the USSR. The discovery of the ternary phases $BaNd_2Ti_3O_{10}$ (1:1:3) and $BaNd_2Ti_5O_{14}$ (1:1:5) was reportedly confirmed by Kolar *et al.* [2] and at about the same time an intermediate compound with the compositional ratio of 1:1:4 ($BaNd_2Ti_4O_{12}$) was observed in the USSR by Razgon *et al.* [3] and Mudrolyubova *et al*. [4] Since then solid solutions in the system $BaO–Ln_2O_3–TiO_2$

Microwave Materials and Applications, First Edition.
Edited by Mailadil T. Sebastian, Rick Ubic and Heli Jantunen.
© 2017 John Wiley & Sons, Ltd. Published 2017 by John Wiley & Sons, Ltd.

have attracted much scientific and commercial interest due to their high permittivity, high quality factor, and low temperature coefficient of resonant frequency.

The composition and stoichiometry of the ternary phases were the subject of some debate, as has been documented by Ubic *et al.* [5] in a thorough review. Bolton [6] was the first to thoroughly investigate the $BaO–Ln_2O_3–TiO_2$ system (Ln = lanthanide rare-earth metal). He found, among various binary phases, two unknown ternary compounds, one of which had a molar compositional ratio of approximately 1:0.71:3. More than ten years later, Kolar *et al.* maintained [2, 7, 8] that both a 1:1:3 and a 1:1:5 compound existed, although their X-ray diffraction (XRD) data were not definitive in that Kolar *et al*. [2], Polyakov *et al.* [9], and Fukuda *et al.* [10] all assigned the 1:1:5 compound $BaNd_2Ti_5O_{14}$ orthorhombic lattice parameters practically coinciding with those of Gens *et al.* [11] for the 1:1:4 $BaNd_2Ti_4O_{12}$, a stoichiometry first suggested by Razgon *et al.* [3]. In 1986 it was proposed by Jaakola *et al.* [12] that the true stoichiometry for the 1:1:4/1:1:5 phase must be closer to 15:19:72 ($Ba_{3.75}Nd_{9.5}Ti_{18}O_{54}$). They found that the 1:1:5 composition did not lead to a single-phase ceramic, but contained ~15% $BaTi_4O_9$ and TiO_2 as secondary phases. These results were later verified by Chen *et al.*, who found [13] small amounts of $Nd_2Ti_2O_7$ and TiO_2 impurities in 1:1:5 powders. Contrarily, Polyakov *et al.* [9] found 1:1:4 powders to be multiphase and that 1:1:5 compositions were single phase. This 1:1:4/1:1:5 discrepancy had long since been noted in Russia and the crystallography of an isostructural compound of praseodymium ($Ba_{3.75}Pr_{9.5}Ti_{18}O_{54}$) had already been proposed by Matveeva *et al.* [14]; however, many workers [10, 15–21] have made subsequent reference to the 1:1:5 phase. The small error in one of the 4c oxygen positions reported by Matveeva *et al.* [14] was later corrected by Ubic *et al.* [5].

The XRD evidence of Guha [22] indicated that the stoichiometry of the La-based phase was, in fact, 1:1:4.25, but in the same year Takahashi *et al.* [23, 24] used a modified coprecipitation method to establish that the correct composition of the compound was $BaO{\cdot}R_2O_3{\cdot}4TiO_2$ (R = La, Nd, and Sm) using transmission electron microscopy (TEM), XRD, and Raman spectroscopy. Valant and his coworkers also reported [25, 26] the occurrence of the 1:1:4 phase in the Gd system.

Recently, $Ba_{3.75}Nd_{9.5}Ti_{18}O_{54}$ and $BaNd_2Ti_4O_{12}$ compounds were explained [27] as merely specific compositions of the solid-solution phase $Ba_{6-3x}Nd_{8+2x}Ti_{18}O_{54}$ (BNT) $0 \leq x \leq 0.75$. Ohsato *et al.* reported [28] the same phase five years later. Curiously, the x values reported then were $0 \leq x \leq 0.70$, which includes $BaNd_2Ti_4O_{12}$ ($x = 0.5$) but precludes the compound $Ba_{3.75}Nd_{9.5}Ti_{18}O_{54}$ ($x = 0.75$). This discrepancy probably stems from the fact that they tested various x values in intervals of 0.1, so the compositions $x = 0.7$ and $x = 0.8$ were tested, but not $x = 0.75$. Later, Negas and Davies [29] tested $x = 0.75$ and found it to be multiphase, although this may have been caused by processing temperatures too low (or heating cycles too short) for the solid solution to encompass $x = 0.75$. The solubility limits they reported were $0.2 \leq x \leq 0.7$. The discrepancy between this lower limit of solubility and that published by Ohsato *et al*. [28] was noted, but as Q was found to increase with increasing x, the anomaly was left as academic. Later, Suvorov *et al*. suggested [30] that the upper limit extended to $x = 0.75$. Recently, Cruickshank *et al*. have observed [31] that the upper limit of solubility increases with increased processing temperature, and reaches $x = 0.80$ at 1400 °C. Ubic *et al*. found [32] the solubility range to extend at least between $0.25 \leq x \leq 0.75$ at 1400 °C. Conversely, Belous and Ovchar reported [33] that the $x = 1$

composition forms initially in the $Ba_{6-3x}Nd_{8+2x}Ti_{18}O_{54}$ system, with other compositions ($0.5 < x < 1$) forming by reaction with $BaTiO_3$ and/or $BaTi_4O_9$.

Some authors have reported [6,20,33] apparently single-phase ceramics for compositions far outside the range of $Ba_{6+3x}Nd_{8-2x}Ti_{18}O_{54}$, suggesting that the solid solution might exist in a much larger compositional range than previously thought (an *area* on the isothermal section of the ternary diagram instead of a *line*). Belous and Ovchar claimed [33] to have obtained single-phase ceramics in the $BaO–Nd_2O_3–nTiO_2$ system for $0 \leq n \leq 4.5$. If true, the equivalency $Ba^{+2} + 2Nd^{+3} = 2Ti^{+4}$ must be considered, although this possibility seems already to have been discounted by Nenasheva *et al*. [34] and Cruickshank *et al*. [31]. Additionally, the excess TiO_2 present for $n > 4$ cannot be accommodated by any crystal model of BNT so far proposed.

4.2.1 Crystal Structure of $Ba_{6-3x}Ln_{8+2x}Ti_{18}O_{54}$

It is now generally agreed that, as well as the 1:1:3 phase ($BaLn_2Ti_3O_{10}$), a ternary solid–solution phase exists [35,36]. Although various structural models differ in their detail, there is a consensus that the crystal structure essentially consists of a three-dimensional framework of corner-sharing perovskite-like TiO_6 octahedra joined according to a pattern similar to that of the tetragonal tungsten bronzes (Figure 4.1).

The tungsten bronze structure family is probably the second largest family of oxygen octahedra-based ferroelectrics (next to perovskites) [39]. In fact, there are at least 150 known compounds or solid-solutions with this structure [40], including $Ba_2NaNb_5O_{15}$, $Sr_2KNb_5O_{15}$, $K_3Li_2Nb_5O_{15}$, $Pb_2KNb_5O_{15}$, and $Sr_{1-x}Ba_xNb_2O_6$. The structure is typified by oxygen octahedra linked at the corners in a complex way to yield three types of openings: large pentagonal sites, diamond sites, and tiny triangular sites. It can be described chemically by the formula $[(A1)_2A2C_2][B1(B2)_4]O_{15}$. Combinations of large monovalent (e.g., K^+, Na^+, Rb^+), divalent (e.g., Pb^{+2}, Ba^{+2}, Sr^{+2}, Ca^{+2}), and trivalent (e.g., La^{+3}, Nd^{+3}, Eu^{+3}, Gd^{+3}) cations occupy the pentagonal (A2) and diamond (A1) sites. The pentagonal

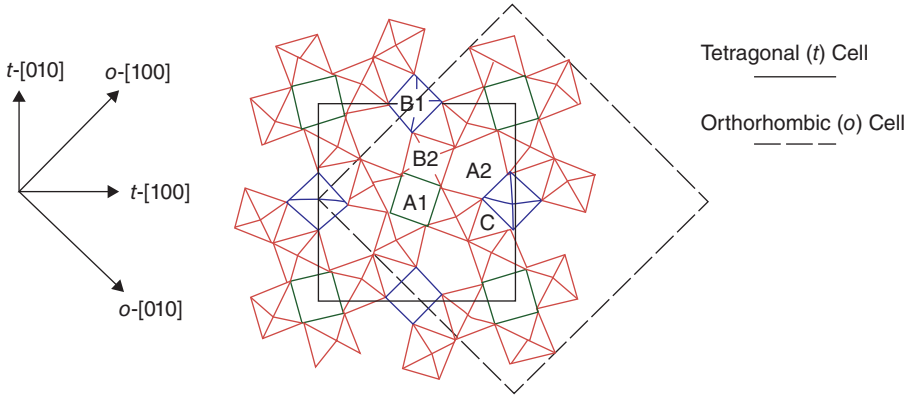

Figure 4.1 *Schematic diagram of the tungsten bronze structure. After Subbarao* et al. *[37] and Jamieson* et al. *[38].*

sites (A2) have a coordination of 15 and there are two per cell. There are four diamond sites (A1) per unit cell, each with a coordination of 12. Only very small cations like Li^{+} can occupy the triangular (C) sites, and highly charged cations like Nb^{+5}, Ta^{+5}, Ti^{+4}, and Zr^{+4} occupy the octahedral (B1 and B2) sites. There are four triangular (C) sites per unit cell, each with nine nearest O^{-2} neighbours. The two B1 and eight B2 octahedral sites all have, of course, sixfold coordination.

Frequently, consistent with charge neutrality, not all sites are fully occupied, as is the case with BNT [14, 41]. The large variation in cation radii is the reason for the many complex end-member compounds and solid solutions [42]. The only known compounds in which all five crystallographic sites are filled are $K_3Li_2Nb_5O_{15}$ and $K_3Li_2Ta_5O_{15}$. These compounds are termed "stuffed bronzes." All other tungsten bronzes are called either "filled" or "unfilled" bronzes where the C sites are completely vacant and the A1 and A2 sites are either fully or partially occupied. For example, strontium barium niobate, $(Sr_{1-x}Ba_x)_5Nb_{10}O_{30}$ is an "unfilled" bronze in which the A sites are only $^5/_6$ filled. It is likely, in this case, that Ba^{+2} predominantly occupies the pentagonal sites [40] since Ba^{+2} (1.61 Å) is substantially larger than Sr^{+2} (1.44 Å) [43].

A model based on the Pr analog (BPT) to the solid-solution BNT phase reported by Matveeva *et al.* [14] is shown in Figure 4.2 (also shown in the Plate Section). According to this model, the structure of $Ba_{3.75}Pr_{9.5}Ti_{18}O_{54}$ is orthorhombic with formula $A1_4A2_{10}Ti_{18}O_{54}$. It is similar to the tetragonal tungsten bronze structure, but with 3×3 rather than 2×2 octahedral units of perovskite structure in columns parallel to [001]. In both structures, the perovskite-like columns are joined at their corners to form alternating three- and five-membered rings of octahedra enclosing cavities that can accommodate cations. Within the columns, four-membered rings are present. Although the TiO_6 framework of BNT and the tetragonal tungsten bronze MO_6 framework are not identical, the essential features of the two crystal structures remain the same. There are four important aspects of the unit cell. First, the four pure barium sites (A2) are only 81.25% occupied. Second, there are ten atomic positions (A1) that are randomly occupied by either Pr^{+3} or Ba^{+2}.

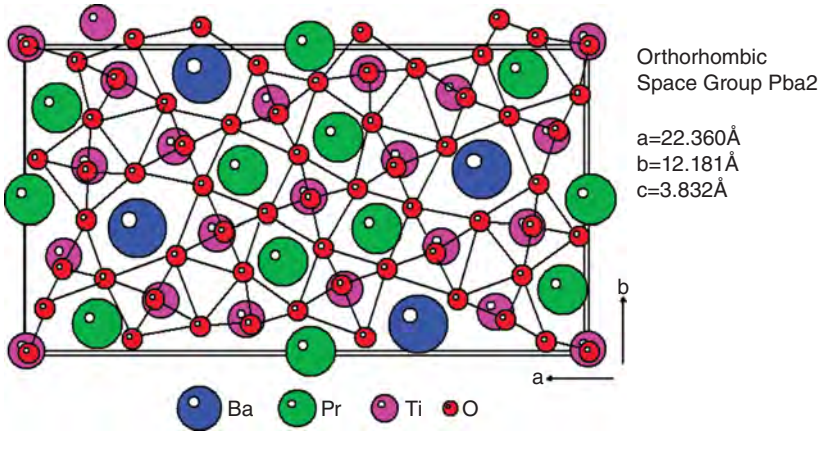

Figure 4.2 *Proposed crystal structure of $Ba_{3.75}Pr_{9.5}Ti_{18}O_{54}$. Source: Adapted from Matveeva* et al. *1984 [14]. This figure is also shown in the Plate Section.*

Third, there is no crystallographic distinction between B1 and B2 sites and, fourth, C sites are vacant. The structural formula can therefore be written as $[Ba_{4-x}][Pr_{8+2x}Ba_{2-2x}]Ti_{18}O_{54}$. The small error in one of the 4c oxygen positions reported by Matveeva *et al.* [14] was later corrected by Ubic *et al.* [5].

A few years after this model was put forward, Roth *et al.* [41] proposed a slightly different structural model, which can be written as either $Ba_4Nd_8[Ba_{2x}+Nd_{4/3-4/3x}]Ti_{18}O_{54}$ ($0 \leq x \leq 1$) or simply $Ba_{4+2x}Nd_{91/3-4/3x}Ti_{18}O_{54}$. Unlike the previous model, this one maintains full Ba^{+2} occupancy in the pentagonal A2 sites, which have a coordination of ten. Also, the A1 sites, which have eightfold coordination, are of two kinds. Of the ten A1 sites in the unit cell, eight are occupied by Nd^{+3}, whilst the other two are only partially occupied and shared by Ba^{+2} and Nd^{+3}. This formula precludes the 15:19:72 composition, that is, $Ba_{3.75}Nd_{9.5}Ti_{18}O_{54}$, and effectively limits the solid solution to $x \leq {}^2/_3$ (x as defined by Matveeva *et al.* [14]).

Azough *et al.* [44] modified the model of Matveeva *et al.* [14] to account for the cell doubling along z observed by high-resolution X-ray diffraction in $Ba_{3.75}Nd_{9.5}Ti_{18}O_{54}$ samples. Their study suggested a much more complex distribution of cations than had been previously been proposed. According to the new model, the large pentagonal A2 sites are primarily occupied by Ba^{+2}, although Nd^{+3} also shares these sites. The A1 sites are divided into three types, two of which are shared by Ba^{+2} and Nd^{+3}, the third of which is occupied only by Nd^{+3}. On careful examination of the atomic positions, it becomes clear that the closest pentagonal A2 sites are separated only by 0.18 Å, and the A1 sites by 0.05–0.21 Å. Given that the radius of a Ba^{+2} ion is around 1.61 Å [43], it seems clear that this model is flawed.

An alternative crystal structural formula, similar to that of Roth *et al.* [41], was suggested by Ohsato *et al.* [45] and differs from that of Matveeva *et al.* [14] and Azough *et al.* [44] in that the A2 sites are only occupied by Ba^{+2} and the A1 sites are only partially occupied by Ba^{+2} and Nd^{+3}. According to this model, for $0 \leq x \leq {}^2/_3$ the A1 sites are fully occupied by Ba^{+2} and the A2 sites become richer in Ln^{+3} until, at $x \leq {}^2/_3$, the cations are fully ordered with only Ba^{+2} occupying A2 sites and only Ln^{+3} in A1 sites. For ${}^2/_3 < x \leq 1$, the A2 sites are also only partially occupied. The arrangement can be written as:

$$\begin{aligned} &[Ba_4][Ln_{8+2x}Ba_{2-3x}]Ti_{18}O_{54}, && 0 \leq x \leq {}^2/_3 \\ &[Ba_{4-3(x-2/3)}][Ln_{9+1/3+2(x-2/3)}]Ti_{18}O_{54}, && {}^2/_3 \leq x \leq 1 \end{aligned}$$

Using this model, Ohsato and coworkers explained [45,46] data showing that the maximum Q in some compositions occurs for $x = {}^2/_3$ by arguing that both the ordering of cations on A1 and A2 sites as well as the reduction of internal strain at $x = {}^2/_3$ results in the highest Q. While this structural model may be sound, in the cases of Nd and La-based compositions, Q increased from $x = 0.6$ to $x = 0.7$, and the decrease for Pr is almost indiscernable. Many of the samples tested were [47] almost certainly multiphase, as the graph of unit-cell volume to composition seems to disobey Vegard's law for $x < 0.2$ and $x > 0.7$. Compositions in these regions cannot be single-phase, and any electrical data acquired from such samples would be unreliable. The decrease in Q for Sm-based ceramics for which $x = 0.7$ is probably due to the formation of a secondary phase, possibly $Sm_4Ti_9O_{24}$. The Nd analog of this compound has been reported as a secondary phase in $Ba_{6-3x}Nd_{8+2x}Ti_{18}O_{54}$ ceramics by several authors [28, 41, 48]. In addition, as the calculation of internal strain requires a knowledge of the

crystallite size, which can only be approximately known, there is a possibility for error. More recently Wunderlich and Ohsato attributed [49] the discontinuous change in dielectric properties between Eu and Sm when doping with different rare-earth elements to electron–phonon interaction.

The space group of the solid–solution phase has been variously reported by different authors. Based on the systematic absences observed in single-crystal XRD of an La-based 1:1:4 crystal, Gens *et al.* reported [11] the probable space groups *Pba*2 (No. 32) or *Pbam* (No. 55). The lattice parameters calculated for the Nd analog were $a = 22.21$, $b = 12.30$, $c = 3.84$ Å. Matveeva *et al.* later confirmed [14] these results by single-crystal XRD and X-ray spectroscopic studies of a Pr-based 15:19:72 crystal, reporting the same space groups and lattice constants: $a = 22.360 \pm 0.007$, $b = 12.181 \pm 0.004$, $c = 3.832 \pm 0.004$ Å. Based on their data of 1990 measured peaks, they calculated atomic positions using space group *Pba*2. Approximately 400 additional peaks corresponding to a doubling of the period along z were also identified, but significantly were omitted from the structural refinement.

Ohsato *et al.* also observed [35] superlattice XRD peaks in Nd-based 15:19:72 crystals and reported orthorhombic lattice constants $a = 12.189$, $b = 22.319$, $c = 7.677$ Å. The space group of their fundamental lattice agreed with that of Matveeva *et al.* [14], but that of the doubled cell was reported as either $Pbn2_1$ (No. 33) or *Pbnm* (No. 62). Kolar *et al.*'s work [50] later confirmed the findings of Matveeva *et al.* [14].

Azough *et al.* published the first TEM studies of the Nd-15:19:72 compound [44] and the Pr-1:1:4 compound [51] in 1995. Reorienting the unit cell, they reported the lattice constants as $a = 22.2$, $b = 12.2$, $c = 7.6$ Å. By observing the systematic absences in microdiffraction patterns, they also determined the space group to be either $Pna2_1$ (No. 33) or *Pnam* (No. 62). Since these two space groups have different point symmetries, convergent beam electron diffraction (CBED) was used parallel to [100] to distinguish between them. They concluded that the observed *2mm* symmetry of the zero-order Laue zone (ZOLZ) and the whole pattern confirmed that the space group must be *Pnam* (No. 62). They also observed antiphase boundaries (APBs) with displacement vectors of $c/2$ in these crystals and went on to suggest that since *Pnam* is a maximal non-isomorphous subgroup of *Pbam* ($c = 2c'$), the material probably underwent a phase transition on cooling from *Pbam* to *Pnam* in which the c axis doubled. Azough *et al.* [52] later used high-resolution XRD to calculate lattice constants for the Nd-15:19:72 compound as $a = 22.3475$, $b = 12.1938$, $c = 7.6771$ Å, but found the best fit to the XRD data using space group *Pbam*, in disagreement with their own previous work [44], which showed identical lattice constants but space group *Pnam*. They also noted the appearance of a strong XRD peak at $d = 3.45$ Å at 780 °C for Pr-1:1:4, which they could not identify.

Rawn [53], also accounting for the c-axis doubling and reorienting the unit cells into the standard setting for each space group, used Rietveld analysis on powder XRD data of La- and Gd-1:1:4 analogs to determine the space groups as $Pna2_1$ (No. 33) for La-1:1:4 and *Pnma* (No. 62) for Gd-1:1:4.

4.2.2 Tolerance Factor and Its Effect on the Temperature Coefficient

The tolerance factor (t) for the perovskite (ABO_3) crystal structure, discussed in Chapter 3, can be used to predict the onset of tilt transitions in perovskites and is the major factor that influences the behavior of the temperature coefficient of the dielectric constant ($\tau\varepsilon_r$) and,

by implication, τ_f, by allowing for steady thermal expansion with little modification of the octahedral volume. Although BNT has a more complicated structure, it is perovskite-related and the same phenomena can be invoked in tuning its τ_f. Because the crystal structure of BNT is comprised to a great extent of $(Nd_{4/5+x/5}Ba_{1/5-x/5}TiO_3)^{+(x/5+4/5)}$ perovskite-like octahedra [14], the tolerance factor can be calculated as if for a complex perovskite as

$$t = \frac{\left[(4/5 + x/5)R_{Nd^{+3}} + (1/5 - x/5)R_{Ba^{+2}}\right] + R_{O^{-2}}}{\sqrt{2}\left(R_{Ti^{+4}} + R_{O^{-2}}\right)} \tag{4.1}$$

By changing the size of the various crystallographic sites, the octahedra can be forced to tilt. Although it is rarely invoked by name, this is the strategy employed by researchers producing doped BNT ceramics.

4.2.3 Microwave Dielectric Properties of $BaO–Ln_2O_3–TiO_2$ System

The compounds in this system possess a high dielectric constant in the range of 65–110 with reasonably good quality factors. Eu, Sm, and Nd based compounds have high quality factors (*Qf*) up to about 14 000 GHz and the La-based ceramics show the highest relative permittivity [1, 5, 29, 45, 49, 54, 55]. It was observed that, in general, the relative permittivity and τ_f decreases and the quality factor increases with a decrease in ionic radii of the rare-earth ion. A detailed investigation of the dielectric properties of $Ba_{6-3x}Ln_{8+2x}Ti_{18}O_{54}$ solid solutions was done by Ohsato and coworkers [45]. The dependence of the dielectric constant, quality factor, and temperature coefficient of resonant frequency on x is shown in Figure 4.3. The ε_r and τ_f decreased with x whereas *Qf* increased with x and the maxima value is obtained at about $x = 2/3$ and thereafter it decreased. The increase in *Qf* at $x = 2/3$ can be attributed to the ordering of RE and Ba ions in the A1 and A2 sites, respectively, and a reduction in the internal strain, which result in a non-linear variation of *Qf* [45]. In the

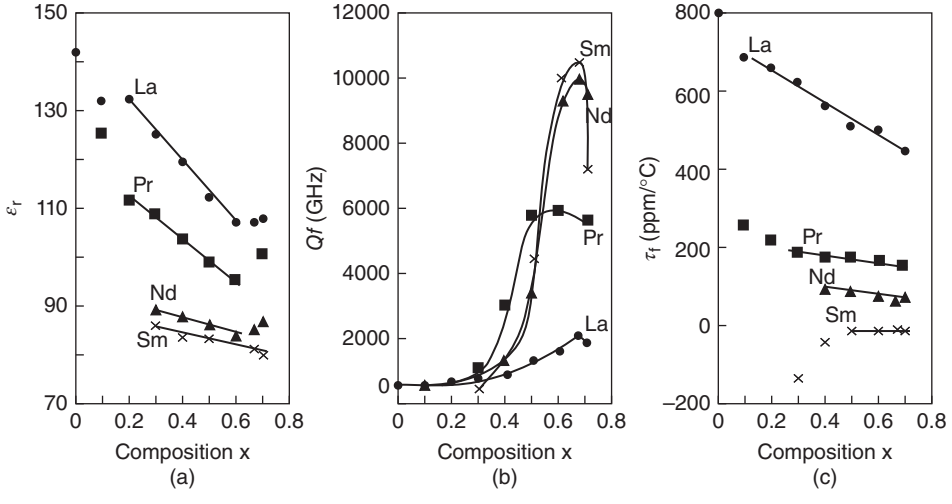

Figure 4.3 *Microwave dielectric properties of $Ba_{6-3x}Ln_{8+2x}Ti_{18}O_{54}$ (Ln = La, Pr, Nd, and Sm), Source: Adapted from Ohsato 2001 [45].*

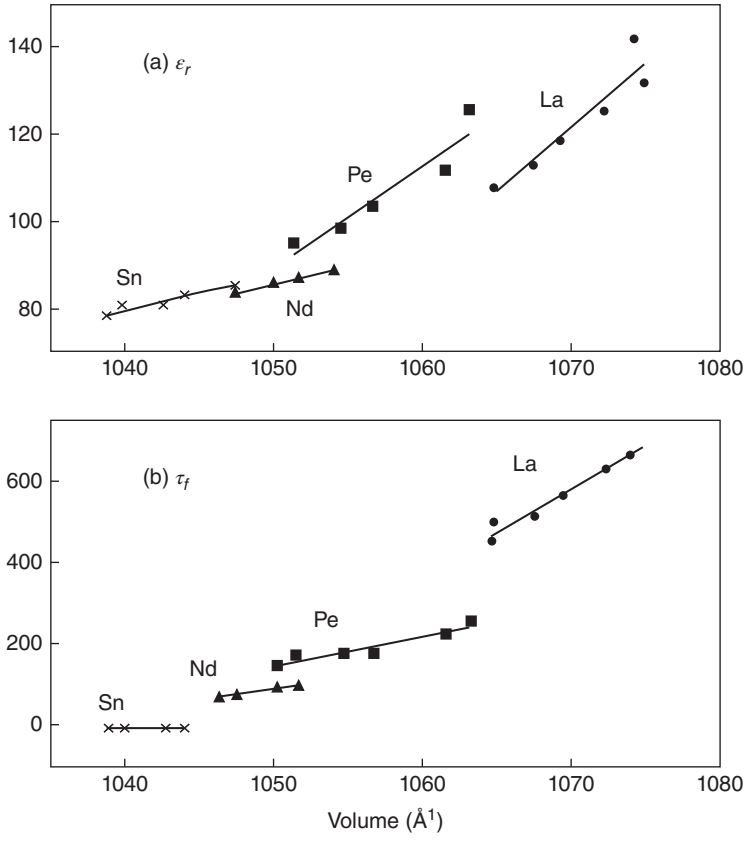

Figure 4.4 *Dependence of (a) ε_r and (b) τ_f on the unit cell volume. Source: Adapted from Ohsato 2001 [45].*

$BaO–Ln_2O_3–TiO_2$ system dielectric constants are found to be affected by three factors: (a) volume of the octahedron, (b) tilting of the octahedron, and (c) polarizabilities of Ln and Ba ions. The relative permittivity is found to increase with lattice parameters or cell volumes, as shown in Figure 4.4. It is worth to note that the dielectric constant and temperature coefficient of resonant frequency increase almost linearly with cell volume [45].

Ohsato *et al.* [56] investigated the effect of partial substitution of Eu, Dy, Ho, Er, and Yb for Nd in $Ba_{6-3x}(Nd_{1-y}–Ln_y)_{8+2x}Ti_{18}O_{54}$ ceramics for $x = 2/3$ and $y = 0.0$ to 1. The sintered samples formed solid solutions in the whole range of y. The volume of the unit cell decreased linearly with composition y for all Ln ions except for Yb. All Ln ions occupy A1 sites, but Yb ions occupy different smaller sites such as B and C sites after occupying the A1 sites. The occupancy of the A1 sites by Ln ions was revealed by the decrease of the lattice parameters and volume values. In the case of Yb, which has the smallest ionic radius, the volume starts increasing in the vicinity of $y = 0.4$, indicating that Yb ions occupy smaller sites such as trigonal and octahedral sites. The Qf improved up to $y = 0.3$ for all Ln ions substituted for Nd. The τ_f values of all Ln compounds improved with y. Figure 4.5a

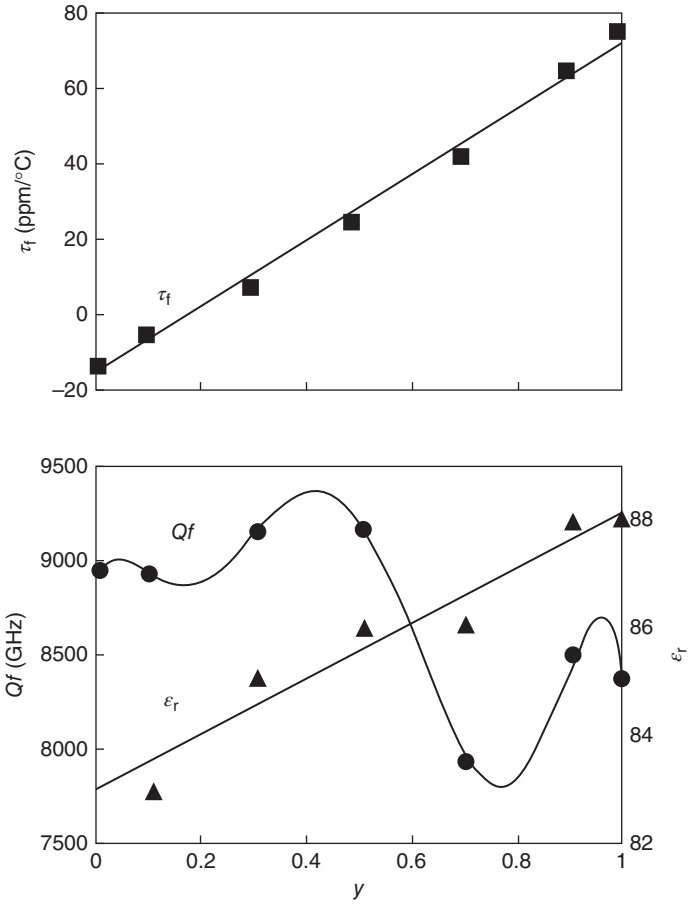

Figure 4.5 *Variation of quality factor (Qf) and τ_f of $Ba_4(Nd_{28/3-y}Sm_y)Ti_{18}O_{54}$ for y = 1. Source: Adapted from Ohsato* et al. *1995 [57].*

and b shows the variation of *Qf* and τ_f with ionic radii of Ln for $y = 1$ composition. The Eu series exhibited the best *Qf* for y = 1, with $\varepsilon_r = 83$, *Qf* = 10 500 GHz, and $\tau_f = 47$ ppm/°C. It may be noted that Negas and Davies [29] reported a high *Qf* value of 14 000 GHz for the Eu-based ceramics. In the case of Yb having the smallest ionic radius, the *Qf* values deteriorated at $y = 1$ because the Yb ions substitute into octahedral or triangular C sites. Several authors [57–61] improved the τ_f by partially substituting Sm by Nd. Ohsato *et al.* [57] studied the effect of substitution of La and Nd for Sm in $Ba_{6-3x}Sm_{8+2x}Ti_{18}O_{54}$ ($x = 0.6$). The lattice parameters changed linearly in both Sm–La and Sm–Nd series, indicating the formation of solid–solution phases. Both the La- and Nd-based ceramics have positive τ_f and the Sm-based ceramic has a negative τ_f. Thus partial La and Nd substitution for Sm resulted in a temperature-stable ceramic. $Ba_{6-3x}(Sm_{0.8}Nd_{0.2})_{8+2x}Ti_{18}O_{54}$ ceramic showed [57,58] $\varepsilon_r = 84$, *Qf* of 9000 GHz, and $\tau_f = 0$ and $Ba_{6-3x}(Sm_{0.9}La_{0.1})_{8+2x}Ti_{18}O_{54}$ has $\varepsilon_r = 84$, *Qf* = 9000 GHz, and $\tau_f = 1.6$ ppm/°C. Figure 4.6 shows the variation of ε_r, τ_f, and *Qf*

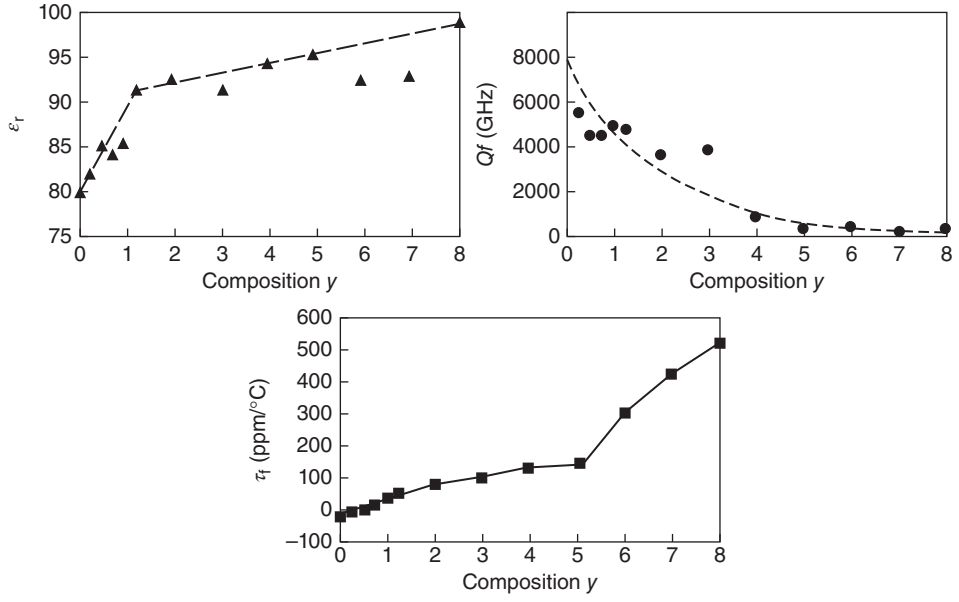

Figure 4.6 *Variation of ε_r, Qf, and τ_f as a function of composition in $Ba_4Sm_{(28-y)/3}Li_yTi_{18}O_{54}$ solid solution. Source: Adapted from Ohasto* et al. *2004 [102].*

of the Sm–Nd series. Ichinose and Amada [62] prepared BaO–$(Sm_{1-x}La_x)_2O_3$–$5TiO_2$ for $x = 0$ to 1. At $x = 0.1$ the composition has $\varepsilon_r = 91$, $Qf = 8900$ GHz, and $\tau_f = 4.2$ ppm/°C. La substitution increases ε_r and decreases Qf and changes the negative τ_f to a positive one. In general it has been found that as the ionic radius of the lanthanide decreases (atomic number increases) τ_f decreases.

4.2.3.1 The Effect of Dopants and Additives on Electrical Properties

Much attention has been given to doping ternary compositions to effect substitution on either the rare-earth oxide sites or the barium sites to maximize dielectric properties. The effect of additives on the sintering temperature, densification, and microwave dielectric properties of $Ba_{6-3x}Ln_{8+2x}Ti_{18}O_{54}$ ceramics has been extensive investigated by many workers [30, 63–100]. The additives that improved the dielectric properties of $Ba_{6-3x}Ln_{8+2x}Ti_{18}O_{54}$ are PbO, Bi_2O_3 or $Bi_4Ti_3O_{12}$, and TiO_2. The $Ba_{6-3x}Sm_{8+2x}Ti_{18}O_{54}$ for $x = 2/3$ has good properties: $\varepsilon_r = 80.4$, $Qf > 9000$ GHz. However, the τ_f is –13 ppm/°C and hence TiO_2, which has a high positive τ_f, was added to tailor its negative τ_f [65]. Addition of rutile considerably decreased the sintering temperature and improved the dielectric properties and could tune τ_f close to zero with ε_r of about 82 and $Qf = 9000$–12 000 GHz [65]. XRD and electron probe microanalysis (EPMA) studies showed the presence of $Ba_2Ti_9O_{20}$ and TiO_2 secondary phases in addition to $Ba_{6-3x}Sm_{8+2x}Ti_{18}O_{54}$. The most common dopant on the rare-earth sites, apart from other rare-earths [36, 37], has been bismuth [8, 16, 25, 61, 101], although some workers [44] have substituted Bi^{+3} for Ba^{+2}. In

all cases, adding Bi_2O_3 to ternary compositions increased ε_r but lowered Q and depressed τ_f. Kolar *et al.* [8] also reported that Bi_2O_3 aided processing by broadening the sintering interval and Azough *et al.* found [44] it to improve densification.

The beneficial influence of Bi_2O_3 or Bi_2O_3–TiO_2 addition in improving densification and τ_f of $Ba_{6-3x}Ln_{8+2x}Ti_{18}O_{54}$ ceramics has been reported by several researchers [5, 21, 30, 42, 73, 76–79, 92, 93]. Suvorov *et al.* [30] reported that zero τ_f can be achieved by the addition of 2.3 mol% Bi_2O_3 to the $Ba_{6-3x}Nd_{8+2x}Ti_{18}O_{54}$ ($x = 0.5$) compound. This amount of Bi coincides with the solid solubility limit of Bi, which substitutes for Nd in $Ba_{6-3x}Nd_{8+2x}Ti_{18}O_{54}$ ($x = 0.5$). Further addition of Bi caused the formation of the Bi-rich phase, accompanied with considerable decrease of Qf value and increase of τ_f. They also reported that the properties of Bi containing $Ba_{6-3x}Nd_{8+2x}Ti_{18}O_{54}$ ($x = 0.5$) ceramics can be significantly improved by leaching off the unreacted secondary phases prior to sintering. This increased Qf to about 5800 GHz with $\varepsilon_r = 88$ and $\tau_f = 0$ ppm/°C. Addition of small amounts of Mn and WO_3 further improved Qf to about 7000 GHz. Wu and Chen found [73] that the addition of $Bi_4Ti_3O_{12}$ led to the formation of $BaTi_4O_9$ secondary phase whereas Bi_2O_3 addition gave a single-phase material. EXAFS investigation of the local environment of Bi^{3+} ions incorporated in $Ba_{4.5}Nd_9Ti_{18}O_{54}$ showed [93] that Bi^{3+} ions selectively substitute for the Nd^{3+} ions. Zheng *et al.* [66] studied the effect of Bi addition in $Ba_{6-3x}(Sm_{0.2}Nd_{0.8})_{8+2x}Ti_{18}O_{54}$ ($x = 2/3$). Bi_2O_3 addition lowered the sintering temperature, increased ε_r, and lowered τ_f and improved the Qf up to 1 wt% Bi_2O_3 addition. Addition of 1 wt% Bi_2O_3 and sintered at 1200 °C/3 h gave a Qf of 8500 GHz and $\tau_f = -17$ ppm/°C, whereas 2 wt% Bi_2O_3 addition lowered the sintering temperature to 1175 °C/3 h and the ceramics had $\varepsilon_r = 83.5$, $Qf = 7600$ GHz, and $\tau_f = 14$ ppm/°C. A secondary phase of $Ba_2Ti_9O_{20}$ formed when 2 wt% Bi_2O_3 was added. The *b*-axis lattice parameter and cell volume decreased with Bi_2O_3 addition, indicating that Ba ions in the A2 pentagonal sites were substituted by Bi since Bi is smaller than Ba. A small amount of Bi_2O_3 addition lowered the sintering temperature and improved the microwave dielectric properties.

Ohsato *et al.* studied [102] the effect of Li substitution for Sm in $Ba_{6-3x}Sm_{8+2x}Ti_{18}O_{54}$ ($x = 2/3$). An X-ray diffraction study showed that a single-phase $Ba_4Sm_{(28-y)/3}Li_yTi_{18}O_{54}$ formed for $y \leq 7$. The lattice parameters a and c decreased sharply until $y = 1$ and then increased linearly up to $y = 7$. In the range $0 \leq y \leq 1$ the lattice parameters decreased, indicating that Li ions occupied only the A1 sites. In the region $1 \leq y \leq 7$, the a and c lattice parameters increased, indicating that Li ions occupied C sites. The site occupancy of Li changes at $y = 1$. One samarium ion can be substituted by three Li ions forming two vacancies. At $y = 1$, the vacancies of the A1 sites were fully occupied by Li ions. For $y > 1$, Li ions also occupy the C sites after filling the A1 sites. The dielectric properties of $Ba_4Sm_{(28-y)/3}Li_yTi_{18}O_{54}$ vary in relation to the variation in lattice parameters and are given in Figure 4.8 as a function of y. The ε_r increased with an increase in y whereas the Qf decreased. In the vicinity of $y = 0.3$, $\varepsilon_r = 83$, $Qf = 5000$ GHz, and $\tau_f = 0$ ppm/°C.

Yao *et al.* reported [97] that MgO or Al_2O_3 addition acts as an acceptor, could effectively suppress the reduction of Ti^{4+} ions, and significantly improve the Qf values of BST ceramics at the cost of the dielectric constant. MnO_2 as an oxidant had also improved the Qf values without affecting the relative permittivity. Excellent microwave dielectric properties were achieved in $Ba_{4.2}Sm_{9.2}Ti_{18}O_{54}$ ceramics doped with 0.2 wt% Al_2O_3 sintered at 1340 °C for 3 h: $\varepsilon_r = 76.9$, $Qf = 10\,120$ GHz, and $\tau_f = 22$ ppm/°C.

4.2.3.2 Substitution for Ba

Several authors [15, 18, 29, 87, 103–105] reported that addition of Pb improves the microwave dielectric properties of $Ba_{6-3x}Ln_{8+2x}Ti_{18}O_{54}$ ceramics. It has been reported that Pb^{2+} enters the Ba^{2+} sites [15, 29, 86, 87, 104] and the lattice parameters decrease since Pb^{2+} has a smaller ionic size than Ba^{2+}. The high dielectric polarizability of Pb^{2+} increased ε_r with a decrease in τ_f. However, Ubic *et al.* [106,107] reported a slight decrease in ε_r with Pb substitution. It was reported [104] that volatilization of PbO leads to the formation of secondary phases such as TiO_2. Belous and coworkers [87,105] investigated solid solubility limits of $(Ba_{1-y}Pb_y)_{6-x}La_{8+2/3x}Ti_{18}O_{54}$, $(Ba_{1-y}Pb_y)_{6-x}Nd_{8+2/3x}Ti_{18}O_{54}$, and $(Ba_{1-y}Ca_y)_{6-x}Ln_{8+2/3x}Ti_{18}O_{54}$ for a wide range of y and x. The Pb^{2+} and Ca^{2+} ions, when partially substituting for Ba^{2+} ions, occupy first the A1 sites and then the pentagonal A2 sites. Dielectric properties of the $(Ba_{1-y}M_y)_{6-3x}Ln_{8+2x}Ti_{18}O_{54}$ (R = La, Nd, Sm and M = Pb, Ca) materials strongly depend on the distribution of the Pb^{2+} and Ca^{2+} ions at different crystallographic sites. By partial isovalent substitution of Pb^{2+} and Ca^{2+} for Ba^{2+}, the τ_f of $(Ba_{1-y}M_y)_{6-3x}Ln_{8+2x}Ti_{18}O_{54}$ can be tuned to zero. Belous, Ovchar, and others [87, 105] reported that $(Ba_{1-y}Pb_y)_{6-x}Nd_{8+2/3x}Ti_{18}O_{54}$ samples sintered at 1330–1380 °C for 2–3 hours were single phase for the region $0 < y < 0.7$ at $x = 0$, $0 < y < 0.6$ at $x = 0.25$, and $0 < y < 0.4$ at $x = 0.5$. $Nd_4Ti_9O_{24}$ secondary phase was observed [86,87,104,105] outside the single-phase region. It was found that the dielectric properties varied non-linearly with Pb content due to the location of Pb^{2+} ions in different crystallographic sites in the unit cell. EXAFS studies by Valant *et al.* [93] on $Ba_{4.5-y}Pb_yNd_9Ti_{18}O_{54}$ revealed that Pb^{2+} does not substitute for Nd^{3+} or Ba^{2+} randomly on all possible sites. The Pb^{2+} selectively enters the A1 site previously shared by Ba^{2+} and Nd^{3+}; however, for larger concentrations of Pb, it also substitutes for Ba in the A2 sites [105].

Several workers [17, 19, 85, 107–113] investigated the effect of Sr substitution for Ba in $Ba_{6-3x}Sm_{8+2x}Ti_{18}O_{54}$. Sun *et al.* [19] reported that it is possible to tune the τ_f from –13 to +30 ppm/°C by adjusting the Sr content from 0 to 25 mol% in the $0.15(Ba_{1-x}Sr_x)O$–$0.15Sm_2O_3$–$0.7TiO_2$. The τ_f became zero for $x = 0.07$. Nishigaki *et al.* reported [17] that $Ba_{1-x}Sr_xSm_2Ti_{4.7}O_{14}$ with $x = 0.05$ sintered at 1350–1380 °C/2 h showed excellent dielectric properties, that is, $\varepsilon_r = 80$, $Qf = 11\,000$ GHz, and τ_f zero. The sintered ceramic showed the presence of small amounts of TiO_2 and $Ba_2Ti_9O_{20}$ secondary phases in accordance with the finding that 1:1:4.7 is not a single-phase compound. The presence of TiO_2 with high positive τ_f makes the 1:1:4.7 ceramics more positive.

The partial substitution of Ca for Ba in $Ba_{6-3x}Ln_{8+2x}Ti_{18}O_{54}$ considerably improved [87, 88, 105] τ_f with slight improvement in ε_r and Qf. The composition $(Ba_{0.95}Ca_{0.05})$–Sm_2O_3–$4.5TiO_2$ showed $\varepsilon_r = 81$, $Qf = 11\,000$ GHz, and $\tau_f = 2$ppm/°C [88]. Ubic *et al.* [106, 107] found that the substitution of Ca and Sr for Ba in $Ba_{6-3x}Nd_{8+2x}Ti_{18}O_{54}$ severely degraded the Qf but increased ε_r and τ_f. $Nd_4Ti_9O_{24}$ and $NdTiO_3$ were found as secondary phases. The synthesis of Bi- and Pb-substituted $Ba_{6-3x}Ln_{8+2x}Ti_{18}O_{54}$ is related to the conditions necessary to maintain exact stoichiometry and reproducibility due to the high partial pressure of Bi_2O_3 and PbO at elevated temperatures [83]. Slight changes in stoichiometry can lead to dramatic changes in the microstructural development during sintering. Incomplete substitution of Pb for Ba and Bi for Nd due to the evaporation of PbO or Bi_2O_3 during sintering leads to the formation of multiphase ceramics. In such ceramics the resultant dielectric properties depend on the properties of each individual single phase.

The most frequently added divalent cations have been strontium (usually added to Sm-based compositions) and lead (usually added to Nd-based compositions), substituted on barium sites. Nishigaki *et al.* [17] and Sun *et al.* [19] found that strontium doping in Sm-based 1:1:5 compositions increased ε_r while lowering Q and raising τ_f. Wakino *et al*. reported [15] that addition of PbO to 1:1:5 Nd-based powders increased both ε_r and Q at 3 GHz. Suvorov *et al.* [61] achieved some success in tuning dielectric properties by doping La-1:1:4 ceramics with Sr, Ca, or Zn, and by adding up to 10 wt% $Bi_2Ti_2O_7$. Ubic [114] has shown that, for single-phase BNT ceramics, as x increases, ε_r and τ_f decrease and Q increases. In the same work, doping the $x = 0.75$ composition with PbO was shown to result in a lowering of τ_f, even through zero, with only modest reductions in Q and, contrary to Wakino *et al.* [15], ε_r. Doping with Ca or Sr was also tried and found to lead to the formation of an additional phase. The resulting ceramics showed an increase in ε_r and τ_f and a drastic lowering of Q, in agreement with Nishigaki *et al.* [17] and Sun *et al.* [19]. Samples doped with Zr or Hf showed the presence of $Nd_2Zr_2O_7$ and $Nd_2Hf_2O_7$ and resulted in very poor resonance.

4.2.3.3 Substitution for Ti

The microwave dielectric properties of $Ba_{6-3x}Ln_{8+2x}Ti_{18}O_{54}$ can also be tailored by suitable substitution at the B site. Attempts were made to substitute Al, Sn, Zr, and Hf for Ti [86, 89, 98, 115, 116]. Mizuta *et al.* [89] prepared $(Ba_{4.2}Sm_{9.2})_\alpha Ti_{18-y}Al_yO_{54}$ $(0 < y < 1.61)$ and $(\alpha = 1 + y/36)$ where the B site is substituted by Al. The ε_r and Qf decreased and τ_f became more negative with Al substitution. The results indicate the possibility of tuning τ_f to zero in the La- and Nd-based ceramics by partial aluminum substitution at B sites. Azough *et al.* [71] reported that the addition of up to 1 wt% Al_2O_3 to the starting mixtures reduced the sintering temperatures by about 100 °C with an increase in Qf. The substitution of a small amount of Al on the Ti sites led to a decrease in ε_r and improvement in τ_f [71, 89]. Chen *et al.* [86, 116] made A- and B-site substitutions in $Ba_{6-3x}Sm_{8+2x}Ti_{18}O_{54}$ by preparing $Ba_{6-3x}Sm_{8+2x}(Ti_{1-z}Sn_z)_{18}O_{54}$ $(x = 2/3,\ z = 0.05,\ 0.1,\ 0.2,\ 0.3,\ 0.5,\ 0.8)$ and Ba_{6-3x} $(Sm_{1-y}Nd_y)_{8+2x}(Ti_{1-z}Sn_z)_{18}O_{54}$ $(x = 2/3,\ z = 0.05,\ y = 0.1,\ 0.3,\ 0.5,\ 0.8)$. In $Ba_{6-3x}(Sm_{1-y}Nd_y)_{8+2x}(Ti_{1-z}Sn_z)_{18}O_{54}$ with $z = 0.05$, the ε_r, Qf, and τ_f increased with increases in y. The ceramic $Ba_{6-3x}(Sm_{1-y}Nd_y)_{8+2x}(Ti_{1-z}Sn_z)_{18}O_{54}$ $(x = 2/3)$ with $y = 0.8$, $z = 0.05$ sintered at 1360 °C/12 h showed $\varepsilon_r = 80$, $Qf = 10\,600$ GHz, and $\tau_f = +11$ ppm/°C. The ε_r and Qf decreased with increases in z.

4.2.3.4 Effect of Glass Addition

Several authors studied [68, 69, 80, 82–84, 91, 117–120] the effect of addition of different glasses on the sintering temperature and the dielectric properties of $Ba_{6-3x}Ln_{8+2x}Ti_{18}O_{54}$ ceramics. The glass addition lowered the sintering temperature and changed the dielectric properties. Lu and Huang [120] reported that the addition of less than 2 wt% B_2O_3 in $Ba_{6-3x}Nd_{8+2x}Ti_{18}O_{54}$ lowered the sintering temperature by about 200 °C and improved densification whereas addition of more than 5 wt% B_2O_3 considerably decreased ε_r and led to the formation of $Ba_2Ti_9O_{20}$ secondary phases. Ota *et al.* [68] reported the effect of addition of crystalline and glassy B_2O_3 and GeO_2 in $Ba_{6-3x}Sm_{8+2x}Ti_{18}O_{54}$. Addition of 0.5 wt% B_2O_3 lowered the sintering temperature from 1400 to about 1170 °C with $\varepsilon_r = 76$, $Qf =$ 10 500 GHz, and $\tau_f = -19.4$ ppm/°C and 0.5 wt% of GeO_2 reduced the sintering temperature to about 1150 °C with $\varepsilon_r = 77$, $Qf = 8900$ GHz, and $\tau_f = -19.7$ ppm/°C. However, addition

of 0.5 wt% B_2O_3 + 0.5 wt% GeO_2 reduced the *Qf* to 5200 GHz. Addition of 0.5 wt% glassy B_2O_3 considerably reduced the *Qf* to about 4300 GHz and ε_r to 69.6 when sintered at 1200 °C. Chang *et al.* [81, 117] reported that the addition of alumina-doped silica glass to $Ba_{6-3x}(Nd,Sm)_{8+2x}Ti_{18}O_{54}$ ceramic lowered the sintering temperature and permittivity and improved the *Qf*. Addition of 20 wt% alumina-doped silica and sintered at 1250 °C gave $\varepsilon_r = 30$ and $Qf \sim 8700$ GHz. Santha *et al.* [69] investigated the effect of several glass systems on the sintering temperature, microwave dielectric, and elastic properties of $Ba_{6-3x}Sm_{8+2x}Ti_{18}O_{54}$ ceramics. It was found that addition of 3–4 wt% Al_2O_3–B_2O_3–SiO_2 and sintered at 1175 °C resulted in a ceramic with $\varepsilon_r = 64$, $Qf = 8500$ GHz, and zero τ_f. The Youngs modulus decreased with increasing amount of glass irrespective of the composition of the glass [69].

4.3 The Effect of Processing Parameters on Electrical Properties

Wu *et al.* [18] used various processing parameters to tune the properties of Sr-doped BNT. They were also the first to report the reaction sequence on calcination of an Sm-based 1:1:5 composition, although no thermal analysis was used to verify their reaction temperatures. They concluded that the $BaCO_3$ reacted with the TiO_2 to form $BaTi_4O_9$ at 900 °C. At 950 °C, $Sm_2Ti_2O_7$ formed and at 1000 °C, the $BaTi_4O_9$ and Sm_2O_3 reacted to form $Ba_4Ti_{13}O_{30}$ and more $Sm_2Ti_2O_7$. The ternary phase finally formed at 1050 °C. $Ba_2Ti_9O_{20}$ formed during sintering at 1325–1375 °C, and sintered pellets were found to contain a ternary compound, $Ba_2Ti_9O_{20}$, and TiO_2. The reaction mechanism proposed by Ubic [114] for the BNT system is in partial agreement with this work. He found that by first reacting a 1:1 stoichiometric amount of $BaCO_3$ and TiO_2 to form $BaTiO_3$, the formation of barium polytitanates was prevented. Similarly, by then adding the Nd_2O_3 and remaining TiO_2 to the $BaTiO_3$, milling in distilled water, drying, and heating to 600 °C, the $Nd(OH)_3$ (an inevitable consequence of wet milling hexagonal Nd_2O_3) decomposes in two stages, first to NdOOH (400 °C) and ultimately to the cubic form of Nd_2O_3 (550 °C), a much less hydratable polymorph of the oxide, which is stable up to 950 °C. Further confirmation of the two-stage decomposition of $Nd(OH)_3$ can be inferred by data extrapolated from work by Shafer and Roy [121]. It is possible that the formation of *c*-Nd_2O_3 in this way prevented the formation of the previously reported [16] $Nd_2Ti_2O_7$ impurity phase in the BNT system. The Sm_2O_3 used by Wu *et al.* [18] did not undergo appreciable hydration, as they milled in alcohol, not water. Using this method [114], sintered pellets typically contained only the ternary phase, although $Nd_4Ti_9O_{24}$ was observed as a secondary phase in BNT ($x = 0.75$) samples sintered below 1400 °C.

Low-temperature calcinations [114] of these pre-reacted powders generally led to incomplete reaction and the presence of two binary phases, *t*-$BaTiO_3$ and Ba_2TiO_4, as well as BNT. $BaTi_4O_9$ was previously observed by Chen *et al.* [20] (along with $Nd_2Ti_2O_7$) and $Nd_4Ti_9O_{24}$ by Ohsato *et al.* [28] and Roth *et al.* [41] in similar experiments with *un*-pre-reacted powder.

The microstructure of BNT ceramics (Figure 4.7) is dominated by acicular grains, which tend to hinder densification, especially at very high temperatures (≥ 1400 °C). Exaggerated grain growth can lead to desintering where the larger grains eventually touch and push each other apart [18, 19]. The observation of an acicular grain structure has been made by

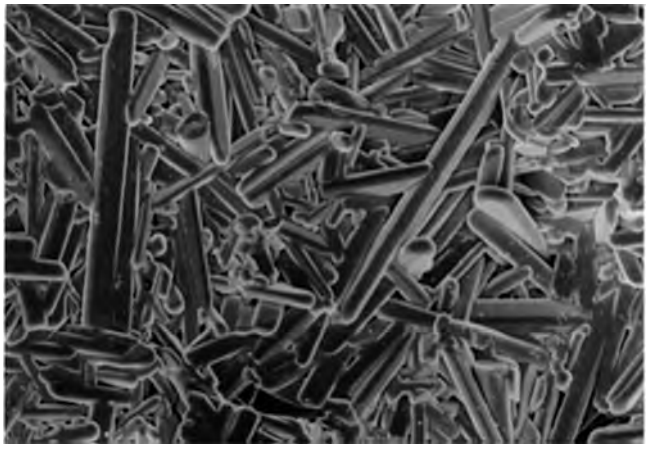

Figure 4.7 *The microstructure of* $(Ba_{0.5}Pb_{0.5})_{3.75}Nd_{9.5}Ti_{18}O_{54}$ *was sintered in air at 1400 °C for four hours. Source: Adapted from Ubic* et al. *1998 [5].*

Suvorov *et al*. [30] in 1:1:4 ceramics, by Chen *et al*. [20] in 1:1:5 ceramics, and by Ubic *et al.* in various compositions [56].

Negas and Davies incorporated [29] the effect of processing on the properties of the solid-solution phase. By inserting a tie-line between TiO_2 and the solid solution in the Nd and Sm system phase diagrams, various authors explained the appearance of $Ba_2Ti_9O_{20}$ and TiO_2 "metastable" impurities [17–19] for 1:1:5 "compounds." The appearance of these secondary phases explains why these ceramics can show such large variability in τ_f. Wu *et al.* [18] and Sun *et al.* [19] sintered ceramics, unknowingly, near and above peritectic melting, and the microstructures observed [17–19] also show evidence of transitory melts. Partial melting can help to improve densification by allowing liquid-phase sintering, but can also lead to local exaggerated grain growth if mixing is not homogeneous.

Negas and Davies [29] also investigated anisotropy of dielectric properties caused by forming techniques in 1:1:5 Sm-based ceramics. Isostatically pressed pellets never exhibited anisotropy, and die-pressed pellets and extruded parts only showed anisotropy above a critical calcination temperature (CCT). XRD evidence confirmed that this CCT (1025–1050 °C) corresponded to the first appearance of the solid–solution phase as a reaction product. Above CCT the concentration of solid solution increases and explains an increase in the anisotropies observed. At all temperatures, the anisotropy in extruded parts was (predictably) greater than that in die-pressed pellets. In the case of Bi- or Pb-containing compositions, the solid solution developed in the range 975–1025 °C, and by 1150 °C powders were almost fully reacted. In this case, the measured anisotropies were much larger.

Control of atmosphere is usually critical in avoiding high dielectric losses caused by reduction. Oxygen deficiency in titanate systems is well known and is thought to be compensated by the formation of Ti^{+3} ions [122]. These Ti^{+3} ions in barium titanates are considered to be the cause of conduction and of higher dielectric losses [123]. Oxygen heat treatments can eliminate the formation of Ti^{+3} ions and thus decrease the dielectric loss by 10–20% in $BaTi_4O_9$ [124] and by 5–20% in $Ba_2Ti_9O_{20}$ [125, 126]. The dielectric loss of $(Zr,Sn)TiO_4$ is also reportedly [127] affected by O^{-2} deficiencies. Ubic *et al.* [103] have

also seen evidence of chemical reduction in the $BaO–Nd_2O_3–TiO_2$ system in the form of a divalently doped $NdTiO_3$ impurity phase. This phase is almost certainly related to the A-deficient perovskite $Nd_{2/3}TiO_3$ which can be stabilized by the addition of various dopants.

4.4 Titania

Titanium dioxide crystallizes in three different forms, namely rutile, brookite, and anatase. When heated above 700 °C brookite and anatase converts irreversibly to rutile. TiO_2 single crystals possess a relative permittivity of 89 and 173 along the perpendicular and parallel to the *c* axis, respectively. However, it averages to 100 in polycrystalline samples. In 1962 Okaya and Barash were the first to experiment a dielectric resonator and did it using a rutile single crystal [128]. In 1968 Cohen [129] for the first time experimentally determined the microwave dielectric properties of the rutile resonator and reported that it has $\varepsilon_r = 100$, $Q = 10\,000$ at 3.45 GHz and $\tau_f = 400$ ppm/°C. Egerton and Thomson [130] reported dense rutile ceramics having low loss at the microwave frequency range prepared by hot-pressing the rutile powder in a graphite die. In the year of 2000 Templeton *et al.* [131] prepared TiO_2-based dielectric resonators using rutile raw powder as the starting material. Rutile powder was mixed with dopants, ball-milled, and sintered to almost full density at 1500 °C. Figure 4.8 shows the plot of Q of undoped sintered TiO_2 as a function of porosity. Depending on the porosity content two regions were present. In region 1 the quality factor steadily increased from a porosity of 30% to a value of about 6%. However, in region 2 at a porosity <6% the Q value rapidly decreased. This was due to oxygen deficiency in the dense or almost fully dense material. During sintering at high temperatures of about 1500 °C the material achieves >97% of the theoretical density and there is no interconnected porosity. At these temperature rutile is slightly oxygen deficient and the diffusion coefficient is too low to allow oxygenation of TiO_2 disk [132, 133].

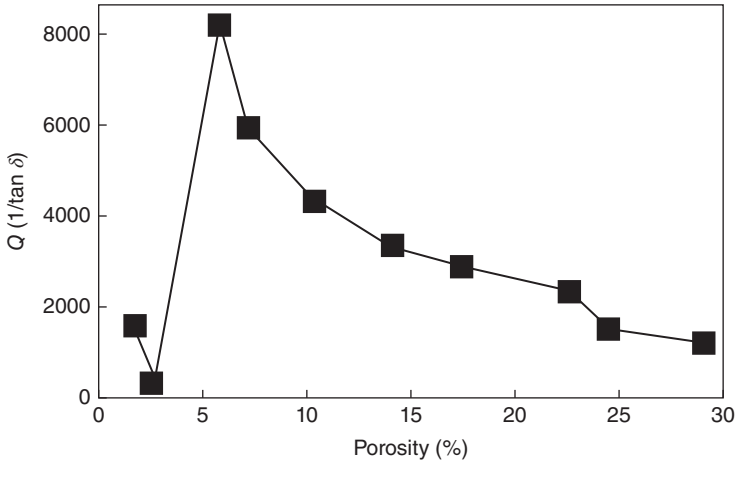

Figure 4.8 *Effect of porosity on the quality factor value of sintered TiO_2 disks measured at 3 GHz. Source: Adapted from Templeton* et al. *2000 [131].*

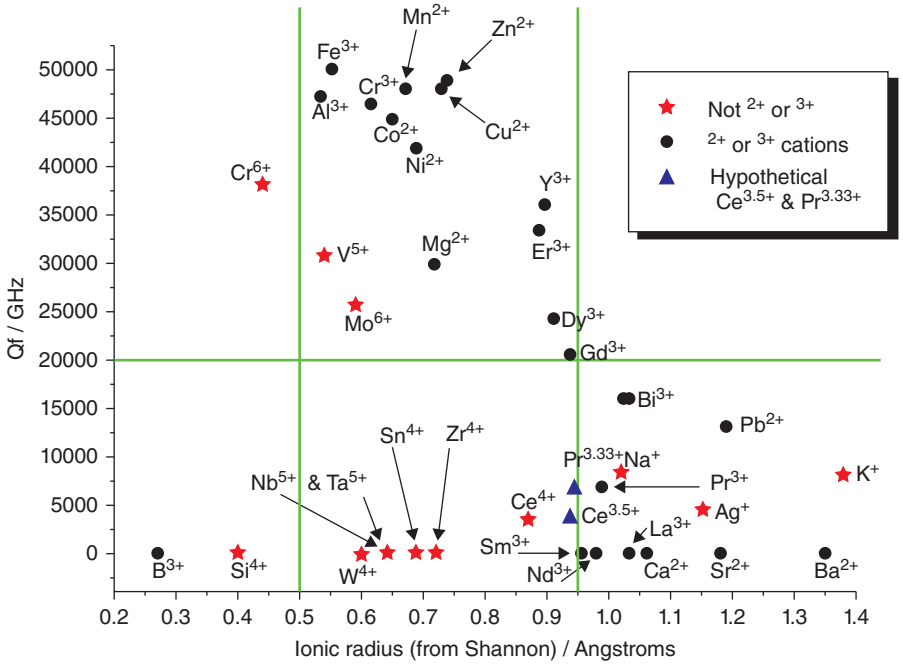

Figure 4.9 *Qf versus six coordinate ionic radii for doped TiO_2. The lines indicate ideal range for ionic radii [8] for the dopants to get high Q. Source: Pullar* et al. *2009 [34]. Reprinted with permission from Elsevier.*

Templeton *et al.* [131] also investigated the effect of different dopants on microwave dielectric properties of TiO_2. Later on Pullar *et al.* [134] carried out a comprehensive analysis of the influence of dopants on microwave dielectric properties of TiO_2. Dopants with a range of valence state and ionic radii were all added at 0.05 mol% to TiO_2. All the doped samples had densities greater than 95%, except those with Pb and Bi. In agreement with the densification all doped samples except Pb and Bi has permittivity close 100. Figure 4.9 shows the plot of *Qf* against ionic radii [43] of dopants, which is divided into two groups. The first group consists of dopants having ionic radii between 0.5 and 0.95 Å exhibited quality factor above 200 000 GHz. However, the second group with ionic radii outside this limit showed a quality factor much less than 20 000 GHz. Most of the samples doped with divalent or trivalent cations showed a high quality factor with the exception of V^{5+}, Cr^{6+}, and Mo^{6+}. In the case of V^{5+} and Cr^{6+} the reduction to lower oxidation might have occurred, ensuring that the ionic radii was between the ideal range of 0.5–0.95 Å. Rare-earth doped titania exhibited an anomalous decrease of *Q* from a Gd (0.94 Å) doped sample to an Sm (0.96 Å) doped one. Pr^{3+} and Ce^{4+} were exceptions, which might be due to their multiple valence state. In the conclusion the high quality factor can be obtained in TiO_2 by doping with ions having a +2 and +3 oxidation state and the dopant cation should have ionic radii between 0.5 and 0.95 Å. Even though the upper limit of 0.95 Å is quite discrete with no effect of dopants if ionic radii >0.96 Å, the ions with larger ionic radii and a +1 oxidation state exhibited measurable quality factors. Since TiO_2 possesses a high temperature

coefficient of resonant frequency of about +400 ppm/°C it is widely used to tailor τ_f of materials having a negative temperature coefficient of resonant frequency [1, 135, 136].

Klein *et al.* [137] studied MW dielectric properties of single-crystal rutile. High-purity rutile single crystals show extremely low losses at microwave frequencies and cryogenic temperatures. Tobar *et al.* [138] used WGM to measure the Q of rutile single crystals at low temperatures. The rutile had $Q = 10^4$ at 300 K, 10^5 at 80 K, and 10^7 at 10 K. It also showed anisotropy both in permittivity and loss factor. Tobar *et al.* [138, 139] also reported a high Q sapphire–rutile frequency-compensated dielectric resonator with a Q-factor of the order of a few million below 90 K.

4.5 $Sr_{1-3x/2}Ce_xTiO_3$ Ceramics

In the field of microwave communications, high permittivity materials ($\varepsilon_r > 100$) are required for miniaturization, and there are only a few classes of materials that show simultaneously high permittivity and high quality factor with temperature stability [1]. Among the high-permittivity materials, perovskite-based titanates such as $CaTiO_3$ and $SrTiO_3$ are widely studied systems. Sreemoolanadhan *et al*. [140] reported the microwave dielectric properties of ceramics in the $BaO–2CeO_2–nTiO_2$ system; however, most of these materials were not phase-pure [140, 141]. Bamberger *et al.* [142] reported the existence of a new compound, $Sr_2Ce_2Ti_5O_{16}$, and a series of solid solutions of the type $Sr_{2+n}Ce_2Ti_{5+n}O_{16+3n}$ ($n \leq 7$). In both cases, Ce is necessarily present as Ce^{4+}; however, the crystal structure and phase purity of these compounds were not well established. It was determined in subsequent work [143, 144] that such ceramics prepared via the route described by Bamberger *et al.* [142] largely contain Ce^{3+} rather than Ce^{4+}, so the formula is more correctly written as $Sr_{2+n}Ce_2Ti_{5+n}O_{15+3n}$ or more simply as $Sr_{1-3x/2}Ce_xTiO_3$, where $x = 2/(n + 5)$. The $Sr_2Ce_2Ti_5O_{16}$ compound is simply the $x = 0.4$ member of this series, which reportedly [145, 146] is a different structure than compositions for which $x < 0.4$.

Indeed, many Ce-based compounds synthesized in air contain both Ce^{3+} and Ce^{4+}; therefore, it is reasonable to expect that a finite amount of Ce^{4+} could be reduced to Ce^{3+} in these compositions, as observed previously in some Ba-polytitanates sintered in air at high temperatures [147]. The XPS spectra (Figure 4.10) performed in the Ce-3d binding energy region showed that more than 90% of the surface Ce existed as Ce^{3+}, explaining the formation of stable, phase-pure perovskites. The presence of Ti^{3+} ions was not detected in any sample. The quantification of the amounts of Ce^{3+} and Ce^{4+} are given in Table 4.1. The reduction of Ce^{4+} upon annealing has also been observed by Beyreuther *et al.* [148]. Subodh *et al.* obtained [144] well-sintered samples with good dielectric properties by sintering in the temperature range of 1300 to 1400 °C.

4.5.1 Crystal Structure of $Sr_{1-3x/2}Ce_xTiO_3$ System

X-ray diffraction data and vibrational spectroscopy of $Sr_{1-3x/2}Ce_xTiO_3$ ($0.1333 \leq x \leq 0.4$) ceramics [144, 149] seemed to show cubic symmetry in space group $Pm\bar{3}m$; however, these techniques are not very sensitive to subtle oxygen displacements. The similar $Sr_{1-3x/2}La_xTiO_3$ system was previously investigated by Howard *et al.* [150], who found that

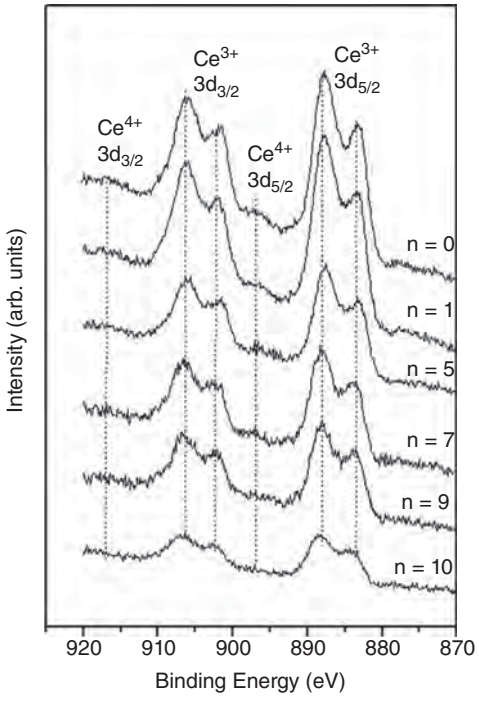

Figure 4.10 *XPS spectra in the Ce-3d binding energy region for selected samples, from x = 0.400 to 0.133. Peaks linked to Ce^{3+} and Ce^{4+} cations are indicated. Source: Adapted from Subodh* et al. *2007 [144].*

Table 4.1 *Ce^{4+} content in $Sr_{1-3x/2}Ce_xTiO_3$ ceramics.*

x	Sintering temperature (°C)	Ce^{4+}/Ce_{total}
0.400	1300	0.10
0.333	1375	0.07
0.286	1375	0.07
0.250	1375	0.06
0.222	1375	0.06
0.200	1375	0.08
0.182	1375	0.05
0.167	1375	0.05
0.154	1400	0.04
0.143	1400	0.04
0.133	1400	0.03
$SrTiO_3$		0

at room temperature antiphase octahedral tilting about one axis drives a $Pm\bar{3}m \rightarrow I4/mcm$ transition at $x \approx 0.2$, and cation ordering drives a further transition to C*mmm* at $x \geq 0.55$.

4.5.1.1 Electron Diffraction

All compositions ($0.1333 \leq x \leq 0.4$) tested by Ubic *et al*. [145] appeared to be single-phase, essentially consisting of a solid solution of $SrTiO_3$ and $Ce_2Ti_3O_9$. The $Ce_2Ti_3O_9$ compound has been variously reported as either an undistorted perovskite with $Pm\bar{3}m$ symmetry [151] or a doubled perovskite with *Pmmm* symmetry [152]. The oxygen-deficient versions of this phase are also typically reported in orthorhombic settings. Figure 4.11 shows selected area electron diffraction patterns (SADPs) of $Sr_{0.625}Ce_{0.25}TiO_3$ parallel to the pseudocubic directions [001], [101], and [111].

Both the [001] and [111] patterns can be indexed unambiguously according to a primitive simple cubic perovskite unit cell in $Pm\bar{3}m$; however, faint superlattice reflections in the [101] pattern cannot be explained by this structure. The extra reflections closest to the central transmitted spot correspond to $\frac{1}{2}\{111\}$, a fact that clearly indicates that the lattice

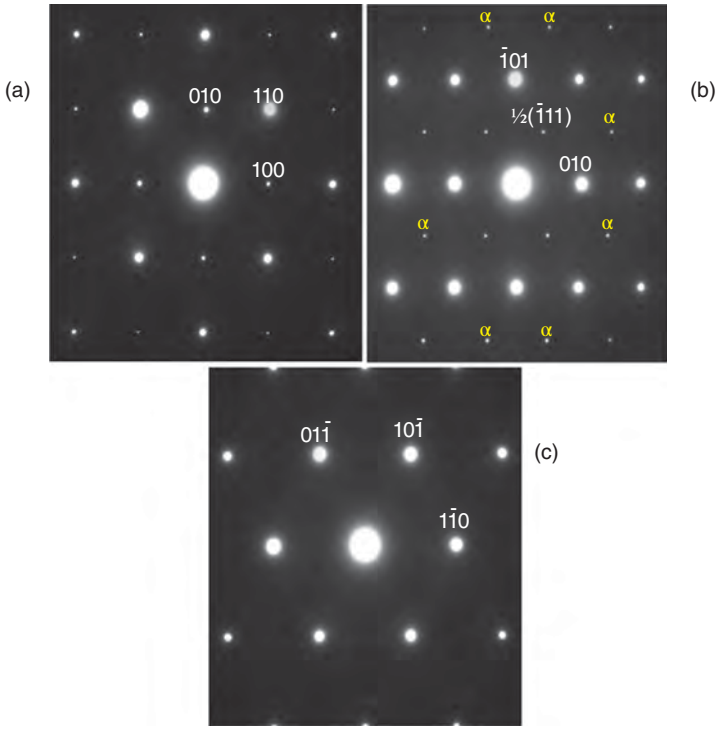

Figure 4.11 *Selected-area electron diffraction patterns from grains of the x = 0.25 composition corresponding to (a) [001], (b) [101], and (c) [111] pseudocubic directions. Superlattice reflections caused by antiphase tilting of octahedra are denoted with an α in (b). Source: Adapted from Ubic* et al. *2008 [145].*

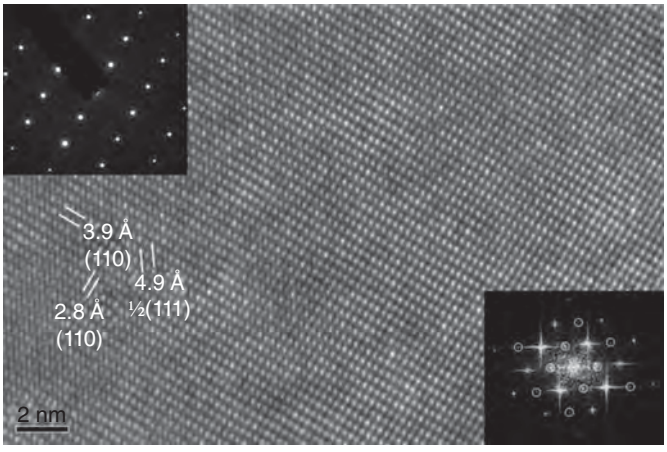

Figure 4.12 *High-resolution image of the x = 0.25 composition parallel to the pseudocubic [110]. The lower-right inset is a Fourier transform of the image with superlattice spots circled. Source: Adapted from Ubic* et al. *2008 [145].*

constant must be doubled and the symmetry lowered. Similar patterns were obtained for every composition examined by Ubic *et al.* [145]. Only $R\bar{3}c$, corresponding to antiphase tilts of equal magnitude about each pseudocubic axis (tilt system $a^-a^-a^-$), was able to consistently index all the observed diffraction patterns, with the [001], [101], and [111] pseudocubic patterns corresponding to [241], [$\bar{1}$11], and [001], respectively. The pattern in Figure 4.11 can be indexed based on a trigonal unit cell in $R\bar{3}c$. In such a tilt system, it is found empirically that the octahedra are generally flattened down their rotation axis [153].

Figure 4.12 is a high-resolution image of the $x = 0.25$ composition parallel to a pseudocubic <110>. The Fourier transform of the image appears in the inset and clearly demonstrates the existence of a non-cubic superlattice. The pseudocubic $\{100\}$ spacing measures consistently at about 3.9 Å from the image, in agreement with the XRD data. The measured $\{110\}$ spacing (2.8 Å) is close to what one would expect for such a cubic crystal; however, the $\{111\}$ spacing appears stretched. For a cubic crystal with a lattice constant of 3.9 Å, one would expect a $\{111\}$ spacing of 2.3 Å. A simply doubled $\{111\}$ would then be about 4.5 Å, but the $\frac{1}{2}\{111\}$ measured on this image is closer to 4.9 Å, indicating a stretch along a pseudocubic <111> (trigonal [001]), which would suggest a lowering of the symmetry to trigonal (and a trigonal *c*-axis of about 13.5 Å).

The tolerance factors of these compounds, if the vacancies were neglected, would be between 0.991 ($x = 0.4$) and 1.004 ($x = 0.1333$), indicating an untilted cubic structure. On the other hand, if partial and mixed occupancy of the A site is taken into account, these values would decrease to between 0.8905 ($x = 0.4$) and 0.9696 ($x = 0.1333$), consistent with the presence of a superlattice due to antiphase tilts such as that observed in Figure 4.11. Grains for which $0.1333 \leq x \leq 0.25$ looked relatively defect-free; however, in the case of $x = 0.4$ grains were very defective. Streaks were visible in diffraction patterns and very faint $\frac{1}{2}\{odd, even, even\}$ β-reflections were observed in <110> patterns (Figure 4.13),

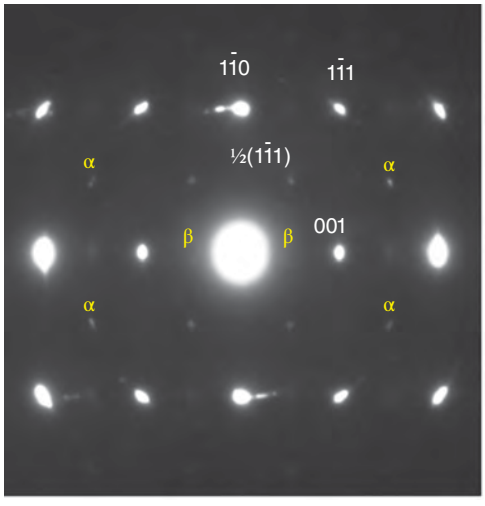

Figure 4.13 *Pseudocubic [110] selected area diffraction pattern of the x = 0.4 composition with α and β superlattice reflections indicated. Source: Adapted from Ubic* et al. *2009 [146].*

usually indicative of either ordering or antiparallel displacements of A-site cations. The latter is not allowed in $R\bar{3}c$.

4.5.1.2 Neutron Diffraction

Ubic *et al.* [145] used neutron diffraction to refine the unit cell parameters, atomic positions, and isotropic displacement parameters (IDPs) for the various $Sr_{1-3x/2}Ce_xTiO_3$ ($x = 0.1333$, 0.1667, 0.25, 0.4) compositions in space group $R\bar{3}c$. Table 4.2 summarizes the refinement results for each composition. A charge-balance analysis of the refinement results agrees well with the XPS data, although there is a small anomaly in the charge balance for $x = 0.4$, which would actually suggest a negative amount of Ce^{4+}. This anomaly is undoubtedly the result of a structural change between $0.25 \leq x \leq 0.4$. The A-site bond valence sums were found to decrease from 2.0273 at $x = 0.1333$ to 1.9029 for $x = 0.4$, whilst the Ti bond valence sums increase from 4.1736 at $x = 0.1333$ to 4.2258 at $x = 0.4$.

Figure 4.14 illustrates the observed and calculated neutron diffraction patterns for $Sr_{1-3x/2}Ce_xTiO_3$ ($x = 0.1333$, 0.1667, 0.25, 0.4). The arrowed peak in Figure 4.14b indicates a superlattice reflection at ≈2.35 Å corresponding to the same pseudocubic $\frac{1}{2}\{311\}$ also indicated by the symbols in Figure 4.14b. In this model, the positions of the cations are fixed.

There is only one degree of freedom (x), which is in the 18e oxygen positions. Ideally $x = 0.5$, and the size of the deviation away from 0.5 is related to the severity of octahedral tilting. Ubic *et al.* [145] calculated that the first superlattice XRD (Cu–Kα) peak for $Sr_{0.625}Ce_{0.25}TiO_3$ ($x = 0.25$) would be the extremely weak for the $\frac{1}{2}\{311\}$ peak at 38.38° ($I \sim 0.23\%$), and all the other allowed superlattice peaks would be so weak as to be nonexistent. The $x = 0.4$ composition was more closely analyzed later [146] and found to be closer to *C2/c*; however, very weak, diffuse β reflections, attributed to a short-range

Table 4.2 *Unit cell parameters and refinement results for $Sr_{1-3x/2}Ce_xTiO_3$ at room temperature.*

Composition (x)	0.1333	0.1667	0.25	0.4
Refined cell parameters (Å)	$a = b = 5.5091(2)$ $c = 3.5071(3)$	$a = b = 5.5062(2)$ $c = 3.4989(3)$	$a = b = 5.5005(2)$ $c = 13.4797(3)$	$a = b = 5.4860(2)$ $c = 3.4539(3)$
x position for the O[a]	0.5108(2)	0.5137(2)	0.5184(2)	0.5237(3)
Angle of tilt	1.2°	1.5°	2.0°	2.6°
Sr/Ce U_{iso}	0.008(1)	0.008(1)	0.008(1)	0.008(1)
Ti U_{iso}	0.006(1)	0.006(1)	0.007(1)	0.007(1)
O U_{iso}	0.0114(4)	0.0119(5)	0.0137(5)	0.0162(6)
$[Ce^{4+}]/[Ce_{total}]$	0.03	0.05	0.06	0.10
Sr occupation refined/expected	0.795(7)/0.8	0.744(6)/0.75	0.601(7)/0.625	0.352(5)/0.4
Ce occupation refined/expected	0.133/0.133	0.167/0.166	0.269/0.25	0.445/0.4
Sr/Ce–O average bond length (Å)	2.7557	2.7544	2.7516	2.7457
Ti–O average bond length (Å)	1.9493	1.9488	1.9477	1.9447
Sr–O bond valence sum	1.7132	1.6154	1.3258	0.7988
Ce–O bond valence sum	0.3141	0.3964	0.6487	1.1041
Ti–O bond valence sum	4.1736	4.1793	4.1917	4.2258
Over all Gof /Rwp	1.94/3.77 %	2.07/3.90 %	2.18/4.46 %	11.43/5.16%

[a] Sr and Ce in 0, 0, $\frac{1}{4}$, Ti in 0, 0, 0, and O in x, 0, $\frac{1}{4}$.

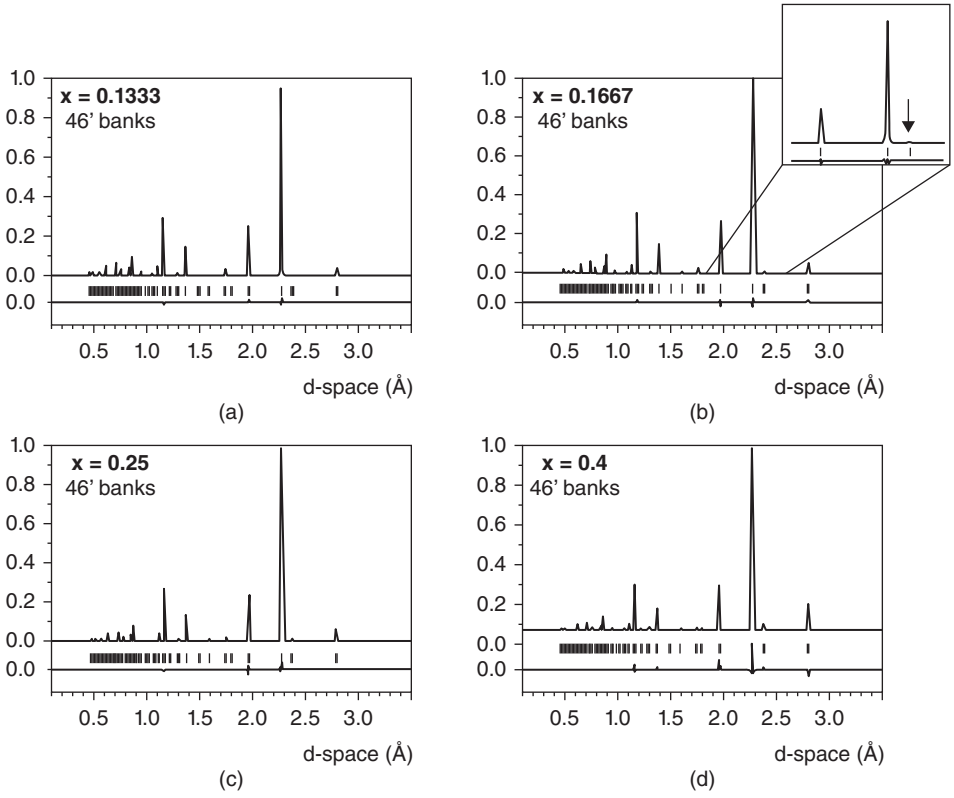

Figure 4.14 *ToF neutron powder diffraction patterns for d-spacings between 0.5 and 3 Å for* $Sr_{1-3x/2}Ce_xTiO_3$ *(x = 0.1333, 0.1667, 0.25, 0.4) taken from data obtained with the 46° bank detectors. Observed data are represented by crosses; calculated results are represented by solid lines. The difference curve is illustrated on the same scale. The arrow in the inset (b) shows, as an example, a weak superlattice reflection at ≈2.35 Å corresponding to the pseudocubic* $\frac{1}{2}\{311\}$*. Source: Adapted from Ubic* et al. *2008 [145].*

ordering effect, were not accounted for in the refinement. They may be related to the incipient ferroelectric nature of $Sr_{0.4}Ce_{0.4}TiO_3$.

4.5.2 Microstructure and Dielectric Properties of SCT ceramics

Recently Subodh *et al.* [143, 144] and Ubic *et al.* [145, 146] investigated the crystal structures and microwave dielectric properties of members of this solid–solution series and found all of them to possess high dielectric constants with reasonably good quality factors. The SEM images of thermally etched $Sr_{1-3x/2}Ce_xTiO_3$ ceramics with $x = 0.167$, 0.200, 0.25, 0.25, and 0.333 are shown in Figure 4.15. Optimized microwave dielectric properties of these ceramics at 2 GHz with respect to Ce content is given in Figure 4.16. The observed decrease in permittivity with x would likely be due to the hardening of the soft mode phonon caused by the extrinsic Ce^{3+}/Ce^{4+} ions and their associated vacancies. The initial increase

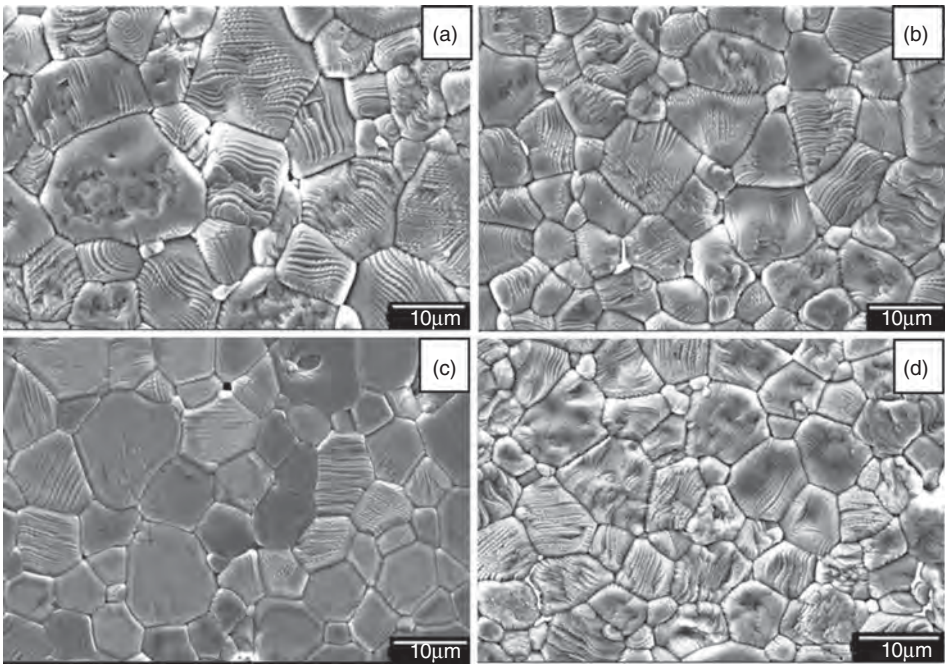

Figure 4.15 *SEM micrographs for the $Sr_{1-3x/2}Ce_xTiO_3$ samples sintered at 1375 °C/2 h, for (a) x = 0.1667, (b) x = 0.2, (c) x = 0.25, (d) x = 0.333. Source: Adapted from Subodh* et al. *2007 [144].*

in quality factor with x may also be a consequence of the soft mode hardening; however, above $x = 0.25$ its decrease in the disorder introduced in the system would reduce the phonon lifetimes of the different polar phonon modes.

As is well known, $SrTiO_3$ is an incipient ferroelectric [154], which explains its relatively high permittivity. For this reason, it does not obey Shannon's additive polarizability rule for determining the permittivity of oxides [155]. From the Clausius-Mosotti equation, a permittivity of just 40.0 is obtained for $SrTiO_3$. For all the $Sr_{1-3x/2}Ce_xTiO_3$ materials reported by Subodh *et al.* [144], predicted permittivities vary from 40.0 ($x = 0$) to 36.7 ($x = 0.40$). Since the measured relative permittivity values are far above these predicted values, it may be concluded that $Sr_{1-3x/2}Ce_xTiO_3$ materials are also incipient ferroelectrics, which is further confirmed by investigating the low-temperature microwave properties [156]. The low-temperature dielectric properties of $Sr_{1-3x/2}$ Ce_xTiO_3 ($x = 0.133$ to 0. 400) were measured at 2–4 GHz. The static dielectric permittivity of all samples presents typical behavior of incipient ferroelectric materials, increasing up to a high-saturated value on cooling, as seen in $SrTiO_3$.

4.5.3 $(Sr_{0.75-x}Pb_xCe_{0.167})TiO_3$

All $Sr_{1-3x/2}Ce_xTiO_3$ ceramics have reasonably high permittivity values ($\varepsilon_r > 100$). As the ionic radius of Pb^{2+} (1.49 Å) and Sr^{2+} (1.44 Å) in cuboctahedral coordination are a good

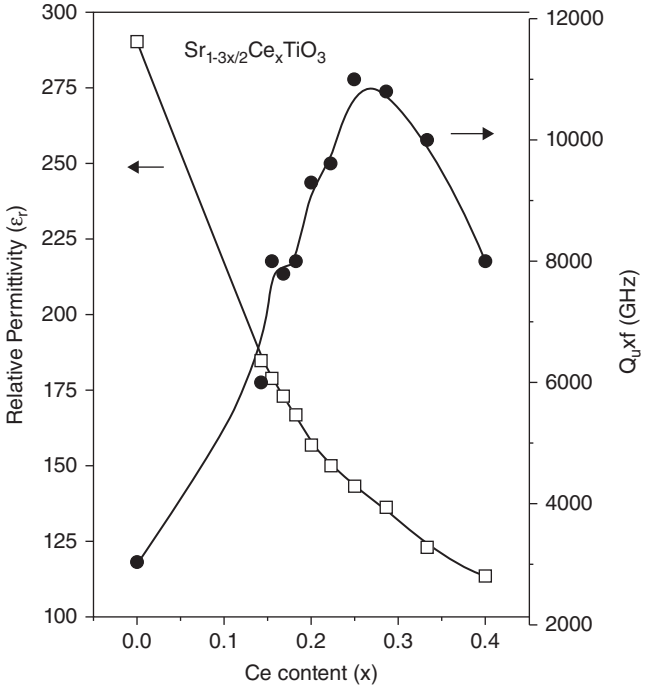

Figure 4.16 *Dependence of microwave ε_r and Qf with Ce^{3+} content (x) for the $Sr_{2+n}Ce_2Ti_{5+n}O_{15+n}$ (renamed as $Sr_{1-3x/2}Ce_xTiO_3$) solid solutions, at optimized sintering temperatures. $SrTiO_3$ values are included for x = 0. Source: Adapted from Subodh* et al. *2008 [144].*

match, and as Pb^{2+} has a high ionic polarizability (6.58 Å^3) [155], Pb^{2+} was chosen by Kamba *et al.* [157] to add substitutionally for Sr^{2+} in $Sr_{0.75}Ce_{0.167}TiO_3$. They investigated the temperature dependence of the dielectric response in $(Sr_{0.75-x}Pb_xCe_{0.167})TiO_3$ ceramics between 100 Hz and 3.2 GHz. Representative curves for all ten samples ($y = 0 – 0.75$) are shown in Figure 4.17. No dielectric dispersion, i.e., change of permittivity with frequency, was observed in high-frequency and microwave data; therefore, the curves were plotted only at 100 MHz. Room-temperature microwave dielectric properties are summarized in Figure 4.18. Microwave dielectric resonances were obtained in all $Sr_{0.75-x}Pb_xCe_{0.1667}TiO_3$ ceramics with the exception of the $x = 0.5$ sample, which exhibits high dielectric loss ε'' due to the proximity to room temperature of its T_C. The best Qf was obtained for the $x =$ 1 sample, where $Qf = 5800$ GHz and $\varepsilon_r = 240$; however, its τ_f of 920 ppm/°C, although about half the value for $SrTiO_3$, is still too high for microwave applications.

4.6 $Pb_n(Nb_{1-x}Ta_x)O_{5+n}$

The pyrochlore structure, space group $Fd\bar{3}m$ (No. 227), is well understood. Stoichiometrically pyrochlore is usually written as $A_2B_2O_7$, consisting of large (radius ≈1 Å) A-site

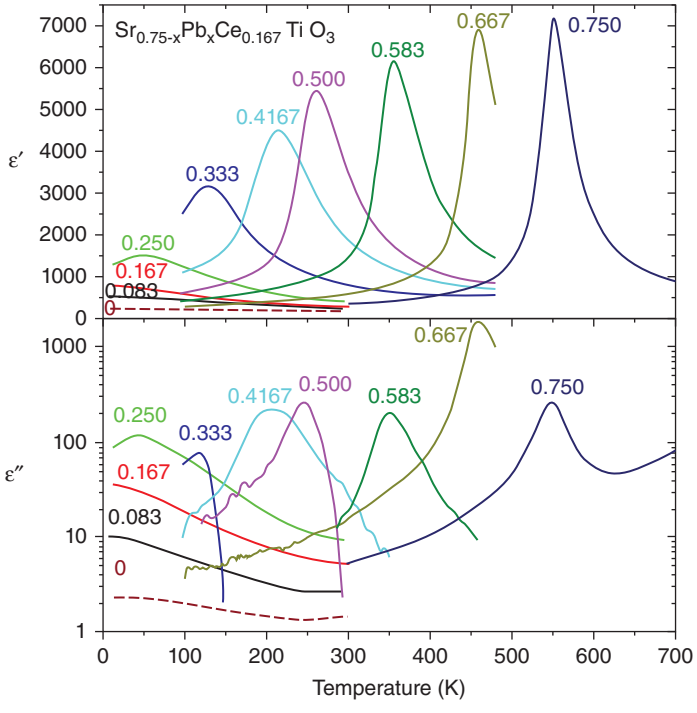

Figure 4.17 *Temperature dependences of real and imaginary parts of complex permittivity in* $Sr_{0.75-x}Pb_xCe_{0.1667}TiO_3$ *(x = 0–0.75) ceramics. Data were taken at 100 kHz (y = 0–0.25, 0.75) and at 100 MHz (y = 0.3333–0.6667). Source: Adapted from Kamba* et al. *2009 [157].*

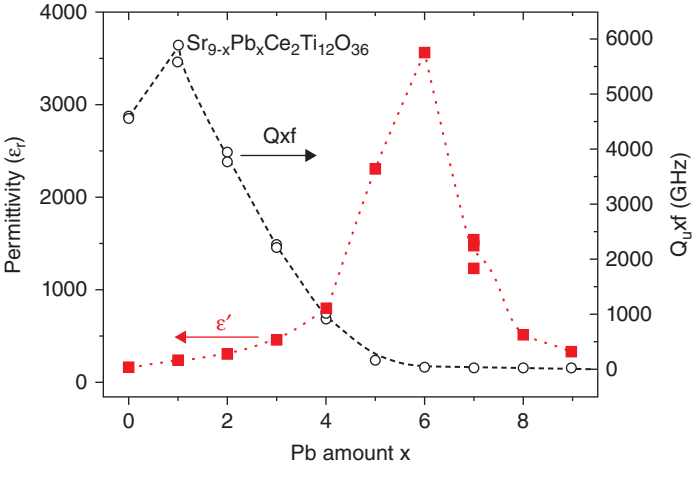

Figure 4.18 *Concentration dependence of microwave permittivity and Qf factor in* $Sr_{0.75-x}Pb_xCe_{0.6667}TiO_3$ *(x = 0–0.75) ceramics. Data were collected at room temperature between 0.9 and 3.2 GHz. Source: Adapted from Kamba* et al. *2009 [157].*

cation species in eightfold coordination and a network of oxygen octahedra (actually trigonal antiprisms) enclosing smaller (radius ≈0.6 Å) B-site cations. The only crystallographic variable is in the 48f oxygen sites, the positions of which have one degree of freedom called x. The cubic form of lead pyroniobate is PbO-deficient, with only 75% of A sites occupied ($Pb_{1.5}Nb_2O_{6.5}$). Introducing more PbO into this structure ($Pb_nNb_2O_{5+n}$, $n > 1.5$) causes a rhombohedral distortion of the pyrochlore structure, the nature of which is still not completely understood. For this reason, stoichiometric $Pb_2Nb_2O_7$ does not have the cubic pyrochlore structure. Beech *et al.* [158] suggested that $Pb_nM_2O_{5+n}$ (M = Nb, Ta) pyrochlore may exist over the range $1.33 \leq n \leq 1.6$, but Ubic and Reaney [159] found the $n = 1.33$ composition to yield a diphasic mixture of $PbNb_2O_6$ and $Pb_{1.5}Nb_2O_{6.5}$.

4.6.1 $Pb_nNb_2O_{5+n}$ ($1.5 \leq n < 2$)

Cook and Jaffe [160] measured the lattice constant of the cubic pyrochlore $Pb_{1.5}Nb_2O_{6.5}$ as $a = 10.561 \pm 0.001$ Å and $\varepsilon_r = 200$ at room temperature (and $\varepsilon_r = 500$ at –196 °C). Roth found [161] this phase to melt incongruently at 1233 °C to liquid plus tetragonal $PbNb_2O_6$. In 1971 Brusset *et al.* [162] confirmed the existence of the cubic pyrochlore compound $Pb_{1.5}Nb_2O_{6.5}$ and reported a lattice constant of $a = 10.56$ Å. It was subsequently found [159] to have $a = 10.5604$, $\varepsilon_r = 259$, $Q_f = 3015$ GHz, and $\tau_f = 1239$ ppm/°C. High-resolution XRD scans and neutron diffraction of the cubic $Pb_{1.5}Nb_2O_{6.5}$ phase by Ubic and Reaney revealed [163] a lattice constant of 10.5622 Å and a crystallographic x parameter for the 48f oxygen positions of 0.313, significantly lower than some early authors have reported [164] but in excellent agreement with later work [158, 165]. For this composition, selected area diffraction patterns (SADPs) can be indexed according to the cubic pyrochlore structure (Figure 4.19a); however, with increasing Pb content, crystallographic layers appear in the structure on {111} planes, lowering the symmetry of the crystal (Figure 4.19b to h).

Compositions for which $1.5 < n \leq 2.5$ contain discreet PbO-rich layers on pseudocubic {111} planes between alternating slabs of pyrochlore (Figure 4.19b to g), similar in appearance to Ruddlesden-Popper phases [163]. For $n = 1.6$, a streaking of intensity is visible along cubic <111>, which is associated with one-dimensional disorder in those directions (Figure 4.19b). For $1.6 \leq n < 3$, discreet extra reflections appear corresponding to a multiplication of the {111} spacing (Figure 4.19c to g). The defects that cause these effects are visible in the dynamical dark-field images of Figure 4.20, which show a $Pb_{1.6}Nb_2O_{6.6}$ grain near a <111> orientation. Regions of undefected pyrochlore still remain but are separated by clusters of highly defective material. Using the invisibility criterion, it can be shown that a different set of defect {111} planes is visible in each micrograph. The high-resolution <110> projections in Figure 4.19b to g reveal a pyrochlore structure separated and sheared by defect layers. The one-dimensional disorder in the $n = 1.6$ composition can be clearly seen as an aperiodic arrangement of defect layers. Leroux *et al.* suggested [166] that PbO-rich layers may form as planar defects in the lead niobate lattice. The increase in the defect density observed with increasing n (PbO content) points to a similar conclusion. For $1.5 < n < 2.0$, regions of undefected cubic pyrochlore still remain. As n increases, these regions shrink until, at $n = 2$, none are left; however, perfect periodicity is still not achieved. The periodicity of defect layers does not become homogeneous for compositions where $n < \sim 2.2$. Even in $Pb_2Nb_2O_7$, although no undefected regions are found, the defect spacing is not constant within a grain. This observation seems to indicate that the stability

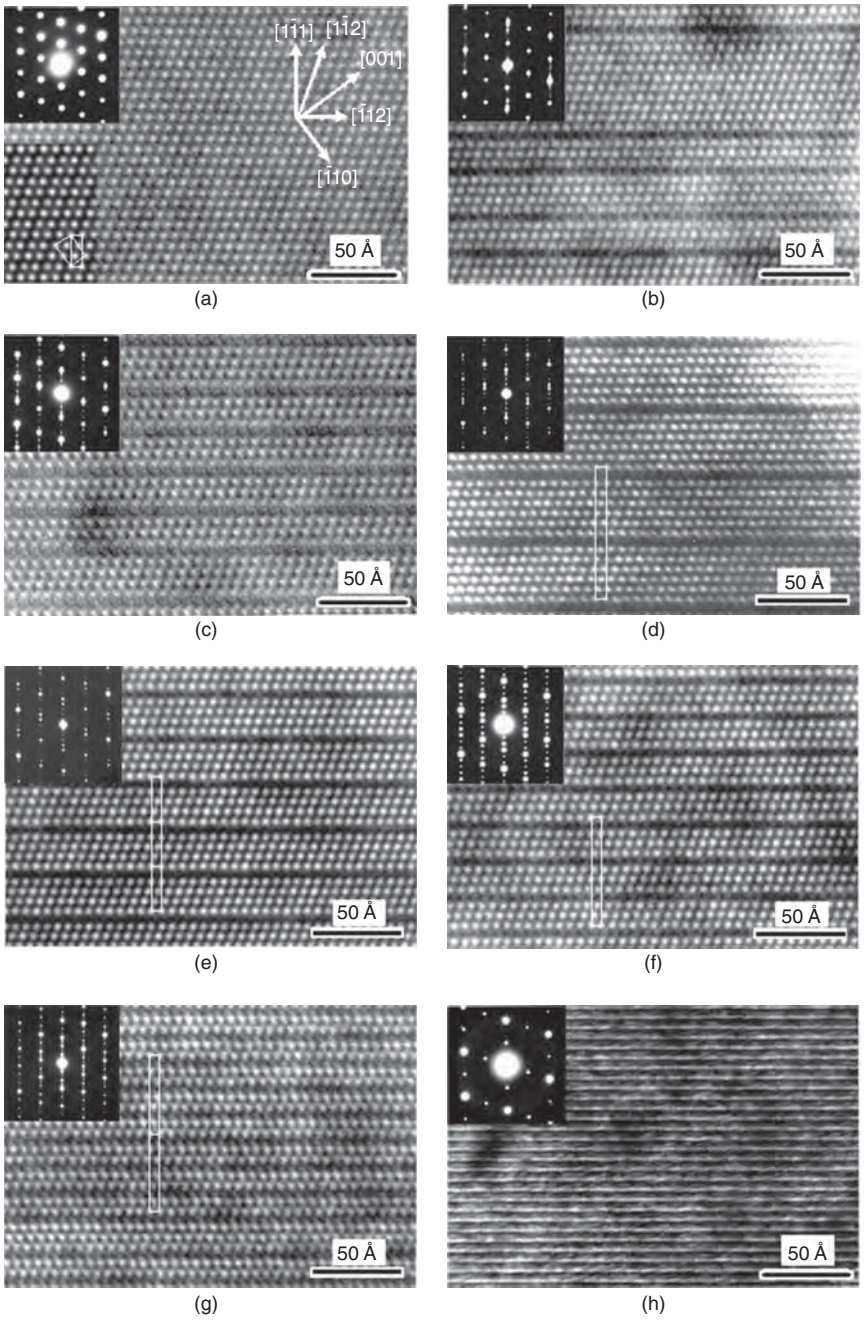

Figure 4.19 *High-resolution TEM images and the corresponding SADPs of grains from $Pb_nNb_2O_{5+n}$ ceramics with the nominal compositions (a) n = 1.5, (b) n = 1.6, (c) n = 1.75, (d) and (e) n = 2.0, (f) n = 2.2, (g) n = 2.5, and (h) n = 3.0. A simulation of the n = 1.5 structure is shown inset in (a) and outline unit cells are drawn for both the cubic and trigonal settings. Crystallographic directions are labeled with reference to the cubic unit Cell. Source: Adapted from Ubic and Reaney 2002 [163].*

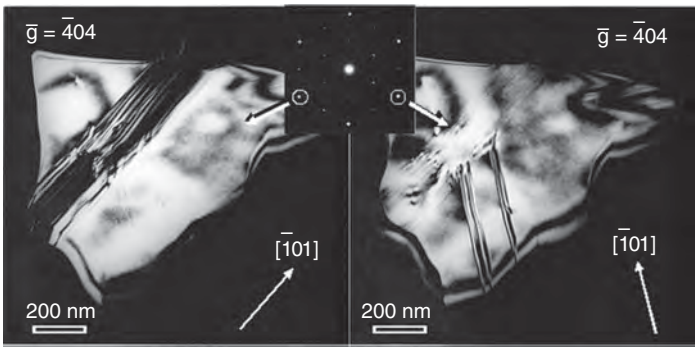

Figure 4.20 *Dynamical dark-field TEM images of a $Pb_{1.6}Nb_2O_{6.6}$ grain near the <111>$_{cubic}$ zone. Source: Adapted from Ubic and Reaney 2002 [163].*

of the layered structure decreases as the separation of the defects increases (n decreases), which is what one would expect from a thermodynamic point of view. Long-range Coloumb interactions are not strong enough in this system to create long periodic structures (low n), unlike, for example, in $Bi_4Ti_3O_{12}$-based materials, where strain and charge minimization produce a periodic distribution of rock-salt-structured planar defects, which separate and shear perovskite blocks [167].

The images in Figure 4.19d to g show four distinct structures, each one differing by the spacing of the defect layers, which seems to decrease with increasing n from infinity for $n = 1.5$ to 9.1 Å for $n = 2.5$. Similarly, X-ray diffraction results (Figure 4.21) for these compositions clearly show a progression from one structure (cubic pyrochlore) to another ($Pb_3Nb_2O_8$) with increasing n.

Simulated XRD patterns corresponding to the crystal models of references are shown [164, 166] along with an experimental trace for a $Pb_2Nb_2O_7$ pellet in Figure 4.22 It is clear

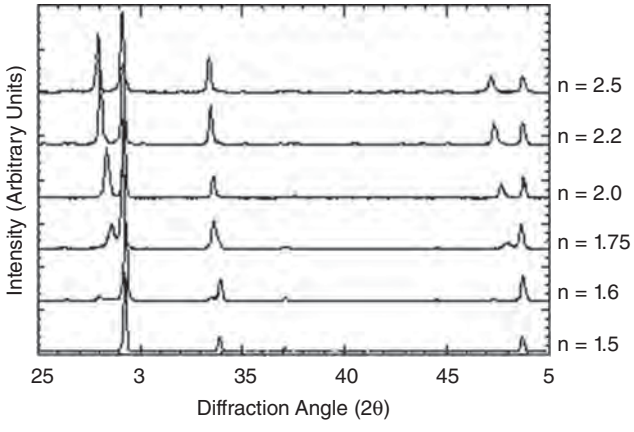

Figure 4.21 *XRD traces of crushed pellets with nominal compositions corresponding to $Pb_nNb_2O_{5+n}$ where n = 1.5, 1.6, 1.75, 2.0, 2.2, and 2.5. Source: Adapted from Ubic and Reaney 2002 [163].*

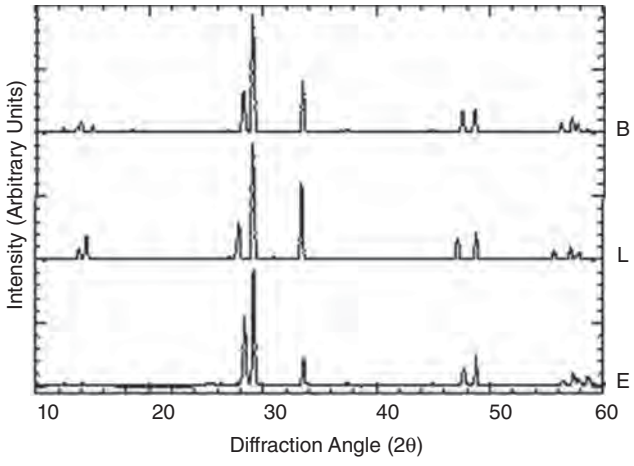

Figure 4.22 *A comparison of the simulated XRD patterns for the $Pb_2Nb_2O_7$ models proposed by Bernotat-Wulf and Hoffmann [172] (marked B), Leroux* et al. *[166] (marked L), and an experimental trace for a crushed $Pb_2Nb_2O_7$ pellet (marked E). Source: Adapted from Ubic and Reaney 2002 [163].*

that neither model is a very good match. On close inspection and considering the site occupancies reported, Bernotat-Wulf and Hoffmann's "$Pb_2Nb_2O_7$" model [164] would actually have the stoichiometry $Pb_{2.37}Nb_2O_{8.82}$, which is not a charge-balanced composition. In addition, the $c = 19.2$ Å axis of Leroux *et al.*'s [166] model cannot accommodate the ≈27 Å spacing clearly observable in the SADP and high-resolution image for this composition in Figure 4.19d and e. Finally, Ubic and Reaney have shown [163] that high-resolution TEM simulations of these models are unable to reproduce the images in Figure 4.19d and e. Leroux *et al.*'s [166] model for $Pb_{2.5}Nb_2O_{7.5}$ is a reasonable match for $Pb_2Nb_2O_7$ (Figure 4.19e) but does not show the shearing of pyrochlore slabs by defect layers evident in the experimental images. A reasonable inference from Figure 4.19 is that, for $n > 1.5$, the cubic pyrochlore remains largely unchanged and that slabs of it are separated and sheared by PbO-rich defect layers, the number of which increases with PbO content.

The cubic pyrochlore structure can be described equally well in a trigonal setting, with a unit cell $a = 7.4686$ Å ($d_{110\text{-cubic}}$) and $c = 18.2943$ Å ($3 \times d_{111\text{-cubic}}$) or with rhombohedral axes, $a_r = 7.4686$ Å, $\varepsilon_r = 60°$. Such a setting makes it easily comparable to the defective structures, as the introduction of defect layers removes all but one of the cubic triads.

4.6.2 $Pb_2Nb_2O_7$

Cook and Jaffe were the first to report [160] the existence of $Pb_2Nb_2O_7$. Their work showed it to have a distorted fluorite structure of rhombohedral symmetry, $a = 5.285 \pm 0.003$ Å, $\alpha = 89.25°$. In 1972 Brusset *et al.* reported [171] observing $Pb_2Nb_2O_7$ as single crystals formed from a melt at 1300°C. The symmetry they reported was monoclinic, with lattice parameters $a = 13.021 \pm 0.012$ Å, $b = 7.483 \pm 0.006$ Å, $c = 34.634 \pm 0.018$ Å, $\beta = 125.18° \pm 0.04$,[1] and possible space groups *C*2/*m*, *C*2, or *Cm*. Bernotat-Wulf and Hoffmann later concluded [172] that $Pb_2Nb_2O_7$ was trigonal, space group *P*3*m*1 (No. 156), with

$a = 7.472$ Å and $c = 28.351$ Å. Li *et al.* [173] were able to obtain monoclinic $Pb_2Nb_2O_7$ only by molten salt synthesis, while obtaining the rhombohedral variant by solid-state synthesis. Saine *et al.* conducted [174] a study of the PbO–Nb_2O_5 system and found $Pb_2Nb_2O_7$ in both a cubic ($a = 10.508$ Å) and rhombohedral ($a = 7.464$ Å, $c = 18.88$ Å) forms, although Wakiya *et al.* suggested [168] that full occupancy of the A-site by Pb^{+2} would not be stable in the pyrochlore structure due to its $(6s)^2$ lone pair. Subramanian *et al.* calculated [169] that the ratio of cation sizes must fall between 1.4 and 2.2 to form a stable +2,+5 pyrochlore. In the case of $Pb_2Nb_2O_7$, this ratio is 2.02, but the effect of the $(6s)^2$ electrons is to cause substantial departure from the centrosymmetric $Fd\bar{3}m$ space group. Bernotat-Wulf and Hoffmann published [164] the atomic positions of their $Pb_2Nb_2O_7$ model in 1982. More than a decade later, Leroux *et al.* reported [166, 170] a trigonal cell with $a = 7.46$ Å and $c = 19.2$ Å. Both models are shown in Figure 4.23.

Ubic and Reaney observed [163] two structures with different defect-layer densities but with almost identical lattice constants in pellets with nominal composition $Pb_2Nb_2O_7$ (Figure 4.19d and e). The SADP in Figure 4.19d can be indexed according to a trigonal unit cell with dimensions $a = 7.469$ Å and $c = 27.664$ Å; however, the high-resolution image clearly shows a repeat in the c-direction of 82.991 Å, indicating that for (00l) type reflections, $l = 3n$. There are 11 possible trigonal space groups that have this selection rule, but

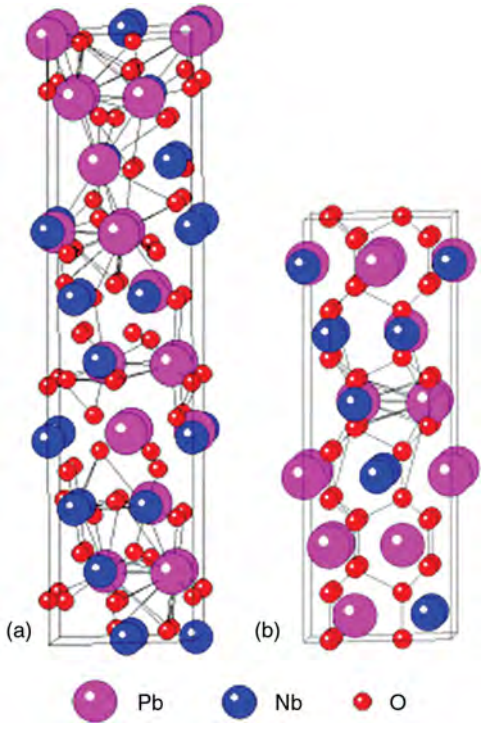

Figure 4.23 *Crystal models of the $Pb_2Nb_2O_7$ structure as proposed in references [164] (a) and [166] (b), viewed along <100>.*

the space group suggested by Bernotat-Wulf and Hoffmann [172], $P3m1$, is not among them. Figure 4.19e shows the other structure observed in $Pb_2Nb_2O_7$ and its SADP can be indexed according to $a = 7.436$ Å and $c = 27.561$ Å. The corresponding high-resolution image shows a similar c-repeat distance, which, when trebled, becomes $c = 82.682$ Å and again yields the rule $(00l)$: $l = 3n$.

Cook and Jaffe measured [160] the electrical properties of $Pb_2Nb_2O_7$ and found $\varepsilon_r = 110$ at room temperature with $\tan\delta = 0.004$ at 100 kHz. The temperature dependence of ε_r was strongly negative and non-linear. A year later, Goodman used [175] a sulfate route to form $Pb_2Nb_2O_7$ and $PbNb_2O_6$ in order to decrease PbO loss in calcining and also used additions of TiO_2 and ZrO_2 to obtain dense pellets on sintering. The rate of thermal expansion was nearly constant up to 1000 °C and yielded $\tau_f = 2.66$ ppm/°C. At about the same time, Shirane and Pepinsky reported [176] that $Pb_2Nb_2O_7$ was probably not ferroelectric, unlike $Cd_2Nb_2O_7$, despite the small maximum observed in the dielectric constant at –259 °C. The room-temperature dielectric constant they measured was $\varepsilon_r = 185$. Hulm also studied [177] this dielectric anomaly in $Pb_2Nb_2O_7$ and suggested that it might be attributed to an antiferroelectric transition. Siegwarth *et al.* used [178] a sulfate route similar to Goodman's [175] to obtain $Pb_2Nb_2O_7$, but, unlike Goodman, they used no sintering aids and could only obtain samples of approximately 75% of theoretical density. The peak in ε_r was observed at –256 °C, but at a value of only 53 due to the poor densification. Based on specific heat measurements, they suggested that the peak was the result of a low-frequency dielectric relaxation and not an antiferroelectric transition. As the frequency of the field increased, the peak decreased and was shifted to higher temperatures – the classic sign of relaxation. While most workers [176, 178–180] seem to agree that the pyrochlore-type compounds in the system are not ferroelectric, Sekiya *et al.* have reported [181] that $Pb_2Nb_2O_7$ is ferroelectric.

4.6.3 Pb-Rich Phases ($n > 2$)

Roth was the first to report [161] the existence of $Pb_3Nb_2O_8$, to which he ascribed a distorted pyrochlore-type structure with pseudotetragonal symmetry. The true symmetry could not be determined at the time. Vandenborre later reported [182] that it had a distorted pyrochlore-type structure with tetragonal space group $I4_1/amd$ (No. 141) and lattice constants $a = 7.53$ Å, $c = 10.82$ Å. Roth [161] was also the first to observe the existence of $Pb_5Nb_4O_{15}$. Its symmetry was reported as similar to the rhombohedrally-distorted pyrochlore $Pb_2Nb_2O_7$, but with an even greater distortion. The lattice parameters measured were $a = 10.709$ Å, $\alpha = 88.23°$. This stoichiometry is derived from the pyrochlore structure by removing the loosely bonded oxygens on the 8b sites and charge compensating by removing Nb^{+5}. The result is $Pb_2Nb_{1.6}O_6$, or $Pb_5Nb_4O_{15}$. Later, Brusset *et al.* listed [171] monoclinic lattice parameters for $Pb_5Nb_4O_{15}$ as $a = 12.948 \pm 0.009$ Å, $b = 7.419 \pm 0.005$ Å, $c = 39.700 \pm 0.017$ Å, $\beta = 126.66° \pm 0.03$ Å. Leroux *et al.* proposed [166] that the Pb-rich niobates form the homologous series $Pb_{2n+1}Nb_{2n}O_{7n+1}$, where 0 (PbO) $\leq n \leq \infty$ ($Pb_2Nb_2O_7$), by the alternate stacking of Pb-rich and Nb-rich planes. Later, the series $Pb_{2n+1}Nb_{2n-1}O_{7n-1}$ was discussed [170], with compounds reported for $n = 5$, 7, 9, and 11. Charge compensation is apparently achieved via oxygen vacancies. No defect layers were observed for $Pb_2Nb_2O_7$ ($n = \infty$). Samples in that study were powders prepared in small quantities by calcining in evacuated quartz tubes, all of which would surely lead to severe PbO-loss and

so to an overestimation of the PbO content left in the sample. Indeed, an over-estimation of the PbO content would explain differences in their work with that of other workers, which have shown evidence for defect layers in $Pb_2Nb_2O_7$ compositions [164, 172] and even $Pb_{1.6}Nb_2O_{6.6}$ [159, 183–185]. The effects of PbO loss could be reduced by increasing the mass of reactants, calcining in an air-filled closed cavity, and preparing microscopy samples from sintered pellets, as was been done subsequently by Ubic and Reaney [163].

Ubic and Reaney interpreted [163] the electron diffraction patterns and high-resolution images (Figure 4.19d to g) corresponding to $2 \leq n \leq 2.5$ compounds as arising from trigonal structures obeying the selection rule $00l$: $l = 3n$. Both $R\bar{3}m$ and $R3m$ are subgroups of $Fd\bar{3}m$ and require that for $00l$: $l = 3n$ when expressed in the hexagonal setting. $R\bar{3}m$ is a maximal non-isomorphic subgroup of $Fd\bar{3}m$ and so is the likely symmetry of these materials.

The properties of Pb-rich phases were reported by Ubic and Reaney [159]. In addition, Jawahar *et al.* published [186] microwave properties of $A_{2.5}B_2O_{7.5}$ (A = Ba, Sr, Ca, Mg, Zn; B = Nb, Ta) and found some compositions to have modestly high ε_r ($14 \leq \varepsilon_r \leq 41$), high Q ($2396 \leq Q_f \leq 76\,440$ GHz), and low τ_f (–58 ppm/°C $\leq \tau_f \leq$ +140 ppm/°C).

4.6.4 Doping Studies

In 1971, Krause *et al.* reported [187] that $Pb(Mg_{1/3}Nb_{2/3})O_3$ (PMN) was a cubic perovskite crystal with $a = 4.049$ Å. Ten years later, Pfoertsch *et al.* observed [188] a cubic pyrochlore XRD pattern from a MgO-doped $Pb_{1.5}Nb_2O_{6.5}$ material with an apparent stoichiometry of $Pb_{1.83}Nb_{1.71}Mg_{0.29}O_{6.39}$. The lattice constant they measured was $a = 10.5988$ Å. The same material was later studied by Shrout and Swartz, who confirmed [179] these findings and reported a room-temperature dielectric constant of 130 with an anomalous peak near 200 at –253 °C due to relaxation. The dielectric loss at room temperature was $\tan \delta < 0.002$.

The solubility of Mg^{2+} in the pyrochlore phase has been studied by several workers. Wakiya *et al.* found [168] the solubility limit of Mg^{+2} in pyrochlore $Pb_{(3+3x)/2}Mg_xNb_{(2-x)}O_{6.5}$ to be $x = 0.24$. Additionally, they measured a gradient in the cubic lattice constant in sintered pellets with depth which indicated that pyrochlores with various compositions must form in the system. Earlier work indicated [165] the existence of a pyrochlore at the $x = 0.24$ composition with a lattice constant of 10.6029 Å. No cation ordering was found on the A or B site. Other workers found pyrochlores containing more Mg^{2+}, including $Pb_2(Mg_{0.25}Nb_{1.75})O_{6.625}$ [189] $Pb_{1.83}Mg_{0.29}Nb_{1.71}O_{6.39}$ [179], and $Pb_2Mg_{0.32}Nb_{1.87}O_7$ [190]. The ε_r of these pyrochlores is generally reported as 200. Some ceramics have been produced [180, 189, 191, 192], which have comprised both lead magnesium niobate perovskite (negative τ_f) and pyrochlore (positive τ_f) phases, either by accident or purposely, to affect dielectric properties.

To date, very little effort has been expended in studying the tantalate analogs of these niobates, although they may actually be more promising. It has been shown [159] that Ta^{+5} doping on the Nb^{+5} sites can decrease τ_f dramatically, while increasing **Q** at the expense of ε_r.

4.6.5 Microwave Properties

Figure 4.24 shows the effect of Pb content on τ_f for the entire $Pb_nNb_2O_{5+n}$ ($1.5 \leq n \leq 3.0$) series. The origin of the minimum at $n = 2$ is unknown, although it may be due to the relative stability of this phase or the spacing of the crystallographic layers. A phase change occurs

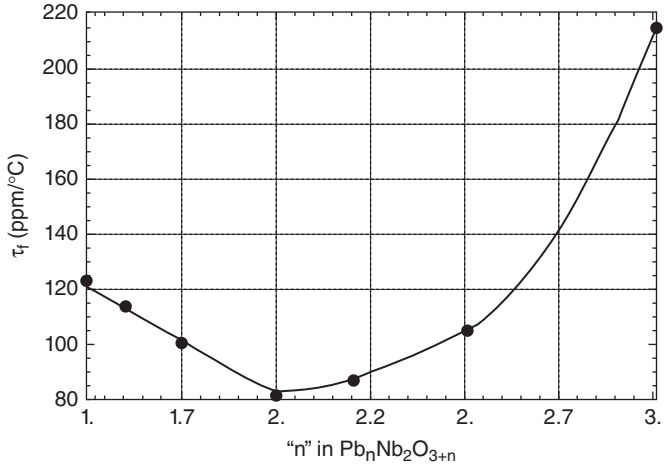

Figure 4.24 *The effect of Pb concentration (n) on the τ_f of $Pb_nNb_2O_{5+n}$. Source: Adapted from Ubic and Reaney 2002 [163].*

at $n = 3.0$, where $Pb_3Nb_2O_8$ is stable. This phase has a very high τ_f (2161 ppm/°C) and the proximity of this phase boundary may also account for the increase in τ_f as n increases from 2 to 3.

The effect of PbO content on ε_r and Q is shown in Figure 4.25. As the amount of PbO increases, ε_r is suppressed and Q increases, with Q at a maximum at about $n = 2.2$. Ubic and Reaney reported [163] that data on Q and, therefore ε_r, were unobtainable for $n = 3$ due to a very poor resonance response.

Figure 4.26 shows the effect of Ta doping on the τ_f of both the $n = 1.5$ and $n = 2$ compositions. In both cases, a clear trend is obvious, with τ_f decreasing significantly with increasing

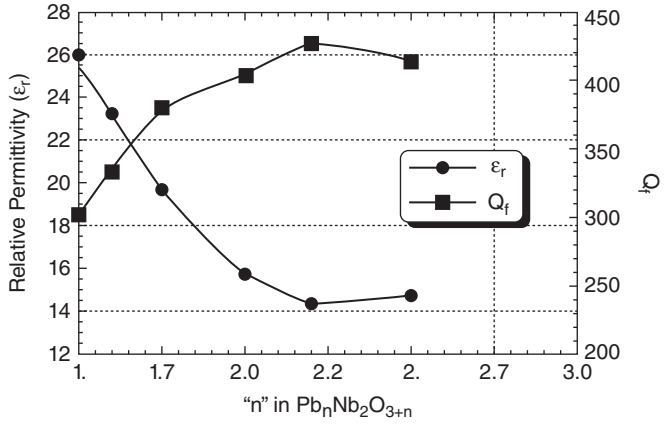

Figure 4.25 *The effect of Pb concentration (n) on the ε_r and Q of $Pb_nNb_2O_{5+n}$. Source: Adapted from Ubic and Reaney 2002 [163].*

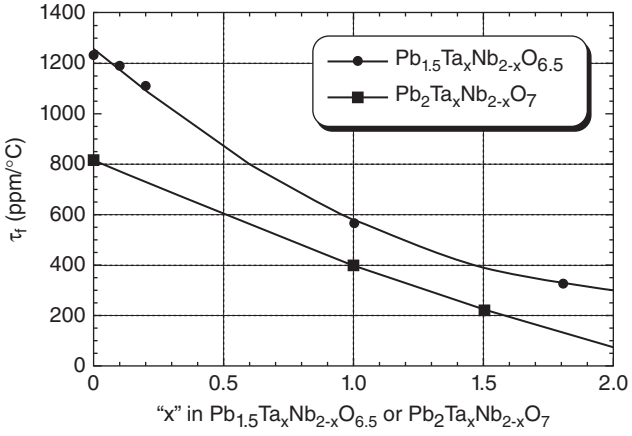

Figure 4.26 *The effect of Ta^{5+} doping on the τ_f of $Pb_{1.5}Nb_2O_{6.5}$ and $Pb_2Nb_2O_7$. Source: Adapted from Ubic and Reaney 2002 [163].*

Ta content. This trend can be explained in terms of the crystal chemistry of the system. As the ionic sizes of six-coordinated Nb^{5+} and Ta^{5+} are virtually identical, the change is associated with a dampening of ionic mobility (rather than octahedral tilting or other effects). The more massive Ta^{5+} ion, despite having a higher ionic polarizability [193] than Nb^{5+}, gives rise to weaker interactions with the microwave field (as well as lower-frequency fields) and hence lower permittivity and a flatter ε_r versus temperature curve. In this way, doping with Ta has the effect of dampening $\tau_{\varepsilon r}$ and thus τ_f. Along with the inevitable decrease in ε_r, Ubic and Reaney also observed [163] a corresponding increase in Q (Figures 4.27 and 4.28), with the exception of the $Pb_{1.5}Ta_{1.8}Nb_{0.2}O_{6.5}$ composition. The origin of the

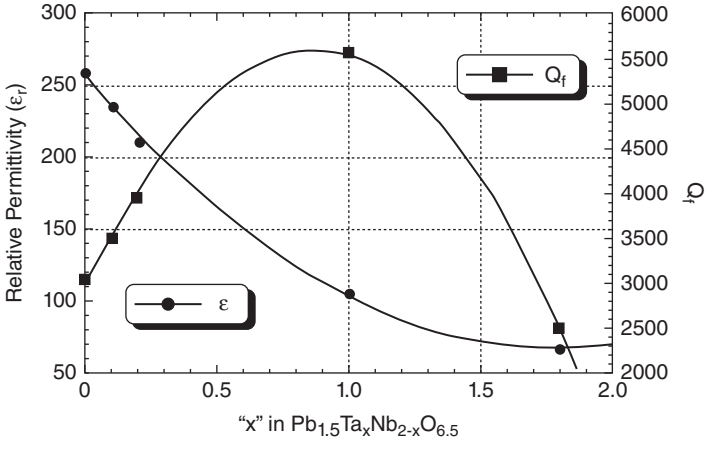

Figure 4.27 *The effect of Ta^{5+} doping on the ε_r and Q of $Pb_{1.5}Nb_2O_{6.5}$. Source: Adapted from Ubic and Reaney 2002 [163].*

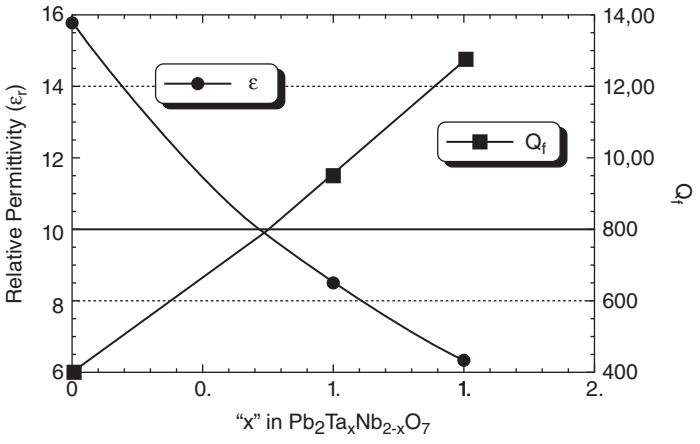

Figure 4.28 *The effect of Ta^{5+} doping on the ε_r and Q of $Pb_2Nb_2O_7$. Source: Adapted from Ubic and Reaney 2002 [163].*

peak in Q_f for $Pb_{1.5}TaNbO_{6.5}$ is unknown, although Cava *et al.* have reported [194] a phase change in the $Ca_2Ta_xNb_{2-x}O_7$ system near $x = 1.62$, which may also occur in this system. The composition which showed the best combination of properties was $n = 2$ and $x = 1.5$ ($Pb_2Ta_{1.5}Nb_{0.5}O_7$), for which $\tau_f = 223$ ppm/°C, $\varepsilon_r = 64$, and $Q_{2.5GHz} = 5200$ ($Q_f = 12\,800$ GHz).

Mg-doping is even more effective in reducing τ_f, with a 38% reduction shown with just 12% of the B sites occupied by Mg [163]. Unfortunately, the effects on ε_r and Q_f are not as good, both decreasing by about 40%. This deleterious effect is almost certainly related to the introduction of additional oxygen vacancies required for charge compensation, according to $Pb_{1.5}(Mg_yNb_{2-y})O_{6.5\text{-}1.5y}$.

4.7 $(Pb_{1-x}Ca_x)(Fe_{1/2}B_{1/2})O_3$ [B = Nb, Ta]

The lead-based relaxor materials such as (Pb,Ca)ZrO_3, (Pb,Ca)HfO_3, and (Pb,Ca)(Fe,Nb)O_3 having a high relative permittivity and small temperature coefficient of permittivities are extensively investigated for multilayer capacitor applications [195,196]. Several workers reported [196–201] $Pb_{1-x}Ca_x(Fe_{1/2}Nb/Ta_{1/2})O_3$ as single-phase perovskites with high ε_r and low-loss factors in the microwave frequency range. The ε_r and τ_f decreased and the Qf increased with increasing Ca substitution. At $x = 0.55$, the ceramic has $\varepsilon_r = 91$, $Qf =$ 4950 GHz, $\tau_f = 2$ ppm/°C. The (Pb, Ca)$(M_{1/2}Nb_{1/2})O_3$ (M = Al, Cr) are not perovskite and have low quality factors. It has been reported that partial substitution of La^{3+} and Nd^{3+} at the A site of $(Pb_{0.5}Ca_{0.5})(Fe_{1/2}Nb_{1/2})O_3$ improves the microwave dielectric properties [202]. The $[(Pb_{0.5}Ca_{0.5})_{1-x}(La_{0.5}Nd_{0.5})_x]$ $(Fe_{1/2}Nb_{1/2})O_{3+\delta}$ with $x = 0.06$ showed $\varepsilon_r = 100$, $Qf = 5820$ GHz, and $\tau_f = 0$ ppm/°C when sintered at 1150 °C. A pyrochlore secondary phase was formed for $x > 0.04$, degrading the dielectric properties. The ε_r decreased with increasing amount of (La, $Nd)^{3+}$ substitution. Yang *et al.* [202, 203] suggested that

substitution of a small amount of $(La,Nd)^{3+}$ for $(Pb,Ca)^{2+}$ could eliminate oxygen vacancies and improve the quality factor. Substitution of Ti^{4+} for $(Fe_{1/2}, Nb_{1/2})$ leads to a single-phase compound and increase ε_r and τ_f [204]. $[(Pb_{0.5}Ca_{0.5})_{0.95}La_{0.05}][(Fe_{1/2}Nb_{1/2})_{1-y}Ti_y]O_{3+\delta}$ [PCLFNT] with $y = 0.1$ showed ε_r =117, Qf = 4950 GHz, and τ_f =17 ppm/°C. The substitution of Ti for $(Fe, Nb)^{4+}$ increased the ε_r although the ionic polarizability of Ti is low and is attributed to the increase in rattling of B-site ions by the smaller Ti^{4+} [204]. Kucheiko *et al.* [205] reported that substitution of Fe^{3+}/Nb^{5+} by Sn^{4+} at the B site of the perovskite $(Pb,Ca)(Fe,Nb)O_3$ considerably improves the quality factor without appreciable changes in the τ_f and ε_r. The $[Pb_{1-x}Ca_x][(Fe_{1/2}Nb_{1/2})_{1-y}Sn_y]O_3$ with $x = 0.55$ and $y = 0.1$ sintered at 1150 °C has ε_r =85, Qf = 8600 GHz, τ_f = 0 ppm/°C. Choi *et al.* obtained [206] a single-phase compound, $(Pb_{0.4}Ca_{0.6})[(Mg_{1/3}Nb_{2/3})_{1-x}Sn_x]O_3$, which forms a single-phase tetragonal perovskite structure on sintering at 1280 °C. The Sn substitution increased the Qf but ε_r and τ_f decreased. The composition with $x = 0.1$ has ε_r = 52, Qf = 8200 GHz, and τ_f = –3 ppm/°C. Suitable substitutions at A or B sites and by the addition of dopants are found to improve the properties of $[Pb_{1-x}Ca_x]$ $[(Fe_{1/2}Ta_{1/2})$ (PCFT) and $[Pb_{1-x}Ca_x][(Fe_{1/2}Nb_{1/2})$ (PCFN) [202, 203, 205, 207–220]. The microwave dielectric properties of these compositions are given in the Appendix. The partial substitution of La for Pb in $Pb(Mg_{1/2}Nb_{1/2})O_3$ improves ordering [218–221]. However, the La substitution increases the τ_f [222]. Hence, Liu and Wu [212] introduced smaller Ca for Pb by forming $Pb_{1-x}Ca_x(Mg_{1/2}Nb_{1/2})O_3$. They prepared $[(Pb_{1\,x}Ca_x)_{1/2}La_{1/2}]$ $[Mg_{1/2}Nb_{1/2}]O_3$ with $x = 0.01$–0.5 by sintering at 1350 °C. An X-ray diffraction study showed that all the compositions have an $A(B'_{1/2}\ B''_{1/2})O_3$-type perovskite structure. However, the space group changed from Fm3m to Pa3 by the substitution of 10 mol% Ca. As the Ca content is increased to 50 mol% the symmetry changed to R3. The ε_r decreased from 80 to 44 and Qf increased from 50 000 to 90 000 GHz for $x = 0.4$ and τ_f changed from 120 to –30 ppm/°C. $[(Pb_{1-x}Ca_x)_{1/2}La_{1/2}]$ $[Mg_{1/2}Nb_{1/2}]O_3$ for $x = 0.3$ sintered at 1350 °C/3 h showed ε_r = 50, Qf = 86 000 GHz, and τ_f = 0 ppm/°C.

Nakano *et al.* [223] modified the low-temperature fireable ferroelectric $Pb(Fe_{2/3}W_{1/3})O_3$–$(Pb(Fe_{1/2}Nb_{1/2})O_3$ to a paraelectric at room temperature by the partial substitution of Pb by Ca. When Pb was partially substituted by Ca, a single phase (Pb, Ca)(W, Fe, Nb)O_3 (PCWFN) was formed with high relative permittivity and low dielectric loss. The $yPb(Fe_{2/3}W_{1/3})O_3$–$(1-y)(Pb_{1-x}Ca_x)(Fe_{1/2}Nb_{1/2})O_3$ (PFW–PFN) solid solutions sintered at temperatures in the range 930–1000 °C ceramics have ε_r in the range 71–128, Qf up to 3800 GHz, and τ_f of –30 to +90 ppm/°C, depending on the values of x and y and the sintering temperature [223,224]. Kucheiko *et al.* [225] found that partial substitution of Fe and Nb by Sn improves the microwave dielectric properties. The (Pb_{1-x}, Ca_x)(Fe, Nb, Sn) ceramics have [225] ε_r = 86–90, Qf = 7500–8600 GHz, and τ_f = 0–9 ppm/°C when sintered at 1165 °C. Ha *et al.* [226] added CuO–Bi_2O_3 in $[(Pb_{0.45}Ca_{0.55})(Fe_{0.5}Nb_{0.5})_{0.9}Sn_{0.1}]O_3$ (PCFNS) ceramics to lower its sintering temperature. Addition of 0.2 wt% CuO and 0.1 wt% Bi_2O_3 lowered the sintering temperature to 1000 °C/3 h with ε_r = 83, Qf = 6085 GHz and τ_f = 8 ppm/°C. An increase in Bi_2O_3 content led to the formation of secondary phases and increased relative permittivity but lowered the quality factor and τ_f. The $[(Pb_{0.5}Ca_{0.5})_{1-x}La_x](Fe_{0.5}Nb_{0.5})O_3$ can be sintered at 1150 °C with $\varepsilon_r > 90$, $Qf \sim 5500$ GHz, and τ_f in the range 7–15 ppm/°C [227, 228]. Yang *et al.* [227] reported that addition of 1 wt% of PbO–B_2O_3–V_2O_5 (PBV) glass to PCLFN (Pb, Ca, La)(Fe, Nb)O_3 can lower the sintering temperature to 1050 °C with ε_r = 101, Qf = 5400 GHz, and τ_f = 5.9 ppm/°C. Zhe *et al.* [229] found that addition of

$Bi_2O_3 + MnO_2$ to the $[(Pb_{0.5}Ca_{0.5})_{0.92}La_{0.08}](Fe_{0.5}Nb_{0.5})O_3$ (PCLFN) system lowered the sintering temperature to 1050 °C with $\varepsilon_r = 91.1$, $Qf = 4870$ GHz, and $\tau_f = 18.5$ ppm/°C.

4.8 $Ag(Nb_{1-x}Ta_x)O_3$

Recently $Ag(Nb_{1-x}Ta_x)O_3$ was reported [230–233] as a high permittivity and low-loss dielectrics for microwave applications. The $Ag(Nb_{1/2}Ta_{1/2})O_3$ is monoclinic with space group P2/m [233]. The $Ag(Nb_{1-x}Ta_x)O_3$ ceramics are prepared by initially mixing Nb_2O_5 and Ta_2O_5 and pre-reacting at about 1200 °C. This will give a homogeneous solid solution of $(Nb_{1-x}Ta_x)_2O_5$ [234]. It is then ground and mixed well with an appropriate amount of Ag_2O and calcined at about 1100 °C. The ground powder is compacted and then sintered at temperatures in the range 1200–1300 °C. As the amount of Ta content increases, the sintering temperature also increases. It was reported that with increasing sintering temperature, an increasing amount of black silver precipitates in the ceramic [233, 234]. One of the problems with Ag(Nb, Ta)O_3 dielectric is its decomposition during sintering, which leads to degradation of properties [233] and can be controlled by processing in an oxygen atmosphere [230, 233]. The decomposition of Ag(Nb, Ta)O_3 is due to volatilization of silver [230, 233, 234]. In order to avoid decomposition, Valant and Suvorov kept the pressed samples in a corundum tube or crucible during sintering [230, 233]. The other technique to prevent decomposition at high temperatures is to lower the sintering temperature. The sintering temperature can be lowered using fine powder obtained by wet chemical methods such as the alkoxide and citrate route [235, 236], use of low melting additives such as CuO [237] or glasses [238]. Li *et al.* [238] reported that addition of 2 wt% glass lowered the sintering temperature to about 960 °C and prevented the silver decomposition problem. However, they do not reveal what glass they have used. Guo *et al.* [239] found that addition of 2.5 wt% Sb_2O_5 lowers the dielectric loss. The unusually high ε_r, fairly low dielectric loss, and low sintering temperature makes this material important for passive dielectric components. However, the temperature dependence of permittivity is relatively high. Recently Valant and coworkers [240–242] deliberately generated an inhomegeneity on the B sites of Ag(Nb, Ta)O_3 by controlling the powder morphology and carefully selecting the firing conditions. The different Ag(Nb, Ta)O_3 phases present in such ceramics exhibited different temperature dependencies of the permittivity, which produced a compensated overall temperature dependence of such ceramics. Valant *et al.* [240] suppressed the high temperature dependence of permittivity in Ag(Nb, Ta)O_3-based ceramics by preparing a mixture of $Ag(Nb_{0.65}Ta_{0.35})O_3$ and $Ag(Nb_{0.35}Ta_{0.65})O_3$, which have monotonically increasing and decreasing permittivity variation with temperature. By mixing a mixture of 45 wt% of $Ag(Nb_{0.65}Ta_{0.35})O_3$ and 55wt% $Ag(Nb_{0.35}Ta_{0.65})O_3$ and controlling its microstructure by using coarse grains and preventing the reaction to form $Ag(Nb_{0.5}Ta_{0.5})O_3$, they could achieve an ε_r of 430, $Qf = 700$ GHz, and temperature dependence of permittivity of only 40 ppm/°C. The microwave dielectric properties of $Ag(Nb_{1-x}Ta_x)O_3$ for various values of x and additives are given in the Appendix. Porokhonsky *et al.* [243] studied the dielectric properties of $AgNbO_3$ and $Ag_{1-x}Li_xNbO_3$ in the millimeter wavelength region. Substitution of 5% of Ag with Li induces an orthorhombic to rhombohedral phase transition. The temperature characteristics of the ε_r significantly vary with Li substitution and the material becomes a useful ferroelectric ceramic [244–246] having surprisingly high

piezoelectric properties [247]. Hence it is a potential lead-free piezoelectric ceramic although costwise it is not attractive. Recently it was shown that the compositions $Ag(Nb_{0.8}Ta_{0.2})O_3$ and $Ag(Nb_{0.9}Ta_{0.1})O_3$ are useful for possible applications in tunable microwave devices such as phase shifters, tunable filters, and varactors [248–251]. You and Koh [252] prepared highly polar axis oriented $Ag(Ta_{0.38}\ Nb_{0.62})O_3$ films on $LaAlO_3$ single crystals by pulsed laser ablation. The $Ag(Ta_{0.38}\ Nb_{0.62})O_3/LaAlO_3$ thin-film capacitors exhibited superior overall performance – low-loss tangent with ε_r of 224. The Au/Cr/Ag(Ta, Nb)O_3/$LaAlO_3$ interdigital capacitors show a low-loss tangent of about 0.0033 at 1 MHz and a high figure of merit (K factor) greater than 48 at 40 V. The Ag(Nb, Ta)O_3 is also reported as a photocatalyst with the ability to split water into oxygen and hydrogen [253, 254]. Silver niobate is a weak ferroelectric and antiferroelectric undergoing a rich sequence of phase transitions from a simple perovskite cubic above 853 K to an antiferroelectric M3 phase below 620 K, a disordered antiferroelectric M2 below 530 K, and a weak ferroelectric M1 phase below 340 K. This sequence of displacive phase transitions occur due to tilting of the oxygen octahedra [255–261] and these phase transitions considerably influence the dielectric properties. This material is useful for several microwave electronic components such as bandpass filters and high-capacity NPO multilayer capacitors. Addition of 1 wt% CuO to $Ag(Nb_{1/2}Ta_{1/2})O_3$ lowers the sintering temperature to 900 °C [237] and hence is a promising material for LTCC technology. However, it was shown later that Cu ions incorporate into the Ag(Nb, Ta)O_3 crystal structure [262].

In Ag(NbTa)O_3 ceramics, the $AgNbO_3$ and $AgTaO_3$ compounds undergo a series of structural phase transitions as they cool from the prototypic cubic perovskite phase [263]. $AgNbO_3$ exhibits a weak ferroelectric behavior at room temperature [263]. These materials have a high relative permittivity >400 and Qf in the range 600–900 GHz [264–266]. Composite microstructures consisting of 45 wt% $Ag(Nb_{0.65}Ta_{0.35})O_3$ and 55 wt% $Ag(Nb_{0.35}Ta_{0.65})O_3$ have $\varepsilon_r = 430$ and $Qf = 700$ GHz. A large grain size helps to minimize the reaction between these two phases during sintering [266]. Moreover, the evaporation and reduction of Ag_2O at high temperature and in oxygen-deficient atmospheres severely affect the densification and microwave properties [266]. To lower the sintering temperature, Sakabe *et al.* [267] added V_2O_5 and substituted Li for silver in $Ag(Nb_xTa_{1-x})O_3$. More recently, Kim *et al*. [268] succeeded in lowering the sintering temperature to below 950 °C by liquid phase sintering with the addition of 1 wt% CuO. They adjusted [268] the temperature coefficient of capacitance by adjusting the Nb/Ta ratio in the solid solution and by creating composite microstructures. They prepared a two-phase assemblage consisting of $Ag(Nb_{3/4}Ta_{1/4})O_3$ (ANT-31) and $Ag(Nb_{1/4}Ta_{3/4})O_3$ (ANT-13) to get a temperature-stable composite. The CuO added temperature-stable composite had a relative permittivity of about 390 and Qf of about 800 GHz. SEM and EDAX analysis revealed that CuO segregated at the grain boundaries. Figure 4.29 shows the variation of relative permittivity with temperature for $Ag(Nb_{3/4}Ta_{1/4})O_3$–$Ag(Nb_{1/4}Ta_{3/4})O_3$ (45:55 mol% mixing ratio) composite and the end members $Ag(Nb_{3/4}Ta_{1/4})O_3$ (ANT-31) and $Ag(Nb_{1/4}Ta_{3/4})O_3$ (ANT-13). The composite showed a very nominal variation in the relative permittivity with temperatures ranging from –50 °C to 100 °C. Figure 4.30 shows the variation of temperature coefficient of capacitance for Ag(Nb, Ta)O_3 end members and composite. The ANT-31–13 sintered at 900 °C/2 h is nearly temperature stable. The $Ag(Nb_{2/4}Ta_{2/4})O_3$ (ANT-22) + 1 wt% CuO and sintered at 900 °C showed an $\varepsilon_r = 398$ and $Qf = 400$ GHz at 2.24 GHz. The ANT-31-13+1 wt% CuO and sintered at 875 °C showed an $\varepsilon_r = 378$ and $Qf = 410$ GHz.

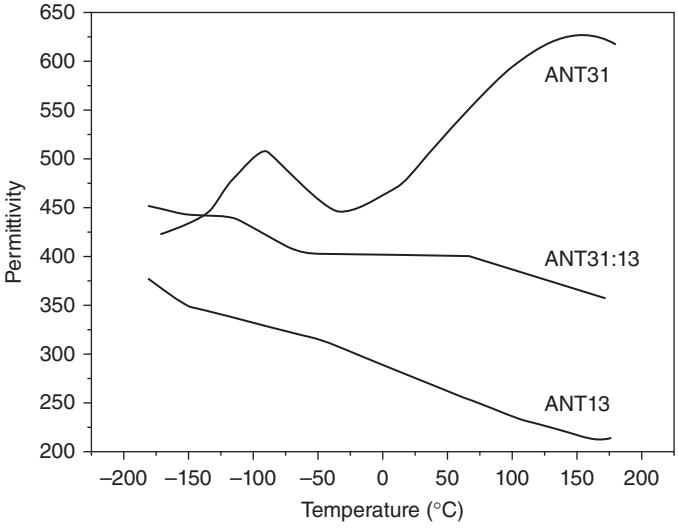

Figure 4.29 *Temperature dependence of relative permittivity for ANT 31:13 end members and composites. Source: Kim* et al. *2002 [268].*

It was found that the material did not react with silver conductor. Guo *et al.* [269] reported that partial substitution of Sb for Nb/Ta lower the tan δ and improve the temperature stability of the dielectric ceramic. Kim *et al.* [268] proposed $Ag(Nb_{1-x}Ta_x)O_3$ solid solution and composites as promising candidates as embedded capacitors for high-frequency applications.

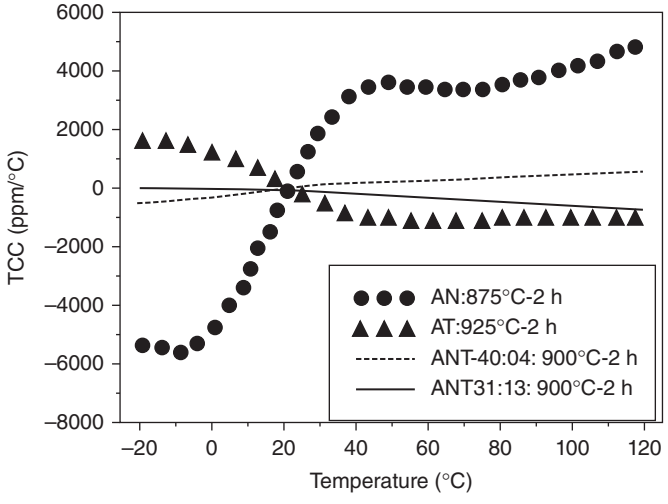

Figure 4.30 *Variation of temperature coefficient of capacitance for $Ag(Nb, Ta)O_3$ end members and composite. Source: Kim* et al. *2002 [268].*

4.9 Summary

There are about 600 resonator materials with relative permittivities above 70. The $Ba_{0.6}Sr_{0.4}TiO_3$ + 0.5 wt% $MgCo_2(VO_4)_2$ composite has the highest reported room-temperature relative permittivity at 2763 with a *Qf* factor of 300 GHz at 1 GHz. The high relative permittivity of the resonator enables the miniaturization of mobile handsets; however, in general most of the high-permittivity materials have high positive τ_f values. Some high-permittivity materials such as TiO_2, TiO_2–$Bi_2Ti_4O_{11}$, $Ca_{(1-x)}Ln_{2x/3}TiO_3$, $(Sm_{1/2}Na_{1/2})TiO_3$, $La(Mg_{1/2}Ti_{1/2})O_3$–$CaTiO_3$, and $Sr_{1-3x/2}Ce_xTiO_3$ also have high quality factors, but among the high-permittivity materials, tungsten bronze-type materials such as $Ba_{6-3x}(Sm,Nd)_{8+2x}Ti_{18}O_{54}$ ceramics ($x = 2/3$) have the best combination of high quality factor and low τ_f and so are commercially manufactured for production of mobile phone handsets.

References

1. Sebastian, M.T. (2008) *Dielectric Materials for Wireless Communication*, Elsevier, Oxford, UK.
2. Kolar, D., Gaberščček, S., Volavšek, B., *et al.* (1981) Synthesis and crystal chemistry of $BaNd_2Ti_3O_{10}$, $BaNd_2Ti_5O_{14}$ and $Nd_4Ti_5O_{24}$. *Journal of Solid State Chemistry*, **38**, 158–164.
3. Razgon, S., Gens, A.M., Varfolomeev, M.B., *et al.* (1980) The complex barium and lanthanum titanates. *Russian Journal of Inorganic Chemistry*, **25**, 945–947.
4. Mudrolyubova, P., Rotenberg, B.A., Kartenko, N.F., *et al.* (1981) The physicochemical properties of specimens of the $BaTiO_3 \cdot Ln_2O_3 \cdot 3TiO_2$ system. *Izvestiya Akademii Nauk SSSR, Neorganicheskie Materialy*, **17** (4), 683–686.
5. Ubic, R., Reaney, I. M., and Lee, W.E. (1998) The microwave dielectric solid-solution phase in the system BaO–Ln_2O_3–TiO_2 (Ln = lanthanide cation). *International Materials Reviews*, **43** (5), 205–219.
6. Bolton, R.L. (1968) Temperature compensating ceramic capacitors in the system barium rare-earth oxide-titania. PhD Thesis, The University of Illinois.
7. Kolar, D., Stadler, Z., Gaberščček, S., and Suvorov, D. (1978) Ceramic and dielectric properties of selected compositions in the BaO–TiO_2–Nd_2O_3 system. *Berichts der Deutsche Keramische Gesellschaft*, **55** (7), 346–348.
8. Kolar, D., Gaberščček, S., Stadler, Z., and Suvorov, D. (1988) High stability, low loss dielectrics in the system BaO–Nd_2O_3–TiO_2–Bi_2O_3. *Ferroelectrics*, **27**, 269–272.
9. Polyakov, S.M., Gindin, E.I., Prokhvatilov, V.G., and Shtel'makh, S.V. (1983) Composition and structure of a "barium lanthanide tetratitanate." *Russian Journal of Inorganic Chemistry*, **28** (11), 1686–1687.
10. Fukuda, K., Fujii, I., Kitoh, R., *et al.* (1993) Influence of rare earth ions on BaO–TiO_2–rare earth oxide ceramics for microwave applications. *Japanese Journal of Applied Physics*, **32** (Part 1: 4), 1712–1715.
11. Gens, A.M., Varfolomeev, M.B., Kostomarov, V.S., and Korovin, S.S. (1981) Crystal-chemical and electrophysical properties of complex titanates of barium and the lanthanides. *Russian Journal of Inorganic Chemistry*, (**4**), 482–484.
12. Jaakola, T., Uusimäki, A., Rautioahu, R., and Leppävuori, S. (1986) Matrix phase in ceramics with composition near $BaO \cdot Nd_2O_3 \cdot 5TiO_2$. *Journal of the American Ceramic Society*, **69** (10), C234–C235.
13. Chen, X.M., Suzuki, Y., and Sato, N. (1995) Microstructures and microwave dielectric characteristics of ceramics with the composition $BaO \cdot Nd_2O_3 \cdot 5TiO_2$. *Journal of Materials Science: Materials in Electronics*, **6**, 10–16.

14. Matveeva, R.G., Varfolomeev, M.B., and Il'yushenko, L.S. (1984) Refinement of the composition and crystal structure of $Ba_{3.75}Pr_{9.5}Ti_{18}O_{54}$. *Russian Journal of Inorganic Chemistry*, **29** (1), 17–19.
15. Wakino, K., Minai, K., and Tamura, H. (1984) Microwave characteristics of (Zr, Sn)TiO_4 and BaO–PbO–Nd_2O_3–TiO_2 dielectric resonators. *Journal of the American Ceramic Society*, **67** (4), 278–281.
16. Durand, J.M. and Boilot, J.P. (1987) Microwave characteristics of BaO–Bi_2O_3–TiO_2–Nd_2O_3 dielectric resonators. *Journal of Materials Science Letters*, **6**, 134–136.
17. Nishigaki, S., Kato, H., Yano, S., and Kamimura, R. (1987) Microwave dielectric properties of (Ba,Sr)O–Sm_2O_3–TiO_2 ceramics. *American Ceramic Society Bulletin*, **66** (9), 1405–1410.
18. Wu, J.-M., Chang, M.-C., and Yao, P.-C. (1990) Reaction sequence and effects of calcination and sintering on microwave properties of (Ba,Sr)O–Sm_2O_3–TiO_2 ceramics. *Journal of the American Ceramic Society*, **73** (6), 1599–1605.
19. Sun, J.-S., Wei, C.-C., and Wu, L. (1992) Dielectric properties of (Ba,Sr)O–$(Sm,La)_2O_3$–TiO_2 ceramics at microwave frequencies. *Journal of Materials Science*, **27**, 5818–5822.
20. Chen, X.M., Suzuki, Y., and Sato, N. (1993) Preparation and densification of $BaNd_2Ti_5O_{14}$ dielectric ceramics. *Materials Letters*, **16**, 75–78.
21. Sreemoolanadhan, H., Sebastian, M.T., and Mohanan, P. (1996) Dielectric resonators in BaO–Ln_2O_3–$5TiO_2$ system (Ln = –La, Pr, Nd, Sm). *British Ceramic Transactions*, **95** (2), 79–81.
22. Guha, J.P. (1991) Synthesis and characterisation of barium lanthanum titanates. *Journal of the American Ceramic Society*, **74** (4), 878–880.
23. Takashi, J., Ikegami, T., and Kageyama, K. (1991) Occurrence of dielectric 1:1:4 compound in the ternary system BaO–Ln_2O_3–TiO_2 (Ln = La, Nd, and Sm): I, An improved coprecipitation method for preparing a single-phase powder of ternary compound in the BaO–La_2O_3–TiO_2 system. *Journal of the American Ceramic Society*, **74** (8), 1868–1872.
24. Takahashi, J., Ikegami, T., and Kageyama, K. (1991) Occurrence of dielectric 1:1:4 compound in the ternary system BaO–Ln_2O_3–TiO_2 (Ln = La, Nd, and Sm): II, Re-examination of formation of isostructural ternary compounds in identical systems. *Journal of the American Ceramic Society*, **74** (8), 1873–1879.
25. Valant, M., Suvorov, D., and Kolar, D. (1995) Chemical characteristics of the compound $Ba_{4.5}Gd_9Ti_{18}O_{54}$, in *Proceedings of the Fourth Euroceramics* (eds G. Gusmano and E. Traversa), September–October 1995, Riccione, Italy, vol. 5, pp. 211–218, European Ceramic Society.
26. Valant, M., Suvorov, D., and Kolar, D. (1994) High permittivity microwave ceramics – The influence of $Ba_{4.5}Gd_9Ti_{18}O_{54}$ addition on the temperature stability of dielectric properties, in *Proceedings of the 4th International Conference on Electronic Ceramics and Applications (Electroceramics IV)* (ed. R. Wasser), September 5–7, 1994, Aachen, Germany, pp. 69–72, Institut für Werkstoffe der Elektrotechnik, Aachen.
27. Varfolomeev, M.B., Mironov, A.S., Kostomarov, V.S., *et al.* (1988) The synthesis and homogeneity ranges of the phases $Ba_{6-x}Nd_{8+2x/3}Ti_{18}O_{54}$. *Russian Journal of Inorganic Chemistry*, **33** (4), 607–608.
28. Ohsato, H., Ohhashi, T., Nishigaki, S., *et al.* (1993) Formation of solid solutions of new tungsten bronze-type microwave dielectric compounds $Ba_{6-3x}R_{8+2x}Ti_{18}O_{54}$ (R = Nd and Sm, $0 \leq x \leq 1$). *Japanese Journal of Applied Physics*, **32** (Part 1: 9b), 4323–4326.
29. Negas, T. and Davies, P.K. (1995) Influence of chemistry and processing on the electrical properties of $Ba_{6-3x}Ln_{8+2x}Ti_{18}O_{54}$ solid solutions. *Ceramic Transactions*, **53**, 179–196.
30. Suvorov, D., Valant, M., and Kola, D. (1995) Chemistry and microwave properties of Bi_2O_3 doped $Ba_{4.5}Nd_9Ti_{18}O_{54}$ based ceramics. *Ceramic Transactions*, **53**, 197–206.
31. Cruickshank, K.M., Jing, X., Wood, G., *et al.* (1996) Phase equilibria studies of $Ba_{6-3x}Nd_{8+2x}Ti_{18}O_{54}$ solid solution. *Journal of the American Ceramic Society*, **79** (6), 1605–1610.
32. Ubic, R., Reaney, I.M., Lee, W.E., *et al.* (1999) Properties of the microwave dielectric phase $Ba_{6-3x}Nd_{8+2x}Ti_{18}O_{54}$. *Ferroelectrics*, **228** (1–4), 271–282.
33. Belous, A.G. and Ovchar, O.V. (1997) MW ceramic dielectrics based on the system BaO–$(Nd,Sm)_2O_3$–TiO_2. *Key Engineering Materials*, **132–136**, 1191–1194.
34. Nenasheva, E.A., Sidorova, N.M., Kartenko, N.F., *et al.* (1985) Compounds in the systems $BaLa_2O_4$–TiO_2, $BaNd_2O_4$–TiO_2. *Inorganic Materials*, **21**, 1330–1333.

35. Ohsato, H., Nishigaki, S., and Okuda, T. (1992) Superlattice and dielectric properties of BaO–R_2O_3–TiO_2 (R = La, Nd, and Sm) microwave dielectric compounds. *Japanese Journal of Applied Physics*, **31** (9b), 3136–3138.
36. Laffez, P., Desgardin, G., and Raveau, B. (1995) Microwave dielectric properties of doped $Ba_{6-x}(Sm_{1-y},Nd_y)_{8+2x/3}Ti_{18}O_{54}$ oxides. *Journal of Materials Science*, **30** (1), 267–273.
37. Subbarao, S.C., Shirane, G., and Jona, F. (1960) X-ray, dielectric, and optical study of ferroelectric lead metatantalate and related compounds. *Acta Crystallographica*, **13**, 226–231.
38. Jamieson, P.B., Abrahams, S.C., and Bernstein, J.L. (1968) Ferroelectric tungsten bronze-type crystal structures. I. Barium strontium niobate $Ba_{0.27}Sr_{0.75}Nb_2O_{5.78}$. *Journal of Chemical Physics*, **48** (11), 5048–5057.
39. Lines, M.E. and Glass, A.M. (1977) *Principles and Applications of Ferroelectrics and Related Materials*, Oxford University Press, Oxford.
40. Neurgaonkar, R.R., Oliver, J.R., Cory, W.K., *et al.* (1994) Piezoelectricity in tungsten bronze crystals. *Ferroelectrics*, **160**, 265–276.
41. Roth, R.S., Beach, F., Santoro, A., *et al.* (1987) Structure of the nonstoichiometric solid solutions $Ba_2RE_4[Ba_x+RE_{2/3-2/3x}]Ti_9O_{27}$ (RE = Nd, Sm). *Acta Crystallogrtaphica*, **A43**, C138–C139.
42. Randall, C.A., Guo, R., Bhalla, A.S., and Cross, L.E. (1991) Microstructure–property relations in tungsten bronze lead barium niobate, $Pb_{1-x}Ba_xNb_2O_6$. *Journal of Materials Research*, **6** (8), 1720–1728.
43. Shanon, R. D. (1976) Revised effective ionic radii and systematic studies of interatomic distances in halides and chalcogenides. *Acta Crystallographica*, **A32**, 751–767.
44. Azough, F., Setasuwon, P., and Freer, R. (1995) The structure and microwave dielectric properties of ceramics based on $Ba_{3.75}Nd_{9.5}Ti_{18}O_{54}$. *Ceramic Transactions*, **53**, 215–227.
45. Ohsato, H. (2001) Science of tungsten bronze type like $Ba_{6-3x}R_{8+2x}Ti_{18}O_{54}$ (R = rare earth) microwave dielectric solid solutions. *Journal of the European Ceramic Society*, **21**, 2703–2711.
46. Ohsato, H., Mizuta, M., Ikoma, T., *et al.* (1998) Microwave dielectric properties of tungsten bronze type $Ba_{6-3x}R_{8+2x}Ti_{18}O_{54}$ (R = La, Pr, Nd, and Sm) solid solutions. *Journal of the Ceramic Society of Japan*, **106**, 178–182.
47. Ohsato, H., Imaeda, M., Komura, A., *et al.* (1999) Non-linear microwave quality factor change based on the site occupancy of cations on the tungstenbronze-type $Ba_{6-3x}R_{8+2x}Ti_{18}O_{54}$ (R = rare earth) solid solutions. *Ceramic Transactions*, **100**, 41–50.
48. Ubic, R., Reaney, I.M., and Lee, W.E. (1997) Microwave resonators in the system $BaO{\cdot}Nd_2O_3{\cdot}TiO_2$, in *Institute of Physics Conference Series* (ed. J.M. Rodenburg), September 2–5, 1997, Cambridge, vol. 153, pp. 613–616, Institute of Physics Publishing, Bristol.
49. Wunderlich, W. and Ohsato, H. (2013) Enhanced microwave resonance properties of pseudo-tungsten-bronze $Ba_{6-3x}RE_{8+2x}Ti_{18}O_{54}$ (R = rare earth) solid solutions explained by electron–phonon interaction. *Japanese Journal of Applied Physics*, **52** (9), 09KH04.
50. Kolar, D., Gabecek, S., and Suvorov, D. (1993) Structural and dielectric properties of perovskite-like rare earth titanates, in *Proceedings of the Third European Ceramic Society Conference* (eds P. Duran and J.F. Fernandez), September 12–17, 1993, Madrid, Spain, vol. 2, pp. 229–234, Faenza Editrice Ibérica, Castellón de la Plana, Spain.
51. Azough, F., Champness, P.E., and Freer, R. (1995) Determination of the space group of ceramic $BaO{\cdot}Pr_2O_3{\cdot}4TiO_2$ by electron diffraction. *Journal of Applied Crystallography*, **28** (5), 577–581.
52. Azough, F., Freer, R., Tang, C.C. (1997) Determination of the structures of Ba-Ln-Ti-O microwave dielectric ceramics using synchrotron high resolution X-ray diffraction. *British Ceramics Proceedings*, **57**, 111–117.
53. Rawn, C.J. (1996) Structure of $Ba_{6-x}Ln_{8+2/3x}Ti_{18}O_{54}$ microwave dielectrics, in *Proceedings of the Fifth International Conference on Electronic Ceramics and Applications* (eds J.L. Baptista, J.A. Labrincha, and P.M. Vilarinho), September 2–4, 1996, Aveiro, Portugal, pp. 67–70, Department of Ceramics Engineering, University of Aveiro, Aveiro.
54. Qin, N., Chen, X.M., and Liu, X.Q. (2006) Dielectric anomaly and phase transition in $Ba_{6-3x}(Sm_{1-y}La_y)_{6+2x}Ti_{18}O_{54}$ ($x = 0.5$) ceramics. *Journal of the American Ceramic Society*, **89** (9), 2796–2803.

55. Wu, Y.J. and Chen, X.M. (2000) Bi/Sm co-substituted $Ba_{6-3x}Nd_{8+2x}Ti_{18}O_{54}$ microwave dielectric ceramics. *Journal of the American Ceramic Society*, **83**, 1837–1839.
56. Ohsato, H., Sugino, J., Komura, A., *et al.* (1999) Microwave dielectric properties of $Ba_4(Nd_{28/3-y}R_y)Ti_{18}O_{54}$ (R = Eu, Dy, Ho, Er, and Yb) solid solutions. *Japanese Journal of Applied Physics*, **38**, 5625–5628.
57. Ohsato, H., Kato, H., Mizuta, M., *et al.* (1995) Microwave dielectric properties of the $Ba_{6-3x}(Sm_{1-y}R_y)_{8+2x}Ti_{18}O_{54}$ (R = Nd and La) solid solutions with zero temperature coefficient of the resonant frequency. *Japanese Journal of Applied Physics*, **34**, 5413–5417.
58. Li, Y. and Chen, X.M. (2002) Effects of sintering conditions on microstructures and microwave dielectric properties of $Ba_{6-3x}(Sm_{1-y}Nd_y)_{8+2x}Ti_{18}O_{54}$ ceramics ($x = 2/3$). *Journal of the European Ceramic Society*, **22**, 715–719.
59. Mercurio, J.P., Manir, M., and Frit, B. (1989) Microwave dielectric properties of $BaNd_{(2-x)}Sm_{2x}Ti_5O_{14}$ ceramics. *Materials Letters*, **8**, 112–114.
60. Satheesh, V., Murigavel, P., Murthy, V.R.K., and Viswanathan, B. (1997) Synthesis and role of Nd and Sm on the microwave dielectric properties of $BaNd_{2(1-x)}Sm_{2x}Ti_5O_{14}$ dielectric resonator. *Materials Science and Engineering, B*, **48**, 202–204.
61. Suvorov, D., Valant, M., and Kolar, D. (1997) The role of dopants in tailoring the microwave properties of $Ba_{6-3x}R_{8+2x}Ti_{18}O_{54}$ (R = La–Gd) ceramics. *Journal of Materials Science*, **32**, 6483–6488.
62. Ichinose, N. and Amada, H. (2001) Preparation and microwave dielectric properties of the $BaO(Sm_{1-x}La_x)_2O_3$–$5TiO_2$ ceramic system. *Journal of the European Ceramic Society*, **21**, 2751–2753.
63. Yamada, A., Utsumi, Y., and Watarai, H. (1991) Effect of Mn addition on dielectric properties and microstructure of BaO–Nd_2O_3–TiO_2 ceramics. *Japanese Journal of Applied Physics*, **30**, 2350–2353.
64. Silva, A., Azough, F., Freer, R., and Leach, C. (2000) Microwave dielectric ceramics in the system BaO–Li_2O–Nd_2O_3–TiO_2. *Journal of the European Ceramic Society*, **20**, 2727–2734.
65. Ohsato, H., Komura, A., Takagi, Y., *et al.* (1998) Microwave dielectric properties and sintering of $Ba_{6-3x}R_{8+2x}Ti_{18}O_{54}$ (R = Sm, $x = 2/3$) solid solution with added rutile. *Japanese Journal of Applied Physics*, **37**, 5357–5359.
66. Zheng, Y., Zhao, X., Lei, W., and Wang, S. (2005) Effects of Bi_2O_3 addition on the microstructures and microwave dielectric characteristics of $Ba_{6-3x}(Sm_{0.2}Nd_{0.8})_{(8+2x)}Ti_{18}O_{54}$ ($x = 2/3$) ceramics. *Materials Letters*, **60**, 459–463.
67. Okawa, T., Imaeda, M., and Ohsato, H. (2002) Microwave dielectric properties of $Ba_4(Sm_{1-y}Bi_y)_{9+1/3}Ti_{18}O_{54}$ solid solutions. *Key Engineering Materials*, **214–215**, 37–42.
68. Ota, Y., Kakimoto, K.-I., Ohsato, H., and Okawa, T. (2004) Low-temperature sintering of $Ba_{6-3x}Sm_{8+2x}Ti_{18}O_{54}$ microwave dielectric ceramics by B_2O_3 and GeO_2 addition. *Journal of the European Ceramic Society*, **24**, 1755–1760.
69. Santha, N., Sebastian, M.T., George, V., and Philip, J. (2006) Microwave dielectric and elastic properties of glass-added $Ba_{6-3x}R_{8+2x}Ti_{18}O_{54}$ ($x = 2/3$). *Materials Chemistry and Physics*, **100**, 423–429.
70. Chang, L.-C. and Chiou, B.-S. (2004) Effect of B_2O_3 nano coating on the sintering behaviour and electrical microwave properties of $Ba(Nd_{2-x}Sm_x)Ti_4O_{12}$ ceramics. *Journal of Electroceramics*, **13**, 829–837.
71. Azough, F., Lowe, T., and Freer, R. (2005) Control of microwave dielectric properties in the system BaO Nd_2O_3 $4TiO_2$–BaO Al_2O_3 $4TiO_2$. *Journal of Electroceramics*, **15**, 183–192.
72. Huang, L., Tsai, J.T., and Li, J.-L. (2000) Microwave dielectric properties of $(1-x)$CaO–xBaO–Li_2O–$(1-y)Sm_2O_3$–yNd_2O_3–TiO_2 ceramics system. *Journal of Materials Science*, **35**, 4901–4905.
73. Wu, Y.J. and Chen, X.M. (1999) Modified $Ba_{6-3x}Nd_{8+2x}Ti_{18}O_{54}$ microwave dielectric ceramics. *Journal of the European Ceramic Society*, **19**, 1123–1126.
74. Yang, C.-F. (2000) Microwave properties of $(Ba_{1-x}Sr_x)Sm_2Ti_4O_{12}$ ceramics and its application as dielectric resonator antenna. *Japanese Journal of Applied Physics*, **39**, 1430–1434.

75. Wu, Y.J. and Chen, X.M. (2001) Structures and microwave dielectric properties of $Ba_{6-3x}(Nd, Bi_y)_{8+2x}Ti_{18}O_{54}$ ($x = 2/3$) solid solution. *Journal of Materials Research*, **16**, 1734–1738.
76. Okawa, T., Imaeda, M., and Ohsato, H. (2000) Microwave dielectric properties of Bi added $Ba_4Nd_{9+1/3}Ti_{18}O_{54}$ solid solutions. *Japanese Journal of Applied Physics*, **39**, 5645–5649.
77. Valant, M. and Suvorov, D. (2001) Incorporation of bismuth into $Ba_{6-3x}R_{8+2x}Ti_{18}O_{54}$ (R = Nd,Gd). *Journal of Materials Science*, **36**, 2991–2997.
78. Cho, I.-S., Kim, D.-W., Kim, J.-R., and Hong, K.S. (2004) Low temperature sintering and microwave dielectric properties of $BaO–(Nd_{1-x}Bi_x)_2O_3–4TiO_2$ by the glass additions. *Ceramics International*, **30**, 1181–1185.
79. Wu, Y.J. and Chen, X.M. (2000) Bismuth/samarium cosubstitutied $Ba_{6-3x}Nd_{8+2x}Ti_{18}O_{54}$ microwave dielectric ceramics. *Journal of the American Ceramic Society*, **83**, 1837–1839.
80. Cho, I.-S., Kim, D.-W., Kim, J.-R., and Hong, K.S. (2004) Low temperature sintering and microwave dielectric properties of BaO $(Nd_{1-x}Bi_x)_2O_3$ $4TiO_2$ by the glass additions. *Ceramics International*, **30**, 1181–1185.
81. Chang, L.-E., Chiou, B.-S., and Lee, W.-H. (2004) Effect of glass additions on the sintering behaviour and electrical microwave properties of $BaO–Nd_2O_3–Sm_2O_3–TiO_2$ ceramics. *Journal of Materials Science: Materials in Electronics*, **15**, 153–158.
82. Lee, C.C. and Lin, P. (1998) Effect of glass addition on microwave properties of $BaO–La_2O_3–4.7TiO_2$. *Japanese Journal of Applied Physics*, **37**, 6048–6054.
83. Dernovsek, O., Naeini, A., Preu, G., *et al.* (2001) LTCC glass ceramic composites for microwave application. *Journal of the European Ceramic Society*, **21**, 1693–1697.
84. Jung, B.-H., Hwang, S.-J., and Kim, H.-S. (2005) Glass-ceramic for low temperature co-fired dielectric ceramic materials based on $La_2O_3–B_2O_3–TiO_2$ glass with BNT ceramics. *Journal of the European Ceramic Society*, **25**, 3187–3193.
85. Imaeda, M., Ito, K., Mizuta, M., *et al.* (1997) Microwave dielectric properties of $Ba_{6-3x}Sm_{8+2x}Ti_{18}O_{54}$ solid solutions with Sr substituted for Ba. *Japanese Journal of Applied Physics*, **36**, 6012–6015.
86. Chen, X.M. and Li, Y. (2002) A- and B-site cosubstituted $Ba_{6-3x}Sm_{8+2x}Ti_{18}O_{54}$ microwave dielectric ceramics. *Journal of the American Ceramic Society*, **85**, 579–584.
87. Belous, A.G., Ovchar, O., Valant, M., *et al.* (2001) The effect of partial isovalent substitution in the A sublattice on MW properties of materials based on $Ba_{6-x}Ln_{8+2x/3}Ti_{18}O_{54}$ solid solutions. *Journal of the European Ceramic Society*, **21**, 2723–2730.
88. Belous, A.G. and Ovchar, O.V. (1999) MW dielectrics with perovskite like structure based on Sm containing systems. *Journal of the European Ceramic Society*, **19**, 1119–1122.
89. Mizuta, M., Uenoyama, K., Ohsato, H., *et al.* (1996) Formation of tungsten bronze type $(Ba_{6-3x}Sm_{8+2x})Ti_{18-y}Al_yO_{54}$ ($a = 1 + y/36$) solid solutions and microwave dielectric properties. *Japanese Journal of Applied Physics*, **35**, 5065–5068.
90. Suvorov, D., Valant, M., and Kolar, D. (1997) The role of dopants in tailoring the microwave properties of $Ba_{6-3x}R_{8+2x}Ti_{18}O_{54}$ (R = La–Gd) ceramics. *Journal of Materials Science*, **32**, 6483–6485.
91. Cheng, C.-C., Hsieh, T.E., Lin, I.-N. (2004) Effects of composition on low temperature sinterable Ba–Nd–Sm–Ti–O microwave dielectric materials. *Journal of the European Ceramic Society*, **24**, 1787–1790.
92. Okawa, T., Imaeda, M., Ohsato, H., Harada, A. (2003) Site occupancy of Bi ions and microwave dielectric properties of Bi doped $Ba_{6-3x}R_{8+2x}Ti_{18}O_{54}$ (R = rare earth, $x = 2/3$) solid solutions. *Materials Chemistry and Physics*, **79**, 199–203.
93. Valant, M., Arcon, I., Suvorov, D., *et al.* (1997) Extended X-ray absorption fine structure study of incorporation of Bi and Pb atoms into the crystal structure of $Ba_{4.5}Nd_9Ti_{18}O_{54}$. *Journal of Materials Research*, **12**, 799–804.
94. Huang, B., Wang, Z., Chen, T., and Wang, L. (2014) Effect of MnO_2 doping on the microstructure and microwave dielectric properties of $Ba_{4.2}Nd_{9.2}Ti_{18}O_{54}$ ceramics. *Journal of Materials Science: Materials in Electronics*, **25**, 5264–5268.
95. Ohsato, H., Komura, A., and Nishigaki, S. (2004) Occupation in the trigonal columns of tungsten bronze like $Ba_{6-3x}Sm_{8+2x}Ti_{18}O_{54}$ solid solutions. *Journal of the Ceramic Society of Japan*, **112** (Suppl. 1), 1618–1621.

96. Chang, G., Zhou, X.-H., Zhang, S.-R., *et al.* (2015) Effect of TiO_2 and Al_2O_3 doping on sintering behavior and microwave dielectric properties of $Ba_4(Sm_{0.5}Nd_{0.5})_{28/3}Ti_{18+x}O_{54+2x}$ ceramics. *Journal of Materials Science: Materials in Electronics*, **25** (10), 4439–4443.
97. Yao, X., Lin, H., Chen, W., and Luo, L. (2012) Anti reduction of Ti^{4+} in $Ba_{4.2}Sm_{9.2}Ti_{18}O_{54}$ ceramics by doping with MgO, Al_2O_3 and MnO_2. *Ceramics International*, **38**, 3011–3016.
98. Gao, X. and Tai, Q. (2010) Microwave dielectric properties of $Ba_{6-3x}La_{8+2x}(Ti_{1-z}Zr_z)_{18}O_{54}$ ($x = 2/3$) ceramics. *Journal of Rare Earths*, **28** (3), 411–415.
99. Zhu, J., Lu, W., Lei, W., and Wan, S. (2009) Effects of $SrTiO_3$ additives on the structure and microwave dielectric properties of $Ba_{4.2}Sm_{9.2}Ti_{18}O_{54}$ ceramics. *Ceramics International*, **35**, 855–860.
100. Hsiang, H.-I. and Chen, T.-H. (2009) Influence of glass additives on the sintering behaviour and dielectric properties of $BaO{\cdot}(Nd_{0.8}Bi_{0.2})_2O_3{\cdot}4TiO_2$ ceramics. *Journal of Alloys and Compounds*, **467**, 485–490.
101. Valant, M., Suvorov, D., and Kolar, D. (1996) Role of Bi_2O_3 in optimizing the dielectric properties of $Ba_{4.5}Nd_9Ti_{18}O_{54}$ based microwave ceramics. *Journal of Materials Research*, **11** (4), 928–931.
102. Ohsato, H., Komura, A., and Nishigaki, S. (2004) Occupation in the trigonal columns of tungsten bronze like $Ba_{6-3x}Sm_{8+2x}Ti_{18}O_{54}$ solid solutions. *Journal of the Ceramic Society of Japan*, **112** (Suppl. 1), 1618–1621.
103. Ubic, R., Reaney, I.M., Lee, W.E., *et al.* (1996) Effect of divalent dopants on properties of $Ba_{3.75}Nd_{9.5}Ti_{18}O_{54}$ microwave dielectric resonators, in *Proceedings of the MRS Symposium on Solid-State Chemistry of Inorganic Materials* (eds P.K. Davies, A.J. Jacobson, C.C. Torardi, and T.A. Vanderah), December 2–5, 1996, Boston, Materials Research Society, Pittsburgh.
104. Podlinik, M., Valant, M., and Suvorov, D. (1997) The influence of isovalent doping on the microwave dielectric properties of $Ba_{6-3x}Nd_{8+2x}Ti_{18}O_{54}$ based ceramics. *Key Engineering Materials*, **132–136**, 1211–1214.
105. Belous, G. and Ovchar, O.V. (2000) Pb-induced temperature stabilization of high dielectric constant in barium neodymium titanates. *Ferroelectrics*, **238**, 9–16.
106. Ubic, R., Reaney, I.M., Lee, W.E., *et al.* (1999) Properties of the microwave dielectric phase $Ba_{6-3x}Nd_{8+2x}Ti_{18}O_{54}$. *Ferroelectrics*, **228**, 271–282.
107. Ubic, R., Reaney, I.M., and Lee, W.E., *et al.* (1999) $Ba_{6-3x}Nd_{8+2x}Ti_{18}O_{54}$ microwave dielectric resonators. *Ferroelectrics*, **223**, 293–300.
108. Ubic, R., Reaney, I.M., Lee, W.E. (1999) Perovskite. $NdTiO_3$ in Sr- and Ca-doped BaO–Nd_2O_3–TiO_2 microwave dielectric ceramics. *Journal of Materials Research*, **14**, 1576–1580.
109. Takahashi, J., Kageyama, K., and Kodaira, K. (1993) Microwave dielectric properties of lanthanide titanate ceramics. *Japanese Journal of Applied Physics*, **32**, 4327–4331.
110. Lee, C.C. and Lin, P. (1998) Microwave dielectric properties and microstructures of $(Ba_{1-x}Pb_x)O{\cdot}La_2O_3{\cdot}4.7TiO_2$ ceramics. *Japanese Journal of Applied Physics*, **37**, 878–884.
111. Mercurio, D., Abou-Salama, M., and Mercurio, J.-P. (2001) Investigations of the tungsten bronze-type $(Ba_{1-\alpha}Sr_\alpha)_{6-x}La_{8+2x/3}Ti_{18}O_{54}$ ($0 \le x \le 1$) solid solutions. *Journal of the European Ceramic Society*, **21**, 2713–2716.
112. Nagatomo, T., Otagiri, T., Suzuki, M., and Ohsato, H. (2006) Microwave dielectric properties and crystal structure of the tungsten bronze type $(Ba_{1-\alpha}Sr_\alpha)_6(Nd_{1-\beta}Y_\beta)_8Ti_{18}O_{54}$ solid solutions. *Journal of the European Ceramic Society*, **26**, 1865–1898.
113. Suzuki, M., Ohsato, H., Nagatomo, T., *et al.* (2006) Crystal structure and microwave dielectric properties of the tungstenbronze-type like $(Ba_{1-\alpha}Sr_\alpha)_6(Nd_{1-\beta}Y_\beta)_8Ti_{18}O_{54}$ solid solutions. *Journal of the European Ceramic Society*, **26**, 2035–2038.
114. Ubic, F.J. (1997) Processing and analysis of microwave dielectric resonators in the system BaO–Nd_2O_3–TiO_2. PhD Thesis, The University of Sheffield.
115. Wu, Y.J. and Chen, X.M. (1999) Dielectric ceramics of $Ba_{6-3x}Nd_{8+2x}$ (Zr, Ti)$_{18}O_{54}$. *Ferroelectrics*, **233**, 271–277.
116. Wu, S.Y., Li, Y., and Chen, X.M. (2004) Raman spectra of Nd/Sn cosubstituted $Ba_{6-3x}Sm_{8+2x}Ti_{18}O_{54}$ microwave dielectric ceramics. *Journal of Applied Physics*, **96**, 5683–5686.

117. Chang, L.-C. and Chiou, B.-S. (2005) Electrical behaviour of $BaO–Nd_2O_3–Sm_2O_3–TiO_2$ with glass/oxide additives analysed by impedance spectroscopy. *Journal of Electroceramics*, **15**, 75–81.
118. Cheng, C.-C., Hsieh, T.-E., and Lin, I.-N. (2003) Microwave dielectric properties of glass ceramics composites for low temperature cofirable ceramics. *Journal of the European Ceramic Society*, **23**, 2553–2558.
119. Cheng, C.-C., Hsieh, T.-E., Lin, I.-N. (2003) The effect of composition on Ba–Nd–Sm–Ti–O microwave dielectric materials for LTCC application. *Materials Chemistry and Physics*, **79**, 119–123.
120. Lu, C.-H. and Huang, Y.-H. (2003) Densification and dielectric properties of barium neodymium titanate oxide ceramics. *Materials Science and Engineering, B*, **98**, 33–37.
121. Shafer, M.W. and Roy, R. (1959) Rare-earth polymorphism and phase equilibria in rare-earth oxide water systems. *Journal of the American Ceramic Society*, **42** (11), 563–570.
122. Monneraye, M., Serindat, J., and Jouwersma, (1968) Control of dielectric losses and temperature coefficient of permittivity by doping in some glass-ceramic materials. *Glass Technology*, **9** (3), 70–77.
123. Newnham, R. (1983) Structure-property relations in ceramic capacitors. *Journal of Materials Education*, **5** (6), 947–982.
124. Mhaisalkar, S.G., Lee, W.E., and Readey, D.W. (1989) Processing and characterization of $BaTi_4O_9$. *Journal of the American Ceramic Society*, **72** (11), 2154–2158.
125. O'Bryan, H.M., Thomson, J., and Plourde, J.K. (1974) New $BaO–TiO_2$ compound with temperature-stable high permittivity and low microwave loss. *Journal of the American Ceramic Society*, **57** (10), 450–453.
126. Nomura, S., Tomaya, K., and Kaneta, K. (1983) Effect of Mn doping on the dielectric properties of $Ba_2Ti_9O_{20}$ ceramics at microwave frequency. *Japanese Journal of Applied Physics*, **22** (Part 1: 7), 1125–1128.
127. Hirano, S.-I., Hayashi, T., and Hattori, A. (1991) Chemical processing and microwave characteristics of (Zr, Sn)TiO_4 microwave dielectrics. *Journal of the American Ceramic Society*, **74** (6), 1320–1324.
128. Okaya, A. and Barash, L.F. (1962) The dielectric microwave resonator. *Proceedings of the IRE*, **50** (10), 2081–2092.
129. Cohen, S.B. (1968) Microwave band pass filters containing high *Q* dielectric resonators. *IEEE Transactions on Microwave Theory and Techniques*, **16**, 218–227.
130. Egerton, C. and Thomson, J. (1971) Preparation of high density ceramic TiO_2 having low dielectric loss at microwave frequencies. *American Ceramic Society Bulletin*, **50** (11), 924.
131. Templeton, A., Wang, X., Webb, S.J., *et al.* (2000) Microwave dielectric loss of titanium oxide. *Journal of the American Ceramic Society*, **83** (1), 95–148.
132. Grant, F.A. (1959) Properties of rutile. *Reviews of Modern Physics*, **31** (3), 646–674.
133. Kingery, W.D., Bowen, H.K., and Uhlman, D.R. (1976) *Introduction to Ceramics*, 2nd edn, John Wiley & Sons, Inc., New York.
134. Pullar, R.C., Penn, S.J., Wang, X., *et al*. (2009) Dielectric loss caused by oxygen vacancies in titania ceramics. *Journal of the European Ceramic Society*, **29**, 419–424.
135. Tsunooka, T., Androu, M., Higashida, Y., *et al.* (2003) Effects of TiO_2 on sinterability and dielectric properties of high-*Q* forsterite ceramics. *Journal of the European Ceramic Society*, **23**, 2573–2578.
136. Li, F., Liu, P., Ruan, P., *et al.* (2015) Microwave dielectric properties of $(1 - x)SiO_2–xTiO_2$ ceramics, *Ceramic International*, **41**, S582–S587.
137. Klein, N., Zuccaro, C., Dahe, U., *et al.* (1995) Dielectric properties of rutile and its use in high temperature superconducting resonators. *Journal of Applied Physics*, **78**, 6683–6686.
138. Tobar, M.E., Krupka, J., Ivanov, E.N., and Woode, R.A. (1998) Anisotropic complex permittivity measurement of monocrystalline rutile. *Journal of Applied Physics*, **83**, 1604–1609.
139. Tobar, M.E., Krupka, J., Hartnett, J.G., and Woode, R.A. (1998) High Q sapphire rutile frequency temperature compensated microwave dielectric resonators. *IEEE Transactions on Ultrasonic and Ferroelectrics and Frequency Control*, **45**, 830–835.

140. Sremoolanadhan, H., Sebastian, M.T., Ratheesh, R., *et al.* (2004) Microwave dielectric properties of $BaO-2CeO_2-nTiO_2$ ceramics. *Journal of Solid State Chemistry*, **177**, 3995–4000.
141. Guha, J. P. and Kolar, D. (1973) Subsolidus equilibria in the system $BaO–CeO_2–TiO_2$. *Journal of American Ceramic Society*. **56**, 5–6.
142. Bamberger, C.E., Haverlock, T.J. and Kopp, O.C. (1994) Synthesis and characterization of $Sr_2Ce_2Ti_5O_{16}$ in the system $SrO–CeO_2–TiO_2$. *Journal of American Ceramic Society*, **77**, 1659–1661.
143. Subodh, G. and Sebastian, M.T. (2007) Microwave dielectric properties of $Sr_2Ce_2Ti_5O_{16}$ ceramics. *Materials Science and Engineering B*, **136**, 50–56.
144. Subodh, G., James, J., Sebastian, M.T., *et al.* (2007) Structure and microwave dielectric properties of $Sr_{2+n}Ce_2Ti_{5+n}O_{15+3n}$ ($n \leq 10$) homologous series. *Chemistry of Materials*, **19**, 4077–4082.
145. Ubic, R., Subodh, G., Sebastian, M.T., *et al*. (2008) Structure of compounds in the $Sr_{1-3x/2}Ce_xTiO_3$ homologous series. *Chemistry of Materials*, **20**, 3127–3133.
146. Ubic, R., Subodh, G., Sebastian, M.T., *et al*. (2009) Structure of $Sr_{0.4}Ce_{0.4}TiO_3$. *Chemistry of Materials*, **21**, 4706–4710.
147. Kolar, D. (1997) Phase equilibria and dielectric properties of rare earth containing $BaTiO_3$ ceramics. *Proceedings of Materials Research Symposium*, **453**, 425.
148. Beyreuther, E., Grafström, S., Eng, L.M., *et al.* (2006) XPS investigation of Mn valence in lanthanum manganite thin films under variation of oxygen content. *Physical Review B*, **73**, 155425.
149. Moreira, R.L., Lobo, R.P.S.M., Subodh, G., *et al.* (2007) Optical phonon modes and dielectric behavior of $Sr_{1-3x/2}Ce_xTiO_3$ microwave ceramics. *Chemistry of Materials*, **19**, 6548–5654.
150. Howard, C.J., Lumpkin, G.R., Smith, R.I., and Zhang, Z.J. (2004) Crystal structures and phase transition in the system $SrTiO_3–La_{2/3}TiO_3$. *Journal of Solid State Chemistry*. **177**, 2726.
151. Leonov, A.I., Piryutko, M.M. and Keler, E.K. (1966) Bulletin of the Academy of Science (USSR), *Division of Chemical Sciences*, **5**, 756.
152. Yoshii, K. (2000) Structural and magnetic studies of the lanthanide deficient perovskite $Ce_{2/3}TiO_3$. *Journal of Alloys and Compounds*, **305**, 72–75.
153. Howard, C.J., Kennedy, B.J., and Chakoumakos, B.C. (2000) Neutron powder diffraction study of rhombohedral rare-earth aluminates and the rhombohedral to cubic phase transition. *Journal of Physics: Condensed Matter*, **12**, 349–365.
154. Müller, K.A. and Burkard, H. (1979) $SrTiO_3$: an intrinsic quantum paraelectric below 4 K. *Physical Review B*, **19**, 3593–3602.
155. Shannon, R.D. (1993) Dielectric polarizabilities of ions in oxides and fluorides *Journal of Applied Physics*, **73**, 348–366.
156. Moreira, R.L., Lobo, R.P.S.M., Subodh, G., *et al.* (2009) Microwave and infrared dielectric properties of $Sr_{1-x/2}Ce_xTiO_3$ ($x = 0.154$ to 0.400) incipient ferroelectrics at cryogenic temperatures. *Journal of Physics D. Applied Physics*, **42**, 75411–75419.
157. Kamba, S., Savinov, S.M., Tkáč, O., *et al.* (2009) Ferroelectric and incipient ferroelectric properties of a novel $Sr_{9-x}Pb_xCe_2Ti_2O_{36}$ ($x = 0–9$) ceramic system.*Chemistry of Materials*, **21**, 811–819.
158. Beech, F., Jordan, W.M., Catlow, C.R., *et al.* (1988) Neutron powder diffraction structure and electrical properties of the defect pyrochlores $Pb_{1.5}M_2O_{6.5}$ (M = Nb, Ta). *Journal of Solid State Chemistry*, **77**, 322–335.
159. Ubic, R. and Reaney, I.M. (2000) Lead niobate ceramics for microwave dielectric resonators, in *Ceramic Transactions*, vol. 106, *Electronic Ceramic Materials and Devices* (eds K.M. Nair and A.S. Bhalla), American Ceramic Society, Westerville, OH, pp. 263–275.
160. Cook, W.R., Jr and Jaffe, H. (1952) Ferroelectricity in oxides of fluorite structure. *Physical Review*, **88** (6), 1426.
161. Roth, R.S. (1959) Phase equilibrium relations in the binary system lead oxide–niobium pentoxide. *Journal of Research National Bureau of Standards*, **62** (1), 27–38.
162. Brusset, H., Gillier-Pandraud, H., Mahé, R., and Voliotis, S.D. (1971) Etude de systemes binaires et pseudo-binaires definis entre Nb_2O_5 et PbO, SrO, BaO. *Materials Research Bulletin*, **6**, 413–424.

163. Ubic, R. and Reaney, I.M. (2002) Structure and dielectric properties of lead Pyrochlores. *Journal of American Ceramic Society*. **85**, 2472–7248.
164. Bernotat-Wulf, H. and Hoffmann, W. (1982) Die Kristallstrukturen der Bleiniobate vom Pyrochlor-Typ. *Zeit Fur Kristallographia*, **158**, 101–117.
165. Wakiya, N., Saiki, A., Ishizawa, N., *et al.* (1993) Crystal growth, crystal structure and chemical composition of a pyrochlore type compound in lead–magnesium–niobium–oxygen system. *Materials Research Bulletin*, **28**, 137–143.
166. Leroux, Ch., Tatarenko, H., and Nihoul, G. (1996) High-resolution electron microscopy and modelling of homologous series in nonstoichiometric lead–niobium oxides. *Physical Review B: Condensed Matter*, **53** (18), 11993–12005.
167. Aurivillius, B. (1949) Mixed bismuth oxides with layer lattices. *Arkiv for Kemi*, **59**, 499–512.
168. Wakiya, N., Kim, B.H., Shinozaki, K., and Mizutani, N. (1994) Composition range of cubic pyrochlore type compound in leadmagnesium–niobium–oxygen system. *Journal of Ceramic Society Japan*, **102**, 612–615.
169. Subramanian, M.A., Aravamudan, G., and Subba Rao, G.V. (1983) Oxide pyrochlores – A review. *Progress in Solid State Chemistry*, **15**, 55–144.
170. Leroux, Ch., Badeche, T., Nihoul, G., *et al.* (1999) A homologous series $Pb_{2n+1}Nb_{2n-1}O_{7n-1}$ studied by electron microscopy. *European Physics Journal:Applied Physics*, **7**, 33–40.
171. Brusset, H. Mahe, R., and Aung Kyi, U. (1972) Charactérization et comparison structurales de niobates de type pyrochlore. *C.R. Academy Science C.*, **C275**, 327–330.
172. Bernotat-Wulf, H. and Hoffmann, W. (1980) Ein neuartiges Bauprinzip in den Kristallstrukturen der Bleiniobate vom Pyrochlor-Typ. *Naturwissenschaften*, **67**, 141–142.
173. Li, C.C., Chiu, C.C. and Desu, S.B. (1991) Formation of lead niobates in molten salt systems. *Journal of American Ceramic Society*, **74**, 42–47.
174. Saine, M.C., Gasperin, M., and Brusset, H. (1981) Étude cristallochimique de cinq phases de niobates de plomb dérivant de la structure pyrochlore. *Review. Chimica Minineralogy*, **18**, 587–592.
175. Goodman, G. (1953) Ferroelectric properties of lead metaniobate. *Journal of American Ceramic Society*, **36**, 368–372.
176. Shirane, G. and Pepinsky, R. (1953) Dielectric properties and phase transitions of $Cd_2Nb_2O_7$ and $Pb_2Nb_2O_7$. *Physical Review*, **92**, 504.
177. Hulm, J.K. (1953) Low-temperature dielectric properties of cadmium and lead niobates. *Physical Review*, **92**, 504–505.
178. Siegwarth, J.D., Lawless, W.N., and Morrow, A.J. (1976) Dielectric and thermal properties of $Pb_2Nb_2O_7$ at low temperature. *Journal of Applied Physics*, **47**, 3789–3791.
179. Shrout, T.R. and Swartz, S.L. (1983) Dielectric properties of pyrochlore lead magnesium niobate. *Materials Research Bulletin*, **18**, 663–667.
180. Mergen, A. and Lee, W.E. (1997) Fabrication, characterisation and formation mechanism of $Pb_{1.83}Mg_{0.29}Nb_{1.71}O_{6.39}$ pyrochlore. *Journal of European Ceramic Society*, **17**, 1033–1047.
181. Sekiya, T., Tsuzuki, A., Kawakami, S., and Torii, Y. (1989) Preparation and properties of rapidly quenched films in the $PbO–Nb_2O_5$ system. *Materials Research Bulletin*, **24**, 63–69.
182. Vandenborre, M.T., Chubb, M., Mahé, R., and Brusset, H. (1977) Etude structurale de composes $3PbO–B_2O_5$ (B = Nb, Ta) de type pyrochlore. *C.R. Hebd. Seances Acad. Sci.*, *Serie C*, **284**, 179–182.
183. Ubic, R. and Reaney, I.M. (1999) Crystal structure of lead pyroniobate. *Institute of Physics Conference Series*, **161**, 157–160.
184. Ubic, R. and Reaney, I.M. (2001) Electron microscopy of lead pyroniobate. *Journal of European Ceramic Society*, **21**, 2123–2126.
185. Ubic, R. and Reaney, I.M. (2001) Microwave properties of doped lead pyroniobate. *Journal of European Ceramic Society*, **21**, 2659–2662.
186. Jawahar. I.N., Sebastian, M.T., George, J., *et al.* (1998) The $A_5B_4O_{15}$ (A = Ba, Sr, Ca, Mg, Zn; B = Nb, Ta) microwave ceramic dielectric resonators. *Bulletin of Electrochemistry*, **14**, 364–365.
187. Krause, H.B. and Gibbon, D.L. (1971) Ordering of Mg and Nb in the octahedral positions of the "cubic" perovskite structure of $Pb_3MgNb_2O_9$. *Zeit Fur Kristallogafiyar*, **134**, 44–53.

188. Pfoertsch, R. (1981) *Joint Committee on Powder Diffraction Standards*, card #33-0769.
189. Chen, J. and Harmer, M.P. (1990) Microstructure and dielectric properties of lead magnesium niobate–pyrochlore diphasic mixtures. *Journal of American Ceramic Society*, **73**, 68–73.
190. Adrianova, I.I., Berezhnoi, A.A., Nefedova, E.V., *et al*. (1974) electrooptical effect in lead magnesium niobate crystals of pyrochlore structure. *Optical Spectroscopy*, **36**, 547–548.
191. Cava, R.J., Peck, W.F., Jr, and Krajewski, J.J. (1995) Pyrochlore based oxides with high dielectric constant and low temperature coefficient. *Journal of Applied Physics*, **78**, 7231–7233.
192. Mergen, A., Reaney, I.M., and Lee, W.E. (1997) Microstructures of pyrochlore–perovskite mixtures in PbO–MgO–Nb_2O_5 system. *British Ceramic Transactions*, **96**, 41–49.
193. Shannon, R.D. (1993) Dielectric polarizabilities of ions in oxides and fluorides. *Journal of Applied Physics*, **73**, 348–366.
194. Cava, R.J., Krajewski, J.J., and Roth, R.S. (1998) Low temperature coefficient bulk dielectrics in the $Ca_2Nb_2O_7$–$Ca_2Ta_2O_7$ system. *Materials Research Bulletin*, **33**, 527–532.
195. Kato, J., Kagata, H., and Nishimoto, K. (1991) Dielectric properties of lead–alkaline earth zirconate at microwave frequencies. *Japanese Journal of Applied Physics*, **30**, 2343–2346.
196. Kato, J., Kagata, H., and Nishimoto, K. (1992) Dielectric properties of (Pb, Ca)(Me, Nb)O_3 at microwave frequency. *Japanese Journal of Applied Physics*, **31**, 3144–3147.
197. Kagata, H., Kato, J., and Nishimoto, K. (1992) Rap. Technical Meeting. *Dielectric and electrical insulation*. IEE Japan, Tsukuba. DEI-92–32 (in Japanese).
198. Kagata, H., Kato, J., Nishimoto, K., and Inoue, T. (1993) Dielectric properties of Pb based perovskite substituted by Ti for B site at microwave frequencies. *Japanese Journal of Applied Physics*, **32**, 4332–4334.
199. Kim, E.S., Jeon, J.S., and Yoon, K.H. (2003) Effect of sintering method on the microwave dielectric properties of $(Pb_{0.45}Ca_{0.55})(Fe_{0.5}Nb_{0.5})O_3$ ceramics. *Journal of European Ceramic Society*, **23**, 2583–2587.
200. Kim, E.S., Park, H.S., and Yoon, K.H. (2003) Porosity dependence of microwave dielectric properties of complex perovskite $(Pb_{0.5}Ca_{0.5})$ $(Fe_{0.5}Ta_{0.5})O_3$ ceramics. *Materials Chemistry and Physics*, **79**, 213–217.
201. Yoon, K.H., Park, H.S., Cho, J.Y., and Kim, E.S. (2003) Microwave dielectric properties of $(Pb_{0.4}Ca_{0.6})(Fe_{0.5}Ta_{0.5})O_3$ ceramics by mechanochemical processing. *Journal of European Ceramic Society*, **23**, 2579–2582.
202. Yang, Q., Kim, E.S., Xu, J., and Meng, Z. (2004) Effect of La^{3+} and Nd^{3+} on the microwave dielectric properties of $(Pb_{0.5}Ca_{0.5})(Fe_{0.5}Nb_{0.5})O_3$ ceramics. *Materials Science and Engineering B*, **99**, 259–261.
203. Yang, O.H., Kim, E.S., and Xu, J. (2004) Effect of Nd^{3+} on the microwave dielectric properties of $(Pb_{0.5}Ca_{0.5})(Fe_{0.5}Nb_{0.5})O_3$ ceramics. *Materials Science and Engineering B*, **113**, 224–227.
204. Yang, Q., Kim, E.S., Xu, J., and Meng, Z. (2003) Microwave dielectric properties of (Pb, Ca, La)(Fe, Nb)O_{3+d} ceramics substituted by Ti in B site. *Materials Science and Engineering B*, **99**, 332–335.
205. Kucheiko, S., Choi, J.W., Kim, H.-J., *et al.* (1997) Microwave characteristics of (Pb, Ca)(Fe, Nb, Sn)O_3 dielectric materials. *Journal of American Ceramic Society*, **80**, 2937–2940.
206. Choi, J.W., Ha, J.-Y., Kang, C.Y., *et al.* (2000) Microwave dielectric properties of (Pb, Ca)(Mg, Nb, Sn)O_3 ceramics. *Japanese Journal of Applied Physics*, **39**, 5923–5926.
207. Yang, Q.H., Kim, E.S., Kim,Y.J., and Kim, P.K. (2003) Effect of PbO–B_2O_3–V_2O_5 glass on the microwave dielectric properties of (Pb, Ca, La) (Fe, Nb)O_3 ceramics. *Materials Chemistry and Physics*, **79**, 239–242.
208. Ha, J.-Y., Choi, J.W., Kim, H.-J., *et al.* (2003) The effect of sintered aid CuO–Bi_2O_3 on the microwave dielectric properties of $(Pb_{0.45}Ca_{0.55})$ $[(Fe_{0.5}Nb_{0.5})_{0.9}$ $Sn_{0.1}]O_3$ ceramics. *Materials Chemistry and Physics*, **79**, 261–265.
209. Zhe, H.M., Xiang, Z.D., Huang, G.H., *et al.* (2005) Influence of Bi_2O_3 and MnO_2 doping on the microwave properties of [(Pb, Ca, La)][Fe, Nb]O_3 dielectric ceramics. *Materials Science and Engineering B*, **117**, 199–204.
210. Xiang, Z.D., Zhe, H.M., Lin, J.S., and Jing, H. (2004) Microwave properties of CeO_2 modified (Pb, Ca)(Fe, Nb)O_3 dielectric ceramics. *Materials Letters*, **58**, 2684–2687.

211. Hu, M., Zhou, D., Zhang, D., *et al*. (2003) Microwave dielectric properties of (Pb,Ca)(Fe,Nb,Zr)O_3 ceramics. *Materials Science and Engineering B*, **99**, 403–407.
212. Liu, C.-L. and Wu, J.-B. (2001) Effects of calcium substitutions on the structure and microwave dielectric characteristics of $[(Pb_{1-x}Ca_x)_{1/2}La_{1/2}](Mg_{1/2}Nb_{1/2})O_3$ ceramics. *Journal of American Ceramic Society*, **84**, 1291–1295.
213. Yang, Q.H., Kim, E.S., and Xu, J. (2004) (Effect of Nd^{3+} on the microwave dielectric properties of $(Pb_{0.5}Ca_{0.5})(Fe_{0.5}Nb_{0.5})O_3$ ceramics. *Materials Science and Engineering B*, **113**, 224–227.
214. Yoon, K.H., Kim, E.S. and Jeon, J.S. (2003) Understanding the microwave dielectric properties of $(Pb_{0.45}Ca_{0.55})[(Fe_{0.5}(Nb_{1-x}Ta_x)_{0.5}]O_3$ ceramics. *Journal of European Ceramic Society*, **23**, 2391–2396.
215. Hu, X. and Chen, X.M. (2004) Microstructure and dielectric properties of $Ca(Fe_{1/2}Nb_{1/2})O_3$ modified by $PbZrO_3$ ceramics. *Japanese Journal of Applied Physics*, **43**, 215–218.
216. Cho, Y.S., Yoon, K.H., Lee, B.D., *et al.* (2004) Understanding microwave dielectric properties of Pb based perovskite ceramics via bond valence. *Ceramic International*, **30**, 2247–2250.
217. Nakano, M., Suzuki, K., Miura, T., and Kobayashi, M. (1993) Low temperature fireable dielectric material $Pb(Fe_{1/2}W_{1/2})O_3$–$(PbCa)(Fe_{1/2}Nb_{1/2})O_3$ for microwave use. *Japanese Journal of Applied Physics*, **32**, 4314–4318.
218. Chen, J., Chen, H.M. and Harmer, M.P. (1989) Ordering and dielectric properties of undoped and La/Na doped $(Pb(Mg1/2Nb2/3)O_3$ ceramics. *Journal of American Ceramic Society*, **72**, 593–598.
219. Kim, N., Huebner, W., Jang, S.J., and Shrout, T.R. (1989) Dielectric and piezoelectric properties of lanthanum modified lead magnesium niobate and lead titanate ceramics. *Ferroelectrics*, **93**, 341–349.
220. de Nathan, N., Hausson, E., Gaucher, P., and Morel, A. (1990) Modification of the B site order of $Pb(Mg_{1/3}Nb_{2/3})O_3$ ceramics by thermal annealing or by La doping. *Materials Research Bulletin*, **25**, 427–434.
221. Lin, L.J. and Wu, T.B. (1990) Ordering behaviour of lead magnesium niobate ceramics with A site substitution. *Journal of American Ceramic Society*, **73**, 1253–1254.
222. Lin, L.J. (1991) Structure and dielectric properties of $Pb(Mg_{1/3}Nb_{2/3})O_3$–$La(Mg_{2/3}Nb_{1/3})O_3$–$PbTiO_3$. PhD Thesis, National Hua University, Taiwan.
223. Nakano, M., Suzuki, K., Miura, T., and Kobayashi, M. (1993) Low temperature fireable dielectric material $Pb(Fe_{2/3}W_{1/3})O_3$–$(PbCa)(Fe_{1/2}Nb_{1/2})O_3$ for microwave use. *Japanese Journal of Applied Physics*, **32**, 4314–4318.
224. Kato, J., Kagata, H., and Nishimoto, K. (1992) Dielectric properties of (Pb, Ca) (Me, Nb)O_3 at microwave frequencies. *Japanese Journal of Applied Physics*, **31**, 3144–3147.
225. Kucheiko, S., Choi, J.W., Kim, H.J., *et al.* (1997) Microwave characteristics of (Pb, Ca) (Fe, Nb, Sn)O_3 dielectric materials. *Journal of American Ceramic Society*, **80**, 2937–2940.
226. Ha, J.-Y., Choi, J.-W., Kim, H.-J., Yoon, S.-J., and Yoon, K.H. (2003) The effect of sintering and CuO–Bi_2O_3 on microwave dielectric properties of $(Pb_{0.45}Ca_{0.55})$ $[(Fe_{0.5}Nb_{0.5})_{0.9}Sn_{0.1}]O_3$ ceramics. *Materials Chemistry and Physics*, **79**, 261–265.
227. Yang, Q.H., Kim, E.S., Kim, Y.J. and Kim, P. K. (2003) Effect of PbO–B_2O_3–V_2O_5 glass on the microwave dielectric properties of (Pb, Ca, La)(Fe, Nb)O_3 ceramics. *Materials Chemistry and Physics*, **79**, 236–238.
228. Wei, C -H. and Jean, J.-H. (2003) Low fire processing $(Ca_{1-x}$ $Nd_{2x/3})TiO_3$ microwave ceramics. *Journal of American Ceramic Society*, **86**, 93–98.
229. Zhe, H.M., Xiang, Z.D., Shuang, G.H., *et al.* (2005) Influence of Bi_2O_3 and MnO_2 doping on microwave properties of [(Pb, Ca)La] (Fe, Nb)O_3 dielectric ceramics. *Materials Science and Engineering B*, **117**, 199–204.
230. Valant, M. and Suvorov, D. (1999) New high permittivity $AgNb_{1-x}Ta_xO_3$ microwave ceramics. Part II: Dielectric characteristics. *Journal of American Ceramic Society*, **82**, 88–93.
231. Petzel, J., Kamba, S., Buixaders, E., *et al*. (1999) Infrared and microwave dielectric response of disordered and antiferroelectric Ag(Ta,Nb)O_3 system. *Ferroelectrics*, **223**, 235–246.
232. Kim, H.T., Shrout, T., Rindall, C., and Lanagan, M. (2002) Low temperature sintering and dielectric properties of Ag(Nb,Ta)O_3 composite ceramics. *Journal of American Ceramic Society*, **85**, 2738–2744.

233. Valant, M. and Suvorov, D. (1998) A new high permittivity $AgNb_{1-x}Ta_xO_3$ microwave ceramics. Part-1. Crystal structures and phase composition relations. *Journal of European Ceramic Society*, **82**, 81–87.
234. Valant, M., Axelsson, A.-K. and Alford, N. (2007) Review of $Ag(Nb,Ta)O_3$ as a functional material. *Journal of European Ceramic Society*, **27**, 2549–2560.
235. Telli, M.B. (2005) Chemical solution deposition of silver tantalate niobate $Ag(Ta_xNb_{1-x})O_3$ thin films. Doctoral Thesis, Pennsylvannia State University, USA.
236. Xiao, M., Wu, X.M., and Song, K.X. (2005) $Ag_{1-x}Na_x(Nb_{1-y}Ta_y)O_3$ dielectric ceramic prepared through citrate precursor method. *Key Engineering Materials*, **280–283**, 15–17.
237. Kim, H.T., Shrout, T., Rindall, C., and Lanagan, M. (2002) Low temperature sintering and dielectric properties of $Ag(Nb.Ta)O_3$ composite ceramics. *Journal of American Ceramic Society*, **85**, 2738–2744.
238. Li, L., Wang, D., and Wu, X. (2006) Temperature stable and high *k* dielectric ceramics based on $Ag(Nb_{1-x}Ta_x)O_3$. *Journal of European Ceramic Society*, **26**, 1991–1993.
239. Guo, X., Xiao, M., Ding, N., and Zhang, Z. (2006) The effect of Sb_2O_5 additions on the dielectric properties of $Ag(Nb_{0.8}Nb_{0.2})O_3$ ceramics. *Materials Letters*, **60**, 3651–3654.
240. Valant, M., Suvorov, D., Hoffmann, C., and Sommaria, H. (2001) $Ag(Nb, Ta)O_3$ based ceramics with suppressed temperature dependence of permittivity. *Journal of European Ceramic Society*, **21**, 2647–2651.
241. Valant, M., Suvorov, D., Hoffmann, C., and Sommaria, H. (2002) Method for producing a ceramic silver niobium tantalate body. US Patent 6,843,956, German Patent 10042349.
242. Hoffmann, C., Sommaria, H., Suvorov, D., and Valant, M. (2005) Metalized ceramics. US Patent 6,956,001.
243. Porokhonsky, V., Bovtun, V., Kamba, S., *et al.* (2000) Microwave dielectric properties of the $Ag_{1-x}Li_xNbO_3$ ($x = 0$–0.06) ceramics. *Ferroelectrics*, **238**, 134–138.
244. Sakabe, Y., Ogiso, Y., and Wada, N. (2001) Ferroelectric properties of $(Ag, Li)(Nb, Ta)O_3$ ceramics. *Japanese Journal of Applied Physics*, **40**, 5675–5678.
245. Kanaria, A. (2001) Dielectric properties of $Ag_{1-x}A_xNbO_3$ [A = K, Na, Li] and $AgNb_{1-x}Ta_xO_3$ solid solutions in the vicinity of diffuse phase transitions. *Journal of Physics D*, **34**, 1447–1455.
246. Kanaria, A. and Miga, S. (2001) Preparation and dielectric properties of $Ag_{1-x}Li_xNbO_3$ (ALN) solid solutions ceramics. *Materials Science and Engineering B*, **86**, 128–133.
247. Takada, T., Takahashi, Y., Wada, N., and Sakabe, Y. (2003) Effects of substitution of Na, K ions for Ag ion in $(Ag, Li)NbO_3$ ceramics. *Japanese Journal of Applied Physics*, **42**, 6023–6026.
248. Zimmermann, F., Menesklou, W., and Ivers-Tiffee, E. (2004) Investigation of $Ag(Ta, Nb)O_3$ as tuneable microwave dielectrics. *Journal of European Ceramic Society*, **24**, 1811–1814.
249. Zimmermann, F., Menesklou, W., and Ivers-Tiffee, E. (2002) Electrical properties of silver tantaliteniobate thick films. *Integated Ferroelectrics*, **50**, 181–188.
250. Koh, J.H. and Grishin, A. (2001) Electrically tuneable $Ag(Ta,Nb)O_3$ thin film structures on oxide substrates. *Integrated Ferroelectrics*, **39**, 1281–1288.
251. Koh, J.H. and Grishin, A. (2001) $Ag(Ta, Nb)O_3$ thin film low loss variable interdigital capacitors. *Applied Physics Letters*, **79**, 2234–2236.
252. You, H.W. and Koh, J.-H. (2007) $Ag(Ta,Nb)O_3$ thin film interdigital capacitors for microwave applications. *Microelectronics Journal*, **38**, 222–226.
253. Kato, H., Kobayashi, H., and Kudo, A. (2002) Role of Ag^+ in the band structures and photocatalytic properties of $AgMO_3$ (M = Ta, Nb) with the persovskite structure. *Journal of Physical Chemistry B*, **106**, 12441.
254. Kudo, A. (2006) Development of photocatalyst materials for water splitting. *International Journal of Hydrogen Energy*, **31**, 197–202.
255. Francombe, M.H. and Lewis, B. (1958) Structural and electrical properties of silver niobate and silver tantalite. *Acta Crystallographica*, **11**, 175–178.
256. Kanaria, A. (1998) An additional phase transition in silver niobate. *Ferroelectrics*, **205**, 19–28.
257. Lukaszewski, M., Pawelczyk, M., and Kanaria, A. (1983) On the phase transition in silver niobate $AgNbO_3$. *Phase Transitions*, **3**, 247–258.
258. Pawelczyk, M. (199) Phase transitions in $AgTa_xNb_{1-x}O_3$ solid solutions. *Phase Transitions*, **8**, 273–292.

259. Kugel, G.E., Fontana, M.D., Hafid, M., *et al.* (1987) A Raman study of silver tantalite ($AgTaO_3$) and its structural phase transition sequence. *Journal of Physics C. Solid State Physics*, **20**, 1217–1230.
260. Ratuszna, A., Pawluk, J., and Kanaria, A. (2003) Temperature evolution of the crystal structure of $AgNbO_3$. *Phase Transitions*, **76**, 611–620.
261. Sciau, P., Kanaria, A., Dkhil, B., *et al.* (2004) Structural investigation of $AgNbO_3$ phase using X-ray and neutron diffraction. *Journal of Physics Condensed Matter*, **16**, 2795–2810.
262. Duguey, S., Leburgeois, R., Grattepain, C., *et al.* (2007) Study of copper substitution in $Ag(Nb_xTa_{1-x})O_3$. *Journal of European Ceramic Society*, **27**, 1171–1175.
263. Framcombe, M.H. and Lewis, B. (1958) Structural and electrical properties of silver niobate and silver tantalite. *Acta Crystallographica*, **11**, 175.
264. Valant, M., Suvorov, D., and Meden, A. (1998) New high permittivity $AgNb_{1-x}Ta_xO_3$ microwave ceramics. Part-1. Crystal structures and phase-decomposition relations. *Journal of American Ceramic Society*, **82**, 81–87.
265. Valant, M., Suvorov, D., and Meden, A. (1999) New high permittivity $AgNb_{1-x}Ta_xO_3$ microwave ceramics. Part-2. Dielectric characteristics. *Journal of American Ceramic Society*, **82**, 88–93.
266. Valant, M., Suvorov, D., Hoffmann, C., and Sommariva, H. (2001) $Ag(NbTa)O_3$ based ceramics with suppressed temperature dependence of permittivity. *Journal of European Ceramic Society*, **21**, 2647–2651.
267. Sakabe, Y., Takeda, T., Ogio, Y., and Wada, N. (2001) Dielectric and ferroelectric properties of (Ag, Li)(Nb, Ta)O_3 ceramics, in *Proceedings of 10th US–Japanese Seminar on Dielectric and Piezoelectric Ceramics*, September 26–29, 2011, Providence, RI, pp. 63–66.
268. Kim, H.T., Shrout, T.R., Rindall, C., and Lanagan, M. (2002) Low temperature sintering and dielectric properties of Ag(Nb, Ta)O_3 composite ceramics. *Journal of American Ceramic Society*, **85**, 2738–2744.
269. Guo, X., Zhu, N., Xiao, M., and Wu, X. (2007) Structural and dielectric properties of $Ag(Nb_{0.8}–Ta_{0.2})_{1-x}Sb_xO_3$ ($x = 0.08$) ceramics. *Journal of American Ceramic Society*, **90**, 2467–2471.

5

Millimeter-Wave Materials

Hitoshi Ohsato
Nagoya Industrial Science Research Institute and Nagoya Institute of Technology, Nagoya, Japan
Microelectronics Research Unit, University of Oulu, Oulu, Finland

5.1 Introduction: New Frontiers of Millimeter-Wave Dielectrics

In 2013, *Nikkei Electronics* (NE) magazine [1] reported that millimeter-wave wireless communications has begun to spread to public welfare systems in Japan. Millimeter-wave communications have reached runways to takeoff after many twists and turns. Figure 5.1 shows the frequency assignments made by the Ministry of Internal Affairs and Communications (MIC) for millimeter waves from 30 GHz (1 cm) to 300 GHz (1 mm) [2]. The wireless gigabite (WiGig) for millimeter-wave wireless communications uses 60 (57 to 66) GHz and vehicle radar use 60 (60–61) GHz, 76 (76–77) GHz, and 79 (77–81) GHz.

The standard millimeter-wave communication in the 60 GHz zone converges to "IEE802.11ad.," because of its usage in a public welfare apparatus as WiGig. This has the highest data communication speed of 7 G bits per second at a short communication distance of approximately 10 m with advanced properties such as security and power control. Non-compressed millimeter-wave wireless communications with a high data transfer rate [3] have been developed to support the individual system interface, which connects PC peripheral devices and a data bus for high definition television (HDTV), monitors, and projectors, as shown in Figure 5.2a. Furthermore, millimeter-wave communication can be applied to radar for pre-crash safety systems [4], as shown in Figure 5.2b. Although the 60 GHz zone was assigned in Japan in 1995, the 76 GHz zone is used now, which is also the assigned one internationally. The 79 GHz zone is designed for next generation millimeter-wave radar. The 79 GHz radar is better than the 76 GHz radar in terms of distance, speed, and angle resolutions. However, the detection distance of 76 GHz is better than that of

Microwave Materials and Applications, First Edition.
Edited by Mailadil T. Sebastian, Rick Ubic and Heli Jantunen.
© 2017 John Wiley & Sons, Ltd. Published 2017 by John Wiley & Sons, Ltd.

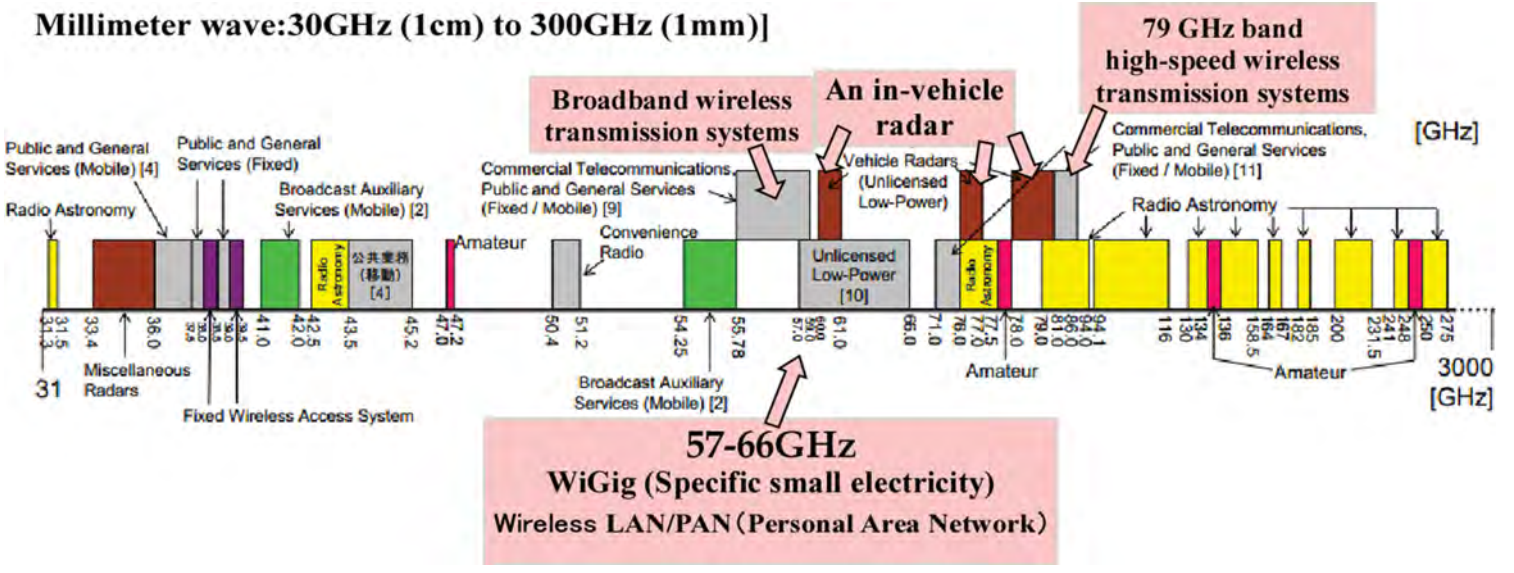

Figure 5.1 *Millimeter-wave layout list of 30 GHz (1 cm) to 300 GHz (1 mm) of Ministry of Public Management, Home Affairs, Posts and Telecommunications in Japan [2].*

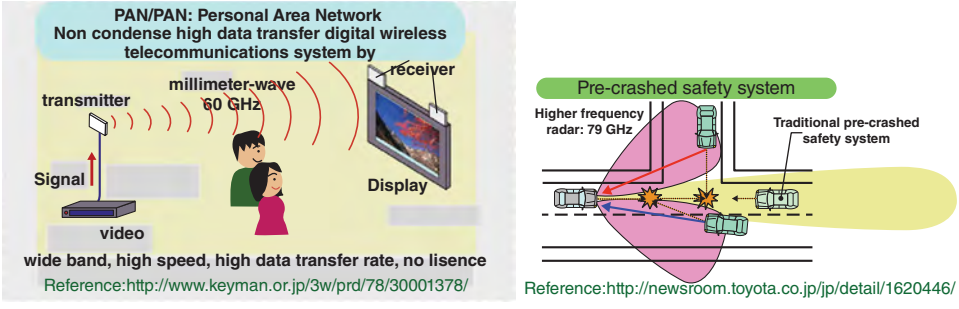

(a) (b)

Figure 5.2 *Usage of millimeter-wave: (a) Non-condense high data transfer digital wireless telecommunications system (LAN/PAN) [3]. (b) Millimeter-wave radar on the pre-crashed safety system [4]. Source: Reproduced with permission of TOYOTA News Release 2009.*

79 GHz. Hence the 76 GHz band is better for the detection of a distant car. On the other hand, the 79 GHz band is better for the detection of near people. Vehicle radar systems such as the advanced emergency braking system and autonomous emergency braking (AEB) are increasingly becoming essential internationally [5].

Table 5.1 shows the properties of ceramics and resin substrates for millimeter-wave communications. The ceramics exhibit superior properties on dielectric losses ($\tan\delta$), temperature coefficient of resonant frequency (τ_f), thermal conductivity, and linear expansion (CTE). The dielectric losses ($\tan\delta$) of ceramics are smaller than that of resin by one order

Table 5.1 *Properties of ceramics and resin-based substrate*

	Ceramics			Ceramics + resin	Resin	
Properties	A443 (Kyocera)	Willemite	Willemite–11 wt% TiO_2	AD1000 (Arlon)	MEGTRON4 (Panasonic)	FR-4
ε_r	9.6	6.6	9.39 (60 GHz)	10.7 (10 GHz)	3.8	4.3
$\tan\delta$	5×10^{-4}	6.8×10^{-5}	4.8×10^{-4}	23×10^{-4}	5×10^{-3}	$1.6\ 10^{-2}$
τ_f (ppm/K)	–60	–61	–0.69	178	–	–
T_g (K)	None	None	None	–	176	170
Thermal conductivity (W/mK)	–	–	3.3	0.81	–	0.34
$\sigma(x)$	6.9	–	–	8	12–14	11–13
$\sigma(z)$	6.9	10	10	20	35	60
Dimensional precision (μm)	15	–	–	–	50	75

T_g: glass-transition temperature, σ: linear expansion coefficient, –: not available.

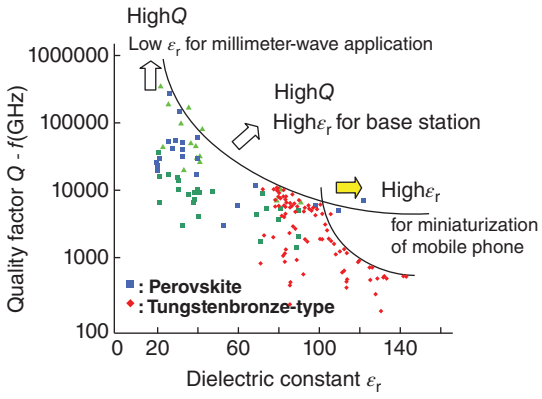

Figure 5.3 *Direction of development of microwave dielectrics designed on a figure: Qf as a function of ε_r. Source: Adapted from Ohsato et al. 2004 [9].*

of magnitude: especially, tan δ is 6.8×10^{-5} (15 GHz) for normal willemite [6,7] and 4.8×10^{-4} (60 GHz) for willemite with near zero τ_f. The τ_f is achieved near zero –0.69 ppm/K at 57.95 GHz, which is the allowable frequency for millimeter-wave radar for a vehicle [8], and for picture transmission as described in Section 5.4.2. Moreover, the thermal conductivity is also superior by three times, which is a very important property for high-density integrated devices. The linear expansion coefficient is also small by 1/6 as compared with FR-4 resin. Therefore, the use of ceramic substrates is strongly recommended for the high-quality devices in millimeter-wave communications. Moreover, mobile equipment applying low-temperature co-fired ceramics (LTCC) are integrated and reduce the size while producing high performance.

Figure 5.3 shows the three development directions of microwave dielectrics, which is presented in the variation of quality factor (Qf) as a function of the dielectric constant ε_r [9]. The Qf and ε_r are discussed in Section 5.2. The curve in Figure 5.3 shows the outline of the upper limit of Qf obtained for a given ε_r. The first direction with a high ε_r is mainly used in the miniaturization of mobile phone components. The second one, with a high Q and a high ε_r, is in demand for use in mobile phone base stations. The third direction, with a high Q and a low ε_r, is for devices working in the millimeter-wave range. This direction is the new frontiers of microwave dielectrics [5], because the utilizable frequency region is expanding towards the millimeter wave due to the shortage of conventional radio frequency (RF) regions.

Dielectrics for the microwave region [10] have been researched for a long time, with some excellent materials [11–16] developed and used for practical applications. Some of them, such as complex perovskite [14] with high quality factors are used for millimeter-wave wireless communication. Recently, millimeter applications have received much attention. The dielectrics with a high quality factor (Q), low dielectric constant (ε_r), and near-zero temperature coefficients of the resonant frequency (τ_f) are desired for usage as vehicles for millimeter-wave communication [17, 18]. Most of the useful candidate materials with low ε_r and high Qf exist in the silicates such as forsterite (Mg_2SiO_4) [19–22], willemite (Zn_2SiO_4) [23], and cordierite/indialite ($Mg_2Al_4Si_5O_{18}$) [24, 25]. The low ε_r and high Qf

is attributed to the reduced rattling in the silicate tetrahedra based on covalency, as described in Section 5.4.5 [25–28].

In this chapter, the dielectric properties for millimeter-wave materials with emphasis on silicates such as forsterite, willemite, cordierite/indialite glass ceramics and other dielectrics such as alumina, spinel, etc. are discussed.

5.2 Dielectric Properties for Millimeter Wave [29]

5.2.1 Quality Factor *Q*

Microwave dielectric materials for millimeter-wave applications are termed as millimeter-wave dielectrics [17]. The wave number increases in the millimeter-wave region, as shown in Figure 5.4a and b. Dielectric losses are generated by dielectric polarization accompanied by the electromagnetic wave. Therefore, as the wave number increases, dielectric losses also increase. The dielectric materials with low loss ($\tan\delta$), that is, high Q, are desirable for practical applications. The quality factor $Q = 1/\tan\delta$.

The presence of defects and impurities in crystals that produce polars increase losses, as shown in Figure 5.5a and b, respectively. The example of impurities present in the forsterite ceramics synthesized using high purity raw materials are given in Section 5.4.1 [17]. The presence of grain boundaries also produce polars (Figure 5.5c). Therefore the grain growth in the ceramics decreases the dielectric losses. In the case of Al_2O_3, it is found [30, 31] that the Qf values increased with grain size, as seen in Figure 5.43b. These losses, which are based on impurities and defects, are of extrinsic origin whereas intrinsic losses are based on the crystal structure such as symmetry and ordering. In the case of complex perovskite such as $Ba(Mg_{1/3}Ta_{2/3})O_3$ (BMT), $Ba(Zn_{1/3}Ta_{2/3})O_3$ (BZT), and $Ba(Zn_{1/3}Nb_{2/3})O_3$ (BZN) with order–disorder transition, high symmetry brings low loss/high Q instead of ordering [32]. The cordierite/indialite ceramics [24] is also an example of high Q materials according to high symmetry, as described at Section 5.4.3. In the case of pseudotungstenbronze solid solutions without phase transition, the compositional ordering brings low loss/high Q.

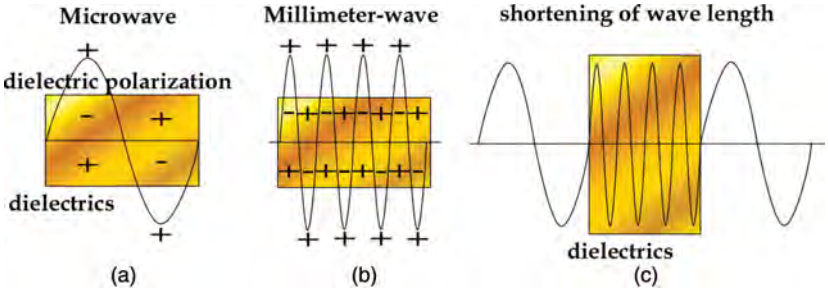

Figure 5.4 *(a) When irradiated by electromagnetic waves, the materials should resonate due to changing dielectric polarization under alternating electromagnetic fields. (b) Dielectric losses increase with an increase in frequency. (c) ε_r causes a shortening of wavelength λ in dielectrics. Source: Adapted from Ohsato [17, 32].*

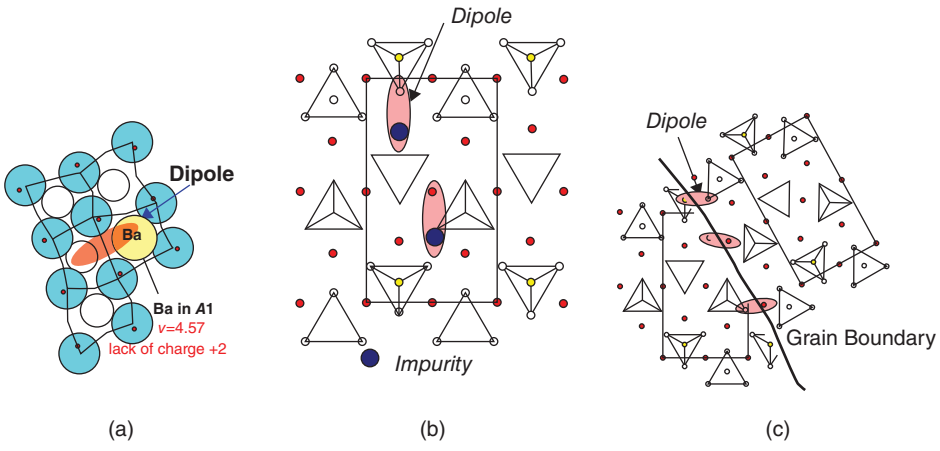

Figure 5.5 *Origin of extrinsic losses produced by (a) defects, (b) impurities), and (c) grain boundary.*

5.2.2 Dielectric Constant ε_r

The dielectric constant ε_r causes a shortening of wavelength λ in dielectrics, as shown in Figure 5.4c according to the following equation:

$$\lambda = \lambda_0/\varepsilon_r^{1/2} \tag{5.1}$$

Here, λ_0 is the wavelength in a vacuum. In the microwave region, the ε_r value is expected to be large for the miniaturization of mobile communication equipment. In the millimeter-wave region, the ε_r value is expected to be small. As the wavelength is in the millimeter order, miniaturization is not needed. There are other more important phenomena such as the time delay T_{PD} according to the following equation:

$$T_{PD} = \sqrt{\varepsilon_r}/c \tag{5.2}$$

Here, ε_r is the dielectric constant and c is the velocity of light. The time delay is desirable in order to improve the speed of the signal.

5.2.3 Temperature Coefficient of Resonant Frequency τ_f

The τ_f is required to be near 0 ppm/°C for global usage in different environmental temperatures. Millimeter-wave radar for an anticollision system is located in the extreme condition in front of the radiator, with a high temperature from the radiator and high and low temperatures from outside air in the summer time and winter time, respectively. Therefore, near zero τ_f is needed. The τ_f has a relationship with the temperature coefficient of dielectric constant τ_ε as follows:

$$\tau_f = -(\alpha + \tau_\varepsilon/2) \tag{5.3}$$

where α is the thermal expansion coefficient.

Most millimeter-wave compounds with a low ε_r have a large negative τ_f, such as alumina: –65 ppm/°C and forsterite: –70 ppm/°C. The τ_f of these millimeter-wave dielectrics was improved by two different methods. The first requires the addition of materials with the opposite sign (i.e., a positive τ_f). The addition of rutile with $\tau_f = +450$ ppm/°C can adjust the τ_f of the compound in question [19, 20, 23, 33]. The second method is to adjust the τ_f to near 0 ppm/°C by the formation of the solid–solution phases [34]. This is the preferred method because of the small degradation of *Qf*.

5.3 Candidates of Millimeter-Wave Dielectrics

The origin of ε_r was considered by differences of crystal structures, as shown in Figure 5.6 [17]. Silicates with a low ε_r are formed by the tetrahedral framework of SiO_4 (Figure 5.6a), with 45% ionic bonds and 55% covalent bonds, described later in Section 5.4.5. Covalent bonds reduce ε_r because the rattling effect of the cations in a polyhedron should reduce as a result of the high bond strength. On the other hand, titanates (Figure 5.6c), with a large ε_r such as $SrTiO_3$, are formed by a TiO_6 octahedral framework, which is almost of ionic bond and has space for ionic displacement. In the case of aluminates, although Al ions also occupy an octahedral framework, the Al ions located in the pair octahedral on the threefold axis repel each other, as shown in Figure 5.6b. The Al ions are immovable in the octahedron and produce a medium ε_r. The order of ε_r is as follows:

$$\varepsilon_{r\ \text{silicate}} < \varepsilon_{r\ \text{aluminate}} < \varepsilon_{r\ \text{titanate}}$$

Silicates with a low ε_r are good candidates for millimeter-wave dielectrics [17], and germanate and phosphate also are constructed with GeO_4 and PO_4 tetrahedron with covalent features described later in Sections 5.4.5 and 5.4.8, respectively. The important millimeter-wave dielectrics are listed in Table 5.2.

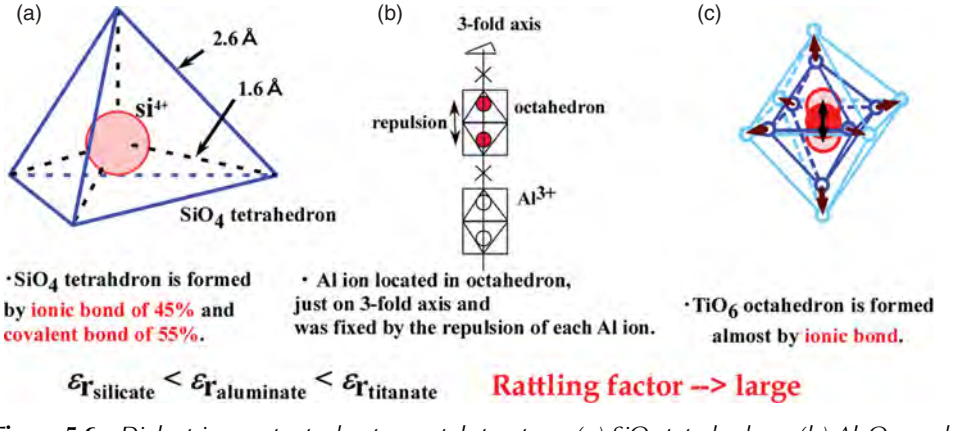

Figure 5.6 *Dielectric constants due to crystal structure: (a) SiO_4 tetrahedron, (b) Al_2O_3, and (c) TiO_6 octahedron. Source: Adapted from Ohsato 2005 [17].*

Table 5.2 *Main millimeter-wave dielectrics*

Material	ST (°C)	Crystal system	SG	ε_r	Qf (GHz)	τ_f (ppm/°C)	Reference
Mg_2SiO_4 (fosterite)	1450	Orthorhombic	*Pbnm*	6.8	270000	−67	77*
Zn_2SiO_4 (willemite)	1340	Trigonal	$R\bar{3}$	6.6	219000	−61	23
$Mg_2Al_4Si_5O_{18}$ (cordierite)	1440	Orthorhombic	*Cccm*	6.2	40000	−25	34*
Ni-doped cordierite (deform to indialite)	1390–1440	Orthorhombic/ hexagonal	*Cccm*/ *P6mcc*	6.2	99110	−30	51
Indialite (glass ceremics)	1300	Hexagonal	*P6/mcc*	4.7	210000	−27	24
$Ca_{0.99}Mg_{0.01}SiO_3$ (wollastonite)	1290/2 h	Monoclinic	$P2_1/a$	6.5	62400	−43	53*
$CaSiO_3$ + 1 wt% Al_2O_3 (wollastonite)	1250	Monoclinic	$P2_1/a$	6.7	24600		72*
α-$CaSiO_3$ (wollastonite)	1500/2 h	Monoclinic	*C2/c*	6.8	42200	−19	26
$SrSiO_3$	1540/2 h	Monoclinic	*C2/c*	6.8	13100	−66	26
$(Ca_{1-x}Sr_x)SiO_3$ ($x = 0.8$)	1490/2 h	Monoclinic	*C2/c*	6.62	66700	−40	26
$CaMgSi_2O_6$ (diopside)	1300/3 h	Monoclinic	*C2/c*	7.4	59700	−42	118*
$CaMgSi_2O_6$ (diopside)	CIP:1300	Monoclinic	*C2/c*	7.6	121380	−66	27
$MgSiO_3$ (enstatite)	1380/13 h	Orthorhombic	*Pbnm*	6.7	121200	−17	71*
Zn_2GeO_4 (Ge–willemite, olivine)	1300	Trigonal	$R\bar{3}$	6.9	102700	−32	65*
Mg_2GeO_4 (Ge–forsterite) + 3 wt% B_2O_3 (olivine)	1200/4 h	Orthorhombic	*Pnma*	6.5	91000	−28	54*
$NaAlSi_3O_8$ (albite)	1025	Triclinic	$C\bar{1}(P\bar{1})$	5.5	11200	−5	25*
$Na_{0.8}Ca_{0.2}Al_{1.2}Si_{2.8}O_8$ (plagioclase)	1100	Orthorhombic	$P\bar{1}$	5.8	17600	−7	71
$K_{0.67}Ba_{0.33}Ga_{1.33}Ge_{2.67}O_8$ (feldspar)	1020	Monoclinic	$P2_1/a$	5.9	94100	−25	72
Al_2O_3+0.5wt%TiO_2	1550/5 h	Trigonal	$R\bar{3}c$	10	453000	9	76
Al_2O_3 (corundum)	1550/5 h	Trigonal	$R\bar{3}c$	10	335000	−60	247*
Al_2O_3 (corundum)	1550	Trigonal	$R\bar{3}c$	10.1	680000	−60	18, 30
Al_2O_3 (corundum)	1400/8 h	Trigonal	$R\bar{3}c$	10	634000	−40	75
Al_2O_3 + 500 ppm TiO_2 (corundum)		Trigonal	$R\bar{3}c$	10	500000	10	74
Nano Al_2O_3 + 0.5 wt% TiO_2 (corundum)	1400	Trigonal	$R\bar{3}c$	10.8	680000	14	285
$0.9Al_2O_3$–$0.1TiO_2$ (corundum)	1300/2 h	Trigonal	$R\bar{3}c$	12.4	148000	2	77
Al_2O_3–TiO_2:MnO (corundum)	1300	Trigonal	$R\bar{3}c$	12.4	274000	0	336
$Mg_4Nb_2O_9$ (corundum)	1200/10 h	Trigonal	$P\bar{3}c1$	12.4	194000	−71	79

(*continued*)

Table 5.2 *(Continued)*

Material	ST (°C)	Crystal system	SG	ε_r	Qf (GHz)	τ_f (ppm/°C)	Reference
$Mg_4Ta_2O_9$ (corundum)	1450	Trigonal	$P\bar{3}c1$	11.5	347000	−70	80
Mg_4NbSbO_9 (corundum)	1500	Trigonal	$P\bar{3}c1$	12.5	280000	−45	338
$Mg_4(Nb_{2-x}V_x)O_9$ (x = 0.0625) (corundum)	1025	Trigonal	$P\bar{3}c1$	11.6	160250	−75	310
$Mg_4Nb_2O_{9+3}$ wt% LiF (corundum)	950/10 h	Trigonal	$P\bar{3}c1$	12.6	116410	−72	248
$MgAl_2O_4$ (spinel)	1650/3 h	Cubic	$Fd\bar{3}m$	8.5	105000	−63	85
$ZnAl_2O_4$ (spinel)	1375	Cubic	$Fd\bar{3}m$	8.5	56000	−79	33
$0.79ZnAl_2O_4$–$0.21Mg_2TiO_4$ (spinel)	1550	Cubic	$Fd\bar{3}m$	9.6	160800	−65	226∗
$MgGa_2O_4$ (Mg–gallium spinel)	1410	Cubic	$Fd\bar{3}m$	9.5	117000	−4	86
$ZnGa_2O_4$ (Zn–gallium spinel)	1385	Cubic	$Fd\bar{3}m$	10.4	94600	−27	87
$MgGa_2O_4$ (Mg–gallium spinel)	1560	Cubic	$Fd\bar{3}m$	9.2	298000	−63.5	89
$MgZn_2O_4$ (Zn–gallium spinel)	1550	Cubic	$Fd\bar{3}m$	9.8	220000	−64	88
$Mg_3B_2O_6$(MgO–25 mol% B_2O_3) (kotoite)	1320	Orthorhombic	$Pnmn$	7.2	310000	−60.6	95
$Zn_3B_2O_6$	925/4 h	Triclinic	$I2/c$	6.7	58500	−58	98
$LaBO_3$	1300	Orthorhombic	$Pmcn$	11.8	76900	−52	100
$LiMgPO_4$ (olivine)	950	Orthorhombic	$Pmnb$	6.6	79100	−60	58
$LiMg_{0.95}Co_{0.05}PO_4$ (olivine)	875/2 h	Orthorhombic	$Pmnb$	7	111200	−54	102
$SrCuP_2O_7$	925	Monoclinic	$P2_1/n$	7	101110	−62	104
$YbPO_4$ (xenotime)	1600	Tetragonal	$I4_1/amd$	8.2	71600	−28	133
$CePO_4$ (monazite)	1400/2 h	Monoclinic	$P2_1/n$	11.6	68300	−46	133
$Ca_{2+x}La_6(SiO_4)4(PO_4)O_2$ (x=2) (apatite)	1475/4 h	Hexagonal	$P6_3/m$	13.8	27900	−11	313
$Mg_3(VO_4)_2$	1050	Orthorhombic	$Cmca$	9.4	65500	−90	106
$Mg_2Co(VO_4)_2$	1000	Orthorhombic	$Cmca$	9.2	107500	−97	106
$MgCo_2(VO_4)_2$	900/5 h	Orthorhombic	$Cmca$	9.4	78900	−95	221∗
$Mg_3(VO_4)_2$–$0.2Ba_3(VO_4)_2$	950/5 h	Orthorhombic	$Cmca$	11	114000	−58	107
$Mg_3(VO_4)_2$–$0.5Ba_3(VO_4)_2$ + 0.0625 wt%	950/5 h	Orthorhombic	$Cmca$	13	74000	−6	107
$Ca_5Co_4(VO_4)_6$ (garnet)	875	Cubic	$Ia\bar{3}d$	10.1	95200	−63	259∗
MgO (periclase)	1490	Cubic	$Fm3m$	7.9	113600	16.4	141∗
MgO (periclase)	1490	Cubic	$Fm3m$	7.9	113600	16.4	141∗

ST: synthesis temperature, SG: space group,∗: Reference [42].

5.4 Specialized Study

In this section, silicate compounds, such as forsterite, willemite, indialite/cordierite glass ceramics, and other silicates such as wollastonite and diopside, are presented first. Although feldspar ceramics are mainly silicates, they are presented in the "substituted Ge for Si" section because feldspar ceramics with good properties are Ge-substituted for Si. As the germanates also show similar properties to those of silicates in terms of ionicity and covalency, Ge-forsterite, Ge-willemite, and feldspar-substituted Ge for Si are presented. Moreover, non-silicates with low ε_r and high Q, such as alumina including new-type corundum, spinel, borates, and phosphates are presented.

5.4.1 Forsterite

5.4.1.1 Synthesized High-Q Forsterite

Forsterite ceramics synthesized using high-purity raw materials are compared with commercially available materials in Table 5.3. The synthesized high-purity forsterite ceramics showed lower dielectric losses of $\tan\delta = 9.6 \times 10^{-5}$ measured at 23 GHz frequency than a commercial one of $\tan\delta = 8.4$ to 17×10^{-4} for 23 GHz, which are comparable with a quality factor Qf of 240 000 and approximately 10 000 GHz, respectively, as shown in Figure 5.7. The synthesized forsterite was single phase with high relative density of 96 to 98% [17, 35, 36]. Surface microstructures of a commercially available forsterite and that of a high-purity one are shown in Figure 5.8a and b, respectively. The higher dielectric losses of the commercial one was due to a very glassy phase among the grains, as seen in Figure 5.8a. On the other hand, synthesized forsterite ceramics have a fine grain boundary, which leads to low dielectric losses. In the texture of the grain boundaries, different configurations of grains are observed. The grains of a commercial one have many facets of crystal surface accompanied by a veryglassy phase in grain boundaries. The grains with facets, called euhedral (idiomorphic) in crystallography, appeared as the result of crystal

Table 5.3 *Dielectric, resistivity and thermal properties of commercial forsterite ceramics and high-purity forsterite ceramics sintered at 1360 °C for 2 hours*

Properties	Commercial	High purity
ε_r (23 GHz)	6.5 ~ 6.6	6.8
$\tan\delta$ (23 GHz)	$8.4 \sim 17 \times 10^{-4}$	0.96×10^{-4}
Volume resistivity (Ωm)		
100 °C	5.0×10^{11}	8.5×10^{12}
300 °C	7.0×10^{9}	1.8×10^{10}
500 °C	1.0×10^{9}	4.4×10^{8}
Coefficient of thermal expansion (ppm/°C)	25 ~ 700 °C 11.2	25 ~ 700 °C 9.4
Thermal conductivity (w/m °C) at room temperature	3.2	9.1

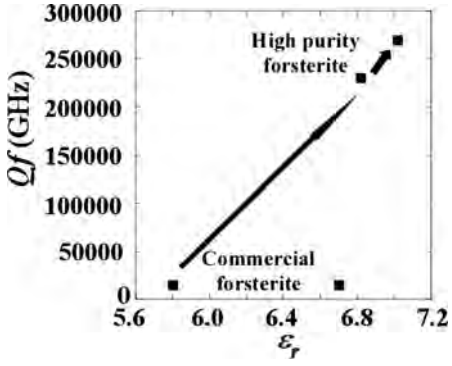

Figure 5.7 *Qf of high purity forsterite ceramics and commercial forsterite ceramics against ε_r. Dielectric losses of commercial forsterite ceramics and high Q forsterite ceramics against dielectric constants. Source: Adapted from Ohsato 2007 [35].*

growth in the liquid phase, which is introduced by impurity. The liquid phase remains as a glassy phase, as shown in Figure 5.8a. On the other hand, the high-purity forsterite ceramics have grains without facets, called anhedral (allotriomorphic), which may be due to direct contact of grains. In Table 5.3, the volume resistivity of commercial forsterite ceramics is lower than that of the high-purity one and found to depend on the glassy phase. Thermal conductivity of the high-purity one is about three times that of the commercial grade.

5.4.1.2 Adjust the Temperature Coefficient of Resonant Frequency on Forsterite

The large negative τ_f (−65 ppm/°C) of forsterite can be adjusted to near zero ppm/°C by adding rutile, which has a large positive τ_f (450 ppm/°C) [19, 20, 37]. Although pure forsterite ceramics are sintered at 1360 °C (see Table 5.3), 30 wt% rutile added to forsterite

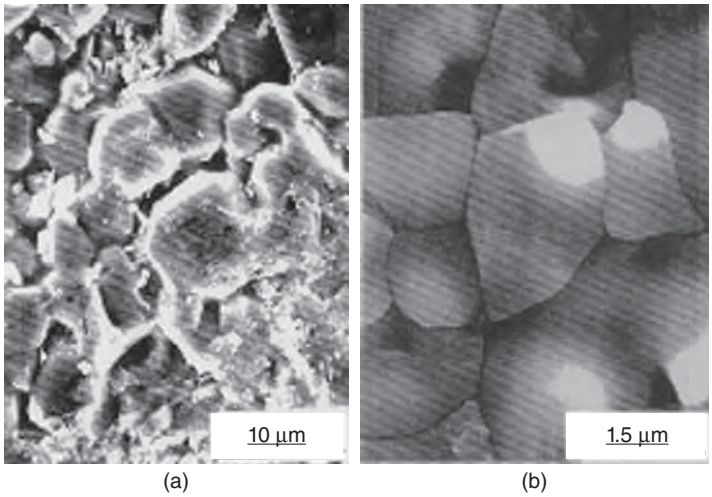

Figure 5.8 *SEM photographs of (a) commercial forsterite ceramics and (b) high purity forsterite ceramics sintered at 1360 °C. Source: Adapted from Ohsato 2007 [35].*

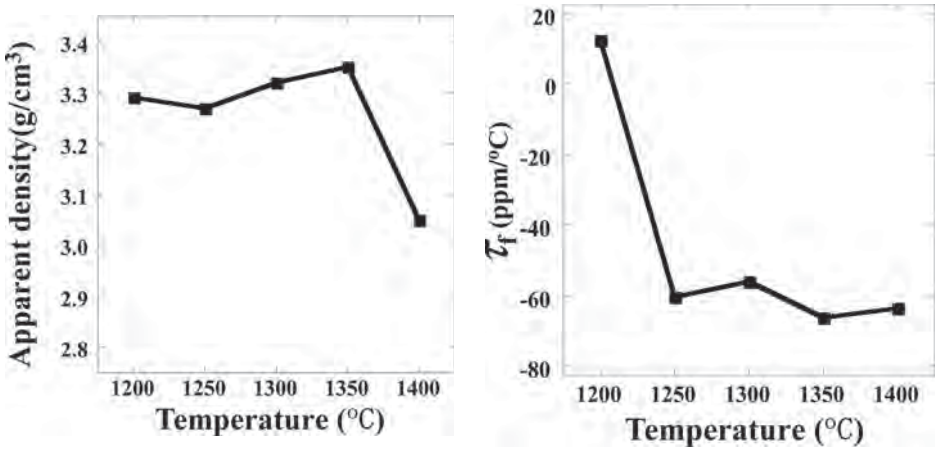

Figure 5.9 *(a) Apparent density and (b) temperature coefficient of resonant frequency of the forsterite ceramics with added 30 wt% rutile as a function of the sintering temperature. Source: Adapted from Tsunooka et al. 2004 [20].*

ceramics could be sintered at 1200 °C with high apparent density of 3.3 g/cm^3, as shown in Figure 5.9a. The added rutile acts as a sintering aid for improving the sinterability of forsterite. The τ_f of the sample sintered at 1200 °C is 12.7 ppm/°C, but the value is degraded to –60 ppm/°C suddenly on increasing the sintering temperature (Figure 5.9b). This is due to the disappearance of rutile based on the following reaction [20]:

$$Mg_2SiO_4 + 2TiO_2 \rightarrow MgTi_2O_5 + MgSiO_3 \tag{5.4}$$

As the compositions of forsterite added rutile locate in the compositional triangle Mg_2SiO_4—$MgTi_2O_5$—$MgSiO_3$ in the ternary phase diagram [39], as shown in Figure 5.10, rutile reacts with forsterite to make $MgTi_2O_5$ and enstatite as in chemical reaction (5.4).

Figure 5.11a shows τ_f and ε_r of the samples sintered at 1200 °C for 2 hours as a function of rutile content [20, 38]. The τ_f of forsterite ceramics added rutile increased linearly with the amount of rutile addition, as shown in Figure 5.11a. The τ_f changed from negative to positive values between 20 and 25 wt% addition of rutile. The τ_f showed 3.95 ppm/°C in the case of 25 wt% addition of rutile. Although ε_r values shift to a high value of 11.5 with increasing amounts of rutile (Figure 5.11b), the *Qf* values also keep a relatively high value of 80 000 HGz (Figure 5.11a). The increase of apparent density is attributed to the addition of rutile, which has a higher density (4.24 g/cm^3) than forsterite (3.22 g/cm^3). The fosterite composite with 24 wt% rutile has $\tau_f = 0$ ppm/°C, $\varepsilon_r = 11$, and $Qf = 82\,000$ GHz when sintered at 1200 °C for 2 hours. Figure 5.11c shows a backscattered SEM photograph of the forsterite with 25 wt% rutile ceramic composite sintered at 1200 °C for 2 hours. The microstructure was composed by grains of forsterite (light gray grains) and rutile crystals (white grains) and densified in the state of pore and glassy-phase free at grain boundaries. This appears to be due to the enhanced sinterability by excess rutile addition.

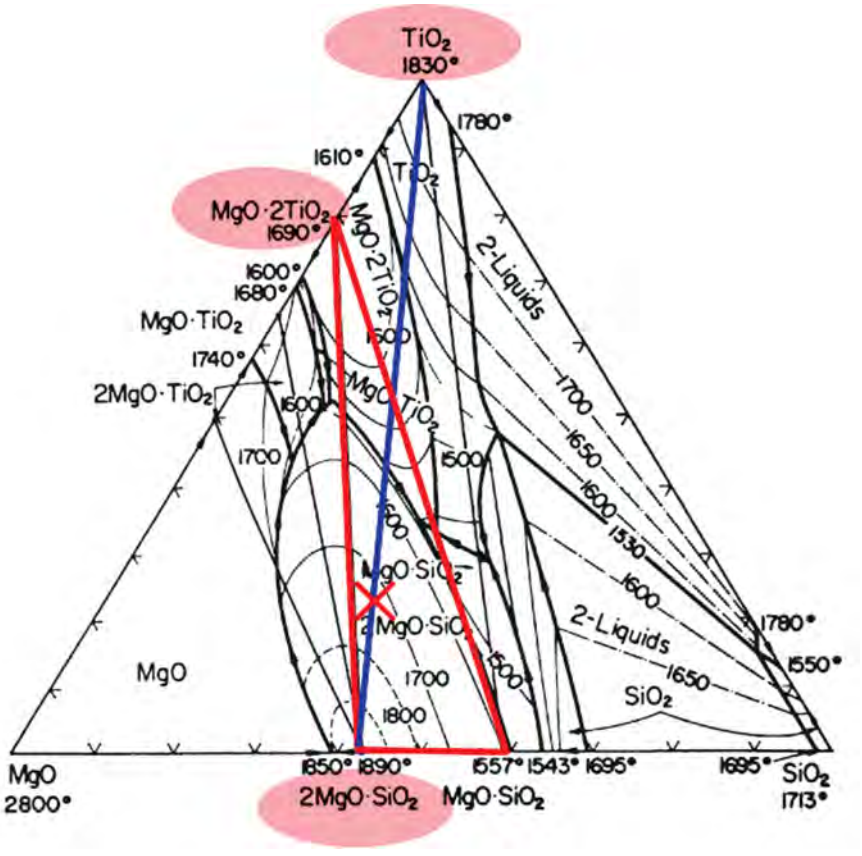

Figure 5.10 *Rutile added to forsterite located in the $2MgO{\cdot}SiO_2$—$MgO{\cdot}2TiO_2{\cdot}MgO{\cdot}SiO_2$ compositional triangle. Source: Adapted from Tsunooka et al. 2013 [38].*

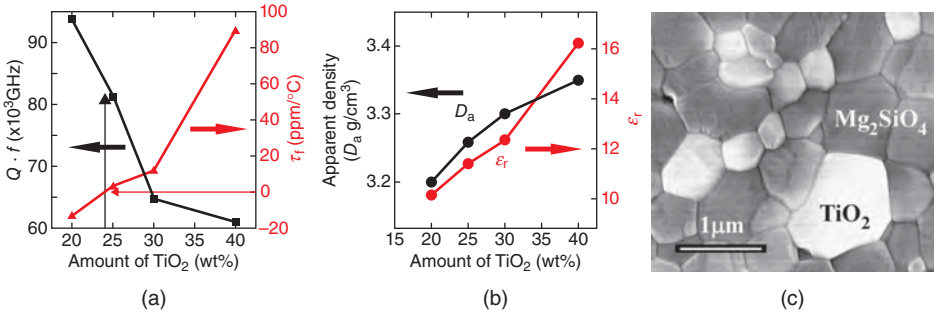

Figure 5.11 *Qf and τ_f (a) and Da and ε_r (b) of rutile added forsterite as a function of amount of TiO_2. (c) A backscattered SEM photograph of the forsterite ceramics composite with 25 wt% rutile sintered at 1,200 °C for 2 hours. Source: Adapted from Tsunooka et al. [20, 38].*

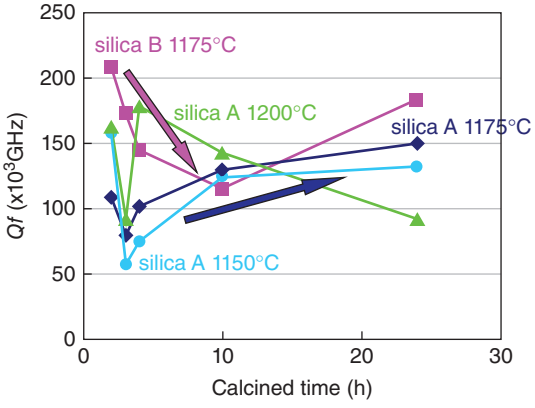

Figure 5.12 *Qf values of sintered at 1400 °C for 2 hours as a function of calcined hours. Source: Ando et al. [21, 22].*

5.4.1.3 Diffusion of Si and Mg Ions on the Formation of Forsterite

Generally, synthesis of silicates is very difficult and needs good knowledge of the raw materials with phase, shape and size, calcination and sintering conditions, pressing conditions, etc. The effects of diffusion of different elements on the formation of forsterite and the properties have been verified [21, 22]. Figure 5.12 shows the variation of *Qf* of forsterite sintered at 1400 °C for 2 hours as a function of calcination time (2–24 hours). The specimens are calcined at 1150, 1175, and 1200 °C for silica A with a crystalline form and large grain size of 0.82 μm for SiO_2 raw material and 1175 °C for silica B with an amorphous form and small size of 0.25 μm. In the case of silica A, the *Qf* values initially decrease for 2 to 4 hours calcined samples and then increase for calcination for 4 to 24 hours. Figure 5.13a and b shows XRPD patterns of specimens: silica A and silica B, respectively, which reveal two kinds of diffraction patterns for calcined and sintered specimens with different calcination duration. The XRPD patterns for calcined powder are indicated by "cal *n*h, for $n = 2, 3, 4, 10, 24$." Sintered ceramic using calcined powder "cal *n*h" is denoted by "sin *n*h." All ceramics are sintered at 1400 °C for 2 hours. All the crystalline XRPD patterns are mainly composed of forsterite. An enstatite ($MgSiO_3$) observed for silica A specimens and its content decreased with calcination duration and almost disappeared after 24 hours of calcination, resulting in a single phase forsterite, as shown in Figure 5.13a. The calcined samples show unreacted raw materials: periclase (MgO) and quartz (SiO_2). The enstatite phase was also detected in sintered specimen silica B, as shown in Figure 5.13b. However, the amount of enstatite in sintered specimens did not decrease but increased with calcination duration up to 10 hours and suddenly almost disappeared at 24 hours of calcination. The calcined samples of silica B contained only unreacted raw material of MgO as revealed by XRPD and resulted in a single phase of forsterite when the calcination duration was 24 hours. The silica may remain with MgO as an amorphous particle for up to 10 hours of calcination and cannot be detected by XRPD due to the amorphous nature. However, the amount of unreacted raw materials was reduced by means of using the amorphous silica with a spherical shape.

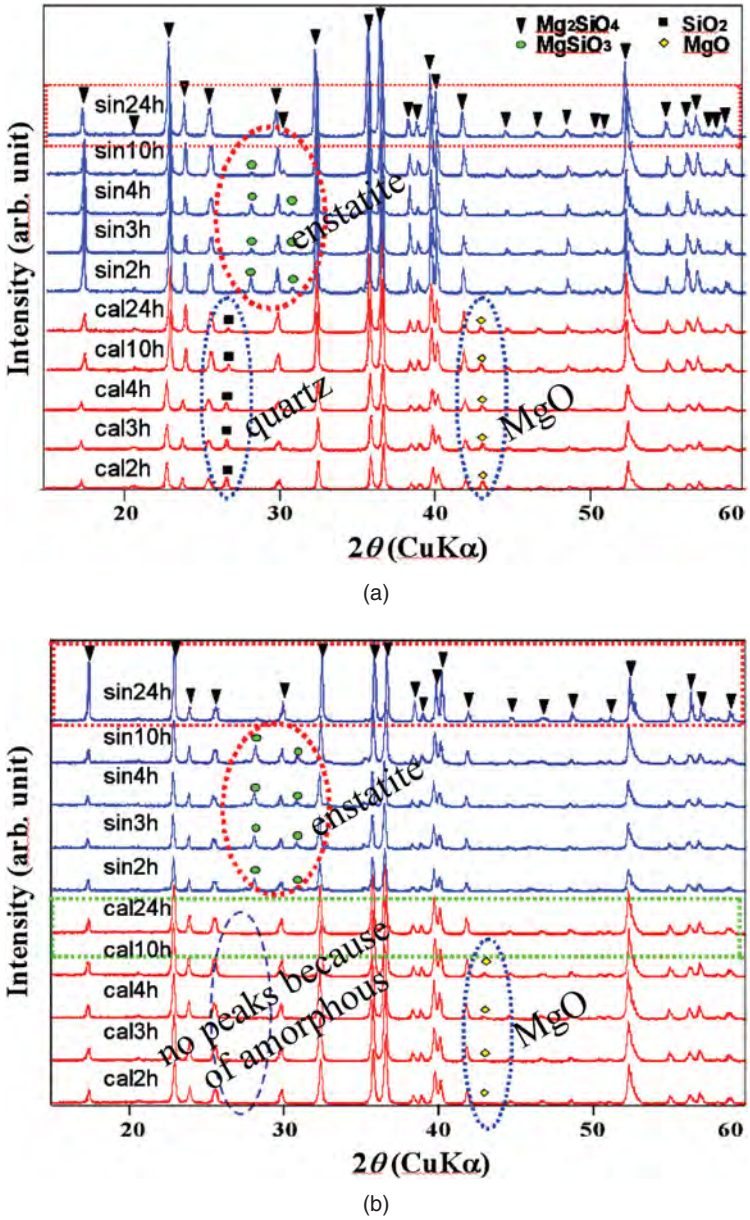

Figure 5.13 *XRPD patterns of powders applied: (a) silica A and (b) silica B. XRPD patterns as shown below half way in (a) and (b) represent the difference in calcined powder at 1175 °C for 2, 3, 4, 10, and 24 hours and are indicated as "cal nh". Above halfway in (a) and (b), 1175 °C, samples, which are sintered at 1400 °C for 2 hours after, are denoted as "sin nh." Source: Ando et al. [21, 22].*

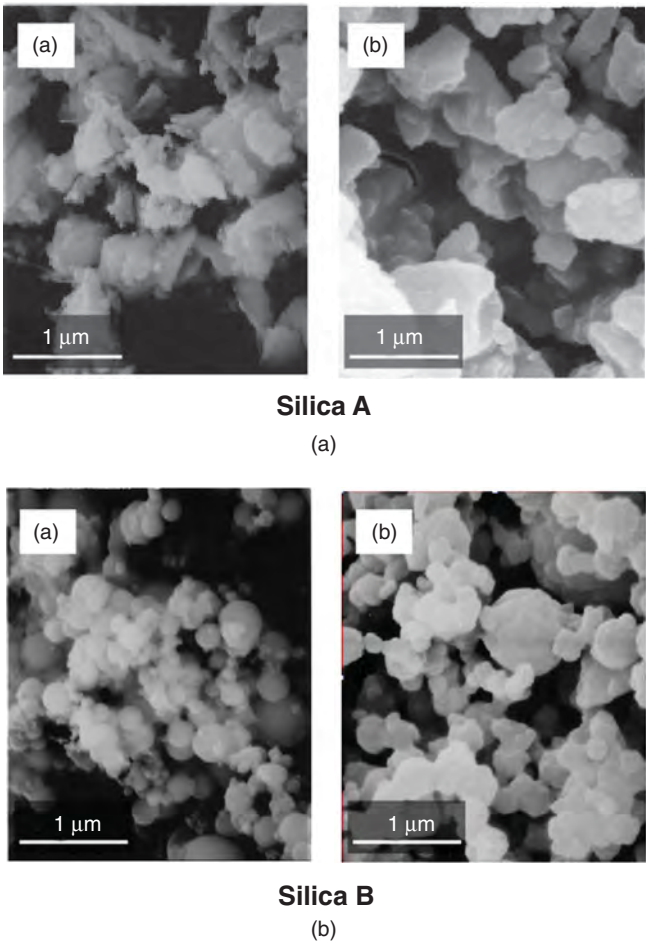

Figure 5.14 *SEM image of silica A and silica B: (a) raw materials and (b) calcined powder. Source: Ando et al. [21, 22].*

Figure 5.14 shows the SEM images of raw SiO_2 (a) and the calcined powder (b) and silica A and B. The shapes of calcined forsterite are the same as the configuration of SiO_2 raw materials, and the size becomes large. This phenomenon is considered as follows: diffusion of Mg ion is more than that of Si ion. This is because Si ion forms SiO_4 tetrahedron due to a half covalent bonding and a half ionic bonding, but Mg ion forms a single ion due to ionic bonding.

To determine the reason for the change in *Qf* as a function of calcination time, the powder calcined at 1175 °C for 2 hours is examined. SEM images in Figure 5.15a and b show the cross-section of the powder grains calcined using silica A and silica B, respectively. Both figures show that the raw silica materials maintain their shape. The shape of the calcined powder using silica A is irregular and that using silica B is spherical. EPMA line analysis is done on Si and Mg of the cross-section of the grains (3.2 μm for silica A and 1.3 μm

for silica B). The concentrations of Si and Mg showed peaks at the core and shell of the grains, respectively. This suggests that forsterite (Mg_2SiO_4) is formed at the shell part of the grains and silica (SiO_2) remains at the core part of the grains. Figure 5.15c shows a small grain (0.86 μm) prepared using silica A calcined at 1175 °C for 2 hours. In this case, the concentrations of Mg and Si are almost the same all over the grains. In the final stage of calcination, forsterite should be completely formed. Figure 5.16 shows the average grain size of the samples sintered at 1400 °C for 2 hours using silica A and silica B as a function of calcination time. Both of the samples synthesized showed maximum grain sizes at calcination times of 4 and 10 hours, respectively. The calcination time at maximum grain sizes just fits those at the lowest *Qf*. The origin of low *Qf* might be concerned with these grain sizes. As shown in scanning electron microscopy (SEM) images in Figure 5.17, the grain size of the sample with the lowest *Qf* is fairly large and the surface morphology shows

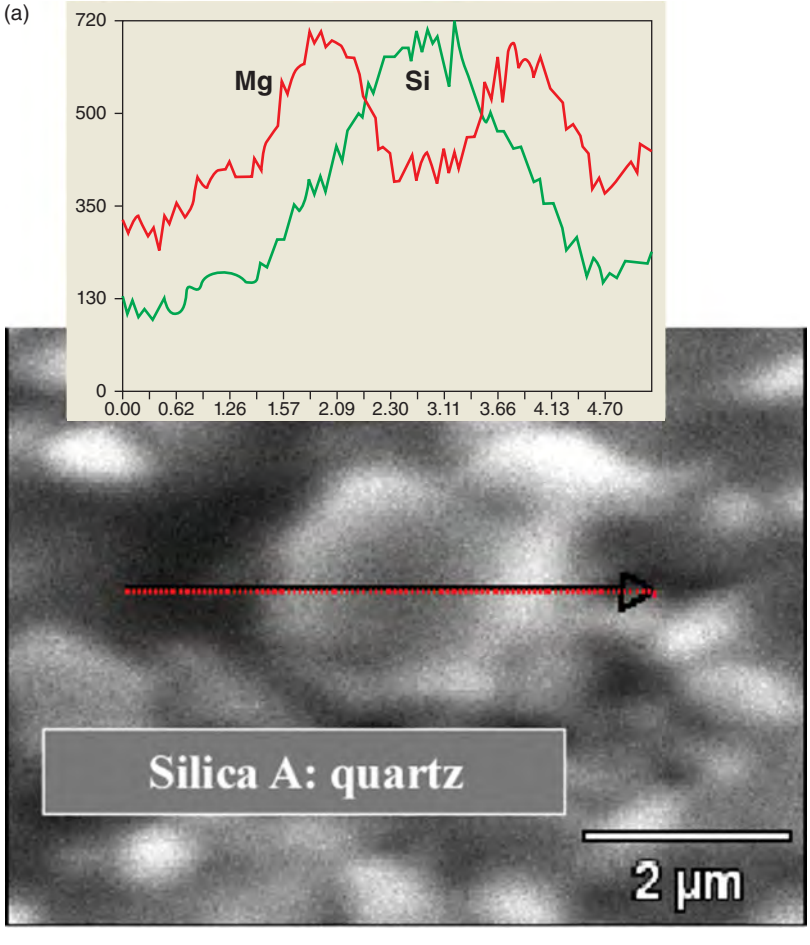

Figure 5.15 *SEM images of the section of grains calcined at 1175 °C for 2 h with EPMA line analysis of Si and Mg: (a) silica A, (b) silica B, and (c) small grains of silica A. Source: Ando et al. [21, 22].*

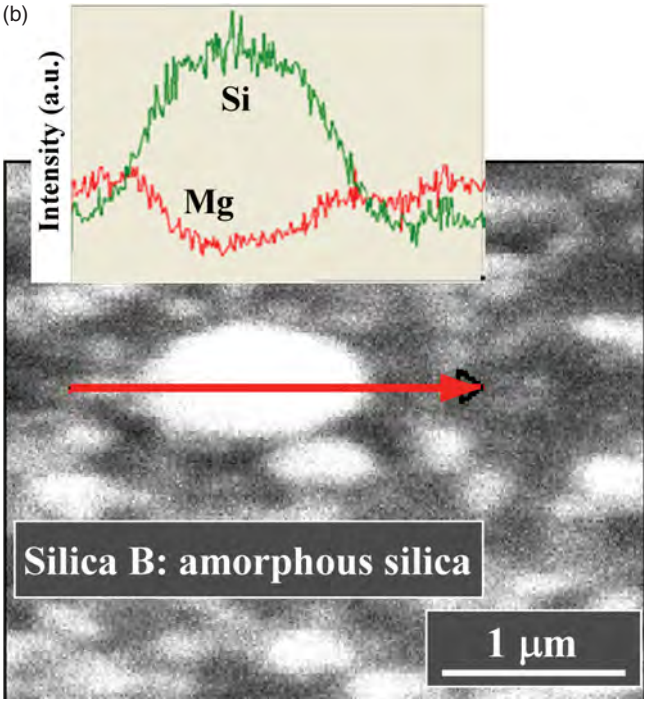

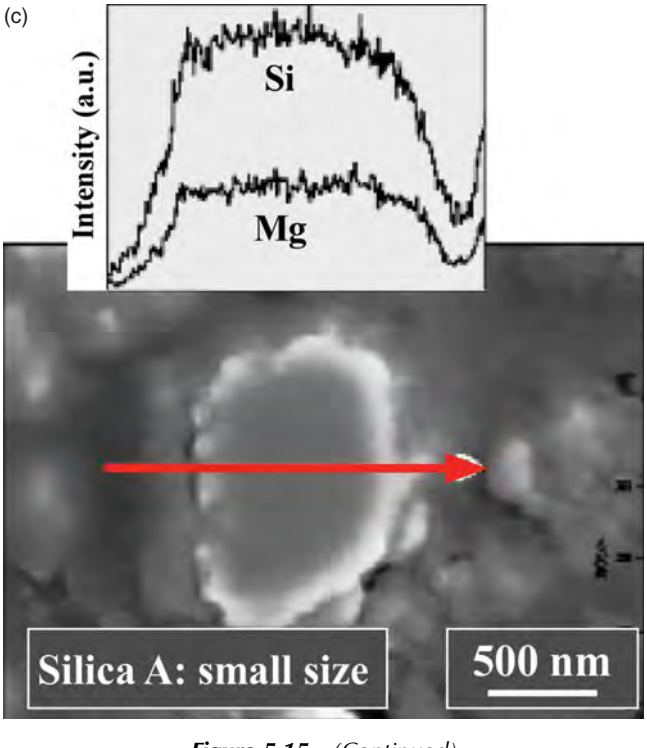

Figure 5.15 *(Continued)*

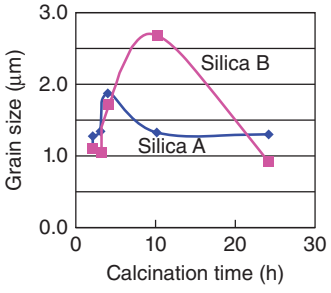

Figure 5.16 *The average grain size of the samples sintered at 1400 °C for 2 hours using silica A and silica B as a function of calcination time. Source: Ando et al. [21, 22].*

a glassy phase. The origin of the glassy phase is residual silica in the core part of the calcined grains. In the SiO_2-rich part in the binary phase diagram of MgO–SiO_2, the eutectic point is about 1546 °C, as shown in Figure 5.18 [40]. Because the sintering temperature is 1400 °C near the eutectic point, the glassy phase must arise from the silica-rich core of the grains including magnesia, as shown in Figure 5.17c and d on silica A and B, respectively. In the early stage of calcination, because the diffusion of Mg is weak, the core part of the grains is occupied mainly by pure silica with a melting point of 1728 °C, which makes the glassy-phase formation difficult. Also, in the final stage of calcination at 24 hours, because all the silica phase reacts with MgO to form forsterite, no glassy phase appears. Thus, the sintered samples on both end-sides of the calcination time show small grains, as shown in Figure 5.17a and e on both silica A and B, and high *Qf* values.

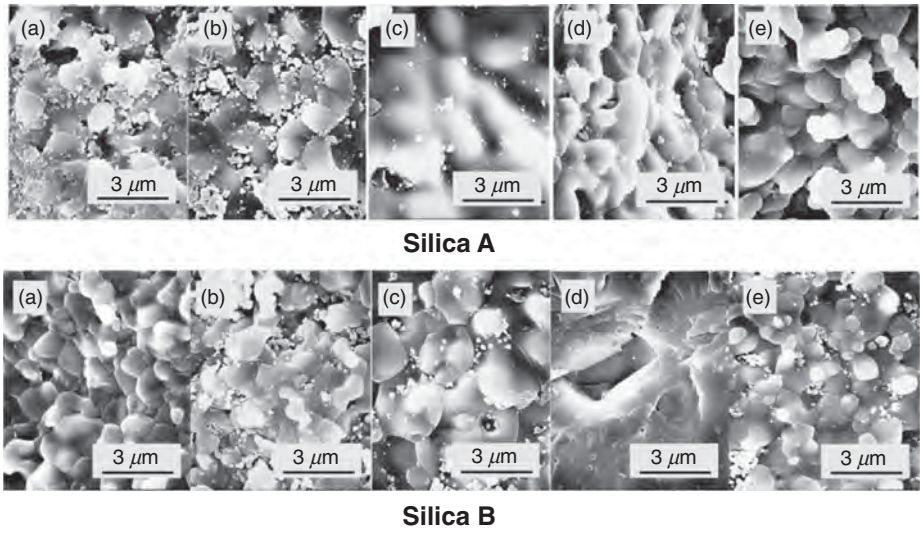

Figure 5.17 *Surface SEM images of specimens prepared by using silica A and silica B sintered at 1400 °C for 2 hours as a function of calcination time and at 1175 °C for (a) 2, (b) 3, (c) 4, (d) 10, and (e) 24 hours. Source: Ando et al. [21, 22].*

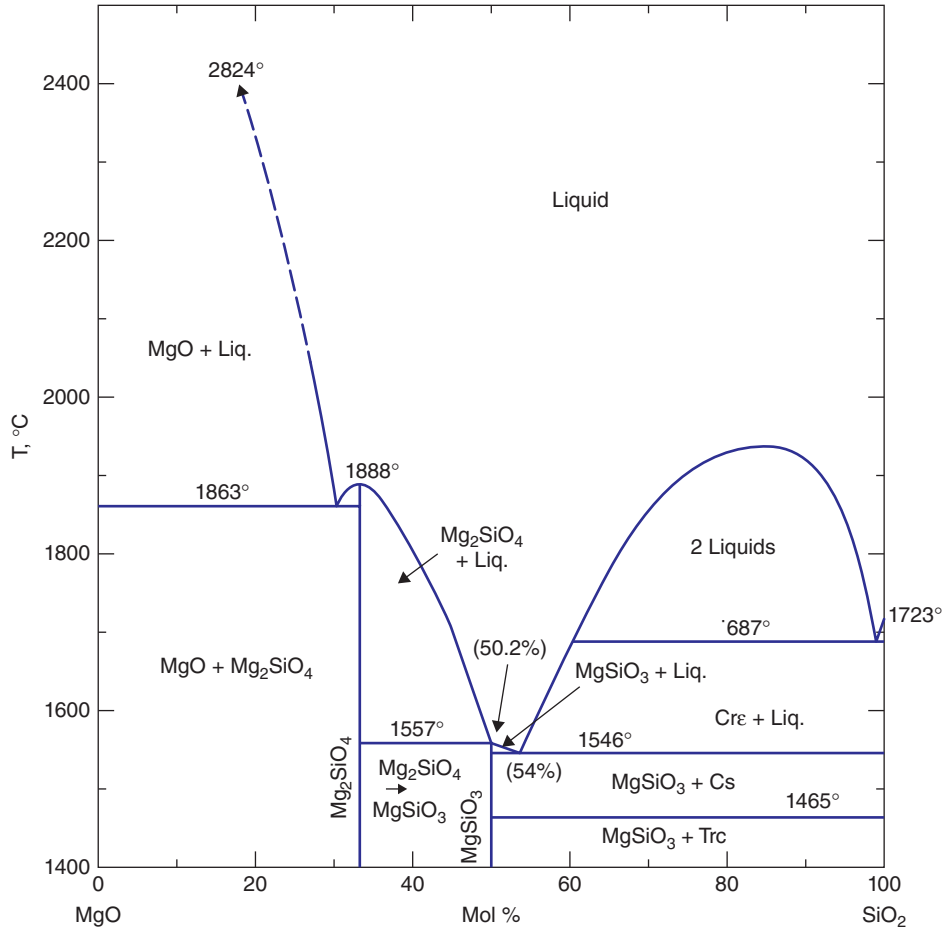

Figure 5.18 *Phase diagram of the MgO—SiO_2 binary system. Source: Adapted from Wu et al. 1993 [40].*

5.4.2 Willemite

5.4.2.1 Synthesis of Willemite with High Q

Guo *et al*. reported willemite (Zn_2SiO_4) ceramics with ultra-high *Qf* of 219 000 GHz [23]. It has a low ε_r of 6.6, which is lower than forsterite. Glass-free willemite ceramics have been sintered at 1340 °C using high-purity ZnO raw materials, as shown in Figure 5.19. The sintering temperature is lower than that of forsterite and is 1400 °C. Ultra-high *Q* of this compound comes from high-purity raw materials and is same as for forsterite described earlier in Section 5.4.1. The ceramics are well sintered with 96 to 98% of theoretical density. Commercial ceramics usually contain a glassy phase. Inclusions and impurities from the glass phase form dipoles with anions (Figure 5.5b) and the *Qf* is degraded by the dipoles turning over under the alternating electromagnetic wave, as shown in Figure 5.4a and b.

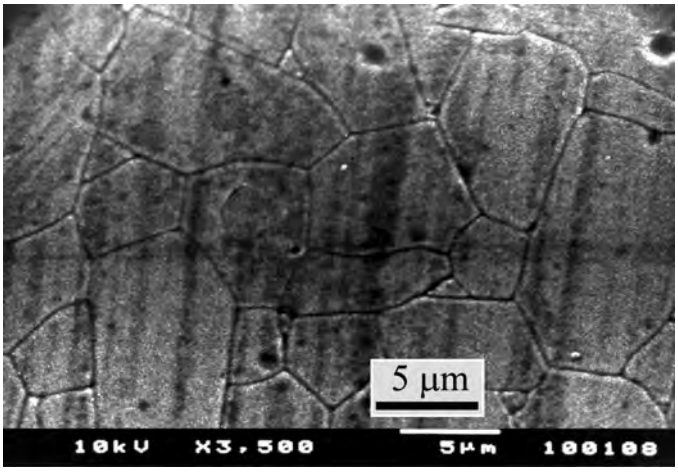

Figure 5.19 *SEM micrograph of willemite ceramic sintered at 1340 °C for 2 h. Source: Adapted from Guo et al. 2006 [23].*

5.4.2.2 *Adjustment of the Temperature Coefficient of Resonant Frequency τ_f of Willemite*

The variation of τ_f of TiO_2-added willemite as a function of TiO_2 (wt%) content is shown in Figure 5.20b. The τ_f changes linearly with TiO_2 content in the range of ±30 ppm/°C, which is the usable region. With 11 wt% of TiO_2, a τ_f value of 1.0 ppm/°C, ε_r value of 9.3, and a *Qf* value of 113 000 GHz are obtained on sintering at 1250 °C. Dong *et al*. [41] also reported willemite ceramics containing 11 wt% of TiO_2 sintered at 1200 °C prepared by the sol–gel process. They also reported excellent microwave dielectric properties: a τ_f value of –1.0 ppm/°C, ε_r value of 9.1, and *Qf* value of 150 000 GHz, and is similar as Guo's data. More exciting, chemical reactions between willemite and rutile could not be

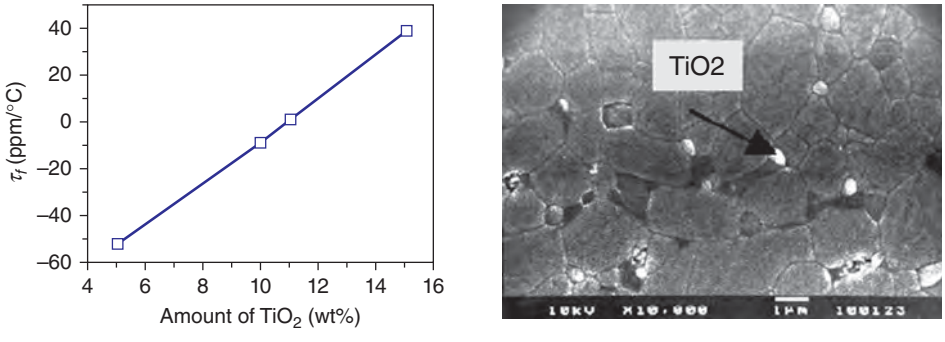

Figure 5.20 *(a) The τ_f of rutile added willemite as a function of amount of TiO_2. (b) SEM photograph of rutile added willemite. These samples were sintered at 1250 °C for 2 h. After Guo et al. [23].*

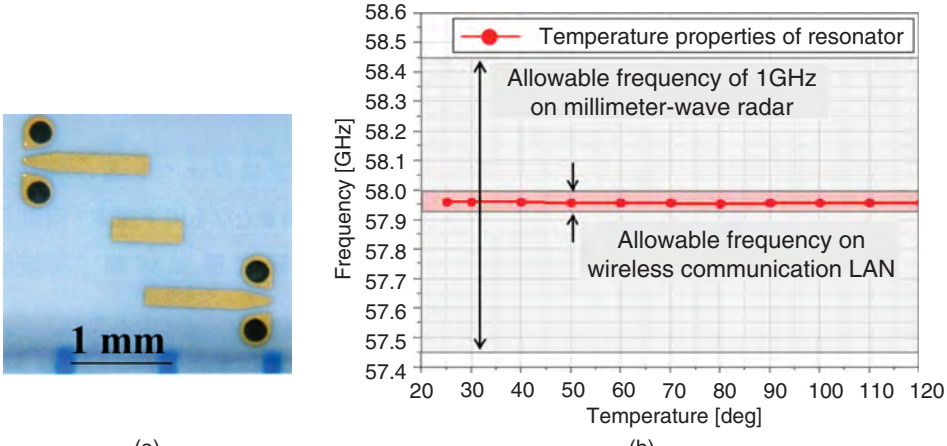

Figure 5.21 *(a) Millimeter-wave dielectric strip resonator with 3 μm thickness electrode on the substrate with 0.2 mm thickness for trial manufacture. (b) Resonant frequency depending on temperature. Source: Adapted from Nakazawa and Shimakata 2011 [8].*

observed at the sintering temperature of 1250 °C. In the case of forsterite, it reacts with TiO_2, producing $MgTi_2O_5$, since the compositions of TiO_2 added to forsterite locate in the $MgTi_2O_5$—Mg_2SiO_4—$MgSiO_3$ subcompositional triangle, as shown in Figure 5.10 [38]. Therefore the τ_f of forsterite is degraded, as shown in Figure 5.9b. On the other hand, in the case of willemite, the τ_f is very stable in a wide sintering temperature range [23]. In a SEM photograph (Figure 5.20b), the rutile particles with white color and submicrometer size are located among grains of willemite. Rutile-added pure willemite substrates for a millimeter-wave resonator with superior τ_f, as shown in Figure 5.20a, are researched and developed in The Supporting Industry Project of Japan by the Ministry of Economy, Trade and Industry of Japan (METI) [7]. On the substrate with 0.2 mm thickness for trial manufacture, a millimeter-wave dielectric strip resonator was fabricated by electrodes with 3 μm thickness, as shown in 5.21a [8]. The $\tau_f = -0.69$ ppm/°C between 20 to 120 °C, as shown in Figure 5.21b, which was under $\Delta f = 0.009$ GHz (difference of frequency) and far lower than allowable frequency of 1 GHz on the millimeter-wave radar for a vehicle. The properties of the substrates are satisfactory as compared to standard substrates for millimeter-wave picture transmission. The substrates show low thermal expansion of 2 to 3 ppm/°C, which is suitable for a millimeter-wave circuit board.

5.4.2.3 Willemite LTCC Substrate

Some examples of LTCC materials appeared in the database by Sebastian *et al.* [42]. Kim *et al*. reported willemite ceramics for LTCC by adding B_2O_3 and V_2O_5 [43, 44]. They added 25.0 mol% B_2O_3 to $Zn_{2-x}SiO_{4-x}$ ceramics (x = 0.2–0.3), resulting with Qf = 70 000 GHz, ε_r = 6.0, and $\tau_f = -21.9$ ppm/°C. Addition of 12 mol% V_2O_5 and sintered

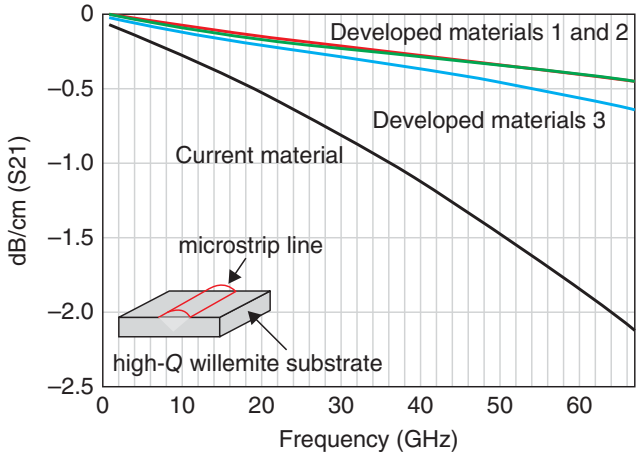

Figure 5.22 *Transmission loss in the microstrip line using high-Q willemite substrate. The loss is 1/9 that in the current substrates [7].*

at 875 °C showed $Qf = 17\,500$ GHz, $\varepsilon_r = 7.3$, and $\tau_f = -28$ ppm/°C. Dou *et al*. reported $0.95Zn_2SiO_4$–$0.05CaTiO_3$ ceramics for LTCC by adding 4 wt% Li_2CO_3–H_3BO_3 sintered at 950 °C, which showed $Qf = 26\,300$ GHz, $\varepsilon_r = 7.1$, and $\tau_f = -4.5$ ppm/°C [45].

The Supporting Industry Project by the METI in Japan has researched on willemite LTCC by using CaB_2O_4 and Li_2O–B_2O_3 low-temperature sintering agents [7]. The project leader Fujimoto [6] compared the transmission loss in the microstrip line fabricated on the willemite substrate with a current material, as shown in Figure 5.22. The transmission loss is 0.5 dB/cm (Ag) at 67 GHz, which is champion data in the world 1/9 losses against current substrate. These data are presented in the following web pages such as: http://www.chubu.meti.go.jp/kikai/sapoin/seika/23fy/23-13.pdf. The products report (outline version: March 2014) "Development for high integration LTCC substrates with high Q and low dielectric constant" by the Japan Fine Ceramics Center (JFCC) was based on the support industries of Japan (2013) by METI, Japan [7].

Low-temperature sintering agents such as Ca–borate (CaB_2O_4), B_2O_3–LiO_2, and $LiBO_2$ for LTCC substrates formed superior low-loss LTCC materials. These agents can sinter the LTCC materials without glass phases. Suvorov *et al.* reported that addition of 10 wt% Ca–borate lowered sintering to 880 °C for 5 hours [46]. In the Supporting Industry Project, 5 wt % Ca–borate was added to willemite for developing LTCC substrates, which showed a low ε_r of 6.7 and high Qf of 25 000 GHz (measurement frequency of 17 GHz). This high Q of 1470 at 17 GHz is superior to $\tan\delta$ of 0.00068 at 1 GHz. In the case of B_2O_3–Li_2O, a low sintering agent, willemite LTCC materials also achieved ε_r lower than 7 and a high Qf around of 35 000 GHz on sintering at 850 to 880 °C. Moreover, the $LiBO_2$ sintering agent with added LTCC substrate was used for fabricating millimeter-wave LTCC slot array antenna on an experimental basis employing gold electrode instead of silver, which has the problem of migration. Ando *et al.* reported silica-boric acid-added willemite LTCC substrates [47].

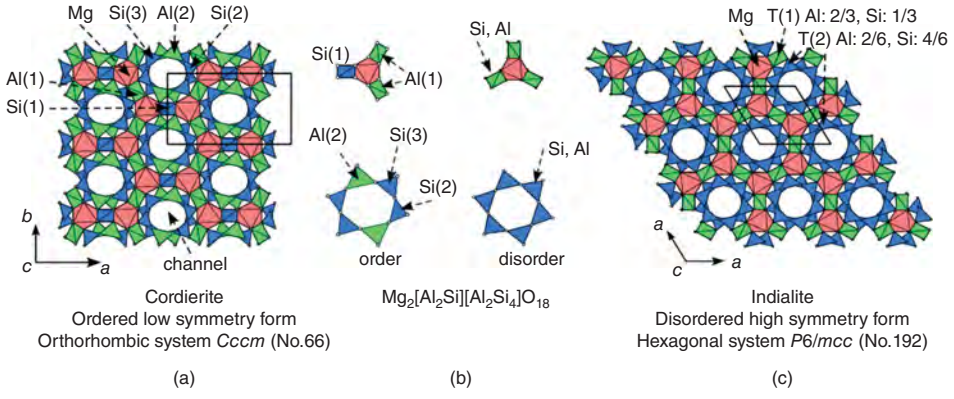

Figure 5.23 *Crystal structure of (a) cordierite and (c) indialite, and (b) ordering/disordering of AlO_4/SiO_4. Source: Adapted from Ohsato et al. 2013 [25].*

5.4.3 Indialite/Cordierite Glass Ceramics

5.4.3.1 Indialite/Cordierite Glass Ceramics with High Q Improved by Ni-Doping

Cordierite ($Mg_2Al_4Si_5O_{18}$) has two polymorphs: cordierite and indialite, as shown in Figure 5.23a and c, respectively. Cordierite is of low symmetry form: an orthorhombic crystal system *Cccm* (No. 66), which has $Si_4Al_2O_{18}$ six-membered tetrahedron rings with ordered SiO_4 and AlO_4 tetrahedra, as shown in Figure 5.23a. On the other hand, indialite is of high symmetry form: hexagonal crystal system *P6/mcc* (No. 192), which has disordered $Si_4Al_2O_{18}$ equilateral hexagonal rings, as shown in Figure 5.23c [48, 49]. Usually in compounds with an order–disorder phase transition, the disordered form is the high-temperature form and the ordered form is the low-temperature form. However, in cordierite, the order–disorder transition point is not clear, because the transition temperature is located near the incongruent melting temperature to mullite and the liquid phase. On the other hand, indialite precipitates as an intermediate phase during the crystallization process from glass to cordierite, which is metastable phase transforming to cordierite at a higher temperature under heating.

Cordierite is characterized by a lower ε_r of 6.19 depending on the silicates, and by near-zero τ_f of –24 ppm/°C [50] as compared to other silicates. Based on these properties, Terada *et al*. carried out extensive research on these microwave dielectrics [51]. They reported a good *Qf* by doping Ni, as shown in Figure 5.24a. The *Qf* was improved from 39 900 to 99 110 GHz by doping Ni of $x = 0.1$ in $(Mg_{1-x}Ni_x)_2Al_4Si_5O_{18}$. The Ni substitution did not change the ε_r value considerably but τ_f was degraded from –24 to –30 ppm/°C. For $x > 0.1$, the properties were affected by the formation of the secondary phase of $NiAl_2O_4$. Terada *et al*. also analyzed the crystal structure of Ni-substituted cordierite by the Rietveld method [52] in order to clarify the origin of the improved *Qf* value. The crystal structure analysis was performed by the Rietveld method using the synchrotron radiation XRPD pattern obtained using the multidetector system (MDS) [53] in the "Photon Factory" of the National Laboratory for High Energy Physics in Tsukuba, Japan. Figure 5.25 shows the crystal structures of Ni-substituted cordierite $(Mg_{1-x}Ni_x)_2Al_4Si_5O_{18}$ with $x = 0$, 0.05, and

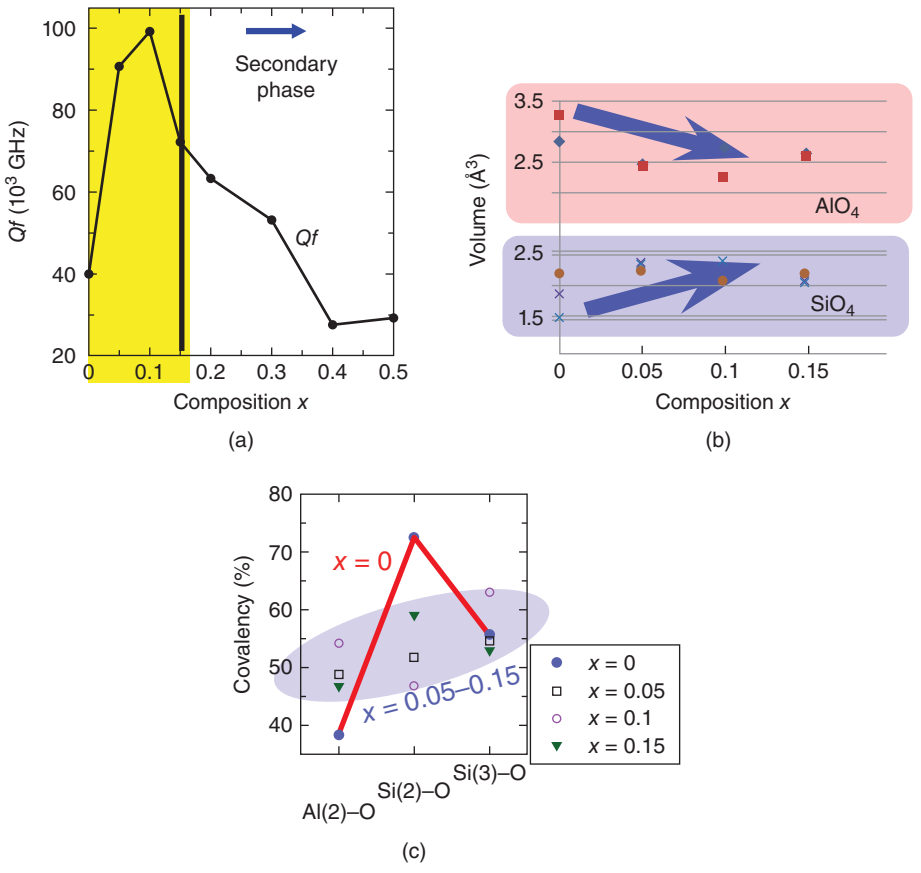

Figure 5.24 *(a) Qf as a function of Ni-doped cordierite, (b) volume of AlO_4 and SiO_4 as a function of Ni-doped cordierite, and (c) covalencies of Si—O and Al—O as a function of composition x. Source: Adapted from Ohsato et al. 2013 [25].*

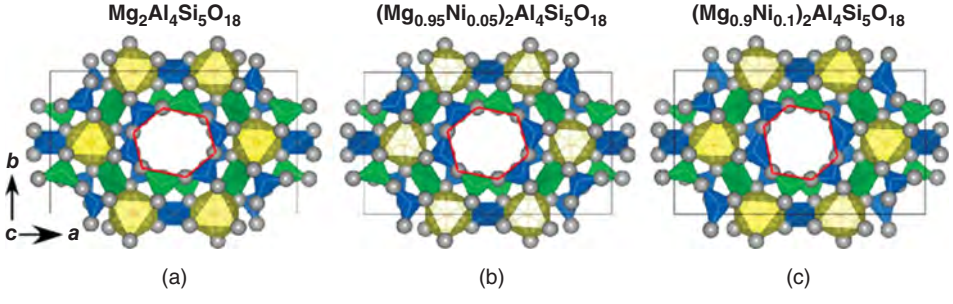

Figure 5.25 *Crystal structure of Ni-doped cordierite $(Mg_{1-x}Ni_x)_2Al_4Si_5O_{18}$, (a) x = 0, (b) 0.05, and (c) 0.1. Source: Adapted from Ohsato et al. 2010 [28].*

0.1. The crystal structure showed a tendency to deform to indialite with high symmetry on the hexagonal ring composed of corner-sharing (Si,Al)O_4 tetrahedra in the *a–b* plane. Ni-substituted cordierite $(Mg_{1-x}Ni_x)_2Al_4Si_5O_{18}$ with composition $x = 0.1$ (see Figure 5.25c) was obviously close to equilateral hexagonal rings compared to $(Mg_{0.95}Ni_{0.05})_2Al_4Si_5O_{18}$ (Figure 5.25b) and $Mg_2Al_4Si_5O_{18}$ (Figure 5.25a). The ratio of disordering between SiO_4 and AlO_4 tetrahedra is shown by volumes and covalencies of SiO_4 and AlO_4 tetrahedra, indicating transformation from cordierite to indialite [28]. The covalency (*fc*) of the cation–oxygen bond was estimated from the following equation [54]:

$$fc = as^M \tag{5.5}$$

where *a* and *M* are empirical constants, which depend on the number of inner-shell electrons of ions reported by Brawn and Wu [55]. Here, $a = 0.54$ v.u. and $M = 1.64$ for the inner-shell electrons number 10. The bond strength *s* is obtained from the following equation:

$$s = (R/R1)^{-N} \tag{5.6}$$

Here, *R* is defined as the bond length. *R*1 and *N* are the empirical parameters that depend on the cation site and the each cation–anion pair, respectively.

Figure 5.24b and c show the calculated volumes and covalency of SiO_4 and AlO_4 octahedra, respectively. On the cordierite $Mg_2Al_4Si_5O_{18}$, as shown in Figure 5.23a, SiO_4 and AlO_4 tetrahedra are located on the hexagonal rings and among the rings by ordering as shown in Figure 5.23b; the volumes of these tetrahedra show different values, as shown in Figure 5.24b. With increasing amounts of Ni substitution in cordierite, those values (Figure 5.24b) become similar and the rings have a tendency to become equilaterally hexagonal, as shown in Figure 5.25c. The covalencies of Si and Al in the (Si, Al)O_4 tetrahedra also become similar, as shown in Figure 5.24 (c). These phenomena mean the orthorhombic crystal system of cordierite (Figure 5.23a) changes to the hexagonal one of indialite (Figure 5.23c). The improvement of *Qf* should be based on the high symmetry instead of ordering by order–disorder transition, as reported in previous papers concerning complex perovskite [32].

5.4.3.2 Indialite Glass Ceramics with High Q

The *Qf* value of indialite derived by Ni-doped cordierite was improved three times from cordierite, as described before in Section 5.4.3.1. Ohsato *et al*. had an idea about synthesis of indialite for high *Q* [25]. Pure indialite could not be synthesized by a solid-state reaction because the order–disorder phase transition is hindered by the incongruent melting to form mullite and liquid. It is well known that indialite is an intermediate phase during the crystallization process from glass with cordierite composition to cordierite. Therefore, fabrication of indialite glass ceramics has been attempted: the glass with cordierite composition was melted at 1550 °C and then kept at 1600 °C for 1 hour. The melted glass was cast into a rod with diameter $\phi = 10$, $l = 30$ mm in a graphite mold. The cast glass rods were annealed at 760 °C under the glass transition point of 778 °C in order to avoid fracture by internal strain, as shown in Figure 5.26a and b. The glass rod with 10 mm diameter was cut to form a resonator with a height of 6 mm (Figure 5.26c).

The glass pellets were then crystallized at temperatures in the range of 1200 to 1470 °C for 10 and 20 hours. The crystallized pellets have two problems: deformation (Figure 5.27a)

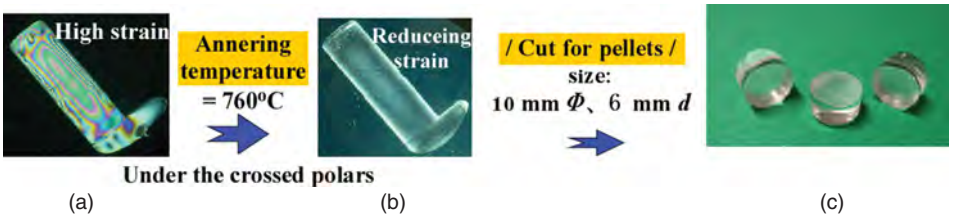

Figure 5.26 *(a) Just-casted glass rod with internal strain under the crossed polars, (b) annealed glass without strain free, and (c) glass pellets cut for resonator. Source: Adapted from Ohsato et al. 2013 [25].*

by formation of a glass phase and cracking (Figure 5.27a) by crystal growth from the surface (Figure 5.27b) [25]. Figure 27b shows photographs by a polarizing microscope of the thin section of crystallized samples. The needle-like crystals grown from the surface have an orientation with *c*-axis elongation. As the thermal expansions of *c*-direction and perpendicular to the *c*-axis are of opposite signs, as shown in Figure 5.27c, the cracking has appeared as shown in Figure 5.27a. The microwave dielectric properties of the sample with cracking had a wide scattering range of the data [25].

Microwave dielectric properties of indialite/cordierite glass ceramics showed extremely high *Qf* values of more than 200 000 GHz, as shown in Figure 5.28b [24], which is much

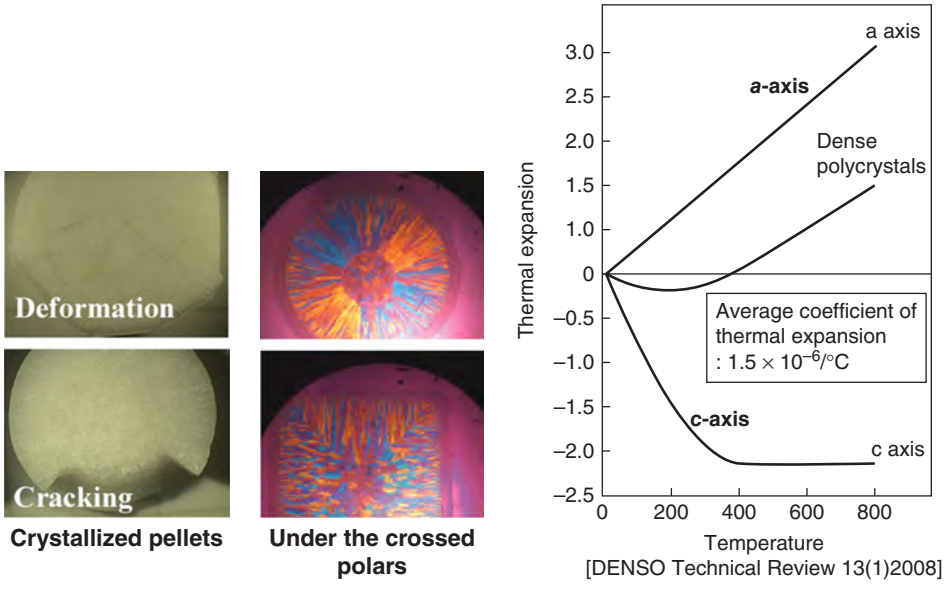

Figure 5.27 *(a) Deformation and cracking of crystallized pellets, (b) anisotropic crystal growth of the pellets crystallized from the surface of the glass pellets under the crossed polars, and (c) thermal expansion of crystallographic axes on cordierite. Source: Adapted from Ohsato et al. 2013 [25].*

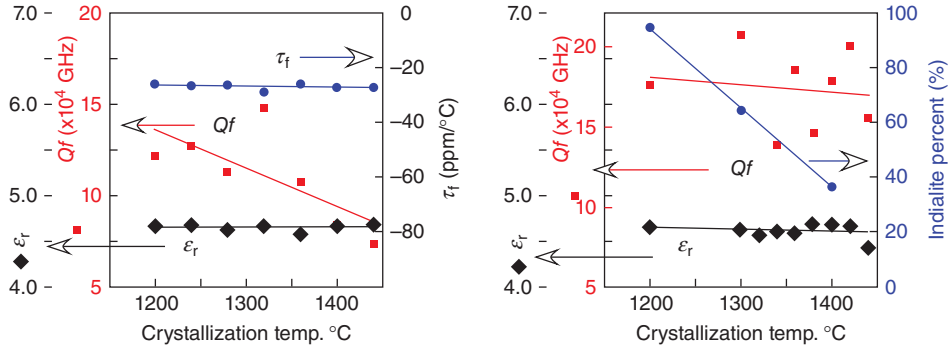

Figure 5.28 *Microwave dielectric properties of indialite/cordierite glass ceramics crystallized for (a) 10 and (b) 20 hours, and indialite percentage (b) as a function of the crystallization temperature. Source: Adapted from Ohsato et al. 2013 [25].*

better than the highest *Qf* value of 90 000 GHz obtained by doping Ni using the conventional solid-state reaction as described before (Figure 5.24a), which is a suitable level for millimeter-wave dielectrics. However, the measured *Qf* values in these samples showed a wide scattering range, as described above. The *Qf* values decrease as a function of crystallization temperature. From the relationship between the *Qf* and the phase proportions, as shown in Figure 5.28, it is clear that the indialite glass ceramics exhibit a higher quality factor than the cordierite ones. The dielectric constant ε_r is lowest at 4.7 among the silicates and the τ_f was –27 ppm/°C, as shown in Figure 5.28a. The amount of indialite/cordierite was analyzed by the Rietveld method, which is calculated using two phases such as indialite and cordierite. Here, the amount of residual % corresponds to that of cordierite. At 1200 °C, about 95% of the precipitated phase is indialite and the amount of indialite decreases and that of cordierite increases along with increasing temperature. Therefore, from these figures, indialite shows a higher *Qf* than cordierite. This τ_f value of –27 ppm/°C is better than that of other substrates having a low dielectric constant of approximately –60 ppm/°C as shown in Table 5.2 [24].

The amount of indialite could be estimated from ordering of Al/SiO_4 tetrahedra, which show a difference of volume and covalency from AlO_4 and SiO_4 tetrahedra as described before in the case of Ni-doped cordierite [28]. The volume and covalency can be calculated based on the atomic coordinates obtained using indialite and cordierite mixed models by the Rietveld method. Figure 5.29a and b show the volume and covalency of Si/AlO_4 tetrahedra for indialite and cordierite phases, respectively, formed at 1200, 1300, and 1400 °C [25]. There are two sites of tetrahedra in indialite: one is *T*(1) located among the rings and another is *T*(2) in the hexagonal ring, as shown in Figure 5.23c. There are also five sites of tetrahedra in cordierite: Al(1) and Si(1) locate among the hexagonal rings, while Al(2), Si(2), and Si(3) locate inside the ring, as shown in Figure 5.23b. All the volumes of the tetrahedra at 1200 °C converged to a range of 2.2–2.5Å^3, as shown in Figure 5.29a, which indicates disordering of Si and Al ions. *T*(1), Al(1), and Al(2) increase to around 2.6 Å^3 at 1400 °C. On the other hand, *T*(2), Si(1), Si(2), and Si(3) decrease to around 2.2 Å^3. Here, ionic radii of Al^{3+} and Si^{4+} with coordination number (CN) 4 are 0.39 and 0.26 Å, respectively. Therefore, the changes in the tetrahedral volumes depend on the ratio Al and Si in these sites. In the case

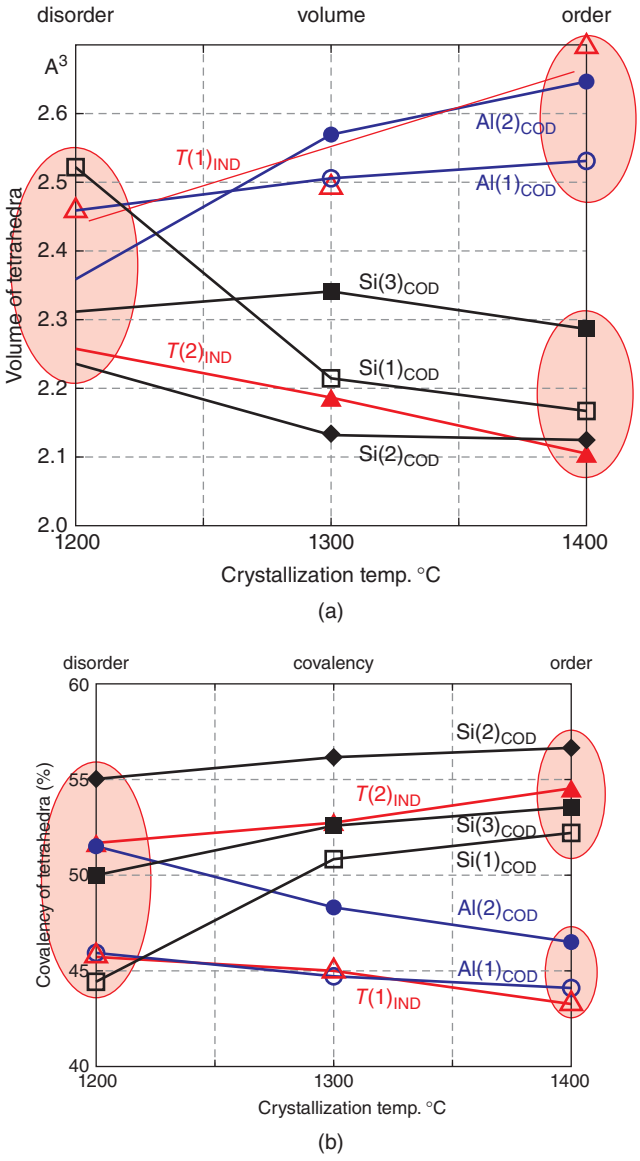

Figure 5.29 *Estimating the ordering ratios of Si and Al in tetrahedra by (a) volumes and (b) covalencies of Si/AlO_4 tetrahedra. Source: Adapted from Ohsato et al. 2013 [25].*

of covalencies, *T*(2), Si(1), Si(2), and Si(3) increase, while *T*(1), Al(1), and Al(2) decrease as a function of crystallization temperature. Usually covalency of the SiO_4 is larger than that of the AlO_4 tetrahedron. Hence, the increase of covalencies of *T*(2), Si(1), Si(2), and Si(3) sites at 1400 °C indicate that Si ions dominantly occupy these sites. On the other hand, the decrease of the covalencies of *T*(1), Al(1), and Al(2) should indicate that Al ions occupy these sites.

(a)

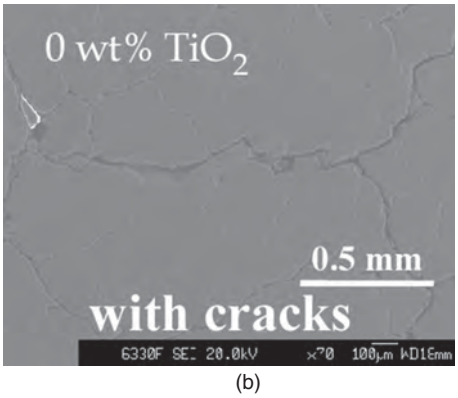

(b)

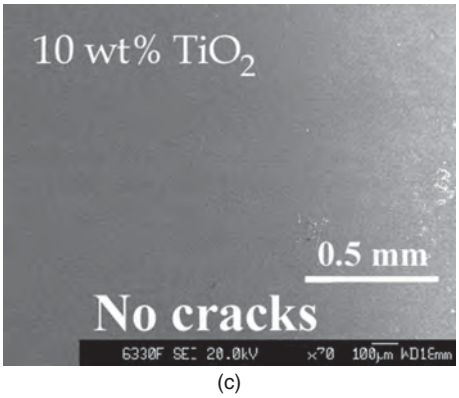

(c)

Figure 5.30 *(a) Optical and (b) and (c) SEM photographs of indialite/cordierite glass ceramics crystallized at 1200 °C for 10 hours; (a) and (c) with 10 wt% TiO_2 show no cracks and no deformations, but (b) without TiO_2 shows cracks. Source: Adapted from Kagomiya and Ohsato 2014 [56].*

5.4.3.3 Control of Deformation, Cracking, and τ_f by Adding Rutile

In order to avoid the deformation and cracking of indialite/cordierite glass ceramics stated above, volume crystallization was performed by adding a nucleating agent such as rutile [56]. Figure 5.30a shows photographs of 10 wt% rutile added to glass ceramics crystallized at 1200 °C for 10 hours, indicating the absence of deformation and cracks. The SEM figure of the glass ceramics also did not show cracking (Figure 5.30b). Figure 5.31 shows microwave dielectric properties of the glass ceramics with rutile of 0, 10, and 20 wt% crystallized at 1200 °C for 10 hours. The τ_f was adjusted to 0 ppm/°C by adding 12 wt% of rutile, which has a high τ_f of 450 ppm/°C. The Qf value was found to decrease to 100 000 GHz and ε_r increased to 5.8 by rutile addition.

5.4.4 Other Silicates

5.4.4.1 Wollastonite

Pseudowollastonite (α-$CaSiO_3$) of high temperature form is also characterized by a lower ε_r of 7.0 and by a near-zero τ_f of –21 ppm/°C, which are good properties for

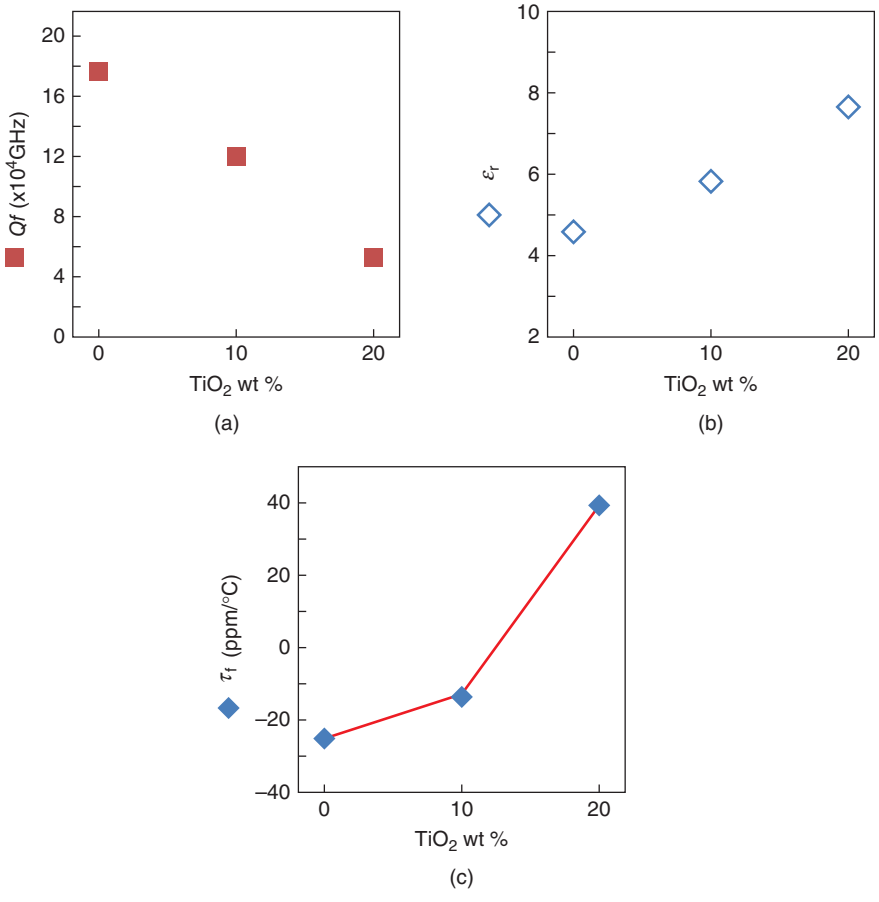

Figure 5.31 *Microwave dielectric properties of indialite/cordierite glass ceramics with rutile 0, 10, 20 wt% crystallized at 1200 °C for 10 hours. Source: Adapted from Kagomiya and Ohsato 2014 [56].*

millimeter-wave dielectrics. The *Qf* value of 36 000 GHz was improved to 67 000 GHz at $x = 0.8$ on the $Ca_{1-x}Sr_xSiO_3$ substituted Sr for Ca [26].

Wollastonite $CaSiO_3$ possesses two polymorphs: one is a low-temperature form composed of a chain structure of SiO_4 tetrahedra and the second one is a high-temperature form (pseudowollastonite α-$CaSiO_3$) with three-membered ternary rings of SiO_4 tetrahedra, as shown in Figure 5.32. Among the silicates, cordierite composed of six-membered SiO_4 hexagonal rings shows τ_f close to zero, suggesting that the SiO_4 ring framework contributes to a lower absolute value of τ_f. As silicates with a ring framework are expected to be a near-zero τ_f, detailed investigation was done on the microwave dielectric properties of α-$CaSiO_3$. In addition, $SrSiO_3$ substituted Sr for Ca was focused, which is composed of a three-membered ternary ring of SiO_4 tetrahedra. Both α-$CaSiO_3$ and $SrSiO_3$ belong to the same monoclinic space group *C*2/*c*. However, the detailed structures are different: the former is composed of a four-layered structure (Figure 5.32a) [57] and the latter a six-layered structure (Figure 5.32b) [58]. α-$CaSiO_3$ and $SrSiO_3$ are end-members of a eutectic binary

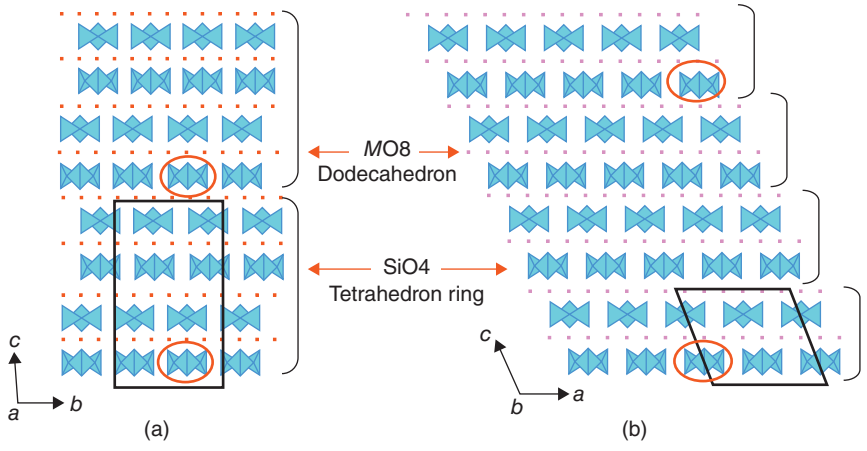

Figure 5.32 *Crystal structure of (a) α-$CaSiO_3$ and (b) $SrSiO_3$ solid solutions. Source: Adapted from Kagomiya et al. 2009 [26].*

phase diagram (ACerS-NIST Phase Equilibria Diagrams No. 6680) [59]. The end-members form a wide range of solid solutions called $CaSiO_3$ solid solutions (s.s.) and $SrSiO_3$ s.s. from $x = 0$ to 0.4 and 0.6 to 1.0, respectively.

The dielectric properties of $(Ca_{1-x}Sr_x)SiO_3$ are shown in Figure 5.33 [26]. Although the *Qf* value of α-$CaSiO_3$ solid solutions was decreased with composition x, that of $SrSiO_3$ solid solutions was increased to 66 700 GHz at $x = 0.8$ on the $(Ca_{1-x}Sr_x)SiO_3$, as described above. Although the relative density increased to 95%, ε_r shows the lowest value at $x = 0.8$. The reason for the lowest ε_r and highest *Qf* is based on the covalence of the SiO_4 tetrahedra. The average covalencies of Si(1)–O and Si(2)–O at $x = 0.8$ are 55.3 and 53.1, respectively. On the other hand, those at $x = 1.0$ are 54.9 and 52.1. As the covalencies of SiO_4 tetrahedra at $x = 0.8$ are larger than those at $x = 1.0$, the ε_r values are low. The *Qf* values are high based on the crystal structure stabilized by the high covalencies of the SiO_4 tetrahedra.

5.4.4.2 *Diopside*

The ε_r of diopside ($CaMgSi_2O_6$) is low at 7.6, which is suitable for millimeter-wave dielectric applications. By controlled synthesis the *Qf* of diopside can be improved from 59 700 to 121 380 GHz, which will be described later [27]. Figure 5.34 shows microwave dielectric properties of diopside ceramics as a function of calcination temperature. When the calcination temperature is 1200 °C, the best *Qf* value of 121 380 GHz was obtained. This composition has the best sintering condition with the highest relative density, as shown in Figure 5.35c. The dielectric constants ε_r were increased from 6.9 to 7.6 with an increase in calcination temperatures up to 1200 °C and then decreased to 7.4 at 1250 °C. These ε_r values are synchronized with *Qf* values and also relative densities. Although ε_r are usually synchronized with relative density, it is very interesting for ε_r to be accompanied by *Qf*. The reason for this phenomenon is expected to be clarified in the future. The temperature coefficient of the resonant frequency τ_f was about –60 ppm/°C, which is similar to the negative large values for most of the resonators with a low ε_r, such as forsterite, willemite, alumina, etc.

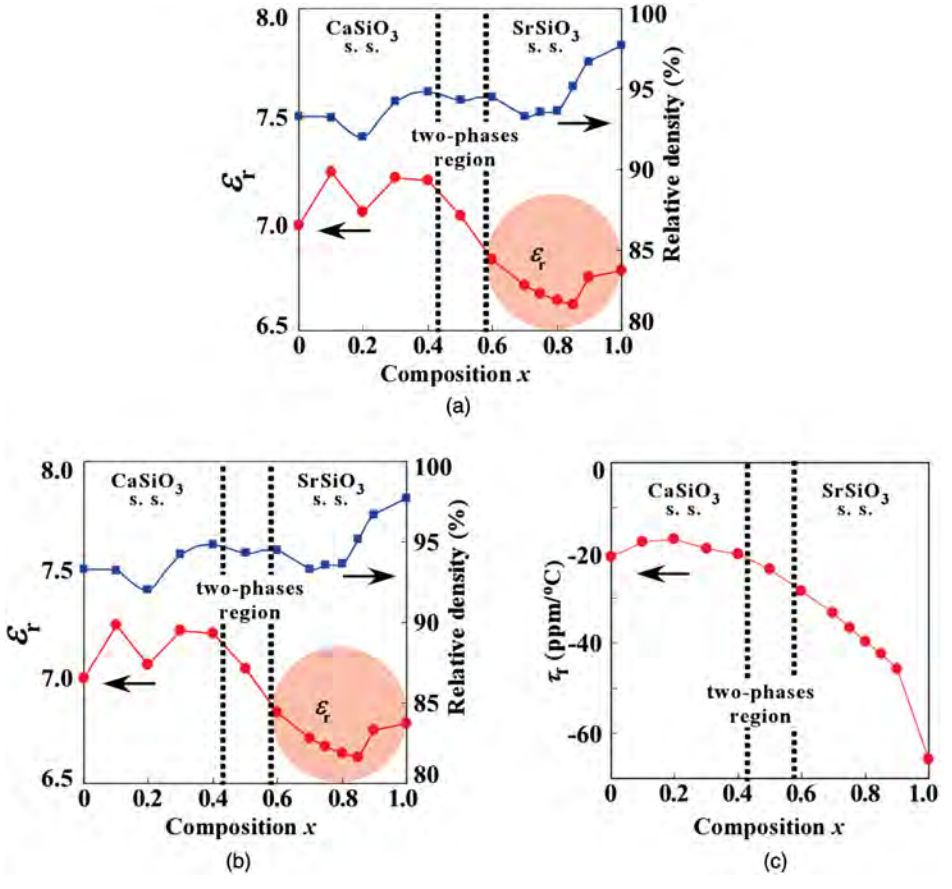

Figure 5.33 *Relative density and microwave dielectric properties, ε_r, Qf, and τ_f, of $(Ca_{1-x}Sr_x)SiO_3$ solid solutions as functions of composition x. Source: Adapted from Kagomiya et al. 2009 [26].*

The *Qf* values are affected by the fine calcined isolated grain powders without necking. The powder was prepared by calcining at 1200 °C for 2 hours, by which time the highest *Qf* diopside ceramics with a high relative density of 96.7% were formed on sintering at 1300 °C for 2 hours, as shown in Figure 5.35c. The high density was brought about by a high bulk green density of 1.8 g/cm^3 (Figure 5.35b) using fine calcined isolated grain powder sintered without necking at 1200 °C, as shown in Figure 5.36c. The necking resulting from sintering at 1250 °C was observed in the marked circle shown in Figure 5.36d, which might be formed by the eutectic melts (1357 °C) in the diopside–akermanite–mullite subcompositional triangle. The starting composition of diopside should be shifted to a composition with less SiO_2 in the subcompositional triangle owing to the formation of a core–shell structure on the quartz grain, as described earlier in Section 5.4.1.3 and now shown in Figure 5.37 [21,22].

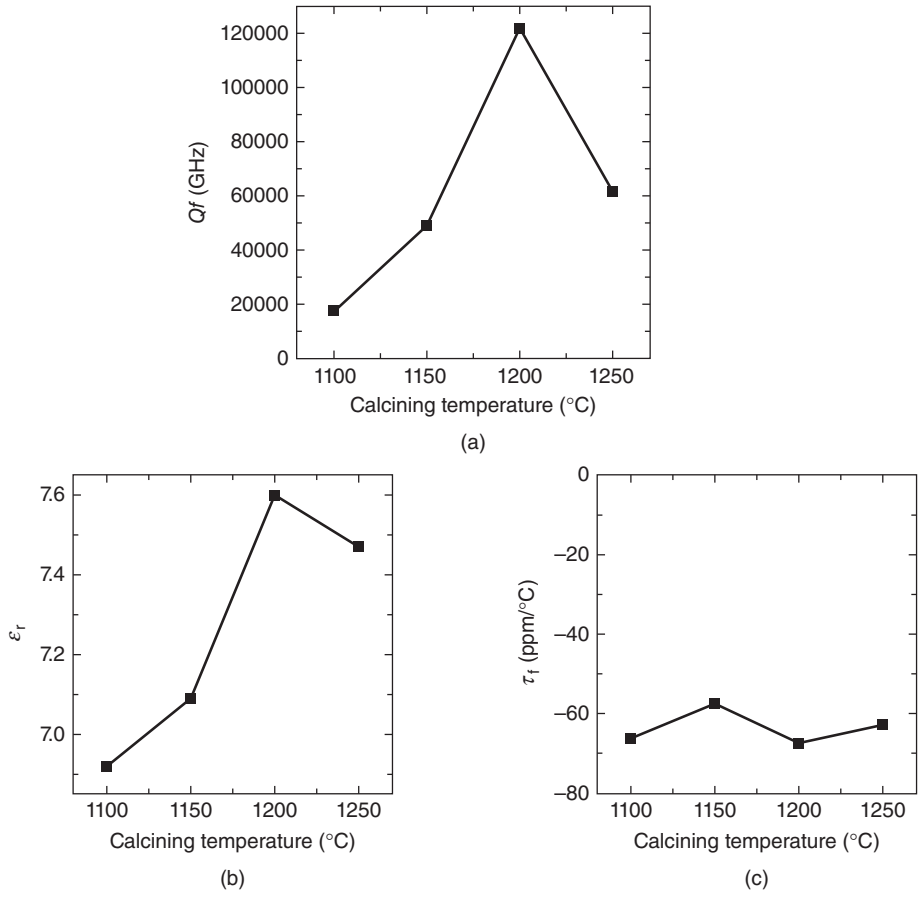

Figure 5.34 *(a) Qf, (b) ε_r and (c) τ_f of $CaMgSi_2O_6$ ceramics sintered at 1300 °C, as a function of calcining temperature. Source: Adapted from Ohsato et al. 2012 [27].*

5.4.5 Substituted Ge for Si

5.4.5.1 Ionicity and Covalency

The feature of the SiO_4 tetrahedron is that it brings low ε_r for important properties of millimeter-wave dielectrics, as described in Section 5.2.2. In this section, it is presented that the GeO_4 tetrahedron substituted for Si also brings low ε_r. Ionicity and covalence of the SiO_4 tetrahedron are 44% and 56%, respectively, which are derived based on the electronegativity difference between Si and O as following procedure and are discussed in a paper by Pauling [60]. Figure 5.38b shows the amount of ionic character as a function of the difference of electronegativity $|x_A - x_B|$ between the A–B bond presented based on the following equation by Pauling [61]:

$$\text{Amount of ionic character } p = 1 - e^{-c(x_A - x_B)} \tag{5.7}$$

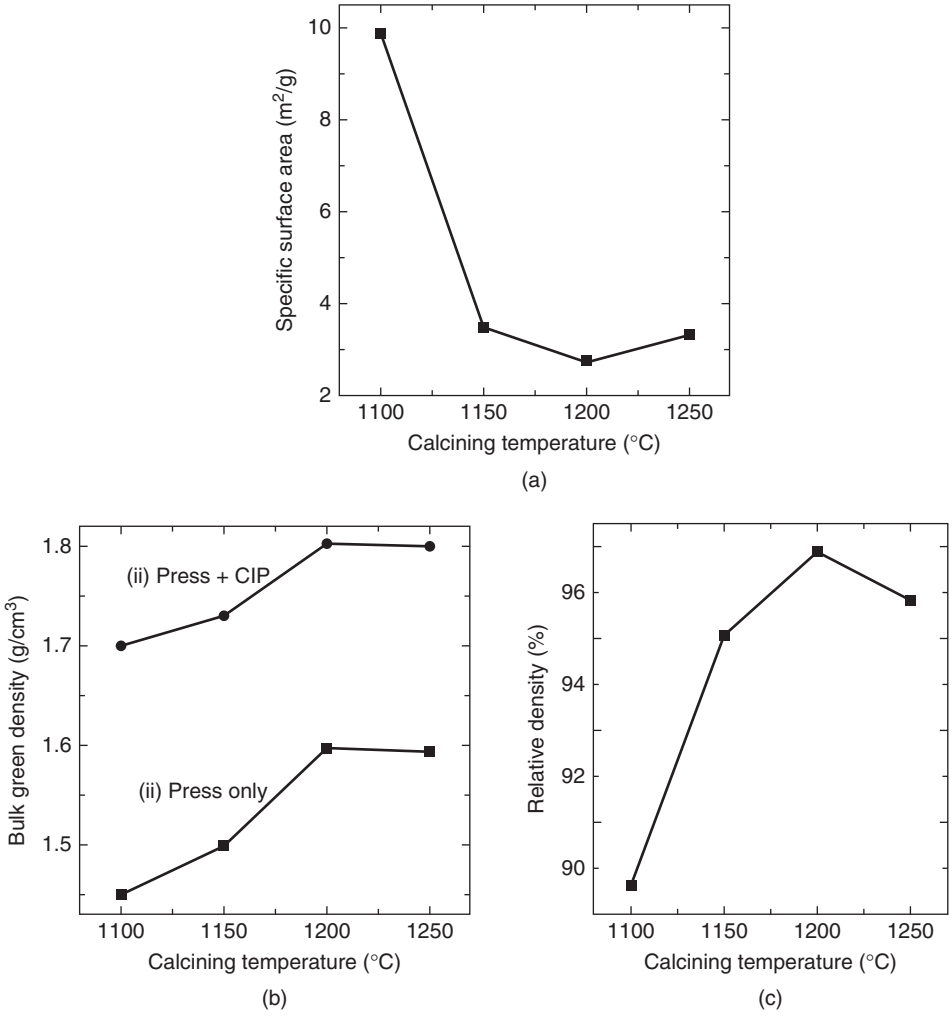

Figure 5.35 *(a) Specific surface area, (b) bulk green density, and (c) relative density of sintering temperature at 1300 °C for 2 h. Source: Adapted from Ohsato et al. 2012 [27].*

in which c has the value 1/4. According to this curve [62], the bonds in the case of Si—O with $|x_A - x_B| = 1.7$ have a 50% ionic character and a 50% covalent character. Equation (5.7) was modified based on the dipole moment of HF measured by Hannay and Smith [63] as follows:

$$p = 16|x_A - x_B| + 3.5|x_A - x_B|^2 \tag{5.8}$$

According to this equation, p of Si—O with $|x_A - x_B| = 1.7$ was 37.3% smaller than the value of Poling, and $p = 50\%$ was obtained by $|x_A - x_B| = 2.1$. An electronegativity difference of about 2.1 corresponds to a bond that is 50% ionic. Bonds with a larger

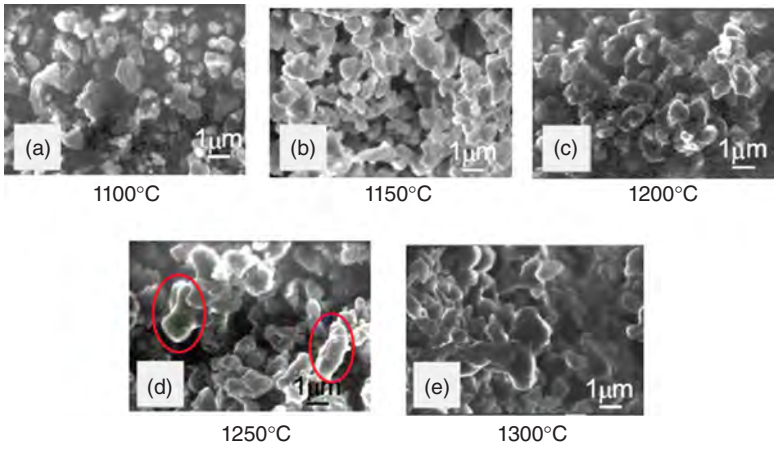

Figure 5.36 *SEM figures of diopside powders calcined at 1100–1300 °C for 2 h. Source: Ohsato et al. 2012 [27].*

electronegativity difference are therefore primarily ionic; those with a smaller difference are primarily covalent.

If atomic coordinates are obtained by crystal structure analysis, covalency f_c can be calculated more quantitatively using bond strength s, which is presented in Section 5.4.3.2). In the case of cordierite presented in Section 5.4.4, covalency values of Si—O bonds are located around 50.3 to 80.6% averaged to 63.22% and those of Al—O around 34.5 to 47.5% averaged to 39.3%. When Ni 0.1 mol% was doped to cordierite, covalency values of Si—O bonds were located around 37.13 to 83.9% averaged to 54.8%,

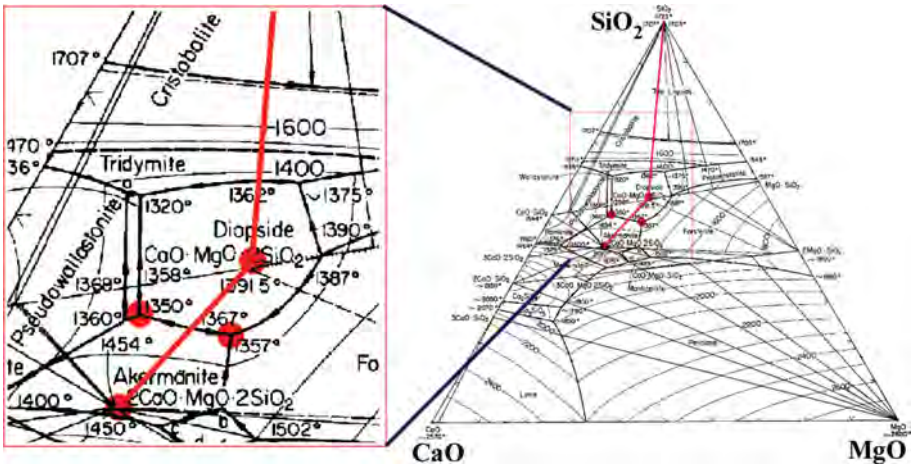

Figure 5.37 *Phase diagram of CaO—MgO—SiO_2 ternary system. A part around the diopside and akermanite is magnified including triple points at 1350 and 1357 °C. Source: Adapted from Ohsato et al. 2012 [27].*

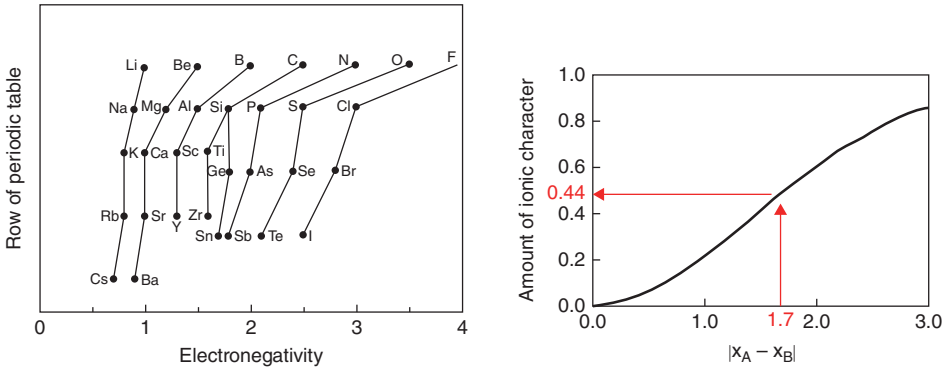

Figure 5.38 *(a) The electronegativity scale of the elements, showing the relation to the periodic table. The electronegativities are plotted against the horizontal scale, and different columns of the periodic table are separated vertically. (b) Curve relating an amount of ionic character of a bond A—B to the difference in electronegativity $x_A - x_B$ of the atoms [61, 62].*

and those of Al—O around 36.5 to 50.4% averaged to 49.2% [28, 64]. Based on these data, it was revealed that by reducing the differences between Si—O and Al—O covalency values, disordering of Si/AlO_4 tetrahedra by phase transition from cordierite to indialite had been clarified. In the case of a phase change by the crystallization temperature, as stated in Section 5.4.3.2, the covalency values also clarified the change [25]. In another case of Sr–wollastonite $SrSiO_3$ and $(Ca_{0.2}Sr_{0.8})SiO_3$ presented in Section 5.4.4.1, covalency values of Si—O bonds around 46.75 to 69.27% average to 53.5% and around 47.18 to 69.45% average to 54.2% were obtained, respectively [26]. The reason for high *Qf* on the $(Ca_{0.2}Sr_{0.8})SiO_3$ were discussed.

5.4.5.2 Ge–Forsterite and Ge–Willemite

Some examples with GeO_4 tetrahedra for LTCC materials appeared in the database by Sebastian [42] and are Zn_2GeO_4 (Ge–willemite) ceramics [65] with the same structure of willemite (Zn_2SiO_4) and with the same space group of trigonal $R\bar{3}$(No. 148). The properties are ε_r of 6.87 similar to 6.6 of willemite depending of same electronegativity value of 1.8, *Qf* of 102 700 GHz, and τ_f of –32.4 ppm/°C. The B_2O_3-added Mg_2GeO_4 (Ge–forsterite) [66] has the same structure with forsterite as the space group of orthorhombic *Pnma* (No.62), with ε_r of 6.8 similar to forsterite, *Qf* of 95 000 GHz, and τ_f of –28.7 ppm/°C.

5.4.5.3 Feldspar

The feldspars have a general formula MT_4O_8. Here T = Si and Al, located in the tetrahedron site, and $M = Na^+$, K^+, Rb^+, Ca^{2+}, Sr^{2+}, or Ba^{2+}. Also, T sites could be occupied by Ge^{4+} and Ga^{3+} instead of Si^{4+} and Al^{3+}, respectively. Most natural feldspars lie in the $KAlSi_3O_8$ (Orthoclase: Or)–$NaAlSi_3O_8$ (Albite: Ab)–$CaAl_2Si_2O_8$–(Anorthite: An), triangle, as shown in Figure 5.39 [67]. TO_2 makes the framework similar to various SiO_2 crystal structures, and substitution of Al^{3+} for Si^{4+} introduces large cations Na^+ (or K^+ or Ca^{2+})

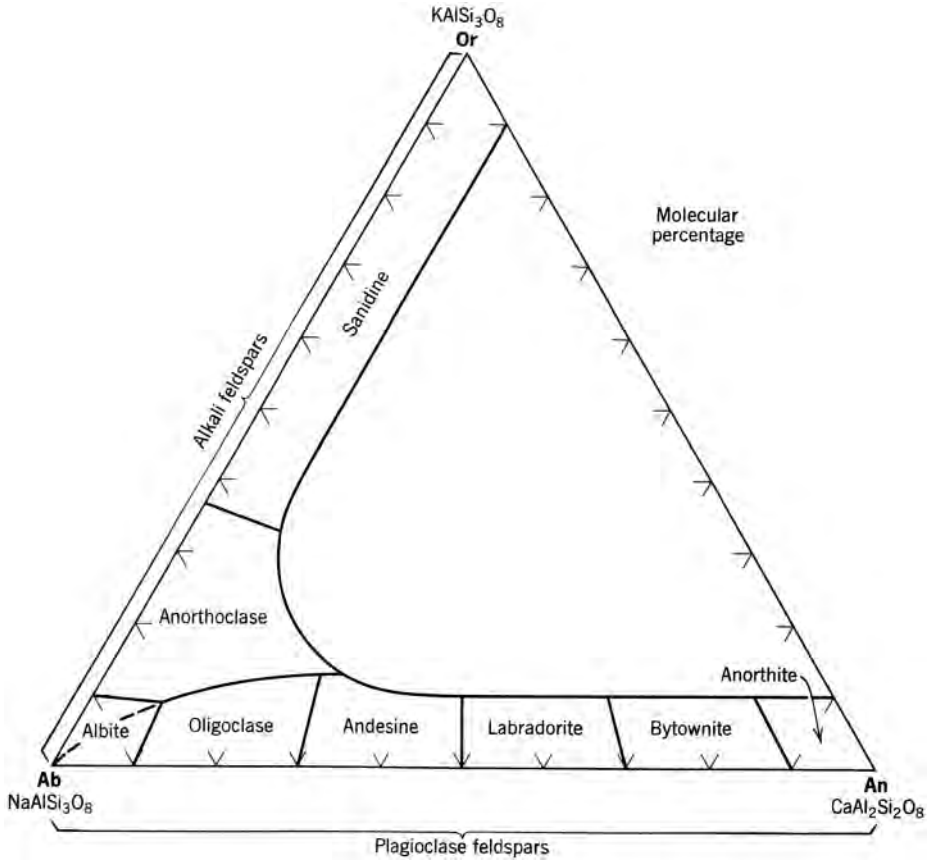

Figure 5.39 *The solid solutions in alkali and plagioclase feldspars at high temperature. Source: Adapted from Hurlbut 1971 [67].*

to maintain electrostatic charge valances. Anorthite feldspar was presented for a new glass of LTCC (LFC) at the International Society for Hybrid Microelectronics (ISHM) 1985 [68] and 1986 [69] by Nishigaki *et al*., who got the Best Paper Awards in 1985 and 1986 at the Conferences. The anorthite feldspar has good properties such as a low dielectric constant of 7.0, low thermal expansion (CTE) of 4.5×10^{-6}/ °C and high temperature resistance at 1300 °C. The composition of the LFC (low temperature fireable ceramics) is the G1 point, adding the Al_2O_3 filler as shown in Figure 5.40 [70], which meets the eutectic point of 1170 °C due to dissolution of Al_2O_3 and melts under 900 °C by the effect of adding B_2O_3 at 10 wt%. This LFC technology was handed to Bosch and bone fruit to μ-Hybrid (LTCC-ECU) in 1995 [70]. Recently, Krzmanc *et al*. [71] presented microwave dielectric characterization of plagioclase feldspars $Na_xCa_{1-x}Al_{2-x}Si_{2+x}O_8$ s.s., which were prepared under subsolidus conditions; they revealed some advantages of sodium-rich $Na_xCa_{1-x}Al_{2-x}Si_{2+x}O_8$ s.s. ($0.8 \leq x \leq 1$) over anorthite ($x = 0$). The sintering temperature decreased with increases in x from 1300 °C for anorthite to 1000 °C for albite ($x = 1$), which were affected by

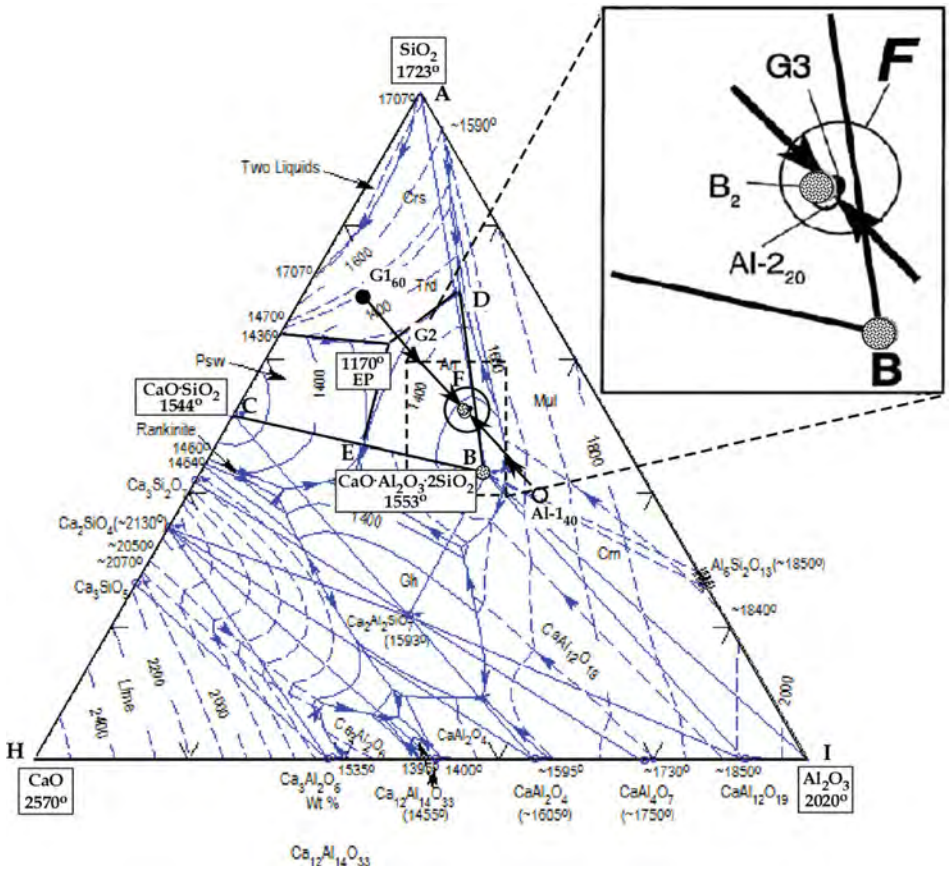

Figure 5.40 *Sintering process of LFC containing anorthite as the main composition; start composition: •60% Gl_{60} + ○40% Al_2O_3 + 10 wt% B_2O_3, final composition: anorthite (•B_2) + 20%Al_2O_3(○Al-2_{20}) + glass (•G3:B_2O_3•SiO_2) [70]. Source: Reproduced with permission from Nishigaki 2005.*

eutectic points located between albite–nepheline and albite–SiO_2. The dielectric properties are shown in Figure 5.41. The τ_f of anorthite ($x = 0$) was –140 ppm/°C, and the values approached near to zero ppm/°C with increasing x. The dielectric constants ε_r were decreased gradually because of the higher dielectric polarizability of Ca^{2+} compared with Na^+. These values were obtained from the samples (solid circles as shown in the figure) and cooled quickly, which means uncontrolled cooling in an oven by natural convection, conduction, and radiation to room temperature. The dielectric constants of slow cooled samples are also shown in the figure by squares, which are almost the same values. The *Qf* values of the samples are shown in Figure 5.41b as solid circles for uncontrolled cooling and squares for cooling with a rate of 0.5 °C/min. The slow-cooling samples showed nearly two times higher *Qf* values than that of first-cooling samples in the sodium-rich $Na_xCa_{1-x}Al_{2-x}Si_{2+x}O_8$ s.s. ($0.8 \leq x \leq 1$). The improvement might be due to short-range ordering (SRO) of Al/Si,

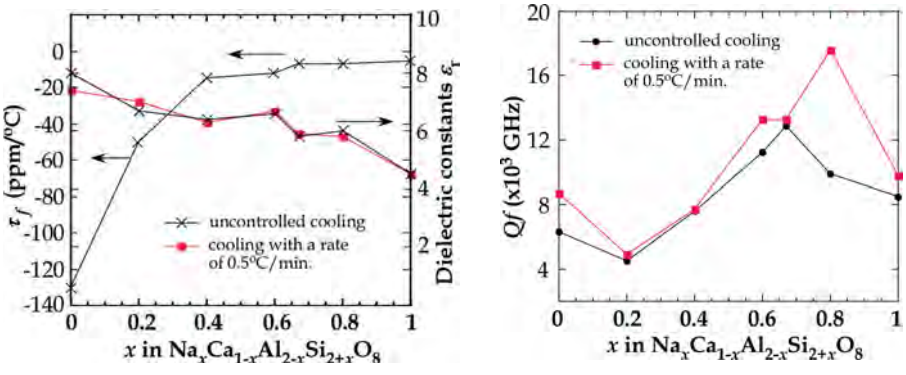

Figure 5.41 *Dielectric properties of plagioclase feldspars $Na_xCa_{1-x}Al_{2-x}Si_{2+x}O_8$ s.s: (a) τ_f and ε_r, (b) Qf as a function of x. Source: Adapted from Krzmanc 2005 [71].*

but there is no evidence from the XRPD data for any increase in the long-range ordering (LRO).

On the other hand, in this section, effects of substitution of Ge for Si are considered on the point of view of covalencies affecting the dielectric constant and quality factor. Additional effects of the substitution of Ge for Si on the feldspars are now presented. One effect is on the point of view of LTCC technology because of their sintering temperature and the tetrahedral ordering that strongly influences the dielectric losses in the microwave frequency range. Krzmanc also presented Ge-plagioclase feldspars $K_xBa_{1-x}Ga_{2-x}Ge_{2+x}O_8$ s.s. concerning Ge and Ga instead of Si and Al on the theme of this section [72]. The Ge–feldspars were also synthesized under subsolidus conditions using a solid-state reaction technology. In this series, there are two types of crystal structure, $C2/m$ (No. 12) and $P2_1/a$ (No. 14). The first one is stable up to the melting point, which is disordered Ga and Ge ions in the 8*j* Wyckoff notation positions. The second one is obtained by annealing in the temperature range 800–900 °C for $x = 1$, 0.9, and 0.67, and observed up to near the melting point at $x = 0.4$ and 0, which is probably more ordered than the $C2/m$ structure but the ordering could not be determined by the Rietveld method. The $P2_1/a$ (No. 14) modification on $x = 0.67$ exhibited a three-times-higher Qf value and a lower ε_r than the $C2/m$ (No. 12) modification. At the same time, there is no significant change of τ_f. $P2_1/a$ (No. 14) Ge–feldspars exhibiting ε_r of 5.9–7.0, Qf values of 95 000–106 000 GHz, and a τ_f of –25 ppm/°C are promising candidates for microwave applications and LTCC technology.

5.4.6 Corundum

5.4.6.1 Alumina

Alumina is a good candidate for millimeter-wave dielectrics because of the high Qf of 680 000 GHz and low ε_r of 10.05 [18]. The Qf of a single crystal was reported to be 1 000 000 GHz [73, 74]. Huang *et al.* [75] reported Al_2O_3 ceramics with a high Qf of 634 000 GHz using high purity nano $(\alpha + \theta)$–Al_2O_3 powders and Alford *et al.* [74] 500 ppm doped Al_2O_3 with a high Qf of 500 000 GHz.

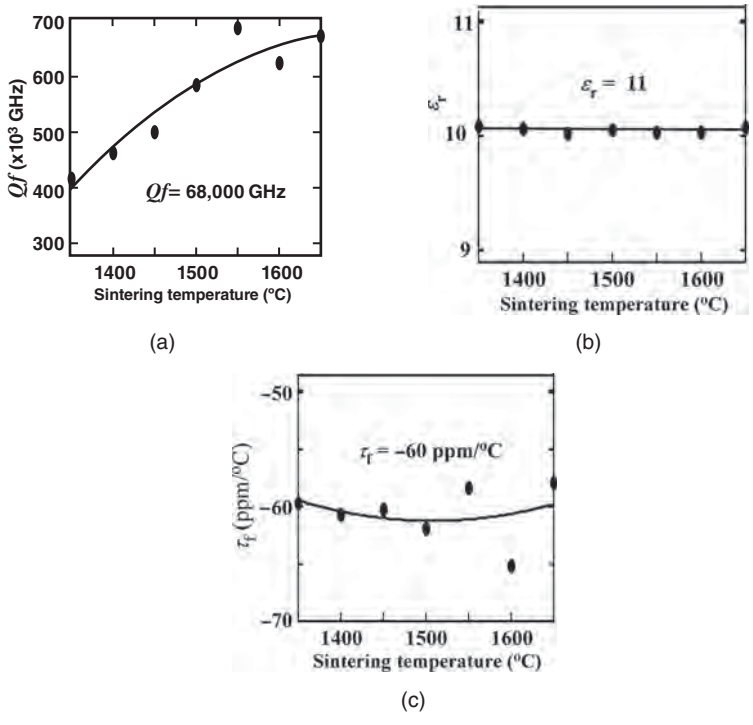

Figure 5.42 *Microwave dielectric properties of alumina ceramics: (a) Qf, (b) ε_r, and (c) τ_f as a function of the sintering temperature. Source: Adapted from Ohsato et al. 2003 [18].*

Figure 5.42 shows the microwave dielectric properties of alumina ceramics as a function of sintering temperature [18, 30]. The *Qf* value increases with an increase in sintering temperature. In the temperature range higher than 1500 °C, the *Qf* values are improved to more than 600 000 GHz and the highest *Qf* value of 680 000 GHz was obtained when sintered in the temperature range of 1550 to 1650 °C. This value is the highest *Qf* in the world as far as we know for single-phase alumina ceramics with the exception of a single crystal. These samples were well sintered with a high relative density, more than 99.5%, as shown in Figure 5.43a. The mean grain size measured using SEM figures were also increased with the sintering temperature, as shown in Figure 5.43b. The relationship between *Qf* and grain size is shown in Figure 5.43c. The *Qf* values increased almost linearly to 600 000 GHz up to 3 μm grain size, and showed the highest value of 680 000 GHz at a mean grain size of 5 μm. The *Qf* value of 370 000 GHz presented by Alford *et al.* [76] is fitted on the curve of a 1 to 2 μm grain size, which was measured from the SEM figure presented in their papers.

5.4.6.2 Improvement of τ_f of Alumina

The τ_f of alumina is expected to decrease to near zero ppm/°C by adding rutile with τ_f = +450 ppm/°C. Although the formation of Al_2TiO_4 prevents near-zero τ_f, annealing brings

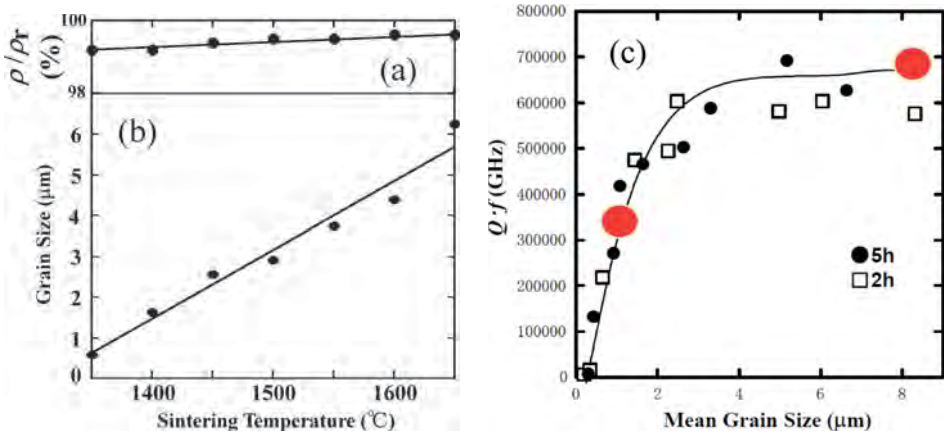

Figure 5.43 *(a) Density and (b) mean grain size of alumina ceramics as a function of sintering temperature, and (c) Qf values as a function of mean grain size of alumina ceramics. Source: Adapted from Miyauchi 2008 [30].*

the decomposition of Al_2TiO_4 and achieved near-zero τ_f [18, 77]. Figure 5.44 is a phase diagram for TiO_2–Al_2O_3 [78], which shows Al_2TiO_5 as a stable phase above 1200 °C. Addition of 10 mol% TiO_2 to alumina (10 mol% TiO_2–90 mol% Al_2O_3) adjusted τ_f to near zero when sintered at 1350 °C for 5 hours. Figure 5.45a and b show τ_f and ε_r as a function of sintering temperature. The τ_f values of a sintered sample (solid circle) decrease at above 1300 °C due to the formation of Al_2TiO_5. Therefore, Miyauchi *et al.* [77] annealed the samples at a lower temperature of 1100 °C to decompose Al_2TiO_5. The τ_f improved from –40 to near zero ppm/°C on annealing at 1350 °C, as shown in Figure 5.45a. The *Qf* and ε_r also changed from 142 000 to 114 000 GHz and 11.6 to 12.4, respectively.

5.4.6.3 New-Type Corundum with Ordered Structure

A new corundum-type $Mg_4Nb_2O_9$ (MN) compound shows a high *Qf* of 194 000 GHz with a low ε_r of 12.4 and is a candidate for millimeter-wave dielectrics [79]. Ogawa *et al.* found

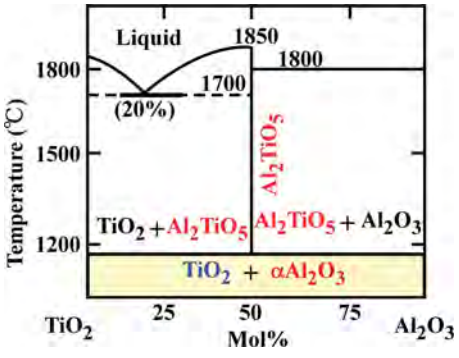

Figure 5.44 *TiO_2—Al_2O_3 phase diagram. Source: Adapted from Levin 1975 [78].*

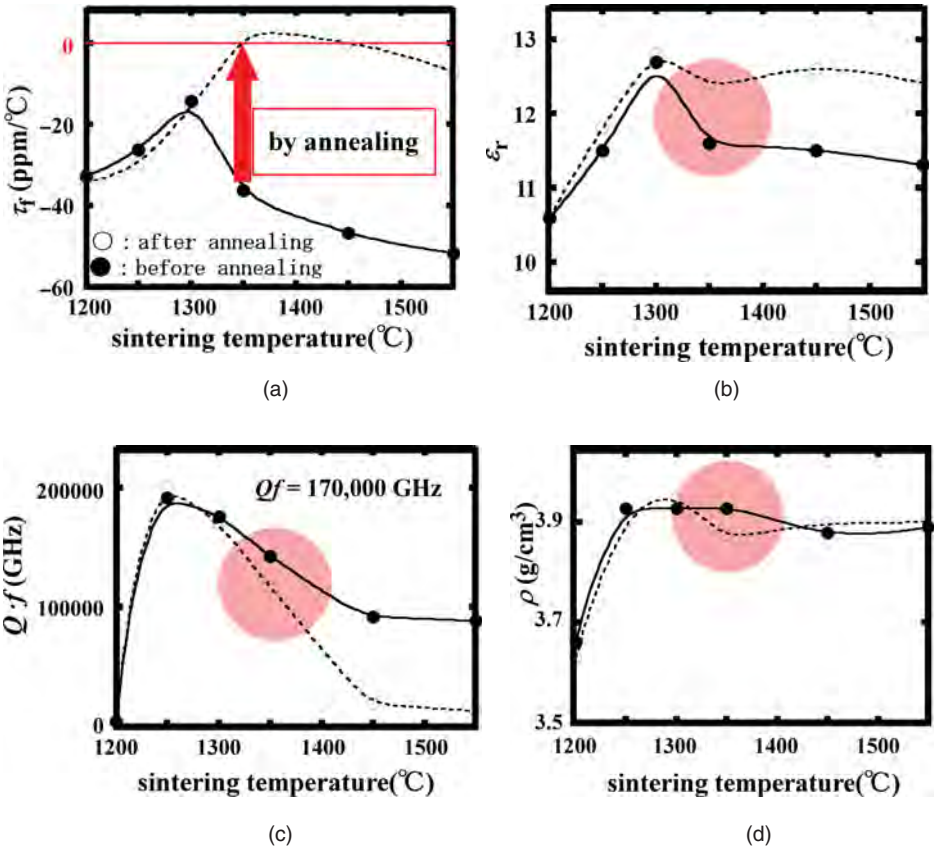

Figure 5.45 *(a) τ_f, (b) ε_r, (c) Qf, and (d) ρ of TiO_2-added alumina as a function of sintering temperature. Solid and open circles show data before and after annealing, respectively. Source: Adapted from Miyauchi et al. 2006 [77].*

this compound with a high *Qf* for the substrate of a high-temperature superconductor film. It was found that $Mg_4(Nb_{2-x}Ta_x)O_9$ (MNT s.s., $0 \le x \le 2$) and $Mg_4(Nb_{2-x}Sb_x)O_9$ (MNS s.s., $0 \le x \le 1$) solid solutions have the highest *Qf* of 350 000 GHz at $x = 2$ and 280 000 GHz at $x = 1$, respectively [80, 81].

Figure 5.46 shows the crystal structure of alumina and the new-type corundum [82]. Crystal data of corundum are as follows: crystal system: trigonal, space group: *R*3*c* (No. 167), lattice parameter: $a = 4.758$, $c = 13.991$ Å. This crystal structure is composed of octahedrals stacked along the *c*-axis in a threefold manner, and two-thirds of the face-shared octahedrals are occupied by Al ions. The crystal data of the new-type corundum are as follows: crystal system: trigonal, space group: $P\bar{3}c1$(No. 165), lattice parameter: $a = 5.1612(7)$, $c = 14.028(1)$ Å. This crystal structure is the ordered corundum structure, in which cations are ordered at two-thirds of octahedral sites in the hexagonal closest packed oxygen array along the *c*-axis. The cation stacking along the *c*-axis is the manner of –Mg(1)–(Mg(2), Nd)–Vacancy–(Mg(2), Nd)–Mg(1)–, with the $Mg(1)O_6$ octahedron being

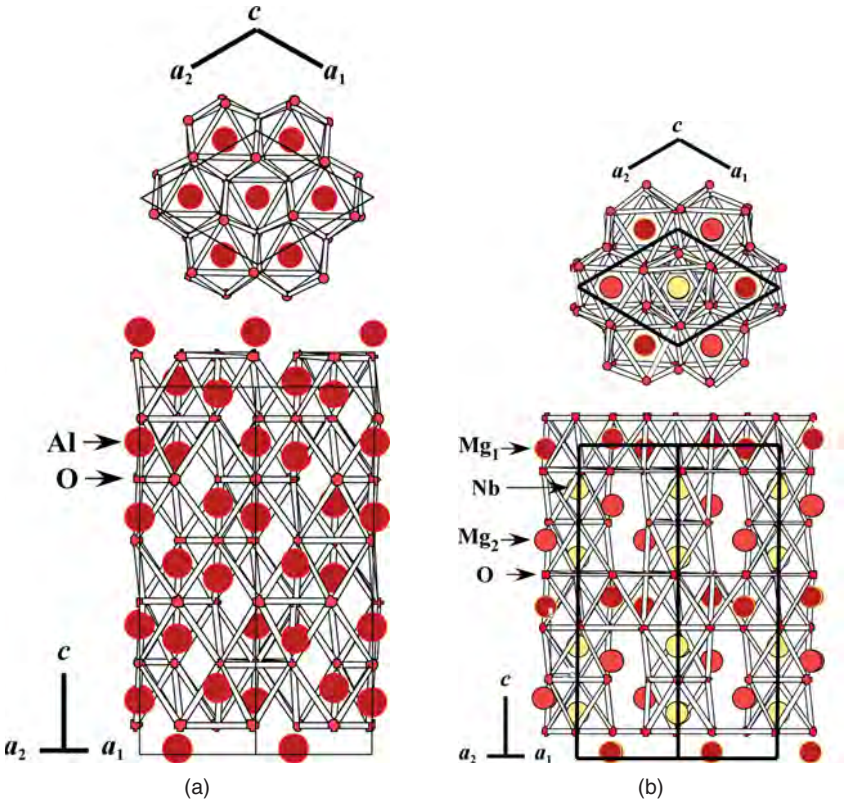

Figure 5.46 *Crystal structure of (a) alumina and (b) new-type corundum.*

face-shared with the $Mg(2)O_6$ octahedron and edge-shared with the $Mg(1)O_6$ octahedron, while the NbO_6 octahedron is face-shared with the NbO_6 octahedron and edge-shared with the $Mg(2)O_6$ octahedron.

Origins of high Q and low ε_r of the new-type corundum ceramics are presented using bond strengths derived on the bases of the bond valence theorem [54, 55] and the discrete variable X_a(DV–X_a) method [83,84]. In this section, the two solid solution series described above are reviewed based on the researches of Ogawa's group. In the case of MNT solid solutions [80], these solid solutions are made in the whole range of $x = 0$–2 because they have the same ionic radius of 0.64 Å. The total density of states (DOS) and the energy level diagrams of MN ($x = 0$) and MT ($x = 2$) are calculated using the cluster model of $(Mg_4M_2O_{62})^{-26}$ (M = Nb and Ta) by the discrete variable X_a(DV–X_a) method, as shown in Figure 5.47. In the energy-level diagrams, the solid and dotted lines indicate the occupied and unoccupied molecular orbitals, respectively. The highest occupied molecular orbital (HOMO) levels lie on the top of the O–2p valence band; the occupied bands located from –7 to 0 eV and from –20 to –15 eV are mainly composed of O–2p and O–2s orbitals, respectively. The unoccupied orbitals located above 5 eV of MN and MT are made up of Mg–3s, Nb–4d, and Ta–5d orbitals, as shown in Figure 5.47. Significant amounts of Nb–4d

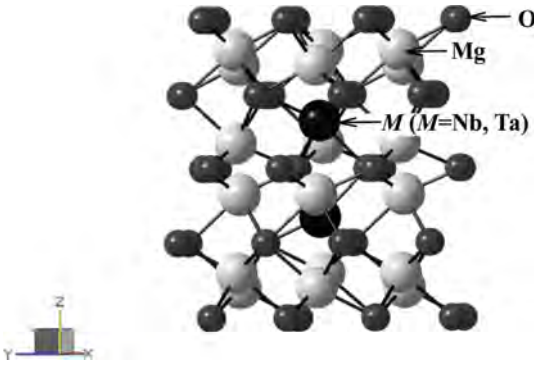

(a)

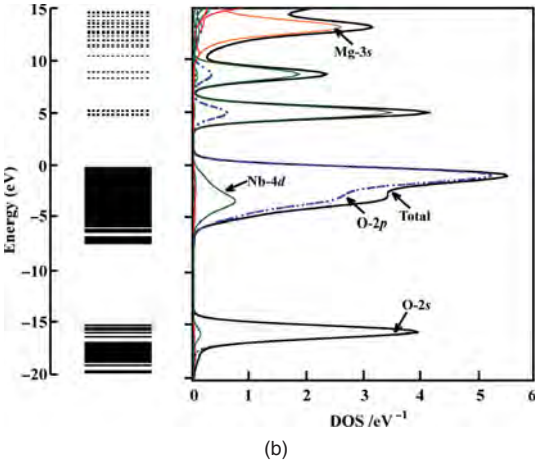

(b)

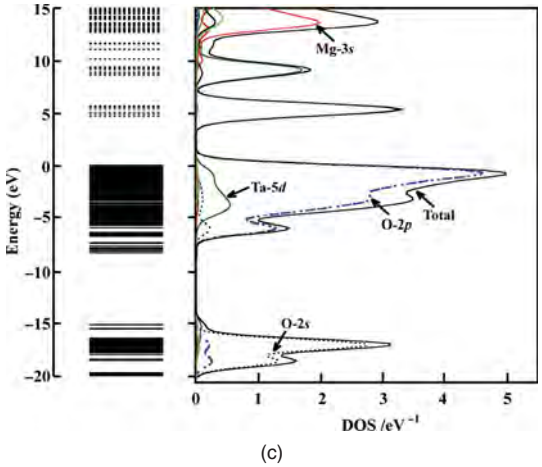

(c)

Figure 5.47 *(a) Cluster model used in the calculation: $(Mg_4M_2O_{22})^{-26}$ (M = Nb and Ta). Energy level diagrams and total and partial density state of (b) MN and (c) MT by $(Mg_{18}M_2O_{60})^{-74}$. Source: Adapted from Ogawa et al. 2003 [80].*

and Ta–5d states in the O–2p band are found, suggesting that the Nb—O and Ta—O bonds are covalent. The net charges, which define the ionicity of atoms, for the Nb and Mg ions at MN were 2.55 and 1.81, respectively, and those of the Ta and Mg ions at MT were 2.55 and 1.82, respectively. Thus, the covalent interactions of the Nb—O and Ta—O bonds are considered to be strong and the Mg—O bond at MN and MT may be an ionic interaction. From these results, it is considered that the Ta substitution for Nb in the MNT s.s. exerts an influence on the average bond strength of the Nb—O and Ta—O bonds in the NbO_6 and TaO_6 octahedra. The bond order, which represents the strength of covalent Nb—O and Ta—O bonding in NbO_6 and TaO_6 octahedra, were determined in order to discuss the covalent interactions in more detail. The bond order of Ta—O bonds (0.180) is larger than that of the Nb—O bonds (0.133), whereas those of the Mg—O bonds in $Mg(1)O_6$ and $Mg(2)O_6$ did not change with Ta substitution for Nb. From these results it is evident that the Ta—O bond became more covalent than that of the Nb—O bond. The ε_r of MT is found to be lower than that of MN, as shown in Figure 5.48a. The variation of the ε_r values with x is similar to that of ionic polarizability (α_{obs}), as shown in Figure 5.48b, which are estimated by the Clausius–Mossotti equation as follows:

$$\alpha_{obs} = 1/b[V_m(\varepsilon - 1)/(\varepsilon + 2)] \tag{5.9}$$

where ε and V_m represent the measured dielectric constants and molecular volumes, and the constant value b is $4\pi/3$. The Qf values of MNT increase drastically from 194 000 to

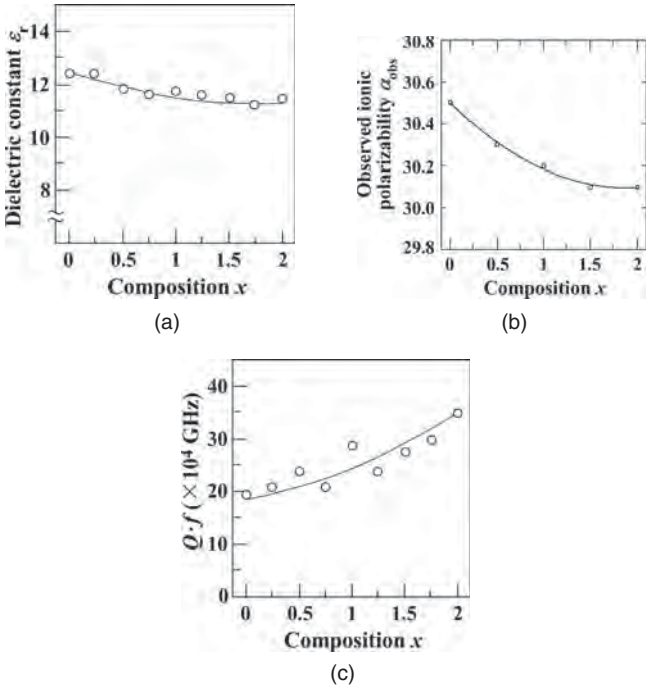

Figure 5.48 *(a) ε_r, (b) α_{obs}, and (c) Qf of MNT s.s. as a function of composition x. Source: Adapted from Ogawa et al. 2003 [80].*

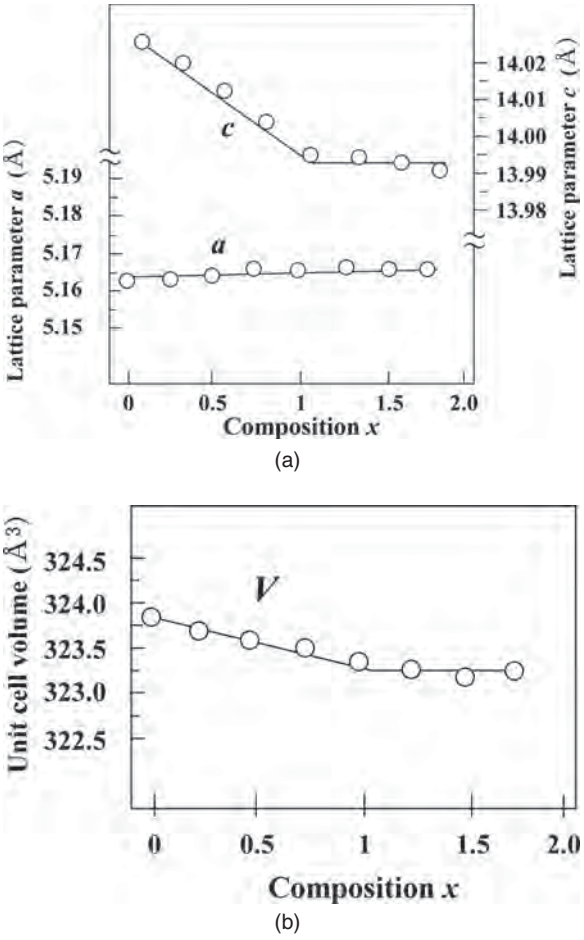

Figure 5.49 *(a) Lattice parameters and (b) volumes of MNS s.s. as a function of composition x. Source: Adapted from Ogawa et al. 2005 [81].*

347 000 GHz with increasing composition x, as shown in Figure 5.48c. The *Qf* also might be increased by decreasing the dielectric losses based on reducing the rattling due to the covalency of MT stated above.

In the case of $Mg_4(Nb_{2-x}Sb_x)O_9$ (MNS) system [81], the MNS compound makes s.s. in the composition range x from 0 to 1. It is revealed by Vegard's rule that the applied lattice parameter changes as shown in Figure 5.49. The normalized covalency of the Sb–O bond is higher than that of Nb—O bond, although normalized covalency of the Mg—O bond was not observed and differences in the composition range $x = 0$ to 1 are as shown in Figure 5.50. The covalencies are calculated using Equation (5.5) of bond strength theory stated in Section 5.4.3. The total and partial DOS of the Nb- and Sb-centered cluster models with $(AMg_{12}O_{45})^{-61}$ (A = Nb and Sb) clusters are shown in Figure 5.51, which are calculated in the same way as MNT s.s. stated above. The mixture of Nb–4d and Sb–5p states in the

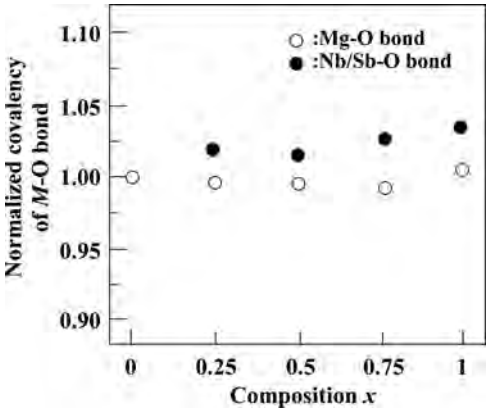

Figure 5.50 *Normalized covalency of Mg—O and (Nb/Sb)–O bonds as a function of composition x. Source: Adapted from Ogawa et al. 2005 [81].*

O–2p band suggests the strong covalent interaction between pentavalent cations (Nb and Sb) and oxygen. The ionicities of MN and MS are almost the same, which were determined from the net charge. The covalency of the Sb–O bond is larger than that of the Nb—O bond based on the bond order: that of Sb–O is 0.180 and that of Nb—O is 0.133. As a result, the Sb substitution for Nb in MNS strengthens the covalency as evaluated based on the normalized covalency of Nb/Sb–O bond (Figure 5.50).

Figure 5.52 shows the microwave dielectric properties of MNS s.s. as a function of composition x [81]. The ε_r values are decreased from 13 to 10 with x, which are expected to increase by the increase in the ionic polarizability: 3.97 A^3 for Nb^{5+} ion and 4.27 A^3 for Sb^{5+} ion. The decrease in the ε_r may relate to the variations in the covalency of Nb/Sb–O in $(NbSb)O_6$ octahedra calculated by the bond valence theorem and the discrete variable $X_a(DV\text{–}X_a)$ described earlier. The Qf values of MNS s.s. are increased from 193 000 to 283 000 GHz in the single-phase region with composition x from 0 to 1 as shown in Figure 5.52a. The improvement in the Qf value of MNS s.s. exhibited a similar tendency to those of MNT s.s., which is exerted by the enhancement of covalency of the Sb/Nb—O bonds. The τ_f of MNT locates approximately at –70 ppm/°C in the single-phase region, which is not influenced by the substitution of Sb for Nb.

5.4.7 Spinel

Aluminate spinel (AAl_2O_4) and gallium spinel (AGa_2O_4) (A = Mg, Zn) are reported for millimeter-wave dielectrics with high Qf and low ε_r. Mg– and Zn–aluminate spinel ceramics show high Qf of 105 000 and 56 000 GHz, low ε_r of 8.5 and 8.5, and τ_f of –63 and –79 ppm/°C, respectively [33, 85]. Moreover, Mg– and Zn–gallium spinel ceramics show a high Qf of 117 000 and 94 600 GHz, low ε_r of 9.5 and 10.4, and τ_f of –4 and –27 ppm/°C, respectively [86, 87]. More recently, Mg– and Zn–gallium spinel ceramics sintered at 1475 and 1550 °C showed a high Qf of 298 000 and 220 000 GHz and low ε_r of 9.2 and 9.8, respectively [88]. Figure 5.53 shows the crystal structure of the AB_2O_4 spinel [89] viewed from perpendicular to the [111] direction (this figure is also in the Plate Section). The red

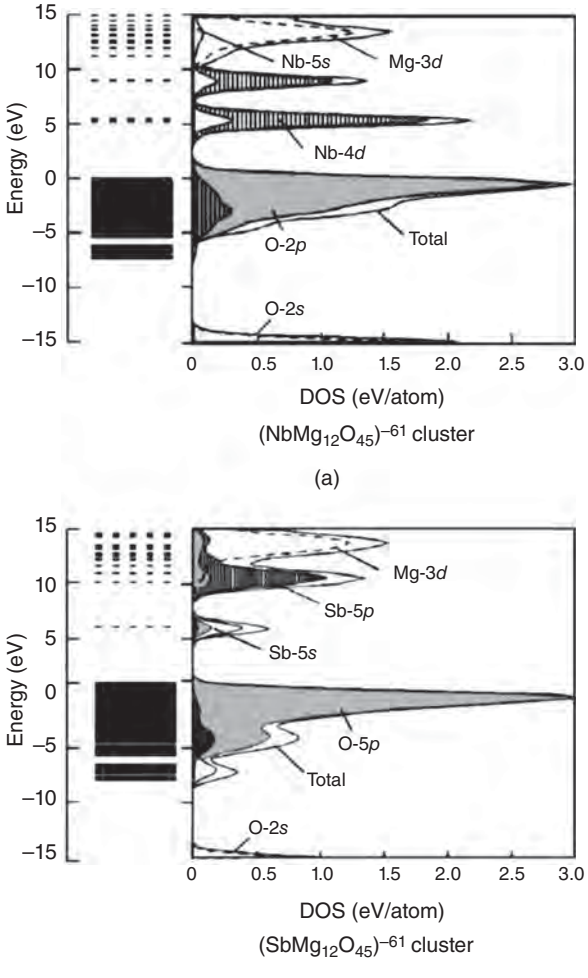

Figure 5.51 *Energy-level diagrams and total and partial density of states of (a) $Mg_4Nb_2O_9$ and (b) $Mg_4Sb_2O_9$ by $(AMg_{12}O_{45})^{-61}$ (A = Nb and Sb) cluster. Source: Adapted from Ogawa et al. 2005 [81].*

balls are oxygen ions, which form the closest packing layers, the green ones are *B* ions located in octahedra (*O*), and the yellow ones are *A* ions located in tetrahedra (*T*). Among the oxygen closest packing layers, AO_4 *T*-sites and BO_6 *O*-sites are located, whose positions are 8*a* and 16*d* in the Wyckoff notation in the $Fd\bar{3}m$ (No. 227) space group [90], respectively. There are two different layers: one is occupied by only the BO_6 octahedron and another is occupied by the BO_6 octahedron and AO_4 tetrehedon. The crystal structure of $A[B_2]O_4$ stated here is named as the "normal spinel" and that of $B[AB]O_4$ is named as the "inverse spinel." In the crystal structure of the inverse spinel, half of *B* ions occupy the *T*-sites and the residual half of *B* ions and *A* ions occupy the Osites. Moreover, there is an "intermediate spinel" $AB[AB]O_4$ between the normal and inverse spinels [92].

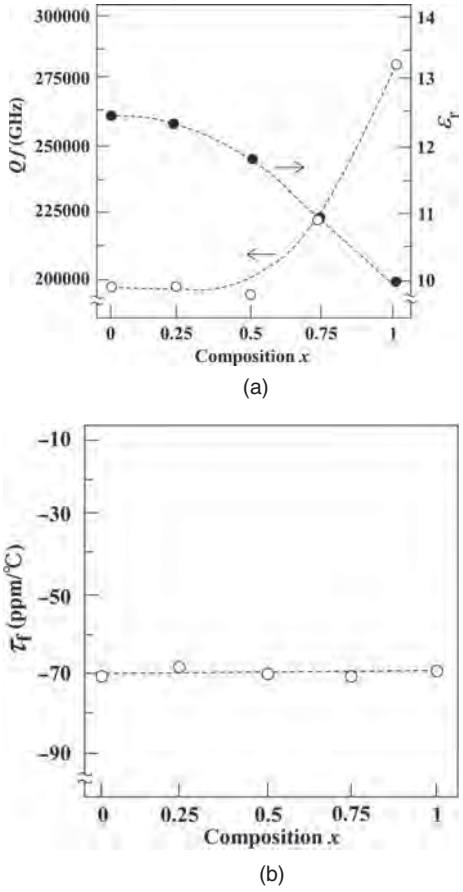

Figure 5.52 *(a) The Qf and ε_r values and (b) τ_f of MNS s.s. as a function of composition x. Source: Adapted from Ogawa et al. 2005 [81].*

Kan *et al*. [91] studied cation distributions and microwave dielectric properties of the $MgGa_2O_4$ intermediate spinel. Figure 5.54 shows the microwave dielectric properties of $MgGa_2O_4$ as a function of firing temperature from 1500 to 1600 °C. The *Qf* values considerably increased from 92 000 to 298000 GHz with an increasing firing temperature. Well-sintered samples at temperatures above 1540 °C with 96% relative densities showed excellent *Qf* in the range 250 000 to 300 000 GHz and low dielectric constants of 9.0–9.3. Figure 5.55a shows the lattice parameters and degree of inversion *x*, Figure 5.55b the volume values of *T* and *O* sites, and Figure 5.55c the covalencies of *T* and *O* sites as a function of the firing temperature from 1500 to 1600 °C. The degree of inversion *x* in the $Mg_{1-x}Ga_x[Mg_xGa_{2-x}]O_4$ intermediate spinel estimated from the site occupancies of *T* and *O* sites obtained by Rietveld crystal structure analysis are slightly decreased from 0.88 to 0.84 with firing temperature (Figure 5.55a). The obtained structural formulas of the intermediate $MgGa_2O_4$ spinel are $Mg_{0.12}Ga_{0.88}[Mg_{0.88}Ga_{1.12}]O_4$ and $Mg_{0.16}Ga_{0.84}[Mg_{0.84}Ga_{1.16}]O_4$, at 1500 and 1600 °C, respectively. The amount of the Mg^{2+} cations increases in *T* sites and

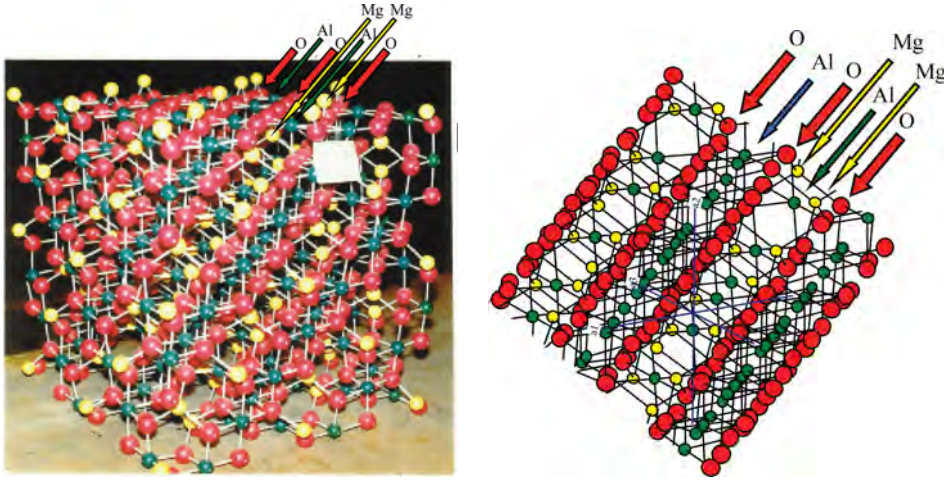

(a) (b)

Figure 5.53 *(a) Model of crystal structure of spinel, which is exhibited in KEK Tsukuba, made by Dr Y. Kudoh and students of Professor Y. Takeuchi's group at the University of Tokyo. (b) Illustrated spinel structure from perpendicular to [111] direction with the same angle as (a). This figure is also in the Plate Section.*

that of the Ga^{3+} cations increases in *O* sites with firing temperature. Covalency values of a *T*-site increase and those of an *O*-site decrease with the firing temperature (Figure 5.55c), which are calculated using Equation (5.5) in Section 5.4.3.1. The covalence value of the *T* site increasing at 1600 °C might affect the *Qf* values as in the case of indialite (Figure 5.29) and Sr–wollastonite discussed in Sections 5.4.3.1 and 5.4.4.1, respectively. The increase in the lattice parameters as shown in Figure 5.55a could not be explained by using the radius of the ion in the polyhedron, but it could be explained by increasing the volume of the *O* site, which depends on decreasing covalencies, as shown in Figure 5.55b and c.

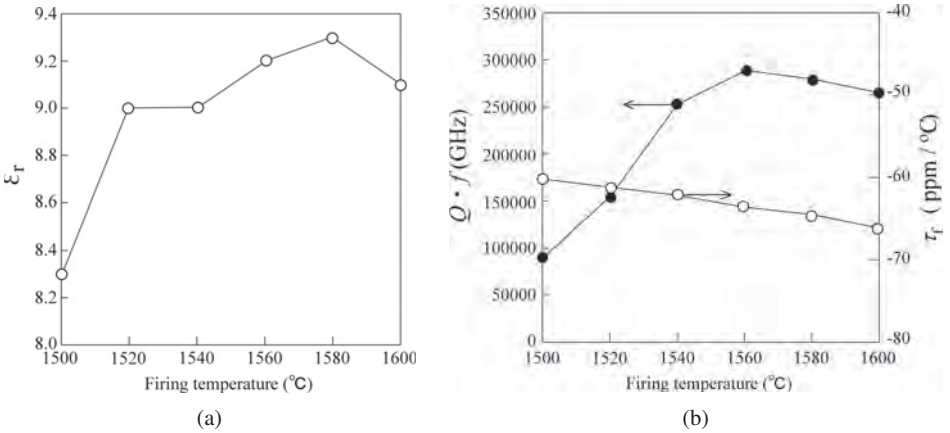

(a) (b)

Figure 5.54 *Microwave dielectric properties of $MgGa_2O_4$. Source: Kan et al. 2013 [91].*

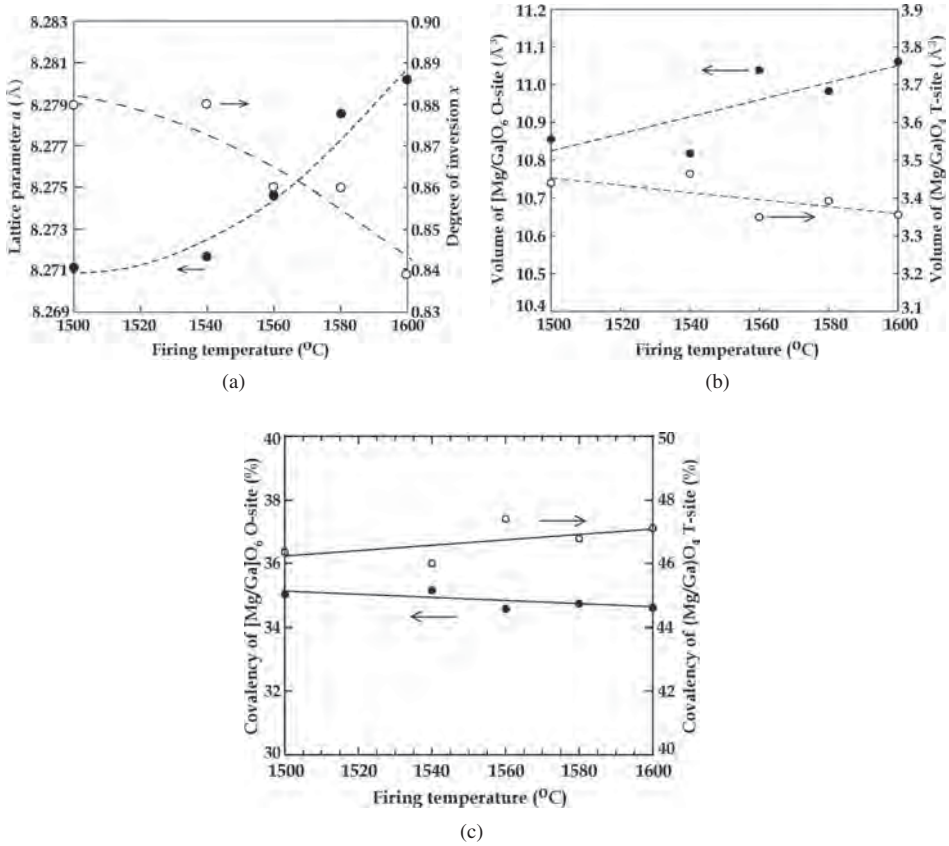

Figure 5.55 *(a) Lattice parameter of $MgGa_2O_4$ and degree of inversion x of $Mg_{1-x}Ga_x[Mg_xGa_{2-x}]O_4$, (b) volume values and (c) covalency of T- and O-sites of $MgGa_2O_4$. Source: Kan et al. 2013 [91].*

Kan *et al*. [88] also studied crystal structures and microwave dielectric properties of spinel-structured $(Mg_{1-x}Zn_x)Ga_2O_4$ s.s. One of the end members, $MgGa_2O_4$ ceramics sintered at 1500 °C, is an intermediate spinel with a degree of inversion of 0.88, as described earlier, and $ZnGa_2O_4$ ceramics are normal spinels with a degree of inversion of 1.0 [86, 87]. These compounds reveal whole s.s. by the linearly increased lattice parameter due to Vegard's law, as shown in Figure 5.56a. Figure 5.56b and c show volumes and covalencies of *O* and *T*, respectively, which are estimated from the refined atomic coordinates and lattice parameters stated earlier. The change of covalency with composition *x* are also confirmed by volume changes of *O* and *T* with composition *x*. In the tetrahedron, the covalency of the cation–oxygen bond slightly decreased depending on the Zn ions occupied preferentially. As the electronegativity of the Zn ion (1.6) is larger than that of Mg (1.2), ionicity of the Zn–O bond showing opposite character is becoming large. This is consistant with the change of covalency. Figure 5.57a, b, and c show the relative density, dielectric constant, and quality factor *Qf* values, respectively, as a function of the firing temperature. The variations of ε_r values are similar to those of relative density.

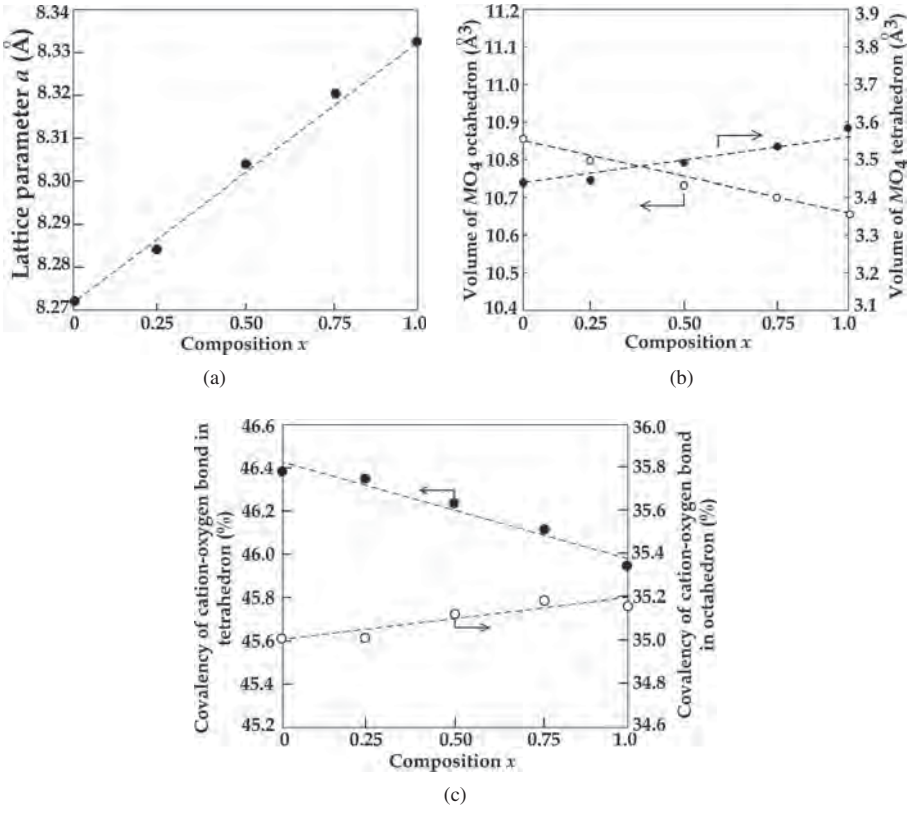

Figure 5.56 *(a) Lattice parameter, (b) volume of MO_4 tetrahedron and MO_6 octahedron, and (c) covalency of the M–O bond in MO_4 tetrahedron and MO_6 (M = Mg, Zn, Ga) octahedron as a function of composition x of $(1 - x)MgGa_2O_4$–$xZnGa_2O_4$ ceramics fired at 1500 °C for 2 h in air. Source: Kan et al. 2014 [88].*

Above 1475 °C, the relative densities in the composition range of 0.25 to 1.0 are saturated and the *Qf* value of $ZnGa_2O_4$ of $x = 1.0$ showed an excellent 240 000 GHz and those of $0.25 \leq x \leq 0.75$ approximately 180 000 GHz. In the case of $MgGa_2O_4$, the relative density and *Qf* values of random variations with the firing temperature are shown in Figure 5.57c, and the *Qf* value at 1550 °C shows a very high value of 298 000 GHz. These *Qf* values of $(Mg_{1-x}Zn_x)Ga_2O_4$ s.s. are much higher than those of $ZnAl_2O_4$ [93] and $MgAl_2O_4$ [85] spinel ceramics. The dielectric constants ε_r of $(Mg_{1-x}Zn_x)Ga_2O_4$ s.s. are approximately 9.8, being suitable for millimeter-wave dielectrics, but the τ_f values show around –64 ppm/°C. Further research is needed to improve τ_f for commercial applications.

5.4.8 Borate, Phosphate, and Vanadate

5.4.8.1 Borate

There are several borate materials such as $A_3B_2O_6$ (A = Mg, Zn), AB_2O_4 (A = Ca, Sr, Ba), RBO_3 (R = La, Nd, Sm, Dy, Ho, Y) with high *Qf* and low ε_r useful for millimeter dielectric

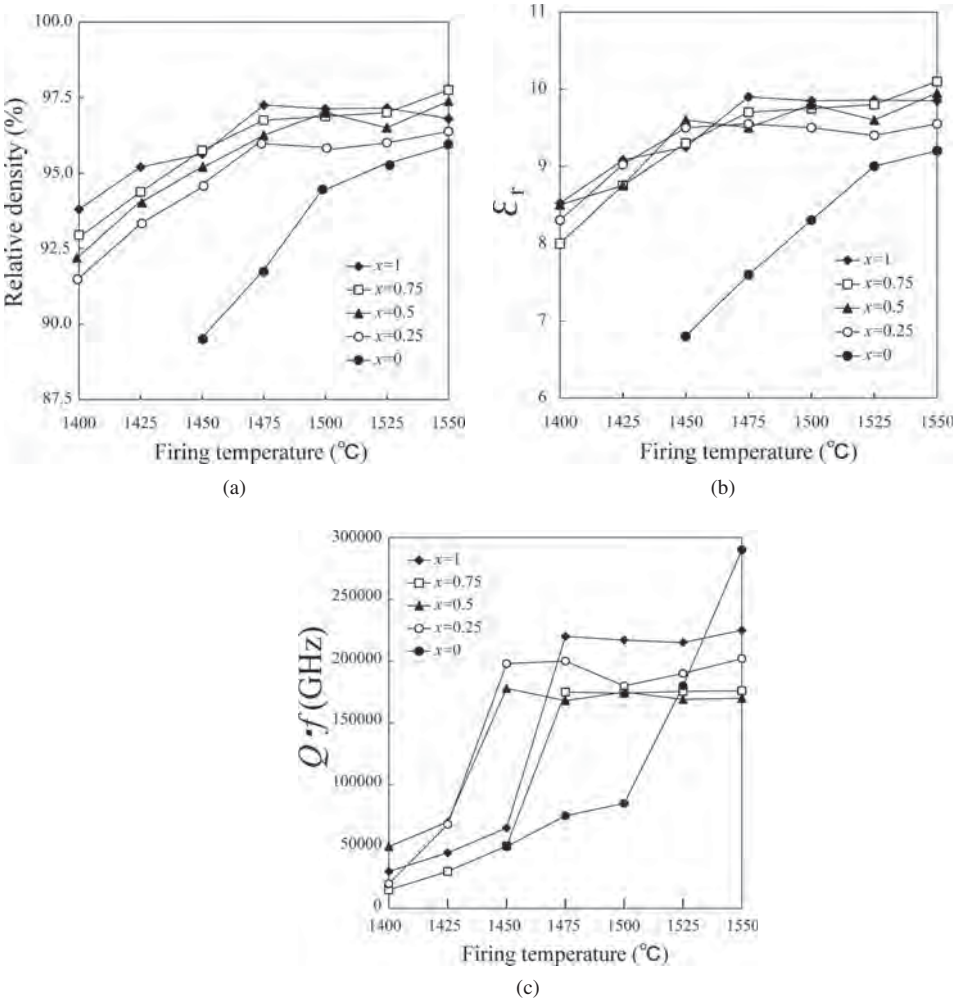

Figure 5.57 *(a) Relative density, (b) the ε_r values, and (c) Qf of $(Mg_{1-x}Zn_x)Ga_2O_4$ s.s. as a function of the firing temperature. Source: Kan et al. 2014 [88].*

applications. Magnesium borate $Mg_3B_2O_6$ (Kotoite) was originally found during research on new glass-ceramics for LTCC by Mori *et al*. (2006) [94]. $Mg_3B_2O_6$ has good microwave dielectric properties with $Qf = 150\ 400$ GHz, $\varepsilon_r = 7.2$. Nishizuka *et al.* [95] synthesized $Mg_3B_2O_6$ from the nominal composition of MgO–25 mol% B_2O_3 by sintering at 1320 °C. It has the best Qf value of 310 000 GHz, $\varepsilon_r = 7.2$, and $\tau_f = -60.6$ ppm/°C. The $Mg_3B_2O_6$ compound also precipitated with MgO at 1330 °C for 2 hours from the nominal composition of MgO–33 mol% B_2O_3 ($Mg_2B_2O_5$) with properties of $Qf = 260\ 100$ GHz, $\varepsilon_r = 7.4$, and $\tau_f = -60.0$ ppm/°C [95]. The $Mg_3B_2O_6$ ceramics obtained from $Mg_3B_2O_6$–5 wt% $Mg_2B_2O_5$ composition showed 10 times larger grains and showed a high Qf of 240 000 GHz

and $\varepsilon_r = 7$ [96]. Doslar *et al*. [97] also reported similar properties on the $Mg_3B_2O_6$ ceramics synthesized by a solid-state reaction. $Zn_3B_2O_6$ ceramics, with Zn substituted for Mg, is also a promising candidate for LTCC substrate application, which shows the properties of *Qf* value of 58 535 GHz, $\varepsilon_r = 6.8$, and $\tau_f = -58$ ppm/°C [98]. AB_2O_4 compounds are used as a low sintering agent, but there are no data on Sebastian's database. On the other hand, $LaBO_3$ ceramics in the RBO_3 (R = La, Nd, Sm, Dy, Ho, Y) series [99, 100] show a high *Qf* of 76 900 GHz, $\varepsilon_r = 11.8$, $\tau_f = -52$ ppm/°C.

5.4.8.2 Phosphate

Phosphate also exhibits a low dielectric constant because the crystal structure is composed by a PO_4 tetrahedron similar to an SiO_4 tetrahedron [101]. The amount of P–O ionic character (p) is 30% calculated by Equation (5.8) in Section 5.4.5. The dielectric constant varies in the range 6 to 12, which is larger than that of silicates. Hence, the phosphates are also candidates for millimeter-wave dielectrics. The phosphates join with PO_4 tetrahedra to form similar structures of silicates. Aluminum phosphate $AlPO_4$ (berlinite) is a similar structure to quartz SiO_2 and is composed of a three-dimensional framework of tetrahedra, with a low *Qf* as compared with quartz with a high *Qf* [102]. The $LiMgPO_4$ compound also has a similar structure with forsterite, which is called as olivine-type compound. The $LiMgPO_4$ compound substituted Zn for Mg exhibits a high *Qf* of 99 700 GHz with a low $\varepsilon_r = 6.7$ and $\tau_f = -62$ ppm/°C [103]. The τ_f was improved to –5 ppm/°C by adding a 0.12 volume fraction of TiO_2 with dielectric properties $\varepsilon_r = 10.1$ and $Qf = 52\,900$ GHz [103].

Complex pyrophosphate compounds AMP_2O_7 (A = Ca, Sr; M = Zn, Cu) [104] could be densified below 950 °C without any glass addition and exhibit a low $\varepsilon_r < 8$, a high *Qf* value and negative τ_f. The $SrCuP_2O_7$ ceramics sintered at 925 °C for 2 hours exhibited the highest *Qf* value of 101100 GHz in this compound series, $\varepsilon_r = 7.04$, and $\tau_f = -64$ ppm/°C. However, this compound seriously reacts with silver at 700 °C, although $SrZnP_2O_7$ could be co-fired with copper in a reduced atmosphere and exhibits $\varepsilon_r = 7.06$, $Qf = 52\,781$ GHz, and $\tau_f = -70$ ppm/°C. Various rare-earth orthophosphates (RPO_4) [105], such as monazite (R = La, Ce, Pr, Nd, Sm, Eu) and xenotime (R = Tb, Dy, Ho, Er, Tm, Yb, Y), exhibited low permittivity, high *Qf*, and negative τ_f values. The higher ε_r and more negative τ_f value of monazite than those of xenotime are attributed to a decrease in *R*–O bond strength. However, the *Qf* value was not affected by the crystal structure and both monazite and xenotime had a similar *Qf* value of approximately 60 000 GHz.

5.4.8.3 Vanadate

The magnesium orthovanadate $Mg_3(VO_4)_2$ ceramics [106] could be sintered at 750 to 1050 °C without any glass addition; the maximum *Qf* value of 65 440 GHz was obtained at 1050 °C accompanied with grain growth of approximately 10 μm. The $(Mg_{3-x}Co_x)(VO_4)_2$ compound with $x = 2$ sintered at 900 °C showed an improvement in *Qf* (78 900 GHz) with a low ε_r of 9.5 and negative τ_f of –94.5 ppm/°C [106]. Figure 5.58a, b, c, and d show, respectively. the bulk density, ε_r, *Qf*, and τ_f as a function of the sintering temperature. The effects of the substitution are exhibited clearly at 850 for $x = 3$, 900 for $x = 2$, and 1000 °C

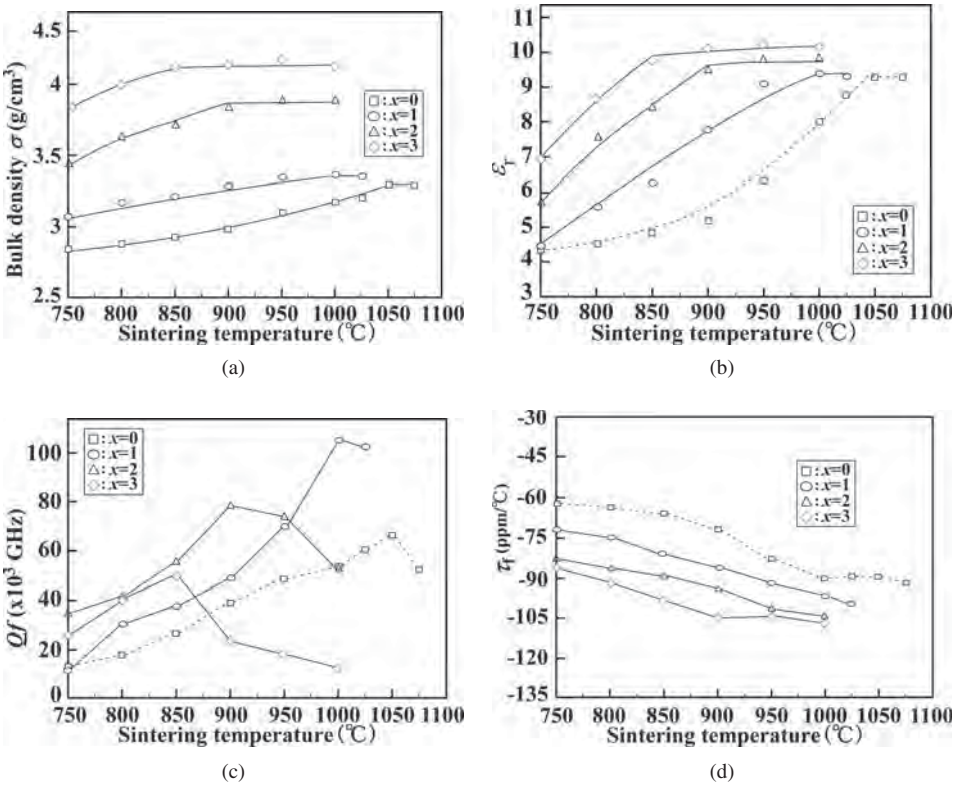

Figure 5.58 *The effects of Co substitution for Mg on (a) the bulk density, (b) ε_r, (c) Qf, and (d) τ_f of $(Mg_{3-x}Co_x)(VO_4)_2$ ceramics sintered for 5 h in air. Source: Umemura et al. 2005 [106].*

for $x = 1$ in the three figures. They depend on the amount of $Co_3(VO_3)_2$ ceramics, which form the liquid phase at approximately 850 °C. The ceramics with $x = 1$ exhibited the highest *Qf* value of > 100 000 GHz, lowest ε_r of 9.0, and $\tau_f = -90$ ppm/°C [106]. These solid solutions are excellent materials for LTCC because the composition of the ceramics could be selected depending of the sintering temperature.

Ogawa *et al*. [107] also reported $Mg_3(VO_4)_2$–$xBa_3(VO_4)_2$ ceramics with high *Qf* values, with near-zero τ_f by adding Li_2CO_3 as the sintering agent. Figure 5.59a, b, c, and d show, respectively, the density, ε_r, *Qf*, and τ_f as a function of composition x. The highest *Qf* value was obtained at $x = 0.2$, and is higher than 100 000 GHz, as shown in Figure 5.59c. The ε_r and τ_f values are 11.0, –58 ppm/°C, respectively. The near-zero τ_f value is obtained at $x = 0.5$. The variation of these values depend on the existence of the intermediate compound $BaMg_2(VO_4)_2$ and the high decompositional temperature of 1610 °C of $Ba_3(VO_4)_2$. Moreover, in order to reduce the sintering temperature, the sintering conditions are improved by adding Li_2CO_3. The $x = 0.5$ ceramics with 0.0625 wt% Li_2CO_3 exhibit good properties of $Qf = 74\,437$ GHz, $\varepsilon_r = 12.6$, $\tau_f = -5.8$ ppm/°C, which ceramics sintered at 950 °C for 5 hours in air [107].

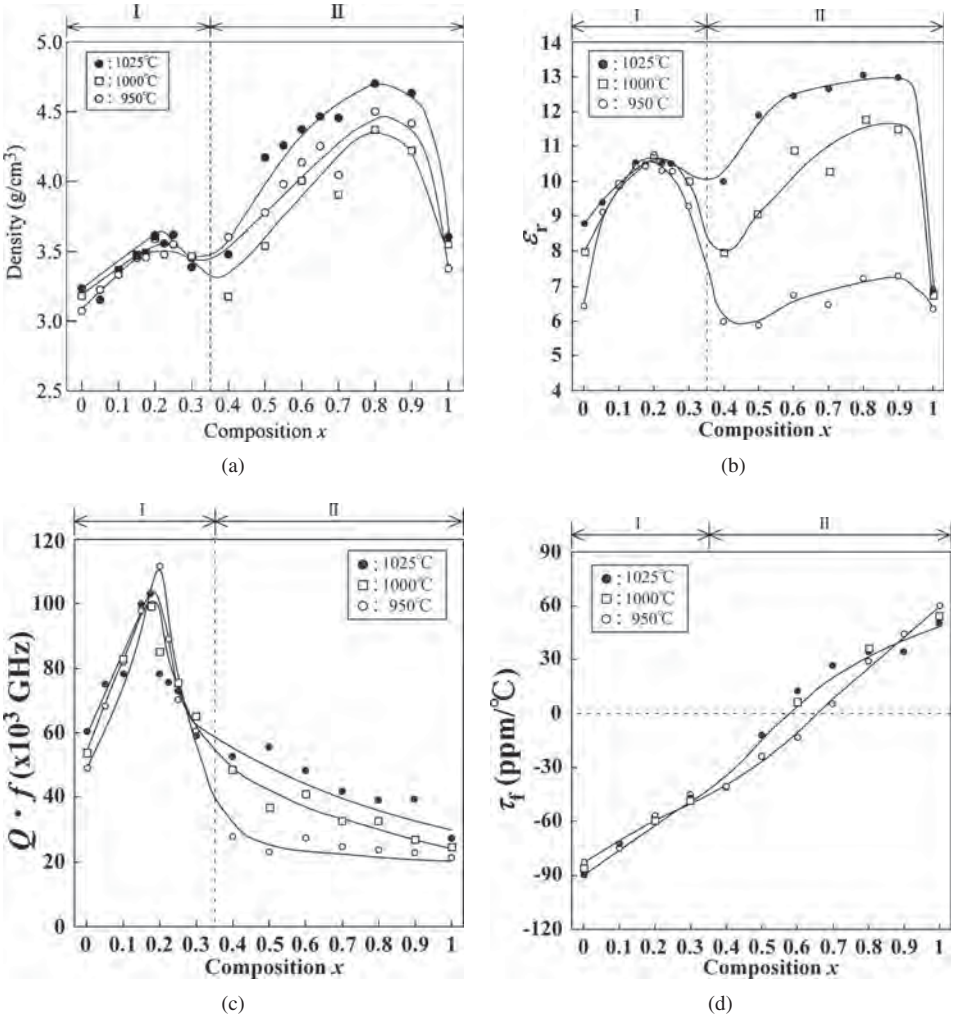

Figure 5.59 *(a) Bulk density, (b) ε_r, (c) Qf, and (d) τ_f of $Mg_3(VO_4)_2$–$xBa_3(VO_4)_2$ ceramics sintered at 950, 1000, and 1025 °C for 5 h in air. After Ogawa et al. [107]*

Acknowledgments

The author would like to thank Professors Hirotaka Ogawa and Akinori Kan at Meijyo University for preparing some data.

References

1. Editor (2013) Take off on WiGig! (in Japanese) *Nikkei Electronics* No. 1123 (December 9, 2013).

2. Ministry of Public Management, Home Affairs, Posts and Telecommunications in Japan. http://www.tele.soumu.go.jp/resource/search/myuse/use/ika.pdf, http://www.tele.soumu.go.jp/e/index.htm.
3. Editor (2008) What is a millimeter-wave? (in Japanese) *J-Net*. http://j-net21.smrj.go.jp/develop/digital/entry/001-20081119-06.html/ (accessed March 28, 2016).
4. Toyota News Release (in Japanese) (February 26, 2009).
5. Nikkei Electronics (2014) Millimeter wave forefront (in Japanese), Nikkei BP, ISBN: 978-4-8222-7694-2.
6. Fujimoto, M., Yasufuku, Y., Kan, A., *et al.* (2015) Low loss LTCC substrates for millimeter-wave application (in Japanese). Speech presented at the 150th Electronic Ceramic Process Meeting in Bannkokubashi Comvension Center, Yokohama, February 14, 2015.
7. Japan Fine Ceramics Center (2014) Development for high integration LTCC substrates with high Q and low dielectric constant (in Japanese). Report of Support Industrial Project 2014. METI, Japan, March 30, 2014.
8. Nakazawa, H. and Shimakata, Y. (2011) Forsterite- and willemite-based ceramic substrates with low thermal expansion coefficient and high thermal conductivity (IV) — The evaluation of MSL, BPF and the resonator for millimeter wave bands (in Japanese). Speech presented at IEICE Society Conference 2011, Hokkaido University, Sapporo, Japan, September 13–16, 2011.
9. Ohsato, H., Tsunooka, T., Kan, A., *et al*. (2004) Microwave-millimeterwave dielectric materials. *Key Engineering Materials*, **269**, 195–198.
10. Sebastian, M.T. (2008) *Dielectric Materials for Wireless Communication*, Elsevier Science Publishers, Amsterdam.
11. Kolar, D., Stadler, Z., Gaberscek, S., and Suvorov, D. (1978) Ceramic and dielectric properties of selected compositions in the $BaO–TiO_2–Nd_2O_3$ system. *Berichte der Deutschen Keramischen Gesellschaft*, **55**, 346–347.
12. Ohsato, H., Ohhashi, T., Nishigaki, S., *et al*. (1993) Formation of solid solutions of new tungsten bronze-type microwave dielectric compounds $Ba_{6-3x}R_{8+2x}Ti_{18}O_{54}$ (R = Nd and Sm, $0 < x < 1$). *Japanese Journal of Applied Physics*, **32** (9B), 4324–4326.
13. Ohsato, H., Ohhashi, T., Kato, H., *et al*. (1995) Microwave dielectric properties and structure of the $Ba_{6-3x}R_{8+2x}Ti_{18}O_{54}$ solid solutions. *Japanese Journal of Applied Physics*, **34**, 187–191.
14. Koga, E. and Moriwake, H. (2003) Effects of superlattice ordering and ceramics microstructure on the microwave Q factor of complex perovskite-type oxide $Ba(Zn_{1/3}Ta_{2/3})O_3$ (in Japanese). *Journal of Ceramic Society of Japan*, **111** (Suppl.), 767–775.
15. Ohsato, H., Koga, E., Kagomiya, I., and Kakimoto, K. (2010) Origin of high Q for microwave complex perovskite. *Key Engineering Materials*, **421-422**, 77–80.
16. Tohdo, Y., Kakimoto, K., Ohsato, H., *et al.* (2006) Microwave dielectric properties and crystal structure of homologous compounds $ALa_4Ti_4O_{15}$ (A = Ba, Sr and Ca) for base station applications. *Journal of the European Ceramic Society*, **26**, 2039–2043.
17. Ohsato, H. (2005) Microwave materials with high Q and low dielectric constant for wireless communications. *Proceedings of the Materials Research Society Symposium*, **833**, 55–62.
18. Ohsato, H., Tsunooka, T., Ohishi, Y., *et al*. (2003) Millimeter-wave dielectric ceramics of alumina and forsterite with high quality factor and low dielectric constant. *Journal of Korean Ceramic Society*, **40** (4), 350–353.
19. Tsunooka, T., Andou, M., Higashida, Y., *et al.* (2003) Effects of TiO_2 on sinterability and dielectric properties of high-Q forsterite ceramics. *Journal of the European Ceramic Society*, **23** (14), 2573–2578.
20. Tsunooka, T., Sugiyama, H., Kakimoto, K., *et al*. (2004) Zero temperature coefficient τ_f and sinterability of forsterite ceramics by rutile addition *Journal Ceramic Society of Japan*, **112** (Suppl.), S1637–S1640.
21. Ando, M., Himura, K., Tsunooka, T., *et al*. (2007) Synthesis of high-quality forsterite. *Japanese Journal of Applied Physics*, **46** (10B), 7112–7116.

22. Ando, M., Ohsato, H., Kagomiya, I., and Tsunooka, T. (2008) Quality factor of forsterite for ultrahigh frequency dielectrics depending on synthesis process. *Japanese Journal of Applied Physics*, **47** (9), 7729–7731.
23. Guo, Y., Ohsato, H., and Kakimoto, K. (2006) Characterization and dielectric behavior of willemite and TiO_2-doped willemite ceramics at millimeter-wave frequency. *Journal of the European Ceramic Society*, **26**, 1827–1830.
24. Ohsato, H., Kim, J.S., Kim, A.Y., *et al*. (2011) Millimeter-wave dielectric properties of cordierite/indialite glass ceramics. *Japanese Journal of Applied Physics*, **50** (9), 09NF01-1-5.
25. Ohsato, H., Kim, J.S., Cheon, C.I., and Kagomiya, I. (2013) Millimeter-wave dielectrics of indialite/cordierite glass ceramics: estimating Si/Al ordering by volume and covalency of Si/Al octahedron. *Journal Ceramic Society of Japan*, **121**, 649–654.
26. Kagomiya, I., Suzuki, I., and Ohsato, H. (2009) Microwave dielectric properties of $(Ca_{1-x}Sr_x)SiO_3$ ring silicate solid solutions. *Japanese Journal of Applied Physics*, **48**, 09KE02-1-4.
27. Ohsato, H., Terada, M., and Kawamura, K. (2012) Fabrication conditions of diopside for millimeterwave dielectrics. *Japanese Journal of Applied Physics*, **51** (9), 09LF02-1-4.
28. Ohsato, H., Kagomiya, I., Terada, M., and Kakimoto, K. (2010) Origin of improvement of Q based on high symmetry accompanying Si–Al disordering in cordierite millimeter-wave ceramics. *Journal of the European Ceramic Society*, **30**, 315–318.
29. Kajfez, D. and Guillon, P. (1998) *Dielectric Resonators*, 2nd edn, Noble Publishing Corporation, Atlanta, GA.
30. Miyauchi, T. (2008) Research for microwave–millimeter-wave alumina ceramics (in Japanese). Dr Thesis, Nagoya Institute of Technology, p. 29.
31. Ohsato, H. (2014) Design of microwave dielectrics based on crystallography, in *Advances in Multifunctional Materials and Systems II*, Ceramic Transaction 245 (eds J. Akedo, X.M. Chen, and T. Tseng), John Wiley & Sons, Inc., Hoboken, NJ, pp. 87–100.
32. Ohsato, H. (2016) Microwave dielectrics with perovskite-type structure, in *Perovskite Materials* (eds L. Pan and G. Zhu), INTEC, 2016, Croatia, Chapter 9. Open Access: http://cdn.intechopen.com/pdfs-wm/49723.pdf.
33. Surendran, K.P., Santha, N., Mohanan, P., and Sebastian, M. (2004) Temperature stable low loss ceramic dielectrics in $(1 - x)\ ZnAl_2O_4$–$xTiO_2$ system for microwave substrate applications. *European Physical Journal, B*, **41**, 301–306.
34. Ohsato, H., Kato, K., Mizuta, M., *et al*. (1995) Microwave dielectric properties of the $Ba_{6-3x}(Sm_{1-y}, R_y)_{8+2x}Ti_{18}O_{54}$ (R = Nd and La) solid solutions with zero temperature coefficient of the resonant frequency. *Japanese Journal of Applied Physics*, **34** (9B), 5413–5417.
35. Ohsato, H., Ando, M., and Tsunooka, T. (2007) Synthesis of forsterite with high Q and near zero TCf for microwave/millimeterwave dielectrics. *Journal of Korean Ceramic Society*, **44** (11), 597–606.
36. Ohsato H. (2005) Research and development of microwave dielectric ceramics for wireless communications. *Journal of Ceramic Society of Japan*, **113**, 703–711.
37. Tsunooka, T., Sugiyama, T., Ohsato, H., *et al.* (2004) Development of forsterite with high Q and zero temperature coefficient τ_f for millimeterwave dielectric ceramics. *Key Engineering Materials*, **269**, 199–202.
38. Tsunooka, T., Ando, M., Suzuki, S., *et al*. (2013) Research and developments for millimeterwave dielectric forsterite with low dielectric constant, high Q, and zero temperature coefficient of resonant frequency. *Japanese Journal of Applied Physics*, **52** (9), 09KH02-1-4.
39. Massazza, F, and Sirchia, E. (1958) Phase diagrams for ceramics No.723, Dhim. Ind. (Milan), 40 466, 86.
40. Wu, P., Erikson, G., Pelton, A.D., and Blander, M. (1993) Prediction of the thermodynamic properties and phase diagrams of silicate systems – Evaluation of the FeO–MgO–SiO_2 system. *The Iron and Steel Institute of Japan International*, **33**, 26–35.
41. Dong, M., Yue, Z., Zhuang, H., *et al.* (2008) Microstructure and microwave dielectric properties of TiO_2 doped Zn_2SiO_4 ceramics synthesized through the sol–gel process. *Journal of American Ceramic Society*, **91**, 3981–3985.

42. Sebastian, M.T., Ubic, R., and Jantunen, H. (2015) Low-loss dielectric ceramic materials and their properties. *International Materials Review*, **60**, 395–415.
43. Kim, J.-S., Song, M.-E., Joung, M.-R., *et al.* (2010) Effect of B_2O_3 addition on the sintering temperature and microwave dielectric properties of Zn_2SiO_4 ceramics. *Journal of the European Ceramic Society*, **30**, 375–379.
44. Kim, J.-S., Song, M.-E., Joung, M.-R., *et al.* (2008) Low temperature sintering and microwave dielectric properties of V_2O_5 added Zn_2SiO_4 ceramics. *Journal of American Ceramic Society*, **91**, 4133–4136.
45. Dou, G., Zhou, D., and Gong, S. (2012) Low temperature sintered Zn_2SiO_4–$CaTiO_3$ ceramic with near zero temperature coefficient of resonant frequency. *Journal of Alloys and Compounds*, **513**, 466–473.
46. Suvorov, D. (2010) Contemporary materials for electronic applications, in *The 6th Microwave Materials and Their Applications*, Warsaw, Poland, September 1–4, 2010.
47. Ando, M., Ohsato, H., Igimi, D., *et al*. (2015) Low-temperature sintering of silica–boric acid-doped willemite and microwave dielectric properties. *Japanese Journal of Applied Physics*, **54**, 10NE03-1-6.
48. Miyashiro, A. (1957) Cordierite–indialite relations. *American Journal of Science*, **255**, 43–62.
49. Gibbs, G.V. (1966) Polymorphism of cordierite. I. Crystal structure of low cordierite. *American Mineralogist*, **51**, 1068–1087.
50. Wu, J.-M. and Huang, H.L. (2000) Effect of crystallization on microwave dielectric properties of stoichiometric cordierite glasses containing B_2O_3 and P_2O_5 glasses. *Journal of Materials Research*, **15**, 222–227.
51. Terada, M., Kawamura, K., Kagomiya, I., *et al*. (2007) Effect of Ni substitution on the microwave dielectric properties of cordierite. *Journal of the European Ceramic Society*, **27**, 3045–3148.
52. Izumi, F. and Ikeda, T. (2000) A Rietveld-analysis program RIETAN-98 and its applications to zeolites. *Materials Science Forum*, **321–324**, 198–203.
53. Toraya, H., Hibino, H., and Ohsumi, K. (1996) A new powder diffractometer for synchrotron radiation with multiple-detector system. *Journal of Synchrotron Radiation*, **3**, 75–83.
54. Brown, I.D. and Shannon, R.D. (1973) Empirical bond-strength–bond-length curves for oxides. *Acta Crystallographica*, **A29**, 266–282.
55. Brown, I.D. and Wu, K-K. (1976) Empirical parameters for calculating cation–oxygen bond valences. *Acta Crystallographica*, **B32**, 1957–1959.
56. Kagomiya, I. and Ohsato, H. (2014) Crystallized glass ceramic dielectrics for high frequency. Japanese Patent Application No. 2014-164285, filed August 12, 2014.
57. Yang, H. and Prewitt, C.T. (1999) On the crystal structure of pseudowollastonite ($CaSiO_3$). *American Mineralogist*, **84**, 929–932.
58. Nishi, F. (1997) Strontium metasilicate, $SrSiO_3$. *Acta Crystallographica*, **C53**, 534–536.
59. Moir, G.K. and Glasser, F.P. (1974) System $CaSiO_3$–$SrSiO_3$. *Transactions and Journal of the British Ceramic Society*, **73**, 199–206.
60. Pauling, L. (1980) The nature of silicon–oxygen bonds. *American Mineralogists*, **65**, 321–323.
61. Pauling, L. (1967) *The Chemical Bond*, Cornell University Press, New York, pp. 69–73.
62. Kittel, C. (1956) *Introduction to Solid State Physics*, 2nd edn, John Wiley & Sons, Inc., New York, p. 57.
63. Hannay, N.B. and Smith, C.P. (1946) The dipole moment of hydrogen fluoride and the ionic character of bonds. *Journal of American Chemistry Society*, **68** (2), 171–173. doi: 10.1021/ja01206a003.
64. Terada, M. (2007) Crystal structure and microwave dielectric properties of cordierite ceramics. Master Thesis, Nagoya Institute of Technology.
65. Wu, S. and Ma, Q. (2013) Synthesis characterization and microwave dielectric properties of Zn_2GeO_4. *Journal of Alloys and compounds*, **567**, 40–46.
66. Chen, C.X., Wu, S.P., and Li, J.H. (2013) Synthesis and microwave dielectric properties of B_2O_3 doped Mg_2GeO_4. *Journal of Alloys and Compounds*, **578**, 153–156.

67. Hurlbut, Jr, C.S., and Cornelis, K. (1971) *Manual of Mineralogy (after James D. Dana)*, 19th edn, John Wiley & Sons, Inc., New York, pp. 420–431.
68. Nishigaki, S., Yanao, S., Fukuta, J., *et al*. (1985) A new multilayered low temperature fireable ceramic substrate, in *Proceedings of International Symposium of Hybrid Microelectrics* (*ISHM*), Anaheim, CA, vol. 85, pp. 225–234.
69. Nishigaki, S., Fukuta, J., Yanao, S., Kawabe, H.K. Noda, and M. Fukaya (1986) A new low temperature fireable Ag multilayer ceramic substrate having post-fired Cu conductor, in *Proceedings of the International Symposium of Hybrid Microelectrics* (*ISHM*86), pp. 429–437.
70. Nishigaki, S. (2005) u-Hybrid as ECUs for next generation automotives using LTCC (LFC) material system (in Japanese). *Ceramics*, **40**, 137–123.
71. Krzmanc, M.M., Valant, M., Jancar, B., and Suvorov, D. (2005) Subsolidus synthesis and microwave dielectric characterisation of plagioclase feldspars. *Journal of American Ceramic Society*, **88**, 2472–2479.
72. Krzmanc, M.M., Meden, A., and Suvorov, D. (2007) The correlation between the structure and the dielectric properties of $K_xBa_{1-x}Ga_{2-x}Ge_{2+x}O_8$ ceramics. *Journal of the European Ceramic Society*, **27** (8–9), 2957–2961.
73. Krupka, J., Derzakowski, K., Tobar, M.E., *et al*. (1999) Complex permittivity of some ultralow loss dielectric crystals at cryogenic temperatures. *Measurement of Science and Technology*, **10**, 387.
74. Alford, N.Mc.N., Breeze, J., Wang, X., *et al*. (2001) Dielectric loss of oxide single crystals and polycrystalline analogues from 10 to 320 K. *Journal of the European Ceramic Society*, **21**, 2605–2611.
75. Huang, C.-L., Wang, J.-J., Yen, F.-S., and Huang, C.-Y. (2008) Microwave dielectric properties and sintering behavior of nano scaled $(\alpha + \theta)$–Al_2O_3 ceramics. *Material Research Bulletin*, **43**, 1463–1471.
76. Alford, N.McN,N. and Penn, S.J. (1996) Sintered alumina with low dielectric loss. *Journal of Applied Physics*, **80**, 5895–5898.
77. Miyauchi, Y., Ohishi, Y., Miyake, S., and Ohsato, H. (2006) Improvement of the dielectric properties of rutile-doped Al_2O_3 ceramics by annealing treatment. *Journal of the European Ceramic Society*, **26**, 2093–2096.
78. Levin, E.M. and McMurdie, H.F. (1975) Phase diagrams for ceramists. *American Ceramic Society*, **3**, 135.
79. Kan, A., Ogawa, H., and Ohsato, H. (2004) Relationship between bond strength and microwave dielectric properties of corundum type $(Mg_{4-x}Co_x)Nb_2O_9$ and $Mg_4(Nb_{2-y}Ta_y)O_9$ solid solutions. *Journal Ceramic Society of Japan*, **112** (Suppl. 1), S1622–S1626.
80. Ogawa, H., Kan, A., Ishihara, S., and Higashida, Y. (2003) Crystal structure of corundum type $Mg_4(Nb_{2-x}Ta_x)O_9$ microwave dielectric ceramics with low dielectric loss. *Journal of the European Ceramic Society*, **23**, 2485–2488.
81. Ogawa, H., Taketani, H., Kan, A., *et al*. (2005) Evaluation of electronic state of $Mg_4(Nb_{2-x}Sb_x)O_9$ microwave dielectric ceramics by first principal calculation method. *Journal of the European Ceramic Society*, **25**, 2859–2863.
82. Kumada, N., Taki, K., and Kinomura, N. (2000) Single crystal structure refinement of a magnesium niobium oxide: $Mg_4Nb_2O_9$. *Materials Research Bulletin*, **35**, 1017–1021.
83. Adachi, H., Shiokawa, S., Tsukada, M., *et al*. (1979) Discrete variational Xα cluster calculations. III. Application to transition metal complexes. *Journal of the Physical Society of Japan*, **47**, 1528–1537.
84. Adachi, H., Tsukada, M., and Satoko, C. (1978) Discrete variational Xα cluster calculations. I. Application to metal clusters, *Journal of the Physical Society of Japan*, **45**, 875–883.
85. Surendran, K.P., Bijumon, P.V., Mohanan, P., and Sebastian, M.T. (2005) $(1-x)MgAl_2O_{4-x}TiO_2$ dielectrics for microwave and millimeter wave applications. *Applied Physics*, **A81**, 823–826.

86. Wu, X., Xue, J., Wang, R., and Li, J. (2014) Synthesis, characterization and microwave dielectric properties of spinel $MgGa_2O_4$ ceramic material. *Journal of Alloys and Compounds*, **585**, 542–548.
87. Xue, J., Wu, S., and Li, J. (2013) Synthesis microstructure and microwave dielectric properties of spinel ZnGa2O4 ceramics. *Journal of American Ceramic Society*, **96**, 2481–2485.
88. Kan, A., Takahashi, S., Moriyama, T., and Ogawa, H. (2014) Influence of Zn substitution for Mg on microwave dielectric properties of spinel-structured $(Mg_{1-x}Zn_x)Ga_2O_4$ solid solutions. *Japanese Journal of Applied Physics*, **53**, 09PB03.
89. Putnis, A. (1992) *Introduction to Mineral Sciences*, Cambridge University Press, 134 pp.
90. Hahn, T. (ed.) (2002) *International Table for Crystallography*, vol. A, *Space-Group Symmetry*, 5th edn, Published for The International Union of Crystallography (IUCr) by Kluwer Academic Publishers, Dordrecht, pp.696–703.
91. Kan, A., Moriyama, T., Takahashi, S., and Ogawa, H. (2013) Cation distributions and microwave dielectric properties of spinel-structured $MgGa_2O_4$ ceramics. *Japanese Journal of Applied Physics*, **52**, 09KH01.
92. Hill, R.J., Craig, J.R., and Gibbs, G.V. (1979) Systematics of the spinel structure type. *Physics and Chemistry of Minerals*, **4**, 317–339.
93. Surendran, K.P., Sebastian, M.T., Manjusha, M.V., and Philip, J. (2005) A low loss, dielectric substrate in $ZnAl_2O_4$–TiO_2 system for microelectronic applications. *Journal of Applied Physics*, **98**, 44101.
94. Mori, N., Sugimoto, Y., Harada, J., and Higuchi. Y. (2006) Dielectric properties of new glass-ceramic for LTCC applied to microwave or millimeter-wave frequencies. *Journal of the European Ceramic Society*, **26**, 1925–1928.
95. Nishizuka, M., Ogawa, H., Kan, A., and Sugino, M. (2009) Synthesis and microwave dielectric properties of MgO–x mol% B_2O_3 (x = 33 and 25) ceramics in MgO–B_2O_3 system. *Ferroelectrics*, **388**, 101–108.
96. Dosler, U., Krzmanc, M.M., Jancar, B., and Suvorov, D. (2011) A high Q microwave dielectric materials based on $Mg_3B_2O_6$. *Journal of American Ceramic Society*, **93**, 3788–3792.
97. Dosler, U., Krzmanc, M.M., and Suvorov, D. (2010) The synthesis and microwave dielectric properties of $Mg_3B_2O_6$ and $Mg_2B_2O_5$ ceramics. *Journal of the European Ceramic Society*, **30**, 413–418.
98. Wu, X.G., Wang, H., Chen, Y.H., and Zhou, D. (2012) Synthesis and microwave dielectric properties of $Zn_3B_2O_6$ ceramics for substrate applications. *Journal of American Ceramic Society*, **95**, 1793–1795.
99. Takada, T., Yamamoto, H., and Kageyama, K. (2003) Synthesis and microwave dielectric properties of $x$$Re_2O_3$–$y$$B_2O_3$ (Re = La, Nd, Sm, Dy, Ho and Y) compounds. *Japanese Journal of Applied Physics*, **42**, 6162–6167.
100. Chen, X.M., Bai, S., Li, M., and Zhang, W. (2013) Synthesis, characterization and dielectric properties of low loss $LaBO_3$ ceramics. *Journal of the European Ceramic Society*, **33**, 3001–3006.
101. Zachariasen, W.H. (1948) The crystal structure of the normal orthophosphates of barium and strontium. *Acta Crystallographica*, **1**, 263–265.
102. Abhilash, P., Thomas, D., and Sebastian, M.T. (2013) Sintering and microwave dielectric properties of $AlPO_4$–MgF_2 ceramic composites. *International Journal of Modern Physics*, Conference Series **22**, 159–163.
103. Thomas, D. and Sebastian, M.T. (2010) Temperature compensated LiMgPO4: a new glass free low temperature cofired ceramic. *Journal of American Ceramic Society*, **93**, 3828–3831.
104. Bian, J.J., Kim, D.W., and Hong, K.S. (2005) Glass free LTCC microwave dielectric ceramics. *Materials Research Bulletin*, **40**, 2120–2129.
105. Cho, I.S., Choi, G.K., An, J.S., *et al*. (2009) Sintering microstructure and microwave dielectric properties of rare earth phosphates $RePO_4$ (Re = La, Ce, Nd, Sm, Tb, Dy, Y, Yb). *Materials Research Bulletin*, **44**, 173–178.

106. Umemura R., Ogawa, H., Ohsato, H., *et al.* (2005) Microwave dielectric properties of low temperature sintered $Mg_3(VO_4)_2$ ceramics. *Journal of the European Ceramic Society*, **25**, 2865–2870.
107. Ogawa, H., Yokoi, A., Unemura, R., and Kan, S. (2007) Microwave dielectric properties of $Mg_3(VO_4)_2$–$xBa_3(VO_4)_2$ ceramics for LTCC with near zero temperature coefficient of resonant frequency. *Journal of the European Ceramic Society*, **27**, 3099–3104.

6

Other Important Materials

M.T. Sebastian[1] *and R.C. Pullar*[2]
[1]*Microelectronics Research Unit, Faculty of Information Technology and Electrical Engineering, University of Oulu, Oulu, Finland*
[2]*Department of Materials and Ceramic Engineering/CICECO – Aveiro Institute of Materials, University of Aveiro, Campus Universitário de Santiago, Aveiro, Portugal*

6.1 Spinel

The compounds with the general formula AM_2O_4 (A = Mg, Zn, Co, Ni, Cu; M = Al, Ga, Fe) are referred to as spinels [1], which belong to the face-centered cubic symmetry group $F\,d\,\overline{3}\,mn$. Their cubic cell contains a close-packed array of 32 oxygen atoms with cations in the tetrahedral and octahedral interstices. In the normal spinel structure, tetrahedral sites are occupied by divalent cations whereas octahedral sites are occupied by trivalent cations. The crystal structure of spinel is given in detail in Chapter 5 in Section 5.4.7.

6.1.1 $ZnAl_2O_4$

The zinc aluminate spinels are finding versatile applications in industrial ceramics, radiation resistant matrices in nuclear bombardments, and supports for Pt catalysts. The mixture characteristics of $ZnAl_2O_4$–TiO_2 were also investigated to explore the possibility of developing ultrafiltration membranes with the aim of increasing the electrical interaction of $ZnAl_2O_4$ and TiO_2 layers towards the filtered ionic species [2]. Zinc aluminate has very low electrical conductance (5.4×10^{-6} ohm^{-1}) [3], which is a unique characteristic of low-loss dielectrics. Van der Laaga *et al.* reported [4] that ε_r of $ZnAl_2O_4$ was 9.46 at a frequency of 10 MHz and Surendran *et al.* [5, 6] were the first to report the microwave dielectric properties of MAl_2O_4 (M = Zn, Mg) ceramics. The $ZnAl_2O_4$ sintered into a dense ceramics at 1425 °C with a densification of about 96%. The sintered $ZnAl_2O_4$ has $\varepsilon_r = 8.5$, $Qf = 56$ 300 GHz, and τ_f of –79 ppm/°C [5]. In synthetic spinels, a disordered distribution of cations

Microwave Materials and Applications, First Edition.
Edited by Mailadil T. Sebastian, Rick Ubic and Heli Jantunen.
© 2017 John Wiley & Sons, Ltd. Published 2017 by John Wiley & Sons, Ltd.

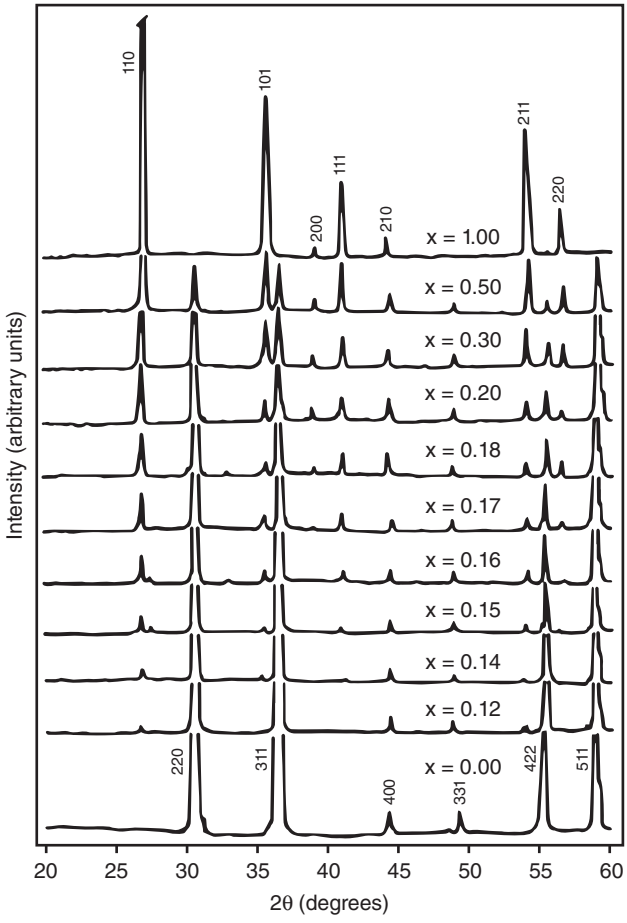

Figure 6.1 *Powder diffraction patterns of (1 – x)$ZnAl_2O_4$–xTiO_2 mixed phases for x = 0.0, 0.12, 0.14, 0.15, 0.16, 0.17, 0.18, 0.2, 0.3, 0.5, 1.0. Source: Adapted from Surendran* et al. *2004 [5].*

exists systematically in such a way that a fraction of trivalent aluminum ions may occupy tetrahedral sites for zinc. Therefore the sintered samples were annealed at 1000 °C for 5 hours. It was reported that addition of 1 wt% $CaCO_3$ improved the *Qf* to about 58 000 GHz [5]. The high negative τ_f of $ZnAl_2O_4$ has been tailored by adding TiO_2 [5]. Figure 6.1 shows the XRD patterns recorded from samples for $x = 0.0$, 0.12, 0.15, 0.16, 0.17, 0.18, 0.2, 0.3, 0.4, 0.5, and 1.0 in $(1 - x)ZnAl_2O_4$–$xTiO_2$ composite sintered at 1425 °C. The crystal structure of TiO_2 (rutile) is tetragonal. The intensity of the XRD peaks of spinel phase decreases and that of rutile (ilmenite) increase with an increase in x. The bulk density of the composite initially increased and reaches a maximum when $x = 0.17$, as shown in Figure 6.2. From the figure it is evident that the density of $ZnAl_2O_4$ samples increase when TiO_2 addition reaches a maximum for $x = 0.17$ in $(1 - x)$ $ZnAl_2O_4$–$xTiO_2$ and thereafter it decreases. It has been reported [7] that the densification behavior of TiO_2 is hindered due to the anatase to rutile phase transition consequent to the reduction of Ti^{4+} to Ti^{3+} state. It is believed [8] that addition of dopants with valencies 2 and 3 improves its densification

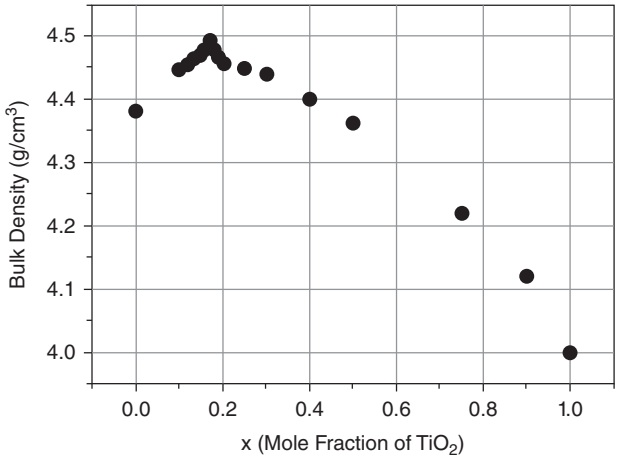

Figure 6.2 *Variation of the bulk density of (1 – x)$ZnAl_2O_4$–xTiO_2 with x. Source: Adapted from Surendran* et al. *2004 [5].*

process, which can compensate its oxygen vacancy that could be developed at the time of sintering. The anatase titania starting material was doped with 1 mol% additive Fe_2O_3, which improved the densification process. The anatase phase transformed to rutile on sintering at high temperature.

The microwave dielectric properties of zinc aluminate spinel are found to be quite interesting since the dielectric loss factor of this ceramic is found to be low enough for microwave substrate and mm wave applications. The variation of the dielectric constant of $ZnAl_2O_4$ with TiO_2 addition is shown in Figure 6.3 and is compared with different mixing models such as serial, logarithmic, and parallel mixing models (described in Chapter 2). The behavior of the dielectric constant of $ZnAl_2O_4$–TiO_2 mixture does not follow any of the

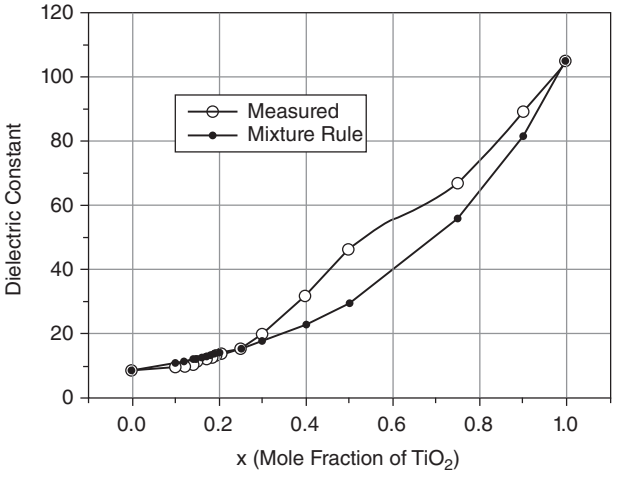

Figure 6.3 *Variation of the ε_r of (1 – x)$ZnAl_2O_4$–xTiO_2 with x. Source: Adapted from Surendran* et al. *2004 [5].*

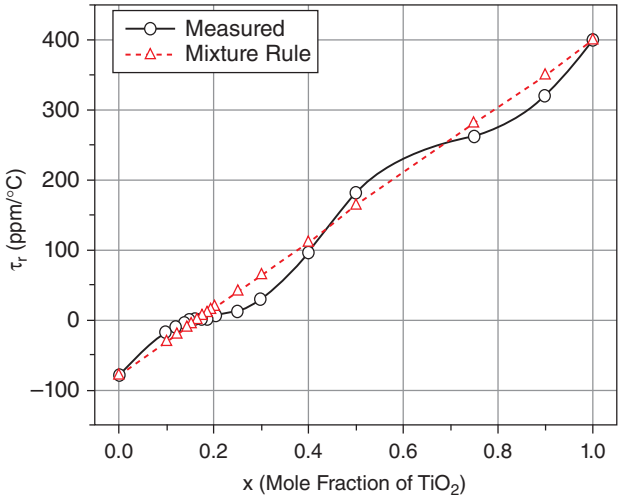

Figure 6.4 *Variation of the temperature coefficient of resonant frequency of (1 – x) $ZnAl_2O_4$–xTiO_2 with x. Source: Adapted from Surendran* et al. *2004 [5].*

mixture rules of random binary phase materials. The dielectric constant shows reasonably good agreement with the logarithmic mixing rule for smaller values of x while it shows noticeable deviation as the value of x increases. The temperature coefficient of resonant frequency (τ_f) of pure $ZnAl_2O_4$ is –79 ppm/°C. It has been shown that variation of τ_f in a random mixture is proportional to the molar variation of the constituent phases [8]. Hence the τ_f of the mixture phases can be computed using a general mixture formula [9]:

$$\tau_{f(\text{eff})} = v_1\tau_{f1} + v_2\tau_{f2}$$

The variation of τ_f of the mixed phases of $ZnAl_2O_4$–TiO_2 is shown in Figure 6.4, from which it is obvious that the variation of mixed phases swinged around the straight line corresponding to the rule of mixtures. The composition $0.83ZnAl_2O_4$–$0.17TiO_2$ shows τ_f of 1 ppm/°C. The variation of the unloaded quality factor of the various mixture phases are plotted in Figure 6.5 as a function of increasing TiO_2 content. The product Qf is maximum (~100 200 GHz) at around $x = 0.17$ in $(1 - x)ZnAl_2O_4$–$xTiO_2$, where the τ_f assumes a minimum value (zero). It is worthwhile to note that the intermediate phases show better quality factors compared to the end phase components, which is unusual in dielectric mixtures. From Figure 6.5, it is clear that the drop in the quality factor is more for the TiO_2-rich compositions since rutile has a lower Qf. Thomas *et al.* found [10] that increasing the sintering temperature to 1450 °C increased the Qf to 91 000 GHz with $\varepsilon_r = 11.7$ with $\tau_f = 1$ ppm/°C. Addition of a small amount of BBSZ glass (0.2 wt%) and sintered at 1400 °C/4h improved the Qf to 120 000 GHz, but the τ_f increased to –7 ppm/°C. Addition of 10 wt% BBSZ lowered the sintering temperature to 950 °C with $\varepsilon_r = 10.9$, $Qf = 12000$ GHz, and $\tau_f =$ –23 ppm/°C. Figure 6.6 shows the backscattered SEM images of $0.83ZnAl_2O_4$–$0.17TiO_2$ sintered at 1450 °C/4 h and $0.83ZnAl_2O_4$–$0.17TiO_2$ + 10 wt% BBSZ glass sintered at 950 °C/10 h.

Huang *et al.* [11] reported a very high Qf of 277 000 GHz for the composition for $x = 0.5$ with τ_f of 177 ppm/°C. As x increased the ε_r and τ_f gradually increased but the Qf increased

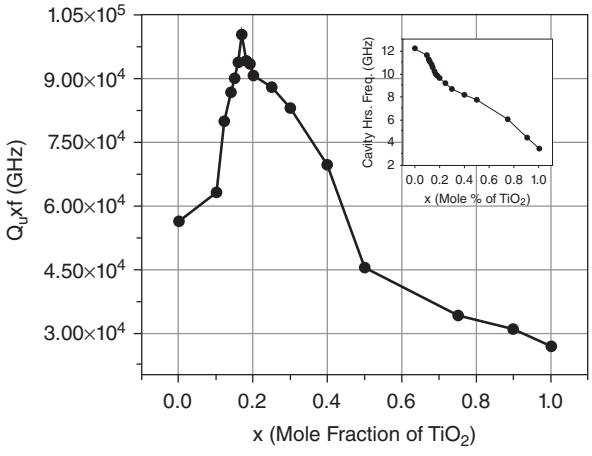

Figure 6.5 *Variation of the unloaded quality factor and resonant frequency of $(1-x)ZnAl_2O_4$–$xTiO_2$ with x. Source: Adapted from Surendran* et al. *2004 [5].*

up to $x = 0.5$ and then decreased with a further increase in x. The high τ_f was tailored to about 2 by adding $MgTiO_3$ or $Mg_4Nb_2O_9$, which lowered the Qf to about 200 000 GHz. Figure 6.7 shows the microstructure of $(1-x)ZnAl_2O_4$–$xTiO_2$ for different values of x. The effect of additives and partial substitutions on the microwave dielectric properties $ZnAl_2O_4$ are given in Table 6.1. Addition of Mg_2TiO_4, $Co_2TiO_4 + TiO_2$ in $ZnAl_2O_4$ are also found to improve Qf but the τ_f is badly affected [12, 13]. The temperature coefficient of relative permittivity of $0.83ZnAl_2O_4$–$0.17TiO_2$ is –16 ppm/°C. The coefficient of thermal expansion of the substrate material $0.83ZnAl_2O_4$–$0.17TiO_2$ in the temperature range 30–1250 °C was found to be 6.3 ppm/°C, which is comparable to that of metallic silicon (4 ppm/°C). The composition $0.83ZnAl_2O_4$–$0.17\ TiO_2$ is an ideal temperature stable, high Q dielectric resonator, which is comparable to many of the conventional low dielectric constant microwave dielectrics like Al_2O_3. In spite of the fact that that alumina has a high quality factor at the microwave frequency range, its τ_f is –60 ppm/°C and, being a well-known refractory, its processing temperature is high (>1700 °C). The $0.83ZnAl_2O_4$–$0.17TiO_2$ rutile–spinel

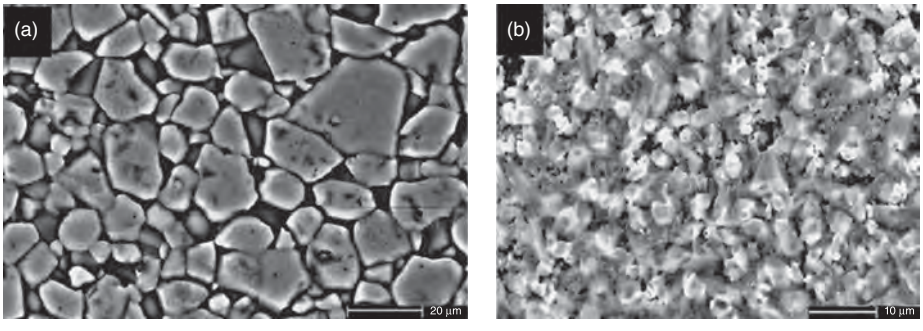

Figure 6.6 *(a) Backscattered SEM micrographs of $0.83ZnAl_2O_4$–$0.17TiO_2$ sintered at 1450 °C, (b) $0.83ZnAl_2O_4$–$0.17TiO_2$ + 10 wt% BBSZ sintered a 950 °C. Source: Adapted from Thomas* et al. *2008 [10].*

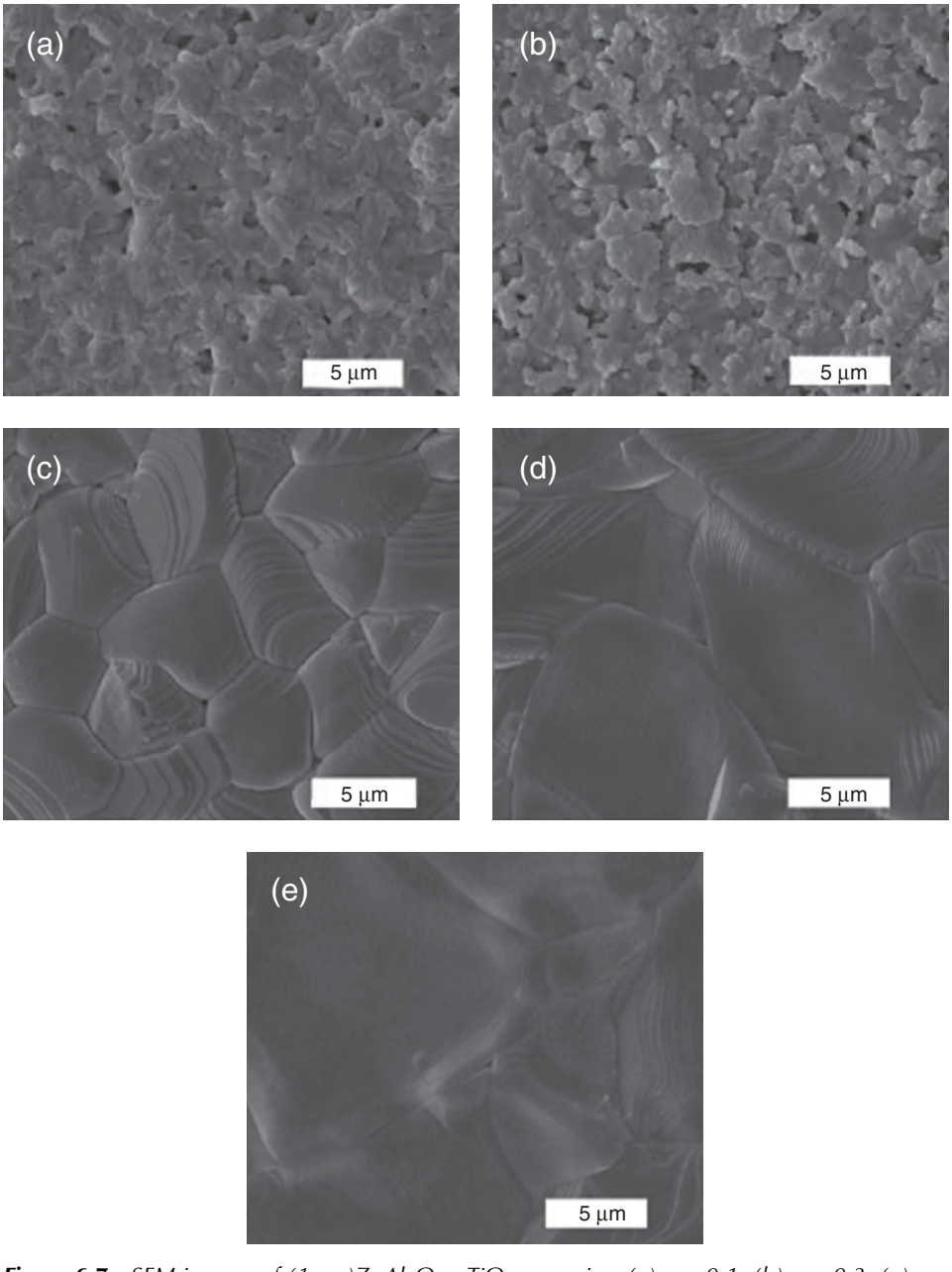

Figure 6.7 *SEM images of $(1 - x)ZnAl_2O_4$–$xTiO_2$ ceramics: (a) x = 0.1, (b) x = 0.3, (c) x = 0.5, (d) x = 0.7, and (e) x = 0.9, sintered at 1390 °C/4 h. Source: Huang* et al. *2009 [11].*

Table 6.1 *Microwave dielectric properties of spinels.*

Material	Additive	ST (°C)	ε_r	Qf (GHz)	τ_f (ppm/°C)	Reference
$ZnAl_2O_4$	Annealed 1000 °C/5 h	1425	8.5	56 300	–79	[5]
$ZnAl_2O_4$	–	1700/3 h	8.6	106 000	–	[26]
$0.83ZnAl_2O_4$–$0.17TiO_2$	Annealed at 1000 °C/5 h		12.7	100 250	1	[5]
$ZnAl_2O_4$	Annealed at 1000 °C/5 h	1425	8.5	56 300	–79	[5]
$0.79ZnAl_2O_4$–$0.21Co_2TiO_4$		1500	9.9	94 000	–66	[11]
$0.79ZnAl_2O_4$–$0.21Mg_2TiO_4$		1550	9.6	160 800	–65	[11]
$0.79ZnAl_2O_4$–$0.21Co_2TiO_4$		1500	9.9	94 000	–66	[27]
$0.79ZnAl_2O_4$–$0.21Co_2TiO_4$		1500	9.9	94 000	–66	[11]
$(1–x)ZnAl_2O_4$–xCo_2TiO_4 (x=0.8)		1425	14.0	148 800	–56	[12]
$1–x)ZnAl_2O_4$–xCo_2TiO_4 (x=0.2)		1525	10.0	147 600	–65	[12]
$(0.5ZnAl_2O_4–0.5TiO_2)$		1390/4 h	25.2	277 000	177	[13]
$0.23MgTiO_3–0.77(0.5ZnAl_2O_4–0.5TiO_2)$		1360/4 h	18.7	190 000	–2	[13]
$0.47Mg_4Nb_2O_9–0.53(0.5ZnAl_2O_4–0.5TiO_2)$		1390/4 h	13.4	210 000	2	[13]
$0.79ZnAl_2O_4$–$0.21Mn_2TiO_4$	SPS	1300	9.6	30 600		[26]
$(1–x)ZnAl_2O_4$–$xTiO_2$ (x=0.21)	–	1500	11.6	74 000	0	[27], [29]
$ZnAl_2O_4$	1 mol% $CaCO_3$	1400	8.5	58 000	–81	[5]
$0.83ZnAl_2O_4$–$0.17TiO_2$	0. 2 wt% $27B_2O_3$–$35Bi_2O_3$ –$6SiO_2$– $32ZnO$	1400/4 h	11.7	120 000	–7	[10]
$0.79ZnAl_2O_4$–$0.21Co_2TiO_4$	13 mol% TiO_2	1350	10.7	86 700	–62	[28]
$0.79ZnAl_2O_4$–$0.21Co_2TiO_4$	20 mol% TiO_2	1350	11.1	98 700	–63	[28]
$0.94(0.79ZnAl_2O_4$-$0.21Mg_2TiO_4)+0.06CaTiO_3$		1400	11.8	88 000	–8	[30]
$0.9(0.79ZnAl_2O_4–0.21Mg_2TiO_4)+0.1TiO_2$		1450	10.2	158 000	–64	[30]
$MgAl_2O_4$		1700	7.9	82 000		[26]
$MgAl_2O_4$	Annealed at 1000 °C		8.8	68 900	–75	[20]
$(1–x)MgAl_2O_4$–$xTiO_2$ (x=0.25)	Annealed at 1000 °C		11.0	105 400	–12	[20]
$MgAl_2O_4$ (SPS method)		1325	8.4	54 000	–74	[31]
$MgAl_2O_4$		1700	7.9	82 000		[26]
$(Mg_{1-x}Zn_x)Al_2O_4$ (x=0.6)		1700	8.3	93 000		[26]

(*continued*)

Table 6.1 *(Continued)*

Material	Additive	ST (°C)	ε_r	Qf (GHz)	τ_f (ppm/°C)	Reference
$(Mg_{1/2}Zn_{1/2})Al_2O_4$		1600/4 h	8.6	95 000	–52	[32]
$(Mg_{1-x}Zn_x)Al_2O_4$ (x=0.6)		1700	8.3	93 000		[26]
$(Mg_{0.95}Zn_{0.05})Al_2O_4$		1570	8.1	156 000	–70	[25]
$(Mg_{1-x}Ni_x)Al_2O_4$ (x=0.25)		1510/3 h	8.2	130 000	54	[23]
$(Mg_{1/2}Co_{1/2})Al_2O_4$		1600/4 h	8.8	107 300	–54	[24]
$Mg_{1-x}Co_xAl_2O_4$ (x=0.2)		1475	8.0	49 300	–50	[33]
Mg_2TiO_4		1500	14.2	160 000	–50	[34]
Mg_2TiO_4	1.5 wt% CeO_2	1300	14.6	167 000		[49]
$Mg2TiO_4$		–	14.4	55 000	–	[50]
$0.94Mg_2TiO_4$–$0.06SrTiO_3$		1440/4 h	17.8	70 900	–3	[51]
$0.93(Mg_{0.98}Co_{0.02})_2TiO_4$–$0.07CaTiO_3$		1400	13.0	105 000		[34]
$0.93(Mg_{0.95}Co_{0.02})_2TiO_4$–$0.07CaTiO_3$		1400	19.2	90 000		[34]
$0.93(Mg_{0.98}Co_{0.02})_2TiO_4$–$0.07CaTiO_3$	5 wt% ZnO–B_2O_3	1200	18.6	80 000		[34]
$(Mg_{1-x}Zn_x)_2TiO_4$ (x=0.01)		1330/4 h	15.1	153 600	–48	[43]
$0.93(Mg_{0.98}Co_{0.02})_2TiO_4$–$0.07CaTiO_3$		1400	13.0	105 000		[34]
$(Mg_{1-x}Zn_x)_2TiO_4$ (x=0.03)		1330/4 h	15.2	203 800	–42	[43]
$(Mg_{1-x}Zn_x)_2TiO_4$ (x=0.05)		1330/4 h	15.5	275 300	–34	[43]
$(Mg_{1-x}Zn_x)_2TiO_4$ (x=0.07)		1330/4 h	15.4	223 600	–29	[43]
$(Mg_{1-x}Zn_x)_2TiO_4$ (x=0.09)		1330/4 h	15.1	165 500	–24	[43]
$0.94(Mg_{0.95}Zn_{0.05})_2TiO_4$–$0.04SrTiO_3$		1270	18.0	125 600	0	[36]
$(1-x)Mg_2(Ti_{0.95}Sn_{0.05})O_4$–$xCaTiO_3$ (x=0.03)		1300/4 h	17.2	162 500	–36	[37]
$(1-x)Mg_2(Ti_{0.95}Sn_{0.05})O_4$–$xCaTiO_3$ (x=0.09)		1300/4 h	18.1	92 000	0	[37]
$0.93(Mg_{0.95}Co_{0.05})_2TiO_4$–$0.07SrTiO_3$		1300/4 h	18.4	102 200	1	[38]
$[(Mg_{0.5}Zn_{0.5})_{0.95}Co_{0.05}]_2TiO_4$		1225/4 h	18.2	206 000	–21	[52]
$(Mg_{1-x}Co_x)_{1.8}Ti_{1.1}O_4$ (x=0.05)		1390/4 h	16.1	207 500	–53	[44]
$(Mg_{1-x}Co_x)_{1.8}Ti_{1.1}O_4$ (x=1)		1210/4 h	19.5	76 400	–51	[44]
$(Mg_{1-x}Zn_x)_{1.8}Ti_{1.1}O_4$ (x=0.06)		1360/4 h	16.5	210 700	–62	[53]
$(Mg_{0.95}Zn_{0.05})_{1.8}Ti_{1.1}O_4$		1375/4 h	15.0	185 000	–45	[54]
$0.93(Mg_{0.95}Zn_{0.05})_{1.8}Ti_{1.1}O_4$–$0.07CaTiO_3$		1375	18.3	96 000	–5	[54]
$(Mg_{0.97}Zn_{0.03})_2(Ti_{0.95}Sn_{0.05})O_4$		1390/4 h	14.6	183 500	–44	[35]

$0.93(Mg_{0.97}Zn_{0.03})_2(Ti_{0.95}Sn_{0.05})O_4$–$0.07CaTiO_3$		1390/4 h	18.3	94 700	–4	[35]
$Mg_2(Ti_{1-x}Sn_x)O_4$ (x=0.05)		1390/4 h	15.6	317 500	–45	[40]
$(Mg_{1-x}Co_x)_2TiO_4$ (x=0.05)		1390/4 h	15.7	286 000	–53	[45]
$(Mg_{1-x}Mn_x)_2TiO_4$ (x=0.05)		1330/4 h	15.7	276 200	–53	[46]
$(Mg_{0.95}Zn_{0.05})_2(Ti_{0.8}Sn_{0.2})O_4$		1325/4 h	13.1	131 200	–56	[41]
$(Mg_{0.95}Zn_{0.05})_2(Ti_{0.8}Sn_{0.2})O_4$	3 wt% LiF	1150/5 h	13.0	119 300	–59	[42]
Zn_2SnO_4	1 wt% B_2O_3	975	9.3	62 000	–50	[55]
$Zn_2(Sn_{0.99}Zr_{0.01})O_4$		1225/4 h	9.6	87 000	–51	[56]
$ZnGa_2O_4$		1385	10.4	94 600	–27	[48]
$MgGa_2O_4$		1410/4 h	9.5	117 000	–4	[47]
Mg_2SnO_4		1550/4 h	8.4	55 100	–62	[57]
$(Mg_{0.93}Zn_{0.07})_2SnO_4$		1550/4 h	8.5	186 100	–61	[58]
$Li_2MgTi_3O_8$	–	1075/4 h	27.2	42 000	3.2	[60]
$Li_2Mg_{0.9}Zn_{0.1}Ti_3O_8$	–	1075/4 h	27.0	62 000	1	[61]
$Li_2MgTi_3O_8$	1 wt% LMZBS	950	25.2	55 000	1	[62]
$Li_2MgTi_3O_8$	Reaction sintering	1100/5 h	23.0	54 000	2	[89]
$Li_2(Mg_{0.96}Zn_{0.04})Ti_3O_8$		1200	28.7	151 200	–3	[66]
$Li_2(Mg_{1-x}Co_x)Ti_3O_8$ (x=0.05)		1170	26.7	82 000	–3	[66]
$Li_2(Mg_{0.94}Zn_{0.06})Ti_3O_8$		1075	27.1	44 800	2	[67]
$Li_2(Mg_{0.94}Co_{0.06})Ti_3O_8$		1075	26.6	43 500	4	[67]
$Li_2Mg(Ti_{1-x}Sn_x)_3O_8$ (x=0.15)		1100/4 h	26.0	74 700	–5	[90]
$0.4LiFe_5O_8$–$0.6Li_2MgTi_3O_8$		1050/2 h	16.1	28 500		[68]
$Li_2ZnTi_3O_8$		1075/4 h	25.6	72 000	–11	[60]
$Li_2ZnTi_3O_8$	3wt% LMZBS	900/4 h	23.2	31 300	–16	[62]
$Li_2ZnTi_3O_8$	0.25Wt% CuO–$1.5Bi_2O_3$–$1.5V_2O_5$	875	25.6	53 400	–5	[91]
$Li_2ZnTi_3O_8$	B_2O_3+TiO_2	900	25.9	46 500	0	[92]
$Li_2ZnTi_3O_8$	H_3BO_3	880	25.9	50 200	–7	[93]
$Li_2ZnTi_3O_8$	MgO–B_2O_3–SiO_2	900	25.0	56 200	–10	[94]
$Li_2ZnTi_3O_8$	ZnO–B_2O_3–SiO_2	925	25.6	51 600	–12	[95]
$Li_2ZnTi_3O_8$	ZnO–B_2O_3	950	25.3	61 700	–13	[96]
$Li_2ZnTi_3O_8$	Annealed at 1000 °C /4 h	1075/4 h	25.8	90 000	–10	[64]
0.6 $Li_2ZnTi_3O_8$–$0.4Li_2TiO_3$	1 wt% ZBS		25.4	86 400	–1	[69]

(*continued*)

Table 6.1 *(Continued)*

Material	Additive	ST (°C)	ε_r	Qf (GHz)	τ_f (ppm/°C)	Reference
$Li_2ZnTi_3O_8$ +3 wt% TiO_2	1.5 wt% B_2O_3	900	25.9	46 500	0	[71]
$Li_2ZnTi_3O_8$ +3.5 wt%TiO_2	1 wt% LBS	875	26.0	44 000	–4	[70]
$(1–x)Li_2ZnTi_3O_8–xTiO_2$ (x=0.1)		1100	26.0	45 000	–1	[72]
$Li_2ZnTi_3O_8$+ 4 wt% nano-TiO_2		1050/4 h	28.0	68 000	–2	[73]
$Li_2ZnTi_{3+x}O_{8+2x}$ (x = 0.17)		1160/5 h	28.5	58 500	2	[74]
$Li_2ZnTi_3O_8$		1075	26.6	83 600	–12	[96]
$Li_2ZnTi_3O_8$		1075	23.5	71 000	–4	[97]
$Li_2ZnTi_3O_8$			30.2	70 000	–17	[98]
$Li_2Zn(Ti_{0.9}Sn_{0.1})_3O_8$		1120	23.3	71 000	–22	[79]
$(1–x)LiZn_{0.5}Ti_{1.5}O_4$ (LZT)–$xTiO_2$ (x=0.1)		1075	26.0	45 000	–1	[80]
$Li_2(Zn_{0.94}Mg_{0.06})Ti_3O_8$		1140	26.1	150 000	–14	[81]
$Li_2(Zn_{0.92}Co_{0.08})Ti_3O_8$		1140	24.7	140 000	–13	[81]
$Li_2ZnTi_3O_8$	Reaction sintering	1100/2 h	25.8	78 200	–11	[99], [100]
$Li_2Zn(Ti_{1-x}Zr_x)_3O_8$ (x = 0–0.07)		1100/4 h	25.4	122 000	–16	[81]
$Li_2CoTi_3O_8$		1025	28.9	52 600	7	[81]
$Li_2CoTi_3O_8$	2 wt% B_2O_3	900	26.6	21 300	2	[84]
$Li_2Zn_xCo_{1-x}Ti_3O_8$ (x=0.4)		1050/2 h	27.7	57 100	–1	[85]
$Li_2(Mg_{0.3}Zn_{0.7})Ti_3O_8–xTiO_2$ (x=0.12)	3 wt% ZBS	900/3 h	25.1	19 600	–2	[86]
$(1–x)Li_2Zn_3Ti_4O_{12}–xTiO_2$ (x=0.6)			15.1	62 000	–5	[88]
$Li_2Zn_3Ti_4O_{12}$		1075	20.6	106 700	–12	[101]
$Li_2Zn_3Ti_4O_{12}$	+1.5 wt% $BaCu(B_2O_5)$	900/2 h	19.4	57 600	–48	[101]
$0.4Li_2Zn_3Ti_4O_{12}–0.6Ba_3(VO_4)_2$		950/4 h	16.9	51 300	3	[102]
$0.7Li_2Zn_3Ti_4O_{12}–0.3Ba_3(VO_4)_2$		1000	18.1	88 900	–18	[102]
$0.8Li_2Zn_3Ti_4O_{12}–0.2Li_2TiO_3$		1160/2 h	18.0	100 000	–48	[103]
$0.8Li_2Zn_3Ti_4O_{12}–0.2Li_2TiO_3$	2.0 wt% $0.4B_2O_3$–0.6CuO	925/2 h	17.5	71 000	–44	[103]
$Li_2Zn_3Ti_4O_{12}$	1.5 wt% LZB	900/2 h	19.1	63 750	–49	[104]
$Li_2Zn_3Ti_4O_{12}$		1075/2 h	20.6	106 700	–48	[101]
$Li_2Mg_3Ti_4O_{12}$		1125/2 h	20.2	62 300	–27	[105]
$0.95Li_2Mg_3Ti_4O_{12}–0.05CaTiO_3$		1200/2 h	22.6	48 000	–2	[105]

mixture composition is advantageous over Al_2O_3 in respect to temperature compensation, which is a necessary requirement for microwave dielectric substrate applications.

6.1.2 $MgAl_2O_4$

Magnesium aluminate ($MgAl_2O_4$) spinel is a potential refractory material with excellent high-temperature mechanical, thermal, and chemical properties. The development of magnesium aluminate spinel bodies and method of fabricating spinel refractories were available from about a century ago. It has a high melting point (2130 °C) and low thermal expansivity (7.45 ppm/°C). The phase diagram of the MgO–Al_2O_3 system was established as early as 1916. Extensive work has been done to improve the densification and physical properties of this material. Dense sintered products of magnesium aluminate spinel were also reported through the addition of rare earth oxides [14] like Yb_2O_3, Y_2O_3, and Dy_2O_3. The effect of addition of TiO_2 on the development of magnesium aluminate spinel is also available in the literature. It was reported [15] that the sintering of magnesium aluminate in the presence of TiO_2 is beneficial in improving the densification [15, 16]. The dielectric properties of $MgAl_2O_4$ was studied by many authors [17, 18]. In 1991, Shannon and Rossman measured [19] the dielectric loss factor (0.0008 at 1 MHz) and dielectric constant (8.3) of single crystal $MgAl_2O_4$ using a two-terminal method. The $(1 - x)MgAl_2O_4$–$xTiO_2$ ceramics can be prepared by the conventional mixed oxide route by sintering in the temperature range 1400–1460 °C for 4 hours [20]. The sintered samples were annealed at 1000 °C for 5 hours [20]. The $MgAl_2O_4$ sintered and annealed showed a densification of about 97% of its theoretical density [20] (3.58 g/cm^3). The bulk density of $MgAl_2O_4$ increases with x, reaches a maximum at $x = 0.5$ and then gradually deceased until $x = 0.3$. It then increased since the density of rutile is higher than $MgAl_2O_4$. Figure 6.8 shows the variation of bulk density

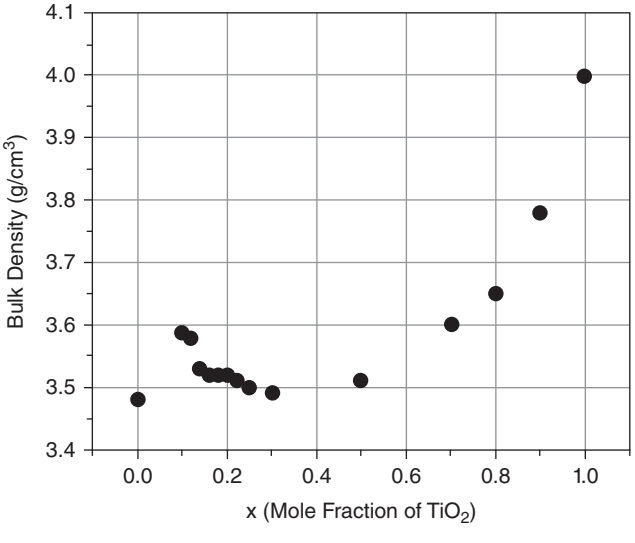

Figure 6.8 *Variation of bulk density of $MgAl_2O_4$ with mole fraction of TiO_2 addition. Source: Adapted from Surendran* et al. *2005 [20].*

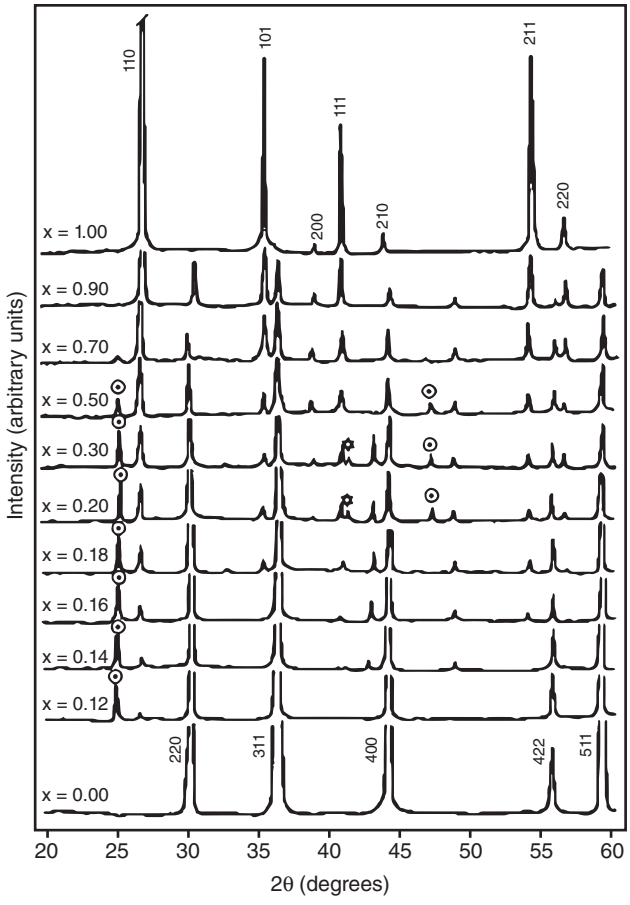

Figure 6.9 *Powder diffraction pattern of $(1 - x)MgAl_2O_4$–$xTiO_2$ system for x = 0.0, 0.12, 0.14, 0.16, 0.18, 0.20, 0.30, 0.50, 0.70, 0.90, and 1.0. ⊙ represents $MgTiO_3$ and ∗ represents Mg_2TiO_4 phases. Source: Adapted from Surendran* et al. *2005 [20].*

of $(1 - x)MgAl_2O_4$–$xTiO_2$ phases as a function of x. The X-ray diffractograms recorded from $(1 - x)MgAl_2O_4$–$xTiO_2$ are given in Figure 6.9. The $MgAl_2O_4$ has a fcc cubic crystal structure. As the concentration of TiO_2 in $MgAl_2O_4$ increases an additional phase $MgTiO_3$ is formed consequent to the reaction between spinel and rutile. For 20 and 30 mol% of TiO_2 additions the presence of another phase, Mg_2TiO_4, is also detected in the XRD patterns. The formation of low dielectric constant and high Q phases like $MgTiO_3$ and Mg_2TiO_4 on the addition of TiO_2 into $MgAl_2O_4$ was confirmed in later studies [21].

The dielectric constant of pure $MgAl_2O_4$ is measured to be 8.75. The dielectric constant of TiO_2 doped with Fe_2O_3 is 105. Using the rule of mixtures such as the serial mixture rule, logarithmic rule, and parallel mixture rule the dielectric constant of the mixture has been calculated and is plotted as a function of the mole fraction of TiO_2, as shown in Figure 6.10. The deviation from the ideal curve fitting plots are believed to be due to the presence of additional phases. It is interesting to note that the dielectric constant is ∼20 for the mixture

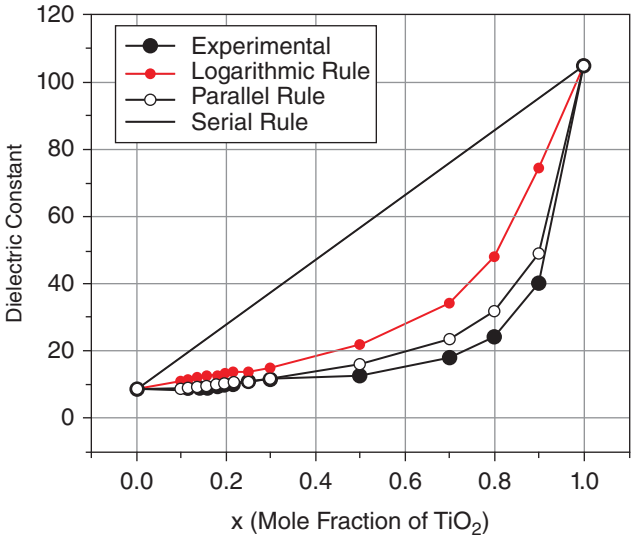

Figure 6.10 *Variation of ε_r of $MgAl_2O_4$ with mole fraction of TiO_2 addition. Source: Adapted from Surendran* et al. *2005 [20].*

phases between 0.7 and 0.8 in $(1 - x)MgAl_2O_4$–$xTiO_2$ ceramics, where the τ_f approaches zero value. The unloaded quality factor and τ_f of $MgAl_2O_4$ are plotted in Figure 6.11 with increasing TiO_2 content. $MgAl_2O_4$ has Qf of 68 900 GHz. As the TiO_2 content in $MgAl_2O_4$ increases, the microwave quality factor also increases, reaching a maximum value of $Qf = 105\,400$ GHz for $x = 0.25$ in $(1 - x)MgAl_2O_4$–$xTiO_2$. For higher TiO_2 contents, the

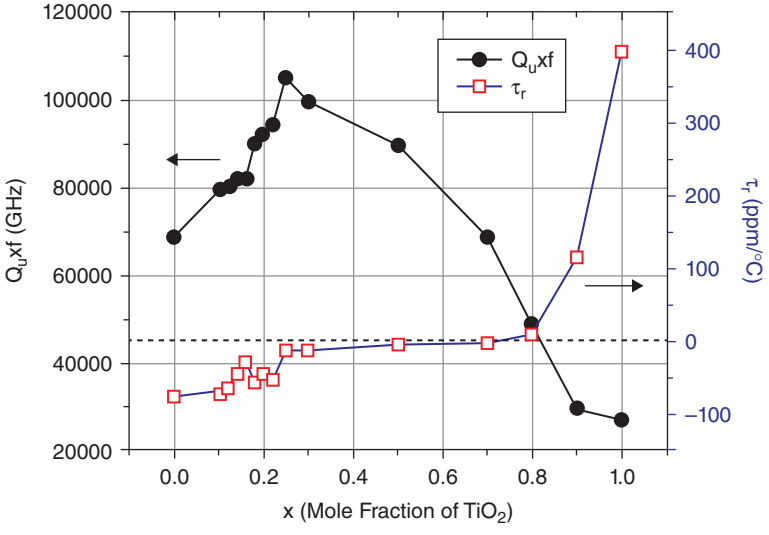

Figure 6.11 *Variation of Q_u and τ_f of $MgAl_2O_4$ with mole fraction of TiO_2 addition. Source: Adapted from Surendran* et al. *2005 [20].*

quality factor decreases as evident from Figure 6.11. Compositions in the mixture region between $x = 0.7$ and 0.8 in $(1 - x)\ MgAl_2O_4$–$xTiO_2$, where the τ_f approaches minimum values, are having reasonably good quality factors ($Qf = 49\,000$ to 69 000 GHz) [20]. The temperature coefficient of resonant frequency (τ_f) of pure $MgAl_2O_4$ is –75 ppm/°C. The TiO_2 has a high τ_f of about 400 ppm/°C. As the TiO_2 content in $MgAl_2O_4$ increases the τ_f must assume less negative values owing to a general mixture rule. However, it can be seen from Figure 6.11 that for $x = 0.16$ τ_f is –27 ppm/°C but for $x = 0.18$ it again shifted to –57 ppm/°C. The fluctuating nature of the temperature coefficient of TiO_2 added to $MgAl_2O_4$ may be attributed to the formation of $MgTiO_3$ and Mg_2TiO_4 secondary phases, which are also low-loss dielectric with negative τ_f. Partial substitution of Mg by Zn, Ni, and Co is found to improve the Qf of $MgAl_2O_4$ to larger than 100 000 GHz [22–25].

6.1.3 A_2TiO_4 (A = Mg, Zn)

In 2007 Belous *et al.* [34] reported that the spinel Mg_2TiO_4 has a high Qf of 160 000 GHz with an ε_r of 14.2. However, it has a relatively large negative τ_f of 50 ppm/°C. They reported that the τ_f can be tailored by forming materials of the system $0.93[(1 - x)\ Mg_2TiO_4$–$xCo_2TiO_4]$–$0.07CaTiO_3$ with τ_f within the range of −5 to −10 ppm/°C [34]. Partial substitution of Ti by Sn and addition of $SrTiO_3$ or $CaTiO_3$ in $(Mg,Zn)_2TiO_4$ improved the τ_f close to zero with a quality factor close to 100 000 GHz [35–38]. A small amount of ilmenite $MgTiO_3$ second phase is often formed when sintered below 1400 °C. This is in agreement with the thermal decomposition mechanism

$$Mg_2TiO_4 = Mg_{2+2d}Ti_{1-d}O_4 + MgTiO_3$$

The thermal decomposition of Mg_2TiO_4, however, becomes negligible at temperatures exceeding 1400 °C [34, 39]. It may be noted that $MgTiO_3$ is also a high Q material. Partial substitution of Ti by Sn is also found to improve the quality factor [35, 37, 40, 41]. The $(Mg_{0.95}Zn_{0.05})_2(Ti_{0.8}Sn_{0.2})O_4$ ceramics sintered at 1325 °C possesses good microwave dielectric properties with $\varepsilon_r = 13.1$, $Qf = 131\,170$ GHz, and $\tau_f = -56$ ppm/°C [41]. Addition of 0.3 wt% LiF lowers the sintering temperature to about 1150 °C with ε_r =13.0, Qf = 119 300, and τ_f of –59 ppm/°C [42]. The τ_f can be tailored close to zero by adding a small amount of $CaTiO_3$. Partial substitution of Mg by Zn, Co, or Mn is reported to further improve the quality factor to about 200 000 GHz [43–46]. The $0.93(Mg_{0.97}Zn_{0.03})_2(Ti_{0.95}Sn_{0.05})O_4$–$0.07CaTiO_3$ has a Qf of 94 700 GHz with τ_f of –4 ppm/°C [35]. The spinels $ZnGa_2O_4$ and $MgGa_2O_4$ have a high Qf, relatively low τ_f, and are suitable for millimeter-wave applications [47, 48].

6.2 $Li_2ATi_3O_8$ (A = Mg, Zn) Ceramics

The spinel structure $Li_2ZnTi_3O_8$ ($LiZn_{1/2}Ti_{3/2}O_4$) has been investigated extensively as an anode material for rechargeable lithium-ion batteries [59]. George and Sebastian reported [60–62] $Li_2ATi_3O_8$ (A = Mg, Zn) as a novel temperature-stable low-cost high-Q dielectric ceramic. Since then several authors investigated these materials extensively and tailored the dielectric properties by suitable substitutions and by adding dopants or glasses. The $Li_2ATi_3O_8$ (A = Zn, Mg) ceramic can be prepared by the conventional solid-state ceramic

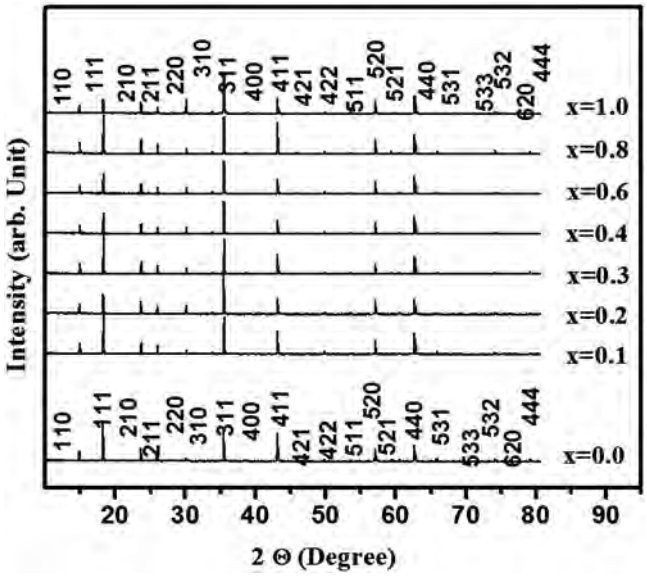

Figure 6.12 *X-ray diffraction patterns of $Li_2Mg_{1-x}Zn_xTi_3O_8$ (x = 0, 0.1, 0.2, 0.3, 0.4, 0.6, 0.8, 1) ceramics sintered at 1075 °C/4 h. Source: Adapted from George and Sebastian 2010 [61].*

route by sintering at a relatively high temperature of 1075 °C/4 h [60–62]. These compacts were prepared by muffling the samples by powder of the same composition during sintering to prevent the escape of volatile lithium at elevated sintering temperatures [60–62]. The sintered samples showed a densification > 96%. The Mg- and Zn-based ceramics form a complete series of solid solutions. Figure 6.12 shows the X-ray diffraction pattern of $Li_2Mg_{1-x}Zn_xTi_3O_8$ (x = 0, 0.1, 0.2, 0.3, 0.4, 0.6, 0.8, 1) ceramics sintered at its optimized sintering temperature of 1075 °C/4 h. All the peaks can be indexed based on the JCPDS file number 48-0263 for $Li_2MgTi_3O_8$ and 86-1512 for $Li_2ZnTi_3O_8$ with cubic crystal symmetry. It forms a complete series of solid solutions. Figure 6.13 shows the SEM images of thermally etched ceramics of $Li_2MgTi_3O_8$ and $Li_2ZnTi_3O_8$ ceramics sintered at 1075 °C/4 h. The grains are closely packed and most of the grains have an average size of 30–40 μm. Figure 6.13 also shows the SEM micrograph of $Li_2Mg_{1-x}Zn_xTi_3O_8$ with (c) x = 0.2, (d) 0.4, (e) 0.6, and (f) 0.8. Figure 6.13g is the magnified image of a part of Figure 6.13e.

Figure 6.14 shows the variation of (a) relative permittivity, (b) quality factor, and (c) temperature coefficient of resonant frequency of $Li_2MgTi_3O_8$ (LMT) and $Li_2ZnTi_3O_8$ (LZT) ceramics as a function of the sintering temperature. The ceramics showed the best densification on sintering at 1075 °C for 4 hours [60–62]. As the sintering temperature increases to 1075 °C, the relative permittivity and quality factor reaches a maximum value and the temperature coefficient of resonant frequency is found to be minimum. However, a subsequent increase in the sintering temperature degrades the microwave dielectric properties. The improvements in microwave dielectric properties are attributed to the improvement in densification. On the other hand, the dielectric properties are degraded due to the decreased densification by the evaporation of a volatile element like lithium at elevated temperature

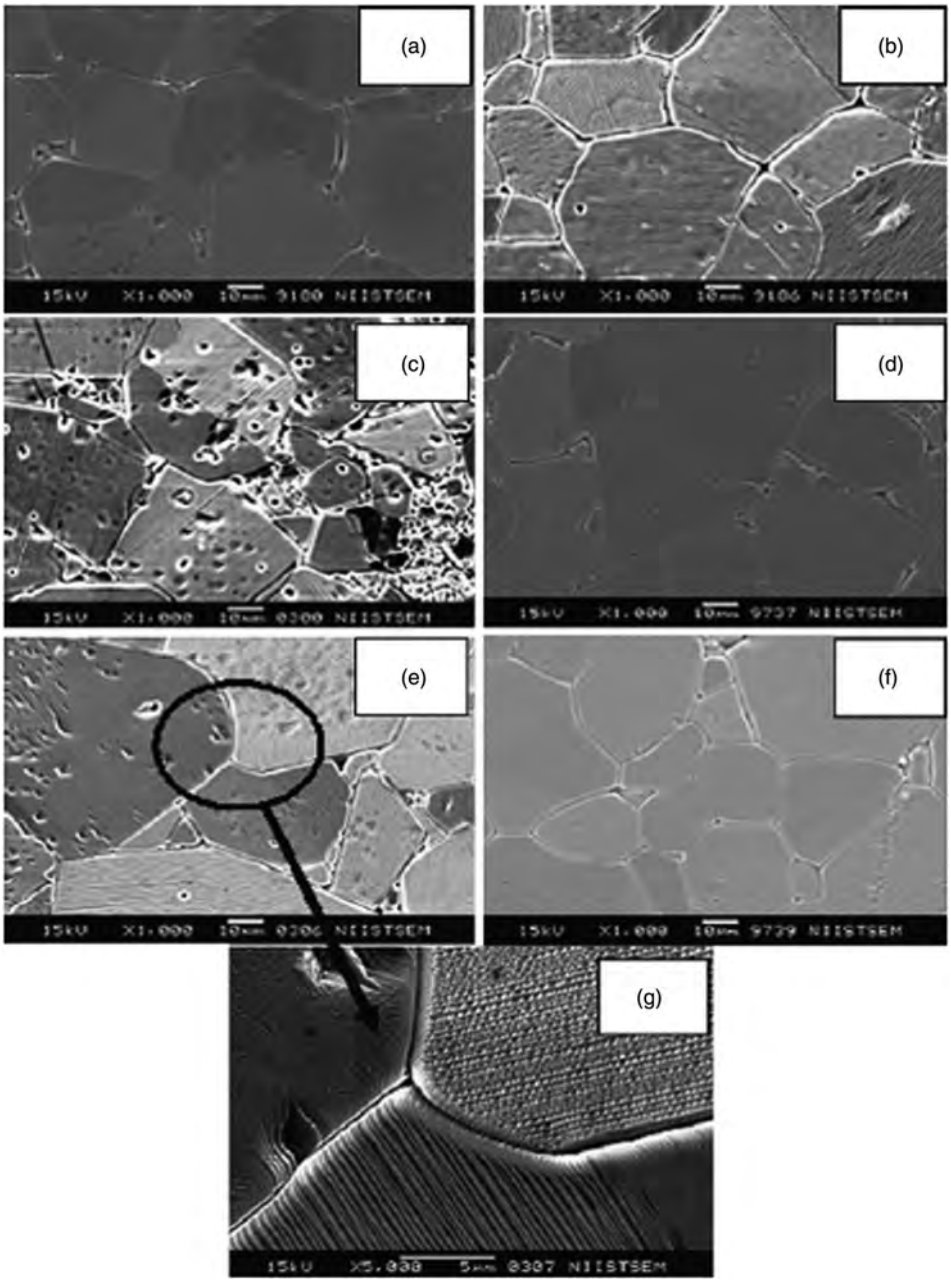

Figure 6.13 *Shows the SEM images of thermally etched (25 °C below the sintering temperature): (a) $Li_2MgTi_3O_8$ and (b) $Li_2ZnTi_3O_8$ ceramics sintered at 1075 °C/4 h. The figure also shows the SEM micrograph of $Li_2Mg_{1-x}Zn_xTi_3O_8$ for (c) x = 0.2, (d) 0.4, (e) 0.6, and (f) 0.8; (g) is the magnified image of a part of (e). Source: Adapted from George and Sebastian 2010 [61].*

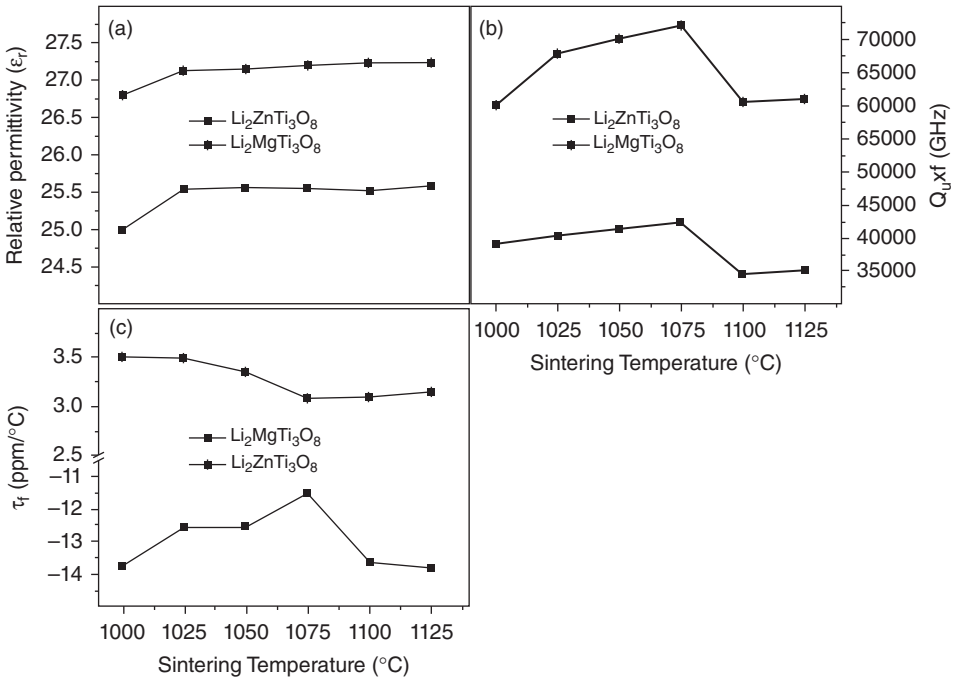

Figure 6.14 *The variation of (a) relative permittivity, (b) quality factor, and (c) temperature coefficient of resonant frequency of $Li_2MgTi_3O_8$ and $Li_2ZnTi_3O_8$ ceramics as a function of sintering temperature. Source: Adapted from George and Sebastian 2010 [60].*

above 1075 °C. Hence the samples were sintered by muffling with calcined powder. It was found that muffling the samples with the same powder gives a better quality factor than adding extra Li_2CO_3. The $Li_2MgTi_3O_8$ ceramics sintered at 1075 °C have $\varepsilon_r = 27.2$, $Qf = 42\,000$ GHz, and $\tau_f = (+)\ 3$ ppm/°C at 5 GHz. The $Li_2ZnTi_3O_8$ ceramics sintered at 1075 °C shows $\varepsilon_r = 25.6$, $Qf = 72\,000$ GHz, and $\tau_f = (-)\ 11$ ppm/°C at 5 GHz. Most of the titanium-based ceramics have a high processing temperature (>1400 °C). The high sintering temperature results in a coring effect in titanium-based ceramics. This phenomenon has been observed in zirconium tin titanate ($Zr_{0.8}Sn_{0.2}TiO_4$), $BaTi_4O_9$, and $Ba_2Ti_9O_{20}$ ceramics [63]. The coring effect is due to the reduction of Ti^{4+} to Ti^{3+} and the associated oxygen deficiency. This causes the degradation of the quality factor of microwave dielectric ceramics. In the case of $Li_2ZnTi_3O_8$ ceramics the sintering temperature is relatively low for titanium reduction. However, Armaki *et al.* [64] reported an increase in quality factor on annealing $Li_2ZnTi_3O_8$ at 1000 °C for 4 hours.

The well-known microwave dielectric materials with a high quality factor in general need a high sintering temperature together with a long soaking time. However, the $Li_2MgTi_3O_8$ and $Li_2ZnTi_3O_8$ dielectric ceramics show excellent dielectric properties at a relatively low sintering temperature of 1075 °C/4 h. The $Li_2MgTi_3O_8$ and $Li_2ZnTi_3O_8$ ceramics show excellent microwave dielectric properties with a temperature coefficient of resonant frequency of +3 ppm/°C and –11 ppm/°C, respectively. George and Sebastian [60–62] tuned

the dielectric properties by forming a solid solution between $Li_2MgTi_3O_8$ and $Li_2ZnTi_3O_8$ ceramics and obtained a zero τ_f composition. As x increases from 0 to 1, the relative permittivity of $Li_2Mg_{1-x}Zn_xTi_3O_8$ ceramics decreases from 27 to 25.5. At $x = 0.1$, the quality factor of $Li_2Mg_{1-x}Zn_xTi_3O_8$ ceramics increases to 62 000 GHz. As x increases from 0 to 1, the τ_f decreases linearly from +3 to –11 ppm/°C with an increase of x from 0 to 1 and showed a zero τ_f at $x = 0.2$. The Ca substitution at the Mg or Zn site by forming $Li_2(A_{1-x}Ca_x)Ti_3O_8$ ceramics (A = Mg, Zn and $x = 0$, 0.05, 0.1, 0.15, 0.20) led to the formation of a $CaTiO_3$ secondary phase for $x > 0.05$ [61]. This is due to the large ionic radii of Ca as compared to that of Mg or Zn. The relative permittivity is found to increase with an increase in the calcium substitution for both the $Li_2(Mg_{1-x}Ca_x)Ti_3O_8$ and $Li_2(Zn_{1-x}Ca_x)Ti_3O_8$ ceramics. This is due to the presence of the $CaTiO_3$ second phase, which has a high permittivity of about 174 [63]. As x increases from 0 to 0.2, the relative permittivity of $Li_2(Mg_{1-x}Ca_x)Ti_3O_8$ and $Li_2(Zn_{1-x}Ca_x)Ti_3O_8$ ceramics increases from 27.2 to 32.8 and 25.6 to 30.8, respectively. The quality factor of both $Li_2(Mg_{1-x}Ca_x)Ti_3O_8$ and $Li_2(Zn_{1-x}Ca_x)Ti_3O_8$ ceramics is found to decrease with an increase in x. The $CaTiO_3$ has a low quality factor of about 3600 GHz [63] as compared to $Li_2MgTi_3O_8$ and $Li_2ZnTi_3O_8$ ceramics, which led to a decrease in the quality factor. The τ_f of $Li_2(Mg_{1-x}Ca_x)Ti_3O_8$ increases from +3 to 51 ppm/°C whereas the τ_f of $Li_2(Zn_{1-x}Ca_x)Ti_3O_8$ shifts from –11 to +38 ppm/°C. The $CaTiO_3$ has a high positive τ_f of about +800 ppm/°C and is commonly used to tune the temperature coefficient of resonant frequency of microwave dielectric ceramics that are having a negative τ_f [63]. Many authors [65–88] tailored the microwave dielectric properties of $Li_2ZnTi_3O_8$ and $Li_2MgTi_3O_8$ by suitable substitution or using different additives. The microwave dielectric properties of these materials are given in Table 6.1. Addition of a small amount of TiO_2 improved the τ_f and increased ε_r but lowered the quality factor [65,70–73,75,80,86,87]. Partial substitution of Mg with Zn and Co is found to improve the quality factor [61, 66, 67] in $Li_2MgTi_3O_8$ ceramics. In $Li_2ZnTi_3O_8$, partial substitution of Zn by Mg, Co, Zr [81, 82] improved the quality factor. In fact, by suitable substitution it is possible to get a low-cost ceramic with ε_r in the range 23–28 with Qf of about 100 000 GHz at a low τ_f close to zero.

6.2.1 Effect of Glass Addition in $Li_2ATi_3O_8$ (A = Mg, Zn)

Addition of glasses such as LMZBS (20:Li_2O, 20:MgO, 20:ZnO, 20:B_2O_3, 20:SiO_2), BBS (BaO–B_2O_3–SiO_2), ZBS (ZnO–B_2O_3–SiO_2), CBS (CaO–B_2O_3–SiO_2), MBS (MgO–B_2O_3–SiO_2), BBSZ (Bi_2O_3–B_2O_3–SiO_2–ZnO), H_3BO_3, CuO–Bi_2O_3–V_2O_5, B_2O_3, Bi_2O_3, LBS, Li_2O–Al_2O_3–B_2O_3, CuO–B_2O_3, ZnO–La_2O_3–B_2O_3, and $BaCu(B_2O_5)$) are found to lower the sintering temperature below the melting point of silver electrode material (960 °C) suitable for LTCC applications. However, the addition of glasses lowered the quality factor.

The sintering temperature of the $Li_2MgTi_3O_8$ and $Li_2ZnTi_3O_8$ ceramics were lowered [62] by the addition of lithium magnesium zinc borosilicate (20:Li_2O, 20:MgO, 20:ZnO, 20:B_2O_3, 20:SiO_2) (LMZBS) glass. This glass was chosen since the elements in the glass were lithium, magnesium, and zinc, which were also present in the parent material. This may avoid the formation of a second phase in the final product. Different weight percentages of LMZBS glass were added to the fine powder of calcined $Li_2MgTi_3O_8$ and $Li_2ZnTi_3O_8$ ceramics. These compacts were muffled by calcined powder of the same composition and sintered at different temperatures in the range 850–1075 °C for 4 hours.

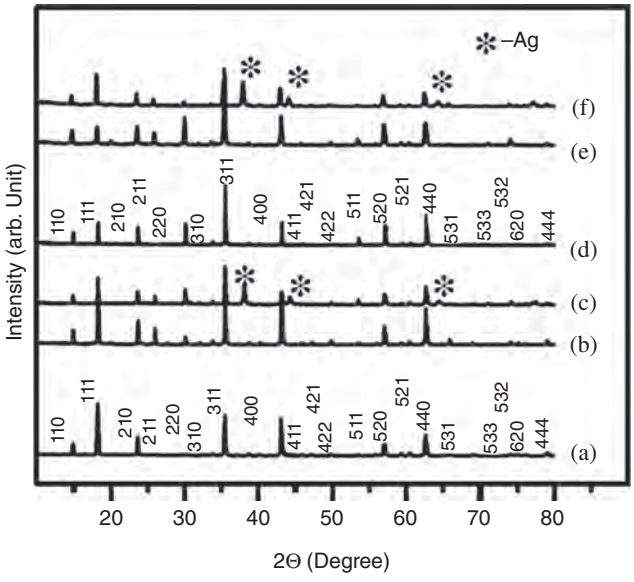

Figure 6.15 *The X-ray diffraction pattern of (a) $Li_2MgTi_3O_8$ sintered at 1075 °C/4 h, (b) $Li_2MgTi_3O_8$ + 3 wt% of LMZBS sintered at 925 °C/4 h, (c) $Li_2MgTi_3O_8$ + 3 wt% of LMZBS + 20 wt% of Ag sintered at 925 °C/4 h, (d) $Li_2ZnTi_3O_8$ sintered at 1075 °C/4 h, (e) $Li_2ZnTi_3O_8$ + 3 wt% of LMZBS sintered at 900 °C/4 h, and (f) $Li_2ZnTi_3O_8$ + 3 wt% of LMZBS + 20 wt% of Ag sintered at 900 °C/4 h. Source: Adapted from George and Sebastian 2011 [62]*

The sintering temperature of the ceramic glass composite was optimized for the best density and dielectric properties. Addition of 3 wt% of LMZBS decreases the sintering temperature of $Li_2MgTi_3O_8$ from 1075 °C/4 h to 925 °C/4 h and that of $Li_2ZnTi_3O_8$ ceramics from 1075 °C/4 h to 900 °C/4 h. Addition of 3 wt% LMZBS glass lowers the sintering temperature to well below the melting point of Ag.

Generally, addition of glass in ceramics degrades the microwave dielectric properties by the formation of secondary phases while sintering. Figure 6.15 shows the X-ray diffraction pattern of (a) $Li_2MgTi_3O_8$ sintered at 1075 °C/4 h, (b) $Li_2MgTi_3O_8$ + 3 wt% of LMZBS sintered at 925 °C/4 h, (c) $Li_2MgTi_3O_8$ + 3 wt% of LMZBS + 20 wt% of Ag sintered at 925 °C/4 h, (d) $Li_2ZnTi_3O_8$ sintered at 1075 °C/4 h, (e) $Li_2ZnTi_3O_8$ + 3 wt% of LMZBS sintered at 900 °C/4 h, and (f) $Li_2ZnTi_3O_8$ + 3 wt% of LMZBS + 20 wt% of Ag sintered at 900 °C/4 h. It is found that addition of LMZBS glass does not lead to the formation of any secondary phase. All the peaks in the XRD pattern are indexed based on JCPDS file number 48-0263 for the $Li_2MgTi_3O_8$ + LMZBS system and JCPDS file number 86-1512 for the $Li_2ZnTi_3O_8$ + LMZBS system with cubic crystal symmetry. For LTCC applications the electrode material should not react with the ceramic material during co-firing. The X-ray diffraction pattern of dielectric ceramics and electrode material sintered at its optimized sintering temperature is an acceptable way to study the interface reaction. It is observed from Figure 6.15c and f that there is no additional phase other than metallic silver and $Li_2MgTi_3O_8$ or $Li_2ZnTi_3O_8$ (JCPDS file number 86-1512) phases. Since the formation of

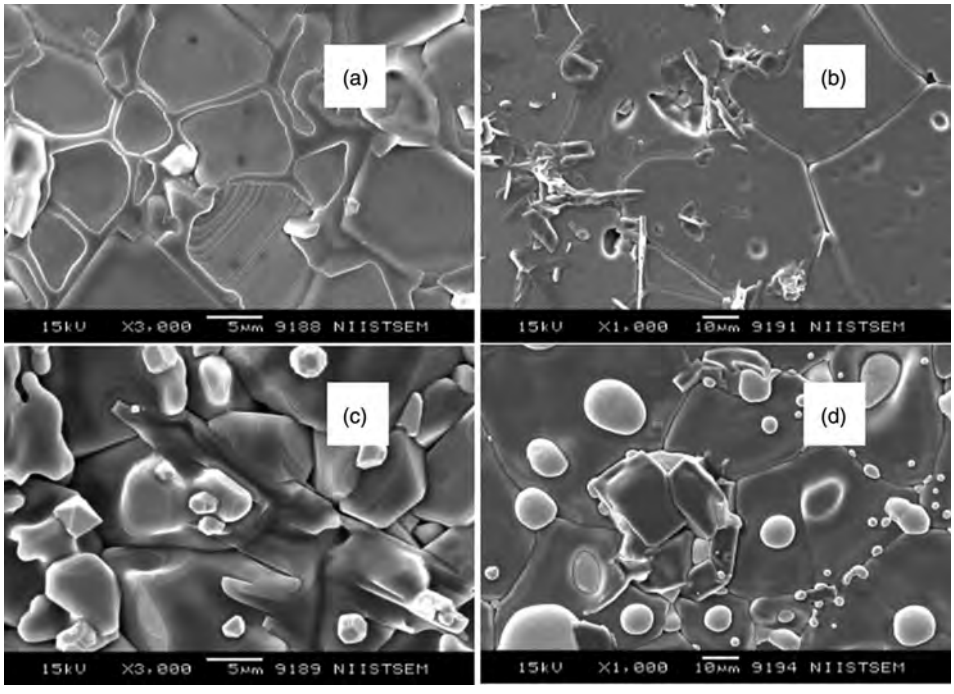

Figure 6.16 *SEM images thermally etched: (a) 3 wt% of LMZBS glass added to LMT ceramics sintered at 925 °C/4 h, (b) 3 wt% of LMZBS glass added to LZT ceramics sintered at 900 °C/4 h, (c) LMT + 3wt% of LMZBS + 20 wt% of Ag sintered at 925 °C/4 h, and (d) LZT + 3 wt% of LMZBS + 20 wt% of Ag sintered at 900 °C/4 h. Source: Adapted from George and Sebastian 2011 [62].*

the secondary phase is not observed in the pattern, it may be possible to use Ag as the electrode material for these ceramic–glass composites.

Figure 6.16 shows the scanning electron micrograph of thermally etched 3 wt% of LMZBS glass added to (a) $Li_2MgTi_3O_8$ ceramics sintered at 925 °C/4 h and (b) $Li_2ZnTi_3O_8$ ceramics sintered at 900 °C/4 h. The influence of glass addition in ceramics varies from material to material. Figure 6.16a is a typical example of liquid phase sintering in which the glass melts and wets the grains and flows between the grains of $Li_2MgTi_3O_8$ ceramics. The LMT ceramics sintered at 1075 °C/4 h has a grain size of about 30–40 μm whereas the 3 wt% of LMZBS glass-added LMT ceramics sintered at 925 has a grain size of about 8 to 10 μm. The effect of LMZBS glass addition in $Li_2ZnTi_3O_8$ ceramics is different from that of $Li_2MgTi_3O_8$ ceramics. It can be observed from Figure 6.17 that the glass is concentrated mainly at the grain boundaries and there is no significant change in the grain size compared to pure LZT sintered at 1075 °C/4 h. Figure 6.16 shows the micrograph of (c) $Li_2MgTi_3O_8$ + 3 wt% of LMZBS + 20 wt% of Ag sintered at 925 °C/4 h and (d) $Li_2ZnTi_3O_8$ + 3 wt% of LMZBS + 20 wt% of Ag sintered at 900 °C/4 h. The silver did not react with the ceramic–glass composites and are distributed randomly. This micrograph strongly supports the results of non-reactivity of silver with the ceramic glass system as evidenced from the X-ray diffraction pattern (see Figure 6.15).

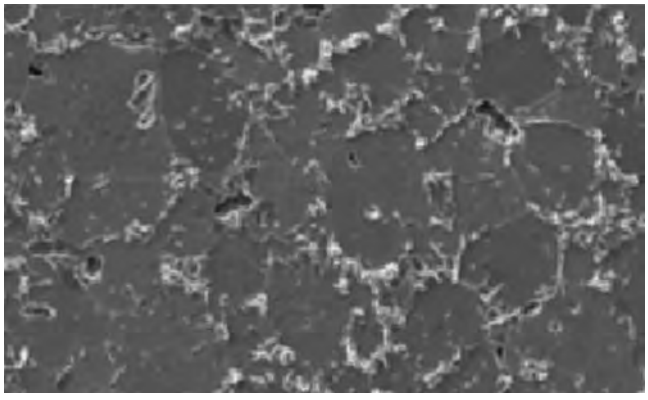

Figure 6.17 *The low magnification image of $Li_2ZnTi_3O_8$ + 3 wt% of LMZBS glass sintered at 900 °C/4 h. Source: Adapted from George and Sebastian 2011 [62].*

The effect of glass addition on the microwave dielectric properties of dielectric ceramics depend strongly on the chemistry of glass, the chemical reaction, the phase change during sintering, and the final density [106]. Generally, the *Qf* value of the ceramic glass composite decreased with increasing glass content despite the increase in the density. Figure 6.18 shows the relative permittivity and quality factor of (a) LMT and (b) LZT ceramics as a function of LMZBS glass addition. It is found that the dielectric properties change in a manner similar to that of densification. As the LMZBS glass content increases from 0 to 5 wt%, the relative permittivity of LMT decreases from 27.2 to 23.7 and that of LZT decreases from 25.7 to 22.8. The decrease in the permittivity of both the LMT + LMZBS and LZT + LMZBS ceramic glass composites is expected since the permittivity of LMZBS glass is ($\varepsilon_r = 6.9$) lower than that of LMT and LZT ceramics. Figure 6.18 also illustrates the variation of quality factor of (a) LMT and (b) LZT ceramics as a function of LMZBS glass fluxing. It is found that a small amount of glass (1 wt%) increases the quality factor of LMT ceramics from 42 000 GHz to 52 000 GHz and further addition of LMZBS glass (5 wt%) decreases the quality factor of LMT to 38 000 GHz. For LZT + LMZBS ceramic glass composites, a gradual decrease in the quality factor is observed along with a decrease in sintering temperature. The quality factor of LZT ceramics decreases from 72 000 GHz to 27 000 GHz with the addition of 5 wt% of LMZBS glass. The added glasses not only acted as the sintering aid but also as an impurity phase with a low quality factor and ε_r, which can adversely affect the microwave dielectric properties. It has been reported that the microwave dielectric loss is mainly caused not only by the lattice vibrations but also by the pores, the grain morphology, and the second phase [63]. During sintering the impurities are concentrated at the grain boundary intersections and this accumulation of impurities increases the loss factor [106]. In addition, the dielectric loss of glasses is much higher than that of LMT and LZT ceramics. The relatively higher dielectric loss of the glass and the low densification could be the reason for the decrease in the quality factor of LMT and LZT ceramics with LMZBS glass composite. Addition of 3 wt% of LMZBS glass in LMT and LZT shows the quality factor of 43 000 GHz and 30 000 GHz when sintered at 925 °C/4 h and 900 °C/4 h, respectively.

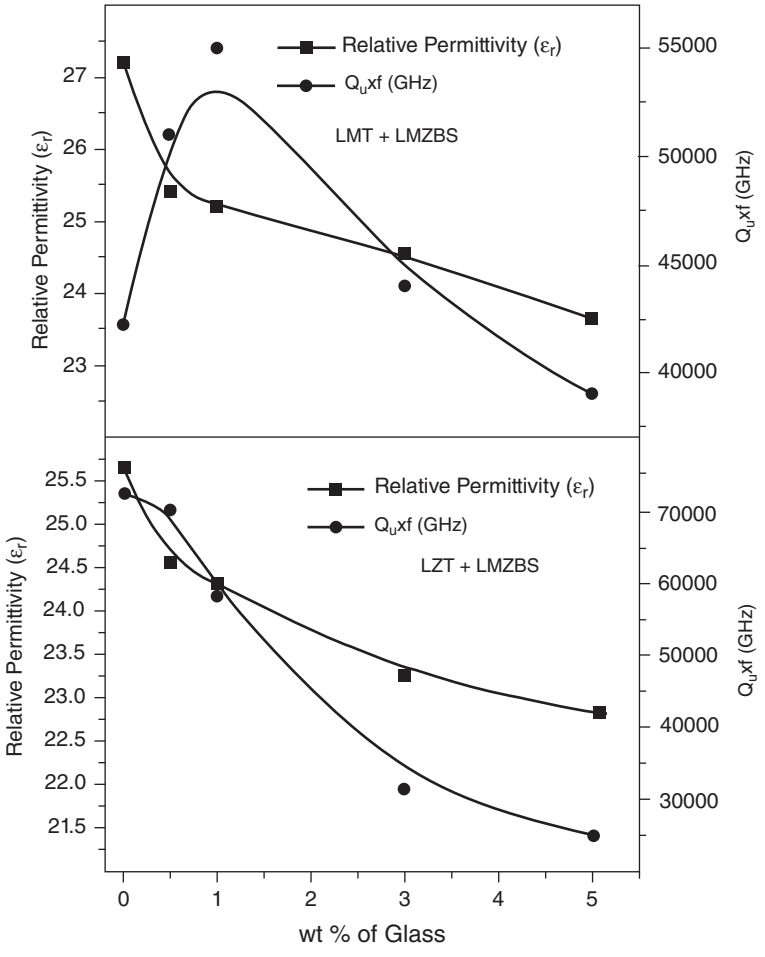

Figure 6.18 *Variation of relative permittivity and quality factor of (a) LMT and (b) LZT ceramics as a function of LMZBS glass addition. Source: Adapted from George and Sebastian 2011 [62].*

The stability of the resonant frequency of a resonator or filter with ambient temperature is important when the design and performance of the microelectronic devices are concerned. Figure 6.19 shows the variation of the temperature coefficient of resonant frequency of LMT and LZT ceramics with different wt% values of LMZBS glass. It is observed that the addition of 5 wt% LMZBS glass in LMT decreases the τ_f from +3 to +0.5 ppm/°C and that of LZT varies from –11 to –16.5 ppm/°C. The decrease in the τ_f of the present ceramic glass system is due to the relatively high negative τ_f of LMZBS glass as compared to LMT and LZT ceramics. The LMT with 1 wt% LMZBS sintered at 950 °C has an ε_r of 25.2, Qf of 55 000 GHz and $\tau_f = 1$ ppm/°C [62], and LZT with a small amount of $CuO–Bi_2O_3–V_2O_5$, H_3BO_3, $MgO–B_2O_3–SiO_2$,B_2O_3, $ZnO–B_2O_3$ showed a quality factor above 40 000 GHz with a sintering temperature suitable for LTCC applications. The relatively high ε_r of about 22 to 27, low sintering temperature, $Qf >$ 40 000 GHz, τ_f close

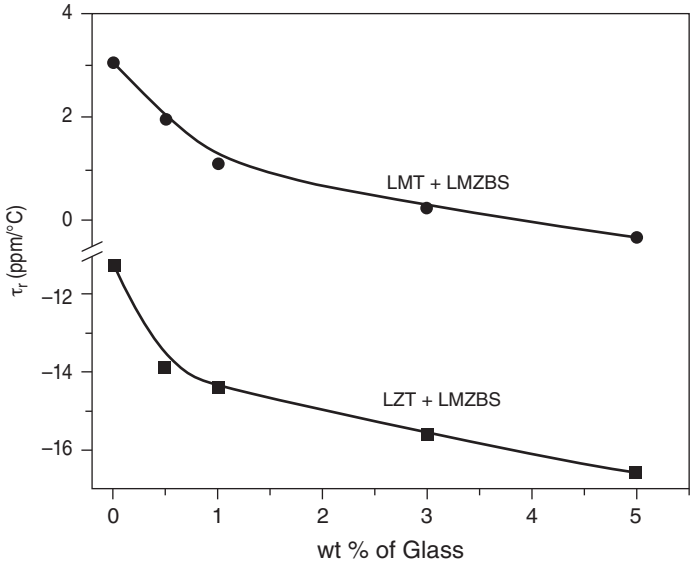

Figure 6.19 *The variation of temperature coefficient of resonant frequency of LMT and LZT ceramics as a function of LMZBS glass. Source: Adapted from George and Sebastian 2011 [62].*

to zero, and non-reactivity with Ag electrode material make these excellent materials for LTCC applications as compared to current commercial LTCC compositions. There are several lithium-based compounds with low sintering temperatures and the properties of these compounds are given in the Appendix (which appears at the end of Volume II) and are also discussed in Chapter 8. The $Li_2ATi_3O_8$ (A = Mg, Zn) materials are excellent in terms of dielectric properties, sintering temperature, and cost of raw materials as compared to commercially available high-Q dielectric resonators. The addition of glasses lower the sintering temperature below the melting point of Ag and its non-reactivity with the electrode make these materials suitable for dielectric resonator and LTCC applications.

6.3 $Li_2Zn_3Ti_4O_{12}$

Recently $ZnLi_{2/3}Ti_{4/3}O_4$ ($Li_2Zn_3Ti_4O_{12}$) was reported as a high-Q microwave material [88, 101–104]. Figure 6.20 shows the X-ray diffraction pattern of the ceramic. It has a cubic structure with space group Fd-3m similar to $MgFe_2O_4$ with lattice parameters of $a = 8.40172$ °A and density = 4.43 g/cm^3. Inset is the SEM of ceramic sintered at 1075 °C for 2 h [101]. The material sintered into dense ceramic at 1075 °C/2 h. The SEM shows that the grains are relatively large at 50–100 μm in size. The $ZnLi_{2/3}Ti_{4/3}O_4$ ceramic sintered at 1075 °C for 2 h has good microwave dielectric properties of $\varepsilon_r = 20.6$, $Qf = 106\,700$ GHz, $\tau_f = -48$ ppm/°C [101]. Addition of 15 wt% of $BaCu(B_2O_5)$ lowered the sintering temperature to 900 °C with reasonably good microwave dielectric properties of $\varepsilon_r = 19.4$, $Qf = 57\,600$ GHz and $\tau_f = -39.5$ ppm/°C. It was found that the $ZnLi_{2/3}Ti_{4/3}O_4$–$BaCu(B_2O_5)$

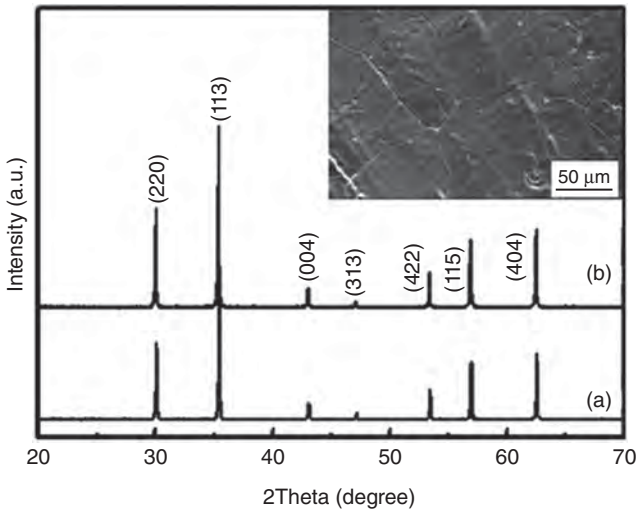

Figure 6.20 *XRD of $ZnLi_{2/3}Ti_{4/3}O_4$ (a) powders calcined at 900 °C and (b) ceramic sintered at 1075 °C for 2 h. Source: Zhou* et al. *2012 [101]. Reproduced with permission of Elsevier.*

composite is chemically compatible with Ag electrode material. Liu *et al.* [88] reported that addition of a small amount of rutile can tailor the τ_f of the compound. $0.4ZnLi_{2/3}Ti_{4/3}O_4$–$0.6TiO_2$ ceramic has excellent microwave dielectric properties with ε_r of 25.1, a high *Qf* of 62 000 GHz, and a near-zero τ_f of −5 ppm/°C when sintered at 1075 °C. Addition of $Ba_3(VO_4)_2$, B_2O_3–CuO, Li_2TiO_3 + B_2O_3–CuO, or Li_2O–ZnO-B_2O_3 are found to lower the sintering temperature to a level suitable for LTCC applications with reasonably good microwave dielectric properties [102–104]. The 0.8 $ZnLi_{2/3}Ti_{4/3}O_4$–$0.2Li_2TiO_3$ + 2 wt% B_2O_3–CuO composite sintered at 925 °C has ε_r = 17.5 with *Qf* of 71 000 GHz and τ_f of –44 ppm/°C [103]. The addition of LZB glass also lowers the sintering temperature to about 900 °C with ε_r = 19.1, *Qf* of 63 800 GH,z and τ_f of –49 ppm/°C and is chemically compatible with Ag [104].

In general the spinels are found to have excellent microwave dielectric properties and are suitable for substrate and mm-wave applications. There are several compositions with *Qf* greater than 100,000 GHz with relatively low sintering temperatures as compared to well-known materials like Al_2O_3, BMT, or BZT. Addition of suitable glass further lowers the sintering temperatures suitable for LTCC applications and these materials are chemically compatible with silver electrode material. The relatively low sintering temperatures and inexpensive raw materials make spinels important for commercial applications.

6.4 Apatites

Apatites have long been studied for their catalytic activity, luminescent properties, and bioceramic applications [107, 108]. In recent times, considerable attention has been paid to rare earth containing silicate and germanate apatites due to their high oxide ion

conductivity. The apatite-based silicates find much interest in technological applications such as fuel cells, oxygen sensors, etc. [108]. The doped apatite compounds have been established as promising candidates for use in fluorescent lamp phosphors and laser technology [109]. Shannon and Rossman reported that fluroapatite minerals have a low dielectric loss and ε_r of about 10 at 1 MHz [110]. Recently Sebastian and coworkers made a detailed investigation on the microwave dielectric properties of apatites with substitutions at different sites [111–115].

The apatites form a large family of compounds with general formula $A_{10}(BO_4)_6X_2$ with A being a monovalent to trivalent cation (Na^+, K^+, Ca^{2+}, Sr^{2+}, La^{3+}, Pr^{3+}, etc.), (BO_4) a trivalent or tetravalent anion ($(PO_4)^{3-}$, $(VO_4)^{3-}$, $(SiO_4)^{4-}$, etc.), and X a monovalent or divalent anion (OH^-, F^-, Cl^-, O^{2-}, etc.). Most of the apatite materials crystallize in the $P6_3/m$ space group with hexagonal symmetry [116]. However, a few exceptions form compounds with lower symmetry such as $P6_3$ and $P2_1/m$. The structure consists of isolated BO_4 tetrahedra arranged in such a way as to form two distinct channels running along the *c*-axis direction, as shown in Figure 6.21 (also shown in the Plate Section). The smaller channel is occupied by the A cations and the larger channel contains a ring of A cations with the oxygen anion occupying the positions in the channel centre. Thus the A cation has two possible sites, A(I) with ninefold coordination (4*f*) and A(II) with sevenfold coordination (6*h*) [116, 117]. The distribution of cations between the two non-equivalent A sites has been addressed in several studies [118, 119]. The average covalency of the A(II) site is higher than that of A(I) site [120]. Large number of possible substitutions in all of the three sites make apatites an attractive class of materials for functional applications. Some of these substitutions can be realized without any change of cationic or anionic charge. It is possible to substitute a bivalent cation with a trivalent cation and trivalent anion (PO_4^{3-})

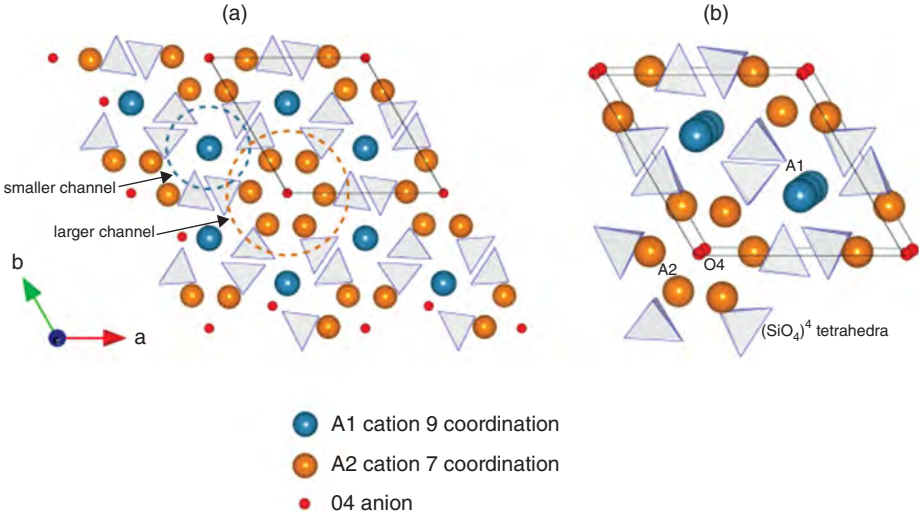

Figure 6.21 *The apatite crystal structure is shown with $(SiO_4)_4$–polyhedra shown as grey tetrahedra, the AII (6h) sites are in orange, the AI (4f) sites are in blue, and the large and small channels. Source: Qu* et al. *[129]. This figure is also shown in the Plate Section.*

with a tetravalent anion (SiO_4^{4-}) and a solid solution exists between phosphate and silicate apatites [113, 114, 121].

6.4.1 $A_2RE_8(SiO_4)_6O_2$ ceramics

In rare-earth oxyapatites $A_2RE_8(SiO_4)_6O_2$ (A = Mg, Ca, Sr, Ba) Mg and Ca ions can occupy A(II) sites whilst larger Sr and Ba ions occupy only the A(I) site [122]. The alkaline-earth ions reside in A(I) site except when the RE^{3+} ions are large (e.g., La^{3+}) and A^{2+} ions are small (e.g., Mg^{2+}), where A^{2+} ions may also be accommodated in A(II) [122]. Blasse [122] reported that by doping these compounds with Eu^{3+}, the Eu^{3+} ions enter the A(II) sites in $A_2La_8(SiO_4)_6O_2$ and A(I) sites in $A_2Y_8(SiO_4)_6O_2$ (A = Mg, Ca), respectively. This is due to the fact that the Eu^{3+} is smaller than La^{3+} and larger than Y^{3+}. In later reports, the doping rare-earth ions (Ce^{3+}, Pr^{3+}) have been found to occupy both the A(I) and A(II) sites in $A_2Y_8(SiO_4)_6O_2$ (A = Mg, Ca, Sr) by luminescence spectroscopy [123]. The apatite rare–earth silicate is often written as $A(I)_4A(II)_6(SiO_4)_6O_2$. Recently Thomas and coworkers made a detailed investigation [111,112,124] of the structure $(Sr_2RE_2)RE_6Si_6O_{26}$ (RE = rare earth) ceramics by X-ray diffraction along with Rietveld refinement and electron diffraction. Figure 6.22 shows the TEM images of $(Sr_2RE_2)RE_6Si_6O_{26}$ (RE = Tm, Y, Tb, and Pr) ceramics. These samples are dense ceramics, as indicated by the clear grain boundaries. Figure 6.23 shows the XRD pattern of $(Sr_2RE_2)RE_6Si_6O_{26}$ (RE = La, Pr, Nd,

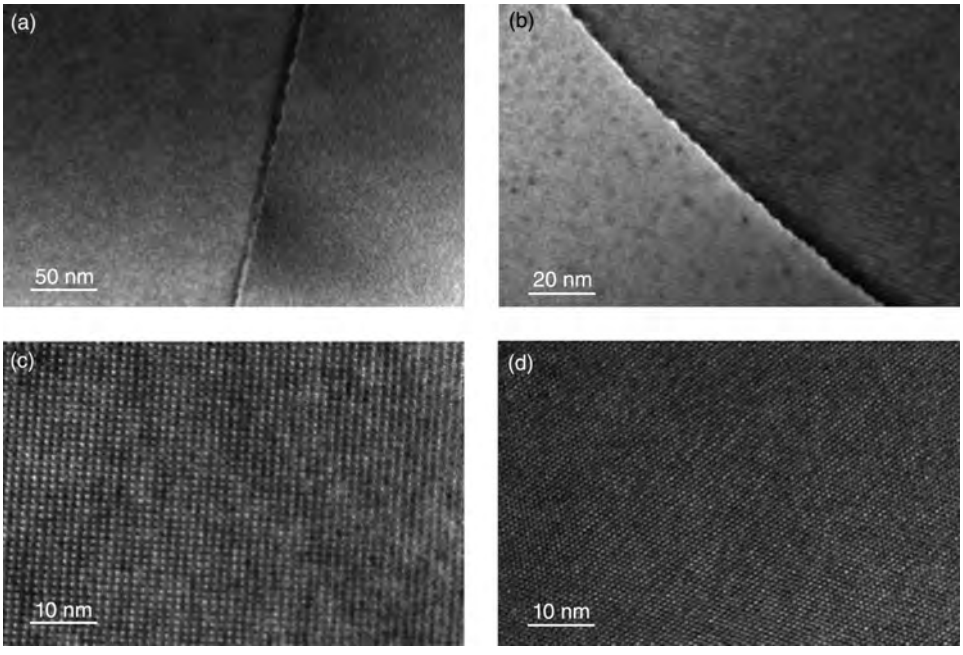

Figure 6.22 *TEM images of (a) $(Sr_2Tm_2)Tm_6Si_6O_{26}$, (b) $(Sr_2Y_2)Y_6Si_6O_{26}$, (c) $(Sr_2Tb_2)Tb_6Si_6O_{26}$, and (d) $(Sr_2Pr_2)Pr_6Si_6O_{26}$. Source: Adapted from Leu* et al. *2011 [111].*

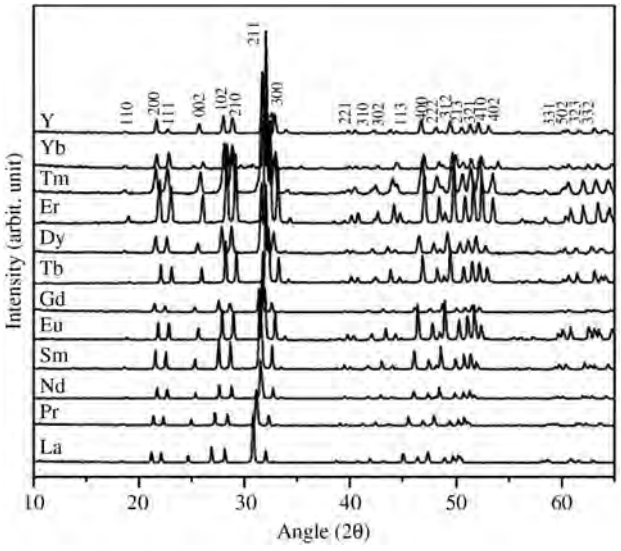

Figure 6.23 *X-ray diffraction patterns of $Sr_2RE_8Si_6O_{26}$ (RE = La, Pr, Nd, Sm, Eu, Gd, Tb, Er, Tm, Yb, and Y) ceramics. Source: Adapted from Thomas and Sebastian 2009 [112].*

Sm, Eu, Gd, Tb, Dy, Er, Tm, Yb, and Y) ceramics. Figure 6.24 shows selected area electron diffraction patterns (SADPs) of a representative material, $(Sr_2Y_2)Y_6Si_6O_{26}$, obtained with the beam parallel to (a) [110], (b) [011], (c) [120], and (d) [001]. The diffraction patterns are identical for all of the materials. Detailed analysis of electron diffraction and X-ray diffraction indicated a hexagonal structure with the $P6_3/m$ space group [111,125,126]. Both *a* and *c* lattice constants show a linear dilation with increasing ionic radius of the rare-earth element in VI coordination [111]. The structural refinement of $(Sr_2RE_2)(RE_6)(SiO_4)_6O_2$ and $Ca_2La_8(SiO_4)_6O_2$ has shown that A(II) sites are solely occupied by La^{3+} ions, whereas A(I) sites are occupied equally by La^{3+} and Ca^{2+} ions [111,118]. The structural refinements of $(Sr_2RE_2)RE_6Si_6O_{26}$ confirms the hexagonal structure with space group $P6_3/m$ (No. 176) [111,125].

The $A_2RE_4Si_6O_{26}$ (A = Sr, Ca, and Ba; RE = rare earths) ceramics were prepared by the conventional solid-state ceramic route by sintering at temperatures in the range 1325–1650 °C for 4 hours [111,112,124]. Rare-earth ions having a lower ionic radius exhibit a higher sintering temperature (> 1500 °C). The $Sr_2RE_8Si_6O_{26}$ (RE = La, Pr, Nd, Sm, Eu, Tb, Yb) shows a relative density in the range 90–95% while $Sr_2RE_8Si_6O_{26}$ (RE = Gd, Dy, Er, Tm, Y) shows a low value of relative density (< 85%). Addition of a small amount (0.5 wt%) of zinc borosilicate (ZBS) glass improved the density of these materials considerably [112]. Figure 6.25a and b shows the SEM images of $Sr_2La_8Si_6O_{26}$ and $Sr_2Dy_8Si_6O_{26}$ sintered at 1325 °C and 1475 °C, respectively. Both microstructures reveal the single-phase nature of the materials. The ceramics have a grain size varying from 1 to 3 μm. Figure 6.25c shows the SEM image of 0.5 wt% zinc borosilicate (ZBS) glass added to $Sr_2Dy_8Si_6O_{26}$ ceramics. No secondary phases are observed while an increase in the grain size is noted by the addition

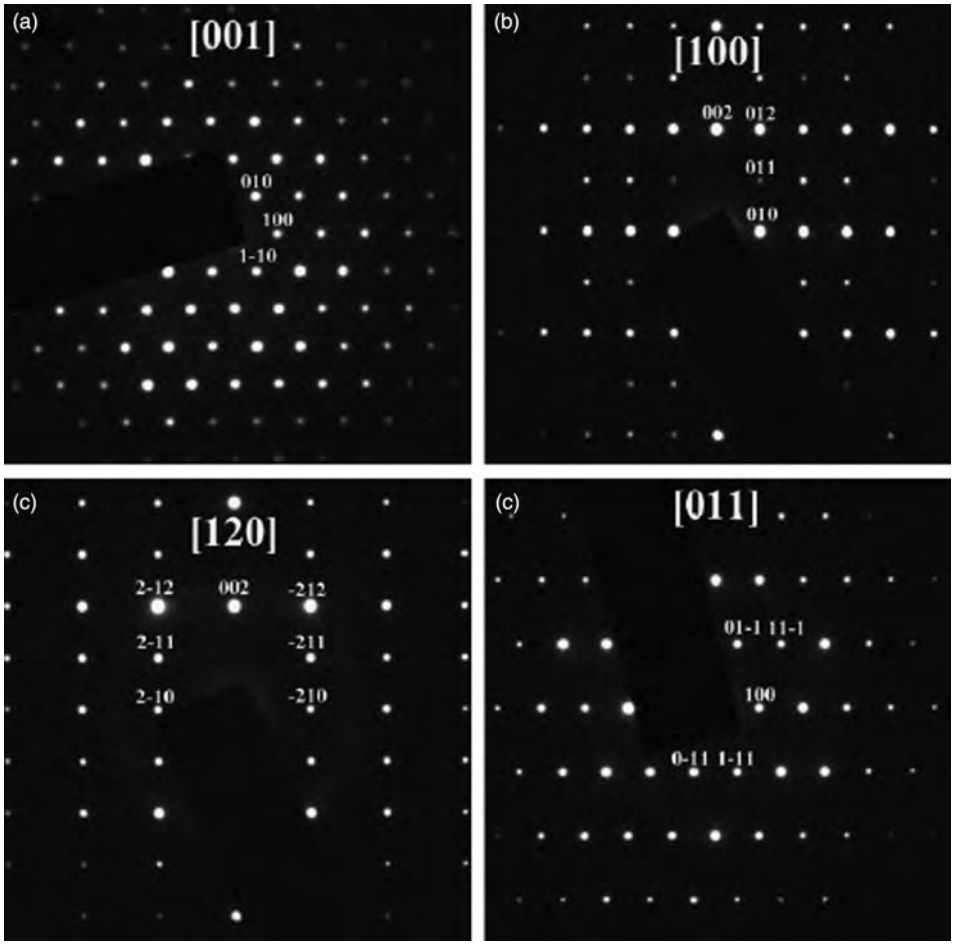

Figure 6.24 *Electron diffraction patterns of* $(Sr_2Pr_2)Pr_6Si_6O_{26}$ *ceramic along (a) [001], (b) [100], (c) [120], and (d) [011] zones. Source: Leu* et al. *2011 [111].*

of glass frits [112]. The $Sr_2RE_8Si_6O_{26}$ (RE = La, Pr, Nd, Sm, Eu, Gd, Tb, Dy, Er, Tm, Yb, and Y) ceramics have relative permittivity in the range 9.6 to 15.6. The microwave dielectric properties of all apatites are given in the Appendix. The ceramic composed of rare earths with a higher ionic radius exhibited a higher relative permittivity than the smaller ones. The ε_r is highest for $Sr_2Pr_8Si_6O_{26}$ and lowest for $Sr_2Dy_8Si_6O_{26}$ ceramics. The relative permittivity is not only dependent on the ionic polarizabilities but also on the rattling effect, which could be explained based on the bond valence of the materials [111]. The covalency of the various bonds are calculated by the method proposed by Brown and Shannon [127] showed that the Si–O bond shows a covalence character of about 59% for $Sr_2La_8Si_6O_{26}$, which decreases gradually as the RE^{3+} ionic radius decreases [111]. Thus with the decrease in covalency an increase in relative permittivity is expected. $Sr_2RE_8Si_6O_{26}$ (RE = La, Nd, Sm, Eu, and Y) ceramics have $Qf >$ 20 000 GHz with a maximum value of 26 300 GHz

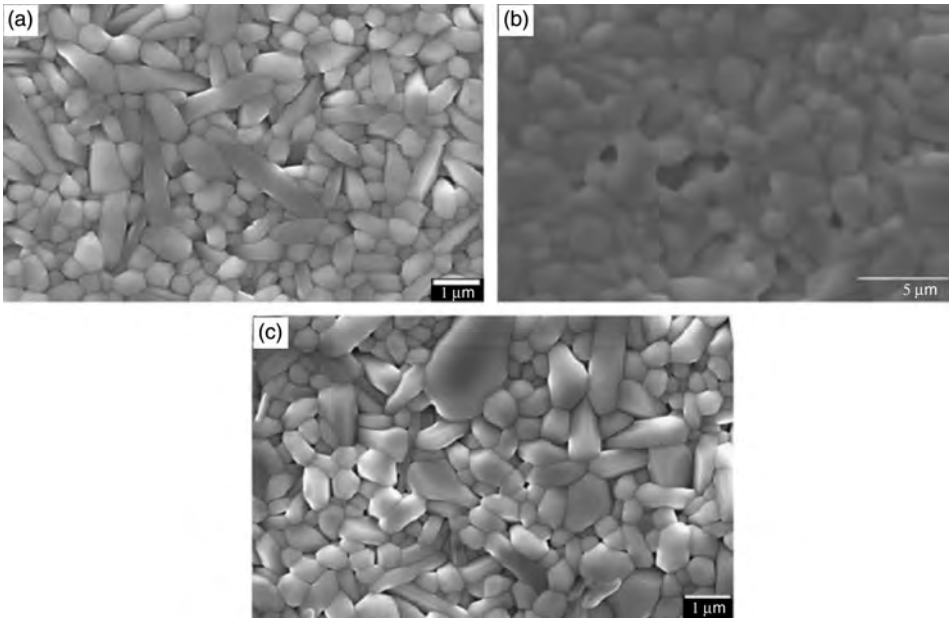

Figure 6.25 *SEM images of (a) $Sr_2La_8Si_6O_{26}$ sintered at 1325 °C/2 h, (b) $Sr_2Dy_8Si_6O_{26}$ sintered at 1475 °C/2 h, and (c) $Sr_2Dy_8Si_6O_{26}$ + 0.5 wt% ZBS sintered at 1450 °C/2 h. Source: Adapted from Thomas and Sebastian 2009 [112].*

for the $Sr_2La_8Si_6O_{26}$ ceramic. The temperature coefficient of resonant frequency of the ceramics varied in the range 10 to –40 ppm/°C. The high negative τ_f of the ceramics have been tailored by adding a small amount of rutile, which has a high positive τ_f [112].

6.4.2 $(Ca, Ba)_2RE_8Si_6O_{26}$ (RE = Rare Earths)

Figure 6.26 shows the XRD patterns of $Ca_2RE_8Si_6O_{26}$ and $Ba_2RE_8Si_6O_{26}$ ceramics. The $Ca_2RE_8Si_6O_{26}$ (RE = La, Pr, Nd, Sm, Eu, Tb, Dy, Tm, Yb, and Y) and $Ba_2RE_8Si_6O_{26}$ (RE = La, Pr, Nd, Sm) ceramic compounds belong to the hexagonal symmetry with space group $P6_3/m$ similar to $Sr_2RE_8Si_6O_{26}$ [124]. However, it is found that as the ionic radii of the A-site ion decreases from Ba to Ca, definite changes are visible in the XRD of these materials. The intensity of one of the reflections (110) in the XRD pattern decreases from the $Ba_2RE_8Si_6O_{26}$ series to the Sr series and finally disappears for $Ca_2RE_8Si_6O_{26}$. Even though single-phase compounds are obtained in this system, further studies are needed to elucidate the exact crystal structure of these compositions. It is expected that as the ionic radius of the rare earth decreases from La to Yb, the lattice parameters (a and c) must also decrease. However, the "a" values deviate considerably from the linear trend while "c" shows an almost regular decrease with the ionic radius [124]. This can be due to the multiple site occupancy of various ions that are found in apatite-type structures.

The $Ca_2RE_8Si_6O_{26}$ have relative densities up to about 95% but $Ca_2Tb_8Si_6O_{26}$, $Ca_2Dy_8Si_6O_{26}$ and $Ca_2Tm_8Si_6O_{26}$ are found to be difficult to densify [124]. The

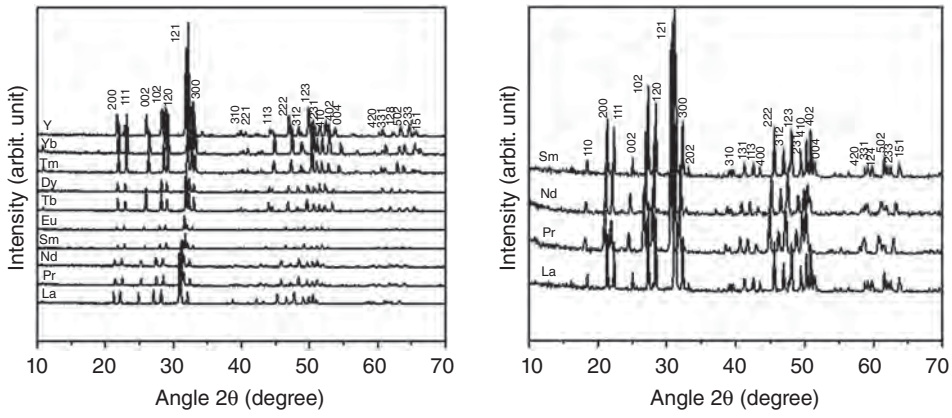

Figure 6.26 *XRD patterns of (A) $CaRE_4Si_3O_{13}$ (RE = La, Pr, Nd, Sm, Eu, Tb, Dy, Tm, Yb, and Y) and (B) $BaRE_4Si_3O_{13}$ (RE = La, Pr, Nd, Sm) ceramics. Source: Adapted from Thomas 2011 [124].*

relative densities show that $Ba_2RE_8Si_6O_{26}$ ceramics possess a higher relative density with a maximum of 98%, except for $Ba_2La_8Si_6O_{26}$. Figure 6.27a and b show the microstructure of $Ca_2La_8Si_6O_{26}$ and $Ca_2Y_8Si_6O_{26}$ sintered at 1325 °C and 1475 °C, respectively. Both of them revealed a uniform single phase and a well-packed microstructure. The $Ca_2La_8Si_6O_{26}$ ceramics has an average grain size less than 1 μm whereas $Ca_2Y_8Si_6O_{26}$ shows a comparatively higher grain size (~ 2–3 μm). Figure 6.27c shows the microstructure of $Ba_2La_8Si_6O_{26}$ sintered at 1325 °C. From the SEM images it can be inferred that the material possesses a highly dense microstructure. The Ca-based apatites have a relative permittivity in the range 11.9 to 14.9, Qf up to 24 800 GHz, and τ_f in the range –39 to +10 ppm/°C [124]. In the case of Ba series only four of the rare earth-based silicates are found to exhibit resonance at the microwave frequency. Very few reports are available on the existence or formation of phase-pure $Ba_2RE_8Si_6O_{26}$ apatites. The $Ba_2RE_8Si_6O_{26}$ (RE = La, Pr, Nd, Sm) possess a high value of relative permittivity as compared with those of Ca- and

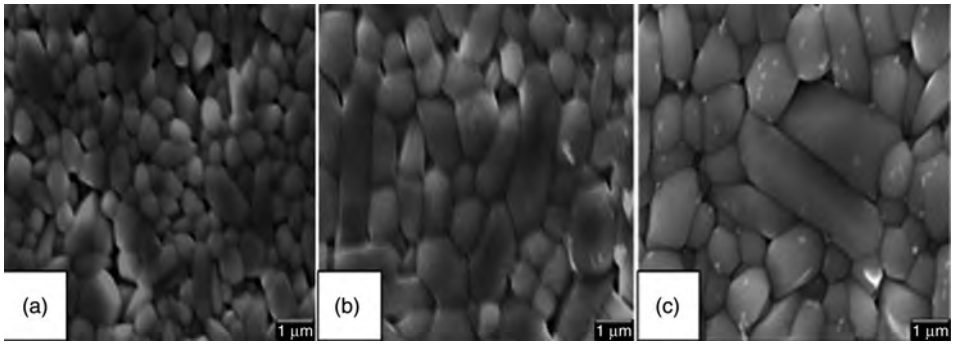

Figure 6.27 *SEM images of (a) $Ca_2La_8Si_6O_{26}$ sintered at 1325 °C/2 h, (b) $Ca_2Y_8Si_6O_{26}$ sintered at 1475 °C/2 h, and (c) $Ba_2La_8Si_6O_{26}$ sintered at 1325 °C/2 h. Source: Adapted from Thomas 2011 [124].*

Sr-based rare-earth silicates. This is due to the high ionic polarizability of Ba^{2+} (α_D = 6.4 Å^3). A maximum value of relative permittivity of about 16.8 is obtained for $Ba_2Pr_8Si_6O_{26}$. The quality factor of $Ca_2RE_8Si_6O_{26}$ varies from 13 000 to 31 000 GHz. In both $Ca_2RE_8Si_6O_{26}$ and $Ba_2RE_8Si_6O_{26}$ series, as the RE^{3+} ionic radii decreases, the quality factor is found to decrease gradually. This may be due to the increasing ionic character as observed in the case of $Sr_2RE_8Si_6O_{26}$.

6.4.3 $Ca_{2+x}RE_{8-x}(SiO_4)_{6-x}(PO_4)_xO_2$ (RE = Rare Earths)

Thomas *et al.* [113, 114] prepared $Ca_{2+x}RE_{8-x}(SiO_4)_{6-x}(PO_4)_xO_2$ (x = 0, 2, 4, and 6) ceramics by the solid-state ceramic route and sintered at temperatures in the range 1375–1675 °C for 4 hours. The sintering temperature is found to vary with x. The ceramics showed a densification in the range 93 to 98% for different RE and different x values. Figure 6.28 shows the powder XRD patterns of $Ca_{2+x}La_{8-x}(SiO_4)_{6-x}(PO_4)_xO_2$ ceramics for RE = La. The ceramics crystallize with hexagonal symmetry and belong to the $P6_3/m$ space group. It is found that the XRD patterns of all ceramics are similar except for the small shift towards the higher angles with the increase in the value of x. The magnitude of the peak shift decreases with the decrease in ionic radius of the RE ion. Figure 6.29 shows the variation of lattice parameters as a function of x for all the rare-earth series. The lattice parameters "a" and "c" decreases gradually with x for the series containing larger RE ions (La to Eu). However, the slope of both lattice parameter variations decreases with the decrease in ionic radius of the rare earth ion. Finally, for the smaller RE ion (Tb) the lattice parameter variation with x becomes marginal. It is also noteworthy that the lattice parameter "c" varies irregularly with x for $Ca_{2+x}Gd_{8-x}(SiO_4)_{6-x}(PO_4)_xO_2$, although the variation

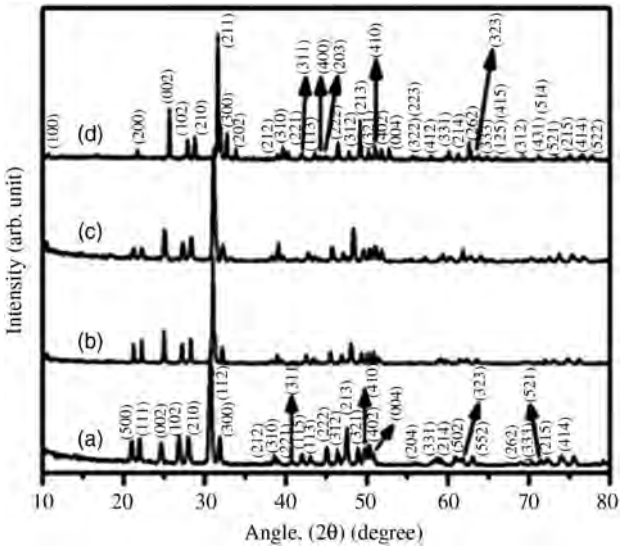

Figure 6.28 *Powder XRD patterns of $Ca_{2+x}La_{8-x}(SiO_4)_{6-x}(PO_4)_xO_2$ with (a) x = 0 sintered at 1475 °C/4 h, (b) x = 2 sintered at 1475 °C/4 h, (c) x = 4 sintered at 1675 °C/4 h, and (d) x = 6 sintered at 1425 °C/4 h. Source: Adapted from Thomas and Sebastian 2011 [113].*

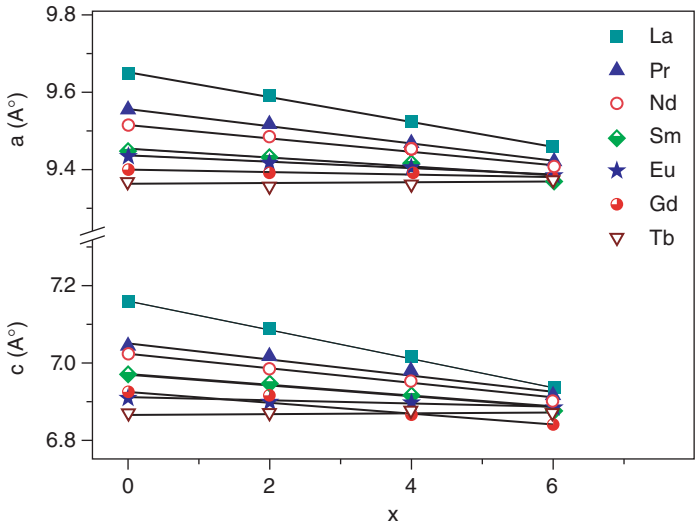

Figure 6.29 *Lattice parameter variation of* $Ca_{2+x}RE_{8-x}(SiO_4)_{6-x}(PO_4)_xO_2$ *with the value of* x. *Source: Adapted from Thomas* et al. *2013 [114].*

is small. It has been reported earlier that for apatites, the lattice parameter variation is sensitive to the distribution of cations among the M(I) and M(II) sites [128]. From Figure 6.29 it is also obvious that the variation of lattice parameters for $Ca_{2+x}RE_{8-x}(SiO_4)_{6-x}(PO_4)_xO_2$ with the change in RE ion is more pronounced at the silicate end ($x = 0$) compared to the phosphate end ($x = 6$). The number of RE ions per unit cell decreases as the value of x increases and hence the effect of RE substitution on the lattice parameters may be relatively low for higher values of x. The unit cell volume varies with x in a similar way, as do the lattice parameters. The variation of cell volume with x diminishes as La is replaced with smaller RE ions and the variation becomes negligible for the Tb series. The microstructure of $Ca_{2+x}La_{8-x}(SiO_4)_{6-x}(PO_4)_xO_2$ ceramics is shown in Figure 6.30. The microstructure of the composition with $x = 0$ (Figure 6.30a) contains grains of size randomly varying from less than 1 μm to ~8 μm. The SEM image of the surface of the ceramic with $x = 4$ (Figure 6.30 c) shows still larger grains of size greater than 10 μm. It is found that the average grain size increases with increasing value of x, as shown in Figure 6.30a to d. The microstructure of other RE = Pr, Sm, Tb, etc., also showed a similar behavior.

The $Ca_{2+x}RE_{8-x}(SiO_4)_{6-x}(PO_4)_xO_2$ ceramics have low thermal expansion (CTE ≤ 7 ppm/°C). The value of CTE increases with x for all the RE series. The $x = 0$ has the lowest CTE and CTE increase with an increase in x. The relative permittivity of $Ca_{2+x}RE_{8-x}(SiO_4)_{6-x}(PO_4)_xO_2$ ceramics at microwave frequencies varies in the range 9.2 to 14.8 for different RE for $x = 0$ to 6. The ε_r decreases gradually with the increase of x. This may be mainly due to the decrease in number of RE^{3+} ions with relatively large ionic polarizability [63] in the unit cell as the value of x increases. Figure 6.31a depicts the variation of Qf as a function of x for $Ca_{2+x}RE_{8-x}(SiO_4)_{6-x}(PO_4)_xO_2$. For $Ca_{2+x}La_{8-x}(SiO_4)_{6-x}(PO_4)_xO_2$, Qf decreases gradually from 33 100 GHz (at $x = 0$) to 12 700 GHz (at $x = 6$). Similarly for $Ca_{2+x}Tb_{8-x}(SiO_4)_{6-x}(PO_4)_xO_2$ the

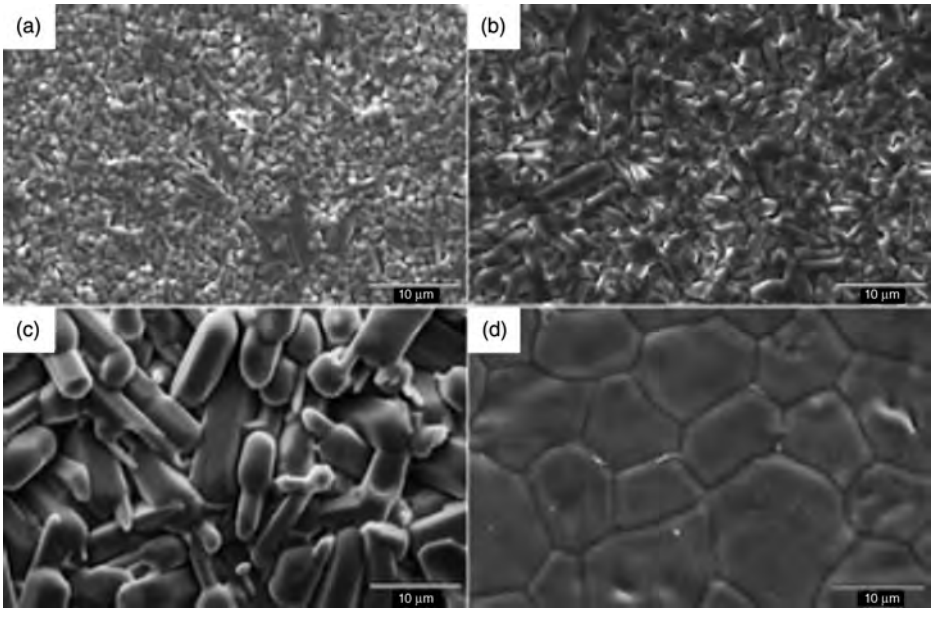

Figure 6.30 *SEM images of $Ca_{2+x}La_{8-x}(SiO_4)_{6-x}(PO_4)_xO_2$ with (a) x = 0 sintered at 1475 °C/4 h, (b) x = 2 sintered at 1475 °C/4 h, (c) x = 4 sintered at 1675 °C/4 h, and (d) x = 6 sintered at 1425 °C/4 h. Source: Adapted from Thomas* et al. *2013 [114].*

quality factor decreases from 20 800 GHz (at $x = 0$) to 14 200 GHz (at $x = 6$). For $Ca_{2+x}RE_{8-x}(SiO_4)_{6-x}(PO_4)_xO_2$ with RE = Pr, Nd, Sm, and Eu, Qf decreases with x, reaches the minimum value at $x = 4$ and then increases for $x = 6$ (Figure 6.31). The variation of Qf for $Ca_{2+x}Gd_{8-x}(SiO_4)_{6-x}(PO_4)_xO_2$ also follows a similar trend, showing the minimum value at $x = 2$. The variation in Qf with x is small for the Gd series compared

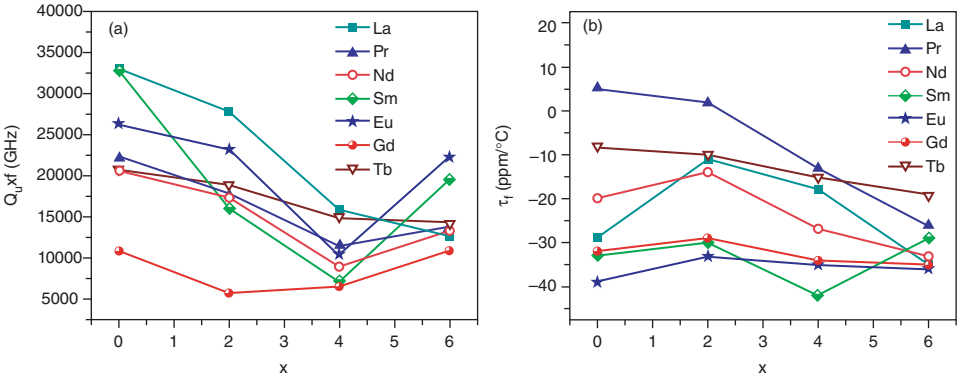

Figure 6.31 *(a) Variation of $Q_u f$ with x for $Ca_{2+x}RE_{8-x}(SiO_4)_{6-x}(PO_4)_xO_2$ ceramics and (b) variation of τ_f with x for $Ca_{2+x}RE_{8-x}(SiO_4)_{6-x}(PO_4)_xO_2$ ceramics. Source: Adapted from Thomas* et al. *2013 [114].*

to the other series. A reasonably good quality factor ($Qf > 20\,000$ GHz) is obtained for the compositions $Ca_{2+x}La_{8-x}(SiO_4)_{6-x}(PO_4)_xO_2$ ($x = 0$, 2), $Ca_2Pr_8(SiO_4)_6O_2$ ($x = 0$), $Ca_2Nd_8(SiO_4)_6O_2$ ($x = 0$), $Ca_2Sm_8(SiO_4)_6O_2$ ($x = 0$), $Ca_{2+x}Eu_{8-x}(SiO_4)_{6-x}(PO_4)_xO_2$ ($x = 0$, 2. and 6), and $Ca_2Tb_8(SiO_4)_6O_2$ ($x = 0$). Among the various RE series studied, the Gd series show a relatively poor quality factor, with the maximum value being 10 900 GHz for $Ca_2Gd_8(SiO_4)_6O_2$ ($x = 0$).

The variation of τ_f with x for the ceramics is shown in Figure 6.31b. All the ceramics except $Ca_{2+x}Pr_{8-x}(SiO_4)_{6-x}(PO_4)_xO_2$ ($x = 0$, 2) show a negative value of t_f. For $Ca_{2+x}Pr_{8-x}(SiO_4)_{6-x}(PO_4)_xO_2$ the value of t_f decreases with x from 5 ppm/°C at $x = 0$ and shows a negative value from $x = 4$ onwards. From Figure 6.31b it can be observed that for the ceramics containing La, Nd, Eu, and Gd, the magnitude of t_f decreases initially with x up to $x = 2$ and then increases from $x = 4$ onwards. The value of t_f decreases linearly with x for $Ca_{2+x}Tb_{8-x}(SiO_4)_{6-x}(PO_4)_xO_2$. For $Ca_{2+x}Sm_{8-x}(SiO_4)_{6-x}(PO_4)_xO_2$ the t_f shows irregular variations with x, which may be due to multiple substitutions at different sites. Among the various compositions developed, $Ca_4La_6(SiO_4)_4(PO_4)_2O_2$ is found to have good densification (98.7%) and microwave dielectric properties ($\varepsilon_r = 13.8$, $Qf = 27\,900$ GHz, and $\tau_f = -11$ ppm/°C). Such an inherently low value of τ_f is very attractive for practical applications.

6.4.4 Effect of Isovalent Substitutions in $Ca_4La_6(SiO_4)_4(PO_4)_2O_2$

The microwave dielectric properties of $Ca_4La_6(SiO_4)_4(PO_4)_2O_2$ changes with the isovalent substitutions for the cations: Ca^{2+}, La^{3+} and for the anions: $(SiO_4)^{4-}$, $(PO_4)^{3-}$. The compositions studied are $(Ca_{4-x}Sr_x)La_6(SiO_4)_4(PO_4)_2O_2$ ($x = 0$, 2, 4), $Ca_4(La_{6-x}Pr_x)(SiO_4)_4(PO_4)_2O_2$ ($x = 0$, 2, 4, 6), $Ca_4La_6(SiO_4)_{4-x}(GeO_4)_x(PO_4)_2O_2$ ($x = 0$, 2, 4), and $Ca_4La_6(SiO_4)_4(PO_4)_{2-x}(VO_4)_xO_2$ ($x = 0$, 1, 2). The ceramics were prepared by the solid-state ceramic route. The compacts were then sintered in air at temperatures in the range 1350–1600 °C for 4 hours [114]. Figure 6.32 shows the SEM images of the compositions derived from $Ca_4La_6(SiO_4)_4(PO_4)_2O_2$ by fully replacing Ca^{2+} with Sr^{2+} (Figure 6.32a), La^{3+} with Pr^{3+} (Figure 6.32b), $(SiO_4)^{4-}$ with $(GeO_4)^{4-}$ (Figure 6.32c), and $(PO_4)^{3-}$ with $(VO_4)^{3-}$ (Figure 6.32d). All these ceramics have good sinterability and sintered densities were between 96 and 99%. The CTE of the ceramics were between 4 and 5 ppm/°C. The SEM images of the compositions with Sr^{2+} and $(GeO_4)^{4-}$ (Figure 6.32a and c) reveal dense microstructures with well-packed polygonal grains. For $Sr_4La_6(SiO_4)_4(PO_4)_2O_2$ the grain size varies from < 1 μm to ~5 μm. $Ca_4La_6(GeO_4)_4(PO_4)_2O_2$ shows a broader grain size distribution with the size varying from ~1 μm to ~15 μm. The microstructure of $Ca_4Pr_6(SiO_4)_4(PO_4)_2O_2$ (Figure 6.32b) and $Ca_4La_6(SiO_4)_4(VO_4)_2O_2$ (Figure 6.32d) shows rather elongated grains with the maximum grain size of ~5 μm and ~8 μm, respectively.

The substitution of Sr^{2+} and $(GeO_4)^{4-}$ increases the sintering temperature. On the other hand, the sintering temperature decreases with the substitution of Pr^{3+} and $(VO_4)^{3-}$. The relative density decreases for all the substitutions. However, the variation in relative density is marginal for Sr^{2+} substitution and all the compositions in this series maintain a densification ≥ 98%. The ceramics show only a small thermal expansion with the values of CTE in the range 4–5 ppm/°C.

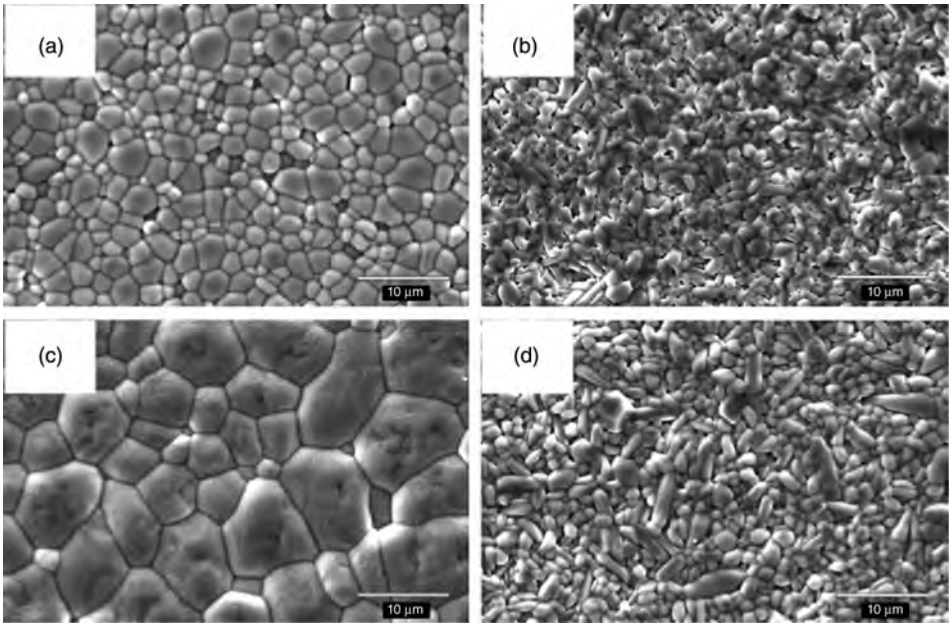

Figure 6.32 *SEM images of (a) $Sr_4La_6(SiO_4)_4(PO_4)_2O_2$, (b) $Ca_4Pr_6(SiO_4)_4(PO_4)_2O_2$, (c) $Ca_4La_6(GeO_4)_4(PO_4)_2O_2$, and (d) $Ca_4La_6(SiO_4)_4(VO_4)_2O_2$. Source: Adapted from Thomas* et al. *2013 [114].*

The ε_r decreases gradually with x for Sr^{2+} substitution. On the other hand, ε_r increases with the substitution of $(GeO_4)^{4-}$ and $(VO_4)^{3-}$. The ε_r does not show considerable variation with Pr^{3+} substitution. The *Qf* shows a substantial decrease from 27 900 GHz to 12 900 GHz as the value of x increases from 0 to 4, although the ceramics are very dense. Hence some other extrinsic factors might be responsible for such behavior. In the apatite structure, the divalent cation has two possible sites 4f with ninefold coordination and 6h with sevenfold coordination [117]. The ordering of the ions among these sites may influence the dielectric response of the system. From Figure 6.33b, it can be observed that Q decreases from 27 900 GHz at $x = 0$ to 17 800 GHz at $x = 6$ with the Pr^{3+} substitution. $(GeO_4)^{4-}$ substitution first decreases *Qf* from 27 900 GHz for $x = 0$ to 14 700 GHz for $x = 2$ and then increases to 20 400 GHz for $x = 4$. *Qf* decreases initially with the $(VO_4)^{3-}$ substitution and saturates at 22 900 GHz from $x = 1$ onwards. It is found that all substitutions leads to a decrease in the Q-factor.

The variation of τ_f with different substitutions is shown in Figure 6.34. The τ_f increases linearly with x for Sr^{2+} and $(VO_4)^{3-}$ substitution (Figure 6.34a and d, respectively). The Pr^{3+} substitution gradually increases τ_f from –11 ppm/°C at $x = 0$ to + 2 ppm/°C at $x = 6$ (Figure 6.34b). The partial substitution of Pr^{3+} for La^{3+} in $Ca_4La_6(SiO_4)_4(PO_4)_2O_2$ effectively reduces the τ_f without much altering the values of ε_r and *Qf*. The composition $Ca_4La_6(SiO_4)_4(PO_4)_2O_2$ is found to have the highest densification (98.7%) and good microwave dielectric properties with $\varepsilon_r = 13.8$, $Qf = 27\,900$ GHz, and $\tau_f = -11$ ppm/°C.

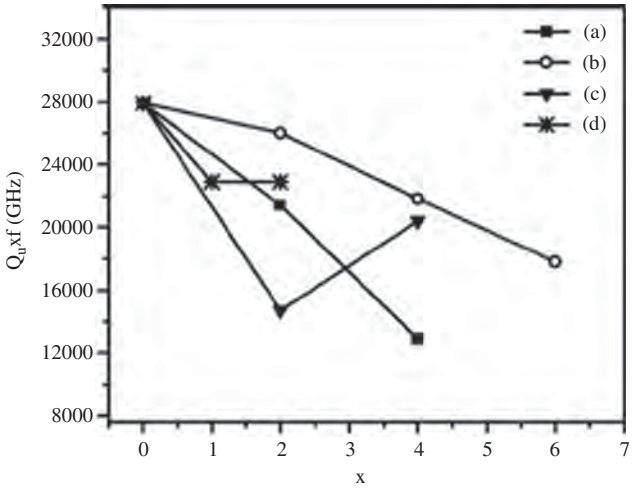

Figure 6.33 *Dependence of Qf on x for (a) $(Ca_{4-x}Sr_x)La_6(SiO_4)_4(PO_4)_2O_2$, (b) $Ca_4La_{6-x}Pr_x)(SiO_4)_4(PO_4)_2O_2$, (c) $Ca_4La_6(SiO_4)_{4-x}(GeO_4)_x(PO_4)_2O_2$, and (d) $Ca_4La_6(SiO_4)_4(PO_4)_{2-x}(VO_4)_xO_2$. Source: Adapted from Thomas* et al. *2013 [114]*

6.4.5 $LiRE_9(SiO_4)_6O_2$ (RE = Rare Earths)

$LiRE_9(SiO_4)_6O_2$ (RE = La, Pr, Nd, Sm, Eu, Gd, and Er) ceramics have sintering temperatures in the range 1175–1275 °C for 4 hours [115]. The sintering was done by muffling the samples with the powder of same composition in order to avoid the escape of volatile lithium. The $LiLa_9(SiO_4)_6O_2$ showed poor densification and addition of 1 wt%

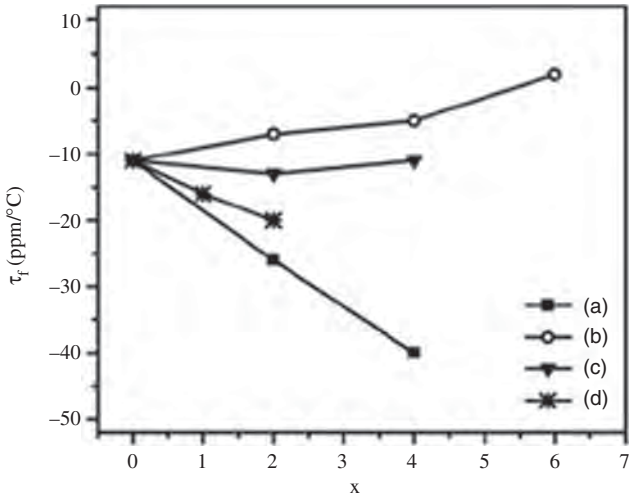

Figure 6.34 *Variation of τ_f with x for (a) $(Ca_{4-x}Sr_x)La_6(SiO_4)_4(PO_4)_2O_2$, (b) $Ca_4(La_{6-x}Pr_x)(SiO_4)_4(PO_4)_2O_2$, (c) $Ca_4La_6(SiO_4)_{4-x}(GeO_4)_x(PO_4)_2O_2$, and (d) $Ca_4La_6(SiO_4)_4(PO_4)_{2-x}(VO_4)_xO_2$ ceramics. Source: Adapted from Thomas* et al. *2013 [114].*

LiF improved the densification to above 90% The ceramics have a hexagonal crystal structure with space group $P6_3/m$. As compositions progress through the lanthanide series from La to Er, the peaks show a gradual shift towards higher angles due to the corresponding decrease in the ionic radius of RE^{3+} ions. The ceramics have relative permittivity in the range 12.8 to 15.3, Qf up to 13 000 GHz and τ_f varies in the range 2 to 33 ppm/°C [115]. It was reported [129] that the random distribution of divalent and trivalent ions over equivalent site contributes to the dielectric losses even when electronic and ionic conduction are completely suppressed. These materials with apatite structure have a random distribution of ions in the A(I) and A(II) sites that may contribute to dielectric losses. Apatites are well known for bioceramic applications. The biocompatibility of the present ceramics are not investigated. Biocompatible apatites are useful for fabrication of implantable devices such as antenna.

6.5 Alumina

Alumina ceramic has excellent properties such as low dielectric loss, ε_r of about 10, high thermal conductivity, a high melting point of about 2050 °C, and good chemical stability, and is extensively used as microwave substrates in different applications. Extensive work has also been done on the microwave dielectric properties of alumina [130–140]. The quality factor of alumina is found to vary considerably from sample to sample prepared from a wide range of sources, although the relative permittivity and physical properties remain nearly the same. Powder purity is an important factor in obtaining low-loss alumina [130–132]. The quality factor of alumina ceramic is found to decrease dramatically [133,134] by the presence of a very small amount of alkali ions and metallic impurities such as K, Na, Fe, etc., but the presence of a very small amount of TiO_2 considerably improves the quality factor [130, 133, 135–140]. Ohsato *et al.* reported a very high Qf value of 680 000 GHz in alumina sintered at 1550 °C [140] and the high quality factor is attributed [140] to the high purity of the initial alumina raw material. It was found [130] that addition of 0.5 wt% TiO_2 lowers the sintering temperature with considerable improvement in the quality factor. However, addition of more than 0.5 mol% TiO_2 considerably lowers the quality factor. Huang *et al.* [138, 139] found that use of nano-TiO_2 additive in nano-alumina powder can considerably lower the sintering temperature with an excellent quality factor. The sample containing 8 wt% of nano-TiO_2 sintered at 1350 °C for 4 h showed ε_r of 10.8 with Qf of 338 000 GHz, and a τ_f of 1 ppm/°C. Huang *et al.* [138,139] sintered nano-powders of alumina with 0.5 wt% nano-powders of TiO_2 at 1550 °C and reported a Qf of 680 000 GHz with a τ_f of –49 ppm/°C. Addition of larger amounts of TiO_2 adversely affected the quality factor [130,138,139]. Breeze *et al.* showed [141] that grain boundaries in alumina have only a limited influence on the dielectric loss provided there is no deleterious impurities. They reported that high-purity, fine-grained polycrystalline alumina possess very low dielectric loss of about 8.33×10^{-6} at 10 GHz at 300 K. It is difficult to densify pure alumina without sintering aids. It is therefore important that these sintering aids do not adversely affect the loss. Alford and Penn showed [130] that the dielectric loss of sintered materials can approach that measured in single crystals. Several authors [130, 142, 143] investigated the loss factor of alumina of different purity levels and concluded that impure alumina always gives a poor loss. However, use of high-purity raw material with proper doping and good

Table 6.2 *Qf of alumina and sapphire and the effect of additives on the quality factor.*

Material	Sintering temperature (°C)	ε_r	*Qf* (GHz)	τ_f (ppm/°C)	Reference
Al_2O_3	1550	10	335 000	–60	[130]
Al_2O_3	1550	10.1	680 000	–60	[140]
Al_2O_3+1500 ppm MgO+300 ppm La_2O_3		9.7	300 000		[161]
Al_2O_3+500 ppmTiO_2		10	500 000		[133]
Al_2O_3+0.15V_f TiO_2		10	300 000	0	[157]
Al_2O_3–TiO_2 doped		10.2	119 150		[141]
Al_2O_3+0.1TiO_2:MnO	1300	12.4	274 000	1.5	[135]
Al_2O_3+0.1TiO_2	1300	12.4	148 000	0	[142]
Al_2O_3+0.1TiO_2 annealed at 1000 °C	1350	12.4	117 000	1.5	[145]
0.895Al_2O_3–0.105TiO_2	1350	12.5	340 000	2	[136]
0.9Al_2O_3–0.1TiO_2	1300	12.7	176 000	–14	[145]
0.89Al_2O_3–0.11TiO_2+0.5 wt% ZnO	1350	12.9	187 000	–2	[138]
Al_2O_3+500 ppm MgO+500 ppm Nb_2O_5	1550	9.9	216 900		[162]
Al_2O_3+0.5 wt% TiO_2	1550	10.0	453 000		[130]
Nano-Al_2O_3+8 wt% nano-TiO_2	1350	10.8	338 000	1	[138], [139]
Nano-Al_2O_3+0.5 wt% nano-TiO_2	1400	9.8	680 000		[139]
Nano-Al_2O_3	1400	10.0	634 000	–40	[166]
Sapphire (measured at 297 K)			1.2×10^6		[163]
Sapphire (measured at 1.55 K)			10.54×10^{10}		[164]
Sapphire (measured at 4.55 K)			1.2×10^{10}		[165]

microstructure are required for low dielectric loss. The Q-factor of alumina varies from manufacturer to manufacturer. The results indicate that purity alone is not a good indicator of the resulting dielectric loss tangent. It is found that purity influences the quality factor but purity alone is not a guarantee for a low-loss factor [130, 142, 143]. Several authors reported [130, 131, 134, 140, 144–147] low dielectric loss in alumina at the microwave frequency range using different additives, which are given in Table 6.2. The ε_r and τ_f are not much affected by the variation in the sintering temperature whereas the *Qf* is temperature dependent. Alford *et al.* [148] found that the quality factor varies considerably with the use of different binders. The PEG 3350 and PEG 20000 are found to give the highest quality factor. However, porosity left by the binders and the impurities present in the binders can affect the quality factor considerably [148]. Several authors lowered the sintering temperature of alumina by adding low melting glasses and are discussed in Chapter 8 on LTCC materials.

Molla *et al.* [132] studied the effect of moisture on tan δ in alumina. They prepared 42% porous alumina and measured the microwave dielectric loss in both dry and moist atmospheres at 15 GHz. Figure 6.35 shows the variation of tan δ with time in porous alumina

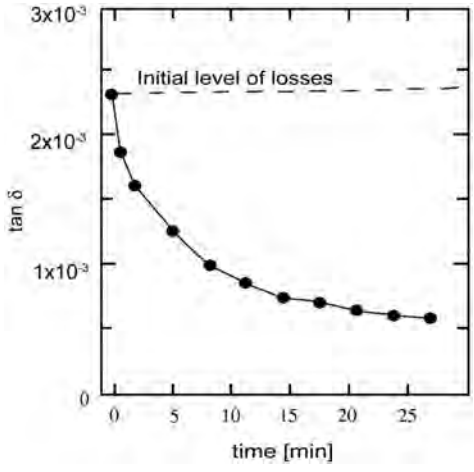

Figure 6.35 *Variation of tan δ with time in 42% porous alumina after introduction of dry N_2 gas. Source: Adapted from Molla* et al. *1999 [132].*

after introduction of dry nitrogen gas in to the resonant measuring cavity. The result indicates that moisture in the cavity increased tan δ. They attributed the ionic conductivity on the water surface to be the reason for the origin of high dielectric losses in porous alumina. The loss factor decreases with an increase in density in polycrystalline alumina [130]. The presence of porosity has a tremendous influence on the quality factor. Alford and coworkers [133, 134] studied the effect of porosity and grain size on the microwave dielectric properties of sintered alumina. The purity of the starting powder, the porosity, and the grain size have been varied and the influence of these variations on ε_r and tan δ were investigated. In order to vary the porosity and thus the density, they sintered the alumina samples at different temperatures in the range 1000–1600 °C for up to 30 h. Figure 6.36 shows the effect of porosity on the loss factor in polycrystalline alumina [133, 134]. The relative permittivity decreases with an increase in pore volume, as expected. The dielectric loss was found to depend strongly on the porosity. A variation in the grain size did not affect the permittivity in nearly dense samples and caused an increase in the dielectric loss when the grain size in the alumina exceeded approximately 3–4 μm. The polycrystalline ceramics always exhibit higher losses than single crystals but in high-quality ceramics the difference can be small. Polycrystalline alumina with an extremely low microwave dielectric loss is reported with properties analogous to a theoretical ensemble of randomly oriented single-crystal sapphire grains [133]. Braginsky and Ilschenko [149] have shown that below 50 K the loss is strongly dependent on the level of crystal perfection as determined by the rate of crystal growth. Ikeda and Miura [150] studied the tan δ of single crystals of alumina and reported that alumina without disorientation showed a low tan δ, in agreement with the theory of Gurevich and Tagantsev [151]. Several people studied [152–154] the quality factor of sapphire crystal using the "whispering gallery mode" (WGM) method. WGM measurements at high-order modes showed unloaded quality factors in the range 10^7 to 10^9 at the X band in the liquid nitrogen to helium temperature range [133, 152–155]. Woode *et al.* [156] reported a sapphire loaded cavity resonator with a Q of 6×10^7 at 8.95 GHz at 77 K.

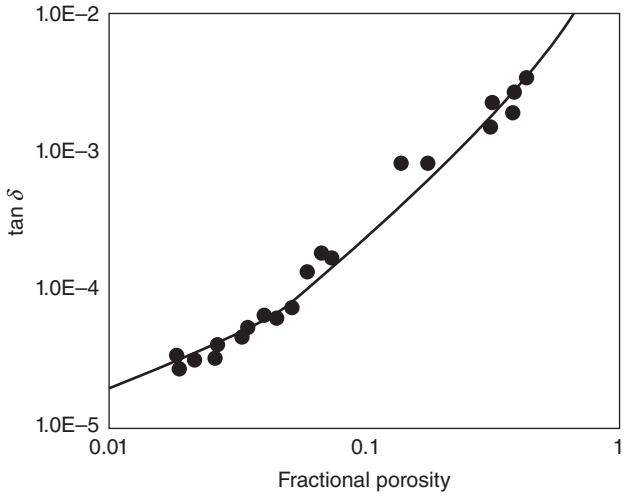

Figure 6.36 *Variation of tan δ with fractional porosity. Source: Adapted from Alford* et al. *2001 [133].*

A sapphire WGM mode resonator shows a Q as high as 200 000 at ambient temperature, better than 10 million at 77 °K [154] and 8.3×10^9 at 12.7 GHz at 1.55 K.

A suitable relative permittivity, very low loss factor, and high thermal conductivity (30 W/m K) of alumina make it an excellent material for electronic packaging applications. Alumina has a high τ_f of –60 ppm/°C at room temperature and TiO_2 has a high Qf of 48 000 GHz, $\varepsilon_r = 100$, and a positive τ_f of 450 ppm/°C [157]. Hence it is possible to tune the τ_f of alumina with the use of rutile as a compensator [130, 135–137, 139, 141, 142, 144, 145, 153, 157–159]. Alford and coworkers [157, 158] compensated the high τ_f of alumina by coating a film of TiO_2 over the surface of the alumina disk. The composite resonators obtained by firing at 1400 °C showed temperature compensation depending on the volume fraction of TiO_2. A volume fraction of 0.015 yielded zero τ_f with a Q value of 30 000 GHz. Tobar *et al.* [155] used thin $SrTiO_3$ wafers to compensate for the τ_f dependence in sapphire with Q-factors varying in the range 20 000 to 50 000 GHz. Residual paramagnetic impurities in sapphire resonators can be a useful method to compensate for the effect of temperature fluctuations on the frequency [160]. High-purity sapphire single crystals at cryogenic temperatures provide an excellent dielectric for high-stability resonator applications such as ultra-low noise, ultra-stable microwave oscillators, and owing to its mechanical rigidity, low thermal expansion and very low dielectric loss [152, 161–166].

6.6 Zirconium Tin Titanate

Zirconium titanate solid solutions have a variety of applications such as wireless communications, catalysts, high-temperature pigments, sensors, optics, and as gate dielectrics [167–170]. In 1941 Rath [171] reported $ZrTiO_4$ as a useful temperature-stable dielectric ceramic. In the 1950s ZrO_2–TiO_2–SnO_2 solid solutions were investigated for a low-temperature coefficient of capacitance applications [172]. Wakino and coworkers [173,

174] first reported $Zr_xTi_ySn_zO_4$ as a temperature-stable low-loss dielectric material for microwave applications. The composition $Zr_{0.8}Sn_{0.2}TiO_4$ gives the best microwave dielectric properties. The $Zr_{1-x}Sn_xTiO_4$ ceramic is usually prepared [175,176] by the conventional solid-state ceramic route by calcining at about 1100 °C followed by sintering the pucks at temperatures in the range 1400 to 1700 °C depending on the composition. $Zr_{0.8}Sn_{0.2}TiO_4$ powders do not readily sinter by the solid-state method. It is difficult to fully densify $Zr_{0.8}Sn_{0.2}TiO_4$ without sintering aids if the powder is prepared by the mixed oxide route. Hence ZnO is usually added as a sintering aid. Several authors reported the preparation of dense zirconium tin titanate by chemical and hydrothermal methods [177–182] at relatively lower temperatures. There are a number of publications [183–189] that report the efficacy of liquid-phase sintering aids, such as $BaCuO_2 + CuO$, CuO, ZnO, Bi_2O_3, SiO_2, B_2O_3, $5ZnO–2B_2O_3$, and V_2O_5. The $ZrTiO_4$ is orthorhombic having the space group *Pbcn* [175, 190] with a theoretical density of 5.15 gm/cm^3. The $ZrTiO_4$ undergoes an order–disorder phase transition [190–193] at a temperature between 1100 and 1200 °C. This transition is from an α-PbO_2-type high-temperature phase with a random distribution of Zr and Ti ions to the low-temperature phase with a commensurate or incommensurate ordered phase of cations [194]. Partial substitution of Zr by Sn inhibits the order–disorder transition. The transition to the incommensurate (IC) phase is initiated by the formation of short-range cation ordered clusters in the disordered matrix. As the transformation proceeds, the growing ordered region will be surrounded by a disordered boundary region. Finally, the faulted boundary region becomes a sharp faulted boundary having one atomic layer that is characterized by a wrong-site occupation of Zr and Ti cations. Thus the incommensurately ordered structure can be viewed as a commensurately 1:1 cation ordered structure with the interface modulation along the *a*-axis surrounded by faulted boundaries [194]. Wolfram and Gobel investigated [175] the detailed phase diagram of the system $ZrO_2–TiO_2–SnO_2$ ($Zr_xTi_ySn_zO_4$), where $x + y + z = 2$, and reported that single-phase ceramics existed over a limited range of composition. The single phase region was formed from a solid solution with orthorhombic $ZrTiO_4$. The substitution of Sn in $ZrTiO_4$ stabilizes the high-temperature phase with a random arrangement of cations [181] and broadening of the phase transition in $ZrTiO_4$ [195].

Several authors [175, 176, 181, 194, 196, 197] reported microwave dielectric properties of $ZrTiO_4$ ceramics prepared by both solid-state ceramic and wet chemical methods. The $ZrTiO_4$ has $\varepsilon_r = 42$, $Qf = 28\,000$ GHz, and $\tau_f = 58$ ppm/°C. Wolfram and Gobel [175] reported the microwave dielectric properties of $Zr_xTi_ySn_zO_4$ ($x + y + z = 2$) containing 1 wt% ZnO and 1.5 wt% La_2O_3 as sintering aids and sintered in the range 1300–1350 °C for 4 hours. The ε_r decreased initially up to $z = 0.4$ and then it increased for $y = 1$. The quality factor increased with Sn content up to $z = 0.4$ and for $y = 1$, as shown in Figure 6.37. Figure 6.38 shows the variation of τ_f as a function of Sn content (z). The τ_f decreased for $y = 1$ with an increasing amount of Sn (z) up to $z = 0.3$ and a further increase in z considerably increased the τ_f. Compositions in the range $0.15 < z < 0.3$ and $1 - z/2 < y < 1.05$ were found to be useful for dielectric resonator application since they have high quality factors, low τ_f, and a high ε_r of greater than 35. The relationship between composition of the solid solution and its dielectric properties is very complex. However, in general, increasing the TiO_2 content at the expense of ZrO_2 or SnO_2 increased the quality factor and ε_r, whereas increasing the SnO_2 content at the expense of ZrO_2 increased the quality factor with little effect on ε_r [175, 198]. The composition $Zr_{0.8}Sn_{0.2}TiO_4$, which has excellent microwave

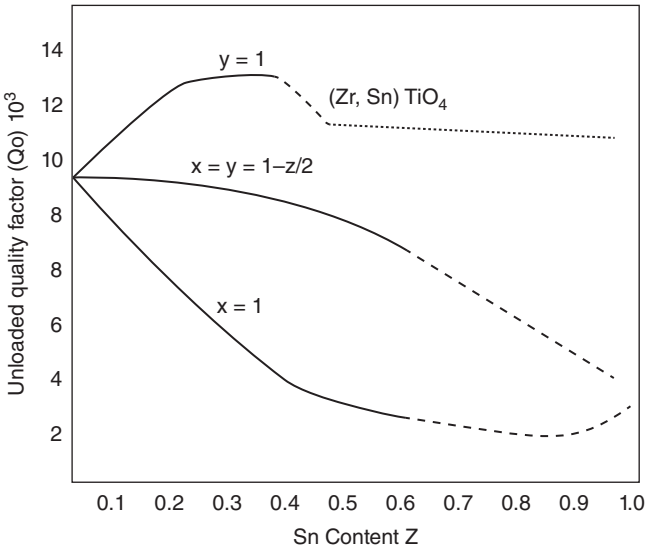

Figure 6.37 *Variation of the unloaded quality factor with Sn in $Zr_xSn_zTi_yO_4$ ceramics. Source: Adapted from Wolfram and Gobel 1981 [175].*

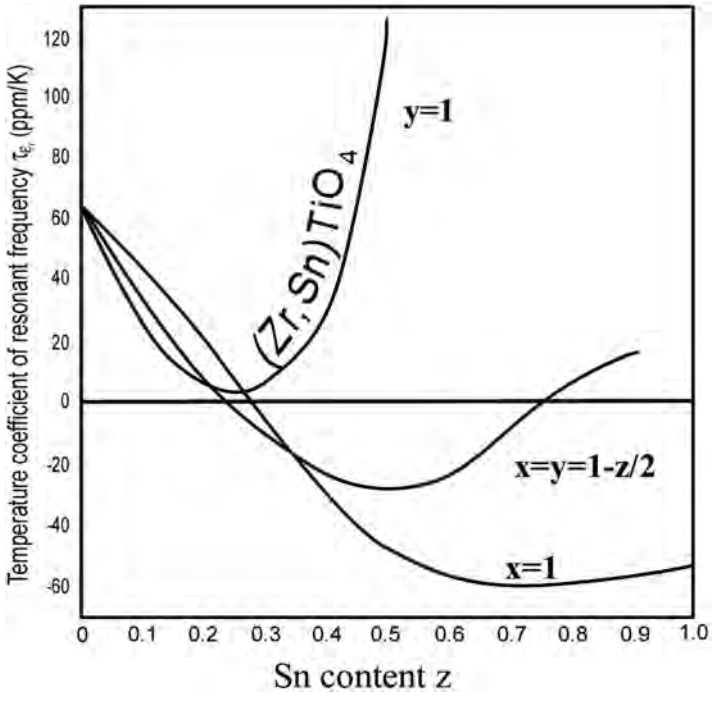

Figure 6.38 *Variation of the temperature coefficient of resonance frequency τ_f with Sn content. Source: Adapted from Wolfram and Gobel 1981 [175].*

dielectric properties such as $\tau_f \sim 0$ ppm/°C, $\varepsilon_r = 38$, and $Qf = 49\,000$ GHz [167], is useful for practical applications.

$Zr_{0.8}Sn_{0.2}TiO_4$ ceramics are one of the most popular commercial dielectric materials for microwave devices [63, 176, 199]. However, a major disadvantage of pure $Zr_{0.8}Sn_{0.2}TiO_4$ ceramics is their poor sinterability at <1600 °C. Hence extensive research [179, 180, 183, 189, 197, 200–205] was done on adding dopants to the $Zr_{0.8}Sn_{0.2}TiO_4$ system to lower the sintering temperature and to improve densification without much degradation of the required dielectric properties. Therefore sintering aids such as ZnO have been invariably added to achieve good densification at temperatures between 1200 and 1500 °C. Although addition of ZnO considerably improves densification at a relatively lower temperature [167,179,200,201,206] of 1400 °C, the microwave quality factor is not improved. McHale *et al.* [206] proposed a defect model in which a limited solubility of the sintering aid or dopant significantly affects the final state of densification. A combination of two or more sintering aids are found to be effective in improving the quality factor, as given in Table 6.3. Several authors studied [207–209] the effect of annealing on the dielectric properties of $Zr_{0.8}Sn_{0.2}TiO_4$ ceramics. It was found that a slow-cooled ceramic has a much higher quality factor as compared to a rapidly cooled ceramic. Azough and Freer [207] selected $Zr_{0.8}Sn_{0.2}TiO_4$ samples containing 1.5 wt% of ZnO and sintered at 1400 °C/4 h and annealed in the 700–1100 °C range for up to 1000 h. Rapid cooling from the sintering temperature yielded a disordered structure having a low *Qf* value. The permittivity was nearly independent of the cooling rate but the quality factor increased considerably with slow cooling. Ahn *et al.* reported [209] that slow-cooled $Zr_{0.8}Sn_{0.2}TiO_4$ ceramics containing 0.35 wt% B_2O_3–Li_2O aided sintering and WO_3 and Sb_2O_5 dopants showed a *Qf* greater than 60 000 GHz. The increase in *Qf* with a decrease of cooling rate is attributed to ordering of cations with slow cooling.

Tamura and coworkers investigated [167,202–210] the role of lattice defects such as oxygen vacancy in $Zr_{0.8}Sn_{0.2}TiO_4$. The lattice defects were introduced by annealing in oxygen-free atmospheres that introduced about 1000 ppm oxygen vacancies, samples prepared by doping with 1.3 mol% Fe_2O_3 and 0.5 mol% Ta_2O_5. The tan δ was found to be higher for samples annealed in an oxygen-free atmosphere. The samples doped with 1.3 mol% Fe_2O_3 had a much higher tan δ whereas that doped with Ta_2O_5 had a tan δ close to the benchmark. The addition of Fe ions creates oxygen vacancies, which led to an increase in tan δ. Addition of a small amount of Fe_2O_3 drastically reduced the *Qf* factor [167,202]. Fe ions in the grain occupy the Zr^{4+}, Ti^{4+}, and Sn^{4+} sites as Fe^{3+} creates oxygen vacancies to maintain charge neutrality leading to an increase in the loss factor [202]. Figure 6.39 represents a defect model of Fe^{3+} and Ta^{5+} doped $Zr_{0.8}Sn_{0.2}TiO_4$ where M and O denote Ti^{4+} and oxygens. The substitution of Ta^{5+} leads to a positive charge and Fe^{3+} leads to a negative charge. The presence of oxygen vacancies gives positive charges. The presence of Fe ions and the associated oxygen vacancies degrade the quality factor. The high-temperature sintering may lead to a reduction of Ti^{4+} to Ti^{3+}. In Ta-doped $Zr_{0.8}Sn_{0.2}TiO_4$, the Ta^{5+} may compensate for Ti^{3+} to maintain charge neutrality [202,211,212]. This is supported by the fact that doping with Nb_2O_5, Sb_2O_5, V_2O_5, and WO_3 increases the quality factor (see Table 6.4). Additives such as ZnO + NiO + Ta_2O_5, ZnO + Ta_2O_5, ZnO + Nb_2O_5, ZnO + Sb_2O_5, Sb_2O_5 + B_2O_3 + Li_2O, WO_3 + B_2O_3 + Li_2O, ZnO + NiO improve *Qf* [202, 203, 209, 212, 213]. Iddles *et al.* [201] reported that donor ions such as Nb^{5+} reduced the number of oxygen vacancies and improve quality factor, while acceptor ions such as La^{3+} produced electrons and

Table 6.3 *Dielectric properties of $(Zr_{0.8}Sn_{0.2}T)iO_4$ with different dopants.*

Sintering temperature (°C)	Ddopants	ε_r	Qf (GHz)	τ_f (ppm/°C)	Reference
1600/4 h	No dopant	38.9	51 500	1	[218]
1360/6 h	1 wt% CdO +0.5 wt% NiO+0.5 wt%La_2O_3	35.5	42 750	–7	[219]
1370/2 h	2 wt% La_2O_3, 1 wt% NiO	37	62 000	–9	[214], [215]
1370/20 h	La_2O_3, NiO+annealing	37.1	50 000		[208]
1400/4 h	1 wt% $BaCO_3$	39.5	47 500	0	[218]
1400/4 h	1 wt% $SrCO_3$	38.6	44 500	9	[218]
1400/4 h	1 wt% $CaCO_3$	39.2	46 500	0	[218]
1380/4 h	0.5 wt% ZnO+0.2 wt% NiO	38	58 800	0	[176], [202]
1280/2 h	1 wt% ZnO+2 wt% La_2O_3+0.2 wt% NiO	35.9	56 576	–	[205]
1220	1 wt% ZnO+1 wt% CuO	38	50 000	3	[183]–[185]
1500/2 h	0.5 wt% B_2O_3+0.3 wt% La_2O_3+1 wt% $NiTa_2O_6$	39.3	52 000	1	[220]
1400	1.5 wt% ZnO +slow cooled	36	51 000	–	[207]
1400/5 h	1 wt% ZnO+1 mol% Sb_2O_5	40.8	60 900		[211], [212]
1400/5 h	1 wt% ZnO+0.5 wt% Nb_2O_5	38	47 600		[211], [212]
1450/5 h	1 wt% ZnO+1 mol% Ta_2O_5	40.5	53 200		[212]
1400/5 h	1 wt% ZnO+1 mol% Nb_2O_5	40	47 600		[212]
1400/2 h	2 mol% ZnO+0.5 mol% Nb_2O_5	37	48 000	–4	[213]
1400/4 h	1 wt% ZnO+0.5 wt%Ta_2O_5	38.5	53 200		[211], [212]
1380/4 h	0.5 wt% ZnO+0.2 wt% NiO+Ta_2O_5	37.8	60 200	–	[202]
1340/3 h	1 wt% ZnO+0.25 wt% WO_3	37.8	61 000	–4	[203]
1300/3 h	1 wt% ZnO +1 wt% V_2O_5	37.2	51 200	–2	[183]
1300/5 h	1 mol% Sb_2O_5+0.35wt% B_2O_3–Li_2O+slow cooled	37	62 000	–	[209]
1300/5 h	1 mol% WO_3+0.35 wt% B_2O_3–Li_2O+slow cooled	37	60 000	–	[209]
–	2 wt% $MnCO_3$	35	51 000	26	[221]
1250	Coprecipitation	40.9	49 000	–2	[180]
1600/3 h	Alkoxide	40	50 000	3	[181]
1300/3 h	Sol–gel+0.5 wt% ZnO	38	55 000	1	[182]
1325/16 h	0.15 wt% (La_2O_3+ZnO) Coprecipitation	37.6	53 750	–3	[179]
130/20 h	1 wt% NiO+2 wt% La_2O_3+industrial attrition milled	37	62 000	–9	[212], [214]
1140	$(Zr_{1-x}Sn_x)(Li_{1/4}Nb_{3/4})_{0.4}Ti_{0.6}O_4$ (x=0.3)	31.8	58 300	–33	[222]
1300/3 h	32 wt% Nano ZST	39.2	72 900	–	[223]
1150/3 h	1 wt% ZnO+0.2 wt% B_2O_3	38.7	61 500	–	[224]

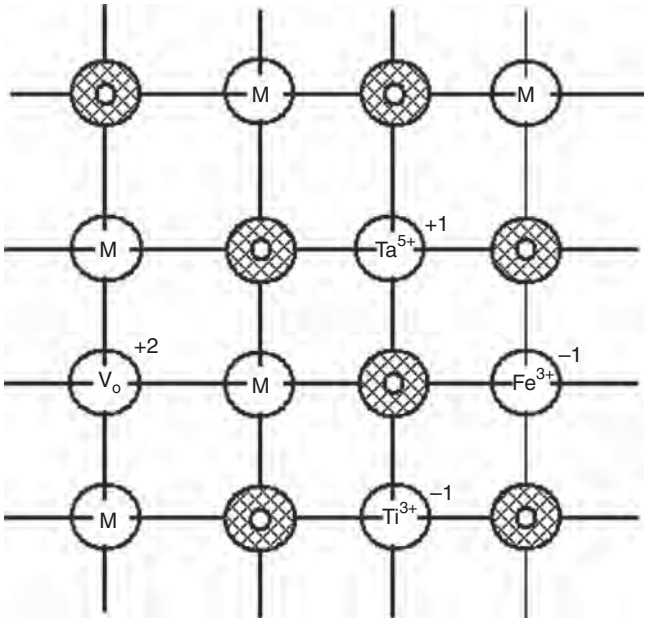

Figure 6.39 *Simplified defect model for charge deviation of substitution of Ta^{5+} and Fe^{3+} for tetravalent cations and of oxygen vacancies. M and O denote cation and oxygen, respectively. Source: Adapted from Tamura 2006 [210].*

decrease quality factor. The Nb^{5+}, Ta^{5+}, and Sb^{5+} ions could substitute for Zr^{4+}, Sn^{4+}, Ti^{4+} ions in the $Zr_{0.8}Sn_{0.2}TiO_4$ lattice because they all have a similar ionic radius. Yoon *et al.* [211, 212] studied the microwave dielectric properties of $Zr_{0.8}Sn_{0.2}TiO_4$ as a function of the amount of additives such as Nb_2O_5, Ta_2O_5, and Sb_2O_5. 1 wt% ZnO was also added as a sintering aid and the samples were sintered at 1400 °C/5 h. Figure 6.40 shows the variation of *Qf* as a function of mol% of different additives. As the amount of additives increased up to 1 mol% the unloaded *Qf* increased due to a decrease in oxygen vacancies [201, 208] in the $Zr_{0.8}Sn_{0.2}TiO_4$ lattice and an increase in density. The *Qf* then decreased with the further addition of dopants. The Sb_2O_5 added samples showed the highest unloaded *Qf*. It was found that Sb_2O_5 addition increased the *Qf* factor and addition of Sb_2O_3 decreased the *Qf* value [204]. Huang and coworkers [183–186] reported that addition of CuO, Bi_2O_3, and V_2O_5 in $Zr_{0.8}Sn_{0.2}TiO_4$ reduced the sintering temperature to 1220 °C due to liquid phase effects. The ε_r and τ_f are not significantly affected but the *Qf* is very much affected. Bi_2O_3 addition reduced the *Qf* considerably whereas 1 wt% CuO and V_2O_5 addition gave an excellent quality factor. Houivet *et al.* [214] reported that $Zr_{0.8}Sn_{0.2}TiO_4$ prepared by milling in an industrial attrition mill using zirconia grinding media gave very low porosity <0.1% and the samples had $\varepsilon_r = 37$, $Qf = 55000$ GHz. The *Qf* increased to 62 000 GHz when the grinding media was magnesia stabilized zirconia balls [215].

Table 6.4 *Microwave dielectric properties of in $BaO–TiO_2$ ceramics.*

$BaTi_4O_9$+dopants	Sintering temperature (°C)	ε_r	*Qf* (GHz)	τ_f (ppm/°C)	Reference
$BaTi_4O_9$	1300/2 h	37	22 700	15	[229]
$BaTi_4O_9$+2 mol% $BaWO_4$	1400/2 h	35	50 400	0	[236]
$BaTi_4O_9$+$ZnO–Ta_2O_5$ +0.1 wt% Mn	1275	36	45 000	0	[237]
$0.62BaTi_4O_9–0.35ZnO–0.3Ta_2O_5$ +0.3 wt% Mn	1280/2 h	35.4	48 150	1	[235], 237]
$0.62BaTi_4O_9–0.35ZnO–0.3Nb_2O_5$+0.3 wt%Mn	1280/2 h	35.8	50 760	1	[235], [237]
$0.615BaTi_4O_9–0.35ZnO–0.3Nb_2O_5$+0.3 wt%Mn	1280/2 h	35.8	50 800	1	[235]
$BaO–4TiO_2–0.1WO_3$	1360/in O_2	36	43 900	–	[238]
$BaO–4TiO_2–0.1WO_3$	1360/in air	36	44 500	–	[238]
$BaO–4TiO_2–0.1WO_3$	1400/2 h in O_2	35	50 400	–1	[236]
$BaO–4TiO_2–0.1WO_3$+5 wt% B_2O_3	1200	35	70 550		[238]
$BaTi_4O_9$+3 wt% MCAS glass	1200/4 h	34.6	42 050	14	[241]
$BaTi_4O_9$+citrate route	1250/10 h	36	50 500	16	[233]
$BaTi_4O_9$ polymer precursor route	1250/3 h	35.6	42 000	12	[231]
$BaTi_5O_{11}$ (alkoxide+hot pressed)	1050/48 h	41	46 000	40	[252]
$Ba_{0.79}Sr_{0.21}Ti_5O_{11}$ hot pressed	1050/72 h	42	39 000	44	[265]
$BaTi_5O_{11}$ (alkoxide)	1120/48 h	42	61 110	39	[250]
$BaTi_5O_{11}$+1 wt% CuO	1100	40.5	44 500	39	[282]
$Ba_2Ti_9O_{20}$	1350/3 h	39	32 000	2	[257], [265]
Reacting $BaTi_4O_9$ with TiO_2	1390	39	42 000	5	[266]
$Ba_2Ti_9O_{20}$+1 mol% Mn+annealing at 1000°C/24 h in O_2	1200/10 h	41	46 800	3	[246]
$Ba_2Ti_9O_{20}$+6 wt% ZrO_2	1390/6 h	39	40 000		[257]
$Ba_2Ti_9O_{20}$+1.64 mol%ZrO_2	1390/6 h in O_2	39.5	41 700	2	[256], [276]
$Ba_2Ti_9O_{20}$+1.64 mol% SnO_2	1390/6 h in O_2	39.3	38 400	–	[276]
$Ba_2Ti_9O_{20}$+2.46 mol% SnO_2	1390/6 h in O_2	38.8	38 700	1	[250]
$Ba_2Ti_9O_{20}$ (citrate route)	1300/10 h	37	57 000	–6	[233]
$Ba_2Ti_9O_{20}$+5 wt% B_2O_3	1200	36.5	40 200	38	[283]

(*continued*)

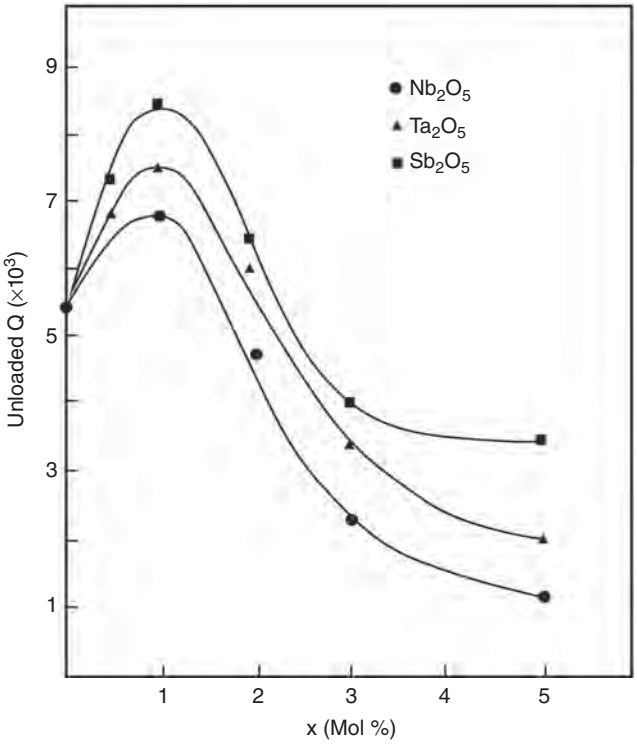

Figure 6.40 *Variation of unloaded quality factor at 7 GHz with the amount of Nb_2O_5 (•) Ta_2O_5(▲) and Sb_2O_5 (◆) for sintered $Zr_{0.8}Sn_{0.2}TiO_4$. Source: Adapted from Yoon* et al. *1995 [212].*

Several authors reported [179–182, 216] that the quality factor of $Zr_{0.8}Sn_{0.2}TiO_4$ prepared by wet chemical methods are comparable or higher than those prepared by the conventional solid state method. Hirano *et al.* [178] reported that $Zr_{0.8}Sn_{0.2}TiO_4$ prepared by a metal alkoxide route and sintered at 1600 °C for 3 h had $\varepsilon_r = 40$, $Qf = 50\,000$ GHz, and $\tau_f = 3$ ppm/K. The Qf was increased to 53 000 GHz by annealing the samples in O_2 at 1450 °C for 15 h. The unannealed material has a lower Qf due to the presence of oxygen defects. This is in agreement with Wakino [216], who noted that large specimens of $Zr_{0.8}Sn_{0.2}TiO_4$ exhibit a color change from surface to core (coring) that was caused by oxygen vacancies. Hirano *et al.* [178] quenched samples from 1600 °C and found they were black in color. This is characteristic of a ceramic sample containing reduced titanium. Alford *et al.* reported [217] that tan δ of undoped $Zr_{0.8}Sn_{0.2}TiO_4$ decreased approximately linearly down to the lowest temperature measured (15 K), as shown in Figure 6.41. A decrease in tan δ on cooling to low temperatures is expected since lattice vibrations are suppressed at low temperatures.

$Zr_{0.8}Sn_{0.2}TiO_4$ has a high sintering temperature of about 1600 °C and is difficult to densify. Hence ZnO is usually added as a sintering aid. However, ZnO leads to the formation of a lossy secondary phase that degrades the quality factor. Moreover, sintering at high temperature leads to a reduction of Ti^{4+} to Ti^{3+} and creation of oxygen vacancies. The presence

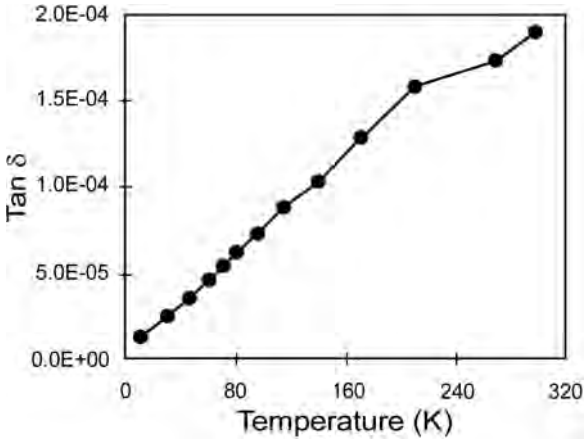

Figure 6.41 *The temperature dependence of tan δ of ZST normalized to 10 GHz. Source: Adapted from Alford* et al. *1995 [217].*

of oxygen vacancies also reduces the quality factor. Hence pentavalent metal oxides such as Ta_2O_5, Sb_2O_5, Nb_2O_5, or WO_3 are added in small quantities to compensate for the titanium reduction and oxygen vacancies. The pentavalent dopants substitute for Ti^{4+} and the remaining one + charge compensates for the T^{3+} making the crystal electrically neutral and thereby improving the quality factor. By careful preparation and using pentavalent doping one can achieve a temperature-stable $Zr_{0.8}Sn_{0.2}TiO_4$ with a *Qf* factor of about 60 000 GHz. The ceramics prepared by wet chemical methods, although expensive, also give a reasonably good quality factor. Zirconium tin titanate is an important dielectric material with excellent properties useful for applications in wireless communication. The raw materials required for its commercial production are not expensive.

6.7 Dielectric Materials in the $BaO–TiO_2$ System

Barium titanate compounds in the $BaO–TiO_2$ system are well known in electronic ceramics, especially in the ceramic capacitor industry. The Ti-rich compounds in the $BaO–TiO_2$ system exhibit [225–227] good temperature compensation with very good relative permittivity and low dielectric loss. In 1947, Bunting and coworkers reported [225] a low-loss temperature-compensated composition containing 83.3 mol% TiO_2 with $\varepsilon_r = 37$ at 1 MHz. Later in 1958 Jonker and Kwestroo [226] reported a promising combination of dielectric properties at 1 MHz for ternary compositions in the $BaO–TiO_2–SnO_2/ZrO_2$ system containing 18.5 mol% BaO and 4 mol% SnO_2/ZrO_2. During 1966 to 1971 $BaTi_4O_9$ was reported as a temperature-compensated dielectric ceramic compound [227]. Several compounds were reported in the TiO_2-rich region of the $BaO–TiO_2$ system, as shown in Figure 6.42. In the following we discuss the three important low-loss dielectric ceramics. $BaTi_4O_9$, $BaTi_5O_{11}$, and $Ba_2Ti_9O_{20}$ have low dielectric loss and high relative permittivity, useful for dielectric resonator and capacitor applications.

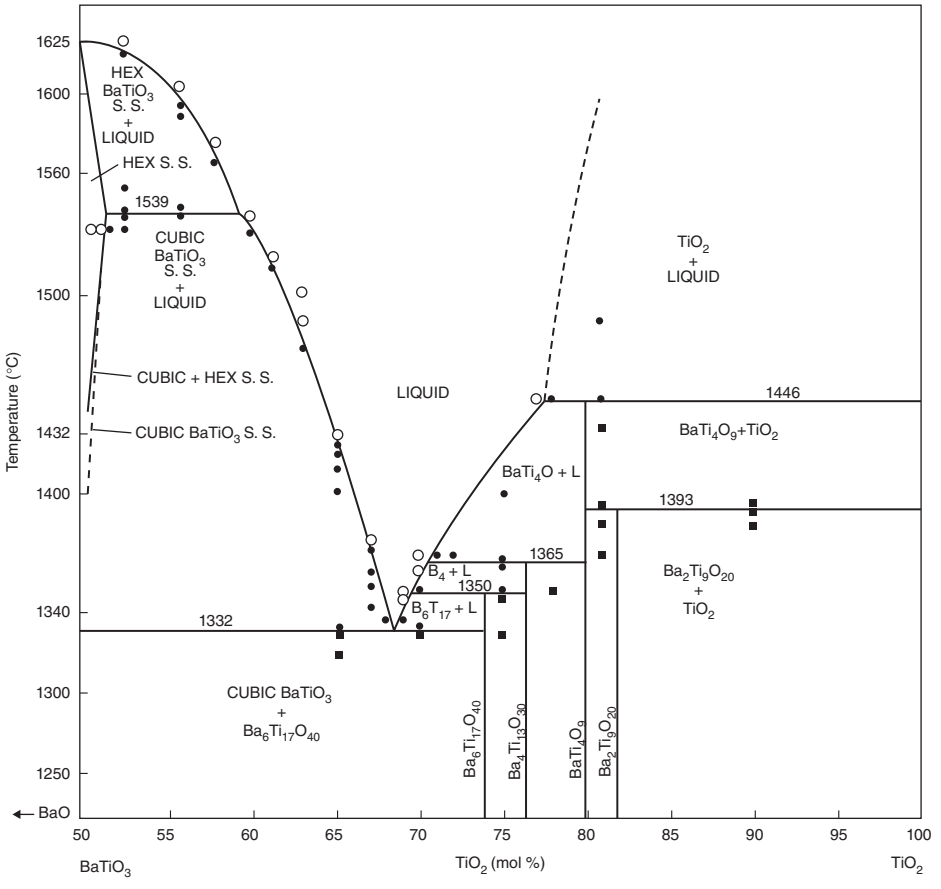

Figure 6.42 *Phase diagram of $BaTiO_3$–TiO_2 system. Source: Adapted from Kirby and Wechsler 1991 [228].*

6.7.1 $BaTi_4O_9$

$BaTi_4O_9$ is prepared by the conventional solid-state ceramic route by calcining at about 1100 °C followed by sintering the shaped pucks at about 1350 °C/2 h [229, 230]. A small amount of $Ba_2Ti_9O_{20}$ is often found to form as a secondary phase in $BaTi_4O_9$ [230]. Several authors [231–234] reported synthesis of $BaTi_4O_9$ by wet chemical methods. $BaTi_4O_9$ is orthorhombic with the *Pnmn* space group. It was Masse *et al.* [227] who first pointed out that $BaTi_4O_9$ is a suitable material for microwave dielectric resonator applications. The $BaTi_4O_9$ has ε_r of 37, Qf of 22 700 GHz, and $\tau_f = +15$ ppm/ °C [229]. Several authors studied [229, 235–240] the effect of dopants on the dielectric properties of $BaTi_4O_9$. The dielectric properties of $BaTi_4O_9$ are improved by the addition of certain dopants and are given in Table 6.4. Addition of a small amount of $BaWO_4$, WO_3, MnO_2, ZnO–Ta_2O_5, and WO_3–B_2O_3 considerably improved the quality factor [229, 235–238]. Doping has not much effect on ε_r and τ_f, although the Qf very much depends on it. The solubility of WO_3

in $BaTiO_3$ is extremely small (<0.1%) and the addition of WO_3 to $BaTiO_3$ increases the loss tangent of the ceramics [240]. However, $BaO–4TiO_2–0.1WO_3$ ceramic was found to possess excellent microwave properties [236, 238]. Addition of [241, 242] MCAS ($MgO–CaO–Al_2O_3–SiO_2$) glass in the ratio (5:19:26:50) to $BaTi_4O_9$ improved densification and lowered the sintering temperature. For 3 wt% addition of MCAS, the sintering temperature decreased to 1200 °C from 1350 °C and has $\varepsilon_r = 34.6$, $Qf = 42\,050$ GHz, and $\tau_f = 14$ ppm/°C. Sintering at high temperatures is also known to reduce Ti^{4+} to Ti^{3+}, which degrades the quality factor. It is well known that oxygen is lost from titanate systems during sintering in an atmosphere of low oxygen content [230, 243–245]. The formation of oxygen vacancies in titanates accompanies the formation of electrons, which results in the reduction of Ti^{4+} into Ti^{3+} [230]. The presence of Ti^{3+} ions in $BaO–TiO_2$ systems is considered to be the reason for a low quality factor. Firing pure $BaTi_4O_9$ ceramics in an oxygen atmosphere decreased the loss by an order of magnitude [230]. Mn doping and heat treatment in an oxygen atmosphere can convert Ti^{3+} ions to Ti^{4+} [230, 246]. The ceramics prepared with WO_3 and $ZnO–Nb_2O_5$ or $ZnO–Ta_2O_5$ dopants show the best quality factors. It may be noted that the $BaTi_4O_9$ usually contains secondary phases and their amounts vary depending on the preparation conditions and initial raw materials. Pure $BaTi_4O_9$ does not have an optimum performance as a DR since its τ_f is relatively high. Hence the $BaTi_4O_9$ material is often modified by using additives [237, 247, 248].

6.7.2 $BaTi_5O_{11}$

It is difficult to obtain $BaTi_5O_{11}$ as a single-phase material by the solid-state reaction method [249, 250]. However, single-phase $BaTi_5O_{11}$ was prepared by wet chemical methods [233, 250–253]. Javadpour and Eror [251] observed the same stability range for $BaTi_5O_{11}$ and $BaTi_4O_9$ ceramics. The $BaTi_5O_{11}$ has a monoclinic structure with $P2_1/n$ space group. The sol–gel prepared $BaTi_5O_{11}$ samples have $\varepsilon_r = 40$, $Qf > 60\,000$ GHz, and $\tau_f = 39$/ppm/°C [250]. Hirano and Otsuko [252] obtained dense ceramics with $Qf = 46\,000$ GHz by hot pressing at 1050 °C for 48 hours under 8.5 MPa. $(Ba_{1-x}Sr_x)Ti_5O_{11}$ and $BaTi_{1-x}Sn_xO_{11}$ were synthesized as single-phase materials by heating the fine particles prepared by the controlled hydrolysis of metal alkoxides [254] using barium, strontium–butoxide, and titanium isopropoxide or titanium ethoxide and tin isoproxide. The $(Ba_{0.79}Sr_{0.21})Ti_5O_{11}$ has excellent properties with $Qf = 39\,000$ GHz. The microwave dielectric properties of $BaTi_5O_{11}$ prepared by different methods and sintering temperatures are given in Table 6.4.

6.7.3 $Ba_2Ti_9O_{20}$

The $Ba_2Ti_9O_{20}$ can be prepared by mixing $BaCO_3$ and TiO_2 in stoichiometric proportions and calcining at about 1200 °C followed by sintering the shaped pellets at about 1400 °C/3 h [255–257]. The preparation of dense and phase-pure $Ba_2Ti_9O_{20}$ is generally difficult using the solid-state method due to the existence of the thermodynamically stable $BaTi_4O_9$ compound in the vicinity of the desired composition. Generally the ceramics contain certain amounts of secondary phases consisting of $BaTi_4O_9$, rutile, and traces of $BaTi_5O_{11}$. It is known from the phase diagram of the $BaO–TiO_2$ system that $Ba_2Ti_9O_{20}$ decomposes to $BaTi_4O_9 + TiO_2$ above 1420 °C. Several authors reported the preparation of $Ba_2Ti_9O_{20}$ by wet chemical methods [253, 258–264]. In order to eliminate secondary phases of $BaTi_4O_9$

and $BaTi_5O_{11}$ in $Ba_2Ti_9O_{20}$ a calcination temperature >1200 °C and longer time >10 h are needed. $Ba_2Ti_9O_{20}$ has a triclinic cell with space group $P\bar{1}$.

$Ba_2Ti_9O_{20}$ has relative permittivity of 39, *Qf* of about 32 000 GHz, and τ_f of 2 ppm/°C [257, 265, 266]. Varma *et al.* [267] studied the effect of the purity of raw materials and reported that the properties vary considerably with the purity of the initial raw materials. The dielectric properties vary depending on the amount of secondary phases present in the final product. Usually single-phase $Ba_2Ti_9O_{20}$ is prepared by adding dopants. In such cases, the dielectric properties depend on the nature and amount of dopants added. Several authors studied [233, 246, 256, 257, 268–272] the effects of dopant addition in $Ba_2Ti_9O_{20}$. The dielectric properties of the sintered ceramics containing different dopants are given in Table 6.4. It is found that addition of a small amount of ZrO_2, MnO_2, SnO_2, and B_2O_3 improve the quality factor [254, 256, 257, 265, 268, 273]. The calcination temperature has considerable influence on the amount of secondary phase [255, 265, 274]. $Ba_2Ti_9O_{20}$ has been difficult to synthesize in the single phase without additives that form a solid solution. Tin ion dopants have been used in the form of SnO_2 and $BaSnO_3$ additives in several studies [256–258, 275–277] to stabilize $Ba_2Ti_9O_{20}$ and their microwave dielectric properties have been evaluated. The substitution of Sn^{4+} cations for Ti $^{4+}$ cations reduced the τ_f without degrading ε_r considerably [256–258, 265, 268, 274–277]. Addition of a small amount of Al_2O_3, Bi_2O_3, SnO_2, or ZrO_2 promote the formation of $Ba_2Ti_9O_{20}$ [226, 258, 273]. SnO_2 doping of up to 2.5 mol% increased *Qf* whereas it increased with doping of up to 1.64 mol% of Zr and reduced with further doping of Zr. The solubility of Sn in $Ba_2Ti_9O_{20}$ was higher than that of Zr [256]. The $Ba_2Ti_9O_{20}$ with 1.64 mol% of Sn showed a *Qf* of value of 38 700 GHz whereas it was 41 700 GHz for 1.64 mol% of Zr doping, both sintered at 1390 °C for 6 h. The conventional high-temperature sintering route leads to compositional and structural fluctuations due to the reduction of Ti^{4+} to Ti^{3+}. This gives rise to degradation of the dielectric properties. Pure $Ba_2Ti_9O_{20}$ has a grey color whereas with Mn addition the color changed from pale brown to dark brown. There was no appreciable change in ε_r and τ_f by Mn addition but *Qf* increased considerably [246]. The Mn acts as an oxidizing agent. Mn behaves as a compensator in defect equilibrium, probably helping to maintain Ti^{4+}. Mn added after calcination gave the best *Qf*. Nomura *et al.* reported [278] the maximum *Qf* for 0.5 mol% Mn addition whereas Srivastava *et al.* observed [279] a high Qf at about 3 mol% Mn. In ZnO/Ta_2O_5 added samples with the highest *Qf* were found for about 0.1 mol% Mn addition [237]. Annealing 6–12h at 1000–1275 °C increases the *Qf* [246, 265, 280] by as much as 50%. The *Qf* increased with annealing in O_2. To be most effective the sintered samples after cooling below 600 °C should be annealed at temperatures between 1000 and 1275 °C for 6–12 h. The cooling rates should be less than 200 °C/h.

Addition of a small amount of $BaWO_4$ to $BaTi_4O_9$ considerably improved the microwave dielectric properties [236, 238]. An X-ray diffraction study showed that the sintered ceramics is a multiphase and consists of $BaTi_4O_9$, $Ba_2Ti_9O_{20}$, and $BaWO_4$. The composition $BaO–4TiO_2–0.1WO_3$ showed [238] excellent dielectric properties and is commercially known as N-35. It consists of 9.9 vol% $BaTi_4O_9$, 84.4 vol% $Ba_2Ti_9O_{20}$, and 5.7 vol% $BaWO_4$, with $\varepsilon_r = 36$, $Qf = 52\ 000$ GHz, and $\tau_f \sim 0$ [238]. Takada *et al.* [238] added 5–30 wt% glasses such as B_2O_3, SiO_2, $5ZnO–2B_2O_3$ and commercial glasses to $BaO–TiO_2–WO_3$ ceramic (N-35). The density increased with sintering temperature and showed maximum density when sintered in the temperature range 1000–1200 °C. As the sintering temperature increased the TiO_2 content decreased and $Ba_2Ti_9O_{20}$ content increased

for ceramics without glass addition. B_2O_3 addition lowered the sintering temperature and increased ε_r, which may be due to the increased TiO_2 content. The density and *Qf* increased with glass addition but larger amounts of B_2O_3 decreased *Qf* and ε_r. The maximum density, ε_r, and *Q* were found for samples containing 5 wt% B_2O_3 and sintered at 1200 °C. The sintered samples contain $BaTi_4O_9$, $Ba_2Ti_9O_{20}$, $BaWO_4$, and TiO_2. Recently $BaTi_4O_9/Ba_2Ti_9O_{20}$ composites containing substantial amounts of ZnO/Ta_2O_5 have been reported [235] with *Qf* values 20–25% higher. Negas *et al.* [237] and Lee *et al.* [235, 281] reported excellent properties for $0.62BaTi_4O_9$–$0.35ZnO$–$0.3Ta_2O_5$ sintered at 1280 °C. X-ray diffraction analysis revealed that samples sintered at 1250–1300 °C contained a mixture of four phases: $BaTi_4Zn_2O_{11}$, $BaTi_{4-x}Zn_{x/3}Ta_{2x/3}O_9$, $Ba_2Ti_{9-x}Zn_{x/3}Ta_{2x/3}O_{20}$, and a small amount of $Ba_3Ti_{4+5x}Ta_{4-4x}O_{21}$. Undoped samples had *Qf* <10 000 GHz whereas Mn doping increased *Qf* up to 50 000 GHz for $x = 0.1$. It was found that the samples calcined at 1000 °C and sintered at 1280 °C have negative τ_f and samples calcined at 1100 °C and sintered at 1280 °C have positive τ_f. Lee *et al.* [235, 281] believe that samples calcined at 1000 °C have more $BaZn_2Ti_4O_{11}$, which has a negative τ_f [237] as compared to those calcined at 1100 °C. Hence it is possible to slightly tune τ_f by varying the calcination temperature. Less expensive Nb can be used instead of Ta, which slightly increased ε_r [237]. The $0.62BaTi_4O_9$–$0.35ZnO$–$0.3Nb_2O_5$ had $\varepsilon_r = 36.4$, $Qf = 48\,150$ GHz and $\tau_f = 0$ [237]. A small amount of Mn doping considerably improves *Qf* values. The 0.1 wt% Mn doped $0.615BaTi_4O_9 + 0.35ZnO + 0.035Ta_2O_5$ calcined at 1000 °C and sintered at 1280 °C/2 h showed a *Qf* of 50 700 GHz, τ_f of 5 ppm/°C, and $\varepsilon_r = 35.8$. Addition of 0.02 to 0.1 wt% Mn yields an unscored high *Qf* product. The addition of Mn helps to maintain Ti^{4+} as the Mn can trap electrons associated with intrinsic oxygen vacancies of titanates within the grains. Mn thus behaves as a compensator in defect equilibrium by helping to maintain Ti^{4+}.

The BaO–TiO_2 system has three low-loss dielectric compounds, which are $BaTi_4O_9$, $BaTi_5O_{11}$, and $Ba_2Ti_9O_{20}$. It is difficult to produce these compounds in single-phase form by the conventional solid-state method since there are several compounds in the vicinity of the desired composition. These compositions have relative permittivity between 35 and 39 with reasonably good *Qf* in the range 35 000–60 000 GHz depending on the dopants and relatively low τ_f. These materials also have a sintering temperature in the range 1300–1400 °C. The BaO–TiO_2-based dielectric resonators sintered at high temperatures usually have oxygen vacancies associated with the reduction of Ti^{4+} to Ti^{3+}. Hence sintering in an oxygen atmosphere or annealing improves the quality factor. Addition of a small amount of MnO (<1 wt%), which is an oxidizing agent, is also known to improve the quality factor. Addition of dopants such as ZrO_2, SnO_2, Ta_2O_5, and WO_3 in small quantities also improves the quality factor. Zr, Sn, Ta, and W have ionic radii close to that of titanium and they substitute at the Ti site.

6.8 Columbite Niobates ($M^{2+}Nb_2O_6$)

At the beginning of the twenty-first century, the best available microwave dielectrics, with ε_r around 30–35, near-zero t_f, and $Qf = 150\,000$–$300\,000$ GHz, were tantalum-based complex perovskites, such as $BaZn_{0.33}Ta_{0.67}O_3$ (BZT) [284] and $BaMg_{0.33}Ta_{0.67}O_3$ (BMT) [285]. However, as the mobile and wireless communications boom of the late 1990s created a massive need for more tantalum, the price of tantalite ore (~60% Ta_2O_5) rapidly increased

from \$75/kg in 1999 to a peak of over \$500/kg in 2000 [286]. This led to a great interest in alternative materials – in the case of microwave dielectrics, those based on niobium such as $BaZn_{0.33}Nb_{0.67}O_3$ (BZN) and $Ba(Zn/Co)_{0.33}Nb_{0.67}O_3$ (BZCN), as well as the columbite niobates such as $ZnNb_2O_6$. While their microwave dielectric properties were inferior to the tantalum-based perovskites ($t_f = -30$ ppm/°C, $Qf \sim 100\,000$ GHz for BZN) [287], columbite ore was only \$8/kg in 2001/2, with 80% coming from Brazil [286]. Since then more sources of tantalum have been discovered and the prices of tantalite and niobium ores have remained steady at around \$70/kg and \$15/kg, respectively [288], so niobium is still significantly less expensive than tantalum, and the interest in niobate dielectric ceramics, such as the columbites, has continued [289].

The binary niobate ceramics have the formula MNb_2O_6, where M is a $^{2+}$ cation and are one of the end members of the perovskite $BaM_{0.33}Nb_{0.67}O_3$ group (the other being BaO). They are mostly isostructural with the orthorhombic mineral columbite, the two exceptions being $SrNb_2O_6$ and $BaNb_2O_6$, which due to the larger sizes of their M^{2+} ions have Type I and Type II orthorhombic structures, respectively [290], and as they are not columbites they will not be discussed in this chapter. However, very recently, in 2016, the mixed strontium/calcium niobate $Ca_{0.5}Sr_{0.5}Nb_2O_6$ has been reported as having a columbite structure, although its sintering and microwave properties have not yet been explored [291]. It was formed as a powder by coprecipitation and calcination at 650 °C.

The transition metal columbite niobates have been found to sinter at temperatures of 1100–1200 °C, much lower than the perovskites, and this can be lowered even more when Cu^{2+} is used as one of the TMs. They have only a superficial degree of ordering and do not require the complex processing needed for many perovskite microwave dielectrics. Although *Qf* of the niobate perovskites is lower than the tantalate perovskites, the best columbite niobates have *Qf* values similar to those of BZN and BCZN, and are significantly superior to the binary $M^{2+}Ta_2O_6$ compounds, which do not have the columbite structure [292]. The columbites all have ε_r between 17 and 25 and negative t_f values of smaller than –80 ppm/°C, and require lower processing temperatures – indeed, with the incorporation of Cu^{2+} they are approaching LTCC temperatures. Furthermore, $MgNb_2O_6$ is in wide use as a precursor to synthesize single-phase PMN ($Pb(Mg_{1/3}Nb_{2/3})O_3$) in the "columbite" process [293, 294].

The mineral columbite (the ore from which niobium is extracted) has the nominal formula $[(Fe/Mn/Mg)(Nb/Ta)_2O_6]$. The tantalum-rich form is the ore tantalite. It is a black mineral with an orthorhombic crystal structure, space group = *Pnca* (60) [295]. The microwave dielectric columbites are binary niobate ceramics with the formula MNb_2O_6, where M = 2+ cation. In the AB_2O_6 columbite structure, the A and B cations are at the center of the octahedra surrounded by six oxygen atoms. The AO_6 and BO_6 octahedra form independent zigzag chains by sharing edges, and the chains are connected by sharing corners in the order AO_6 chain–BO_6 chain–BO_6 chain (Figure 6.43). In the fully ordered state, this form repeats ABBABB octahedral layers, with an orthorhombic α-PbO_2-type structure, first solved by Sturdivant [295]. The unit cell is orthorhombic, space group 60 (either *Pbcn* or *Pcan*), with lattice parameter ratios of approximately 1:1.14:2.5 (Figure 6.44) [296]. Unlike the others, $CuNb_2O_6$ has two polymorphs, the black orthorhombic columbite form, normally forming above 900 °C, and a yellowish-green monoclinic form, present between 700 and 900 °C [297]. Between these temperatures the two forms can coexist, although annealing at 800–900 °C can complete conversion into the orthorhombic $CuNb_2O_6$ [298]. It has been shown

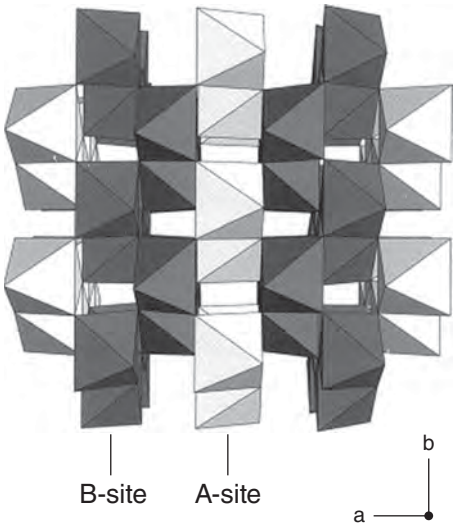

Figure 6.43 *Columbite octahedral structure ($A = M^{2+}$, $B = Nb^{5+}$) projected along the c [001] axis. Source: Adapted from Pullar 2009 [289].*

that substitution of just 10% of the Cu^{2+} ions in $CuNb_2O_6$ with Zn^{2+} leads to a monoclinic compound being formed [291], even after heating over 900 °C.

6.8.1 Synthesis of Columbite Ceramics

The columbites are mostly easy to make from a simple solid-state reaction of stoichiometric oxides (or carbonates), reacted together in a calcination step, then milled to reduced particle size before sintering. The transition metal columbites usually need sintering temperatures of 1100–1200 °C, whereas the group II metals need higher temperatures of 1300–1400 °C [292, 296, 300, 301]. The exceptions to this are $CdNb_2O_6$, which required only 1000 °C/12 h to form [302], and $CuNb_2O_6$, which can form a monoclinic phase as low as 600 °C [303], partially converting to the orthorhombic columbite phase above 800 °C [301].

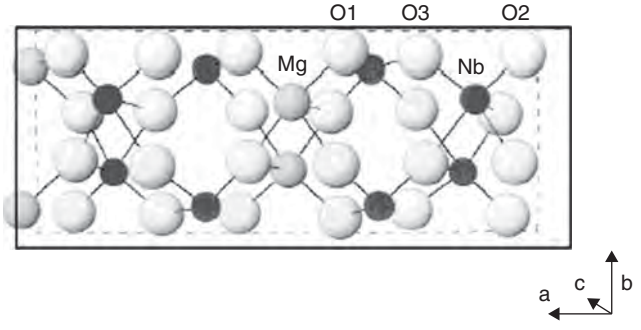

Figure 6.44 *Unit cell of columbite $MgNb_2O_6$. Source: Adapted from Pullar 2009 [289].*

However, many do not form by a simple one-step process, for example, $MgNb_2O_6$ can be difficult to form in the single phase [304], with the corundum $Mg_4Nb_2O_9$ phase sometimes forming alongside the columbite [305], but this can be avoided by using higher calcination times and temperatures (1200 °C/ > 4 h) [301, 305], or calcining at 1000 °C/4 h and heating/cooling rapidly at rates of 30 °C/min [306]. It is suggested [307] that $MgNb_2O_6$ forms in a two-step process: both $MgNb_2O_6$ and $Mg_4Nb_2O_9$ form simultaneously above 700 °C and then at >1100° C/6 h the corundum phase reacts with residual Nb_2O_5 to produce single-phase $MgNb_2O_6$. It seems that $CoNb_2O_6$ forms by a similar two-step process between 700 and 900 °C, after the initial formation of $CoNb_2O_6$ at 550 °C, with the corundum reacting with residual Nb_2O_5 above 900 °C and single-phase $CoNb_2O_6$ obtained after >2 h at 1100 °C [307, 308]. Pullar *et al.* also demonstrated that it makes no difference if CoO or Co_3O_4 is used in the formation of $CoNb_2O_6$ [301]. It also seems that $NiNb_2O_6$ does not tend to form in a simple one-step process, with the minor phases of unreacted NiO and Nb_2O_5 precursors and the corundum $Ni_4Nb_2O_9$ phase tending to form, together with the columbite $NiNb_2O_6$ [309], at 600 °C, leading to single-phase columbite at ∼900 °C/4 h. $MnNb_2O_6$ forms two non-stoichiometric compositions, with slight excesses of either manganese or niobium, instead of stoichiomeric $MnNb_2O_6$ [310], indicating the instability of the nominal composition. If Fe_2O_3 is reacted with Nb_2O_5 in a 1:1 ratio, $FeNb_2O_3$ forms at 800 °C, becoming single phase at 1100 °C [311], so Fe^{2+} ions need to be present to ensure the formation of $FeNb_2O_6$. $CuNb_2O_6$ is hard to make as a single-phase material, as both orthorhombic and monoclinic forms can coexist up to 900 °C. Pullar *et al.* [301] reported a mixed phase $CuNb_2O_6$ up to 1200 °C, when it melted, and above 950 °C a liquid phase leads to exaggerated or discontinuous grain growth (DGG). It has been suggested that once the monoclinic phase has been formed it is hard to obtain the single orthorhombic phase, although it can be obtained through processing variations [312–315]. In contrast, Belous *et al.* state that $ZnNb_2O_6$ forms as a single phase directly between 500 and 800 °C [307]. $ZnNb_2O_6$ nanopowders were made by ball-milling stoichiometric oxides in a planetary mill for 20 hours and then heating them to 650 °C in a conventional oven, or at 550 °C in a microwave furnace. These formed the columbite phase directly, with particle sizes of 83 and 86 nm, respectively, but their sintering behavior and microwave properties were not measured [313].

Other synthetic techniques for columbite ceramics include high-energy ball-milling/mechanochemical synthesis [318], molten salt methods [316, 317], the reaction sintering process [318–324], coprecipitation routes [319–320], oxalate routes [312, 321, 322], sol–gel/citrate gel/Pechini methods [323–324], and solvothermal synthesis [325]. $MgNb_2O_6$ thin films have been produced by pulsed laser deposition (PLD) [326] and $MgNb_2O_6$ [327] and $ZnNb_2O_6$ [328] thin films were also made from sol–gel methods. Columbite single crystals have been grown from fluxes [329] and by floating-zone [330], Czochralski technique [331], and laser-heated pedestal growth (LHPG) techniques [332].

Hydrothermal synthesis, carrying out a reaction at relatively low temperatures in water contained in a sealed autoclave (creating very high pressures) for extended periods (typically, one day or more), is a well-established way of making nanoparticles of materials that otherwise require much higher temperatures to form. Ellipsoidal $MnNb_2O_6$ nanocrystals (10–20 nm diameter) were reported in 2014, made from hydrothermal synthesis in an autoclave at 150 °C/24 h [333], and $CoNb_2O_6$, $NiNb_2O_6$, and $FeNb_2O_6$ nanocrystals (50–100 nm) were reported by Lei *et al.* in 2014, made by a hydrothermal reaction at 180 °C/12 h

followed by annealing at 800 °C/2 h [334]. Hydrothermal nanosynthesis has also been used to make micrometer-scale flower- or "rose-like" $ZnNb_2O_6$ structures formed from $ZnNb_2O_6$ nanocrystals/nanosheets, under hydrothermal conditions at 240 °C/5 h by Hirano and Okamoto in 2015 [335], similar flower-like $MnNb_2O_6$ and $ZnNb_2O_6$ were made under hydrothermal conditions at 240°C/5 days by Huang *et al.* in 2014 [336], and metastable rutile $CoNb_2O_6$ at 240 °C/3 days in 2011 by Ma *et al.*, which was transformed to columbite by annealing at 800 °C [337]. A range of hierarchical $CaNb_2O_6$ micro- and nanostructures were earlier also reported by Zhang *et al.* in 2010, made from hydrothermal synthesis at 200 °C/3 days [338], and $MnNb_2O_6$ six-teeth nanogears (resembling 500 nm diameter, six-pointed, columbite "snowflakes") were hydrothermally synthesized by Hu *et al.* in 2012 [339]. None of these hydrothermal columbites have been explored as microwave dielectrics to date, although Huang *et al.* did calcine their $MnNb_2O_6$ and $ZnNb_2O_6$ at 1000–1050 °C/10 h to produce micrometer-scale columbite grains.

6.8.2 Microwave Dielectric Properties of Columbites

Maeda *et al.* first created interest in columbites as microwave dielectric ceramics in 1987 [296] and reported reasonably high values of $Qf = 44\,000$ GHz for $ZnNb_2O_6$, despite it only being 91% dense. However, they reported low values for a poorly sintered (88% dense) $CoNb_2O_6$ of $Qf = 6800$ GHz and extremely low values of $Qf = 1280$ GHz for $MgNb_2O_6$ with 95% density. All three samples had $\varepsilon_r = 20$ to 21 and $\tau_f = -70$ to –85 ppm/°C. Since then there have been many reports of the microwave dielectric properties of columbites, with the most in-depth studies carried out by Lee *et al.* [292,300] and Pullar *et al.* [301,340], but while they largely agree on ε_r values, reported values for Qf and τ_f can vary greatly. Although Lee's samples had higher permittivities, all were stated to be >95% of theoretical density, and the trend demonstrated is identical to that reported by Pullar *et al.*, attributed by Lee to a correlation between ε_r and the electronegativity of the compound [292]. The variation in Q and τ_f is because, while ε_r is largely dependent on the intrinsic polarizability of the constituent ions and density, dielectric loss and τ_f are affected by many more factors other than porosity. As well as the intrinsic losses due to phonon–lattice interactions and point defects that occur in single crystals, in a polycrystalline ceramic losses due to grain boundaries, dislocations, pores, secondary phases, etc., dominate, meaning that processing conditions and microstructure can have an enormous effect on Q. Furthermore, the processes that contribute to τ_f in columbites are not fully understood, and this can largely explain the variation in properties reported for these compounds. Although most articles specify the sintering conditions, some do not give density data, and very few give details of microstructure, which is so important to Q values.

Another important factor, which is often underestimated in microwave measurements, is the measurement technique involved, and many authors who are expert in materials chemistry clearly have less experience in dielectric measurements at GHz frequencies. The most common methods are the Hakki–Coleman/Courtney method, the post-resonator method, the transmission open cavity method, and the resonant cavity method. Furthermore, nearly all authors calculate τ_f by measuring f at just two points, usually 25 °C and 85 °C, ignoring the possible non-linearity of this behavior and leaving the behavior at common operating temperatures below 25 °C unknown. By far the most detailed experimental procedure for microwave measurements is given by Pullar *et al.* [301], who not only give details of the

cavities used but also uniquely subtract losses due to the cavity and measurement setup to give the actual Q of the ceramic, compensate ε_r for geometric effects of the sample and cavity, and measure τ_f continuously over a range of 250–310 K, deriving it from a least-squares linear fit with a level of confidence greater than 99.999%.

The low Qf values for $ZnNb_2O_6$ and $CoNb_2O_6$ reported by Maeda *et al.* [296] could be due to the low density of their samples and associated microstructural effects. Without more information on the microstructure, phase purity, or stoichiometry of the sample, it is hard to comment on the very low Qf values reported for their $MgNb_2O_6$ sample, but it is in great contrast to the much higher values reported by all other studies, despite its high density. Pullar *et al.* reported a detailed study on Zn-, Mg-, Co-, Ca-, Mn-, Ni-, and $CuNb_2O_6$ ceramics [301], with ε_r values between 17.1 and 23.2 and negative t_f values between –45.1 and –75.8 ppm/°C, these two extremes being for $CuNb_2O_6$ and $ZnNb_2O_6$, respectively. The Qf values reported by Pullar *et al.* are shown in Figure 6.45, and it can be seen that the four outstanding samples were $ZnNb_2O_6$ (84 500 GHz), $MgNb_2O_6$ (79 600 GHz), $CaNb_2O_6$ (49 600 GHz), and $CoNb_2O_6$ (41 700 GHz) after being fired to 1200, 1300, 1350, and 1150 °C, respectively, for 2 hours. The other columbites all had relatively high losses, and $CuNb_2O_6$ was so poor it was not included on this diagram. The maximum Q coincided with the highest degree of sintering, but as density was lost slightly with oversintering at higher temperatures, Q decayed rapidly as the discontinuous grain growth (DGG) process resulted in some massively enlarged grains. This was the first direct evidence linking a sudden decrease in Q with the onset of DGG, the uneven growth of some massive grains, despite little change in density or ε_r. Little or no improvement was seen with increased

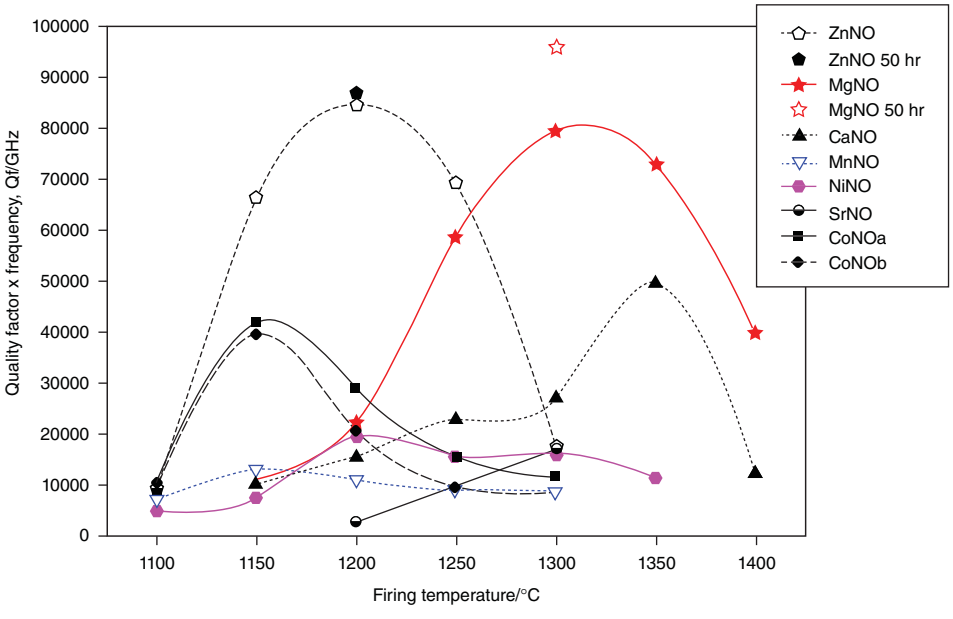

Figure 6.45 *Variation in Qf with firing temperature of binary niobate (NO = Nb_2O_6) ceramics. CoNOa and b made with CoO and Co_3O_4, respectively. Source: Adapted from Pullar* et al. *2005 [301].*

firing times, except for $MgNb_2O_6$, in which Q had increased to 95 900 GHz after firing at 1300 °C/50 h. This was thought unlikely to be due to ordering, as is the case in complex perovskites, and there was little change in microstructure (no DGG occurred), but it was tentatively attributed to defects from oxygen vacancies being reduced with extended firing, as has been observed in titania dielectric ceramics [341, 342].

With the exception of Maeda *et al.* [296] and Butee *et al.* [343], all other studies [292, 301, 307, 344–345, 357] roughly agree with the Qf values for $ZnNb_2O_6$ reported by Pullar *et al.* [301]. The exceptionally high Qf value of 103 730 GHz reported by Butee *et al.* was for a highly sintered (97%) sample with large grains (21 μm), but smaller than the massive grains >40 μm observed by Pullar *et al.* from DGG. The sample was also sintered with a sacrificial ZnO puck to eliminate zinc loss, and one of these factors may account for the high Qf of this sample. The Qf values reported for $MgNb_2O_6$ samples by Lee *et al.* [292], Tzou *et al.* [346], and Wu *et al.* [347] match the 50 h sintered sample by Pullar *et al.* [301], but Khalam *et al.* reported higher Qf values of 104 000 GHz [348]. Again, this was for a very well sintered sample (98%, sintered at 1400 °C/4 h), with a surprisingly large and varied grain size of 20–100 μm, but on sintering at 1425 °C/4 h the authors report that Qf decreased as the grain size increased even further. Some other authors report lower Qf values of around 55 GHz for samples sintered between 1350 and 1450 °C [349].

Qf data for other columbites vary greatly between studies. The Qf values Lee *et al.* [292, 300] reported for $CaNb_2O_6$ and $CoNb_2O_6$ are, respectively, only 43% and 27% of those of Pullar *et al.* [301] while Lee's Qf values for $MnNb_2O_6$ and $NiNb_2O_6$ are more than double those reported by Pullar *et al*. Liou *et al.* [318] and Butee *et al.* [343] reported similar Qf values to Pullar *et al.* for $NiNb_2O_6$, even though these samples were better sintered. Liou *et al.* [318] agreed with the Qf values of Lee *et al.* for $CaNb_2O_6$, despite the low density and ε_r of this sample, while Chen *et al.* agree with Pullar *et al.*, reporting a maximum Qf of 50 000 GHz for $CaNb_2O_6$ sintered at 1400 °C/4 h [350]. Belous *et al.* [307] reported Qf values for $CoNb_2O_6$ (81000 GHz), double those of Pullar *et al.* [301], for a sample sintered at a high temperature of 1400 °C/8h. Belous *et al.* suggest that their unusually high sintering temperature and time totally removes the presence of any $Co_4Nb_2O_9$ left from the formation process [308], which drastically reduces Q, so their Qf values may in fact be nearer the true value for single-phase $CoNb_2O_6$. It is known that variations in sintering time and temperature, or even heating and cooling rates, and impurities present can all have a profound impact on the dielectric losses of complex perovskites, due to either the ordering of cations in sites within the crystal lattice or oversintering causing grain growth or the loss of material [351, 352]. Pullar *et al.* have shown Q to vary greatly in some cases with firing time, although due to a change in microstructure rather than an ordering phenomenon. Unfortunately, most authors do not supply any microstructural details, and the observation of Lee *et al.* [300] that Q is related to the number of electrons in the 3d orbitals of the divalent cations is not supported by other author's results, although it is accepted that Zn^{2+} and Mg^{2+} produce complex perovskites with high Q because they have full outer electron shells [353]. Lee *et al.* did show that their $CoNb_2O_6$ sample had a conductivity an order or magnitude higher than their $ZnNb_2O_6$ sample, which could explain the higher losses of their $CoNb_2O_6$ sample [300]. However, Butee *et al.* have demonstrated that their $NiNb_2O_6$ and $ZnNb_2O_6$ samples had equal conductivity, but a fivefold difference in Qf [343]. No microwave dielectric properties have been reported for $FeNb_2O_6$ or $CdNb_2O_6$. Although their microwave dielectric resonance was not measured, the ellipsoidal $MnNb_2O_6$ nanocrystals made by Lei *et al.* [333] were found to be microwave absorbers when

assembled in a layer 3.5 mm thick. They showed a reflection loss of –11.6 dB at 7.8 GHz, around the same frequency as their dielectric resonance occurred as reported by Pullar *et al.* [301] (6.77 GHz), measured on sintered pucks of ~4 mm thickness.

Discrepancies between the τ_f results could partly be explained by variations in the measurement technique, and although there are sizeable variations between some of the values reported, at least they are all of the same sign and approximate magnitude, except for the $CaNb_2O_6$ sample reported by Lee *et al.* [292, 300]. They found this to have a positive τ_f, whereas all other reported τ_f values for columbites are negative. *Lee* et al. observed a correlation between unit cell volume of the columbite and τ_f (increasing in the order $NiNb_2O_6 < CoNb_2O_6 < ZnNb_2O_6 < MnNb_2O_6 < CaNb_2O_6$), which is not apparent in data from other authors. Lee was puzzled by this change of sign of τ_f, but suggested it may be due to tilting of MO_6 octahedra caused by the much larger ionic radius of the Ca^{2+} cation compared to the transition metal divalent cations [300] that had been observed in BZN-based complex perovskites [354], as a correlation to the tolerance factor. It remains unexplained why this phenomenon of positive τ_f for $CaNb_2O_6$ had not been observed by any other authors, and it remains a highly anomalous result. However, the mechanism behind τ_f in these ceramics is not fully understood, and variations in processing and the resulting microstructure and stoichiometry will surely have an effect upon τ_f.

6.8.3 Microwave Properties of Solid Solutions and Non-stoichiometric Columbites

A detailed study of the effects of non-stoichiometry on Zn-, Mg-, and $CoNb_2O_6$ has been published by Belous *et al.* [307]. They showed that variations of $-0.04 \leq x \leq 0.04$ affected Q in a very non-linear fashion in the system $M_{1+x}Nb_2O_6$, where M = Zn, Mg, and Co. As x increased in steps of 0.01 there was little change in ε_r, and a slight but general trend of increasing τ_f with $ZnNb_2O_6$ and $MgNb_2O_6$, and decreasing τ_f with $CoNb_2O_6$. In all cases with $x < 0$ the excess niobium formed as an Nb_2O_5 secondary phase, with a corresponding large drop in Qf. In $ZnNb_2O_6$ a single phase existed between $0 \leq x \leq 0.005$, above which a zinc-rich secondary phase formed along with a reduced porosity up to $x = 0.01$. This coincided with a peak Qf of 120 000 GHz at $x = 0.01$, 50% greater than the $x = 0$ sample and the highest ever reported for $ZnNb_2O_6$. This large Q was attributed to the lower porosity and the decrease in Q with $x > 0.01$ to the presence of the zinc-rich phase, although values were still higher than in the $x = 0$ sample. $MgNb_2O_6$ had a wider single-phase range of $0 \leq x \leq 0.03$, forming $Mg_4Nb_2O_9$ above this as a secondary phase. The Qf showed a steady increase as x increases, from a low value of 58 000 GHz at $x = 0$ to 121 000 GHz at $x = 0.03$, again the highest value ever reported for $MgNb_2O_6$. This increase begins before the formation of $Mg_4Nb_2O_9$ at $x = 0.03$, which is an excellent microwave ceramic in its own right ($\varepsilon_r = 12$, $Qf = 210\,000$ GHz [355]), and no explanation is given for this. $CoNb_2O_6$ had a single-phase range of $0 \leq x \leq 0.01$, after which a Co-rich phase appeared. Unlike the Zn and Mg ceramics, Qf reached a maximum of 81 000 GHz (already double any other reported values) at $x = 0$, and steadily decreased with increasing x. These fascinating results, demonstrating the huge effect small changes in stoichiometry can have on Q, are shown in Figure 6.46. The τ_ε data were also reported for $Co_{1+x}Nb_2O_6$, and showed that while the existence of Nb_2O_5 at $x < 0$ had little effect, the Co-rich phase at $x > 0$ reduced τ_ε and the Co-rich phase was identified as $Co_4Nb_2O_9$ [308].

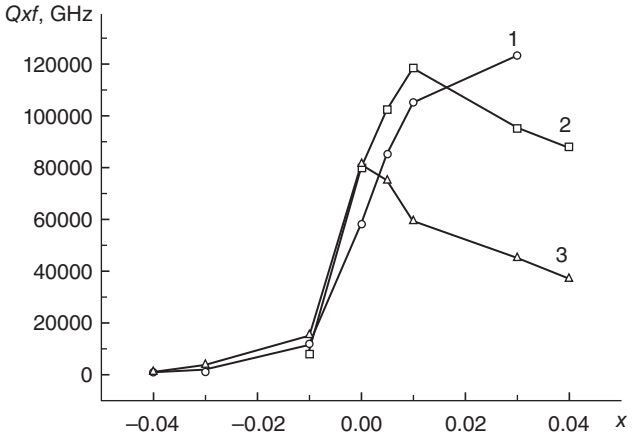

Figure 6.46 *The product Qf for the columbites $A_{1+x}Nb_2O_6$, where A = Mg (1), Zn (2), and Co (3), as a function of x. The samples were sintered in air for 8 h at 1400 °C (1 and 3) and 1300 °C (2). Source: Belous* et al. *2007 [307]. Reproduced with permission of Elsevier.*

The $Zn_{1-x}Mg_xNb_2O_6$ solid solution was studied by Zhang *et al.* [356], who found that the sintering temperature increased and ε_r decreased with x, as one would expect. Also, the grain shape changed from larger, equiaxed grains to smaller, elongated grains as x increased from 0 to 0.5 (sintered at 1150 °C). At $x > 0.6$ a higher temperature of 1300 °C was needed, and DGG was observed, with some grains up to several tens of μm long (see Figure 6.47). This may account for the relatively low *Qf* values of 49 807 GHz and 68 805 GHz reported

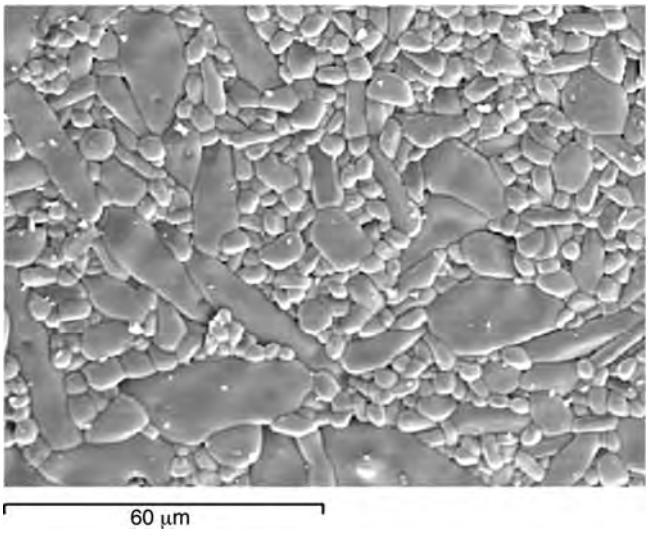

Figure 6.47 *SEM micrograph of $Zn_{1-x}Mg_xNb_2O_6$ ceramic, x = 0.7, sintered at 1300 °C, demonstrating DGG. Source: Zhang* et al. *2004 [356]. Reproduced with permission of Elsevier.*

for $x = 0.7$ and $x = 1$, respectively. Although the sintering temperature required for maximum Qf increased with x as expected, the actual peak Qf values dropped to a minimum of 31 112 GHz at $x = 0.5$ (sintered at 1250 °C), and then steadily increased again with $x > 0.5$, independent of density. The τ_f showed a corresponding minimum of –29.5 ppm at $x = 0.5$, attributed to the tilting of MO_6 octahedra during substitution.

The $Ni_{1-x}Zn_xNb_2O_6$ solid solution was investigated by Butee *et al.* [343], with $0 \leq x \leq 1$ in steps of 0.2. As x increased, the grain size increased from 7.6 to 21 μm, with a corresponding increase in intergranular pore size, and the optimum sintering temperature decreased from 1300 to 1200 °C. All samples were over 97% dense, the unit cell parameters and cell volume increased with x, and the microwave properties ε_r, Qf, and τ_f also increased with x (measured at 4–5 GHz).

The $Zn(Nb_{1-x}Ta_x)_2O_6$ system was sintered at 1250 °C/2 h and investigated as a function of x by Zhang *et al.* [357]. They found that a columbite solid solution exists between $x = 0$ and $x = 0.4$, beyond which the tantalite trirutile structure dominates. Sintering temperature, density, and ε_r increased with x, but Qf and τ_f decreased, with $ZnNb_{0.6}Ta_{0.4}O_6$ having $\varepsilon_r = 23$, $Qf = \sim$74 000 GHz (at 6–10 GHz), and $\tau_f = -40$ ppm. More recently, Fu *et al.* have reported that a mixture of $(ZnTa_2O_6)_{0.8}(MgNb_2O_6)_{0.2}$ sintered at 1350 °C/2 h has $\varepsilon_r = 35.58$, $Qf = \sim$65 500 GHz, and a near-zero $\tau_f = 1.02$ ppm [358]. RiaziKhoei *et al.* [359] have shown that the $(1-x)ZrTiO_6$–$xZnNb_2O_6$ system is ordered columbite for values of $x \geq 0.85$, with $\varepsilon_r = 27$, $Qf = 58\,000$ GHz, and $\tau_f = -20$ ppm, for $x = 0.85$ sintered at 1260 °C/4 h (measured at 3.5 GHz).

Khalam *et al.* studied the MgO–$(1-x)Nb_2O_5$–$(5x/2)TiO_2$ ($(x)Nb_2O_5$ was substituted by $(5x/2)TiO_2$ for charge compensation) sintered at 1400 °C [348]. The lattice constants of $MgNb_2O_6$ decreased with x because the ionic radius of Ti^{4+} (0.605 Å) is smaller than that of Nb^{5+} (0.64 Å). Beyond $x = 0.2$, the orthorhombic phase of $MgNb_2O_6$ changes to tetragonal phases of $MgTiO_3$ and TiO_2, which coexist with ever-decreasing amounts of columbite. With the substitution of 1 mole of TiO_2 ($x = 0.4$), $MgTiO_3$ became the major phase, and some additional traces of Nb_2O_5 were observed. When $x = 0.6$ (1.5 moles of TiO_2), the $MgNb_2O_6$ grains with sharp boundaries disappeared and the TiO_2 rutile phase appeared. Addition of more TiO_2 reduced the grain size due to the formation of $MgTiO_3$. Q increased with $x \leq 4$, as $MgTiO_3$ has $\varepsilon_r = 18$, $Qf = 140\,000$ GHz, and $\tau_f = -50$ ppm. At $x > 0.4$ the formation of rutile decreases Q and τ_f, and increases ε_r; the $x = 0.6$ composition has $\varepsilon_r = 34.5$, $Qf = 81\,300$ GHz, and $\tau_f = -2$ ppm. Further substitution of TiO_2 shifts the τ_f to the positive, but it is no longer a columbite phase. In the $(1-x)ZnNb_2O_6$–$xTiO_2$ system sintered at 1250 °C/2 h, Kim *et al.* observed a columbite phase up to $x = 0.4$, above which the ixolite $ZnTiNb_2O_8$ phase appeared, a disordered modification of the columbite structure containing all the cations distributed over all the metal sites. Then, above $x = 0.57$ rutile TiO_2 also forms [360].

Acknowledgments

R.C. Pullar was supported by FCT Grant SFRH/BPD/97115/2013 for this work, which was developed in the scope of the project CICECO−Aveiro Institute of Materials (FCT UID/CTM/50011/2013), financed by national funds through the FCT/MEC and when applicable cofinanced by FEDER under the PT2020 Partnership Agreement.

References

1. Buschbaum, H.M. (2003) The crystal chemistry of AM O oxometallates. *Journal of Alloys and Compounds*, **349**, 49–104.
2. Elamarraki, Y., Cretin, M., Persin, M., *et al.* (2001) Elaboration and properties of TiO_2–$ZnAl_2O_4$ ultrafiltration membranes. *Materials Research Bulletin*, **36**, 227–237.
3. Buchanan, R.C. (1996) *Ceramic Materials for Electronics*, Marcel Dekker, New York.
4. van der Laaga, N.J. Snela, M.D., and Magusinb, M.M. (2004) Structural, elastic, thermophysical and dielectric properties of zinc aluminate ($ZnAl_2O_4$). *Journal of European Ceramic Society*, **24**, 2417–2424.
5. Surendran, K.P., Santha, N., Mohanan, P., *et al.* (2004) Temperature stable low permittivity ceramic dielectrics in $(1 - x)ZnAl_2O_4$–$xTiO_2$ system for microwave substrate applications. *European Physics Journal B*, **41**, 301–306.
6. Surendran, K.P., Mohanan, P., Manjusha, M.V., *et al*. (2005) A low loss dielectric substrate in $ZnAlO_4$–TiO_2 system for microelectronic applications. *Journal of Applied Physics* **98**, 044101.
7. Shannon, R.D. and Pask, J.A. (1965) Kinetics of anatase–rutile transformation. *Journal of the American Ceramic Society*, **48**, 391–398.
8. Templeton, A., Wang, X., Penn, S.J., *et al.* (2000) Microwave dielectric loss of titanium oxide. *Journal of the American Ceramic Society*, **83**, 95–100.
9. Paladino, A.E. (1971) Temperature compensated $MgTi_2O_5$–TiO_2 dielectrics. *Journal of the American Ceramic Society*, **54**, 168–171.
10. Thomas, S. and Sebastian, M.T. (2008) Effect of B_2O_3–Bi_2O_3–SiO_2–ZnO glass on the sintering and microwave dielectric properties of $0.83ZnAl_2O_4$–$0.17TiO_2$. *Materials Research Bulletin*, **43**, 843–851.
11. Huang, C.L., Yang, T.J., and Huang, C.C. (2009) Low dielectric loss ceramics in the $ZnAl_2O_4$–TiO_2 system as a T_f compensator. *Journal of the American Ceramic Society*, **92**, 119–124.
12. Lei, W., Lu, W.Z., Hua, J.H., *et al.* (2008) Modification of $ZnAl_2O_4$-based low permittivity microwave dielectric ceramics by adding 2MO–TiO_2 (M = Co, Mg, and Mn). *Journal of the American Ceramic Society*, **91**, 1958–1961.
13. Lei, W., Zhong, W.Z., Wang, X.-H., *et al.* (2011) Phase composition and microwave dielectric properties of $ZnAl_2O_4$–Co_2TiO_4 low permittivity ceramics with high quality factor. *Journal of the American Ceramic Society*, **94**, 20–23.
14. Skomorovskaya, L.A. (1993) Magnesia spinel ceramics alloyed with rare earth oxides. *Glass and Ceramics*, **3–4**, 165–168.
15. Baik, Y.H. (1985) Sintering of $MgAl_2O_4$ spinel and its characteristics. *Yoop Hikoech*, **22**, 29–36.
16. Sarkar, R. and Bannerjee, G. (2000) Effect of addition of TiO_2 on reaction sintered MgO–Al_2O_3 spinels. *Journal of European Ceramic Society*, **20**, 2133–2141.
17. Grimes, N.W. (1992) Analysis of oxide dielectric data and the quantum theory of atomic polarizability. *Journal of Physics: Condensed Matter*, **4**, L567–L570.
18. Kennedy, C., Mollá, J., Ibarra, A., *et al*. (1991) The effect of ZrO_2 doping on mechanical and dielectric properties of Al_2O_3 and $MgAl_2O_4$. *Journal of Nuclear Materials*, **179-181**, 375–378.
19. Shannon, R.D. and Rossman, G.R. (1991) Dielectric constant of $MgAl_2O_4$ spinel and the oxide additivity rule. *Journal of Physics and Chemistry of Solids*, **52**, 1055–1059.
20. Surendran, K.P., Bijumon, P.C., Mohanan, P., *et al.* (2005) $(1 - x)MgAl_2O_4$–$xTiO_2$ dielectrics for microwave and millimeter wave applications. *Applied Physics A*, **A81**, 823–826.
21. Petrova, M.A., Mikirticheva, G.A., Novikova, A.S., *et al.* (1997) Spinel solid solutions in the systems $MgAl_2O_4$–$ZnAl_2O_4$ and $MgAl_2O_4$–Mg_2TiO_4. *Journal of Materials Research*, **12**, 2584–2588.
22. Huang, C.-L., Tai, C.-Y., Huang, C.Y., *et al.* (2010) Low loss microwave dielectrics in the spinel structured $(Mg_{1-x}Ni_x)Al_2O_4$ solid solutions. *Journal of the American Ceramic Society*, **93**, 1999–2003.
23. Husu, C.H., Tung, T.H., and Hsu, C.K. (2011) Dielectric characteristics of $(Mg_{1/2}Co_{1/2})Al_2O_4$ ceramics at microwave frequencies. *Materials Chemistry and Physics*, **131**, 1–3.
24. Huang, C.-L., Chien, Y.H., Tsai, C.-Y., *et al.* (2011) High Q microwave dielectrics in the $(Mg_{1-x}Zn_x)Al_2O_4$ ($x = 0 – 0.1$) system. *Journal of Alloys and Compounds*, **509**, L150–L152.

25. Zheng, S.W., Fan, X.C., and Chen, X.M. (2008) Analysis of infrared reflection spectra of $Mg_{1-x}Zn_xAl_2O_4$ microwave dielectric ceramics. *Journal of the American Ceramic Society*, **91**, 490–493.
26. Lorite, I., Rodriguez, M.A., Azough, F., *et al.* (2012) $ZnAl_2O_4$ and $ZnAl_2O_4$ – (0.21) Mn_2TiO_4 microwave dielectric ceramics prepared by hot pressing and spark plasma sintering. *Journal of the American Ceramic Society*, **95**, 1023–1028.
27. Lei, W., Lu, W.Z., Zhu, J.Z., *et al.* (2009) Effects of heating rate on microstructures and microwave dielectric properties of $(1 - x)ZnAl_2O_4$–$xTiO_2$ ($x = 0.21$) ceramics. *Ceramic International*, **35**, 277–280.
28. Lei, W., Lu, W.Z., and Wang, X.C. (2012). Temperature compensating $ZnAlO_4$–Co_2TiO_4 spinel based low permittivity microwave dielectric ceramics. *Ceramic International*, **38**, 99–103.
29. Lu, W.Z., Lei, W., Zhu, J.H., *et al.* (2007) Calcining temperature dependence of microwave dielectric properties of $(1 - x)ZnAl_2O_4$–$xTiO_2$ ($x = 0.21$) ceramics. *Japanese Journal of Applied Physics*, **46**, L724–L726.
30. Lei, W., Lu, W.-Z., Liu, D., *et al.* (2009) Phase evolution and microwave dielectric properties of $(1 - x)ZnAl_2O_4$–$xMgTiO_4$ ceramics. *Journal of the American Ceramic Society*, **92**, 105–109.
31. Fu, P., Lu, W., Lei, W., *et al.* (2013) Transparent poly-crycristalline $MgAl_2O_4$ ceramic fabricated by spark plasma sintering: microwave dielectric and optical properties. *Ceramic International*, **39**, 2481–2487
32. Tseng, C.F., Tung, H.H., Hsu, C.-K., *et al*. (2010) Dielectric characteristics of $(Mg_{1/2}Zn_{1/2})Al_2O_4$ ceramics at microwave frequencies. *Journal of Alloys and Compounds*, **502**, 136–138.
33. Tsai, W.C., Liou, Y.-H., and Liou, Y.-C. (2012) Microwave dielectric properties of $MgAl_2O_4$–$CoAl_2O_4$ spinel compounds prepared by reaction sintering process. *Materials Science and Engineering B*, **177**, 1133–1137.
34. Belous, A., Ovchar, O., Durylin, D., *et al.* (2007) Microwave composite dielectrics based on magnesium titanates. *Journal of European Ceramic Society*, 2007, **27**, 2963–2966.
35. Li, H., Tang, B., Zhang, S., *et al.* (2014) Composite dielectrics $(1 - x)(Mg_{0.97}Zn_{0.03})_2(Ti_{0.95}Sn_{0.05})O_4$–$xCaTiO_3$ suitable for microwave application. *Journal of Materials Science: Materials in Electronics*, **25**, 3318–3323.
36. Huang, C.-L., Liu, S.S., and Chen, S.H. (2009) Dielectric properties of a low loss $(1 - x)(Mg_{0.95}Zn_{0.05})_2TiO_4$–$xSrTiO_4$ ceramic system at microwave frequencies. *Journal of Alloys and Compounds*, **480**, 794–797.
37. Huang, C.-L., Chen, J.-Y., Li, J.B. (2011) Effect of $CaTiO_3$ addition on microwave dielectric properties of $Mg_2(Ti_{0.95}Sn_{0.05})O_4$ ceramics. *Journal of Alloys and Compounds*, **509**, 4247–4251.
38. Huang, C.-L. and Chen, J.Y. (2009) Low loss microwave dielectrics using $SrTiO_3$ modified $(Mg_{0.95}Co_{0.05})_2TiO_4$ ceramics. *Journal of Alloys and Compounds*, **485**, 706–710.
39. Petrova, A.A., Mikirticheva, G.A., Novikova, A.S., *et al.* (1997) Spinel solid solutions in the systems $MgAl_2O_4$–$ZnAl_2O_4$ and $MgAl_2O_4$–Mg_2TiO_4. *Journal of Materials Research*, **12**, 2584–2588.
40. Huang, C.-L. and Chen, J.-Y. (2009) Low loss microwave dielectrics using $Mg_2(Ti_{1-x}Sn_x)O_4$ ($x = 0.01$–0.09) solid solution. *Journal of the American Ceramic Society*, **92**, 2237–2241.
41. Yao, G.G. and Liu, P. (2011) Microwave dielectric properties of low-loss $(Mg_{0.95}Zn_{0.05})_2(Ti_{0.8}Sn_{0.2})O_4$ ceramics. *Journal of Functional Materials*, **42**, 732–733.
42. Yao, G.G. and Liu, P. (2012) Effects of LiF addition on sintering behavior and microwave dielectric properties of $(Mg_{0.95}Zn_{0.05})_2(Ti_{0.8}Sn_{0.2})O_4$ ceramics. *Ceramic International*, **38**, 2239–2242.
43. Huang, C.-L. and Liu., S.S. (2008) Low loss microwave dielectrics in the $(Mg_{1-x}Zn_x)_2TiO_4$ ceramics. *Journal of the American Ceramic Society*, **91**, 3428–3430.
44. Huang, C.-L., Tseng, Y.-W., and Kuo, Y.C. (2011) Low loss microwave dielectrics in the $(Mg_{1-x}Co_x)_{1.8}Ti_{1.1}O_4$ ($x = 0.03$–1) solid solutions. *Journal of the American Ceramic Society*, **94**, 2963–2967.
45. Huang, C.-L. and Chen, J.Y. (2009) High Q microwave dielectrics in the $(Mg_{1-x}Co_x)_2TiO_4$ ceramics. *Journal of the American Ceramic Society*, **92**, 379–383.

46. Huang, C.-L. and Chen, J.-Y. (2009) Low loss microwave dielectric ceramics using $(Mg_{1-x}Mn_x)_2TiO_4$ (x = 0.02–0.1) solid solution. *Journal of the American Ceramic Society*, **92**, 675–678.
47. Wu, X., Xue, J., Wang, R., and Li, J. (2014) Synthesis, characterization and microwave dielectric properties of spinel $MgGa_2O_4$ ceramic material. *Journal of Alloys and Compounds*, **585**, 542–548.
48. Xue, J., Wu, S., and Li, J. (2013) Synthesis microstructure and microwave dielectric properties of spinel $ZnGa_2O_4$ ceramics. *Journal of the American Ceramic Society*, **96**, 2481–2485.
49. Bhuyan, R.K., Santhoshkumar, T., Goswami, D., *et al.* (2013) Enhanced densification and microwave dielectric properties of Mg_2TiO_4 ceramics added with CeO_2 nanoparticles. *Materials Science and Engineering B*, **178**, 471–476.
50. Shin, H.K., Shin, H.S., Jung, H.S., *et al.* (2005) Role of lithium borosilicate glass in the decomposition of $MgTiO_3$ based dielectric ceramics during sintering. *Materials Research Bulletin*, **41**, 1206–1214.
51. Huang, C.-L. and Liu, S.-S. (2009) Dielectric characteristics of the $(1 - x)Mg_2TiO_4$–$xSrTiO_3$ ceramic system at microwave frequencies. *Journal of Alloys and Compounds*, **47**1, L9–L12.
52. Chen, Y.B. (2012) Dielectric properties and crystal structure of Mg_2TiO_4 ceramics substituting for Mg with Zn and Co. *Journal of Alloys and Compounds*, **513**, 481–486.
53. Huang, C.-L., Tseng, Y.W., Chen, J.Y., *et al.* (2012) Dielectric properties of high-Q $(Mg_{1-x}Zn_x)_{1.8}Ti_{1.1}O_4$ ceramics at microwave frequency. *Journal of European Ceramic Society*, **32**, 2365–2371.
54. Li, L., Zhang, M., Liao, Q., *et al.* (2012) Composite dielectrics $(1 - y)$ $(Mg_{0.95}Zn_{0.05})_{1.8}Ti_{1.1}O_4$–$yCaTiO_3$ suitable for microwave applications. *Journal of Alloys and Compounds*, **531**, 18–22.
55. Ma, Q., Wu, S., and Fan, Y. (2014) Synthesis and microwave dielectric properties of Zn_2SnO_4 ceramics. *Ceramic International*, **40**, 1073–1080.
56. Chen, Y.-C., Weng, M.-Z., and Hong, J.-M. (2014) Effect of Zr substitution on microwave dielectric properties of Zn_2SnO_4 ceramics. *Journal of Materials Science: Materials in Electronics*, **25**, 5000–5005.
57. Chen, Y.-C., Wang, Y.N., and Hsu, C.-H. (2011) Elucidating the dielectric properties of $MgSnO_4$ ceramics at microwave frequency. *Journal of Alloys and Compounds*, **509**, 9650–9653.
58. Chen, Y.-C. (2012) Elucidating the microwave dielectric properties of $(Mg_{1-x}Zn_x)_2SnO_4$ ceramics. *Journal of Alloys and Compounds*, **527**, 84–89.
59. Hong, Z.S., Wei, M.D., Ding, X.K., *et al.* (2010) $Li_2ZnTi_3O_8$ nanorods: a new anode material for lithium-ion battery. *Electrochemistry Communications*, **12**, 720.
60. George, S. and Sebastian, M.T. (2010) Synthesis and microwave dielectric properties of novel temperature stable high Q $Li_2ATi_3O_8$ (A = Mg, Zn) ceramics. *Journal of the American Ceramic Society*, **93**, 2164–2166.
61. George, S. and Sebastian, M.T. (2010) Microwave dielectric properties of novel temperature stable high Q $Li_2Mg_{1-x}Zn_xTi_3O_8$ and $Li_2A_{1-x}Ca_xTi_3O_8$ (A = Mg, Zn) ceramics. *Journal of European Ceramic Society*, **30**, 2585–2592.
62. George, S. and Sebastian, M.T. (2011) Low temperature sintering and microwave dielectric properties of $Li_2ATi_3O_8$ (A = Mg, Zn) ceramics. *International Journal of Applied Ceramic Technology*, **8**, 1400–1407.
63. Sebastian, M.T. (2008) *Dielectric Materials for Wireless Communications*, Elsevier Publishers, Oxford, UK.
64. Armaki, H.T., Nassaj, E.T., and Bari, M. (2013) Phase analysis and improvement of quality factor of $Li_2ZnTi_3O_8$ ceramics by annealing treatment. *Journal of Alloys and Compounds*, **581**, 757–761.
65. Tong, J., Zhang, B., Huang, W., and Yang, H. (2013) The effect of composition on $Li_2(Mg_{0.3}Zn_{0.7})Ti_3O_8$–$xTiO_2$ microwave dielectric ceramics follow temperature co-fired ceramics technology application. *Materials Letters*, **95**, 168–171.
66. Su, C.H., Ho, Y.-D., and Huang, C.-L. (2014) Low loss and temperature stable microwave dielectrics using $Li_2(Mg_{1-x}A_x)Ti_3O_8$ (A^{2+} = Zn, Co; x = 0.02–0.1) ceramics. *Journal of Alloys and Compounds*, **607**, 67–72.

67. Wang, L., Sun, Q., Ma, W., and Huan, Z. (2013) Microwave dielectric characteristics of $Li_2(Mg_{0.94}M_{0.06})Ti_3O_8$ (M = Zn, Co, Mn) ceramics. *Ceramic International*, **39**, 5185–5190.
68. He, L., Zhou, D., Feng, X., *et al.* (2013) A novel magnetodielectric solid solution ceramic $0.4LiFe_2O_8$–$0.6Li_2MgTi_3O_8$ with excellent microwave dielectric properties. *Journal of the American Ceramic Society*, **96**, 3027–3030.
69. Lu, X., Zheng, Y., Dong, Z., and Huang, Q. (2014) Low temperature sintering and microwave dielectric properties of $0.6Li_2ZnTi_3O_8$–$0.4Li_2TiO_3$ ceramics doped with ZnO–B_2O_3–SiO_2 glass. *Materials Letters*, **131**, 1–4.
70. Hou, M.-Z., Chen, G.H., Bao, Y., *et al.* (2012) Low-temperature firing and microwave dielectric properties of LBS glass-added $Li_2ZnTi_3O_8$ ceramics with TiO_2. *Journal of Materials Science: Materials in Electronics*, **23**, 1722–1727.
71. He, M. and Zhang, H. (2013) Low-temperature firing and microwave properties of TiO_2 modified $Li_2ZnTi_3O_8$ ceramics doped with B_2O_3. *Journal of Materials Science: Materials in Electronics*, **24**, 3303–3308.
72. Wang, W., Zhou, H., Chen, X., *et al.* (2014) Crystal structure and optimized microwave dielectric properties of $(1 - x)LiZn_{0.5}Ti_{1.5}O_4$–$xTiO_2$ ceramics for applications in dielectric resonator. *Journal of Materials Science: Materials in Electronics*, **24**, 2641–2645.
73. Bari, M., Taheri-Nassaj, E., and Taghipour-Armaki, H. (2013) Role of nano- and micron-sized particles of TiO_2 additive on microwave dielectric properties of $Li_2ZnTi_3O_8$–4 wt% TiO_2 ceramics. *Journal of the American Ceramic Society*, **96**, 3737–3741.
74. Li, Y.X., Li, H., Li, J., *et al.* (2014) Effect of TiO_2 ratio on the phase and microwave dielectric properties of $Li_2ZnTi_{3+x}O_{8+2x}$ ceramics. *Journal of Electronic Materials*, **43**, 1107–1111.
75. Li, Y.X., Qin, Z.J., Tang, B., *et al.* (2015) Microwave dielectric properties of TiO_2-added $Li_2ZnTi_3O_8$ ceramics doped with Li_2O–Al_2O_3–B_2O_3 glass. *Journal of Electronic Materials*, **44**, 281–286.
76. Fang, L., Liu, Q., Su, C., *et al.* (2012) Microwave dielectric properties and compatibility with silver of low-fired $Li_2Cu_{0.1}Zn_{0.9}Ti_3O_8$ ceramic. *Materials Letters*, **81**, 34–36.
77. Fang, L., Liu, Q., Tang, Y., and Zhang, H. (2012) Adjustable dielectric properties of $Li_2Cu_xZn_{1-x}Ti_3O_8$ ($x = 0$ to 1) ceramics with low sintering temperature. *Ceramic International*, **38**, 6431–6434.
78. Tang, Y., Fang, L., Zhou, H., *et al.* (2013) Microwave dielectric properties and chemical compatibility with silver electrode of low fired $Li_2Cu_{0.2}Mg_{0.8}Ti_3O_8$ ceramics. *Ceramic International*, **39**, 8503–8506.
79. Wu, Y., Zhou, D., Guo, J., *et al.* (2013) Microwave dielectric properties and low temperature sintering of $Li_2Zn(Ti_{1-x}Sn_x)_2O_8$ ($x < 0.2$) ceramics with B_2O_3–CuO addition. *Journal of Materials Science: Materials in Electronics*, **24**, 4942–4946.
80. Wang, W., Zhou, H., Chen, X., *et al.* (2013) Crystal structure and optimized microwave dielectric properties of $(1 - x)$ $LiZn_{0.5}Ti_{1.5}O_{4-x}TiO_2$ ceramics for application in dielectric resonator. *Journal of Materials Science: Materials in Electronics*, **24**, 2641–2645.
81. Huang, C.-L., Su, C.H., and Chang, C.M. (2011) High *Q* microwave dielectric ceramics in the $Li_2(Zn_{1-x}A_x)Ti_3O_8$ (A = Mg, C0; $x = 0.02$–0.1) system. *Journal of the American Ceramic Society*, **94**, 4146–4149.
82. Zhang, J. and Zuo, R. (2016) Effects of Zr substitution on the microstructure and microwave dielectric properties of $Li_2Zn(Ti_{1-x}Zr_x)_3O_8$ ceramics. *Journal of Materials Science: Materials in Electronics*, in press.
83. Fang, L., Chu, D., Zhou, H., *et al.* (2011) Microwave dielectric properties and low temperature sintering behaviour of $Li_2CoTi_3O_8$ ceramic. *Journal of Alloys and Compounds*, **505**, 1880–1888.
84. Fang, L., Tang, Y., Chu, D., *et al.* (2012) Effect of B_2O_3 addition on the microstructure and miocrowave dielectric properties of $Li_2CoTi_3O_8$ ceramics. *Journal of Materials Science: Materials in Electronics*, **23**, 478–483.
85. Fang, L., Chu, D., Zhou, H., *et al.* (2011) Microwave dielectric properties of temperature stable $Li_2Zn_xCo_{1-x}Ti_3O_8$ ceramics. *Journal of Alloys and Compounds*, **509**, 8840–8844.

86. Tong, J., Zhang, B., Huang, W., and Yang, H. (2013) The effect of composition of $Li_2(Mg_{0.3}Zn_{0.7})Ti_3O_8$–$xTiO_2$ microwave dielectric ceramic for LTCC applications. *Materials Letters*, **95**, 168–171.
87. Li, Y., Li, J., Tang, B., *et al.* (2014) Low temperature sintering and dielectric properties of $Li_2ZnTi_3O_8$–TiO_2 composite ceramics doped with CaO–B_2O_3–SiO_2 glass. *Journal of Materials Science: Materials in Electronics*, **25**, 2780–2785.
88. Liu, X., Zhou, H., Chen, X., *et al.* (2012) Phase structure and microwave dielectric properties of $(1 - x)Li_2Zn_3Ti_4O_{12}$–$xTiO_2$ ceramics. *Journal of Alloys and Compounds*, **515**, 22–25.
89. Yao, G.G., Liu, P., Zhang, H.W. (2013) Microwave dielectric properties of $Li_2MgTi_3O_8$ ceramics produced by reaction-sintering method. *Journal of Materials Science: Materials in Electronics*, **24**, 1128–1131.
90. Zhang, P., Wang, Y., Liu, J., *et al.* (2014) A high improved quality factor of $Li_2MgTi_3O_8$ microwave dielectric ceramics system. *Materials Letters*, **123**, 195–197.
91. He, M. and Zhang, H. (2014) Microwave properties of low fired $Li_2ZnTi_3O_8$ ceramics doped with CuO–Bi_2O_3–V_2O_5. *Journal of Alloys and Compounds*, **586**, 627–632.
92. He, M. and Zhang, H. (2013) Low temperature firing and microwave properties of TiO_2 modified $Li_2ZnTi_3O_8$ ceramics doped with B_2O_3. *Journal of Materials Science: Materials in Electronics*, **24**, 3303–3308.
93. Chen, G.H., Zhen, M., and Yang, H.Y. (2012). Effect of H_3BO_3 on the low temperature sintering and microwave dielectric properties of $Li_2ZnTi_3O_8$ ceramics. *Journal of Alloys and Compounds*, **534**, 9–12.
94. Zhang, P., Wang, Y., Hua, Y., *et al.* (2013) Low temperature sintering and microwave dielectric properties of $Li_2ZnTi_3O_8$. *Materials Letters*, **107**, 351–353.
95. Lv, X., Zheng, Y., Zhou, B., *et al.* (2013) Microwave dielectric properties of $Li_2ZnTi_3O_8$ ceramics doped with ZnO–B_2O_3–SiO_2 glass. *Materials Letters*, **91**, 217–219.
96. Li, H., Lu, W., and Lei, W. (2012) Microwave dielectric properties of $Li_2ZnTi_3O_8$ ceramics doped with ZnO–B_2O_3 frit. *Materials Letters*, **71**, 148–150.
97. Bari, M., Nassaj, E.T., and Armaki, H.T. (2015) Phase evolution, microstructure, and microwave dielectric properties of reaction-sintered $Li_2ZnTi_3O_8$ ceramic obtained using nanosized TiO_2 reagent. *Journal of Electronic Materials*, **44**, 3670–3676.
98. Singh, S.K., Kiran, S.R., and Murthy, V.R.K. (2013). Structural, Raman spectroscopic and microwave dielectric studies on spinel $Li_2Zn_{(1-x)}Ni_xTi_3O_8$ compounds. *Materials Chemistry and Physics*, **141**, 822e827.
99. Shahraki, A.S., Taheri, E., Bafrood, H.B., *et al.* (2014) Microwave dielectric properties of $Li_2ZnTi_3O_8$ ceramic prepared by reaction sintering process. *Journal of Materials Science: Materials in Electronics*, **25**, 1117–1121.
100. Lu, X., Zheng, Y., Dong, Z., *et al.* (2014) Microstructures and microwave dielectric properties of $Li_2ZnTi_3O_8$ ceramics prepared by reaction-sintering process. *Journal of Materials Science: Materials in Electronics*, **25**, 3358–3363.
101. Zhou, H., Liu, X., Chen, X., *et al.* (2012) $ZnLi_{2/3}Ti_{4/3}O_3$: a new low loss spinel microwave dielectric ceramic. *Journal of European Ceramic Society*, **32**, 261–265.
102. Zhang, T., Zuo, R., and Wang, Y. (2014) $Li_2Zn_3Ti_4O_{12}$–$Ba_3(VO_4)_2$ microwave delectric ceramics sintered at low temperature without glass additives. *Journal of Materials Science: Materials in Electronics*, **25**, 5570–5575.
103. Wu, Y., Zhou, D., Guo, J., and Pang, L.X. (2013) Microwave dielectric properties and low temperature firing of $(1 - x)Li_2Zn_3Ti_3O_8$–xLi_2TiO_3 $(0.2 < x < 0.8)$ ceramics with B_2O_3–CuO addition. *Journal of Materials Science: Materials in Electronics*, **24**, 1505–1510.
104. Sayyadi-Shahraki, A., Taheri-Nassaj, E., Hassanzadeh-Tabrizi, S.A., *et al.* (2014) Low temperature cofireable $Li_2Zn_3Ti_4O_{12}$ microwave dielectric ceramic with Li_2O–ZnO–B_2O_3 glass additive. *Journal of Materials Science: Materials in Electronics*, **25**, 355–360.
105. Zhou, H., Liu, X., Chen, X., *et al.* (2012) Preparation phase structure and microwave dielectric properties of a new low cost $MgLi_{2/3}Ti_{4/3}O_4$ compound. *Materials Chemistry and Physics*, **137**, 22–25.
106. Sebastian, M.T. and Jantunen, H. (2008) Low loss dielectric materials for LTCC pplications: a review. *International Materials Review*, **53**, 57–90.

107. Wanmaker, W.L., Ter Vrugt, J.W., and Verlijsdonk, J.G. (1971) Luminescence of alkaline earth yttrium and lanthanum phosphate–silicates with apatite structure. *Journal of Solid State Chemistry*, **3**, 452–457.
108. Monma, H. (1982) Catalytic behavior of calcium phosphates for decompositions of 2-propanol and ethanol. *Journal of Catalysis*, **75**, 200–203.
109. Panteix, P.J., Béchade, E., Julien, I., *et al.* (2008) Influence of anionic vacancies on the ionic conductivity of silicated rare earth apatites. *Materials Research Bulletin*, **43**, 1223–1231.
110. Shannon, R.D. and Rossman, G.R. (1992) Dielectric constants of apatite, epidote, vesuvianite, and zoisite, and the oxide additivity rule. *Physics and Chemistry of Minerals*, **19**, 157–165.
111. Leu, L.C., Thomas, S., Sebastian, M.T., *et al.* (2011) Crystal structure of apatite type rare-earth silicate $(Sr_2RE_2)(RE_6)(SiO_4)_6O_2$ (RE = La, Pr, Tb, Tm, and Y). *Journal of the American Ceramic Society*, **94** (8), 2625–2632.
112. Thomas, S. and Sebastian, M.T. (2009) Microwave dielectric properties of $SrRE_4Si_3O_{13}$ (RE = La, Pr, Nd, Sm, Eu, Gd, Tb, Dy, Er, Tm, Yb, and Y) ceramics. *Journal of the American Ceramic Society*, **92**, 2975–2981.
113. Thomas, D. and Sebastian, M.T. (2011). Microwave dielectric properties of $Ca_{2+x}La_{8-x}(SiO_4)_{6-x}(PO_4)_xO_2$ solid solution. *Journal of the American Ceramic Society*, **94**, 2276–2278.
114. Thomas, D., Abhilash, P., and Sebastian, M.T. (2013). Effect of isovalent substitutions on the microwave dielectric properties of $Ca_4La_6(SiO_4)_4(PO_4)_2O_2$ apatite. *Journal of Alloys and Compounds*, **546**, 72–76.
115. Manu, K.M., Karthik, C., Leu, L.C., *et al.* (2013) Crystal structure and microwave dielectric properties of $LiRE_9(SiO_4)_6O_2$ ceramics (RE = La, Pr, Nd, Sm, Eu, Gd, and Er). *Journal of the American Ceramic Society*, **96**, 1504–1511.
116. Serret, A., Cabañas, M.V., and Vallet-Regí, M. (2000) Stabilization of calcium oxyapatites with lanthanum(III)-created anionic vacancies. *Chemistry of Materials*, **12**, 3836–3841.
117. Felsche, J. (1972) Rare earth silicates with the apatite structure. *Journal of Solid State Chemistry*, **5**, 266–275.
118. Schroeder, L.W. and Mathew, M. (1978) Cation ordering in $Ca_2La_8(SiO_4)_6O_2$. *Journal of Solid State Chemistry*, **26**, 383–387.
119. Hughes, J.M., Cameron, M., and Crowley, K.D. (1991) Ordering of divalent cations in the apatite structure; crystal structure refinements of natural Mn- and Sr-bearing apatite. *American Mineralogist*, **76**, 1857–1862.
120. Boyer, L., Piriou, B., Carpena, J., *et al.* (2000) Study of sites occupation and chemical environment of Eu^{3+} in phosphate–silicates oxyapatites by luminescence. *Journal of Alloys and Compounds*, **311**, 143–152.
121. Boyer, L., Carpena, J., and Lacout, J.L. (1997) Synthesis of phosphate–silicate apatites at atmospheric pressure. *Solid State Ionics*, **95**, 121–129.
122. Blasse, G. (1975) Influence of local charge compensation on site occupation and luminescence of apatites. *Journal of Solid State Chemistry*, **14**, 181–184.
123. van Vliet, J.P.M. and Blasse, G. (1990) Luminescence from Pr^{3+} in barium lanthanum oxyapatite. *Materials Research Bulletin*, **25**, 391–394.
124. Thomas, S. (2011) Silicate and aluminate based dielectric ceramics for microwave communication. PhD Thesis, Cochin University of Science and Technology.
125. Shen, Y.Q., Tok, A., and Dong, Z.L. (2010) Synthesis and crystal structure characterization of silicate apatite $Sr_2Y_8(SiO_4)_6O_2$. *Journal of the American Ceramic Society*, **93**, 1176–1182.
126. Masubuchi, Y. Higuchi, M., Katase, H., Takeda, T., *et al.* (2004) Oxide ion conduction in $Nd_{9.33}(SiO_4)_6O_2$ and $Sr_2Nd_8(SiO_4)_6O_2$ single crystals grown by floating zone method. *Solid State Ionics*, **166**, 213–217.
127. Brown, I.D. and Shannon, R.D. (1973). Empirical bond-strength–bond-length curves for oxides. *Acta Crystallographics Section A: Foundation Crystallographics*, **29**, 266–282.
128. Chartier, A., Meis, C., and Gale, J.D. (2001) Computational study of Cs immobilization in the apatites $Ca_{10}(PO_4)_6F_2$, $Ca_4La_6(SiO_4)_6F_2$ and $Ca_2La_8(SiO_4)_6O_2$. *Physical Review B*, **64**, 085110.
129. Schlomann, E., (1964) Dielectric losses in ionic crystals with disordered charge distributions. *Physical Review*, **135**, A413–A419.

130. Alford, N.McN. and Penn, S.J. (1996) Sintered alumina with low dielectric loss. *Journal of Applied Physics*, **80**, 5895–5898.
131. Molla, J., Heidenger, R., and Ibarro, A. (1994) Alumina ceramics for heating systems. *Journal of Nuclear Materials*, **212/215**, 1029–1034.
132. Molla, J., Gonzalez, M., Vila, R., *et al.* (1999) Effect of humidity on microwave dielectric losses of porous alumina. *Journal of Applied Physics*, **85**, 1727–1730.
133. Alford, N.McN., Breeze, J., Wang, X., *et al.* (2001) Dielectric loss of oxide single crystals and polycrystalline analogues from 10 to 320 K. *Journal of European Ceramic Society*, **21**, 2605–2611.
134. Penn, S.J., Alford, N.McN., Templeton, A., *et al.* (1997) Effect of porosity and grain size on the microwave dielectric properties of sintered alumina. *Journal of the American Ceramic Society*, **80**, 1885–1888.
135. Kono, M., Takagi, H., Tatekawa, T., *et al.* (2006) High *Q* dielectric resonator material with low dielectric constant for millimeter wave applications. *Journal of European Ceramic Society*, **26**, 1909–1912.
136. Kolodiazhnyi, T., Annino, G., Spreitzer, M., *et al.* (2009) Development of Al_2O_3–TiO_2 composite ceramics for high power millimeter wave applications. *Acta Meeterialia*, **57**, 3402–3409.
137. Ohishi, Y., Miyauchi, Y., Kakimoto, K., and Ohsato, H. (2005) Microwave dielectric properties of Al_2O_3–TiO_2 improved by addition of ZnO. *Journal of Ferroelectrics*, **327**, 27–31.
138. Huang, C.-L., Huang, J.J., and Huang, C.Y. (2005) Sintering behaviour and microwave dielectric properties of nano-alpha alumina. *Materials Letters*, **59**, 3746–3749.
139. Huang, C.-L., Wang, J.J., and Huang, C.-Y. (2007) Microwave dielectric properties of sintered alumina using nano scaled powders of α-alumina and TiO_2. *Journal of American Ceramic Society*, **90**, 1487–1493.
140. Ohsato, H., Tsunooka, T., Ando, M., *et al.* (2003) Millimeter-wave dielectric ceramics of alumina and fosterite with high quality factor and low dielectric constant. *Journal of Korean Ceramic Society*, **40**, 350–353.
141. Breeze, J., Aupi, X., and Alford, N.McN. (2002) Ultralow loss polycrystalline alumina. *Applied Physics Letters*, **81**, 5021–5023.
142. Woode, R.A., Ivanov, E.N., Tobar, M.E., *et al.* (1994) Measurement of dielectric loss tangent of alumina at microwave frequencies and room temperature. *Electronic Letters*, **30**, 2120–2122.
143. Giordano, V., Kersale, Y., Monaco, O., *et al.* (1999) Progress report on the development of microwave spectral references at the LPMO. *European Journal of Applied Physics*, **8**, 269–274.
144. Miyauchi, Y., Ohishi, Y., Miyake, S., *et al.* (2006) Improvement of the dielectric properties of rutile-doped Al_2O_3 ceramics by annealing treatment. *Journal of European Ceramic Society*, **26**, 2093–2096.
145. Ohishi, Y. Miyauchi, Y., Ohsato, H., *et al.* (2004) Controlled temperature coefficient of resonant frequency of Al_2O_3–TiO_2 ceramics by annealing treatment. *Japanese Journal of Applied Physics*, **43**, L749–L751.
146. Woode, R.A., Ivanov, E.V., Tobar, M.E., *et al.* (1994) Cryogenic sapphire microwave Resonator–oscillator with exceptional stability. *Electronic Letters*, **30**, 417–419.
147. Kobayashi, Y. (1985) Microwave measurement of dielectric properties of low loss materials by the dielectric rod resonator method. *IEEE Transactions on Microwave Theory and Technology*, **MTT-33**, 586–592.
148. Alford, N.McN., Wang, X., Penn, S.J., *et al.* (2000) Effect of ceramic binders on microwave dielectric loss of alumina. *British Ceramic Transactions*, **99**, 212–214.
149. Braginsky, V.B. and Ilschenko, V.S. (1987) Experimental observation of fundamental microwave absorption in high quality dielectric crystals. *Physics Letters A*, **120**, 300–305.
150. Ikeda, M. and Miura, T. (1998) Measurement of complex dielectric constant above room temperature and its application to determination of intrinsic dielectric loss. *Japanese Journal of Applied Physics*, **37**, 5353–5356.
151. Gurevich, V.I. and Tagantsev, A.K. (1991) Intrinsic dielectric loss in crystals. *Advances in Physics*, **40**, 719–767.

152. Dick, G.J. and Saunders, J. (1990) Measurement and analysis of a microwave oscillator stabilized by a sapphire dielectric ring resonator for ultra-low noise. *IEEE Transactions on Ultrasonics Ferroelectric and Frequency Control*, **37**, 339–346.
153. Tobar, M.E., Krupka, J., Hartnett, J.G., *et al.* (1999) High *Q* sapphire rutile frequency compensated microwave dielectric resonators. *IEEE Transactions on Microwave Theory and Technology*, **MTT-45**, 830–835.
154. Luiten, A.N., Mann, A.G., and Blair, D.G. (1993) Ultra-high *Q* factor cryogenic sapphire resonator. *Electronic Letters*, **29**, 879–881.
155. Tobar, M.E., Giles, A.G., Edwards, S.J., *et al.* (1994) High *Q* TE stabilized sapphire microwave resonators for low noise applications. *IEEE Transactions on Ultrasonics Ferroelectric and Frequency Control*, **41**, 391–396.
156. Woode, R.A., Tobar, M.E., Ivanov, E.N., *et al.* (1996) An ultralow noise microwave oscillator based on a high *Q* liquid nitrogen cooled sapphire resonator. *IEEE Transactions on Microwave Theory and Technology*, **MTT-43**, 936–941.
157. Breeze, J., Penn, S.J., Poole, M., *et al.* (2000) Layered Al_2O_3–TiO_2 composite dielectric resonators. *Electronic Letters*, **36**, 883–884.
158. Alford, N.McN., Breeze, J., Penn, S.J., *et al.* (2000) Layered Al_2O_3–TiO_2 composite dielectric resonators with tuneable temperature coefficient for microwave applications. *IEEE Proceedings of Measurement Science and Technology*, **147**, 269–273.
159. Hartnett, J., Tobar, M.E., Ivanov, E.N., *et al.* (2000) High frequency temperature compensated sapphire/rutile resonator. *Electronic Letters*, **36**, 726–727.
160. Mann, A.G., Giles, A.J., Blair, D.G., *et al.* (1992) Ultra-stable cryogenic dielectric microwave resonators. Mode frequency temperature compensation by residual paramagnetic impurities. *Journal of Physics D*, **5**, 1105–1109.
161. Yuan, L., Wang, H., Lin, H., *et al.* (2014) Effect of MgO/La_2O_3 co-doping on the microstructure, transmittance and microwave dielectric properties of translucent polycrystalline alumina. *Ceramic International*, **40**, 2109–2113.
162. Zhang, K., Yuan, L., Fu, Y., *et al.* (2016) Microwave dielectric properties of Al_2O_3 ceramics co-doped with MgO and Nb_2O_5. *Journal of Materials Science: Materials in Electronics*, in press.
163. Krupka, J., Derzakowski, K., Tobar, M.E., *et al.* (1999) Complex permittivity of some ultralow loss dielectric crystals at cryogenic temperature. *Measurement Science and Technology*, **10**, 387–392.
164. Luiten, A.N., Mann, A.G., and Blair, D.G. (1993) Ultra-high *Q* factor cryogenic sapphire resonator. *Electronic Lett*. **29**, 879-881
165. Hartnett, J. G., Locke, C. R., Ivanov, E. N., *et al.* (2006) Cryogenic sapphire oscillator with exceptionally high long term frequency stability. *Applied Physics Letters*, **89**, 203513–203515.
166. Huang, C.-L., Wang, J.-J., Yen, F.-S., *et al.* (2008) Microwave dielectric properties and sintering behavior of nano scaled ($\alpha + o$)-Al_2O_3 ceramics. *Materials Research Bulletin*, **43**, 1463–1471.
167. Wakino, K., Minai, K., and Tamura, H. (1984) Microwave characteristics of (Zr,Sn)TiO_4 and BaO-PbO-Nd_2O_3-TiO_2 dielectric resonator. *Journal of American Ceramic Society*, **67**, 278–281.
168. Yang, S. and Wu, J.M. (1991) ZrO_2–TiO_2 ceramic humidity sensors. *Journal of Materials Science*, **26**, 631–636.
169. Van Dover, R.B., Schneemeyer, L.F., and Fleming, R.M. (1998) Discovery of a useful thin-film dielectric using a composition-spread approach. *Nature*, **392**, 162–164.
170. Eichler, J.F., Just, O., and Rees, W.S. (2004) The design and synthesis of heterometallic Alkoxide–amides and their application in the MOCVD of zirconium–tin–titanate (ZTT). *Journal of Materials Chemistry*, **14**, 3139–3143.
171. Rath, W. (1941) Keramische Sindermassen fur die Elektronik Fortschritter auf dem Greblet der Keramischen Isollerstoff fur die Electroteknik II. *Keram. Radsch.*, **49**, 137–139.
172. British Patent No. 692468 (1952).
173. Wakino, K., Nishikawa, T., Tamura, S., *et al*. (1975) Microwave band pass filters containing dielectric resonators with improved temperature stability and spurious response, in *Proceedings of the IEEE Microwave Theory and Technology Symposium*, New York, pp. 63–65,

174. Wakino, K., Nishikawa, T., Tamura, S., *et al.* (1978) Miniaturised band pass filters using half wave dielectric resonators with improved spurious response, in *Proceedings of the IEEE MTT Symposium*, pp. 230–132.
175. Wolfram, W. and Gobel, H.E. (1981) Existence range, structural and dielectric properties of $Zr_xTi_ySn_zO_4$ ceramics ($x + y + z = 4$). *Materials Research Bulletin*, **16**, 1455–1463.
176. Tamura, H. (1994) Microwave loss quality of $(Zr_{0.8}Sn_{0.2})TiO_4$. *American Ceramic Society Bulletin*, **73**, 92–95.
177. Bianco, A., Viticoli, M., Gusmano, G., *et al.* (2001) Zirconium tin titanate thin films via aqueous polymeric precursor route. *Materials Science and Engineering C*, **15**, 211–213.
178. Hirano, S., Hayashi, T., and Hattori, A. (1991) Chemical processing and microwave characteristics of (Zr, Sn)TiO_4 microwave dielectrics. *Journal of the American Ceramic Society*, **74**, 1320–1324.
179. Khairulla, F. and Phule, P. (1992) Chemical synthesis and structural evolution of zirconium titanate. *Materials Science and Engineering B*, **12**, 327–336.
180. Leoni, M., Viviani, M., Battilana, G., *et al.* (2001) Aqueous synthesis and sintering of zirconium titanate powders for microwave components. *Journal of European Ceramic Society*, **21**, 1739–1741.
181. Han, K.R., Jang, J.W., and Cho, S.-Y. (1998) Preparation and dielectric properties of low temperature-sinterable $(Zr_{0.8}Sn_{0.2})TiO_4$ powder. *Journal of the American Ceramic Society*, **81**, 1209–1214.
182. Chen, D., Jiao, X., and Zhang, M. (2000) Hydrothermal synthesis and characterization of $(Zr_{1-x}Sn_x)TiO_4$ ($x = 0.05$–0.20) powders. *Materials Research Bulletin*, **35**, 2101–2108.
183. Huang, C.-L., Weng, M.-H. and Chen, H.L. (2001) Effects of additives on microstructures and microwave dielectric properties of (Zr, Sn) TiO_4 ceramics. *Materials Chemistry and Physics*, **71**, 17–22.
184. Huang, C.-L. and Weng, M.-H. (2000) Liquid phase sintering of (Zr, Sn)TiO_4 microwave dielectric ceramics. *Materials Research Bulletin*, **35**, 1881–1888.
185. Huang, C.-L., Weng, M.-H., and Wu, C.C. (2001) Microwave dielectric properties and microstructures of V_2O_5 modified $Zr_{0.8}Sn_{0.2}TiO_4$ ceramics. *Japanese Journal of Applied Physics*, **40**, 698–702.
186. Huang, C.-L. and Weng, M.H. (2001) Liquid phase sintering of (Zr, Sn)TiO_4 microwave dielectric ceramics. *Materials Research Bulletin*, **35**, 1881–1888.
187. Jean, J.-H. and Lin, S.-C. (2000) Low fire processing of ZrO_2–SnO_2–TiO_2 ceramics. *Journal of the American Ceramic Society*, **83**, 1417–1422.
188. Takada, T., Wang, S.F., Yoshikawa, S., *et al.* (1994) Effect of glass additions on BaO–TiO_2–WO_3 microwave ceramics, *Journal of the American Ceramic Society*, **77**, 1909–1916.
189. Takada, T., Wang, S.F., Yoshikawa, S., *et al.* (1994) Effects of glass on (Zr, Sn)TiO_4 for microwave applications. *Journal of the American Ceramic Society*, **77**, 2485–2488.
190. Newnham, R.E. (1967) Crystal structure of $ZrTiO_4$. *Journal of the American Ceramic Society*, **50**, 216.
191. McHale, A.E. and Roth, R. S. (1983) Investigation of the phase transition in $ZrTiO_4$ and $ZrTiO_4$-SnO_2 solid solutions. *Journal of the American Ceramic Society*, **66**, C-18-20;
192. Park, Y. (1995) Influence of order disorder transition on microwave characteristics of tin- modified zirconium titanate. *Journal of Materials Science Letters*, **14**, 873–875.
193. Yamamoto, A., Yamada, T., Ikada, H., *et al.* (1991) Modulated structure of zirconium titanate. *Acta Crystallographica*, **C-47**, 1588–1591.
194. Christerfferson, R. and Davies, P.K. (1992) Structure of commensurate and incommensurate ordered phase in the system $ZrTiO_4$–$Zr_5Ti_7O_{24}$. *Journal of the American Ceramic Society*, **75**, 563–569.
195. Park, Y. and Kim, Y. (1996) Order–disorder transition of tin-modified zirconium titanate. *Materials Research Bulletin*, **31**, 7–15.
196. Ho, Y., Weng, M.-H., Dai, B.-T., and Wang, S.-S. (2005) Nanopowder and microwave dielectric properties of sol–gel derived $Zr_{.8}Sn_{.2}TiO_4$ ceramics. *Japanese Journal of Applied Physics*, **44**, 6152–6155.

197. Azough, F., Freer, R., Wang, C.L., *et al.* (1996) The relationship between the microstrucutre and microwave dielectric properties of zirconium titanate ceramics. *Journal of Materials Science*, **31**, 2539–2549.
198. Kudesia, R., Snyder, R.L., and Condrate, R.A. (1993) Structural study of $Zr_{0.8}Zn_{0.2}TiO_4$. *Journal of Physics and Chemistry of Solids*, **54**, 671.
199. Wersing, W. (1991) High frequency ceramic dielectrics and their applications for microwave components, in: *Electroceramics* (ed. B.C.H. Steele), Elsevier Applied Sciences, pp. 67–119.
200. Azough, F. and Freer, R. (1989) The microstructure and low frequency dielectric properties of some zirconium titanate stannate (ZTS) ceramics. *British Ceramic Society*, **42**, 225–233.
201. Iddles, D.M., Bell, A., and Moulson, A.J. (1992) Relationship between dopants, microstructure and the microwave dielectric properties of ZrO_2–TiO_2–SnO_2 ceramics. *Journal of Materials Science*, **27**, 6303–6310.
202. Michiura, N., Tatekawa, T. Higuchi, Y., and Tamura, H. (1995) Role of donor and acceptor ions in the dielectric loss tangent of $(Zr_{0.8}Sn_{0.2})TiO_4$ dielectric resonator materials. *Journal of American Ceramic Society*, **78**, 793–796.
203. Huang, C.-L., Hsu, C.-S., and Lin, R.–J. (2001) Improved high-*Q* microwave dielectric resonator using ZnO and WO_3-doped $Zr_{0.8}Sn_{0.2}TiO_4$ ceramics. *Materials Research Bulletin*, **36**, 1985–1993.
204. Kim, W.S., Kim, T.H., Kim, E.S., *et al.* (1998) Microwave dielectric properties and far infrared reflectivity spectra of the $(Zr_{0.8}Sn_{0.2})TiO_4$ ceramics with additives. *Japanese Journal of Applied Physics*, **37**, 5367–5371.
205. Ioachin, A., Banau, M.G., Toacsan, M.I., *et al.* (2005) Nickel doped $(Zr_{.8}Sn_{.2})TiO_4$ for microwave and millimeter wave applications. *Materials Science and Enginerring B*, **118**, 205–209.
206. McHale, A.E., Kudesia, R., and Lee, A.H. (1994) In *Proceedings of the Symposium on Electroceramics and Solid State Ionics* (eds H.L. Tuller and D.M. Smythe), The Electrochemical Society.
207. Azough, F. and Freer, R. (1990) Microstructural development and microwave dielectric properties of $ZrTiO_4$ based ceramics, in *Proceedings of the 7th IEEE International Symposium on Applied Ferroelectrics*, Illionois, pp. 198–201.
208. Houivet, D., Fallah, E.E., Lamagenere, B., *et al.* (2001) Effect of annealing on the microwave properties of (Zr, Sn)TiO_4 ceramics. *Journal of European Ceramic Society*, **21**, 1727–1730.
209. Ahn, Y.S., Yoon, K.H., and Kim, E.S. (2003) Effect of cooling rate on loss quality of $(Zr_{0.8}Sn_{0.2})TiO_4$ ceramics with additives. *Journal of European Ceramic Society*, **23**, 2519–2523.
210. Tamura, H. (2006) Microwave dielectric losses caused by lattice defects. *Journal of European Ceramic Society*, **26**, 1775–1780.
211. Yoon, K.H. and Kim, E.S. (1995) Dielectric characteristics of zirconium tin titanate ceramics at microwave frequencies. *Materials Research Bulletin*, **30**, 813–820.
212. Yoon, K.H., Kim, Y.S., and Kim, E.S. (1995) Microwave dielectric properties of $(Zr_{0.8}Sn_{0.2})TiO_4$ ceramics with pentavalent additives. *Journal of Materials Research*, **10**, 2085–2090.
213. Park, J.Y.H., Ryu, J.M, Shin, M.Y., *et al.* (2001) Effect of Nb_2O_5/ZnO addition on microwave properties of $(Zr_{0.8}Sn_{0.2})TiO_4$ ceramics. *Journal of the American Ceramic Society*, **84**, 2542–2546.
214. Houivet, D., Fallah, J.E., and Haussonne, J.M. (1997) Effect of the grinding process on different characteristics of (Zr, Sn)TiO_4 microwave dielectric ceramics. *Key Engineering Materials*, **132–136**, 1199–1202, Trans-Tech publication.
215. Houivet, D., Fallah, J.E., and Haussonne, J.M. (1999) Phases in La_2O_3 and NiO doped (Zr, Sn)TiO_4 microwave dielectric ceramics. *Journal of the European Ceramic Society*, **19**, 1095–1099.
216. Wakino, K. (1990) Ceramic Transactions -8, in *Ceramic Dielectrics, Composition, Processing and Properties* (eds H.C. Ling and M.F. Fan). *American Ceramic Society*, **1**, 305.
217. Alford, N.McN., Penn, S.J., Templeton, A., *et al.* (1998) Materials and processing developments in microwave ceramics, in *Proceedings of the 9th CIMTEC, World Ceramics Congress and Forum on New Materials*, Florence, June 14–19, 1998.

218. Kim, D.-J., Hahn, J.-W., Han, G-P., *et al.* (2000) Effects of alkaline–earth–metal addition on the sinterability and microwave characteristics of (Zr, Sn)TiO_4 dielectrics. *Journal of the American Ceramic Society*, **83**, 1010–1012.
219. Heiao, Y.C.,L. Wu, L., and Wei, C.C. (1988) Microwave dielectric properties of (ZrSn)TiO_4 ceramic. *Materials Research Bulletin*, **23**, 1687–1692.
220. Yoon, J.-R., Kim, K,-Y., and Lee, H.-Y. (1997) In *Proceedings of 5th Intlernational Conference on Properties and Applications of Dielectric Materials*, Seoul, Korea, 960 pp.
221. Yu, H.G., Song, C.X., Shen, Z.H., *et al.* (2005) Dielectric properties of zirconium tin titanate with additives of ZnO, CuO, $MnCO_3$, and Bi_2O_3. *Key Engineering Materials*, **280–283**, 91–94.
222. Pang, L.-X., Zhou, D., Chen, Y.H., and Wang, H. (2011) Structural and microwave dielectric behavior of ($Li_{1/4}Nb_{3/4}$) substituted $Zr_xSn_yTi_2O_4$ ($x + y + z = 2$) system. *Materials Physics and Chemistry*, **125**, 641–645.
223. Pamu, D., Rao, L.N., and Raju, K.C.J. (2011) Enhanced microwave dielectric properties of ($Zr_{0.8}Sn_{0.2}$)TiO_4 ceramics with the addition of its own nanoparticles. *Journal of the American Ceramic Society*, **95**, 126–132.
224. Pamu, D., Rao, L.N., and Raju, K.C.J. (2011) Low temperature processing of ($Zr_{0.8}Sn_{0.2}$)TiO_4 ceramics with improved *Q* factor. *Journal of Alloys and Compounds*, **509**, 9289–9295.
225. Bunting, L.N., Shelton, G.A., and Creamer, A.S. (1947) Properties of barium strontium titanate dielectrics. *Journal of the American Ceramic Society*, **30**, 114–125.
226. Jonker, G.H. and Kwestroo, W. (1958) Ternary systems BaO–TiO_2–SnO_2 and BaO–TiO_2–ZrO_2, *Journal of the American Ceramic Society*, **41**, 390–394.
227. Masse, D.J., Purcel, R.A., Readey, D.W. (1971) New low loss high *k* temperature compensated dielectric for microwave applications. *Proceedings of IEEE*, **59**, 1628–1629.
228. Kirby, K.W. and Wechsler, B.A. (1991) Phase relations in the barium titanate–titanium oxide system. *Journal of the American Ceramic Society*, **74**, 1841–1847
229. Mhaisalker, S.G., Readey, D.W., and Akbar, S.A. (1991) Microwave dielectric properties of doped $BaTi_4O_9$. *Journal of the American Ceramic Society*, **74**, 1894–1898.
230. Mhaisalker, S.G., Readey, D.W., and Akbar, S.A. (1989) Processing and characterization of $BaTi_4O_9$. *Journal of the American Ceramic Society*, **72**, 2154–2158.
231. Weng, M.H., Liang, T.-J., and Huang, C.-L. (2002) Lowering of sintering temperature andmicrowave dielectric proprties of $BaTi_4O_9$ ceramics prepared by the polymeric precursor method. *Journal of European Ceramic Society*, **22**, 1693–1698.
232. Lu, S.G., Kwok, K.W., and Chen, H.L. (2003) Structural and electrical properties of $BaTi_4O_9$ microwave ceramics incorporated with glass phase. *Materials Science and Engineering*, **B99**, 491–494.
233. Choy, J.-H., Han, Y.-S., Kim, J-T., *et al.* (1995) Citrate route to ultrafine barium polytitanates with microwave dielectric properties. *Journal of Materials Chemistry*, **51**, 57–63.
234. Choy, J.H., Han, Y.-S., and Hwang, S.-H., *et al.* (1998) Citrate route to Sn doped $BaTi_4O_9$ with microwave dielectric properties. *Journal of the American Ceramic Society*, **81**, 3197–3204.
235. Lee, M.J., You, B.D., and King, D.S. (1965) Properties of Mn doped $BaTi_4O_9$–ZnO–Ta_2O_5 ceramics. Part 1. Reaction sequence, microstructural analysis and microwave dielectric properties. *Journal of Materials Science: Materials in Electronics*, **6**, 165–172.
236. Nishigaki, S., Yano, S., Kato, H., *et al.* (1988) BaO–TiO_2–WO_3 microwave ceramics and crystalline $BaWO_4$. *Journal of the American Ceramic Society*, **71**, C11–C17.
237. Negas, T., Yeager, G., Bell, S., *et al.* (1993) $BaTi_4O_9$/$Ba_2Ti_9O_{20}$ based ceramics resurrected for modern microwave applications. *American Ceramic Society Bulletin*, **72**, 80–89.
238. Takada, T., Wang, S.F., Yoshikawa, S., *et al*. (1994) Effect of glass additions on BaO–TiO_2–WO_3 microwave ceramics. *Journal of the American Ceramic Society*, **77**, 1909–1916.
239. Mashima, K., Shinohara, M., Kageyama, K., *et al.* (1991) Influence of some oxide addition on dielectric properties of $BaTi_4O_9$. *Huntai Oyobi Hummatsuyakin*, **38**, 735.
240. Ern, V. and Newnham, R.E. (1961) Effect of WO_3 on dielectric properties of $BaTiO_3$ ceramics. *Journal of the American Ceramic Society*, **44**, 199.
241. Yang, C.F. (1999) Microwave characteristics of glass-$BaTi_4O_9$ ceramics. *Japanese Journal of Applied Physics*, **38**, 3576–3579.

242. Cheng, C.-C., Yang, C.-F., Lo, S.-H., *et al.* (2000) Sintering of $BaTi_4O_9/Ba_2Ti_9O_{20}$ based ceramics by glass addition. *Journal of European Ceramic Society*, **20**, 1061–1067.
243. Panlener, R.J. and Blumenthal, R.W. (1971) Ti rich nonstoichiometric $BaTiO_3$–III. High temperature thermodynamic and X-ray diffraction measurements. *Journal of the American Ceramic Society*, **54**, 610–614.
244. Burn, I. (1979) Mn-doped polycrystalline $BaTiO_3$. *Journal of Materials Science*, **14**, 2453–2458.
245. Monneraye, M. (1968) The control of dielectric losses and temperature coefficient of permitivitty by doping in some glass-ceramic materials. *Journal of Serindat and C. Jouwersma, Glass Technology*, **9**, 70–77.
246. Nomura, S., Tomoya, K., and Kaneta, K. (1983) Effect of Mn doping on the dielectric properties of $Ba_2Ti_9O_{20}$ ceramics at microwave frequency. *Japanese Journal of Applied Physics*, **22**, 1125–1128.
247. Fukuda, K., Kitoh, R., and Awai, I. (1995) Microwave characteristics of mixed phases of $BaTi_4O_9$–$BaPr_2Ti_4O_{12}$ ceramics. *Journal of Materials Science*, **30**, 1209–1216.
248. Negas, T., Yeager, G., Bell, S., *et al.* (1991) Chemistry and properties of temperature compensated microwave dielectrics. National Institute of Standards (USA), Special Publication No. 804, p. 21.
249. Negas, T., Roth, R.S., Parker, H.S., *et al.* (1974) Subsolidus phase relations in the $BaTiO_3$–TiO_2 system. *Journal of Solid State Chemistry*, **9**, 297–307.
250. Fukui, T., Sakurai, C., and Okayama, M. (1992) Effects of heating rate on sintering of alkoxide derived $BaTi_5O_{11}$ powder. *Journal of Materials Research*, **7**, 192–196.
251. Javadpour, J. and Eror, N.G. (1988) Raman spectroscopy of higher titanate phases in the $BaTiO_3$–TiO_2 system. *Journal of the American Ceramic Society*, **71**, 206–213.
252. Hirano, S. and Otsuka, J. (1989) Sol–gel processing and properties of $BaTi_5O_{11}$ microwave dielectrics. Annual Meeting of American Ceramic Society, Indianopolis, IN.
253. Lu, H.-C., Burkhart, L.E., and Schrader, G.L. (1991) Sol–gel process for the preparation of $Ba_2Ti_9O_{20}$ and $BaTi_5O_{11}$. *Journal of the American Ceramic Society*, **74**, 968–972.
254. Hirano, S., Hayashi, T., Kikuta, K., and Otsuka, J. (1990) Chemical processing and properties of $BaTi_5O_{11}$ microwave dielectrics. *Ceramic Transactions*, **12**, 733–740.
255. Hennings, D. and Schnabel, P. (1983) Dielectric characterisation of $Ba_2Ti_9O_{20}$ type ceramics at microwave frequencies. *Philips Research Journal*, **38**, 295–311.
256. Lin, W.-Y., Speyer, R.F., Hackenberger, W.S., *et al.* (1999) Microwave properties of $Ba_2Ti_9O_{20}$ doped with zirconium and tin oxide. *Journal of the American Ceramic Society*, **82**, 1207–1211.
257. Wang, S.F., Hsu, Y.F., Weng, T.-H., *et al.* (2003) Effects of additives on the microstructure and dielectric properties of $Ba_2Ti_9O_{20}$ microwave ceramics. *Journal of Materials Research*, **18**, 1179–1187.
258. Wu, J.-M. and Wang, H.-W. (1988) Factors affecting the formation of $Ba_2Ti_9O_{20}$. *Journal of the American Ceramic Society*, **71**, 869–875.
259. Teoreanu, I., Andronescu, E., and Folea, A. (1996) Microwave processing of $Ba_2Ti_9O_{20}$ ceramic. *Ceramic International*, **22**, 305–307.
260. Gormikov, Y.I., Makarova, Z.Y., Belous, A.G., *et al.* (1984) Effect of zinc oxide additions on the phase compositions and dielectric properties of barium tetratitanate. *Soviet Progress in Chemistry*, **50**, 1243.
261. Chu, L.W., Hsiue, G.-H., Chiang, Y.-J., *et al.* (2004) Ultrafine $Ba_2Ti_9O_{20}$ microwave dielectric materials synthesized by chemical process. *Journal of European Ceramic Society*, **24**, 1781–1785.
262. Wang, H.W. and Chung, M.-R. (2002) Formation of $Ba_2Ti_9O_{20}$ ceramics from EDTA gel derived powders. *Materials Chemistry and Physics*, **77**, 853–859.
263. Chu, L.-W., Hsiue, G.-H., Chiang, Y.-J., *et al.* (2005) Ultrafine $Ba_2Ti_9O_{20}$ powders synthesized by inverse microemulsion processing and their microwave dielectric properties. *Journal of the American Ceramic Society*, **88**, 3405–3411.
264. Huang, J.R., Xiong, Z.X., Fang, C., *et al.* (2003) Hydrothermal synthesis of $Ba_2Ti_9O_{20}$ nanopowder for microwave ceramics. *Materials Science and Engineering B*, **99**, 226–229.

265. O'Bryan, H.M., Thomson Jr, J., and Plourde, J.K. (1974) A new $BaO–TiO_2$ compound with temperature-stable high permittivity and low microwave loss. *Journal of the American Ceramic Society*, **57**, 450–453.
266. Fang, R.-T., Shiue, J.-J., and Liou, S.-C. (2002) Formation mechanism and sintering behaviour of $Ba_2Ti_9O_{20}$. *Journal of European Ceramic Society*, **22**, 79–85.
267. Varma, M.R., Sreemoolanathan, H., and Chandrasekharan, V. (2004) Effect of different raw materials on the microwave dielectric properties of $Ba_2Ti_9O_{20}$ ceramics. *Journal of Materials Science: Materials in Electronics*, **15**, 345–349.
268. Lin, W.-Y. and Speyer, R.F. (1999) Dielectric properties of microstructure controlled $Ba_2Ti_9O_{20}$ resonators. *Journal of the American Ceramic Society*, **82**, 325–330.
269. Jaakola, T., Mottonan, J., Uusimaki, A., Rautioaho, R., and Leppavuori, S. (1987) Preparation of Nd doped $Ba_2Ti_9O_{20}$ ceramics for use in microwave applications. *Ceramic International* **13**, 151–157.
270. Wu, S., Wang, G., Zhao, Y., and Su, H. (2003) $BaO–TiO_2$ microwave ceramics. *Journal of European Ceramic Society*, **23**, 2565–2568.
271. Wang, S.-F., Yang, T.C.K., Chiang, C.-C., *et al.* (2003) Effects of additives on the phase formation and microstructural evolution of $Ba_2Ti_9O_{20}$ microwave ceramic. *Ceramic International*, **29**, 77–81.
272. Lin, W., Gerhardt, R., and Speyer, R. (1999) Thermal processing and properties of $BaTi_4O_9$ and $Ba_2Ti_9O_{20}$ dielectric resonators. *Journal of Materials Science*, **34**, 3021–3025.
273. Huang, W., Liu, K.-S., Chu, L.-W., *et al.* (2003) Microwave dielectric properties of LTCC materials consisting of glass-$Ba_2Ti_9O_{20}$ composites. *Journal of European Ceramic Society*, **23**, 2559–2563.
274. O'Bryan, H.M., Thomson Jr, J., and Plourde, J.K. (1978) Effects of chemical treatment on loss quality of microwave dielectric ceramics. *Ber. Dt. Keramik Ges.*, **55**, 348–351.
275. Lin, W.-Y., Gerhardt, R.A., Speyer, R.F., *et al.* (1999) Thermal processing and properties of $BaTi_4O_9$ and $Ba_2Ti_9O_{20}$ dielectric resonators. *Journal of Materials Science*, **34**, 3021–3025.
276. Yoon, KH., Kim, J.B. and Kim, E.S. (1996) Effect of $BaSnO_3$ on the microwave dielectric properties of $Ba_2Ti_9O_{20}$. *Journal of Materials Research*, **11**, 1996–2001.
277. O'Bryan, H. M., Plourde, J.K., and Thomson, J. (1986) Dielectric for microwave applications. US Patent No. 4563 661.
278. Nomura, S., Kaneta, K., Kuwata, J., *et al.* (1981) Piezoelectric ceramics of the $PbTiO_3–La(Me_{2/3}Nb_{1/3})O_3$ (Me = Mg, Zn) solid solution system. *Ferroelectrics*, **37**, 587–590.
279. Srivastava, G.P., Srivastava, M., Tyagi, G.S., *et al.* (1996) Studies on Mn doped barium nanotitanate dielectric resonators. *Journal of Materials Science Letters*, **15**, 1134–1136.
280. O'Bryan, H.M.O. (1987) Identification of surface phases on $BaTiO_3–TiO_2$ ceramics. *American Ceramic Society Bulletin*, **66**, 677–680.
281. Lee, M.J., Kim, C.Y., You, B.D., *et al*. (1995) Properties of Mn doped $BaTi_4O_9–ZnO–Ta_2O_5$ ceramics. Part II. Defect chemical relations. *Journal of Materials Science: Materials in Electronics*, **6**, 173–177.
282. Zhou, F., Liu, X., Wang, H., *et al.* (2013) Phase stability, low temperature cofiring and microwave dielectric properties of $BaTi_5O_{11}$ ceramics with $BaCu(B_2O_5)$ addition. *Journal of Materials Science: Materials in Electronics*, 2013, **24**, 299–304.
283. Huang, C.-L., M.-H., Lion, C.-T., *et al.* (2000) Low temperature sintering and microwave dielectric properties of $Ba_2Ti_9O_{20}$ ceramics using glass additions. *Materials Research Bulletin*, **35**, 2445–2456.
284. Kawashima, S., Nishida, M., Ueda, I., and Ouchi, H. (1983) $Ba(Zn_{1/3}Ta_{2/3})O_3$ ceramics with low dielectric loss at microwave-frequencies. *Journal of the American Ceramic Society*, **66** (6), 241–243.
285. Matsumoto, K., Hiuga, T., Takada K., and Ichimura, H. (1986) $Ba(M_{1/3}Ta_{2/3})O_3$ ceramics with ultra-low loss at microwave-frequencies, in *IEEE Conference Proceedings: Sixth IEEE International Symposium on Applications of Ferroelectrics*, **1986**, 118–121.
286. Cunningham, L.D. (2002) Columbium (niobium) and tantalum. *US Geological Survey Minerals Year Book 2002*. Available at: http://minerals.usgs.gov/minerals/pubs/commodity/niobium/niobimyb02r.pdf.

287. Nomura, S. (1983) Ceramics for microwave dielectric resonators. *Ferroelectrics*, **49**, 61–70.
288. Niobium (Columbium) and Tantalum Statistics and Information (1996–2008) *US Geological Survey*. Available at: http://minerals.usgs.gov/minerals/pubs/commodity/niobium/#pubs.
289. Pullar, R.C. (2009) The synthesis, properties and applications of columbite niobates ($M^{2+}Nb_2O_6$): a critical review. *Journal of the American Ceramic Society*, **92**, 563–577.
290. Repelin, Y., Husson, E., and Brusset, H. (1979) Etude par spectroscopies d'absorption i.r. et de diffusion Raman des composes $A^{II}B_2O_6$ de structure de type "blocs 1×2" – I. Etude du niobate de baryum $BaNb_2O_6$. *Spectrochimica Acta*, **35**, 937–948.
291. Dudhe, C.M., Nagdeote, S.B., and Palikundwar, U.A. (2016) Synthesis and characterization of a novel alkaline earth niobate $Ca_{0.5}Sr_{0.5}Nb_2O_6$. *Journal of Alloys and Compounds*, **658**, 55–60.
292. Lee, H.-J., Kim, I.-T., and Hong, K.-S. (1997) Dielectric properties of AB_2O_6 compounds at microwave frequencies (A = Ca, Mg, Mn, Co, Ni, Zn and B = Nb, Ta). *Japanese Journal of Applied Physics Part 2*, **36** (10A), L318–320.
293. Sreedhar, K. and Mitra, A. (1997) Formation of lead magnesium niobate perovskite from $MgNb_2O_6$ and $Pb_3Nb_2O_8$ precursors. *Materials Research Bulletin*, **32**, 1643–1649.
294. Hong, Y.-S., Park, H.-B., and Kim, S.-J. (1998) Preparation of $Pb(Mg_{1/3}Nb_{2/3})O_3$ powder using a citrate-gel derived columbite $MgNb_2O_6$ precursor and its dielectric properties. *Journal of the European Ceramic Society*, **18**, 613–619.
295. Sturdivant, J.H. (1930) The crystal structure of columbite. *Zeitschrift fur Kristallographie*, **75**, 88–105.
296. Maeda, M., Yamamura, T., and Ikeda, T. (1987) Dielectric characteristics of several complex oxide ceramics at microwave frequencies. *Japanese Journal of Applied Physics Part 1 – Supplemental*, **26-2**, 76–79.
297. Wahlstrom, E. and Marinder, B.-O. (1977) Phase analysis studies in the copper–niobium–oxygen system. *Inorganic and Nuclear Chemistry Letters*, **13**, 559–564.
298. Langbein, H., Bremer, M., and Krabbes, I. (1997) CuX_2O_6 and $BacuX_2O_9$ (X = Nb, Ta): influence of the preparation conditions on phase formation and phase composition. *Solid State Ionics*, **101–103** (1), 579–584.
299. Kodama, K., Harashina, H., Sasaki, S., *et al.* (1999) Magnetic excitations of $CuNb_2O_6$. *Journal of Physics and Chemistry of Solids*, **60** (8–9), 1129–1132.
300. Lee, H.-J., Hong, K.-S., Kim, S.-J., and Kim, I.-T. (1997) Dielectric properties of MNb_2O_6 compounds (where M = Ca, Mn, Co, Ni or Zn). *Materials Research Bulletin*, **32** (7), 847–855.
301. Pullar, R.C., Breeze, J.D., and Alford, N.M. (2005) Characterization and microwave dielectric properties of $M^{2+}Nb_2O_6$ ceramics. *Journal of the American Ceramic Society*, **88**, 2466–2471.
302. Martinez-de la Cruz, A., Lopez Alcaraz, N., Fuentes, A.F., and Torres-Martınez, L.M. (1999) Electrochemical lithium insertion in some niobates MNb_2O_6 (M = Mn, Co, Ni, Cu, Zn and Cd). *Journal of Power Sources*, **81–82**, 255–258.
303. Zhang, Y.C., Fua, B.J., and Liu, Q. (2009) Preparation of $CuNb_2O_6$ nanocrystalline powders by sol–gel method. *Journal of Alloys and Compounds*, **477**, 716–719.
304. Kim, N.-K. (1997) Synthesis chemistry of $MgNb_2O_6$ and $Pb(Mg_{1/3}Nb_{2/3})O_3$. *Materials Letters*, **32**, 127–130.
305. Ananta, S., Brydson, R., and Thomas, N.W. (1999) Synthesis, formation and characterisation of $MgNb_2O_6$ powder in a columbite-like phase. *Journal of the European Ceramic Society*, **19**, 355–362.
306. Ananta, S. (2004) Phase and morphology of magnesium niobate powders synthesized by solid state reaction. *Materials Letters*, **58**, 2781–2786.
307. Belous, A., Ovchar, O., Jancar, B., and Bezjak, J. (2007) The effect of non-stoichiometry on the microstructure and microwave dielectric properties of the columbites $A^{2+}Nb_2O_6$. *Journal of the European Ceramic Society*, **27**, 2933–2936.
308. Belous, A.G., Ovchar, O.V., Kramarenko, A.V., *et al.* (2006) Effect of nonstoichiometry on the structure and microwave dielectric properties of cobalt metaniobate. *Inorganic Materials*, **42**, 1369–1373.
309. Khamman, O., Yimnirun, R., and Ananta, S. (2007) Effect of calcination conditions on phase formation and particle size of nickel niobate powders synthesized by solid-state reaction. *Materials Letters*, **61**, 639–643.

310. Garcıa-Alvarado, F., Orera, A., Canales-Vazquez, J., and Irvine, J.T.S. (2006) On the electrical properties of synthetic manganocolumbite $MnNb_2O_{6-\delta}$. *Chemistry of Materials*, **18**, 3827–3834.
311. Yu, Y., Feng, C., Li, C., *et al.* (2001) Formation of columbite-type precursors in the mixture of MgO–Fe_2O_3–Nb_2O_5 and the effects on fabrication of perovskites. *Materials Letters*, **51**, 490–499.
312. Langbein, H. and Wolki, G. (1995) Preparation of copper niobates by thermal decomposition of freeze-dried complex oxalate solutions. *Thermochimica Acta*, **264**, 67–73.
313. Barzegar Bafrooei, H., Taheri Nassaj, E., Ebadzadeh, T., and Hu, C.F. (2014) A comparative study of $ZnNb_2O_6$ nanoceramics synthesized by high energy ball milling and subsequent conventional and microwave annealing. *Journal of Materials Science: Materials for Electronics*, **25**, 1770–1777.
314. Kong, L.B., Ma, J., Huang, H., and Zhang, R.F. (2002) Crystallization of magnesium niobate from mechanochemically derived amorphous phase. *Journal of Alloys and Compounds*, **340**, L1–L4.
315. Davaadorj, B.-E., Jeon, H., and Lee, J. (2012) Mechanochemical synthesis of manganocolumbite ($MnNb_2O_6$) from manganese (II) oxide and niobium pentoxide. *Journal of Alloys and Compounds*, **527**, 122–126.
316. Guo, L., Dai, J., Tian, J., and He, T. (2008) Synthesis of $ZnNb_2O_6$ powder with rod-like particle morphologies. *Ceramics International*, **34**, 1783–1785.
317. Shanker, V. and Ganguli, A.K. (2003) Comparative study of dielectric properties of $MgNb_2O_6$ prepared by molten salt and ceramic method. *Bulletin of Materials Science*, **26** (7), 741–744.
318. Liou, Y.-C., Shiue, C.-Y., and Weng, M.-H. (2008) Synthesis and properties of TiO_2 added $NiNb_2O_6$ microwave dielectric ceramics using a simple process. *Journal of the European Ceramic Society*, **29** (6), 1165–1171.
319. Mulla, I.S., Natarajan, N., Gaikwad, A.B., *et al.* (2007) A coprecipitation technique to prepare $CoTa_2O_6$ and $CoNb_2O_6$. *Materials Letters*, **61**, 2127–2129.
320. Balamurugan, C., Maheswari, A.R., and Lee, D.-W. (2014) Structural, optical, and selective ethanol sensing properties of p-type semiconducting $CoNb_2O_6$ nanopowder. *Sensors and Actuators B*, **205**, 289–297.
321. Srisombat, L., Ananta, S., and Phanichphant, S. (2004) Chemical synthesis of magnesium niobate powders. *Materials Letters*, **58**, 853–858.
322. Ravi, V. and Navale, S.C. (2006) A co-precipitation technique to prepare $CaNb_2O_6$. *Ceramics International*, **32** (4), 475–477.
323. Zhou, Y., Lu, M., Qiu, Z., *et al.* (2007) Photoluminescence of $NiNb_2O_6$ nanoparticles prepared by combustion method. *Materials Science and Engineering B*, **140**, 128–131.
324. Wu, W., Liang, S., and Ding, Z. (2011) A new approach to the preparation of microcrystalline $ZnNb_2O_6$ photocatalysts via a water-soluble niobium–citrate–peroxo compound. *Solid State Sciences*, **13**, 2019–2023.
325. Cho, I.-S., Bae, S.T., Yim, D.K., *et al.* (2009) Preparation, characterization, and photocatalytic properties of $CaNb_2O_6$ nanoparticles. *Journal of the American Ceramic Society*, **92** (2), 506–510.
326. Sun, D., Senz, S., and Hesse, D. (2003) Topotaxial formation of $Mg_4Nb_2O_9$ and $MgNb_2O_6$ thin films on MgO (001) single crystals by vapor–solid reaction. *Journal of the American Ceramic Society*, **86** (6), 1049–1051.
327. Ho, Y.-D., Chen, K.-R., and Huang, C.-L. (2013) Sol–gel-derived amorphous-$MgNb_2O_6$ thin films for transparent microelectronics. *Journal of the American Ceramic Society*, **96** (11), 3375–3378.
328. Hsu, C.-H. and Yan, S.-F. (2011) Fabrication and characterization of $ZnNb_2O_6$ thin films using sol–gel method. *Journal of the American Ceramic Society*, **94** (3), 822–826.
329. Greenblatt, M., Wanklyn, B.M., and Garrard, B.J. (1982) Flux growth of MNb_2O_6 (M = Mg, Zn, Ba) single crystals. *Journal of Crystal Growth*, **58** (2), 463–464.
330. Prabhakaran, D., Wondre, F.R., and Boothroyd, A.T. (2003) Preparation of large single crystals of ANb_2O_6 (A = Ni, Co, Fe, Mn) by the floating-zone method. *Journal of Crystal Growth*, **250**, 72–76.

331. Ballman, A.A. (1965) Growth of piezoelectric and ferroelectric materials by the CzochraIski technique. *Journal of the American Ceramic Society*, **48**, 112–113.
332. de Almeida Silva, R., de Camargo, A.S.S., Cusat, C., *et al.* (2004) Growth and characterization of columbite $CaNb_2O_6$ high quality single crystal fiber. *Journal of Crystal Growth*, **262**, 246–250.
333. Lei, S., Guo, D., Wang, C., *et al.* (2014) Preparation and magnetic and microwave absorption properties of $MnNb_2O_6$ ellipsoid-like hierarchical structures. *Crystal Engineering Communications*, **16**, 7949–7955.
334. Lei, S., Wang, W., Guo, D., *et al.* (2014) Synthesis and magnetic properties of MNb_2O_6 (M = Fe, Co, Ni) nanoparticles. *RSC Advances*, **4**, 52740–52748.
335. Hirano, M. and Okamoto, T. (2015) Synthesis, morphology, and luminescence of $ZnNb_2O_6$ nanocrystals by hydrothermal method. *Nano-Structures and Nano-Objects*, available online 8 December 2015 at http://dxdoi.org.10.1016/j.nanoso.2015.11.001.
336. Huang, X., Jing, Y., and Yang, J. (2014) Flower-like nanostructure MNb_2O_6 (M = Mn, Zn) with high surface area: hydrothermal synthesis and enhanced photocatalytic performance. *Materials Research Bulletin*, **51**, 271–276.
337. Ma, R., Cao, F., Wang, J., *et al.* (2011) Hydrothermal synthesis and phase stability of $CoNb_2O_6$ with a rutile structure. *Materials Letters*, **65**, 2880–2882.
338. Zhang, Y., Liu, C., and Pang, G. (2010) Hydrothermal synthesis of a $CaNb_2O_6$ hierarchical micro/nanostructure and its enhanced photocatalytic activity. *European Journal of Inorganic Chemistry*, **2010**, 1275–1282.
339. Hu, W., Cui, Z., and Mi, Y. (2012) 3-D $MnNb_2O_6$ nanogears from 1-D Nb_2O_5 nanorods. *Materials Chemistry and Physics*, **133**, 599–604.
340. Pullar, R.C., Breeze, J.D., and Alford, N.M. (2002) Microwave dielectric properties of columbite-structure niobate ceramics, $M^{2+}Nb_2O_6$. *Key Engineering Materials*, **224-6**, 1–4.
341. Templeton, A., Wang, X., Penn, S.J., *et al.* (2000) Microwave dielectric loss of titanium dioxide. *Journal of the American Ceramic Society*, **83** (1), 95–100.
342. Pullar, R.C., Penn, S.J., Wang, X., *et al.* (2009) Dielectric loss caused by oxygen deficiency in titania ceramics. *Journal of the European Ceramic Society*, **29**, 419–424.
343. Butee, S., Kulkarni, A., Prakash, O., *et al.* (2009) High *Q* microwave dielectric ceramics in $(Ni_{1-x}Zn_x)Nb_2O_6$ system. *Journal of the American Ceramic Society*, **92** (5), 1047–1053.
344. Jawahar, N., Sebastian, M.T., Binoy, G.S., and Mohanan, P. (2000) A novel method for tuning the microwave dielectric properties by stacked dielectric resonators. *Proceedings of APSYM 2000*, 173–175.
345. Shahgholin, N., Asadian, K., and Ebadzadeh, T. (2014) Microstructural and microwave dielectric properties of $ZnNb_2O_6$ ceramics prepared through microwave sintering. *Ceramics International*, **40**, 14335–14339.
346. Tzou, W.-C., Chen, Y.-C., Yang, C.-F., and Cheng, C.-M. (2006) Microwave dielectric characteristics of $Mg(Ta_{1-x}Nb_x)_2O_6$ ceramics. *Materials Research Bulletin*, **41**, 1357–1363.
347. Wu, H.T., Jiang, Y.S., Wu, W.B., *et al.* (2012) Synthesis and microwave dielectric properties of columbite-structure $MgNb_2O_6$ ceramics by aqueous sol–gel technique. *Journal of Electroceramics*, **28**, 191–196.
348. Khalam, L.A., Thomas, S., and Sebastian, M.T. (2007) Tailoring the microwave dielectric properties of $MgNb_2O_6$ and $Mg_4Nb_2O_9$ ceramics. *International Journal of Applied Ceramic Technology*, **4** (4), 359–366.
349. Kim, E.S. and Kim, S.J. (2009) Effect of sintering temperature on the microwave dielectric properties of MgB_2O_6 (B = Nb^{5+}, Ta^{5+}) ceramics. *Ferroelectrics*, **388** (1), 93–100.
350. Chen, Y.-C., Weng, M.-Z., and Chang, K.-C. (2014) Effect of sintering temperature and time on microwave dielectric properties of $CaNb_2O_6$ ceramics. *Journal of Materials Science: Materials for Electronics*, **25**, 844–851.
351. Akbas, M.A. and Davies, P.K. (1998) Ordering-induced microstructures and microwave dielectric properties of the $Ba(Mg_{1/3}Nb_{2/3})O_3$–$BaZrO_3$ system. *Journal of the American Ceramic Society*, **81** (3), 670–676.

352. Kim, I.-T., Hong, K.-S., and Yoon, S.-J. (1995) Effect of nonstoichiometry and chemical inhomogeneity on the order–disorder phase formation in the complex perovskite compounds, $Ba(Ni_{1/3}Nb_{2/3})O_3$ and $Ba(Zn_{1/3}Nb_{2/3})O_3$. *Journal of Materials Science*, **30** (2), 514–521.
353. Kageyama, K. (1992) Crystal-structure and microwave dielectric properties of $Ba(Zn_{1/3}Ta_{2/3})O_3$–$(Sr,Ba)(Ga_{1/2}Ta_{1/2})O_3$ ceramics. *Journal of the American Ceramic Society*, **75** (7), 1767–1771.
354. Colla, E.L., Reaney, I.M., and Setter, N. (1992) The temperature coefficient of the relative permittivity of complex perovskites and its relation to structural transformations. *Ferroelectrics*, **133**, 217–222.
355. Ogawa, H., Kan, A., Ishihara, S., and Higashida, Y. (2003) Crystal structure of corundum type $Mg_4(Nb_{2-x}Ta_x)O_9$ microwave dielectric ceramics with low dielectric loss. *Journal of the European Ceramic Society*, **23**, 2485–2488.
356. Zhang, Y.C., Wang, J., Yue, Z.X., *et al.* (2004) Effects of Mg^{2+} substitution on microstructure and microwave dielectric properties of $(Zn_{1-x}Mg_x)Nb_2O_6$ ceramics. *Ceramics International*, **30**, 87–91.
357. Zhang, Y.C., Yue, Z.X., Qi, X., *et al.* (2004) Microwave dielectric properties of $Zn(Nb_{1-x}Ta_x)_2O_6$ ceramics. *Materials Letters*, **58**, 1392–1395.
358. Fu, B., Zhang, Y. and Yue, H. (2013) Microwave dielectric properties of $(1 - x)ZnTa_2O_6$–$xMgNb_2O_6$ ceramics. *Ceramics International*, **39**, 3789–3793.
359. Riazikhoei,P., Azough, F., and Freer, R. (2006) The influence of $ZnNb_2O_6$ on the microwave dielectric properties of $ZrTiO_6$ ceramics. *Journal of American Ceramic Society*, **89**, 216–223.
360. Kim, D.-W., Kim, D.-Y., and Hong, K.S. (2000) Phase relations and microwave dielectric properties of $ZnNb_2O6$-TiO_2. *Journal of Materials Research*, **15**, 1331–1335.

7

Microwave Dielectric Properties of Glasses and Bulk Glass Ceramics

Martin Letz
SCHOTT AG, Research and Technology Development, Mainz, Germany

7.1 Glasses

The reason why glasses and glass ceramics are considered for microwave applications are that glasses have in comparison to polymers improved thermal properties and in comparison to ceramics improved material homogeneity. These advantages of glasses are usually accompanied by larger dielectric losses and a limited range of dielectric constants that is available to glasses. Glass ceramic systems can combine the advantages of glasses with an increased range of dielectric constants and reduced losses. Typical glasses and glass ceramics for application in microwave electronics are derived from optic glass production. This means that 3d transition elements, which usually lead to optic absorption in the visible range of the spectrum, are reduced in such glasses to a very small level of a few ppm (parts per million). Since among such 3d transition elements magnetic impurities like iron, manganese, or nickel are also present, the level of magnetic impurities in such glasses and glass ceramics can be very low. Such a low level of magnetic impurities leads to a low level of material non-linearities (intermodulation), which makes these material classes applicable at high field strength in, for example, base station antennas and filter elements. Glasses are usually obtained using a melting process and are systems out of thermodynamic equilibrium, which are produced via supercooling a liquid. Under fast enough cooling rates the static structure of the liquid is mainly preserved while the dynamic is frozen. The system loses ergodicity, which means that a particle is caught in the cage provided by its nearest neighbors and cannot escape from there. Due to its thermal history glasses have a high degree of structural disorder, which leads to an increase in phonon scattering and a decrease in phonon

Microwave Materials and Applications, First Edition.
Edited by Mailadil T. Sebastian, Rick Ubic and Heli Jantunen.
© 2017 John Wiley & Sons, Ltd. Published 2017 by John Wiley & Sons, Ltd.

lifetime. Since phonon–phonon scattering processes are a dominant loss mechanism in the GHz spectral range, glasses are in principal expected to have a higher dielectric loss compared to ceramics or single crystals with the same composition. On the other hand, glasses can be made with excellent homogeneity, which becomes increasingly advantageous when designs in microwave electronics become more sophisticated, when narrowband applications like global navigation systems, GNS, need to target specific frequency bands with high accuracy, or when frequencies increase leading to smaller structures.

When optic glasses are manufactured the material homogeneity is probed by measuring the refractive index n in the visible range of the spectrum. A homogeneity of lens blanks of 30 cm diameter of the order of $\Delta n/n < 10^{-5}$ is a standard quality. Since the refractive index is related to the dielectric constant as

$$\varepsilon_r = n^2 \tag{7.1}$$

the homogeneity measured in the visible range is a good measure for the homogeneity of the dielectric properties, even if optical frequencies are on the high-frequency site of the infrared absorptions in materials and are three orders of magnitude larger than frequencies of typical electronic applications in GHz. The temperature coefficient of an eigenresonance in a material, τ_f, is related to the linear thermal expansion, α_L, and the temperature coefficient of the dielectric constant

$$\tau_\varepsilon = \frac{1}{T}\frac{\mathrm{d}\varepsilon}{\mathrm{d}T}$$

The linear thermal expansion is

$$\alpha_L = \frac{1}{L}\frac{\mathrm{d}L}{\mathrm{d}T} = \frac{1}{3}\frac{1}{V}\frac{\mathrm{d}V}{\mathrm{d}T} = \frac{1}{3}\alpha_V \tag{7.2}$$

where L is the length of a sample, V the volume, and α_L and α_V are linear and volume thermal expansion of the material, respectively. The τ_f is approximately given as

$$\tau_f \sim -\frac{1}{2}\tau_\varepsilon - \alpha_L \tag{7.3}$$

a relation that becomes exact if one considers eigenresonances in a plate with infinite lateral dimensions. However, in standard Hakki–Coleman experiments, which use eigenresonances of cylindrical samples, Equation (7.3) can also be applied. Oxide glasses have in general a small thermal expansion in the order of –1 ppm/K $< \alpha_L <$ 10 ppm/K, which often results in negative τ_f values.

7.1.1 Silica Glass, a Special Glass System

The major exception to the rule that a disordered structure like a glass always has a relatively high dielectric loss and therefore a low Q value is pure quartz glass, SiO_2, which contains only two types of atoms, Si and O. It can be produced by melting or fusing natural quartz crystals, which gives it the name fused silica. Higher qualities are available mostly for deep UV optics in the range of 193 nm wavelength where the quartz glass is obtained in extreme high purity from the gas phase. For all microwave applications the standard quality should be good enough. Typical brand names of high-purity silica glass are HPFS (Corning) or Suprasil, Infrasil, and Spectrosil (Haereus). In Table 7.1 the properties of quartz glass are shown. The particular quality, especially the highest quality grades that are made for

Table 7.1 *The Haereus data of fused silica according to reference [1] at 30 GHz.*

Material	T_g [°C]	ε_r	tan δ	Q	Qf [GHz]	τ_f [ppm/K]	Reference
Fused silica	1200	3.81	4×10^{-4}	2500	75 000	–15	[1]

deep ultraviolet optic applications, are not needed in microwave applications. Some of the synthetic quartz glasses have a content of a few parts per million (ppm) of residual water, which might affect the microwave loss.

7.1.2 Multicomponent Glasses

Glass forming occurs in a large number of composition ranges, mostly in oxide systems. A key to leave thermodynamic equilibrium and solidify in an amorphous structure is disorder of composition. Therefore increasing the number of different chemical components very often increases the probability to find stable glasses. For this reason a large number of multicomponent glasses exist. The largest variety of such glasses was developed for the optic industry. Here color compensation for achromatic and apochromatic lens systems was the driver for the large variety of existing glass systems together with the search for high refractive index glasses. Most often glasses that have a high refractive index in the optic range of the spectrum will also have a high dielectric constant, since the atomic polarizability affects both frequency ranges, the optic range of several THz and the electronic GHz frequency range. The dielectric constants of glasses are in the range between $3.6 < \varepsilon_r < 21$. Therefore glasses span a wide range of dielectric constants, which is in general larger than that of polymers. However, glasses do not reach the very high dielectric constant ranges above 20 that many ceramic phases have. Glasses containing silicate and borate usually have low thermal expansion, α_L, of the order of 2 ppm/K $< \alpha_L <$ 10 ppm/K. Together with the weak temperature dependence of the dielectric constant of glasses this often results according to Equation (7.3) in slightly negative temperature coefficients τ_f or temperature coefficients that are close to zero [2]. These small temperature coefficients are a clear advantage of glasses over polymers, which in general have a much larger thermal expansion. A number of glasses that are used for electronic applications are adjusted with their thermal expansion to the thermal expansion of silicon, which is $\alpha_{silicon} = 3.6$ ppm/K. These glasses are often bonded or co-processed within semiconductor processes. Typical glasses with this property are borofloat 33 (BF33) with $\alpha_{BF33} = 3.3$ ppm/K and AF32eco with $\alpha_{AF32} = 3.2$ ppm/K. The production of glasses via highly homogeneous melting processes can lead to very good homogeneity and reproducibility. Optic glasses are often produced with a variation of the refractive index $\Delta n/n < 10^{-5}$ over lens blanks with a 30 cm diameter. Such a high homogeneity and reproducibility is a clear advantage over ceramic processes. Glasses are isotropic and can have surface roughness in the nanometer range, even without polishing. Such a smooth surface gives well-defined boundary conditions for the electrical field if a metallization is applied. Metallization can be made by sputtering, vapor deposition, screen printing, or galvanic processes. The chemical and thermal stability of glasses is in general quite high and and even if some glass systems like phosphate glasses and chalcogenide glasses exist that can be relatively vulnerable against chemical attack.

Table 7.2 *Dielectric properties of multicomponent glasses.*

Material	ε_r	tan δ	Measured frequency	Qf [GHz]
SCHOTT P-LAK35	10	3.7×10^{-3}	1.1	297
SCHOTT P-LAK35	10	4.1×10^{-3}	1.869	456
SCHOTT P-LAK35	10	5.3×10^{-3}	4.928	930
SCHOTT P-LASF35	19.9	4.2×10^{-3}	1.088	259
SCHOTT P-LASF35	19.7	4.7×10^{-3}	1.844	392
SCHOTT P-LASF35	19.6	6.5×10^{-3}	4.705	724
SCHOTT N-LAK22	8.7	2.5×10^{-3}	1.101	440
SCHOTT N-LAK22	8.7	2.8×10^{-3}	1.872	669
SCHOTT N-LAK22	8.7	3.5×10^{-3}	4.959	1417
SCHOTT N-SF66	21.1	2.8×10^{-3}	1.092	390
SCHOTT N-SF66	21.0	3.1×10^{-3}	1.842	594
SCHOTT N-SF66	20.9	4.8×10^{-3}	4.687	976
SCHOTT MEMpax®	4.4	5.7×10^{-3}	1.109	195
SCHOTT MEMpax®	4.4	6.4×10^{-3}	1.89	295
SCHOTT MEMpax®	4.4	7.3×10^{-3}	5.094	698
SCHOTT BOROFLOAT®33	4.5	5.1×10^{-3}	1.096	215
SCHOTT BOROFLOAT®33	4.5	5.7×10^{-3}	1.874	329
SCHOTT BOROFLOAT®33	4.5	7.3×10^{-3}	5.094	698
SCHOTT FOTURAN®$\text{II}_{(\text{glass})}$	4.4	8.4×10^{-3}	1.098	131
SCHOTT FOTURAN®$\text{II}_{(\text{glass})}$	4.4	9.0×10^{-3}	1.871	208
SCHOTT FOTURAN®$\text{II}_{(\text{glass})}$	4.4	10.9×10^{-3}	4.954	454
SCHOTT B 270®	6.6	5.2×10^{-3}	1.106	213
SCHOTT B 270®	6.6	5.9×10^{-3}	1.884	319
SCHOTT B 270®	6.6	7.7×10^{-3}	5.068	658
SCHOTT B 270®i	6.7	5.9×10^{-3}	1.104	187
SCHOTT B 270®i	6.7	6.6×10^{-3}	1.878	285
SCHOTT B 270®i	6.7	8.4×10^{-3}	5.012	597
SCHOTT AF 32®eco	5.1	3.5×10^{-3}	1.107	316
SCHOTT AF 32®eco	5.1	3.9×10^{-3}	1.886	484
SCHOTT AF 32®eco	5.1	4.9×10^{-3}	5.087	1038
SCHOTT D 263®T eco	6.4	7.4×10^{-3}	1.107	150
SCHOTT D 263®T eco	6.4	8.4×10^{-3}	1.884	233
SCHOTT D 263®T eco	6.3	10.1×10^{-3}	5.072	502
Corning Gorilla 4 (see reference [3])	7.39	2.5×10^{-2}	–	–

A disadvantage of glasses is that the intrinsic disorder leads to a broad range of phonon modes, which strongly increases the probability of phonon–phonon scattering processes. These scattering processes will lead to a loss mechanism, which is relevant in the GHz range. Also ionic conductivity mostly by alkali ions (Li, Na, K, etc.) can become a relevant loss mechanism in the GHz range of the electromagnetic spectrum. Therefore alkaline ion free glass compositions like AF32 show a much smaller loss than alkali containing compositions like D263 or Gorilla from Corning. Table 7.2 gives the dielectric properties of a number of different glasses at GHz frequencies.

Glasses find applications as substrates on which microstrip lines and feedthroughs are structured. In this case a low dielectric constant, at least lower than the one of silicon, $\varepsilon_{Si} = 11.7$, is needed to reduce parasitic capacities. They are also used as substrates on which antenna structures are made. In this case a higher dielectric constant can lead to miniaturization and/or can reduce perturbation of the antenna near field, for example, by human tissue (body loading). At larger frequencies the high homogeneity of glasses allows accurate designs to be made. Due to the low thermal expansion of glasses antenna arrays can also be structured on glasses that barely change their radiation characteristic under temperature changes. Also windows that are highly transparent for electromagnetic radiation can be made. In this case the glass has the function of hermetic sealing and can protect radar electronics in a harsh environment. Due to their relatively high dielectric loss, multicomponent glasses are not well suited for resonators and filter elements.

7.1.3 Solder Glasses, Sealing Glasses, Glass Joins, Passivation Glasses, and Glass Powder Additives

There are a number of glass systems that are mainly applied as glass powders or glass pastes. The most important property in many applications is adjusting the thermal expansion of such a glass to an adjacent metal of ceramic compounds. In this way seals and joins with defined mechanical properties like zero stress or a defined compressive stress can be obtained which are vacuum proof within a defined temperature range. Many of these glass powders have good properties in the GHz range and are used for high-frequency feedthroughs. Especially alkaline free or low alkaline containing compositions show a low dielectric loss. Also as additions for liquid phase sintering at temperatures well below 900°C in ceramic [4,5]. processes for low-temperature co-fired ceramics (LTCC) applications such glass powders can find applications [6, 7]. For LTCC applications a large number of further glass solutions are used and discussed [8–11]. Since a large part of the present book is devoted to ceramics, which are produced via a sintering process and where often glass additions can be used as sinter aids [12–14], we will not go into further details of solder glasses in the present section but will rather return to pore-free bulk materials. Some of the glass powders crystallize during sintering and form a sinter glass ceramic [15]. The advantages of such crystallizing glasses are improved high-temperature properties together with usually a decrease of dielectric loss with increasing crystalline content.

7.2 Bulk Glass Ceramics

In the present section we introduce a class of materials that is rather new as dielectric material for high-frequency applications. These are bulk glass ceramics, which are defined via their production process. The production of a bulk glass ceramic is done via a glass melt, a liquid phase. The glass is shaped using methods that are common to glass production, like casting or pressing or maybe even floating or drawing. In this way a homogeneous glass with a true amorphous structure is made. This glass does not yet have the final dielectric properties. Glasses are in a meta-stable state from a thermodynamic point of view. This means that there is always a number of crystalline structures that are thermodynamically more stable

than the amorphous glass. This is used for making a glass ceramic. In a second and independent production step such glasses are treated with a well-defined time–temperature profile. During this temperature treatment crystals grow inside the glass, which is often called ceramming of the glass. Usually ceramming temperatures slightly above the calorimetric glass transition temperature are applied. In this way crystalline phases grow inside the glass. The crystalline phases with their dielectric properties will now alter the dielectric properties of the glass. Often the crystalline phases have a much lower dielectric loss in comparison with the original glass and a higher dielectric constant. The choice of composition and the ceramming temperature controls the crystalline phases that grow in such a glass ceramic. The use of nucleating agents together with an adjustment of heating rates and details of the time–temperature profile allows the size of the crystallites, the packing fraction, and the size distribution to be controlled. The situation in the phase diagram is shown in Figure 7.1 in an oversimplified way to illustrate the interplay between glass formation and crystallization of a particular phase. In this way highly homogeneous materials completely free of pores are created, which allow accurate designs to be made with well-defined metal to dielectric interfaces.

Besides the superior homogeneity and pore-free structure there is a limitation to glass ceramics in comparison to their ceramic counterparts. This is the fact that there will always be a residual glass phase present or sometimes also a mixture of different crystalline phases with different dielectric properties. This increased disorder leads to a slightly increased

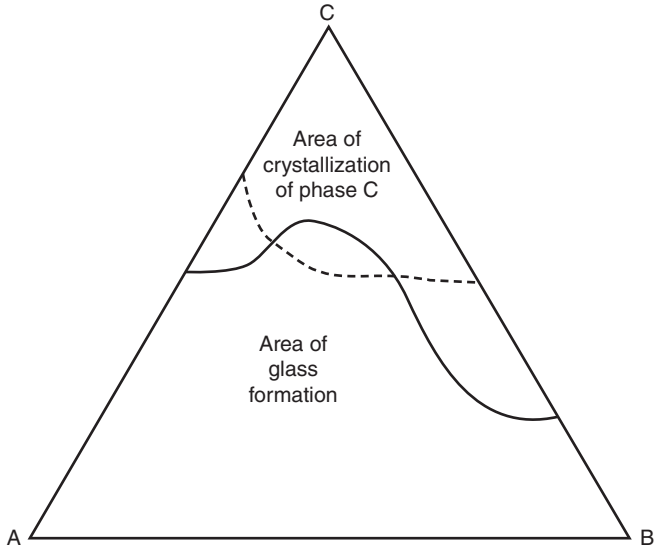

Figure 7.1 *A schematic situation is shown where C denotes the targeted crystalline phase one likes to obtain in a glass ceramic and A and B are glass-forming components like, for example, SiO_2 or B_2O_3. The thin solid line shows the boundary of the region where glass formation is observed under standard laboratory conditions and the dashed line shows the field of crystallization of the phase C. In the rare cases where the field of crystallization of C overlaps with the glass-forming area a stable glass can be molten, which crystallizes the phase C under heat treatment.*

dielectric loss. It further limits the maximum dielectric constant that can be obtained. A random mixture of components with different permittivities is electrically a random arrangement of parallel and serial positioned capacitors. Therefore the total permittivity ϵ_{tot} of a multiphase system will always be in between the two extrema, parallel positioning

$$\epsilon_{par} = \sum_i V_i \epsilon_i$$

and serial positioning

$$\epsilon_{ser} = \left(\sum_i V_i \epsilon_i^{-1} \right)^{-1} :$$

$$\sum_i V_i \epsilon_i > \epsilon_{tot} > \left(\sum_i V_i \epsilon_i^{-1} \right)^{-1} \tag{7.4}$$

A model that seems to work quite well and can be motivated mathematically by the use of the approximation for small n, $x^n \sim 1 + n \ln(x)$, is the Lichtenecker model [16, 17]

$$\ln(\epsilon_{tot}) = \sum_i V_i \ln(\epsilon_i) \tag{7.5}$$

Equation (7.5) means that even at 80% volume filling of a crystalline phase with a high dielectric constant in a glass ceramic one would only reach around half of the permittivity that one could reach with a ceramic material that contains only the high-permittivity crystalline phase. This restricts the range of dielectric constants for low loss in the GHz range, which can be addressed with glass ceramics to approximately

$$4 < \varepsilon_{\text{glass-ceramic}} < 40 \tag{7.6}$$

Using ferroelectric crystalline phases can extend this range towards even higher dielectric constant values, but will lead to strongly induced dielectric loss together with non-linear material properties. Therefore Equation (7.6) gives the range of permittivities for which glass ceramic systems can be found that are usable in GHz electronics.

7.2.1 The $BiNbO_4$ System

The first glass ceramic system that was developed and optimized for electronic applications in the GHz range as a high ε_r dielectric material was the $BiNbO_4$ system. There is early work on this system [18] that did not target the low dielectric loss at GHz frequencies. Mirsaneh *et al.* [19] investigated the system in detail and optimized it for low values of τ_f together with a dielectric constant $\varepsilon_r > 20$. The motivation for the development was the limited homogeneity, the batch-to-batch variations and the barely controllable sinter shrinkage of conventional sinter ceramics [20]. It was for the first time possible to make working antennas out of a bulk glass ceramic material using the $BiNbO_4$ system.

7.2.2 The $La_4Ti_9O_{24}$ and $La_2Ti_2SiO_9$ System

In the La–Ti–Si phase diagram it is possible to obtain stable glasses in the field of crystallization of the two crystalline phases $La_4Ti_9O_{24}$ and $La_2Ti_2SiO_9$, which is shown in the

Table 7.3 *Dielectric properties of glass ceramics.*

Material	ε_r	tan δ	Measured frequency	*Qf* (GHz)
SCHOTT FORTURAN®II (cerammed 560°C)	5.8	5.80×10^{-3}	1.103	190
SCHOTT FORTURAN®II (cerammed 560°C)	5.9	6.50×10^{-3}	1.876	289
SCHOTT FORTURAN®II (cerammed 560°C)	5.8	7.90×10^{-3}	4.993	632
SCHOTT FORTURAN®II (cerammed 810°C)	5.4	3.90×10^{-3}	1.103	283
SCHOTT FORTURAN®II (cerammed 810°C)	5.5	4.40×10^{-3}	1.877	427
SCHOTT FORTURAN®II (cerammed 810°C)	5.4	5.50×10^{-3}	5.005	910
SCOTT NEXTREMA®724-3 transparent	6.4	5.40×10^{-2}	1.089	20
SCOTT NEXTREMA®724-3 transparent	6.5	3.70×10^{-2}	1.884	51
SCOTT NEXTREMA®724-3 transparent	6.3	4.40×10^{-2}	4.953	113
SCOTT NEXTREMA®724-8 opaque white	6.2	2.50×10^{-3}	1.09	436
SCOTT NEXTREMA®724-8 opaque white	6.3	4.00×10^{-3}	1.844	461
SCOTT NEXTREMA®724-8 opaque white	6.2	9.30×10^{-3}	4.946	532
SCOTT NEXTREMA®712-3 tinted	6.9	6.40×10^{-2}	1.087	17
SCOTT NEXTREMA®712-3 tinted	7.0	4.90×10^{-2}	1.839	38
SCOTT NEXTREMA®712-3 tinted	6.7	5.50×10^{-2}	4.933	90
SCOTT NEXTREMA®712-6 translucent blue grey	6.7	3.00×10^{-3}	1.089	363
SCOTT NEXTREMA®712-6 translucent blue grey	6.7	4.00×10^{-3}	1.842	461
SCOTT NEXTREMA®712-6 translucent blue grey	6.7	8.40×10^{-3}	4.931	587
SCOTT NEXTREMA®712-8 opaque grey	6.8	3.10×10^{-3}	1.088	351
SCOTT NEXTREMA®712-8 opaque grey	6.8	4.30×10^{-3}	1.84	428
SCOTT NEXTREMA®712-8 opaque grey	6.7	1.00×10^{-2}	4.929	493

work of Braun *et al.* [21]. In this system one can reach values of $20 < \varepsilon_r < 30$ together with *Qf* values of more than 9000 GHz. The glasses are stabilized using SiO_2 and B_2O_3 as glass formers and additional disorder within the crystalline phase.

7.2.3 Properties of Glass Ceramics from the Lithium Aluminum Silicate System

Lithium aluminum silicate (LAS) glass ceramic systems are usually optimized for zero or close to zero thermal expansion. The normal, slightly positive thermal expansion is compensated by high-quartz solid-solution crystalline phases, which in a large temperature range around room temperature have a negative thermal expansion. Since the alkali ion lithium is of particular importance in these systems, the dielectric loss is only moderate. In Table 7.3 the NEXTREMA type of glass ceramics are from the family of the LAS glass ceramic systems. However, when ceramized at higher temperatures, where the thermal expansion increases slightly, a different crystalline phase, the Keatite, occurs, which strongly improves the dielectric loss in the GHz range. When ceramized into the Keatite the glass ceramics are mostly opaque and lose their transparency.

7.2.4 Photosensitive Crystallizing Glasses

A further glass ceramic system that is of particular interest is a silver and Ce containing glass system that allows photostructuring. An example for such a glass system is Foturan

[22, 23]. In its glassy state it can be illuminated using UV light. In a second step crystals from chain silicates grow in the illuminated areas under application of a well-defined time–temperature profile, which can be easily etched away. The three-dimensional structure, which is obtained in this way, can be heat treated a second time with a higher temperature than the first ceramization process. In this way one obtains a photostructured three-dimensional object that is used for high-frequency filters, MEMS (microelectromechanical systems) with relatively low dielectric losses in the GHz frequency range. An example for such a structuring can be found in reference [24]. In Table 7.3 the dielectric properties of Foturan are shown.

References

1. Data sheet from Haereus quarzglas. URL http://www.heraeus-quarzglas.de/de/quarzglas/electricalproperties/Electrical_properties.aspx.
2. Wu, J.M. and Huang, H.L. (1999) Microwave properties of zinc, barium and lead borosilicate glasses. *Journal of Non-Crystalline Solids*, **260** (1–2), 116–124.
3. Data sheet from corning gorilla. URL http: //www.corninggorillaglass. com/uploads/kcfinder/files/Corning%20Gorilla%20Glass% 204_PI%20Sheet_090315_E.pdf.
4. Rajesh, S., Jantunen, H., Letz, M., and Pichler-Willhelm, S. (2012) Low temperature sintering and dielectric properties of alumina filled glass composites for LTCC applications. *International Journal of Applied Ceramic Technology*, **9** (1), 52.
5. Kim, H.T., Kim, S.H., Nahm, S., Byun, J.D., and Kim, Y. (1999) Low-temperature sintering and microwave dielectric properties of zinc metatitanate–rutile mixtures using boron. *Journal of the American Ceramic Society*, **82** (11), 3043–3048.
6. Jantunen, H., Rautioaho, R., Uusimäki, A., and Leppävuori, S. (2000) Compositions of $MgTiO_3$–$CaTiO_3$ ceramic with two borosilicate glasses for {LTCC} technology. *Journal of the European Ceramic Society*, **20** (14–15), 2331–2336.
7. Cheng, C.C., Hsieh, T.E., and Lin, I.N. (2003) Microwave dielectric properties of glass–ceramic composites for low temperature co-firable ceramics. *Journal of the European Ceramic Society*, **23** (14), 2553–2558.
8. Abhilash, P., Thomas, D., Surendran, K.P., and Sebastian, M.T. (2016) Facile synthesis of "quench-free glass" and ceramic–glass composite for LTCC applications. *Journal of the American Ceramic Society*, **96** (5), 1533–1537.
9. Dernovsek, O., Eberstein, M., Schiller, W., Naeini, A., Preu, G., and Wersing, W. (2001) {LTCC} glass–ceramic composites for microwave application. *Journal of the European Ceramic Society*, **21** (10–11), 1693–1697.
10. Takada, T., Wang, S.F., Yoshikawa, S., Jang, S.J., and Newnham, R.E. (1994) Effect of glass additions on BaO–TiO_2–WO_3 microwave ceramics. *Journal of the American Ceramic Society*, **77** (7), 1909–1916.
11. Surendran, K., Mohanan, P., and Sebastian, M. T. (2004) The effect of glass additives on the microwave dielectric properties of $Ba(Mg_{1/3}Ta_{2/3})O_3$ ceramics. *Journal of Solid State Chemistry*, **177** (11), 4031–4046.
12. Huang, C.L., Weng, M.H., Lion, C.T., and Wu, C.C. (2000) Low temperature sintering and microwave dielectric properties of $Ba_2Ti_9O_{20}$ ceramics using glass additions. *Materials Research Bulletin*, **35** (14–15), 2445–2456.
13. Huang, C.L. and Weng, M.H. (2001) Improved high Q value of $MgTiO_3$–catio 3 microwave dielectric ceramics at low sintering temperature. *Materials Research Bulletin*, **36** (15), 2741–2750.
14. Kim, D.W., Lee, D.G., and Hong, K.S. (2001) Low-temperature firing and microwave dielectric properties of $BaTi_4O_9$ with Zn–B–O glass system. *Materials Research Bulletin*, **36** (3–4), 585–595.

15. Lo, C.L., Duh, J.G., Chiou, B.S., and Lee, W.H. (2002) Low-temperature sintering and microwave dielectric properties of anorthite-based glass-ceramics. *Journal of the American Ceramic Society*, **85** (9), 2230–2235.
16. Prasad, A. and Prasad, K. (2007) Effective permittivity of random composite media a comparative study. *Physica B: Cond. Materials*, **396** (1–2), 132.
17. Braun, H. (2015) Titanate based paraelectric glass-ceramics for applications in GHz electronics. University of Mainz, Germany.
18. Gerth, K. and Rüssel, C. (1999) Crystallization of $Bi_3Ti_nBO_9$ from glasses in the system $Bi_2O_3/TiO_2/Nb_2O_5/B_2O_3/SiO_2$. *Journal of Non-Crystalline Solids*, **243** (1), 52–60.
19. Mirsaneh, M., Leisten, O.P., Zalinska, B., and Reaney, I.M. (2008) Circularly polarized dielectric-loaded antennas: current technology and future challenges. *Advanced Functional Materials*, **18** (16), 2293–2300.
20. Zalinska, B., Leisten, O.P., and Reaney, I.M. (2014) Fabrication of multilayer dielectrically loaded antennas using aqueous electrophorectic deposition of polyether ether ketone. *Journal of Materials Science*, **49** (11), 4121–4126.
21. Braun, H., *et al. (*2016) in Journal of European Ceramic Society (in press).
22. Wikipedia Schott Foturan. URL http://www.en.wikipedia.org/ wiki/Foturan.
23. Höland, W. and Beall, G. (2012) *Glass–Ceramic Technology*, John Wiley & Sons, Inc., Hoboken, NJ, 254 pp.
24. He, F., Sun, H., Huang, M., *et al. (*2009) Rapid fabrication of optical volume gratings in Foturan glass by femtosecond laser machining. *Applied Physics A*, **97**, 853–857.

8

High Temperature Cofired Ceramic (HTCC), Low Temperature Cofired Ceramic (LTCC), and Ultralow Temperature Cofired Ceramic (ULTCC) Materials

M.T. Sebastian and Heli Jantunen
Microelectronics Research Unit, Faculty of Information Technology and Electrical Engineering, University of Oulu, Oulu, Finland

8.1 High Temperature Cofired Ceramics (HTCC)

8.1.1 Introduction

Traditionally microwave devices have been fabricated from metals with coaxial RF connections which are bulky and expensive. Recently modern electronic devices based on an integrated circuit consisting of millions of interconnected components (resistors, transistors, etc.) kept on a tiny silicon chip have been developed. This circuit is then assembled on insulating substrates and packages. Electrical connections are then made to the microscopic electronic components through the base of the substrate. The package helps to seal the circuit from the surrounding and make it a single compact unit, which helps to maintain the reliability of the device. Alumina is commonly used as the material for substrates and packages because of its high resistivity, good mechanical and thermal properties, high dielectric strength, and thermal and chemical stability. The high temperature cofired ceramic (HTCC) alumina substrate and packages have been commonly used in microelectronic packages for

Microwave Materials and Applications, First Edition.
Edited by Mailadil T. Sebastian, Rick Ubic and Heli Jantunen.
© 2017 John Wiley & Sons, Ltd. Published 2017 by John Wiley & Sons, Ltd.

decades. This is because of its excellent properties, cost, and ease of manufacture. It can also be used to fabricate complex micro components, suitable for high temperature applications. Substrates with thickness larger than 1.5 mm are made by dry pressing and sintering. Substrates with a thickness less than 1.5 mm are made by tape casting/doctor blade techniques. The green tapes are hole-punched or laser-cut, via hole coated (vias are conductive pathways between layers), and metallized with tungsten or molybdenum by screen printing. The conductor metal is selected based on the sintering temperature, conductivity, and non-reactivity with substrates. Several layers of the tapes are stacked to get the desired thickness and then laminated into multilayer structures. It is then cofired at temperatures greater than 1500 °C in a hydrogen–nitrogen atmosphere to prevent the conductor metals from oxidation. The resulting sintered compact is a monolithic package with internal conductor paths and the silicon chip is mounted on it and the package is hermetically sealed with a glass or metal lid. The integrated circuit package containing the silicon device can be connected to the external electric circuit. The packaging material should have low ε_r in order to increase the signal speed but a higher ε_r is useful for miniaturization. In the case of electronic substrate and dielectric packaging applications, the relative permittivity should be less than 15 and are ideal for MMICs. The thermal expansion coefficient should match with the silicon chip and conducting metals. A higher thermal conductivity (TC) is needed to dissipate the heat generated. AlN has a higher TC than alumina but has a higher sintering temperature with problems in the cofiring process. BeO has a very high thermal conductivity in the range 250–330 W/m K with good dielectric properties ($\varepsilon_r = 6.5$, tan $\delta = 0.001$, and CTE = 7 ppm/°C). The high TC of BeO substrates is desirable for high power microelectronic applications. However, it is not being used in practical applications due to its toxicity and high cost.

The rapid development in the microelectronic industry has created a high demand for low loss microwave ceramics due to their reliability, high integration potential, and good dielectric properties. Today, the telecommunication industry requires high volume efficiency without affecting the electrical performance of the devices. HTCC substrate-based components cover a wide range of application fields. Examples are electronic components (multilayer capacitors, multilayer actuators and R-C filters), 3D multichip modules (engineering management systems, gearbox control in automotive applications, high frequency applications in aerospace and medical engineering), intelligent 3D packages (Si-chip and microelectromechanical systems (MEMSs) packaging), as well as lab-on-chip systems. HTCC is extensively used for hermetic packaging because of its good electrical properties, and mechanical and thermally conducting properties. The HTCC technology permits hermetic straight-through vias and dense metal interconnects. HTCC packages are most commonly used in military, aerospace, medical device, and high temperature applications, especially in automotive, high power, wireless communication and RF packages.

Multilayer ceramic technology can be divided into three parts: HTCC (sintering temperature >950 °C), LTCC (sintering temperature 700–950 °C), and ULTCC (sintering temperature <700 °C). LTCC usually contains glass, which lowers the firing temperature compatible with silver and gold. LTCC and HTCC technologies are extensively used in the fabrication of hybrids in microelectronic devices. Both HTCC and LTCC tapes are manufactured in a very similar manner but the tape content and applications are different. HTCC is fired at higher temperatures >1500 °C and is used in applications where higher chemical and thermal stabilities are needed. Hence HTCC is suitable mainly in high temperature applications such as automotive ones. HTCC is relatively more expensive. The green tapes

are machined using punchers and lasers for fabricating 3D structures. It is then printed with conductive paths and the tapes are aligned, laminated, and fired. The slurry composition decides the mechanical and electrical properties of green and sintered tapes of both HTCC and LTCC.

Commercial LTCC tapes are produced by the tape casting process based on organic solvents whereas HTCC can be produced by water-based techniques. Organic solvents have low boiling points and have a faster drying process. Water-based tape casting is more environment friendly, inexpensive, and limits the CO_2 emissions as compared to the organic solvent-based tape casting. A wide range of water soluble binders such as derivatives of cellulose ethers, polyvinyl alcohol, acrylic polymers, and acrylic polymer emulsion have been examined for tape casting [1, 2]. During firing, the ceramic particles sinter to a hard material, the sample shrinks by about 15–20%, and the grains grow and lower the porosity. However, a higher sintering temperature and duration increase the grain size. An increase in grain size adversely affects the mechanical properties and decreases the strength. Hence it is desirable to keep the grain size as small as possible.

Cofired ceramic packages are fabricated through four distinct processing stages that include material preparation, green processing, sintering, and post-fire processing. Material preparation consists of milling raw materials (ceramic particle size in the range 0.1 to 1 μm), formulation of slurry, and tape casting, as well as deposition of conductive inks. Green processing consists of punching cavities, via punch, via fill, screen printing, and lamination. Once the green process is complete, the ceramic/metal composite is cofired in a carefully controlled atmosphere. Post-fire processing consists of additional printing, sawing, machining, and brazing. The packages are then plated with suitable conducting metal plates for solder and wire bond applications. The packages can be designed for crystal/oscillator/surface acoustic wave (SAW) frequency control devices, complimentary metal oxide semiconductors (CMOSs), charge coupled devices (CCDs), infrared and ultraviolet image sensors, hermetic ceramic feedthroughs for DC to Ka band high frequency applications, HTCC packages for microwave applications in the L through Ka band frequency ranges, pin grid array packaging for semiconductor microprocessors, as well as high temperature, optoelectronic, and multichip module applications.

8.2 HTCC Alumina

Extensive work has been done on HTCC alumina and several companies are commercially manufacturing HTCC alumina tapes; some of the important players are given in Table 8.1.

Table 8.1 *Alumina and AlN HTCC manufacturers*

CoorsTek	Lea Tec.
Maruwa	Fine Ceramic Co. Ltd
Technical Products Inc.	Semiconductor Wafer Inc.
MTI Corp.	Ceram Tech.
ATP Applied Thin Film Products	Valey Design Corp.
Kyocera	Advanced Technical Ceramics
GM Components	NEO Tech.
Centreline Technologies	NEVZ-CERAMICS Russia
ORTECH Advanced Ceramics	ESL ElectroScience

HTCC alumina substrates were processed by non-aqueous or aqueous tape casting [1–5]. In the non-aqueous method as a typical example, the fine alumina powder of about 62 wt% is made into a slurry by ball milling in dispersant (fish oil) and solvents such as xylene and anhydrous ethyl alcohol. It is then mixed with binder (polyvinyl butyral) and plasticizers butylbenzyl phthalate and poly(alkylne glycol) and again milled. The slurry is yielded and cast by the doctor blade technique. There are several dispersants, plasticizers, solvents, and binders available for tape casting and the solid loading depends on the organics and their wt % used in the tape casting process. An aqueous slurry is usually prepared with a cellulosic binder. This binder was used to achieve slurries with a low viscosity and a shear thinning rheological behavior. In the aqueous method the alumina powder is ball milled with plasticizers such as polypropylene glycol, glycerin dispersant ammonium polyelectrolyte, and distilled water. The mixed slurry is then milled with binder methyl cellulose and water. This slurry is then cast to form sheets of uniform thickness (about 50–700 μm). Once dried, these so-called "green sheets" can be easily cut, rolled up for transport, and processed further. For more details of tape casting the reader is referred to the book of Mistler and Twiname [3]. The presence of the organic phase in the green tapes influence the properties. The tensile strength increases, whereas the apparent density decreases, when the binder content increases. The tensile strength decreases, whereas the apparent density increases, when the powder content in the suspension increases. Kristofferson *et al.* [4] investigated the suitability of different binders such as latexes, polyvinyl alcohol, and cellulose on water-based tape casting of alumina. It was found that latexes result in low viscosity suspensions with less foaming problems. The use of latex binders enable the highest solid loading with quick drying and high green density. The sintering behavior and resulting microstructure were found to be different for different binders. They found significant variation in shrinkage in thickness direction, casting direction transverse to the casting direction, and also in the relative sintered density for the different binders. The shrinkage was found to be larger in the thickness direction. The anisotropic bahavior in sintering shrinkage is attributed to the orientation of alumina particles/polymer and pores during casting and drying. The z shrinkage during debinding is reported to be ten times higher than the in-plane shrinkage [6]. The transverse (y) shrinkage is slightly higher than that in the casting direction during binder burnout [6]. A small amount of additives is usually added as sintering aids and their presence influences the dielectric properties. Also, 96% alumina thick film and 99% alumina thin film substrates are commercially manufactured by type casting for thick and thin film integration. Tok *et al.* [7] reported that a better accuracy of tape thickness can be achieved by casting at lower casting speeds. However, the accuracy decreases when thinner tapes are cast. They suggested to optimize the casting speed and blade height to achieve accurate and reproducible results for cast tapes. The properties of HTCC alumina are given in Table 8.2.

The next step in the production involves the introduction of electrically conducting lines. Depending on the design, the sheets are punched to form cavities and vias, which can be filled with a metal paste. These vias create vertical connections for the electrical feedthroughs. The planar electrical lines are defined on the ceramic sheets by screen-printing, again using refractory metal pastes.

Once the various metal structures are defined, the ceramic sheets are stacked in a specific order and laminated. This process connects the individual, basically two-dimensional sheets and ends up in a three-dimensional structure with hermetic electrical feedthroughs. High temperature multilayer ceramics are sintered at temperatures in the range 1500–1800 °C.

Table 8.2 *Physical and electrical properties of HTCC Al_2O_3, AlN, and $ZrSiO_4$*

Properties	Alumina	AlN	$ZrSiO_4$
ε_r	9.5–9.9 (10 GHz)	8.0–9.2 (1 MHz)	9.2 (5 GHz)
tan δ	0.0001–0.0004 (10 GHz)	0.001 (1 MHz)	0.0003 (5 GHz)
Density (gm/cm^3)	3.8–3.95	3.25–3.3	4.2–4.3
Thermal conductivity (W/m K)	25–35	200–230	15
Poisson's ratio	0.2 to 0.23	0.25	
CTE (ppm/°C)	6–8	4.2–5.8	–2.5
Flexural strength MPa	450–650	300–450	150–200
Hardness Moh's	9.0	7.0	6.5–7.5
Volume resistivity RT	1×10^{14}	$>10^{13}$	–
Dielectric breakdown voltage	>15 KV/mm	>15 KV/mm	–
Water absorption	Nil	Nil	Nil
Color	White	White/gray	White
Sintering temperature (°C)	1500–1700	1700–1900	1600

The driving force for innovative packaging solutions with ceramic multilayer feedthrough are: miniaturization, cost savings, and HF applications.

High temperature cofired ceramic differs from LTCC because their firing temperatures are greater than 1500 °C and this restricts the types of metallizations that can be cofired. If gold and silver were cofired at 1500 °C, they would melt and run off the ceramic. Thus only refractory metals are cofired above 1000 °C, such as tungsten and molybdenum. These metals have high resistivity, as shown in Table 8.3. This indicates that metal losses in HTCC circuits at high frequencies can be severe. HTCC can easily provide hermiticity, unlike LTCC.

8.3 Aluminium Nitride HTCC

Aluminum nitride has been extensively investigated for HTCC applications because of its excellent thermal conductivity, good dielectric and physical properties, and a matching

Table 8.3 *Resistivity and melting point of common electrode materials*

Metal	Resistivity (μΩ-cm)	Melting point (°C)
W	5.6	3410
Mo	5.2	2610
Pt	10.5	1769
Pd	10.8	1552
Cu	1.7	1083
Au	2.3	1063
Ag	1.6	961

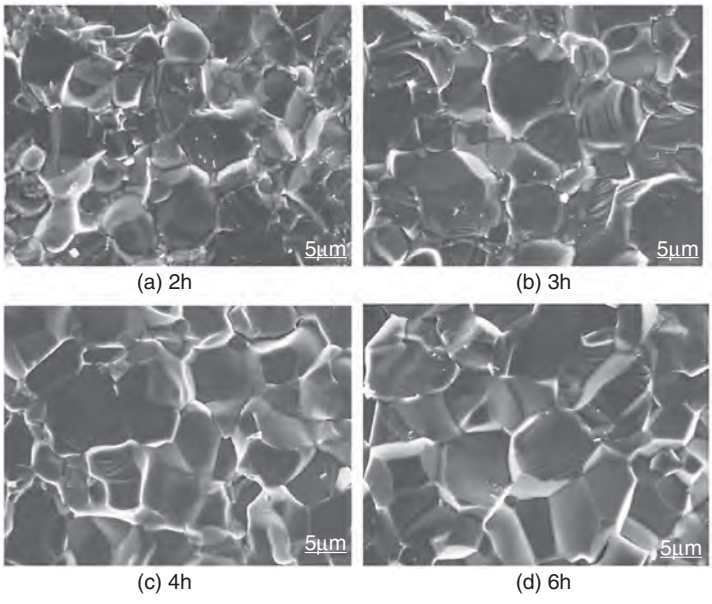

Figure 8.1 *SEM micrograph of aluminum nitride substrate sintered at 185 °C for different holding times: (A) 2 h, (B) 3 h, (C) 4 h, and (D) 6 h. Source: Luo* et al. *2006 [12]. Reproduced with permission of John Wiley & Sons.*

thermal expansion coefficient with that of silicon (see Table 8.2). Several authors reported [8–12] the casting of green AlN tapes. The predominant covalent bonding of AlN leads to high sintering temperatures (1800–2000 °C) and Y_2O_3 and CaO or CaF_2 and YF_3 are frequently used as sintering aids to improve densification and lower the sintering temperature [13–15]. The AlN tapes are sintered in inert atmospheres/nitrogen to prevent oxidation. AlN green tapes can be prepared in a way similar to alumina. AlN becomes hydrolyzed by water and Olhero *et al.* reported that soaking AlN powders in aqueous solution of aluminum dihydrogen orthophosphate can prevent hydrolysis [15]. Luo *et al.* [12] reported that initial surface treatment of AlN powder with DP270 improved stabilization of the powder (lower oxygen content) in aqueous ball milling media. They reported improvement in the microstructure and thermal conductivity with an increase in sintering duration at 1850 °C. Figure 8.1 shows the microstructure of a fractured surface of AlN substrate sintered for different durations. The grain size increased with a clean grain boundary with an increase in sintering duration. The thermal conductivity (TC) increased with an increase in holding time, as shown in Figure 8.2. Aluminum nitride is replacing BeO in several applications because of the toxicity and high cost of the latter. Hybrid circuit designers prefer AlN, which is the only other ceramic with high thermal conductivity up to 230 W/m K. AlN substrates can be used wherever thermomechanical or power dissipation properties are important, such as highly integrated thick and thin film components, power converters, and transmitter and HF diode substrates for use in satellite systems. AlN substrates are extensively used as heatsinks for semiconductor devices, power electronics, mobile communications, and multichip modules.

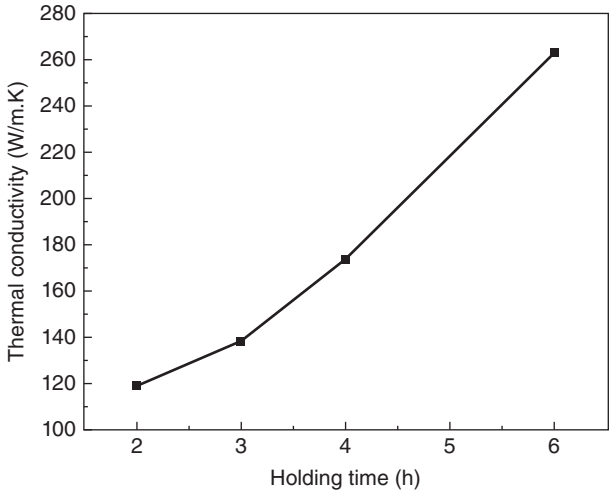

Figure 8.2 *Variation of thermal conductivity of AlN substrate with sintering duration at 1850 °C. Source: Luo* et al. *2006 [12]. Reproduced with permission of John Wiley & Sons.*

8.4 $ZrSiO_4$

$ZrSiO_4$ has tetragonal symmetry and belongs to the *I*41/*amd* space group. Recently $ZrSiO_4$ was reported as a low loss dielectric material with useful properties for microwave substrate applications [16]. $ZrSiO_4$ is available as such in nature. It is a byproduct of the mining and processing of heavy mineral sands, which are primarily extracted for rare earth, radioactive elements, titanium, ilmenite, and tin minerals. The major end use of $ZrSiO_4$ is refractory purpose, foundry sands, and ceramic opacification. The major advantages of $ZrSiO_4$ are that it resists metal penetration and burn-in, ensures dimensional accuracy, machinability, high thermal conductivity, low thermal expansion, corrosion resistance, longer life, and high thermal and mechanical stability. The preliminary reports on its dimensional, thermal, and mechanical stability suggest it as a good alternative material for alumina-based HTCC substrates for MCM-C (multichip module–ceramics) fabrications. Recently Varghese and Sebastian [17, 18] reported the preparation of HTCC $ZrSiO_4$ tapes using both commercial (Aldrich) and natural raw powders.

For an effective tape casting, well-dispersed and stable ceramic slurry is essential. The preparation of $ZrSiO_4$ slurry was based on an already optimized composition of HTCC alumina tape casting slurry. The 61.94 wt% of $ZrSiO_4$ powder in anhydrous ethanol/xylene solvent of 15.3/15.3 wt% (in the ratio 50:50 by weight) solvent with 1.24 wt% of dispersant (fish oil) were ball milled for 12 hours in the first stage of slurry preparation. The second stage of the $ZrSiO_4$ slurry compositions were PVB (polyvinyl butyral) binder of 3.09 wt%, type 1 BBP (butyl benzyl phthalate) and type 2 PEG (polyethylene glycol) plasticizer of 1.55 wt% each with respect to the filler loading. These were added into the first stage slurry and ball milled for another 12 hours. Table 8.4 shows the commercial and mineral $ZrSiO_4$ tape casting slurry compositions. The pseudoplastic behavior is essential for the tape casting slurry for efficient tape casting. The viscosity of the slurry decreases with an increase in

Table 8.4 *$ZrSiO_4$ tape casting slurry compositions. Source: Adapted from Varghese 2015 [17]*

Component	Composition (wt%)	Function
First stage		
$ZrSiO_4$	61.94	
Fish oil	1.24	Dispersant
Xylene	15.31	Solvent
Ethanol	15.31	Solvent
Second stage		
Polyvinyl butyral, grade B-98	3.09	Binder
Butyl benzyl phthalate	1.55	Plasticizer (Type I)
Polyethylene glycol	1.55	Plasticizer (Type II)

the shear rate, a behavior called shear thinning (pseudoplastic). The pseudoplastic behavior of $ZrSiO_4$ tape casting slurry is evident from the viscosity measurement of ceramic slurry, as shown in Figure 8.3. Figure 8.4 shows the SEM microstructure of green tapes. The single layer green tape of commercial (Figure 8.4e) and natural (Figure 8.4f) $ZrSiO_4$ have thicknesses of 81 and 78 μm, respectively, and is clear from the cross-sectional microstructure of the tapes. The surface morphology of green tape indicates more or less uniformly distributed commercial and natural $ZrSiO_4$ ceramic particles connected through polymer bridges with some porosity.

The surface roughness of the green tape is one of the parameter concerns while printing the circuit patterns [19]. The AFM images of the surface of the green tape cast from commercial commercial and mineral $ZrSiO_4$ are shown in Figure 8.5 (also shown in the Plate Section). The cast green tape has an average surface roughness (S_a) of 75 and 100 nm,

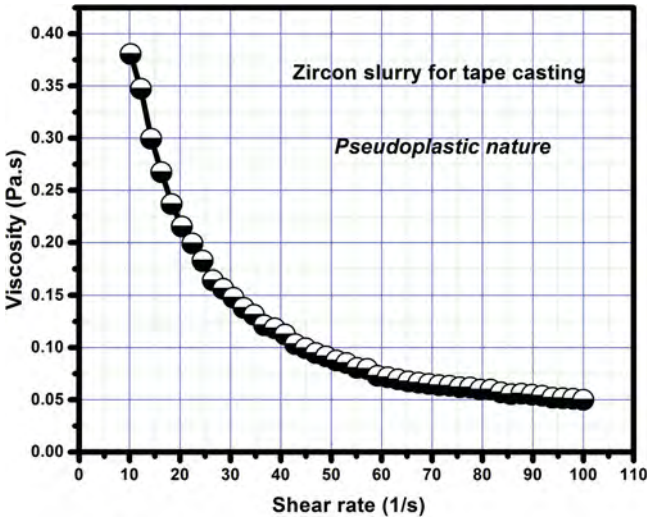

Figure 8.3 *Viscosity analysis of $ZrSiO_4$ slurry. Source: Adapted from Varghese* et al. *2015 [17].*

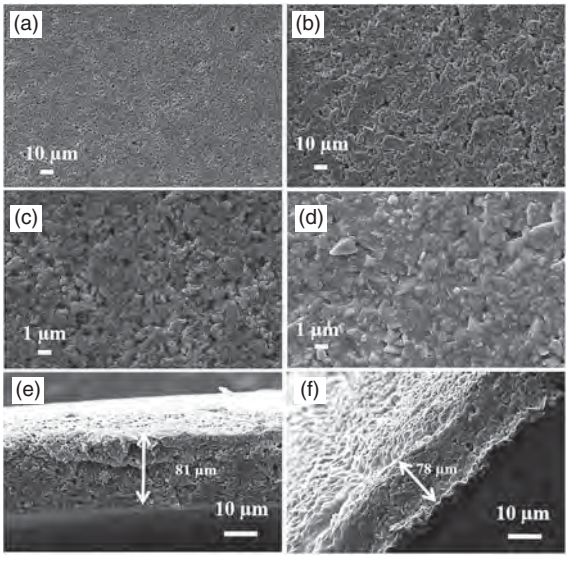

Figure 8.4 *Microstructure of single layer of Aldrich and IRE $ZrSiO_4$ cast green tape (a) surface of Aldrich zircon tape (b) surface of mineral zircon tape (c) Aldrich tape surface magnified (d) mineral tape surface magnified (e) Aldrich tape cross sectional (f) mineral tape cross sectional. Source: Adapted from Varghese* et al. *2015 [17].*

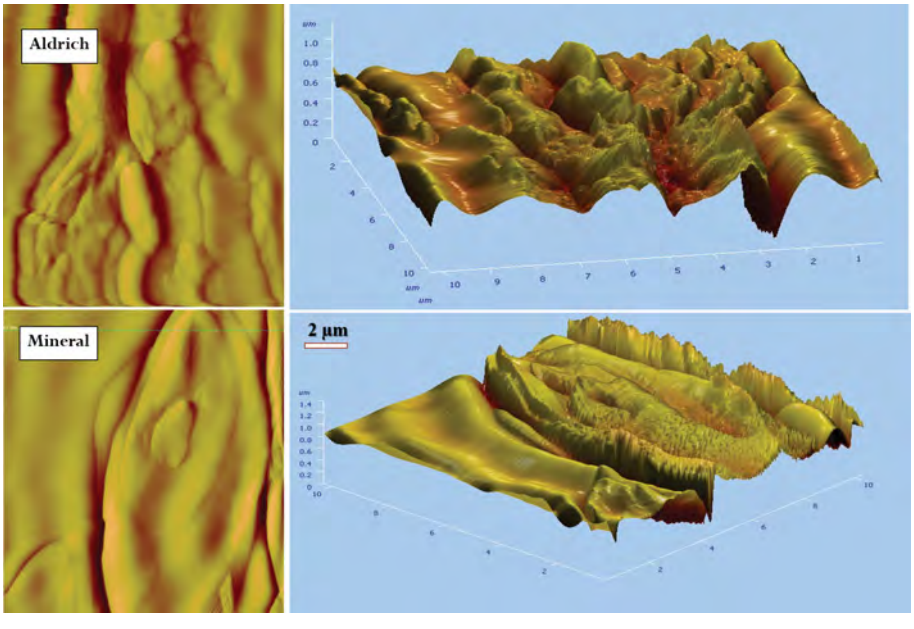

Figure 8.5 *Surface roughness of Aldrich and mineral $ZrSiO_4$ cast green tape. Source: Adapted from Varghese* et al. *2015 [17]. This figure is also shown in the Plate Section.*

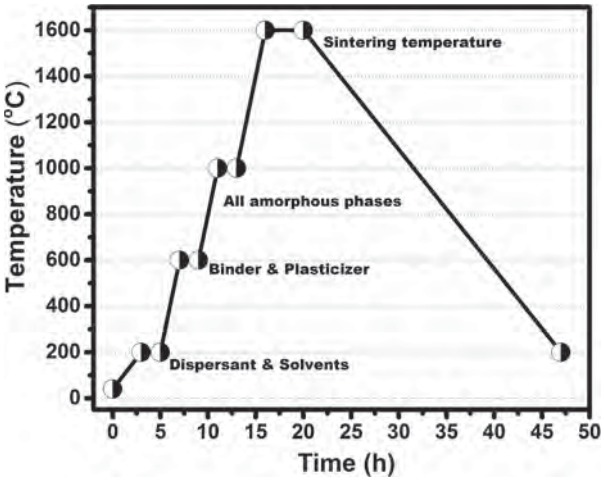

Figure 8.6 *Sintering profile of $ZrSiO_4$ HTCC ceramic substrate. Source: Adapted from Varghese* et al. *2015 [17].*

respectively, for commercial and mineral $ZrSiO_4$. The prominently obvious features of the surface of the green $ZrSiO_4$ tape in 2D and 3D surface geometry are shown in Figure 8.5. The RMS deviations of surface (Sq) is nearly 104 and 140 nm respectively for commercial and mineral $ZrSiO_4$ tape and are depicted in the inset table of Figure 8.5. The kurtosis of the topographic height distribution (Sku) of commercial and mineral $ZrSiO_4$ is nearly 4.1275 and 3.5164, respectively. This indicates that the surfaces of green $ZrSiO_4$ tape is almost uniform as the kurtosis of a well-spread distribution is greater than 3. Skewness of topographic height distribution (Ssk) is the measure of asymmetry of the surface deviations about a reference plane. The Ssk of commercial and mineral $ZrSiO_4$ is –0.2471 and –0.6876, respectively, where the negative value of skewness generally indicates that the surface distribution has a longer tail at the lower side of the reference plane [20]. Figure 8.6 shows the sintering profile of $ZrSiO_4$ green tapes. A slow heating rate of 1 °C/min is given up to 1000 °C with three intermediate dwells of about 30 minutes each at 200 °C, 600 °C, and 1000 °C for the complete burnout of organics. Heating rate of 2 °C/min is employed up to 1600 °C and the sample is cooled at a rate of 2 °C/min after the dwell at 1600 °C for 2 hours. The inset on Figure 8.6 depicts the photograph of sintered HTCC $ZrSiO_4$ substrate. Substantial grain growth occurs during sintering and hence the microstructure of the commercial and mineral $ZrSiO_4$ tapes (Figure 8.7) shows well-packed grains with fractional porosity. In the SEM image of the cross-section of thermolaminated stacks (Figure 8.7e and f), no interlayer boundary is visible. This means that under the conditions of thermolamination, the polymer in the matrix softens and the layers diffuse one into another, making the laminate homogeneous [21]. It is clear from the microstructure that the stack densified to form a single module.

The microwave dielectric properties of the green as well as sintered commercial and mineral $ZrSiO_4$ tapes are given in Tables 8.5 and 8.6 respectively. The green tape shows low relative permittivity and high dielectric loss tangent due to the presence of organic additives. After thermolamination, the relative permittivity of 4.2, 4.0 and dielectric loss of 0.05, 0.07 are obtained at 5 and 15 GHz, respectively, for a four-layer laminated

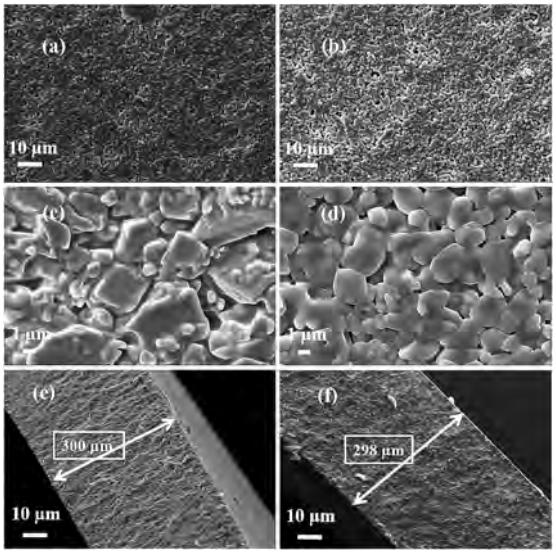

Figure 8.7 *Sintered microstructure of Aldrich and mineral $ZrSiO_4$ HTCC substrates (a) mineral $ZrSiO_4$ (b) Aldrich $ZrSiO_4$ (c) mineral magnified (d) Aldrich magnified (e) mineral cross sectional (f) Aldrich cross sectional. Source: Adapted from Varghese* et al. *2015 [17].*

Table 8.5 *Microwave dielectric properties of green $ZrSiO_4$ tape laminated*

		5 GHz		15 GHz	
Material	Thickness (µm)	ε_r	tan δ	ε_r	tan δ
Aldrich $ZrSiO_4$ Fout-layer stack	395	4.2	0.05	4.0	0.07
Mineral $ZrSiO_4$ Four-layer stack	389	4.0	0.07	3.9	0.09

stack of commercial $ZrSiO_4$ tapes. Similarly for the mineral $ZrSiO_4$ sample, relative permittivity is 4.0, 3.9 and dielectric loss is 0.07, 0.09, respectively, at 5 and 15 GHz. During thermolamination, the polymers present in the green tape softens and the laminate shrinks, bringing the ceramic particles close to each other due to the applied pressure,

Table 8.6 *Microwave dielectric properties of sintered $ZrSiO_4$ HTCC substrate. Source: Adapted from Varghese 2015 [17]*

			5 GHz		15 GHz	
Material	Density (%)	Thickness (µm)	ε_r	tan δ	ε_r	tan δ
Aldrich $ZrSiO_4$ Four-layer stack	96	298	9.2	0.0003	9.0	0.0004
Mineral $ZrSiO_4$ Four-layer stack	94	300	8.3	0.0005	8.1	0.0006

Table 8.7 *Thermal and mechanical properties of sintered $ZrSiO_4$ HTCC substrates. Source: Adapted from Varghese 2015 [17]*

	Mechanical properties		Thermal properties	
Material	Tensile strength (MPa)	Flexural strength (MPa)	Thermal conductivity (W/m K)	CTE (ppm/°C)
Aldrich $ZrSiO_4$ Four-layer stack	18	146	15	–2.5
Mineral $ZrSiO_4$ Four-layer stack	16	143	14	–2.1

which makes the laminate denser. The laminate of both commercial and mineral $ZrSiO_4$ sintered at 1600 °C/2 h shows good densification of 96 and 94%, respectively, due to grain growth and the subsequent removal of porosity. The variation in the densification is also evident in the property of the sintered samples. The sintered laminate shows good microwave dielectric properties with ε_r of 9.2, 8.3, respectively, for commercial and mineral $ZrSiO_4$ sintered at 1600 °C/2 h and tan δ of 0.0003, 0.0005, respectively, at 5 GHz. At this frequency the porosity corrected ε_r is 9.7 (commercial $ZrSiO_4$) and 8.9 (mineral $ZrSiO_4$). This difference in properties is attributed to the presence of impurities in mineral $ZrSiO_4$. At a higher frequency of 15 GHz, ε_r of sintered tape is 9.0, 8.1, respectively, for commercial and mineral $ZrSiO_4$. Similarly, corresponding tan δ values of these tapes are 0.0004 and 0.0006, respectively, at 15 GHz. The porosity corrected ε_r at 15 GHz is 9.5 and 8.8 for commercial and mineral $ZrSiO_4$, respectively.

Mechanical and thermal properties of sintered $ZrSiO_4$ (1600 °C/2 h) tapes are given in Table 8.7. The tensile, three-probe bending, thermal conductivity, and coefficient of thermal expansion are very important for the different device development processes in microelectronics. Generally the refractory materials have moderately high thermal and mechanical properties. The sintered $ZrSiO_4$ HTCC substrates show tensile strengths of 18 and 16 MPa while they have good flexural strengths of 146 and 143 MPa, respectively, for commercial and mineral samples. The substrates fabricated using commercial and mineral $ZrSiO_4$ starting powders show high thermal conductivity of 15 and 14 W/m K, respectively. Both substrates show low negative thermal expansion coefficients. Table 8.2 compares the fired properties of $ZrSiO_4$ tapes with that of commercially available alumina, aluminum nitride HTCC substrates. The $ZrSiO_4$ HTCC substrates have excellent mechanical and thermal properties with ultralow thermal expansivity.

8.5 Low Temperature Cofired Ceramics (LTCC)

8.5.1 Introduction

The multilayer cofired ceramic technology is used to fabricate several devices such as bandpass filters, oscillators, waveguides, antennas, etc., for miniaturization of microwave components in wireless communication. The important characteristics required for practical applications are suitable relative permittivity (high for miniaturization and low for fast signal transmission), low dielectric loss, temperature stable dielectric properties,

matched CTE with other materials in integrations, low sintering temperature below that of the electrode materials, high thermal conductivity, chemical compatibility with electrode material, low cost, and non-toxic. A large number of low loss ceramic dielectric materials are reported in the literature [22–24]. However, most of these materials have high sintering temperatures, which preclude their usage and integration with other materials such as low melting electrodes, semiconductors such as silicon or GaAs, and polymer-based substrates. The HTCC tapes have high sintering temperatures >1500 °C and need high melting point conductors such as tungsten or molybdenum for cofiring. The resistivity of these conductors are relatively high. Recently considerable attention has been paid to miniaturization. When the device size decreases, the conductor line size also decreases. When the size of the conductor lines decreases to a very small size, the resistivity increases. Hence one needs to use highly conducting metal conductors such as silver. However, silver has a low melting point of 961 °C. Hence silver will melt when cofired with HTCC tapes. The use of silver electrodes necessitated the need for bringing down the sintering temperature to below 960 °C. The high sintering temperature of crystalline ceramic materials can be lowered by adding low melting low loss glasses or additives. There are low loss glass-free ceramics with inherently low sintering temperatures. In LTCC the green dielectric tape with passive components is cofired with the common electrode silver at temperatures less than the melting point of silver (961 °C). Slightly higher cofiring temperatures are possible with copper or gold electrodes. The low sintering temperature enables the fabrication of embedded microwave components and transmission lines using highly conductive metals such as silver with low conductor loss and electrical resistance at high frequencies. LTCC is a multilayer capable substrate technology offering excellent RF and microwave performance characteristics. The excellent mechanical and electrical properties of LTCC substrates, combined with the ability to embed passive components, offer superior RF performance and device miniaturization for high frequency applications.

LTCC technology has become very important for modern compact electronic products. For high frequency applications low permittivity materials are required for increasing the signal speed and to minimize parasitic capacitances. The increase in frequency leads to a decrease in the widths of lines in printed circuits and is too narrow to realize by screen printing, especially when the relative permittivity is high. The lowest relative permittivity reported among the LTCC materials is 4.0 for $KGaGe_3O_8$ with Qf of 10 200 GHz. Among the commercially available LTCC systems, the Electro-Science Lab 41110 and Alcoa have the lowest relative permittivity of 4.2 with a loss tangent of about 0.003 at 3 GHz. One method to lower the permittivity is by introducing porosity. Hence recently Sobocinski *et al.* [25] lowered the relative permittivity of LTCC by porosification with poly(methyl methacrylate) microspheres. However, introduction of porosity affects the loss factor, mechanical properties, and leads to diffusion of conductor pastes. In LTCC, the introduction of porosity by lowering the sintering temperature is not advisable for the use of commercial thick film pastes.

8.5.2 Important Characteristics of LTCC

The LTCC tapes are fabricated in a way similar to HTCC tapes. However, the ceramic filler contents are different. In the LTCC fabrication process, a slurry containing ceramic powder or with low loss glass and/or sintering aids is initially prepared with suitable binders and organic solvents. It is then cast under “doctor blades” to obtain green tapes with a suitable

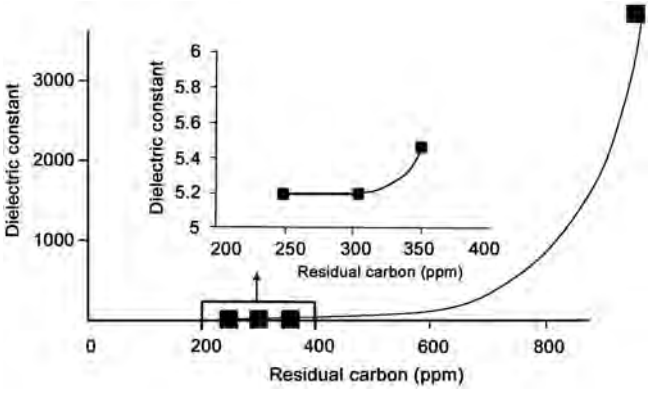

Figure 8.8 *Variation of relative permittivity as a function of residual carbon in glass–ceramics. Source: Adapted from Tummula 1991 [27].*

thickness, usually in the range 50 to 300 μm. Then holes or vias are made on the tape by mechanically punching or laser-aided micromachining followed by filling with a conductive paste. Stencil and screen printing processes are used to generate conductive patterns. The ceramic tapes thus obtained are then stacked, laminated, and sintered followed by post-firing metallization, electrical testing, and final assembly. For details the reader is referred to references [3] and [26]. Although the LTCC technology is advantageous for high frequency applications, there is rigorous demands on the materials requirement and properties.

In the glass–ceramic composites, the main phase is a dielectric material having a high sintering temperature. Addition of a suitable glass phase can lower the sintering temperature of the dielectric to a required level depending on the amount and type of the glass composition. In these composites, the crystalline phase makes a significant contribution to the dielectric properties. The glass phase lowers relative permittivity and increases the dielectric loss. The selection of glass materials is very important and influences the mechanical and dielectric properties of the composites [26]. The densification or crystallization of the composite should be at temperatures above 800 °C in order to enable the evaporation of the organics and solvents used in conductive pastes and binder and plasticizers causing residual carbon traces in the microstructure [27, 28]. The presence of residual carbon that may form during binder decomposition if left in the LTCC would adversely affect the dielectric properties, as shown in Figure 8.8. The residual carbon content should be below 300 ppm to get the useful dielectric properties [27]. Figure 8.9 shows that the removal of last traces of carbon from the green sheet extends up to about 800 °C. Hence the densification of the ceramic should start above 800 °C [27]. Thus complete carbon removal makes the selection and identification of a suitable composition very challenging. The functionality of a particular LTCC material depends on the dielectric properties. For substrate applications low relative permittivity materials with ε_r in the range of 4–12 are used whereas high permittivity materials are used mainly for capacitor layers or resonating structures. Signal propagation is one of the most important aspects in electronic packaging and is related to the relative permittivity. The signal propagation delay t_d is given by [29]

$$t_d \sim l(\varepsilon_r)^{1/2}/c$$

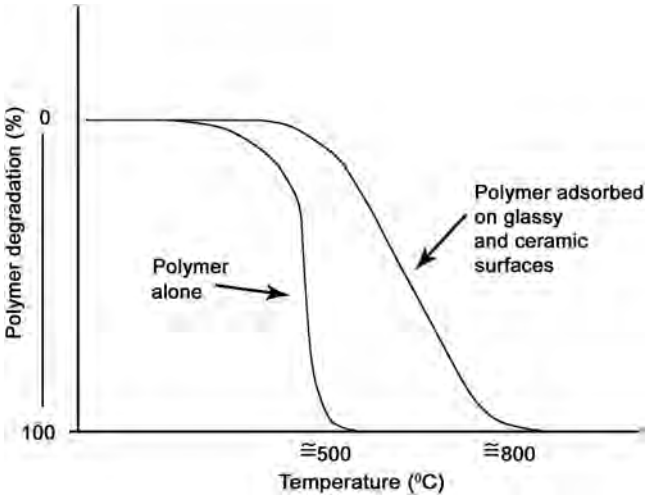

Figure 8.9 *Polymer degradation in neutral atmosphere. Source: Adapted from Tummula 1991 [27].*

where l is the line length, ε_r is the relative permittivity of the substrate, and c is the speed of light. Hence a low relative permittivity LTCC substrate is required for increasing the signal speed [27]. Figure 8.10 shows the variation of propagation delay as a function of the relative permittivity of the ceramic materials. There are LTCC materials with high permittivity that can enable small embedded capacitors, inductors, filters and antennas [23,24,30]. In LTCC technology, the main losses are conductor losses and their role increases with increasing frequency.

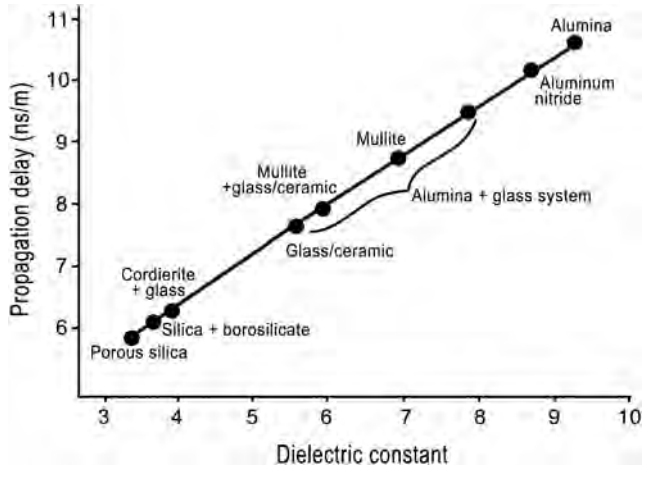

Figure 8.10 *Signal propagation delay as a function of relative permittivity with different ceramic materials. Source: Adapted from Tummula 1991 [27].*

The thermal conductivity of LTCC should be high in order to remove the heat generated by the device during operation and is critical for the efficient and reliable functioning of the device. The heat removal is more critical in the fabrication of high density and high power devices that can operate at high speed. The LTCC has low thermal conductivity usually of the order of 2–5 W/m K [31], but is 10 times higher than that of organic laminates. In high power applications, such as microwave amplifier packages, the low thermal conductivity of LTCCs considerably affects the performance. The coefficient of thermal expansion (CTE) of the LTCC should match with the systems based on silicon chips and other components mounted on the substrate. A thermal expansion mismatch would give rise to failure of solder connections between the chip and the substrate. The CTE should thus be chosen such that it matches the value of the mounting board and chip. Table 8.8 gives a list of commercially available LTCCs and their properties. These materials have relative permittivity in the range 4 to 25 with low loss tangents down to 0.0001.

8.5.3 Glass–Ceramic Composites

Most of the low loss dielectric ceramics have relatively high sintering temperatures. There are several methods to lower the sintering temperature of ceramics, such as use of glasses with low melting temperatures, addition of low melting oxides as sintering aids, chemical processing, and using starting materials with a small particle size. The chemical processing method or the use of small particles are less commonly used for LTCC technology. The use of glasses is found to be an effective way to decrease the firing temperature and is the most commonly employed method. The important low loss glasses and glass ceramics are discussed in Chapter 7. In practice, there are two approaches to exploit glasses to obtain ceramic compositions sinterable below 950 °C. The first approach is via the glass–ceramic route, which starts with a fully glassy system that devitrifies almost completely during the sintering process. The devitrification of glass greatly increases the viscosity of the system during firing, thereby improving the resistance to distortion [32]. The starting materials used in this approach are pure glasses, such as cordierite glass [32], which densifies first, followed by crystallization. The physical properties of the resulting composition are controlled by the degree of crystallization, which can be enhanced by the addition of a small amount of crystalline phase, which acts as a nucleating agent. During sintering, the glass recrystallizes to low loss phases and produces a low dielectric loss ceramic body [33]. The glass is transformed into a dense glass–ceramic during sintering and there should be a reasonable amount of crystallization to get a low loss composite. For example, during sintering of Ferro A6M, which contains $CaO—SiO_2—B_2O_3$ glass, wollastonite ($CaSiO_3$) crystallites are formed with some residual borosilicate glass in the sintered product. This type of dielectric tape has low losses and is suitable for 20–30 GHz applications such as in military and aerospace applications. In the glass–ceramic approach, the starting material consists of a low softening point glass and a crystalline ceramic [22, 32, 34, 35]. The glass–ceramic densifies by a three-stage liquid phase sintering by particle rearrangement, dissolution and precipitation, and solid-state sintering [35–39]. The glass–ceramic composite sinters by reactive and non-reactive liquid phase sintering depending on the amount of glass and type of glass [40]. The densification mechanism of glass–ceramic can be further classified as non-reactive, partially reactive, and completely reactive system, depending on the reactivity between the glass and ceramics. In non-reactive systems, such as borosilicate

Table 8.8 *Commercial LTCC tapes*

LTCC supplier	Composition	k	tan δ/Q (f)
Schott AG	Al_2O_3+glass	7–8	0.005 (10 GHz)
KOA	–	7	0.003 (1 MHz)
Dupont 943	–	7.5	0.001 (3 GHz)
Dupont 951	(Al_2O_3+$CaZrO_3$+glass)	7.8	0.006 (6 GHz)
Dupont 9K7	Al_2O_3+glass	7.2	0.002 (9 GHz)
Fujitsu	Al_2O_3+BSG	7.8	–
	Al_2O_3+SiO_2–B_2O_3	4.9	–
Asahi glass	Al_2O_3+Fosterit+BSG	7.4	800(10 GHz)
Murata	$CaZrO_3$+glass	25	700 (5 GHz)
	BaO–Al_2O_3–SiO_2	6.1	300 (2 GHz)
	BaO–Al_2O_3–SiO_2–B_2O_3–CaO	6.1	0.0007
Sumitomo metal	CaO–Al_2O_3–SiO_2–B_2O_3+Al_2O_3	7.7	–
Hitachi	Pb–aluminobrosilicate+Al_2O_3,$CaZrO_3$	9.0–12.0	0.001–0.003
	BaO–Al_2O_3–B_2O_3–	7.0	–
	SiO_2+Al_2O_3+$ZrSiO_4$		
Niko	NL–AgII	7.8	>300 (1 MHz)
	NL–AgIII	7.2	>300 (1 MHz)
Maruwa	HA-995	9.7	–
Ferro	A6M	5.9	500 (3 GHz)
	A6–B	6.5	0.005
Electro-Science	41020-70C	7–8	200 (1 MHz)
Lab	41110	4.2	0.0037 (3 GHz)
Heraeus	CT700	7.5–7.9	450 (1 GHz)
	CT2000	9.1	1000 (450 MHz)
Alcoa	Borosilicate glass+SiO_2+dopants	3.9–4.2	<0.003
Shoei	$BaZr(BO_3)_2$	7.0	0.001
Noritake	Al_2O_3–fosterite+glass	7.4	
Toshiba	BaO–SnO_2–TiO_2–B_2O_3	7–13	0.0005–0.0008
Tektronix	MgO–CaO–silicate+Al_2O_3	5.8	0.0016
Motorola	T2000	9.1	0.003
Amkor	GCS 50	5.0	0.001 (10 GHz)
	GCS 71	7.1	0.005 (10 GHz)
	GCS60	6.0	0.001 (10 GHz)
	GCS44	4.4	0.001 (10 GHz)
	GCS2000	18.0	0.006 (10 GHz)
Taiyudan	Al_2O_3–CaO–SiO_2–ZrO_2–MgO–B_2O_3	6.7	0.001
	Al_2O_3–SiO_2–ZrO_2–MgO	7.3	0.002
EPCOS	K8	7.8	0.001
EMCA	T8800	7.2	0.002
Matsushita	MKE–100 (PbO–glass+Al_2O_3)	7.8	500 (1 MHz)
NTK	GC-11	7.9	200 (3 GHz)
	NOC–F1	6.3	0.0028 (40
	GC–21	7.6	GHz)
			0.003 (3 GHz)

(*continued*)

Table 8.8 *(Continued)*

LTCC supplier	Composition	k	tan δ/Q (f)
NEC	MLS–25M (Al_2O_3–B_2O_3–SiO_2)	4.7	300 (2.4 GHz)
	MLS–41 (Nd_2O_3–TiO_2–SiO_2)	19.0	500 (2.4 GHz)
	MLS–61	8.0	500 (2.4 GHz)
	GCS 78 (PbO–Al_2O_3–SiO_2)	8.1	150 (2.4 GHz)
	GCS 71	7.8	>300 (1 MHz)
	GCS 60	7.1	>300 (1 MHz)
Kyocera	G55 (BSG+SiO_2+Al_2O_3+cordierite)	5.0	800 (10 GHz)
	GL 660	9.5	300 (10 GHz)
	JHB 62 (Pb-borosilicate	7.9	0.0002 (2 GHz)
	glass+Al_2O_3+SiO_2)	18.7	0.00025 (2 GHz)
	JLB 62	9.4	0.0005 (3.2 GHz)
	AAB 62	6.0	0.0017
	GL560	4.9	0.0006 (2 GHZ)
	GL 530		

glass (BSG)–cordierite, the densification mainly occurs by particle rearrangement [41,42]. The amount of glass content required for densification decreases with an increase in the particle size ratio between the ceramic filler and glass [43]. In certain systems, the glass not only serves as a bonding agent to hold the ceramic particles but also reacts with filler ceramic at the sintering temperature to form high Q crystalline phases. In this type of reactive system, the sintering conditions, like heating rate, sintering temperature, and duration, control the microstructure, phases, and final properties. The liquification of glass takes a dominant role in the viscous flow mechanism among constituents and so the selection of suitable glass is important for good sinterability. The liquification of the glass is the key mechanism for sintering in glass ceramic composites. The glass penetrates the 3D mesh structure formed by the ceramic particles and facilitates the wetting of each ceramic particle surface with glass melt. The amount of glass content, its softening temperature, and particle size are important for densification of glass ceramic composites [44,45]. The ceramic has the effect of hindering the flow of the glass and hence the use of ceramic with a large particle size lowers the specific surface area, and is beneficial in improving the sintered density.

SiO_2 and B_2O_3 glasses commonly form the network structures of glass. The SiO_2, for example, has a high melting point and high viscosity. Thus when the SiO_2 content is large, the glass has a high transition temperature, low thermal expansion, and better chemical stability. The addition of B_2O_3 to silica glass lowers the viscosity. Na_2O, PbO, K_2O, Li_2O, CaO, MgO, and BaO are modifier oxides. Na_2O lowers the softening point considerably, but it increases the CTE and degrades the stability. However, the addition of Na_2O and Li_2O modifiers increases the ionic conductivity and the Li_2O crystallizes readily. Al_2O_3 can form AlO_4 tetrahedrons and connect to the network structure and has the effect of controlling crystallization. The glass basically only softens and wets the ceramic powder during sintering, providing a dense hermetic structure. The volume fraction of the added glass determines the sintering characteristics and the crystalline filler is a major determinant of electrical properties, also increasing viscosity during sintering and thereby minimizing distortion. The crystalline phase also increases the mechanical strength of the final LTCC. Thus the properties of the final glass–ceramic are controlled by the ratio of glass to ceramic

and the individual properties of the mixtures. The use of glass or sintering aids, although an effective method to develop LTCC systems by lowering the sintering temperature of an original dielectric ceramic, is usually accompanied by an abrupt degradation of the dielectric properties due to the formation of secondary phases. Only in a few cases could the sintering temperature be reduced without degradation of the dielectric properties due to the enhancement of the density of the ceramics or elimination of oxygen vacancies [46]. The effectiveness of sintering aids depends on several factors, such as sintering temperature, viscosity, solubility, and glass wettability [47]. The main requirement for liquid phase sintering is that the liquid phase should wet the grains of the ceramics.

8.5.4 Microwave Dielectric Properties of Glasses

The microwave dielectric properties of ceramics with glass additives strongly depends on the densification, microstructure, and interactions between glass and ceramics. Single components with a low melting point are often used as sintering aids, but they easily form complex compounds with matrix ceramics, degrading the dielectric properties [48]. However, complex additives and multicomponent glasses are much more effective in reducing the sintering temperature of ceramics with good microwave dielectric properties [49]. Generally, low softening temperature glass materials were mixed with the ceramic materials to reduce the firing temperature. However, network formers contained in the glass materials may absorb the microwave power profoundly in the high frequency region, degrading the quality factor for the material [50]. At least three types of loss for glasses have been distinguished [51]: resonance type vibration losses at very high frequency, migration losses caused by the movement of mobile ions (mainly alkali ions), and deformation losses by defect or deformation of the basic silicon oxide network. Resonant type vibration losses are particularly important in the microwave region. Among the glasses, silica glass has the lowest tan δ in the microwave region [52,53]. The tan δ of fused silica is less than 0.0001 in the microwave frequency region [54]. However, silica when used alone is not an effective flux to lower the sintering temperature for low loss dielectric ceramics. To lower the melting point, the rigid bonds in SiO_2 need to be broken by suitable modifiers such as alkali ions in order to lower the melting point. However, the use of alkali ions adversely affects the loss factor [53, 55]. The tan δ of silica-based binary glasses such as borosilicate (B_2O_3–SiO_2) is about 0.001 at 3 GHz [56]. The ternary glasses such as lithium borosilicate, aluminum borosilicate, and soda borosilicate have a loss tangent in the range 0.001 to 0.004 at 3 GHz [53, 56]. Wu and Huang [57] investigated the microwave dielectric properties of several low melting borosilicate glasses based on Pb, Zn, and Ba. They have ε_r in the range 7–19.5 depending on the composition and losses of the order of 1×10^{-3} and have negative τ_f.

Several authors investigated [58–70] the crystallization behavior and dielectric properties of $CaO—SiO_2—B_2O_3$, $BaO—CaO—Al_2O_3—B_2O_3—SiO_2$, $MgO—Al_2O_3—B_2O_3—SiO_2$, $BaO—SrO—SiO_2$, $BaO—Al_2O_3—B_2O_3—SiO_2$, and $Li_2O—Al_2O_3—SiO_2$ glass—ceramics and the effect of doping with TiO_2, ZnO, P_2O_5, Na_2O, PbO, etc. The glass transition and crystallization temperatures depend on the network modifiers or dopants. These glass–ceramics densify at temperatures in the range 700–950 °C with ε_r in the range 6 to 11 and loss tangent less than 10^{-3}. During sintering several low loss crystalline phases are formed, which control the dielectric and thermal properties. Takada *et al.* [71, 72] reported that the *Qf* improved when a mixture of amorphous melt and crystalline mixtures of $La_2O_3—B_2O_3$

was fired. The best dielectric properties, $Qf = 72\,000$ GHz and $\varepsilon_r = 8$ at 13 GHz, with low firing temperatures of 900 °C, were found when the mixing ratio of La_2O_3—$2B_2O_3$—0.5ZnO was 20% crystalline melt and 80% amorphous melt. Kagata *et al.* [73] reported that MgO—Sm_2O_3—Al_2O_3 ($MgSmAl_{11}O_{19}$) and Al_2O_3—SiO_2—B_2O_3 in equal amounts and sintering at 920 °C resulted in LTCC with $\varepsilon_r = 7.8$, $Qf = 10\,000$ GHz, and $\tau_f = 11$ ppm/°C.

8.5.5 LTCC Materials and Their Properties

In 1994, Takada *et al.* [64] reported for the first time the effect of glass additions on the microwave properties of dielectric ceramics. Since then, several different types of low melting glasses and sintering aids have been added to several low loss dielectric ceramics to bring down the sintering temperature below 950 °C. It may be noted that there are several dielectric materials with inherently low sintering temperatures less than 950 °C and are discussed in a subsequent section. The following sections explain the important compositions researched and the microwave properties thus reported. There are about 1000 low loss dielectric materials with sintering temperatures in the range 700 to 950 °C and are tabulated with properties in the Appendix, which appears at the end of Volume II.

8.5.5.1 Alumina

Alumina, which has a relative permittivity of 9.5 with a very high quality factor, although having a relatively high τ_f (–60 ppm/°C) and high sintering temperature (1550°C), is widely used as a substrate material for high frequency applications. It is a good basic material to start development of low permittivity LTCC [74]. Many authors investigated [73,75–91] the effect of various glass additions, such as ZnO—B_2O_3 (ZB), MgO—Al_2O_3—SiO_2—GeO_2 + ZB, ZnO—La_2O_3—B_2O_3, La_2O_3—B_2O_3, ZnO—Nd_2O_3—B_2O_3, Al_2O_3—B_2O_3—SiO_2, CaO—La_2O_3—B_2O_3, CaO—Al_2O_3—SiO_2—TiO_2—B_2O_3, MgO—La_2O_3—B_2O_3, CaO—Al_2O_3—SiO_2—B_2O_3, Bi_2O_3—B_2O_3—ZnO—SiO_2 (BBSZ), CaO—B_2O_3—SiO_2, etc., on the sintering behavior and microwave dielectric properties of alumina. The firing temperature is a dominant factor in controlling the dielectric properties due to the formation of crystalline phases at certain temperatures and hence should thus be carefully controlled to get useful properties. Dai reported [92] that the heating rate has a profound influence on the crystallization process, densification, shrinkage, and dielectric properties of Dupont 9k7 LTCC tapes, which consist of Al_2O_3 filler, crystallizable glass, and organic vehicles. Figure 8.11 shows the Z shrinkage of laminated tapes in the temperature range 600 to 800 °C. Although the shrinkage of all samples are completed below 800 °C, the onset and end of shrinkage is found to depend on the heating rate. The shrinkage and density are found to increase with an increase in the heating rate. Figure 8.12 shows the variation of X, Y, and Z shrinkage and bulk density as a function of the heating rate. The relative permittivity increased when the heating rate increased and the *Qf* showed only a small variation, as shown in Figure 8.13. An X-ray diffraction study showed multiple crystallization of $LaBO_3$, $AlPO_4$, $CaAl_2B_2O_7$, and $LaPO_4$ at all heating rates. Figure 8.14 shows the TEM images of 9k7 sintered by heating at 10 °C/min and 5 °C/min. The different crystallized phases are evident in the microstructure. Dai suggested that an optimized sintering profile with an appropriate heating rate is needed for good densification prior to onset of crystallization followed by full crystallization to limit the amount of residual glass for improved dielectric properties.

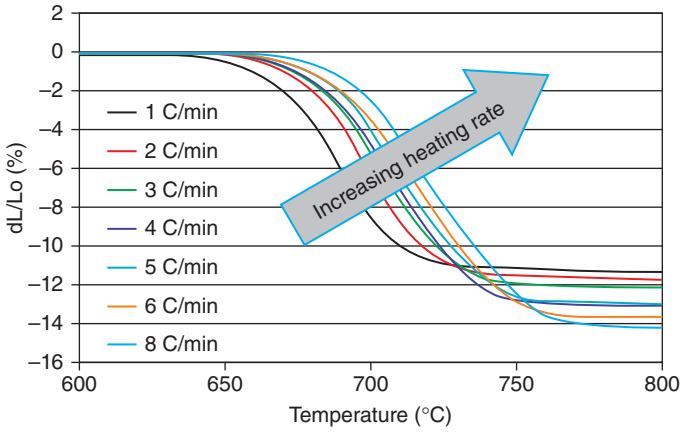

Figure 8.11 *Variation of Z shrinkage of 9K7 at different heating rates on sintering at 800 °C. Source: Dai 2012 [92]. Reproduced with permission of John Wiley & Sons.*

The Motorola LTCC T2000 consists of alumina filler with B_2O_3—K_2O—SiO_2—CaO—SrO—BaO glass and the large negative τ_f of alumina glass–ceramic compensated with TiO_2, which has a positive τ_f. An X-ray diffraction study of T2000 revealed that during sintering Al_2O_3 reacted with the glass and formed anorthite type crystalline phases $MSi_2Al_2O_8$ (M = Ca, Sr, or Ba) [93]. The consumption of SiO_2, CaO, SrO, and BaO to form anorthite greatly decreased the amount of glass in the final product and results in a high Qf. The dissolution of Al_2O_3 into the glass and subsequent formation of crystalline phases via a diffusion controlled process were observed [94]. The T2000 dielectric has $\varepsilon_r = 9.1$ and $Qf = 2500$ GHz. Figure 8.15 shows how the τ_f of T2000 can be adjusted over a wide range,

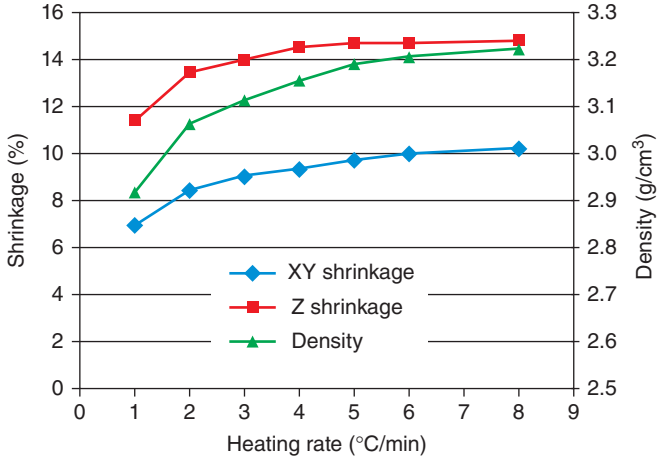

Figure 8.12 *Variation of XY and Z shrinkage and bulk density with heating rate sintered at 800 °C. Source: Dai 2012 [92]. Reproduced with permission of John Wiley & Sons.*

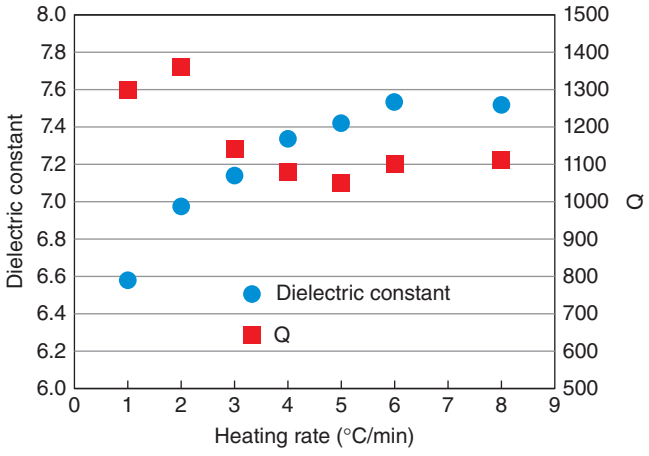

Figure 8.13 *Variation of dielectric constant and quality factor Q with heating rate on sintering at 800 °C. Source: Dai 2012 [92]. Reproduced with permission of John Wiley & Sons.*

depending on the amount of TiO_2 in the composite. The composite has τ_f of –80 ppm/°C in the absence of TiO_2. They suggested from extensive TEM and EDS analysis that during sintering, part of the TiO_2 dissolves in the glass matrix and acts as nucleation agents for the subsequent growth of the titanium-rich crystalline phases. The compensating mechanism of TiO_2 for τ_f can be significantly different from that of a TiO_2 addition to a non-reactive LTCC dielectric. Dai *et al.* [93, 94] proposed that the τ_f of T2000 is adjusted by the combined effect of residual TiO_2, titanium in the glass matrix, and the titanium-rich crystalline phases. The TiO_2 dissolves into the glass during sintering and forms titanium-rich plate-like crystalline phases via a nucleation and growth process. This process makes the τ_f modification more efficient than a simple mixing of TiO_2 into the composition.

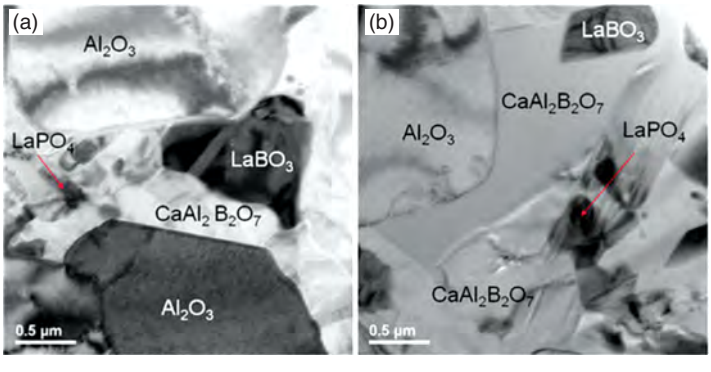

Figure 8.14 *TEM images of the microstructure 9K7 sintered by heating at (a) rate of 1 °C and (b) 5 °C/min. Source: Dai 2012 [92]. Reproduced with permission of John Wiley & Sons.*

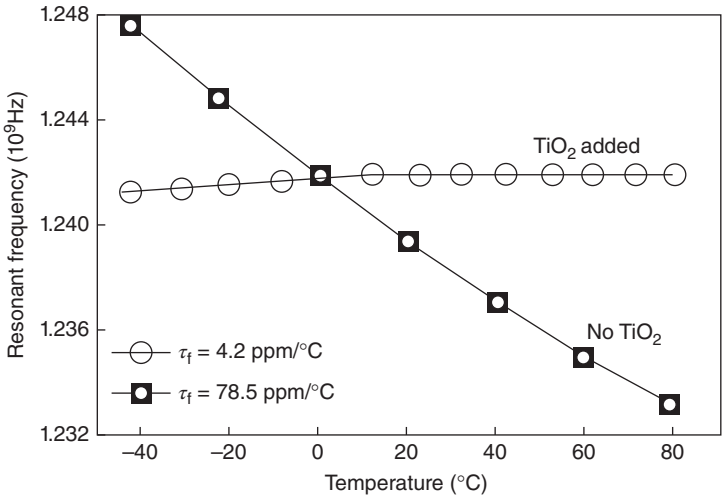

Figure 8.15 *Variation of resonant frequency with and without TiO_2 addition in T2000 glass–ceramic system. Source: Dai 2002 [93]. Reproduced with permission of John Wiley & Sons.*

8.5.5.2 TiO_2

The TiO_2 is widely researched as a basic ceramic for high permittivity LTCCs. Several approaches including monosized [95] or nanosized [96] TiO_2 have been attempted in order to sinter the TiO_2 ceramics at temperatures lower than 1000 °C. Kim *et al.* in 1992 reported [97] that the addition of about 2 wt% CuO to TiO_2 significantly lowered the sintering temperature to 900 °C, resulting with $\varepsilon_r = 98$, *Qf* of 14 000 GHz, and τ_f of 374 ppm/°C. Several authors studied [98–101] TiO_2 with borosilicate glass (BSG), which are the most commonly used glass materials in glass–ceramic composites for microelectronic packaging. Yoon *et al.* [99] prepared composites of anatase TiO_2 with 20 wt% of borosilicate glass and zinc borosilicate glass (ZBSG), and studied their sintering behavior, phase evolution, and microwave dielectric properties. It was found that the wetting behaviou of a glass with the basic ceramic has an important role in the properties. The BSG did not react with TiO_2 but ZBSG reacted with TiO_2, forming a second phase of Zn_2SiO_4 that affected the microwave properties of the composite. The highest *Qf* (11 000 GHz) value was achieved with the non-reactive system (TiO_2 with BSG) when sintered at 900 °C, and the material showed a relative permittivity of about 55 with a relatively high τ_f over 300 ppm/°C. The addition of ZBSG resulted in ε_r of about 75 with *Qf* of about 8000 GHz. On the other hand, Jean and Lin [100] studied the effects of borosilicate addition on the densification and dielectric and thermal expansion properties of TiO_2 using both in rutile and anatase phases. They reported that anatase has better wetting properties with BSG and hence results in a larger densification than rutile [100]. The densification was controlled by viscous flow of BSG. Yano *et al.* [98] reported the modification of τ_f by adding TiO_2 in glass–ceramic in which the reaction of TiO_2 with glass was purposely minimized by coarsening the TiO_2 particles via heat treatment. They reported that 15 wt%TiO_2 was necessary to decrease the original τ_f of an undoped LTCC dielectric from 250 ppm/°C to almost 0 ppm/°C. Miyauchi and Arashi

[102] reported that the viscosity of the glass–ceramics increased with decreasing TiO_2 average particle size and the effect was attributed to the ability of smaller particles to more effectively obstruct glass liquefaction. Several authors investigated [103–107] the anorthite ($CaO—Al_2O_3—2SiO_2$:$CaAl_2Si_2O_8$) glass–ceramic system with TiO_2 as a potential material for LTCC applications. The anorthite is an important material for LTCC substrates due to its lower CTE and low relative permittivity as compared to alumina [104]. Lo *et al.* [108] and Marques *et al.* [109] reported a low temperature anorthite glass–ceramic composite by reducing the particle size of glass powders to the submicrometer scale. Addition of TiO_2 into this glass powder has been reported to play the role of nucleating agents to reduce the crystallization temperature below 900 °C [106]. Lo *et al.* [107] investigated the sintering behavior of TiO_2 nucleated anorthite-based glass–ceramics ($CA—Al_2O_3—SiO_2—TiO_2$) with different compositions. They reported that the anorthite glass densified and crystallized on sintering at 950 °C and the glass–ceramic showed a CTE in the range 4–5 ppm/°C, which is very close to silicon. The relative permittivity of the composite, however, increased with TiO_2 content, but in this case the temperature dependence of the permittivity was only slightly influenced.

8.5.5.3 *Bi_2O_3-Based Compounds*

Among the bismuth-based ceramics, $Bi_2O_3—ZnO—Nb_2O_5$ (BZN) ternary oxides received considerable attention. Several research groups [110–113] studied the structure and properties of $BiO—ZnO—Nb_2O_5$ ceramics. There are two main phases in BZN, a cubic pyrochlore phase $Bi_{1.5}ZnNb_{1.5}O_7$ (α-phase) with ε_r of about 150 and τ_ε of about −400 ppm/°C, and a monoclinic zirconolite-like phase $Bi_2Zn_{2/3}Nb_{4/3}O_7$ (β-phase) with ε_r of about 80 and $\tau_\varepsilon \sim +150$ ppm/°C. Several authors [114–120] reported that the sintering temperature of $Bi_2O_3—ZnO—Nb_2O_5/Ta_2O_5$ can be lowered by suitable doping, such as B_2O_3, V_2O_5, $CuO—V_2O_5$, $BaCO_3—CuO$, $MoO_3—CuO$, $PbO—Bi_2O_3—B_2O_3—ZnO—TiO_2$, etc. The 0.5 wt% addition of B_2O_3 lowers the sintering temperature of $Bi_2(Zn_{1/3}Ta_{2/3})_2O_7$ to about 850 °C, forming a low temperature monoclinic phase with ε_r of about 63, $Qf = 3500$ GHz, and $\tau_f = -14$ ppm/°C [114]. Although a vanadate-based addition lowers the sintering temperature considerably, it must be noted that silver is reactive [121, 122] with V_2O_5 and hence not suitable for LTCC. Youn *et al.* [112] formulated high relative permittivity bismuth pyrochlore dielectric composition with low dielectric loss at microwave frequencies. These compositions closely matched [123, 124] the shrinkage profiles with certain commercially available LTCC systems, allowing cofiring of systems with two materials. The high ε_r bismuth-based compounds were integrated into a low ε_r LTCC matrix and cofired to produce a miniaturized, microstrip bandpass filter with excellent characteristics. Baker and coworkers [123, 124] used a series of loop inductors and parallel plate capacitors to develop a unique miniaturized patch antenna with antenna size reduction up to 93% with good bandwidth and gain characteristics. The incorporation of high ε_r bismuth pyrochlore capacitors in low ε_r LTCC substrates was found [123, 124] to decrease the bandpass filter size with improvement in the overall filter characteristics. Several authors [30, 125–129] also investigated the microwave dielectric properties of $BiAO_4$ (A = Nb/Ta) with small amounts of CuO or V_2O_5, CuV_2O_6, B_2O_3 to lower the sintering temperature and reported dense ceramics with ε_r in the range 40–45, Qf up to 30 000 GHz, and low τ_f when sintered at 950 °C.

8.5.5.4 $BaO—TiO_2$ System

Several groups [130–141] studied the effect of adding glasses, such as B_2O_3, BBS, LBS, ZB, glass frit, $PbO—B_2O_3—SiO_2$, BCB + CuO, BaB_2O_4, etc., in $Ba_2Ti_9O_{20}$, $BaTi_4O_9$, and $BaTi_5O_{11}$ ceramics. It was found that addition of 5 wt%B_2O_3 and sintered at 900 °C gave single phase $Ba_2Ti_9O_{20}$. However, the addition of larger amounts of B_2O_3 led to the formation of $BaTi(BO_3)_2$ and rutile secondary phases. The best composition with $BaTi_4O_9$ was reported by Zhou and Jean [134]. They increased the BaO content in the barium zinc borate (BZB) glass addition of 0—20 mol% BaO content in 90 vol.% $BaTi_4O_9$, resulting in the variation of ε_r in the range 28–33 and Qf in the range 15000–20000 GHz. The $BaTi_5O_{11}$ containing 1 wt% CuO and 4 wt% BCB and sintered at 925 °C showed ε_r of 37.4 with Qf of 25 500 GHz and τ_f of 33 ppm/°C [141].

Tungsten bronze type $BaO—Ln_2O_3—TiO_2$ ceramics (Ln = Nd/Sm) sintered at about 1400 °C are well-known microwave compositions having moderately high relative permittivity (70–100), high Qf (>7000 GHz) and zero τ_f. $BaO—Ln_2O_3—TiO_2$ (Ln = Sm/Nd) in 1:1:4 or 1:1:5 compositions are especially suitable for dielectric resonators in mobile phone handsets [142]. These compositions have also been investigated by several authors [143–153] as a basic dielectric for LTCCs. The sintering temperatures of tungsten bronze-type materials have been lowered by adding different additives such as $BaCu(B_2O_5)$, $La_2O_3—B_2O_3—TiO_2$, BBSZ, $BaO—B_2O_3—SiO_2$, $Li_2O—ZnO—B_2O_3$, B_2O_3, $Li_2O—B_2O_3—SiO_2$, $Li_2O—B_2O_3—SiO_2—Al_2O_3—CaO$, GeO_2, etc. Dernovsek *et al.* [148] reported the effect of addition of $B_2O_3—Bi_2O_3—SiO_2—ZnO$ (BBSZ) and $La_2O_3—B_2O_3—TiO_2$ (LBT) modified by BaO, ZrO_2, and SrO on the densification and microwave dielectric properties of $BaNd_2Ti_4O_{12}$ ceramics. The addition of 10 vol.% BBSZ lowered the sintering temperature to 900 °C, producing a composition with ε_r of 68, Qf above 6000 GHz, and zero τ_f. An even higher Qf (8500 GHz) was achieved by Cheng *et al.* [153, 154] with the addition of $42BaO–45B_2O_3–13SiO_2$ in $Ba(Nd, Sm, Bi)_2Ti_5O_{14}$. Sintering performed at about 900 °C, however, resulted in a decrease of ε_r to 40. It was also found that the wetting ability of the glass by recalcining the glass–ceramic mixture improved the microwave dielectric properties [153]. The highest Qf values in tungsten bronze-based LTCCs was reported by Park *et al.* [155]. They reported the relative permittivity and Qf value of 32 and 9000 GHz, respectively, to the composition made of MBRT-90 ($Ba(Nd, Sm, Bi)_2Ti_4O_{12}$) with 10 wt% $52.45Li_2O—31.06B_2O_3—11.99SiO_2—2CaO—2.5Al_2O_3$ and sintered at 875 °C. However, these microwave ceramics easily formed secondary phases with glasses that were added to decrease the sintering temperature. The secondary phases thus formed altered the relative permittivity [143, 150, 151] and the microstructure.

8.5.5.5 Columbites

The columbites MNb_2O_6 (M = Ca, Co, Mn, Ni, or Zn) ceramics are known [156, 157] as useful microwave dielectric materials. The $ZnNb_2O_6$ sintered at 1150 °C for 2 h has Qf of 83 700 GHz and ε_r of 25 [157]. Several authors reported [158–166] low temperature sintering of columbites by using additives such as $ZnCuB_2O_5$, $B_2O_3—SiO_2$, $ZnO—V_2O_5$, $CuO—B_2O_5$, $V_2O_5—Bi_2O_3—CuO$, TiO_2 + CuO, etc. Kim *et al.* [158] reported that addition of 5 wt% CuO to $ZnNb_2O_6$ resulted in the formation of $(ZnCu_2)Nb_2O_8$ secondary phase, which has a low melting point and lowered the sintering temperature to about 900 °C

through liquid phase sintering. The $(ZnCu_2)Nb_2O_8$ phase has excellent dielectric properties ($\varepsilon_r = 16.7$, $Qf = 41\,000$ GHz, and $\tau_f = -76$ ppm/°C) and addition of CuO was able to reach a composition with $\varepsilon_r = 22.1$, $Qf = 59\,500$ GHz, and $\tau_f = -66$ ppm/°C. It was also found [159, 160] that addition or substitution of V_2O_5 to $ZnNb_2O_6$ lowers the sintering temperature to about 900 °C, but with a lossy secondary phase degrading the quality factor. However, partial substitution of V for Nb lowered the sintering temperature to 875 °C and $Zn(Nb_{0.942}V_{0.06})_2O_6$ samples showed a single phase columbite structure with ε_r of 23.9, Qf of 65 000 GHz, and τ_f of –73 ppm/°C. The $(1-x)ZnNb_2O_6$—$xTiO_2$ ($x = 0.58$) with 10 wt% CuO sintered at 875 °C showed Qf of 17 000 GHz, ε_r of 37, and τ_f of 27 ppm/°C [161].

8.5.5.6 *$ATiO_3$ (A = Mg, Ca, Zn)*

(Mg, Ca)TiO_3 is a very useful dielectric material for high frequency antenna applications. The (Mg, Ca)TiO_3 sintered at 1350 °C has $\varepsilon_r = 20$, $Qf > 85\,000$ GHz, and τ_f is 23 ppm/°C [22]. Several authors [167–174] studied the densification and microwave dielectric properties of (Mg, Ca)TiO_3 and related materials by adding ZBS, LBS, $BaCu(B_2O_5)$, Bi_2O_3—V_2O_5, CuO—Bi_2O_3—V_2O_5, LiF—Fe_2O_3–V_2O_5, etc. The additives, such as Bi_2O_3—V_2O_5, enable liquid phase sintering and usually produce secondary phases with decreasing ε_r. Decomposition of the $MgTiO_3$ to $MgTi_2O_5$ and Mg_2TiO_4 during liquid phase sintering using lithium borosilicate glass was also observed [175]. However, this decomposition does not adversely affect the dielectric properties since $MgTi_2O_5$ has $\varepsilon_r = 17.4$ and $Qf = 47\,000$ GHz and Mg_2TiO_4 has $\varepsilon_r = 14.4$ and $Qf = 55\,000$ GHz. Jantunen *et al.* [167, 168, 176, 177] made a detailed study of the effects of different glass compositions on the tape casting and the microwave dielectric properties. Nearly full density (97%) was achieved when ZSB glass ($60.3ZnO$—$27.1SiO_2$—$12.6B_2O_3$) was mixed with the (Mg, Ca)TiO_3. The fired ceramics was found to contain crystalline phases of $ZnTiO_3$, Zn_2SiO_4, $Mg_{4/3}Zn_{2/3}B_2O_5$, and TiO_2. The optimized compositions sintered at 900 °C showed excellent microwave properties such as $\varepsilon_r = 8.5$–9.5 and dielectric loss of 0.001 at 7 GHz. Jantunen *et al.* [177] prepared this composition also without adding a separate glass phase. The ceramic powder with 70 wt% glass composed of oxides ZnO, SiO_2, and B_2O_3 in the ratio of 60.3:12.6:27.1 mol.% was mixed in a ball mill, dried, pressed, and sintered at 900 °C. The samples prepared in this method were found to have better properties than those prepared by mixing glass with ceramic powder. Choi *et al.* reported [178] that addition of lithium borosilicate glass to the $CaZrO_3$—$CaTiO_3$ system lowered the sintering temperature from 1450 to 900 °C.

The ZnO—TiO_2 system contains $ZnTiO_3$ (hexagonal), Zn_2TiO_4 (cubic), and $Zn_2Ti_3O_8$ (cubic) [179]. The preparation of $ZnTiO_3$ from a mixture of ZnO and TiO_2 is difficult because the compound decomposes into Zn_2TiO_4 and rutile at about 945 °C [180]. Haga *et al.* [181] in 1992 reported for the first time the microwave dielectric properties of ZnO—TiO_2 ceramics. $ZnTiO_3$ has a negative τ_f and addition of rutile improves the τ_f close to zero [182, 183]. Several authors [182–184] studied the effect of glass addition on the sinterability and microwave dielectric properties of $ZnTiO_3$ ceramics. Addition of B_2O_3, ZnO—B_2O_3—SiO_2, ZnO—B_2O_3, B_2O_3 + LiF, etc., all lowered the sintering temperature with reasonably good dielectric properties. The best properties, $\varepsilon_r = 30$, $Qf = 56\,000$ GHz, and $\tau_f = 10$ ppm/°C, was obtained with 1 wt% addition of B_2O_3 sintered at 875 °C for 4 h [182]. The addition of 2 wt% ZBS lowered the sintering temperature to 900 °C for 3 h with

good dielectric properties of $\varepsilon_r = 27$, $Qf = 20\,000$ GHz, and $\tau_f = 2$ ppm/°C and is chemically compatible with silver [183]. The microwave dielectric properties of $ZnTiO_3$ can be improved by substituting Mg for Zn [185–188]. Zero τ_f can be obtained in $Zn_{1-x}Mg_xTiO_3$ for x in the range 0–0.1 when sintered at about 925 °C [187]. X-ray diffraction and thermal analysis showed that the stability range of the hexagonal phase increased to higher temperatures as the Mg content increased. Sintering (Zn, Mg)TiO_3 above 950 °C led to the formation of (Zn, Mg)$_2TiO_4$ and rutile, the latter enabling material with zero τ_f. Lee and Lee [187] reported that addition of 1 wt% of zinc borate ($3ZnO—B_2O_3$) to $Zn_{0.95}Mg_{0.05}TiO_3—0.25TiO_2$ lowered the sintering temperature to 900 °C, which significantly improved the density and microwave dielectric properties ($\varepsilon_r = 23.6$, $Qf = 31\,000$ GHz, and $\tau_f = -8$ ppm/°C). The $(Zn_{0.9}Mg_{0.1})TiO_3$ + 0.5 wt% ZBS ceramic sintered at 900 °C shows the best dielectric properties [188]: $\varepsilon_r = 20.53$, $Qf = 61\,600$ GHz (at 7.44 GHz), and $\tau_f = 76$ ppm/°C. Addition of TiO_2 tuned the τ_f from negative to near zero. The $(Zn_{0.9}Mg_{0.1})TiO_3$ + 3 wt% ZBS + 10 wt% TiO_2 sintered at 900 °C have $\varepsilon_r = 24.83$, Qf = 44 300 GHz (at 6.65 GHz), and $\tau_f = 3$ ppm/°C.

8.5.5.7 Lithium-Based Composites

In 2002 Borisevich and Davies reported [189–191] that $Li_{1+x-y}M_{1-x-3y}Ti_{x+4y}O_3$ (M = Nb/Ta; $x = 0.1$; $y = 0.05$–0.175) solid solutions are potential candidate materials for LTCC applications with a quality factor up to 10 500 GHz when sintered at 1100 °C. However, volatile Li has a deleterious effect on dielectric properties in Li-based ceramics and the deficiency of Li lead to a decrease in density and lattice defects. Nevertheless, several groups have reported LTCC compositions based on the $Li_2O—M_2O_5—TiO_2$ system [192–194]. A lower sintering temperature was achieved by addition of oxides or their combinations, such as Li_2O, V_2O_5, B_2O_3, and other glasses. The relative permittivity values were in the range of 20 to 65, with the *Qf* value even up to 50 000 GHz. One good example is $5Li_2O—0.583Nb_2O_5—3.248TiO_2$ + 1 wt%V_2O_5 sintered at 920 °C with $\varepsilon_r = 21.5$, $Qf = 33\,000$ GHz, and $\tau_f = 6.1$ ppm /°C [194].

George and Sebastian reported [195, 196] $Li_2ATi_3O_8$ (A = Mg, Zn) spinels that have excellent microwave dielectric properties with a sintering temperature of about 1100 °C. Addition of a small amount of low melting glasses and dopants such as LBS, LMZBS, $CuO—B_2O_3$, $ZnO—B_2O_3$, ZBS, H_3BO_3, $B_2O_3 + TiO_2$, CBS, Li_2WO_4, Bi_2O_3, etc., lower the sintering temperature below 950 °C with excellent dielectric properties [195–204]. The low temperature sintered ceramics have relative permittivity in the range 21 to 28 with *Qf* in the range 40 000 to 86 000 GHz and τ_f between 0 and –14. Figure 8.16 shows the SEM microstructure of $Li_2ZnTi_3O_8$ (LZT) and $Li_2MgTi_3O_8$ (LMT) containing different amounts of LMZBS glasses. X-ray diffraction and SEM analysis showed that the ceramics are chemically compatible with silver electrode material. Figures 8.17 and 8.18 show the variation of sintering temperature and microwave dielectric properties of LZT and LMT as a function of LMBZS glass content. This family of materials are excellent for LTCC applications and the raw materials are relatively inexpensive. In this family the composite $0.6Li_2ZnTi_3O_8—0.4Li_2TiO_3$ + 1 wt% $ZnO—B_2O_3—SiO_2$ sintered at 900 °C has a relative permittivity of 25.4, *Qf* of 86 400 GHz, and $\tau_f = -1$ ppm/°C [201]. The $Li_2Zn_3Ti_4O_{12}$ is another spinel material that shows good microwave properties and can be sintered at about 900 °C by adding glasses such as BCB and LZB [205–208]. This composites have

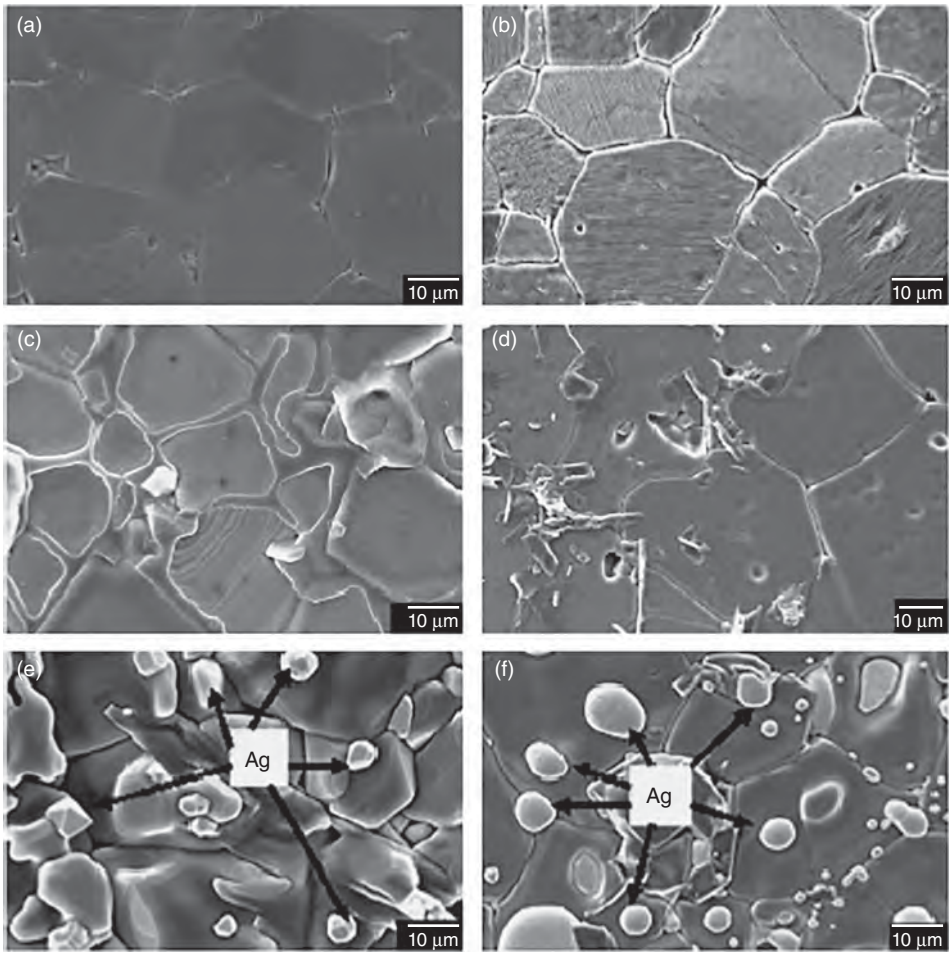

Figure 8.16 *SEM micrographs of thermally etched: (a) $Li_2MgTi_3O_8$ ceramics sintered at 1075 °C, (b) $Li_2ZnTi_3O_8$ ceramics sintered at 1075 °C, (c) $Li_2MgTi_3O_8$ + 3 wt% LMZBS glass sintered at 925 °C/4 h, (d) $Li_2ZnTi_3O_8$ + 3 wt% LMZBS glass sintered at 900 °C/4 h and $Li_2MgTi_3O_8$ + 3 wt% LMZBS glass sintered at 925 °C/4 h, (e) $Li_2MgTi_3O_8$ + 3 wt% LMZBS glass + 20 wt% Ag sintered at 925 °C/4 h, and (f) $Li_2ZnTi_3O_8$ + 3 wt% LMZBS glass + 20 wt% Ag sintered at 900 °C/4 h. Source: Adapted from George* et al. *2011 [195].*

a relative permittivity of about 17 to 19 depending on the glass additives and *Qf* up to 70 000 GHz.

The Li_2CaSiO_4 (LCS) and Li_2MgSiO_4 (LMS) are yet another family of high *Q* materials. Addition glasses such as LBS, LMZBS, ZB, PBS, LBS, and BBS lower the sintering temperatures to the range 875–950 °C with excellent microwave dielectric properties [209–213]. These composites have a relatively low relative permittivity in the range 5–7 and quality factor up to about 100 000 GHz. X-ray diffraction and SEM analysis showed the non-reactivity of silver with the LMS ceramic–glass composites. Figure 8.19 shows

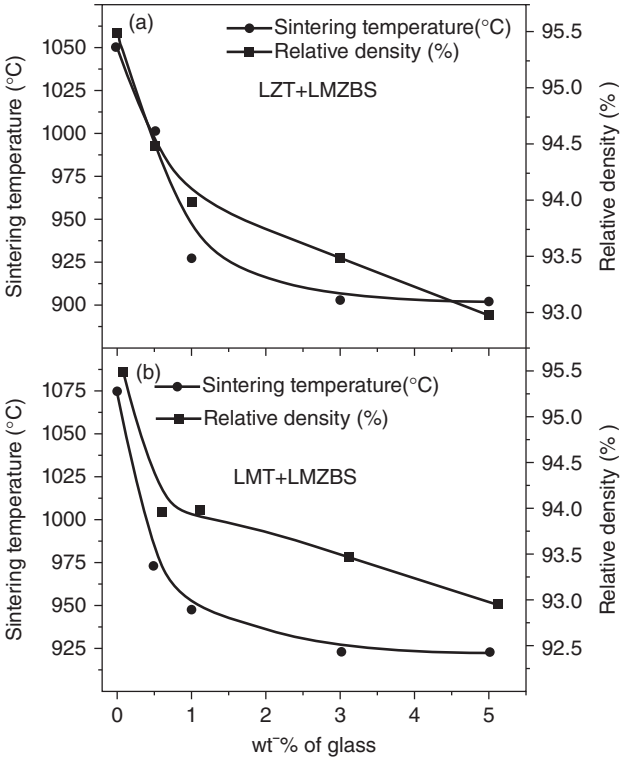

Figure 8.17 *The variation of sintering temperature and relative density of (a) $Li_2MgTi_3O_8$ and (b) $Li_2ZnTi_3O_8$ ceramics as a function of LMZBS glass. Source: Adapted from George and Sebastian 2011 [195].*

the microstructure of LMS sintered with different amounts of LBS and LMZBS glass and silver electrode material. The glass-added ceramics have a relatively dense microstructure with a grain size in the range of 5–10 μm. It is observed that both glasses melt to form a liquid phase and wet the grains of LMS, thereby promoting the densification of LMS. Figure 8.19e and f shows the SEM images of 20 wt% silver-added LMS with 1 wt% LBS and 2 wt% LMZBS glasses sintered at 925 °C/2 h and 875 °C/2 h, respectively. It is observed that the silver does not react with the glass–ceramic composite and is distributed randomly. Table 8.9 gives the dielectric properties of LMS–glass composites in the microwave frequency range. The composite containing 1 wt% LMZBS or LMS glass has a loss tangent of the order of 10^{-5} at 8 GHz [210]. Figure 8.20 shows the variation of relative permittivity of LMS and LMS with glass additive in the temperature range –40 to 120 °C measured at 1 MHz and the variations are only marginal. Another similar material is $LiAlSiO_4$ (LAS) and when sintered with 12 mol% B_2O_3 at 950 °C showed an ultrahigh *Qf* of 212 000 GHz with a relative permittivity of 5.3 and τ_f of –8 ppm/°C [214]. The LMS, LCS, and LAS composites have a low relative permittivity and are useful as a low ε_r material for increasing the signal transmission speed. However, the LTCC tapes of the composites have not been reported in the literature.

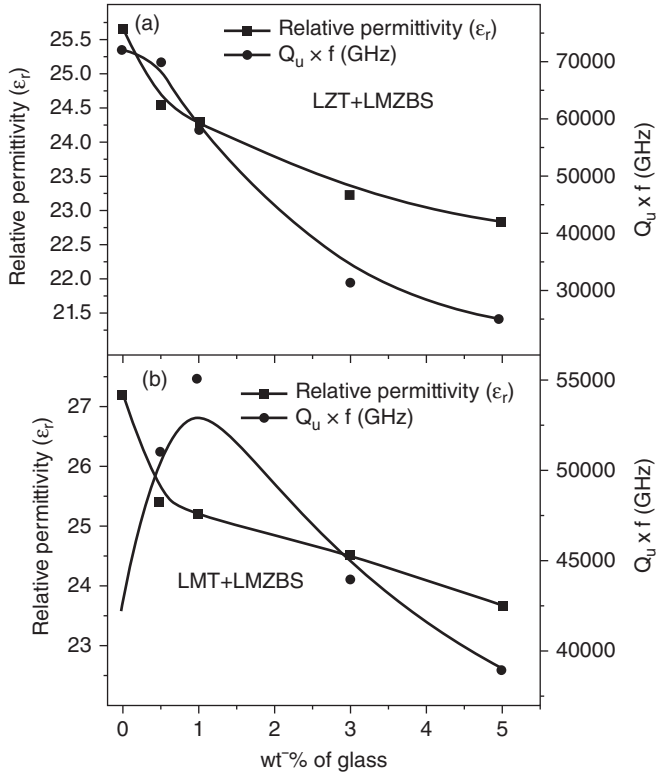

Figure 8.18 *The variation of sintering temperature and relative permittivity and quality factor of $Li_2MgTi_3O_8$ and (b) $Li_2ZnTi_3O_8$ ceramics as a function of LMZBS glass addition. Source: Adapted from George and Sebastian 2011 [195].*

Table 8.9 *Microwave dielectric properties of lithium-based LTCC materials*

Material	ε_r	tan δ/*Qf*	τ_f	Sintering temperature (°C)	Reference
Li_2MgSiO_4	5.1	0.0005 (8GHz)	–	1250	210
Li_2MgSiO_4 + 1 wt% LBS	5.5	0.00007 (8GHz)	–	925	210
Li_2MgSiO_4 + 2 wt% LMZBS	5.9	0.000067 (8GHz)	–	875	210
Li_2CaSiO_4	4.4	0.003 (8GHz)	–	1000	209
Li_2CaSiO_4 + 3 wt% BBS	8.1	004 (8GHz)	–	900	209
Li_2CaSiO_4 + 3 wt% ZBS	7.1	004 (8GHz)	–	875	209
Li_2CaSiO_4 + 3 wt% PBS	7.8	003 (8GHz)	–	900	209
Li_2CaSiO_4 + 1 wt% LBS	7.2	002 (8GHz)	–	925	209
Li_2CaSiO_4 + 3 wt% BZBS	7.3	005 (8GHz)	–	900	209
$LiAlSiO_4$	4.8	36000 GHz	8	1350	211
$LiAlSiO_4$ + 12 mol% B_2O_3	5.3	212000 GHz	−8	950	211
Li_2ZnSiO_4	5.8	14700 GHz	−97	1250	212
Li_2ZnSiO_4 + 25 wt% ZnO-B_2O_3	5.5	10800 GHz	−47	950	212

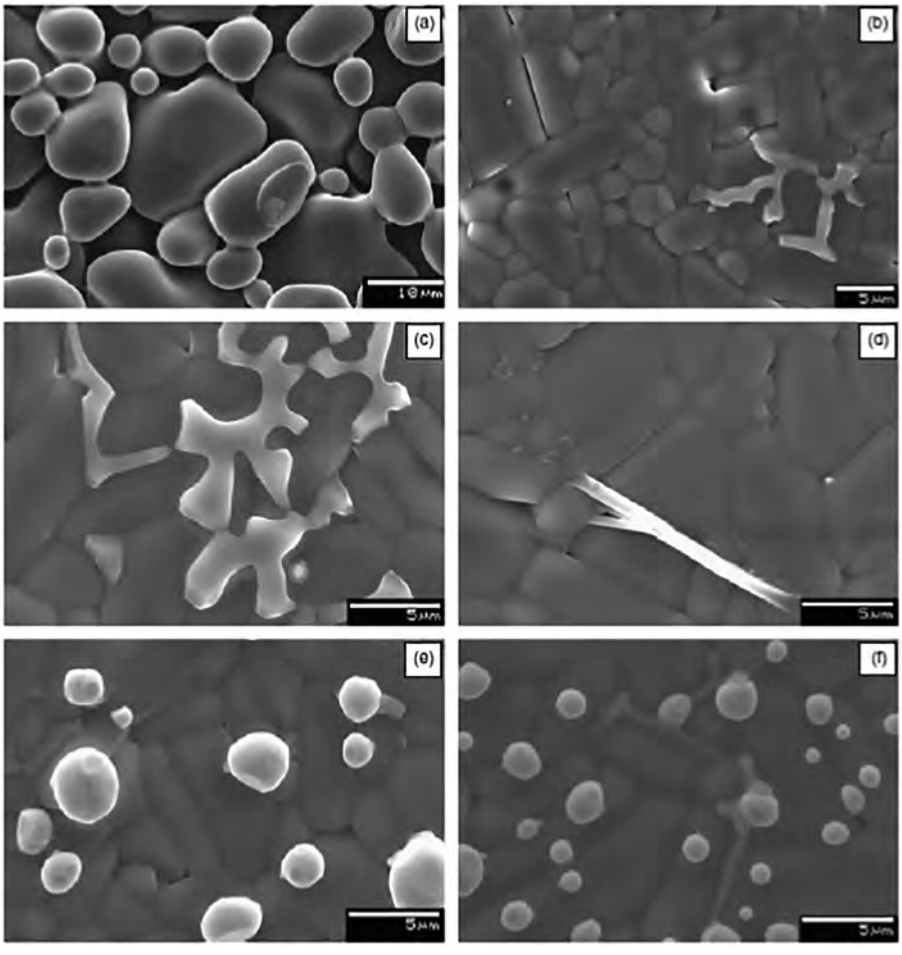

Figure 8.19 *SEM micrographs of sintered (a) Li_2MgSiO_4 (LMS), (b) LMS + 0.5 wt% LBS, (c) LMS + 1 wt% LBS, (d) LMS + 2 wt% LMZBS, (e) LMS + 1 wt % LBS + 20 wt% Ag, and (f) LMS + 2 wt% LMZBS + 20 wt% Ag. Source: Adapted from George* et al. *2009 [210].*

8.5.5.8 Glass-Free LTCC Materials

The $A_2P_2O_7$ (A = Mg, Mn, Zn) thortveitite forms are reported [215–217] to have good microwave dielectric properties. Bian *et al.* [215, 217, 218] reported that some of the $A_2P_2O_7$, such as $CaCuP_2O_7$, $SrCuP_2O_7$, $Mn_2P_2O_7$, $Zn_2P_2O_7$, $CaZnP_2O_7$, and $SrZnP_2O_7$, are suitable glass-free LTCC materials. They can be sintered at temperatures of ~900 °C with a low ε_r of about 7, *Qf* up to 100 000 GHz, and negative τ_f of about –70 ppm/°C. $SrCuP_2O_7$ sintered at 925 °C has the highest *Qf* of greater than 101 100 GHz, and the lowest τ_f of −62 ppm/°C. They all react with silver but $SrZnP_2O_7$ and $CaZnP_2O_7$ do not react with Cu. Recently Thomas and coworkers [219–221] reported another glass-free LTCC material: $LiMgPO_4$ (LMP), with very good microwave dielectric properties. The LMP sintered

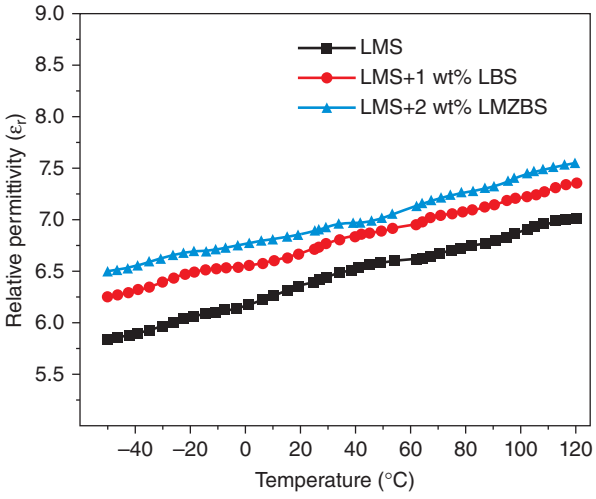

Figure 8.20 *Variation of relative permittivity (1 MHz) with temperature for Li_2MgSiO_4 and with the addition of LBS and LMZBS glasses. Source: Adapted from George* et al. *2009 [210].*

at 950 °C showed a relative permittivity of 6.6, $Qf = 79\,100$ GHz, and τ_f of –55 ppm/°C [219]. Addition of a 0.12 volume fraction of TiO_2 could lower the τ_f to about 1 ppm/°C with relative permittivity of 10 and Qf of 26 900 GHz. The LMP is chemically compatible with an Ag electrode material. Figure 8.21 shows the XRD pattern of LMP with TiO_2 and Ag additives and sintered at 950 °C. The LMP has an orthorhombic crystal structure. Thomas

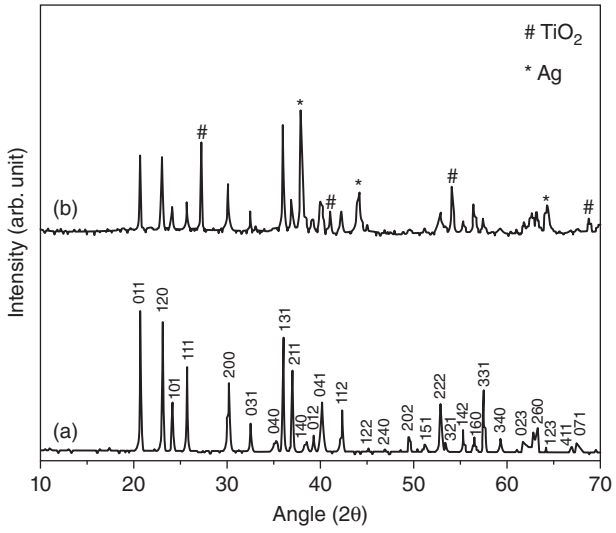

Figure 8.21 *XRD pattern of (a) $LiMgPO_4$ sintered at 950 °C/2 h and (b) $LiMgPO_4$ + 0.15 volume fraction of TiO_2 + 20 wt% Ag and sintered at 950 °C/6 h. Source: Adapted from Thomas and Sebastian 2010 [219].*

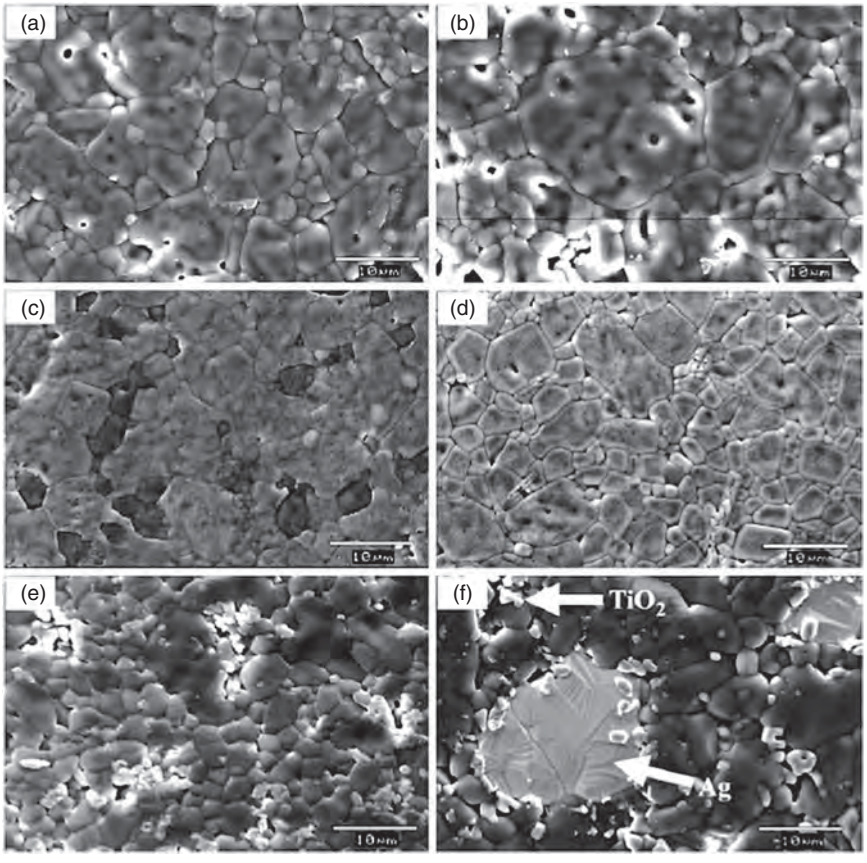

Figure 8.22 *SEM micrographs of (a) $LiMg_{0.9}Zn_{0.1}PO_4$ sintered at 925 °C/4 h, (b) $LiMg_{0.8}Zn_{0.2}PO_4$ sintered at 900 °C/4 h, (c) $LiMg_{0.2}Zn_{0.8}PO_4$ sintered at 850 °C/4 h, (d) $LiZnPO_4$ sintered at 825 °C/4 h, (d) $LiMg_{0.9}Zn_{0.1}PO_4$ + 0.12 volume fraction of TiO_2 sintered at 950 °C/4 h, and (f) $LiMg_{0.9}Zn_{0.1}PO_4$ + 0.12V_f TiO_2 +20 wt% Ag sintered at 950 °C/6 h. Source: Adapted from Thomas and Sebastian 2012 [220].*

and Sebastian reported [220] that partial substitution of Mg by Zn improved the quality factor considerably. The $LiMg(1 - x)Zn_xPO_4$ ceramic retains the orthorhombic structure up to $x = 0.2$. The compositions with $0.3 \leq x \leq 0.8$ exist as a mixture of orthorhombic and monoclinic phases. When Mg^{2+} is fully replaced with Zn^{2+} ($x = 1.0$) complete transition to the monoclinic phase occurs. The SEM images of the sintered and thermally etched surfaces of the ceramics with $x = 0.1$, 0.2, 0.8, and 1.0 are shown in Figure 8.22a to d, respectively. The images reveal a microstructure containing grains of size randomly varying from ~1 μm to >10 μm. From the surface morphology of the composition with $x = 0.8$ (Figure 8.22c) it is obvious that the ceramic is a mixture of two phases. Figure 8.22e shows the microstructure of $LiMg_{0.9}Zn_{0.1}PO_4$ cofired with 0.12 volume fraction of TiO_2 at 950 °C for 4 h. Large grains of $LiMg_{0.9}Zn_{0.1}PO_4$ and small grains of TiO_2 can be observed in the image. The sintering temperature of TiO_2 is very high (~1500 °C) and hence no

Table 8.10 *Slurry composition for LiMgPO4 tape casting [227]*

Component	Composition (wt%)	Function
First stage	34.87	Ceramic
$LiMgPO_4$	0.70	Dispersant
Fish oil	26.16	Solvent
Xylene	26.16	Solvent
Ethanol		
Second stage	5.23	Binder
Polyvinyl butyral	2.61	Plasticizer type I
Butyl benzyl phalate	3.92	Plasticizer type II
Polyethylene glycol	0.35	Homogenizer
Cyclohexanone		

substantial grain growth occurs for TiO_2 at 950 °C. The SEM image of the composite of $LiMg_{0.9}Zn_{0.1}PO_4$ with 0.12 volume fraction ofTiO_2 and 20 wt% Ag sintered at 950 °C for 6 h is shown in Figure 8.22f, in which all the constituent phases can be separately identified, which indicates that no significant reaction occurs between these phases. The ceramic with $x = 0.1$ ($LiMg_{0.9}Zn_{0.1}PO_4$) sintered at 925 °C exhibits a low relative permittivity (ε_r) of 6.7, a high quality factor (Qf of 99700 GHz) with a temperature coefficient of resonant frequency (τ_f) of −62 ppm/°C. The slightly large τ_f is adjusted nearly to zero with the addition of TiO_2. $LiMg_{0.9}Zn_{0.1}PO_4$—TiO_2 composite with 0.12 volume fraction TiO_2 sintered at 950 °C shows good microwave dielectric properties: $\varepsilon_r = 10.1$, $Qf = 52\,900$ GHz, and $\tau_f = -5$ ppm/°C. The ceramic is found to be chemically compatible with silver. Thomas *et al.* fabricated [221] $LiMgPO_4$ LTCC tapes by the doctor blade technique. The tape casting slurry of $LiMgPO_4$ with a typical pseudoplastic behavior has been prepared and cast into thin tapes of thickness 70 μm. Table 8.10 gives the composition of tape casting slurry.

$LiMgPO_4$ green tape shows a tensile strength of 0.22 MPa and average surface roughness of 0.25 μm. Figure 8.23a and b shows the SEM images of the surface of green and sintered tapes, respectively. Similarly, Figure 8.23c and d shows the SEM images of the cross-section of a thermolaminated stack (four layers) before and after sintering, respectively. The surface morphology of green tape reveals more or less uniformly distributed LMP ceramic grains connected through polymer bridges and some porosity. Substantial grain growth occurs during sintering and hence the microstructure of the sintered tape (Figure 8.23b) shows well-packed grains. In the SEM image of the cross-section of the thermolaminated stack (Figure 8.23c), no interlayer boundary is visible. This means that under the conditions of thermolamination, the polymer in the matrix softens and the layers diffuse one into another, making the laminate homogeneous. From the microstructure of the fractured surface of the sintered stack (Figure 8.23d), it is clear that the stack densifies to form a single module. The green tape has ε_r of 3.2 and tan δ of 0.0688 at 5 GHz. The thermolaminated tape (four layers) sintered at 950 °C/2 h shows good microwave dielectric properties: $\varepsilon_r = 6.4$ and tan $\delta = 0.0002$. $LiMgPO_4$ has a coefficient of thermal expansion of 10.5 ppm/°C and thermal conductivity of 7.1 W/m K. The $LiMgPO_4$ family of materials are excellent low cost materials for LTCC applications.

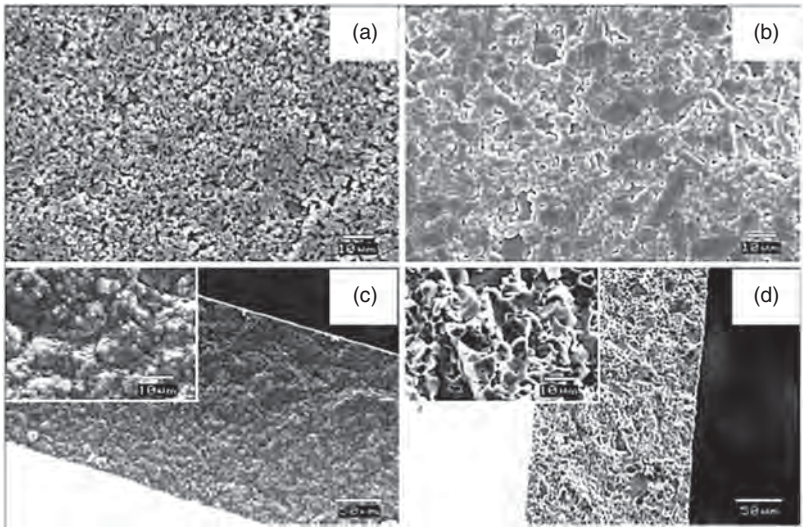

Figure 8.23 *SEM images of (a) and (b) cross-sections of thermolaminated tape (four layers) having different magnification; (e) and (f) are surfaces of green and sintered tapes respectively. Source: Adapted from Thomas* et al. *2013 [221].*

$Bi_4(SiO_4)_3$ (BSO) was recently reported as a glass-free LTCC material with $\varepsilon_r = 14.9$ and $Qf = 36\ 100$ GHz [222, 223]. Recently Abhilash *et al.* [222] reported the preparation of glass-free LTCC tapes of $Bi_4(SiO_4)_3$. The as-prepared green tape of thickness 70 μm has an average surface roughness of 320 nm and a tensile strength of 0.37 MPa. The microwave dielectric properties of the green tape ($\varepsilon_r = 6.2$ and tan $\delta = 0.0390$) and sintered tape ($\varepsilon_r = 13.3$ and tan $\delta = 0.0007$) were measured at 15 GHz. A close look at the morphology of a sintered tape (Figure 8.24d) reveals the presence of well-formed grains during sintering, where the grains appear to be very closely packed with minimal porosity. The average grain size comes at about 3–4 μm. The delamination of the laminated tape is the challenging issue in LTCC processing. The cross-sectional SEM images of the laminated tape are recorded in order to confirm the absence of individual layer delamination, which is presented in Figure 8.24a and c. From both images with low and high magnification (Figure 8.24a and c, respectively) a crack-free and debonding-free microstructure could be observed, which clearly indicates that the reported laminating conditions are good enough to form a non-delaminating stack for LTCC fabrication. The BSO ceramic has promising thermal properties, with a thermal conductivity of 2.82 W/m K and an average CTE of 7.1 ppm/°C. The microwave dielectric properties of the green tape ($\varepsilon_r = 6.2$ and tan $\delta = 0.0390$), thermolaminated tape ($\varepsilon_r = 7.8$ and tan $\delta = 0.0536$), and laminated tape sintered at 900 °C/4 h ($\varepsilon_r = 13.3$ and tan $\delta = 0.0007$) at 15 GHz were measured. Table 8.11 gives the properties of the recently developed LTCC tapes. More recently $LiMBO_3$ (M = Ca, Sr) have been reported as high Q low k glass-free LTCC materials [224]. The $LiCaBO_3$ and $LiSrBO_3$ sintered at 800 °C showed $\varepsilon_r = 8.7$, $Qf = 75\ 000$ GHz, $\tau f = -150$ ppm/°C, and $\varepsilon_r = 8.6$, $Qf = 60\ 000$ GHz, $\tau f = -39$ ppm/°C, respectively. $LiMBO_3$ (M = Ca, Sr) ceramics are chemically compatible with Ag after sintering at 800 °C/2 h,

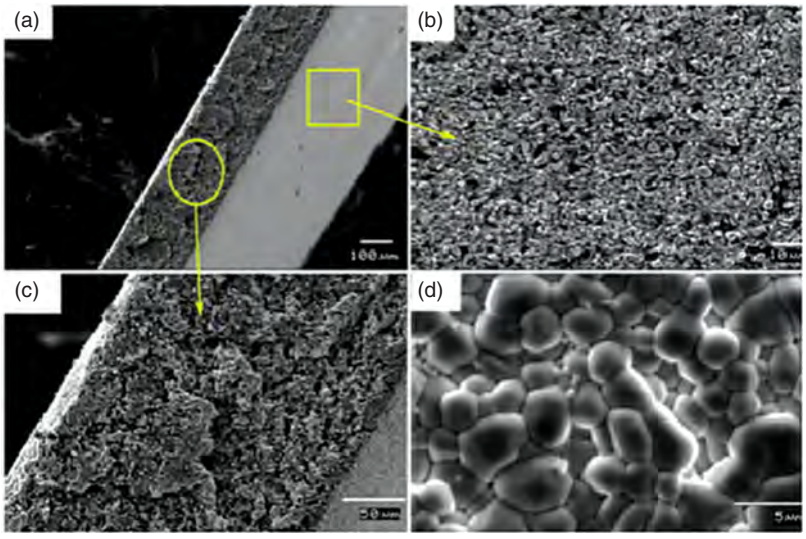

Figure 8.24 *SEM images of (a) and (c) cross-section of thermolaminated tape (four layers) having different magnification; (b) and (d) are surfaces of green and sintered* $Bi_4(SiO_4)_3$ *tapes, respectively. Source: Adapted from Abhilash* et al. *2015 [222].*

while $0.81Mg_2Si_{0.9}V_{0.1}O_4 - 0.19Ca_{0.8}Sr_{0.2}TiO_3$ + 4 wt% LiF sintered at 900 °C shows ε_r of 11, Qf = 49 000 GHz, and τf = –7 ppm/°C [225]. Manu and Sebastian reported [226] $SrCuSi_4O_{10}$ (SCS)–LMZBS glass composite for LTCC applications. The SCS ceramic with 5 wt% LMZBS glass sintered at 900 °C had $\varepsilon_r = 5.0$ and tan $\delta = 1.9 \times 10^{-3}$ at 5 GHz. The green tape had ε_r of 2.2 and tan δ of 1.8×10^{-2} at 5 GHz. The thermolaminated tape sintered at 900 °C showed $\varepsilon_r = 4.8$ and tan $\delta = 1.6 \times 10^{-3}$ at 5 GHz and 4.7 and 1.9×10^{-3} at 15 GHz, respectively. The composite showed chemical compatibility with the silver electrode material and showed a nearly zero coefficient of linear thermal expansion (CTE). Joseph *et al.* reported that the thickness of the LTCC tapes influence the relative permittivity [227]. Figure 8.25 shows the variation of relative permittivity of $Sr_2ZnSi_2O_7$ + 15 wt% LMZBS glass sintered at 825 °C having different thicknesses as a function of temperature. The LTCC tape, which has greater thickness showed higher relative permittivity and lower loss tangent and this may be due to the difference in porosity.

8.5.6 Constrained Sintering

The LTCC tapes shrink in all three directions during a free sintering process, being 12–16% in the *X–Y* (radian) direction and slightly more in the thickness (axial) direction. The shrinkage limits the size of the substrates that can be processed, imposes limitations on embedded passive components, and introduces complexity in the processing. The constrained sintering technology was consequently proposed as a solution, referring to various techniques used in LTCC: pressure-assisted sintering (PAS), pressureless assisted sintering (PLAS), self-constrained sintering, and the LTCC-M approach. In the LTCC-M, a metal substrate is used as a constraint [228–231]. Except for the PAS technique, all use either an internal

Table 8.11 *Properties of LTCC tapes measured at 5 GHz*

Material	No. of layers	Thickness (μm)	Measurement frequency GHz	k	tan δ	TC (W/m K)	CTE (ppm/°C)	Reference
$40Al_2O_3$—60BBSZ								82
green tape	1	103	5	5.9	0.07			
Laminated tape	5	446	5	7.6	0.08			
Sintered at 850 °C	5	408	5	10.9	0.009	7.2	6.9	
$SrCuSi_4O_{10}$ + 5 wt% LMZBS								232
green tape	1	70	5	2.2	0.018			
Laminated tape	3	220	5	2.8	0.015			
Sintered at 900 °C	3	190	5	4.8	0.0016	–	–1	
$LiMgPO_4$								227
green tape	1	70		3.2	0.0688			
Laminated tape	4	240		4.1	0.0680			
Sintered at 950 °C	4	190		6.4	0.0002	7.1	10.5	
$Bi_4(SiO_4)_3$								228
green tape	1	70		6.2	0.0396			
Laminated tape	4	240		7.8	0.0536			
Sintered tape at 900 °C	4	170		13.3	0.0007	2.82	7.1	
$Sr_2ZnSi_2O_7$+ 15wt% LMZBS tape sintered at 825 °C		500	20	6.9	0.0015	–	–	233

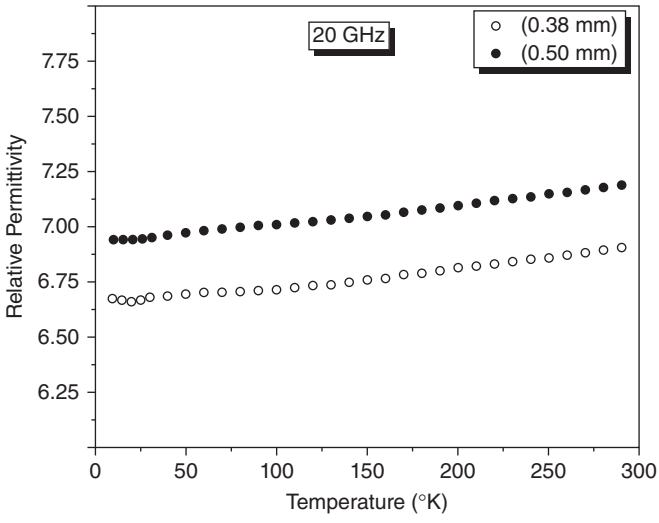

Figure 8.25 *Variation of relative permittivity of $Sr_2ZnSi_2O_7$ + 15 wt% LMZBS glass sintered at 825 °C having thicknes 0.5 and 0.38 mm as a function of temperature. Source: Adapted from Joseph* et al. *2011 [227].*

or external non-sintering material to constrain in-plane shrinkage of the LTCC, to achieve zero shrinkage in the *X–Y* direction. The concept of constrained sintering or zero shrinkage technology has recently become important in LTCC for the precise control and maintenance of sintering shrinkage and tight dimensional tolerances [229–231]. During normal cofiring, stresses develop because of the mismatch in sintering behavior of different components [232–234]. These stresses can lead to warped and non-uniform shrinkage, leading to dimensional variations. The zero shrinkage technology is thus an attractive option as it completely inhibits the transverse shrinkage, resulting in extremely low dimensional changes in the plane of the structure, thus maintaining tight tolerances. Kagata *et al.* [73] succeeded in making non-shrinkage LTCC by firing the laminated sheet with HTCC alumina or magnesia green sheets on both sides and then removing the non-sintered HTCC. The glass–ceramic sheet shrinks only in the *Z* direction and not in the *X–Y* direction due to the constraining effects of the HTCC layers.

There are about 1000 low loss dielectric materials (see the Appendix) reported with a sintering temperature in the range 700 to 950 °C. Figures 8.26 and 8.27 show the variation of their Qf and τ_f as a function of relative permittivity. In general the quality factor decreases with increasing ε_r. Some of these materials, such as $LiAlSiO_4$ + 12 mol% B_2O_3, Li_2MgSiO_4 + 1 wt% LBS/LMZBS, $K_xBa_{1-x}Ga_{2-x}Ge_{2+x}O_8$, $SrCuP_2O_7$, $SrZnP_2O_7$, $Li_2Ca_2Mo_3O_{12}$, 0.96MgO–0.04LiF, $Mg_4Nb_2O_9$ + 3 wt% LiF, $0.8Mg_3(VO_4)_2$–$0.2Ba_3(VO_4)_2$, $LiCeO_3$, $Li_2Zn_3Ti_4O_{12}$, and $0.87Li_2TiO_3$–0.05MgO–0.08LiF, have a high Qf > 100 000 GHz. The 0.96MgO–0.04LiF sintered at 950 °C showed the highest quality factor (Qf = 282 200 GHz) with ε_r of 9.6 and τ_f of –63 ppm/°C. There are several temperature-compensated compositions, such as $LiAlSiO_4$ + B_2O_3, $CaO—MgO—SiO_2—TiO_2$ + $Li_2CO_3—V_2O_5$, and $LiMg_{0.9}Zn_{0.1}PO_4$ + 0.12 volume fraction of TiO_2, and several others need only a slight adjustment using additives. Most of the LTCC

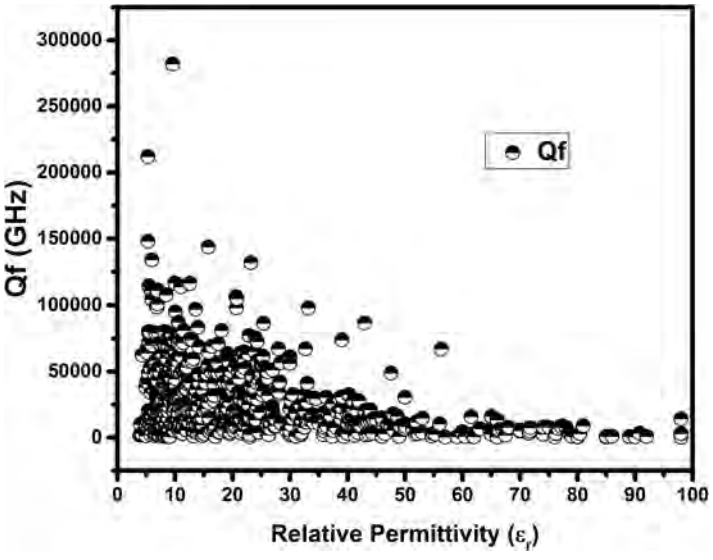

Figure 8.26 *Variation of Qf of LTCC materials with relative permittivity.*

materials having high *Qf* and high ε_r have a sintering temperature close to 950 °C, as shown in Figure 8.28. Although several authors reported success in reducing the sintering temperature to the level suitable for LTCC, tapes of these ceramics are not made. Furthermore, very little attention was paid to find their chemical compatibility with electrode materials and silicon, thermal expansion, shrinkage, thermal conductivity, etc.

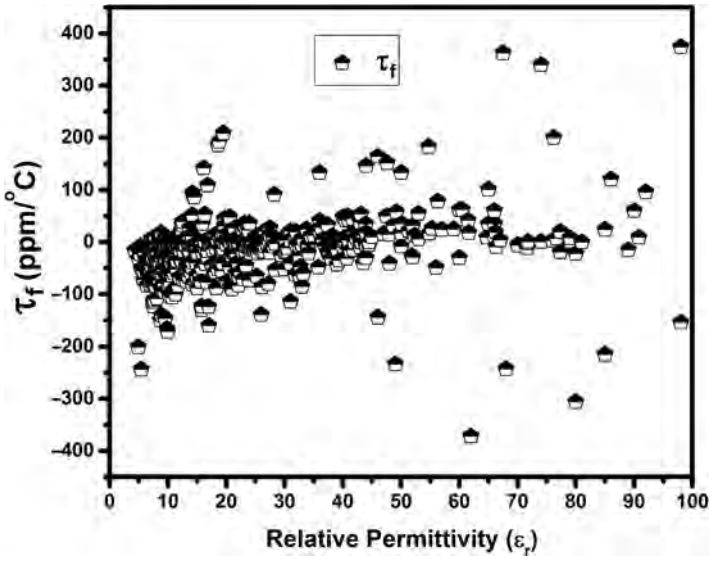

Figure 8.27 *Variation of τ_f of LTCC materials with relative permittivity*

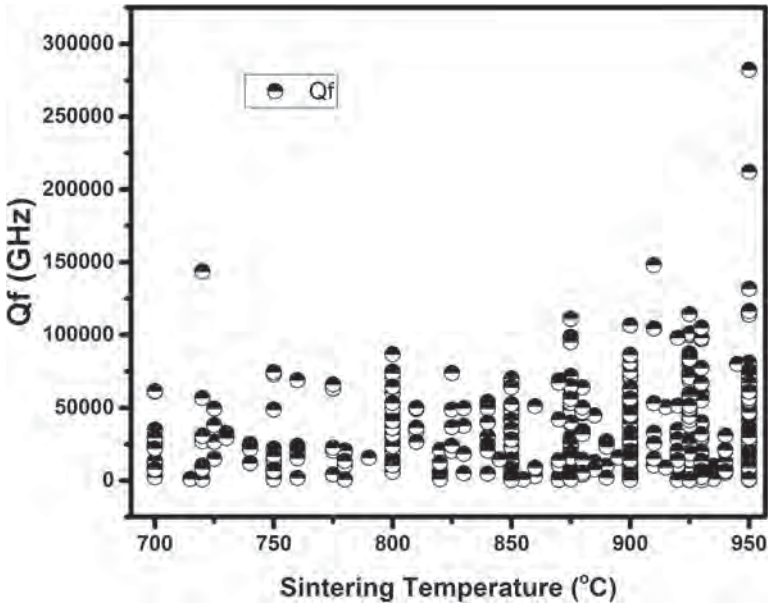

(a)

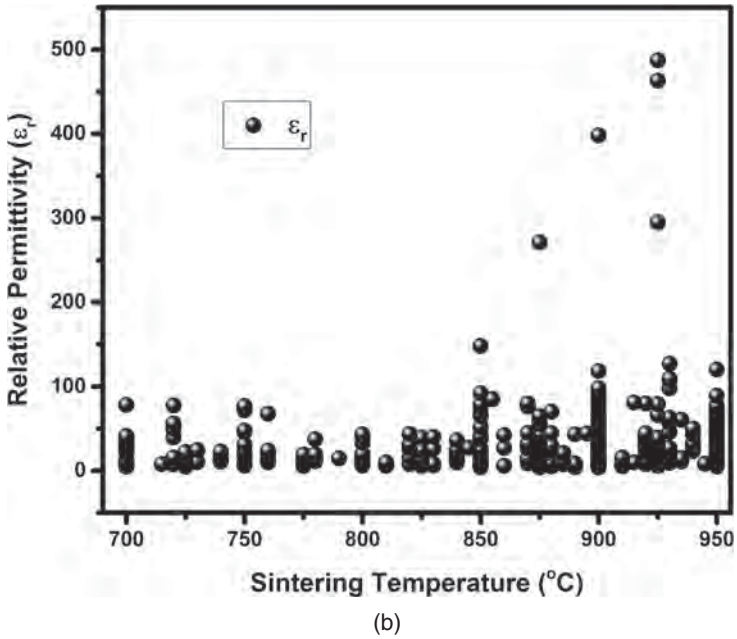

(b)

Figure 8.28 *Variation of (a) Qf and (b) relative permittivity of LTCC materials with sintering temperature.*

8.6 Ultralow Temperature Cofired Ceramics (ULTCC)

8.6.1 Introduction

The ceramics that densify at temperatures less than 700 °C are considered as ultra-low temperature cofired ceramics (ULTCCs). The low temperature sintering enables cofiring with semiconductive or organic structures using aluminum or nanosilver ink conductor electrode materials. Multilayer packages made with much lower sintering temperatures would save energy, reduce processing time, and enable integration with semiconductors or even plastic into the package using Al or Ag nanoinks. Recently several electroceramic materials with low sintering temperatures less than 700 °C have been reported and are given in the Appendix. These materials are divided into two categories. In the ULTCC category I (ULTCC-I), with a sintering temperature at 400 °C or below, only a few materials are reported. The category II covers compositions having a sintering temperature in the range 400 to 700 °C. This category of materials enable cofiring with Al or different metal mixture electrodes with a relatively low conductivity. Both categories of materials can be cofired with silver-based inks. Currently an intensive search is going on to find materials with ultralow firing temperatures and the number of papers published on ULTCC is rapidly increasing. Most of the high quality factor (Q) dielectric materials have high sintering temperatures and can be lowered by adding low melting glasses, but it often degrades the microwave dielectric properties. The densification in this case is achieved by liquid phase sintering. Addition of low melting compounds TeO_2, Bi_2O_3, B_2O_3, Li_2O, V_2O_5, MoO_3, etc., can also lower the sintering temperature of parent materials, but large amounts of these low melting sintering aids usually degrade the microwave dielectric properties. However, there are materials with inherently ultralow sintering temperatures. The ULTCC materials can be grouped into (a) materials with originally low sintering temperatures, (b) glass + ceramic composites, and (c) glass or glass–ceramic. Valant and Suvorov were the first to report [235] an ULTCC material based on sillenite $Bi_{12}PbO_{19}$ with a sintering temperature of 680 °C. This material has ε_r of 38.6, a low Qf of 2900 GHz, and τ_f of –84 ppm/°C. Zhou *et al.* reported that pure Bi_2O_3 can be sintered at 680 °C with a relative permittivity of 33.5, Qf of 18 700 GHz, and a high negative τ_f of 235 ppm/°C [236]. The reported materials with ULTCC materials are found to be mostly based on tellurates, molybdates, vanadates, and tungstates in combination with Bi, K, Na, Ag, Li, Ba, etc., and glasses or glass ceramic composites [237]. Most of these materials are found to react with the common electrode silver. Although several ULTCC category II (ULTCC-II) materials are reported, only a handful of materials are found under category I (ULTCC-I) with sintering temperatures less than 400 °C.

8.6.2 Ultralow Temperature Cofireable Ceramics (ULTCC Category II)

8.6.2.1 Glasses and Glass–Ceramic Composites

There are several dielectric materials with excellent microwaved dielectric properties but have high sintering temperatures [24]. Commonly the high sintering temperatures of ceramics is lowered to a level suitable for ULTCC by adding glasses with a low softening temperature. The network formers in the glasses may absorb microwave energy considerably at high frequencies that increases the loss factor of the composite. However, there are several

glasses with a relatively low loss tangent in the microwave frequency range. The ULTCC materials based on glasses are usually multiphase and properties depend on the individual phases, microstructure, morphology, and connectivity of each phase. The ULTCC should have good densification and crystallinity for useful dielectric and mechanical properties. The effectiveness of glass additives on sintering depends on several factors such as the sintering temperature, viscosity, solubility, wetting behavior, etc. There are two basic methods to prepare glass-based ULTCC: glass–ceramic and glass + ceramic routes [237, 238]. The glass–ceramic system starts with a glassy material that devitrifies almost completely to crystalline phases during the sintering process. The properties of the sintered composite depend on the degree of crystallization and can be controlled by the addition of a small amount of suitable nucleating agent. In the glass + ceramic route, a low softening point glass and a crystalline ceramic are initially mixed and heat treated. The glass melts and penetrates the 3D mesh structure of the ceramic and wets the ceramic particles to effect the densification of the ceramic body. The end product consists of ceramic particles in a glassy matrix. Generally borosilicate glasses having low softening temperatures and good dielectric properties are used as flux materials.

In 1999, Wu and Huang [239] made a detailed study on the microwave dielectric properties of ULTCC-based barium, zinc, and lead borosilicate glasses of different compositions. The glass transition temperature (T_g) decreases with an increase in B_2O_3 content in ZBS ($ZnO—B_2O_3—SiO_2$) and BBS ($BaO—B_2O_3—SiO_2$) glasses, as shown in Figure 8.29a. Figure 8.29b shows the variation of relative permittivity with B_2O_3 content and the variations are marginal. The *Qf* varied in the range 1200 to 3500 GHz and τ_f in the range –5 to about –120 ppm/°C with B_2O_3 content. Figure 8.30a and b shows the variation of T_g and relative permittivity of PBS ($PbO—B_2O_3—SiO_2$) glass with PbO content. In Pb-based glass an increase in Pb content lowered the glass transition temperature (T_g) from 500 to 312 °C. The relative permittivity of Pb-based glass increased from about 9 to about 20 and the *Qf* decreased from about 1700 to about 500 GHz when the Pb content increased from 30 to 70 mol%. The τ_f decreased from –10 to about –150 ppm/°C with an increase in Pb content. The τ_f became more negative with increasing amounts of BaO and PbO while it became less negative with ZnO content. It was found [239] that the microwave dielectric properties ε_r and *Qf* mainly depend on the network modifiers in the glasses.

Chen *et al.* [240] reported the microwave dielectric properties of $MO—B_2O_3—SiO_2$ (M = Mg, Ca, Ba, or Sr) glasses. These glasses have a softening temperature (T_s) in the range 560 to 613 °C with the lowest temperature for Ba and the highest for Mg. These glasses have a relative permittivity in the range 6.6 to 7.6. The Ba-based glass has the highest relative permittivity (ε_r) of 7.6 with a quality factor (*Qf*) of about 4100 GHz and Mg based glass has the lowest relative permittivity of 6.6 with the lowest *Qf* of 2100 GHz. Yu and coworkers [241–244] reported that $3ZnO—2B_2O_3$ glass–ceramic sintered at 650 °C for 30 minutes has excellent dielectric properties. The sintered composite comprised two crystalline phases: $Zn_3B_2O_6$ and α-$Zn(BO_2)_2$. The glass + ceramic composites showed ε_r of 7.5 and tan δ of 6×10^{-4} at 10 MHz. Addition of 15 wt% SiO_2 and sintered at 650 °C for 30 minutes lowered ε_r to 6.1 with tan $\delta = 1.3 \times 10^{-3}$ at 1 MHz. Yu *et al.* [243] also prepared SiO_2-filled zinc borate glass composite ULTCC tapes. The laminated five-layer ULTCC tape sintered at 650 °C showed ε_r of 6.4 with tan δ of 0.001 at 1 MHz. Figure 8.31a shows the SEM cross-section micrograph of $3ZnO—2B_2O_3$ + 15 wt% SiO_2 laminated ceramic tapes cofired with silver electrode at 650 °C for 30 minutes. The $ZnO—B_2O_3$-based

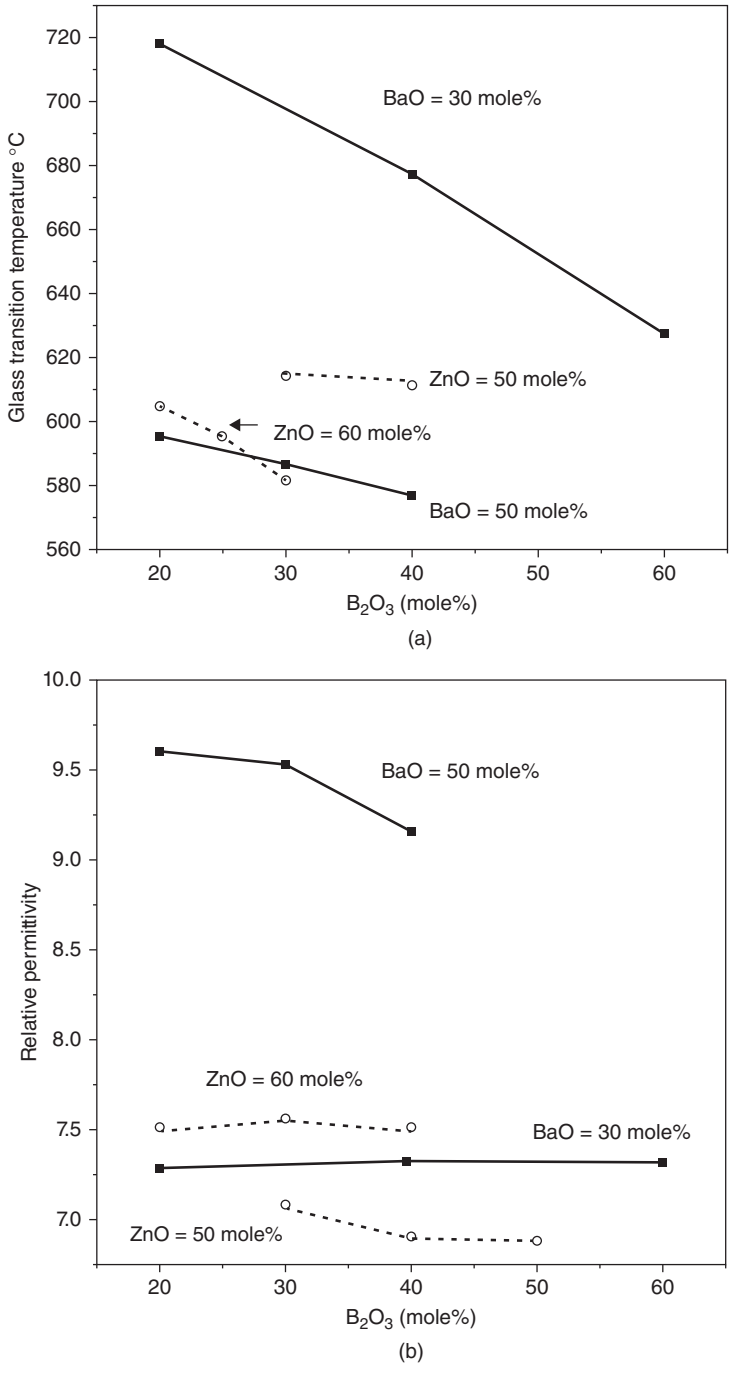

Figure 8.29 *Variation (a) of glass transition temperature as a function of B_2O_3 content (O) $ZnO—B_2O_3—SiO_2$, ■ $BaO—B_2O_3—SiO_2$ glasses; (b) relative permittivity as a function of B_2O_3 content (O) $ZnO—B_2O_3—SiO_2$, ■ $BaO—B_2O_3—SiO_2$ glasses. Source: Wu and Huang 1999 [239]. Reproduced with permission from Elsevier.*

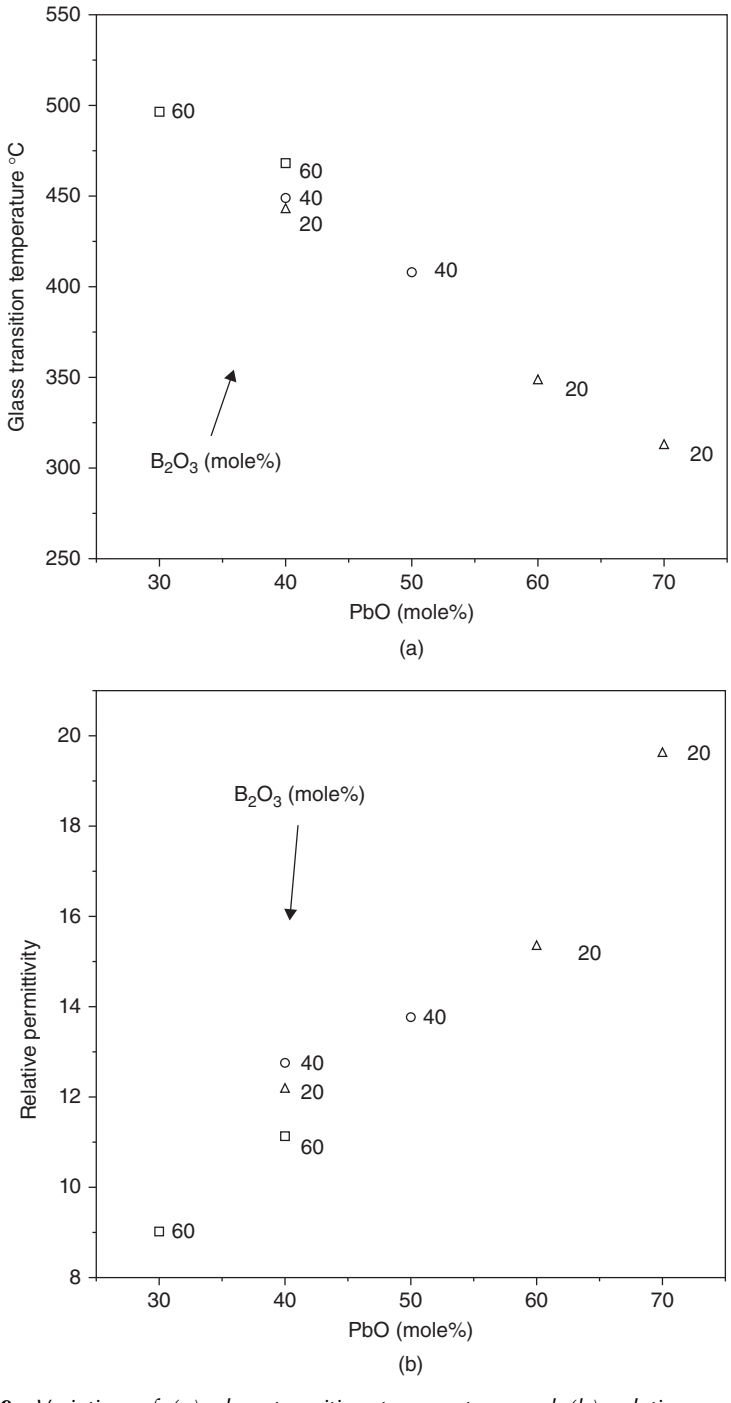

Figure 8.30 *Variation of (a) glass transition temperature and (b) relative permittivity of PbO—B_2O_3—SiO_2 glasses as a function of PbO content. Source: Wu and Huang 1999 [239]. Reproduced with permission from Elsevier.*

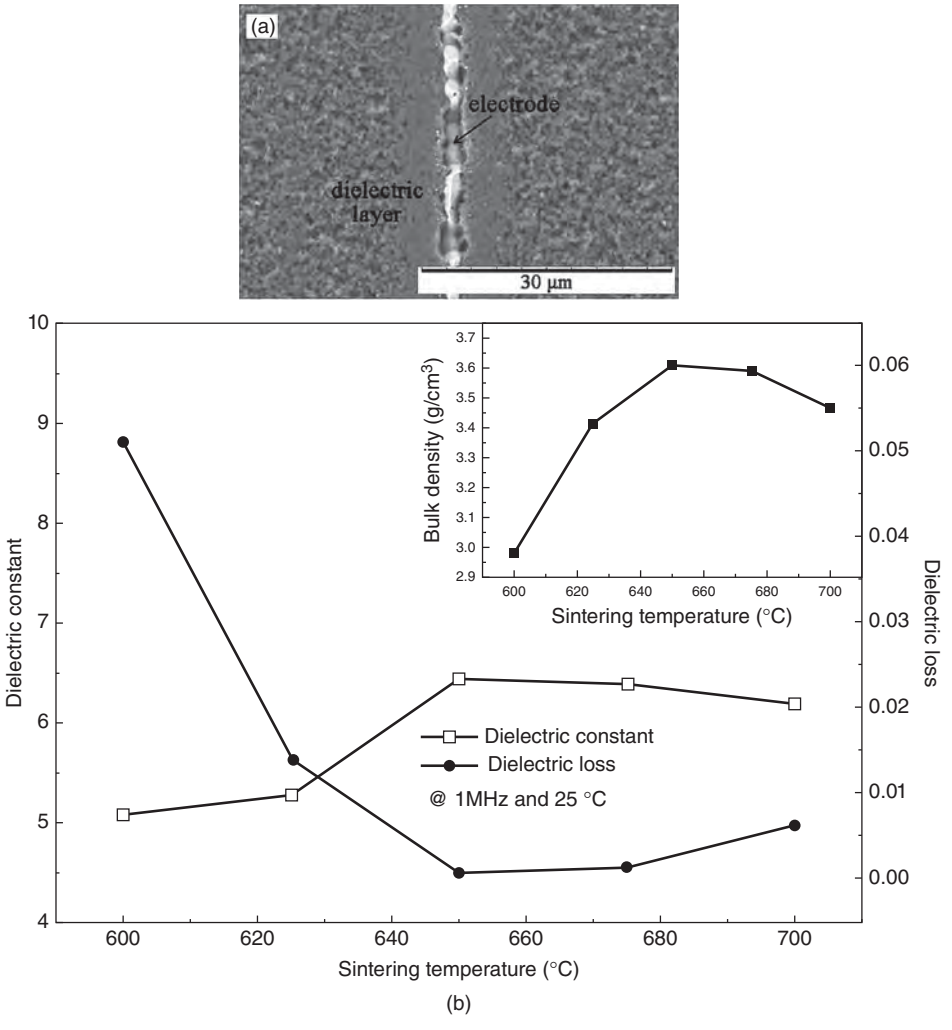

Figure 8.31 *(a) Scanning electron micrograph of the cross-section of $3ZnO—2B_2O_3—15$ wt% SiO_2 ULTCC laminated tape cofired with Ag at 650 °C for 30 min. (b) Dielectric properties of $3ZnO—2B_2O_3—SiO_2$ bulk ceramics sintered at different temperatures for 30 min. The inset shows the variation of bulk density. Source: Yu* et al. *2014 [243]. Reproduced with permission from Springer.*

glass–ceramic is chemically compatible with silver electrode material and is a suitable candidate for ULTCC applications. Figure 8.31b shows the variation of dielectric properties and bulk densities of silica-filled zinc borate glass sintered at different temperatures for 30 minutes. The composite shows the best dielectric properties and density when sintered at 650 °C for 30 minutes.

Rajesh *et al.* [245] prepared silver cofireable glass + alumina composites with ultralow sintering temperatures. They used the commercial glasses G018-249 and G018-250 with

glass transition temperatures T_g of 365 and 380 °C, respectively. The G018-249 glass frit is alkali free and contains a large amount of Bi_2O_3 and ZnO whereas the G018-250 is a solder glass containing Li_2O and Bi_2O_3. The alumina filler used was about 50 wt% and the composite well densified on sintering at 650 °C. The composites were found to be chemically compatible with silver electrode material on sintering at 650 °C. The G018-249 and G018-250 composites with alumina sintered at 650 °C showed a relative permittivity of 9.5 and 8.85, loss tangents of 0.0068 and 0.0087 at 1 MHz, and bulk densities of 3.62 and 3.99 g/cm^3, respectively. The composites showed only marginal variation in loss tangent and relative permittivity with temperatures in the range 0 to 80 °C.

Addition of a large amount of BBSZ ($27B_2O_3$—$35Bi_2O_3$—$6SiO_2$—32ZnO in mol%) glass is reported to lower the sintering temperature of Al_2O_3 and $BaTiO_3$ [246, 247] to a level for ULTCC applications. The BBSZ glass has a relative permittivity of about 21 [148] and hence its addition increases the relative permittivity of alumina composite and decreases that of $BaTiO_3$-based composite. The $BaTiO_3$ composite containing 50 wt% BBSZ glass sintered at 450 °C had $\varepsilon_r = 136$ with tan δ of 0.020 at 100 MHz. X-ray diffraction study of the BBSZ—Al_2O_3 and BBSZ—$BaTiO_3$ composites sintered at 450 °C revealed the presence of $Bi_{24}Si_2O_{40}$ secondary phase, which influenced the dielectric properties [246, 247]. The relative permittivity of the composite can be tailored by the amount of ceramic fillers keeping the sintering temperature close to 450 °C. The ε_r of BBSZ—alumina increases above that of BBSZ and is attributed to the presence of secondary phase $Bi_{24}Si_2O_{40}$, which has a high ε_r of 37.6 with *Qf* of 8100 GHz [235]. However, Kim *et al.* observed $ZnAl_2O_4$ secondary phase instead of $Bi_{24}Si_2O_{40}$ in BBSZN with a slightly different composition and containing a small amount of Na_2O ($22.7Bi_2O_3$–$23.3B_2O_3$–$13.5SiO_2$–37.9ZnO—$2.6Na_2O$ mol%) [248]. The BBSZN has a low ε_r of 15.3, *Qf* of 1500 GHz, and τ_f of –40 ppm/°C. The BBSZN with 50 vol% Al_2O_3 sintered at 700 °C showed ε_r of about 9.5, $Qf = 3200$ GHz, and $\tau_f = 119$ ppm/°C [248]. The glass-based ceramic materials are potential candidates for packaging applications using silver- or aluminum-based electrodes. Recently $Li_3AlB_2O_6$ ceramic, which has a triclinic crystal structure, is reported [249] as a useful ULTCC material. The microwave dielectric properties are found to depend on the sintering temperature and the degree of crystallization. The ε_r and *Qf* improved with increasing sintering temperature whereas the τ_f becomes more negative. The degree of crystallization increases and density decreases with an increase in the sintering temperature. The increase in ε_r and *Qf* is attributed to improvement in crystallization. The sample sintered at 700 °C has $\varepsilon_r = 4.9$, $Qf = 12\,600$ GHz, and $\tau_f = -201$ ppm/°C. It is found that addition of 5 wt% TiB and sintered at 675 °C for 10 h considerably improved the microwave dielectric properties with τ_f of 10 ppm/°C, $\varepsilon_r = 4.2$, and $Qf = 13\,000$ GHz.

8.6.2.2 Vanadates

In 2000, Valant and Suvorov reported [250] that $BiVO_4$ ceramic has good microwave dielectric properties with a low sintering temperature. Since then several vanadate compounds such as $LiMgVO_4$, $LiZnVO_4$, BaV_2O_6, $A_{16}V_{18}O_{61}$ (A = Ba, Sr, Ca), $Ba_3V_4O_{13}$, and $Na_2BiMg_2V_3O_{12}$ have been reported [250–261] for ultra-low temperature cofired applications with sintering temperatures less than 700 °C. The orthorhombic BaV_2O_6 can be well sintered at 550 °C for 1 h with excellent microwave dielectric properties [259]. This material with a relative permittivity ε_r of 11.2, high quality factor of 42 800 GHz, and τ_f

of 28 ppm/°C is a potential candidate for ULTCC application utilizing Al electrodes. Monoclinic CaV_2O_6 is another similar compound with a very high quality factor having ε_r of 10.2, *Qf* of 123 000 GHz, and τ_f of –60 ppm/°C when sintered at 675 °C [260]. This material has the highest *Qf* among the vanadates. The $Ba_3V_4O_{13}$ has a monoclinic crystal structure and the ceramic sintered at 600 °C for 1 h shows excellent microwave dielectric properties. It has ε_r of 9.6, *Qf* of 56 100 GHz, and τ_f of –42 ppm/°C and is cofireable with Al [257]. The $A_{16}V_{18}O_{61}$ (A = Ba, Sr, Ca) ceramics have an excellent quality factor in the range 75 600–80 100 GHz, ε_r = 9.7–11.1, and τ_f = –40 to –78 ppm/°C [261]. The $LiZnVO_4$ is rhombohedral and sinters at a higher sintering temperature of 750 °C with ε_r of 7.6 and *Qf* of 22 000 GHz, but addition of rutile lowers the sintering temperature with improvement in microwave dielectric properties [255]. The $0.7LiZnVO_4$—$0.3TiO_2$ ceramic sintered at 680 °C has a permittivity of 12.6, *Qf* of 38 000 GHz and a τ_f of 5 ppm/°C. However, it is not known how rutile, which has a high sintering temperature, can lower the sintering temperature of $LiZnVO_4$. Although this composite has excellent microwave dielectric properties with a low sintering temperature, it reacts with Ag electrode material. The compounds rich in vanadium and niobium react with silver, unlike the ones that are rich in bismuth in both V and Nb systems [250]. In general, vanadates react with silver electrode material and most of them are chemically compatible with Al although its conductivity is lower than silver.

8.6.2.3 Tungstates

Recently several tungstate-based ceramics with low sintering temperature have been reported for ULTCC applications [262–268]. Many of the tungstate-based materials in combination with molybdates, Li, Bi, and Te have ultralow sintering temperatures. Li_2WO_4, which has a rhombohedral crystal structure, sinters at about 650 °C and has ε_r of 5.5 with a high *Qf* of 62 000 GHz and a high negative τ_f of –146 ppm/°C [262]. It does not react with silver and aluminum conductors [262]. $Li_2A_2W_3O_{12}$ (A = Mg, Zn) is another group of tungstate compounds, which can be sintered at about 700 °C [264]. $Li_2Zn_2W_3O_{12}$ does not form as a single phase material but is composed of $ZnWO_4$ and Li_2WO_4 with a relative permittivity of 11.3, *Qf* of 24 500 GHz, and τ_f of –100 ppm/°C when sintered at 700 °C. The $Li_2Mg_2W_3O_{12}$ is single phase and densifies well at 720 °C with a relative permittivity of 8.4, *Qf* of 56 700 GHz, and τ_f of –73 ppm/°C. The PbO—WO_3 binary system has two low melting phases: $PbWO_4$ and Pb_2WO_5 [269]. The Pb_2WO_5 has a monoclinic crystal structure and a relative permittivity of 16.4, *Qf* of 14 800 GHz with a τ_f of –95 ppm/°C when sintered at 520 °C. The $PbWO_4$ has a slightly higher sintering temperature of 620 °C and a higher relative permittivity of 21.4 with *Qf* of 43 000 GHz and a low τ_f of –7 ppm/°C. Figure 8.32 shows the SEM microstructure of Pb_2WO_5 and $PbWO_4$ ceramics sintered at 520 and 620 °C for 2 h, respectively. Both the materials do not react with Ag or Al electrode materials.

8.6.2.4 Molybdates

Recently several authors reported the microwave dielectric properties of bismuth based molybdates, such as Bi_2O_3—$4MoO_3$, $Bi_2Mo_3O_{12}$, Bi_2O_3—$2.2MoO_3$, $Bi_2Mo_2O_9$, $(ABi)_{1/2}MoO_4$ (A = Li, Na, K, Rb, Ag), $Bi_{12}PbO_{19}$, $(Ca_{1-3x}Bi_{2x}A\phi_x)MoO_4$ (x = 0.15, ϕ = an A site vacancy), $Li_{0.5}Bi_{0.5}(W_{1-x}Mo_x)O_4$, $(Bi_{1-x}RE_x)_2Mo_2O_9$ (RE = La, Nd), and $(Ag_{0.5}Bi_{0.5}(Mo_{0.5}W_{0.5})O_4$, with low sintering temperatures [266, 270–276]. Figure 8.33a

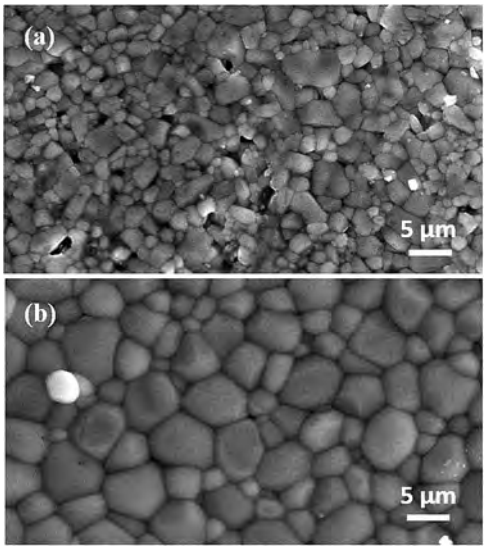

Figure 8.32 *SEM micrograph of (a) Pb_2WO_5 sintered at 530 °C and (b) $PbWO_4$ sintered at 620 °C. Source: Xie* et al. *2015 [269]. Reproduced with permission from John Wiley & Sons.*

shows the variation of the relative permittivity of the Bi_2O_3—MoO_3 materials as a function of composition. Among the compounds in this system, $Bi_2Mo_2O_9$ has the highest relative permittivity and has positive τ_f. The τ_f varies almost linearly with relative permittivity, as shown in Figure 8.33b. As permittivity decreases the τ_f deceases and becomes negative. The quality factors of these materials are in the range 9300 to 12 500 GHz. The Bi_2O_3—MoO_3 compositions are found to react with Ag but are compatible with Al electrodes. Zhou *et al.* reported [236] Ag and Al electrode compatible materials, such as

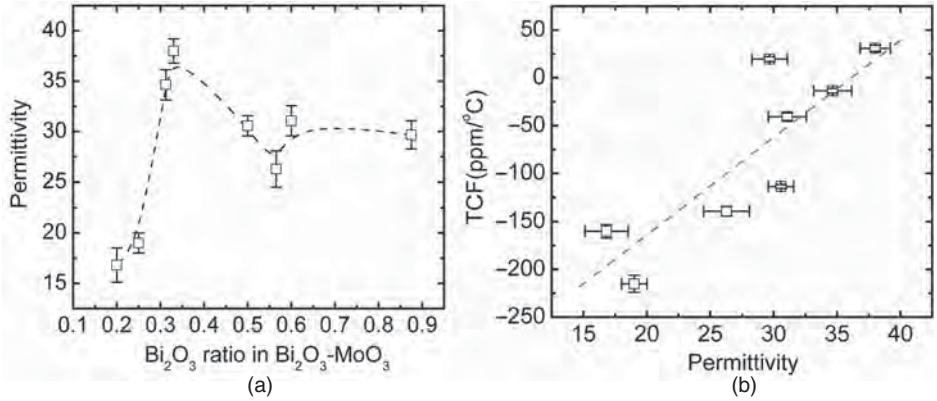

Figure 8.33 *Variation of relative permittivity, Qf and sintering temperature as a function of MoO_3 ratio in Na_2O—MoO_3 system. Source: Zhang* et al. *2015 [277].*

Li_2MoO_4, $Li_2Mo_4O_{13}$, $Li_3BiMo_3O_{12}$, and $Li_8Bi_2Mo_7O_{28}$ in the Li_2O—Bi_2O_3—MoO_3 system, with ultra-low sintering temperatures in the range 520–540 °C. These compositions have ε_r in the range 5.5 to 44.4, Qf = 3000 to 46 000 GHz, and τ_f in the range –235 to +245 ppm/°C. The Na_2O—MoO_3 system also comprise three compositions, Na_2MoO_4, $Na_2Mo_2O_7$, and $Na_6MoO_{11}O_{36}$, with ultralow sintering temperatures in the range 500–660 °C have interesting microwave dielectric properties [277]. These compounds, which are chemically compatible with Al electrodes, have relative permittivities in the range 4 to 13.4, Qf up to 62 400 GHz, and τ_f in the range –57 to –115 ppm/°C.

The substitution of Ca, Zn, Al, In, Fe, etc., at the Bi site in $Li_3BiMo_3O_{12}$ ceramics resulted in a significant improvement of the microwave dielectric properties [278, 279]. $Li_2Zn_2Mo_3O_{12}$, $Li_3AlMo_3O_{12}$, and $Li_3InMo_3O_{12}$ have a Lyonsite-related crystal structure. The $Li_2Ca_2Mo_3O_{12}$ did not form and resulted in a multiphase ceramic (Li_2MoO_4 + $CaMoO_4$) with a very high quality factor of 108 000 GHz. The Li_2MoO_4 sinteredat has ε_r = 5.5, Qf = 46 000 GHz, and τ_f = –160 ppm/°C, The τ_f of Li_2MoO_4 can be improved by composite formation with TiO_2 without much degradation of the quality factor. The $0.55Li_2MoO_4$—$0.45TiO_2$ sintered at 700 °C showed a τ_f of –5 ppm/°C with ε_r = 10.6 and Qf = 30 100 GHz [280]. The simultaneous substitution of the A site Li by Bi and B site Mo by W or V in Li_2MoO_4 considerably improved the dielectric constant and τ_f with ultralow sintering temperatures [266, 281]. Figure 8.34 shows the variation of relative permittivity,

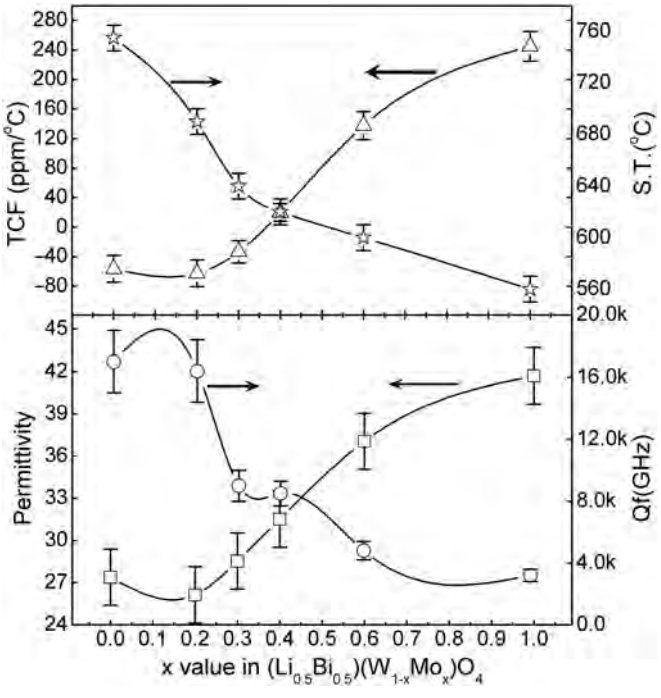

Figure 8.34 *Variation of microwave dielectric properties of $(Li_{0.5}Bi_{0.5})(W_{1-x}Mo_x)O_4$ as a function x. Source: Zhou* et al. *2012 [266]. Reproduced with permission from World Scientific Publishers.*

τ_f, sintering temperature, and quality factor as a function of the x value. The sintering temperature and quality factor decrease with the x value whereas the τ_f and relative permittivity increase with the x value.

Zhou and coworkers [267, 273, 282, 283] reported microwave dielectric properties of $(ABi)_{1/2}MoO_4$ (A = Li, Na, K, Rb, Ag, Ca) that can easily be sintered at temperatures below 700 °C. Most of them have relatively low quality factors (less than 13 000 GHz) and react with silver. However, the Ca-substituted composition with $x = 0.15$ $[(Ca_{1-3x}Bi_{2x}\phi_x)MoO_4]$ (ϕ = an A site vacancy) has excellent properties with $\varepsilon_r = 21.2$, $Qf = 29300$ GHz, $\tau_f = -1$ ppm/°C when sintered at 700 °C. It is found [274] that the sintering temperature of $(Ag_{0.5}Bi_{0.5})MoO_4$ could be effectively lowered from 610 °C to about 520 °C by forming a solid solution with $BiVO_4$. The K_2O—MoO_3 binary system consists of a few ultralow temperature sinterable compositions such as $K_2Mo_2O_7$, $K_2Mo_3O_{10}$, and $K_2Mo_4O_{13}$ [284] with τ_f in the range –63 to –92 ppm/°C. All these ceramics have a low sintering temperature, are chemically compatible with Al electrode material, and good dielectric properties. The $K_2Mo_2O_7$, which has a triclinic crystal structure, show the lowest sintering temperature of 460 °C. It has relative permittivity of 7.5 and $Qf = 22\,000$ GHz. The $(K_{0.5}La_{0.5})MoO_4$ is another interesting material which can be densified at 660 °C exhibiting a high quality factor of about 59 000 GHz [285]. Rare earth molybdates such as $Nd_2Mo_4O_{15}$ and $Sm_2Mo_4O_{15}$ have very good quality factors (about 60 000 GHz) but their sintering temperatures are relatively high at about 690–700 °C and their τ_f are close to –50 ppm/°C [285]. The pure Te_2MoO_7 has a relative permittivity of 13.6, Qf of 46 900 GHz, and τ_f of −36 ppm/°C. Partial substitution of Mo by W improved the τ_f but degraded the quality factor. The monoclinic $Te_2(Mo_{1-x}W_x)O_7$ can be well sintered at 520 °C with interesting microwave dielectric properties with $\varepsilon_r = 13.9$, $Qf = 25\,800$ GHz, and τ_f of –13 ppm/°C for $x = 0.05$ [268].

8.6.2.5 Tellurates

The first low loss tellurate-based dielectric material ($TiTe_3O_8$) was reported by Maeda *et al.* in 1987 [156]. Later several authors reported the microwave dielectric properties of many tellurate compounds [287–302]. The TeO_2 with predominant covalent bonding is difficult to densify and the sample sintered at 640 °C for 15 h; having a porosity of 20% showed ε_r of 19.3, Qf of 30 000 GHz, and τ_f of –119 ppm/°C [287]. The high negative value of τ_f has been tuned [297] close to zero by the addition of 10 wt% of $CaTiO_3$ and 15 wt% of $SrTiO_3$ by sintering at 645 and 610 °C, respectively. The addition of $CaTiO_3$ and $SrTiO_3$ to TeO_2 led to the formation of secondary phases $TiTeO_3$, $CaTe_2O_5$, and $SeTe_2O_5$, lowering the quality factor. The monoclinic $Bi_2Te_2O_8$ ceramic sintered in oxygen atmosphere at 650 °C for 10 h showed ε_r value of 39, Qf of 23 000 GHz, and τ_f of –43 ppm/°C [288]. Kwon *et al.* [291,292] made a detailed study of the structure and properties of materials in the BaO—TeO_2 system. The compounds $BaTe_4O_9$ and $BaTe_2O_6$ have low sintering temperatures of 550 and 650 °C, respectively, and have high quality factors whereas the compounds $BaTeO_3$ and Ba_2TeO_5 have sintering temperatures above 700 °C. The $BaTe_4O_9$ has ε_r of 17.5, high Qf of 54 700 GHz, and τ_f of –90 ppm/°C. The ceramic is found to react with silver but is compatible with aluminum electrodes. The high negative τ_f of $BaTe_4O_9$ has been compensated by forming a composite with $TiTe_3O_8$ and has a relative permittivity of 50, Qf of 30 600 GHz, and a positive τ_f of 133 ppm/°C [296]. The $BaTe_4O_9$ + 40 wt% $TiTe_3O_8$ sintered at 575 °C has ε_r of 25, Qf of 19 300 GHz, and τ_f of –3 ppm/°C [251].

Table 8.12 *Slurry composition in tape casting (wt%) for $Zn_2Te_3O_8$ + 4 wt% TiO_2. After Honkamo* et al. *[302]*

ZTT powder	Ethanol + xylene	Fish oil	PVB (B98)	Butyl benzyl phthalate (S160)	Polyalkylene glycol (UCON 50HB2000)
62.9	15.4 + 15.4	1.3	3.4	0.8	0.8

The ATe_3O_8 (A=Sn, Zr, Zn) ceramics have recently been reported [293,294] as ultralow temperature sinterable materials. The $Zn_2Te_3O_8$ ceramic sintered at 585 °C has $\varepsilon_r = 16.2$, $Qf = 66\,000$ GHz, and τ_f of –60 ppm/°C. The high negative τ_f of $Zn_2Te_3O_8$ has been tailored by forming composites with TiO_2 and $TiTe_3O_8$. Addition of 4 wt% TiO_2 improved the τ_f to –9 ppm/°C [292,293], but the quality factor decreased to 27 000 GHz with an increase in relative permittivity to 19.3. However, addition of $TiTe_3O_8$ improved the τ_f without much degradation in the microwave dielectric properties [299]. The $Zn_2Te_3O_8$ + 30 wt% $TiTe_3O_8$ composite has τ_f of 3 ppm/°C with $\varepsilon_r = 19.8$ and Qf of 50 000 GHz. Honkamo *et al.* [302] were the first to fabricate ULTCC tapes. They prepared a composite of $Zn_2Te_3O_8$ + 4 wt% TiO_2 (ZTT) by the solid-state ceramic route. The slurry composition for tape casting is given in Table 8.12. The slurry composition was optimized based on several experiments on different kinds of ceramic powders with a PVB-based organic system [303]. Honkamo *et al.* proposed [302] a relationship for the amount of the organic PVB-based systemas a function of the specific surface area (SSA) of the ceramic powder. It was found that the SSA value can give a rough estimate of the desired amounts of dispersant and binder in tape casting slurry. They suggested that for small SSA values the amount of binder can be varied in a moderately wide range and the dispersant amount should be close to 1 wt% in relation to the ceramic powder. The SSA value of the ceramic powder was 1.28 m^2/g. The thickness of the tape was about 80 μm and the surface roughness was about 0.1 μm.

The cast tapes were laminated with ten layers at a temperature of 70 °C and pressure of 17 MPa with a dwell time of 20 min. The green density of the stack was 3.4 gm/cm^3, which is about 69% of the sintered density (4.9 gm/cm^3). The sintering temperature was optimized at 660 °C for 4 h with a linear shrinkage in the plane of 14.65 and 13.7% in thickness. Figure 8.35a shows the microstructure of the green and sintered tapes. The green tape had an average grain size of about 1 μm and the sintered tape showed a grain size of about 5 μm. The ZTT is found to react with the common electrode material Ag but is chemically compatible with the Al electrode at 660 °C, as revealed by the SEM microstructure in Figure 8.35c. The stacked and sintered tapes formed a monolithic multilayer without any trace of lamination, indicating the possibility of practical application for multilayer modules. Figure 8.36 shows the variation of relative permittivity and loss tangent of the sintered tape as a function of temperature in the range 0 to 70 °C. The loss tangent shows slight variations with temperature whereas the relative permittivity nearly remains constant. At 7 GHz the sintered tape showed a relative permittivity of 17.3 and loss tangent of 0.0064 and are suitable for Al electrode-based applications. However, the toxicity and reactivity of most of the tellurates with silver electrodes to form Ag_6TeO_6, Ag_2TeO_3 and $Ag_3Te_2O_7$ and the high cost makes them less attractive for commercial applications. The $MgTe_2O_5$, which has an orthorhombic crystal structure, can be sintered into a dense ceramic at 700 °C

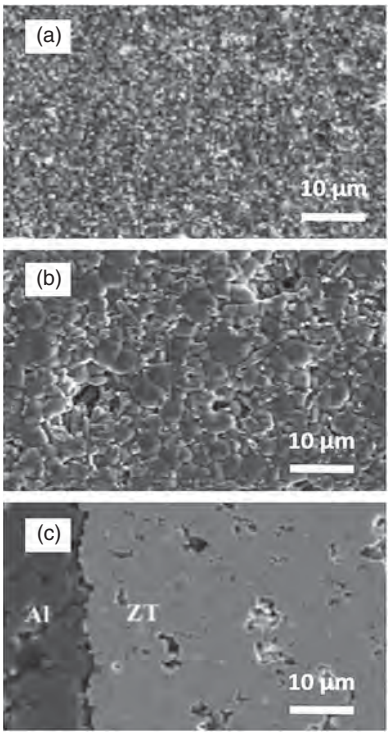

Figure 8.35 *Surface morphology of (a) green $Zn_2Te_2O_8$ + 4wt% TiO_2 tapes, (b) tape sintered at 660 °C, and (c) cross-sectional view of the interface between ZT and Al sintered at 660 °C. Source: Adapted from Honkamo* et al. *2009 [302].*

[295]. The $MgTe_2O_5$ has ε_r of 10.5, $Qf = 61\,000$ GHz, and $\tau_f = -45$ ppm/°C. Subodh *et al.* [295] reported that the relative permittivity decreased and the quality factor and τ_f increased on cooling to cryogenic temperatures, as shown in Figure 8.37. The ceramic showed ε_r of 9.5 and quality factor of 132 000 GHz at 15 K with a high negative τ_f of 277 ppm/°C. The increase in the quality factor on cooling is attributed to the decreased interaction of phonons with microwave.

8.6.3 ULTCC Category I

There are only a handful of materials under category I that can be sintered at temperatures of 400 °C or less. Recently it was reported that silver-based molybdate has a very low sintering temperature [304, 305]. The Ag_2MoO_4 can be densified at 450 °C and has relative permittivity of 8.1, $Qf = 17\,000$ GHz, and τ_f of –133 ppm/°C. It is chemically compatible with silver but reacts with Al. Partial substitution of Ag with Na further lowers the sintering temperature to 400 °C with considerable improvement in the microwave dielectric properties [305]. The $NaAgMoO_4$ has a spinel structure and does not react with electrode materials such as Ag and Al. The $NaAgMoO_4$ ceramics has the lowest sintering temperature among the ULTCC materials. The permittivity and quality factor increase with an increase in the sintering temperature, reached a maximum at 400 °C, and then decreased.

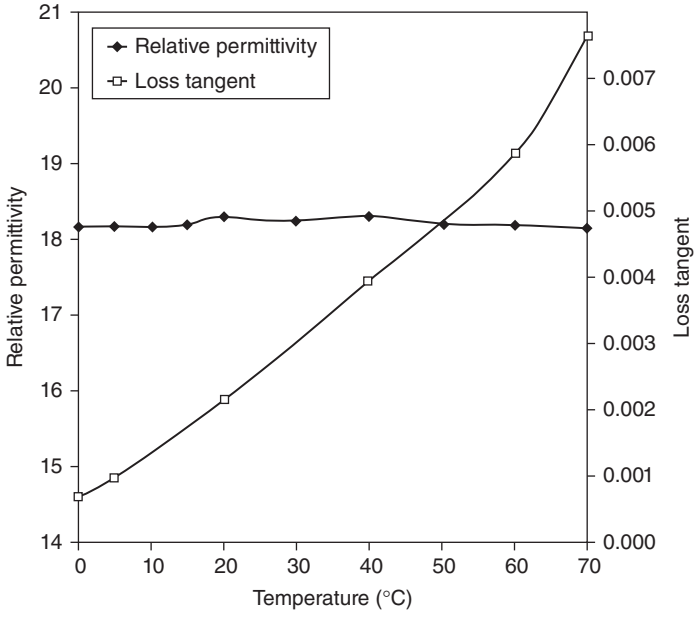

Figure 8.36 *Variation of relative permittivity and loss tangent of $Zn_2Te_2O_8$ + 4wt% TiO_2 laminated tape sintered at 660 °C measured at 1 MHz. Source: Adapted from Honkamo 2009* et al. *[302].*

The ceramic sintered at 400 °C exhibits a permittivity of 7.9, *Qf* value of 33 000 GHz, and τ_f of –120 ppm/°C.

Recently Kahari *et al.* reported [306,307] a novel method for preparing Li_2MoO_4 ceramics at room temperature by moistening the water soluble Li_2MoO_4 powder using deionized

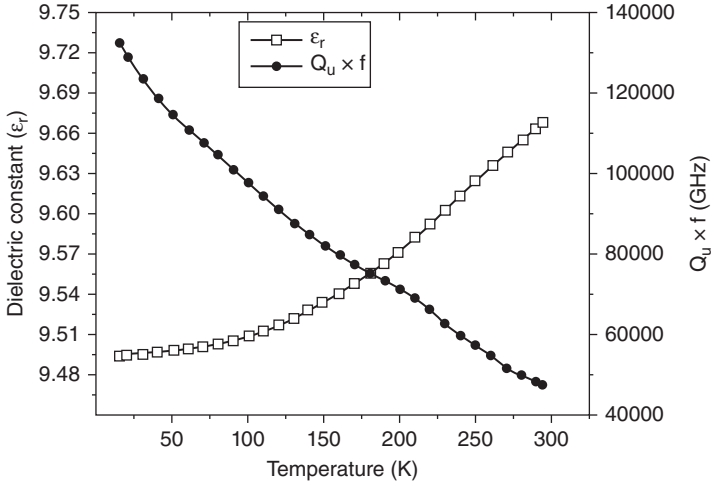

Figure 8.37 *Variation of dielectric constant and quality factor of $MgTe_2O_5$ ceramics at cryogenic temperatures. Source: Adapted from Subodh* et al. *2008 [295].*

water and pressing under a pressure of about 130 MPa. The samples were then dried at room temperature. The samples were also prepared by sintering at 540 °C. There was no appreciable difference in the sintered density of the samples dried at room temperature or sintered at 540 °C. The amount of water in the pressed samples was about 2–3 wt% before drying or sintering. It is believed that the densification of the samples occurred during pressing. X-ray diffraction study showed that the crystal structure remains the same and water did not react to form any hydrates. The samples showed a relative permittivity in the range of 4.6 to 5.2 at 9.6 GHz. The room temperature dried samples showed a *Qf* value of about 10 200 GHz and that sintered at 540 °C had 18 500 GHz, respectively. This difference in dielectric properties is attributed to the presence of small amounts of residual water. It was found [306] that the ceramic powder particle size has a great influence on preparation, densification, and dielectric properties. Larger particles are advantageous in fabricating Li_2MoO_4 ceramics by moistening and then pressing method. Smaller particles lead to clay-like clusters, leading to non-uniform densification, warpage, and cracking. Kahari *et al.* [307] tailored the dielectric properties by adding TiO_2 and $BaTiO_3$ in Li_2MoO_4 with an optimized room temperature preparation method.

8.7 Discussion and Conclusion

ULTCC materials with sintering temperature, crystal structure, relative permittivity, quality factor–frequency product, measurement frequency, temperature variation of resonant frequency, and references so far reported are given in the Appendix. There are about 170 ULTCC compositions with sintering temperatures less than 700 °C. About 34% of ULTCC materials are based on molybdates, 25% on tellurates, about 9% contain vanadium, and 5% contain tungsten. Na_2MoO_4 ceramic has the lowest ε_r of 4.1, *Qf* of 35 000 GHz, and τ_f of –76 ppm/°C with a sintering temperature 660 °C [277]. CaV_2O_6 has the highest *Qf* (123 000 GHz) with $\varepsilon_r = 10.2$ and τ_f of –60 ppm/°C [260]. The $Zn_2Te_3O_8$ + 30 wt% $TiTe_3O_8$ sintered at 600 °C has the best τ_f (3 ppm/°C) with ε_r of 19.8, *Qf* of 50 000 GHz [299]. $BaTiTe_3O_9$ has the highest negative τ_f (–372 ppm/°C) with ε_r of 29.0, $Qf = 1700$ GHz [291]. $(Li_{0.5}Bi_{0.5})MoO_4$ has the highest positive τ_f (240 ppm/°C) with ε_r of 44.4 and *Qf* of 3200 GHz [236]. $[(Li_{0.5}Bi_{0.5})_xBi_x][Mo_xV_{1-x}]$ with $x = 0.098$ has the highest ε_r (81) among the crystalline ULTCC materials [281]. There are only a couple of materials under ULTCC category I: $NaAgMoO_4$ and room temperature prepared Li_2MoO_4 by the moistening and pressing technique. As expected, the reported quality factors of the microwave dielectric ceramics decrease significantly with increasing relative permittivity, as shown in Figure 8.38. Most of the ULTCC materials have ε_r <40 with moderate *Qf*, as shown in Region I of Figure 8.38. The *Qf* of the materials with $\varepsilon_r > 40$ are relatively small. There are only a handful of materials with *Qf* > 50 000 GHz, as revealed by Figure 8.38.

In general the τ_f is found to increase with increasing relative permittivity, as shown in Figure 8.39. It is evident from Figure 8.39 that most of the ULTCC materials have negative τ_f. However, there are a reasonable number of materials with τ_f close to zero and most of these materials have ε_r in the range 5 to 40. Figure 8.40 shows the variation of relative permittivity, quality factor, and τ_f as a function of sintering temperature of the ceramics. Most of the ULTCC materials have a sintering temperature >600 °C and they have relatively large ε_r (Figure 8.40a). The ULTCC compositions are feasible for cofiring with organic or

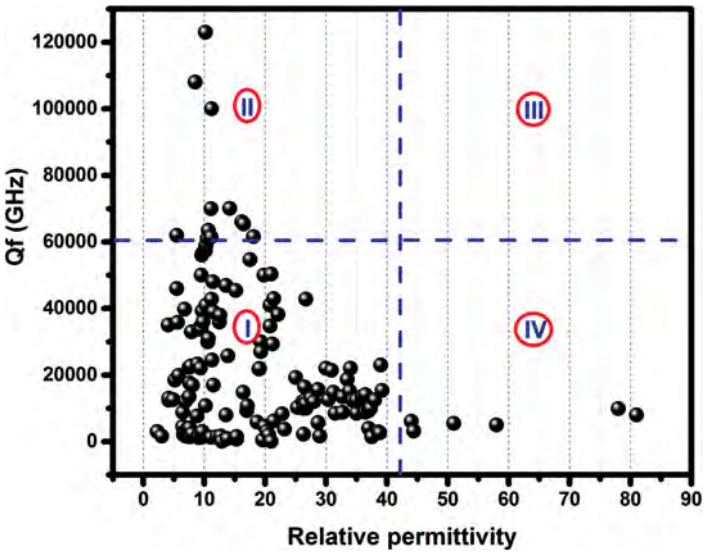

Figure 8.38 *Variation of quality factor frequency product with relative permittivity.*

semiconductive structures using aluminum or less than 400 °C using nanosilver ink electrodes. In semiconductors, metal electrodes should be deposited on top of the dielectric layers with a low temperature process. Multilayer packages made by LTCC technology but with a much lower sintering temperature would enable cofiring of semiconductor devices into the package.

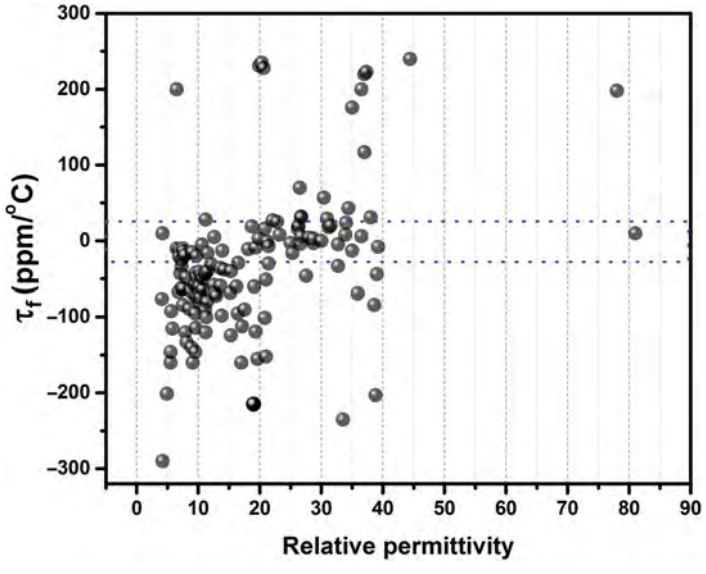

Figure 8.39 *Variation of τ_f with relative permittivity.*

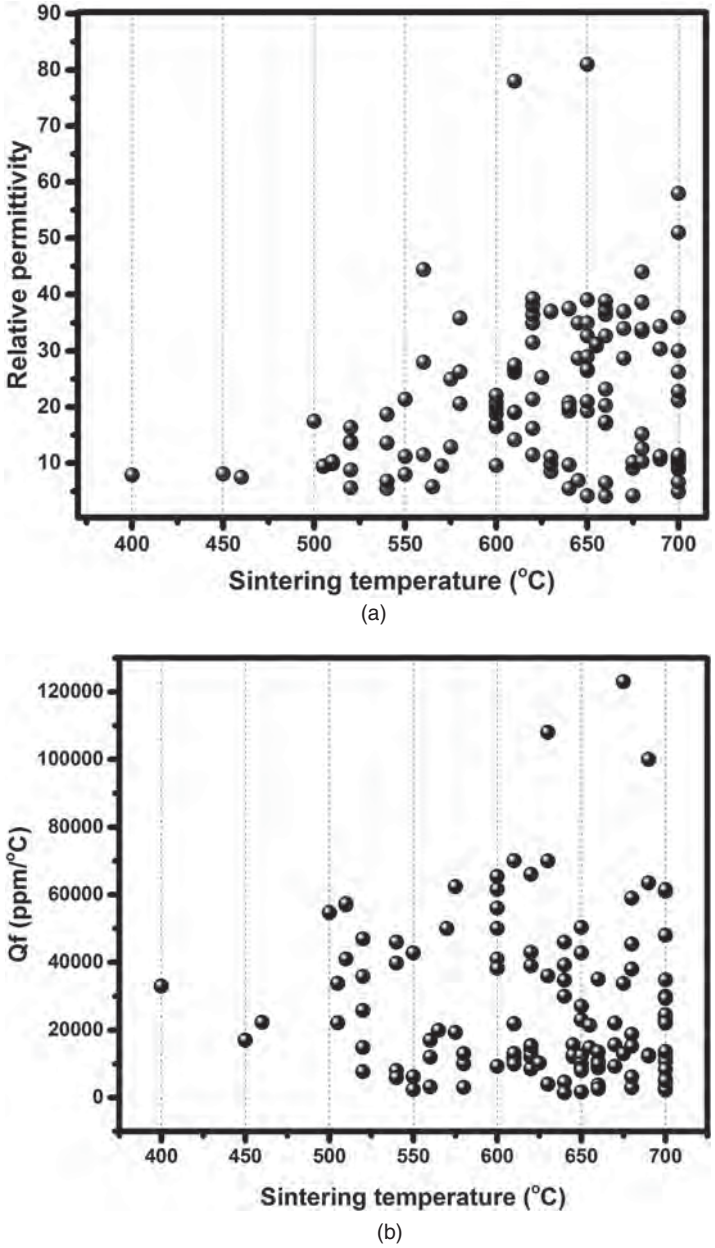

Figure 8.40 *Variation of microwave dielectric properties as a function of sintering temperature: (a) ε_r, (b) Qf, and (c) τ_f.*

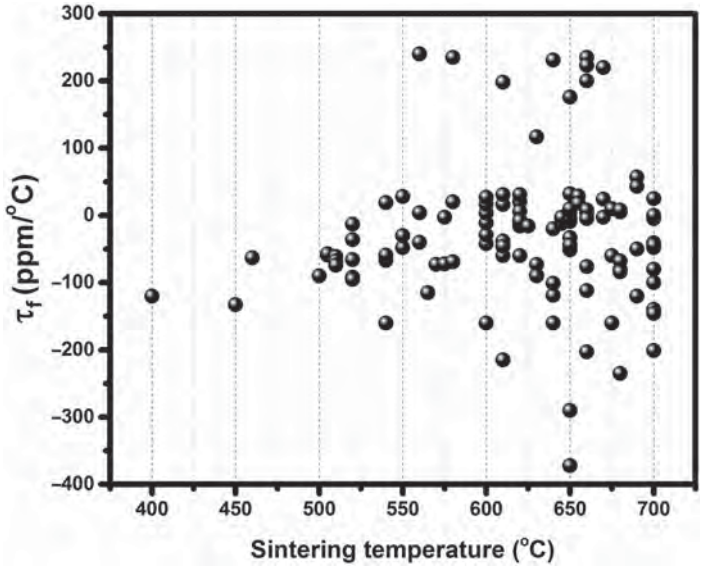

(c)

Figure 8.40 *(Continued)*

The materials under category I (ULTCC-I), with a sintering temperature at 400 °C or below, should be feasible with commercially available highly conductive nanosilver inks in cofiring. These compositions have inherently ultralow sintering temperatures. Although only very few compositions so far belonging to this category are reported, they will in the future provide great opportunities with integrated applications with semiconductor devices or on organic substrates. One challenge with the ULTCC materials is that most of them based on vanadates and molybdates are soluble in water. This means the ultimate device needs suitable encapsulation. These materials need to be tape cast for practical applications. In addition the low sintering temperature causes extra challenge in tape casting, which means the need for suitable binders, dispersants, and plasticizers that can burn out before shrinkage. The research and development of ULTCC-I materials are still however in their initial stage. Attempts should be also made to lower the cost of production of microwave materials with emphasis on the use of environment friendly materials with the possibility of recycling. In the near future, the new emerging communication applications like 5G network machine-to-machine connection and Internet of Things (IoT) will need novel dielectric ceramics with feasible component fabrication technologies. This means that the low loss ULTCC microwave ceramics will continue to be an active area of research in years to come. The future will show their importance for improved performance with cost-efficient and miniaturized devices.

References

1. Kristofferson, A. and Carlstrom, E. (1997) Tape casting of alumina in water with an acrylic latex binder. *Journal of European Ceramic Society*, **17**, 289–297.

2. Chartier, T. and Bruneau, A. (1993) Aqueous tape casting of alumina substrates. *Journal of European Ceramic Society* **12**, 243–247.
3. Mistler, R.E., and Twiname. E.R. (2000) Tape casting. Theory and practice. The American Ceramic Society, Westerville, OH, USA.
4. Kristoffersson, A., Roncar, E., and Galassi, C. (1998) Comparison of different binders for water based tape casting of alumina. *Journal of European Ceramic Society*, **18**, 2123–2131.
5. Hotz, D. and Greil, P. (1995) Aqueous tape casting of ceramic powders. *Review. Materials Science and Engineering A*, **202**, 206–217.
6. Fu, Z. and Roosen, A. (2015) Shrinkage of tape cast products during binder burnouts. *Journal of American Ceramic Society*, **98**, 20–29.
7. Tok, A.I.Y., Boey, F Y.C., and Akhor, M.K. (1999) Tape casting of high dielectric ceramic substrates for microelectronic packaging. *Journal of Materials Engineering and Performance*, **8**, 469–472.
8. Luo, X.-J., Zhang, B.-L., Li, W.-L., *et al*. (2004) Preparation of aluminum nitride green sheets by aqueous tape casting. *Ceramic International*, **30**, 2099–2103.
9. Streicher, E. and Chartier, T. (1990) Influence of organic components on properties of tape-cast aluminum nitride substrates. *Ceramic International*, **16**, 247–252.
10. Streicher, E. and Chartier. T. (1992) Preparation and characterization of tape cast aluminium nitride substrates. *Journal of European Ceramic Society*, **9**, 231–242.
11. Olhero, S. and Fereira. J. (2005) Rheological characterization of water based AlN slurries for tape casting process. *Journal of Materials Processing Technology*, **69**, 206–213.
12. Luo, X., Li, J., Zhang, B., *et al.* (2006) High thermal conductivity aluminum nitride substrates prepared by aqueous tape casting. *Journal of American Ceramic Society*, 836–841.
13. Qiao, L., Heping, Z., Xue, H., *et al.* (2003) Effect of Y_2O_3 on low temperature sintering and thermal conductivity of AlN ceramics. *Journal of European Ceramic Society*, **23**, 61–67.
14. Baranda, P., Knudsen, A., and Ruh, E. (1994) Effect of yttria on the thermal conductivity of aluminum nitride. *Journal of American Ceramic Society*, **77**, 1846–1850.
15. Olhero, S., Alves, F.L., and Fereira, J.M.F. (2011) Last advances in aqueous processing of aluminum nitride (AlN) – a review, in *Advances in Ceramics* (ed. C. Cikalidis), Intechopen, pp. 207–242.
16. Varghese, J., Joseph, T., and Sebastian, M.T. (2011) $ZrSiO_4$ ceramics for microwave integrated circuit applications. *Materials Letters*, **65**, 1092–1094.
17. Varghese, J. (2015) Fabrication of microwave substrates and formulation of dielectric inks for microelectronic applications. PhD Thesis, Cochin University of Science and Technology, India.
18. Varghese, J. and Sebastian, M.T. (2016) To be published.
19. Bhushan, B. (1995) *Handbook of Micro/nanotribology*, CRC Press, New York.
20. Saif, R.A.A., Ramli, N., and Poopalan, P. (2010) AFM study of multilayer sol–gel $Ba_xSr_{1-x}TiO_3$ thin films. *Jordan Journal of Physics*, **3**, 61–68.
21. Salam, L.A., Matthews, R.D., and Robertson, H. (2000) Optimisation of thermoelectric green tape characteristics made by the tape casting method. *Materials Chemistry and Physics*, **62**, 263–272.
22. Sebastian, M.T. (2008) *Dielectric Materials for Wireless Communication*, Elsevier, Oxford.
23. Sebastian M.T. and Jantunen, H. (2008) Low loss dielectric materials for LTCC applications: a review. *International Materials Reviews*, **53**, 57–90.
24. Sebastian M.T., Ubic, R., and Jantunen, H. (2015) Low loss dielectric ceramic materials and their applications. *International Materials Reviews*, **60**, 392–411.
25. Sobocinski, M., Teirikangas, M., Perantie, J., *et al.* (2015) Decreasing the relative permittivity of LTCC by porosification with poly(methyl methcrylate) microspheres. *Ceramic International*, **41**, 10871–10877.
26. Imanaka, Y. (2005) *Multilayers Low Temperature Cofired Ceramics (LTCC) Technology*, Chapter 2, Springer, New York.
27. Tummala, R.R. (1991) Ceramic and glass packagings in the 1990s. *Journal of American Ceramic Society*, **74**, 895–908.
28. Gektin, V., Bar-Cohen, A., and Witzman, S. (1998) Coffin–Manson based fatigue analysis of underfilled DCAS. *IEEE Transactions on Components and Packaging Technology A*, **21A**, 577–584.

29. Schwartz, B. (1984) Microelectronic packaging. *American Ceramic Society Bulletin*, **63**, 577–581.
30. Kagata, H., Inoue T., and Kato, J (1992) Low-fire bismuth-based dielectric ceramics for microwave use. *Japanese Journal of Applied Physics*, **31**, 3152–3155.
31. Wang, Y., Zhang, G., and Ma, J. (2002) Research of LTCC/Cu, Ag multilayer substrate in microelectronic packaging. *Materials Science and Engineering B*, **94**, 48–53.
32. Knickerbocker, S., Kumar, A.H., and Herron, W. (1993) Cordierite glass–ceramics for multilayer ceramic packaging. *American Ceramic Society Bulletin*, **72**, 90–95.
33. Ferro Corporation (1996) *FERRO-TAPE-A6"*, Technical Publication, Ferro Corporation, Santa Barbara, CA.
34. Niwa, K., Imanaka, Y., Kamehara, N., *et al.* (1989) In *Advances in Ceramics* (eds M.P. Yan *et al.*), vol. 26, Columbus, The American Ceramic Society, Columbus, USA, p. 323.
35. Kwon, O.-H. and Messing, G.L. (1990) Kinetic analysis of solution precipitation during liquid phase sintering of alumina. *Journal of American Ceramic Society*, **73**, 275–281.
36. Singh, V.K. (1981) Densification of alumina and silica in the presence of liquid phase. *Journal of American Ceramic Society*, **64**, C133–C135.
37. Kingery, W.D., Niki, E., and Narasimhan, M.D. (1961) Sintering of oxide and carbide–metal compositions in presence of a liquid phase. *Journal of American Ceramic Society*, **44**, 29–34.
38. German, R.M. (1985) *Liquid Phase Sintering*, Plenum Press, New York, pp. 65–151.
39. Jean, J.-H. and Lin, S.-C. (1999) Densification kinetics of borosilicate glass + TiO_2. *Journal of Materials Research*, **14**, 1359–1363.
40. Eberstein, M. and Schiller, W.A. (2003) Development of high permittivity glasses for microwave LTCC tapes. *Glass Science and Technology*, **76**, 8–16.
41. Jean, J.-H. and Gupta, T.K. (1992) Liquid phase sintering in glass–cordierite system. *Journal of Materials Science*, **27**, 1575–1584.
42. Eustice, A.L., Horowitz, S.J., Stewart, J.J., *et al.* (1986) Low temperature cofired ceramics: a new approach to electronic packaging, in *Proceedings of 36th Conference on Electronic Component*, Seattle, WA, IEEE, pp. 37–67.
43. Jean, J.-H. and Gupta, T.K. (1992) Liquid phase sintering of glass–cordierite system: particle size effects. *Journal of Materials Science*, **27**, 4967–4973.
44. Kuczynski, G.C. and Zaplatynsky, I. (1956) Sintering of glass. *Journal of American Ceramic Society*, **39**, 349–350.
45. Ohsato, H. (2005) Research and development of microwave dielectric ceramics for wireless communications. *Journal of Ceramic Society Japan*, **113**, 703–711.
46. Yoon, K.H., Yoo, S.J., Kim, W.S., *et al.* (1999) Effect of BaO/WO_3 on the microwave loss quality of $Ba(Mg_{1/3}Ta_{2/3})O_3$. *Japanese Journal of Applied Physics*, **38**, 5616–5620.
47. Kingery, W.D. (1959) Densification during sintering in the presence of a liquid phase. *I. Theory. Journal of Applied Physics*, **30**, 301–306.
48. Ichinose, N. and Yamamota, H. (1997) Effective of additives on microwave dielectric properties of low temperature firing of (Mg, Ca)TiO_3 based ceramics. *Ferroelectrics*, **201**, 255–262.
49. Tamura, H., Kagata, H., Inoue, T., *et al.* (1992) Low fire bismuth based dielectric ceramic for microwave use. *Japanese Journal of Applied Physics*, **31**, 3152–3155.
50. Navias, L. and Green, R.L. (1946) Dielectric properties of glasses at ultrahigh frequencies and their relation to composition. *Journal of American Ceramic Society*, **29**, 267–276.
51. Israd, J.O. (1961) A study of migration loss in glass and a generalized method of calculating the rise of dielectric loss with temperature, in *Proceedings of International Conference Composite Materials in Electronic Packaging Engineering*, IEEE, p. 3636.
52. Wakino, K. (1992) Dielectric materals and Applications, in *Proceedings of ISIF* (ed. A.R. von Hipple), MIT Press, Cambridge, MA, pp. 308–335
53. Von Hippel, A.R. (ed.) (1954) *Dielectric Materials and Applications*, MIT Press, Cambridge, MA.
54. Li, L., Fang, Y., Xiao, Q., Wu, Y.J., *et al.* (2014) Microwave dielectric properties of fused silica prepared by different approaches. *International Journal of Applied Ceramic Technology*, **11**, 193– 199.
55. Kinser, D.L. (1971) In *Physics of Electronic Ceramics: Part A* (eds L.L. Hench *et al.*), Marcel & Dekker, New York.

56. Berezhoni, A.I. (1970) In *Glass Ceramics and Photo-citalls* (ed. A.G. Pincus), Translated from Russian, Plenum Press, New York
57. Wu, J.M.and and Huang, H.L. (1999) Microwave properties of zinc, barium and lead borosilicate glasses. *Journal of Non-crystalline Solid*, **260**, 116–124.
58. Zhu, H., Lu, M., Zhou, H., Li, L., and Lv, A. (2006) Preparation and properties of low-temperature co-fired ceramic of $CaO–SiO_2–B_2O_3$ system. *Journal of Materials Science: Materials in Electronics*, **17**, 637–641.
59. Kim, S.-G., Park, J.S., An, J.S., *et al.* (2006) Effects of the addition of different types of fillers on the properties of $BaO–ZnO–B_2O_3–SiO_2$ glass composites for application to barrier ribs of plasma display anels. *Journal of American Ceramic Society*, **89**, 902–907.
60. Chang, C.R. and Jean, J.H. (1999) Crystallization kinetics and mechanism of low-dielectric, low-temperature, cofirable $CaO–B_2O_3–SiO_2$ glass–ceramics. *Journal of American Ceramic Society*, **82**, 1725–1732.
61. Kobayashi, Y. and Kato, E. (1994) Low temperature fabrication of anorthite ceramics. *Journal of the American Ceramic Society*, **77**, 833–834.
62. Lo, C.L., Duh, J.-G., Chiou, B.S., *et al.* (2002) Low-temperature sintering and microwave dielectric properties of anorthite-based glass–ceramics. *Journal of American Ceramic Society*, **85**, 2230–2235.
63. Lim, E.S., Kim, B.S., Lee, J.H., *et al.* (2006) Effect of BaO content on the sintering and physical properties of $BaO–B_2O_3–SiO_2$ glasses. *Journal of Non-crystalline Solids*, **352**, 821–826.
64. Takada, T., Wang, S.F., Yoshikawa S., *et al*. (1994) Effect of glass additions on $BaO–TiO_2–WO_3$ microwave ceramics. *Journal of American Ceramic Society*, **77**, 1909–1916.
65. Ren, L., Zhou, H., Li, X., *et al*. (2015) Synthesis and characteristics of borosilicate based glass–ceramics with different SiO_2 and Na_2O contents. *Journal of Alloys and Compounds*, **646**, 780–786.
66. Li, B., Long, Q., and Duan, D. (2016) Effects of ZrO_2 on properties of $BaO–Al_2O_3–B_2O_3–SiO_2$ composites for LTCC applications. *Journal of Materials Science: Materials in Electronics*, **27**, 2824–2829.
67. Li, B., Qing, Z., Li, Y., *et al*. (2016) Effect of CaO content on structure and properties of low temperature cofired glass–ceramic in the $Li_2O–Al_2O_3–SiO_2$ system. *Journal of Materials Science: Materials in Electronics*, **27**, 2455–2459.
68. Li, B., Duan, D., and Long, Q. (2016) Influence of ZrO_2 on microstructures and properties of $Li_2O–Al_2O_3–SiO_2$ glass–ceramic for LTCC applications. *Journal of Materials Science: Materials in Electronics*, **27**, 134–139.
69. Li, B., Xu, M., and Tang, B. (2016) Effects of ZnO on crystallization microstructures and properties of $BaO–Al_2O_3–B_2O_3–SiO_2$ glass–ceramics. *Journal of Materials Science: Materials in Electronics*, **27**, 70–76.
70. Liu, J.-Z., Wu, X.-F., Xu, N.-X., *et al.* (2015) Crystallization sinterability and dielectric properties of $CaO–B_2O_3–SiO_2$ glass ceramics with Al_2O_3 additives. *Journal of Materials Science: Materials in Electronics*, **26**, 8899–8903.
71. Takada, T. and Kageyama, K. (2005) Synthesis and microwave dielectric properties of $La_2O_3–xB_2O_3$-based melt mixtures for low-temperature cofired ceramics. *Japanese Journal of Applied Physics*, **44**, 6629–6635.
72. Takada, T., Yammoto, H., and Kageyama, K. (2003) Synthesis and microwave dielectric properties of $xRe_2O_3–yB_2O_3$ (Re = La, Nd, Sm, Dy, Ho and Y) compounds. *Japanese Journal of Applied Physics*, **42**, 6162–6167.
73. Kagata, H., Saito, R., and Katsumura, H. (2004) $Al_2O_3–MgO–ReOx$ (Re = rare earth) based LTCC and its applications to multilayer non-shrinkage substrate for microwave devices. *Journal of Electroceramics*, **13**, 277–280.
74. Ohsato, H., Tsunooka, T., Ando, M., *et al.* (2003) Millimeter wave dielectric ceramics of alumina and fosterite with high quality factor and low dielectric constant. *Journal of Korean Ceramic Society*, **40**, 350–353.
75. Jei, W.C.J., Chen, C.L., and Roosen, A. (2005) $La_2O_3–Al_2O_3–B_2O_3$ based glass ceramics for LTCC application. *Key Engineering Materials*, **280–283**, 929–934.

76. Seo, J.J., Shin, D.J., and Cho, Y.S. (2006) Phase evolution and microwave dielectric properties of lanthanum borate based low temperature cofired ceramic materials. *Journal of American Ceramic Society*, **89**, 2352–2355.
77. Chen, C.-L., Wei, W.-J., and Roosen, A. (2006) Wetting, densification and phase transformation of $La_2O_3/A_2O_3/B_2O_3$-based glass–ceramics. *Journal of European Ceramic Society*, **26**, 59–65.
78. Chakraborty, I.N., Shelby, J.E., and Condrate, R.A. (1984) Properties and structure of lanthanum borate glasses. *Journal of American Ceramic Society*, **67**, 782–785.
79. Fang, Y.C. and Jean, J.-H. (2006) Compositional design of lead-free, low temperature cofired ceramic dielectric composite. *Japanese Journal of Applied Physics*, **45**, 6357–6361.
80. Nair, I.J, Abhilash, P, Arun, S., *et al*. (2015) LTCC tapes based on Al_2O_3–BBSZ glass with improved thermal conductivity. *Ceramic International*, **41**, 13572–13581.
81. Liu, J.-Z., Wu, X.-F., Xu, N.-X., *et al*. (2015) Crystallization, sinterability and dielectric properties of $CaO–B_2O_3–SiO_2$ glass ceramics with Al_2O_3 additives. *Journal of Materials Science: Materials in Electronics*, **26**, 8899–8903.
82. Choi, Y.-J., Park, J.H., Ko, W.-J., *et al*. (2006) Cofiring and shrinkage matching in low and middle permittivity dielectric compositions for a low temperature cofired ceramics system. *Journal of American Ceramic Society*, **89**, 562–567.
83. Yoon, S.O., Shim, S.H., Kim, K.S., *et al*. (2009) Low temperature preparation and microwave dielectric properties of ZBS glass–Al_2O_3 composite. *Ceramic International*, **35**, 1271–1275.
84. Doo, S.H., Jo, Y.H., Lee, J.S., *et al*. (2010) Enhanced quality factor of zinc lanthanum borate based dielectrics via the control of ZnO/B_2O_3 ratio. *Journal of American Ceramic Society*, **93**, 334–337.
85. Tzou, W.-C., Chang, S.-L., Yang, C.-F., *et al*. (2003) Sintering and dielectric properties of $0.88Al_2O_3–0.12TiO_2$ microwave ceramics by glass addition. *Materials Research Bulletin*, **38**, 981–989.
86. Fang, C.-F., Chen, Y.C., Tzou, W.C., *et al*. (2003) Sintering and microwave dielectric characteristics of MCAS glass-added $0.84Al_2O_3–0.16TiO_2$ ceramics. *Materials Letters*, **57**, 2945–2949.
87. Lim, M.-H., Park, J.-H., Kim, H.-G., *et al*. (2003) *In Proceedings of IEEE International Conference on Properties and Applications of Dielectric Materials*, vol. 2, pp. 757–760.
88. Hu, W., Liun, H., Hao, H., *et al*. (2015) Influence of TiO_2 additive on the microwave dielectric properties of α-$CaSiO_3–Al_2O_3$ ceramics. *Ceramics International*, **41**, S510–S514.
89. Lo, C.L., Duh, J.-G., Chou, B.-S., *et al*. (2002) Low temperature sintering and microwave dielectric properties of anorthite based glass-ceramics. *Journal of American Ceramic Society*, **85**, 2230-2235.
90. Jo, Y.H., Kang, M.S., Chung, K.W., *et al*. (2008) Chemical stability and dielectric properties of $RO–La_2O_3–B_2O_3$ (R = Ca, Mg, Zn) based ceramics. *Materials Research Bulletin*, **43**, 361–369.
91. Nekoute, K.A., Khosroshahi, R.A., and Musavian, R.T. (2016) Sintering behavior and microwave dielectric properties of $SiO_2–MgO–Al_2O_3–TiO_2$ ceramics. *Journal of Materials Science: Materials in Electronics*, in press.
92. Dai, S. (2012) Densification and crystallization in crystallizable low temperature co-fired ceramics. *Journal of Materials Science*, **47**, 4579–4584.
93. Dai, S., Huang, R.F., and Wilcox, D.L. (2002) Use of titanates to achieve a temperature-stable low-temperature cofired ceramic dielectric for wireless applications. *Journal of American Ceramic Society*, **85**, 828–832.
94. Wilcox, D., Huang, R.F., and Dai, S. (1998) Multilayer electronic ceramic devices, in *Ceramic Transactions* (eds J.-H. Jean *et al.*), vol.97, The American Ceramic Society, Westerville, OH, pp. 201–213.
95. Barringer, E.A. and Bowen, H.K. (1982) Formation, packing, and sintering of monodisperse TiO_2 powders. *Journal of American Ceramic Society*, **65**, C199–C201.
96. Hahn, H., Logas, J., and Averback, R.S (1990) Sintering characteristics of nanocrystalline TiO_2. *Journal of Materials Research*, **5**, 609–614.
97. Kim, D.W., Kim, T.G., and Hong, K.S. (1999) Low firing of CuO doped anatase. *Materials Research Bulletin*, **34**, 771–781.
98. Yano, S., Hirofumi, N., Komaki, Y., *et al*. (1993) Distributed constant circuit board using ceramic substrate material. US Patent 5232765.

99. Yoon, S.H., Kim, D.W., Cho, S.Y., *et al*. (2003) Phase analysis and microwave dielectric properties of LTCC TiO_2 with glass system. *Journal of European Ceramic Society*, **23**, 2549–2552.
100. Jean, J.H. and Lin, S.C. (1999) Effects of borosilicate glass on densification and properties of borosilicate glass + TiO_2 ceramics. *Journal of Materials Research*, **14**, 1359–1363.
101. Cui, X.M., Zhou, J., Miao, C.L., *et al*. (2005) The study on fabrication of dielectric materials for low temperature cofired ceramics. *Rare Earth Materials Engineering*, **34**, 410–415.
102. Miyauchi, Y. and Arashi, T. (2005) The particle size effect of filler on sintering characteristics in glass–ceramics. *Journal of Japanese Society for Powder Metallurgy*, **52**, 271–275.
103. Mattox, D.M., Gurkovich, S.R., Olenik, J.A., *et al*. (1988) *Ceramic Engineering Science*, **9**, 1567–1578.
104. Gudla, R.A. (1971) Anorthite ceramic dielectrics. *American Ceramic Society Bulletin*, **50**, 555–557.
105. Ismail, M.G.U. and Aria, H. (1992) Sol gel synthesis of B_2O_3 doped anorthite and its characteristics. *Journal Ceramic Society Japan*, **100**, 1385–1389.
106. Lo, C.L., Duh, J.G., Chiou, B.S., *et al*. (2002) Microstructure characteristics of anorthite composite glass with nucleating agents of TiO_2 under non-isothermal crystallization. *Materials Research Bulletin*, **37**, 1949–1960.
107. Lo, C.L., Duh, J.G., Chiou, B.S., *et al*. (2002) Low-temperature sintering and microwave dielectric properties of anorthite-based glass–ceramics. *Journal of American Ceramic Society*, **85**, 2230–2235
108. Lo, C.L., Duh, J.G., Chiou, B.S., *et al*. (2002) Low temperature sintering and crystallisation behaviour of low loss anorthite-based glass–ceramics. *Journal of Materials Science*, **38**, 693–698.
109. Marques, V.M.F., Tulyaganov, D.U., Agathopoulos, S., *et al*. (2006) Low temperature synthesis of anorthite based glass-ceramics via sintering and crystallization of glass–powder compacts. *Journal of European Ceramic Society*, **26**, 2503–2510.
110. Levin, I., Amos, T.G., Nino, J.C., *et al*. (2002) Crystal structure of the compound $Bi_2Zn_{2/3}Nb_{4/3}O_7$. *Journal of Materials Research*, **17**, 1406–1411.
111. Valant, M. and Davies, P.K. (2000) Crystal chemistry and dielectric properties of chemically substituted $(Bi_{1.5}Zn_{1.0}Nb_{1.5})O_7$ and $Bi_2(Zn_{2/3}Nb_{4/3})O_7$ pyrochlores. *Journal of American Ceramic Society*, **83**, 147–153.
112. Youn, H.J., Sogabe, T., Randall, C.A., *et al*. (2001) Phase relations and dielectric roperties in the Bi_2O_3—ZnO—Ta_2O_5 system. *Journal of American Ceramic Society*, **84**, 2557–2562.
113. Du, H., Yao, X., and Zhang, L. (2002) Structure, IR spectra and dielectric properties of Bi_2O_3–ZnO–SnO_2–Nb_2O_5 quarternary pyrochlore. *Ceramic International*, **28**, 231–234.
114. Hong, H.B., Kim, D.W., and Hong, K.S. (2003) Microwave dielectric properties of $Bi_2(Zn_{1/3}Ta_{2/3})_2O_7$ polymorphs. *Japanese Journal of Applied Physics*, **42**, 5172–5175.
115. Wang, H., Du, H., Peng, Z., *et al*. (2004) Improvements of sintering and dielectric properties on Bi_2O_3–ZnO–Nb_2O_5 pyrochlore ceramics by V_2O_5 substitution. *Ceramic International*, **30**, 1225–1229.
116. Shen, B., Yao, X., Kang, L., *et al*. (2004) Effect of CuO or/and V_2O_5 oxide additives on Bi_2O_3–ZnO–Ta_2O_5 based ceramics. *Ceramic International*, **30**, 1203–1206.
117. Wang, H., Peng, Z., Du, H., Yao, T., and Yao, X. (2004) Mn^{4+} and W^{6+} substitution on Bi_2O_3–ZnO–Nb_2O_5-based low firing ceramics. *Ceramic International*, **30**, 1219–1223.
118. Chen, S.Y. and Lin, Y.J. (2001) Effect of CuO-based oxide additives on Bi_2O_3–ZnO–Nb_2O_5 microwave ceramics. *Japanese Journal of Applied Physics*, **40**, 3305–3310.
119. Choi, G.K., Kim, D.W., Cho, S.Y., *et al*. (2004) Influence of V_2O_5 substitutions to $Bi_2(Zn_{1/3}Nb_{2/3})_2O_7$ pyrochlore on sintering temperature and dielectric properties. *Ceramic International*, **30**, 1187–1190.
120. Nenesheva, E.A. and Kartenko, N.F. (2006) Low-sintering ceramic materials based on Bi_2O_3–ZnO–Nb_2O_5 compounds. *Journal of European Ceramic Society*, **26**, 1929–1922.
121. Ling, H.C., Yan, M.F., and Rhodes, W.W. (1990) High dielectric constant and small temperature coefficient bismuth-based dielectric compositions. *Journal of Materials Research*, **5**, 1752–1762.

122. Su, W.F. and Lin, S.C. (2003) Biomimetic Mg- and Mg,CO_3-substituted hydroxyapatites: synthesis characterization and *in vitro* behavior. *Journal of European Ceramic Society*, **23**, 2593–2596.
123. Randall, C.A., Nino, J.C., Baker, A., *et al*. (2003) *American Ceramic Society Bulletin*, **82**, 644–652.
124. Baker, A., Lanagan, M.T., Randall, C.A., *et al*. (2005) Integration concepts for the fabrication of LTCC structures. *International Journal of Applied Ceramic Technology*, **2**, 514–520.
125. Wang, N., Zhao, M.Y., Li, W., *et al*. (2004) The sintering behavior and microwave dielectric properties of $Bi(Nb,Sb)O_4$ ceramics. *Ceramic International*, **30**, 1017–1022.
126. Lee, H.R., Yoon, K.H., and Kim, E.S. (2003) Low temperature sintering and microwave dielectric properties of $BiNbO_4$–$ZnNb_2O_6$ ceramics with CuV_2O_6 additive. *Japanese Journal of Applied Physics*, **42**, 6168–6171.
127. Kim, E.S. and Choi, W. (2006) Effect of phase transition on the microwave dielectric properties of $BiNbO_4$. *Journal of European Ceramic Society*, **26**, 1761–1766.
128. Wang, N., Zhao, M.Y., Yin, Z.W., *et al.* (2004) Effects of complex substitution of La and Nd for Bi on the microwave dielectric properties of $BiNbO_4$ ceramics. *Materials Research Bulletin*, **39**, 439–448.
129. Shihua, D., Xi, Y., and Yang, Y. (2004) Dielectric properties of B_2O_3-doped $BiNbO_4$ ceramics. *Ceramic International*, **30**, 1195–1198.
130. Wang, S.-F., Chiang, C.C., and Wang, C.H. (2003) Effects of B_2O_3 on the phase formation of $Ba_2Ti_9O_{20}$ ceramic. *Materials Chemistry and Physics*, **79**, 256–260.
131. Huang, W., Liu, K.S., Chu, L.-W., *et al*. (2003) Microwave dielectric properties of glass–ceramic composites for low temperature cofireable ceramics. *Journal of European Ceramic Society*, **23**, 2559–2564.
132. Lee, J.A., Lee, J.H., and Kim, J.J. (2006) Low-temperature sintering and microwave dielectric characteristics of $Ba_2Ti_9O_{20}$ ceramics. *Journal of European Ceramic Society*, **26**, 2111–2115.
133. Choi, Y.G. Park, J.H., Ko, W.J., *et al*. (2005) Low temperature sintering of $BaTi_4O_9$ based middle k dielectric composition for LTCC applications. *Journal of Electroceramics*. **14**, 157–162
134. Zhou, M.-Z. and Jean, J.H. (2006) Low-fire processing of microwave $BaTi_4O_9$ dielectric with BaO–ZnO–B_2O_3 glass. *Journal of American Ceramic Society*, **89**, 786–791.
135. Lee, J.A., Lee, J.H., and Kim, J.J. (2006) Low temperature sintering and microwave dielectric characteristics of $Ba_2Ti_9O_{20}$ ceramics. *Journal of European Ceramic Society*, **26**, 2111–2115.
136. Lee, Y.C., Lee, W.H., and Shie, F.S. (2003) Effects of B_2O_3 addition on the microwave dielectric properties of $Ba_2Ti_9O_{20}$ ceramics. *Japanese Journal of Applied Physics*, **42**, 1311–1314.
137. Lee, Y.C., Lee, W.H., and Shie, F.S. (2005) Microwave dielectric properties and microstructures of $Ba_2Ti_9O_{20}$ based with 3ZnO–B_2O_3 addition. *Journal of European Ceramic Society*, **25**, 3459–3468.
138. Huang, C.L., Weng, M.H., Lion, C.T., *et al*. (2000) Low temperature sintering and microwave dielectric properties of $Ba_2Ti_9O_{20}$ ceramics using glass additions. *Materials Research Bulletin*, **35**, 2445–2456.
139. Kim, D.W., Lee, D.G., and Hong, K.S. (2001) Low temperature firing and microwave dielectric properties of $BaTi_4O_9$ with Zn–B–O glass system. *Materials Research Bulletin*, **36**, 585–595.
140. Lu, S.G. Kwok, K.W., Chen, H.L.W., *et al*. (2003) Structural and electrical properties of $BaTi_4O_9$ microwave ceramics incorporated with glass phase. *Materials Science and Engineering B*, **99**, 491–494.
141. Zhou, F., Liu, X., Wang, H., *et al*. (2013) Phase stability, low temperature cofiring and microwave dielectric properties of $BaTi_5O_{11}$ ceramics with $BaCu(B_2O_5)$ addition. *Journal of Materials Science: Materials in Electronics*, **24**, 299–304.
142. Ohsato, H. (2005) Research and development of microwave dielectric ceramics for wireless communications. *Journal of Ceramic Society Japan*, **113**, 703–711.
143. Jung, B.H., Hwang, S.J., and Kim, H.S. (2005) Glass–ceramic for low temperature cofired dielectric ceramic materials based on La_2O_3–B_2O_3–TiO_2 glass with BNT ceramics. *Journal of European Ceramic Society*, **25**, 3187–3193.

144. Hwang, S. and Kim, H. (2007) Effect of frit size on microwave properties of glass ceramic in low temperature cofired ceramics. *Thermochemica Acta*, **A45**, 119–112.
145. Cheng, C.C., Hsieh, T.E., and Lin, I.N. (2003) Microwave dielectric properties of glass ceramic composites for low temperature cofireable ceramics. *Journal of European Ceramic Society*, **23**, 2553–2558.
146. Santha, N.I. (2008) Effect of bismuth borate and LiF on the sintering, thermal and microwave dielectric properties of $Ba_{6-3x}Sm_{8+2x}Ti_{18}O_{54}$ ($x = 2/3$) solid solution. *International Journal of Applied Ceramic Technology*, **5**, 334–340.
147. Kim, M.H., Lim, J.B., Nahm, S., *et al.* (2007) Low temperature sintering of $BaCu(B_2O_5)$–added $BaO–Re_2O_3–TiO_2$ (Re = Sm, Nd) ceramics. *Journal of European Ceramic Society*, **27**, 3033–3037.
148. Dernovsek, O., Naeini, A., Preu, G., *et al.* (2001) LTCC glass–ceramic composites for microwave application. *Journal of European Ceramic Society*, **21**, 1693–1697.
149. Ota, Y., Kakimoto, K., Ohsato, H. *et al.* (2004) Low temperature sintering of $Ba_{6-3x}Sm_{8+2x}Ti_{18}O_{54}$ microwave dielectric ceramics by B_2O_3 and GeO_2 addition. *Journal of European Ceramic Society*, **24**, 1755-1760.
150. Yoon, J.M., Lee, J.A., Lee, J.H., *et al.* (2006) Sintering behavior and microwave dielectric characteristics of $BaO–Sm_2O_3–4TiO_2$ ceramics with B_2O_3 and BaB_2O_4 addition. *Journal of European Ceramic Society*, **26**, 2129–2133.
151. Lim, J.B., Cho, K.H., Nahm, S., *et al.* (2006) Effect of $BaCu(B_2O_5)$ on the sintering temperature and microwave dielectric properties of $BaO–Ln_2O_3–TiO_2$ (Ln = Sm, Nd) ceramics. *Materials Research Bulletin*, **41**, 1868–1874.
152. Cho, I.S., Kim, D.W., Kim, J.R., *et al.* (2004) Low-temperature sintering and microwave dielectric properties of $BaO·(Nd_{1-x}Bi_x)_2O_3·4TiO_2$ by the glass additions. *Ceramic International*, **30**, 1181–1185.
153. Cheng, C.C., Hsieh, T., and Lin, I.N. (2004) Effects of composition on low temperature sinterable Ba–Nd–Sm–Ti–O microwave dielectric materials. *Journal of European Ceramic Society*, **24**, 1787–1790.
154. Cheng, C.C., Hsieh, T., and Lin, I.N. (2003) Microwave dielectric properties of glass-ceramic composites for low temperature co-firable ceramics. *Journal of European Ceramic Society*, **23**, 2553–2558.
155. Park, J.H., Choi, Y.J., and Park, J.-H. (2004) Low-fire dielectric compositions with permittivity 20–60 for LTCC applications. *Materials Chemistry and Physics*, **88**, 308–312.
156. Maeda, M., Yamamura, T., and Ikeda, T. (1987) Dielectric characteristics of several complex oxide ceramics at microwave frequencies. *Japanese Journal of Applied Physics*, **26**, 76–79.
157. Lee, H.J., Hong, K.S., Kim, S.J., *et al.* (1997) Dielectric properties of MNb_2O_6 compounds (M = Ca, Mn, Co, Ni, or Zn). *Materials Research Bulletin*, **32**, 847–855.
158. Kim, D.W., Ko, K.H., and Hong, K.S. (2001) Influence of copper (II) oxide additions to zinc niobate microwave ceramics on sintering temperature and dielectric properties. *Journal of American Ceramic Society*, **84**, 1286–1290.
159. Wee, S.H., Kim, D.W., Yoo, S.I., *et al.* (2004) Low temperature sintering of V_2O_5 added and substituted $ZnNb_2O_6$ microwave ceramics. *Japanese Journal of Applied Physics*, **43**, 3511–3515.
160. Wang, J., Yue, Z., Gui, Z., and Li, L. (2005) Low temperature sintered $Zn_3(Nb_{1-x}V_{x/2})_2O_{6-2.5x}$ microwave dielectric ceramics with high Q value for LTCC applications. *Journal of Alloys and Compounds*, **392**, 263–267.
161. Kim, D.W., Hong, H.B., and Hong, K.S. (2002) Structural transition and microwave dielectric properties of $ZnNb_2O_6–TiO_2$ sintered at low temperatures. *Japanese Journal of Applied Physics*, **41**, 1465–1469.
162. Choi, Y.J., Park, J.H., Ko, W.J., *et al.* (2006) Cofiring and shrinkage matching in low and middle permittivity dielectric compositions for a low temperature cofired ceramics system. *Journal of American Ceramic Society*, **89**, 562–567.
163. Anjana, P.S., Jawahar, I.N., and Sebastian, M.T. (2009) Low loss temperature stable ceramics in $ZnNb_2O_6–Zn_3Nb_2O_8–ZnTa_2O_6$ system. *Journal of Materials Science: Materials in Electronics*, **20**, 587–596.

164. Wang, J., Yue, Z., Gui, Z., *et al*. (2005) Low temperature sintered $ZnNb_2O_6$ microwave dielectric ceramics doped with $ZnO–V_2O_5$ additives. *Journal of Materials Science: Materials in Electronics*, **40**, 6581–6583.
165. Fang, G., Jiaji, L., Rongzi, H., *et al*. (2009) Microstructure and dielectric properties of low temperature sintered $ZnNb_2O_6$ microwave ceramics. *Ceramic International*, **35**, 2687–2692.
166. Zhang, Y.C., Yue, Z.X., Gui, L., and Li, L. (2005) Microwave dielectric properties of $CuO–V_2O_5–Bi_2O_3$ doped $ZnNb_2O_6$ ceramics with low sintering temperature. *Journal of Electroceramics*, **14**, 67–74.
167. Jantunen, H., Uusumaki, A., Rautioaho, R., *et al*. (2000) Compositions of $MgTiO_3–CaTiO_3$ ceramic with two borosilicate glasses for LTCC technology. *Journal of European Ceramic Society*, **20**, 2331-2336.
168. Jantunen, H., Uusumaki, A., Rautioaho, R., *et al*. (2002) Temperature coefficient of microwave resonance frequency of a low temperature cofired (LTCC) system. *Journal of American Ceramic Society*, **85**, 697–699.
169. Yao, G., Liu, P., and Zhang, H. (2013) Low temperature sintering and microwave dielectric properties of $(Mg_{0.95}Zn_{0.05})_2(Ti_{0.8}Sn_{0.2})O_4–(Ca_{0.8}Sr_{0.2})TiO_3$ composite ceramics. *Journal of American Ceramic Society*, **96**, 3114–3119.
170. Chen, Y.B. (2012) Microwave dielectric properties of $[(Mg_{0.5}Zn_{0.5})_{0.95}Co_{0.05}]_2TiO_4$ ceramics with $BaCu(B_2O_5)$ sintered at low temperatures. *Journal of Alloys and Compounds*, **543**, 125–128.
171. Zhang, Q.L. and Yang, H. (2007). Low temperature sintering and microwave dielectric properties of $MgTiO_3$ ceramics. *Journal of Materials Science: Materials in Electronics*, **18**, 967–971.
172. Chen, Y.B. (2011) Low temperature sintering and microwave dielectric properties of $(Mg_{0.7}Zn_{0.03})_{0.95}Co_{0.05}TiO_3$ ceramics with $BaCu(B_2O_5)$ additions. *Journal of Alloys and Compounds*, **509**, 6884–6888.
173. Shin, H.K., Shin, S.-T., and Bae, S., *et al*. (2008) Effect of oxygen partial pressure during liquid phase sintering on the dielectric properties of $0.9MgTiO_3–0.1CaTiO_3$. *Journal of American Ceramic Society*, **91**, 132–138.
174. Zhang, Q.L., Yang, H., and Tong, J.X. (2005) Low temperature sintering and microwave dielectric properties of $MgTiO_3$ ceramics with Bi_2O_3 and V_2O_5. *Materials Letters*, **60**, 1188–1191.
175. Shin, H.K., Shin, H., Jung, H.S., *et al*. (2006) Role of lithium borosilicate glass in the decomposition of $MgTiO_3$-based dielectric ceramic during sintering. *Materials Research Bulletin*, **41**, 1206–1214.
176. Hu, T., Rautioaho, R., Jantunen, H., *et al*. (2005) Optimization of $MgTiO_3–CaTiO_3$ based LTCC tapes containing B_2O_3 for use in microwave applications. *Ceramic International*, **31**, 85–93.
177. Jantunen, H., Rautioaho, R., Uusimaaki, A., *et al.* (2000) Preparing low-loss low-temperature cofired ceramic material without glass addition. *Journal of American Ceramic Society*, **83**, 2855–2857.
178. Choi, Y.J., Park, J.-H., Park, J.H., and Park, J.G. (2004) Middle-permittivity LTCC dielectric compositions with adjustable temperature coefficient. *Materials Letters*, **58**, 3102–3106.
179. Yamaguchi, O., Morimi, M., Kawabata, H., *et al.* (1987) Formation and transformation in $ZnTiO_3$. *Journal of American Ceramic Society*, **70**, C-97–C-98.
180. Chang, Y.S., Chang, Y.H., Chen, I.G., *et al*. (2003) The structure and properties of zinc titanate doped with strontium. *Journal of Alloys and Compounds*, **354**, 303–309.
181. Haga, K., Ishiji, T., Mashiyama, J., *et al.* (1992) Dielectric properties of two-phase mixture ceramics composed of rutile and its compounds. *Japanese Journal of Applied Physics*, **31**, 3156–3159.
182. Kim, H.T., Kim, S.H., Nahm, S., *et al.* (1999) Low-temperature sintering and microwave dielectric properties of zinc metatitanate–rutile mixtures using boron. *Journal of American Ceramic Society*, **82**, 3043–3048.
183. Zhang, Q.L., Yang, H., Zoua, J.L., *et al.* (2005) Sintering and microwave dielectric properties of LTCC–zinc titanate multilayers. *Materials Letters*, **59**, 880–884.
184. Chaouchi, A., Aliouat, M., Marinel, S., *et al.* (2007) Effects of additives on the sintering temperature and dielectric properties of $ZnTiO_3$ based ceramic. *Ceramic International*, **33**, 245–248.

185. Kim, H.T., Nahm, S., Byun, J.D., *et al.* (1999) Low-fired (Zn, Mg)TiO_3 microwave dielectrics. *Journal of American Ceramic Society*, **82**, 3476–3480.
186. Lee, Y.C., Lee, W.H., and Shiao, F.T. (2004) Microwave dielectric properties of $Zn_{0.95}Mg_{0.05}TiO_3 + 0.25TiO_2$ ceramics with $3ZnO–B_2O_3$ addition. *Japanese Journal of Applied Physics*, **43**, 7596–7599.
187. Lee, Y.C. and Lee, W.H. (2005) Effects of glass addition on microwave dielectric properties of $Zn_{0.95}Mg_{0.05}TiO_3 + 0.25TiO_2$ ceramics. *Japanese Journal of Applied Physics*, **44**, 1838–1843.
188. Li, E., Zhang, P., Duan, S., Wang, J., *et al*. (2015) Low temperature sintering of low-loss $ZnTiO_3$ microwave dielectric ceramics with Zn–B–Si glass. *Journal of Alloys and Compounds*, **647**, 866–872.
189. Borisevich, A. and Davies, P.K. (2000*)* Microwave dielectric properties of $Li_{1+x-y}M_{1-x-3y}Ti_{x+4y}O_3$ ($M = Nb^{5+}$, Ta^{5+}) solid solutions. *Journal of European Ceramic Society*, **21**, 1719–1722.
190. Borisevich, A. and Davies, P.K. (2002) Synthesis and dielectric properties of $Li_{1-x+y}Ta_{1-x-3y}Ti_{x+4y}O_3$ M-phase solid solutions. *Journal of American Ceramic Society*, **85**, 2487–2491.
191. Borisevich, A. and Davies, P.K. (2002) Crystalline structure and dielectric properties of $Li_{1+x-y}Nb_{1-x-3y}Ti_{x+4y}O_3$ M-phase solid solutions. *Journal of American Ceramic Society*, **85**, 573–578.
192. Kang, D.H., Nahm, K.C., and Cha, H.J. (2006) Effect of $Li_2O–V_2O_5$ on the low temperature sintering and microwave dielectric properties of $Li_{1.0}Nb_{0.6}Ti_{0.5}O_3$ ceramics. *Journal of European Ceramic Society*, **26**, 2117–2121.
193. Zeng, Q., Li, W., Shi, J. L., *et al.* (2006) A new microwave dielectric ceramic for LTCC applications. *Journal of American Ceramic Society*, **89**, 1733–1735.
194. Zeng, Q., Li, W., Shi, J.L., *et al.* (2006) Microwave dielectric properties of $5Li_2O–0.583Nb_2O_5–3.248TiO_2$ ceramics with V_2O_5. *Journal of American Ceramic Society*, **89**, 3305–3307.
195. George, S. and Sebastian, M.T. (2011) Low temperature sintering and microwave dielectric properties of $Li_2ATi_3O_8$ (A = Mg, Zn) ceramics. *International Journal of Applied Ceramic Technology*, **8**, 1400–1407.
196. George, S. and Sebastian, M.T. (2010) Synthesis and microwave dielectric properties of novel temperature stable high Q $Li_2ATi_3O_8$ (A = Mg, Zn) ceramics. *Journal of American Ceramic Society*, **93**, 2164–2166.
197. Wu, Y., Zhou, D., Guo, J. and Pang, L.-X. (2013) Microwave dielectric properties and low temperature sintering of $Li_2Zn(Ti_{1-x}Sn_x)_3O_8 (x < 0.2)$ ceramics with B_2O_3–CuO addition. *Journal of Materials Science: Materials in Electronics*, 2013, **24**, 4942–4946.
198. Lu, X., Zheng, Y., Dong, Z., *et al.* (2014) Low temperature sintering and microwave dielectric properties of $Li_2ZnTi_3O_8$ ceramics doped with $ZnO–La_2O_3–B_2O_3$ glass. *Ceramic International*. **40**, 7087–7092.
199. Zhang, P., Wang, Y., Hua, Y., *et al.* (2013) Low temperature sintering and microwave dielectric properties of $Li_2ZnTi_3O_8$. *Materials Letters*, **107**, 351–353.
200. Lu, X., Zheng, Y., and Zhou, B. (2013) Effect of B_2O_3 addition on the microwave dielectric properties of $Li_2ZnTi_3O_8$ ceramics. *Journal of Electroceramics*, **31**, 360–363.
201. Lu, X., Zhang, Y., Dong, Z., *et al*. (2014) Low temperature sintering and microwave dielectric properties of $0.6Li_2ZnTi_3O_{206}–0.4Li_2TiO_3$ ceramics. *Materials Letters*, **131**, 1–4.
202. He, M. and Zhang, H. (2016) Microwave properties of low fired $Li_2ZnTi_3O_8$ ceramics doped with $CuO–Bi_2O_3–V_2O_5$. *Journal of Alloys and Compounds*, in press.
203. He, M. and Zhang, H. (2013) Low temperature firing and microwave properties of TiO_2 modified $Li_2ZnTi_3O_8$ ceramics doped with B_2O_3. *Journal of Materials Science: Materials in Electronics*, **24**, 3303–3308.
204. Li, Y.X., Li, H., Tang, B., *et al.* (2015) Microwave dielectric properties of low fired $Li_2ZnTi_3O_8–TiO_2$ composite ceramics with Li_2WO_4 addition. *Journal of Materials Science: Materials in Electronics* **26**, 1181–1185.
205. Zhou, H., Liu, X., Chen, X., *et al.* (2012) $ZnLi_{2/3}Ti_{4/3}O_3$: a new low loss spinel microwave dielectric ceramic. *Journal of European Ceramic Society*, **32**, 261–265.

206. Wu, Y., Zhou, D., Guo, J., *et al.* (2013) Microwave dielectric properties and low temperature firing of $(1-x)Li_2Zn_3Ti_3O_8$–xLi_2TiO_3 ($0.2< x <0.8$) ceramics with B_2O_3–CuO addition. *Journal of Materials Science: Materials in Electronics*, **24**, 1505–1510.
207. Zhang, T., Zuo, R., and Wang, Y. (2014) $Li_2Zn_3Ti_4O_{12}$–$Ba_3(VO_4)_2$ microwave dielectric ceramics sintered at low temperature without glass additives. *Journal of Materials Science: Materials in Electronics*, **25**, 5570–5575.
208. Sayyadi-Shahraki, A., Taheri-Nassaj, E., Hassanzadeh-Tabrizi, S.A. *et al*. (2014) Low temperature cofireable $Li_2Zn_3Ti_4O_{12}$ microwave dielectric ceramic with Li_2O–ZnO–B_2O_3 glass additive. *Journal of Materials Science: Materials in Electronics*, **25**, 355–360.
209. George, S., Sebastian, M.T., Raman, S., *et al* (2011) Novel low loss low permittivity glass-composites for LTCC applications. *International Journal of Applied Ceramic Technology*, **8**, 172–179.
210. George, S., Anjana, P.S., Deepu, V.N., *et al.* (2009) Low temperature sintering and microwave dielectric properties of Li_2MgSiO_4 ceramics. *Journal of American Ceramic Society*, **92**, 1244–1249.
211. Kweon, S.H., Joung, M.R., Kim, J.S., *et al.* (2011) Low temperature sintering and microwave dielectric properties of B_2O_3 added $LiAlSiO_4$ ceramics. *Journal of American Ceramic Society*, **94**, 1995–1998.
212. Dou, G., Zhou, D., Gong, S., *et al.* (2013) Low temperature sintering and microwave dielectric properties of Li_2ZnSiO_4 ceramics with ZB glass. *Journal of Materials Science: Materials in Electronics*, **24**, 1601–1607.
213. Busuioc, C. and Jinga, S. L. (2014) Preparation and characterization of $Li_xZn_{2-x}V_xSi_{1-x}O_4$ ceramics. *Ceramic International*, **40**, 5931–5936.
214. Kweon, S.H., Joung, M.R., Kim,J.S., *et al.* (2011) Low temperature sintering and microwave dielectric properties of B_2O_3 added $LiAlSiO_4$ ceramics. *Journal of American Ceramic Society*, **94**, 1995–1998.
215. Bian, J.J., Kim, D.W., and Hong, K.S. (2005) Glass free LTCC microwave dielectric ceramics. *Materials Research Bulletin*, **40**, 2120–2129.
216. Cho, I.S., Kang, S.K., Kim, D.W., *et al.* (2006) Mixture behaviour and microwave dielectric properties of $(1-x)Ca_2P_2O_7$–$xTiO_2$. *Journal of European Ceramic Society*, **26**, 2007–2010.
217. Bian, J.J., Kim, D.W., and Hong, K.S. (2005) Mixture behaviour and microwave dielectric properties of $(Ca_{1-x}Zn_x)_2P_2O_7$. *Materials Letters*, **59**, 257–260.
218. Bian, J.J., Kim, D.W., and Hong, K.S. (2004) Microwave dielectric properties of $A_2P_2O_7$ (A = Ca, Sr, Ba, Zn, Mn). *Japanese Journal of Applied Physics*, **43**, 3521–3525.
219. Thomas, D. and Sebastian, M.T. (2010) Temperature-compensated $LiMgPO_4$: a new glass-free low-temperature cofired ceramic. *Journal of American Ceramic Society*, **93**, 3828–3831.
220. Thomas, D. and Sebastian, M.T. (2012) Effect of Zn^{2+} substitution on the microwave dielectric properties of $LiMgPO_4$ and the development of a new temperature stable glass free LTCC. *Journal of the European Ceramic Society*, **32**, 2359–2364.
221. Thomas, D., Abhilash, P., and Sebastian, M.T. (2013) Casting and characterization of $LiMgPO_4$ glass free LTCC tape for microwave applications. *Journal of the European Ceramic Society*, **33**, 87–93.
222. Abhilash, P., Sebastian, M.T., and Surendran, K.P. (2015) Glass free, non-aqueous LTCC tapes of $Bi_4(SiO_4)_3$ with high solid loading. *Journal of the European Ceramic Society*, **35**, 2313–2320.
223. Kim, J.-S., Joung, M.-R., Song, M.-E., *et al*. (2008) Synthesis and microwave dielectric properties of $Bi_4(SiO_4)_3$ ceramics. *Journal of American Ceramic Society*, **91**, 3461–3464.
224. Liu, Y., Wang, Y., Li., Y., and Bian, J.J. (2016) Low temperature sintering and microwave dielectric properties of $LiMBO_3$ (M = Ca, Sr) ceramics. *Ceramic International*, in press.
225. Fu, Z., Liu, E., Ma, J., *et al*. (2016) Microwave dielectric properties of low-fired $(1-x)Mg_2Si_{0.9}V_{0.1}O_4$–$xCa_{0.8}Sr_{0.2}TiO_3$ composite ceramics. *Materials Physics Chemistry*, **170**, 118–122.
226. Manu, K. and Sebastian, M.T. (2016) Tape casting of low permittivity Wesselsite–glass composite for LTCC based microwave applications. *Ceramic International*, **42**, 1210–1216.

227. Joseph, T., Sebastian M.T., Jantunen, H., *et al.* (2011) Tape casting and dielectric properties of $Sr_2ZnSi_2O_7$-based ceramic–glass composite for low-temperature co-fired ceramics applications. *International Journal of Applied Ceramic Technology*, **8**, 854.
228. Needs, C.R., Wang, C.B., Hang, K.W., *et al.* (2003) In *Proceedings of Conference on Ceramic Interconnect Technology*, Denver, CO, IMAPS, 126 pp.
229. Lautzenhiser, F. and Amaya, E. (2002) In *Proceedings of SPIE – International Society of Optical Engineering*, vol. 4828, pp. 143–149.
230. Mohanram, A., Lee, S.J., Messing, G.L., *et al.* (2006) Constrained sintering of low-temperature Co-fired ceramics. *Journal of American Ceramic Society*, **89**, 1923–1929.
231. Mohanram, A., Lee, S.J., Messing, G.L., *et al.* (2006) A novel use of constrained sintering to determine the viscous Poisson's ratio of densifying materials. *Acta Materialia*, **53**, 2413–5418.
232. Lu, G.Q., Sutterlin, R.C., and Gupta, T.K. (1993) Effect of mismatched sintering kinetics on camber in a low-temperature cofired ceramic package. *Journal of American Ceramic Society*, **76**, 1907–1914.
233. Mohanram, A., Lee, S. J. and Messing, G. L. (2002) In *Proceedings of International Conference on Microelectronic Packaging Society*, Washington, DC, IMAPS, pp. 772–777.
234. Garino, T.J. (2003) In *Proceedings of SPIE – International Society for Optical Engineering*, vol. 5231, pp. 171–176.
235. Valant, M. and Suvorov, D. (2001) Processing and dielectric properties of sillenite compounds $Bi_{12}Mo_{20-d}$ (M = Si, Ge, Ti, Pb, Mn, $B_{1/2}$, $P_{1/2}$). *Journal of American Ceramic Society*, **84**, 2900–2904
236. Zhou, D., Randall, C.A., Wang, H., *et al.* (2010) Microwave dielectric ceramics in Li_2O–Bi_2O_3–MoO_3 system with ultra-low sintering temperatures. *Journal of American Ceramic Society*, **93**, 1096–1100.
237. Sebastian, M.T., Wang, H., and Jantunen, H. (2016) Low temperature co-fired ceramics with ultra-low sintering temperature. A review. *Current Opinion in Solid State and Materials Science*, in press.
238. Kemethmuller, S., Hagyamasi, M., Stiegelschmitt, A., *et al*. (2007) Viscous flow as the driving force for the densification of low temperature cofired ceramics. *Journal of American Ceramic Society*, **90**, 64–70.
239. Wu, J.M. and Huang, H.L. (1999) Microwave properties of zinc, barium and lead borosilicate glasses. *Journal of Non-crystalline Solids*, **260**, 116–124.
240. Chen, C.-C., Chou, C.C., Shih, W.J., *et al*. (2003) Microwave dielectric properties of glass–ceramic composites for low temperature cofireable ceramics. *Materials Chemistry and Physics*, **79**, 129–134.
241. Ju, K., Yu, H., Ye, L., and Xu, G. (2013) Ultra low temperature sintering and dielectric properties of SiO_2 filled glass composites. *Journal of American Ceramic Society*, **96**, 3563–3568.
242. Yu, H., Ju, K., and Wang, K. (2014) A novel glass–ceramic with ultra-low sintering temperature for LTCC application. *Journal of American Ceramic Society*, **97**, 704–707.
243. Yu, H., Ju, K., Liu, J., and Li, Y. (2014) Tape casting and dielectric properties of SiO_2 filled glass composite ceramic with an ultralow sintering temperature. *Journal of Materials Science: Materials in Electronics*, **25**, 5114–5118.
244. Yu, H., Liu, J., Zhang, W., and Zhang, S. (2016) Ultra-low sintering temperature ceramics for LTCC applications: a review. *Journal of Materials Science: Materials in Electronics*, in press.
245. Rajesh, S., Jantunen, H., Letz, M., *et al.* (2012) Low temperature sintering and dielectric properties of alumina filled glass composites for LTCC applications. *International Journal of Applied Ceramic Technology*, **9**, 52–59.
246. Chen, M.Y., Juuti, J., Hsi, C.S., *et al.* (2015) Dielectric $BaTiO_3$–BBSZ glass ceramic composition with ultra-low sintering temperature. *Journal of European Ceramic Society*, **35**, 139–144.
247. Chen, M.Y., Juuti, J., Hsi, C.S., *et al.* (2015) Dielectric properties of ultra-low sintering temperature Al_2O_3–BBSZ glass composite. *Journal of European Ceramic Society*, **98**, 1133–1136.
248. Kim, K.S., Shim, S.H., Kim, S., *et al.* (2010) Microwave dielectric properties of ceramic/glass composites with bismuth–zinc borosilicate glass. *Journal of Ceramic Processing Research*, **11**, 47–51.

249. Ohashi, M., Ogawa, H., Kan, A., *et al*. (2005) Microwave dielectric properties of low temperature sintered $Li_3AlB_2O_6$ ceramic. *Journal of European Ceramic Society*, **25**, 2877–2881.
250. Valant, M. and Suvorov, D. (2000) Chemical compatibility between silver electrodes and low-firing binary-oxide compounds: conceptual study. *Journal of American Ceramic Society*, **83**, 2721–2729.
251. Zhou, H., He, F., Chen, X., *et al.* (2014) Series of thermally stable $Li_{1+2x}Mg_{4-x}V_3O_{12}$ ceramics. Low temperature sintering characteristic, crystal structure and microwave dielectric properties. *Journal of Materials Science: Materials in Electronics*, **25**, 1480–1484.
252. Yao, G.G. Liu, P., and Zhang, H.W. (2013) Novel series of low firing microwave dielectric ceramics $Ca_5A_4(VO_4)_6$ (A = Mg, Zn). *Journal of American Ceramic Society*, **96**, 1691–1693.
253. Fang, L., Wei, Z., Su, C., *et al.* (2016) Novel low firing microwave dielectric ceramic: $BaMV_2O_7$ (M = Mg,Zn). *Ceramic International*, in press.
254. Zhou, H., Miao, Y., Chen, J., *et al.* (2014) Sintering characteristic, crystal structure and microwave dielectric properties of a novel thermally stable ultralow firing $Na_2BiMg_2V_3O_{12}$ ceramic. *Journal of Materials Science: Materials in Electronics*, **25**, 2470–2474.
255. Li, W.B., Xi, H.H., and Zhou, D. (2015) Microwave dielectric properties of $LiMVO_4$ (M = Mg,Zn) ceramics with low sintering temperatures. *Ceramic International*, **41**, 9063–9068.
256. Yao, G.G., Hu, X.S., Tian, X.L., *et al.* (2015) Low temperature sintering and microwave dielectric properties of $LiMgVO_4$ ceramics. *Journal of Materials Science: Materials in Electronics*, **26**, 1795–1798.
257. Kalathil, S.E., Neelakantan, A., and Ratheesh, R. (2014) Microwave dielectric properties of ultralow temperature cofireable $Ba_3V_4O_{13}$ ceramics. *Journal of American Ceramic Society*, **97**, 1530–1533.
258. Jiang, X., Fang, L., Xiang, H., *et al.* (2016) A novel low-firing microwave dielectric ceramic $NaMg_4V_3O_{12}$ and its chemical compatibility with silver electrode. *Ceramic International*, in press.
259. Neelakantan, U.A., Kalathil, S.E., and Ratheesh, R. (2015) Structure and microwave dielectric properties of ultra-low cofireable BaV_2O_6 ceramics. *European Journal of Inorganic Chemistry*, **2015** (2), 305–310.
260. Yao, G.-G., Pei, C.-J., Xu, J.G., *et al*. (2016) Microwave dielectric properties of CaV_2O_6 ceramics with low dielectric loss. *Journal of Materials Science: Materials in Electronics*, in press.
261. Suresh, E.K., Prasad, K., Arun, N.S., *et al*. (2016). Synthesis and microwave dielectric properties of $A_{16}V_{18}O_{61}$ (A = Ba, Sr, and Ca) ceramics for LTCC applications. *Journal of Electronic Materials*, in press.
262. Zhou, D., Randall, C.A., Pang, L.X., *et al*. (2011) Microwave dielectric properties of Li_2WO_4 ceramic with ultra-low sintering temperature. *Journal of American Ceramic Society*, **94**, 348–350.
263. Zhou, H., Chen, X., Fang, L., Liu, X., *et al.* (2010) Microwave dielectric properties of $LiBiW_2O_8$ ceramics with low sintering temperature. *Journal of American Ceramic Society*, **93**, 3976–3979.
264. Fang, L., Wei, Z., Guo, H., *et al.* (2016) Phase composition and microwave dielectric properties of low firing $Li_2A_2W_3O_{12}$ (A = Zn, Mg) ceramics. *Journal of Materials Science: Materials in Electronics*, in press.
265. Zhou, D., Pang, L. X., Xie, H. D., *et al*. (2014) Crystal structure and microwave dielectric properties of an ultralow temperature fired $(AgBi)_{0.5}WO_4$ ceramic. *European Journal of Inorganic Chemistry*, 296- 301
266. Zhou, D., Guo, J., Yao, X., *et al.* (2012) Phase evolution and microwave dielectric properties of $(Li_{0.5}Bi_{0.5})(W_{1-x}Mo_x)O_4$ ($0.0 \leq x \leq 1.0$) ceramics with ultra-low sintering temperatures. *Functional Materials Letters*, **5**, 1250042.
267. Zhou, D., Li, W.B., Guo, J., *et al.* (2014) Structure phase evolution and microwave dielectric properties of $(Ag_{0.5}Bi_{0.5})(Mo_{0.5}W_{0.5})O_4$ ceramic with ultra-low sintering temperature. *Inorganic Chemistry*, **53**, 5712–5716.
268. Wang, S.F., Wang, Y.R., Hsu, Y.F., *et al.* (2010) Ultra low fire $Te_2(Mo_{1-x}W_x)O_7$ ceramics: microstructure and microwave dielectric properties. *Journal of American Ceramic Society*, **93**, 4071–4074.

269. Xie, H.D., Xi, H.H., Chen, C., *et al.* (2015) Microwave dielectric properties of two low temperature sintering ceramics in the PbO–WO_3 binary system. *Ceramic International*, **41**, 1087–1092.
270. Zhou, D., Wang, H., Pang, L.X., *et al.* (2009) Bi_2O_3–MoO_3 binary system: an alternative ultralow sintering temperature microwave dielectric. *Journal of American Ceramic Society*, **92**, 2242–2246.
271. Zhou, D., Randall, C.A., Wang, H., *et al.* (2009) Microwave dielectric properties trends in a solid solution $(Bi_{1-x}Ln_x)_2Mo_2O_9$ (Ln = La, Nd, $0.0 \leq x \leq 0.2$) system. *Journal of American Ceramic Society*, **92**, 2931–2936.
272. Zhou, D., Randall, C.A., Pang, L.X., *et al.* (2011) Microwave dielectric properties of $(ABi)_{1/2}MoO_4$ (A = Li, Na, K, Rb, Ag) type ceramics with ultra-low firing temperatures. *Materials Chemistry and Physics*, **129**, 688–692.
273. Guo, J., Randall, C.A., Zhang, G., *et al.* (2014) Synthesis, structure and characterization of new low firing microwave dielectric ceramics: $(Ca_{1-3x}Bi_{2x}\Phi_x)MoO_4$. *Journal of Materials Chemistry C*, **2**, 7364–7372.
274. Zhou, D., Pang, L.X. and Qi, Z.M. (2014) Crystal structure and microwave dielectric behaviours of ultra-low temperature fired $x(Ag_{0.5}Bi_{0.5})MoO_4$–$(1-x)BiVO_4$ ($0.0 \leq x \leq 1.0$) solid solution withscheelite structure. *Inorganic Chemistry*, **53**, 9222–9227.
275. Zhou, D., Li, W.B., Guo, J., *et al.* (2014) Structure phase evolution and microwave dielectric properties of $(Ag_{0.5}Bi_{0.5})(Mo_{0.5}W_{0.5})O_4$ ceramic with ultralow sintering. *Inorganic Chemistry*, **53**, 5712–5716.
276. Liu, W., Wang, H., Zhou, D., and Li, K. (2010) Dielectric properties of low firing $Bi_2Mo_2O_9$ thick films screen printed on Al foils and alumina substrates. *Journal of American Ceramic Society*, **93**, 2202–2206.
277. Zhang, G.Q., Wang, H., Guo, J., *et al.* (2015) Ultra low sintering temperature microwave dielectric ceramics based on Na_2O–MoO_3 binary system. *Journal of American Ceramic Society*, **98**, 528–533.
278. Zhou, D., Randall, C.A., Pang, L.X., *et al.* (2011) Microwave dielectric properties of $Li_2(M^{2+})_2Mo_3O_{12}$ and $Li_3(M^{3+})Mo_3O_{12}$ (M = Zn, Ca, Al and In) lyonsite related type ceramics with ultra-low sintering temperature. *Journal of American Ceramic Society*, **94**, 802–805.
279. Liao, Q., Wang, Y., Jiang, F., and Guo, D. (2014) Ultra-low glass free $Li_3FeMo_3O_{12}$ microwave dielectrics. *Journal of American Ceramic Society*, **97**, 2394–2396.
280. Guo, J., Zou, D., Zou, S.L., *et al.* (2014) Microwave dielectric ceramics Li_2MoO_4–TiO_2 (M = Mo, W) with low sintering temperature. *Journal of American Ceramic Society*, **97**, 1819–1822.
281. Zhou, D., Randall, C.A., Wang, H., *et al.* (2010) Ultra low firing high *k* structures based on $[(Li_{0.5}Bi_{0.5})_xBi_{1-x}][Mo_xV_{1-x}]O_4$ microwave dielectric ceramics. *Journal of American Ceramic Society*, **93**, 2147–2150.
282. Zhou, D., Pang, L.X., Wang, H., *et al.* (2011) Phase transitions, Raman spectra, infrared spectra, band gap, and microwave dielectric properties of low temperature firing $(Na_{0.5x}Bi_{1-5x})(Mo_xV_{1-x})O_4$ solid solution ceramics with scheelite structures. *Journal of Materials Chemistry*, **21**, 18412–18420.
283. Zhou, D., Pang, L.X., Guo, J., *et al.* (2011) Phase evolution, phase transition, Raman spectra, infrared spectra, and microwave dielectric properties of low temperature firing $(K_{0.5x}Bi_{1-0.5x})(Mo_xV_{1-x})O_4$ ceramics with scheelite related structure. *Inorganic Chemistry*, **50**, 12733–12738.
284. Zhang, G Q., Guo, J., He, L., *et al.* (2014) Preparation and microwave dielectric properties of ultralow temperature sintering ceramics in K_2O–MoO_3 binary system. *Journal of American Ceramic Society*, **97**, 241–245.
285. Pang, L.X., Zhou, D., Cai, C.-L., *et al.* (2013) Infrared spectroscopy and microwave dielectric properties of ultra low temperature firing $(K_{0.5}La_{0.5})MoO_4$ ceramics. *Materials Letters*, **92**, 36–38.
286. Surjith, A., Suresh, E.K, Freddy, S., *et al.* (2013) Microwave dielectric properties of low temperature sinterable $RE_2Mo_4O_{15}$ (RE = Nd, Sm) ceramics for LTCC applications. *Journal of Materials Science: Materials in Electronics*, **24**, 1818–1822.
287. Udovic, M., Valant, M., and Suvorov, D. (2001) Dielectric characterization of ceramics from the TiO_2–TeO_2 system. *Journal of European Ceramic Society*, **21**, 1735–1738.

288. Udovic, M., Valant, M., and Suvorov, D. (2004) Phase formation and dielectric characterization of the Bi_2O_3–TeO_2 system prepared in an oxygen atmosphere. *Journal of American Ceramic Society*, **87**, 591–597.
289. Valant, M. and Suvorov, D. (2004) Glass free low temperature cofired ceramics: calcium germinates, silicates and tellurates. *Journal of European Ceramic Society*, **24**, 1715–1719.
290. Kwon, D.K., Lanagan, M.T., and Shrout, T.R. (2005) Microwave dielectric properties and low temperature cofiring of $BaTe_4O_9$ with aluminum metal electrodes. *Journal of American Ceramic Society*, **88**, 3419–3422.
291. Kwon, D.K., Lanagan, M.T., and Shrout, T.R. (2005) Synthesis of $BaTiTe_3O_9$ ceramics for LTCC application and its dielectric properties. *Journal of Ceramic Society Japan*, **113**, 216–219.
292. Kwon, D.K., Lanagan, M.T., and Shrout, T.R. (2007) Microwave dielectric properties of BaO–TeO_2 binary compounds. *Materials Letters*, **61**, 1827–1831.
293. Subodh, G. and Sebastian, M.T. (2007) Glass-free $Zn_2Te_3O_8$ microwave ceramic for LTCC applications. *Journal of American Ceramic Society*, **90**, 2266–2268.
294. Subodh, G. and Sebastian, M.T. (2008) Microwave dielectric properties of ATe_3O_8 (A = Sn, Zr) ceramics. *Japanese Journal of Applied Physics*, **47**, 7943–7946.
295. Subodh, G., Jacob, M.V., and Sebastian, M.T. (2008) Microwave dielectric properties and vibrational spectroscopic analysis of $MgTe_2O_5$ ceramics. *Journal of Materials Research*, **23**, 1551–1556.
296. Wang, S.F., Wang, Y.R., Hsu, Y.F., *et al.* (2010) Densification, microstructure and microwave dielectric properties of ultra-low fire $BaTe_4O_9$–$TiTe_3O_8$ ceramic composites. *Journal of European Ceramic Society*, **30**, 17371741.
297. Jiao, X., Zhong, C., Zhang, S., *et al.* (2010) Microwave dielectric properties of BaO–TiO_2–TeO_2 ternary system. *Journal of Materials Science*, **45**, 3331–3335.
298. Wang, S.-F., Huang, C.Y., and Liu, Y.L. (2010) Effects of $CaTiO_3$ and $SrTiO_3$ additions on the microstructure and microwave dielectric properties of ultralow fire TeO_2 ceramics. *Journal of American Ceramic Society*, **93**, 3272–3277.
299. Wang, S.-F., Hsu, Y.-F., Wang, Y.-R., *et al.* (2011) Ultra low fire $Zn_2Te_3O_8$–$TiTe_3O_8$ ceramic composites. *Journal of American Ceramic Society*, **94**, 812–816.
300. Schileo, G., Dias, A., Moreira, R.L., *et al.* (2014) Structure and microwave dielectric properties of low firing $Bi_2Te_2W_3O_{16}$ ceramics. *Journal of American Ceramic Society*, **97**, 1096–1102.
301. Cao, X., Gao, F., Hu, G., *et al.* (2013) The phase transitions and dielectric properties of low temperature sintered $ZnNb_2O_6$–$Zn_3Nb_2O_6$–$TiTe_3O_8$ microwave ceramics. *Journal of Materials Science: Materials in Electronics*, **24**, 3021–3028.
302. Honkamo, J., Jantunen, H., Subodh, G., *et al.* (2009) Tape casting and dielectric properties of $Zn_2Te_3O_8$ based ceramics with an ultra-low sintering temperature. *International Journal of Applied Ceramic Technology*, **6**, 531–536.
303. Jantuen, H., Hu, T., Uusimakki, A., *et al.* (2004) Tape casting of ferroelectric, dielectric, ferroelectric and ferromagnetic materials. *Journal of European Ceramic Society*, **24**, 1077–1081.
304. Zhou, D., Li, W.B., Pang, L.X., *et al.* (2014) Sintering behavior and dielectric properties of ultra-low temperature fired silver molybdate ceramics. *Journal of American Ceramic Society*, **97**, 3597–3601.
305. Zhou, D., Pang, L.X., Qi, Z.M., *et al.* (2014) Novel ultra-low temperature cofired microwave dielectric ceramic at 400 degrees and its chemical compatibility with base metal. *Scientific Reports*, **4**, 5980.
306. Kahari, H., Teirikangas, M., Juuti, J., *et al.* (2014) Dielectric properties of lithium molybdenate ceramic fabricated at room temperature. *Journal of American Ceramic Society*, **97**, 3378–3379.
307. Kahari, H., Teirikangas, M., Juuti, J., *et al.* (2015) Improvements and modifications to room temperature fabrication method for dielectric Li_2MoO_4 ceramics. *Journal of American Ceramic Society*, **98**, 687–689.

Microwave Materials and Applications

Wiley Series in Materials for Electronic and Optoelectronic Applications

www.wiley.com/go/meoa

Series Editors

Professor Arthur Willoughby, *University of Southampton, Southampton, UK*

Dr Peter Capper, *SELEX Galileo Infrared Ltd, Southampton, UK*

Professor Safa Kasap, *University of Saskatchewan, Saskatoon, Canada*

Published Titles

Bulk Crystal Growth of Electronic, Optical and Optoelectronic Materials, Edited by P. Capper

Properties of Group-IV, III–V and II–VI Semiconductors, S. Adachi

Charge Transport in Disordered Solids with Applications in Electronics, Edited by S. Baranovski

Optical Properties of Condensed Matter and Applications, Edited by J. Singh

Thin Film Solar Cells: Fabrication, Characterization, and Applications, Edited by J. Poortmans and V. Arkhipov

Dielectric Films for Advanced Microelectronics, Edited by M. R. Baklanov, M. Green, and K. Maex

Liquid Phase Epitaxy of Electronic, Optical and Optoelectronic Materials, Edited by P. Capper and M. Mauk

Molecular Electronics: From Principles to Practice, M. Petty

CVD Diamond for Electronic Devices and Sensors, Edited by R. S. Sussmann

Properties of Semiconductor Alloys: Group-IV, III–V, and II–VI Semiconductors, S. Adachi

Mercury Cadmium Telluride, Edited by P. Capper and J. Garland

Zinc Oxide Materials for Electronic and Optoelectronic Device Applications, Edited by C. Litton, D. C. Reynolds, and T. C. Collins

Lead-Free Solders: Materials Reliability for Electronics, Edited by K. N. Subramanian

Silicon Photonics: Fundamentals and Devices, M. Jamal Deen and P. K. Basu

Nanostructured and Subwavelength Waveguides: Fundamentals and Applications, M. Skorobogatiy

Photovoltaic Materials: From Crystalline Silicon to Third-Generation Approaches, Edited by G. Conibeer and A. Willoughby

Glancing Angle Deposition of Thin Films: Engineering the Nanoscale, Matthew M. Hawkeye, Michael T. Taschuk, and Michael J. Brett

Microwave Materials and Applications

Volume II

Edited by

MAILADIL T. SEBASTIAN
University of Oulu, Finland

RICK UBIC
Boise State University, ID, US

HELI JANTUNEN
University of Oulu, Finland

WILEY

This edition first published 2017
© 2017 John Wiley & Sons, Ltd

All rights reserved. No part of this publication may be reproduced, stored in a retrieval system, or transmitted, in any form or by any means, electronic, mechanical, photocopying, recording or otherwise, except as permitted by law. Advice on how to obtain permission to reuse material from this title is available at http://www.wiley.com/go/permissions.

The right of Mailadil T. Sebastian, Heli Jantunen and Rick Ubic to be identified as the authors of the editorial material in this work has been asserted in accordance with law.

Registered Offices
John Wiley & Sons, Inc., 111 River Street, Hoboken, NJ 07030, USA
John Wiley & Sons Ltd, The Atrium, Southern Gate, Chichester, West Sussex, PO19 8SQ, UK

Editorial Office
The Atrium, Southern Gate, Chichester, West Sussex, PO19 8SQ, UK

For details of our global editorial offices, customer services, and more information about Wiley products visit us at www.wiley.com.

Wiley also publishes its books in a variety of electronic formats and by print-on-demand. Some content that appears in standard print versions of this book may not be available in other formats.

Limit of Liability/Disclaimer of Warranty: While the publisher and authors have used their best efforts in preparing this book, they make no representations or warranties with respect to the accuracy or completeness of the contents of this book and specifically disclaim any implied warranties of merchantability or fitness for a particular purpose. It is sold on the understanding that the publisher is not engaged in rendering professional services and neither the publisher nor the authors shall be liable for damages arising herefrom. If professional advice or other expert assistance is required, the services of a competent professional should be sought.

Library of Congress Cataloging-in-Publication Data

Names: Sebastian, M. T., 1952– editor. | Jantunen, Heli, editor. | Ubic, Rick, editor.
Title: Microwave materials and applications / edited by Dr. Mailadil T. Sebastian, Dr. Heli Jantunen, Dr. Rick Ubic.
Description: Chichester, UK ; Hoboken, NJ : John Wiley & Sons, 2017. | Includes bibliographical references and index.
Identifiers: LCCN 2016052142 | ISBN 9781119208525 (cloth) | ISBN 9781119208556 (epub)
Subjects: LCSH: Microwave devices–Materials. | Dielectrics.
Classification: LCC TK7876 .M2545 2017 | DDC 621.381/30284–dc23
LC record available at https://lccn.loc.gov/2016052142

A catalogue record for this book is available from the British Library.

ISBN: 9781119208525

Set in 10/12pt TimesLTStd by Aptara Inc., New Delhi, India

10 9 8 7 6 5 4 3 2 1

Contents

VOLUME I

List of Contributors **xv**
Series Preface **xvii**
Preface **xix**

1. Measurement of Microwave Dielectric Properties and Factors Affecting Them **1**
M.T. Sebastian, M.A.S. Silva, and A.S.B. Sombra

1.1 Introduction 1
1.2 Permittivity (ε_r) and quality factor (Q) 2
1.3 Measurement of Microwave Dielectric Properties 7
1.4 Methods of Measurement 8
1.4.1 Hakki and Coleman (Courtney) Method 8
1.4.2 $TE_{01\delta}$ Mode Dielectric Resonator Method 11
1.4.3 Measurement of the Quality Factor by a Strip Line Excited Using the Cavity Method 14
1.4.4 Whispering Gallery Mode (WGM) Resonators 17
1.4.5 Split Post Dielectric Resonator (SPDR) 18
1.4.6 Cavity Perturbation Method 20
1.4.7 TM_{0n0} Mode and Re-entrant Cavity Methods 21
1.4.8 TE_{01n} Mode Cavities 22
1.4.9 Thin Samples and Free-Space Methods 24
1.5 Measurement of EMI Shielding Effectiveness 29
1.5.1 Waveguide Method 29
1.6 Terahertz and Millimeter Wave Measurements 31
1.6.1 Backward Wave Oscillator (BWO) 31
1.6.2 Terahertz Time-Domain Spectroscopy (THz-TDS) 32
1.7 Measurement of Dielectric Properties of Powder Samples 34
1.8 Estimation of Dielectric Loss by Spectroscopic Methods 35
1.9 Factors Affecting Dielectric Loss 39
1.10 Measurement of Temperature Coefficient of Resonant Frequency 41
1.11 Tuning of the Resonant Frequency 42
References 45

2. Modeling of Microwave Dielectric Properties of Composites **53**
Marko Tuhkala, Merja Teirikangas, and Jari Juuti

2.1 Introduction 53
2.2 Connectivity 54
2.3 Electrostatic Theory 56
2.3.1 Polarizability 56
2.3.2 Scattering 56
2.3.3 Orientation 57
2.4 Mixing Equations 59
2.4.1 Clausius–Mossotti 60
2.4.2 Maxwell–Garnett 60
2.4.3 Bruggeman Symmetric 63
2.4.4 Bruggeman Non-symmetric 64
2.4.5 Sen Scala–Cohen 64
2.4.6 Coherent Potential 64
2.4.7 Looyenga 65
2.4.8 Lichtenecker 65
2.4.9 Modified Lichtenecker 66
2.4.10 Differential 66
2.4.11 General Mixing Model 67
2.4.12 Effective Medium Theory (EMT) 68
2.4.13 Jayasundere–Smith 69
2.4.14 Vo–Shi 70
2.4.15 Interphase Power Law (IPL) 71
2.5 Effect of Porosity 71
2.5.1 Permittivity 72
2.5.2 Dielectric Losses 73
2.5.3 Dielectric Properties of Powders 74
2.6 Conclusion 77
References 77

3. Perovskites **81**
K.P. Surendran and Rick Ubic

3.1 Introduction 81
3.2 Lattice Constant Prediction 83
3.3 Tolerance Factor 84
3.4 Octahedral Tilting 86
3.5 Simple Perovskites 87
3.5.1 $LnAlO_3$ Type Materials 87
3.5.2 $Ag(Nb_{1-x}Ta_x)O_3$ Type Materials 88
3.5.3 Ca-Based Perovskites 89
3.6 Cation Ordering 89
3.6.1 1:1 Ordered Perovskites 90
3.6.2 1:2 Ordering 103

3.6.3 1:3 Ordering 130
3.6.4 1:2:1 Ordering 132
3.7 Cation Deficient Perovskites 133
3.8 Summary 135
References 136

4. High Permittivity Materials 149
Rick Ubic, G. Subodh, and M.T. Sebastian

4.1 Introduction 149
4.2 The $BaO–Ln_2O_3–TiO_2$ System 149
4.2.1 Crystal Structure of $Ba_{6-3x}Ln_{8+2x}Ti_{18}O_{54}$ 151
4.2.2 Tolerance Factor and Its Effect on the Temperature Coefficient 154
4.2.3 Microwave Dielectric Properties of $BaO–Ln_2O_3–TiO_2$ System 155
4.3 The Effect of Processing Parameters on Electrical Properties 162
4.4 Titania 164
4.5 $Sr_{1-3x/2}Ce_xTiO_3$ Ceramics 166
4.5.1 Crystal Structure of $Sr_{1-3x/2}Ce_xTiO_3$ System 166
4.5.2 Microstructure and Dielectric Properties of SCT ceramics 172
4.5.3 $(Sr_{0.75-x}Pb_xCe_{0.167})TiO_3$ 173
4.6 $Pb_n(Nb_{1-x}Ta_x)O_{5+n}$ 174
4.6.1 $Pb_nNb_2O_{5+n}$ $(1.5 \leq n < 2)$ 176
4.6.2 $Pb_2Nb_2O_7$ 179
4.6.3 Pb-Rich Phases $(n > 2)$ 181
4.6.4 Doping Studies 182
4.6.5 Microwave Properties 182
4.7 $(Pb_{1-x}Ca_x)(Fe_{1/2}B_{1/2})O_3$ [B = Nb, Ta] 185
4.8 $Ag(Nb_{1-x}Ta_x)O_3$ 187
4.9 Summary 190
References 190

5. Millimeter-Wave Materials 203
Hitoshi Ohsato

5.1 Introduction: New Frontiers of Millimeter-Wave Dielectrics 203
5.2 Dielectric Properties for Millimeter Wave 207
5.2.1 Quality Factor Q 207
5.2.2 Dielectric Constant ε_2 208
5.2.3 Temperature Coefficient of Resonant Frequency τ_f 208
5.3 Candidates of Millimeter-Wave Dielectrics 209
5.4 Specialized Study 212
5.4.1 Forsterite 212
5.4.2 Willemite 222
5.4.3 Indialite/Cordierite Glass Ceramics 226
5.4.4 Other Silicates 232
5.4.5 Substituted Ge for Si 236

5.4.6 Corundum 242
5.4.7 Spinel 250
5.4.8 Borate, Phosphate, and Vanadate 255
Acknowledgments 259
References 259

6. Other Important Materials 267
M.T. Sebastian and R.C. Pullar

6.1 Spinel 267
6.1.1 $ZnAl_2O_4$ 267
6.1.2 $MgAl_2O_4$ 277
6.1.3 A_2TiO_4 (A = Mg, Zn) 280
6.2 $Li_2ATi_3O_8$ (A = Mg, Zn) Ceramics 280
6.2.1 Effect of Glass Addition in $Li_2ATi_3O_8$ (A = Mg, Zn) 284
6.3 $Li_2Zn_3Ti_4O_{12}$ 289
6.4 Apatites 290
6.4.1 $A_2RE_8(SiO_4)_6O_2$ ceramics 292
6.4.2 $(Ca, Ba)_2RE_8Si_6O_{26}$ (RE = Rare Earths) 295
6.4.3 $Ca_{2+x}RE_{8-x}(SiO_4)_{6-x}(PO_4)_xO_2$ (RE = Rare Earths) 297
6.4.4 Effect of Isovalent Substitutions in $Ca_4La_6(SiO_4)_4(PO_4)_2O_2$ 300
6.4.5 $LiRE_9(SiO_4)_6O_2$ (RE = Rare Earths) 302
6.5 Alumina 303
6.6 Zirconium Tin Titanate 306
6.7 Dielectric Materials in the $BaO–TiO_2$ System 314
6.7.1 $BaTi_4O_9$ 315
6.7.2 $BaTi_5O_{11}$ 316
6.7.3 $Ba_2Ti_9O_{20}$ 316
6.8 Columbite Niobates ($M^{2+}Nb_2O_6$) 318
6.8.1 Synthesis of Columbite Ceramics 320
6.8.2 Microwave Dielectric Properties of Columbites 322
6.8.3 Microwave Properties of Solid Solutions and Non-stoichiometric Columbites 325
Acknowledgments 327
References 328

7. Microwave Dielectric Properties of Glasses and Bulk Glass Ceramics 345
Martin Letz

7.1 Glasses 345
7.1.1 Silica Glass, a Special Glass System 346
7.1.2 Multicomponent Glasses 347
7.1.3 Solder Glasses, Sealing Glasses, Glass Joins, Passivation Glasses, and Glass Powder Additives 349
7.2 Bulk Glass Ceramics 349
7.2.1 The $BiNbO_4$ System 351
7.2.2 The $La_4Ti_9O_{24}$ and $La_2Ti_2SiO_9$ System 351

7.2.3 Properties of Glass Ceramics from the Lithium Aluminum Silicate System 352
7.2.4 Photosensitive Crystallizing Glasses 352
References 353

8. High Temperature Cofired Ceramic (HTCC), Low Temperature Cofired Ceramic (LTCC), and Ultralow Temperature Cofired Ceramic (ULTCC) Materials 355
M.T. Sebastian and Heli Jantunen

8.1 High Temperature Cofired Ceramics (HTCC) 355
8.1.1 Introduction 355
8.2 HTCC Alumina 357
8.3 Aluminium Nitride HTCC 359
8.4 $ZrSiO_4$ 361
8.5 Low Temperature Cofired Ceramics (LTCC) 366
8.5.1 Introduction 366
8.5.2 Important Characteristics of LTCC 367
8.5.3 Glass–Ceramic Composites 370
8.5.4 Microwave Dielectric Properties of Glasses 373
8.5.5 LTCC Materials and Their Properties 374
8.5.6 Constrained Sintering 390
8.6 Ultralow Temperature Cofired Ceramics (ULTCC) 395
8.6.1 Introduction 395
8.6.2 Ultralow Temperature Cofireable Ceramics (ULTCC Category II) 395
8.6.3 ULTCC Category I 406
8.7 Discussion and Conclusion 408
References 411

Index **i1**

VOLUME II

List of Contributors **xv**
Series Preface **xvii**
Preface **xix**

9. Voltage Tunable Microwave Dielectrics for Frequency and Phase Agile Devices 427
K. Sudheendran and K.C. James Raju

9.1 Introduction to Voltage Tunable Materials 427
9.2 Different Classes of Voltage Tunable Materials 428
9.2.1 Ferroelectric-Based Voltage Tunable Materials 428
9.2.2 Non-ferroelectric Voltage Tunable Materials 428
9.2.3 Multiferroic Voltage Tunable Materials 430

9.3 Importance of Voltage Tunable Materials in Frequency and Phase Agile Devices 432
9.3.1 Varactors in Frequency and Phase Agile Devices 432
9.4 Growth Techniques for Voltage Tunable Thin Films on Various Substrates 434
9.4.1 Pulsed Laser Deposition Technique 434
9.4.2 Sputter Deposition Techniques 435
9.4.3 Chemical solution deposition technique (CSD) 436
9.5 Characterization techniques 437
9.5.1 Low-Frequency Measurement of Ferroelectric Thin Films 438
9.6 High-Frequency Characterization 438
9.6.1 Modified Cavity Perturbation Technique 439
9.6.2 Calibration Comparison Technique 441
9.6.3 Extraction of the Conductor Loss 443
9.6.4 Tunability Measurement 446
9.6.5 Reflection Measurements 446
9.7 Design and Realization Aspects of Varactors Using Tunable Materials 449
9.7.1 Planar and Parallel Plate Structures 449
9.7.2 Realization and Characterization of the Varactors 451
9.8 Conclusions 454
Acknowledgment 454
References 454

10. Dielectric Inks 457
J. Varghese and M.T. Sebastian

10.1 Introduction 457
10.2 Methodology 461
10.2.1 Formulation of Printing Inks 461
10.3 Dielectric Inks and Their Properties 462
10.3.1 Preliminary Treatment of Ceramic Particles 462
10.3.2 Raw Materials Selection and Optimization for Screen Printable Ink 465
10.3.3 Rheology of Dielectric Inks 466
10.3.4 Microstructure and Surface Roughness of Printed Layers 467
10.3.5 Dielectric Properties of Printed Layers 470
10.4 Polymer-Based Dielectric Inks, Properties and Applications 473
10.5 Commercially Available Dielectric Inks, Properties and Applications 475
10.6 Conclusion 475
Acknowledgment 477
References 477

11. Polymer–Ceramic Composites for Microwave Applications 481
R. Ratheesh and M.T. Sebastian

11.1 Introduction: Microwave Substrates 481
11.2 Types of Polymer–Ceramic Composites 483

11.3 Thermoplastic Matrix and Composites 485
11.3.1 Poly(tertrafluoroethylene) 485
11.4 PTFE/Ceramic Composites 489
11.4.1 Preparation and Dielectric Properties 489
11.4.2 Temperature Variation of Relative Permittivity 496
11.4.3 Moisture Absorption Characteristics 498
11.4.4 Coefficient of Thermal Expansion 499
11.4.5 Mechanical Properties 501
11.5 Polyethylene–Ceramic Composites 502
11.6 Polystyrene–Ceramic Composites 507
11.7 Epoxy-Ceramic Composites 510
11.8 Liquid Crystal Polymer (LCP) 513
11.9 Thermal Conductivity 514
11.9.1 Geometric Mean Model 515
11.9.2 Effective Medium Theory (EMT) Model 515
11.9.3 Cheng–Vachon Model 515
11.9.4 Maxwell–Eucken Model 516
11.9.5 Nielson Model 516
11.9.6 Agari–Uno Model 516
11.10 Polymer Nanoceramic Composites 518
11.11 Ultrawideband Antenna Design Using Copper Cladded Ceramic-Filled PTFE Substrates 521
11.11.1 Antenna Configuration 522
11.12 Conclusion 526
References 527

12. Rubber–Ceramic Composites 537
M.T. Sebastian and L.K. Namitha

12.1 Introduction 537
12.2 Silicone Rubber 539
12.2.1 Introduction 539
12.2.2 Composite Preparation 541
12.2.3 Dielectric Properties 543
12.2.4 Mechanical Properties 549
12.2.5 Coefficient of Thermal Expansion (CTE) 550
12.2.6 Thermal Conductivity 550
12.2.7 Moisture Absorption of Composites 552
12.3 Butyl Rubber (BR) 553
12.3.1 Introduction 553
12.3.2 Preparation of Butyl Rubber (BR)–Ceramic Composites 554
12.3.3 Dielectric Properties 556
12.3.4 Bending 561
12.3.5 Thermal Conductivity 563
12.3.6 Mechanical Properties 564

12.3.7 Moisture Absorption of Composites 565
12.3.8 Coefficient of Thermal Expansion (CTE) 566
12.4 Fabrication of Flexible Microstrip Antenna 567
12.5 Conclusions 570
References 570

13. Designing of Materials for EMI Shielding Applications 575
Swati Varshney and S.K. Dhawan

13.1 Electromagnetic Shielding and Microwave Absorption Mechanism 577
13.2 Shielding Effectiveness (SE) 577
13.3 Measurement of Shielding Effectiveness 578
13.4 Electromagnetic Shielding Materials 581
13.5 New Insight into Designing of Materials for Microwave Shielding 583
13.6 Nanostructured Graphene/Fe_3O_4 Incorporated Polyaniline for EMI Shielding 584
13.7 Designing of Polypyrrole–γ-Fe_2O_3 Nanocomposite Wave Absorber 586
13.7.1 Magnetic Measurements 586
13.7.2 Microwave Absorption Investigations 587
13.7.3 Dielectric and Permeability Studies 588
13.8 Designing of Conducting Polymer Composite by Incorporating Ferrofluid 590
13.9 Designing of Polypyrrole–Aqueous Ferrofluid (PFF) Nanocomposite Microwave Absorber 593
13.9.1 Magnetic Measurements 593
13.9.2 Microwave Absorption Investigations 594
13.9.3 Dielectric and Permeability Studies 596
13.10 Conclusions 596
Acknowledgments 598
References 598

14. Microwave Ferrites and Applications 603
Vincent G. Harris

14.1 Introduction 603
14.2 Structure, chemistry, magnetism, and gyromagnetic properties 604
14.3 Ferrite Materials Processing for Microwave Applications 611
14.3.1 Ferrite Processing as Bulk Polycrystalline Substrates 612
14.3.2 Thin-Film Processing 612
14.3.3 Thick-Film Processing of Ferrites 617
14.4 Semiconductor Integration of Ferrite Thin and Thick Films for MIC Development 620
14.4.1 Selection of Semiconductor Substrate Materials 621
14.4.2 Ferrite Film Growth on Semiconductor Substrates 622
14.5 Ferrite–Based Microwave Device Development 628
14.5.1 Monolithic Integrated Circuits (MICs) 629
14.5.2 Microwave Materials Property Needs 630

14.5.3 Circulators and Isolators 632
14.5.4 Phase Shifters 635
14.5.5 Filters 639
14.6 Outlook 642
References 643

15. Applications of Microwave Dielectrics 653
Heike Bartsch, Alexander Schulz, Jens Müller, Alexander Ebert, Steffen Spira, Frank Wollenschläger, and Matthias Hein

15.1 General Requirements for Microwave Applications 653
15.2 LTCC Microwave Components and Materials 654
15.2.1 Conductor Patterning Technologies 654
15.2.2 Transmission Lines and Transitions 656
15.2.3 Lumped Passive Integrated Components 659
15.2.4 Integrated Functional Materials for Passives 663
15.3 LTCC Application Examples 666
15.3.1 Power Dividers 666
15.3.2 A 60 GHz Stripline Parallel Coupled Bandpass Filter 667
15.3.3 Integrated Antennas 671
15.3.4 Microwave Modules 674
References 676

16. Applications of Dielectric Resonators 683
P. Mohanan and S. Mridula

16.1 Introduction 683
16.2 Dielectric Resonator Antenna (DRA) 684
16.2.1 Excitation Techniques 686
16.2.2 Rectangular Dielectric Resonator Antenna 688
16.2.3 Resonant Modes of the DRA 693
16.2.4 Cylindrical DRA 696
16.2.5 Hemispherical DRA 696
16.3 Applications of Dielectric Resonator in Microwave Oscillators 698
16.3.1 Diode Oscillators 699
16.3.2 Transistor Oscillators 699
16.3.3 State of the Art DROs 702
16.4 Application of Dielectric Resonators in Microwave Filters 703
16.4.1 Dielectric Resonator Bandpass Filters 704
16.4.2 Tunable Dielectric Resonator Filters 706
16.4.3 State of the Art DR Filters 709
References 710

Appendix: List of Low-Loss Ceramic Dielectric Materials and Their Properties 715
M.T. Sebastian

Index **i1**

List of Contributors

Heike Bartsch, Electronics Technology Group, Department of Electrical Engineering and Information Technology, Technische Universität Ilmenau, lmenau, Germany

S.K. Dhawan, Polymeric and Soft Materials Section, National Physical Laboratory (CSIR), New Delhi, India

Alexander Ebert, RF and Microwave Research Laboratory, Department of Electrical Engineering and Information Technology, Technische Universität Ilmenau, lmenau, Germany

Vincent G. Harris, Center for Microwave Magnetic Materials and Integrated Circuits, Department of Electrical and Computer Engineering, Northeastern University, Boston, Massachusetts, USA

Matthias Hein, RF and Microwave Research Laboratory, Department of Electrical Engineering and Information Technology, Technische Universität Ilmenau, lmenau, Germany

K.C. James Raju, CASEST, School of Physics, University of Hyderabad, Hyderabad, India

Heli Jantunen, Microelectronics Research Unit, Faculty of Information Technology and Electrical Engineering, University of Oulu, Oulu, Finland

Jari Juuti, Microelectronics Research Unit, University of Oulu, Oulu, Finland

Martin Letz, SCHOTT AG, Research and Technology Development, Mainz, Germany

P. Mohanan, Department of Electronics, Cochin University of Science and Technology, Kochi, India

S. Mridula, Department of Electronics, Cochin University of Science and Technology, Kochi, India

Jens Müller, Electronics Technology Group, Department of Electrical Engineering and Information Technology, Technische Universität Ilmenau, lmenau, Germany

L.K. Namitha, Materials Science and Technology Division, CSIR-NIIST, Trivandrum, India

Hitoshi Ohsato, Nagoya Industrial Science Research Institute and Nagoya Institute of Technology, Nagoya, Japan; Microelectronics Research Unit, University of Oulu, Oulu, Finland

R.C. Pullar, Department of Materials and Ceramic Engineering/CICECO – Aveiro Institute of Materials, University of Aveiro, Campus Universitário de Santiago, Aveiro, Portugal

R. Ratheesh, Centre for Materials for Electronics Technology (CMET), Microwave Materials Division, Thrissur, India

Alexander Schulz, Electronics Technology Group, Department of Electrical Engineering and Information Technology, Technische Universität Ilmenau, lmenau, Germany

M.T. Sebastian, Microelectronics Research Unit, Faculty of Information Technology and Electrical Engineering, University of Oulu, Oulu, Finland

M.A.S. Silva, LOCEM–Laboratory of Telecommunications and Materials Science and Engineering, Physics Department, Federal University of Ceará (UFC), Ceará, Brazil

A.S.B Sombra, LOCEM–Laboratory of Telecommunications and Materials Science and Engineering, Physics Department, Federal University of Ceará (UFC), Ceará, Brazil

Steffen Spira, RF and Microwave Research Laboratory, Department of Electrical Engineering and Information Technology, Technische Universität Ilmenau, lmenau, Germany

G. Subodh, Department of Physics, Kerala Univeriversity, Trivandrum, India

K. Sudheendran, Department of Physics, Sree Kerala Varma College, University of Calicut, Thrissur, India

K.P. Surendran, Materials Science and Technology Division, CSIR NIIST, Trivandrum, India

Merja Teirikangas, Microelectronics Research Unit, University of Oulu, Oulu, Finland

Marko Tuhkala, Microelectronics Research Unit, University of Oulu, Oulu, Finland

Rick Ubic, Micron School of Materials Science and Engineering, Boise State University, Idaho, USA

J. Varghese, Microelectronics Research Unit, Faculty of Information Technology and Electrical Engineering, University of Oulu, Oulu, Finland

Swati Varshney, Polymeric and Soft Materials Section, National Physical Laboratory (CSIR), New Delhi, India; Department of Chemistry, Delhi Institute of Tool Engineering, Okhla, New Delhi, India

Frank Wollenschläger, RF and Microwave Research Laboratory, Department of Electrical Engineering and Information Technology, Technische Universität Ilmenau, lmenau, Germany

Series Preface

Wiley Series in Materials for Electronic and Optoelectronic Applications

This book series is devoted to the rapidly developing class of materials used for electronic and optoelectronic applications. It is designed to provide much-needed information on the fundamental scientific principles of these materials, together with how these are employed in technological applications. The books are aimed at (postgraduate) students, researchers, and technologists, engaged in research, development, and the study of materials in electronics and photonics, and industrial scientists developing new materials, devices, and circuits for the electronic, optoelectronic, and communications industries.

The development of new electronic and optoelectronic materials depends not only on materials engineering at a practical level but also on a clear understanding of the properties of materials and the fundamental science behind these properties. It is the properties of a material that eventually determine its usefulness in an application. The series therefore also includes such titles as electrical conduction in solids, optical properties, thermal properties, and so on, all with applications and examples of materials in electronics and optoelectronics.

The characterization of materials is also covered within the series in as much as it is impossible to develop new materials without the proper characterization of their structure and properties. Structure–property relationships have always been fundamentally and intrinsically important to materials science and engineering.

Materials science is well known for being one of the most interdisciplinary sciences. It is the interdisciplinary aspect of materials science that has led to many exciting discoveries, new materials, and new applications. It is not unusual to find scientists with a chemical engineering background working on materials projects with applications in electronics. In selecting titles for the series, we have tried to maintain the interdisciplinary aspect of the field, and hence its excitement to researchers in this field.

Arthur Willoughby
Peter Capper
Safa Kasap

Preface

A large number of papers continue to be published in the area of microwave materials and applications; however, there have hitherto been no books in the open literature that treat the different types of microwave materials, such as low-loss dielectric ceramics, glass ceramics, polymer- and elastomer-based composites, cofired ceramics, electromagnetic interference (EMI) shielding materials, tunable dielectrics, dielectric inks, or microwave ferrites. Our purpose here is to provide a comprehensive and self-consistent volume whereby the aforementioned lack of a reference book in the open literature can be remedied.

Microwave dielectric materials play a key role in global society, with a wide range of applications straddling terrestrial and satellite communications, including Internet of Things (IoT), software radio, GPS, DBS TV, environmental monitoring via satellite, etc. The mobile phone is one of the most widely spread technologies on the planet. In many countries the number of mobile subscriptions exceeds the population. The IoT is posed to make an explosive growth in the near future. In this paradigm, many everyday objects will be networked via radio-frequency identification (RFID), printed electronics, and sensor network technologies. Fifth generation (5G) mobile networks or wireless systems represent the next major phase of mobile telecommunication standards beyond the current 4G/IMT-Advanced standards. In addition to providing greater speeds, 5G networks will also need to meet the needs of new uses, such as the IoT as well as broadcast-like services and lifeline communications for times of natural disaster. According to GSMA Intelligence, the revenue for mobile network operators from interconnected devices in the segments of automotive, health, utilities, and consumer electronics will be $1.3 trillion by 2020. The worldwide data volume in mobile communication systems doubles nearly every year. To address this challenge, higher frequency bands will be used for which broadband and multiband equipment is required. The new standard Long Term Evolution (LTE-A) and the standardization process for 5G mobile communications necessitates changes in the technology of antennas and filters. In order to meet the specifications of future systems, new designs and improved or new microwave dielectric components are required. The recent progress in the IoT, microwave telecommunications, satellite broadcasting, and intelligent transport systems (ITSs) has resulted in an increasing demand for low-loss dielectric materials, tunable dielectrics, microwave ferrites, and EMI shielding materials. Low-loss dielectric oxide ceramics have revolutionized the microwave wireless communication industry by reducing the size and cost of filter, oscillator, and antenna components in applications ranging from cellular phones to the IoT. Wireless communication technology demands materials with highly specialized properties. Recently the demand for materials with low sintering temperatures has increased not only to lower the energy cost of devices but also to integrate with polymers and silver-based electrodes. Several polymer-based (polymer–ceramic) composites have also recently been developed for wireless communication technology.

A dielectric resonator is an electromagnetic component that exhibits resonance for a narrow range of frequencies. The resonance is similar to that of a circular hollow metallic waveguide except that the boundary is defined by a large change in permittivity rather than by a conductor. Dielectric resonators (DRs) generally consist of a puck of ceramic that has a high permittivity and a low dissipation factor (tan δ). The resonant frequency is determined by the overall physical dimensions of the puck, the permittivity of the material, and its immediate surroundings. The key properties required for a dielectric resonator are high quality factor ($Q \sim 1/\tan \delta$), high relative permittivity (ε_r), and near-zero temperature coefficient of resonant frequency (τ_f). The first chapter describes the different techniques for measuring the microwave properties of materials. Chapter 2 discusses the modeling of relative permittivity of composites using different mixing rules. Developing dielectric resonator materials in which these three properties are simultaneously optimized is difficult. Low-permittivity ceramics are used for millimeter-wave communications and also as substrates for microwave integrated circuits. The medium permittivity ceramics with ε_r in the range 25–50 are used for satellite communication and in cell phone base stations. High-ε_r materials are used in mobile phones where miniaturization of components is very important. For millimeter-wave applications, temperature-stable, low-permittivity, and high-Q (low-loss) substrates are required for high-speed signal transmission with minimum attenuation. Chapters 3 to 6 describes such materials.

The term dielectric resonator (DR) first appeared in 1939 when Richtmeyer showed that a suitably shaped dielectric piece can function as a microwave resonator; however, it took more than 20 years to generate further interest in DRs and to verify Richtmeyer's prediction experimentally. In the early 1960s Okaya and Barash rediscovered DRs while working on rutile single crystals. They measured the permittivity and Q of TiO_2 single crystals at room temperature down to 50 K in the microwave frequency range using the commensurate transmission line technique. In the early 1960s Cohn and his co-workers performed extensive theoretical and experimental work on DRs. Rutile ceramics that had an isotropic permittivity of about 100 were used for their experiments, but TiO_2 has a poor (+450 ppm/^{o}C) resonant frequency stability that prevented its commercial exploitation. The first microwave filter using TiO_2 ceramics was proposed by Cohen in 1968, but this filter was not useful for practical applications because of its high ε_r and frequency instability with temperature. A real breakthrough in dielectric resonator ceramic technology occurred in the early 1970s when the first temperature-stable low-loss barium tetratitanate ($BaTi_4O_9$) ceramics were developed by the Raytheon Company. Later, barium nanotitanate ($Ba_2Ti_9O_{20}$) with improved performance was reported by Bell Laboratories. The next breakthrough came from Japan when Murata Manufacturing Company produced (Zr, Sn)TiO_4 ceramics. Commercial production of dielectric resonators started in the early 1980s.

In the last two decades there has been extensive progress in the development of terahertz (THz) technology. This progress has enabled a multitude of potential applications, be it communications, biomedical, imaging, security, quality control of food and agricultural products, matter and light control, or chemical agent detection – in every application it has emerged as one of the most promising areas of interest. The terahertz region of the electromagnetic spectrum, referring roughly to the frequencies from 100 GHz or 0.1 THz to 30 THz, is the bridge between the microwave and infrared spectral bands. The promise of THz radiation resides in its unique properties and characteristics: its non-ionizing nature; its submillimeter spatial resolution; its transmission through dielectric materials that are

transparent to it; its interaction with water molecules, making it useful for certain medical diagnoses; its unique signature for molecular and rotational energy levels of many biological and chemical agents; and its potential for wireless communications. Although a large number of materials have been characterized in the microwave frequency range, relatively little attention has been paid to millimeter-wave or terahertz characterization of materials, possibly due to the relatively expensive facilities required. Chapter 5 discusses mm-wave material systems and applications of this technology.

Glasses have good thermal properties compared to polymers and better material homogeneity in comparison to ceramics, and hence they are considered for microwave applications; however, glasses in general have higher dielectric losses and a limited range of dielectric constants. Glass–ceramic composites have the advantage of an increased range of dielectric constants and reduced losses. They can be made with excellent homogeneity to produce sophisticated miniaturized microwave electronic devices. Chapter 7 discusses microwave dielectric properties of important glasses and glass–ceramics.

In the past, microwave devices have been traditionally machined from metal, and coaxial RF connections were made with metallic connectors, generally leading to expensive, heavy, and bulky packages. Moreover, today's electronic circuits for the automotive industry, entertainment electronics, and telecommunications have to handle a steadily increasing level of functionality whilst occupying the smallest volume possible. In the development of complex miniaturized circuits, flexible glass/ceramic or ceramic tapes with sintering aids made of high-temperature cofired ceramics (HTCCs), low-temperature cofired ceramics (LTCCs), and ultralow-temperature cofired ceramics (ULTCCs) play a decisive role as base materials. The choice of HTCC, LTCC, or ULTCC tapes is based on the electrode materials used and cofiring temperature. Cofired ceramics have become crucial in the development of various modules and substrates. In this technology, several thin layers of low-permittivity ceramics or glass/ceramic composites and conductors are combined, and the resulting multilayered modules are generally used in the form of a 3D wiring circuit board. These materials also enable a versatile mix of passive microwave components like microstrips, striplines, antennas, filters, resonators, capacitors, inductors, phase shifters, and dividers, making possible a whole matrix of designs that are not practical on regular alumina or any soft substrates. Thus these integrated components enable, for example, interconnection with 3D stripline circuitry. Chapter 8 describes the preparation characterization and properties of important HTCC, LTCC, and ULTCC ceramics.

Tunable microwave materials are extensively being investigated and utilized to meet the stringent requirements of modern wireless communication systems. The potential of tunable materials has been established for a variety of microwave applications such as tunable phase shifters (which introduce a controllable phase shift between the input and output of the device) and delay lines. The high power handling capabilities of ferroelectric varactors (variable capacitors) make these devices highly desirable for tunable matching networks. Tunable dielectric materials are also used in antenna beam steering as an efficient and cost-effective replacement for expensive and bulky phased array designs. Significant progress has been made in the development of more sensitive, low-loss, and versatile tunable materials. Bulk ferroelectric materials have relatively high loss tangents, limiting their applications in the microwave regime; however, thin films of ferroelectric materials have been investigated for extra-high tunability and temperature stability. The dielectric properties of thin films are significantly different from those of the bulk material of the

same composition. Moreover, very high electric fields can be applied to these thin films to achieve high tunability. Among the ferroelectric materials, barium strontium titanate (BST) is the dominant candidate for microwave tunable applications. Chapter 9 discusses the recent advances in tunable microwave dielectric materials.

Recently, there has been an increasing trend towards printing for the manufacture of low-cost consumer electronics due to the high flexibility of the printing process, providing significant advantages over conventional manufacturing processes including the possibility of low-cost flexible electronic devices. Applications for printed electronics include smart packages, flexible displays, distributed sensors, and antennas. Different types of inks based on advanced materials such as capacitor materials with a high relative permittivity, insulator layers with a low relative permittivity, and sealing glasses with a low melting point have been reported if the inorganic materials are considered. Screen printing is a simple and low-cost manufacturing method widely used for the fabrication of ceramic thick films in the range 10–100 μm. The screen printable ceramic ink consists of ceramic fillers with suitable organic solvents, dispersants, and binders. The high- and low-relative permittivity inks are extensively used in dynamic random access memory (DRAM) capacitors, photovoltaics and multilayer ceramic (MLC) circuits. Chapter 10 discusses the preparation and properties of important low-loss dielectric inks.

Materials used in microelectronic packaging have to simultaneously fulfill diverse requirements, such as low dielectric loss (tan δ), moderate relative permittivity (ε_r), low thermal dependence of permittivity (τ_ε), moisture absorption resistance, low coefficient of thermal expansion (CTE), and high dimensional stability and mechanical stiffness. Polymer–ceramic composites, especially type 0–3, are a potential material group suitable for producing demanding and functional packages that combine the electrical properties of ceramics and the mechanical flexibility, chemical stability, and processing possibilities of polymers. It is well known that the connectivity between the phases in the composite materials is very important in achieving the desired properties. The preparation of 0–3 type composite materials by combining a dielectric or a ferroelectric ceramic and a polymer for suitable properties means not only choosing the right materials, processed in a particular way, but also coupling them with the best possible design structure. This concept of connectivity describes the interspatial relationships in a multiphase material controlling the mechanical and electrical properties and thermal fluxes between the phases. Additionally, the filler particle size, interfacial properties, percolation level, and porosity effects can also play a role in the composite properties. Interfacial effects can occur between the ceramic grains and the polymer matrix, leading to large dielectric relaxations normally at low frequencies. The properties of the polymer–ceramic composites are determined by the number of phases and the way in which the phases are interconnected. The response of a ceramic–polymer composite to an external excitation (electric field, temperature, stress, etc.) depends on the response of individual phases, their interfaces as well as the connectivity concept. Chapter 11 describes the preparation, characterization, and properties of important polymer–ceramic composites with 0–3 connectivity for electronic circuits.

Flexible electronics constitute an important research area for the next generation of consumer electronics and is becoming a part of our day-to-day life. They are increasingly being used in a number of applications that benefit from their low profile, light weight, and good dielectric properties. These applications and potential applications are in various societal sectors, including healthcare, the automotive industry, human–machine interfaces, mobile

communications, and computing. Flexible circuits make portable devices more resilient. For some applications, particularly in the biomedical field, electronic circuits are conformally wrapped around curved surfaces. The dielectric materials used for flexible electronic applications must have mechanical flexibility, optimum relative permittivity, low-loss tangent, temperature stability of relative permittivity, low coefficient of thermal expansion (CTE), and high thermal conductivity. It is very difficult to identify a single material that possesses all of these properties simultaneously. Ceramics with high permittivity and low loss are available, but their high processing temperatures and brittle nature preclude their use as a single phase. At the same time low-loss elastomers with good flexibility and easy processing are available, but their high CTE, low permittivity, and low thermal conductivity limits their single-phase use; however, through the composite approach one can improve or tailor the individual properties of both elastomer and ceramics. In such systems, the circuits must not only be flexible but also stretchable. Chapter 12 describes synthesis, characterization, and properties of elastomer–ceramic composites.

The explosive growth in wireless communication systems has led to an increased use of electronic equipment, which in turn has caused a widespread problem of electromagnetic interference (EMI). EMI affects human health and reduces the lifetime and performance of electronic instruments. It also leads to malfunctioning of electronic devices used all over the planet and even in space exploration. This EMI problem can be solved by shielding electronic equipment against electromagnetic radiation. Extensive research has been done in order to develop lightweight microwave shielding materials with high efficiency and strength. Chapter 13 discusses the recent advances in EMI shielding materials.

Ferrite materials are insulating magnetic oxides with both high permeability and moderate permittivity in the range 5–20 at wavelengths from DC to the millimeter range. Due to their low eddy-current losses, there exist no other materials with such a wide range of electronic applications in terms of power generation, conditioning, and conversion. Electromagnetic waves can pass through ferrites with negligible attenuation but undergo a phase shift that can be influenced by DC magnetic fields. Ferrites are extensively used in the fabrication of microwave isolators, circulators, switches, inductors, and EMI shields. The ability to process thick-film ferrites having perpendicular magnetic anisotropy and self-bias properties allows for the redesign of conventional microwave passive components as lightweight planar constructs. Low-loss ferrites are also used in tunable microwave electronics that are small in size, profile, and weight. Microwave materials and device technologies are in a state of significant positive change with the potential to greatly impact a wide range of technologies that involve the sending, receiving, and manipulation of electromagnetic signals. Chapter 14 describes the preparation, characterization, and properties of important microwave ferrite materials.

Chapters 15 and 16 discuss briefly the different applications of microwave materials.

The topics covered in this book include microwave measurements, dielectric resonators, microwave substrates, tunable dielectrics, and EMI shielding materials. The book also has a data table (Appendix) listing the reported low-loss dielectric materials with properties and references arranged in order of increasing permittivity. Although the title of the book is microwave materials, it may be noted that the materials discussed in this book are useful for several other applications, such as capacitors and gate dielectrics. Actually, several thousand research papers are published annually on microwave materials, so the data or many very useful materials are scattered; hence, it is the purpose of this book to bring the

data and science of these useful microwave materials together for the benefit of researchers and technologists across the world.

In conclusion we thank all contributing authors for their great zeal and hard work in compiling their respective chapters. This book has been realized only due to their willingness to participate in this collaborative effort. A book project of this magnitude cannot see the light of day without a constant source of encouragement and support; hence, we express our gratitude to our families, friends, and colleagues. We also thank John Wiley & Sons Ltd for publishing this book.

M.T. Sebastian, R. Ubic, and H. Jantunen

9

Voltage Tunable Microwave Dielectrics for Frequency and Phase Agile Devices

K. Sudheendran[1] *and K.C. James Raju*[2]
[1]*Department of Physics, Sree Kerala Varma College, University of Calicut, Thrissur, India*
[2]*CASEST, School of Physics, University of Hyderabad, Hyderabad, India*

9.1 Introduction to Voltage Tunable Materials

The dielectric materials, which have a voltage-dependent dielectric constant, are termed as tunable dielectric materials [1]. Generally this class of materials exhibits a large change in dielectric constant with an applied DC electric field. The major class of materials being considered for tunable dielectric applications are ferroelectrics in their paraelectric state. The dielectric materials have been investigated for device application for many years. Only recently, monolithically compatible processing of these materials in thin-film form became possible, and has generated great interest and promise for designing a new class of electronic devices, especially for high-frequency applications. For a microwave engineer the main attraction of a tunable material is the strong dependence of their dielectric permittivity ε on the applied bias electric field E. This characteristic is commonly described by a parameter named tunability n, defined as the ratio of the permittivity of the material at zero electric field $\varepsilon(0)$ to its permittivity at some non-zero electric field $\varepsilon(E)$ as given by Equation (9.1). The relative tunability n_r is defined by Equation (9.2) [2]:

$$n = \frac{\varepsilon(0)}{\varepsilon(E)} \tag{9.1}$$

$$n_r = \frac{\varepsilon(0) - \varepsilon(E)}{\varepsilon(0)} \tag{9.2}$$

Microwave Materials and Applications, First Edition.
Edited by Mailadil T. Sebastian, Rick Ubic and Heli Jantunen.
© 2017 John Wiley & Sons, Ltd. Published 2017 by John Wiley & Sons, Ltd.

The dielectric loss of a tunable dielectric material is also dependent on the applied DC electric field. Experiments show that a ferroelectric material with a higher loss tangent usually has larger tunability. Since the loss tangent of a material is an important factor affecting the performance of the electric circuit, in the development of electrically tunable ferroelectric microwave devices, a figure of merit K (K-factor) is defined by K = tunability/tan δ

$$K = \frac{\varepsilon(0) - \varepsilon(E)}{\varepsilon(0)} \times \frac{1}{\tan\delta} \tag{9.3}$$

is often used to indicate the quality of the tunable dielectric material. Usually, in the calculation of K, the loss tangent at the maximum external DC electric field is used [3].

9.2 Different Classes of Voltage Tunable Materials

9.2.1 Ferroelectric-Based Voltage Tunable Materials

There are several ferroelectric materials that have been considered as possible candidates for tunable microwave devices. The most attention has been paid to $SrTiO_3$ and its solid solutions with $BaTiO_3$ and $PbTiO_3$ [4]. The bulk form of $SrTiO_3$ exhibits large tunabilities at cryogenic temperatures while at room temperature a large electric field is required for its tuning [5]. Voltage tunable (Ba, Sr)TiO_3 thin films and ceramics have been extensively investigated due to their high power handling capacity and large tunability over a wide frequency range. Thin films of BST-type materials are desirable, because they can be easily integrated with standard IC processing procedures and can therefore be scaled for mass production [6]. In addition to barium strontium titanate (BST), lead strontium titanate (PST) has been proposed as a potential candidate material for high-frequency tunable devices [7]. Ferroelectric sodium potassium niobium oxide $Na_xK_{(1-x)}NbO_3$ is another candidate material considered for tunable applications [8]. It is a continuous solid solution of $KNbO_3$ and $NaNbO_3$, having a pervoskite structure for $x < 0.97$. The dielectric properties of these ceramics were well studied by many researchers. The NKN thin films deposited on various oxide substrates have shown high dielectric permittivity and voltage tunability. Because of their excellent crystallinity and electrical properties, NKN films were studied for memory and tunable microwave device applications.

Barium strontium titanate ((Ba_x, Sr_{1-x})TiO_3, BST) is one of the most intensively studied materials for tunable microwave devices. This material is of particular interest because of low loss, high tunability, composition (i.e., Ba/Sr ratio), and controllable Curie temperature (T_c) [9]. Thin films of BST also show a high breakdown field, high time-dependent dielectric breakdown (TDDB), low leakage current, and low fatigue and ageing. These properties depend on the microstructures of the films such as grain size, strain, crystallite size, and, more importantly, composition and crystallinity and its orientation. To date, BST thin-film varactors have been employed in microwave phase shifters, delay lines, tunable switches, tunable matching networks, tunable filters, and resonators [10]. A typical voltage tunability characteristics of BST thin films is shown in Figure 9.1.

9.2.2 Non-ferroelectric Voltage Tunable Materials

To date, almost exclusively, BST and $SrTiO_3$ have been investigated for tunable microwave application. Most of the literature on RF applications of tunable dielectrics has focused on

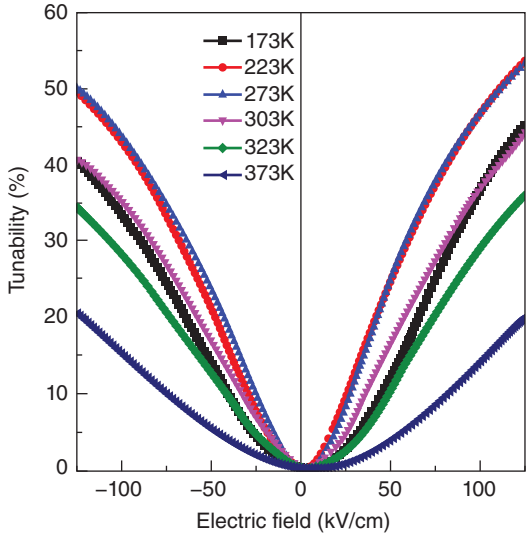

Figure 9.1 *A typical voltage tunability characteristics of BST thin films. Source: Sudheendran* et al. *2015 [26].*

the $Ba_xSr_{1-x}TiO_3$ (BST) thin films, and numerous devices and circuit demonstrations have been reported [11]. A promising RF performance has been achieved but, in general, the RF losses of BST-based devices are relatively higher. All these tunable dielectric materials investigated to date fall under the group of ferroelectrics and they exhibit temperature-dependent structure and dielectric properties. They also exhibit the phenomena of hysteresis in their ferroelectric state. The dielectric properties of ferroelectric thin films are found to be highly thickness dependent. All these things put together make such materials relatively lossier at microwave frequencies. If one can employ a non-ferroelectric material for tunable microwave applications, one can avoid the loss originating from the coupling of the soft lattice modes with electromagnetic fields, which is a characteristic feature of all ferroelectrics. Also, ferroelectric thin films are more vulnerable to the process-related strain and impurities, which in effect would increase the dielectric losses in these thin films [12]. These limitations of the ferroelectric thin films enhance the search for non-ferroelectric tunable materials having low loss at the microwave frequencies, even if the tunability is relatively lower since the low losses could lead to a higher *K* factor.

Bismuth-based pyrochlore ceramics were discovered in the early 1970s and have attracted additional study during the last 10 years due to their possible applications in high-frequency capacitors and microwave resonators [13]. Recently, researchers are showing much interest in the ternary oxides of the Bi_2O_3—ZnO—Nb_2O_5 (BZN) system, which exhibits a high dielectric permittivity (ε_r), relatively low dielectric loss ($\tan\delta$), and a compositionally tunable temperature coefficient of capacitance (τ_c) [14]. There are two main phases in the Bi_2O_3—ZnO—Nb_2O_5 system: $Bi_{1.5}Zn_{1.0}Nb_{1.5}O_7$ (c-BZN) with a cubic pyrochlore structure, in which at least some Zn atoms occupy A site positions with $\varepsilon_r \sim 160$ at room temperatures, and $Bi_2Zn_{2/3}Nb_{4/3}O_7$ (m-BZN), which has $\varepsilon_r \sim 80$ with a monoclinic zirconolite-like structure. Bi_2O_3—ZnO—Nb_2O_5-based pyrochlore

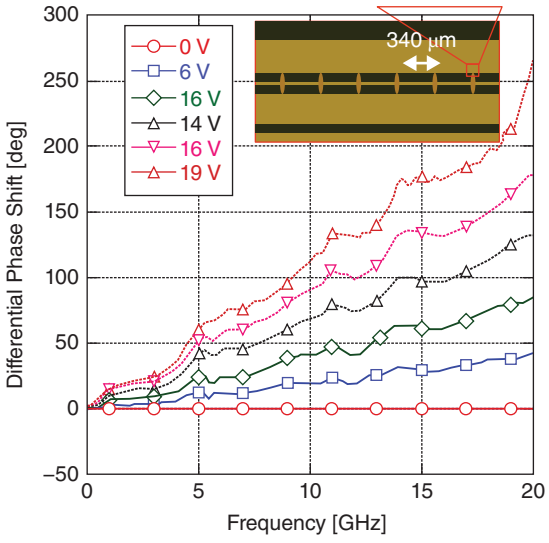

Figure 9.2 *Photograph and differential phase shifts with applied DC bias of c-BZN phase shifter fabricated and displayed by Professor Stemmer. Reproduced with permission from Professor Susanne Stemmer UCSB.*

ceramics are presently being considered as smart microwave material because of their unique dielectric properties in the microwave range. It is one of the few non-ferroelectric materials known today exhibiting voltage-dependent dielectric permittivity. Because of being non-ferroelectric, this material exhibits low loss and a high figure of merit in the microwave frequency region. A monolithic Ku-band phase shifter employing a voltage tunable c-BZN thin-film parallel plate capacitor is reported by Jaehoon Park *et al.* [15]. They have designed a nine section distributed coplanar waveguide loaded line phase shifter, as shown in Figure 9.2.

These phase shifters were reported to have a differential phase shift of 175° with a maximum insertion loss of 3.5 dB at 15 GHz. As per their report, insertion loss is significantly better than that of the BST 5-based phase shifters using a similar design. The BST phase shifter had an insertion loss of 3 dB at 10 GHz [16] whereas the BZN phase shifter had an insertion loss of only 1.8 dB at 10 GHz. This shows that the BZN thin-film devices maintain relatively low losses well into the microwave frequency region.

9.2.3 Multiferroic Voltage Tunable Materials

The magnetism that can be controlled by the application of an electric field has been attracting a great amount of interest recently due to its potential technological impact. The coexistence of electrical polarization and magnetization in multiferroic materials provides great opportunities for realizing effective electric field control over magnetization, or vice versa, through a strain mediated magnetoelectric interaction effect in layered magnetic/ferroelectric multiferroic heterostructures. Ferroelectric and magnetic characteristics of BST—CFO heterostructures is shown in Figure 9.3.

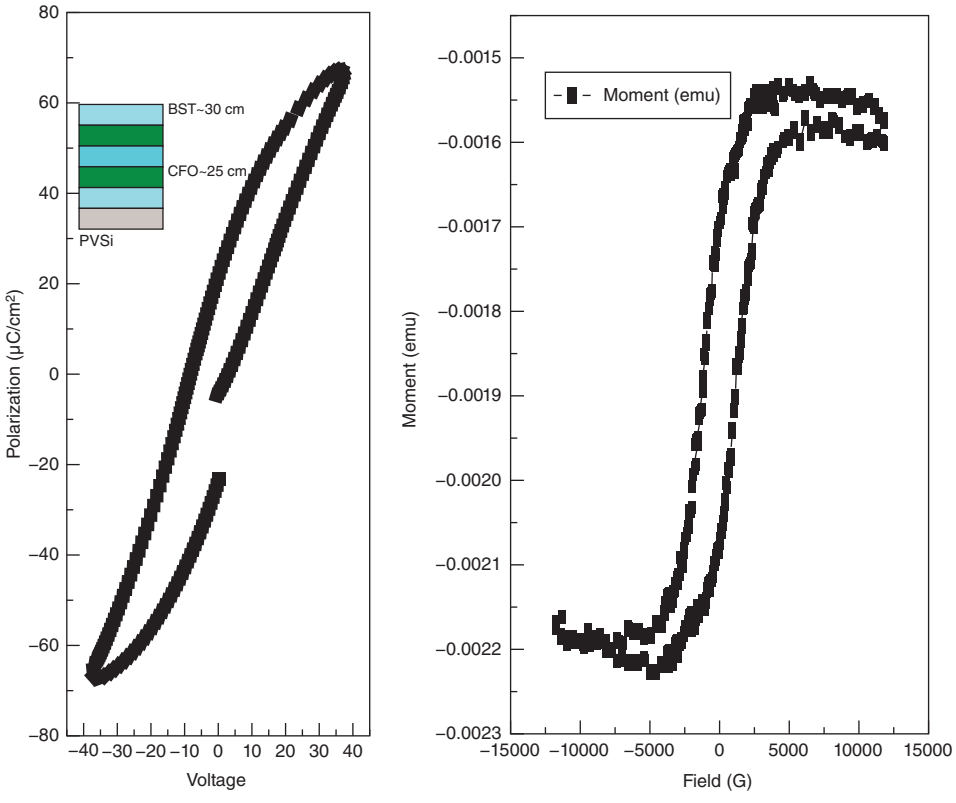

Figure 9.3 *Room temperature ferroelectric and magnetic characteristics of BST—CFO heterostructures fabricated by the present authors.*

Strong magnetoelectric coupling has been the enabling factor for different multiferroic devices, which, however, has been hard to achieve, particularly at RF/microwave frequencies. Exchange coupled multiferroic heterostructures have already demonstrated a sort of deterministic magnetization switching. New multiferroic devices include multiferroic voltage tunable bandpass filters, voltage tunable inductors, tunable bandstop filters, and spintronic devices, which are being demonstrated for microwave applications. The basic working principle of these multiferroic microwave devices are the dynamic magnetization switching at room temperature in the antiferromagnetic/ferromagnetic/ferroelectric/multiferroic heterostructures. Through an active competition between the E-field uniaxial anisotropy and unidirectional anisotropy, large E-field induced tunable exchange field results. Besides the new materials aspect, the multiferroic devices have many benefits in comparison with the conventional devices. They include fast wide-bandwidth tuning with low insertion loss in the microwave and millimeter wave frequency range, planar integrability, and negligible power consumption. These benefits make them potential candidates for practical information storage, logic devices, radars, satellites, and telecommunication applications [17].

9.3 Importance of Voltage Tunable Materials in Frequency and Phase Agile Devices

By utilizing the non-linear dielectric agility of these materials in thin-film form in microwave devices, one can tune either the frequency or phase of a signal. Frequency and phase agile circuits in many cases provide a new capability or offer the potential for lower cost alternatives in satellite and terrestrial communications and sensor applications. Frequency agile circuits have wide applications in microwave systems. A frequency agile circuit could be used in K-band satellite communication subsystems such as a receiver front end. BST materials can be easily tuned in a wide range of frequency with an application of a very small amount of voltage. Frequency agile circuits also includes resonators, filters, oscillators, etc. A phase agile circuit is used to provide a variable insertion phase in a microwave signal path without changing the physical path of the signal. These circuits are used in many different applications. The most common ones are phased array radars, synthetic aperture radars, diverse power combining schemes, and adaptive antenna configurations.

9.3.1 Varactors in Frequency and Phase Agile Devices

Varactor is a non-linear device that provides a capacitance that varies in response to an applied control voltage. The capacitance of a varactor, when within its operating parameters, decreases as the voltage applied to the device increases. Varactors can be used to fabricate reconfigurable components for RF and microwave applications [18]. The established technology for microwave varactors is based on semiconductors typically employing GaAs or silicon technology.

A semiconductor varactor is a p–n junction diode or a PIN diode made of gallium–arsenide (GaAs), silicon (Si), or silicon–germanium (SiGe). The depletion area in the p–n junction forms a capacitor, whose capacitance can be varied by changing the reverse bias voltage across the diode. A schematic diagram of the p–n junction and PIN diodes are shown in Figure 9.4. As a mature varactor technology, varactor diodes are commercially available at very low cost. The advantages of varactor diodes include large tunability, a small footprint, fast tuning speed, and low control voltage. Semiconductor varactors are widely

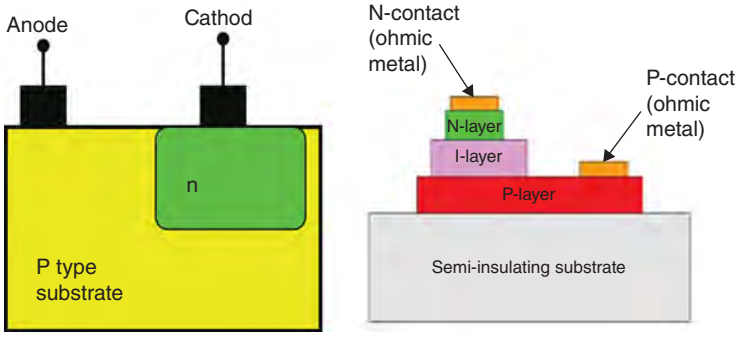

Figure 9.4 *Schematic diagram of a simple p–n junction diode and a PIN diode. Source: Adapted from Sudheendran 2014 [17].*

used in electrical and electronic circuits in a variety of applications, including voltage-variable tuned circuits, voltage-controlled oscillators, phase shifters, frequency multipliers, etc. Varactors are commonly used in the voltage-controlled oscillator (VCO) circuits of phase-locked loops (PLLs), which, in turn, are commonly used in high-frequency applications, such as with cellular phones. The varactor diode can be supplied at a low price because of a structure suitable for mass production using a semiconductor process, and furthermore the variable amount of capacitance available is large. However, their disadvantage is the poor Q-factor, which decreases as the operating frequency increases. Tunable circuits using varactor diodes exhibit a considerable amount of loss beyond 5 GHz. Another drawback of semiconductor varactors is their poor power handling capability because the reverse bias requirement does not allow for a large RF voltage swing across the diode.

Microelectromechanical systems (MEMSs) is the technology of very small mechanical devices driven by electricity. MEMS technology is finding wider and deeper application day by day. The variation of capacitance in a MEMS varactor is achieved by the mechanical movements of the electrodes on the application of an electric voltage. Processing methods are available that make them work well along with coplanar waveguides (CPWs), which are mostly used in monolithic microwave integrated circuits (MMICs). The development of MEMS in RF applications started in the beginning of the 1990s with switching devices [19]. Nowadays even variable inductances and capacitances are possible with MEMS devices. The advantages of MEMS varactors to RF and microwave technology are their high linearity, high Q, large capacitance variation (tunability), the ability to handle high RF power, along with size and weight reduction The disadvantages are in general a high control voltage, a large temperature dependence, durability, and the slow switching speed in comparison to other devices. A schematic diagram and microphotograph of a MEMS varactor is shown in Figure 9.5.

Voltage tunable dielectric material based varactors have recently been identified as a potential technology competing with the existing varactor technologies. When a direct current (DC) voltage is applied to these materials, the dielectric constant of the materials can be decreased by nearly an order of magnitude, changing the high-frequency wavelength in the microwave device. Ferroelectric materials are one of the most prominent and most widely studied candidate materials for voltage tunable applications. When a voltage is applied across a ferroelectric capacitor its capacitance will decrease accordingly. A typical

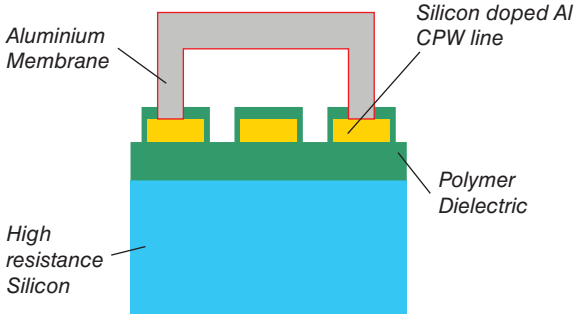

Figure 9.5 *Schematic diagram of a MEMS aractor. Source: Adapted from Sudheendran 2014 [17].*

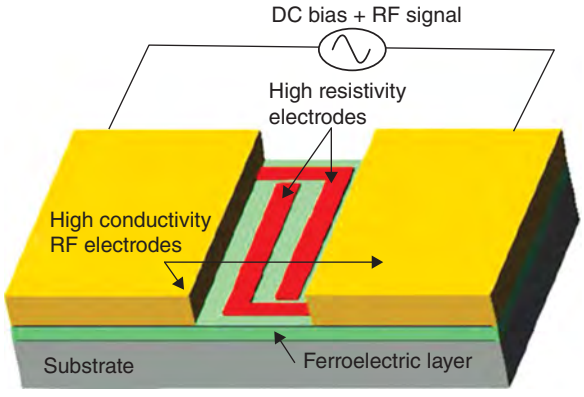

Figure 9.6 *Typical ferroelectric varactor used for microwave applications.*

ferroelectric varactor is shown in Figure 9.6. Recent advances in film growth have demonstrated high-quality ferroelectric thin films. This technology may allow microwave devices that have very low power consumption and are compact, lightweight, simple, robust, planar, voltage tunable, and affordable.

9.4 Growth Techniques for Voltage Tunable Thin Films on Various Substrates

It is also worth mentioning that a variety of techniques exist to examine the growth of voltage tunable thin films used in these devices. Some of the most widely used growth methods includes PLD, RF magnetron sputtering, molecular-beam epitaxy (MBE), chemical solution deposition (CSD), and metal organic chemical vapour deposition (MOCVD). Each method has its own advantages and disadvantages. A brief description of some of these techniques are given in the following sections.

9.4.1 Pulsed Laser Deposition Technique

In a pulsed laser deposition process the material will be repeatedly targeted by a very intense UV laser pulse and hence the material becomes ablated, keeping the chemical composition of the film the same as the target. The microstructure and physical properties of films can be tailored by the growth parameters during the PLD process, such as the growth temperature, oxygen ambient pressure, substrate–target distance, laser repetition rate, and the laser energy [21]. The typical growth conditions optimized by the authors for BST thin films are a growth temperature of 750 °C, laser fluence at the target of 1.5 J/cm^2, and oxygen ambient pressure of 0.1 mbar. Given that the laser may be shared between several deposition systems, the PLD method is widely regarded as one of the cheapest deposition methods for research purposes [22]. Compared with RF magnetron sputtering, PLD has the disadvantage ofa small-area deposition capability but has precise thickness control [23].

The advantages of pulsed laser deposition for oxide film growth and of molecular beam epitaxy for two-dimensional film growth can be combined to develop a method for

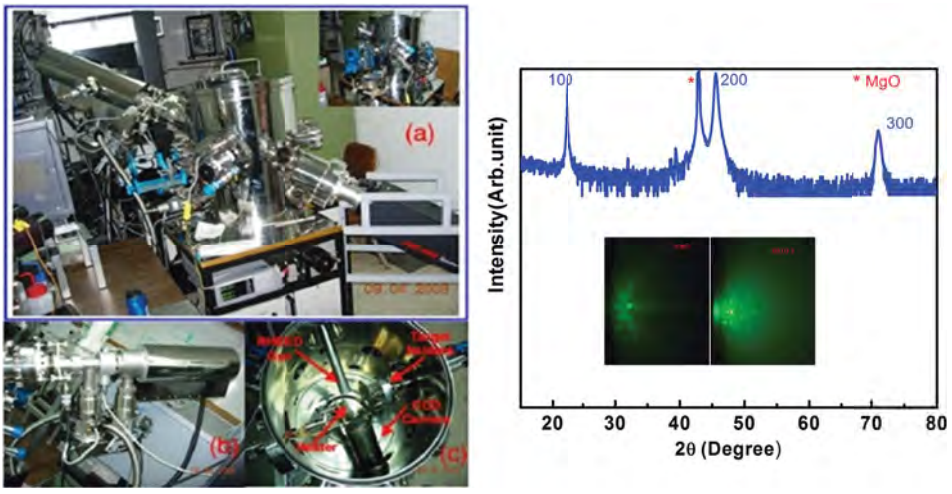

Figure 9.7 *In situ monitoring of epitaxial growth of BST thin films on MgO substrate using laser MBE.*

atomically controlled layer-by-layer epitaxy of complex oxides and other ceramic thin films. This is termed the laser MBE method and has been proved to be particularly useful for the growth of voltage tunable epitaxial thin films. Two-dimensional molecular layer epitaxy can be verified by the clear observation of RHEED intensity oscillations for the growth of various ceramics including perovskites, infinite-layer cuprates, rock salt oxides, corundum, and fluorites on oxide substrates. The authors could achieve the epitaxial growth of BST thin films on MgO and ALO substrates at low as well as high temperatures, as shown in Figure 9.7. Some phenomena indicating novel quantum effects were observed in high-quality ZnO film and $SrTiO_3/SrVO_3$ superlattice, both fabricated by laser MBE. In view of the versatility and structure-sensitive properties of oxides, lattice engineering by laser MBE is expected to be a promising technology for opening a new field of oxide electronics.

9.4.2 Sputter Deposition Techniques

Sputter deposition is a physical vapor deposition process for depositing thin films. Sputtering means ejecting material from a target and depositing it on a substrate such as a silicon wafer. The target is the source material. Substrates are placed in a vacuum chamber and are pumped down at a prescribed process pressure. Sputtering starts when a negative charge is applied to the target material, causing a plasma or glow discharge. Positive-charged gas ions generated in the plasma region are attracted to the negatively biased target plate at a very high speed. This collision creates a momentum transfer and ejects atomic size particles from the target. These particles are deposited as a thin film on to the surface of the substrates. Sputtering is extensively used in the semiconductor industry to deposit thin films of various materials in integrated circuits processing. Thin antireflection coatings on glass, which are useful for optical applications, are also deposited by sputtering. Because of the low substrate temperatures used, sputtering is an ideal method to deposit contact metals for

Figure 9.8 *Photograph of (a) the sputtering system, (b) inner view of the triple targets system, (c) the sputtering targets, and (d) RF plasma generated during the functional oxide deposition.*

thin-film transistors. This technique is also used to fabricate thin-film sensors, photovoltaic thin films (solar cells), metal cantilevers and interconnects, etc. The photograph of the triple target sputtering unit available from the authors' research lab for the growth of tunable thin films is shown in Figure 9.8.

Magnetron sputtering can be done either in DC or RF modes. DC sputtering is done with conducting materials. If the target is a non-conducting material the positive charge will build up on the material and it will stop sputtering. RF sputtering can be done with both conducting and non-conducting materials. Here, magnets are used to increase the percentage of electrons that take part in ionization events and thereby increase the probability of electrons striking the qargon atoms, increase the length of the electron path, and hence increase the ionization efficiency significantly. In the RF magnetron sputtering method, the stoichiometry of films sputtered is normally different from that of the target and therefore can be difficult to control precisely.

9.4.3 Chemical solution deposition technique (CSD)

The chemical solution deposition method (CSD) has also been used for the deposition of ferroelectric thin films for tunable microwave device applications. The low cost, effectiveness, and large-area deposition capability make it attractive [24]. The stoichiometry of the film can be well controlled and dopants can be introduced into the films easily. In the CSD

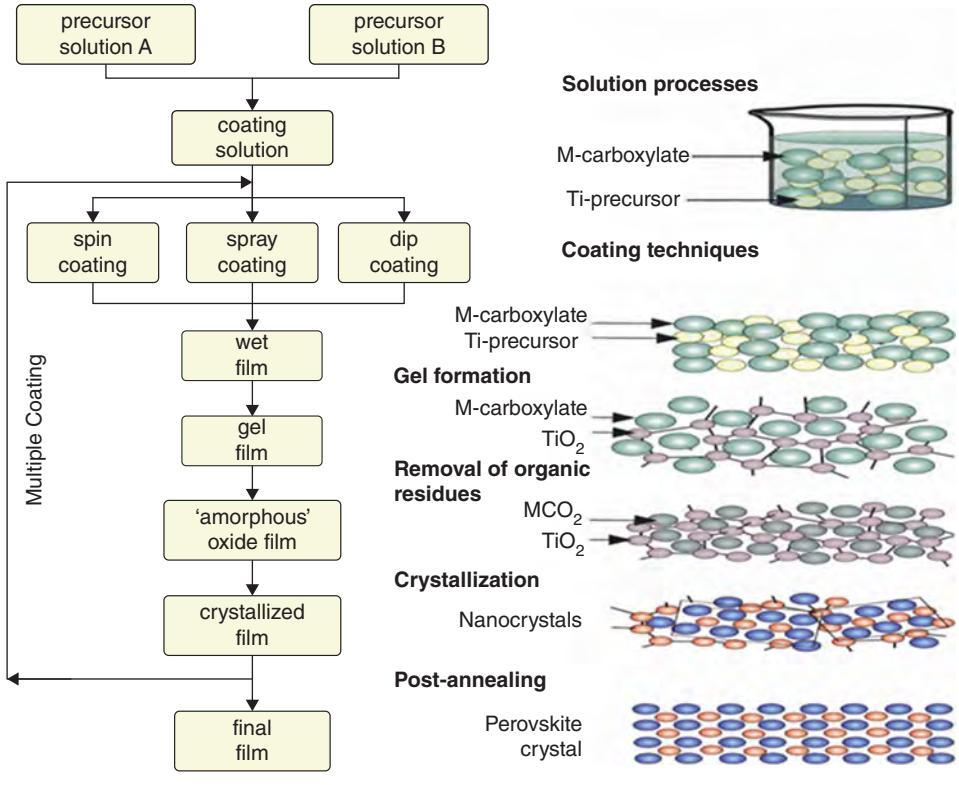

Figure 9.9 *Flowchart of the principle steps of the chemical solution deposition (CSD) method. Source: Waser* et al. *[25]. Reproduced with permission of Springer.*

process a solution containing organic compounds of the metal ions is deposited on the substrate by dip, spray, or spin coating. The wet film is either first pyrolyzed or directly crystallized. A sequence of deposition and heat treatment procedures followed by a final postannealing step results in the crystalline film. Thin films fabricated by the CSD method are susceptible to surface thickness non-uniformity, surface roughness, voids, and possibly the existence of cracks. However, the CSD method is a very flexible technique giving high reproducibility. With optimized process parameters, dense and homogeneous crystalline thin films of high quality have been grown. They are suitable for integration on the micrometer size scale as thin-film capacitors in MMICs or as piezoelectric elements in MEMS. A flowchart of the principal steps of the chemical solution deposition (CSD) method is shown in Figure 9.9 [25].

9.5 Characterization techniques

At the low-frequency regions (up to a few MHz) the thin-film dielectrics are characterized by making a metal–insulator–metal (MIM) capacitor structure. The dielectric constant and loss factor are calculated by directly measuring the capacitance and dissipation factor using an impedance analyzer or LCR meter [26]. This method cannot be directly used in

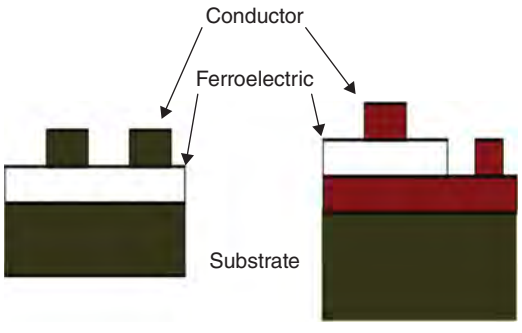

Figure 9.10 *Schematic diagram of planar and parallel plate capacitor test structures. Figure from the PhD Thesis of K. Sudheendran submitted to University of Hyderabad.*

the microwave frequencies because of the following limitations. At microwave frequencies, the dimensions of the capacitor become comparable with the wavelength of the electromagnetic wave used for the measurement and hence the capacitors can no more be considered as lumped elements but will have to be considered as distributed elements. Also, at these frequencies the impedance of the capacitor will be very small compared to the resolution of the impedance analyzers. Hence, special techniques are to be used for the measurement of the dielectric parameters of thin films at microwave frequencies.

9.5.1 Low-Frequency Measurement of Ferroelectric Thin Films

There are essentially two structures for measuring the DC or low-frequency dielectric properties of films: the coplanar capacitor or parallel plate capacitor. Figure 9.10 shows these two geometries. The shape of the surface electrode is important for determining the capacitance of the structure and for the parallel plate configuration it is generally square or rectangle. The capacitance is usually fairly large owing to the thickness of the ferroelectric film being small. For the coplanar structure the electrodes need to be close together to maximize the field within the ferroelectrics. If we want to increase the capacitance further we can use an interdigital finger structure. The properties of the ferroelectric materials can be extracted from the measured real and imaginary part of capacitance using a conformal mapping technique. The measurement is typically performed at frequencies between 100 kHz and 1 MHz. The dielectric and ferroelectric properties of BST thin films grown by the authors on Pt/Si substrate measured by the parallel plate capacitor technique is shown in Figure 9.11.

9.6 High-Frequency Characterization

Many researchers are trying to study the microwave dielectric properties of thin films by employing various methods. Most of the measurement methods used for the determination of the complex permittivity and loss tangent of dielectric thin films involve two steps. Firstly, the electrical characteristics of the dielectric thin film containing the test structure is monitored. Secondly, the dielectric permittivity and loss tangent of the material are derived from the obtained test structure data. The measurement techniques can be broadly classified

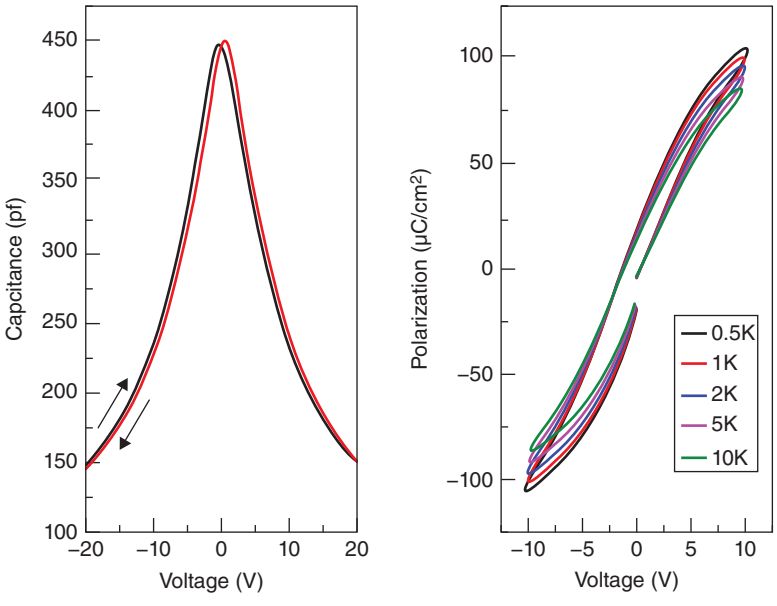

Figure 9.11 *Measured capacitance and polarization of ferroelectric capacitors at low frequencies. Source: Sudheendran* et al. *2015 [26].*

into three different groups, such as reflection measurements, transmission measurements, and resonance measurements [27]. In reflection measurement, the reflection coefficient of the thin-film capacitor is measured while in the transmission measurement techniques, the transmission characteristics of the thin-film-based planar transmission lines are measured using a vector network analyzer. In the resonance method, the characteristics of a resonator containing the thin-film material are investigated.

9.6.1 Modified Cavity Perturbation Technique

The cavity perturbation technique is widely used in the measurement of dielectric parameters of materials [28]. This technique has also been used effectively to determine the complex permittivity of liquids [29]. In the conventional cavity perturbation technique, the changes in the resonant frequency and quality factor Q when a material is introduced into the cavity give a measure of the complex permittivity of the material [30]. For materials having a complex permittivity $\varepsilon' - j\varepsilon''$, these changes may be expressed as

$$\frac{f_1 - f_2}{f_2} = (\varepsilon' - 1)\frac{\int_{V_S} E_1^2 \, dV}{\int_{Vc} E_1^2 \, dV} \tag{9.4}$$

$$\left[\frac{1}{Q_2} - \frac{1}{Q_1}\right] = \varepsilon'' \frac{\int_{V_S} E_1^2 dV}{\int_{Vc} E_1^2 dV} \tag{9.5}$$

where

$$E_1 = E_{10} \sin\left(\pi x/a\right) \sin\left(n\pi z/L\right) \tag{9.6}$$

and f_1, f_2 are the resonance frequencies without and with the specimen, respectively, Q_1 and Q_2 are the corresponding quality factors of the cavity, and V_s and V_c are the sample and cavity volumes, respectively. The conventional cavity perturbation technique can be extended to measure the complex permittivity of larger samples, provided the field perturbation by the sample lies within the prescribed limits [31]. In this case, the length of the sample is not small and the field E_1 in Equations (9.4) and (9.5) is no longer a constant but varies sinusoidally along the sample length. This method therefore involves solving the eigenvalue problem of a dielectric sample in a rectangular cavity. In our experiments we consider the substrate as a part of the cavity. The field inside the cavity with the substrate is taken as the initial field E_1. This approach has been used for quite a long time for the determination of the dielectric properties of liquids/solids in the powder form. A hole is drilled through the top surface of the cavity at the $E_{\max}$ position and a sample holder is inserted through that hole. The cavity with the sample holder is taken as the initial cavity, which has a resonance frequency f_1 with the sample holder [32]. Now the samples whose dielectric properties have to be determined are introduced into this sample holder and the properties are extracted from the shift in the resonance frequency and the shift in the quality factor of the cavity. In our approach, the uncoated substrate can be considered as a part of the cavity, provided the substrate is of a low dielectric constant material. The cavity with the film-coated substrate inside is taken as the perturbed cavity with a resonance frequency f_2. Q_1 and Q_2 are the corresponding quality factors of the cavity.

The main assumption of this method is that the dimension of the sample is small compared to the wavelength, which is always true in the case of thin films. If the sample surface lies across the cavity and everywhere else is tangential to the electric field, then the dielectric constant is given as [33]

$$\varepsilon' = K\frac{L}{\tau}\frac{\Delta f}{f_{0s}} + 1 \tag{9.7}$$

where L is the cavity length, τ is the film thickness, Δf is the frequency shift, f_{0s} and f_0 are the resonance frequencies of the cavity with the substrate and the film-coated substrate, respectively. The coefficient K is a measure of the area of the sample with respect to the cross-sectional area of the cavity. It is equal to unity when the whole cross-section is occupied by the film and is less than unity when the cross-section is partially filled with a film. Similarly, the dielectric loss is given as

$$\varepsilon'' = K\frac{L}{2\tau}\left[\frac{1}{Q_{L_s}} - \frac{1}{Q_{L_0}}\right] \tag{9.8}$$

where Q_{Ls} and Q_{L0} denote the unloaded Q factor of the cavity with and without the film-coated substrate, respectively. This means that in this method the uncoated substrate is considered as a part of the cavity, giving a net resonant frequency f_0, provided the substrate is a low dielectric constant material. The cavity with the film-coated substrate inside is taken as the perturbed cavity with a resonance frequency f_{0s} and Q_{L0} and Q_{Ls} are the corresponding quality factors of the cavity. It was assumed that the shift in the resonance frequency and

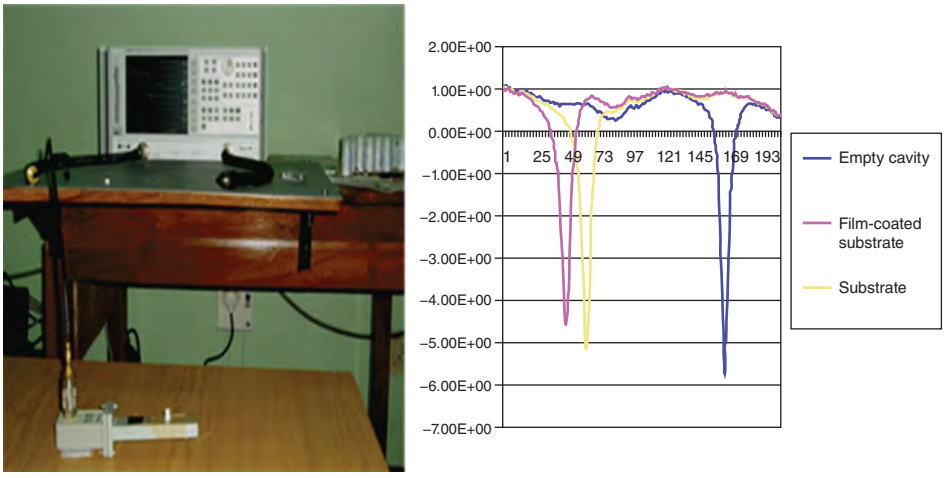

Figure 9.12 *Picture of the cavity perturbation measurement set up with the resonance characteristics of the cavity under different perturbations.*

the quality factor from (f_0, Q_{L_0}) to (f_{Ls}, Q_{Ls}) is only due to the properties of the film since the substrate is considered as a part of the cavity. Hence Equations (9.7) and (9.8) can be applied directly to find out the dielectric constant and loss of the thin films coated on low dielectric constant substrates. This is a quick method to measure the complex permittivity of the film at spot frequencies. However, the tunability cannot be measured by this method as there is no provision to apply the DC bias voltage. A picture of the cavity perturbation measurement set up with the resonance characteristics of the cavity under different perturbations is shown in Figure 9.12.

9.6.2 Calibration Comparison Technique

This is a broadband technique that can be used for the extraction of dielectric properties of thin films on a substrate. This technique can also be employed to extract the voltage-dependent dielectric properties. The calibration comparison technique makes use of two identical coplanar waveguides (CPW) patterned on the surface of the film [34] and on the bare substrate.Two CPW test structures of a 100 micrometer gap and 200 micrometer width were patterned simultaneously, one on the test film and the other on the bare substrate by a liftoff process. The scattering parameters of these CPW transmission lines were measured using a VNA and a probe station (LMS-2709) mounted with the GSG probes of a 250 micrometer pitch. A picture of the CPW transmission lines fabricated for on-wafer measurement is shown in Figure 9.13.

The test structure fabricated was designed and simulated using the full-wave simulator momentum of the Keysight ADS. The characteristic impedance of the CPW transmission lines was obtained from the electromagnetic simulation of the CPW line on the reference sample. A typical simulated result for the CPW line on a 0.5 mm thick $LaAlO_3$ substrate using ADS momentum is shown in Figure 9.14.

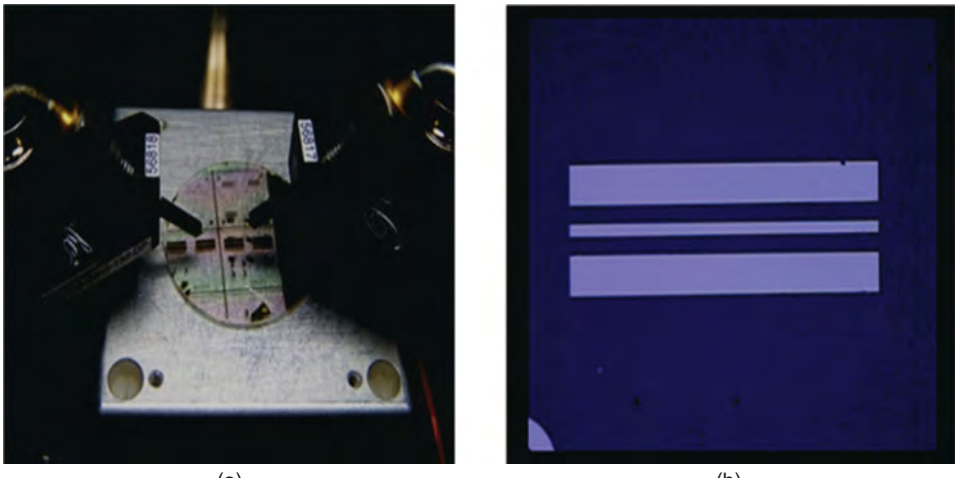

Figure 9.13 *(a) Picture of the CPW transmission lines fabricated for on-wafer measurement, mounted on the probe station. (b) The fabricated CPW line. Source: Sudheendran and James Raju 2010 [27].*

The method used in this study compares the propagation characteristics of the transmission lines fabricated on the bare substrate (reference sample) and the substrate with the thin film of BST (test sample). This technique has been successfully used in the past for the characterization of low k as well as high k dielectric thin films [35]. The resistance and inductance of the reference and test CPW lines were assumed to be the same. Also the loss tangent of the low-loss microwave substrate is assumed to be negligible. The ratio of the propagation constants of the CPW lines in both cases is given as

$$\frac{\gamma_{test}}{\gamma_{ref}} = \frac{\sqrt{[(R_{test} + j\omega L_{test})(G_{test} + j\omega C_{test})]}}{\sqrt{[(R_{ref} + j\omega L_{ref})(G_{ref} + j\omega C_{ref})]}} \tag{9.9}$$

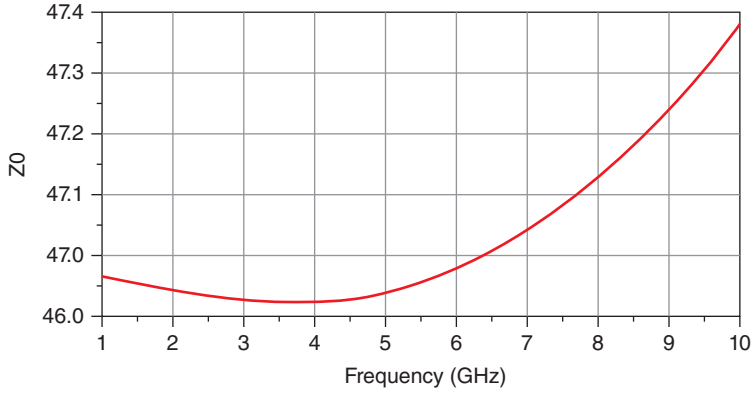

Figure 9.14 *Simulated results for the characteristic impedance of the reference CPW line.*

This can also be written as

$$\frac{(\alpha_{test} + j\beta_{test})}{(\alpha_{ref} + j\beta_{ref})} = \frac{\sqrt{[G_{test} + j\omega C_{test}]}}{\sqrt{(j\omega C_{ref})}} \tag{9.10}$$

where α and β are the frequency-dependent attenuation and the phase constant, respectively. The R, L, C, and G are the resistance, inductance, capacitance, and conductance per unit length of the CPW transmission line and are all frequency-dependent parameters. The conductance per unit length of the test sample can be expressed as

$$G_{test} = \omega(C_{test} \tan \delta_{eff}) \tag{9.11}$$

where $\tan \delta_{eff}$ is the effective loss tangent of the CPW structure. Substituting G_{test} from Equation (9.11) and $C_{test} = C_{film} + C_{ref}$ in Equation (9.10) and comparing the real and imaginary parts of the left- and right-hand sides and solving them, we get the capacitance of the film (C_{film}). The dielectric constant of the film ε_{film} is determined from C_{film} using the conformal mapping technique [36]. In the limit of the dielectric film thickness $t \ll s$, where s is the spacing between the center conductor and the ground line,

$$\varepsilon_{film} = (sC_{film}/(2\varepsilon_0 t)) - \varepsilon_{substrate} \tag{9.12}$$

and the loss tangent of the film is given as

$$\tan \delta_{film} \approx \tan \delta_{eff}(1 + C_{ref}/C_{film}) \tag{9.13}$$

The frequency-dependent attenuation and phase constants α and β for the test and reference lines are calculated from the measured magnitude and phase of the S_{21} for the reference and test sample. A typical measured S_{21} for the BST thin films is given in Figure 9.15.

9.6.3 Extraction of the Conductor Loss

A distributed circuit model for the CPW test structure is shown in Figure 9.16. During the broadband characterization it has observed that the attenuation in the test CPW line is very high. The attenuation in the CPW line is a combined effect of both conductor and dielectric losses. We have therefore tried to separate out the attenuation characteristic of the CPW lines in terms of conductor losses and dielectric losses. The method developed is briefly described below. The measured data are used to calculate the distributed line parameters for the test and reference samples. For the test sample the CPW transmission line is defined over the film and in the case of the reference sample the CPW line is defined only on the bare substrate. The resistance per cm for the CPW transmission line is obtained from the attenuation due to the conductor losses (α_c), which are equal to the attenuation in the reference sample:

$$\alpha_c = R/Z_{Cref}(Np/\text{cm}) \tag{9.14}$$

From the calculated distributed line parameters the dielectric loss can be separated from the total loss in the test sample. The dielectric loss in the test sample was calculated using the following equations:

$$\alpha_d = 8.686 * \pi/\lambda_g * (\tan \delta_{eff}) \qquad (\text{dB/cm}) \tag{9.15}$$

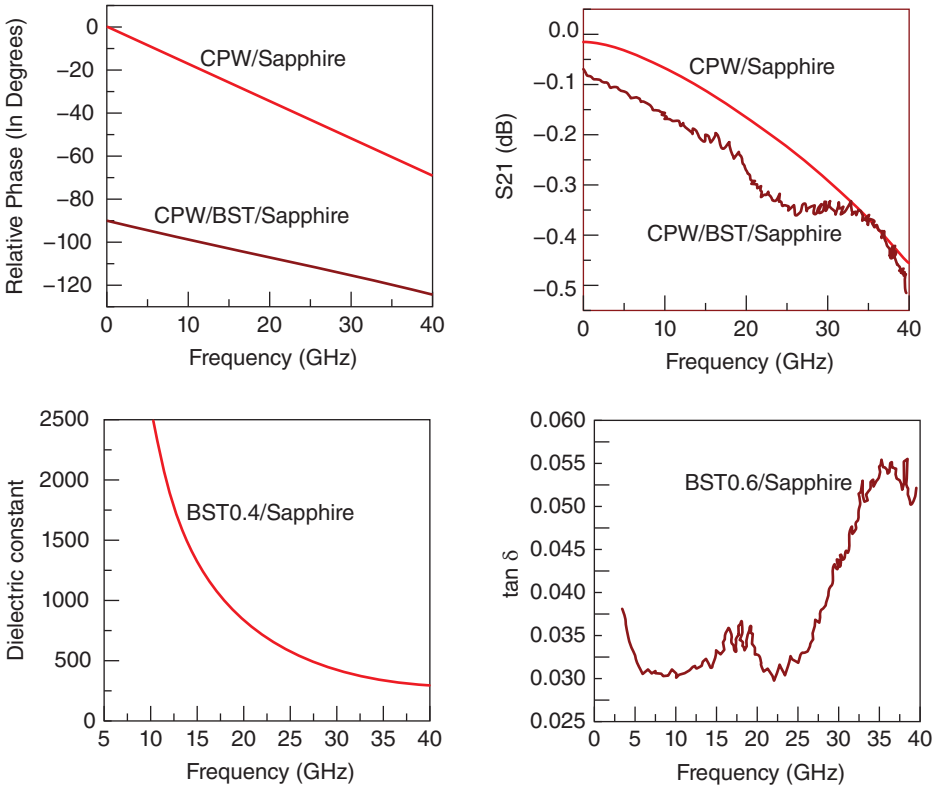

Figure 9.15 *Measured S_{21} phase and magnitude for the test and reference line fabricated for the BST thin films deposited on the sapphire substrate and the extracted dielectric permittivity and loss tangent for the films.*

Substituting for the guide wavelength λ_g in terms of β_{test} we can obtain

$$\alpha_d = 8.686 * (\beta_{test}/2) * \tan\delta_{eff} \quad (\text{dB/cm}) \tag{9.16}$$

Once the dielectric loss was obtained the conductor loss from the reference sample was added in order to calculate the expected total losses. Figures 9.17 and 9.18 show these

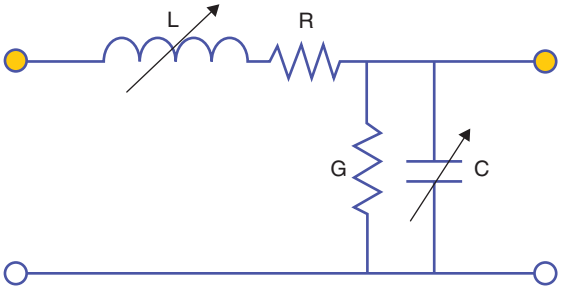

Figure 9.16 *Distributed circuit model for the CPW test structure.*

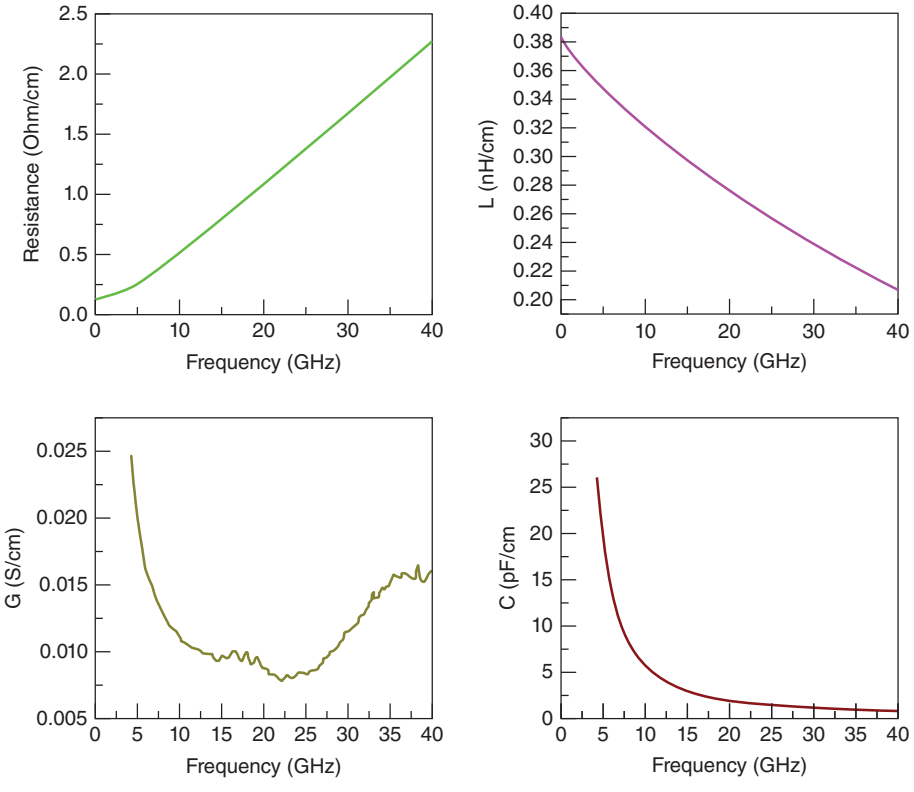

Figure 9.17 *Calculated distributed line parameters for the test samples.*

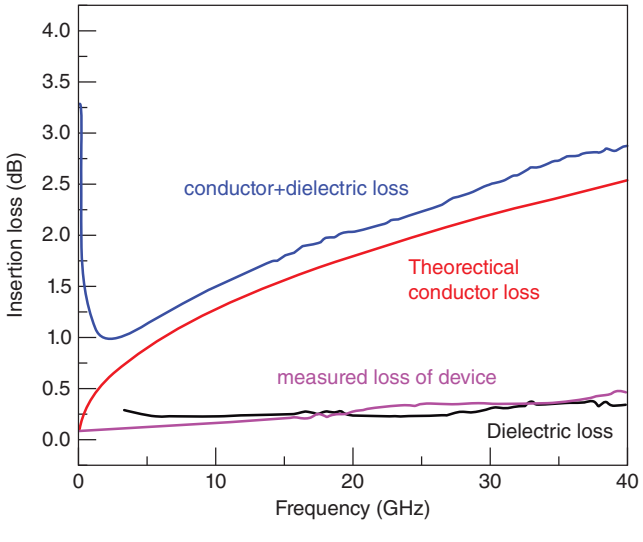

Figure 9.18 *Figure shows the distribution of various loss parameters extracted for the test device.*

characteristics of the test structure. From the above study it came to light that the conductor properties will also play a crucial role in the device performance. Since most of the electrodes/metallization is being carried out by the physical vapor deposition route we decided to study the effect of process parameters on the electrical properties of the metallic thin films [37].

The microwave conductivity is determined by the resistance per unit length of the transmission line, which is derived from the measured propagation constant of the CPW transmission lines. We make use of the distributed circuit model in order to determine the resistance per unit length of the transmission line. The resistance per cm (R) of the CPW transmission line is obtained from the attenuation due to the conductor losses (α_c), which is equal to the attenuation in the reference sample itself:

$$\alpha_c = R/Z_{Cref} \ (Np/\text{cm}) \tag{9.17}$$

where Z_{Cref} is the characteristic impedance of the reference CPW line.

The surface resistance (R_s) of the metallic thin film can be related to the attenuation α as follows [38]:

$$\alpha = 40 - 20\log(R_s) \tag{9.18}$$

The surface resistance of the film is a function of its conductivity σ_f and t, the thickness, which is given by

$$\sigma_f = 1/(R_s t) \tag{9.19}$$

The frequency-dependent conductivity of these thin films was derived using Equations (9.17) to (9.19).

9.6.4 Tunability Measurement

The calibration comparison method can also be extended to measure the dielectric properties of the films under an applied electric field (tunability measurements) [39, 40]. For the microwave tunability measurements, a DC bias voltage was applied to the CPW lines through the high-voltage bias tees. DC blocking capacitors were used at both ports of the VNA to give additional protection during these measurements. The magnitude and phase of the S_{21} of the CPW lines patterned on the c-BZN thin films were measured under a bias voltage of 100 V. This voltage was able to produce a field of around 10 kV/cm only in the test structures employed. For a higher field strength, either the CPW of a smaller gap or bias tees of higher a voltage rating are to be employed in this method. A block diagram of the tunability measurement setup is shown in Figure 9.19.

9.6.5 Reflection Measurements

This method is also known as a direct measurement method. In this technique the reflection measurements are carried out directly on a capacitor made out of the films whose characteristics are to be evaluated. The capacitors can have either a planar, parallel plate, or interdigitated configuration. The capacitances of these capacitors are calculated directly from the measured complex reflection coefficient (S_{11}). Appropriate modeling has to be done to extract the dielectric permittivity and loss tangent of the films from the calculated capacitance. In the present study we have used parallel plate capacitors in the circular patch capacitor geometry for characterizing the BZN thin films grown on platinized silicon

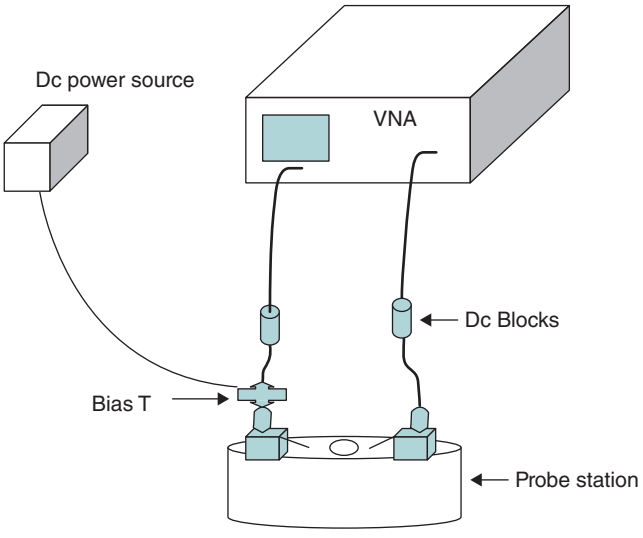

Figure 9.19 *Block diagram of the tunability measurement setup. Figure from the PhD Thesis of K. Sudheendran submitted to University of Hyderabad.*

substrates. Circular patch capacitor (CPC)-based measurements is a commonly used reflection-based measurement procedure for ferroelectric films. The cross-section of the electrode layout of the test structures used for the experiment is shown in Figure 9.20. In this structure the total capacitance measured between the center patch and the surrounding concentric electrode is

$$C = (C_f C_{out})/(C_f + C_{out}) \tag{9.20}$$

where C_f is the capacitance between the center patch and the bottom plate and C_{out} is the capacitance between the top outer electrode and the bottom plate. Typically $C_{out} \gg C_f$ and the top outer electrode provides an effective microwave connection to the bottom plate, resulting in [41]

$$C \approx C_f \tag{9.21}$$

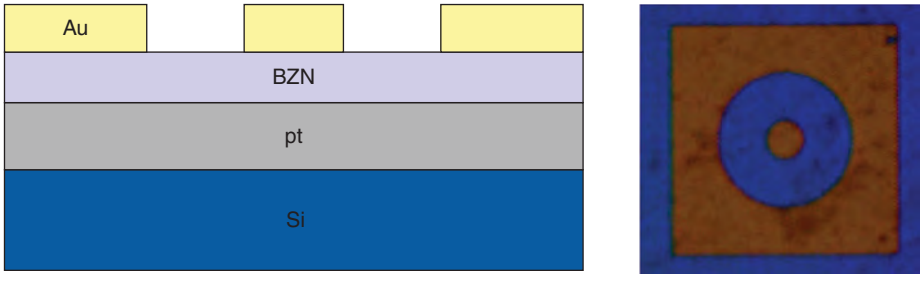

Figure 9.20 *Cross-section and microphotograph of the tunable capacitor fabricated using BZN thin films. Source: Adapted from Sudheendran* et al. *2010 [50].*

All microwave measurements are carried out at room temperature using the VNA and GSG probes. A one port open short load calibration procedure is used to measure the S_{11} parameters of the test structures between the central patch and the circular electrode surrounding it. The measured reflection coefficient S_{11} is converted into impedance for the test structure Z_T using [42]

$$Z_T = Z_0 \frac{1 + S_{11}}{1 - S_{11}} = R + jX \tag{9.22}$$

Here, $Z_0 = 50$ ohm. The capacitance and loss tangent of the capacitor can be derived from the complex impedance using the following relations:

$$C = -\frac{1}{\omega X}, \qquad \tan\delta = -\frac{R}{X} \tag{9.23}$$

The relative permittivity of the materials can be calculated using the simple parallel plate model. The real and imaginary parts of the permittivity can also be computed using the ADS momentum electromagnetic simulation tool by fitting the simulated S parameters to the measured one. The dielectric permittivity of these films can also be determined using the analytical procedure developed by Georgian *et al.* [43].

The main task in this measurement procedure is to extract the capacitance C_F and the loss tangent $\tan\delta_f$ of the dielectric films from the calculated capacitance C and the dissipation factor of the test device. These calculated parameters include the parasitic capacitance from the top and outer electrodes and the parasitic resistance between them. To avoid the parasitic effect, a number of CPC structures were designed on the same thin films of thickness t with the same outer electrode radius but with different inner electrode radii a_1. The dielectric constant of the film can be calculated using

$$\varepsilon' = \frac{t\left(\frac{1}{a_2^2} - \frac{1}{a_1^2}\right)(X_1 - X_2)}{\omega\pi\varepsilon_0 \left\{(X_1 - X_2)^2 + \left[R_1 - R_2 - \frac{R_s}{2\pi}\ln\left(\frac{a_2}{a_1}\right)\right]^2\right\}} \tag{9.24}$$

Here X_1, X_2, R_1, and R_2 can be calculated from the measured S_{11} of the CPC structures having the inner radii a_1 and a_2, using Equation (9.24), where R_s is the surface resistance of the bottom electrode.

Similarly, the loss tangent of the film is given by

$$\tan\delta_f = \frac{1}{\omega C_f R_f} = \frac{\frac{R_s}{2\pi}\ln\left(\frac{a_2}{a_1}\right) - R_1 + R_2}{X_1 - X_2} \tag{9.25}$$

The measurement structure consists of a BZN thin film (in the thickness range of 200–350 nm) on top of a 200 nm thick Pt film. The top electrode consists of a 500 nm gold film. Circular patches with different inner diameters ranging from 80 μm to 120 μm and a concentric ground plane with a constant diameter of 300 μm are photolithographically defined without damaging the BZN thin films. The real and imaginary part of the complex reflection coefficient is measured using VNA and a J Microtechnology make LMS-2709 RF

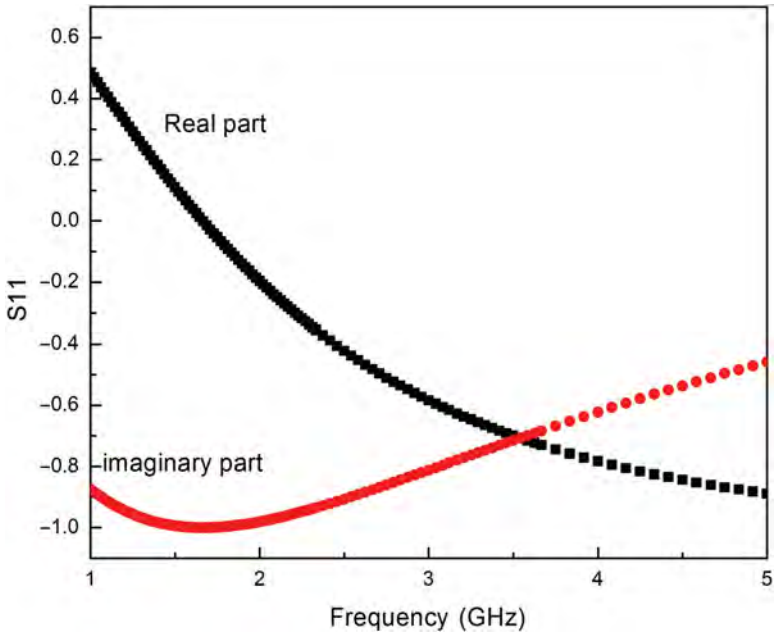

Figure 9.21 *Measured real and imaginary parts of the S_{11} parameter of the CPC capacitor fabricated using c-BZN thin films. Source: Adapted from Sudheendran* et al. *2010 [50].*

probe station mounted with a GSG probe of 250 micrometer pitch. Typical measured real and imaginary parts of the S_{11} parameters of the CPC varactors are shown in Figure 9.21.

9.7 Design and Realization Aspects of Varactors Using Tunable Materials

Varactors are the basic tunable circuit elements in the microwave circuits based on tunable dielectric thin films [44]. Two different approaches are available for the realization of tunable varactors based on the voltage-dependent dielectric materials. The first approach is to place the tunable dielectric thin films between the top and bottom electrodes, which is termed the parallel plate circuit approach and the second approach is to fabricate a set of electrodes on top of the tunable dielectric thin films, which is known as the planar circuit approach [45]. Transmission-line structures with the coplanar-type electrodes is a simple example of the planar-type varactors and the interdigitated electrodes are another type of planar varactor.

This section describes the realization and characterization of parallel plate and interdigitated varactors using cubic bismuth–zinc–niobate (c-BZN) thin films.

9.7.1 Planar and Parallel Plate Structures

A schematic diagram of a typical interdigitated varactor is shown in Figure 9.22. For the interdigitated varactor fabrication, the c-BZN thin film is deposited directly on to the

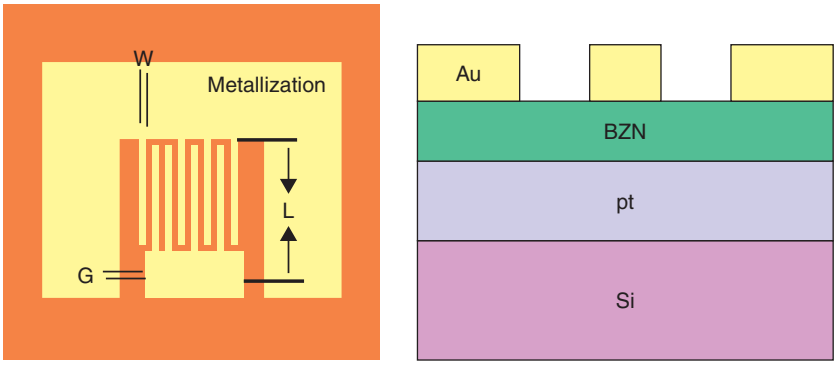

Figure 9.22 *Schematic diagram of the interdigitated and parallel plate varactor in the GSG configuration. Source: Sudheendran 2014 [17].*

substrate and the electrode metallization is patterned on top of the c-BZN thin films. In the interdigitated varactors the minimum gap between the electrodes can be up to 2–3 micrometers using the standard photolithographic techniques. Each IDC varactor realized in this chapter had six pairs of interdigital electrodes having a width (W) of 12 μm and a gap (G) of 8 μm with an overlapping length (L) of 320 μm. These varactors were designed in such a way that they can be probed using a ground signal ground (GSG) probe of 250 μm pitch.

The schematic diagram of the parallel plate c-BZN varactor in the CPC configuration is shown in Figure 9.23. In this configuration the bias field is applied across the thickness of the film, resulting in a lower bias voltage requirement compared to that of an interdigitated capacitor. An advantage of the parallel plate approach is that the integration of tunable components on an industrially important Si substrate can be achieved easily. For the characterization purpose we have designed a parallel plate varactor having circular patch capacitor geometry (CPC). The inner circular patch had diameters of 80, 100, and 120 μm while the outer circular ring had a diameter of 300 μm. The outer circular patch acts as a virtual RF

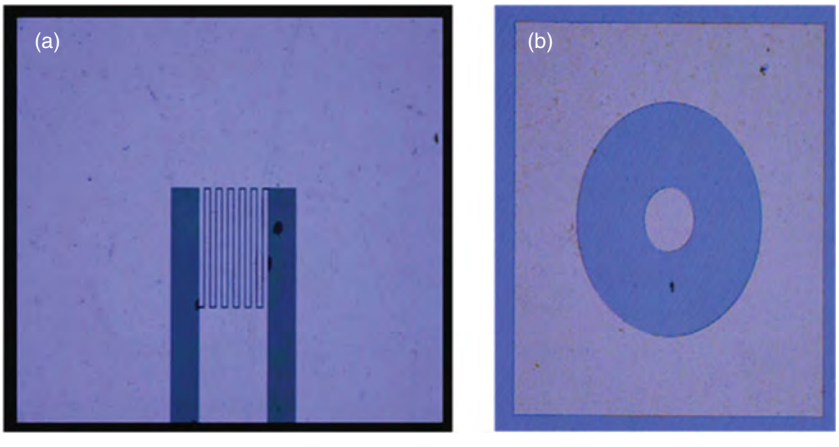

Figure 9.23 *Microphotograph of the fabricated (a) IDC and (b) CPC varactors. Source: Adapted from Sudheendran* et al. *2010 [50].*

ground for the device. These devices were characterized using the GSG probes of 250 μm pitch.

9.7.2 Realization and Characterization of the Varactors

Tunable dielectric thin-film-based varactors have been fabricated on different substrates by various deposition methods, including pulsed laser deposition (PLD), magnetron sputtering, chemical solution deposition (CSD), and metal organic chemical vapor deposition (MOCVD). A typical film thickness is of the order of 500 nm [46]. The pulsed laser deposition (PLD) technique was used to deposit BZN thin films on fused silica and platinized silicon substrates for the realization of an interdigital and parallel plate varactor. Laser power density of 3 J/cm^2 was used in all cases at a repetition rate of 5 Hz. Films were grown in pure oxygen atmosphere at a pressure ranging from 1 to 12 mtorr. The substrate was maintained at ambient temperature during deposition and the films were postdeposition annealed in a furnace at 600 °C in air for 30 minutes. The thickness of the films was measured using a stylus profiler and the films had a thickness of 350 nm.

Standard photolithography and a metal liftoff process were used to define the structure of the interdigital capacitors (IDCs) on the BZN-coated fused silica substrates as well as the parallel plate varactors having the circular patch capacitor (CPC) structures on platinized silicon substrates. A line-positive photoresist from Arch chemicals was used to make a thick layer of photoresist of about 1 micrometer. After the standard UV exposure and development of photoresist, 0.5 μm thick gold electrodes were deposited by RF magnetron sputtering at room temperature followed by a liftoff process to remove the metals in the unwanted places.

The optical microscopic images of the realized IDC and CPC varactors using c-BZN thin films are shown in Figure 9.24. The Agilent 8722ES vector network analyzer (VNA) connected to a J Micro technology make RF probe station mounted with GSG probes from GGB industries was used to characterize the microwave properties of the IDC varactors fabricated using the c-BZN thin films deposited on fused silica substrates. Prior to the testing, the 250 μm pitch GSG probe was calibrated using the CS-5 calibration substrate from GGB industries.

Figure 9.25 shows the calculated capacitance from the measured reflection from the fabricated CPC structure. The capacitance is calculated assuming a parallel resistor–capacitor model for which the admittance is given by coefficient S_{11} of the IDC varactor:

$$Y = Y_0 \frac{1 - S_{11}}{1 + S_{11}} = j\omega C \tag{9.26}$$

Here Y_0 is the reference admittance and S_{11} is the reflection coefficient. The calculated capacitance of the IDC varactor at 4 GHz with 0 V DC bias was 1.067 pF, which was changed to 0.969 pF by application of a 1.2 MV/cm field exhibiting a tunability of 9%. The observed quality factor for the IDC varactors at 4 GHz was about 38. The quality factor of the c-BZN varactors on amorphous fused silica is comparable to that of the reported quality factors of the BST-based varactors [47] on single-crystal sapphire substrates.

The Agilent 4294A impedance analyzer was used to measure the voltage-dependent capacitance and loss tangent values of the CPC varactors fabricated using c-BZN films at low frequencies. A voltage sweep was done from −15 to +15 V for CPC structures. Figure 9.24 shows the capacitance versus voltage characteristics of the CPC structure

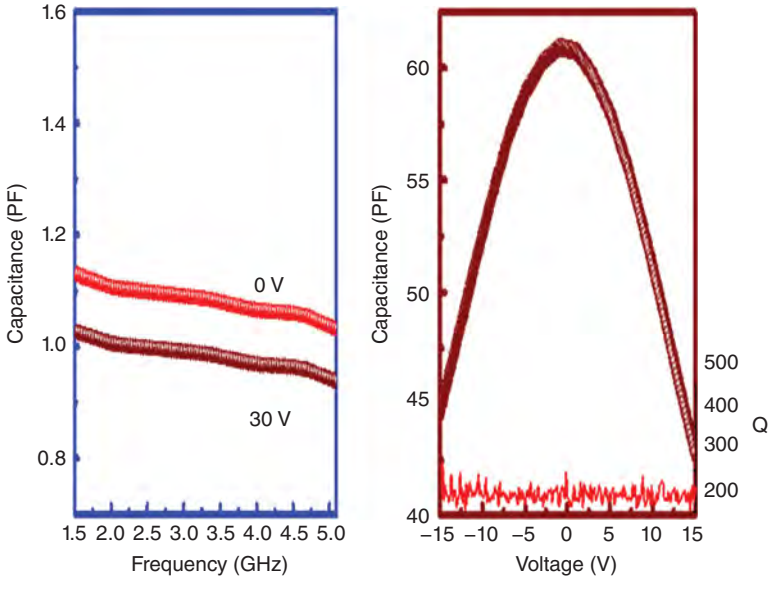

Figure 9.24 *Frequency dependence of capacitance for the IDC varactors fabricated using the c-BZN films measured at different bias fields. Source: Adapted from Sudheendran and James Raju 2010 [50].*

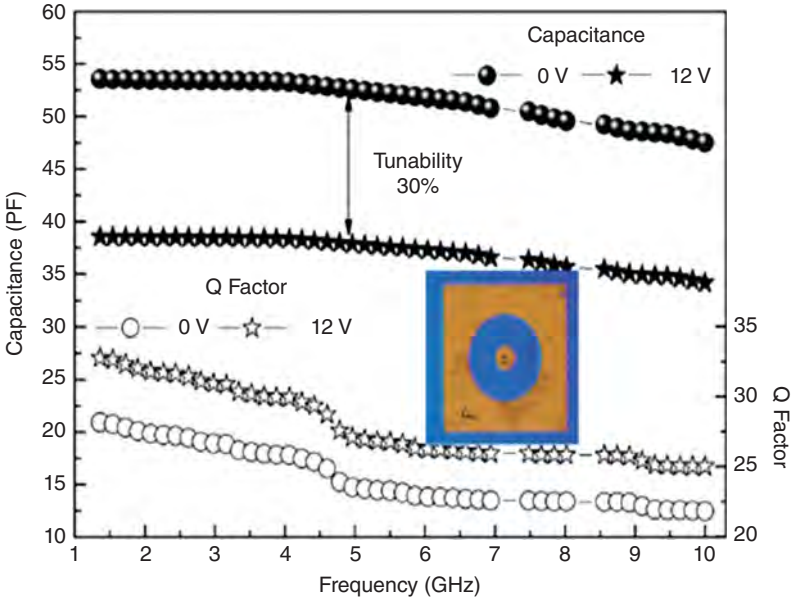

Figure 9.25 *Variation of capacitance and loss tangent with voltage for the CPC varactors fabricated using the BST thin films. Source: Saravanan* et al. *2012 [49].*

fabricated and measured at 1 MHz. The capacitance is changed from 60.8 pF at 0 V to 44.58 pF at 15 V. The percentage of tunability is defined as

$$n = \left[\frac{(C_{0V} - C_{15V})}{C_{0v}}\right] \times 100 \tag{9.27}$$

where C_{0V} and C_{15V} are the capacitance at 0 volt and 15 volts, respectively. Hence the tunability is around 25% at 15 V bias.

The microwave characteristics of the CPC varactors were determined using the Agilent 8722ES VNA connected to a 250 micrometer pitch GSG probe mounted on a J Micro technology make RF probe station. The complex reflection coefficient of the CPC varactors was measured after the standard short–open–load calibration using the CS-5 calibration substrate. The measured reflection coefficient S_{11} is converted into impedance for the test structure Z_T using [48]

$$Z_T = Z_0 \frac{1 + S_{11}}{1 - S_{11}} = R + jX \tag{9.28}$$

where $Z_0 = 50$ ohms. The capacitance and loss tangent of the capacitor can be derived from the complex impedance using the following relations:

$$C = -\frac{1}{\omega X}, \qquad \tan\delta = -\frac{R}{X} \tag{9.29}$$

Figure 9.26 shows the measured voltage-dependent characteristics of the CPC varactors fabricated by the authors using BST [49] and C-BZN films [50] on Pt/Si substrates. It can

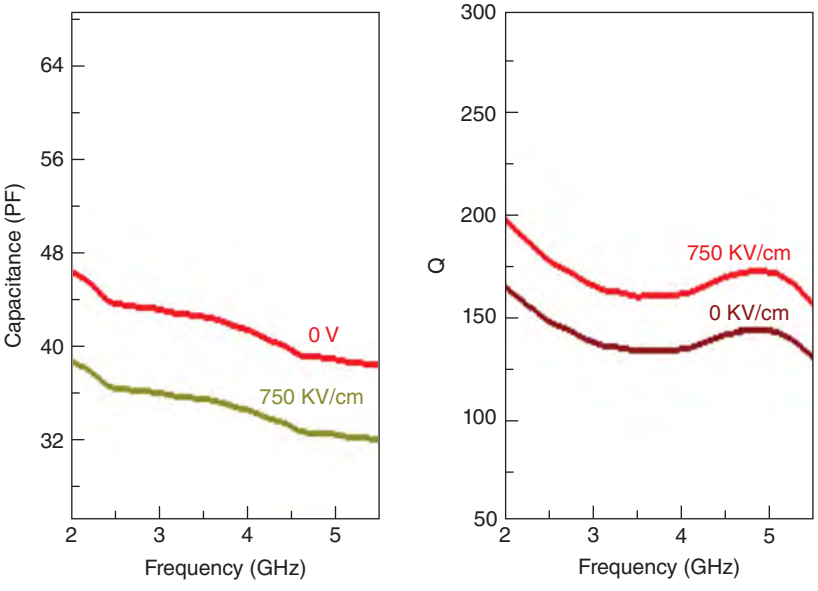

Figure 9.26 *Frequency dependence of capacitance and Q factor for the CPC varactors fabricated using the c-BZN films measured at different bias fields. Figure from the PhD Thesis of K. Sudheendran submitted to University of Hyderabad.*

be seen from the figure that the CPC varactor had a capacitance of 38.78 pF at 5 GHz, which has changed to 32.32 pF with the application of a bias voltage of 15 V, resulting in a capacitive tunability of 16.6%.

9.8 Conclusions

This chapter presented a detailed description about the preparation and characterization of voltage tunable materials for frequency and phase agile microwave devices. Ferroelectric, non-ferroelectric, and multiferroic materials can be used to provide frequency and phase agility for microwave devices. The tunable devices that make use of these agile materials as tuning elements have a good integration advantage since they can be used in thin-film forms suitable for highly integrated microwave devices compatible with planar circuits, with high tuning speeds. It is seen that the metal layer contributes to most of the associated losses compared to the tunable dielectric thin films. Some non-ferroelectric materials also exhibit tunability with lower losses. Multiferroic films are being explored at present for achieving electric field control over magnetic properties as it is more compatible with miniaturization. A continuous effort is being carried out to obtain a ferroelectric material with a low-loss tangent and a high-permittivity tuning range, as this would improve the device performance to a greater extent [51]. A proof-of-concept microwave varactor has been designed, fabricated, and tested with voltage tunable dielectric and ferroelectric material. The demonstrated varactors were showing very good voltage tunability, which is essential for device applications.

Acknowledgment

The authors express their sincere thanks to Prof. Ram S. Katiyar, University of Puerto Rico, Prof. Guru Subramanyam, University of Dayton, and Dr. Venkata Saravanan, Central University of Tamilnadu, for some of the experimental data used in this chapter. KS acknowledges the Science and Engineering Research Board (SERB) of the Government of India for a research project.

References

1. Alexandru, H.V., Berbecaru, C., Ioachim, A., *et al.* (2004) Oxides ferroelectric (Ba, Sr)TiO_3 for microwave devices. *Materials Science and Engineering B*, **109**, 152–159.
2. Gevorgian, S.S. and Kollberg, E.L. (2001) Do we really need ferroelectrics in paraelectric phase only in electrically controlled microwave devices? *IEEE Transactions on Microwave Theory and Techniques*, **49** (11), 2117–2124.
3. Mueller, C.H., Romanofsky, R.R., and Miranda, F.A. (2001) Ferroelectric thin film and broadband satellite systems. *IEEE Potent.*, **1**, 36–39.
4. Wolf, S.A. and Treger, D. (2002) Frequency agile materials for electronics (FAME) – progress in the DARPA program. *Integrated Ferroelectrics*, **42**, 39–55.
5. Miranda, F.A., van Keuls, F.W., Romanofsky, R.R., *et al.* (2002) Ferroelectric thin films-based technology for frequency- and phase-agile microwave communication applications. *Integrated Ferroelectrics*, **42**, 131–149.

6. Subramanyam, G., Van Keuls, F.W., and Miranda, F.A. (2000) A *K*-band frequency agile microstrip bandpass filter using a thin-film HTS/ferroelectric/dielectric multiplayer configuration. *IEEE Transactions on Microwave Theory and Techniques*, **48** (4), 525–530.
7. Tagantsev, A.K., Sherman, V.O., Astafiev, K.F., *et al.* (2003) Ferroelectric materials for microwave tunable applications. *Journal of Electroceramics*, **11**, 5–66.
8. Xi, X.X., Li, H.C., Si, W., *et al.* (2000) Oxide thin films for tunable microwave devices. *Journal of Electroceramics*, **4** (2–3), 393–405.
9. Xu, J., Menesklou, W., and Ivers-Tiffee, E. (2004) Processing and properties of BST thin films for tunable microwave devices. *Journal of European Ceramics Society*, **24**, 1735–1739.
10. Tombak, A., Ayguavives, F.T., Maria, J.P., *et al.* (2001) Tunable RF filters using thin film barium strontium titanate based capacitors. *IEEE MTT-S Digest*, 1453–1456.
11. Subramanyam, G., Mohsina, N., Al Zaman, A., *et al.* (2001) Ferroelectric thin-film based electrically tunable *Ku*-band coplanar waveguide components. *IEEE MTT-S Digest*, 471–474.
12. Chen, W., Yao, X., and Wei, X.Y. (2007) Tunability and ferroelectric relaxor properties of bismuth strontium titanate ceramics. *Applied Physics Letters*, **90** (18), 182902-1-3.
13. Wang, X., Wang, H., and Yao, X. (1997) Structures, phase transformations, and dielectric properties of pyrochlores containing bismuth. *Journal of the American Ceramic Society*, **80** (10), 2745–2748.
14. Wang, H., Elsebrock, R., Schneller, R.T., *et al.* (2004) Bismuth zinc niobate ($Bi_{1.5}ZnNb_{1.5}O_7$) ceramics derived from metallo-organic decomposition precursor solution. *Solid State Communications*, **132**, 481–486.
15. Park, J., Lu, J.W., Stemmer, S., *et al.* (2005) Microwave dielectric properties of tunable capacitors employing bismuth zinc niobate thin films. *Journal of Applied Physics*, **97** (8), 24672.
16. Park, J., Lu, J.W., Boesch, D.S., *et al.* (2006) Distributed phase shifter with pyrochlore bismuth zinc niobate thin films. *IEEE Microwave and Wireless Components Letters*, **16** (5), 264–266.
17. Sudheendran, K. (2014) Recent trends in voltage tunable microwave devices with multiferroic materials. *Recent Patents on Materials Science*, **7** (3), 214–219.
18. Soukup, R.J. (1976) Capacitance of a hyper abrupt tuning varactor diode. *IEEE Transactions on Electron Devices*, **23** (3), 361–363.
19. Dec, A. and Suyama, K. (1998) Micro-machined electro-mechanically tunable capacitors and their applications to RF ICs. *IEEE Transactions on Microwave Theory and Techniques*, **46** (12), 2587–2596.
20. Rijks, G.S.M, Steeneken, P.G., van Beek, J.T.M., *et al.* (2006) Micro-electro mechanical tunable capacitors for reconfigurable RF architectures. *Journal of Micromechanics and Microengineering*, **16**, 601–611.
21. Sudheendran, K., Krishna, M.G., and James Raju, K.C. (2009) Effect of process parameters and post-deposition annealing on the microwave dielectric and optical properties of pulsed laser deposited $Bi_{1.5}Zn_{1.0}Nb_{1.5}O_7$ thin films. *Applied Physics A*, **95**, 485–495.
22. Chrisey, D.B., Hubler, G.K. (1994) *Pulsed Laser Deposition of Thin Films*, John Wiley & Sons.
23. Pavunny, S.P., Misra, P., Scott, J.F., and Katiyar, R.S. (2013) Advanced high-*k* dielectric amorphous $LaGdO_3$ based high density metal–nsulator–metal capacitors with sub-nanometer capacitance equivalent thickness. *Applied Physics Letters*, **102** (25), 252905.
24. Schneller, T., Waser, R., Kosec, M., Payne, D. (eds) (2013) *Chemical Solution Deposition of Functional Oxide Thin Films*, ISBN 978-3-211-99310-1, Springer.
25. http://www.emrl.de/r_m_6.html.
26. Sudheendran, S., Pavunny, S.P, Instan, A.A., and Katiyar, R.S. (2015) The thermal stability of voltage tunability in pulsed laser deposited $Ba_{0.6}Sr_{0.4}TiO_3$ thin films. *Integrated Ferroelectrics*, **166** (1), 140–149.
27. Sudheendran, K. and James Raju, K.C. (2010) Microwave characterization technique for high *K* thin films. *Key Engineering Materials*, **421**, 73–76.
28. Altschuler, H.M. (1963) In *Handbook of Microwave Measurements*, vol. 2, Brooklyn Polytechnic Press, New York, p. 530.
29. Sudheendran, K., Pamu, D., Krishna, M.G., and James Raju, K.C. (2010) Determination of dielectric constant and loss of high-*K* thin films in microwave frequencies. *Measurement*, **43**, 556–562.

30. Thomas, R. and Dube, D.C. (1997) Extended technique for complex permittivity measurement of dielectric films in the microwave region. *Electronics Letters*, **33**, 218–220.
31. Subrahmanian, V., Bellubai, B.S., and Sobhanadri, J. (1993) A new technique of measuring the complex dielectric permittivity of liquids at microwave frequencies. *Reviews of Scientific Instruments*, **64**, 231–233.
32. Dube, C., Lanagan, M.T., Kim, J.H., and Jang, S.J. (1988) Dielectric measurement on substrate materials at microwave frequencies using a cavity perturbation technique. *Journal of Applied Physics*, **63**, 2466–2468.
33. Chen, L., Ong, C.K., and Tan, B.T.G. (1999) Amendment of cavity perturbation method for permittivity measurement of extremely low-loss dielectrics. *IEEE Transactions on Instruments and Measurements*, **48**, 1031–1037.
34. Subramanyam, G., Heckman, E., Grote, J., and Hopkins, F.K. (2005) Dielectric properties of DNA based polymers between 10 and 30 GHz. *IEEE Microwave Wireless Technology Letters*, **15**, 232–234.
35. Gevorgian, S.S. (1994) Basic characteristics of two layered substrate coplanar waveguides. *Electronics Letters*, **30** (5), 1236.
36. Lue, H.T. and Tseng, T.Y. (2001) Application of on-wafer TRL calibration on the measurement of microwave properties of $Ba_{0.5}Sr_{0.5}TiO_3$ thin films. *IEEE Transactions on Ultrasonic, Ferroelectrics, and Frequency Control*, **48** (6), 1640.
37. Holloway, C.L. and Kuester, E.F. (1995) A quasi-closed form expression for the conductor loss of CPW lines, with an investigation of edge shape effects. *IEEE Transactions on Microwave Theory and Techniques*, **43** (12), 2695.
38. Lancaster, M.J., Powell, J., and Porch, A. (1998) Thin-film ferroelectric microwave devices. *Superconductor Science and Technology*, **11** (11), 1323–1343.
39. Defay, E., *et al.* (2009) Ferroelectric properties of Pb(Zr, Ti)O_3 thin films until 40 GHz. *Applied Physics Letters*, **94**, 4563.
40. Suherman, P.M., *et al.* (2006) Microwave properties of $Ba_{0.5}Sr_{0.5}TiO_3$ thin film coplanar phase shifters. *Journal of Applied Physics*, **99**, 104101.
41. Ikuta, K., Umeda, Y., and Ishii, Y. (1995) Measurement of high-frequency dielectric characteristics in the mm-wave band for dielectric thin films on semiconductor substrates. *Japan Journal of Applied Physics*, **34**, L1211.
42. Ma, Z.X., Becker, A.J., Polakos, P., *et al.* (1998) RF measurement technique for characterizing thin dielectric films. *IEEE Transactions on Electrical Devices*, **45**, 1811.
43. Vorobiev, A., Kuylenstierna, D., Rundqvist, P., and Gevorgian, S. (2006) In *Proceedings of the 36th European Microwave Conference*, Manchester, UK, pp. 843–886.
44. Rundqvist, P., Vorobiev, A., Gevorgian, S., and Khamchane, K. (2004) Nondestructive microwave characterization of ferroelectric films on conductive substrates. *Integrated Ferroelectrics*, **60**, 1.
45. Saad, M.M., Baxter, P., Bowman, R.M., Gregg, J.M., Morrison, F.D., and Scott, J.F. (2004) Intrinsic dielectric response in ferroelectric nano-capacitors. *Journal of Physics: Condensed Matter*, **16**, L451.
46. Zhang, X.Y., Wang, P., Sheng, S., *et al.* (2008) Ferroelectric $Ba_xSr1\text{-}xTiO_3$ thin-film varactors with parallel-plate and interdigital electrodes for microwave applications. *Journal of Applied Physics*, **104**, 124110.
47. Vorobiev, A., Rundqvist, P., Khamchane, K. and Gevorgian, S. (2004) Microwave loss mechanisms in $Ba_{0.25}Sr_{0.75}TiO_3$ thin film varactors. *J. Applied Physics*, **96**, 4642.
48. Khamchane, K., Vorobiev, A., Claeson, T., and Gevorgian, S. (2006) $Ba_{0.25}Sr_{0.75}TiO_3$ thin-film varactors on $SrRuO_3$ bottom electrode. *Journal of Applied Physics*, **99**, 034103.
49. Saravanan, V., Sudheendran, K., and James Raju, K.C. (2012) Tunable dielectric characteristics of (111)-oriented barium strontium titanate thin films deposited on platinized Si substrates. *Electronic Materials Letters* **8** (6), 571–575.
50. Sudheendran, K. and James Raju, K.C. (2010) Realization of tunable varactors using bismuth zinc niobate thin films. *Key Engineering Materials*, **422**, 153–156.
51. Guru, S., Cole, M.W., Nian, X., *et al.* (2013) Challenges and opportunities for multi-functional oxide thin films for voltage tunable radio frequency/microwave components. *Journal of Applied Physics*, **114**, 191301.

10
Dielectric Inks

J. Varghese and M.T. Sebastian
Microelectronics Research Unit, Faculty of Information Technology and Electrical Engineering, University of Oulu, Oulu, Finland

10.1 Introduction

In the early 1800s, Thomas Edison described a method for producing conductors on linen paper, which is the first mention of ink in the literature. Specifically, the first conductive ink was patented by Voigt and Haeffner in 1899 [1]. The first article published on printed circuits dates back to the mid-1940s. Based on these publications, the printing of conductors was not only for circuits but also for resistors, capacitors, inductors, and combinations of them [2, 3]. The era of printed electronics from the past, present, and future is shown in Figure 10.1 [4]. The past nineteenth century to the present twenty-first century highlights the major development of printed electronic devices starting from a conductor on linen paper, RFID tags, photovoltaics, flexible display, immune sensor, printed 3D antenna, storage devices, printed supercapacitor, printed loudspeaker, etc. Nowadays, there is considerable interest in printed electronics, from partially printed to fully printed devices. This includes printed OLED displays [5], RFIDs [6], sensors [7], thin-film transistors [8], solar cells [9], batteries [10], and many other components.

In principle, printed electronic circuits (PEC) involve a direct printing process using conductive/dielectric paste on flexible substrates such as polymer–ceramic laminates and hence eliminate the required traditional subtractive wet process such as etching, stripping, metallization, and copper plating used in the current "silicon electronics". The traditional method is a time-consuming process, often requiring a high vacuum with material wastage greater than 90%. This increases the cost due to the excess disposal of the waste material. On the other hand, a printed electronic circuit uses about 20% of the current labour requirement

Microwave Materials and Applications, First Edition.
Edited by Mailadil T. Sebastian, Rick Ubic and Heli Jantunen.
© 2017 John Wiley & Sons, Ltd. Published 2017 by John Wiley & Sons, Ltd.

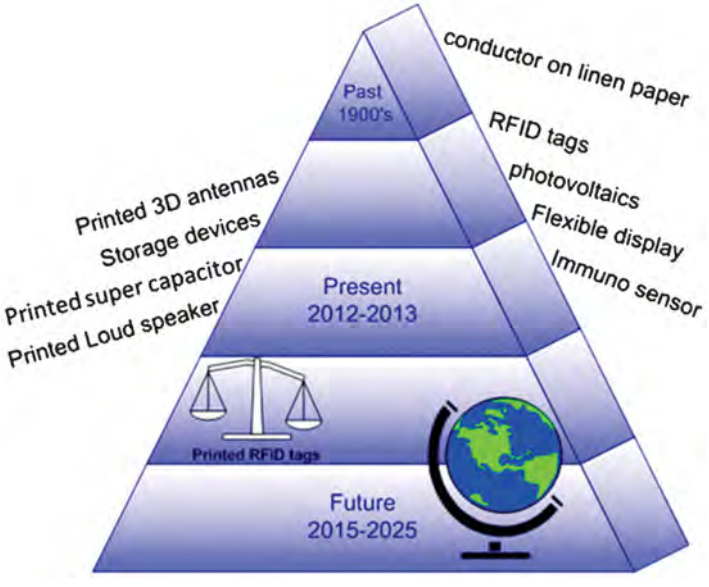

Figure 10.1 *Printed electronics: past, present, and future.*

for the traditional method. Printing technology has several advantages such as different materials patterning, high throughput, low cost, and minimum material wastage.

These advantages of printed electronics and possibly future low-cost technology are attracting substantial research attention. The number of papers published in the area of printed electronics considerably increased, as shown in Figure 10.2, during 1975–2014. The above publication survey is based on the publication types, such as research articles, conference papers, reviews, books, etc., reported in the Scopus database. Recently a few reviews on printed electronics have been reported in the literature [11–14]. The need for further miniaturization, technological advances, and portability demands of electronic devices in different sectors such as telecommunication, intelligent packaging, automotive industry, and medicine are driving the demand for printed electronic products in the market. According to a printed electronic market survey, the printed electronics market is estimated to grow at a CAGR of 33.8% from 2014 to 2020 and it is estimated to reach $40.2 billion by 2020 [15]. The tantalizing goals such as the projected multibillion dollar market for low-cost printing technologies arrives as no surprise as tremendous effort has been directed towards the development of affordable grooming methods of printing ink. Many new industries such as DuPont, Nova Centrix, NTERA, RADTECH, etc., have opened up recently in this growing area. The increasing number of publications every year as well as market growth indicates the demand for suitable ink materials, devices, and new printing techniques for printed electronics.

The most common applications of printing inks are for conducting channels. Silver is used as a common conductor ink, but aluminium, copper, gold, and platinum are also used for certain specific purposes [16–20]. In addition to conductor inks, dielectric thick film inks are mainly used in three primary applications such as circuit protection from the

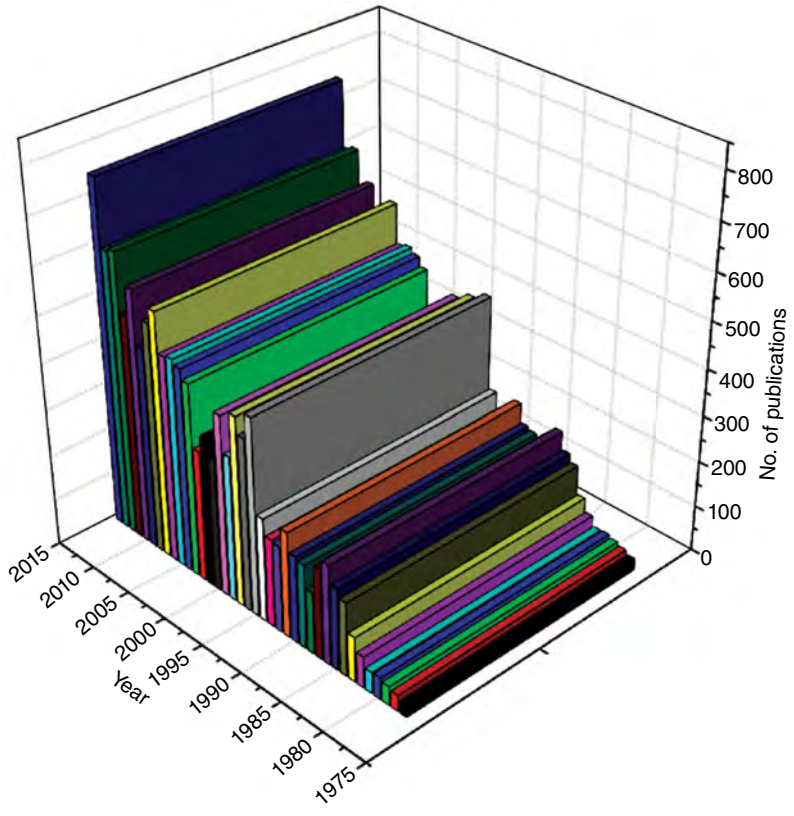

Figure 10.2 *Publication survey of printed electronics.*

hostile environment, crossover and multilayer insulation, and capacitors. One of the early reviews of Finch in 1969 states that dispersion of dielectric powder can be screened and heat treated to produce hermetic seals, overglazes, crossovers, and capacitors [21]. Most of the reported ink compositions are based on ceramic–glass composites [21]. During 2000 and 2001 Thiele *et al.* reported the dielectric, piezoelectric, and ferroelectric properties of screen printed layers of lead zirconate titanate [22, 23]. This ink consists of PZT (BM500 grade) with 3 wt% of B_2O_3–Bi_2O_3–CdO and borosilicate glass, respectively. In addition to filler, they used terpinol as solvent, ethyl cellulose as binder, and phosphate ester as dispersant in the colloidal suspension [23]. More recently dielectric thick films have been widely used in photovoltaics as a photoelectrode in dye-sensitized solar cells (DSSC) [24]. Low and high *k* dielectrics are used as a gate electrode in thin-film transistors (TFTs) as well as in memory devices [25, 26].

Recently several low and high relative permittivity screen printable inks have been reported. Hou *et al.* have reported screen-printable P(VDF–TrFE)/PMMA/$BaTiO_3$/silica (SII) dielectric ink for organic field-effect transistors (OFETs) [27]. The epoxy/$BaTiO_3$ nanocomposite dielectric is reported to have a capacitance of 6 nF/cm^2 with high relative permittivity of 35 at 30 kHz [28]. It has also been reported that increasing the loading of

nanopowders in P(VDF–TrFE) results in relative permittivity up to 51.5 [29]. Recently, Sun *et al.* reported electrical properties of screen-printed doped ceria interlayer for IT-SOFC (intermediate temperature–solid oxide fuel cells) applications [30]. Low-frequency passive components including resistors, capacitors, and inductors have been reported for printed electronic applications up to 10 MHz [31]. However, multilayer printed MIM (metal–insulator–metal) structures have not yet been realized with optimized properties for microwave applications. Despite the enormous demand, very little attention was paid to the development of low-permittivity and low-loss screen printable inks for microwave applications. Recently a few low-loss printable dielectric materials have been reported and are given in Table 10.1. The microwave dielectric properties of printed layers were first reported

Table 10.1 *Dielectric properties of printed layers*

Serial number	Printed dielectric layers with substrates	ε_r with frequency	tan δ	Reference
1	SiO_2 on BoPET	2.4–2.3 (8.2–18 GHz)	0.003–0.006	32
2	$ZrSiO_4$ on BoPET	3.4–3.3 (8.2–18 GHz)	0.003–0.0057	33
3	TiO_2 on PET	17.9 (100 kHz)	Unknown	34
4	Barium titanate filled LuxPrint-8153 on polyester (DuPont)	35	Unknown	35
5	$BaTiO_3$–lanthanum nitrate hexahydrate–63 wt% PbO–25 wt% B_2O_3–12 wt% SiO_2	78 (1 MHz)	0.02	36
6	$BaTiO_3$–antimony acetate–63 wt% PbO–25 wt% B_2O_3–12 wt% SiO2	38 (1 MHz)	0.02	36
7	$BaTiO_3$–63 wt% PbO–25 wt% B_2O_3–12 wt% SiO_2	112 (1 MHz)	0.02	36
8	TiO_2 on BoPET	6.9 (15.1 GHz)	0.08	37
9	PZT 40 vol.%+ PVDF–TrFE copolymer	34 (1 MHz)	0.09	38
10	Al_2O_3 on BoPET	2.9 (15 GHz)	0.004	39
11	Al_2O_3 on photographic paper	3.3 (15 GHz)	0.08	39
12	α-$MnMoO_4$ on organic substrate	12 (1 GHz)	0.1	40
13	PZT on Polyimide	~ 80 (1 KHz)	~ 0.03	41
14	BST–ZnO–B_2O_3 composite layer	144 (10 GHz)	0.03	42
15	$Bi_2Mo_2O_9$ on Al_2O_3 Substrate	35 (5–19 GHz)	0.001	43

by Liu *et al.* in 2010 [43]. They developed screen printable $Bi_2Mo_2O_9$ dielectric ink suitable for firing temperature at 645 °C. At a low frequency of 5 MHz a printed $Bi_2Mo_2O_9$ layer on Al foil sintered at 645 °C shows a relative permittivity of 38 and dielectric loss of 0.7%. The printed $Bi_2Mo_2O_9$ layer on alumina substrate shows a relative permittivity of ∼ 35 and quality factor ∼ 12 500 GHz using a split post dielectric resonator technique [43]. The microwave dielectric properties of room temperature curable and screen printable dielectric ink formulation was reported by Varghese *et al.* in 2014 [32, 33]. In this chapter we discuss the formulation and characterization of room temperature curable dielectric inks based on SiO_2, $ZrSiO_4$, and Al_2O_3 ceramics for screen printable microwave applications. A brief summary about low-temperature polymer-based and commercial dielectric inks, properties, and applications are also discussed in this chapter.

10.2 Methodology

10.2.1 Formulation of Printing Inks

Printing uses a typical paste or ink with low or high viscosity that ensures adequate colloidal stability for various printing methods such as screen, inkjet, gravure, flexo, offset, and 3D printing. Most of the printing inks designed should have both pseudoplastic and thixotropic properties. The viscosity of such materials decreases upon shear rate and recover to high viscosity upon removal of the shear stress after a short period. In general, most of the inks were prepared in a two-stage process, as shown in Figure 10.3. The first stage of a process flowchart is the ball milling of filler for 6–12 hours with solvent and dispersant. Initially, the filler particle is dispersed in the solvent and dispersant with adequate sedimentation control. In the second stage, the binder is added and milled again for 6–12 hours with controlled

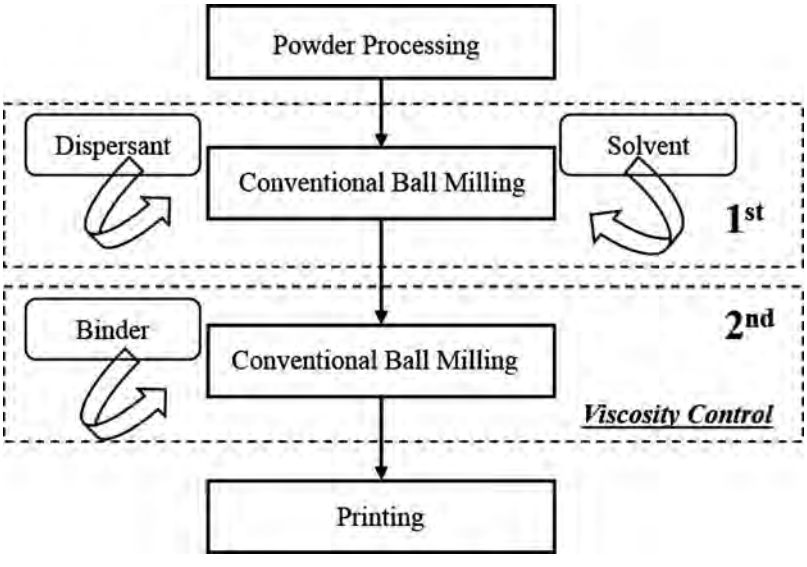

Figure 10.3 *Process flowchart of printing ink.*

Table 10.2 *Parameters for various printing methods*

Printing	Layer thickness (μm)	Resolution (μm)	Viscosity (mPa s)	Reference
Screen	3–100	20–100	500–50000	44
Inkjet	0.3–20	20–50	1–30	44
Gravure	0.8–8	75	50–200	44
Flexo	0.8–2.5	80	50–500	44
Offset	0.5–2	20–50	30 000–100 000	44
3D	100+	100	1–500	45

viscosity, while in the case of a polymer-based dielectric ink, filler, which is a polymer, is directly dissolved in the solvent and is a one-stage process. In the case of 3D printing, the system combines mechanical and pneumatic devices so that a higher force can be applied to the printing materials.

The process flowchart of ink formulation given in Table 10.2 is suitable for all printing methods except 3D printing. The printing parameters such as layer thickness, resolution, and ink viscosity for various printing methods such as screen, inkjet, gravure, flexo, offset, and 3D printing are given in Table 10.2. Screen printing and inkjet printing techniques are most commonly used for the fabrication of functional layered products. The 3D printing is the technique for future functional front end products. The final composition of the dielectric ink is ready for printing after the completion of the second stage of milling. The ideal behavior of a printing ink is difficult to set and can be controlled by selection of a high molecular weight polymer as well as a suitable solvent combination. The use of ceramic filler constituents of proper particle size and addition of dispersant and binder are also important factors governing the behavior of the printing inks. Table 10.3 represents the commonly used solvents, dispersants, and binders used for good colloidal stability of the printing ink.

In the present chapter, we discuss in detail the high-purity SiO_2, $ZrSiO_4$, and Al_2O_3 ceramic-based screen printing ink prepared by the tumbling ball milling technique. The ceramic powders were preheated at 600 °C for 30 minutes to remove the moisture and organic contaminants during powder processing. A mixture of anhydrous xylene/ethanol was used as an organic solvent for preparation of the dielectric ink. Fish oil was used as the dispersant and polyvinyl butyral as the binder in the colloidal suspension.

10.3 Dielectric Inks and Their Properties

10.3.1 Preliminary Treatment of Ceramic Particles

In a colloidal ink, a small filler particle size, low density, and a uniform distribution of filler are required to promote good stability of the suspension, for obvious reasons. In this regard, three key parameters to be controlled in powder processing are the phase purity, average particle size, and distribution. The structure, dielectric, and thermal properties of the bulk SiO_2, $ZrSiO_4$, and Al_2O_3 powders are given in Table 10.4.

Figure 10.4a and b shows the particle size distribution of preheated and phase pure SiO_2 and $ZrSiO_4$ ceramics. In Figure 10.4a, s1, s2, and s3 represent the particle size distribution

Table 10.3 *Commonly used screen printing solvents, dispersants, and binders*

Serial number	Solvent	Dispersant	Binder	Reference
1	Cyclopentanone	NA	Photoresist (SU-8)	31
2	1-Hexanol	Poly melamine–co-formaldehyde	Poly (4-vinylphenol) (PVP)	31
3	Xylene/ethanol	Fish oil	Polyvinyl butyral B-98	46
4	Water	PEG, glycerol, PPG	PVA	46
5	Texanol ester alcohol	Hypermer KD15	Ethyl cellulose N7 grade	46
6	Methyl ethyl ketone/ethyl alcohol	Polyester/ polyamine copolymer	Acrylic copolymer: methyl ethyl ketone (50:50 wt%)	46
7	Water	NA	Cellulose ether	47
8	Terpinol	NA	Ethyl cellulose	47
9	Glycol or Polyglycol	NA	Xantangum/ modified cellulose	47
10	Methyl ethyl ketone	NA	Ethyl methacrylate co-polymer:MEK (50:50 wt%)	47
11	*N*-methyl-2 pyrrolidone (NMP)	NA	Poly(vinylidene fluride) PVDF	47
12	Naptha (PC/SN)	NA	Poly (carbonate)	47
13	Ethylene glycol diacetate (EGDA)	NA	Poly (methyl methacrylate) (PMMA)	47
14	Dimethyl acetamide (DMAC)	NA	Poly (sulfone) (PS)	47
15	Alpha-terpineol	NA	Ethyl cellulose (EC)	47

of preheated SiO_2 at different concentrations in order to confirm the average particle size distribution. Evidently, the particle size distribution is in a broad range of 100–1000 nm with an average particle size of 420 nm. The microstructure of the filler particle distribution is shown in the inset and is consistent with the particle size distribution determined through particle size analysis. Raw correlation data in the measurement accuracy of the particle size analysis are given in Figure 10.4a. Similarly, Figure 10.4b represents the particle size distribution of preheated $ZrSiO_4$; the average particle size distribution is in the broad range of 500–1000 nm with an average particle size of 776 nm. The average particle size distribution of preheated Al_2O_3 ceramics is 260 nm [39]. The particle size and phase purity are

Table 10.4 *Structure dielectric and thermal properties of SiO_2, $ZrSiO_4$, and Al_2O_3 ceramics*

		Dielectric properties at 1 MHz		Thermal Properties		
Materials	Structure	ϵ_r	tan δ	Thermal conductivity at 25 °C (W/m K)	Coefficient of thermal expansion 25–300 °C (ppm/°C)	Reference
SiO_2	Hexagonal	3.8–5.4	0.003	1.25	0.3–0.4	48
Al_2O_3	Trigonal	8.8–10.1	0.0003–0.002	25–30	8	48
$ZrSiO_4$	Tetragonal	8.6–11	0.001	15	±2	4, 49

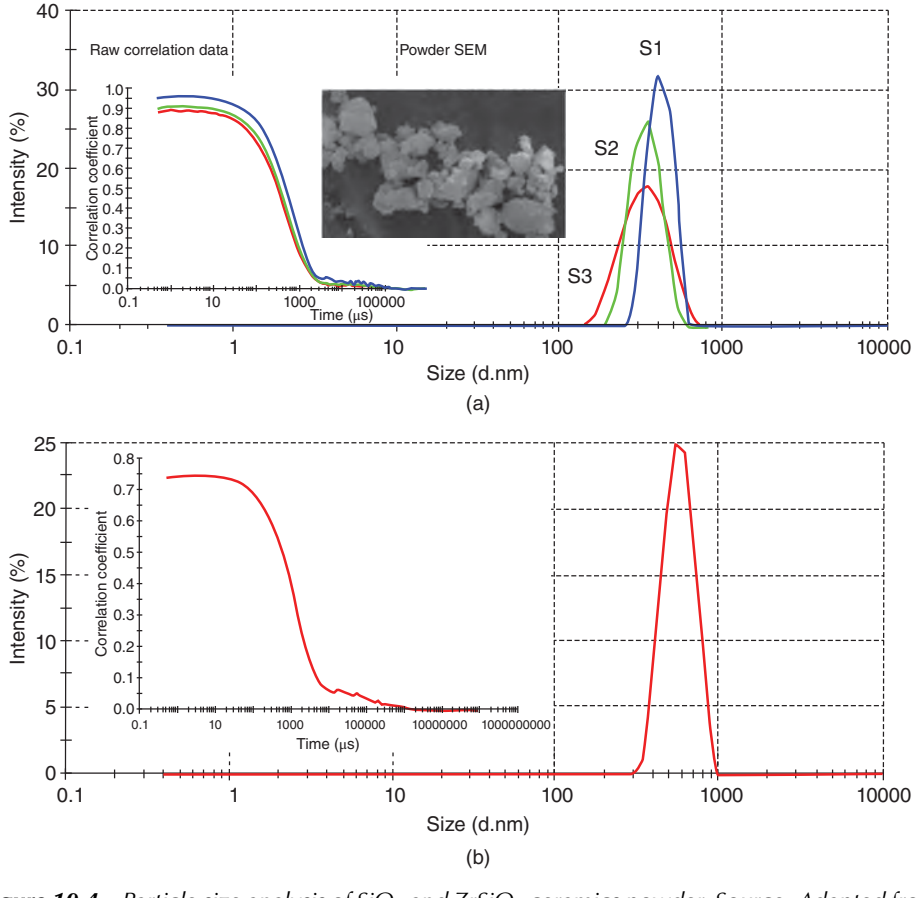

Figure 10.4 *Particle size analysis of SiO_2 and $ZrSiO_4$ ceramics powder. Source: Adapted from Varghese* et al. *[32, 33].*

two important parameters that control the colloidal stability of the suspension [32,33]. The particle size required for the screen printing application is in the range 100–1000 nm.

10.3.2 Raw Materials Selection and Optimization for Screen Printable Ink

A screen printing ink requires a very careful balance of formulation to meet the stringent requirements of the printing process and the end use properties. Many of these properties are controlled by a suitable choice of the solvent, dispersant, and binder that constitute the ink vehicle. A proper combination of these components with maximal filler loading can generate a well-dispersed colloidal mixture, possessing an ideal range of viscosity (5–10 Pa s at 10 1/s) [44, 48, 50,51] suitable for screen printing. In the ink composition, the dispersant is used to avoid particle coagulation. Solvents are the ink vehicle that is essential for printing, drying, and storage. Polymeric binders supply the network that holds the entire chemical system.

An equimolar mixture of anhydrous xylene and ethanol is chosen as the ideal solvent system in the preparation of SiO_2 and $ZrSiO_4$ based dielectric ink, which is found to be facilitating a fast drying rate at room temperature [32, 33]. It is found that [32, 33, 39] the use of multiple solvents in colloidal ink formulation is advantageous because of its high solubility, greater control over drying rate, and cost effectiveness. Moreover, the anhydrous xylene/ethanol solvent mixture is fairly non-reactive with most of the ceramics [46].

Fish oil is chosen as the dispersant for dielectric ink formulation and its concentration is optimized by rheology measurements. Figure 10.5a shows the variation of viscosity as a function of shear rate of the colloidal mixture. The rheology measurement were performed by fixing the filler loading (SiO_2) as a constant at 60 wt% of the total ink weight and gradually varying the concentration of the dispersant with respect to the dielectric filler loading. The viscosity of the colloidal mixture is found to be decreasing with an increase in shear rate and maintains a pseudoplastic nature for 1 wt% fish oil. The optimal viscosity of 7 Pa s at 10 1/s shear rate is observed, which is in the suitable range of viscosity required for screen printing inks. The viscosity analysis for dispersant optimization reveals that 1 wt% dispersant is enough to effectively disperse the SiO_2 particles prior to the binder addition. For filler

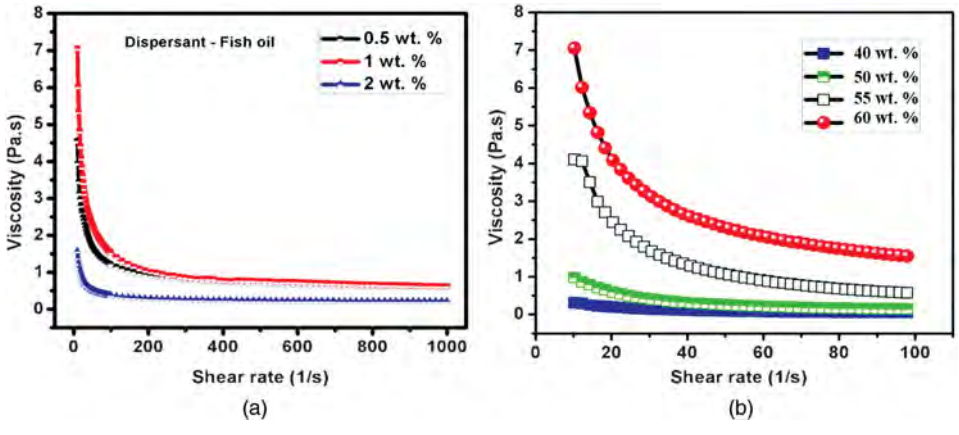

Figure 10.5 *(a) Dispersant and (b) filler (SiO_2) optimization. Source: Adapted from Varghese* et al. *[32, 33]*

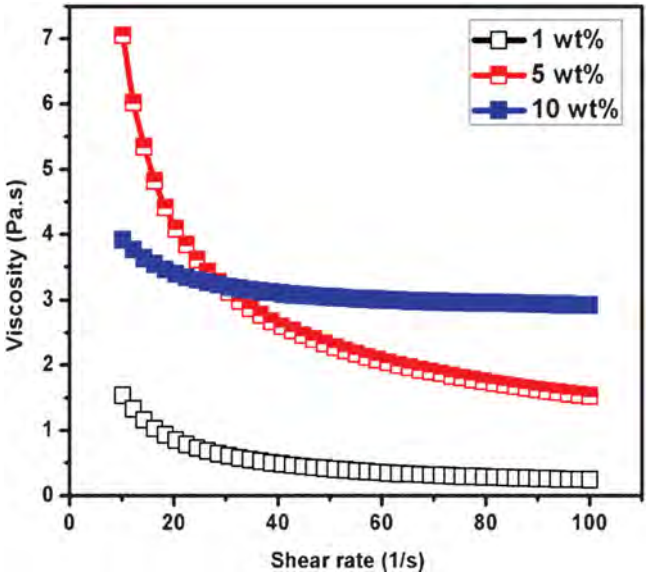

Figure 10.6 *Binder optimization for SiO_2 ink. Source: Adapted from Varghese* et al. *[32, 33]*

loading optimization, the concentrations of the dispersant (fish oil) and binder (polyvinyl butyral) were fixed arbitrarily with respect to the filler loading at 1 wt% and 5 wt%, respectively. Figure 10.5b shows the variation of viscosity as a function of shear rate for various filler loadings ranging from 40 to 60 wt%. A shear-thinning behavior, which is typical of the colloidal inks, can be observed in Figure 10.5b. It is found that the maximum attainable SiO_2 filler loading in the ink formulation is 60 wt% and further increases in the filler content may lead to clogging [32, 33].

Polyvinyl butyral (PVB), a commonly used binder for printing in the textile industry, is qualified as the binder in the silica ink formulation because of its outstanding binding efficiency, optical clarity, better adhesion to a number of surfaces, and toughness combined with flexibility. The use of PVB for ink formulation can bring about considerable influence over the strength, flexibility, plasticity, printability, and smoothness of the printed surface [46]. The binder loading is optimized by keeping the concentration of the filler and dispersant as constants. As seen in Figure 10.6, the concentration of the binder is varied from 1 to 10 wt% with respect to the maximum filler loading. A viscosity of about 1.5 Pa s is achieved by the addition of 1 wt% binder and increases to nearly 7 Pa s when the binder content is increased to about 5 wt% at a shear rate of 10 1/s. Further increase in the binder content decreases the viscosity of the ink, which limits the smooth screen printing.

10.3.3 Rheology of Dielectric Inks

The ink consisted of 60 wt% of SiO_2 or $ZrSiO_4$ ceramic filler, 35 wt% of anhydrous xylene/ethanol (solvent system), 1 wt% of dispersant (fish oil), and 5 wt% of polyvinyl butyral (binder) with respect to the filler. Similarly, for Al_2O_3 the ink composition consisted of 70 wt% of Al_2O_3 ceramic filler, 30 wt% of anhydrous xylene/ethanol (solvent system),

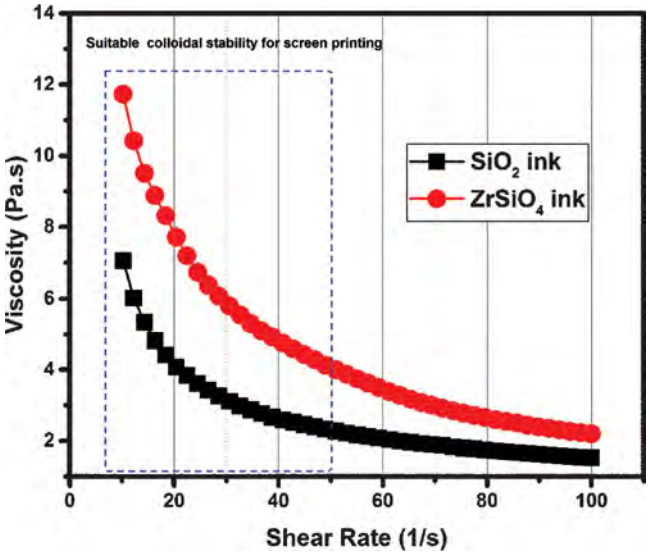

Figure 10.7 *Final dielectric ink rheology. Source: Adapted from Varghese* et al. *[32, 33].*

2.5 wt% of dispersant (fish oil), and 5 wt% of polyvinyl butyral (binder) with respect to the filler [39]. Generally, viscosity required for screen printing application is above 5 Pa s at the shear rate of above 10/s with a pseudoplastic nature of suspension [32,33, 50,51]. Figure 10.7 shows the rheological characteristics of optimized SiO_2 and $ZrSiO_4$ and ceramic inks. Both inks showed a pseudoplastic nature, that is, the viscosity decreased with increasing shear rate. The formulated ink showed a viscosity of about 7 and 12 Pa s at a lower shear rate of 10/s, respectively, for SiO_2 and $ZrSiO_4$ ink, while at a higher shear rate of 100/s the viscosity decreased down to below 3 Pa s. The viscosity of the inks proved to be feasible for screen printing and maintained colloidal stability. It is found that both the SiO_2 and $ZrSiO_4$ ceramic inks cure in less than 10 minutes depending on the atmospheric conditions.

10.3.4 Microstructure and Surface Roughness of Printed Layers

The adhesion strength of the screen printed SiO_2, and Al_2O_3 ink on BoPET film was studied using a scotch test analysis, which was performed on freshly printed patterns after 5, 10, 15, 20, 25, and 30 minutes after printing. The scotch tape test qualitatively confirms that the screen printed layers show good adhesion to the BoPET film even for a single print stroke. Figure 10.8 shows the scotch tape test before and after analysis of Al_2O_3 dielectric ink printed on BoPET substrate [39].

The print quality of the ink is examined by optical microscopy images of the printed patterns. The optical micrograph of the patterns manually printed on BoPET film is shown in Figure 10.9a) to d. In manual screen printing, it is difficult to control the levelling time and snap-off. Mesh openings are clearly visible in the optical image (Figure 10.9a and c) of the printed SiO_2 and $ZrSiO_4$ ink surfaces obtained by the first print stroke. The surface finish of the printed layer can be improved by performing multiple printing strokes. This is

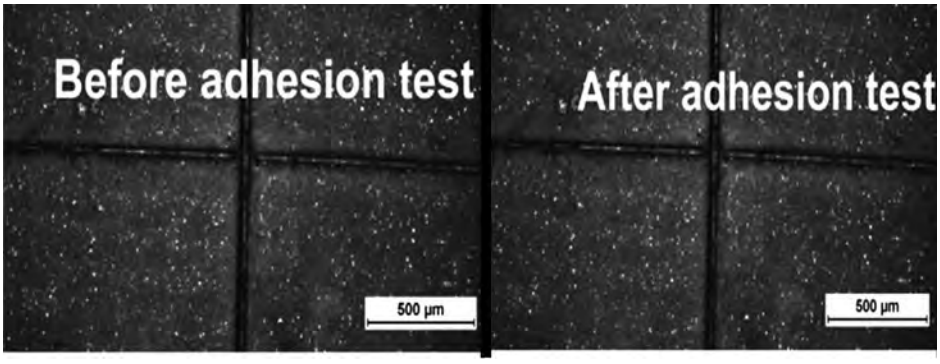

Figure 10.8 *Optical microscopy image before and after adhesion test of Al_2O_3 layer on BoPET. Source: Adapted from Nair* et al. *2016 [39].*

clear from Figure 10.9b and d, where fewer mesh openings are only visible with a printed layer of nearly 50 µm thickness, which is achieved by two-stroke printing. The two-stroke printed SiO_2 and $ZrSiO_4$ inks are chosen for further characterization. The surface morphology of the printed layer is an important factor governing the performance of advanced printed electronic devices. The microstructure of SiO_2 and $ZrSiO_4$ inks and BoPET film

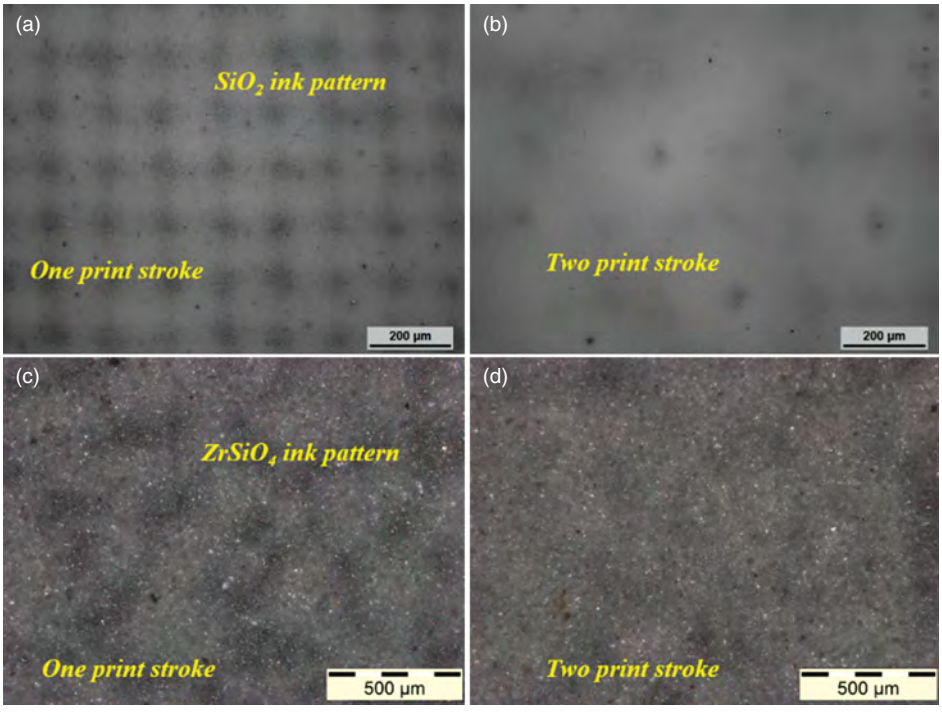

Figure 10.9 *Optical microscopy image of printed layers. Source: Adapted from Varghese* et al. *[32, 33].*

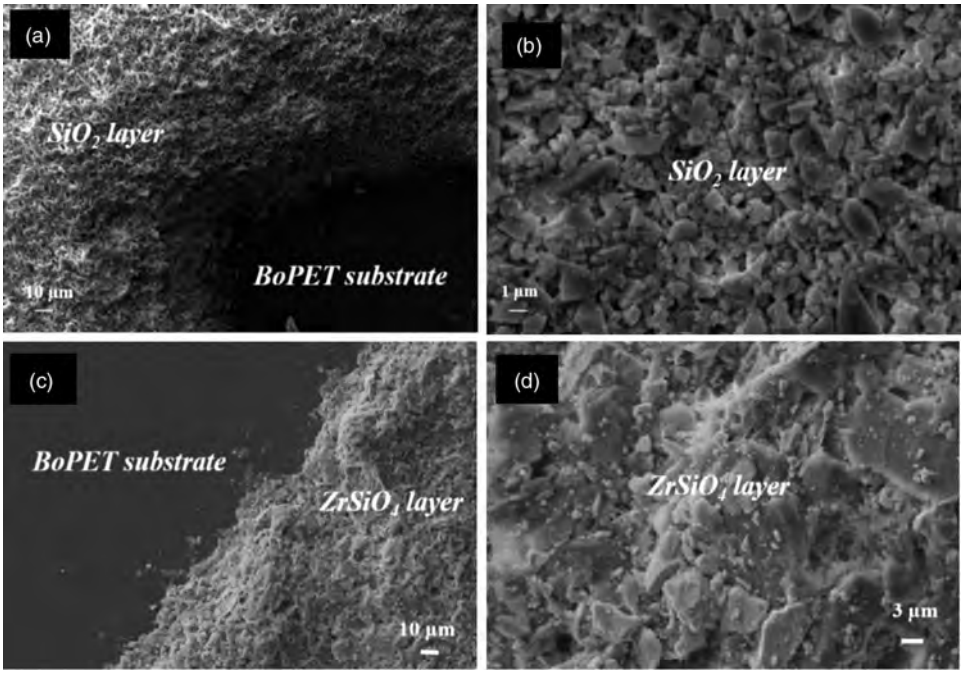

Figure 10.10 *SEM images of printed layers. Source: Adapted from Varghese* et al. *[32, 33].*

are distinctly different, as shown in Figure 10.10a and b. The edges of printed patterns after a print with the SiO_2 and $ZrSiO_4$ inks on BoPET substrate are visible in Figure 10.10a and b. The microstructure of the screen printed layer in Figure 10.10a and b presents a porous behavior with a uniform distribution of SiO_2 and $ZrSiO_4$ particles. The porous microstructure is believed to originate from the low solid loading as well as volatilization of the organic solvents. The boundary between BoPET film and the SiO_2 and $ZrSiO_4$ coating is clearly visible in the microstructure depicted in Figure 10.10a and c, while the SiO_2 and $ZrSiO_4$ crystallites are visible at higher magnification, shown in Figure 10.10b and d.

Figure 10.11a and b (also shown in the Plate Section) illustrates the surface roughness of the screen printed SiO_2 and $ZrSiO_4$ layer measured using atomic force microscopy (AFM) in the tapping mode. A more prominently obvious microstructure of the printed SiO_2 and $ZrSiO_4$ ink surfaces are clear from 2D and 3D AFM images. The average surface roughness (Ra) of screen printed SiO_2 is about 370 nm and the root mean square (RMS) deviation of surface roughness (Rq) is nearly 478 nm, while Ra and Rq of the $ZrSiO_4$ layer are of the order of 160 and 200 nm, respectively, as shown in Figure 10.11a and b. The kurtosis of the topography height distribution (Sku) is found to be nearly 0.546 and 2.97 nm, which indicates the uneven surfaces of the printed layer. The bumpy nature with mountains and valleys of the surface of the printed ink is more evident in the 3D images in Figure 10.11a and b. If the kurtosis distribution is less than 3, the distribution curve is called platykurtoic and has relatively few high mountains and low valleys [52]. If the kurtosis distribution is greater than 3, the distribution curve is said to be leptokurtoic and has many high peaks and

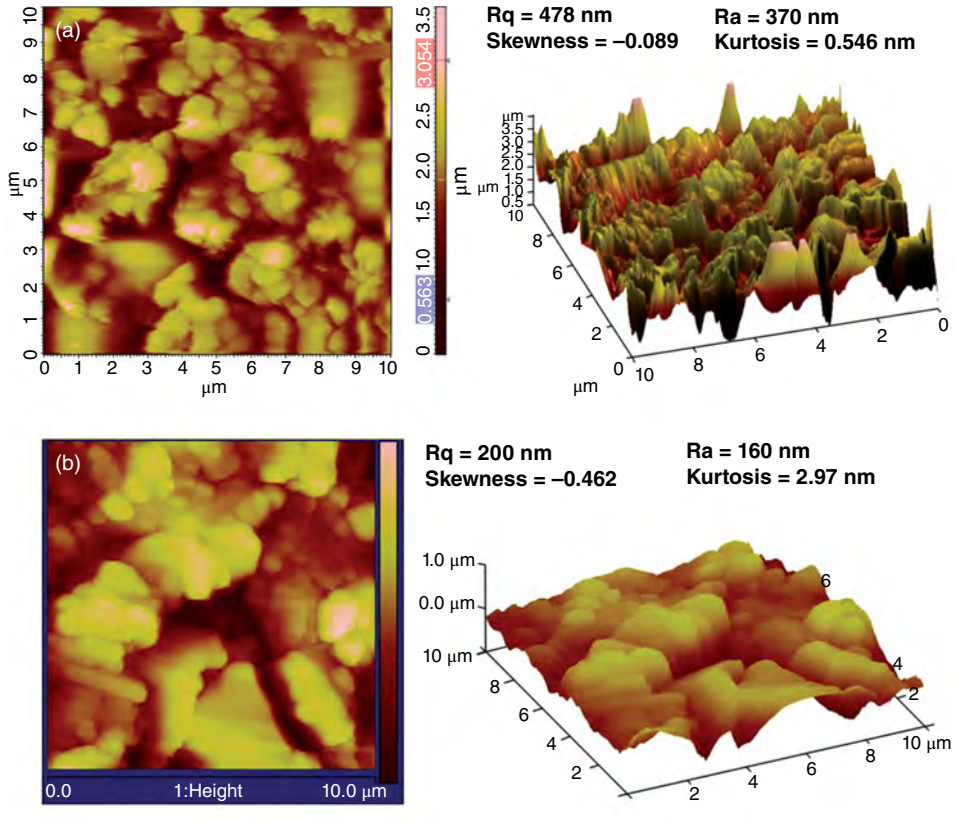

Figure 10.11 *AFM surface roughness of printed layers. Source: Adapted from Varghese* et al. *[32, 33]. This figure is also shown in the Plate Section.*

low valleys. In the printed patterns, the skewness, which is a measure of the asymmetry of the surface, is –0.089 and –0.462, respectively, for SiO_2 and $ZrSiO_4$. The negative value of skewness (Ssk) generally indicates that the surface distribution has a longer tail on the lower side of the reference plane. Similarly, the Al_2O_3 printed layer shows Ra of 400 nm, Sku of 2.45, and Ssk of –0.248 on the BoPET substrate [39]. Surface properties of the printed layers are very important in the various fabrication steps involved in the printed electronic devices.

10.3.5 Dielectric Properties of Printed Layers

The dielectric properties of SiO_2 and $ZrSiO_4$ ink patterns printed on BoPET film is characterized using standard procedures. The variation of relative permittivity (ε_r), dielectric loss (tan δ) and impedance (Z) of printed SiO_2 and $ZrSiO_4$ inks on BoPET film in the radio frequency range of 600 Hz to 3 MHz are shown in Figure 10.12a and b. The relative permittivity and dielectric loss tangents show a decreasing trend with an increase in frequency.

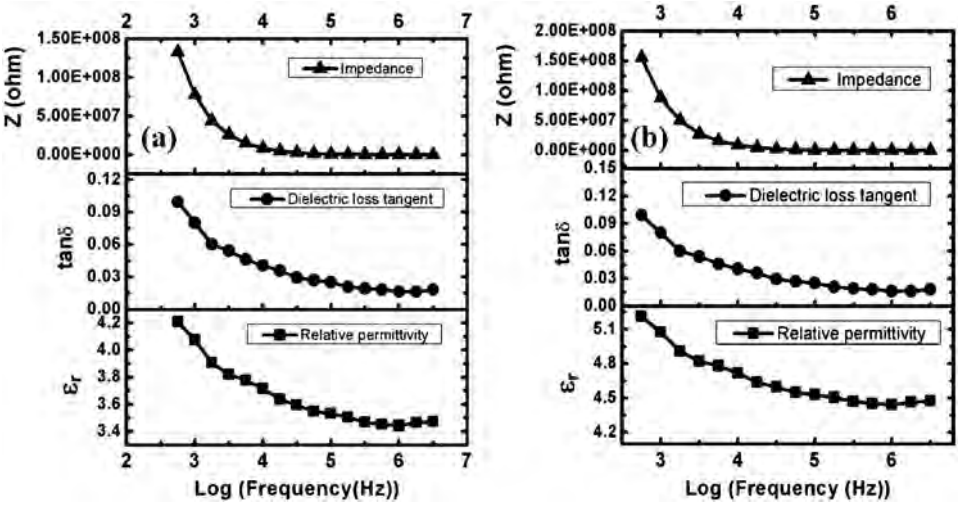

Figure 10.12 *Dielectric properties of SiO_2 and $ZrSiO_4$ dried ink. Source: Adapted from Varghese* et al. *[32, 33].*

The printed SiO_2 ink on BoPET film has ε_r of 3.4 and tan δ of 0.02 at 1 MHz, while the printed $ZrSiO_4$ layer on BoPET film has ε_r of 4.5 and tan δ of 0.02 at 1 MHz. The Al_2O_3 layer on BoPET substrate shows ε_r of 5.2 and tan δ of 0.02 at 1 MHz [39].

The values of relative permittivity and dielectric loss tangent of the printed SiO_2 layer measured at X (8.2–12.4 GHz) and Ku-band (12.4–18 GHz) frequency ranges, as well as their temperature variation of relative permittivity at 15 GHz, are shown in Figure 10.13a and b, respectively. The frequency variation of the relative permittivity of printed SiO_2 ink on BoPET film is found to be non-linear with a decreasing trend that varies from 2.4 to 2.3 in the measured frequency range of 8.2–18 GHz, where the polarization mechanisms are mainly dictated by ionic and electronic polarization. The temperature coefficient of relative

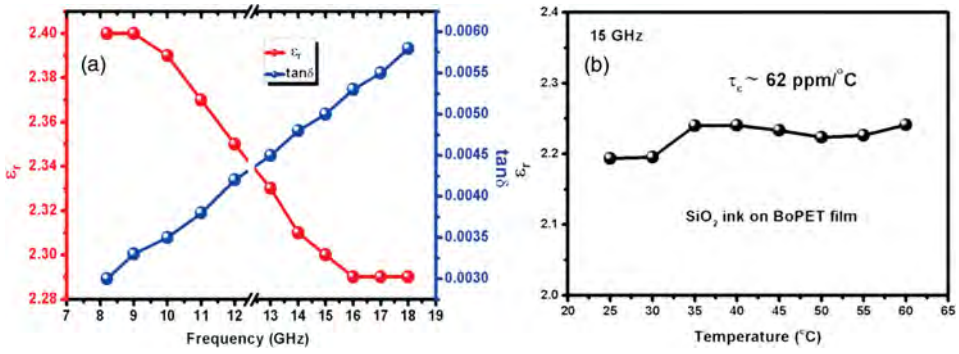

Figure 10.13 *(a) Relative permittivity and dielectric loss of printed SiO_2 layer on BoPET film at x and Ku band frequency range and (b) temperature variation of relative permittivity of printed SiO_2 layer on BoPET film at 15 GHz. Source: Adapted from Varghese* et al. *[32, 33].*

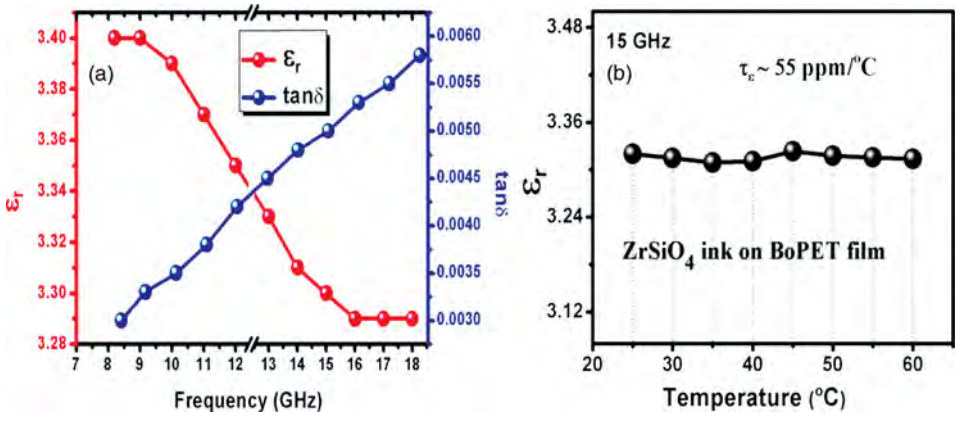

Figure 10.14 *(a) Relative permittivity and dielectric loss of printed $ZrSiO_4$ layer on BoPET film at and Ku band frequency range and (b) temperature variation of relative permittivity of printed $ZrSiO_4$ layer on BoPET film at 15 GHz. Source: Adapted from Varghese* et al. *[32, 33].*

permittivity (τ_ε) is one of the crucial parameters required for the stability of the signal in communication devices. The variation of the relative permittivity of the printed SiO_2 layer on BoPET substrate with respect to the temperature range (25–60 °C) is shown in Figure 10.13b and gives a τ_ε of 62 ppm/°C.

Similarly, Figure 10.14a shows that $ZrSiO_4$ ink on BoPET film has a relative permittivity variation of 3.40 to 3.29 at this frequency range. The dielectric loss tangent of printed $ZrSiO_4$ ink on BoPET film increases with an increase in frequency, as depicted in Figure 10.14a, while the Al_2O_3 ink on BoPET substrate shows a relative permittivity of 2.93 and dielectric loss tangent of 0.004 at 15 GHz [39]. The external factors such as porosity, humidity, impurities, etc., can greatly influence the dielectric loss of the material. The variation of the relative permittivity of printed $ZrSiO_4$ ink on BoPET film and BoPET film with respect to operating temperature (25–60 °C) are shown in Figure 10.14b and gives a τ_ε of 55 ppm/°C. The Al_2O_3 ink on BoPET substrate shows τ_ε of 66 ppm/°C at 5 GHz [39]. The low relative permittivity, low dielectric loss and good temperature stability on dielectric properties of the printed SiO_2, $ZrSiO_4$, and Al_2O_3 layer on BoPET make them suitable candidates for printed microwave wireless communications.

Recently, Liu *et al.* reported RF and microwave dielectric properties of sintered $Bi_2Mo_2O_9$ ceramic thick film screen printed on Al foil and alumina substrates [43]. Figure 10.15a and b shows the cross-sectional and surface microstructure of $Bi_2Mo_2O_9$ ceramic thick film sintered at 645 °C/3 h. The microstructure reveals that the printed thick film shows a thickness of 15–20 μm and is well sintered with limited porosity and good contact with Al foil. Figure 10.15c depicts the frequency-dependent relative permittivity and dielectric loss of $Bi_2Mo_2O_9$ ceramic thick film on Al foil. It is found that the relative permittivity increases from 15 to 38 when the sintering temperature increases from 550 to 645 °C measured at radio frequency in the range 1 kHz to nearly 1 MHz. Similar observations are also evident from Figure 10.15d, which shows that the relative permittivity and *Qf* of $Bi_2Mo_2O_9$ ceramic thick film screen printed on alumina substrate sintered in the temperature 550–645 °C. The relative permittivity varied from 15 to 35, and *Qf* increased from 208

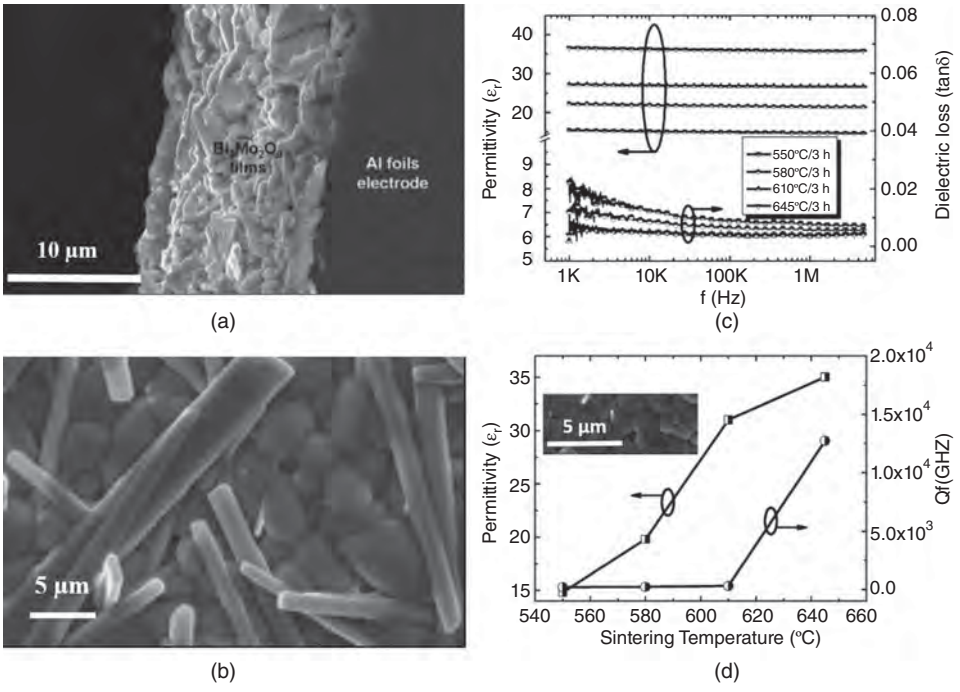

Figure 10.15 *(a) Cross-sectional, (b) surface microstructure of $Bi_2Mo_2O_9$ ceramic thick film screen printed on Al foil and (c) RF and (d) microwave dielectric properties of $Bi_2Mo_2O_9$ ceramic thick film at various sintering temperatures. Inset (d) shows the microstructure of $Bi_2Mo_2O_9$ ceramic thick film on alumina substrate at 645 °C. Source: Liu* et al. *2010 [43]. Reproduced with permission of John Wiley & Sons.*

to 12 700 GHz. The $Bi_2Mo_2O_9$ ceramic thick film printed and sintered at 645 °C has a τ_ε of 124 ppm/°C. The inset of Figure 10.15d shows the microstructure of $Bi_2Mo_2O_9$ ceramic thick film on alumina substrate. The structural, RF, and microwave dielectric properties of $Bi_2Mo_2O_9$ ceramic thick film suggest that these low-temperature fired ceramic thick films have potential applications in LTCC technology [43].

10.4 Polymer-Based Dielectric Inks, Properties and Applications

Polymer-based dielectric inks are used for several printed electronic applications. Recently Cook *et al.* reported inkjet printed dielectric polymer for the fabrication of multilayer capacitors operated at 3 GHz. The formulated ink based on commercially available SU-8 (UV curable photoresist) with ε_r of about 4 and PVP (poly (4-vinylphenol)) ε_r relative permittivity of 3 is used [31]. The SU-8 ink consisting of 29–45 wt% polymer filler in the solvent Cyclopentanone is mixed in 80–20 wt% to obtain the required colloidal stability for inkjet printing (viscosity of 9 mPa s) [31]. The PVP ink consists of 0.55 wt% PVP powder and 0.05 wt% of 1-Hexanol with the addition of polymelamine–co-formaldehyde as a heat-activated crosslinker for the required colloidal stability. The dielectric measurements indicate that a microwave capacitor based on the above polymer dielectric ink has

capacitance values up to 50 μF and self-resonant frequency of up to 3 GHz. These results make it suitable to use in the 800 MHz RFID and 2.4 GHz band [31]. Very recently, Ostfeld *et al.* reported [53] screen printed passive components for flexible power electronic applications. They report that they demonstrated the integration of passive components such as an inductor, resistor, and capacitor for flexible power electronic applications. They used BT-101 dielectric ink for the fabrication of a flexible capacitor [53]. Recently Ng *et al.* reported [54] the importance of dielectric inks for printed electronics devices, especially printed organic complementary transistors. They described a high-*k* PVDF terpolymer dielectric used as an effective gate dielectric for complementary devices. Similarly, there are several reports on the use of dielectric ink in several electronic devices such as all-polymer thin-film transistors [55–57], MIM capacitors [58], microfluidic devices [59], OLEDs [60], etc.

More recently Joseph *et al.* reported a screen printable and room temperature curable polyaniline nanofiber-based microwave absorbing ink [61]. Figure 10.16a and b shows the

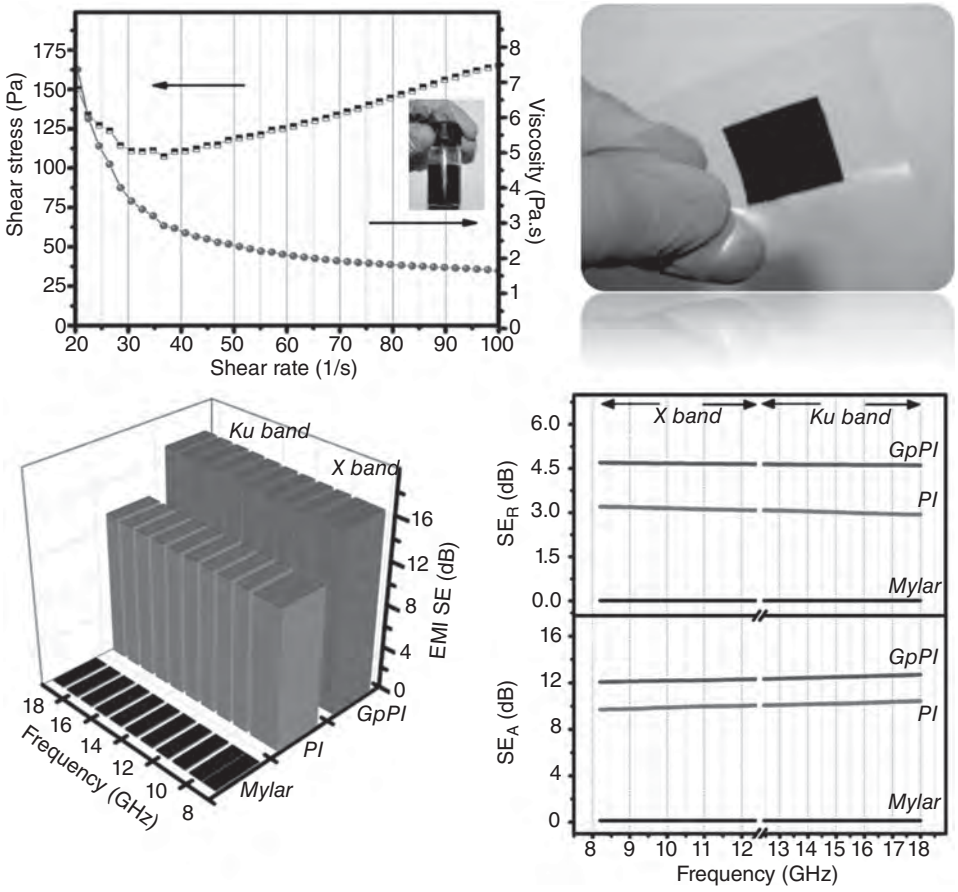

Figure 10.16 *(a) Rheology of polyaniline nanofiber-based screen printing, (b) screen printed polyaniline nanofiber layer on Mylar substrate and (c) and (d) microwave EMI shielding properties of the screen printed polyaniline based ink. Source: Joseph* et al. *2016 [61].*

rheological properties and screen printed layer of polyaniline nanofiber ink on Mylar substrate, respectively. The rheology studies reveals that the developed ink shows good colloidal stability for screen printing. The screen printable ink consists of polyaniline nanofiber and polyaniline nanofiber–graphite composite as fillers, and toluene and sodium dodecyl benzene sulfonate (SDBS) as solvent and dispersant, respectively. Figure 10.16d and e shows the electromagnetic interference shielding effectiveness (EMI SE) and reflection (SER) and absorption (SEA) shielding effectiveness of Mylar, polyaniline nanofiber (PI), and polyaniline nanofiber graphite composite (GP PI) layer on Mylar substrates at X and Ku band frequency ranges. The Mylar substrate has an EMI SE of 0.1 dB, which indicates that it is transparent to the electromagnetic radiation in the microwave frequency range of 8–18 GHz. However, the screen printed polyaniline nanofiber layer has a significant EMI SE of above 13 dB, resulting in electromagnetic wave attenuation of above 95% even at a small thickness of 50 μm. GpPI has an EMI SE of 17 dB, equal to the electromagnetic wave attenuation of about 98% in the measured frequency range, which is fairly good at this low thickness value. The screen printed polyaniline nanofiber and polyaniline nanofiber–graphite composite-based layers can prove to be a potential absorbing shielding material to meet the commercial EMI shielding applications in the microwave frequency range [61].

10.5 Commercially Available Dielectric Inks, Properties and Applications

Printable dielectric inks are used extensively to provide good electrical isolation between conductive layers to avoid short circuits and reduce electromagnetic coupling that might interfere in the operation of the printed electronic devices. Most of the dielectric inks are designed in electronic circuits for component protection from exposure to UV radiation, oxidation, abrasion, moisture, thermal shock, etc. Some of the commercially available dielectric inks, and their applications and properties are given in Table 10.5 [62–70]. DuPont 5951 is a commercially available multilayer dielectric ink with a relative permittivity in the range of 6–10 and dielectric loss of 0.005 after firing [63]. A few thermally conductive dielectric inks are also available in the markets [67]. CALDONCONTROLS, CCD 120 A series dielectric ink has a relative permittivity in the range of 4–4.2 and an ink with a thermal conductivity in the range of 1.5–20 W/m K [67]. Applied Technologies supplies dielectric inks for the UV protection and transparent coating for electronic devices, which were based on polyester, silicone, urethane, epoxy, acrylic, and fluoropolymer [69]. Most of the commercially available dielectric inks are used for interconnecting purposes in multilayer circuit boards. It is also clear from Table 10.5 that most of them are UV curable and their properties in microwave regions are unknown. The dielectric properties of the printed inks with suitable relative permittivity, low dielectric loss, and good temperature stability of dielectric properties make them useful for microwave applications.

10.6 Conclusion

The present chapter discusses a low-cost preparation procedure for the development of SiO_2, $ZrSiO_4$, and Al_2O_3 dielectric inks that are screen printable on flexible substrates.

Table 10.5 *Commercial dielectric inks, properties and applications*

Number	Commercial product and vendors	Applications	Dielectric strength (V/mils)	Viscosity (Pa s)	Curability (UV/solvent/ water)	Reference
1	DI-7502, DI-7521 (Acrylic) - EMS Inc. NAGASEAMERICA	Electric short protection, membrane switches	>1000	10–12	UV	62
2	5951-DuPont	Interconnect	>700	20–30	Solvent/150 °C at air	63
3	1020A, 452SS, PF455B, M7000 A BLU E&C LOCTITE EDAG	Keyboards and flexible circuits, display and flexible solar, RFID, rigid circuits and LEDs	–	–	UV and solvent/ 165 °C at air	64
4	BT-101-CONDUCTIVE COMPONUDS	Capacitive dielectric	>500	10	Solvent/130 °C at air	65
5	InkA-1220, 1201 (Inkjet)	Protective coating	~381	13–16	UV	66
6	CCD 120A-20, 30, 40, and 50 - CALDON CONTROLS Ltd.	LED lighting circuits, power supply, solar panels, solid-state relay, motor drives	2500	–	150 °C at air	67
7	D2080121P12, D2151013D1-D4-GWENT GROUP	Insulating layer for flexible polymer	–	1–14	UV and 150 °C at air	68
8	3200 UVR-2, 3240, 3180, 3245, 3310, 3330, 3400, 3410, 3450, 3810 UVR, FO 120C, FO121CA-Applied Technologies	UV blocking overcoat for electronics, transparent	>500	6–75	100–150 °C at air	69
9	125-17, 116-20, 113-48, 111-27, 118-02, 122-01, 119-07, 118-08, 118-12	Insulating layer and membrane switches	365, 525, 1300	20	UV, 25–200 °C at air	70

The colloidal ink comprises SiO_2, $ZrSiO_4$, and Al_2O_3 as the dielectric fillers with suitable organic vehicles. A suitable blending of solvent mixture (anhydrous xylene/ethanol), silica filler (60 wt% of SiO_2 or $ZrSiO_4$ or Al_2O_3 with respect to total weight), dispersant (1 wt% of natural fish oil with respect to filler), and binder (5 wt% of polyvinyl butyral with respect to filler) constitute the final ink composition. The room temperature curing, low dielectric loss, and low relative permittivity of the printed layer make them suitable for printed microwave applications. The inks are advantageous over water-based dielectric inks in terms of ease of synthesis, cost-effectiveness, and faster curing time. The recent progress in wireless communication, IoTs, and 5G and smart technologies, etc., may require low-loss dielectric inks of varying relative permittivity.

Acknowledgment

The authors are grateful for ERC Project No. 24001893 for financial assistance.

References

1. Voigt, J.F.H. and Haeffner, J.A. (1899) Electrical resistance. US Patent 617375A.
2. Deyrup, A.J., Kermit, H., Ballard, K., *et al.* (1945) Preparation of electrical capacitors. US Patent 2389419.
3. Hoffman, L.C. (1984) An overview of thick-film hybrid materials, *American Ceramic Bulletin*, **63**, 572-576.
4. Varghese, J. (2015) Fabrication of microwave substrates and formulation of dielectric ink for microelectronic applications. Doctoral Thesis, Cochin University of Science and Technology, Kerala, India.
5. Sekitani, T., Nakajima, H., Maeda, H., *et al.* (2009) Stretchable active-matrix organic light-emitting diode display using printable elastic conductors. *Nature Materials*, **8**, 494–499.
6. Shin, D.Y., Lee, Y., and Kim, C.H. (2009) Performance characterization of screen printed radio frequency identification antennas with silver nano paste. *Thin Solid Films*, **517**, 6112–6118.
7. Vyas, R., Lakafosis, V., Rida, A., Chaisilwattana, N., *et al.* (2009) Paper-based RFID-enabled wireless platforms for sensing applications. *IEEE Transaction on Microwave Theory and Technology*, **57**, 1370–1382.
8. Noh, J., Jung, M., Lee, G., *et al.* (2011) Integrable single-walled carbon nanotube (SWNT) network based thin film transistors using roll-to-roll gravure and inkjet. *Organic Electronics*, **12**, 2185–2191.
9. Angmo, D., Larsen-Olsen, T.T., Jørgensen, M., *et al.* (2013) Roll-to-roll inkjet printing and photonic sintering of electrodes for ITO-free polymer solar cell modules and facile product integration. *Advanced Energy Materials*, **3**,172–175.
10. Gaikwad, A.M., Steingart, D.A., and Ng, T.N. (2013) A flexible high potential printed battery for powering printed electronics. *Applied Physics Letters*, **102**, 233302, doi: 10.1063/1.4810974.
11. Li, Z., Liu, H., Ouyang, C., *et al.* (2016) Recent advances in pen-based writing electronics and their applications. *Advanced Functional Materials*, **26**, 165–180.
12. Teichler, A., Perelaer, J., and Schubert, U.S. (2013) Inkjet printing of organic electronics – comparison of deposition techniques and state-of-the-art developments. *Journal of Materials Chemistry C*, **1**, 1910–1925.
13. Singh, M., Haverinen, H.M., Dhagat, P., *et al.* (2010) Inkjet printing-process and its applications. *Advanced Materials*, **22**, 673–685.
14. Kurra, N. and Kulkarni, G. (2013) Pencil-on-paper: electronic devices. *Lab Chip*, **13**, 2866–2873.
15. MARKETSANDMARKETS: Printed electronics market worth $40.2 billion by 2020. Available at: http://www.marketsandmarkets.com/PressReleases/printed-electronics-market.asp.

16. Perelaer, J., Smith, P.J., Mager, D., *et al.* (2010) Printed electronics: the challenges involved in printing devices, interconnects, and contacts based on inorganic materials. *Journal of Material Chemistry*, **20**, 8446–8453.
17. Hong, C.M., Gleskova, H., and Wagner, S. (1997) Direct writing and lift-off patterning of copper lines at 200 °C maximum process temperature. *Materials Research Society Symposium Proceedings*, **471**, doi: http://dx.doi.org/10.1557/PROC-471-35.
18. Redinger, D.R., Molesa, S., and Yin, S. (2004) An ink-jet-deposited passive component process for RFID. *IEEE Transactions on Electron Devices*, **51**(12), 1978–1983.
19. O'Connell, C.D., Higgins, M.J., Sullivan, R.P., *et al.* (2013) Nanoscale platinum printing on insulating substrates. *Nanotechnology*, **24** (50), 505301–505311.
20. Fei, F., Zhuang, J., Wu, W., *et al.* (2015) A printed aluminium cathode with low sintering temperature for organic light-emitting diodes. *RSC Advances*, **5**, 608–611.
21. Finch, R.G. (1968) Thick film materials. *Thin Solid Films*, **3**, 189–199.
22. Thiele, E.S. and Setter, N. (2000) Lead zirconate titanate particle dispersion in thick-film ink formulation. *Journal of American Ceramic Society*, **83**, 1407–1412.
23. Thiele, E.S., Damjanovic, D., and Setter, N. (2001) Processing and properties of lead zirconate titanate piezoelectric thick films on electroded silicon. *Journal of American Ceramic Society*, **84** (12), 2863–2868.
24. Papageorgiou, N., Grätzel, M., and Infelta, P.P. (1996) On the relevance of mass transport in thin layer nanocrystalline photoelectrochemical solar cells. *Solar Energy Materials and Solar Cells*, **44**, 405–438.
25. Ng, T.N., Schwartz, D.E., Lavery, L.L., *et al.* (2012) Scalable printed electronics: an organic decoder addressing ferroelectric non-volatile memory. *Nature Scientific Reports*, **2**, 585, doi: 10.1038/srep00585.
26. Nelo, M., Sloma, M., Kelloniemi, J., *et al.* (2013) Inkjet-printed memristor: printing process development, *Japanese Journal of Applied Physics*, **52** (5S1), 05DB21.
27. Hou, X., Ng, S.C., Zhang, J., *et al.* (2015) Polymer nanocomposite dielectric based on P(VDF–TrFE)/PMMA/$BaTiO_3$ for TIPs–pentacene OFETs. *Organic Electronics*, **17**, 247–252.
28. Rasul, A., Zhang, J., Gamota, D., *et al.* (2010) Flexible high capacitance nanocomposite gate insulator for printed organic field-effect transistors. *Thin Solid Films*, **518**, 7024–7028.
29. Yildirim, F.A., Ucurum, C., Schliewe, R.R., *et al.* (2007) Spin-cast composite gate insulation for low driving voltages and memory effect in organic field-effect transistors. *Applied Physics Letters*, **90**, 083501. Available at: http://dx.doi.org/10.1063/1.2591314.
30. Sun, J.L., Wang, J.X., He, C.R., *et al.* (2015) Synthesis and electrical properties of screen-printed doped ceria interlayer for IT-SOFC applications. *Journal of Alloys and Compounds*, **628**, 450–457.
31. Cook, B.S., Cooper, J.R., and Tentzeris, M.M. (2013) Multi-layer RF capacitors on flexible substrates utilizing inkjet printed dielectric polymers. *IEEE Microwave and Wireless Components Letters*, **23**, 353–355.
32. Varghese, J., Surendran, K.P., Sebastian, M.T. (2014) Room temperature curable silica ink. *RSC Advances*, **4** (88), 47701–47707.
33. Varghese, J., Teirikangas, M., Puustinen, J., *et al.* (2015) Room temperature curable zirconium silicate dielectric ink for electronic applications. *Journal of Materials Chemistry C*, **3** (35), 9240–9246.
34. Mandal, S., Sharma. R., and Katiyar, M. (2012) A hybrid dielectric ink consisting of up to 50 wt% of TiO_2 nanoparticles in polyvinyl alcohol (PVA). *Journal of Chemistry and Chemical Engineering*, **6**, 625–630.
35. DuPont (2009) LuxPrint 8153, Technical data sheet, MCM8153.
36. Mirjana, M., Vijatović, J.D., Bobić, B.D., *et al.* (2010) Barium titanate thick films prepared by screen printing technique. *Processing and Application of Ceramics*, **4** (2), 53–58.
37. Anoop, S.P. (2012) Titania dielectric ink for printed electronics. MPhil Thesis, University of Kerala, Kerala, India.
38. Siponkoski, T., Nelo, M., Palosaari, J., *et al.* (2015) Electromechanical properties of PZT/P(VDF–TrFE) composite ink printed on a flexible organic substrate. *Composites Part B*, **80**, 217–222.

39. Nair, I.I.J., Varma, M.R., and Sebastian M. T. (2016) Low cost, room temperature curable alumina ink for printed electronic applications. *Journal of Materials Science: Materials in Electronics*, **27**, 9891–9899.
40. Kähäri, H., Juuti, J., Myllymäki, S., *et al.* (2013) Preparation of α-$MnMoO_4$ at a ultra-low temperature on an organic substrate. *Material Research Bulletin*, **48**, 2403–2405.
41. Bretos, I., Jimenez, R., Wu, A., Kingon, I.A., *et al.* (2014) Activated solutions enabling low-temperature processing of functional ferroelectric oxides for flexible electronics. *Advanced Materials*, **26**, 1405–1409.
42. Nikfalazar, M., Kohler, C., Weins, A., *et al.* (2016) Beam steering phased array antenna with fully printed phase shifters based on low-temperature sintered BST–composite thick films. *IEEE Microwave and Wireless Component Letters*, **26** (1), 70–72.
43. Liu, W., Wang, H., Zhou, D., *et al.* (2010) Dielectric properties of low-firing $Bi_2Mo_2O_9$ thick films screen printed on Al foils and alumina substrates. *Journal of American Ceramic Society*, **93** (8), 2202–2206.
44. Nelo M. (2015) Inks based on inorganic nanomaterials for printed electronics applications. Doctoral Thesis, University of Oulu, Oulu, Finland.
45. Yang, H., He, Y., Tuck, C., *et al.* (2013) High viscosity jetting system for 3D reactive inkjet printing, in *Solid Free from Fabrication Proceedings*, University of Texas, Austin, pp. 505–513.
46. Mistler, R.E., Twiname, E.R. (2000) Tape casting: theory and practice. *The American Ceramic Society*, Ohio, USA.
47. Alkire, R.C., Bartlett, P.N., and Lipkowski, J. (eds) (2015) *Electrochemistry of Carbon Electrodes*, vol. 16, Chapter 12, Wiley-VCH.
48. Buchanan, R.C. (2004) *Ceramic Materials for Electronics*, Marcel Dekker, USA.
49. Varghese, J., Joseph, T., Sebastian, M.T. (2011) $ZrSiO_4$ ceramics for microwave integrated circuit applications. *Materials Letters*, **65**, 1092–1094.
50. Yen, T.-S. and Sacks, M.D. (1988) Effect of particle size distribution on the sintering of alumina. *Journal of American Ceramic Society*, **71** (12), 484–487.
51. Kunjappu, J.T. (2001) *Essays in Ink Chemistry*, Nova Science Publishers, New York.
52. Gadelmawla, E.S., Koura, M.M., Maksoud, T.M.A., *et al.* (2002) Roughness parameters. *Journal of Materials Processing Technology*, **123** (1), 133–145.
53. Ostfeld, A.E., Deckman, I., Gaikwad, A.M., *et al.* (2015) Screen printed passive components for flexible power electronics. *Nature Scientific Report*, **5**, 15959, doi: 10.1038/srep15959.
54. Ng, T.N., Mei, P., Whiting G.L., *et al.* (2015) Comparison of conductor and dielectric inks in printed organic complementary transistors. *Proceedings of SPIE*, **9185**, 918501–918506.
55. Kawase, T., Shimoda, T., Newsome, C., *et al.* (2003) Inkjet printing of polymer thin film transistors. *Thin Solid Films*, **438-439**, 279– 287.
56. Dadvand, A., Lu, J., Py, C., *et al.* (2016) Inkjet printable and low annealing temperature gate-dielectric based on polymethylsilsesquioxane for flexible n-channel OFETs. *Organic Electronics: Physics, Materials, Applications*, **30**, 213–218.
57. Alsaif, M.M.Y.A., Chrimes, A.R., Daeneke, T., *et al.* (2016) High-performance field effect transistors using electronic inks of 2D molybdenum oxide nanoflakes. *Advanced Functional Materials*, **26**, 91–100.
58. Lim, J., Kim, J., Yoon, Y.J., *et al.* (2012) All-inkjet-printed metal–insulator–metal (MIM) capacitor. *Current Applied Physics*, **12**, e14–e17.
59. Hamad, E.M., Bilatto, S.E.R., Adly, N.Y., *et al.* (2016) Inkjet printing of UV-curable adhesive and dielectric inks for microfluidic devices. *Lab on a Chip – Miniaturisation for Chemistry and Biology*, **16** (1), 70–74.
60. Tait, J.G., Witkowska, E., Hirade, M., *et al.* (2015) Uniform aerosol jet printed polymer lines with 30 μm width for 140 ppi resolution RGB organic light emitting diodes. *Organic Electronics*, **22**, 40–43.
61. Joseph, N., Varghese, J., and Sebastian, M.T. (2016) A facile formulation and excellent electromagnetic absorption of room temperature curable polyaniline nanofiber based inks. *Journal of Materials Chemistry C*, **4**, 999–1008.
62. NAGASEAMERICA, http://nagaseamerica.com/product/dielectric-inks.

63. DuPont (2013) 5951, MCM5951, Technical Data Sheet. Multilayer Dielectric. Available at: http://www.dupont.com/content/dam/dupont/products-and-services/electronic-and-electrical-materials/documents/prodlib/5951.pdf.
64. LOCTITE Henkel's Printed Electronic Inks. Available at: http://www.henkel-adhesives.com/com/content_data/326281_LT5980_Printed_Electronic_Inks_F_LR615251_Updated.pdf.
65. CONDUCTIVE COMPOUNDS, BT-101Capacitive dielectric ink. Available at: http://www.conductivecompounds.com/pdf/bt-101-el-dielectric.pdf.
66. POLITECHNICO DI TORNIO. Available at: http://www.politronica.eu/products/dielectric_inks/index_html.html.
67. CALDONCONTRILS, Dielectric Inks. Available at: http://www.caledoncontrols.com/uploads/3/0/7/8/3078706/ccd_120a.pdf.
68. GWENT GROUP, Dielectric Inks. Available at: http://www.gwent.org/gem_membrane.html
69. Applied Technologies, Dielectric Inks. Available at: http://www.applied-technologies.net/}!dielectric-insulator-inks/c1owo.
70. CREATIVE MATERIALS, Dielectric Inks. Available at: http://www.creativematerials.com/products/dielectric-inks.

11

Polymer–Ceramic Composites for Microwave Applications

R. Ratheesh[1] *and M.T. Sebastian*[2]
[1]*Centre for Materials for Electronics Technology (CMET), Microwave Materials Division, Thrissur, India*
[2]*Microelectronics Research Unit, Faculty of Information Technology and Electrical Engineering, University of Oulu, Oulu, Finland*

11.1 Introduction: Microwave Substrates

Microwave substrates are solid dielectric media having stable relative permittivity and low-loss tangent at microwave frequencies. Dielectric substrates for microwave applications differ in many ways from the conventional printed circuit boards (PCBs) used at low frequencies. The PCBs have the primary functions of conveying signals/voltages and providing mechanical support to the circuit traces and lumped element (L, C, R) components, etc. Microwave packaging technology demands substrate materials with high-frequency compatibility, minimal dielectric losses, low coefficient of thermal expansion, and high thermal conductivity. Relative permittivity is a critical parameter since the signal transmission rate impedance of the circuit largely depends on the substrate relative permittivity. The loss tangent of the base dielectric substrates are generally not of much importance while designing circuits below 1 GHz and therefore are comparatively cheap PCB materials made from epoxy/woven fabric composites (with a trade name FR4), which are often used as substrates [1–6]. However, as the operational frequencies exceed 1 GHz, the dissipative signal loss in the substrate becomes more significant and the tan δ parameter of the substrate cannot be overlooked. Moreover, the ε_r value of the substrate material also has a profound influence on signal propagation as the speed of the signal (v_s) passing through the dielectric medium

Microwave Materials and Applications, First Edition.
Edited by Mailadil T. Sebastian, Rick Ubic and Heli Jantunen.
© 2017 John Wiley & Sons, Ltd. Published 2017 by John Wiley & Sons, Ltd.

is inversely proportional to the square root of ε_r ($v_s = c/\sqrt{(\varepsilon_r \mu_r}$, where c is the speed of light and $\mu_r \sim 1$ for non-magnetic materials). Thus, the choice of the substrate material becomes very important at the designing stage of a microwave circuit. Hence, unlike conventional PCBs, the substrate material itself is an integral part of the microwave circuit, as its properties decide the dimensions of the circuit and, thereby, the characteristics of the components/devices that result [1, 3–10]. The following equations show the importance of substrate parameters in designing a microwave device [6, 7]:

$$Z_0 = \ln\left(\frac{h}{(w+t)}\right)\frac{1}{\sqrt{\varepsilon_r}} \tag{11.1}$$

where Z_0 is the characteristic impedance of the line, ε_r is the relative permittivity of the base substrate, h is the dielectric thickness from the signal to ground plane, w is the line width, and t is the line thickness. The power loss or signal attenuation a_d in dB/cm for a stripline circuit is

$$a_d = 10.75\frac{f}{c}\sqrt{(\varepsilon_r \tan\delta)} \tag{11.2}$$

where f is the frequency, c is the speed of light, ε_r and tan δ are the relative permittivity and loss tangent of the substrate, respectively. The equation shows that power loss increases linearly with frequency and to the square root of ε_r and tan δ. Consequently, for microwave circuitry, where f is necessarily high, low tan δ is a very important factor to reduce signal loss.

Various state-of-the-art electronic and communication devices used in defense, avionics, and information technology (IT) related fields require base substrates of high reliability, stability, low microwave losses, and appropriate ε_r values. Wireless access applications that use next-generation cell phones (4G/5G), blue-tooth equipped devices, wireless LAN, collision prevention millimeter wave radar, as well as peripheral electronic devices need microwave dielectric, substrates with improved properties [1–3, 8]. Such substrates are used as the base dielectrics for power amplifier circuits used in particle accelerator, mobile base stations, personal communication system (PCS), and patch antennas (for high-speed digital transmit–receive applications) [2–6].

Presently, the microwave component industry uses several substrate materials comprising hard and soft substrates [1, 8, 11]. Hard substrates usually comprise α-alumina, magnesia, aluminum nitride, fused silica (quartz), cordierite, GaAs, and beryllia. The ceramic (or quartz) substrates have the advantage of withstanding the localized heat caused during the wire-bonding process. Although hard substrates are highly isotropic and have very high operating temperatures besides high thermal conductivity (k) and comparable CTE, they exhibit brittleness, difficulty in machining and a relatively high cost of chemically and thermally compatible conducting layer. Certain applications such as patch antenna, base station circuitry necessitate substrates with larger sizes, wherein hard substrates are seldom used. In order to overcome these disadvantages, soft substrates comprising polymer composites made out of both thermoset plastic and thermoplastic have been developed [1, 6, 9, 11]. These materials generally have easy machinability, better shock resistance, a low-cost conduction/metallization layer, tailor-made properties, and tight tolerance in their electrical properties. Further, soft substrates based on some thermoplastic composites have

more flexibility compared to thermoset-based substrates and are generally known as flexible substrates or laminates.

11.2 Types of Polymer–Ceramic Composites

The dielectric materials used in microelectronic packaging need to simultaneously satisfy diverse requirements such as low-loss tangent, moderate relative permittivity, low-temperature variation of relative permittivity, low or no moisture absorption, low coefficient of thermal expansion (CTE), and high dimensional stability and mechanical stiffness. Soft substrates are generally polymer matrix composites wherein polymers are filled with either ceramic particulates or woven glass materials. Soft substrates are advantageous over hard substrates in terms of low-temperature processing, flexibility, easy machinability, cheap conductor patterns, etc. [10]. The polymers have a low dielectric constant, low loss tangent but a high CTE, high-temperature variation of relative permittivity τ_ε, very low thermal conductivity, and good mechanical properties. The ceramics in general have a relatively high relative permittivity, low-loss tangent, relatively high thermal conductivity, low CTE, and low τ_ε but is very brittle. Hence, by using the composite approach, one can get reasonably good properties for practical applications in microelectronics. It is well known that connectivity between the phases in the composite materials are very important in achieving the desired properties and are discussed in Chapter 2. The concept of connectivity describes the interspatial relationships in a multiphase material controlling the mechanical and electrical properties and thermal fluxes between the phases. The filler particle size, shape, interfacial properties, percolation level, and porosity play a crucial role on the properties of the composite [11]. Polymer matrix composites can be classified into two categories depending on the nature of the matrix used, that is, thermoset or thermoplastic. Thermoplastic materials have a melt temperature associated with them, whereas dimensional behavior of thermosets are characterized by its glass transition temperature (T_g). Among them, thermoset matrix composites are most preferred for low-end applications whereas thermoplastic composites are the choice of preference for high-end microwave circuit applications. The main advantage of thermoplastic matrix composites compared with thermoset matrix composites are an unlimited shelf life and does not require curing, reprocessability, chemical inertness, lower moisture absorption, higher service temperature, and high environmental tolerance. However, the processing difficulties and relatively high viscosity are some drawbacks of thermoplastic materials. The recent explosive growth in wireless market and advances in high-speed digital technology have brought new thermoset as well as thermoplastic materials with superior electrical performance to address these needs [12, 13].

Most common base substrate used for microwave circuit fabrication is the epoxy/glass substrate (FR-4) having a relative permittivity of 4.4 with loss tangent of 0.05 at 800 MHz. FR-4 is fabricated through hot pressing of woven fabric/brominated epoxy composites [14]. However, the use of FR-4 substrates at high frequencies (>1 GHz) are restricted due to their higher loss tangent [15]. Polystyrene is a low-loss material and hence can be used for high-frequency applications. Alumina-filled polystyrene composites are reported as substrate material for microwave applications [11], but the low service temperature and crack formation make polystyrene unfavorable in practical applications [16]. The microwave dielectric properties of several low-loss polymers are given in Table 11.1.

Table 11.1 *Dielectric properties of low-loss polymers*

Material	Relative permittivity	Loss tangent	Frequency
PTFE	2.1	0.0001	10 GHz
Polystyrene	2.5–2.6	0.0003	3 GHz
Polyimide	3.00	0.004	10 GHz
Polypropylene	2.25	0.0003–0.0004	1 MHz
polycarbonate	2.8–3.4	0.0006–0.001	
HDPE	2.34	0.0001	10 GHz
COC	2.4	0.0001	1 GHz
Polyphenlene sulphide (PPS)	3.0–3.05	0.002	1 GHz
PEEK	3.3	0.0040	10 GHz
POE	2.1	0.0002	5 GHZ
Poly(methymethocrylate)	2.61	0.01	11 GHz
Metallocene cyclic olefin copolymer	2.35	0.00088	1 MHz
LCP	3.00	0.002	10 GHz
Epoxy	3.4–4.0	0.02	1 MHz–1 GHz

Several materials based on thermosetting polymer matrix are available for high-frequency applications [11,17]. Thermosetting polyimide is one of the most preferred matrices for fabricating such substrates. One of the most common PCBs for high-frequency application is filled poly(1,2-butadiene) composites [18]. These composites exhibit a low porosity content even at a filler loading of 60 vol.%. Poly(1,2-butadiene)-based substrates having dielectric constants of 3.27, 4.5, 6, 9.2, and 9.8 with a loss tangent <0.0025 at 10 GHz are commercially available. Table 11.2 shows the properties of some of the poly(1,2-butadiene)-based high-frequency substrate materials that are commercially available. Laminates based on thermoset polymers need only ordinary processing techniques but suffer from a high moisture absorption content and low tensile strength. Long-term exposure of these thermoset matrix substrates to a highly oxidative environment may lead to change in

Table 11.2 *Properties of some thermoset polymer-based microwave substrates**

Properties	TMM3	TMM4	TMM6	TMM10	TMM10i
Dielectric constant	3.27 ± 0.03	4.5 ± 0.04	6.0 ± 0.08	9.2 ± 0.23	9.8 ± 0.24
Loss tangent	0.002	0.002	0.0023	0.0022	0.002
τ_{ε_r} (ppm/°C)	+37	+15	−11	−38	−43
CTE (ppm/°C)	23	21	26	20	20
Moisture absorption (%)	0.12	0.18	0.2	0.2	0.13
Thermal conductivity (W/m K)	0.70	0.70	0.72	0.76	0.76
Glass transition temperature (°C)	425	425	425	425	425

*TMM is the registered trademark of poly(1,2-butadiene)-based substrates by M/s. Rogers Corporation, USA.

the dielectric properties of hydrocarbons and hence the substrates. It is difficult to use this class of materials in an extreme chemical environment [19].

Thermoplastic materials have advantages over thermoset matrices in their chemical inertness and high service temperature. Various thermoplastics having low-loss tangent are used as the matrix for making flexible microwave substrates. Poly(tetrafluoroethylene) (PTFE), polyphenylene oxide (PPO), polyetherimide (PEI), etc., are the major thermoplastic polymer matrices having stable dielectric properties in the microwave frequency region [20].

11.3 Thermoplastic Matrix and Composites

11.3.1 Poly(tertrafluoroethylene)

Poly(tetrafluoroethylene) was discovered by Roy Plunkett at DuPont laboratory in 1938 [21]. PTFE is synthesized through emulsion polymerization of tetrafluoroethylene (TFE) monomers ($-CF_2-CF_2-$) under pressure using free radical catalysis. At room temperature TFE is extremely unsafe to handle unless it is inhibited with 1–2 wt% of limonene or other radical scavenger [22]. Due to the uniqueness in its electrical, mechanical, and thermal properties, PTFE finds application from aerospace components to mechanical bearings to cooking wear. PTFE is found to be resistant even to corrosion due to uranium hexafluoride (UF_6), which is a well-known corrodent and an intermediate material for the production of highly enriched uranium. The carbon–carbon skeleton is completely covered with the fluorine outer layer in a helical conformation as shown in Figure 11.1. The carbon–fluorine bond energy (116 kcal/mol) is the highest currently known among organic compounds. This contributes to the high solvent resistance of PTFE molecules [23].

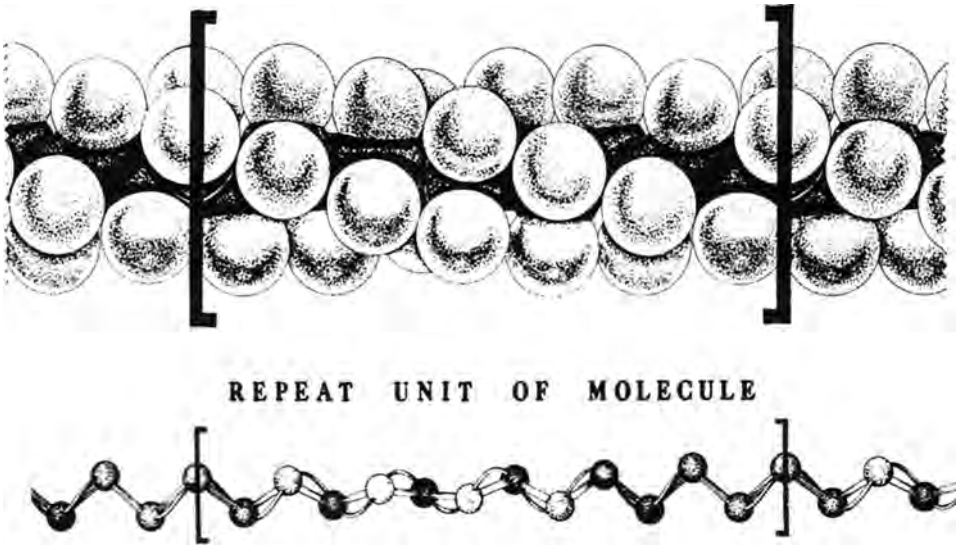

Figure 11.1 *Schematic representation of the helical arrangement of PTFE with fluorine atoms covering the carbon backbone. Source: Clark [25]. Reproduced with permission of Elsevier.*

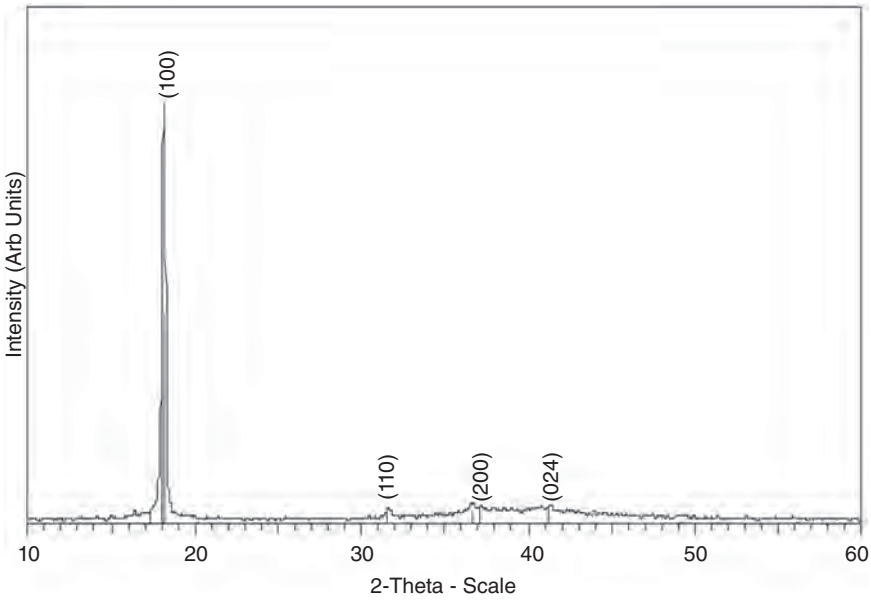

Figure 11.2 *Powder X-ray diffraction pattern of PTFE.*

PTFE is a highly crystalline polymer with crystallinity varying from 40 to 98% [24]. The very high crystallinity of PTFE is an indication of its unbranched chain structure. The fluorine atoms are too large to allow a planar zigzag structure, which would permit chain flexibility, and hence the chains are rigid. Irrespective of its hydrocarbons (polyethylene), fluorine atoms in PTFE are arranged in a helical conformation over the zigzag carbon skeleton. The van der Waals radius of fluorine atom is higher (1.35 Å) than that of hydrogen (1.1 Å). Hence, a helical conformation of C—F molecules results when hydrogen is replaced with carbon. The helical structure is due to rotation around the chain bonds, which takes place to increase the distance between the fluorine atoms [22, 25–27]. Figure 11.2 shows the powder X-ray diffraction pattern of 50 μm size PTFE powder recorded using CuKα radiation. PTFE has sharp peaks at 2θ angles of 17.9°, and weak peaks at 31.4°, 36.9°, and 41.2°, indicating the crystal ordering of the samples [24, 28]. PTFE has three crystalline phases at atmospheric pressure, which is shown in Figure 11.3. The atmospheric crystalline phases are triclinic (<19 °C), hexagonal (19–30 °C), and pseudohexagonal (> 30 °C). At high pressure (>0.5 GPa), a fourth state is also reported where PTFE appears as a planar zigzag crystal [29–31]. The phase transition observed for PTFE from triclinic to hexagonal lattice at 19 °C is reported as first order. Depending on the pressure, there is a slight increase in the transition temperature. The conformation of fluorine atoms around the carbon skeleton is a non-commensurable helix and the conformation cannot be expressed as a ratio of simple whole numbers. Instead, it is 13/6 helix where the atoms are evenly spaced along a helix, having six turns per 13 atoms to form the repeat unit below 19 °C. From triclinic to hexagonal transition, the helical conformation untwisted from 13/6 to 15/7 [30].

One of the key factors that provides wide applicability for PTFE is its high service temperature. It has been reported that PTFE can be used up to 200 °C for electronic applications

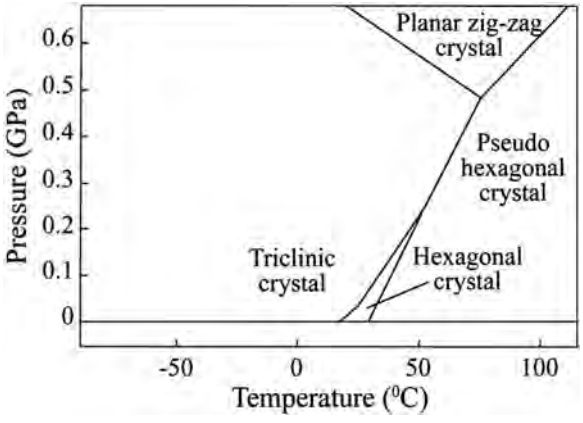

Figure 11.3 *Different crystalline phases of PTFE. Source: Brown and Dattelbaum 2005 [24]. Reproduced with permission of Elsevier.*

[21]. It is difficult to see the glass transition (T_g) temperature of PTFE in the TG/DSC curve due to its peculiar crystalline arrangement. T_g is reported to be between 130 to 180 °C, but a very clear melting point (T_m) is observed [32,33] from the TG/DSC analysis around 327 °C, as shown in Figure 11.4. It is reported that the melting point of PTFE increases with increasing applied pressure at a rate of 1.52 °C/MPa. It is observed from the TG/DSC analysis that the decomposition of PTFE starts only after 500 °C [34]. The decomposition temperature increases with an increase in pressure. The decomposition temperature is 700 °C at 2 kbar and increases to 800 °C at 30 kbar [35]. Different byproducts are released during

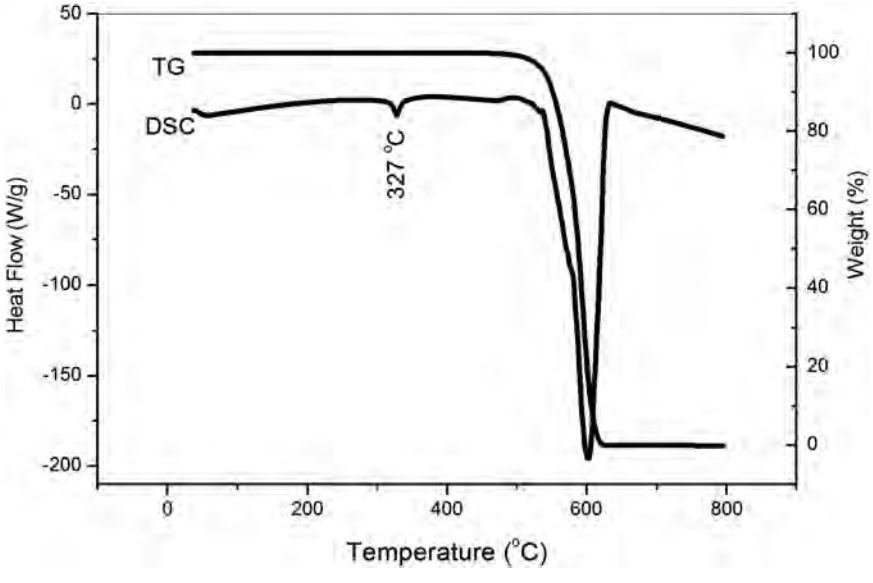

Figure 11.4 *TG/DSC plot of PTFE powder. Source: Rajesh 2009 [62].*

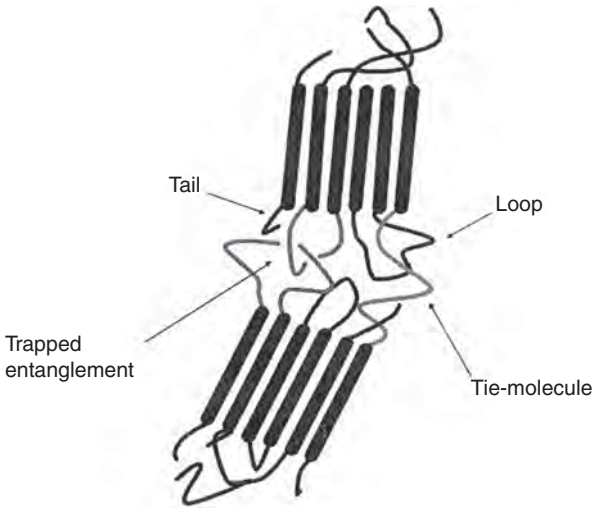

Figure 11.5 *Schematic representation of two microcrystals connected by tie-molecule and a trapped entanglement. Source: Adapted from Gossi 2006 [39].*

decomposition depending on the decomposing atmosphere. Under vacuum PTFE first decomposes to its nearly pure monomer TFE. The monomer further decomposes into perfluoropropylene and perfluoroisobutylene [34, 36]. Thermal decomposition in air produces mainly carbonyl fluoride, which is highly toxic when inhaled. The degradation is always accelerated by oxygen. Decomposition of PTFE in glass or quartz vessels can yield products such as silicon tetrafluoride, carbon monoxide, carbon dioxide, etc. [37]. The thermal rate of depolymerization is always proportional to the weight of the samples and hence thin PTFE specimens will decompose at a faster rate [34–36].

The outstanding mechanical properties of PTFE are closely linked to its unique crystal structure. Bunn *et al.* reported that the structure of PTFE consists of polycrystalline aggregate in which the individual crystallites are composed of long-chain molecules assembled side by side to form fairly thin sheets [38]. Molecules of PTFE are aligned in the form of fibrous crystals or folded ribbons forming lamellae. The lamellar crystals are connected with tie molecules, which are shown in Figure 11.5. The ultrahigh molecular weight ($>10^7$–10^8 g/mol) provides sufficient macromolecular connectivity and gives tough mechanical behavior [37]. The enhanced connectivity due to ultrahigh molecular weight provides a very high melt viscosity (10^{11} Pa s). PTFE has an ultimate tensile strength of 25–30 MPa with 200–300% elongation with respect to molecular weight. However, the tensile properties very much depend on the crystallinity of the polymer. It is reported that tensile strength and elongation increase with decreasing crystallinity [37–39]. The excellent electrical properties of PTFE make it one of the most favorable candidates in the microwave industry. PTFE has a dielectric constant of 2.1, which is constant over a wide range of frequencies (up to 20 GHz) [40]. However, two relaxation peaks at 19 and 30 °C have been reported in the real part of dielectric constant associated with the first-order crystalline phase transition. PTFE has the lowest loss tangent (<0.0003 at 10 GHz) among all known polymer materials. The low-loss tangent is a consequence of the symmetrical conformation of the polymer

Table 11.3 *Important physical properties of PTFE*

Properties	Value
Dielectric constant	2.1 at 10 GHz
Loss tangent	0.0003 at 10 GHz
$\tau_{\varepsilon r}$	−400 ppm/°C
CTE	+109 ppm/°C
Thermal conductivity	0.1–0.25 W/m K
Density	2.17 g/cm^3
Moisture absorption	0.001%
Tensile strength	25–30 MPa
Elongation	200–400%
Volume resistivity	10^{15} ohm
Melting point	327 °C

backbone, which effectively neutralizes the dipole forces of the C—F bonds, yielding a net zero dipole moment [41]. The only contribution towards the loss tangent in PTFE is the presence of impurity and polar end groups.

PTFE has a biphasic nature consisting of amorphous and crystalline phases. Crystalline regions have high electrical resistivity because the molecular chains are arranged in a compact and orderly manner whereas the charge carriers migrate through the amorphous region. This means that the DC resistivity of PTFE will increase with respect to crystallinity. At a high field charge carriers will be trapped by the interface region between crystalline and amorphous regions, which provide a high space charge polarization [29]. Some of the relevant physical properties of PTFE are given in Table 11.3.

11.4 PTFE/Ceramic Composites

11.4.1 Preparation and Dielectric Properties

The preparation and dielectric properties of ceramic-filled PTFE composites have been investigated by many authors [42–72]. Chen *et al.* reported PTFE-reinforced SiO_2 composites fabricated through rolling followed by pressureless sintering [42–44]. Chen and coworkers also prepared SiO_2-reinforced PTFE using a PTFE suspension and silica powders (5 μm or 25 μm SiO_2) [43]. The composite filled with 25 μm SiO_2 at 60 wt% filler content showed acceptable dielectric properties ($\varepsilon_r \sim 2.8$, tan $\delta \sim 0.0025$). The tensile modulus, water absorption, and dielectric constant increased with an increase in SiO_2 filler content. The composites filled with small-size filler (5 μm) showed a higher tan δ (0.006) as a result of a higher SiO_2 surface area. On loading 60 wt% silica in PTFE matrix, crystallinity of PTFE is found to decrease to ∼ 40%. Chen and coworkers [44] modified the surface of silica powder and reinforced PTFE with 60 wt % silica coated with silane. The silane content for coating on the filler was optimized as 1 wt%, wherein the acceptable properties (low moisture absorption ∼ 0.1 wt% and minimum CTE) are obtained for the composite. Although moisture absorption is slightly decreased, a fairly good increase in tensile

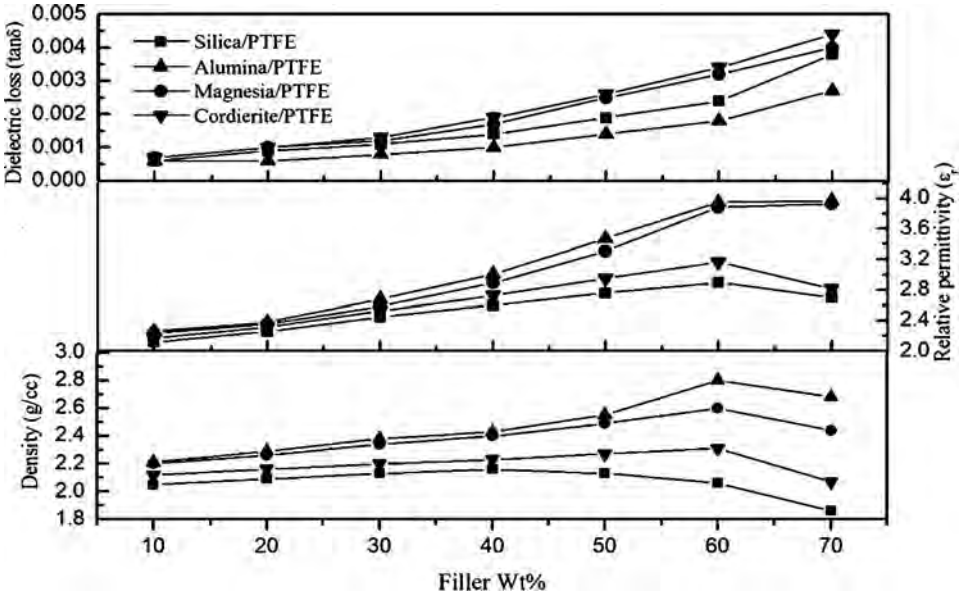

Figure 11.6 *Density, dielectric constant and loss tangent of SiO_2, Al_2O_3, MgO, and cordierite filled PTFE composites. Source: Murali* et al. *2009 [47].*

properties is observed on a further increase in silane content. However, an increase in CTE restricted the optimum silane content to 1 wt%. Murali *et al.* prepared [46] PTFE with nano- and micrometer-sized silica composites through the SMECH process, which comprises sigma mixing, extrusion, calendering, and hot pressing and reported that the PTFE/silica nanocomposites have a lower density, higher losses, and higher ε_r for <30 wt% of filler as compared to that of a micrometer-sized filler. They also reported [47] α-alumina and MgO-filled PTFE substrates. PTFE/Al_2O_3 composite has a dielectric constant of 4.30 and a loss tangent of 0.0021, whereas PTFE/MgO composite has a dielectric constant of 3.35 and a loss tangent of 0.015, respectively, at an optimum filler loading (Figure 11.6). Brucite phase formation during silane coating is expected to be the reason for the inferior loss tangent of MgO-filled PTFE composites [47]. Studies on the cordierite-filled PTFE ceramics exhibited a relative permittivity of 3.17 and a loss tangent of 0.0034 at X-band [51]. The PTFE composites prepared by these fillers exhibit low relative permittivity values ($\varepsilon_r < 5$). The microwave dielectric properties of ceramic-filled PTFE are given in Table 11.4. The density and relative permittivity increase with ceramic filler content up to about 60 wt% (about 0.5 volume fraction) of filler, beyond which they decrease as shown in Figures 11.6 and 11.7, which are typical examples for materials having low and high relative permittivities. The loss tangents in general increase with filler content.

Several authors reported [48–50, 52, 53, 68] the preparation characterization and properties of PTFE reinforced with ceramics such as TeO_2, CeO_2, $ZnAl_2O_4$—TiO_2, $Ba(Mg_{1/3}Ta_{2/3})O_3$, Mg_2SiO_4, $Sm_2Si_2O_7$, $MgTiO_3$, etc., for possible microwave applications. These researchers focused on the effect of filler concentration on a PTFE matrix for improving the dielectric as well as thermal properties of the composite systems. The powder

Table 11.4 *Ceramic-filled polymer Composites*

Polymer	Filler	V_f	ε_r	$\tan\delta$	F_0	Reference
PTFE	CeO_2	0.6	5.0	0.0064	7 GHz	Anjana *et al.* [49]
PTFE	SiO_2	60 wt%	2.9	0.0024	8 GHz	Chen *et al.* [43,44]
PTFE	$ZnAl_2O_4$—TiO_2	0.6	4.8	0.008	7 GHz	Thomas *et al.* [50]
PTFE	$SrTiO_3$	63 wt%	13.1	0.0055	10 GHz	Rajesh *et al.* [61]
PTFE	Modified $SrTiO_3$	60 wt%	12.19	Qf = 1930 GHz		Jin *et al.* [67]
PTFE	TiO_2	0.67	10.2	0.022	10 GHz	Rajesh *et al.* [56]
PTFE	$2MgO$—$2Al_2O_3$—$5SIO_2$	60 wt%	3.17	0.0034	10 GHz	Murali *et al.* [51]
PTFE	Bi_2O_3—ZnO—Nb_2O_5	0.6	12.5	0.001	800 MHz	Xiang *et al.* [63]
PTFE	Al_2O_3	0.66	4.3	0.0021	10 GHz	Murali *et al.* [47]
PTFE	MgO	0.56	3.35	0.015	10 GHz	Murali *et al.* [47]
PTFE	$CaTiO_3$		11.8	0.0036	10 GHz	Rajesh *et al.* [59]
PTFE	$BaNdSmTi_4O_{12}$	67 wt%	8.04	0.009	10 GHz	Stanley *et al.* [64]
PTFE	$Sr_2Ce_2Ti_5O_{16}$	0.4	7.72	0.08	7 GHz	Subodh *et al.* [66]
PTFE	$MgTiO_3$	50 wt%	4.34	0.0009	10 GHz	Yuan *et al.* [53]
PTFE	$CaTiO_3$	0.4	13	0.001	2–7.5 GHz	Hu *et al.* [60]
PTFE	TiO_2/SiO_2	5 wt%/50 wt%	2.87	0.00075	10 GHz	Yuan *et al.* [58]
PTFE	$Sr_2ZnSi_2O_7$	0.5 vol.%	4.4	0.003	4–6 GHz	Joseph *et al.* [72]
PTFE	$BaWO_4$	74 wt%	4.30	0.004	10 GHz	Nijesh *et al.* [65]
PTFE	BMT	67 wt %	6.7	0.0018		Nijesh *et al.* [52]
PTFE	TeO_2	0.6	5.4	0.006		Subodh *et al.* [48]
PTFE	$Sm_2Si_2O_7$	0.4	3.9	0.0054		Thomas *et al.* [68]
PTFE	AlN	0.5	4.2	0.006	1 MHz	Pan *et al.* [155]
PTFE	Mg_2SiO_4	0.5	3.2	0.009	5	Sasikala *et al.* [126]
PTFE	Nano Mg_2SiO_4	0.3	2.8	0.03	5 GHz	Sasikala *et al.* [126]
Polyethylene	$Sm_2Si_2O_7$	0.4	4.81	0.0055	8 GHz	Thomas *et al.* [73]
Polyethylene	$Ca([Li_{1/3}Nb_{2/3})_{0.8}Ti_{0.2}]O_3$	0.4	7.72	0.004	8 GHz	George and Sebastian [76]
Polyethylene	Li_2MgSiO_4	0.4	3.54	0.0032	8 GHz	George *et al.* [74]
Polyethylene	$Sr_9Ce_2Ti_{12}O_{36}$	0.4	12.1	0.004	8 GHz	Subodh *et al.* [75]

(*continued*)

Table 11.4 *(Continued)*

Polymer	Filler	V_f	ε_r	$\tan\delta$	F_0	Reference
Polysterene	Li_2MgSiO_4	0.4	3.84	0.012	8 GHz	George *et al.* [74]
Polysterene	$Sm_2Si_2O_7$	0.4	4.34	0.0101	8 GHz	Thomas *et al.* [73]
Polysterene	$Sr_2Ce_2Ti_5O_{15}$	0.5	13.6	0.0004	8 GHz	Subodh *et al.* [90]
Polysterene	$Ca([Li_{1/3}Nb_{2/3})_{0.8}Ti_{0.2}]O_3$	0.4	7.4	0.003	8 GHz	George and Sebastian [76]
Polystyrene	Mg_2SiO_4	0.5	4.0	0.006	5 GHz	Sasikala *et al.* [91]
HDPE	$Sr_2Ce_2Ti_5O_{15}$	0.4	11.0	0.006	8 GHz	Subodh *et al.* [80]
HDPE	$Ca_4La_6(SiO_4)_4(PO_4)_2O_2$	0.4	5.1	0.0023	5 GHz	Thomas *et al.* [78]
HDPE	CeO_2	0.4	11.0	0.006	8 GHz	Anjana *et al.* [79]
HDPE	$Mg_{0.95}Ca_{0.05}TiO_3$	0.5	7.32	0.001	8.4 GHz	Shi *et al.* [82]
HDPE	$Li_2MgSiO4$	0.4	3.54	0.0032	5 GHz	George *et al.* [74]
HDPE	$Sm_2Si_2O_7$	0.5	5.3	0.009	8 GHz	Thomas *et al.* [73]
HDPE	$ZrSiO_4$	0.4	4.8	0.0018	5 GHz	Varghese *et al.*[84]
HDPE	$BaTiO_3$	0.5	18.0	0.1	10 MHz	Su and Zhang [77]
POE	$SrTiO_3$	0.4	11.0	0.010	0.9 GHz	Xiang *et al.* [159]
POE	$SrTiO_3$—NiZn ferrite		5.4	0.0018	100 Hz	Yang *et al.* [145]
PEEK	TiO_2	25 wt%	4.99	0.0087	8 GHz	Rajesh *et al.* [146]
PEEK	SrTiO3	27 wt%	5.27	0.003	1 MHz	Nisa *et al.* [127]
Poly(methymetho crylate)	$Ba_{0.6}Sr_{0.4}TiO_3$	0.416	1212	0.026	10 kHz	Xiang *et al.* [147]
Metallocene cyclic olefin copolymer	Soda lime borosilicate	0.36	1.92	0.0009	1 MHz	Yang *et al.* [148]
Cyclo-olefin polymer	MgO	0.3	3.8	0.0005	12 GHz	Takahashi *et al.* [156]
COC	BST	0.25	6.0	0.0023	1 GHz	Hu *et al.* [150]
Polyphenelene sulphide (PPS)	BST	0.7	13.5	0.0025	1 GHz	Hu *et al.* [151]
PPS	Mica/$SrTiO_3$	0.38	6.4	0.0052	210 GHz	Che *et al.* [152]
PPS	Mica/$SrTiO_3$	24/14 vol.%	6.4	0.0053	10 GHz	Walpta *et al.* [153]
Polyimide	$BaTiO_3$	0.9	117.0		1 MHz	Devaraju *et al.* [154]
Polyimide	$BaTiO_3$	0.1	35.0	0.0082	10 kHz	Devaraju *et al.* [154]
LCP	–	–	3.00	0.002	10 GHz	Takata *et al.* [100]
DGEBA	Mg_2SiO_4	0.4	3.8	0.014	7 GHz	Sasikala [157]

Epoxy	$Sr_9Ce_2Ti_{12}O_{36}$	0.4	14.1	0.022	8 GHz	Subodh *et al.* [75]
Epoxy	PMN—PT/$BaTiO_3$(3:1)	0.7	89.0	0.017	10 KHz	Bhalla *et al.* [158]
Epoxy	$BaTiO_3$	0.6	45.0	0.035	–	Ramajo *et al.* [134]
Epoxy	$BaTiO_3$	0.45	13.1	0.025	1 GHz	Lee *et al.* [135]
Epoxy	$SrTiO_3$	0.5	21.0		10 GHz	Lee *et al.* [135]
Epoxy	PMN—PT—$BaTiO_3$	0.7	110.0	0.016	–	Rao *et al.* [136]
Epoxy	Ca(Li,Nb,Ti)O_3	0.3	8.0	0.009	1 MHz	George and Sebastian [137]
Epoxy	Ca(Li, Nb,Ti)O_3—Ag	0.26 Ag	72.3	0.065	1 MHz	George and Sebastian [137]
Epoxy	$(Ba_{0.9}Sr_{0.1})(Ti_{0.9}Zr_{0.1})O_3$	70 wt%	25.2	0.035	1 MHz	Yang *et al.* [138]
Polypropylene	Zn_2SiO_4	0.335	2.98	0.00018	12 GHz	Takahashi *et al.* [139]
Polypropylene	$MgAl_2O_4$	0.2	3.0	0.00017	12 GHz	Takahashi *et al.* [140]
RT Duroid 6010 LM	PTFE–ceramic	–	10.24	0.0018		Rogers
RT Duroid 5880	PTFE–glass microfibers	–	2.2	–	2 GHz	Rogers
RT Duroid 5870	PTFE–glass microfibers	–	2.33	0.0023	10 GHz	Rogers
RT Duroid 6002		–	2.94	0.0012	10 GHz	Rogers
RO 4533			3.3	0.0020		Rogers
RO 4534			3.4	0.0022		Rogers
RO 4535			3.5	0.0032		Rogers
RO 4350			3.45	0.004	10 GHz	Rogers
FR4	Fiber glass reinforced epoxy		4.2	0.020	10 GHz	Rogers
TFG			3.2	0.003	10 GHz	Rogers
TPG30			2.87	0.0027	10 GHz	Taconic
TLG-29,TLG-30, TLG-32, TLG-33, TLG-34, TLG-35			2.87–3.5	0.0024–0.0029	10 GHz	Taconic
TLT	PTFE–fiber glass fabric		2.5	0.0006	1 MHz	Taconic
TLP	PTFE–fiber glass fabric		2.17	0.0009	10 GHz	Taconic
TLC			2.75–3.20	0.0030	10 GHz	Taconic
TLE			2.95–3.00	0.0028	10 GHz	Taconic
RF-35			3.5	0.0028	10 GHz	Taconic

(*continued*)

Table 11.4 *(Continued)*

Polymer	Filler	V_f	ε_r	$\tan\delta$	F_0	Reference
RF-35P			3.5	0.0035	10 GHz	Taconic
TSM-30			2.94	0.0012	10 GHz	Taconic
TLY	PTFE–woven glass		2.17–2.4	0.0009	10 GHz	Taconic
TLX	PTFE–woven glass		2.45–2.65	0.0019	10 GHZ	Taconic
Taclamplus			2.1	0.0004	10 GHz	Taconic
RF-60A			6.15	0.0038	10 GHz	Taconic
RF-41, RF-43, RF-45			4.10–4.50	0.0033–0.0038	10 GHz	Taconic
TRF -41, TRF-43, TRF-45	PTFE–woven glass reinforced		4.1–4.5	0.0035	10 GHz	Taconic
RF-30			3.00	0.0014	1.9 GHz	Taconic
HyRelex			2.6	0.0020	10 GHz	Taconic
C_εr-10			10.0	0.0035	10 GHz	Taconic
Arlon 25FR and 25N			3.38	0.0025	10 GHz	Arlon
FASTRISE 27			2.7	0.0020	10 GHz	Taconic
TSM29			2.94	0.0014	10 GHz	Taconic
CLTE			2.94–3.00	0.0012–0.0023		Arlon
TC350			3.5	0.0020		Arlon
TC600			6.15	0.0020		Arlon
AD255A, AD260, AD300A, AD320A, AD350A, AD410A, AD430A			2.55–4.3	0.0015–0.0035		Arlon
AD1000A			10.2	0.0023		Arlon
AD600			6.00	0.003		Arlon
AR1000			9.8	0.003		Arlon
25N			3.38	0.0025		Arlon
25FR			3.58	0.0035		Arlon
DiClad 880-PIM			2.17	0.0009		Arlon
IsoClad 917			2.17	0.0013		Arlon
CuClad 250 GT			2.40	0.001		Arlon
Nelco N4000-13			3.70	0.008		Nelco
Nelco 4000-13SI			3.4	0.008	10 GHz	Nelco
Nelco 400013SI			3.30	0.007		Nelco

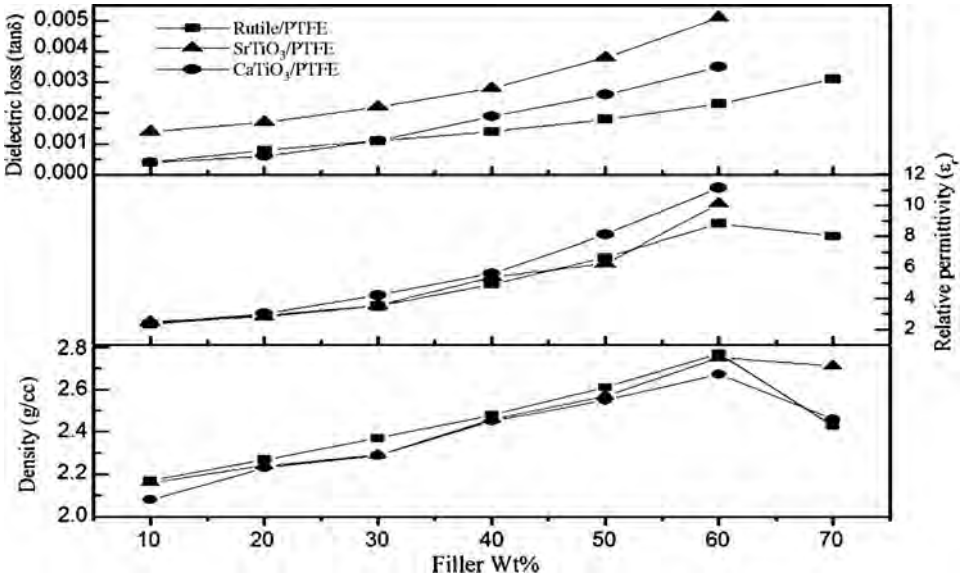

Figure 11.7 *Density, relative permittivity, and loss tangent of TiO_2, and $SrTiO_3$ filled PTFE composites.*

processing method was employed for the preparation of the composites wherein the matrix and filler are mixed thoroughly in the presence of a suitable solvent followed by compaction and hot pressing. The effects of different volume fractions of filler on the dielectric properties of the composites are investigated at radio and microwave frequencies. The microwave dielectric properties of the composites are given in Table 11.4. $Ba(Mg_{1/3},Ta_{2/3})O_3$ (BMT) ceramic-filled PTFE microwave substrate has a dielectric constant of 6.7 for 67 wt% BMT loading together with a loss tangent of 0.003 in the X-band frequency [52]. Sintered and powdered BMT ceramic-filled PTFE ceramic composite exhibited a lower loss tangent (tan $\delta = 0.0018$) compared to calcined BMT ceramic-filled composites (tan $\delta = 0.003$) due to the better structural ordering of the former. $MgTiO_3$-filled PTFE composites were prepared by Yuan *et al.* through the cold pressing and hot treating process for the fabrication of flexible composites for microwave substrate applications. Dielectric properties, density, moisture absorption, and thermal properties of the composites were reported from 30 to 70 wt% filler loading. The thermal expansion coefficient decreases whereas the moisture absorption increases as a function of filler fraction. The composite has a dielectric constant of 4.34 and a loss tangent of 0.00097 at 50 wt% filler loading [53].

Rajesh *et al.* reported [56] the effect of rutile grade TiO_2 filler on the microwave dielectric properties of PTFE composites. The optimum filler loading in the PTFE matrix using 3 μm rutile powder was observed to be around 67 wt%. At optimum filler loading, the PTFE/rutile composite has a dielectric constant of 10.2 with a loss tangent of 0.0022 at the X-band frequency region (Figure 11.7). Yuan *et al.* prepared [58] a composite substrate by dispersing TiO_2 and SiO_2 in colloidal PTFE in varying weight percentages for microwave application. The total content of TiO_2 and SiO_2 fillers was fixed at 55 wt% and the content of TiO_2 in the PTFE matrix varied from 1 wt% to 9 wt%. The influence of TiO_2 filler

loading on the microstructure, density, moisture absorption, microwave dielectric properties, and coefficient of thermal expansion of filled PTFE composites were investigated. The results revealed that the TiO_2- and SiO_2-filled PTFE composites exhibited good dielectric properties ($\varepsilon_r \sim 2.87$, $\tan\delta \sim 0.00075$) at a filler loading of 5 wt% TiO_2 and 50 wt% SiO_2 [58]. Rajesh *et al.* prepared [59] $CaTiO_3$-filled PTFE composites and found that the optimum loading possible with a 3 μm-sized filler in the PTFE matrix is around 61 wt%. Dimensionally stable microwave substrate with a relative permittivity of 11.8 and a loss tangent of 0.0036 at 10 GHz was realized at optimum filler loading. Hu *et al.* also prepared [60] $CaTiO_3$-filled PTFE composites by the powder processing technique for microwave frequency applications. The dielectric constant and the τ_f value of composites increased, while the *Qf* value decreased with increasing volume fraction of $CaTiO_3$ in composites. Composites with 40 vol.% $CaTiO_3$ exhibit $\varepsilon_r = 13$, $Qf = 930$ GHz, and $\tau_f = 260$ ppm/°C.

In order to improve the relative permittivity further, $SrTiO_3$-filled PTFE composite substrates have been prepared through the SMECH process by Rajesh *et al.* [61]. The effect of filler loading on the microwave dielectric properties of the composite substrates has been studied at the X-band region using the waveguide cavity perturbation technique. The optimum loading possible in the PTFE matrix with 5 μm $SrTiO_3$ filler was found to be around 63 wt%, wherein the composite sample exhibited a relative permittivity of 13.1 and a loss tangent of 0.0055 at 10 GHz.

Thomas *et al.* investigated [68] the effect of a coupling agent on properties of PTFE/$Sm_2Si_2O_7$ composites. The filler surface was chemically modified using phenyl trimethoxy silane (PTMS) as the coupling agent. The microstructural study using scanning electron microscopy (SEM) showed that the particles were well dispersed in the matrix when treated with phenyl trimethoxy silane (PTMS), as shown in Figure 11.8. The surface modification led to an improvement in the dielectric properties. The PTFE/$Sm_2Si_2O_7$ composites are prepared by the powder processing technique. The filler/matrix interaction was improved by modification of the filler surface using a PTMS coupling agent. The relative permittivity and dielectric loss increase with an increase in the filler content. It is seen that the surface modification leads to an improvement in the dielectric properties. The relative permittivity and dielectric loss of untreated PTFE/0.4 Vf $Sm_2Si_2O_7$ and silane coupled PTFE/0.4 V_f $Sm_2Si_2O_7$ composite are 3.78, 0.011 and 3.92, 0.0054, respectively. The experimental values of relative permittivity are found to match well with the effective medium theory even for a higher volume fraction of silane-treated filler. Porosity correction was applied to the effective relative permittivity of the composites. It was found that the addition of silane coupling agent is very effective in improving the thermal properties of the PTFE/$Sm_2Si_2O_7$ composites. Moreover, the CTE values of the silane-coupled composites are much lower when compared to that of the untreated one, which attracts much practical interest.

11.4.2 Temperature Variation of Relative Permittivity

The temperature coefficient of relative permittivity ($\tau_{\varepsilon_r'\varepsilon}$) is an important parameter since it affects the operating frequency while the substrate is used for outdoor wireless applications [69]. The $\tau_{\varepsilon_r'}$ of unfilled PTFE is about 400 ppm/°C whereas that of $SrTiO_3$ filler is around −3000 ppm/°C. The variation of $\tau_{\varepsilon_r'}$ of $SrTiO_3$-filled PTFE substrates in the temperature range 0 to 100 °C with filler loading is shown in Figure 11.9. Since the $\tau_{\varepsilon_r'}$ of the filler

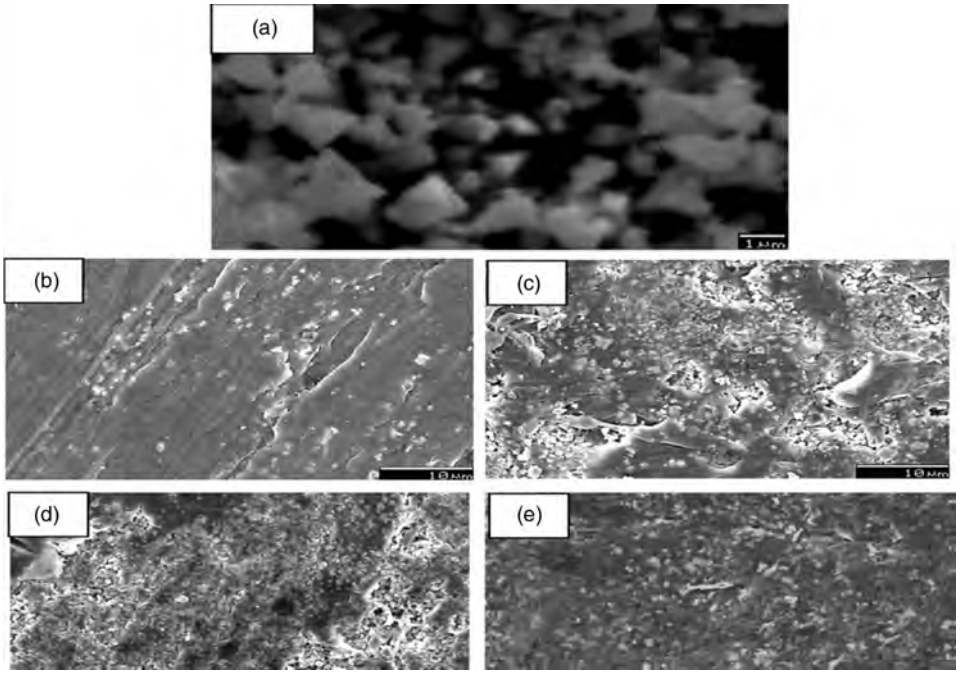

Figure 11.8 *SEM images of (a) $Sm_2Si_2O_7$ powder, PTFE loaded with (b) 0.1 V_f $Sm_2Si_2O_7$, (c) 0.3 V_f $Sm_2Si_2O_7$, (d) 0.5 V_f $Sm_2Si_2O_7$, and (e) 0.3 V_f silane-treated $Sm_2Si_2O_7$. Source: Thomas* et al. *2010 [68]. Reproduced with permission of Springer.*

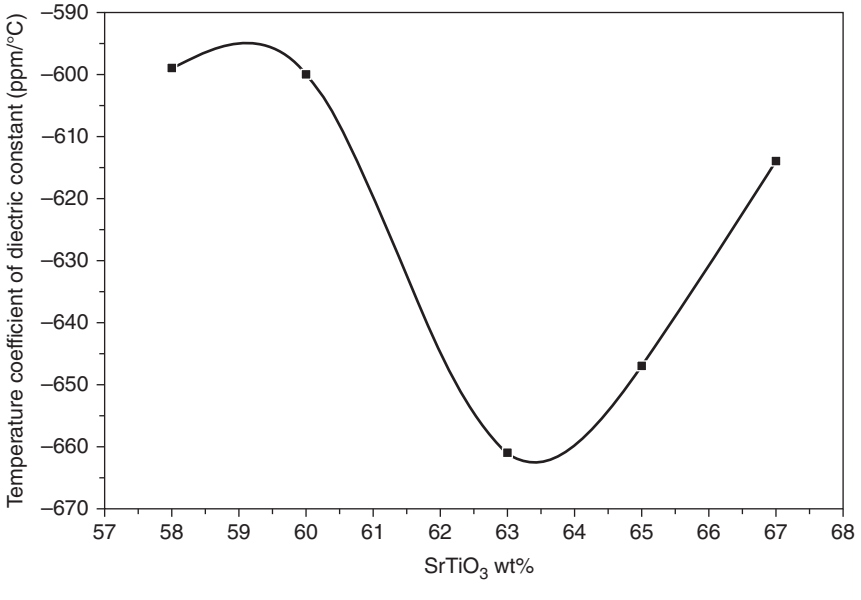

Figure 11.9 *Variation of dielectric constant and density with $SrTiO_3$ loading from 59 to 67 wt% at X-band. Source: Adapted from Rajesh* et al. *2009 [61].*

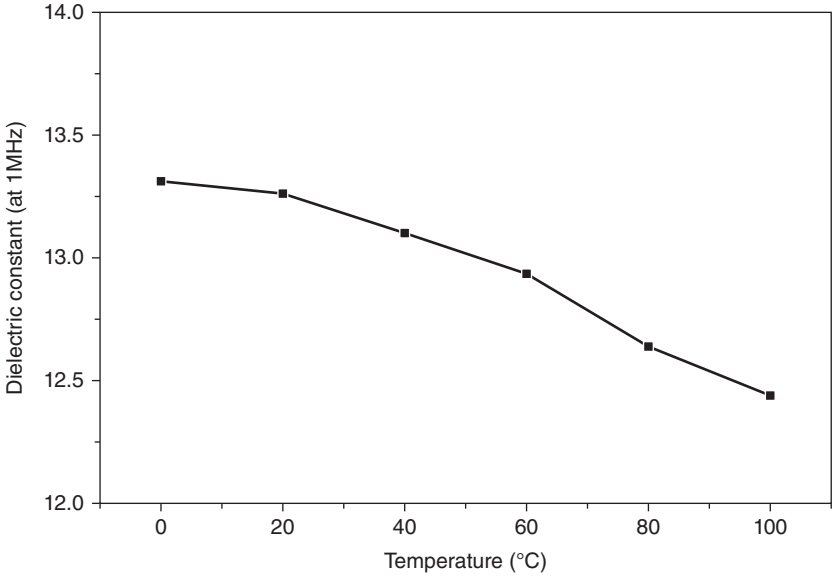

Figure 11.10 *Variation of relative permittivity with temperature for 63 wt% PTFE/$SrTiO_3$ composite. Source: Adapted from Rajesh 2009 [62].*

is a high negative value, the temperature coefficient of relative permittivity of composite system also changed to the negative direction. The $\tau_{\varepsilon_r'}$ of the optimum filler loaded (63 wt%) composite is reported as −661 ppm/°C [61, 62, 70]. The decrease in $\tau_{\varepsilon_r'}$ towards the negative direction after 63 wt% loading is due to the void formation since the composite has an optimum density at 63 wt%. The change in relative permittivity with respect to temperature for a 63 wt% $SrTiO_3$ loaded sample is shown in Figure 11.10. The change in relative permittivity is relatively high after 20 °C, which is reported as due to the phase change occurring in the PTFE matrix after the PTFE changes from triclinic to hexagonal crystal structure at around 19 °C [31]. The temperature coefficient of other high dielectric composites such as TiO_2- and $CaTiO_3$-filled PTFE composites [56, 57, 59] are shown in Figure 11.11.

11.4.3 Moisture Absorption Characteristics

Water is a polar molecule with non-linear H—O—H bonding and hence a high relative permittivity of about 78 for water with a high dielectric loss. Hence, absorption of water during circuit operation at high humid conditions may harm the dielectric properties of microwave substrates. Moisture absorption of the composites and associated degradation of electrical properties of PTFE composites have been studied by many authors [47, 53, 56, 57]. Moisture absorption of silane coated and uncoated rutile-filled PTFE composites are studied and reported as per IPC-TM-650 2.6.2 standards [71]. Samples having a dimension of 2 inch × 2 inch ($l \times b$) are taken for measurements. The weight gain by each composite after immersing in water for 24 h was noted using an electronic balance having four-digit accuracy and

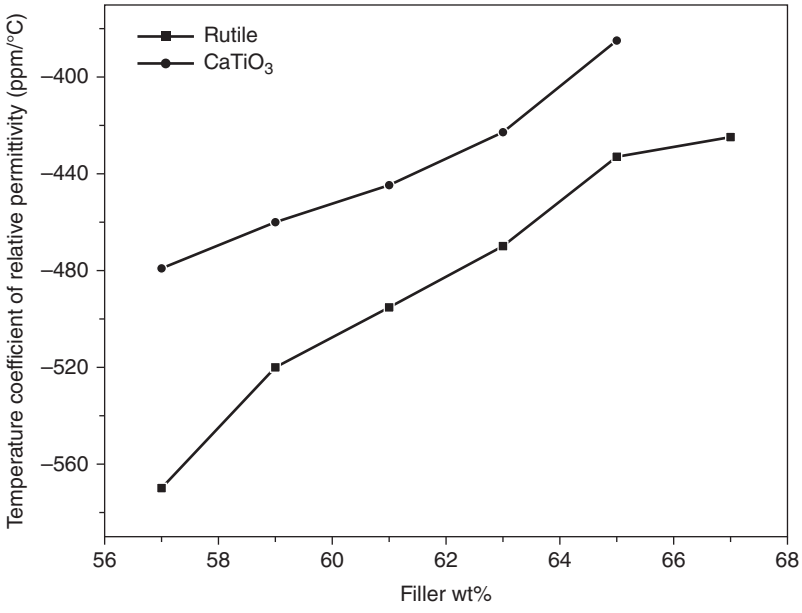

Figure 11.11 *Variation of $\tau\varepsilon_r$ with respect to filler concentration of TiO_2 and $CaTiO_3$. Source: Adapted from Rajesh 2009 [62].*

the moisture absorption percentage was calculated using the relation

$$\%\text{aAbsorption} = \frac{(\text{Final weight} - \text{Initial weight})}{\text{Final weight}} \times 100 \tag{11.3}$$

The moisture absorption of PTFE/rutile composites with silane-coated filler increases with filler loading (Figure 11.12). PTFE is a highly hydrophobic polymer matrix. Hence, the main contribution of the moisture absorption comes from the adsorbed water by the ceramic fillers and by the internal pores in the composite structures. Ceramics are in general hydrophilic and hence the main contribution to moisture absorption is by the adsorbed hydroxyl group in the ceramic surfaces. It is clear from the figure that the silane-coated rutile-filled PTFE composites exhibited a lower moisture content of 0.05% at optimum loading, which is within the accepted range for microwave substrate applications [56].

11.4.4 Coefficient of Thermal Expansion

The coefficient of thermal expansion (CTE) of polymer/ceramic composites is an important parameter that is used in packaging technology. Any mismatch between the CTE of the substrate and the outer conducting layer will lead to the peeling off from the circuit pattern during continuous operating cycles. In addition, a high CTE will result in poor stress relief and hence the solder and the interconnects will be affected by thermal shock. Hence, CTE has a very critical role in controlling the circuit performance of the composite substrates when used at very high frequencies. In order to match the CTE of the conducting copper layer, the CTE of the composite has to match with that of copper. Figure 11.13 shows the

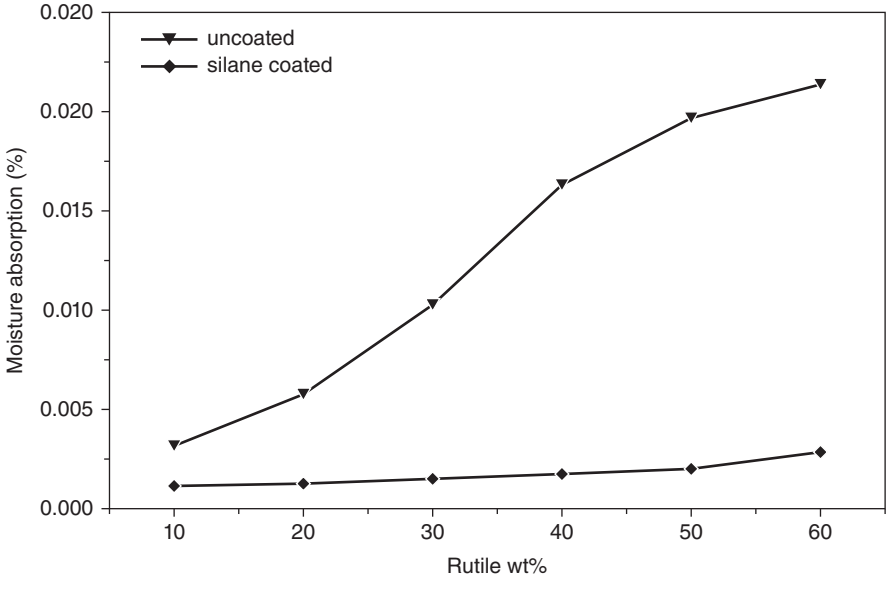

Figure 11.12 *Moisture absorption characteristics of silane coated and uncoated rutile-filled PTFE composites. Source: Adapted from Rajesh 2009 [62].*

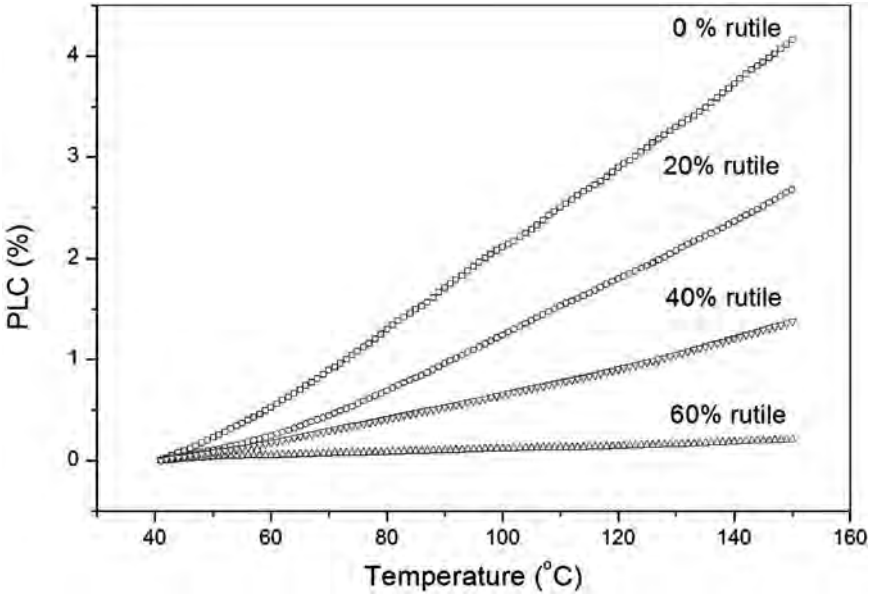

Figure 11.13 *Variation of percentage change in length with temperature at different rutile filler loadings. Source: Adapted from Rajesh 2009 [56].*

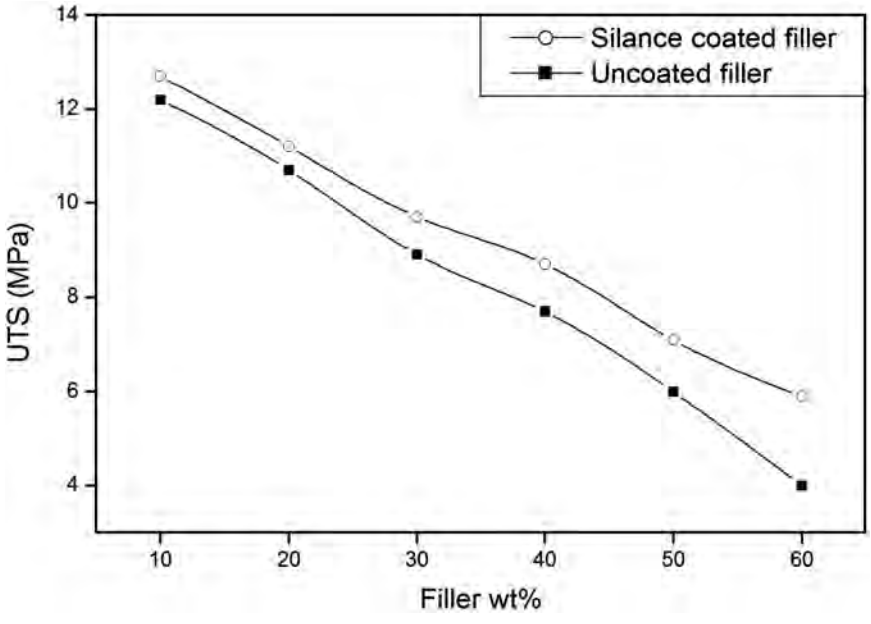

Figure 11.14 *Comparison of ultimate tensile strength of the PTFE-based composites prepared using the silane coated and uncoated fused silica as fillers. Source: Murali* et al. *2009 [46].*

variation of percentage change in length (PLC) with temperature at different filler loadings. A significant difference is not observed in the PLC between 20 and 40 wt% loaded composites, whereas PTFE loaded with 60 wt% rutile shows a significant reduction in the slope of the curve. It is clear that the coefficient of thermal expansion is reduced from 110 ppm/°C for virgin PTFE to 27 ppm/°C for 60 wt% rutile-loaded PTFE composites. At optimum filler loading the CTE is further reduced to 18 ppm/°C, which is comparable with that of a copper conducting layer [56].

11.4.5 Mechanical Properties

Figure 11.14 shows the comparison of ultimate tensile strength (UTS) with respect to filler loading for both the coated and the uncoated fused silica-filled composites. Silane-coated samples show higher UTS as compared to uncoated samples [46]. The reason for a comparatively high UTS obtained for silane-coated samples is due to an improved PTFE-fused silica–microfiber glass interface. However, PTFE does not make any chemical attachment with the phenyl group of the silane coupling agent (PTMS) used and the heavy phenyl group entangles with PTFE chains. The other end of the silane coupling agent makes the Si—O—Si bond with fused silica and the microfiber glass surface. The physical adhesion through phenyl group entanglement at one end and chemical adhesion with the fused silica on the other end of the silane coupling agent results in a good PTFE filler interface, which improves the mechanical strength of the composites prepared using the silane-coated filler.

11.5 Polyethylene–Ceramic Composites

The ceramic-filled polyethylene composites have been studied by several workers using $ZrSiO_4$, $Sm_2Si_2O_7$, CeO_2, $Sr_2Ce_2Ti_5O_{16}$, $Ca_4La_6(SiO_4)_4(PO_4)_2O_2$, $Mg_{0.95}Ca_{0.05}TiO_3$, $BaTiO_3$, and Li_2MgSiO_4 ceramic fillers for possible microwave substrate applications [73–84]. The ceramic-filled polyethylene composites were prepared by melt mixing and hot pressing techniques. The dielectric properties of the composites studied at radio and microwave frequencies show that as the amount of filler content increases the density and relative permittivity increases. The variation of relative permittivity with volume fraction of the filler at radio frequency is depicted in Figure 11.15 as a typical example for HDPE—$Sm_2Si_2O_7$ composites. The polyethylene/$Sm_2Si_2O_7$ composite exhibits a relative permittivity and loss tangent of 5.28 and 0.0091 at 8 GHz even at a higher filler content of 0.5 volume fraction. The microwave dielectric properties of HDPE–ceramic composites are given in Table 11.4. The relative permittivity and loss tangent increases with an increase in filler content.

Su and Zhang reported that the incorporation of $BaTiO_3$ into HDPE can result in composites with a high relative permittivity and low dielectric loss [77]. The addition of 50 vol.% $BaTiO_3$ increases the dielectric constant and loss of HDPE composite at 10 MHz from 2.5 and 0.02 to 18.5 and 0.10, respectively. The addition of 50 vol.% $BaTiO_3$ decreases the volume resistivity of HDPE composite from 3.6×10^{13} Ωm to 3.5×10^{11} Ωm, which exhibits the non-conducting nature of the composite even at 50 vol.% $BaTiO_3$ loading. In terms of

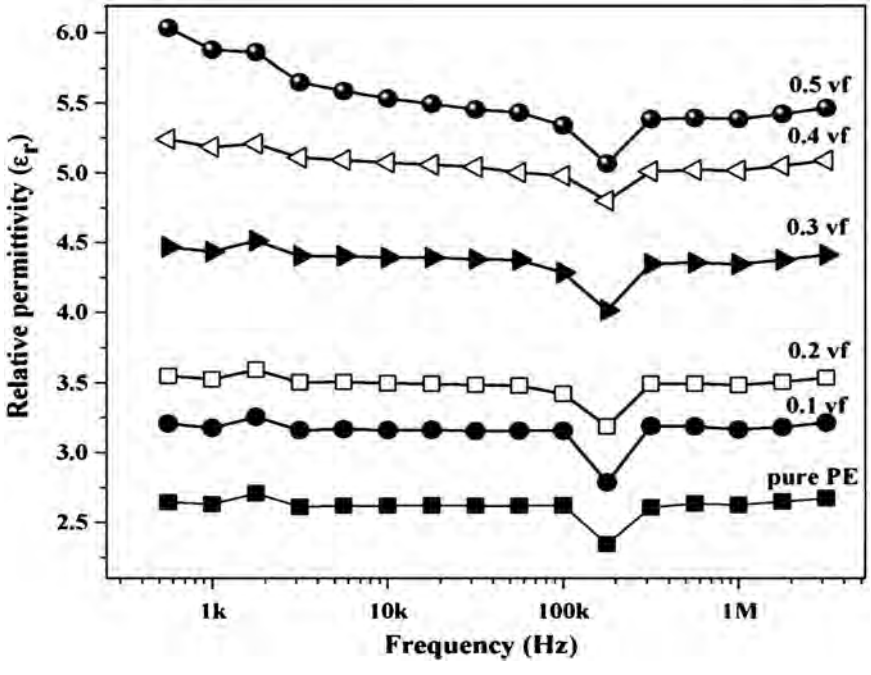

Figure 11.15 *Variation of relative permittivity with frequency for PE—$Sm_2Si_2O_7$ composites. Source: Adapted from Joseph* et al. *2011 [72].*

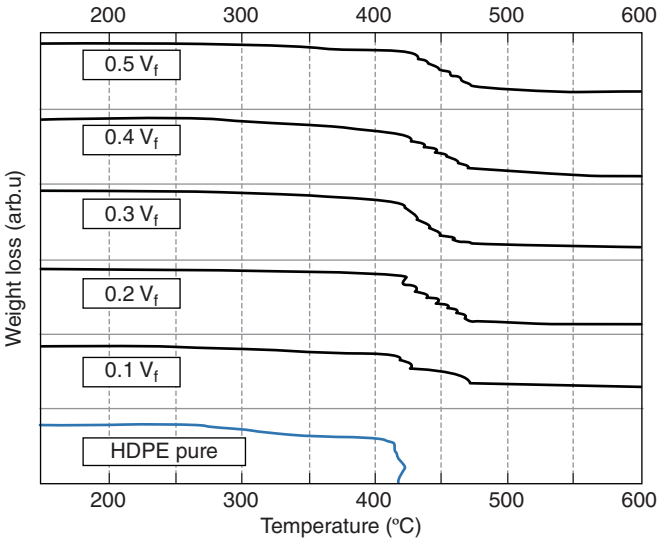

Figure 11.16 *TGA curve of HDPE matrix and its composite with $ZrSiO_4$ composites having different ceramic volume fractions. Source: Adapted from Varghese* et al. *2015 [84].*

mechanical properties, the increased amount of modified $BaTiO_3$ can increase the flexural strength and modulus of HDPE composites from 8 and 90 MPa to 14 and 780 MPa, respectively.

Varghese *et al.* [84] made a detailed study of the electrical, thermal, and mechanical properties of HDPE—$ZrSiO_4$ composites. Figure 11.16 shows the thermogravimetric analysis (TGA) of HDPE—$ZrSiO_4$ composites for different volume fractions of filler ceramic. The beginning of decomposition is the same for pure and for all volume fractions of $ZrSiO_4$ fillers while ending is extended between 400 and 500 °C. As the filler content increases the temperature at which weight loss occurs also increases. The TGA measurements of pure HDPE demonstrate that the weight loss starts at around 280 °C and becomes complete at around 400–450 °C. However, it has been reported that the thermal degradation of 99 wt% polymers starts at 402.84 °C for pure HDPE and 420 °C for reprocessed HDPE [85]. The degradation temperature of pure HDPE is around 405 °C and is increased by the addition of $ZrSiO_4$ fillers with the HDPE matrix. The degradation of HDPE—$ZrSiO_4$ composites completes at around 420 °C, as shown in Figure 11.16. The relative permittivity and dielectric loss tangent at 5 GHz increases with an increase in the volume fraction of the filler. The composite with a maximum filler loading of 0.5 volume fraction of $ZrSiO_4$ has an ϵ_r of 5.6 and a tan δ of 0.003. The dielectric loss tangent is the primary factor affecting the frequency selectivity of materials. The factors such as the anharmonic interaction of the electric field with the phonon system, imperfections in a crystal lattice, order–disorder, and impurities influence the loss tangent [86]. Considering the composite as a whole, additional effects arising from the heterogeneity, the porosity, and the matrix–filler interphase region may also affect the loss factor [86, 87].

The prediction of effective relative permittivity of polymer–ceramic composites is very important for engineering applications. Several numerical relations have been proposed to

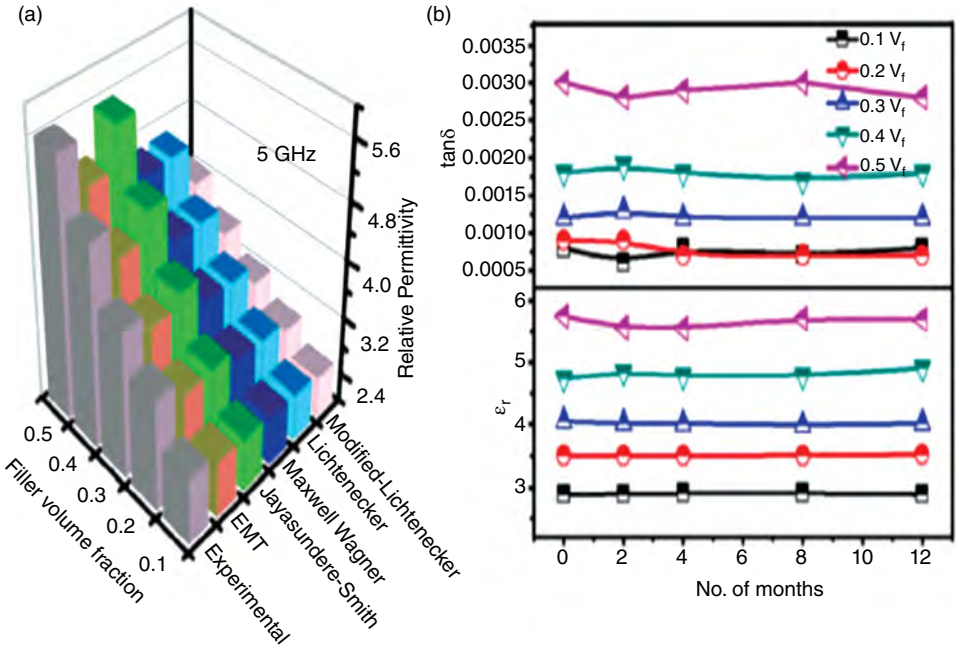

Figure 11.17 *(a) Comparison of experimental and theoretical relative permittivity, (b) effect of aging on microwave dielectric properties of HDPE—$ZrSiO_4$ composites at 5 GHz. Source: Adapted from Varghese* et al. *2015 [84].*

predict the relative permittivity of these structures and are discussed in Chapter 2. These models can be used to determine the extent of filler dispersion and filler–matrix compatibility by comparing the predicted values with the experimental data. In order to understand the physical mechanisms controlling the relative permittivity of the composites, the experimental values of ε_r are compared with values predicted using different theoretical models. Figure 11.17a depicts the comparison of the experimentally observed values of relative permittivity at 5 GHz with the theoretical predictions for HDPE–$ZrSiO_4$ composites. The Lichtenecker model shows a wide deviation from the experimental values even for low filler loadings. The Lichtenecker model describes the composite system as a continuous matrix with randomly oriented spheroids. This model does not provide an appropriate match to the experimentally observed values of relative permittivity for HDPE—$ZrSiO_4$. The conventional mixing rule and the Lichtenecker model do not explain the filler matrix interactions. The modified Lichtenecker equation describes the filler matrix interaction by introducing a correction factor. However, the modified Lichtenecker model also shows a considerable deviation in the experimental and theoretical values and may be due to the difference in the basic concept of the models. The values of relative permittivity obtained using Maxwell–Wagner and EMT models show a considerable difference between the experimentally observed values, especially at higher filler loading. The values of relative permittivity obtained using the Jayasundere–Smith model are found to match the experimental data. This model assumed a biphase system consisting of dielectric spheres dispersed in a continuous medium of the matrix and hence is suitable for both lower and higher filler loadings.

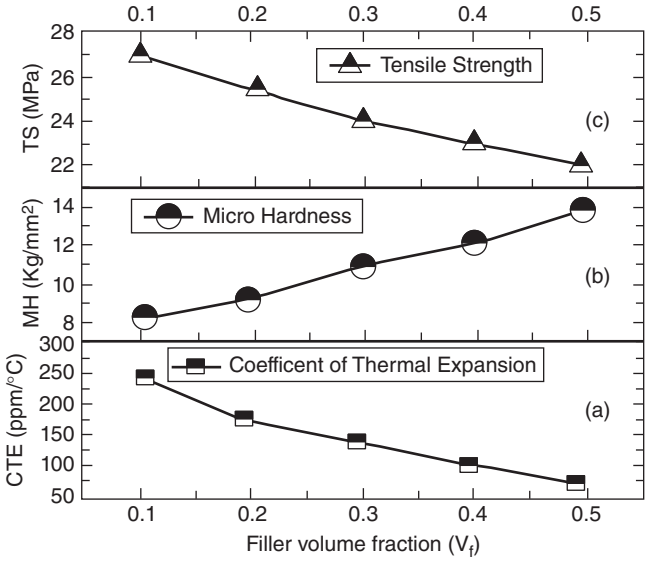

Figure 11.18 *Variation of (a) linear thermal expansion, (b) microhardness, and (c) tensile strength with filler volume fraction of HDPE—$ZrSiO_4$ composites. Source: Adapted from Varghese* et al. *2015 [84].*

However, the effective permittivity will depend on the permittivity of each phase in the mixture, volume fraction, shape and size of the filler particle, porosity, and interface between the matrix and the filler. The aging of microwave dielectric properties of the HDPE—$ZrSiO_4$ composite is important for practical applications. Figure 11.17b depicts the effect of the shelf life on microwave dielectric properties of HDPE—$ZrSiO_4$ composites at 5 GHz. From Figure 11.17b, it is evident that over a period of one year, a relative permittivity and a dielectric loss tangent of HDPE—$ZrSiO_4$ composites exhibit only a marginal deviation and are within the error limits of microwave measurements. The variation in the dielectric loss of 0.1 volume fraction after 2 months of measurement may be due the atmospheric humidity and moisture absorption within the sample.

Figure 11.18a shows the variation of the linear coefficient of thermal expansion (CTE) of HDPE—$ZrSiO_4$ composites with the filler volume fraction. The CTE value decreases gradually with an increase in filler volume fraction and is due to the very low CTE value possessed by the $ZrSiO_4$ filler as compared to the polymer matrix. It is evident from the figure that CTE decreases almost linearly from 243 to 70 ppm/°C as the filler loading increases from 0.1 to 0.5 volume fraction. This is due to the higher CTE of the HDPE matrix (250 ppm/°C) [72] than that of the $ZrSiO_4$ filler (–2.5 ppm°C) [88]. During heating of the composites, the polymer matrix will undergo more expansion as compared to ceramic fillers. However, the matrix–filler interphases are able to transmit the thermal stress and the expansion of the matrix will reduce. The CTE of the matrix will be lowered if the interfaces between the matrix and the filler are capable of transmitting the stress developed [130,131]. In HDPE—$ZrSiO_4$ composites, the linear decrease in CTE with the filler volume fraction indicates that the matrix–filler adhesion is good enough to withstand the thermal stress.

Microhardness testing with a point indenter is a simple method to measure the mechanical properties of the soft substrates. Figure 11.18b shows the variation of microhardness of HDPE matrix composites with $ZrSiO_4$ ceramic filler addition. Microhardness of $ZrSiO_4$ is reported to be in the range of 800–1200 kg/mm^2 [132] while a pure HDPE matrix has only 7 kg/mm^2. As the volume fraction of $ZrSiO_4$ increases, the hardness of HDPE—$ZrSiO_4$ composites also increases. Microhardness increases from 8.2 to 13.9 kg/mm^2 for the variation in the filler loading from 0.1 to 0.5 volume fraction with a standard deviation of 0.45. Figure 11.18c shows the variation of tensile strength of the HDPE—$ZrSiO_4$ composites with filler loading. The tensile strength decreases from 27 to 22 MPa as the filler concentration increases from 0.1 to 0.5 volume fraction. The mechanical strength of HDPE is mainly due to its semicrystalline structure. When the polymers are loaded with more and more inorganic fillers, the deformation area in the matrix decreases, which in turn reduces the tensile strength [133]. Moreover, the increase in porosity with filler loading may also bring about a reduction in tensile strength as the presence of air in the composites weakens the filler–matrix interface [46]. The weak interface is one of the reasons for reduced tensile strength. The interface volume increases at a higher filler loading, which leads to more filler–filler interaction and hence weakens the filler–matrix interface of the composite.

Sarmah *et al.* reported [89] the microwave dielectric properties of the titania-filled low-density polyethylene composite system at 10 GHz as an alternative substrate for microstrip patch antennas (MPAs) for handheld devices. Morphological, thermal, and microwave characterization of the composite have been studied for different volume fractions of TiO_2 in the polymer matrix. The relative permittivity of the TiO_2-filled LDPE composite has increased from 2.27 to 2.49 and the loss tangent from 0.0038 to 0.0053 while varying the filler concentration from 0 to 6%. The microstrip patch antenna fabricated using LDPE/TiO_2 substrate showed a return loss of −17 dB at 10 GHz (Figure 11.19).

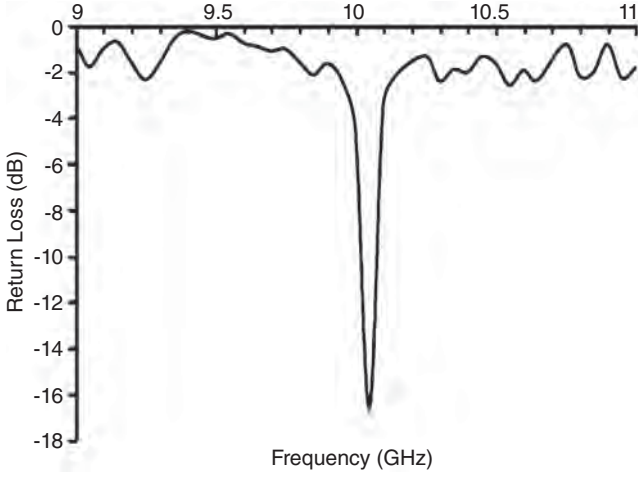

Figure 11.19 *Return loss study of rectangular microstrip patch antenna designed with 4% V_f of TiO_2 in LDPE substrate at 10 GHz. Source: Adapted from Sarmah* et al. *2010 [89]. Reproduced with permission of Springer.*

11.6 Polystyrene–Ceramic Composites

Several researchers investigated [72, 74, 76, 90, 91] the microwave dielectric properties of polystyrene reinforced with ceramics such as $Sm_2Si_2O_7$, Li_2MgSiO_4, $Ca[(Li_{1/3}Nb_{2/3})_{0.8}Ti_{0.2}]O_{3-\delta}$, and $Sr_2Ce_2Ti_5O_{15}$, and Mg_2SiO_4. The polystyrene (PS) ceramic composites are prepared by melt mixing followed by hot pressing. The microwave dielectric properties of the PS–ceramic composites are given in Table 11.4. Recently Sasikala and Sebastian [91] reported forsterite of (Mg_2SiO_4)-filled polystyrene composites. Figure 11.20 shows the typical microstructure polystyrene–Mg_2SiO_4 composites revealing the surface morphology and filler distribution with different volume percentages of filler loading. At a low filler loading, uniform dispersion of ceramic particles can be observed (Figure 11.20a and c). Hence, the continuous matrix phase provides a major contribution to the dielectric and thermal properties of these composites. As the filler content is increased, the interparticle distance decreased, which in turn increased the connectivity between the ceramic particles. The connectivity of the individual components is important because it controls the electric flux pattern as well as the mechanical and thermal properties. However, beyond the 40 vol.% filler loading, the packing of the particles grew denser, leading to agglomeration (Figure 11.20b and d). The fractured surface of PS–Mg_2SiO_4 composite revealed a weak interface region at a higher filler loading (Figure 11.20d).

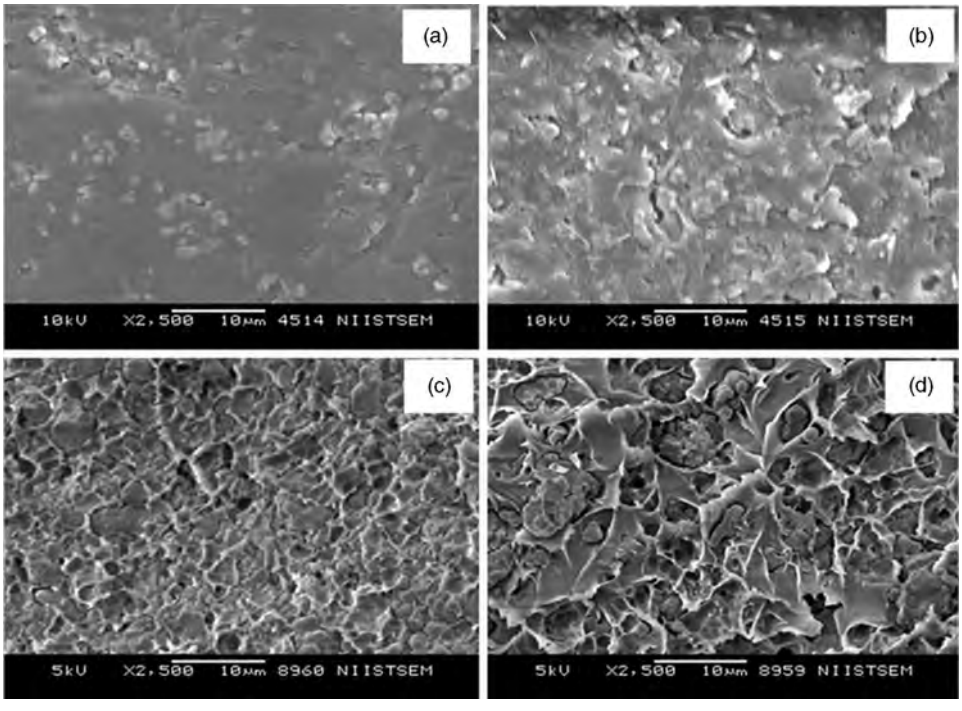

Figure 11.20 *SEM images of (a) PS–10 vol.% Mg_2SiO_4, (b) PS–50 vol.% Mg_2SiO_4, (c) fractured surface of PS–10 vol.% Mg_2SiO_4, and (d) fractured surface of PS–50 vol.% Mg_2SiO_4. Source: Adapted from Sasikala and Sebastian 2016 [91].*

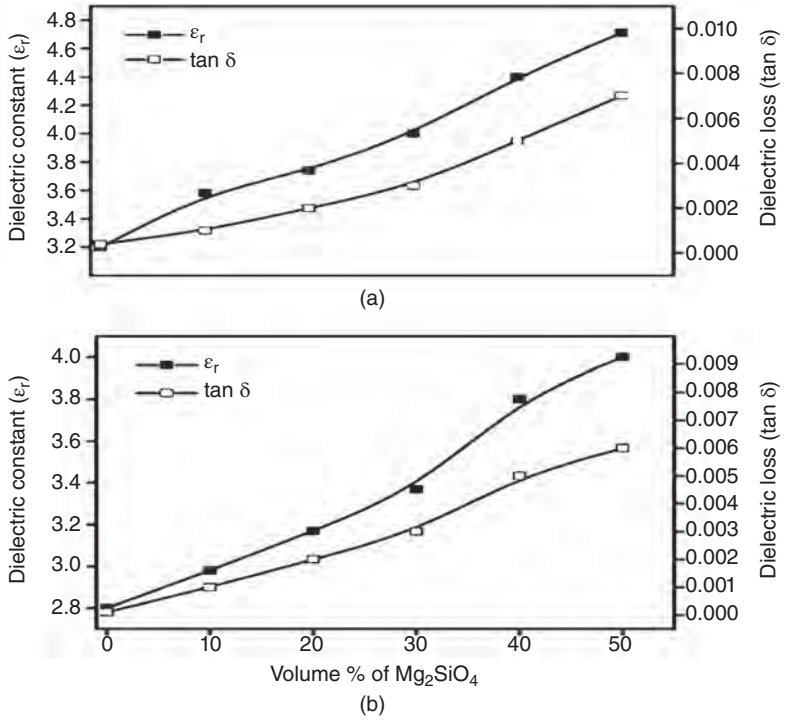

Figure 11.21 *Variation of dielectric constant and loss tangent of PS—Mg_2SiO_4: (a) 1 MHz and (b) 5 GHz as a function ceramic filler content. Source: Adapted from Sasikala and Sebastian 2016 [91].*

It was found that the relative permittivity and loss tangent increased with an increase in filler content. Figure 11.21 shows the variation of relative permittivity and loss tangent of polystyrene–Mg_2SiO_4 composites as a function of filler volume fraction as a typical example. Figure 11.21a and b shows the dielectric properties of the PS—Mg_2SiO_4 composites at 1 MHz and 5 GHz, respectively. In both cases, a gradual increase in the dielectric constant and dielectric loss is observed with increasing ceramic loading. The increase in the dielectric constant of the PS—Mg_2SiO_4 composites is due to the relatively higher dielectric constant of Mg_2SiO_4 as compared with PS. The dielectric constant increased from 3.2 to 4.7 at 1 MHz and from 2.8 to 4 at 5 GHz as the filler content was varied from 0 to 50 vol.%. The dielectric loss depends on intrinsic and extrinsic factors. The intrinsic factors are mainly due to the interaction of the alternating current (AC) electric field with phonons. Extrinsic factors such as defects, interfaces, micropores, and the size and shape of the filler also contribute to the dielectric loss. Agglomeration of filler particles and entrapped porosity may be the reasons for the increase in the tan δ values of the composites with increasing filler loading. The composite containing 0.5 volume fraction of filler shows a relative permittivity of 4.0 and tan δ of 0.006 at 5 GHz. In a similar way the ε_r and tan δ of $Sm_2Si_2O_7$, Li_2MgSiO_4, $Ca[(Li_{1/3}Nb_{2/3})_{0.8}Ti_{0.2}]O_{3-\delta}$, and $Sr_2Ce_2Ti_5O_{15}$ are found to increase with an increase in filler loading [72, 74, 76, 90].

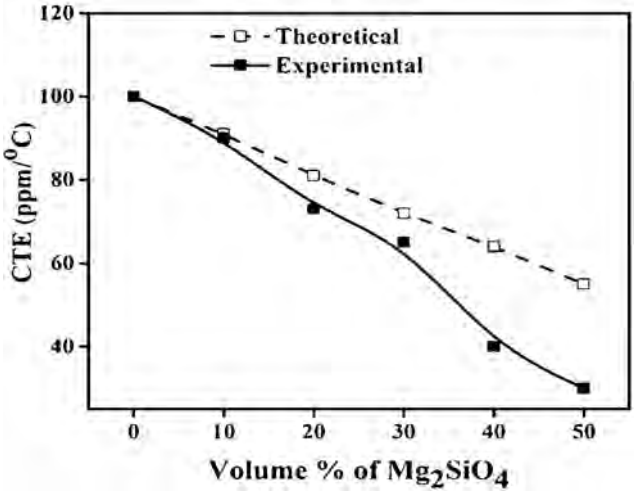

Figure 11.22 *Variation of CTE of PS—Mg_2SiO_4 composites with filler loading. Source: Adapted from Sasikala and Sebastian 2016 [91].*

The thermal expansion coefficient of the composite is very important in relation to its dimensional stability, compatibility with metal electrodes, mechanical robustness, etc., when applied to microwave substrate applications. Figure 11.22 shows the variation of the CTE of the PS—Mg_2SiO_4 composites with the filler loading. Mg_2SiO_4 has a CTE of 9 ppm/°C in the temperature range of 25 to 120 °C, while PS has a relatively high value of 100 ppm/°C. Incorporation of Mg_2SiO_4 resulted in the reduction of the CTE from 100 ppm/°C for PS to 30 ppm/°C for the composite at 50 vol.% filler loading. The presence of ceramic with low CTE causes the polymer chains to become arrested and unable to expand with temperature. A considerable amount of work has been done on predicting the thermal expansion coefficient of composites [92, 93]. The rule of mixtures serves as a first-order approximation to the overall calculation of the CTE of the composite:

$$\alpha_c = \upsilon_f \alpha_f + (1 - \upsilon_f)\alpha_m \tag{11.4}$$

where α_c, α_m, and α_f are the CTE of the composite, matrix, and filler, respectively.

The experimental results were compared with the theoretical prediction using the rule of mixtures given by Equation (11.4). The experimental values show a large deviation from the theoretical predictions, especially at high filler loadings where the porosity is relatively high. In a similar way the CTE of $Sm_2Si_2O_7$, Li_2MgSiO_4, $Ca[(Li_{1/3}Nb_{2/3})_{0.8}Ti_{0.2}]O_{3-\delta}$, and $Sr_2Ce_2Ti_5O_{15}$ are found to decrease with the filler loading. The thermal stability of PS was found to increase with the filler loading and PS—Mg_2SiO_4 composites were found to be thermally stable up to 300 °C. A typical differential scanning calorimetry (DSC) thermogram of the PS–40 vol.% Mg_2SiO_4 composite in the heating mode is shown in Figure 11.23. The glass-transition temperature (T_g) of PS is 94 °C and is not affected by incorporation of even 40 vol.% Mg_2SiO_4.

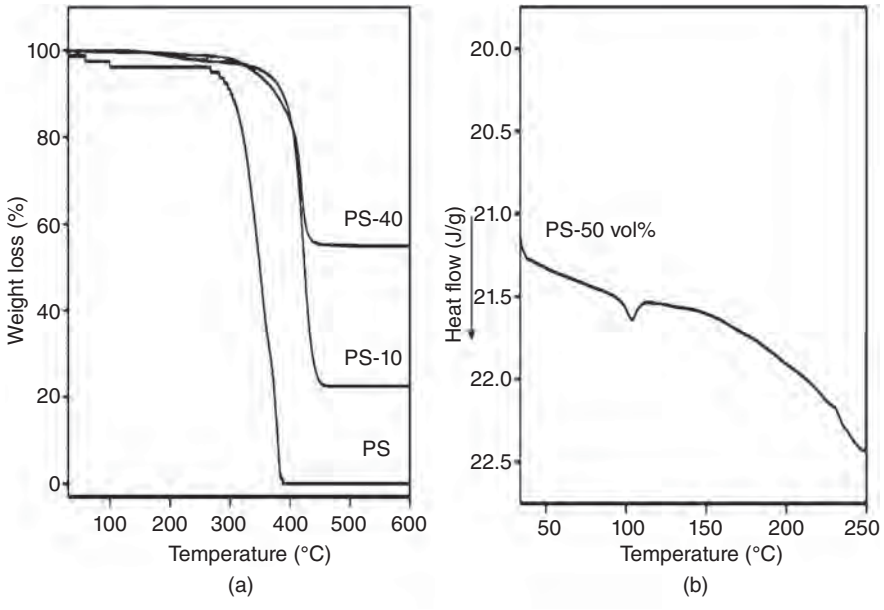

Figure 11.23 *(a) TGA and (b) DSC plot of PS—Mg_2SiO_4 composites. Source: Adapted from Sasikala and Sebastian 2016 [91].*

11.7 Epoxy Ceramic Composites

Ceramic-filled epoxy resin with tailored dielectric and thermal properties have been studied by various research groups [75,94–98] using fillers such as boron nitride, $SrTiO_3$, Mg_2SiO_4, $(Zr_{0.8}Sn_{0.2})TiO_4$, $Ca[(Li_{1/3}Nb_{2/3})O_{0.8}Ti_{0.2}]O_{3-\delta}$, and $Sr_9Ce_2Ti_{12}O_{36}$. Sasikala *et al.* prepared [94] diglycidyl ether of bisphenol A (DGEBA)–forsterite composites through the mechanical mixing process and investigated the influence of silane coupling agent on the microstructure, dielectric, and thermal properties. Phase pure forsterite (Mg_2SiO_4) powder was prepared through the solid-state ceramic route and the filling fraction of forsterite in the DGEBA matrix was varied from 10 to 40 vol.%.

SEM micrographs of fractured samples of DGEB–forsterite composites are shown in Figure 11.24. There are areas without filler and small trials of microporosity are observed in samples made without surface-coated fillers. In these samples, particle distribution is not homogeneous and particle agglomeration appears at higher filler volume fractions (Figure 11.24a and b). Composites prepared using silane-treated fillers result in a more homogeneous distribution of filler (Figure 11.24c and d).

The aminosilane treatment increased the relative permittivity and dielectric loss of the composites in both microwave and radio frequency ranges compared to composites prepared using untreated powders. A 40 vol.% silane-treated forsterite-filled DGEBA composite exhibited a relative permittivity of 3.9 and a loss tangent of 0.016 at 7 GHz. Figures 11.25 and 11.26 show, respectively, the variation of relative permittivity and loss factor with volume fraction of forsterite for both silane treated and untreated DGEBA forsterite

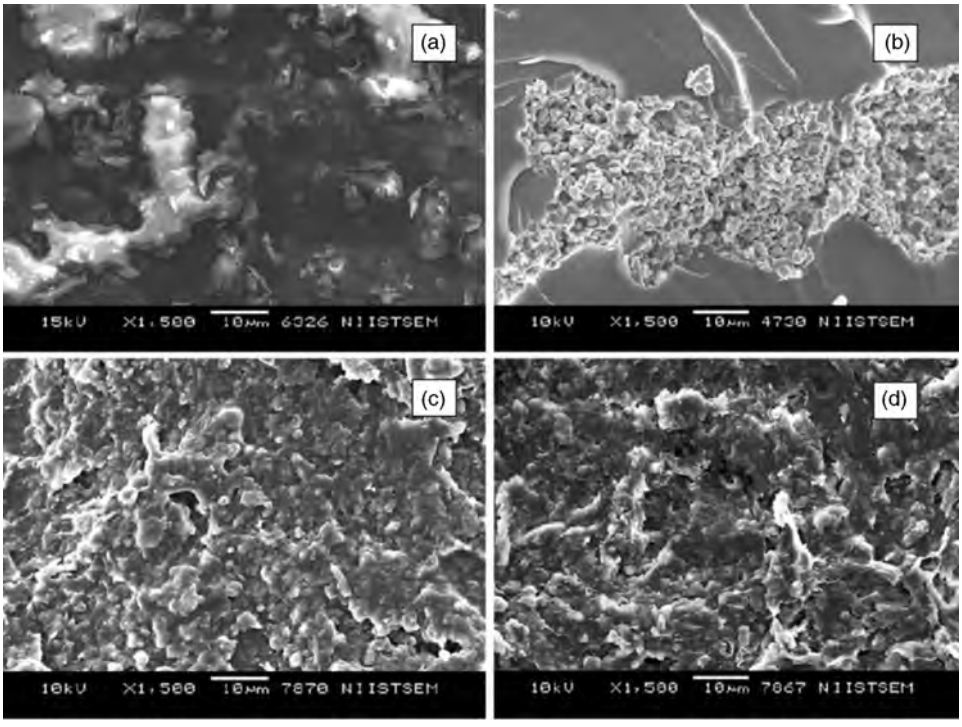

Figure 11.24 *SEM images of fractured surface of DGEBA: (a) 10 vol.% Mg_2SiO_4 (untreated), (b) 40 vol.% forsterite (untreated), (c) 10 vol.% fosterite silane (treated), and (d) 40 vol.% forsterite silane (treated). Source: Adapted from Sasikala* et al. *2011 [94].*

composites at radio and microwave frequency ranges. The relative permittivity increased gradually with an increase in the ceramic content, while the loss factor decreases as expected since the ceramic has a lower loss factor than the DGEBA. It is found that aminosilane treatment increased the relative permittivity and loss factor of the composites in both microwave and low-frequency ranges compared to composites prepared using untreated powders. The increase in relative permittivity can be attributed to the uniform dispersion of the forsterite powder in the DGEBA matrix, lower porosity, and the enhanced polarization from the dipole–dipole interaction of closely packed powders, as compared with untreated forsterite–DGEBA composites.

Huang *et al.* reported [95] the epoxy composites with boron nitride spheres and flakes as filler materials with distinct characteristics and loading levels (0, 10, 20, and 30 wt%). The relative permittivity and loss tangent remain low in both boron nitride spheres and flakes-loaded composites, even at higher loading levels of 30 wt%. The 30 wt% boron nitride flakes-filled epoxy composites exhibited a very high thermal conductivity of 0.933 W/m K, which is 366.8% that of the neat epoxy (0.259 W/m K). The preparation and microwave dielectric properties of $Ca[(Li_{1/3}Nb_{2/3})O_{0.8}Ti_{0.2}]O_{3-\delta}$ epoxy-filled polymer composites for microwave substrate applications is reported by George *et al.* [97]. The epoxy of CLNT exhibited a relative permittivity of 7.1 and a loss tangent of 0.01 at 9 GHz. A coplanar

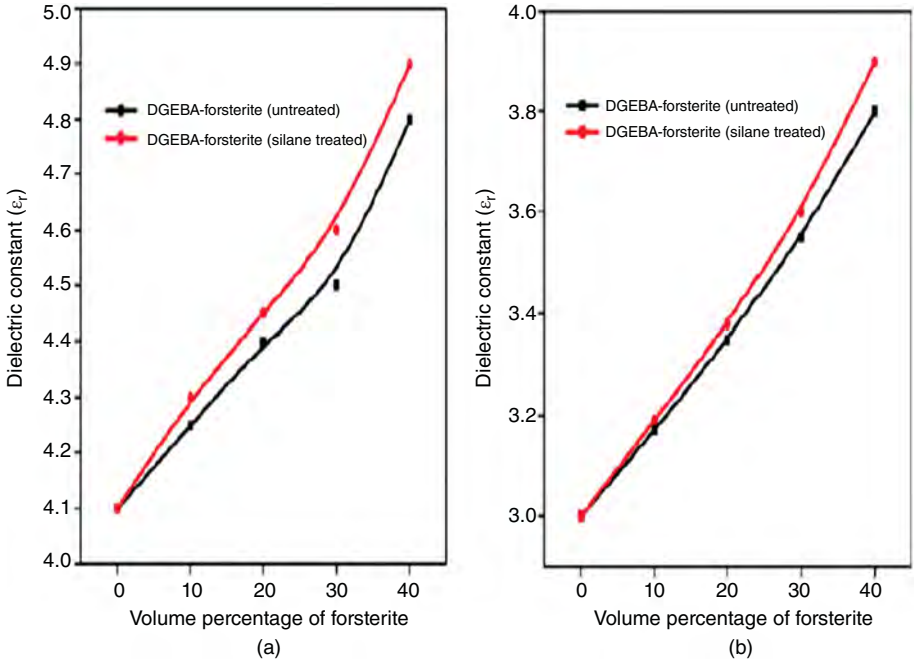

Figure 11.25 *Variation of relative permittivity of DGEBA with vol.% of fosterite for both silane treated and untreated measured at (a) 1 MHz and (b) 7 GHz. Source: Adapted from Sasikala* et al. *2011 [94].*

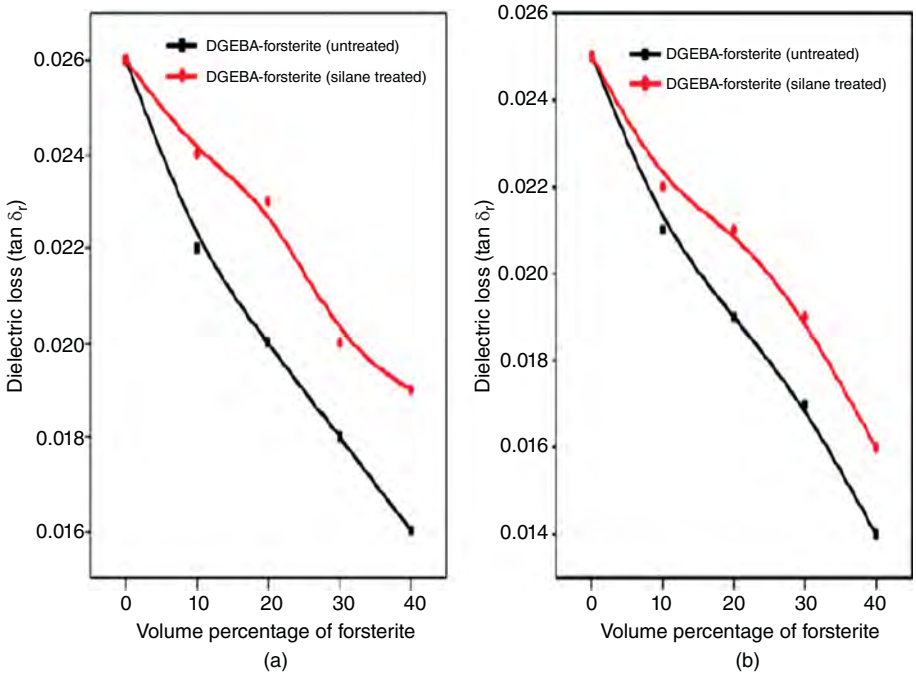

Figure 11.26 *Variation of loss tangent of DGEBA with vol.% of fosterite for both silane treated and untreated measured at (a) 1 MHz and (b) 7 GHz. Source: Adapted from Sasikala* et al. *2011 [94].*

waveguide monopole antenna has been designed and fabricated using epoxy–CLNT composite and its response was compared with standard FR-4 epoxy. Subodh *et al.* reported [75] the dielectric response of the $Sr_9Ce_2Ti_{12}O_{36}$ ceramics loaded in epoxy resin. 40 vol.% ceramic loaded epoxy composite has a relative permittivity of 14.1 and a loss tangent of 0.022, respectively, at 8 GHz. Epoxy/$SrTiO_3$ composite embedded capacitor films (ECFs) were fabricated by Lee *et al.* [98] for high-frequency applications. Relative permittivities of epoxy $SrTiO_3$ composite embedded capacitor films with various $SrTiO_3$ particle loadings were measured using a rectangular cavity resonator method. At microwave frequencies, 50 vol.% of $SrTiO_3$-filled epoxy composites exhibited a relative permittivity of ∼20, which is stable in the 2 to 10 GHz range, whereas $BaTiO_3$-filled epoxy composites showed a decrease in relative permittivity as a function of frequency.

11.8 Liquid Crystal Polymer (LCP)

Liquid crystal polymer (LCP) has gained much attention recently as an organic dielectric material for flexible microwave substrate and also for packaging applications. LCPs are interesting theomoplastic polymers whose molecules can be mutually aligned and organized, whereas the bulk LCP can flow like a liquid in the molten stage. The liquid crystal state results from the rigid nature of the segments of the LCP molecules. When LCP flows in the liquid crystal state, the rigid segments of the molecules align next to one another in the shear flow direction, creating locally oriented regions. Once the oriented regions are formed, their direction and structure persisits even when the LCP approaches the melt tempererature as a result of the long relaxation time of the stiff chain LCP molecules. Farell and Lawrence [99] reported biaxially oriented LCP substrates suitable for microwave and millimeter wave circuit designs. LCP possesses unique features such as a low relative permittivity, low-loss tangent, extremely low moisture absorption, high operating temperature, and chemical resistance, together with a hermetic nature. In addition, adhesive-free conductor clad laminates can be realized because of their thermoplastic nature. LCP is also environment friendly and recyclable [99–103].

The dielectric properties of LCP and the performance of various planar transmission lines on LCP substrates have been characterized up to 110 GHz by Thompson *et al.* [101]. Microstrip ring resonators and cavity resonators have been measured in order to characterize the relative permittivity (ε_r) and loss tangent ($\tan\delta$) of LCP above 30 GHz. The measured relative permittivity up to 106.4 GHz is shown to be steady near 3.16, and the loss tangent stays below 0.0049. Broadband extraction was found to be reliable using both ring and cavity resonators, but the cavity resonator measurement is found to be the most accurate method for loss-tangent extraction at millimeter wave frequencies. Transmission lines of various impedances and types on different LCP substrate thicknesses show a maximum attenuation of 0.88–2.55 dB/cm at 110 GHz. LCP is shown to be very attractive as a high-performance low-cost substrate and as a packaging material for various applications throughout the millimeter wave frequency spectrum [101]. Takata and Pham reported [100] the design and fabrication of various planar transmission lines including ring resonators, T-resonators, and microstrip lines on LCP films to demonstrate the electrical performance. They also demonstrated compact bandpass filters using LCP flex and compared the characteristics with that of LTCC. Kingstey [102] reported that LCP is the forerunner in

microwave materials, especially for applications requiring flexible or conformal electronics. LCP offers low-loss performance through W-band, dielectric stability, and low cost. LCP is also an excellent packaging material and fabrication of the multilayer device is a straightforward process since a low melting temperature bond ply is available. In addition, very few design considerations need to be given to the packaging effects since the relative permittivity of LCP is low. Park *et al.* [103] reported the dielectric properties of $(100 - x)$ LCP–x $BaNd_2Ti_4O_{12}$ ($x = 0, 10, 20, 30, 40$ vol.%) composites. LCP resin was initially melt mixed in a twin screw extruder and BNT filler is dispersed with the melted LCP resin. The composite specimens are prepared by hot pressing the LCP–BNT granules at 310 °C. At 30 vol.% filler loading the composite exhibits a relative permittivity of 6.3 and a loss tangent of 0.013 at 1 MHz.

11.9 Thermal Conductivity

Materials for electronic packaging require high thermal conductivity in order to dissipate heat generated in the devices, especially during switching on/off of the devices. Thus, there is a need to predict and model the thermal conductivity of the composites in a number of industrial processes. The thermal conductivity of polymers is generally very low as compared to ceramics. Polymer–ceramic composites are commonly used as substrates for packaging as dissipation of the heat generated is essential in electronic devices. It is well known that the addition of a high thermal conductivity material such as aluminum nitride as a filler effectively improves the thermal conductivity of polymers or polymer composites [104–106]. Epoxy–silica composites has been extensively used for electronic packaging applications since they have excellent mechanical and electrical properties with ease of fabrication and low cost. Silica has a relatively low thermal conductivity of 1.5 W/m K. Wong and Bollampally incorporated thermally conducting fillers such as alumina, aluminum nitride in epoxy, to improve the thermal conductivity [104]. Figure 11.27 shows

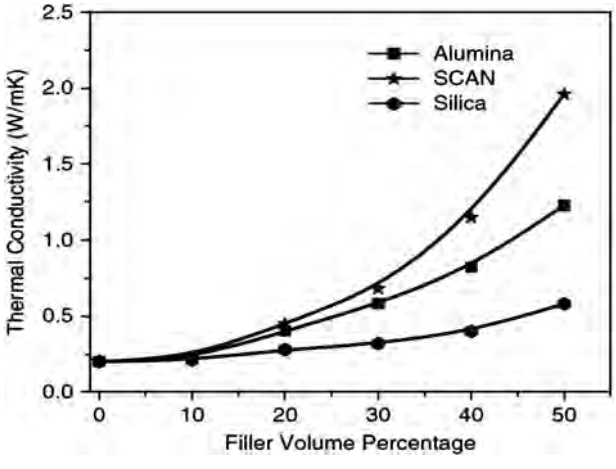

Figure 11.27 *The variation of thermal conductivity of epoxy composite as a function of volume percentages of different fillers. Source: Adapted from Wong and Bollampally 1999 [104].*

the variation of thermal conductivity as a function of volume fraction of alumina, silica, and silica-coated aluminum nitride. Addition of 50 vol.% of silica-coated aluminum nitride increased the thermal conductivity ten times as compared to pure epoxy.

The effective thermal conductivity of a heterogeneous material depends on its composition, crystal structure, intrinsic thermal conductivities, filler particle size and shape, and interfacial thermal resistance distribution within the medium and contact between particles. Several models and experimental methods have been reported [107–118] to predict and determine the thermal conductivity of composite materials. The following models are used to calculate the effective thermal conductivity of polymer–ceramic composites.

11.9.1 Geometric Mean Model

This is a simple model to predict the thermal conductivity of a two-phase composite [107] and is given by

$$k_{eff} = k_f^{V_f} k_m^{1-V_f} \tag{11.5}$$

where k_{eff}, k_f, and k_m are the thermal conductivities of the composite, filler, and matrix, respectively.

11.9.2 Effective Medium Theory (EMT) Model

The EMT model assumes that the composite system is a homogeneous medium and the equation for thermal conductivity can be derived through the Laplace equation for thermal transfer, which can be expressed as [109, 110]

$$V_m \frac{k_m - k_{eff}}{k_m + 2k_{eff}} + V_f \frac{k_f - k_{eff}}{k_f + 2k_{eff}} = 0 \tag{11.6}$$

where V_m is the volume fraction (V_f) of the polymer matrix in the composite.

11.9.3 Cheng–Vachon Model

This model is based on Tsao's model, which gives the thermal conductivity of a two-phase solid mixture [111]. The Cheng and Vachon model assumes a parabolic distribution of the discontinuous phase in the continuous phase [117]. The constants of this parabolic distribution can be determined and presented as a function of the discontinuous phase volume fraction. The thermal conductivity of the two-phase solid mixture is derived in terms of the distribution function and the thermal conductivity of the constituent phases.

For $f_f > k_m$,

$$\frac{1}{k_c} = \frac{1}{\sqrt{C(k_m - k_f)[k_m + B(k_f - k_m)]}} \times \ln \frac{\sqrt{[k_m + B(k_f - k_m)]} + \frac{B}{2}\sqrt{C(k_f - k_m)}}{\sqrt{[k_m + B(k_f - k_m)]} - \frac{B}{2}\sqrt{C(k_m - k_f)}} + \frac{1 - B}{k_m} \tag{11.7}$$

where

$$B = \sqrt{3V_f/2}, \qquad C = -4\sqrt{2/3V_f}.$$

11.9.4 Maxwell–Eucken Model

Maxwell obtained [107,118] a simple relationship for the thermal conductivity of randomly distributed non-interacting particles homogeneousy filled in the polymers by solving the Laplace equation. This model assumes that the particles are well dispersed and the potential around each sphere will not be influenced by the presence of each particle (most parts are not touching each other). These conditions are fulfilled only for low filler loadings:

$$k_c = k_m \left[\frac{k_f + 2k_m + 2V_f(k_f - k_m)}{k_f + 2k_m - V_f(k_f - k_m)} \right] \tag{11.8}$$

11.9.5 Nielson Model

Nielson obtained [113, 114] a semitheoretical model by introducing the shape, size, and orientation of the particles into the composite and modifying the Halpin–Tsai equation [115]:

$$\begin{gathered} k_c = k_m \left[\frac{1 + ABV_f}{1 - BV_f\psi} \right], \\ B = \frac{k_f/k_m - 1}{k_f/k_m + A}, \qquad \psi = 1 + \left(\frac{1 - \phi_m}{\phi_m^2} \right) V_f \end{gathered} \tag{11.9}$$

The constant A is a function of the geometry of the filler particles and ϕ_m is the maximum filler content possible while still maintaining a continuous matrix phase. B is a constant related to the relative conductivity of the components. The values of A and ϕ_m for many geometric shapes and orientations are reported by Kumlutas *et al.* [116].

11.9.6 Agari–Uno Model

Agari and Uno [112] developed a model that considers a parallel and series conducting mechanism in the particle-filled polymer composites:

$$\log k_c = V_f C_2 \log k_f + (1 - V_f) \log(C_1 k_m) \tag{11.10}$$

where C_1 is the coefficient of the effect on crystallinity and crystal size of the polymer and C_2 is a measure of the ease with which the particles form conductive chains of the filler.

In general, ceramics have a relatively higher thermal conductivity as compared to polymers. Hence, the thermal conductivity of the composite increases with the increase in the filler content [72,79,84,104,119]. Figure 11.28 shows the variation of the thermal conductivity of a typical polymer–ceramic HDPE—$ZrSiO_4$ composite. As the V_f of the ceramic increases, the thermal conductivity gradually increases. For a high V_f (>0.4), the thermal conductivity increases rather fast [72,79,84,104,119] due to the presence of more connecting paths between the filler ceramic. A comparison of experimental and predicted values of the thermal conductivities of HDPE—$ZrSiO_4$ composites with varying filler contents is given in Figure 11.28. For HDPE—$ZrSiO_4$ composites, thermal conductivity increases with an increase in filler loading due to the high thermal conductivity of the $ZrSiO_4$ ceramic filler (15 W/m K) compared to the HDPE matrix. The thermal conductivity of the HDPE—$ZrSiO_4$ composite increases from 0.45 W/m K for pure HDPE to 0.74 and 2.3 W/m K, respectively, for 0.1 and 0.5V_f of $ZrSiO_4$ in the HDPE matrix. The presence of more connecting paths

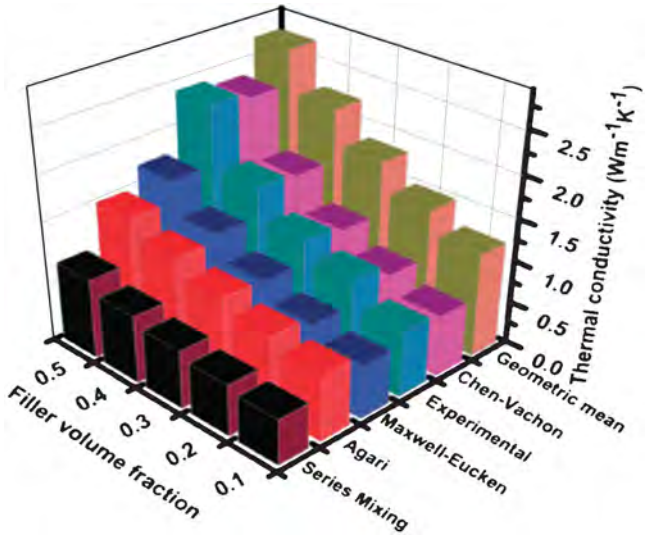

Figure 11.28 *Variation of thermal conductivity of HDPE—$ZrSiO_4$ composite with filler volume fraction and comparison with theoretical models. Source: Adapted from Varghese* et al. *2015 [84].*

between the filler particles also contributes to the increase in the thermal conductivity of the composites at a higher filler loading. The experimental results of HDPE—$ZrSiO_4$ composites are close to the predictions of Chen–Vachon as well as the geometric mean model. The increase in the volume fraction of $ZrSiO_4$ results in the agglomeration of ceramic particles, thereby increasing the mismatch between the experimental and theoretical values. The predicted thermal conductivity using Maxwell–Eucken, series mixing, and Agari models holds, matching thermal conductivity at a lower filler loading, and these models deviate from the experimental results for a higher filler loading. The Maxwell–Eucken model predicts values significantly below experimental data of HDPE—$ZrSiO_4$ composites, which is because it does not account for differences in the morphology as well as the effects of chain formation.

In the case of HDPE—CeO_2, the experimental thermal conductivity matches with the EMT model. A similar observation of variation of thermal conductivity is reported by Kim *et al.* [108] for AlN–epoxy composites. For PTFE—$Sr_2Ce_2Ti_5O_{15}$, a good fitting of the experimental results is found with the Nielson model [119]. This model includes the shape parameters of the filler ceramic particles. In the case of polyethylene–Li_2MgSiO_4, the Agari–Uno model was found to be close to the experimental observation [74]. As the volume fraction of the filler increases, the mismatch between the matrix and the filler in the form of an interfacial gap becomes drastic, which reduces heat conduction [120]. Generally, all theoretical predictions are valid for low filler contents [116]. Agari *et al.* [121] reported that the powder properties of particles (the ease of forming an aggregate of particles, limit of packing, etc.) considerably affect the thermal conductivity of the composites. The theoretical models consider variations in the size, shape, intrinsic thermal conductivity, and state of dispersion of the filler. The wide variations in filler geometry, orientation, and dispersion make it difficult to compare composites filled with different materials. Moreover, the interfacial boundary thermal resistance between the filler particles and the matrix, referred

to as Kapitza resistance [122] is not taken into account while evaluating the thermal conductivity of composites. It takes place in the molecular level and is difficult to measure. Moreover, the theoretical models explained above do not consider the porosity of the composites. As a result, experimental and theoretical thermal conductivity data are often not in agreement [123, 124].

11.10 Polymer Nanoceramic Composites

Extensive researches have been reported on polymer–nanoceramic composites [44–46, 125–127]. It was found that polymer–nanoceramic composites have a higher moisture absorption in comparison with microceramic composites. The sensitivity of polymer ceramic composites to humidity is indeed a serious matter of concern. Absorption of moisture will degrade the dielectric properties since water is a polar molecule with a high relative permittivity. It is reported that < 0.1% moisture absorption is not problematic for packaging applications [1]. The PTFE—Mg_2SiO_4 microcomposite shows low moisture absorption (<0.08 wt%) even at 50 vol.% loading. However, PTFE—Mg_2SiO_4 nanocomposite shows significant moisture absorption (Figure 11.29) of 0.1 wt% at 30 vol.% loading [126]. As compared to PTFE—Mg_2SiO_4 microcomposite, the nanocomposite has a much larger interface area between the filler and the matrix, resulting in significant moisture absorption. The increased polymer dynamics in the nanocomposite also helps in moisture diffusion [125]. Figure 11.30 shows the variation of loss tangent of PTFE—Mg_2SiO_4 (micro and nano) composites. It is found that PTFE—Mg_2SiO_4 nanocomposites show a higher loss tangent as

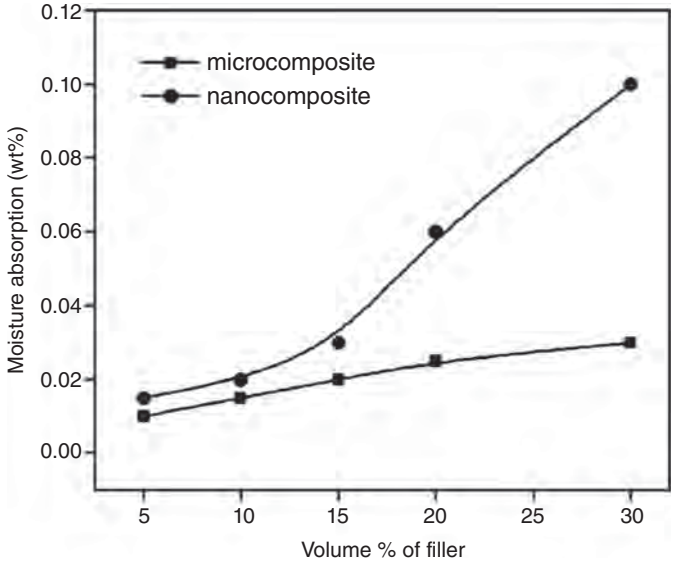

Figure 11.29 *Variation of moisture absorption in PTFE—Mg_2SiO_4 micro and nanocomposites silane treated. Source: Adapted from Sasikala and Sebastian 2016 [126].*

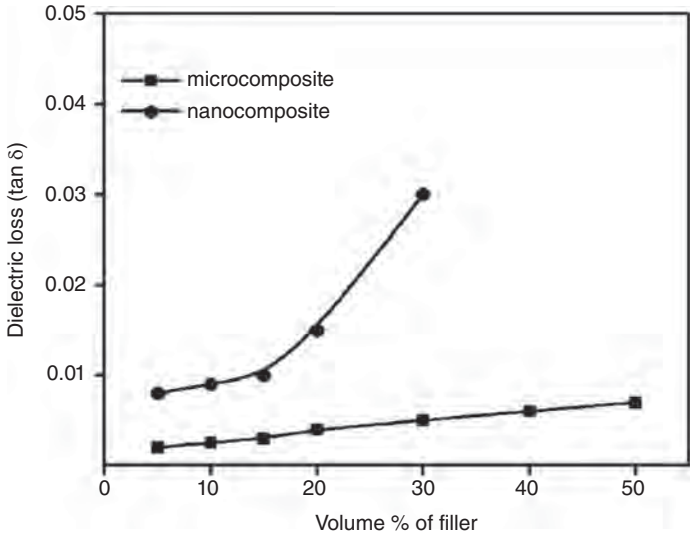

Figure 11.30 *Variation of loss tangent with filler loading in PTFE—Mg_2SiO_4 micro and nanocomposite. Source: Adapted from Sasikala and Sebastian 2016 [126].*

compared to corresponding microcomposites [126]. The relatively high loss tangent exhibited by nanocomposites is due to their high moisture absorption and porosity. The large interface volume of a nanocomposite causes anharmonicity in the composite system, which in turn increases the loss tangent [46]. In addition, the lattice defects present in the nanofiller can also increase the loss tangent of the composites [127].

Figure 11.31 shows the variation of Vickers microhardness as a function of filler loading. It shows that microcomposites have a higher hardness than nanocomposites. The

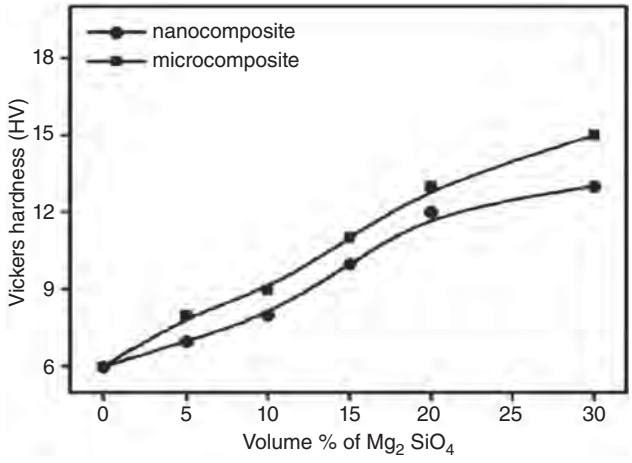

Figure 11.31 *Vickers microhardness of PTFE—Mg_2SiO_4 micro and nanocomposites. Source: Adapted from Sasikala and Sebastian 2016 [126].*

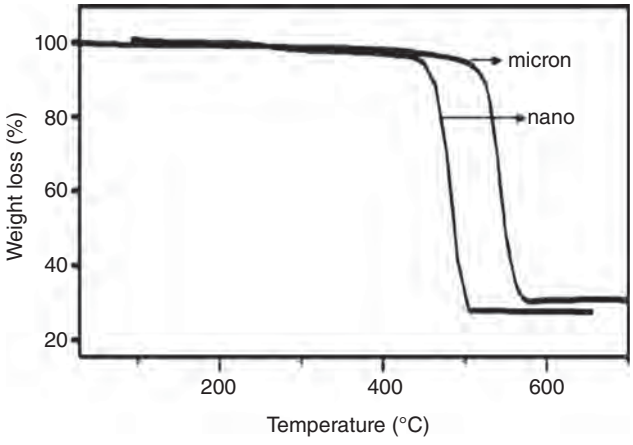

Figure 11.32 *Thermogravimetric profile of PTFE—Mg_2SiO_4 micro and nanocomposites. Source: Adapted from Sasikala and Sebastian 2016 [126].*

nanocomposites have a higher porosity and the higher moisture absorption can affect the strength of composites. At 30 vol.% loading, PTFE—Mg_2SiO_4 micro- and nanocomposites show an average hardness of 15 and 12 HV, respectively. Thermal stability of composites were analyzed by thermogravimetric analysis (Figure 11.32). Compared to composites filled with surface-treated Mg_2SiO_4 micropowder, those with surface-treated nanopowder exhibit a lower degradation temperature and more weight loss. This indicates that more silane coupling agent has been absorbed and reacted with Mg_2SiO_4 nanopowder because of a relatively large specific surface area of smaller particles [128]. Figure 11.33 shows the

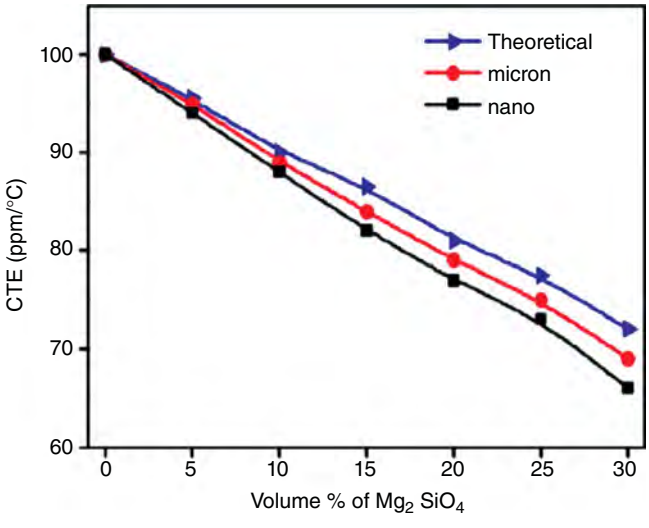

Figure 11.33 *Variation of CTE of PTFE—Mg_2SiO_4 micro and nanocomposites with filler content. Source: Adapted from Sasikala and Sebastian 2016 [126].*

variation of CTE of PTFE—Mg_2SiO_4 micro- and nanocomposites and their comparison with a theoretical prediction using mixture rules. Both composites show a gradual decrease in CTE with an increase in filler content and is expected since the expansion of the matrix is constrained by the presence of filler. It is to be noted that for the same filler content, a nanocomposite exhibits a slightly lower CTE than a microcomposite. This may be due to the increased interaction between the nanofiller and matrix [129]. A similar trend has been reported in the case of PTFE—SiO_2 composites [43]. It is evident from Figure 11.33 that the calculated CTE values are slightly higher than experimental data, especially at high filler loadings. In actual practice the presence of air/posity in the sample can reduce the CTE of polymer/ceramic composites. This may be the reason for deviation of the experimental values of CTE from the theoretical ones, especially at higher filler loadings, where the porosity is relatively large.

Chen *et al.* modified [42] the silica powder by silane treatment. The silylation process replaced SiO—OH (hydrophilic) with Si—CH_3 (hydrophobic) on the surface of the TEOS-derived silica colloidal particle and the hydrophobic property is stable even up to 400 °C [42]. The results also showed that the silylated PTFE/SiO_2 composites had high porosity (53.7%) with nanosize (10–40 nm) pores while incorporating nanosize SiO_2 particles (20–50 nm). The composites also exhibited low ε_r ($\sim$ 1.9) due to porosity, CTE of 66.5 ppm/°C, tensile modulus of 114 MPa, and high thermal stability. The effects of nanosize rutile filler on the microwave dielectric properties of PTFE composites were also investigated [57] and the results were compared with those of micrometer-size rutile-filled composites. The nano-sized composites show higher relative permittivity and loss tangent than micrometer-size rutile-filled composites. The increase in relative permittivity is attributed to the high polarizability of nanofillers and an increase in the interface volume of the nanorutile-filled composites.

11.11 Ultrawideband Antenna Design Using Copper Cladded Ceramic-Filled PTFE Substrates

The rapid growth in wireless communication systems has made ultrawideband (UWB) an outstanding technology to replace the conventional wireless technologies in today's use, such as that of Bluetooth and wireless (local area networks, LANs), etc. Extensive research has been done to develop UWB LNAs, mixers, and entire front ends but not much effort has been done to develop UWB antennas. To implement UWB technology, there are many challenges to overcome. UWB has a significant effect on antenna design. It has attracted a surge of interest in antenna design by providing new challenges and opportunities for antenna designers as UWB systems require antenna with an operating bandwidth covering the entire UWB (3.1–10.6 GHz) and capable of receiving associated frequencies at the same time [141]. Consequently, the antenna behavior and performance have to be consistent and predictable across the UWB. Moreover, UWB is a technology that modulates impulse-based waveforms rather than continuous carrier waves. Hence, the design of UWB antennas requires different considerations from those used in designing narrowband antennas. The hardest challenge in designing a UWB antenna is to attain a wide impedance bandwidth with high radiation efficiency. A return loss of less than -10 dB is necessary in order to obtain high radiation efficiency.

A compact ultrawideband multiple input and multiple output MIMO antenna of size 30.5×38 mm^2 having a band notch function at WiMAX band and WLAN band is fabricated using ceramic-filled PTFE substrates having an effective relative permittivity of 4.4 and loss tangent of 0.0018 at 10 GHz. A split ring slot etched on the radiating patch gives WiMAX band rejection and a U-shaped slot on the feed line gives WLAN band rejection. A T-shaped stub on the ground plane is introduced to obtain high isolation (< -20 dB) in the entire operating band.

11.11.1 Antenna Configuration

The geometry of the ultrawideband MIMO antenna with WiMAX and WLAN rejection is shown in Figure 11.34. The proposed antenna is fabricated on a substrate having dielectric constant 4.4, loss tangent 0.0018, and thickness 1.6 mm. An MIMO antenna consists of two identical planar monopole elements having an ultrawide bandwidth. Both monopoles are fed by a 50 Ω microstrip transmission line having a width of $W_f = 3$ mm. The UWB MIMO antenna is fabricated and tested for validating the antenna performance [141]. A prototype of the fabricated antenna is shown in Figure 11.35. During the measurement of antenna parameters, one port is excited and the other is terminated with 50 Ω impedance. Simulated and measured reflection coefficients are shown in Figure 11.36. Measured S_{11}

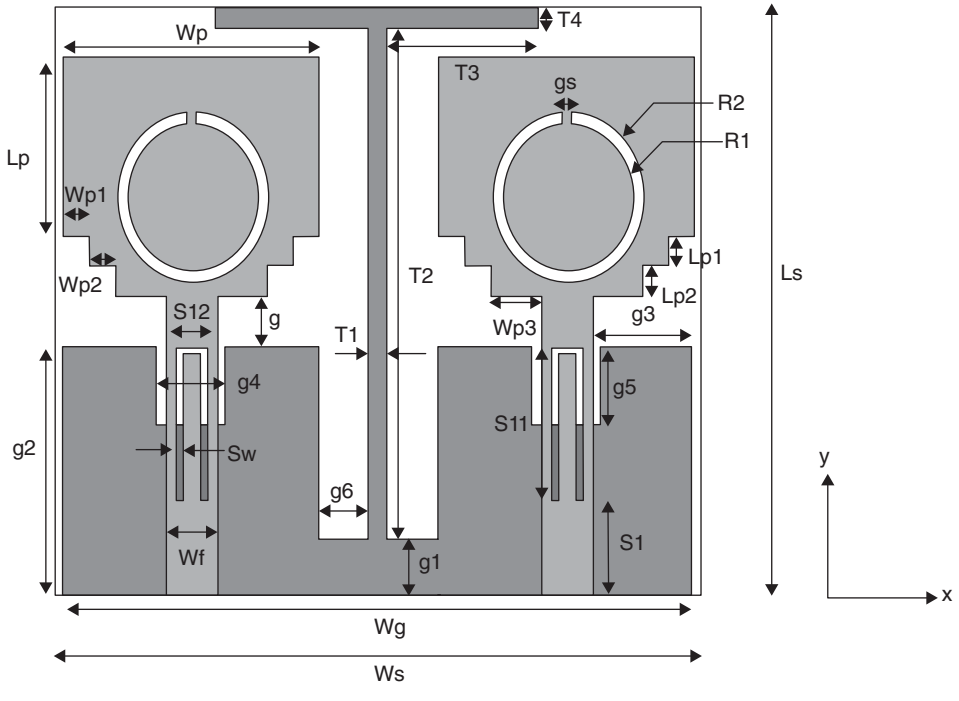

Figure 11.34 *Geometry of the dual-band notched UWB MIMO antenna. Source: Joseph* et al. *2015 [141].*

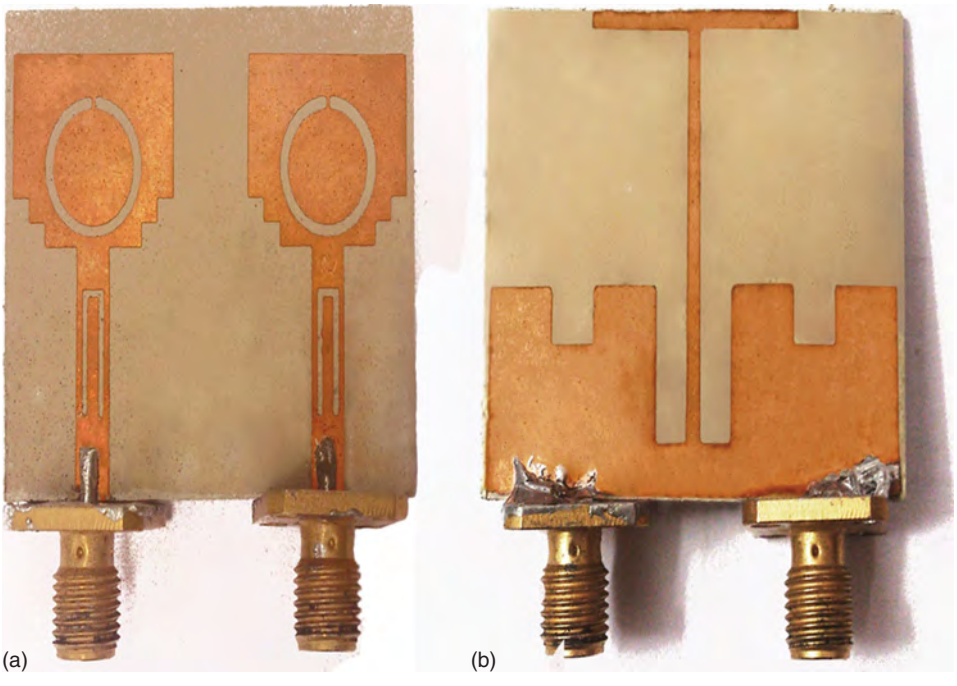

Figure 11.35 *Photograph of fabricated UWB antenna: (a) front view and (b) rear view.*

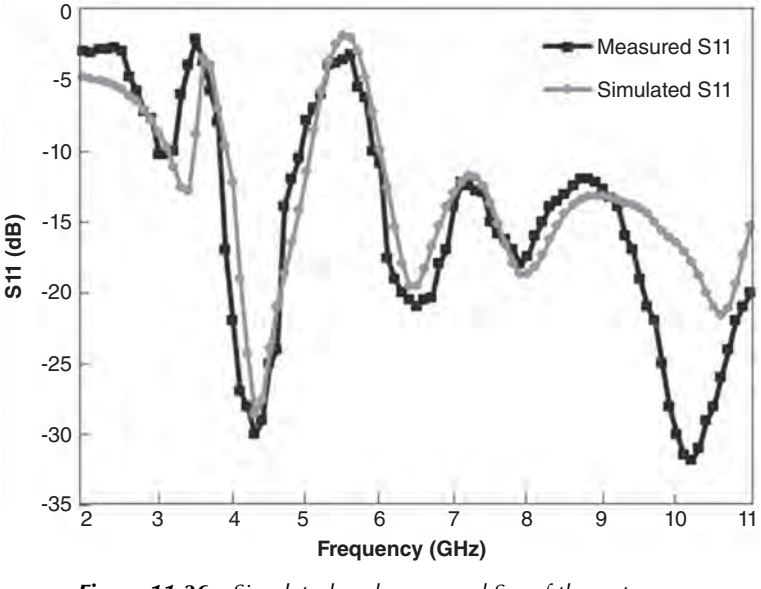

Figure 11.36 *Simulated and measured S_{11} of the antenna.*

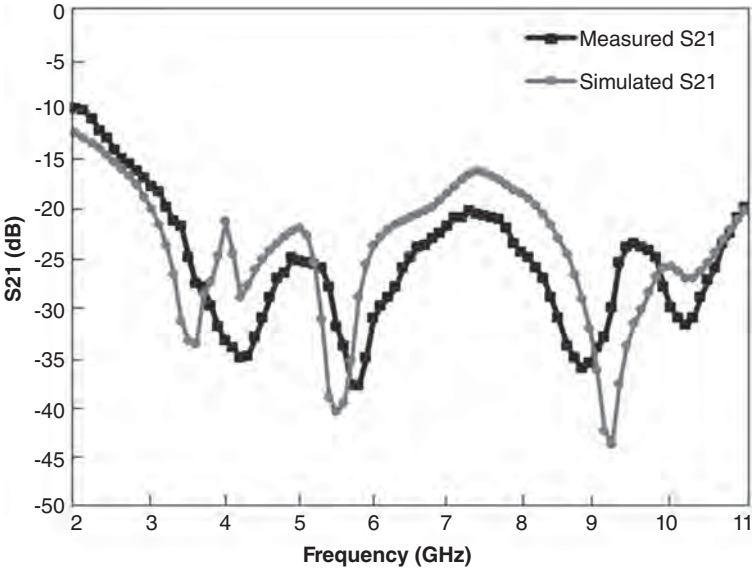

Figure 11.37 *Simulated and measured S_{21} of the antenna.*

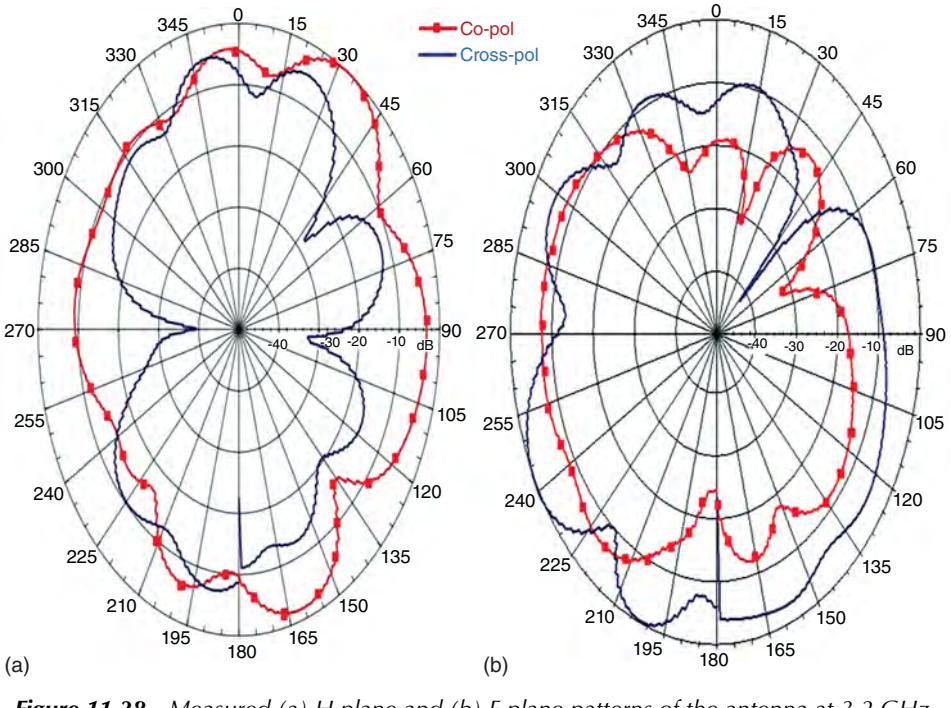

Figure 11.38 *Measured (a) H plane and (b) E plane patterns of the antenna at 3.2 GHz.*

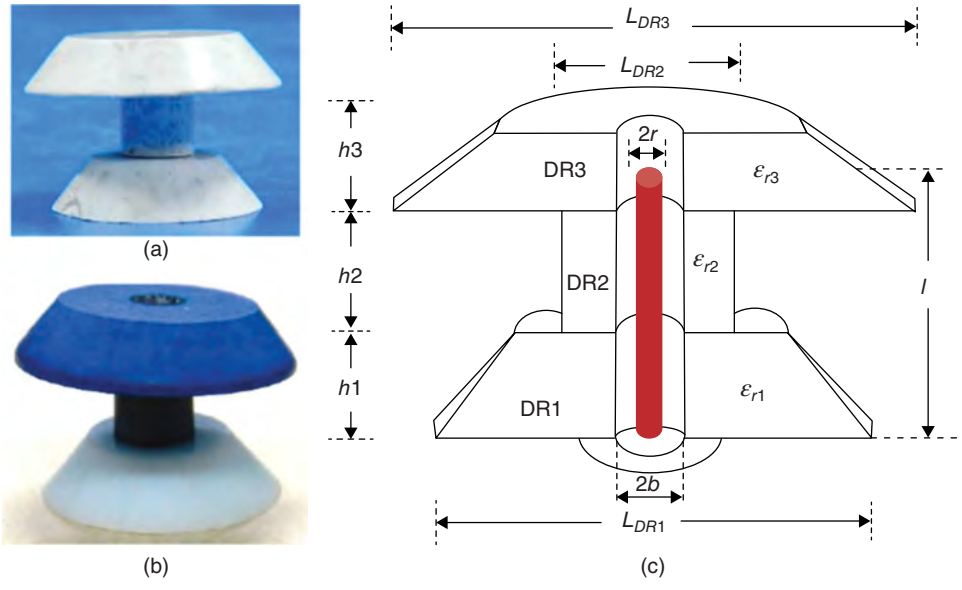

Figure 11.39 *Fabricated mushroom DRA: (a) prototype-A and (b) prototype-B, with h1 = 4.2, h2 = 5.1, h3 = 4.2, LDR1 = 17.6, LDR2 = 6, LDR3 = 22.2, b = 1.57, ε_{r1} = 6.5, ε_{r2} = 4.5, ε_{r2} = 4, l = 11 (all parameters are in mm). (c) Schematic sketch of the mushroom-shaped monopole-DRA for ultrawideband cross-sectional view. Source: Adapted from Ganguly* et al. *2016 [143].*

is less than −10 dB in the entire UWB operating range except at WiMAX and WLAN bands. Also the proposed antenna achieves a good isolation of S_{21} less than −20 dB in the entire 3.1 to 10.6 GHz frequency band (Figure 11.37). Good matching between the simulated and measured frequency responses ensure that the operating band of the fabricated antenna satisfies the design requirement. Measured E plane (*YZ*-plane) and H plane (*XZ*-plane) radiation patterns of the antenna at 3.2 GHz are shown in Fig. 11.38. The proposed antenna has a nearly omnidirectional radiation pattern in the entire operating band, which is desired for UWB systems [142]. Therefore the UWB MIMO antenna fabricated using ceramic-filled PTFE substrates effectively rejects WiMAX and WLAN bands and exhibits excellent antenna characteristics.

More recently Ganguly *et al.* [143] reported a mushroom-shaped antenna with about 137% bandwidth with monopole-like radiation and 6–10 dBi gain over the entire band. Figure 11.39a and b shows two fabricated mushroom-shaped antennas (prototype a and b), which consist of three resonators with varying relative permittivities ($\varepsilon_{r1} = 6.5$, $\varepsilon_{r2} = 4.5$, $\varepsilon_{r3} = 4.1$). Figure 11.39c shows the schematic sketch of the antenna with cross-sectional view. The antenna is made of polyethylene–$SrTiO_3$ and $SrCuSi_4O_{10}$ ceramic composites of different wt% to obtain varying relative permittivities. Figure 11.40 shows the E-plane radiation pattern exhibiting the peak gain at different frequencies. The simulated and measured return loss characteristics for the mushroom-shaped antenna are in good agreement, as shown in Figure 11.41.

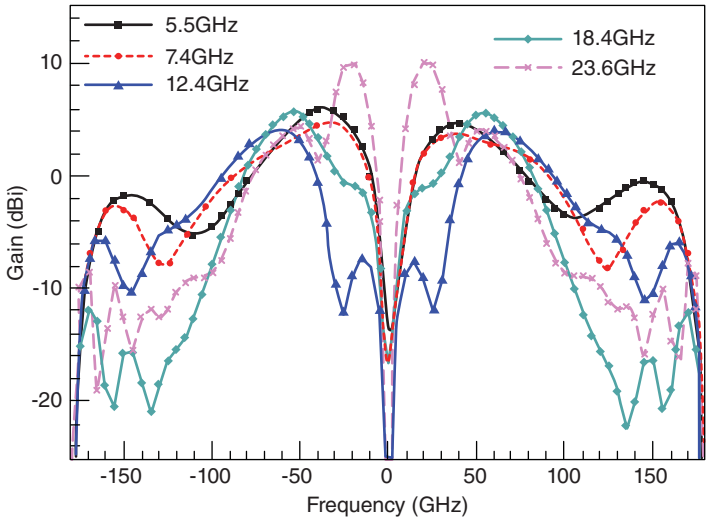

Figure 11.40 *E-plane radiation pattern showing peak gain at different frequencies. Source: Adapted from Ganguly* et al. *2016 [143].*

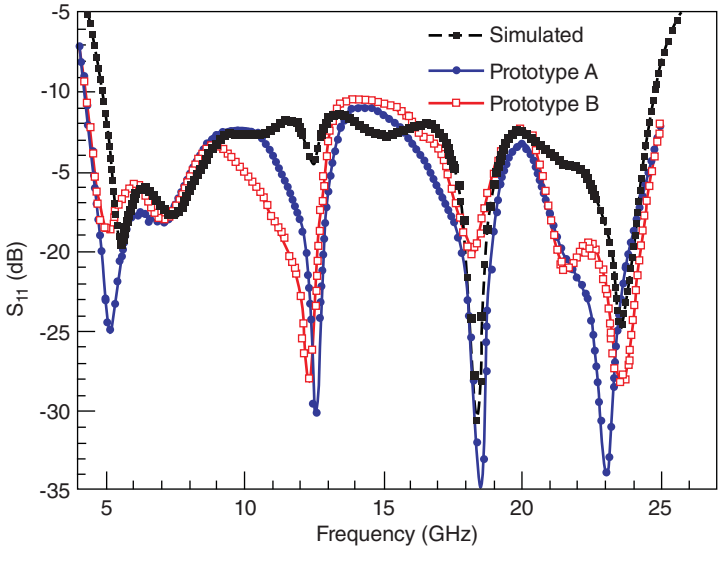

Figure 11.41 *Simulated and measured return loss characteristics for mushroom prototypes shown in Figure 11.39. Source: Adapted from Ganguly* et al. *2016 [143].*

11.12 Conclusion

A composite with three-dimensionally connected polymer phase loaded with isolated ceramic particles (0–3 connectivity) finds extensive applications in microelectronic industry. The polymer–ceramic composites combine the electrical, thermal, and mechanical

properties of both the polymers and ceramics with ease of manufacturing. One of the biggest advantages is the possibility of adjusting the electrical, thermal, and mechanical properties continuously as a function of ceramic loading, enabling unique freedom to component designers. The relative permittivity and thermal conductivity increases with ceramic loading whereas the CTE decreases. The loss tangent in general increases with ceramic loading. The dielectric properties are mainly dependent on the polymer matrix until the level of the percolation limit. Usually the filler addition is limited to about 50–60 volume fraction. Preparation of composites with a larger volume fraction of filler (more than 50–60) is difficult and the amount of porosity increases. In the case of nano-based fillers, the electrical properties are inferior with a relatively higher moisture absorption and only a relatively smaller amount of filler can be reinforced. The polymer–ceramic composites facilitate the fabrication of inexpensive and very complex three-dimensional (3D) structures. This offers a tremendous application potential in 3D antennas.

The relative permittivity of polymer–ceramic composites cannot increase to a very high value, even at maximum filler loading [144] since the 0–3 type composite follows an exponential relationship between relative permittivity of the composite and the volume fraction of the filler. At low volume fractions, the filler particles are randomly distributed in the polymer matrix with poor connectivity between the ceramic particles. At higher volume fractions or near the percolation threshold, the ceramic filler particles are connected and hence the relative permittivity shows an abrupt increase. However, it is difficult to mix large amounts of filler ceramics in the polymer matrix. It was found that the use of a coupling agent, such as silane treatment to modify the surface of the filler powders, although slightly improves the relative permittivity and mechanical properties degrades the microwave dielectric loss factor. The silane treatment is found to lower the porosity. The volume fraction of the ceramic that can be incorporated into the polymer depends on the density, powder particle size, and shape or morphology of the ceramic powder. When the powder particle size is very small, they have a high surface area and only a small volume fraction can be incorporated. The nanofillers have a high surface area and hence the possibility of agglomeration of nanoparticles increases with filler loading. This makes the processing of polymer nanofiller composites difficult at higher filler loadings.

References

1. Laverghetta, T.S. (1985) *Microwave Materials and Fabrication Techniques*, Artech House, Dedham, MA, USA.
2. Daigle, B. (1996) Printed circuit board material and design consideration for wireless application, in *Proceedings of 46th IEEE Electronic Components and Technology Conference*, Orlando, FL, USA, pp. 354–357.
3. Sharma, J., Choate, M., Peters, S., and La Crosse, W.L. (2002) Laminate materials with low dielectric properties, in *IPC Printed Circuit Exposition*, La Crosse, WI, pp. S05-1–8.
4. Fiedziuszko, S.J., Hunter, I.C., Itoh, T., Kobayashi, Y., Nishikawa, T., Stitzer, S.N., and Wakino, K. (2002) Dielectric materials, devices and circuits. *IEEE Transactions on Microwave Theory Techniques*, **50**, 706–719.
5. Aguilar, J.R., Beadle, M., Thompson, P.T., and Shelley, M.W. (1998) The microwave and RF characteristics of FR4 substrates, in *IEEE Colloquium on Low Cost Antenna Technology*, Ref. No. 1998/206, Pub. IEE, Savoy Place, London, pp. 2/1–2/6.

6. Jarvis, J.B., Riddle, B, and Janezic, M.D. (1999) Dielectric and magnetic properties of printed wiring boards and other substrate materials, Technical Note 1512, Radio Frequency Technology Division, National Institute of Standards and Technology (NIST), Boulder, CO, USA.
7. Singh, R. and Ulrich, R.K. (1999) High and low dielectric constant materials. *Electrochemical Society Interface*, **8**, 26–30.
8. Chung, D.D.L. (1995) *Materials for Electronic Packaging*, Butterworth-Heinemann, Newton, MA, p. 199.
9. Farguhar, O.S., Seman, A.M., and Poliks, M.D. (1999) Manufacturing experience with high performance mixed dielectric circuit boards. *IEEE Transactions on Advanced Packaging*, **22**, 153–159.
10. Light, D.N. and Wilcox, J.R. (1995) *IEEE Transactions on Composites and Packaging Technology A*, **18** (1), 118.
11. Sebastian, M.T. and Jantunen, H. (2010) Polymer–ceramic composites of 0–3 connectivity for circuits in electronics: a review. *International Journal of Applied Ceramic Technology*, **7**, 415–434.
12. Chung, D.D.L. (2003) *Composite Materials: Functional Materials for Modern Technologies*, Springer.
13. Chung, D.D.L. (2000) Composite materials for electronics functions, *Materials Science Foundation*, vol. 12, Trans Tech Publications Inc.
14. Wall, L.A. (1972) *Fluoropolymers*, John Wiley & Sons, Inc., New York.
15. Willis, O.R. (2008) *Characterizing Fluoropolymeric Materials for Microelectronics and MEMS Packaging*, ProQuest Information and Learning Company, USA
16. Deka, J.R. and Bhattacharyya, N.S. (2005) Microwave characterization of alumina filled polystyrene composite, in *Proceedings of URSI*. Available at: http://www.ursi.org/proceedings/procga05/pdf/D04.6(0652).pdf
17. Bur, A.J. (1985) Dielectric properties of polymers at microwave frequencies: a review. *Polymer*, **26**, 963–977.
18. Allen,F.H. III, Robert, L.B., and Michael, E. (1996) Ceramic filled composite polymeric electrical substrate materials exhibiting high dielectric constant and low thermal coefficient of dielectric constant, US Patent No. 5552210.
19. Allen, F.H. III (1994) Fluoropolymeric electrical substrate material exhibiting low thermal coefficient of dielectric constant, US Patent No. 5358775.
20. Brydson, J.A. (1989) *Plastic Materials (V)*, Butterworths.
21. Plunket, R.J. (1941) Tetrafluoroethylene polymers, US Patent No. 2230654.
22. Pascale, J.V., Hermann, D.B., and Miner, R.J. (1963) High-energy electron radiation resistance of plastics. *Modern Plastics*, **41** (2), 239.
23. Drobny, J.G. (2001) Blends and composites based on fluoropolymers, *Macromolecular Symposium*, **170**, 149–156.
24. Brown, E.N. and Dattelbaum, D.M. (2005) The role of crystalline phase on fracture and microstructure evolution of polytetrafluoroethylene (PTFE). *Polymer*, **46**, 3056–3068.
25. Clark, E.S. (1999) The molecular conformations of polytetrafluoroethelene: forms II and IV. *Polymer*, **40**, 4659–4665.
26. Springborg, M. and Lev, M. (1989). Electronic structures of polyethylene and polytetrafluoroethylene. *Physical Review B*, **40** (5), 3333–3339.
27. Bunn, C.W. and Howells, E.R. (1954) Structures of molecules and crystals of fluoro-carbons. *Nature*, **174**, 549–551.
28. Lei, C, Wang, X., Fang, Q., and Gao, Y. (2007) Space charge distribution and crystalline structure in quenched polytetrafluoroethylene. *European Polymer Journal*, **43**, 4523–4529.
29. Brown, E.N. and Dattelbaum, D.M. (2005) The role of crystalline phase on fracture and microstructure evolution of polytetrafluoroethylene (PTFE). *Polymer*, **46**, 3056–3058.
30. Bouznik, V.M., Kirik, D.D., Solovyv, L.A., and Tsvetnikov, A.K. (2004) A crystal structure of ultra-dispersed form of polytetrafluoroethylene based on X-ray powder diffraction data. *Powder Diffraction*, **19**, 219–224.
31. Weeks, J.J., Clark, E.S., and Eby, R.K. (1981) Crystal structure of the low temperature phase (II) of polytetrafluoroethylene. *Polymer*, **22**, 1480–1486.

32. Tordella, J.P. (1963) An unusual mechanism of extrusion of polytetrafluoroethylene at high temperature and pressure. *Transactions of the Society of Rheology*, **7**, 231–239.
33. Bernier, G.A., Kline, D.E., and Sauer, J.A. (1967) Effect of nuclear radiation on the mechanical relaxation behavior of polytetrafluoroethylene *Journal of Macromolecule Science*, **B1** (2), 335–372.
34. Lewis, R.F. and Nayalor, A. (1947) Pyrolysis of polytetrafluoroethylene. *Journal of the American Chemical Society*, **69**, 1968–1970.
35. Tamayama, M., Anderson, T.N., and Eyring, H. (1967) The melting and pyrolysis of teflon and the melting of silver chloride and iodine under high pressure. *Proceedings of the National Academy of Sciences*, **57**, 554–561.
36. Wall, L.A. and Michaelson, J.D. (1956) Thermal decomposition of polytetrafluoroethylene in various gaseous atmospheres. *Journal of Research of the NBS*, **56**, 27–34.
37. Tobolsky, A.V., Katz, D., and Eisenberg, A. (1963) Maximum relaxation times in polytetrafluoroethylene. *Journal of Applied Polymer Sciences*, **07**, 468–474.
38. Bunn, C.W., Cobbold, A.J., and Palmer, R.P. (1958) The fine structure of polytetrafluoroethylene. *Journal of Polymer Sciences*, **28**, 365–376.
39. Gossi, M.D. (2006) Melt processable poly(tetrafluoroethylenes). PhD Thesis, Eidgenossische Technische Hochschule Zurich, Zurich, Switzerland.
40. Eby, R.K. and Wilson, F.C. (1962) Relaxations in copolymers of tetrafluoroethylene and hexafluropropylene. *Journal of Applied Physics*, **33**, 2951–2955.
41. Ehrlich, P. (1953) Dielectric properties of Teflon from room temperature to 314 °C and frequencies of 10^2 to 10^5 c/s. *Journal of Research of the NBS*, **51**, 185.
42. Chen, Y.C., Tsai, C.C., and Lee, Y.D. (2004) Preparation and properties of silylated PTFE/SiO_2 organic–inorganic hybrids via sol–gel process. *Journal of Polymer Science, Polymer Chemistry*, **42**, 1789–1807.
43. Chen, Y.C., Lin, H.C., and Lee, Y.D. (2003) The effect of filler content and size on the properties of PTFE/SiO_2 composites. *Journal of Polymer Research*, **10**, 247–258.
44. Chen, Y.C., Lin, H.C., and Lee, Y.D. (2004) The effects of phenyltrimethoxysilane coupling agents on the properties of PTFE/silica composites. *Journal of Polymer Research*, **11**, 1–7.
45. Huang, S.I., Chen, T.H., and Chen, H. (2006) Study on the composites of two sized silica filled in PTFE. *Journal of Reinforced Plastics and Composites*, **25**, 1053–1058.
46. Murali, K.P., Rajesh, S., Prakash, O., Kulkarni, A.K., and Ratheesh, R. (2009), Preparation and properties of silica filled PTFE flexible laminates for microwave circuit applications. *Composites: Part A*, **40**, 1179–1185.
47. Murali, K.P., Rajesh, S., Prakash, O., Kulkarni, A.K., and Ratheesh, R. (2009) Comparison of alumina and magnesia filled PTFE composites for microwave substrate applications. *Materials Chemistry and Physics*, **113**, 290–295.
48. Subodh, G., Joseph, M., Mohanan, P., and Sebastian, M.T. (2007) Low dielectric loss polytetrafluoroethylene/TeO_2 polymer ceramic composites. *Journal of American Ceramic Society*, **90**, 3507–3511.
49. Anjana, P.S., Sebastian, M.T., Suma, N., and Mohanan, P. (2008) Low dielectric loss PTFE/CeO_2 ceramic composites for microwave communication applications. *International Journal of Applied Ceramic Technology*, **5**, 325–333.
50. Thomas, S., Deepu, V.N., Mohanan, P., and Sebastian, M.T. (2008) Effect of filler content on the dielectric properties of PTFE/$ZnAl_2O_4$–TiO_2 composites. *Journal of American Ceramic Society*, **91**, 1971–1975.
51. Murali, K.P., Rajesh, S., Stanly, J.K., Prakash, O., Kulkarni, A.K., and Ratheesh, R. (2010) Preparation and characterization of cordierite filled PTFE laminates for microwave substrate applications. *Journal of Materials Science: Materials in Electronics*, **21**, 192–198.
52. Nijesh, K.J., Stanley, J.K., Murali, K.P., and Ratheesh, R. (2010) $Ba(Mg_{1/3}, Ta_{2/3})O_3$ filled PTFE composites for microwave substrates applications. *Materials Chemistry and Physics*, **122**, 507–511.
53. Yuan, Y, Zhang, S.R., Zhou, X.H., and Li, E.Z. (2013) $MgTiO_3$ filled PTFE composites for microwave substrate applications. *Materials Chemistry and Physics*, **141**, 175–179.

54. Aguilar, J.R., Beadle, M., Thompson, P.T., and Shelley, M.W. (1998) The microwave and RF characteristics of FR4 substrates, in *IEE Colloquium on Low Cost Antenna Technology*, Ref. No. 1998/206, Pub. IEE, Savoy Place, London, pp. 2/1–2/6.
55. Bessede, J.L., Klkoun, S., Stochmil, C., and Etienne, S. (2000) Dielectric properties of PTFE-based composite insulating materials: interfaces effects. *Conference on Electrical Insulation and Dielectric Phenomena*, France, vol. 2, pp. 772–775.
56. Rajesh, S., Murali, K.P., Priyadarsini, V., Potty, S.N., and Ratheesh, R. (2009) Rutile filled PTFE composites for flexible microwave substrate applications. *Materials Science and Engineering B*, **163**, 1–7.
57. Rajesh, S., Nisa, V.S., Murali, K.P, and Ratheesh, R. (2009) Microwave dielectric properties of PTFE/rutile nanocomposites. *Journal of Alloys and Compounds*, **477**, 677–682.
58. Yuan, Y., Cui, Y.R., Wu, K.T., Huang, Q.Q., and Zhang, S.R. (2014), TiO_2 and SiO_2 filled PTFE compositions for microwave substrate applications. *Journal of Polymer Research*, 21, **366**, 1–6.
59. Rajesh, S., Murali, K.P., and Ratheesh, R. (2009) Preparation and characterization of high permittivity and low loss PTFE/$CaTiO_3$ microwave laminates. *Polymer Composites*, 1480–1485.
60. Hu, Y., Zhang, Y., Liu, H., and Zhou, D. (2011) Microwave dielectric properties of PTFE/$CaTiO_3$ polymer ceramic composites. *Ceramic International*, **37**, 1609–1613.
61. Rajesh, S., Murali, K.P., Rajani, K.V., and Ratheesh, R. (2009) $SrTiO_3$ filled PTFE composite laminates for microwave substrate application. *International Journal of Applied Ceramic Technology*, **6** (5), 553–561.
62. Rajesh, S. (2009) Development and characterization of high dielectric flexible PTFE/ceramic substrates for microwave circuit applications. PhD Thesis, Mahatma Gandhi University, India.
63. Xiang, F., Wang, H., and Yao, X. (2006) Preparation and dielectric properties of bismuth based dielectric/PTFE microwave composites. *Journal of European Ceramic Society*, **26**, 1999–2002.
64. Stanley, J.K., Satheesh, R., and Ratheesh, R. (2009) Preparation and microwave characterization of $BaNd_{2-x}Sm_xTi_4O_{12}$ ($0 \leq x \leq 2$) ceramics and their effect on the temperature coefficient of dielectric constant in polytetrafluoroethylene composites. *Materials Research Bulletin*, **44** (10), 2022–2026.
65. Nijesh, K.J., Stanley, J.K., Murali, K.P., and Ratheesh, R. (2010). Preparation and microwave characterization of $BaWO_4$ filled poly tetrafluoroethylene laminates for microwave substrate applications. *Journal of Materials Science: Materials in Electronics*, **21**, 1255–1261.
66. Subodh, G., Pavithran, C., Mohanan, P., and Sebastian, M.T. (2006) PTFE/$Sr_2Ce_2Ti_5O_{16}$ polymer ceramic composite for electronic packaging applications. *Journal of European Ceramic Society*, **27**(8), 3039–3044.
67. Jin, S., Wang, L., Wang, Z., Haung, B., Zhang, Q., and Fu, Z. (2015) Dielectric properties of modified $SrTiO_3$/PTFE composites for microwave RF antenna applications. *Journal of Materials Science: Materials in Electronics*, **26** (10), 7431–7437.
68. Thomas, S., Raman, S., Mohanan, P., and Sebastian, M.T. (2010) Effect of coupling agent on the thermal and dielectric properties of PTFE/$Sm_2Si_2O_7$ composites. *Composites: Part A* **41**, 1148–1155.
69. Rajesh, S., Murali, K.P., and Ratheesh, R. (2011) Temperature stable low loss PTFE/rutile composites using secondary polymer. *Applied Physics A*, **104**, 159–164.
70. Rajesh, S., Murali, K.P., Jantunen, H., and Ratheesh, R. (2011) The effect of filler on the temperature coefficient of relative permittivity of PTFE/ceramic composites. *Physica B: Condensed Matter*, **406** (22), 4312–4316.
71. Test Method Manual IPC-TM-650, 2.6.2, Moisture absorption, flexible printed wiring, Institute for Interconnecting and Packaging Electronic Circuitry.
72. Joseph, T., Uma, S., Philip, J., and Sebastian, M.T. (2011) Electrical and thermal properties of PTFE–$Sr_2ZnSi_2O_7$ composites. *Journal of Materials Science: Materials in Electronics*, **22**, 1000–1009.
73. Thomas, S., Deepu, V., Uma, S., Mohanan, P., Philip, J., Sebastian, M.T. (2009) Preparation and characterization of $Sm_2Si_2O_7$ loaded polymer composites for microelectronics applications. *Materials Science and Engineering B*, **163**, 67–75.
74. George, S., Anjana, P.S., Sebastian, M.T., Krupka, J., Uma, S., and Philip, J. (2010) Dielectric, mechanical and thermal properties of low-permittivity polymer–ceramic composites for

microelectronic applications. *International Journal of Applied Ceramic Technology*, **7** (4), 461–474.
75. Subodh, G., Deepu, V., Mohanan, P., and Sebastian, M.T. (2009) Dielectric response of high permittivity polymer ceramic composite with low loss tangent. *Applied Physics Letters*, **95**, 062903–062905.
76. George, S., Deepu, V., Mohanan, P., and Sebastian, M.T. (2010) Influence of $Ca[Li_{1/3}Nb_{2/3})_{0.8}Ti_{0.2}]O_{3-\delta}$ filler on the microwave dielectric properties of polyethylene and polystyrene for microelectronics applications. *Polymer Engineering and Science*, **50** (3), 570–576.
77. Su, J. and Zhang, J. (2016) Preparation and properties of barium titanate ($BaTiO_3$) reinforced high density polyethylene (HDPE) composite for electronic applications. *Journal of Materials Science: Materials in Electronics*, **27**, 4344–4350.
78. Thomas, D. and Sebastian, M.T. (2014) HDPE matrix composites filled with $Ca_4La_6(SiO_4)_4(PO_4)_2O_2$ for microwave substrate applications. *Journal of Electronic Packaging*, **136**, 031002-1–031002-5.
79. Anjana, P.S., Deepu, V., Uma, S., Mohanan, P., Philip, J., and Sebastian, M.T. (2010) Dielectric, thermal and mechanical properties of CeO_2 filled HDPE composites for microwave substrate applications. *Journal of Polymer Science, Part B, Polymer Physics*, **48**, 998–1008.
80. Subodh, G., Deepu. V., Mohanan, P., and Sebastian, M.T. (2009), Dielectric response of $Sr_2Ce_2Ti_5O_{15}$ ceramic reinforced high density polyethylene. *Journal of Physics D, Applied Physics*, **42**, 225501–225505.
81. Ossama, E.G., Sohair, F.M., Ahmed, A.E., and Ahmed, S.H. (2014) Improving the dielectric properties of high density polyethylene by incorporating clay–nanofibres. *World Journal of Engineering and Technology*, **2**, 289–297.
82. Shi, Y., Zhang, L., and Yue, Z. (2015) Dielectric response of $Mg_{0.95}Ca_{0.05}TiO_3$ ceramic filled HDPE composites with low dielectric loss. *Ceramic International*, **41**, S504–S509.
83. Seeger, K. (1991) Microwave measurement of the dielectric constant of high density polyethylene. *IEEE Transactions on Microwave Theory and Techniques*, **39**, 353–354.
84. Varghese, J., Nair, D.R., Mohanan, P. and Sebastian, M.T. (2015) Dielectric, thermal and mechanical properties of zirconium silicate reinforced high density polyethylene composites for antenna applications. *Physical Chemistry and Chemical Physics*, **17**, 14943–14950.
85. Oza, S., Wang, R., and Lu, N. (2011), Thermal and mechanical properties of recycled high density polyethylene/hemp fiber composites. *International Journal of Applied Science Technology*, **1**, 31–36.
86. Sebastian, M.T. (2008) *Dielectric Materials for Wireless Communications*. Elsevier Science and Technology Publishers, Oxford, UK.
87. Gemant, A. (1938) The role of solid friction in synthetic dielectric. *Journal of Applied Physics*, **9**, 730–734.
88. Varghese, J., Joseph, T., and Sebastian, M.T. (2011) $ZrSiO_4$ ceramics for microwave integrated circuit applications. *Materials Letters*, **65**, 1092–1094.
89. Sarmah, D., Deka, J.R., and Bhattacharyya, N.S. (2010) Study of LDPE/TiO_2 and PS/TiO_2 composites as potential substrates for microstrip patch antennas. *Journal of Electronic Materials*, **39** (10), 2359–2364.
90. Subodh, G., Deepu, V., Mohanan, P., and Sebastian, M.T. (2009) Polystyrene/$SrCe_2Ti_5O_{15}$ composites with low dielectric loss for microwave substrate applications. *Polymer Engineering and Science*, **49** (6), 1218–1224.
91. Sasikala, T.S. and Sebastian, M.T. (2016) Microwave dielectric properties of polystyrene–forsterite (Mg_2SiO_4) composite. *Journal of Electronic Materials*, **45**, 731–735.
92. Wakashima, K., Otsuka, M., and Umekawa, S. (1974) Thermal expansion of heterogenous solids containing aligned ellipsoidal inclusions. *Journal of Composite Materials*, **8**, 391–404.
93. Ishikawa, T., Koyama, K., and Kobayashi, S.J. (1978). Thermal expansion coefficients of unidirectional composites. *Journal of Composite Materials*, **12**, 153–168.
94. Sasikala, T.S., Raman, S., Mohanan, P., Pavithran, C., and Sebastian, M.T. (2011) Effect of silane coupling agent on the dielectric and thermal properties of DGEBA–forsterite composites *Journal of Polymer Research*, **18**, 811–819.

95. Huang, L., Zhu, P., Li, G., Zhou, F., Lu, D., Sun, R., and Wong, C. (2015) Spherical and flake-like BN filled epoxy composites: morphological effect on the thermal conductivity, thermo-mechanical and dielectric properties. *Journal of Materials Science: Materials Electronics*, **26**, 3564–3572.
96. Chaudhary, R.K., Baskey, H.B., Srivastava, K.V., and Biswas, A. (2012) Synthesis and microwave characterisation of $(Zr_{0.8}Sn_{0.2})TiO_4$–epoxy composite and its application in wide-band stacked rectangular dielectric resonator antenna. *IET Microwave Antennas Propagation*, **6** (7), 740–746.
97. George, S., Raman, S., Mohanan, P., Sebastian, M.T. (2010) Polymer ceramic composites for microwave substrate and antenna applications, in *Proceedings of Indian Antenna Week*, Puri, India. Available at: ieeexplore.ieee.org/iel5/5530013/5545939/05545948.pdf.
98. Lee, S., Hyun, J.-G., Kim, H., and Paik, K.-W. (2007) A study on dielectric constant of epoxy/$SrTiO_3$ composite for embedded capacitor films (ECF). *IEEE Transactions on Advanced Packaging*, **30** (3), 428–433.
99. Farrell, B. and Lawrence, M. (2002) Processing of liquid crystalline polymer printed circuits, in *IEEE Electronic Components and Technology Conference*, pp. 667–671. Available at: ieeexplore.ieee.org/iel5/7890/21740/01008168.pdf
100. Takata, K. and Pham, A.-V. (2007) Electrical properties and practical applications of liquid crystal polymer flex, in *Proceedings of IEEE Polytronic Conference*. Available at: ieeexplore.ieee.org/document/4339140/.
101. Thompson, D.C., Tantot, O., Jallageas, H., *et al.* (2004) Characterization of liquid crystal polymer (LCP) material and transmission lines on LCP substrates from 30 to 110 GHz. *IEE Transactions on Microwave Theory and Technology*, **52** (4), 1343–1351.
102. Kingsley, N. (2008) Liquid crystal polymer: enabling next generation conformal and multilayer electronics. *Microwave Journal*, 188–200.
103. Park, M.-S., Chun, M.-P., Cho, J.-H., Nam, J.-H., Choi, B.-H., and Nahm, S. (2009) Preparation and dielectric properties of ceramic (BNT)–polymer (LCP) composite. *Journal of KIEEME* (in Korean), **22** (11), 935–940.
104. Wong, C.P. and Bollampally, R.S. (1999) Thermal conductivity, elastic modulus, and coefficient of thermal expansion of polymer composites filled with ceramic particles for electronic packaging. *Journal of Applied Polymer Science*, **74**, 3396–3403.
105. Kume, S., Yamada, Y., Watari, K., Harada, I., and Mitsuishi, K. (2009) High thermal conductivity AlN filler for polymer/ceramic composites. *Journal of American Ceramic Society*, **92**, S153–S156.
106. Lee, E.S., Lee, S.M., Shanfield, D.J., and Canno, W.G. (2008) Enhanced thermal conductivity of polymer matrix composites via high solid loading of aluminum nitride in epoxy resin. *Journal of American Ceramic Society*, **91**, 1169–1174.
107. Progelnof, R.C., Throne, J.L., and Reutsch, R.R. (1976) Methods of predicting the thermal conductivity of composite systems: a review. *Polymer Engineering Science*, **16**, 615–625.
108. Kim, W., Bae, J.W., Choi, D., and Yong, S.K. (1999) Thermally conductive EMC (epoxy moulding compound) for microelectronic encapsulation. *Polymer Engineering. Science*, **39**, 756–766.
109. Hakansson, B. and Ross, R.G. (1990) Effective thermal conductivity of binary dispersed composites over wide ranges of volume fraction temperature and pressure. *Journal of Applied Physics*, **68**, 3285–3292.
110. Landauer, R. (1978) In *Proceedings of the Conference on Electrical Transport and Optical Properties of Inhomogeneous Media* (eds J.C. Garland and B.B. Tanner), American Institute of Physics, New York.
111. Tsao, T.N.G. (1961) Thermal conductivity of two phase materials. *Industrial Engineering Chemistry*, **53**, 395–397.
112. Agari, Y. and Uno, T. (1986) Estimation on thermal conductivities of filled polymers. *Journal of Applied Polymer Science*, **32**, 5705–5712.
113. Nielson, L. (1973) Thermal conductivity of particulate filled polymers. *Journal of Applied Polymer Science*, **17**, 1819–1820.
114. Nielson, L. (1974) The thermal and electrical conductivity of two phase systems, *Industrial Engineering Chemistry Fund*, **13**, 17–20.

115. Halpin, J.C. and Kardos, J.L. (1976) The Halpin–Tsai equations: a review. *Polymer Engineering and Science*, **16**, 344–352.
116. Kumlutas, D., Tavman, I.H., and Coban, M.T. (2003) Thermal conductivity of particle filled polyethylene composite materials. *Composite Science Technology*, **63**, 113–117.
117. Cheng, S.C. and Vachon, R.I. (1969) The prediction of the thermal conductivity of two and three phase solid heterogeneous mixtures. *International Journal of Heat Mass Transfer*, **12**, 249–264.
118. Maxwell, J.C. (1954) *A Treatise on Electricity and Magnetism*, Dover, New York, 1954.
119. Subodh, G., Manjusha, M.V., Philip, J., and Sebastian, M.T. (2008) Thermal properties of polytetrafluoroethylene/$Sr_2Ce_2Ti_5O_{16}$ polymer/ceramic composites. *Journal Applied Polymer Science*, **108**, 1716–1721.
120. He, H., Fu, R., Han, Y., Shen, Y., and Song, X. (2007) Thermal conductivity of ceramic particle filled polymer composites and theoretical predictions. *Journal of Materials Science*, **42**, 6749–6754.
121. Agari, Y., Ueda, A., Tanaka, M., and Nagai, S. (1990) Thermal conductivity of polymer filled with particles in the wide range from low to super high volume content. *Journal of Applied Polymer Science*, **40**, 929–941.
122. Beneviste, Y. and Miloh, T. (1986) The effective conductivity of composites with imperfect thermal contact at constituent interfaces. *International Journal of Engineering Science*, **24**, 1537–1552.
123. Hill, R. and Supancic, P.H. (2002) Thermal conductivity of platelet-filled polymer composites. *Journal American Ceramic Society*, **85**, 851–857.
124. Hill, R. and Supancic, P.H. (2004) Determination of the thermal resistance of the polymer–ceramic interface of alumina filled polymer composites. *Journal of American Ceramic Society*, **87**, 1831–1835.
125. Sun, Y.Y., Zhang, Z.Q., and Wong, C.P. (2005) Influence of interphase and moisture on the dielectric spectroscopy of epoxy/silica composites. *Polymer* **46**, 2297–2305
126. Sasikala, T.S. and Sebastian, M.T. (2016) Mechanical, thermal and microwave dielectric properties of Mg_2SiO_6 filled polyteterafluoroethylene composites. *Ceramic International*, **42**, 7551–7563.
127. Nisa, V.S., Rajesh, S., Murali, K.P., Priyadarsini, V., Potty, S.N., and Ratheesh, R. (2008) Preparation, characterization and dielectric properties of temperature stable $SrTiO_3$/PEEK composites for microwave substrate applications. *Composite Science and Technology*, **68**, 106–112.
128. Xu, Y. and Chung, D.D. (2000) Increasing the thermal conductivity of boron nitride and aluminum nitride particle epoxy–matrix composites by particle surface treatments. *Composite Interface*, **7**, 243–256.
129. Zhou, W., Yu,D., Wang, C., An, Q., and Qi, S. (2008) Effect of filler size distribution on the mechanical and physical properties of alumina-filled silicone rubber, *Polymer Engineering Science*.**48**, 1381–1388.
130. Holliday, L. and Robinson, D. (1973) The thermal expansion of composites based on polymers: review. *Journal of Materials Science*, **8** (3), 301–311.
131. Raghava, R.S. (1988) Thermal expansion of organic and inorganic matrix composites: a review of theoretical and experimental studies. *Polymer Composites*, **9** (1), 1–11.
132. Patnaik, P. (2002) *Handbook of Inorganic Chemicals*, McGraw-Hill Professional, p. 1002.
133. Rusu, M., Sofian, N., and Rusu, D. (2001) Mechanical and thermal properties of zinc powder filled high density polyethylene composites. *Polymer Testing*, **20** (4), 409–417.
134. Ramajo, L., Rebedo, M., Santiago, D., Castro, M., and Ramajo, D. (2008) Computational approach of dielectric permittivities in $BaTiO_3$–epoxy composites. *J. Composite Materials*, **42**, 2027–2037.
135. Lee, S., Hun, J.G., Kim, H.S., and Paik, K.W. (2007) A study on dielectric constants of epoxy/$SrTiO_3$ composite for embedded capacitor films (ECFs). *IEEE Transactions on Advanced Packaging*, **30**, 428–433.
136. Rao, Y., Ogitani, S., Kohl, P., and Wong, C.P. (2002) Novel polymer–ceramic nanocomposite based on high dielectric constant epoxy formula for embedded capacitor application. *Journal of Applied Polymer Science*, **83**, 1084–1090.

137. George, S. and Sebastian, M.T. (2009) Three-phase polymer–ceramic–metal composite for embedded capacitor applications. *Composite Science Technology*, **69**, 1298–1302.
138. Yang, C.-F., Wu, C.-C., Su, C.-C., and Chen, Y.C. (2009) The development of prediction method for the permittivity of epoxy/$(Ba_{0.9}Sr_{0.1})(Ti_{0.9}Zr_{0.1})O_{3.}$ composites. *Applied Physics A*, **97**, 455–460.
139. Takahashi, S., Imai, Y., Kan, A., Hotta, Y., and Ogawa, H. (2016) Effects of hollow Zn_2SiO_4 particles addition on the dielectric properties of isostatic polypropylene–HW composites. *Materials Science and Engineering B*, in press.
140. Takahashi, S., Imai, Y., Kan, A., Hotta, Y., and Ogawa, H. (2015) Microwave dielectric properties of composites consisting of $MgAl_2O_4$ filler synthesized by molten salt method and isotactic polypriplylene polymer matrix. *Japanese Journal of Applied Physics*, **54**, 10NE02-1–10NE02-5.
141. Joseph, S., Sreekumari Amma, P., Modal, A.K., and Ratheesh, R. (2015) Compact UWB antenna with WiMAX and WLAN rejection, in *IEEE International Microwave and RF Conference (IMaRC)*, Hyderbad, India.
142. Quing, X., Chia, M.Y.W, and Wu, X. (2003) Wide slot antenna for UWB applications. *Proceedings of IEEE Antennas and Propagation Society International Symposium*, **1**, 834–837.
143. Ganguly, D., Guha, D., George, S., *et al.* (2016) New design approach for hybrid monopole antenna to achieve increased ultra-wide bandwidth. *Antennas and Propagation Magazine*, in press.
144. Popielarz, R. and Chiang, C.K. (2007) Polymer composites with dielectric constant comparable to that of barium titanate ceramics. *Materials Science and Engineering B*, **139**, 48–54.
145. Yang, H., Wang, H., Xiang, F., and Yao, X. (2009) Multifunctional $SrTiO_3$/NiZn ferrite/POE composite with electromagnetic and flexible properties for RF applications. *Journal of Ceramics*, 221–226.
146. Rajesh, S., Murali, K.P., Priyadarsini, V., Potty, S.N., and Ratheesh, R. (2008). Microwave dielectric properties of rutile filled PEEK composites. *Polymer-Plastics Technology and Engineering*, **47**, 242–246.
147. Xiang, F., Wang, H., Li, K., Chen, Y., Zhang, M., Shen, Z., and Yao, X. (2007) Dielectric tunability of $Ba_{0.6}Sr_{0.4}TiO_3$/poly(methyl methocrylate) composites in 1–3 type structure. *Applied Physics Letters*, **91**, 192907.
148. Yang, T.C.-K., Tsai, S.H.-Y., Wang, S.-F., and Juan, C.-C. (2002) Dielectric and thermal studies of inorganic microfillers on polymer microwave substrates– metallocene cyclic olefin copolymers (COC). *Composite Science and Technology*, **62**, 6.
149. Takahashi, S., Imai, Y., Kan, A., Hotta, Y., and Ogawa, H. (2015) High frequency dielectric and mechanical properties of cyclo-olefin polymer/MgO composites. *Polymer Bulletin*, **72** (7), 1595–1601.
150. Hu, T., Juuti, J., Jantunen, H., and Vikman, T. (2007) Dielectric properties of BST/polymer composite. *Journal of European Ceramic Society*, **27**, 3997–4001.
151. Hu, T., Juuti, J., and Jantunen, H. (2007) RF properties of BST–PPS composites. *European Ceramic Society*, **27**, 2923–2926.
152. Che, S., Kanada, I., and Sakamoto, N. (2005) Dielectric properties of spherical dielectric oxide powder and its ceramic–polymer composites. *Japanese Journal of Applied Physics*, **44**, 7107–7110.
153. Walpita, L.M., Ahern, M.R., Chen, P., Goldberg, H., *et al.* (1999) Temperature-compensated thermoplastic high dielectric constant microwave laminates. *IEEE Transactions on Microwave Theory and Techniques*, **47**, 1577–1584.
154. Devaraju, N.G., Kim, E.S., and Lee, B., (2001) The synthesis and dielectric study of $BaTiO_3$/polyimide nanocomposite films. *Microelectronic Engineering*, **82**, 71–83.
155. Pan, C., Kou, K., Wu, G., Zhang, Y., and Wang, Y. (2016) Fabrication and characterization of AlN/PTFE composites with low dielectric constant and high thermal stability for electronic packaging. *Journal of Materials Science: Materials in Electronics*, **27**, 286–292.
156. Takahashi, S., Imai, Y., Kan, A., Hotta, Y., and Ogawa, H. (2015) High frequency dielectric and mechanical properties of cyclo-olefin polymer/MgO composites. *Polymer Bulletin*, **72**, 1595–1601.

157. Sasikala, T.S., Pavithran, C., Raman, S., Mohanan, P., and Sebastian, M.T. (2011) Effect of silane coupling agent on the dielectric and thermal properties of polymer–ceramic composites. *Journal of Polymer Research*, **18**, 811–819.
158. Bhalla, A.S., Newnham, R.E., Cross, L.E., and Schulze, W.A. (1981) Pyroelectric PZT polymer composites *Ferroelectrics*, **33**, 139–146.
159. Xiang, F. and Wang, H, (2007) Dielectric properties of $SrTiO_3$/POE flexible composites for microwave applications. *Journal of the European Ceramic Society*, **27** (8–9), 3093–3097.

12

Rubber–Ceramic Composites

M.T. Sebastian[1] *and L.K. Namitha*[2]
[1]*Microelectronics Research Unit, Faculty of Information Technology and Electrical Engineering, University of Oulu, Oulu, Finland*
[2]*Materials Science and Technology Division, CSIR-NIIST, Trivandrum, India*

12.1 Introduction

The future of electronics is expected to be soft and rubbery. Extensive research has been devoted to the development and advancement of flexible electronics and their applications. Devices based on this new technology are stretchable, twistable and deformable into curvilinear shapes, thereby enabling applications that would be impossible to achieve by using the hard and rigid substrates [1]. The development of flexible electronic devices continues to advance at great speeds. Recently electronic systems that can cover large areas on flexible substrates have received increasing attention because they enable a wide range of applications such as flexible displays, electronic textiles, sensory skins and active antennas etc. [2]. The potential applications of flexible electronics are in various societal sectors, including healthcare, automotive industry, human–machine interfaces, mobile communications and computing platforms. The flexible circuitry would be able to do many things that rigid circuits cannot. Flexible circuits make portable devices more resilient. For many applications, particularly in the biomedical field and body-worn antenna, electronic circuits are to be conformally wrapped around curved surfaces. In such systems, the circuits must be not only flexible but also stretchable [3]. Flexible electronics is an emerging field in the electronic industry that enables a wide range of applications such as capacitors for energy storage, wireless communication, electronic packaging and electromagnetic interference (EMI) shielding. Modern electronic industry requires systems that can be fitted into nonplanar forms that can be folded and unfolded for packaging or storage [3, 4]. The flexible substrates have many potential applications from neural prosthetics in the medical field

Microwave Materials and Applications, First Edition.
Edited by Mailadil T. Sebastian, Rick Ubic and Heli Jantunen.
© 2017 John Wiley & Sons, Ltd. Published 2017 by John Wiley & Sons, Ltd.

to microwave devices in electronics, which provides the advantage of three-dimensional designs of conformal structures [5, 6]. Conventional polymers filled with ceramic are rigid and cannot be bent or stretched. Stretchability means that the circuits should have the capacity to absorb large levels of strain without degradation in their electronic properties. In this context, the elastomer–ceramic composites can be used for stretchable and bendable electronic applications.

The requirements of a material to be used as a flexible dielectric are good mechanical flexibility, high thermal conductivity and low coefficient of thermal expansion. In addition, an ideal microwave substrate material needs optimum permittivity (low ε_r for fast signal speed and high ε_r for miniaturization), good processability, low dielectric loss and low cost [4]. It is very difficult to identify a single material that possesses all these properties simultaneously. Ceramics with high permittivity and low loss are available but their high processing temperature and brittle nature preclude their single-phase use. At the same time low-loss elastomers with good flexibility and ease of processing are available but their high CTE, low ε_r and low thermal conductivity (TC) limits their single-phase use. However, through the composite approach one can improve or tailor the individual properties of both elastomer and ceramics. There are a number of ceramic materials with high relative permittivity and low dielectric loss that are available, but are brittle in nature [7]. Butyl and silicone rubbers have low dielectric loss with good mechanical flexibility and stretchability, but they have low relative permittivity, low TC and high CTE. Therefore, the practical applications of elastomer or a ceramic alone is limited. By integrating the flexibility, stretchability and low processing temperature of butyl and silicone rubbers with high relative permittivity, low loss and low CTE of ceramics, a composite may be formed that can deliver an improved performance. Composite technology, where novel artificial materials are fabricated by combining at least two constituent phases such as ceramic–ceramic or ceramic–polymer in an ordered or randomly distributed manner, is being used widely, for example, in electronics, sonars, medical diagnostics and non-destructive testing (NDT) applications. Composite electroceramics introduce not only new functionalities but also an extremely wide range of properties that can be seamlessly adjusted in addition to a significant flexibility in fabrication. Connectivity among the different phases has a key role in the development of composites for practical applications. The physical properties of the composite materials can change by many orders of magnitude depending on the manner in which the connections are made.

The relative permittivity of butyl rubber and silicone rubber can be tailored over a wide range by reinforcing with low-loss ceramics having different ranges of relative permittivity. For electronic packaging and substrate applications, materials must have a low relative permittivity to minimize capacitive coupling and signal delay along with a low-loss tangent to reduce signal attenuation. High-permittivity ceramic materials can be used to make butyl rubber composites for flexible dielectric waveguide and capacitor applications. Elastomer–ceramic composites can combine the advantageous properties of both elastomer and ceramics that can satisfy diverse requirements of the present-day electronic industry. One of the very attractive features of these ceramic-filled elastomers is that the electrical and physical properties can be varied over a wide range by choosing the appropriate type, shape, particle size and connectivity or volume fraction of the fillers in the rubber matrix [8]. The performance of the composites strongly depends on the extent of homogeneous dispersion of the filler particles and interfacial properties. Although extensive researches were done on the microwave dielectric properties of rigid polymer–ceramic composites [4], very little

attention was paid to elastomer–ceramic composites. In this chapter, we discuss the recent advances in low-loss silicone and butyl rubber composites with ceramics for microwave applications.

12.2 Silicone Rubber

12.2.1 Introduction

Silicone rubber is a well-known dielectric elastomer, widely used in electronics and microfluidics due to its elasticity, biocompatibility, optical transparency, permeability, UV transmission and availability [5]. Silicones play a key role in all fields including the automotive, cosmetics, electronic, chemicals, foods, textiles and construction industries [5, 9]. Polydimethylsiloxane (PDMS) is the basic polymer for silicone rubber (SR), the hydrocarbon methyl groups being hydrophobic and water repellent. Pure silicone rubber shows little tracking and erosion resistance. Some properties of silicone rubber must be improved for practical applications. The specific properties of the polymers can be improved by the use of fillers and this can also help to reduce cost. Silicones manifest highly elastic behavior due to the high flexibility of the siloxane bond. The Si—O bond polarizability in polydimethylsiloxane (PDMS) is higher than that of non-polar organic polymers (e.g., polyfluroethylene) and the side methyl groups prevent Si—O dipoles from approaching each other too closely [6]; thus the relative permittivity of PDMS is very low. Silicones are highly functional materials that exhibit both inorganic and organic characteristics. Every silicone consists of organic group side chains attached to a main chain of siloxane bonds (—Si—O—Si—), as shown in Figure 12.1. Siloxane bonds have a much higher bond energy than the C—C and C—O bonds forming the main chains of organic polymers. Having high bond energy, Si—O bonds will not break, even at temperatures around 200 °C. Silicones are highly resistant to heat up to a temperature of 200 °C, are resistant to UV rays, are chemically stable, are water repellent and show a range of other characteristics. The molecular structure gives silicone unique properties, including water-repellency, cold-resistance, and easy release (non-adhesiveness) and is largely temperature stable. The moisture absorption of silicone rubber is about 0.039 vol.%. Among the available elastomers silicone rubber has a prominent position due to its unique properties, such as [9] good dielectric properties, high binding energy, high elasticity, resistance to extreme environments such as heat, ozone, weather, chemical

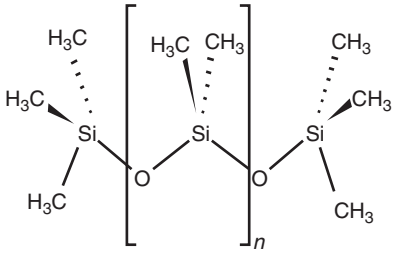

Figure 12.1 *Silicone rubber (polydimethyl siloxane).*

stability, moisture and steam resistance, good electrical insulation, exceptional weatherability, gas permeability, biocompatibility and a physiologically inert character. Silicone rubbers are extensively used in industry for development of a wide variety of products, including automotive applications, cooking, baking and food storage products, apparels, electronics, medical devices and implants and in home repair and hardware, with products such as silicone sealants [10].

In the pure form silicone elastomer is a thermoset polymer; once cross-linked it cannot be brought back to its former shape. Silicone rubber molecules exist above their glass transition temperature and hence considerable segmental motions are possible. The glass transition temperature of silicone elastomer is −127 °C. The long polymer chains will cross-link during curing and the process is known as vulcanization. Dicumyl peroxide is used for the vulcanization of silicone rubber. The elastomer exhibit large elongation from which they recover rapidly on the removal of the applied stress.

Materials having variable relative permittivity are required for practical applications in the electronic industry. The incorporation of ceramic fillers in a polymer matrix is a well-known technique to improve the dielectric and mechanical properties of the material [11]. Depending on the type and volume fraction, the filler can change the permittivity values of the final composite material [12, 13]. Pure silicone rubber shows poor thermal and dielectric properties. Different types of fillers are added to the rubber to improve the properties. The dielectric properties of silicone rubber can be tailored over a wide range by reinforcing with ceramics having different ranges of relative permittivities, that is, ceramic particles with (i) a high permittivity, (ii) a medium permittivity and (iii) a low permittivity. In applications like electronic packaging and substrate, the materials should have a low relative permittivity to increase the signal transmission speed. High relative permittivity materials are used for the manufacture of an embedded capacitor as well as dielectric wave guide applications [4]. The thermal properties of the rubber can be improved by the use of ceramic fillers since they have a high thermal conductivity and low coefficient of thermal expansion. However, through the composite approach one can improve or tailor the individual properties of both elastomer and ceramics. Although a considerable amount of work has been reported on silicone rubber–ceramic composites, very little attention has been paid to their microwave dielectric properties [13–20]. Recently Namitha and coworkers reported [21–25] the microwave dielectric properties of silicone rubber filled with Al_2O_3, $Ba(Zn_{1/3}Ta_{2/3})O_3$ (BZT), $Ba(Mg_{1/3}Ta_{2/3})O_3$ (BMT), $Li_2ZnTi_3O_8$ (LZT) AlN, fused SiO_2, $Ca_{0.61}Nd_{0.26}TiO_3$ (CNT), $SrTiO_3$ (ST) and $BaTiO_3$ (BT). The microwave properties of silicone rubber and fillers are given in Table 12.1. Namitha and coworkers investigated the physical and electrical properties of silicone rubber–ceramic composites using fillers based on their relative permittivity, that is, fillers having low permittivity (<10), medium permittivity (<100) and high permittivity (≥100). Silica, alumina and aluminum nitride fall in the first category while BZT, LZT and BMT fall in the second category and the last category includes CNT, $BaTiO_3$, and $SrTiO_3$.

Among the available low permittivity ceramics, Al_2O_3 and AlN are used for the preparation of low permittivity silicone rubber–ceramic composites since they have a relatively low loss factor. Alumina is a well-known ceramic having good dielectric properties, low CTE (7 ppm/°C), high thermal conductivity (30 W/m K) and low cost. It offers a combination of good electrical and mechanical properties leading to a wide range of applications in many fields, like electrical, electronics, biomedical, chemical industries, etc. The tan δ

Table 12.1 *Microwave dielectric and thermal properties of filler ceramics and elastomers*

Material	Density (g/cm^3)	ε_r	tan δ	TC (W/m K)	CTE (ppm/°C)
Silicone rubber	1.16	3.0	10^{-2}	0.19	266
Butyl rubber	0.96	2.4	10^{-3}	0.13	191
Fused silica	2.20	3.8	10^{-4}	1.5	0.5
AlN	3.26	8.0	10^{-3}	220.0	4.5
Al_2O_3	3.95	9.8	10^{-5}	30.0	7.0
$Li_2ZnTi_3O_8$	3.97	25.6	10^{-3}	5.4	11.7
$Ba(Mg_{1/3}Ta_{2/3})O_3$ (BMT)	7.64	24.0	10^{-3}	4.5	8.0
$Ba(Zn_{1/3}Ta_{2/3})O_3$ (BZT)	7.90	29.0	10^{-3}	3.9	4.2
$Ca_{0.61}Nd_{0.26}TiO_3$	~4.5	98.0	10^{-3}	2.4	10.3
TiO_2	4.23	104.0	10^{-4}	11.0	9.2
$Sr_2Ce_2Ti_5O_{16}$	5.0	113.0	10^{-4}	2.9	1.7
$SrTiO_3$	5.11	290.0	10^{-2}	12.0	9.4
$BaTiO_3$	6.02	1500.0	10^{-2}	2.6	5.4
$Ba_{0.7}Sr_{0.3}TiO_3$	~5.7	2850.0	10^{-2}	4.4	3.0

of alumina is 1×10^{-5} and τ_ε of about 130 ppm/°C at room temperature [7, 26]. Recently Namitha and coworkers [21–25] and Sebastian and Chameswary [27] studied the effect of filler particle size of alumina on microwave dielectric, thermal, and mechanical properties of silicone rubber as well as in butyl rubber. Zhou *et al*. also studied the effect of alumina filler on the properties of silicone rubber [28, 29]. Aluminum nitride is a ceramic with very high thermal conductivity (70–210 W/m K) and hence it finds potential application in the field of microelectronics. $Ba(Zn_{1/3}Ta_{2/3})O_3$ (BZT) and $Ba(Mg_{1/3}Ta_{2/3})O_3$ (BMT) are the most widely studied materials in the perovskite family and are commercially produced for applications in wireless communication [7]. BZT and BMT possesses excellent physical and dielectric properties such as low-loss tangent (10^{-4}), dielectric constant (25–30) and a small temperature coefficient of dielectric constant ($\tau_\varepsilon < 6$ ppm/°C) for microwave applications [7, 30]. Pervoskite barium titanate (BT) is one such ferroelectric material widely utilized in the manufacture of electronic components. $BaTiO_3$ has a relatively high permittivity greater than 1500, high dielectric loss factor and thermal properties such as TC = 2.6 W/m K and CTE = 5.4 ppm/°C. $SrTiO_3$ is a well-known ceramic with a very large value of ε_r (290) and low value (10^{-3}) of tan δ [31].

12.2.2 Composite Preparation

Methyl end-blocked silicone rubber was used for the present study. Both Al_2O_3 and AlN powders were heat-treated at 100 °C for 24 h before using for composite preparation. The $Ba(Mg_{1/3}Ta_{2/3})O_3$ (BMT), $Ba(Zn_{1/3}Ta_{2/3})O_3$ (BZT), $BaTiO_3$ and $SrTiO_3$ etc., were prepared by a conventional solid-state ceramic method. The stoichiometrically weighed chemicals were mixed by wet ball milling and dried. The mixtures were then calcined at appropriate temperatures and ground well to get a particle size in the range 0.5–2 μm. The resultant powders were used for composite preparation with silicone rubber. The rubber was

Table 12.2 *Formulations of composites (ingredients in phr[a])*

Silicone rubber	100	100	100	100	100	100
Dicumyl peroxide (DCP)	2	2	2	2	2	2
$SRAl_2O_3$ (SRL_1)	$SRAL_0$	$SRAL_1$	$SRAL_2$	$SRAL_3$	$SRAL_4$	$SRAL_5$
[]^b	0[0]	10[0.02]	50[0.12]	100[0.22]	200[0.35]	300[0.45]
SR—AlN (SRL_2)	$SRAN_0$	$SRAN_1$	$SRAN_2$	$SRAN_3$	$SRAN_4$	
[]^b	0[0]	10[0.03]	50[0.15]	100[0.26]	200[0.41]	
SR—BZT(SRM_1) $Ba(Zn_{1/3}Ta_{2/3})O_3$	$SRBZ_0$	$SRBZ_1$	$SRBZ_2$	$SRBZ_3$	$SRBZ_4$	
[]^b	0[0]	10[0.014]	50[0.066]	100[0.124]	200[0.220]	300[0.299]
SR—BMT(SRM_2) $Ba(Mg_{1/3}Ta_{2/3})O_3$	$SRBM_0$	$SRBM_1$	$SRBM_2$	$SRBM_3$	$SRBM_4$	
[]^b	0[0]	10[0.015]	50[0.072]	100[0.134]	200[0.233]	
SR—BT(SRH_1) $BaTiO_3$	$SRBT_0$	$SRBT_1$	$SRBT_2$	$SRBT_3$	$SRBT_4$	
[]^b	0[0]	10[0.04]	50[0.09]	100[0.16]	200[0.28]	
SR—ST(SRH_2) $SrTiO_3$	$SRST_0$	$SRST_1$	$SRST_2$	$SRST_3$	$SRST_4$	
[]^b	0[0]	10[0.02]	50[0.09]	100[0.18]	200[0.30]	

[a] Parts per hundred of rubber.
[b] Volume fractions of filler given in brackets.

first masticated through the counter-rotating sigma blades in order to make it soft. Then the pure rubber is vulcanized using dicumyl peroxide (DCP). Finally, appropriate amount of fillers were mixed by sigma mixing in a kneading machine at room temperature with the rotation speed of 25 rpm for 45 minutes. The mixtures thus obtained were then hot-pressed at 200 °C for 90 minutes under a pressure of 2 MPa with appropriate molds or dies. The formulations of composites are shown the Table 12.2. The optimization of preparation temperature and duration were done by studying the cross-linking behavior.

The composites fall under three categories [21–25]: (i) composites with low permittivity (SR—Al_2O_3, SR—AlN), (ii) composites with medium permittivity (SR—BMT, SR—BZT) and (iii) composites with high permittivity (SR—BT, SR—ST). The dielectric properties of AlN are not very attractive but it has a high thermal conductivity, which is important for certain electronic applications. BMT and BZT are well-known ceramics with low dielectric loss, optimum relative permittivity, low CTE and good thermal conductivity, whereas BT and ST have very high relative permittivity, good thermal properties and optimum dielectric loss. The composites of SR—Al_2O_3 are represented as SRL_1 and SR—AlN composite as SRL_2, SR—BZT composite as SRM_1 and SR—BMT composite as SRM_2, SR—BT composite as SRH_1 and SR—ST composite as SRH_2. The amount or volume fraction of filler ceramic that can be added to silicone rubber depends on the density and filler particle size. A maximum filler loading of about 0.45 V_f is attained for SRL_1 composites and 0.41 V_f for SRL_2 composites. In the case of SRM_1 and SRM_2 composites it is possible to mix up to

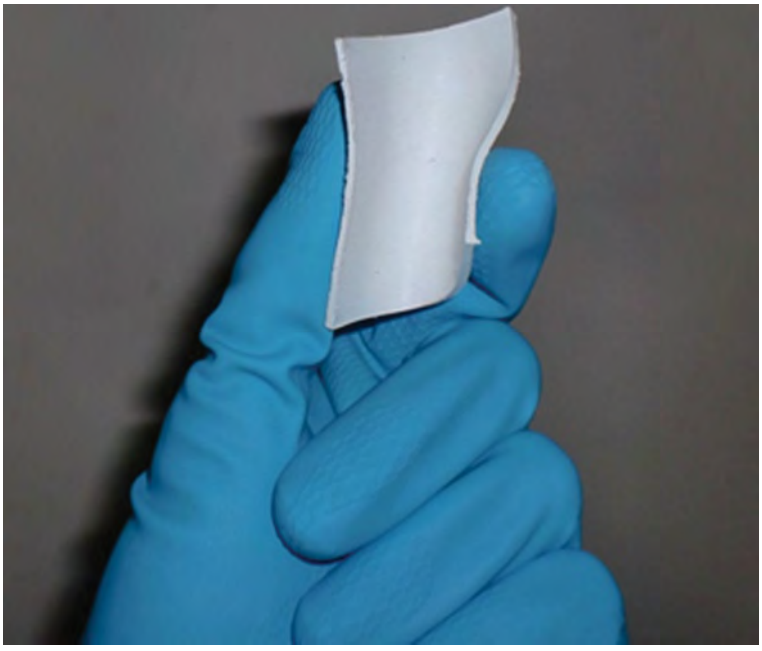

Figure 12.2 *Photograph of silicone rubber–BZT composite.*

0.3 V_f and 0.36 V_f, respectively. Mixing is found to be difficult for more than 0.28 V_f for SR—$BaTiO_3$ and 0.30 V_f fo SR—$SrTiO_3$ composites. Larger amounts of filler lead to inhomogeneous mixing, hardening and difficulty in mixing and also degradation of the mechanical properties [19]. Ceramic fillers can be incorporated in the rubber matrix only up to a certain loading fraction beyond which the composite becomes porous as a result of insufficient rubber to encapsulate the filler. Figure 12.2 shows a typical photograph of silicone rubber ceramic composites exhibiting flexibility. The optimum filler loading also depends on the particle size, distribution and morphology of the filler. Figure 12.3 represents the SEM images of BZT powder and fractograms of 4+ silicone rubber composites having different filler contents [22]. Figure 12.3a shows the microstructure of BZT powder. Figure 12.3b to d shows the fractograms of SR—0.01 V_f BZT, SR—0.12 V_f BZT, and SR—0.299 V_f BZT composites, respectively. BZT particles are uniformly dispersed throughout the matrix at low volume fractions. As the filler content increases, the agglomeration of ceramic particles increases, which leads to porosity. At a lower filler loading the matrix covers the ceramic particles but as the filler loading increases the interparticle distance decreases, which may lead to the agglomeration of filler particles.

12.2.3 Dielectric Properties

Dielectric sheets having dimensions of 30 mm × 30 mm and thickness of about 1.8 mm were used for the microwave measurements using the SPDR method described in Chapter 2. The radio frequency measurements were done by the parallel plate capacitor method using thin

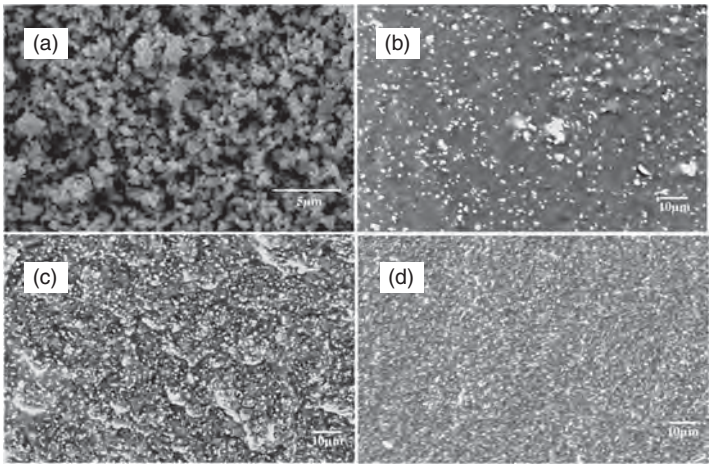

Figure 12.3 *SEM micrographs of silicone rubber–$Ba(Zn_{1/3}Ta_{2/3})O_3$ composites: (a) $Ba(Zn_{1/3}Ta_{2/3})O_3$ Powder, (b) V_f = 0.014, (c) 0.124, and (d) 0.299. Source: Adapted from Namitha and Sebastian 2013 [22].*

samples of about 1 mm in thickness. The variation of relative permittivity and the dielectric loss of the composites with varying filler fractions at the radio frequency region (1 MHz) are shown Figure 12.4a and b. It is clear from the figure that relative permittivity increases with filler fraction, which is due to the high relative permittivity of the ceramic compared to the silicone rubber matrix and the increased connectivity among the filler particles. A similar trend was observed in polymer–ceramic composites [32, 33] and are discussed in Chapter 11. The increase in the relative permittivity depends on ceramic filler loading, permittivity of the ceramic and the frequency of measurement. The dielectric loss decreases with an increase in the volume fraction for some composites and is due to the low-loss factor of the ceramic filler as compared to the rubber matrix. In the case of SR—AlN and SR—$BaTiO_3$ the dielectric losses increase [23,25] with filler content. This is due to the high dielectric loss of the AlN and $BaTiO_3$ fillers.

Figure 12.5a and b shows the relative permittivity and dielectric loss of the composites at microwave frequency with varying filler fractions. The trend is similar to that at the radio frequency region and the permittivity increases with filler loading. The addition of ceramic fillers gradually increases the relative permittivity. Even though the ε_r of $BaTiO_3$ is much higher than that of the matrix, the composite cannot attain relative permittivity of more than about 15. The dielectric loss of a polymer–ceramic composite depends on the factors such as interface between two components in the composite, moisture content and porosity. The dielectric properties of the rubber composites depends on the volume fraction, size, connectivity between the filler particles and shape of the ceramic fillers and also the preparation methods [34]. The reason for the relatively low permittivity of the rubber–ceramic composites may be due to the depolarization of the filler while incorporating it in the rubber matrix since the rubber matrix obscures the polarizability of the ceramic filler [35] and the poor connectivity between the ceramic filler particles [34]. Even at maximum filler loading the relative permittivity of the elastomer–ceramic composite cannot increase to a very

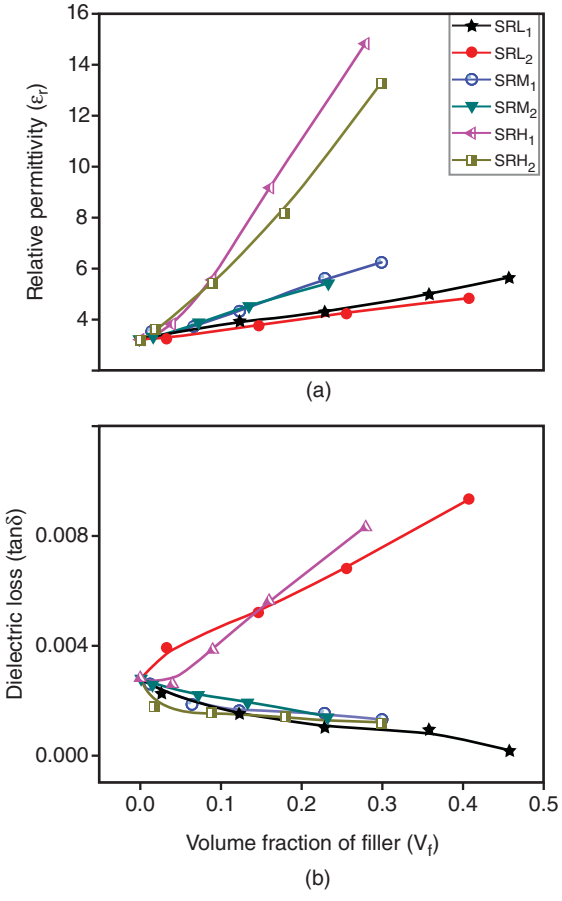

Figure 12.4 *Variations of dielectric properties of silicone rubber composites at 1 MHz: (a) relative permittivity, (b) loss tangent: SRL_1: SR—Al_2O_3; SRL_2: SR—AlN; SRM_1: SR—BZT; SRM_2: SR—BMT; SRH_1: SR—$BaTiO_3$; SRH_2: SR—$SrTiO_3$.*

high value [36]. This is because the 0–3 type composite follows an exponential relationship between the volume fraction of the filler and relative permittivity of the composite. The logarithm of the relative permittivity of polymer–dielectric ceramic composites (ε_r composite) is linearly proportional to the volume fraction of the filler (V_f) with the slope dependent on the dielectric properties of both components [37]:

$$\log \varepsilon_{r\,\text{composite}} = V_{f\,\text{filler}} \log(\varepsilon_{r\,\text{filler}}/\varepsilon_{r\,\text{polymer}}) + \log \varepsilon_{r\,\text{polymer}} \tag{12.1}$$

In the case of dielectric loss, the SRL_2 and SRH_1 composites show an increasing trend with filler addition since the loss tangents of AlN and $BaTiO_3$ are higher than that of silicone rubber. Moreover, the presence of porosity and the interface between the rubber matrix and ceramics can lead to additional loss. However, all other compositions show a decreasing trend with filler loading due to the low-loss factor of the filler.

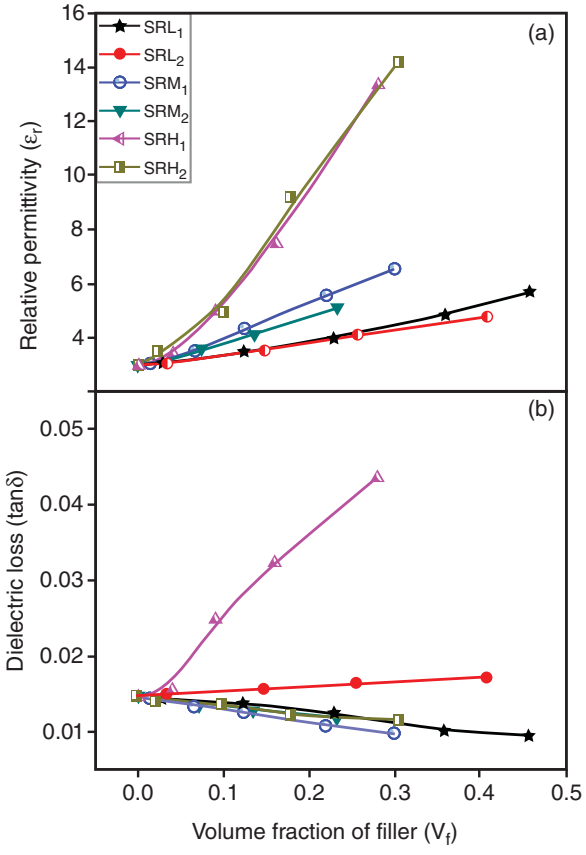

Figure 12.5 *Variations of dielectric properties of silicone rubber composites at 5 GHz: SRL_1: SR—Al_2O_3; SRL_2: SR—AlN; SRM_1: SR—BZT; SRM_2: SR-BMT; SRH_1: SR—$BaTiO_3$; SRH_2: SR—$SrTiO_3$.*

12.2.3.1 Theoretical Modeling of Relative Permittivity

The precise prediction of the effective relative permittivity of the composite is very important for electronic packaging applications. Numerous relations have been used to predict the relative permittivity of polymer–ceramic composites and are discussed in detail in Chapter 2. The theoretical models follow certain assumptions, which are related to dielectric properties of individual components, the connectivity of polymer–ceramic composites, size and shape of the filler and morphology. The following relations were used to compare the experimentally observed values of relative permittivity of composites at 5 GHz in the present study.

Maxwell Garnet [38]:

$$\frac{\varepsilon_{eff} - \varepsilon_m}{\varepsilon_{eff} + 2\varepsilon_m} = V_f \frac{\varepsilon_i - \varepsilon_m}{\varepsilon_i + 2\varepsilon_m} \tag{12.2}$$

Jayasundere–Smith equation [39]:

$$\varepsilon_{eff} = \frac{\varepsilon_m(1-V_f) + \varepsilon_i V_f \left[\frac{3\varepsilon_m}{\varepsilon_i + 2\varepsilon_m}\right]\left[1 + \left(\frac{3V_f[\varepsilon_i - \varepsilon_m]}{\varepsilon_i + 2\varepsilon_m}\right)\right]}{(1-V_f) + V_f \left[\frac{3\varepsilon_m}{\varepsilon_i + 2\varepsilon_m}\right]\left[1 + \left(\frac{3V_f[\varepsilon_i - \varepsilon_m]}{\varepsilon_i + 2\varepsilon_m}\right)\right]} \tag{12.3}$$

Lichtenecker equation [40]:

$$\ln \varepsilon_{eff} = (1-V_f)\ln \varepsilon_m + V_f \ln \varepsilon_f \tag{12.4}$$

Modified Lichtenecker equation [41]:

$$\log \varepsilon_{eff} = \log \varepsilon_m + f(1-k)\log\left(\frac{\varepsilon_f}{\varepsilon_m}\right) \tag{12.5}$$

Effective medium heory (EMT) [42]:

$$\varepsilon_{eff} = \varepsilon_m \left[1 + \frac{V_f(\varepsilon_f - \varepsilon_m)}{\varepsilon_m + n(1-V_f)(\varepsilon_f - \varepsilon_m)}\right] \tag{12.6}$$

where ε_{eff}, ε_m, and ε_f are the relative permittivities of composite, matrix and filler respectively and V_f is the volume fraction of the filler. Figure 12.6 shows the comparison of experimental results with theoretical values of relative permittivity obtained from various models at 5 GHz for BZT (SRM_1) composites. Maxwell Garnet relations predict a lower ε_r compared to the experimental data and this relation is suitable for a low volume fraction of ceramic particles. The Lichtenecker equation [40] considers the composites as random mixtures of spherical particles dispersed in a continuous medium. In the modified Lichtenecker equation [41] the fitting factor k gives the interaction between filler and matrix and is sensitive to the polymer and matrix. The Jayasundere–Smith model [39] considers all

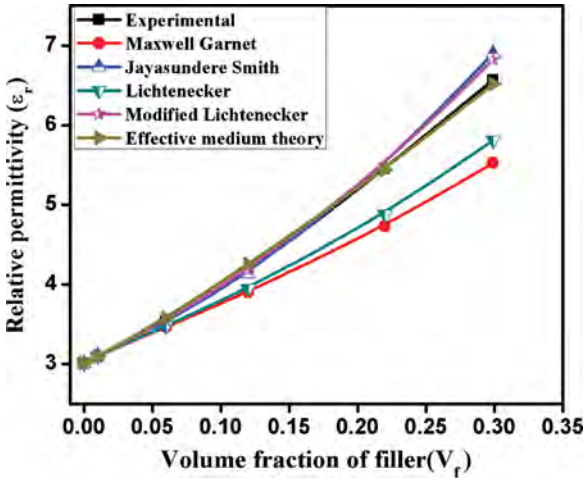

Figure 12.6 *Comparisons between experimental and theoretical permittivity of SR—BZT omposites at 5 GHz. Source: Adapted from Namitha and Sebastian 2013 [22].*

filler particles to be spherical. The Jayasundere-Smith model and modified Lichtenecker equation show good agreement with experimental results but show deviation at higher volume fractions. The entrapped air and imperfect dispersion of filler in the composites may be the reason. The EMT model [42] fits well with the experimental results. This model includes a morphology factor n, which can be obtained by empirical calculations. In the EMT model, composites are treated as an effective medium whose relative permittivity is the average of the relative permittivity of the constituents. The effective permittivity of a composite depends on various factors such as relative permittivity of individual components in the system, porosity, their volume fractions, size, shape, interphase polarizability, and interphase volume fractions [42]. All these parameters cannot be accounted for in a single equation.

12.2.3.2 Effect of Bending on Microwave Dielectric Properties

The effect of bending on dielectric properties is very important for flexible electronic applications. Bending measurements of the composites were carried out by bending the samples manually in such a way that every part of the sample had undergone 180° bending. The bending cycle was repeated 125 times and the microwave dielectric properties were measured by the SPDR method after every 25 cycles. Figure 12.7a and b shows the variation

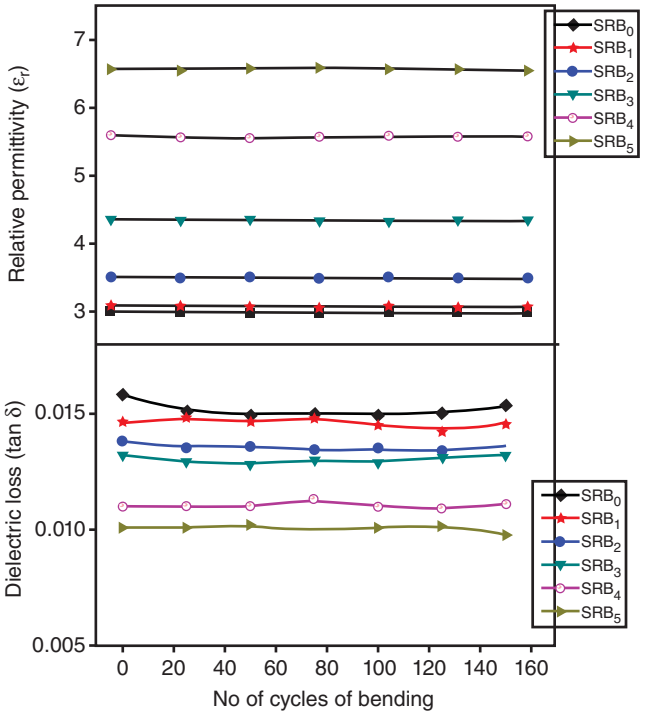

Figure 12.7 *Variations of dielectric properties of SR—BZT composites with bending measured at 5 GHz. SRBo $V_f = 0$; SRB_1 $V_f = 0.014$; SRB_2 $V_f = 0.66$; SRB_3 $V_f = 0.124$; SRB_4 $V_f = 0.22$; SRB_5 $V_f = 0.299$. Source: Adapted from Namitha and Sebastian 2013 [22].*

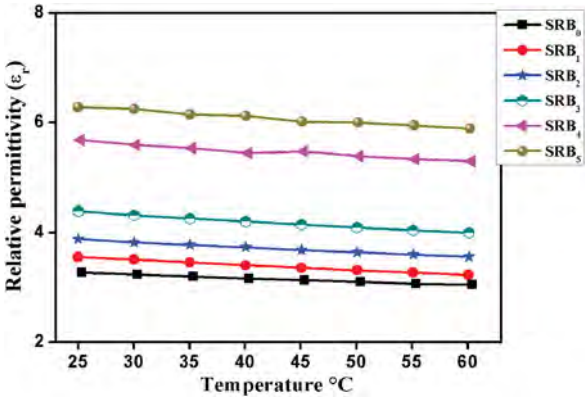

Figure 12.8 *Variation of relative permittivity of SR—BZT composites with temperature at 5 GHz. SRBo $V_f = 0$; SRB_1 $V_f = 0.014$; SRB_2 $V_f = 0.66$; SRB_3 $V_f = 0.124$; SRB_4 $V_f = 0.22$; SRB_5 $V_f = 0.299$. Source: Adapted from Namitha and Sebastian 2013 [22].*

of dielectric properties of (SR—BZT (SRM_1) composites with bending [22]. It is obvious from the figure that relative permittivity is nearly independent of the effect of bending. The dielectric loss of composites shows a small variation with repeated bending. At a higher filler loading there may be some agglomerations that, on bending, release the stress that leads to a slight variation, but this variation is only marginal. The bending of the composites does not considerably affect the microwave dielectric properties and hence they are suitable for flexible electronic applications.

12.2.3.3 Temperature Variation of Relative Permittivity

The temperature dependence of relative permittivity on SR—BZT (SRM_1) composites at 5 GHz is shown in Figure 12.8. The thermal stability of relative permittivity is one of the important properties of substrate material that controls the overall performance of the material. The variation of relative permittivity with temperature should be small for practical applications. The composites show reasonable stability with temperature at low filler loadings but a slight decrease of ε_r is observed with temperature at higher filler loadings [22]. All the composites are almost thermally stable within the measured temperature range, as evident from the figure. The decrease in moisture content and CTE with temperature may also affect the temperature variation of relative permittivity.

12.2.4 Mechanical Properties

For practical applications, good mechanical properties of the elastomer are essential and are normally improved by the addition of fillers. The stress–strain curves of pure elastomer and the different composites are shown in Figure 12.9. BZT (SRM_1) composite is taken as a representative for all composite systems [22]. The stress–strain properties of the composites were measured using a universal testing machine with a rate of grip separation of 500 mm/min. Tensile tests were conducted using dumbbell-shaped samples of width 4 mm and thickness in the range 1.5–2 mm. The elastomer exhibits good flexibility and good

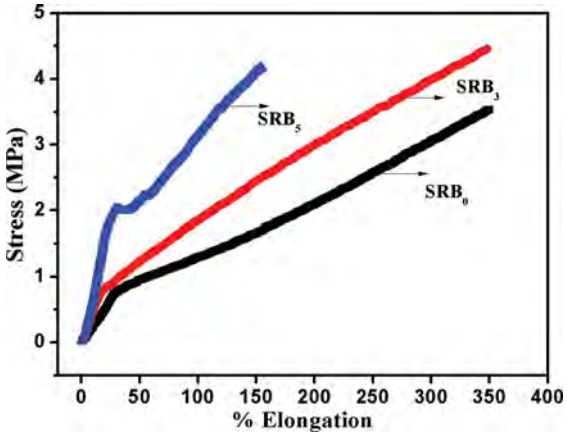

Figure 12.9 *The stress–strain curve of SR—BZT composites. SRBo V_f = 0; SRB_1 V_f = 0.014; SRB_2 V_f = 0.66; SRB_3 V_f = 0.124; SRB_4 V_f = 0.22; SRB_5 V_f = 0.299. Source: Adapted from Namitha and Sebastian 2013 [22].*

mechanical strength. The incorporation of filler particles enhance the stiffness, that is, the stress for elongation increases with filler loading. This is attributed to the filler–matrix and filler–filler interactions, which restrict the mobility of the elastomer matrix. Filler parameters like size, shape, interfacial adhesion between filler and matrix and the aspect ratio, have a strong impact on the mechanical response of the composites [43].

12.2.5 Coefficient of Thermal Expansion (CTE)

The variation in coefficient of thermal expansion (CTE) is an important factor for electronic packaging applications. The variations in CTE of ceramic-filled silicone rubber composites are shown in Figure 12.10. A reduction in CTE was observed with an increase in filler loading [21–25]. The filler ceramics have a very low CTE < 8 ppm/°C whereas the silicone rubber has a high CTE of 266 ppm/°C. Hence incorporation of ceramic fillers decreases the CTE of the composite. Additionally there exists a mechanical interaction between filler and matrix that binds the matrix together, leading to a lowering of thermal expansion.

12.2.6 Thermal Conductivity

The thermal conductivity (*Tc*) of the composites is measured using a laser thermal property analyzer using alumina as the reference sample:

$$\boldsymbol{Tc} = \lambda \times \boldsymbol{Cp} \times \boldsymbol{\rho} \tag{12.7}$$

where thermal conductivity, specific heat capacity and thermal diffusivity measurements are done at room temperature. Figure 12.11 shows the variation of thermal conductivity of the different silicone rubber composites with the volume fraction of the filler. The effective thermal conductivity of the composite is strongly influenced by its structure, intrinsic thermal conductivities, composition, filler particle shape and size, interfacial thermal

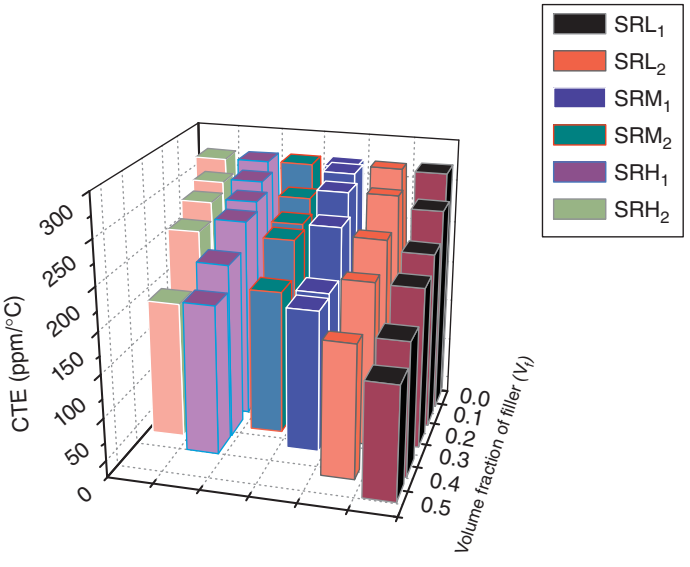

Figure 12.10 *Variation of CTE of silicone rubber composites with ceramic filler content.*

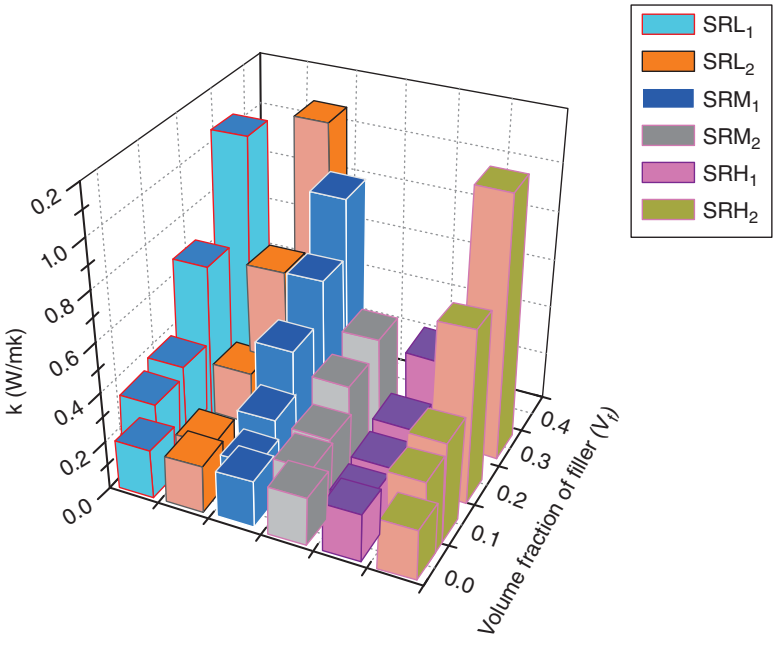

Figure 12.11 *Variation of thermal conductivity of silicone rubber composites with ceramic filler content.*

resistance, etc. [44]. It is evident from the figure that thermal conductivity of the composites is increased with an increase in filler content. At lower volume fractions the matrix covers the heat conductive filler particles and they cannot touch each other, due to the low thermal conductivity. When the filler loading increases filler particles begin to touch each other and form a thermally conductive network, increasing thermal conductivity.

12.2.7 Moisture Absorption of Composites

For practical applications moisture absorption of the composites is an important parameter since it adversely affects the dielectric properties of substrate [45]. The ASTM D 570-98 procedure was used for the moisture absorption characteristic of the composites. The volume % of water absorption was calculated using the relation,

$$\text{Volume \% of moisture absorption} = \frac{(W_f - W_i)/\rho_w}{\dfrac{W_f - W_i}{\rho_w} + \dfrac{W_i}{\rho_c}} \times 100 \tag{12.8}$$

where W_f and W_i are the final and initial weights of the sample and ρ_w and ρ_c are the densities of water and composite, respectively. The density of the composites was measured using Archimedes method. It was reported by Laverghetta that the upper limit of moisture absorption for electronic packaging applications is about 0.1% [46]. The variation of moisture absorption of silicone rubber composites as a function of ceramic loading is shown in Figure 12.12. It is clear from the figure that the moisture absorption of the composites increases with filler loading. The increase of moisture absorption may be due to the increase in porosity with filler loading and the hydrophilic nature of the ceramic particles. The

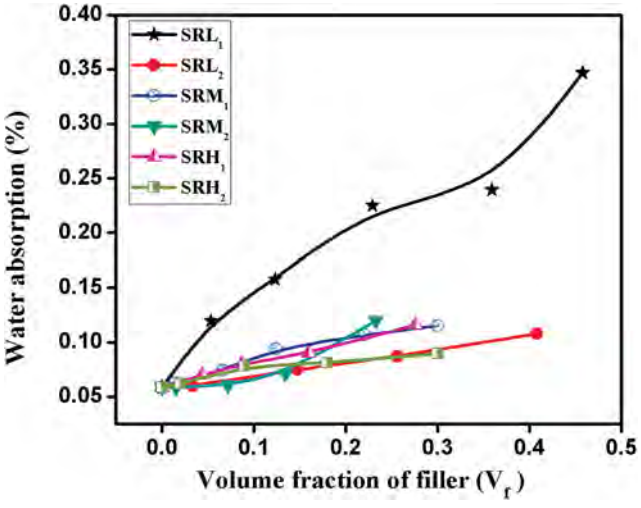

Figure 12.12 *Variation of moisture absorption of silicone rubber composites with filler loading SRL_1: SR—Al_2O_3; SRL_2: SR—AlN; SRM_1: SR—BZT; SRM_2: SR—BMT; SRH_1: SR—$BaTiO_3$; SRH_2: SR—$SrTiO_3$.*

Table 12.3 *Microwave dielectric, thermal and physical properties of silicone rubber–ceramic composites*

Material	Average powder particle size (μm)	V_f of filler	ε_r	tan δ	CTE (ppm/°C)	TC (W/m K)	Moisture absorption (vol.%)
$SRAL_5$: Al_2O_3	2.0	0.458	5.79	0.0095	114	1.60	0.347
$SRAN_4$: AlN	1.3	0.408	4.79	0.0172	138	1.06	0.108
$SRBZ_5$: $Ba(Zn_{1/3}Ta_{2/3})O_3$	0.75	0.299	6.57	0.0098	149	0.92	0.115
$SRBM_4$: $Ba(Mg_{1/3}Ta_{2/3})O_3$	0.55	0.233	5.14	0.0118	152	0.49	0.119
$SRBT_4$: $BaTiO_3$	0.90	0.272	13.38	0.0435	188	0.40	0.116
$SRST_4$: $SrTiO_3$	0.80	0.305	14.21	0.0116	142	1.07	0.089
$SRFS_4$: SiO_2	0.50	0.506	3.35	0.0085	116	0.52	0.100
$SRLT_4$: $Li_2ZnTi_3O_8$	0.70	0.363	7.49	0.0098	144	0.83	0.112
$SRCT_4$: $Ca_{0.61}Nd_{0.26}TiO_3$	0.90	0.434	11.9	0.0115	156	0.58	0.072

silicone rubber–ceramic composites are bendable and stretchable. They are possible candidates for microwave flexible substrate applications. The physical and microwave dielectric properties of the silicone rubber–ceramic composites are summarized in Table 12.3.

12.3 Butyl Rubber (BR)

12.3.1 Introduction

Butyl rubber is a copolymer of 98% polyisobutylene with 2% isoprene distributed randomly in the polymer chain, as shown in Figure 12.13. Polymerization of isoprene results in the incorporation of a double bond or unsaturation into the polymer chain. These double bonds serve as cross-linking sites. Vulcanization of the butyl rubber with sulfur results in the formation of a network structure in the form of a cross-linked rubber. Butyl rubber is a thermoset polymer and once vulcanized it cannot be reformed into a new shape [47, 48]. Butyl rubber is amorphous and viscoelastic with low Young's modulus and high yield strain as compared to other polymer materials due to its weak intermolecular attractive forces. Butyl rubber exists above the glass transition temperature and hence considerable segmental

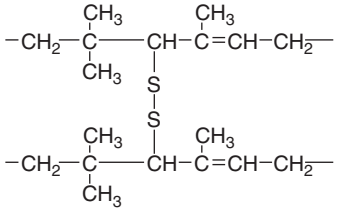

Figure 12.13 *Butyl rubber.*

motion is possible. The glass transition temperature of butyl rubber is around −63 °C. At ambient temperatures, rubbers are relatively soft and deformable. The chain segments of elastomers can undergo high local mobility, but the gross mobility of chains is restricted by the introduction of a few cross-links into the structure during vulcanization. The covalent cross-linkages ensure that the elastomer will return to its original configuration when the stress is removed. In the absence of applied stress [49], molecules of elastomers usually assume coiled shapes. Consequently, elastomers exhibit large elongation (up to about 1000%) from which they recover rapidly on removal of the applied stress. Among elastomers, vulcanized butyl rubber has excellent dielectric properties, high damping properties at ambient temperatures, is mechanically flexible, air tight and gas impermeable, has a low glass transition temperature, good resistance to oxidizing chemicals, good weathering and heat and chemical resistance. The main use of butyl rubber is in tyre-curing bladders and inner tubes and is also used for seals, adhesives, molded flexible parts, etc. [50–52]. The moisture absorption of butyl rubber is about 0.039 vol.%.

Recently Chameswary and coworkers reported the microwave dielectric properties of butyl rubber composites with $SrTiO_3$, $Sr_2Ce_2Ti_5O_{16}$, SiO_2, $Ba(Zn_{1/3}Ta_{2/3})O_3$, $Ba_{0.7}Sr_{0.3}TiO_3$, Al_2O_3, $BaTiO_3$ and TiO_2 fillers [27, 53–60]. The microwave dielectric properties of the ceramics used and butyl rubber are given in Table 12.1. Elastomer–alumina composites are well studied for their mechanical and curing characteristics [26,61,62]. Silica is a low-permittivity ceramic with excellent dielectric properties ($\varepsilon_r = 3.8$, $\tan\delta > 10^{-4}$) [63] and good thermal properties such as $Tc = 1.4$ W/m K and CTE = 0.5 ppm/°C. Silica is an important reinforcing filler in elastomers for industrial applications. The effect of silica on dielectric properties of styrene–butadiene rubber was investigated by Hanna *et al.* [64] in the frequency range of 60–108 Hz at room temperature. $Ba(Zn_{1/3}Ta_{2/3})O_3$ is a complex perovskite ceramic with $\varepsilon_r = 28$, $\tan\delta = 10^{-4}$, and a low coefficient of relative permittivity of about 12 ppm/°C. Butyl rubber is a synthetic elastomer with excellent dielectric properties at microwave frequencies ($\varepsilon_r = 2.4$, $\tan\delta > 10^{-3}$) with good mechanical flexibility. The ceramics TiO_2, $SrTiO_3$, $BaTiO_3$, $SrCe_2Ti_5O_{16}$, $Ba_{0.7}Sr_{0.3}TiO_3$ have relatively high permittivities [7].

12.3.2 Preparation of Butyl Rubber (BR)–Ceramic Composites

The ceramics $Ba(Zn_{1/3}Ta_{2/3})O_3$ (BZT), $Sr_2Ce_2Ti_5O_{15}$ (SCT), $SrTiO_3$, $BaTiO_3$, and $Ba_{0.7}Sr_{0.3}TiO_3$ were prepared by the conventional solid-state ceramic route using high-purity raw materials. The stoichiometric amount of chemicals were mixed by ball milling and dried. The mixtures were then calcined followed by sintering at appropriate temperatures and ground well. The powders had an average particle size in the range 0.5 to 5 μm and were used for preparing butyl rubber–ceramic composites [53–60]. The nanoalumina powder (<50 nm particle size), nanorutile (100 nm) and nano-$BaTiO_3$ (~80 nm) were used for preparing butyl rubber–nano composites. The fused silica and nanopowders were dried at 100 °C for 24 h before use. The process involving incorporation of ingredients such as activators, accelerators, vulcanizing agent and fillers into the virgin rubber is known as compounding of rubber. The compounding of butyl rubber mix was done by the sigma blend method using a kneading machine. The butyl rubber of IIR grade was first masticated through the two counter-rotating sigma blades in order to make it soft and more processable. Then the additives are incorporated one by one as per the order given in Table 12.4.

Table 12.4 *Formulation of the rubber mix*

Ingredients	phr[a]
Butyl rubber	100.0
Zinc oxide	5.0
Stearic acid	3.0
Tetramethylthiuram disulfide	1.0
Sulfur	0.5

[a]Parts per hundred.

The additives such as zinc oxide and stearic acid act as activators for vulcanization, tetramethylthiuram disulfide acts as an accelerator and sulfur acts as the vulcanizing agent. Finally, different volume fractions of ceramic fillers are added. The mixing was done for about 30 min to obtain uniform composites. Then obtained composites are hot-pressed at 200 °C for 90 min in suitable dies or molds under a pressure of 2 MPa. Figure 12.14 shows a photograph of a typical butyl rubber–ceramic composite exhibiting good flexibility.

The volume fraction of the ceramic that can be incorporated into the butyl rubber depends on the density, powder particle size and shape or morphology of the ceramic powder. When the powder particle size is very small, they have a high surface area and only a smaller volume fraction can be incorporated. The nanofillers have a high surface area and hence the possibility of agglomeration of nanoparticles increases with filler loading. This makes the processing of butyl rubber (BR) nanofiller composites difficult at higher filler

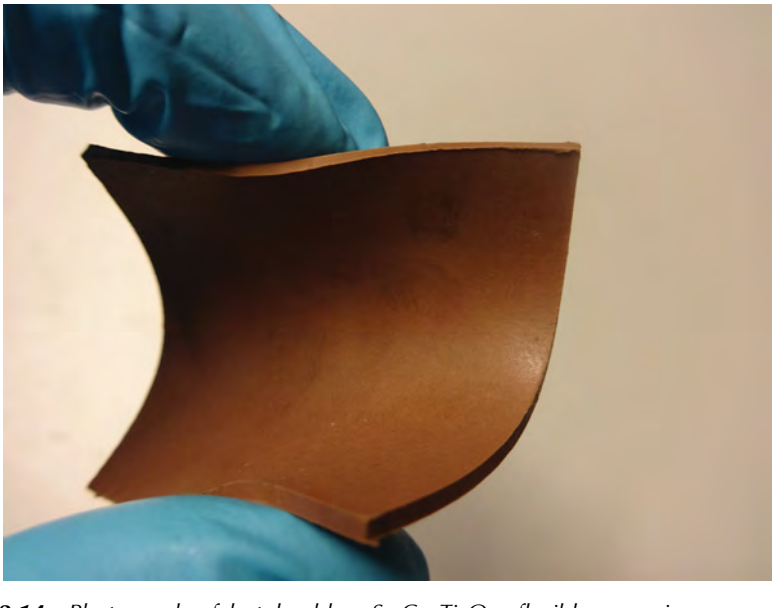

Figure 12.14 *Photograph of butyl rubber–$Sr_2Ce_2Ti_5O_{16}$ flexible ceramic composites. This figure is also shown in the Plate Section.*

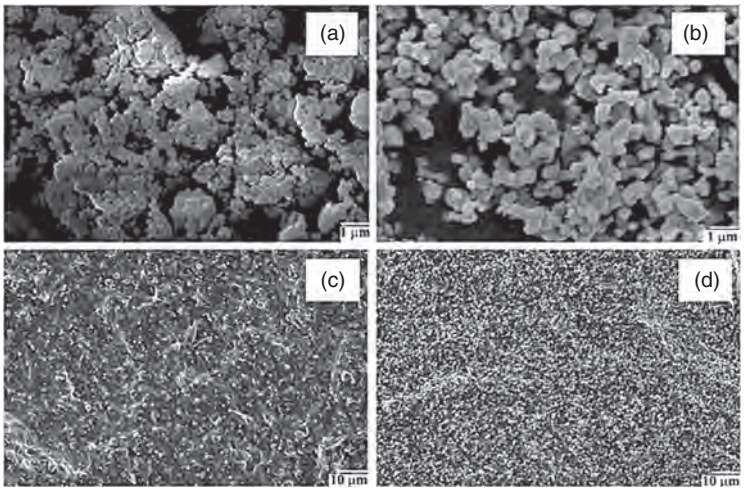

Figure 12.15 *SEM image of (a) SiO_2 powder, (b) $Ba(Zn_{1/3}Ta_{2/3})O_3$ powder, (c) fractured surface of BRS-5 and (d) BR–BZT-7. Source: Adapted from Chameswary and Sebastian 2013 [55].*

loading [57–60]. Hence, a maximum loading of 0.1 volume fraction (V_f) of nanoalumina (<50 nm) was possible in the case of BR–nanoalumina composites. In the case of $BaTiO_3$ nanopowder (~80 nm) $V_f = 0.24$ whereas for nanorutile (100 nm) $V_f = 0.3$ [60]. It was found that the use of a coupling agent such as silane to modify the surface of the filler powders slightly improves the relative permittivity and mechanical properties but degrades the microwave dielectric loss factor [59]. Figure 12.15 represents typical SEM micrographs of BZT and SiO_2 reinforced butyl rubber composites. Figure 12.15a and b shows the SEM images of silica and BZT powders, respectively. Both silica and BZT particles are irregularly shaped and are <1 μm in size. Figure 12.15c and d represents fractured SEM images of BR–0.42 V_f of SiO_2 and BR–0.32 V_f BZT, respectively. From the figure it is clear that the filler particles are randomly distributed in the rubber matrix of both composites.

12.3.3 Dielectric Properties

The addition of ceramic fillers in butyl rubber gradually increased the relative permittivity. The increase in the relative permittivity depends on the amount of ceramic filler, its relative permittivity and the frequency of measurement. Figure 12.16 shows the variation of relative permittivity of butyl rubber ceramic composites as a function of filler volume fraction measured at 5 GHz by the SPDR method described in Chapter 2. As the relative permittivities of the fillers are higher than that of the butyl rubber, the ε_r of BR composites show an increasing trend with filler content. The microwave dielectric properties of butyl rubber–ceramic composites with the highest volume fraction with homogeneous dispersion of fillers are given in Table 12.5. Although relative permittivity of filler ceramics is much higher than that of matrix, the composite cannot attain a high relative permittivity. The relative permittivities of $BaTiO_3$ and $Ba_{0.7}Sr_{0.3}TiO_3$ are higher than 1000 but the composites with about 0.4 volume fraction can achieve a relative permittivity of about 13 only. The

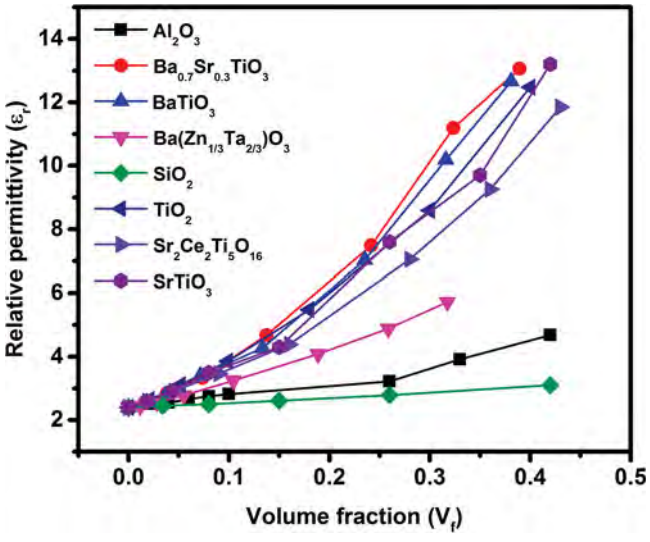

Figure 12.16 *Variation of relative permittivity with volume fraction of ceramic fillers in butyl rubber–ceramic composites.*

relative permittivities of polymer–ceramic composites cannot increase to a very high value even at maximum filler loading [37] since the 0–3 type composite follows an exponential relationship between relative permittivity of composite and the volume fraction of the filler, as given in Equation (12.1). At low volume fractions, the filler particles are randomly distributed in the rubber matrix with poor connectivity between the ceramic particles. At higher volume fractions or near the percolation threshold the ceramic filler particles are connected and hence the relative permittivity shows an abrupt increase. However, it is difficult to mix large amount of filler ceramics in the rubber matrix.

Table 12.5 *Butyl rubber–ceramic composites (5 GHz)*

Filler	Powder particle size	V_f	ε_r	tan δ	CTE	Water absorption (vol.%)	*Tc* (W/m K)
SiO_2	<1 μm	0.4	3.1	0.0045	80	0.09	0.56
Al_2O_3	~1 μm	0.4	4.7	0.0026	55	0.08	0.58
$Ba(Zn_{1/3}Ta_{2/3})O_3$	<1 μm	0.32	5.8	0.0025	86	0.05	0.35
$Sr_2Ce_2Ti_5O_{16}$	~5 μm	0.43	11.0	0.0018	30	0.07	0.45
TiO_2	~2 μm	0.40	12.5	0.0027	108	0.08	0.72
$SrTiO_3$	~5 μm	0.42	13.2	0.0025	26	0.08	0.55
$Ba_{0.7}Sr_{0.3}TiO_3$	<5 μm	0.39	13.1	0.009	29	0.06	0.41
$BaTiO_3$	~1 μm	0.38	12.7	0.02	33	0.12	0.43
Nano-Al_2O_3	<50 nm	0.10	3.15	0.014	–	0.75	–
Nano-$BaTiO_3$	~80 nm	0.24	8.79	0.019	–	0.091	–
Nano-TiO_2	~100 nm	0.3	7.6	0.003	–	0.11	–

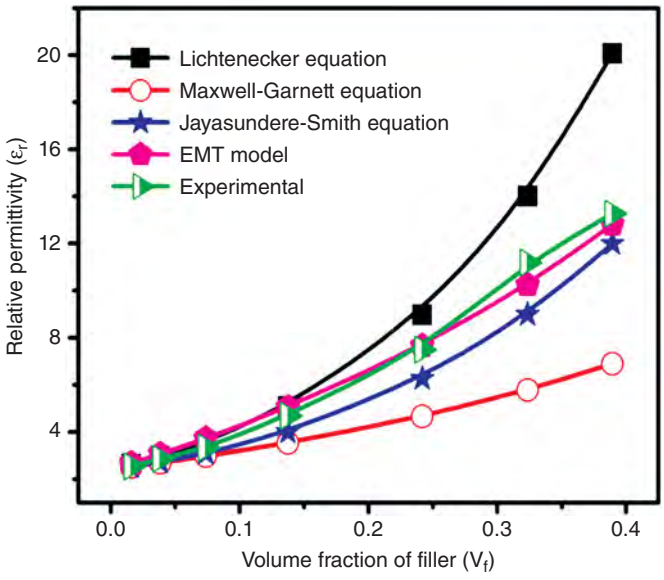

Figure 12.17 *Comparison between experimental and theoretical relative permittivity with BST loading at 5 GHz. Source: Adapted from Chameswary and Sebastian 2013 [56].*

The prediction of effective relative permittivity of polymer–ceramic composites is very important for engineering applications. Several numerical relations have been proposed to predict the relative permittivity of these structures [35, 38–42, 65]. These models can be used to determine the extent of filler dispersion and filler–matrix compatibility by comparing the predicted values with the experimental data. In order to understand the physical mechanisms controlling the relative permittivity of a heterogeneous system, the experimental values of ε_r are compared with values predicted using different theoretical models. Figure 12.17 represents a typical example of comparing the experimental relative permittivity of butyl rubber–$Ba_{0.7}Sr_{0.3}TiO_3$ composites with that computed using different theoretical models, described in Chapter 2. The figure shows that Lichtenecker and Maxwell Garnet equations [38,41] hold only for low volume fractions of the filler and deviate at higher filler contents. This may be due to the inhomogeneous dispersion of powder particles at higher filler loadings. The Jayasundere–Smith equation [39] also shows a mismatch with the experimental plot. In the Jayasundere–Smith model all of the ceramic particles are considered to be spherical in shape. The BST particles are irregularly shaped and hence this model shows deviation from the experimental profile [53]. The experimental profile shows reasonable agreement with the EMT model [42]. This model considers a shape or morphology factor n and the model matches the experimental plot. The deviation of all theoretical models at higher filler loading is due to the imperfect dispersion of filler particles in the butyl rubber matrix. The relative permittivity of the composites is influenced not only by the relative permittivity of the individual components but also other factors such as morphology, size and shape of filler particles, volume fraction of phases, degree of dispersion, agglomerates, interphase polarizability and interphase volume fractions, mechanical and chemical coupling between rubber and filler, porosity, presence of moisture, impurities, and dispersion,

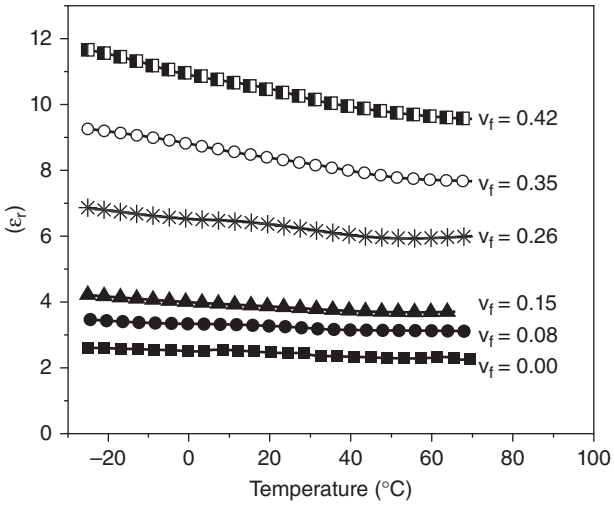

Figure 12.18 *Variation of relative permittivity of butyl rubber–$SrTiO_3$ composites as a function of temperature measured at 1 MHz. Source: Adapted from Thomas* et al. *2011 [53].*

and interaction between the two phases [34,42,66–71], and hence the prediction of relative permittivity of composites is very difficult. All these parameters cannot be accounted for in a single equation. Therefore the experimental results show a deviation from the theoretical values at a higher filler content. In addition, the deviation at higher filler loading may be due to the inhomogenous dispersion of filler particles in the rubber matrix.

The relative permittivity of a material should be stable within the operational temperature range of the electronic device for practical applications. The variation of relative permittivity of butyl rubber–ceramic composites with temperature measured by the parallel plate capacitor method at 1 MHz showed a slight decrease with an increase in temperature. The decrease will be more with an increase in filler loading. Figure 12.18 shows the temperature dependence of relative permittivity of butyl rubber–$SrTiO_3$ composites measured in the range 25 to 75 °C. From the figure, it is clear that all of the composites are nearly thermally stable within the measured temperature range.

The loss tangent is an important factor affecting the frequency selectivity of materials. Figure 12.19 shows the variation of loss tangent of butyl rubber composites as a function of volume fraction of filler ceramics measured at 5 GHz. In general the loss tangent increases with the increase in filler content for all rubber–ceramic composites. The loss tangent increases considerably for $BaTiO_3$ since it is a lossy ferroelectric material. The increase is relatively small for alumna, silica, rutile, etc., since they are low-loss ceramics. The increase in loss of the composites with increasing filler loading may be due to the presence of porosity, an increase in the interphase region, and moisture content. The water absorption and porosity of all composites are found to increase with the filler volume fraction. The dipole relaxation of water molecules in the microwave frequency contributes to dielectric loss [69]. It is found that the loss increases with thermal aging of the composites whereas the relative permittivity remains nearly the same [56]. Figure 12.20 shows the variation of relative permittivity and loss tangent with thermal aging at 75 °C for different

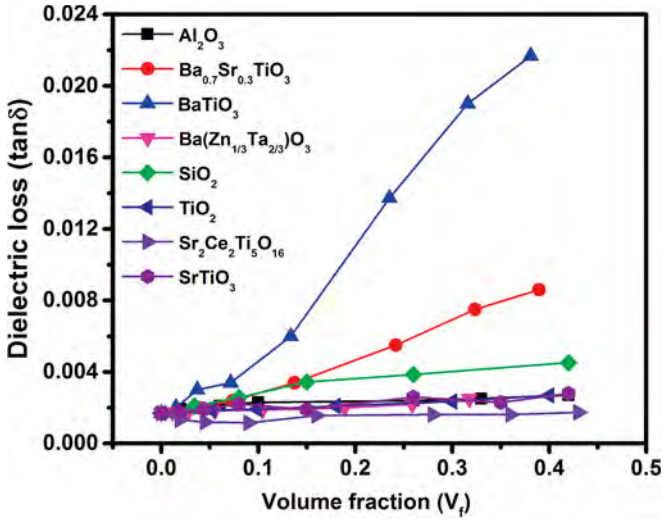

Figure 12.19 *Variation of tan δ with volume fraction of ceramic fillers in butyl rubber–ceramic composites.*

durations of butyl rubber-—$Ba_{0.7}Sr_{0.3}TiO_3$ composites. The permittivity is almost independent of thermal aging, but the loss factor increases with aging time. This may be due to some chemical reactions occurring during aging [72]. Overton *et al*. reported a similar observation in Teflon films [73].

It is found that the relative permittivity and loss tangent are higher for nanofillers such as alumina, rutile and $BaTiO_3$ [57, 58, 60]. Figure 12.21 shows the variation of relative permittivity and loss tangent of $BaTiO_3$-based butyl rubber composites. The relative permittivity of BR–micrometer $BaTiO_3$ composite is 7.03 for ceramic loading of 0.24 V_f and that of BR–nano $BaTiO_3$ composite is 8.79 for the same loading of nano-$BaTiO_3$. The nanoceramic-filled butyl rubber composites have a higher relative permittivity than micrometer composite. Similar behavior was observed in PTFE–silica, PTFE–rutile and PEEK–$SrTiO_3$ composites [32, 74–75]. It was reported that the nanofillers have more polarization at the interphase region due to their large surface area and interface region between the filler and matrix [66]. The nanocomposites have a high moisture content due to their large surface area. The composites filled with nanoparticles have a large interfacial area, which promotes the interfacial polarization mechanism leading to a higher relative permittivity of the composites. The accumulation of charges at the interfaces causes polarization in heterogeneous systems and the relaxation of this polarization causes loss at low frequencies. As the filler content increases the interfacial area increases and consequently the loss tangent of composites increases. It is also noted that the loss tangent in BR–nano-$BaTiO_3$ composite is higher than that of BR–micro-$BaTiO_3$ composites. The increased lattice strain due to the high surface area of nanoparticles and the higher moisture content in the butyl rubber–nano-$BaTiO_3$ composites contribute to a higher loss tangent of the composites. The loss tangent is the main factor affecting the frequency selectivity of a material and is influenced by many factors such as porosity, microstructure and defects [7].

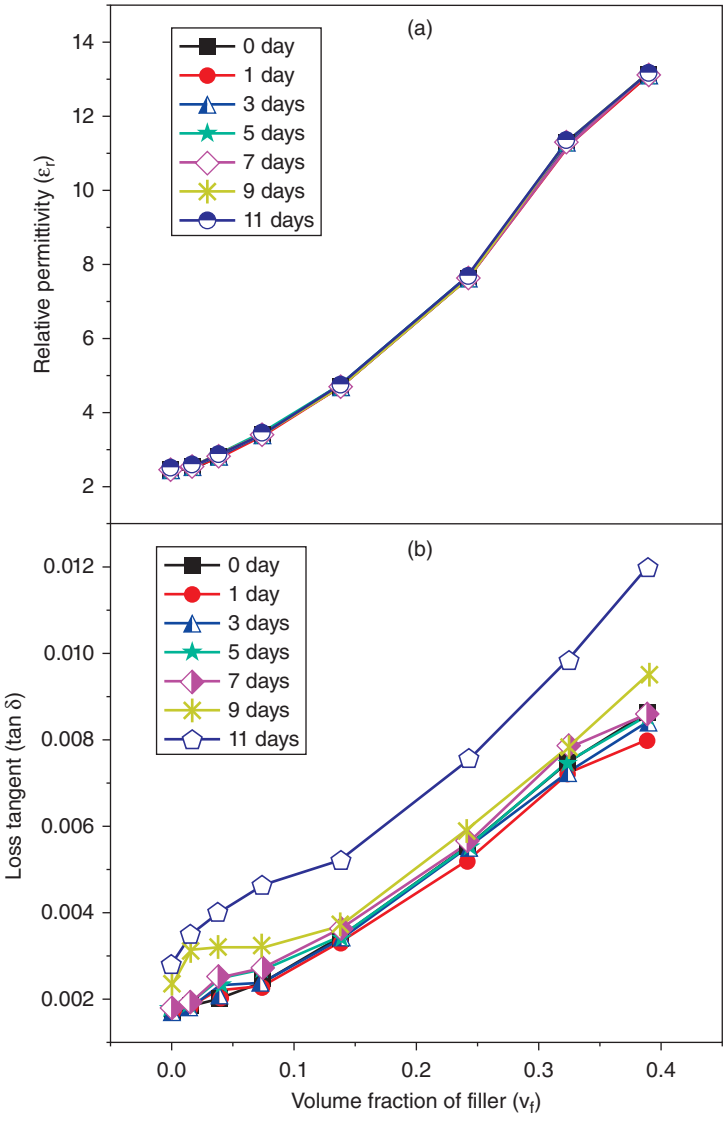

Figure 12.20 *Variation of (a) relative permittivity and (b) loss tangent with aging at 75 °C for different durations for all BST compositions measured at 5 GHz. Source: Adapted from Chameswary and Sebastian 2013 [56].*

12.3.4 Bending

The bending effect on dielectric properties is important for flexible electronic applications. Bending measurements of the composites were carried out by bending the samples manually in such a way that every part of the sample had undergone 180° bending. The bending cycle was repeated for 125 times and the microwave dielectric properties were measured

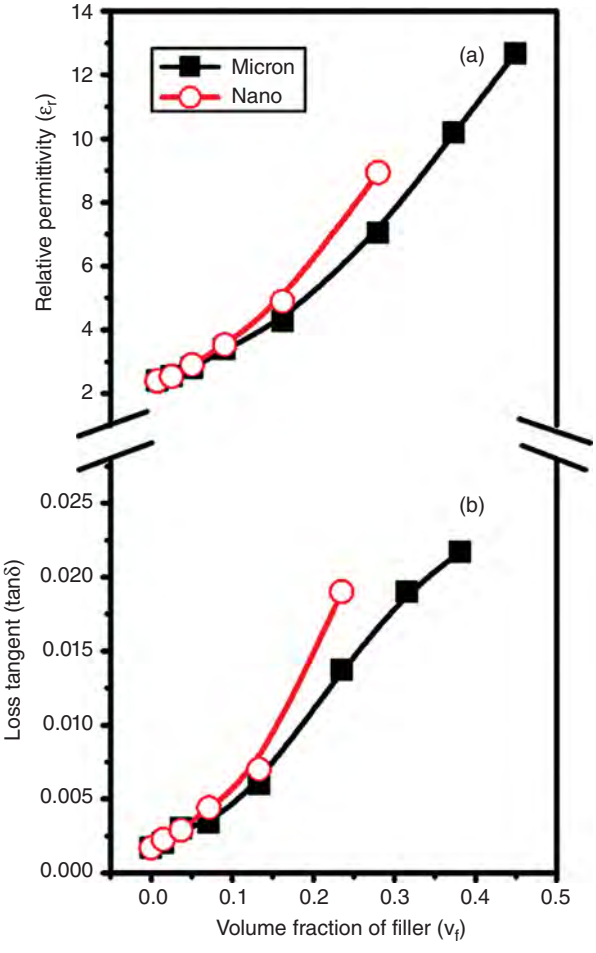

Figure 12.21 *Variation of (a) relative permittivity and (b) loss tangent of BR/BT and BR/nBT composites at 5 GHz. Source: Adapted from Chameswary and Sebastian 2015 [60].*

by the after every 25 cycles. It was reported that the relative permittivity of butyl rubber—ceramic composites is nearly independent of bending up to 125 cycles but the loss tangent shows small variations and the variations increase with an increase in filler loading [53–60]. Figure 12.22 shows the variation of relative permittivity and loss factor of butyl rubber–$Ba_{0.7}Sr_{0.3}TiO_3$ as a function of cycles of bending. It is clear from the figure that the relative permittivity of all the composites is nearly independent of bending. The loss tangent of the composites shows only small variations with repeated bending. Vrejoiu *et al*. [76] observed a similar behavior in PFCB (perfluorocyclobutene (poly(1,1,1)-triphenyl ethane perfluorocyclobutyl ether)−$BaTiO_3$ composites. They observed that repeated mechanical bending up to 50 cycles does not change ε_r and tan δ of the composites. The bending of the composites does not considerably affect the microwave dielectric properties and hence they are suitable for flexible electronic applications.

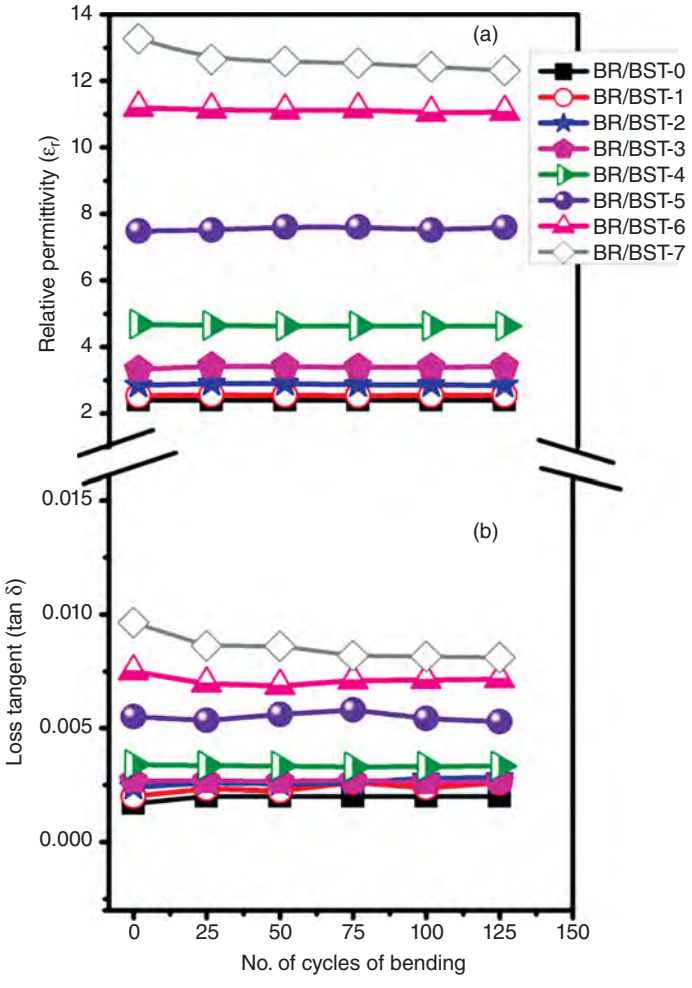

Figure 12.22 *Variation of (a) relative permittivity and (b) loss tangent of butyl rubber–$Ba_{0.7}Sr_{0.3}TiO_3$ composites with bending. BST-0: $V_f = 0$; BST-1: $V_f = 0.02$; BST-2: $V_f = 0.04$; BST-3: $V_f = 0.07$; BST-4: $V_f = 0.14$; BST-5: $V_f = 0.24$; BST-6: $V_f = 0.32$; BST-7: $V_f = 0.39$. Source: Adapted from Chameswary and Sebastian 2013 [56].*

12.3.5 Thermal Conductivity

Heat dissipation from integrated circuits is a crucial problem for the electronic industry that affects potential miniaturization, speed and reliability. The thermal conductivity (TC) of polymers is very low, ranging from 0.14 to 0.60 W/m K [77] and can be improved by the addition of ceramic fillers since the TC of ceramics is higher than that of polymers. The TC of the composites depends on the intrinsic thermal conductivities of filler and matrix, shape and size of the filler and the loading level of filler and filler connectivity [20]. The TC of butyl rubber–ceramic composites is found to increase with an increase in filler loading. This is quite expected since the TC of ceramics is higher than that of butyl rubber

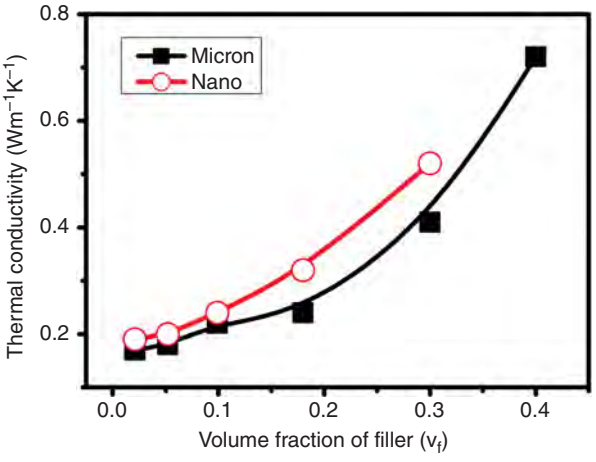

Figure 12.23 *Variation of thermal conductivity of BR/RT and BR/nRT composites with ceramic loading. Source: Adapted from Chameswary and Sebastian 2014 [58].*

matrix (0.13 W/m K). Figure 12.23 shows the variation of TCof butyl rubber–rutile as a function of ceramic loading. As the filler loading increases, the distance between the filler particles decreases and thus the filler becomes the main channels for thermal conduction. The increase in TC of the composites at a higher filler content is due to the presence of more connecting paths between the filler particles. The TC of the composite can be further enhanced by adding high TC fillers such as aluminum nitride, silicon nitride, etc. The TC of nano-based composites are found to be higher than that of micrometer sized filler-based composites [57, 58, 60]. The matrix/filler interface plays a critical role in nanocomposites due to its large surface area. The number of particles increases with decreasing particle size for the same filler content [78, 79]. This will lead to the formation of a large number of heat-conductive channels in nanofiller-added composites. Hence, the TC of a nano-based composite is higher than micrometer-based composites. The effective TC of a heterogeneous system is strongly affected by the TC of individual components, composition, crystal structure, distribution within the medium and contact between the particles. Numerous theoretical models were proposed for predicting the TC of composites [44, 80].

12.3.6 Mechanical Properties

The mechanical flexibility is the prime requirement for flexible electronic applications. The tensile test is useful to evaluate mechanical properties of materials in which the sample is pulled to failure in a relatively short period of time. Figure 12.24 shows the stress–strain curves of BR-0, BR/rutile and BR/nanorutile. It is found that the stress needed for elongation increases with filler content. It is also evident that the stress needed for nanorutile-filled butyl rubber composite is higher than that of microrutile-filled butyl rubber composites. Fu *et al*. reported that the particle size, particle–matrix interface adhesion and particle loading are the main factors that affect the mechanical properties of particulate-filled polymer composites [43]. The more uniform dispersion of nanoparticles in the rubber matrix is

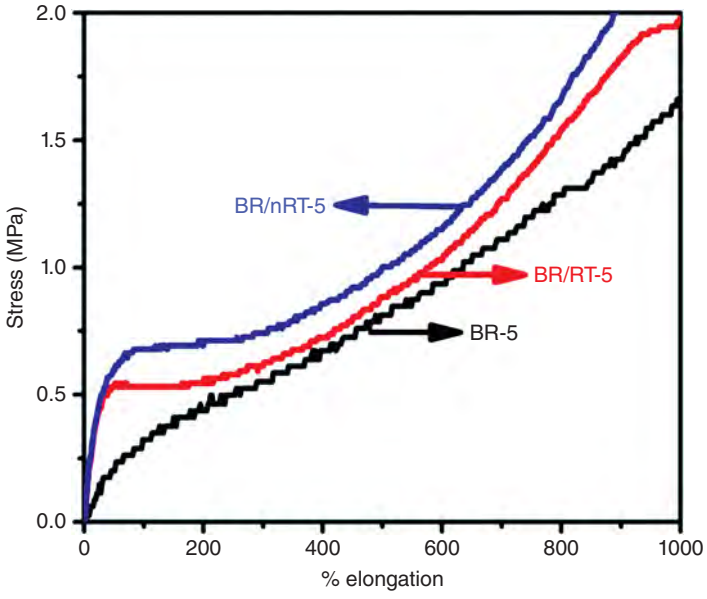

Figure 12.24 *Stress–strain curves of butyl rubber–rutile (RT) and nanorutile (nRT) composites (MRT-5: microrutile $V_f = 0.3$, NRT-5: nanorutile $V_f = 0.3$. Source: Adapted from Chameswary and Sebastian 2014 [58].*

responsible for the high stiffness of BR/NRT-5 (nano $V_f = 0.3$) composite. This may be due to the more homogeneous dispersion of nanoparticles in the rubber matrix. Chee *et al*. [81] reported that at lower filler loading the nanoalumina particle orient along the direction of stress and this would reinforce and increase the stiffness of the nanocomposite. All the composites remain unbroken even up to an elongation of 1000% [53–58]. Hence, the composite is suitable for flexible applications. The stress needed for elongation increases with filler content. The interfacial adhesion plays a major role in mechanical properties of the composites. Todorova *et al*. [82] reported that the interfacial adhesion increases with filler loading, which in turn increases the effectiveness of the stress transfer from rubber chains. Salaeh *et al*. [83] reported that the mobility of molecular chains decreases due to the incorporation of ceramic particles and hence the increase in stiffness of the composite.

12.3.7 Moisture Absorption of Composites

The moisture content is an important parameter for materials used for practical applications. Absorption of moisture from the working atmosphere will degrade the dielectric properties since water is a polar molecule. The moisture absorption characteristics of the composites were measured by the method described in Section 12.2.7 using the samples with dimensions 50 mm × 50 mm × 2 mm. It is reported that as the filler content increases, the volume % of water content increases for butyl rubber ceramic composites since the ceramic is hydrophilic in nature. Compared to the micrometer composite, nanocomposites have a high tendency to absorb moisture due to the large surface area and higher nanofiller loading also

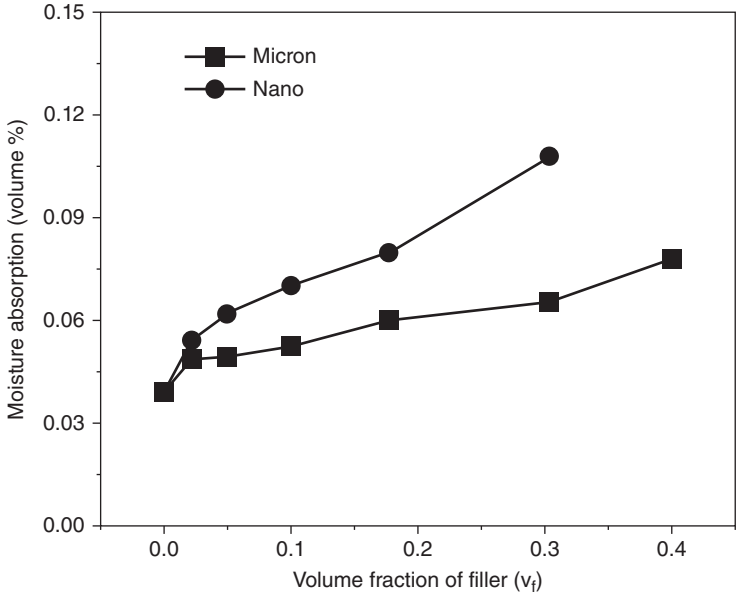

Figure 12.25 *Variation of moisture absorption with ceramic loading of butyl rubber–rutile composites with nano- and micrometer-sized fillers. Source: Adapted from Chameswary and Sebastian 2014 [58].*

leads to the formation of pores in the composites due to agglomeration of the particles. The loss tangent and moisture absorption of butyl rubber–nanoceramic composites are much higher as compared to the micrometer composites. The dielectric properties of the composites are affected by the presence of moisture content. The absorbed moisture interacts with polymer matrix and also with the filler–matrix interface [84–86] and thus affects the dielectric properties of composites. Figure 12.25 shows the variation of moisture absorption with filler loading in butyl rubber–rutile composites for both nano- and micrometer-sized powder particles. The moisture content significantly influences the electrical properties of the composites because the relative permittivity and loss tangent of water are high.

12.3.8 Coefficient of Thermal Expansion (CTE)

The CTE of butyl rubber–ceramic composites decreases with an increase in the ceramic filler content. Figure 12.26 shows the variation of coefficient of thermal expansion (CTE) of butyl rubber–ceramic composites as a function of filler content. The CTE of the composites decreases with ceramic loading since the CTE value of the ceramics is smaller than that of rubber matrix and also the mobility of loose molecular bonds in the polymer chains is restrained by the ceramic loading [87, 88]. In polymer–ceramic composites, there is a region of tightly bound polymer chains in the immediate vicinity of the filler particles followed by a region of loosely bound polymer chains. The filler particles will largely restrict the thermal expansion of polymer chains tightly bound to them, but the thermal expansion of loosely bound polymer chains may not be constrained very much. The addition

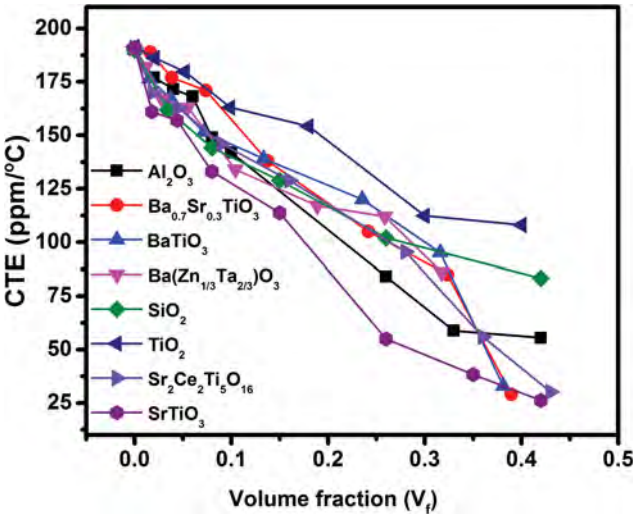

Figure 12.26 *Variation of CTE with volume fraction of ceramic fillers in butyl rubber–ceramic composites.*

of more filler leads to the reduction in volume fraction of loosely bound polymer chains. Consequently, the thermal expansion of the composite will become suppressed. The interfacial properties of the filler significantly affect the CTE of the composites. The thermal expansion of composites is more reduced in a strong interfacial system than that in a poor interface system. Recently Goyal *et al*. [88] reported that the unconstrained polymer chains become constrained upon the addition of a ceramic, which reduces the thermal expansion of composites.

The physical cross-linking points are more in the case of nanoparticles because of their high specific surface area and this will increase the mechanical interaction between the filler and rubber matrix [28]. Hence, the nanocomposites have a lower CTE than the microcomposites.

12.4 Fabrication of Flexible Microstrip Antenna

The recent explosive growth in wireless communication has increased the demand for suitable antennas. The conformability of antennas requires reconfigurable and stretchable antennas that can be mounted on non-planar spaces [89–91]. The substrate flexibility metallized patch determines the conformality limits. A microstrip patch antenna is fabricated using silicone rubber $-0.134\ V_f\ Ba(Mg_{1/3}Ta_{2/3})O_3$ substrate and is shown in Figure 12.27. It has $\varepsilon_r = 4.75$, $\tan\delta = 0.0122$ at 5 GHz, and thickness of 1.092 mm and density of 2.03 g/cm^3. The design of a microstrip antenna was done with Ansoft HFSS (high frequency structure simulator) software and the antenna was fabricated using the screen printing technique [24]. The measurement of a fabricated antenna was carried out in an anechoic chamber using a network analyzer. Figure 12.28 illustrates the simulated and experimental return loss as well as the radiation pattern of a microstrip patch antenna. The experimental

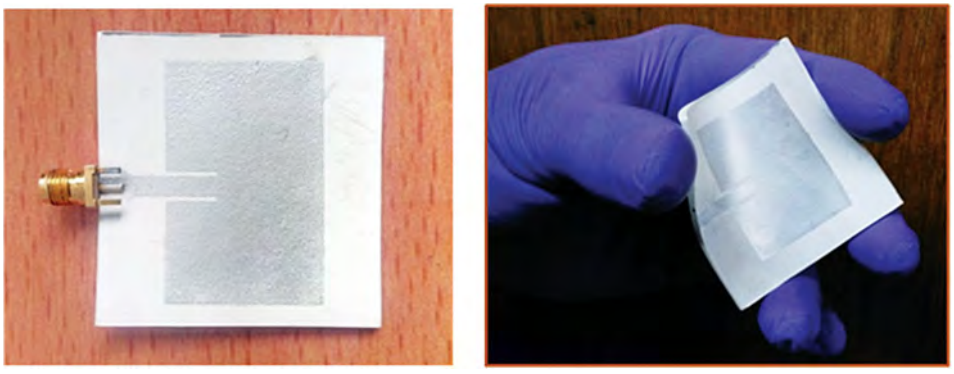

Figure 12.27 *Photograph of fabricated flexible patch antenna.*

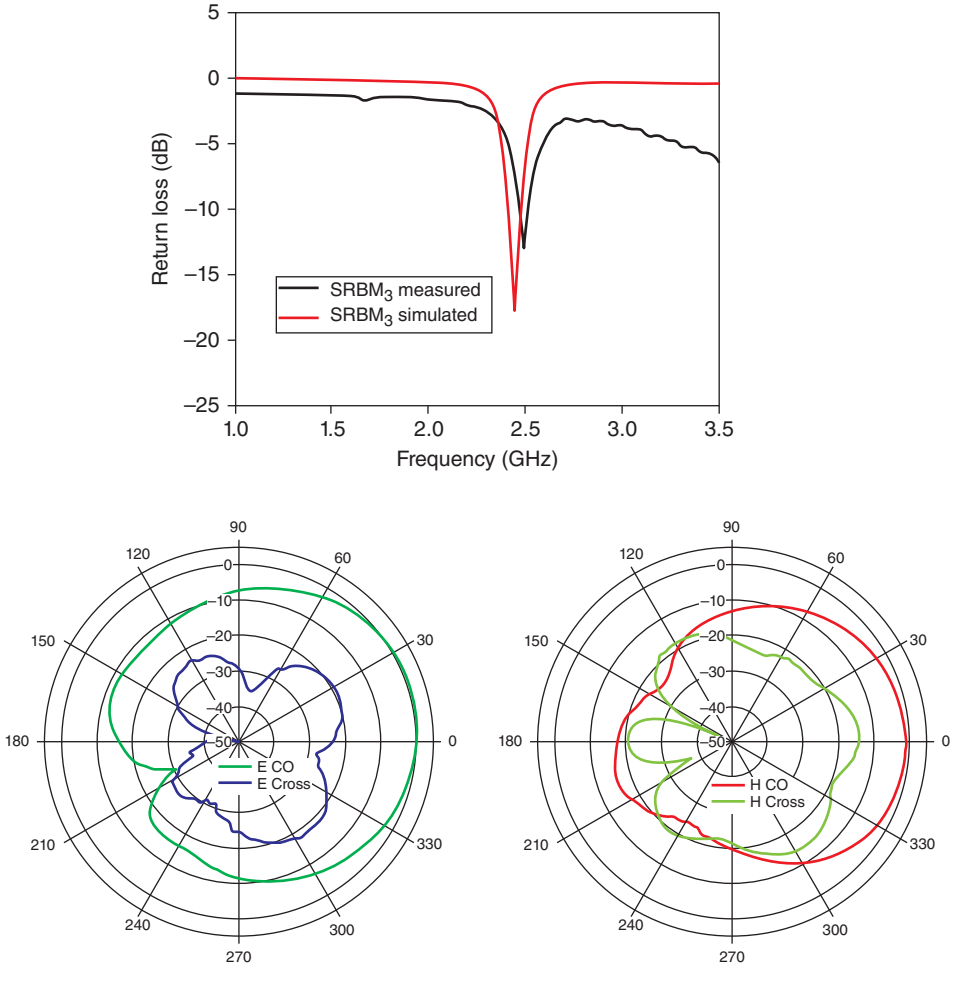

Figure 12.28 *Comparison of experimental and simulated return loss and radiation pattern of SR-0.134 V_f $Ba(Mg_{1/3}Ta_{2/3})O_3$ composites, with $\varepsilon_r = 4.75$, $\tan\delta = 0.0122$ at 5 GHz. Thickness of 1.092 mm and density of 2.03 g/cm^3.*

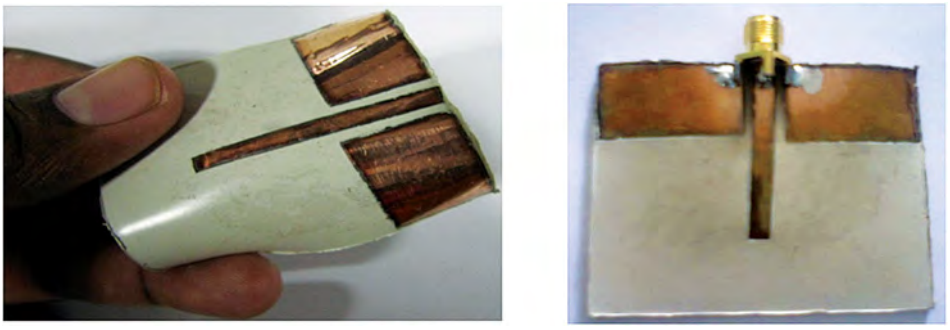

Figure 12.29 *Photograph of fabricated patch antenna.*

and simulated results show a good match and the antenna resonates at 2.48 GHz with a return loss of about −12.9 dB. A butyl rubber-based patch antenna has also been fabricated using BR+0.15 V_f of $SrTiO_3$ composite having a relative permittivity of 4.3 and tan δ = 0.002 at 5 GHz [59]. The antenna dimensions were optimized using a high-frequency structure simulator (HFSS) to get good impedance matching. The optimized dimension of the resonating element is 35 mm length and 3 mm width. The antenna was fed with a coplanar waveguide with a ground plane of 22 mm × 15 mm size and as the ground plane is on the same plane it can be easily fabricated. The copper cladding was done by hot pressing as per the simulated design in Figure 12.29. Figure 12.30 shows the simulated and measured reflection characteristics of the antenna. The simulated and measured reflection

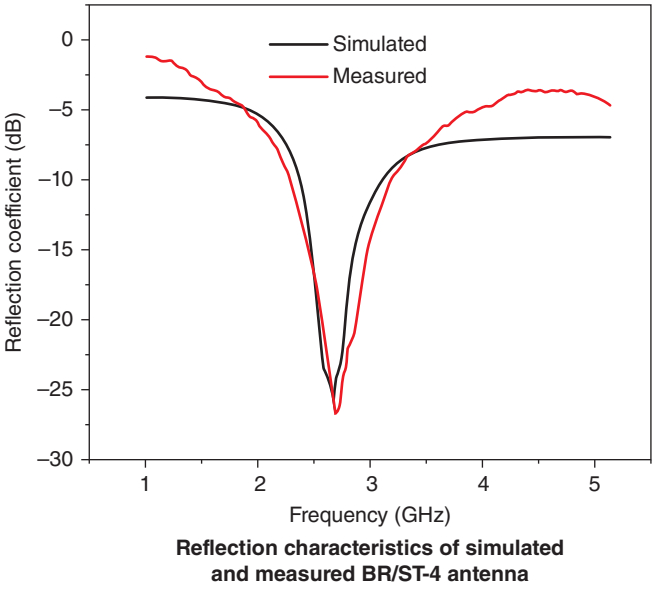

Figure 12.30 *Reflection characteristics of simulated and measured BR+0.15 v_f of $SrTiO_3$ antenna. Relative permittivity of 4.3 and tan δ = 0.002 at 5 GHz. Source: Chameswary 2015 [59].*

characteristics are in good agreement. The measured sample has a return loss of −26.75 dB at 2.68 GHz. The bandwidth of butyl rubber–$SrTiO_3$ at the −10 dB level is 16.9%. The results indicate that the silicone and butyl rubber–ceramic composite-based substrates can be used as a cost-effective, flexible microwave antenna substrate.

12.5 Conclusions

Mechanically flexible and stretchable silicone and butyl rubber–ceramic composites can be prepared by mixing in a kneading machine followed by hot pressing. The composites are found to be flexible, bendable and stretchable. The microwave dielectric and thermal properties are improved with ceramic loading. The composite preparation is difficult for ceramic loading higher than 40 vol.%. The nanopowder can be loaded to a much lower level. The relative permittivity of composites depends on the rubber matrix and the volume fraction and permittivity of the filler ceramics. It is found that one can get only a relative permittivity of about 14 even with maximum loading with high-permittivity ceramics. The thermal conductivity increases and coefficient of thermal expansion decreases with an increase in filler content. The water absorption increases with an increase in ceramic loading. The composites are found to have good dielectric properties, flexibility and are suitable antenna fabrication and capacitative applications. The composite with nanoceramic filler has inferior microwave dielectric properties. The physical and microwave dielectric properties of the silicone rubber and butyl rubber ceramic composites are summarized in Tables 12.3 and 12.5. One of the most attractive features of these particulate composites is that their electrical and physical properties can be varied over a wide range by choosing the appropriate shape, size and connectivity or volume fraction of the fillers in the rubber matrix.

References

1. Rogers, J.A. and Huang, Y. (2009) A curvy, stretchy future for electronics. *Proceedings of the National Academy of Sciences*, **106**, 10875–10876.
2. Sun, Y. and Rogers, J.A. (2007) Inorganic semiconductors for flexible electronics. *Advanced Materials*, **19**, 1897–1916.
3. Seol, Y.G., Noh, H,Y., and Lee, S.S., *et al*. (2008) Mechanically flexible low-leakage multilayer gate dielectrics for flexible organic thin film transistor. *Applied Physics Letters*, **93**, 013305-1–013305-3.
4. Sebastian, M.T. and Jantunen, H. (2010) Polymer–ceramic composites of 0–3 connectivity for circuits in electronics: a review. *International Journal of Applied Ceramic Technology*, **7** (4), 415–434.
5. Yang, S. and Jiang, K. (2012) In *Elastomer Application in Microsystem and Microfluidics in Advanced Elastomers – Technology, Properties and Applications*, Chapter 8, *InTech. Open Science/Open Mind*, pp. 203–222.
6. Gubbels, F., De Jaeger, R., and Gleria, M. (2007) Inorganic polymers, in *Silicones in Industrial Applications* (eds R. De Jaeger and M. Gleria), Chapter 2, Nova Science Publishers, pp. 61–162.
7. Sebastian, M.T. (2008) *Dielectric Materials for Wireless Communication*, Elsevier, Oxford, UK.
8. Sebastian, M.T., Ananthalumar, S., Subodh, D., Juuti, J., Teirinkangas, M., and Jantunen, H. (2012) Composite electroceramics, in *Wiley Encyclopedia of Composites*, 2nd edn (eds L. Nicolais and A. Borzacchiello), John Wiley & Sons, Inc.
9. Characteristic Properties of Silicone Rubber Compounds. Copyright belongs to Shin-Etsu Co. Ltd. Available at: http://www. Silicone.jp/.

10. Handbook on Rubber and Allied Products (with Project profiles) NPCS Board–2013, published by NIIR Project Consultancy Services, pp. 11–12. Available at: https://books.google.co.in/books?isbn=9381039267.
11. Stiubianua, G., Belea, A., Cazacua, M., *et al*. (2015). Dielectric silicone elastomers with mixed ceramic nanoparticles. *Materials Research Bulletin*, **71**, 67–74.
12. Momen, G. and Farzaneh, M. (2011) Survey of micro/nano filler use to improve silicone rubber for outdoor insulators. *Reviews on Advanced Materials Science*, **27**, 1–13.
13. Gallone, G., Carpi, F., De Rossi., D., *et al*. (2007) Dielectric constant enhancement in a silicone elastomer filled with lead magnesium niobate–lead titanate. *Materials Science and Engineering C*, **27**, 110–116.
14. Qin, F. and Brosseau, C. (2012) A review and analysis of microwave absorption in polymer composites filled with carbonaceous particles. *Journal of Applied Physics*, **111**, 061301(1)–061301(24).
15. Zhou, W.Y., Qi, S.H., and Tu, C.C. (2007) Novel heat-conductive composite silicone rubber. *Journal of Applied Polymer Science*, **104** (4), 2478–2483.
16. Koulouridis, S., Kiziltas, G., and Zhou, Y. (2006) Polymer–ceramic composites for microwave applications: fabrication and performance assessment. *IEEE Transactions on Microwave Theory and Techniques*, **54** (12), 544202–544208.
17. Babu, S., Singh, K., and Govindan, A. (2012) Dielectric properties of $CaCu_3Ti_4O_{12}$–silicone resin composites. *Applied Physics A*, **107** (3), 697–700.
18. Sim, L.C., Ramanan, S.L., and Ismail, H. (2005) Thermal characterization of Al_2O_3 and ZnO reinforced silicone rubber as thermal pads for heat dissipation purposes. *Thermochimica Acta*, **430** (1–2), 155–165.
19. Zhou, W., Qi, S., Zhao, H.Z., and Liu, N.L. (2007) Thermally conductive silicone rubber reinforced with boron nitride particle. *Polymer Composites*, **28** (1), 23–28.
20. Kemaloglu, S., Ozkoc, G., and Aytac, A. (2010) Properties of thermally conductive micro and nano size boron nitride reinforced silicon rubber composites. *Thermochimica Acta*, **499** (1–2), 40–47.
21. Namitha, L.K., Chameswary, J., Ananthakumar, S., and Sebastian, M.T. (2013) Effect of micro- and nano-fillers on the properties of silicone rubber–alumina flexible microwave substrate. *Ceramic International*, **39**, 7077–7087.
22. Namitha, L.K. and Sebastian, M.T. (2013) Microwave dielectric properties of flexible silicone rubber–$Ba(Zn_{1/3}Ta_{2/3})O_3$ composite substrates. *Materials Research Bulletin*, **48**, 4911–4916.
23. Namitha, L.K., Ananthakumar, S., and Sebastian, M.T. (2015) Aluminum nitride filled flexible silicone rubber composites for microwave substrate applications. *Journal of Materials Science Materials in Electronics*, **26**, 891–897.
24. Namitha, L.K. and Sebastian, M.T. (2015) Fused silica filled silicone rubber composites for flexible electronic applications. *Materials Science Forum*, **830–831**, 537–540.
25. Namitha, L.K. (2016) *Ceramic Reinforced Silicone Elastomer Composites for Flexible Microwave Applications*. PhD Thesis, University of Kerala.
26. Alford, N.M. and Penn, S.J. (1996) Sintered alumina with low dielectric loss. *Journal of Applied Physics*, **80** (10), 5895–5898.
27. Sebastian, M.T. and Chameswary, J. (2016) *Polyisobutylene-co-Isoprene Composites for Flexible Electronic Applications. Flexible and Stretchable Electronic Composites* (eds D. Ponnamma *et al*.), Springer Series on Polymer and Composite Materials, Springer International Publishing, Switzerland.
28. Zhou, W., Qi, S., Tu, C., *et al*. (2007) Effect of the particle size of Al_2O_3 on the properties of filled heat conductive silicone rubber. *Journal of Applied Polymer Science*, **104**, 1312–1318.
29. Zhou, W., Yu, D., Wang, C., *et al*. (2008) Effect of filler size distribution on the mechanical and physical properties of alumina-filled silicone rubber. *Polymer Engineering and Science*, **48** (7), 1381–1388.
30. Surendran, K.P., Varma, P.C.R., and Varma, M.R. (2007). Solid state and solution synthesis of $Ba(Mg_{1/3}Ta_{2/3})O_3$: a comparative study, *Materials Research Bulletin*, **42**, 1831–1844.
31. Wise, P.L., Reaney, I.M., and Lee, W.E. (2001) Structure-microwave property relations of Ca and Sr titanates, *Journal of European Ceramic Society*, **21**, 2629–2632.

32. Murali, K.P., Rajesh, S., Om Prakash, A., *et al*. (2009) Preparation and properties of silica filled PTFE flexible laminates for microwave circuit applications. *Composites A*, **40**, 1179–1185.
33. Subodh, G., Joseph, M., Mohanan, P., and Sebastian, M.T. (2007) Low dielectric loss polytetrafluoroethylene/TeO_2 polymer ceramic composites. *Journal of American Ceramic Society*, **90**, 3507–3511.
34. Brosseau, C., Queffelec, P., and Talbot, P. (2001) Microwave characterization of filled polymers. *Journal of Applied Physics*, **89**, 4532–4540.
35. Jayasundere, N. and Smith, B.V. (1993) Dielectric constant for binary piezoelectric 0–3 composites. *Journal of Applied Physics*, **73**, 2462–2466.
36. Popielarz, R. and Chiang, C.K. (2007) Polymer composites with dielectric constant comparable to that of barium titanate ceramics. *Materials Science and Engineering B*, **139**, 48–54.
37. Popielarz, R., Chiang, C.K., Nozaki, R., and Obrzut, J. (2001) Dielectric properties of polymer/ferroelectric ceramic composites from 100 Hz to 10 GHz. *Macromolecules*, **34**, 5910–5915.
38. Maxwell Garnett, J.C. (1904) Colours in metal glasses and in metallic films. *Philosophical Transactions of the Royal Society of London. Series A, Containing Papers of a Mathematical or Physical Character*, **203**, 385–420.
39. Jayasundere, N. and Smith, B.V. (1993) Dielectric constant for binary piezoelectric 0–3 composites. *Journal of Applied Physics*, **73**, 2462–2466.
40. Lichtenecker, K. and Rother, K. (1931) Die Herleitung des logarithmischen Mischungs-gesetzes aus allegemeinen Prinzipien der stationaren Stromung, *Physics Zeitschrift*, **XXXII**, 255–260, 1931.
41. Shivola, H. (1989) Self consistency aspects of dielectric mixing theories. *IEE Transactions of Geoscience and Remote Sensing*, **27**, 403–415.
42. Rao, Y., Qu, J., Marinis, T.C., and Wong, P. (2000) A precise numerical prediction of effective dielectric constant for polymer–ceramic composite based on effective-medium theory. *IEEE Transactions on Components and Packaging Technologies*, **23**, 680–683.
43. Fu, S., Feng, B., Lauke, B., and Mai, Y. (2008) Effects of particle size, particle/matrix interface adhesion and particle loading on mechanical properties of particulate–polymer composites. *Composites Part B*, **19**, 933–961.
44. Popielarz, R., Chiang, C.K. (2007) Polymer composites with dielectric constant comparable to that of barium titanate ceramics. *Materials Science and Engineering B*, **139**, 48–54.
45. Rajesh, S., Murali, K.P., Rajani, K.V., and Ratheesh, R. (2009) $SrTiO_3$-filled PTFE composite laminates for microwave substrate applications. *International Journal of Applied Ceramic Technology*, **6**, 553–561.
46. Laverghetta, T.S. (1984) *Microwave Materials and Fabrication Techniques*, Artech House, USA, pp. 9–21.
47. Thomas, R.M. and Sparks, W.J. (1944) Mixed olefinic polymerization process and product. US Patent 2,356,128.
48. http://en.wikipedia.org/wiki/Butyl_rubber.
49. Ebewele, R.O. (2000) *Polymer Science and Technology*, CRC Press, FL.
50. http://en.wikipedia.org/wiki/Elastomer.
51. Billmeyer, F.W. (1962). *Text Book of Polymer Science*, Wiley Interscience Publishers, New York and London.
52. Duffy, J. and Wilson, G.J. (1993) Synthesis of butyl rubber by cationic polymerization, in *Ullman's Encyclopedia of Industrial Chemistry*, 5th edn, Elsevier, Amsterdam.
53. Thomas, D., Chameswary, J., and Sebastian, M.T. (2011) Mechanically flexible butyl rubber–$SrTiO_3$ composites for microwave applications. *International Journal of Applied Ceramic Technology*, **8**, 1099–1107.
54. Chameswary, J., Thomas, D., Subodh, G., Harshan, S., Philip, J., and Sebastian, M.T. (2012) Microwave dielectric properties of flexible butyl rubber–strontium cerium titanate composites. *Journal of Applied Polymer Science*, **124**, 3426–3433.
55. Chameswary, J. and Sebastian, M.T. (2013) Effect of $Ba(Zn_{1/3}Ta_{2/3})O_3$ and SiO_2 ceramic fillers on the microwave dielectric properties of butyl rubber composites. *Journal of Materials Scince: Materials in Electronics*, **24**, 4351–4360.

56. Chameswary, J. and Sebastian, M.T. (2013) Butyl rubber–$Ba_{0.7}Sr_{0.3}TiO_3$ composites for flexible microwave electronic applications. *Ceramic International*, **39**, 2795–2802.
57. Chameswary, J., Namitha, L.K., Brahmakumar, M., and Sebastian, M.T. (2014) Material characterization and microwave substrate applications of alumina filled butyl rubber composites. *International Journal of Applied Ceramic Technology*, **11**, 919–926.
58. Chameswary, J. and Sebastian, M.T. (2014) Development of butyl rubber–rutile composites for flexible microwave substrate applications. *Ceramic International*, **40**, 7439–7448.
59. Chameswary, J. (2015) Butyl rubber–ceramic composites for flexible electronic applications. PhD Thesis, Cochin University of Science and Technology, India.
60. Chameswary, J. and Sebastian, M.T. (2015) Preparation and properties of $BaTiO_3$ filled butyl rubber composites for flexible electronic circuit applications. *Journal of Materials Science*: *Materials in Electronics*, **26**, 4629–4637.
61. Mohamad, N., Muchtar, A., Ghazali, M.J., Dahlan, H.M., and Azhari, C.H. (2009) Epoxidised natural Rubber–alumina nanoparticle composites (ENRAN): effect of filler loading on the tensile properties. *Solid State Science and Technology*, **17**, 133–143.
62. Mohamad, N., Muchtar, A., Ghazali, M.J., Mohd, D.H., and Azhari, C.H. (2008) The effect of filler on epoxidised natural rubber–alumina nanoparticles composites. *European Journal of Scientific Research*, **24**, 538–547.
63. Li, L., Fang, Y., Xiao, Q., Wu, Y.J., Wang, N., Chen, X.M. (2014) Microwave dielectric properties of fused silica prepared by different approaches. *International Journal of Applied Ceramic Technology*, **11**, 193–199.
64. Hanna, F.F., Yehiab, A.A., and About-Bakr, A.F. (1973) Dielectric properties of polar rubber mixtures. *British Polymer Journal*, **5**, 49–53.
65. Sareni, B., Krahenubuh, L., Beroul, A., and Brosseau, C. (1997) Effective dielectric constant of random composite material. *Journal of Applied Physics*, **81**, 2375–2383.
66. Todd, M.G. and Shi, F.G. (2002) Validation of a novel dielectric constant simulation model and the determination of its physical parameters. *Microelectronic Journal*, **33**, 627–632.
67. Xie, L., Huang, X., Wu, C., and Jiang, P. (2011) Core shell structured poly(polymethyl methalycrate) nanocomposites prepared by in situ atom transfer radical polymerization: a route to high dielectric constant materials with inherent low loss of the base polymer. *Journal of Materials Chemistry*, **21**, 5897–5906.
68. Teirikangas, M., Juuti, J., Hu, T., and Jantunen, H. (2009) Extrinsic influences of the polymer matrix on electrical properties of high frequency composites. *Ferroelectrics*, **387**, 70–76.
69. Xiang, F., Wang, H., and Yao, X. (2006) Preparation and dielectric properties of bismuth based dielectric/PTFE microwave composite. *Journal of European Ceramic Society*, **26**, 1999–2002.
70. Murugaraj, P., Mainwaring, D., and Mora-Huertas, N. (2005) Dielectric enhancement in Polymer–nanoparticle composites through interphase polarizability. *Journal of Applied Physics*, **98**, 054304-1–054304-6
71. Valant, M. and Suvorov, D. (2003) Microstructural phenomena in low firing ceramics. *Materials Chemistry Physics*, **79**, 104–110.
72. Sun, Y.Y., Luo, S., and Wong, C.P. (2003) Electrical and mechanical properties of carbon black filled ethylene propylene rubber during thermal oxidation ageing, in *Electronic Components and Technology Conference*, pp. 1644–1647.
73. Overton, E., Hammoud, A.N., Baumann, E.D., and Myers, I.T. (1993) Thermal aging effects on the electrical properties of film and ceramic capacitors, in *Electrical Electronics Insulation Conference and Electrical manufacturing and Coil Winding Conference*, pp. 201–205.
74. Rajesh, S., Nisa, V.S., Murali, K.P., and Ratheesh, R. (2009) Microwave dielectric properties of PTFE/rutile nanocomposites. *Journal of Alloys and Compounds*, **477**, 677–682.
75. Nisa, V.S., Rajesh, S., Murali, K.P., Priyadarsini, V., Potty, S.N., and Ratheesh, R. (2008) Preparation, characterization and dielectric properties of temperature stable SrTiO3/PEEK composites for microwave substrate applications. *Composite Science and Technology*, **68**, 106–112.
76. Vrejoiu, I., Pedarnig, J.D., Dinescu, M., Gogonea, S.B., Bäuerle, D. (2002) Flexible ceramic–polymercomposite films with temperature-insensitive and tunable dielectric permittivity. *Applied Physics A*, **74**, 407–409.

77. Tavman, I.H. (1998) Effective thermal conductivity of isotropic polymer composites. *International Communication in Heat Mass Transfer*, **25**, 723–732.
78. Zhou, W., Qi, S., Li, H., and Shao, S. (2007) Study on insulating thermal conductive BN/HDPE composites. *Thermochimica Acta*, **452**, 36–42.
79. Ling, W., Gu, A., Liang, G., and Yuan, L. (2010) New composites with high thermal conductivity and low dielectric constant for microelectronic packaging. *Polymer Composites*, **31**, 307–313.
80. Richerson, D.W. (2006) Modern ceramic engineering properties, in *Processing and Use in Design*, Taylor and Francis, CRC Press, London.
81. Chee, C.Y., Song, N.L., Abdullah, L.C., *et al*. (2012) Characterization of mechanical roperties: low-density polyethylene nanocomposite using nano alumina particle as filler. *Journal of Nanomaterials*, 215978–215984.
82. Todorova, Z., Dishovsky, N., Dimitrov, R., Tantawy, F.E., Aal, A.N., Al-Hajry, A., and Bououdina, M. (2008) Natural rubber filled SiC and B_4C ceramic composites as a new NTC thermistor and piezoresistive sensor materials. *Polymer Composites*, **29**, 109–118.
83. Salaeh, S., Muensit, N., Bomlai, P., and Nakason, C. (2011) Ceramic/natural rubber composites: influence types of rubber and ceramic materials on curing, mechanical, morphological, and dielectric properties. *Journal of Materials Science*, **46**, 1723–1731.
84. Zhao, H., and Li, R.K.Y. (2008) Effect of water absorption on the mechanical and dielectric properties of nano-alumina filled epoxy nanocomposites. *Composite A: Applied Science and Manufacturing*, **39**, 602–611.
85. Gonon, P., Pham Hong, T., Lesaint, O., Bourdelais, S., and Debruyne, H. (2005) Influence of high levels of water absorption on the resistivity and dielectric permittivity of epoxy composites. *Polymer Testing*, **24**, 799–804.
86. Zhao, H. and Li, R.K.Y. (2008) Effect of water absorption on the mechanical and dielectric properties of nano-alumina filled epoxy nano composites. *Composites: Part A*, **39**, 602–611.
87. Li, T.L. and Hsu, S.L.C. (2010) Enhanced thermal conductivity of polyimide films via a hybrid of micro and nano sizes boron nitride. *Journal of Physical Chemistry B*, **114**, 6825–6829.
88. Goyal, R. K., Jadhav, P., and Tiwari, A.N. (2011) Preparation and properties of new polyphenelyne sulfide/AlN composite for electronic packaging. *Journal of Electronic Packaging*, **40**, 1377–1383.
89. Kubo, M., Li, X., Kim, C., *et al*. (2010) Stretchable microfluidic radio frequency antennas. *Advanced Functional Materials*, **22**, 2749–2752.
90. Tiercelin, N., Coquet, P., Sauleau, R., *et al*. (2006). *Journal of Micromechanical and Microengineering*, **16**, 2389.
91. Cetiner, B.A., Jafarkhani, H., Qian, J.-Y., *et al*. (2004) Multifunctional reconfigurable MEMS integrated antennas for adaptive MIMO systems. *IEEE Communications Magazine*, **42**, 62–70.

13

Designing of Materials for EMI Shielding Applications

Swati Varshney[1,2] *and S.K. Dhawan*[1]
[1]*Polymeric and Soft Materials Section, National Physical Laboratory (CSIR), New Delhi, India*
[2]*Department of Chemistry, Delhi Institute of Tool Engineering, Okhla, New Delhi, India*

The technological development based on material engineering has been revolutionizing the electronics industry due to the expansion of small and efficient electronic/communication devices. These electronic equipments are used in a high operating frequency and bandwidth. This may lead to the possibility of deterioration of the radio wave atmosphere, which is known as electromagnetic interference (EMI). EMI consists of many unwanted radiated signals, which may be highly damaging to the electronic system or equipment performance [1]. Due to this, EM wave absorbing materials have attracted much attention for the proper functioning of electronics, radio frequency radiation sources in all commercial, military equipment, scientific electronic devices, communication instruments, and radiation sources. Also, the EMI shielding materials should be lightweight potential absorbers of the radiation, able to protect aircraft avionics and health hazards in humans. Therefore, in the last decades, a range of materials including very thin sheets of metals, different forms of carbon, for example, graphite and its exotic forms such as expanded graphite, reduced graphene oxide (RGO), carbon black, graphene, carbon fibers, single- and multiwalled carbon nanotubes (CNTs) [2–13] and conducting polymers, dielectric, magnetic materials and their composites, have been used for EMI shielding in automotive applications. However, metals are expensive, heavy, and prone to corrosion, while adding to the complexity and cost of manufacturing processes. Therefore, as an alternative, intrinsically conducting polymer-based composites with a wide range of electrical conductivity, permittivity (ε) or permeability (μ) have been suggested for microwave absorption. Thus, EM

Microwave Materials and Applications, First Edition.
Edited by Mailadil T. Sebastian, Rick Ubic and Heli Jantunen.
© 2017 John Wiley & Sons, Ltd. Published 2017 by John Wiley & Sons, Ltd.

absorption properties of various polymer composites incorporated in dielectric or magnetic materials have been widely investigated. Among the nanostructures, conducting polymers, along with some magnetic and dielectric fillers, exhibit very good EM absorption properties. Conducting polymers like polyaniline, polypyrrole, polythiophene, and PEDOT show potential for commercial applications because of their higher conductivity, good environmental stability, and facile synthesis. In a recent approach, conducting polymer composites along with carbon nanotubes and graphene matrix have been studied extensively, which find applications in microwave absorption and electromagnetic interference shielding. Yang *et al.* reported carbon nanofiber and CNT–polystyrene composite for a shielding application [14] but CNT-based nanocomposites are synthesized by a complex process that is not favorable for commercial applications as absorbing candidates. However organic polymers, having an extended π-conjugated system, can be a better substitute for designing a shield due to their easy processability, light weight, and better corrosion resistance. Moreover, conjugated polymers show conductivity in the semiconductor regime. The high conductivity and dielectric constant of the materials contribute to a high EMI shielding efficiency. The only critical obstacle is the mechanical strength of the polymer, which can be conquered by combining with magnetic nanoparticles to form ferromagnetic nanocomposites that provide a system with novel functionality for better microwave absorption application [15–17]. The insertion of ferromagnetic nanoparticles not only improves various properties of host materials owing to their intriguing properties arising from small size and large surface area but also reduces the tendency of agglomeration of nanoparticles [18] due to its dispersion into the polymer matrix. These composites possess many advantages as the relatively high conductivity, very light weight, flexibility, reasonably facile processability, and a wide diversity of synthetic methods allow various complex structures conforming to various constraints to be designed [19]. Dhawan and others have investigated the microwave absorption properties of the γ-Fe_2O_3 incorporated polyaniline and PEDOT nanocomposites with different ferrite loadings [20, 21]. Among conducting polymers, polypyrrole (PPy) is a widely used conducting polymer for commercial applications because of its good conductivity and good environmental stability [22–25]. A number of articles have been reported the synthesis of polypyrrole [26–30] and its composite by incorporating ferrite particles in the polymer matrix [15, 31–37]. Bidan *et al.* has reported the electrochemical method of preparing polypyrrole composite showing magnetic and conducting properties [38]. A polypyrrole/ferrospinel ($NiFe_2O_4$) nanocomposite with a core-shell structure was prepared by in situ chemical polymerization of pyrrole in the presence of $NiFe_2O_4$ nanoparticles [39]. Wuang *et al.* demonstrated the emulsion polymerization technique to synthesize Fe_3O_4 and polypyrrole nanocomposites using polyvinyl alcohol as a surfactant, resulting in magnetic core–shell nanostructures of spherical shape [40]. Li *et al.* reported in situ chemical oxidative polymerization of $ZnFe_2O_4$/polypyrrole core–shell structured nanocomposite by using ammonium persulfate as oxidant [41]. The properties of these ferromagnetic polymer composites depend on their micro/nanostructures and morphologies, which can be easily controlled by the synthesis method. Several articles have appeared recently covering different aspects of ferrite reinforcement in various polymer matrix systems. Today it is very difficult to avoid electromagnetic radiations because we are living in the broth of electromagnetic radiations. This chapter will throw some light on the design of effective polymeric shielding materials that can be used to reduce these harmful effects.

A part of the chapter is focused on the synthesis and characterization of nanostructured polyaniline, polypyrrole, and its composite with γ-Fe_2O_3 nanoparticles. A study has also been devoted towards designing ferrite particles of different shapes in the graphene oxide matrix to obtain the desired shielding characteristics.

Another section of the chapter describes the preparation of water-based ferrofluid and synthesis of lightweight nanoengineered polypyrrole composites. The optimized composite sample with an appropriate amount of aqueous ferrofluid shows absorption-dominated shielding effectiveness in the 12.4–18 GHz frequency range. Attention has been paid to the structural development of polypyrrole nanocomposites having dielectric and magnetic losses by the incorporation of γ-Fe_2O_3/Fe_3O_4 nanoparticles in the polypyrrole matrix.

13.1 Electromagnetic Shielding and Microwave Absorption Mechanism

The shielding of the radiated EMI has caused increased concern today as any electronic device that transmits or utilizes any form of electrical energy could be a source of electromagnetic interference (EMI). This EMI may degrade the performance of electronic equipments. Hence, these equipments must be shielded to avoid such types of EMI degradation. The shield is a barrier that provides reflection and/or absorption of electromagnetic radiation. In fact the shield acts as a guard and prevents the penetration of electromagnetic radiation.

13.2 Shielding Effectiveness (SE)

SE is the primary aspect of evaluating the feature of EMI shielding materials. The effectiveness of a shield and its resulting EMI attenuation are based on the frequency, the distance of the shield from the source, the thickness of the shield, and the shield material and can be expressed in dB units as [42–45]

$$SE\,(\text{dB}) = -10\,\log\,(P_T/P_I) = -20\,\log\,(E_T/E_I) \tag{13.1}$$

where P_T (E_T) and P_I (E_I) are the power (electric field intensity) of the transmitted and incident electromagnetic waves, respectively. Three shielding mechanisms are observed with any type of electromagnetic interference. When a plane wave is incident on a shield, part of the wave is reflected from the front surface of the shield, part is absorbed within the shielding material and part is reflected at various surfaces or interfaces in the shield, where it can aid or hinder the effectiveness of the shield depending on its phase relationship with the incident wave, as shown in Figure 13.1. On the basis of these proposed mechanisms, the total shielding effectiveness can be expressed as

$$SE\,(\text{dB}) = SE_A + SE_R + SE_M \tag{13.2}$$

where SE_A, SE_R, and SE_M are the absorption factor, reflection factor, and multiple reflection factor in thin shields, respectively [46–49]. All the terms in the equation are expressed in dB.

Absorption loss, SE_A in Equation (13.2) is the result of ohmic loss and heating loss induced due to the action between electric and/or magnetic dipoles in the shield with the

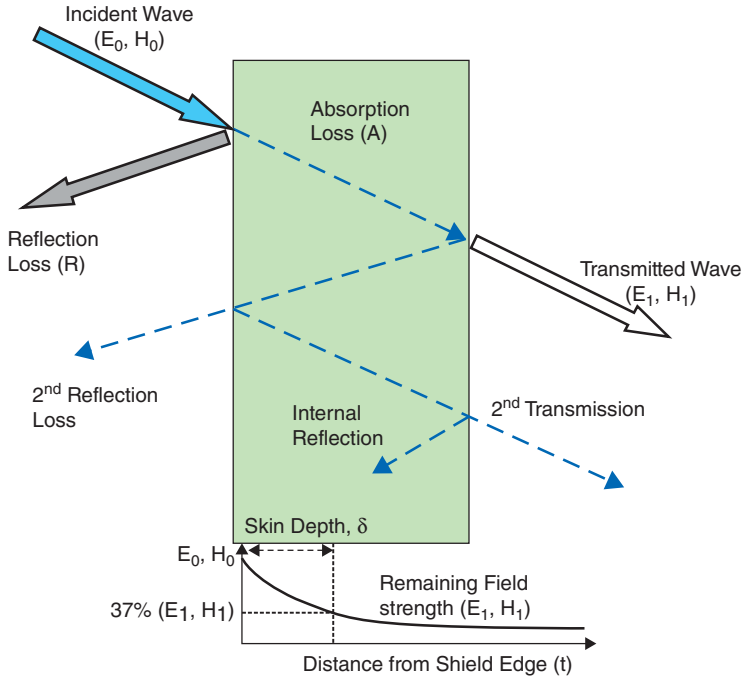

Figure 13.1 *Graphical representation of EMI shielding.*

electromagnetic fields, as it is a function of the product of $\sigma_r\mu_r$, where σ_r is the electrical conductivity of the shield relative to copper and μ_r is the magnetic permeability of the shield to free space. From the absorption loss point of view, a good material for a shield will have high conductivity and high permeability. On the other hand, reflection loss, SE_R, arises due to interaction between conducting particles in the conducting material and electromagnetic field and can be represented as a function of the ratio σ_r/μ_r. As a result, for a larger reflection loss, a shield tends to be electrically conducting, having a lower magnetic permeability. Other than reflection and absorption losses, a third loss is due to multiple reflection (SE_M). The factor SE_M can be mathematically positive or negative (in practice, it is always negative) and becomes insignificant when the absorption loss $SE_A > 10$ dB. It is usually only important when metals are thin and at low frequencies (i.e., below approximately 20 kHz).

13.3 Measurement of Shielding Effectiveness

There are various methods for the measurement of shielding effectiveness by calculating permittivity and permeability from *S*-parameters. The selection of the conversion technique /measurement method depends on the desired properties, rate of conversion, and required precision. Table 13.1 gives a summary of the conversion techniques utilizing various sets of *S*-parameters to find out the dielectric properties, that is, permittivity (ε) and permeability (μ).

Table 13.1 *Conversion techniques*

Conversion technique	*S*-parameters	Dielectric properties
NRW	(S_{11}, S_{21}, S_{12}, S_{22}) or a pair (S_{11}, S_{21})	ε_r and μ_r
NIST iterative	(S_{11}, S_{21}, S_{12}, S_{22}) or a pair (S_{11}, S_{21})	ε_r and $\mu_r = 1$
New non-iterative	(S_{11}, S_{21}, S_{12}, S_{22}) or a pair (S_{11}, S_{21})	ε_r and $\mu_r = 1$
SCL	S_{11}	ε_r

Electromagnetic shielding and dielectric properties have been measured by using an Agilent E8362B vector network analyzer (VNA) in the frequency range of 12.4–18 GHz (Ku-band). Powder composite samples have been pressed in the form of rectangular pellets (15.8×7.9 mm^2), inserted in a copper sample holder, and then connected between the waveguide flanges of a network analyzer, as shown in Figure 13.2.

To analyze the shielding mechanism, complex permittivity and permeability have been calculated by using scattering parameters, that is, (S_{11} (or S_{22}) and S_{12} (or S_{21}), based on the calculations given in the Nicholson–Ross–Weir (NRW) method. The NRW method is the most frequently used technique by using sets of *S*-parameters (Table 13.1) in order to calculate the reflection coefficient (R) and the transmission coefficient (T) of the material under test, that is, $T = |E_T/E_I|^2 = |S_{12}|^2 = |S_{21}|^2$, $R = |E_R/E_I|^2 = |S_{11}|^2 = |S_{22}|^2$ and the absorption coefficient (A) = $(1 - R - T)$. Here, it is noted that the absorption coefficient is given with respect to the power of the incident EM wave. If the effect of multiple reflection between both interfaces of the material is negligible, the relative intensity of the effectively incident EM wave inside the materials after reflection is based on the quantity as $1 - R$. Therefore, the effective absorbance (A_{eff}) can be described as $A_{eff} = (1 - R - T)/(1 - R)$ with respect to the power of the effectively incident EM wave inside the shielding material. It is convenient to express the reflectance and effective absorbance in the form of $-10 \log (1 - R)$ and $-10 \log (1 - A_{eff})$ in decibel (dB), respectively, which give SE_R and SE_A as

$$SE_R = -10 \log (1 - R) \tag{13.3}$$

$$SE_A = -10 \log (1 - A_{eff}) = -10 \log \frac{T}{1 - R} \tag{13.4}$$

For the material, the skin depth (δ) is the distance up to which the intensity of the electromagnetic wave decreases to $1/e$ of its original strength. The skin depth is related to the attenuation constant (β) of the wave propagation vector $\delta = 1/\beta = \sqrt{2/\omega\sigma\mu_{AC}}$, with the approximations that $\sigma \gg \omega\varepsilon$. As $\delta \propto \omega^{-1/2}$, at low frequencies for electrically thin samples ($d \ll \delta$) the shielding effectiveness of the sample is therefore described as

$$SE\,(\text{dB}) = 20 \log \left(1 + \frac{1}{2} Z_0 d\sigma\right) \tag{13.5}$$

where σ is the AC conductivity, Z_0 is free space impedance, and d is the sample thickness. For higher frequencies, sample thickness (electrically thick samples) is sufficiently greater

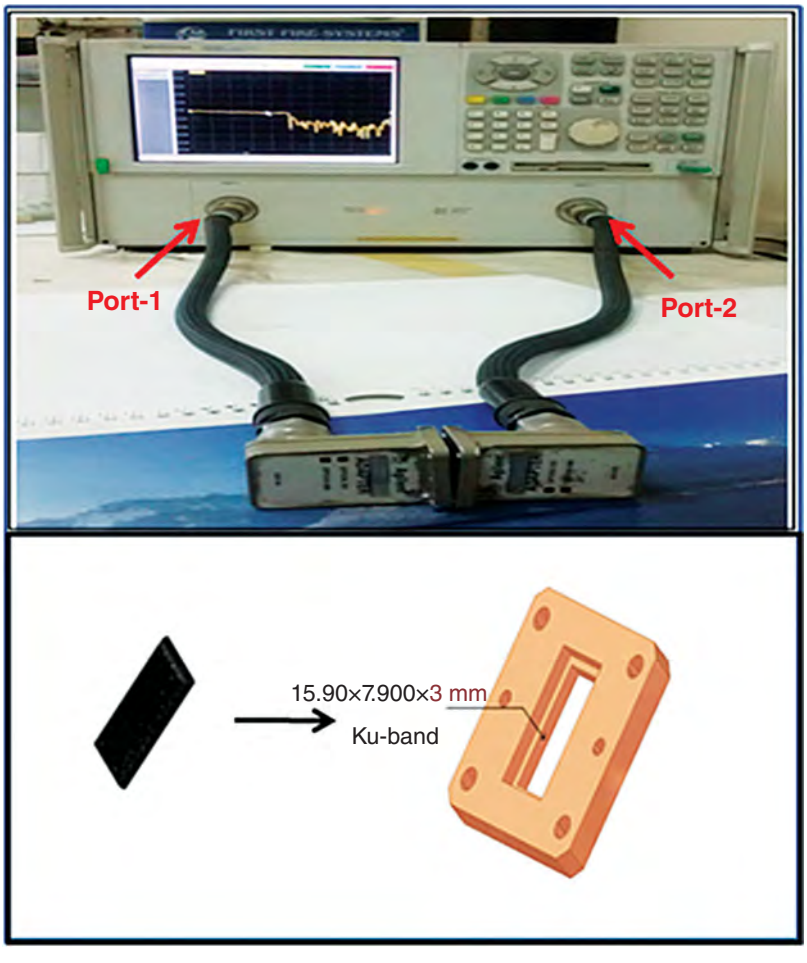

Figure 13.2 *Two-port vector network analyzer.*

than skin depth and EMI shielding effectiveness for the plane electromagnetic wave is given as

$$SE\ (\text{dB}) = SE_R\ (\text{dB}) + SE_A\ (\text{dB}) \tag{13.6}$$

$$SE_R(\text{dB}) \approx 10 \log \left(\frac{\sigma_{\text{AC}}}{16\omega\varepsilon_0\mu_r} \right) \tag{13.7}$$

$$SE_A(\text{dB}) = 20\frac{d}{\delta} \log e \tag{13.8}$$

where σ_{AC} depends upon the dielectric properties ($\sigma_{AC} = \omega\varepsilon_0\varepsilon''$) of the material, ω is the angular frequency ($\omega = 2\pi f$), ε_0 is the free space permittivity, and μ_r is the relative magnetic permeability of the sample. In Equation (13.6), the first term is related to the reflection of the EM wave and contributes as the shielding effectiveness due to reflection. The second

term expresses the loss due to the absorption of the wave when it passes through the shielding material. In a microwave range, the contribution of the second part becomes more as compared to the reflection term.

13.4 Electromagnetic Shielding Materials

As mentioned in Equation (13.6), the first term is related to the reflection of the EM wave and contributes as the shielding effectiveness due to reflection. The second term expresses the loss due to the absorption of the wave when it passes through the shielding material. In the microwave range, the contribution of the second part becomes more as compared to the reflection term. It is observed from Equations (13.7) and (13.8) that at a particular frequency, the high conductivity, magnetic permeability, thickness, and dielectric constant are important parameters for excellent microwave shielding. For this reason, metals were used as the shielding material, but some drawbacks are associated with the usage of metals, like corrosion, heavy weight, difficult processability, and a reflection-dominated shielding mechanism. On the other hand, carbon-based materials offer an absorption-dominated shielding mechanism. Among these carbon-based materials, graphite, graphene oxide, MWCNT, carbon fibers, and conducting polymers are extensively used materials for shielding application along with some dielectric and magnetic fillers in order to tune the microwave absorption properties [50–53]. Addition of dielectric filler in the composite enhances the dielectric constant of the material, which ends up with high dielectric losses. Several types of dielectric fillers have been reported in various research works. Some of them are TiO_2, fly ash, SiO_2, and $BaTiO_3$ [54–57]. High permeability is another requisite property for effective shielding so as to increase magnetic losses in composite. This property can be easily achieved by incorporation of soft ferrite particles like Fe_3O_4, Fe_2O_3, and barium ferrite [56–58]. Conductive polymeric materials offer a balanced combination of electrical and other properties like light weight, corrosion resistance, easy processability, and design flexibility as compared to other commercially available microwave shielding materials. A synergistic combination of conducting materials along with nanostructured ferrite particles enhances the total shielding efficiency (SE) of the polymer composite. As a result, around the world, various research groups are working to design an effective shield against electromagnetic radiation by using various magnetic fillers with a conducting polymer matrix. The properties of conducting ferromagnetic composite can be easily controlled by selecting an appropriate polymer matrix, synthesis technique, synthesis conditions, reinforcement type, and polymer-to-reinforcement ratio. As absorption-dominated shielding effectiveness depends on conductivity and magnetic permeability, it has been concluded that the amalgamation of conducting polymer matrix along with magnetic and dielectric fillers make possible an excellent microwave absorbing material for shielding applications. Furthermore, Table 13.2 describes various composite materials being used for electromagnetic shielding applications.

A recent review by Idris *et al.* [79] has highlighted the various parameters used in designing the nanomaterials, which play an important role in developing new microwave absorption materials. These materials provide the properties of strong absorption, wide frequency range, low density, and thin samples. Recently, more and more researchers have devoted their studies to nanocomposite materials. By incorporating different nanomaterials, a new

Table 13.2 *Various composite materials used for an electromagnetic shielding application*

S number	Year	Polymer *M* matrix	Reinforcement	Shielding effectiveness, thickness, working frequency	Reference
1	1993	Polyethersulfone	Ni particles	23 dB, 2.8 mm, 1–2 GHz	59
2	1994	Polyethersulfone	Carbon fibers	19 dB, 2.8 mm, 1–2 GHz	60
3	2004	Cement	Steel fibers	70 dB, 9.5 mm, 1.5 GHz	61
4	2007	Epoxy	SWCNT	28 dB, 2 mm, 8.2–12.4 GHz	62
5	2009	Polyaniline	TiO_2/barium ferrite particles	58 dB, 2 mm, 12–18.4 GHz	63
6	2009	Polypropylene	MWCNT	34.8 dB, 1 mm, 8–12.4 GHz	64
7	2010	Polyaniline	γ- Fe_2O_3	11.2 dB, 3 mm, 8.2–12.4 GHz	65
8	2010	Poly(3,4-ethylenedioxy thiophene	Barium ferrite	24.4 dB, 2 mm, 12–18.4 GHz	66
9	2010	Polystyrene	Polyaniline/ clay	16.2 dB, 10 mm, 8 GHz	67
10	2010	Polyvinyl chloride	Graphite/Cu nanoparticles	70 dB, 2 mm, 1–20 GHz	68
11	2011	Cement	Graphene oxide/ aqueous ferrofluid	46 dB, 2.5 mm, 8.2–124 GHz	69
12	2011	Silicone rubber	TiB_2	29 dB, 2 mm, 1–12 GHz	70
13	2012	Polyaniline	1. Graphene sheet 2. SWCNT	34.2 dB, 2.4 mm, 2–18 GHz 31.5 dB, 2.4 mm, 2–18 GHz	71
14	2012	Polypyrrole	γ- Fe_2O_3	28.4 dB, 1.5 mm, 12.4–18 GHz	36
15	2012	Polyaniline	Natural rubber	60 dB, 1 mm, 1–12 GHz	72
16	2013	Polyurethane	MWCNT	41.6 dB, 2.5 mm, 8.2–12.4 GHz	73
17	2013	Phenolic resin (Novolac)	Polypyrrole/ carbon fibres	23 dB, 1.25 mm, 12.4–18 GHz	44
18	2013	ABS	1. MWCNT 2. Carbon nanofibers 3. Carbon black nanoparticles	40.7 dB, 1.1 mm, 8.2–12.4 GHz 26.1 dB, 1.1 mm, 8.2–12.4 GHz 15.3 dB, 1.1 mm, 8.2–12.4 GHz	74
19	2013	Polystyrene	Carbon nanofibers	24 dB, 2 mm, 0.05–1.5 GHz	75
20	2014	Polypyrrole	Aqueous ferrofluid	23.5 dB, 2 mm, 12.4–18 GHz	37
21	2014	Graphene nanoribbons	MnO_2	57 dB, 3 mm, 12.4–18 GHz	76
22	2015	UHMWPE	CNT	50 dB, 1 mm, 8–12.4 GHz	77
23	2015	Poly(3,4-ethylenedioxythiophene)	MWCNT	58 dB, 2.8 mm, 12.4–18 GHz	78

composite material can be designed that shows excellent electromagnetic wave absorber performance in the GHz range.

Selection of material possessing good EMI shielding properties depends upon various parameters like dielectric behavior, being moderately electrically conductive, and offering ferromagnetic attributes. In addition, electromagnetic wave absorption characteristics of a material depend on its dielectric properties, like permittivity and permeability. By incorporation of dielectric and magnetic fillers, the electromagnetic properties of such materials can be improved to obtain a maximum absorption of electromagnetic energy. These composite materials are useful as microwave absorbers due to their advantages with respect to lighter weight, lower cost, design flexibility, and adjustable microwave properties over intrinsic ferrites. A ferrite material encapsulated in a conducting matrix is an ideal material for application in microwave absorption. Moreover, various parameters have to be optimized in designing a perfect microwave absorbing material. Therefore, a new aspect is being explored by many researchers where conducting polymers have been incorporated with nanomaterials in order to design good EMI shielding materials.

13.5 New Insight into Designing of Materials for Microwave Shielding

Various approaches for the shape-controlled synthesis of iron oxide-reduced graphene oxide (RGO) composites have been formulated to evaluate the effect of different morphologies on their microwave shielding properties. Graphene oxide offers conducting properties, high strength, and high thermal stability, but lacks in magnetic properties, which are essential for electromagnetic shielding. Hence, composites of graphene oxide with magnetic nanoparticles have been attracting attention for shielding applications. The presence of functional groups present in reduced graphene oxide helps to improve electromagnetic wave absorption. In the light of this, electromagnetic interference (EMI) shielding effectiveness of iron oxide of different shapes coated with reduced graphene oxide was investigated in the Ku-band frequency range (12.4–18 GHz) [80].

The experimental measurements reveal that the shielding effectiveness values for flakes, cubes, and rods of iron oxide are found to be 2.83, 4.27, and 5.40 dB, respectively. When these structures are covered with RGO, the SE values of RFlakes RCubes, and RRods are found to be 27.42, 30.96, and 33.30 dB, respectively. These results are associated with the shape and size of iron oxide, as shown in Figure 13.3. Thus the maximum total SE achieved for the RRods, due to the improved microwave shielding properties of the RRods, may be ascribed to the rod-shaped nature of iron oxide.

The results suggest that the systems are promising EMI absorption materials in the microwave frequency range. In addition, the enhanced microwave shielding properties of the iron oxide microstructures may be due to the specific rod-shaped structures. The assembly of these rods is believed to increase the geometrical effect and lead to enhanced shielding effectiveness with the incidence of microwaves. Furthermore, RRods offer a higher aspect ratio in comparison to the RCubes and RFlakes. The rod-shaped nature of iron oxide also allows it to be aligned in a specific direction to maximize the attenuation of an EM wave, while the cubes and flakes are randomly scattered and are not able to maximize the attenuation of microwaves. The plausible proposed mechanism for the enhancement of the EMI shielding by the nanorod shape in comparison to the other structures is shown in

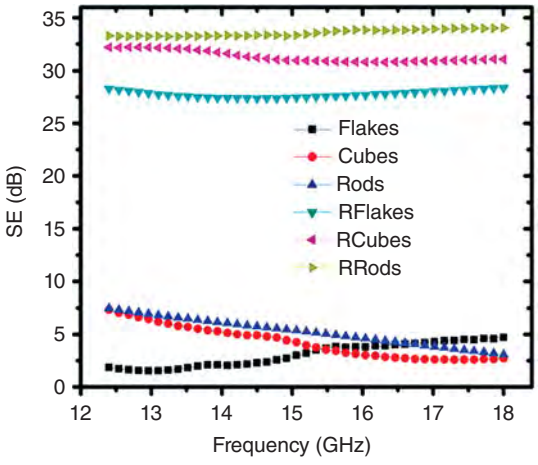

Figure 13.3 *Variation of the total shielding effectiveness of different ferrites encapsulated with reduced graphene oxide. Source: Adapted from Gupta* et al. *2014 [80].*

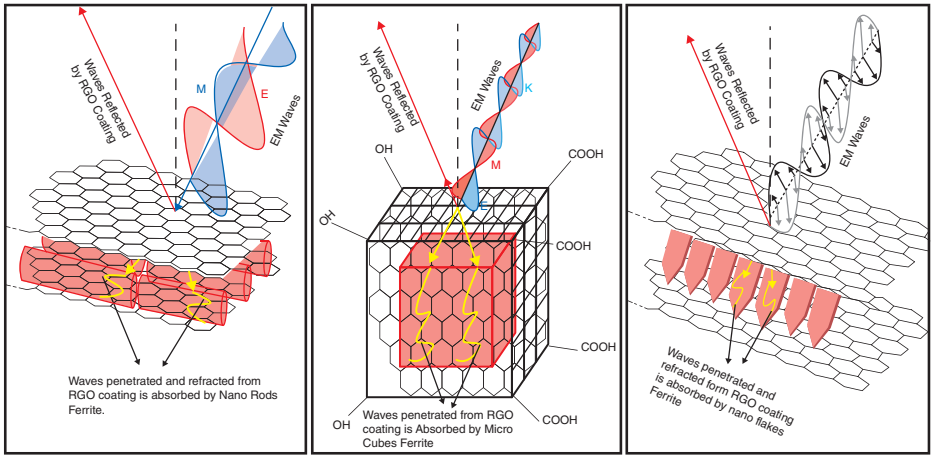

Figure 13.4 *Schematic representation of the interaction of microwave with different shaped RGO coated iron oxide. Source: Adapted from Gupta* et al. *2014 [80].*

Figure 13.4. In other words, one-dimensional nanostructures with a large effective surface area (due to the high aspect ratio) appear to be good candidates for microwave shielding [80].

13.6 Nanostructured Graphene/Fe_3O_4 Incorporated Polyaniline for EMI Shielding

A three-dimensional (3D) nanostructure consisting of chemically modified graphene/Fe_3O_4 (GF) incorporated polyaniline has also been studied by Singh *et al.* [81]. Intercalated GF

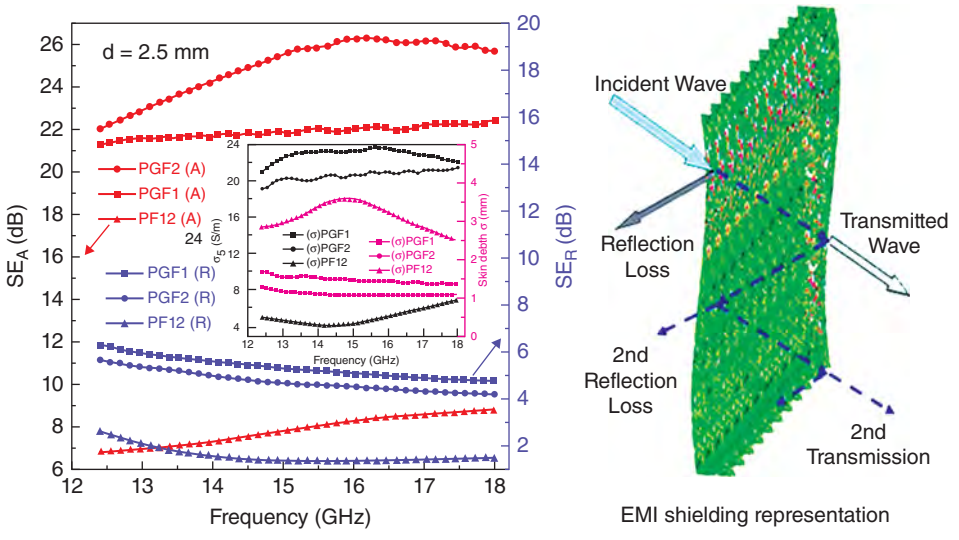

Figure 13.5 *Dependence of shielding effectiveness (SE_A and SE_R) of polymer ferrite 12, polymer graphene ferrite (PGF 1) and polymer graphene ferrite (PGF 2) composites as a function of frequency for sample thickness d ~ 2.5 mm and EMI shielding representation. The inset illustrates the variation of microwave conductivity and skin depth with frequency. Source: Adapted from Singh* et al. *2013 [81]. Reproduced with permission of Elsevier.*

was synthesized by the in situ generation of Fe_3O_4 nanoparticles in a graphene oxide suspension followed by hydrazine reduction and further in situ polymerization with aniline to form a polyaniline composite. In Figure 13.5, the variation of the shielding effectiveness with frequency for the different ratios of [aniline]/[graphene–ferrite] is shown. It is interesting to note that, in polymer graphene ferrite composites, the contribution to SE values mainly comes from the absorption rather than reflection, as observed in metals. Polymer graphene ferrite composites (PGF) have shown excellent frequency stability in the measured frequency range, which was found to increase with increasing GF content. Polymer composites having different weight ratios of monomer to GF have been prepared, namely, aniline: GF: 1:1 (PGF1) and 1:2 (PGF 2). Besides these, polyaniline with Fe_3O_4 in the weight ratio of 1:2 (PF12) was also synthesized in a similar manner without GF. The results indicate that the PGF2 sample has a higher SE_A of 22–26 dB (left black scale) with an SE_R of 4.7–6.3 dB (right blue scale) as compared to PGF1 ($SE_A \sim 21$ dB and $SE_R \sim 4.5$ dB) in the 12.4–18 GHz range, while PF12 has a lower value shielding effectiveness ($SE_A \sim$ 7–9 dB and $SE_R \sim 1.5$–2.5 dB) in comparison to polymer graphene ferrite composites in the same frequency range having a thickness of 2.5 mm.

Complex permittivity and the permeability of composites were calculated using scattering parameters (S_{11} and S_{21}) based on the theoretical calculations given by Nicholson, Ross, and Weir [82, 83]. The real part (ε') is mainly associated with the amount of polarization occurring in the material and the imaginary part (ε'') is related to the dissipation of energy. Here, graphene along with the Fe_3O_4 nanoparticles were incorporated in the polyaniline matrix having different conductivities and dielectric constants and

therefore show interfacial polarization in the applied frequency range. The presence of insulating Fe_3O_4 in the conducting matrix results in the formation of an increased interface and a heterogeneous system, wherein some space charge accumulates at the interface, contributing to the higher microwave absorption. As a result, polyaniline nanocomposites with graphene/Fe_3O_4 hybrids provide promising properties as a new type of sheath material for electromagnetic pollution in the high-frequency range, maintaining strong absorption.

13.7 Designing of Polypyrrole–γ-Fe_2O_3 Nanocomposite Wave Absorber

Stick-shaped polypyrrole nanocomposite has been synthesized by in situ emulsion polymerization. Prior to the synthesis of polypyrrole composite, magnetic γ-Fe_2O_3 nanoparticles have been synthesized by the co-precipitation method [84, 85]. Then γ-Fe_2O_3 nanoparticles have been homogenized in the aqueous medium of sodium lauryl sulfate (SLS) and stirred for 1 hour to form an emulsion. To this solution, pyrrole has been added. Thereafter, oxidant $FeCl_3$ has been added to the above solution. As a result micelles are formed via cooperative interaction between aqueous $FeCl_3$ solution and SLS in aqueous solvent. The incorporation of γ-Fe_2O_3 into SLS emulsions strongly affects the micelle aggregation number and second critical micelle concentration. In this heterogeneous polymerization system, water is the continuous phase and surfactant SLS acts as the discontinuous phase. The monomer pyrrole is emulsified along with the γ-Fe_2O_3 particles to form the micromicelles and on addition of oxidant $FeCl_3$ the polymerization takes place at the interface boundary of the micelles. As polymerization proceeds, the micelles grow by the addition of monomer from the aqueous solution and addition of the $FeCl_3$ leads to the formation of cationic free radicals, which combine with another monomer moiety to form a dimer, which on further oxidation and combination with another cation radical forms a termer and ultimately to a long chain of polymer. For a comparative study, polypyrrole (PPy) without γ-Fe_2O_3 along with several compositions of the PPyFe nanocomposites having different weight ratios of Py:γ-Fe_2O_3 – 1:1 (PPyFe 11), 1:2 (PPyFe 12), and 1:3 (PPyFe 13) have also been synthesized by the same procedure as described above in order to check the effect of loading ferrite constituents in the polymer matrix on microwave absorption properties. The room temperature conductivity of polypyrrole doped with SLS has been found to be 0.15 S/cm, which decreases with an increase of γ-Fe_2O_3 nanoparticles loading to 0.09 S/cm for PPyFe 11 and 0.05 S/cm for PPyFe 12.

13.7.1 Magnetic Measurements

Figure 13.6 shows the room temperature magnetization behavior of PPyFe 11 nanocomposite with varying concentration of γ-Fe_2O_3. The negligible retentivity (M_r) and coercivity (H_c) of the materials indicate the superparamagnetic behavior of these nanocomposites, which can be attributed to the small size of γ-Fe_2O_3 particles, that is, approaching the single domain limit. The saturation magnetization (M_s) value of the γ-Fe_2O_3 has been found to 60 emu/g at an external field of 5 kG with no hysteresis loop, placing it in the category of a superparamagnetic soft ferrite. When these γ-Fe_2O_3 nanoparticles have been incorporated in the polymer matrix in the weight ratio of 1:1 of Py: γ-Fe_2O_3 (PPyFe 11), the saturation magnetization (M_s) value has been found to be 11 emu/g and increases to 20 emu/g

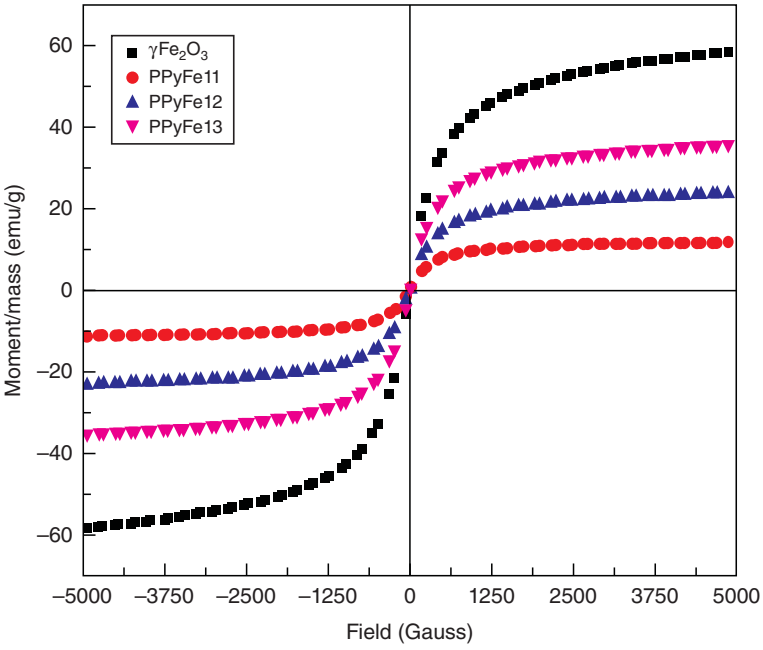

Figure 13.6 *Magnetization curves of γ-Fe_2O_3, PPyFe 11, PPyFe 12, and PPyFe 13 nanocomposites. Source: Varshney* et al. *2012 [36]. Reproduced with permission of Elsevier.*

for PPyFe 12 having twice the γ-Fe_2O_3 content, while the M_s value has been increased to 35 emu/g for the PPyFe 13 nanocomposite.

Figure 13.7 shows transmission electron microscopy (TEM) images and a selected area electron diffraction (SAED) pattern of PPy and PPyFe nanocomposites. TEM images of PPy show the marigold flower-like structure of nearly 100 nm size (Figure 13.7a and b) while the diffused SAED pattern of polypyrrole confirms its semicrystalline nature (Figure 13.7c). Figure 13.7d and e and g and h shows that ferrite nanoparticles are homogeneously dispersed in the PPy matrix for PPyFe 12 and PPyFe 13 samples. The existence of encapsulated magnetic and dielectric core into the conducting crust is very helpful in improving the absorption of the EM wave. The crystalline nature of the nanocomposites has been confirmed by the diffused SAED pattern, showing in Figure 13.7f and i for PPyFe 12 and PPyFe 13 samples, respectively.

13.7.2 Microwave Absorption Investigations

Figure 13.8 shows the dependence of the shielding effectiveness with frequency in the 12.4–18 GHz range for the different ratios of the [PPy]/[γ-Fe_2O_3]. Figure 13.8a shows that SE_A values for the composite increase with the ferrite loading from 17.0 to 22.6 dB while SE_R values decrease with the ferrite loading from 7.5 to 5.8 dB in the measured frequency range of 12.4 to 18 GHz. From Figure 13.8a and before it is clear that the shielding due to absorption of SE_A is dominant over reflection shielding. The nanocomposite PPyFe 13 with a higher amount of ferrite shows the highest value for total shielding effectiveness with SE_A

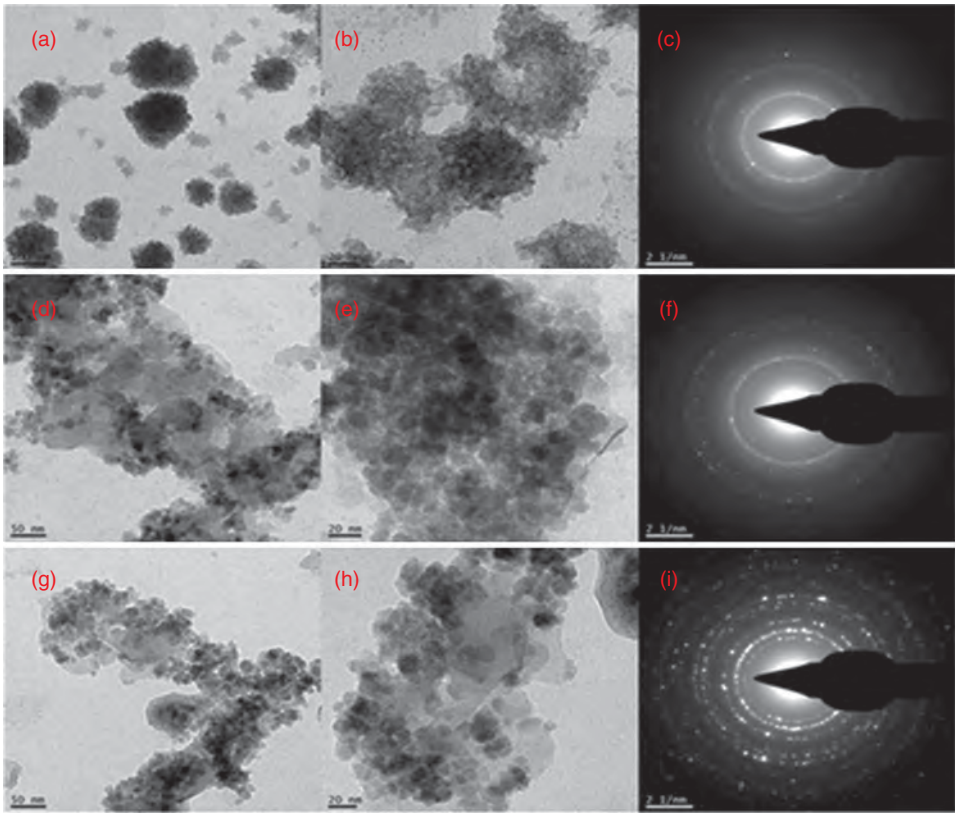

Figure 13.7 *Transmission electron micrograph of (a and b) polypyrrole, (d and e) PPyFe 12, (g and h) PPyFe 13, and (c, f, and i) the selected area diffracted (SAED) patterns of polypyrrole, PPyFe 12, and PPyFe 13. Source: Varshney* et al. *2012 [36]. Reproduced with permission of Elsevier.*

of 22.6 dB and SE_R of 5.8 dB. The increase in the absorption part with the addition of ferrite particles may be attributed to the higher dielectric and magnetic losses.

13.7.3 Dielectric and Permeability Studies

The electromagnetic absorption behavior of material depends on complex permittivity ($\varepsilon_r = \varepsilon' - j\varepsilon''$) and permeability ($\mu_r = \mu' - j\mu''$). The Nicholson–Ross–Weir method was used to determine complex permittivity and permeability of the nanocomposites [82, 83]. The real part (ε') of permittivity is mostly related to the amount of polarization within the material and the dissipation of energy is associated with the imaginary part (ε'') of permittivity.

The dielectric performance of the material depends on ionic, electronic, orientation, and space charge polarization. Due to the heterogeneity of the composite material, space charge polarization is dominant as compared to others. In conjugated polymers, the conduction mechanism can be explained by the polaron/bipolaron system. The polaron/bipolaron system has one mobile charge species and others are fixed charges (dipoles) with restricted

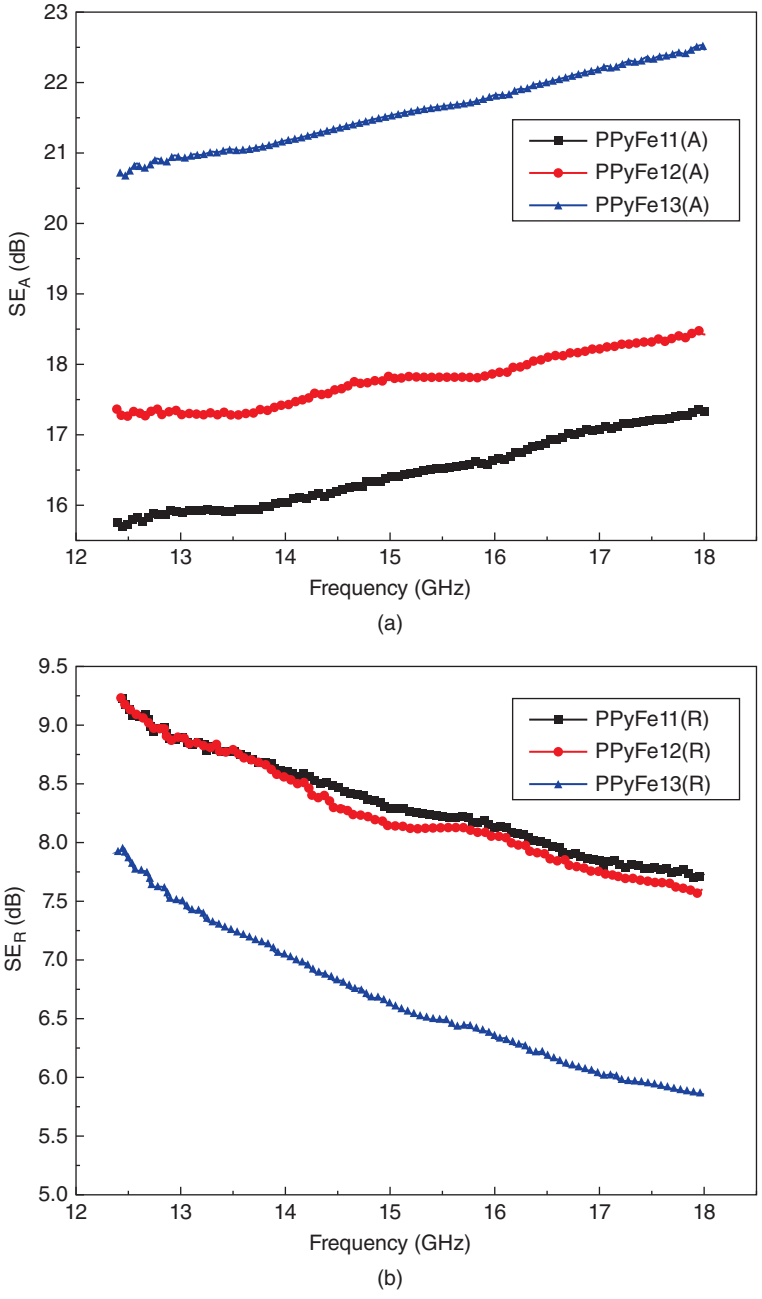

Figure 13.8 *Dependence of shielding effectiveness (SE_A and SE_R) as a function of frequency. Source: Varshney* et al. *2012 [36]. Reproduced with permission of Elsevier.*

mobility. Mobile charge species are free to move along the polymer chain. This arrangement of charges results in strong polarization in the system. On the increase of frequency, the dipoles present in the system cannot reorient themselves fast enough to respond to the applied electric field and, accordingly, the dielectric constant decreases. From Figure 13.9a and b, it is observed that in the case of PPy/γ-Fe_2O_3 composites, incorporation of insulating γ-Fe_2O_3 in the conducting matrix leads to higher values of the dielectric constant ($\varepsilon' = 38$) and dielectric loss ($\varepsilon'' = 23$) for PPyFe 12. The difference in the relative dielectric constant of γ-Fe_2O_3 and polypyrrole results in more accretion of space charge and strong orientational polarization, which accordingly results in improved microwave absorption values.

Figure 13.10 shows the behavior of real (μ') and imaginary (μ'') parts of permeability with frequency for the PPy/γ-Fe_2O_3 composites. The real part of the permeability shows negligible variation in the measured frequency range, whereas the magnetic loss part slightly decreases with the frequency. Higher values of μ'' have been observed for PPyFe 13 as compared to PPyFe 11, which confirms the existence of greater magnetic losses in PPyFe 13 nanocomposite. The magnetic loss is expressed by the imaginary part of complex permeability, which mainly occurs because of magnetic hysteresis and domain-wall displacement in the material.

The permeability for the hexagonal ferrites having the *c*-axis as the preferred direction of magnetization is defined as

$$\frac{\mu - 1}{4\pi} = \left(\frac{2}{3}\right)\frac{M_s}{H_A} \tag{13.9}$$

where M_s is the saturation magnetization and H_A is the anisotropy field. As the frequency increases, μ remains equal to its static (DC) value up to a critical frequency and then decreases with a further increase in frequency, whereas the imaginary part of permeability (μ'') starts to increase near the critical frequency and has a maximum at the resonance frequency, which demonstrates the maximum power loss.

In γ-Fe_2O_3, due to the large anisotropy field, the coupling of the magnetic dipole is strong. When the frequency of the applied field increases the magnetic dipole tries to rotate with the frequency, but at higher frequencies, due to strong anisotropy, the induced magnetization (B) lags behind the applied field (H), which results in magnetic losses. The larger the anisotropy, the higher is the difference in B and H and the more are the magnetic losses occurring in the material [86]. The desired property of EM matching in composites results from the dielectric and magnetic loss in the whole frequency range, which also confirms that the improved microwave absorption properties definitely result from the mutual effect of PPy and γ-Fe_2O_3 in the composite.

13.8 Designing of Conducting Polymer Composite by Incorporating Ferrofluid

A ferrofluid is a collection of super paramagnetic nanoparticles suspended in a liquid with no aggregation. Ferrofluid shows both fluid property and magnetic property, which can be easily controlled by the influence of moderate magnetic fields. This ferromagnetic system has many important and unusual properties and reacts to an external magnetic field, which is able to change its physical characteristics. No natural existing fluid offers these properties.

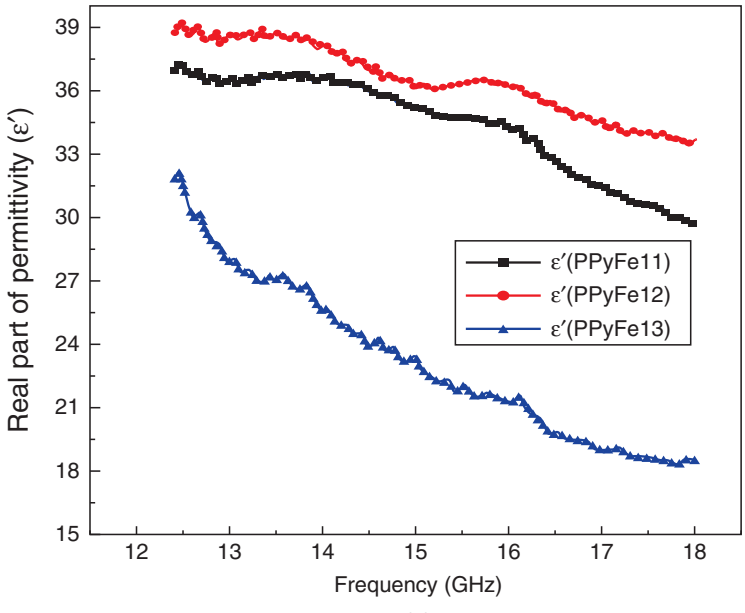

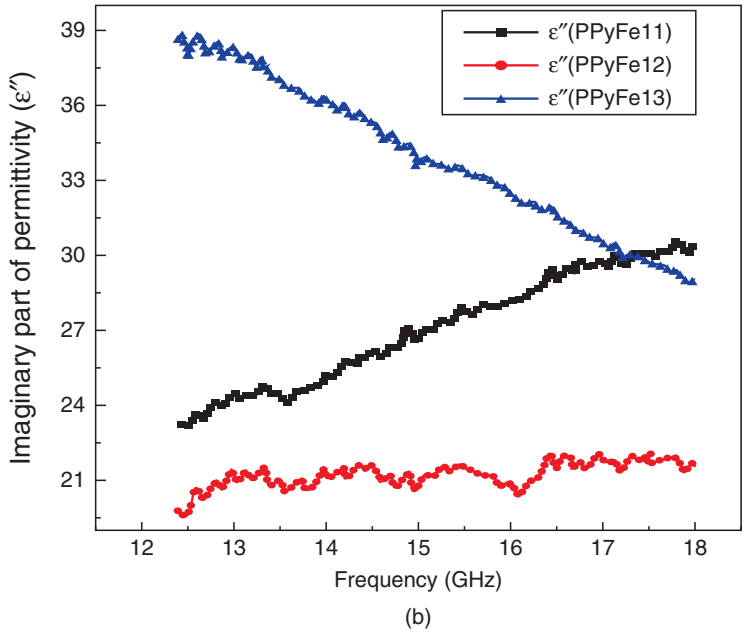

Figure 13.9 *Behavior of real and imaginary parts of permittivity of PPyFe composites as a function of frequency. Source: Varshney* et al. *2012 [36]. Reproduced with permission of Elsevier.*

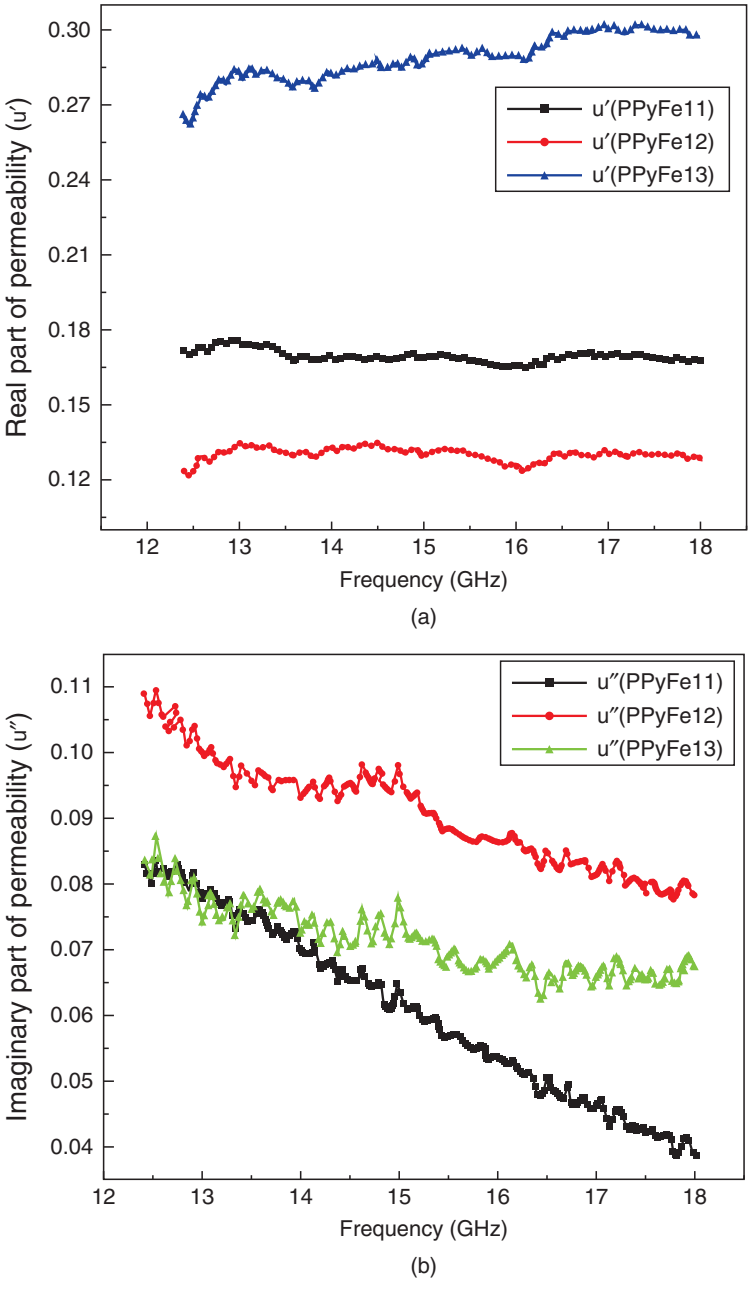

Figure 13.10 *Variation of (a) real and (b) imaginary parts of magnetic permeability of PPyFe nanocomposites as a function of frequency. Source: Varshney* et al. *2012 [36]. Reproduced with permission of Elsevier.*

The magnetic fluid research was initiated by Papell who reported the first ferrofluid by grinding magnetite in a ball mill in the presence of oleic acid (surfactant) and kerosene [87].

In the same year, Rosensweig *et al.* reported the composition of ferrofluid and the method of preparation by a co-precipitation technique for the energy conservation application [88]. The co-precipitation technique is still used as a basis for producing high-value colloid magnetic suspensions in a range of liquid carrier fluids. Ferrofluid with a variety of magnetic materials and solvents prepared by different techniques for different technological applications are currently available. When polymer molecules are able to adsorb or combine with ferrofluid magnetic particles, a magneto polymer system is formed. Such ferrofluid–polymer systems are quite interesting for many practical technological applications. A number of articles have been published on the synthesis of ferrofluid–polymer systems for different technological applications. Alam *et al.* reported a chemical method for the synthesis of Fe_3O_4/PANI nanocomposite [89]. Fang *et al.* developed free-standing electromagnetic composite films based on a conductive polypyrrole (PPy) hydrosponge and the Fe_3O_4 ferrofluid via self-assembly in the presence of β-cyclodextrin sulfate and under static condition [90].

13.9 Designing of Polypyrrole–Aqueous Ferrofluid (PFF) Nanocomposite Microwave Absorber

Ferrofluids (FF) can be designed in the presence of suitable surfactant-like tetramethylammonium hydroxide (TMAH), dextran, and oleic acid. The surfactant provides the coating of magnetic nanoparticles in a micelle-like fashion, which interact with the conducting polymer via hydrogen bonding. The pyrrole cationic free radicals are adsorbed on the surface of the Fe_3O_4 and polymerized continuously, which subsequently combine with another unit to form a neutral dimer. Schematic representation of the incorporation of FF in polypyrrole matrix is shown in Figure 13.11. Due to the core–shell type of morphology, it is observed that DC conductivity at room temperature of these composites does not deteriorate too much after incorporation of ferrofluid as compared to the polypyrrole. The conductivity value of 0.11, 0.08, and 0.05 S/cm has been calculated for PFF 11, PFF 12, and PFF 13 composites respectively.

13.9.1 Magnetic Measurements

The magnetic properties of the ferrofluid and PFF composites have been studied by using the M–H curves (Figure 13.12). The saturation magnetization (M_s) value of the aqueous FF was found to be 9.05 emu/g at an external field of 5 kOe with a small value of coercivity and negligible retentivity with no hysteresis loop, which confirms its superparamagnetic nature. When these nanoferrite particles have been encapsulated in the polypyrrole matrix in a weight-to-volume ratio of 1:1 (PFF 11), the M_s value was observed to be 1.3 emu/g. However, on increasing the loading of FF in the composite the magnetization value was increased to 2.8 emu/g and 5.5 emu/g for PFF 12 and PFF 13, respectively. With these observations, it is confirmed that the saturation magnetization value depends on the ferrite concentration. The increase in M_s value is due to the high poly-dispersivity of the ferrofluid

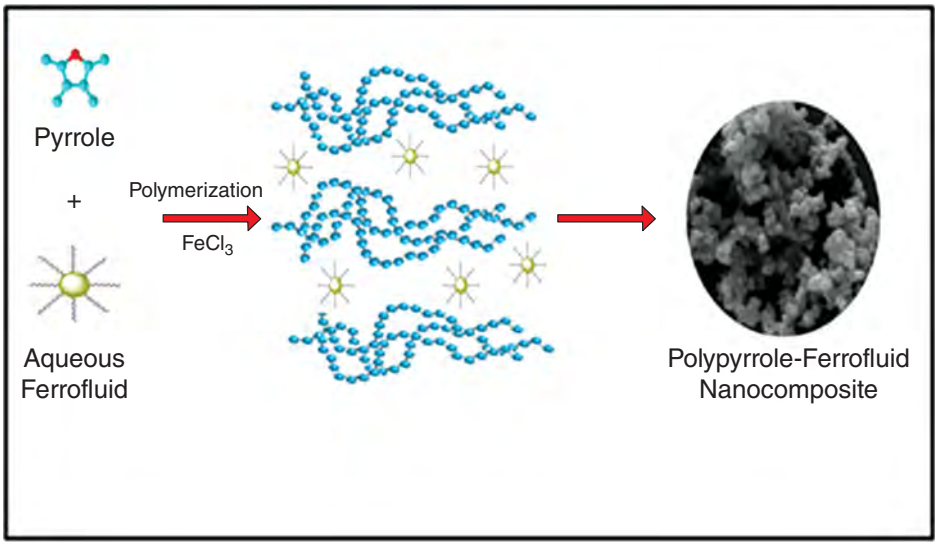

Figure 13.11 *Schematic representation for the synthesis of polypyrrole–ferrofluid (PFF) nanocomposites.*

in the polymer matrix, which arises due to the functionalization of nanoferrite particles with sodium lauryl sulfate.

13.9.2 Microwave Absorption Investigations

Figure 13.13a shows the variation of the SE_A and SE_R with frequency in the range of 12.4–18 GHz (Ku-band). From the figure, it has been observed that incorporation of

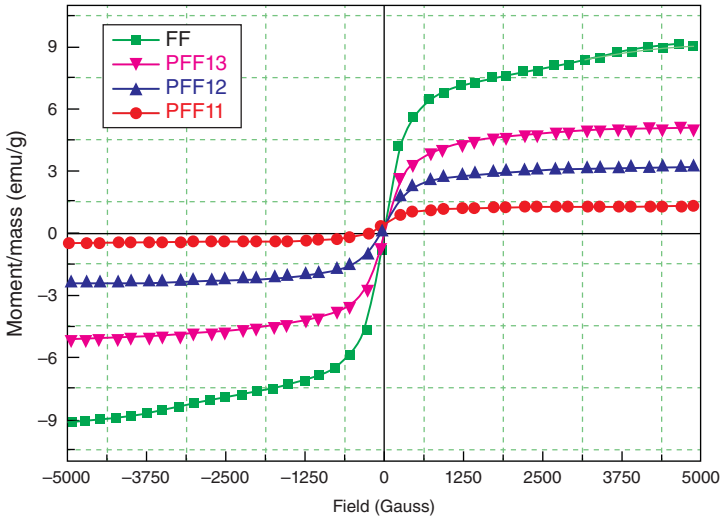

Figure 13.12 *Magnetization curves of ferrofluid, PFF 11, PFF 12, and PFF 13 nanocomposites. Source: Varshney* et al. *2014 [37]. Reproduced with permission of Elsevier.*

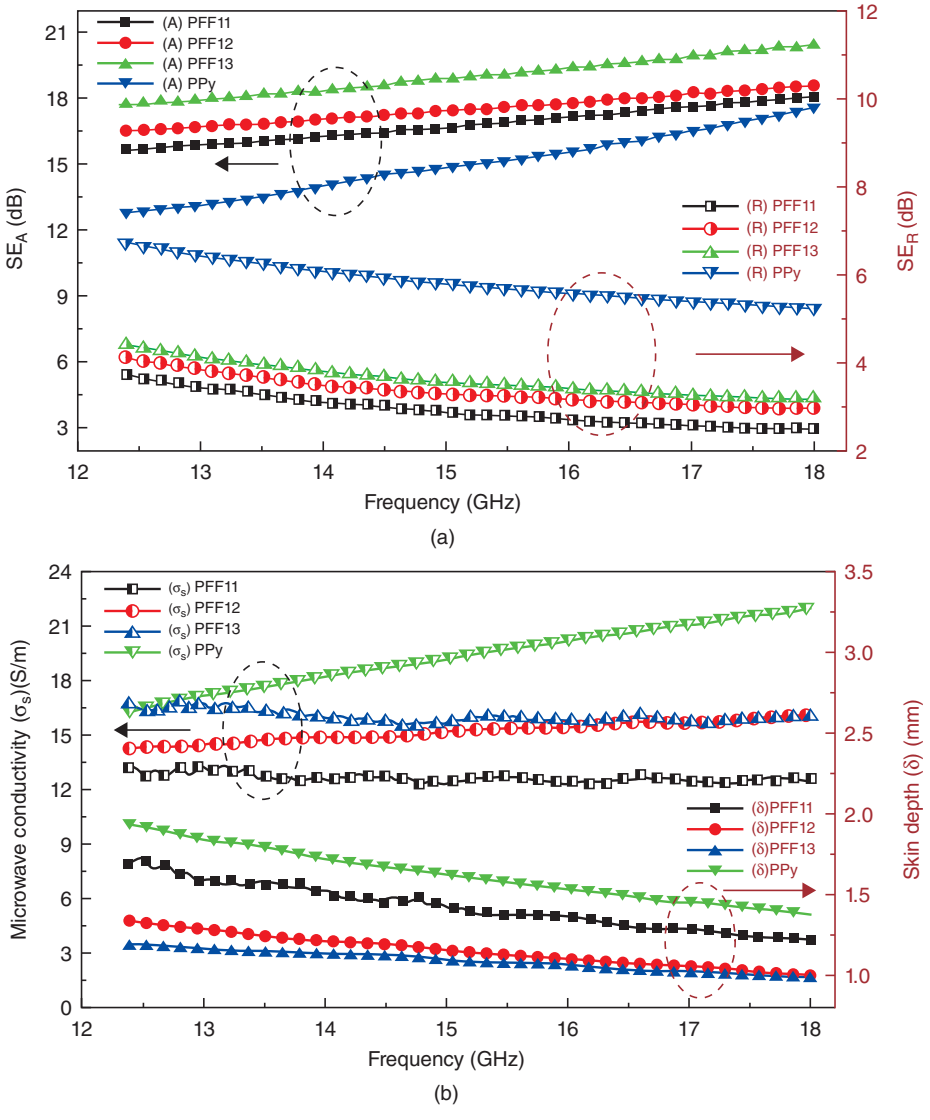

Figure 13.13 *(a) Dependence of shielding effectiveness (SEA and SER) of PPy and PFF composites as a function of frequency, showing the effect of ferrofluid concentration on the SE value of the nanocomposites. (b) Variation of microwave conductivity and skin depth of PPy and PFF composites as a function of frequency. Source: Varshney* et al. *2014 [37]. Reproduced with permission of Elsevier.*

Fe_3O_4 nanoparticles in PFF composites exhibits a much better performance since showing absorption-dominated SE rather than reflection. Polypyrrole shows an SE_A of 17.6 dB while for polypyrrole nanocomposite, that is, PFF 13, the maximum SE due to absorption ($SE_{A(\max)}$) has been observed to be 20.4 dB at 18.0 GHz with a matching thickness of 2 mm. For the reflection part, SE_R has been 3.1 dB and 5.2 dB for PFF 13 and PPy, respectively, at a frequency of 18.0 GHz. The results demonstrate that the absorption of microwave and

overall shielding effectiveness ($SE = SE_A + SE_R$) up to 23.5 dB (99.5% attenuation) for PFF 13 increase with the concentration of the ferrofluid in the composite. The increase in the absorption with the addition of ferrofluid to PFF samples may be attributed to the higher dielectric and magnetic losses induced by the presence of Fe_3O_4 nanoparticles in ferrofluid. In the case of PPy, absorption is still the dominating factor, but the reflection part is on the higher side, which makes it less favorable as a microwave absorbing material. Increased attention in the case of PFF samples may be attributed to the higher dielectric loss induced in the samples. Figure 13.13b demonstrates the variation of microwave conductivity ($\sigma_S = \omega\varepsilon_0\varepsilon''$) and frequency depth with frequency, which is calculated by using the equation ($\delta = \sqrt{2/\mu_r\omega\sigma_S}$). This relation shows the dependence of skin depth on the conductivity and magnetic permeability. It means that for highly conducting and magnetic material, the skin depth is very small. From Figure 13.13b, it is observed that the microwave conductivity and the skin depth almost remain constant in measurements of the frequency range. A higher value of σ_s has been observed for the PPy due to the higher dielectric loss as compared to PFF composites, but PFF composites are more prone to the absorption because of the combined effect of dielectric and magnetic loss.

13.9.3 Dielectric and Permeability Studies

The concept of the Nicholson, Ross, and Weir technique [82, 83] has been used to calculate complex permittivity ($\varepsilon_r = \varepsilon' - j\varepsilon''$) and permeability ($\mu_r = \mu' - j\mu''$) for further analysis of the shielding mechanism. The higher value of the dielectric loss in the case of PFF nanocomposite is attributed to the orientation and space charge polarization. Figure 13.14a reveals that ε' and ε'' decrease with an increase in frequency of the applied field. In PFF 13, incorporation of ferrofluid in the conducting polypyrrole matrix leads to higher values of dielectric constant ($\varepsilon' = 23.1$) and dielectric loss ($\varepsilon'' = 24.3$). This arises due to strong orientational polarization, which consequently leads to the improved shielding effectiveness due to absorption.

The variation in the real (μ') and imaginary (μ'') parts of permeability with frequency is shown in Figure 13.14b. Both the real and imaginary parts of the permeability remain constant with a little fluctuation in the measured frequency range. These magnetic losses are induced due to the presence of magnetic Fe_3O_4 nanoparticles in the ferrofluid. The eddy current effect, anisotropy energy, and natural resonance are responsible for magnetic losses in the composite. In the microwave range, the presence of nano-sized ferrite particles in the polymer matrix is the main reason for the eddy current while effective anisotropy energy can enhance significantly with small particle size due to the surface effect of nano-sized ferrite particles [91]. In addition to this, the coating of ferrite particles with polymer also ends with additional interfaces and more polarization charges on the surface. The above-mentioned factors contribute to the enhancement of microwave absorption.

13.10 Conclusions

In conclusion, materials decorated with different types of magnetic particles that have moderate electrical conductivity show excellent absorption-dominated electromagnetic shielding effectiveness. It has been observed that all the shapes of iron oxide covered with RGO

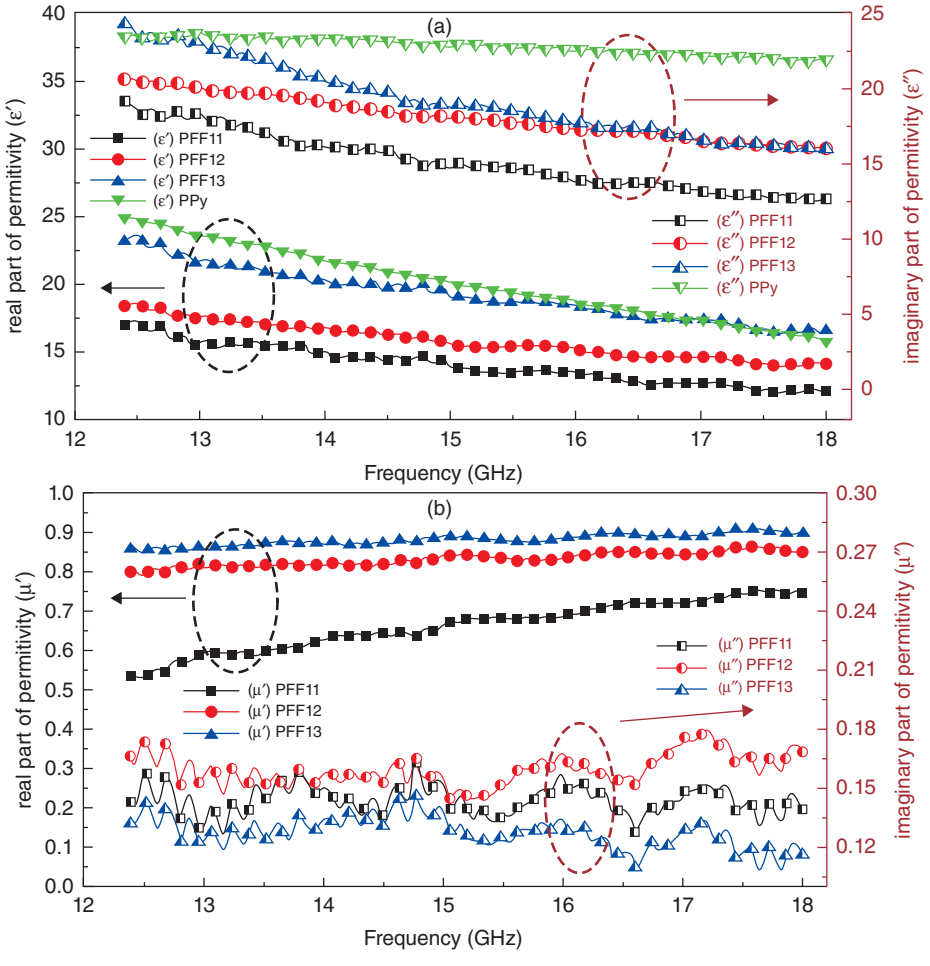

Figure 13.14 *Behaviour of (a) real (ε′) and (b) imaginary (ε″) parts of complex permittivity of PPy and PFF composites as a function of frequency. Dependence of real (μ′) and imaginary (μ″) parts of magnetic permeability of PFF composites on frequency. Source: Varshney* et al. *2014 [37]. Reproduced with permission of Elsevier.*

exhibit promising EMI shielding performance. The iron oxide nanorods covered with RGO show higher EMI shielding values than the composites based on other structures. The presence of RGO plays a crucial role in enhancing the dielectric loss. The enhanced dielectric loss can be attributed to the natural resonance, dipole relaxation, electron polarization related relaxation, interfacial polarization, residual defects in thinner RGO sheets and higher conductivity of the composite. Additionally, the associated magnetic losses of the composites are mainly caused by natural resonance and eddy currents. Thus, these new composites provide new insights into EMI shielding materials and may represent suitable morphologies for applications in next-generation EMI shielding applications.

The amalgamation of conducting polypyrrole with different magnetic nanoparticles provides a successful way to synthesize composite materials with improved processability and

greater potential in the field of EMI shielding applications. The high absorption properties mainly result from the high dielectric and magnetic losses in the composites and depend on the concentration of magnetic nanoparticles in the polymer composite.The incorporation of γ-Fe_2O_3/Fe_3O_4 particles in the polymer system leads to more interfacial dipolar polarization and higher anisotropic energy due to nano-size that consequently contributes to the high values of shielding effectiveness due to absorption.

In spite of these interesting developments, a lot remains to be done with regard to both fundamental understanding and the much needed improvement of the method of the designing electromagnetic shielding materials to operate at higher frequencies for their application.

Acknowledgments

The authors wish to thank Prof. R.C. Budhani, Director NPL and Director DITE for their keen interest in the work. The authors also thank Dr R.K. Kotnala for VSM measurements, Dr Vijjian for recording XRD data, and Dr K.N. Sood for recording the SEM micrograph.

References

1. Naishadham, K. (1992) Shielding effectiveness of conducting polymers. *IEEE Transactions on Electromagnetic Compatibility, EMC*, **34**, 47–50.
2. Liu, G., Wang, L., Chen, G., *et al.* (2012) Enhanced electromagnetic absorption properties of carbon nanotubes and zinc oxide whisker microwave absorber. *Journal of Alloys and Compounds*, **514**, 183–188.
3. Li, B.W., Shen, Y., Yue, Z.X., *et al.* (2006) Enhanced microwave absorption in nickel/hexagonal–ferrite/polymer composites. *Applied Physics Letters*, **89**, 132504-2.
4. Wang, C., Lv, R., Huang, Z., *et al.* (2011) Synthesis and microwave absorbing properties of FeCo alloy particles/graphite nanoflake composites. *Journal of Alloys and Compounds*, **509**, 494–498.
5. Liu, X.G., Geng, D.Y., Meng, H., *et al.* (2008) Microwave-absorption properties of ZnO-coated iron nanocapsules. *Applied Physics Letters*, **92**, 173117-3.
6. Chen, W., Zheng, J., Li, Y., *et al.* (2012) Synthesis and electromagnetic characteristics of $BaFe_{12}O_{19}$/ZnO composite material. *Journal of Alloys and Compounds*, **513**, 420–424.
7. Yang, Y., Gupta, M.C., Dudley, K.L., *et al.* (2005) A comparative study of EMI shielding properties of carbon nanofiber and multi-walled carbon nanotube filled polymer composites. *Journal of Nanoscience and Nanotechnology*, **5**, 927–931.
8. Zhou, J., He, J., Wang, T., *et al.* (2011) Design of mesostructured γ-Fe_2O_3/carbon nanocomposites for electromagnetic wave absorption applications. *Journal of Alloys and Compounds*, **509**, 8211–8214.
9. Che, R.C., Zhi, C.Y., Liang, C.Y. *et al.* (2006) Fabrication and microwave absorption of carbon nanotubes/$CoFe_2O_4$ spinel nanocomposite. *Applied Physics Letters*, **88**, 033105-3.
10. Xu, H., Anlage, S.M., Hu, L., *et al.* (2007) Microwave shielding of transparent and conducting single-walled carbon nanotube films. *Applied Physics Letters*, **90**, 183119-3.
11. Xie, S., Jin, G.Q., Meng, S., *et al.* (2012) Microwave absorption properties of in situ grown CNTs/SiC composites. *Journal of Alloys and Compounds*, **520**, 295–300.
12. Jun, Z., Huiquing, F., Yangli, W., *et al.* (2012) Ferromagnetic and microwave absorption properties of copper oxide/cobalt/carbon fiber multilayer film composites. *Thin Solid Films*, **520**, 5053–5059.

13. Zeng, J., Fan, H., Wang, Y., *et al.* (2012) Oxidized electroplating zinc-covered carbon fibers as microwave absorption materials. *Journal of Alloys and Compounds*, **524**, 59–62.
14. Yang, Y., Gupta, M.C., Dudley, K.L., *et al.* (2005) Novel carbon nanotube—polystyrene foam composites for electromagnetic interference shielding. *Nano Letters*, **5**(11), 2131–2134.
15. Ohlan, A., Singh, K., Chandra, A., *et al.* (2010) Microwave absorption behavior of core–shell structured poly(3,4-ethylenedioxy thiophene)–barium ferrite nanocomposites. *ACS Applied Materials and Interfaces*, **2**, 927–933.
16. Cui, C., Du, Y., Li, T., *et al.* (2012) Synthesis of electromagnetic functionalized Fe_3O_4 microspheres/polyaniline composites by two-step oxidative polymerization. *Journal of Physical Chemistry B*, **116**, 9523–9531.
17. Cao, M.S., Yang, J., Song, W.L., *et al.* (2012) Ferroferric oxide/multiwalled carbon nanotube vs polyaniline/ferroferric oxide/multiwalled carbon nanotube multiheterostructures for highly effective microwave absorption. *ACS Applied Materials and Interfaces*, **4**, 6949–6956.
18. Sharma, R., Lamba, S., Annapoorni, S., *et al.* (2005) Magnetic properties of polypyrrole-coated iron oxide nanoparticles. *Journal of Physics D: Applied Physics*, **38**, 3354–3359.
19. Joo, J. and Epstein, A.J. (1994) Electromagnetic radiation shielding by intrinsically conducting polymers. *Applied Physics Letters*, **65**, 2278–2280.
20. Singh, K., Ohlan, A., Bakhshi, A.K., and Dhawan, S.K. (2010) Synthesis of conducting ferromagnetic nanocomposite with improved microwave absorption properties. *Materials Chemistry and Physics*, **119**, 201–207.
21. Ohlan, A., Singh, K., Chandra, A., and Dhawan, S.K. (2010) Microwave absorption behavior of core–shell structured poly(3,4-ethylenedioxy thiophene)–barium ferrite nanocomposites. *ACS Applied Materials and Interfaces*, **2**, 927–933.
22. Carrasco, P.M., Grande, H.J., Cortazar, M., *et al.* (2006) Structure–conductivity relationships in chemical polypyrroles of low, medium and high conductivity. *Synthetic Metals*, **156**, 420–425.
23. Su, N., Li, H.B., Yuan, S.J., *et al.* (2012) Synthesis and characterization of polypyrrole doped with anionic spherical polyelectrolyte brushes. *eXPRESS Polymer Letters*, **6**, 697–705.
24. Wu, T.-M. and Lin, S.-H. (2006) Synthesis, characterization, and electrical properties of polypyrrole/multiwalled carbon nanotube composites. *Journal of Polymer Science Part A: Polymer Chemistry*, **44**, 6449–6457.
25. Skotheim, T.A. and Reynolds, J.R. (2007) Recent advances in polypyrrole. *Handbook of Conducting Polymers*, vol. 3, CRC Press, Taylor & Francis Group, NW, pp. 260–344.
26. Wei, L., Sevilla, M., Fuertes, A.B., *et al.* (2012) Polypyrrole-derived activated carbons for high performance electrical double-layer capacitors with ionic liquid electrolyte. *Advanced Functional Materials*, **22**, 827–834.
27. Brezoi, D.-V. (2010) Polypyrrole films prepared by chemical oxidation of pyrrole in aqueous $FeCl_3$ solution. *Journal of Science and Arts*, **1** (12), 53–58.
28. Kaur, A., Ishpal, R., and Dhawan, S.K. (2012) Tuning of EMI shielding properties of polypyrrole nanoparticles with surfactant concentration. *Synthetic Metals*, **162**, 1471–1477.
29. Li, G.R., Feng, Z.P., Zhong, J.H., *et al.* (2010) Electrochemical synthesis of polyaniline nanobelts with predominant electrochemical performances. *Macromolecules*, **43**, 2178–2183.
30. Chougule, M.A., Pawar, S.G., Godse, P.R., *et al.* (2011) Synthesis and characterization of polypyrrole (PPy) thin films. *Soft Nanoscience Letters*, **1**, 6–10.
31. Turcu, R., Pana, O., Nan, A., *et al.* (2008) Polypyrrole coated magnetite nanoparticles from water based nanofluids. *Journal of Physics D: Applied Physics*, **41**, 245002-9.
32. Xiao, H.-M., Zhang, W.-D., Wan, M.-X., *et al.* (2009) Novel electromagnetic functionalized γ-Fe_2O_3/polypyrrole composite nanostructures with high conductivity. *Journal of Polymer Science Part A: Polymer Chemistry*, **47**, 4446–4453.
33. Kanwal, F., Siddiqi, S.A., Batool, A., *et al.* (2011) Synthesis of polypyrrole–ferric oxide (Ppy–Fe_2O_3) composites and study of their structural and conducting properties. *Synthetic Metals*, **161**, 335–339.
34. Liu, J. and Wan, M. (2000) Composites of polypyrrole with conducting and ferromagnetic behaviors. *Journal of Polymer Science Part A: Polymer Chemistry*, **38**, 2734–2739.
35. Brezoi, D.-V. and Ion, R.-M. (2005) Phase evolution induced by polypyrrole in iron oxide–polypyrrole nanocomposite. *Sensors and Actuators B: Chemical*, **109**, 171–175.

36. Varshney, S., Singh, K., Ohlan, A., *et al.* (2012) Synthesis, characterization and surface properties of Fe_2O_3 decorated ferromagnetic polypyrrole nanocomposites. *Journal of Alloys and Compounds*, **538**, 107–114.
37. Varshney, S., Ohlan, A., Jain, V.K., *et al.* (2014) Synthesis of ferrofluid based nanoarchitectured polypyrrole composites and its application for electromagnetic shielding. *Material Chemistry and Physics*, **143**, 806–813.
38. Bidan, G., Jarjayes, O., Fruchart, J.M., *et al.* (1994) New nanocomposites based on "tailor dressed" magnetic particles in a polypyrrole matrix. *Advanced Materials*, **6**, 152–155.
39. Jiang, J., Ai, L.H., and Zheng, J.L. (2010) Preparation and characterization of polypyrrole/ferrospinel nanocomposites by W/O microemulsion pathway. *Journal of Macromolecular Science, Part B: Physics*, **49**, 652–657.
40. Wuang, S.C., Neoh, K.G., Kang, E.T., *et al.* (2007) Synthesis and functionalization of polypyrrole–Fe_3O_4 nanoparticles for applications in biomedicine. *Journal of Materials Chemistry*, **17**, 3354–3362.
41. Li, Y., Yi, R., Yan, A., *et al.* (2009) Facile synthesis and properties of $ZnFe_2O_4$ and $ZnFe_2O_4$/polypyrrole core–shell nanoparticles. *Solid State Sciences*, **11**, 1319–1324.
42. Singh, A.P., Garg, P., Alam, F., *et al.* (2012) Phenolic resin-based composite sheets filled with mixtures of reduced graphene oxide, γ-Fe_2O_3 and carbon fibers for excellent electromagnetic interference shielding in the X-band. *Carbon*, **50**, 3868–3875.
43. Varshney, S., Ohlan, A., Singh, K., *et al.* (2013) Robust multifunctional free standing polypyrrole sheet for electromagnetic shielding. *Science of Advanced Materials*, **5**, 881–890.
44. Sachdev, V.K., Patel, K., Bhattacharya, S., *et al.* Electromagnetic interference shielding of graphite/acrylonitrile butadiene styrene composites. *Journal of Applied Polymer Science*, **120**, 1100–1105.
45. Schelkunoff, S.A. (1943) *Electromagnetic Waves*, Van Nostrand, Princeton, NJ, pp. 241–335.
46. Schulz, R.B., Plantz, V.C., and Brush, D.R. (1988) Shielding theory and practice. *IEEE Transactions on Electromagnetic Compatibility*, **30**, 187–201.
47. Paul, C.R. (2004) *Electromagnetics for Engineers*, John Wiley & Sons, Inc., Hoboken, NJ, pp. 713–731.
48. Ott, H.W. (1988) *Noise Reduction Techniques in Electronic Systems*, John Wiley & Sons, Inc., New York, pp.159–182.
49. Colaneri, N.F. and Shacklette, L.W. (1992) EMI shielding measurements of conductive polymer blends. *IEEE Transactions on Instrumentation and Measurement*, **41**, 291–297.
50. Mishra, M., Singh, A.P., and Dhawan, S.K. (2013) Expanded graphite–nanoferrite–fly ash composites for shielding of electromagnetic pollution. *Journal of Alloys and Compounds*, **557**, 244–251.
51. Yuan, B., Yu, L., Sheng, L., *et al.* (2012) Comparison of electromagnetic interference shielding properties between single-wall carbon nanotube and graphene sheet/polyaniline composites. *Journal of Physics D: Applied Physics*, **45**, 235108– 235108-6.
52. Yonglai, Y., Mool, C.G. and Kenneth, L.D. (2007) Towards cost-efficient EMI shielding materials using carbon nanostructure-based nanocomposites. *Nanotechnology*, **18** (34), 345701-4.
53. Narayanan, T., Sunny, V., Shaijumon, M., *et al.* (2009) Enhanced microwave absorption in nickel-filled multiwall carbon nanotubes in the S band. *Electrochemical and Solid-State Letters*, **12** (4), K21–K4.
54. Joseph, N., Janardhanan, C., and Sebastian, M.T., *et al.* (2014) Electromagnetic interference shielding properties of butyl rubber-single walled carbon nanotube composites. *Composites Science and Technology*, **101**, 139–144.
55. Huang, X., Chen, Z., Tong, L., *et al.* (2013) Preparation and microwave absorption properties of $BaTiO_3$–MWCNTs core/shell heterostructure. *Materials Letters*, **111**, 24–27.
56. Dhawan, S.K., Singh, K., Bakhshi, A.K., *et al.* (2009) Conducting polymer embedded with nanoferrite and titanium dioxide nanoparticles for microwave absorption. *Synthetic Metals*, **159** (21–22), 2259–2262.
57. Varshney, S., Ohlan, A., Jain, V.K., *et al.* (2014) In situ synthesis of polypyrrole–γ-Fe_2O_3–fly ash nanocomposites for protection against EMI pollution. *Industrial and Engineering Chemistry Research*, **53**, 14282–14290.

58. Li, Q., Pang, J., Wang, B., *et al.* (2013) Preparation, characterization and microwave absorption properties of barium–ferrite–coated fly-ash cenospheres. *Advanced Powder Technology*, **24** (1), 288–294.
59. Li, L. and Chung, D.D.L. (1993) Effect of viscosity on the electrical properties of conducting thermoplastic composites made by compression molding of a powder mixture. *Polymer Composites*, **14** (6), 467–472.
60. Li, L. and Chung, D.D.L. (1994) Electrical and mechanical properties of electrically conductive polyethersulfone composite. *Composites*, **25** (3), 215–224.
61. Wen, S. and Chung, D.D.L. (2004) Electromagnetic interference shielding reaching 70 dB in steel fiber cement. *Cement and Concrete Research*, **34**, 329–332.
62. Huang, Y., Li, N., Ma, Y., *et al.* (2007) The influence of single-walled carbon nanotube structure on the electromagnetic interference shielding efficiency of its epoxy composites. *Carbon*, **45**, 1614–1621.
63. Ohlan, A., Singh, K., Chandra, A., *et al.* (2009) Conjugated polymer nanocomposites: synthesis, dielectric, and microwave absorption studies. *Journal of Applied Physics*, **106**, 044305–044311.
64. Al-Saleh, M.H. and Sundararaj, U. (2009) Electromagnetic interference shielding mechanisms of CNT/polymer composites. *Carbon*, **47**, 1738–1746.
65. Sudha, J.D., Sivakala, S., Patel, K., *et al.* (2010) Development of electromagnetic shielding materials from the conductive blends of polystyrene polyaniline–clay nanocomposite. *Composites: Part A*, **41**, 1647–1652.
66. Al-Ghamdi, A.A. and El-Tantawy, F. (2010) New electromagnetic wave shielding effectiveness at microwave frequency of polyvinyl chloride reinforced graphite/copper nanoparticles. *Composites: Part A*, **41**, 1693–1701.
67. Singh, A.P., Mishra, M., Chandra, A., *et al.* (2011) Graphene oxide/ferrofluid/cement composites for electromagnetic interference shielding application. *Nanotechnology*, **22**, 465701-9.
68. Al-Ghamdi, A. and El-Tantawy, F. (2010) New electromagnetic wave shielding effectiveness at microwave frequency of polyvinyl chloride reinforced graphite/copper nanoparticles. *Composites: Part A*, **41**, 1693–1701.
69. Singh, A.P., Mishra, M. Chandra, A., *et al.* (2011) Graphene oxide/ferrofluid/cement composites for electromagnetic interference shielding application. *Nanotechnology*, **22**, 465701-9.
70. Al-Hartomy, O., Al-Solamy, F., Al-Ghamdi, A., Dishovsky, N., Iliev, V., and El-Tantawy, F. (2011) Dielectric and microwave properties of silicone rubber/TiB_2 nanocomposites, KGK, April 13–18, 2011.
71. Yuan, B., Yu, L., Sheng, L., *et al.* (2012) Comparison of electromagnetic interference shielding properties between single-wall carbon nanotube and graphene sheet/polyaniline composites. *Journal of Physics D: Applied Physics*, **45**, 235108-6.
72. Al-Ghamdi, A., Al-Hartomy, O., Al-Solamy, F., *et al.* (2012) On the prospects of conducting polyaniline/natural rubber composites for electromagnetic shielding effectiveness applications. *Journal of Thermoplastic Composite Materials*, **27**, 765–782.
73. Gupta, T., Singh, B.P., Teotia, S., *et al.* (2013) Designing of multiwalled carbon nanotubes reinforced polyurethane composites as electromagnetic interference shielding materials. *Journal of Polymer Research*, **20**, 169–177.
74. Al-Saleh, M.H., Saadeh, W.H., and Sundararaj, U. (2013) EMI shielding effectiveness of carbon based nanostructured polymeric materials: a comparative study. *Carbon*, **60**, 146–156.
75. Al-Saleh, M.H. and Sundararaj, U. (2013) Morphological, electrical and electromagnetic interference shielding characterization of vapor grown carbon nanofiber/polystyrene nanocomposites. *Polymer International*, **62**, 601–607.
76. Gupta, T., Singh, B.P., Singh, V.N., *et al.* (2014) MnO_2 decorated graphene nanoribbons with superior permittivity and excellent microwave shielding properties. *Journal of Materials Chemistry A*, **2**, 4256–4263.
77. Al-Saleh, M.H. (2015) Influence of conductive network structure on the EMI shielding and electrical percolation of carbon nanotube/polymer nanocomposites. *Synthetic Metals*, **205**, 78–84.
78. Farukh, M., Singh, A.P., and Dhawan, S.K. (2015) Enhanced electromagnetic shielding behavior of multi-walled carbon nanotube entrenched poly(3,4-ethylenedioxythiophene) nanocomposites. *Composites Science and Technology*, **114**, 94–102.

79. Idris, F.M., Hashim, M., Abbas, Z.F., *et al.* (2016) Recent developments of smart electromagnetic absorbers based polymer–composites at gigahertz frequencies. *Journal of Magnetism and Magnetic Materials*, **405**, 197–218.
80. Gupta, A., Singh, A.P., Varshney, S., *et al.* (2014) New insight into the shape-controlled synthesis and microwave shielding properties of iron oxide covered with reduced graphene oxide. *RSC Advances*, **4**, 62413–62422.
81. Singh, K., Ohlan, A., Pham, V.H., *et al.* (2013) Nanostructured graphene/Fe_3O_4 incorporated polyaniline as a high performance shield against electromagnetic pollution. *Nanoscale*, **5**, 2411–2420.
82. Nicolson, A.M. and Ross, G.F. (1970) Measurement of the intrinsic properties of materials by time-domain techniques. *IEEE Transactions on Instrumentation and Measurement*, **19**, 377–382.
83. Weir, W.B. (1974) Automatic measurement of complex dielectric constant and permeability. *Proceedings of the IEEE*, **62**, 33–36.
84. Cornell, R.M. and Schertmann, U. (2000) *Iron Oxides in the Laboratory Preparation and Characterization*, 2nd edn, John Wiley & Sons, Inc., New York, pp. 188.
85. Singh, K., Ohlan, A., Kotnala, R.K., *et al.* (2008) Dielectric and magnetic properties of conducting ferromagnetic composite of polyaniline with γ-Fe_2O_3 nanoparticles. *Materials Chemistry and Physics*, **112**, 651–658.
86. Ishino, K. and Narumiya, Y. (1987) Development of magnetic ferrites: control and application of losses. *Ceramic Bulletin*, **66**, 1469–1474.
87. Papell, S.S. (1965) Low viscosity magnetic fluid obtained by the colloidal suspension of magnetic particles. US Patent 3,215,572.
88. Rosensweig, R.E., Nestor, R.E., and Timmins, J.W. (1965) Ferrohydrodynamic fluids for direct conversation of heat energy, in *Materials Association Direct Energy Conversion Symposium Proceedings*, AIChE-I. Chemistry Series 5, pp. 104–118.
89. Alam, J., Riaz, U., and Ahmad, S. (2007) Effect of ferrofluid concentration on electrical and magnetic properties of the Fe_3O_4/PANI nanocomposites. *Journal of Magnetism and Magnetic Materials*, **314**, 93–99.
90. Fang, L., Dai, T., and Lu, Y. (2009) Electromagnetic composite films based on polypyrrole hydrosponge and Fe_3O_4, ferrofluid. *Synthetic Metals*, **159**, 2101–2107.
91. Dimitrov, D.A. and Wysin, G.M. (1995) Magnetic properties of spherical fcc clusters with radial surface anisotropy. *Physical Review B*, **51**, 11947–11950.

14

Microwave Ferrites and Applications

Vincent G. Harris
Center for Microwave Magnetic Materials and Integrated Circuits, Department of Electrical and Computer Engineering, Northeastern University, Boston, Massachusetts, USA

14.1 Introduction

Microwave ferrites are a unique class of magnetic materials that possess moderate values of magnetization and permeability, low radio frequency (rf) conduction losses, and gyromagnetic properties that provide them with non-reciprocal behavior that has found ubiquitous utility in a broad range of rf devices such as circulators, isolators, phase shifters, directional couplers, power limiters, and filters, among others.

Although mature in development, having been first industrialized in the 1950s, modern ferrites are now processed using new and improved techniques that provide them with unique functional properties that include: tuning of resistivity over many decades, magnetoelectric effect, multiferroicity, and a giant magneto dielectric effect. Such novel processing schemes include chemical processing of particles having unique shapes and sizes; thin and thick film processed using pulsed laser deposition, molecular beam epitaxy, magnetron sputtering, liquid phase epitaxy, and various variants of the chemical vapor deposition technique; and the development of crystallographically produced texture ferrites using screen printing or topochemical ordering, among others.

These techniques, ferrite materials, and a sampling of unique rf devices will be considered and reviewed in this chapter. We will begin with a review of basic principles of chemistry, magnetism, and gyromagnetic properties.

Microwave Materials and Applications, First Edition.
Edited by Mailadil T. Sebastian, Rick Ubic and Heli Jantunen.
© 2017 John Wiley & Sons, Ltd. Published 2017 by John Wiley & Sons, Ltd.

14.2 Structure, chemistry, magnetism, and gyromagnetic properties

Let us consider magnetic ceramics, such as the microwave ferrites, that possess both significant permittivity and permeability concomitant with low microwave dielectric and magnetic losses. They exist in a variety of crystal structures that include the cubic spinels (Figure 14.1a, space group: *Fd3m*), garnets (Figure 14.1b, space group: Ia_3d), and the hexaferrite magnetoplumbite (Figure 14.2a to c, space group: Pb_3/mmc, also shown in the Plate Section) phases [1–2]. It is noteworthy that the hexaferrite structure and its many variants consist in part of an assembly of spinel and distorted spinel subunits (S, R, T; * denotes 180° rotation) that are aligned or rotated about a common axis. Crystal symmetry is broken in these structures by the inclusion of large barium (or strontium) ions, giving rise to hexagonal symmetry and profound magnetic anisotropy energies and correspondingly high magnetic anisotropy fields. The latter properties will be shown to be quite useful in device design at frequencies above the Ku-band.

The ferrite structure, be it spinel, garnet, or hexaferrite, has as its structural backbone a close-packed arrangement of oxygen anions. Metallic cations, magnetic and non-magnetic, and typically divalent and trivalent, reside on the interstices of the close-packed oxygen lattice, in some cases filling all available sites while in others preferentially filling select sites. In the case of unoccupied cation sites, vacancies and defects permit the stabilization of higher-order valence states that give rise to anomalous local anisotropic fields.

Ferrites find a wide variety of uses in military and commercial radar and communication electronics as well as inductors and power conditioning and conversion applications. They are integral materials in switch mode power supplies, transformers, power converters, inductor cores, filters, etc., as well as passive electronics used in transmit and receive modules such as isolators, circulators, phase shifters, filters, directional couplers, power limiters, etc.

Radar applications have obvious military applications but may also be used in commercial systems for aviation, severe weather warning radar, oceanographic satellite radar, and automobile anticollision radar, to name a few. Other applications include satellite communication uplinks and downlinks over a broad range of frequencies (see Figure 14.3).

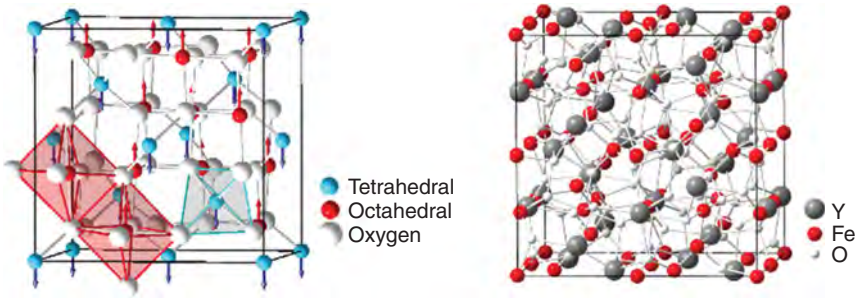

Figure 14.1 *Schematic representation of (a) the spinel ferrite unit cell and (b) garnet (YIG) unit cell structures. Source: Adapted from Harris 2012 [1].*

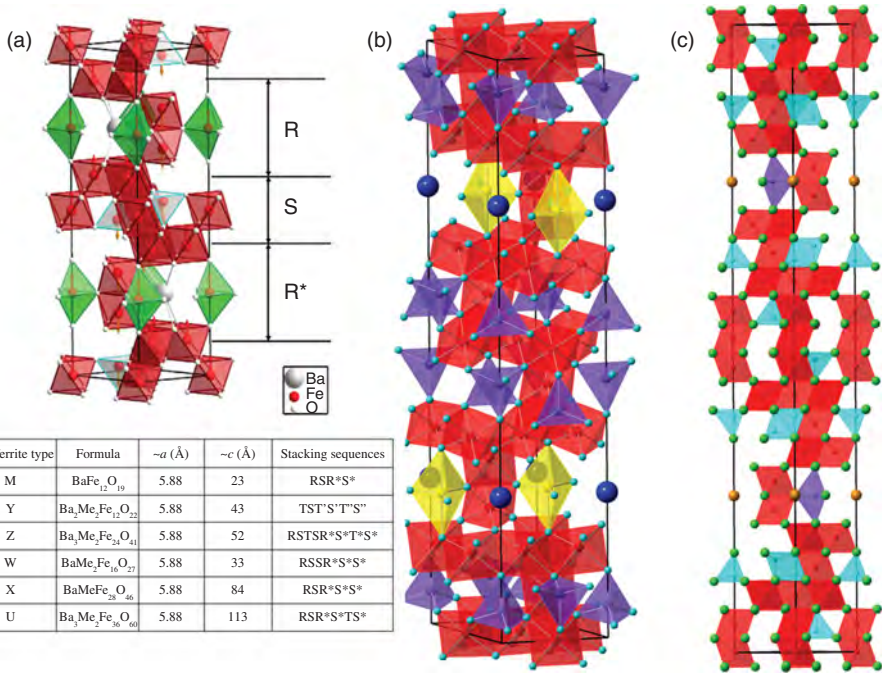

Hexaferrite type	Formula	~a (Å)	~c (Å)	Stacking sequences
M	$BaFe_{12}O_{19}$	5.88	23	RSR*S*
Y	$Ba_2Me_2Fe_{12}O_{22}$	5.88	43	TST'S'T"S"
Z	$Ba_3Me_2Fe_{24}O_{41}$	5.88	52	RSTSR*S*T*S*
W	$BaMe_2Fe_{16}O_{27}$	5.88	33	RSSR*S*S*
X	$BaMeFe_{28}O_{46}$	5.88	84	RSR*S*S*
U	$Ba_3Me_2Fe_{36}O_{60}$	5.88	113	RSR*S*TS*

Figure 14.2 *Schematic representation of hexaferrite structures of (a) M-type, (b) Y-type, and (c) Z-type variants. Table 1 presents structures and lattice constants for the hexaferrite structures including M, Y, Z, W, X, and U-type ferrites as the inset to this figure. This figure is also shown in the Plate Section.*

Magnetism in the ferrites derives from the exchange energy, J, between spins of neighboring magnetic ions. Because J is negative, the antiparallel alignment of spins is the lowest energy configuration. Since the distance between metal ions is too great to support direct exchange, such as that experienced in most magnetic metals (e.g., Fe, Co, Ni), the exchange is mediated by the oxygen anion that resides between the two cations and is thus considered an indirect exchange, that is, a superexchange [3]. Three factors principally affect the strength of the exchange, which include the distance, direction, and angle of the cations with respect to the anion. While the direction and angle are defined by the relationship between Me–O–Me, the critical distance is that between Me–O not Me–Me, the latter having little impact on J. All three factors determine the degree of orbital overlap between the extending 2p orbitals of oxygen and the 3d orbitals of the cations, and hence the magnitude of J. By examining p- and d-orbital alignments one can readily conclude that larger Me–O–Me angles produce a stronger negative exchange, while angles that approach 90° produce a weak exchange. This is seen in the spinel ferrite systems where, for example, the exchange J_{AB} corresponds to the largest A–O–B angle, ~154°, which is far larger than that of the B–O–B angle, J_{BB} ~125° [1]. Magnetization results from an imbalance of spins on the ferrimagnetically coupled sublattices [4]. One approach to increasing the net magnetization is to populate one sublattice preferential to the other with non-magnetic cations,

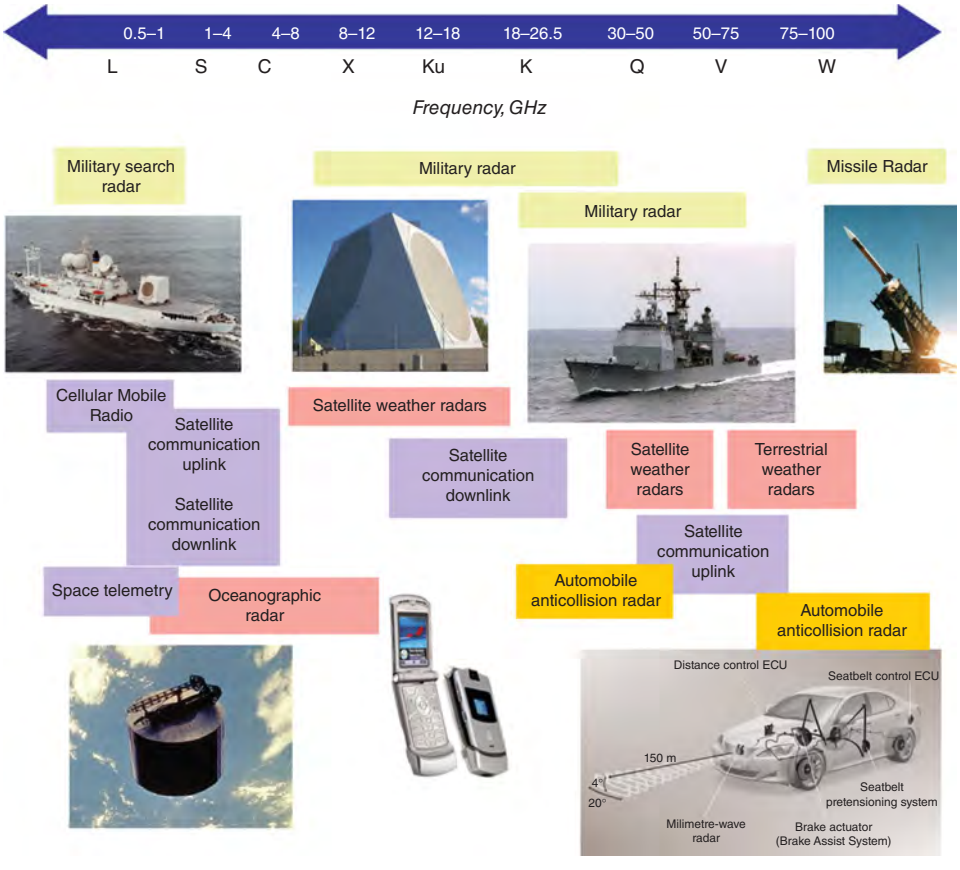

Figure 14.3 *Varied rf, microwave and millimeter-wave applications as they appear across the frequency spectrum from L to W bands. Source: Adapted from Harris 2012 [1].*

while concomitantly maintaining a strong exchange energy, J, to minimize spin canting [5]. Alternatively, one may populate one sublattice relative to the other with high spin moments. For a thorough treatment of the sources of magnetism in ferrites and other oxide systems, the reader is directed to a recent text by Dionne [6].

Because the hexaferrites [7] are among the only ferrites possessing strong magnetocrystalline anisotropy, we focus here on the engineering of both magnetic and structural anisotropies in this class of materials.

Importantly, when processed with strong anisotropy in both magnetic polarization and structure, hexaferrites experience a magnetic easy axis that may align along the crystallographic c-axis, as is the case with M- and U-type ferrites, or align in the basal plane, as is the case with, for example, the Y- and Z-type ferrites. These ferrites can find great utility in passive rf devices such as circulator/isolators, phase shifters, filters, and antenna substrates, among other applications [8]. They are the select materials for use above the X-band because their high magnetic anisotropy leads to high ferromagnetic resonance frequencies. Hexaferrites also find applications as permanent magnets [9], magnetic recording [10], and

EMI (electromagnetic interference) absorbers [11], to name only three other applications. We will not focus on these applications and material variants but instead limit the scope of this article to ferrite systems used for off-resonance rf device applications, where it is very important to minimize dielectric and magnetic losses while maximizing permeability and magnetization and controlling crystallographic and magnetic texture.

It has been established by careful experimental studies by numerous researchers that certain substitutions for the Fe cation leads to dramatic changes in magnetic anisotropy energy, K_u, and the magnetic anisotropy field, H_A, and consequently the ferromagnetic resonance (FMR) condition [12]. In order to appreciate the interrelationship between H_A and f_{FMR}, we will provide the following background information.

The FMR condition for ferrite materials is described by the susceptibility tensor of the form:

$$[\chi_v] = \frac{M}{(H_1 H_2 - \omega^2/\gamma^2)} \begin{bmatrix} H_1 & -j\omega/\gamma \\ j\omega/\gamma & H_2 \end{bmatrix} \equiv \begin{bmatrix} \chi_{11} & \chi_{12} \\ \chi_{21} & \chi_{22} \end{bmatrix} \tag{14.1}$$

where M is the saturation magnetization, ω is the radial frequency, γ is the gyromagnetic ratio, and H_1 and H_2 are effective internal magnetic fields. The real and imaginary components of permeability in the frequency domain are depicted in Figure 14.4. The FMR frequency is expressed as

$$f_{FMR} = \frac{\gamma}{2\pi}\sqrt{H_1 H_2} \tag{14.2}$$

where the internal magnetic fields, H_1 and H_2, are given in the table of Figure 14.4 for spinel and garnets as well as M-type and Y- and Z-type hexaferrites. Trends in resonant frequency (i.e., f_{FMR}) as a function of H_A and bias field (H) are depicted in Figure 14.5. This figure makes clear the impressive variation in resonant frequency as a function of applied fields and magnetic anisotropy fields [13].

It is essential to operate a passive rf device far from the peak in μ", while at the same time close enough to benefit from a high differential real permeability. Operating too close to the peak in μ" leads to a high device insertion loss (see Figure 14.4). Any insertion loss greater than 1 dB is likely to be seen as too lossy, thus limiting the device's utility and wide acceptance. We have shown by the iterative electromagnetic finite element method analysis of designs, in which the FMR loss of the magnetic material (as FMR linewidth) is adjusted, that a 1 dB insertion loss roughly correlates to an FMR linewidth of approximately 500 Oe (for the case of an X-band circulator). This rather crude demonstration depends upon other critical factors such as the operational frequency band relative to FMR, impedance matching, and conduction losses (among others) that may not be included in the linewidth calculation.

The FMR linewidth, ΔH, in turn depends upon the intrinsic magnetic anisotropy and extrinsic parameters such as crystal quality, grain orientation, porosity, etc. [14]. The latter properties are often reflected in the coercivity of the ferrite, which in turn has been shown to determine in part the remanent magnetization leading to self-biased properties. Both magnetization and the anisotropy field are determined in part from atomic -level parameters and interactions. For example, fundamental sources of anisotropy include: magnetocrystalline, dipolar, spin–orbit coupling, single ion, pair order, etc. These in turn are affected by the proportion, type, and valence of cations, as well as the bond angle and distance between cation and anion. Point, line, and volume defects also contribute to changes in exchange

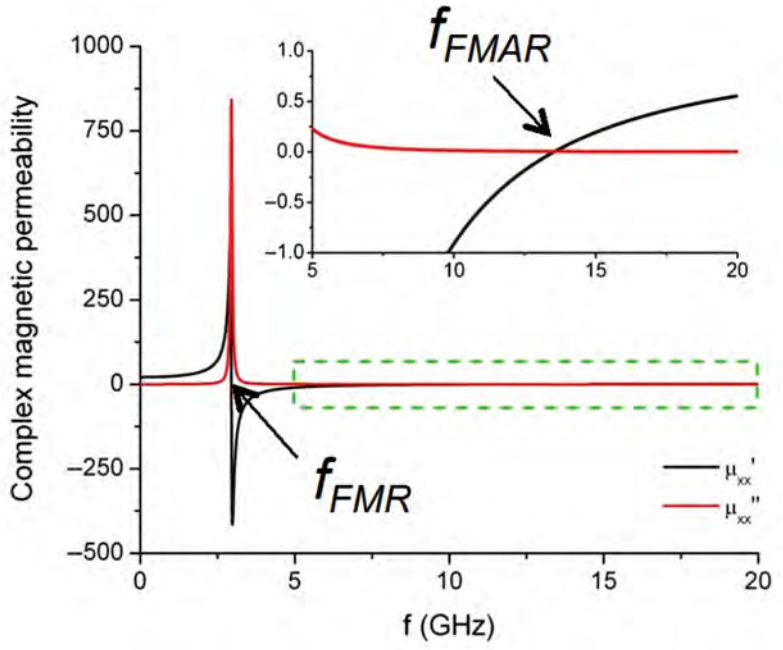

	H_1	H_2
Spinel and garnet	$H + 4\pi M$	H
M-type	$H + H_A - 4\pi M$	$H + H_A - 4\pi M$
Y- and Z-type	$H + H_\theta - 4\pi M$	H

Figure 14.4 *The real and imaginary components of permeability in the frequency domain near the ferrimagnetic resonance (FMR) and ferrimagnetic antiresonance (FMAR).*

that in turn affect magnetic anisotropy, magnetization, thermomagnetic behavior, and FMR linewidth [15]. In this way, one can appreciate the care in preparation that must be afforded the processing of magnetic materials for use at rf frequencies.

The FMR condition depends strongly upon the strength of H_A (i.e., the magnetic anisotropy field), intrinsic magnetization (M_s), and the applied field (H). Variations in the applied field and H_A act to shift the FMR frequency, allowing the tailoring of device operational frequency and performance for applications over a wide range of frequencies. For example, the work by Albanese and Deriu in 1979 showed an unambiguous trend in which Fe ion substitutions with Al and Ga lead to FMR frequencies as high as the W-band [16]. Similarly, it was shown by these same researchers that substitutions of In and Sc can shift the FMR frequency to below the X-band. Cobalt and Ti, as Co(x)/Ti(x) [17], have also been shown to reduce the magnetic anisotropy energy, thereby reducing the FMR frequency while retaining the easy magnetic direction along the crystallographic c-axis. Recently, Hu

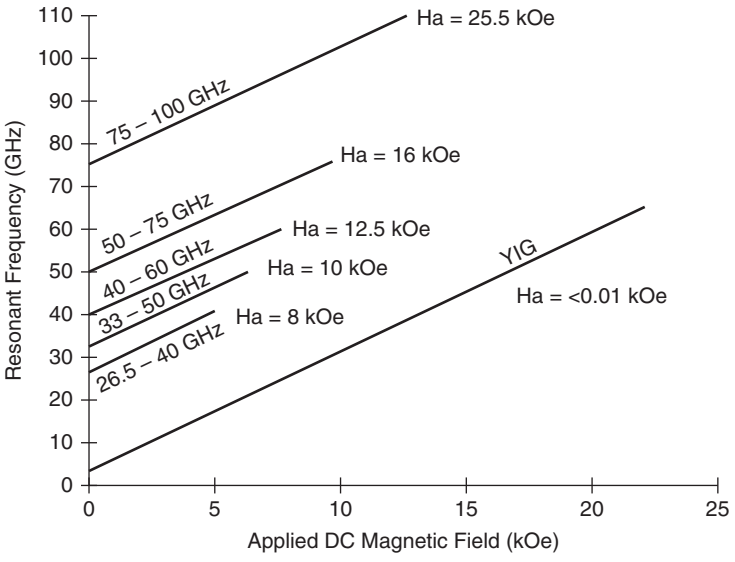

Figure 14.5 *Trends in resonant frequency (i.e., f_{FMR}) as a function of H_A and bias field (H). This figure makes clear the variation in resonant frequency as a function of applied fields and magnetic anisotropy fields in accordance with the equations presented in Figure 20.4.*

et al. [18] reported the properties of (Zr, Zn)-doped BaM films deposited by the pulsed laser deposition technique, demonstrating the manipulation of H_A from 8 to 18 kOe. However, at high substitution levels the *c*-axis alignment weakens H_A to the point that the ferrite becomes ferroxplanar with the magnetic easy axis aligning within the crystallographic basal plane. Similarly, the addition of Ir and Co (as Co(x)/Ir(x)) reveals clear trends in which increasing x reduces H_A from >15 kOe to <1.2 kOe to the point where for $x > 0.65$ the H_A is poorly defined and aligns in the basal plane [14]. Li *et al.* [19], in substituting Zn and Zr (as Zn(x/2)/Zr(x/2)), also found a pronounced reduction in H_A from ~16 to <10 kOe. Daigle *et al.* [20] has experimented with the substitution of Co ions in both Y and Z hexaferrites as choice materials for low profile antenna substrates for UHF to S-band applications. Recently, W-type ferrites have drawn new attention for use as a self-biased microwave material, especially for application in low-frequency devices. Su *et al.* [21] first reported the low-frequency self-biased characteristics of a W-type hexaferrite having hysteresis squareness values of >80% and H_A values ranging from 6 to 12 kOe. These studies represent progress in developing self-biased microwave ferrites with perpendicular anisotropy, that is, easy magnetic polarization direction aligns along the c-axis. W-type hexaferrites may prove effective alternatives to the well-known self-biased (Sr, Ba)M or Sc-doped (Sr, Ba)M ferrites.

It is important to realize the essential role of magnetic and structural anisotropy in establishing the strength and direction of the easy magnetic polarization. In the presence of large magnetocrystalline anisotropy energy the magnetic easy polarization aligns along the crystallographic *c*-axis for M type and aligns in the basal plane for Y and Z hexaferrites. Hence, often the problem facing the rf materials engineer reduces to the successful processing of crystallographic texture.

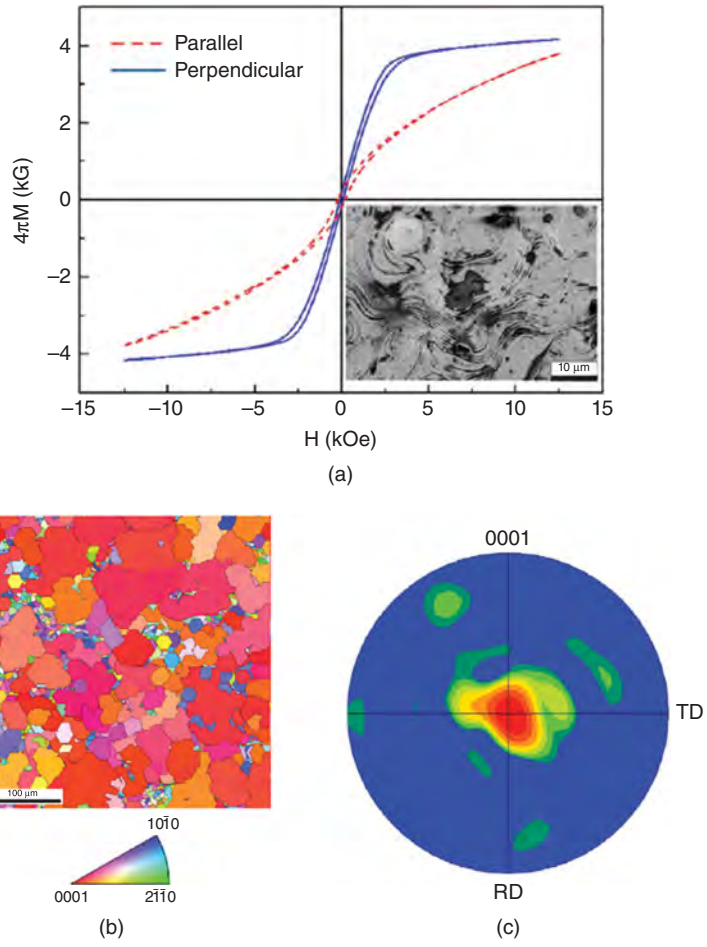

Figure 14.6 *(a) Magnetic hysteresis loops and SEM image of the surface morphology for the BaM compact sintered at 1350 °C for 10 hours by the topochemical growth process. Perpendicular and parallel refer to the orientation of the applied magnetic field with respect to the sample surface. (b) Orientation map along the [0001] direction measured by EBSD for the BaM ferrite sintered by the topochemical growth process. The color code for the crystallographic orientations is given in the stereographic triangle below the map. (c) Pole figure along the [0001] direction for the BaM ferrite sintered by the topochemical growth process. Source: Adapted from Y. Chen* et al. *2007 [24]. This figure is also shown in the Plate Section.*

As discussed, the role of crystallographic texture is often a vehicle to manipulation of magnetic anisotropy that in turn allows for the tuning of the operating frequency, bandwidth, and loss characteristics, among other properties. Figure 14.6 (also shown in the Plate Section) is a plot of ferrite operational bands versus frequency. In Figure 14.6 we see the impact of cation dopants, anisotropy energy, and texture in the choice of available materials for certain frequency bands. This qualitative depiction reflects the flexibility of the hexagonal ferrite and the other spinels and garnets in covering large swaths of frequency space by

adjusting magnetocrystalline anisotropy (K_u) via cation substitution. One notices that the garnets and spinels appear on the low-frequency side of the frequency spectrum. This is due to the lack of strong magnetocrystalline anisotropy in these cubic symmetry systems. The NiZn–ferrite is seen to possess utility beyond the MnZn–ferrite due to its far superior insulating properties, leading to low conduction-related losses. Alternatively, MnZn–ferrites remain the choice materials for inductor core applications below 1 MHz in power converters and conditioners due to their high permeability and saturation induction. YIG, the ferrite having among the lowest rf losses, is widely used below the Ku-band. Beyond Ku-band frequencies the required bias magnets become prohibitively expensive, large, and cumbersome. The hexaferrite systems cover many decades of frequency space depending upon the nature of cation substitution and the intrinsic magnetocrystalline anisotropy energy. Variants of the magnetoplumbite structure are listed in the inset Table1 in Figure 14.2 and include M, Y, Z, U, and W. Each finds utility for a wide range of applications and over a broad range of frequencies. With the recent importance placed on millimeter-wave device technology, the hexaferrites are expected to receive considerable attention for use in transmit and receive module passive components and other applications.

14.3 Ferrite Materials Processing for Microwave Applications

As alluded to earlier, ferrites are groups of irreplaceable electronic materials having advanced properties related to high permeability, non-reciprocal electromagnetic properties, and low eddy current losses. Ferrite devices in bulk form have long been utilized in various types of high-frequency and high-power applications, while it continues to remain a challenge to develop planar film devices towards ferrite–MIC integration [22]. A key enabler for integration is the growth of oriented epitaxial ferrite films on semiconductor substrates. Different strategies have been pursued to this end. Unfortunately, most ferrite preparation techniques involve high-temperature processing in oxygen-rich environments that are incompatible with most semiconductor materials and technologies. Until now, there have been no ferrite film-based integrated microwave devices in either commercial or military markets. Research demonstrations have demonstrated only limited advantages over existing well-developed technologies in terms of performance, form factor, and production costs, among other properties.

Today, there are emerging markets in high-frequency, high-power, wireless and satellite communications (GPS, Bluetooth, WLAN, commercial radar, etc.), as well as many defense applications. As a result, high-quality ferrite film materials and related planar devices are in high demand. Meanwhile, given commercially available advanced semiconductor substrates and new innovative ferrite film growth techniques developed in recent years, many of the obstacles inhibiting monolithic integration of ferrites are being remediated. Indeed, research activity towards this goal has been revitalized.

Advances made in materials are often the catalyst to technological revolution. Accordingly, our discussion will begin with a review of the recent development of ferrite and semiconductor materials relevant to our goals. We will then examine past and recent progress in the growth and patterning of ferrite films on semiconductor substrates with the goal of integrating ferrites with active semiconductor devices compatible with MICs. This will be the topic of discussion in Section 14.4.

14.3.1 Ferrite Processing as Bulk Polycrystalline Substrates

The use of polycrystalline ferrite substrates rather than that of single crystal substrates has numerous benefits including potential ease of processing and cost reduction. The processing of crystallographically textured ferrite polycrystalline bulk samples requires a much different approach that is equally challenging.

In order to align polycrystals one must either seed the growth of crystals, in essence taking advantage of epitaxy between the seed and the ferrite grain, or in the case with magnetic systems, such as ferrites, a magnetic field may be used to produce a torque on particles to align them along the magnetic flux direction and subsequently achieve crystallographic texture and a magnetic easy direction of magnetic polarization. A third technique involves the alignment of polycrystals by mechanical shear forces and although this has been shown to work to some degree (~70% remanence squareness) it remains inadequate to meet the needs of rf engineers (>90% remanence squareness).

Y. Chen *et al.* [23] demonstrated the approach of epitaxial seeding in the growth of highly textured barium hexaferrite. In that example, goethite, that is, α-FeOOH nanorods mixed with $BaCO_3$, were dispersed in a polymer solution and oriented under a 90 kOe magnetic field during polymerization. The magnetic orientation arose principally from the interaction of the strong magnetic field with the anisotropic antiferromagnetism of the goethite particles. The orientated antiferromagnetic particles resulted in the topochemical growth of $BaFe_{12}O_{19}$ ferrite grains along the [0001] direction by a one-step sintering process. The degree of grain orientation was determined using magnetic measurements (see Figure 14.7a) and orientation distribution functions (Figure 14.7b) and pole figures (Figure 14.7c) deduced by electron backscatter diffraction analysis.

In addition to the hexaferrite compacts for self-biased microwave devices, a quasi-single crystal (QSC) Sc-doped $BaFe_{12}O_{19}$ ferrite has attracted interest from the microwave engineering community [24]. The material was fabricated by a single solid-state reaction technique that included the alignment of ferrite particles as seed crystals by the application of an external magnetic field of 10 kOe and a pressure of 1500 psi. This technique was shown to be cost-effective in producing future microwave devices compared with those that employ BaM single crystals. Figure 14.8a to c depicts an SEM image illustrating a collection of large, coalesced crystals having strong *c*-axes alignment out of the sample plane (see Figure 14.8b). The QSC ferrite bulk samples show similar static magnetic properties to those of single crystals (see Figure 14.8c). However, the FMR linewidths are ~300 Oe at U-band frequencies, broader than Ba ferrite single crystals, <100 Oe. Nevertheless, a 300 Oe linewidth is acceptable for many microwave and millimeter-wave device applications.

14.3.2 Thin-Film Processing

14.3.2.1 Thin-Film Processing Using PLD and AT-LAD

Pulsed laser deposition (PLD) is a well-established method for growing ferrite films. In conventional PLD, laser pulses from a high-energy laser (e.g., typically an Excimer gas-based laser but Nd–YAG solid-state lasers have proven effective) ablate a homogeneous target, forming a molecular flux (or plume). The substrate intercepts the plume allowing for film growth on selected, often lattice matched, substrates. PLD has been used in the

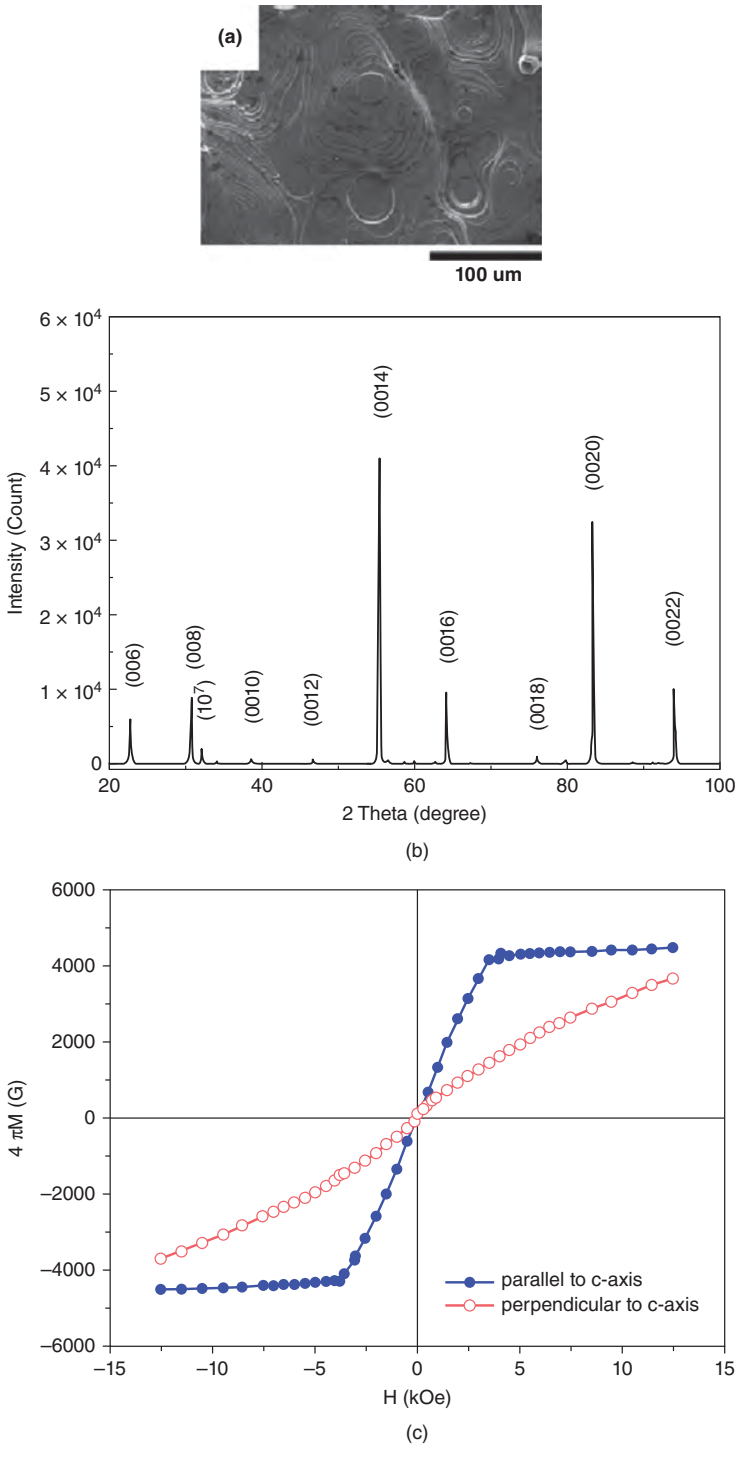

Figure 14.7 *(a) SEM micrograph for the surface of a BaM–ferrite quasi-single-crystal. (b) X-ray diffraction pattern of a* $BaFe_{12}O_{19}$ *BaM quasi-single-crystal. (c) Hysteresis loops of a Ba–ferrite quasi-single-crystal when an external field is parallel and perpendicular to the c axis. Source: Adapted from Y. Chen* et al. *[24].*

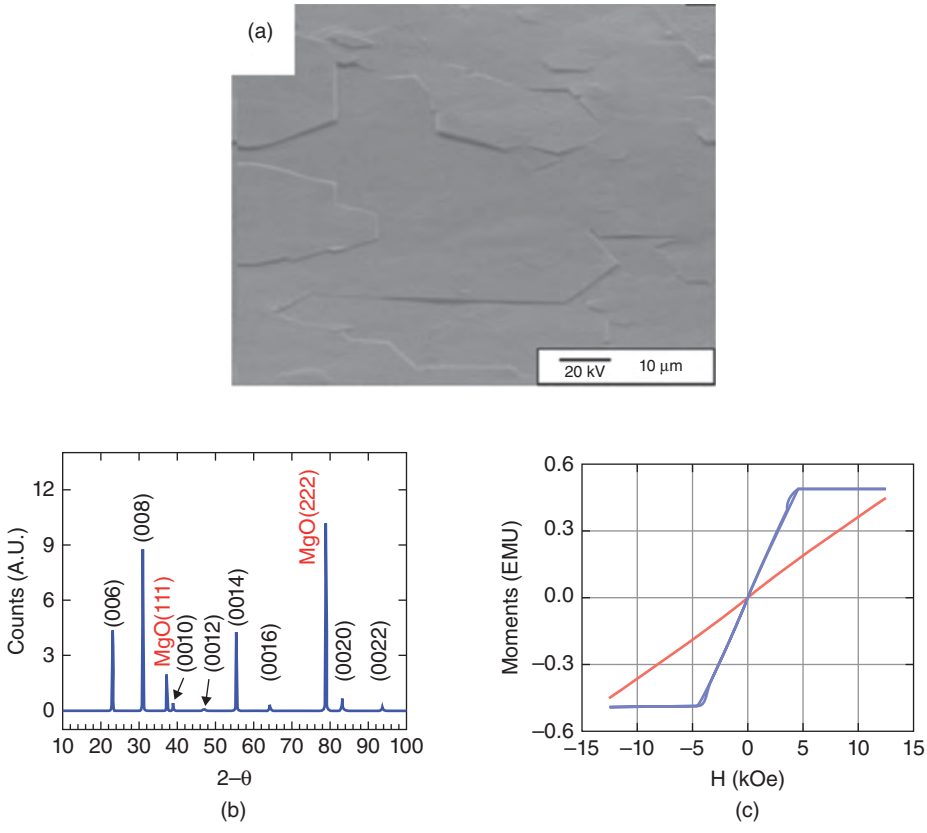

Figure 14.8 *(a) SEM micrograph of a faceted surface of an LPE grown thick film; (b) the X-ray diffraction data, and (c) magnetic hysteresis loops, respectively, of an LPE grown thick film of BaM. XRD clearly supports a very strong crystalline texture, which gives rise to the single-crystal-like magnetic properties in the hysteresis loops. Source: Adapted from Yoon* et al. *2004 [82].*

deposition of garnet, spinel, and hexaferrite ferrites. The deposition of epitaxial yttrium iron garnet (YIG) films by PLD was first attempted by Dorsey *et al.* in 1993 [25, 26]. Films with a thickness of about 1 µm were deposited on (111) gadolinium gallium garnet (GGG) substrates. Narrow FMR linewidths of <1 Oe were observed in films deposited under low oxygen pressure (<250 mTorr) and high substrate temperature (>800 °C). Thin films of $Bi_3Fe_5O_{12}$ (i.e., BIG), $Eu_1Bi_2Fe_5O_{19}$ (i.e., EBIG) as well as YIG/BIG and YIG/EBIG heterostructures, have been investigated by Simion *et al.* [27]. Increased saturation magnetization was observed in the YIG/BIG heterostructures compared to that of single layer films [28]. Thick (~50 µm) epitaxial YIG films with a linewidth of 5.7 Oe were deposited on (111) GGG substrates at a high rate by Buhay *et al.* [29]. In the same paper, the deposition of polycrystalline thick (50–100 µm) films on 3 inch gold-coated (100) Si wafers followed by rapid thermal annealing for monolithic device fabrication was reported. More recently, the magneto-optical properties of Ce [30, 31] and Bi [32, 33] substituted YIG films and YIG/GGG superlattices [34] grown by PLD on (111) GGG substrates have been investigated.

Growth of ferrite films using PLD was first proposed by Vittoria in 1991 [35], inspired by the PLD growth of high-T_c superconducting films. The first BaM hexaferrite films grown by PLD were reported by Dorsey *et al.* in 1992 [36]. In the years following this work many researchers have applied PLD to ferrite film synthesis. Among the highest quality BaM films made are those by Song *et al*. [37], who achieved perpendicular magnetic anisotropy and an FMR linewidth of ~16 Oe at 60.3 GHz.

The above-mentioned studies had strived to align the crystallographic *c*-axis and the magnetic easy axis perpendicular to the film plane. In-plane orientation can be achieved by using suitable substrates that are chosen for their lattice matching (e.g., *a*- or *m*-cut sapphire). Welch *et al.* reported in 1995 that the *c*-axis of BaM films deposited on the in-plane substrate was randomly distributed in the film plane [38]. Yoon *et al.* subsequently reported in 2003 that the *c*-axis of the ScM (scandium-doped BaM) films deposited on *a*-cut sapphire was in the film plane parallel to the *c*-axis of the substrate [39].

A long-sought goal of the ferrite community has been the integration of ferrite-based microwave passive devices with semiconductor electronics. This requires the growth of ferrites on semiconductor substrates. Oriented hexaferrite films deposited on semiconductor substrates are made difficult by the high temperatures required to grow a ferrite having low microwave loss. Further difficulties arise from the formation of native oxides on the substrate surface, leading to a loss of epitaxy when growing the ferrite. Liu *et al.* reported in 2005 the growth of oriented BaM films on silicon substrates with an MgO buffer layer [40]. Z. Chen *et al.* reported in 2006 the growth of oriented BaM thin films on 6H-SiC substrates with and without an MgO buffer layer [41, 42]. The latter studies included the growth of BaM having perpendicular magnetic anisotropy and an FMR linewidth (peak-to-peak in the power derivative) of less than 100 Oe at 53 GHz. A more detailed discussion of ferrite growth on semiconductors appears in Section 14.4 of this chapter.

Besides BaM, many hexaferrite materials have been deposited by PLD. Other M-type hexaferrites, strontium and lead hexaferrites (SrM and PbM), have been studied [43, 44]. Scandium-doped BaM films were deposited to control the magnetic anisotropy [45], whereas cobalt- and titanium-co-doped BaM and aluminum-doped SrM films were deposited for the optimization of the magneto-optical properties [46, 47].

Growth of spinel ferrites using PLD was first realized by Tanaka *et al.* in 1991. In this work, nickel zinc ferrite ($Ni_xZn_{1-x}Fe_2O_4$) polycrystalline films were deposited on glass substrates [48]. Johnson *et al*. reported in 1999 the growth of nickel ferrite ($NiFe_2O_4$) on *c*-cut sapphire substrates using both PLD and ATLAD [49]. Chinnasamy *et al*. reported in 2007 the PLD growth of Ni-ferrite films on MgO (111) substrates. In this study, as in others, post-annealing was found to enhance the magnetic properties of the films, including increasing the magnetization and reducing the FMR linewidth [50].

Balestrino *et al.* reported in 1995 the PLD growth of lithium ferrite ($Li_{0.5}Fe_{2.5}O_4$) and Mn- and Zn-doped lithium ferrite films [51]. Cillessen *et al*. reported in 1996 the epitaxial growth of MnZn–ferrite films on $SrTiO_3$ with and without $BaZrO_3$ buffer layers [52].

Guyot *et al.* reported in 1996 the growth of cobalt ferrite films [53]. In 2004, Terzzoli *et al.* reported the growth of Co–ferrite films on Si (100) substrates with a strong (111) crystal texture in spite of the formation of a native oxide layer at the substrate surface [54]. Yang *et al.* illustrated enhanced magnetization in PLD Cu-ferrite films as a function of working gas pressure-induced cation disorder [54].

A variant to conventional PLD that will be discussed here involves the sequential ablation from multiple targets. This allows one to control cation distribution in the unit cell

leading to the stabilization of ferrites having far from equilibrium structures. This technique has been referred to as alternating target laser ablation deposition, or ATLAD. In recent years, ATLAD has been used by Zuo *et al.* [55] and Yang *et al.* [56] to realize far from equilibrium cation distributions within the spinel lattice for Mn–ferrite and Cu–ferrite film systems, respectively. In the case of Mn–ferrite films, low oxygen pressure processing led to a low cation inversion and large single ion anisotropy, increasing H_A from ~20 to >1000 Oe. In contrast, at high pressures the cation inversion increases, distorting the cubic structure, breaking the crystal symmetry, and stabilizing a perpendicular magnetic anisotropy field of ~1000 Oe. This affords these films unique potential for microwave applications at lower frequencies. In the Cu–ferrite film system, Yang *et al.* were able to redistribute the Cu ions from predominantly octahedral sites (~85%) to predominantly tetrahedral sites (~60%). This created an imbalance of spins between the A- and B-sublattices resulting in a magnetization increase of up to 65%. Such a significant increase was predicted by Zuo *et al.* from first principles band structure calculations [57].

Limitations of PLD and ATLAD (alternating target laser ablation deposition) ferrite film fabrication include film thickness, typically <2 μm, and high-temperature processing, typically >700 °C. At these thicknesses the films are not well suited for device applications, while at these high temperatures the process is not compatible with semiconductor device fabrication. As a result, PLD remains a valuable research tool but does not adequately address the materials needs of the microwave device community. During the last decade, Abe and coworkers have developed a wet chemistry deposition technique: spin spray ferrite plating that allows low-temperature processing of thicker ferrite films. We next discuss the advantages and disadvantages of this technique.

14.3.2.2 Spin Spray Ferrite Plating

In spin spray plating (SSP) the nucleation and growth of a solid phase film is facilitated by hydrolysis without pyrolysis. Abe and coworkers first began developing SSP during the mid-1980s as a means of processing ferrite films at low temperatures [58]. The advantages of SSP include rapid growth rates, thick dense films, low-temperature processing, and a myriad of suitable substrate materials that range from plastics to ceramics. By ferrite plating one can prepare polycrystalline films having the spinel structure ($(M, Fe)_3O_4$, M = Fe, Co, Ni, Zn, Mn, etc.) directly from an aqueous solution. This technique has recently been extended to the deposition of ferrites on to rolls of plastic sheet [59].

Requiring no post-deposition heat treatments, SSP opened the door to depositing ferrite films on such non-heat-resistant materials as semiconductor substrates [60] and polymer sheets [61] for EMI suppression and other purposes.

The Abe research group has developed NiZn–ferrite noise suppressors, which absorb noise currents by magnetic losses before they radiate electromagnetic noise, for applications in the low microwave bands. In one approach, ferrite films are deposited on to polyimide sheets, which are cut and pasted on to noise sources. In a second approach, NiZn–ferrite films are deposited directly on to printed circuit boards, covering potential noise sources such as ICs and conducting wires [62].

SSP NiZn ferrite films, 3 μm thick, have been shown to suppress GHz noise more effectively than commercialized noise suppressors consisting of composite sheets in which fine magnetic metal flakes are embedded in polymer sheets. The sheet-type noise suppressors, made by the roll spray ferrite plating process, have attractive properties, including surface

resistivity higher than 1×10^5 Ω/cm^2, stability to temperatures greater than 260 °C (lead-free soldering temperature), and the ability to withstand the standard bend test (JIS C5016: no peel-off occurred after one million cycles of bending at a 3 mm radius of curvature) [63]. Spin sprayed NiZnCo–ferrite films have been shown to have very high natural resonance frequencies from 3 to 5 GHz and values of μ' from 5 to 8 up to a few GHz. These films are promising as magnetic field shields to improve, for example, the sensitivity of 900 MHz RFID tags for next-generation applications [64].

Even with the thicker films one obtains when using SSP, these samples still fall short of the needs for many microwave device applications. The FMR linewidths of SSP films are higher than those processed by PLD with the losses attributed to contaminants from the chemical processing. Liquid phase epitaxy (LPE) is a technique that has been shown to provide both thick films and high crystal quality. We next examine the LPE growth of ferrites in Section 14.3.3.1.

14.3.2.3 Sputter Deposition

Sputter deposition has often been used to deposit ferrite materials for magnetic storage applications. In more recent years, sputter deposition has been used to deposit microwave-compatible ferrites on silicon, with some success. Recently, hexagonal barium ferrite films were deposited on Si (111) substrates by radio-frequency magnetron sputter deposition for possible microwave frequency applications. These films exhibited strong *c*-axis perpendicular orientation benefiting from a Pt buffer layer revealing ferromagnetic resonance linewidths, ΔH, 400–600 Oe at 40–60 GHz [65]. Although these properties hold promise for microwave applications, this technique tends to produce films of limited thickness, 200–500 nm, which make it ill-suited for many microwave applications.

A discussion of the details of these studies is presented in Section 14.4.2 of this chapter.

14.3.3 Thick-Film Processing of Ferrites

14.3.3.1 Liquid Phase Epitaxial Processing of Ferrites

In liquid phase epitaxy (LPE), oxide compounds such as ferrites are mixed and dissolved in solvents or fluxes (i.e., common fluxes include boron oxide (B_2O_3), barium oxide (BaO) and B_2O_3, lead oxide (PbO), or a mixture of B_2O_3/PbO). In general, the composition of the flux mixtures is chosen so that the melt temperature for most ferrites is about 1000 °C or less. The substrate acts as a seed on to which the ferrite film grows. Appropriate lattice matching is considered to minimize strain-induced crystal defects.

LPE was first employed to produce high-quality yttrium iron garnet (YIG: $Y_3Fe_5O_{12}$) films by Linaries in 1968 [66]. LPE grown garnets continue to receive a great deal of attention for high-frequency applications such as microwave and millimeter-wave devices and optical Faraday isolators [67–68]. Growth rates in LPE can be about 60 μm/h, leading to film thicknesses of 200 μm or more [69]. This is a definite advantage over other deposition techniques including physical vapor deposition or chemical vapor deposition methods. In all film deposition-processing methods that aim to maintain epitaxy a common difficulty is the lattice mismatch between ferrites and crystal substrates. A favored substrate for the deposition of garnets, gadolinium gallium garnet (GGG), has the garnet crystal structure with a close match to the thermal expansion coefficient of YIG, in addition to a lattice mismatch of only 0.06 % [49, 54]. Further, GGG is among the most crystallographically perfect

of commercially available substrates having wafer diameters up to 3 inches. Although the lattice mismatch is exceedingly small compared to the mismatches of many epitaxial semiconductor materials or oxides (i.e., spinels and hexaferrites), these mismatches can have deleterious effects upon film structure and properties. However, the growth of YIG by LPE on double-sided GGG provides a cancellation of in-plane tensile stress that results in film thicknesses in excess of 200 μm. These films have been measured to have FMR linewidths of less than 1 Oe at ~ 9 GHz [69]. The success of LPE in the growth of high-quality YIG films led to similar LPE processing of spinel ferrite films. A number of spinel ferrites have been grown by LPE [70–71], but crystal quality and thickness of the films has yet to reach the level of the garnets. This may be due to crystal defects resulting from mismatches in substrate lattice parameters and/or thermal expansion coefficients. As a result, it has been difficult to consistently deposit high-quality and reasonably thick spinel ferrite films, such as $LiFe_2O_4$, having linewidths consistently below 20 Oe. Notwithstanding these limitations, the smallest recorded FMR linewidth for LPE-grown Li–ferrite is below 10 Oe [71].

Furthermore, the approach taken to thin- and thick-film fabrication and bulk compacts and engineered components take on very different approaches.

The principal motivation for the growth of low-loss ferrites as thin and thick films and compacts is their use in microwave control devices such as phase shifters, filters, circulators/isolators, power limiters, etc. Further motivation stems from a long-time goal of using the strong uniaxial magnetic anisotropy to stabilize high magnetic polarization in the remanent state. Such a material property, known as self-bias, would eliminate the need for bulky and expensive biasing magnets such as those used in circulators and isolators. The most direct way of realizing magnetic anisotropy is through crystallographic texture. For thin-film ferrites the goal is to grow films as either seed crystals or engineered films ready for further processing on lattice-matched substrates. The epitaxial growth of ferrites on such substrates typically leads to low dislocation densities and the minimization of other point and volume defects. As a result, microwave losses (as ΔH) tend to be low – for spinel and garnets in the ones of Oe and for the hexaferrites in the tens of Oe. Most studies of the epitaxial growth of spinels and garnets involve their growth on select microwave oxide substrates including MgO [26], STO [72], sapphire, GGG [73], etc.

LPE-grown hexagonal ferrites, especially barium hexaferrite, have received great attention [74–75]. The smallest linewidths obtained for LPE-grown epitaxial barium hexaferrite on single crystal hexagallates ($SrGa_{12}O_{19}$) substrates were ~45 Oe at 60 GHz [76]. These values should be compared with ΔH <10 Oe for the best barium hexaferrite single crystal sphere [77, 78] and a value of ~10 Oe predicted for Mn-doped hexagonal ferrite [79, 80]. Recently, hexagonal ferrite films having the *c*-axis perpendicular to the substrate plane have been grown by LPE on PLD-grown seed layers on commercially available substrates [81–82] The best ΔH value, 28 Oe, was measured from a 45 μm film grown on double-sided (111) MgO [95]. Alternatively, a 200 μm BaM film with the *c*-axis aligned along the in-plane direction, grown on double-sided *m*-plane Al_2O_3 [39], had a ΔH of 70 Oe at 60 GHz. Figure 14.8a to c presents an SEM image of a faceted surface of an LPE-grown Ba–hexaferrite thick film with panels b and c presenting the X-ray diffraction data and the magnetic hysteresis loops, respectively. XRD clearly supports a very strong crystalline texture that gives rise to the single-crystal-like magnetic properties in the hysteresis loops.

The LPE technique has clear advantages over other physical and chemical deposition techniques, producing very thick films (>200 μm) having high crystal quality that in some

cases approach that of single crystals. These films are very well suited for microwave and millimeter-wave devices that require low losses. However, they continue to require a biasing magnet to saturate the film, thus adding size, weight, and assembly cost to devices. We next examine a second technique that provided film thicknesses in the 100s of micrometers but has traditionally offered poor crystalline quality and high microwave losses.

14.3.3.2 Screen Printing Processing of Ferrites

$BaFe_{12}O_{19}$–hexaferrite thick film samples, processed through the use of the screen printing technique have high hysteresis loop squareness (M_r/M_s ~97%, Figure 14.9c) and low

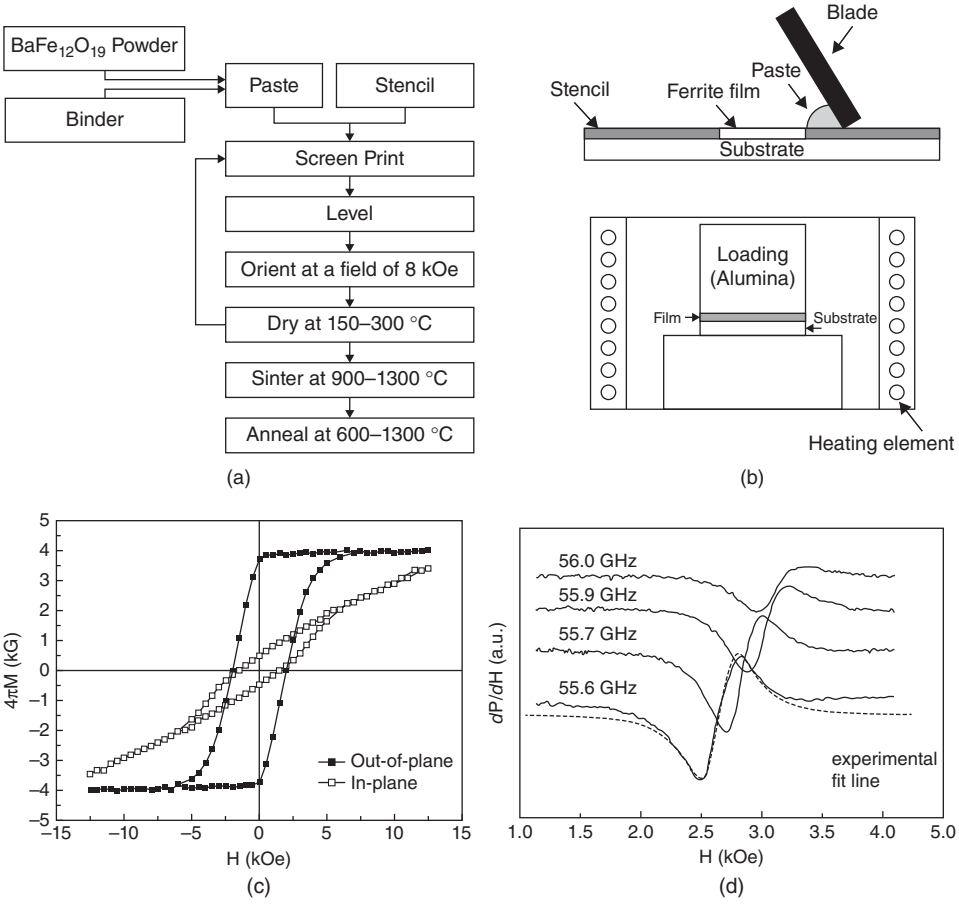

Figure 14.9 *(a) Flowchart detailing the process steps of the screen printing of hexaferrites, (b) schematic illustrating screen printing of the paste through a stencil and its subsequent sintering, (c) magnetic hysteresis loops collected with the applied magnetic field aligned parallel (hollow symbols) and perpendicular (solid symbols) to the plane of the film, indicating both a perpendicular magnetic anisotropy and self-bias properties, (d) FMR spectra for samples at different frequencies and SEM micrographs of (e) the thick film surface and (f) the cross-section. Source: Adapted from Y. Chen* et al. *[15].*

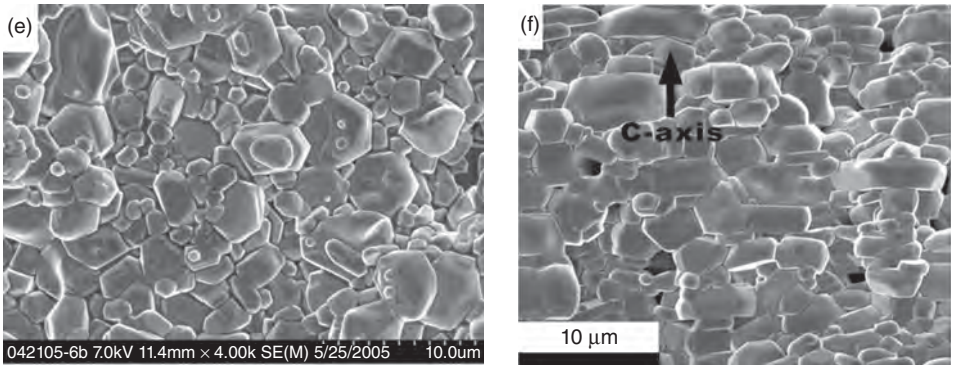

Figure 14.9 *(Continued).*

ferromagnetic resonance (FMR) linewidths of about 210 Oe (Figure 14.9d). Scanning electron microscopy (SEM, Figure 14.9e and f) and X-ray diffraction (XRD) measurements (not shown here) exhibit strong crystallographic *c*-axis alignment of crystals perpendicular to the film plane. Theoretical estimates suggest that such narrow linewidths can be attributed to the reduction in porosity and the improvement in *c*-axis orientation of crystallites in polycrystalline barium–ferrite films. As such, hexaferrite materials prepared using this technique offer new opportunities in the development of the next generation of self-biased planar microwave devices.

14.4 Semiconductor Integration of Ferrite Thin and Thick Films for MIC Development

During the past half century, the rapid development of solid-state devices has dramatically shaped large-scale electronic systems. Similar to the evolution of silicon technology for consumer electronics, one such example in microwave applications is the advancement of active electronically scanned array (AESA) radars based on GaAs microwave monolithic integrated circuits (MMICs) (c. 1980s) [83]. These advances were enabled by the unabated development of smaller and faster electronic components and systems largely through the means of devices miniaturization and integration. However, in contrast to solid-state devices based on Si and GaAs, ferrite-based microwave and millimter-wave devices, such as isolators, circulators, phase shifters, filters, etc., have remained largely unchanged.

A review by Z. Chen and Harris in 2012 [84] examined the historical development of ferrite thin-film growth on semiconductors and other functional substrates. In that review, the work of Z. Chen *et al.* was reviewed in which hexagonal ferrites were epitaxially grown on SiC [85] and GaN [86]. In an impressive demonstration, Z. Chen *et al.* showed via pole figure analysis a confirmation of the epitaxial growth of barium hexaferrite on GaN. Cross-section transmission electron microscopy imaging of the hexaferrite/MgO/GaN/sapphire structure revealed limited interdiffusion and defects.

The growth of high-quality hexagonal ferrite films on GaN substrates was further affirmed by the FMR peak-to-peak linewidth values of less than 90 Oe at the U-band. A

linewidth of <100 Oe is consistent with microwave insertion losses well below 1 dB in such devices as circulators and isolators. This development provides a pathway to realizing integration of active and passive devices on a single wafer – a long-sought goal of rf system engineers. Remaining challenges to realizing wide-scale integration is the development of large-diameter GaN substrate materials (i.e., $\geq$ 4 inch diameter) together with the transition from a research-scale pulsed laser deposition to industrial acceptable deposition growth technologies.

14.4.1 Selection of Semiconductor Substrate Materials

Let us next consider the other side of the ferrite integration problem, namely, the appropriate selection of semiconductor material substrates.

In the early 1940s, the demand for sensitive crystal detectors for radar applications motivated intensive research effort in the preparation of elemental semiconductor materials like Si [87] and Ge [88, 89]. This research eventually led to the invention of the junction transistor by Shockley, Bardeen, and Brattain in 1947 [90] and set the stage for the semiconductor electronics era. Today, semiconductors are arguably the most widely used materials in consumer, industrial, and military electronics.

Semiconductor materials can be classified into two groups: (1) single element semiconductors such as Si and Ge from Group IV of the periodic table and (2) compound semiconductors like SiC (Group IV), GaAs, GaN, InP from Groups III to V, and CdTe and ZnSe from Groups II and VI. Among these, Si has by far been the single most dominant material since the inception of semiconductor technology. Driven by the massive consumer electronics and personal computer markets, Si-based integrated circuit technology has made tremendous progress, resulting in the development of smaller, cheaper, and faster electronics. This progress has been accurately captured by Moore's law [91, 92], which states that the number of transistors that can be placed on an integrated circuit has doubled approximately every two years, a trend that has been shown to continue for decades and is not expected to stop until 2018 or later. However, as Si technology is being pushed to its processing limits, that is, ~22 nm node [93], alternative ways other than size reduction is needed to sustain technical advances. One such approach is the use of novel semiconductor materials. In fact, from the beginning of the semiconductor era, scientists have been in search of materials that offer complimentary or superior properties to Si [94]. For instance, Goups III to V compounds such as GaAs exhibit superior electrical properties and special optical properties that have been utilized in high-frequency MMIC and other applications [95]. The use of SiGe as a replacement for classic silicon bipolar devices has also attracted attention [96]. Regardless of their successful development as materials for high-frequency applications, both GaAs and SiGe suffer from limited power handling capabilities. The ultimate material has to meet challenges of both high speed and high power handling. Johnson has argued that the basic limitation on various transistor characteristics is set by the product of the breakdown electric field and the saturated electron drift velocity. The combination of these variables, captured in Johnson's figure of merit (JFOM) [97] will determine cutoff frequency and maximum power handling ability. Keys [98] later introduced another important parameter, that is, thermal conductivity, into his figure of merit (KFOM). The properties of several semiconductor materials, along with their respective figures of merit, are listed in Table 14.1.

Table 14.1 *The properties of the most common semiconductor materials (Note: H in 6H-SiC denotes hexagonal, C in 3C denotes cubic.)*

	EB (V/cm) $\times 10^5$	V_{sat} (cm/s) $\times 10^7$	σT 300K (W/s)	K	Eg (eV)	JFOM (WΩ/s^2) $\times 10^{23}$	KFOM (Ws$^{1/2}$/cm$^{1/2}$) $\times 10^2$
Si	3	1	1.5	11.8	1.1	0.9	1.381
GaAs	4	2	0.5	12.8	1.43	6.5	0.625
GaN	20	2.5	1.5	9.5	3.45	253.3	2.433
6H-SiC	40	2	5	10	3.1	648.5	7.071
3C-SiC	40	2.5	5	9.7	2.4	1013.2	8.027
C	100	2.7	20	5.5	5.45	7386.3	44.313

In Table 14.1, SiC and GaN, also classified as wide-bandgap semiconductors due to their large gap energy (i.e., >1.7 eV), have significant advantages over other semiconductor materials including Si and GaAs in terms of high-temperature, high-frequency, and high-power applications [99–100]. The GaN/SiC and SiC have also been shown to possess superior thermal conductivity to that of copper, which could enhance the power handling capability at the system level. The only materials with superior properties to SiC and GaN are diamond or graphene, which are currently not yet mature enough to be considered for practical device development.

The successful epitaxial growth of wide-bandgap semiconductor films (e.g., GaN, SiC) on SiC and GaN single crystal substrates [101, 102] make them among the most competitive materials for next-generation high-frequency, high-power circuits. The idea of depositing ferrites on such agile and versatile substrates arose within the microwave engineering community with the goal of incorporating ferrite devices with active semiconductor devices into monolithic structures. Not only do SiC and GaN, with wide- bandgap structures, cause less conduction loss than Si and GaAs at high frequencies, but also they bring more thermal stability to high-temperature processing, which is comparable with ferrite device fabrication protocols. What makes these two materials even more attractive is the fact that both SiC and GaN adopt the hexagonal structure, similar to BaM–hexaferrite, with corresponding lattice mismatches of 4.38% and 7.00%, respectively. Such properties are required to realize the epitaxial growth of hexaferrite films.

14.4.2 Ferrite Film Growth on Semiconductor Substrates

Ever since the first systematic studies by Snoek and others in circa 1940 [103], ferrites have been successfully used as bulk materials in discrete elements for applications at microwave and millimeter-wave frequencies. However, there has been a growing interest in using ferrites as films rather than in bulk form for several reasons. First, films provide superior surface uniformity and roughness to bulk compacts. Second, films provide lower process cost, smaller size, and enhanced compatibility with planar circuit designs compared with three-dimensional constructs. The research on high-quality ferrite films for microwave and millimeter-wave applications has lagged far behind semiconductor film development. Until the 1970s [104], driven by the rapid development of various forms of magnetic recording

and bubble memory technologies, extensive work on preparing yttrium iron garnet (YIG) films was begun and was later extended to other ferrite film systems. As a consequence, YIG became the first group of ferrite materials that could be prepared as films to near-perfect crystalline quality and applied in tunable microwave filters and magnetostatic wave devices [105].

In the following sections, past studies of ferrite film growth on different semiconductor substrates will be reviewed. Potential approaches to MIC fabrication, such as recent studies on hexaferrite film processing on GaN and SiC, including ferrite film growth and patterning, will be discussed.

14.4.2.1 Preparation of Ferrite Films on Si Substrates

The growth of ferrite materials on semiconductor substrates was first motivated by memory and recording media applications. BaM–hexaferrite was for decades considered among the top candidates for magnetic recording media because of its high anisotropy field, high coercivity, mechanical hardness, and chemical stability. For conventional longitudinal recording, high coercivity and small grain size are highly desirable. In 1993, Sui *et al.* reported coercivity values as high as 4100 Oe achieved in BaM films grown on silicon by the RF sputtering technique [106]. In 1994, Hylton *et al.* found that doping Cr_2O_3 reduced the grain size to ~20 nm while concomitantly maintaining coercivity in excess of 4000 Oe [107]. In 2002, Morisako *et al.* reported that the grain size of BaM films deposited on an AlN underlayer was reduced to ~50 nm [108]. Later in 2004, He *et al.* reported that using Al_2O_3 as the buffer layer instead of AlN resulted in a further reduction of grain size [109]. As the grain size reduces to the onset of superparamagntism the written bits are no longer stable. At this point, perpendicular magnetic recording, which requires BaM films prepared with *c*-axis orientation normal to the film plane, become more attractive in further improving storage density. In 1985, Matsuoka *et al.* reported the growth of BaM/ZnO/SiO_2/Si structures for perpendicular recording application [110]. In 1997, Morisako *et al.* reported the improvement of the *c*-axis orientation and the alleviation of Ba and Fe diffusion by the use of amorphous Ba–Fe–O buffer layers [111]. In 2001, Lisfi and Lodder showed that BaM films grown directly on SiO_2/Si exhibit a granular structure with two easy axes (in-plane and perpendicular) and strong magnetic coupling [112]. A ZnO underlayer promoted orientation of the *c*-axis perpendicular to the film plane with a low exchange coupling achieved by separating grains.

The deposition of ferrite films on Si for microwave applications are more challenging than those for the recording industry in terms of the requirement of high crystal quality, preferred orientation and greater film thicknesses. In 1991, Lacroix *et al.* [113] proposed using SiO_2, ZnO, GGG, and $A1_2O_3$ as buffer layers for growth on Si. Among these, ZnO gave rise to the best BaM film orientation for in situ crystallized films grown on Si by PLD. However, the best BaM films were still unsuitable for either device applications or as seed layers for liquid phase epitaxy (LPE); the later will be addressed shortly. In 2000, Wane *et al.* [114] reported the growth of BaM films by e-beam evaporation used for integrated permanent magnets in MMIC circulators. It was also reported that a layer of Au or Cu was needed to improve the adhesion of the film on Si. In 2004, Le Berre *et al.* [115] reported the growth of 10 μm thick BaM for use in a passive isolator with 3.3 dB/cm of loss at 50 GHz. In 2005, Liu *et al.* reported [116] the growth of barium ferrite films by PLD on MgO buffered

Si substrates for microwave applications. Besides BaM ferrite, spinel and garnet ferrites have also been explored for integration on silicon. In 1995, Adam *et al.* [117] first reported the growth of 100 mm thick YIG film on Si for the monolithic integration of an X-band circulator. The film was grown at 500 °C, followed by rapid thermal annealing at 850 °C for 20 seconds. In 2004, Xi *et al.* [118] reported polycrystalline NiZn–ferrite films fabricated on Si (111) substrates by PLD and observed a preferential (400) orientation of the films. In 2005, Sorescu *et al.* [119] investigated NiZn– and Zn–ferrite films deposited on Si (100) substrates. In 2006, Calle *et al.* [120] studied NiZn–ferrite films deposited on (100) Si substrates using the magneto-optical Kerr effect. In 2008, Y. Chen *et al.* [121] investigated polycrystalline BaM films having thicknesses of 100–150 μm deposited on Al_2O_3/Si or SiO_2/Si substrates by the screen printing technique. Due to a relatively low density, that is, ~87% of theoretical, and the misalignment of grains, the BaM films exhibited a microwave linewidth of ~300 Oe. Although this value is far below those ever attained by polycrystalline coatings and compacts, they remain comparatively high to those films produced by PLD and LPE on microwave substrates. In 2010, Zhang *et al.* employed radio-frequency magnetron sputter-deposition of barium hexaferrite films on Pt-coated Si substrates that had FMR linewidths suitable for microwave device applications [122].

14.4.2.2 Preparation of Ferrite Films on GaAs Substrates

As a microwave substrate, GaAs is more attractive than Si, due to its relatively lower conductivity and its successful processing in MMICs. In 1987, Abe *et al.* [123] fabricated a microstrip junction circulator using NiZn–ferrite films deposited by spin -spray plating on to GaAs. In 1990, Yoo and Talisa [124] demonstrated the spin-spray deposition and patterning of NiZn–ferrite films on a portion of a GaAs wafer containing several MMIC circuits. Because thick films with low losses are in high demand for practical device applications, a 25 μm thick NiZn–ferrite film was deposited by employing multiple spin-spray deposition cycles with intermediate drying steps. Unfortunately, low resistivity and high dielectric loss at microwave frequencies was measured and attributed to poor crystal quality. In 1995, Buhay *et al.* [125] reported the deposition of YIG films using high-rate PLD on GaAs. The poor microwave performance (i.e., high attenuation) was attributed to poor surface morphology and excessive cracking of thick YIG films. In 1996, Adam *et al.* [126] reported the development of K-band circulators operating at 20 and 35 GHz that were monolithically integrated with both GaAs and epitaxial GaAs-on-Si wafers.

Despite these efforts, no device has been achieved to be adequate for practical use. As discussed earlier, poor crystal quality has a detrimental effect on device performance. In polycrystalline ferrites, impurity defects, random local anisotropy fields, and residual porosity act to broaden the FMR linewidth and increase microwave loss. To ensure better microwave performance, near single crystal quality films are needed. The produced films mentioned above are mostly polycrystalline in nature, in some cases amorphous, resulting in poor device performance compared with other competing technologies. The successful single crystal ferrite film growth requires high-temperature processing, which is beyond the tolerance of Si and GaAs substrates. It is well known that GaAs dissociates at ~450 °C and Si easily alloys under heat treatments at high temperatures for long durations. Even by introducing SiO_2 and Si_3N_4 as protective layers [63], GaAs still cannot be exposed to temperatures approaching 900 °C without degradation. Such temperatures, for example, are necessary for the growth of high-quality ferrite films. Attempts to mitigate these problems

by employing a two-step deposition of BaM at a temperature under 500 °C, followed by annealing, was unsuccessful. Similarly, rapid thermal annealing for several seconds at elevated temperatures was also shown to be ineffective. It remains now as an ongoing challenge to identify optimal film growth techniques that ensure high crystal quality ferrites on GaAs and Si.

14.4.2.3 Preparation of Ferrite Films on SiC and GaN Substrates

As was discussed previously, GaN and SiC accommodate higher power levels than other competitors, which could eliminate the need, for example, of separate power amplifiers that are necessary for Groups III to V compounds such as GaAs and Group IV compounds such as SiGe [127] in circuits design. The well-established SiC and GaN [128–129] processing treatments follow those of most conventional semiconductor protocols. The demonstration of passive ferrite devices fabricated on GaN and SiC substrates would enable the integration of complete circuit assemblies on a single semiconductor substrate without sacrifice to performance, in other words, a true MIC. As a result, the development of ferrite epitaxial film growth on WBG semiconductor substrates would represent an important technological advance.

Notwithstanding their superior properties, as reported by Madar [130], difficulties in material preparation, crystal quality, and cost have prevented SiC and GaN from being until recently commercially exploited. Z. Chen *et al.* reported the growth of oriented BaM thin films on 6H-SiC [22, 131] and Ohodnicki *et al.* on GaN [132]. The hexagonal structure of SiC and GaN provides a matched template to assist oriented single crystal film deposition of hexaferrite phases. However, the lattice mismatch that ranges from 4.38% (SiC) to 7.00% (GaN) remains a serious problem to the growth of low-loss ferrites on WBG substrates. Additionally, the formation of native oxides on the SiC substrate surface was shown to lead to a loss of epitaxy during the early stages of PLD film growth. In the case of GaN, adhesion of the film to the substrate becomes problematic for deposition temperatures above 900 °C, which is a typical growth temperature for BaM [132, 133]. Z. Chen *et al.* applied an interwoven MgO/BaM buffer heterostructure on SiC to successfully relieve the strain induced by lattice mismatch and reduce interdiffusion between the film and substrate [147]. Further studies of these samples were reported by Cai *et al.* [134]. The long-term stability of the buffer heterostructure was demonstrated in which films deposited on SiC without such a buffer experienced a dramatic deterioration of soft magnetic properties upon prolonged room temperature aging [135]. It was not until Z. Chen *et al.* introduced a low temperature MBE grown MgO buffer layer between the ferrite film and SiC substrate that a high quality BaM film having an FMR linewidth consistently less than 100 Oe (i.e., $f = 53$ GHz) resulted [136]. In the case of GaN, Z. Chen and Harrissuccessfully addressed the film adhesion problem by applying an MgO buffer layer deposited by PLD using N_2O [137]. The resulting films are among the highest quality reported BaM grown on semiconductor substrates and have FMR linewidths consistently less than 90 Oe at 53 GHz [138]. This high crystal quality and epitaxy were demonstrated in the XRD pole figure measurements of Figure 14.10a to d. Quantitative analysis of the (006) pole figure by peak angular integration suggests that more than 95% of the BaM grains have *c*-axes aligned within 5° degrees of the film normal.

The key to these films on SiC and GaN is in controlling the chemical sharpness and strain of the interfacial region between the film and substrate. For the case of BaM films grown on

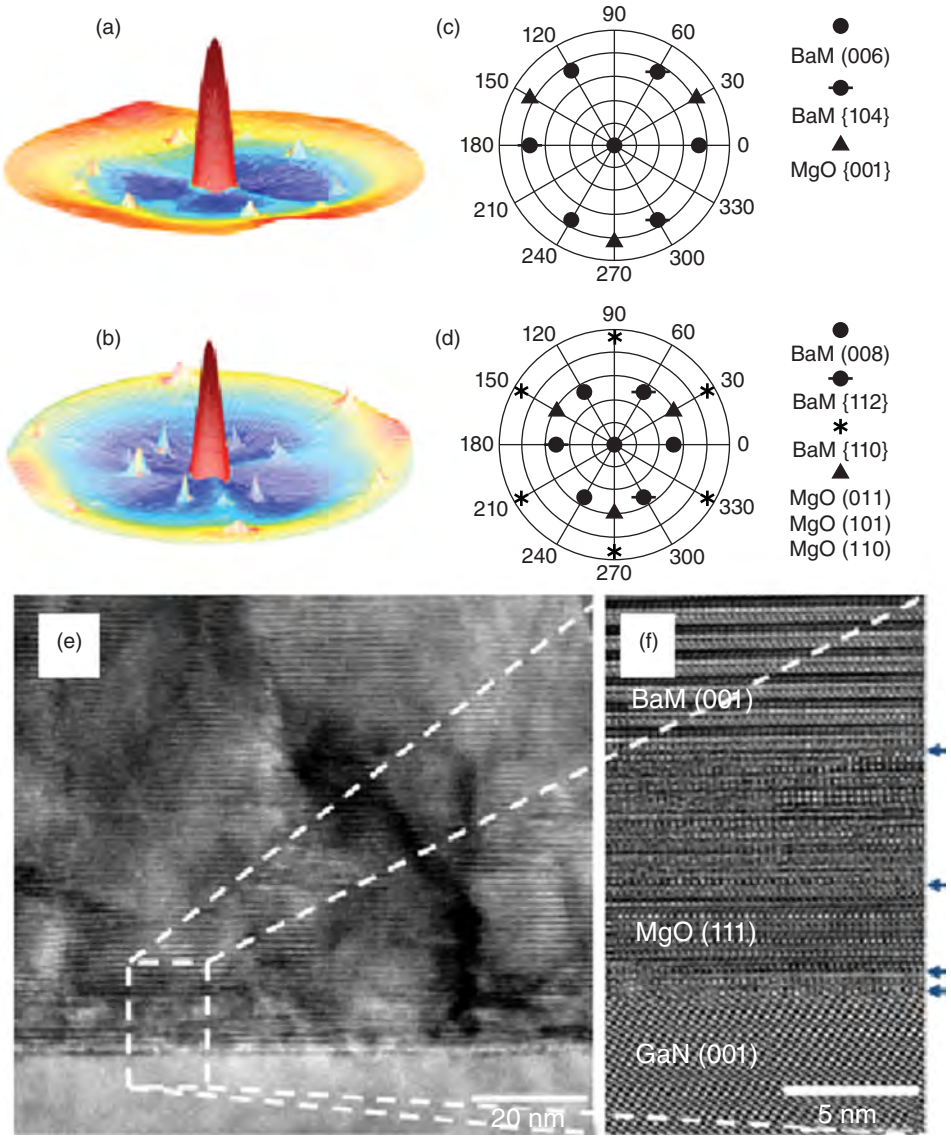

Figure 14.10 *Pole figures obtained for (a) the (006) and (b) the (008) reflections, and the corresponding 2D projections (c) and (d), with 2θ values fixed at 23.00° and 30.30°, respectively. The single dominant peak in (a) corresponds to $\phi = \xi = 0°$ for the BaM (006) reflection. The weaker peaks in (a) and (c) exhibiting six-fold symmetry correspond to closely spaced BaM (104) reflections. The minor peaks exhibiting threefold symmetry in (a) and (c) derive from closely spaced MgO (100) reflections illustrating the epitaxial nature of the BaM films grown on MgO/GaN/Al_2O_3. Similarly, (b) and (d) show similar data for the (008) reflection, further supporting the epitaxial growth of films. (e) Transmission electron microscopy images of the BaM film grown on MgO/GaN/Al_2O_3 in cross-section. The image (f) is an expanded view of the section denoted in (e). The regions denoted by arrows signify intermixing. Source: Adapted from Z. Chen* et al. *[86].*

GaN, the crystal BaM can be clearly observed in the high-resolution transmission electron microscopy cross-sectional image of Figure 14.10e and f. Importantly, the images reveal regions of GaN, MgO, and hexaferrite phases having sharp interfaces. It is noteworthy that a spinel phase appears to have stabilized between the MgO and BaM film. This has proven not to be detrimental to the performance of these materials for microwave and millimeter-wave applications.

The same results were revealed in the BaM film deposited on SiC by MBE techniques [139, 140]. Unlike semiconductor devices, microwave ferrite devices commonly require films to have thicknesses greater than 10 μm depending on the specific operational frequency. It is not uncommon for the ferrite layers to be >50 μm. To meet this requirement, Z. Chen and coworkers have recently grown an 8 μm thick film by PLD that had an FMR linewidth of <150 Oe after a post-deposition heat treatment. An attempt to extend film thicknesses to > 15 μm was found to result in wide-scale cracking. This trend was also found to be the case when thick BaM films were grown by PLD on other substrates [141]. Cracking is attributed to the brittle nature of BaM. At a critical thickness it becomes energetically favorable for accumulated strain to be released through fracture during the cooling period of growth. The cracking tends to be diminished by a perfect match of thermal expansion constant between the films and selected substrates or by innovative interface treatments. To further investigate the growth of high-quality BaM thick films on GaN and SiC, Z. Chen used the LPE technique following the PLD deposition of seed layer films. Unfortunately, like Si, SiC substrates proved unstable in the BaM flux melts used in LPE processing. This was attributed in large part to the chemical affinity of Si and Fe, as evidenced by the eutectic transition observed in the Fe–Si phase diagram at temperatures near 875 °C. In contrast, GaN is more compatible with the LPE technique and its associated flux compositions.

As mentioned, many ferrite devices require external magnetic fields to saturate spins and eliminate lossy magnetic domain walls. The needed bias magnets add considerable size, weight to device fabrication, and related assemblies cost as well as limiting attempts to realize integration of non-reciprocal passive and active devices. The external magnets can only be removed from designs when ferrites possess a sufficiently large internal remnant magnetization that provides magnetic polarization in the absence of an external magnetic field. Such materials and devices that employ them are typically referred to as being self-biased. Self-biased circulators, based on textured polycrystalline barium and strontium hexaferrites, have been demonstrated [142 143]. The difficulty in obtaining self-bias properties in ferrite films originates from the demagnetizing energy inherent in film geometries that acts to hold the magnetization in the film plane. In 2006, Y. Chen *et al.* [144] demonstrated a large remnant magnetization in BaM thick films produced by screenprinting followed by magnetic field annealing and sintering processes. Although this technology represents a promising path forward, surface roughness and cracking pose challenges to device fabrication and system integration. To date, much attention has been paid to maximizing magnetocrystalline anisotropy to offset the demagnetizing energy by processing enhanced crystal texture. It has been shown by Z. Chen *et al.* [145] that increased remnant fields are possible by utilizing shape anisotropy from artificial structures. Using gas mixtures of CHF_3 and SF_6, Z. Chen was first to demonstrate reactive ion etching (RIE) of BaM ferrite (see Figure 14.11a to e). Damages resulting from the RIE process lead to an increased coercive field and FMR linewidth. This trend was reversed by a post-process heat treatment that ultimately led to properties superior to the as-processed PLD films.

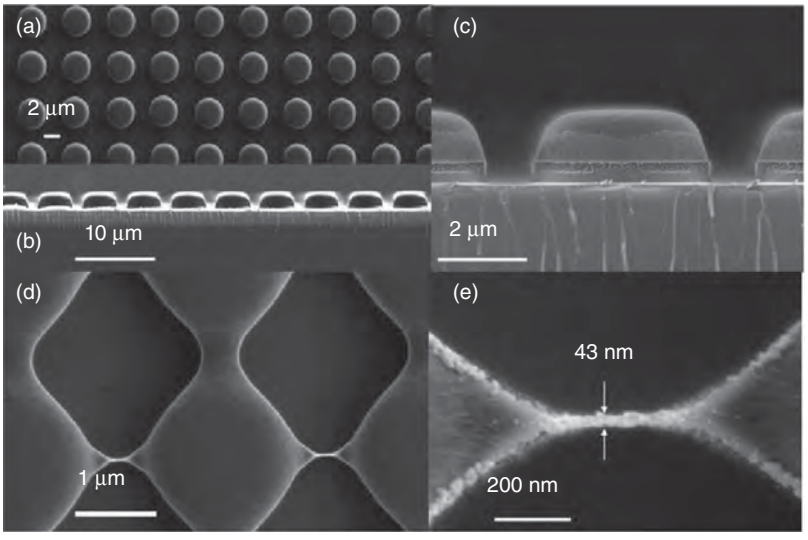

Figure 14.11 *(a) Top-view SEM image of the patterned BaM film array consisting of of ~3 μm diameter pillars at a ~4 μm center-to-center spacing. (b) Side view SEM image of the same sample. (c) An expanded view of one pillar consisting of a BaM cylinder with the height-to-diameter aspect ratio of 0.2 having a photoresist cap on the surface. The "frost" on the element is a thin PtPd coating used to reduce fluorescence during SEM imaging. (d) Top view SEM image of a test pattern designed to evaluate minimum lateral features. (e) An expanded view of the minimal lateral feature of ~43 nm (at the necked region). Source: Adapted from Z. Chen* et al. *[145].*

Ferrite film deposition on GaN and SiC has so far been limited to BaM–hexaferrite. However, the BaM ferrite film could be used for variant-doped BaM–hexaferrite LPE growth as well as for other types (Y, Z, W, U, etc.) because it shares the same crystal structure with other members of the hexaferrite family. As is well known, the substitution of Fe by other cations in the Ba hexaferrite unit cell provides remarkable flexibility in tailoring the magnitude of the anisotropy field and thus tuning operating frequency. For example (see Figure 14.6), the substitution of Sc or In for Fe reduces the anisotropy field allowing for applications from C-, X-, Ku-, K-, to K_a-bands. [146] On the other hand, substitutions of Al or Ga increase the value of H_a and allow for device applications up to U-, E-, W-bands and beyond [147]. In recent years, alternating target laser ablation deposition (ATLAD) has been practiced by Zuo *et al.* [148], Yang *et al.* [149], and Geiler *et al.* [150] to grow various types of ferrite materials including spinel ferrites and M-type ferrites. In these studies cation distribution was successfully manipulated by layer-by-layer growth under controlled growth conditions. This technique has been shown to provide an opportunity to tune H_a by controlling the type and distribution of cations.

14.5 Ferrite–Based Microwave Device Development

As already alluded to, it is because ferrite materials possess moderate to high magnetization, high permeability, moderate to high permittivity, and high electrical resistivity, that they are

uniquely suited for high-frequency applications over many decades of frequency. At lower frequencies, for example, DC $< f <$ 10 MHz, spinel ferrites commonly function as inductor cores in power generation, conditioning, and conversion, while at higher frequencies, for example, 1 GHz $< f <$ 100 GHz, they function as passive and active devices that send, receive, and manipulate electromagnetic signals. Other applications not falling into these categories include EMI shielding and absorbers, among others.

Ferrites find a wide variety of uses in military and commercial radar and communication electronics as integral materials in traveling wave tubes, switch mode power supplies, transformers, power converters, inductor cores, filters, etc., as well as passive electronics used in transmit and receive modules in isolators, circulators, phase shifters, filters, directional couplers, power limiters, etc.

Radar applications have obvious military applications but may also be used in commercial systems for applications in commercial aviation, severe weather warning radar, oceanographic satellite radar, and automobile anticollision radar. Other applications include satellite communication uplinks and downlinks over a broad range of frequencies (see Figure 14.3).

In the quest to take advantage of ferrite dielectric properties, as early as the mid-1950s a wide variety of microwave ferrite devices, including circulators, isolators, phase shifters, directional couplers, power limiters, etc., based on polycrystalline spinel ferrites, were reported [151]. Early on it was understood that the FMR linewidth played a large role in determining magnetic loss and performance of rf and microwave devices [152]. The introduction of a new family of rare earth ferrites of the garnet structure possessing very low FMR linewidths was very significant [153]. Ferrites of hexagonal crystal structure were identified as candidates for application at higher frequencies due to the high magnetic anisotropy fields that serve to bias these materials in the microwave and millimeter-wave bands [154].

Figure 14.3 presents a frequency scale from ∼0.5 to ∼110 GHz in which different applications are presented (circa 2010). The applications include a broadband assortment of military and commercial systems and technologies including military radar, commercial radar, military and commercial communication, and automotive anticollision radar, to name a few. This figure naturally omits the many classified military applications that span these frequency bands.

We next examine the material needs of microwave devices. We limit ourselves here to those devices that are based on magnetic materials to provide necessary permeability, nonreciprocal behavior and self-bias, among other properties.

14.5.1 Monolithic Integrated Circuits (MICs)

Monolithic integrated circuits have both passive and active components and their interconnections fabricated on a common substrate, preferably, a semiconductor. Let us consider transmit and receive modules used in radar system front ends. T/R modules include: passive devices such as circulators, isolators, phase shifters, and delay lines, and MMICs such as low-noise amplifiers (LNA), high-power amplifiers (HPA), and CMOS devices and heat sinks for HPAs.

These passive devices are usually fabricated on insulating oxides substrates, while MMICs use GaAs substrates and CMOS employ Si substrates. For heat sinks, copper or

other metals are usually employed. Each phased array has potentially thousands of T/R modules. A goal of the microwave community is to make the module smaller in size, less costly to fabricate and assemble, with enhanced performance. In order to meet these needs, a monolithic construct is desired.

In fact, the idea of passive–active integration on a common substrate emerged soon after the demonstration of the first GaAs metal epitaxial semiconductor field effect transistor (MESFET) [155]. In 1994, a YIG/Si circulator was fabricated by bonding a 130 μm thick single crystal YIG film to a metalized Si wafer followed by the removal of the underlying GGG substrate [156]. Later in 2001, a planar microstrip Y-junction circulator was fabricated from a metalized 130 μm thick self-biased polycrystalline strontium hexaferrite ceramic that was then bonded to a silicon substrate to yield an integrated circulator [157].

These demonstrations were either hybrid structures or conventional MMICs with the ferrite and semiconductor components processed separately and assembled afterwards by attaching or bonding, etc. A high-level integration, exercising complete integration on one substrate, would provide enhanced circuit reliability, higher power efficiency, greater design flexibility, improved impedance matching, and the realization of two-dimensional processing. Logically, there are three approaches to realizing these goals:

(a) The deposition of high-quality ferrite films and semiconductor films on a common microwave substrate.
(b) The deposition of high-quality semiconductor films on ferrite substrates.
(c) The deposition of high-quality ferrite films on semiconductor substrates.

For the first approach, ferrite film deposition on oxides such as MgO, Al_2O_3, and GGG has been extensively studied and routinely demonstrated. Similarly, epitaxial films of Si [158], GaAs [159], and InP [160] grown on the GGG substrate have been reported. For the second approach effort, it was reported from 1999 to 2004 by Ito, Ohta, and coworkers that GaAs [161], GaN [162], AlN [163], InAs [164], and InSb [165] epitaxial films were successfully grown on MnZn–ferrite substrates using MnAs buffer layers. Despite these demonstrations, integrated devices of this architecture have not yet obtained major success nor widescale acceptance. The third approach, namely, the growth of ferrites on semiconductor substrates, has garnered much attention and is the focus of the remainder of this chapter.

14.5.2 Microwave Materials Property Needs

The specific needs of ferrite materials for microwave devices naturally vary depending upon the intended use of the materials. One challenge to scientists and engineers is the chasm that exists between the vernacular employed by engineer and physicist (or chemist, materials scientist, etc.). Often the functional needs of the microwave engineer are not easily communicated to the solid-state physicist who designs ferrite materials, and vice versa. For example, the microwave engineer may require an insertion loss of less than 1 dB for a Y-junction circulator. To the physicist/materials scientist this constraint is difficult to translate to properties that they have control over in the design and processing of ferrite materials such as anisotropy fields, coercivity, magnetization, etc. However, we have shown by iterative finite element method (FEM) designs, in which the FMR loss of the material (as FMR linewidth) is adjusted, that a 1 dB insertion loss roughly correlates to an FMR linewidth

of nearly 500 Oe (at X-band). This rather crude demonstration depends upon other critical factors such as the operational frequency band relative to FMR, impedance matching, and conductive losses (among others) that may not be included in the linewidth calculation. The FMR linewidth in turn depends upon the intrinsic magnetic anisotropy and extrinsic parameters such as crystal quality, grain orientation, porosity, etc. [166]. The later properties are often reflected in the coercivity of the ferrite that in turn has been shown to determine in part the remanent magnetization leading to self-biased properties. The operating frequency is often determined by the FMR frequency, which is dependent upon the magnetization, anisotropy field, and applied magnetic fields. Both magnetization and anisotropy field are determined in part from atomic level parameters and interactions. For example, fundamental sources of anisotropy include: magnetocrystalline, dipolar, spin–orbit coupling, single ion, pair order, etc. These in turn are affected by the proportion, type and valence of cations, as well as the bond angle and distance between cations and anions. Point, line, and volume defects also contribute to changes in exchange, which in turn affect magnetic anisotropy, magnetization, thermomagnetic behavior, and FMR linewidth. In this way, one can appreciate the care in preparation that must be afforded magnetic materials for use at ultrahigh frequencies.

This correlation between engineering, or functional performance, and underlying physical properties is essential to the development of advanced materials that will address next-generation microwave engineering needs.

Prior to the 1980s, ferrite materials were prepared predominantly in bulk form and often as powders, and were used principally as compacts and cores. During the late 1980s to early 1990s, ferrite materials were developed for the first time as thin films using such techniques as magnetron sputtering, pulsed laser deposition, and liquid phase epitaxy.

Sputtered ferrites, having polycrystalline microstructures, found utility in early generations of magnetic recording media [167]. Typically, films deposited by this technique possess copious grain boundaries (valued for recording media) leading to excessive DC and rf losses and little application value at microwave frequencies.

Pulsed laser deposition, a technique that was developed and applied largely to oxide-based superconductors, has been applied to ferrite systems with great success [168, 169]. Pulsed laser deposition is effective at producing near single crystal quality thin films but is largely relegated to research studies since the films, like in sputter deposition, are limited in thickness. PLD also suffers from limited substrate surface area. Processing techniques leading to thick films, coatings, and layers, such as liquid phase epitaxy (LPE), screen printing, tape casting, and ceramic compaction, remain the dominant means of industrial-scale processing of ferrite materials for high-frequency commercial and military applications. For microwave passive device deposition tools must provide control of the direction and amplitude of the magnetic anisotropy field, FMR linewidth, remanent magnetization, and, importantly, the film/substrate thickness to greater than tens of micrometers. A paradox is faced in the refinement of ferrite materials in that many of these properties are optimized by the growth of near single crystal structures (e.g. anisotropy fields and low FMR linewidths) whereas other properties (e.g. high remanent magnetization needed for self-bias operation) require high coercive fields that are often inherent in materials having copious grain boundaries and defects. This dichotomy requires compromise in the choice of materials processing methods and conditions. The fact that these materials must be tens of micrometers in thickness provides additional growth challenges.

So far, we have been most concerned with devices operating off-resonance in which high permeability, high magnetization, and low FMR linewidth are highly valued. In contrast, for the case of electromagnetic interference (EMI) suppression and absorbers, material properties require high permeability but also high losses that readily allow for broadband absorption of electromagnetic signals. It is also desirable to either deposit magnetic materials directly over circuit board elements or create flexible sheets that can be affixed over radiating elements. These processing methods have until recently proven elusive. Materials processing technologies are discussed in greater detail in Section 14.3 of this chapter.

Having discussed materials needs, we next turn to key elements of transmit and receive modules for applications in radar and communication systems, including circulators, isolators, phase shifters, filters, etc. In these elements there has been a trend towards microstrip designs. In the following sections we discuss the merits of ferrite-based microstrip device designs keeping in mind that there exists a plethora of other devices and topologies that include prominently waveguide, transmission line, and stripline.

14.5.3 Circulators and Isolators

Our discussion of devices begins with a brief description of the microwave isolator as a transmission line with non-reciprocal attenuation. In its most simplistic manifestation, it consists of a conductor positioned over a magnetic material, typically a ferrite, biased by an external magnetic field aligned perpendicular to the plane of the device and conductor. Although ferrite isolators consist of these basic elements they can operate on different principles: Faraday rotation, field displacement, and resonance absorption [170]. Most isolators make use of resonant absorption (or FMR). In contrast, a circulator has three of more ports and the non-reciprocal properties of the ferrite lead to standing waves that shunt electromagnetic power from one port to another while isolating the third (see Figure 14.12a).

The frequency-dependent permeability of ferrites, including spinels, garnets, and hexaferrites, assumes a tensor form due to the gyromagnetic nature of ferrites. Because the direction of precessional motion of magnetic dipole moments is dependent upon the sense of rotation for a given magnetic bias field direction, reversing the field direction reverses the sense of rotation. Hence, the rotational motion does not obey time reversal symmetry and results in non-reciprocal wave propagation properties. The frequency of the precessional motion, that is, the ferromagnetic resonance (FMR) frequency, is proportional to the magnitude of the magnetic bias field, in addition to the externally applied magnetic field, the demagnetizing field, and the magnetocrystalline anisotropy field. Since reversing the propagation direction is equivalent to reversing the sense of rotation in a circularly polarized wave, only one propagation direction will interact strongly with the ferrite. This direction-dependent nature of wave propagation in ferrite materials allows various non-reciprocal behaviors, such as that observed in isolators and circulators [185]. The strength of the interaction between the ferrite and the wave can be controlled by an external field, allowing various tunable devices, such as phase shifters and filters. The strongest interaction occurs at FMR, resulting in a strong attenuation of the wave. This property of ferrites is exploited in the design of various absorber devices.

We next examine the isolator/circulator as a key ferrite control element that finds a wide range of applications in the transmission, reception, and manipulation of electromagnetic signals. The use of isolators play an important role in radar systems where they are used to

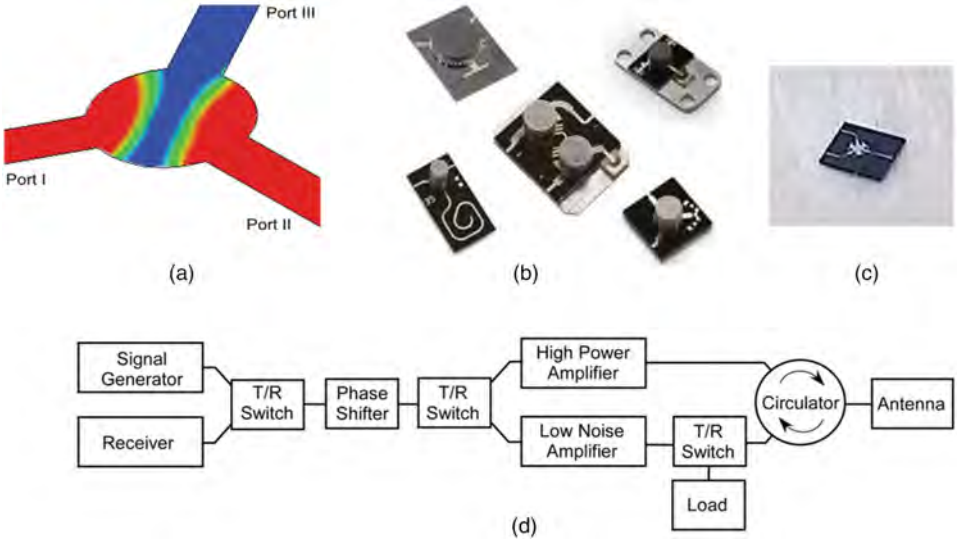

Figure 14.12 *(a) Magnitude of the electric field in the stripline Y-junction circulator calculated by finite element methods. Low insertion loss in the forward direction of propagation (port I to port II) and high isolation in the reverse direction (port I to port III) are observed. (b) Photograph of several microstripline circulator products of Saisum Technology Co. Ltd (from www.saisum.en.china.cn) illustrating a traditional design with prominent bias magnets positioned atop the conductor patterns of the circulators. (c) Self-biased circulator offered by Metamagnetics Inc. (from www.mtmgx.com) that operates without bias magnets. (d) Simplified block diagram of a T/R module. Switches and a circulator are utilized to guide the high-power transmitted signal to the antenna in the transmit mode and to guide the low-power signal from the antenna to the low-noise amplifier and the receiver in the receive mode.*

control the voltage standing wave ratio (VSWR) seen by amplifiers and to mitigate reflected power from the antenna. In this case, dedicated isolators (two port non-reciprocal devices) or circulators (three, or more, port nonreciprocal devices) can be used. In the case of a circulator, the third port is terminated by a matched load, thereby allowing operation as an isolator. Depending upon system needs, space, and volume, dedicated isolators may be more desirable. The circulator, one of the most frequently utilized ferrite devices in modern microwave systems, is a passive non-reciprocal multiport device used to control the power flow and to isolate various components in high-frequency systems.

A typical electric field configuration in a ferrite-loaded microstripline Y-junction computed by finite element methods is shown in Figure 14.12a. Here one sees the stabilization of a standing wave that acts to shunt the flow of power from one port to another while concomitantly isolating the third. Wu and Rosenbaum demonstrated the conditions necessary for circulation over a full octave bandwidth in microstrip devices [171]. The extensive literature on circulator theory and design is reviewed in the annotated bibliography by Knerr [172] and in texts by von Aulock and Fay [173] and Helszajn [174].

The Y-junction circulators, pictured in a microstripline configuration in Figure 14.12b) by courtesy of Saisum Technology Co. Ltd of China, are often utilized in transmit–receive

(T/R) modules of phased array radar systems [175]. Figure 14.12c is a recent development in circulator design by Metamagnetics Inc. of the United States that is constructed using a self-biased ferrite and therefore does not require a biasing magnet, thus saving space, weight, and assembly costs. T/R modules, a simplified block diagram of which is shown in Figure 14.12d, combine monolithic microwave integrated circuits (MMICs) and digital circuitry fabricated on high-frequency semiconductor substrates, such as gallium–arsenide and gallium–nitride, to produce high performance, high efficiency, low weight, low cost, and small sized modules [176]. In many modern T/R modules the one arm of the circulator has a matched load and the circulator acts as an isolator. In this case the send and receive functions are switched as opposed to being operated in a STAR mode (simultaneous transmit and receive).

The ferrite is the material that interacts strongly with the EM signal and provides non-reciprocal behavior. Non-reciprocal microstrip devices such as isolators and circulators require the ferrite to have a magnetization vector aligned perpendicular to the device/film plane. A relatively new circulator design, the ferrite coupled line circulator, allows for in-plane alignment of the magnetization but suffers from higher insertion loss and therefore has yet to become a viable option to the Y-junction circulator.

The first waveguide Y-junction circulators were reported in the late 1950s [177] with stripline designs following soon thereafter [178]. The first monolithic microstrip circulator on a garnet substrate was introduced in 1967 [179]. The theory of stripline Y-junction circulators was developed by Bosma [180, 181], and Fay and Comstock [182]. These theories explain the non-reciprocal behavior of the ferrite loaded stripline Y-junction in terms of the splitting of counter-rotating dielectric resonance modes in the ferrite material due to the off-diagonal elements of the permeability tensor proposed by Polder [183, 184].

The need to miniaturize circulator devices, to facilitate broader integration with monolithic microwave circuits, and to extend the applicable frequency range into the millimeter-wave regime has motivated studies in utilizing the unique properties of hexagonal ferrites. Textured polycrystalline hexagonal ferrites, such as barium and strontium hexaferrite, can be produced with permanent magnet properties such that they will remain in a stable magnetized state in the absence of an external bias field (i.e., self-biased). High uniaxial magnetic anisotropy fields in these materials, which can exceed 40 kOe, are utilized to decrease or eliminate the external biasing field requirement according to Kittel's [185] resonance equation, which incorporates both dipolar and magnetocrystalline anisotropy interactions [186].

Polycrystalline textured strontium hexaferrite (SrM), having a remnant magnetization of approximately 3.5 kG, uniaxial anisotropy field of 18.4 kOe, and FMR linewidth of approximately 2 kOe, was utilized to develop a self-biased waveguide junction circulator operating at 73.5 GHz by Akaiwa and Okazaki [187]. The reported insertion loss was 1.1 dB with isolation exceeding 20 dB over a 2.4 GHz bandwidth. In 1989, polycrystalline SrM was utilized to develop a self-biased waveguide circulator operating at 30.7 GHz with an insertion loss of less than 1 dB and isolation of more than 20 dB over a 1% bandwidth [188]. In 1992, a textured barium/strontium ferrite with remanent magnetization of 3.5 kG and uniaxial anisotropy field of 21 kOe was utilized to design microstrip and stripline circulators operating at 37 and 32 GHz, respectively [189]. In 2001, an integrated self-biased microstrip circulator was fabricated through bonding of textured SrM platelets to silicon substrates in a low-temperature process compatible with semiconductor fabrication

protocols [190]. Insertion loss of 2.8 dB and isolation of 33 dB were measured at 28.9 GHz with a 20 dB bandwidth of 1%. Circulator designs utilizing single crystal platelets of ScM with saturation magnetization of 3.9 kG, uniaxial anisotropy field of 8.7 kOe, and linewidth of 100 Oe embedded into glass–microwave integrated circuit wafers resulted in operation at 22.2 GHz with a minimum insertion loss of 2 dB and isolation of 21 dB. This performance was obtained with ferrite platelets partially saturated by an externally applied magnetic field of 2 kOe (55% saturation) [191, 192]. Recently, Wang *et al.* [193] developed a self-biased Ku-band circulator. This two-dimensional construct employed a self-biased SrM-type hexaferrite and demonstrated an insertion loss of less than 2 dB with a corresponding isolation of 20 dB over a bandwidth of 500 MHz with a center frequency of 13.5 GHz. This was the first such demonstration of a self-biased circulator operating at a frequency less than 20 GHz.

As mentioned previously, the circulator design that has great potential for monolithic microwave circuit integration and self-bias operation is the ferrite coupled-line (FCL) circulator. First developed in the 1980s, in contrast to Y-junction circulators, FCL circulators utilize longitudinally magnetized ferrite to couple modes between closely spaced wave guiding lines [194]. The non-reciprocity of ferrite coupled-line waveguides was first explained in terms of coupled mode theory by Marcuse [195].

Ferrite coupled-line circulators have the additional advantages of broad bandwidths, planar form factors, and small biasing fields [196]. Self-bias designs utilizing hexagonal ferrites have also been reported [197]. Due in part to a lower demagnetizing factor associated with a longitudinally magnetized film, self-biased hexaferrite films are easier to produce to thicknesses necessary for FCL device fabrication. Therefore, self-biased FCL circulators have the potential for true monolithic integration where the ferrite film is deposited and metalized with proper circuitry during device fabrication. There is no doubt that circulator designs described here, as well as other high-frequency ferrite devices, will continue to benefit from further advances in ferrite materials to result in true microwave monolithic integrated circuits.

14.5.4 Phase Shifters

Phase shifters are critical elements for electronically scanned phased array (ESPA) antennas and are devices that allow the antenna beam to be steered without physically repositioning the antennae. Existing phase shifter technologies, for example, ferroelectric, semiconductor-MMIC, and MEMS, each suffer shortcomings or operational constraints that limit their wide-scale deployment across varied military and commercial platforms. The key figures of merit include: phase shift per dB of insertion loss, power budget, power handling, and size, weight, and cost. Here, we target phase shifter applications in which high performance is demanded in low-profile lightweight devices that handle high power loads (tens of watts average power). Such applications include radar and communication phased array systems on aircraft, satellite, ships, and, importantly, next-generation unmanned systems. Of the key elements of T/R channels, the semiconductor-based phase shifter introduces a disproportionate insertion loss. Clearly, enhanced T/R module performance would be realized by the reduction in insertion loss of phase shifters. This is one driving force in the development of next-generation phase shifter device technology. Semiconductor phase shifter technologies (i.e., diode and FET-based) suffer from low-power handling (<1 W),

high-power dissipation (1–2 W), high insertion loss (6–8 dB at X-band), poor phase resolution (~4 bits), and often costly hermetic packaging. As target frequencies approach and surpass Ku-band, increases in insertion loss due to conduction losses in the semiconductor become prohibitive. Benefits of semiconductor phase shifters include broadband operation and low cost. In comparison, advantages of existing ferrite phase shifter technology include very low-loss operation, < 1 dB insertion loss, high power handling capabilities (100s of W_{ave}, 1000s of $W_{pk\text{-}pk}$ for waveguide technology), reliability, and radiation hardness. However, these devices are large/heavy, require large power budgets (up to 10 W), and are costly to fabricate. As a result they are used principally in specialized applications such as high-power passive phased arrays.

Recent breakthroughs in microwave materials and device technologies include:

(a) The ability to process near single crystal quality ferrite thick films and ceramic compacts suitable for application in ultralow-loss microwave passive device applications.
(b) The ability to process high-quality ferrites having self-biased properties while maintaining low microwave losses
(c) Microstrip passive phase shifter designs that require significantly smaller bias fields.
(d) Computational advances that have set the groundwork to successfully and accurately describe EM wave propagation in highly anisotropic magnetic materials
(e) Novel voltage and current-driven transducer technologies that produce magnetic bias fields that enable active tuning of devices with minimal power loads.

The phase shifter technology described here combines the low-loss, high-power handling, reliability, and radiation hardness of today's ferrite waveguide phase shifters in a planar, cost-effective, high-power handling–low-power consumption microstripline topology. In contrast to other phase shifter technologies, ferrite phase shifters are characterized as having superior insertion loss performance and microwave power handling capabilities. These devices are also highly reliable and radiation-tolerant properties are valued for space-related applications. Ferrite phase shifters rely on electromagnetic wave propagation in low-loss magnetic materials, such as yttrium iron garnet (YIG) and spinel ferrites, typically substituted with non-magnetic cations of lithium, magnesium, nickel, and zinc. Such devices require magnetic fields to bias and actively tune the phase angle. These fields may be generated by permanent magnets for static bias fields or by current-driven coils for dynamic tuning. For operation at high frequencies (at or above X-band), permanent magnets are large, heavy, and costly. Tunable ferrite components, in addition to being comparatively large, experience high DC power consumption and slow response times due to the large inductance of current-driven coils. Improved response times and reduced DC power consumption are achieved in latching-type ferrite phase shifters, where short current pulses are used to set the phase [87].

A recent development that may significantly impact the tuning of microwave magnetic devices is multiferroic (MF) materials exhibiting the magnetoelectric (ME) effect [198]. Among the numerous investigations appearing in the literature, multiferroic (MF) metamaterials, constructed as multilayered or granular heterostructures, have drawn the most attention [199]. Multiferroic heterostructures have indeed been shown to offer unique opportunities in the development of many new multifunctional devices, including electric field controlled (EFC) magnetic memory elements [200]. EFC microwave devices [201] and E- and H-field transducers having magnetically modulated piezoelectricity or electrically

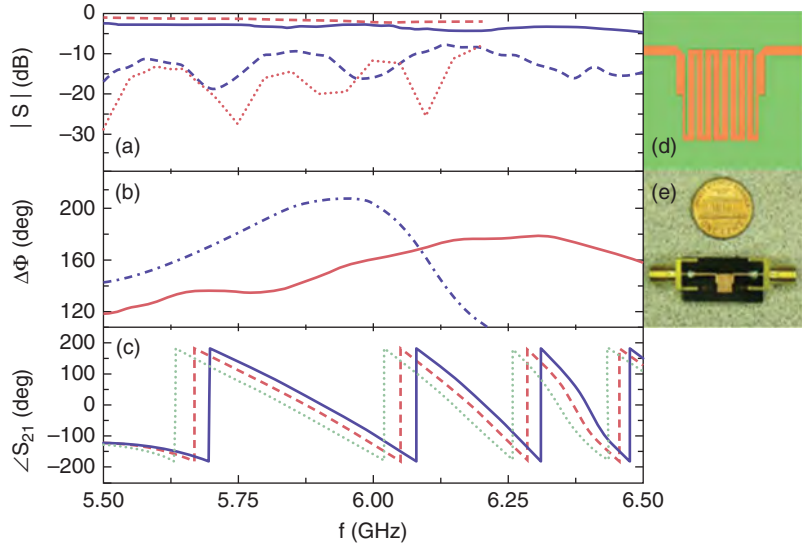

Figure 14.13 *S parameters collected from the meanderline phase shifter of Geiler* et al. *(a) Calculated dotted-dashed and measured solid insertion loss. Calculated (dotted) and measured (dashed) return loss. (b) Calculated (dotted-dashed) and measured (solid) differential phase shift. (c) Measured insertion phase at an applied electric field of 0 (solid), 3 (dashed), and 6 (dotted) kV/cm. (d) Finite element model of the microstrip circuit. (e) Fabricated device with coaxial edge mount SMA connectors. This phase shifter is designed to operate with a multiferroic transducer where dynamic tuning is provided by a voltage excitation. Source: Adapted from Geiler* et al. *[204].*

modulated magnetoelectricity [202, 203]. In many of these examples, mechanical coupling between piezoelectric (e.g., PZT, PMN–PT, etc.) and magnetostrictive (e.g., Terfenol-D^{TM}, Galfenol, Metglas^{TM}, etc.) layers provide electric field induced magnetic polarization of the magnetostrictive layer(s) and magnetic field induced electric polarization of the piezoelectric layer. Alternatively, Geiler *et al.* [204] have demonstrated the generation of magnetic fringe fields by MF heterostructures that act on nearby microwave devices that are decoupled from the transducer. In both instances the MF heterostructures may eliminate the need for voluminous and costly magnetic field coils to actively tune magnetic components. These developments represent a disruptive advance in the field of multifunctional electronics.

Geiler's voltage tuning of a meander line ferrite phase shifter (see Figure 14.13a and e) was realized by affixing a YIG substrate to an MF heterostructure consisting of PMN–PT/Terfenol-D/PMN–PT. This geometry allowed the YIG substrate to see the voltage-induced magnetic fields emanating from the MF heterostructure without experiencing any strain or microwave electromagnetic coupling. A magnetic bias field of 200 Oe was applied along the length of the MF heterostructure and along the meander line elements by an electromagnet. Measured insertion and return loss are superimposed with calculated spectra in Figure 14.13 a. At a frequency of 6.3 GHz, the insertion loss and the return loss were measured to be 3.2 and 13 dB, respectively, while a differential phase shift of 180° was measured at 6.3 GHz. Out of the 3.2 dB of insertion loss, 0.5 dB is attributed to impedance mismatch

loss. The remaining 1 dB between calculated and measured insertion loss is attributed to connector effects, imperfections associated with the device fabrication process, and variations in the material properties from those assumed in the finite element model. The contribution of the MF heterostructure to the insertion loss was less than 0.2 dB. The magnetic fringe field was non-uniform and varied from 330 Oe near the edge of the 1.3 cm YIG substrate to 210 Oe near the center. The differential phase shift was calculated by subtracting the insertion phase at zero internal field from the insertion phase at 100 Oe internal field. A differential phase shift of 210° was calculated at the design frequency (Figure 14.13b). As the electric field increased from 0 to 6 kV/cm, a linear tunable phase shift of more than 65° was observed (Figure 14.13c). This phase change was due to the fact that the magnetic fringe fields from the MF heterostructure varied by approximately 20% with the applied electric field. These results demonstrate the potential of MF heterostructures as external tuning elements for microwave magnetic devices.

A different path was taken by Tatarenko *et al.* [205] who demonstrated an electric field tunable yttrium iron garnet YIG–lead zirconate titanate PZT phase shifter based on the tuning of ferromagnetic resonance at X-band. The electric field control of the phase shift arose through a magnetoelectric interaction in which a piezoelectric deformation in PZT occurred under the application of an electric field E, leading to a shift in the FMR frequency in YIG. A phase shift of 90 to 180° and an insertion loss of 1.5–4 dB was measured corresponding to an $E = 5$–8 kV/cm applied across PZT. This approach represents a new path towards realizing high performance EFC phase shifter devices.

The discovery of metamaterials possessing a negative index of refraction (NIM) has allowed for the development of novel microwave technologies [206]. A significant recent development is the fabrication of tunable negative index metamaterials (TNIMs) utilizing high-quality ferrite materials [207, 208]. One such example of a microwave device making use of a ferrite-based TNIM is the He *et al.* phase shifter [226–228]. As discussed previously, there is significant demand in the microwave industry for affordable, lightweight, high-power phase shifters. In ferrite phase shifters a change in permeability by the application of a magnetic field causes a change in the phase velocity of the microwave signal traveling through the phase shifter. Traditional ferrite phase shifters operate at frequencies far from the FMR in order to avoid absorption losses. As a result, the real part of the complex permeability, μ', is necessarily small. Experimental and theoretical investigations of field tunable negative refractive index metamaterial (NIM) using a yttrium iron garnet (YIG) film and an array of copper wires in waveguides were carried out by both P. He *et al.* and Y. He *et al*. A key feature of magnetic field tunability of the NIM in the microwave frequency region was demonstrated. Transmission passbands were realized in the negative refractive index region that could be tuned by an external magnetic field. The permeability of the NIM was simultaneously tuned along with the refractive index. The change in permeability leads to a change in the phase velocity of the signal and, therefore, the phase of the transmission coefficient.

The advantage of using a ferrite NIM for phase shifter applications is that it allows for low-loss operation over frequencies near FMR where μ' is negative and relatively high. In the field tunable NIM, the effect of the ferrite is to provide a tunable negative permeability over a continuous range of frequencies on the high-frequency side of FMR. Complementary negative permittivity, ε', was achieved using a single periodic array of copper thin wires deposited on Kapton^{TM}. A negative refractive index region of 0.5 GHz in width at K-band

was demonstrated. Increasing the volume of the YIG increased the absorption and therefore a tradeoff between bandwidth for the negative index region and low-loss was realized. Additionally, the dielectric permittivity of the YIG slabs reduced the effective negative permittivity obtained from the plasmonic copper wires. For a 1 cm long NIM, when the applied magnetic field was varied from 6.0 to 7.0 kOe, the phase varied 160° with the insertion loss varying from 4.3 to 6.3 dB at 24 GHz.

A tunable negative refractive index metamaterial and miniature phase shifter were also designed and fabricated in a microstripline configuration for applications in rf, microwave, and millimeterwave integrated circuits [208]. The metamaterial consisted similarly of plasmonic copper wires and YIG slabs having an insertion loss of 5 dB at the center of the transmission band. The YIG enabled magnetic field tuning of the negative refractive index from 7.0 to 11.0 GHz. The insertion phase was tuned by 45° continuously by varying the bias field from 3.8 to 4.6 kOe at 9.0 GHz. Figure 14.14a to e illustrates a schematic of the device with a photograph (see Figure14.14a) and the device's phase shift and transmitted signal (i.e., passband) (see Figure 14.14b). In Figure 14.14c to e one sees the simulated and experimental passbands signaling the occurrence of negative index. This passband was shown to shift under the application of a magnetic field demonstrating broadband tunability of the NIM. H-field tuning was shown to be broadband and linear (see Figure 14.14e).

14.5.5 Filters

Microwave filter designs have been a topic of great interest for more than seven decades [209] and continue to grow as high-performance materials and increasingly complex designs are investigated to meet stringent modern-day requirements. A major development to the field of microwave filters was the advent of tunable bandwidth parameters allowing for a single device to operate at user-defined frequencies [211]. The tuning mechanisms in these filters vary from static mechanical methods such as plungers, screw-tuned cavities, and conductor–conductor positioning, to active methods such as applied E-field and H-field tuning, with each method offering distinct benefits. Active methods, such as E-field and H-field tuning, allow for remote device performance tuning as well as the ability to automate band tuning for frequency-modulated applications. Active tuning also enables high-speed precision bandpass adjustments and better repeatability than mechanical tuning methods. The advantages of H-field tunable filters over E-field tunable varactors or MEMS devices include low insertion loss and high power handling. YIG filters, based on single crystal resonators, are among the most widely utilized H-field tuned devices offering multioctave band tunability and high Q-factors.

Next, we examine a highly versatile, planar, low-loss, and low-cost alternative to YIG single crystal resonator filters with a low externally applied H-field requirement. The proposed design consists of a multipole Chebyshev bandpass filter implemented in microstrip hairpin-line coupled resonator geometry on a polycrystalline YIG substrate biased and tuned with an externally applied H-field above the FMR frequency (see Figure 14.15a to c) [211].

The hairpin-line bandpass filters are essentially parallel-coupled half-wavelength resonators folded into a "U" shape and follow the same set of design equations that govern parallel-coupled half-wavelength resonator filters. For example, a five-pole Chebyshev equiripple response is considered, but Butterworth, elliptical, and other filter response types are equally applicable.

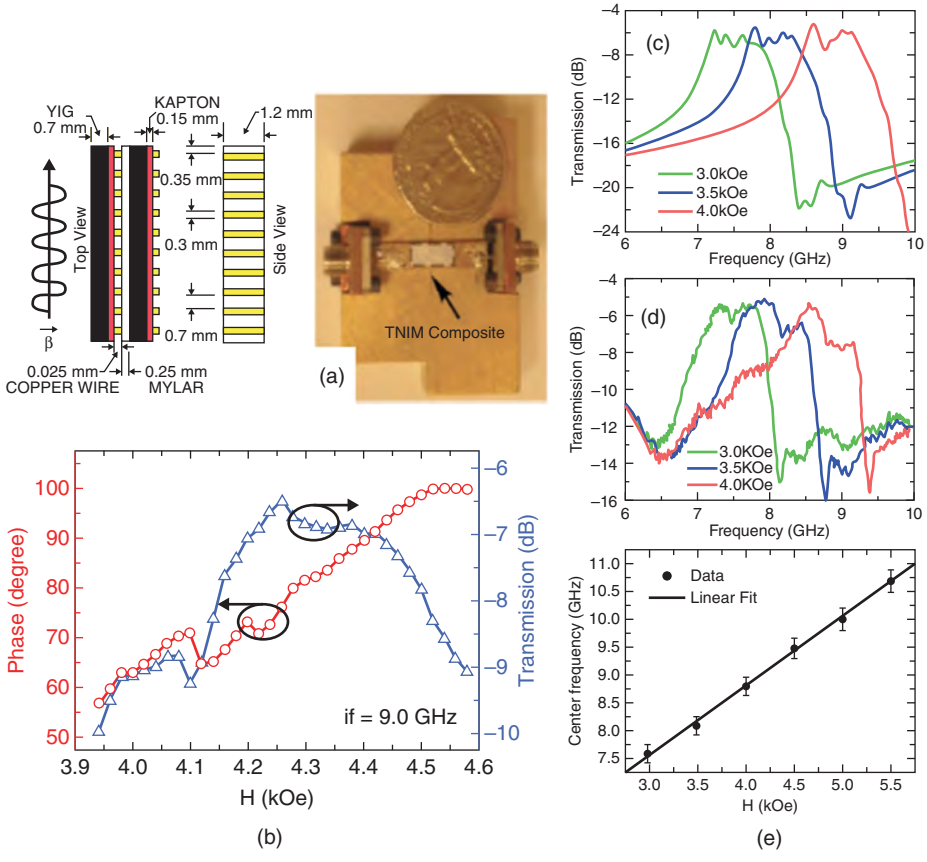

Figure 14.14 *(a) Schematic top and side views of the 10.0 × 2.0 × 1.2 mm³ TNIM (i.e., tunable negative index material) composite. Photograph of the microstrip test fixture, a 5 × 25 mm² upper strip on the brass ground base relative to a US quarter provided for a visual size comparison. The TNIM composite is mounted under the center of the upper strip. (b) Measured phase shift and corresponding transmission versus the magnetic bias field of the TNIM composite at 9.0 GHz. The insertion phase shifts 45° while the transmission varies from −6 to −10 dB. (c) Simulated and (d) measured 1.0 GHz wide TNIM passbands of over −8 dB transmission centered at 7.5, 8.0, and 8.8 GHz at magnetic bias fields of 3.0, 3.5, and 4.0 kOe, respectively. (e) Center frequency of the TNIM passband increases linearly from 7.6 to 10.7 GHz with the bias field changing from 3.0 to 5.5 kOe. Adapted from He* et al. *[208].*

The dynamic tuning of the proposed device is realized by varying the magnetic permeability of the substrate by applying an external magnetic field. The variation in permeability with applied field is strongest below the FMR frequency and above the ferromagnetic antiresonance (FMAR) frequency. Operation sufficiently far from both resonance conditions is necessary to achieve low-loss performance.

The measured insertion loss of a ferrite microstrip hairpin-line bandpass filter is compared with the predictions of the numerical model in Figure 14.15d. Good agreement in

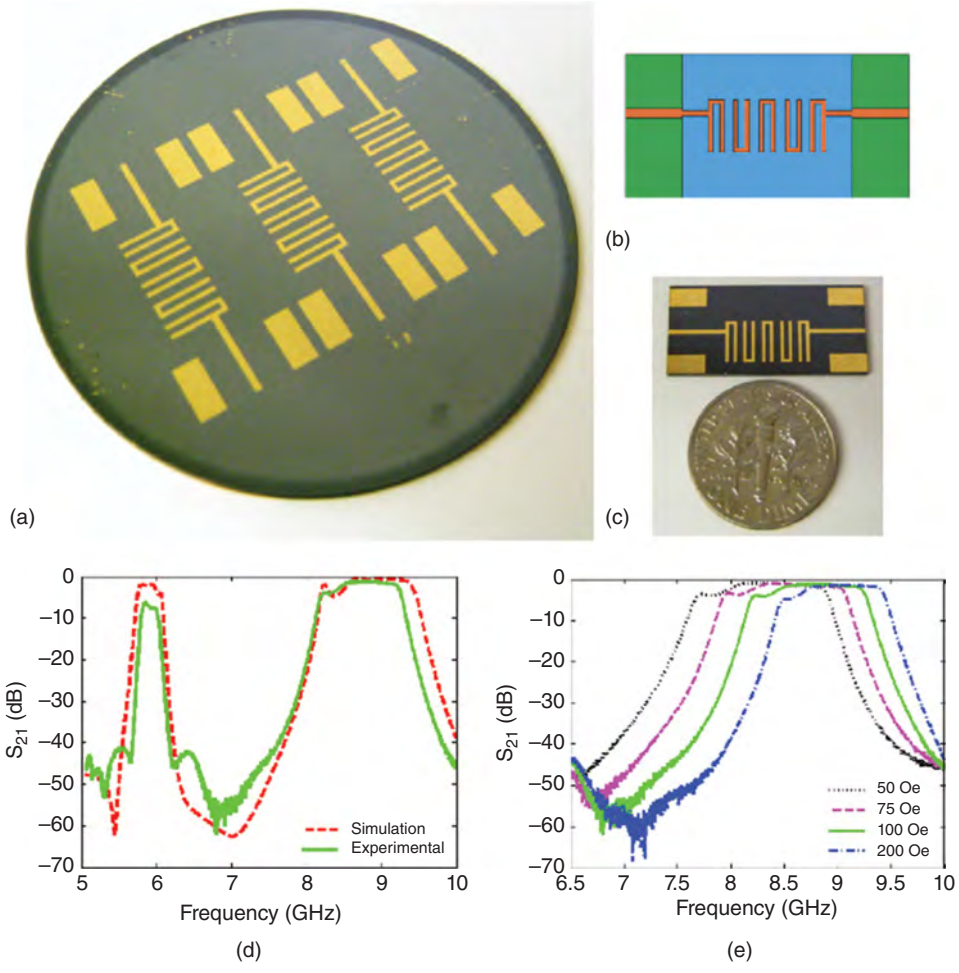

Figure 14.15 *(a) Photograph of the patterned 50 mm diameter YIG wafer. (b) Outline of the hairpin-line resonator bandpass filter design used in numerical modeling. (c) Photograph of the fabricated bandpass filter device. (d) Simulated and measured passband characteristics of the ferrite microstrip hairpin-line coupled resonator bandpass filter. A measured spectrum is collected under an applied magnetic field of 100 Oe. (e) Passband characteristics of the ferrite microstrip hairpinline coupled resonator bandpass filter under an applied magnetic field from 50 to 200 Oe. Adapted from Gillette* et al. *[211].*

the frequency range of interest is observed. Under an externally applied field of 100 Oe, an insertion loss of 1.3 dB was measured at 8.8 GHz compared to 0.9 dB predicted by the numerical model.

H-field tuning of the ferrite microstrip hairpin-line bandpass filter is demonstrated (Figure 14.15e). The device exhibits passband tunability with the center frequency varying from 8.3 to 9 GHz under applied H-fields of 50 to 200 Oe. The insertion loss at the passband center frequency varies between 1 and 1.4 dB as a function of applied H-fields. While a

bandpass filter design with a fractional bandwidth ($\Delta f/f_{center}$) of approximately 10% at X-band is demonstrated, the proposed approach lends itself to the realization of a broad range of filter responses, including low-pass, high-pass, band-pass, and bandstop, as well as pass band characteristics, including center frequency, fractional bandwidth, passband ripple, out-of-band rejection, etc. Furthermore, due to the low H-field requirement, the proposed filter design has the potential for high-speed and low-power operations, in addition to possessing radiation-tolerant properties, making them well-suited for space-related applications.

Multiferroic (MF) heterostructures that demonstrate the magnetoelectric effect (ME) can also be adapted as tunable microwave filters [212]. ME resonators, consisting of 110 μm thick (111) yttrium iron garnet (YIG) on a GGG substrate bonded to PZT, have been demonstrated. In that example, YIG, having a saturation induction 4πM of 1750 G and an FMR linewidth of ~ 1 Oe, was bonded to a PZT plate poled in an electric field of 10 kV/cm perpendicular to the sample plane. The heterostructure consisted of a YIG film bonded to a PZT crystal with ethyl cyanoacrylate. The heterostructure was placed between transducers and was subjected to an H-field parallel to the sample plane and perpendicular to the microstrips. The frequency dependence on the insertion loss was measured from 4 to 10 GHz as a function of H- and E-fields applied across the PZT. The maximum ME coupling was observed at $f_r = 6.77$ GHz corresponding to FMR in YIG. A frequency shift was observed and attributed to the strain at the YIG–PZT interface caused by the piezoelectric response of the PZT. A near-linear variation in δf with E was observed. A maximum shift of 120 MHz for $E = 3$ kV/cm corresponding to 2% of the center frequency of the filter was measured [232].

14.6 Outlook

The fabrication of film-based ferrite devices on semiconductor substrates remain under development and unanticipated challenges maybe exist for the next circuit level integration. Could one expect to use semiconductor devices to replace all ferrite components as an alternative way for future MIC technology? Earlier researchers employed a static magnetic field on a semiconductor material to create a magnetoplasma and demonstrate non-reciprocity [213]. MMIC active circulators based on MESFET and HEMT [214–215] have also been reported. Semiconductor FETs, diodes, and switch-based devices are widely used as replacements for ferrite phase shifters in electronically steerable phase array radars for many applications. In fact, most semiconductor transmit/receive modules are widely employed in low-frequency low-power applications such as the consumer mobile phone industry. It appears that semiconductor counterpart devices will continue to be exploited in many applications due to the established fabrication technology as well as economic considerations. However, the likelihood of using semiconductor devices to replace all ferrite components is not at all promising. At high frequencies, such as the 8-mm-wave range and above, insulating materials like ferrites are essential to ensure low-loss propagation of electromagnetic signals. Additionally, no semiconductor devices have the power handling capability of ferrite circulators. The suggested implementation of GaN switches to replace ferrite circulators would limit the power capability of single T/R modules. Together with an anticipated large insertion loss of GaN switches, such a replacement would significantly degrade system performance. In recent years, there has been much attention paid to

the development of simultaneous transmit and receive (STAR) technology for use in radar and communication phased array platforms. STAR employs the same aperture to send and receive EM signals simultaneously. The non-reciprocity of the circulator is a key property of STAR technology and for the foreseeable future only the ferrite circulator fulfills this need. Consequently, ferrite-based microwave components, such as isolators, circulators, filters, phase shifters, etc., will be in high demand in film form to integrate with semiconductor technology in the coming years.

In this chapter, we have focused on the development of a new generation of ferrite materials for rf, microwave, and millimeter-wave frequencies. Such research endeavors, intended to merge both passive and active electronic components on to a common semiconductor substrate and thus providing lower process costs, smaller size, enhanced compatibility with planar circuit designs, lead to enhanced system and assembly integration.

References

1. Harris, V.G. (2012) Modern microwave ferrites. *IEEE Transactions on Magnetism*, **48** (3), 1075.
2. Harris, V.G., Chen, Z., Chen, Y., *et al.* (2006) Ba-hexaferrite films for next generation of microwave devices. *Journal of Applied Physics*, **99**, 08M911.
3. Anderson, P.W. (1950) Antiferromagnetism. Theory of superexchange Interaction. *Physics Review*, **79**, 350.
4. Néel, L. (1948) Propertietes magnetiques des ferrites – ferrimagnetisme et antiferromagnetisme. *Annales de Physique*, **3**, 137.
5. Yafet, Y. and Kittel, C. (1952) Antiferromagnetic arrangements in ferrites. *Physics Review*, **87**, 290–294.
6. Dionne, G.F. (2009) *Magnetic Oxides*, Springer, New York.
7. Recent developments in the epsilon phase of Fe_2O_3 show this phase to also have very high coercive field and anisotropy constant. We omit a discussion of this phase as it is beyond the scope of this chapter. For further details see: Jin, J., Ohkoshi, S., and Hashimoto, K. (2004) Giant coercive field of nanometer-sized iron oxide. *Advanced Materials*, 16, 48–51.
8. Geiler, A., Daigle, A., Wang, J., *et al.* (2012) Consequences of magnetic anisotropy in realizing practical microwave hexaferrite devices. *Journal of Magnetism and Magnetic Materials*, **324**, 3393–3397.
9. Kirchmayr, H.R. (1996) Permanent magnets and hard magnetic materials. *Journal of Physics D: Applied Physics*, **29**, 2763.
10. Sui, X., Scherge, M., Kryder, M.H., *et al.* (1996) Barium ferrite thin-film recording media. *Journal of Magnetism and Magnetic Materials*, **155**, 132.
11. Koledintseva, M., Drewniak, J., Zhang, Y., *et al.* (2009) Modeling of ferrite-based materials for shielding enclosures. *Journal of Magnetism and Magnetic Materials*, **321**, 730–733.
12. Smit, J. and Wijn, H.P.J. (1959) *Ferrites*, John Wiley & Sons, Inc., New York, and references contained within.
13. Nicholson, D.B. (1990) Hexagonal ferrites for millimeter-wave applications. *Hewlett-Packard Journal*, **41**, 59.
14. Chen, Y., Geiler, A., Sakai, T., *et al*. (2006) Microwave and magnetic properties of self-biased barium hexaferrite screen printed thick films. *Journal of Applied Physics*, **99**, 08M904.
15. Chen, Y., *et al*. (2006) Screen printed thick self-biased, low-loss, barium hexaferrite films by hot-press sintering. *Journal of Applied Physics*, **100**, 043907.
16. Albanese, G. and Deriu, A. (1979) Magnetic properties of Al, Ga, Sc, In substituted barium ferrites: a comparative analysis. *Ceramurgia International*, **5**, 3–10.
17. Li, Z.W., *et al.* (2006) Co_2 +Ti_4 + substituted Z-type barium ferrite with enhanced imaginary permeability and resonance frequency. *Journal of Applied Physics*, **99**, 063905.

18. Hu, B., Chen, Y., Su, Z., *et al.* (2013) Magnetocrystalline anisotropy and FMR linewidth of Zr and Zn-doped Ba-hexaferrite films grown on MgO (111). *IEEE Transactions on Magnetics*, **49**, 4234–4237.
19. Li, Z.W., Ong, C.K., Yang, Z., *et al*. (2000) Site preference and magnetic properties for a perpendicular recording material: $BaFe_{12}–xZn_{x/2}–Zr_{x/2}–O_{19}$ nanoparticles. *Physics Review B*, **62**, 6530–6537.
20. Daigle, A.P., Geiler, M., Geiler, A., *et al.* (2012) Permeability spectra of Co_2Z hexaferrite compacts produced via a modified aqueous co-precipitation technique. *Journal of Magnetism and Magnetic Materials*, **324**, 3719–3722.
21. Su, Z., Chen, Y., Hu, B., *et al.* (2013) Crystallographically textured self-biased W-type hexaferrites for X band microwave applications. *Journal of Applied Physics*, **113** (17), 17B305.
22. Chen, Z., Yang, A., Yoon, S.D., *et al.* (2006) Epitaxial growth of Ba-hexaferrite films on single crystal 6-H SiC. *Journal of Magnetism and Magnetic Materials*, **301**, 166.
23. Chen, Y., Fitchorov, T., Koblischka-Veneva, A., *et al.* (2009) Topochemical growth of textured polycrystalline barium hexaferrite from oriented antiferromagnetic α-FeOOH nanorods. *Nanotechnology*, **20**, 445606.
24. Chen, Y., Geiler, A.L., Chen, T., *et al.* (2007) Low-loss barium ferrite quasi-single-crystals for microwave application. *Journal of Applied Physics*, **101**, 09M501.
25. Dorsey, P.C., Bushnell, S.E., Seed, R.G., *et al*. (1993) Epitaxial yttrium iron garnet films grown by pulsed laser deposition. *Journal of Applied Physics*, **74**, 1242.
26. Dorsey, P.C., Bushnell, S.E., Seed, R.G., *et al*. (1993) Magnetic and structural characteristics of pulsed laser deposited epitaxial $Y_3Fe_5O_{12}$ films. *IEEE Transactions on Magnetism*, **29**, 3069.
27. Simion, B.M., Ramesh, R., Keramidas, V.G., *et al*. (1994) Magnetic characterization of epitaxial $Y_5Fe_3O_{12}/Bi_3Fe_5O_{12}$ and $Y_5Fe_3O_{12}/Eu_1Bi_2Fe_5O_{12}$ heterostructures grown by pulsed laser deposition. *Journal of Applied Physics*, **76**, 6287.
28. Simion, B.M., Thomas, G., Ramesh, R., *et al.* (1995) Growth and characterization of ($Y_3Fe_5O_{12}–Bi_3Fe_5O_{12}$) heterostructures by pulsed laser deposition. *Applied Physics Letters*, **66**, 830.
29. Buhay, H., Adam, J.D., Daniel, M.R., *et al.* (1995) Thick yttrium–iron–garnet (YIG) films produced by pulsed laser deposition for integration applications. *IEEE Transactions on Magnetism*, **31**, 3832.
30. Nakata, Y., Tashiro, Y., Okada, T., *et al.* (2000) Fabrication of Ce:YIG film for electric and magnetic field sensor by pulsed-laser deposition and laser-induced forward transfer. *Proceedings of SPIE*, **4088**, 333.
31. Higuchi, S., Ueda, K., Yahiro, F., *et al*. (2001) Fabrications of cerium-substituted YIG thin films for magnetic field sensor by pulsed-laser deposition. *IEEE Transactions on Magnetism*, **37**, 2451.
32. Hayashi, H., Iwasa, S., Vasa, N.J., *et al.* (2002) Characteristics of Bi:YIG magneto-optic thin films fabricated by pulsed laser deposition method for an optical current transformer. *Japanese Journal of Applied Physics*, **41**, 410.
33. Hayashi, H., Iwasa, S., Vasa, N.J. *et al.* (2002) Fabrication of Bi-doped YIG optical thin film for electric current sensor by pulsed laser deposition. *Surface Science*, **197**, 463.
34. Chern, M.Y., Lee, W. S., and Liou, D.R. (1997) Curie temperatures of $Y_3Fe_5O_{12}/Gd_3Fe_5O_{12}$ superlattices. Letter to the Editor. *Journal of Magnetism and Magnetic Materials*, **170** (3), L243–L247.
35. Vittoria, C. (1993) Pulsed laser deposition of ferrite materials. US Patent No. 5,227,204.
36. Dorsey, P., Seed, R., Vittoria, C., *et al.*, (1992) Oriented barium hexaferrite thin films prepared by pulsed laser deposition. *IEEE Transactions on Magnetism*, **28** (5), 3216–3218.
37. Song, Y., Kalarickal, S., and Patton, C.E. (2003) Optimized pulsed laser deposited barium ferrite thin films with narrow ferromagnetic resonance linewidths. *Journal of Applied Physics*, **94**, 5103.
38. Welch, R., Jackson, T., and Palmer, S. (1995) Barium hexaferrite films prepared by pulsed laser deposition. *IEEE Transactions on Magnetism*, **31** (6), 2752.

39. Yoon, S.D., Vittoria, C., and Oliver, S.A. (2003) Magnetization behavior of scandium-substituted barium hexaferrite films having uniaxial axis in the film plane. *Journal of Magnetism and Magnetic Material*, **265** (2), 130–137.
40. Liu, X.H., Hong, M.H., Song, W.D., *et al*. (2005) Barium ferrite ($BaFe_{12}O_{19}$) thin films prepared by pulsed laser deposition on MgO buffered Si substrates. *Applied Physics A*, **80**, 611–614.
41. Chen, Z.H., Yang, A., Yoon, S.D., *et al*. (2006) Growth of Ba–hexaferrite films on single crystal 6-H SiC. *Journal of Magnetism and Magnetic Materials*, **301** (1), 166–170.
42. Chen, Z.H., Yang, A., Cai, Z.H., *et al*. (2006) Structure and magnetism of Ba–hexaferrite films grown on single crystal 6-H SiC with graduated interfacial MgO buffer layers. *IEEE Transactions on Magnetism*, **42** (10), 2855–2857.
43. Koleva, M., Zotova, S., Atanasov, P., *et al.* (2000) Sr–ferrite thin films grown on sapphire by pulsed laser deposition. *Applied Surface Science*, **168** (1–4), 108–113.
44. Faloh-Gandarilla, J.C., Diaz-Castanon, S., Leccabue, F., *et al*. (2004) Magnetic properties of polycrystalline Sr–M and Pb–M hexaferrites thin films grown by pulsed laser deposition on Si/SiO_2 substrates. *Journal of Alloy Composites*, **369** (1–2), 195–197.
45. Oliver, S., Chen, M., Vittoria, C., *et al.* (1999) Properties of pulsed laser deposited scandium-doped barium hexaferrite films. *Journal of Applied Physics*, **85** (8), 4630–4632.
46. Atkinson, R., Papakonstantinou, P., Salter, I., *et al.* (1994) Optical and magneto-optical properties of Co–Ti-substituted barium hexaferrite single crystals and thin films produced by laser ablation deposition. *Journal of Magnetism and Magnetic Materials*, **138** (1–2), 222–231.
47. Heczko, O., Gerber, R., and Simsa, Z. (2000) Structural, magnetic and magneto-optical properties of $SrFe_{12-x}Al_xO_{19}$ hexaferrite thin films prepared by laser ablation deposition. *Thin Solid Films*, **358** (1–2), 206-214.
48. Tanaka, K., Omata, Y., Nishikawa, Y., *et al.* (1991) Formation of Ni–Zn–ferrite films using laser ablation. *IEEE Transactions on Magnetism, Japan*, **6** (11), 1001.
49. Johnson, M.T., Kotula, P.G., and Carter, C.B. (1999) Growth of nickel ferrite thin films using pulsed-laser deposition. *Journal of Crystal Growth*, **206** (4), 299–307.
50. Chinnasamy, C.N., Yoon, S.D., Yang, A., *et al.* (2007) Effect of growth temperature on the magnetic, microwave, and cation inversion properties on $NiFe_2O_4$ thin films deposited by pulsed laser ablation deposition. *Journal of Applied Physics*, **101** (9), 09M517.
51. Balestrino, G., Martellucci, S., Paoletti, A., *et al.* (1995) Lithium ferrite epitaxial films grown by pulsed laser deposition: structural and electrical transport properties. *Solid State Communications*, **96** (12), 997–1002.
52. Cillessen, J., Wolf, R., Giesbers, J., *et al.* (1996) Growth, structuring and characterisation of all-oxide thin film devices prepared by pulsed laser deposition. *Applied Surface Science*, **96–98**, 744–751.
53. Guyot, M., Lisfi, A., Krishnan, R., *et al.* (1996) Ferrimagnetic thin films prepared by pulsed laser deposition. *Applied Surface Science*, **96–98**, 802–806 ; Terzzoli, M.C., Duhalde, S. Jacobo, L., *et al.* (2004) High perpendicular coercive field of $CoFe_2O_4$ thin films deposited by PLD. *Journal of Alloys and Compounds*, **369**, 209–212.
54. Yang, A., Chen, Z., Zuo, X., *et al.* (2005) Cation-disorder-enhanced magnetization in pulsed-laser-deposited $CuFe_2O_4$ films. *Applied Physics Letters*, **86**, 252510.
55. Zuo, X., Yang, A., Yoon, S.D. *et al.* (2005) Large induced magnetic anisotropy in manganese spinel ferrite films. *Applied Physics Letters*, **87**, 152505.
56. Yang, A., Chen, Z., Islam, S.M., *et al.* (2008) Cation engineering of Cu–ferrite films deposited by alternating target laser ablation deposition. *Journal of Applied Physics*, **103** (7), 07E509.
57. Zuo, X., Yang, A., Vittoria, C., *et al.* (2006) Computational study of copper ferrite ($CuFe_2O_4$). *Journal of Applied Physics*, **99**, 08M909.
58. Abe, M. and Tamaura, Y. (1984) Ferrite plating in aqueous solution: new technique for preparing magnetic thin film. *Journal of Applied Physics*, **55** (6), 2614; Abe, M., Tamaura, Y., Goto, Y., *et al.* (1987) High speed deposition of high-quality ferrite films from aqueous solution at low temperatures ($\leq$90 °C). *Journal of Applied Physics*, **61**, 3211.

59. Kondo, K., Numata, Y., Chiba, T., *et al*. (2005) Spin-sprayed ferrite films highly permeable in the GHz range, with excellent heat resistance. *Transactions on the Magnetism Society of Japan*, **5** (4), 161–164.
60. Abe, M., Itoh, T., Tamaura, Y., *et al.* (1987) Ferrite plating on GaAs for microwave monolithic integrated circuit. *IEEE Transactions on Magnetism*, **23** (5), 3736.
61. Kondo, K., Chiba, T., Ono, H., *et al.* (2006) Conducted noise suppression up to GHz range by spin-sprayed $Ni_{0.2}Zn_xFe_{2.8-x}O_4$ ($x = 0.3$, 0.6) films having different natural resonance frequencies. *Journal of Magnetism and Magnetic Materials*, **301**, 107–111.
62. Kondo, K., Chiba, T., Ono, H., *et al.* (2003) Conducted noise suppression effect up to 3 GHz by NiZn ferrite film plated at 90 °C directly onto printed circuit board. *Journal of Applied Physics*, **93**, 7130.
63. Matsishita, N., Kondo, K., Yoshida, S., *et al.* (2006) Ni–Zn ferrite films synthesized from aqueous solution usable for sheet-type conducted noise suppressors in GHz range. *Journal of Electroceramics*, **16**, 557–560.
64. Kondo, K., Yoshida, S., Ono, H., *et al.* (2007) Spin sprayed Ni(–Zn)–Co ferrite films with natural resonance frequency exceeding 3 GHz. *Journal of Applied Physics*, **101** (9), 09M502–09M502-3.
65. Zhang, L., Su, X.D., Chen, Y., *et al.* (2010) Radio-frequency magnetron sputter-deposited barium hexaferrite films on Pt-coated Si substrates suitable for microwave applications. *Scripta Materialia*, **63**, 492–495.
66. Linares, R.C. (1968) Epitaxial growth of narrow linewidth yttrium iron garnet films. *Journal of Crystal Growth*, **3–4**, 443–446.
67. Hibiya, T. (1983) Surface morphologies and quality of thick liquid phase epitaxial garnet films for magneto-optic devices. *Journal of Crystal Growth*, **62** (1), 87–94.
68. Webb, M.R. (1989) *International Journal of Infrared and Millimeter Waves*, **10**, 1317.
69. Glass, H.L. (1988) Ferrite films for microwave and millimeter-wave devices. *Proceedings IEEE*, **76** (2), 151.
70. Robertson, J.M., Jansen, M., Hoekstra, B., *et al.* (1977) Growth of spinel ferrite films by liquid phase epitaxy. *Journal of Crystal Growth*, **41** (1), 29–35.
71. van der Straten, P.J.M. and Metselaar, R. (1980) Liquid phase epitaxial growth of lithium ferrite-aluminate films. *Journal of Crystal Growth*, **48** (1), 114.
72. Suzuki, Y., van Dover, R.B., Gyorgy, E.M., *et al.* (1996) Structure and magnetic properties of epitaxial spinel ferrite thin films. *Applied Physics Letters*, **68**, 714.
73. Dorsey, P.C., Bushnell, S.E., Seed, R.E., *et al.* (1993) Epitaxial yttrium iron garnet films grown by pulsed laser deposition. *Journal of Applied Physics*, **74**, 1242.
74. Stearns, F.S. and Glass, H.L. (1976) Liquid phase epitaxy of hexagonal ferrites and spinel ferrites on non-magnetic spinel substrates. *Materials Research Bulletin*, **11** (10), 1319–1325.
75. Kramer, W.E., Stewart, A.M., Hopkins, R.H., *et al.* (1986) Investigation of hexagonal ferrite substrate and film growth. *IEEE Transactions on Magnetism*, **22** (5), 981.
76. Dotsch, H., Mateika, D., Roschmann P., *et al.* (1983) Growth and properties of epitaxial barium hexaferrite films. *Materials Research Bulletin*, **18** (10), 1209–1216.
77. Mita, M. (1962) *Journal of Physics Society of Japan*, **18**, 155.
78. Morgenthaler, F.R. (1962) Microwave phonon instabilities associated with ferromagnetic resonance. *Proceedings of IRE*, **50** (10), 2139.
79. Labeyrie, M., Mage, J.C., Simonet, W., *et al.* (1984) FMR linewidth of barium hexaferrite at millimeter wavelengths. *IEEE Transactions on Magnetism*, **20** (5), 1224.
80. Silber, L.M. and Wilber, W.D. (1986) Temperature and frequency dependence of linewidth in $BaFe_{12}O_{19}$. *IEEE Transactions on Magnetism*, **22**, 984.
81. Yuan, M.S., Glass, H.L. and Adkins, L.R. (1988) Epitaxial barium hexaferrite on sapphire by sputter deposition. *Applied Physics Letters*, **53**, 340.
82. Yoon, S.D. and Vittoria, C. (2004) Thick M-type barium hexaferrite films grown on garnet substrates. *Journal of Applied Physics*, **96** (4), 2131–2135.
83. Brookner, E. (2006) Phased arrays and radars – past, present and future. *Microwave Journal*, **49**, 1.

84. Chen, Z. and Harris, V.G. (2012) Ferrite film growth on semiconductor substrates towards microwave and millimeter wave integrated circuits. *Journal of Applied Physics*, **112** (8), 081101.
85. Chen, Z. *et al.* (2007) Epitaxial growth of M-type Ba–hexaferrite films on MgO (111) SiC (0001) with low ferromagnetic resonance linewidths. *Applied Physics Letters*, **91** (18), 182505-3.
86. Chen, Z. *et al.* (2010) Structure, magnetic, and microwave properties of thick Ba–hexaferrite films epitaxially grown on GaN/Al_2O_3 substrates. *Applied Physics Letters*, **96** (24), 242502-3.
87. Scaff, J.H. and Ohl, R.S. (1947) Development of silicon crystal rectifiers for microwave radar receivers. *Bell System Technical Journal*, **26** (1), 1–30.
88. Johnson, V.A. and Lark-Horovitz, K. (1969) *Pioneer in Solid State Physics*, Pergamon Press, New York.
89. Seitz, F. (1995) Research on silicon and germanium in World War II. *Physics Today*, January, 22–27.
90. Shockley, W., Bardeen, J., and Brattain, W. Semiconductor amplifier. US Patent 2502488.
91. Moore, G. (1965) Cramming more components onto integrated circuits. *Electronics Magazine*, **38** (8).
92. Moore, G. (1975) Progress in digital integrated electronics. *IEEE, IEDM Technology Digest*, 11–13.
93. Schmid, G.M., Stewart, M.D., Wang, C.-Y., *et al.* (2004) Resolution limitations in chemically amplified photoresist systems. *Proceedings of SPIE*, **5376**, 333–342.
94. Alferov, Z.I. (2000) Nobel Lecture: the double heterostructure concept and its applications in physics, electronics, and technology. *Review of Modern Physics*, **73**, 767.
95. Kondoh, H. (1998) Recent trends and status of Japanese RFIC's for commercial applications, in *IEEE Radio Frequency Integrated Circuits Symposium.*
96. Thompson, S.E., Chau, R.S., Ghani, T., *et al.* (2005) In search of "Forever," continued transistor scaling one new material at a time. *IEEE Transactions on Semiconductor Manufacturing*, **18** (1), 26–36.
97. Johnson, E.O. (1963) *RCA Review*, **26**,163–177.
98. Keyes, R.W. (1972) Figure of merit for semiconductors for high-speed switches. *Proceedings of IEEE*, **60** (2), 225.
99. Bhatnagar, M. and Baliga, B.J. (1993) Comparison of 6H-SiC, 3C-SiC, and Si for power devices. *IEEE Transactions on Electron Devices*, **40**, 645−655.
100. Matsunami, H. (2006) Current SiC technology for power electronic devices beyond Si. *Microelectronic Engineering*, **83** (1), 2–4.
101. Wetzel, C., *et al.* (1994) GaN epitaxial layers grown on 6H-SiC by the sublimation sandwich technique. *Applied Physics Letters*, **65** (8), 1033–1035.
102. http:www.CREE.com, Product Data sheet.
103. Snoek, J.L. (1936) Magnetic and electrical properties of the binary systems MO.Fe_2O_3. *Physica*, **3** (6), 463–483; Snoek, J.L. (1946) Non-metallic magnetic material for high frequencies, *Philips Technology Review*, **8**, 353; see also the review by Adam, J.D., Davis, L.E., Dionne, G., *et al.* (2002) Ferrite devices and materials. *IEEE Transactions on Microwave Theory and Techniques*, **50** (3), 721–737.
104. Heinz, D.M., Besser, P., Owens, I.M., *et al.* (1971) Mobile cylindrical magnetic domains in epitaxial garnet films. *Applied Physics*, **42**, 1243–1251.
105. Mee, J.E., Besser, P.J., and Pizzarello, F.A. (1970) Epitaxial growth of ferromagnetic garnets. Air Force Avionics Laboratory Technical Report AFAL-TR-70-194.
106. Sui, X. and Kryder, M.H. (1993) Magnetic easy axis randomly in-plane oriented barium hexaferrite thin film media. *Applied Physics Letters*, **63**, 1582.
107. Hylton, T.L., Parker, M.A., Ullah, M., *et al.* (1994) Ba–ferrite thin-film media for high-density longitudinal recording. *Journal of Applied Physics*, **75** (10), 5960–5965.
108. Morisako, A., Naka, T., Ito, K., *et al.* (2002) Properties of Ba-ferrite/AlN double layered films for perpendicular magnetic recording media. *Journal of Magnetism and Magnetic Materials*, **242–245**, 304–310.
109. Morisako, A., Shams, N.N., Miuraa, Y., *et al.* (2004) *C*-axis oriented Ba–ferrite thin film with small grain for perpendicular magnetic recording. *Journal of Magnetism and Magnetic Materials*, **272–276**, 2191–2193.

110. Matsuoka, M., Naoe, M., and Hoshi, Y. (1985) Ba–ferrite thin-film disk for perpendicular magnetic recording. *Journal of Applied Physics*, **57** (8), 4040–4042.
111. Morisako, A., Liu, X., Matsumoto, M., *et al*. (1997) The effect of underlayer for Ba–ferrite sputtered films on c-axis orientation. *Journal of Applied Physics*, **81**, 4374–4376.
112. Lisfi, A. and Lodder, J.C. (2001) The effects of ZnO underlayer on microstructural and magnetic properties of $BaFe_{12}O_{19}$ thin films. *Journal of Physics: Condensing Matter*, **13** (26), 5917–5922.
113. Lacroix, E., Gerard, P., Marest, G., *et al*. (1991) Substrate effects on the crystalline orientation of barium hexaferrite films. *Journal of Applied Physics*, **69** (8), 4770–4772.
114. Wane, I., Bessaudou, A., Cosset, F., *et al*. (2000) Thick barium hexaferrite (Ba-M) films prepared by electron-beam evaporation for microwave application. *Journal of Magnetism and Magnetic Materials*, **211**, 309–313.
115. Le Berre, M., Capraro, S., Chatelon, J.P., *et al.* (2004) In *Materials Research Society Symposium Proceedings*, 783.
116. Liu, X., Hong, M.H., Song, W.D., *et al*. (2005) *Applied Physics A*, **80**, 611–614.
117. Adam, J.D., Buhay, H., Daniel, M.R., *et al.* (1995) Thick yttrium–iron–garnet (YIG) films produced by pulsed laser deposition (PLD) for integration applications. *IEEE Transactions on Magnetics*, **31**, 3832–3834.
118. Xi, X.W., Chen, Y.J., and Zhang, X.Y. (2004) Growth and magnetic properties of soft ferrite films by pulsed laser deposition. *Vacuum*, **75**, 161–165.
119. Sorescu, M., Diamandescu, L., Swaminathan, R., *et al*. (2005) Structural and magnetic properties of NiZn and Zn ferrite thin films obtained by laser ablation deposition. *Journal of Applied Physics*, **97**, 10G105.
120. Calle, C., Calle, V.H., Cué llar, F., *et al*. (2006) Magneto-optical Kerr effect in NiZn ferrite films of variable thickness. *Physica B*, **384**, 103–105.
121. Chen, Y., Smith, I., Geiler, A.L., *et al*. (2008) Realization of hexagonal barium ferrite thick films on Si substrates using a screen printing technique. *Journal of Physics D: Applied Physics*, **41**, 095006.
122. Zhang, L., Su, X.D., Chen, Y., *et al.* (2010) Radio-frequency magnetron sputter-deposited barium hexaferrite films on Pt-coated Si substrates suitable for microwave applications. *Scripta Materialia*, **63**, 492–495.
123. Abe, M., Itoh, T., Tamaura, Y., *et al*. (1988) Ferrite–organic multilayer film for microwave monolithic integrate circuits prepared by ferrite plating based on the spray-spin-coating method. *Journal of Applied Physics*, **63**, 3774–3777.
124. Yoo, K.C. and Talisa, S.H. (1990) Spin-spray plating of spinel ferrite films on semiconductor substrates. *Proceedings of SPIE, Electro-Optical Materials for Switches, Coatings, Sensor Optics, and Detectors*, **134**, 1307.
125. Buhay, H., Adam, J.D., Daniel, M.R., *et al*. (1995) Thick yttrium–iron–garnet (YIG) films produced by pulsed laser deposition (PLD) for integration applications. *IEEE Transactions on Magnetism*, **31**, 3832–3834.
126. Adam, J.D., Buhay, H., Daniel, M.R., *et al*. (1996) K-band circulators on semiconductor wafers. *IEEE MTT-S Digest*, **1**, 113–115.
127. Neudeck, P.G. (1999) SiC Technology, in *The VLSI Handbook, The Electrical Engineering Handbook Series* (ed. W.K. Chen), CRC Press and IEEE Press, Boca Raton, FL, pp. 6.1–6.24.
128. Spry, D., Neudeck, P., Okojie, R., *et al.* (2004) Electrical operation of 6H-SiC MESFET at 500 °C for 500 hours in air ambient, in *2004 IMAPS International High Temperature Electronics Conference*, Santa Fe, NM, May 18–20.
129. Treu, M., Rupp, R., Blaschitz, P., and Hilsenbeck, J. (2006) Commercial SiC device processing: status and requirements with respect to SiC based power devices. *Superlattices and Microstructures*, **40**, 380–387.
130. Madar, R. (2004) Materials science: silicon carbide in contention. *Nature*, **430**, 974.
131. Chen, Z., Yang, A., Cai, Z., *et al*. (2006) Structure and magnetism of Ba–hexaferrite films grown on single crystal 6-H SiC. *IEEE Transactions on Magnetism*, **42**, 2855.

132. Ohodnicki, P.O., Goh, K.Y., Hanlumyuang, Y., *et al.* (2007) Magnetic anisotropy and crystalline texture in $BaO(Fe_2O_3)6$ thin films deposited on GaN/Al_2O_3. *Journal of Applied Physics*, **101**, 09M521.
133. Chen, Z., Yang, A., Mahalingam, K., *et al.* (2010) Structure, magnetic, and microwave properties of thick Ba-hexaferrite films epitaxially grown on GaN/Al_2O_3 substrates. *Applied Physics Letters*, **96**, 242502.
134. Cai, Z., Chen, Z., Goodrich, T.L., *et al.* (2007) Chemical and structural characterization of barium hexaferrite films deposited on 6H-SiC with and without MgO/BaM interwoven layers. *Journal of Crystal Growth*, **307** (2), 321.
135. Chen, Z., Cai, Z., Yang, A., *et al.* (2008) The effects of room temperature aging upon the magnetic properties of Ba–hexaferrite films grown on 6H-SiC substrates. *Journal of Applied Physics*, **103**, 07E513.
136. Chen, Z., Yang, A., Geiler, A., *et al.* (2007) Epitaxial growth of M-type Ba–hexaferrite films on MgO (111)/SiC (0001) with low ferromagnetic resonance line widths. *Applied Physics Letters*, **91**, 182505.
137. Chen, Z. and Harris, V.G. (2010) Unpublished.
138. Chen, Z., Yang, A., Mahalingam, K., *et al.* (2010) Structure, magnetic, and microwave properties of thick Ba–hexaferrite films epitaxially grown on GaN/Al_2O_3 substrates. *Applied Physics Letters*, **96**, 242502.
139. Cai, Z., Goodrich, T.L., Chen, Z., *et al.* (2009) Epitaxial growth of barium hexaferrite film on wide bandgap semiconductor 6H-SiC by molecular beam epitaxy. *Journal of Physics D: Applied Physics*, **43**, 095002.
140. Cai, Z., Goodrich, T.L., Sun, B., *et al.* (2007) Role of magnesium oxide interface layer in heteroepitaxial growth of barium hexaferrite on 6HSiC (0001). *Journal of Crystal Growth*, **307**, 321–327.
141. Chen, Z. and Harris, V.G. (2012) Ferrite film growth on semiconductor substrates towards microwave and millimeter wave integrated circuits. *Journal of Applied Physics*, **112**, 081101.
142. Akaiwa, Y. and Okazaki, T. (1974) An application of a hexagonal ferrite to a millimeter-wave Y circulator. *IEEE Transactions on Magnetism*, **10**, 374.
143. Oliver, S.A., Shi, P., Hu, W., *et al.* (2001) Integrated self-biased hexaferrite microstrip circulators for millimeter-wavelength applications. *IEEE Transactions on Microwave Theory and Techniques*, **49**, 385–389.
144. Chen, Y., Sakai, T., Chen, T., *et al*. (2006) Oriented barium hexaferrite thick films with narrow ferromagnetic resonance linewidth. *Applied Physics Letters*, **88**, 062516.
145. Chen, Z., Xie, C., Yang, Q., *et al*. (2009) High-rate reactive ion etching of barium hexaferrite films using optimal CHF_3/SF_6 gas mixtures. *Applied Physics Letters*, **94**, 112505.
146. Perekarima, T.M. and Cheparin, V.P. (1967) *Fiz. Tverd. Tela*., 9, 3205, as reported in *Landolt-Bornstein Part C: Hexagonal Ferrites*, Springer, Berlin and Heidelberg, pp. 1615–1925; Albanese, G. and Deriu, A. (1979) Magnetic properties of Al, Ga, Sc, In substituted barium ferrites: a comparative analysis. *Ceramargia International*, 5, 3–10.
147. Van Uitert, L.G. and Swanekamp, F.W. (1957). Permanent magnet oxides containing divalent metal ions. *Journal Applied Physics*, 28, 482; Mones. A.H. and Banks, E. (1958) Cation substitutions in BaFe12O19. *Journal Physics Chemical Solids*, 4, 217; Haneda, K. and Kojima, H. (1973). Intrinsic coercivity of substituted $BaFe_{12}O_{19.}$ *Journal Applied Physics*, 12, 355.
148. Zuo, X., Yang, A., Yoon, S.D., *et al.* (2005). Large induced magnetic anisotropy in manganese spinel ferrite films. *Applied Physics Letters*, **87**, 152505.
149. Yang, A., Chen, Z., Arena, D., *et al.* (2005) Cation-disorder-enhanced magnetization in PLD Cu-ferrite films. *Appl. Phys. Lett*., **86**, 252510.
150. Geiler, A.L., Yoon, S.D., Chinnasamy, C.N. (2007) $BaFe_{12}O_{19}$ thin films grown at the atomic scale from $BaFe_2O_4$ and Fe_2O_3 targets. *Applied Physics Letters*, **91**, 162510.
151. Rodrigue, G.P. (1988) A generation of microwave ferrite devices. *Proceedings of the IEEE*, **76** (2), 121–137.
152. Lax, B. (1956) Frequency and loss characteristics of microwave ferrite devices. *Proceedings of IRE*, **44**, 1368–1386.

153. Bertaut, F. and Pauthenet, R. (1957) Crystalline structure and magnetic properties of ferrites having the general formula $5Fe_2O_3 \cdot 3M_2O_3$. *Proceedings of the Institute of Electrical Engineers*, **104B**, 261–264.
154. DeBitetto, D.J., DePre, F.K., and Brockman, F.G. (1959) Highly anistropic materials for millimeter wave applications. *Proceedings of the Symposium on Millimeter Waves*, **9**, 95.
155. Pengely, R.S. and Turner, J.A. (1976) Monolithic broadband GaAs FET amplifiers. *Electronics Letters*, **12** (10), 251–252.
156. Oliver, S.A., Zavracky, P.M., McGruer, N.E., and Schmidt, R. (1994) *IEEE Transactions on Magnetism*, **30**, 4551–4554.
157. Oliver, S.A., Shi, P., Hu, W., *et al.* (2001) Integrated self-biased hexaferrite microstrip circulators for millimeter-wavelength applications. *IEEE Transactions on Microwave Theory and Techniques*, **49** (2), 385–387.
158. Rasky, P.H.L., Greve, D.W., and Kryder, M.H. (1985) The feasibility of silicon on garnet technology. *Journal of Applied Physics*, **57** (1), 4077.
159. Manasevit, H.M. (1983) Epitaxial composite and method of making. US Patent 4 368 098.
160. Razeghi, M., Meunier, P.-L., and Maure, P. (1986) Crowth of CaInAs–InP multiple quantum wells on garnet (GGC = Gd,Ca,O_{12}) substrate by metalorganic chemical vapor deposition. *Journal of Applied Physics*, **59**, 2261–2263.
161. Ito, S., Fujioka, H., and Oshima, M. (2004) Characterization of heterointerfaces in GaAs/MnAs/MnZn–ferrite structures. *Journal of Crystal Growth*, **260**, 384–387.
162. Ohta, J., Fujioka, H., Takahashi, H., and Oshima, M. (2001) Crystal growth of GaN on (Mn, Zn) Fe_2O_4 substrates. *Physical Status Solidi (a)*, **188**, 497–500.
163. Ohta, J., Fujioka, H., Ito, S., and Oshima, M. (2002) Room-temperature epitaxial growth of AlN films. *Applied Physics Letters*, **81**, 2373–2375.
164. Ikeda, T., Fujioka, H., Hayakawa, S., *et al.* (1999) Epitaxial growth of InAs on single-crystalline Mn–Zn ferrite substrates. *Japanese Jounal of Applied Physics*, **38**, L854.
165. Fujioka, H., Ikeda, T., Ito, S., Oshima, M. (2002) Characteristics of InSb grown on single crystalline Mn–Zn ferrite substrates. *Journal of Crystal Growth*, **241**, 309.
166. Chen, Y., Geiler, A.L., Sakai, T., *et al.* (2006) Microwave and magnetic properties of self-biased barium hexaferrite screen printed thick films. *Journal of Applied Physics*, **99** (8), 08M904.
167. Sui, X., Scherge, M., Kryder, M.H., *et al.* (1996) Barium ferrite thin-film recording media. *Journal of Magnetism and Magnetic Materials*, **155** (1–3), 132–139.
168. Tanaka, K., Omata, Y., Nishikawa, Y., *et al.* (1991) Formation of Ni–Zn–ferrite films using laser ablation. *Journal of Magnetism and Magnetic Materials*, **6** (11), 1001–1006.
169. Vittoria, C. (1993) Fabrication of ferrite films using laser deposition. US Patent 5,227,204.
170. Adam, J.D., Davis, L.E., Dionne, G.F., *et al.* (2002) Ferrite devices and materials. *IEEE Transactions on Microwave Theory and Techniques*, **50** (3), 721–737.
171. Wu, Y.S. and Rosenbaum, F.J. (1974) Wideband operation of microstrip circulators. *IEEE Transactions on Microwave Theory and Techniques*, **22**, 849.
172. Knerr, R.H. (1975) An annotated bibliography of microwave circulators and isolators – 1968–1975. *IEEE Transactions on Microwave Theory and Techniques*, **23**, 818–825.
173. von Aulock, W.H. and Fay, C.E. (1968). *Linear Ferrite Devices for Microwave Applications*, Academic Press, New York.
174. Helszajn, J. (1975) *Nonreciprocal Microwave Junctions and Circulators*, John Wiley & Sons, Inc., New York.
175. Schloemann, E.F. (1988) Circulators for microwave and millimeter-wave integrated circuit. *Proceedings of the IEEE*, **76** (2), 188–200.
176. Fenn, A.J., Temme, D.H., Delaney, W.P., *et al.* (2000) The development of phased-array radar development. *Lincoln Laboratory Journal*, **12**, 321.
177. Schaug-Pettersen, T. (1957) Norwegian Electronic Research. *ONR Technology Report ONRL*, **111**, 57.
178. Davis, L., Milano, J.U., and Saunders, J. (1960) A strip-line L-band compact circulator, *Proceedings of IRE*, **48**, 115.
179. Hershenov, B. (1967) All garnet microstrip circulators for integrated circuits. *IEEE-1967 G-MTT International Microwave Symposium Digest*, 142–144.

180. Bosma, H. (1962) On the principle of stripline circulation. *Proceedings of IEE*, **109**, 137.
181. Bosma, H. (1964) On stripline Y-circulation at UHF. *IRE Transactions on Microwave Theory and Techniques*, **12** (1), 61–72.
182. Fay, C.E. and Comstock, R.L. (1965) Operation of the ferrite junction circulator. *IEEE Transactions on Microwave Theory and Techniques*, **13** (1), 15–27.
183. Polder, D. (1948) On the phenomenology of ferromagnetic resonance. *Physics Review*, **73** (9), 1120.
184. Polder, D. (1949) On the theory of ferromagnetic resonance. *Philosophical Magazine*, **40** (2), 99–115.
185. Kittel, C. (1948) On the theory of ferromagnetic resonance absorption. *Physics Review*, **73** (2), 155.
186. Harris, V.G., Geiler, A., Chen, Y., *et al.* (2009). Recent advances in processing and applications of microwave ferrites. *Journal of Magnetism and Magnetic Materials*, **321** (14), 2035–2047.
187. Akaiwa, Y. and Okazaki, T. (1974) An application of a hexagonal ferrite to a millimeter-wave Y circulator. *IEEE Transactions on Magnetism*, **10** (2), 374–378.
188. Weiss, J.A., Watson, N.G., and Dionne, G.F. (1989) New uniaxial-ferrite millimeter-wave junction circulators. *IEEE MTT-S Digest*, **1**, 145.
189. Zeina, N., How, H., and Vittoria, C. (1992) Self-biasing circulators operating at Ka-band utilizing M-type hexagonal ferrites. *IEEE Transactions on Magnetism*, **28** (5), 3219.
190. Oliver, S.A., Shi, P., Hu, W., *et al.* (2001) Integrated self-biased hexaferrite microstrip circulators for millimeter-wavelength applications. *IEEE Transactions on Microwave Theory and Techniques*, **49** (2), 385.
191. Shi, P., Yoon, S.D., Zuo, X., Kozulin, I., *et al.* (2000) Microwave properties of pulsed laser deposited Sc-doped barium hexaferrite films. *Journal of Applied Physics*, **87** (9), 4981.
192. Shi, P., How, H., Zuo, X., *et al*. (2001) MMIC circulators using hexaferrites. *IEEE Transactions on Magnetism*, **37** (4), 2389.
193. Wang, J.W., Geiler, A.L., Harris, V.G., *et al.*, (2011) Self biased Y-junction circulator at Ku band. *IEEE Microwave and Wireless Components Letters*, **21**, 292–294.
194. Davis, L.E. and Sillars, D. (1986) Millimetric nonreciprocal coupled-slot finline components. *IEEE Transactions on Microwave Theory and Techniques*, **34**, (7), 804–808.
195. Marcuse, D. (1975) Coupled-mode theory for anisotropic optical waveguides. *Bell System Technology Journal*, **54** (6), 985.
196. Queck, C.K. and Davis, L.E. (2002) Microstrip and stripline ferrite-coupled-line (FCL) circulators. *IEEE Transactions on Microwave Theory and Techniques*, **50** (12), 2910.
197. Queck, C.K. and Davis, L.E. (2003) Self-biased hexagonal ferrite coupled line circulators. *Electronics Letters*, **39** (22), 1595.
198. Bichurin, M.I., Viehland, D., and Srinivasan, G. (2007) Magnetoelectric interactions in ferromagnetic-piezoelectric layered structures: phenomena and devices. *Journal of Electroceramics*, **19** (4), 243–250.
199. Nan, C.W, Bichurin, M.I., Dong, S., and Viehland, D. (2008) Multiferroic magnetoelectric composites: historical perspective, status, and future directions. *Journal of Applied Physics*, **103** (3), 031101.
200. Eerenstein, W., Mathur, N.D., and Scott, J.F. (2006) Multiferroic and magnetoelectric materials. *Nature*, **442**, 759.
201. Fetisov, Y.K. and Srinivasan, G. (2006) Electric field tuning characteristics of a ferrite–piezoelectric microwave resonator. *Applied Physics Letters*, **88**, 143505.
202. Chen, Y., Fitchorov, T., Vittoria, C., *et al.* (2010) Electrically controlled magnetization switching in a multiferroic heterostructure. *Applied Physics Letters*, **97**, 052502.
203. Dong, S., Zhai, J., Li, J., and Viehland, D. (2006) Near-ideal magnetoelectricity in high-permeability 4242 magnetostrictive/piezofiber laminates with a (2–1) connectivity. *Applied Physics Letters*, **89** (25), 252904.
204. Geiler, A.L., Gillette, S.M, Chen, Y., *et al.* (2010) Multiferroic heterostructure fringe field tuning of meander line microstrip ferrite phase shifter. *Applied Physics Letters*, **96** (5), 053508.
205. Tatarenko, A.S., Srinivasan, G., and Bichurin, M.I. (2006) Magnetoelectric microwave phase shifter. *Applied Physics Letters*, **88**, (18), 183507.

206. Smith, D.R., Pendry, J.B., Wiltshire, M.C.K. (2004) Metamaterials and negative refractive index. *Science*, **305**, 788–792.
207. He, Y., He, P., Harris, V.G., and Vittoria, C. (2006) Role of ferrites in negative index materials. *IEEE Trans.actions on Magnetism*, **42** (10), 2852–2854.
208. He, P., Gao, J., Chen, Y., *et al*. (2009) Q-band tunable negative refractive index metamaterials using Sc-doped BaM hexaferrite. *Journal of Physics D: Applied Physics*, **42**, 155005.
209. Levy, R. and Cohn, S.B. (1984) A history of microwave filter research, design, and development. *IEEE Transactions on Microwave Theory and Techniques*, **32**, 1055–1067.
210. Uher, J. and Hoefer, W.J.R. (1991) Tunable microwave and millimeter-wave band-pass filters. *IEEE Transactions on Microwave Theory and Techniques*, **39** (4), 643–653.
211. Gillette, S., Geiler, A.L., and Chen, Z., *et al*. (2011) Active tuning of a microstrip hairpin-line microwave band pass filter on a polycrystalline YIG substrate using small magnetic fields. *Journal of Applied Physics*, **109**, 07A513.
212. Tatarenko, A.S., Gheevarughese, V., and Srinivasan, G. (2006) Magnetoelectric microwave band pass filter. *Electronics Letters*, 20060167.
213. Sloan, R., Yong, C.K., and Davis, L.E. (1995) Planar millimetric semiconductor junction circulators. *IEEE Colloquium on Terahertz Technology*, **13**, 1–6.
214. Pyndiah, R. and Van Den BoGaart, F. (1989) Novel multioctave MMIC active isolator (1–20 GHz). *Electronics Letters*, **25**, 1420–1422.
215. Berg, M., Hackbarth, T., Maile, B.E., *et al.* (1996) Active circulator MMIC in CPW technology using quarter micron InAlAs/InGaAs/InP HFETs, in *Eighth International Conference on Indium Phosphide and Related Materials*, pp. 68–71.

15

Applications of Microwave Dielectrics

Heike Bartsch,[1] Alexander Schulz,[1] Jens Müller,[1] Alexander Ebert,[2]
Steffen Spira,[2] Frank Wollenschläger,[2] and Matthias Hein[2]
[1]Electronics Technology Group and
[2]RF and Microwave Research Laboratory, Department of Electrical Engineering and Information Technology, Technische Universität Ilmenau, lmenau, Germany

15.1 General Requirements for Microwave Applications

Substrates for microwave circuits are required to have a low dielectric loss tangent ($\tan \delta < 0.001$ across the range of frequencies of interest) and high frequency and temperature stability of permittivity. This allows for low signal losses and dispersion-free signal transmission. Depending on the specific application either low or high-k materials are necessary. Low-k materials ($k < 10$) are typically requested for microwave applications since they improve radiation, provide faster signal propagation (phase velocity), and offer a higher degree of freedom for structuring technologies to achieve distributed elements and components due to the fact that the wavelength-related structures are large enough. Mid-k and high-k materials are candidates for integrated capacitors and compact resonant components for applications in the lower gigahertz range. Thus such components can be realized very compact.

Besides these dielectric properties the substrate itself has to be mechanically stable and should have a temperature coefficient of expansion matching those of semiconductor materials applied in microwave circuits. The thermal conductivity of the substrate needs to be as high as possible to spread the heat and remove the dissipated power. The surface roughness influences the skin effect related conductor loss, the structural resolution for photolithographic processes, and the potential adhesion of the conductor itself. For smallest skin losses the substrate surface should be as smooth as possible. Substrate bow, waviness, and warpage might influence the photolithographic process as well since glass or chromium masks cannot be ideally aligned to the substrate surface. Furthermore, tight thickness control of

Microwave Materials and Applications, First Edition.
Edited by Mailadil T. Sebastian, Rick Ubic and Heli Jantunen.
© 2017 John Wiley & Sons, Ltd. Published 2017 by John Wiley & Sons, Ltd.

dielectric layers is essential for reproducible microwave properties (e.g., wave impedance control and hence achievable operational bandwidth).

Metals with high electrical conductivity such as copper, silver, or gold are required for transmission lines and vertical through holes (vias) with low insertion loss. The dielectric substrate needs to be compatible with the deposition and structuring technology of these metals in terms of process conditions like annealing or sintering temperatures. Pattern accuracy and tolerances of lines or gaps between lines as well as their reproducibility, have an important impact on the microwave behavior of integrated structures and scale with frequency. The edge roughness of transmission lines might significantly contribute to the skin effect related loss and coupling gaps between lines determine the stray fields and mutual coupling between neighboring lines.

Multilayer ceramic technologies such as LTCC or HTCC offer options to implement three-dimensional waveguide, biasing, and control structures and components in addition to better shielding opportunities. Vertical shielding is typically accomplished by via fences. The achievable via density and thus frequency limit is directly related to the process of generating smallest holes and their filling procedure. The stability of LTCC dielectric properties versus processing conditions is very much dependent on the material composition of the tape itself (e.g., crystallization behavior) [1]. Reference [2] lists some typical electrical, mechanical, and thermal properties of LTCC materials from commercial suppliers.

Finally, the dielectric substrates and their metallization shall ensure subsequent assembly steps to mount passive or active devices by soldering or wire or flip chip bonding.

15.2 LTCC Microwave Components and Materials

15.2.1 Conductor Patterning Technologies

The conductor pattern resolution directly influences the capability to implement microwave functions on LTCC. Both lateral (line widths and gaps) and vertical structures (vias) contribute to the microwave performance of transmission lines, line transitions, and passive components. Vertical interconnects between layers in LTCC are made of metal paste filled holes. Their typical diameter in volume production is in the range from 100 to 200 μm [3]. Critical aspects and limitations that come with much smaller via diameters are the processes to create smaller holes, the filling of these holes with metal paste, and the stack alignment of layers. The latter is not only a matter of positioning tolerances. Tape handling and shrinkage during previous process steps may lead to local distortions and poor via-to-via coverage [4]. Holes are either mechanically punched or laser drilled. The minimum hole diameter is about 50 μm for mechanical punching [3–5]. Laser drilling results depend on the laser source [3, 5] and machine parameters [6]. Holes with a diameter of about 35 μm are demonstrated in reference [6]. However, the shape of laser drilled holes is conical compared to the straight walls of punched vias, which poses problems for via filling. As a general rule the ratio tape thickness-to-hole diameter should be below 2:1 to achieve clean holes and to allow for sufficient metal paste filling.

The following subsections provide an overview about different technologies to structure the lateral conductor pattern on LTCC tapes and substrates.

15.2.1.1 Additive Processes

Thick film screen printing is the dominant method used to structure the lateral metallization on LTCC since it is a fast, material efficient additive process. The line resolution depends on screen parameters such as wire diameter, mesh count, wire orientation, screen aperture and type of photo emulsion, paste parameters such as rheology, metal content, and particle size distribution, and screen printing parameters such as printing speed, force, and screen snap-off. For typical thick film screen printing of structures larger than 125 μm stainless steel fabrics with a wire diameter of 24 μm and 325 meshes/inch are used. For fine line printing the wire diameter is reduced to 18 μm or even 15 μm and the mesh count is increased to 400–500 meshes/inch. However, the smaller wire diameter reduces the mechanical stability and durability of such screens. The concept of a combination of fine metal mesh and polymer mesh (trampoline mesh) is applied to prevent plastic deformation of the metal wires [7]. Conductor lines and spaces of approximately 50 μm are possible by fine line screen printing [8]. Straight structures yield better printing results compared to curved structures where parts of the pattern are blocked by the wire and wire crossings [9]. Schwanke *et al.* [7, 10] demonstrated a solution using fine line screens coated with a hydrophobic nanolayer. The coating improves paste release and lines with 30 μm width could be successfully printed.

An alternative approach to circumvent the mesh orientation effect is based on a stepped or dual-layer stencil [11]. This stencil is also being used to combine screen printing and via filling in one step with a line resolution of 75 μm across 8 inch × 8 inch tapes.

Gravure offset printing is also adapted for thick film structures [12]. Line widths of about 35 μm are demonstrated. However, due to the paste release behavior in gravure offset printing the line thickness of narrow lines tends to be low.

Inkjet and aerosoljet printing are maskless processes with high flexibility for layout changes and fast prototyping [13, 14]. Using silver nanoinks line widths of less than 20 μm are demonstrated with aerosoljet printing [14]. In order to obtain several micrometer thick lines multiple printing passes are required. Inkjetting can even be combined with screen printing, as shown in reference [15].

15.2.1.2 Semiadditive Processes

Semiadditive techniques are made up of a combination of thin layer deposition, photo resist application, lithography, and galvanic or electrochemical methods to build up high resolution structures with sufficient thickness. Due to the wet chemical processes this technique can only be applied on sintered LTCC substrates and therefore only on outer layers. Sputtered thin film-based process sequences with gold or copper metal lines result in a line and gap resolution of 10 μm on as-fired LTCC (no grinding or polishing) [8]. The thin film layer sequence with adhesion layer and plating base permits the integration of thin film resistors [16] but does not allow for additional sintering steps at 850 °C.

An alternative concept is based on screen printing and sintering gold-based resinate pastes as plating base [17, 18]. The sintered base layer thickness is below one micrometer. Gold electrodeposition is used to increase the thickness for conductor lines and line widths below 15 μm can be achieved with chromium masks [17]. Figure 15.1 shows a line resolution test structure with line widths from 5 to 10 μm. Due to the fact that the layer structure is monometallic the substrate may be re-fired and subsequent layers can be added in a tape-on-substrate process [19].

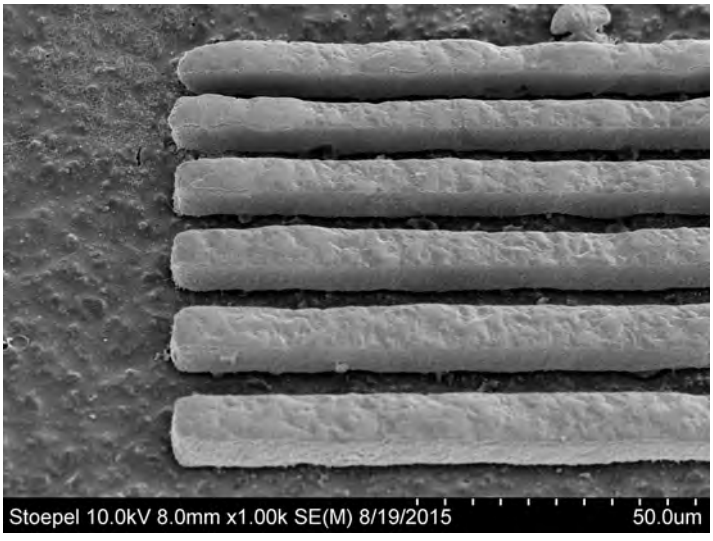

Figure 15.1 *Line resolution test pattern on LTCC GreenTape™ 951 based on Au resinate layer (RP 181208 Heraeus) and approximately 6 μm electrodeposited Au (AURUNA® 558).*

15.2.1.3 Subtractive processes

Alternatively, sintered thick films may be etched or photoimageable pastes can be applied to improve the line resolution. Etching of thick film pastes requires additional photolithographic steps (photoresist deposition, exposure, resist development). The resolution is about 30 μm for lines and gaps between lines [8]. Compared to high resolution screen printing the edge quality is much better but the process is only compatible with sintered films on the top or bottom layer of the substrate.

Photoimageable pastes can also be used on green ceramic foils [20] and therefore in inner layers of the LTCC stack. Due to edge curl effects during sintering the minimum line width is slightly smaller than the minimum gap between lines (30 μm versus 40 μm). Both technologies are based on subtractive processes with high material consumption and waste.

Laser structuring of green or fired thick films can be combined with standard screen printing. Only the areas around critical structures are enlarged and laser ablated. Line widths and spaces of about 30 μm are achieved with good repeatability [21].

15.2.2 Transmission Lines and Transitions

15.2.2.1 Line Types

The multilayered dielectric LTCC substrate allows integrating planar RF-transmission line structures such as microstrip lines, coplanar lines, and striplines. An overview of a transmission lines is given in reference [22].Technology-independent parameters for impedance controlled designs are summarized in reference [23]. However, compared to microwave theory the real transmission line implementations differ according to the size-limited extension

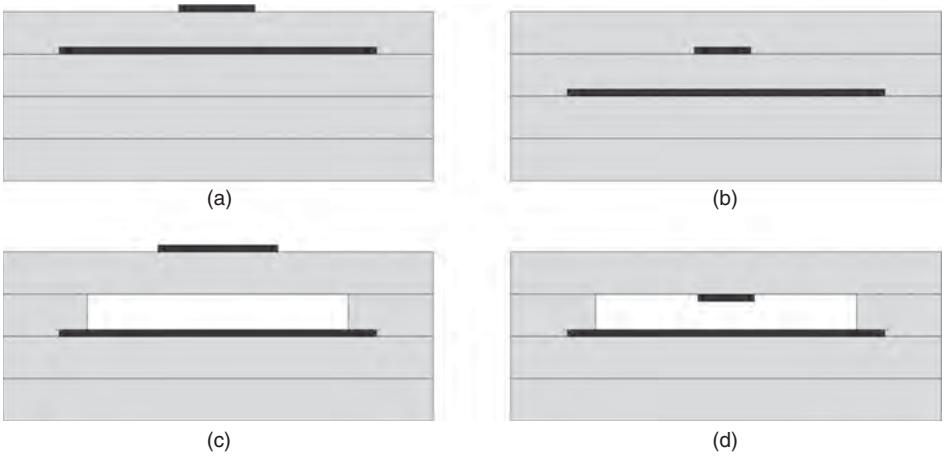

Figure 15.2 *Microstrip line configurations in LTCC: (a) standard microstrip line, (b) embedded microstrip, (c) suspended microstrip, and (d) inverted microstrip.*

of ground planes and the non-ideal interconnections among ground layers, since LTCC vias provide a good electrical connection only locally.

15.2.2.2 Microstrip Lines

The classical microstrip line consists of a conductor line guided above a ground plane (Figure 15.2a). The effective permittivity is considerably smaller than the substrate permittivity and the wave impedance is defined by the line width-to-tape thickness ratio. For typical LTCC materials with a k-value smaller than eight the line width is larger than the tape thickness. This large line width sometimes causes problems for interconnecting integrated circuits due to the mismatch in the contact pitches. If the conductor is covered by an additional substrate layer the line is called an embedded or buried microstrip line (Figure 15.2b). This line type has an increased permittivity compared to the standard microstrip line. Suspended or inverted microstrip lines have a much lower effective permittivity due to the air gap in the layer stack (Figure 15.2c and d) [24]. In addition, these line types exhibit very low dielectric losses since air offers the ultimate microwave performance. Their implementation in LTCC is possible by machining a channel or cavity in one LTCC tape. This concept is locally applied to optimize the quality factor of a strip line resonator in reference [25]. Inverted and suspended microstrip lines in LTCC can also be deployed for permittivity measurement of fluids [26] and may be applied for tunable phase shifters [27].

15.2.2.3 Coplanar Waveguide (CPW)

A planar ground–signal–ground configuration is used for the coplanar line (Figure 15.3a). This line type is very suitable for single layer circuits. In LTCC designs the grounded coplanar line type (Figure 15.3b) is often in use in order to separate the coplanar line from signals in other LTCC layers. Via fences are necessary to connect the inner ground plane with the ground plane layers on the top. The pitch of the vias as well as the distance of the two via

Figure 15.3 *Coplanar line configurations in LTCC: (a) standard coplanar line, and (b) grounded coplanar line.*

rows influence the maximum operating frequency [28]. The wave impedance is defined by the substrate permittivity, the signal line width, the lateral spacing to the ground planes, and for the grounded version the distance to the ground plane underneath. This line type therefore provides better options to adapt the signal line width to the interconnect pitch of integrated circuits.

15.2.2.4 Striplines and Substrate Integrated Waveguides

LTCC striplines consist of at least two tape layers (Figure 15.4a). The stripline is fully enclosed by the LTCC dielectrics and the effective permittivity of this line is equal to the substrate permittivity. Via fences provide contact between the ground plane layers and shielding [29–31]. Similar to the grounded coplanar line the distance between the two via rows and via pitch of the fences themselves have a strong influence on the upper frequency limit of this line [28]. Small vias with a tight pitch are recommended. Better shielding is achieved by connecting the via fences with conductor strips in the center layer (Figure 15.4b) [32]. The suppression of via fence-related resonances is obtained by combining the coplanar line and stripline as shown in Figure 15.4c [33]. In order to enhance shielding and isolation of striplines the via fences may be replaced with full metals walls [34].

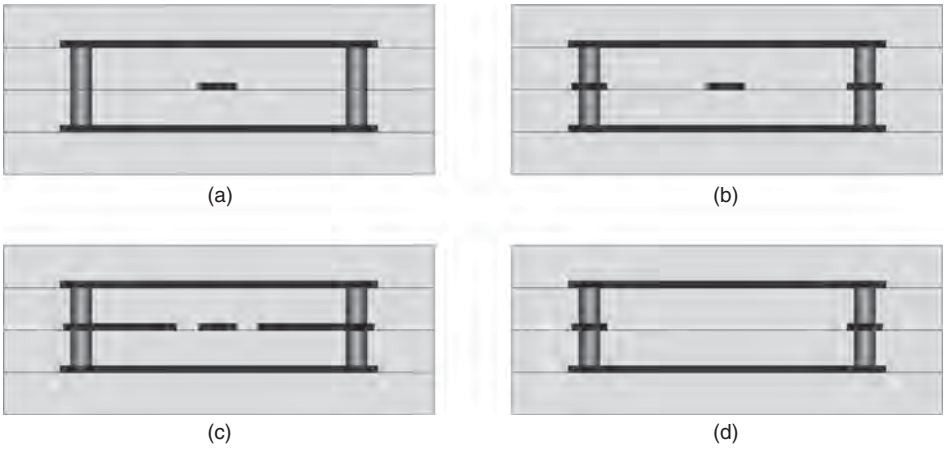

Figure 15.4 *Stripline and SIW configurations in LTCC: (a) standard stripline, (b) stripline with ground connecting strips, adapted from Gipprich 2001 [32], (c) coplanar stripline, adapted from Trabert 2007 [33], and (d) SIW.*

The wave impedance is defined by the substrate permittivity and the line width-to-thickness ratio, where the thickness is the distance between the ground planes. With *k*-values of about eight the line width of a 50 ohm LTCC stripline embedded between 100 μm thick tape layers becomes smaller than 50 μm and fine line printing techniques need to be employed.

LTCC substrate-integrated waveguides (SIW) are similar in design and manufacturing to the stripline despite the fact that no inner line is required (Figure 15.4d). The propagating wave modes depend on the substrate permittivity and the cross-sectional dimensions of the waveguide (width and height) [35]. SIWs provide a high quality factor and are used in LTCC designs for substrate integrated filters [36, 37] or for interconnecting the substrate to rectangular metal waveguides [47].

15.2.2.5 Line Transitions

The substrate embedded line types such as embedded microstrip line, inverted microstrip line, stripline, and substrate integrated waveguide cannot be directly accessed and need to be connected by surface-integrated transmission lines. These line transitions represent discontinuities for the electromagnetic fields and cause signal reflections or excitation of other wave modes. In order to reduce these effects the transition should be as small as possible and the wave impedance of the transition should be matched closely to the line impedance.

Microstrip to stripline transitions are described in references [38] and [39]. The microstrip ground layer serves also as an upper ground plane for the stripline and the vertical interconnect passing through the ground plane layer is designed in the style of a coaxial line. Transitions from one side of the substrate to the other include microstrip-to-microstrip, CPW-to-CPW, and CPW-to-microstrip combinations [40, 41]. Such transitions are required for interconnections between the inside of a microwave package and the bottom of the package. The grounded CPW-to-stripline transition offers high design flexibility. For maximum shielding between the top layer and the stripline layer the vertical transition passes through the lower ground plane layer of the CPW line. Compensation of the parasitic via capacitance is achieved by introducing a window or opening in the lower ground plane [42] (Figure 15.5a). In combination with a locally higher inductance per unit length of the stripline the impedance can be matched to a certain frequency band. A wider bandwidth is achieved by reducing the via diameter [28] (Figure 15.5b). An alternative technological solution to reduce the via capacitance is based on embedded air cavities [43].

In the case of a grounded CPW line consisting of two LTCC layers, the ground planes can also be used for the stripline. Thus, the vertical interconnection is very short (one layer only). Using the parasitic capacitance compensation with an aperture in the lower ground plane a bandwidth of up to 100 GHz is obtained [44].

References [45] and [39] describe microstrip-to-SIW and CPW-to-SIW transitions, respectively. A direct transition design from the microstrip to an attached metal waveguide is given in reference [46] and an SIW-to-metal waveguide is proposed in reference [47].

15.2.3 Lumped Passive Integrated Components

Integrated passives are usually applied to improve system miniaturization and performance, for example, with respect to harmonic distortion or reliability. For RF- and microwave circuits the main advantage to use integrated lumped components such as capacitors, resistors, or inductors is their short interconnection length with reduced parasitics within a circuit.

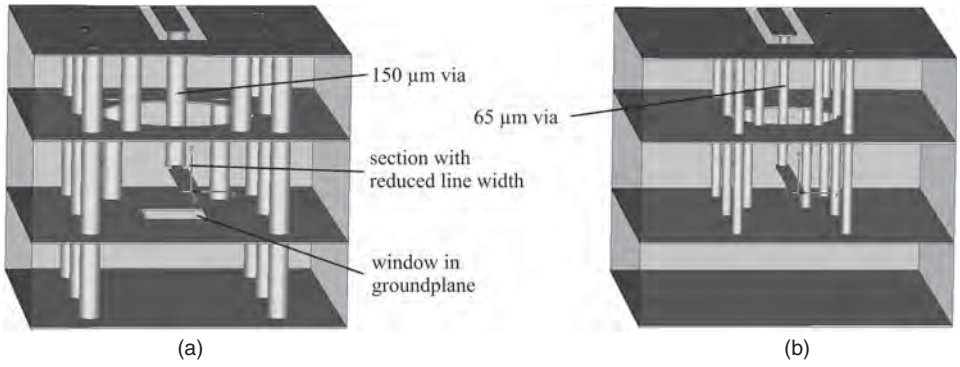

Figure 15.5 *Coplanar-to-stripline transitions in LTCC: (a) with window in the ground plane to reduce capacitance in combination with a high impedance stripline section, adapted from Perrone 2005 [42] and (b) with smaller via diameter to reduce the parasitic capacitance, adapted from Perrone 2006 [28].*

To consider them lumped or concentrated, their physical size needs to be small in relation to the wavelength, which means that requirements on structural resolution increase with increasing frequency.

15.2.3.1 Thick Film Resistors

Printed thick film resistors consist of two metal electrodes and an overlapping area with specific resistivity or sheet resistance (Figure 15.6). Such resistors are either co- or post-fired on top of an LTCC substrate or co-fired inside the multilayer stack. Their fired resistance value and other properties such as the temperature coefficient of resistance are heavily influenced by processing conditions [48]. Resistors on the substrate surface are laser trimmed to their target value with a tolerance of less than one percent over a range from several ohms to megaohms. The main challenge for embedded resistors is to achieve the desired resistance value and to control the tolerances due to potential chemical interactions between resistor paste and surrounding tapes during sintering [49,50]. Subsequent laser trimming is not easily possible. An alternative method to trim resistors by high voltage pulses has been demonstrated but is difficult to implement in rf and microwave designs [51]. Due to the physical size constraints for microwave applications such resistors often have to be much smaller

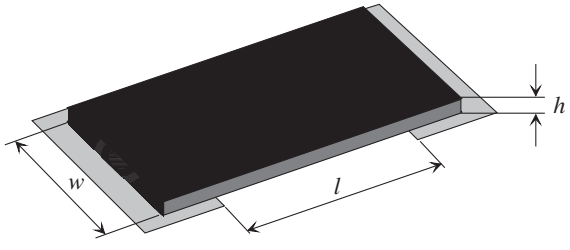

Figure 15.6 *Typical structure of a printed thick film resistor.*

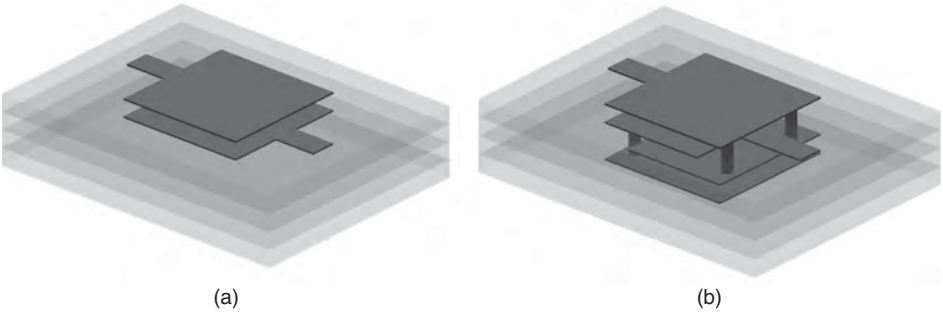

Figure 15.7 *Plate capacitors in LTCC: (a) plate capacitor with two electrodes and (b) multilayer capacitor with four electrodes.*

than recommended by material suppliers, which makes manufacturing more challenging. Printed resistors in microwave applications are used as load or matching components, in power dividers, and as attenuators.

15.2.3.2 Capacitors

Capacitors are integrated in an LTCC as a plate or interdigital type. The plate capacitor, also referred to as a metal–insulator–metal (MIM) capacitor, consists of at least two electrodes separated by an LTCC layer (Figure 15.7). Due to the low permittivity of the LTCC tapes and the typical layer thickness of 100 μm the capacitance density is very low (less than 2 pF/mm^2) [52]. Very thin tapes [53] or multilayer electrodes are applied in order to minimize their physical size. The self-resonant frequency of such capacitors is heavily influenced by the plate and via inductance [52].

Interdigital capacitors or finger capacitors only need one conductor layer. In the simplest form they are printed on the substrate surface (Figure 15.8a). The capacitance depends on the coupling gap between fingers, the coupling length, the number of fingers, and the dielectric boundary conditions [54]. Printed on the surface, the effective permittivity is smaller than the substrate permittivity. If embedded in the LTCC stack the capacitance density is increased (Figure 15.8b). Provided that the coupling gap is smaller than the thickness of the cover layer the capacitance can be doubled [55]. By adding an identical interdigital capacitor in an adjacent layer the capacitance density is doubled again (superposition principle, Figure 15.8c). The highest capacitance density is achieved by arranging the second interdigital capacitor in an antiparallel way (Figure 15.8d) due to the fact that both edge-coupling between fingers in one plane as well as side-coupling between fingers in two layers prevail. This woven wire or quasi-fractal concept is theoretically investigated in reference [56]. Higher capacitance densities are only possible by integrating high-k pastes or high-k tapes in the LTCC layer stack.

15.2.3.3 Inductors

Inductors are made of a conductive pattern and are therefore easy to implement in LTCC designs. The multilayer capability in combination with small via diameters allow for various shapes (Figure 15.9). The quality factor of inductors is mainly influenced by the

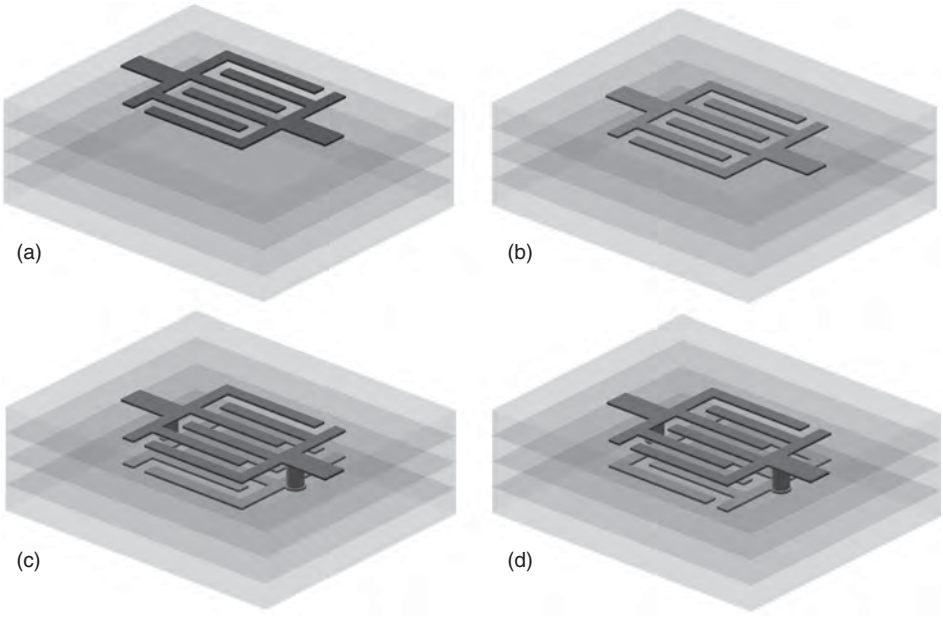

Figure 15.8 *Interdigital capacitors in LTCC: (a) top layer, (b) buried, (c) two capacitors in parallel buried, and (d) two capacitors in antiparallel buried.*

conductivity of the metal traces. Quality factors as high as 140 have been measured with silver conductors [57]. The self-resonant frequency of integrated inductors depends on the design (e.g., line width and distance) and the permittivity of the substrate that influences the parasitic capacitance. Concepts to implement air cavities are applied to increase the self-resonant frequency [58, 59]. Using fine line structuring techniques self-resonant frequencies beyond 10 GHz are achievable [53].

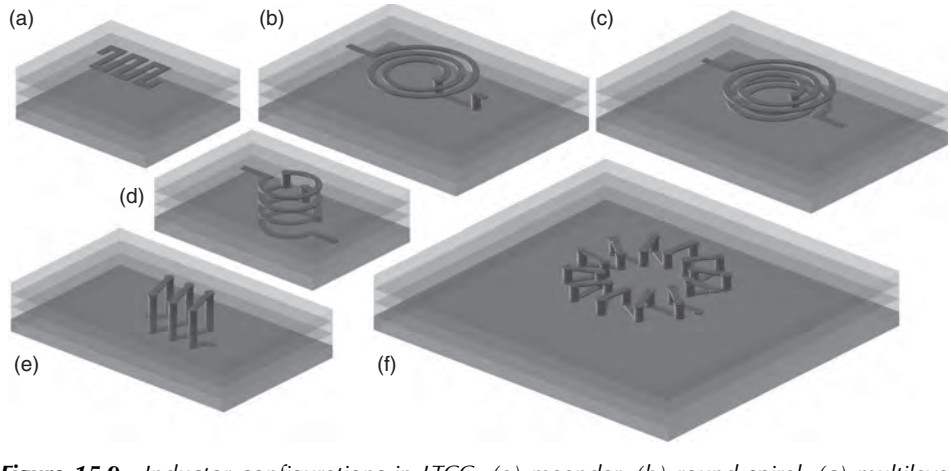

Figure 15.9 *Inductor configurations in LTCC: (a) meander, (b) round spiral, (c) multilayer spiral, (d) vertical helix, (e) horizontal helix, and (f) toroidal.*

15.2.4 Integrated Functional Materials for Passives

15.2.4.1 Integration Strategies for Mixed Materials

Mixed material structures combine the features of functional regions with high and low permittivity or high permeability. While impedance matching transmission lines require low permittivity to minimize cross-talk, high permittivity or high permeability materials increase the energy density of the respective substrate area and thus allow a miniaturization of lumped components such as coils and capacitors or fulfill electromagnetic compatibility functions. The possible size reduction is significant; reference [60] demonstrated a bandpass filter, which is reduced in size from 20 mm × 20 mm without high-*k* materials to 4.1 mm × 5.6 mm using high-*k* patches with a permittivity of 50–150. Further application examples use mixed materials for the size reduction of components with a given wavelength or for lowering the operational frequency for given dimensions [60–62].

The technological challenge for the realization of such mixed material structures consists in lowering the sinter temperature of functional materials to 900 °C and below and controlling possible material interactions and stress due to mismatch in the temperature coefficients of expansion (TCE) and chemical reactions [63]. The properties of commercially available functional tapes co-fired with commercially available standard tapes cover permittivity ranges from 13 to 250 and permeability values from 50 to more than 1100 [64]. Since the resulting properties depend on the sinter profile, layout and post-fire treatments it is necessary to evaluate the specific properties for the single case and adapt the design [65, 66].

Several integration strategies can be applied to co-fire different materials. Figure 15.10 gives an overview of these methods. The easiest and cheapest way is the direct screen printing of functional pastes and subsequent co-firing. However, the screen printed layers have limited thickness consistency and components such as capacitors are failure-prone,

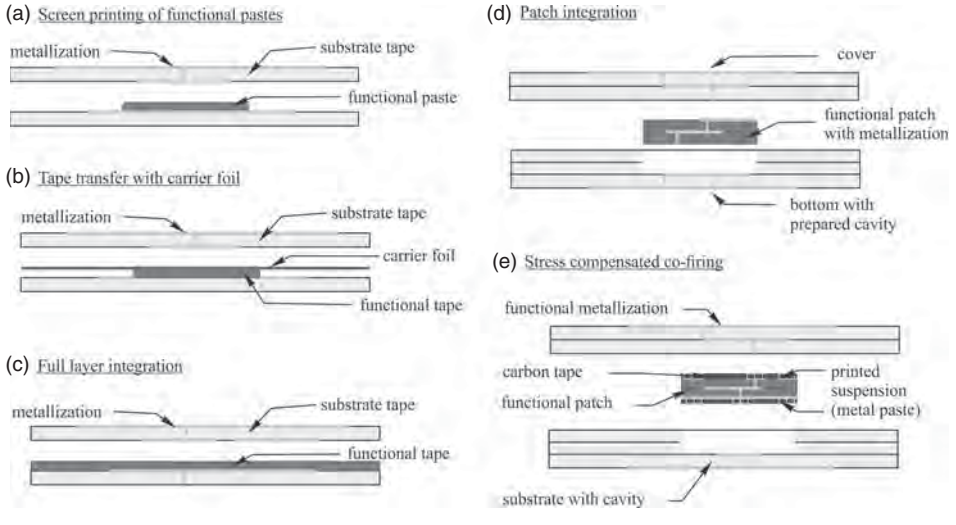

Figure 15.10 *Integration methods for co-firing of functional materials in LTCC multilayer circuits: (a) via screen printing, (b) by tape transfer, (c) as full layer, (d) as pre-processed multilayer, and (e) as pre-processed multilayer with decoupling layers.*

because pinholes are often generated, which may lead to electrical short-circuits. This failure is prevented by the use of thin functional tapes, which are cast on a carrier foil and structured by laser cut [67]. The unnecessary material is stripped from the carrier and the functional patch is laminated on the substrate tape. Subsequently, the tape is treated in the same way as a screen printed one. Both methods are limited to thin functional layers (10 to 30 μm) and induce minor stress. A further method is the lamination of a full layer over the whole substrate. In this way, numerous components of the same type can be integrated, for instance decoupling capacitors, which are necessary on various places on a board, or shielding elements. However, the use of this method requires a very good adaptation of the shrinkage behavior and thermal expansion of the substrate tape and the functional tape. Non-matching shrinkage can be addressed by applying a zero shrinkage process, such as pressure-assisted sintering [68]. Less stress is generated if patches with pre-manufactured components are inserted into a prepared substrate tape. Both parts are laser cut. The prepared functional components can be inserted into cavities in the green state. Electrical connections are formed during the lamination. The subsequent co-firing creates compact circuits. Nevertheless, a large TCE mismatch can lead to a crack forming and the use of substrate tapes with adapted thermal expansion may be necessary [69]. Since it is complicated to meet all these requirements, thermal expansion match, sinter profile adaption, and functional requirements for signal routing, it might be advisable to use substrate tapes with optimized microwave performance and compensate for the stress. One method to achieve this compensation is the use of fugitive tapes, such as carbon black, as a decoupling layer. The carbon black tape is equipped with metal paste via connections and screen printed metallization. These act as a ductile suspension after the burnout of the carbon and allow stress compensation. The functional metallization conducts the signal and is connected over similar metal structures with the component metallization of the functional patch. An example for the integration of coils is given in reference [70].

15.2.4.2 Decoupling Capacitors

The filtering of noise generated by different components is a task that is typically solved by ceramic capacitors. Ceramic capacitors for this purpose usually have values of 1 nF and more and complex circuits require a huge number of such components. Consequently, a considerable area reduction can be achieved by burying those capacitors. Parasitic inductances are reduced due to short interconnections if the capacitor is located directly underneath the integrated circuit. Often the tolerance of a decoupling capacitor is not critical, but a crucial parameter is the insertion loss.

A suitable high-k material for the construction of decoupling capacitors is barium strontium titanate. The material can be co-fired with different commercially available LTCC tapes at temperatures around 900 °C [71, 72]. Sinter additives influence the temperature characteristics strongly; dependent on the composition, X7R class (EIA RS-198-Code) is reachable [73]. Material interaction at the interface between high-k dielectric and metallization, as well as between high-k and low-k material, leads to a dependency on capacitance density from layout and sinter conditions [65,66]. The achievable k-values of co-fired buried BST capacitors can reach values of 1000 and above and a loss tangent between 4 and 2%, dependent on sintering conditions and composition. For instance, the capacitance density of buried shunt capacitors in CT 700 tape (Heraeus) exceeds 100 pF/mm [74].

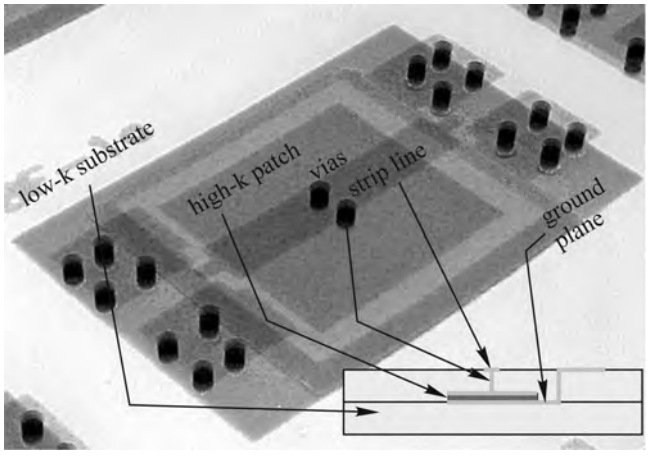

Figure 15.11 *X-ray image of a buried, co-fired ceramic shunt capacitor in CT 700 (Heraeus).*

Figure 15.11 depicts an X-ray picture of a buried shunt component. The high-k material is inserted between the electrodes using tape transfer with a carrier foil (Figure 15.10b). The fired thickness of the dielectric amounts to 30 μm. The depicted test component connects the transmission line at the top of the substrate with the ground plane at the bottom. Figure 15.12 compares the measured insertion loss of a co-fired capacitor for two layouts. Capacitors with one and two via connections between the conductor line and upper plate are presented. The reduction of the parasitic via inductance resulting from the parallel connection leads to an increase of the resonance frequency.

15.2.4.3 Multilayer Inductors Based on BaFe12-2xCoxTixO19–M Ferrite Tape

Co–Ti-doped barium ferrite materials were traditionally used as storage materials for magnetic storages and in recent years they became important as absorbers [75–77]. The

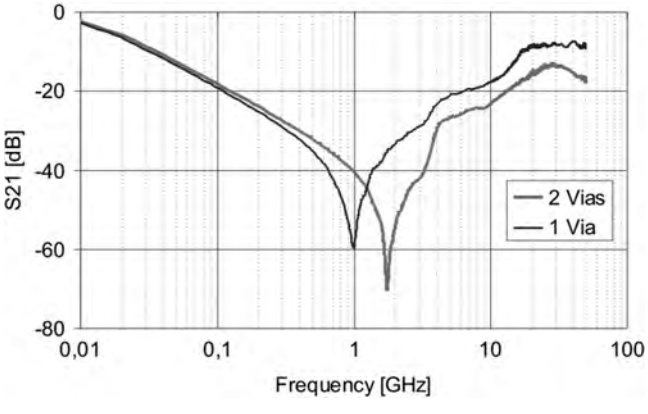

Figure 15.12 *Insertion loss of a barium hexaferrite capacitor, connected as a shunt element with one and two vias. Source: Adapted from Bartsch 2010 [66].*

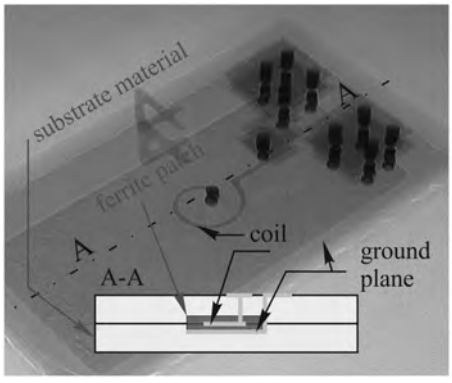

Figure 15.13 *Co-fired coil, printed on an M-type ferrite patch, integrated in a TCE-adapted zinc titanate substrate tape.*

electromagnetic adsorbing behavior of M-type ferrites at frequencies above 8 GHz due to interactive loss mechanisms with reflections of 96 % is reported in reference [78]. The direct integration of these absorbers into LTCC multilayers offers the possibility to integrate electromagnetic shielding components efficiently in a very confined space.

LTCC tapes with the composition $BaCo_{1.3}Ti_{1.3}Fe_{9.4}O_{19}$ show a permeability $\mu' = 17$ and a cut-off frequency of 1 GHz. The use of Bi_2O_3, B_2O_3, SiO_2, and ZnO as additives lowers the sintering temperature successfully down to 900 °C and allows the use of commercially available silver metallization without affecting the magnetic performance [79]. Measurements on multilayer inductances show that the properties of the tape agree well with ring core measurements and can be specified as: permittivity $\varepsilon_r = 21$, loss tangent = 0.0004, complex permeability $\mu' = 16$ (real part) and $\mu'' = 0.025$ (imaginary part).

The integration of the ferrite material into commercially available substrate tapes is challenging because of its high TCE. While the adaptation of the sintering point can be achieved by suitable sintering additives, the TCE mismatch leads to cracks and component failure. One strategy to overcome this limitation is the use of polycrystalline zinc titanate as substrate tape, which has a matched TCE [69]. Patches with coil structures can be successfully co-fired with this substrate tape. Simulations and measurements on buried patch components (see Figure 15.13) confirm the material data determined on ring cores and indicate that material interactions can be controlled. However, the properties of these TCE-adapted materials are not optimized for RF applications and thus complex circuits are subject to design limitations and performance loss. Therefore, a stress-compensated co-firing can be the solution here (see Figure 15.10e).

15.3 LTCC Application Examples

15.3.1 Power Dividers

Power dividers provide in-phase output signals, usually with an equal power division ratio of 3 dB. A fundamental and simple variant is the T-junction power divider [80], which can be realized with any type of transmission line. A 60 GHz microstrip feeding network for an

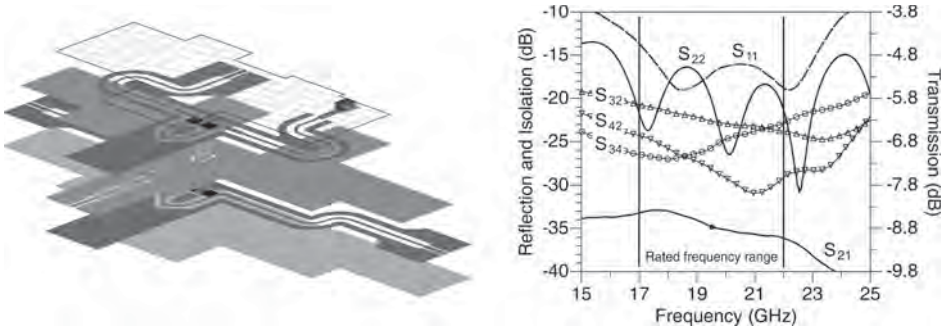

Figure 15.14 *(a) 3D-exploded layout of a one-stage four-way Wilkinson power divider, showing five metallization layers, indicated ground vias, and coplanar test ports. (b) Measured S-parameters of a fabricated sample.*

antenna patch array on a DuPont DP943^{TM} LTCC substrate demonstrates the application of this power divider type [81]. A simultaneous match of all ports and isolation between the output ports with a lossless operation under matched load conditions accomplishes the Wilkinson power divider [82]. Planar versions of the two-way divider are widely used. Numerous articles were published for the enhancement of the basic topology [83–85]. A 20 GHz one-stage four-way Wilkinson power divider can be beneficially implemented in a compact manner in multilayer LTCC technology [86, 87]. Figure 15.14a shows the 3D-exploded view of the shielded stripline divider fabricated on a sixfold layered GreenTape^{TM} 951-PX LTCC substrate. In this technology the maximum line impedance is limited to about 50 Ω. Quarter wavelength transformers are used at all ports for matching the 24 Ω divider reference impedance to 50 Ω termination impedance. Measured S-parameters of this divider are shown in Figure 15.14b. The quasi-lumped resistors in this design are printed buried resistors and require stable process conditions for maintaining the envisaged tolerances.

In the case of a mismatched output load, the reflected power is absorbed by the resistor of the Wilkinson divider. The Gysel power divider [88] was proposed to accommodate this condition in high-power applications. Figure 15.15a shows the schematic of a two-way Gysel divider. The design of Z_1 and Z_2 is carried out according to the rules valid also for a Wilkinson divider, whereas Z_3, Z_4, and R are to be optimized for the required values for isolation and output return loss. The load resistance R can also be implemented as a termination of a transmission line with an impedance $Z_L = R$. This termination may dissipate the requested power, on the one hand, and can be realized, on the other hand, by printing buried resistive structures with much higher tolerances while obtaining a high return loss. An appropriate Gysel divider for 30 GHz operation was proposed and simulated for the GreenTape^{TM} 951 system [89], the simplified layout of which is depicted in Figure 15.15b.

15.3.2 A 60 GHz Stripline Parallel Coupled Bandpass Filter

Microwave filters can be manufactured from lumped or distributed components or a combination of them and can be easily designed to the required response. Some elementary filter types are high-, low- and bandpass as well as band rejection filters.

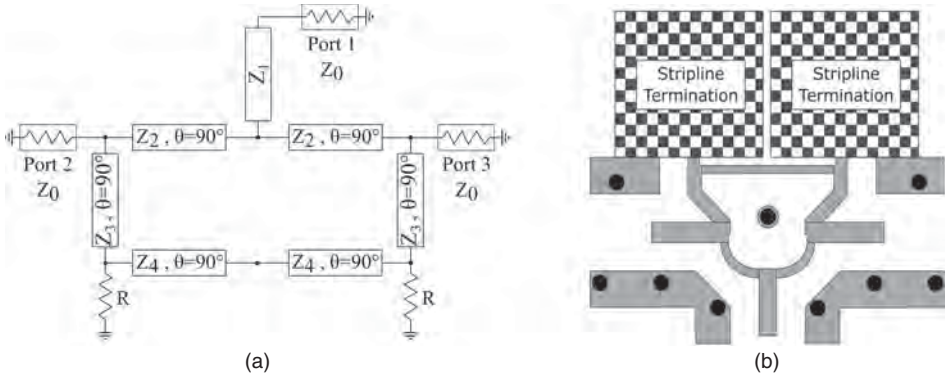

Figure 15.15 *Gysel power divider. (a) Schematic of a two-way divider. (b) Simplified layout of a proposed 30 GHz divider realizing the left-hand schematic. Source: Adapted from Klein 2014 [89].*

Bandpass filters (BPF) are fundamental passive RF structures having a characteristic transmission behavior at their operating frequency band. Below and above the operating band the transmitted signal should be attenuated to a level as required by the respective application. The filter roll-off or shape factor is defined as the ratio of the bandwidth evaluated for two different attenuation values and quantifies the rise of the frequency response. All electric filter properties must be designed according to the intended filter application. Filters are also essential in millimeter-wave systems around 60 GHz and can be realized with transmission lines or waveguide structures applying reactive elements, which are periodically loaded. Lumped element filters are difficult to manufacture in LTCC since the required physical dimensions at 60 GHz are too small even for fine line structuring methods. The growing data rates in digital communication networks that have to handle the growing amount of information requires broadband applications. A design based on coupled transmission lines offers high flexibility in this regard and the implementation on LTCC package level using fine structuring technologies is feasible [90].

A fully embedded line coupled stripline filter in inner LTCC layers features several advantages like reduced cross-coupling to other inner millimeter-wave structures and low radiation losses due to the shielding capabilities in LTCC. The electrical interconnections between the BPF and the antenna or to other surface-mounted devices can be easily realized by vertical via transitions and transmission lines.

Figure 15.16 depicts the schematic layout of a five-pole Chebyshev stripline parallel coupled BPF. The target specification for the filter optimization process comprises a center frequency at 58 GHz and a bandwidth larger than 10 GHz to meet the specifications for a broadband communication system. Additional theoretical aspects in filter synthesis and design are covered in references [91] and [92].

The most critical structures in terms of manufacturability for this particular filter design are the 30 μm coupling gaps of the first and last filter sections (marked in Figure 15.16). In order to allow screen printing for the filter pattern these gaps need to be wider and alternative ways to achieve the tight coupling need to be introduced. Nishikawa *et al.* [93] suggest using floating areas above and underneath the critical sections. In reference [94] active coupling patches with connections to the feed lines are added above and below the

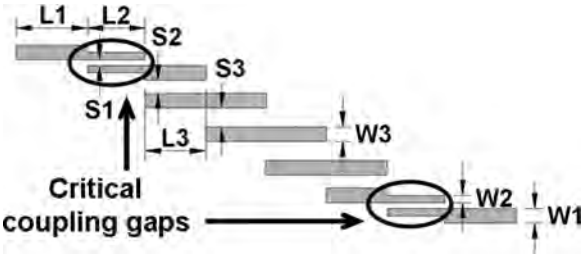

Figure 15.16 *Schematic layout of the BPF (L: segment length, W: conductor width, S: spacing) with critical filter coupling gaps marked (coupling plates are not shown).*

first and last filter sections (Figure 15.17). In order to be compatible with the 100 μm wide feeding line the via diameters are reduced to 68 μm (fired dimension). As a result these critical gap dimensions are enlarged to 40 μm, which enables structuring by fine line screen printing. The final design parameters can be examined in reference [94]. Solid metallization layers on top and bottom as well as via fences on both filter sides are applied to suppress unwanted wave modes and to reduce cross-coupling and radiation effects. All shielding fences are based on 130 μm (fired diameter) vias with a pitch of 330 μm. A 3D view of the four-layer stripline BPF design with a shielding via fence is illustrated in Figure 15.17.

DuPont's LTCC material GreenTape^{TM} 9k7V and the gold paste system were used for the BPF implementation. In order to allow S-parameter measurement with 250 μm pitch coplanar wave probes grounded CPW-to-stripline transitions were added in the final design. The overall filter dimensions are $5.75 \times 2.2 \times 0.42$ mm^3 including transitions and measurement ports (Figure 15.18).

The measured and simulated scattering parameters of the BPF from 50 to 67 GHz are shown in Figure 15.19. The measured insertion loss is less than 1.5 dB at the center frequency of 58 GHz, including the transition loss. The calculated 3 dB bandwidth of the

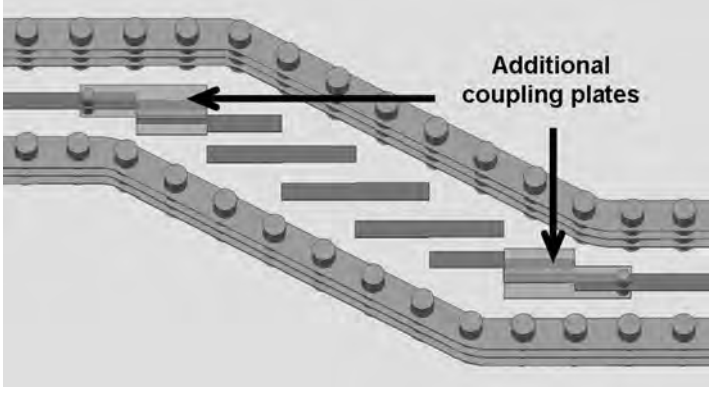

Figure 15.17 *3D view of 60 GHz stripline BPF including via fences and coupling plates (top and bottom metallization are not shown).*

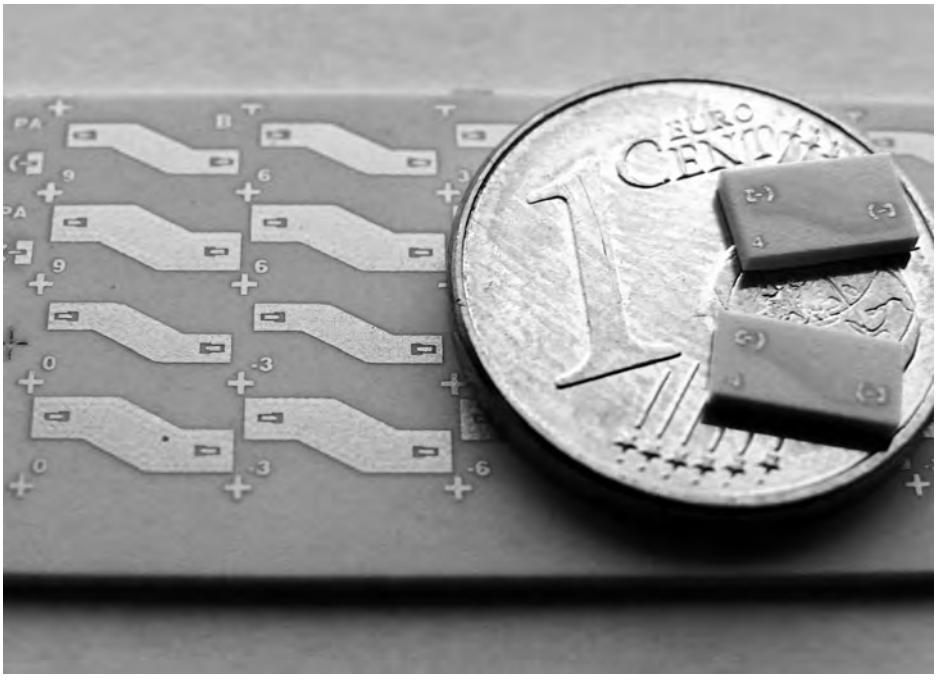

Figure 15.18 *A 60 GHz stripline BPF implemented in LTCC compared to the size of a euro cent coin.*

filter is about 11 GHz, which indicates wideband capabilities. The reflection coefficients are higher than predicted (> –15 dB between 55 and 58 GHz), which is most likely attributed to manufacturing tolerances. A slightly better shape factor of 1.42 is evaluated compared to the simulation.

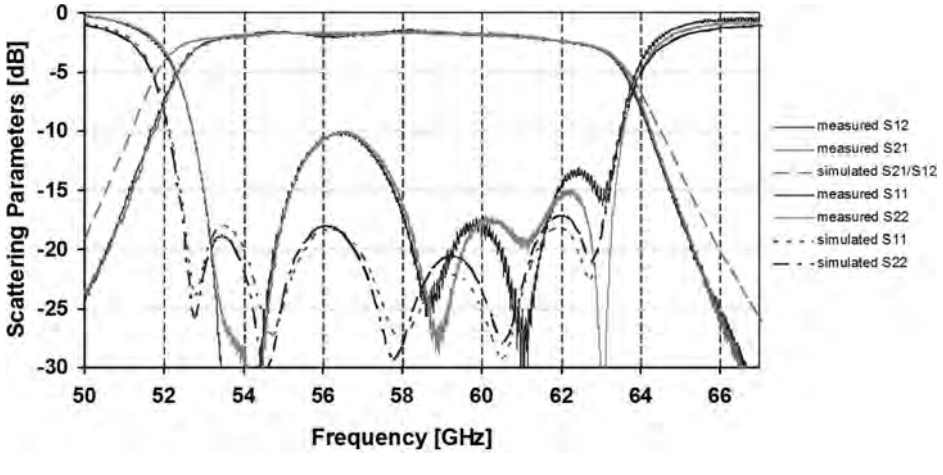

Figure 15.19 *Measured and simulated scattering parameters of the stripline BPF.*

15.3.3 Integrated Antennas

Antenna integration directly in LTCC technology possesses several advantages as well as disadvantages. The advantages include the multilayer and 3D structuring capabilities, which allow for compact realization of antennas with complex feed networks, integration in the direct vicinity of MMICs, significantly reducing the total losses by transmission lines. and the shrinking of structures due to the dielectric constant.

The high dielectric constant of LTCC can, however, also be a disadvantage for antenna implementations. At millimeter-wave frequencies, the scaling starts to raise problems with precision and resolution of conducting structures. For resonant antennas, small variations can cause deviations from the design frequency, comparable to filter structures.

In addition, high-k substrates tend to propagate substrate modes and surface waves. These generally reduce the effective gain of the antenna, and thus the overall performance. With the inclusion of special structures the losses due to these parasitic effects can often be reduced.

There exists a large number of different antenna types that have been implemented in LTCC technology. A recent overview including a large number of different antenna types can be found in reference [95]. Two antenna designs specifically for communication applications are presented in reference [96]. As an example of a resonant antenna radiation perpendicular to the surface of the LTCC substrate a 2×2 dual-polarized, symmetrically fed patch antenna array is presented here. A more detailed description can be found in reference [97]. The antenna was designed to cover most of the 60 GHz ISM-band, more specifically 59.5 to 66.5 GHz. To benefit from future improvements of MMIC technology and performance, and to offer some robustness against fabrication tolerances, larger bandwidths are always preferable. To achieve this relatively high bandwidth, an approach based on aperture-fed, stacked patches was pursued (Figure 15.20a). The whole antenna design requires at least five substrate layers, and hence is specifically suited for an LTCC implementation. The antenna was originally designed for the DuPont^{TM} 9K7 substrate material with a sintered layer thickness of 105 μm.

As previously mentioned, antennas on high-k materials tend to excite surface waves. This effect is especially pronounced for patches. To reduce this effect the entire array is encompassed by a metallic wall consisting of grounded via fences and metallized rings on each layer of LTCC (Figure 15.20b). These walls inhibit the propagation of surface waves

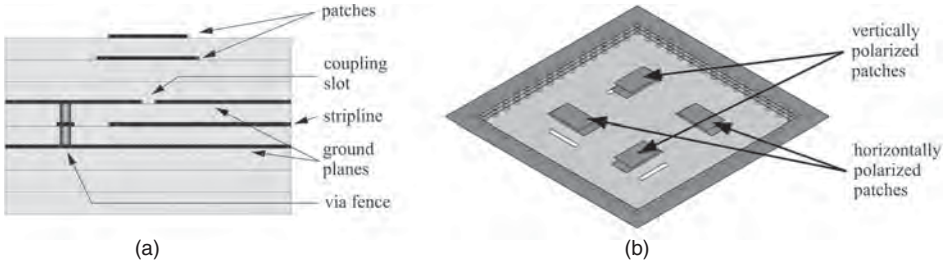

Figure 15.20 *(a) Layer stack of the patch array. The antenna requires a total of five substrate and six metallization layers and was extended by three additional substrate layers to increase the robustness of the test substrate. (b) Isometric view of the 2 × 2 patch array configuration. Each pair of diagonally located patches radiates in one polarization, as indicated in the figure.*

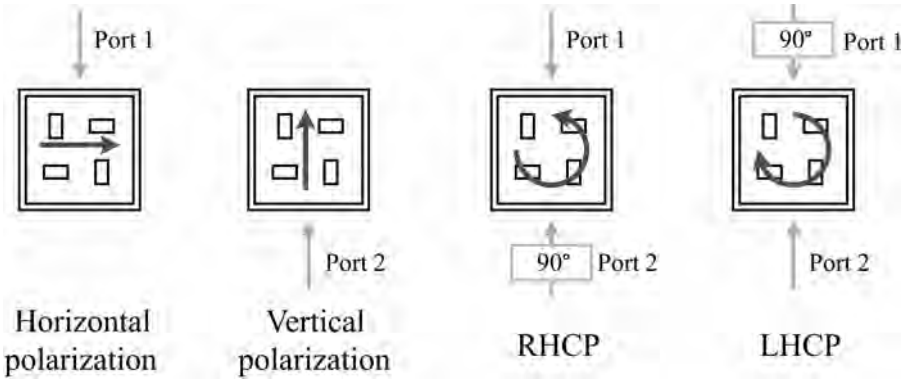

Figure 15.21 *Basic operation modes of the patch antenna array. The array can radiate dual linear polarizations directly from signals fed to the two ports as well as circular right-handed and left-handed polarizations (RHCP and LHCP) if an appropriate phase shift is provided by external components.*

across the substrate and reduce unwanted radiation from its edges, improving the radiation pattern of the antenna.

As depicted in Figure 15.20b, the four elements are placed symmetrically in a square configuration. Each pair of elements is responsible for one of the orthogonal polarizations. The pairs share a common phase center, improving the cross-polarization discrimination (XPD) of the antenna for linear polarizations, and thus allowing the antenna to be properly utilized for dual circular polarizations if an external phase shift of 90° between the two differential input signals is provided. The basic operation modes of the antenna are summarized in Figure 15.21.

To verify the design, several samples of the antenna in two different implementations were fabricated. The first variant provides 50 Ω coaxial MMPX connectors for the individual ports, allowing a straightforward test with standard S-parameter measurement equipment. A second implementation utilizes on-substrate waveguide transitions for direct interfacing with standard WR15 waveguide components. The waveguide variant features lower losses, better matching, and higher bandwidth, and requires no soldering or gluing processes.

The S-parameters were measured utilizing an Agilent E8362B vector network analyzer and are displayed in Figure 15.22. The waveguide-fed antenna is matched better than −10 dB between 56 and 63.5 GHz, while the coaxially fed antenna could only be found to have a return loss better than −10 dB for one of the ports between 53 and 59 GHz. Additionally, the coaxial implementation showed a larger variation across several test substrates. The coupling between the feeding ports for the individual polarizations was lower than −30 dB for the frequency range of interest.

The radiation patterns of both antenna variants were measured in an anechoic chamber utilizing a frequency conversion technique (Figure 15.23). The measurement equipment featured mixers with waveguide interfaces, and thus no additional adapters were required for the waveguide-fed antennas. The antennas have a radiation efficiency of about 60 to 65% in the target frequency band.

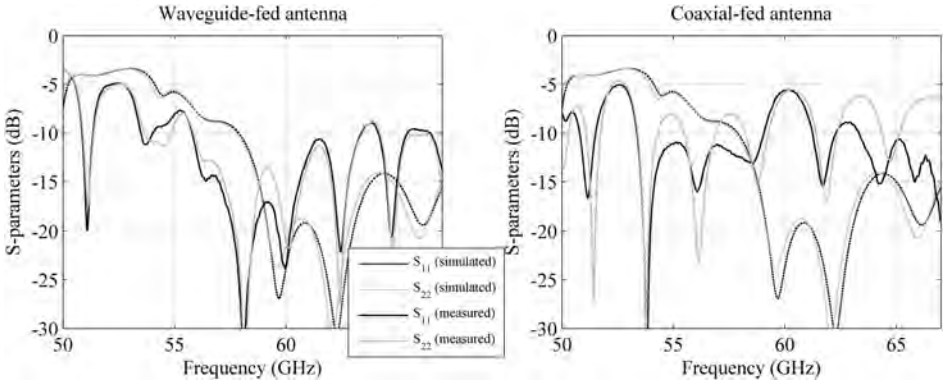

Figure 15.22 *Simulated (dotted lines) and measured (solid lines) reflection coefficients of the antenna substrates with waveguide transitions on the left-hand side and coaxial connectors on the right-hand side. The waveguide implementation features reflections less than −10 dB between 56 and 63.5 GHz and generally provides improved parameters compared to the coaxial variant.*

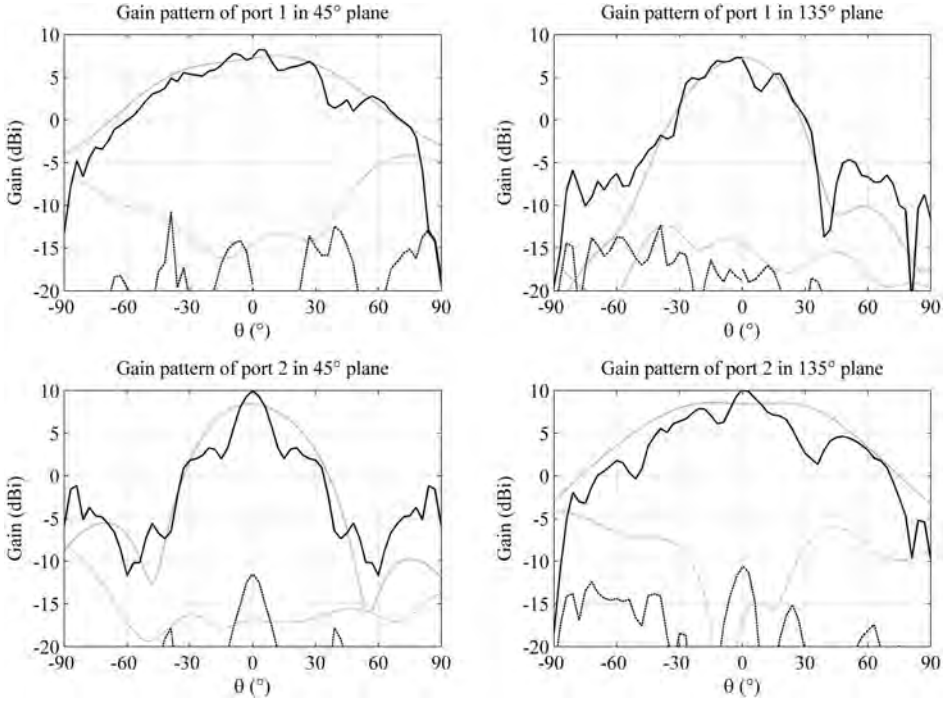

Figure 15.23 *Simulated (grey curves) and measured (black curves) antenna radiation patterns at 60 GHz for the co-polarized (solid lines) and cross-polarized (dashed lines) radiation in the 45° and 135° planes. The co-polarization for the individual ports is oriented according to Figure 15.21. Resulting from the diagonally arranged pairs of patches, the 45° and 135° planes correspond to the widest and narrowest beam width for the individual pairs.*

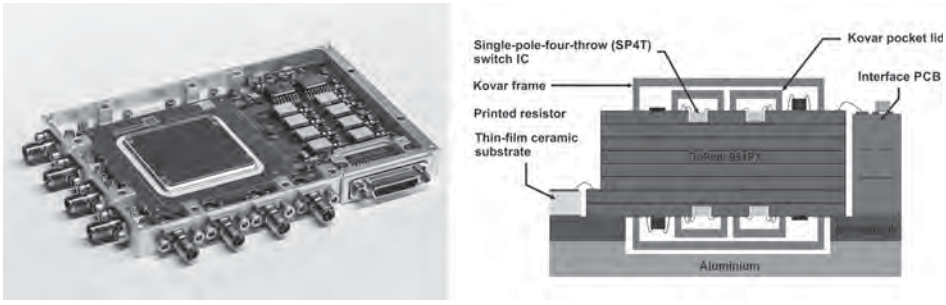

Figure 15.24 *LTCC-based electronic 4 × 4 switch matrix for geostationary satellite communications in Ka-band. (a) Photograph of the assembled switch matrix module, with mechanic housing, LTCC-based ceramic package, interface PCB, and coaxial connectors. Outer dimensions are 126 mm × 87 mm × 11 mm. (b) Vertical cross-section of the ceramic package with double-sided assembly.*

15.3.4 Microwave Modules

15.3.4.1 A 4 × 4 Ka-Band Switch Matrix

The use of LTCC is a promising technology for the realization of satellite payload modules and subsystems, since it provides good microwave performance, multilayer capabilities with three-dimensional microwave circuitry and high wiring densities, moderate production costs, and hermetic packaging. Especially implementations of electronic switch matrices benefit from the multilayer capability of LTCC substrates, since signal-line crossovers can naturally be realized with buried waveguides on different layers, which results in an increased compactness and high isolation [98]. Figure 15.24a depicts an optical photograph of an electronic 4 × 4 switch matrix module for geostationary satellite communications in Ka-band. The module comprises the ceramic package and a printed circuit board (PCB), acting as an interface, inside the housing. The overall dimensions of the module measure 126 mm × 87 mm × 11 mm, with a total mass of 193 g. Figure 15.24b shows a vertical cross-section of the module. The ceramic package consist of eight layers Dupont^{TM} GreenTape^{TM} 951PX, which has a total fired thickness of 1.6 mm and uses cavities on both sides of the substrate to accommodate the pin diode switch matrix. The footprint area of the ceramic package measures 58 mm × 58 mm. In order to optimize the compactness of the switch matrix as well as the insertion loss, a double-sided mounting technology was applied [99]. In order to mitigate the thermal mismatch between the ceramic material and the aluminum housing, the substrate was mounted on a molybdenum heat-sink [100]. All necessary components for the basic switching functionality, that is, the switch MMICs, driver circuitry, and chip capacitors were integrated in the ceramic package by consistently using chip-and-wire technology. For the adjustment of necessary bias currents printed resistors were incorporated, which were fine-adjusted by laser trimming to a value of 300 Ω ± 2 %. For hermetic sealing of the bare-die components, gold-plated kovar frames with inner dimensions of 34 mm × 34 mm × 1.5 mm were soldered on both sides and sealed by laser-welding kovar lids on top. In order to achieve good microwave isolation properties, small kovar pocket-lids were placed around each switch MMIC. The insertion loss of the module amounts to 18 dB,

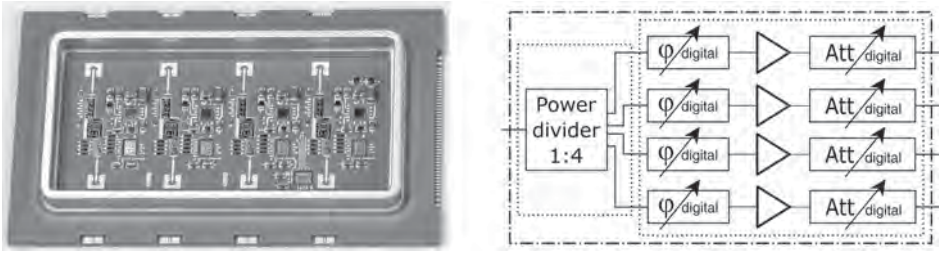

Figure 15.25 *Four-way vectorial steering module, operating at Ka-band satellite downlink frequencies from 17 to 22 GHz. (a) Photograph of an assembled part comprising a substrate with six layers DuPont™ 951-PX GreenTape™. Outer dimensions are 26 mm × 44.5 mm. (b) Block diagram with an integrated power divider.*

while the return loss remains above 11.5 dB in the frequency range of interest from 17 to 22 GHz. Due to the exclusive use of buried striplines the isolation between the different switching paths is better than 50 dB [101].

15.3.4.2 Vectorial Steering Module

Payload flexibility is a demanding requirement in modern satellite communications, upcoming vehicular radar (autonomous driving), and mobile communication systems (5G) as well. Array antennas offer variable beam patterns by changing the excitation of the individual feeds [102]. The dedicated beamforming network comprises as building blocks high-order power dividing structures and a large number of control elements for the signal phases and amplitudes. Size and mass constitute important design constraints, so that the aggregation of multiple actuators into one subassembly is an inevitable consequence. The vectorial steering elements are often exposed to low signal power levels only, and hybrid integration of MMIC and passive structures in LTCC technology becomes attractive for versatile system layout. Commercial off-the-shelf (COTS) space-qualified MMIC, in addition to custom-designed devices [103, 104], increase the design flexibility and shorten design cycles. Figure 15.25a shows a photograph of a compact four-way vectorial steering module employing 5-bit digital phase shifters and attenuators and GaAs amplifier MMIC, as well as control and bias integrated circuits. The associated block diagram in Figure 15.25b indicates also the convenient integration of a power divider into the module itself. The four-way stripline Wilkinson divider presented in Section 15.3.1 would be an eligible variant for this purpose. The vectorial transmission parameters of the module can be adjusted by 344° for phase and 15.5 dB for amplitude at step sizes of 11.25° and 0.5 dB, respectively. Measured results reveal a worst-case RMS phase and amplitude errors of 3.8°, respectively 0.23 dB, for all steering paths. All digital phase and amplitude control bits are directly accessible via a TTL interface.

15.3.4.3 A 60 GHz Front-End Receiver Module

The frequency band around 60 GHz is considered to be suitable for high data rate communications and massive MIMO links in future mobile communication systems [96]. Moreover,

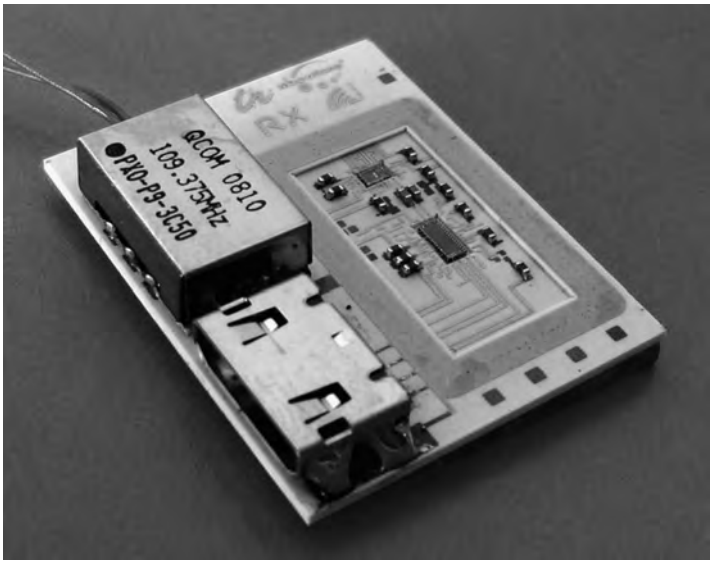

Figure 15.26 *LTCC 60 GHz receiver module with back-side integrated antennas and heat spreader.*

the high atmospheric attenuation at this frequency allows for small cells and multiple use of channels in close vicinity. Within the project EASY-A [105] the implementation of such a system for an in-flight entertainment system in aircrafts and fast wireless data links for consumer applications was pursued. Figure 15.26 shows an rf front-end receiver module based on LTCC. The module contains different transmission lines and transitions (single-ended and differential lines), impedance transformers for antenna matching, antennas at the back side, two monolithic microwave integrated circuits (MMIC), and heat management concepts. Cavities in the LTCC are used to align the MMIC surface to the substrate surface. Thus, the wire-bond connections are reduced in length. The microwave circuit part can be hermetically closed with a metal lid to protect the MMICs and to shield this circuit section.

References

1. Walker, J., Malony, J., Gleason, C., *et al.* (2016) The effect of firing temperature on structure and electrical properties in low temperature co-fired ceramics, in *Proceedings of the 12th CICMT*, April 19–21, 2016, Denver, CO, USA.
2. Jones, W.K., Liu, Y., Larsen, B., *et al.* (2000) Chemical, structural, and mechanical properties of the LTCC tapes. *The International Journal of Microcircuits and Electronic Packaging*, **23** (4), Fourth Quarter, ISSN 1063-1674.
3. Wolter, K.-J., Rebenklau, L., Hagen, G. (2005) Via formation in LTCC tape: a comparison of technologies, in *Proceedings of ACerS/IMAPS 1st International Conference on Ceramic Interconnect and Ceramic Microsystems Technologies*, April 2005, Baltimore, MD, USA.
4. Wang, G., Folk, E.C., Barlow, F., and Elshabini, A. (2006) Fabrication of microvias for multilayer LTCC substrates. *IEEE Transactions on Electronics Packaging Manufacturing*, **29**, 32–41.

5. Hagen, G. and Rebenklau, L. (2006) Fabrication of smallest vias in LTCC tape, in *Proceedings of Electronics System Integration Technology Conference*, 2006, pp. 642–647, Dresden, Germany.
6. Drüe, K.-H. (2005) Precise drilling and structuring of LTCC materials using a 355 nm YAG-laser, in *Proceedings of EMPC 2005*, June 2005, Brugge, Belgium.
7. Schwanke, D., Lang, A., Pohlner, J., *et al.* (2010) Entwicklung nanotechnologischer Siebbeschichtungen und daran angepasster Pastensysteme für den Fine-Line-Druck von keramischen Schaltungsträgern, in *Ergebnisbericht des BMBF-Verbundprojekts "nanoSieb" Book Series, System Integration in Electronic Packaging* (eds K.-J. Wolter, T. Zerna, and S. Wiese), vol. 12, Verlag Dr Markus A. Detert, Templin, ISSN 1860-4145.
8. Müller, J., Perrone, R., Thust, H., *et al.* (2006) Technology benchmarking of high resolution structures on LTCC for microwave circuits, in *Proceedings of Electronics System Integration Technology Conference*, September 5–7, 2006, pp. 111–117, Dresden, Germany.
9. Müller, J., Perrone, R., Rentsch, S., *et al.* (2006) Improved RF performance for embedded passives in LTCC by fine line structuring methods, in *Proceedings of XXX International Conference of IMAPS*, September 24–27, 2006, Kraków, Poland.
10. Schwanke, D., Pohlner, J., Wonisch, A., *et al.* (2009) Enhancement of fine line print resolution due to coating of screen. *Journal of Microelectronics and Electronic Packaging,* **6**, 13−19.
11. Brunner, S., Stadler, M., Leitner, M., and Aichholzer, K. (2012) Advanced high frequency LTCC technology for applications beyond 60 GHz, in *Proceedings of 8th International Conference on Ceramic Interconnect and Ceramic Microsystems Technologies (CICMT)*, 2012, pp. 77–81, Erfurt, Germany.
12. Hagberg, J., Pudas, M., Leppävuori, S., *et al.* (2001) Gravure offset printing development for fine line thick film circuits. *Microelectronics International*, **18** (3), 32–35.
13. Sitek, J., Futera, K., Belavič, D., *et al.* (2011) An investigation of the conductive lines quality deposited by inkjet printing on different substrates, in *Proceedings of IMAPS – IEEE CPMT Poland Conference*, 2011, pp. 307–310, Gdansk-Sobieszewo, Poland.
14. Ihle, M., Partsch, U., and Mosch, S. (2012) Aerosol printed co- and post-fired functional films for LTCC-multilayer components, in *Proceedings of 8th International Conference on Ceramic Interconnect and Ceramic Microsystems Technologies (CICMT)*, 2012, pp. 71–76, Erfurt, Germany.
15. Albertsen, A., Koiwai, K., Kobayashi, K., *et al.* (2009) Combined manufacture methods for high density LTCC substrates: thick film screen printing, ink jet, postfiring thin film processes, and laser-drilled fine vias. *Journal of Microelectronics and Electronic Packaging*, **6**, 6–12.
16. Reppe, G., Müller, J., Pohlner, J., *et al.* (2005) Development and Evaluation of Fine Line Structuring Methods for Microwave Packages in Satellite Applications, in *15th European Microelectronics and Packaging Conference and Exhibition*, June 12–15, 2005, Oud Sint Jan, Brugge, Belgium.
17. Stöpel, D., Drüe, K.-H., Humbla, S., *et al.* (2010) Fine-line structuring of microwave components on LTCC substrates, in *Proceedings of Electronics System–Integration Technology Conferences (ESTC)*, September 2010, Berlin, Germany.
18. Müller, J., Stöpel, D., Mache, T., *et al.* (2011) Fineline structuring on LTCC-substrates for 60 GHz line coupled filters, in *Proceedings of European Microelectronics Packaging Conference*, September 12–15, 2011, Brighton, United Kingdom.
19. Schulz, A., Gutzeit, N., Stöpel, D., *et al.* (2016) High resolution patterning of LTCC based microwave structures for Q/V-band satellite applications, in *Proceedings of German Microwave Conference GeMiC*, March 14–16, 2016, Bochum, Germany.
20. Perrone, R., Thust, H., and Drüe, K.-H. (2004) Progress in the integration of planar and 3D coils on LTCC by using photoimageable inks, in *Proceedings of 37th International Symposium on Microelectronics*, November 14–18, 2004, Long Beach, CA, USA.
21. Gutzeit, N., Welker, T., Drüe, K.-H., and Müller, J. (2016) High resolution LTCC laser processing in the green and fired state for future technologies, in *Proceedings of 12th International Conference on Ceramic Interconnect and Ceramic Microsystems Technologies (CICMT)*, 2016, pp. 103–106, Denver, CO, USA.

22. Maloratsky, L.G. (2011) Using modified microstrip lines to improve circuit performance. *Journal of High Frequency Electronics*, March **2011**, 36–52.
23. Wadell, B.C. (1991) *Transmission Line Design Handbook*, Artech House, ISBN 0890064369, 9780890064368.
24. Schellenberg, J.M. (1995) CAD models for suspended and inverted microstrip. *Journal of IEEE Transactions on Microwave Theory and Techniques*, **43** (6), June 1995, 1247–1252.
25. Lee, Y.C. and Park, C.S. (2003) A new millimeter-wave stripline resonator with embedded air cavities in LTCC multilayer structure. *Microwave Symposium Digest*, 2003 IEEE MTT-S International, June 2003, vol. **3**, pp. 2027–2030.
26. Müller, J. (2014) Wide band measurement of dielectric properties of electronic assembly materials inside an LTCC fluidic structure. *Journal of Microelectronics and Electronic Packaging*, **11**, 64–69, doi: 10.4071/imaps40.
27. Weil, C., Lüssem, G., and Jakoby, R. (2002) Tunable inverted-microstrip phase shifter device using nematic liquid crystals, in *IEEE MTT-S International Microwave Symposium*, June 2002, pp. 367–370.
28. Perrone, R., Müller, J., Thust, H. and Trabert, J. (2006) 3D interconnection technology for LTCC RF modules up to 60 GHz, in *Proceedings of the 2006 IMAPS/ACerS International Conference on Ceramic Interconnect and Ceramic Microsystems Technologies*, April 24–27, 2006, Denver, CO, USA.
29. Ponchak, G.E., Chen, D., Yook, J.-G., and Katehi, L.P.B (1998) Characterization of plated via hole fences for isolation between stripline circuits in LTCC packages, in *IEEE MTT-S International Microwave Symposium Digest*, 1998, pp. 1831–1834.
30. Ponchak, G.E., Chun, D., Yook, J., and Katehi, L.P.B. (2000) The use of metal filled via holes for improving isolation in LTCC RF and wireless multichip packages, *Journal IEEE Transactions on Advanced Packaging*, **2000**, 88–99.
31. Aguirre, J., Garland, P., Mobley, T., *et al.* (2006) Full-wave analysis and characterization of via grounding techniques used to isolate striplines for embedded passive interconnects, in *Proceedings of Ceramic Interconnect and Ceramic Microsystems Technologies (CICMT)*, April 24–27, 2006, Denver, CO, USA.
32. Gipprich, J. and Stevens, D. (2001) A new via fence structure for crosstalk reduction in high density stripline packages, in *Microwave Symposium Digest, 2001 IEEE MTT-S International*, vol. 3, May 2001, pp. 1719–1722, doi: 10.1109/MWSYM.2001.967237.
33. Trabert, J., Drüe, K.-H., Müller, J., *et al.* (2007) High performance 3-dimensional hybrid-integrated switch matrix for Ka-band satellite communication applications based on ceramic multilayer technology, in *Proceedings of IMAPS International Symposium on Microelectronics*, November 11–15, 2007, San Jose, CA, USA.
34. Peterson, K.A., Knudson, R., Duverneay, B., *et al.* (2009) Improved isolation for LTCC transceiver modules using full tape thickness features, in *Proceedings of 5th International Conference and Exhibition on Ceramic Interconnect and Ceramic Microsystems Technologies (CICMT)*, April 21–23, 2009, Denver, CO, USA.
35. Collin, R.E. (1990) *Field Theory of Guided Waves*, 2nd edn, Wiley-IEEE Press, December 1990.
36. Li, H., Hong, W., Cui, T.J., and Wu, K. (2003) Propagation characteristics of substrate integrated waveguide integrated waveguide based on LTCC. *IEEE MTT-S Technical Digest*, **3**, 2045–2048.
37. Chen, X.-P. and Wu, K. (2014) Substrate integrated waveguide filters: design techniques and structure innovations. *IEEE Microwave Magazine*, **15** (6), 121–133.
38. Schmückle, F.J., Jentzsch, A., Heinrich, W., *et al.* (2001) LTCC as MCM substrate: design of strip-line structures and flip-chip interconnects. *IEEE MTT-S, International Microwave Symposium Digest*, **3**, 1903–1906.
39. Valois, R., Baillargeat, D., Verdeyme, S., *et al.* (2005) High performances of shielded LTCC vertical transitions from DC up to 50 GHz. *IEEE Transactions on Microwave Theory and Techniques*, **53** (6), 2026–2032.
40. Heyen, J., Gordiyenko, A., Heide, P., and Jacob, A.F. (2003) Vertical feedthroughs for millimeter-wave LTCC modules, in *33rd European Microwave Conference Proceedings*, 2003, pp. 411–414.

41. Kangasvieri, T., Halme, J., Vähäkangas, J., and Lahti, M. (2006) Ultrawideband shielded vertical via transitions from DC up to the Vband, in *IEEE European Microwave Conference*, September 2006, pp. 476–479.
42. Perrone, R., Drüe, K.-H., Thust, H., Trabert, J., and Hein, M. (2005) Development and evaluation of photodefined elements for microwave modules in LTCC for space applications, in *Proceedings of European Microelectronics and Packaging Conference*, June 12–15, 2005, Brugge, Belgium.
43. Lee, Y.C. and Park, C.S. (2005) A novel CPW-to-stripline vertical via transition using a stagger via structure and embedded air cavities for V-band LTCC SiP applications, in *Proceedings of the 2005 Asia Pacific Microwave Conference*, vol. 2.
44. Nair, D.M., McKinzie, W.E., Thrasher, B.A., *et al.* (2013) A 10 MHz to 100 GHz LTCC CPW-to-stripline vertical transition, in *IEEE International Microwave Symposium*, 2013, pp. 1–4.
45. Yang, T.-H., Chen, C.F., Huang, T.-Y., *et al.* (2005) A 60 GHz LTCC transition between microstrip line and substrate integrated waveguide, in *IEEE Asia Pacific Microwave Conference (APMC) Proceedings*, 2005.
46. Grabherr, W. and Menzel, W. (1991) A new transition from microstrip to rectangular waveguide, in *Proceedings of the 22nd European Microwave Conference*, 1991, pp. 1170–1175.
47. Wang, X. and Stelzer, A. (2010) A 79-GHz LTCC laminated waveguide to metallic rectangular waveguide transition using high permittivity material, in *Proceedings of the European Microwave Conference (EuMC)*, 2010, pp. 664–667.
48. Birol, H., Maeder, T., and Ryser, P. (2006) Influence of processing and conduction materials on properties of co-fired resistors in LTCC structures. *Journal of the European Ceramic Society*, **26** (10–11), 1937–1941.
49. Rodriguez, M.A., Yang, P., Kotula, P., and Dimos, D. (2000) Microstructure and phase development of buried resistors in low temperature co-fired ceramic. *Journal of Electroceramics*, **5** (3), 217–223.
50. Kretzschmar, C. and Partsch, U. (2007) Dickschichtwiderstände, in *Proceedings of DKG-Jahrestagung*, March 19–20, 2007, Dresden, Germany.
51. Ehrhardt, W. and Thust, H. (2001) Trimming of thick-film resistors by energy of high voltage pulses and its influence on microstructure, in *Proceedings of 13th European Microelectronics and Packaging Conference*, May 31–June 1, 2011, pp. 403–407, Strasbourg, France.
52. Thust, H. and Müller, J. (2007) Integrated passive devices in ceramic substrates, in *Ceramic Interconnect Technology Handbook* (eds F. Barlow and A. Elshabini), Chapter 9, CRC Press, Boca Raton, FL, USA, ISBN 10-8493-3557-4.
53. Perrone, R. and Müller, J. (2008) Compact RF-filter-modules with lumped elements in LTCC for applications up to 10 GHz, in *Proceedings of 2nd IEEE-ESTC*, September 1–4, 2008, pp. 491–495, Greenwich, United Kingdom, ISBN 978-1-4244-2814-4.
54. Alley, G.D. (1970) Interdigital capacitors and their application to lumped-element microwave integrated circuits. *IEEE Transactions on Microwave Theory and Techniques*, **18** (12), December 1970.
55. Perrone, R. (2007) Erweiterung des Frequenzbereichs und der Integrationsdichte von LTCC-Modulen mittels Photostrukturierung und Designoptimierung. Dissertation TU Ilmenau, ISBN 978-3-938843-30-7, Verlag ISLE 2007.
56. Aparicio, R. and Hajimiri, A. (2002) Capacity limits and matching properties of integrated capacitors. *Journal IEEE of Solid-State Circuits*, **37** (3), March 2002.
57. Simine, A., Kholodnyak, D., Turalchuk, P., *et al.* (2005) Enhancement of inductance Q-factor for LTCC filter design, in *Proceedings of IEEE European Microwave Conference*, October 4–6, 2005, pp. 1319–1322, Paris, France.
58. Eun, K.C. and Park, C.S. (2004) Air cavity incorporation to LTCC spiral inductor for high Q-factor and SRF. *International Journal of Electronics and Communications (AEÜ)*, **58**, 434–436.
59. Perrone, R., Thust, H., and Drüe, K.-H. (2004) Progress in passive integration of planar and 3D coils by using photoimageable inks on and into LTCC, in *IMAPS, 37th International Symposium on Microelectronics*, November 2004, Long Beach, CA, USA.
60. Baker, A., Lanagan, M., Randall, C., *et al.* (2005) Integration concepts for the fabrication of LTCC structures. *International Journal of Applied Ceramic Technology*, **2** (6), 514–520.

61. Kim, K. and Varadan, V.V. (2008) Microstrip patch antenna on LTCC metamaterial substrates in millimeter wave bands, in *IEEE Antennas and Propagation Society International Symposium*, 2008, pp. 1–4.
62. Perrone, R., Kapitanova, P., Kholodnyak, D., *et al.* (2009) Miniaturisation of a LTCC high-frequency rat-race-ring by using 3-dimensional integrated passives and embedded high-*k* capacitors, in *Microelectronics and Packaging Conference*, June 16–18, 2009, pp. 1–6, Rimini, Italy.
63. Megherhi, M.H., Dougherty, J.P., Dayton, G.O., and Newnham, R.E. (1990) Electrical properties of co-fired high and low dielectric constant multilayer package materials, in *Proceedings of IEEE 7th International Symposium on Applications of Ferroelectrics*, June 6–8, 1990, doi: 10.1109/ISAF.1990.200194.
64. Feingold, A.H., Heinz, M., Wahlers, R.L., and Stein, M.A. (2003) Materials for capacitive and inductive components integrated with commercially available LTCC systems, in *Proceedings of Conference on Microelectronics and Packaging (IMAPS)*, June 18, 2003, Hrezelia, Israel.
65. Rentsch, S., Müller, J., and Hein, M. (2013) Tunability, frequency, and temperature behavior of cofired LTCC-integrated barium–strontium–titanate shunt capacitors up to 8 GHz. *Journal of Microelectronics and Electronic Packaging*, **10** (1), 23–29.
66. Bartsch, H., Grieseler, R., Müller, J., *et al.* (2010) Properties of high-*k* materials embedded in low temperature cofired ceramics, in *Proceedings of IEEE (Ed.) Electronic System-Integration Technology Conference (ESTC)*, September 13–16, 2010, pp. 1–5, Berlin, Germany.
67. Müller, J., Mach, M., and Perrone, R. (2008) Novel method for embedding high quality LTCC RF-capacitors using mid-*k* tapes, in *Proceedings of 4th Ceramic Interconnect Ceramic Microsystems Technology Conference (CICMT)*, April 21–24, 2008, pp. 223–227, München, Germany, ISBN 0-930815-83-1.
68. Hintz, M., Albrecht, A., Thust, H., and Tschernev, R. (2004) Advanced LTCC processes using pressure assisted sintering (PAS), in *SMTA Pan Pacific Conference*, 2004, Hawaii, USA.
69. Bierlich, S., Reimann, T., Barth, S., *et al.* (2016) Integration of high-frequency M-type hexagonal ferrite inductors in LTCC multilayer modules. *International Journal of Applied Ceramic Technology*, pp. 540–548.
70. Bartsch, H., Töpfer, J., Löhnert, R., *et al.* (2013) Integrierte LC-Glieder in keramischen LTCC-Schaltungsträgern, in *MikroSystemTechnik Kongress 2013: Von Bauelementen zu Systemen*, October 14–16, 2013, pp. 283–286, Aachen, Germany.
71. Barth, S., Arnold, M., Grützmann, D., *et al.* (2009) Low-sintering high-*k* materials for an LTCC application. *International Journal of Applied Ceramic Technology*, **6** (1), 35–40.
72. Hu, T. (2004) BST-based low temperature co-fired ceramic (LTCC) modules for microwave tunable components. Dissertation, Oulu.
73. Naghib-Zadeh, H. (2011) Low temperature sintering of barium titanate based ceramics with high dielectric constant for LTCC applications. *Journal of the European Ceramic Society*, **31** (4), 589–596.
74. Bartsch, H., Barth, S., and Müller, J. (2012) Embedded ceramic capacitors in LTCC, in *Proceedings of IMAPS/ACerS (Ed.), Ceramic Interconnect and Ceramic Microsystems Technologies (CICMT)*, 2012, Erfurt, Germany.
75. Batlle, X., Garcia del Muro, M., Tejada, J., *et al.* (1994) Static magnetic properties of nanocrystalline Co–Ti doped barium ferrite $BaFe_{12-2x}Co_x/Ti_xO_{19}$ ($x = 0.8$). *Journal IEEE Transactions on Magnetics*, **30** (2), 708–710.
76. Vinnik, D.A., Zherebtsov, D.A., Mashkovtseva, L.S., *et al.* (2015) Growth, structural and magnetic characterization of Co- and Ni-substituted barium hexaferrite single crystals. *Journal of Alloys and Compounds*, **628**, 480–484.
77. Gutzeit, N., Halbedel, B., Romanus, H., and Müller, J. (2015) Sputtered thin films of Ti substituted barium hexaferrit for miniaturized components of electronic devices in the microwave range, in *Proceedings of 20th International Conference on Magnetism (ICM)*, July 5–10, 2015, Barcelona, Spain.
78. Kaur, H., Singh, C., Kaur, R., *et al.* (2015) Microwave and electrical properties of Co–Ti substituted M-type Ba hexagonal ferrite. *The European Physical Journal B*, **88** (10).

79. Bierlich, S., Reimann, T., Bartsch, H., and Töpfer, J. (2015) Co/Ti-substituted M-type hexagonal ferrites for high-frequency multilayer inductors. *Journal of Magnetism and Magnetic Materials*, **384**, 1–5.
80. Pozar, D.M. (2012) *Power Dividers and Directional Couplers in Microwave Engineering*, 4th edn, pp. 317–379, John Wiley & Sons, Inc.
81. Wollenschläger, F., Alhouri, L., Xia, L., *et al.* (2009) Measurement of a 60 GHz antenna array fed by a planar waveguide-to-microstrip transition integrated in low-temperature co-fired ceramics, in *Proceedings of 3rd European Conference on Antennas and Propagation*, March 2009, pp. 1001–1005, Berlin, Germany.
82. Wilkinson, E.J. (1960) An N-way hybrid power divider. *IRE Transactions on MTT*, **8**, 116–118.
83. Horst, S., Bairavasubramanian, R., Tentzeris, M.M., and Papapolymerou, J. (2007) Modified Wilkinson Power Dividers for Millimeter-Wave Integrated Circuits. *IEEE Transactions on Microwave Theory and Techniques*, **55**, 2439–2446.
84. Miralles, E., Schönlinner, B., Ziegler, V., and Ellinger, F. (2015) Fast design method and validation of very wideband tapered Wilkinson divider, in *Proceedings of 45th European Microwave Conference*, September 2015, pp. 119–122, Paris, France.
85. Wu, L., Sun, Z., Yilmaz, H., and Berroth, M. (2006) A dual-frequency Wilkinson power divider. *IEEE Transactions on Microwave Theory and Techniques*, **54**, 278–284.
86. Spira, S., Welker, T., Müller, J., and Hein, M.A. (2015) Compact 1-stage 4-way Wilkinson power divider at Ka-band utilising LTCC technology, in *Proceedings of IMAPS Nordic Conference*, June 8–9, 2015, Helsingør, Denmark.
87. Spira, S., Schneider, M., Welker, T., *et al.* (2016) Compact three-dimensional four-way vectorial steering module for Ka-band multiple feeds-per-beam satellite payload applications, in *IEEE MTT-S International Microwave Symposium*, May 22–27, 2016, San Francisco, CA, USA.
88. Gysel, U.H. (1975) A new N-way power divider/combiner suitable for high-power applications, in *IEEE MTT-S International Microwave Symposium Digest*, May 1975, pp. 116–118, Palo Alto, CA, USA.
89. Klein, T., Uhlig, P., Günner, C., and Kulke, R. (2014) Substrate-integrated divider networks in LTCC with optimized tolerance/isolation properties for Ka-band satellite systems, in *Proceedings of 47th International Symposium on Microelectronics*, October 2014, pp. 816–819, San Diego, CA, USA.
90. Müller, J., Stöpel, D., Mache, T., *et al.* (2011) Fineline structuring on LTCC-substrates for 60 GHz line coupled filters, in *Proceedings of European Microelectronics Packaging Conference*, September 12–15, 2011, Brighton, United Kingdom.
91. David, P.M. (2005) *Microwave Engineering*, 3rd edn, John Wiley & Sons, Inc., New York, USA.
92. George, M., Leo, Y., and Jones E.M.T. (1980) *Microwave Filters, Impedance-Matching Networks, and Coupling Structures*, 1st edn, Artech House, Norwood, MA, USA.
93. Nishikawa, K., Seki, T., Toyoda, I., and Kubota, S. (2007) Compact 60-GHz LTCC stripline parallel-coupled bandpass filter with parasitic elements for millimeter-wave system-on-package, in *IEEE MTT-S International Microwave Symposium*, June 3–8, 2007, pp. 1649–1652, Honolulu, USA.
94. Schulz, A., Rentsch, S., Xia, L., *et al.* (2012) A low-loss fully embedded stripline parallel coupled BPF for applications using the 60 GHz band. *International Journal of Applied Ceramic Technology*, New York, USA, publication [online] http://onlinelibrary.wiley.com/doi/10.1111/j.1744-7402.2011.02738.x/full, Wiley-Blackwell, 2012.
95. Ullah, U., Mahyuddin, N., Arifin, Z., *et al.* (2015) Antenna in LTCC technologies: a review and the current state of the art. *Journal of IEEE Antennas and Propagation Magazine*, **57** (2), 241–260, April 2015. doi: 10.1109/MAP.2015.2414668.
96. Martínez-Vázquez, M., Oikonomopoulos-Zachos, C., Maulwurf, K., *et al.* (2011) Highly integrated antennas and front-ends for 60 GHz WLAN applications. *International Journal of Microwave and Wireless Technologies*, **3** (2), 157–170.
97. Wollenschläger, F., Stephan, R., Xia, L., *et al.* (2011) A compact dual-polarized wideband patch antenna array for the unlicensed 60 GHz band. *Proceedings of the 5th European Conference on Antennas and Propagation (EUCAP)*, April 11–15, 2001, pp. 1873–1877, Rome, Italy.

98. Humbla, S., Stephan, R., Stöpel, D., *et al.* (2013) Low-Earth-orbit verification of a reconfigurable 4×4 switch matrix and potential applications for satellite communications, in *IEEE-APS Topical Conference on Antennas and Propagation in Wireless Communications*, September 2103, pp. 851–854, Torino, Italy.
99. Kaleem, S., Rentsch, S., Humbla, S., *et al.* (2014) Highly integrated reconfigurable microwave switch matrix module for geostationary satellites, in *Proceedings of the 44th European Microwave Conference*, October 2014, pp. 992–995, Rome, Italy.
100. Kirsch, M., Häussermann, B., and Konrath, W. (2014) Buried microwave designs using LTCC multilayer technology for high density integrated space hybrids, in *Micro- and Millimetre Wave Technology and Techniques Workshop at ESTEC*, November 2014, Noordwijk, Netherlands.
101. Ebert, A., Kaleem, S., Müller, J., *et al.* (2015) An industry-level implementation of a compact microwave diode switch matrix for flexible input multiplexing of a geo-stationary satellite payload, in *COMCAS International Conference on Microwaves, Communications, Antennas and Electronics Systems*, November 2015, Tel Aviv, Israel.
102. Angeletti, P., Mangenot, C., and Toso, G. (2013) Recent advances on array antennas for multibeam space Applications. Proceedings of IEEE Antennas and Propagation Society International Symposium, July 2013, pp. 2233–2234, Orlando, FL, USA.
103. Nagasaka, M., Nakazawa, S., Kamei, M., *et al.* (2015) Prototype of 21-GHz band beam forming network for array-fed imaging reflector antenna, in *Proceedings of 45th European Microwave Conference*, September 2015, pp. 1455–1458, Paris, France.
104. Shin, D.-H., Jeong, J.-C., Moon, S.-M., *et al.* (2015) Compact Ku-band GaAs multifunction chip for SATCOM phased arrays, in *Proceedings of 45th European Microwave Conference*, September 2015, pp. 1471–1474, Paris, France.
105. EASY-A: enablers for ambient services and systems. Part A – 60 GHz, broadband links. Available at: http://www.easy-a.de/.

16

Applications of Dielectric Resonators

P. Mohanan and S. Mridula
Department of Electronics, Cochin University of Science and Technology, Kochi, India

16.1 Introduction

In the early days of microwave research, guided electromagnetic wave propagation in dielectric media received widespread attention. The term "dielectric resonator (DR)" was coined by Richtmyer [1] of Stanford University in 1939, when he showed that non-metallic dielectric materials functioned as microwave resonators. However, his theoretical work failed to generate significant interest, and practically nothing happened in this field for more than 25 years. In the early 1960s, Okaya and Barash of Columbia University rediscovered dielectric resonators, while working on high dielectric materials (single-crystal TiO_2 rutile). Their report [2] provided the first analysis of dielectric resonator design and the modes inside the resonator. DR is usually a puck of low-loss ceramic material having high relative permittivity with very high Q. However, in spite of the high Q and small size, rutile dielectric resonators were not considered for use in microwave devices, due to their poor temperature stability. The development of the first temperature stable, low loss, barium tetratitanate ceramics, followed by $(Zr{-}Sn)TiO_4$ ceramics from Murata Manufacturing Company, Japan, in the early 1970s was a real breakthrough in ceramic technology [3, 4]. The miniaturization of microwave circuits due to high dielectric constant materials has aided the popularization of DRs. Together, these technologies permit the realization of small, reliable, lightweight, and stable microwave systems, offering new design opportunities for microwave engineers. Fiedziuszko *et al.* [5] have critically reviewed a sequential evolution of the application of dielectric materials in various microwave devices.

DRs have been employed for the measurement of material properties [6–9]. High resolution, high sensitivity, and a large dynamic range of test systems are the striking features of such measurements. Small size, low loss, light weight, and ease of integration with

Microwave Materials and Applications, First Edition.
Edited by Mailadil T. Sebastian, Rick Ubic and Heli Jantunen.
© 2017 John Wiley & Sons, Ltd. Published 2017 by John Wiley & Sons, Ltd.

Table 16.1 *Properties of resonators*

Resonator	Size	Q-factor	τ_f	Integrability with MICs
Metallic cavity	Large	High	Low	Non-integrable
Microstrip resonators	Small	Very low	High	Integrable
DR	Very small	Very high	Very low	Integrable

planar transmission lines make dielectric resonators widely useful for achieving excellent performance as frequency discriminators, filters, and oscillators in wireless, satellite, and broadcast communication systems [10, 11]. Dielectric resonators are an attractive, low-cost alternative to traditional metallic resonant cavities in many microwave applications. They have the advantage of size reduction without compromising the electromagnetic performance. They also exhibit a significantly higher Q-factor than conventional transmission line resonators due to the absence of conductor loss. In addition, temperature variation of the resonant frequency of DRs can be engineered to a desired value to meet the requirements of the circuit designer. Table 16.1 compares the properties of various resonators. The ceramic-based dielectric technology is also being developed as a means of building high-performance antennas for WLAN and handset applications. Large multielement antenna arrays for millimeter wave bands with excellent radiation characteristics can be realized using microstrip-fed dielectric resonators. The versatile nature of DRAs makes them adaptable to numerous wireless communication applications by appropriate choice of design parameters [12–17]. The DR can be employed in a dielectric resonator antenna (DRA), dielectric resonator oscillator (DRO), and dielectric resonator filters.

16.2 Dielectric Resonator Antenna (DRA)

The early studies on DRs laid emphasis on the structure as an energy storage device. Low loss ($\tan\delta < 10^{-4}$) and high relative permittivity ($10 \leq \varepsilon_r \leq 100$) DRs were widely used in shielded microwave circuits, where they exhibit a very high unloaded Q-factor, given by

$$Q_u = \frac{1}{\tan\delta} \tag{16.1}$$

Long *et al.* [18] proposed the use of resonators for antenna applications. For details of dielectric resonator antennas (DRAs), the reader is referred to recent reviews [12, 18–23].

The ceramic dielectric resonators are often enclosed inside metal cavities to confine radiation and to maintain a high quality factor, which is important for filter and oscillator applications. However, when the cavity is not enclosed by metallic walls, electromagnetic fields do exist beyond the geometrical boundary of the cavity. Open dielectric resonators thus offer attractive features as antenna elements [18], since the Q-factors of the lowest-order modes of the resonator are reduced significantly due to the power lost in the radiated fields. Instead of confining the field inside the resonator, open DR can radiate electromagnetic energy like an antenna. According to the IEEE Standard for terms and definition for antennas, the dielectric resonator antenna is defined as "An antenna where the radiation pattern is controlled by electromagnetic resonances in a dielectric material excited by a probe or a

slot in a ground screen placed under it" [24]. Use of lower dielectric constant materials and proper choice of the resonator dimensions enhance these radiation fields, lowering the radiation Q-factor (Q_r), corresponding to a wider bandwidth and higher radiation efficiency. This is made possible by minimizing the volume-to-surface ratio. The radiation Q-factors of isolated spherical DRs were reported by Gastine *et al.* in 1967 [25]. The possibility of constructing very small antennas using DRs was first considered by Sager and Tisi [26]. The radiating mechanism in a dielectric resonator antenna (DRA) is the displacement current circulating in a dielectric medium, usually a ceramic pellet. The stored energy inside the dielectric is extremely high and it is difficult for external objects to detune the device [27–29] due to a highly confined near field. Unlike patch antennas, they can radiate from all surfaces, rendering high radiation efficiency and low Q-factor. Since its birth in the early 1980s, there has been a steady progress of research in this area over the years.

The early experimental study of the dielectric resonator antenna (DRA) by Long *et al.* [18], followed by a numerical computation of the radiation characteristics of dielectric resonators by Kishk *et al.* [31], have shown that the DRA is an efficient radiator at microwave frequencies. A proper selection of the resonator shape mitigates the effect of increasing the dielectric constant, while keeping the antenna size very compact. For example, a rectangular resonator with a flat tile shape has a wider bandwidth than a dielectric cube resonating at the same frequency. Ring structures, conical DRA, stepped DRAs, stacking of DRAs, use of parasitic DRs, and metal strips added to the DR surface enhance the bandwidth performance. Bandwidth can also be enlarged by designing a resonator supporting different modes with closely spaced resonant frequencies [32–41]. A good overview of the early work on DRAs is given by Soren *et al.* [21], Huitema and Monediere [22], and Mongia *et al.* [42]. Extensive research by the antenna engineers in this field has led to the development of several novel DRAs offering significant enhancements in bandwidth, gain, and coupling [43, 44].

Dielectric resonator antennas of various geometries, parameters, and excitation methods have been studied extensively. Different resonant modes have distinct electromagnetic field distributions within the DRA, and each mode may provide a different radiation pattern. The dimensional degrees of freedom are considered in comparing various DR geometries. It is found that for hemispherical, circular cylindrical, and rectangular shapes, the tunable dimensions are one, two, and three, respectively. A single tunable dimension makes hemispherical DRAs easy to design but difficult to optimize for particular requirements, limiting their use. For example, the radius of a hemispherical DRA, of a certain material, singularly determines its resonant frequency. The radius–height pair determines the behavior of circular cylindrical DRAs. The structural symmetry in hemispheres and circular cylinders normally supports degenerate resonant modes. These modes may increase the cross-polarization level, which may be undesirable for most of the applications, but may be advantageous for dual or circular polarization designs. The existence of two independent aspect ratios in a rectangular DRA offers better design flexibility [45]. Proper choice of the dimensions can also avoid the mode degeneracy problem, leading to low cross-polarization. However, it is relatively uneasy to form a DR with configurations precisely suitable for a specific resonant frequency. Also, the native hardness of the material makes it difficult to make slight geometrical modifications to the constructed DRA to compensate for manufacturing tolerances or fabrication errors. The features of the DRA can be fully exploited when the frequencies of operation are of the order of several GHz or higher. To obtain a

reasonable antenna size in such bands, a very high dielectric constant would be required, since the size of a DRA is proportional to $\varepsilon_r^{-1/2}$. High permittivity is also a requirement for integration with printed technology – to achieve strong direct coupling from microstrip lines to DRAs. However, the Q of the antenna increases as $\varepsilon_r^{3/2}$, thereby causing an unacceptable reduction in bandwidth. Nevertheless, the advantage offered by this phenomenon is the reduction of the interaction between antenna elements in DRA arrays [46] due to high stored energy and highly confined near field.

Several attractive features of DRA are listed below.

- Small size and light weight
- Absence of conductor losses and surface wave losses leading to high radiation efficiency, especially at higher frequencies
- Moderate bandwidth ~10%
- Freedom in controlling the size and bandwidth of the DRA by choosing from a wide range of permittivity and resonator shapes.
- Ease of integration to various existing planar and IC technologies
- Shaping the radiation pattern as per the requirement by controlling the modes.

16.2.1 Excitation Techniques

Widely adopted excitation schemes of DRAs include conducting probes, direct microstrip line coupling, microstrip slot (aperture), and coplanar waveguide, as shown in Figure 16.1a to d.

16.2.1.1 Coaxial Probe Excitation

The probe excitation requires drilling of a hole into the DR to insert the probe, as shown in Figure 16.1a. The probe length, position, and depth of penetration are the factors controlling the impedance matching. Keeping the conducting probes near the outer surface can also

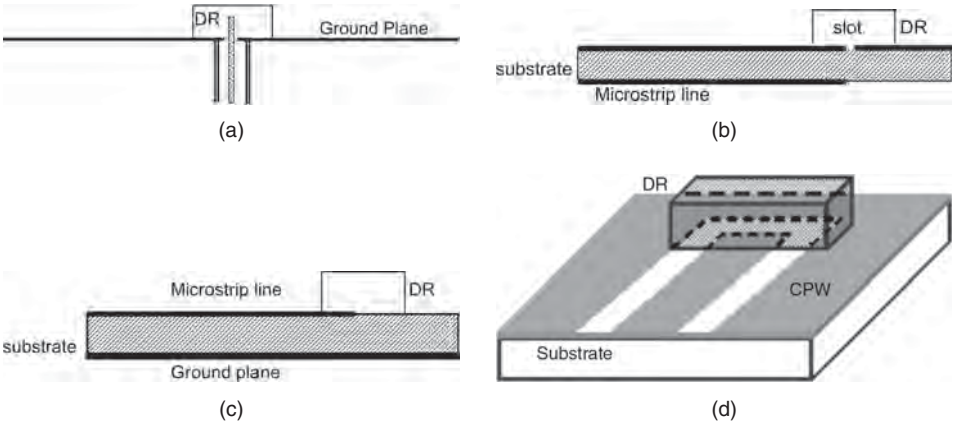

Figure 16.1 *(a) Coaxial probe excited DRA on a conducting ground plane, (b) Microstrip slot excited DRA, (c) microstrip line excited DRA, (d) co-planar waveguide excited DRA.*

efficiently excite a high permittivity DRA. This greatly simplifies the construction of the antenna since this avoids drilling a hole inside the dielectric.

Good coupling can be achieved by adjusting the location, length of the probe, and aligning the probe properly along the electric field orientation. Due to the air gap between the probe and the dielectric material, a via hole probe may show a small drift in resonant frequency and usually lowers the resonant frequency. However, the coaxial probe feed is not normally acceptable at high frequencies due to large probe self-reactance.

16.2.1.2 Microstrip Line Excitation

This is a simple and inexpensive method applicable to frequencies well within the millimetre wave bands. This feeding technique allows the DRA to be integrated with MMICs without the need for a coupling slot [47]. In the direct microstrip coupling scheme, the far open circuit end of a microstrip line is terminated on the DRA, as shown in Figure 16.1b. The overlap distance of the DR on the microstrip line is the critical parameter that determines the amount of coupling and the particular mode of excitation in the DRA.

This structurally simplified feed configuration has the merit of low back lobe radiation in antenna arrays. Moreover, it provides a relatively wide bandwidth in comparison with the conventional aperture-coupled DRA. However, this method inevitably introduces an undesirable air gap which may slightly change the radiation characteristics. A microstrip line fed conformal strip method is also used to excite a DRA [48]. The strip cut from a conducting adhesive tape has the same width as the microstrip line. This method shares the merits of using a coaxial probe, but avoids the need for drilling a hole to accommodate the probe. Although this feature can be obtained, by placing the probe near the outer surface of a DRA with a high dielectric constant ($\varepsilon_r \geq 20$). Furthermore, it allows very easy post-manufacturing trimmings, as the conformal strip can be easily cut shorter without leaving an air gap or extended longer without the need for deepening the hole.

16.2.1.3 Microstrip-Slot (Aperture) Excitation

The aperture-coupling mechanism depicted in Figure 16.1c, has been widely used to separate the feed line structure from the DRA and thus provides flexibility in the design of the feed line and the DRA. The radiation from the feeding circuit is drastically reduced, enhancing the polarization quality. Drilling a hole in a hard DR to accommodate the probe penetration is no longer necessary.

This type of excitation scheme avoids large probe self-reactance at millimeter wave frequencies and potentially helps the integration of DRAs with MMICs. A much wider impedance bandwidth is exhibited by annular slot-fed DRAs instead of rectangular slots. However, the back lobe radiation through the substrate is of major concern.

16.2.1.4 Coplanar Waveguide (CPW) Excitation

The coplanar waveguide excitation, as illustrated in Figure 16.1d, is uniplanar and less dispersive in nature. Like other microstrip feeds, it provides convenience in integration of the DRA with active circuitry since shunt/series components can be connected on the same side of the substrate without via holes [49].

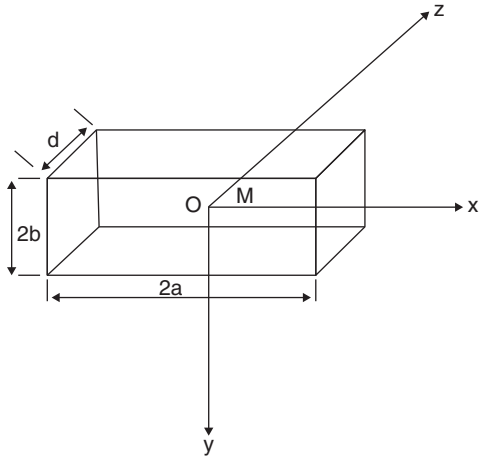

Figure 16.2 *Geometry of rectangular DRA, where the smaller dimension d is aligned along the z axis.*

The CPW feeding is characterized by low conductor losses, low radiation leakage, and is particularly suited for millimeter wave applications because of reduced surface wave excitation in electrically thick substrates compared to microstrip feed. The impedance matching may be difficult with low permittivity DRAs in this type of feeding. However, a vertical strip extended from the centre strip of the CPW on to the surface of the DRA is found to improve the coupling. A slot line can also be used to feed DRA in certain applications [50].

16.2.2 Rectangular Dielectric Resonator Antenna

The geometry of a rectangular DRA is illustrated in Figure 16.2. Usually different TE and TM modes are excited in the DRA as in a rectangular metallic cavity. By properly selecting the modes, different radiation characteristics can be easily achieved. The dominant mode for the above DRA with smaller dimension d aligned along the z axis is TE^z_{111}, that is, one half-wave variation of E or H filed along the x, y, and z directions.

For this mode the fields are [42]

$$H_z = A\cos(k_x x)\ \cos(k_y y)\ \cos(k_z z) \tag{16.2}$$

$$E_z = 0 \tag{16.3}$$

where the corresponding wave numbers along the x, y, and z directions inside the DRA are given by

$$\begin{aligned} k_x &= \frac{\pi}{2a}, \qquad k_y = \frac{\pi}{2b} \\ k_z \tan\left(\frac{k_z d}{2}\right) &= \sqrt{(\varepsilon_r - 1)k_0^2 - k_z^2} \end{aligned} \tag{16.4}$$

where ε_r and, k_0 are the relative dielectric constant of DRA and the free space wave number at the resonant frequency f_0, respectively.

The performance of the rectangular DRA is determined by the following parameters:

- Dimensions of the DR
- Material properties of the DR
- Orientation of the DR with respect to the feed line
- Position of the DR upon the feed line
- Dimensions of the feed line
- Dimensions of the ground plane.

The rectangular DRA proposed by Mridula and coworkers [51, 52] comprises a rectangular dielectric resonator of dimensions ($a \times b \times d$) = 2.25 cm × 1.19 cm × 0.555 cm, made of low-loss ceramic material $Ca_5Nb_2TiO_{12}$ ($\varepsilon_r = 48$). The DR is prepared using the conventional solid-state ceramic route at a sintering temperature of 1550 °C. The low density of the material (4.05 g/cm^3) ensures a light weight of the antenna configuration. The DR is excited directly by a 50 Ω microstrip line of width 3 mm, fabricated on a substrate of dielectric constant $\varepsilon_{rs} = 4.28$ and thickness 1.6 mm. The antenna geometry and excitation technique are shown in Figure 16.3.

The return loss for different positions of the DR placed in different orientations along the feed line is measured and optimized for a maximum 2:1 VSWR bandwidth. The measurements are done using an HP 8510C network analyser. Different resonant frequencies are excited as the DR is moved along the feed line. The overall size of the antenna configuration is decided by the aspect ratio of the DR, the dimensions of the feed line, and the ground plane. Table 16.2 lists the aspect ratio of the DR in various orientations.

The *b–a–d* orientation illustrated in Figure 16.3 is a low profile orientation, corresponding to the least value of aspect ratio of the DR (0.25). The distance of the reference vertex [**p**] from the feed axis and the open feed end (d_x, d_y) indicate the position of the DR along the *x* and *y* axes, respectively. In order to arrive at a compact antenna configuration, a truncated ground plane may be used. The radiation characteristics of the 2 cm line excited DRA in the *b–a–d* orientation of the resonator is discussed in this section.

The numerically computed (FDTD) return loss characteristics are plotted in Figure 16.4 along with the experimentally observed results. The numerical computations indicate a

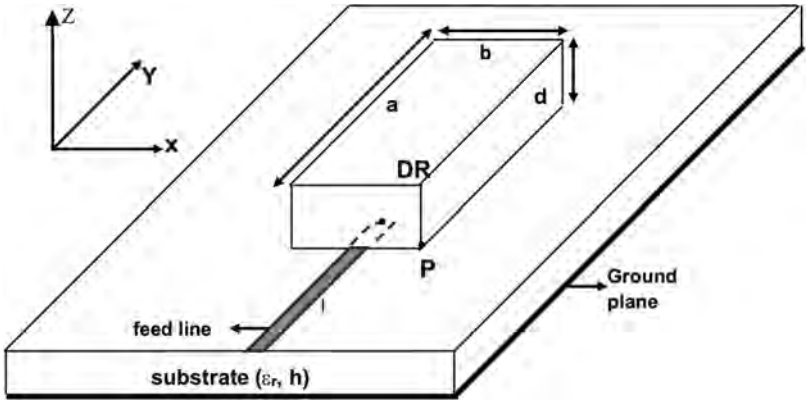

Figure 16.3 *The b–a–d orientation of the rectangular dielectric resonator on a microstrip ine.*

Table 16.2 *Aspect ratio of the DR in different orientations [$Ca_5Nb_2TiO_{12}$, $\varepsilon_r = 48$], [$a \times b \times d$] = [2.25 × 1.19 × 0.555] cm^3*

	Orientation					
Dimensions along x–y–z axes ⇒	*b–a–d*	*a–b–d*	*d–a–b*	*d–b–a*	*a–d–b*	*b–d–a*
Aspect ratio $\frac{\text{Height}}{\text{Width}}$ ⇒	0.25	0.47	0.53	1.9	2.14	4.05

resonance at 3.202 GHz with a bandwidth of 6.1% (3.098 to 3.2931 GHz). The experimentally measured resonance is at 3.175 GHz with a band width of 10.2% (2.956 to 3.281 GHz). A lower resonant mode at 3.04 GHz is also observed in the operating band.

Antennas for mobile communication applications ought to radiate equally in all directions. However, in many wireless applications the pattern shape plays a secondary role with respect to bandwidth. The numerically predicted (FDTD) and experimentally measured radiation patterns in the *b–a–d* orientation of the resonator are shown in Figure 16.5. The patterns are broad in both planes with a front-to-back ratio of 15 dB and cross-polarization better than –20 dB in both principal planes along the maxima.

The DRA is found to exhibit linear polarization within the band. The polarization of the resonant modes at 3.04 and 3.175 GHz is along the longer dimension *a* of the DR, parallel to the feed axis. The measured gain characteristics of the DRA at the optimum bandwidth position is shown in Figure 16.6. The average gain of the antenna is nearly 7 dBi.

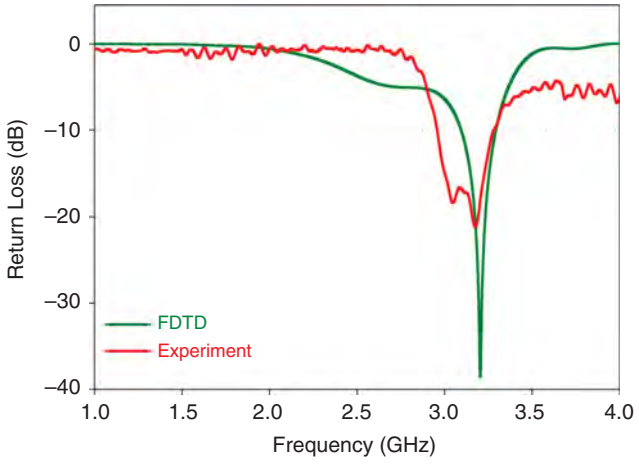

Figure 16.4 *Return loss characteristics of the rectangular DRA at the optimum bandwidth position, with large ground plane 4 × 4 cm^2, feed line length = 2 cm, (dx, dy) = (0.5, 1.5) cm, $\varepsilon_r = 48$.*

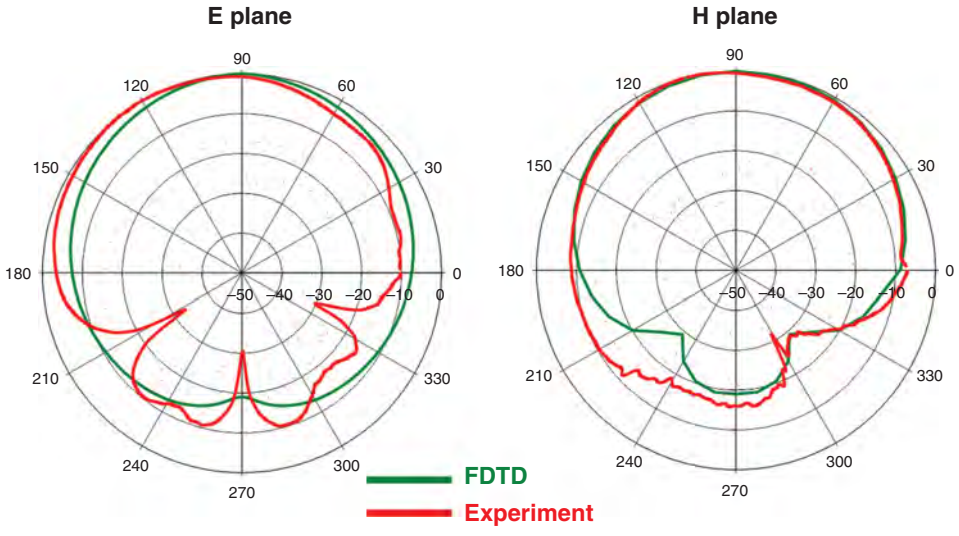

Figure 16.5 *Radiation pattern of the rectangular DRA (detailed in Figure 16.4) at the optimum bandwidth position at resonance (f = 3.175 GHz): —- co-polar, ... cross-polar.*

The reflection characteristics and gain of the same DRA on a truncated ground plane is shown in Figure 16.7. It is noted that the resonant frequency is slightly shifted to the lower side for this case (3.115 GHz) and the gain has reduced drastically (average gain of 2.1 dBi). The patterns are broad in both planes, with maxima along the broad side direction. The front-to-back ratio is 8 dB with a cross-polarization better than −14 dB along the maxima in both the planes.

Even though the truncation of the ground plane results in a reduction of gain of the antenna, the radiation pattern is broad and the configuration is therefore highly desirable

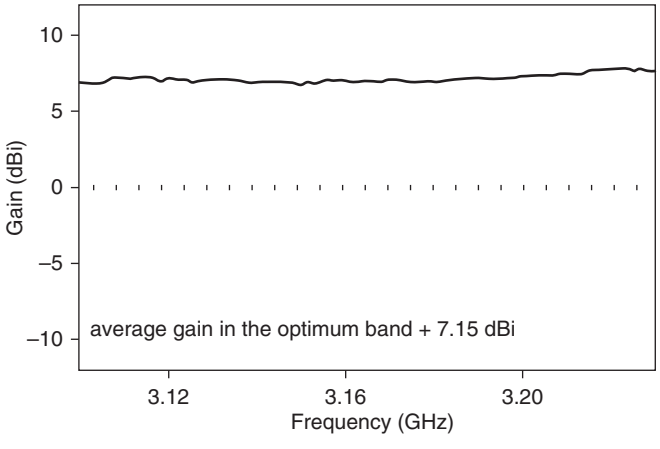

Figure 16.6 *Gain of the rectangular DRA measured at the optimum bandwidth position.*

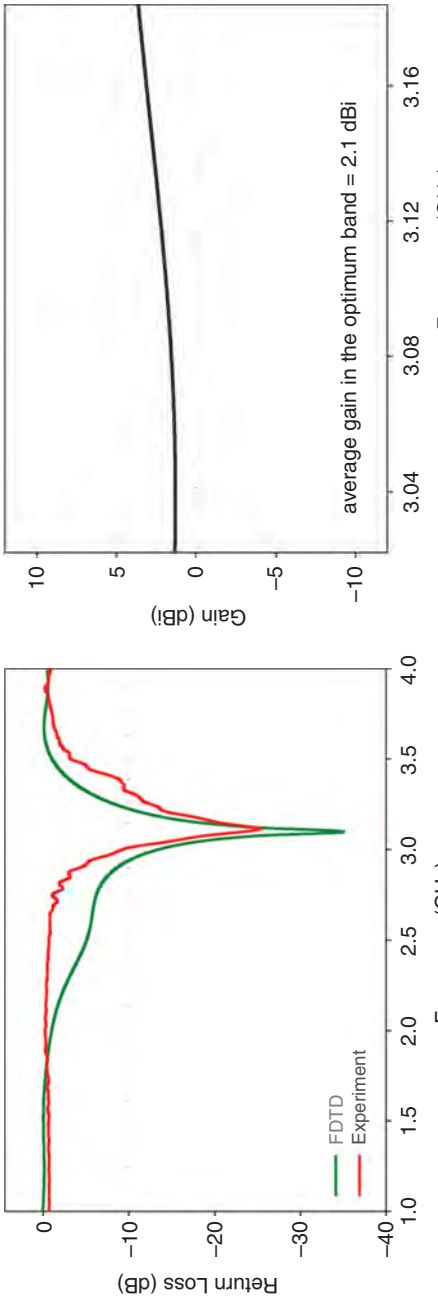

Figure 16.7 *Characteristics of the rectangular DRA measured at the optimum bandwidth position, with a truncated ground plane 2 × 4 cm², feed line length = 2 cm, orientation: b–a–d, (dx, dy) = (0.6, 1.2) cm: (a) return loss and (b) gain.*

for mobile communication applications where active circuitry can be incorporated for compensating the reduced gain.

16.2.3 Resonant Modes of the DRA

The modes of the rectangular DRA are identified from the field distributions within the DR at the resonant frequency (3.202 GHz) predicted numerically (FDTD) in different plane cuts (*xy*, *yz*, and *xz* planes), as illustrated in Figure 16.8a to c. The $TE^{z}_{m,n,p}$ mode is identified,

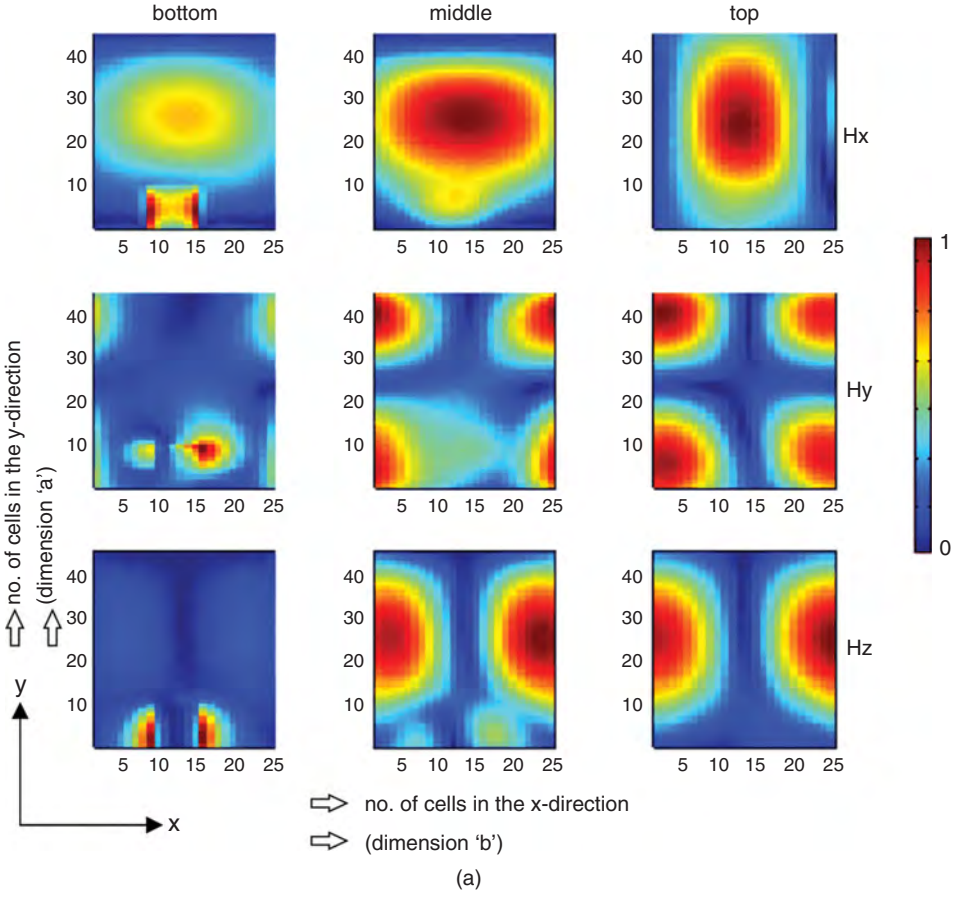

Figure 16.8 *(a) Field distribution within the DRA predicted using FDTD in the x–y plane at three different zlayers at f = 3.202 GHz, feed line length = 2 cm, ground plane: 4 × 4 cm² (large ground plane), orientation: b–a–d, (dx, dy) = (0.5, 1.5) cm. (b) Field distribution within the DRA predicted using FDTD in the y–z plane at different x layers at f = 3.202 GHz, feed line length = 2 cm, ground plane: 4 × 4 cm² (large ground plane), orientation: b–a–d, (dx, dy) = (0.5, 1.5) cm. (c) Field distribution within the DRA predicted using FDTD in the x–z plane at different y layers at f = 3.202 GHz, feed line length = 2 cm, ground plane: 4 × 4 cm² (large ground plane), orientation: b–a–d, (dx, dy) = (0.5, 1.5) cm. Source: Adapted from Mridula 2005 [51].*

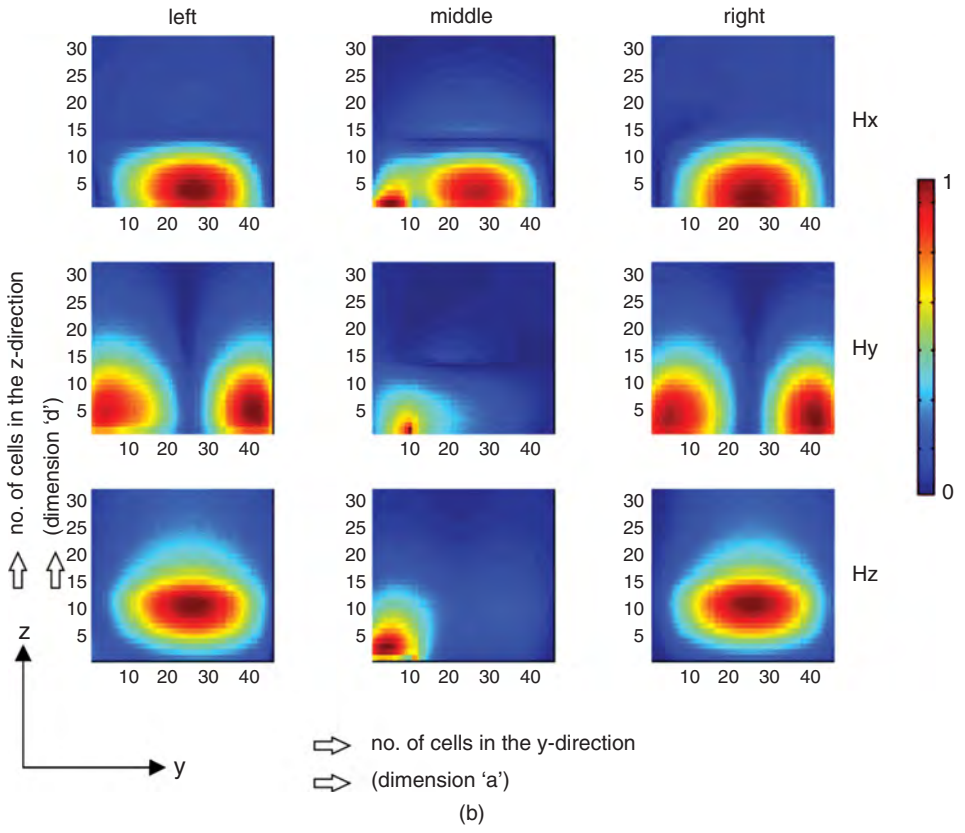

Figure 16.8 *(Continued)*

where the indices denote the number of half-wave intensity variations of the magnetic field along the dimensions a, b, and d of the DR, respectively ($a > b > d$).

The first, second, and third rows of figures in Figure 16.8a illustrate the variation of the Hx, Hy, and Hz components, respectively, in the x–y plane. The first, second, and third columns of the figures correspond to the H-field variation in the x–y plane at the bottom, middle, and top layers of the DR. The one half-wave variation of all the three field components along the dimensions a and b is evident from the field distribution at the top layer (column 3).

In Figure 16.8b the first, second, and third columns correspond to the H-field variation in the y–z plane at the left, middle, and right layers of the DR. The one half-wave variation of all the three field components along the dimension a and less than one half-wave variation along the dimension d is evident from the field distribution at the right-most layer (column 3).

In Figure 16.8c the first, second, and third columns correspond to the H-field variation in the x–z plane at the front (source end), middle, and back (feed end) layers of the DR. The one half-wave variation of all the three field components along the dimension b and less

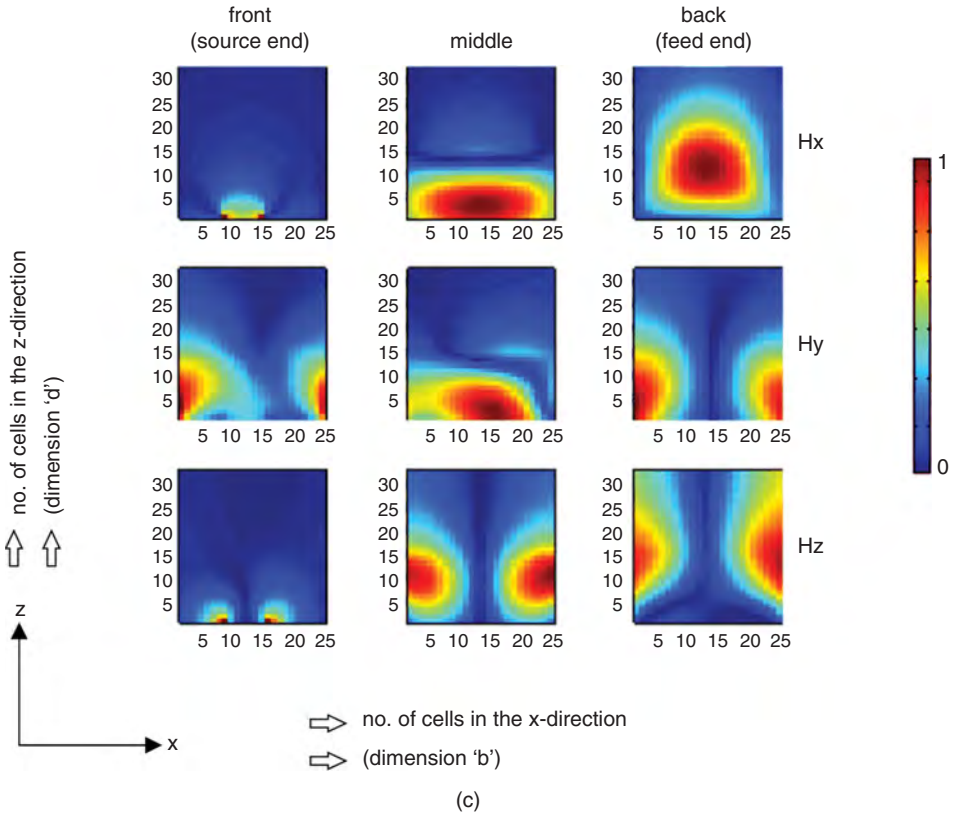

Figure 16.8 *(Continued)*

than one half-wave variation along the dimension d is evident from the field distribution at the back layer (column 3).

The one half-wave variation along the dimensions a and b and less than a half-wave variation (δ) along the dimension d, as illustrated in Figure 16.8a to c confirm the presence of $TE^{z}_{11\delta}$ mode. Simulation using the commercially available software HFSS^{TM} also gives similar results, as shown in Figure 16.9.

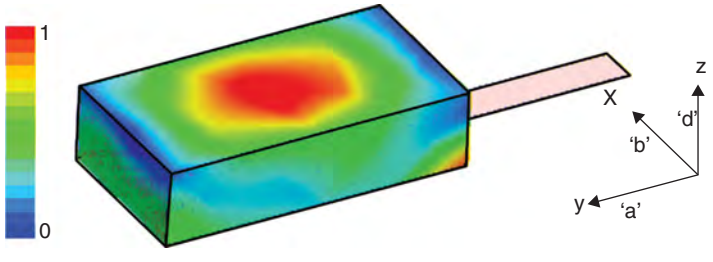

Figure 16.9 *Simulated H field distribution within the DR at f = 3.202 GHz. Source: Adapted from Mridula 2005 [51]. This figure is also shown in the Plate Section.*

16.2.4 Cylindrical DRA

Radiation characteristics of a cylindrical DRA have been reported by McAllister and Long [18]. The radiation pattern and input impedance of the antenna have been measured for different aspect ratios, materials, and coaxial feed probes. The magnetic wall boundary condition is used to theoretically predict the radiation characteristics. The resonant frequency of the antenna for different modes can be calculated from the following equations [18]:

$$\psi_{TE_{npm}} = J_n\left(\frac{X_{np}}{a}\rho\right)\left\{\begin{matrix}\sin n\varphi \\ \cos n\varphi\end{matrix}\right\}\sin\left[\frac{(2m+1)\pi}{2d}\right] \tag{16.5}$$

$$\psi_{TM_{npm}} = J_n'\left(\frac{X_{np}'}{a}\rho\right)\left\{\begin{matrix}\sin n\varphi \\ \cos n\varphi\end{matrix}\right\}\cos\left[\frac{(2m+1)\pi}{2d}\right] \tag{16.6}$$

where $J_n(X_{np}) = 0$, $J_n'(X_{np})' = 0$ and $n = 1, 2, 3, \ldots$, $p = 1, 2, 3, \ldots$, $m = 0, 1, 2, 3, \ldots$, and

$$k_\rho^2 + k_z^2 = k^2 = \omega^2\varepsilon\mu$$

$$f_{npm} = \frac{1}{2\pi a\sqrt{\varepsilon\mu}}\sqrt{\left\{\begin{matrix}X_{np}^2 \\ X_{np}'^2\end{matrix}\right\} + \left[\frac{\pi a}{2d}(2m+1)\right]^2} \tag{16.7}$$

The typical coaxial feeding technique for the cylindrical DRA is shown in Figure 16.10. It is found that for large *a*/*d* ratios, the pattern is omnidirectional in nature. The radiation pattern is found to be broadside in nature with high efficiency.

A broadband cylindrical dielectric resonator antenna excited by a modified microstrip line with 20% bandwidth is presented by Bijumon *et al.* [53]. The geometry of the antenna along with its reflection characteristics are shown in Figure 16.11, while the radiation pattern of the antenna along the principle planes at 2.62 GHz are shown in Figure 16.12.

16.2.5 Hemispherical DRA

Hemispherical DRAs are usually placed on a ground plane and hence can be treated as spherical DRAs. Since this is a standard geometry, closed-form Green's functions are

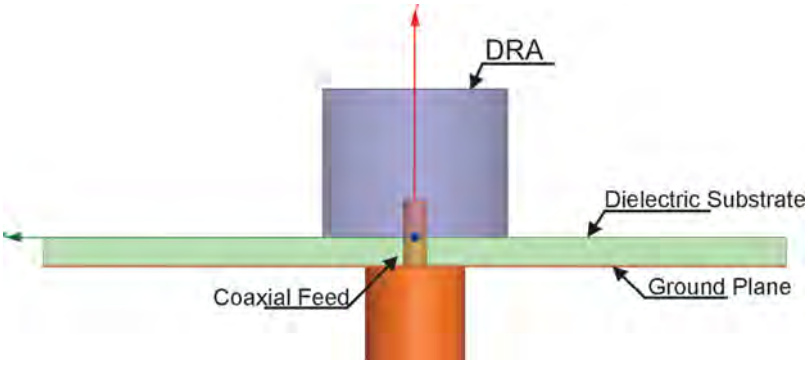

Figure 16.10 *Typical coaxial feeding used for exciting cylindrical DRA with conducting ground plane.*

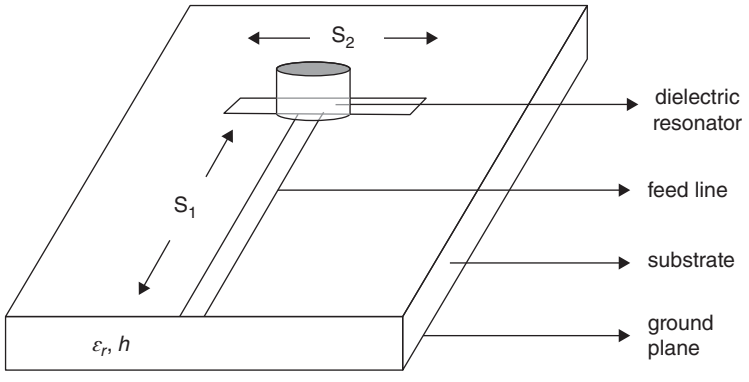

(a)

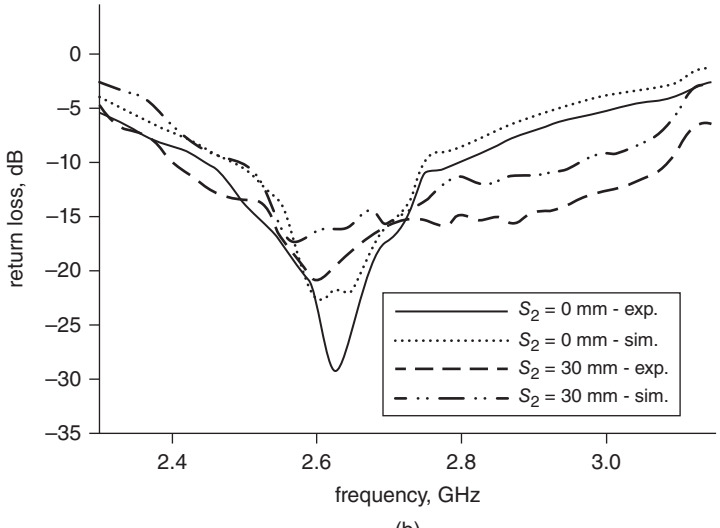

(b)

Figure 16.11 *(a) The geometry of the cylindrical DRA on a modified microstrip line and (b) the return loss of the antenna. Source: Adapted from Bijumon 2005 [53].*

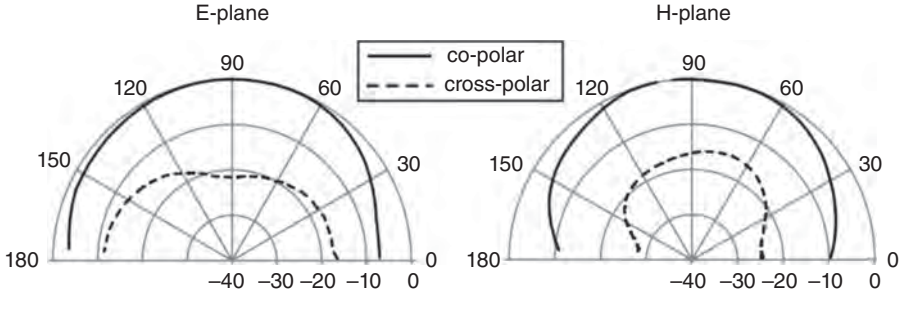

Figure 16.12 *The radiation pattern of the cylindrical DRA at 2.62 GHz along the principle planes. Source: Adapted from Bijumon 2005 [53].*

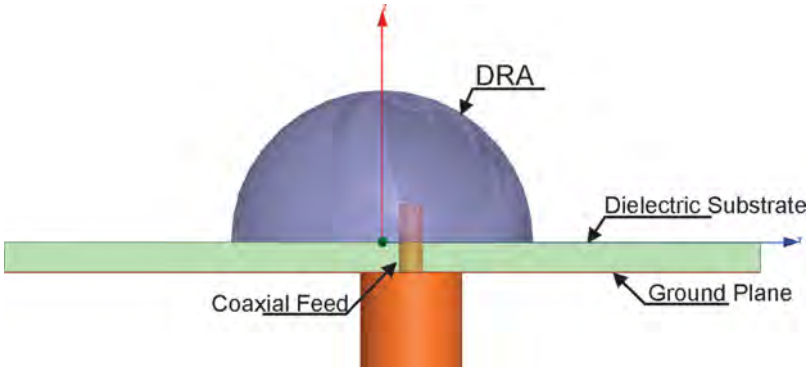

Figure 16.13 *Geometry of the hemispherical DRA excited with coaxial feed.*

available and method of moments (MoM) can be easily used for theoretical analysis. Geometry of a hemispherical DRA is shown in Figure 16.13. The resonance frequency of a hemispherical DRA having radius a and fed at a distance r from the centre is given by [54]

$$f_r = \frac{4.775 \times 10^7 Re\,(ka)}{\sqrt{\varepsilon_r} a} \tag{16.8}$$

where k is the wave number in dielectric and is given as $k_0\sqrt{\varepsilon_r}$.

Generally it is noted that a reduction in the dielectric constant of a DRA can increase the radiation properties over a relatively wide range of frequencies. Hence, low dielectric constant low-loss materials are preferred for wideband applications. High dielectric constant materials (ε_r = 80–100) are preferred for low profile applications, provided that the bandwidth is not a major constraint. For a rectangular DRA the bandwidth is normally 20–40% and for a cylindrical DRA is 35–40%. For typical antenna applications it is recommended to use a low-loss material with dielectric constant $8 \leq \varepsilon_r \geq 20$.

The lowest frequency of operation of DRA reported to date is at 55 MHz, by Kingsley and O'Keefe, using a water-filled multiprobe cylindrical VHF DRA, which has an unloaded Q-factor of approximately 28.4 [55]. The highest operating frequency of a DRA reported is at 94 GHz [56], which is a micromachined subarray fabricated on high-resistivity silicon and used as a feed for a reflector antenna.

16.3 Applications of Dielectric Resonator in Microwave Oscillators

A microwave oscillator is an important component in any communication, radar, remote sensing systems, etc., as it is the element that acts as the signal source. High Q tuning circuits are used for improving the stability of oscillators. The dielectric resonators have a very high Q in the range of several thousands, when compared with other conventional resonators like lumped element resonators, microstrip lines and stubs, cavity resonators [57], etc. The advantages of using dielectric resonator oscillators (DROs) over other oscillators are a high frequency stability, temperature stability, reduced noise, high efficiency,

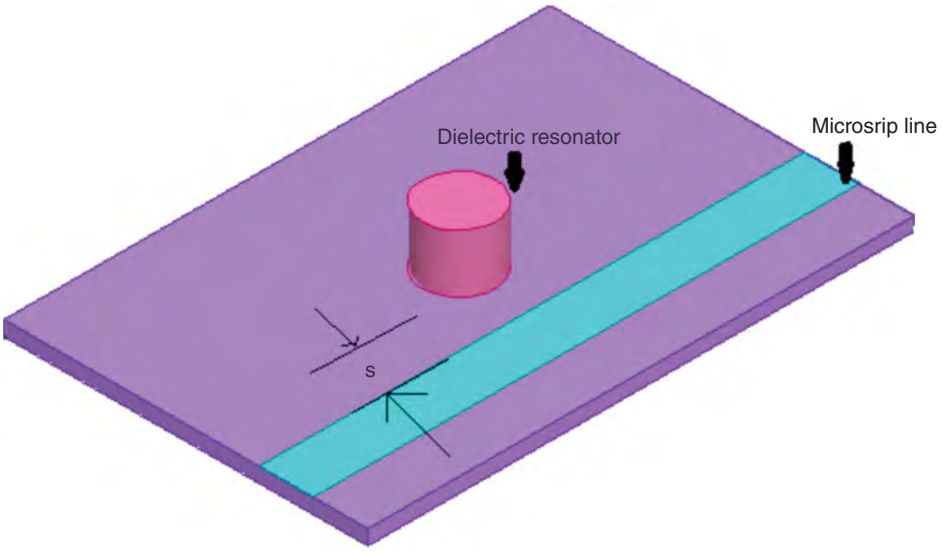

Figure 16.14 *A dielectric resonator kept in proximity of a transmission line.*

and small size [4, 58, 59]. Because of these reasons DROs are commonly used for many applications in microwave and millimeter wave frequencies.

A DR coupled to a microstrip transmission line is shown in Figure 16.14. The parameter s indicates the spacing between the DR and microstrip transmission line. The resonator is magnetically coupled to the transmission line. The amount of energy coupling is determined by the spacing s. In the equivalent circuit, a transmission line loaded with DR can be modeled as a parallel RLC circuit [57]. The DR can also be employed to produce a steady and stable oscillation at its resonant frequency with diode oscillators and other active circuit elements.

16.3.1 Diode Oscillators

Dielectric resonators are used in Gunn diode oscillators to reduce frequency variations arising from temperature or bias changes and to lower the oscillator phase noise. The typical oscillator configuration employing DR is shown in Figure 16.15. The configuration reported in reference [60] offers a stability of 0.5 ppm/°C at 10 GHz. Another application of DR in diode oscillators is the stabilization of a high-power IMPATT oscillator, employing two dielectric resonators. This allows independent control of fundamental and harmonic frequencies of the oscillator [60, 61]. A typical oscillator using a IMPATT diode and DR is shown in Figure 16.16.

16.3.2 Transistor Oscillators

These types of DR oscillators using active devices like FET or BJT are classified as reflection or feedback type depending on the position of the DR.

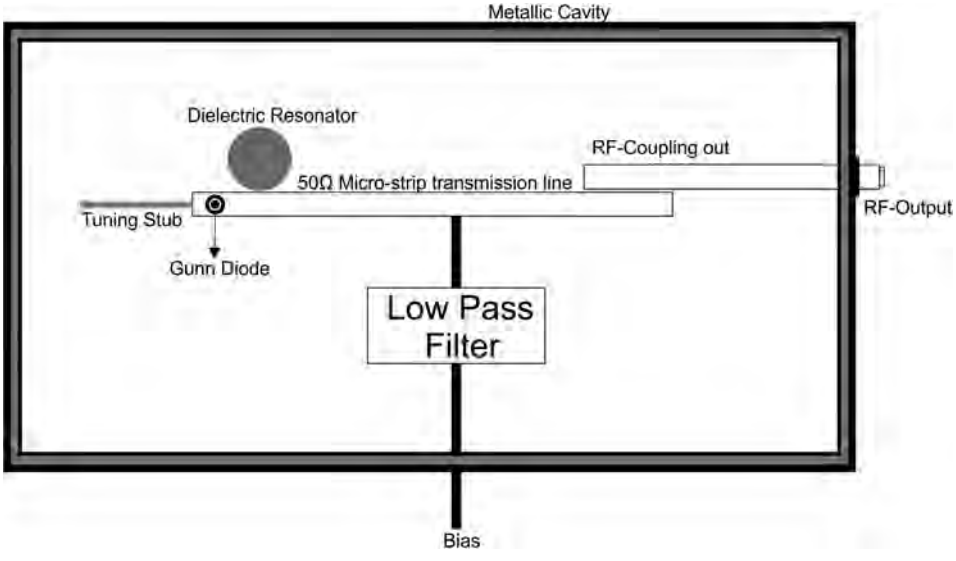

Figure 16.15 *Gunn diode oscillator using dielectric resonator.*

16.3.2.1 Reflection Type Oscillator

In the reflection type oscillator, the DR is placed approximately half a wavelength away from the transistor, as shown in Figure 16.17. Here the DR acts as a weakly coupled band-stop filter with a high Q. A part of the output energy is reflected towards the device and such a self-injected oscillator will generate a signal at the resonant frequency of the dielectric resonator. Typical reflection oscillators exhibit very good phase noise characteristics

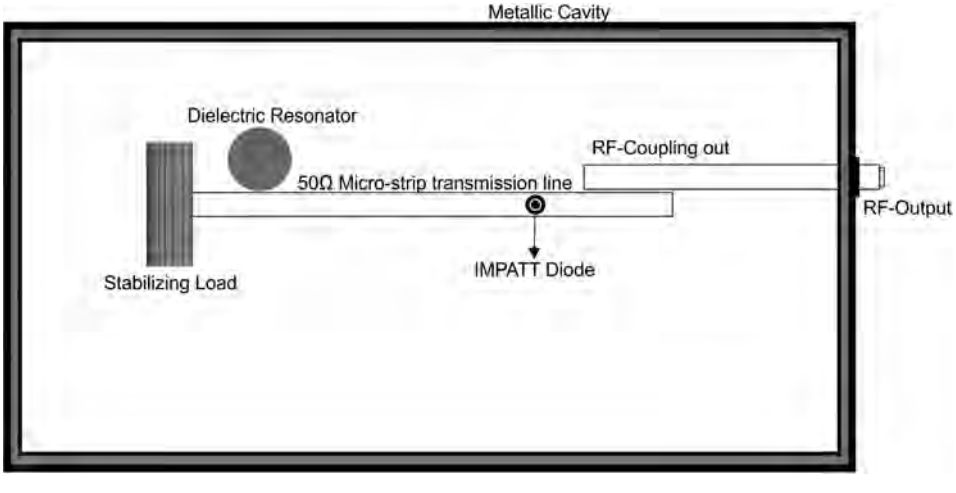

Figure 16.16 *IMPATT diode oscillator employing dielectric resonator.*

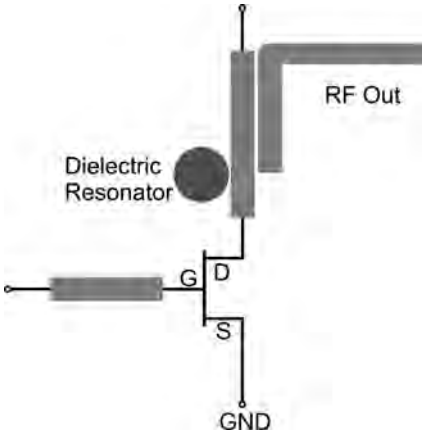

Figure 16.17 *Reflection type oscillator configuration.*

and frequency stability of approximately 1.5 ppm/°C. Because of the reflective mode of operation, these designs are sensitive to load changes and require an output isolator or buffer amplifier [60, 61].

16.3.2.2 Feedback Type Oscillator

In the feedback type oscillator, the DR is placed between the input and output, thereby creating a feedback network. The DR oscillators can be designed in two types of feedback configurations: (1) series feedback and (2) shunt/parallel feedback, as shown in Figure 16.18a and b. The parallel configuration uses a resonator coupled to two microstrip lines, functioning as a high-Q bandpass filter that couples a portion of the transistor output back to its input. The amount of coupling is controlled by the spacing between the resonator and the lines, and the phase is controlled by the length of the lines [57]. In the shunt feedback configuration, the resonator is strongly coupled to the drain and gate transmission

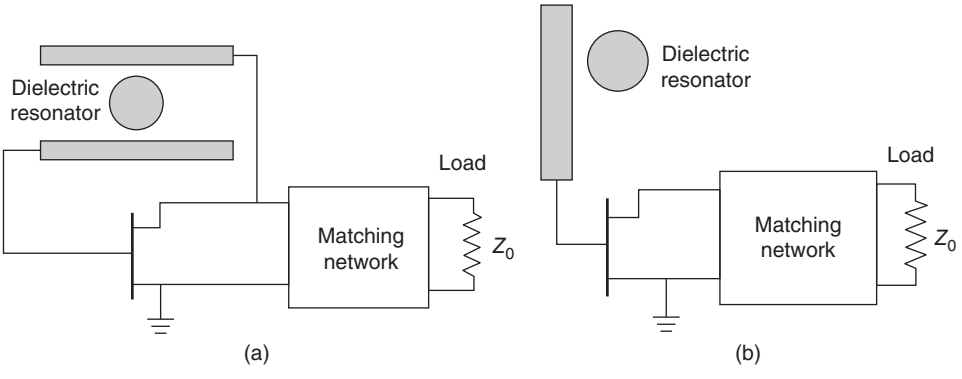

Figure 16.18 *(a) Parallel feedback configuration and (b) Series feedback configuration.*

Table 16.3 *Performance comparison of various DRO circuit configurations*

Parameter	Reflection	Series feedback	Shunt feedback
Mechanical tuning range	Fair	Good	Poor
FM noise	Fair	Good	Best
Output power	Good	Good	Fair
Load pulling	Poor	Best	Good

lines. Therefore, the loaded Q of the circuit is quite low and phase noise performance is degraded [60].

The series feedback configuration is simpler, using only a single microstrip feedline, but typically does not have a tuning range as wide as that obtained with parallel feedback [57]. The placement of the dielectric resonator on the gate port is critical, where it is isolated from the output circuits by the very low drain to gate capacitance inherent in the device. This isolation minimizes interaction between the output and input port, which allows the resonator to be lightly coupled to the gate, resulting in a very high loaded Q and, therefore, minimum phase noise [4]. The performance comparison of various DRO circuit configurations is shown in Table 16.3 [61].

To increase the stability of the oscillator further and improve close-in phase noise, phase-locked systems are becoming increasingly popular. In such systems, a tunable (e.g., varactor) dielectric-resonator oscillator is phase locked to a low-frequency crystal source or digital synthesizer, typically in application-specified integrated circuit (ASIC) form. This approach significantly enhances the overall performance of doubly resonant oscillators allowing their use in all communication systems including the most stringent and demanding satellite receiver systems [4].

16.3.3 State of the Art DROs

Hosoya *et al.* [62] developed a $TE_{01\delta}$ mode Ba (Mg, Ta) O_3 cylindrical DR combined with a 0.15 μm heterojunction field effect transistor to achieve low phase noise, high power, and excellent temperature stability in V-band. The reported DRO exhibits a low phase noise of −90 dBc/Hz at 100 kHz offset, a high output power of 10.0 dBm, and an excellent frequency stability of 1.6 ppm/°C at an oscillation frequency of 59.6 GHz. A tunable low phase noise oscillator presented with a substrate integrated waveguide (SIW)-based dielectric resonator having a high Q-factor [63] reported a phase noise of −121.7 dBc/Hz at a 10 kHz offset. An oscillator using the higher HEM_{221} mode of a rectangular dielectric resonator operating at 24.7 GHz with output power delivered is 4.5 dBm and phase noise −100 dBc/Hz at 100 kHz offset was reported by Haase and Hoffmann [64]. A harmonic dielectric resonator oscillator using a parallel feedback structure using a single DR to obtain an operating frequency of 9.45 GHz is reported in reference [65]. Zhou *et al.* have used $BaTiO_3$ resonators for developing broad tuning ultralow phase noise oscillators incorporating a cascaded SiGe amplifier, resonator, and phase shifter [66]. The reported phase noise is −135 dBc/Hz at 10 kHz offset.

In push–push oscillators [67–71], odd multiples of frequency are cancelled out and even multiples are added constructively. A 14 GHz push–push DRO using an SIW power combiner achieved high harmonic suppression with a frequency tuning range of 30 MHz and phase noise −98.01 dBc/Hz [67]. Low-temperature co-fired ceramic (LTCC) technology was employed to manufacture push–push voltage-controlled DR oscillators to reduce the circuit size [68, 69]. The phase noise reported is −103 dBc/Hz at 100 kHz offset, the fundamental frequency suppression is 30 dBc, and the output power is 0.5 dBm [68]. The oscillator reported by Ryu and Kim [69] works at 16 GHz with phase noise −97.5 dBc/Hz at 100 kHz offset. Sinnesbichler *et al.* reported [70] a 58 GHz push–push oscillator with a maximum output power of −8 dBm and a phase noise of −105 dBc/Hz at an offset frequency of 1 MHz. The mechanical tuning range of the oscillator is approximately 500 MHz. A 22 GHz DRO using an MMIC with a low phase noise of −114 dBc/Hz at 100 kHz offset is presented by Chang *et al.* [71].

Locke *et al.* [72] presented an ultrastable cryogenically cooled sapphire dielectric resonator oscillator at 11 GHz. The phase noise reported is −97 rad^2/Hz at an offset of 1 Hz from the carrier, and the frequency stability is better than 1×10^{-15} at an average time of 1 second.

16.3.3.1 Frequency Stability

DRs exhibit excellent frequency stability characteristics by virtue of a low temperature coefficient of frequency shift. Frequency stability is expressed in terms of ppm/°C. Because of the high Q nature of the dielectric resonator, the frequency pulling characteristics are better than other free running oscillators. The frequency pulling figure for an unbuffered (at 10 GHz) DRO is typically less than 5 MHz peak-to-peak for a 1.5:1 VSWR varying through all phases [73]. Frequency pulling can be minimized by isolating the oscillator from the load. Many modern DROs have buffer amplifiers or isolators to reduce the effect of frequency pulling. For example, DRO 1000 series dielectric resonator oscillators manufactured by Microwave Dynamics is buffered by a cascaded low-noise driver and power amplifiers for minimum load pulling and maximum isolation and power. To ensure oscillator stability over the full temperature range, high-Q low dielectric constant resonators are chosen with a proper temperature coefficient to compensate for frequency drift. When extreme stability is required, a miniature heater can be provided to ensure constant temperature and minimum drift. These DROs are internally voltage regulated to avoid reverse bias, frequency pushing, bias modulation, and voltage transients [74].

16.4 Application of Dielectric Resonators in Microwave Filters

Dielectric resonators (DRs) are commonly used in the design and development of high Q bandpass, bandstop, and tunable filters. DR filters find applications in many microwave systems. The main advantages of DR filters are high frequency stability, very small fractional bandwidth, high power handling capacity, and low insertion loss. These characteristics are very much required in modern communication systems such as satellite communications. DR-based filters can be designed by arranging suitable dielectric resonators of

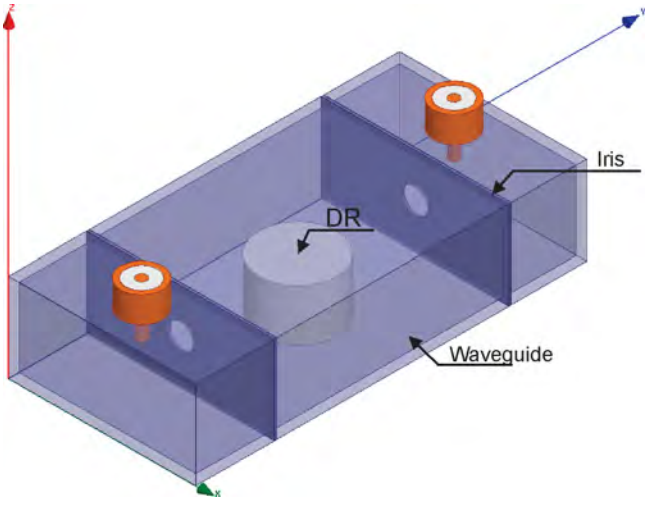

Figure 16.19 *Configuration of a typical dielectric resonator filter. This figure is also shown in Plate Section.*

the required shape inside a cylindrical metallic cavity [75]. A typical configuration of a rectangular cavity-based DR filter is shown in Figure 16.19.

Mansour reported a dielectric resonator filter consisting of a number of dielectric resonators mounted inside cavities operating below cut-off, to avoid cavity modes, as shown in Figure 16.20. The cavities are separated by irises to provide the necessary coupling between resonators [76]. Resonators of different shapes are chosen based on filter requirements.

16.4.1 Dielectric Resonator Bandpass Filters

16.4.1.1 Single Mode Filters

Single mode filters make use of the $TE_{01\delta}$ fundamental mode of the DR. The advantages of these fundamental mode filters are design simplicity, flexibility in layout options, and low manufacturing cost. The TE mode filter can have a layout suitable for mass production and tuning. An example of the TE mode filter arrangement is shown in Figure 16.21. This is a five-pole TE mode DR filter with three non-adjacent aperture couplings, including both inductive and capacitive couplings. It exhibits an elliptical frequency response with three transmission zeros all at the lower side of the passband [4, 77, 78].

16.4.1.2 Dual Mode Filters

Dual mode filters usually use the low attenuation hybrid $HE_{11\delta}$ mode of the DR. The dual-mode filter can halve the number of physical resonator cavities, therefore significantly reducing the weight and volume of the unit. It has been widely used in satellite communication systems. The dual mode filter can be used to realize high-performance elliptic function filters that require coupling between nonadjacent cavities. A typical filter configuration using $HE_{11\delta}$ mode is shown in Figure 16.22. Coupling between modes within a single cavity is achieved via a mode-coupling screw with an angular location of 45°, with

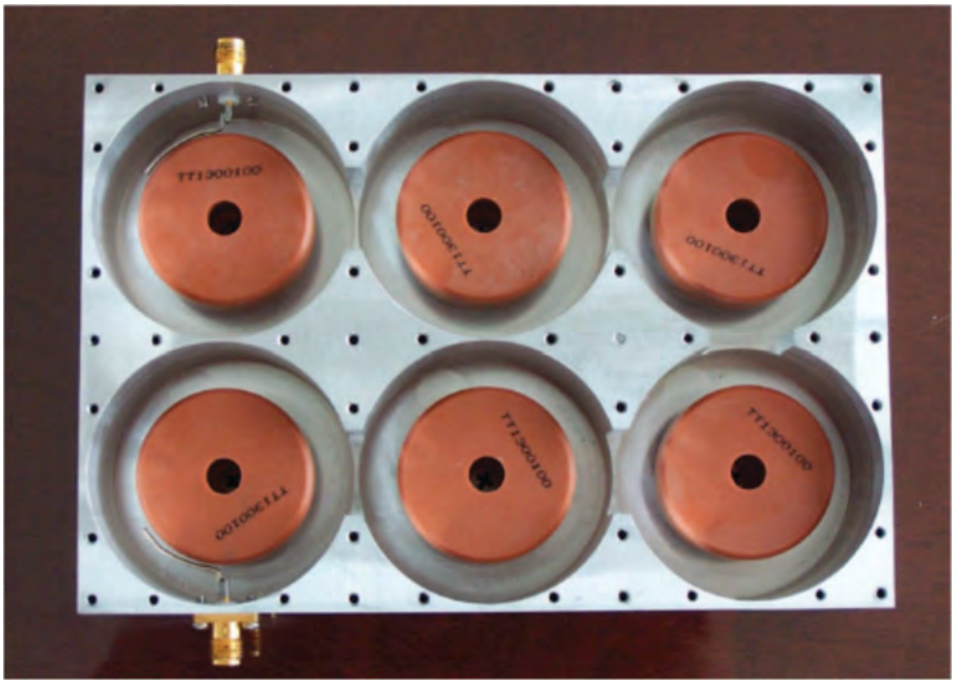

Figure 16.20 *A filter configuration realized using dielectric resonators. Source: Mansour 2009 [76]. Reproduced with permission of IEEE. This figure is also shown in Plate Section.*

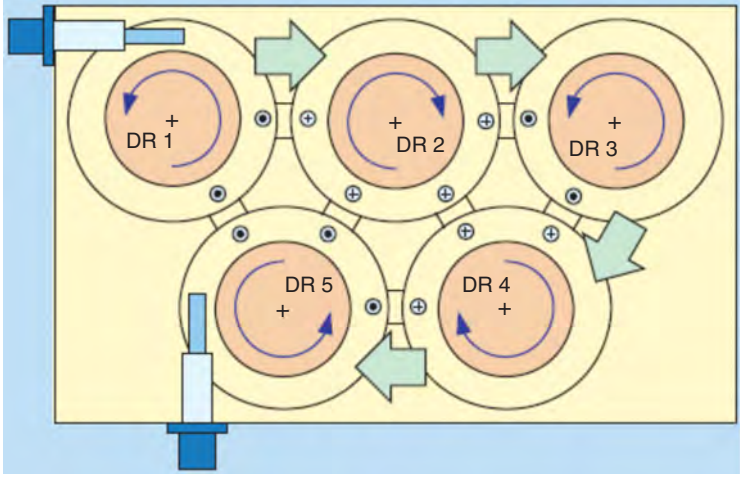

Figure 16.21 *Schematic of TE single mode filter with five poles. Source: Wang 2007 [77]. Reproduced with permission of IEEE.*

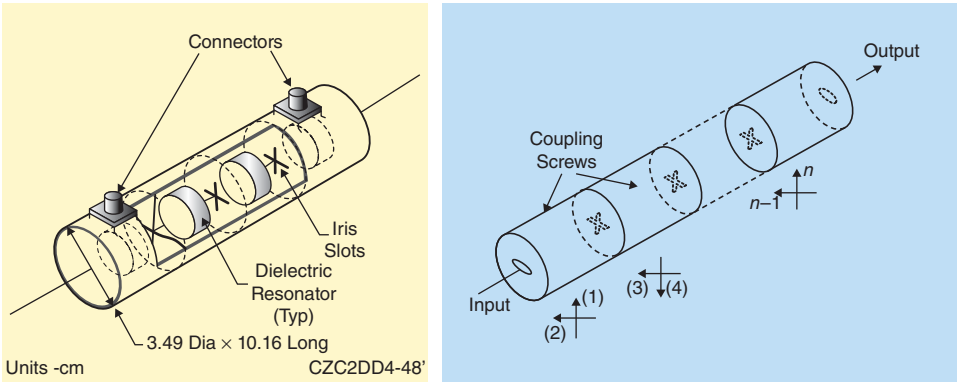

Figure 16.22 *Dual mode dielectric resonator filter. Source: Wang 2007 [77]. Reproduced with permission of IEEE.*

respect to orthogonal tuning screws [77]. Intercavity coupling is provided by coupling slots. DRs are mounted axially in the center of each evanescent circular cavity. A low-loss stable mounting is required to ensure good electrical and temperature performance [4, 77].

16.4.1.3 Mixed Mode Filters

Both the TE_{01} mode and HE_{11} mode filters have very limited spurious free performance. Mixing the TE_{01} mode and HE_{11} mode of the DR cavities and offsetting the spurious frequencies of two types of resonators can improve the spurious performance of the filter while maintaining the advantages of elliptic function filters [4, 77–79].

A schematic of a six-pole quasi-elliptic function filter using dielectric loaded cavities is shown in Figure 16.23. The principle can be easily extended to higher-order filters [77].

16.4.2 Tunable Dielectric Resonator Filters

Modern communication systems demand devices that can adapt to different requirements. This is also applicable for filters, which is the reason for the huge demand for tunable filters in the market. DRs are a good choice in the design of tunable filters as they can operate at various modes. DRs are available in various shapes, which can be used to enhance the tunability and add flexibility of integration of several tuning techniques [76].

16.4.2.1 MEMS-Based Tunable DR Filter

Yan and Mansour reported [80] a tunable dielectric resonator filter consisting of a DR operating at $TE_{01\delta}$ mode, a tuning disk, and multiple MEMS. The MEMS actuators along with the disk are employed to replace the tuning screws typically used in conventional DR filters. All the components are contained in a metallic cavity, as shown in Figure 16.24 [76]. Tunability is achieved by moving the tuning disk along the z-axis with the use of a MEMS

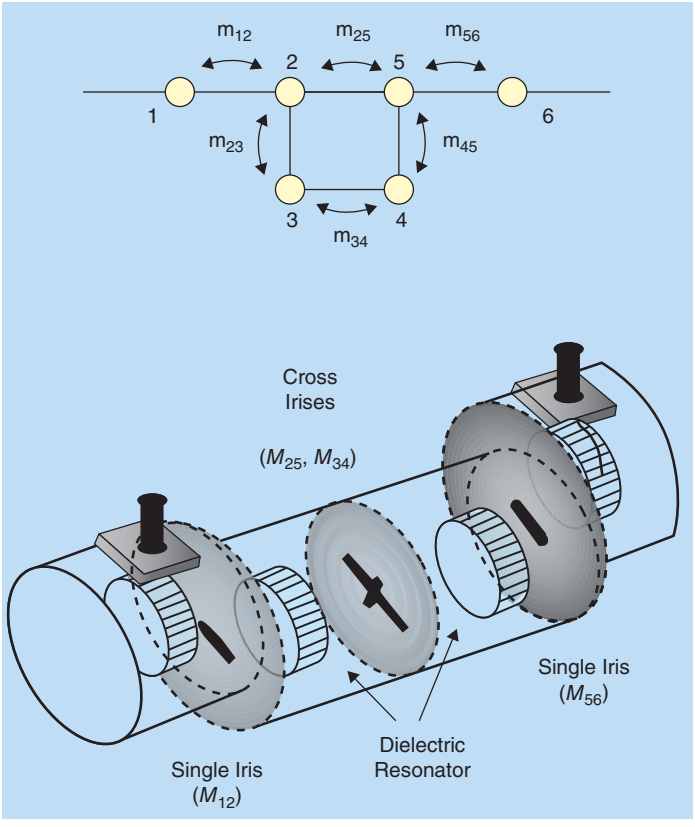

Figure 16.23 *Mixed mode dielectric resonator filter. Source: Wang 2007 [77]. Reproduced with permission of IEEE.*

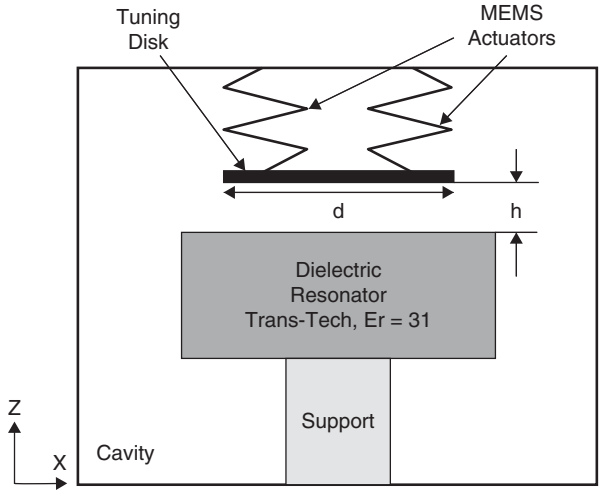

Figure 16.24 *MEMS-based tunable dielectric resonator. Source: Mansour 2009 [76]. Reproduced with permission of IEEE.*

actuator. With no DC bias applied to the MEMS actuator, the tuning disk is at the closest position to the dielectric resonator, that is, the value of the tuning gap h is at a minimum. This state corresponds to the highest resonant frequency. When a DC voltage is applied to the MEMS actuator, the tuning disk is pulled away from the dielectric resonator and the resonant frequency begins to decrease. A tuning range of 400 MHz is obtained by using 2 mm × 2 mm tuning disks.

16.4.2.2 Magnetically Tuned DR Filter

Methods of tuning the frequency by changing the magnetic field surrounding the DR by using ferrites is reported in references [81] and [82]. A schematic of the DR with ferrite rods for tuning is shown in Figure 16.25 [76].

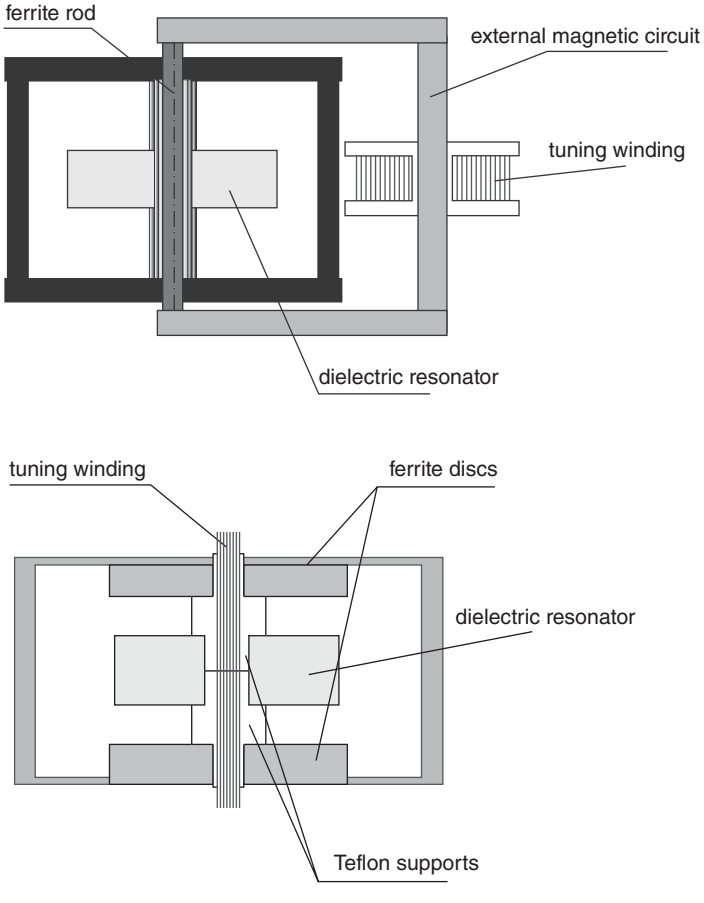

Figure 16.25 *Tunable dielectric resonator using ferrites. Source: Mansour 2009 [76]. Reproduced with permission of IEEE.*

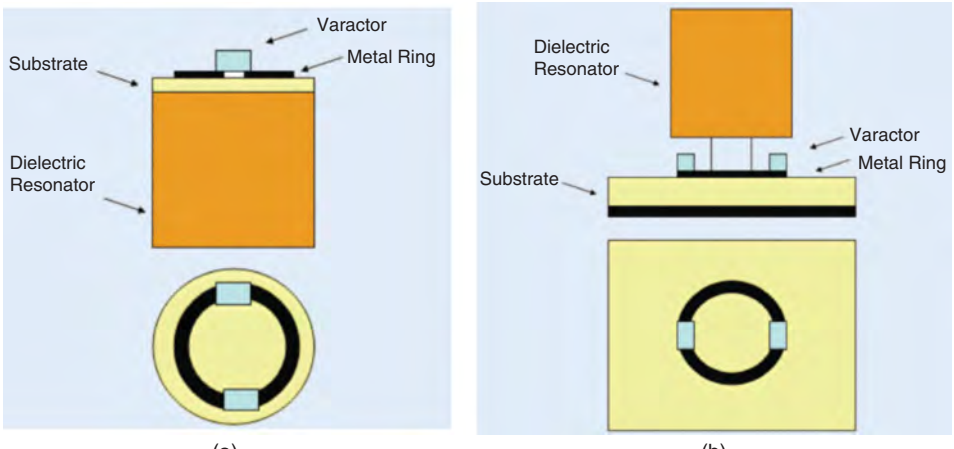

Figure 16.26 *Tunable dielectric resonator using varactor diodes. (a) Varactor is coupled to the top of DRA, (b) Varactors are integrated proximity of the DRA. Source: Mansour 2009 [76]. Reproduced with permission of IEEE.*

16.4.2.3 Varactor Tuned DR Filter

The schematic of a varactor tuned filter is shown in Figure 16.26. The field distribution in the vicinity of the dielectric resonator is changed by varying the boundary conditions on the metal ring through the use of varactors. Use of varactor diodes as a tuning element is elaborately discussed in references [83] and [84].

16.4.3 State of the Art DR Filters

A quadruple mode dielectric resonator filter using cylindrical resonators is presented by Memarian and Mansour [85]. The center frequency of the filter is 3.666 GHz and the fractional bandwidth is 1%. A spurious free window of 480 MHz and insertion loss varying between 0.4 to 0.6 dB over the passband is observed. The authors have also reported a half-cut dual-mode dielectric resonator filter derived from the quad-mode resonator. Zhang and Mansour have reported a dual-band filter with center frequencies of 5 and 5.6 GHz [86]. The fractional bandwidth is 1% for both passbands. The proposed filter is a two-pole filter with a maximum insertion loss of 0.25 dB in the first passband and 0.27 dB in the second passband. The spurious-free stop band is 700 MHz. The authors have extended their study by developing a threepole dualband filter that operates at 2.6 and 3.5 GHz with fractional bandwidths 0.7 and 1.1%, respectively. Bastioli and Snyder have reported a new class of dielectric resonator filters with an in-line structure and pseudo-elliptic response [87]. This uses a $TE_{01\delta}$ single mode, cascaded along an evanescent mode waveguide and oriented along orthogonal directions. The authors also report triple, quadruple and quintuple resonator filter configurations.

The $TE_{01\delta}$ mode is differentially excited to create the fundamental passband of a band-pass filter [88,89]. Chen *et al.* reported a narrow-band balanced bandpass filter using a rectangular dielectric resonator with center frequency 3.967 GHz, fractional bandwidth 0.5%,

and better than 20 dB common-mode suppression in the passband [88]. A 40 dB common mode suppression level at a center frequency of 1.75 GHz and fractional bandwidth 1.3% is presented by Zhan *et al.* [89]. Dielectric resonators are used in tunable bandpass filters [80,90,91]. MEMS switches as the tuning element are used in a tunable three-pole filter with center frequency 15.6 GHz and 1% fractional bandwidth [80]. The tuning range reported by the authors is 400 MHz. Three tunable filters with an MEMS contact-type switch, GaAs varactor and MEMS varactor are reported [90]. The four-pole tunable dielectric resonator filter operating at 5.2 GHz with 1% fractional bandwidth presented in reference [91] uses piezoelectric transducer actuators as the tuning element. Aswathi *et al.* reported [92] a dual bandstop filter designed using the $TE_{01\delta}$ mode. The rejection frequencies are 9.96 and 10.15 GHz with bandwidths of 1.6 and 0.6%, respectively.

References

1. Richtmyer, R.D. (1939) Dielectric resonators. *Journal of Applied Physics*, **10**, 391–398.
2. Okaya, A. and Barash, L.F. (1962) The dielectric microwave resonator. *Proceedings of IRE*, **50**, 2081–2092.
3. Masse, D.J., Purcel, R.A., Ready, D.W., *et al.* (1971) A new low loss high *K* temperature compensated dielectric for microwave applications. *Proceedings of IEEE*, **59**, 1628–1629.
4. Fiedziuszko, J.S. and Stephen Holme, S. (2001) Dielectric resonators – raise your high- *Q*. *IEEE Microwave Magazine*, **2**, 51–60.
5. Fiedziuszko, J.S., Hunter, I.C., Itoh, T., *et. al.* (2002) Dielectric materials, devices and circuits. *IEEE Transactions on Microwave Theory and Techniques*, **50**, 706–720.
6. Shu, Y. and Wong, T.Y. (1995) Perturbation of dielectric resonator for material measurement. *Electronics Letters*, **31**, 704–705.
7. Fargeot, S., Veronjanne, A., Auborg, M., *et al.* (1998) Cylindrical dielectric resonator antenna for material characterization. *Microwave Optical Technology Letters*, **17**, 273–275.
8. Semouchkina, E., Cao, W., Lanagan, M., *et al.* (2001) Combining FDTD simulations with measurements of microstrip ring resonators for characterization of low and high *K* dielectrics at microwaves. *Microwave Optical Technology Letters*, **29**, 21–24.
9. Jacob, M.V., Mazierska, J., Leong, K., *et al.* (2001) Novel method for calculation and measurement of unloaded Q-factor of superconducting dielectric resonators, in *IEEE Antennas and Propagation Society International Symposium*, Boston, MA, vol. 3, pp. 1993–1996.
10. Yuksel, E.Y., and Wong, T.T.Y. (2003) A phase-shifting frequency discriminator employing dielectric resonator. *Microwave Optical Technology Letters*, **36**, 87–89.
11. Liu, J.-C., Cheng, C.-S., and Yao, L. (2003) Dual-mode double ring resonator for microstrip band-pass filter design. *Microwave Optical Technology Letters*, **36**, 310–314.
12. Petosa, A. (2007) *Dielectric Resonator Antenna Handbook*, Artech House.
13. Chair, R., Kisk, A.A., Lee, K.F., *et al.* (2006) Performance comparison between dielectric resonator antennas and printed microstrip patch antennas at X band. *Microwave Journal*, **49**, 90–104.
14. Aleksiejunas, R. and Ivaska, V. (1997) Leaky mode cylindrical dielectric resonator antenna. *Electronics Letters*, **33**, 547–548.
15. Pang, K.K., Lo, H.Y., Leung, K.W., *et al.* (2000) Circularly polarized dielectric resonator antenna subarrays. *Microwave Optical Technology Letters*, **27**, 377–379.
16. Wong, K.-L., Su, S.-W., Choiu, T.-W., *et al.* (2002) Dual-band plastic chip antenna for GSM/DCS mobile phones. *Microwave Optical Technology Letters*, **33**, 330–332.
17. Yung, T.-S., Chang, T.-H., Wu, W.-Z., *et al.* (2004) Dual-band dielectric resonator antenna, in *IEEE Antennas and Propagation Society International Symposium*, Monterrey, CA, vol. 2, pp. 1351–1354.
18. Long, S.A., McAllister, M.W., and Sheen, C. (1983) The resonant cylindrical dielectric cavity antenna. *IEEE Transactions on Antennas and Propagation*, **31**, 406–412.

19. Petosa, A. and Ittipiboon, A. (2010) Dielectric resonator antennas. A historical review and the current state of the art. *IEEE Antennas and Propagation Magazine*, **52**, 91–116.
20. https://www.ieee.li/pdf/viewgraphs/development_of_dielectric_resonator_antenna.pdf.
21. Soren, D., Ghatak, R., Mishra, R.K., *et. al.* (2014) Dielectric resonator antennas: designs and advances. *Progress in Electromagnetism Research B.*, **60**, 195–213.
22. Huitema, L. and Monediere, T. (2012) *Dielectric Materials for Compact Dielectric Resonator Antenna Applications* (ed. M.A. Silaghi), InTech Publishers, pp. 27–58, ISBN 978-953-51-0764-4.
23. Sebastan, M.T., Ubic, R., and Jantunen, H. (2015) Low loss dielectric ceramic materials and their properties. *International Materials Review*, **60**, 392.
24. IEEE (2013) IEEE Standard for Definitions of Terms for Antennas, IEEE Std 145™, IEEE Standard Association, IEEE Antennas and Propagation Society.
25. Gastine, M., Courtois, L., and Dormann, J.J. (1967) Electromagnetic resonances of free dielectric spheres. *IEEE Transactions on Microwave Theory and Technique*, **15**, 694–700.
26. Sager, O. and Tisi, F. (1968) On eigen modes and forced resonance-modes of dielectric spheres. *Proceedings of IEEE*, **56**, 1593–1594.
27. Petosa, A., Simons, N., Siushansian, R., *et al.* (2000) Design and analysis of multisegment dielectric resonator antennas. *IEEE Transactions on Antennas and Propagation*, **48**, 738–742.
28. Lee, M.T., Luk, K.M., Leung, K.W., *et al.* (2002) A small dielectric resonator antenna, *IEEE Transactions on Antennas and Propagation*, **50**, 1485–1487.
29. Denidni, T.A., Rao, Q., and Sebak, A.R. (2004) Multi-eccentric ring slot fed dielectric resonator antenna for multi-frequency operations, in *IEEE Antennas and Propagation Society International Symposium*, Monterrey, CA, vol. 2, pp. 1379–1382.
30. Mridula, S., Sreedevi, K.M., Mohanan, P., *et al*. (2004) Characteristics of a microstrip excited high-permittivity rectangular dielectric resonator antenna. *Microwave Optical Technology Letters*, **40**, 316–318.
31. Kishk, A.A., Auda, H.A., and Ahn, B.C. (1987) Accurate prediction of radiation patterns of dielectric-resonator antennas. *Electronics Letters*, **23**, 1374–1375.
32. Verplanken, M. and Van Bladel, J. (1976) The electric-dipole resonances of ring resonators of very high permittivity. *IEEE Transactions on Microwave Theory and Techniques*, **24**, 108–112.
33. Lee, R.Q. and Simons, R.N. (1993) Bandwidth enhancement of dielectric resonator Antennas, in *IEEE Antennas and Propagation Society International Symposium*, Michigan, vol. 3, pp. 1500–1503.
34. Shum, S.M. and Luk, K.M. (1995) Stacked annular ring dielectric resonator antennas for wideband applications. *IEEE Transactions on Antennas and Propagation*, **43**, 889–892.
35. Fan, Z., Antar, Y.M.M., Ittipiboon, A., *et al.* (1996) Parasitic coplanar three-element dielectric resonator antenna subarray, *Electronics Letters*, **32**, 789–790.
36. Hsiao, F.-R., Kuo, J.-S., Chiou, T.-W., *et al.* (2002) A broadband very-high-permittivity dielectric resonator antenna for WLAN application in the 5.2 GHz band. *Microwave Optical Technology Letters*, **32**, 426–427.
37. Kishk, A.A., Tin, Y., and Glisson, A.W. (2002) Conical dielectric resonator antennas for wideband applications. *IEEE Transactions on Antennas and Propagation*, **50**, 469–474.
38. Bit-Babik, B., Di Nallo, C., and Faraone, A. (2004) Multimode dielectric resonator antenna of very high permittivity, in *IEEE Antennas and Propagation Society International Symposium*, Monterrey, CA, vol. 2, pp. 1383–1386.
39. Pliakostathis, K. and Mirshekar-Syahkal, D. (2004) Stepped dielectric resonator antennas for wideband applications, in *IEEE Antennas and Propagation Society International Symposium*, Monterrey, CA, vol. 2, 1367–1370.
40. Chair, R., Kishk, A.A., Lee, K.F., *et al.* (2004) Broadband aperture coupled flipped staired pyramid and conical dielectric resonator antennas, in *IEEE Antennas and Propagation Society International Symposium*, Monterrey, CA, vol. 2, pp. 1375–1378.
41. Al Sharkawy, M., Elsherbeni, A.Z., and Smith, C.E. (2004) Stacked elliptical dielectric resonator antennas for wideband applications, in *IEEE Antennas and Propagation Society International Symposium*, Monterrey, CA, vol. 2, pp. 1371–1374.

42. Mongia, R.K. and Bhartia, P. (1994) Dielectric resonator antennas – a review and general design relations for resonant frequency and bandwidth. *International Journal of Microwave and Millimeter-Wave Computer-Aided Engineering*, **4**, 230–247.
43. Petosa, A., Ittipiboon, A., Antar, Y.M.M., *et al.* (1998) Recent advances in dielectric resonator antenna technology. *IEEE Antennas and Propagation Magazine*, **40**, 35–48.
44. Ghosh, I.S., Hilgers, A., Schlenker, T., *et al.* (2001) Ceramic microwave antennas for mobile applications. *Journal of the European Ceramic Society*, **21**, 2621–2628.
45. Mongia, R.K., Ittipiboon, A., Cuhaci, M. (1994) Low profile dielectric resonator antennas using a very high permittivity material. *Electronics Letters*, **30**, 1362–1363.
46. Gentili, G.B., Morini, M., and Selleri, S. (2003) Relevance of coupling effects on DRA array design. *IEEE Transactions on Antennas and Propagation*, **51**, 399–404.
47. Luk, K.M., Lee, M.T., Leung, K.W., *et al.* (1999) Technique for improving coupling between microstripline and dielectric resonator antenna. *Electronics Letters*, **35**, 357–358.
48. Leung, K.W., Wong, W.C., Luk, K.M., *et al.* (2000) Circular-polarised dielectric resonator antenna excited by dual conformal strips. *Electronics Letters*, **36**, 484–486.
49. Guo, Y.X. and Luk, K.-M. (2003) On improving coupling between a coplanar waveguide feed and a dielectric resonator antenna. *IEEE Transactions on Antennas and Propagation*, **51**, 2142–2144.
50. Lo, H.Y., Leung, K.W., and Luk, K.M. (2001) Slot-line-excited equilateral-triangular dielectric resonator antenna of very high permittivity. *Microwave and Optical Technology Letters*, **29**, 230–231.
51. Mridula S. (2005) Investigations on a microstrip excited rectangular dielectric resonator antenna. PhD Thesis, Cochin University of Science and Technology, Cochin, Kerala, India.
52. Mohanan, P., Mridula, S., and Binu, P. (2007) FDTD analysis of rectangular dielectric resonator antenna. *Journal of the European Ceramic Society*, **27**, 2753–2757.
53. Bijumon, P.V., Menon, S.K., Suma, M.N., *et al.* (2005) Broadband cylindrical dielectric resonator antenna excited by modified microstrip line. *Electronics Letters*, **41**, 385–387.
54. McAllister, M.W. and Long, S.A. (1984) Resonant hemispherical dielectric antenna. *Electronics Letters*, **20**, 657–659.
55. Kingsley, S.P. and O'Keefe, S.G. (1999) Beam steering and monopulse processing of probe fed dielectric resonator antenna. *Proceedings of Rada Sonar Navigation*, **146**, 121–125.
56. Svedin, J., Huss, L.G., Karlen, D., *et al.* (2007) A micromachined 94 GHz dielectric resonator antenna for focal plane array applications, in *IEEE International Microwave Symposium*, Honolulu, Hawaii, pp. 1375–1378.
57. Pozar, D.M. (2011) *Microwave Engineering*, 4th edn, John Wiley & Sons, Inc.
58. Plourde, J.K. and Ren C.L. (1981) Application of dielectric resonators in microwave components. *IEEE Transactions on Microwave Theory and Techniques*, **29**, 754–770.
59. Ugurlu, S.S. (2011) Dielectric resonator oscillator design and realization at 4.25 GHz, in *7th International Conference on Electrical and Electronics Engineering*, Bursa, Turkey, pp. II-205II-208.
60. Golio, M. and Golio, J. (2007) *RF and Microwave Passive and Active Technologies*, 2nd edn, CRC Press.
61. Smith, B.L. and Carpentier, M.H. (1993) *Microwave Engineering Handbook: Microwave Circuits, Antennas, and Propagation*, vol. 2, Van Nostrand Reinhold, New York.
62. Hosoya, K., Ohata, K., Funabashi, M., *et al.* (2003) V-band HJFET MMIC DROs with low phase noise, high power, and excellent temperature stability. *IEEE Transactions on Microwave Theory and Techniques*, **51**, 2250–2258.
63. Zhou, L., Yin, W.Y., Wang, J., *et al.* (2013) Dielectric resonators with high Q-factor for tunable low phase noise oscillators. *IEEE Transactions on Components, Packaging and Manufacturing Technology*, **3**, 1008–1015.
64. Haase, M. and Hoffmann, K. (2013) Transistor oscillator 24.7 GHz stabilized by HEM_{221} mode of rectangular dielectric resonator, in *13th Conference on Microwave Techniques*, Pardubice, Czech Republic, pp. 62–64.
65. Du, Y.C., Tang, Z.X., Zhang, B., *et al.* (2012) K-band harmonic dielectric resonator oscillator using parallel feedback structure. *Progress in Electromagnetics Research Letters*, **34**, 83–90.

66. Zhou, L., Wu, Z., and Sallin, M. (2007) Broad tuning ultra-low phase noise dielectric resonator oscillators using SiGe amplifier and ceramic-based resonators. *IET Microwave Antennas Propagation*, **1**, 1064–1070.
67. Su, P., Tang, Z.X., and Zhang, B. (2012) Push–push dielectric resonator oscillator using substrate integrated waveguide power combiner. *Progress in Electromagnetics Research Letters*, **30**, 105–113.
68. Yom, I.B., Shin, D.H, Oh, S.H, *et al*. (2007) Push–push voltage controlled dielectric resonator oscillator using a LTCC technology. *Microwave and Optical Technology Letters*, **49**, 1824–1827.
69. Ryu, K.K. and Kim, S.C. (2015) Push–push voltage controlled dielectric resonator using a broadside coupler. *Journal of Information and Communication Convergence Engineering*, **13** (2), 139–143.
70. Sinnesbichler, F.X., Hautz, B., and Olbrich, G.R. (2000) A Si/SiGe HBT dielectric resonator push–push oscillator at 58 GHz. *IEEE Microwave and Guided Wave Letters*, **10**, 145–147.
71. Chang, H.Y., Wang, H., Wang, Y.C., *et al*. (2004) A 22-GHz ultra-low phase noise push–push dielectric resonator oscillator using MMICs, in *12th GAAS Symposium*, Amsterdam, pp. 33–36.
72. Locke, C.R., Motohiro, K., Hiroyuki, I., *et al.* (2010) Ultra-stable cryogenically cooled sapphire-dielectric resonator oscillator and associated synthesis chain for frequency dissemination. *Journal of the National Institute of Information and Communications Technology*, **57**, 47–59.
73. https://www.miteq.com/docs/D210B.PDF.
74. http://microwave-dynamics.com/datasheets/DRO%201000.pdf.
75. Saliminejad, R. and Ghafourifard, M.R. (2008) A novel and accurate method for designing dielectric resonator filter. *Progress in Electromagnetics Research B*, **8**, 293–306.
76. Mansour, R.R. (2009) High-Q tunable dielectric resonator filters. *IEEE Microwave Magazine*, **10**, 84–98.
77. Wang, C. and Zaki, K.A. (2007) Dielectric resonators and filters. *IEEE Microwave Magazine*, **8**, 115–127.
78. Liang, J.F. and Blair, W.D. (1998) High-Q TE_{01} mode DR filters for PCS wireless base stations. *IEEE Transactions on Microwave Theory and Techniques*, **46**, 2493–2500.
79. Liang, J.F. and Zaki, K.A. (1994) Mixed modes dielectric resonator filters. *IEEE Transactions on Microwave Theory and Techniques*, **42**, 2449–2454.
80. Yan, W.D. and Mansour, R.R. (2007) Tunable dielectric resonator bandpass filter with embedded MEMS tuning elements. *IEEE Transactions on Microwave Theory and Techniques*, **55**, 154–160.
81. Faar, A.N., Blackie, G.N., and Williams, D. (1983) Novel techniques for electronic tuning of dielectric resonators, in *Proceedings of 13th European Microwave Conference*, pp. 791–796.
82. Krupka, J., Abramowicz, A., and Derzakowski, K. (2006) Magnetically tunable filters for cellular communication terminals. *IEEE Transactions on Microwave Theory and Techniques*, **54**, 2329–2335.
83. Virdee, B.S. (1997) Effective technique for electronically tuning a dielectric resonator. *Electronic Letters*, **33**, 301–302.
84. Virdee, B.S., Virdeet, A., and Trinogga, L.A. (2003) Novel invasive electronic tuning of dielectric resonators. *IEEE MTT-S Digest*, **1**, 51–54.
85. Memarian, M. and Mansour, R.R. (2009) Quad-mode and dual-mode dielectric resonator filters. *IEEE Transactions on Microwave Theory and Techniques*, **57**, 3418–3426.
86. Zhang R. and Mansour, R.R. (2009) Dual-band dielectric resonator filters. *IEEE Transactions on Microwave Theory and Techniques*, **57**, 1760–1766.
87. Bastioli, S. and Snyder, R.V. (2012) Inline pseudoelliptic $TE_{01\delta}$ mode dielectric resonator filters using multiple evanescent modes to selectively bypass orthogonal resonators. *IEEE Transactions on Microwave Theory and Techniques*, **60**, 3988–4001.
88. Chen, J.X., Zhan, Y., Qin, W., *et al.* (2015) Novel narrow-band balanced bandpass filter using rectangular dielectric resonator. *IEEE Microwave and Wireless Components Letters*, **25**, 289–291.
89. Zhan, Y., Li, J., Qin, W., *et al.* (2015) Low-loss differential bandpass filter using $TE_{01\delta}$-mode dielectric resonators. *Electronics Letters*, **51**, 1001–1003.

90. Huang, F., Fouladi, S., and Mansour, R.R. (2011) High-Q tunable dielectric resonator filters using MEMS technology. *IEEE Transactions on Microwave Theory and Techniques*, **59**, 3401–3409.
91. Huang, F. and Mansour, R.R. (2009) Tunable compact dielectric resonator filters, in *Proceedings of the 39th European Microwave Conference*, pp. 559–562.
92. Awasthi, S., Biswas, A., and Akhtar, M.J. (2015) Dual-band dielectric resonator bandstop filters. *International Journal of RF and Microwave Computer-Aided Engineering*, **25**, 282–288.

Appendix

List of Low-Loss Ceramic Dielectric Materials and Their Properties

M.T. Sebastian

Abbreviations

ST = sintering temperature (°C)
ε_r = relative permittivity
f = measurement frequency (GHz)
τ_f = coefficient of temperature variation of resonant frequency (ppm/°C)
No. = serial number
Qf = quality factor frequency product (GHz)

The table lists the key property data of microwave dielectric materials available from published materials. These data are the relative permittivity (ε_r), the product of the Q-factor and the frequency (Qf), the frequency of measurement (f), and the temperature coefficient of the resonant frequency (τ_f). In tabulating these data, we make no judgment on the measurement method and the reliability of the result. It is known that the ceramic properties such as porosity, grain size, raw materials used, impurities, measurement methods, and equipment used for measurements affect the dielectric properties and readers should be aware that exact comparison of data on materials of identical composition and manufactured in different laboratories using different processing conditions and measured by different methods would be expected to lead to small variations in properties. The data of dielectric measurements carried out using impedance methods at low (MHz) frequency is excluded as the errors in these methods mean that a loss tangent less than 10^{-3} is unreliable. The data are arranged in the order of increasing relative permittivity. The quality factor of the microwave dielectric ceramics decrease significantly with increasing relative permittivity, as shown in Figure A.1. The inset in the figure shows the variation of quality factor frequency product with

Microwave Materials and Applications, First Edition.
Edited by Mailadil T. Sebastian, Rick Ubic and Heli Jantunen.
© 2017 John Wiley & Sons, Ltd. Published 2017 by John Wiley & Sons, Ltd.

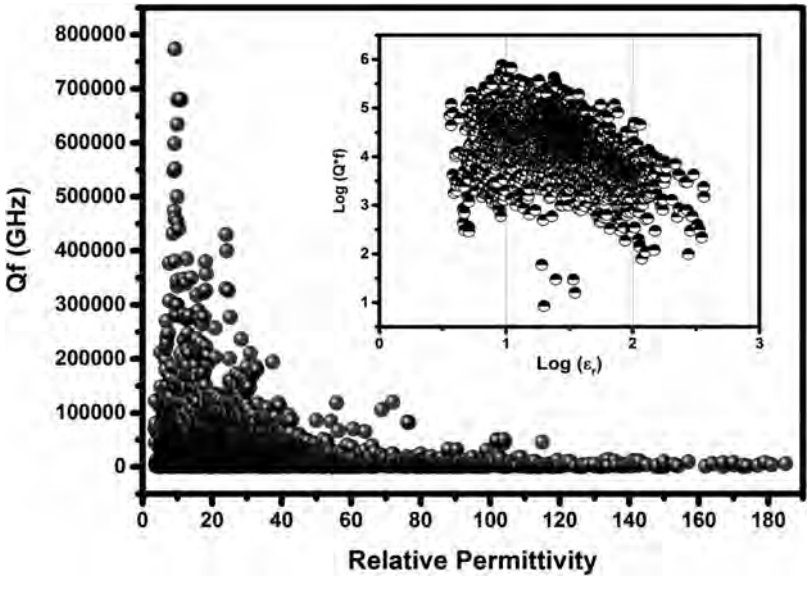

Figure A.1 *Variation of quality factor frequency product as a function of relative permittivity. The inset in the figure shows the variation of quality factor frequency product with relative permittivity in the logarithmic scale.*

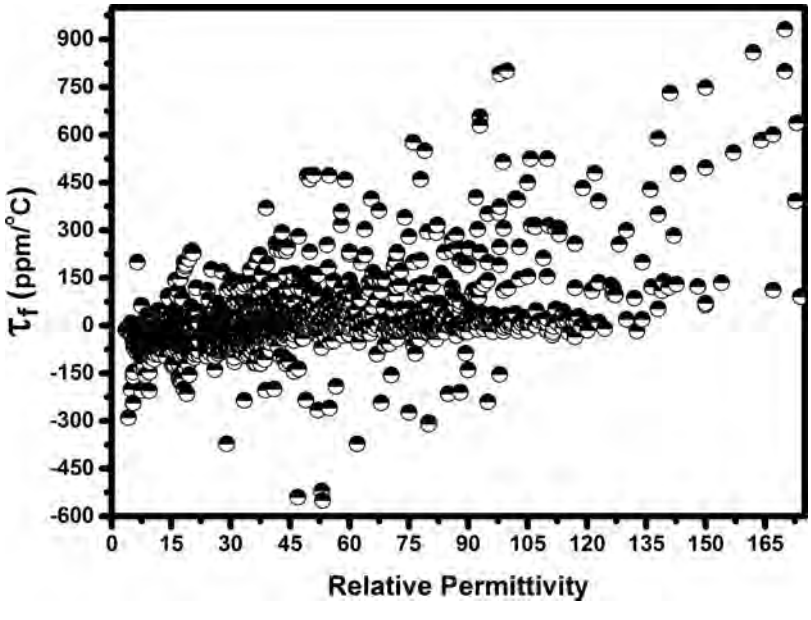

Figure A.2 *Variation of coefficient of temperature variation of resonant frequency in ppm/°C as a function of relative permittivity.*

relative permittivity in the logarithmic scale. The $0.993MgO–0.007B_2O_3$ has the highest Qf ($Qf = 773\,700$ GHz with $\varepsilon_r = 9.3$ and $\tau_f = -55$ ppm/°C). On the other hand, $AlPO_4$ has the lowest relative permittivity wth $\varepsilon_r = 3.0$ and $Qf = 900$ GHz. SiO_2 has $\varepsilon_r = 3.5$ with Qf of 92400 GHz and $\tau_f = -15$ ppm/°C. In general, the low ε_r materials have negative τ_f and high ε_r materials with positive τ_f, as shown in Figure A.2. The DR table is an updated version of the table in Appendix II in *Dielectric Materials for Wireless Communication* by M.T, Sebastian, published by Elsevier in 2008 and the supplementary file by M.T. Sebastian, Rick Ubic, and H. Jantunen, in *International Materials Review*, vol. 60, (2015), p.392. There are several low-loss single crystal materials and the reader is referred to Appendix II in the above referred book.

No.	Material	ST (°C)	Crystal structure	ε_r	Qf (GHz)	f_0	τ_f	Reference
1	$AlPO_4$+5 wt% MgF_2	1450	Orthorhombic	3.0	900	5.8	–	1
2	50%Li_2CO_3-40.24%B_2O_3-9.76%SiO_2	600	glass	3.2	10500		−79	2
3	SiO_2 sol-gel	1550	Tetragonal cristobalite	3.5	92400		−15	3
4	0.2B_2O_3-0.8SiO_2	1100	Amorphous (fused silica)	3.6	70600			4
5	SiO_2 (solid state method)	1100	fused silica	3.7	44300		−15	5
6	SiO_2melt method		Fused silica	3.7	122100			5
7	10.5CaO-22.2B_2O_3-67.3SiO_2	1035	Glass	3.8	4300	12.9		6
8	SiO_2	1650	Trigonal $P3_121$	3.8	80400		−16	7
9	CaO-B_2O_3-SiO_2 (29.3:9.3:61.4 mol%)	900	Glass	3.9	1800	9.9		8
10	27.8CaO-27B_2O_3-45.2SiO_2	875	Glass	4.0	3200	12.8		8
11	$KGaGe_3O_8$	890	Monoclinic $P2_1/a$	4.0	10200	13		9
12	$SrCuSi_4O_{10}$	1100	Gillespite Tetragonal P4/ncc	4.0	11500			10
13	CaO-B_2O_3-SiO_2 (19.8:30.9:49.3 mol%)	900	Glass	4.1	2000	9.9		8
14	CaO-B_2O_3-SiO_2 (10.5:22.2:67.3 mol%)	900	Glass	4.1	2600	9.9		8
15	Na_2MoO_4	660	Cubic Fd-3m	4.1	35000		−76	11
16	$Li_3AlB_2O_6$	650	Triclinic	4.2	12460	16.8	−290	12
17	27.8CaO-27B_2O_3-45.3SiO_2	850	Glass	4.2	3200	12.8		6
18	$LiAlSiO_4$+15 wt% Bi_2O_3	900	α-eucryptite Rhombohedral R3	4.3	62400		−16	13
19	Li_2CaSiO_4	1000	Tetragonal I-42m	4.4	2500			14
20	BF33 glass	–	Glass	4.6	440	4		15
21	BF33 glass	–	Glass	4.6	860	5		15
22	BF33 glass	–	Glass	4.6	2900	24		15
23	BF33 glass	–	Glass	4.6	4560	77		15
24	$Mg_2Al_4Si_5O_{18}$ Indialite recrystallized	1320	Hexagonal P6/mcc	4.6	207800	19	−27	16
25	MEMPAX glass	–	Glass	4.7	310	2		15
26	MEMPAX glass	–	Glass	4.7	700	5		15
27	MEMPAX glass	–	Glass	4.7	2400	24		15
28	MEMPAX glass	–	Glass	4.7	5130	77		15
29	$K_{0.9}Ba_{0.1}Ga_{1.1}Ge_{2.9}O_8$	990	Monoclinic C2/m	4.7	10600	13	−18	9
30	$LiAlSiO_4$	1350	α-eucryptite Rhombohedral R3	4.8	36000		8	17

31	$Li_3AlB_2O_6$	700	Triclinic	4.9	12600	16.9	−201	12
32	(cordierite) $Mg_2Al_4Si_5O_{18}$+7 wt% Yb_2O_3	1420	Orthorhombic Cccm	4.9	112500	18		18
33	Li_2MgSiO_4+5 wt% LMZBS	850/2h	Orthorhombic	4.9	8000	8		19
34	Zn_2SiO_4-SiO_2-H_3BO_3 (30:55:15 wt%)	725		4.9	38100	18.49		20
35	$SrCuSi_4O_{10}$+5 wt% LMZBS	900/6h	Tetragonal Gillespite P4/ncc	5.0	4000			10
36	30 wt% Al_2O_3+70 wt% [3ZnO-2B_2O_3]	850	Composite	5.0	8000	7	−32	21
37	Mg_2SiO_4+15 wt% LBS	950	Orthorhombic Pbnm	5.0	1500			22
38	Li_2MgSiO_4+3 wt% LMZBS	850/2h	Orthorhombic	5.0	10000	8		19
39	$SrCuSi_4O_{10}$+3 wt% LMZBS	975/6h	Tetragonal Gillespite P4/ncc	5.1	5000			10
40	Li_2MgSiO_4	1250/2h	Orthorhombic	5.1	16000	8		19
41	Cordierite+15 wt% CaO-B_2O_3	1020	Cordierite composite	5.1	4500	10.3		23
42	Li_2MgSiO_4+3 wt% LBS	850/2h	Orthorhombic	5.1	42100	8		19
43	Li_2MgSiO_4+2 wt% LBS	850/2h	Orthorhombic	5.1	67000	8		19
44	AF32 glass	–	Glass	5.1	360	1		15
45	AF32 glass	–	Glass	5.1	290	4		15
46	AF32 glass	–	Glass	5.1	1190	5		15
47	AF32 glass	–	Glass	5.1	3470	24		15
48	AF32 glass	–	Glass	5.1	7230	77		15
49	$KGaGe_3O_8$+0.3 wt% H_3BO_3	880	Monoclinic $P2_1/a$	5.2	64000	13	−23	9
50	Li_2MgSiO_4+5 wt% LBS	850/2h	Orthorhombic	5.2	12500	8		19
51	Li_2MoO_4	Room Temp	Trigonal R-3	5.2	18500	9.6		24
52	$LiAlSiO_4$+12 mol%B_2O_3	950	α-eucryptite Rhombohedral R3	5.3	212000		−8	17
53	Li_2MgSiO_4 citrate gel method	1175	Orthorhombic	5.3	9000	9		25
54	$K_{0.9}Ba_{0.1}Ga_{1.1}Ge_{2.9}O_8$	910/20h	Monoclinic $P2_1/a$	5.3	148100	13		9
55	$SrCuSi_4O_{10}$+1 wt% LMZBS	1075/6h	Tetragonal Gillespite P4/ncc	5.3	6500			10
56	sillimanite (Al_2SiO_5)	1525		5.3	37500		−17	26
57	$Li_3AlB_2O_6$	775/10h	Triclinic P-1	5.4	20450	17.4	−244	12
58	Li_2MgSiO_4+0.5 wt% LBS	925/2h	Orthorhombic	5.4	80000	8		19
59	40 wt% Al_2O_3+60 wt% (SiO_2-B_2O_3-Al_2O_3)	875	Composite	5.4	8000	–	−50	27

(*continued*)

No.	Material	ST (°C)	Crystal structure	ε_r	Qf (GHz)	f_0	τ_f	Reference
60	$0.85SiO_2$-$0.15TiO_2$ core shell structure	1200	Composite	5.4	40500		0	28
61	Zn_2SiO_4-SiO_2-H_3BO_3 (33:59::8 wt%)	825		5.4	48800	17.7		20
62	Zn_2SiO_4-SiO_2-H_3BO_3 (33:59:8 wt%)	875		5.5	40500	17.49		20
63	$NaAlSi_3O_8$ (albite)	1025	Triclinic C-1	5.5	11200		−5	29
64	Li_2MoO_4	540	Trigonal R-3	5.5	46000	13	−160	30
65	Li_2MgSiO_4+1 wt% LBS	925/2h	Orthorhombic	5.5	114300	8		19
66	Li_2MgSiO_4+0.5 wt% LMZBS	925/2h	Orthorhombic	5.5	72700	8		19
67	CaO-SiO_2-B_2O_3+0.5 wt% ZrO_2		Composite	5.5	28500	11.1		31
68	Li_2WO_4	640	Monoclinic C2/c	5.5	62000	15.7	−146	32
69	$K_{0.9}Ba_{0.1}Ga_{1.1}Ge_{2.9}O_8$+0.1 wt% H_3BO_3	910	Monoclinic $P2_1/a$	5.6	10400	13		9
70	Li_2MgSiO_4+1 wt% LMZBS	925/2h	Orthorhombic	5.6	80000	8		19
71	$K_2Mo_3O_{10}$	520	Monoclinic p-1	5.6	39300		−67	33
72	$Zn_{1.8}SiO_{3.8}$+20 mol% B_2O_3	900	Rhombohedral	5.7	53000		−16	34
73	Al_2O_3+50 vol% ZBS glass	900	Composite	5.7	17800	12.6		35
74	$Mg_5TaO_3(BO_3)_3$+1 wt% LiF	1300/2h	Orthorhombic Pnma warwickite	5.7	27000			36
75	$Al_2W_{3-x}Mo_xO_{12}$ (x=1)	810	Orthorhombic Pbcn	5.8	33810		−72	37
76	μ-cordierite+B_2O_3-P_2O_5	860	Composite	5.8	3000		−55	38
77	α-cordierite+B_2O_3-P_2O_5	950	Composite	5.8	6000		−15	38
78	Li_2CaSiO_4+1 wt% ZBS	975	Tetragonal I-42m	5.8	2000			14
79	$K_{0.67}Ba_{0.33}Ga_{1.33}Ge_{2.67}O_8$	1020	Monoclinic C2/m	5.9	94100		−25	39
80	Al_2O_3+MgO-Al_2O_3-SiO_2-GeO_2+ ZnO-B_2O_3	900	Composite	5.9	5590	8.4		40
81	Li_2MgSiO_4+2 wt% LMZBS glass	875/2h	Orthorhombic	5.9	111000	8		19
82	MgO-B_2O_3-SiO_2+10 wt% TiO_2	1050	Composite	5.9	16500			41
83	$0.84SiO_2$- $0.16TiO_2$	1275/3h	Composite	5.9	36700	12.5	−5	42
84	Al_2O_3+50 vol% ZBS glass	800	Composite	6.0	14400	12.5		35
85	$Zn_{2-x}SiO_{4-x}$+25 mol% B_2O_3	900	Composite	6.0	70000		−22	43
86	CaO-B_2O_3-SiO_2	830	Glass	6.0	5000	10		44
87	Al_2O_3+50 vol% ZBS glass	850	Composite	6.0	16950	12.5		35
88	Al_2O_3+50 vol% ZBS glass	750	Composite	6.0	9200	12.4		35

89	$K_{0.67}Ba_{0.33}Ga_{1.33}Ge_{2.67}O_8$	970	Monoclinic $P2_1/a$	6.0	134000	13	−22	9
90	$K_xBa_{1-x}Ga_{2-x}Ge_{2+x}O_8$ (x=0.67)	910	Monoclinic C2/m	6.0	104500		−20	9
91	$Na_{0.8}Ca_{0.2}Al_{1.2}Si_{2.8}O_8$	1100	Triclinic P-1	6.0	17600		0	45
92	$MgO\text{-}Al_2O_3\text{-}B_2O_3\text{-}SiO_2\text{-}TiO_2$		Composite	6.1	4200			46
93	α- $Mg_2P_2O_7$	1150	Throtveitite type Monoclinic $P2_1/c$	6.1	38180		−746	47
94	$CaWO_4$+0.5 wt% B_2O_3	1050	Sheelite Tetragonal $I4_1/a$	6.1	38100		−47	48,49
95	$(Mg_{0.9}Ni_{0.1})_2Al_4Si_5O_{18}$	1440/2h	Orthorhombic Cccm	6.1	99100		−32	50
96	$MgO\text{-}B_2O_3\text{-}SiO_3$ glass ceramic		Glass	6.1	11300			51
97	$K_{0.6}Ba_{0.4}Ga_{1.4}Ge_{2.6}O_8$	970	Monoclinic $P2_1/a$	6.1	120900	13	−23	9
98	$Mg_2B_2O_5$	1310	Monoclinic $P2_1/c$	6.2	32000		−45	52
99	$KGaGe_3O_8$	970	Monoclinic P21/a	6.2	19800		−21	39
100	$Mg_2Al_4Si_5O_{18}$ cordierite	1440	Orthorhombic Cccm	6.2	40000		−25	38
101	50 wt% Al_2O_3+50 wt% $(SiO_2\text{-}B_2O_3\text{-}Al_2O_3)$	875	Composite	6.2	11400	–	−35	27
102	45 wt% Al_2O_3+55 wt% $(SiO_2\text{-}B_2O_3\text{-}Al_2O_3)$	875	Composite	6.3	11500	–	−33	27
103	$AlSbO_4$	1100/3h	Tetragonal $P4_2/mnm$	6.3	3200	4	–	53
104	$CaO\text{-}B_2O_3\text{-}SiO_2$+4 wt% $La_2O_3\text{-}B_2O_3$	850	Glass	6.3	10000			54
105	$Al_2W_{3-x}Mo_xO_{12}$ (x=0)	1100	Orthorhombic Pbcn	6.3	9600		−67	37
106	$Al_2W_{3-x}Mo_xO_{12}$ (x=2)	810	Orthorhombic Pbcn	6.3	36500		−55	37
107	$0.9Mg_2Al_4Si_5O_{18}\text{-}0.1TiO_2$		Composite	6.3	55400	17.6	−21	55
108	$42.5SiO_2\text{-}21MgO\text{-}20Al_2O_3\text{-}16.5TiO_2$		Composite	6.3	27000	9.7	−6	56
109	$Al_2W_{3-x}Mo_xO_{12}$ (x=3)	810	Monoclinic $P2_1/a$	6.4	49200		−41	37
110	55 wt% Al_2O_3+45 wt% $(SiO_2\text{-}B_2O_3\text{-}Al_2O_3)$	900	Composite	6.4	13000	–	−58	27
111	$Mg_3(VO_4)_2$	950/5h	Orthorhombic Cmca	6.4	48800	–	−83	57
112	$K_{0.9}Ba_{0.1}Ga_{1.1}Ge_{2.9}O_8$	1040	Monoclinic C2/m	6.4	94700	12	−23	39
113	$Y_2BaCu_{0.75}Ni_{0.25}O_5$		Orthorhombic	6.4	8350	13.5	−40	58
114	$K_{0.4}Ba_{0.6}Ga_{1.6}Ge_{2.4}O_8$	1040	Monoclinic $P2_1/a$	6.4	94700	12	−23	39
115	$BaAl_2Si_2O_8$	1475/3h	Hexagonal P6/mmm	6.4	44800		−47	59

(*continued*)

No.	Material	ST (°C)	Crystal structure	ε_r	Qf (GHz)	f_0	τ_f	Reference
116	$Ca_{0.99}Mg_{0.01}SiO_3$	1290/2h	Wollastonite Monoclinic $P2_1/a$	6.5	62400		−43	60
117	Mg_2GeO_4+3 wt% B_2O_3	1200/4h	Orthorombic Pnma	6.5	91000		−28	61
118	ZnO-B_2O_3-SiO_2 glass (60.3:27.1:12.6)		Glass	6.5	4500	17.1	−10	35
119	0.3TeO_2-$SnTe_3O_8$	660	Composite	6.5	8800		200	62
120	Li_2CaSiO_4+0.5 wt% BBS	925	Tetragonal I-42m	6.5	5500			14
121	Li_2CaSiO_4+0.5 wt% PBS	925	Tetragonal I-42m	6.5	1500			14
122	0.15ZnO-0.25Nd_2O_3-0.6B_2O_3+ 50 wt% Al_2O_3	850	Composite	6.5	22500	18.9		63
123	$Mg_3B_3O_6$+35 wt% LMBS	950	Composite	6.5	21000		−50	64
124	$(Zn_{1-x}Co_x)_2SiO_4$ (x=0.05)	900	Willimite Rhombic R3	6.5	5700		−55	65
125	$(Zn_{0.095}Co_{0.05})_2SiO_4$+2 wt% Li_2O–B_2O_3–SiO_2–CaO–Al_2O_3	900	Willimite	6.5	57000		−55	66
126	$LiMgPO_4$	950	Orthorhombic Pmnb	6.6	79100		−60	67
127	$(Mg_{0.4}Zn_{0.6})_2SiO_4$		Trigonal R-3	6.6	95650		−60	68
128	Zn_2SiO_4+sol-gel	1325	Trigonal R-3	6.6	198400		−42	69
129	$Sr_2Al_2Si_{0.9}Ge_{0.1}O_7$	1525	Tetragonal Gehhlenite type $P\text{-}42_1m$	6.6	22900		−28	70
130	Al_2O_3+50 vol % ZBS glass	700	Composite	6.6	2600	11.8		35
131	$Ca_{1-x}Sr_xSiO_3$ (x=0.8)		Monoclinic $P2_1/a$	6.6	66700		−40	71
132	MgO-B_2O_3-SiO_2 (42:45:13)		Glass	6.6	2100	6.88		72
133	Willemite (Zn_2SiO_4)	1340	Trigonal R-3	6.6	219000		−61	73
134	$CaWO_4$+1 wt% $MnSO_4$	1050	Scheelite $I4_1/a$	6.6	129540		−56	48,49
135	$K_{0.9}Ba_{0.1}Ga_{1.1}Ge_{2.9}O_8$	990	Monoclinic C2/m	6.6	12700		−21	39
136	$Zn_{1.8}SiO_{3.8}$	1300/3h	WillemiteTrigonal R-3	6.6	147000		−22	74
137	MgO-B_2O_3-SiO_2 (42:45:13) glass		Glass	6.6	2130	6.9		75
138	ZnO-0.6 SiO_2+Bi_2O_3-Li_2CO_3	910/2h	Glass	6.7	33000	11	−33	76
139	CaO-SiO_2	1320	Glass ceramic	6.7	25400			77
140	50 wt% (La_2O_3-B_2O_3))+50 wt% Al_2O_3	850	Glass	6.7	2800	17.7		78
141	$Mg_{1.975}Mn_{0.025}SiO_4$ Fosterite	1400	Orthorhombic Pbnm	6.7	180000		−71	79

142	$MgSiO_3$	1380/13h	Orthorhombic Pbnm	6.7	121200		−17	80
143	$CaSiO_3$+1 wt% Al_2O_3	1250	Wollastonite Monoclinic $P2_1/a$	6.7	24600			81
144	$LiMg_{0.9}Zn_{0.1}PO_4$	925	Orthorhombic Pmnb Olivine type	6.7	99700		−62	82
145	$Zn_3B_2O_6$	925/4h	Triclinic I2/c	6.7	58500		−58	83
146	$(Mg_{0.95}La_{0.05})_2Al_4Si_5O_{18+0.05}$		Orthorhombic	6.7	78500	14.3	−22	84
147	Mg_2SiO_4+15 wt% LMZBS glass	950	Composite	6.8	30600			85
148	$Mg_2B_2O_5$+55 wt% LMZBS glass	950	Composite	6.8	50000	7.28	−64	86
149	Mg_2SiO_4Fosterite	1450	Orthorhombic Pbnm	6.8	270000		−67	87
150	Li_2ZnSiO_4+20 wt% ZnO-B_2O_3	950/3h	Composite	6.8	9300		−51	88
151	Li_2ZnSiO_4+25 wt% ZnO-B_2O_3	950/3h	Composite	6.8	10800		−47	88
152	α-$CaSiO_3$	1500	Monoclinic C2/c wollastonite	6.8	42200		−19	89
153	$SrSiO_3$	1500	Monoclinic C2/c	6.8	13100		−66	89
154	Mg_2GeO_4+B_2O_3	1250	Orthorhombic Pnma	6.8	95000		−29	90
155	$K_2Mo_4O_{13}$	540	Triclinic p-1	6.8	39800		−67	33
156	$0.9Ca_{0.9}Mg_{0.1}SiO_3$-$0.1CaMgSi_2O_6$	1290/2h		6.9	118000			91
157	$Mg_{1.93}Ca_{0.07}SiO_4$ Fosterite	1400	Orthorhombic Pbnm	6.9	105000		−72	79
158	ZnO:B_2O_3 (50:50) glass	<800	Glass	6.9	1733	16.4	−10	92
159	$K_{0.67}Ba_{0.33}Ga_{1.33}Ge_{2.67}O_8$	1020	Monoclinic C2/m	6.9	32600	12	−27	39
160	ZnO:B_2O_3:SiO_2 (50:40:10) glass	611	Glass	6.9	1710	15.8	−21	92
161	$BaGa_2Ge_2O_8$	1100/12h	Monoclinic $P2_1/a$	6.9	10640		−26	39
162	xMgO-(1-x)B_2O_3 (x=0.75)	1350/4h	Orthorhombic Pnmn	6.9	119600		−69	93
163	MgO-B_2O_3-SiO_2+10 wt% TiO_2		Composite	6.9	16500			51
164	3ZnO-B_2O_3	950/1h	Glass	6.9	20600	6.35	−80	94
165	$(Ca_{0.9}Mg_{0.1})SiO_3$+Li_2CO_3-Bi_2O_3	890/2h	Mixed phases	6.9	27000		−40	95
166	16ZnO-16La_2O_3-68B_2O_3+50 wt% Al_2O_3	950	Composite	6.9	12100	18.1	−12	96
167	$Sm_2Si_2O_7$+15 wt% LMZBS	950/2h	Tetragonal $P4_1$	6.9	5000	10		97
168	Zn_2GeO_4	1300	Trigonal R-3	6.9	102700		−32	98
169	$LiMg_{0.95}Ni_{0.05}PO_4$	875	Orthorhombic olivine type	6.9	98600		−55	99

(*continued*)

No.	Material	ST (°C)	Crystal structure	ε_r	Qf (GHz)	f_0	τ_f	Reference
170	$(Mg_{0.95}Ni_{0.05})_2SiO_4$+12 wt% Li_2CO_3-V_2O_5	1150/4h	Orthorhombic	6.9	99800		−50	100
171	$HfSiO_4$		Tetragonal amd	7.0	25000	10	−44	101
172	$Sr_{0.05}Ba_{0.95}Al_2Si_2O_8$	1600/162h	Monoclinic celsian I2/c	7.0	92600		−22	102
173	$Mg_3B_2O_6$+5 wt% $Mg_2B_2O_5$	1310/20h	Kotoite Orthorhombic Pnmn	7.0	241000		−18	52,103
174	$SrCuP_2O_7$	925	Monoclinic $P2_1/n$	7.0	101110		−62	104
175	$CaMgSi_2O_6$	900/1h	Monoclinic C2/c	7.0	43200		−22	105
176	$CaMgSi_2O_6$+8.5 wt% ZrO_2	950	Composite	7.0	7300			106
177	Mg_2SiO_4+1 wt% TiO_2 Fosterite	1300	Orthorhombic Pbnm	7.0	230000		−65	107
178	$Ba_2V_2O_7$	950	Anorthic Triclinic P-1	7.0	19000		−74	108
179	δ-$Ba_2P_2O_7$	1150	Dichromatic type Hexagonal P-62m	7.0	12300			47
180	$Ba_2MgSi_2O_7$	1350/10h	Tetragonal P-421m	7.0	31000		−60	109
181	$Sr_2Al_2SiO_7$	1525	Tetragonal $P4\text{-}2_1m$	7.0	33000		−34	110
182	$LiMg_{0.95}Co_{0.05}PO_4$	875/2h	Orthorhombic olivine type	7.0	111200		−54	111
183	$SrZnP_2O_7$	950	Monoclinic $P2_1/n$	7.1	52780		−70	104,112
184	$MgMoO_4$	900	Wolframite Monoclinic C2/m	7.1	79100		−46	113
185	ZnO:B_2O_3:SiO_2 (50:30:20) glass	614Td	Glass	7.1	1670	15.9	−43	92
186	α-$Sr_2P_2O_7$	1150	Dichromatic type Orthorhombic Pnam	7.1	33500		−23	47
187	SrO-B_2O_3-SiO_2 (32.85:52.09:15.05) glass		Glass	7.1	3600	6.7		72
188	$MgTiO_3$+15 wt% $CaTiO_3$+ZnO-B_2O_3-SiO_2(35:25:40)	900/0.5h	Composite	7.1	3500	16	6	114
189	$0.95Zn_2SiO_4$-$0.05CaTiO_3$+Li_2CO_3-H_3BO_3	950	Trigonal R-3	7.1	26300		−5	115
190	Li_2CaSiO_4+3 wt% ZBS	875	Tetragonal I-42m	7.1	2000			14
191	$0.88(Mg_{0.4}Zn_{0.6})_2SiO_4$–$0.12CaTiO_3$+4 wt% Li_2CO_3–H_3BO_3	950	Composite	7.1	28600		−6	116
192	$Mg_3B_2O_6$		Kotoite Orthorhombic Pnmn	7.2	150400	16		117

193	$BaAl_2Si_2O_8$	1500/12h	Monoclinic	7.2	70600	10.5	−22	118
194	$Sr_{0.05}Ba_{0.95}Al_2Si_2O_8$	1500/40h	Monocelsian Hexagonal P6/mmm	7.2	77000	10.5		118
195	Li_2CaSiO_4+1 wt% LBS	925	Tetragonal I-42m	7.2	4000			14
196	$Sr_2Al_2SiO_7$	1525	Gehlenite Tetragonal P-42_1m	7.2	33000		−37	119
197	CaO-MgO-SiO_2+10 wt% Li_2O-Bi_2O_3 (Sol gel)	890	Composite	7.2	25600		−69	120
198	$Sr_2Al_{1.9}Ga_{0.1}SiO_7$	1525	Tetragonal P-42_1m	7.2	21500		−41	70
199	Mg_2SiO_4+0.5 wt% LMZBS glass Fosterite	1525	Orthorhombic Pbnm	7.3	121200			85
200	Li_2CaSiO_4+3 wt% BZBS	900	Tetragonal I-42m	7.3	1700			14
201	$Sr_2Al_2SiO_7$+0.5 wt% LMZBS glass	1500	Gehlenite P4-2_1m, Tetragonal	7.3	34200		−36	70
202	$Sr_2Al_2SiO_7$+1 wt% LMZBS glass	1500	Gehlenite P4-2_1m, Tetragonal	7.3	36300		−23	70
203	$Sr_{2-x}Ca_xAl_2SiO_7$ (x=0.25)	1450	Tetragonal P4-2_1m	7.3	26000		−34	110
204	$SrZnP_2O_7$	925/2h	Monoclinic $P2_1/n$	7.3	71520		−64	104
205	BaO:B_2O_3:SiO_2 (30:20:50) glass	717 Td	Glass	7.3	1840	14.8	−62	92
206	$BaCu(B_2O_5)$	810		7.3	50000		−32	121
207	CaO-B_2O_3-SiO_2 (69.7:16.2:14.1 mol%)	900	Glass	7.3	2300	9.6		8
208	CaO-B_2O_3-SiO_2 (38.3:31.5:30.2 mol%)	900	Glass	7.3	1800	9.6		8
209	BaO:B_2O_3:SiO_2 (30:40:30) glass	677 Td	Glass	7.3	2700	15.4	−34	92
210	BaO:B_2O_3:SiO_2 (30:60:10) glass	627 Td	Glass	7.3	3390	14.9	−25	92
211	$CaCuP_2O_7$	900/2h	Monoclinic $P2_1/n$	7.3	71620		−76	104
212	$Mn_2P_2O_7$	1150	Monoclinic C2/m	7.3	23850		−96	47
213	$Zn_{1.8}SiO_{3.8}$+12 wt% V_2O_5	875/2h	Trigonal R-3	7.3	17500		−28	122
214	$Y_2BaCu_{0.6}Mg_{0.4}O_5$		Orthorhombic Pmmm	7.4	25320	12.9	−56	58,123
215	$CaAl_2Si_2O_8$ (Anorthite)	1500	Triclinic P-1	7.4	12000		−130	29
216	$MgAl_2O_4$+Li-Mg-Zn-B-Si-O glass	1000	Glass-ceramic	7.4	48000	24	−90	124
217	$Mg_2Si_{0.9}Ti_{0.1}O_4$Fosterite	1425	Orthorhombic Pbnm	7.4	73760	15	−60	125
218	$ZrSiO_4$	1550	Tetragonal $I4_1$	7.4	8500	5.15	−50	126
219	19ZnO-13La_2O_3-68B_2O_3+40 wt% Al_2O_3		Composite	7.4	18100			127
220	xMgO-(1-x)B_2O_3 (x=0.8)	1350/4h	Composite	7.4	247880		−65	93

(*continued*)

No.	Material	ST (°C)	Crystal structure	ε_r	Qf (GHz)	f_0	τ_f	Reference
221	$CaMgSi_2O_6$	1300/3h	Monoclinic C2/c	7.4	59700		−42	128
222	$Sr_{2-x}Ca_xAl_2SiO_7$ (x=0.5)	1450	Tetragonal P4-2_1m	7.4	25000		−33	110
223	Alpha $CaSiO_3$+6 wt% SiO_2	1350		7.4	33700		−11	129
224	$Mg_{2.15}SnO_4$	1620/4h	Spinel Cubic Fd3m	7.4	76800		−50	130
225	BaCu (B_2O_5)	850		7.4	23000		−75	131
226	$LiZnVO_4$ (UsingV_2O_5)	800	Trigonal phenakite R-3	7.5	25400		−123	132
227	CaO-B_2O_3-SiO_2 (42:45:13)		Composite	7.5	2400	6.24		72
228	20ZnO-16La_2O_3-64B_2O_3+50 wt% Al_2O_3	950	Composite	7.5	13500		−10	96
229	$BaAl_2Ge_2O_8$	1350/12h	Monoclinic I2/c	7.5	74100		−32	102
230	$SrSiO_3$-NiO	1375	Monoclinic C2	7.5	56500		64	133
231	$HfSiO_4$+2 wt% LMZBS	1400/4h	Tetragonal $I4_1$/amd	7.5	7500	5		134
232	CaO-B_2O_3-SiO_2 (42:45:13) glass		Glass	7.5	2380	6.2		72
233	$DyBO_3$,$HoBO_3$,YBO_3		Vaterite Hexagonal $P6_3$/mmc	7.5	10000			135
234	α-$Zn_2P_2O_7$	1150	Throtveitit Monoclinic C2/m	7.5	50000		−204	47
235	$Mg_{2.05}SiO_4$ Fosterite	1550/3h	Orthorhombic Pbnm	7.5	114700	10.6	−59	75
236	$Ba_2ZnSi_2O_7$	1350	Monoclinic	7.5	48000		−74	109
237	$K_2Mo_2O_7$	460	Triclinic	7.5	22300		−63	33
238	ZnO:B_2O_3:SiO_2 (60:20:20) glass	<800	Glass	7.5	1410	15.4	−84	92
239	ZnO:B_2O_3 (60:40) glass	<800	Glass	7.5	1430	15.1	−3	92
240	$LiZnVO_4$ (Using NH_3VO_3)	720	Trigonal phenakite R-3	7.5	27600		−114	132
241	ZnO:B_2O_3:SiO_2 (60:30:10) glass	<800	Glass	7.6	1440	15.5	−21	92
242	$CaZnP_2O_7$	900/2h	Pyrophosphate	7.6	63130		−82	136
243	20CaO-20La_2O_3-60B_2O_3+40 wt% Al_2O_3	850	Composite	7.6	5000	17.4		137
244	BaO-B_2O_3-SiO_2 (42:45:13) glass		Glass	7.6	4100	6.65		72
245	$BaGa_2Si_2O_8$	1350/12h	Monoclinic I2/c	7.6	62300		−32	102
246	24ZnO-16La_2O_3-60B_2O_3+50 wt% Al_2O_3	950	Glass	7.6	17600	16.9	−14	96
247	$CaMgSi_2O_6$	1300 CIP	Monoclinic C12/c1	7.6	121380		−66	138

248	Zn_2SiO_4+8 mol% Bi_2O_3	885/2h	Trigonal R-3	7.6	12600		−22	139
249	BaO-B_2O_3-SiO_2 (42:45:13)		Glass	7.6	4000	6.65		72
250	$LiZnVO_4$	750/2h	Rhombohedral R3	7.6	22000		−110	140
251	xMgO-(1-x)B_2O_3 (x=0.9)	1350/4h	Orthorhombic Pnmn	7.7	376800		−58	93
252	$Y_2BaCu_{0.9}Mg_{0.1}O_{5\ CIP}$	1250	Orthorhombic Pbnm	7.7	37500	14.5	−37	123
253	$CaMg_{0.9}Zn_{0.1}Si_2O_6$+0.6 wt% LiF	900	Monoclinic C12/c1	7.7	70000		−25	141
254	0.91Mg_2SiO_4-0.09$CaTiO_3$+12 wt% Bi_2O_3-Li_2CO_3-H_3BO_3	950	Fosterite composite	7.7	11300	6.1	−5	142
255	$Li_2Mg_2(WO_4)_3$	875	Orthorhombic Pnma	7.7	29600	6	−16	143
256	α-$Ca_2P_2O_7$	1290/4h	Monoclinic $P2_1/n$	7.8	14100		−97	144
257	Li_2CaSiO_4+3 wt% PBS	900	Tetragonal I-42m	7.8	2700			14
258	$Mg_3Sm_4Al_{44}O_{75}$+B_2O_3-SiO_2-Al_2O_3	920	Mgnetoplumbite	7.8	10000		11	145
259	$DyPO_4$	1600	Xenotime tetragonal $I4_1/amd$	7.8	28700		−17	146
260	$TbPO_4$	1600	Xenotime tetragonal $I4_1/amd$	7.8	20100		−18	146
261	27ZnO-16La_2O_3-57B_2O_3+50 wt% Al_2O_3	950	Composite	7.8	22700	16.8	−19	96
262	45CaO-31.7B_2O_3-23.3SiO_2	715	Composite	7.8	1130	12.5		6
263	27ZnO-16La_2O_3-57B_2O_3 glass+50 wt% Al_2O_3		Composite	7.8	1350	16.8		96
264	xMgO-(1-x)B_2O_3 (x=0.85)	1350/4h	Composite	7.8	307600		−58	93
265	$Li_xZn_{2-x}V_xSi_{1-x}O_4$ (x=0.8)	820		7.8	21100	11.5		147
266	$CaMg_{0.9}Zn_{0.1}Si_2O_6$+5 wt% MgF_2	1050		7.8	169800	11.7	−26	148
267	Yb_2BaCuO_5		Orthorhombic Pnma	7.9	7290		−44	149
268	$LiMgPO_4$+0.05 vfTiO_2	950	Orthorhombic Pmnb	7.9	63600		−36	67
269	$SrWO_4$	1150	Tetragonal $I4_1/a$	7.9	56000		−55	150
270	$Mg_3(VO_4)_2$	950/10h	Orthorhombic Cmca	7.9	53000		−84	57
271	CaO-B_2O_3-SiO_2(50.1:22.2:67.3 mol%)	900	Composite	7.9	2100	9.6		8
272	$CaMg_{0.9}Zn_{0.1}Si_2O_6$	1200	Monoclinic C2/c	7.9	76100		−22	141
273	$ZnAl_2O_4$	1700	Spinel cubic Fd3m	7.9	82000		−63	151
274	$Sr_2ZnSi_2O_7$+15 wt% LMZBS	875	Composite	7.9	39000	12.71	−54	152
275	MgO	1490	Cubic Fm3m	7.9	113600	16.4		153

(*continued*)

No.	Material	ST (°C)	Crystal structure	ε_r	Qf (GHz)	f_0	τ_f	Reference
276	Nd_2SiO_5	1500	Monoclinic $P2_1/c$	7.9	38800	18.35	−53	154
277	$Ca(Sn_{0.1}Si_{0.9})O_3$	1375	Monoclinic $P2_1/a$	7.9	58000		−43	155
278	α-$CaSiO_3$+2 wt% TiO_2	1300	Mixture	7.9	16500		1	156
279	$Ca(Mg_{1-x}Al_x)(Si_{1-x/2}Al_{x/2})_2O_6$ (x=0.08)	1275	Monoclinic C2/c	7.9	59800		−42	157
280	$NaAgMoO_4$	400	Spinel Fd-3m	7.9	33000		−120	158
281	Mg_2SnO_4+LiF-Fe_2O_3-V_2O_5	1050	Cubic Fd3m	7.9	41400		−82	159
282	α-$CaSiO_3$+2 wt% Al_2O_3+2.5 wt% TiO_2	1250	Composite	7.9	24000		−1	160
283	5ZnO-2B_2O_3+6 mol% $Pb_{1.5}Nb_2O_{6.5}$	910	Composite	7.9	15000	7.4	−7	161
284	CAS-T5 glass (CaO:Al_2O_3:SiO_2:TiO_2:B_2O_3)	950	Composite	8.0	22500	10	−20	163
285	$CaMgSi_2O_6$+15 wt% LBS glass	925/2h	Monoclinic C2/c	8.0	15000	10.17	−49	164
286	$Ca_{1-x}Cd_xMoO_4$ (x=0)	1075	Sheelite fergusonite type Tetragonal $I4_1/a$	8.0	46500		−20	165
287	$CaAl_2Si_2O_8$+5 wt% TiO_2	900	Anorthic I-1	8.0	22500		−50	163
288	$CaMgSi_2O_6$+12 wt% Al_2O_3	1250	Composite	8.0	60100		−48	166
289	Li_2O-B_2O_3-SiO_2-Al_2O_3-CaO	550	Composite	8.0	2400		−48	167,168
290	La_2O_3-2B_2O_3-0.5ZnO	900	Composite	8.0	72000	13		169
291	YPO_4	1600	Xenotime tetragonal $I4_1/amd$	8.0	67900		−35	146
292	$Sr_{2-x}Ca_xAl_2SiO_7$ (x=1)	1475	Tetragonal P4-2_1m	8.0	27500		−42	110
293	0.94Mg_2SiO_4-0.06$Ca_{0.9}Sr_{0.1}TiO_3$	1440/3h	Composite	8.0	53400	14.4	−4	170
294	20MgO-20La_2O_3-60B_2O_3+40 wt% Al_2O_3	950	Composite	8.1	19000			137
295	$BaWO_4$	1150	Scheelite Tetragonal $I4_1/a$	8.1	56000		−55	150,171
296	$SrWO_4$	1150	Tetragonal $I4_1/a$	8.1	57500		−78	150
297	$MgZn_2(VO_4)_2$	800/5h	Orthorhombic Cmca	8.1	44700		−108	172
298	Li_2CaSiO_4+3 wt% BBS	900	Tetragonal I-42m	8.1	2000			14
299	60 wt% La_2O_3-B_2O_3+40 wt% Al_2O_3	850	Composite	8.1	4500	17.5		78
300	$CaZrB_2O_6$	1075	Dolomite type borate	8.1	39400		3	173
301	$Mg_{0.8}Zn_{0.2}Al_2O_4$		Spinel Cubic Fd3m	8.1	87000			174

302	$20MgO\text{-}20La_2O_3\text{-}60B_2O_3$+40 wt% Al_2O_3	950	Composite	8.1	19000	16.1		137
303	$(Mg_{0.95}Zn_{0.05})Al_2O_4$	1580	Spinel cubic Fd3m	8.1	165000		−68	175
304	Ag_2MoO_4	450 2h	Cubic Fd3-m	8.1	17000		−133	176
305	$MgTiO_3\text{-}CaTiO_3$ (MMT-20)+ $SiO_2\text{-}B_2O_3\text{-}BaO$	875	Composite	8.2	3000	7		177
306	$BaWO_4$+0.5 wt% B_2O_3	950	Scheelite Tetragonal $I4_1/a$	8.2	32700		−18	48,49
307	$20ZnO\text{-}20La_2O_3\text{-}60B_2O_3$+40 wt% Al_2O_3	950	Composite	8.2	20000	17.1		137
308	$CaMgSi_2O_6$+15 wt% LMZBS glass	900/2h	Monoclinic C2/c	8.2	32000	10.15	−48	164
309	$Mg_{0.6}Zn_{0.4}Al_2O_4$		Spinel Cubic Fd3m	8.2	93000			174
310	$LiMg_{0.9}Zn_{0.1}PO_4$+0.05 Vf TiO_2	925	Orthorhombic Pmnb Olivine type	8.2	80200		−39	82
311	$Nd_2Mo_3O_{12}$	945	Monoclinic C2/c	8.2	80000		−60	178
312	$Mg_2V_2O_7$+6 mol %Li_2CO_3	800	Monoclinic $P2_1/c$	8.2	70600		−35	179
313	$LiInSiO_4$	1150	Orthorhombic Pnma	8.2	12600		−55	180
314	$Zn_2(Sn_{1-x}Si_x)O_4$ (x=0.07)	1175/4h		8.2	55500		−120	181
315	$BaMgV_2O_7$	830	Orthorhombic	8.2	37600	11.7	−35	182
316	$YbPO_4$	1600	Xenotime tetragonal $I4_1/amd$	8.2	71600		−28	146
317	70 wt% $La_2O_3\text{-}B_2O_3$+30 wt% Al_2O_3	850	Composite	8.3	5500	17.2		78
318	Li_2CaSiO_4+1 wt% BBS	925	Tetragonal I-42m	8.3	10000			14
319	Y_2BaCuO_5 (CIP)		Orthorhombic Pbnm	8.3	53300		−40	123
320	$20ZnO\text{-}20La_2O_3\text{-}60B_2O_3$+40 wt% Al_2O_3	950	Composite	8.3	18600	17		137
321	$Mg_{0.75}Ni_{0.25}Al_2O_4$		Spinel cubic Fd3m	8.3	130000	15.4	−53	183
322	$CaMgSi_2O_6$	1300/2h	Monoclinic C2/c	8.3	53000	10.27	−45	164
323	$Mg_{0.4}Zn_{0.6}Al_2O_4$		Spinel cubic Fd3m	8.3	93000			174
324	$Sr_2MgSi_2O_7$	1550	Akermite Tetragonal $P4\text{-}2_1m$	8.3	55000		−48	133
325	$20ZnO\text{-}20La_2O_3\text{-}60B_2O_3$+40 wt% Al_2O_3	850	Composite	8.3	1100	17.1		137
326	$LiInSiO_4$+1 wt% LMZBS	1100	Orthorhombic Pnma	8.4	22000		−45	180

(*continued*)

No.	Material	ST (°C)	Crystal structure	ε_r	Qf (GHz)	f_0	τ_f	Reference
327	$Ca_3SnSi_2O_9$	1525	Cuspidine $P2_1/c$	8.4	92000		−60	184
328	$Mg_{0.2}Zn_{0.8}Al_2O_4$		Spinel cubic Fd3m	8.4	98000			174
329	Sm_2SiO_5	1500	Monoclinic $P2_1/c$	8.4	64000		−37	185
330	Mg_2SnO_4	1550/4h	Cubic spinel Fd3m	8.4	55100		−62	186
331	$MgAl_2O_4$ (SPS)	1325	Spinel cubic Fd3m	8.4	54000		−74	187
332	(1-x)$Ba_3(VO_4)_2$-xMg_2SiO_4 (x=0.65)	1200	Composite	8.4	52200		−7	188
333	80 wt% La_2O_3-B_2O_3+20 wt% Al_2O_3	850	Composite	8.4	9800	17.6		78
334	$CaSiO_3$	1300	Wollastonite Monoclinic $P2_1/a$	8.4	16000	10		189
335	$Ca_3SnSi_2O_9$	1400	Monoclinic $P2_1/c$	8.4	93300		−70	189
336	$Sr_2ZnSi_2O_7$	1475	Akermite Tetragonal P4-2_1m	8.4	105000		−52	133
337	β-$Ca_2P_2O_7$	1150/2h	Tetragonal $P4_1$ dichromatic type	8.4	53500		−53	104
338	$Ca_2Al_2SiO_7$	1500	Tetragonal P4-2_1m	8.4	33000		−34	110
339	0.86$(Mg_{0.4}Zn_{0.6})_2SiO_4-0.14CaTiO_3$	1180/4h	Composite	8.4	28100		−6	190
340	$Li_2Mg_2W_3O_{12}$	720	Lyonsite-type orthorhombic	8.4	56700		−73	191
341	$BaZnP_2O_7$	875/2h	Triclinic P-1	8.4	27900	11.1	−57	192
342	$Li_2Mg_2W_3O_{12}$	720	Orthorhombic lyonsite	8.4	56700		−73	193
343	$Yb_2Ba(Cu_{0.5}Ni_{0.5})O_5$			8.5	13300		−46	194
344	$TbPO_4$	1650/2h	Tetragonal $I4_1/amd$	8.5	20100		−17	146
345	$MgAl_2O_4$	1650/3h	Spinel Cubic Fd3m	8.5	105000		−63	195
346	Li_2MgSiO_4		Orthorhombic	8.5	30000	15		117
347	Li_2O-B_2O_3-SiO_2 frit glass	<800	Glass	8.5	1800		−157	196
348	$MgTiO_3$-$CaTiO_3$ (MMT)-20-ZnO-B_2O_3-SiO_2 (44.57:17.32:6.95:30.16)	875	Composite	8.5	7000	7	6	177,197
349	$ZnAl_2O_4$	1375	Spinel Cubic Fd3m	8.5	56000	12.3	−79	198
350	ZnO-B_2O_3-SiO_2-MMT-20 (44.57:17.32:6.95:30.16)	875	Composite	8.5	3000	7	6	197
351	$Mg_4Nb_2O_9$ (Precipitation)	950	Corundum type P-3c1	8.5	50000			199
352	$CaMgSi_2O_6$+1 wt% LBS glass	1300/2h	Monoclinic C2/c	8.5	64000	10.27	−45	164
353	0.84Al_2O_3-0.16TiO_2+8 wt% MCAS glass	1250	Composite	8.5	9900		−2	200
354	$MnMoO_4$	900	Wolframite Monoclinic C2/m	8.5	54100		−74	113

355	Mn_2SiO_4	1100/N_2	Orthorhombic Pbnm	8.5	50000		−90	79,201
356	$Ca_{0.8}Sr_{0.2}SnO_3$	1540	Perovskite Orthorhombic Pbnm	8.5	6700		−44	202
357	13CaO-19La_2O_3-68B_2O_3+40 wt% Al_2O_3		Composite	8.5	8100			127
358	$(Zn_{0.8}Mg_{0.2})_2SiO_4$-$TiO_2$+3 wt% Li_2O-B_2O_3-SiO_2 glass	870/2h	Composite	8.5	11500		0	203
359	$(Mg_{0.93}Zn_{0.07})_2SnO_4$	1550/4h	Cubic spinel Fd3m	8.5	186100		−61	204
360	$Mg_{0.8}Co_{0.2}Al_2O_4$	1475	Spinel cubic Fd3m	8.5	50000		−60	205
361	$CaW_{1-x}Te_xO_4$ (x=0.15)	900	Scheelite $I4_1/a$	8.5	44000			206
362	$Sr_2ZnSi_2O_7$	1475	P-42_1/m Hardystonite	8.5	105000		−52	133,152
363	$Li_2Ca_2Mo_3O_{12}$	630	Lyonsite orthorhombic	8.5	108000	13.2	−89	207
364	$Y_2BaCu_{0.25}Ni_{0.75}O_5$		Orthorhombic Immm	8.6	31290	12.5	−36	58
365	0.88Al_2O_3-0.12TiO_2+2 wt% MCAS glass	1250	Composite	8.6	9580		5	208
366	$(Mg_{1/2}Zn_{1/2})Al_2O_4$	1600/4h	Spinel Cubic Fd3m	8.6	95000		−52	209
367	Ca_2SiO_4	1450	Orthorhombic $P2_1/n$	8.6	26100		−89	210
368	$SrW_{1-x}Te_xO_4$ (x=0.2)	800	Scheelite Tetragonal $I4_1/a$	8.6	38400			206
369	$SrW_{1-x}Te_xO_4$ (x=0.0)	900	Scheelite Tetragonal $I4_1/a$	8.6	37900		−57	206
370	0.96$Sr_2Al_2SiO_7$-0.04$CaTiO_3$	1500	Tetragonal P-42_1m	8.6	20400		9	119
371	$LiSrBO_3$	800	Monoclinic $P2_1/c$	8.6	60000		−39	211
372	Li_4WO_5	890	Orthorhombic rocksalt	8.6	23100	11	−3	212
373	$LiCaBO_3$	800	Orthorhombic Pbca	8.7	75000		−150	211
374	$ZnMoO_4$	800	Wolframite Triclinic P-1	8.7	49900		−87	113
375	$CaWO_4$+0.5 wt% Bi_2O_3+9 wt% H_3BO_3	850	Scheelite Tetragonal $I4_1/a$	8.7	70220		−15	213
376	$CaWO_4$	1200	Scheelite Tetragonal $I4_1/a$	8.7	75000		−54	150
377	$(Al_{1/2}Ta_{1/2})O_2$	1600	Tetragonal P4/nmm	8.7	60800		−55	214
378	Ca-Al-B-Si-O+Al_2O_3 (K8)	870	Composite	8.7	900	3	–	215
379	$NdPO_4$	1300	Monoclinic $P2_1/n$	8.7	59500		−47	146
380	$(Mg_{0.95}Ni_{0.005})_2SnO_4$	1550/4h	Cubic Spinel Fd3m	8.7	103100		−63	216
381	$ZnAl_2O_4$SPS		Spinel Cubic Fd3m	8.7	57000			151
382	$SrW_{1-x}Te_xO_4$ (x=0.1)	800	Scheelite $I4_1/a$	8.7	40300			206
383	$(Mg_{1/2}Co_{1/2})Al_2O_4$	1600	Spinel Cubic Fd3m	8.8	107300		−54	217

(*continued*)

No.	Material	ST (°C)	Crystal structure	ε_r	Qf (GHz)	f_0	τ_f	Reference
384	$Sr_2MnSi_2O_7$	1375	Akermite Tetragonal P4-2_1m	8.8	32000		−59	133
385	$Ca_{0.5}Sr_{0.5}Zr_4P_6O_{24}$	1400	Trigonal R-3	8.8	1200	11	−32	218
386	$Li_2Mo_4O_{13}$	520	Anorthic P-1	8.8	7700	10.7	−66	30
387	xMgO-(1-x)B_2O_3 (x=0.95)	1350/4h	Orthorhombic Pnmn	8.8	432000		−55	93
388	BaO-ZnO-SiO_2	1275	Composite	8.8	34000		−58	133
389	$Sr_2ZnSi_2O_7$+2 wt% $SrTiO_3$	1450	Akermite Tetragonal P4-2_1m	8.8	60000		−13	133
390	0.4$Ba_3(VO_4)_2$-0.6Mg_2SiO_4	1200	Composite	8.8	55900		−1	188
391	$(Zn_{0.8}Mg_{0.2})_2SiO_4$-$TiO_2$+3 wt% Li_2O-B_2O_3	900	Mixed phases	8.8	15500		18	219
392	CaO-Al_2O_3-SiO_2-B_2O_3+Al_2O_3	900	Composite	8.8	1500			220
393	Zn_2SnO_4+0.5 wt% $BaCuB_2O_5$	1150/4h	Spinel Fd-3m	8.8	30900		−88	221
394	$Li_2Mg_3SnO_6$	1360	Cubic rocksalt Fm-3m	8.8	123000	10.7	−32	222
395	$Sr_2CoSi_2O_7$	1375	Akermite Tetragonal P4-2_1m	8.9	34000		−57	133
396	ZnO-B_2O_3-SiO_2-MMT-20 (46.34:17.09:6.85:29.72)	900	Composite	8.9	7000	8	−24	197
397	$CaGeO_3$	1200	Orthorhombic Pbnm	8.9	32200	10		223
398	ZnO-B_2O_3-SiO_2-MMT-20(44.97:17.2:6.9:29.93)	900	Composite	8.9	810	8	−15	177,197
399	ZnO-B_2O_3-SiO_2-MMT-20(46.34:17.09:6.85:29.72)	900	Composite	8.9	800	8	−24	177,197
400	$ZnTiO_3$+1 wt% B_2O_3	900/4h	Trigonl R-3	8.9	49000		−32	224
401	$CaSiO_3$+1 wt% Al_2O_3+1.5 wt% Li_2CO_3+0.2 wt% CuO+10 wt% $CaTiO_3$	900	Composite	8.9	19800		−1	225
402	$Mg(Al_{1-x}Ga_x)_2O_4$ (x=0.6)	1485	Cubic Fd3m	8.9	107000	14.8	−16	226
403	$LiMgVO_4$	700/4h	Orthorhombic	8.9	23300	10.2	−140	227
404	xMgO-(1-x)B_2O_3 (x=0.97)	1350/4h	Orthorhombic Pnmn	9.0	547700		−55	93
405	$Ca_{1-x}Cd_xMoO_4$ (x=0.2)		Scheelite Tetragonal I4$_1$/a	9.0	32500		−40	165
406	$BaWO_4$		Scheelite Tetragonal I4$_1$/a	9.0	32200			228
407	$BaMoO_4$	900	Scheelite Tetragonal I4$_1$/a	9.0	37100		−90	229

408	$SrWO_4$		Scheelite Tetragonal $I4_1/a$	9.0	62600			228
409	$(1-x)Ba_3(VO_4)_2$-xMg_2SiO_4 (x=0.55)	1175	Composite	9.0	52500		0	188
410	ZnO-B_2O_3-SiO_2-MMT-20(49.21:16.15:6.49:28.15)	900	Composite	9.0	7000	8	−62	197
411	Co_3O_4-Nb_2O_5-TiO_2	1010	Mixture	9.0	41000	7.5	−59	230
412	$MgTiO_3$-$CaTiO_3$-ZnO-B_2O_3-SiO_2		Composite	9.0	7000	7	−55	197
413	PbO:B_2O_3:SiO_2 (30:60:10) glass		Glass	9.0	1700	13.5	−15	92
414	$5ZnO$-Ta_2O_5-TiO_2	1150	Composite	9.0	9000	7.9	−45	230
415	$0.9CaWO_4$-$0.1Li_2WO_4$	1150	Composite	9.0	117600		−55	231
416	Yb_2BaNiO_5		Orthorhombic Pnma	9.1	44600		−37	149
417	K_2O-B_2O_3-SiO_2-CaO-SrO-BaO (glass)+Al_2O_3	900	Composite	9.1	600	0.5	0	232
418	Yb_2BaZnO_5		Orthorhombic Pnma	9.1	44600		−38	149
419	$DyPO_4$	1650/2h	Tetragonal $I4_1/amd$	9.1	28600		−17	146
420	α-$Ca_3(PO_4)_2$	1500/10min	Monoclinic $P2_1/a$	9.1	22000		−97	233
421	$xMgO$-$(1-x)B_2O_3$ (x=0.96)	1350/4h	Orthorhombic Pnmn	9.1	473890		−57	93
422	$CaSnSiO_5$	1525	Monoclinic A2/a	9.1	61000		35	234
423	$Mg_3(VO_4)_2$	950/50h	Orthorhombic Cmca	9.1	64100	–	−93	57
424	Zn_2SiO_4+11 wt% TiO_2	1200	Composite	9.1	150800		−1	69
425	$0.89Zn_2SiO_4$-$0.11TiO_2$		Composite	9.1	118000		1	235
426	$Ba_3(PO_4)_2$-$0.2BaWO_4$+0.8 wt% B_2O_3	925	Composite	9.1	45500		−2	236
427	$LiMgVO_4$	675/2h	Orthorhombic Cmcm	9.1	33700		−160	140
428	$0.95Sr_2Al_2SiO_7$-$0.05CaTiO_3$	1475	Gehlenite Tetragonal $P\text{-}42_1m$	9.2	14400		24	119
429	$BaMoO_4$	800	Scheelite Tetragonal $I4_1/a$	9.2	26600		−17	49
430	CaO-MgO-SiO_2-TiO_2+1 wt% Li_2CO_3-V_2O_5	880	Composite	9.2	46200		1.3	128
431	$xMgO$-$(1-x)B_2O_3$ (x=0.98)	1350/4h	Orthorhombic Pnmn	9.2	598370		−54	93
432	$Ca_{1-x}Cd_xMoO_4$ (x=0.4)	1025	Scheelite Tetragonal $I4_1/a$	9.2	38500		−40	165
433	BaO:B_2O_3:SiO_2 (50:40:10) glass	<800	Glass	9.2	1220	13.1	−43	92
434	$Ca_5Mg_4(VO_4)_6$	800	Cubic garnet Ia-3d	9.2	53300	10.6	−50	237
435	$Y_2BaCu_{0.9}Mg_{0.1}O_5$	1250	Orthorhombic Pbnm	9.2	36798		−36	123

(*continued*)

No.	Material	ST (°C)	Crystal structure	ε_r	Qf (GHz)	f_0	τ_f	Reference
436	(1-x)$LiYW_2O_8$-x$BaWO_4$+y wt% B_2O_3 (x=0.48, y=0.5)	930	Mixed phases	9.2	28100		−52	48
437	0.88$CaMgSi_2O_5$-0.12$CaTiO_3$+1 wt% Li_2CO_3-V_2O_5	880/2h	Composite	9.2	46200		1	128
438	1.8MgO-1.2Al_2O_2-2.8SiO_2-1.2TiO_2-0.4La_2O_3	1200	Composite	9.2	28600		−99	238
439	$SmBO_3$		Vaterite Hexagonal $P6_3/mmc$	9.3	11000			135
440	$LiMgPO_4$+0.1 vfTiO_2	950	Orthorhombic Pmnb	9.3	45400		−12	67
441	0.84$MgAl_2O_4$-0.16TiO_2	1410	Composite	9.3	82200	10.1	−27	187
442	$BaMoO_4$	900	Scheelite Tetragonal I41/a	9.3	37200		−79	113
443	Zn_2SiO_4+11 wt% TiO_2	1250	Composite	9.3	113000		1	73
444	xMgO-(1-x)B_2O_3 (x=0.993)	1350/4h	Orthorhombic Pnmn	9.3	773700		−55	93
445	xMgO-(1-x)B_2O_3 (x=0.995)	1350/4h	Orthorhombic Pnmn	9.3	551700		−56	93
446	xMgO-(1-x)B_2O_3 (x=0.999)	1350/4h	Cubic Fm3m	9.3	380400		−56	93
447	$Ca(Sn_{0.4}Si_{0.6})O_3$	1450	Monoclinic $P2_1/a$	9.3	63000		−52	155
448	0.8$ZnAl_2O_4$-0.2Co_2TiO_4		Spinal Cubic Fd3m	9.3	147000		−65	239
449	$Ba_3(VO_4)_2$+40 wt% $Zn_{1.87}SiO_{3.87}$	1100	Composite	9.3	23000		0	240
450	Zn_2SnO_4+1 wt% B_2O_3	975	Cubic Fd3m	9.3	62000		−59	241
451	Al_2O_3+20 wt% $CaSiO_3$	1325	Composite	9.4	13700			242
452	$Ba_3MgSb_2O_9$		Complex perovskite Hexagonal $P6_3/mmc$	9.4	6700	8.98		243
453	0.84Al_2O_3-0.16TiO_2+4 wt% MCAS glass	1250	Composite	9.4	8200		10	200
454	Y_2BaCuO_5		Orthorhombic Pbnm	9.4	3830	12	−35	244
455	α-$Ca_3(PO_4)_2$ Fluoro apatite	1500/8h	Trigonal R-3m	9.4	15200		−97	233
456	0.88$CaMgSi_2O_5$-0.12$CaTiO_3$	1300/2h	Composite	9.4	50800		6	128
457	$Mg_3(VO_4)_2$	1050	Orthorhombic Cmca	9.4	65500		−90	57
458	$MgCo_2(VO_4)_2$	900/5h	Orthorhombic Cmca	9.4	78900		−95	245
459	$SrMoO_4$	1050	Scheelite Tetragonal $I4_1/a$	9.5	61000		−67	113
460	La_2O_3-2B_2O_3-0.5ZnO+La_2O_3-3B_2O_3-0.5ZnO	900	Glass	9-10	72000	13		169

461	$BaO:B_2O_3:SiO_2$ (50:30:20) glass		Glass	9.5	1256	13.5	−95	92
462	$Y_2BaCu_{0.8}Mg_{.0.2}O_5$		Orthorhombic Pbnm	9.5	42300	−38		123
463	(1-x)$Ba_3(VO_4)_2$-xMg_2SiO_4 (x=0.5)	1175	Composite	9.5	46600		6	188
464	$Li_3AlMo_3O_{12}$	570	Lyonsite Psudohexagonal	9.5	50000	14.1	−73	207
465	$Ca_{1-x}Cd_xMoO_4$ (x=0.6)	1000	Scheelite Tetragonal $I4_1/a$	9.5	35700		−48	165
466	Sr_2SiO_4	1575	Monoclinic $P2_1/n$	9.5	19100		−205	210
467	$CaMoO_4$-xY_2O_3-xLi_2O (x=0.306)	775	Composite	9.5	63200		7	246
468	$MgGa_2O_4$	1410	Spinel Fd3m	9.5	117000	14.7	−4	247
469	$LiMgVO_4$	700	Orthorhombic Cmcm	9.5	34800		−146	248
470	$LiMg_{0.9}Zn_{0.1}PO_4$+0.1 Vf TiO_2	950	Orthorhombic Pmnb Olivine type	9.5	69500		−15	82
471	$CaWO_4$+0.12 wt% $BaCu(B_2O_5)$	875		9.5			−41	249
472	0.75Li_2ZnSiO_4-0.25$CaTiO_3$+25 wt% ZnO-B_2O_3	950	Composite	9.5	11800	7.8	−5	250
473	0.79$ZnAl_2O_4$-0.21 Mg_2TiO_4	1550	Composite	9.6	160800		−65	251
474	0.79$ZnAl_2O_4$-0.21Mn_2TiO_4	1300 SPS	Composite	9.6	30630		–	151
475	0.96 MgO-0.04LiF	950	Cubic Fm3m	9.6	282230		−63	252
476	$Ba_3CaSb_2O_9$		Complex perovskite Monoclinic C2/c	9.6	3400	9.2		243
477	$SrDy_4Si_3O_{13}$	1475/4h	Hexagonal apatite $P6_3/m$	9.6	9200		28	253
478	$BaO:B_2O_3:SiO_2$ (50:20:30) glass		Glass	9.6	1310	14.3	−114	92
479	$Ba_3V_4O_{13}$	6001h	Monoclinc I2/a	9.6	56000		−42	254
480	$Ba_2V_2O_7$	840/1h	Triclinic	9.6	30300		−32	255
481	$Zn_2(Sn_{0.99}Zr_{0.01})O_4$	1225/4h	Cubic Fd-3m	9.6	87000		−51	256
482	RE mixPO_4	1250	Monoclinic $P2_1/n$	9.6	45200	13.5	−35	257
483	$Ca(Mg_{0.92}Al_{0.08})(Si_{0.96}Al_{0.04})_2O_6$+10 wt% $CaTiO_3$	1250	Mixture	9.6	32600		−1	258
484	ZnO-B_2O_3-SiO_2-MMT-20(44.77:17.59:7.05:30.59)	900	Composite	9.7	7000	8	9	197
485	$CrTaO_4$		Rutile type Tetragonal $P4_2/mnm$	9.7	1600	4		53
486	$Y_2BaCu_{0.6}Ni_{0.4}O_5$	1270/3h	Orthorhombic Pnma	9.7	36000		−27	259

(*continued*)

No.	Material	ST (°C)	Crystal structure	ε_r	Qf (GHz)	f_0	τ_f	Reference
487	β-$Ca_3(PO_4)_2$	1125/8h	Rhombohedral R3C	9.7	10300		−47	233
488	0.79$ZnAl_2O_4$-0.21 Mn_2TiO_4	1400	Composite	9.7	23500		−63	251
489	$(K_{0.5}Sm_{0.5})MoO_4$	800/2h	Monoclinic I2/b	9.7	20000		−65	260
490	Al_2O_3+1500 ppm MgO+300 ppm La_2O_3			9.7	300000			261
491	0.55$Ba_3(VO_4)_2$-0.45$LiMgPO_4$	850	Composite	9.7	50700		1	262
492	0.8$LiZnVO_4$-0.2TiO_2	640	Composite	9.7	39200		−20	140
493	$Li_3InMo_3O_{12}$	630	Lyonsite Orthorhombic Pcn	9.8	36000	15	−73	207
494	$CaSiO_3$+1 wt% Al_2O_3+10 wt% $CaTiO_3$+1 wt% Li_2CO_3-CuO	900	Composite	9.8	19800		−1	263
495	$LiMgVO_4$ (UsingV_2O_5)	810	Orthorhombic Cmcm	9.8	26500		−166	132
496	$LiMgVO_4$ (Using NH_3VO_3)	720	Orthorhombic Cmcm	9.9	30800		−171	132
497	$Y_2BaCu_{0.8}Mg_{.0.2}O_{5\ CIP}$	1250	Orthorhombic Pbnm	9.9	49200	12.8	−40	123
498	$(K_{0.5}Nd_{0.5})MoO_4$	760/2h	Monoclinic I2/b	9.9	69000		−62	260
499	$(Mg_{1/2}Ca_{1/2})WO_4$+1 wt% Li_2WO_4	950	Wolframite P2/c	9.9	30150		−63	48
500	$MgWO_4$	950	Wolframite Monoclinic P2/c	9.9	5400			264
501	0.79$ZnAl_2O_4$-0.21 Co_2TiO_4	1500	Spinel cubic Fd3m	9.9	94000		−66	251
502	$Ca_{1-x}Cd_xMoO_4$ (x=0.8)	925	Sheelite Tetragonal I41/a	9.9	34000		−50	165
503	$CaW_{1-x}Te_xO_4$ (x=0.05)	900	Scheelite Tetragonal $I4_1/a$	9.9	53600			206
504	$Sr_2V_2O_7$+1 mol% Li_2CO_3	800	Anorthic P-1	9.9	73800		−29	265
505	0.96$CaWO_4$-0.04$Na_2W_2O_7$	875	Wolframite Monoclinic P2/c	9.9	64400			266
506	$Nd_4Si_3O_{12}$	1450	Hexagonal $P6_3/m$	9.9	6300	11.7	−12	154
507	$Zn_2(Sn_{0.95}Ti_{0.05})O_4$	1225/4h		9.9	76900		−38	267
508	$Li(Mg_{1-x}Ni_x)PO_4$ (x=0.05)	875	Orthohombic	9.9	50800		−1	99
509	$LiMg_{0.95}Ni_{0.05}PO_4$+11 wt% TiO_2	875	Orthorhombic olivine type	9.9	50800		−1	99
510	$Na_6Mo_{11}O_{36}$	510	Anorthic P-1	9.9	57000		−68	11
511	$BiCaVO_6$	900	$Cmc2_1$	9.9	23600		−71	540
512	$CaWO_4$	1290	Wolframite Monoclinic P2/c	10.0	50800		−50	264,266
513	$LiMgPO_4$+0.12TiO_2	950	Composite	10.0	26900		1	67
514	$Ba_3Nb_2P_4O_{18}$	1150	P-1	10.0	58400		−34	268

515	$0.83ZnAl_2O_4$-$0.17TiO_2$+10 wt% BBSZ glass	950	Composite	10.0	10000		−23	269
516	Al_2O_3	1400/8h	Trigonal R-3c	10.0	634000	14	−40	270
517	$CaW_{1-x}Te_xO_4$ (x=0.15)	850	Scheelite Tetragonal $I4_1/a$	10.0	42000		−61	206
518	$0.5Ba_3(VO_4)$-$0.5Zn_{1.87}SiO_{3.87}$+3 wt% B_2O_3		Composite	10.0	40800		0.5	271
519	TiO_2-$CaAlSi_2O_8$	960/0.5h	Composite	10.0	22500		−10	163
520	$Y_2Ba(Cu_{0.8}Mg_{0.2})O_5$ (CIP)			10.0	49180		−40	123
521	CAS-T10 glass ($CaO:Al_2O_3:SiO_2:TiO_2:B_2O_3$)	950	Composite	10.0	22500	10	−15	163
522	Al_2O_3+0.5 wt% TiO_2	1550/5h	Composite	10.0	453000	9		272
523	Al_2O_3	1550/5h	Trigonal R-3c	10.0	335000		−60	272
524	CaO-4ZnO-Ta_2O_5-TiO_2	1225	Mixture	10.0	15000	8.4	−60	230
525	$Mg_4Nb_2O_9$+3 wt% LiF	950/10H	Corundum type Hexagonal P-3c1	10.0	116420		−72	273
526	$LiMgPO_4$+0.12 vfTiO_2	950	Orthorhombic Pmnb	10.0	26900		−1	67
527	$Mg_4Ta_2O_9$	1450	Corundum trigonal P-3c1	10.0	345000		−70	274
528	Al_2O_3+500 ppm TiO_2		Hexagonal R-3c	10.0	500000	10		275
529	Mg_4NbSbO_9	1450/10h	Corundum type P-3c1	10.0	280000		−70	276
530	$BaTeO_3$	800	Orthorhombic Pnma	10.0	34000		−54	277
531	$Sm_2Si_2O_7$	1375	Tetragonal $P4_1$	10.0	2000	10		97
532	Al_2O_3+0.015 vf TiO_2		Composite	10.0	300000	10	0	278
533	$CaWO_4$	1150	Scheelite Tetragonal $I4_1/a$	10.0	75000		−24	150,279
534	$NaCa_2Mg_2V_3O_{12}$	915/4h	Cubic garnet Ia3d	10.0	50600		−47	280
535	45Vol% $LiMg_{0.9}Zn_{0.}1PO_4$+$Ba_3(VO_4)_2$	800	Composite	10.0	64500		−2	281
536	$LiMg_{0.95}Co_{0.05}PO_4$+16.1 wt% TiO_2	875/2h	Composite	10.0	58200		1	111
537	Al_2O_3	1550	Hexagonal R-3c	10.1	680000		−60	201
538	$Y_2BaCu_{0.1}Ni_{0.9}O_5$		Orthorhombic Immm	10.1	5830	12.3	−36	58
539	$Mg_5Nb_4O_{15}$		$A_nB_{n-1}O_{3n}$ perovskite Orthorhombic	10.1	32300		−24	282
540	$CaW_{1-x}Te_xO_4$ (x=0.05)	850	Scheelite Teragonal $I4_1/a$	10.1	40500		−61	206

(*continued*)

No.	Material	ST (°C)	Crystal structure	ε_r	Qf (GHz)	f_0	τ_f	Reference
541	$CaW_{1-x}Te_xO_4$ (x=0.2)	850	Scheelite Tetragonal $I4_1/a$	10.1	44300		−60	206
542	$Ca_{1-x}Cd_xMoO_4$ (x=1)	900	Tetragonal $I4_1/a$	10.1	53200		−57	165
543	$LiMg_{0.9}Zn_{0.1}PO_4$+0.12 Vf TiO_2	950	Orthorhombic Pmnb Olivine type	10.1	52900		−5	82
544	$La_2Mo_3O_{12}$	930	Monoclinic C2/c	10.1	60000		−80	178
545	$0.55Li_2WO_4$-$0.45TiO_2$	730	Mixture	10.1	32800		−17	283
546	$Ca_5Co_4(VO_4)_6$	875	Cubic garnet Ia-3d	10.1	95200	10.6	−63	284
547	$CaMoO_4$-xY_2O_3-xLi_2O (x=0.066)	775	Composite	10.1	66000		−57	246
548	$AlTeO_6$-TeO_2	900/2h+ anneal/750		10.2	24300	13.3		285
549	$Y_3Al_5O_{12}$+1.3 wt% TiO_2	1550	Garnet Cubic Ia3d	10.2	80100		−30	286
550	$Bi_6B_{10}O_{24}$	700	Orthorhombic Pnma	10.2	10750		−41	287
551	$0.9(0.79ZnAl_2O_4$-$0.21Mg_2TiO_4)$-$0.1TiO_2$	1450	Composite	10.2	158000		−64	288
552	Al_2O_3, TiO_2 doped		Trigonal R-3c	10.2	119150			289
553	(1-x)$LiYW_2O_8$-x$BaWO_4$+y wt% B_2O_3 (x=0.46, y=0.5)	900	Mixed phases	10.2	24300		−21	48
554	$Ce_2(WO_4)_3$	1025	Monoclinic C2/c	10.2	10500		−25	290
555	$Ba_3ZrV_4O_{15}$	800	Orthorhombic Pnma	10.2	30600	8.5	−102	291
556	CaV_2O_6	675		10.2	123000	10.2	−60	292
557	$0.88ZnAl_2O_4$-$0.12TiO_2$	1380	Composite	10.3	79800	11.1	−22	198
558	$Mg_3Yb_4Al_{44}O_{75}$	1680	Magnetoplumbite	10.3	41000		−57	145
559	$Mg_3Dy_4Al_{44}O_{75}$	1680	Magnetoplumbite	10.3	28000		−49	145
560	$CaMo_{1.02}O_4$	1300/2h	Tetragonal $I4_1/a$	10.3	71000			293
561	$NdPO_4$	1300/2h	$P12_1/n1$ Monozite	10.3	59500		−47	146
562	$SmPO_4$	1400	Monoclinic $P2_1/n$	10.3	60500		−54	146
563	Li_3SbO_4+1 wt% B_2O_3	930	Monoclinic P2/c	10.3	14600	13.5	−28	294
564	$BaLa_2(MoO_4)$	800	Monoclinic	10.3	29800		−76	295
565	$(K_{0.5}La_{0.5})MoO_4$	680	Tetragonal $I4_1/a$	10.3	59000		−81	296
566	$Yb_3A_{l2}O_{12}$	1650	Cubic Garnet Ia-3d	10.3	12900		−70	297

567	$LaPO_4$	1400	Monoclinic $P2_1/n$	10.4	64500		−56	146
568	$SrEr_4Si_3O_{13}$	1500/4h	Hexagonal apatite $P6_3/m$	10.4	18100		−24	253
569	$Sr_2V_2O_7$	1000	Anorthic P-1	10.4	19500		−35	299
570	$Ba_2V_2O_7$	920/10h	Anorthic P-1	10.4	51600		−20	299
571	$Y_3Al_5O_{12}$	1650/24h	Cubic Ia3d	10.4	440000		−50	300
572	$SrCe_2(MoO_4)_4$	840		10.4	54100	8.08	−46	301
573	MgO-1.2Al_2O_3-2.8SiO_2-1.2TiO_2-0.8CeO_2	1150/2h	Composite	10.4	15300		−5	302
574	$ZnGa_2O_4$	1385	Cubic spinel Fd3m	10.4	94600		−27	303
575	$CaWO_4$	1100	Scheelite Tetragonal $I4_1/a$	10.4	76500		−24	49
576	CAS-TB glass (CaO:Al_2O_3:SiO_2:TiO_2:B_2O_3)	950	Composite	10.5	14200	10	−20	163
577	0.83$ZnAl_2O_4$-0.17TiO_2+10 wt% BBSZ+0.3 wt% LiF	925/10	Composite	10.5	14500	5.5	−28	269
578	$MgTe_2O_5$	700/4h	Orthorhombic Pbcn	10.5	61000	5.3	−45	304
579	$LiCa_3MgV_3O_{12}$	900	Cubic garnet Cubic Ia3d	10.5	74700		−61	305
580	$Mg_2V_2O_7$	950/10h	Triclinic Anorthic P-1	10.5	58200		−27	306
581	$Er_3Al_2O_{12}$	1600	Cubic Garnet Ia-3d	10.5	11700		−45	297
582	$Yb_3Al_2O_{12}$+1 wt% Ga_2O_3	1600	Cubic Garnet	10.5	50000		−50	297
583	$Na_{0.5}Nd_{0.5}MoO_4$	760		10.5	19600	9.15	−49	307
584	0.96$CaWO_4$-0.04$YLiF_4$	750/2h		10.5	73000		−38	308
585	0.83$ZnAl_2O_4$-0.17TiO_2+15 wt% BBSZ glass	950/10h	Composite	10.6	9300	5.5	−29	269
586	$MgTiO_3$-$CaTiO_3$ (MMT-20)+ SiO_2-B_2O_3-BaO	900	Composite	10.6	6000	7		177
587	$Ca_3ZrSi_2O_9$	1400	Monoclinic $P2_1/a$	10.6	93300		−77	189
588	$CaZrB_2O_6$+3 wt% Bi_2O_3-CuO	925		10.6	87350		2	173
589	$Ba_3SrSb_2O_9$		Complex perovskte Triclinic P-I	10.6	4600	9		243
590	0.8$SrMoO_4$-TiO_2.+3 wt% H_3BO_3-CuO	875	Composite	10.6	72000		−19	309
591	$Y_2BaCu_{0.7}Mg_{0.3}O_5$ CIP	1250	Orthorhombic Pbnm	10.6	29300	12.3	−44	123
592	0.8$BaMoO_4$-0.2TiO_2	1275	Composite	10.6	51800		−56	229

(*continued*)

No.	Material	ST (°C)	Crystal structure	ε_r	Qf (GHz)	f_0	τ_f	Reference
593	$0.55Li_2MoO_4$-$0.45TiO_2$	700	Mixture	10.6	30000		−5	283
594	$0.75MgAl_2O_4$-$0.25TiO_2$	1450	Composite	10.7	105400	7.5	−12	195
595	$CoWO_4$	1200	Wolframite Monoclinic P2/c	10.7	38600			264
596	$0.87[0.79ZnAl_2O_4$-$0.21Co_2TiO_4]$-$0.13TiO_2$	1350	Composite	10.7	86700		−62	310
597	$Ba_3ZrV_4O_{15}$	800	Orthorhombic Pnma	10.7	30600		−106	291
598	$Sm_2Mo_4O_{15}$	690	Triclinic (PI-)	10.7	63500	11.6	−50	311
599	$LiMg_4V_3O_{12}$	740/4h	Tetragonal	10.7	24000	9.65	−12	312
600	$BaZnV_2O_7$	720	Orthorhombic	10.7	31000	11.7	−64	182
601	$0.9ZnAl_2O_4$-$0.08CaTiO_3$		Composite	10.8	32300		0	313
602	$CaMoO_4$	1100	Scheelite Tetragonal $I4_1/a$	10.8	89700		−23	49,228
603	Nano Al_2O_3+0.5 wt% TiO_2	1400	Trigonal R-3c	10.8	680000	14		314
604	$CaCu_2Nb_2O_8$+3 wt% V_2O_5	935		10.8	9300		−16	315
605	$Er_3Al_2O_{12}$+1 wt% Ga_2O_3	1550	Cubic Garnet	10.8	12600		−37	297
606	$CaGe_2O_5$	1180	Monoclinic Pbam	10.9	39000	10		223
607	$Y_3Al_2O_{12}$+1 wt% Ga_2O_3	1600	Cubic Garnet	10.9	25000		−33	297
608	$0.7Ca_2P_2O_7$-$0.3TiO_2$	1200/2h	Composite	10.9	44000		−11	316
609	$0.83ZnAl_2O_4$-$0.17TiO_2$+10 wt% BBSZ glass	950/10h	Composite	10.9	12000	5.5	−23	269
610	$Ba_2V_2O_7$+6 mol% Li_2CO_3	750	Anorthic P-1	10.9	74500		−20	317
611	$CaWO_4$		Scheelite tetragonal $I4_1/a$	10.9	105600			228
612	Sr_2ZnTeO_6+1 wt% ZnO-B_2O_3-P_2O_5-TeO_2 glass	950	Not available	10.9	4250		−57	318
613	Mg_2YVO_6	1290/4h	Tetragonal $I4_1/amd$	10.9	68300		−54	298
614	$Ca_2ZnSi_2O_7$	1300	Tetragonal $P\text{-}42_1m$	11.0	13500		−64	133
615	MgO-Al_2O_3-SiO_2-TiO_2-CeO_2	1100/2h	Composite	11.0	12100		26	320
616	$0.76Mg_2SiO_4$-$0.24TiO_2$		Composite	11.0	85000		0	107,321
617	$Mg_3(VO_4)_2$-$0.2Ba_3(VO_4)_2$	950/5h	Composite	11.0	114000		−58	322
618	Sm_2BaCuO_5:Co		Orthorhombic Pnma	11.0	89000		−7	323
619	$NdBO_3$		Aragonite Orthorhombic	11.0	17000			135

620	Ba_2MgTeO_6+0.2 wt% B_2O_3	1200	Orthorhombic Pnam	11.0	25000	5.5	−16	324
621	$Sr_2CaSi_2O_7$	1300	Akermite Tetragonal P4-2$_1$m	11.0	13500		−64	133
622	Mg_2SiO_4+24 wt% TiO_2	1200	Composite	11.0	82000		0	87
623	Al_2O_3	1550	Trgonal R-3c	11.0	680000		−65	235
624	TiO_2-B_2O_3-: Ca-Al-Si-) glass		Glass	11.0	1400	10		163
625	$Mg_5Ta_4O_{15}$ (MgO calcined)	1560	Psuedo-brookite Orthorhombic Cmcm	11.0	18100	9.06	−54	325
626	$Mg_5Nb_4O_{15}$ (MgO calcined)	1450	Psuedo-brookite Orthorhombic Cmcm	11.0	37400	8.3	−53	325
627	$Mg_4Nb_2O_9$	1300	Trigonal P-3c1	11.0	210000		−70	274
628	0.50Li_2WO_4-0.5TiO_2	730	Mixture	11.0	32000		−3	283
629	TiP_2O_7	1250	Pyrophosphate	11.0	77000		−14	326
630	$Na_{0.5}La_{0.5}MoO_4$	740/2h		11.0	25100	8.83	−59	327
631	0.81$Mg_2Si_{0.9}V_{0.1}O_4$-0.19$Ca_{0.8}Sr_{0.2}TiO_3$+4 wt% LiF	900/4h	Multiphase	11.0	49000	9.5	−7	328
632	$(Mg_{4-x}Mn_x)Nb_2O_9$		Corundum Trigonal P-3c1	11-16	21000-50000			329
633	PbO:B_2O_3 (40:60) glass	469Td	Glass	11.1	1320	12.22	−43	92
634	$CePO_4$	1400/2h	Monoclinic P2$_1$/n	11.1	68500		−46	146
635	$Nd_4Mo_4O_{15}$	700	Triclinic (PI$^-$)	11.1	61500	12	−44	311
636	0.35$Ba_3(VO_4)_2$-0.65$BaWO_4$	925	Composite	11.1	79100		−2	330
637	0.8(0.79$ZnAl_2O_4$-0.21Mg_2TiO_4)-0.2TiO_2	1450	Composite	11.1	155100		−62	288
638	$Li_2Zn_2Mo_3O_{12}$	630	Lyonsite Orthorhombic Pnma	11.1	70000	14.6	−90	207
639	0.8[0.79$ZnAl_2O_4$-0.21 Co_2TiO_4]-0.2TiO_2	1350	Composite	11.1	98700		−63	310
640	$Tb_2Al_2O_{12}$+1 wt% Ga_2O_3	1500	Cubic Garnet	11.1	30000		−32	297
641	$Y_3Al_2O_{12}$+1 wt% Nb_2O_5	1625	Cubic Garnet	11.2	120000		−48	297
642	$NiCu_2Nb_2O_8$+3 wt% V_2O_5	935		11.2	5760		−11	315
643	$Cu_3Nb_2O_8$	910	Anorthic	11.2	25560		−4	315
644	$SrTm_4Si_3O_{13}$	1650/4h	Monoclinic apatiteP2$_1$/m	11.2	14400		−20	253

(*continued*)

No.	Material	ST (°C)	Crystal structure	ε_r	Qf (GHz)	f_0	τ_f	Reference
645	$SrEr_4Si_3O_{13}$+0.5 wt% ZBS glass		Hexagonal apatite $P6_3/m$	11.2	21000		−20	253
646	$Ba_3(PO_4)_2$-0.2$BaWO_4$	1100	Composite	11.2	71985		1.5	236
647	$Na_{0.5}Ce_{0.5}MoO_4$	780		11.2	19400	8.98	−44	331
648	$Mg_5Nb_4O_{15}$Sol-gel	1300	Psuedo brookite Orthorhombic	11.3	43300		−58	332
649	0.7$BaMoO_4$-0.3TiO_2	1285	Composite	11.3	52600		−34	229
650	$MgCu_2Nb_2O_8$+3 wt% V_2O_5	935		11.3	2900		−27	315
651	0.4$Ba_3(VO_4)_2$-0.6$BaWO_4$	925	Composite	11.3	75100		3	330
652	0.83$ZnAl_2O_4$-0.17TiO_2+3 wt% BBSZ	1300/4	Composite	11.3	35000		−14	269
653	$Li_2Zn_2W_3O_{12}$	700	Li_2WO_4+$ZnWO_4$	11.3	24500		−100	193
654	$ZnCu_2Nb_2O_8$+3 wt% V_2O_5	935	Not available	11.4	10200		−23	315
655	$LiMgPO_4$+0.15 vf TiO_2	950	Orthorhombic Pmnb	11.4	21100		4	67
656	$CaCe_2(MoO_4)_4$	840	Not available	11.4	52100	6.9	−44	301
657	(1-x)$Ba_2V_2O_7$-x$Ba_3(VO_4)_2$ (x=0.42)	875/4h	Composite	11.4	71700		−1	333
658	Li_2SnO_3	1325	Rock salt C2/c(15)	11.4	13100		14	334
659	Zn_2SnO_4+3 wt% ZnO-B_2O_3-SiO_2	1075/4h	Cubic spinel Fd-3m	11.4	33000		−107	335
660	$BaPr_2(MoO_4)_4$			11.5	24800			337
661	0.8$SrMoO_4$-0.2TiO_2	1300	Composite	11.5	19200		8	309
662	$Y_2BaCu_{0.4}Ni_{0.6}O_5$	1360/3h	Orthorhombic Pnma	11.5	45200	13.11	−20	259
663	$BaTi(BO_3)_2$	1000/2h	Trigonal R-3	11.5	2300			338
664	$Mg_4Ta_2O_9$	1450	Corundum Trigonal P-3c1	11.5	347000		−70	339
665	$Yb_3Ga_5O_{12}$	1400	Garnet Cubic Ia3d	11.5	60300		−12	340
666	$Mg_4Nb_{0.5}Ta_{1.5}O_9$	1100	Corundum type Trigonal P-3c1	11.5	25520			339
667	0.8$NaCa_2Mg_2V_3O_{12}$-0.2$CaTiO_3$	930/4h	Cubic garnet	11.5	37500		2	280
668	$LiCa_3ZnV_3O_{12}$	900	Cubic Garnet	11.5	81100	−72	–	341
669	$Li_3FeMo_3O_{12}$	580	Orthorhombiv Pnma	11.5	12000		−20	342
670	$(Na_{0.5}Bi_{0.5})_{0.1}Ca_{0.9}MoO_4$	850	Tetragonal Scheelite	11.5	35100		−52	343
671	$BaY_2(MO_4)_4$	925/2h	Monoclinic	11.5	47200	10.3	−35	344
672	$LiKSm_2(MoO_4)_4$	620	Monoclinic Sheelite	11.5	39000		−16	345
673	$Mg_4(Nb_{2-x}V_x)O_9$ (x=0.0625)	1025	Corundum type Trigonal P-3c1	11.6	160250		−75	346

674	$0.83ZnAl_2O_4$-$0.17TiO_2$+1 wt% BBSZ glass	1300/4h	Composite	11.6	49000		−10	269
675	$ZnAlO_4$-$0.21TiO_2$	1500/3h	Composite	11.6	74000	6.5	0	347
676	$CaCu_2Nb_2O_8$	1110		11.6	2300		−17	315
677	$CePO_4$	1400/2h	Monoclinic $P2_1/n$	11.6	68300		−46	146
678	$SrEr_4Si_3O_{13}$+0.5 wt% LBS glass	1475/4h	Hexagonal apatite $P6_3/m$	11.6	21000		−20	253
679	$0.88Al_2O_3$-$0.12TiO_2$+8 wt% MCAS glass	1350	Composite	11.6	11500		−3	348
680	$Ca_{2+x}La_{8-x}(SiO_4)_{6-x}(PO_4)O_2$ (x=6)	1425/4h	Hexagonal $P6_3/m$ apatite	11.6	12700		−35	349
681	$0.79ZnAl_2O_4$-$0.21TiO_2$	1500/3h	Composite	11.6	74000	6.5	0	350
682	$0.95[0.79ZnAl_2O_4$-$0.21Co_2TiO_4]$-$0.05SrTiO_3$	1425	Composite	11.6	49950		−2	310
683	$0.95(0.79ZnAl_2O_4$-$0.21Mg_2TiO_4)$-$0.05SrTiO_3$	1450	Composite	11.6	55000		9	288
684	$0.6LiYW_2O_8$-$0.4BaWO_4$	900	Mixed phases	11.7	19750		14	48
685	$Ca_5Zn_4(VO_4)_6$	725	Cubic garnet Ia3d	11.7	49400	9.7	−83	237
686	$Yb_2Ba(Cu_{0.75}Zn_{0.25})O_5$		Orthorhombic Pnma	11.7	11200		−43	149
687	$BaDy(MoO_4)_4$		Monoclinic	11.7	11500			337
688	$CaMoO_4$ (hot pressed)	1100	Tetragonal scheelite $I4_1/a$	11.7	55000		−60	293
689	$Ca_{0.8}(Nd_{0.5}Li_{0.5})_{0.2}WO_4$	825/2h	Tetragonal scheelite $I4_1/a$	11.7	36700		5	351
690	$0.83ZnAl_2O_4$-$0.17TiO_2$+0.2 wt% BBSZ	1400/4	Mixture	11.7	120000		−7	269
691	$0.83ZnAl_2O_4$-$0.17TiO_2$+0.1 wt% BBSZ	1425/4	Mixture	11.7	96000		−4	269
692	$BaNd_2(MoO_4)$	960	Monoclinic	11.7	45000	9.9	−41	352
693	$LiMg_{0.9}Zn_{0.1}PO_4$+0.15 Vf TiO_2	975	Orthorhombic Pmnb Olivine type	11.7	49800		17	82
694	MgO-$1.2Al_2O_3$-$2.8SiO_2$-$0.6CeO_2$	1200	Composite	11.7	17300		48	320
695	$(Mg_{4-x}Co_x)Nb_2O_9$ (x=0.5)	1200/10h	Corundum type Trigonal P-3c1	11.7	50700		−68	353
696	$Sr_2NaMg_2V_3O_{12}$	900/4h	Cubic garnet Ia-3d	11.7	37900		−3	354
697	$BaSm_2(MoO_4)$	960	Monoclinic	11.8	20000	9.7	−34	352
698	$0.9Al_2O_3$-$0.1TiO_2$+0.3 wt% Nb_2O_5	1550	Composite	11.8	8000		2	355
699	$0.94(0.79ZnAl_2O_4$-$0.21Mg_2TiO_4)$-$0.06CaTiO_3$	1400	Composite	11.8	88080		−8	288

(*continued*)

No.	Material	ST (°C)	Crystal structure	ε_r	Qf (GHz)	f_0	τ_f	Reference
700	$La(Mg_{1/2}Ti_{1/2})O_3$+B_2O_3-La_2O_3-MgO	800	Composite	11.8	14700		7.4	356
701	ZnO-B_2O_3-P_2O_5-TeO_2 glass annealed			11.8	3500		−90	318
702	0.85$CaWO_4$-0.15$LaNbO_4$+3 wt% H_3BO_3-1 wt% Li_2CO_3	900	Scheelite+second phases	11.8	45200		−23	357
703	$La(Mg_{0.5}Ti_{0.5})O_3$+0.6B_2O_3-0.12La_2O_3-0.28MgO	850/2h	Composite	11.8	14700		7	356
704	Y_2BaCuO_5	1250	Orthorhombic Pnma	11.8	3200	10.7	−38	244
705	Mg_4NbTaO_9	1100	Corundum type P-3c1	11.8	281670		−66	358
706	$LaBO_3$	1300	Orthorhombic Pmcn	11.8	76900	15	−52	359
707	$Mg_4Nb_{1.5}Ta_{.5}O_9$	1100	Corundum type Trigonal P-3c1	11.9	234520		−67	358
708	Li_2MnO_3+2 wt% BCB	1200/4h	Monoclinic C2/c	11.9	80600		0	360
709	BaO-SrO-SiO_2-ZrO_2	<1000	Composite	12.0	1000	5		361
710	$CoCu_2Nb_2O_8$+3 wt% V_2O_5	885		12.0	7530		−18	315
711	CaO-4Co_3O_4-Nb_2O_5-TiO_2	1100	Mixture	12.0	28000	6.9	−42	230
712	$Mg_4(TaNb_{1-x}V_x)O_9$ (x=0.025)	1200	Corundum type Trigonal P-3c1	12.0	200000		−73	362
713	$Mg_4Ta_2O_9$	1250	Corundum type P-3c1	12.0	347000		−65	235
714	$AlNbO_4$	1250	Monoclinic fergusonite C2/m	12.0	34000		−56	363
715	0.85$CaWO_4$-0.$SmNbO_4$+1 wt% Li_2WO_4	800	Composite	12.0	13300		−28	364
716	$Ba_3(VO_4)_2$+60 wt% $CaWO_4$	900	Composite	12.0	37000		−1	365
717	$Ba_3V_4O_{13}$	700/4h	Monoclinic C2/c	12.0	22500		−67	366
718	$Ca_4Tb_6(SiO_4)_4(PO_4)_2O_2$		Hexagonal Apatite $P6_3/m$	12.0	19000		−10	367
719	$Mg_{3-x}Ca_xV_2O_8$ (x=9/4)	950		12.0	5700		15	368
720	$Ca_2V_2O_7$	920	Anorthic Triclinic P-1	12.1	15400		−32	299
721	0.8$CaMoO_4$-0.2TiO_2+3 wt% H_3BO_3-CuO	875	Composite	12.1	53300		−16	309
722	0662$BaMoO_4$-0.338TiO_2	1285	Composite	12.1	41600		−25	229
723	0.76$SrMoO_4$-0.24TiO_2+3 wt% H_3BO_3-CuO	900	Composite	12.1	40700		10	309
724	PbO:B_2O_3:SiO_2 (40:20:40) glass		Glass	12.1	1420	12.2	−31	92

725	$MgWO_4$	1200	Wolframite Monoclinic P-2/c	12.1	41800		−45	48,49
726	$Li_{0.8}Mg_{4.1}V_3O_{12}$	760	Tetragonal	12.1	21800		2	248
727	$5BaO\text{-}2V_2O_5$	900/1h	Composite	12.1	26800		7	255
728	$Ca(Mg_{0.92}Al_{0.08})(Si_{0.96}Al_{0.04})_2O_6$+22 wt% TiO_2	1225	Mixture	12.1	6000		2	258
729	$Y_2BaCu_{0.75}Zn_{0.25}O_5$	1250	Orthorhombic Pnma	12.2	25660	11.5	−40	244
730	$Dy_3Ga_5O_{12}$	1450	Cubic Garnet Ia3d	12.2	42100	14.6	−22	340,369
731	$0.76SrMoO_4\text{-}0.24TiO_2$	1300	Composite	12.2	21700		40	309
732	$0.92MgAl_2O_4–0.08(Ca_{0.8}Sr_{0.2})TiO_3$	1440/ 20 min	Composite	12.2	56200		−3	370
733	$0.88Al_2O_3\text{-}0.12TiO_2$+2 wt% MCAS glass	1350	Composite	12.3	20485		2.5	348
734	$BaCe_2(MoO_4)_4$	840	Monoclinic	12.3	24700	7.5	−37	301,371
735	$Mg_4Nb_2O_9$ sol-gel	1250	Corundum type P-3c1	12.3	165000		−48	372
736	$Ca_{2+x}La_{8-x}(SiO_4)_{6-x}(PO_4)O_2$ (x=4)	1675/4h	Hexagonal $P6_3/m$ apatite	12.3	15900		−28	349
737	$Mg_3CoNb_2O_9$	1150	Corundum type P-3c1	12.3	34560		−64	358
738	Yb_2BaZnO_5		Orthorhombic Pnma	12.3	27000		−60	149
739	$0.72Ba(Mg_{1/2}W_{1/2})O_3\text{-}0.28BaTiO_3$	1500/6h	Perovskite	12.3	11000		−5	373
740	$Sm_3Ga_5O_{12}$+TiO_2	1450	Garnet cubic Ia3d	12.3	234700	14.1	−16	369
741	$Sm_3Ga_5O_{12}$	1450	Garnet cubic Ia3d	12.3	192200	14	−19	369
742	$(Mg_{4-x}Co_x)Nb_2O_9$ (x=1)	1200/10h	Corundum typeTrigonal P-3c1	12.3	34500		−64	358
743	$Ba_3V_2O_8$	1300/1h	Hexagonal	12.3	52200		42	255
744	$0.50Li_2MoO_4\text{-}0.5TiO_2$	720	Mixture	12.3	27000		23	283
745	$CeVO_4$	950	Tetragonal zircon	12.3	41500		−35	374
746	$Na_2YMg_2V_3O_{12}$	850	Cubic garnet Ia-3d	12.3	23200	10.2	−4	375
747	$Nd_3Ga_5O_{12}$	1400	Garnet Cubic Ia-3d	12.4	137800	13.8	−33	369
748	$0.9Al_2O_3\text{-}0.1TiO_2$Annealed at 1000 C	1350	Composite	12.4	117000		1.5	376
749	$Al_2O_3\text{-}TiO_2$:MnO	1300	Composite	12.4	274000	76	0	377
750	$0.9Al_2O_3\text{-}0.1TiO_2$	1300/2h	Composite	12.4	148000		2	378
751	$(1\text{-}x)LiYW_2O_8\text{-}xBaWO_4$+y wt% B_2O_3 (x=0.2, y=0)	900	Mixed phases	12.4	12100		33	48
752	$Ce_2(WO_4)_3$	1000	Monoclinic C2/c	12.4	10500	4.8	−39	290

(*continued*)

No.	Material	ST (°C)	Crystal structure	ε_r	Qf (GHz)	f_0	τ_f	Reference
753	$0.9LiCa_3MgV_3O_{12}$+0.1$CaTiO_3$	925/4h	Cubic garnet Ia3d	12.4	57600		3	305
754	$Mg_4Nb_2O_9$	1200/10h	Corundum typeTrigonal P-3c1	12.4	192200		−71	358
755	Mg_4NbSbO_9	1500	Corundum type Trigonal P-3c1	12.5	275000		−45	379
756	$0.895Al_2O_3$-$0.105TiO_2$	1350	Composite	12.5	340000	80	2	380
757	$Eu_3Ga_5O_{12}$	1400	Garnet cubic Ia3d	12.5	169100	14.6	−17	369
758	$LaBO_3$		Orthorhombic Pncn	12.5	53000			135
759	$Ba_3ZnNb_{2-x}Sb_xO_9$ (x=1.875)		Perovskite Pm3m cubic	12.5	2290	7.6		381
760	$Ba_3(VO_4)_2$+0.5 wt% B_2O_3	950	Trigonal R-32m	12.5	41065		39	108
761	$NaMg_4V_3O_{12}$	690	Tetragonal I-42d	12.5	35900	10.5	−58	382
762	$Mg_4Nb_2O_9$+3 wt% LiF	950/10h	Corundum type Trigonal P-3c1	12.6	116410		−72	273
763	$0.83ZnAl_2O_4$-$0.17TiO_2$	1410	Composite	12.6	100200	10	0	198,383
764	$Yb_2Ba(Cu_{0.25}Ni_{0.75})O_5$		Orthorhombic Immm	12.6	50040		−41	149
765	$YSmBaCuO_5$		Orthorhombic	12.6	25130	11	−30	384
766	$Mg_3(VO_4)_2$-$0.5Ba_3(VO_4)_2$+0.0625 wt% Li_2CO_3	950/5h	Composite	12.6	74400		−6	322
767	$SrGd_4Si_3O_{13}$	1525/4h	Hexagonal apatite $P6_3/m$	12.6	8800		−20	253
768	1-x($0.79ZnAlO_4$-$0.21Co_2TiO_4$)-x$CaTiO_3$ (x=0.08)	1400	Composite	12.6	67500		−1	310
769	$SrY_4Si_3O_{13}$	1575/4h	Hexagonal apatite $P6_3/m$	12.6	20500		−18	253
770	$0.7LiZnVO_4$-$0.3TiO_2$	680	Composite	12.6	38000		5	140
771	$Li_2Mg_3ZrO_6$	1380	Cubic rocksalt Fm-3m	12.6	86000	9.3	−36	222
772	$Mg_4Nb_2O_9$/MgO	1400	Composite	12.6	196700		−47	385
773	$(La_{0.5}Na_{0.5})_{1-x}$-$(Na_{0.5}Nd_{0.5})_xWO_4$ (x=0.3)	800/2h	Composite	12.7	23500		−1	386
774	$0.9Al_2O_3$-$0.1TiO_2$	1300	Composite	12.7	176000		−14	387
775	$YTmBaCuO_5$		Orthorhombic	12.7	17900	10.6	−27	384
776	$PbO:B_2O_3:SiO_2$ (40:40:20) glass		Glass	12.7	1700	12	−69	92
777	$[(Li_{0.5}Bi_{0.5})_{0.1}Ca_{0.9}]MoO_4$	850	Scheelite Tetragonal $I4_1/a$	12.7	41300	10	−17	388
778	$(Mg_{0.95}Zn_{0.05})_4Ta_2O_5$			12.7	385000		−62	389
779	Tm_2BaCuO_5	1250	Orthorhombic Pmna	12.8	14400	9.77	−15	384
780	$NiCu_2Nb_2O_8$	985		12.8	4240		481	315

781	$SrTm_4Si_3O_{13}$+0.5 wt% LBS glass	1575/4h	Apatite monoclinic $P2_1/m$	12.8	16500		−26	253
782	$0.8CaMoO_4$-$0.2TiO_2$	1325	Composite	12.8	29310		10	309
783	Li_2SnO_3	1230	Monoclinic C2/c	12.8	20800		27	390
784	$(Mg_{4-x}Co_x)Nb_2O_9$ (x=1.5)	1200/10h	Corundum typeTrigonal P-3c1	12.8	20500		−63	358
785	$LiEr_9(SiO_4)_6O_2$	1250/4h	Apatite, Hexagonal $P6_3/_m$	12.8	1300		17	391
786	$SrYb_4Si_3O_{13}$+0.5 wt% LBS glass	1425/4h	Hexagonal apatite $P6_3/m$	12.9	12000		−27	253
787	$BaTa_2P_2O_{11}$	1200	Rhombohedral R-3c	12.9	28900		−29	392
788	$Y_2Ba_{0.7}Sr_{0.3}CuO_5$		Orthorhombic Pnma	12.9	2960	10.7	2	393
789	$0.89Al_2O_3$-$0.11TiO_2$-0.5 wt% ZnO	1350	Composite	12.9	187000		−2	394
790	$Mg_4Nb_2O_9$	1300/10h	Trigonal P-3c1	12.9	217390	–	−70	346,358
791	$Na_2Mo_2O_7$	575	Orthorhombic Cmca	12.9	62400		−72	11
792	$Mg_3La_4Al_{44}O_{75}$	1680	Magnetoplumbite	13.0	7700		3	145
793	2CaO-3ZnO-Ta_2O_5-TiO_2	1300	Composite	13.0	20000	6.6	−24	230
794	$Ba_3ZnNb_{2-x}Sb_xO_9$ (x=2)		Perovskite	13.0	1550	7.7		381
795	$Ba_3(VO_4)_2$	1200	Rhombohedral $R3_2/m$	13.0	46700		17	322
796	$Mg_3(VO_4)_2$-$0.5Ba_3(VO_4)_2$+0.0625 wt% Li_2CO_3	950/5h	Composite	13.0	74000		−6	322
797	$SrDy_4Si_3O_{13}$+0.5 wt% LBS glass	1425/4h	Hexagonal apatite $P6_3/m$	13.0	9500		28	253
798	Mg_4NbSbO_9	1500	Corundum type Trigonal P-3c1	13.0	275000			395
799	$(Mg_{0.95}Zn_{0.05})_4Nb_2O_9$	1340/4h	Corundum Trigonal P-3c1	13.0	247000		−67	396
800	$0.77CaMoO_4$-$0.23TiO_2$+3 wt% H_3BO_3-CuO	900	Composite	13.0	57400		−5	309
801	$Li_3(Mg_{0.95}Mn_{0.05})_2NbO_6$	1140/4h	Fdd	15.6	52200	8.9	−20	397
802	$(Mg_{0.95}Zn_{0.05})_2(Ti_{0.8}Sn_{0.2})O_4$	1150/5h	Spinel Cubic Fd3m	13.1	119310	10	−59	398
803	$SrYb_4Si_3O_{13}$	1525/4h	Hexagonal apatite $P6_3/m$	13.1	11400		−25	253
804	Sr_2ZnTeO_6+2 wt% ZnO-B_2O_3-P_2O_5-TeO_2 glass	950	Composite	13.1	4300		−53	318
805	$0.67Ba(Mg_{1/2}W_{1/2})O_3$-$0.33BaTiO_3$	1500/6h	Perovskite	13.1	35000		−6	373
806	$MgWO_4$	1150	Wolframite MonoclinicP12/c1	13.1	69000		−58	150
807	$MgWO_4$+9 wt% Li_2CO_3	950	Composite	13.1	20000		−75	399
808	Ba_2SiO_4	1525	Orthorhombic Pmcn	13.1	17900		−17	210

(*continued*)

No.	Material	ST (°C)	Crystal structure	ε_r	Qf (GHz)	f_0	τ_f	Reference
809	Al_2O_3-WO_3-TiO_2	1150	Multiphase	13.2	3580	6.9	12	400
810	$Mg_2Co_2Nb_2O_9$		Corundum type Trigonal P-3c1	13.2	14300		−51	358
811	CeO_2+20 wt% B_2O_3	900	Cubic flurite Fm3m	13.2	24200	4.3	−46	401
812	$(Mg_{0.95}Ca_{0.05})TiO_3$+BaO-$B_2O_3$-$SiO_2$(50:50 wt%)	900	Composite	13.2	10000		–	402
813	Ca_2MgTeO_6+0.2 wt% B_2O_3	1250	Perovskite	13.2	81000	5.5	−81	324
814	$LiGd_9(SiO_4)_6O_2$	1250/4h	Apatite, Hexagonal $P6_3/m$	13.2	6900		23	391
815	$Ba_2Ti_9O_{20}$+50 vol% BBS glass	900	Composite	13.2	1150			338
816	$LiCa_3ZnV_3O_{12}$-0.2$CaTiO_3$	925	Cubic Garnet	13.2	59600	1		341
817	0.5$MgAl_2O_4$-0.5TiO_2	1460	Composite	13.2	88000	6.8	−4	195
818	$Ni_{1-x}(Zn_{1/2}Zr_{1/2})_xW_{1-x}Nb_xO_4$ (x=0.25)		Monoclinic Wolframite P2/c	13.2	28700		−29	403
819	$YErBaCuO_5$		Orthorhombic	13.3	16050	10.6	−34	384
820	$NiWO_4$	1200	Wolframite Monoclinic P2/c	13.3	24900			264
821	0.7$CaWO_4$-0.3$LaNbO_4$	1150	Composite	13.3	50000		−9	279
822	$(Na_{0.5}Bi_{0.5})_{0.2}Ca_{0.8}MoO_4$	850	Scheelite Tetragonal	13.3	32900		−42	343
823	0.8$Mg_{1.9}Cu_{0.1}SiO_4$-0.2$(La_{0.5}Na_{0.5})TiO_3$+4 wt% LiF	950	Orthorhombic	13.3	14400		6	404
824	$Sm_2BaCu_{0.5}Zn_{0.5}O_5$	1280	Orthorhombic Pnma	13.4	65740	10.6	−6	405
825	Sr_2ZnTeO_6+5 wt% ZnO-B_2O_3-P_2O_5-$Te0_2$ glass	950	Composite	13.4	4500		−52	318
826	$BaTa_2P_2O_{11}$+5 wt% TiO_2	1250	Rhombohedral R-3c	13.4	17200		−6	392
827	0.47$Mg_4Nb_2O_9$–0.53(0.5$ZnAl_2O_4$-0.5TiO_2)	1390/4h	Composite	13.4	210000		−2	406
828	0.77$CaMoO_4$-0.23TiO_2	1325	Composite	13.4	31300		33	309
829	Sr_2ZnTeO_6+5 wt% ZnO-B_2O_3-P_2O_5-TeO_2 glass	950	Composite	13.4	4500		−2	318
830	$Mg_5Nb_4O_{15}$+5 wt% B_2O_3	1300/4h	Multiphase	13.4	55700		−55	319
831	Er_2BaCuO_5		Orthorhombic Pnma	13.5	12560	11	−26	384
832	0.64$Ba(Mg_{1/2}W_{1/2})O_3$-0.36$BaTiO_3$	1500/6h	Perovskite	13.5	14000		−6	373,407

833	$ZnWO_4$	1200	Wolframite Monoclinic P2/c	13.5	62800			264
834	$SrSm_4Si_3O_{13}$	1375/4h	Hexagonal apatite $P6_3/m$	13.5	20800		−28	253
835	$Mg_4Nb_2O_9$+0.75 wt% Fe_2O_3	1240	Corundum type Trigonal P-3c1	13.5	280000		−62	408
836	Li_2SnO_3		Monoclinic C2/c	13.5	61600		29	409
837	$SrY_4Si_3O_{13}$+0.5 wt% LBS glass	1475/4h	Hexagonal apatite $P6_3/m$	13.5	21500		−18	253
838	$ZnW_{1-x}Te_xO_4$ (x=0.05)	900	Wolframite $P2_1/n$	13.5	22500		−66	206
839	$MgWO_4$	1050	Monoclinic P2/c	13.5	69000		−58	150
840	$Li_8Bi_2Mo_7O_{28}$	540	Tetragonal	13.6	8000	9.2	−59	30
841	Te_2MoO_7	520	Monoclinic $P2_1/c$	13.6	46900		−36	410
842	$Ba_3TiV_4O_{15}$	800	Orthorhombic Pnma	13.6	31800	8.6	10	291
843	Li_2MnO_3	930/4h	Monoclinic C2/c	13.6	97000		−5	360
844	$BaY_2(MoO_4)_4$-0.5TiO_2	970/2h	Composite	13.6	30800	9.6	1	411
845	$Ce_2(WO_4)_3$+0.2 wt% ZBS	900	Monoclinic C2/c	13.7	20200		−25	290
846	Li_2SnO_3+1 wt% BaO-CuO	900	Monoclinic C2/c	13.7	36400		27	390
847	$Ca_{2+x}La_{8-x}(SiO_4)_{6-x}(PO_4)O_2$ (x=0)	1475/4h	Hexagonal $P6_3/m$ apatite	13.7	33100		−29	349
848	$ZnMnW_2O_8$	950		13.7	10670		−17	48
849	PbO:B_2O_3:SiO_2 (50:40:10) glass	409 Td	Glass	13.8	880	10.7	−98	92
850	$Y_2BaCu_{0.2}Ni_{0.8}O_5$	1390/3h	Othorhombic Pnma	13.8	87200	12.8	−17	259
851	$Ba_2CeV_3O_{11}$	1025		13.8	10000		−14	366
852	$Ca_{2+x}La_6(SiO_4)_4(PO_4)O_2$ (x=2)	1475/4h	Hexagonal $P6_3/m$ apatite	13.8	27900		−11	349
853	$Ca_4La_4Pr_2(SiO_4)_4(PO_4)_2O_2$	1475	Hexagonal apatite $P6_3/m$	13.8	26000		−7	367
854	$Ca_4La_2Pr_4(SiO_4)_4(PO_4)_2O_2$	1475	Hexagonal apatite $P6_3/m$	13.8	21800		−5	367
855	0.6$BaMoO_4$-0.4TiO_2	1285	Composite	13.8	40500		−6	229
856	Nd_2MoO_6	1350/4h	Tetragonal I-42m	13.8	66400		−53	412
857	$Te_2(Mo_{0.95}W_{0.05})O_7$	520	Monoclinic $P2_1/c$	13.9	25800		−13	410
858	Sr_2ZnTeO_6+10 wt% ZnO-B_2O_3-P_2O_5-TeO_2	900	Composite	13.9	3300		−58	318
859	$SrNdSi_3O_{13}$+0.5 wt% LBS glass	1350/4h	Hexagonal apatite $P6_3/m$	13.9	20500		−33	253
860	$SrSm_4Si_3O_{13}$+0.5 wt% LBS glass	1350/4h	Hexagonal apatite $P6_3/m$	13.9	21800		−28	253
861	1-xCeO_2-xY_2O_3 (x=0.5)	1650	Cubic flurite Fm3m	13.9	35000		−53	413
862	$YHoBaCuO_5$		Orthorhombic	13.9	12056	10.7	−30	384

(*continued*)

No.	Material	ST (°C)	Crystal structure	ε_r	Qf (GHz)	f_0	τ_f	Reference
863	$Mg_4Ta_2O_9$	1200	Corundum type P-3c1	14.0	350000	–	−60	339
864	$YDyBaCuO_5$		Orthorhombic	14.0	42600	10.8	−22	384
865	$LaMgAl_{11}O_{19}$	1700	Hexagonal P63/mmc	14.0	28000	7	−12	414
866	$Y_2BaCu_{0.75}Zn_{0.25}O_5$	1270	Orthorhombic Pnma	14.0	56230	10.8	−39	244
867	$Mg_5Nb_4O_{15}$	1475	Psuedobrookite Orthorhombic Cmcm	14.0	14600	7.3	−58	325
868	$5Co_3O_4$-Ta_2O_5-TiO_2	1150	Mixture	14.0	48000	6.5	−43	230
869	$0.2ZnAl_2O_4$-$0.8Co_2TiO_4$		Not available	14.0	148800		−52	239
870	$Mg_3Ce_4Al_{44}O_{75}$	1680	Magnetoplumbite	14.0	9000		11	145
871	$Ba_3NiSb_2O_9$		Perovskite	14.0	41840	7.8	−5	381
872	$YGdBaCuO_5$		Orthorhombic	14.0	14300	10.9	−35	384
873	$0.80ZnAl_2O_4$-$0.20TiO_2$	1420	Spinal cubic Fd3m composite	14.0	90700	9.66	6	198
874	$Ba[Ti_{0.39}(Co_{0.5}W_{0.5})_{0.61}]O_3$	1400	Perovskite	14.0	7700		−14	415
875	$Li_3(Mg_{0.92}Zn_{0.08})2NbO_6$+0.5 wt% $0.17Li_2O$-$0.83V_2O_5$	925/2h	Orthorhombic Fddd	14.0	83400		−37	416
876	$0.662BaMoO_4$-$0.338TiO_2$+5 wt% H_3BO_3+1 wt% CuO	875	Composite	14.0	48300		14	229
877	Li_2ZrO_3	1200	Tetragonal	14.1	17600		39	390
878	Li_3TaO_4+1 wt% B_2O_3	930	Rock salt type	14.1	29900	12.4	−48	294
879	$LiEu_9(SiO_4)_6O_2$	1250/4h	Apatite, Hexagonal $P6_3/m$	14.1	7100		8	391
880	$[(Li_{0.5}Bi_{0.5})_{0.15}Ca_{0.85}]MoO_4$	760	Scheelite tetragonal $I4_1/a$	14.1	24000	10.3	11	388
881	$Yb_2Ba(Cu_{0.5}Zn_{0.5})O_5$			14.2	20630		−48	149
882	$Y_2BaCu_{0.5}Zn_{0.5}O_5$	1270	Orthorhombic Pnma	14.2	110660	10.7	−42	244
883	Mg_2TiO_4	1500	Cubic spinel Fd3m	14.2	160000		−50	417,418
884	$0.8(Al_{1/2}Ta_{1/2})O_2$-$0.2(Mg_{1/3}Ta_{2/3})O_2$	1450	Composite	14.2	62150		−41	214
885	80 wt% (La_2O_3-B_2O_3-TiO_2 in 20:60: 20 mol%)+20 wt % $BaNd_2Ti_5O_{14}$	850	Composite	14.2	9800	7.5	94	419
886	$SrLa_4Si_3O_{13}$	1325/4h	Hexagonal apatite $P6_3/m$	14.2	26300		−46	253
887	$SrEu_4Si_3O_{13}$+0.5 wt% LBS glass	1425/4h	Hexagonal apatite $P6_3/m$	14.2	19800		−22	253
888	$LiLa_9(SiO_4)_6O_2$	1250/4h	Apatite, hexagonal $P6_3/m$	14.2	7300		18	391

889	$LiSm_9(SiO_4)_6O_2$	1250/4h	Apatite, Hexagonal $P6_3/m$	14.2	8500		2	391
890	$LiNd_9(SiO_4)_6O_2$	1250/4h	Apatite, Hexagonal $P6_3/m$	14.2	6400		12	391
891	$Ba_3(VO_4)_2$	925	Trigonal R-3_2/m	14.2	42200		52	330
892	$Ba_2BiV_3O_{11}$	870	Monoclinic $P2_1/c$	14.2	68700	8.7	−81	420
893	$LaVO_4$	850	Monoclinic Monazite	14.2	48200		−38	374
894	$SrTb_4Si_3O_{13}$+0.5 wt% LBS glass	1425/4h	Hexagonal apatite $P6_3/m$	14.3	23500		10	253
895	$0.2ZnAl_2O_4$-$0.8Co_2TiO_4$		Composite	14.3	148000		−53	239
896	$SrTb_4Si_3O_{13}$	1500/4h	Hexagonal apatite $P6_3/m$	14.3	19300		6	253
897	$LiY(W_{1-x}Te_x)_2O_8$ (x=0.2)	850	Monoclinic	14.3	4000		−6	421
898	$Mg_{0.95}Co_{0.05}TiO_3$	1275/4h	Ilmenite Trigonal R-3	14.3	128000	7	−51	422
899	Sr_2MgTeO_6+0.2 wt% B_2O_3	1250	Cubic Fm3m	14.3	27400	5.5	−60	324
900	BaO-0.35MgO-0.33WO_3-0.32TiO_2	1500/6h	Perovskite Hexagonal	14.4	74000		−9	373
901	BaO+0.34MgO-0.32WO_3-0.34TiO_2	1500/6h	Perovskite Hexagonal	14.4	87000		−7	373
902	$Sm_2BaCu_{0.75}Zn_{0.25}O_5$	1280	Orthorhombic Pnma	14.4	47000	10.6	−7	405
903	$La_2Sn_2O_7$	1580/34h	Cubic Fd3m	14.4	40500		−54	423
904	$Ca_{1-x}(La_{0.5}Na_{0.5})_xWO_4$+30 mol%$TiO_2$ (x=0.9)	850/2h	Composite	14.4	14300		−9	424
905	80 wt% (La_2O_3-B_2O_3-TiO_2 in 20:60:20 mol%)+20 wt % $BaNd_2Ti_5O_{14}$	800	Composite	14.5	9100	7.5	86	419
906	BaO-0.34MgO-0.32WO_3-0.34TiO_2	1500/12h	Perovskite Hexagonal	14.5	107000		−8	373,407
907	$Mg_3Pr_4Al_{44}O_{75}$	1680	Magnetoplumbite	14.5	10000		23	145
908	$Y_2BaCu_{0.6}Ni_{0.4}O_5$	1340	Orthorhombic Pnma	14.5	36000	14.5	26	259
909	$MnWO_4$	1000	Monoclinic P2/c	14.5	32000		−64	150
910	Ba_2SiO_4	1525/4h	Orthorhombic Pmcn	14.5	17900		−17	210
911	Ca_4La_6 $(SiO_4)_4(VO_4)_2O_2$	1475	Hexagonal apatite $P6_3/m$	14.5	22000		−20	367
912	Mg_2TiO_4+1.5 wt% CeO_2 nano particles		Spinel Fd3m	14.6	167000			425
913	$(Mg_{0.97}Zn_{0.03})(Ti_{0.95}Sn_{0.05})O_4$	1390/4h	Cubic spinel	14.6	183500		−44	426
914	$Ba_3MgNb_{2-x}Sb_xO_9$ (x=0.5)		Perovskite	14.7	81300	6.3	5	381
915	$Zn_3Nb_2O_8$+3 wt% (0.29$BaCO_3$+0.71CuO)	950	Monoclinic C2/c	14.7	8200	8.3		427
916	$SrLa_4Si_3O_{13}$+0.5 wt% LBS glass	1300/4h	Hexagonal apatite $P6_3/m$	14.7	25800		−40	253

(*continued*)

No.	Material	ST (°C)	Crystal structure	ε_r	Qf (GHz)	f_0	τ_f	Reference
917	$Cu_2ZnNb_2O_8$+1 wt% LBS glass	935	Triclinic	14.7	5100		−18	428
918	$Cu_2ZnNb_2O_8$+0.7 wt% LMZBS glass	935	Triclinic	14.8	2500		−39	428
919	$SrEu_4Si_3O_{13}$	1450/4h	Hexagonal apatite $P6_3/m$	14.8	20700		−24	253
920	$LiYW_2O_8$	900	Monoclinic	14.8	9550		−64	48
921	$0.2(Li_{1/2}Nd_{1/2})WO_4$-$0.8ZnWO_4$	850/4h	Tetragonal $I4_1/n$	14.8	1370		−20	429
922	$Li_2Zn_2W_2O_9$	790	Corundum	14.7	15700	9.7	−77	430
923	$Ni_{1-x}(Zn_{1/2}Zr_{1/2})_xW_{1-x}Nb_xO_4$ (x=0.5)		Monoclinic wolframite P2/c	14.8	32650		−35	403
924	$Ba_3NiNb_{2-x}Sb_xO_9$ (x=1.875)		Perovskite	14.8	38380	6.8	−10	381
925	$Yb_2Ba(Cu_{0.25}Zn_{0.75})O_5$			14.9	52810		−45	149
926	Dy_2BaCuO_5		Orthorhombic Pnma	14.9	31610	10.56	−6	384
927	1-xCeO_2-xGd_2O_3 (x=0.5)	1650	Cubic flurite Fm3m	14.9	15300		−62	413
928	$0.1ZnAl_2O_4$-$0.9Co_2TiO_4$		Composite	14.9	130000		−50	239
929	$Ba_2CeV_3O_{11}$	1025		14.9	12700	5	−15	366
930	$Bi_4(SiO_4)_3$	900	Cubic I-43d	14.9	36000		−9	431
931	$ZnW_{1-x}Te_xO_4$ (x=0.1)	900	Wolframite $P2_1/n$	14.9	27700		−65	206
932	$0.8ZnAl_2O_4$-$0.2Co_2TiO_4$		Composite	15.0	148000		−50	239
933	Sr_2TiO_4	1300/5h	Tetragonal I4/mmm	15.0	1600	4		53
934	5MgO-Nb_2O_5-TiO_2	1325	Mixture	15.0	59000	6.8	−77	230
935	$Mg_3Nd_4Al_{44}O_{75}$	1680	Magnetoplumbite	15.0	11000		35	145
936	$Ba_3MgNb_{2-x}Sb_xO_9$ (x=1.875)		Perovskite	15.0	84100	7.25	2.8	381
937	$Ba(Mg_{1/2}W_{1/2})O_3$	1550	Perovskite cubic Fm3m	15.0	57300	12.7		432
938	$BiZn_2VO_6$	780/4h	Triclinic P-1	15.0	20650		−88	433
939	BaO-0.34MgO-0.33WO_3-0.33TiO_2	1500/6h	Perovskite hexagonal	15.1	72000		−13	373
940	Al_2O_3+Ca-Al-B-Si-O+Ba-(Sm,Nd)-Ti-O	870	Composite	15.1	2800	3		215
941	$Ba_2CeV_3O_{11}$+1 wt% ZnO-B_2O_3-SiO_2	825		15.1	20300	4.9	−21	366
942	$CeTe_2O_6$	680	Monoclinic $P2_1/n$	15.2	45400		−68	434
943	$Y_2BaCu_{0.25}Zn_{0.75}O_5$	1270	Orthorhombic Pnma	15.2	70080	9.95	−42	244
944	$(Mg_{4-x}Co_x)Nb_2O_9$ (x=3)	1200/10h	Corundum typeTrigonal P-3c1	15.2	2200		−36	358
945	Ca_4La_6 $(GeO_4)_4(PO_4)_2O_2$	1475	Hexagonal apatite $P6_3/m$	15.2	20400		−11	367
946	$Ni_{1-x}(Zn_{1/2}Zr_{1/2})_xW_{1-x}Nb_xO_4$ (x=0.75)		Monoclinic Wolframite P2/c	15.2	41250		−45	403

947	$Li_3(Mg_{0.95}Ni_{0.05})_2NbO_6$	1140/4H	Fdd	15.2	84800	8.9	−23	397
948	$Li_2Mg_3TiO_6$	1280	Cubic rocksalt Fm-3m	15.2	152000	8.3	−39	222
949	Ho_2BaCuO_5		Orthorhombic Pbnm	15.3	9360	10.48	−19	384
950	$LaSrAlO_4$	1375	Tetragonal I4/mmm	15.3	32820		−17	435
951	$PbO:B_2O_3:SiO_2$ (60:20:20) glass	348 Td	Glass	15.3	650	11.72	−124	92
952	$LiPr_9(SiO_4)_6O_2$	1250/4h	Apatite, hexagonal $P6_3/m$	15.3	6400		33	391
953	Ca_3WO_6	1275	Monoclinic $P2_1/n$	15.3	29200		−30	436
954	$ZnW_{1-x}Te_xO_4$ (x=0.15)	900	Wolframite Monoclinic $P2_1/n$	15.3	41700		−61	206
955	$0.8(Mg_{0.95}Co_{0.05})_4Ta_2O_9$-$0.2CaTiO_3$	1375/4h	composite	15.3	390500		−35	437
956	Y_2BaZnO_5	1270	Orthorhombic Pnma	15.4	189000	10	−41	244
957	$Y_2Ba(Cu_{1/4}Zn_{3/4})O_5$		Orthorhombic Pbnm	15.4	220000		−65	235
958	BaO-$0.35MgO$-$0.34WO_3$-$0.31TiO_2$	1500/6h	Perovskite hexagonal	15.4	77000		−8	373
959	$Ba(Mg_{1/3}Ta_{(2-2x)/3}W_{x/3}Ti_{/3})O_3$ (x=1)	1550/4h	Perovskite Trigonal P-3m1	15.4	35400		−25	438
960	$0.8MgTiO_3$−$0.2Mg_{2.05}SiO_{4.05}$− $0.06CaTiO_3$	1380/4h	Composite	15.4	72700		−1	439
961	$Li_3(Mg_{0.95}Zn_{.05})_2NbO_6$	1140/4H	Fdd	15.4	82200	8.9	−19	397
962	$Sm_2Ba(Cu_{0.985}Co_{0.015})O_5$		Orthorhombic Pnma	15.5	59300	10.3	−8	323
963	$SrSmAlO_4$		K_2NiF_4 type tetragonal I4/mmm	15.5	95300		−1	440
964	$0.91MgWO_4$-$0.09CaTiO_3$+5 wt% Li_2CO_3-$4H_3BO_3$	950		15.5	20800		0	441
965	$(Mg_{0.95}Zn_{0.05})_2TiO_4$	1330	Cubic Fd3m	15.5	275300		−34	442
966	$(Mg_{0.9}Mn_{0.1})_2TiO_4$	1330	Cubic Fd3m	15.5	172000		−57	443
967	$SrNd_4Si_3O_{13}$	1400/4h	Hexagonal apatite $P6_3/m$	15.5	21000		−29	253
968	$ZnW_{1-x}Te_xO_4$ (x=0.2)	900	Wolframite Monoclinic $P2_1/n$	15.5	24600		−60	206
969	$0.91MgWO_4$-$0.09CaTiO_3$	950	Composite	15.5	20800	7.1	0	441
970	$SrTe_2O_5$	580		15.5	8700		−116	444
971	$Cu_3Nb_2O_8$	900/2h	Anorthic	15.6	48400		−75	445
972	$(Mg_{0.9}Co_{.0.1})_2TiO_4$	1390/4h	Cubic Fd3m	15.6	162000	10.4	−47	446
973	$(Mg_{0.96}Mn_{0.04})_2TiO_4$	1330	Cubic Fd3m	15.6	237000		−52	443
974	BaO-$0.33MgO$-$0.34WO_3$-$0.33TiO_2$	1500/6h	Perovskite hexagonal	15.6	67000		−10	373
975	$SrPr_4Si_3O_{13}$	1325/4h	Hexagonal apatite $P6_3/m$	15.6	12200		−9	253

(*continued*)

No.	Material	ST (°C)	Crystal structure	ε_r	Qf (GHz)	f_0	τ_f	Reference
976	$Mg_2(Ti_{0.95}Sn_{0.05})O_4$	1390	Cubic Fd3m	15.6	318000	10.8	−45	447
977	$Bi_4(SiO_4)_3$+3 mol% B_2O_3		Cubic I-43d	15.6	36300		−22	448
978	$SmNb_{1-x}(Si_{1/2}Mo_{1/2})_xO_4$ (x=0.69)		Tetragonal scheelite $I4_1/a$	15.6	32800		−38	449
979	$Li_3(Mg_{0.95}Ca_{0.05})_2NbO_6$	1140	Fdd	15.6	96200	8.9	−18	397
980	$LiZnNbO_4$	1070	Tetragonal	15.6	85300	9.1	−64	450
981	$(Mg_{0.95}Co_{.0.05})_2TiO_4$	1390/4h	Cubic Fd3m	15.7	286000	10.4	−52	446
982	$(Mg_{0.95}Mn_{0.05})_2TiO_4$	1330	Cubic Fd3m	15.7	276000		−53	443
983	$Mg_{1.8}Ti_{1.1}O_4$	1450/4h	Tetragonal $P4_122$	15.7	141000	10.57	−52	451
984	$YAlO_3$	1650/2h	Perovskite Hexagonal P63/mmc	15.7	58000	10	−59	452
985	$Mg_4Nb_2O_9$+3 wt% LiF+6 wt% $CaTiO_3$	950/5h	Corundum type+mixtures	15.7	22100		−3	453
986	(1-x)$(Al_{1/2}Ta_{1/2})O_2$-x$(Mg_{1/3}Ta_{2/3})O_2$ (x=0.2)	1550	Orthorhombic Pbcn	15.7	103600		−40	454
987	$LaTi_2Al_9O_{19}$	1600	Monoclinic	15.7	68200		−22	455
988	$0.7Ba_2BiV_3O_{11}$-$0.3TiO_2$	910	Composite	15.7	53200	8.57	−2	420
989	$Li_3Bi_2P_3O_{12}$	725	Cubic I-43m	15.8	26600		−130	456
990	Li_3NbO_4	930/2h	Cubic I-43m	15.8	55000		−49	457
991	$Y_2Ba_{0.7}Sr_{0.3}Cu_{0.25}Zn_{0.75}O_5$		Orthorhombic Pnma	15.8	20700	10.5	−13	393
992	Li_2CeO_3	720/4h	Cubic Fm3-m	15.8	143700		−123	458
993	Li_2TiO_3-13 wt% MgO+4 wt% LiF	850/4h		15.8	64500		0	459
994	$SrNdAlO_4$		K_2NiF_4 type Tetragonal I4/mmm	15.9	110000		−15	440
995	$Ca(Ta_{2-x}Nb_x)O_6$ (x=1.5)	1425	Cubic Pm3	15.9	102500		−56	460
996	$YSmBaZnO_5$		Orthorhombic	15.9	63210	9.9	−23	58
997	$Y_2Ba_{0.7}Sr_{0.3}Cu_{0.75}Zn_{0.25}O_5$		Orthorhombic Pnma	15.9	12450		0.8	393
998	$MgCu_2Nb_2O_8$	1010	Not available	15.9	6780		−46	315
999	$Ba_3Ti_5Nb_6O_{28}$+5 wt% B_2O_3	900/2h	Monoclinic $P2_1/c$	15.9	14000		−13	461
1000	$SmNb_{1-x}(Si_{1/2}Mo_{1/2})_xO_4$ (x=0.68)		Monoclinic+Tetragonal	15.9	33400		−39	449
1001	$(0.4Bi_2O_3$-La_2O_3-MgO-$TiO_2)$-$0.6La(Mg_{0.5}Ti_{0.5})O_3$	900	Composite	15.9	14300		35	462
1002	$BaNb_{2-x}Ta_xP_2O_{11}$ (x=1.5)	1250	Rhombohedral R-3c	15.9	13200		−25	392

1003	75 wt% $ZnNb_2O_6$-TiO_2+25 wt% (SiO_2- B_2O_3_Al_2O_3)	875	Composite	15.9	15000		−20	27
1004	Gd_2BaCuO_5		Orthorhombic Pbnm	16.0	3320	11.05	−27	384
1005	$Mn_4Nb_2O_9$	–	Corundum Trigonal P-3c1	16.0	50000		–	329
1006	3CaO-2ZnO-Ta_2O_5-TiO_2	1325	Composite	16.0	34500	6.2	−49	230
1007	$NdYBaZn_{0.45}Cu_{0.55}O_5$	1250/50h	Orthorhombic Pnma	16.0	100270		–	463
1008	$Ba_{10}Ta_{7.04}Sn_{1.2}O_{30}$		Trigonal P-3m1	16.0	30000		20	464
1009	$Co_4Nb_2O_9$	1200	Corundum Trigonal P-3c1	16.0	5000		−10	274
1010	$(Mg_{0.95}Zn_{0.05})TiO_3$	1320/4h	Ilmenite Trigonal R-3	16.0	210000		−60	465
1011	$Y_{1.5}Sm_{0.5}BaZnO_5$		Orthorhombic Pbnm	16.0	120000	−32		466
1012	$Ba_{2-2x}Sr_{2x}SmSbO_6$ (x=0.1)	1500	Perovskite	16.0	93000		−50	467
1013	Sr_2SmSbO_6	1550	Perovskite	16.0	93000		−50	467
1014	(1-y)Li_3NbO_4+yLi_2SnO_3 (y=0.7)		Composite	16.0	75300		3	409
1015	Tm_2BaZnO_5		Orthorhombic Pnma	16.1	8040	9.9	−20	58
1016	$Sm_2Ba(Cu_{0.995}Co_{0.005})O_5$		Orthorhombic Pbn	16.1	87800	10	−8	323
1017	$(Li_{1/2}Nd_{1/2})WO_4$	775/4h	Tetragonal $I4_1/n$	16.1	4210		142	429
1018	$MgTiO_3$	1350/4h	Ilmenite Trigonal R-3	16.1	289400		−54	468
1019	$(Mg_{0.095}Co_{0.05})_{1.8}Ti_{1.1}O_4$	1390/4h	Spinel cubic Fd3m	16.1	207500	10.7	−53	469
1020	0.4$LiFe_5O_8$-0.6$Li_2MgTi_3O_8$	1050/2h	Disordered spinel	16.1	28500		–	470
1021	$Nd_2BaZn_{0.5}Cu_{0.5}O_5$		Orthorhombic Pnma	16.2	36570		−13	468
1022	$Zn_2Te_3O_8$	620	Monoclinic C2/c	16.2	66000	4.9	−60	471
1023	$(Mg_{0.95}Ca_{0.05})TiO_3$+3 mol% V_2O_5	1100	Ilmenite Trigonal R-3	16.2	62000		50	472
1024	Er_2BaZnO_5	1300	Orthorhombic Pnma	16.3	6836	9.9	−28	58
1025	$ErAlO_3$	1650/2h	Perovskite Orthorhombic Pbnm	16.3	44200	10	−40	452
1026	BaO-0.33MgO-0.35WO_3-0.32TiO_2	1500	Perovskite Hexagonal	16.3	77000		−10	373
1027	$Ba_3MgNb_{2-x}Sb_xO_9$ (x=1)		Perovskite	16.3	33400	6.7	−4	381
1028	0.9$(Mg_{0.95}Zn_{0.05})_2(Ti_{0.8}Sn_{0.2})O_4$-0.1 ($Ca_{0.8}Sr_{0.2}$)$TiO_3$+5.3LiF-$Fe_2O_3$-$V_2O_5$	950	Composite	16.3	30800	8.3	−10	473
1029	$(Li_{0.5}Yb_{0.5})MoO_4$	820	Tetragonal Scheelite	16.3	6350		53	474
1030	0.7$Li_3(Mg_{0.92}Zn_{0.08})_2NbO_6-0.3Ba_3(VO_4)_2$	950	Composite	16.3	50000	8.6	2	475

(*continued*)

No.	Material	ST (°C)	Crystal structure	ε_r	Qf (GHz)	f_0	τ_f	Reference
1031	Pb_2WO_5	520	Monoclinic	16.4	14800	7.6	−95	476
1032	$Co_4Nb_2O_9$	1100/10H	Corundum type Trigonal P-3c1	16.4	5000		−11	358,477
1033	Li_3NbO_4	1150	Cubic I-43m	16.4	47100	10	−45	478,479
1034	$0.8Li_2Zn_3Ti_4O_{12}$-$0.2Li_2TiO_3$+2 wt% $0.1.5B_2O_3$-0.6CuO	925/5h	Composite	16.4	69000		−42	480
1035	Li_2TiO_3-13 wt% MgO	1325/4h		16.4	87500		−1	459
1036	$(Mg_{1-x}Zn_x)_{1.8}Ti_{1.1}O_4$ (x=0.06)	1360/4h	Cubic Fd3m	16.5	210700		−62	451
1037	$Ca(Ta_{2-x}Nb_x)O_6$ (x=1.4)	1425	Orthorhombic Pbcn	16.5	84080		−49	460
1038	$0.5BaMoO_4$-$0.5TiO_2$	1285	Composite	16.5	25200		46	229
1039	$ZnW_{1-x}Te_xO_4$ (x=0.0)	1100	Wolframite $P2_1/n$	16.5	20500		−70	206
1040	$Y_2Ba_{0.7}Sr_{0.3}Cu_{0.5}Zn_{0.5}O_5$		Orthorhombic Pnma	16.5	17670	10.1	−2	393
1041	$Y_2Ba_{0.7}Sr_{0.3}Cu_{0.15}Zn_{0.85}O_5$		Orthorhombic Pnma	16.5	23640	10.5	−18	393
1042	Sm_2BaCuO_5		Orthorhombic Pnma	16.5	53200	9.9	−5	323
1043	$Mg_3Sm_4Al_{44}O_{75}$	1680	Magnetoplumbite	16.5	11000		95	145
1044	$MgTiO_3$ (slow cooled 1°/min)	1350	Ilmenite Trigonal R-3	16.5	220000		−55	481
1045	$0.84Ba(Mg_{1/2}W_{1/2})O_3$-$0.16BaTiO_3$	1500	Perovskite hexagonal	16.6	12000		−11	373
1046	$CoCu_2Nb_2O_8$	985	Not available	16.6	36800		−37	315
1047	$(Mg_{0.95}Ca_{0.05})TiO_3$+5 mol% V_2O_5	1000	Ilmenite Hexagonal R-3	16.6	13700		−50	472
1048	$ErNbO_4$	1500	Monoclinic fergusonite	16.6	43900		−64	363
1049	$Li_{3-3x}Mg_{4x}Nb_{(1-x)}O_4$ (x=0.2)	1300/2h		16.6	85160	10	−32	479
1050	$SrLaAlO_4$		Tetragonal I4/mmm	16.7	149400		−32	440
1051	$Mg(Ti_{0.95}Sn_{0.05})O_3$		Ilmenite Trigonal R-3	16.7	275000	10.3	−53	447
1052	$Ba(Mg_{1/2}W_{1/2})O_3$	1500/6h	Perovskite cubic Fm3m	16.7	42000		34	373
1053	$0.6Ba(Mg_{1/2}W_{1/2})O_3$-$0.4BaTiO_3$	1500/6h	Perovskite Hexagonal	16.7	15000		12	373
1054	$Y_2Ba_{0.7}Sr_{0.3}ZnO_5$		Orthorhombic Pnma	16.7	4920	10.8	−35	393
1055	$ZnCu_2Nb_2O_8$	900/2h		16.7	41000		−77	482
1056	$Sm_2BaCu_{0.99}Co_{0.01}O_5$		Orthorhombic Pnma	16.8	90700	9.9	−9	58,323
1057	$Y_2Ba_{0.7}Sr_{0.3}Cu_{0.1}Zn_{0.9}O_5$		Orthorhombic Pnma	16.8	23600	10.5	−21	393
1058	70 wt% (La_2O_3-B_2O_3-TiO_2 in 20:60:20 mol%)+30 wt % $BaNd_2Ti_5O_{14}$	800	Composite	16.8	5900	7.1	109	419

1059	$(Mg_{0.95}Co_{0.05})TiO_3$		Ilmenite Trigonal R-3	16.8	230000	10	−54	483
1060	$SmNb_{1-x}(Si_{1/2}Mo_{1/2})_xO_4$ (x=0.04)		Monoclini+Tetragonal	16.8	45300		−45	449
1061	$1\text{-}xCeO_2\text{-}xSm_2O_3$ (x=0.25)	1650	Cubic flurite Fm3m	16.8	29650		−56	413
1062	$Li_{3-3x}Mg_{4x}Nb_{(1-x)}O_4$ (x=1/3)	1300/2h		16.8	79600	10	−22	479
1063	$[Mg_{0.5}Zn_{0.5})_{0.95}Co_{0.05}]_2TiO_4$+8 wt% BCB	925	Composite	16.8	28000		−29	484
1064	$(Na_{0.5}Bi_{0.5})_{0.4}Ca_{0.6}MoO_4$	800	Tetragonal scheelite	16.8	31800		−17	343
1065	$0.36Ba_5Nb_4O_{15}\text{-}0.64BaWO_4$	1100	Composite	16.9	56700		−4	485
1066	$Co_2La_4Ti_3Si_{(4-x)}O_{22-d}$ (x=0)	1275	Perrierite Monoclinic $P2_1/a$	16.9	35100	4.73	−164	486
1067	$(1\text{-}x)CeO_2\text{-}xEu_2O_3$ (x=0.85)	1600	Cubic flurite Fm3m	16.9	64700		−39	413
1068	$Sm_2BaCu_{0.25}Zn_{0.75}O_5$	1300/2h	Orthorhombic Pnma	16.9	42200	−4.6		405
1069	$0.4Li_2Zn_3Ti_4O_{12}\text{-}0.6Ba_3(VO_4)_2$	950	Composite	16.9	51300		3	487
1070	$3CaO\text{-}2ZnO\text{-}Ta_2O_5\text{-}TiO_2$	1400	Mixture	17.0	30000	6.6	−47	230
1071	$CeO_2\text{-}0.5WO_3\text{-}0.5TiO_2$	1130	Mixture	17.0	45500		7	488
1072	$Mg_5Ta_4O_{15}$	1550	Psuedo-brookite Orthorhombic Cmcm	17.0	14400	7.2	−15	325
1073	$BaNb_2O_6$		Columbite Orthorhombic $C222_1$	17.0	2600	7.01		489
1074	$Ba(Mg_{1/2}W_{1/2})O_3$	1550/6h	Perovskite Fm3m	17.0	57000		−34	373,432
1075	$Ca_5Ta_2HfO_{12}$	1700	Perovskite Orthorhombic Pnma	17.0	18000	5.9	−32	490
1076	$MgTiO_3$		Ilmenite Trigonal R-3	17.0	166400		−50	491,492
1077	$Mg_{0.95}Co_{0.05}TiO_3$	1200/3h	Ilmenite Trigonal R-3	17.0	170000	9.4	−40	493
1078	$ErAlO_3$		Perovskite Orthorhombic Pbnm	17.0	44200	10	−40	452
1079	$Bi_2O_3\text{-}4MoO_3$	600	Mixture	17.0	9300		−160	494
1080	Ba_2TeO_5	950	Monoclinic	17.0	49600	12	−124	277
1081	30 vol% Al_2O_3+BaO-ZnO-SrO-CaO-Nd_2O_3-TiO_2-B_2O_3-SiO_2 glass	900	Composite	17.0	800		−2	495
1082	$Nd_2Sn_2O_7$	1550/9h	Cubic	17.0	33100		−55	496
1083	Dy_2BaZnO_5	1320	Orthorhombic	17.1	29669	9.9	−2	58
1084	$CuNb_2O_6$	1000	Columbite Pbcn	17.1	7100	7.4	−45	489
1085	$BaO\text{-}0.34\ MgO\text{-}0.35\ WO_3\text{-}0.31TiO_2$	1500/6h	Perovskite Hexagonal	17.1	75000		−8	373
1086	Eu_2BaCuO_5		Orthorhombic Pbnm	17.1	9820		−25	497

(*continued*)

No.	Material	ST (°C)	Crystal structure	ε_r	Qf (GHz)	f_0	τ_f	Reference
1087	$LaSrAlO_4$	1450	Tetragonal K_2NiF_4 type	17.1	30770	10.77	3	435
1088	$(Mg_{0.95}Zn_{0.05})TiO_3$	1300	Ilmenite Trigonal R-3	17.1	264000	7	−40	498
1089	$NdYBaZn_{0.45}Cu_{0.55}O_5$			17.1	100300	−30		463
1090	$Ba(Ni_{1/2}W_{1/2})O_3$	1450	Perovskite Cubic Fm3m	17.1	36300	13.3	−68	432
1091	$SmNb_{1-x}(Si_{1/2}Mo_{1/2})_xO_4$ (x=0.03)		Monoclinic+Tetragonal	17.1	46200		−46	449
1092	In_2O_3-WO_3-TiO_2	1175	Multphase	17.2	5100	6.4	−68	400
1093	Gd_2BaZnO_5	1280	Orthorhombic Pbnm	17.2	2580	9.8	−27	58
1094	$Eu_2BaCu_{0.25}Zn_{0.75}O_5$		Orthorhombic Pbnm	17.2	57920		−29	497
1095	Ho_2BaZnO_5	1300	Orthorhombic Pbnm	17.2	6200	9.8	−23	58
1096	$Li_3(Mg_{0.92}Zn_{0.08})2NbO_6$	1120/4h	Orthorhombic Fddd	17.2	142300		−23	416
1097	$CaNb_2O_6$	1350	Columbite Pbcn	17.3	49600	6.9	−53	489
1098	$Mg_3Eu_4Al_{44}O_{75}$	1680	Magnetoplumbite	17.3	11000		147	145
1099	Li_2MgTiO_4	1360	Rock salt	17.3	97300	9.8	−27	499
1100	1-xCeO_2-xTm_2O_3 (x=0.25)	1650	Cubic flurite Fm3m	17.3	27850		−40	413
1101	$Co_2La_4Ti_3Si_{(4-x)}O_{22-d}$ (x=0.05)	1300	Perrierite Monoclinic $P2_1/a$	17.3	46600	4.75	−177	486
1102	$MgTiO_3$ (Pecchini mehod)+0.1 mol% Cr	1150	Ilmenite Trigonal R-3	17.3	136400			500
1103	$CoZnTiO_4$	1200	Cubic Spinel Fd-3m	17.3	97600	8.8	−36	501
1104	$Co_2La_4Ti_3Si_{(4-x)}O_{22-d}$ (x=0.1)	1300	Perrierite monoclinic $P2_1/a$	17.4	48700	4.68	−155	486
1105	$Mg(Sn_{0.05}Ti_{0.95})O_3$	1390/4h	Trigonal Ilmenite R-3H	17.4	322000		−54	502
1106	$Ba_8Zn(Nb_{6-x}Sb_x)O_{24}$ (x=2.4)	1425	Not available	17.4	9800		−3	503
1107	$LuNbO_4$	1500	Monoclinic fergusonite I2	17.4	56600		−64	363
1108	$Ba(Mg_{0.33}Ta_{0.13}Ti_{0.267}W_{0.267})O_3$	1560	Perovskite Hexagonal P-3m1	17.4	43780	7.1	−29	438
1109	$CaTeO_3$	840		17.4	49300	10		223
1110	$MgTi_2O_5$	1500/3h	Orthorhombic Psuedobrookite Bbmm	17.4	47000		−66	418
1111	$MgTiO_3$ (Chemical Pecchini mehod)	1150	Ilmenite, trigonal R-3H	17.4	166400		–	500
1112	0.5$Li_2Zn_3Ti_4O_{12}$-0.5$Ba_3(VO_4)_2$	950	Composite	17.4	56500		−5	487
1113	0.6$Li_2Zn_3Ti_4O_{12}$-0.4$Ba_3(VO_4)_2$	975	Compposite	17.5	73100		−16	487
1114	$BaTe_4O_9$	500	Monoclinic	17.5	54700		−90	277,504
1115	0.96$MgTiO_3$-0.036$SrTiO_3$+4 wt% CuO	1070/2h	Composite	17.5	25100		0	505

1116	$0.74CaWO_4$-$0.26TiO_2$	1250	Composite	17.5	27000		0	506
1117	$(Zn_{1-x}Cu_x)_2TiO_4$ (x=0.005)	1060/4h	Cubic Fd3m	17.5	7300		–	507
1118	$0.95MgTiO_3$-$0.05CaTiO_3$+5 wt% B_2O_3	1050	Composite	17.5	22000		−2	508
1119	$0.8Li_2Zn_3Ti_4O_{12}$-$0.2Li_2TiO_3$+2 wt% $0.4B_2O_3$-$0.6CuO$	925/5h	Composite	17.5	71000		−44	480
1120	$Mg(Zr_{0.05}Ti_{0.95})O_3$+1 wt% B_2O_3	1270	Ilmenite Cubic R-3	17.6	108000		2	509
1121	$DyAlO_3$	1650/2h	Perovskite Orthorhombic Pnma	17.6	38000	10	−34	452
1122	Nd_2BaCuO_5		Tetragonal I4/mcm	17.6	2200		−18	463
1123	$ZnWO_4$	1100	Monoclinic P2/c	17.6	65000		−60	150
1124	Ba_aMgWO_6		Perovskite Cubic Fm3m	17.6	45200	10.1		432
1125	$Co_2La_4Ti_3Si_{(4-x)}O_{22-d}$ (x=0.02)	1275	Perrierite Monoclinic $P2_1/a$	17.6	40800	4.73	−174	486
1126	MWF-38+10 wt% Li_2O-B_2O_3-SiO_2-CaO-Al_2O_3 (28:27:30:5:10)	875	Composite	17.7	3700		−15	510
1127	$MgTiO_3$+1 mol% Nb_2O_5	1350	Ilmenite R-3H, Trigonal	17.7	175000		–	511
1128	$0.95MgTiO_3$-$0.05CaTiO_3$+15 wt% LMZBS	1050	composite	17.7	29000		−10	508
1129	$Ca(Nb_{0.93}Ta_{0.07})_2O_6$	14004h	Othrorhombic columbite Pbcn	17.7	117000		−51	512
1130	$Mg_{0.97}Zn_{0.03}TiO_3$+0.5 mol% Zn	1275	Ilmenite	17.7	277500	8.5	−55	513
1131	Li_2ZrO_3+1 wt% BaO-CuO	900	Monoclinic C2/c	17.8	4300		12	390
1132	$0.94Mg_2TiO_4$-$0.6SrTiO_3$	1440/4h	Composite	17.8	70900	10	−3	514
1133	$Co_2La_4Ti_3Si_{(4-x)}O_{22-d}$ (x=0.25)	1250	Perrierite Monoclinic $P2_1/a$	17.8	30700	4.7	−150	486
1134	CeO_2-WO_3-TiO_2	1025	Multiphase	17.8	13100	6.2	85	400
1135	$DyNbO_4$	1250	Monoclinic fergusonite I2	17.8	38500		−66	363
1136	$(Zr_{0.8}Sn_{0.2})TiO_4$+10 wt% BaO-B_2O_3-SiO_2-Li_2O-CuO	950/4h	Composite	17.8	12700		1	515
1137	$NiTiO_3$	1475/4h	Trigonal R-3 Ilmenite	17.8	13900		−51	516
1138	$0.96MgTiO_3$-$0.036SrTiO_3$	1170/2h	Composite	17.9	30400	9	5	505
1139	$Eu_2BaCu_{0.5}Zn_{0.5}O_5$		Orthorhombic Pnma	17.9	49849		−30	497
1140	$(Zn_{1-x}Cu_x)_2TiO_4$ (x=0.01)	1060/4h	Cubic Fd3m	17.9	7500			517
1141	$MgTiO_3/CaTiO_3$ layered		Layered-composite	17.9	61400	9.64	0	518

(*continued*)

No.	Material	ST (°C)	Crystal structure	ε_r	Qf (GHz)	f_0	τ_f	Reference
1142	$Ba[Ti_{1-x}(Co_{0.5}W_{0.5})_xO_3$ (x=0.61)		Perovskite	18.0	7700		−14	519
1143	$0.94(Mg_{0.95}Zn_{0.05})_2TiO_4$-$0.06SrTiO_3$	1270	Cubic spinel	18.0	125600	10	0	520
1144	$(Zn_{0.95}Cu_{0.05})_2TiO_4$	1060	Cubic Fd3m	18.0	9700	7.4	−166	517
1145	$0.91Mg_2(Ti_{0.95}Sn_{0.05})O_4$-$0.09CaTiO_3$		Composite	18.0	92000		0	521
1146	$2/3LaCa_{0.5}Zr_{0.5}O_3$-$1/3CaTiO_3$	1575	Composite	18.0	26000	5.3	−75	522
1147	$5MgO$-Ta_2O_5-TiO_2	1325	Mixture	18.0	114000	6.61	−56	230
1148	$Zn_{0.6}Mg_{0.4}TiO_3$+5 wt% B_2O_3-SiO_2-ZnO-K_2O	1100	Composite	18.0	29400		–	523
1149	$Sm_2BaCu_{0.5}Zn_{0.5}O_5$		Orthorhombic Pbnm	18.0	65700	−6.4		524
1150	$(1-x)LaCa_{0.5}Zr_{0.5}O_3$-$xCaTiO_3$ (x=1/3)		Composite	18.0	16000		−75	522
1151	$0.5CeO_2$-$0.5Sm_2O_3$	1650	Composite	18.0	90000		−30	525
1152	$5ZnO$-Nb_2O_5-TiO_2	1050	Mixture	18.0	6000	5.9	−57	230
1153	$5MgO$-Ta_2O_5-TiO_2	1325	Mixture	18.0	114000	6.6	−47	230
1154	CeO_2-$0.5NiO$-$0.5TiO_2$	1200	Mixture	18.0	25300		−58	488
1155	$0.8Li_2Zn_3Ti_4O_{12}$-$0.2Li_2TiO_3$	1160	Cubic $P4_232$	18.0	100000		−48	480
1156	$Ca_9Nd_2W_4O_{24}$	1450	Tetragonal scheelite 141/a	18.0	4050			526
1157	Eu_2BaZnO_5		Orthorhombic Pnma	18.1	23360		−25	497
1158	$0.7Li_2Zn_3Ti_4O_{12}$-$0.3Ba_3(VO_4)_2$	1000	Composite	18.1	88980		−25	487
1159	$MgTiO_3/CaTiO_3$ /$MgTiO_3$ layered		Layered-composite	18.1	61400	9.6	0	518
1160	$MgTiO_3$+6 wt% CuO-Bi_2O_3-V_2O_5	900/2h	Ilmenite Trigonal R-3	18.1	20300		−57	527
1161	$Nd_2BaZn_{0.25}Cu_{0.75}O_5$	1250/10h	Tetragonal I4/mcm	18.1	25170		−18	463
1162	BaO-$0.32MgO$-$0.28WO_3$-$0.4TiO_2$	1500/6h	Composite	18.1	48000		−3	407
1163	$Ba(Ni_{1/2}W_{1/2})O_3$	1450	Perovskite cubic Fm3m	18.1	52000	8.22	−45	528
1164	$0.92(Mg_{0.95}Co_{0.05})_2TiO_4$-$0.08(Ca_{0.8}Sr_{0.2})TiO_3$+0.5 wt% B_2O_3	1200/4h	Composite	18.1	95000	9.5	−5	529
1165	$0.91(Mg_{0.97}Co_{0.03})2(Ti_{0.95}Sn_{0.05})O_4$-$0.09CaTiO_3$	1390/4h	Composite	18.1	87600		4	530
1166	$Sr_{1-x}Ca_xLaAlO_4$ (x=0.4)	1475	Tetragonal I4/mmm	18.1	150500		−26	531
1167	$Mg(Zr_{0.05}Ti_{0.95})O_3$	1420	Ilmenite Trigonal R-3	18.1	380000		−50	532
1168	$0.85Li_2TiO_3$-$0.5Li_2WO_4$	950	Mixture	18.1	81000		2	533

1169	$CaNb_2O_6$	1400/4h	Orthorhombic columbite Pbcn	18.1	50000		−54	534
1170	$(Zn_{1-x}Cu_x)_2TiO_4$ (x=0.05)	1060/4h	Cubic Fd3m	18.2	7500		−82	507
1171	$Mg(Zr_{0.05}Ti_{0.95})O_3$+1.5 wt% CuO	1300	Ilmenite Trigonal R-3	18.2	223000		−2	535
1172	$(Zn_{0.95}Mn_{0.05})_2TiO_4$	1180	Cubic Fd3m	18.2	9550	7.5	−200	517
1173	$Mg_{1+\delta}TiO_{3+\delta}$ (δ=0.03)	1400	Ilmenite Trigonal R-3	18.2	326600		−50	536
1174	$CaSmAlO_4$		K_2NiF_4 type Tetragonal I4/mmm	18.2	51060		−3	537
1175	$CaNdAlO_4$		K_2NiF_4 type Tetragonal I4/mmm	18.2	17980		−52	537
1176	$0.9(Mg_{0.95}Zn_{0.05})_2(Ti_{0.8}Sn_{0.2})O_4$-$0.1(Ca_{0.8}Sr_{0.2})TiO_3$	950	Spinel+Perovskite Composite	18.2	49100	8.1	15	473
1177	$SrLa_2Al_2O_7$		Tetragonal R-P phase	18.2	71700		−22	538
1178	$Zn(Mn_{1-x}Ti_x)3O_7$ (x=0.68)+5 wt% ZnO-B_2O_3	900	Multiphase	18.2	12000		−4	539
1179	$0.6LiMgVO_4$-$0.4TiO_2$	740	Composite	18.2	21600		−11	140
1180	$BiCuVO_6$	675	Monoclinic $P2_1/n$	18.2	7800	7.7	−177	540
1181	0.995MgO-0.005BaO-TiO_2	1320	Cubic Fm3m	18.3	18500	9.83		541
1182	$Mg_3Gd_4Al_{44}O_{75}$	1680	Magnetoplumbite	18.3	4800		175	145
1183	$Mg_3Tb_4Al_{44}O_{75}$	1680	Magnetoplumbite	18.3	5900		200	145
1184	$0.5ZnNb_2O_6$-$0.5Zn_3Nb_2O_8$-12 wt% $ZnCuB_2O_5$	875	Orthorhombic mixture	18.3	39750	5.9	−88	542
1185	$Sr(Ni_{1/2}W_{1/2})O_3$	1570	Perovskite Cubic Fm3m	18.3	56000	8.4	−50	528
1186	(1-x)CeO_2-xNd_2O_3 (x=0.7)	1600	Cubic flurite Fm3m	18.3	44700		−62	413
1187	$Mg_{1+\delta}T\ iO_{3+\delta}$ (δ=0.02)	1400	Ilmenite Hexagonal R-3	18.3	357600		−50	536
1188	$0.93(Mg_{0.95}Zn_{0.05})_{1.8}Ti_{1.1}O_4$-$0.07CaTiO_3$	1375	Composite	18.3	96000		−5	543
1189	$0.93(Mg_{0.97}Zn_{0.03})(Ti_{0.95}Sn_{0.05})O_4$-$0.07CaTiO_3$	1390/4h	Cubic spinel	18.3	94700		−4	426
1190	$0.91Mg_2TiO_4$-$0.1(Ca_{0.8}Sr_{0.2})TiO_3$	1300/4h	Composite	18.3	90500	9.5	0	544
1191	$0.8MgNb_2O_6$-$0.2CaTiO_3$	1300	Composite	18.4		73700	−45	545
1192	$GdAlO_3$	1650/2h	Perovskite Orthorhombic	18.4	11000	10	−54	452
1193	$(Zr_{0.8}Sn_{0.2})TiO_4$+10 wt% BaO-B_2O_3-SiO_2-Li_2O-CuO	950/8h	Composite	18.4	10500		−0	515
1194	$BaNd_2Ti_5O_{14}$+La_2O_3-B_2O_3-TiO_2	750	Composite	18.4	6100		4	546

(*continued*)

No.	Material	ST (°C)	Crystal structure	ε_r	Qf (GHz)	f_0	τ_f	Reference
1195	$0.93(Mg_{0.95}Co_{0.05})TiO_4$-$0.07SrTiO_3$		Composite	18.4	102200	9.5	1	547
1196	$0.88Mg_2TiO_4$-$0.12CaTiO_3$+4 wt% $ZnNb_2O_6$	1360/6h	Composite	18.4	31000	6	0	548
1197	Sm_2BaZnO_5		Orthorhombic Pnma	18.5	35500	9.5	−6	549
1198	$Sr_{1+x}La_{1-x}Al_{1-x}Ti_xO_4$	1500		18.5	95000		−9	550
1199	(1-x)CeO_2-xSm_2O_3 (x=0.85)	1600	Cubic flurite Fm3m	18.5	44700		−55	413
1200	$(Zn_{1-x}Cu_x)_2TiO_4$ (x=0.2)	1060/4h	Cubic Fd3m	18.5	7400		−15	507
1201	$(Mg_{0.7}Zn_{0.03})_{0.95}Co_{0.05}TiO_3$+7 wt% $BaCu(B_2O_5)$	950/4h	Composite	18.5	35000		−51	551
1202	$Mg_{0.95}Zn_{0.05}Ti_2O_5$	1450/4h	Orthorhombic Bbmn	18.5	45000		−41	552
1203	$0.2Li_2Zn_3Ti_4O_{12}$-$0.8Li_2TiO_3$+3 wt% $0.4B_2O_3$-0.6CuO	925/5h	Cubic composite	18.5	42000		−38	480
1204	$Li_2Zn_3Ti_4O_{12}$+2 wt% BCB	900	Cubic Fd-3m	18.5	31100		−36	553
1205	$Mg_{0.95}Co_{0.05}Ti_2O_5$	1425/4h	Orthorhombic Bbmn	18.6	68000		−39	552
1206	$(Li_{0.5}Er_{0.5})MoO_4$	800	Tetragonal Scheelite	18.6	10650		186	474
1207	$(Ca_{1+x}Sm_{1-x})(Al_{1-x}Ti_x)O_4$ (x=0.02)	1450	K_2NiF_4 type Tetragonal I4/mmm	18.6	74600		−11	454
1208	$Co_2La_4Ti_3Si_{(4-x)}O_{22-d}$ (x=0.5)	1250	Perrierite monoclinic $P2_1/a$	18.6	20700	4.6	−131	486
1209	$0.77(0.5ZnAl_2O_4$-$0.5TiO_2)$-$0.23MgTiO_3$	1390/4h	Composite	18.7	190000		−2	406
1210	$DyTiNb_xTa_{1-x}O_6$ (x=0.05)	1575	Orthorhombic Pbcn	18.7	31000	5.7	−28	555
1211	$0.96MgTiO_3$-$0.036SrTiO_3$+4.5 Wt% CuO	1070/2h	Ilmenite Trigonal R-3	18.7	19600	9		505
1212	(1-x)$(Mg_{0.95}Ni_{0.05})TiO_3$-x$SrTiO_3$ (x=0.01)	1300/4h	Composite	18.7	105000		−38	556
1213	$Nd_2BaZn_{045}Cu_{0.55}O_5$	1250/10h	Tetragonal+Orthrohombic	18.8	44100		−20	463
1214	$SmNbO_4$	1250	Orthorhombic Ima2	18.8	56300		−40	363
1215	$CaNb_2O_6$	1350	Orthorhombic Pbcn	18.8	49600		−53	557
1216	$[(Mg_{0.5}Zn_{0.5})_{0.95}Co_{0.05}]_2TiO_4$	1225	Cubic spinel Fd3m	18.8	206000		−21	558
1217	$0.9MgTiO_3$-$0.1CaTiO_3$+5 wt% Li_2O-B_2O_3-SiO_2	950	Composite	18.8	19000		10	559
1218	$Mg_{0.95}Ni_{0.05}Ti_2O_5$	1425/4h	Orthorhombic bbmn	18.8	50000		−48	552
1219	$(Li_{0.5}Y_{0.5})MoO_4$	780	Tetragonal Scheelite	18.8	10400		193	474

1220	(1-x)$Li_3Bi_2P_3O_{12}$-xTiO_2 (x=0.45)	750	Monoclinic $P2_1/m$	18.9	13700		−43	456
1221	$CaYAlO_4$	1450/3h	K_2NiF_4 type Tetragonal I4/mmm	18.9	39980		6	537
1222	$Sr_{1-x}Ca_xNdAlO_4$ (x=0.6)	1450/3h	K_2NiF_4 structure	18.9	91300		−13	560
1223	$Sr_{0.6}Ca_{0.4}LaAlO_4$+0.15 wt% B_2O_3	1300	K_2NiF_4 structure	18.9	63000		−25	561
1224	$(Ca_{1+x}Sm_{1-x})(Al_{1-x}Ti_x)O_4$ (x=0)	1400	K_2NiF_4 type Tetragonal I4/mmm	19.0	54600		−15	554
1225	Sr_2AlNbO_6 (oxygen atm)	1550	Perovskite	19.0	16000	8.3	−5	562
1226	$YTiNbO_6$	1400	Aschenite Orthorhombic Pbcn	19.0	8820	8.2	−45	563
1227	$Sm_{0.1}Y_{0.9}TiNbO_6$	1420	Aschenite Orthorhombic Pbcn	19.0	11700		−42	564
1228	$Zn_{0.6}Mg_{0.4}TiO_3$+5 wt% B-Si-Zn-K glass	950	Trigonal R-3	19.0	18950			565
1229	$ZnTiO_3$	1100	Trigonal R-3	19.0	30000	10	−55	566
1230	0.96$MgTiO_3$-0.036$SrTiO_3$+2 Wt% B_2O_3	1170/2h	Composite	19.0	75300	9	−9	505
1231	$Bi_2Mo_3O_{12}$	610	Monoclinic $P2_1/n$	19.0	21800	7.6	−215	494
1232	$(Zn_{0.95}Co_{0.05})_2TiO_4$	1180	Cubic spinel Fd3m	19.0	2100	7.3		517
1233	$Ba_{2-2x}Sr_{2x}SmSbO_6$ (x=0.4)	1500	Perovskite	19.0	30000		−40	467
1234	$Ba(Zn_{1/2}W_{1/2})O_3$	1250/4h	Cubic perovskite Fm3m	19.0	14000		−35	567
1235	$Ca_{1-3x/2}La_x(Mg_{1/2}W_{1/2})O_3$ (x=0.02)	1375/2h	Complex perovskite Monoclinic	19.0	55000	–	−75	568
1236	0.4$Li_2Zn_3Ti_4O_{12}$-0.6Li_2TiO_3+3 wt% 0.4B_2O_3-0.6CuO	900/5h	Composite	19.0	29000		−38	480
1237	$(Nd_{0.99}Co_{0.015})_{1.02}Nb_{0.988}O_4$	1250/4h	Monoclinic fergusonite I2/a	19.0	43300		−48	569
1238	$Ca_9Sm_2W_4O_{24}$	1450	Tetragonal scheelite 141/a	19.0	3100			526
1239	$(Ba_xMg_{1-x})(Sn_{0.0}5Ti_{0.95})O_3$ (x=0.01)	1210/4h	Ilmenite type Trigonal	19.0	120000		−42	570
1240	0.75$ZnWO_4$-0.25TiO_2+0.5 wt% Li_2CO_3-H_3BO_3	950/2h	Composite	19.0	13500		−11	571
1241	$(Nd_{0.99}Mn_{0.015})_{1.02}Nb_{0.988}O_4$	1250/4h	Monoclinic fergusonite I2/a	19.1	38600		−43	569
1242	$(Nd_{0.99}Ca_{0.015})_{1.02}Nb_{0.988}O_4$	1250/4h	Monoclinic fergusonite I2/a	19.1	35300		−38	569
1243	(1-x)$MgTiO_3$-x$Ca_{0.8}Sr_{0.2}TiO_3$ (x=0.02)		Composite	19.1	110600		−38	572
1244	$Tb(Ti_{1/2}W_{1/2})O_4$	1375	Tetragonal Scheelite	19.1	5900	6.6	−6	400
1245	0.99MgO-0.01BaO-TiO_2	1320	Composite	19.1	21500	9.53		541
1246	80 wt% $ZnNb_2O_{6-}TiO_2$+20 wt% (SiO_2- $B_2O_{3_}Al_2O_3$)	875	Composite	19.1	9600		9	27
1247	0.25Li_5FeO_8-0.75$Li_2ZnTi_3O_8$	1050	Composite	19.1	11770	6.84	−60	573

(*continued*)

No.	Material	ST (°C)	Crystal structure	ε_r	Qf (GHz)	f_0	τ_f	Reference
1248	$Nd(Mg_{0.47}Ba_{0.03}Sn_{0.5})O_3$	1600/4h	Cubic perovskite	19.1	97500		−64	574
1249	$Li_2Zn_3Ti_4O_{12}$+1.5 wt% Li_2O-ZnO-B_2O_3 glass	900/2h	Cubic $P4_232$	19.1	63800	9	−49	575
1250	Pb_2MoO_5	610/2h	Monoclinic	19.1	21960	7.46	−60	576
1251	$(Na_{0.5}Bi_{0.5})_{0.5}Ca_{0.5}MoO_4$	775	Tetragonal scheelite	19.1	22700		−10	343
1252	$(Ba_xMg_{1-x})(Zr_{0.05}Ti_{0.95})O_3$ (x=0.01)	1210/4h	Ilmenite type Trigonal	19.1	180000		−38	570
1253	$(Ba_xMg_{1-x})(Zr_{0.05}Ti_{0.95})O_3$ (x=0.03)	1210/4h	Ilmenite type Trigonal	19.2	156000		−35	570
1254	85 wt% $ZnNb_2O_6$-TiO_2+15 wt% (CaO- B_2O_3-SiO_2)	875	Composite	19.2	11000		17	27
1255	CaO-Sm_2O_3-Al_2O_3	1425	Composite	19.2	120000		−10	577
1256	$0.76Li_2TiO_3$-0.24MgO	1250	Rocksalt Monoclinic C2c	19.2	106220		4	578
1257	1-xCeO_2-xLa_2O_3 (x=0.25)	1650	Cubic flurite Fm3m	19.2	14700		−64	413
1258	$(Mg_{0.95}Co_{0.05})_2TiO_4-0.08(Ca_{0.8}Sr_{0.2})TiO_3$		Composite	19.2	123200	9.2	3	579
1259	$Nd(Mg_{0.45}Co_{0.05}Sn_{0.5})O_3$	1550	Perovskite	19.2	68900		−67	580
1260	$Bi(Sb_{1-x}Ta_x)O_4$ (x=0.05)	960	Monoclinic I2/c	19.2	60,000		−55	581
1261	$Li_{2.081}Ti_{0.676}Nb_{0.243}O_3$+5 wt% LBS glass	850	Composite	19.2	41400		−2	582
1262	$YbTiTaO_6$	1560	Euxenite Orthorhombic Pbcn	19.3	31800	6.2	−41	583
1263	$CaTe_2O_5$	780	Monoclinic	19.3	13400	10		223
1264	$BiSbO_4$	1080/2h	Monoclinic I2/c	19.3	70000		−62	584
1265	$Nd(Mg_{0.5}Sn_{0.5})O_3$	1550/4h	Perovskite	19.3	43300		−57	585
1266	$MgTi_2O_5$+10 wt% LBS glass	950/2h	Composite	19.3	6800	–	−16	167
1267	$Ba(Co_{1/2}W_{1/2})O_3$	1390	Perovskite Cubic Fm3m	19.3	21000	7.76	−55	528
1268	TeO_2	640/15h	Tetragonal $P4_12_12$	19.3	30000	4	−119	586
1269	$Zn_2Te_3O_8$+4 wt% TiO_2	650/2h	Monoclinic C2/c	19.3	27000	5.14	−9	471
1270	$LaNbO_4$	1250	Fergusonite Monoclinic I2/a	19.3	54400		9	363
1271	$Y(Ti_{1/2}W_{1/2})O_4$	1425	Tetragonal Scheelite	19.3	6200		−19	400
1272	$0.4Li_2Zn_3Ti_4O_{12}$-$0.6Li_2TiO_3$	1240	Composite	19.3	28000		−31	480
1273	$Nd_{2.9/3}Ca_{0.05}(Mg_{0.5}Sn_{0.5})O_3$	1550/4h	Cubic	19.3	99000		−65	587
1274	$(Ba_{0.05}Mg_{0.95})(Zr_{0.05}Ti_{0.95})O_3$	1210/4h	Ilmenite type	19.3	132000		−32	570
1275	$LiNi_{0.5}Ti_{0.5}O_2$	1275/6h	Fm-3m	19.3	51300		−20	588

1276	$La(Mg_{0.5}Sn_{0.5})O_3$+2 wt% ZBS glass	1400/4h	Cubic	19.4	35800		−86	589
1277	$(Ca_{1+x}Sm_{1-x})(Al_{1-x}Ti_x)O_4$ (x=0.06)	1500	K_2NiF_4 type Tetragonal I4/mmm	19.4	120700		−9	554
1278	$(Nd_{0.99}Sr_{0.015})_{1.02}Nb_{0.988}O_4$	1250/4h	Monoclinic fergusonite I2/a	19.4	33100		−30	569
1279	$Li_2Zn_3Ti_4O_{12}$+1.5 wt% BCB	900	Cubic Fd-3m	19.4	57600		−40	553
1280	$0.94CaNb_2O_6$-$0.06CaTiO_3$	1300	Composite	19.5	69500		−65	545
1281	$Ca(La_{1/2}Ta_{1/2})O_3$	1500	Perovskite Monoclinic $P2_1/n$	19.5	30000	9.8	−41	590
1282	$CoTiO_3$	1375/5h	Trigonal R-3 Ilmenite	19.5	62500		−49	516
1283	Sm_2BaZnO_5	1320/2h	Orthorhombic Pmna	19.5	35500	−6.4		405
1284	$ZnTiO_3$+0.25 wt% V_2O_5	900	Trigonal R-3	19.5	2700	7.4		591
1285	90 wt% $ZnNb_2O_6$-TiO_2+10 wt% (SiO_2- B_2O_3-Al_2O_3)	900	Composite	19.5	9200		18	27
1286	90 wt% (Mg,Ca)TiO_3+10 wt% Li_2O-B_2O_3-SiO_2	950	Composite	19.5	26700		−12	592
1287	$Ca_{1+x}Nd_{1-x}Al_{1-x}O_4$ (x=0.15)		Tetragonal I4/mmm	19.5	93400		−2	593
1288	$Nd(Mg_{0.4}Zn_{0.1}Sn_{0.5})O_3$	1500/4h	Perovskite	19.5	129200		−66	594
1289	$(Zn_{0.95}Ni_{0.05})_2TiO_4$	1180	Cubic Fd3m	19.5	2200	7.3		517
1290	$LaNbO_4$+3 wt% CuO	950/2h	Monoclinic fergusonite I2/a	19.5	49000		1	595
1291	$Li_{2+x}Ti_{1-4x}Nb_{3x}O_3$ (x=0.07)	1300	Monoclinic rock salt	19.5	84800		−1	596
1292	$SrLaAlO_4$ (co-precipitation PH=8)	1425	Tetragonal I4/mmm	19.5	56500		−33	597
1293	$Nd(Mg_{0.43}Ca_{0.07}Sn_{0.5})O_3$	1550/4h	Perovskite	19.5	100400			598
1294	$(Li_{0.5}Gd_{0.5})MoO_4$	750	Tetragonal Scheelite	19.5	3900		209	474
1295	PbO:B_2O_3:SiO_2 (70:20:10) glass		Glass	19.6	500	10.3	−155	92
1296	$NdNbO_4$	1250	Monoclinic fergusonite I2/a	19.6	33000		−24	363
1297	Sm_2BaCuO_5		Orthorhombic Pnma	19.6	3400	11.36	−9	384
1298	$(Ca_{1+x}Sm_{1-x})(Al_{1-x}Ti_x)O_4$ (x=0.1)	1500	K_2NiF_4 type Tetragonal I4/mmm	19.6	113700		−6	554
1299	$(Mg_{0.95}Ca_{.05})TiO_3$+5 mol% B_2O_3	1200	IlmeniteTrigonal R-3	19.6	86000	10	−3	472
1300	$0.92Ba(Mg_{1/2}W_{1/2})O_3$-$0.08BaTiO_3$	1500/6h	Perovskite Cubic Fm3m	19.6	37000		−19	373
1301	$Nd_{0.5}La_{1.5}BaZnO_5$			19.6	16320		−1	599
1302	$CaNb_2O_6$	1400	Columbite Pbcn	19.6	21500		13	600
1303	$Ca(Sm_{1/2}Ta_{1/2})O_3$	1500	Perovskite	19.6	26500	9.8	−24	590
1304	$CaTe_2O_5$			19.6	12600		−89	444

(*continued*)

No.	Material	ST (°C)	Crystal structure	ε_r	Qf (GHz)	f_0	τ_f	Reference
1305	$LiYbW_2O_8$	900	Monoclinic P2/n	19.7	8720		45	48
1306	$Ba(Mg_{0.33}Ta_{0.33}Ti_{0.167}W_{0.167})O_3$	1580	Perovskite Trigonal R-3	19.7	58200	6.5	−11	438
1307	$(1\text{-}y)Li_3NbO_{4\text{-}y}Li_2TiO_3$ (y=0.6)		Composite	19.7	91200		24	409
1308	$La(Mg_{0.5}Sn_{0.5})O_3$+0.5 wt% B_2O_3	1500/4h	Perovskite	19.7	45000		−85	601
1309	Li_2TiO_3+1 wt% BaO-CuO	900	Monoclinic C2/c	19.7	46300		31	390
1310	$La_4Ti_3O_{12}$		Hexagonal	19.7	9950		−10	602
1311	$(Ba_xMg_{1\text{-}x})(Zr_{0.05}Ti_{0.95})O_3$ (x=0.07)	1210/4h	Ilmennite type Trigonal	19.7	100000		−31	570
1312	Li_2TiO_3	1230	Monoclinic C2/c	19.8	23600		39	390
1313	$Zn_2Te_3O_8$+30 wt% $TiTe_3O_8$	600	Composite	19.8	50000		3	603
1314	$(1\text{-}y)Li_3NbO_4$-+yLi_2TiO_3 (y=0.6)		Composite	19.8	91200		−24	409
1315	$Ca_{1.15}Sm_{0.85}Al_{0.85}Ti_{0.15}O_4$+0.15 wt% B_2O_3	1325	Tetragonal I4/mmm	19.8	89400		−1	604
1316	$Dy(Ti_{1/2}W_{1/2})O_4$	1425	Tetragonal Scheelite	19.9	6000	6.6	−5	400
1317	$MgNb_2O_6$+2 wt% CuO	1170	Columbite Orthorhombic Pbcn	19.9	110000	10	−44	605
1318	$BaNd_2Ti_5O_{14}$: $(20La_2O_3\text{-}60B_2O_3\text{-}20TiO_2)$ (60:40 wt%)	850	Tungsten bronze	19.9	8200			606
1319	$1\text{-}xCeO_2\text{-}xNd_2O_3$ (x=0.4)	1650	Cubic flurite Fm3m	19.9	34100		−55	413
1320	$Ba_8Zn(Nb_{6\text{-}x}Sb_x)O_{24}$ (x=1.8)	1425		19.9	18600		6	503
1321	$La_{0.97}Sm_{0.03}(Mg_{0.5}Sn_{0.5})O_3$	1500/4h		19.9	70200		−77	607
1322	$(Li_{0.5}Sm_{0.5})MoO_4$	640	Tetragonal Scheelite	19.9	4600		231	474
1323	$(Sr_{1\text{-}x}Ca_x)La_2Al_2O_7$ (x=0.1)	1600/3h	R-P I4/mmm	19.9	135400		−19	608
1324	$Ca(Al_{1/2}Ta_{1/2})O_3$		Complex perovskite	20.0	8500	–	−90	609
1325	$Ca[(Li_{1/3}Nb_{2/3})_{0.95}Ti_{0.05}]O_{3\text{-}d}$+5 wt% Bi_2O_3	900/3h	Perovskite	20.0	6500		−4	610
1326	$La_{0.9}Nd_{0.1}NbO_4$	1250	Monoclinic fergusonite I2/a	20.0	45000		−1	363
1327	$Ca(Nd_{1/2}Ta_{1/2})O_3$	1500	Perovskite Monoclinic $P2_1/n$	20.0	2400	9.7	−16	590
1328	$0.95MgTiO_3\text{-}0.05CaTiO_3$+0.25 wt% CuO	1275/4h	Composite	20.0	51000	7	−8	611
1329	$Ca(Nd_{1/2}Nb_{1/2})O_3$	1500	Complex perovskite	20.0	17500	9.6	−33	590

1330	$GdTiNbO_6$	1385	Aschenite Orthorhombic Pbcn	20.0	9050	7.27	−52	563
1331	$MgO\text{-}SiO_2\text{-}TiO_2$+15 wt% $ZnO\text{-}B_2O_3$+2.4 wt% Co_2O_3	1160	Composite	20.0	100000	10		612
1332	$Sm_{0.3}Y_{0.7}TiNbO_6$	1420	Orthorhombic Pbnm	20.0	19200		−33	564
1333	$LaNbO_4$		Monoclinic I2/a	20.0	15000		50	279
1334	$Li_{2.081}Ti_{0.676}Nb_{0.243}O_3$	1100	Monoclinic	20.0	50000		13	613
1335	$CaO\text{-}4ZnO\text{-}Nb_2O_5\text{-}TiO_2$	1125	Composite	20.0	9000	5.9	−47	230
1336	$5NiO\text{-}Nb_2O_5\text{-}TiO_2$	1125	Composite	20.0	8200	5.9	−64	230
1337	$CaO\text{-}4MgO\text{-}Ta_2O_5\text{-}TiO_2$	1360	Composite	20.0	50000	5.6	−33	230
1338	$5NiO\text{-}Ta_2O_5\text{-}TiO_2$	1300	Composite	20.0	14000	5.9	−53	230
1339	$Sr_3Zn_{0.75}Mg_{0.25}Nb_2O_9$	1300	Hexagonal, perovskite	20.0	8500		−16	614
1340	$CaO\text{-}4Co_3O_4\text{-}Ta_2O_5\text{-}TiO_2$	1210	Composite	20.0	26000	5.8	−30	230
1341	$Ba_{1-3x/2}La_x(Mg_{1/2}W_{1/2})O_3$ (x=0.02)	1450/2h	Complex perovskite cubic Fm3m	20.0	87680	–	−1	568
1342	$xBa(Mg_{1/2}W_{1/2})O_3\text{-}(1\text{-}x)BaTiO_3$ (x=0.92)	1500/6h	Perovskite Fm3m	20.0	37000		−19	373
1343	$0.95MgTiO_3\text{-}0.05CaTiO_3$	1400	Ilmenite Trigonal R-3	20.0	56000		0	615
1344	$0.94MgTiO_3\text{-}0.06CaTiO_3$+0.25 wt% CuO	1275	Ilmenite Trigonal R-3	20.0	48000		−3	611
1345	$0.75MgAl_2O_4\text{-}0.25TiO_2$		Composite	20.0	10500		0	195
1346	$Ba(Mg_{1/3}Ta_{(2\text{-}2x)/3}W_{x/3}Ti_{x/3})O_3$ (x=0.15)	1550/4h	Perovskite Trigonal R-3	20.0	90000		0	438
1347	$Ba[Ti_{1-x}(Ni_{1/2}W_{1/2})_x]O_3$ (x=0.6)	1425	Perovskite Hexagonal $P6_3/mmc$	20.0	42000		−10	616
1348	$Zn_3Nb_2O_8$+2 wt% V_2O_5+0.5 wt% CuO	800	Monoclinic C2/c	20.0	36000	11.8	–	617
1349	$BiSbO_4+V_2O_5\text{-}CuO$	930	Monoclinic I2/c	20.0	40000		−75	618
1350	$La_{2.98/3}Sr_{0.01}(Mg_{0.5}Sn_{0.5})O_3$	1550/4h		20.0	57100		−77	619
1351	$Ba(Mg_{1/2}W_{1/2})O_3$	1550/2h	Perovskite Cubic Fm3m	20.0	120000		−28	620
1352	$Ba(Zn_{0.49}W_{0.5})O_{2.995}$	1360/4h	Perovskite Cubic Fm3m	20.0	40000		−35	567
1353	$Zn_{1.8}Ti_{1.1}O_4$	1090	Cubic Fd3m	20.0	20200		−58	451
1354	$La_{2.98/3}Ba_{0.01}(Mg_{0.5}Sn_{0.5})O_3$+0.25 wt% CuO	1500/4h		20.0	50000		−78	621
1355	$0.5Mg_4Nb_2O_9\text{-}0.5CaTiO_3$+1.7 wt% V_2O_5	1150/5h	Composite	20.0	48000		−12	622
1356	$(Co_{0.95}Zn_{0.05})TiO_3$	1350/3h	Trigonal R-3	20.0	107000	9.27	60	623

(*continued*)

No.	Material	ST (°C)	Crystal structure	ε_r	Qf (GHz)	f_0	τ_f	Reference
1357	$La_{2.98/3}Ba_{0.01}(Mg_{0.5}Sn_{0.5})O_3$+0.25 wt% CuO	1500/4h	Not available	20.0	50100		−78	621
1358	$0.95MgTiO_3$-$0.05CaTiO_3$+1 wt% ZnO	1300	Composite composite	20.0	65000	7	−6	624
1359	$Ba(Mg_{1/2}W_{1/2})O_3$+x$Ba(Y_{1/3}W_{1/3})O_3$+ (x=0.02)	1575	Cubic Fm-3m Perovskite	20.0	160000		−21	625
1360	$ZnNb_2O_6$-$0.2CaTiO_3$+4 wt% $BaCu(B_2O_5)$	950/4h	Composite	20.0	12500		3	626
1361	$0.95MgTiO_3$-$0.05CaTiO_3$+1 wt% ZnO+0.5 wt% WO_3	1310		20.0	62000	7	−5	627
1362	$La(MgSn)_{0.5}O_3$	1600/4h	Perovskite Monoclinic $P2_1/n$	20.1	63000		−78	628
1363	$La(Mg_{0.43}Ba_{0.07}Sn_{0.5})O_3$	1550/2h	Cubic perovskite	20.1	51600	−82	−8	629
1364	$(Ba_xMg_{1-x})(Sn_{0.05}Ti_{0.95})O_3$ (x=0.03)	1210/4h	Ilmenite type Trigonal	20.1	100000		−26	570
1365	$0.96Mg_{0.95}Co_{0.05}TiO_3$-$0.04SrTiO_3$+1 wt% ZnO	1250	Composite	20.1	74000		−8	630
1366	$NdNbO_4$+2 wt% CaF_2	1225	Monoclinic fergusonite I2/a	20.1	75000		−19	631
1367	(1-x)$(Mg_{0.95}Ni_{0.05})TiO_3$-x$SrTiO_3$ (x=0.03)	1300/4h	Composite	20.1	85000		−11	556
1368	$SrNb_2O_6$	1300	Columbite Monoclinic $P2_1/c$	20.1	16900	6.5	–	489
1369	$0.55LiMgVO_4$-$0.45TiO_2$	760	Composite	20.1	20100		16	140
1370	Zn_2TiO_4	1300/2h	Cubic Fd3m	20.2	19000		−55	632
1371	$(Ca_{1+x}Sm_{1-x})(Al_{1-x}Ti_x)O_4$ (x=0.15)	1400	K_2NiF_4 type Tetragonal I4/mmm	20.2	97800		−0.5	554
1372	$Ba_3NiNb_{2-x}Sb_xO_9$ (x=0.5)		Cubic Pm3m	20.2	16780	6	−29	381
1373	$La_{1-x}Bi_x(Mg_{0.5}Sn_{0.5})O_3$ (x=0.1)			20.2	58100		−84	633
1374	$La(Mg_{0.4}Ca_{0.1}Sn_{0.5})O_3$	1500	Perovskite	20.2	80500		−79	634
1375	$La(Mg_{0.4}Ni_{0.1}Sn_{0.5})O_3$	1550/4h		20.2	74600		−85	635
1376	$La_{0.97}Yb_{0.03}(Mg_{0.5}Sn_{0.5})O_3$			20.2	56800		−79	636
1377	$MgLi_{2/3}Ti_{4/3}O_4$	1125/2h	Cubic Fd-3m	20.2	62300		−27	637
1378	(1-x)$MgTiO_3$-x$Ca_{0.8}Sr_{0.2}TiO_3$ (x=0.04)		Ilmenite Hexagonal R-3	20.2	97200		−21	572
1379	$0.2Li_2Zn_3Ti_4O_{12}$-$0.8Li_2TiO_3$	1240	Composite	20.2	24000		−11	480
1380	$(Ba_xMg_{1-x})(Sn_{0.05}Ti_{0.95})O_3$ (x=0.05)	1210/4h	Ilmenite type Trigonal	20.2	84000		−17	570
1381	$(Ba_xMg_{1-x})(Sn_{0.05}Ti_{0.95})O_3$ (x=0.07)	1210/4h	Ilmenite type Trigonal	20.3	75000		−14	570

1382	$SrLaGaO_4$	1275/3h	Tetragonal I4/mmm	20.3	16200		−34	638
1383	La_2BaZnO_5		Tetragonal I4/mcm	20.3	17800		−0.9	599,639
1384	$NdLaBaZnO_5$		Orthorhombic	20.3	7900		−5	599
1385	$ZnTiO_3$+0.5 wt% V_2O_5	900	Hexagonal R-3	20.3	5200	7.8		591
1386	90 wt% $ZnNb_2O_6$-TiO_2+10 wt% (Li_2O- B_2O_3-SiO_2)	875	Composite	20.3	8200		5	27
1387	$0.95(Mg_{.95}Co_{.05})TiO_3-0.05CaTiO_3$	1275/4h	Ilmenite Hexagonal R-3	20.3	107000	7	−23	422
1388	CeO_2.(at 30K)	1675	Cubic flurite Fm3m	20.3	600000	5.5		640
1389	$Pr(Ti_{1/2}W_{1/2})O_4$	1300	Tetragonal Scheelite	20.3	6900	6.53	−20	400
1390	$MnTa_2O_6$	1350	Columbite Orthorhombic Pbcn	20.3	16500		−44	600
1391	$(Li_{0.5}Nd_{0.5})MoO_4$	660	Tetragonal Scheelite	20.3	3000		235	474
1392	(1-x)$Mg_{0.95}Ni_{0.05}Ti_{0.98}Zr_{0.02}O_3$-x$SrTiO_3$ (x=0.04)		Composite	20.3	85400		3	641
1393	$SmAlO_3$	1650/2h	Orthorhombic Pbnm	20.4	65000	10	−74	452
1394	$MnTiO_3$	1350/2h	Hexagonal R-3(148) Ilmenite	20.4	15200		−56	516
1395	$Ba_3NiNb_{2-x}Sb_xO_9$ (x=1)		Hxagonal $P6_3mc$	20.4	43880	6.3	−18	381
1396	$CoNb_2O_6$	1300/4h	Columbite Pbcn	20.5	81000		−70	489,642
1397	$(Ba_xMg_{1-x})(Sn_{0.05}Ti_{0.95})O_3$ (x=0.1)	1210/4h	Ilmenite type Trigonal	20.5	37000		−3	570
1398	$Li_2Ti_{1-x}(Zn_{1/3}Nb_{2/3})_xO_3$ (x=0.2)		Monoclinic C2/c	20.5	75300		15	643
1399	$Sm_{0.4}Y_{0.6}TiNbO_6$	1400		20.5	15000		−30	564
1400	$Co_{1+0.01}Nb_2O_6$ (sintered in O_2)	1400	Columbite Pbcn	20.5	114000		−60	644
1401	$Sr_2La_2MgW_2O_{12}$	1525	Trigonal R-3m	20.5	35000		−83	645
1402	$SrNd_2Al_2O_7$		Tetragonal R-P phase	20.5	65500		−4	538
1403	$(Ba_{0.1}Mg_{0.9})(Zr_{0.05}Ti_{0.95})O_3$	1210/4h	Ilmenite type	20.6	25000		−28	570
1404	$ZnLi_{2/3}Ti_{4/3}O_4$	1075	Cubic Fd-3m	20.6	106700		−48	553
1405	0.5CeO_2-0.5$BaTi_4O_9$+12 wt% B_2O_3+1 wt% CuO	950/4h	Cubic flurite Fm3m+Orthorhombic Pnmm	20.6	17000	5.7	48	646
1406	$ErTiTaO_6$	1560	Euxenite orthorhombic	20.6	85500		−29	583
1407	$(Li_{0.5}Ce_{0.5})MoO_4$	580	Tetragonal Scheelite	20.6	2000		228	474
1408	$Ca(La_{1/2}Nb_{1/2})O_3$	1500	Perovskite	20.6	38000	9.4	−51	590

(*continued*)

No.	Material	ST (°C)	Crystal structure	ε_r	Qf (GHz)	f_0	τ_f	Reference
1409	$MgTiO_3$+5 mol% Bi_2O_3-7 mol% V_2O_5	875	Ilmnite Trigonal R-3+second phase	20.6	10420	6.3		647
1410	0.97MgO-0.03BaO-TiO_2	1320	Mixture phases	20.6	32600	9.35		541
1411	$(Ba_xMg_{1-x})(Zr_{0.05}Ti_{0.95})O_3$ (x=0.1)	1210/4h	Ilmneite type Trigonal	20.6	25000		−28	570
1412	$ZnTiO_3$+0.75 wt% V_2O_5	900	Trigonal R-3	20.6	8800	8.2		591
1413	$(Ba_{0.75}Sr_{0.25})(Mg_{0.5}W_{0.5})O_3$	1400	multiphase	20.6	152600		24	648
1414	$Nd_2BaZn_{0.8}Cu_{0.2}O_5$		Tetragonal I4/mcm	20.7	11680		−2	463
1415	$Sr_3ZnNb_2O_9$	1300	Complex perovskite Cubic Pm3m	20.7	7500		−27	614
1416	$LaAlO_3$+0.25 wt% CuO	1460	Perovskite Trigonal R-3m	20.7	48000		−80	649
1417	$(Ca_{1+x}Sm_{1-x})(Al_{1-x}Ti_x)O_4$ (x=0.2)	1500	K_2NiF_4 type Tetragonal I4/mmm	20.7	99400		1	554
1418	$CeAlO_3$	1500	Tetragonal P4/mmm	20.7	40110	9.5	−57	650
1419	$Ba_4Ti_3P_2O_{15}$	1200/4h	Monoclinic	20.7	42200		37	651
1420	Ba_2SmSbO_6	1500	Perovskite Cubic Fm3m	20.7	86500		25	467
1421	$Sr_{1-3x/2}La_x(Mg_{1/2}W_{1/2})O_3$ (x=0.01)	1550/2h	Complex perovskite Tetragonal	20.7	60000	–	−40	568
1422	Li_2TiO_3+2 wt% Li_2O-ZnO-B_2O_3+35 wt% $LiZnNbO_4$	900	Composite	20.7	19300		0	652
1423	$(Zn_{0.95}Ni_{0.05})_3Nb_2O_8$+4 wt% B_2O_3-CuO	930/2h	Monoclinic	20.7	98000		−85	653
1424	$Ba_2Mg_{0.9}Ca_{0.1}WO_6$	1500	Perovskite Cubic Fm3m	20.8	120700		0	441
1425	TeO_2		Tetragonal $P4_12_12$	20.8	34700		−101	444
1426	0.964$MgTiO_3$-0.036$SrTiO_3$	1270	Ilmenite Trigonal R-3+Perovskite	20.8	71000		−1	654
1427	$La_{2-x/3}Na_x(Mg_{1/2}W_{1/2})O_3$ (x=0.5)	1450	Perovskite Orthorhombic I222	20.8	5700		−47	655
1428	$Nd_2BaZn_{0.7}Cu_{0.3}O_5$		Tetragonal I4/mcm	20.8	19793		−3	463
1429	0.96$Mg(Zr_{0.05}Ti_{0.95})O_3-0.04SrTiO_3$		Composite	20.8	257000		0	656
1430	$(Zn_{0.95}Co_{0.05})Nb_2O_8$+4 wt% B_2O_3-CuO	930	Composite	20.8	105000		−84	657
1431	0.94$(Mg_{0.95}Co_{0.05})TiO_3-0.06CaTiO_3$	1275/4h	Composite	20.9	102000	7	−10	422
1432	$Ca(Sm_{1/2}Nb_{1/2})O_3$	1500	Perovskite	20.9	24500	9.4	−28	590
1433	0.95MgO-0.05BaO-TiO_2	1320	Composite	20.9	32500	9.06		541
1434	0.96$MgTiO_3$-0.04$SrTiO_3$	1300/4h	Composite	20.9	135000	9	0	658
1435	$Zn_{1.01}Nb_2O_6$	1300/4h	Columbite Pbcn	20.9	120000		−74	642

1436	$MnNb_2O_6$	1150	Columbite Pbcn	20.9	12900	6.8	−74	557
1437	$Li_{2.081}Ti_{0.676}Nb_{0.243}O_3$+1.5 wt% B_2O_3	880	Monoclinic	20.9	34100		8	613
1438	$0.95Mg(Zr_{0.05}Ti_{0.95})O_3$-$0.05SrTiO_3$	1390	Composite	20.9	203000	6.8	2	659
1439	$CoLi_{2/3}Ti_{4/3}O_4$+1.5 wt% $BaCu(B_2O_5)$	900	Cubic spinel Fd-3m	20.9	27800		−24	660
1440	$(1-x)Li_3Bi_2P_3O_{12}$-$xTiO_2$ (x=0.50)	750	Monoclinic $P2_1/m$	20.9	14000		−25	456
1441	$Li_2ZnTi_3O_8$-0.2 SnO_2	1080/4h	Cubic spinel	10.9	89500		−24	661
1442	$(1-x)(Mg_{0.95}Ni_{0.05})TiO_3$-$xSrTiO_3$ (x=0.04)	1300/4h	Composite	20.1	73000		1	556
1443	$Mg_{1.03}Nb_2O_6$	1400/4h	Columbite Pcan	21.0	121000		−60	642
1444	$0.964MgTiO_3$-$0.036SrTiO_3$	1270	Composite	21.0	71000		−1	654
1445	$BaTe_2O_6$	650	Orthorhombic Cmcm	21.0	50300		−51	277
1446	$Ca(Mg_{1/3}Ta_{2/3})O_3$		Complex perovskite	21.0	78000	–	−61	609
1447	$Zn_3Nb_2O_8$	1150/2h	Monoclinic C2/c	21.0	83300		−71	445,632
1448	$0.95MgTiO_3$-$0.05CaTiO_3$	1450	Composite	21.0	56000	7	0	611
1449	$5NiO$-Nb_2O_5-TiO_2	1125	Mixture	21.0	8200	5.08	−64	230
1450	$TbTiNbO_6$	1385	Aschenite Orthorhombic Pbcn	21.0	15700	7.58	−45	563
1451	$5ZnO$-$2Nb_2O_5$	1220	Mixed phases	21.0	88000	6.98	−73	325
1452	$Sm_{0.6}Y_{0.4}TiNbO_6$	1400	Euxenite Orthorhombic Pbnm	21.0	11500		−4	564
1453	$Ca_5Ta_2ZrO_{12}$	1700	Perovskite	21.0	23800	5.38	−27	662
1454	$ZnTiO_3$	925	Trigonal R-3	21.0	30000		−90	663
1455	$Ca[(Li_{0.33}Nb_{0.67})_{0.9}Ti_{0.1}]\ O_{3-\delta}$+20 wt% LiF	840	Composite	21.0	20400		−18	664
1456	$Ba_{0.95}(Zn_{1/2}W_{1/2})O_{2.95}$	1250/4h	Cubic perovskite Fm3m	21.0	25000		−40	567
1457	$NiNb_2O_6$	1200	Columbite Pbcn	21.0	19300	6.5	−71	557
1458	$Mg_{0.95}Ca_{0.05}TiO_3$+0.2 mol% Bi_2O_3	1250	Ilmenite Trigonal R-3	21.0	55600	7	−12	665
1459	$0.96(Mg_{0.95}Ni_{0.05})TiO_3$-$0.04SrTiO_3$	1300/4h	Ilmenite Trigonal R-3	21.0	73000		1	666
1460	$SrLa_4Si_3O_{13}$+8 wt% TiO_2	1225/4h	Composite	21.0	13000		−10	253
1461	$0.54BaWO_4$-$0.46Ba_5Nb_4O_{15}$	1100	Composite	21.0	49500		9	485
1462	$Mg_{1+0.01}Nb_2O_6$	1400	Columbite Pcan	21.0	121000	10	−60	644
1463	$0.6Mg_4Nb_2O_9$-$0.4SrTiO_3$	1300/4h	Composite	21.0	112000	9.7	2	667
1464	$x(Mg_{0.96}Co_{0.04})TiO_3$-$(1-x)SrTiO_3$ (x=0.94)	1360/6h	Composite	21.0	97000		2	668

(*continued*)

No.	Material	ST (°C)	Crystal structure	ε_r	Qf (GHz)	f_0	τ_f	Reference
1465	$Nd(Mg_{0.5}Sn_{0.4}Ti_{0.1})O_3$	1550/4h	Perovskite	21.1	50000		−60	669
1466	$(Sr_{1-x}Ca_x)Nd_2Al_2O_7$ (x=0.5)		Ruddlesden-Popper solid solution	21.1	68200		0	670
1467	$0.4BaTa_2V_2O_{11}$-$0.6Ba_2BiV_3O_{11}$	885	Composite	21.1	44750		2	670b
1468	$Ba[Ti_{1-x}(Zn_{1/2}W_{1/2})_x]O_3$ (x=0.6)	1420	Hexagonal $P6_3/mmc$ perovskite	21.2	26800		−3	695
1469	$Mg_{0.95}Ca_{0.05}TiO_3$+2 wt% B_2O_3	1200	Ilmenite Trigonal R-3	21.2	62000	8	4	615
1470	(1-x)$MgTiO_3$-x$Ca_{0.8}Sr_{0.2}TiO_3$ (x=0.06)	1300/4h	Composite	21.2	110900	9.3	−1	696
1471	$Ca(Yb_{1/2}Ta_{1/2})O_3$	1500	Perovskite	21.2	24000	9.6	−38	590
1472	$SmZrTaO_6$	1650		21.2	24190		−58	671
1473	$CaTa_2O_6$	1600	Cubic Pm3m	21.2	11600		1	600
1474	$Sr(Co_{1/2}W_{1/2})O_3$	1450	Perovskite Cubic Fm3m	21.2	14000	7.72	−73	528
1475	$Li_2Zn(Ti_{0.9}Sn_{0.1})_3O_8$+1.5 wt% $0.4B_2O_3$-0.6CuO	875	Cubic spinel	21.2	12000		−20	672
1476	$Ca_{1-3x}Bi_{2x}A_x)MoO_4$ (x=0.15, A=A site vacancy)	700	Tetragonal Scheelite	21.2	29300		−1	673
1477	$Ca[Li_{0.33}Nb_{0.67}]_{0.9}Ti_{0.1}]O_{3-\delta}$+20 wt% LiF	840	Perovskite	21.3	20450	4.59	−18	664
1478	$ZnTiO_3$+1 wt% V_2O_5	900	Trigonal R-3	21.3	8000	8.8		591
1479	$Nd(Ti_{1/2}W_{1/2})O_4$	1285	Tetragonal Scheelite $I4_1/a$	21.3	10600	5.5	−22	400
1480	$0.98CeO_2$-$0.02CaTiO_3$+0.25 wt% B_2O_3	1380/4h	Fluorite Cubic Fm3m	21.3	60000	8	−41	674
1481	$0.34BaMoO_4$-$0.66TiO_2$	1300	Composite	21.3	20700		119	229
1482	(1-x)$MgTiO_3$-x$Ca_{0.8}Sr_{0.2}TiO_3$ (x=0.06)		Ilmenite Trigonal R-3	21.4	83700		−2	572
1483	$PbWO_4$	620	Tetragonal	21.4	43000	7	−7	476
1484	$CaHfO_3$	1750/6h	Orthorhombic perovskite Pnma	21.4	15950	8.9	−33	675
1485	Li_2TiO_3+5 wt% Li_2O-MgO-B_2O_3	850	Monoclinic C2/c	21.4	64100		27	676
1486	$(Rb,Bi)_{1/2}MoO_4$	550	Scheelite Monoclinic $P2_1/c$	21.4	6200	7.5	−30	677
1487	$CoLi_{2/3}Ti_{4/3}O_4$	1050	Cubic spinel Fd-3m	21.4	35000		−22	660
1488	$0.5CeO_2$-$0.25MgO$-$0.25TiO_2$: 1 WO_3	1400	Mixture phases	21.4	90000	5.57	−50	488
1489	$SrNdGaO_4$	1300/3h	Tetragonal I4/mmm	21.4	16600		7.1	638
1490	$0.9ZnNb_2O_6$-$0.1(ZnO$-$V_2O_5)$	950	Columbite Pbcn	21.4	29500			678
1491	$MgNb_2O_6$	1300	Columbite Orthorhombic Pcan	21.4	93800		−70	600

1492	$MgTiO_3$-$CaTiO_3$ (MMT-20)	1360	Composite	21.4	26000	7		177
1493	$0.5BaCaV_2O_7$-$0.5TiO_2$	950	Composite	21.4	14600		4	679
1494	$0.95(Mg_{0.98}Zn_{0.02})TiO_3$-$0.05CaTiO_3$+4 wt% CBS glass	1240/2h	Composite	21.4	59200		−2	680
1495	$Sm(Ti_{1/2}W_{1/2})O_4$	1300	Tetragonal Scheelite	21.5	7100	5.5	−14	400
1496	BaO-0.32MgO-0.26WO_3-0.42TiO_2	1500/6h	Composite	21.5	49000		1	407
1497	$MgNb_2O_6$+0.25 wt% B_2O_3	1260/3h	Columbite Orthorhombic Pcan	21.5	115800		−48	681
1498	$5Li_2O$-$0.583Nb_2O_5$-$3.248TiO_2$+1 wt% V_2O_5	920	M phase	21.5	32950		6.1	682
1499	85 wt% $Ba_5Nb_4O_{15}$+15 wt% Li_2O-B_2O_3-SiO_2-CaO-Al_2O_3	875	Composite	21.5	3400		−15	592
1500	$NdAlO_3$+0.25 wt% V_2O_5	1410	Perovskite Trigonal R-3m	21.5	64000	9	−30	683
1501	$ZnNb_2O_6$	1200	Columbite Orthorhombic Pbcn	21.5	84500	6.3	−75	557
1502	$Ba_3MgSb_2O_9$		Perovskite Hexagonal $P6_3/mmc$	21.5	23020	5.1	−6	381
1503	$MgNb_2O_6$+2 wt% CuO-B_2O_3	1050	Columbite Orthorhombic Pcan	21.5	108000		−44	684
1504	$Zn_3Nb_2O_8$	1150/2h	Monoclinic C2/c	21.6	83300		−71	632
1505	$PbWO_4$	850	Scheelite Tetragonal $I4_1/a$	21.6	34500		−22	49
1506	$0.93(Mg_{0.95}Co_{0.05})TiO_3$-$0.07CaTiO_3$	1275/4h	Ilmnite Trigonal R-3	21.6	92000	7	−2	685
1507	$Ba[Ti_{1-x}(Ni_{1/2}W_{1/2})_x]O_3$ (x=0.55)	1425	Perovskite	21.6	38400		−8	616
1508	$0.93(Mg_{0.95}Co_{0.05})TiO_3$-$0.07Ca_{0.8}Sr_{0.2}TiO_3$	1275	Composite	21.6	98900		1	686
1509	$SrSm_2Al_2O_7$		Tetragonal R-P phase	21.6	64700		4	538
1510	$(Zn_{0.7}Mg_{0.3})TiO_3$+1 wt% Li_2O-B_2O_3-SiO_2-CaO-Al_2O_3- glass	900	Mixture	21.6	62000		−60	687
1511	$0.93Li_2Mg_2W_2O_9$-$0.07CaTiO_3$	920	Trigonal P-3c1 Corundum	21.6	20700		−1	688
1512	$Mg_{0.95}Ca_{0.05}TiO_3$+0.5 mol%Bi_2O_3	1250	Ilmenite Trigonal R-3	21.7	52400	7	−29	665
1513	$1\text{-}x(Mg_{0.95}Ni_{0.05})TiO_3$-$x(Ca_{0.8}Sr_{0.2})TiO_3$	1275/4h	Composite	21.7	94000		5	689
1514	$1\text{-}xCeO_2$-xEr_2O_3 (x=0.15)	1650	Cubic Flurite Fm3m	21.7	23000		−40	413
1515	$SrNb_2O_6$	1300	Columbite Monoclinic $P2_1/c$	21.7	16900	6.51	–	557
1516	$(1\text{-}x)CeO_2$-xEr_2O_3 (x=0.7)	1650	Cubic flurite Fm3m	21.7	23000		−40	413

(*continued*)

No.	Material	ST (°C)	Crystal structure	ε_r	Qf (GHz)	f_0	τ_f	Reference
1517	CeO_2+1 wt% CuO	1580	Cubic flurite Fm3m	21.7	50000	9	−59	690
1518	$0.9Mg_{0.95}Co_{0.05}TiO_3$-$0.1Ca_{0.6}La_{0.8/3}TiO_3$+ 0.25 wt% V_2O_5	1250	Composite	21.7	58000	2.0	−10	691
1519	MgO-TiO_2-ZnO-CaO+10 wt% Li_2O-B_2O_3-SiO_2	900	Composite	21.7	50000		−22	692
1520	$MgTiO_3$–$(K_{0.5}La_{0.5})TiO_3$+0.5 wt% ZnO	1300/4h	Multiphase	21.7	68000	8	1	693
1521	$0.56Ba(Mg_{1/2}W_{1/2})O_3-0.44BaTiO_3$	1500	Composite	21.8	13000		44	373
1522	$0.9(Mg_{0.95}Co_{0.05})TiO_3$-$0.1Ca_{0.6}La_{0.8/3}TiO_3$	1350/4h	Composite	21.8	131000	7	−16	694
1523	$(Ca_{1+x}Sm_{1-x})(Al_{1-x}Ti_x)O_4$ (x=0.3)	1500	K_2NiF_4 type Tetragonal I4/mmm	21.8	83100		10	554
1524	99 wt% $BiSbO_4$+1 wt% $CaTiO_3$	1100	Monoclinic I2/c	21.8	61150		−40	697
1525	$0.94MgTiO_3$-$0.06Ca_{0.8}Sr_{0.2}TiO_3$	1300	Composite	21.9	128000		−68	698
1526	$Mg_{0.95}Ca_{0.05}TiO_3$+1 mol% Bi_2O_3	1250	Ilmenite Trigonal R-3	21.9	41100	7	0	665
1527	90 wt% $CaZrO_3$+10 wt% Li_2O-B_2O_3-SiO_2	875	Composite	21.9	4700		−39	592
1528	Li_3NbO_4-0.15$CaTiO_3$		Composite	21.9	24900		−58	699
1529	$(Na_{0.5}Bi_{0.5})_{0.6}Ca_{0.4}MoO_4$	750	Tetragonal scheelite	21.9	20660		8	343
1530	$Ca(Ca_{1/3}Ta_{2/3})O_3$		Perovskite	22.0	22000	–	6	609
1531	$Li_{2.081}Ti_{0.676}Nb_{0.243}O_3$+0.5 wt% B_2O_3	880	M phase	22.0	32000		−41	700
1532	$Sr(Ca_{1/3}Ta_{2/3})O_3$		Complex perovskite Trigonal P-3m1	22.0	27300	7	10	701
1533	$Ca(Ni_{1/3}Ta_{2/3})O_3$		Complex perovskite	22.0	21000	–	−91	609
1534	$CrNbO_4$	1300/5h	Tetragonal $P4_2/mmm$	22.0	4000	4	−80	53
1535	$(Zn_{0.7}Mg_{0.3})TiO_3$	950	Trigonal R-3	22.0	65000		−80	663
1536	$Sr(Mg_{1/3}Ta_{2/3})O_3$		Complex perovskite Hexagonal	22.0	5600	7	−50	701
1537	$Y(Mg_{1/2}Ti_{1/2})O_3$	1650/2h	Perovskite Cubic Fd3m	22.0	33700	10	−46	702
1538	$NdGaO_3$		Perovskite Orthorhombic Pbnm	22.0	85000			703
1539	Sr_4AlNbO_8	1525		22.0	3700	10.25		562

1540	$(Zn_{0.3}Co_{0.7})TiO_3$	1150	Trigonal R-3	22.0	80000		−60	704
1541	$DyTiNbO_6$	1385	Aschenite Orthorhombic Pbcn	22.0	19100	7.76	−42	563
1542	$YbTiNbO_6$	1400	Aschenite Orthorhombic Pbcn	22.0	11000	7.4	−63	563
1543	$Sm_{0.71}Y_{0.29}TiNbO_6$	1400	Orthorhombic Pbnm	22.0	1400		−2	564
1544	$Ca_5Nb_2HfO_{12}$	1700	Perovskite	22.0	16000	5.4	−29	490
1545	$0.5CeO_2$-$0.25ZnO$-$0.25TiO_2$:4 Co_3O_4	1250	Mixed phases	22.0	32100	5.5	−48	490
1546	CeO_2-$0.5CoO$-$0.5TiO_2$	1200	Mixed phases	22.0	50000		−47	488
1547	$CoNb_2O_6$	1150	Columbite Orthorhombic Pbcn	22.0	41700	6.7	−66	489,600
1548	$Zn_{0.5}Mg_{0.5}Nb_2O_6$	1150	Columbite Pbcn	22.0	33100		−29	705
1549	$Ca_{1-x}Bi_xW_{1-x}VxO_4$ (x=0.3)	950/2h	Tetragonal Scheelite ($I4_1/a$)	22.0	16700		2	706
1550	$(1-x)(Mg_{0.95}Zn_{0.05})TiO_3$-$xCa_{0.6}La_{0.8/3}TiO_3$ (x=0.1)	1320/4h	Composite	22.0	94000		−20	465
1551	$5Li_2O$-$0.58Nb_2O_5$-$3.23TiO_2$+0.5 wt% B_2O_3	900	M phase	22.0	32000		10	707
1552	$(1-x)(Mg_{0.95}Ni_{0.05})TiO_3$-$xCa_{0.6}La_{0.8/3}TiO_3$ (x=0.1)	1325	Composite	22.0	118000		−25	708
1553	Li_2TiO_3		Monoclinic rocksalt C2/c	22.0	63500		20	709
1554	Li_2TiO_3+20 vol% $Li_2Zn_3Ti_4O_{12}$	900	Composite	22.0	28400		−2	710
1555	$NdAlO_3$		Perovskite Trigonal R-3m	22.0	58000		−35	711
1556	$ZnNb_2O_6$+10 wt% V_2O_5	900/2h	Columbite Orthorhombic Pnca	22.1	10300		−83	712,713
1557	$La_{2-x/3}Na_x(Mg_{1/2}W_{1/2})O_3$ (x=0.4)	1450	Perovskite Composite	22.1	5500		−45	655
1558	$YTiTaO_6$	1625	Euxenite Orthorhombic	22.1	51400		−20	583
1559	$0.6(Al_{1/2}Ta_{1/2})O_2$-$0.4(Mg_{1/2}Ta_{2/3})O_2$	1450	Orthorhombic Pbcn	22.1	90930		−16	214
1560	$0.92(Mg_{0.95}Co_{0.05})TiO_3$-$0.08CaTiO_3$	1275/4h	Composite	22.1	86400	7	5.4	422
1561	Nd_2BaCuO_5		Tetragonal I4/mcm	22.1	4910		4.6	463
1562	$Nd_2Ba(Zn_{1-x}Cu_x)O_5$ (x=0.15)		Tetragonal I4/mcm	22.1	7700	2		463
1563	$ZnNb_2O_6$+5 wt% CuO	925/2h	Columbite Orthorhombic Pbcn	22.1	59500		−65	482
1564	$Ba(Yb_{1/2}Ta_{1/2})O_3$	1700	Perovskite Cubic Fm3m	22.1	14000	6.7	89	590
1565	$Sm_2Ba_{0.95}Sr_{0.05}ZnO_5$		Orthorhombic	22.1	10000		30	549
1566	Li_2TiO_3		Monoclinic rocksalt C2/c	22.1	63500		20	714

(*continued*)

No.	Material	ST (°C)	Crystal structure	ε_r	Qf (GHz)	f_0	τ_f	Reference
1567	$Bi[Sb_{1-x}(Nb_{0.992}V_{0.008})_x]O_4$ (x=0.05)		Monoclinic I2/c	22.1	41000		−54	715
1568	$Ca_{1-x}Bi_xW_{1-x}V_xO_4$ (x=0.3)	950/2h		22.1	16700		2	706
1569	$(1-x)Li_3Bi_2P_3O_{12}$-$xTiO_2$ (x=0.55)	725	Monocklinic $P2_1/m$	22.1	14900		−3	456
1570	$La_3Ti_5Al_{15}O_{37}$	1420	Monoclinic Cc	22.1	57100		19	455
1571	$(1-x)(Mg(Sn_{0.05}Ti_{9.5})O_3$-$x(Ca_{0.8}Sr_{0.2})TiO_3$-ywt% $ZnNb_2O_6$ (x=0.7, y=4)	1320/2h	Composite	22.1	60600	7	0	716
1572	$0.95MgTiO_3$–$0.05(Ca_{0.8}Sr_{0.2})(Zr_{0.1}Ti_{0.9})O_3$	1300/4h	Composite		116000		5	717
1573	$ZnTiO_3$+5 wt% B_2O_3-SiO_2	850	Composite	22.2	52460	6		718
1574	$Mg_{0.93}Ca_{0.07}TiO_3$	1350/3h	IlmeniteTrigonal R-3	22.2	68550		6	719
1575	$Gd(Ti_{1/2}W_{1/2})O_4$	1375	Tetragonal Scheelite	22.2	5000	5.5	−16	400
1576	$Mg_{0.95}Ca_{0.05}TiO_3$+5 mol%Bi_2O_3	1250	Ilmenite Trigonal R-3	22.3	22500	7	−110	665
1577	$NdAlO_3$	1650/2h	Perovskite Trigonal R-3m	22.3	58000	10	−33	452
1578	$Sr_3Zn_{0.5}Mg_{0.5}Nb_2O_9$	1300	Trigonal, complex perovskite P-3m1	22.3	8200		4	614
1579	$Nd_2BaZn_{095}Cu_{0.05}O_5$	1250/10h	Tetragonal I4/mcm	22.4	6340		2	463
1580	$NdAlO_3$+0.25 wt% CuO	1420/2h	Trigonal R-3m	22.4	63000	10	−35	720
1581	$MnNb_2O_6$	1150	Columbite orthorhombic Pbcn	22.4	34300		−60	600
1582	$0.5CeO_2$-$0.25MgO$-$0.25TiO_2$	1400	Mixture phases	22.4	17500	5.5	−62	488
1583	$Zn_3Nb_2O_8$+2 mol% V_2O_5	850-1000	Monoclinic C2/c	22.4	67500			712
1584	CeO_2+10 wt% Bi_2O_3-B_2O_3-ZnO-SiO_2	950	Cubic flurite Fm3m	22.4	12000	4.5	−57	401
1585	$LaLuO_3$	1525	Orthorhombic Pnma	22.4	14400		−7.5	721
1586	$(1-y)Li_{2.02}Ti_{0.92}Nb_{0.06}O_3$ (y=0.2)	1070	M phase	22.5	13600		14	722
1587	$0.91(Mg_{0.7}Zn_{0.03})TiO_3$-$0.09CaTiO_3$	1310/3h	Ilmenite trigonal R-3	22.5	86000	7.5	3	723
1588	$Zn_{1+0.005}Nb_2O_6$	1300	Pbcn Columbite	22.5	122000	70	−75	644
1589	ZnO-B_2O_3-P_2O_5-TeO_2 glass		Glass	22.5	1500	7	−100	318
1590	$0.95(Mg_{0.7}Zn_{0.3})_{0.95}Co_{0.05}TiO_3$-$0.05Ca_{0.8}Sr_{0.2}TiO_3$	1150	Composite	22.5	90000	9	0	724
1591	$0.9(Mg_{0.95}Co_{0.05})TiO_3$-$0.1Ca_{0.8}Sm_{0.4/3}TiO_3$	1275	Composite	22.5	108000	8	−8	725

1592	$0.75ZnNb_2O_6$-$0.25TiO_2$	1200	Columbite-Orthorhombic Pnca	22.5	15000		−15	545
1593	$0.91(Mg_{0.7}Zn_{0.3})TiO_3$-$0.09CaTiO_3$	1310/3h	Composite	22.5	86000	7.5	3	726
1594	$La_{5/3}MgTaO_6$	1500/6h	Perovskite	22.5	5000	7.2	−80	727
1595	$0.95(Mg_{0.95}Zn_{0.05})TiO_3$-$0.05CaTiO_3$+1 Mol% $LaAlO_3$	1200/4h	Mixture	22.6	89000		−7	728
1596	$NiNb_2O_6$	1150	Columbite Orthorhombic Pbcn	22.6	40100		−38	729
1597	Nd_2BaZnO_5		Tetragonal I4/mcm	22.6	12451	8.9	4.6	730
1598	$La_{2-x/3}Na_x(Mg_{1/2}W_{1/2})O_3$ (x=0.1)	1400	Perovskite	22.6	19700		−34	655
1599	$La_{2-x/3}Na_x(Mg_{1/2}W_{1/2})O_3$ (x=0.2)	1400	Perovskite	22.6	16600		−27	655
1600	$0.94MgTiO_3$-$0.06CaTiO_3$+0.2 mol% Bi_2O_3	1250	Ilmenite Trigonal R-3	22.6	53000	7	−3	665
1601	$0.95MgLi_{2/3}Ti_{4/3}O_4$-$0.05CaTiO_3$	1200/2h	Composite	22.6	48000		−2	637
1602	$0.93(Mg_{0.95}Zn_{0.05})TiO_3$-$0.07CaTiO_3$	1300/4h	Composite	22.6	93000	10	−3	731
1603	$0.7Mg_{0.95}Co_{0.05}TiO_3$-$0.3Zn_{0.975}Ca_{0.025}TiO_3$	1200	Composite	22.6	57000		0	732
1604	$Ca[(Li_{1/3}Nb_{2/3})_{1-x}Sn_x]O_3$ (x=0.3)	1150	Perovskite Orthorhombic	22.6	46300		−39	733
1605	$0.5ZnNb_2O_6$-$0.5Zn_3Nb_2O_8$	1200	Orthorhombic (mixture)	22.7	95500		−65	542
1606	$0.9(Mg_{0.95}Zn_{0.05}Ti)O_3$-$0.1Ca_{0.8}Sm_{0.4/3}TiO_3$	1300	Composite	22.7	124000		−6	734
1607	$0.93(Mg_{0.95}Mn_{0.05})TiO_3$-$0.07CaTiO_3$	1270/4h	Composite	22.7	90700		0.8	735
1608	(1-x)$MgTiO_3$-x$Ca_{0.8}Sr_{0.2}TiO_3$ (x=0.08)		Composite	22.7	72400		14	572
1609	$0.9(Mg_{0.95}Co_{0.05}TiO_3$-$0.1Ca_{0.6}La_{0.8/3}TiO_3$	1225	Composite	22.7	76000		−12	736
1610	$BiCu_2VO_6$	740	Monoclinic $P2_1/n$	22.7	12000	11	−17	737
1611	$0.45TiO_2$-$0.55CeTe_2O_6$	700	Composite	22.8	8300		25	434
1612	$Li_2ZnTi_3O_8$+5 wt% LMZBS	900	Ternary spinel Cubic P4332	22.8	25000		−17	738
1613	$LaAlO_3$+10 mol% $Sr_2Nb_2O_7$	1575/3h	Composite	22.8	18610	7.6	46	739
1614	$CoNb_2O_6$	1100	Columbite Pbcn	22.8	93800		−45	600
1615	$0.92CoNb_2O_6$-$0.08TiO_2$	1150	Columbite Orthorhombic Pnca	22.8	29000		−12	545
1616	$La_{2-x/3}Na_x(Mg_{1/2}W_{1/2})O_3$ (x=0.3)		Perovskite	22.8	11500		45	655

(*continued*)

No.	Material	ST (°C)	Crystal structure	ε_r	Qf (GHz)	f_0	τ_f	Reference
1617	CeO_2:1 mol% Nd_2O_3	1650	Cubic flurite Fm3m	22.8	51000		−63	525
1618	$Li_{2.08}TiO_3$+0.13LiF	900/2h	Monoclinic Rock salt C2/c	22.8	63000		1	740
1619	$0.89MgTiO_3$-$0.11(Ca_{0.6}Na_{0.2}Sm_{0.2})TiO_3$	1250	Mixture	22.8	76000	8	−3	741
1620	$Zn(Nb_{0.95}Ta_{0.05})_2O_6$+4.5 wt% CuO	930	Columbite Orthorhombic Pnca	22.9	77200		−71	742
1621	$Ba[Ti_{1-x}(Zn_{1/2}W_{1/2})_x]O_3$ (x=0.55)	1420	Hexagonal perovskite $P6_3/mmc$	22.9	15200		−1	665
1622	$0.9(Mg_{0.95}Ni_{0.05})TiO_3$-$0.1Ca_{0.8}Sm_{0.4/3}TiO_3$	1275/4h	Composite	22.9	92000		−5	743
1623	$(Ca_{1+x}Sm_{1-x})(Al_{1-x}Ti_x)O_4$ (x=0.4)	1400	K_2NiF_4 type Tetragonal I4/mmm	22.9	49100		15	554
1624	$0.7Li_2TiO_3$-0.3ZnO		Composite	23.0	99800	8.91	0	744
1625	Nd_2O_3-TiO_2+BaO-SiO_2-B_2O_3-ZnO-SrO glass	900	Glass	23.0	600			745
1626	Sm_2O_3	1650/2h	Monoclinic C2/m	23.0	46000		22	525
1627	$(Zn_{0.65}Mg_{0.35})TiO_3$+1.5 wt% $BiVO_4$+5 wt% $CaTiO_3$	930	Composite	23.0	16200		1	746
1628	$Ca(Cu_{1/3}Ta_{2/3})O_3$		Complex perovskite	23.0	5500	–	–	609
1629	$0.93MgTiO_3$-$0.07CaTiO_3$ (SPS sintering)	1150/ 10 min	Composite	23.0	7000		–	747
1630	$Ca(Co_{1/3}Ta_{2/3})O_3$		Complex perovskite	23.0	12000	–	−65	609,701
1631	$Ba_{0.99}(Zn_{1/2}W_{1/2})O_{2.99}$	1250/4h	Cubic perovskite Fm3m	23.0	22000		−35	567
1632	$Sr(Ni_{1/3}Ta_{2/3})O_3$		Complex perovskite Trigonal P-3m1	23.0	49000	7	−18	701
1633	$Sr(Co_{1/3}Ta_{2/3})O_3$		Complex perovskite Trigonal P-3m1	23.0	17500	7	−71	701
1634	$Ba(Ni_{1/3}Ta_{2/3})O_3$		Complex perovskite Trigonal P-3m1	23.0	49700	7	−18	701
1635	$La(Co_{1/2}Ti_{1/2})O_3$		Perovskite	23.0	32000		−57	748
1636	$Dy(Mg_{1/2}Ti_{1/2})O_3$	1650/2h	Perovoskite	23.0	36800	10	−6	702
1637	$0.7MgTiO_3$-$0.3MgTa_2O_6$	1460/3h	Mixed phases	23.0	81000		−2	749
1638	$Ca(La_{1/2}Ta_{1/2})O_3$	1600/4h	Complex perovskite Monoclinic $P2_1/n$	23.0	20600		−32	750

1639	$CaTiO_3$-$CaZrO_3$+frit glass (70:15:15)	875	Composite	23.0	2400		0	196
1640	$Sm_2Ba_{0.9}Sr_{0.1}ZnO_5$		Tetragonal	23.0	8520		36	549
1641	CeO_2-CoO_4-TiO_2+0.5 wt% CuO	1050	Mixture	23.0	45000		−55	366
1642	CaO-4NiO-Ta_2O_5-TiO_2	1340	Mixture	23.0	8500	5.5	−48	230
1643	$CoNb_2O_6$	1150	Columbite Orthorhombic Pbcn	23.0	40000		−35	729
1644	$0.4(0.5ZnNb_2O_6$-$0.5Zn_3Nb_2O_8)$-$0.6ZnTa_2O_6$	1275	Composite	23.0	9300		−55	542
1645	CaO-4MgO-Nb_2O_5-TiO_2	1340	Mixture	23.0	52000	5.5	−30	230
1646	2CaO-3ZnO-Nb_2O_5-TiO_2	1140	Mixture	23.0	15000	5.5	−34	230
1647	$Nd(Mg_{1/2}Ti_{1/2})O_3$	1650/2h	Perovskite	23.0	36900	10	−49	702
1648	$Li_2MgTi_3O_8$	1100/5h	Cubic spinel $P4_332$	23.0	54050	7.29	2	751
1649	$Ca[(Li_{1/3}Nb_{2/3})_{1-x}Sn_x]$ $O_{3-\delta}$ (x=0.3)	1150/3h	Perovskite	23.0	46300		−39	752
1650	$0.93(Mg_{0.6}Zn_{0.4})_{0.95}Co_{0.05}TiO_3$-0.07 $CaTiO_3$	1200	Composite	23.0	79400		1	753
1651	$0.93MgTiO_3$-$0.07CaTiO_3$ SPS method	1150/ 10 min	Ilmenite+Perovskite	23.0	70000			754
1652	CeO_2	1675	Cubic flurite Fm3m	23.0	65000		−55	640
1653	Li_2TiO_3+2 wt% ZnO-B_2O_3 frit+0.9 wt% CeO_2	920/4h	Composite	23.0	34900		33	755
1654	$HoTiTaO_6$	1550	Euxenite Orthorhombic	23.1	46900		−8	583
1655	$Nd_{1.95}La_{0\cdot.5}BaZnO_5$		Orthorhombic Pnma	23.1	7165		2	599
1656	Li_2TiO_3+2.5 wt% ZnO-B_2O_3	900/2h	Monoclinic C2/c	23.1	32300		36	756
1657	$Ba_5Li_2W_3O_{13}$+4 wt% $BaCu((B_2O_5)$	900	Hexagonal Perovskite	23.1	34300		4	757
1658	$Li_2ZnTi_3O_8$+3 wt% LMZBS	900	Cubic $P4_332$	23.2	31300		−16	738
1659	$0.87(Mg_{0.95}Ni_{0.05})TiO_3$-$0.13(La_{0.5}Na_{0.5})TiO_3$	1275/4h	Composite	23.2	86500		3	758
1660	$Li_{2.08}TiO_3$(sol-gel)	1050	Monoclinic C2/c	23.2	56400		38	759
1661	$PrAlO_3$	1650/2h	Perovskite Trigonal R-3m	23.2	51000	10	−25	452
1662	$ZnNb_2O_6$	1200	Columbite Orthorhombic Pnca	23.2	84500	6.3	−76	557
1663	Li_2TiO_3+2 wt% Li_2O-ZnO-B_2O_3	900	Monoclinic C2/c	23.2	38900		30	652

(*continued*)

No.	Material	ST (°C)	Crystal structure	ε_r	Qf (GHz)	f_0	τ_f	Reference
1664	$0.2(LiNb_{0.8}Ti_{0.5}O_3)+0.8(Li_{2.02}Nb_{0.06}Ti_{0.92})O_3$	1100	Composite	23.2	14900		14	760
1665	$Na_2BiMg_2V_3O_{12}$	660/4h	Cubic garnet	23.2	3700		8	761
1666	$0.87Li_2TiO_3$-0.05MgO-0.08LiF	950	Composite	23.2	131700		0	762
1667	$Zn(Nb_{1-x}V_{x/2})_2O_{6-2.5x}$ (x=0.15)	975/2h	Columbite Orthorhombic Pbcn	23.3	37000		−71	712
1668	$Ca[(Li_{1/3}Nb_{2/3})_{1-x}Sn_x]O_3$ (x=0.2)	1150/3h	Perovskite	23.3	50600		−30	752
1669	$Ca(La_{1/2}Nb_{1/2})O_3$	1550/4h	Perovskite Monoclinic	23.3	31000		−43	763
1670	$ZnNb_2O_6$+5 wt% CuO+4B_2O_3	900	Columbite Orthorhombic Pnca	23.3	46800		−7	764
1671	$Ca(Li_{1/3}Ta_{2/3})O_3$-δ+6 wt% B_2O_3	1100	Perovskite	23.3	27900	10.99		765
1672	$Ba_2Ca_{1-x}Sr_xWO_6$ (x=0.5)	1200	Perovskite Cubic Fm3m	23.3	45200		−14	766
1673	$Li_2Zn(Ti_{0.9}Sn_{0.1})_3O_8$	1120	Cubic spinel	23.3	71000		−22	672
1674	$ZnNb_2O_6$+1 wt% V_2O_5+1 wt% Bi_2O_3+2.5 wt% CuO	880	Columbite Orthorhombic Pnca	23.4	47000		−45	767
1675	$0.88(Mg_{0.95}Zn_{0.05})TiO_3$-$0.12(Na_{0.5}La_{0.5})TiO_3$		Composite	23.4	103000	9	1	768
1676	$LaAlO_3$+5 mol% $Sr_2Nb_2O_7$	1575/3h	Composite	23.4	20790	10.81	−25	769
1677	$LaAlO_3$	1650/2h	Perovskite Hexagonal R-3m	23.4	68000	10	−44	452
1678	CeO_2:1 mol% Er_2O_3	1650	Cubic flurite Fm3m	23.5	74000		−60	525
1679	$La_6Mg_4Ta_2W_2O_{24}$	1350/4h	$A_{1-d}BO_3$ perovskite Monoclinic	23.5	13600	5.4	−46	770
1680	$0.96(Mg_{0.6}Zn_{0.4})_{0.95}Co_{0.05}TiO_3$-$0.04SrTiO_3$	1250	Mixture phases	23.5	92000		−2	771
1681	$SrHfO_3$	1750/6h	Orthorhombic perovskite Pnma	23.5	33500	9.3	−63	675
1682	$Ba_2Ca_{1-x}Sr_xWO_6$ (x=0.1)	1200	Perovskite Cubic Fm3m	23.5	60100		−16	766
1683	$0.3Li_2TiO_3$-$0.7Li(Zn_{0.5}Ti_{0.5})O_4$	1100	Composite	23.5	88360		0	772
1684	$Ba(Mg_{0.33}Ta_{0.53}Ti_{0.067}W_{0.067})O_3$	1590	Perovskite	23.6	75900	5.7	−3	438
1685	$La_{2/3}(Mg_{1/2}W_{1/2})O_3$	1250	Orthorhombic I222	23.6	32500		−43	655,773
1686	(1-x)Li_2TiO_3+xLiF (x=0.1)	1100/2h	Composite	23.6	10800		4	774
1687	$La_{2/3}(Mg_{1/2}W_{1/2})O_3$+2 mol% TiO_2	1330	Orthorhombic I222	23.6	14800		−10	775
1688	$Zn_{0.95}Mg_{0.05}TiO_3$+0.25 TiO_2+1 wt% 3ZnO-B_2O_3	940/2h	Composite	23.6	30990	7.75	−8	776

1689	$Sr_{1-x}Nd_{1-x}Al_{1-x}Ti_xO_4$ (x=0.6)		Tetragonal I4/mmm	23.6	86300		11	777
1690	$(Ni_{1-x}Zn_x)Nb_2O_6$ (x=0.2)	1300	Columbite Orhorhombic Pbcn	23.6	18900		−62	778
1691	$(Zn_{1-x}Mg_x)Nb_2O_6$	1150-1350	Columbite Orthorhombic Pnca	23.6-19.2	81220-33110		−71 to −29	705
1692	$SrLa_2Mg_2W_2O_{12}$	1525	Orthorhombic	23.7	15900		0	645
1693	$Li_2MgTi_3O_8$+5 wt% LMZBS	925	Ternary spinel Cubic $P4_332$	23.7	38000		0	738
1694	(1-x)$Li_3Bi_2P_3O_{12}$-xTiO_2 (x=0.6)	760	Monoclinic $P2_1/m$	23.8	15300		23	456
1695	$CaZrO_3$ (nanopowder)	1500/4h	Perovskite Pbnm	23.8	30600	5.65	1.4	779
1696	$Zn(Nb_{1-x}V_{x/2})_2O_{6-2.5x}$ (x=0.025)	1000/2h	Columbite Orthorhombic Pnca	23.8	64000		−50	712
1697	$Zn_{1+x}Nb_2O_6$ (x=0.01)	1250	Columbite Orthorhombic Pnca	23.8	120000		−73	780
1698	$NiZrNb_2O_8$	1200	Monoclinic Wolframite P2/c	23.8	40300		−28	781
1699	$MgZrNb_2O_8$+1 wt% H_3BO_3	1200/4h	Monoclinic P2/c	23.8	58900		−13	782
1700	$Zn(Nb_{0.94}V_{0.06})_2O_6$	875/2h	Columbite Orthorhombic Pbcn	23.9	65000		−73	713
1701	CeO_2:1 mol% Sm_2O_3	1650	Cubic flurite Fm3m	23.9	90000		−50	525
1702	$Sr_2La_2MgW_2O_{12}$	1525	Orthorhombic	23.9	35000		−83	645
1703	$Ba_2Ca_{0.975}Sr_{0.025}WO_6$	1250	Perovskite Cubic Fm3m	23.9	80200		18	766
1704	$Ba_2Ca_{1-x}Sr_xWO_6$ (x=0.05)	1225	Perovskite Cubic Fm3m	24.0	77800		−20	766
1705	$Ba[Ti_{1-x}(Co_{0.5}W_{0.5})_x]O_3$ (x=0.9)	1425	Perovskite	24.0	20700		−18	519
1706	$Ba_{0.98}(Zn_{1/2}W_{1/2})O_{2.98}$	1250/4h	Cubic perovskite Fm3m	24.0	31000		−40	567
1707	$0.85(Mg_{0.95}Ni_{0.05})TiO_3$-$0.15Ca_{0.61}Nd_{0.26}TiO_3$	1350	Composite	24.0	67000		−9	783
1708	Li_2TiO_3+2.5 wt% LiF	950	Monoclinic C2/c	24.0	75500		36	784
1709	CeO_2: 1mol% CaO	1675	Cubic flurite Fm3m	24.0	120000	5.48	−60	640
1710	CeO_2+1 mol% Sm_2O_3	1650/2h	Cubic flurite Fm3m	24.0	90000		−50	525
1711	2CaO-3CoO-Ta_2O_5-TiO_2	1260	Mixture	24.0	13500	5.3	−19	230
1712	$Ba_8Ta_6Ni_{0.25}Mg_{0.75}O_{24}$			24.0	93000		25	785
1713	$Ca(Li_{1/3}Ta_{2/3})O_3$-δ	1200	Perovskite	24.0	42300	10.8		765
1714	BaO-TiO_2-WO_3+5 wt%% ZnO-$2B_2O_3$	1100	Composite	24.0	13000	9.4		786
1715	BaO-0.32MgO-0.25WO_3-0.43TiO_2	1500/6h	Composite	24.0	19500		34	407
1716	$Ba(Mg_{1/3}Ta_{2/3})O_3$	1640/20h	Complex perovskite Trigonal P-3m1	24.0	430000	10	5	787

(*continued*)

No.	Material	ST (°C)	Crystal structure	ε_r	Qf (GHz)	f_0	τ_f	Reference
1717	$Ca(In_{1/2}Ta_{1/2})O_3$	1600/4h	Complex perovskite Monoclinic $P2_1/n$	24.0	16700		−35	750
1718	$Ca(Pr_{1/2}Ta_{1/2})O_3$	1600/4h	Complex perovskite Monoclinic $P2_1/n$	24.0	22200		−31	750
1719	$LiNb_3O_8$	1075	α-PbO_2 type Monoclinic $P2_1/a$	24.0	58000		−96	788
1720	$Nd_{0.3}Dy_{0.7}TiNbO_6$			24.0	27750		−22	564
1721	$Ca(Li_{1/3}Ta_{2/3})O_3$-δ+3 wt% B_2O_3	1100	Perovskite	24.0	40300	10.86		765
1722	$(Zn_{0.3}Co_{0.7})Ti_{1-x}Sn_xO_3$ (x=0.02)	1220/4h	Cubic spinel+rutile	24.0	66700		−5	789
1723	$0.75(Al_{1/2}Ta_{1/2})O_2$-$0.25(Ti_{1-x}Sn_x)O_2$	1450/3h	Tetragonal TiO_2 type	24-30	55000-80000		−25 to 15	790
1724	$0.85Ba(Mg_{1/3}Ta_{2/3})O_3$-$0.15BaSnO_3$	1640/20h	Complex perovskite Trigonal P-3m1	24.0	330000		−1	791
1725	$La_{3/4}Mg_{2/4}Ta_{1/4}W_{1/4}O_3$	1350/4h		24.0	13600		−46	770
1726	$La_{2/3}(Mg_{1/2}W_{1/2})O_3$+2 mol% TiO_2		Orthorhombic I222	24.0	14800	6	10	775
1727	Sm_2SrZnO_5		Tetragonal	24.1	19283	8.1	−97	549
1728	$Ca(Li_{1/3}Ta_{2/3})O_3$-δ+1 wt% B_2O_3	1100	Perovskite	24.1	38900	10.8		765
1729	$0.20MgAl_2O_4$-$0.80TiO_2$	1460	Composite	24.1	48900	5.5	11	195
1730	$Ca[(Li_{1/3}Nb_{2/3})_{0.8}Ti_{0.2}]O_{3-d}$+15 wt% LMZBS	900	Complex Perovskite Orthorhombic	24.1	13500		−21	792
1731	$Li_2(Mg_{0.3}Zn_{0.7})Ti_3O_8$-$0.12TiO_2$+2 wt% BaO-$B_2O_3$-$SiO_2$	900	Spinel	24.1	22000		−4	793
1732	$Ba(Sn,MgTa)O_3$		Complex perovskite Hexagonal P-3m1	24.2	120000	6.0		794
1733	$Ca(Pr_{1/2}Nb_{1/2})O_3$	1550/4h	Complex perovskite Monoclinic	24.2	31500		−39	763
1734	$Ba[Ti_{1-x}(Ni_{1/2}W_{1/2})_x]O_3$ (x=0.5)	1425	Perovskite	24.2	35000		−6	616
1735	$Ba_8Ta_6(Ni_{1-x}Mg_x)O_{24}$ (x=0.75)		Complex perovskite	24.2	93100		26	785
1736	$Ba(Mg_{1/2}Ta_{2/3})O_3$:0.5mol% $Ba(Mg_{1/2}W_{1/2})O_3$		Complex perovskite Trigonal P-3m1	24.2	400000	10		795
1737	(1-x)$MgTiO_3$-x$Ca_{0.8}Sr_{0.2}TiO_3$ (x=0.1)		Composite	24.2	59200		35	572

1738	$Bi[Sb_{1-x}(Nb_{0.992}V_{0.008})_x]O_4$ (x=0.1)		Monoclinic I2/c	24.2	33000		−46	715
1739	$BaHfO_3$	1750/6h	Cubic perovskite Pm-3m	24.2	14250	8.9	111	675
1740	$Li_2ZnTi_3O_8$+1 wt% LMZBS	925	Ternary spinel Cubic $P4_332$	24.3	58000		−14	738
1741	$Li_2ZnTi_3O_8$+1 wt% LZB	925	Ternary spinel Cubic $P4_332$	24.3	41400		−13	796
1742	$Sm_2Ba_{0.75}Sr_{0.25}ZnO_5$		Orthorhombic Pnma	24.3	8670	8.17	30	549
1743	$0.85(Mg_{0.95}Zn_{0.05})TiO_3$-$0.15Ca_{0.61}Nd_{0.26}TiO_3$	1300	Mixed phases	24.3	112000	8	−10	797
1744	$0.9ZnNb_2O_6$-0.1(2ZnO-V_2O_5)	950	Columbite Orthorhombic	24.3	72800		–	678
1745	In_2O_3-TiO_2-Ta_2O_5	1525	Composite	24.3	15400		39	583
1746	$0.5Zn_3Nb_2O_8$-$0.5ZnNb_2O_6$	1200/2h	Composite	24.3	95500		−65	542
1747	$0.82BiSbO_4$-$0.18Bi_2Mo_2O_9$	825	Composite	24.3	24000		−4	798
1748	$0.92NaMg_4V_3O_{12}$-$0.08CaTiO_3$	730/4h	Composite	24.3	29200	10.5	−4	382
1749	$LaTiTaO_6$	1530	Multphase	24.4	45300		−39	583
1750	$Sm_2Ba_{0.15}Sr_{0.85}ZnO_5$		Orthorhombic Pnma	24.4	12200	8.19	3	549
1751	$(Ca_2Mg_3)Ta_2(Ti_{0.75}Zr_{0.25})O_{12}$	1375		24.4	12400		−32	799
1752	$Ca(Nd_{1/2}Ta_{1/2})O_3$	1600/4h	Complex perovskite Monoclinic $P2_1/n$	24.4	22400		−30	750
1753	$0.84(Mg_{0.95}Co_{0.05})TiO_3$-$0.16(Na_{0.5}Nd_{0.5})TiO_3$		Ilmenite Trigonal R-3	24.4	70000		2	800
1754	$(Ni_{1-x}Zn_x)Nb_2O_6$ (x=0.2)	1280	Columbite Orthorhombic Pbcn	24.4	24300		−64	778
1755	$Li_2MgTi_3O_8$+3 wt% LMZBS	925	Ternary spinel cubic $P4_332$	24.5	44000		0	738
1756	$0.99(Mg_{0.7}Zn_{0.3})_{0.95}Co_{0.05}TiO_3$-0.1 $(La_{0.5}Na_{0.5})TiO_3$	1150/4h	Composite	24.5	68000		0	801
1757	$Sm_2Ba_{0.1}Sr_{0.9}ZnO_5$		Orthorhombic Pnma	24.5	14950	8.2	−36	549
1758	$Ba(Mg_{0.33}Ta_{0.63}Ti_{0.017}W_{0.017})O_3$	1600	Complex perovskite Trigonal P-3m1	24.5	100700	5.4	13	438
1759	$Ca(Nd_{1/2}Nb_{1/2})O_3$	1550/4h	Complex perovskite Monoclinic	24.5	31800		−37	763
1760	$Sm_2Ba_{0.05}Sr_{0.95}ZnO_5$		Orthorhombic Pnma	24.6	8690	8.2	82	549
1761	$Li_{2+x}TiO_3$ (x=0.08)		Monoclinic C2/c	24.6	66000		22	802
1762	$Ba_4LiNb_{3-x}Sb_xO_{12}$ (x=1)	1400/4h	Cubic Im3m	24.6	52100		0	803

(*continued*)

No.	Material	ST (°C)	Crystal structure	ε_r	Qf (GHz)	f_0	τ_f	Reference
1763	$0.85(Mg_{0.95}Ni_{0.05})TiO_3$-$0.15Ca_{0.6}La_{0.8/3}TiO_3$	1325	Composite	24.6	102000		−4	804
1764	$Zn_{0.95}Mg_{0.05}TiO_3$+0.25TiO_2+1 wt% 3ZnO-B_2O_3	880	Composite	24.6	4000		−14	805
1765	$Li_2ZnTi_3O_8$+0.5 wt% LMZBS	1000	Ternary spinel Cubic $P4_332$	24.6	70000		−14	738
1766	(1-x)$(Mg_{0.95}Ni_{0.05})TiO_3$-x$Ca_{0.6}La_{0.8/3}TiO_3$ (x=0.15)	1325	Ilmenite Trigonal R-3	24.6	102000		−4	708
1767	(1-x)$(Mg_{0.095}Zn_{0.05})TiO_3$-x $(Na_{0.5}Nd_{0.5})TiO_3$ (x=0.16)	1300	Composite	24.7	82000	9	0	806
1768	$Mg_4Al_2Ti_9O_{25}$		Psuedobrookite Bbmm	24.7	30,000			807
1769	$Ba(Mg_{1/3}Ta_{2/3})O_3$ Annealed 1500/50h WGM		Complex perovskite Trigonal P-3m1	24.7	326250	13.05	8	808
1770	$Ba_{0.9925}(Mg_{0.33}Ta_{0.67})O_3$	1600	Complex perovskite Trigonal P-3m1	24.7	152, 00	5.7	1	809
1771	$La(Mg_{2/3}Ta_{1/3})O_3$	1600	Perovskite	24.7	65500	10	−65	810
1772	$Li_2(Zn_{0.92}Co_{0.08})Ti_3O_8$	1140	Ternary spinel Cubic $P4_332$	24.7	140000		−13	811
1773	$Ca(Sm_{1/2}Nb_{1/2})O_3$	1550/4h	Complex perovskite Monoclinic	24.7	33200		−34	763
1774	0.5$Mg_4Nb_2O_9$-0.5$CaTiO_3$		Composite	24.8	82000	9.1	0	812
1775	$Mg_{0.95}Co_{0.05}Ti_2O_4-0.78TiO_2$		Composite	24.8	38500		−1	813
1776	$Ca[Li_{0.33}Nb_{0.67}]_{0.9}Ti_{0.1}]O_{3-\delta}$+10 wt% LiF	900	Composite	24.8	19300	4.2	−15	664
1777	$SmTaTi_{0.25}Zr_{0.75}O_6$			24.9	25200		−44	671
1778	$Ba(Zn_{1/6}Co_{1/6}Ta_{2/9}Nb_{2/9}Sb_{2/9})O_3$	1575/6h	Perovskite	24.9	83000		−13	814
1779	$(Ni_{1-x}Zn_x)Nb_2O_6$ (x=0.4)	1220	Columbite Orthorhombic Pbcn	24.9	35400		−66	778
1780	0.85$MgTiO_3$-0.15$Ca_{0.6}La_{0.8/3}TiO_3$+0.5 wt% ZnO	1250	Composite	24.9	65200	8	0	815
1781	0.93$(Mg_{0.95}Ni_{0.05})_2TiO_4-0.07SrTiO_3$	13404h	Composite	24.9	98000	9.8	1	816
1782	$Ba[Mg_{1-x}Zn_x]_{1/3}Ta_{2/3}]O_3$		Complex perovskite Trigonal P-3m1	24-26	200000-300000	8	−2	817
1783	CaO-ZrO_2-glass		Glass	25.0	3500			818

1784	$Ba(Co_{1/3}Ta_{2/3})O_3$	1500	Perovskite Trigonal P-3m1	25.0	71400		−16	701
1785	$Ca(Eu_{1/2}Nb_{1/2})O_3$	1550/4h	Complex perovskite Monoclinic	25.0	35800		−30	763
1786	$La(Co_{1/2}Ti_{1/2})O_3$	1550	Complex perovskite	25.0	67000		−42	748,819
1787	$Ca(Ga_{1/2}Ta_{1/2})O_3$	1500/2h	Complex perovskite Orthorhombic Pnma	25.0	80000		−81	820
1788	$Ca(Al_{1/2}Nb_{1/2})O_3$	–	Complex perovskite Orthorhombic	25.0	7500		−87	609
1789	Sr_2AlNbO_6	1600	Complex perovskite	25.0	4100		−3	562
1790	$Ca(Zn_{1/3}Ta_{2/3})O_3$		Complex perovskite	25.0	25,000	–	−66	609
1791	$ZnNb_2O_6$	1150/2h	Columbite Orthorhombic Pnca	25.0	83700		−56	729
1792	$NiTa_2O_6$	1600	Tetragonal $P4_2/mmm$	25.0	31000		35	600
1793	$Pr_{0.1}Gd_{0.9}TiNbO_6$	1385	Aeschenite Orthorhombic Pcan	25.0	3450		−15	564
1794	$Ca[(Li_{1/3}Nb_{2/3})_{1-x}Sn_x]\ O_{3-\delta}$ (x=0.15)	1150/3h	Perovskite	25.0	49100		−25	752
1795	$(Sr_{2/3}La_{1/3})(Li_{1/3}Ta_{2/3})O_3$		Perovskite	25.0	25000			821
1796	$La_6Mg_4Nb_2W_2O_{24}$	1400/4h	Perovskite Monoclinic	25.0	16400	5.4	−56	770
1797	$(Zn_{0.9}Mg_{0.1})TiO_3$+4 wt% Bi_2O_3	1000/4h	Composite	25.0	70000		−10	822
1798	$Sr(In_{1/2}Nb_{1/2})O_3$+0.2 wt% B_2O_3	1350/4h	Complex perovskite	25.0	38600		−63	823
1799	$Sm(Mg_{1/2}Ti_{1/2})O_3$	1650/2h	Perovskite Orthorhombic $Pnm2_1$	25.0	65500	10	−26	702
1800	$BaO\text{-}TiO_2\text{-}WO_3$ (N-35):5 wt% $PbO\text{-}SiO_2\text{-}B_2O_3$	1100	Composite	25.0	6500	6	–	786
1801	$Ba_3MgNb_{2-x}Sb_xO_9$ (x=0.25)		Perovskite Trigonal P-3m1	25.0	96290	5.6	6	381
1802	$Sr_{2/3}La_{2/3}[Li_{1/3}Ta_{2/3}]O_3$	1350	Monoclinic $P2_1/c$	25.0	25200	10.2	−25	821,824
1803	$(1\text{-}x)(Mg_{0.95}Zn_{0.05})TiO_3\text{-}xCa_{0.6}La_{0.8/3}TiO_3$ (x=0.15)	1320/4h	Composite	25.0	86000		1	465
1804	$(Zn_{0.65}Mg_{0.35})TiO_3\text{-}0.15TiO_2$+1 wt% $CaO\text{-}B_2O_3\text{-}SiO_2$	950	Composite	25.0	47000		10	825
1805	$BaTe_4O_9$+40 wt% $TiTe_3O_8$	575	Composite	25.0	19300		−3	826
1806	$Ba_{4-5x}Mg_xNb_{2-y}O_9$ (x=0.425, y=0.002)	1320	Trigonal P-3m1	25.0	160000		1	827
1807	$(Ni_{1-x}Zn_x)Nb_2O_6$ (x=0.6)	1260	Columbite Orthorhombic Pbcn	25.0	53400		−68	778
1808	$La(Co_{1/2}Ti_{1/2})O_3$	1550	Perovskite Orthorhombic Pbnm	25.0	38000		−42	828

(*continued*)

No.	Material	ST (°C)	Crystal structure	ε_r	Qf (GHz)	f_0	τ_f	Reference
1809	$Li_2ZnTi_3O_8$+2 wt% MgO-B_2O_3-SiO_2	900/4h	Ternary spinel Cubic $P4_332$	25.0	56200		−10	829
1810	$Li_2ZnTi_3O_8$+1.5 wt% B_2O_3	925/4h	Ternary spinel Cubic $P4_332$	25.0	49600		−11	830
1811	$0.4Li_2Zn_3Ti_4O_{12}$-$0.6TiO_2$	1175	Composite	25.1	62000		−5	831
1812	$0.9LaAlO_3$-$0.1SrTiO_3$	1680	Perovskite Composite	25.1	128000	10	−51	832
1813	$Sm_2Ba_{0.25}Sr_{0.75}ZnO_5$		Tetragonal	25.1	1900	8.17	18	549
1814	$Ba(Mg_{0.3183}Ta_{0.67})O_3$	1600	Perovskite Hexagonal P-3m1	25.1	120500	5.6	3	809
1815	$Ba_4LiTa_2SbO_{12}$	1480	Hexagonal Perovskite $P6_3mc$	25.1	77700		−4	833
1816	$Li_2(Mg_{0.3}Zn_{0.7})Ti_3O_8$-$0.12TiO_2$+3 wt% ZBS	900/3h	Ternary spinel Cubic $P4_332$	25.1	19600		2	834
1817	$Ca[(Li_{1/3}Nb_{2/3})_{1-x}Sn_x]O_3$ (x=0.1)	1150/3h	Perovskite	25.2	48200		−14	752
1818	$0.17Ba_5Nb_4O_{15}$-$0.83BaNb_2O_6$	1300	Composite	25.2	59300		0	835
1819	90 wt% $CoNb_2O_6$+10 wt% $CaTiO_3$	1150	Composite	25.2	21700		2	545
1820	$0.5ZnAl_2O_4$-$0.5TiO_2$		Composite	25.2	277000		177	406
1821	$Bi(In_{1/3}Mo_{2/3})O_4$	840	Monoclinic C2/c	25.2	40000		−65	836
1822	1-xCeO_2-xYb_2O_3 (x=0.25)	1650	Cubic flurite Fm3m	25.2	47800		−60	413
1823	$Li_2MgTi_3O_8$+1 wt% LMZBS	950	Ternary spinel Cubic $P4_332$	25.2	55000		1	738
1824	$Li_2Cu_{0.1}Zn_{0.9}Ti_3O_8$	950	Ternary spinel Cubic $P4_332$	25.2	32100		2	837
1825	$Sm_2Ba_{0.5}Sr_{0\cdot5}ZnO_5$		Tetragonal	25.3	10075	8.1	30	549
1826	$Li_2ZnTi_3O_8$+0.25 wt% ZnO-B_2O_3	950	Ternary spinel Cubic $P4_332$	25.3	61600		−13	838
1827	TeO_2+7.5 wt% $CaTiO_3$		Composite	25.3	10200		−16	444
1828	$0.9MgNb_2O_6$-$0.1TiO_2$	1300	Composite	25.4	19000		−23	545
1829	1-xCeO_2-xEu_2O_3 (x=0.1)	1650	Cubic flurite Fm3m	25.4	70300		−64	413
1830	$Ba[Ti_{1-x}(Zn_{1/2}W_{1/2})_x]O_3$ (x=0.5)	1420	Cubic perovskite Pm3-m	25.4	11800		9	695
1831	$Li_2MgTi_3O_8$+0.5 wt% LMZBS	975	Ternary spinel Cubic $P4_332$	25.4	51000		2	738
1832	$PbMoO_4$	850	Scheelite Tetragonal $I4_1/a$	25.4	35200		−21	49
1833	$La(Mg_{0.5}Ti_{0.5})O_3$+30 wt% La_2O_3-B_2O_3-TiO_2 glass	1200/3h	Composite	25.4	13200		−55	839
1834	$Ba_5Li_2W_3O_{13}[Ba(Li_{2/5}W_{3/5})O_3]$	1120	Hexagonal Perovskite	25.4	39000		10	757

1835	$0.6Li_2ZnTi_3O_8$-$0.4Li_2TiO_3$+1 wt% ZnO-B_2O_3-SiO_2	900	Mixture	25.4	86400		−1	840
1836	$Nd_2Ba_{0.5}Sr_{0.5}ZnO_5$		Tetragonal I4/mcm	25.5	6120		26	730
1837	$Sm(Co_{1/2}Ti_{1/2})O_3$	1360/4h	Perovskite Orthorhombic $Pnm2_1$	25.5	76000	10	−16	841
1838	$Ba[Mg_{1/3}(Nb_{1/4}Ta_{3/4})_{2/3}]O_3$		Complex perovskite Triagonal P-3m1	25.5	140600		5	842
1839	$Ca_2Mg_3(Ta_{1.75}Sb_{0.25})TiO_{12}$	1375	Mixture phases	25.5	13500		−24	843
1840	$0.85MgTiO_3$-$0.15Ca_{0.6}La_{0.8/3}TiO_3$	1275/4h	Composite	25.5	82500		0	844
1841	$Ba(In_{1/2}Ta_{1/2})O_3$+0.5 wt% Nb_2O_5	1575	Complex perovskite cubic Fm3m	25.5	40050		26	845
1842	$BaMg_{1/3}Nb_{2/3}O_3$-$Mg_4Nb_2O_9$	1320	Composite	25.5	160000		0	846
1843	$Ca(Gd_{1/2}Nb_{1/2})O_3$	1550/4h	Complex perovskite Monoclinic	25.5	11000		−26	763
1844	$(Ni_{1-x}Zn_x)Nb_2O_6$ (x=0.8)	1220	Columbite Orthorhombic Pbcn	25.6	90400		−71	778
1845	$Ba_{10}Ta_{7.04}Ti_{.045}Sn_{0.75}O_{30}$		Hexagonal $P6_3mmc$	25.6	59100		30	464
1846	$(Zr_{0.8}Sn_{0.2})TiO_4$+10 wt% BaO-B_2O_3-SiO_2-Li_2O-CuO	1000/4h	Composite	25.6	13000		−8	515
1847	$Li_2ZnTi_3O_8$	1075	Ternary spinel Cubic $P4_332$	25.6	72000		−11	847
1848	$Li_2ZnTi_3O_8$+0.75 wt% ZnO-B_2O_3-SiO_2	925	Ternary spinel Cubic $P4_332$	25.6	51600		−11	848
1849	$Li_2ZnTi_3O_8$+1.5 wt% Bi_2O_3+0.25 wt% CuO+1.5 wt% V_2O_5	875	Spinel cubic $P4_332$	25.6	53400		−5	849
1850	$CaHfO_3$	1750	Orthorhombic	25.6	15900	9.7	−33	850
1851	Nd_2SrZnO_5			25.7	25830	9.7	−80	58,730
1852	$Ba_5Nb_3TaO_{15}$	1500	Trigonal P-3m1 perovskite	25.7	21600	4.93	16	851
1853	$LiMgTi_3O_8$+3 wt% MgO-3 wt% LiF	825	Spinel cubic	25.7	57100		−4	852
1854	$0.4(Al_{1/2}Ta_{1/2})O_2$-$0.6(Mg_{1/2}Ta_{2/3})O_2$	1450	Tetragonal	25.8	111230		−5	214
1855	$0.8Mg_{0.95}Co_{0.05}TiO_3$-$0.2Ca_{0.6}La_{0.8/3}TiO_3$	1300	Composite	25.8	80000	0	−11	853
1856	$La_6Mg_4Ta_2W_2O_{24}$	1400/4h		25.8	16400		−56	770
1857	$Ca(Sm_{1/2}Ta_{1/2})O_3$	1600/4h	Complex perovskite Monoclinic $P2_1/n$	25.8	25000		−25	750
1858	$Ca(Yb_{1/2}Ta_{1/2})O_3$	1600/4h	Complex perovskite Monoclinic $P2_1/n$	25.8	59200		−21	750

(*continued*)

No.	Material	ST (°C)	Crystal structure	ε_r	Qf (GHz)	f_0	τ_f	Reference
1859	$Li_2ZnTi_3O_8$	1100	Spinel cubic $P4_332$	25.8	78200		−11	854
1860	$Li_2(Mg_{0.94}Mn_{0.06})Ti_3O_8$	1075	Ternary spinel cubic $P4_332$	25.8	39400		−13	855
1861	$0.4(Mg_{0.95}Co_{0.05})_4Ta_2O_9$-$0.6CaTiO_3$	1375/4h	Composite	25.8	200000		−5	437
1862	$Li_3ZnTi_3O_8$+1 wt% H_3BO_3	880/4h	Ternary spinel Cubic $P4_332$	25.9	50200		−7	856
1863	$Li_2ZnTi_3O_8$+1.5 wt% B_2O_3+3 wt% TiO_2	900	Ternary spinel Cubic $P4_332$	25.9	46500		0	857
1864	$Li_2Mg_{0.4}Zn_{0.6}Ti_3O_8$	1075/4h	Ternary spinel Cubic $P4_332$	25.9	65000		−8	858
1865	$Sr(Yb_{0.5}Ta_{0.5})O_3$+0.5 wt% Nb_2O_5	1600/4h	Complex perovskite Orthorhombic Pnma	25.9	32300		−79	859
1866	$Ca(Ni_{1/3}Nb_{2/3})O_3$		Complex perovskite Orthorhombic	26.0	11000	–	−78	609
1867	85 wt% $BaTi_4O_9$+15 wt% Li_2O-B_2O_3-SiO_2-CaO-Al_2O_3	875	Composite	26.0	10200		0	592
1868	$0.85(Mg_{0.95}Zn_{0.05})TiO_3$-$0.15Ca_{0.6}La_{0.8/3}TiO_3$	1320/4h	Composite	26.0	86000		0.5	465
1869	$0.5LaCa_{0.5}Zr_{0.5}O_3$-$0.5CaTiO_3$	1575	Composite	26.0	13500	4.5	−67	522
1870	$Nd(Mg_{1/2}Ti_{1/2})O_3$	1650/2h	Perovskite Monoclinic P21/n	26.0	60000		−72	702,860
1871	$Ca(Sm_{1/2}Ta_{1/2})O_3$	1600/4h	Complex perovsite	26.0	25000		−25	750
1872	$Ca(Er_{1/2}Ta_{1/2})O_3$	1600/4h	Complex perovskite	26.0	29600		−12	750
1873	$Ca(Yb_{1/2}Ta_{1/2})O_3$	1600/4h	Complex perovskite	26.0	59200		−21	750
1874	$Sr(Yb_{1/2}Ta_{1/2})O_3$	1600/4h	Complex perovskite	26.0	32300		−79	861
1875	$Sr(In_{1/2}Nb_{1/2})O_3$	1600/4h	Perovskite	26.0	32700		−62	823
1876	BaO-TiO_2-WO_3 (N-35):5 wt% BaO-SiO_2-B_2O_3	1100	Composite	26.0	8400	6.1	–	862
1877	$Sr_3Ti_2O_7$	1300/5h	Tetragonal I4/mmm	26.0	2400	4		53
1878	$LaYbO_3$	1600/4h	Orthorhombic Pnma	26.0	20600	7	−22	863
1879	$0.75Ca_2AlNbO_6$-$0.25Ca_3Nb_2O_8$		Mixture phases	26.0	13200	6.97	−14	864
1880	$2CaO$-$3NiO$-Ta_2O_5-TiO_2	1410	Composite	26.0	11000	4.9	−41	230
1881	$Ca_5Nb_2ZrO_{12}$	1690	Perovskite	26.0	22800	4.8	−25	662
1882	$3CaO$-$2ZnO$-Nb_2O_5-TiO_2	1325	Composite	26.0	22000	5.3	−25	230

1883	$2CaO\text{-}3MgO\text{-}Ta_2O_5\text{-}TiO_2$	1450	Composite	26.0	30000	5.1	−28	230
1884	$0.2CaTiO_3\text{-}0.8Sm(Mg_{0.5}Ti_{0.5})O_3$	1550	Composite	26.0	13500	6	−33	865
1885	MWF-38+10 wt% $Li_2O\text{-}B_2O_3\text{-}SiO_2\text{-}CaO\text{-}Al_2O_3$ (52.45:31.06:11.99:2:2.5)	875	Composite	26.0	10200		−4	510
1886	$Ca(Ta_{2-x}Nb_x)O_6$ (x=1.2)	1450	Orthorhombic Pbcn	26.0	25300		54	460
1887	$1.3Bi_2O_3\text{-}MoO_3$	820	P2/a	26.0	4000		−139	494
1888	$Ba_3Co_{1+y}Nb_2O_9$+y (y=0.07)	1470	Perovskite Trigonal P-3m1	26.0	90000	10	−5	866
1889	$Sr(In_{1/2}Nb_{1/2})O_3$+0.5 wt% CeO_2	1600/4h	Complex perovskite Orthorhombic	26.0	32700		−62	823
1890	$Ba(Zn_{1/3}Ta_{2/3})O_3$+5 mol% B_2O_3+10 mol% CuO	870/2h	Complex perovskite Trigonal P-3m1	26.0	11000		0	867
1891	$MgZrNb_2O_8$	1340/4h	Wolframite Monoclinic P2/c	26.0	120800	6.85	−50	868
1892	$MgZrNb_2O_8$+2 wt% $BaCu(B_2O_5)$	1100/4h	Monoclinic P2/c	26.0	65100	8.7	−47	869
1893	$Ba_{10}Ta_{7.04}Sn_{0.75}O_{30}$		Hexagonal $P6_3mmc$	26.0	59100		–	870
1894	$Li_2Mg(Ti_{1-x}Sn_xg_{0.06})_3O_8$ (x=0.15)	1100/4h	Spinel Cubic $P4_332$	26.0	74700		−5	871
1895	$0.5CeO_2\text{-}0.25ZnO\text{-}0.25TiO_2$	1250	Mixture phases	26.1	24100	5.1	−43	488
1896	$Ca[(Li_{1/3}Ta_{2/3})_{.95}Ti_{0.05}]O_{3\text{-}d}$+3 wt% B_2O_3	1050/4h	Perovskite	26.1	22000	10.3	−97	765
1897	$0.35(Al_{1/2}Ta_{1/2})O_2\text{-}0.65(Mg_{1/3}Ta_{2/3})O_2$	1450	Composite	26.1	112500		0	214
1898	$ZnNb_2O_6$	1200	Columbite Orthorhombic Pbcn	26.1	103730		−73	778
1899	$Li_2(Zn_{0.94}Mg_{0.06})Ti_3O_8$	1140	Ternary spinel Cubic $P4_332$	26.1	150000		−14	811
1900	$0.9Li_2ZnTi_3O_8\text{-}0.1TiO_2$	1100	Ternary spinel Cubic $P4_332$	26.1	44500		−1	872
1901	$0.81Mg_{0.95}Ni_{0.05}TiO_3$-$0.19Nd_{0.5}Na_{0.5}TiO_3$	1300	Composite	26.1	69100		−6	873
1902	$Li_2ZnTi_3O_8$+1 wt% LZB+3.5 wt% TiO_2	900/4h	Ternary spinel Cubic $P4_332$	26.1	45200		−4	874
1903	$0.8(Mg_{0.95}Zn_{0.05})TiO_3$-$0.2Ca_{0.61}Nd_{0.26}TiO_3$+1 wt% V_2O_5	1275	Composite	26.1	46000	8	2	875
1904	$Bi(Ga_{1/3}Mo_{2/3})O_4$	830	Monoclinic sheelite C2/c	26.1	49800		−86	876
1905	$Ca_2Mg_3Nb_4TiO_{17}$	1525		26.2	13750		−24	877

(*continued*)

No.	Material	ST (°C)	Crystal structure	ε_r	Qf (GHz)	f_0	τ_f	Reference
1906	$MgTa_{1.3}Nb_{0.7}O_6$	1450	Columbite tetragonal $P4_2/mmm$	26.2	43100		−4	878
1907	$Nd(Mg_{0.5}Ti_{0.5})O_3$+10 mol% B_2O_3	1325	Monoclinic $P2_1/n$	26.2	61300	9.63	−46	879
1908	1-xCeO_2-xDy_2O_3 (x=0.20)	1650	Cubic flurite Fm3m	26.2	70150		−57	413
1909	0.87$(Mg_{0.7}Zn_{0.3})TiO_3$-0.13$(Ca_{0.61}La_{0.26})TiO_3$	1270	Composite	26.2	120000		−3	880
1910	$(Zn_{0.65}Mg_{0.35})TiO_3$+1 wt% CuV_2O_6+9 wt% TiO_2	930	Composite	26.2	31930		−0	881
1911	$Li_2ZnTi_3O_8$	1050	Ternary spinel Cubic $P4_332$	26.2	62000		−15	882
1912	TeO_2+17.5 wt% $SrTiO_3$	610	Composite	26.2	12000		16	444
1913	$Ca[(Li_{1/3}Nb_{2/3})_{0.8}Ti_{0.2}]O_{3\text{-}d}$+12 wt% LMZBS glass	900/4h	Composite	26.2	13000	4.8	−20	792
1914	$Ba(Mg_{0.30}Ta_{0.60}Ti_{0.10})O_3$	1600	Complex perovskite Trigonal P-3m1	26.3	100000	5.2	14	883
1915	0.5CeO_2-0.25MnO-0.25TiO_2	1200	Mixture phases	26.3	17100	5	−30	488
1916	(1-x)$(Mg_{0.95}Zn_{0.05})TiO_3$-x$(Ca_{0.6}La_{0.8/3})TiO_3$ (x=0.21)		Composite	26.3	60700	6.44	0	884
1917	$(Ca_2Mg_{3.75}Pb_{0/.25})Ta_2(Ti_{0.75}Zr_{0.25})O_{12}$	1375		26.3	14000		−22	799
1918	$(Ag_{0.5}Bi_{0.5})(Mo_{0.5}W_{0.5})O_4$	580	Tetragonal Scheelite I41/A	26.3	10000		20	885
1919	$Bi_2Te_2W_3O_{16}$	700/6h	Monoclinic C2/c	26.3	2250	7.9		886
1920	$ZnZr(Nb_{1-x}Sb_x)_2O_8$ (x=0.08)	1250/4h	Monoclinic wolframite	26.3	89400		−57	887
1921	0.75$(Al_{1/2}Ta_{1/2})O_2$-0.25$(Ti_{1-x}Sn_x)O_2$ (x=0.05-0.3)		Tetragonal	26.3-30.0	63400-70700		<10	790
1922	$Nd_2Ba_{0.5}Ca_{0.5}ZnO_5$			26.4	6185		24	730
1923	$Ca(Er_{1/2}Ta_{1/2})O_3$	1600/4h	Complex perovskite Monoclinic $P2_1/n$	26.4	29600		−12	750
1924	$Ba[Ti_{1-x}(Zn_{1/2}W_{1/2})_x]O_3$ (x=0.7)	1420	Perovskite	26.4	22900		−2	695
1925	$LiBiW_2O_8$	650	Monoclinic	26.5	16400		70	888
1926	$Ca[(Li_{1/3}Nb_{2/3})_{0.8}Ti_{0.2}]O_{3\text{-}d}$+12 wt% LBS	920	Perovskite Orthorhombic	26.5	7000		−18	792
1927	0.2$(Al_{1/2}Ta_{1/2})O_2$-0.8$(Mg_{1/3}Ta_{2/3})O_2$	1450		26.5	103190		25	214

1928	$Ba_3NiNb_{2-x}Sb_xO_9$ (x=0.1)		Perovskite Cubic Pm3m	26.5	31110	5	−13	381
1929	$(1-x)La(Mg_{1/2}Ti_{1/2})O_3$-$xLa_{2/3}TiO_3$ (x=0.1)		Perovskite Monoclinic $P2_1/n$	26.5	30580	8.3		889
1930	$Ba[Ti_{1-x}(Ni_{1/2}W_{1/2})_x]O_3$ (x=0.45)	1425	Perovskite	26.5	30800		−3	616
1931	BaO-Sm_2O_3-$4TiO_2$+10 wt% B_2O_3	1100/2h	Composite	26.5	11800		−10	890
1932	$Ca(Tb_{1/2}Nb_{1/2})O_3$	1550/4h	Complex perovskite Monoclinic	26.5	34600		−13	763
1933	$Ba_3Ti_5Nb_6O_{28}$+5 wt% CuO	900/2h	Monoclinic $P2_1/c$	26.6	14100		21	461
1934	$Ba_8Ta_6(Ni_{1-x}Mg_x)O_{24}$ (x=0.5)		Hexagonal $P6_3cm$	26.6	86800		31	785
1935	$Ba_8Ta_6MgO_{24}$		Hexagonal $P6_3cm$	26.6	80900		18	785
1936	$Li_2CoTi_3O_8$+2 wt% B_2O_3	900	Cubic spinel $P4_332$	26.6	21300		2	891
1937	$Li_2(Mg_{0.94}Co_{0.06})Ti_3O_8$	1075	Cubic spinel $P4_332$	26.6	43600		4	855
1938	$0.8Mg_{0.95}Zn_{0.05})TiO_3$-$0.2Ca_{0.61}Nd_{0.26}TiO_3$+1 wt% B_2O_3	1175	Composite	26.6	54900	9	9	892
1939	$Ba_2Ti_9O_{20}$+20 wt% BaO-B_2O_3-ZnO glass	900	Composite	26.6	11950		−7	893
1940	TeO_2+15 wt% $SrTiO_3$	610	Composite	26.6	12400		−4	444
1941	$Ca_xZn_{1-x}Zr_{0.8}Sn_{0.2}Nb_2O_8$ (x=0.15)	1275	Mixture	26.6	61350		−21	894
1942	$Sr_6Ta_4ZrO_{18}$+3 wt% Bi_2O_3-B_2O_3	1625/2h	$A_6B_5O_{18}$ type perovskite	26.7	9100		−39	895
1943	$0.8LaAlO_3$-$0.2SrTiO_3$	1680	Composite	26.7	139000	10	−50	832
1944	$0.9TeO_2$-$SnTe_3O_8$	650	Mixture phase	26.7	10000		32	62
1945	TeO_2+20 wt% $SrTiO_3$	610	Composite	26.7	11400		31	444
1946	$Li_2Mg_{0.95}Co_{0.05}Ti_3O_8$	1170	Cubic Spinel	26.7	82000		−3	896
1947	$PbMoO_4$	650/2h	Tetragonal $I4_1/a$	26.7	42800	6.2	6	897
1948	$Sm(Mg_{0.5}Ti_{0.5})O_3$+10 mol% B_2O_3		Perovskite	26.8	20000		−18	898
1949	$Ca(Eu_{1/2}Ta_{1/2})O_3$	1600/4h	Complex perovskite Monoclinic $P2_1/n$	26.8	23600		−22	750
1950	$La(Mg_{2/3}Nb_{1/3})O_3$	1500/4h	Perovskite Rhombohedral	26.8	52000		−86	899
1951	$(Zr_{0.8}Sn_{0.2})TiO_4$+10 wt% BaO-B_2O_3-SiO_2-Li_2O-CuO	1000/8h	Composite	26.8	21900		−1	515
1952	$Li_2ZnTi_3O_8$+4 wt% TiO_2+1 wt% CBS glass	900/4h	Cubic+rutile	26.9	23600		−1	900

(*continued*)

No.	Material	ST (°C)	Crystal structure	ε_r	Qf (GHz)	f_0	τ_f	Reference
1953	$Ca(Cu_{1/3}Nb_{2/3})O_3$		Complex perovskite Orthorhombic	27.0	3300	–	–	609
1954	$Li_2Mg_{0.2}Zn_{0.8}Ti_3O_8$	1075/4h	Ternary spinel Cubic $P4_332$	27.0	66500		−50	858
1955	$Sr(Ga_{1/2}Ta_{1/2})O_3$	1500/3h	Perovskite	27.0	91000		–	901
1956	$La(Mg_{1/2}Ti_{1/2})O_3$ sol-gel	–	Monoclinic Perovskite $P2_1/n$	27.0	74500		−9	902
1957	$Ca(Y_{1/2}Ta_{1/2})O_3$	1600/4h	Perovskite Monoclinic $P2_1/n$	27.0	42300		−1	750
1958	$0.6Ca(Y_{1/2}Ta_{1/2})O_3$-0.4 $Ba(Y_{1/2}Ta_{1/2})O_3$	1600/4h	Perovskite	27.0	42000		−77	750
1959	$Sr(Er_{1/2}Ta_{1/2})O_3$	1600/4h	Pervoskite	27.0	22100		−88	861
1960	Ca_2AlNbO_6		Perovskite Monoclinic $P2_1/n$	27.0	14000	7.02	0	864
1961	$Ba(Mg_{1/3}Ta_{2/3})O_3$-$Ba(Zn_{1/3},Ta_{2/3})O_3$		Complex perovskite Trigonal P-3m1	27.0	150000	10		903
1962	BaO-TiO_2-WO_3 (N-35)+5 wt% ZnO-B_2O_3-SiO_2	1000	Composite	27.0	8400	7.0		786,862
1963	$Ca(Yb_{1/2}Nb_{1/2})O_3$	1500	Perovskite	27.0	7200	8.4	−30	590
1964	BaO-TiO_2-WO_3 (N-35):5 wt% PbO-Al_2O_3-SiO_2	1100	Composite	27.0	8400	6.1	–	786,862
1965	$Ba_8Ta_6Ni_{0.25}Zn_{0.75}O_{24}$		Trigonal $P6_3cm$	27.0	91730		35	785
1966	$BaTi_4O_9$+20 wt% B_2O_3-ZnO-La_2O_3	900/3h	Composite	27.0	20000		7	904
1967	$Nd(Co_{1/2}Ti_{1/2})O_3$	1440/4h	Monoclinic $P2_1/n$	27.0	140000	9	−46	905
1968	$Ba_6Ta_4TiO_{18}$	1625/2h		27.0	27500		45	895
1969	$CaZrO_3$		Perovskite Orthorhombic Pcmn	27.0	20800			906
1970	$Ba(Mn_{1/3}Ta_{2/3})O_3$	1600/air	Perovskite Trigonal P-3m1	27.0	15500		45	907
1971	$Ba(Mn_{1/3}Ta_{2/3})O_3$	1600/N_2	Perovskite Trigonal P-3m1	27.0	104000		45	907
1972	$0.3CaTiO_3$-$0.7Sm(Mg_{0.5}Ti_{0.5})O_3$	1550	Composite	27.0	11970	5.8	−29	865
1973	ZnO-TiO_2-2 wt% ZnO-B_2O_3-SiO_2	930/3h	Composite	27.0	20000		2	908
1974	BaO-$2CeO_2$-$4TiO_2$	1250	Composite	27.0	18560		9	909
1975	$Ba_5Nb_2Ta_2O_{15}$	1475	Trigonal P-3m1 perovskite	27.0	10600	4.7	22	851
1976	$Li_2ZnTi_3O_8$+2 wt% Li_2WO_4	860/4h	Composite	27.0	51100		−4	910
1977	$Nd_5Ti_4CrO_{17}$	1600/4h	Monoclinic	27.0	6400		−94	911

1978	$CaO\text{-}4NiO\text{-}Nb_2O_5\text{-}TiO_2$	1185	Composite	27.0	4000	4.6	−58	230
1979	$Ba_3NiNb_{2-x}Sb_xO_9$ (x=0.25)		Perovskite Cubic Pm3m	27.0	27370	5	−21	381
1980	$LaGaO_3$		Perovskite Orthorhombic Pnma	27.0	97000	5	−80	912
1981	$Ba(Zn_{1/2}Ta_{2/3})O_3$+1 mol% CeO_2	1525/6h, 1350/5h	Complex perovskite Trigonal P-3m1	27.0	123000		14	913
1982	$Ba[(Mg_{0.4}Zn_{0.6})Ta_{2/3}]O_3$	1600/4h	Perovskite Trigonal P-3m1	27.0	109900		4	883
1983	$0.7Ba(Mg_{1/3}Ta_{2/3})O_3$-$0.3Ba(Co_{1/3}Nb_{2/3})O_3$	1530/5h	Complex perovskite Trigonal P-3m1	27.0	172700		−1	914
1984	$Li_2Mg_{0.9}Zn_{0.1}Ti_3O_8$	1075/4h	Ternary spinel Cubic $P4_332$	27.0	62000		1	858
1985	$Li_2Zn_{0.95}Ca_{0.05}Ti_3O_8$	1075/4h	Ternary spinel Cubic $P4_332$	27.0	51100		−2	858
1986	$Bi(Sb_{0.6}Ta_{0.4})O_4$	1000	Monoclinic I2/c	27.0	35000		−15	915
1987	$Ca(Zr_xTi_{1-x})O_3$ (x=1)	1515/15h	Perovskite Orthorhombic Pcnmn	27.0	16500	5.35	−20	916
1988	$Ba_3LiTa_{3-x}Sb_xTi_5O_{21}$ (x=3)	1220	Hexagonal $P6_3/mcm$	27.0	29400		−25	917
1989	$Nd(Co_{1/2}Ti_{1/2})O_3$+1 wt% P_2O_5-ZnO-La_2O_3-Al_2O_3-Na_2O-MgO-Yb_2O_3 glass	1300	Monoclinic $P2_1/n$ Perovskite	27.0	64000		−29	918
1990	$Ba_{1/3}Pr_{2/3}Zn_{1/3}Ti_{2/3}O_3$		Not available	27.0	1000	5.07	−22	919
1991	$Ba_{1/2}Sr_{1/2}(Zn_{1/6}Co_{1/6}Ta_{2/9}Nb_{2/9}Sb_{2/9})O_3$	1550/6h	Perovskite	27.0	32100		−23	814
1992	$Ba_8NiTa_6O_{24}$		Hexagonal $P6_3cm$	27.0	81800			785
1993	$Ba_5Sr_2Ta_4ZrO_{21}$		$A_nB_{n-1}O_{3n}$ Hexagonal Perovskite	27.0	9800			920
1994	$Ba(La_{1/2}Ta_{1/2})O_3$	1450	Perovskite Cubic Fm3m	27.1	18000	8.7	51	590
1995	$Sr(La_{1/2}Ta_{1/2})O_3$	1500	Perovskite Cubic Fm3m	27.1	2600	8.4	−29	590
1996	$(Mg_{1/3}Ta_{2/3})O_2$	1550	Tetragonal $P4_2mmm$	27.1	95360		51	454
1997	$Li_2(Mg_{0.94}Zn_{0.06})Ti_3O_8$	1075	Cubic spinel $P4_332$	27.1	44800		2	855
1998	$Sr(Nd_{1/2}Ta_{1/2})O_3$	1500	Perovskite ubic Fm3m	27.1	25000	8.3	−68	590
1999	$Sr(Er_{0.5}Ta_{0.5})O_3$+0.5 wt% Nb_2O_5	1600/4h	Complex perovskite Tetragonal	27.1	22100		−77	859
2000	$Mg_{0.5}Zn_{0.5}ZrNb_2O_8$	1260	Monoclinic P2/c	27.1	91100		−18	921
2001	$Ca(Gd_{1/2}Ta_{1/2})O_3$	1600/4h	Complex perovskite Monoclinic	27.2	26000		−16	750
2002	$Nd(Co_{1/2}Ti_{1/2})O_3$+0.75 wt% B_2O_3	1320/4h	Perovskite Monoclinic $P2_1/n$	27.2	153000	9	0	922
2003	$Ba_3LiSb_3Ti_5O_{21}$	1220	Hexagonal $P6_3/mcm$	27.2	29400		−25	923

(*continued*)

No.	Material	ST (°C)	Crystal structure	ε_r	Qf (GHz)	f_0	τ_f	Reference
2004	$Li_2MgTi_3O_8$	1075	Ternary spinel Cubic $P4_332$	27.2	42000		3	847
2005	$Bi_3FeMo_2O_{12}$	845/2h	Monoclnic sheelite C2/c	27.2	14500		−80	924
2006	$Ba_2Ti_9O_{20}$+1 wt% ZnO-B_2O_3	940/2h	Monoclinic P-1	27.3	8300	7.2	3	925
2007	$MgTa_{1.4}Nb_{0.6}O_6$	1450	Columbite Tetragonal $P4_2/mmm$	27.3	40800		−3	926
2008	$Ba_8Ta_6(Ni_{1-x}Zn_x)O_{24}$ (x=0.5)		Hexagonal $P6_3cm$	27.4	83800		36	785
2009	$Nd(Co_{1/2}Ti_{1/2})O_3$+0.5 wt% ZnO	1350	Perovskite Monoclinic $P2_1/n$	27.4	147000	8	−30	927
2010	$ZnZr_{0.8}Sn_{0.2}Nb_2O_8$	1275/6h	Monoclinic P2/c	27.4	76800	7	−55	928
2011	TeO_2+10 wt% $SrTiO_3$		Composite	27.5	13100		−46	444
2012	$Ba_8Ta_6NiO_{24}$		Hexagonal $P6_3cm$	27.5	81750		33	785
2013	$Sr(La_{1/2}Nb_{1/2})O_3$	1500	Perovskite Cubic Fm3m	27.5	2000	8.3	−33	590
2014	$Sr(Zn_{1/2}W_{1/2})O_3$	1360	Perovskite Cubic Fm3m	27.5	51000	7.0	−45	528
2015	0.8$La(Mg_{1/2}Ti_{1/2})O_3$-0.2$La_{2/3}TiO_3$	1500/2h	Composite	27.5	16600	7.9		929
2016	$Ba(Mg_{1/3}Nb_{2/3})O_3+B_2O_3$	900	Perovskite Trigonal P-3m1	27.5	8500		27	930
2017	(1-x)$La(Mg_{1/2}Ti_{1/2})O_3$-x$La_{2/3}TiO_3$ (x=0.2)		Perovskite Monoclinic $P2_1/n$	27.5	16600	7.89		889
2018	$Sr(Y_{0.5}Ta_{0.5})O_3$+0.5 wt% Nb_2O_5	1600/4h	Complex perovskite Rhombohedral R3m	27.5	54300		−77	859
2019	90 wt%(Zr,Sn)TiO_4+10 wt% Li_2O-B_2O_3-SiO_2	875	Composite	27.5	9000		14	592
2020	$ZnTiO_3$-0.25TiO_2	925	Composite	27.5	14000		−20	931
2021	$Ba_8Ta_6(Ni_{1-x}Zn_x)O_{24}$ (x=0.75)		Hexagonal $P6_3mc$	27.6	91700		37	785
2022	$Ca[(Li_{1/3}Ta_{2/3})_{.9-}Ti_{0.1}]O_{3-d}$+3 wt% B_2O_3	1000/4h	Perovskite	27.6	9800	10.2	–	765
2023	$La(Mg_{1/2}Ti_{1/2})O_3$	1600	Monoclinic perovskite $P2_1/n$	27.6	114300	7.1	−81	932,933
2024	$(Ca_2Mg_3)Nb_2(Ti_{0.75}Zr_{0.25})O_{12}$	1275		27.6	7600		−36	799
2025	$Li_2Zn_xCo_{1-x}Ti_3O_8$ (x=0.4)	1050/2h	Cubic spinel $P4_332$	27.7	57100		1	934
2026	$Li_2Zn_{0.9}Ca_{0.1}Ti_3O_8$	1075/4h	Ternary spinel Cubic $P4_332$	27.7	44500		11	858
2027	$Sr(Sm_{1/2}Ta_{1/2})O_3$	1500	Perovskite	27.7	59000	8.5	−63	590
2028	$Sr(Ho_{0.5}Ta_{0.5})O_3$+0.5 wt% Nb_2O_5	1600/4h	Complex perovskite Tetragonal	27.7	38800		−75	859
2029	$Ba[(Mg_{0.4}Zn_{0.6})Ta_{2/3}]O_3$	1575	Complex perovskite Trigonal P-3m1	27.7	109900	4.6	6.3	883

2030	$Ba_6Ta_4ZrO_{18}$+2 wt% Bi_2O_3-B_2O_3	1625/2h	$A_6B_5O_{18}$ type perovskite	27.8	41000		5	895
2031	$Li_2ZnTi_3O_8$+2 wt% Bi_2O_3	950	Cubic $P4_332$	27.8	36400			935
2032	$Ba_5SrTa_4ZrO_{18}$+2 wt% Bi_2O_3-B_2O_3	1625/2h	$A_6B_5O_{18}$ type perovskite	27.8	18500		37	895
2033	$Sm_{0.78}Y_{0.22}TiNbO_6$	1400	Orthorhombic Pbnm	27.9	2300		11	564
2034	$MgNb_2O_6$	1450	Columbite Orthorhombic Pcan	27.9	91500			926
2035	$MgTa_{1.5}Nb_{0.5}O_6$	1450	Columbite Tetragonal $P4_2/mmm$	27.9	33100		−1	926
2036	0.8($Mg_{0.95}Co_{0.05}$)TiO_3-0.2($Ca_{0.6}La_{0.8/3}TiO_3$+1 wt% ZnO	1250	Mixed phases	27.9	36000	8	14	936
2037	$Ba_8Ta_6(Ni_{1-x}Mg_x)O_{24}$ (x=0.25)		Hexagonal $P6_3cm$	27.9	81500		32	785
2038	$Sr_{1-x}Ca_x(Ga_{1/2}Ta_{1/2})O_3$		Perovskite	26-28	18000-90000	8	−50 to−97	937
2039	$Zn_{0.9}Co_{0.1}ZrNb_2O_8$	1240/4h	Monoclinic P2/c	27.9	68600	6.95	−62	938
2040	$BaTi_4O_9$-10 mol% BaO-ZnO-B_2O_3 glass	925	Composite	28-33	20000	6.6		939
2041	$Nd(Mg_{1/2}Ti_{1/2})O_3$	1650/2h	Monoclinic perovskite $P2_1/n$	28.0	36900	10	−49	702
2042	$Ba_{1/3}Nd_{2/3}Zn_{1/3}Ti_{2/3}O_3$			28.0	1500	5.03	−19	919
2043	($Zn_{0.9}Mg_{0.1}$)TiO_3+1 wt% V_2O_5	950/4h	Trigonal R-3	28.0	67200		−8	940
2044	$Ba_4LiNb_{3-x}Ta_xO_{12}$ (x=3)	1450	Hexagonal perovskite $P6_3mc$	28.0	103600		25	941
2045	0.47$BaTe_4O_9$-0.53$TiTe_3O_8$	560	Composite	28.0	12000	10	4	942
2046	$Ca(Zr_xTi_{1-x})O_3$ (x=0.8)	1470/15h	Perovskite Cubic Pm3m	28.0	3500	4.35	170	916
2047	$Ba(Tb_{1/2}Ta_{1/2})O_3$	1625	Perovskite	28.0	28200		−38	943
2048	$Ca(Mg_{1/3}Nb_{2/3})O_3$		Complex perovskite Orthorhombic	28.0	58000	–	−48	609,944
2049	$Sr(Zn_{1/3}Ta_{2/3})O_3$	1500	Perovskite Cubic Pm3m	28.0	21700		−54	701
2050	$Ba(Zn_{1/3}Ta_{2/3})O_3$	1350/120h	Complex perovskite Trigonal P-3m1	28.0	168000		1	903
2051	0.6$Ca(Yb_{1/2}Ta_{1/2})O_3$-0.4 $Ba(Yb_{1/2}Ta_{1/2})O_3$	1600/4h	Perovskite	28.0	48000		2	750
2052	$Ca(Yb_{1/2}Ta_{1/2})O_3$+4 mol% $CaTiO_3$	1600/4h	Perovskite	28.0	41000		−2	750

(*continued*)

No.	Material	ST (°C)	Crystal structure	ε_r	Qf (GHz)	f_0	τ_f	Reference
2053	$Ba[Zr_{0.0645}\ Ni_{0.1625}Zn_{0.816}Ta_{1.957}]O_3$	1520/48h	Perovskite Trigonal P-3m1	28.0	136770		−3	945
2054	$Ba(Zn_{1/3}Ta_{2/3})O_3$+1 mol% Cr_2O_3	1525/6h	Complex perovskite Hexagonal P-3m1	28.0	125500		−2	913
2055	$Ca(Ho_{1/2}Ta_{1/2})O_3$	1600/4h	Perovskite Monoclinic $P2_1/n$	28.0	23700		−8	750
2056	$Sr(Dy_{1/2}Ta_{1/2})O_3$	1600/4h	Perovskite	28.0	34200		−73	861
2057	$Sr(Ho_{1/2}Ta_{1/2})O_3$	1600/4h	Perovskite	28.0	38800		−75	861
2058	$Sr(Y_{1/2}Ta_{1/2})O_3$	1600/4h	Perovskite Monoclinic $P2_1/n$	28.0	54300		−77	861
2059	$Ca(Ca_{1/3}Nb_{2/3})O_3$		Perovskite Monoclinic	28.0	17000	–	−22	609
2060	$Zn(Nb_{0.35}Ta_{0.65})_2O_6$	1300	Columbite Orthorhombic Pbcn	28.0	50000		0	946
2061	$0.5Ca_2AlNbO_6$-$0.5Ca_3Nb_2O_8$		Mixture phases	28.0	8900	6.86	36	864
2062	$MgTa_2O_6$+0.5 wt% CuO	1400	Trirutile structure Tetragonal $P4_2/mmm$	28.0	58000		18	947
2063	$Zn_{0.4}Co_{0.6}TiO_3$	1200	Spinel+rutile	28.0	70000			948
2064	$Pr(Mg_{1/2}Ti_{1/2})O_3$	1650/2h	Perovskite	28.0	27800	10	−17	702
2065	$Ba_5Ta_4O_{15}(A_nB_{n-1}O_{3n})$	1550	Trigonal P-3m1 perovskite	28.0	31600	5.55	12	325,851
2066	3CaO-2CoO-Ta_2O_5-TiO_2	1400	Mixture	28.0	19500	4.8	−14	230
2067	$0.75(Al_{1/2}Ta_{1/2}O_2)$-$0.25(Ti_{0.85}Sn_{0.15})O_2$	1450/3h	Composite	28.0	68000		0	949
2068	$(1-x)LaMg_{1/2}Ti_{1/2}O_3$-$xLa_{2/3}TiO_3$ (x=0.1)		Perovskite	28.0	56000	6.6	−66	950
2069	$(1-x)Sr(Li_{1/4}Nb_{3/4})O_3$-$xSr(Li_{2/3}W_{3/5})O_3$ (x=0.283)	1450	Provskite Monoclinic $P2_1/c$	28.0	23800	9.1	30	951
2070	$Ba_8Li_2Ta_6O_{24}$		Hexagonal $P6_3mmc$	28.0	103600		−29	952
2071	$MgZr_{1.32}Nb_2O_{8.64}$	1320/6h	Wolframite	28.0	68600		1	953
2072	$La_5AlTi_3O_{15}$	1600	Hexagonal perovskite	28.1	28600	3.4	−39	954
2073	$0.09[0.5ZnNb_2O_6$-$0.5Zn_3Nb_2O_8]$-*0.91*$ZnTa_2O_6$+5 wt% ZBS	900	Composite	28.1	32800		−8	955
2074	$Ba(Zn_{1/2}W_{1/2})O_3$	1340	Perovskite Cubic Fm3m	28.1	22700	8		432
2075	Al_2O_3-TiO_2-Ta_2O_5	1575	Composite	28.1	1000		20	583
2076	$SrHfO_3$	1750	Cubic Pm3m	28.1	33500	9.3	−63	850
2077	$Ba(Ti_{0.5}Mn_{0.5})O_3$+5 wt% Li_2CO_3	1200	Perovskite Hexagonal	28.1	5300		35	956
2078	$Li_2Cu_{0.2}Mg_{0.8}Ti_3O_8$	950	Cubic $P4_332$	28.1	34300		9	957

2079	$Ba[Ti_{1-x}(Zn_{1/2}W_{1/2})_x]O_3$ (x=1)	1380	Cubic perovskite $Fm3^{-}m$	28.2	15200		−16	695
2080	$Ba_{10}Mg_{0.25}Ta_{7.9}O_{30}$	1600/12h	Hexagonal $P6_3mc$	28.2	33500		29	958
2081	$Sr(Dy_{0.5}Ta_{0.5})O_3$+0.5 wt% Nb_2O_5	1600/4h	Complex perovskite tetragonal	28.2	34200		−73	859
2082	$Ca(Ho_{1/2}Ta_{1/2})O_3$	1600/4h	Complex perovskite Monoclinic $P2_1/n$	28.2	23700		−8	750
2083	$BaTa_2V_2O_{11}$	870	Rhombohedral R-3m	28.2	41950		91	336
2084	$La(Zn_{1/2}Ti_{1/2})O_3$ (sol gel)		Perovskite	28.3	66500			959
2085	$La_2Ti_2SiO_9$	1325	Monoclinic C2/m	28.3	29500		23	960
2086	$Ba(Zn_{1/3}Ta_{2/3})O_3$+1 wt% V_2O_3	1600	Perovskite Trigonal P-3m1	28.4	236000			961
2087	$Li_2Mg_{0.95}Ca_{0.05}Ti_3O_8$	1075/4h	Ternary spinel cubic $P4_332$	28.4	40000		14	858
2088	$Ca[(Li_{1/3}Nb_{2/3})_{0.75}Ti_{0.25}]O_{3-d}$+12 wt% LMZBS glass	920/4h	Perovskite	28.4	11000	4.8	−3	792
2089	$Ca[(Li_{1/3}Ta_{2/3})_{.8}Ti_{0.2}]O_{3-d}$+3 wt% B_2O_3	1050	Perovskite	28.4	12900	9.9	−15	765
2090	$Sr_6Ta_4ZrO_{18}$+3 wt% Bi_2O_3-B_2O_3 glass	1625/2h		28.4	9100		−39	895
2091	$ZnZrNb_2O_8$+3 wt% $BaCu(B_2O_5)$	950/4h	Monoclinic	28.4	56700		−53	962
2092	$Ba_3MgNb_{2-x}Sb_xO_9$ (x=0.125)		Perovskite Trigonal P-3m1	28.5	101300	4.7	14	381
2093	$0.8(Mg_{0.5}Zn_{0.4})_{0.95}Co_{0.05}TiO_3$-$0.2Ca_{0.61}Nd_{0.26}TiO_3$	1250	Mixed phases	28.6	80600		4	963
2094	TeO_2+10 wt% $CaTiO_3$	645	Composite	28.7	15600		−3	444
2095	$0.6[0.7ZnNb_2O_6$-$0.3Zn_3Nb_2O_8]$-$0.4TiTe_3O_8$	670	Composite	28.7	5700		3	964
2096	$(Mg_{0.95}Ni_{0.05})Ta_2O_6$	1525	Tetragonal $P4_2/mmm$	28.7	88300		45	965
2097	$(Pb_{1-3x/2}La_x)(Mg_{1/2}W_{1/2})O_3$ (x=0.56)	1200	Perovskite Orthorhombic	28.7	18100		−6	966
2098	$Li_2Mg_{0.96}Zn_{0.04}Ti_3O_8$	1200	Cubic Spinal	28.7	151200		−3	896
2099	$Sr(Tb_{0.5}Ta_{0.5})O_3$+0.5 wt% Nb_2O_5	1600/4h	Complex perovskite Tetragonal	28.8	46200		−70	859
2100	$Mg_{0.3}Co_{0.7}Ta_2O_6$	1500/2h	Tetragonal $P4_2/mmm$	28.8	22900		34	967
2101	$Li_2CoTi_3O_8$	1025	Cubic spinel $P4_332$	28.9	52600		7	968
2102	$Ba_8Ta_6ZnO_{24}$		Hexagonal $P6_3cm$	28.9	85000		40	785
2103	$SmTaTi_{0.6}Zr_{0.4}O_6$			28.9	38320		−12	671
2104	$0.7LaAlO_3$-$0.3SrTiO_3$	1680	Composite	28.9	120000	9.9	−44	832
2105	$Zn_{0.95}Ni_{0.05}ZrNb_2O_8$			29.0	83600		−49	969

(*continued*)

No.	Material	ST (°C)	Crystal structure	ε_r	Qf (GHz)	f_0	τ_f	Reference
2106	$Ca(Co_{1/3}Nb_{2/3})O_3$		Complex perovskite Orthorhombic	29.0	6200	–	−65	609
2107	$BaO\text{-}TiO_2\text{-}WO_3$ (N-35): $ZnO\text{-}B_2O_3$	1100	Composite	29.0	7000	5.8	–	786,862
2108	$CoTa_2O_6$	1500	Trirutile Tetragonal $P4_2/mmm$	29.0	2300		23	600
2109	$La(Mg_{1/2}Ti_{1/2})O_3$	1650/2h	Perovskite Monoclinic $P2_1/n$	29.0	114000		−81	933
2110	$Ba(Zn_{1/2}Ta_{2/3})O_3$+0.3 mol% Ta_2O_5	1620/10h	Complex perovskite Trigonal P-3m1	29.0	152000			162
2111	0.95 $Ba(Zn_{1/2}Ta_{2/3})O_3$-0.05Sr $(Ga_{1/2}Ta_{1/2})O_3$	1550/2h, 1450/24h	Perovskite	29.0	162000		0	970,971
2112	$Ba_3(Zr_{0.0645}Zn_{0.816}Ni_{0.1625}Ta_{1.957})O_9$	1510/24h	Complex perovskite Trigonal P-3m1	29.0	126860		−2	972
2113	$Sr(Tb_{1/2}Ta_{1/2})O_3$	1600/4h	Perovskite	29.0	34200		−70	861
2114	$3CaO\text{-}2NiO\text{-}Ta_2O_5\text{-}TiO_2$	1500	Composite	29.0	18800	4.9	−33	230
2115	$2CaO\text{-}3CoO\text{-}Ta_2O_5\text{-}TiO_2$	1175	Composite	29.0	18500	4.9	−28	230
2116	$La_{10}MgTi_9O_{34}$		Perovskite slab series	29.0	13000	5.9	−22	950
2117	$BaTiTe_3O_9$	650		29.0	1700	7.6	−372	973
2118	$(1\text{-}x)Ca(Li_{1/4}Nb_{3/4})O_3\text{-}xCa(Li_{2/3}W_{3/5})O_3$ (x=0.333)	1150	Provskite Trigonal $P2_1/c$	29.0	15700	9.7	−35	951
2119	$(Sr_{2/3}La_{1/3})(Li_{1/3}Nb_{2/3})O_3$	1300	Not available	29.0	6300	8.9	−76	824
2120	CeO_2+0.06$CaTiO_3$	1650/2h	Cubic flurite Fm3m	29.0	25000		0	525
2121	$La(Mg_{1-x}Zn_x)_{1/2}Ti_{1/2}O_3$ (x=0.3)	1475/4h	Perovskite Cubic Pa3	29.0	74000		−63	974
2122	$Sr_{4-m}La_mTi_{m-1}Ta_{4-m}O_{12}$ (m=1)	1560	Cation deficient Hexagonal perovskite	29.0	16050		−43	975
2123	$Mg(Nb_{0.7}Ta_{1.3})O_6$		Columbite	29.0	67800		1	976
2124	$Ba_8Ga_{0.8}Ta_{5.92}O_{24}$	1450/24h	Hexagonal $P6_3cm$	29.0	29000		11	952
2125	$Ba_8CoTa_6O_{24}$		Hexagonal $P6_3cm$	29.0	69400			952
2126	$Ba_8CuTa_6O_{24}$		Hexagonal $P6_3cm$	29.0	8600			952
2127	$0.5CeO_2\text{-}0.25MnO\text{-}0.25TiO_2$:0.4 Sb_2O_3	1200	Composite	29.1	7000	4.9221	−1	488
2128	$Ba(Zn_{1/2}W_{1/2})O_3$	1330	Perovskite cubic Fm3m	29.1	36000	6.8	−31	528
2129	$La(Mg_{1-x}Co_x)_{1/2}TiO_3$ (x=1)+1 wt% ZnO	1375/4h	Perovskite	29.1	80000		−59	977

2130	$BaHfO_3$	1750	Cubic perovskite Pm3m	29.1	5400	8.85	111	850
2131	$Zn_{0.95}Mg_{0.05}ZrNb_2O_8$			29.1	81200			969
2132	$Ca_2Mg_3(Nb_{1.75}Sb_{0.25})TiO_{12}$	1250	Mixture phases	29.2	18800		−22	843
2133	$Pr_2Ti_2SiO_9$	1325	Monoclinic C2/m	29.2	33700		20	960
2134	$0.9La(Mg_{1/3}Ti_{1/3})O_3$-$0.1SrTiO_3$		Perovskite Pbnm	29.2	14500	7.33		978
2135	$0.9Nd(Co_{1/2}Ti_{1/2})O_3$-$0.1SrTiO_3$	1440/4h	Perovskite mixtures	29.3	80900		0	979
2136	$Ba_6Ta_4TiO_{18}$	1550/2h	Not available	29.3	27500		45	895
2137	$(1-x)La(Mg_{1/2}Ti_{1/2})O_3$-$xLa_{2/3}TiO_3$ (x=0.3)		Perovskite Orthorhombic Pnma	29.3	6500	8.3		889
2138	$Sm(Mg_{0.5}Ti_{0.5})O_3$+10 mol% Bi_2O_3	1300	Composite	29.3	26300	8.84	−33	898
2139	$Mg_{0.7}Co_{0.3}Ta_2O_6$	1500/2h	Tetragonal $P4_2/mmm$	29.3	45700		40	967
2140	$SrYb_{1/2}Nb_{1/2})O_3$+0.2 wt% B_2O_3	1350/4h	Complex perovskite Orthorhombic	29.3	30600		−75	823
2141	$Ca[(Li_{1/3}Nb_{2/3})_{0.95}Zr_{0.15}]O_{3+d}$+5 wt% Li_2O-B_2O_3-SiO_2-CaO-Al_2O_3 glass	940	Perovskite	29.4	5400		−25	980
2142	$Sr(Yb_{1/2}Nb_{1/2})O_3$	1500	Perovskite Hexagonal	29.4	50000	8.1	−72	590
2143	$0.8(Al_{1/2}Ta_{1/2})O_2$-$0.2TiO_2$	1450/3h	Tetragonal	29.4	75470		0	981
2144	$Ca[(Li_{1/3}Ta_{2/3})_{.85}Ti_{0.15}]O_{3-d}$+3 wt% B_2O_3	1050/4h	Perovskite	29.4	20700	10.47	−57	765
2145	$Ba_6Ti_{1-x}Sn_xNb_4O_{18}$ (x=1)	1530	Trigonal R-3m	29.5	28500	6.06	0	982
2146	$Sr(Gd_{0.5}Ta_{0.5})O_3$+0.5 wt% Nb_2O_5	1600/4h	Complex perovskite Tetragonal	29.5	4000		−66	859
2147	$BaZn_{1.98}Cu_{0.02}Ti_4O_{11}$	1190/2h	Orthorhombic Pbcn	29.5	51400		−34	983
2148	$0.85(Mg_{0.7}Zn_{0.3})_{0.95}Co_{0.05}TiO_3$-$0.15Ca_{0.8}Sm_{0.4/3}TiO_3$		Composite	29.5	65000	9	1	984
2149	$ZnZrNb_2O_8$			29.5	61000		−53	969
2150	$Pr_xY_{1-x}TiTaO_6$ (x=0.23)	1600		29.6	41000		5	985
2151	$Zn_{0.95}Co_{0.05}ZrNb_2O_8$			29.6	60500			969
2152	$0.94CoNb_2O_6$-$0.06TiO_2$	1150	Composite	29.6	20300		4	545
2153	$0.78ZnNb_2O_6$-$0.22TiO_2$	1200	Composite	29.6	27700		22	545
2154	$Ca[Li_{1/3}Nb_{2/3}]O_3$	1150/3h	Perovskite	29.6	40000		−21	752
2155	$Ca(In_{1/2}Nb_{1/2})O_3$	1550/4h	Complex perovskite Orthorhombic	29.6	37900		−33	763
2156	$La(Mg_{1/2}Ti_{1/2})O_3$+1 wt% CuO	1450	Perovskite $P2_1/n$	29.6	33800		−68	986

(*continued*)

No.	Material	ST (°C)	Crystal structure	ε_r	Qf (GHz)	f_0	τ_f	Reference
2157	$Sr(Nd_{1/2}Nb_{1/2})O_3$	1500	Perovskite	29.7	2500	8.1	−32	590
2158	$SmTaTi_{0.5}Zr_{0.5}O_6$			29.7	32173		−21	671
2159	$Ba_{10}Co_{0.25}Ta_{7.9}O_{30}$	1600/24h	Hexagonal $P6_3mc$	29.7	36700		29	865
2160	$0.23BaWO_4$-$0.77Ba_5Nb_4O_{15}$	1100	Composite	29.7	44600		28	485
2161	$(1-y)Li_{2.02}Ti_{0.92}Nb_{0.06}O_3$ (y=0.4)	1070		29.8	10000		24	722
2162	$Mg_{0.93}Co_{0.07}Ta_2O_6$	1500/2h	Tetragonal $P4_2/mmm$	29.8	68200		42	967
2163	$Ca[(Li_{1/3}Nb_{2/3})_{0.9}Zr_{0.1}]O_{3-d}$	1150	Perovskite	29.8	36300		−5	987
2164	$Ba[Ti_{1-x}(Ni_{1/2}W_{1/2})_x]O_3$ (x=0.4)	1425	Perovskite Hexagonal $P6_3/mmc$	29.8	26700		7	695
2165	$0.9La(Mg_{1/2}Ti_{1/2})O_3$-$0.1CaTiO_3$	1600	Perovskite $P2_1/n$	29.8	16700	6.9	−70	932
2166	$La(Co_{1/2}Ti_{1/2})O_3$+0.25 wt% CuO	1380	Orthorhombic Pnm_{21}	29.8	64000	8	−56	988
2167	$NdNbO_4$	1150	Fergusonite	29.8	49000		53	989
2168	$Zn_{0.95}Mn_{0.05}ZrNb_2O_8$			29.8	59800		−40	969
2169	$Ba_3YNb_3O_{12}$	1450		29.9	39500		24	990
2170	$Ca[(Li_{1/3}Nb_{2/3})_{1-x}Zr_x]O_3$ (x=0.05)	1150	Perovskite orthorombic	29.9	46300		−20	733
2171	$La(Mg_{1-x}Zn_x)_{1/2}Ti_{1/2}O_3$+1 wt% B_2O_3	1475	Perovskite Cubic Pa3	30.0	74000		−63	991
2172	$7Bi_2O_3$-MoO_3	820	Composite	30.0	1900		−20	494
2173	$Ca(Dy_{1/2}Ta_{1/2})O_3$	1600/4h	Complex perovskite Monoclinic $P2_1/n$	30.0	26500		−6	750
2174	$ZnZrNb_2O_8$	950	Monoclinic P2/c	30.0	61000		−52	992
2175	$Ba(Yb_{1/2}Nb_{1/2})O_3$	1700	Complex perovskite Orthorhombic	30.0	16500	8.7	118	590
2176	Nb_2O_5-$Zn_{0.95}Mg_{0.05}TiO_3$+0.25TiO_2+5 wt% Bi_2O_3	960	Composite	30.0	12000		−12	993
2177	$Ba_4LiNb_{3-x}Ta_xO_{12}$ (x=2)	1400	Hexagonal perovskite	30.0	37500		34	941
2178	$Sr(Al_{1/2}Nb_{1/2})O_3$+0.2 wt% B_2O_3	1350/4h	Complex perovskite	30.0	22500		−2	823
2179	$La_4Ba_2Ti_5O_{18}$+B_2O_3		Hexagonal R	30.0	20000		55	994
2180	$Ba(Zn,Ta)O_3$-$Ba(Zn,Nb)O_3$		Complex perovskite Trigonal P-3m1	30.0	164000	12	0	903
2181	$Ba(Ca_{1/3}Ta_{2/3})O_3$		Perovskite Hexagonal	30.0	27400	7	145	701
2182	$BaNb_2O_6$	1300	Orthorhombic $C222_1$	30.0	43000		−45	995
2183	$Pb_{0.5}Ca_{0.5}(Al_{1/2}Nb_{1/2})O_3$		Perovskite	30.0	1500	5.1	−23	996

2184	$CaZrO_3$		Perovskite Pcmn Orthorhombic	30.0	26400	11	−27	997,998
2185	$SrZrO_3$		Perovskite Orthorhombic Pcmn	30.0	13600	11	−67	997,998
2186	$La(Co_{1/2}Ti_{1/2})O_3$	1440/6h	Perovskite Orthorhombic $Pnm2_1$	30.0	67000	10	−64	819
2187	$Ba_8Li_2Nb_2Ta_4O_{24}$		Hexagonal $P6_3mmc$	30.0	37500			952
2188	$Ca[(Li_{1/3}Nb_{2/3})_{0.9}\ Zr_{0.1}]O_{3-\delta}$	1150	Perovskite	30.0	36300		−5	999
2189	$(1-x)Sr(Li_{1/4}Nb_{3/4})O_3$-$xSr(Li_{2/5}W_{3/5})O_3$ (x=0.385)	1450	Provskite monoclinic $P2_1/c$	30.0	21200		−33	951
2190	$(1-x)Ca(Li_{1/4}Nb_{3/4})O_3$-$xCa(Li_{2/5}W_{3/5})O_3$ (x=0.238)	1150	Perovskite	30.0	22700		−33	951
2191	$ZnTiO_3$+0.25TiO_2+1 wt% B_2O_3	875/4h	Mixture	30.0	56000		10	1000
2192	$Sm_{0.8}Y_{0.2}TiNbO_6$	1400	Orthorhombic Pbnm	30.0	11000		17	564
2193	$Ba_5Ta_4O_{15}$	1550/40h	Hexagonal perovskite	30.0	31600		12	325
2194	$Bi_2ZnNb_2O_9$+$ZnNb_2O_6$+3 wt% PbO-Bi_2O_3-B_2O_3-ZnO-TiO_2 glass	900	Composite	30.0	3500	6		1001
2195	$Ba_2Ti_9O_{20}$+9 wt% B_2O_3	1050/2h	Monoclinic $P2_1/m$	30.0	13700		6	1002
2196	$Ba(Zn_{1/3}Ta_{2/3})O_3$+1 mol% Mn	1550	Perovskite Trigonal P-3m1	30.0	145000		0	787
2197	$Ba_3[Zr_{0.09}Ni_{0.125}Zn_{0.845}Ta_{1.94}]O_3$	1520/48h	Perovskite Trigonal P-3m1	30.0	138710		−1	945
2198	$Ba(Zr_{0.05}Zn_{0.32}Ta_{0.63})O_3$	1500/4h	Complex perovskite Trigonal P-3m1	30.0	148000		8	1003
2199	0.15$TiTe_3O_8$-0.85TeO_2	700	Composite	30.0	22000	5	0	586
2200	BaO-CeO_2-TiO_2+1.5 wt% CuO	1050	Composite	30.0	32000		−11	366
2201	$Ca_{1-x}Nd_{2x/3})TiO_3$+3ZnO-2B_2O_3 glass (20-40 mol%)	880	Perovskite Tetragonal	30-60	200-5500		20-60	1004
2202	3CaO-2MgO-Ta_2O_5-TiO_2	1550	Composite	30.0	185000	4.6	−24	230
2203	$La(Zn_{1/2}Ti_{1/2})O_3$sol-gel	1350	Perovskite Orthorhombic	30.0	60000		−71	1005
2204	$Ca(Yb_{1/2}Nb_{1/2})O_3$	1550/4h	Complex perovskite Orhorhombic	30.0	32500		−25	763
2205	$Sr(Eu_{1/2}Ta_{1/2})O_3$	1600/4h	Complex perovskite	30.0	45500		−43	861
2206	$Sr(Gd_{1/2}Ta_{1/2})O_3$	1600/4h	Complex perovskite	30.0	4000		−66	861
2207	$Ca(Dy_{1/2}Ta_{1/2})O_3$	1600/4h	Complex perovskite	30.0	26500		−6	750
2208	$BaZn_2Ti_4O_{11}$	1200	Orthorhombic Pbcn	30.0	68000		−30	1006

(*continued*)

No.	Material	ST (°C)	Crystal structure	ε_r	Qf (GHz)	f_0	τ_f	Reference
2209	$Ba_5SrTa_4ZrO_{18}$+2 wt% Bi_2O_3-B_2O_3 glass	1525/4h	Trigonal R-3m	30.0	18500		37	895
2210	$BaZn_{1.95}Ti_4O_{10.95}$	1200	Orthorhombic Pbcn	30.0	110000			1006
2211	$La(Co_{1/2}Ti_{1/2})O_3$+0.25 wt% B_2O_3	1350/6h	Perovskite	30.0	64600	8	−48	1007
2212	(1-x)$Sr(Li_{1/4}Nb_{3/4})O_3$-x$Sr(Li_{2/5}W_{3/5})O_3$ (x=0.385)	1450	Perovskite	30.0	21200	9.2	−33	951
2213	$(Ca_{2/3}La_{1/3})(Li_{1/3}Nb_{2/3})O_3$	1250	Monoclinic $P2_1/c$	30.0	26500	8.7	−26	824
2214	(1-x)$CaTiO_3$-x$Sm(Mg_{1/2}Ti_{1/2})O_3$ (x=0.8)		Orthorhombic Pnm1 Perovskite	30.0	13000		−20	1008
2215	$BaZn_{2-x}Ti_4O_{11-x}$ (x=0-0.1)	1250/4h	Orthorhombic Pbcn	30.0	83000		−30	1006
2216	$Ba_{10}Co_{0.25}Ta_{7.9}O_{30}$	1550	$P6_3mc$	30.0	36700	3.78	29	958
2217	$Sr(Eu_{0.5}Ta_{0.5})O_3$+0.5 wt% Nb_2O_5	1600/4h	Complex perovskite Tetragonal	30.0	45500		−63	859
2218	$Nd_5Ti_4FeO_{17}$	1400	Monoclinic P21/b	30.0	7400		−104	911
2219	$Ba_6Ta_4ZrO_{18}$+2 wt% Bi_2O_3-B_2O_3 glass	1625/2h		30.1	41000		5	895
2220	La_2O_3-WO_3-TiO_2	1350	Multiphase	30.1	9225	5.8	−17	400
2221	$Nd_2Ti_2SiO_9$	1300	Monoclinic C2/m	30.1	19600		10	960
2222	TeO_2+15 wt% $CaTiO_3$		Composite	30.1	21400		29	444
2223	$MgTa_2O_6$ (Sol-gel)	1200	Columbite Tetragonal $P4_2/mmm$	30.1	57300		29	1009
2224	$Ca[(Li_{1/3}Nb_{2/3})_{1-x}Zr_x]O_3$ (x=0.1)	1150	Perovskite Orthorhombic	30.1	36000		−5	733
2225	0.8$Sm(Mg_{0.5}Ti_{0.5})O_3$-0.2$Ca_{0.8}Sr_{0.2}TiO_3$	1550/3h	Perovskite	30.1	115000		9	1010
2226	$LiBiW_2O_8$+30 mol% TiO_2	700/2h	Composite	30.2	13000		−9	888
2227	$La(Co_{1/2}Ti_{1/2})O_3$+0.75 wt% ZnO	1320	Perovskite	30.2	73000	8	−35	1011
2228	MWF-38+10 wt% Li_2O-B_2O_3-SiO_2-(56.92:37.59:5.49)	875	Composite	30.2	9500		3	510
2229	$BaLi_2Ti_6O_{14}$+0.5 wt% $BaCu(B_3O_5)$	920	Orthorhombic Cmca	30.2	28400		−18	1012
2230	$MgTa_2O_6$	1550	Tetragonal $P4_2/mmm$	30.3	59600		30	600
2231	$ZnTa_2O_6$	1400	Orthorhombic Pbcn	30.3	87580		9	1013
2232	$Eu(Zr_{1/3}Ti_{2/3})O_6$	1600	Aeschyenite Orthorhombic Pnma	30.4	11000	4.5	−4	1014
2233	$Nd(Zn_{1/2}Ti_{1/2})O_3$+1.5 wt% CuO	1240	Complex perovskite Monoclinic	30.4	14000	8	−44	1015
2234	$(AgBi)_{1/2}MoO_4$	690	Tetragonal $I4_1/a$	30.4	12600	8.7	57	677
2235	$Mg_{0.99}Co_{0.01}Ta_2O_6$	1500/2h	Tetragonal $P4_2/mmm$	30.4	72500		44	967
2236	$Eu(Zr_{1/3}Ti_{2/3})O_6$	1600/4h	Aeschyenite Orthorhombic Pnma	30.4	11000		−4	1014

2237	$Ba_{1-x}La_{2x/3}ZrO_3$ (x=0.1)	1430/15h	Cubic Pm3m	30.4	9000	4.7	165	1016
2238	$Ca[(Li_{1/3}Nb_{2/3})_{0.8}Ti_{0.2}]O_{3-d}$+5 wt% LBS glass	950/4h	Complex perovskite Orthorhombic	30.5	14700	4.6	−18	792
2239	$Ba(Y_{1/2}Ta_{1/2})O_3$		Complex perovskite	30.5	38500	9.4	135	1017
2239	$Ba(Y_{1/2}Ta_{1/2})O_3$		Complex perovskite	30.5	38500	9.4	135	1017
2240	$Sr(Al_{1/2}Nb_{1/2})O_3$	1600/4h	Complex perovskite	30.5	10800		−27	823
2241	$0.09[0.5ZnNb_2O_6$-$0.5Zn_3Nb_2O_8]$-*0.91*$ZnTa_2O_6$+3 wt% BBS	950	Composite	30.5	32600		−11	955
2242	$Ba_8ZnTa_6O_{24}$	1400	Hexagonal perovskite	30.5	62000	8.9	36	818
2243	$Sr(Sm_{0.5}Ta_{0.5})O_3$+0.5 wt% Nb_2O_5	1600/4h	Complex perovskite Tetragonal	30.5	45200		−61	859
2244	$Ca(Li_{1/3}Nb_{2/3})O_{3-d}$+4 wt% B_2O_3	1000	Perovskite orthorhombic	30.6	31000		−18	1018
2245	$MgTa_2O_6$	1550	Tetragonal $P4_2/mmm$	30.6	58200		29	926
2246	$Mg_{0.97}Co_{0.03}Ta_2O_6$	1500/2h	Tetragonal $P4_2/mmm$	30.6	89000		43	967
2247	$Sr(Ho_{1/2}Nb_{1/2})O_3$+0.2 wt% B_2O_3	1350/4h	Perovskite Tetragonal	30.6	16650		−66	823
2248	$Sr(Y_{1/2}Nb_{1/2})O_3$+0.2 wt% B_2O_3	1350/4h	Complex perovskite Orthorhombic	30.7	42500		−67	823
2249	$Mg_{0.95}Co_{0.05}Ta_2O_6$	1500/2h	Tetragonal $P4_2/mmm$	30.7	106200		43	967
2250	$Sr(Yb_{1/2}Nb_{1/2})O_3$+0.5 wt% CeO_2	1600/4h	Complex perovskite Orthorhombic Pnma	30.7	26600		−73	823
2251	$Nd(Zn_{1/2}Ti_{1/2})O_3$+1 wt% CuO	1270	Complex perovskite Monoclinic	30.7	158000	8	−45	1015
2252	$Ca(Fe_{1/2}Ta_{1/2})O_3$		Complex perovskite	30.7	3000	5.38		1019
2253	$Mg_{0.5}Zn_{0.5}TiNb_2O_8$	1120/6h	Not available	30.7	66900		−4	1020
2254	$Ca[(Li_{1/3}Nb_{2/3})_{0.8}Ti_{0.2}]O_{3-d}$+5 wt% LMZBS	975	Complex perovskite Orthorhombic	30.7	22600		−18	792
2255	$Sr_6Ta_4ZrO_{18}$+3 wt% Bi_2O_3-B_2O_3	1625/2h	$A_6B_5O_{18}$ type perovskite	30.8	5600		−19	895
2256	$Nd(Zn_{1/2}Ti_{1/2})O_3$+0.75 wt% CuO	1300	Complex perovskite Monoclinic	30.8	147500	8	−45	1015
2257	$Zn(Ti_{1-x}Sn_x)Nb_2O_8$		Orthorhombic Pbcn	30.9	43500		−54	1021
2258	$0.8Li_2ZnTi_3O_8$-$0.2TiO_2$	1100	Ternary spinel cubic $P4_332$	30.9	56100		29	872

(*continued*)

No.	Material	ST (°C)	Crystal structure	ε_r	Qf (GHz)	f_0	τ_f	Reference
2259	$0.1BaTiO_3$-$0.9La(Mg_{1/2}Ti_{1/2})O_3$		Perovskite Pbnm	30.9	16330	8.29	−72	933
2260	$Li_{0.774}Zr_{0.057}NbO_3$	1150	Orthorhombic Pnma	30.9	3550		−16	1022
2261	$Ba_3ZnNb_{2-x}Sb_xO_9$ (x=0.75)		Perovskite Cubic Pm3m	30.9	23700	5	0	381
2262	$Ba_3ZnNb_{2-x}Sb_xO_9$ (x=0.5)		Perovskite Cubic Pm3m	30.9	35620	5.3	−11	381
2263	$0.85BaTi_4O_9$-$0.15BaZn_2Ti_4O_{11}$+11 wt% $BaCu(B_2O_5)$	900	Composite	30.9	20200		12	1023
2264	$Ba_{1-x}Ca_x(Nd_{1/2}Nb_{1/2})O_3$		Perovskite Cubic Fm3m	30-42	25000-5000			1017
2265	$Ba_{1-x}Ca_x(Y_{1/2}Ta_{1/2})O_3$		Perovskite	30-22				1017
2266	(1-x)$LaMg_{1/2}Ti_{1/2}$-x$La_{2/3}TiO_3$ (x=0.2)		Perovskite	31.0	43000	6.3	−54	950
2267	2CaO-3NiO-Nb_2O_5-TiO_2	1275	Composite	31.0	7500	4.3	−49	230
2268	(1-x)$Sr(Li_{1/4}Nb_{3/4})O_3$-x$Sr(Li_{2/3}W_{3/5})O_3$ (x=0.333)	1450	Perovskite monoclinic $P2_1/c$	31.0	27400	8.7	−23	951
2269	$(Sr_{0.15}Ba_{0.85})(Yb_{0.5}Ta_{0.5})O_3$	1600/4h	Complex perovskite	31.0	32100		0	859
2270	(1-x)$Ca(Li_{1/4}Nb_{3/4})O_3$-x$Ca(Li_{2/3}W_{3/5})O_3$ (x=0.238)	1150	Provskite monoclinic $P2_1/c$	31.0	22700	10.3	−33	951
2271	(1-x)Ba $(Li_{1/4}Nb_{3/4})O_3$-x$Ba(Li_{2/3}W_{3/5})O_3$ (x=0.333)	1470	Perovskite Cubic P-3m1	31.0	19000	7.8	18	1024
2272	$Sm(Zn_{1/2}Ti_{1/2})O_3$	1310/2h	Perovskite Orthorhombic Pnm	31.0	37000	8	−19	1025
2273	$Ba_3Zn_7Ti_{12}O_{34}$	1150/4h		31.0	4300		−25	1026
2274	BaO-TiO_2-WO_3 (N-35):5 wt% Al_2O_3-SiO_2-B_2O_3	1100	Composite	31.0	5400	5.7	–	786,862
2275	$Ba(Mg_{1/3}Nb_{2/3})O_3$+2 mol% B_2O_3+10 mol% CuO	875	Perovskite composite	31.0	21500		21	1027
2276	$0.5Ba(Mg_{1/2}W_{1/2})O_3$-$0.5BaTiO_3$		Perovskite composite	31.0	8200	–	125	373
2277	$Ba_8Zn(Nb_{6-x}Sb_x)O_{24}$ (x=0.9)	1425		31.0	11550		21	503
2278	Bi_2MoO_6	750	Monoclinic $P2_1/n$	31.0	16700	6.4	−114	494
2279	$(Zr_{0.8}Sn_{0.2})TiO_4$+MnO_2	1350/4h	Orthorhombic Pbcn	31.0	93000	9.3		1028
2280	3Bi_2O_3-2MoO_3	820		31.0	1000		−41	494
2281	$Mg_4La_2Ti_5O_{17}$	1350/4h		31.0	15000		4	1029

2282	$BaO\text{-}4.3TiO_2\text{-}0.5ZnO$+7 wt% BCB	900	Composite	31.0	18200		4	1030
2283	$(Zn_{0.5}Co_{0.5})TiO_3$	1150	Perovskite	31.0	60000		75	704
2284	$0.75(Al_{1/2}Ta_{1/2})O_2\text{-}0.25(Ti_{1-x}\ Sn_x)O_2$	1450/3h	Composite	31-26	54600-70700		13 to −9	949
2285	$0.95Ba(Zn_{1/2}Ta_{2/3})O_3\text{-}0.05[Sr_{0.25}Ba_{0.75}](Ga_{1/2}Ta_{1/2})O_3$	1500	Perovskite	31.0	210000			971
2286	$Ba_3Zn_7Ti_{12}O_{34}$	1150/4h	Orthorhombic	31.0	4300	10	−25	1026
2287	$Ba_{0.85}Sr_{0.15}(Y_{1/2}Ta_{1/2})O_3$	1600	Complex perovskite	31.0	32000		0	861
2288	$Sr(La_{1/2}Ta_{1/2})O_3$	1600/4h	Complex perovskite	31.0	4500		−42	861
2289	$Sr(Sm_{1/2}Ta_{1/2})O_3$	1600/4h	Complex perovskite	31.0	45200		−61	861
2290	$Sr(Al_{1/2}Nb_{1/2})O_3$	1600/24h	Complex perovskite	31.0	10800		−27	823,1031
2291	$Ca(Y_{1/2}Nb_{1/2})O_3$	1550/4h	Perovskite Orhorhombic	31.0	35000		−13	763
2292	$Sr(Yb_{1/2}Nb_{1/2})O_3$	1600/4h	Complex perovskite	31.0	26600		−73	823
2293	$Ca(Li_{1/3}Nb_{2/3})O_{3\text{-}\delta}$+4 wt% B_2O_3	1000	Complex perovskite	31.0	31000		−18	1018
2294	$0.4CaTiO_3\text{-}0.6Sm(Mg_{0.5}Ti_{0.5})O_3$	1550	Perovskite	31.0	12000	5.3	−28	865
2295	$2CaO\text{-}3MgO\text{-}Nb_2O_5\text{-}TiO_2$	1325	Composite	31.0	33000	4.6	−10	230
2296	$Ca_4MgTa_2TiO_{12}$	1625	Perovskite	31.0	43000	4.7	−62	230
2297	$Ba(Li_{1/4}Nb_{3/4})O_3\text{-}Ba(Li_{2/3}W_{3/5})O_3$	1470	Perovskite Cubic	31.0	19000	7.8	18	1024
2298	$Ca_4NiTa_2TiO_{12}$	1625	Perovskite Orthorhombic Pnma	31.0	40000	4.7	−26	230
2299	$Ba(Ni_{1/3}Nb_{2/3})O_3$	1400	Complex perovskite Cubic Pm3m	31.0	48000		−18	1032
2300	$Ba(Mg_{1/3}Nb_{2/3})O_3$	1350	Complex perovskite P-3m1 Hexagonal	31.0	46000		18	1033
2301	$Ba_4SrTa_4O_{15}$ $(A_nB_{n-1}O_{3n})$	1575	Trigonal P3m1 perovskite	31.1	9500	5.2	8	851
2302	$Pr_{0.16}Gd_{0.8}TiNbO_6$	1400	Orthorhombic	31.1	3180		−8	564
2303	$SrEr_{1/2}Nb_{1/2})O_3$+0.2 wt% B_2O_3	1350/4h	Complex perovskite Orthorhombic	31.1	38400		−71	823
2304	$SmTaTi_{0.7}Zr_{0.3}O_6$			31.1	37481		−2	671
2305	$Ca[(Li_{1/3}Nb_{2/3})_{1-x}Zr_x]O_3$ (x=0.3)	1150	Perovskite orthorombic	31.1	27100		−15	733
2306	TeO_2+12.5 wt% $CaTiO_3$		Composite	31.2	14800		18	444
2307	$ZnTa_2O_6$+0.25 wt% CaF_2	1225/4h	Orthorhombic Pbcn	31.3	73600	6.8	−7	1034
2308	$0.5Ba(Mg_{1/2}W_{1/2})O_3\text{-}0.5BaTiO_3$	1500/6h	Perovskite Hexagonal	31.2	8200		125	373

(*continued*)

No.	Material	ST (°C)	Crystal structure	ε_r	Qf (GHz)	f_0	τ_f	Reference
2309	$Sr(La_{0.5}Ta_{0.5})O_3$+0.5 wt% Nb_2O_5	1600/4h	Rhombohedral R3m complex Perovskite	31.2	4500		−42	859
2310	$Sr(Dy_{1/2}Nb_{1/2})O_3$+0.2 wt% B_2O_3	1350/4h	Complex perovskite Tetragonal	31.2	30300		−63	823
2311	$0.75(Al_{1/2}Ta_{1/2})O_2-0.25TiO_2$	1450	Composite	31.2	54600		13	949
2312	$Nd(Zr_{1/3}Ti_{2/3})O_6$	1600	Aeschyenite Orthorhombic Pnma	31.4	15800	4.3	6	1014
2313	$(Zr_{0.8}Sn_{0.2})TiO_4$+10 wt% BaO-B_2O_3-SiO_2-Li_2O-CuO	1050/4h	Orthorhombic Pbcn	31.4	32200		−1	515
2314	$Nd(Zr_{1/3}Ti_{1/3})O_6$	1600/4h	Aeschyenite Orthorhombic Pnma	31.4	15800		6	1014
2315	$Ca(Ho_{1/2}Nb_{1/2})O_3$	1550/4h	Complex perovskite Orthorhombic	31.4	32000		3	763
2316	$Bi[Sb_{1-x}(Nb_{0.992}V_{0.008})_x]O_4$ (x=0.2)		Monoclinic I2/c	31.4	8000		8	715
2317	$Ba[Ti_{1-x}(Zn_{1/2}W_{1/2})_x]O_3$ (x=1)	1420	Cubic perovskite $Fm3^-m$	31.4	20900		−1	695
2318	$0.9Ba(Zn_{1/3}Ta_{2/3})O_3-0.1BaTi_4O_9$	1320	Perovskite Hexagonal Composite	31.5	68500	6	4	1035
2319	$Ba[(Mg_{1-x}Co_x)_{1/3}Nb_{2/3}]O_3$ (x=0.05)		Perovskite Trigonal P-3m1	31.5	45000		17	1036
2320	$(Zr_{1-x}Sn_x)(Li_{1/3}Nb_{3/4})_{0.4}Ti_{0.6}O_4$ (x=0.3)	1140	–	31.5	58300		−33	1037
2321	$Sr(Nd_{0.5}Ta_{0.5})O_3$+0.5 wt% Nb_2O_5	1600/4h	Complex perovskite Tetragonal	31.5	38500		−55	859
2322	$(Li_{0.5}Bi_{0.5})(W_{0.6}Mo_{0.4})O_4$	620		31.5	8500	8.2	20	1038
2323	$Nd(Zn_{1/2}Ti_{1/2})O_3$	1330/4h	Pervskite Monoclinic	31.6	170000	8.5	−42	1039
2324	$Sr(Sm_{0.5}Ta_{0.5})O_3$+0.5 wt% Nb_2O_5 0.2 wt% TiO_2	1600/4h	Complex perovskite Tetragonal	31.6	46400		−55	859
2325	$SmTaTi_{0.8}Zr_{0.2}O_6$		Cubic Fd3m	31.7	30654		6	671
2326	$(Zr_{0.8}Sn_{0.2})TiO_4$+10 wt% BaO-B_2O_3-SiO_2-Li_2O-CuO	1050/12h	Composite	31.7	29700		−2	1040
2327	$Ba_5NbTa_3O_{15}$ ($A_nB_{n-1}O_{3n}$)	1500	Trigonal P3m1 perovskite	31.7	21500		16	851
2328	$BaSr_4Ta_4O_{15}$($A_nB_{n-1}O_{3n}$)	1600	Trigonal P3m1 perovskite	31.7	2800	5.34	−60	851
2329	90 wt% $BaTi_4O_9$+10 wt% Li_2O-B_2O_3-SiO_2	875	Composite	31.7	9000		10	592
2330	$Ba[(Mg_{1-x}Co_x)]_{1/3}Nb_{2/3}]O_3$ (x=0.8)		Perovskite	31.7	76900		3	1041
2331	$BaLi_2Ti_6O_{14}$	1025	Orthorhombic Cmca	31.7	23300	7.3	−15	1012
2332	$Sr(Sm_{1/2}Nb_{1/2})O_3$	1500	Complex perovskite Monoclinic $P2_1/n$	31.8	41000	8.1	−45	590

2333	$Nd[(Co_{0.02}Zn_{0.8})_{1/2}Ti_{1/2}]O_3$		Perovskite monoclinic	31.8	176000	9.0	−43	1042
2334	$BaNb_2P_2O_{11}$	1150	Trigonal R3-c	31.8	24100		45	268
2335	$(Zr_{1-x}Sn_x)(Li_{1/4}Nb_{3/4})_{0.4}Ti_{0.6}O_4$ (x=0.3)		–	31.8	58300		−33	1043
2336	$ZnTiNb_2O_8$+2 wt% Li_2O-ZnO-B_2O_3	875	Ixiolite	31.8	25000		−62	1044
2337	$Ba[(Ni_{1/3}Nb_{2/3})_{1-x}Zr_x]O_3$ (x=0.1)	1650	Perovskite	31.8	36100		8	1045
2338	MBRT-90+10 wt% Li_2O-B_2O_3-SiO_2-CaO-Al_2O_3 (28:27:30:5:10)	875	Composite	31.9	2200		20	510
2339	$Ba(Mg_{1/3}Nb_{2/3})O_3$		Complex perovskite Trigonal P-3m1	32.0	55500	10	33	787
2340	$Sr(Pr_{0.5}Ta_{0.5})O_3$+0.5 wt% Nb_2O_5	1600/4h	Complex perovskite Tetragonal	32.0	8400		−50	859
2341	$Ba(Yb_{1/2}Ta_{1/2})O_3$+0.5 wt% Nb_2O_5	1575	Complex perovskite	32.0	35850		112	845
2342	$Ca[(Li_{1/3}Nb_{2/3})_{0.95}Zr_{0.15}]O_{3+d}$+15 wt% ZnO-$B_2O_3$-$SiO_2$ glass rit	940/4h	Perovskite orthorhombic	32.0	66400		−27	1046
2343	$La_6Mg_{0.913}Ti_{4.04}O_{18}$		Perovskite slab series	32.0	31000	6.1	−46	950
2344	$Ca_5Nb_2Ti_{0.4}Hf_{0.6}O_{12}$	1675	Perovskite Orthorhombic Pnma	32.0	22000	4.5	±0.5	490
2345	$Ba(Mg_{1/3-x}Nb_{2/3})O_{3-\delta}$ (x=0.02)	1450	Complex perovskite Trigonal P-3m1	32.0	96000		30	1047
2346	$Ba(Co_{1/3}Nb_{2/3})O_3$	1400	Complex perovskite Trigonal P-3m1	32.0	78000		−12	1048,1049
2347	$Ba(Yb_{1/2}Ta_{1/2})O_3$	1625/4h	Complex perovskite	32.0	35900		112	943
2348	$Ca(Fe_{1/2}Ta_{1/2})O_3$	–	Complex perovskite Orthorhombic Pbnm	32.0	20000		−61	609
2349	$Ca(Er_{1/2}Nb_{1/2})O_3$	1550/4h	Complex perovskite	32.0	31800		−18	763
2350	$Ca(Dy_{1/2}Nb_{1/2})O_3$	1550/4h	Complex perovskite Orthorhombic	32.0	32500		5	763
2351	$Sr(Sm_{1/2}Ta_{1/2})O_3$+0.2 wt% TiO_2	1600	Complex perovskite	32.0	46400		−46	861
2352	$Sr(Pr_{1/2}Ta_{1/2})O_3$	1600/4h	Complex perovskite	32.0	8400		−50	861
2353	$Sr(Nd_{1/2}Ta_{1/2})O_3$	1600/4h	Complex perovskite	32.0	38500		−55	861
2354	$Sr(Ho_{1/2}Nb_{1/2})O_3$	1600/4h	Complex Perovskite	32.0	20400		−65	823
2355	$Sr(Y_{1/2}Nb_{1/2})O_3$	1600/4h	Complex Perovskite	32.0	38800		−66	823
2356	$Sr(Er_{1/2}Nb_{1/2})O_3$	1575/4h	Complex perovskite	32.0	36100		−67	823

(*continued*)

No.	Material	ST (°C)	Crystal structure	ε_r	Qf (GHz)	f_0	τ_f	Reference
2357	$BaO\text{-}2CeO_2\text{-}5TiO_2$	1250	Composite	32.0	19100		41	909
2358	$EuTiNbO_6$	1370	Orthorhombic Pbnm	32.0	17250	5.3	5	563
2359	$5CaO\text{-}2Nb_2O_5$	1500	Mixed phases	32.0	6500	6.48	−37	325
2360	$BaTi_4O_9$+10 wt% glass frit	875	Composite	32.0	9000		10	1050
2361	$0.1(Na_{0.5}La_{0.5})TiO_3\text{-}0.9CeO_2$	1400	Mixed phases	32.0	8200		0	1051
2362	$SrLi_2Ti_6O_{14}$+0.5 wt% BCB	900	Orthorhombic Cmca	32.0	12900		−5	1012
2363	$3CaO\text{-}2CoO\text{-}Nb_2O_5\text{-}TiO_2$	1400	Composite	32.0	15000	4.3	−18	230
2364	$0.25Ca_2AlNbO_6\text{-}0.75Ca_3Nb_2O_8$		Mixture phases	32.0	7500	6.34	64	864
2365	$ZnTa_2O_6/MgNb_2O_6/ZnTa_2O_6$ (6:1:6) Vf layered	–	Composite	32.0	82800		0	1052
2366	$La_5Ti_4CrO_{17}$	1600/2h	Orthorhombic Pnnm	32.0	5700		−24	911
2367	$Ba(Cd_{1/3}Ta_{2/3})O_3+B_2O_3$	1350	Complex perovskite Cubic Pm3m	32.0	50000	2	80	1053
2368	$Ca_5Nb_2Ti_{0.4}Hf_{0.6}O_{12}$	1675	Perovskite Orthorhombic Pnma	32.0	22000	4.458	≈0	490
2369	$BaO\text{-}TiO_2\text{-}WO_3$ (N-35):5 wt% $Al_2O_3\text{-}SiO_2$	1100	Composite	32.0	11000	5.6	–	862
2370	$Ca[(Li_{1/3}Nb_{2/3})_{0.8}Ti_{0.2}]O_{3\text{-}d}$+3 wt% LBS	1025	Complex perovskite orthorhombic	32.0	20000		−18	792
2371	$SnTe_3O_8$	700/15h	Cubic Ia3	32.0	13200	4		53
2372	$La_6Mg_{0.913}Ti_{4.04}O_{18}$			32.0	31000	6.1	−46	950
2373	$Ba(Sn_{0.226}Zn_{0.258}Nb_{0.516})O_3$	1500	Perovskite Cubic Pm3m	32.0	97000		12	1054
2374	$Ba(Zn_{1/3}Nb_{2/3})O_3$+5 mol% B_2O	900	Perovskite Cubic Pm3m	32.0	3500		20	1055
2375	$Sr(Sm_{0.5}Ta_{0.5})O_3$+0.5 wt% Nb_2O_5 0.25 wt% TiO_2	1600/4h	Complex perovskite Tetragonal	32.1	38600		−46	859
2376	$(Ca_2Mg_{2.75}Pb_{0.25})Nb_2(Ti_{0.75}Zr_{0.25})O_{12}$	1275		32.2	12250		−35	799
2377	$Sr(Er_{1/2}Nb_{1/2})O_3$+0.5 wt% CeO_2	1600/4h	Perovskite Orthorhombic	32.2	36100		−67	823
2378	$Sr(Y_{1/2}Nb_{1/2})O_3$+0.5 wt% CeO_2	1600/4h	Complex perovskite Orthorhombic	32.2	38850		−66	823
2379	$Ba_5Nb_3TaO_{15}$	1435	Trigonal P-3m1 perovskite	32.2	4700	4.4	35	851
2380	$Sr(Ho_{1/2}Nb_{1/2})O_3$+0.5 wt% CeO_2	1600/4h	Complex perovskite Tetragonal	32.3	20400		−65	823

2381	$Sr(Tb_{1/2}Nb_{1/2})O_3$+0.2 wt% B_2O_3	1350/4h	Complex perovskite Tetragonal	32.3	33500		−64	823
2382	$Ba_6Nb_4ZrO_{18}$	1625/2h	$A_6B_5O_{18}$ type perovskite Trigonal R-3m	32.4	52000		25	895
2383	$(Zr_{1-x}Sn_x)(Li_{1/4}Nb_{3/4})_{0.4}Ti_{0.06}O_4$ (x=0.2)		Not available	32.4	50300		−24	1037
2384	$Bi_2W_2O_9$	875	Orthorhombic Pbn21	32.5	7700	5.5	−63	1056
2385	$(Sr_{0.05}Ba_{0.95})(Y_{0.5}Ta_{0.5})O_3$	1600/4h	Complex perovskite	32.5	47300		0	859
2386	$Ca[(Li_{1/3}Nb_{2/3})_{0.8}Ti_{0.2}]O_{3-d}$+5 wt% ZnB_2O_4 glass	940	Perovskite Orthorhombic	32.5	20600		−26	1057
2387	$0.6Ba(Co_{1/3}Nb_{2/3})O_3$-$0.4Ba(Ni_{1/3}Nb_{2/3})O_3$+0.5 wt% CuO	1270	Composite	32.5	82000	9	−21	1058
2388	$0.09[0.5ZnNb_2O_6$-$0.5Zn_3Nb_2O_8]$-*0.91*$ZnTa_2O_6$+3 wt% ZBS	950	Composite	32.5	32400		−7	955
2389	$Ba_6Ti_{1-x}Sn_xNb_4O_{18}$ (x=0.75)	1510	Trigonal R-3m	32.6	25800	6.2	18	982
2390	$0.9MgTiO_3$-$0.1BaTiO_3$	1325	Composite	32.7	31700		−85	1059
2391	$ZnTiNb_2O_8$+$BaCu(B_2O_5)$	950	Orthorhombic Pbcn	32.6	20100	5.1	−64	1060
2392	$Nd[(Zn_{0.925}Co_{0.075})_{0.5}Ti_{0.5}]O_3$	1390/4h	Not available	32.6	185300		31	1061
2393	$ZnNb_2O_6$+1.5 wt% (CuO-V_2O_5-Bi_2O_3)	870/2h	Orthorhombic columbite Pbcn	32.7	67100		−47	1062
2394	$0.7TeO_2$-$SnTe_3O_8$	650	Mixture phases	32.7	8800		−33	62
2395	$(Bi_{0.8}La_{0.2})_2Mo_2O_9$		MonoclinicP21/n	32.7	13500		−5	1063
2396	$(Zr_{1-x}Sn_x)(Li_{1/4}Nb_{3/4})_{0.4}Ti_{0.6}O_4$ (x=0.2)		–	32.7	47900		−4	1043
2397	$0.09[0.5ZnNb_2O_6$-$0.5Zn_3Nb_2O_8]$-*0.91*$ZnTa_2O_6$+1 wt% ZBS	1050	Composite	32.7	41000		−22	955
2398	$Ca[(Li_{1/3}Nb_{2/3})_{0.75}Ti_{0.25}]O_{3-d}$+5 wt% LBS glass	950/4h	Perovskite Orthorhombic	32.8	11500	4.5	−3	792
2399	$0.Ba(Zn_{1/3}Nb_{2/3})O_3$-$0.7ZnNb_2O_6$	1200/8h	Composite	32.8	34100		−10	1064
2400	$Ba_{1-z}Sr_z[Zn_{1/3}(Ta_pNb_{1-p}]_-Sr_{1-x}Ca_x(Ga_{1/2}Ta_{1/2})]O_3$		Perovskite	32-34	180000-80000	7	0-10	1065
2401	$Sr(Mg_{1/3}Nb_{2/3})O_3$:Mn		Perovskite Trigonal P-3m1	33.0	23700	10.3	−14	787
2402	$BaTi_4O_9$+5 wt% ZnO-B_2O_3 glass	900/2h	Orthorhombic+$Zn(BO_2)_2$ second phase Pmmn	33.0	27000		7	1066
2403	$3CaO$-$2CoO$-Nb_2O_5-TiO_2	1400	Composite	33.0	15000	4.3	−18	230

(*continued*)

No.	Material	ST (°C)	Crystal structure	ε_r	Qf (GHz)	f_0	τ_f	Reference
2404	$Sr(Dy_{1/2}Nb_{1/2})O_3$	1575/4h	Complex perovskite	33.0	32700		−63	823
2405	$Ba[(Ni_{0.6}Zn_{0.4)1/3}Nb_{2/3}]O_3$+1 mol% B_2O_3	1300	Perovskite Cubic Pm3m	33.0	39700		−4	1067
2406	$Ba[Ti_{1-x}(Zn_{1/2}W_{1/2})_x]O_3$ (x=0.9)	1380	Cubic perovskite $Fm3^-m$	33.0	19900		0	695
2407	$Ba_{0.95}Sr_{0.05}(Y_{1/2}Ta_{1/2})O_3$	1600	Complex perovskite	33.0	47300		0	861
2408	$Ba(Y_{1/2}Ta_{1/2})O_3$	1625/4h	Complex perovskite cubic	33.0	50200		120	943
2409	(1-x)$LaMg_{1/2}Ti_{1/2}O_3$-x$La_{2/3}TiO_3$ (x=0.3)		Perovskite	33.0	43000	6.3	−54	950
2410	$Bi_6Te_2O_{15}$(oxygen atm)	800/15h	Orthorhombic	33.0	41000		−85	1068
2411	$Ca[Li_{1/3}Nb_{2/3}]_{0.75}Ti_{0.25}]O_{3-\delta}$+5 wt% Li_2O-B_2O_3-SiO_2	950/4h	Perovskite Orthorhombic	33.0	11500		−5	792
2412	$Ba(Cd_{1/3}Ta_{2/3})O_3$+2 wt% ZnO	1550	Complex perovskite Cubic Pm3m	33.0	37500		80	1069
2413	$La_5AlTi_3O_{15}$	1600/3h	Not available	33.0	28600		−39	954
2414	$Li_{0.774}Zr_{0.057}NbO_3$	1150	Perovskite Orthorhombic	33.0	4460		−28	1070
2415	$Ba_{1/3}La_{2/3}Zn_{1/3}Ti_{2/3}O_3$		Perovskite	33.0	19000	6.7	−11	919
2416	0.5$SrTiO_3$-0.5$LaAlO_3$	1550/20h	Psuedo Cubic perovskite	33.0	54000			1071
2417	$Sr(Dy_{1/2}Nb_{1/2})O_3$+0.5 wt% CeO_2	1575/4h	Complex Perovskite	33.0	32700		−63	823
2418	$Ba(Y_{1/2}Ta_{1/2})O_3$+0.5 wt% Nb_2O_5	1575	Complex perovskite	33.0	50150		120	845
2419	$Ba_3Sr_2Ta_4O_{15}(A_nB_{n-1}O_{3n})$	1575	Hexagonal perovskite	33.2	4300	5.2	−15	851
2420	$Sr_5Nb_2Ta_2O_{15}(A_nB_{n-1}O_{3n})$	1575	Hexagonal perovskite	33.2	2500	5.65	−2	851
2421	$Ba_3ZnNb_{2-x}Sb_xO_9$ (x=0.375)		Perovskite	33.2	44940		−3	381
2422	(1-x)$La(Mg_{1/2}Ti_{1/2})O_3$-x$La_{2/3}TiO_3$ (x=0.37)		Orthorhombic Imma	33.2	8560	8.3		889
2423	$La_5CrTi_3O_{15}$	1625/2	$A_5B_4O_{15}$ type cation deficient perovskite Trigonal P3m	33.2	27500	4.88	−34	1072
2424	$La_4PrCrTi_3O_{15}$	1575/2	$A_5B_4O_{15}$ type cation deficient Perovskite Trigonal P3m	33.2	23700	4.7	−22	1072
2425	$Ba_5SrTa_4TiO_{18}$	1550/2h	$A_6B_5O_{18}$ type perovskite	33.2	33000		65	895
2426	$Ba_2Ti_3Nb_4O_{15}$+3 wt% ZBS	925	Tetragonal	33.2	13600		6	1073

2427	$Ba[(Y_{0.85}Pr_{0.15})_{1/2}Ta_{1/2}]O_3$+0.5 wt% Nb_2O_5	1575	Complex perovskite	33.2	51500		0	845
2428	$Ba((Co_{0.6-x/2}Zn_{0.4-x/2}Mg_x)_{1/3}Nb_{2/3})O_3$ (x=0.3)	annealed 1400/12h	Complex perovskite	33.2	117200		14	1074
2429	$Pr(Zr_{1/3}Ti_{2/3})O_6$	1600/4h	Aeschyenite Orthorhombic Pnma	33.3	16200	4.3	14	1014
2430	(Ba0.95Sr0.05)(Co1/3Nb2/3)O3		Perovskite	33.3	87100		4	1075
2431	$Ce(Zr_{1/3}Ti_{1/3})O_6$	1600/4h	Aeschyenite Orthorhombic Pnma	33.4	15800		14	1014
2432	$Zr_{0.8}Sn_{0.2}TiO_4$+4 wt% WO_3	1400	Orthorhombic Pbcn	33.4	56000		0	1076
2433	Bi_2O_3	680	Tetragonal P-42_1c	33.5	18700	8.7	−235	30
2434	$Ba(Ho_{1/2}Ta_{1/2})O_3$+0.5 wt% Nb_2O_5	1575	Perovskite	33.5	24050		130	845
2435	$La_4NdCrTi_3O_{15}$	1600/2		33.5	18000	4.7	−36	1072
2436	$Ba(Ho_{/2}Ta_{1/2})O_3$	1625	Complex perovskite Tetragonal	33.5	24000		130	943
2437	$Sr(Gd_{1/2}Nb_{1/2})O_3$+0.2 wt% B_2O_3	1350/4h	Complex perovskite Tetragonal	33.5	8350		−60	823
2438	$Ba_8Zn(Nb_{6-x}Sb_x)O_{24}$ (x=0.6)	1425	Perovskite	33.6	11500		30	503
2439	$SrLi_2Ti_6O_{14}$	1000	Orthorhombic Cmca	33.6	8700	6.8	−3	1012
2440	$Zn_{0.85}Co_{0.15}Ta_2O_6$	1325/2h	Orthorhombic Pbcn	33.7	53300		42	1077
2441	$BaTi_4O_9$+10 wt% BaO-Li_2O-B_2O_3-SiO_2-ZnO glass	925	Composite	33.7	14500			1078
2442	$Ba_{1+x}[(Co_{0.7}Zn_{0.3})_{1/3}Nb_{2/3}]O_3$ (x=-0.01)	1450/10h	Perovskite Trigonal P-3m1	33.7	70900		−4	1079
2443	$Ba[(Co_{0.6-x/2}Zn_{0.4-x/2}Mg_x)_{1/3}Nb_{2/3}]O_3$ (x=0.3)		Perovskite Trigonal P-3m1	33.7	93800		10	1080
2444	$Ba_2Sr_3Ta_4O_{15}(A_nB_{n-1}O_{3n})$	1600	Trigonal P-3m1 perovskite	33.7	2400	5	−25	851
2445	$(Sr_{0.1}Ba_{0.9})(Ti_{0.1}Zn_{0.3}Ta_{0.6})O_3$		–	33.7	36000	7	23	1003
2446	$ZnTa_2O_6$	1400/10h	Orthorhombic Pbcn	33.7	79310	8.5	9	1081
2447	$Sr(Tb_{1/2}Nb_{1/2})O_3$+0.5 wt% CeO_2	1575/4h	Complex perovskite Tetragonal	33.7	36300		−61	823
2448	$Zn_{0.87}Co_{0.13}Ta_2O_6$	1325/2h	Orthorhombic Pbcn	33.8	66300		43	1077
2449	93 wt% $BaTi_4O_9$+10 wt% Li_2O-B_2O_3-SiO_2	950	Composite	33.8	12700		25	592
2450	$(Sr_{1-x}Ba_x)(Y_{1/2}Nb_{1/2})O_3$ (x=0.65)	1600/4h	Complex perovskite	33.8	45600		0	823
2451	$Ba_4ZnTi_{11}O_{27}$+4 wt% BaCu)B_2O_5)	1200/2h	Monoclinic C2/m	33.8	12200	6.18	7	1082

(*continued*)

No.	Material	ST (°C)	Crystal structure	ε_r	Qf (GHz)	f_0	τ_f	Reference
2452	$Sr_6Nb_4ZrO_{18}$+2 wt% Bi_2O_3-B_2O_3	1625/2h	$A_6B_5O_{18}$ type perovskite	33.9	21000		−8	895
2453	$(Bi_{0.9}Nd_{0.1})_2Mo_2O_9$		Monoclinic $P2_1/n$	33.9	15200		8	1063
2454	$Ba_{1-x}La_{2x/3}(Co_{0.7}Zn_{0.3})_{1/3}$ $Nb_{2/3}O_3$ (x=0.01)	1425/10h	Complex perovskite	34.0	63000		5	1083
2455	$Ba_4LiNb_{3-x}Ta_xO_{12}$ (x=1)	1350	Hexagonal perovskite $P6_3mc$	34.0	56000		43	941
2456	$Ba(Dy_{1/2}Ta_{1/2})O_3$+0.5 wt% Nb_2O_5	1575	Complex perovskite	34.0	20650		−48	845
2457	$Sr_{4-m}La_mTi_{m-1}Ta_{4-m}O_{12}$ (m=2)	1580	Not available	34.0	35000		−15	975
2458	$Ba_8Li_2Nb_2Ta_4O_{24}$		Hexagonal $P6_3mmc$	34.0	56000			952
2459	$Bi(Sb_{1-x}Ta_x)O_4$ (x=0.6)	960	Orthorhombic $Pc2_1n$	34.0	30,000		−16	581
2460	$ZnTiNb_2O_8$	1250/2h	Orthorhombic Pbcn	34.0	42500		−52	632
2461	$0.2TiTe_3O_8$-$0.8TeO_2$	670	Composite	34.0	22000		24	586
2462	BaO-TiO_2-WO_3 (N-35): B_2O_3	1200		34.0	70500	8.5	–	786, 862
2463	$La(Zn_{1/2}Ti_{1/2})O_3$	1550	Perovskite	34.0	59000	10	−52	1084, 1085
2464	$Ba_{10}Ta_{8-0.8x}Ti_xO_{30}$ (x=0.6)	1400/40h	$A_nB_{n-1}O_{3n}$ Hexagonal Perovskite $P6_3/mmc$	34.0	30820		57	920
2465	$Ca_5Ta_2Ti_{0.6}Hf_{0.4}O_{12}$	1675	Complex perovskite Orthorhombic Pnma	34.0	26000	4.4	0	490
2466	$Ca_5Nb_2Ti_{0.2}Zr_{0.8}O_{12}$	1670	Complex perovskite Orthorhombic Pnma	34.0	24000	4.4	0	662
2467	$0.25Ba(Zn_{1/3}Nb_{2/3})O_3$-$0.75Ba(Mg_{1/3}Nb_{2/3})O_3$+$B_2O_3$-LiF	1350	Perovskite Trigonal P-3m1	34.0	76700	7.6	−4	1086
2468	$La_5Mg_{0.5}Ti_{3.5}O_{15}$		Trigonal P-3m1	34.0	31000	6	−16	950, 958
2469	$La_4SmCrTi_3O_{15}$	1575/2		34.0	15900	4.89	−38	1072
2470	$0.5CaTiO_3$-$0.5Sm(Mg_{0.5}Ti_{0.5})O_3$	1550	Perovskite	34.0	10400	4.91	−24	865
2471	$(1-x)(Mg_{0.95}Zn_{0.05})TiO_3$-$xCa_{0.6}La_{0.8/3}TiO_3$ (x=0.3)	1320/4h		34.0	61000		66	465
2472	$Ca[(Li_{1/3}Nb_{2/3})_{0.84}Ti_{0.16}]O_{3-\delta}$+2 wt% LiF+3 wt% B_2O_3	900/2h	Perovskite	34.0	17400		−5	752
2473	$Ba(Dy_{1/2}Ta_{1/2})O_3$	1625	Complex perovskite Tetragonal	34.0	20600		−48	943

2474	$Sr(Gd_{1/2}Nb_{1/2})O_3$	1575/4h	Perovskite	34.0	8800		−56	823
2475	$0.99Ba(Co_{1/3}Nb_{2/3})O_3$-$0.01Ba(Y_{1/2}Nb_{1/2})O_3$	1380	Perovskite	34.0	38690			1087
2476	$0.95Ba(Yb_{1/2}Nb_{1/2})O_3$-$0.05Ca(Y_{1/2}Nb_{1/2})O_3$	1600	Perovskite	34.0	47500		1	763
2477	$Sr(Tb_{1/2}Nb_{1/2})O_3$	1575/4h	Perovskite	34.0	36300		−61	823
2478	$Ca_5Nb_2Ti_{0.2}Zr_{0.8}O_{12}$	1670	Perovskite Pnma Orthorhombic	34.0	24000	4.4	0	662
2479	$Ca_5Ta_2Ti_{0.6}Hf_{0.4}O_{12}$	1675	Perovskite Pnma Orthorhombic	34.0	26000	4.4	0	490
2480	$xBa(Zn_{1/3}Nb_{2/3})O_3$-(1-x)Ba $(Mg_{1/3}Nb_{2/3})O_3$ (x=0.25)	1500	Perovskite Hexagonal P-3m1	34.0	76700		−4	1086
2481	$Ba[(Ni_{0.6}Zn_{0.4)1/3}Nb_{2/3}]O_3$+0.5 mol% B_2O_3	1340	Perovskite Hexagonal P-3m1	34.0	42100		−8	1067
2482	$LiNb_3O_8$	1075/3h	Monoclinic $P2_1/a$	34.0	58000		−96	788
2483	$Zr_{0.034}Hf_{0.966}TiO_4$		Orthorhombic Pbcn	34.1	34000	9.9		1088
2484	$0.09[0.5ZnNb_2O_6$-$0.5Zn_3Nb_2O_8]$-*0.91*$ZnTa_2O_6$+1 wt% ZBS	1000	Composite	34.1	37100		−3	955
2485	$ZnTi(Nb_{1-x}Ta_x)_2O_8$ (x=0.05)	1140/6h	Orthorhombic Pbcn	34.1	40000		−66	1089
2486	$Ca[(Li_{1/3}Nb_{2/3})_{0.8}Ti_{0.2}]O_{3-d}$+15 wt% LMZBS	900	Composite	34.1	11500		−21	792
2487	$Ba_2SrYNb_3O_{12}$	1450	Perovskite Trigonal R-3	34.1	31900		74	990
2488	$Ba_8Ta_4Ti_3O_{24}$			34.2	23050		76	920
2489	$Ba_5Nb_2Ta_2O_{15}$	1475	Perovskite	34.2	10500		22	1090
2490	$0.7BaTi_4O_9$-$0.3BaZn_2Ti_4O_{11}$	1240/3h	Composite	34.2	60600		−2	1091
2491	$Ca[(Li_{1/3}Nb_{2/3})_{0.8}Ti0._2]O_{3-d}$+1 wt% LBS	1100	Perovskite Orthorhombic	34.2	22900		−10	792
2492	$Ca[(Li_{1/3}Nb_{2/3})_{0.8}Ti_{0.2}]O_{3-d}$+3 wt% LMZBS	1025	Complex Perovskite Orthorhombic	34.2	24500		−5	792
2493	$Ba(Sm_{1/2}Ta_{1/2})O_3$	1500	Perovskite	34.3	27000	7.7	5	590
2494	$Ba[Ni_{0.6}Zn_{0.4}]_{0.33}Nb_{0.67}]O_3$+0.5 mol% B_2O_3	1350	Perovskite Hexagonal P-3m1	34.3	42100		−3	1067
2495	$0.5ZnNb_2O_6$-$0.5TiO_2$	1250/2h	Composite	34.3	42500		−52	1092
2496	$ZnTiNb_2O_8$	1250	Orthorhombic Pbcn	34.3	42500		−52	1093

(*continued*)

No.	Material	ST (°C)	Crystal structure	ε_r	Qf (GHz)	f_0	τ_f	Reference
2497	$Zn_{0.89}Co_{0.11}Ta_2O_6$	1325/2h	Tri rutile Tetragonal	34.3	72000		44	1077
2498	$Ca[(Li_{1/3}Nb_{2/3})_{0.84}Ti_{0.16}]O_{3-\delta}$+2 wt% LiF+3 wt% ZnO-$B_2O_3$-$SiO_2$	900/2h	Complex Perovskite Orthorhombic	34.3	17400		−5	1094
2499	$Ba_3Sr_2Ta_4O_{15}$	1575		34.3	4000		−15	1090
2500	$Sr(Gd_{1/2}Nb_{1/2})O_3$+0.5 wt% CeO_2	1575/4h	Complex perovskite Tetragonal	34.3	8800		−56	823
2501	$Sr(Eu_{1/2}Nb_{1/2})O_3$+0.2 wt% B_2O_3	1350/4h	Complex perovskite Tetragonal	34.3	37600		−54	823
2502	$Ca(Zn_{0.333}Nb_{0.662}V_{0.005})O_3$	1200/3h		34.3	16400		−17	1095
2503	$0.5La_{2/3}TiO_3$-$0.5LaAlO_3$	1425	Perovskite Orthorhomic	34.4	45000	6.7	−23	1096
2504	$(NaBi)_{1/2}MoO_4$	690	Tetragonal $I4_1/a$	34.4	12300	7.5	43	677
2505	$(Zr_{1-x}Sn_x)(Li_{1/4}Nb_{3/4})_{0.4}Ti_{0.06}O_4$ (x=0.5)			34.4	44500		−14	1043
2506	$Bi_2Te_2W_3O_{16}$		Monoclinic C2/c	34.5	3200		−92	886
2507	$Ba_3Co_{0.7}Zn_{0.3}Nb_2O_9$+0.4 wt% CeO_2	1450/4h	Perovskite Trigonal P-3m1	34.5	84000	4	0	1097
2508	$0.7Ba(Co_{1/3}Nb_{2/3})O_3$-$0.3Ba(Zn_{1/3}Nb_{2/3})O_3$	1400/20h	Complex perovskite Trigonal P-3m1	34.5	97000	6.5	0	1097, 1098
2509	$0.5LaAlO_3$-$0.5SrTiO_3$+0.25 wt% B_2O_3	1430/2h	Perovskite Psuedocubic	34.5	43200	7	−11	1099
2510	$Ba_3Co_{.7}Zn_{.3}Nb_2O_9$+$V_2O_5$	1450	Perovskite Trigonal P-3m1	34.5	85000	4	0	1097
2511	$La_4SmCrTi_3O_{15}$	1650	Hexagonal P3m	34.5	17300	4.7	−38	1072
2512	MgO-$0.4Nb_2O_5$-$1.5TiO_2$		Composite	34.5	81300		−2	976
2513	$Ba_4LiNb_3O_{12}$+4 wt% BCB	950	Hexagonal $P6_3mc$	34.5	29600		12	1100
2514	$0.5CeO_2$-$0.5BaTi_4O_9$	1260/4h	Cubic flurite Fm3m+ Orthorhombic Pnmm	34.5	20050	4.2	2	646
2515	$NdTiSb_xTa_{1-x}O_6$ (x=0.2)	1480		34.6	14500	4.2	41	1101
2516	$ZnTa_2O_6$+0.5 wt% CuO	1230	Orthorhombic Pbcn	34.6	65500		5	1102
2517	$DyTiTaO_6$	1500	Aeschneite Orthorhombic	34.6	40100		7	583
2518	$BaTi_4O_9$+3 wt% MCAS glass	1200	Orthorhombic Pnmm	34.6	42050	7	14	1103
2519	$La_4PrCrTi_3O_{15}$	1575	Trigonal P3m	34.6	23700	4.8	−22	1072
2520	$0.09(0.5ZnNb_2O_6$-$0.5Zn_3Nb_2O_8)$-$0.91ZnTa_2O_6$	1350	Orthorhombic mixtures	34.7	41950		0	542
2521	$Bi[Sb_{1-x}(Nb_{0.992}V_{0.008})_x]O_4$ (x=0.4)		Monoclinic I2/c	34.7	16000		16	715
2522	$Sr(Eu_{1/2}Nb_{1/2})O_3$+0.5 wt% CeO_2	1575/4h	Complex perovskite Tetragonal	34.7	44000		−52	823

2523	$BaSr_2YNb_3O_{12}$	1450	Perovskite Trigonal R-3	34.7	26200		−8	990
2524	$La_5CrTi_3O_{15}$	1650	Trigonal P3m	34.8	34000	4.8	−35	1072
2525	$Sr_6Ta_4TiO_{18}$+3 wt% Bi_2O_3-B_2O_3 glass	1625/2h		34.8	5600		−19	895
2526	$BiNbO_4$+0.03 wt% CuV_2O_6	1050	Monoclinic P-1	34.9	9870		−3	1104
2527	$Ba_5SrTa_4TiO_{18}$	1550/4h		34.9	33000		65	895
2528	$Sr_3YNb_3O_{12}$	1450		34.9	15300		46	990
2529	0.09[0.5$ZnNb_2O_6$-0.5$Zn_3Nb_2O_8$]-*0.91*$ZnTa_2O_6$+0.5 wt% ZBS	1250	Composite	34.9	53900		−2	955
2530	Bi_2O_3-2.2MoO_3	620	Mixture	35.0	12000		−13	494
2531	$Ca[(Li_{1/3}Ta_{2/3})_{0.7}Ti_{0.3}]O_{3-d}$+3 wt% B_2O_3	1050	Perovskite Orthorhombic	35.0	22800	9.45	−4	765
2532	$Ca[(Li_{1/3}Nb_{2/3})_{0.9}Ti_{0.1}]O_{3-\delta}$+0.7 wt% B_2O_3	1000	Perovskite Orthorhombic	35.0	22100		−5	765
2533	$Ca[(Li_{1/3}Nb_{2/3})_{1-x}Ti_x]$ $O_{3-\delta}$ (x=0.1)	1150/3h	Perovskite Orthorhombic	35.0	27200		−2	752
2534	0.5TeO_2-0.5$SnTe_3O_8$	650	Mixture phases	35.0	8500		176	62
2535	$BaTi_4O_9$-0.1WO_3	1400	Orthorhombic Pmmn	35.0	52000	8	−1	171
2536	0.46$LaAlO_3$-0.54$SrTiO_3$+2 wt% B_2O_3	1460/2h	Perovskite Psuedo cubic	35.0	38000	7	−1	1105
2537	0.5$LaAlO_3$-0.5$SrTiO_3$		Psudocubic perovskite	35.0	27000		−18	1106
2538	$Ca[(Li_{1/3}Nb_{2/3})_{0.8}Ti_{0.2}]O_{3-d}$+5 wt% Bi_2O_3	900/3h	Perovskite Orthorhombic	35.0	11000		13	610
2539	$BaZrO_3$		Perovskite Cubic P23	35.0	8800			906
2540	$Ba_{10}Ta_{8-0.8x}Ti_xO_{30}$ (x=1.2)	1400/40h	Hexagonal perovskite	35.0	25760		64	920
2541	$Ca(Zn_{1/3}Nb_{2/3})O_3$		Perovskite	35.0	16,000	–	−43	609
2542	0.42$Zn_3Nb_2O_8$-0.58TiO_2	1250	Composite	35.0	48000		0	1092
2543	$Pb_{0.75}Ca_{0.25}(Al_{1/2}Nb_{1/2})O_3$		Perovskite	35.0	1100	4.7	133	996
2544	$Ca_{4.75}Ni_{0.25}Ta_2TiO_{12}$	1625	Perovskite Orthorhombic Pnma	35.0	34000	4.5	±0.5	230
2545	0.5CeO_2-0.25CaO-0.25TiO_2:6.5Cr_2O_3	1550	Composite	35.0	4300	4.4	0	488
2546	$Sr(Cr_{1/2}Nb_{1/2})O_3$	1600/4h	Perovskite Cubic Pm3m	35.0	6400		−80	823
2547	$Sr(Eu_{1/2}Nb_{1/2})O_3$	1575/4h	Perovskite Monoclinic $P2_1/n$	35.0	44000		−52	823
2548	0.9$Ba(Zn_{0.6}Co_{0.4})_{0.33}Nb_{0.67}]O_3-0.1Ba(Ga_{1/2}Ta_{1/2})O_3$		Perovskite	35.0	93550	3.06	0	1107
2549	BaO-4TiO_2-0.1WO_3		Composite	35.0	52400	6	0	171

(*continued*)

No.	Material	ST (°C)	Crystal structure	ε_r	Qf (GHz)	f_0	τ_f	Reference
2550	$Ba[(Zn_{0.3}Co_{0.7})_{1/3}Nb_{2/3}O_3$+0.25 wt% V_2O_5	1450/4h	Perovskite Trigonal P-3m1	35.0	85000		0	1108
2551	$Ba([(Co_{0.7}Zn_{0.3})_{1/3}Nb_{2/3}]O_3$ +0.4 wt% CeO_2	1450	Perovskite Trigonal P-3m1	35.0	84000		0	1097
2552	$0.9Ba[(Zn_{0.6}Co_{0.4})_{1/3}Nb_{2/3}]O_3$-$0.1Ba(Ga_{1/2}Ta_{1/2})O_3$		Perovskite	35.0	97600		0	1109
2553	$0.35Ba(Ni_{1/3}Nb_{2/3})O_3$-$0.65Ba(Zn_{1/3}Nb_{2/3})O_3$	1450/4h	Perovskite Trigonal P-3m1	35.0	25000		1	1110
2554	$BaO\text{-}Al_2O_3\text{-}4TiO_2$		–	35.0	5000	–	−15	1111
2555	$Ca_{4.75}Ni_{0.25}Ta_2TiO_{12}$	1625	Complex perovskite	35.0	34000	4.49	0	230, 1112
2556	$BaO\text{-}4TiO_2\text{-}0.1WO_3$	1400/2h in O_2	Composite	35.0	50400		−0.5	171
2557	$0.5LaAlO_3\text{-}0.5SrTiO_3$+0.25 wt% B_2O_3	1430	Psuedo Cubic perovskite	35.0	43200		−11	1099
2558	$0.46LaAlO_3\text{-}0.54SrTiO_3$+0.25 wt% B_2O_3	1460/2h	Psuedo Cubic perovskite	35.0	38000		−1	1113
2559	$La_5GaTi_3O_{15}$	1550	$A_5B_4O_{15}$ type cation deficient Perovskite	35.0	30300	3.09	−55	954
2560	$ZnTa_2O_6$	1200	Orthorhombic Pbcn	35.1	50600		10	1114
2561	$Zn_{0.9}Ti_{0.8\text{-}x}Sn_xNb_{2.2}O_8$ (x=0.05)	1120/6h	Orthorhombic Pbcn	35.1	49100		−28	1115
2562	$(1\text{-}x)La(Mg_{1/2}Ti_{1/2})O_3\text{-}xLa_{2/3}TiO_3$ (x=0.4)		Perovskite I2/a	35.1	6700	7.9		889
2563	$Sr(Cr_{1/2}Nb_{1/2})O_3$+0.2 wt% B_2O_3	1350/4h	Complex perovskite Cubic Pm3m	35.1	12500		−73	823
2564	$0.17Ba_5Nb_4O_{15}\text{-}0.83BaNb_2O_6$(hex)	1250/2h	Hexagonal perovskite	35.2	59300		0	1116
2565	$BaTi_{4.35}Zn_{0.55}O_{10.25}$	1260/6h		35.2	5000		36	1117
2566	$Ba_2Sr_3Ta_4O_{15}$	1575	Hexagonal perovskite	35.2	2400		−25	1090
2567	$0.05Ca(Y_{1/2}Nb_{1/2})O_3$-$0.95Ba((Y_{1/2}Nb_{1/2})O_3$	1550/4h	Complex perovskite	35.2	48300		1	763
2568	$PrTiSb_xTa_{1\text{-}x}O_6$ (x=0.2)	1480		35.2	12700	4.2	48	1101
2569	$Ca_4La_2Ti_{5\text{-}x}(Mg_{1/3}Nb_{2/3})_xO_{17}$ (x=4)	1540	Orthorhombic Pbnm	35.2	21300		−17	1118

2570	$Ca[(Li_{1/3}Nb_{2/3})_{0.8}Ti_{0.2}]O_{3-d}$+0.1 wt% LMZBS	1050	Complex perovskite Orthorhombic	35.2	22800		−4	792
2571	$Sr(Cr_{1/2}Nb_{1/2})O_3$	1600/4h	Complex perovskite	35.3	6400		−80	823
2572	$0.6Ba(Zn_{1/3}Nb_{2/3})O_3$-$0.4Ba(Co_{1/3}Nb_{2/3})O_3$	1450	Perovskite	35.5	86000	2	0	1119
2573	$Sr(Sm_{1/2}Nb_{1/2})O_3$+0.2 wt% B_2O_3	1350/4h	Complex perovskite Tetragonal	35.5	34500		−48	823
2574	$Ba(Tb_{1/2}Ta_{1/2})O_3$	1625	Complex perovskite Tetragonal	35.5	31900		−38	943
2575	$Ba(Tb_{1/2}Ta_{1/2})O_3$+0.5 wt% Nb_2O_5	1575	Complex perovskite Tetragonal	35.5	31900		−38	845
2576	$(Zr_{1-x}Sn_x)(Li_{1/4}Nb_{3/4})_{0.4}Ti_{0.6}O_4$ (x=0.1)			35.5	37800		−5	1043
2577	$0.8ZnTa_2O_6$-$0.2MgNb_2O_6$	1350/2h	Composite	35.6	65500		0	1120
2578	$La_4NdCrTi_3O_{15}$	1650	Trigonal P3m	35.6	19400	4.7	−34	1072
2579	$Dy(W_{0.5}Ti_{1.5})O_6$	1450	Orthorhombic Pnma Aeschynite type	35.6	20200		10	1121
2580	$Ba(Sc_{1/2}Nb_{1/2})O_3$	1700/12h	Perovskite	35.7	20000			1122
2581	$Ba_3ZnNb_{2-x}Sb_xO_9$ (x=0.125)		Perovskite Hexagonal P-3m1	35.7	56980	4.8	14	381
2582	$SmTaTi_{0.9}Zr_{0.1}O_6$			35.8	27730		15	671
2583	$Ba_3ZnNb_{2-x}Sb_xO_9$ (x=0.25)		Perovskite Trigonal P-3m1	35.8	35090	5.4	6	381
2584	$0.615BaTi_4O_9$-0.35ZnO-$0.3Nb_2O_5$+0.3 wt% Mn	1280/2h	Composite	35.8	50800		1	1123
2585	$Bi(Nb_{0.7}Ta_{0.3})O_4$	900	Orthorhombic Pnma	35.8	2200		−48	1124
2586	$Sr(Sm_{1/2}Nb_{1/2})O_3$+0.5 wt% CeO_2	1575/4h	Complex perovskite Tetragonal	35.8	32300		−47	823
2587	$Ba_{3-x}Sr_xLaNb_3O_{12}$ (x=3)	1430	Trigonal R-3m	35.8	44300		−9	1125
2588	BaO-0.6ZnO-$3TiO_2$	1180	Composite	35.8	21300		1	1126
2589	$Zn_{0.7}Co_{0.3}TiNb_2O_8$	1075/4h	Orthorhombic Pbcn	35.9	35100		0	1127
2590	$Ba_8Zn(Nb_{6-x}Sb_x)O_{24}$ (x=1.5)	1425		35.9	16900		9	503
2591	$0.5LaAlO_3$-$0.5SrTiO_3$	1680	Perovskite	35.9	108800	9.7	−21	832
2592	$(Zr_{0.8}Sn_{0.2})TiO_4$+0.2 wt% NiO	1280	Orthorhombic Pbcn	35.9	56700	9.2		1128
2593	$Ba_6Nb_4ZrO_{18}$	1625/2h	Trigonal R-3m	35.9	52000		25	895
2594	$(Ag_{0.5}Bi_{0.5})MoO_4$	580	Wolframite Monoclinic C12/m1	35.9	13000	7.5	−69	1129
2595	BaO-TiO_2-WO_3 (N-35)		Composite	36.0	50400	6	0	862

(*continued*)

No.	Material	ST (°C)	Crystal structure	ε_r	Qf (GHz)	f_0	τ_f	Reference
2596	$Ba_{1-x}Ca_x(Sc_{1/2}Nb_{1/2})O_3$		Perovskite	36-55	20000-55000			1122
2597	$Sr(La_{1/2}Nb_{1/2})O_3$+0.2 wt% B_2O_3	1350/4h	Complex perovskite Tetragonal	36.0	5200		−22	823
2598	$Ba(Nd_{1/2}Ta_{1/2})O_3$	1500	Complex perovskite	36.0	18000	7.3	2.9	590
2599	$Sr(Sm_{0.5}Ta_{0.5})O_3$+0.5 wt% Nb_2O_5+wt% TiO_2	1600/4h	Complex perovskite Tetragonal	36.0	22300		−38	859
2600	$Ba_2Ti_9O_{20}$+9 wt% BaB_2O_4	1050/2h	Monoclinic $P2_1/m$	36.0	12600		−2	1002
2601	$Ba(Zn_{1/3}Nb_{2/3})O_3$+5 mol% B_2O_3+CuO	875	Perovskite	36.0	19000		21	1130
2602	Bi_2TiTeO_8	840/10h		36.0	4700	5.7	41	1131
2603	$BaTi_4O_9$ -Citrate route	1250/10h	Orthorhombic Pnmm	36.0	50470		16	1132
2604	$Ba_{10}Ta_{7.04}Ti_{1.2}O_{30}$		Hexagonal $P6_3/mmc$	36.0	30000		52	464
2605	$BaTi_4O_9$-ZnO-Ta_2O_5+0.1 wt% Mn	1280	Orthorhombic Pnmm	36.0	45000	4.5	0	1133
2606	$Nd(Zn_{1/2}Ti_{1/2})O_3$		Perovskite	36.0	42300		−47	1134
2607	$TiTe_3O_8$	700/5h	Cubic Ia3	36.0	13600	4	133	53
2608	$0.25Zn_3Nb_2O_8$-$0.75TiO_2$	1200/2h	Composite	36.0	5160		4	632
2609	BaO-TiO_2-WO_3 (N-35)+5 wt% SiO_2	1200	Composite	36.0	4500	8.5		786
2610	$ZrTiO_4$ (polymer route)+0.5 wt% Hf	1600	Orthorhombic Pbcn	36.0	29700	5.3		1135
2611	$Ba(Yb_{1/2}Nb_{1/2})O_3$	1600	Complex perovskite	36.0	38100		2	1136
2612	$Nd_2Ti_2O_7$	1300	Monoclinic $P2_1$	36.0	16400		−118	1137, 1138
2613	$Ba(Gd_{1/2}Ta_{1/2})O_3$	1625/4h	Complex perovskite Tetragonal	36.0	3200		−18	943
2614	$Ba(Tb_{1/2}Ta_{1/2})O_3$	1625/4h	Complex perovskite Tetragonal	36.0	31900		−38	943
2615	$(Pb_{0.2}Ca_{0.8})(Ca_{1/3}Nb_{2/3})O_3$	1350	Perovskite	36.0	12500		−27	1139
2616	$0.6Ba(Zn_{1/3}Nb_{2/3})O_3$-$0.4Ba(Co_{1/3}Nb_{2/3})O_3$	1400	Perovskite Trigonal P-3m1	36.0	86000		0	1119
2617	$Sr(Sm_{1/2}Nb_{1/2})O_3$	1575/4h	Complex perovskite	36.0	32300		−47	823
2618	$Ca_4NiNb_2TiO_{12}$	1550	Perovskite Orthorhombic	36.0	31500	4.1	−30	230
2619	$Ca_{4.88}Co_{0.12}Ta_2TiO_{12}$	1625	Orthorhombic Pnma Perovskite	36.0	35000	4.49	0	230, 1112
2620	$Ca_5Ta_2Ti_{0.7}Zr_{0.3}O_{12}$	1650	Perovskite Pnma Orthorhombic	36.0	28000	4.4	0	662

2621	$La_4MgTi_3O_{12}$		Perovskite slab series	36.0	26000	5.8	−39	950
2622	$0.2CaTiO_3$-$0.8Ca(Mg_{1/3}Nb_{2/3})O_3$	1450	Composite	36.0	39000	7.7	−30	944
2623	Li_2O-Nb_2O_5-TiO_2+1 wt% B_2O_3	1100		36.0	10450	5.9	12	1140
2624	$5Li_2O$-Nb_2O_5-$5TiO_2$	1120		36.0	10500		12	760
2625	$Ba_2Ti_{9-x}[La_{0.5}Ta_{.5}]_xO_{20}$ (x=0.05)	1350	Monoclinic P-1	36.0	60000		12	1141
2626	$Ba_8Ta_{4+0.8x}Ti_{3-x}O_{24}$ (x=0=0.4)	1400/40h	$A_nB_{n-1}O_{3n}$ Hexagonal Perovskite	36.0	12000		–	1142
2627	$Ba_{7/12}La_{5/12}Zn_{1/3}Ti_{5/12}Nb_{3/12}O_3$	1400		36.0	1100	5.01	−14	919
2628	$Sr_3LaNb_3O_{12}$	1430	Hexagonal perovskite	36.0	45000		−9	1143
2629	$Ba(Gd_{1/2}Ta_{1/2})O_3$+0.5 wt% Nb_2O_5	1575	Complex perovskite Tetragonal	36.0	3150		−18	845
2630	$Ba[(Zn_{0.6}Mg_{0.4})Nb_{2/3}]O_3$		Perovskite Hexagonal P-3m1	36.0	94400		29	1144
2631	TiO_2+50 vol% ZBS glass	900	Composite	36.0	7500			1145
2632	$Ba(Ti_{0.5}Mn_{0.5})O_3$+5 wt% Bi_2O_3	1200	Perovskite	36.0	6800		25	956
2633	$0.6La_{1/2}Mg_{1/2}TiO_3$-$0.4La_{1/2}Na_{1/2}TiO_3$+1 wt% B_2O_3	1475	Composite	36.0	15500	8	−5	1146
2634	$Ba_8(Mg_{1-x}Zn_x)Nb_6O_{24}$ (x=0.2)			36.0	16950		57	1147
2635	$NdTiSb_xTa_{1-x}O_6$ (x=0.1)	1480/4h		36.0	17600	4.19	48	1101
2636	$Ba_4MgTi_{11}O_{27}$	1275	Monoclinic C2/m	36.1	19600		15	1148
2637	$Ba_8Zn(Nb_{6-x}Sb_x)O_{24}$ (x=0)	1425		36.2	10900		50	503
2638	$Ba_3LiNb_{0.5}Sb_{2.5}Ti_5O_{21}$	1200	Hexagonal $P6_3/mcm$	36.2	27000		20	923
2639	$Ba_8(Mg_{1-x}Zn_x)Nb_6O_{24}$ (x=1)			36.2	10900		50	1147
2640	$Sr_5NbTa_3O_{15}$	1575	Hexagonal perovskite P-3m1	36.2	6900	5.14	31	851
2641	$La_5GaTi_3O_{15}$	1600/30h	$A_5B_4O_{15}$ type cation deficient Perovskite	36.2	30300		−55	954
2642	$BaTi_4O_9$+5 mol% CuO+2 mol% B_2O_3	900/2h	Orthorhombic Pmmn	36.3	30500		28	1149
2643	$La_6MgTi_4O_{18}$	1625/2h	$A_6B_5O_{18}$ type perovskite	36.3	27350		−39	895
2644	$ZnTiNbTaO_8$	1140/6h	Orthorhombic Pbcn	36.3	67000		58	1150
2645	$CeTiSb_xTa_{1-x}O_6$ (x=0.05)	1480/4h		36.3	11500	3.99	63	1101
2646	$(Sr_{1-x}Ba_x)(Y_{1/2}Nb_{1/2})O_3$ (x=0.95)	1600/4h	Complex perovskite	36.3	48600		0	823
2647	$0.85BaTi_4O_9$-$0.15BaZn_2Ti_4O_{11}$+1 wt% CuO	1150/3h	Composie	36.4	62600		0	1151
2648	$CaTi_{0.3}(Al_{1/2}Nb_{1/2})_{0.7}O_3$+1 wt% Li_3NbO_4	1300/5h	Perovskite Orthorhombic	36.4	38900	7	−57	1152

(*continued*)

No.	Material	ST (°C)	Crystal structure	ε_r	Qf (GHz)	f_0	τ_f	Reference
2649	$Sr_6Nb_4ZrO_{18}$+2 wt% Bi_2O_3-B_2O_3 glass	1625/2h		36.4	21000		−8	895
2650	$5Li_2O$-$1Nb_2O_5$-$5TiO_2$+1 wt% B_2O_3+4 wt% ZnO	920	Multiphase	36.4	8800		4	1153
2651	$Nd_2Ti_2O_7$		Monoclinic $P2_1/n$	36.5	16400	9.1	−118	1137
2652	$Bi_2Mo_2O_9$+2 mol% Nb_2O_5	620	Monoclinic $P2_1/n$	36.5	14100		6	1154
2653	$Ba(Eu_{1/2}Ta_{1/2})O_3$+0.5 wt% Nb_2O_5	1575	Perovskite Tetragonal	36.5	41200		−16	845
2654	$Ba_2Ti_9O_{20}$+5 wt% B_2O_3	1200	Monoclinic $P2_1/n$	36.5	40200		38	1149
2655	BaO-TiO_2-ZnO+0.5 mol% $MnCO_3$+0.24 mol% SnO_2	1160/6h	Mixture phases	36.5	42000	4.7	2	1117
2656	$La_5Zn_{0.5}Ti_{3.5}O_{15}$	1500		36.5	23000	5.3	−39	954
2657	$BaTi_{4.35}Zn_{0.55}O_{10.25}$+0.5 mol% SnO_2	1160/6h		36.5	42000		2	1117
2658	$0.3TeO_2$-$0.7SnTe_3O_8$	660/2h	Mixture phases	36.5	8800		200	62
2659	$Sr(Nd_{1/2}Nb_{1/2})O_3$+0.2 wt% B_2O_3	1350/4h	Complex perovskite Cubic	36.5	22200		−42	823
2660	$Ca_5Ta_2TiO_{12}$+1 wt% Co_3O_4	1625/4h	Complex perovskite Orthorhombic Pnma	36.5	38500		6	1155
2661	$0.7SrTiO_3$-$0.3LaAlO_3$+10 wt% ZnO-B_2O_3	1100/3h		36.6	10800		−4	1156
2662	$Ba_3Ti_5Nb_6O_{28}$+3 wt% ZnB_2O_4	925	Monoclinic $P2_1/c$	36.6	19100		5	1157
2663	$Sr(La_{1/2}Nb_{1/2})O_3$+0.5 wt% CeO_2	1575/4h	Complex perovskite Cubic	36.6	4025		−20	823
2664	$0.6ZrO_2$-$0.4(Zn_{1/3}Nb_{2/3})O_2$-$0.2SnO_2$-$0.8TiO_2$	1220	Tetragonal	36.6	43200		−6	1158
2665	(5-x)BaO-xMgO-$2Nb_2O_5$ (x=0.5)	1200	Mixed phases	36.7	20000		61	1159
2666	$(Zr_{0.8}Sn_{0.2})TiO_4$+0.2 wt% MgO	1320	Orthorhombic Pbcn	36.7	60000	6.5		1160
2667	$Sr(Pr_{1/2}Nb_{1/2})O_3$+0.2 wt% B_2O_3	1350/4h	Complex perovskite Cubic	36.7	4600		−35	823
2668	$Ba_6Ti_{1-x}Sn_xNb_4O_{18}$ (x=0.5)	1500	Monoclinic $P2_1/c$	36.7	21400	5.7	34	982
2669	$ZnTiNb_2O_8$	1075/5h	Orthorhombic Ixiolite Pbcn	36.7	54000		−70	1161
2670	$Ba_4ZnTi_{11}O_{27}$	1200/2h	Monoclinic C2/m	36.8	16460		17	1082
2671	$Ba_3LaTa_3O_{12}$		$A_4B_4O_{12}$ Cation deficient perovskite	36.8	22000	6.4	−50	1162
2672	$NdTiSb_xTa_{1-x}O_6$ (x=0.05)	1480/4h		36.8	15700	4.13	48	1101

2673	$CaTi_{0.3}(Al_{1/2}Nb_{1/2})_{0.7}O_3$	1500/5h	Perovskite	36.8	29800	7	−61	1152
2674	$Ca(Fe_{1/2}Nb_{1/2})O_3$		Perovskite Orthorhombic Pbnm	36.8	15800	8.2	−93	1163, 1164
2675	$TbTiTaO_6$	1525	Orthorhombic	36.8	32300		10	583
2676	$BaO\text{-}ZnO\text{-}TiO_2$+0.5 mol% $MnCO_3$	1250		36.8	39000		−7	1117
2677	$Ba(Zn_{1/3}Nb_{2/3})O_3$+1 mol SnO_2 annealed at 1325	1450/4h	Perovskite Trigonal P-3m1	36.8	83200		29	1165
2678	$CeTiSb_xTa_{1-x}O_6$ (x=0.1)	1480/4h		36.9	10100	3.98	67	1101
2679	$Sr(Nd_{1/2}Nb_{1/2})O_3$+0.5 wt% CeO_2	1575/4h	Complex perovskite Cubic	36.9	20100		−40	823
2680	$La_4Ti_9O_{24}$	1350	Orthorhombic Fddd	37.0	24800	8.1	15	1137, 1138
2681	$Ba(La_{1/2}Ta_{1/2})O_3$	1625/4h	Complex perovskite	37.0	20950		−36	943
2682	$Ba(Eu_{1/2}Ta_{1/2})O_3$	1625/4h	Complex perovskite	37.0	41200		−16	943
2683	$Sr(La_{1/2}Nb_{1/2})O_3$	1575/4h	Complex perovskite	37.0	4000		−20	823
2684	$Sr(Nd_{1/2}Nb_{1/2})O_3$	1575/4h	Complex perovskite	37.0	20100		−40	823
2685	$0.9Ba(Co_{1/3}Nb_{2/3})O_3\text{-}0.1Ba(Y_{1/2}Nb_{1/2})O_3$	1380	Perovskite	37.0	25560			1087
2686	$0.35CaTiO_3\text{-}0.65LaAlO_3$	1600	Perovskite Rhombohedral	37.0	47000		−2	1166
2687	$0.42ZnNb_2O_6\text{-}0.58TiO_2$+10 wt% CuO	875	Composite	37.0	17000		−7	1167
2688	$Ba_2Ti_9O_{20}$(citrate route)	1300/2h	Monoclinic $P2_{1/}m$	37.0	57000	10.7	−6	1132
2689	$0.9Ba(Zn_{1/3}Nb_{2/3})O_3\text{-}0.1Ba(Ga_{1/2}Ta_{1/2})O_3$		Perovskite	37.0	93500	2.9	15	1107
2690	$Ba(Y_{1/2}Nb_{1/2})O_3$	1600	Complex perovskite	37.0	49600		15	1136
2691	$Zr_{0.8}Sn_{0.2}TiO_4$+1 mol% Sb_2O_5+0.35 wt% $B_2O_3\text{-}Li_2O$+slow cooled	1300/5h	Orthorhombic Pbcn	37.0	62000		–	1168
2692	$Ca_{4.18}Co_{0.82}Nb_2TiO_{12}$	1550	Complex perovskite Orthorhombic Pnma	37.0	30000	4.31	0	230, 1112
2693	$Ca_{4.85}Zn_{0.15}Ta_2TiO_{12}$	1625	Complex perovskite Orthorhombic Pnma	37.0	35000	4.15	0	230, 1112
2694	$Ca_{4.82}Mg_{0.18}Ta_2TiO_{12}$	1625	Complex perovskite Orthorhombic Pnma	37.0	36000	4.356	0	230, 1112

(*continued*)

No.	Material	ST (°C)	Crystal structure	ε_r	Qf (GHz)	f_0	τ_f	Reference
2695	$Zr_{0.8}Sn_{0.2}TiO_4$+2 wt% La_2O_3, 1 wt% NiO	1370/2h	Orthorhombic Pbcn	37.0	62000		−9	1169
2696	$Zr_{0.648}Sn_{0.332}TiO_4$+$La_2O_3$+NiO	1370/20h	Orthorhombic Pbcn	37.0	41500		–	1170
2697	3CaO-2MgO-Nb_2O_5-TiO_2	1340	Composite	37.0	19000	4.2	−20	230
2698	0.1TeO_2-$SnTe_3O_8$	670/2h	Cubic Ia3, mixture	37.0	9300		220	62
2699	$NdTiSb_xTa_{1-x}O_6$ (x=0.0)	1480/4h		37.0	11200	3.96	54	1101
2700	$(KBi)_{1/2}MoO_4$	630	Tetragonal $I4_1/a$	37.0	4000	7.5	117	677
2701	0.6$Sm(Co_{1/2}Ti_{1/2})O_3$-0.4$CaTiO_3$	1420	Perovskite	37.0	43000		1	1171
2702	$Ba_3Ti_5Nb_6O_{28}$	1250	Monoclinic $P2_1/c$	37.0	11400		−8	1172
2703	$Ba_8Li_2Nb_6O_{24}$		Hexagonal $P6_3mmc$	37.0	57500			952
2704	$Ba_4LiNb_{3-x}Ta_xO_{12}$ (x=0)	1275	Hexagonal perovskite $P6_3/mc$	37.0	57600		65	941
2705	$Ba_8(Mg_{1-x}Zn_x)Nb_6O_{24}$ (x=0.6)			37.0	14600		53	1147
2706	$La_5Ti_4FeO_{17}$	1500	Orthorhombic Pnnm	37.0	60000		−27	911
2707	$Ba(La_{1/2}Ta_{1/2})O_3$	1625	Complex perovskite Orthorhombic	37.1	18200		−35	943
2708	$Ba(La_{1/2}Ta_{1/2})O_3$+0.5 wt% Nb_2O_5	1575	Complex perovskite Orthorhombic	37.1	20950		−36	845
2709	$Ca[(Li_{1/3}Nb_{2/3})_{0.8}Ti_{0.2}]O_{3-d}$+0.5 wt% LMZBS	1125	Complex perovskite Orthorhombic	37.1	22100		2	792
2710	$Ba_{3-x}Sr_xLaNb_3O_{12}$ (x=2)	1415	Trigonal R-3m	37.1	33900		−18	1125
2711	$Ba_8(Mg_{1-x}Zn_x)Nb_6O_{24}$ (x=0.4)		Not available	37.1	16900		55	1147
2712	$Ca[(Li_{1/3}Nb_{2/3})_{0.8}Ti_{0.2}]O_{3-d}$+0.5 wt% LBS	1125	Complex perovskite Orthorhombic	37.2	21800		−5	792
2713	$Zr_{0.8}Sn_{0.2}TiO_4$+1 wt% V_2O_5	1300	Orthorhombic Pbcn	37.2	51000	7	−2	1173
2714	0.6$CaTiO_3$-0.4$NdAlO_3$	1450/10h	Perovskite Orthorhombic	37.2	40750		114	1174
2715	0.7$La(Mg_{1/2}Ti_{1/2})O_3$-0.3$CaTiO_3$	1600	Perovskite Monoclinic $P2_1/n$	37.2	15300	6.3	−54	932
2716	$Ba_5Nb_3TaO_{15}$	1435	Hexagonal	37.2	4500		35	1090
2717	$Ba(In_{1/2}Ta_{1/2})O_3$	1625	Perovskite	37.2	35500		25	943
2718	$Ba(Y_{1/2}Ta_{1/2})O_3$	1625	Perovskite	37.3	45900		120	943
2719	0.6$Ca(Al_{0.5}Nb_{0.5})O_3$-+0.5$SrTiO_3$	1500	Perovskite	37.3	25400		22	1175

2720	$0.6Li_2ZnTi_3O_8$-$0.4TiO_2$	1100	Spinel Cubic+rutile	37.3	11700		102	872
2721	$SnTe_3O_8$	660/2h	Cubic Ia3	37.3	10000		223	62
2722	$Bi_{12}(B_{0.5}P_{0.5})O_{20}$	780	Sillenite	37.4	850		−19	1176
2723	$BaTi_5O_{11}$+1 wt% CuO+4 wt% $BaCu(B_2O_5)$	925	Monoclinic $P2_1/n$	37.4	25500		33	1177
2724	$Ba(La_{1/2}Nb_{1/2})O_3$	1650	Perovskite	37.4	8000	7.2	−8	590
2725	Sr_2TiO_4 ($Sr_{n+1}Ti_nO_{3n+1}$)		Perovskite	37.4	8160	3.1	137	1358
2726	$Zn_{0.5}Ti_{0.5}NbO_4$	1100	Orthorhombic Ixiolite Pbcn	37.4	194000		−58	1179
2727	$Nd_4Ti_9O_{24}$	1300	Orthorhombic Fddd	37.5	24100	8	65	1137, 1138
2728	$Ca_3Mg_2Nb_4TiO_{17}$	1225		37.5	22500	3.9	−4	877
2729	$Sr(Pr_{2/}Nb_{1/2})O_3$+0.5 wt% CeO_2	1575/4h	Complex perovskite cubic	37.5	3250		−34	823
2730	$CeTiSb_xTa_{1-x}O_6$ (x=0.2)	1480		37.5	8400	4	53	1101
2731	$Ba_8Ti_3Nb_{4-x}Sb_xO_{24}$ (x=1.5)			37.5	38000		15	1178
2732	$0.425La_{0.97}Sm_{0.03}(Mg_{0.5}Sn_{0.5})O_3$-$0.575Ca_{0.8}Sm_{0.4/3}TiO_3$	1600		37.5	40300		2	1180
2733	$Bi_2Mo_2O_9$+3 mol%Y_2O_3	640	Monoclinic $P2_1/n$	37.5	14750			1176
2734	$ZnTa_2O_6$	1350	Tri-α PbO_2Orthorhombic Pbcn	37.6	65200		9	600
2735	$Ba(Sm_{1/2}Ta_{1/2})O_3$	1625	Complex perovskite Tetragonal	37.6	15000		−10	943
2736	$Ba_5SrNb_4ZrO_{18}$	1600/2h	$A_6B_5O_{18}$ type perovskite Trigonal R-3m	37.6	36000		68	895
2737	$Bi_{12}SiO_{20}$	850	Cubic I23	37.6	8100		−20	1176
2738	Beta-Bi_3SbO_7	960	Orthorhombic	37.6	5080		−120	1181
2739	$Ca_5Ta_2TiO_{12}$+1 wt% NiO	1625/4h	Complex perovskite Orthorhombic Pnma	37.6	38000		7	1155
2740	$Ba(Sm_{1/2}Ta_{1/2})O_3$+0.5 wt% Nb_2O_5	1575	Complex Perovskite Tetragonal	37.6	16000		−10	845
2741	$CeTiSb_xTa_{1-x}O_6$ (x=0.15)	1480/4h		37.7	9300	3.98	64	1101
2742	$Ca_5Ta_2TiO_{12}$+0.5 wt% CuO	1625/4h	Complex perovskite Orthorhombic Pnma	37.7	38000		12	1155
2743	$La_6ZnTi_4O_{18}$	1600/4h	$A_6B_5O_{18}$ type perovskite	37.7	21850		−37	895

(*continued*)

No.	Material	ST (°C)	Crystal structure	ε_r	Qf (GHz)	f_0	τ_f	Reference
2744	$(Zr_{0.8}Sn_{0.2})TiO_4$+1 wt% ZnO, 0.25 wt% WO_3	1340	Orthorhombic Pbcn	37.8	61000	7	−4	1182
2745	$Ba_2La_2TiTa_2O_{12}$	1520	Trigonal P-3m1 perovskite	37.8	36200	5.7	−52	1183
2746	$GdTiTaO_6$	1540	Aeschneite Orthorhombic	37.9	12900		11	583
2747	$Gd(W_{0.5}Ti_{1.5})O_6$	1375	Orthorhombic Pnma Aeschynite type	37.9	2600		−7	1121
2748	$Ca_5Ta_2TiO_{12}$+1 wt% ZnO	1625/4h	Complex perovskite Orthorhombic Pnma	37.9	39000		5	1155
2749	$Ca_{5-x}Zn_xNb_4TiO_{17}$ (x=0.2)	1340	$A_nB_n3_{n+2}$ type Perovskite $P2_1/C$	37.9	22000		−62	1184
2750	$Ba_2Ti_3Nb_4O_{18}$	1220	Monoclinic $P2_1/c$	38.0	23700	4.8	−3	1185
2751	$Zr_{0.8}Sn_{0.2}TiO_4+B_2O_3$		Orthorhombic pbcn	38.0	61500			1186
2752	$Bi_2Mo_2O_9$	620	Monoclinic $P2_1/n$	38.0	12500		31	494
2753	$Ba_2Ti_9O_{20}$ (Hydrothermal)	150	Monoclinic $P2_1/m$	38.0	1200	5.6	6	1187
2754	$Ca(Zr_xTi_{1-x})O_3$ (x=0.7)	1470/15h	Perovskite	38.0	2900	3.9	168	916
2755	$0.95Ba(Zn_{1/3}Nb_{2/3})O_3$-$0.05Ba(Ga_{1/2}Ta_{1/2})O_3$		Perovskite	38.0	102950	2.9	19	1107
2756	$Bi_{12}GeO_{20}$	850	Cubic I23 Sillenite	38.0	7800		−31	1176
2757	$Ba(Sm_{1/2}Ta_{1/2})O_3$	1625/4h	Complex perovskite	38.0	15000		−10	943
2758	$Ba(Ho_{1/2}Nb_{1/2})O_3$	1600	Complex perovskite	38.0	21600		−11	1136
2759	$Sr(Pr_{1/2}Nb_{1/2})O_3$	1575/4h	Complex perovskite	38.0	3300		−34	823
2760	$Ca_3Nb_2O_8$		Tetragonal P4/nnc	38.0	7100	5.9	113	864
2761	$Zr_{0.8}Sn_{0.2}TiO_4$		Orthorhombic Pbcn	38.0	62000	4	0	1188
2762	$0.24Li_2O$-$0.71Nb_2O_5$-$0.05TiO_2$	1350	M phase	38.0	40000		−99	760
2763	$Zr_{0.8}Sn_{0.2}TiO_4$ sol-gel derived	1300	Orthorhombic Pbcn	38.0	55000	6	1	1189
2764	$0.5LaCa_{0.5}Zr_{0.5}O_3$-$0.5SrTiO_3$	1575	Composite	38.0	7000	3.8	8	522
2765	BaO-$2CeO_2$-$3TiO_2$	1250	Composite	38.0	7200		159	909
2766	$Ca_5Ta_2TiO_{12}$	1625	Complex perovskite Orthorhombic Pnma	38.0	33000	4.2	10	1190, 1191
2767	$Ca_5Ta_2TiO_{12}$+0.2 wt% Al_2O_3-B_2O_3-SiO_2	1550	Complex perovskite Orthorhombic Pnma	38.0	38000		8	1191

2768	$Ca_5Ta_2TiO_{12}$+0.1 wt% $2MgO\text{-}Al_2O_3\text{-}5SiO_2$	1550	Complex perovskite Orthorhombic Pnma	38.0	40000		5	1191
2769	$Ba(Zn_{1/3}Nb_{2/3})_{0.9}Zr_{0.1}O_3$	1400	Perovskite Cubic Pm3m	38.0	61000	10	15	1192
2770	$Ca_5Ta_2TiO_{12}$+0.5 wt% MgO	1625/4h	Complex perovskite Orthorhombic Pnma	38.0	40000		6	1155
2771	$La_{0.42}Ca_{0.58}[Ca_{0.05}Mg_{0.16}Ti_{0.79}]O_3$		Perovskite	38.0	20000	5.3	25	950
2772	$Ca_{(1-x)}Y_xTi_{1-x}Al_xO_3$ (x=0.3)		Perovskite Orthorhombic	38.0	14200		−14	1193
2773	$Ba_{0.2}Sr_{0.71}(Zr_{0.951}Ti_{0.039}Ta_{0.01})O_3$		Perovskite Orthorhombic	38.0	1700		0	1194
2774	$Ba_{0.29}Sr_{0.71}(Zr_{0.973}Ti_{0.027})O_3$		Perovskite Orthorhombic	38.0	2000		−40	1194
2775	$Ba(Zn_{1/3}Nb_{2/3})O_3$+1 mol% WO_3	1450	Perovskite Cubic Pm3m	38.0	95150		39	1165
2776	$0.4Nd_{1525/4}Yb_{0.04}(Mg_{0.5}Sn_{0.5})O_3\text{-}0.6Ca_{0.08}Sr_{0.2}TiO_3$+1.25 wt% B_2O_3	1525/4h	Composite	38.0	68600		2	1195
2777	$Ba_2Ti_3Nb_4O_{18}$		Monoclinic $P2_1/c$	38.1	14200		−11	1196
2778	$Ba_3Ti_5Nb_6O_{28}$+$BaCu(B_2O_5)$	925	Monoclinic $P2_1/c$	38.2	19200		12	1172
2779	$Ca[(Li_{1/3}Nb_{2/3})_{0.8}Ti_{0.2}]O_{3\text{-}d}$+0.2 wt% LBS	1125	Complex perovskite Orthorhombic	38.2	21500		−2	792
2780	$Ba_4NdTiNb_3O_{15}$	1430/3h	Hexagonal perovskite	38.2	18700	5.4	12	1352
2781	$BaO\text{-}ZnO\text{-}TiO_2$	1250		38.2	5000		36	1117
2782	$Sr_{1-x}Ca_x[(Li_{1/4}Nb_{3/4})_{1-y}Ti_y]O_3$		Perovskite	38.2-45.8	35000		30 to -70	1197
2783	$0.7La(Mg_{1/2}Ti_{1/2})O_3\text{-}0.3SrTiO_3$		Perovskite Pbnm	38.3	10550	6.6		978
2784	$0.87La(Mg_{1/2}Ti_{1/2})O_3\text{-}0.13Ca_{0.8}Sr_{0.2}TiO_3$+0.5 wt% B_2O_3	1475	Composite	38.3	67000	8	0	1198
2785	$Zn_{0.97}Co_{0.03}Ta_2O_6$		Orthorhombic Pbcn	38.3	109200		10	1077
2786	$PrTiSb_xTa_{1-x}O_6$ (x=0.15)	1480/4h	Not available	38.3	12300	4.05	60	1101
2787	$0.4Nd(Mg_{0.4}Zn_{0.1}Sn_{0.5})O_3\text{-}0.6Ca_{0.8}Sr_{0.2}TiO_3$	1350/4h	Composite	38.3	35000		−5	1199
2788	$Ba(Zn_{1/3}Nb_{2/3})O_3$+1 mol%WO_3 annealed at 1325	1450/4h	Perovskite Cubic Pm3m	38.4	95150		38	1165

(*continued*)

No.	Material	ST (°C)	Crystal structure	ε_r	Qf (GHz)	f_0	τ_f	Reference
2789	$Ba(Pr_{1/2}Ta_{1/2})O_3$	1625	Complex perovskite Orthrohombic	38.5	42800		−8	943
2790	$Sm(Nb_{0.25}Ta_{0.75})TiO_6$			38.5	22100		26	671
2791	$Zn_{0.95}Co_{0.05}Ta_2O_6$		Orthorhombic Pbcn	38.5	112000		11	1077
2792	$(Zn_{0.95}Mn_{0.05})Ta_2O_6$	1325	Orthorhombic Pbcn	38.5	92700		9	1200
2793	$Ba(Pr_{1/2}Ta_{1/2})O_3$+0.5 wt% Nb_2O_5	1575	Complex perovskite Orthorhombic	38.5	47150		−39	845
2794	$(Sm_{0.5}Y_{0.5})(Ti_{1.5}W_{0.5})O_6$	1400/10h	Not available	38.5	36900		−6	1201
2795	$Eu(W_{0.5}Ti_{1.5})O_6$	1375	Orthorhombic Pnma Aeschynite type	38.6	30500		3	1121
2796	$0.5Ba(Y_{1/2}Nb_{1/2})O_3$-$0.5Ba(Ca_{1/9}Y_{3/9}Nb_{5/9})O_3$		Perovskite	38.6	17400	8.1		1202
2797	MWF-38	1360	Composite	38.6	44500		1.3	510
2798	$Bi_{12}PbO_{19}$		Cubic I23 sillenite	38.6	2900		−84	1176
2799	$Ca[(Li_{1/3}Nb_{2/3})_{1-x}Ti_x]O_3$ (x=0.2)	1150/3h	Perovskite	38.6	26100		0	752
2800	$Ba_3Ti_5Nb_6O_{28}$+3 wt% B_2O_3+1 wt% CuO	900/2h	Monoclinic $P2_1/c$	38.6	29800		5	1203
2801	$Ca_5Ta_2TiO_{12}$+0.5 wt% Al_2O_3	1625/4h	Complex perovskite Orthorhombic Pnma	38.6	36000		6	1155
2802	$Ca(Fe_{1/2}Nb_{1/2})O_3$	1250/3h	Perovskite Orthorhombic Pbnm	38.6	1830	5.9	−107	1164
2803	$Ba(Nd_{1/2}Ta_{1/2})O_3$+0.5 wt% Nb_2O_5	1575	Complex perovskite Tetragonal	38.7	12050		−4	845
2804	$Zr_{0.8}Sn_{0.2}TiO_4$+1 wt% ZnO+0.2 wt% B_2O_3	1150/3h	Orthorhombic Pbcn	38.7	61500			1186
2805	$PrTiSb_xTa_{1-x}O_6$ (x=0.1)	1480/4h		38.7	12800	4.02	64	1101
2806	$Bi_4B_2O_9$	660	Monoclinic $P2_1/c$	38.8	2620		−203	287
2807	$Ba(Eu_{1/2}Ta_{1/2})O_3$	1625	Complex perovskite	38.8	36200		−10	943
2808	$Ba(Dy_{1/2}Nb_{1/2})O_3$	1600	Complex perovskite	38.9	20600		−4	1136
2809	$Zr_{0.8}Sn_{0.2}TiO_4$	1600/4h	Orthorhombic Pbcn	38.9	51500		0.7	1204
2810	$Ba_{3-x}Sr_xLaNb_3O_{12}$ (x=1.5)	1405	Hexagonal perovskite R-3m	38.9	25800		−35	1125

2811	$ZnTiNb_2O_8$-0.8TiO_2+2 wt% $BaCu(B_2O_5)$	950	Orthorhombic Pbcn	38.9	14500	4.71	0	1205
2812	$Ba(In_{1/2}Nb_{1/2})O_3$+MoO_3 additive	1600	Complex perovskite	39.0	30700		17	1136
2813	$Ba_5Nb_4O_{15}$ ($A_nB_{n-1}O_{3n}$)	1380	Hexagonal perovskite P-3m1	39.0	23700	4.7	78	325
2814	$Ba_5Nb_4O_{15}$+6.3 vol% $BaNb_2O_6$+3 wt% B_2O_3	925/2h	Composite	39.0	18700		0	1206
2815	(1-x)$Ba_3(ZnNb_2)O_9$-x$Ba_3W_2O_9$ (x=0.007)	1380	Perovskite	39.0	118000		21	1207
2816	$Ca[(Li_{1/3}Nb_{2/3})_{1-x}Ti_x]$ $O_{3-\delta}$ (x=0.15)	1150/3h	Perovskite	39.0	26100		0	752
2817	$Ba(Tb_{1/2}Nb_{1/2})O_3$	1600	Complex perovskite	39.0	52400		−2	1136
2818	$Ba_3Ti_5Ta_6O_{28}$	1430		39.0	4000	5.3	30	1208
2819	$Ca_4SrTa_2TiO_{12}$	1625	Complex Perovskite Orthorhombic Pnma	39.0	21000	3.59	12	1209
2820	$Ba(Mn_{1/3}Nb_{2/3})O_3$		Trigonal P-3m1 Perovskite	39.0	9300	9.3	27	787
2821	$Ba_4LaSnNb_3O_{15}$ ($A_5B_4O_{15}$)	1480/4h	Hexagonal perovskite	39.0	14800	5.9	−29	1210
2822	(1-x)$LaMg_{1/2}Ti_{1/2}$-x$La_{2/3}TiO_3$ (x=0.48)		Perovskite	39.0	3800	4.6	23	950
2823	$Li_{0.774}Zr_{0.057}NbO_3$	1150	Orthorhombic Pnma	39.0	4500	6	−17	1070
2824	$Ca_5Ta_2TiO_{12}$+0.1 wt% 2MgO-Al_2O_3-5SiO_2	1600	Perovskite Orthorhombic Pnma	39.0	40000	5	8	1211
2825	$Ca_5Ta_2TiO_{12}$+0.1 wt% B_2O_3-Al_2O_3-5SiO_2	1600	Complex perovskite Orthorhombic Pnma	39.0	38000	5	7	1211
2826	$Ca_5Ta_2TiO_{12}$+0.1 wt% SiO_2	1600	Complex perovskite Orthorhombic Pnma	39.0	35000	5	9	1211
2827	$Ca_5Ta_2TiO_{12}$+1 wt% SnO_2	1625/4h	Complex perovskite Orthorhombic Pnma	39.0	35500		2	1155
2828	$Ca_5Ta_2TiO_{12}$+1 wt% Cr_2O_3	1625/4h	Complex perovskite Orthorhombic Pnma	39.0	40500		13	1155
2829	$Ca_5Ta_2TiO_{12}$+1 wt% In_2O_3	1625/4h	Complex perovskite Orthorhombic Pnma	39.0	37000		2	1155
2830	$SrTiO_3$-$LaAlO_3$		Perovskite	39.0	60000		0	1212

(*continued*)

No.	Material	ST (°C)	Crystal structure	ε_r	Qf (GHz)	f_0	τ_f	Reference
2831	$Sr(Sm_{0.5}Ta_{0.5})O_3$+0.5 wt% Nb_2O_5+2 wt% TiO_2	1600/4h	Complex perovskite Tetragonal	39.0	11600		−20	859
2832	$BaMg_6Ti_6O_{19}$	1450	Hexagonal $P6_3/mmc$	39.0	20000	2	370	1213
2833	$Ba_2Ti_9O_{20}$	1350/3h	Monoclinic $P2_1/m$	39.0	32000	2		1214, 1215
2834	$Ba_5Nb_4O_{15}$+3 wt% B_2O_3	925	Perovskite Hexagonal P-3m1	39.0	18700		0	1206
2835	$Bi_2Te_2O_8$(oxygen atm)	650/10h	Monoclinic C2/c	39.0	23000		−43	1216
2836	$0.9BiNbO_4$-$0.1ZnNb_2O_6$+$0.8CuV_2O_6$	900	Mixture phases	39.0	31000		−10	1217
2837	$Ba_{9/12}La_{3/12}Zn_{1/3}Ti_{3/12}Nb_{5/12}O_3$	1400		39.0	1500	5.46	−42	919
2838	$Sr_2La_2TiNb_2O_{12}$	1450	Hexagonal perovskite	39.0	40600		−5	1143
2839	$Sr_{4-m}La_mTi_{m-1}Ta_{4-m}O_{12}$ (m=3)	1600		39.0	42000		−8	975
2840	$0.6La(Mg_{1/2}Ti_{1/2})TO_3$-$0.4Ca_{0.6}Nd_{0.8/3}TiO_3$+0.5 wt% B_2O_3	1475	Composite	39.0	41000	8	−3	1218
2841	$Bi_{11.8}SiO_{19.7}$	825/4h	Cubic I23	39.0	74000		−14	1219
2842	$Bi_4B_2O_9$	660	Monoclinic $P2_1/c$	39.0	2600		−203	287
2843	$Ba(Dy_{1/2}Ta_{1/2})O_3$	1625	Complex perovskite	39.1	18200		−48	943
2844	$0.8BaZn_2Ti_4O_{11}$-$0.2BaNd_2Ti_4O_{12}$	1250	Composite	39.1	37850		−9	1220
2845	$(Zr_{0.8}Sn)TiO_4$+2 wt% ZST nano	1300/3h	Orthorhombic Pbcn	39.2	72900		–	1221
2846	$Sr_{1.6}Ca_{0.4}TiO_4$	1600	Tetragonal I4/mmm	39.2	8100	3	195	1222
2847	(5-x)BaO-xMgO-$2Nb_2O_5$ (x=1)+1 wt% CuO	1200	Composite	39.2	43800		38	1159
2848	$Sr_2La_4Ti_5O_{18}$	1625/2h	$A_6B_5O_{18}$ type perovskite	39.2	27350		20	895
2849	$Sm(Nb_{0.5}Ta_{0.5})TiO_6$			39.3	19600		33	671
2850	$Ca_5Ta_2TiO_{12}$+1 wt% Sb_2O_3	1625/4h	Complex perovskite Orthorhombic Pnma	39.3	36800		7	1155
2851	$Ba_2Ti_9O_{20}$+1.64 mol%SnO_2	1390/6h in O_2	Monoclinic P-1	39.3	38400		–	1223
2852	$Ba_3LaTa_3O_{12}$	1500	$A_nB_{n-1}O_{3n}$ perovskite Trigonal R3m	39.4	26800	6	−46	1224

2853	$Bi_{12}MnO_{20-d}$	720	Cubic I23 Sillimanite	39.4	800		−35	1176
2854	$PrTiSb_xTa_{1-x}O_6$ (x=0.05)	1480/4h		39.4	14800	4.001	65	1101
2855	$Sm(W_{0.5}Ti_{1.5})O_6$	1350	Orthorhombic Pnma Aeschynite type	39.4	35500		−1	1121
2856	$5.7Li_2O$-Nb_2O_5-$7.3TiO_2$	1100	M phase	39.5	16200		65	1225
2857	$CeTiSb_xTa_{1-x}O_6$ (x=0)			39.5	11400	3.81	60	1101
2858	$Ba_{3-x}Sr_xLaNb_3O_{12}$ (x=1)	1400	Perovskite Trigonal R-3m	39.5	22600		−56	1125
2859	$Ba_{1-x}La_x[Zn_{(1+x)/3}Nb_{(2-x)/3}]O_3$ (x=0)	1350/4h		39.5	112280		19	1226
2860	$Ba_2Ti_9O_{20}$+1.64 mol% ZrO_2	1390/6h O_2	Monoclinic $P2_1/m$	39.5	41700		2	1227
2861	$Ba_5SrNb_4ZrO_{18}$	1600/4h	Trigonal R-3m	39.5	36000		68	895
2862	$Ba[Zn_{1/4}Ti_{1/4}Ta_{1/2}]O_3$	1500	Perovskite cubic	39.6	15000	7.4		1228
2863	$0.6La_{2/3}TiO_3$-$0.4LaAlO_3$	1400/33h	Perovskite Orthorhomic	39.6	42200	6	−15	1096
2864	$Ba(Ho_{1/2}Ta_{1/2})O_3$	1625	Complex perovskite	39.6	21900		130	943
2865	$PrTiSb_xTa_{1-x}O_6$ (x=0.0)	1480/4h		39.6	12500	3.97	56	1101
2866	$0.95Ba(Zn_{1/3}Nb_{2/3})O_3$-$0.05BaZrO_3$+1 wt% CuO	1360/2h	Perovskite cubic Pm3m	39.7	70000	7	17	1229
2867	$Ba(Sm_{1/2}Nb_{1/2})O_3$	1500	Complex perovskite	39.7	21500	7.1	21	590
2868	$(1-x)La(Mg_{1/2}Ti_{1/2})O_3$-$xLa_{2/3}TiO_3$ (x=0.45)		Perovskite I2/a	39.7	5800	7.6		889
2869	$Ba(Yb_{1/2}Ta_{1/2})O_3$	1625	Complex perovskite	39.7	31700		112	943
2870	$0.65CaTiO_3$-$0.35Sm_{0.9}Nd_{0.1}AlO_3$	1415/3h	Orthorhombic Perovskite	39.7	50000		−7	1230
2871	$Ba_6Ti_{1-x}Sn_xNb_4O_{18}$ (x=0.25)	1480	Hxagonal R-3m	39.8	19800	5.5	46	982
2872	$GdTiTaO_6$	1540		39.9	12900		11	583
2873	$Ba(Gd_{1/2}Nb_{1/2})O_3$	1600	Complex perovskite	40.0	5700		5	1136
2874	$Ca_5Nb_{0.5}Ta_{1.5}TiO_{12}$	1600	Complex perovskite Orthorhombic Pnma	40.0	31500		19	1231
2875	$Ba(Eu_{1/2}Nb_{1/2})O_3$	1600	Complex perovskite	40.0	40200		7	1136
2876	$Ba_3Ti_5Nb_3Ta_3O_{28}$	1375		40.0	8000	4.8	9	1208
2877	$Ba_5Nb_4O_{15}$	–	Trigonal perovskite P-3m1	40.0	53000		78	1232-1234
2878	$Ca_4ZnNb_2TiO_{12}$	1550	Perovskite Orthorhombic Pnma	40.0	30500	4.2458	−37	230

(*continued*)

No.	Material	ST (°C)	Crystal structure	ε_r	Qf (GHz)	f_0	τ_f	Reference
2879	$Sr_5Nb_4O_{15}(A_nB_{n-1}O_{3n})$	1400	Trigonal P-3c1 perovskite	40.0	19400	4.84	55	325
2880	$Ca(Fe_{1/2}Nb_{1/2})O_3$	1500/6h	Complex perovskite Orthorhombic Pbnm	40.0	20000		−76	609
2881	$Ca[(Li_{1/3}Nb_{2/3})_{0.8}Ti_{0.2}]O_{3-\delta}$	920	Orthorhombic perovskite	40.0	20500	8	5	1235
2882	$Ca[(Li_{1/3}Nb_{2/3})_{0.8}Ti_{0.2}]O_{3-\delta}$+12 wt% B_2O_3-ZnO-SiO_2-PbO frit glass	900	Composite	40.0	12500		−8	1236
2883	$Sr(Zn_{1/3}Nb_{2/3})O_3$		Perovskite Cubic Pm3m	40.0	36800	9.2	−39	787
2884	$0.3Sr(Eu_{1/2}Nb_{1/2})O_3$-$0.7Sr(Fe_{1/2}Nb_{1/2})O_3$	1600/4h	Complex perovskite	40.0	22600		−4	823
2885	$Ba[(Zn_{0.8}Co_{0.2})_{1/3}Nb_{2/3}]O_3$	1410	Perovskite Cubic Pm3m	40.0	50135		18	1130
2886	$Ba(Zn_{1/3}Nb_{2/3})O_3$	1390	Perovskite Cubic Pm3m	40.0	87000		30	787, 1237
2887	$Ba_{0.3}Sr_{0.7}(Zn_{1/3}Nb_{2/3})O_3$	1500/1h	Perovskite Cubic Pm3m	40.0	30500	10	−5	1238
2888	$0.7Ca(Mg_{1/3}Nb_{2/3})O_3$-$0.3CaTiO_3$		Perovskite	40.0	27900	3.8	−15	1238
2889	$(Zr,Sn)TiO_4$	1600	Orthorhombic Pbcn	40.0	53000	10	0	1240
2890	$Ba_8Ta_{4+0.8x}Ti_{3-x}O_{24}$ (x=0)	1400/40h	$A_nB_{n-1}O_{3n}$ hexagonal Perovskite P63/mcm	40.0	12960			920
2891	$0.6La_{2/3}TiO_3$-$0.4LaAlO_3$(oxygen)	1400/33h	Perovskite Orthorhombic	40.0	50800	6	−15	1096
2892	$Ba_{0.75}Sr_{0.25}(Zn_{1/3}Ta_{2/3})_{0.94}Ti_{0.06}O_3$	1400	Perovskite	40.0	65000	10	−13	1194
2893	$Ba_5Nb_4O_{15}$+0.3 wt% ZnB_2O_4 glass	900	Hexagonal Perovskite	40.0	12100		48	1241
2894	Ba-Nd-Sm-Bi-Ti-O+9 wt% BaO-B_2O_3-SiO_2	950/2.5h	Composite	40.0	3000			1242
2895	$ZnNb_2O_6$-$1.8TiO_2$+4 wt% $BaCu(B_2O_5)$	950/4h	Composite	40.0	11000		2	626
2896	$Bi(V_{0.008}Nb_{0.992})O_4$	830	Orthorhombic Pnma	40.0	18500			1243
2897	$La(Mg_{0.3}Ti_{0.5})O_3$+15 mol% Bi_2O_3	1325	Composite	40.1	60200		70	1244
2898	$Ca_5Ta_4TiO_{17}$	1525	Monoclinic $P2_1/c$	40.1	16450	4.22	−54	877, 1245
2899	$Ba_3Ti_5Nb_6O_{28}$+2 wt% B_2O_3+2 wt% CuO	900/2h	Monoclinic $P2_1/c$	40.2	32200		5	461
2900	$La_6MgTi_4O_{18}$	1625/2h		40.2	35000		−39	895
2901	$Ba_5Nb_4O_{15}$+1.5 wt% $BaCu(B_2O_5)$		Hexagonal perovskite	40.2	28600		60	1246
2902	BaO-CeO_2-$3TiO_2$	1300	Composite	40.3	19900		22	1247

2903	$Ba(Zn_{1/3}Nb_{2/3})O_3$+1 mol% ZrO_2 annealed at 1325	1450/4h	Complex perovskite trigonal	40.3	77800		26	1165
2904	$Ba_3Ti_5Nb_6O_{28}$+1 wt% B_2O_3+3 wt% CuO	900/2h	Monoclinic $P2_1/c$	40.3	32500		9	461
2905	2.5ZnO-0.2SnO_2-4.8TiO_2-2.5Nb_2O_5+4 wt% $BaCu(B_2O_5)$	900	Composite	40.4	19000		−1	1248
2906	5.7Li_2O-Nb_2O_5-7.3TiO_2+1 wt% B_2O_3	900	M phase+Li_2TiO_3	40.5	13900		42	1225
2907	$ZnTi(Nb_{1-x}Ta_x)_2O_8$ (x=0.8)	1200/2h	Orthorhombic Pbcn	40.5	41000		0	1249
2908	$Ca_4La_2Ti_{5-x}(Mg_{1/3}Nb_{2/3})_xO_{17}$ (x=3)	1540	Orthorhombic Pbnm	40.5	19100		1	1118
2909	$BaTi_5O_{11}$+1 wt% CuO	1100	Monoclinic $P2_1/n$	40.5	44500		39	1177
2910	$Ca_4MgNb_4TiO_{17}$	1250		40.6	18250		1.5	877
2911	$Ga_{0.5}Ta_{0.5}TiO_4$	1400	Tetragonal P42/mnm	40.6	17500		110	1250
2912	$BiNb_{0.6}Sb_{0.4}O_4$	920	Orthorhombic Pnna	40.7	9500		−31	1251
2913	$Zr_{0.8}Sn_{0.2}TiO_4$+1 wt% ZnO+1 mol% Sb_2O_5	1400/5h	Orthrhombic Pbcn	40.8	60900			1252
2914	5.5Li_2O-Nb_2O_5-7.5TiO_2+1 wt% B_2O_3	875		40.8	15500	5.78	50	1253
2915	$La_6ZnTi_4O_{18}$	1600/4h		40.8	21900		−37	895
2916	$Ni_{0.35}Zn_{0.65}TiNb_2O_8$	1100/6h	–	40.9	40900		1	1254
2917	0.8ZrO_2-0.4$(Zn_{1/3}Nb_{2/3}O_2$-0.8TiO_2	1320/3h		40.9	43300		−4	1255
2918	5Li_2O-1Nb_2O_5-5TiO_3+1 wt% B_2O_3	900		41.0	9880		43	1256
2919	$Ba_2Ti_3Nb_4O_{18+}$ 1.5 wt% $MnCO_3$-CuO+0.5 wt% LBS	900/2h	Composite	41.0	15000	4.8	4	1185
2920	$Ba_{1/2}La_{1/2}Zn_{1/3}Ti_{1/2}Nb_{1/6}O_3$	1400		41.0	1550	5.04	18	919
2921	$SrLa_3Ti_2NbO_{12}$	1480	Hexagonal perovskite	41.0	33600		3	1143
2922	$Ba_2Ti_9O_{20}$:Mn		Monoclinic $P2_1/m$	41.0	45000	9	2	1254
2923	$Ba(Zn_{1/3}Nb_{2/3})O_3$+1 mol% CeO_2 annealed at 1325	1450/4h	Complex perovskite Cubic Pm3m	41.0	69500		41	1165
2924	$Ca_{4.35}Mg_{0.65}Nb_2TiO_{12}$	1550	Orthorhombic perovskite Pnma	41.0	33000	4.1	0	230
2925	$Ba(Zn_{1/3}Nb_{2/3})O_3$ Annealed in N_2	1500	Perovskite cubic Pm3m	41.0	90000		4	787
2926	$(Ti_{0.8}Sn_{0.2})Te_3O_8$	700/5h	Cubic Ia3	41.0	22000	4		53
2927	$Bi_{0.95}Sm_{0.05}NbO_4$	1040	Orthorhombic Pnma	41.0	5200		−200	1258

(*continued*)

No.	Material	ST (°C)	Crystal structure	ε_r	Qf (GHz)	f_0	τ_f	Reference
2928	$Bi_{12}TiO_{20}$	800/5h	Cubic I23 sillenite	41.0	10400		−11	1176, 1259
2929	$0.65CaTiO_3$-$0.35SmAlO_3$	1450/12h	Perovskite Orthorhombic	41.0	42000		−18	1174
2930	$0.9BiNbO_4$-$0.12ZnNb_2O_6$+1.2 wt% CuV_2O_6	850	Composite	41.0	28120		4	1217
2931	$BaTi_5O_{11}$ (hot pressed)	1050/48	Monoclinic $P2_1/n$	41.0	46000	10	40	1260
2932	$0.65CaTiO_3$-$0.35LaAlO_3$	1450/12h	Perovskite Orthorhombic	41.0	33000		−17	1174
2933	$Sr_5Ta_4O_{15}(A_nB_{n-1}O_{3n})$	1610	Hexagonal perovskite P-3m1	41.0	2400	5.99	–	325
2934	$Ca_3Nb_2O_8$		Cubic	41.0	8700	8.6	123	864
2935	$Ba_3Ti_5Nb_6O_{28}$	1300	Monoclinic $P2_1/c$	41.0	4500	5.4	8	1208
2936	$Zr_{0.513}Hf_{0.487}TiO_4$	1600	Orthorhombic Pbcn	41.0	20400		13	1057
2937	$5CaO$-$2Ta_2O_5$	1550	Mixed phases	41.0	5900	5.9	140	325
2938	$NaCa_4Ta_5O_{17}$	1350	Monoclinic (P21/b)	41.0	11600		−14	1261
2939	$CaLa_4Ti_4O_{15}$ $(A_nB_{n-1}O_{3n})$	1550/24h	Hexagonal perovskite P-3c1	41.1	50240		−25	1262
2940	$CaTi_{0.4}(Al_{1/2}Nb_{1/2})_{.6}O_3$+1 wt% Li_3NbO_4	1300/5h	Perovskite Orthorhombic	41.1	36200	7	−36	1152
2941	$Ba(Zn_{1/3}Nb_{2/3})O_3$	1390	Perovskite Cubic Pm3m	41.1	86900	9.5	31	787, 1238
2942	$BaTi_5O_{11}$ (reaction sintering)	1100	Monoclinic $P2_1/n$	41.2	47400		36	1263
2943	$0.4La(Mg_{0.4}Sr_{0.1}Sn_{0.5})O_3$-$0.6Ca_{0.8}Sr_{0.2}TiO_3$	1550/4h	Composite	41.2	56900		−6	1264
2944	$CaTi_{0.4}(Al_{1/2}Nb_{1/2})_{.6}O_3$	1500/5h	Perovskite Orthorhombic	41.3	27100	7	−44	1152
2945	$EuTiTaO_6$	1525	Aeschynite Orthorhombic	41.3	59500		19	583
2946	Li_2O-Nb_2O_5-TiO_2 (5:1:5)+1 wt% B_2O_3	900		41.3	9320			1140
2947	ZnO-Nb_2O_5-$0.08SnO_2$-$1.92TiO_2$+1 mol% MnO_2+4 wt% $BaCuB_2O_5$	850	composite	41.3	1690		−16	1265
2948	$CaTi_{0.5}(Al_{1/2}Ta_{1/2})_{0.5}O_3$	1500/15h	Perovskite Orthorhombic	41.4	26100	8	−20	1266
2949	$Zn_{0.7}Ni_{0.3}TiNb_2O_8$	1125/4h	Orthorhomic Pbcn	41.4	31800		−9	1267
2950	$Ba_{0.9}Ca_{0.1}(Y_{.285}Nb_{1/2})O_{3+\delta}$		Perovskite	41.5	48860	7.85	258	1202
2951	$BiNbO_4$:0.4 wt% B_2O_3	960/2h	Orthorhombic Pnma	41.5	21000		−2	1268
2952	$0.7CaTiO_3$-$0.3(La_{0.5}Nd_{0.5})AlO_3$		Rhombic perovskite	41.5	37000	8	4	1269
2953	$Ca_2Zn_4Ti_{15}O_{36}$+8 wt% B_2O_3	990	Hexagonal	41.5	11400		95	1270

2954	$Ca[Ti_{1-x}(Mg_{1/3}Nb_{2/3})_x]O_3$ (x=0.7)	14504h		41.6	29450		−12	1271
2955	$Sm(Nb_{0.75}Ta_{0.25})TiO_6$			41.6	18900		36	671
2956	$CaLa_4Ti_3O_{15}$	1450	$A_nB_{n-1}O_{3n}$ Hexagonal Perovskite P-3m	41.6	8100	4.31	−25	1272
2957	$5Li_2O$-Nb_2O_5-$5TiO_2$+1 wt% V_2O_5	900/6h	M phase+Li_2TiO_3	41.7	7800		45	1273
2958	$(LiBi)_{1/2}MoO_4$	560	Scheelite	41.7	3200	5.5	240	677
2959	$0.8Ba_{0.6}Sr_{0.4}La_4Ti_4O_{15}$-$0.2Ba_5Nb_4O_{15}$	1475	Hexagonal Perovskite	41.7	25100		2	1274
2960	$Zr(Zn_{1/3}Nb_{2/3})_{0.6}Ti_{1.4}O_6$		$ZrTi_2O_6$ type Orthorhombic Pbcn	41.7	42100		−16	1275
2961	$SmTiTaO_6$	1500	Aeschneite Orthorhombic	41.8	24500		24	583
2962	$(Ni_{1/3}Ta_{2/3})_{1-x}Ti_xO_2$ (x=0.3)	1300	Rutile Tetragonal $P4_2/mmm$	41.8	20600		35	1276
2963	$BiNb_{1-x}Mo_xO_4$ (x=0.01)	950	Orthorhombic Pnma	41.8	3500		−15	1277
2964	$Pr_{0.2}Gd_{0.8}TiNbO_6$	1400	Orthorhombic Pnma	41.9	9500		35	564
2965	$Ba(Nd_{1/2}Nb_{1/2})O_3$	1500/96h	Perovskite	41.9	15000	6.8	13	590
2966	$Ba_{3-x}Sr_xLaNb_3O_{12}$ (x=0.5)	1390	Trigonal R-3m	41.9	19400		−65	1125
2967	$0.67CaTiO_3$-$0.33NdAlO_3$	1450/10h	Perovskite Orthohombic	42.0	42900		45	1174
2968	$ZrTiO_4$	1400	Orthorhombic Pbcn	42.0	31000	7	58	1188
2969	$Ca_{4.38}Ni_{0.62}Nb_2TiO_{12}$	1550	Perovskite Orthorhombic Pnma	42.0	28200	4	≈0	230
2970	$Sr_4Ti_3O_{10}$	1300/5h	Tetragonal I4/mmm	42.0	960	4		53
2971	$0.95Ba(Zn_{1/3}Nb_{2/3})O_3$-$0.05BaZrO_3$	1450/2h	Perovskite Perovskite Cubic Pm3m	42.0	96000	7	27	1278
2972	$0.84Ba_5Nb_4O_{15}$-$0.16BaNb_2O_6$+0.3 wt% B_2O_3	900	Composite	42.0	28000		0	835
2973	$Ba_xLa_4Ti_{3+x}O_{12+3x}$ (x=0.2)	–		42.0	86000		−17	1279
2974	$BaTi_5O_{11}$	1120/24	Monoclinic $P2_1/n$	42.0	61100	–	40	1280
2975	$La_{0.43}Ca_{0.57}[Ca_{0.08}Mg_{0.14}Ti_{0.78}]O_3$		Perovskite	42.0	18000	5.0	9	950
2976	$La_9Mg_{0.5}Ti_{8.5}O_{31}$		Perovskite slab series	42.0	15000	8.4	−11	950
2977	$0.6CaTiO_3$-$0.4SmGaO_3$	1450/12h	Perovskite, multiphase	42.0	35000		−11	1174
2978	(1-x)$LaMg_{1/2}Ti_{1/2}O_3$-x$La_{2/3}TiO_3$ (x=0.45)		Perovskite	42.0	4500	4.8	−30	950
2979	$BaNb_2O_6$ (hex)	1050	Hexagonal columbite	42.0	4000		−800	835, 995
2980	$Ba_{0.79}Sr_{0.21}Ti_5O_{11}$(hot pressed)	1050/72h	Monoclinic $P2_1/n$	42.0	39000	10	44	1260

(*continued*)

No.	Material	ST (°C)	Crystal structure	ε_r	Qf (GHz)	f_0	τ_f	Reference
2981	$Ca_{4.38}Ni_{0.62}Nb_2TiO_{12}$	1550	Perovskite	42.0	28200	4	0	230, 1112
2982	$Sr(Sm_{0.5}Ta_{0.5})O_3$+0.5 wt% Nb_2O_5+3 wt% TiO_2	1600/4h	Complex perovskite Tetragonal	42.0	8750		3	859
2983	$Ca_3Sr_2Ta_2TiO_{12}$	1600	Perovskite Orthorhombic Pnma	42.0	16000	3.5	14	1209
2984	$0.6CaTiO_3$-$0.4Sm(Mg_{0.5}Ti_{0.5})O_3$	1550	composite	42.0	9200	4.8	6	865
2985	$Ba_{0.8}Sr_{0.2}(Zn_{1/3}Ta_{2/3})_{0.94}Ti_{0.06}O_3$	1400	Perovskite	42.0	82000	10	−13	1192
2986	$Ca_{0.6}(Li_{.5}Nd_{.5})_{0.4})_{0.45}Zn_{.55}TiO_3$+2 wt% $0.33ZnO$-$0.67H_3BO_3$	900/4h	Multi phase	42.0	10300		19	1281
2987	$0.1CaTiO_3$-$0.9Nd(Mg_{1/2}Ti_{1/2})O_3$	1400	Perovskite Orthorhombic	42.0	35000		−10	1282
2988	$Sr(Sm_{1/2}Ta_{1/2})O_3$+3 wt% TiO_2	1600	Perovskite	42.0	8800		3	861
2989	$0.76ZrTi_2O_6$-$0.24ZnNb_2O_6$	1300/4h	Composite	42.0	22976			1283
2990	$Nd(W_{0.5}Ti_{1.5})O_6$	1350	Orthorhombic Pnma Aeschynite type	42.0	26200		9	1121
2991	$0.4La(Mg_{1/2}Ti_{1/2})O_3$-$0.6(Na_{0.5}Nd_{0.5})TiO_3$+1 wt% B_2O_3	1475	Composite	42.0	33000	8	1	1284
2992	$5.5Li_2O$-Nb_2O_5-$7.5TiO_2$	1075		42.0	16900	5.75	64	1253
2993	$Ca^{(}Zr_xTi_{1-x})O_3$ (x=0.9)	1515/15h	Perovskite Orthorhombic Pcmn	42.0	10700	4.6	82	916
2994	$0.36Ca_4La_2Ti_5O_{17}$-$0.64LaAlO_3$	1560/4h	Composite	42.0	12500		0	1285
2995	$0.4LaAlO_3$-$0.6SrTiO_3$	1680	Perovskite	42.1	83000	9.5	8	832
2996	$Ba_5Nb_{4-x}(W_{1/2}Ti_{1/2})O_{15}$ (x=0.4)		Perovskite	42.2	38600		53	1286
2997	$Ba_4LaTiTaO_{15}$	1540/6h	Trigonal P-3m1	42.3	28790		33	1287
2998	$Ca(La_{0.5}Nd_{0.5})_4Ti_4O_{15}$ ($A_nB_{n-1}O_{3n}$)	1525	Hexagonal Perovskite	42.3	15200	8.3	−6	1288
2999	$Ba_{11}TiNb_8O_{33}$	1400		42.3	27000		47	1289, 1290
3000	$CaLa_{0.5}Nd_{0.5}Ti_4O_{15}$	1525	Hexagonal Perovskite	42.3	15200	8.3	−6	1288
3001	$Ba_4LaTiTa_3O_{15}$	1540/6h	Perovskite Hexagonal	42.3	28800		33	1291
3002	$Sr_{0.92}[Li_{1/4}Nb_{3/4}]_{0.92}Ti_{0.08}O_3$	1350/2h	Perovskite	42.3	31500	9	–	1197
3003	ZnO-Nb_2O_5-TiO_2-SnO_2+1.5 wt% CuO-V_2O_5	860	Mixture phases	42.3	9000		8	1292

3004	$Ba_{1-x}La_x[Zn_{(1+x)/3}Nb_{(2-x)/3}]O_3$ (x=0.05)	1350/4h	Perovskite	42.4	46530		35	1226
3005	$BaLa_3Ti_2NbO_{12}$	1460/6h	Hexagonal perovskite	42.4	33600		6	1293
3006	$Zr_{0.7}(Zn_{1/3}Ta_{2/3})_{0.3}TiO_4$	1300	Orthorhombic α-PbO_2	42.5	40200	5	1	1294
3007	$0.3BaTiO_3$-$0.7La(Mg_{1/2}Ti_{1/2})O_3$		Perovskite I4/mcm	42.5	14225	7.23	−34	933
3008	$5.5Li_2O$-Nb_2O_5-$7.5TiO_2$	1100		42.6	16800		66	1253
3009	$SrLaSm_3Ti_5O_{17}$	1350		42.6	7300		−96	1295
3010	$Ba_2La_2TiNb_2O_{12}$	1440		42.7	31130		−4	1296
3011	$Ba_{21}Nb_{16}TiO_{63}$			42.7	19000		25	1289
3012	$Ba_2La_3Ti_3NbO_{15}(A_5B_4O_{15})$	1460	Hexagonal perovskite	42.8	21700	5.85	−8	1297
3013	$Ba_{16}Nb_{12}TiO_{48}$		Not available	42.9	29000		25	1289
3014	$Ba_{0.9}Ca_{0.1}(Y_{0.315}Nb_{1/2})O_{3+\delta}$		Perovskite	42.9	63500	7.78	235	1202
3015	$Ba_6Ti_{1-x}Sn_xNb_4O_{18}$ (x=0)	1460	Trigonal R-3m	43.0	11530	5.6	64	982
3016	$Bi_{12}SiO_{20}$	800/5h	Cubic I23	43.0	86800		−10	1298
3017	$Sr_4LaTiNb_3O_{15}$	1460	Hexagonal perovskite	43.0	44700	5.18	13	1299
3018	$Li_{0.215}Nb_{0.645}Ti_{0.14}O_2$	1020		43.0	14500		−15	1300
3019	$Ba_{2-x}Sr_xLa_3Ti_3NbO_{15}$ (x=1)	1520		43.0	39100		1	1301
3020	$Pb_{0.5}Ca_{0.5}(Cr_{1/2}Nb_{1/2})O_3$		Perovskite	43.0	3800	4.6	293	996
3021	$BiNbO_4$	875	Orthorhombic Pnma	43.0	15700	4.3	38	1302, 1303
3022	$0.7CaTiO_3$-$0.3NdAlO_3$		Perovskite Orthorhombic	43.0	47000	–	0	1304, 1305
3023	$Sr(Zn,Nb)O_3$-$SrTiO_3$		Perovskite	43.0	25000	5	−5 to 5	1306
3024	$La_{0.57}Ca_{0.43}[Ca_{0.11}Mg_{0.18}Ti_{0.71}]O_3$		Perovskite	43.0	26000	3.5	−19	950
3025	$Ca_4BaTa_2TiO_{12}$	1575	Orthorhombic Pnma	43.0	5000	3.9	14	1307
3026	$0.16BaNb_2O_6$-$0.84Ba_5Nb_4O_{15}$+0.3 wt% B_2O_3+0.3 wt% V_2O_5	900	Composite	43.0	19500		0	835
3027	$Ca_5NbTaTiO_{12}$	1580	Complex perovskite Orthorhombic Pnma	43.0	30000	–	28	1209, 1231
3028	$Ba(Nd_{0.8}Sm_{0.2})_2Ti_4O_{12}$+1 wt% B_2O_3	1020	Tungsten Bronze	43.0	5500			1308
3029	$Ca_{4.36}Zn_{0.64}Nb_2TiO_{12}$	1550	Orthorhombic perovskite Pnma	43.0	29000	4.0	0	230
3030	$Ba_6Nb_4TiO_{18}$	1625/2h	$A_6B_5O_{18}$ type perovskite	43.0	9500		53	895
3031	$Sr_6Nb_4TiO_{18}$	1625/2h	$A_6B_5O_{18}$ type perovskite	43.0	6700		26	895

(*continued*)

No.	Material	ST (°C)	Crystal structure	ε_r	Qf (GHz)	f_0	τ_f	Reference
3032	$Zr_{0.7}(ZnTa)_{0.3}TiO_4$	1300/3h	Orthorhombic Pbcn	43.0	40200		1	1294
3033	$Ba(Sm_{1/2}Nb_{1/2})O_3$	1600	Perovskite Cubic Fm3m	43.0	18400		9	1136
3034	$Sm_{0.9}Y_{0.1}TiNbO_6$	1560	Aeschneite Orthorhombic	43.0	10230		47	564
3035	$0.52Nd(Co_{1/2}Ti_{1/2}O_3$-$0.48CaTiO_3$	1550	Composite	43.0	4000		0	1309
3036	$Ba_xLa_4Ti_{3+x}O_{12+3x}$ (x=2.3)			43.0	23480		−17	1310
3037	$La_2Ti_2O_7$		Monoclinic $P2_1$	43.0	2200	5.5	−6	950
3038	$0.7CaTiO_3$-$0.3La(Ga_{0.5}Al_{0.5})O_3$	1540	Composite	43.0	40000		13	1269
3039	$BiNbO_4$+0.4 wt% V_2O_5+0.1 wt% CuO	900	Orthorhombic Pnma Stibiotantalite	43.0	20400		8	1311
3040	$0.5La(Mg_{1/2}Ti_{1/2})O_3$-$0.5CaTiO_3$	1600	Composite	43.0	28000	5.5	−13	1312
3041	$Ca_{4.5}Mg_{0.5}Nb_4TiO_{17}$	1250		43.0	17850		−33	877
3042	$NdTiTaO_6$	1550	Aeschneite Orthorhombic	43.1	26400		30	583
3043	$Ca[(Li_{1/3}Nb_{2/3})_{0.7}Ti_{0.3}]O_{3\text{-}d}$+6 wt% Bi_2O_3, 2 wt% B_2O_3	920	Perovskite	43.1	10600	7.68	10	1235
3044	$Ca[(Li_{1/3}Nb_{2/3})_{0.7}Ti_{0.3}]O_{3\text{-}d}$+3 wt% Bi_2O_3; 2 wt% B_2O_3	940	Perovskite	43.1	12900	7.73	54	1235
3045	$Zr_{0.752}Hf_{0.248}TiO_4$		Orthorhombic Pbcn	43.2	20000	8.5	–	1088
3046	Alpha-Bi_3SbO_7	890	Anorthic	43.2	2080		0	1181
3047	$BiNbO_4$+0.5 wt% CuO	900	Orthorhombic Pnma Stibiotantalite	43.3	13000	6.3	15	1313
3048	$Ca[La_{0.875}Nd_{0.125})_4Ti_4O_{15}$ ($A_nB_{n-1}O_{3n}$)	1550	Hexagonal perovskite	43.4	32900	7.52	−13	1288
3049	$(1\text{-}x)Ca(Mg_{1/3}Ta_{2/3})O_3$-$x(Ca_{0.8}Sr_{0.2})TiO_3$ (x=0.4)	1425/2h	Composite	43.4	46000	6.8	−3	1314
3050	$Ba_3LaNb_3O_{12}$	1500	Hexagonal perovskite R-3m	43.5	9000		−100	1315, 1316
3051	$Sr_5Ta_4O_{15}$	1510	Hexagonal perovskite	43.5	2400		–	1090
3052	$0.7CaTiO_3$-$0.3NdAlO_3$		Perovskite	43.5	30000	8	−2	1269
3053	$Ba_{11}Nb_8TiO_{33}$			43.5	12000		33	1289
3054	$BiTaO_4$	950	Triclinic	43.5	12000		−40	1317
3055	$Bi_{0.99}(La_{0.38}Nd_{0.62})_{0.01}NbO_4$	820	Orthorhombic+Triclinic	43.5	12300		13	1318
3056	$0.66CaTiO_3$-$0.34(La_{0.5}Nd_{0.5})GaO_3$		Perovskite Rhombic	43.6	43000	8	−10	1269

3057	$CaLa_4Ti_4O_{15}$ ($A_nB_{n-1}O_{3n}$)	1550	Hexagonal perovskite	43.6	33850	7.8	−17	1288
3058	$0.7CaTiO_3$-$0.3NdAlO_3$	1450/10h	Rhombic perovskite	43.7	34800		14	1174
3059	$Ba(Ti_{0.85}Mn_{0.15})O_3$+15 wt% Li_2CO_3	950	Perovskite	43.7	2500		−30	1319
3060	$(Sr_{0.2}Ca_{0.488}Nd_{0.2}0_8)Ti_{1-x}Ga_{4x/3}O_3$ (x=0.5)	1350/4h	Orthorhombic Perovskite Pnma	43.7	60000	4.7	8	1320
3061	$0.7Ca(Mg_{1/3}Nb_{2/3})O_3$-$0.3(Ca_{0.8}Sr_{0.2})TiO_3$		Perovskite	43.8	45200	7.2	−4	1321
3062	$Zn_{0.17}Nb_{0.33}Ti_{0.5}O_2$	1080	–	43.8	35000	9		1322
3063	$SrLa_4Ti_4O_{15}$ ($A_nB_{n-1}O_{3n}$)		Hexagonal perovskite P-3m	43.8	50200	4.15	−14	1262, 1272
3064	$Ba_{1-x}La_x[Zn_{(1+x)/3}Nb_{(2-x)/3}]O_3$ (x=0.35)	1350/4h	Perovskite	43.8	2180		−10	1226
3065	$Bi_{0.992}Gd_{.0.008}NbO_4$	900/3h	Orthorhombic Pnma	43.8	16850	4.3	0	1323
3066	$Ca[(Li_{1/3}Nb_{2/3})_{0.7}Ti_{0\cdot.3}]O_{3-\delta}$+1 wt% Bi_2O_{3+} 1 wt% B_2O_3	960	Perovskite	43.9	16600	7.6	35	1235
3067	$Ca_4MgNb_2TiO_{12}$-$xCaTiO_3$ (x=0.3)		Composite	43.9	20200		−7	1324
3068	$0.66Ca(Mg_{1/3}Nb_{2/3})O_3$-$0.34CaTiO_3$+ 0.25 wt% B_2O_3	1250	Composite	44.0	30000	6.7	−2	1325
3069	$0.1CaTiO_3$-$0.9Nd(Mg_{1/2}Ti_{1/2})O_3$+0.5 wt% ZnO	1325	Composite	44.0	43800		1	1326
3070	$0.32Nd(Zn_{0.45}Mg_{0.05}Ti_{0.5})O_3$-$0.1NdAlO_3$-$0.58CaTiO_3$		Composite	44.0	32200	1.97	0	1327
3071	$Bi_2Ti_3TeO_{12}$	900/10h		44.0	12500		146	1131
3072	$ZrTiO_4$-$ZnNb_2O_6$		Composite	44.0	48000		0	1283
3073	$Ca_2Sr_3Ta_2TiO_{12}$	1575	Perovskite Orthrohombic Pnma	44.0	8500	3.5	18	1209
3074	$BaTiNb_4O_{13}$	1250	Orthorhombic Pbma	44.0	9000	4.7	15	1208
3075	$Sr_2Zn_4Ti_{15}O_{36}$	1150/8h	Trigonal R-3m	44.0	3600	10	160	1026
3076	$Ba_8Ta_{4+0.8x}Ti_{3-x}O_{24}$ (x=0.8)	1400/40h		44.0	9720			920
3077	$Ba(Nd_{1/2}Nb_{1/2})O_3$	1600	Complex perovskite	44.0	11700		10	1136
3078	$Ca_{0.7}Nd_{0.3}T_{0.7}Al_{0\cdot.3}O_3$		Perovskite Orthorhombic	44.0	40000		0	1328
3079	$Ba(La_{0.99}Al_{0.11})_4Ti_4O_{15}(A_nB_{n-1}O_{3n})$		Hexagonal perovskite	44.0	47000		1	1329
3080	$066CaTiO_3$-$0.34LaAlO_3$	1450/12h	Perovskite Orthorhombic	44.0	30000		−3	1174
3081	$Ba_{0.9}Ca_{0.1}(Y_{0.33}Nb_{1/2})O_{3+\delta}$		Complex perovskite	44.0	41210	7.7	234	1202
3082	$0.7Ca(Li_{1/4}Nb_{3/4})O_3$-$0.3CaTiO_3$	1250	Composite	44.0	12000		−9	1330

(*continued*)

No.	Material	ST (°C)	Crystal structure	ε_r	Qf (GHz)	f_0	τ_f	Reference
3083	$Sr_2La_4Ti_5O_{18}$+0.3 wt% Bi_2O_3-B_2O_3	1625/2h		44.0	23000		22	895
3084	0.6$CaTiO_3$-0.4$NdGaO_3$	1450/12h	Perovskite	44.0	30000		−18	1174
3085	$BiNbO_4$+0.5 wt% V_2O_5	895	Orthorhombic Pnma	44.0	15800	7	18	1311
3086	$BiNbO_4$+0.25 wt% CuO+V_2O_5	900	Orthorhombic Pnma	44.0	18660		−8	1311
3087	$Bi_{0.95}Sm_{0.05}NbO_4$+0.5 wt% CuO	900	Orthorhombic Pnma	44.0	12900		−4	1331
3088	$BiNb_{0.4}Ta_{0.6}O_4$	940	Orthorhombic Pnma	44.0	21000		−30	1332
3089	0.5$La(Mg_{1/2}Ti_{1/2})O_3$-0.5$CaTiO_3$+1 wt% B_2O_3	1400	Perovskite	44.0	28000	7	−8	1312
3090	0.225Li_2O-0.67Nb_2O_5-0.1TiO_2	1350		44.0	28000		−20	760
3091	$Na_{1-x}K_xCa_4Nb_5O_{17}$ (x=0)	1200	Monoclinic P21/a $A_nB_nO_{3n+2}$	44.0	13800		−120	1333
3092	$Ba_8Nb_4Ti_3O_{24}$	1450	Hexagonal $P6_3/mmc$	44.1	22000		115	1334
3093	0.66$CaTiO_3$-0.34$(La_{0.5}Nd_{0.5})GaO_3$		Rhombic perovskite	44.1	43000	8	1	1269
3094	$Ba_2La_2TiNb_2O_{12}$	1350/6h	Hexagonal perovskite	44.2	31660	6.9	−5	1316
3095	$Ca[Ti_{1-x}(Mg_{1/3}Nb_{2/3})_x]O_3$ (x=0.65)	14504h	Perovskite	44.2	28340		−2	1335
3096	$CaLa_4Ti_4O_{15}$+1 wt% $BiVO_4$	1425		44.3	51400		−9	1336
3097	$BaLa_4Ti_4O_{15}(A_nB_{n-1}O_{3n})$	1600/2h	Hexagonal perovskite P-3c1	44.4	41000		−26	1262, 1329 ,1337
3098	$Bi_{0.95}Sm_{0.05}NbO_4$	950	Orthorhombic Pnma	44.4	13000	7.2	−4	1338
3099	$(Li_{0.5}Bi_{0.5})MoO_4$	560	Scheelite	44.4	3200	5.5	245	30
3100	$Ca_4La_2Ti_{5-x}(Mg_{1/3}Nb_{2/3})_xO_{17}$ (x=2.5)	1540	Orthorhombic Pbnm	44.4	16400		15	1118
3101	0.67$ZrTi_2O_6$-0.33$ZnNb_2O_6$+0.7 wt% $MnCO_3$	1270	Composite	44.4	44800		−7	1339
3102	0.5$Nd(Co_{1/2}Ti_{1/2})O_3$-0.5$(Ca_{0.8}Sr_{0.2})TiO_3$	1340/4h	Composite	44.5	20000		0	1340
3103	$BiNb_{0.95}Sb_{.05}O_4$	880	Orthorhombic Pnma	44.5	14300		−5	1251
3104	$BiNb_{0.88}Ta_{0.12}O_4$+0.5 wt% CuO	920	Orthorhombic Pnma	44.5	14000		−0	1313
3105	$Ba(Pr_{1/2}Nb_{1/2})O_3$	1600	Complex perovskite	44.5	28500		−22	1136
3106	$Ba(Y_{0.3}Bi_{0.2}Nb_{.5})O_3$	1300	Complex perovskite	44.6	2000		6	1341
3107	$Ba_4Nd_2Ti_3Nb_2O_{18}$	1450/8h		44.6	13100		18	1342
3108	$Ba_{1-x}La_x[Zn_{(1+x)/3}Nb_{(2-x)/3}]O_3$ (x=0.3)	1350/4h	Perovskite	44.7	1990		7.7	1226

3109	$Ca_2La_4Ti_5O_{18}$		$A_nB_{n-1}O_{3n}$ Trigonal perovskite R-3m	44.7	20100	4.19	6	1272
3110	$Ca_2Zn_4Ti_{15}O_{36}$+4 wt% CaO-B_2O_3-SiO_2	1050/2h	Trigonal R-3	44.7	31000			1343
3111	0.67$CaTiO_3$-0.33$(La_{0.5}Nd_{0.5})GaO_3$		Rhombic perovskite	44.7	41000	8	6.3	1269
3112	$Ca[(Li_{1/3}Nb_{2/3})_{1-x}Ti_x]O_3$ (x=0.3)	1150/3h	Perovskite	44.7	22500		20	752
3113	$Ba_6Nb_4TiO_{18}$	1450	Trigonal R-3m	44.9	12000		33	895
3114	$Sr(Fe_{1/2}Nb_{1/2})O_3$+0.2 wt% B_2O_3	1350/4h	Complex perovskite Cubic Pm3m	44.9	10600		−15	823
3115	$Sr(Fe_{1/2}Nb_{1/2})O_3$	1600/4h	Complex perovskite Cubic Pm3m	44.9	4800		−24	823
3116	0.7$La_{2/3}TiO_3$-0.3$LaAlO_3$	1400/33h	Perovskite Orthorhombic	44.9	33000	6	7	1096
3117	$Ca_5Nb_4TiO_{17}$	1475	Monoclinic $P2_1/c$	44.9	17600		−113	877, 1245
3118	$BiNbO_4$+0.03 wt% $CuV_2O_{6\ (Ortho)}$	1000	Orthorhombic Pnma	44.9	16100		−3	1104
3119	0.55$Ca(Mg_{1/3}Ta_{2/3})O_3$-0.45$Ca_{0.8}Sm_{0.4/3}TiO_3$	1450	Composite	45.0	41700	6.6	0	1344
3120	$Ba_{2/3}La_{1/3}Zn_{1/3}Ti_{1/3}Nb_{1/3}O_3$	1400		45.0	6500	6.09	−6	919
3121	$NiNb_2O_6$+30 wt% TiO_2	1300/2h	Orthorhombic Pbcn	45.0	7700	6	73	1345
3122	0.73$CaTiO_3$-0.27$NdAlO_3$	1450/10h	Rhombic perovskite	45.0	31000		−15	1174
3123	$Ca[(Li_{1/3}Ta_{2/3})_{.5}Ti_{0.5}]O_{3-\delta}$+3 wt% B_2O_3	1050	Perovskite	45.0	12300	8	75	765
3124	$Na_{1-x}K_xCa_4Nb_5O_{17}$ (x=0.25)	1300	Monoclinic$P2_1/a$ $A_nB_nO_{3n+2}$	45.0	4600		34	1333
3125	0.81$BiVO_4$-0.19YVO_4	87072h	Monoclinic+Tetragonal	45.0	14000		10	1346
3126	$Na_{1-x}K_xCa_4Nb_5O_{17}$ (x=0.75)	1300	Monoclinic$P2_1/a$ $A_nB_nO_{3n+2}$	45.0	3700		123	1333
3127	0.58$ZnNb_2O_6$-0.42TiO_2	1250/2h	Composite	45.0	6000		0	1092
3128	0.42$ZnNb_2O_6$-0.58TiO_2	1250	Composite	45.0	48000	8	0	1092
3129	0.45$Nd_3Ga_5O_{12}$ -0.65$CaTiO_3$	1450	Composite	45.0	46000	5	−2	340
3130	0.7$CaTiO_3$-0.3$SmAlO_3$	1450/12h	Perovskite Orthorhombic Pbnm	45.0	42000		1	1174
3131	0.7$CaTiO_3$-0.3$NdAlO_3$	1450/10h	Perovskite Orthorhombic Pbnm	45.0	44000		3	1174
3132	$Ba(La_{1/2}Nb_{1/2})O_3$	1600	Complex perovskite Monoclinic	45.0	5700		7	1136
3133	$BaLa_4Ti_4O_{15}(A_nB_{n-1}O_{3n})$		Trigonal perovskite P-3m1	45.0	48000			1329
3134	$Sr(Fe_{1/2}Nb_{1/2})O_3$	1450/4h	Perovskite Cubic Pm3m	45.0	4800		−24	1163
3135	$CaSr_4Ta_2TiO_{12}$	1550	Perovskite Orthorhombic Pnma	45.0	15500	3.4220	21	1209

(*continued*)

No.	Material	ST (°C)	Crystal structure	ε_r	Qf (GHz)	f_0	τ_f	Reference
3136	$Ba_xLa_4Ti_{3+x}O_{12+3x}$ (x=0.4)	–	Trgonal perovskite P-3m1	45.0	60000		−15	1279
3137	$Ba_xLa_4Ti_{3+x}O_{12+3x}$ (x=0.6)	–	Trigonal perovskite P-3m1	45.0	50000		−13	1279
3138	$BaTiTa_2Nb_2O_{13}$	1350	Orthorhombic Pbma	45.0	3500	5.2	96	1208
3139	$BaSr_4Nb_4O_{15}(A_nB_{n-1}O_{3n})$	1400	Trigonal Perovskite P-3m1	45.0	23300	4.57	82	325
3140	$0.2CaTiO_3$-$0.8Sr(Mg_{1/3}Nb_{2/3})O_3$	1600	Perovskite	45.0	9000		0	1347
3141	$Ba_2La_3Ti_3TaO_{15}$	1520		45.0	26800		1	1348
3142	$0.6CaTiO_3$-$0.4LaGaO_3$	1450/12h	Perovskite	45.0	34000		−20	1174
3143	$0.65CaTiO_3$-$0.35SmGaO_3$	1450/12h	Perovskite	45.0	34000		1	1174
3144	$SmTiNbO_6$	1400	Euxenite Orthorhombic Pnma	45.0	18000	4.89	50	563
3145	$0.7CaTiO_3$-$03NdAlO_3$	1450/10h	Perovskite Orthorhombic	45.0	44000		0	1349
3146	$0.65CaTiO_3$-$0.35NdGaO_3$	1450	Perovskite Orthorhombic	45.0	46000		−2	1349
3147	$Ca[(Li_{1/3}Nb_{2/3})_{1-x}Ti_x]\ O_{3-\delta}$ (x=0.3)	1150/3h	Perovskite	45.0	22500		20	752
3148	$La_{2/3}TiO_3$ - $LaAlO_3$			45.0	33000		7	1096
3149	$0.48La(Co_{1/2}Ti_{1/2}O_3$-$0.52CaTiO_3$	1550	$P2_1/n$ Monoclinic perovskite	45.0	5000	7.8	0	1309
3150	$0.5Nd(Zn_{1.2}Ti_{1/2})O_3$-$0.5CaTiO_3$	1300/4h	$P2_1/n$ Monoclinic perovskite	45.0	56000		0	1350
3151	$Ba(Mn_{1/2}Ti_{1/2})O_3$	1450/2h	Perovskite Hexagonal	45.0	11600	5.75	−4	1351
3152	$Ba_3La_2Ti_2Ta_2O_{15}$	1540	Trigonal P-3m1	45.1	31000		−13	1353
3153	$0.71CaTiO_3$-$0.29NdAlO_3$	1450/10h	Perovskite Orthorhombic	45.1	38450		6	1174
3154	$(1\text{-}x)Ca(Mg_{1/3}Ta_{2/3})O_3$-$xCaTiO_3$ (x=0.45)	1550	Perovskite Orthorhmbic Pbnm	45.1	34800		17	1354
3155	$0.7CaTiO_3$-$0.3LaGa_{0.5}Al_{0.5})O_3$		Rhombic perovskite	45.2	40000	8	13	1306
3156	$0.7CaTiO_3$-$0.3\ (La_{.5}Nd_{.5})(Ga_{0.5}Al_{0.5})O_3$		Rhombic perovskite	45.2	43000	8	9	1269
3157	$0.7CaTiO_3$-$0.3Nd(Ga_{0.5}Al_{0.5})O_3$		Rhombic perovskite	45.3	38000	8	11	1269
3158	$Ba_8Nb_4Ti_3O_{24}$	1400	Hexagonal $P6_3/mmc$	45.3	23500	5.6	115	1334
3159	$Ba_4LaNbTa_2O_{15}$		Hexagonal perovskite	45.3	25100		52	1355
3160	$Ba_{1-x}Sr_x\ La_4Ti_4O_{15}$ (x=0.6)	1550	Trigonal P-3m1	45.4	47500		−1	1356
3161	$0.6La(Mg_{1/2}Ti_{1/2})O_3$-$0.4Ca_{0.6}La_{0.8/3}$ TiO_3+w wt% CuO	1450	Composite	45.5	44600	8	2	1357
3162	$Ba_{0.2}Ca_{0.8}(Fe_{1/2}Nb_{1/2})O_3$		Perovskite Orthorhombic Pbnm	45.5	2300	7.4	−34	1163
3163	$(Ba_{1-x}Sr_x)La_4Ti_4O_{15}$ (x=0.4)	1450/4h	Trigonal P-3m1	45.7	44200		−6	1356
3164	$PrTiTaO_6$	1500	Aeschneite Orthorhombic	45.8	32300		33	583
3165	$Pr_{0.5}Gd_{0.5}TiNbO_6$	1400		45.9	9500		41	564

3166	$Zr_{0.992}Hf_{0.008}TiO_4$		Orthorhombic Pbcn	45.9	13000	8.5	53	1088
3167	$Pb_{0.25}Ca_{0.75}(Mg_{1/3}Nb_{2/3})O_3$		Perovskite	46.0	8700	3.7	−34	996
3168	$BaLa_4Ti_4O_{15}$		Hexagonal perovskite P-3m1	46.0	47000		−11	1329, 1337
3169	$Ca_3Ti_2O_7$		Orthorhombic $Ccm2_1$	46.0	2600	2.69	50	1358
3170	$0.1La_2Ti_2O_7$-$0.9La_4Ti_9O_{24}$	1300	Composite	46.0	5500		0	1137, 1138
3171	$BaTiTa_4O_{13}$	1450		46.0	6000	4.6	145	1208
3172	$La_{0.39}Ca_{0.61}[Ca_{0.11}Mg_{0.08}Ti_{0.81}]O_3$		Perovskite	46.0	17000	4.7	36	950
3173	$Ba_2La_4Ti_5O_{18}$	1575/10h	$A_nB_{n-1}O_{3n}$ perovskite Trigonal R-3m	46.0	31850		−36	1234
3174	$Ca_5Nb_{1.5}Ta_{0.5}TiO_{12}$	1560	Complex perovskite Orthorhombic Pnma	46.0	28400		35	1231
3175	$CeTiTaO_6$	1540	Aeschneite orthorhombic	46.0	33300		41	583
3176	$0.3SrTiO_3$-$0.7Ca(Mg_{1/3}Nb_{2/3})O_3$	1475/3h	Perovskite	46.0	29300	6.8	2	1359
3177	$Ca_{0.7}Ti_{0.7}La_{0.3}O_3$+0.25 wt% Al_2O_3	1500	Perovskite Orthorhombic	46.0	38200	4	12	1360
3178	$7Bi_2O_3$-$2TeO_2$ (oxygen atm)	750/15h	–	46.0	1100		−144	1068
3179	$Ca_2Zn_4Ti_{15}O_{36}$+5 wt% V_2O_5	930	Trigonal R-3	46.0	13400		164	1361
3180	$La_3Ti_2TaO_{11}$	1560		46.0	7500		−47	1362
3181	$CaLa_4(Zr_{0.05}Ti_{0.95})_4O_{15}$	1550	Hexagonal	46.0	47500		−10	1363
3182	$Bi_{0.95}Ce_{0.05})NbO_{4.025}$	950	Triclinic+Orthorhombic	46.1	15000			1364
3183	$(Ba_{1-x}Sr_x)La_4Ti_4O_{15}$ (x=0.8)	1600	$A_nB_{n-1}O_{3n}$ Trigonal P-3m1	46.1	52800		−3	1356
3184	$Ba(Er_{03}Bi_{0.2}Nb_{0.5})O_3$	1300	Perovskite	46.1	1500		−27	1341
3185	$0.65LiNb_3O_8$-$0.35TiO_2$	11002h	Composite	46.2	5800		0	788
3186	$Sr_6Nb_4TiO_{18}$	1625/2h	Not available	46.2	6700		26	895
3187	$0.4ZnNb_2O_6$-$0.6TiO_2$	1125	Columbite+rutile	46.2	48000		−1	1365
3188	$0.5ZnTa_2O_6$-$0.5TiO_2$		Composite	46.2	36700		74	1366
3189	$0.55La(Mg_{1/2}Ti_{1/2})O_3$-$0.45SrTiO_3$	1475/4h	Composite	46.3	34000	8	0	1367
3190	$Ba_{2-x}Sr_xLa_3Ti_3NbO_{15}$ (x=0.5)	1500	$A_nB_{n-1}O_{3n}$ Trigonal P-3m1	46.3	33600		4	1301, 1297
3191	$BaLa_4Ti_4O_{15}$	1450	$A_nB_{n-1}O_{3n}$ Trigonal perovskite P-3m1	46.3	16200	5.15	−13	1272

(*continued*)

No.	Material	ST (°C)	Crystal structure	ε_r	Qf (GHz)	f_0	τ_f	Reference
3192	$Ba_{0.2}Sr_{0.8}La_4Ti_{4.2}O_{15}$	1450/5h	Perovskite Trigonal	46.4	36100		−3	1368
3193	$0.64CaTiO_3$-$0.36LaGaO_3$		Rhombic perovskite	46.5	48000	8	−3	1269
3194	$Bi_{0.95}Ce_{0.05}NbO_4$+0.4 mol% CuO	950	Orthorhombic Pnma	46.5	3000			1369
3195	$Ba_3La_2Ti_2Nb_{2-x}Ta_xO_{15}$ (x=1)	1500	Trigonal P-3m1	46.5	27140	–	−4	1353
3196	$CaTi_{0.54}(Al_{1/2}Ta_{1/2})_{0.46}O_3$	1500/15h	Perovskite Orthorhombic	46.5	27300	8	0	1266
3197	$Ca_5Nb_2TiO_{12}$+1 wt% NiO	1550/4h	Complex perovskite Orthorhombic Pnma	46.5	29000		34	1155
3198	$Ca_5Nb_2TiO_{12}$+1 wt% Co_3O_4	1550/4h	Complex perovskite Orthorhombic Pnma	46.5	29000		32	1155
3199	(1-x)$La(Mg_{1/2}Ti_{1/2})O_3$-x$La_{2/3}TiO_3$ (x=0.49)		Perovskite I2/a	46.5	8300	6.2		889
3200	$Sr(Ga_{0.5}Nb_{0.5})_{1-x}Ti_xO_3$ (x=0.3)	1575	Cubic perovskite Fm3m	46.6	42200		5	1370
3201	$Ba_3Nd_2Ti_2Nb_2O_{15}$	1450/3h	Hexagonal perovskite	46.8	19500	5.1	28	1352
3202	(1-y)$Li_{2.02}Ti_{0.92}Nb_{0.06}O_3$ (y=0.6)	1070		46.8	8040		35	722
3203	$(Ba_{1-x}Sr_x)La_4Ti_4O_{15}$ (x=0.2)	1450	Trigonal perovskite P-3m1	46.8	24500		−8	1356
3204	$Ba_{2-x}Sr_xLa_3Ti_3NbO_{15}$ (x=0.75)	1510	Trigonal perovskite P-3m1	46.8	36500		2	1301
3205	$Ba_{1-x}Ca_x(Sc_{1/2}Nb_{1/2})O_3$ (x=0.5)	1650	Perovskite	46.9	28000			1371
3206	$La_2Ti_2O_7$		Monoclinic P21	47.0	8500	7.8	−10	1137
3207	$0.75CaTiO_3$-$0.25LaAlO_3$	1450/12h	Composite	47.0	36000		13	1174
3208	$Bi_2Ti_4O_{11}$		Monoclinic C2/m	47.0	4800		−540	1372
3209	$Ca_2Zn_4Ti_{15}O_{36}$	1150/8h	Hexagonal+residual rutile	47.0	41200	10	120	1026
3210	$Na_{1-x}K_xCa_4Nb_5O_{17}$ (x=0.5)	1300	Monoclinic P21/a $A_nB_nO_{3n+2}$	47.0	5000		−23	1333
3211	$BaTi_{0.3}Ga_{0.35}Nb_{0.35}O_3$	1500/4h	Perovskite-Mixture	47.0	2470	5.5		1373
3212	$0.65CaTiO_3$-$0.35LaGaO_3$	1600	Perovskite Orthorombic Pnma	47.0	40000		0	912
3213	$Ba_{2-x}Sr_xLa_3Ti_3NbO_{15}$ (x=0.25)	1490	Hexagonal P-3m1	47.0	29400		6	1301
3214	$Ba_2La_3Ti_3NbO_{15}$	1470/6h	Hexagonal perovskite P-3m1	47.0	2000		20	1374
3215	$Ba_{2-x}Sr_xLa_3Ti_3NbO_{15}$ (x=0.75)	1510	Trigonal perovskite P-3m1	47.0	36500		2	1297
3216	$Ba_{2-x}Sr_xLa_3Ti_3NbO_{15}$ (x=0.25)	1490	Trigonal perovskite P-3m1	47.0	29400		8	1297
3217	$0.222Li_2O$-$0.668Nb_2O_5$-$0.11TiO_2$	1350		47.0	25000		0	760
3218	$Ca_5Nb_2TiO_{12}$+1 wt% ZnO	1550/4h	Complex perovskite Orthorhombic Pnma	47.0	28000		34	1155

3219	$Ba_3Ti_2(Mg_{1/3}Nb_{2/3})_2Nb_4O_{21}$+5 wt% 2ZnO-$V_2O_5$	900	Hexagonal	47.0	10500		16	1375
3220	0.6$Ca(Mg_{1/3}Nb_{2/3})O_3$-0.4$Ca_{0.61}Nd_{0.26}TiO_3$	1375		47.0	37000		5	1376
3221	$Pr_{0.6}Gd_{0.4}TiNbO_6$	1400	Not available	47.1	9500		44	564
3222	0.76$ZrTi_2O_6$-0.24$ZnNb_2O_6$	1260/4h oxygen	Mixed phases	47.1	34200		0	1283
3223	0.5$La(Mg_{0.5}Ti_{0.5})O_3$-0.5$Ca_{0.0.8}Sr_{0.2}TiO_3$	1475	Composite	47.1	35000		−5	1377
3224	$SrCa_4Nb_4TiO_{17}$	1475	Not available	47.2	12000		−137	1378
3225	$TiFeNbO_6$	1125/5h	Tetragonal	47.2	2300	3.68	281	1379
3226	$Ca[Ti_{1-x}(Mg_{1/3}Nb_{2/3})_x]O_3$ (x=0.6)	14504h	Perovskite	47.3	25630		8	1271
3227	$Ba_3La_3Ti_4NbO_{18}$	1480/6h	Trigonal perovskite P-3m1	47.4	17330	5.18	35	1380
3228	(1-x)$(Ba_{0.6}Sr_{0.4}La_4Ti_4O_{13}$-x TiO_2 (x=0.05)	1550	Hexagonal Perovskite	47.4	46800		−3	1381
3229	Bi_8TiO_{14}			47.4	5400		−16	1382
3230	0.66$CaTiO_3$-0.34$LaGaO_3$		Rhombic perovskite	47.5	46000		4	1269
3231	$Ca_5Nb_2TiO_{12}$+0.5 wt% MgO	1550/4h	Complex perovskite Orthorhombic Pnma	47.5	33000		34	1155
3232	$Ca_5Nb_2TiO_{12}$+0.5 wt% CuO	1550/4h	Complex perovskite Orthorhombic Pnma	47.5	30000		37	1155
3233	11Li_2O-3Nb_2O_5-12TiO_2+LBS glass	900	Mixture	47.5	9600		50	2
3234	0.5$MgTiO_3$-0.5$CaTiO_3$-0.25(Nd_2O_3-TiO_2)		Composite	47.6	30000		8	1383
3235	$TiTe_3O_8$+1 wt% SiO_2	750	Cubic Ia3	47.6	48800		152	1384
3236	$(Ba_{1-x}Ca_x)La_4Ti_4O_{15}$ (x=0.2)	1575/4h	Trional P-3m1 Perovskite	47.7	47100		−8	1356
3237	$(Ba_{1-x}Ca_x)La_4Ti_4O_{15}$ (x=0.4)	1575/4h	Trigonal P-3m1 Perovskite	47.7	47400		−7	1356
3238	0.45$La(Mg_{0.5}Ti_{0.5})O_3$-0.55$Ca_{0.8}Sm_{0.4/3}TiO_3$		Perovskite	47.8	26500	6.2	−2	1385
3239	$Ba_5SrNb_4TiO_{18}$	1450/2h	$A_6B_5O_{18}$ type perovskite	47.9	7000		83	895
3240	$Ba(Gd_{0.3}Bi_{0.2}Nb_{0.5})O_3$	1300	Perovskite	47.9	2100		−3	1341
3241	$Ba_xLa_4Ti_{3+x}O_{12+3x}$ (x=2.5)			47.9	19480			1310
3242	$Ba_3La_2Ti_2Nb_{2-x}Ta_xO_{15}$ (x=0.5)	1480		47.9	25300	–	2	1353
3243	$Bi_{0.75}Ce_{0.25}VO_4$	900	Monoclinic	47.9	18000	7.6	15	1386

(*continued*)

No.	Material	ST (°C)	Crystal structure	ε_r	Qf (GHz)	f_0	τ_f	Reference
3244	$Pb_{0.75}Ca_{0\cdot25}(Cr_{1/2}Nb_{1/2})O_3$		Perovskite	48.0	3600	4.3	8	996
3245	$0.65CaTiO_3$-$0.35LaGaO_3$	1450/12h	Perovskite Orthorhombic	48.0	32000		2	1174
3246	$Ca[(Li_{1/3}Ta_{2/3})_{1-x}Ti_x]O_{3-\delta}$+3 wt% B_2O_3 (x=0.5)	1150	Perovskite	48.0	21000		–	765
3247	$Ca_5Nb_2TiO_{12}$	1550	Complex perovskite Orthorhombic Pnma	48.0	26600	3.7	40	1307
3248	$Ca_3Ba_2Ta_2TiO_{12}$	1540	Complex perovskite Cubic	48.0	3000	3.8	18	1307
3249	$Ba_3Ti_4Ta_4O_{21}$	1380	Hexagonal $P6_3/mcm$	48.0	7000	4.3	50	1208
3250	$(Ca_{1-0.3x}La_{0.2x})[(Mg_{1/3}Ta_{2/3})]_{1-x}Ti_xO_3$ (x=0.5)		Orthorhombic Pnnm complex Perovskite	48.0	21000		2	1387
3251	$Pr_{0.7}Gd_{0.3}TiNbO_6$	1400		48.0	4500		47	564
3252	$Ba_4SrNb_4O_{15}(A_nB_{n-1}O_{3n})$	1400	Hexagonal perovskite	48.0	14600	4.7	140	325
3253	$0.34CaTiO_3$-$0.66Ca(Mg_{1/3}Nb_{2/3})O_3$	1450	Perovskite	48.0	32500		−2	1388
3254	$CaTi_{0.5}(Al_{1/2}Nb_{1/2})_{.5}O_3$	1500/5h	Perovskite orthorhombic	48.0	26100	7	−4	1152
3255	$CaTi_{0.5}(Al_{1/2}Nb_{1/2})_{.5}O_3$+1 wt% Li_3NbO_4	1300/5h	Perovskite orthorhombic	48.0	32100	7	−2	1152
3256	$Ba_8Nb_4Ti_3O_{24}$	1450	Hexagonal $P6_3/mmc$	48.0	23500	5.5	115	1389
3257	$Sr_2La_4Ti_5O_{18}$	1625/2h		48.0	27350		20	895
3258	$Sr_5LaTi_2Nb_3O_{18}$	1520		48.0	27800	4.3		1390
3259	$Ba_4Sm_{9.33}Ti_{18}O_{54}$+15 wt % $BaCu(B_2O_5)$	950	Tungsten Bronze Orthorhombic	48.0	5500		−41	1391
3260	$(Ca_{1-0.3x}La_{0.2x})[Mg_{1/3}Ta_{2/3})O_3$ (x=0.5)		Orthorhombic Pbnm	48.0	21000			1387
3261	$[(Ca,Sr)_x(La,Nd)_{2/3-2x/3}]TiO_3$ (x=0.1)	1350/24h	Tetragonal I4/mcm	48.0	3700		61	1392
3262	$0.5La(Mg_{1/2}Ti_{1/2})O_3$-$0.5SrTiO_3$		Perovskite Pbnm	48.1	5800	6.6		978
3263	$Ba_3LaNb_3O_{12}$	1350/6h	Trigonal R-3m	48.3	38000	6.76	−40	1315
3264	$Ba_{2-x}Sr_xLa_3Ti_3NbO_{15}$ (x=0)	1480	Hexagonal perovskite	48.3	20290		8	1301
3265	$0.2SrTiO_3$-$0.8Ca_{0.61}Nd_{0.26}Ti_{1-x}Al_{4x/3}O_3$ (x=0.5)	1520/4h	Orthorhombic Perovskite	48.3	40700		4	1393
3266	$Ca_2Zn_4Ti_{16}O_{38}$	1100/4h	Trigonal R-3	48.4	31600	6.7	48	1394
3267	$Ca_5Nb_2TiO_{12}$+1 wt% SnO_2	1550/4h	Complex perovskite Orthorhombic Pnma	48.5	28000		36	1155
3268	$CaLa_8Ti_9O_{31}$	1550	Orthorhombic Pbam Perovskite	48.6	19350	3.65	−6	1272
3269	$Ba(Dy_{0\cdot3}Bi_{0.2}Nb_{0.5})O_3$	1300	Perovskite	48.6	2000		6	1341

3270	$0.64CaTiO_3$-$0.36LaGaO_3$	1300	Perovskite	48.7	38000			1395
3271	$Ca_5Nb_2TiO_{12}$+1 wt% Al_2O_3	1550/4h	Complex perovskite Orthorhombic Pnma	48.7	29000		33	1155
3272	$5.7Li_2O$-Nb_2O_5-$14.7TiO_2$+2 wt% B_2O_3-CuO	900		48.7	16350		32	760
3273	$Sr_2La_4Ti_5O_{18}$+0.3 wt% Bi_2O_3-B_2O_3 glass	1625/2h		48.7	23000		22	895
3274	$Ba_{(1-x)}Ca_x)La_4Ti_4O_{15}$ (x=0.4)	1575/4h	Trigonal perovskite P-3m1	48.9	42400		−7	1356
3275	$(Ba_{1-x}Ca_x)La_4Ti_4O_{15}$ (x=0.6)	1575	Trigonal perovskite P-3m1	48.9	41200		−7	1356
3276	$0.45La(Zn_{0.395}Ti_{0.385}Ta_{0.01}Al_{0.21})O_3$-$0.55CaTiO_3$		Composite	49.0	29000	1.957	0	1327
3277	$Ca_5Nb_2TiO_{12}$+1 wt% Cr_2O_3	1550/4h	Complex perovskite Orthorhombic Pnma	49.0	34000		44	1155
3278	$Ca_5Nb_2TiO_{12}$+1 wt% Sb_2O_3	1550/4h	Complex perovskite Orthorhombic Pnma	49.0	30500		36	1155
3279	$0.9Bi_2O_3$-$0.1Nb_2O_5$	900/3h	Flurite δ-Bi_2O_3 Fm-3m	49.0	800		−234	1396
3280	$Ca(Zr_{0.8}Ti_{0.2})O_3$		Perovskite orthorhombic Pcnm	49.0	10800			906
3281	$0.7CaTiO_3$-$0.3NdGaO_3$	1450/12h	Perovskite	49.0	32000		35	1174
3282	$0.66CaTiO_3$-$0.34(La_{0.5}Nd_{0.5})$ GaO_3	1540	Perovskite	49.0	43000		0	1269
3283	$11Li_2O$-$3Nb_2O_5$-$12TiO_2$+0.5 wt% B_2O_3	900	M phase+Li_2TiO_3	49.2	8840		58	1397
3284	$Ca_4La_2Ti_{5-x}(Mg_{1/3}Nb_{2/3})_xO_{17}$ (x=2)	1540	Orthorhombic Pbnm	49.2	16000		32	1152
3285	$Ca_2La_4Ti_5O_{18}$		Trigonal perovskite R	49.3	20100		6	1272
3286	$0.7CaTiO_3$-$0.3LaGaO_3$		Perovskite	49.4	29000	8	22	1269
3287	$CaTi_{0.53}Al_{1/2}Nb_{1/2})_{0.47}O_3$+1 wt% Li_3NbO_4	1300/5h	Perovskite Orthorhombic	49.4	31400	7	12	1152
3288	$Ba_3LiTa_3Ti_5O_{21}$	1200	Perovskite Hexagonal $P6_3/mcm$	49.4	3100		472	1398
3289	$(Ba_{1-x}Ca_x)La_4Ti_4O_{15}$ (x=0.8)	1575	Trigonal perovskite P-3m1	49.5	42400		−5	1356
3290	$Pr_{0.8}Gd_{0.2}TiNbO_6$	1400	Euxenite OrthorhombicPnma	49.5	9500		51	564
3291	$Ba_4LaNb_2TaO_{15}$		Hexagonal perovskite	49.5	24100		75	1355
3292	$(Ni_{1/3}Ta_{2/3})_{1-x}Ti_xO_2$ (x=0.4)	1300	Tetragonal $P4_2/mmm$	49.6	17600		40	1276
3293	$CaTi_{0.53}(Al_{1/2}Nb_{1/2})_{0.47}O_3$	1500/5h	Perovskite	49.8	26000	7	7	1152
3294	$Ba_3La_2Ti_2Nb_2O_{15}$ ($A_5B_4O_{15}$)	1460	Hexagonal perovskite	49.8	22000	5	7	1297

(*continued*)

No.	Material	ST (°C)	Crystal structure	ε_r	Qf (GHz)	f_0	τ_f	Reference
3295	$Li_{1+x+y}Ta_{1-x-3y}Ti_{x+4y}O_3$ (x=0.1, y=0.175)	1175/1h	M-Phase	49.8	10528		32	1399
3296	$Ba_6Ti_{14}Nb_2O_{39}$	1260/4h	Orthorhombic Bm21b	50.0	2600	4	165	1401
3297	$Ca[(Li_{1/3}Nb_{2/3})_{0.9}Ti_{0.3}]O_{3-d}$+1 wt% B_2O_3	940	Perovskite	50.0	6500		−8	1402
3298	$Pb_{0.7}Ca_{0.3}La_{0.5}(Mg_{1/2}Nb_{1/2})O_3$	1350/2h	Perovskite Cubic Fm3m	50.0	86000		0	1403
3299	$0.5La(Mg_{1/2}Ti_{1/2})O_3$-$0.5La_{2/3}TiO_3$	1400/2h	Perovskite	50.0	10000		5	1404
3300	$0.5CaTiO_3$-$0.5La(Zn_{1/2}Ti_{1/2})O_3$	1550/3h	Perovskite Orthorhombic	50.0	38000	7	0	1405
3301	$Ba_2Sr_3Nb_4O_{15}(A_nB_{n-1}O_{3n})$	1400	Hexagonal perovskite	50.0	16500	4.7	232	325
3302	$La_{0.33}TaO_3$	1525	Perovskite Tetragonal P4/mmm	50.0	8000	3.8	144	1406
3303	$Ca_5Nb_2TiO_{12}$+0.1 wt% $2MgO$-Al_2O_3-$5SiO_2$	1520/2h	Orthorhombic Pnma	50.0	30000	4	38	1407
3304	$TiTe_3O_8$	720	Cubic Ia3	50.0	30600	5	133	586
3305	$(1-x)(Mg_{0.95}Zn_{0.05})TiO_3$-$xCa_{0.6}La_{0.8/3}TiO_3$ (x=0.5)	1320/4h		50.0	43500		122	465
3306	$Ba_3Ti_2(Fe_{1/2}Nb_{1/2})Nb_4O_{21}$	1280	Hexagonal	50.0	5200		10	1408
3307	$Ba_3Ti_{4-x}(Mg_{1/3}Nb_{2/3})_xO_{21}$+$BaCu(B_2O_5)$ (x=2)	950	Hexagonal	50.0	10500		18	1409
3308	$Ca_{4-x}Mg_xLa_2T_5O_{17}$ (x=2)			50.0	9450		63	1029
3309	$Ca(Zr_xTi_{1-x})O_3$ (x=0.6)	1470/15h	Perovskite Orthorhombic Pbnm	50.0	3800	3.46	460	916
3310	$NiNb_2O_6$+40 wt% TiO_2	1300/2h	Composite	50.0	5700	6	99	1345
3311	$3Li_2O$-Nb_2O_5-$3TiO_2$+2 wt% B_2O_3-CuO	900	M phase+Li_2TiO_3	50.1	8300		35	1410
3312	$(1-x)La_{2/3}TiO_3$-$xNiTiO_3$ (x=0.2)	1340	Perovskite	50.7	13900	3.5	24	1411
3313	$Sr_5LaTi_2Nb_3O_{18}$	1520		50.7	27800		19	1412
3314	$Ba_{0.2}Sr_{0.8}La_4Ti_4O_{15}$+1 wt% La_2O_3-$0.5B_2O_3$-$0.5TiO_2$	1550/3h	Hexagonal perovskite	50.7	72700		−7	1413
3315	$Ba(Sm_{0.3}Bi_{0.2}Nb_{0.5})O_3$	1300	Perovskite	50.8	1600		14	1341
3316	$Ba_5SrNb_4TiO_{18}$	1450/4h		50.8	7000		83	895
3317	$0.75CaTiO_3$-$0.25SmAlO_3$	1450/12h	Perovskite Orthorhombic	51.0	31000		31	1174
3318	$0.7CaTiO_3$-$0.3SmGaO_3$	1450/12h	Perovskite Orthorhombic	51.0	18000		41	1174
3319	$Ba_3Sr_2Nb_4O_{15}(A_nB_{n-1}O_{3n})$	1400	Hexagonal Perovskite	51.0	21200	4.6	117	325
3320	$Ca_{0.6}(Li_{0.5}Nd_{0.5})_{.4})_{0.45}Zn_{0.55}TiO_3$	1150		51.0	12700		17	1281
3321	$Pr_{0.9}Gd_{0.1}TiNbO_6$	1400	Euxenite Orthorhombic Pnma	51.0	8400		53	564

3322	$Zr_{0.3}(Zn_{1/3}Nb_{2/3})_{0.7}TiO_4$	1290		51.0	26600		70	1414
3323	$Na_{1-x}K_xCa_4Nb_5O_{17}$ (x=1)	1300	MonoclinicP21/a $A_nB_nO_{3n+2}$	51.0	2300		473	1333
3324	$Sr_{0.5}Ba_{0.5}Ca_4Nb_4TiO_{17}$		Orthorhombic Pnnm	51.6	10200	5.37	−14	1415
3325	$0.3La(Mg_{1/2}Ti_{1/2})O_3$-$0.7CaTiO_3$	1500	Perovskite Pbnm	51.2	43800	5.8	–	932
3326	$3Li_2O$-Nb_2O_5-$3TiO_2$+1 wt% $0.83Li_2O$-$0.17V_2O_5$	900	M-Phase+Li_2TiO_3	51.3	7200		22	1416
3327	$TiFeNbO_6$+2 wt% Bi_2O_3	1125/5h	Tetragonal	51.3	1400	3.6	103	1379
3328	$(1-x)La_{2/3}TiO_3$-$xNiTiO_3$ (0.01)	1380	Perovskite	51.4	1600	3.55	25	1411
3329	$Ba_3La_2Ti_2Nb_2O_{15}$	1450		51.5			15	1417
3330	$Ca[(Ga_{1/2}Nb_{1/2})_{1-x}Ti_x]O_3$ (x=0.47)		Pbnm	51.6	34100		0	1418
3331	$(Pb_{0.2}Ca_{0.8})[(Ca_{1/3}Nb_{2/3})_{0.8}Ti_{0.2}]O_3$	1350/3h	Perovskite	51.7	7270		0	1419
3332	$Ba_{0.5}Ca_{0.5}(Fe_{1/2}Nb_{1/2})O_3$		Perovskite	51.7	960	6.9	45	1163
3333	$Bi_2(Zn_{1/3}Ta_{2/3})_2O_7$	850	Cubic Fd3m	51.8	2600		−26	1420
3334	$0.3LaAlO_3$-$0.7SrTiO_3$	1680	Perovskite	52.0	50800	9.3	56	832
3335	$(Li_{1/2}Sm_{1/2})TiO_3$	1300	Perovskite Orthorhombic	52.0	2290	3	−266	1421
3336	$Ca_4SrNb_2TiO_{12}$	1550	Orthorhombic Pnma	52.0	15000	3.59	42	1209
3337	$Ce_{0.33}TaO_3$	1525		52.0	10000	3.58	159	1406
3338	$NdTiNbO_6$	1370	Euxenite Orthorhombic Pnma	52.0	4480	4.93	46	563
3339	$Pr_{0.95}Gd_{0.05}TiNbO_6$	1370	Euxenite Orthorhombic Pnma	52.0	18500		54	564
3340	$CaTi_{0.6}(Al_{1/2}Ta_{1/2})_{0.4}O_3$	1500/15h	Perovskite Orthorhombic	52.0	13200	8	37	1266
3341	$0.7CaTiO_3$-$0.3LaGaO_3$	1450/12h	Perovskite	52.0	27000		40	1174
3342	$Ba_4LaTiNb_3O_{15}(A_5B_4O_{15})$	1450	Hexagonal perovskite	52.0	15600	4.47	93	1210
3343	$Ba_4Sm_{9.33}Ti_{18}O_{54}$+10 wt% $BaCu(B_2O_5)$	950	Orthorhombic	52.0	4000		−29	1422
3344	$Ba_{6-3x}Sm_{8+2x}Ti_{18}O_{54}$ (x=2/3)+3.5 Bi_2O_3-B_2O_3	1050	Tungsten bronze Orthorhombic	52.0	4500		6	1422
3345	$3Li_2O$-$Nb_2O_5$6TiO_2+21 wt% B_2O_3	900		52.0	12000		32	760
3346	$Ca_{5-x}Zn_xNb_4TiO_{17}$ (x=0.4)	1260	Perovskite $A_nB_nO_{3n+2}$	52.0	9950		−9	1423
3347	$Ba_{0.9}Ca_{0.1}(Fe_{1/2}Nb_{1/2})O_3$		Perovskite	52.1	620	6.8	45	1163
3348	$Pb_{0.4}Ca_{0.6}(Mg_{1/3}Nb_{2/3})_{1-x}Sn_x]O_3$ (x=0.1)	1280/2h	Perovskite Tetragonal	52.2	8150	5	−3	1424
3349	$CaTi_{0.5}$ $(Fé_{0.5}Nb_{0.5})_{.5}O_3$+3 wt% B_2O_3	900/2h	Perovskite orthorhombic	52.3	2930		13	1425
3350	$0.4(La_{1/2}Na_{1/2})TiO_3$-$0.6Ca(Mg_{1/3}Nb_{2/3})O_3$	1450	Perovskite Orthorhombic	52.3	29700	6	2	1426

(*continued*)

No.	Material	ST (°C)	Crystal structure	ε_r	Qf (GHz)	f_0	τ_f	Reference
3351	$0.5Ca_{0.6}La_{0.267}TiO_3$-$0.5Ca(Mg_{1/3}Nb_{2/3})O_3$	1490/4h	Perovskite Composite	52.4	36400	5.8	3	1427
3352	$Sr_{1-x}Ca_xLa_4Ti_5O_{17}$ (x=0.85)	1580/6h	Orthorhombic Pnnm	52.4	12600		−23	1428
3353	$Sr_{1-x}Ca_xLa_4Ti_5O_{17}$ (x=1)	1580/6h	Orthorhombic Pnnm	52.7	12700		−37	1428
3354	(1-x)$Sr_{0.2}Na_{0.4}Sm_{0.4}TiO_3$-$SmAlO_3$ (x=0.25)	1470/4h	Orthorhombic perovskite	52.7	9700		2	1429
3355	$Pb_{0.2}Ca_{0\cdot8}(Fe_{1/2}Nb_{1/2})O_3$		Perovskite	53.0	10000	4.1	−69	996
3356	$Bi_2Ti_4O_{11}$	1100	Monoclinic C2/m	53.0	4900		−520	1372
3357	$Ba_3Ti_{4-x}(Zn_{1/3}Nb_{2/3})_xNb_4O_{21}$ (x=2),+1 wt% $MnCO_3$-CuO+1 wt% ZBS	900/2h		53.0	14600		6	1430
3358	$PrTiNbO_6$	1370	Euxenite Orthorhombic Pnma	53.0	12300	4.85	56	563
3359	$Ba_3Ti_{4-x}(Zn_{1/3}Nb_{2/3})_xNb_4O_{21}$ (x=2)+1 wt% ZBS+1 wt% $MnCO_3$-CuO	900/2h	Hexagonal $P6_3/mcm$	53.0	14600		6	1430
3360	$BaLa_4Ti_4O_{15}$ (textured)	1600/2h	Hexagonal Perovskite P-3m1	53.0	41400		−1	1431
3361	$(Ca_{1-x}Nd_{2x/3})TiO_3$ (x=0.3)+2 wt% CaO-ZnO-B_2O_3	900/1h	Perovskite Orthorhombic	53.0	3800		55	1432
3362	$Ca_{0.02}Zn_{1.98}Sn_{0.08}Ti_{1.92}Nb_2O_8$	1120/6h		53.1	48000	21		1433
3363	$0.8TiO_2$-$0.2Bi_2O_3$		Mixture phases	53.2	4500		−550	1434
3364	(1-x)$La_{2/3}TiO_3$-x$NiTiO_3$ (0.15)	1340	Perovskite	53.3	12950	3.4	21	1411
3365	$CaLa_4Ti_5O_{17}$	1550	Perovskite Orthorhombic Pnnm	53.7	17400	3.7	−26	1272
3366	$Sr_{1-x}Ca_xLa_4Ti_5O_{17}$ (x=1)	1580/6h	Orthorhombic Pnnm Perovskite	53.7	11500		−1	1428
3367	$0.8La_{2/3}TiO_3$-$0.2LaAlO_3$	1400	Perovskite Orthorhomic	53.9	29000	5.4	35	1096
3368	$CeTiNbO_6$	1360	Euxenite Orthorhombic Pnma	54.0	6530	4.4	67	563
3369	$0.4CaTiO_3$-$0.6Ca(Mg_{1/3}Nb_{2/3})O_3$	1450	Perovskite	54.0	32000	6.7	18	944
3370	$0.8La_{2/3}TiO_3$-$0.2LaAlO_3$	1400	Perovskite	54.0	29000		35	1096
3371	$Ca_3Sr_2Nb_2TiO_{12}$	1540	Orthorhombic Pnma	54.0	10000	3.5	45	1209
3372	Y_2O_3-$2TiO_2$	1460	Mixed phases	54.0	6565	4.65	−31	1435
3373	$Ba_{6-3x}Sm_{8+2x}Ti_{18}O_{54}$ (x=2/3)+3.5 wt% Bi_2O_3-B_2O_3+1.5 wt% LiF	1050	Tungsten Bronze Orthorhombic	54.0	3400		29	1422
3374	$(Ca_{0.85}Nd_{0.1})[Ti_{0.5}(Mg_{0.33}Nb_{0.67})_{0.5}]O_3$		–	54.1	7660		1	1436
3375	$0.48Nd(Zn_{1/2}Ti_{1/2})O_3$-$0.52SrTiO_3$	1350	Composite	54.2	84000		0	1437

3376	$Ca[Ti_{1-x}(Mg_{1/3}Nb_{2/3})_x]O_3$ (x=0.5)	14504h		54.3	22900		39	1271
3377	$Ba(Ti_{0.85}Mn_{0.15})O_3$+10 wt% B_2O_3	1100	Composite	54.4	3400		254	1319
3378	$Ba_{0·6}Ca_{0.4}(Fe_{1/2}Nb_{1/2})O_3$		Perovskite	54.5	600	6.6	55	1163
3379	$Ba(Ti_{0.85}Mn_{0.15})O_3$+15 wt% Bi_2O_3	900	Perovskite	54.7	1300		183	1319
3380	$Li_{1+x+y}Ta_{1-x-3y}Ti_{x+4y}O_3$ (x=0.1, y=0.15)	1175/1h	M-Phase	54.8	10400		34	1400
3381	$Ba[Zn_{1/4}Ti_{1/4}Nb_{1/2}]O_3$	1400	Perovskite cubic	54.8	13200	6.1		1228
3382	$CaLa_8Ti_9O_{31}$		Orthorhombic Pbam	54.9	19300		−6	1272
3383	$Li_{1+x-y}Nb_{1-x-y}Ti_{x+4y}O_3$ (x=0.1, y=0.175)	1100/1h	M-Phase	54.9	8890	6.2	28	1400, 1438
3384	$Ba_3LiNb_3Ti_5O_{21}$	1200	Hexagonal $P6_3/mcm$	54.9	3200		472	1398
3385	$Ba_{0.75}Sr_{0.25}$ $(Nd_{0.75}Bi_{0.25})_2Ti_4O_{12}$+20 wt% La_2O_3-B_2O_3-ZnO-CaO	900	Multiphase	54.9	2900		17	1439
3386	$Ga_{0.5}Nb_{0.5}TiO_4$	1250	Tetragonal P42/mnm	54.9	16600		165	1250
3387	$Ba_3Ti_4Nb_4O_{21}$	1270	Hexagonal $P6_3/mcm$	55.0	9500	5.5	100	1208
3388	$Sm_{(2-x)/3}Li_xTiO_3$ (x=0.5)	1350	Perovskite	55.0	2000		−260	1440
3389	$Ca[(Li_{1/3}Nb_{2/3})_{1-x}Ti_x]$ $O_{3-\delta}$ (x=0.5)	1150/3h	Perovskite	55.0	18600		83	752
3390	$0.2PbZrO_3$-$0.8Ca(Fe_{1/2}Nb_{1/2})O_3$	1250	Perovskite Orthorhombic Pbnm	55.1	450	5.3	−52	1164
3391	$Ba_4La_2Ti_3Nb_2O_{18}$	1450/6h	$A_nB_{n-1}O_{3n}$ perovskite Trigonal R-3m	55.1	21270	5.1		1441
3392	$Ca[(Li_{1/3}Nb_{2/3})_{1-x}Ti_x]O_3$ (x=0.5)	1150/3h	Perovskite	55.2	18600		83	752
3393	$CaLa_4Ti_5O_{17}$		Orthorhombic Pnnm	55.2	17400		−20	1272
3394	$(Zn_{1/3}Ta_{2/3})_{0.7}Ti_{0.3}O_2$	1200		55.3	17500		30	1442
3395	MBRT-90+10 wt% Li_2O-B_2O_3-SiO_2-(56.92:37.59)	875	Composite	55.3	2500		26	510
3396	$Ba_3LiNb_{3-x}Ta_xTi_9O_{21}$ (x=3)	1180	Hexagonal $P6_3/mcm$	55.6	18500		70	1443
3397	$CaTi_{.6}(Al_{1/2}Nb_{1/2})_{.4}O_3$	1500/5h	Perovskite Orthorhombic	55.7	21800	7	47	1152
3398	$Sr_{1-x}Ca_xLa_4Ti_5O_{17}$ (x=0.5)	1550/6h	Orthorhombic Pnnm	55.8	118000		9	1428
3399	$CaLa_4Ti_{4.95}Zr_{0.05}O_{17}$	1500/4h	Orthorhombic Pnnm	55.9	15600		5	1444
3400	$Ba_{6-3x}Sm_{8+2x}Ti_{18}O_{54}$ (x=2/3)+5 wt% Bi_2O_3-B_2O_3	1050	Tungsten bronze Orthorhombic	56.0	4300		−15	1422
3401	$Ba_{6-3x}Sm_{8+2x}Ti_{18}O_{54}$ (x=2/3)+3.5 wt% Bi_2O_3-B_2O_3+01LiF	1050	Tungsten bronze Orthorhombic	56.0	3900		23	1422

(*continued*)

No.	Material	ST (°C)	Crystal structure	ε_r	Qf (GHz)	f_0	τ_f	Reference
3402	$0.64BaTi_4O_9$-$0.35BaPr_2Ti_4O_{19}$		Composite	56.0	1000			1445
3403	$(Sr_{0.1}Ca_{.9})_3Ti_2O_7$		Orthorhombic $Ccm2_1$	56.0	3000	2.5	141	1358
3404	$BaTi_3Nb_4O_{17}$	1310/4h	Orthorhombic Bbmm	56.0	8400	4	86	1401
3405	$BaTi_{0.95}Ni_{0.05}O_{3-\delta}$	1450/2h	Perovskite	56.0	2400			1446
3406	Bi_2TeO_6 (oxygen atm)	720/15h	Orthorhombic Cmca	56.0	10400		−49	1068
3407	$TiFeNbO_6$+4 wt% Bi_2O_3	1125/5h	Tetragonal	56.1	1000	3.45	17	1379
3408	$Li_{1+x-y}Nb_{1-x-y}Ti_{x+4y}O_3$ (x=0.1, y=0.15)	1100/1h	M-Phase	56.2	8350	6	15	1400, 1438
3409	$0.5MgTiO_3$-$0.5CaTiO_3$-$0.25(Nd_2O_3$-$2TiO_2)$		Composite	56.3	23500		68	1383
3410	$Ca_{0.99}Mg_{0.01}La_4Ti_5O_{17}$	1500	Orthorhombic Pnnm	56.3	12300	6.4	−10	1447
3411	$Ni_{0.5}Ti_{0.5}NbO_4$+2 wt% ZnO	930/6h	Tetragonal $P4_2/mnm$	56.3	67000		78	1448
3412	$Ca_{1-x}Zn_xLa_4Ti_5O_{17}$ (x=0)	1500/4h	Orthorhombic Pnnm	56.5	12500	6.6	4	1449
3413	$Li_{1+x-y}Nb_{1-x-3y}Ti_{x+4y}O_3$ (x=0.1, y=0.1)	1150/10h		56.5	4500		−7	1450
3414	$Sr_{1-x}Ca_xLa_4Ti_5O_{17}$ (x=0.25)	1150/6h	Orthorhombic Pnnm	56.5	10960		39	1428
3415	$CaTi_{.6}(Al_{1/2}Nb_{1/2})_{.4}O_3$+1 wt% Li_3NbO_4	1300/5h	Perovskite Orthorhombic	56.6	28000	7	53	1152
3416	$Ba_xLa_4Ti_{3+x}O_{12+3x}$ (x=3)			56.6	13380		−191	1310
3417	$Ca_{0.97}Mg_{0.03}La_4Ti_5O_{17}$	1450	Orthorhombic Pnnm	56.7	10800	5.3	−16	1447
3418	$Ni_{0.5}Ti_{0.5}NbO_4$	1100/6h		56.8	21100		79	1448
3419	$0.7CaTiO_3$-$0.3Sm(Mg_{0.5}Ti_{0.5})O_3$	1550	Composite	57.0	11150	4.1	54	865
3420	$La_{0.4}Ba_{0.6}Ti_{0.6}Y_{0.4}O_3$	1600/4h		57.0	750		12	1451
3421	Bi_2O_3-CaO-Nb_2O_5 (46.15:23.08:30.77)	950		57.0	470	3.7	24	1452
3422	$Ca_{1-x}Zn_xLa_4Ti_5O_{17}$ (x=0.025)	1500/4h	Orthorhombic Pnnm	57.0	17400	6.7	8	1449
3423	$Ca_{0.99}Zn_{0.01}La_4Ti_5O_{17}$+0.5 wt% CuO	1450	Orthorhombic Pnnm	57.0	15000		−8	1453
3424	$CaLa_4Ti_5O_{17}$	1500	Perovskite Pnnm Orthorhombic	57.0	9000		−10	1454
3425	$Ba_5LaTi_2Nb_3O_{15}$	1420/6h	$A_nB_{n-1}O_{3n}$ perovskite Trigonal R-3m	57.3	18450	4.7		1441
3426	$SrLa_4Ti_{4.9}Zr_{0.1}O_{12}$		Orthorhombic	57.3	9800		70	1455
3427	$Pb_{0.4}Ca_{0.6}(Mg_{1/3}Nb_{2/3})_{1-x}$ $Sn_x]O_3$ (x=0.05)	1280	Perovskite tetragonal	57.4	8120	5	−4	1424
3428	$Ca_{1-x}Zn_xLa_4Ti_5O_{17}$ (x=0.01)	1450	Orthorhombic Pnnm	57.6	17100		5	1449

3429	$Ba_{0.7}Ca_{0.3}(Fe_{1/2}Nb_{1/2})O_3$		Perovskite	57.7	830	7.8	101	1163
3430	$0.85La_{2/3}TiO_3$-$0.15LaAlO_3$	1375	Perovskite Orthorhomic	57.7	27900	5.2	65	1096
3431	$(Zn_{1/3}Nb_{2/3})_{0.4}(Ti_{0.7}Sn_{0.3})_{0.6}O_2$	1150/3h		57.8	14800		58	1456
3432	$Sr_3Ti_2O_7(Sr_{n+1}Ti_nO_{3n+1})$		Perovskite Tetragonal I4/mmm	57.9	18850	2.5	317	1358
3433	$Sr_{2.4}Ca_{0.6}Ti_2O_7$	1600	Tetragonal I4/mmm	57.9	25700	2.5	359	1222
3434	$LiNb_{0.6}Ti_{0.5}O_3$ textured		Not available	57.9	6325		−14	1457
3435	$Ba_{6-3x}Sm_{8+2x}Ti_{18}O_{54}$ (x=2/3)+3.5 wt% Bi_2O_3-B_2O_3+0.5 wt% LiF	1050	Tungsten bronze Orthorhombic	58.0	4500		6	1422
3436	$(Sr_{0.8}Ca_{0.2})_3Ti_2O_7$		Tetragonal I4/mmm	58.0	2500	2.5	359	1358
3437	$0.8Ca_{0.85}Nd_{0.1}TiO_3$-$0.2SmAlO_3$	1400	Perovskite	58.0	14000		13	1458
3438	$4CaO$-BaO-Nb_2O_5-TiO_2	1490	Composite	58.0	4000	3.4	44	1307
3439	Bi_2O_3-CaO-Nb_2O_5 (45.75:21.75:32.5)	1050	Composite	58.0	1060	3.8	20	1452
3440	$(1-x)La_{2/3}TiO_3$-$xNiTiO_3$ (0.075)	1340	Perovskite	58.0	15000	3.4	22	1411
3441	$TiFeNbO_6$+6 wt% Bi_2O_3	1125/5h	Tetragonal	58.1	650	3.32	118	1379
3442	$(Ni_{1/3}Ta_{2/3})_{1-x}Ti_xO_2$ (x=0.5)	1300	Rutile Tetragonal $P4_2/mmm$	58.3	13900		86	1276
3443	$Li_{1+x-y}Nb_{1-x-y}Ti_{x+4y}O_3$ (x=0.05, y=0.1)	1100/1h	M-Phase	58.4	6230	6.3	−31	1400, 1438
3444	$0.3La(Mg_{1/2}Ti_{1/2})O$-$0.7CaTiO_3$	1500	Perovskite Pbnm	58.8	40390	5.5	71	932
3445	$0.8Ca_{0.85}Nd_{0.0.1}TiO_3$-$0.2SmAlO_3$		Perovskite Orthorhombic	58.9	14600		13	1458
3446	$Li_{1+x+y}Ta_{1-x-3y}Ti_{x+4y}O_3$ (x=0.1, y=0.1)	1175/1h	M-Phase	58.9	7720		26	1400, 1438
3447	$0.42(La_{1/2}Na_{1/2})TiO_3$-$0.58Ca(Fe_{1/2}Nb_{1/2})O_3$	1300/10h	Complex perovskite Orthorhombic	58.9	14070	6.6	0	1459
3448	$Pb_{0.4}Ca_{0\cdot6}(Ni_{1/3}Nb_{2/3})O_3$		Perovskite	59.0	7100	4.2	6	996
3449	$Bi_{18}Ca_8Nb_{12}O_{65}$	950		59.0	610	3.7	25	1452
3450	$Ca(Zr_xTi_{1-x})O_3$ (x=0.5)	1470/15h	Perovskite Orthorhombic Pbnm	59.0	4400	3.14	459	916
3451	$(1-y)Li_{2.02}Ti_{0.92}Nb_{0.06}O_3$ (y=0.8)	1070		59.1	6900		36	722
3452	$Li_{1+x-y}Nb_{1-x-y}Ti_{x+4y}O_3$ (x=0.1, y=0.125)	1100/1h	M-Phase	59.2	7560	6	22	1400, 1438
3453	$Ca_4La_2Ti_{5-x}(Mg_{1/3}Nb_{2/3})_xO_{17}$ (x=1)	1540	Orthorhombic Pbnm	59.3	15500		72	1118
3454	$Ba_{0.8}Ca_{0.2}(Fe_{1/2}Nb_{1/2})O_3$		Complex Perovskite	59.5	550	6.3	80	1163
3455	$(1-x)La_{2/3}TiO_3$-$xNiTiO_3$ (0.05)	1360	Perovskite	59.6	14860	3.2	22	1411

(*continued*)

No.	Material	ST (°C)	Crystal structure	ε_r	Qf (GHz)	f_0	τ_f	Reference
3456	$Li_{1+x+y}Ta_{1-x-3y}Ti_{x+4y}O_3$ (x=0.15, y=0.1)	1175/1h	M-Phase	59.6	9100		42	1400, 1438
3457	$Pb_{0.25}Ca_{0.75}[(Mg_{1/3}Nb_{2/3})_{0.75}Ti_{0.25}]O_3$		Perovskite	60.0	11000		0	1460
3458	$Ba(Ti_{0.85}Mn_{0.15})O_3$	1400	Perovskite	60.0	12000		225	1461
3459	$BaSm_2Ti_4O_{12}$+16 mol% $BaCuB_2O_5$	875	Tungsten-Bronze Orthorhombic	60.0	4500		−30	1462
3460	$Ba_4Sm_{9.33}Ti_{18}O_{54}$+8 wt% $BaCu(B_2O_5)$	1050	Tungsten Bronze Orthorhombic	60.0	4100		−26	1391
3461	$(Sr_{0.2}Ca_{0.8})_3Ti_2O_7$		Orthorhombic $Ccm2_1$	60.0	2630	2.5	232	1358
3462	$0.5CaTiO_3$-$0.5Sr(Mg_{1/3}Nb_{2/3})O_3$	1600	Perovskite	60.0	14000		60	1347
3463	$BaNd_2Ti_3O_{10}$		Tungsten bronze	60.0	5300	4.2	140	1463
3464	$Ca_2Sr_3Nb_2TiO_{12}$	1530	Orthorhombic	60.0	6000	3.5	48	1209
3465	$(Ca_{1-x}Nd_{2x/3})TiO_3$ (x=0.3)+25 vol% $3ZnO$-$2B_2O_3$	900	Perovskite	60.0	3700		62	1004
3466	$Ba_3LiNb_2Sb_3Ti_5O_{21}$	1140		60.0	14000		143	923
3467	$Ca[Ti_{0.4}(Mg_{1/3}Ta_{2/3})_{0.6}]O_3$	1350	Perovskite Orthorhombic	60.2	36900		−10	1464
3468	$Ba_3LiNb_{3-x}Ta_xTi_9O_{21}$ (x=2)		Hexagonal $P6_3/mcm$	60.3	15100		100	1443
3469	$Li_{1+x+y}Ta_{1-x-3y}Ti_{x+4y}O_3$ (x=0.1, y=0.075)	1175/1h	M-Phase	60.5	5014		−5	1399, 1400
3470	$7NiNb_2O_6$-$9TiO_2$+3.2 wt% CuO	935	Composite	60.5	1040		62	1465
3471	$0.42(La_{1/2}Na_{1/2})TiO_3$-$0.58Ca(Fe_{1/2}Nb_{1/2})O_3$	1350/10h	Complex perovskite Orthorhombic	60.6	1300	6.6	6.5	1459
3472	$Nd_{0.5}Ti_{0.5}NbO_4$	1140/6h	Tetragonal $P4_2/mnm$	60.6	70100		76	1448
3473	$Ba(Pr_{0.3}Bi_{.02}Nb_{0.5})O_3$	1300	Perovskite	60.7	1500		15	1341
3474	$Sr_{1-x}Ca_xLa_4Ti_5O_{17}$ (x=0)	1500/6h	Orthorhombic Pnnm	60.8	9970		117	1428
3475	$0.5BaTiO_3$-$0.5La(Mg_{1/2}Ti_{1/2})O_3$		Perovskite I4/mcm	60.9	9600	5.2	−2	933
3476	$Ca_2Ba_3Ta_2TiO_{12}$	1525	Cubic perovskite	61.0	1800	3.4	21	1307
3477	$0.2Li_2O$-$0.62Nb_2O_5$-$0.17TiO_2$	1350		61.0	15000		100	760
3478	$_x(Ba_4Nd_{9.33}Ti_{18}O_{54})$-(1-x)$BaLa_4Ti_4O_{15}$ (x=0.75)+Bi_2O_3-B_2O_3-ZnO-SiO_2 glass	1140	Composite	61.0	2300		38	1466
3479	$Ba_4(Sm_{0.5}Nd_{0.5})_{28/3}Ti_{18}O_{54}$+2mol% TiO_2+2 wt% Li_2O-Al_2O_3-B_2O_3 glass		Tungsten Bronze Orthorhombic	61.1	5900		17	1467

3480	$CoTiNb_2O_8$+2 wt% CuO	950	Tetragonal rutile P42/mnm	61.5	15900		42	1468
3481	MBRT-90+10 wt% Li_2O-B_2O_3-SiO_2-CaO-Al_2O_3 (52.45::31.06:11.99:2:2.5)	875	Composite	61.6	2500		18	510
3482	$(Pb_{0.4}Ca_{0.6})(Fe_{1/2}Ta_{1/2})O_3$	1050/3h	Complex perovskite cubic Pm3m	62.0	9000		−15	1469
3483	$0.83Bi_2O_3$-$0.25Nb_2O_5$	900/3h	Flourite Fm-3m	62.0	560		−372	1396
3484	$CaSr_4Nb_2TiO_{12}$	1530		62.0	11500	3.4	51	1209
3485	$Li_{1+x+y}Ta_{1-x-3y}Ti_{x+4y}O_3$ (x=0.15, y=0.075)	1175/1h	M- Phase	62.1	6190		13	1399, 1400
3486	$Li_{1+x-y}Nb_{1-x-y}Ti_{x+4y}O_3$ (x=0.1, y=0.05)	1100/1h	M-Phase	62.4	3750	6.	−53	1399, 1400
3487	$Ba_{0.725}Ca_{0.275}(Fe_{1/2}Nb_{1/2})O_3$		Perovskite	62.4	640	6.3	82	1163
3488	$Ni_{0.3}Zn_{0.2}Ti_{0.5}NbO_4$	1120		62.5	13500	TCF65		1470
3489	$0.9La_{2/3}TiO_3$-$0.1LaAlO_3$	1350	Perovskite Orthorhomic	62.6	26100	4.9	82	1096
3490	$Ca[Ti_{1-x}(Mg_{1/3}Nb_{2/3})_x]O_3$ (x=0.4)	14504h	Perovskite	62.9	12200		92	1271
3491	$Pb_{0.4}Ca_{0.6}(Mg_{1/3}Nb_{2/3})_{1-x}$ $Sn_x]O_3$ (x=0.03)	1280	Perovskite Tetragonal	63.0	7540	5	−4	1424
3492	$Ba_{6-3x}Sm_{8+2x}Ti_{18}O_{54}$ (x=2/3)+3 wt% Bi_2O_3-B_2O_3	1100	Tungsten Bronze	63.0	8500		−19	1422
3493	(1-x)$BaLa_4Ti_4O_{15}$-x$Ba_4Nd_{9.333}Ti_{18}O_{54}$ (x=0.55)		Composite	63.0	10000		−20	1471
3494	$0.9La_{2/3}TiO_3$-$0.1LaAlO_3$	1350	Perovskite	63.0	26100		82	1096
3495	$Bi_2Zn_{2/3}Ta_{4/3}O_7$+0.05 wt% CuO+0.05 wt% V_2O_5	930		63.0	6800	5.35		1472
3496	$Ba_3La_4Ti_6O_{21}$			63.0	9100		198	1473
3497	(1-x)$La_{2/3}TiO_3$-x$NiTiO_3$ (x=0.02)	1380	Perovskite	63.3	6210	3.3	22	1411
3498	$0.4Ba(Mg_{1/2}W_{1/2})O_3$-$0.6BaTiO_3$	1500/6h	Perovskite Hexagonal	63.9	3800		303	373
3499	$CaBa_4Ta_2TiO_{12}$	1500	Cubic perovskite	64.0	1400	3.6	24	1307
3500	$Pb_2Ta_{1.5}Nb_{0.5}O_7$		Hexagonal	64.0	12800		223	1474
3501	Ba_{6-3x} $Sm_{8+2x}Ti_{18}O_{54}$x-$_{2/3}$+3 wt% Al_2O_3-B_2O_3-SiO_2	1175	Tungsten Bronze Orthorhombic	64.0	8500	–	0	1475

(*continued*)

No.	Material	ST (°C)	Crystal structure	ε_r	Qf (GHz)	f_0	τ_f	Reference
3502	$Li_{1+x-y}Nb_{1-x-y}Ti_{x+4y}O_3$ (x=0.15, y=0.075)	1100/1h	M-phase	64.0	4610	5.9	−15	1438
3503	$Co_{0.5}Ti_{0.5}NbO_4$	1120	Tetragonal $P4_2/mnm$	64.0	65300		223	1179
3504	$0.84CaTiO_3$-$0.16Sm_{0.9}Nd_{0.1}AlO_3$+0.4 wt% MgO	1375/3h		64.2	30900		26	1476
3505	$Pb_{.4}Ca_{.6}(Mg_{1/3}Nb_{2/3})_{1-x}$ $Sn_x]O_3$ (x=0.01)	1280	Perovskite Tetragonal	64.7	7130	5	0	1424
3506	$LiNb_{0.6}Ti_{0.5}O_3$+0.5 wt% 0.17 Li_2O-$0.83V_2O_5$	850		64.7	5900		9	1450
3507	$Li_{1+x-y}Nb_{1-x-y}Ti_{x+4y}O_3$ (x=0.1, y=0.1)	1100/1h	M-Phase	64.8	6385	5.7	8	1399, 1400
3508	$La_{2/3}TiO_3$		Perovskite Orthorhombic Pbnm	65.0	15700			1477
3509	$La_{0.4}Ba_{0.6}Ti_{0.6}Yb_{0.4}O_3$	1600/4h	Not available	65.0	4500		1	1451
3510	$Ba_3Ti_4Nb_4O_{21}$+3 wt% CuO+1 wt% B_2O_3	900/2h	Hexagonal $P6_3/mcm$	65.0	16000		101	1478
3511	$Ba_4(Nd_{0.85}Bi_{0.015})_{9.33}Ti_{18}O_{54}$+30 wt% Li_2O-ZnO-B_2O_3	875	Composite	65.0	2500	5.5	35	1479
3512	$(Pb_{0.4}Ca_{0.6})[(Mg_{1/2}Nb_{1/2})O_3Sn_x]$ (x=0.01)	1350	Perovskite	65.0	7100		136	1424
3513	$Ba_4Sm_{9.33}Ti_{18}O_{54}$+6 wt% $BaCu(B_2O_5)$	1075	Orthorhombic	65.0	4200		−24	1391
3514	$Ba[Ti_{1-x}(Co_{0.5}W_{0.5})_xO_3$ (x=0.4)		Perovskite	65.0	3000		45	519
3515	$0.1Pb(Fe_{2/3}W_{1/3})O_3$-$0.9Pb_{0.2}Ca_{0.8}(Fe_{1/2}Nb_{1/2})O_3$	1000	Perovskite	65.3	2270		−24	1480
3516	$CaTi_{0.7}(Al_{1/2}Ta_{1/2})_{0.3}O_3$	1500/15h	Perovskite Orthorhombic	65.4	20000	8	113	1266
3517	$CaTi_{0.7}(Al_{1/2}Nb_{1/2})_{0.3}O_3$	1450/5h	Perovskite Orthorhombic	65.4	19300	7	−2	1152
3518	$0.5CeO_2$-$0.25CaO$-$0.25TiO_2$	1550	Mixture phases	65.5	9500	3.2	399	488
3519	$Ca_3Ba_2Nb_2TiO_{12}$	1475	Cubic perovskite	66.0	2600	3.3	48	1307
3520	$(1-x)(Mg_{0.95}Zn_{0.05})TiO_3$-$xCa_{0.6}La_{0.8/3}TiO_3$ (x=0.7)	1320/4h	Composite	66.0	39000		168	465
3521	$BaTi_{0.4}Ga_{0.3}Nb_{0.3}O_3$	1500/4h	Perovskite Tetragonal P4mm	66.0	3720	4.7		1373
3522	$LiNb_{0.6}Ti_{0.5}O_3$)+2 wt% V_2O_5	900/1h	M-Phase	66.0	3800	5.6	11	1450
3523	Bi_2O_3-CaO-Nb_2O_5 (52.5:17.5:30)	925		66.0	330	3.6	35	1452
3524	$Ba_3Ti_4Nb_4O_{21}$+0.2$MnCO_3$-0.8CuO	950	Hexagonal $P6_3/mcm$	66.0	13400		60	1481
3525	$LiNb_{0.6}Ti_{0.5}O_3$+1 wt% LBS glass	900	Rhombohedral	66.2	5200	4.3	19	1482

3526	$Pb_{0.4}Ca_{0.6}(Mg_{1/3}Nb_{2/3})\ O_3$	1280	Perovskite Tetragonal	66.3	6940	5	3	1424
3527	$Bi_2(Zn_{1/3}Ta_{2/3})_2O_7$	850	Cubic Fd3m	66.3	6200		−9	1472
3528	$(Ni_{1/3}Ta_{2/3})_{1-x}Ti_xO_2$ (x=0.6)	1300	Rutile Tetragonal $P4_2/mmm$	66.4	2180		147	1276
3529	$Ba_{4.2}Nd_{9.2}Ti_{18}O_{54}$+13 wt% $NdAlO_3$+0.3 wt% MnO_2	1380/2h	Tungsten Bronze	66.5	14000		0	1483
3530	$0.92La_{2/3}TiO_3$-$0.08LaAlO_3$	1350	Perovskite Orthorhombic	66.9	28350	4.8	82	1096
3531	$(Ba_{4.2}Sm_{9.2})Ti_{16.6}Al_{1.4}O_{54}$	1440	Tungsten Bronze	67.0	1543	5.4	−90	1484
3532	$BaNd_2Ti_4O_{12}$+B_2O_3-Bi_2O_3-SiO_2-ZnO glass+La_2O_3-B_2O_3-TiO_2	900	Tungsten Bronze	67.0	6000	6	4	1485
3533	$(Ca_{0.3}Li_{0.14}Sm_{0.42})TiO_3$-$Mg_{0.93}Ca_{0.07}TiO_3$ stacked layers	1350	Stacked layers	67.2	7900		0	719
3534	$ZrTe_3O_8$	760/15h	Cubic Ia3	67.5	1800	4	362	53, 62
3535	$CaTi_{0.7}(Al_{1/2}Nb_{1/2})_{0.3}O_3$	1500/5h	Perovskite	67.8	18700		138	1152
3536	$0.8CaTiO_3$- $0.2Sm(Mg_{0.5}Ti_{0.5})O_3$	1550	Perovskite	68.0	12400	3.5	147	865
3537	$Ba_{6-3x}(Sm_{1-y}Nd_y)_{8+2x}(Ti_{1-z}Sn_z)O_{54}$ (x=2/3, y=0, z=0.1)		Tungsten bronze	68.0	4020		20	1486
3538	$0.6CaTiO_3$-$0.4Ca(Mg_{1/3}Nb_{2/3})O_3$	1450	Perovskite	68.0	17000	5.4	108	944
3539	$BiVO_4$	900	Monoclinic I2/b	68.0	8000		−243	1487
3540	$0.3La(Mg_{1/2}Ti_{1/2})O_3$-$0.7SrTiO_3$		Perovskite Imma	68.4	4950	6.6		978
3541	$(Pb_{1-x}Ca_x)[Fe_{1/2}Nb_{1/2}]_{1-y}Zr_yO_3$ (y=0.01, x=0.6)	1150	Perovskite	68.7	6800	4.2	−17	1488
3542	$(Ni_{1/3}Nb_{2/3})_{1-x}Ti_xO_2$ (x=0.3)	1200	Rutile Tetragonal $P4_2/mmm$	68.7	19300		57	1276
3543	$(Ca_{0.2}Sr_{0.8})_3Ti_2O_7$	1460/2h	Tetragonal I4/mmm	68.8	10600			1489
3544	$Ba_4(Sm_{0.5N}d_{0.5})_{28/3}Ti_{18}O_{54}$+$2TiO_2$+5 wt% K_2O-B_2O_3-SiO_2 glass	1075/3h	Orthorhombic Tungsten Bronze	68.8	6800		29	1490
3545	$Ba_4Gd_9Ti_{18}O_{54}$	1350/10h	Orthorhombic Pbam	69.0	3300	1	−60	1491
3546	$CaTi_{0.7}(Al_{1/2}Nb_{1/2})_{0.3}O_3$+1 wt% Li_3NbO_4	1300/5h	Perovskite Orthorhombic	69.0	21500	7	145	1152
3547	(1-x)$La_{2/3}TiO_3$-x$NiTiO_3$ (0.03)	1375	Perovskite	69.4	16960	3.1	18	1411
3548	$Ba_{2-x}Sm_{(4+2/3x)}Ti_9O_{26}$ (x=0.3)	1360/4h	Tunsten Bronze	69.4	9700		6	1493
3549	$(Ba_{4.2}Sm_{.9.2})_aTi_{17.}AlO_{54}$	1440	Tungsten Bronze	70.0	4360	5.22	−57	1484

(*continued*)

No.	Material	ST (°C)	Crystal structure	ε_r	Qf (GHz)	f_0	τ_f	Reference
3550	$LiNb_{0.6}Ti_{0.5}O_3$+1 wt% ZnO-B_2O_3	900	M phase solid solution	70.0	5900		−5	1493
3551	$Ba_4Nd_{9.33}Ti_{18}O_{54}$+2 wt% Al_2O_3	1320/4h	Tungsten Bronze	70.0	12200		20	1494
3552	$Ba_{6-3x}Sm_{8+2x}Ti_{18}O_{54}$ (x=2/3)+1 wt% Bi_2O_3-B_2O_3	1200	Tungsten Bronze	70.0	8500		−13	1422
3553	$Bi_2(Zn_{1/3}Nb_{2/3})_2O_7$+1 wt% of 0.15CuO-0.85$MoO_3$	900		70.0	4800	3		1495
3554	Ba_{6-3x} $Sm_{8+2x}Ti_{18}O_{54}$ (x=2/3)+0.5 wt% (50Al_2O_3-50 SiO_2)	1220	Tungsten Bronze	70.0	8500	–	−21	1475
3555	$Ba_4Sm_{9.33}Ti_{18}O_{54}$+4 wt% $BaCu(B_2O_5)$	1175	Tungsten Bronze	70.0	4700		−16	1391
3556	0.97$La_{2/3}TiO_3$-0.03$NiTiO_3$	1350		70.0	17000		18	1411
3557	Ba_{6-3x} $Sm_{8+2x}Ti_{18}O_{54}$ (x=2/3)+0.5 wt% (44Al_2O_3-30B_2O_3-26SiO_2)	1220	Tungsten Bronze	70.0	8600	–	−12	1475
3558	$LiNb_{0.6}Ti_{0.5}O_3$+1 wt% B_2O_3	880		70.0	5400		−6	1496
3559	$(Ba_{4.2}Sm_{9.2})_\alpha Ti_{18-y}Al_yO_{54}$ (y=1, ∝=1+y/36, x=0.6)	1440	Tungsten Bronze	70.2	4350		−57	1484
3560	$Pb_{0.4}Ca_{.6}[(Fe_{1/2}Nb_{1/2})_{0.9}Sn_{0.1}O_3$	1150/3h	Perovskite Orthorhombic	70.3	8200		−19	1497
3561	0.1$CaTiO_3$-0.5$(Li_{1/2}Nd_{1/2})TiO_3$-0.4$(Dy_{1/3}Nd_{1/3})TiO_3$	1350/3h	Tetragonal P-4b2 Perovskite	70.6	1470		−156	1498
3562	Ba_{6-3x} $Sm_{8+2x}Ti_{18}O_{54}$ (x=2/3)+0.5 wt% (22MgO-22Al_2O_3-56SiO_2)	1200	Tungsten Bronze	71.0	5890	–	−19	1475
3563	Ba_{6-3x} $Sm_{8+2x}Ti_{18}O_{54}$ (x=2/3)+0.5 wt% (35Bi_2O_3- 32ZnO- 6SiO_2-27B_2O_3)	1200	Tungsten Bronze Perovskite	71.0	8900	–	−10	1475
3564	0.14(BaO-Nd_2O_3-4TiO_2)-+0.86(BaO-Al_2O_3- 4TiO_2)			71.0	8200	–	0	1111
3565	$Ba\{Ti_{0.95}Mn_{0.05}\}O_{3-\delta}$	1450/2h	Perovskite	71.1	7700	4.8		1446
3566	$Ba[Ti_{1-x}(Zn_{1/2}W_{1/2})_x]O_3$ (x=0.4)	1420	Cubic perovskite Pm3-m	71.2	4800		48	695
3567	$Cu_{0.5}Ti_{0.5}NbO_4$	960/6h	Tetragonal rutle	71.2	11000		49	1499
3568	SrO-2CeO_2-4TiO_2	1330/3h	Tetragonal	71.3	10400		187	1500
3569	0.2$Pb(Fe_{2/3}W_{1/3})O_3$-0.8$Pb_{.2}Ca_{.8}(Fe_{1/2}Nb_{1/2})O_3$	1000	Perovskite	71.4	1520		−29	1480
3570	$Ba_{(2-x)}Sm_{(4+2/3x)}Ti_9O_{24}$ (x=0.25)	1370		71.5	10700	5.1	4	1501

3571	$Ca_{0.66}La_{0.387}Ti_{0.88}O_3$	1550	Orthorhombic Pbnm	71.5	13400		136	1502
3572	$0.2Ca_{0.8}Sr_{0.2}TiO_3$-$0.8Li_{0.5}Sm_{0.5}TiO_3$+5 wt% $BaCu(B_2O_5)$+1.5 wt% TiO_2	950		71.6	3400		−11	1503
3573	SrO-$2CeO_2$-$5TiO_2$	1330/3h	Mixed phases	71.7	6670		203	1500
3574	$LiNb_{0.63}Ti_{0.4625}O_3$+0.1 wt% B_2O_3-SiO_2	900		71.7	4950		−2	1504
3575	(1-x)$Ca_{0.61}Nd_{0.26}TiO_3$-xNd$(Zn_{0.5}Ti_{0.5})O_3$+x=0.2	1300	Perovskite	71.8	17300		94	1505
3576	$0.92BiVO_4$–$0.08Li_{0.5}Nd_{0.5}WO_4$	750	Monoclinic	71.8	7500		1	1506
3577	$0.96La_{2/3}TiO_3$-$0.04LaAlO_3$	1325	Perovskite Orthorhomic	71.9	23900	4.5	123	1096
3578	$Pb_{0.5}Ca_{0.5}(Na_{1/4}Nb_{3/4})O_3$		Perovskite	72.0	1500	3.5	230	996
3579	$Ba_4Sm_{9.33}Ti_{18}O_{54}$+2 wt% $BaCu(B_2O_5)$	1175	Orthorhombic	72.0	5500		−14	1391
3580	$Pb_{0.5}Ca_{0.5}(Zr_{0.95}Ti_{0.05})O_3$	1350	Perovskite Rhombohdral	72.0	4100	4	2	1507
3581	$0.96La_{2/3}TiO_3$-$0.04LaAlO_3$	1325	Perovskite	72.0	24000		123	1096
3582	$Ba_{6-3x}Sm_{8+2x}Ti_{18}O_{54}$ (x=2/3)+0.5 wt% (60ZnO-30B_2O_3-10SiO_2)	1200	Tungsten-bronze Orthorhombic	72.0	4530	–	−17	1475
3583	$Ba_{6-3x}Sm_{8+2x}Ti_{18}O_{54}$ (x=2/3)+0.5 wt% (40MgO-40B_2O_3-20SiO_2)	1200	Tungsten-Bronze Orthorhombic	72.0	4450	–	−16	1475
3584	Ba_{6-3x} $Sm_{8+2x}Ti_{18}O_{54}$-1.9TiO_2 (x=2/3)	1350/2h	Tungsten Bronze	72.0	10300		7.2	1508
3585	$(Ba_{4.2}Sm_{9.2})_{\alpha}Ti_{18-y}Al_yO_{54}$ (y=0.8, α=1+y/36, x=0.6)	1440	Orthorhombic Tungsten Bronze	72.1	4600		−42	1484
3586	(1-x)$CaTiO_3$-xSm$(Mg_{1/2}Ti_{1/2})O_3$ (x=0.2)		Orthorhombic Pnma	72.0	12000		160	1008
3587	$Pb_{0.5}Ca_{0.5}(Ni_{1/3}Nb_{2/3})O_3$		Perovskite	73.0	5100	3.5	52	996
3588	$Pb_{0.4}Ca_{0.6}(Mg_{1/3}Nb_{2/3})O_3$		Perovskite	73.0	4100	3.1	3.7	996
3589	Ba_{6-3x} $Sm_{8+2x}Ti_{18}O_{54}$ (x=2/3)+0.5 wt% (71ZnO- 29B_2O_3)	1200	Tungsten-Bronze Orthorhombic	73.0	4830	–	−14	1475
3590	$(Pb_{0.5}Ni_{0.5})(Mg_{1/3}Nb_{2/3})O_3$		Perovskite	73.0	4900		52	996
3591	Ba_{6-3x} $Sm_{8+2x}Ti_{18}O_{54}$ (x=2/3)+0.5 wt% (40 B_2O_3- 60SiO_2)	1200	Tungsten-Bronze Orthorhombic	73.0	7900	–	−16	1475
3592	$Ba_{6-3x}Sm_{8+2x}Ti_{18}O_{54}$ (x=2/3)+0.5 wt% B_2O_3	1220	Tungsten Bronze Orthorhombic	73.0	9500	–	−14	1475
3593	$Ba_{0.98}Sr_{0.02})Sm_2Ti_4O_{12}$	1375/6	Tungsten Bronze	73.0	7920		−6	1509

(*continued*)

No.	Material	ST (°C)	Crystal structure	ε_r	Qf (GHz)	f_0	τ_f	Reference
3594	$Ca_4La_2Ti_5O_{17}$	1550/4h	Cubic perovskite	73.0	16000	3.3	127	1118, 1510
3595	$Ba_3LiNb_{3-x}Ta_xTi_5O_{21}$ (x=1)			73.0	13600		172	1443
3596	$Ba_{6-3x}Nd_{8+2x}Ti_{18}O_{54}$ (x=2/3)+2 wt% H_3BO_3-TEOS	1075	Tungsten-Bronze Orthorhombic	73.8	8200		47	1511
3597	$Ba_4Nd_{3.33}Eu_6Ti_{18}O_{54}$	1460	Tungsten-Bronze	73.9	8900		−11	1512
3598	$Ca_{0.8}Sr_{0.2}TiO_3$-$Li_{0.5}Sm_{0.5}TiO_3$+x wt%[YB_2O_3-(1-y)CuO] (x=7.5, y=0.5)	950		74.0	2500		1	1513
3599	$BaTi_{0.95}Co_{0.05}O_{3-\delta}$	1450/2h	Perovskite	74.0	1300			1446
3600	$Pb_{0.5}Ca_{0.5}ZrO_3$	1500	Perovskite	74.0	3900	3.7	−17	1514
3601	$Ba_{6-3x}Sm_{8+2x}Ti_{18}O_{54}$ (x=2/3)+0.5 wt% (50ZnO- 50B_2O_3)	1220	Tungsten bronze	74.0	5330	–	−17	1475
3602	$Ba_{6-3x}Sm_{8+2x}Ti_{18}O_{54}$ (x=2/3)+0.5 wt% (30 BaO- 40B_2O_3+-30SiO_2)	1220	Tungsten Bronze Orthorhombic	74.0	9700	–	−12	1475
3603	TiO_2+zinc borosilcate glass	900	Composite	74.0	8000		340	1515
3604	0.88TiO_2-0.12$Bi_2Ti_4O_{11}$	1200	composite	74.0	9500		3	1372
3605	BaO-Sm_2O_3-TiO_2		Tungsten Bronze	74.0	12000		10	1516
3606	$BaTi_{0.92}Ga_{0.08}O_{2.96}$	1450	Tetragonal Perovskite	74.0	7810	5.5		1517
3607	0.7$Ca_{0.6}La_{0.267}TiO_3$-0.3$Ca(Sm_{0.5}Nb_{0.5})O_3$		Perovskite	74.3	12700		9	1518
3608	$Ba_4(Sm_{0.5}Nd_{0.5})_{28/3}Ti_{18+x}O_{54}-2TiO_2$+2 2x+1.5 wt% Al_2O_3	1260/5h	Mixture	74.3	11900		5	1519
3609	$Ba_{(2-x)}Sm_{(4+2/3x)}Ti_9O_{28}$ (x=0.2)	1370		74.8	10900	5.78	2	1501
3610	$Ca_2Ba_3Nb_2TiO_{12}$	1500	Cubic perovskite	75.0	1600	3.04	53	1307
3611	Ba_{6-3x} $Sm_{8+2x}Ti_{18}O_{54}$ (x=2/3)+0.5 wt% (40PbO-40B_2O_3-20SiO_2)	1200	Tungsten-Bronze Orthorhombic	75.0	6500	–	−17	1475
3612	$(Pb_{0.5}Co_{0.5})(Mg_{1/3}Nb_{2/3})O_3$		Perovskite	75.0	1400		16	996
3613	$(Bi_{1.92}Zn_{0.08})(Zn_{0.64}Nb_{1.36})O_7$	1000	Pyrochlore-Monoclinic	75.0	1800			1520
3614	$Ba_{.98}Sr_{0.02.2}Sm_2Ti_4O_{12}$		Tungsten Bronze	75.0	7920		−6	1509
3615	$Pb_{0.5}Ca_{0.5}(Co_{1/3}Nb_{2/3})O_3$		Perovskite	75.0	1450	3.7	16	996
3616	$Li_{1/2}Nd_{1/2}TiO_3$		Perovskite	75.0	2000		−274	1498

3617	$0.6(Sm_{1/2}Li_{1/2})TiO_3$-$0.4(Sm_{1/2}Na_{1/2}Ti)O_3$	1350		75.0	2000	10		1521
3618	$Ni_{0.15}Nb_{0.3}Ti_{0.55}O_2$	1080	Tetragonal rutile	75.0	12800		280	1522
3619	$xBi_{2/3}MoO_4$-1-x $BiVO_4$ (x=0.5-0.7)	850	Monoclinic/Tetragonal phase boundary	75	8000			1523
3620	$Ba_4Sm_{9.33}Ti_{18}O_{54}$+0.5 wt% GeO_2	1200	Tungsten-Bronze Orthorhombic	75.2	5200		−12	1524
3621	$BaSm_2Ti_4O_{12}$+1 wt% CuO	1160	Tungsten Bronze	75.8	4900		−8	1525
3622	$Ba_{6-3x}(Sm_{1-y}Nd_y)_{8+2x}Ti_{1-z}Sn_z)_{18}O_{54}$ (x=2/3, y=0, z=0.05)		Tungsten Bronze	76.0	6260	4.1	2	1526
3623	$Ba_{6-3x}Sm_{8+2x}Ti_{18}O_{54}$ (x=2/3)+0.5 wt% ($30BaO$-$40B_2O_3$-$30SiO_2$)	1220	Tungsten Bronze Orthorhombic	76.0	9100	–	−7	1475
3624	$Ba_{6-3x}(Sm_{1-y}Nd_y)_{8+2x}Ti_{1-z}Sn_z)_{18}O_{54}$ (x=2/3, y=0.1, z=0.05)		Tungsten-Bronze Orthorhombic	76.0	7130	4.2	6	1526
3625	$(Bi_{1.92}Ca_{0.08})(Zn_{0.64}Nb_{1.36})O_7$	960	Pyrochlore-Monoclinic	76.0	3900			1520
3626	$(Bi_{1.92}Cd_{08})(Zn_{0.64}Nb_{1.36})O_7$	980	Pyrochlore-Monoclinic	76.0	700			1526
3627	$Ba_4Sm_{9.33}Ti_{18}O_{54}$	1350	Tungsten-Bronze Orthorhombic	76.0	10000		−12	1475
3628	$Y_2Ti_2O_7$+8 wt% Bi_2O_3-+1 mol% Nd_2O_3-Nb_2O_5	1350	composite	76.0	18950		26	1527
3629	$Ba_{6-3x}(Sm_{1-y}Nd_y)_{8+2x}(Ti_{1-z}Sn_z)O_{54}$ (x=2/3, y=0, z=0.05)		Tungsten-Bronze Orthorhombic	76.0	6260		2	1526
3630	$Bi_3(Nb_{0.8}V_{0.2})O_7$	870	cubic	76.0	460		3	1528
3631	$Ba_4Sm_{9.33}Ti_{18}O_{54}$+0.5 wt% B_2O_3	1200	Tungsten-Bronze Orthorhombic	76.1	10500		−19	1524
3632	$Ba_{4.5}Gd_9Ti_{18}O_{54}$		Tungsten Bronze	76.1	2050		−35	1529
3633	$Sr_4Ti_3O_{10}(Sr_{n+1}Ti_nO_{3n+1})$		Perovskite Tetragonal I4/mmm	76.1	12700	2.2	576	1358
3634	$Ba_{(2-x)}Sm_{(4+2/3x)}Ti_9O_{24}$ (x=0.15)	1370		76.1	12800	5.2	1	1501
3635	$(Ba_{4.2}Sm_{9.2})_\propto Ti_{18-y}Al_yO_{54}$ (y=0.4, ∝=1+y/36, x=0.6)	1440	Tungsten bronze	76.1	3800		−33	1484
3636	$Bi_2(Zn_{1/3}Nb_{2/3})_2O_7$	950/2h	Monoclinic Pyrochlore	76.2	2980		200	1530
3637	$Li_{1+x-y}Nb_{1-x-y}Ti_{x+4y}O_3$ (x=0.15, y=0)	1100/1h	M -Phase	76.2	1000	5.3	−62	1400, 1438
3638	$Ba_4(Nd_{0.7}Sm_{0.3})_{9.33}Ti_{18}O_{54}$+2 wt% BBS	1000	Tungsten-Bronze Orthorhombic	76.3	8300		18	1531
3639	$Ba_4Sm_{7.33}Eu_2Ti_{18}O_{54}$	1460	Tungsten Bronze	76.4	8990		−16	1512
3640	$Ba_4Nd_{1.33}Eu_8Ti_{18}O_{54}$	1400	Tungsten Bronze	76.6	8590		−21	1512

(*continued*)

No.	Material	ST (°C)	Crystal structure	ε_r	Qf (GHz)	f_0	τ_f	Reference
3641	$Ba(Mg_{0.167}Ta_{0.33}Ti_{0.50})O_3$	1550	Perovskite	76.6	10000	4.1	113	883
3642	$Ba_4(Nd_{0.7}Sm_{0.3})_{9.33}Ti_{18}O_{54}$+1 wt% BBS glass	1100	Tungsten-Bronze Orthorhombic	76.6	8200		13	1531
3643	$Bi_2(Zn_{1/3}Nb_{2/3-x}V_x)_2O_7$ (x=0.001))	990	Pyrochlore Monoclinic	76.7	3580		−88	1532
3644	$0.91BiVO_4$–$0.09Li_{0.5}La_{0.5}WO_4$	750	Monoclinic	76.7	6800		7	1506
3645	$Ba_{4.2}Sm_{9.2}Ti_{18}O_{54}$+0.2 wt% Al_2O_3	1340/3h	Tungsten-Bronze	76.9	10100		−23	1533
3646	$Ba_4Eu_{9.33}Ti_{18}O_{54}$	1400	Tungsten-Bronze Orthorhombic	77.0	6580		34	1512
3647	$Ba_{6-3x}(Sm_{1-y}Nd_y)_{8+2x}Ti_{1-z}Sn_z)_{18}O_{54}$ (x=2/3, y=0.3, z=0.05)		Tungsten Bronze	77.0	7850	4.2	9	1526
3648	$(Ti_{0.9}Zr_{0.1})O_2$	1400/5h	Rutile Tetragonal $P4_2/mmm$	77.0	14000	4		53
3649	24 wt% $BaTiO_3$-76 wt% Nd_2O_3-$3TiO_2$	1220	composite	77.0	11000		123	1534
3650	$(Ba_{1-\alpha}Sm_\alpha)_{4.2}Sm_{9.2}Ti_{18}O_{54}$ α=0.1	1450/2h	Tungsten-Bronze Orthorhombic	77.0	6680		−11	1535
3651	$BaSm_2Ti_5O_{14}$		Tungsten Bronze Orthorhombic Pbam	77.0	9300		12	1536, 1537
3652	$Ba_{6-3x}(Sm_{1-y}Nd_y)_{8+2x}(Ti_{1-z}Sn_z)O_{54}$ (x=2/3, y=0.3, z=0.05)	1360/12	Tungsten-Bronze Orthorhombic Pbam	77.0	8185	4	1	1536
3653	$Ba_4Sm_{9.33}Ti_{18}O_{54}$+0.5 wt% GeO_2	950	Tungsten-Bronze Orthorhombic Pbam	77.3	8900		−19	1524
3654	$Na_{0.5x}Bi_{1-0.5x})(Mo_xV_{1-x})O_4$ (x=0.05)	720		77.3	8000	3.8	20	1538
3655	Ba_{6-3x} $Sm_{8+2x}Ti_{18}O_{54}$+0.5 wt% GeO_2+0.5 wt% B_2O_3 (x=2/3)	1150	Tungsten-Bronze Orthorhombic Pbam	77.3	8900		−13	1524
3656	$Ba_{(2-x)}Sm_{(4+2/3x)}Ti_9O_{24}$ (x=0)	1360		77.5	11200	5.2	−3	1501
3657	$Li_{1+x-y}Nb_{1-x-y}Ti_{x+4y}O_3$ (x=0.05, y=0.05)	1100/1h	M -Phase	77.8	2180	5.2	−42	1400, 1438
3658	$Ba_4Nd_{5.33}Eu_4Ti_{18}O_{54}$	1460	Tungsten-Bronze Orthorhombic Pbam	78.0	10460		10	1512
3659	$(Ba_{4.2}Sm_{.9.2})_aTi_{17.8}Al_{.0.2}O_{54}$	1460	Tungsten-Bronze Orthorhombic	78.0	8233	4.8	−18	1484
3660	$Pb_{0.5}Ca_{0\cdot5}(Li_{1/4}Nb_{3/4})O_3$		Perovskite	78.0	2000	3.7	460	996
3661	$Pb_{0.4}Ca_{0.6}[(Fe_{1/2}Nb_{1/2})_{0.95}Sn_{0.05}O_3$	1150/3h	Perovskite Orthorhombic	78.0	6000		−9	1497
3662	$Ca(Zr_{0.6}Ti_{0.4})O_3$		Perovskite Orthorhombic	78.0	7840			906
3663	$(Ni_{1/3}Nb_{2/3})_{1-x}Ti_xO_2$ (x=0.4)	1200	Rutile Tetragonal $P4_2/mmm$	78.0	17060		98	1276

3664	$Ba_3LiNb_3Ti_5O_{21}$	1100	Hexagonal $P6_3/mcm$	78.0	9800		205	1443
3665	$(Ba_{4.2}Sm_{9.2})_{\propto}Ti_{18-y}Al_yO_{54}$ (y=0.2, $\propto$=1+y/36, x=0.6)	1460	Tungsten-Bronze Orthorhombic Pbam	78.0	8200		−18	1484
3666	$K_{0.5x}Bi_{1-0.5x}(Mo_xV_{1-x})O_4$ (x=0.8-0.1)	700	Scheelite Tetragonal	78.0	7800			1539
3667	$Ba_4(Nd_{28/3-y}Yb_y)Ti_{18}O_{54}$ (y=1)	1480/2h	Tungsten-Bronze Orthorhombic	78.4	6780		53	1542
3668	$Ba_{(2-x)}Sm_{(4+2/3x)}Ti_9O_{24}$ (x=0.05)	1360		78.5	11900	5.2	−2	1501
3669	$Bi_2(Zn_{1/3}Nb_{2/3-x}V_x)_2O_7$ (x=0.001)	850/2	Pyrochlore Monoclinic	78.5	3780			1530
3670	$Ba_4Nd_{8.33}DyTi_{18}O_{54}$	1480	Orthorhombic Pbam	78.6	10040	4.8	34	1537
3671	$Ba_{6-3x}Sm_{8+2x}Ti_{18}O_{54}$ (x=0.75)		Orthorhombic Pbam	78.6	8700		–	1536
3672	$Bi_2(Zn_{1/3}Nb_{2/3-x}V_x)_2O_7$ (x=0.003)	850/2	Pyrochlore monoclinic	78.6	3140			1530
3673	$Ba_4Sm_{8.33}EuTi_{18}O_{54}$	1460	Tungsten-Bronze Orthorhombic Pbam	78.7	9560		−11	1512
3674	$Ba_4Sm_{9.33}Ti_{18}O_{54}$+0.3 mol% TiO_2	1350	Tungsten Bronze Pbam	78.8	10750	4.8	−21	1508
3675	(1-x)$Ca_{0.61}Nd_{0.26}TiO_3$-xNd$(Zn_{0.5}Ti_{0.5})O_3$+x=0.15		Perovskite	78.8	19200		134	1505
3676	$Ba_{6-3x}Sm_{8+2x}Ti_{18}O_{54}$ (x=0.5)		Tungsten-Bronze Orthorhombic Pbam	78.9	8400		−19	1536, 1540
3677	$Pb_{0.5}Ca_{0.5}(Na_{1/4}Nb_{3/4})O_3$		Perovskite	79.0	400	3.7	550	996
3678	$(Ba_{0.97}Ca_{0.03})$-Sm_2O_3-4.5TiO_2		Tungsten Bronze	79.0	10500	10	−5	1536
3679	$Bi_{18}(Ca_{1-x}Zn_x)_8Nb_{12}O_{65}$ (x=0.725)	925		79.0	1000	3.2	1	1452
3680	Bi_3NbO_7+20 wt% $Bi_4B_2O_9$	900	Composite	79.0	1000		8	1541
3681	$Ba_4Nd_{8.33}HoTi_{18}O_{54}$	1480	Tungsten-Bronze Orthorhombic Pbam	79.3	9690	4.7	31	1542
3682	$Ba_4Nd_{8.33}ErTi_{18}O_{54}$	1480	Tungsten-Bronze Orthorhombic	79.5	8290	4.1	53	1542
3683	$Ba_4Nd_{8.33}YbTi_{18}O_{54}$	1480	Tungsten-Bronze Orthorhombic Pbam	79.4	6780	4.7	33	1542
3684	$Ba_{6-3x}La_{8+2x}Ti_{1-z}Zr_x)_{18}O_{54}$ (x=2/3, z=0.1)		Tungsten-Bronze Orthorhombic	79.6	6670	4.83	109	1543
3685	$Ba_{6-3x}Sm_{8+2x}Ti_{18}O_{54}$ (x=2/3)+1 wt% Bi_2O_3 and $Ba_xSr_{1-x}TiO_3$		Tungsten-Bronze Orthorhombic	79.6	10800		2	1544
3686	$Ca_{(1-x)}Nd_{2x/3}TiO_3$ (x=0.3)		Perovskite	79.7	13000		295	1545
3687	Ba_{6-3x} $Sm_{8+2x}Ti_{18}O_{54}$-0.1TiO_2 (x=2/3)	1350/2h	Tungsten-Bronze Orthorhombic	79.8	9880		−18	1508
3688	Bi_3NbO_7		Cubic Fm3m	80.0	300	5		1546

(*continued*)

No.	Material	ST (°C)	Crystal structure	ε_r	Qf (GHz)	f_0	τ_f	Reference
3689	$Ba_4Sm_{9.33}Ti_{18}O_{54}$	1450	Tungsten Bronze	80.0	10700	4.7	−15	1524
3690	$91.9TiO_2$-$8.1Bi_2O_3$		Mixture phases	80.0	9000		21	1434
3691	$0.58(Sm_{1/2}Li_{1/2})TiO_3$-$0.42(Sm_{1/2}Na_{1/2}Ti)O_3$	1350	Tetragonal	80.0	2000	10		1521
3692	$0.8Bi_2O_3$-$0.3Nb_2O_5$	920/3h	Flourite δ-Bi_2O_3 Fm-3m	80.0	420		−306	1396
3693	$(Ti_{0.9}Ge_{0.1})O_2$	1400/5h	Rutile Tetragonal $P4_2/mmm$	80.0	24000	4		53
3694	$(Sm_{1/2}Na_{1/2}Ti)O_3$	1350	Perovskite Tetragonal I4/mmm	80.0	13000	10		1521
3695	$(La_{0.44}Sr_{0.33})TiO_3$	1350	Orthorhombic Ibmm	80.0	7500	3	70	1547
3696	$(Li_{1/2}Nd_{1/2})TiO_3$		Perovskite Orthorhombic	80.0	3100	4	−310	1548
3697	$0.15(Ba_{0.95}Sr_{0.05})$-$0.15Sm_2O_3$-$0.7TiO_2$	1380		80.0	11000	3	0	1549
3698	$Pb_{0.4}Ca_{0\cdot6}(Fe_{1/2}Nb_{1/2})O_3$		Perovskite	80.0	6100	3.2	−25	996
3699	$Ba_{6-3x}(Sm_{1-y}Nd_y)_{8+2x}Ti_{18}O_{54}$ (x=2/3, y=0.1)	1340/6h	Tungsten-Bronze Orthorhombic	80.0	9620	3.75		1550
3700	$Ba_{6-3x}(Sm_{1-y}Nd_y)_{8+2x}(Ti_{1-z}Sn_z)O_{54}$ (x=2/3, y=0.8, z=0.05)	1360/12	Tungsten-Bronze Orthorhombic Pbam	80.0	10600	3.9	11	1526
3701	$Ba_{6-3x}(Sm_{1-y}Nd_y)_{8+2x}(Ti_{1-z}Sn_z)O_{54}$ (x=2/3, y=0.5, z=0.05)	1360/12	Tungsten-Bronze Orthorhombic	80.0	10050	4	5	1526
3702	BaO-Bi_2O_3-Nd_2O_3-TiO_2+0.4 wt% $Mn(CH_3COO)_2$+WO_3	1320		80.0	7000		0	1551
3703	$(Ba_{1-\alpha}Sr_\alpha)_{4.2}Sm_{9.2}Ti_{18}O_{54}$ (α=0.01)	1450/2h	Tungsten-Bronze Orthorhombic	80.0	8890		−11	1535
3704	$(Ba_{1-\alpha}Sr_\alpha)_{6-3x}$ $Sm_{8+2x}Ti_{18}O_{54}$ (α=0.06, x=0.6)		Tungsten-Bronze Orthorhombic	80.0	10075		−7	1535
3705	$Bi_3(Nb_{0.9}V_{0.1})O_7$	870	Tetragonal	80	600		−22	1528
3706	$(Pb_{1-x}Ca_x)ZrO_3$		Perovskite	80-120	2000-4000		–	1460
3707	$Sr(Bi_{1-x}Nd_x)_8Ti_7O_{27}$	1250		80-120	120-2100		–	1552
3708	$(Ba_{0.952}Sr_{.0.048})_{4.2}Sm_{9.2}Ti_{18}O_{54}$		Tungsten-Bronze Orthorhombic Pbam	80.1	10205	4.9	−9	1535
3709	$(Ba_{1-\alpha}Sr_\alpha)_{4.2}Sm_{9.2}Ti_{18}O_{54}$ (α=0.06)	1450/2h	Tungsten-Bronze Orthorhombic Pbam	80.2	10075		−7	1535

3710	$(Ba_{1-\alpha}Sr_{\alpha})_{4.2}Sm_{9.2}Ti_{18}O_{54}$ (α=0.0)	1450/2h	Tungsten-Bronze Orthorhombic Pbam	80.3	9500		−9	1535
3711	$Ca_{0.8}Sr_{0.2}TiO_3$-$Li_{0.5}Sm_{0.5}TiO_3$+x wt% [YB_2O_3-(1-y)CuO] (x=7.5, y=0.5)	900	Perovskite	80.4	3000		–	1513
3712	$(Ba_{1-\alpha}Sr_{\alpha})_{4.2}Sm_{9.2}Ti_{18}O_{54}$ (α=0.04)	1450/2h	Tungsten Bronze	80.6	9590		−12	1535
3713	$Ba_{4.2}Nd_{9.2}Ti_{18-x}Sn_xO_{54}$ (x=0.5)	1340/2h	Tungsten Bronze	80.6	9200		61	1553
3714	$Ba_{6-3x}Sm_{8+2x}Ti_{18}O_{54}$ (x=2/3)	1360/3h	Tungsten-Bronze Orthorhombic	80.8	11330	4	−11	1508, 1554, 1555
3715	$Ba_{6-3x}(Sm_{0.2}Nd_{0.8})_{8+2x}Ti_{18}O_{54}$ (x=2/3)	1330/3h	Tungsten Bronze	80.8	8100		36	1556
3716	BaO-Pr_6O_{11}-TiO_2		Tungsten Bronze	81.0	9000	5	130	1516
3717	$(Ba_{1-x}Ca_x)O$-Sm_2O_3-4.5TiO_2 (x=0.05)		Tungsten Bronze	81.0	9500		2	1557
3718	$Pb_{1-x}Ca_x[(Fe_{1/2}Nb_{1/2})_{1-y}Sn_y]O_3$ (x=0.6, y=0.05)	1150/3h	Perovskite	81.0	4830		3	1497
3719	Bi_2O_3-TiO_2 (1:11.3)+0.112 wt% CuO	915/2h		81.0	8900		0	1558
3720	$Ba_{6-3x}(Sm_{1-y}Nd_y)_{8+2x}Ti_{18}O_{54}$ (x=2/3, y=0.3)	1340/12h	Tungsten Bronze	81.0	9630	3.9		1550
3721	$[(Li_{0.5}Bi_{0.5})xBi_x][Mo_xV_{1-x}]O_4$ (x=0.098)	650	Monoclinic sheelite	81.0	8000		10	1559
3722	$Ba_{3.75}Nd_{9.5}Ti_{17}(Mg_{1/3}Nb_{2/3})O_{54}$	1350/2h	Tugsten Bronze	81.0	7300		17	1560
3723	$Ba_4(Nd_{0.7}Sm_{0.3})_{9.33}Ti_{18}O_{54}$+0.5 wt% Ag	1100	Tungsten Bronze	81.1	11000	4.6	3	1531
3724	$Ba_4Sm_{5.33}Eu_4Ti_{18}O_{54}$	1460	Tungsten Bronze Orthorhombic	81.1	7109		−20	1512
3725	$Ba_4Nd_{7.33}Eu_2Ti_{18}O_{54}$	1460	Tungsten Bronze Orthorhombic	81.1	10660		31	1512
3726	$Ba_4Sm_{3.33}Eu_6Ti_{18}O_{54}$	1400	Tungsten Bronze Orthorhombic	81.2	8604		−26	1512
3727	$Ba_{4.2}Sm_{9.2}Ti_{18}O_{54}$+4 wt% $SrTiO_3$	1360/2h	Tungsten Bronze Orthorhombic	81.2	8470		−2	1561
3728	$Ba_4(Nd_{0.7}Sm_{0.3})_{9.33}Ti_{18}O_{54}$+1 wt% Ag	1100	Tungsten Bronze Orthorhombic	81.2	11000	4.84	1	1531
3729	$Ba_4Sm_{9.33}Ti_{18}O_{54}$(SPS)	1200/ 5mn	Tungsten Bronze	81.2	10099	5	−17	1562
3730	$(Ba_{098}Sr_{.0.02})_{4.2}Sm_{9.2}Ti_{18}O_{54}$		Tungsten Bronze Orthorhombic	81.4	9661	4.8	−11	1535
3731	$Ba_4Sm_{9.33}Ti_{18}O_{54}$+14 mol% TiO_2	1350	Composite	81.5	10415	5	0	1508
3732	Ba_{6-3x} $Sm_{8+2x}Ti_{18}O_{54}$-0.1TiO_2-1.4TiO_2 (x=2/3)	1350/2h	Tungsten Bronze	81.5	10400		0	1508

(*continued*)

No.	Material	ST (°C)	Crystal structure	ε_r	Qf (GHz)	f_0	τ_f	Reference
3733	$Ba_{6-3x}(Sm_{1-y}Nd_y)_{8+2x}Ti_{18}O_{54}$ (x=2/3, y=0.84)	1400/10h	Tungsten Bronze orthorhombic	81.7	10500		2	1563
3734	$LiNb_{0.6}Ti_{0.5}O_3$ textured			81.8	5750		−43	1563b
3735	$(Li_{1/2}Nd_{1/2})TiO_3$		Pervskite Tetragonal	82.0	2220		292	1564
3736	$Ba_{6-x}Sm_{8+2x}Ti_{18}O_{54}$ (x=0.5)	1300	Tungsten bronze	82.0	10150		−17	1563
3737	$(Pb_{0.45}Ca_{0.55})[(Fe_{0.5}(Nb_{.96}Ta_{0.04})_{0.5})O_3$	1150/3h	Perovskite cubic Pm3m	82.0	7650		−5	1565
3738	$Ba_{6-3x}(Sm_{1-y}Nd_y)_{8+2x}Ti_{18}O_{54}$ (x=2/3, y=0.5)	1340/16h	Tungsten Bronze orthorhombic	82.0	9500	3.75		1550
3739	$(Ba_{0.8}Ca_{0.2})_{6-3x}Sm_{8+2x}Ti_{18}O_{54}$ (x=1.5)	1350	Tungsten Bronze orthorhombic	82.0	10000		−20	1566
3740	$Ba_{6-3x}(Sm_{1-y}Nd_y)_{8+2x}Ti_{1-z}Sn_z)_{18}O_{54}$ (x=2/3, y=0.8, z=0.05)	1360/3h	Tungsten Bronze orthorhombic	82.0	1000	4.1	17	1526
3741	$Ba_4Sm_{8.08}Li_{0.25}Ti_{18}O_{54}$	1400	Tungsten Bronze orthorhombic	82.1	5620	4.7	−2	1567
3742	$Ba\{Ti_{0.95}Fe_{0\cdot.05}\}O_{3-d}$	1450	Perovskite	82.1	4800	4		1446
3743	$Ba_{6-3x}(Sm_{0.2}Nd_{0.8})_{8+2x}Ti_{18}O_{54}$ (x=2/3)+1 wt% Bi_2O_3	1200/3h	Tungsten Bronze orthorhombic	82.1	8530		17	1556
3744	$Ba_4La_4Ti_7O_{24}$		Hexagonal	82.2	500		317	1473
3745	$Ba_{6-3x}[Nd_{(8+2x)-y}Bi_y)_]Ti_{18}O_{54}$ (x=2/3, y=0.05)	1380	Tungsten bronze	82.2	9760		62	1519
3746	$(Ba_{0.8}Sr_{0.2})_{4.2}Sm_{9.2}Ti_{18}O_{54}$		Tungsten Bronze orthorhombic	82.3	2860		0	1535
3747	$Ba_4(Sm_{.95}Bi_{.05})_{9+1/3}Ti_{18}O_{54}$	1420	Tungsten Bronze orthorhombic	82.3	8810		−17	1568
3748	$Ba_{6-3x}Sm_{8+2x}Ti_{18}O_{54}$ (x=0.6)	1450	Tungsten Bronze orthorhombic	82.5	10500	4.6	−12	1554
3749	$Ba_4Nd_{9.33}Ti_{18}O_{54}$	1460	Tungsten bronze	82.5	10060		71	1516
3750	$(Pb_{1-x}Ca_x)[Fe_{1/2}Nb_{1/2}]_{1-y}Zr_y]O_3$ (y=0.01, x=0.55)	1150	Perovskite	82.5	6800	3.8	−3	1488
3751	$Ba_4Nd_{8.33}EuTi_{18}O_{54}$	1480	Tungsten Bronze orthorhombic	82.6	10400	4.8	47	1542
3752	$Ba_{6-3x}(Sm_{1-y}Nd_y)_{8+2x}Ti_{18}O_{54}$ (x=2/3, y=0.72)	1400/10h	Tungsten Bronze orthorhombic	82.7	10500		4	1563
3753	$Ba_{4.2}Sm_{9.2}Ti_{18}O_{54}$	1500	Tungsten Bronze orthorhombic	83.0	8950	3.5	−13	1569
3754	$BaO\text{-}Nd_2O_3\text{-}5TiO_2$	1450/2h	Tungsten bronze	83.0	10500		70	1516
3755	$Ba_{4.2}(Sm_{0\cdot.9}Nd_{0\cdot.1})_{9.2}Ti_{18}O_{54}$	1500	Tungsten Bronze orthorhombic	83.0	8936	3.5	−6	1569
3756	$CaBa_4Nb_2TiO_{12}$	1470	Cubic perovskite	83.0	1200	2.9	60	1307

3757	$(Pb_{0.45}Ca_{0.55})[(Fe_{0.5}Nb_{0.5})_{0.9}Sn_{0.1}]O_3$+ 0.2 wt% CuO+0.1 wt% Bi_2O_3	1000/3h	Tungsten Bronze	83.0	6080		8	1570
3758	$(Ni_{1/3}Nb_{2/3})_{1-x}Ti_xO_2$ (x=0.5)	1200	Rutile Tetragonal $P4_2/mmm$	83.1	19300		165	1276
3759	$Ba_{6-3x}(Sm_{1-y}Nd_y)_{8+2x}Ti_{18}O_{54}$ (x=2/3, y=0.6)	1400/10h	Tungsten Bronze Orthorhombic	83.4	10700	4	11	1550
3760	$Ba\{Ti_{0.92}Ga_{0.008}\}O_{3-\delta}$	1450	Perovskite Hexagonal	83.7	4200	4.2		1446
3761	$Ba_{6-3x}(La_{1-y-z}Sm_yBi_z)_{8+2x}Ti_{18}O_{54}$ (x=2/3, y=0.7, z=0)	1350/3h	Tungsten Bronze	83.8	8000	4.0	33	1571
3762	$(Pb_{1/2}Ca_{1/2})(Fe_{1/2}Ta_{1/2})O_3$	1250/ 30 min	Perovskite Cubic	83.9	6680	7		1572
3763	$Ba_4(Nd_{.95}Bi_{.05})_{9.33}Ti_{18}O_{54}$	1360	Tungsten Bronze Orthorhombic	83.9	8330		32	1568
3764	$Ba_{4.2}(Sm_{0.9}La_{0.1})_{9.2}Ti_{18}O_{54}$	1500	Tungsten Bronze Orthorhombic	84.0	9050	3.5	2	1569
3765	Ba_{6-3x} $(Sm_{1-y}Nd_y)_{8+2x}Ti_{18}O_{54}$ (x=0.6, y=0.2)	1500/2h	Tungsten Bronze	84.0	9000		0	1569
3766	$BaO.(Nd_{0.8}Bi_{0.2})_2O_3.4TiO_2$+$Bi_2O_3$-$B_2O_3$-ZnO-$SiO_2$			84.0	3000		24	1573
3767	$Ba_{6-3x}Sm_{8+2x}Ti_{18}O_{54}$ (x=0.7) hotpressed	1200	Tungsten Bronze Orthorhombic	84.0	9960		−14	1574
3768	$0.95TiO_2$-$0.05Bi_2Ti_4O_{11}$	1200		84.0	12500		230	1372
3769	$BaPr_2Ti_5O_{14}$		Tungsten Bronze Orthorhombic	84.0	9000	5	150	1575
3770	$(Ba_{0.9}Ca_{0.1})$-Sm_2O_3-$4.5TiO_2$		Tungsten bronze	84.0	9500	10	25	1557
3771	$Ba_4(Sm_{0.9}Bi_{0.1})_{9+1/3}Ti_{18}O_{54}$	1380	Tungsten Bronze Orthorhombic	84.1	7840		−21	1568
3772	$0.4PbZrO_3$-$0.6Ca(Fe_{1/2}Nb_{1/2})O_3$		Perovskite	84.7	3000	4.2	41	1576
3773	$Ba_{4.2}(Sm_{0.7}Nd_{0.3})_{9.2}Ti_{18}O_{54}$	1500	Tungsten Bronze Orthorhombic	85.0	9160	3.5	9	1569
3774	$Ba_{6-3x}(Sm_{1-y}Nd_y)_{8+2x}Ti_{18}O_{54}$ (x=2/3, y=0.8)	1340/12h	Tungsten Bronze Orthorhombic	85.0	9460	3.9	1	1550
3775	$0.77Bi_2O_3$-$0.23Nb_2O_5$	900/3h	Flourite δ-Bi_2O_3 Fm-3m	85.0	350		−215	1396
3776	$Pb_{1-x}Ca_x[(Fe_{1/2}Nb_{1/2})_{1-y}Sn_y]O_3$ (x=0.55, y=0.1)	1150/3h	Perovskite	85.0	8600		0	1497
3777	$(Pb_{1-x}Ca_x)[(Fe_{1/2}Nb_{1/2})_{1-y}Zr_y]O_3$ (y=0.1, x=0.55)	1200	Perovskite	85.0	8600		−1	1488
3778	$Bi_3Nb_{0.8}Ta_{0.2}O_7$	855/4h		85.0	800		24	1577
3779	$Pb_{0.45}Ca_{.0.55}[(Fe_{1/2}Nb_{1/2})_{0.9}Sn_{0.1}O_3$	1150/3h	Perovskite Orthorhombic	85.3	8600		0	1497

(*continued*)

No.	Material	ST (°C)	Crystal structure	ε_r	Qf (GHz)	f_0	τ_f	Reference
3780	$Ba_4Sm_{8.33}LiTi_{18}O_{54}$	1400	Tungsten Bronze orthorhombic	85.4	5045	4.5	45	1567
3781	$Ba_{4.2}(Sm_{0.5}Nd_{0.5})_{9.2}Ti_{18}O_{54}$	1500	Tungsten Bronze	86.0	9170	3.4	25	215
3782	$Pb_{0.5}Ca_{0\cdot5}(Mg_{1/3}Nb_{2/3})O_3$		Perovskite	86.0	4600	3.0	34	996
3783	$(Pb_{0.45}Ca_{0.55})[(Fe_{0.5}Nb0_{\cdot0.5})_{0.9}Sn_{0.1}]O_3$+ 0.2 wt% CuO+0.4 wt% Bi_2O_3	1000/3h	Perovskite Orthorhombic	86.0	4340		8	1578
3784	$0.74Bi_2O_3$-$0.26Nb_2O_5$	900/2h	Flourite δ-Bi_2O_3 Fm-3m	86.0	1000		120	1396
3785	$BaTi_{0.5}Ga_{0.25}Nb_{0.25}O_3$	1500/4h	Perovskite Tetragonal P4mm	86.0	3050	4		1373
3786	$Ba_{1.37}Na_{063}Nd_2TiO_{10}$	1250	Orthorhombic Amam	86.0	1500		270	1579
3787	$Ba_{6\text{-}3x}$ $Nd_{8+2x}Ti_{18}O_{54}$ (x=0.75)		Tungsten Bronze Orthorhombic	86.0	10450		–	1536
3788	$Ba_{6\text{-}3x}(Sm_{1\text{-}y}Nd_y)_{8+2x}Ti_{18}O_{54}$ (x=0.5, y=0.67)	1400/10h	Tungsten Bronze Orthorhombic	86.0	7850		234	1563
3789	$BaNd_2TiO_{12}$+0.075 wt% $Bi_4B_2O_9$	1200	Orthorhombic	86.0	5400		4	287
3790	BaO-Nd_2O_3-$4TiO_2$+10 wt% $Bi_4B_2O_9$		Tungsten Bronze	86.0	4700		1	1580
3791	$0.15(Ba_{0.93}Sr_{0.07})O$-$0.15(Sm_{0.4}La0.6)_2O_3$-$0.7TiO_2$]	1370		86.2	16700		95	1581
3792	$Pb_{0.45}Ca_{0.55}[(Fe_{1/2}Nb_{1/2})_{0.95}Sn_{0.05}O_3$	1150/3h	Perovskite Orthorhombic	86.3	6250		2	1497
3793	$(Pb_{1\text{-}x}Ca_x)[Fe_{1/2}Nb_{1/2}]_{1\text{-}y}Zr_y]O_3$ (y=0.01, x=0.5)	1150	Perovskite Orthorhombic	86.3	6800	3.7	25	1488
3794	$Pb_{0.45}Ca_{0.55}[(Fe_{1/2}Nb_{1/2})_{0.9}Sn_{0.1}$ O_3	1150/3h	Perovskite Orthorhombic	86.7	7900		0	1497
3795	$Ba_{6\text{-}3x\text{-}z}Sr_zNd_{8+2x\text{-}y}$ $Bi_yTi_{18}O_{54}$ (y=0, z=0.9, x=0.5)		Tungsten Bronze	86.7	7200		63	1582
3796	$Ba_{6\text{-}3x}(La_{1\text{-}y\text{-}z}Sm_yBi_z)_{8+2x}Ti_{18}O_{54}$ (x=2/3, y=0.5, z=0)	1350/3h	Tungsten Bronze Orthorhombic	86.9	7360	3.8	83	1571
3797	$0.9CaTiO_3$-$0.1Sm(Mg_{0.5}Ti_{0.5})O_3$	1550	Perovskite	87.0	9500	3.2	285	865
3798	$(Pb_{1\text{-}x}Ca_x)[(Fe_{1/2}Nb_{1/2})_{1\text{-}y}Zr_y]O_3$ (y=0.05, x=0.55)	1200	Perovskite Orthorhombic	87.0	8500		−10	1488
3799	$Sr(Bi_{1\text{-}x}Nd_x)_8Ti_7O_7$ (x=0.05)			87.0	190			1583
3800	$(Ba_{1\text{-}z}Pb_z)_{6\text{-}x}Nd_{8+2/3x}Ti_{18}O_{54}$ (x=2/3, z=0.4)	1400/2h	Tungsten Bronze Orthorhombic	87.0	4000		−32	1584
3801	$Ca_{(1\text{-}x)}Nd_{2x/3}TiO_3$ (x=0.39)		Perovskite	87.5	12400		242	1545
3802	$Pb_{0.46}Ca_{0.54}[(Fe_{1/2}Nb_{1/2})_{0.9}Sn_{0.1}$ O_3	1150/3h	Perovskite Orthorhombic	87.8	7870		5	1497

3803	$Ba_{4.2}(Sm_{0.1}Nd_{0.9})_{9.2}Ti_{18}O_{54}$	1500	Tungsten Bronze Orthorhombic	88.0	9500	3.44	64	1569
3804	$Ba_{6-x}Nd_{8+2x}Ti_{18}O_{54}$ (x=0.7) hot pressed	1300	Tungsten Bronze	88.0	4920		55	1574
3805	$Ba_{4.2}(Sm_{0.7}La_{0.3})_{9.2}Ti_{18}O_{54}$	1500	Tungsten Bronze Orthorhombic	88.0	8050	3.44	44	1569
3806	$Ba_{6-3x}(Sm_{1-y}Nd_y)_{8+2x}Ti_{18}O_{54}$ (x=0.6, y=0.9)	1500/2h	Tungsten Bronze Orthorhombic	88.0	8500		64	1569
3807	$Ba_{6-3x}(Sm_{1-y}Nd_y)_{8+2x}Ti_{18}O_{54}$ (x=0.6, y=1.0)	1500/2h	Tungsten Bronze Orthorhombic	88.0	8300		76	1569
3808	$BaO\text{-}Bi_2O_3\text{-}TiO_2\text{-}Nd_2O_3$		Tungsten Bronze	88.0	5500		8	1534
3809	$(Ba_{1-3z}Pb_z)_{6-x}Nd_{8+2/3x}Ti_{18}O_{54}$ (x=2/3, z=0.22)	1400/2h	Tungsten Bronze Orthorhombic	88.0	5500		0	1584
3810	$BaO\text{-}Nd_2O_3\text{-}4TiO_2$+0.5 wt% Al_2O_3+8 wt% Bi_2O_3		Tungsten Bronze	88.0	8000	–	0	1111
3811	$(1\text{-}x)(Mg_{0.95}Zn_{0.05})TiO_3\text{-}xCa_{0.6}La_{0.8/3}TiO_3$ (x=0.9)	1320/4h	Composite	88.0	32800		205	465
3812	$Ba_{4.2}Nd_{9.2}Ti_{18}O_{54}$	1500	Tungsten Bronze	88.0	8315	3.4	76	1566
3813	$Li_{0.2}Nd_{0.6}TiO_3$	1450		88.0	2400		−210	1585
3814	$Pb_{0.46}Ca_{0.54}[(Fe_{1/2}Nb_{1/2})_{0.95}Sn_{0.05}\ O_3$	1150/3h	Perovskite Orthorhombic	88.2	6100		7	1497
3815	$Ba_{6-3x}(La_{1-y-z}Sm_yBi_z)_{8+2x}Ti_{18}O_{54}$ (x=2/3, y=0.7, z=0.04)	1350/3h	Tungsten Bronze	88.4	6690	4.4	1	1571
3816	$0.05Pb(Fe_{2/3}W_{1/3})O_3\text{-}0.95Pb_{0.4}Ca_{0.6}(Fe_{1/2}Nb_{1/2})O_3$	1000	Perovskite	88.4	3800		−6	1480
3817	$Ba_4(Sm_{0.85}Bi_{0.15})_{9+1/3}Ti_{18}O_{54}$	1360	Tungsten Bronze Orthorhombic	88.9	6620		−20	1568
3818	$Ba(Nd_{0.82-z}Sm_zBi_{0.18})Ti_4O_{12}$ (z=0.7)	1300/2h	Tungsten Bronze	89.0	6880	4.5		1586
3819	$(Pb_{0.45}Ca_{0.55})[(Fe_{0.5}Nb_{0.5})_{0.9}Sn_{0.1}]O_3$+ 5 wt% BiO_3-LiF	950	Perovskite Orthorhombic	89.0	800		−15	1587
3820	$0.2CaTiO_3\text{-}0.5(Li_{1/2}Nd_{1/2})TiO_3\text{-}0.3(Dy_{1/3}Nd_{1/3})TiO_3$	1350/3h	Tetragonal P-4b2 Perovskite	89.4	4650		−87	1498
3821	$(Ni_{1/3}Nb_{2/3})_{1-x}Ti_xO_2$ (x=0.6)	1200	Rutile Tetragonal $P4_2/mmm$	89.4	12800		193	1276
3822	$Ba_{6-3x}(Nd_{1-y}Bi_y)_{8+2x}Ti_{18}O_{54}$ (x=2/3, y=0.04)	1340/3h	Tungsten Bronze Orthorhombic	89.6	7700	4.0	21	1588
3823	$Ba_{6-3x}Nd_{8+2x}Ti_{18}O_{54}\text{+}PbO/Bi_2O_3$		Tungsten Bronze	90.0	9000	–	0	1569
3824	$BaO\text{-}(Nd_{0.95}Bi_{0.05})_2O_3\text{-}4TiO_2$	1300	Tungsten Bronze type	90.0	7600		33	168

(*continued*)

No.	Material	ST (°C)	Crystal structure	ε_r	Qf (GHz)	f_0	τ_f	Reference
3825	$0.96La_{2/3}TiO_3$-$0.04CaTiO_3$		Perovskite Orthorhombic	90.0	27000	10	190	1589
3826	MBRT-90	1300/2h	Composite	90.0	6100		6	510
3827	$0.75Bi_2O_3$-$0.25Nb_2O_5$	900/3h	Flurite δ-Bi_2O_3 Fm-3m	90.0	630		60	1396
3828	$0.5Sm_{1/2}Li_{1/2}TiO_3$-$0.5Sm_{1/2}Na_{1/2}TiO_3$	1300	Tetragonal	90.0	1500		−140	1521
3829	$BaNd_2Ti_5O_{14}$+25 wt% Nd_2O_3+0.5 mol% PbO	1250/2h	Tungsten Bronze Orthorhombic	90.0	6000		−20	1590
3830	$Ca_{0.61}Nd_{0.26}TiO_3$ (Sol-gel)	1200	Orthorhomic perovskite Pmna	90.2	25200		243	1591
3831	$0.1La(Mg_{1/2}Ti_{1/2})O_3$-$0.9CaTiO_3$	1500	Perovskite Pbnm	90.4	31900	5.8	–	932
3832	$(Pb_{1-x}Ca_x)[Fe_{1/2}Nb_{1/2}]_{1-y}Zr_y]O_3$ (y=0.01,x=0.45)	1150	Perovskite	90.6	2500	3.6	41	1488
3833	$BaSm_{1.8}La_{.2}Ti_5O_{14}$		Orthorhombic Pbam	90.7	8900	–	4	1592
3834	$Ba_{6-3x}(Nd_{(8+2x)-y}Bi_y)Ti_{18}O_{54}$ (x=2/3, y=0.1)	1360	Tungsten Bronze Orthorhombic	90.7	7020		24	1568
3835	$(Pb_{0.5}Ca_{0.5})_{0.92}La_{0.08}(Fe_{0.5}Nb_{0.}5)O_3$	1190/ 2.5h	Perovskite	90.8	5800		15	1593
3836	$(Ca_{0.61}Nd_{0.26})(Ti_{0.98}Sn_{0.2})O_3$-$0.6(Li_{0.5}Nd_{0.5})TiO_3$+5 wt% H_3BO_3-CuO+0.5 wt% Li_2CO_3	900	Composite	90.8	3400		9	1594
3837	$Ba_{6-x}Sm_{8+2x}Ti_{18}O_{54}$ (x=0.5) hot pressed	1300	Tungsten Bronze Orthorhombic	91.0	10870		3	1574
3838	Bi_3NbO_7		Cubic flurite type Fm-3m	91.0	730		100	1595
3839	$(Pb_{0.5}Ca_{0.5})_{0.92}La_{0.08}(Fe_{0.5}Nb_{0.}5)O_3$+1 wt% Bi_2O_3-MnO_2	1050/4h	Perovskite+Pyrochlore	91.1	4870		19	1593
3840	$Ba_4Sm_{6.33}Li_3Ti_{18}O_{54}$	1400	Tungsten Bronze Orthorhombic	91.3	3990	4.4	111	1567
3841	$0.3Pb(Fe_{2/3}W_{1/3})O_3$-$0.7Pb_{0.2}Ca_{0.8}(Fe_{1/2}Nb_{1/2})O_3$	1000	Perovskite	91.3	1650		7	1480
3842	$(Li_{1/2}Pr_{1/2})TiO_3$		Perovskite	92.0	1010		403	1564
3843	$Ba_{4.5}Nd_9Ti_{18}O_{54}$+15mol% $Ba_{4.5}Gd_9Ti_{18}O_{54}$	1350/10h	Tungsten Bronze	92.0	5000		0	1596
3844	$0.75Bi_2O_3$-$0.25Nb_2O_5$	850/3h	Flourite δ-Bi_2O_3 Fm-3m	92.0	720		96	1396
3845	$(Ca_{0.3}Li_{0.14}Sm_{0.42})TiO_3$	1350	Perovskite Orthorhombic	92.1	8292		2.6	719

3846	$Ba_{6-3x}(Nd_{1-y}Bi_y)_{8+2x}Ti_{18}O_{54}$ (x=2/3, y=0.08)		Tungsten Bronze Orthorhombic	92.3	6460	4	10	1588
3847	$Ba_4Sm_{3.33}Li_6Ti_{18}O_{54}$	1350	Tungsten Bronze Orthorhombic	92.4	3580	4.4	303	1567
3848	$Ba_4(Sm_{0.8}Bi_{0.2})_{9+1/3}Ti_{18}O_{54}$	1360	Tungsten Bronze Orthorhombic	92.4	5680		−12	1568
3849	$Ca_{2/5}Sm_{2/5}TiO_3$-$Li_{1/2}Sm_{1/2}TiO_3$-0.8TiO_2	1300/2h		92.5	4900	4	9	1597
3850	$(Pb_{0.45}Ca_{0.55})(Fe_{0.5}Nb_{0.5})O_3$	1100/3h	Perovskite	92.6	5970			996
3851	$Ba_4Sm_{7.33}Li_2Ti_{18}O_{54}$	1400	Tungsten Bronze Orthorhombic	92.7	3720	4.4	89	1567
3852	$CaCu_{2.85}Mn_{0.15}Ti_4O_{12}$	1100	Cubic Im3m	93.0	3950	3.95	657	1598
3853	$Pb_{0.5}Ca_{0.5}$ $(Li_{1/4}Nb_{3/4})O_3$		Perovskite	93.0	2000	3.2	630	996
3854	$Ba_{4.2}(Sm_{0.5}La_{0.5})_{9.2}Ti_{18}O_{54}$	1500	Tungsten Bronze Orthorhombic	93.0	1300	3.3	118	1569
3855	$Ca_{1-x}Nd_{2x/3}TiO_3$ (x=0.42)	1400	Perovskite Orthorhombic	93.0	6940	7	228	1599
3856	0.95TiO_2-0.05$Bi_2Ti_4O_{11}$		Composite	93.0	12500		230	1372
3857	BaO-$(Nd_{1-x}Bi_x)_2O_3$-4TiO_2 (x=0.1)	1300	Tungsten Bronze	93.0	5900		15	168
3858	$Ba_{6-3x-z}Sr_zNd_{8+2x-y}$ $Bi_yTi_{18}O_{54}$ (y=0.5, x=0.5)		Tungsten Bronze Orthorhombic	93.4	5700		40	1582
3859	$(Pb_{0.48}Ca_{0.52})Fe_{1/2}Nb_{1/2})_{0.9}Sn_{0.1}O_3$	1150/3h	Perovskite Orthorhombic	93.6	7100		18	1600
3860	$Ba_4(Nd_{0.85}Bi_{0.15})_{9.33}Ti_{18}O_{54}$	1380	Tungsten Bronze Orthorhombic	93.7	6350		17	1568, 1601
3861	$(Pb_{0.48}Ca_{0.52})(Fe_{1/2}Nb_{1/2})O_3$+2.2 mol% CeO_2	119/2.5h	Perovskite	93.7	6770		2	1600
3862	$Ba_{6-3x}[Nd_{(8+2x)-y}Bi_y)]Ti_{18}O_{54}$ (x=2/3, y=0.15)	1360	Tungsten Bronze Orthorhombic	93.7	6350		17	1568
3863	$Ba_{6-3x}(La_{1-y-z}Sm_yBi_{0.04})_{8+2x}Ti_{18}O_{54}$ (x=2/3,y=0.5,	1340/3h	Tungsten Bronze Orthorhombic	93.9	4337	4	29	1571
3864	$Pb_{0.6}Ca_{0.4}ZrO_3$	1450	Perovskite	94.0	3600	3	−10	1514, 1602
3865	$Pb_{0.6}Ca_{0\cdot4}(Ni_{1/3}Nb_{2/3})O_3$		Perovskite	94.0	3800	3.2	130	996
3866	3SrO-Ta_2O_5-3TiO_2	1400/5h	Composite	94.0	5200			53
3867	$(Pb_{0.6}Ni_{0.4})(Mg_{1/3}Nb_{2/3})O_3$		Perovskite	94.0	3800		130	996
3868	CaO-Sm_2O_3-Li_2O-TiO_2+1 wt% Li_2O-Bi_2O_3-TiO_2	1400		94.0	6000		7	1603
3869	$Pb_{0.48}Ca_{0.52}[(Fe_{1/2}Nb_{1/2})_{0.95}Sn_{0.05}O_3$	1150/3h	Perovskite Orthorhombic	94.3	5950		24	1497

(*continued*)

No.	Material	ST (°C)	Crystal structure	ε_r	Qf (GHz)	f_0	τ_f	Reference
3870	$Ca_{1-x}Sm_{2x/3}TiO_3$ (x=0.6)	1450	Perovskite, Orthorhombic	94.5	14900	5		1604
3871	CaO-BaO-Li_2O-Sm_2O_3-TiO_2 (14:4:9:12:63)	1325		94.5	7400		3	1605
3872	$Ba_{6-3x}Nd_{8+2x}Ti_{18}O_{54}$ x=0.5+10 wt% $Bi_4Ti_3O_{12}$	1300/3h	Tungsten Bronze	94.9	5620		21	1606
3873	$Ba_{6-3x}Pr_{8+2x}Ti_{18}O_{54}$		Tungsten Bronze Orthorhombic	95.0	6000	–	200	1607, 1608
3874	$Ba_4Sm_{5.33}Li_4Ti_{18}O_{54}$	1350	Tungsten Bronze Orthorhombic	95.0	1000	4.4	142	1567
3875	$Ba_{6-3x}(La_{1-y-z}Sm_yBi_z)_{8+2x}Ti_{18}O_{54}$ (x=2/3, y=0.5, z=.08)	1320/3h	Tungsten Bronze Orthorhombic	95.0	3510	3.8	3	1571
3876	$0.3(Sm_{1/2}Li_{1/2})TiO_3$-$0.7(Sm_{1/2}Na_{1/2}Ti)O_3$	1350	Tetragonal	95.0	1000	10		1521
3877	$0.98TiO_2$-$0.02Bi_2Ti_4O_{11}$	1200	Composite	95.0	18000		351	1372
3878	$(Ba_{0.6}Pb_{0.4})_{6-3x}La_{8+2x}Ti_{18}O_{54}$ (x=1.5)	1380	Tungsten Bronze Orthorhombic	95.0	6000		200	1566
3879	$0.3Sm_{1/2}Li_{1/2}TiO_3$-$0.7Sm_{1/2}Na_{1/2}TiO_3$	1300	Perovskite	95.0	1000		−240	1521
3880	Pb,Ca(Fe, W, Nb)O_3	1000	Perovskite	95.7	3840		10	1480
3881	$0.67Ca_{2/5}sm_{2/5}TiO_3$-$0.33Li_{1/2}Sm_{1/2}TiO_3$	1300/3h	Perovskite	95.5	7200		0	1548
3882	$Ba_{6-3x}(Nd_{1-y}Bi_y)_{8+2x}Ti_{18}O_{54}$ (x=2/3, y=0.12)		Tungsten Bronze Orthorhombic	95.8	5820	4	8	1588
3883	$Ba_{6-x}Sm_{8+2x}Ti_{18}O_{54}$ (x=0.3) hot pressed	1300	Tungsten bronze	96.0	1440		−14	1574
3884	CaO-BaO-Li_2O-Sm_2O_3-TiO_2 (14:4:8:12:63)	1325		96.0	7580		−6	1609
3885	$0.92Ba_{4.5}(Nd_{1-y}Bi_y)_9Ti_{18}O_{54}$-$0.08BaTi_4O_9$ (y=0.12)		Tungsten Bronze Orthorhombic	96.0	5590		27	1610
3886	$0.4Ca_{0.6}Sm_{0.8/3}TiO_3$-$0.6(Li_{0.5}Nd_{0.5})TiO_3$+3 wt% $BaCu(B_2O_5)$	1100	Perovskite Orthorhombic	96.3	3100		−20	1611
3887	CaO-SrO-Li_2O-$0.83Sm_2O_3$-$0.17Yb_2O_3$ TiO_2		Perovskite Orthorhombic	96.4	2690	–	36	1612
3888	$Ba_{6-3x-z}Sr_zNd_{8+2x-y}$ $Bi_yTi_{18}O_{54}$ (y=1, x=0.5)		Tungsten Bronze Orthorhombic	97.0	5500		22	1582
3889	$Sr(Bi_{1-x}Nd_x)_8Ti_7O_{27}$ (x=0.1)			97.0	740			1583

3890	$0.3CaTiO_3$-$0.4(Li_{1/2}Nd_{1/2})TiO_3$-$0.3(Dy_{1/3}Nd_{1/3})TiO_3$	1350/3h	Orthorhombic Pbnm Perovskite	97.6	5150		0	1498
3891	$0.98TiO_2$-$0.019Bi_2O_3$		Mixture phases	97.8	3700		354	1434
3892	TiO_2+2 wt% CuO	900/2h	Tetragonal rutile	98.0	14000		374	1613
3893	$0.92Ba_{4.5}(Nd_{1-y}Bi_y)_9Ti_{18}O_{54}$-$0.08BaTi_4O_9$ (y=0.145)		Tungsten Bronze Orthorhombic	98.0	5500		17	1610
3894	$Ca_{1-x}Nd_{2x/3}TiO_3$ (x=0.39)	1400	Perovskite Orthorhombic	98.0	8560	7	247	1599
3895	(1-x)$Ca_{2/5}Sm_{2/5}TiO_3$-x$Li_{1/2}Nd_{1/2}TiO_3$ (x=0.3)	1300/3h	Perovskite Orthorhombic	98.0	5100	5		1614
3896	$0.75Bi_2O_3$-$0.25Nb_2O_5$	930/3h	Flourite δ-Bi_2O_3 Fm-3m	98.0	300		−154	1396
3897	$(Nd_{1/2}Na_{1/2})TiO_3$		Perovskite Orthorhombic	98.0	2700		190	1615
3898	$Ca(Zr_xTi_{1-x})O_3$ (x=0.4)	1430/15h		98.0	5400	2.49	792	916
3899	$Bi_2(Zn_{1-x}Mg_x)_{2/3}Nb_{4/3}O_7$ (x=0.5)	900	Monoclinic+cubic	98.0	3000			1616
3900	$(Ca_{0.275s}Sm_{0.4}Li_{0.25})TiO_3$+0.5 wt% B_2O_3-Li_2O	1200/3h	Perovskite Orthorhombic	98.7	5930		−4	1617
3901	CaO-BaO-Li_2O-Sm_2O_3-TiO_2 (14:2:9:12:63)	1325		98.7	6180		8	1605
3902	$Ba_4Sm_{(28-y)/3}Li_yTi_{18}O_{54}$ (y=8)	1300	Tungsten Bronze Orthorhombic	98.8	280		515	1566
3903	$Ba_{6-3x}(La_{1-y-z}Sm_yBi_z)_{8+2x}Ti_{18}O_{54}$ (x=2/3, y=0.7, z=0.08)	1325/3h	Tungsten Bronze Orthorhombic	99.0	4920	4.38	−18	1571
3904	$0.7Ca_{2/5}Sm_{2/5}TiO_3$-$0.3Li_{1/2}Nd_{1/2}TiO_3$	1200/3h	Perovskite	99.0	6200		9	1614, 1618
3905	$Ba_{6-x}Nd_{8+2x}Ti_{18}O_{54}$ (x=0.3) hot pressed	1300	Tungsten Bronze	99.0	3680		110	1574
3906	$(Ca_{1-x}Nd_{2x/3})TiO_3$ (x=0.6)	1300	Perovskite	99.0	3500	3.2		1619
3907	$Sr_2Ce_2Ti_5O_{16}(Sr_{1-3x/2}Ce_xTiO_3$ x=0.4)+0.4 wt% MoO_3	1300/2h	Psuedocubic	99.0	9700		306	1620
3908	TiO_2 (microwave sint)	1210	Teragonal	99.0	30800	4.42		1621
3909	$Ba_{6-3x}(Nd_{1-y}Bi_y)_{8+2x}Ti_{18}O_{54}$ (x=2/3, y=0.15)		Tungsten Bronze Orthorhombic	99.1	5290		−6	1588
3910	CaO-SrO-Li_2O-0.83Sm_2O_3-0.17Dy_2O_3-TiO_2		Perovskite Orthorhombic	99.5	5930	–	30	1612

(*continued*)

No.	Material	ST (°C)	Crystal structure	ε_r	Qf (GHz)	f_0	τ_f	Reference
3911	$Pb_{0.5}Ca_{0.5}[(Fe_{1/2}Nb_{1/2})_{0.9}Sn_{0.1}O_3$	1150/3h	Perovskite, Orthorhombic	99.6	6570		32	1497
3912	$Sr_5Ti_4O_{13}(Sr_{n+1}Ti_nO_{3n+1})$		Perovskite	99.8	4000	1.9	801	1358
3913	$(Pb_{1/2}Ca_{1/2})_{0.94}(La_{1/2}Nd_{1/2})_{0.06}$ $[Fe_{1/2}Nb_{1/2}]O_{3+d}$	1200/3h	Perovskite Orthorhombic	99.9	5800	5.5	0	1622
3914	$(Ca_{1-x}Nd_{2x/3})TiO_3$ (x=0.5)	1300		100.0	14600	3.2		1619
3915	$Ba(Nd_{0.82-z}Sm_zBi_{0.18})Ti_4O_{12}$ (z=0.1)	1300/2h	Orthorhombic Tungsten Bronze	100.0	3950	4.7		1586
3916	$[(Pb_{0.5}Ca_{0.5})_{0.95}Nd_{0.05}](Fe_{1/2}Nb_{1/2})O_3$		Perovskite	100.0	5800		0	1623
3917	$CaO\text{-}SrO\text{-}Li_2O\text{-}(1\text{-}x)Sm_2O_3\text{-}xDy_2O_3\text{-}TiO_2$ (x=0.17)			100.0	5900		30	1498
3918	$0.45CaTiO_3\text{-}0.35(Li_{1/2}Nd_{1/2})TiO_3\text{-}0.2(Dy_{1/3}Nd_{1/3})TiO_3$	1350/3h	Orthorhombic Pbnm Perovskite	100.1	6430		118	1498
3919	$16CaO\text{-}9Li_2O\text{-}12Sm_2O_3\text{-}63TiO_2$+0.75 wt% V_2O_5	1200/3h	Composite	100.4	5600		7	1624
3920	$0.05Pb(Fe_{2/3}W_{1/3})O_3\text{-}0.95Pb_{0.45}Ca_{0.55}(Fe_{1/2}Nb_{1/2})O_3$	1000	Perovskite	100.8	3250		20	1480
3921	$(Pb,Ca)ZrO_3$		Perovskite	>100	1000	–	–	1602
3922	$Ba_{6-3x-z}Pb_zNd_{8+2x-y}$ $Bi_yTi_{18}O_{54}$ (y=1, z=1.0, x=0.5)		Tungsten Bronze Orthorhombic	101.0	4000		–4	1582
3923	$Bi_{1.733}(Zn_{0.733}Nb_{4/3})O_{6.67}$	1000	Cubic	101.0	4800	4.8		1625
3924	$(Pb_{0.5}Ca_{0.5})_{0.95}La_{0.05}(Fe_{0.5}Nb_{0.5})O_3$+1 wt% $PbO\text{-}B_2O_3\text{-}V_2O_5$	1050/3h	Perovskite Orthorhombic	101.0	5400		6	1626
3925	$0.55Ca_{0.61}Nd_{0.91}TiO_3\text{-}0.45Li_{1/2}Nd_{1/2}TiO_3$	1400/4h	Perovskite Orthorhombic	101.0	5300	7.2	13	1599
3926	$Ca_{1-x}Sm_{2x/3}TiO_3$ (x=0.4)	1450	Perovskite Orthorhombic	101.0	14090	5		1604
3927	$Ca_{(1-x)}Nd_{2x/3}TiO_3$ (x=0.21)			101.0	8000		–	1545
3928	$CaO\text{-}Sm_2O_3\text{-}Li_2O\text{-}TiO_2$+5 wt% $Li_2O\text{-}Bi_2O_3\text{-}TiO_2$	1250		101.9	5000		0	1603
3929	$Pb_{0.5}Ca_{0.5}[(Fe_{1/2}Nb_{1/2})_{0.95}Sn_{0.05}O_3$	1150/3h	Perovskite Orthorhombic	102.0	4900		38	1497
3930	$Ba_{6-x}La_{8+2x}Ti_{18}O_{54}$ (x=0.7) hot pressed	1300	Tungsten Bronze	102.0	2380		399	1574
3931	$Ba(Nd_{0.82-z}Sm_zBi_{0.18})Ti_4O_{12}$ (z=0.03)	1300/2h		102.0	3650	4.74		1586

3932	TiO_2+0.05 mol% Al_2O_3	1500/10h	Tetragonal rutile $P4_2/mmm$	102.0	47100			1628
3933	TiO_2+0.05 mol% Fe_2O_3	1500/10h	Tetragonal rutile $P4_2/mmm$	102.0	50100			1628
3934	TiO_2+0.05 mol% MnO	1500/10h	Tetragonal rutile $P4_2/mmm$	102.0	48000			1628
3935	TiO_2+0.05 mol% CuO	1500/10h	Tetragonal rutile $P4_2/mmm$	102.0	48000			1628
3936	TiO_2+0.05 mol% ZnO	1500/10h	Tetragonal rutile $P4_2/mmm$	102.0	48900			1628
3937	$0.1La(Mg_{1/2}Ti_{1/2})O_3$-$0.9CaTiO_3$	1350	Perovskite	102.5	20200	4.3	395	932
3938	$Ba_{6-3x}(Nd_{1-y}Bi_y)_{8+2x}Ti_{18}O_{54}$ (x=2/3, y=0.18)		Tungsten Bronze Orthorhombic	102.6	4400	4	−17	1588
3939	$[(Pb_{0.5}Ca_{0.5})_{0.95}La_{0.05}][Fe_{0.5}Nb_{0.5})_{1-y}Ti_y]O_{3+d}$ (y=0)	1250	Perovskite Orthorhombic	102.8	5900		7	1593
3940	CaO-BaO-Li_2O-Sm_2O_3-Nd_2O_3-TiO_2 (14:4:8:10:2:63)	1350	Composite	103.0	7200		2	1612
3941	$0.4CaTiO_3$-$0.5(Li_{1/2}Nd_{1/2})TiO_3$-$0.1(Dy_{1/3}Nd_{1/3})TiO_3$	1350/3h	Orthorhombic Pbnm Perovskite	103.0	4214		146	1498
3942	$Ca_{1-x}Nd_{2x/3}TiO_3$ (x=0.39)	1350	Perovskite Orthorhombic Pnma	103.0	15340		247	1629
3943	$(1-x)Li_{1/2}Sm_{1/2}TiO_3$-$xNaNbO_3$ (x=0.1)			103.0	2120		−3	1630
3944	$Na_{0.5}Sm_{0.5}TiO_3$+0.6 wt% CeO_2	1425/2h	Orthorhombic perovskite	103.0	9600		193	1627
3945	$Ba_4(Sm_{0.7}Bi_{0.3})_{9+1/3}Ti_{18}O_{54}$	1320	Tungsten Bronze Orthorhombic	103.3	2980		9	1568
3946	$(Pb_{1/2}Ca_{1/2})_{0.95}La_{0.05}$ $[Fe_{1/2}Nb_{1/2}]O_{3+\delta}$	1150	Perovskite	103.4	5640		7	1622
3947	$Pb_{0.5}Ca_{0.5}(Fe_{1/2}Nb_{1/2})O_3$		Perovskite	104.0	4000	2.8	26	996
3948	TiO_2	1200	Tetragonal rutile	104.0	44000		–	53, 1631
3949	$Sr(Bi_{1-x}Nd_x)_8Ti_7O_{27}$ (x=0.3)			104.0	350			1583
3950	TiO_2+0.05 mol% Fe	1500	Rutile $P4_2/mmm$	104.0	50300			1631
3951	CaO-Li_2O-Sm_2O_3-TiO_2 (16:9:12:63)	1325		104.1	4320		13	1564, 1605
3952	$Ba_{6-3x}La_{8+2x}Ti_{18}O_{54}$		Tungsten bronze	105.0	2000	–	450	1606, 1607
3953	5BaO-Ta_2O_5 -$3TiO_2$	1400/5h	Composite	105.0	800			53
3954	$0.5Ca_{0.6}La_{0.2667}TiO_3$-$0.5Li_{1/2}Nd_{1/2}TiO_3$	1400/4h	Perovskite Cubic	105.0	7000		5	1632
3955	$Ba(Nd_{0.82-z}Sm_zBi_{0.18})Ti_4O_{12}$ (z=0.12)	1300/2h	Tungsten Bronze	105.0	4150	3.64		1586

(*continued*)

No.	Material	ST (°C)	Crystal structure	ε_r	Qf (GHz)	f_0	τ_f	Reference
3956	$Ba_{6-3x}(La_{1-y-z}Sm_yBi_z)_{8+2x}Ti_{18}O_{54}$ (x=2/3, y=0.7, z=0.12)	1325/3h	Tungsten Bronze Orthorhombic	105.1	4170	4.59	−15	1571
3957	$0.45CaTiO_3$-$0.45(Li_{1/2}Nd_{1/2})TiO_3$-$0.1(Dy_{1/3}Nd_{1/3})TiO_3$	1350/3h	Orthorhombic Pbnm Perovskite	105.1	5160		155	1498
3958	$0.7BaTiO_3$-$0.3La(Mg_{1/2}Ti_{1/2})O_3$		Perovskite Pm3m	105.8	6940	4.55	525	933
3959	BaO-$(Nd_{0.8}Bi_{.2})_2O_3$- $4TiO_2$	1300	Tungsten Bronze	106.0	4200		8	168
3960	CaO:BaO:$Li_2O(Sm_{1-y}N_d)_2O_3$:TiO_2 (14:4:8:12:63) (y=0.33)	1400/3h		106.0	6600		22	1609
3961	$0.3Ca_{2/5}Sm_{2/5}TiO_3$-$0.7Li_{1/2}Nd_{1/2}TiO_3$		Perovskite	106.0	3100			1614
3962	$Sr_2Ce_2Ti_5O_{16}(Sr_{1-3x/2}Ce_xTiO_3$ x=0.4)+0.4 wt% NiO	1300/2h	Psuedocubic	106.0	10000		315	1620
3963	$0.5Ca_{2/5}Sm_{2/5}TiO_3$-$0.5Li_{1/2}Nd_{1/2}TiO_3$	1300/3h		106.0	3710	5		1614
3964	$Ca_{1-x}Nd_{2x/3}TiO_3$ (x=0.3)	1400	Perovskite Orthorhombic	107.0	6590	7	316	1599
3965	$Sr_2Ce_2Ti_5O_{16}(Sr_{1-3x/2}Ce_xTiO_3$ x=0.4)+0.4 wt% In_2O_3	1300/2h	Psuedocubic	107.0	9400		310	1620
3966	$Ca_{2/5}Sm_{2/5}TiO_3$-$Li_{1/2}Nd_{1/2}TiO_3$-$0.6TiO_2$	1300/2h		107.0	3300	4	0	1597
3967	CaO-Sm_2O_3-Li_2O-TiO_2 (11:8:5:40)	1250		107.2	5700		0	1633
3968	$0.2Pb(Fe_{2/3}W_{1/3})O_3$-$0.8Pb_{.4}Ca_{.6}(Fe_{1/2}Nb_{1/2})O_3$	930	Perovskite	107.2	3790		48	1480
3969	CaO-SrO-Li_2O-Sm_2O_3-TiO_2		Perovskite Orthorhombic	108.0	5480	–	15	1612
3970	$(Ca_{1-x}Nd_{2x/3})TiO_3$ (x=0.39)	1300	Perovskite	108.0	17200	3		1619
3971	$Sr(Bi_{0.6}Nd_{0.4})_8Ti_7O_{27}$	1260	Aurivillius type	108.0	2000		–	1583
3972	$Ca_{0.6}La_{0.2667}TiO_3$	1400/4h	Perovskite cubic	109.0	17600	4.5	213	1632
3973	$Ba_{3.75}La_{9.5}Ti_{18}O_{54}$		Tungsten Bronze Orthorhombic	109.2	1800	3		1536
3974	$0.1Pb(Fe_{2/3}W_{1/3})O_3$-$0.9Pb_{0.45}Ca_{0.55}(Fe_{1/2}Nb_{1/2})O_3$	930	Perovskite	109.4	3500		5	1480
3975	$Pb_{0.63}Ca_{0.37}ZrO_3$	1450	Perovskite	110.0	3000	2.8		1514
3976	$0.2CaTiO_3$-$0.2(Li_{0.5}Nd_{0.5})TiO_3$	1300	Perovskite	110.0	2600		−15	1634
3977	$(1-x)Ca_{2/5}Sm_{2/5}TiO_3$-$xLi_{1/2}Nd_{1/2}TiO_3$ (x=0.6)	1300/3h	Perovskite	110.0	3400	5	155	1614

3978	$[(Pb_{0.5}Ca_{0.5})_{0.98}Nd_{0.02}](Fe_{1/2}Nb_{1/2})O_3$		Perovskite	110.0	5800		525	1623
3979	$0.15CaO\text{-}0.01SrO\text{-}0.09Li_2O\text{-}0.12Sm_2O_3\text{-}0.63TiO_2$			110.0	4500	3	8	1564
3980	$0.3CaTiO_3\text{-}0.4(Li_{1/2}Nd_{1/2})TiO_3\text{-}0.3La_{1/3}Nd_{1/3}TiO_3$	1350	Perovskite composite	110.0	1400		22	1498
3981	$Ba_{6-x}La_{8+2x}Ti_{18}O_{54}$ (x=0.5) hot pressed	1300	Tungsten Bronze Orthorhombic	110.0	2460			1574
3982	$0.2CaTiO_3\text{-}0.5(Li_{1/2}Nd_{1/2})TiO_3\text{-}0.3(La_{1/3}Nd_{1/3})TiO_3$	1350/3h	Perovskite composite	110.4	1460		315	1498
3983	$Ba_2Sr_2Sm_2Ti_{4+x}Ta_{6-x}O_{30-x/2}$ (x=3)	1340/2h		111.0	200	3.3		1635
3984	$[(Ca_x(La,Nd)_{2/3-2x/3}]TiO_3$ (x=0.9)	1350/24h	Tetragonal I4/mcm	111.3	4500		273	1392
3985	$Ba_{6-3x}(La_{1-y-z}Sm_yBi_z)_{8+2x}Ti_{18}O_{54}$ (x=2/3, y=0.5, z=0.12)	1320/3h	Tungsten Bronze Orthorhombic	111.3	2470	3.7	−30	1571
3986	$Ba_{6-3x}(La_{1-y-z}Sm_yBi_z)_{8+2x}Ti_{18}O_{54}$ (x=2/3, y=0.7, z=0.16)	1300/3h	Tungsten Bronze Orthorhombic	111.4	2530	4.3	−21	1571
3987	$(1\text{-}x)Ca_{0.8}Sr_{0.2}TiO_3\text{-}xLi_{0.5}Nd_{0.5}TiO_3$ (x=0.87)		Perovskite Tetragonal	111.6	2000		−3	1636
3988	$[(Pb_{0.5}Ca_{0.5})_{0.95}La_{0.05}][Fe_{0.5}Nb_{0.5})_{1-y}Ti_y]O_{3+d}$ (y=0.05)	1250	Perovskite Orthorhombic	111.7	5200		24	1593
3989	$0.6(Na,La)TiO_3\text{-}0.4(Li,Sm)TiO_3$		Perovskite	112.0	1060		18	1421
3990	$Sr_2Ce_2Ti_5O_{16}(Sr_{1-3x/2}Ce_xTiO_3$ x=0.4)+0.4 wt% CeO_2	1300/2h	Psuedocubic	112.0	9400		305	1620
3991	$Pb_{0.95}Ca_{.05}ZrO_3$	1250	Perovskite	112.0	720	2.8	–	1514
3992	$Ba_{6-3x-}Nd_{8+2x-y}Bi_yTi_{18}O_{54}$ (y=2, x=0.5)		Tungsten Bronze Orthorhombic	112.0	3000		25	1582
3993	$CaO\text{-}Sm_2O_3\text{-}Li_2O\text{-}TiO_2$+1 wt% $Li_2O\text{-}Bi_2O_3\text{-}TiO_{20}$	1250		112.1	3600		1	1603
3994	$0.05Pb(Fe_{2/3}W_{1/3})O_3\text{-}0.95Pb_{0.5}Ca_{0.5}(Fe_{1/2}Nb_{1/2})O_3$	1000	Perovskite	112.2	2730		52	1480
3995	$CaO\text{-}SrO\text{-}Li_2O\text{-}0.83Sm_2O_3\text{-}0.17Nd_2O_3\text{-}TiO_2$		Perovskite Orthorhombic	112.5	4900	–	13	1612
3996	$[Ca_{0.4}(Li_{1/2}Nd_{1/2})_{0.6}]TiO_3$	1350	Perovskite	112.6	4480		8	1464
3997	$Sr_2Ce_2Ti_5O_{16}(Sr_{1-3x/2}Ce_xTiO_3$ x=0.4)	1300/2h	Psuedocubic	113.0	8000		306	1620

(*continued*)

No.	Material	ST (°C)	Crystal structure	ε_r	Qf (GHz)	f_0	τ_f	Reference
3998	$Sr_2Ce_2Ti_5O_{16}(Sr_{1-3x/2}Ce_xTiO_3$ x=0.4)+0.2 wt% La_2O_3	1300/2h	Psuedocubic	113.0	9700		287	1620
3999	$0.3CaTiO_3$-$0.7Li_{1/2}Sm_{1/2}TiO_3$	1300/3h	Perovskite Orthorhombic	114.0	3700		12	1637
4000	$Ba_2Sr_2Sm_2Ti_{4+x}Ta_{6-x}O_{30-x/2}$ (x=2)	1340/2h		114.0	150	3.63		1635
4001	$Ba_2Sr_2Sm_2Ti_{4+x}Ta_{6-x}O_{30-x/2}$ (x=2.5)	1340/3h		114.0	140		–	1635
4002	$0.25CaTiO_3$-$0.75(Li_{1/2}Nd_{1/2})TiO_3$+10 wt% $Bi_4B_2O_9$	1200		114.0	2830		−8	1638
4003	$Ba_4(Nd_{0.7}Bi_{0.3})_{9.33}Ti_{18}O_{54}$	1320	Tungsten Bronze Orthorhombic	114.1	2700		44	1568
4004	CaO-SrO-Li_2O-$0.83Sm_2O_3$-$0.17Pr_6O_{11}O_3$-TiO_2		Perovskite Orthorhombic	114.3	4850	–	14	1612
4005	BaO-$(Nd_{0.7}Bi_{0.3})_2O_3$-$4TiO_2$	1275	Tungsten Bronze	115.0	2100		26	168
4006	TiO_2	1000	Rutile	115.0	46000			1639
4007	$0.7(Li_{1/2}Nd_{1/2})TiO_3$-$0.3(Na_{1/2}Sm_{1/2})TiO_3$		Orthorhombic	115.0	3800		15	1640
4008	$Ba_{6-3x}(La_{1-y-z}Sm_yBi_z)_{8+2x}Ti_{18}O_{54}$ (x=2/3, y=0.5, z=0.15)	1300/3h	Tungsten Bronze Orthorhombic	115.4	1884	3.58	−22	1571
4009	$0.3CaTiO_3$-$0.4(Li_{1/2}Nd_{1/2})TiO_3$-$0.3(La_{1/3}Nd_{1/3})TiO_3$	1350/3h	Orthorhombic Pbnm Perovskite	116.0	1675		23	1498
4010	$[(Pb_{0.5}Ca_{0.5})_{0.95}La_{0.05}][Fe_{0.5}Nb_{0.5})_{1-y}Ti_y]O_{3+d}$ (y=0.1)	1200	Perovskite Orthorhombic	116.6	4950	17	17	1576
4011	$0.3(Na_{1/2}La_{1/2})TiO_3$-$0.7(Li_{1/2}Sm_{1/2})TiO_3$	1300	Perovskite Orthorhombic	117.0	2280	3	−19	1421
4012	$Ba_{6-3x}(La_{1-y-z}Sm_yBi_z)_{8+2x}Ti_{18}O_{54}$ (x=2/3, y=0.7, z=0.2)	1275/3h	Tungsten Bronze Orthorhombic	117.0	1780	4.29	−36	1571
4013	$0.6CaTiO_3$-$0.1(Li_{1/2}Nd_{1/2})TiO_3$-$0.3(La_{1/3}Nd_{1/3})TiO_3$	1350/3h	Orthorhombic Pbnm Perovskite	117.0	3950		258	1498
4014	$0.4CaTiO_3$-$0.3(Li_{1/2}Nd_{1/2})TiO_3$-$0.3(La_{1/3}Nd_{1/3})TiO_3$	1350/3h	Orthorhombic Pbnm Perovskite	117.0	2070		119	1498
4015	CaO-SrO-Li_2O-$0.83Sm_2O_3$-$0.17Sm_2O_3$-TiO_2		Perovskite Orthorhombic	117.5	4120	–	15	1612
4016	$Ca(Zr_{0.4}Ti_{0.6})O_3$		Perovskite Orthorhombic	118.0	6400			906
4017	$Pb_{0.65}Ca_{0.35}ZrO_3$	1450	Perovskite	118.0	1260	2.8	29	1514

4018	$Sr_{5.7}Al_{0.7}Nb_{9.3}O_{30}$	1375	Tetragonal Tungsten Bronze P4bm	118.0	80	3.1		562
4019	$Bi_{1.5}Zn_{0.92}Nb_{1.5}O_{6.92}$+3 wt% ($0.81MoO_3$-0.19CuO)	900/4h	Cubic	118.2	1000	2.3		1641
4020	$Ba_{0.75}Sr_{0.25}(Nd_xBi_{1-x})_2Ti_4O_{12}$ (x=0.75)	1250		118.5	4900		−1	1642
4021	$Ca_{1-x}Nd_{2x/3}TiO_3$ (x=0.2)	1400/4h	Perovskite Orthorhombic	119.0	4200	7.2	433	1599
4022	$Ca_{1-x}Sm_{2x/3}TiO_3$ (x=0.2)	1450/3h	Perovskite Orthorhombic	119.3	12330	5		1604
4023	(1-x)$Li_{1/2}Sm_{1/2}TiO_3$-x$NaNbO_3$ (x=0.2)			120.0	2300		9	1630
4024	$Bi_{1.5}Zn_{0.92}Nb_{1.5}O_{6.92}$+3 wt% ($0.21BaCO_3$-0.79CuO)	950/4h	Cubic	120.1	1050	2.3		1641
4025	$Ba_{6-3x}(La_{1-y-z}Sm_yBi_z)_{8+2x}Ti_{18}O_{54}$ (x=2/3, y=0.5, z=0.18)	1300/3h	Tungsten Bronze	120.2	1571	3.8	−15	1571
4026	0.4$CaTiO_3$-0.5($Li_{1/2}Nd_{1/2}$)TiO_3-0.1($La_{1/3}Nd_{1/3}$)TiO_3	1350/3h	Orthorhombic Pbnm Perovskite	121.3	3040		113	1498
4027	0.45$CaTiO_3$-0.25($Li_{1/2}Nd_{1/2}$)TiO_3-0.3($Dy_{1/3}Nd_{1/3}$)TiO_3	1350/3h	Orthorhombic Pbnm Perovskite	121.3	3650		109	1498
4028	($La_{1/2}Na_{1/2}$)TiO_3	1300	Cubic perovskite	122.0	9800	3	480	1421
4029	0.15CaO-0.011SrO—0.09Li_2O-13Sm_2O_3-0.63TiO_2			123.0	4150		10.8	1612
4030	0.5$CaTiO_3$-0.4($Li_{1/2}Nd_{1/2}$)TiO_3-0.1($La_{1/3}Nd_{1/3}$)TiO_3	1350/3h	Orthorhombic Pbnm Perovskite	123.0	4148		136	1498
4031	$Sr_3Ce_2Ti_6O_{19}$($Sr_{1-3x/2}Ce_xTiO_3$ x=0.333)	1350/2h	Psuedocubic	123.0	10000		392	1643
4032	$Ba_{6-3x}(La_{1-y-z}Sm_yBi_z)_{8+2x}Ti_{18}O_{54}$ (x=2/3, y=0.5, z=0.2)	1300/3h	Tungsten Bronze Orthorhombic	124.5	1430	3.58	−9	1571
4033	0.4$CaTiO_3$-0.6$Li_{1/2}Nd_{1/2}TiO_3$		Perovskite Orthorhombic	126.0	2600	2.1	127	1644
4034	$Bi_{1.5}Zn_{0.92}Nb_{1.5}O_{6.92}$	1050/4h		126.2	520	2.4		1495
4035	$Ba_3La_3Ti_5Ta_5O_{30}$	1425		126.6	110	3.1	100	1645
4036	$(Pb_{1-x}Ca_x)[Fe_{1/2}Nb_{1/2}]_{1-y}Zr_y]O_3$ (y=0.01, x=0.4)	1150	Perovskite	126.7	3630	3	118	1488
4037	x$Bi_4B_2O_9$-(1-x)(0.2$CaTiO_3$-0.8$Li_{0.5}Nd_{0.5}TiO_3$)		Composite	127.0	2700		−4	287

(*continued*)

No.	Material	ST (°C)	Crystal structure	ε_r	Qf (GHz)	f_0	τ_f	Reference
4038	$0.2Pb(Fe_{2/3}W_{1/3})O_3$-$0.8Pb_{0.45}Ca_{0.55}(Fe_{1/2}Nb_{1/2})O_3$	930	Perovskite	127.2	2300		96	1480
4039	$0.6CaTiO_3$-$0.3(Li_{1/2}Nd_{1/2})TiO_3$-$0.1(La_{1/3}Nd_{1/3})TiO_3$	1350/3h	Orthorhombic Pbnm Perovskite	128.2	4460		256	1498
4040	$0.5(Li_{1/2}Nd_{1/2})TiO_3$-$0.5(Na_{1/2}Nd_{1/2})TiO_3$		Perovskite	130.0	2000		20	1640
4041	$0.2CaTiO_3$-$0.8Li_{.5}Nd_{.5}TiO_3$+5 wt% $Bi_2Ti_2O_7$	1300	Perovskite Orthorhombic Pbnm	130.0	2400		20	1646
4042	$(La_{0.44}Pb_{0.33})TiO_3$	1300	Orthorhombic Ibmm	130.0	5000	3	300	1547
4043	$Ba_4La_2Ti_4Ta_6O_{30}$	1425		131.8	540	3.47	–	1645
4044	$Pb_{07}Ca_{03}ZrO_3$	1400	Perovskite	132.0	1800	2.8	86	1514
4045	$0.2CaTiO_3$-$0.68(Li_{1/2}Nd_{1/2})TiO_3$-$0.12(La_{1/3}Nd_{1/3})TiO_3$	1350/3h	Tetragonal P-4b2 Perovskite	132.6	1450		−17	1498
4046	$Sr_4Ce_2Ti_7O_{22}$	1325	Psuedocubic perovskite	133.0	11100	2.3		1643
4047	$Sr_{0.8}Ca_{0.2}TiO_3$	1400	Perovskite	133.9	3950	1.62	1534	1222
4048	$5CaO$-$2Nb_2O_5$-$3TiO_2$	1300/5h	Composite	134.0	1500			53
4049	$0.8CaTiO_3$-$0.2(Li_{1/2}Nd_{1/2})TiO_3$		Perovskite	134.0	13800		200	1644
4050	$0.5(Ca_{0.7}Nd_{0.2})TiO_3$-$0.5(Li_{1/2}Nd_{1/2})TiO_3$	1150/4h	Composite	134.0	2200		20	1647
4051	$Sr_4Ce_2Ti_7O_{22}(Sr_{1-3x/2}Ce_xTiO_3$ x=0.286)	1350/2h	Psuedocubic perovskite	136.0	10800		428	1643
4052	$0.4CaTiO_3$-$0.48(Li_{1/2}Nd_{1/2})TiO_3$-$0.12(La_{1/3}Nd_{1/3})TiO_3$	1350/3h	Perovskite Orthorhombic Pbnm	136.4	2220		122	1498
4053	$La_{(1-x)/3}Na_xNbO_3$ (x=0.02)	1350.2h	Peerovskite	138.0	1700		350	1648
4054	$Ca(Zr_xTi_{1-x})O_3$ (x=0.3)	1430/15h	Perovskite	138.0	4900	2.3	588	906
4055	$Ca_{0.16}Sr_{0.04}Li_{0.4}Nd_{0.4}TiO_3$+0.75 mol% Li	1270	Perovskite Pnma	138.0	1600		52	1649
4056	$0.4CaTiO_3$-$0.6(LiNd)TiO_3$		Perovskites	139.0	3250		110	1650
4057	$Pb_{0.6}Ca_{0.4}[(Fe_{1/2}Nb_{1/2})_{0.95}Sn_{0.05}O_3$	1150/3h	Perovskite cubic	139.4	2450		140	1497
4058	$PbZrO_3$-CeO_2	1250/4h	Composite	140.0	2500	3	−1080	1651
4059	$0.6PbZrO_3$-$0.4Ca(Fe_{1/2}Nb_{1/2})O_3$	1250/3h	Perovskite	140.7	1776	3.02	120	1576
4060	$(Ca_{1-x}Nd_{2x/3})TiO_3$ (x=0.15)	1300	Perovskite	141.0	11300	2.77		1619
4061	$Ca(Zr_xTi_{1-x})O_3$ (x=0.2)	1430/15h	Perovskite	141.0	5900	2.14	732	906
4062	$(Ca_{1-x}Nd_{2x/3})TiO_3$ (x=0.27)	1300	Perovskite	141.0	10350	3.07		1619

4063	$0.6CaTiO_3$-$0.28(Li_{1/2}Nd_{1/2})TiO_3$-$0.12(La_{1/3}Nd_{1/3})TiO_3$	1350/3h	Perovskite Orthorhombic Pbnm	142.0	3327		283	1498
4064	$Sr_5Ce_2Ti_8O_{25}$	1325	Psuedocubic Perovskite	142.0	11100	2.3		1643
4065	$Pb_{0.6}Ca_{0.4}[(Fe_{1/2}Nb_{1/2})_{0.9}Sn_{0.1}O_3$	1150/3h	Perovskite Cubic	142.6	2520		130	1497
4066	$Sr_5Ce_2Ti_8O_{25}(Sr_{1-3x/2}Ce_xTiO_3$ x=0.25)	1375/2h	Psuedocubic	143.0	11000		478	1643
4067	$Sr_{0.8}Ca_{0.2}TiO_3$		Perovskite Tetragonal I4/mcm	145.0	4050	1.62	1534	1358
4068	$Bi_{1.5}Zn_{0.92}Nb_{1.5}O_{6.92}$+0.6 wt% V_2O_5	850/1h		148.0	120			1495
4069	$0.4CaTiO_3$-$0.5(LiNd)TiO_3$-$0.1(Bi,Na)TiO_3$		Composite	148.0	2650		123	1650
4070	$0.4CaTiO_3$-$0.6Li_{1/2}Nd_{1/2}TiO_3$+15 wt% Bi_2O_3-$2TiO_2$		Composite	150.0	2200		65	1646
4071	$Ca(Zr_xTi_{1-x})O_3$ (x=0.1)	1410/15h	Perovskite	150.0	5000	2.02	749	906
4072	$0.4CaTiO_3$-$0.6Li_{0.5}Nd_{0.5}TiO_3$+10 wt% $Bi_2Ti_2O_7$	1175		150.0	2400		70	1644
4073	$Bi_{1.5}ZnNb_{1.5}O_7$		Cubic	150.0	300	2.9		1652, 1653
4074	$Sr_6Ce_2Ti_9O_{28}(Sr_{1-3x/2}Ce_xTiO_3$ x=0.222)	1375/2h	Psuedocubic Perovskite	150.0	9600		497	1643
4075	$Ca(Zr_{0.2}Ti_{0.8})O_3$		Perovskite Orthorhombic	153.0	4400			906
4076	$Pb_{0.6}Ca_{0.4}(Fe_{1/2}Nb_{1/2})O_3$		Perovskite	154.0	1700	2.3	135	996
4077	$Sr_7Ce_2Ti_{10}O_{31}$ $(Sr_{1-3x/2}Ce_xTiO_3$ x=0.2)	1375/2h	Psuedocubic Perovskite	157.0	9300		544	1643
4078	$CaTiO_3$	1400	Orthorhombic Perovskite Pbnm	162.0	1290	1.5	859	1358
4079	$0.1Pb(Fe_{1/2}Nb_{1/2})O_3$-$0.9CaTiO_3$	1200/3h	Perovskite cubic	164.0	6180	2.8	583	1654
4080	$Pb_{0.75}Ca_{0.25}ZrO_3$	1300	Perovskite	167.0	960	2.4	111	1514
4081	$Sr_8Ce_2Ti_{11}O_{34}$ $(Sr_{1-3x/2}Ce_xTiO_3$ x=0.182)	1375/2h	Psuedocubic Perovskite	167.0	8000		601	1643
4082	$PbZrO_3$-CeO_2 -$SrTiO_3$-NiO-Nb_2O_5	1250/4h		170.0	3600	3	800	1651
4083	$Sr_{0.1}Ca_{0.9}TiO_3$		Orthorhombic Perovskite	170.0	8320	1	931	1358
4084	$0.3Pb(Fe_{1/2}Nb_{1/2})O_3$-$0.7CaTiO_3$	1200/3h	Perovskite Cubic	172.7	810	2.7	392	1654
4085	$Sr_9Ce_2Ti_{12}O_{37}$ $(Sr_{1-3x/2}Ce_xTiO_3$ x=0.167)	1375/2h	Psuedo Cubic Perovskite	173.0	3000		637	1643
4086	$0.4CaTiO_3$-$0.4(LiNd)TiO_3$-$0.2(Bi,Na)TiO_3$			174.0	1300		91	1650
4087	$KTaO_3$	1340	Cubic Pm3m	177.0	2900	3.6		1655

(*continued*)

No.	Material	ST (°C)	Crystal structure	ε_r	Qf (GHz)	f_0	τ_f	Reference
4088	$Sr_{10}Ce_2Ti_{13}O_{40}$ ($Sr_{13x/2}Ce_xTiO_3$ x=0.154)	1400/2h	Psuedo Cubic Perovskite	179.0	8000		724	1643
4089	$Ca_{1.8}Sr_{0.2}Bi_4Ti_5O_{18}$	1175/5h	Orthorhombic	180.0	8000			1656
4090	$Sr_{0.2}Ca_{0.8}TiO_3$		Perovskite	181.0	3900	1.4	991	1358
4091	$Sr_{11}Ce_2Ti_{14}O_{43}$ ($Sr_{1-3x/2}Ce_xTiO_3$ x=0.154)	1400/2h	Psuedo Cubic Perovskite	185.0	6000		789	1643
4092	$0.4CaTiO_3$-$0.3(LiNd)TiO_3$-$0.3(Bi,Na)TiO_3$			204.0	1300		147	1650
4093	$Sr_{0.4}Ca_{0.6}TiO_3$		Perovskite	218.0	7180	1.3	1164	1358
4094	$Ba_{0.5}Sr_{0.5}TiO_3$-$BaWO_4$			225.0	580			1657
4095	$Sr_8Ce_2PbTi_{12}O_{36}$	1300		229.0	4400	2	950	1658
4096	$0.5Pb(Fe_{1/2}Nb_{1/2})O_3$-$0.5CaTiO_3$	1200/3h	Perovskite Cubic	232.1	870	2.3	433	1654
4097	$Sr_{0.5}Ca_{0.5}TiO_3$		Perovskite Orthorhombic Pbnm	236.0	4120	1.2	1234	1358
4098	$0.4CaTiO_3$-$0.2(LiNd)TiO_3$-$0.4(Bi,Na)TiO_3$			253.0	740			1650
4099	$Pb_{1.5}Nb_2O_{6.5}$		Cubic	259.0	3010		1239	1659
4100	$Ca_{0.5}Sr_{0.5}TiO_3$	1350	Orthorhombic	260.0	7000		384	1660
4101	$SrTiO_3$		Cubic perovskite Pm-3m	270.0	3000	2	1500	1358, 1661
4102	$Ag(Nb_{1/3}Ta_{2/3})O_3$+1 wt% CuO	875	Perovskite Orthorhombic pbcm	271.0	800			1662
4103	$BaTi_{0.7}Ga_{0.15}Nb_{0.15}O_3$	1500/4h	Perovskite Tetragonal P4mm	275.0	100	2.4		1373
4104	$Ag(Nb_{2/4}Ta_{2/4})O_3$	1200	Perovskite Pbcm Orthorhombic	285.0	300	2.4		1662
4105	$Ag(Nb_{1/4}Ta_{3/4})O_3$	925	Perovskite Pbcm	295.0	600	2.6		1662
4106	$Sr_7Ce_2Pb_2Ti_{12}O_{37}$	1250		301.0	4300	1.8	1287	1658
4107	40 wt% $Ba_{0.6}Sr_{0.4}TiO_3$-60 wt% $BaZn_6Ti_6O_{19}$	1300	Composite	324	400			1663
4108	$0.8PbZrO_3$-$0.2Ca(Fe_{1/2}Nb_{1/2})O_3$	1250/3h	Perovskite Rhombohedral	335.8	314	2	386	1576
4109	$Bi_6Ti_5TeO_{22}$	1010/10h		350.0	220		2600	1131

4110	$Ba_{0.2}Sr_{0.8}TiO_3$	1450/3h	Cubic perovskite	363.0	2400	2.3		1664
4111	$Ba_{0.3}Sr_{0.7}TiO_3$-10 mol% $MgTiO_3$	1350	Cubic perovskite	365.0	1500			1665
4112	$AgTa_{0.57}Nb_{0.43}O_3$	1200	Perovskite	380.0	800			1666
4113	$Ag(Nb_{2/4}Ta_{2/4})O_3$+1 wt% CuO	900	Perovskite	398.0	400	2.3		1662
4114	$Ag_{0.52}Ta_{0.48}O_3$	1250/20h	Perovskite, Monoclinic P2/m	415.0	430	2		1667
4115	$Ba_{0.5}Sr_{0.5}TiO_3$		Perovskite	420.0	2250			1358
4116	$Sr_6Ce_2Pb_3Ti_{12}O_{36}$	1200		430.0	2300	1.7	2218	1658
4117	$Ba_{0.5}Sr_{0.5}Ti_{1-3y/2}W_yO_3$ (y=0.05)			431.0	365	2.11		1668
4118	$Ba_{0.4}Sr_{0.6}Ti_{0.9}Mn_{0.1}O_3$	1400/4h	Perovkite	449.0	580			1669
4119	$Ag(Nb_{3/4}Ta_{1/4})O_{3-}$ $Ag(Nb_{1/4}Ta_{3/4})O_3$ (5:55)	925	Perovskite Orthorhombic	463.0	200	1.97		1662
4120	$Ag(Nb_{3/4}Ta_{1/4})O_3$	925	Perovskite Orthorhombic Pbcm	487.0	200	1.89		1662
4121	$Ba_{0.8}Sr_{0.2}TiO_3$	1450/3h	Perovskite	560.0	850	1.9		1664
4122	$0.7Pb(Fe_{1/2}Nb_{1/2})O_3$-$0.3CaTiO_3$	1150/3h	Perovskite Cubic	566.0	120	1.42	1075	1654
4123	60 wt% $Ba_{0.6}Sr_{0.4}TiO_3$-40 wt% $BaZn_6Ti_6O_{19}$	1300	Composite	584.0	250			1663
4124	$Ba_{0.4}Sr_{0.6}TiO_3$	1450/3h	Perovskie	672.0	1600	1.7		1664
4125	$BaTi_{0.5}Ga_{0.25}Nb_{0.25}O_3$	1500/4h	Perovskite Tetragonal P4mm	760.0	40	2.4		1373
4126	$Ba_{0.6}Sr_{0.4}TiO_3$	1450/3h	Perovskie	838.0	300	1.6		1664
4127	$Ba_{0.4}Sr_{0.6}TiO_3$		Perovskite	1038.0	720			1670
4128	$Ba_{0.6}Sr_{0.4}TiO_3$+2 mol% $BaCu(B_2O_{5)}$		Perovskite	2553.0	330			1671
4129	$Ba_{0.6}Sr_{0.4}TiO_3$+0.5 wt% $MgCo_2(VO_4)_2$		Perovskite	2763.0	300	1		1672

References

1. Abhilash, P., Thomas, D., and Sebastian, M.T. (2013) *International Journal of Modern Physics. Conference Series*, **22**, 159–163.
2. Li, E., Zhang, P., Duan, S.Y., *et al*. (2015) *Journal of Materials Science: Materials in Electronics*, **26**, 8398–8403.
3. Hu, C. and Liu, P. (2013) *Journal of Alloys & Compounds*, **559**, 129–133.
4. Li, L., Lui, C. H., Zhu J. Y., *et al*. (2016) *Journal of European Ceramic Society*, in press.
5. Li, L., Fang, Y., Xiao, Q., Wu, *et al*. (2014) *International Journal of Applied ceramic Technology*, **11**, 193–199.
6. Wang, S-F., Wang,Y-R., Hsu, Y-F., *et al*. (2012) *Journal of Alloys & Compounds*, **498**, 211–216.
7. Fang, Y., Li, L., Xiao, Q., *et al*. (2012) *Ceramic International*, **38**, 4511–4515.
8. Chiang, S.-C., Wang, S-F., Wang, Y-R., *et al*. (2008) *Ceramic International*, **34**, 599–604.
9. Qin, N., Krzmanc, M. M., and Suvorov, D. (2008) *Journal of American Ceramic Society*, **91**, 2593–2600.
10. Manu, K. M., Anjana, P. S., and Sebastian, M. T. (2011) *Materials Letters*, **65**, 565–567.
11. Zhang, G.Q., Wang, H., Guo, J., *et al*. (2015) *Journal of American Ceramic Society*, **98**, 528–533.
12. Ohsahi, M., Ogawa, H. Kan, A., *et al*. (2005) *Journal of European Ceramic Society*, **25**, 2877–2881.
13. Jeong, B.J., Joung, M-R., Kweon, S-H., *et al*. (2012) *Journal of American Ceramic Society*, **95**, 811–813.
14. George, S., Sebastian, M. T., Raman, S., *et al*. (2011) *International Journal of Appled Ceramic Technology*, **8**, 172–179.
15. Schott AG, Germany.
16. Ohsato, H., Kim, J-S., Kim, A-Y., *et al*. (2011) *Japanese Journal of Applied Physics*, **50**, 09NF01.
17. Kweon, S-H., Joung, M-R., Kim, J-S., *et al*. (2011) *Journal of American Ceramic Society*, **94**, 1995–1998.
18. Okamura, T. and Kishina, T. (1998) *Japanese Journal of Applied Physics*, **37**, 5364–5366.
19. George, S., Anjana, P. S., Deepu, V. N., *et al*. (2009) *Journal of American Ceramic Society*, **92**, 1244–1249.
20. Ando1, M., Ohsato, H., Igimi, D., *et al*. (2015) *Japanese Journal of Applied Physics*, **54**, 10NE04/1-7.
21. Zhou, D., Sun, R., Gong, S., *et al*. (2011) *Ceramic International*, **37**, 2377–2382.
22. Sasikala, T. S., Suma, M. N., Mohanan, P., *et al*. (2008) *Journal of Alloys & Compounds*, **461**, 555–559.
23. Chen, X., Zhao, X., Luo, L., *et al*. (2008) *Japanese Journal of Applied Physics*, **47**, 3572–3575.
24. Kahari, H., Teirikangas,M., Juuti, J., *et al*. (2014) *Journal of American Ceramic Society*, **97**, 3378–3379.
25. George, S., Sajith, V. K., Sebastian, M. T., *et al*. (2011) *Journal of Advanced Dielectrics*, **1**, 209–213.
26. Nair, I. J., and Sebastian, M. T. (2015) *Proceedings of Kerala Science Congress*, India
27. Choi, Y-J., Park, J-H., Ko, W-J., *et al*. (2006) *Journal of American Ceramic Society*, **89**, 562–567.
28. Hu, C., Liu, Y., Zhang, W., *et al*. (2014) *Materials Research Bulletin*, **53**, 54–57.
29. Krzmanc, M. M., Valant, M. and Suvorov, D. (2005) *Journal of European Ceramic Society*, **25**, 2835–2838.
30. Zhou, D., Rindall, C. A., Wang, H., *et al*. (2010) *Journal of American Ceramic Society*, **93**, 1096–1100.
31. He, M., Zhang, S., Zhou, X., *et al*. (2011) *Journal of Alloys & Compounds*, **509**, 4260–4263.
32. Zhou, D., Rindall, C. A., Pang, L-X., *et al*. (2011) *Journal of American Ceramic Society*, **94**, 348–350.

33. Zhang, G-Q., Guo, J., He, L., *et al*. (2014) *Journal of American Ceramic Society*, **97**, 241–245.
34. Kim, J-S., Nguyen, N-H., Lim, J-J., *et al*. (2008) *Journal of American Ceramic Society*, **91**, 671–674.
35. Yoon, S. O., Shim, S. H., Kim, K. S., *et al*. (2009) *Ceramic International*, **35**, 1271–1275.
36. Sebastian, M. T. (Unpublished)
37. Surjith, A., James, N.K., Ratheesh, R. (2011) *Journal of Alloys & Compounds*, **509**, 9992–9995.
38. Wu, J-M. and Huang, H. L. (2000) *Journal of Materials Research*, **15**, 222–227.
39. Krzmanc, M. M., Meden, A., and Suvorov, D. (2007) *Journal of European Ceramic Society*, **27**, 2957–2961.
40. Lim, M-H., Park, J-H., Kim, H-G., *et al*. (2003) *Proceedings of IEEE International Conferenceon Properties and Applications of Dielectric Materials*, **2**, 757–760.
41. Dosler, U., Krzmanc, M. M., and Suvorov, D. (2012) *Ceramic International*, **38**, 1019–1025.
42. Li, F., Liu, P., Ruan, P., *et al*. (2015) *Ceramic International*, **41**, S582–S587.
43. Kim, J-S., Song, M-E., Joung, M-R., *et al*. (2010) *Journal of European Ceramic Society*, **30**, 375–379.
44. Zhu, H., Zhou, H., Liu, M., *et al*. (2009) *Journal of Materials Science: Materials in Electronics*, **20**, 1135–1139.
45. Krzmanc, M. M., Valant, M., Jancar, B., *et al*. (2005) *Journal of American Ceramic Society*, **88**, 2472–2479.
46. Wakino, K., *et al*. (1992) *Proceedings of ISIF-92*, 308.
47. Bian, J.J., Kim, D-W., and Hong, K. S. (2004) *Japanese Journal of Applied Physics*, **43**, 3521–3525.
48. Kim, M-H., Lee, J. C., Cheon, C. I., *et al*. (2006) *Japanese Journal of Applied Physics*, **45**, 7397–7400.
49. Kim, E.S., Chun, B.S., Freer, R., *et al*. (2010) *Journal of European Ceramic Society*, **30**, 1731–1736.
50. Terada, M., Kuwamura, K., Kagomiya, I., *et al*. (2007) *Journal of European Ceramic Society*, **27**, 3045–3048.
51. Dosler, U., Krzmanc, M. M., and Suvorov, D. (2012) *Ceramic International*, **38**, 1019–1025.
52. Dosler, U., Krzmanc, M. M., and Suvorov, D. (2010) *Journal of European Ceramic Society*, **30**, 413–418.
53. Maeda, M., Yamamura, T., and Ikeda, T. (1987) *Journal of Applied Physics* Supl., **26-2**, 76–79.
54. Zhou, X., Li, E., Yang, S., *et al*. (2012) *Ceramic International*, **38**, 5551–5555.
55. Wu, S., Song, K., Liu, P., *et al*. (2015) *Journal of American Ceramic Society*, **98**, 1842–1847.
56. Nekoute, K. A. and Khosroshahi, R. A. (2016) *Journal of Materials Science: Materials in Electronics*, in press.
57. Umemura, R., Ogawa, H., Ohsato, H., *et al*. (2005) *Journal of European Ceramic Society*, **25**, 2865–2870.
58. Kan, A. (2003) PhD Thesis, Meijo University, Japan
59. Lei, W., Ang, R., Wang, X-C., *et al*. (2014) *Materials Research Bulletin*, **50**, 235–239.
60. Sun, H., Zhang, Q., Yang, H., *et al*. (2007) *Materials Science and Engineering*, **B138**, 46–50.
61. Chen, C., Wu, S., and Fan, Y. Z. (2013) *Journal of Alloys & Compounds*, **578**, 153–156.
62. Subodh, G. and Sebastian, M. T. (2008) *Japanese Journal of Applied Physics*, **47**, 7943–7946.
63. Yoon, D. H., Jo, VY.H., Saji, V.S., *et al*. (2009) *Journal of Electroceramics*, **23**, 127–132.
64. Dou, G., Guo, M., Li, Y., *et al*. (2015) *Journal of Materials Science: Materials in Electronics*, **26**, 4207–4211.
65. Chen, H-W., Su, H., Zhang, H-W., *et al*. (2014) *Ceramic International*, **40**, 14655–14659.
66. Chen, H-W., Su, H., Zhang, H-W., *et al*. (2015) *Journal of Materials Science: Materials in Electronics*, **26**, 2820–2823.
67. Thomas, D. and Sebastian, M. T. (2010) *Journal of American Ceramic Society*, **93**, 3828–3831.
68. Song, K.X., Chen, X. M., and Zheng, C.W. (2008) *Ceramic International*, **34**, 917–920.
69. Dong, M., Yue, Z., Zhuang, H., *et al*. (2008) *Journal of American Ceramic Society*, **91**, 3981–3985.

70. Arun, B., Manu, K. M., and Sebastian, M. T. (2013) *Proceedings of International Conference on Ceramics*, Bikaner, India
71. Kagomiya, I., Suzuki, I., and Ohsato, H. (2009) *Japanese Journal of Applied Physics*, **48**, 09KE02–KE04.
72. Chen, C-S., Chou, C-C., Shih, W-J., *et al*. (2003) *Materials Chemistry and Physics*, **79**, 129–134.
73. Guo, Y., Ohsato, H. and Kakimoto, K. (2006) *Journal of European Ceramic Society*, **26**, 1827–1830.
74. Nguyen, N-H., Lim, J-B., Nahm, S., *et al*. (2007) *Journal of American Ceramic Society*, **90**, 3127–3130.
75. Song, K.X. and Chen, X.M. (2007) *Journal of American Ceramic Society*, **90**, 1808–1811.
76. Tzou, J. L., Zhang, Q-L., Yang, H., *et al*. (2006) *Japanese Journal of Applied Physics*, **45**, 4143–4145.
77. Wang, H., Zhang, Q., Yang, H., *et al*. (2008) *Ceramic International*, **34**, 1405–1408.
78. Seo, J. J., Shin, D. J., and Cho, Y.S. (2006) *Journal of American Ceramic Society*, **89**, 2352–2355.
79. Sugiyama, T., Tsunooka, T., Kakimoto, K., *et al*. (2006) *Journal of European Ceramic Society*, **26**, 2097–2100.
80. Song, M-Y., Kim, J-S., Joung, M-R., *et al*. (2008) *Journal of American Ceramic Society*, **91**, 2747–2750.
81. Wang, H., Chen, J., Yang, W., *et al*. (2012) *Journal of European Ceramic Society*, **32**, 541–545.
82. Thomas, D. and Sebastian, M. T. (2012) *Journal of European Ceramic Society*, **32**, 2359–2364.
83. Wu, X-G., Wang, H., Chen, Y-H., *et al*. (2012) *Journal of American Ceramic Society*, **95**, 1793–1795.
84. Songa, K., Liua, P., Lin, H., *et al*. (2016) *Journal of European Ceramic Society*.
85. Sasikala, T. S., Pavithran, C., and Sebastian, M. T. (2010) *Journal of Materials Science: Materials in Electronics*, **21**, 141–114.
86. Zhou, D. X., Sun, F., Hu, Y-X., *et al*. (2012) *Journal of Materials Science: Materials in Electronics*, **23**, 981–989.
87. Tsunooka, T., Sugiyma, H., Kakimoto, K., *et al*. (2004) *Journal of Japanase Ceramic Society*, **112**, S1637–S1640.
88. Dou, G., Zhou, D., Gong, S., *et al*. (2013) *Journal of Materials Science: Materials in Electronics*, **24**, 1601–1607.
89. Kagomiya, I., Suzuki, I., and Ohsato, H. (2009) *Japanese Journal of Applied Physics*, **48**, 09KE02.
90. Chen, S-C. X., Wu, S. P., and Li, J. H. (2013) *Journal of Alloys & Compounds*, **578**, 153–156.
91. Jang, S. W. and Kim, E. S. (2015) *Materials Research Bulletin*, **67**, 239–244.
92. Wu, J-M. and Huang, H-L. (1999) *Journal of Non-Crystalline Solids*, **260**, 116–124.
93. Kan, A., Ogawa, H., Sumino, M., *et al*. (2009) *Japanese Journal of Applied Physics*, **48**, 09KE03.
94. Hu, Y., Wei, D., Fu, Q., *et al*. (2012) *Journal of European Ceramic Society*, **32**, 521–524.
95. Sun, H. P., Zhang, Q-L., and Yang, H. (2009) *Ceramic International*, **35**, 637–641.
96. Doo, S.H.N., Jo, Y. H., Lee, J. S., *et al*. (2010) *Journal of American Ceramic Society*, **93**, 334–337.
97. Renjini, S. N., Thomas, S., Sebastian, M.T., *et al*. (2009) *International Journal of Appled Ceramic Technology*, **6**, 286–294.
98. Wu, S.and Ma, Q. (2013) *Journal of Alloys & Compounds*, **567**, 40–46.
99. Dong, Z. W., Zhen, Y., Cheng, P., *et al*. (2014) *Ceramic International*, **40**, 12983–12988.
100. Zhang, C., Zuo, R., Zhang, J., *et al*. (2015) *Journal of American Ceramic Society*, **98**, 702–710.
101. Varghese, J. and Sebastian, M. T. (2015) *Daltons Trans*., **44**, 5146–5152.
102. Krzmanc, M.M., Jancar, B., and Suvorov, D. (2008) *Journal of European Ceramic Society*, **28**, 3141–3148.
103. Dosler, U., Krzmanc, M. M., Jancar, B., *et al*. (2011) *Journal of American Ceramic Society*, **93**, 3788–3792.
104. Bian, J-J., Kim, D-W., and Hong, K. S., (2005) *Materials Research Bulletin*, **40**, 2120–2129.

105. Choi, B. K., Sun, G. N., and Kim, E. S. (2013) *Ceramic International*, **39**, S677–S680.
106. Feng, K-C., Chou, C-C., Chu, L-W., *et al*. (2013) *Materials Research Bulletin*, **47**, 2851–2855.
107. Tsunooka, T., Andou, M., Higashita, Y., *et al*. (2003) *Journal of European Ceramic Society*, **23**, 2573–2378.
108. Umemura, R., Ogawa, H., Yokoi, A., *et al*. (2006) *Journal of Alloys & Compounds*, **424**, 388–393.
109. Yokoi, A., Ogawa, H., Kan, A., *et al*. (2007) *Journal of European Ceramic Society*, **27**, 2989–2993.
110. Manu, K. M., Karthik, C., Ubic, R., *et al*. (2013) *Journal of American Ceramic Society*, **96**, 1504–1511.
111. Dong, Z. W., Zheng, Y., and Cheng, P. (2014) *Ceramic International*, **40**, 14865–14869.
112. Guo, T., Wu, W., and Wang, Y. (2012) *Ceramic International*, **38S**, S187–S190.
113. Choi, G-K., Kim, J-R., Yoon, S.H., *et al*. (2007) *Journal of European Ceramic Society*, **27**, 3063–3067.
114. Huang, C-L., Pan, C-L., and Lee, W-C. (2008) *Journal of Alloys and Compounds*, **462**, L5–L8.
115. Dou, G., Zhou, D., and Gong, S. (2012) *Journal of Alloys and Compounds*, **513**, 466–473.
116. Wang, W., Li, L., Xiu, S., *et al*. (2015) *Journal of Alloys and Compounds*, **639**, 359–364.
117. Mori, N., Sugimoto, Y., and Harada, J., *et al*. (2006) *Journal of European Ceramic Society*, **26**, 1925–1928.
118. Krzmanc, M. M., Valant, M. and Suvorov, D. (2007) *Journal of European Ceramic Society*, **27**, 1181–1185.
119. Manu, K. M. and Sebastian, M. T. (2012) *Materials Chemistry and Physics*, **133**, 21–23.
120. Wang, H. P., Xu, S-Q., Zhang, B., *et al*. (2009) *Materials Research Bulletin*, **44**, 619–622.
121. Nahm, S., Lim, J-B., Paik, J-H., *et al*. (2006) *Journal of American Ceramic Society*, **89**, 3124–3128.
122. Kim, J-S., Song, M-E., Joung, M-R., *et al*. (2008) *Journal of American Ceramic Society*, **91**, 4133–4136.
123. Mori, K., Ogawa, H., Kan, A., *et al*. (2004) *Journal of European Ceramic Society*, **24**, 1749–1753.
124. Mori, N., Sugimoto, Y., Harada, J., *et al*. (2004) *Journal of Ceramic Society Japan*, **112-1**, S1563–S15666.
125. Song, K. X. and Chen, X. M. (2008) *Materials Letters*, **62**, 520–522.
126. Varghese, J., Joseph, T. and Sebastian, M. T. (2011) *Materials Letters*, **65**, 1092–1094.
127. Jo, Y. H., Doo, S. D., Lee, J. S., *et al*. (2011) *Journal of Alloys & Compounds*, **509**, 849–853.
128. Zhang, Q-L., Yang, H. and Sun, H. P. (2008) *Journal of European Ceramic Society*, **28**, 605–609.
129. Hu, W., Liu, H., Hao, H., *et al*. (2015) *Journal of Materials Science: Materials in Electronics*, **26**, 1977–1981.
130. Zhou, J., Yang, H., Xu, N., *et al*. (2014) *Journal of Materials Science: Materials in Electronics*, **25**, 500–504.
131. Zhou, H. F., Wang, H., Zhang, M. H., *et al*. (2010) *Journal of Materials Research*, **25**, 1793–1798.
132. Li, C., Wei, Z., Luo, H., *et al*. (2015) *Journal of Materials Science: Materials in Electronics*, **26**, 9117–9121.
133. Joseph, T. and Sebastian, M. T. (2010) *Journal of American Ceramic Society*, **93**, 147.
134. Varghese, J., Joseph, T., and Sebastian, M. T. (2015) *Dalton Transactions*, **44**, 5146–5152.
135. Takada, T., Yamamoto, H., and Kageyama, K. (2003) *Japanese Journal of Applied Physics*, **42**, 6162–6167.
136. Zhang Q. L., Yang, H., Zou, J. L., *et al*. (2005) *Materials Letters*, **59**, 257–260.
137. Jo, Y. H., Kang, M. S., Chung, W., *et al*. (2008) *Materials Research Bulletin*, **43**, 361–369.
138. Ohsato, H., Terada, M., and Kawamura, K. (2012) *Japanese Journal of Applied Physics*, **51**, 09LF02–1.
139. Kim, J-S., Nguyen, N-H., Song, M-S., *et al*. (2009) *International Journal of Appled Ceramic Technology*, **6**, 581–586.
140. Li, W-B., Xi, H-H., and Zhou, D. (2015) *Ceramic International*, **41**, 9063–9068.

141. Zhang, J., Zhou, Y., and Yue, Z. (2013) *Ceramic International*, **39**, 2051–2058.
142. Dou, G., Zhou, D., Guo, M., *et al*. (2013) *Journal of Materials Science: Materials in Electronics*, **24**, 1431–1438.
143. Guo, M., Li, Y., Dou, G., *et al*. (2016) *Journal of Materials Science: Materials in Electronics*, in press.
144. Bian, J-J., Kim, D-W., and Hong, K. S., (2003) *Journal of European Ceramic Society*, **23**, 2589–2592.
145. Kagata, H., Saito, R., and Katsumura, H. (2004) *Journal of Electroceramics*, **13**, 277–280.
146. Cho, I-S., Choi, G. K., An, J-S., *et al*. (2009) *Materials Research Bulletin*, **44**, 173–178.
147. Busuioc, C. and Jinga, S. I. (2014) *Ceramic International*, **40**, 5931–5936.
148. Zhang, J., Zhou, X., Peng, B., *et al*. (2014) *Journal of American Ceramic Society*, **97**, 3537–3543.
149. Kan, A., Ogawa, H., Ohsato, H., *et al*. (2001) *Japanese Journal of Applied Physics*, **40**, 5774–5778.
150. Yoon, S. H., Kim, D-W., Cho, S-Y., *et al*. (2006) *Journal of European Ceramic Society*, **26**, 2051–2054.
151. Lorite, I., Rodriguez, M. A., Azough, F., *et al*. (2012) *Journal of American Ceramic Society*, **95**, 1023–1028.
152. Joseph, T., Sebastian, M. T., Jantunen, H., *et al*. (2011) *International Journal of Appled Ceramic Technology*, **8**, 856–864.
153. Chen, J-Y., Hsu, W-H., and Huang, C-L. (2010) *Journal of Alloys & Compounds*, **504**, 284–287.
154. Jiang, C., Wu, S., and Mei, Y. (2012) *Journal of Alloys & Compounds*, **544**, 141–144.
155. Ma, Q., Wu, S., Jiang, C., and Li, J. (2013) *Ceramic International*, **39**, 223–229.
156. Hu, W., Liu, H., Ho, H., *et al*. (2014) *Journal of Materials Science: Materials in Electronics*, **25**, 4730–4734.
157. Wang, H., Li, D., Yang, Q., *et al*. (2014) *Ceramic International*, **40**, 3333–3339.
158. Zhou, D., Pang, L-X., Qi, Z-M., *et al*. (2014) *Scientific Reports*, **4**, 5980.
159. Zhou, J., Xu, N., Zhang, Q., *et al*. (2015) *Materials Letters*, **139**, 169–172.
160. Hu, W., Liun, H., Hao, H., *et al*. (2015) *Ceramic International*, **41**, S510–S514.
161. Hu, Y., Jin, Z., Fu, Q., *et al*. (2015) *Ceramic International*, **41**, 10531–10536.
162. Jeong, Y-H., Kim, M-H., Nahm, S., *et al*. (2005) *Japanese Journal of Applied Physics*, **44**, 956–960.
163. Lo, C-L., Duh, J-G., Chou, B-S., *et al*. (2002) *Journal of American Ceramic Society*, **85**, 2230–2235.
164. Joseph, T., Sebastian, M. T., Sreemoolanathan, H., *et al*. (2010) *International Journal of Appled Ceramic Technology*, **7**, E98–E106.
165. Rao, S.D.R., Kiran, S. R., and Murthy, V R K. (2012) *Journal of American Ceramic Society*, **95**, 3532–3537.
166. Wang, H., Li, D., Yang, Q., *et al*. (2014) *Materials Research Bulletin*, **54**, 66–72.
167. Shin, H., Shin, H-K., Jung, H. S., *et al*. (2005) *Materials Research Bulletin*, **40**, 2021–2028.
168. Cho, I-S., Kim, D-W., Kim, J-R., *et al*. (2004) *Ceramic International*, **30**, 1181–1185.
169. Takada, T. and Kageyama, K. (2005) *Japanese Journal of Applied Physics*, **44**, 6629–6635.
170. Liu, L., Feng, Y., Qiu, T., *et al*. (2015) *Journal of Materials Science: Materials in Electronics*, **26**, 1316–1321.
171. Nishigaki, S., Yano, S., Kato, H., *et al*. (1988) *Journal of American Ceramic Society*, **71**, C-11-C17.
172. Umemura, R., Ogawa, H., and Kan, A. (2006) *Journal of European Ceramic Society*, **26**, 2063–2068.
173. Kim, H. T., Nam, M-H., Kim, J-H., *et al*. (2009) *International Journal of Appled Ceramic Technology*, **6**, 587–592.
174. Zhang, S. W., Fan, X. C., and Chen, X. M. (2008) *Journal of American Ceramic Society*, **91**, 488–493.
175. Huang, C-L., Chien, Y-H., Tsai, C-Y., *et al*. (2011) *Journal of Alloys and Compounds*, **509**, L150–L152.

176. Zhou, D., Li, W-B., Pang, L-X., *et al*. (2014) *Journal of American Ceramic Society*, **97**, 3597–3601.
177. Jantunen, H., Uusumaki, A., Rautioaho, R., *et al*. (2000) *Journal of European Ceramic Society*, **20**, 2331–2336.
178. Pang, L-X., Sun, G. B., and Zhou, D. (2011) *Materials Letters*, **65**, 164–166.
179. Joung, M-R., Kim, J. S., Song, M. E., *et al*. (2009) *Journal of American Ceramic Society*, **2**, 2151–2154.
180. Rose, A., Lazar, A., Manu, K. M., *et al*. (2013) *Journal of Alloys and Compounds*, **552**, 83–87.
181. Chen, Y-C., Su, C-F., Weng, M-Z., *et al*. (2014) *Journal of Materials Science: Materials in Electronics*, **25**, 2120–2125.
182. Fang, L., Wei, Z., Su, C., *et al*. (2014) *Ceramic International*, **40**, 16835–16839.
183. Huang, C-L., Tai, C-Y., Huang, C-Y., *et al*. (2010) *Journal of American Ceramic Society*, **93**, 1999–2003.
184. Wu, S. P., Chen, D. F., Mei, Y. X., *et al*. (2012) *Journal of Alloys & Compounds*, **521**, 8–11.
185. Wu, S. P., Jiang, C., Mei, Y. X., *et al*. (2012) *Journal of American Ceramic Society*, **95**, 37–40.
186. Chen, Y-C., Wang, Y-N., and Hsu, C-H. (2011) *Journal of Alloys & Compounds*, **509**, 9650–9653.
187. Fu, P., Lu, W., Lei. W., *et al*. (2013) *Ceramic International*, **39**, 2481–2487.
188. Meng, S., Yue, Z., Zhuang, H., *et al*. (2010) *Journal of American Ceramic Society*, **93**, 359–361.
189. Kan, A., Ogawa, H., and Ohsato, H. (2007) *Japanese Journal of Applied Physics*, **46**, 7108–7111.
190. Wang, W., Tang, L., Bai, W., *et al*. (2014) *Journal of Materials Science: Materials in Electronics*, **25**, 3601–3607.
191. Fang, L., Wei, Z., Guo, H., *et al*. (2015) *Journal of Materials Science: Materials in Electronics*, **26**, 5892–5895.
192. Xie, H., Chen, C., Tian, R., and Xi, H. (2016) *International Journal of Applied Ceramic Technology*.
193. Fang, L., Wei, Z., Guo, H., *et al*. (2015) *Journal of Materials Science: Materials in Electronics*, **26**, 5892–5895.
194. Kan, A., Ogawa, H., Ohsato, H., *et al*. (2001) *Japanese Journal of Applied Physics*, **40**, 5774–5778.
195. Surendran, K. P., Bijumon, P. V., Mohanan, P., *et al*. (2005) *Applied Physics A*, **A81**, 823–826.
196. Choi, Y-J., Park, J-H., Park, J-H., *et al*. (2004) *Materials Letters*, **58**, 3102–3106.
197. Jantunen, H., Uusumaki, A., Rautioaho, R., *et al*. (2002) *Journal of American Ceramic Society*, **85**, 697–699.
198. Surendran, K. P., Santha, N., Mohanan, P., *et al*. (2004) *European Physics Journal*, **41**, 301–306.
199. Kan, A. and Ogawa, H. (2004) *Journal of Alloys and Compounds*, **364**, 247–249.
200. Fang, C.F., Chen, Y-C., Tzou, W-C., *et al*. (2003) *Materials Letters*, **57**, 2945–2949.
201. Ohsato, H., Tsunooka, T., Ohishi, Y., *et al*. (2003) *Journal of Korean Ceramic Society*, **40**, 350–353.
202. Hsu, C-H. and Chang, C-H. (2012) *Ceramic International*, **38**, 4411–4413.
203. Zhang, Q-L., Yang, H and Zou, J-L. (2008) *Materials Letters*, **62**, 3872–3874.
204. Chen, Y-C. (2012) *Journal of Alloys & Compounds*, **527**, 84–89.
205. Tsai, W-C., Liou, Y-H., and Liou, Y-C. (2012) *Materials Science and Engineering*, **B177**, 1133–1137.
206. Wu, N. X. and Bian, J. J. (2011) *International Journal of Applied Ceramic Technology*, **8**, 1494–1500.
207. Zhou, D., Rindall, C. A., Pang, L-X., *et al*. (2011) *Journal of American Ceramic Society*, **94**, 802–805.
208. Tzou, W-C., Chang, S-L., Yang, C-F., *et al*. (2003) *Materials Research Bulletin*, **38**, 981–989.
209. Tseng, C-F., Tung, H-H., Hsu, C-K., *et al*. (2010) *Journal of Alloys & Compounds*, **502**, 136–138.
210. Joseph, T. and Sebastian, M. T. (2011) *Materials Letters*, **65**, 891–893.

211. Liu, Y., Wang, Y., Li, Y., *et al*. (2016) *Ceramic International*, in press.
212. Lie, J., Fang, L., Luo, H., *et al*. (2016) *Journal of European Ceramic Society*, **36**, 243–246.
213. Kim, S. K., Kim, B.S-H., Lee, B. I. (2006) *Journal of European Ceramic Society*, **26**, 2101–2104.
214. Choi, J. W., Kucheiko, S., Yoon, S-J., *et al*. (2001) *Journal of American Ceramic Society*, **84**, 2570–2572.
215. Higuchi, Y., Sugimoto, Y., Harada, J., *et al*. (2007) *Journal of European Ceramic Society*, **27**, 2785–2788.
216. Chen, Y-C., Wang, Y-N., and Hsu, C-H. (2012) *Materials Chemistry and Physics*, **133**, 829–833.
217. Husu, C-H., Tung, T-H., and Hsu, C-K. (2011) *Materials Chemistry and Physics*, **131**, 1–3.
218. Ajith, M. R., Umerji, A. M., Sreemoolanathan, H., *et al*. (2010) *International Conference Recent Trends in Materials Science & Technology*, Trivandrum, 6.14-6.15
219. Zhang, Q-L., Yang, H., and Zou, J-L. (2009) *Journal of Materials Science: Materials in Electronics*, **20**, 181–185.
220. *Murata Manufacturing Company*, Japan. Product Catalogue
221. Chen, Y-C., You, H-M., and Hang, K-C. (2015) *Journal of Materials Science: Materials in Electronics*, **26**, 7614–7620.
222. Fua, Z., Liua, P., and Ma, J-L., *et al*. (2016) *Journal of European Ceramic Society*, **36**, 625–629.
223. Valant, M. and Suvorov, D. (2004) *Journal of European Ceramic Society*, **24**, 1715–1719.
224. Wu, S. P., Luo, J. H., and Cao, S. X. (2010) *Journal of Alloys & Compounds*, **502**, 147–152.
225. Wang, G., He, Z., Li, D., *et al*. (2013) *Ceramic International*, **40**, 3895–3902.
226. Wu, S., Xue, J., and Fan, Y. (2016) *Journal of American Ceramic Society*.
227. Yao, G. G., Hu, X-S., Tian, X-L., *et al*. (2015) *Journal of Materials Science: Materials in Electronics*, **26**, 1795–1798.
228. Krzmanc, M. C., Logar, M., Budic, B., *et al*. (2011) *Journal of American Ceramic Society*, **94**, 2464–2472.
229. Guo, J., Zhou, D., Wang, H., *et al*. (2012) *Journal of American Ceramic Society*, **95**, 223–237.
230. Bijumon, P. V., Sebastian, M. T., Mohanan, P. (2005) *Journal of Applied Physics*, **98**, 124105.
231. Zhang, Z., Su, H., Tang, X., *et al*. (2013) *Ceramic International*, **40**, 1613–1617.
232. Dai, S. X., Huang, R-F., Wilcox, D. L. (2002) *Journal of American Ceramic Society*, **85**, 828–832.
233. Cho, I-S., Ryu, H-S., Kim, J-R., *et al*. (2007) *Japanese Journal of Applied Physics*, **46**, 2999–3003.
234. Wu, S. P., Chen, D.F., Jiang, C., *et al*. (2012) *Materials Letters*, **91**, 239–241.
235. Ohsato, H. (2010) *Proceedings of Materials Research Sociey Meeting*.
236. Zhen, W. and Bian, J. J. (2014) *Ceramic International*, **40**, 8507–8511.
237. Yao, G-G., Liu, P. and Zhang, H-W. (2013) *Journal of American Ceramic Society*, **96**, 1691–1693.
238. Wang, H-J., Li, B-T., Lin, H-X., *et al*. (2014) *International Journal of Applied Glass Science*, **5**, 436–442.
239. Lei, W., Zhong, W-Z., Wang, X-H., *et al*. (2011) *Journal of American Ceramic Society*, **94**, 20–23.
240. Lv, Y., Zuo, R., and Yue, Z. (2013) *Materials Research Bulletin*, **48**, 2011–2017.
241. Ma, Q., Wu, S. and Fan, Y. (2014) *Ceramic International*, **40**, 1073–1080.
242. Chen, J-M., Wang, H-P., Feng, S-Q., *et al*. (2011) *Ceramic International*, **37**, 989–993.
243. Ling, C. D., Rowda, B., Avdeev, M. *et al*. (2009) *Journal of Solid State Chemistry*, **182**, 479–483.
244. Watanabe, M., Ogawa, H., Ohsato, H., *et al*. (1998) *Japanese Journal of Applied Physics*, **37**, 5360–5363.
245. Bian, J. J. (2007) *Journal of European Ceramic Society*, **27**, 3855–3859.
246. Pang, L-X., Zhou, D., and Liu, W-G. (2014) *Journal of American Ceramic Society*, **97**, 2032–2034.
247. Wu, X., Xue, J., Wang, R., *et al*. (2014) *Journal of Alloys & Compounds*, **585**, 542–548.

248. Zhou, H., He, F., Chen, X., *et al*. (2014) *Journal of Materials Science: Materials in Electronics*, **25**, 1480–1484.
249. Zhang, Z., Su, H., Tang, X., *et al*. (2014) *Ceramic International*, **40**, 10531–10535.
250. Dou, G., Guo, M., and Li, Y. (2016) *Journal of Materials Science: Materials in Electronics*, in press.
251. Lei, W., Lu, W. Z., Hua, J-H., *et al*. (2008) *Journal of American Ceramic Society*, **91**, 1958–1961.
252. Kan, A., Ogawa, H., and Moriyama, T. (2012) *Journal of Materials Research*, **27**, 915–921.
253. Thomas, S. and Sebastian, M. T. (2009) *Journal of American Ceramic Society*, **92**, 2975–2981.
254. Kalathil, S. E., Neelakantan, U. A., and Ratheesh, R. (2014) *Journal of American Ceramic Society*, **97**, 1530–1533.
255. Unnimaya, A. N., Suresh, E. K., Dhanya, J., *et al*. (2014) *Journal of Materials Science: Materials in Electronics*, **25**, 1127–1131.
256. Chen, Y-C., Weng, M-Z. and Hong, J-M. (2014) *Journal of Materials Science: Materials in Electronics*, **25**, 5000–5005.
257. Arun, B., Varghese, J., Surendran, K. P., *et al*. (2014) *Ceramic International*, **40**, 13075–13081.
258. Li, D., Wang, H., Yang, Q., *et al*. (2014) *Ceramic International*, **40**, 14185–14190.
259. Chen, H-C., Weng, M-H., Hung, C-I., *et al*. (2004) *Physica B*, **349**, 304–309.
260. Zhou, D., Pang, L-X., Guo, J., *et al*. (2011) *Journal of European Ceramic Society*, **31**, 2749–2752.
261. Yuan, L., Wang, H., Lin, H., *et al*. (2014) *Ceramic International*, **40**, 2109–2113.
262. Dong, Z. W., Zheng, Y., Cheng, P., *et al*. (2014) *Materials Letters*, **131**, 151–153.
263. Wang, H., He, Z., Li, D., *et al*. (2014) *Ceramic International*, **40**, 3895–3902.
264. Pullar, R. C., Farrah, S., and Alford, N. (2007) *Journal of European Ceramic Society*, **27**, 1059–1063.
265. Joung, J.M-R., Kim, J. S., Song, M. S., *et al*. (2010) *Journal of American Ceramic Society*, **93**, 2132–2135.
266. Wang, L. and Bian, J. J. (2011) *Materials Letters*, **65**, 726–728.
267. Chen, Y-C., Liou, J-M., Weng, M-Z., *et al*. (2014) *Ceramic International*, **40**, 10337–10342.
268. Cho, I-S., Lee, J-S., Bae, S-T., *et al*. (2009) *Journal of Electroceramics*, **23**, 154–158.
269. Thomas, S. and Sebastian, M. T. (2008) *Materials Research Bulletin*, **43**, 843–851.
270. Huang, C-L., Wang, J-J., Yen, F-S., *et al*. (2008) *Materials Research Bulletin*, **43**, 1463–1471.
271. Lv, Y. and Zuo, R. (2013) *Ceramic International*, **39**, 2545–2550.
272. Alford, N. Mc N. and Penn, S. J. (1996) *Journal of Applied Physics*, **80**, 5895–5898.
273. Yokoi, A., Ogawa, H., Kan, A., *et al*. (2004) *Journal of Ceramic Society Japan*, **112**, S-1633–S1636.
274. Kan, A., Ogawa, H., Yokoi, A., *et al*. (2007) *Journal of European Ceramic Society*, **27**, 2977–2981.
275. Alford, N. Mc N., Breeze, J., Wang, X., *et al*. (2001) *Journal of European Ceramic Society*, **21**, 2605–2611.
276. Ogawa, H., Taketani, H., Kan, A., *et al*. (2005) *Journal of European Ceramic Society*, **25**, 2859–2863.
277. Kwon, D-W., Lanagan, M. T., and Shrout, T. R. (2007) *Materials Letters*, **61**, 1827–1831.
278. Breeze, J., Aupi, X., and Alford, N. Mc N. (2000) *Electronic Letters*, **36**, 883–884.
279. Kim, E. S. and Kim, S. H. (2006) *Journal of Electroceramics*, **17**, 471–477.
280. Xiang, F., Fang, L., Su, C., *et al*. (2013) *Ceramic International*, **39**, 9779–9783.
281. Lv, Y., Zuo, R., Cheng, Y., *et al*. (2013) *Journal of American Ceramic Society*, **96**, 3862–3867.
282. Lee, C., Chen, C-T., Huang, C-Y., *et al*. (2008) *Japanese Journal of Applied Physics*, **47**, 4634–4637.
283. Guo, J., Zhou, D., Zou, S-L., *et al*. (2014) *Journal of American Ceramic Society*, **97**, 1819–1822.
284. Yao, G., Li, P., Zhao, X., Zhou, J., *et al*. (2014) *Journal of European Ceramic Society*, **34**, 2983–2987.
285. Kagomiya, I., Kodama, Y., Shimazu, Y., *et al*. (2015) *Journal of Alloys & Compounds*, **640**, 383–387.

286. Zhou, Y., Yue, Z., and Li, L. (2010) *Ferroelectrics*, **407**, 69–74.
287. Chen, X., Zhang, W., Zalinska, B., *et al*. (2012) *Journal of American Ceramic Society*, **95**, 3207–3213.
288. Lei, W., Lu, W-Z., Liu, D., *et al*. (2009) *Journal of American Ceramic Society*, **92**, 105–109.
289. Breeze, J., Aupi, X., and Alford, N. Mc N. (2002) *Applied Physics Letters*, **81**, 5021–5023.
290. Anjana, P. S., Joseph, T., and Sebastian, M. T. (2010) *Ceramic International*, **36**, 1535–1540.
291. Suresh, E. K., Unnimaya, A. N., Surjith, A., *et al*. (2013) *Ceramic International*, **39**, 3635–3639.
292. Yao, G-G., Pei, C-J., Xu, J-G., *et al*. (2015) *Journal of Materials Science: Materials in Electronics*, **26**, 7719–7722.
293. Choi, G-K., Cho, S-Y., An, J-S., *et al*. (2006) *Journal of European Ceramic Society*, **26**, 1969–1971.
294. Pang, L-X., Liou, H., Zhou, D., *et al*. (2012) *Journal of Alloys & Compounds*, **535**, 22–24.
295. Pang, L-X., Liou, H., Zhou, D., *et al*. (2012) *Materials Letters*, **72**, 128–130.
296. Pang, L-X., Zhou, D., Cai, C-L., *et al*. (2012) *Materials Letters*, **92**, 36–38.
297. Sunny, A. R., Viswanath, V., Surendran, K. P., *et al*. (2014) *Ceramic International*, **40**, 311–4317.
298. Su, C-H., Wang, Y-S., and Huang, C-L. (2015) *Journal of Alloys & Compounds*, **641**, 93–98.
299. Joung, M-R., Kim, J-S., Song, M-E., *et al*. (2009) *Journal of American Ceramic Society*, **92**, 3092–3094.
300. Kagoyama, I., Matsuda, Y., Kakimoto, K., *et al*. (2009) *Ferroelectrics*, **387**, 1–6.
301. Surjith, A. and Ratheesh, R. (2013) *Journal of Alloys & Compounds*, **550**, 169–172.
302. Wang, J., Chen, W., and Luo, L. (2007) *Japanese Journal of Applied Physics*, **46**, 5218–5220.
303. Xue, J., Wu, S., and Li, J. (2013) *Journal of American Ceramic Society*, **96**, 2481–2485.
304. Subodh, G., Ratheesh, R., Jacob, M. V., *et al*. (2008) *Journal of Materials Research*, **23**, 1551–1556.
305. Fang, L., Su, C., Zhou, H., *et al*. (2013) *Journal of American Ceramic Society*, **96**, 668–690.
306. Joung, M-R., Kim, J. S., Song, M. E., *et al*. (2009) *Journal of American Ceramic Society*, **92**, 1621–1624.
307. Xi, H-H., Zhou, D., Xie, H-D., *et al*. (2015) *Ceramic International*, **41**, 6103–6107.
308. Bian, J. J. and Ding, Y. M. (2015) *Materials Research Bulletin*, **67**, 245–250.
309. Guo, J., Zhou, D., Wang, L., *et al*. (2013) *Dalton Transactions*, **42**, 1483–1491.
310. Lei, W., Lu, W. Z., and Wang, X-C. (2012) *Ceramic International*, **38**, 99–103.
311. Surjith, A., Suresh, E. K., and Ratheesh, R. (2013) *Journal of Materials Science: Materials in Electronics*, **24**, 1818–1822.
312. Zhou, H., He, F., Chen, X., *et al*. (2014) *Ceramic International*, **40**, 6335–6338.
313. Tseng, C-F. and Tsai, P-S. (2013) *Ceramic International*, **39**, 75–79.
314. Huang, C-L., Wang, J-W., and Huang, C-Y. (2007) *Journal of American Ceramic Society*, **90**, 1487–1493.
315. Pullar, R. C., Azough, F., Freer, R., *et al*. (2007) *Journal of European Ceramic Society*, **26**, 1943–1946.
316. Cho, I-S., Kang, S-K., Kim, D-W., *et al*. (2006) *Journal of European Ceramic Society*, **26**, 2007–2010.
317. Joung, M-R., Song, J-S., Nahm, S., *et al*. (2010) *Journal of American Ceramic Society*, **93**, 934–936.
318. Abhilash, P., Thomas, D., Surendran, K. P., *et al*. (2013) *Journal of American Ceramic Society*, **96**, 1533–1537.
319. Wu, H. T. and Mei, Q. J. (2015) *Journal of Alloys and Compounds*, **651**, 393–398.
320. Wang, J., Chen, W., and Luo, L. (2008) *Journal of Alloys & Compounds*, **464**, 440–445.
321. Ohsato, H., Tsunooka, T., Sugiyama, T., *et al*. (2006) *Journal of Electroceramics*, **17**, 445–450.
322. Ogawa, H., Yokoi, A., Unemura, R., *et al*. (2007) *Journal of European Ceramic Society*, **27**, 3099–3104.
323. Mori, K., Ogawa, H., Kan, A., *et al*. (2003) *Journal of European Ceramic Society*, **23**, 2603–2606.
324. Dias, A., Subodh, G., Sebastian, M. T., *et al*. (2009) *Chemistry of Materials*, **20**, 4347–4355.

325. Jawahar, I. N., Mohanan, P., and Sebastian, M. T. (2003) *Materials Letters*, **57**, 4043–4048.
326. Wang, Y. N. and Bian, J. J. (2015) *Ceramic International*, in press.
327. Xi, H., Zhou, D., Xie, H., and Li, W. (2015) *Materials Letters*, **142**, 221–224.
328. Fu, Z., Liu, P., Ma, J., *et al*. (2016) *Materials Chemistry and Physics*.
329. Kan, A., Ogawa, H., Yokoi, A. (2005) *Journal of Materials Research*, **20**, 2456–2461.
330. Zhuang, H., Yue, Z., Meng, S., *et al*. (2008) *Journal of American Ceramic Society*, **91**, 3738–3741.
331. Xi, H-H., Zhou, D., Yie, H. D., *et al*. (2016) *Ceramic International*.
332. Wu, H. T., Wu, W. B., Yue, Y. L., *et al*. (2012) *Ceramic International*, **38**, 4271–4276.
333. Zhang, C. and Zhuo, R. (2015) *Journal of Alloys & Compounds*, **622**, 362–368.
334. Wang, Y-N., Chen, Y-C., and Syu, R-Y. (2015) *Journal of Materials Science: Materials in Electronics*, **26**, 1494–1499.
335. Chen, Y-C. and You, H-M. (2014) *Journal of Alloys & Compounds*, **616**, 356–362.
336. Fang, L., Guo, H., Fang, W., *et al*. (2015) *Journal of European Ceramic Society*, **35**, 3765–3770.
337. Surjith, A., James, N. K., and Ratheesh, R. (2012) CICMT, Erfurt, Germany
338. Huang, W., Liu, K-S., Chu, L-W., *et al*. (2003) *Journal of European Ceramic Society*, **23**, 2565–2568.
339. Ogawa, H., Kan, A., Ishihara, S., *et al*. (2003) *Journal of European Ceramic Society*, **23**, 2485–2488.
340. Kim, J. C., Kim, M-H., Kim, J-B., *et al*. (2007) *Journal of American Ceramic Society*, **90**, 641–644.
341. Su, C., Fang, L., Wei, Z., *et al*. (2014) *Ceramic International*, **40**, 5015–5018.
342. Liao, Q., Wang, Y., Jiang, F., *et al*. (2014) *Journal of American Ceramic Society*, **97**, 2394–2396.
343. Guo, J., Zhou, D., Li, Y., *et al*. (2014) *Daltons Transactions*, **43**, 11888–11896.
344. Li, W-B., Xi, H-H., and Zhou, D. (2015) *Journal of Materials Science: Materials in Electronics*, **26**, 1608–1611.
345. Zhai, X-L., Zheng, X., Xi, H-H., *et al*. (2015) *Journal of American Ceramic Society*, **98**, 2716–2719.
346. Kan, A., Ogawa, H., Yokoi, A., *et al*. (2003) *Japanese Journal of Applied Physics*, **42**, 6154–6157.
347. Lu, W-Z., Lei, W., Zhu, J-H., *et al*. (2007) *Japanese Journal of Applied Physics*, **46**, L724–L726.
348. Dai, Y., Guo, T., Pei, X., and Chen, W. (2008) *Materials Science and Engineering*, **A475**, 76–80.
349. Thomas, D. and Sebastian, M. T. (2011) *Journal of American Ceramic Society*, **94**, 2276–2278.
350. Lei, W., Lu, W-Z., Zhu, J-Z., *et al*. (2009) *Ceramic International*, **35**, 277–280.
351. Bian, J. J. and Wu, J-Y. (2012) *Journal of American Ceramic Society*, **95**, 318–323.
352. Zhou, D., Pang, L-X., Guo, J., *et al*. (2011) *Journal of American Ceramic Society*, **94**, 2800–2803.
353. Kan, A., Ogawa, H., and Ohsato, H. (2004) *Journal of Ceramic Society Japan*: Suppl. 2004, **112**, S1622–S1626.
354. Xiang, H., Fang, L., Jiang, X., *et al*. (2016) *Journal of American Ceramic Society*, in press.
355. Yue, X., Lei, W., and Lu, W-Z. (2009) *Ceramic International*, **35**, 2131–2134.
356. Lin, H., Yang, A., Luo, L., *et al*. (2008) *Materials Letters*, **62**, 611–614.
357. Jeon, C. J. and Kim, E. S. (2008) *Ceramic International*, **34**, 921–924.
358. Kan, A., Ogawa, H., and Ohsato, H. (2004) *Journal of Ceramic Sociey Japan*: Suppl., **112-1** S1622–S1626.
359. Chen, X. M., Bai, S., Li, M., *et al*. (2013) *Journal of European Ceramic Society*, **33**, 3001–3006.
360. Tseng, C-F., Tseng, P-J., Chang, C-M., *et al*. (2014) *Journal of American Ceramic Society*, **97**, 1918–1922.
361. Mandai, H., *et al*. (1990) In *Proceedings of Ceramic Science & Technlogy Congress*, p. 83
362. Kan, A., Ogawa, H., and Yokoi, A. (2006) *Materials Research Bulletin*, **41**, 1178–1184.

363. Kim, D-W., Kwon, SD-K., Yoon, S. H., *et al*. (2006) *Journal of American Ceramic Society*, **89**, 3861–3864.
364. Kim, S. J. and Kim, E. S. (2008) *Ceramic International*, **35**, 137–141.
365. Lv, Y. and Zuo, R. (2013) *Journal of Materials Science: Materials in Electronics*, **24**, 1225–1230.
366. Anjana, P. S. (2008) Investigations on ceria based dielectric ceramic materials for wireless communication. PhD Thesis. Cochin University of Science & Technology, India.
367. Thomas, S. and Sebastian, M. T. (2012) *Journal of Alloys and Compounds*, **546**, 72–76.
368. Guo, H., Wei, Z., Li, C., *et al*. (2016) *Journal of Materials Science: Materials in Electronics*, **26**, in press.
369. Kim, J. C., Kim, M-H., Nahm, S., *et al*. (2007) *Journal of European Ceramic Society*, **27**, 2865–2870.
370. Yu, J., Shen, C., and Qiu, T. (2015) *Journal of Materials Science: Materials in Electronics*, **26**, 2737–2741.
371. James, N. K. and Ratheesh, R. (2010) *Journal of American Ceramic Society*, **93**, 931–933.
372. Wu, H. T., Li, L-X., Zou, Q., *et al*. (2010) *Journal of Alloys & Compounds*, **509**, 151–155.
373. Takahashi, H., Ayusawa, K., and Sakamoto, N. (1997) *Japanese Journal of Applied Physics*, **36**, 5597–5599.
374. Wang, Y., Zuo, R., Zhang, C., *et al*. (2016) *Journal of American Ceramic Society*, **98**.
375. Xiang, H., Fang, L., Jiang, X., *et al*. (2016) *Ceramic International*, **42**, 3701–3705.
376. Ohishi, Y., Miyauchi, Y., Ohsato, H., *et al*. (2004) *Japanese Journal of Applied Physics*, **43**, L749–L751.
377. Kono, M., Takagi, H., Tatekawa, T., *et al*. (2006) *Journal of European Ceramic Society*, **26**, 1909–1912.
378. Miyauchi, Y., Ohishi, Y., Miyake, S., *et al*. (2006) *Journal of European Ceramic Society*, **26**, 2093–2096.
379. Kan, A. and Ogawa, H. (2009) *Journal of Alloys & Compounds*, **468**, 338–342.
380. Kolodiazhnyi, T., Annino, G., Spreitzer, M., *et al*. (2009) *Acta Metellurgica*, **57**, 3402–3409.
381. Lufasso, M. W., Hopkins, E., Bell, S. M., *et al*. (2005) *Chemistry of Materials*, **17**, 4250–4255.
382. Joang, X. J., Fang, L., Xiang, H., *et al*. (2015) *Ceramic International*, **41**, 13878–13882.
383. Surendran, K. P., Mohanan, P., Manjusha, M. V., *et al*. (2005) *Journal of Applied Physics*, **98**, 044101–9.
384. Kan, A., Ogawa, H., Ohsato, H., *et al*. (2001) *Journal of European Ceramic Society*, **21**, 2593–2598.
385. Yang, T., Han, Z., Liun, P., *et al*. (2015) *Ceramics International*, **41**, S572–S575.
386. Bian, J. J. and Wang, L. (2011) *Journal of American Ceramic Society*, **94**, 3188–3191.
387. Ohishi, Y., Miyauchi, Y., Ohsato, H., *et al*. (2004) *Japanese Journal of Applied Physics*, **43**, L749–L751.
388. Zhou, D., Wang, H., Wang, Q-P., *et al*. (2010) *Functional Letters*, **03**, 253.
389. Huang, C-L., Chu, C. H., Liu, F. S., *et al*. (2014) *Journal of Alloys & Compounds*, **590**, 494–499.
390. Pang, L-X. and Zhou, D. (2010) *Journal of American Ceramic Society*, **93**, 3614–3617.
391. Manu, K. M., Karthik, C., Leu, L-C., *et al*. (2013) *Journal of American Ceramic Society*, **96**, 1504–1511.
392. Thomas, D., Rethika, K. T. and Sebastian, M. T. (2012) *Journal of Materials Science: Materials in Electronics*, **23**, 1268–1271.
393. Kan, A., Ogawa, H., Ohsato, H., *et al*. (2000) *Japanese Journal of Applied Physics*, **39**, 5654–5657.
394. Ohishi, Y., Miyamauchi, Y., Kakimoto, K., *et al*. (2004) *Proceedings of AMF*.
395. Kan, A. and Ogawa, H. (2009) *Journal of Alloys & Compounds*, **468**, 338–342.
396. Huang, C-L. and Yang, W-R. (2011) *Journal of Alloys & Compounds*, **509**, 2269–2272.
397. Zhao, Y. and Zhang, P. (2016) *Journal of Alloys & Compounds*, **658**, 744–748.
398. Yao, G. G. and Liu, P. (2012) *Ceramic International*, **38**, 2239–2242.
399. Guo, M., Li, Y., Dou, G., *et al*. (2015) *Journal of Materials Science; Materials in Electronics*, **26**, 608–612.

400. Bijumon, P. V., Solomon, S., Sebastian, M. T., *et al*. (2003) *Journal of Materials Science: Materials in Electronics*, **14**, 5–8.
401. Anjana, P. S. and Sebastian, M. T. (2009) *Journal of American Ceramic Society*, **92**, 96–104.
402. Shen, C-S., Chou, C-C., Shih, W-J., *et al*. (2003) *Materials Chemistry and Physics*, **79**, 124–128.
403. Ramarao, S. D. and Murthy, V. R. K. (2015) *Daltons Transactions*, **44**, 2311–2324.
404. Li, J., Liu, P., Fu, Z-F., *et al*. (2016) *Journal of Alloys & Compounds*, **660**, 93–98.
405. Kan, A., Ogawa, H., Watanabe, M., *et al*. (1999) *Japanese Journal of Applied Physics*, **38**, 5629–5632.
406. Huang, C-L., Yang, T. J., and Huang, C-C. (2009) *Journal of American Ceramic Society*, **92**, 119–124.
407. Takahashi, H., Ayusawa, K., and Sakamoto, N. (1998) *Japanese Journal of Applied Physics*, **37**, 908–911.
408. Huang, C-L., Yang, W. R., and Chen, Y-R. (2010) *Journal of Alloys & Compounds*, **495**, 15–17.
409. Wu, N. X. and Bian, J. J. (2012) *Materials Science and Engineering B*, **177**, 1793–1798.
410. Wang, S-F., Wang, Y-R., Hsu, Y-F., *et al*. (2010) *Journal of American Ceramic Society*, **93**, 4071–4074.
411. Li, W-B., Xi, H-H., and Zhou, D. (2015) *Journal of Materials Science: Materials in Electronics*, **26**, 1608–1611.
412. Chen, Y. C. and Weng, M-Z. (2015) *Journal of Materials Science: Materials in Electronics*, **26**, 3502–3505.
413. Anjana, P. S., Joseph, T., and Sebastian, M. T. (2010) *Journal of Alloys & Compounds*, **490**, 208–213.
414. Bijumon, P.V., Mohanan, P., and Sebastian, M. T. (2002) *Materials Research Bulletin, Materials Research*, **37**, 2129–2133.
415. Tian, C., Yue, Z., Meng, S., *et al*. (2012) *Journal of American Ceramic Society*, **95**, 1645–1650.
416. Zhang, T. and Zuo, R. (2015) *Ceramic International*, **40**, 15677–15684.
417. Belous, A., Ovchar, O., Durylin, D., *et al*. (2007) *Journal of European Ceramic Society*, **27**, 2963–2966.
418. Shin, H-K., Shin, H. S., Jung, H. S., *et al*. (2005) *Materials Research Bulletin*, **41**, 1206–1214.
419. Hwang, S. J., Kim, Y-J., and Kim, H. S. (2007) *Journal of Electroceramics*, **18**, 121–128.
420. Li, J., Li, C., Wei, Z., *et al*. (2015) *Journal of American Ceramic Society*, **98**, 683–686.
421. Wang, L., Bian, J. J., and Guo, Q. H. (2010) *Materials Chemistry and Physics*, **124**, 748–750.
422. Huang, C-L., Pan, C-L., and Hsu, J-F. (2002) *Materials Research Bulletin*, **37**, 2483–2490.
423. Chen, Y-C., Chen, K. C., and Lee, W. C. (2013) *Journal of Materials Science: Materials in Electronics*, **24**, 1878–1882.
424. Fan, Y. and Bian, J. J. (2014) *Journal of Materials Science: Materials in Electronics*, **25**, 5084–5088.
425. Bhuyan, R. K., Santhoshkumar, T., Goswami, D., *et al*. (2013) *Materials Science and Engineering B*, **178**, 471–476.
426. Li, H., Tang, B., Zhang, S., *et al*. (2014) *Journal of Materials Science: Materials in Electronics*, **25**, 3318–3323.
427. Wu, M-C., Huang, K-T., and Su, W-F. (2006) *Materials Chemistry and Physics*, **98**, 406–409.
428. Varghese, J., Gopinath, S., and Sebastian, M. T. (2013) *Materials Chemistry and Physics*, **137**, 811–815.
429. Zhou, H., Wang, H., Li, K., *et al*. (2010) *Journal of Materials Science: Materials in Electronics*, **21**, 252–255.
430. Guo, H., Fang, L., Jiang, X., *et al*. (2016) *Ceramic International*, in press.
431. Kim, J-S., Joung, M-R., Song, M-E., *et al*. (2008) *Journal of American Ceramic Society*, **91**, 4165–4167.
432. Khalyavin, D. D., Han, J., Senos, A. M. R., *et al*. (2003) *Journal of Materials Research*, **18**, 2600–2607.
433. Luo, H., Li, J., Xu, J., *et al*. (2016) *Journal of Materials Science: Materials in Electronics*, in press.
434. Li, Y. Z., Bian, J. J., and Yuan, L. L. (2009) *Journal of Materials Science*, **44**, 328–330.

435. Liu, X. Q., Chen, X. M., and Xiao, Y. (2003) *Materials Science and Engineering B*, **103**, 276–280.
436. Pang, L-X. and Zhou, D. (2011) *Journal of Materials Science: Materials in Electronics*, **22**, 9807–9810.
437. Li, B-J., Wang, S-Y., Chiu, C-Y., *et al*. (2016) *Journal of Alloys & Compounds*, **661**, 357–362.
438. Surendran, K. P., Mohanan, P., and Sebastian, M. T. (2006) *Materials Research Bulletin*, **41**, 784–790.
439. Li, H., Tang, B., Li, Y. X., *et al*. (2015) *Materials Letters*, **145**, 30–33.
440. Fan, X. C., Chen, X. M., and Liu, X. Q. (2008) *Chemistry of Materials*, **20**, 4092–4098.
441. Guo, M., Dou, G., Gong, S., *et al*. (2012) *Journal of European Ceramic Society*, **32**, 883–890.
442. Huang, C-L. and Liu, S-S. (2008) *Journal of American Ceramic Society*, **91**, 3428–3430.
443. Huang, C-L. and Chen, J-Y. (2009) *Journal of American Ceramic Society*, **92**, 675–678.
444. Wang, S-F., Huang, C-Y., and Liu, Y-L. (2010) *Journal of American Ceramic Society*, **93**, 3272–3277.
445. Kim, D-W., Kim, I-T., Park, B., *et al*. (2001) *Journal of Materials Research*, **16**, 1465–1470.
446. Huang, C-L. and Chen, J. H. (2009) *Journal of American Ceramic Society*, **92**, 379–383.
447. Huang, C-L. and Chen, J. H. (2009) *Journal of American Ceramic Society*, **92**, 2237–2241.
448. Joung, M-R., Kim, J-S., Song, M-E., *et al*. (2008) *Journal of American Ceramic Society*, **91**, 4165–4167.
449. Ramarao, S. D. and Murthy, V. R. K. (2015) *Journal of Physics and Chemistry of Solids*, **17**, 12623–12633.
450. Zhou, H., Gong, J., Fan, G., *et al*. (2016) *Journal of Alloys & Compounds*, in press.
451. Huang, C-L., Tseng, Y-W., Chen, J-Y., *et al*. (2012) *Journal of European Ceramic Society*, **32**, 2365–2371.
452. Cho, S-Y., Kim, I-T., and Hong, K. S. (1999) *Journal of Materials Research*, **14**, 114–119.
453. Yokoi, A., Ogawa, H., Kan, A., *et al*. (2005) *Journal of European Ceramic Society*, **25**, 2871–2875.
454. Choi, J-W., Kang, C-Y., Sim, S-H., *et al*. (2003) *Materials Chemistry and Physics*, **79**, 247–251.
455. Dhanya, J., Unnimaya, A. N., and Ratheesh, R. (2016) *Journal of Materials Science: Materials in Electronics*.
456. Liu, X., Zhou, H., Liang, F., *et al*. (2012) *Journal of American Ceramic Society*, **95**, 3357–3359.
457. Zhou, D., Wang, H., Pang, L-X., *et al*. (2008) *Journal of American Ceramic Society*, **91**, 4115–4120.
458. Tseng, C-F. and Lin, P-A. (2014) *Journal of American Ceramic Society*, **97**, 1020–1022.
459. Ma, J-L., Fu, Z-F., Liu, P., *et al*. (2016) *Materials Science and Engineering B*, **204**, 15–19.
460. Kan, A. and Ogawa, H. (2008) *Journal of Applied Physics*, **47**, 7716–7720.
461. Kim, R., Kim, D-W., Yoon, S. H., *et al*. (2006) *Journal of Electroceramics*, **17**, 439–443.
462. Yang, A., Lin, H., and Chen, W. (2006) *Japanese Journal of Applied Physics*, **45**, 1698–1701.
463. Ogawa, H., Kan, A., Taketani, H., *et al*. (2004) *Journal of Japanese Ceramic Society*, Suppl., **112-1** S1627–S1632.
464. Yokoi, A., Ogawa, H., and Kan, A. (2006) *Journal of European Ceramic Society*, **26**, 2069–2074.
465. Wang, J-J., Huang, C-L., and Li, P-H. (2006) *Japanese Journal of Applied Physics*, **45**, 6352–6356.
466. Tsuji, Y., Kan, A., Ogawa, H., *et al*. (2005) *Journal of European Ceramic Society*, **25**, 2883–2887.
467. Zhou, Y., Tian, C., Meng, S., *et al*. (2012) *Journal of American Ceramic Society*, **95**, 1665–1670.
468. Li, L., Ding, X., and Liao, Q. (2012) *Ceramic International*, **38**, 1937–1941.
469. Huang, C-L., Tseng, Y-W., and Kuo, Y.C. (2011) *Journal of American Ceramic Society*, **94**, 2963–2967.
470. He, L., Zhou, D., Feng, X., *et al*. (2013) *Journal of American Ceramic Society*, **96**, 3027–3030.
471. Subodh, G. and Sebastian, M. T. (2007) *Journal of American Ceramic Society*, **90**, 2266–2268.

472. Ichinose, N. and Yamamoto, H. (1997) *Ferroelectrics*, **201**, 255–262.
473. Yao, G., Liu, P., and Zhang, H. (2013) *Journal of American Ceramic Society*, **96**, 3114–3119.
474. Pang, L-X., Zhou, D., Guo, J., *et al*. (2015) *Journal of American Ceramic Society*, **98**, 130–135.
475. Zhang, T., Zuo, R., and Zhang, C. (2015) *Materials Research Bulletin*, **68**, 109–114.
476. Xie, H-D., Xi, H-H., Chen, C., *et al*. (2015) *Ceramic International*, **41**, 10287–10292.
477. Kan, A., Ogawa, H., Yokoi, A., *et al*. (2007) *Journal of European Ceramic Society*, **27**, 2977–2981.
478. Bian, J. J., Yuan, L. L., Li, Y. Z., *et al*. (2009) *Ferroelectric*, **387**, 1–7.
479. Bian, J. J., Liang, Z., and Wang, L. (2011) *Journal of American Ceramic Society*, **94**, 1447–1453.
480. Wu, Y., Zhou, D., Guo, J., *et al*. (2013) *Journal of Materials Science: Materials in Electronics*, **24**, 1505–1510.
481. Hsieh, M-L., Chen, L-S., Wang, S-M., *et al*. (2005) *Japanese Journal of Applied Physics*, **44**, 5045–5048.
482. Kim, D-W., Ko, K. H., and Hong, K. S. (2001) *Journal of American Ceramic Society*, **84**, 1286–1290.
483. Sohn, J-H., Inaguma, Y., Yoon, S. O., *et al*. (1994) *Japanese Journal of Applied Physics*, **33**, 5466–5470.
484. Chen, Y-B. (2012) *Journal of Alloys & Compounds*, **543**, 125–128.
485. Zhuang, H., You, Z., Zhao, F., *et al*. (2009) *Journal of Alloys & Compounds*, **472**, 411–415.
486. Chameswary, J., Thomas, S., and Sebastian, M. T. (2010) *Journal of American Ceramic Society*, **93**, 1863–1865.
487. Zhang, T., Zuo, R., and Wang, Y. (2014) *Journal of Materials Science: Materials in Electronics*, **25**, 5570–5575.
488. Anjana, P. S., Sebastian, M. T., Axelsson, A-K., *et al*. (2007) *Journal of European Ceramic Society*, **27**, 3445–3452.
489. Pullar, R. C., Breeze, J., and Alford, N. Mc N. (2002) *Key Engineering Materials*, **224-226**, 1–4.
490. Bijumon, P. V., Mohanan, P., and Sebastian, M. T. (2006) *Journal of Electroceramics*, **16**, 239–245.
491. Wakino, K. (1989) *Ferroelectrics*, **91**, 69–86.
492. Ferreira, V. M., Azough, F., Freer, R., *et al*. (1997) *Journal of Materials Research*, **12**, 3293–3299.
493. Kumar, T. S., Gogoi, P., Perumal, A., *et al*. (2014) *Journal of American Ceramic Society*, **97**, 1054–1059.
494. Zhou, D., Wang, H., Pang, L-X., *et al*. (2008) *Journal of American Ceramic Society*, **92**, 2242–2246.
495. Hsiang, H-I., Mei, L-T., Yang, S-W., *et al*. (2011) *Ceramic International*, **37**, 2453–2458.
496. Wang, Y-N., Chen, Y-C., Yao, S-L., *et al*. (2014) *Ceramic International*, **40**, 2641–2645.
497. Kan, A., Ogawa, H., and Ohsato, H. (2002) *Physica*, **B322**, 403–407.
498. Huang, C-L. and Liu, S-S. (2007) *Japanese Journal of Applied Physics*, **46**, 283–285.
499. Tseng, Y-W., Chen, J-Y., Kuo, Y-C., *et al*. (2011) *Journal of Alloys & Compounds*, **509**, L308–L310.
500. Ferrira, V. M., Azough, F., Freer, R., *et al*. (1997) *Journal of Materials Research*, **12**, 3293–3299.
501. Lyu, X., Li, L., Sun, H., *et al*. (2015) *Journal of Materials Science: Materials in Electronics*, **26**, 8663–8666.
502. Tseng, C-F. and Hsu, C-H. (2009) *Journal of American Ceramic Society*, **93**, 1149–1152.
503. Suresh, M. K., John, A., Thomas, J. K., *et al*. (2010) *Materials Research Bulletin*, **45**, 1389–1395.
504. Kwon, D-W., Lanagan, M. T., and Shrout, T. R. (2005) *Journal of American Ceramic Society*, **88**, 3419–3422.
505. Cho, W. W., Kakemoto, K., and Ohsato, H. (2005) *Materials Science and Engineering B*, **121**, 48–53.

506. Yoon, S. H., Choi, G-K., Kim, D-W., *et al*. (2007) *Journal of European Ceramic Society*, **27**, 3087–3091.
507. Butee, S., Kulkarni, A. R., Prakash, Om., *et al*. (2011) *Materials Science and Engineering B*, **176**, 567–572.
508. Sanoj, M. A. and Varma, M. R. (2009) *Journal of Alloys & Compounds*, **477**, 565–569.
509. Tseng, C-F. and Tang, H-J. (2010) *Journal of Alloys & Compounds*, **491**, 314–320.
510. Park, J. H., Choi, Y-J., Park, J-H., *et al*. (2004) *Materials Chemistry and Physics*, **88**, 308–312.
511. Ferreira, V. M. and Baptista, J. L. (1996) *Journal of American Ceramic Society*, **79**, 1697–1698.
512. Chen, Y-C., Weng, M-Z., and Chang, K-C. (2014) *Journal of Materials Science: Materials in Electronics*, **25**, 2475–2481.
513. Li, L., Gao, Z., Ren, Q., *et al*. (2014) *Journal of Alloys & Compounds*, **617**, 841–844.
514. Huang, C-L. and Liu, S-S. (2009) *Journal of Alloys & Compounds*, **471**, L9–L12.
515. Wang, Y-R., Wang, S-F., and Wen, C-K. (2006) *Materials Science and Engineering A*, **426**, 143–146.
516. Anjana, P. S. and Sebastin, M T. (2006) *Journal of American Ceramic Society*, **89**, 2114–2117.
517. Butee, S., Kulkarni, A. K., Prakash, Om., *et al*. (2010) *Materials Science and Engineering B*, **168**, 151–155.
518. Li, L., Chen, X. M., and Fan, X. C. (2005) *Journal of Electroceramics*, **15**, 209–214.
519. Tian, C., Yue, Z., Meng, S., *et al*. (2012) *Journal of American Ceramic Society*, **95**, 1645–1650.
520. Huang, C-L., Liu, S-S., and Chen, S-H. (2009) *Journal of Alloys & Compounds*, **480**, 794–797.
521. Huang, C-L., Chen, J-Y., and Li, B-J. (2011) *Journal of Alloys and Compounds*, **509**, 4247–4251.
522. Levin, I., Vanderah, T. A., and Coutts, R. (2002) *Journal of Materials Research*, **17**, 1729–1734.
523. Wang, Y-R., Wang, S-F., and Lin, Y-M. (2005) *Ceramic International*, **31**, 905–909.
524. Kawaguchi, S., Ogawa, H., Kan, A., *et al*. (2005) *Journal of European Ceramic Society*, **25**, 2853–2858.
525. Sebastian, M. T., Santha, N., Bijumon, P. V., *et al*. (2004) *Journal of European Ceramic Society*, **24**, 2583–2589.
526. Varghese, J., Presumy, M., Sebastian, M. T., *et al*. (2014) *Materials Chemistry and Physics*, **148**, 96–102.
527. Zhang, Q-L. and Yang, H. (2007) *Journal of Materials Science: Materials in Electronics*, **18**, 967–971.
528. Zhao, F., Yue, Z., Gui, Z., *et al*. (2005) *Japanese Journal of Applied Physics*, **44**, 8066–8070.
529. Li, B-J., Chen, J-Y., Huang, G-S., *et al*. (2010) *Journal of Alloys & Compounds*, **505**, 291–296.
530. Li, H., Li, Y., Tang, B., *et al*. (2014) *Journal of Materials Science: Materials in Electronics*, **25**, 717–722.
531. Peng, L. Q., Mao, M. M., and Chen, X. M. (2010) *Journal of American Ceramic Society*, **93**, 4066–4070.
532. Tseng, C-F. (2011) *Journal of Alloys & Compounds*, **509**, 9447–9450.
533. Zhen, W., Li, S., and Bian, J. J. (2013) *Ceramic International*, **39**, 9767–9772.
534. Chen, Y-C., Weng, M-Z., and Chang, K-C. (2014) *Journal of Materials Science: Materials in Electronics*, **25**, 844–853.
535. Tseng, C-F. (2011) *Materials Science Forum*, **687**, 199–203.
536. Huang, C-L., Liu, S., and Chen, S-H. (2011) *Journal of Alloys & Compounds*, **509**, 9702–9707.
537. Xiao, Y., Chen, X. M., and Liu, X. Q. (2004) *Journal of American Ceramic Society*, **87**, 2143–2146.
538. Yi, L., Qiang, X., Li, L., *et al*. (2013) *International Journal of Appled Ceramic Technology*, **10S1**, E177–E185.
539. Cao, Q-S., Lu, W-Z., Wang, X-C., *et al*. (2015) *Ceramic International*, **41**, 9152–9156.
540. Xie, H-D., Chen, C., Xi, H-H., *et al*. (2016) *Ceramic International*, **42**, 989–995.
541. Chen, H-C., Weng, M-H., Huang, C-I., *et al*. (2004) *Japanese Journal of Applied Physics*, **43**, 2564–2567.

542. Anjana, P. S., Jawahar, I. N., and Sebastian, M. T. (2009) *Journal of Materials Science: Materials in Electronics*, **20**, 587–596.
543. Li, L., Zhang, M., Liao, Q., *et al*. (2012) *Journal of Alloys & Compounds*, **531**, 18–22.
544. Huang, C-L., Chen, J-Y., and Jiang, C-Y. (2009) *Journal of Alloys & Compounds*, **487**, 420–424.
545. Pullar, R. C., Okereme, K., and Alford, N. Mc N. (2003) *Journal of European Ceramic Society*, **23**, 2479–2483.
546. Jung, B-H., Hwang, S-J., and Kim, H-S. (2005) *Journal of European Ceramic Society*, **25**, 3187–3193.
547. Huang, C-L. and Chen, J-Y. (2009) *Journal of Alloys & Compounds*, **485**, 706–710.
548. Zhu, H., Lu, W-Z., and Lei, W. (2011) *Ceramic International*, **37**, 1515–1519.
549. Mori, K., Ogawa, H., Kan, A., *et al*. (2004) *Journal of European Ceramic Society*, **24**, 1745–1748.
550. Mao, M. M., Chen, X. M., and Liu, X. Q. (2011) *Journal of American Ceramic Society*, **94**, 3948–3952.
551. Chen, Y-B. (2011) *Journal of Alloys & Compounds*, **509**, 6884–6888.
552. Huang, C-L. and Shen, C-H. (2009) *Journal of American Ceramic Society*, **92**, 384–388.
553. Zhou, H., Liu, X., Chen, X., *et al*. (2012) *Journal of European Ceramic Society*, **32**, 261–265.
554. Fe, X. and Chen, X. M. (2009) *Journal of American Ceramic Society*, **92**, 433–438.
555. Joseph, J. T., Padmakumar, H., Varma, M. R., *et al*. (2008) *Materials Letters*, **62**, 911–913.
556. Shen, C-H. and Huang, C-L. (2010) *International Journal of Appled Ceramic Technology*, **7**, 207–216.
557. Pullar, R. C., Breeze, J., and Alford, N. Mc N. (2005) *Journal of American Ceramic Society*, **88**, 2466–2471.
558. Chen, Y-B. (2012) *Journal of Alloys and Compounds*, **513**, 481–486.
559. Shin, H-K., Shin, H., Bae, S-T., *et al*. (2008) *Journal of American Ceramic Society*, **91**, 132–138.
560. Zhang, C., Yi, L., and Chen, X. M. (2014) *Ceramic International*, **40**, 6077–6082.
561. Li, B., Yi, L., and Chen., X. M. (2015) *Materials Research Bulletin*.
562. Chen, J. Y., Levin, I., Vanderah, T. A., *et al*. (2000) *International Journal of Inorganic Chemistry*, **2**, 107–114.
563. Sebastian, M. T., Solomon, S., Ratheesh, R., *et al*. (2001) *Journal of American Ceramic Society*, **84**, 1487–1489.
564. Surendran, K. P., Varma, M. R., and Sebastian, M. T. (2003) *Journal of American Ceramic Society*, **86**, 1695–1699.
565. Wang, Y-R., Wang, S-F., and Lin, Y-M. (2005) *Ceramic International*, **31**, 905–907.
566. Golovchanski, A., Kim, H. T., and Kim, Y. H. (1998) *Journal of Korean Ceramic Society*, **32**, S1167–S1169.
567. Durilin, D. A., Ovchar, O. V., and Belous, A. G. (2011) *Inorganic Materials*, **47**, 313–316.
568. Bian, J. J., Yan, K., and Dong, Y. F. (2008) *Materials Science and Engineering, B*, **147**, 27–34.
569. Zhang, P., Song, Z., Wang, Y., *et al*. (2014) *Journal of American Ceramic Society*, **97**, 976–981.
570. Tseng, C-F., Wei, T-C., and Lu, S-C. (2014) *Ceramic International*, **40**, 7081–7085.
571. Wang, W., Bai, W., Shen, B., *et al*. (2015) *Ceramic International*, **41**, S435–S440.
572. Chen, J. Y. and Huang, C-L. (2010) *Materials Letters*, **64**, 2585–2588.
573. He, L., Zhou, D., Yang, H., *et al*. (2012) *Journal of American Ceramic Society*, **95**, 3732–3734.
574. Chen, Y-C., Weng, M-Z., and Chen, Y-Y. (2013) *Journal of Materials Science: Materials in Electronics*, **24**, 2970–2975.
575. Sayyadi-Shahraki, A., Taheri, E., Hassanzadeh-Tabrizi, S. A., *et al*. (2014) *Journal of Materials Science: Materials in Electronics*, **25**, 355–360.
576. Xie, H., Xi, H., Chen, C., *et al*. (2014) *Journal of European Ceramic Society*, **34**, 4089–4093.
577. Fan, X. C., Mao, M. M., and Chen, X. M. (2008) *Journal of American Ceramic Society*, **91**, 2917–2922.
578. Bian, J. J. and Dong, Y. F. (2009) *Journal of European Ceramic Society*, **30**, 325–330.
579. Chen, J-Y. and Huang, C-L. (2010) *Journal of Alloys & Compounds*, **496**, L10–L13.

580. Chen, Y-C., Yao, S-L., and Wu, C-Y. (2012) *Journal of Materials Science: Materials in Electronics*, **23**, 1320–1326.
581. Zhou, D., Wang, H., Yao, X., *et al*. (2008) *Journal of American Ceramic Society*, **91**, 2228–2231.
582. Li, E., Niu, N., Wang, J., *et al*. (2015) *Journal of Materials Science: Materials in Electronics*, **26**, 3330–3335.
583. Surendran, K. P., Solomon, S., Varma., M. R., *et al*. (2002) *Journal of Materials Research*, **17**, 2561–2566.
584. Zhou, D., Wang, H., Yao, X., *et al*. (2008) *Journal of American Ceramic Society*, **91**, 1380–1383.
585. Chen, Y-C. and Tsai, R-J. (2011) *Materials Chemistry and Physics*, **129**, 116–120.
586. Udovic, M., Valant, M., and Suvorov, D. (2001) *Journal of European Ceramic Society*, **21**, 1735–1738.
587. Wang, Y-N. (2013) *Journal of Materials Science: Materials in Electronics*, **24**, 4510–4515.
588. Lyu, X., Lin, L., Cai, H., *et al*. (2015) *Ceramics International*, **41**, 9168–9171.
589. Chen, Y-C. and Li, C-H. (2014) *Journal of Materials Science: Materials in Electronics*, **25**, 4312–4318.
590. Tagata, M. and Kageyama, K. (1989) *Journal of American Ceramic Society*, **72**, 1955–1959.
591. Liu, X., Gao, F., Zhao, L., *et al*. (2007) *Journal of Electroceramics*, **18**, 103–109.
592. Choi, Y-C., Park, J-H., Park, J-H., *et al*. (2007) *Journal of European Ceramic Society*, **27**, 2017–2024.
593. Yuan, H. X., Chen, X. M., and Mao, M. M. (2009) *Journal of American Ceramic Society*, **92**, 2286–2290.
594. Chen, Y-C., Chang, K-C., and Yao, S-L. (2012) *Ceramic International*, **38**, 5377–5383.
595. Lee, H-W., Park, J-H., Nahm, S., *et al*. (2010) *Materials Research Bulletin*, **45**, 21–24.
596. Bian, J-J., Wang, L., and Yuan, L. L. (2009) *Materials Science and Engineering*, **B164**, 96–100.
597. Chen, X. N., Wu, S Y., and Chen, X. M. (2013) *Journal of Materials Science: Materials in Electronics*, **24**, 2445–2452.
598. Chen, Y-C., Chen, Y-U., and Yao, S-L. (2013) *Journal of Materials Science: Materials in Electronics*, **24**, 1150–1157.
599. Kan, A., Ogawa, H., Mori, K., *et al*. (2002) *Materials Research Bulletin*, **37**, 1509–1518.
600. Lee, H-J., Kim, I-T., and Hong, K. S. (1997) *Japanese Journal of Applied Physics*, **36**, L1318–L1320.
601. Chen, Y-C. and Chang, Y-H. (2009) *Journal of Alloys & Compounds*, **477**, 450–453.
602. Li, Z., Wu, W., Liu, F., *et al*. (2014) *Materials Letters*, **118**, 24–26.
603. Wang, S. F., Hsu, Y-F., Wang, Y-R., *et al*. (2010) *Journal of American Ceramic Society*, **94**, 812–816.
604. Liu, B., Yi, L., Li, L., *et al*. (2015) *Journal of Alloys & Compounds*, **653**, 351–357.
605. Hsu, C-S., Huang, C-L., Tseng, J-F., *et al*. (2003) *Materials Research Bulletin*, **38**, 1091–1099.
606. Hwang, S. and Kim, H. (2007) *Thermochemica Acta*, **A45**, 119–112.
607. Wang, Y-N., Chen, Y-C., Pan, Y-D., *et al*. (2012) *Ceramic International*, **38**, 3097–3103.
608. Yi, L, Li, L., Qiang, X., *et al*. (2014) *Journal of American Ceramic Society*, **97**, 3531–3536.
609. Kagata, H. and Kato, J. (1994) *Japanese Journal of Applied Physics*, **33**, 5463–5465.
610. Ha, J-Y., Choi, J-W., Yoon, S-J., *et al*. (2003) *Journal of European Ceramic Society*, **23**, 2413–2416.
611. Huang, C-L., Pan, C-L., and Shim, S-J. (2003) *Materials Chemistry and Physics*, **78**, 111–115.
612. Li, L., Wu, X., and Zhu, Z. (to be published)
613. Zeng, Q., Li, W., Shi, J-L., *et al*. (2006) *Journal of American Ceramic Society*, **89**, 1733–1735.
614. Thirumal, M., Jawahar, I. N., Surendran, K. P., *et al*. (2002) *Materials Research Bulletin*, **37**, 185–191.
615. Huang, C-L. and Weng, M-H. (2001) *Materials Research Bulletin*, **36**, 2741–2750.
616. Zhao, F., Yue, Z., Pei, J., *et al*. (2007) *Journal of American Ceramic Society*, **90**, 2461–2466.
617. Shlykhtin, O. A. and Oh, Y-J. (2006) *Journal of American Ceramic Society*, **89**, 3366–3372.
618. Zhou, D., Wang, H., Pang, L-X., *et al*. (2012) *Materials Chemistry and Physics*, **119**, 149–152.

619. Chen, Y-C. and Hsu, W-Y. (2010) *Journal of Alloys & Compounds*, **506**, 441–445.
620. Wu, J. Y. and Bian, J. J. (2013) *Ceramic International*, **39**, 3641–3649.
621. Chen, Y-C. and Hsu, W-Y. (2011) *Ceramic International*, **37**, 55–58.
622. Yao, G-G. and Liu, P. (2010) *Physica*, **B405**, 547–551.
623. Huang, C-L. and Huang, S-H. (2012) *Journal of Alloys & Compounds*, **515**, 8–11.
624. Huang, C-L., Hou, J-L., Pan, C-L., *et al*. (2008) *Journal of Alloys & Compounds*, **450**, 359–363.
625. Wu, J. Y. and Bian, J. J. (2014) *Journal of American Ceramic Society*, **97**, 880–884.
626. Guo, M., Li, Y., Dou, G., *et al*. (2015) *Journal of Materials Science: Materials in Electronics*, **25**, 4319–4325.
627. Xie, W., Zhou, H., Zhu, H., *et al*. (2014) *Ceramic International*, **40**, 6899–6902.
628. Babu, G. S., Subramanian, V., and Murthy, V. R. K. (2007) *Journal of European Ceramic Society*, **27**, 2973–2976.
629. Wang, Y-N. and Chen, M-D. (2013) *Journal of Materials Science: Materials in Electronics*, **24**, 3730–3735.
630. Huang, C-L., Chen, Y-B., and Lee, M-L. (2009) *Journal of Alloys and Compounds*, **469**, 357–361.
631. Zhang, P., Wang, T., Xia, W., *et al*. (2012) *Journal of Alloys and Compounds*, **535**, 1–4.
632. Kim, D-W., Kim, J-H., Kim, J-R., *et al*. (2001) *Japanese Journal of Applied Physics*, **40**, 5994–5998.
633. Chen, Y-C. and Lee, W-C. (2011) *Materials Chemistry and Physics*, **129**, 110–1115.
634. Chen, Y-C. and Chen, M-D. (2011) *Journal of Physics and Chemistry of Solids*, **72**, 1447–1451.
635. Chen, Y-C., Yang, S-K., and Chang, K-C. (2011) *Journal of Alloys and Compounds*, **509**, 9518–9522.
636. Chen, Y-C. (2012) *International Journal of Applied Ceramic Technology*, **9**, 606–614.
637. Zhou, H., Liu, X., Chen, X., *et al*. (2012) *Materials Chemistry and Physics*, **137**, 22–25.
638. Liu, X. Q. and Chen, X. M. (2006) *Journal of European Ceramic Society*, **26**, 1969–1971.
639. Mori, K., Ogawa, H., Kan, A., *et al*. (2002) *Materials Chemistry and Physics*, **79**, 273–275.
640. Santha, N., Sebastian, M. T., Mohanan, P., *et al*. (2004) *Journal of American Ceramic Society*, **87**, 1233–1237.
641. Mannan, A., Khan, D. N., and Ullah, A. (2015) *Journal of Materials Science: Materials in Electronics*, **26**, 2066–2069.
642. Belous, A., Ovchar, O., Jancar, B., *et al*. (2007) *Journal of European Ceramic Society*, **27**, 2933–2936.
643. Chen, G-H., Xu, H-R., and Yuan, C-L. (2013) *Ceramic International*, **39**, 4887–4892.
644. Belous, A., Ovchar, O., Jancar, B., *et al*. (2009) *Journal of Electrochemical Society*, **156**, G206–G212.
645. Venugopal, V., Anjana, P. S., Prakash, Om., *et al*. (2010) *Journal of American Ceramic Society*, **93**, 2467–2469.
646. Anjana, P. S. and Sebastian, M. T. (2008) *International Journal of Appled Ceramic Technology*, **5**, 84–89.
647. Zhang, Q-L., Yang, H., and Tong, J-X. (2005) *Materials Letters*, **60**, 1188–1191.
648. Lina, Y. J., Wang, S-F., Chen, S-H., *et al*. (2015) *Ceramics International*, **41**, 8931–8935.
649. Hsu, C-S. and Huang, C-L. (2001) *Materials Research Bulletin*, **36**, 1939–1947.
650. Feteira, A., Sinclair, D. C., and Lanagan, M. T. (2008) *Journal of Applied Physics*, **101**, 064110.
651. Zhou, H., Wang, H., Zhang, M., *et al*. (2010) *Materials Chemistry and Physics*, **119**, 4–6.
652. Chen, G-H. and Yang, Y. (2013) *Journal of Materials Science: Materials in Electronics*, **24**, 1012–1017.
653. Huang, C-L., Yang, W-R., and Yu, P-C. (2014) *Journal of European Ceramic Society*, **34**, 277–284.
654. Cho, W. W., Kakimoto, K., and Ohsato, H. (2004) *Japanese Journal of Applied Physics*, **43**, 6221–6224.
655. Bian, J. J., Yan, K., and Li, J. (2006) *Journal of European Ceramic Society*, **26**, 1957–1960.
656. Tseng, C-F. and Li, S-C. (2013) *Materials Science and Engineering B*, **178**, 358–362.

657. Yang, W-R., Huang, P-Z., and Huang, C-L. (2015) *Journal of Alloys & Compounds*, **620**, 18–23.
658. Huang, C-L., Wang, J-J., and Chang, Y-P. (2007) *Journal of American Ceramic Society*, **90**, 858–862.
659. Yu, H., Cheng, J., Zhang, W., *et al*. (2012) *Journal of Materials Science: Materials in Electronics*, **23**, 572–575.
660. Zhou, H., Liu, X., Chen, X., *et al*. (2012) *Materials Research Bulletin*, **47**, 1278–1280.
661. Zhang, P. and Zhao, Y. (2016) *Ceramics International*, **42**, 2882–2886.
662. Bijumon, P. V. and Sebastian, M. T. (2004) *Journal of Materials Research*, **19**, 2922–2928.
663. Kim, H. T., Nahm, S., Byun, J. D., *et al*. (1999) *Journal of American Ceramic Society*, **82**, 3476–3480.
664. Tong, J. X., Zhang, Q. L., Yang, H., *et al*. (2005) *Materials Letters*, **59**, 3252–3255.
665. Huang, C-L. and Pan, C-L. (2002) *Japanese Journal of Applied Physics*, **41**, 707–711.
666. Shen, C-H. and Huang, C-L. (2009) *International Journal of Appled Ceramic Technology*, **7**, 207–216.
667. Huang, C-L., Chen, J-Y., and Liang, C-C. (2009) *Journal of Alloys & Compounds*, **478**, 554–558.
668. Tay, K-W. and Wu, W-F. (2012) *Procedia Engineering*, **36**, 462–467.
669. Chen, Y-C., Tsai, R-J., and Wu, C-Y. (2012) *Ceramic International*, **38**, 2927–2934.
670. Lei, Y., Liu, X.Q., and Chen, X. M. (2012) *Materials Chemistry and Physics*, **147**, 162–167.
671. Oishi, T., Kan, A., Ohsato, H., *et al*. (2006) *Journal of European Ceramic Society*, **26**, 2075–2079.
672. Wu, Y., Zhou, D., Guo, J., *et al*. (2013) *Journal of Materials Science: Materials in Electronics*, **24**, 4942–4946.
673. Guo, J., Rindall, C. A., Zhang, G., *et al*. (2014) *Journal of Materials Chemistry*
674. Hsu, C-H. (2008) *Ceramic International*, **34**, 243–247.
675. Feteiro, A., Sinclair, D. C., Raja, K. Z., *et al*. (2008) *Journal of American Ceramic Society*, **91**, 893–901.
676. Chen, G. H., Zhou, M., and Yang, Y. (2012) *Materials Letters*, **89**, 16–18.
677. Zhou, D., Rindall, C. A., Pang, L-X., *et al*. (2011) *Materials Chemistry and Physics*, **129**, 688–692.
678. Wang, J., Yue, Z., Gui, Z., *et al*. (2005) *Journal of Materials Science Letters*, **40**, 6581–6583.
679. Xiang, H., Jiang, X., Fang, L., *et al*. (2015) *Journal of Materials Science: Materials in Electronics*, **26**, 9134–9138.
680. Xie, W., Zhou, H., Jiang, Q., *et al*. (2016) *Journal of Materials Science: Materials in Electronics*, in press.
681. Huang, C-L. and Chiang, K-H. (2008) *Materials Science and Engineering A*, **474**, 243–248.
682. Zeng, Q., Li, W., Shi, J-L., *et al*. (2006) *Journal of American Ceramic Society*, **89**, 3305–3307.
683. Huang, C-L. and Chen, Y-C. (2003) *Journal of European Ceramic Society*, **23**, 167–173.
684. Tian, Z. Q. and Lin, L. (2009) *Journal of Materials Science: Materials in Electronics*, **20**, 867–871.
685. Huang, S. J., Kim, Y-J., and Kim, H. S. (2002) *Materials Research Bulletin*, **37**, 2483–2490.
686. Rajput, S. S. and Keshari, S. (2013) *Journal of Alloys and Compounds*, **581**, 223–229.
687. Ding, Z., Su, H., Tang, X., *et al*. (2015) *Ceramic International*, **41**, 10133–10136.
688. Guo, H., Fang, L., Jiang, X., *et al*. (2015) *Journal of American Ceramic Society*, **98**, 3863–3868.
689. Shen, C-H., Huang, C-L., Chen, W-T., *et al*. (2012) *International Journal of Appled Ceramic Technology*, **9**, 447–453.
690. Chen, W-S., Tseng, C-F., Lee, Y-M., *et al*. (2009) *Journal of Material Processing and Technology*, **209**, 2277–2281.
691. Shen, C-H., Huang, C-L., Lin, L-M., *et al*. (2009) *Journal of Alloys & Compounds*, **489**, 170–174.
692. Zhang, Y., Wu, S., Zhang, B., *et al*. (2014) *Journal of Materials Science: Materials in Electronics*, **25**, 3085–3089.
693. Li, S., Li, L., Lyu, X., *et al*. (2015) *Materials Letters*, **161**, 527–529.

694. Huang, C-L., Pan, C-L., Hsu, J-F., *et al*. (2008) *Journal of Alloys & Compounds*, **461**, 521–528.
695. Tan, C., Yue, Z., Zhou, Y., *et al*. (2013) *Journal of Solid State Chemistry*, **197**, 242–247.
696. Zhang, J., Yue, Z., Zhou, Y., *et al*. (2015) *Journal of American Ceramic Society*, **98**, 1548–1554.
697. Wang, S-F., Chen, J-H., Hsu, Y-F., *et al*. (2013) *Ceramic International*, **39**, 2857–2861.
698. Pan, C-L., Shen, C-H., Chen, P-C., *et al*. (2010) *Journal of Alloys and Compounds*, **503**, 365–369.
699. Zhou, H., Wang, W., Chen, X., *et al*. (2014) *Ceramic International*, **40**, 2103–2107.
700. Zeng, Q., Li, W., Shi, J. L., *et al*. (2006) *Journal of American Ceramic Society*, **89**, 1733–1637.
701. Tamura, H., Konoike, T., Sakabe, Y., *et al*. (1984) *Journal of American Ceramic Society*, **67**, C59–C61.
702. Cho, S-Y., Kim, C-H., Kim, D-W., *et al*. (1999) *Journal of Materials Research*, **14**, 2484–2487.
703. Kim, M-H., Nahm, S., Choi, C-K., *et al*. (2002) *Japanese Journal of Applied Physics*, **41**, 717–721.
704. Kim, H. T. and Lanagan, M. T. (2003) *Journal of American Ceramic Society*, **86**, 1874–1878.
705. Zhang, Y-C., Yue, Z. X., Gui, Z. L., *et al*. (2003) *Materials Letters*, **57**, 4531–4534.
706. Yaomin, D. and Bian, J. J. (2013) *Ceramic International*, **39**, 1555–1560.
707. Zeng, Q., Zhou, Y., and Hou, L. (2011) *Materials Chemistry and Physics*, **129**, 892–895.
708. Shen, C-H., Huang, C-L., Shih, C-F., *et al*. (2010) *International Journal of Appled Ceramic Technology*, **6**, 572–570.
709. Yuan, L. L. and Bian, J. J. (2009) *Ferroelectrics*, **38**, 123–129.
710. Shahraki, E. A. S., Nassaj, E. J., Tabrizi, S. A. H., *et al*. (2014) *Journal of Alloys & Compounds*, **597**, 161–166.
711. Cho, S-Y., Kim, I-T., and Hong, K-S. (1999) *Journal of Materials Research*, **14**, 114–119.
712. Wang, J., Yue, Z., Gui, Z., *et al*. (2005) *Journal of Alloys & Compounds*, **392**, 263–267.
713. Wee, S-H., Kim, D-W., Yoo, S-I., *et al*. (2004) *Japanese Journal of Applied Physics*, **43**, 3511–3515.
714. Bian, J. J., Yuan, L. L., Li, Y. Z., *et al*. (2008) MMA 2008, Hangzhou, China, pp. 79
715. Zhou, D., Wang, H., Yao, X., *et al*. (2009) *Materials Chemistry and Physics*, **113**, 265–268.
716. Xie, W., Zhou, H., Zhu, H., *et al*. (2015) *Journal of Materials Science: Materials in Electronics*, **26**, 3515–3520.
717. Hsun, C-H. and Chang, C-H. (2015) *Ceramics International*, **41**, 6965–6969.
718. Chai, Y-L., Chang, Y-S., Hsiao, Y-J., *et al*. (2008) *Materials Research Bulletin*, **43**, 257–263.
719. Cho, J. Y., Yoon, K. H., and Kim, E. S. (2003) *Materials Chemistry and Physics*, **79**, 286–288.
720. Huang, C-L. and Chen, Y-C. (2002) *Japanese Journal of Applied Physics*, **41**, 1459–1464.
721. Varghese, J., Joseph, T., Sebastian, M. T., *et al*. (2010) *Journal of American Ceramic Society*, **93**, 2960–2963.
722. Zeng, Q., Li, W., Shi, J-L., *et al*. (2008) *Journal of American Ceramic Society*, **91**, 644–647.
723. Su, H. and Wu, S. (2005) *Materials Letters*, **50**, 2337–2341.
724. Huang, C-L., Lin, S-H., Liu, S-S., *et al*. (2010) *Journal of Alloys & Compounds*, **503**, 392–396.
725. Huang, C-L., Shen, C-H., and Lin, T-C. (2009) *Journal of Alloys & Compounds*, **468**, 516–521.
726. Su, H. and Wu, S. (2005) *Materials Letters*, **59**, 2337–2341.
727. Khalyaviv, D. D., Senos, A. M. R., Mantas, P. Q., *et al*. (2007) *Journal of Solid State Chemistry*, **180**, 41–48.
728. Li, L.,Yu, X. L., Sun, H., *et al*. (2015) *Journal of Materials Science: Materials in Electronics*, **26**, 5871–5876.
729. Lee, H-J., Hong, K. S., Kim, S-J., *et al*. (1997) *Materials Research Bulletin*, **32**, 847–855.
730. Ogawa, H., Kan, A., Yokola, S., *et al*. (2001) *Journal of European Ceramic Society*, **21**, 1731–1734.
731. Huang, C-L. and Liu, S-S. (2009) *Materials Letters*, **62**, 3773–3775.
732. Huang, C-L., Chen, Y-B., and Lin, S-H. (2009) *Journal of Alloys & Compounds*, **477**, 712–715.
733. Sumesh, G. and Sebastian, M. T. (2010) In *Perovskite:Structure Properties and Uses* (ed. M. Borowski), pp. 283–317, Nova Science Publishers Inc.
734. Chen, Y-B., Huang, C-L., and Tasi, S-T. (2008) *Materials Letters*, **62**, 2454–2457.
735. Huang, C-L., Chen, J-Y., and Huang, G-S. (2010) *Journal of Alloys & Compounds*, **499**, 48–52.

736. Shen, C-H., Huang, C-L., and Lin, L-M., *et al*. (2010) *Journal of Alloys & Compounds*, **504**, 228–232.
737. Li, C., Xiang, H., and Fang, L. (2016) *Journal of Elecronic Materials*, **45**, 262–266.
738. George, S. and Sebastian, M. T. (2011) *International Journal of Appled Ceramic Technology*, **8**, 1400–1407.
739. Liu, X. Q. and Chen, X. M. (2004) *Journal of European Ceramic Society*, **24**, 1999–2004.
740. Bian, J. J. and Ding, Y. (2014) *Materials Research Bulletin*, **49**, 245–249.
741. Li, L., Li, S., Tian, T., *et al*. (2016) *Journal of Materials Science: Materials in Electronics*, in press.
742. Huang, C-L., Chen, J-Y., and Jiang, C-Y. (2010) *Journal of Mareican Ceramic Society*, **93**, 2755–2759.
743. Shen, C-H. and Huang, C-L. (2009) *Journal of Alloys and Compounds*, **477**, 720–725.
744. Huang, C-L., Tseng, Y-W. and Chen, J-Y. (2012) *Journal of European Ceramic Society*, **32**, 3287–3295.
745. Hsiang, H-I., Mei, L-T., Liao, W-C., *et al*. (2010) *Journal of American Ceramic Society*, **93**, 1714–1717.
746. Li, B., Tang, B., Zhang, S., *et al*. (2010) *Journal of Materials Science*, **45**, 6461–6466.
747. Shim, S. H., Choi, B. G., Kim, S. H., *et al*. (2005) *Japanese Journal of Applied Physics*, **44**, 5073–5075.
748. Cairns, D. L., Reaney, I. M., Zheng, H., *et al*. (2005) *Journal of European Ceramic Society*, **25**, 433–439.
749. Huang, C-L. and Chiang, K-H. (2007) *Journal of Alloys & Compounds*, **431**, 326–330.
750. Khalam, L. A., Thomas, S., and Sebastian, M. T. (2007) *Journal of American Ceramic Society*, **90**, 2476–2486.
751. Yao, G. G., Liu, P., and Zhang, H. W. (2013) *Journal of Materials Science: Materials in Electronics*, **24**, 1128–1131.
752. Choi, J. W., Kang, C-Y., Yoon, S-J., *et al*. (1999) *Journal of Materials Research*, **14**, 3567–3570.
753. Cha, H. J., Kang, D. H., and Cho, Y. S. (2007) *Materials Research Bulletin*, **42**, 265–273.
754. Shim, S. H., Choi, B. G., Yoon, J. W., *et al*. (2005) *Japanese Journal of Applied Physics*, **44**, 5073–5075.
755. Liang, J., Lu, W., Lei, W., *et al*. (2013) *Journal of Materials Science: Materials in Electronics*, **24**, 3625–3628.
756. Liang, J. and Lu, W-Z. (2009) *Journal of American Ceramic Society*, **92**, 952–954.
757. Fang, L., Wei, Z., Liao, W., *et al*. (2014) *Journal of American Ceramic Society*, **97**, 498–500.
758. Shen, C-S., Huang, C-L., Shih, C-F., *et al*. (2010) *International Journal of Appled Ceramic Technology*, **7**, E64–E70.
759. Hao, Y-Z., Zhang, Q-L., Zhang, J., *et al*. (2012) *Journal of Materials Chemistry*, **22**, 23885–23892.
760. Liu, Z., Wang, Y., Wu, W., *et al*. (2013) *Journal of Asian Ceramic Societies*, **1**, 2–8.
761. Zhou, H., Miao, Y., Chen, J., *et al*. (2014) *Journal of Materials Science: Materials in Electronics*, **25**, 2470–2474.
762. Yu, N. X., Zhou, J-H., Yang, H., *et al*. (2014) *Ceramic International*, **40**, 15191–15198.
763. Khalam, L. A. and Sebastian, M. T. (2007) *Journal of American Ceramic Society*, **90**, 1467–1474.
764. Huang, C-L., Lin, R. J., and Wang, H. (2002) *Japanese Journal of Applied Physics*, **41**, 758–762.
765. Liu, P., Ogawa, H., Kim, E. S., *et al*. (2003) *Journal of European Ceramic Society*, **23**, 2417–2421.
766. Zhou, Y., Meng, A., Wu, H., *et al*. (2011) *Journal of American Ceramic Society*, **94**, 2933–2938.
767. Fang, G., Jiaji, L., Rongzi, H., *et al*. (2009) *Ceramic International*, **35**, 2687–2692.
768. Huang, C-L., Li, G-J., and Wang, J-J. (2009) *Journal of Alloys & Compounds*, **472**, 497–501.
769. Liu, X. Q. and Chen, X. M. (2004) *Journal of European Ceramic Society*, **24**, 199–2004.

770. Rajamma, R. and Sebastian, M. T. (2007) *Journal of American Ceramic Society*, **90**, 2472–2475.
771. Wang, J-J., Wang, C-H., and Hsu, T-K. (2009) *Japanese Journal of Applied Physics*, **48**, 081402.
772. Wu, Y., Zhou, D., Guo, J., *et al*. (2011) *Materials Letters*, **65**, 2680–2682.
773. Bian, J. J., Gao, H. B., and Wang, X. W. (2004) *Materials Research Bulletin*, **39**, 2127–2135.
774. Yaomin, D. and Bian, J. J. (2013) *Materials Research Bulletin*, **48**, 2776–2781.
775. Bian, J. J., Yan, K., and Gao, H. B. (2006) *Materials Chemistry and Physics*, **96**, 349–352.
776. Lee, Y-C., Lee, W-H., and Shiao, F-T. (2004) *Japanese Journal of Applied Physics*, **43**, 7596–7599.
777. Zhang, C., Yi, L., Li, L., *et al*. (2013) *International Journal of Applied Ceramic Technology*, E70–E76.
778. Butee, S., Kulkarni, A., Prakash, Om., *et al*. (2009) *Journal of American Ceramic Society*, **92**, 1047–1053.
779. Prasanth, C. S., Kumar, H. P., Pazhani, R., *et al*. (2008) *Journal of Alloys & Compounds*, **464**, 306–309.
780. Belous, A. G., Ovchar, O. V., Kramarenko, A. V., *et al*. (2007) *Inorganic Chemistry*, **43**, 277–280.
781. Xia, W-S., Yang, F-Y., Zhang, G-Y., *et al*. (2016) *Journal of Alloys & Compounds*, **656**, 470–475.
782. Wu, H. T., Guo, J. D., Bi, J. X., *et al*. (2016) *Journal of Alloys and Compounds*, **661**, 535–540.
783. Shen, C-H., Huang, C-L., Shih, C-F., *et al*. (2009) *Journal of Alloys & Compounds*, **475**, 391–395.
784. Hao, Y-Z., Yang, H., Chen, G-H., *et al*. (2013) *Journal of Alloys & Compounds*, **552**, 173–179.
785. Kawaguchi, S., Ogawa, H., Kan, A., *et al*. (2006) *Journal of European Ceramic Society*, **26**, 2045–2049.
786. Takada, T., Wang, S. F., Yoshikawa, S., *et al*. (1994) *Journal of American Ceramic Society*, **77**, 1909–1916.
787. Nomura, S. (1983) *Ferroelectrics*, **49**, 61–70.
788. Yoon, S-O., Yoon, J. H., Shim, S. H., *et al*. (2006) *Journal of European Ceramic Society*, **26**, 2031–2034.
789. Tang, B., Li, Y-X., Li, H., *et al*. (2015) *Journal of Materials Science: Materials in Electronics*, **26**, 2795–2799.
790. Choi, J-W., Ha, J. Y., Yoon, S-J., *et al*. (2003) *Journal of European Ceramic Society*, **23**, 2507–2510.
791. Matsumoto, H., Tamura, H., and Wakino, K. (1991) *Japanese Journal of Applied Physics*, **30**, 2347–2349.
792. George, S. and Sebastian, M. T. (2009) *Journal of Alloys & Compounds*, **473**, 336–340.
793. Tong, J., Zhou, J., Yang, H., *et al*. (2014) *Journal of Materials Science: Materials in Electronics*, **25**, 1293–1297.
794. Tamura, H., Matsumoto, H., and Wakino, K. (1989) *Japanese Journal of Applied Physics*, **28-2**, 21.
795. Furuya, M. and Ochi, A. (1994) *Japanese Journal of Applied Physics*, **33**, 5482–5487.
796. Lu, X., Zheng, Y., Dong, Z., *et al*. (2014) *Ceramic International*, **40**, 7087–7092.
797. Huang, C-L., Tasi, C-F., Chen, Y-B., *et al*. (2008) *Journal of Alloys & Compounds*, **453**, 337–340.
798. Wang, S. F., Hsu, Y-F., Wang, Y-R., *et al*. (2011) *Journal of European Ceramic Society*, **31**, 2975–2980.
799. Suresh, M. K., Padmakumar, H., Warrier, P. R. S., *et al*. (2012) *Journal of Materials Science: Materials in Electronics*, **23**, 200–205.
800. Huang, C-L., Chen, J-Y., and Wang, Y-H. (2009) *Journal of Alloys & Compounds*, **478**, 842–846.
801. Chen, Y-B. (2009) *Journal of Alloys and Compounds*, **489**, 541–544.
802. Bian, J. J. and Dong, Y. F. (2011) *Materials Science and Engineering*, **B176**, 147–151.
803. Zhou, H., Liu, X., Chen, X., *et al*. (2013) *Materials Letters*, **96**, 199–202.

804. Shen, C-H., Huang, C-L., Shih, C-F., *et al*. (2009) *International Journal of Appled Ceramic Technology*, **6**, 562–570.
805. Lee, Y-C. and Lee, W-H. (2005) *Japanese Journal of Applied Physics*, **44**, 1838–1843.
806. Huang, C-L., Wang, J. J., Li, B-J., *et al*. (2008) *Materials Letters*, **62**, 2516–1519.
807. Jayanthi, S. and Kutty, T. R. N. (2008) *Materials Letters*, **62**, 556–560.
808. Ratheesh, R., Sebastian, M. T., Tobar, M. E., *et al*. (1999) *Journal of Physics D*, **32**, 2821–2826.
809. Surendran, K. P., Sebastian, M. T., Mohanan, P., *et al*. (2005) *Chemistry of Materials*, **17**, 142–151.
810. Youn, K-J., Kim, I-T., Hong, K. S., *et al*. (1997) *Ferroelectrics*, **193**, 167–174.
811. Huang, C-L., Su, C-H., and Chang, C-M. (2012) *Journal of American Ceramic Society*, **94**, 4146–4149.
812. Huang, C-L., Chen, J-Y., and Liang, C-C. (2009) *Materials Research Bulletin*, **44**, 1111–1115.
813. Huang, C-L. and Chen, J-H. (2010) *Journal of Alloys and Compounds*, **509**, 6273–6275.
814. Wang, S-F., Wang, Y-R., Liu, C-Y., *et al*. (2012) *Ceramic International*, **38**, 1127–1132.
815. Chen, Y-B. (2009) *Journal of Alloys & Compounds*, **477**, 883–887.
816. Shen, C-H. and Pan, C-L. (2014) *International Journal of Applied Ceramic Technology*.
817. Shimada, T. (2003) *Journal of European Ceramic Society*, **23**, 2647–2652.
818. Mandai, H. and Okube, S. (1992) *Ceramic Transactions*, **32**, 91.
819. Huang, C-L. and Tseng, J-F. (2004) *Materials Letters*, **58**, 3732–3736.
820. Kageyama, K. (1990) *Ferroelectrics*, **109**, 173–178.
821. Davies, P. K., Borosevich, A., and Thirumal, M. (2003) *Journal of European Ceramic Society*, **23**, 2461–2466.
822. Hsieh, M-H., Chen, L-S., Wang, S. M., *et al*. (2005) *Japanese Journal of Applied Physics*, **44**, 5045–5048.
823. Khalam, L. A. and Sebastian, M. T. (2006) *International Journal of Appled Ceramic Technology*, **3**, 364–374.
824. Boriosevic, A. and Davies, P. K. (2004) *Applied Physics Letters*, **84**, 1347–1349.
825. Li, B., Zhang, S., Yuan, Y., *et al*. (2009) *Journal of Materials Science*, **44**, 4993–4998.
826. Wang, S-F., Wang, Y-R., Su, Y-F., *et al*. (2010) *Journal of European Ceramic Society*, **30**, 1737–1741.
827. Kolodiazhnyi, T. (2012) *Journal of European Ceramic Society*, **32**, 4305–4309.
828. Cairns, D. L., Reaney, I. M., Zheng, H., *et al*. (2005) *Journal of European Ceramic Society*, **25**, 433.
829. Zhang, P., Wang, Y., Hua, Y., *et al*. (2013) *Materials Letters*, **107**, 351–353.
830. Lu, X., Zheng, Y., and Zhou, B. (2013) *Journal of Electroceramics*, **31**, 360–363.
831. Liu, X., Zhou, H., Chen, X., *et al*. (2012) *Journal of Alloys & Compounds*, **515**, 22–23.
832. Shimada, T. and Ohtsuki, S. (2004) In *International Conference on Microwave Materials and Their Applications*, Inuyama, Japan.
833. Tang, Y., Gang, L., and Su, C., *et al*. (2014) *Ceramic International*, **40**, 7633–7636.
834. Tong, J., Zhang, B., Huang, W., *et al*. (2013) *Materials Letters*, **95**, 168–171.
835. Kim, D-W., Youn, H. J., Hong, K. S., *et al*. (2002) *Japanese Journal of Applied Physics*, **41**, 3812–3816.
836. Pang, L-X., Zhou, D., Guo, J., *et al*. (2013) *Ceramic International*, **39**, 4719–4722.
837. Fang, L., Liu, Q., Tang, Y., *et al*. (2013) *Ceramic International*, **38**, 6431–6434.
838. Li, H., Lu, W., and Lei, W. (2012) *Materials Letters*, **71**, 148–150.
839. Lin, H., Zhang, Y., Zhao, X., *et al*. (2008) *Japanese Journal of Applied Physics*, **47**, 7243–7245.
840. Lu, X., Zhang, Y., Dong, Z., *et al*. (2014) *Materials Letters*, **131**, 1–4.
841. Song, H-T., Hsu, C-S., Kuo, M-T., *et al*. (2004) *Materials Letters*, **58**, 2829–2833.
842. Lin, C-F., Lu, H-H., Chang, T-I., *et al*. (2006) *Journal of Alloys & Compounds*, **407**, 318–325.
843. Suresh, M. K., Warrier, P. R. S., Thomas, J. K., *et al*. (2010) *Journal of Materials Science: Materials in Electronics*, **21**, 1191–1194.
844. Huang, C-L. and Liu, S-S. (2008) *Materials Letters*, **62**, 3205–3208.
845. Khalam, L. A., Anjana, P. S., and Sebastian, M. T. (2009) *International Journal of Appled Ceramic Technology*, **6**, 571–580.
846. Kolodiazhnyi, T. (2012) *Journal of European Ceramic Society*, **32**, 4306–4309.

847. George, S. and Sebastian, M. T. (2010) *Journal of American Ceramic Society*, **93**, 2164–2166.
848. Lv, X., Zheng, Y., Zhou, B., *et al*. (2013) *Materials Letters*, **91**, 217–219.
849. He, M. and Zhang, H. (2014) *Journal of Alloys & Compounds*, **586**, 627–632.
850. Feteiro, A., Sinclair, D. C., Rajab, K. Z., *et al*. (2008) *Journal of American Ceramic Society*, **91**, 893–901.
851. Jawahar, I. N., Sebastian, M. T., and Mohanan, P. (2004) *Materials Science and Engineering* **B106**, 207–212.
852. Zhang, P., Liu, J., Zhao, Y., *et al*. (2016) *Materials Letters*, **162**, 173–175.
853. Keshri, S. and Rajput, S. S. (to be published)
854. Shahraki, A. S., Taheri-nassaj, E., Bafrood, H. B., *et al*. (2014) *Journal of Materials Science: Materials in Electronics*, **25**, 1117–1121.
855. Wang, L., Sun, Q., Ma, W., *et al*. (2013) *Ceramic International*, **39**, 5185–5190.
856. Zhang, P., Hua, Y., Xia, W., *et al*. (2012) *Journal of Alloys & Compounds*, **534**, 9–12.
857. He, M. and Zhang, H. (2013) *Journal of Materials Science: Materials in Electronics*, **24**, 3303–3308.
858. Sumesh, G. and Sebastian, M. T. (2010) *Journal of European Ceramic Society*, **30**, 2585–2592.
859. Khalam, L. A. and Sebastian, M. T. (2006) *Journal of American Ceramic Society*, **89**, 3689–3695.
860. Kim, J. B., Yoon, K. H., and Cho, Y. S. (2003) *Journal of American Ceramic Society*, **86**, 1159–1161.
861. Kalam, L. A. and Sebastian, M. T. (2006) *Journal of American Ceramic Society*, **89**, 3689–3695.
862. Takada, T., Wang, S. F., Yoshikawa, S., *et al*. (1994) In *Proceedings of 9th International Symposium on Applications of Ferroelectrics*, IEEE, p. 626
863. Feteira, A., Gillie, L. J., Elsebrock, R., *et al*. (2007) *Journal of American Ceramic Society*, **90**, 1475–1482.
864. Vanderah, T. A., Febo, W., Chan, J. Y., *et al*. (2000) *Journal of Solid State Chemistry*, **155**, 78–85.
865. Santha, N., Jawahar, I. N., Mohanan, P., *et al*. (2002) *Materials Letters*, **54**, 318–322.
866. Belous, A. G., Ovchar, O. V., Krameeranko, A. V., *et al*. (2010) *Inorganic Materials*, **46**, 529–533.
867. Kim, M-H., Nahm, S., Sung, W. S., *et al*. (2005) *Japanese Journal of Applied Physics*, **44**, 3091–3094.
868. Cheng, Y., Zuo, R., and Lv, Y. (2013) *Ceramic International*, **39**, 8681–8685.
869. Tang, X., Yang, H., Zhang, Q-I., *et al*. (2016) *International Journal of Appled Ceramic Technology*.
870. Yokoi, A., Ogawa, H., and Kan, A. (2006) *Journal of European Ceramic Society*, **26**, 2069–2074.
871. Zhang, P., Wang, Y., Liu, J., *et al*. (2014) *Materials Letters*, **123**, 195–197.
872. Wang, W., Zhou, H., Chen, X., *et al*. (2014) *Journal of Materials Science: Materials in Electronics*, **24**, 2641–2645.
873. Shen, C-H., Huang, C-L., Shih, C-F., *et al*. (2009) *Current Applied Physics*, **9**, 1042–1045.
874. Chen, G., Hou, M., Bao, Y., *et al*. (2013) *International Journal of Appled Ceramic Technology*, **10**, 492–501.
875. Huang, C-L., Chen, Y-B., and Tasi, C-F. (2008) *Journal of Alloys & Compounds*, **454**, 454–459.
876. Pang, L-X., Liu, W-G., Zhoub, D., *et al*. (2016) *Ceramic International*, **42**, 4574–4577.
877. Anjana, P. S., Joseph, T., and Sebastian, M. T. (2007) Microwave dielectric properties of $Ca_{5-x}Mg_xNb_4TiO_{17}$ ($x = 0$–3) ceramics, in *Proceedings of IEEE AEMC*, Kolkatta.
878. Cheng, C-M., Chen, Y-C., Yang, C-F., *et al*. (2007) *Journal of Electroceramics*, **18**, 155–160.
879. Tay, K-W., Fu, Y-P., and Huang, T-Y. (2009) *Ceramic International*, **35**, 3195–3199.
880. Huang, C-L., Zhao, L., Qiu, T., *et al*. (2012) *Ceramic International*, **38**, 5493–5496.
881. Li, B., Zhou, X., and Zhang, S. (2009) *Journal of Materials Science*, **20**, 1123–1128.
882. Zhou, H., Chu, X., Fang, L., *et al*. (2010) *Journal of Materials Research*, **25**, 1235–1238.
883. Surendran, K. P. and Sebastian, M. T. (2005) *Journal of Materials Research*, **20**, 2919–2928.

884. Rajput, S. S., Keshri, S., and Gupta, V. R. (2013) *Journal of Alloys & Compounds*, **581**, 223–229.
885. Zhou, D., Li, W-B., Guo, J., *et al*. (2014) *Inorganic Chemistry Frontiers*, **53**, 5712–5716.
886. Schileo, G., Dias, A., Moreira, R. L., *et al*. (2014) *Journal of American Ceramic Society*, **97**, 1096–1102.
887. Zhang, P., Zhao, Y., and Wu, H. (2015) *Daltons Transactions*, **44**, 16684–16693.
888. Zhou, H., Chen, X., Fang, L., *et al*. (2010) *Journal of American Ceramic Society*, **93**, 3976–3979.
889. Salak, A. N., Khalyavin, D. D., Mantas, P. W., *et al*. (2005) *Journal of Applied Physics*, **98**, 034101.
890. Yoon, J-M., Lee, J-A., Lee, J-H., *et al*. (2006) *Journal of European Ceramic Society*, **26**, 2129–2133.
891. Fang, L., Tang, Y., Chu, D., *et al*. (2012) *Journal of Materials Science: Materials in Electronics*, **23**, 478–483.
892. Huang, C-L., Chen, Y-B., and Tasi, C-F. (2008) *Journal of Alloys & Compounds*, **460**, 675–679.
893. Zhou, L., Lin, H., Chen, W., *et al*. (2008) *Japanese Journal of Applied Physics*, **47**, 7246–7249.
894. Li, L., Ye, J., Sun, H., *et al*. (2016) *Journal of Materials Science: Materials in Electronics*, in press.
895. Santha, N. and Sebastian, M. T. (2007) *Journal of American Ceramic Society*, **90**, 496–501.
896. Huang, C-L., Su, C-H., and Ho, Y-D. (2014) *Journal of Alloys & Compounds*, **607**, 67–72.
897. Xi, H-H., Zhou, D., He, B., *et al*. (2014) *Journal of American Ceramic Society*, **97**, 1375–1378.
898. Tay, K-W., Fu, Y-P., Huang, J-F., *et al*. (2011) *Ceramic International*, **37**, 1025–1031.
899. Park, J. H., Choi, C., Nahm, S., *et al*. (1999) *Journal of Materials Science Letters*, **18**, 889–993.
900. Li, Y., Li, J., Tang, B., *et al*. (2014) *Journal of Materials Science: Materials in Electronics* **25**, 2780–2785.
901. Takahashi, J., Kageyama, K., Fuji, T., *et al*. (1997) *Journal of Materials Science: Materials in Electronics*, **8**, 79–84.
902. Seabra, M. P. and Ferreira, V. M. (2001) *Key Engieering Materials*, **206-213**, 1501–1504.
903. Kawashima, S., Nishida, N., Ueda, I., *et al*. (1983) *Journal of American Ceramic Society*, **66**, 421–423.
904. Guan, E., Chen, W., and Luo, L. (2007) *Ceramic International*, **33**, 1145–1148.
905. Tseng, C-T., Huang, C-L., Hsu, H. (2007) *Journal of American Ceramic Society*, **90**, 1619–1622.
906. Subramanian, V., Murthy, V. R. K., and Viswanathnan, B. (1997) *Japanese Journal of Applied Physics*, **36**, 194–197.
907. Nomura, S. and Kaneta, K. (1984) *Japanese Journal of Applied Physics*, **33**, 507–508.
908. Zhang, Q. L., Yang, H., Zou, J. L., *et al*. (2005) *Materials Letters*, **59**, 880–884.
909. Sreemoolanathan, H., Sebastian, M. T., Blachnik, R., *et al*. (2004) *Journal of Solid State Chemistry*, **177**, 3995–4000.
910. Li, Y-X., Li, H., Tang, B., *et al*. (2015) *Journal of Materials Science: Materials in Electronics*, **26**, 1181–1185.
911. Muhammed, R., Iqbal, Y., and Rambo, C. R. (2015) *Journal of Materials Science: Materials in Electronics*, **26**, 1918–1922.
912. Zheng, H., Csette, G. D. C., *et al*. (2005) *Journal of Materials Science*, **40**, 5207–5214.
913. Varma, M. R., Reghunathan, R., and Sebastian, M. T. (2005) *Japanese Journal of Applied Physics*, **44**, 298–303.
914. Lee, M. K., Chung, J-H., Ryu, K. W., *et al*. (1998) *Proceedings of International Symposium on Insulating Materials*, Toyahashi, Japan, pp. 139-142
915. Zhou, D., Wang, H., Yao, X., *et al*. (2008) *Journal of American Ceramic Society*, **91**, 2228–2231.
916. Parida, S., Rout, S. K., Gupta, N., *et al*. (2011) *Journal of Alloys & Compounds*, **546**, 216–223.
917. Liao, W., Fang, L., Xiang, F., *et al*. (2013) *Journal of Materials Science: Materials in Electronics*, **24**, 272–276.
918. Hsu, C-H., Chang, Y-H., Yang, H-W., *et al*. (2013) *Ceramic International*, **39**, S203–S208.

919. Sarol, S. L., Rao, G. L. N., Raju, K. C. J., *et al*. (2009) *Japanese Journal of Applied Physics*, **48**, 061401.
920. Baranov, A. N. and Oh, Y. J. (2005) *Journal of European Ceramic Society*, **25**, 3451–3457.
921. Cai, H., Li, L., Sun, H., *et al*. (2015) *Materials Letters*, **144**, 78–81.
922. Tseng, C-F. and Huang, C-L. (2006) *Materials Research Bulletin*, **42**, 9–16.
923. Fang, L., Liao, W., Xu, M., *et al*. (2012) *Materials Letters*, **76**, 73–76.
924. Zhou, D., Pang, L-X., Guo, J., *et al*. (2011) *Journal of Advanced Dielectrics*, **1**, 379–382.
925. Lee, Y-C., Lee, W-H., Shiuc, F-S. (2005) *Journal of European Ceramic Society*, **25**, 3459–3468.
926. Yang, C-F., Chen, C-C., Cheng, C-M., *et al*. (2005) *Journal of European Ceramic Society*, **25**, 2849–2852.
927. Hsu, C-H. and Chang, Y-S. (2009) *Journal of Alloys and Compounds*, **479**, 714–718.
928. Ye, J., Li, L., Li, S., *et al*. (2016) *Journal of Materials Science: Materials in Electronics*
929. Salak, A., Khalyavavin, D. D., Mantas, P. Q., *et al*. (2005) *Journal of Applied Physics*, **98**, 034101.
930. Lim, J. B., Son, J-O., Nahm, S., *et al*. (2004) *Japanese Journal of Applied Physics*, **43**, 5388–5391.
931. Kim, H. T., Kim, S. H., Nahm, S., *et al*. (1999) *Journal of American Ceramic Society*, **82**, 3043–3048.
932. Seabra, M. P., Avdeev, M., Ferreira, V. M., *et al*. (2003) *Journal of European Ceramic Society*, **23**, 2403–2408.
933. Seabra, M. P., Avdeev, M., Ferreira, V. M., *et al*. (2004) *Journal of American Ceramic Society*, **87**, 584–590.
934. Fang, L., Chu, D., Zhou, H., *et al*. (2011) *Journal of Alloys & Compounds*, **509**, 8840–8844.
935. Lu, X., Zheng, Y., Zhou, B., *et al*. (2013) *Ceramic International*, **39**, 9829–9833.
936. Chen, Y-B., Huang, C-L., and Lin, S-H. (2006) *Materials Letters*, **60**, 3591–3595.
937. Shimada, T. (2001) *Journal of European Ceramic Society*, **21**, 2617–2620.
938. Ye, J., Li, L., Li, S., *et al*. (2015) *Journal of Materials Science: Materials in Electronics*, **26**, 8954–8959.
939. Jhou, M-Z. and Jean, J-H. (2006) *Journal of American Ceramic Society*, **89**, 786–791.
940. Hsieh, M-L., Chen, L-S., Hsu, H-S., *et al*. (2008) *Materials Research Bulletin*, **43**, 3122–3129.
941. Fang, L., Li, C., Peng, X., *et al*. (2010) *Journal of American Ceramic Society*, **93**, 1229–1231.
942. Jiao, X., Zhong, C., Zhang, S., *et al*. (2010) *Journal of Materials Science*, **45**, 3331–3335.
943. Moreira, R. L., Khlam, L. A., Sebastian, M. T., *et al*. (2007) *Journal of European Ceramic Society*, **27**, 2803–2810.
944. Huang, C-L., Yang, R-Y., and Weng, M-H. (2000) *Japanese Journal of Applied Physics*, **39**, 6608–6611.
945. Rong, G., Newman, N., Shaw, B., *et al*. (1999) *Journal of Materials Research*, **14**, 4011–4019.
946. Zhang, Y-C., Yue, Z. X., Qi, X., *et al*. (2004) *Materials Letters*, **58**, 1392–1395.
947. Huang, C-L., Chiang, K-H., and Huang, C-Y. (2005) *Materials Chemistry and Physics*, **90**, 373–377.
948. Kim, H. T. and Lanagen, M. T. (2003) *Journal of American Ceramic Society*, **86**, 1874–1878.
949. Choi, J-W., Ha, J-Y., Yoon, S-J., *et al*. (2003) *Journal of European Ceramic Society*, **23**, 2507–2510.
950. Vanderah, T. A., Miller, V. L., Levin, I., *et al*. (2004) *Journal of Solid Chemistry*, **177**, 2023–2038.
951. Wu, H. and Davies, P. K. (2004) *Journal of Solid State Chemistry*, **177**, 4305–4315.
952. Cao, J., Kuang, X., Allix, M., *et al*. (2011) *Chemistry of Materials*, **23**, 5058–5067.
953. Lv, X-S., Li, L-X., Suna, H., *et al*. (2015) *Ceramics International*, **41**, 15287–15291.
954. Kuang, X., Allix, M. B., Claridge, J. B., *et al*. (2006) *Journal of Materials Chemistry*, **16**, 1038–1045.
955. Anjana, P. S., Gopakumar, N., and Sajan, S. (2013) *Journal of Materials Science: Materials in Electronics*, **24**, 2035–2042.
956. Wang, S-F., Hsu, Y-F., Huang, H-S., *et al*. (2011) *Ceramic International*, **37**, 1327–1331.

957. Tang, Y., Fang, L., Zhou, H., *et al*. (2013) *Ceramic International*, **39**, 8503–8506.
958. Mallinson, P., Clridge, J. B., Iddles, D., *et al*. (2006) *Chemistry of Materials*, **18**, 6227–6238.
959. Kucheiko, S., Kim, H-J., Yeo, D-H., *et al*. (1996) *Japanese Journal of Applied Physics*, **35**, 668–672.
960. Thomas, S., Sayoojyam, B., Sebastian, M. T. (2011) *Journal of Materials Science: Materials in Electronics*, **22**, 1340–1345.
961. Jinga, S. I., Stolerin, S., and Busuioc, C. (2012) *Materials Research Bulletin*, **47**, 3713–3718.
962. Tang, X., Yang, H., Zhang, Q-L., *et al*. (2014) *Ceramic International*, **40**, 12875–12881.
963. Wang, J-J. (2009) *Journal of Alloys and Compounds*, **486**, 423–426.
964. Cao, X., Gao, F., Hu, G., *et al*. (2013) *Journal of Materials Science: Materials in Electronics*, **24**, 3021–3028.
965. Huang, C-L. and Chen, J-Y. (2012) *Materials Letters*, **76**, 28–31.
966. Jiang, B. J., Bo, G. H., and Xiaowu, W. (2004) *Materials Research Bulletin*, **39**, 2127–2135.
967. Huang, C-L. and Chen, J-Y. (2010) *Journal of American Ceramic Society*, **93**, 470–473.
968. Fang, L., Chu, D., Zhou, H., *et al*. (2011) *Journal of Alloys & Compounds*, **505**, 1880–1884.
969. Li, L., Sun, H., Cai, H., *et al*. (2015) *Journal of Alloys & Compounds*, **639**, 516–519.
970. Reaney, I. M., Wise, P. L., Qazi, I., *et al*. (2003) *Journal of European Ceramic Society*, **23**, 3021–3034.
971. Kageyama, K. (1992) *Journal of American Ceramic Society*, **75**, 1767–1771.
972. Davies, P. K., Tong, J., and Negas, T. (1997) *Journal of American Ceramic Society*, **80**, 1727–1740.
973. Kwon, D-W., Lanagan, M. T., and Shrout, T. R. (2005) *Journal of Ceramic Society Japan*, **113**, 216–219.
974. Chen, Y-B. (2011) *Journal of Alloys and Compounds*, **509**, 1050–1053.
975. Fang, L., Li, C., Peng, X., *et al*. (2010) *Journal of American Ceramic Society*, **93**, 1884–1887.
976. Khalam, L. A., Thomas, S., and Sebastian, M. T. (2007) *International Journal of Appled Ceramic Technology*, **4**, 356–366.
977. Chen, Y-B. (2011) *Journal of Alloys and Compounds*, **509**, 9226–9229.
978. Sebra, M. P., Salak, A. N., Ferreira,V. M., *et al*. (2004) *Journal of European Ceramic Society*, **24**, 2995–3002.
979. Tseng, C-F. and Huang, C-L. (2007) *Japanese Journal of Applied Physics*, **46**, 1571–1573.
980. Hu, M., Fu, Y., Zhou, D., *et al*. (2012) *Journal of Materials Science: Materials in Electronics*, **23**, 1775–1782.
981. Choi, J-W., Yoon, S., Kim, H-J., *et al*. (2002) *Japanese Journal of Applied Physics*, **41**, 3804–3807.
982. Zhang, H., Fang, L., Su, H., *et al*. (2009) *Journal of American Ceramic Society*, **92**, 238–240.
983. Tans, B., Yu, S., Chen, H., *et al*. (2013) *Journal of Alloys & Compounds*, **551**, 463–467.
984. Chen, Y-B. (2010) *Journal of Alloys and Compounds*, **507**, 286–289.
985. Padmakumar, H., Joseph, J. T., Thomas, J. K., *et al*. (2009) *Journal of Materials Science: Materials in Electronics*, **20**, 551–554.
986. Chen, Y-B., Huang, C-L., and Lo, C-W. (2006) *Materials Science and Engineering B*, **128**, 98–102.
987. Choi, J-W., Ha, J-Y., Yoon, S-J., *et al*. (2004) *Japanese Journal of Applied Physics*, **43**, 223–225.
988. Tsens, C-F and Huang, C-L. (2006) *Japanese Journal of Applied Physics*, **45**, 826–830.
989. Mu, Q. J., Li, C. Y., Guo, J. D., *et al*. (2015) *Ceramic International*, **41**, 907–912.
990. Sithara, S. P., Rajesh, S., Rajani, K. V., *et al*. (2008) *Scripta Materiala*, **59**, 424–427.
991. Chen, Y-B. (2011) *Journal of Alloys & Compounds*, **509**, 1050–1053.
992. Liao, Q., Li, L., Ren, X., *et al*. (2012) *Journal of American Ceramic Society*, **95**, 3363–3365.
993. Lee, Y-C., Chiang, C-S., and Huang, Y-L. (2010) *Journal of European Ceramic Society*, **30**, 963–970.
994. Hsiang, H-I. and Chung, S-H. (2008) *Journal of Alloys & Compounds*, **465**, 356–360.
995. Kim, D-W., Hong, H. B., Hong, K-S., *et al*. (2002) *Japanese Journal of Applied Physics*, **41**, 6045–6048.

996. Kato, J., Kagata, H., and Nishimoto, K. (1992) *Japanese Journal of Applied Physics*, **31**, 3144–3147.
997. Yamaguchi, Y., Komatsu, Y., Otobe, T., *et al*. (1980) *Ferroelectrics*, **27**, 273–276.
998. Choi, Y-J., Park, J-H., and Park, J-G. (2004) *Materials Letters*, **58**, 3102–3106.
999. Choi, J. W., Ha, J-Y., Yoon, S-J., *et al*. (2004) *Japanese Journal of Applied Physics*, **43**, 223–225.
1000. Kim, H. T., Kim, S. H., Nahm, S., *et al*. (1999) *Journal of American Ceramic Society*, **82**, 3043–3048.
1001. Wang, H., Peng, Z., Du, H., *et al*. (2004) *Ceramic International*, **30**, 1219–1223.
1002. Lee, J-A., Lee, J-H., Kim, J-J. (2006) *Journal of European Ceramic Society*, **26**, 2111–2115.
1003. Wakino, K., Murata, M., and Tamura, H. (1986) *Journal of American Ceramic Society*, **69**, 34–37.
1004. Wei, C-H. and Jean, J-H. (2003) *Journal of American Ceramic Society*, **86**, 93–98.
1005. Kucheiko, S., Kim, H-J., Yeo, D-H., *et al*. (1996) *Japanese Journal of Applied Physics*, **35**, 668–675.
1006. Belous, A. G., Ovchar, O. V., Macek-Krzmanc, M., *et al*. (2006) *Journal of European Ceramic Society*, **26**, 3733–3739.
1007. Tseng, C-F. and Huang, C-L. (2006) *Japanese Journal of Applied Physics*, **45**, 8766–8768.
1008. Santha, N., Jawahar, I. N., Mohanan, P., *et al*. (2002) *Materials Letters*, **54**, 318–322.
1009. Wu, H. T., Jiang, Y. S., and Yue, Y. L. (2012) *Ceramic International*, **38**, 5151–5156.
1010. Yao, L., Qiu, T., Wan, W., *et al*. (2014) *Journal of Materials Science: Materials in Electronics*, **25**, 4046–4050.
1011. Hsu, C-H. (2008) *Journal of Alloys and Compounds*, **464**, 412–417.
1012. Su, C., Fang, L., Wei, Z., *et al*. (to be published)
1013. Kan, A., Ogawa, H., and Ohsato, H. (2002) *Journal of Alloys and Compounds*, **337**, 303–308.
1014. Solomon, S., Padmakumar, H., Jacob, L., *et al*. (2008) *Journal of Alloys and Compounds*, **461**, 675–677.
1015. Huang, C-L. and Yang, W-R. (2009) *Materials Letters*, **63**, 103–105.
1016. Bisen, A., Satapathy, A., Parida, S., *et al*. (2014) *Journal of Alloys and Compounds*, **615**, 1006–1012.
1017. Ikawa, H. and Takemoto, M. (2004) *Materials Chemistry and Physics*, **79**, 222–225.
1018. Liu, P., Kim, E. S., and Yoon, K. H. (2001) *Japanese Journal of Applied Physiics*, **40**, 5769–5773.
1019. Lv, X., Wang, Z., and Chen, X. M. (2011) *Ceramic International*, **37**, 1033–1037.
1020. Liao, Q., Ding, X., and Ren, X. (2012) *Journal of American Ceramic Society*, **95**, 1501–1503.
1021. Liao, Q., Li, L., Zhao, P., *et al*. (2011) *Materials Science and Engineering B*, **176**, 41–48.
1022. Lu, C. A., Lin, P. and Wang, S-F. (2007) *Ceramic International*, **33**, 1389–1393.
1023. Tang, B., Guo, X., Yu, S-Q., *et al*. (2015) *Materials Research Bulletin*, **66**, 163–168.
1024. Wu, H. and Davies, P. K. (2004) *Journal of Solid State Chemistry*, **177**, 3469–3478.
1025. Hsu, C-S., Song, H-T., Yu, C-C., *et al*. (2006) *Ceramic International*, **33**, 951–955.
1026. Kim, H. T., Byun, J. D., Kim, Y. (1998) *Materials Research Bulletin*, **33**, 975–986.
1027. Lim, J. B., Kim, D. H., Nahm, S., *et al*. (2006) *Materials Research Bulletin*, **41**, 1199–1205.
1028. Laishram, R., Thakur, O. P., and Bhattacharya, D. K. (2011) *Materials Letters*, **65**, 1678–1680.
1029. Chen, G-H., Di, J. C., Li, M., *et al*. (2012) *Journal of Materials Science: Materials in Electronics*, **23**, 746–752.
1030. Chen, Y., Chen Y., Zeng, Y., *et al*. (2012) *Ceramic International*, **38S**, S147–S152.
1031. Guo, R., Bhalla, S., Sheen, J., *et al*. (1995) *Journal of Materials Research*, **10**, 18–25.
1032. Kim, I-T., Kim, Y. H., and Chung, S. J. (1997) *Journal of Materials Research*, **12**, 518–525.
1033. Kim, Y-W., Park, J-H., and Park, J-G. (2004) *Journal of European Ceramic Society*, **24**, 1775–1779.
1034. Xia, W. S., Li, L-X., Zhang, P., *et al*. (2011) *Materials Letters*, **65**, 3317–3319.
1035. Tzou, W-C., Yang, Y-S., Yang, C-F., *et al*. (2007) *Materials Research Bulletin*, **42**, 1897–1904.
1036. Chen, C-T., Huang, C-Y., Lin, H-J., *et al*. (2012) *Journal of European Ceramic Society*, **32**, 2373–2380.

1037. Pang, L-X., Zhou, D., Chen, Y-A., *et al*. (2011) *Materials Chemistry and Physics*, **125**, 641–645.
1038. Zhou, D., Guo, J., Yao, X., *et al*. (2012) *Functional Materials Letters*, **5**, 125004.
1039. Tseng, C-F., Huang, C-L., Yang, W-R., *et al*. (2006) *Journal of American Ceramic Society*, **89**, 1465–1470.
1040. Wang, Y-R., Wang, S-F., and Ken, C-K. (2006) *Materials Science and Engineering A*, **426**, 3053–3057.
1041. Sun, T. T., Li, L., Mao, M. M., *et al*. (2013) *International Journal of Appled Ceramic Technology*, **10**, E210–218.
1042. Tseng, C-F. (2008) *Journal of American Ceramic Society*, **91**, 4101–4104.
1043. Pang, L-X., Zhou, D., Chen, Y-H., *et al*. (2011) *Materials Chemistry and Physics*, **125**, 641–645.
1044. Li, K., Wang, H., Zhou, H., *et al*. (2010) *International Journal of Appled Ceramic Technology*, **7**, E1494–E1500.
1045. Sun, T., Zhao, Y. F., and Chen, X. M. (2015) *Ceramic International*, **141**, 5872–5880.
1046. Hu, M., Xiong, J., Gu, H., *et al*. (2012) *Ceramic International*, **38**, 3175–3183.
1047. Paik, J. H., Nahm, S., Byulin, J-D., *et al*. (1998) *Journal of Materials Science Letters*, **17**, 1777–1780.
1048. Ahn, C-W., Nahm, N., Lim, Y-S., *et al*. (2002) *Japanese Journal of Applied Physics*, **41**, 5277–5280.
1049. Azough, F., Leach, C., Freer, R. (2006) *Journal of European Ceramic Society*, **26**, 2877–2884.
1050. Choi, Y-G., Park, J-H., Ko, W-J., *et al*. (2005) *Journal of Electroceramics*, **14**, 157–162.
1051. Hu, M-Z., Qian, J., Gu, H-S., *et al*. (2006) *Materials Science and Engineering B*, **134**, 89–93.
1052. Zhang, Y., Fu, B., Hong, M., *et al*. (2014) *Journal of Materials Science: Materials in Electronics*, **25**, 5475–5480.
1053. Li, S., Sun, J., Taylor, R., *et al*. (2004) *Journal of Materials Research*, **19**, 3526–3533.
1054. Sun, J-S., Yu, J-J., You, J-C., *et al*. (1995) *Journal of Materials Science*, **28**, 2163–2168.
1055. Ahn, C. W., Jang, H-J., Nahm, S., *et al*. (2003) *Journal of European Ceramic Society*, **23**, 21473–21478.
1056. Feteira, A. and Sinclair, D. C. (2008) *Journal of American Ceramic Society*, **91**, 1338–1341.
1057. Pang, L-X., Wang, H., Zhou, D., *et al*. (2008) *International Journal of Appled Ceramic Technology*, **5**, 341–346.
1058. Hsu, C-H., Shih, C-F., Yu, C-C., *et al*. (2008) *Journal of Alloys and Compounds*, **461**, 355–359.
1059. Choi, E. S., Lee, Y. H., and Bae, S. G. (2001) *Proceedings of International Symposium on Electrical and Insulating Materials ISEIM-2001*, **PI-5**, 99–102.
1060. Zhou, D., Gou, G., and Gong, S. (2011) *Materials Chemistry and Physics*, **13**, 903–908.
1061. Li, J. and Qiu, T. (2012) *Ceramic International*, **38**, 2597–2600.
1062. Zhang, Y-C., Yue, Z. X., Gui, L., *et al*. (2005) *Journal of Electroceramics*, **14**, 67–74.
1063. Zhou, D., Rindall, C. A., Wang, H., *et al*. (2010) *Journal of American Ceramic Society*, **93**, 2931–2936.
1064. Li, Z., Gao, F., Hu, G. X., *et al*. (2014) *Journal of Materials Science: Materials in Electronics*, **25**, 5020–5026.
1065. Shimada, T. US Patent 6,413896B1.
1066. Kim, D-W., Lee, D-G., and Hong, K. S. (2001) *Materials Research Bulletin*, **36**, 585–595.
1067. Lee, J-H., Jang, Y. I., Youn, H. J., *et al*. (1995) *Jounal of Materials Science*, **34**, 625–628.
1068. Udovic, M., Valant, M., and Suvorov, D. (2004) *Journal of American Ceramic Society*, **87**, 591–597.
1069. Liu, S., Taylor, R., Petrovic, N. S., *et al*. (2005) *Journal of Applied Physics*, **97**, 014105.
1070. Lu, C-A., Lin, P., and Wang, S-F. (2007) *Ceramic International*, **33**, 1389–1393.
1071. Sun, P-H., Nakamura, T., Shun, Y-J., *et al*. (1998) *Japanese Journal of Applied Physics*, **37**, 5625–5629.
1072. Rejini, R. and Sebastian, M. T. (2006) *International Journal of Applied Ceramic Technology*, **3**, 230–235.
1073. Liu, X., Zhou, H., Chen, X., *et al*. (2012) *Journal of Materials Science: Materials in Electronics*, **23**, 640–644.

1074. Ma, P. P., Yi, L., Liu, X. Q., *et al*. (2013) *Journal of American Ceramic Society*, **96**, 3417–3424.
1075. Wang, Z., Huang, B., Wang, L., *et al*. (2015) *Journal of Materials Science: Materials in Electronics*, **26**, 4273–4279.
1076. Tseng, C-F., Hsu, C-H., Huang, C-L., *et al*. (2006) *Japanese Journal of Applied Physics*, **45**, 2680–2682.
1077. Huang, C-L. and Chen, J-Y. (2010) *Journal of American Ceramic Society*, **93**, 1248–1251.
1078. Su, Y-S. and Jean, J. H. (2008) *Japanese Journal of Applied Physics*, **47**, 7254–7256.
1079. Bian, J. J., Song, G. X., and Yan, K. (2007) *Journal of Europen Ceramic Society*, **27**, 2817–2821.
1080. Ma, P. P., Yi, L., Liu, X. Q., *et al*. (2013) *Journal of American Ceramic Society*, **96**, 1795–1800.
1081. Kan, A., Ogawa, H., and Ohsato, H. (2002) *Journal of Alloys and Compounds*, **337**, 303–308.
1082. Zhou, H., Chen, X., Fang, L., *et al*. (2010) *Journal of American Ceramic Society*, **93**, 1537–1539.
1083. Bian, J. J., Dong, Y. F., and Song, G. X. (2008) *Journal of American Ceramic Society*, **91**, 1182–1187.
1084. Cho, S-Y., Seo, M-K., Hong, K. S., *et al*. (1997) *Materials Research Bulletin*, **32**, 725–735.
1085. Ubic, R., Hu, Y., Khamoudshi, K., *et al*. (2006) *Journal of European Ceramic Society*, **26**, 1787–1790.
1086. Veres, A., Marinel, S., and Roulland, F. (2005) *Journal of European Ceramic Society*, **25**, 2759–2762.
1087. Melodetsky, I. and Davies, P. K. (2001) *Journal of European Ceramic Society*, **21**, 2587–2591.
1088. Ikawa, H., Harita, H., and Fukanaga, O. (1990) *Journal of Ceramic Society Japan*, **98**, 860–863.
1089. Liao, W., Li, L., Zhang, P., *et al*. (2011) *Solid State Sciences*, **13**, 1201–1204.
1090. Jawahar, I. N., Sebastian, M. T., Mohanan, P. (2004) *Materials Science and Engineering B*, **106**, 207–212.
1091. Yu, S., Tang, B., Zhang, S., *et al*. (2012) *Materials Letters*, **67**, 293–295.
1092. Kim, D-W., Kim, D-Y., and Hong, K. S. (2000) *Journal of Materials Research*, **15**, 1331–1335.
1093. Lei, Y., Yin, Y., and Liu, Y. (2011) *Advanced Materials Research*, **217-218**, 1235–1238.
1094. Tong, J-X., Zhang, Q-L., Yang, H., *et al*. (2007) *Journal of American Ceramic Society*, **90**, 845–849.
1095. Zhou, H., Chen, X., Fang, L., *et al*. (2014) *Ceramic International*, **40**, 3737–3741.
1096. Suvorov, S., Valant, M., Skapin, S., *et al*. (1998) *Journal of Materials Science*, **33**, 85–89.
1097. Azough, F., Leach, C., and Freer, R. (2006) *Journal of European Ceramic Society*, **26**, 1883–1887.
1098. Ahn, C-W., Jang, H-J., Nahm, S., *et al*. (2003) *Journal of European Ceramic Society*, **23**, 2473–2478.
1099. Huang, C-L. and Hsu, C-S. (2001) *Materials Research Bulletin*, **36**, 2677–2687.
1100. Fang, L., Chu, D., Li, C., *et al*. (2011) *Journal of American Ceramic Society*, **94**, 524–528.
1101. Kumar, H. P., Joseph, S., Solomon, S., *et al*. (2008) *International Journal of Appled Ceramic Technology*, **5**, 347–352.
1102. Huang, C-L. and Chiang, K-H. (2004) *Materials Research Bulletin*, **39**, 1701–1708.
1103. Yang, Y-C. (1999) *Japanese Journal of Applied Physics*, **38**, 3576–579.
1104. Kim, E. S. and Choi, W. (2006) *Journal of European Ceramic Society*, **26**, 1761–1766.
1105. Huang, C-L. and Chiang, K-H. (2002) *Materials Research Bulletin*, **37**, 1941–1948.
1106. Cho, S-Y., Hong, K.S., and Ko, K-H. (1999) *Materials Research Bulletin*, **34**, 511–516.
1107. Hughes, H., Iddles, D. M., and Reaney, I. M. (2001) *Applied Physics Letters*, **79**, 2952–2954.
1108. Azough, F., Leach, L., and Freer, R. (2005) *Journal of European Ceramic Society*, **25**, 2839–2841.
1109. Kamba, S., Hughes, H., Noujini, D., *et al*. (2004) *Journal of Physics D*, **37**, 1980–1986.
1110. Barwick, M., Azough, F., and Freer, R. (2006) *Journal of European Ceramic Society*, **26**, 1767–1773.
1111. Azough, F., Lowe, T., and Freer, R. (2005) *Journal of Electroceramics*, **15**, 183–192.
1112. Bijumon, P. V., Sebastian, M. T., and Mohanan, P. (2005) *Journal of Applied Physics*, **98**, 124105.

1113. Huang, C-L. and Chiang, K-H. (2002) *Materials Research Bulletin*, **37**, 1941–1948.
1114. Zhang, Y-C., Wang, X., Fu, B-J., *et al*. (2012) *Ceramic International*, **38**, S169–S172.
1115. Li, L., Ren, X., and Liao, Q. (2012) *Ceramic International*, **38**, 3985–3989.
1116. Kim, D-W., Hong, K. S., Yoon, C. S., *et al*. (2003) *Journal of European Ceramic Society*, **23**, 2597–2601.
1117. Guoqing, W., Hua, W. S., and Hao, S. (2005) *Materials Letters*, **59**, 2229–2231.
1118. Chen, G. H., Di, J-C., Xu, H-R., *et al*. (2012) *Journal of American Ceramic Society*, **95**, 1394–1397.
1119. Scott, R. J., Thomas, M., and Hampson, C. (2003) *Journal of European Ceramic Society*, **23**, 2467–2471.
1120. Fu, B., Zhang, Y., and Yue, H. (2013) *Ceramic International*, **39**, 3783–3793.
1121. Kan, A., Ogawa, H., Oishi, T., *et al*. (2005) *Japanese Journal of Applied Physics*, **44**, 7103–7106.
1122. Ikawa, H., Ohara, M., Iida, T., *et al*. (2004) *Journal of Ceramic Society Japoan*, Suppl., **12**, S1614–S1616.
1123. Lee, M. J., You, B. D., and King, D. S. (1995) *Journal of Materials Science: Materials in Electronics*, **6**, 165–172.
1124. Kim, D. M., Kim, S., Kim, K. S., *et al*. (2009) *Journal of Electrooceramics*, **23**, 164–168.
1125. Hu, C., Fang, L., Su, H., *et al*. (2009) *Journal of Alloys and Compounds*, **487**, 504–506.
1126. Yu, S., Tang, B., Zhang, S., *et al*. (2010) *Journal of Alloys and Compounds*, **505**, 814–817.
1127. Huan, Z., Sun, Q., Ma, W., *et al*. (2013) *Journal of Alloys and Compounds*, **551**, 630–635.
1128. Iochim, A., Banciu, M. G., Toacsan, M. I., *et al*. (2005) *Materials Science and Engineering B*, **118**, 205–209.
1129. Zhou, D., Pang, L-X., Xie, H. D., *et al*. (2014) *European Journal of Inorganic Chemistry*, 296–301.
1130. Kim, M. H., Jeong, J. H., Kim, H. T., *et al*. (2006) *Journal of European Ceramic Society*, **26**, 2139–2142.
1131. Udovic, M. and Suvorov, D. (2007) *Journal of American Ceramic Society*, **90**, 2404–2408.
1132. Choy, J. H., Han, Y. S., Sohn, J. H., *et al*. (1995) *Journal of American Ceramic Society*, **78**, 1169–1172.
1133. Negas, T., Yeager, G., Bell, S., *et al*. (1993) *American Ceramic Society Bulletin*, **72**, 80–89.
1134. Ubic, R., Khomouski, K., and Spary, A. C. (2004) In *International Conference on Microwave Materials and Their Applications*, MMA 2004, Inuyama, Japan.
1135. Bianco, A., Gusmano, G., Freer, R., *et al*. (1999) *Journal of European Ceramic Society*, **19**, 959–963.
1136. Khalam, L. A., Sreemoolanathan, H., Ratheesh, R., *et al*. (2004) *Materials Science and Engineering B*, **107**, 264–270.
1137. Takahasi, J., Kageyama, K., and Kodaira, K. (1993) *Japanese Journal of Applied Physics*, **32**, 4327–4331.
1138. Takahashi, J., Kageyama, K., and Hayashi, T. (1991) *Japanese Journal of Applied Physics*, **30**, 2354–2358.
1139. Kim, E. S., Kim, Y. H., Chae, J. H., *et al*. (2003) *Materials Chemistry and Physics*, **79**, 230–232.
1140. Zeng, Q., Li, W., Shi, J-L., *et al*. (2006) *Materials Letters*, **60**, 3203–3206.
1141. Parvanova, V. and Iliev, I. (2006) *Journal of Materials Science: Materials in Electronics*, **17**, 815–818.
1142. Baranov, A. N. and Oh, Y-J. (2005) *Journal of European Ceramic Society*, **25**, 3451–3457.
1143. Fang, L., Li, C., Peng, X., *et al*. (2010) *Journal of Materials Research*, **25**, 1239–1242.
1144. Fu, M. S., Liu, X. Q., Chen, X. M., *et al*. (2010) *Journal of American Ceramic Society*, **93**, 787–795.
1145. Kim, K. S., Shim, S. H., Shim, S., *et al*. (2010) *Ceramic International*, **36**, 1571–1575.
1146. Chen, Y. B. (2010) *Journal of Alloys and Compounds*, **496**, 660–664.
1147. Solomon, S., Suresh, M. K., Thomas, J. K., *et al*. (2012) *Ceramic International*, **38**, 6487–6494.
1148. Chen, X., Zhou, H., Fang, L., *et al*. (2010) *Materials Research Bulletin*, **45**, 1509–1512.

1149. Lim, J-J., Nahm, S., Kim, H-T., *et al*. (2005) *Journal of Electroceramics*, **17**, 393–397.
1150. Liao, Q., Li, L., Ren, X., *et al*. (2011) *Journal of American Ceramic Society*, **94**, 3237–3240.
1151. Yu, S. Q., Tang, B., Zhang, X., *et al*. (2012) *Journal of American Ceramic Society*, **95**, 1939–1943.
1152. Kucheiko, S., Yeo, D-H., Choi, J-W., *et al*. (2002) *Journal of American Ceramic Society*, **85**, 1327–1329.
1153. Zeng, Q., Zhang, N., Zhou, Y., *et al*. (2014) *International Journal of Appled Ceramic Technology*, **11**, 200–206.
1154. Lee, Y-C., Chiu, J-D., and Chen, Y. H. (2013) *Journal of American Ceramic Society*, **96**, 1477–1482.
1155. Bijumon, P. V. and Sebastian, M. T. (2007) *International Journal of Appled Ceramic Technology*, **4**, 60–74.
1156. Lei, S., Fan, H., Chen, W., *et al*. (to be published)
1157. Kim, J-R., Kim, D-W., Cho, I-S., *et al*. (2007) *Journal of European Ceramic Society*, **27**, 3075–3079.
1158. Zhu, H., Cui, Z., and Shen, C. (2016) *Journal of Materials Science: Materials in Electronics*, in press.
1159. Liou, Y-C., Shih, C-Y., and Shiu, W-H. (2007) *Materials Research Bulletin*, **42**, 1104–1110.
1160. Ioachim, A., Banciu, M. G., Toacsen, M. I., *et al*. (2006) *Applied Surface Science*, **253**, 335–338.
1161. Bafrooeia, H. B., Taheri Nassaja, E., Ebadzadehb, T., *et al*. (2016) *Ceramic International*, **42**, 3296–3303.
1162. Zhang, H., Wu, Y., Meng, S., *et al*. (2009) *Journal of Alloys and Compounds*, **460**, 460–463.
1163. Ikawa, H., Tsunneyama, T., and Takemoto, M. (2004) In *Microwave Materials and Their Applications*, MMA 2004, Inuyama, Japan.
1164. Hu, X. and Chen, X. M. (2004) *Japanese Journal of Applied Physics*, **43**, 215–218.
1165. Varma, M. R. and Sebastian, M. T. (2007) *Journal of European Ceramic Society*, **27**, 2827–2833.
1166. Moon, J. H., Jung, H. M., Park, H. S., *et al*. (1999) *Japanese Journal of Applied Physics*, **38**, 6821–6827.
1167. Kim, D-W., Hong, H. B., and Hong, K. S. (2002) *Japanese Journal of Applied Physics*, **41**, 1465–1469.
1168. Ahn, Y. S., Yoon, K. H., and Kim, E. S. (2003) *Journal of European Ceramic Society*, **23**, 2519–2523.
1169. Houivet, D., Fallah, J. E., and Haussone, J. M. (199) *Journal of European Ceramic Society*, **19**, 1095–1099.
1170. Houivet, D., Fallah, J. E., and Lamagenere, B., *et al*. (2001) *Journal of European Ceramic Society*, **21**, 1727–1730.
1171. Hsu, C-H. and Ho, H-A. (2010) *Materials Letters*, 396–398.
1172. Zhou, H., Wang, H., Chan, Y., *et al*. (2009) *Materials Chemistry and Physics*, **113**, 1–5.
1173. Yang, R-Y., Weng, M-H., and Kuan, H. (2009) *Ceramic International*, **35**, 39–43.
1174. Suvorov, D., Valant, M., Jancar, B., *et al*. (2001) *Acta Chimie Slovania*, **48**, 87–99.
1175. Hu, M., Fu, Y., Luo, C., *et al*. (2010) *Journal of American Ceramic Society* **93**, 3354–3359.
1176. Valant, M. and Suvorov, D. (2001) *Journal of American Ceramic Society* **84**, 2900–2904.
1177. Zhou, F., Liu, X., Wang, H., *et al*. (2013) *Journal of Materials Science: Materials in Electronics*, **24**, 299–304.
1178. Fang, L., Su, C., Wei, Z., *et al*. (2013) *Ceramic International*, **39**, S579–583.
1179. Tseng, C. F. (2014) *Journal of European Ceramic Society*, **34**, 3641–3648.
1180. Chen, Y-C. and Lee, W-C. (2013) *Journal of Materials Science: Materials in Electronics*, **24**, 345–351.
1181. Pang, L-X. Zhou, D., Wang, H., *et al*. (2011) *Journal of Physics and Chemistry of Solids*, **72**, 882–883.
1182. Huang, C-L., Hsu, C-S., and Lin, R-J. (2001) *Materials Research Bulletin*, **36**, 1985–1993.

1183. Yu, Q., Fang, L., Zhang, H., *et al*. (2009) *Journal of Materials Science: Materials in Electronics*, **20**, 671–674.
1184. Li, C., Wei, X., Yan, H., *et al*. (2013) *Journal of Avanced Dielectrics*, 1320003.
1185. Zhou, D., Zhang, Q., Yang, H., *et al*. (2008) *Journal of European Ceramic Society*, **28**, 2777–2782.
1186. Pamu, D., Rao, G. L. N., and Raju, K. C. J. (2011) *Journal of Alloys and Compounds*, **509**, 9289–9295.
1187. Bijumon, P. V., Antar, Y. M. M., Freundorfer, A. P., *et al*. (2008) *International Journal of Applied Ceramic Technology*, **5**, 382–393.
1188. Tamura, H. (1994) *American Ceramic Society Buletin*, **73**, 94–97.
1189. Ho, Y-S., Weng, M. H., Dai, B-T., *et al*. (2005) *Japanese Journal of Applied Physics*, **44**, 6152–6155.
1190. Bijumon, P. V., Mohanan, P., and Sebastian, M. T. (2002) *Japanese Journal of Applied Physics*, **41**, 3834–3835.
1191. Bijumon, P. V. and Sebastian, M. T. (2005) *Journal of American Ceramic Society*, **88**, 3433–3439.
1192. Parnova, V. D. and Andreev, S. K. (2005) *Journal of Materials Science: Materials in Electronics*, **16**, 249–252.
1193. Feteira, A., Sinclair, D. C., and Lanagan, M. T. (2005) *Journal of Materials Research*, **20**, 2391–2399.
1194. Joseph, J., Vimala, T. M., Raju, K. C. J., *et al*. (1996) *Japanese Journal of Applied Physics*, **35**, 179–181.
1195. Chen, Y-C., Fu, J-Y., Li, C-H., *et al*. (2014) *Journal of Materials Science: Materials in Electronics*, **25**, 4760–4766.
1196. Guo, D., Lin, Z., and Hu, X. (2008) *Ceramic International*, **34**, 1931–1934.
1197. Ichinose, N., Mizutani, T., Hiraki, H., *et al*. (1977) *Ceramuraga International*, 100–102.
1198. Chen, Y-B. (2011) *Journal of Alloys and Compounds*, **509**, 2375–2380.
1199. Chen, Y-C. and Yao, S-L. (2012) *Journal of Physics and Chemistry of Solids* **73**, 1240–1244.
1200. Huang, C-L., Chen, J-Y., Tseng, Y-W., *et al*. (2010) *Journal of American Ceramic Society*, **93**, 3299–3304.
1201. Oishi, T., Ogawa, H., and Kan, A. (2007) *Materials Research Bulletin*, **42**, 2072–2081.
1202. Ikawa, H., Itou, Y., Takei, Y., *et al*. (2003) In *11th US-Japan Seminar on Dielectric & Piezoelectric Ceramics*, Sapporo, Japan, pp. 93–96.
1203. Kim, J-R., Kim, D-W., Yoon, S. H., *et al*. (2006) *Journal of Electrioceramics*, **17**, 439–443.
1204. Kim, D-J., Hahn, J-W., Han, G-P., *et al*. (2000) *Journal of American Ceramic Society*, **83**, 1010–1012.
1205. Guo, M., Gong, S., Dou, G., *et al*. (2011) *Journal of Alloys and Compounds*, **509**, 5988–5995.
1206. Kim, D-W., Kim, J. R., Yoon, S-H., *et al*. (2002) *Journal of American Ceramic Society*, **85**, 2759–2762.
1207. Wu, H. and Davies, P. K. (2006) *Journal of American Ceramic Society*, **89**, 2239–2249.
1208. Sebastian, M. T. (1999) *Journal of Materials Science: Materials in Electronics*, **10**, 475–478.
1209. Bijumon, P. V., Sebastian, M. T., Dias, A., *et al*. (2005) *Japanese Journal of Applied Physics*, **97**, 104–108.
1210. Fang, L., Zhang, H., Huang, T. H., *et al*. (2004) *Materials Research Bulletin*, **39**, 1649–1654.
1211. Bijumon, P. V. and Sebastian, M. T. (2005) *Journal of American Ceramic Society*, **88**, 3433–3439.
1212. Reaney, I. M. and Iddles, D. (2006) *Journal of American Ceramic Society*, **89**, 2063–2072.
1213. Jayanthi, S. and Kutty, T. R. N. (2006) *Materials Letters*, **60**, 796–800.
1214. Plourde, J. K., Lim, D. F., O'Bryan, H. M., *et al*. (1975) *Journal of American Ceramic Society*, **58**, 418–420.
1215. Wang, S. F., Hsu, Y. F., Weng, T-H., *et al*. (2003) *Journal of Materials Research*, **18**, 1179–1187.
1216. Udovic, M., Valant, M., and Suvorov, D. (2004) *Journal of American Ceramic Society*, **87**, 591–597.

1217. Lee, H. R., Yoon, K. H., and Kim, E. S. (2003) *Japanese Journal of Applied Physics*, **42**, 6168–6169.
1218. Chen, Y-B. (2010) *Journal of Alloys and Compounds*, **502**, 153–157.
1219. Jeong, B-J., Joung, M-R., Weon, S-H. K., *et al*. (2013) *Journal of American Ceramic Society*, **96**, 2225–2229.
1220. Yu, S., Zhang, S., Tang, B., *et al*. (2012) *Ceramic International*, **38**, 613–618.
1221. Pamu, D., Rao, L. N., and Raju., K. C. J. (2011) *Journal of American Ceramic Society*, **95**, 126–132.
1222. Wise, P. L., Reaney, I. M., Ubic, R., *et al*. (1999) In *Institute of Physics Conference Series* 161, Electron Microscopy & Analysis Conference EMA G99, Sheffield, 161 pp., IOP Publishing House.
1223. Yoon, K. H., Kim, J. B., and Kim, E.S. (1996) *Journal of Materials Research*, **11**, 1996–2001.
1224. Fang, L., Wu, Y., He, C-Z., *et al*. (2007) *Materials Letters*, **62**, 594–596.
1225. Zhou, H., Wang, H., Li, K., *et al*. (2008) *Journal of Materials Science*, **43**, 3725–3727.
1226. Lee, C-T., Lin, Y-C., Huang, C-Y., *et al*. (2007) *Journal of American Ceramic Society*, **89**, 3662–3668.
1227. Lin, W-Y., Speyer, R. F., Hackenberger, W. S., *et al*. (1999) *Journal of American Ceramic Society*, **82**, 1207–1211.
1228. Marinel, S. and Rolland, F. (2005) *Materials Research Bulletin*, **40**, 962–969.
1229. Weng, J-J., Hsu, C-H., Huang, C-L., *et al*. (2005) *Japanese Journal of Applied Physics*, **44**, 8039–8042.
1230. Yang, X., Wang, X., Yao, G., *et al*. (2013) *Journal of Materials Science: Materials in Electronics*, **24**, 4662–4668.
1231. Bijumon, P. V., Mohanan, P., and Sebastian, M. T. (2003) *Materials Letters*, **57**, 1380–1384.
1232. Ratheesh, R., Sreemoolanathan, H., and Sebastian, M. T. (1997) *Journal of Solid State Chemistry*, **131**, 2–8.
1233. Sreemoolanathan, H., Sebastian, M. T., and Mohanan, P. (1995) *Materials Research Bulletin*, **30**, 653–658.
1234. Vineis, C., Davies, P. K., Negas, T., *et al*. (1996) *Materials Research Bulletin*, **31**, 431–437.
1235. Liu, P., Ogawa, H., Kim, E. S., *et al*. (2004) *Journal of European Ceramic Society*, **24**, 1761–1764.
1236. Ha, J-Y., Choi, J-W., Kang, C-Y., *et al*. (2005) *Japanese Journal of Applied Physics*, **44**, 1322–1325.
1237. Yue, Z., Zhao, F., Zhang, Y., *et al*. (2004) *Materials Letters*, **58**, 1830–1834.
1238. Onoda, M., Kuwata, J., Kanaeta, K., *et al*. (1982) *Japanese Journal of Applied Physics*, **21**, 1707–1710.
1239. Lu, W., Azough, F., and Kipkoch, E. R. (2004) In *International Conference on Microwave Materials and Their Applications*, MMA 2004, Inuyama.
1240. Hirano, S., Hayashi, T., and Hattai, A. (1991) *Journal of American Ceramic Society*, **74**, 1320–1324.
1241. Kim, J-R., Kim, D-W., Jung, H. S., *et al*. (2006) *Journal of European Ceramic Society*, **26**, 2105–2109.
1242. Cheng, C-C., Hsieh, T. E., and Lin, I. N. (2003) *Journal of Europen Ceramic Society*, **23**, 2553–2558.
1243. Zhou, D., Pang, L-X., and Wang, H. (2009) *Materials Chemistry and Physics*, **115**, 126–131.
1244. Tay, K. W., Fu, Y-P., Huang, Q-F., *et al*. (2010) *Ceramic International*, **36**, 1239–1244.
1245. Joseph, T., Anjana, P. S., Ltourneau, S., *et al*. (2010) *Materials Chemistry and Physics*, **121**, 77–82.
1246. Zhou, H., Wang, H., Zhang, M., *et al*. (2010) *Journal of Materials Research*, **25**, 1793–1798.
1247. Xiao, Y., Huang, X., and Zhang, Q. (2012) *Advanced Materials Research*, **197-198**, 323–327.
1248. Zhou, H., Liu, X., Wang, H., *et al*. (2012) *Ceramic International*, **38**, 367–372.
1249. Park, J-H., Choi, Y-J., Nahm, S., *et al*. (2011) *Journal of Alloys and Compounds*, **509**, 6908–6912.
1250. Muhammed, R., Iqbal, Y., and Ali, H. (2015) *Journal of Materials Science: Materials in Electronics*, **26**, 6819–6822.

1251. Wang, N., Zhao, M-Y., Li, W., *et al*. (2004) *Ceramic International*, **30**, 1017–1022.
1252. Yoon, K. H., Kim, Y. S., and Kim, E. S. (1995) *Journal of Materials Research*, **10**, 2085–2090.
1253. Zhou, H., Wang, H., Zhang, M., *et al*. (2009) *Applied Phsics A*, **95**, 513–516.
1254. Cai, H., Li, L., Sun, H., *et al*. (2015) *Journal of Materials Science: Materials in Electronics*, **26**, 998–1003.
1255. Cui, Z., Shen, C., and Qiu, T. (2015) *Journal of Electronic Materials*, **44**, 320–325.
1256. Zeng, Q. and Li, W. (2009) *Materials Science and Engineering B*, **164**, 151–155.
1257. Nomura, S., Tomaya, K., and Kaneta, K. (1983) *Japanese Journal of Applied Physics*, **22**, 1125–1128.
1258. Chen, Y-C., Tzou, W-C., Yang, C-F., *et al*. (2001) *Japanese Journal of Applied Physics*, **40**, 3252–3255.
1259. Jeong, B. J., Joung, M-R., Nahm, S., *et al*. (2013) *Journal of American Ceramic Society*, **96**, 3742–3746.
1260. Hirano, S., Hayashi, T., Kikuta, K., *et al*. (1990) *Ceramic Transactions*, **12**, 733–740.
1261. Muhammad, R., Iqbal, Y., and Rambo, C. R. (2015) *Journal of Materials Science: Materials in Electronics*, **26**, 2161–2166.
1262. Tohdo, Y., Kakimoto, K., Ohsato, H., *et al*. (2006) *Journal of European Ceramic Society*, **26**, 2039–2043.
1263. Zhou, H., Wang, Y., Chen, H., *et al*. (2008) *Journal of American Ceramic Society*, **91**, 3444–3447.
1264. Chen, Y-Y., Chen, Y-C., and Chen, M-D. (2013) *Journal of Materials Science: Materials in Electronics*, **24**, 3126–3131.
1265. Zhang, Y., Dong, X., Chen, H., *et al*. (2016) *Ceramic International*, **42**, 1293–1297.
1266. Kucheiko, S., Choi, J-W., Kim, H-J., *et al*. (1996) *Journal of American Ceramic Society*, **79**, 2739–2743.
1267. Chen, T., Ma, W., Li, R., *et al*. (2014) *Journal of Materials Science: Materials in Electronics*, **25**, 2494–2500.
1268. Shihara, D., Xi, Y., and Yong, Y. (2004) *Ceramic International*, **30**, 1195–1198.
1269. Nenesheva, E. A., Mudroliuba, L. P., Kartenko, N. F. (2003) *Journal of European Ceramic Society*, **23**, 2443–2448.
1270. Yang, H. B., Lin, Y., Zhu, J. F., *et al*. (2009) *Journal of Physics and Chemistry of Solids*, **70**, 55–58.
1271. Zhao, F., Yue, X., Zhang, Y., *et al*. (2005) *Journal of European Ceramic Society*, **25**, 3347–3352.
1272. Jawahar, I. N., Santha, N., Sebastian, M. T., *et al*. (2002) *Journal of Materials Research*, **17**, 3084–3089.
1273. Zeng, Q., Lei, W., Shi, J-I., *et al*. (2007) *Journal of American Ceramic Society*, **90**, 2262–2263.
1274. Zhang, X., Zhang, J., Xie, Z., *et al*. (2015) *Journal of American Ceramic Society*, **98**, 1245–1252.
1275. Tang, B., Yu, S., Chen, H., *et al*. (2013) *Journal of Materials Science: Materials in Electronics*, **24**, 1475–1479.
1276. Kim, E. S., Kang, D. H., and Kim, S. J. (2007) *Japanese Journal of Applied Physics*, **46**, 7101–7104.
1277. Mao, Y., Ding, S. H., Yao, X., *et al*. (2006) *Materials Chemistry and Physics*, **98**, 198–202.
1278. Huang, C-L., Hsu, C-S., Lu, S-J. (2003) *Materials Letters*, **57**, 3602–3605.
1279. Yamada, H., Okawa, T., Tohdo, Y., *et al*. (2007) *Journal of European Ceramic Society*, **26**, 2059–2062.
1280. Fukui, T., Sakurai, C., and Okuyama, M. (1992) *Journal of Materials Research*, **7**, 192–196.
1281. Kim, E. S., Chun, B. S., Kim, J. D., *et al*. (2003) *Materials Science and Engineering B*, **99**, 243–246.
1282. Huang, C-L., Chen, Y-B., and Lin, S-H. (2005) *Solid State Ionics*, **49**, 1921–1924.
1283. Riazikhoei, P., Azough, F., and Freer, R. (2006) *Journal of American Ceramic Society*, **89**, 216–223.
1284. Chen, Y-B. (2010) *Journal of Alloys and Compounds*, **500**, 190–194.

1285. Chen, G-H., Di, J-C., Xu, H-R., *et al*. (2012) *Journal of Materials Science: Materials in Electronics*, **23**, 280–284.
1286. Zhuang, H., Yue, Z., Zhao, F., *et al*. (2008) *Japanese Journal of Applied Physics*, **47**, 4658–4663.
1287. Fang, L., Zhang, G., Hu, C.Z., *et al*. (2008) *Materials Letters*, **62**, 670–672.
1288. Yue, Z., Zhao, F., Gui, Z., *et al*. (2005) *Journal of Alloys and Compounds*, **395**, 126–131.
1289. Zhao, F., Yue, Z., Pei, J., *et al*. (2006) *Applied Physics Letters*, **89**, 202901.
1290. Cho, I-S., Kim, J-R., Kim, D-W., *et al*. (2007) *Journal of European Ceramic Society*, **27**, 3081–3086.
1291. Fang, L., Zhang, G., Hu, C., and Zhang, H. (2008) *Materials Letters*, **62**, 670–672.
1292. Zhang, Q-L. and Yang, H. (2005) *Materials Research Bulletin*, **40**, 1891–1898.
1293. Fang, L., Liu, H-F., Zhang, H., *et al*. (2006) *Materials Research Bulletin*, **41**, 1281–1284.
1294. Kim, W. S., Kim, J. H., Kim, J. H., *et al*. (2003) *Materials Chemistry and Physics*, **79**, 204–207.
1295. Manam, A. and Iqbal, Y. (2011) *Journal of Materials Science: Materials in Electronics*, **22**, 1848–1854.
1296. Fang, L., Meng, S-S., Zhang, H., *et al*. (2006) *Materials Letters*, **60**, 1147–1150.
1297. Fang, L., Zhang, H., Hong, X. K., *et al*. (2004) *Materials Letters*, **58**, 3884–3887.
1298. Joung, M-R., Kweon, S-H., Kim, J-S., *et al*. (2012) *Materials Research Bulletin*, **47**, 4510–4513.
1299. Fang, L., Su, H., Yu, Q., *et al*. (2008) *Journal of American Ceramic Society*, **91**, 2769–2771.
1300. Pang, L-X., Wang, H., Zhou, D., *et al*. (2008) *Journal of American Ceramic Society*, **91**, 2947–2951.
1301. Fang, L., Su, H., Yu, Q., *et al*. (2008) *Materials Letters*, **62**, 4121–4123.
1302. Kagata, A., Inoue, I., Kato, J., *et al*. (1992) *Japanese Journal of Applied Physics*, **31**, 3152–3255.
1303. Kim, E. S. and Choi, W. (2004) In *International Conference on Microwave Materials and Their Applications*, Inuyama, Japan.
1304. Hirahara, S., Fujikawa, N., Enami, S., *et al*. (1994) US Patent 5,356,844.
1305. Jancar, B., Valant, M., and Suvorov, D. (2004) *Chemistry of Materials*, **16**, 1076–1082.
1306. Takasugi, A. and Kitoh, R. (1988) In *National Conference of IECE Japan*, SC-96.
1307. Dias, A., Bijumon, P. V., Sebastian, M. T., *et al*. (2005) *Journal of Applied Physics*, **98**, 084105.
1308. Chang, L. C. and Chiou, B-S. (2004) *Journal of Electroceramics*, **13**, 829–837.
1309. Cairns, D. L., Reaney, I. M., Otten, N., *et al*. (2006) *Journal of European Ceramic Society*, **26**, 875–882.
1310. Ohsato, H., Harada, A., Okawa, T., *et al*. (2005) US Patent 6,905,994.
1311. Huang, C-L., Weng, M-H., and Shan, G-M. (2000) *Journal of Materials Science*, **35**, 5443–5447.
1312. Huang, C-L., Chen, Y-B., and Lo, C-W. (2005) *Japanese Journal of Applied Physics*, **44**, 6706–6708.
1313. Huang, C-L., Weng, M-H., and Yu, C-C. (2001) *Ceramic International*, **27**, 343–350.
1314. Huang, C-L., Chen, Y-T., and Tseng, Y-W. (2010) *Materials Science and Engineering B*, **167**, 142–146.
1315. Rawal, R., Feteira, A., Hyatt, N. C., *et al*. (2006) *Journal of American Ceramic Society*, **89**, 332–335.
1316. Fang, L., Meng, S-S., Zhang, H., *et al*. (2006) *Transactions of Nonferrous Metals Society*, China, **16**, S521–S523.
1317. Huang, C-L. and Weng, M-H. (2000) *Materials Letters*, **43**, 32–35.
1318. Wang, N., Zhao, M-Y., Yin, Z-W., *et al*. (2004) *Materials Research Bulletin*, **39**, 439–448.
1319. Wang, S-F., Wang, Y-R., Wu, Y-C., *et al*. (2009) *Journal of Alloys and Compounds*, **480**, 499–504.
1320. Liu, F., Yuan, C., Liu, X., *et al*. (2015) *Materials Research Bulletin*, **70**, 678–683.
1321. Huang, C-L., Chen, J-H., and Li, B.J. (2009) *Journal of Alloys and Compounds*, **484**, 494–497.
1322. Nenesheva, E. A., Redozubov, S. S., Kartenko, N. F., *et al*. (2011) *Journal of European Ceramic Society*, **31**, 1097–1102.
1323. Pang, Y., Zhong, C., and Zhang, S. (2007) *Journal of Materials Science*, **42**, 7052–7055.

1324. Huang, C-L. and Tseng, Y-W. (2011) *Journal of American Ceramic Society*, **94**, 1824–1828.
1325. Huang, C-L., Wang, J-J., Li, B.J., *et al*. (2009) *Journal of Alloys and Compounds*, **461**, 440–446.
1326. Chen, Y-B. (2009) *Journal of Alloys and Compounds*, **478**, 781–784.
1327. Feteiro, A., Iddles, D., Price, T., *et al*. (2011) *Journal of American Ceramic Society*, **94**, 817–821.
1328. Suvorov, D., Valant, M., Jancar, B., *et al*. (2001) *Acta Chimica Slovania*, **48**, 87–89.
1329. Okawa, H., Kiuchi, K., Okabe, H., *et al*. (2002) *Ferroelectrics*, **272**, 345–350.
1330. Yoon, S-O., Kim, D-M., Kim, S. H., *et al*. (2006) *Journal of European Ceramic Society*, **26**, 2023–2026.
1331. Huang, C-L., Weng, M-H., Wu, C-C., *et al*. (2001) *Materials Research Bulletin*, **35**, 827–835.
1332. Weng, M-H. and Huang, C-L. (2000) *Journal of Materials Science Letters*, **19**, 375–376.
1333. Muhammed, R. and Iqbal, Y. (2013) *Journal of Materials Science: Materials in Electronics*, **24**, 2322–2326.
1334. Rawal, R., Feteira, A., Hyatt, N. C., *et al*. (2006) *Journal of American Ceramic Society*, **89**, 336–339.
1335. Zhao, F., Yue, Z., Zhang, Y., *et al*. (2005) *Journal of European Ceramic Society*, **25**, 3347–3352.
1336. Huang, X., Li, Y. M., Tang, D. P., *et al*. (2015) *Journal of Materials Science: Materials in Electronics*, **26**, 2033–2038.
1337. Okawa, T., Kiuchi, K., Okabe, H., *et al*. (2001) *Japanese Journal of Applied Physics*, **40**, 5779–5782.
1338. Huang, C-L., Weng, M-H., and Wu, C-C. (2001) *Materials Research Bulletin*, **35**, 827–835.
1339. Yu, S., Tang, B., Zhang, W., *et al*. (2012) *Materials Letters*, **80**, 124–126.
1340. Tseng, C-F. and Huang, C-C. (2012) *Journal of Materials Science*, **47**, 3982–3988.
1341. Solomon, S., Nathan, H. S., Sebastian, M. T., *et al*. (1996) *Materials Letters*, **28**, 107–111.
1342. Zhang, H. and Fang, L., Elsebrocke, R., *et al*. (2005) *Journal of Materials Science*, **40**, 4427–4429.
1343. Zhu, H., Shen, W., Jin, Y., *et al*. (2013) *Journal of Materials Science: Materials in Electronics*, **24**, 1090–1094.
1344. Chen, J-Y., Tseng, Y-W., and Huang, C-L. (2010) *Journal of Alloys and Compounds*, **494**, 205–209.
1345. Liou, Y-C., Shiue, C-Y., and Weng, M-H. (2009) *Journal of European Ceramic Society*, **29**, 1165–1171.
1346. Zhou, D., Li, W-B., Xi, H-H., *et al*. (2015) *Journal of Materials Chemistry C*, **3**, 2582–2588.
1347. Badshaw, H., Iddles, D., Quinby, R., *et al*. (2003) *Journal of European Ceramic Society*, **23**, 2435–2441.
1348. Fang, L., Yu, Q., Zhang, H., *et al*. (2007) *Journal of American Ceramic Society*, **90**, 1626–1628.
1349. Jancar, B., Suvorov, D., Valant, M., *et al*. (2003) *Journal of European Ceramic Society*, **23**, 1391–1400.
1350. Tseng, C-F., Huang, C-L., and Yang, W. R. (2007) *Materials Letters*, **61**, 4054–4057.
1351. Keith, G. M., Krik, A. A., Sarma, K., *et al*. (2004) *Chemistry of Materials*, **16**, 2007–2015.
1352. Fang, L., Diao, C-L., Zhang, H., *et al*. (2004) *Journal of Materials Science: Materials in Electronics*, **15**, 803–805.
1353. Fang, Q.L., Yu, Q., Zhang, H., *et al*. (2007) *Materials Letters*, **61**, 3093–3095.
1354. Fu, M. S., Liu, X. Q., Chen, X. M., *et al*. (2008) *Journal of American Ceramic Society*, **91**, 1163–1168.
1355. Gui, D., Zhang, H., and Fang, L. (2008) *Journal of Materials Science: Materials in Electronics*, **19**, 543–546.
1356. Pei, J., Yue, Z., Zhao, F., *et al*. (2008) *Journal of Alloys and Compounds*, **459**, 390–394.
1357. Chen, Y-B. (2009) *Journal of Alloys and Compounds*, **480**, 820–823.
1358. Wise, P. L, Reaney, I. M., Lee, W. E., *et al*. (2001) *Journal of European Ceramic Society*, **21**, 1723–1726.
1359. Wang, J-J. and Huang, C-L. (2006) *Materials Letters*, **60**, 1280–1283.

1360. Ravi, G. A., Azough, F., and Freer, R. (2007) *Journal of European Ceramic Society*, **27**, 2855–2859.
1361. Pang, L-X., Wang, H., Chen, Y-H., *et al*. (2009) *Journal of Materials Science: Materials in Electronics*, **20**, 528–533.
1362. Li, C., Wei, X., Yan, H., *et al*. (2012) *Journal of European Ceramic Society*, **32**, 4015–4020.
1363. Hsu, C-H. and Huang, C-J. (2014) *Journal of Alloys and Compounds*, **587**, 45–49.
1364. Wang, Z., Yao, X., and Zhang, L. (2004) *Ceramic International*, **30**, 1329–1333.
1365. Li, B-J., Chen, J-Y., and Huang, C-L. (2009) *Japanese Journal of Applied Physics*, **48**, 100203.
1366. Park, J-H., Nahm, S., and Park, J-G. (2012) *Journal of Alloys and Compounds*, **537**, 221–226.
1367. Chen, Y-B. (2010) *Journal of Alloys and Compounds*, **491**, 330–334.
1368. Tang, B., Si, F., Li, Y-X., *et al*. (2015) *Journal of Materials Science: Materials in Electronics*, **26**, 2719–2725.
1369. Wang, Z., Yao, X., and Zhang, L. (2004) *Ceramic International*, **30**, 1329–1333.
1370. Ma, P. P., Liu, X. Q., Zhang, F. Q., *et al*. (2015) *Journal of American Ceramic Society*, **98**, 2534–2540.
1371. Ikawa, H., Ohara, M., Iida, T., *et al*. (2005) *Journal of Ceramic Society Japan*, Suppl. Special Issue, **112-1**, S1614–S1616.
1372. Axelsson, A. K., Sebastian, M. T., and Alford, N. Mc N. (2003) *Journal of Korean Ceramic Society*, **40**, 340–345.
1373. Feteiro, A., Sinclair, D. C., Reaney, I. M., *et al*. (2005) *Journal of American Ceramic Society*, **88**, 3055–3062.
1374. Liou, Y. C., Liu, C-Y., and Fung, K. Z. (2008) *Ceramic International*, **34**, 2079–2083.
1375. Zhang, C., Zhuo, R., Sun, Q., *et al*. (2013) *Ceramic International*, **39**, 5675–5679.
1376. Huang, C-L., Chen, Y-H., Shih, C-F., *et al*. (2015) *Materials Research Bulletin*, **63**, 1–5.
1377. Huang, C-L. and Chen, J-Y. (2011) *Journal of Alloys and Compounds*, **509**, L99–L102.
1378. Mann, A. and Reaney, I. M. (2012) *Journal of Materials Science Poland*, **30**, 3415.
1379. Sousa, D. G., Saraiva, G. D., Filho, J. M. S., *et al*. (2014) *Journal of Materials Science: Materials in Electronics*, **25**, 4450–4458.
1380. Fang, L., Zhang, H., Yuan, R. Z., *et al*. (2005) *Materials Letters*, **59**, 535–538.
1381. Zhang, X., Zhang, Y., Peng, B., *et al*. (2014) (to be published)
1382. Nahm, S., Joung, M-R., Jong, B-J., *et al*. (2004) In *Proceedings of Microwave Materials and Applications*, MMA 2014, pp. 21
1383. Takado, T., Kageyama, K., Yonemura, M., *et al*. (2003) *Journal of Materials Science: Materials in Electronics*, **14**, 205–214.
1384. Wang, S-F., Wang, S-J., Wang, Y-R., *et al*. (2009) *Ceramic International*, **35**, 1813–1812.
1385. Chen, J-Y. and Huang, C-L. (2011) *Journal of Alloys and Compounds*, **509**, 426–430.
1386. Zhou, D., Pang, L-X., Guo, J., *et al*. (2014) *Inorgic Chemistry*, **53**, 1048–1055.
1387. Fu, M. S., Nei, L., and Chen, X. M. (2013) *Journal of European Ceramic Society*, **33**, 813–823.
1388. Huang, C-L., Huang, H-L., and Wu, C-C. (2001) *Materials Research Bulletin*, **36**, 1645–1652.
1389. Rawal, A. R., Feteiro, A., Flores, A. A., *et al*. (2005) *Journal of American Ceramic Society*, **89**, 336–339.
1390. Zhang, H., Fang, L., Su, H., *et al*. (2009) *Journal of Materials Science: Materials in Electronics*, **20**, 741.
1391. Santha, N. and Sebastian, M. T. (2008) *Materials Research Bulletin*, **43**, 2278–2284.
1392. Salim, C. M., Iqbal, Y., Qin, S., *et al*. (2014) *Journal of Materials Science: Materials in Electronics*, **25**, 5282–5287.
1393. Qu, J., Liu, F., Yuan, C., *et al*. (2015) *Materials Science and Engineering B*, **191**, 15–20.
1394. Zhao, F., Yue, Z., Pei, J., *et al*. (2006) *Journal of Solid State Chemistry*, **179**, 1719–1725.
1395. Wang, S. F., Wang, Y. R., and Hsu, J-C. (2011) *Journal of Physics and Chemistry of Solids*, **72**, 1011–1014.
1396. Samaoukhima, P., Kamba, S., Santhi, S., *et al*. (2005) *Journal of European Ceramic Society*, **25**, 3085–3088.
1397. Zeng, Q., Li, W., Shi, J., *et al*. (2008) *Materials Research Bulletin*, **43**, 411–417.
1398. Dhanya, T. P., Simna, P. S., and Ratheesh, R (2011) *Journal of Materials Science: Materials in Electronics*, **22**, 974–977.

1399. Borisevich, A. Y. and Davies, P. K. (2002) *Journal of American Ceramic Society*, **85**, 2487–2491.
1400. Borisevich, A. Y. and Davies, P. K. (2001) *Journal of European Ceramic Society*, **21**, 1719–1722.
1401. Ratheesh, R., Sreemoolanathan, H., Suma, S., *et al*. (1998) *Journal of Materials Science: Materials in Electronics*, **9**, 291–294.
1402. Liu, P., Kim, E. S., Kang, S-G., *et al*. (2003) *Materials Chemistry and Physics*, **79**, 270–272.
1403. Liu, C-L. and Wu, T-B. (2001) *Journal of American Ceramic Society*, **84**, 1291–1295.
1404. Salak, A. N., Seabra, M. P., and Ferreira, V. M. (2003) *Journal of European Ceramic Society*, **23**, 2409–2412.
1405. Yeo, D-H., Kim, J. B., Moon, J. H., *et al*. (1996) *Japanese Journal of Applied Physics*, **35**, 663–667.
1406. Gowri, L. (2004) MSc. Project Report, Regional Research Laboratory, Trivandrum.
1407. Bijumon, P. V. and Sebastian, M. T. (2005) *Materials Science and Engineering B*, **123**, 31–40.
1408. Zhou, D., Zhang, Q-L., and Yang, H. (2009) *Journal of Materials Science: Materials in Electronics*, **20**, 756–760.
1409. Zhang, J., Zuo, R., Lv, Y., *et al*. (2012) *Journal of Materials Science: Materials in Electronics*, **23**, 1449–1454.
1410. Zhou, H., Wang, H., Li, K., *et al*. (2009) *Journal of Materials Science: Materials in Electronics*, **20**, 283–288.
1411. Houivet, D., Fallah, J. E., Bernad, J., *et al*. (2001) *Journal of European Ceramic Society*, **21**, 1715–1718.
1412. Zhang, H., Fang, L., Su, H., *et al*. (2009) *Journal of Materials Science: Materials in Electronics*, **20**, 741–744.
1413. Li, Y-X., Si, F., Tang, B., *et al*. (2016) *Journal of Electronic Materials*, in press.
1414. Huang, C-L. and Chien, Y-H. (2011) *Journal of Alloys and Compounds*, **509**, L293–L295.
1415. Manan, A. and Iqbal, Y. (2014) *Bulletin of Materials Science*, **37**, 1215–1219.
1416. Zhou, D., Wang, H., and Ding, X. (2009) *Journal of Materials Science*, **20**, 39–43.
1417. Liou, Y-C. and Liu, C-Y. (2007) *Materials Science and Engineering A*, **448**, 351–355.
1418. Zhang, S. L., Ma, P. P., Liu, X. Q., *et al*. (2015) *Journal of American Ceramic Society*, **98**, 3185–3191.
1419. Kim, E. S., Kim, Y-H., Chun, B. S., *et al*. (2003) *Materials Chemistry and Physics*, **79**, 233–235.
1420. Hong, H. B., Kim, D-W., and Hong, K. S. (2003) *Japanese Journal of Applied Physics*, **42**, 5172–5175.
1421. Ichinose, N. and Mutoh, K. (2003) *Journal of European Ceramic Society*, **23**, 2455–2459.
1422. Santha, N. (2008) *International Journal of Applied Ceramic Technology*, **5**, 334–340.
1423. Li, C., Wei, X., Yan, H., *et al*. (2013) *Journal of Advanced Dielectrics*, **3**, 1320003.
1424. Choi, J-W., Ha, J-Y., Kang, C-Y., *et al*. (2000) *Japanese Journal of Applied Physics*, **39**, 5923–5926.
1425. Wang, K-W., Kim, H. T., Lanangan, M., *et al*. (2006) *Materials Research Bulletin*, **41**, 1385–1391.
1426. Huang, C-L., Liu, S-S., and Chen, C-C. (2009) *Journal of Alloys and Compounds*, **468**, L13–L16.
1427. Xu, P., Yang, J., Li, J., *et al*. (2012) *Ceramic International*, **38**, 3861–3867.
1428. Iqbal, Y., Manan, A., and Reaney, I. M. (2011) *Materials Research Bulletin*, **46**, 1092–1096.
1429. Qui, J-J., Yuan, C., Liu, F., *et al*. (2015) *Journal of Materials Science: Materials in Electronics*, **26**, 4862–4869.
1430. Zhang, Q. L., Zhou, D., and Yang, H. (2011) *Journal of European Ceramic Society*, **31**, 265–272.
1431. Wada, K., Fukami, Y., Kakimoto, K., *et al*. (2005) *Japanese Journal of Applied Physics*, **44**, 7094–7097.
1432. Wei, C-H. and Jean, J-H. (2003) *Journal of American Ceramic Society*, **86**, 93–98.
1433. Li, L., Cai, H., Yu, X., *et al*. (2016) *Journal of Alloys and Compounds*.

1434. Fukuda, K., Kitoh, R., and Awai, I. (1993) *Japanese Journal of Applied Physics*, **32**, 4584–4588.
1435. Ting, T. T., Xi, W-L., and Tu, Z. Q. (2009) *Journal of Alloys and Compounds*, **486**, 606–609.
1436. Kim, E. S., Kim, S. H., Kang, S. G., *et al*. (2004) *Journal of Ceramic Society Japan*, Suppl., **112-1**, S1641–S1644.
1437. Huang, C-L., Tseng, C-F., Yang, W-R., *et al*. (2008) *Journal of American Ceramic Society*, **91**, 2201–2204.
1438. Borisevich, A-Y. and Davies, P. K. (2002) *Journal of American Ceramic Society*, **85**, 573–578.
1439. Tang, B., Xiong, Z., Li, H., *et al*. (2015) *Journal of Materials Science: Materials in Electronics*, **26**, 8017–8021.
1440. Bian, J. J., Yan, K., and Ubic, R. (2007) *Journal of Electroceramics*, 283–288.
1441. Zhang, H., Fang, L., Dronskowski, R., *et al*. (2004) *Journal of Solid State Chemistry*, **177**, 400–412.
1442. Kim, E. S. and Kang, D. H. (2008) *Ceramic International*, **34**, 883–888.
1443. Fang, L., Wu, M., Liu, Q., *et al*. (2012) *Materials Chemistry and Physics*, **76**, 73–76.
1444. Chen, Y-C., Lee, W-C., and Chen, K-C. (2009) *Materials Chemistry and Physics*, **118**, 161–164.
1445. Fukuda, K., Kitoh, R., and Awai, I. (1995) *Journal of Materials Science*, **30**, 1209–1216.
1446. Keith, G. M., Pampling, M. J., Sarma, K., *et al*. (2004) *Journal of European Ceramic Society*, **24**, 1721–1724.
1447. Chen, Y-C., Yao, S-L., Tsai, R-J., *et al*. (2009) *Journal of Alloys and Compounds*, **486**, 410–414.
1448. Tseng, C-F., Chen, C-C., and Lin, C-W. (2014) *Materials Chemistry and Physics*, **147**, 535–539.
1449. Zhao, F., Yue, Z., Gui, Z., *et al*. (2006) *Journal of American Ceramic Society*, **89**, 3421–3423.
1450. Kang, D. H., Nahm, K. C., and Cha, H. J. (2006) *Journal of European Ceramic Society*, **26**, 2117–2121.
1451. Feteira, A., Slsebrock, R., Dias, A., *et al*. (2006) *Journal of European Ceramic Society*, **26**, 1947–1951.
1452. Kagata, H., Inoue, T., and Kato, J. (1992) *Japanese Journal of Applied Physics*, **32**, 3152–3155.
1453. Chen, Y-C. and Tsai, J. M. (2008) *Japanese Journal of Applied Physics*, **47**, 7959.
1454. Chen, Y-C. and Zeng, Y.W. (2009) *Microwave Optical Technology Letters*, **51**, 98.
1455. Iqbal, Y. and Manan, A. (2012) *Journal of Materials Science: Materials in Electronics*, **23**, 536–541.
1456. Kang, D. H. and Kim, E. S. (2008) *Ceramic International*, **34**, 889–892.
1457. Lu, Z., Li, Y., Wang, Y., *et al*. (2011) *Journal of American Ceramic Society*, **94**, 4364–4370.
1458. Kim, E. S., Chun, B. S., and Kang, D. H. (2007) *Journal of European Ceramic Society*, **27**, 3005–3010.
1459. Kim, H-J., Kucheiko, S., Yoon, S-J., *et al*. (1997) *Journal of American Ceramic Society*, **80**, 1316–1318.
1460. Kagata, H., Kato, J., Nishimoto, K., *et al*. (1993) *Japanese Journal of Applied Physics*, **32**, 4332–4334.
1461. Yang, S-F., Chuan, Y-C., Hsu, Y-C., *et al*. (2007) *Japanese Journal of Applied Physics*, **46**, 2978–2983.
1462. Kim, M-H., Lim, J-B., Nahm, S., *et al*. (2007) *Journal of European Ceramic Society*, **27**, 3033–3037.
1463. Ratheesh, R., Nathan, H. S., Sebastian, M. T., *et al*. (1998) *Ferroelectrics*, **211**, 1–8.
1464. Liu, T., Zhao, Z-Z., and Chen, W. (2006) *Journal of American Ceramic Society*, **89**, 1153–1155.
1465. Gong, S., Li, L., Guo, M., *et al*. (2012) *Journal of Materials Science: Materials in Electronics*, **23**, 1346–1351.
1466. Zheng, H., Reaney, I. M., Muir, D., *et al*. (2007) *Journal of European Ceramic Society*, **27**, 4479–4487.

1467. Chang, G., Zhou, X. H., Li, Y-X., *et al*. (2014) *Journal of Materials Science: Materials in Electronics*, **25**, 4750–4754.
1468. Zhang, Y., Zhang, Y. C., Xiang, M., *et al*. (2016) *Ceramic International*, **42**, 3542–3547.
1469. Yoon, K. H., Park, H. S., Cho, J. Y., *et al*. (2003) *Journal of European Ceramic Society*, **23**, 2579–2582.
1470. Chen, T., Ma, W., Sun, Q., *et al*. (2013) *Materials Letters*, **113**, 111–113.
1471. Zheng, H., Reaney, I. M., Muir, D., *et al*. (2005) *Japanese Journal of Applied Physics*, **44**, 3087–3090.
1472. Shen, B., Yao, X., Kang, L., *et al*. (2004) *Ceramic International*, **30**, 1203–1206.
1473. Ohsato, H., Harada, A., Okawa, T., *et al*. European Patent EP1422207A1.
1474. Ubic, R. and Reaney, I. M. (2001) *Journal of European Ceramic Society*, **21**, 2659–2662.
1475. Santha, N., Sebastian, M. T., George, V., *et al*. (2006) *Materials Chemistry and Physics*, **100**, 423–429.
1476. Yang, X., Wang, X., and Li, L. (2015) *Materials Research Bulletin*, **67**, 226–229.
1477. Petzelt, J., Buixaderas, E., Komandin, G., *et al*. (1998) *Materials Science and Engineering* **B57**, 40–45.
1478. Yim, D. K., Kim, J-R., Kim, D-W., *et al*. (2007) *Journal of European Ceramic Society*, **27**, 3053–3057.
1479. Shih, Y-T. and Jean, J. H. (2013) *Journal of American Ceramic Society*, **96**, 3849–3856.
1480. Nakano, M., Suzuki, K., Miura, T., *et al*. (1993) *Japanese Journal of Applied Physics*, **32**, 4314–4318.
1481. Zhou, D., Zhang, Q., Yang, H., *et al*. (2008) *Journal of Materials Science: Materials in Electronics*, **19**, 1000–1004.
1482. Li, E., Zhang, P., Mi, Y., *et al*. (2015) *Journal of Electronic Materials*, **44**, 4316–4321.
1483. Huang, B., Wang, Z., Chen, T., *et al*. (2014) *Journal of Materials Science: Materials in Electronics*, **25**, 5264–5268.
1484. Mizuta, M., Uenoyama, K., Ohsato, H., *et al*. (1996) *Japanese Journal of Applied Physics*, **35**, 5065–5068.
1485. Dernovsek, O., Naeini, A., Preu, G., *et al*. (2001) *Journal of European Ceramic Society*, **21**, 1693–1697.
1486. Chen, X. M. and Li, Y. (2002) *Journal of American Ceramic Society*, **85**, 579–584.
1487. Lee, S. H., Kim, D-W., and Yoo, S. I. (2004) *Journal of American Ceramic Society*, **87**, 871–874.
1488. Hu, M., Zhou, D., Zhang, D., *et al*. (2003) *Materials Science and Engineering B*, **99**, 403–407.
1489. Hsu, C-H. and Chen, Y-C. (2012) *Ferroelectrics*, **43**, 107–112.
1490. Zhou, X., Zhang, Y., and Chang, G., *et al*. (2016) *Journal of Materials Science: Materials in Electronics*, in press.
1491. Valant, M., Suvorov, D., and Kolar, D. (1994) In *Proceedings of the Conference on Euroceramics* (eds Wasser *et al*.), pp. 146-148, RWTH.
1492. Chen, Y-C. and Huang, C-L. (2002) *Materials Science and Engineering A*, **334**, 250–256.
1493. Zhou, H-F., Wang, H., Zhou, D., *et al*. (2008) *Materials Chemistry and Physics*, **109**, 510–514.
1494. Yao, X., Lin, H., Zhao, X., *et al*. (2012) *Ceramic International*, **38**, 6723–6728.
1495. Chen, S-Y. and Lin, Y-J. (2001) *Japanese Journal of Applied Physics*, **40**, 3305–3310.
1496. Zeng, Q., Li, W., Shi, J-I., *et al*. (2007) *Journal of European Ceramic Society*, **27**, 261–265.
1497. Kucheiko, S., Choi, J-W., Kim, H-J., *et al*. (1997) *Journal of American Ceramic Society*, **80**, 2937–2940.
1498. Kim, J-S., Cheon, C. I., Kang, H-J., *et al*. (1999) *Japanese Journal of Applied Physics*, **38**, 5633–5637.
1499. Tseng, C-F. (2015) *Journal of European Ceramic Society*, **35**, 383–387.
1500. Satheesh, R. and Ratheesh, R. (2010) *International Journal of Appled Ceramic Technology*, **7**, E151–E155.
1501. Chen, Y-C. and Huang, C-L. (2002) *Materials Science and Engineering A*, **334**, 250–256.
1502. Muhammed, R. and Iqbal, Y. (2015) *Journal of Materials Science: Materials in Electronics*, **26**, 9092–9096.
1503. Gu, F-F., Chen, G-B., Yuan, C-L., *et al*. (2015) *Materials Research Bulletin*, **61**, 245–251.

1504. Long, Y., Wang, Y., Wu, W., *et al*. (2009) *Journal of American Ceramic Society*, **92**, 2630–2633.
1505. Liang, B., Zheng, X., and Tang, D. (2009) *Journal of Alloys and Compounds*, **488**, 409–413.
1506. Chen, G. H., Gu, F. F., Pan, M., *et al*. (2015) *Journal of Materials Science: Materials in Electronics*, **26**, 6511–6517.
1507. Huang, C-L. and Weng, M-H. (2001) *Materials Research Bulletin*, **36**, 683–691.
1508. Ohsato, H., Komura, A., Takagi, Y., *et al*. (1998) *Japanese Journal of Applied Physics*, **37**, 5357–5359.
1509. Yang, C-F. (2009) *Japanese Journal of Applied Physics*, **39**, 1430–1434.
1510. Rejini, R., Subodh, G., and Sebastian, M. T. (2008) *Journal of Materials Science: Materials in Electronics*, **19**, 1153–1155.
1511. Pang, L-X., Wang, H., Zhou, D., *et al*. (2010) *Materials Chemistry and Physics*, **123**, 727–730.
1512. Futamata, Y., Ohsato, H., Kakimoto, K., *et al*. (2002) *Ferroelectrics*, **272**, 213–218.
1513. Yang, K., Karak, T., and Adachi, M. (2009) *Japanese Journal of Applied Physics*, **48**, 09KE01.
1514. Kato, J. (1991) Material produces small resonators with high dielectric constant, *Journal of Electrical Engineering*, September, 114–118.
1515. Yoon, S-H., Kim, D-W., Cho, S-Y., *et al*. (2003) *Journal of European Ceramic Society*, **23**, 2549–2552.
1516. Fukuda, K., Fijui, I., Kitoh, R., *et al*. (1993) *Japanese Journal of Applied Physics*, **32**, 1712–1715.
1517. Fetira, A., Sarma, K., Alford, N. Mc N., *et al*. (2003) *Journal of American Ceramic Society*, **86**, 511–513.
1518. Li, J. and Qiu, T. (2012) *Ceramic International*, **38**, 4331–4335.
1519. Chang, G., Zhou, X-H., Zhang, S-R., *et al*. (2014) *Journal of Materials Science: Materials in Electronics*, **25**, 4439–4443.
1520. Wang, H., Kamba, S., Zhang, M., *et al*. (2006) *Japanese Journal of Applied Physics*, **100**, 034109.
1521. Belous, A. G. and Ovchar, O. V. (2003) *Journal of European Ceramic Society*, **23**, 2525–2528.
1522. Pang, L-X., Wang, H., Zhou, D., *et al*. (2009) *Journal of Electroceramics*, **23**, 13–18.
1523. Zhou, D., Li, W-B., Pang, L-X., *et al*. (2014) *Daltons Transactions*, **43**, 7290–7297.
1524. Ota, Y., Kakimoto, K., Ohsato, H., *et al*. (2004) *Journal of European Ceramic Society*, **24**, 1755–1760.
1525. Zuo, M. W., Li, W., Shi, J-L., *et al*. (2006) *Materials Research Bulletin*, **41**, 1127–1132.
1526. Chen, X. M. and Li, Y. (2004) *Journal of Applied Physics*, **96**, 5683–5686.
1527. Ding, J., Wang, Z., Gong, Z., *et al*. (2011) *Journal of Rare Earths*, **29**, 683.
1528. Pang, L-X., Zhou, D., and Liu, W-G. (2015) *Ceramic International*, **41**, 5182–5185.
1529. Valant, M. and Suvorov, D. (2001) *Journal of Materials Science*, **36**, 2991–2997.
1530. Choi, G-K., Kim, D-W., Cho, S-Y., *et al*. (2004) *Ceramic International*, **30**, 1187–1190.
1531. Pei, J., Yue, Z., Zhao, F., Gui, Z., *et al*. (2009) *Ceramic International*, **35**, 253–257.
1532. Zhou, D., Wang, H., Yao, X., *et al*. (2008) *Ceramic International*, **34**, 901–904.
1533. Yao, X., Lin, H., Chen, W., *et al*. (2012) *Ceramic International*, **38**, 3011–3016.
1534. Durand, J. M. and Boilot, J. P. (1987) *Journal of Materials Science Letters*, **6**, 134–136.
1535. Imaeda, M., Ito, K., Mizuta, M., *et al*. (1997) *Japanese Journal of Applied Physics*, **36**, 6012–6015.
1536. Ohsato, H., Nishigaki, S., and Okuda, T. (1992) *Japanese Journal of Applied Physics*, **31**, 3136–3138.
1537. Laffezz, P., Desgardin, G., and Raveau, B. (1992) *Journal of Materials Science*, **27**, 5229–5238.
1538. Zhou, D., Pang, L-X., Wang, H., *et al*. (2011) *Journal of Materials Chemistry*, **21**, 18412–18420.
1539. Zhou, D., Pang, L-X., Guo, J., *et al*. (2011) *Inorgic Chemistry*, **50**, 12733–12738.
1540. Cheng, P-S., Yang, C-F., Chen, Y-C., *et al*. (2000) *Ceramic International*, **26**, 877.
1541. Zhang, W., Chen, X., and Bai, S. (2013) *Ceramic International*, **39**, 3957–3963.
1542. Ohsato, H., Sugino, J., Komura, A., *et al*. (1999) *Japanese Journal of Applied Physics*, **38**, 5625–5628.

1543. Gao, X. and Tai, Q. (2010) *Journal of Rare Earths*, **28**, 411.
1544. Zhou, L., Zhou, H., Shao, H., *et al*. (2012) *Journal of Rare Earths*, **30**, 142.
1545. Lowndes, R., Azough, F., Cernik, R., *et al*. (2012) *Journal of European Ceramic Society*, **32**, 3792–3799.
1546. Zhou, D., Wang, H., Yao, X., *et al*. (2008) *Journal of American Ceramic Society*, **91**, 139–143.
1547. Liu, Y-W. and Lin, P. (2006) *Materials Research Bulletin*, **41**, 1845–1853.
1548. Yoon, K. H., Chang, Y. H., Kim, W. S., *et al*. (1996) *Japanese Journal of Applied Physics*, **35**, 5145–5149.
1549. Nishigaki, S., Kato, H., Yano, S., *et al*. (1987) *Amerian Ceramic Society Bulletin*, **66**, 1405–1410.
1550. Li, Y. and Chen, X. M. (2002) *Journal of European Ceramic Society*, **22**, 715–719.
1551. Valant, M., Suvorov, D., and Kolar, D. (1993) *3rd Euroceramics* (eds P. Duram and J. F. Fernandez), vol. 2, pp. 235–240.
1552. Xiong, Z. X., Fang, C., Huang, J. R., *et al*. (2000) *Materials Science and Engineering B*, **99**, 138–142.
1553. Huang, B., Wang, Z., Chen, T., *et al*. (2015) *Journal of Materials Science: Materials in Electronics*, **26**, 3375–3379.
1554. Ohsato, H., Imaeda, M., Takagi, Y., *et al*. (1998) In *Proceedings of Symposium on Applications of Ferroelectrics*, XI, Switzerland, August, pp. 509–512.
1555. Xu, Y., Huang, G., and He, Y. (2005) *Ceramic International*, **31**, 21–25.
1556. Zheng, Y., Zhao, X., Lei, W., *et al*. (2005) *Materials Letters*, **60**, 459–463.
1557. Belous, A. G. and Ovchar, O. V. (1999) *Journal of European Ceramic Society*, **19**, 1119–1122.
1558. Axelsson, A-K. and Alford, N. Mc N. (2006) *Journal of European Ceramic Society*, **26**, 1933–1936.
1559. Zhou, D., Rindall, C. A., Wang, H., *et al*. (2010) *Journal of American Ceramic Society*, **93**, 2147–2150.
1560. Chen, H., Tang, B., Duan, S., Yang, H., *et al*. (2015) *Journal of Electronic Materials*, **44**, 1081–1087.
1561. Zhu, J., Lu, W., Lei, W., *et al*. (2009) *Ceramic International*, **35**, 855–860.
1562. Guo, Y., Kakimoto, K., and Ohsato, H. (2003) *Japanese Journal of Applied Physics*, **42**, 7410–7413.
1563. (a) Webhoffer, A. and Feltz, A. (1999) *Journal of Materials Science Letters*, **18**, 719–721.
1563. (b) Lu, Z., Li, Y., Wang, Y., *et al*. (2011) *Journal of American Ceramic Society*, 4364–4370.
1564. Ezaki, K., Baba, Y., Takahashi, H., *et al*. (1993) *Japanese Journal of Applied Physics*, **32**, 4319–4322.
1565. Yoon, K. H., Kim, E. S., and Jeon, J. S. (2003) *Journal of European Ceramic Society*, **23**, 2391–2396.
1566. Belous, A. G., Ovchar, O., Valant, M., *et al*. (2001) *Journal of European Ceramic Society*, **21**, 2723–2730.
1567. Ohsato, H., Komura, A., and Nishigaki, S. (2004) *Journal of Ceramic Society Japan*, Suppl., **112**, S1616–S1621.
1568. Okawa, T., Imaeda, M., and Ohsato, H. (2000) *Japanese Journal of Applied Physics*, **39**, 5645–5649.
1569. Ohsato, H., Kato, H., Mizuta, M., *et al*. (1995) *Japanese Journal of Applied Physics*, **34**, 5413–5417.
1570. Ha, J-Y., Choi, J-W., Kim, H-J., *et al*. (2003) *Materials Chemistry and Physics*, **79**, 261–265.
1571. Qin, N. and Chen, X. M. (2004) *Materials Science and Engineering B*, **111**, 90–94.
1572. Kim, E. S., Park, H. S., and Yoon, K. H. (2003) *Materials Chemistry and Physics*, **79**, 213–217.
1573. Hsiang, H-I. and Chen, T-H. (2009) *Journal of Alloys and Compounds*, **467**, 485–490.
1574. Hoffmann, C. and Waser, R. (1997) *Ferroelectrics*, **201**, 127–135.
1575. Fukuda, K., Kitoh, R., and Awai, I. (1995) *Journal of Materials Research*, **10**, 312–319.
1576. Yang, Q., Kim, E. S., Xu, J., *et al*. (2003) *Materials Science and Engineering B*, **99**, 332–339.
1577. Skapin, S. D., Pirnat, U., Jancar, B., *et al*. (2015) *Journal of American Ceramic Society*, **98**, 3818–3823.

1578. Choi, W., Kim, H. J., Yoon, S. J., *et al*. (2003) *Materials Chemistry and Physics*, **79**, 261–265.
1579. Yamada, Y., Wada, K., Kagomiya, I., *et al*. (2007) *Journal of European Ceramic Society*, **27**, 3049–3052.
1580. Chen, X., Zhang, W., and Bai, S. (2013) *Journal of Materials Science: Materials in Electronics*, **24**, 224–229.
1581. Sun, J-S., Wei, C-C. and Wu, L. (1992) *Journal of Materials Science*, **27**, 5818–5822.
1582. Negas, T. and Davies, P. K. (1995) *Materials and Processes for Wireless Communication* (eds T. Negas and H. Ling), American Ceramic Society, Westerville, OH, pp. 179–196.
1583. Xiong, Z. X., Fang, C., Huang, J. R., *et al*. (2003) *Materials Science and Engineering B*, **99**, 138–142.
1584. Podlinik, M., Valant, M., and Suvorov, D. (1997) *Key Engineering Materials*, **132-136**, 1211–1214.
1585. Azough, F., Wang, W., Leach, C., *et al*. (2008) *In International Conference on Microwave Materials and Their Applications*, Hangzhou, China, p. 26.
1586. Wu, Y. J. and Chen, X. M. (2000) *Journal of American Ceramic Society*, **83**, 1837–1839.
1587. Qin, C., Yue, Z., Gui, Z., *et al*. (2003) *Materials Science and Engineering B*, **99**, 286–289.
1588. Wu, Y. J. and Chen, X. M. (2001) *Journal of Materials Research*, **16**, 1734–1738.
1589. Kim, I., Jung, W. H., Inaguma, Y., *et al*. (1995) *Materials Research Bulletin*, **30**, 307–316.
1590. Ioachim, A., Toacsan, M. I., Banciu, M. G., *et al*. (2004) *Materials Science and Engineering B*, **109**, 183–187.
1591. Zhong, Q-L., Wu, F., Yang, H., *et al*. (2008) *Journal of Materials Chemistry*, **18**, 5339–5343.
1592. Ichinose, N. and Amada, H. (2001) *Journal of European Ceramic Society*, **21**, 2751–2753.
1593. Zhe, H. M., Xiang, Z. D., Haoshuang, G., *et al*. (2005) *Materials Science and Engineering B*, **117**, 199–204.
1594. Zhang, Q., Sun, H-P., and Yang, H. (2012) *Journal of Alloys and Compounds*, **509**, 9986–9991.
1595. Valant, M. and Suvorov, D. (2003) *Journal of American Ceramic Society*, **86**, 939–944.
1596. Valant, M., Suvorov, D., Kolar, D. (1994) In *Proceedings of the Conference on Euroceramics* (ed. Waser *et al*.), Aachen, pp. 146–147.
1597. Kim, W. S., Kim, E. S., and Yoon, K. H. (1999) *Ferroelectrics*, **223**, 277–284.
1598. Li, M., Feteira, A., Sinclair, D. C., *et al*. (2007) *Applied Physics Letters*, **91**, 132911.
1599. Chen, H-L. and Huang, C-L. (2002) *Japanese Journal of Applied Physics*, **41**, 5650–5653.
1600. Xiang, Z. D., Zue, H. M., Lin, J. S., *et al*. (2004) *Materials Letters*, **58**, 2684–2687.
1601. Okawa, T., Imaeda, M., Ohsato, H. (2002) *Key Engieering Materials*, **214-215**, 37–42.
1602. Kato, J., Kagata, H., Nishimoto, K. (1991) *Japanese Journal of Applied Physics*, **30**, 2343–2346.
1603. Kipoch, E. R., Zhu, J., and Lu, W. (2006) *Journal of Applied Physics*, **100**, 054105.
1604. Kim, W. S., Kim, E. S., and Yoon, K. H. (1999) *Journal of American Ceramic Society*, **82**, 2111–2115.
1605. Chen, Y. C., Cheng, P-S., and Yang, C-F, *et al*. (2001) *Journal of Materials Science Letters*, **20**, 863–865.
1606. Wu, Y. J. and Chen, X. M. (1999) *Journal of European Ceramic Society*, **19**, 1123–1126.
1607. Ohsato, H. (2001) *Journal of European Ceramic Society*, **21**, 2703–2711.
1608. Ohsato, H. and Imaeda, M. (2000) *Materials Chemistry and Physics*, **79**, 208–212.
1609. Huang, C-L., Tsai, J-T., and Li, J-L. (2000) *Journal of Materials Science*, **35**, 4901–4905.
1610. Suvorov, D., Valant, M., and Kolar, D. (1995) Materials and processes for wireless communication, in *Ceramic Transactions* (eds T. Negas and H. Ling), vol. 53, pp. 197–206.
1611. Chen, G-H., Yuan, C-L., Zhou, C-R., *et al*. (2013) *Ceramic International*, **39**, 9763–9766.
1612. Takahashi, H., Baba, Y., Ezaki, K., *et al*. (1996) *Japanese Journal of Applied Physics*, **35**, 5069–5073.
1613. Kim, D-W., Park, B., Chung, J-H., *et al*. (2000) *Japanese Journal of Applied Physics*, **39**, 2696–2700.
1614. Kim, W. S., Yoon, K. H., and Kim, E. S. (2000) *Japanese Journal of Applied Physics*, **39**, 5650–5653.
1615. Takahashi, H., Baba, Y., and Ezaki, K. (1991) *Japanese Journal of Applied Physics*, **30**, 2339–2342.

1616. Li, L., Jin, Y., Dong, H., *et al*. (2014) *Journal of Alloys and Compounds*, **604**, 31–35.
1617. Yoon, K. H., Park, M. S., Cho, J. Y., *et al*. (2003) *Journal of European Ceramic Society*, **23**, 2423–2427.
1618. Huang, G., Zhou, D., Yu, J., *et al*. (2005) *Materials Research Bulletin*, **40**, 13–19.
1619. Yoshida, M., Hara, N., Takada, T., *et al*. (1997) *Japanese Journal of Applied Physics*, **36**, 6818–6823.
1620. Subodh, G. and Sebastian, M. T. (2007) *Materials Science and Engineering B*, **136**, 50–56.
1621. Marinel, S., Choi, D. H., Heuguet, R., *et al*. (2013) *Ceramic International*, **39**, 299–306.
1622. Yang, Q., Kim, E. S., Xu, J., *et al*. (2004) *Materials Science and Engineering B*, **99**, 259–261.
1623. Yang, Q. H., Kim, E. S., and Xu, J. (2004) *Materials Science and Engineering B,* **113**, 224–227.
1624. Gu, Y., Huang, J-L., Li, Q., *et al*. (2008) *Journal of European Ceramic Society*, **28**, 3149–3153.
1625. Schwartz, S. L., and Shrout, T. R. (1995) US Patent 5449652.
1626. Yang, Q. H., Kim, E. S., Kim, Y. J., *et al*. (2003) *Materials Chemistry and Physics*, **79**, 239–242.
1627. Fang, Z-X., Tang, B., Si, F., *et al*. (2016) *Journal of Materials Science*, in press.
1628. Pullar, R. C., Penn, S. J., Wang, X., *et al*. (2009) *Journal of European Ceramic Society*, **29**, 419–424.
1629. Fu, M. S., Liu, X. Q., and Chen, X. M. (2008) *Journal of European Ceramic Society*, **28**, 585–590.
1630. Liang, Z., Yuan, L. L., and Bian, J. J. (2011) *Journal of Alloys and Compounds*, **509**, 1893–1896.
1631. Templeton, A., Wang, X., Penn, S. J., *et al*. (2000) *Journal of American Ceramic Society*, **83**, 95–100.
1632. Huang, C-L., Tsai, J-T., and Chan, Y. B. (2002) *Materials Research Bulletin*, **36**, 547–556.
1633. Kipokoch, E. R. and Lu, W. (2004) In *International Conference on Microwave Materials and Their Applications*, MMA 2004, Inuyama, Japan.
1634. Aziz, D. A., Sterianou, I., and Reaney, I. M. (2009) *Journal of Materials Science*, **44**, 6247–6250.
1635. Li, J., Chen, X. M., and Wu, Y. J. (2002) *Journal of European Ceramic Society*, **22**, 87–91.
1636. Yan, K., Fuji, M., Karaki, T., *et al*. (2007) *Japanese Journal of Applied Physics*, **46**, 7105–7107.
1637. Kim, E. S. and Yoon, K. H. (2003) *Journal of European Ceramic Society*, **23**, 2397–2401.
1638. Chen, X., Bai, X., and Zhang, W. (2012) *Journal of Alloys and Compounds*, **541**, 132–136.
1639. Zhang, L., Shqau, S., Verweiji, H., *et al*. (2010) *Journal of American Ceramic Society*, **93**, 969–972.
1640. Ichonose, N. and Chida, N. (1998) In *Proceedings of IEEE International Symposium on Applications of Ferroelectrics*, pp. 513–516.
1641. Wu, M-C., Huang, Y. C., and Su, W. F. (2006) *Materials Chemistry and Physics*, **100**, 391–394.
1642. Zhu, L. M., Bin, T., Shenquan, Y., *et al*. (to be published)
1643. Subodh, G., James, J., Sebastian, M. T., *et al*. (2007) *Chemistry of Materials*, **19**, 4077–4082.
1644. Lowe, T., Azough, F., and Freer, R. (2003) *Journal of European Ceramic Society*, **23**, 2429–2433.
1645. Chen, X. M., Sun, Y. H., and Zheng, X. H. (2003) *Journal of European Ceramic Society*, **23**, 1571–1575.
1646. Lowe, T., Azough, F., and Freer, R. (2006) *Journal of Electroceramics*, **16**, 257–261.
1647. Kim, E. S., Chun, B. S., Yoon, D-W., *et al*. (2003) *Materials Science and Engineering B*, **99**, 247–251.
1648. Bian, J. J. and Li, Y. Z. (2010) *Materials Chemistry and Physics*, **122**, 617–622.
1649. Yuan, C., Chen, G., Zhou, C., *et al*. (2015) *International Journal of Appled Ceramic Technology*, **12**, E55–E63.
1650. Moon, S. H., Kim, J. S., Cheon, C., *et al*. (2010) *Japanese Journal of Applied Physics*, **49**, 09MC-13-1.
1651. Tatsui, K., Murano, K., Kawamura, T., *et al*. (1987) *Japanese Journal of Applied Physics*, Suppl., **26-2**, 80–82.
1652. Su, W-F. and Lim, S-C. (2003) *Journal of European Ceramic Society*, **23**, 2593–2596.

1653. Nino, J. C., Lanagan, M. T., and Randall, R. C. (2001) *Journal of Applied Physics*, **89**, 4512–4516.
1654. Hu, X., Chen, X. M., and Wu, S-Y. (2003) *Journal of European Ceramic Society*, **23**, 1919–1924.
1655. Axelsson, A-K., Pan, Y., Valant, M., *et al*. (2009) *Journal of American Ceramic Society*, **92**, 1773–1778.
1656. Niu, B., Ma, W., Li, Q., *et al*. (2015) *Journal of Materials Science: Materials in Electronics*, **26**, 916–920.
1657. Zhang, M., Zhai, J., and Yao, X. (2010) *Materials Research Bulletin*, **45**, 1990–95.
1658. Kamba, S., Savinov, M., Luafek, F., *et al*. (2009) *Chemistry of Materials*, **21**, 811–819.
1659. Ubic, R., Reaney, I. M., Lee,W. E., *et al*. (2003) In *Conference Dielectrics for Emerging Technogies*, Institute of Physics, Edinburgh.
1660. Saleem, M., Iqbal, Y., Qin, S., *et al*. (2015) *Journal of Materials Science: Materials in Electronics*, **26**, 1507–1511.
1661. Alford, N. Mc N. London South Bank University (unpublished results)
1662. Kim, H. T., Shrout, T., Rindall, C. A., *et al*. (2002) *Journal of American Ceramic Society*, **85**, 2738–2744.
1663. Wang, S., Zhai, J., Chou, X., *et al*. (2009) *Materials Chemistry and Physics*, **115**, 200–203.
1664. Wu, L., Chen, Y-C., Chen, L-J., *et al*. (1999) *Japanese Journal of Applied Physics*, **38**, 5612–5615.
1665. Lin, T. N., Chu, J. P., and Wang., S-F. (2005) *Materials Letters*, **59**, 2786–2789.
1666. Petzelt, J., Kamba, S., Buixaders, E., *et al*. (1999) *Ferroelectrics*, **223**, 235–246.
1667. Valant, M. and Suvorov, D. (1999) *Journal of American Ceramic Society*, **82**, 88–93.
1668. Zhang, M., Zhai, J., Shen, B., *et al*. (2012) *Journal of Materials Research*, **27**, 910–914.
1669. Zhang, J., Zhai, J., and Yao, X. (2009) *Scripta Materiala*, **61**, 764.
1670. Zhang, Q., Zhai, J., Yao, Z. (2010) *Journal of American Ceramic Society*, **93**, 2560–2562.
1671. Jiang, H., Zhai, J., Zhang, J., *et al*. (2009) *Journal of American Ceramic Society*, **92**, 2319–2322.
1672. Jiang, H., Shen, B., Zhai, J., *et al*. (2012) *Ceramic International*, **38S**, S183–S186.

Index

$A_2B_2O_7$, 174
absorption coefficient, 579
absorption loss, 577–578, 638
agile materials, 622
$Ag_{1-x}Li_xNbO_3$, 187
Ag_2MoO_4, 408
$AgNbO_3$, 187–188
$Ag(Nb_{1-x}Ta_x)O_3$, 187–189
$AgTaO_3$, 188
albite, 210, 239–240
AlN, 361–362, 540–541, 544–546, 552–553, 564
Al_2TiO_4, 244
alumina (Al_2O_3), 70, 73–74, 80, 108–109, 116, 143, 159, 161–162, 207, 209, 212, 234, 243–245, 249, 260–261, 263, 271, 303–306, 359–361, 368, 376–377, 393, 401–402, 460–477, 540–546, 552–554, 557, 559–560, 618, 623–624, 630
anorthite; An, 239–241, 380
antiferromagnetism, 612
anti-phase tilting, 85–87, 100–101
apatites, 290–302
aspect ratio, 685, 689–690, 696

$BaCeO_3$, 117
backward wave oscillator (BWO) method, 31–32
$Ba(Co_{1/3}Nb_{2/3})O_3$, 128
$BaCu(B_2O_5)$, 289, 382
$BaFe_{12}O_{19}$, 612–613, 619
$Ba_2La_8Si_6O_{26}$, 296
Ba_2LnNbO_6, 93–94, 139
Ba_2LnTaO_6, 91–93, 139
$BaNb_2O_6$, 319–329
band-pass filter, 665–668, 701, 704, 709–710, 713
band-rejection filter, 665
$BaNd_2Ti_3O_{10}$, 149
$BaNd_2Ti_4O_{12}$, 149–150, 381
$BaNd_2Ti_5O_{14}$, 149–150
bandwidth, 6, 113, 136, 610, 633–634, 637, 639, 642, 666, 690
$Ba_{6-3x}Ln_{8+2x}Ti_{18}O_{54}$, 151, 155, 158–161
$Ba(Mg_{1/3}Ta_{2/3})O_3$(BMT), 103–118, 123, 126, 135, 143–144, 290, 318, 540, 542, 545–546, 552–553, 567–568
$BaO\text{-}Al_2O_3\text{-}B_2O_3\text{-}SiO_2$, 373, 619
$BaO\text{-}Ln_2O_3\text{-}TiO_2$, 149–150, 155–156
Ba_2PrNbO_6, 94
$Ba_2RE_8Si_6O_{26}$, 296
barium hexaferrite capacitor, 665
$Ba_{6-3x}Sm_{8+2x}Ti_{18}O_{54}$, 157–162
$BaSnO_3$, 116, 144
$Ba_3SrTa_2O_9$, 141
$Ba_{1-x}Sr_xTi_5O_{11}$, 316, 428
$Ba_{0.7}Sr_{0.3}TiO_3$(BST), 66, 78, 554, 556–557, 560, 562–563
$Ba_{0.6}Sr_{0.4}TiO_3$ + 0.5 wt.% $MgCo_2(VO_4)_2$, 190
$Ba_3Ta_2O_8$, 120
$Ba_5Ta_4O_{15}$, 104, 107
Ba_2TbNbO_6, 94
$BaTeO_3$, 406
$BaTe_4O_9$, 406
Ba_2TeO_5, 406

Microwave Materials and Applications, First Edition.
Edited by Mailadil T. Sebastian, Rick Ubic and Heli Jantunen.

© 2017 John Wiley & Sons, Ltd. Published 2017 by John Wiley & Sons, Ltd.

$BaTiO_3$, 82, 87, 100–101, 117, 140, 151, 162, 410, 428, 540–546, 552–557, 559–560, 562
$BaTi_4O_9$, 150–151, 159, 162–163, 283, 314–318, 381
$Ba_2Ti_9O_{20}$, 158–163, 283, 314–318, 381
$BaTi_5O_{11}$, 316, 381
$Ba_3(VO_4)_2$, 258
$BaWO_4$, 121, 126, 129, 144, 146
$Ba_3W_2O_9$, 128, 147
$BaZn_{0.33}Nb_{0.67}O_3$ (BZN), 105, 126–130
$BaZrO_3$, 90, 116–117, 123–124, 128, 144, 146
$Ba_8ZnTa_6O_{24}$, 120, 148
$Ba(Zn_{1/3}Ta_{2/3})O_3$(BZT), 90, 103, 105–106, 109, 118–123, 124, 126, 135, 145–146, 290, 318, 540, 543–550, 552–557, 560
bending, 548–549, 561–563
$Bi_2Mo_2O_9$, 403–404, 460–461, 472–473, 479
$BiNbO_4$, 380
binder, 364, 390, 459, 461–463, 465–467
Bi_2O_3, 158–160, 186–187
Bi_2O_3-B_2O_3-SiO_2-ZnO (BBSZ), 270–271, 376, 381, 393
Bi_2O_3-MoO_3, 403–404
bipolaron, 590
$Bi_4(SiO_4)_3$, 391–393
$Bi_{1.5}ZnNb_{1.5}O_7$, 380
$Bi_2(Zn_{1/3}Ta_{2/3})_2O_7$, 380
B_2O_3, 17, 96–97, 107–108, 128, 130, 161–162, 186, 288, 290, 373
B_2O_3-SiO_2, 375
bond length, 90, 93, 105–106, 119, 228, 262, 674
bond strength, 209, 228, 238, 246
bond-valence, 83–85, 93–94, 170–171, 246, 249, 262
BoPET, 460, 467–472
borosilicate glass (BSG), 107, 143
Bruggeman non-symmetric, 64–65
Bruggeman symmetric, 34, 60, 62, 63–67, 74–76
butyl rubber, 538–539, 553–557, 559–560, 562, 564, 566, 569–570
$CaAl_2Si_2O_8$, 239, 380
CaB_2O_4, 225
$CaCuP_2O_7$, 387
$Ca_2Dy_8Si_6O_{26}$, 293
$Ca_{2+x}Gd_{8-x}(SiO_4)_{6-x}(PO_4)O_2$, 297–300
$Ca_2La_8Si_6O_{26}$, 296
$Ca_4La_6(GeO_4)_4(PO_4)_2O_2$, 297–300
$Ca_{2+x}La_{8-x}(SiO_4)_{6-x}(PO_4)_xO_2$, 297–300
$Ca_4La_6(SiO_4)_4(PO_4)_2O_2$, 297–300
$Ca_4La_6(SiO_4)_4(VO_4)_2O_2$, 297–300
$CaMoO_4$, 210, 234, 236
$Ca_5Nb_2TiO_{12}$, 689–690
$Ca_2Nd_8(SiO_4)_6(PO_4)O_2$, 297–300
$Ca_{0.61}Nd_{0.26}TiO_3$(CNT), 540–541, 553
CaO-B_2O_3-SiO_2 (CBS), 375
$Ca_2Pr_8(SiO_4)_6(PO_4)O_2$, 297–300
$Ca_4Pr_6(SiO_4)_4(PO_4)_2O_2$, 297–300
carbon nanotube (CNT), 575–576, 582
$Ca_2RE_8Si_6O_{26}$, 295, 297
$CaSiO_3$, 210, 231, 233–235, 372
$Ca_2Sm_8(SiO_4)_6(PO_4)O_2$, 297–300
$Ca_{1-x}SrSiO_3$, 233
$Ca_2Tb_8Si_6O_{26}$, 295
$Ca_2Tb_8(SiO_4)_6(PO_4)O_2$, 297–300
$CaTe_2O_5$, 406
$CaTiO_3$, 75–76, 79, 81–82, 84–85, 87–89, 100–101, 133, 135, 137–138, 140–141, 147, 166, 284, 406
cation ordering, 89–90, 95, 101, 104–105, 107–108, 110–111, 113–114, 116, 118–120, 123–124, 128, 132–133, 138–139, 142, 144, 146–147, 168, 182
$Ca_2Tm_8Si_6O_{26}$, 295
cavity perturbation method, 20–21
CaV_2O_6, 410
$Ca_2Y_8Si_6O_{26}$, 295–296
$CaZnP_2O_7$, 387
CeO_2, 95–97, 128, 166
ceramic, 538–550, 551–570, 683–685, 689, 703, 711–713
Cheng–Vachon model, 515
circular polarization, 685, 712
circulators, 618, 620–621, 623–624, 627, 629, 632–635, 642–643
Clausius–Mossotti, 60, 78, 247
coaxial probe, 686–687

cobalt ferrite films, 615
coefficient of thermal expansion (CTE), 538, 540–541, 550, 553, 557, 566–567
coercivity, 607, 623, 630–631
columbite, 318
complex perovskites, 82, 85–86, 90, 93, 98, 103–105, 107, 111–112, 118, 123, 126, 128, 130–132, 136–139
composites, 53–57, 59–63, 65–71, 73–80, 189, 538–570
conducting polymers, 575, 581
conductor loss, 7, 10, 603, 607, 636, 651
conjugated polymers, 576, 588
connectivity, 54–55, 59, 66, 77, 79
constraint sintering, 392, 394
coordination number, 114, 230
coplanar line configuration, 441, 656
coplanar wave guide (CPW), 442, 655, 667, 686–687, 712
cordierite, 206–207, 210, 212, 226–230, 232–233, 238–239, 261–262, 374
corundum, 187, 210–212, 243, 245–246, 263
coupling, 556, 685–688, 699, 701, 704, 706, 712
Courtney method, 8
covalency, 207, 212, 227–228, 230–231, 236, 238–239, 247, 249–250, 253–255, 261
cross polarization, 685, 690–691
Cu-ferrite films, 615
$CuNb_2O_6$, 319–329
$CuO\text{-}Bi_2O_3\text{-}V_2O_5$, 288
$CuO\text{-}B_2O_3$, 383
CuV_2O_6, 380
cylindrical DRA, 685, 696–698

decoupling capacitors, 662
degenerate resonator mode, 685
delay lines, 629
depolarization, 56, 58, 65, 67
dicumyl peroxide (DCP), 540, 542
dielectric inks, 457–480
dielectric loss by spectroscopic methods, 35
dielectric resonator antenna (DRA), 684–685, 688, 696, 710–712
dielectric resonator filter, 135, 684, 704–710, 713–714
dielectric resonator oscillator (DRO), 135, 684, 698, 702–703, 712–713
differential equation, 60, 66
diode, 699–700, 709
diopside, 210, 212, 234–235, 238, 261
dispersant, 363–364, 390, 459, 461–463, 465–467, 475, 477
DuPont, 9K7, 667, 669
DuPont, 943, 665
DuPont, 951, 672–673
dynamic range, 683

eddy current, 596, 611
effect of bending, 548–549, 561–562
effective loss tangent, 68, 75
effective-medium theory (EMT), 63, 65, 68, 78–79, 547–548, 558
effective permittivity, 59, 62–67, 71, 78–79, 548, 655–656, 659
elastomer, 538–540, 554
electromagnetic interference, 1
electronic packaging, 538, 540, 552
EMI materials, 2, 581, 583
EMI shielding, 537, 575, 578, 584–585
EMI shielding effectiveness, 29, 578, 581
enstatite, 214, 216
epoxy ceramic composites, 511–513
epoxy/glass substrate, 511–513
epoxy/$SrTiO_3$, 513
excitation, 685–689

factors affecting dielectric loss, 651, 655
far infrared spectroscopy, 36–37
FDTD, 689–693, 710, 712
feedback type oscillator, 701
$\gamma\text{-}Fe_2O_3$, 576, 586
ferrite, 576, 581, 586, 593
ferroelectric materials, 89, 141, 173
ferrofluid, 577, 590, 593–594
ferromagnetic resonance (FMR), 618–630
ferromagnetic resonance linewidth, 607–617

ferroxplanar, 609
figure of merit, 188, 621
fish oil, 364, 390, 462–463, 465–467
flexible electronics, 537, 561–562
flexible microstrip antenna, 567–568
free space methods, 24–25
front-to-back ratio, 690–691
fused silica, 540–541, 544, 553

GaAs, 369, 620–622, 624–625, 629–630
gain, 685, 690–693
GaN, 620–628, 633, 642
garnets, 604, 607, 610–611, 617–618, 632
general mixing model, 67–68, 74–76
Ge–willemite, 210, 212, 239
GGG substrates, 614, 617–618, 623, 630, 642
glass-ceramic, 345–353, 370, 372, 374
glass transition temperature T_g, 540, 553–554
glassy phase, 350
goethite, 53, 55, 78, 612
graphene, 575–576, 584, 622
graphene oxide, 575, 581, 583–584
gravure offset printing, 653
green tape, 393, 407, 390–391, 408, 665, 672–673
gyromagnetic properties, 603–604, 607, 632
Gysel power divider, 665–666

Hakki and Coleman method, 8–10, 42, 44
H_3BO_3, 288, 383
HDPE-$Sm_2Si_2O_7$, 503
HDPE-$ZrSiO_4$, 503–506
hemispherical DRA, 685, 696, 698, 712
heterostructure, 625, 636–638, 642
hexaferrite, 604, 663
hexagallates ($SrGa_{12}O_{19}$), 618
high frequency structure simulator, HFSS, 540, 567
high-*k* materials, 651, 661, 669, 538
high-*k* pastes, 659
high temperature cofired ceramics (HTCC), 1, 357–368, 652
hydrophilic, 74

IMPATT diode, 699–700
incongruent melting, 226, 228
indialite, 206–207, 210–212, 226, 228–230, 232–233, 239, 254, 261–262
inductor cores, 604, 611, 629
inductors, 604, 658–660, 663
inkjet, 653
in-phase tilting, 86–87, 101
insertion loss, 607, 621, 630, 632, 634–630, 641–642, 652, 662–663, 667, 672
integrated antennas, 669, 674
interconnects, 79, 652
intermediate spinel, 252, 254
internal strain, 153
intrinsic loss factor, 73
inverse spinel, 252

Jayasundere–Smith, 69, 547–548, 558

Kent method, 26
Kerner equation, 69
$KGaGe_3O_8$, 369
K-K relationship, 35–37
$(K_{0.5}La_{0.5})MoO_4$, 406
$K_3Li_2Nb_5O_{15}$, 151–152
$K_2Mo_2O_7$, 406
$K_2Mo_3O_{10}$, 406
Ku-band, 471, 474, 579–580, 604, 606–607, 611, 628, 635–636

$LaAlO_3$, 82, 86–87, 89, 135, 137, 188
$La(Co_{1/2}Ti_{1/2})O_3$, 102, 141
$La(Mg_{0.5}Ti_{0.5})O_3$, 100, 140
Landau–Lifshitz–Looyenga, 65
La_2O-B_2O_3, 375
La_2O_3-B_2O_3-ZnO, 376, 384
$La_4Ti_9O_{24}$, 351
$La_2Ti_2SiO_9$, 351
$La(Zn_{1/2}Ti_{1/2})O_3$(LZT), 86, 101, 137, 141, 540, 553
LCP (liquid crystal polymer) substrates, 513–514
$LiAlSiO_4$, 352, 386
$LiCaBO_3$, 391
Li_2CaSiO_4, 384, 386
$LiCeO_3$, 394

Lichtenecker, 65–66, 68, 558
LiF, 394
$LiLa_9(SiO_4)_6O_2$, 302
$Li_2(Mg,Ca)Ti_3O_8$, 275
$LiMgPO_4$, 211, 257, 264
Li_2MgSiO_4, 384, 386
$Li_2MgTi_3O_8$, 275–276, 280–289, 383–386
$Li(Mg_{0.9},Zn_{0.1})PO_4$, 386–390, 394
$Li_2(MgZn)Ti_3O_8$, 275–276
Li_2MoO_4, 405, 409
Li_2O-Al_2O_3-SiO_2, 375, 394
Li_2O-B_2O_3-SiO_2 (LBS), 384
Li_2O-MgO-ZnO-B_2O_3-SiO_2 (LMZBS), 284–288, 383–387, 394
liquid phase epitaxy (LPE), 603, 617, 623, 631
Li_2TiO_3, 383
Li_2WO_4, 383
$Li_2ZnTi_3O_8$, 275–276, 280–289, 383–386
$Li_2Zn_3Ti_4O_{12}$, 276, 289–290, 383, 394
$LiZnVO_4$, 402–403
Loor formula, 63
Looyenga, 63, 65, 71, 74–76
loss tangent, 56, 68, 74–75, 188
low-k materials, 651, 662
low temperature cofired ceramics (LTCC), 1, 2, 77, 188, 206, 224–225, 239–240, 242, 256–258, 260, 263–264, 289–290, 359, 368–395, 652–674, 703, 713
LTCC module, 652, 672
LTCC stripline, 655–657
LTCC tapes, 652
lumped passive integrated components, 657

magnetic anisotropy energy, 607–608
magnetic anisotropy field, 596, 607, 609, 616, 631
magnetic fillers, 581, 583
magnetic losses, 577, 581, 588, 590, 604, 607, 616
magnetic measurements, 586, 593, 612
magnetic wall, 696
magnetocrystalline, 607, 609, 611, 631–632, 634
magnetoplumbite, 604, 611
magnetostrictive, 637
Maxwell–Garnett, 59–60, 62–63, 65–66, 546, 558
measurement of τ_f, 41–42
mechanical properties, 549–550, 564–565
$MgAl_2O_4$, 211, 255, 263, 273–280
$Mg_2Al_4Si_5O_{18}$, 206, 210, 226–228
$Mg_3B_2O_6$, 211, 256–257, 264
$MgGa_2O_4$, 280
$MgNb_2O_6$, 319–329
$Mg_4Nb_2O_9$, 210–211, 245, 251, 263, 271
$Mg_3(VO_4)_2$, 211, 257–259, 265
MgO, 159, 182, 211, 215–216, 221–222, 238, 256–257, 261, 264, 394
MgO-Al_2O_3-B_2O_3-SiO_2, 376
MgO-B_2O_3-SiO_2 (MBS), 288
$MgSiO_3$, 210, 214, 222, 224
Mg_2SiO_4, 206, 210, 214, 219, 222, 224
$MgTe_2O_5$, 407, 409–410
$MgTiO_3$, 75–76, 79–80, 86, 271, 382
$MgTi_2O_5$, 214, 224, 271, 382
Mg_2TiO_4, 271, 280, 382
micelle, 586, 593
microstrip line, 16, 225, 654–657, 686–689, 697–698, 701, 712
microstrip patch antenna, 567, 669–670
microstrip slot, 686–687
microwave absorption, 577, 587, 595
microwave ferrites, 603–604, 609
microwave filters, 623, 639, 642, 665
microwave modules, 672
microwave monolithic integrated circuits (MMICs), 620–621, 623–624, 629–630, 634–635, 642, 669, 672–674
microwave substrates, 537–538, 540, 552, 570, 624
millimeter-wave, 31, 204–265, 666, 669
mixing equation, 59–60, 63–65, 68, 71–74, 76–77
MMIC, 687, 703, 712–713
modes, 686, 688, 690, 693, 696, 704, 706, 711, 713
modified Lichtenecker, 66, 68, 547–548
moisture adsorption, 74, 539, 552–553, 557, 560, 565–566
molar ratio, 75–76

monazite, 211, 257
monolithic integrated circuits (MICs), 611, 629
Monte Carlo, 68
M-type ferrites, 605, 607, 628, 635, 664
mullite, 226, 228, 235
multilayer inductors, 663
multilayer stack, 658

$NaAgMoO_4$, 408, 410
$NaAlSi_3O_8$, 210, 239
Na_2MoO_4, 405, 410
$Na_2Mo_2O_7$, 405
nanocomposite, 560, 564–565, 567, 577, 586, 593
Nicholson–Ross–Weir method, 579, 588, 596
nickel zinc ferrite, 615
Nielson model, 516
normal spinel, 252, 254

octahedral tilting, 82–86, 94, 101, 124, 133, 137, 139, 147, 168, 170, 184
omnidirectional, 696
open resonator method, 27
ordering, 82, 84, 89–90, 94–96, 100–105, 107–133, 135, 138–139, 141–147, 153, 155, 168, 170, 172, 182, 186, 605
1:3 ordering, 130, 133, 147
1:2 ordering, 89, 103, 109, 118, 120, 123, 125, 127, 133
1:1 ordering, 90, 117, 120, 133
orthoclase, 239

$(Pb,Ca)HfO_3$, 185
$(Pb,Ca)ZrO_3$, 185
$Pb_2Nb_2O_7$, 176, 178–182, 184–185
$Pb_5Nb_4O_{15}$, 181
$Pb_nNb_2O_{5+n}$, 176–178, 182–183
$Pb_n(Nb_{1-x}Ta_x)O_{5+n}$, 174
Pb_2WO_5, 403
$PbWO_4$, 403
PEDOT nanocomposites, 59–60, 67, 72, 76, 576
periclase, 216
permeability, 10, 575, 579, 588, 596, 603–604, 607–608, 611, 628–629, 632, 634, 638, 661, 664
permittivity, 53–54, 56–60, 62–63, 64–74, 76–78, 150, 155–156, 159, 162, 164–166, 172–175, 183–189, 538–539, 541–542, 544–549, 554, 556–563, 566, 569–570, 575, 579, 588, 596, 604, 628, 638–639, 651, 655–664, 683–684, 686–688, 711–712
perovskites, 81–90, 107, 111–112, 116, 118, 123, 126, 128, 130–139, 141–142, 146–147, 151, 154, 166, 185
phase agile device, 432
phase lock, 702
phase shifters, 188, 603–604, 606, 618, 620, 629, 632, 635–636, 638, 642–643, 673
phase transition, 82, 90, 93, 104, 116, 118, 128, 133, 136–137, 139, 142, 154, 187–188, 207, 226, 228, 239
photon factory, 226
photosensitive crystallizing glasses, 352–353
plagioclase, 210, 240, 242, 263
plasmonic, 639
PMN, 182, 319
Polder–Van Santen formula, 63
polyaniline, 474–475, 479, 576, 582, 584
poly dimethyl siloxane (PDMS), 539
polymer-ceramic composites, 481–526
polymorph, 162, 226, 233, 262
polypyrrole, 576, 586, 593
polystyrene-ceramic composites, 507–508
poly(tetrafluoroethylene)(PTFE), 560
polyvinyl butyral, 462–463, 466–467, 477
powder samples dielectric measurements, 34, 63, 74–78, 80
power dividers, 664
power law, 63, 65
precessional motion, 632
printed circuit board, 672
printed electronics, 457–459, 474, 477–478
PS-Mg_2SiO_4, 507–510
PTFE, 65, 78, 490–502, 518–521, 560
PTFE-SiO_2, 490, 560

pulsed laser deposition (PLD), 612, 614–618, 623–625, 627, 631
push–push oscillator, 703, 713
pyrochlore, 174, 176, 178–182, 185

Q-factor, 269, 684–685, 698, 702, 710, 712
Q meter, 20
quartz, 181, 216, 235, 257

radar, 203, 205–206, 208, 224, 604, 606, 611, 621, 629, 632, 634–635, 643, 673
radiation efficiency, 685–686
radiation pattern, 684–685, 690–691, 696–697, 711
rare earth, 86, 98, 137, 139, 150, 154–155, 158, 165, 207, 209, 247
rectangular dielectric resonator antenna (DRA), 88, 711–712
reduced graphene oxide (RGO), 575, 583
reflection type oscillator, 700–701
relative permittivity, 56, 60, 62, 70, 73, 155–156, 159, 164, 173–174, 183–186, 188–189, 459–461, 470–473, 475, 477
rheology, 465–467, 474–475
Rietveld method, 94, 119, 124, 140, 226, 230, 242
rubber–ceramic composites, 537, 540, 544, 553–554, 556–557, 559–560, 562–563, 566, 570
rutile, 158, 164, 166, 209, 213–215, 223–224, 232–233, 244, 260, 263, 683

sapphire, 166, 615, 618, 620
scattering, 56–57, 59, 63, 77–78, 229–230
scattering parameters, 579, 667–668
screen printing, 462–463, 465–467, 474–475, 478, 603, 619, 624, 627, 631, 653–654, 661, 666–667
semiadditive processes, 653
semiconductor, 81, 611, 615–616, 620–623, 625, 627, 629–630, 634–636, 642–643
Sen Scala–Cohen, 64–65
sheet resonator, 26
shielding effectiveness, 577, 587, 596
shielding efficiency, 576, 583
short range order, 172
shrinkage, 392
SiC, 615, 620–622, 625, 627–628
silica, 70, 162, 206–207, 209, 216–219, 221, 225–226, 230, 232, 261–262, 540, 554, 556, 559
silica glass, 162
silicate, 206–207, 209, 212, 216, 226, 230, 232–233, 257, 261–262
silicone rubber, 538–546, 550–553, 567, 570
SiO_2, 54, 162
SiO_4 tetrahedron, 209, 218, 234, 236, 257
skin depth, 578–580
slot line, 688, 712
$(Sm_{1/2}Na_{1/2})TiO_3$, 190
$Sm_4Ti_9O_{24}$, 153
solid solutions, 149, 151–152, 155–156, 166, 174, 186
S parameters, 578–579, 585, 637, 667
spinel, 207, 211–212, 249, 251–255, 264, 267–279, 604–605, 607, 610–611, 614–616, 618, 624, 627–629, 632, 636
spin spray plating (SSP), 616–617
split post dielectric resonator method (SPDR), 18–20, 543, 548, 556, 562, 653
sputter deposition, 617, 631
$SrCe_2Ti_5O_{16}$, 554–555, 557, 560
$Sr_{1-3x/2}Ce_xTiO_3$, 166–167, 170–174, 190
$SrCuP_2O_7$, 211, 257, 267–279
$SrCuSi_4O_{10}$, 392–393
$Sr_2Dy_8Si_6O_{26}$, 293–294
$Sr(Er_{1/2}Nb_{1/2})O_3$, 95
$Sr(In_{1/2}Nb_{1/2})O_3$, 95, 97
$Sr_2KNb_5O_{15}$, 151
$Sr_2La_8Si_6O_{26}$, 294–295
$Sr(Li_{1/4}Ta_{3/4})O_3$, 131
Sr_2LnTaO_6, 95, 139
$SrNb_2O_6$, 319
$(Sr_{0.75-x}Pb_xCe_{0.167})TiO_3$, 173–174
$(Sr_2RE_2)RE_6Si_6O_{26}$, 292–294
$SrSiO_3$, 210, 233–235, 239, 262
$SrTiO_3$, 166–168, 173–174, 540–542, 545–546, 552–554, 557, 559–560, 569–570
$SrZnP_2O_7$, 257, 387, 394

$Sr_2ZnSi_2O_7$, 387, 393
stress–strain curves, 549, 564–565
stripline BPF, 667–668
stripline excited cavity method, 14
striplines, 656, 658, 665, 668, 673
substrate, 53, 78, 81, 87, 100, 137, 140, 360, 362, 367, 537–538, 540, 549, 552–553, 567, 570, 651, 674
subtractive processes, 654
superlattices, 614
surface roughness, 364–365, 467, 469–470, 651
surface wave, 686

tantalite, 86, 91, 93, 95, 108, 113, 133, 138, 143–145
tape casting, 362–363, 367, 631
TE mode, 9, 704
$TE_{01\delta}$ mode dielectric resonator, 9, 13
temperature variation of relative permittivity, 471–472, 549, 554
tenability, 446, 638–639, 641
TeO_2, 406
terahertz measurements, 31–32, 36, 39
terahertz time domain spectroscopy, 32–33
thermal conductivity, 361–363, 368, 464, 514, 518, 538, 540, 542, 550, 552, 563–564, 570, 651
thermal expansion, 155, 181, 464, 538, 540, 550, 566–567, 570, 617–618, 627, 658, 661–662, 672
thick films, 617–618, 620, 624, 627, 631, 636, 654
THz spectroscopy, 32–33
TiO_2 (ilmenite), 66, 77–79, 149, 151, 155–156, 158, 160, 162, 166, 181, 205, 210, 214–215, 223–224, 232–233, 244–245, 257, 260–261, 263–264, 363, 378, 390, 541, 554, 557, 683
$TiTe_3O_8$, 407
TM mode, 9, 688
TM_{0n0} mode method, 21
tolerance factor, 82, 84–88, 91–92, 94–95, 97–98, 100–101, 117, 128, 132, 136, 154–155, 169
topochemical ordering, 603
transmission coefficient, 579
transmission lines, 445, 652, 654, 657, 661, 666, 669, 674
tuning resonant frequency, 42–43

ultralow temperature cofired ceramics (ULTCC), 397–413

varactors, 188
vectorial steering module, 673
Vegard's rule, 247
volume fraction, 58–60, 62–68, 70, 71, 73, 76, 257, 538, 540, 542–549, 551–552, 555–562, 564, 566–567, 570
Vo–Shi equation, 70
VSWR, 689, 703
vulcanization, 540, 553–555

wave guide method, 29–30
whispering gallery mode (WGM) mehod, 166
Wilkinson power divider, 665
willemite, 205–207, 210, 212, 222–225, 234, 239, 260–262
wollastonite, 210, 212, 232–233, 239, 254, 262
W-type ferrites, 609

X-band, 471, 474, 606–608, 624, 630, 636, 638
xenotime, 257, 211
xylene, 364, 390, 462–463, 465–466, 477

YIG/BIG, 614
YIG/EBIG, 614
Yu–Cullen method, 24, 27

zinc borosilicate (ZBS), 66, 78, 108–109, 293, 382–383, 379, 401
$ZnAl_2O_4$, 211, 255, 261, 264, 267–279
$ZnCu_2Nb_2O_8$, 381–382
$ZnGa_2O_4$, 280
(Zn, Mg)TiO_3, 210, 239, 262, 383
$ZnNb_2O_6$, 319–329, 381–382
ZnO-B_2O_3, 288, 382, 398
ZnO-B_2O_3-SiO_2 (ZBS), 376, 395

$ZnSiO_4$, 379, 382
Zn_2SiO_4, 206, 210, 222, 225, 239, 261–262
$ZnTa_2O_6$, 319–329
$ZnTe_3O_8$, 407, 410
$ZnTiO_3$, 382
Zn_2TiO_4, 382
$ZrSiO_4$, 363–368, 460–479
$(Zr_{0.8}Sn_{0.2})TiO_4$, 283, 307–313
$(Zr,Sn)TiO_4$, 683
$ZrTiO_4$, 306–307
Zr_2TiO_6, 65
Z shrinkage, 662

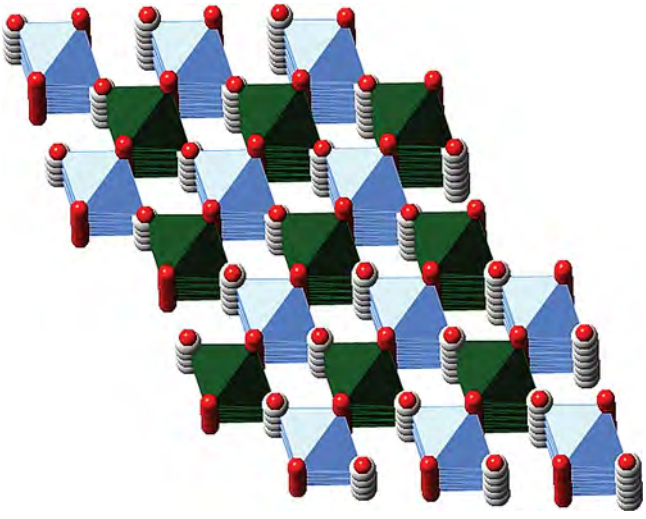

Figure 3.4 *1:1-Ordered double-perovskite $A(B'_{1/2}B''_{1/2})O_3$ structure viewed along $\langle 110 \rangle_c$ to highlight the doubled $\langle 111 \rangle$ repeat of the B′ and B″ cation sites.*

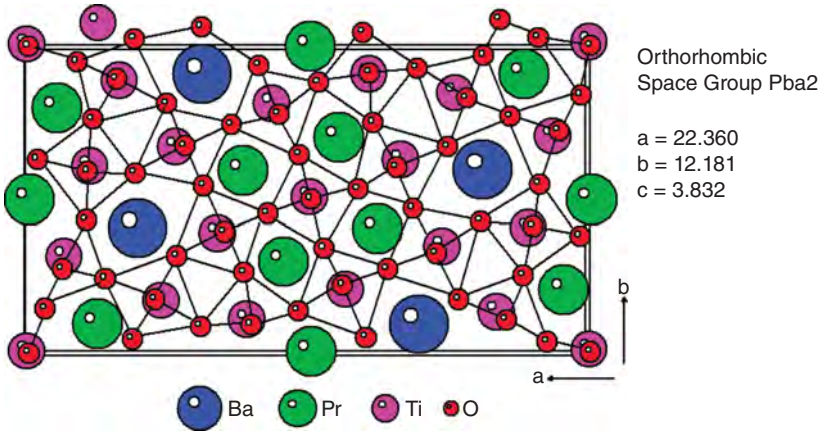

Figure 4.2 *Proposed crystal structure of $Ba_{3.75}Pr_{9.5}Ti_{18}O_{54}$. Source: Adapted from Matveeva* et al. *1984 [14].*

Microwave Materials and Applications, First Edition.
Edited by Mailadil T. Sebastian, Rick Ubic and Heli Jantunen.
© 2017 John Wiley & Sons, Ltd. Published 2017 by John Wiley & Sons, Ltd.

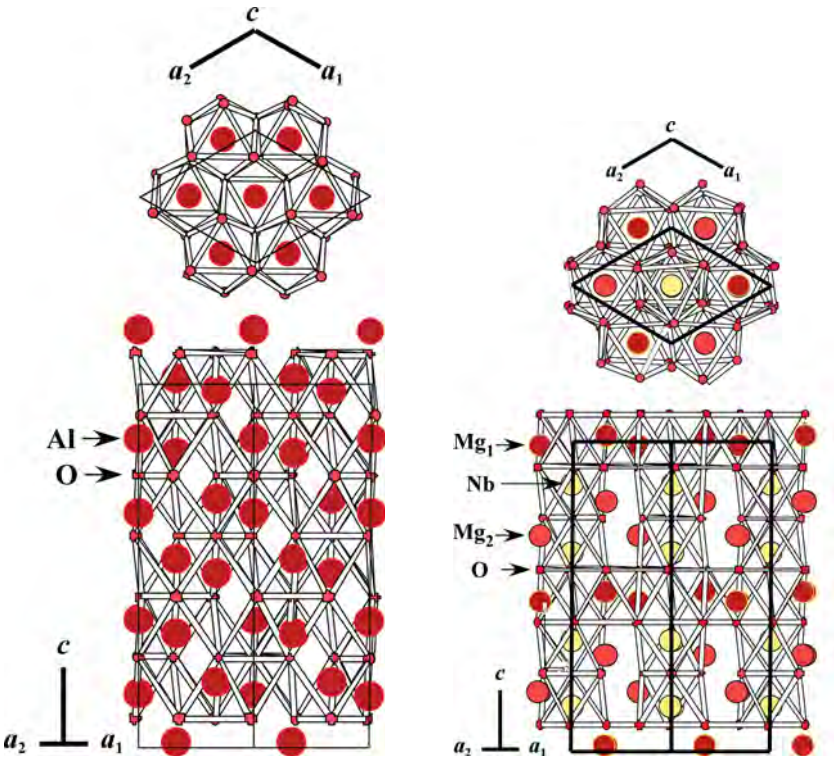

Figure 5.46 *Crystal structure of (a) alumina and (b) new-type corundum.*

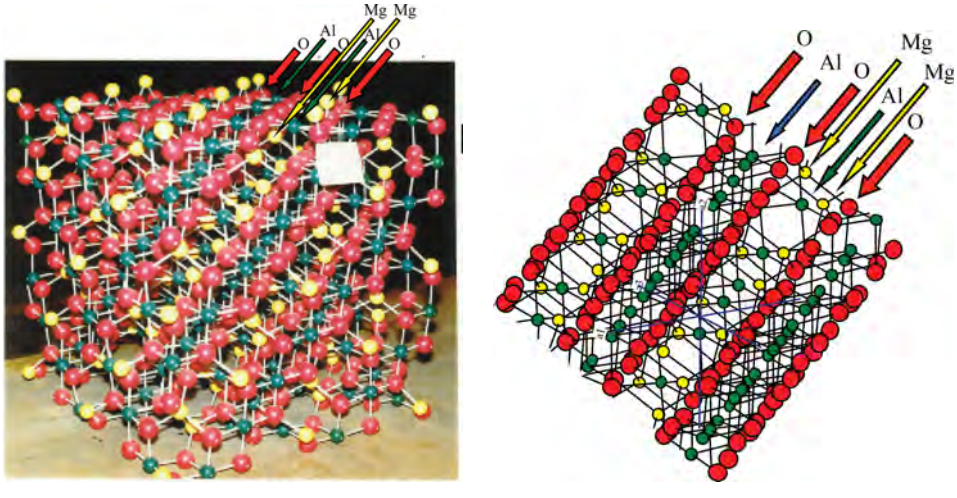

Figure 5.53 *(a) Model of crystal structure of spinel, which is exhibited in KEK Tsukuba, made by Dr Y. Kudoh and students of Professor Y. Takeuchi's group at the University of Tokyo. (b) Illustrated spinel structure from perpendicular to [111] direction with the same angle as (a).*

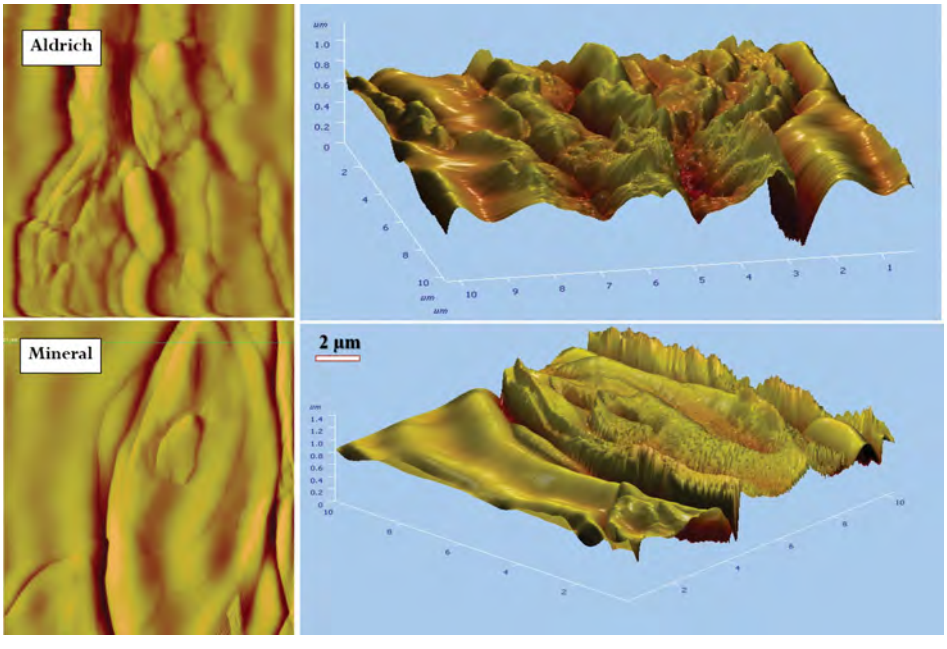

Figure 8.5 *Surface roughness of Aldrich and mineral $ZrSiO_4$ cast green tape. Source: Adapted from Varghese* et al. *2015 [17].*

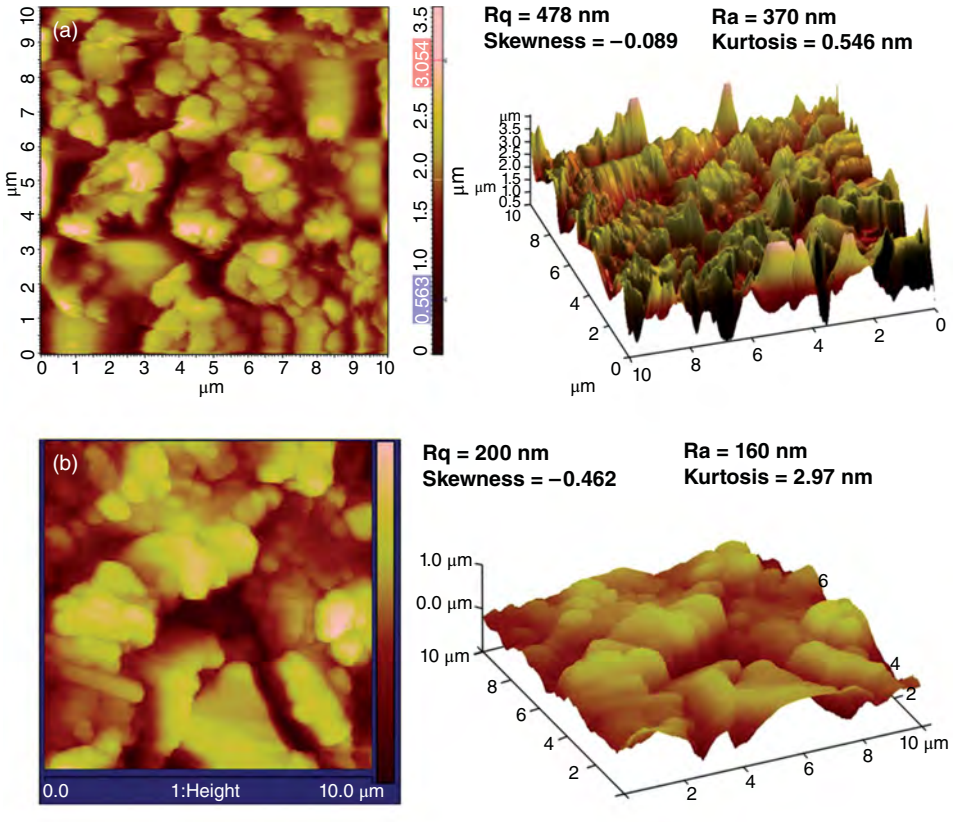

Figure 10.11 *AFM surface roughness of printed layers. Source: Adapted from Varghese* et al. *[32, 33].*

Microwave Materials and Applications, First Edition.
Edited by Mailadil T. Sebastian, Rick Ubic and Heli Jantunen.
© 2017 John Wiley & Sons, Ltd. Published 2017 by John Wiley & Sons, Ltd.

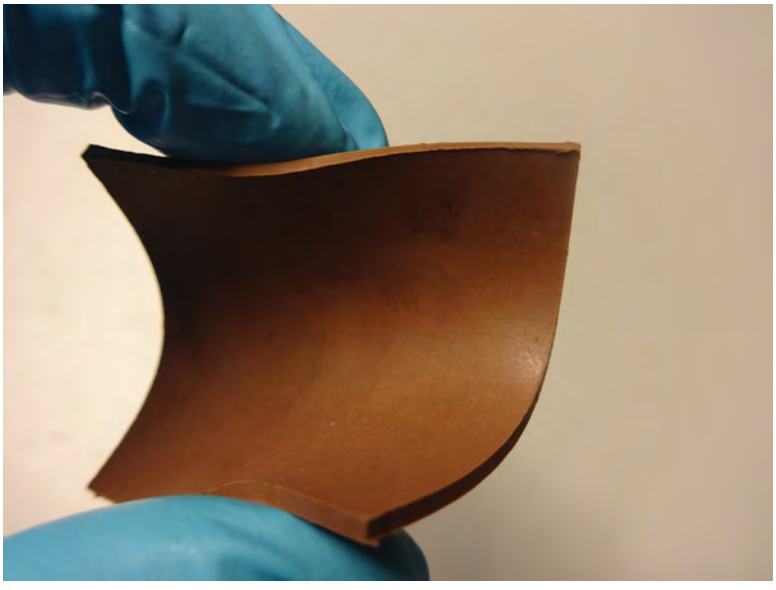

Figure 12.14 *Photograph of butyl rubber–$Sr_2Ce_2Ti_5O_{16}$ flexible ceramic composites.*

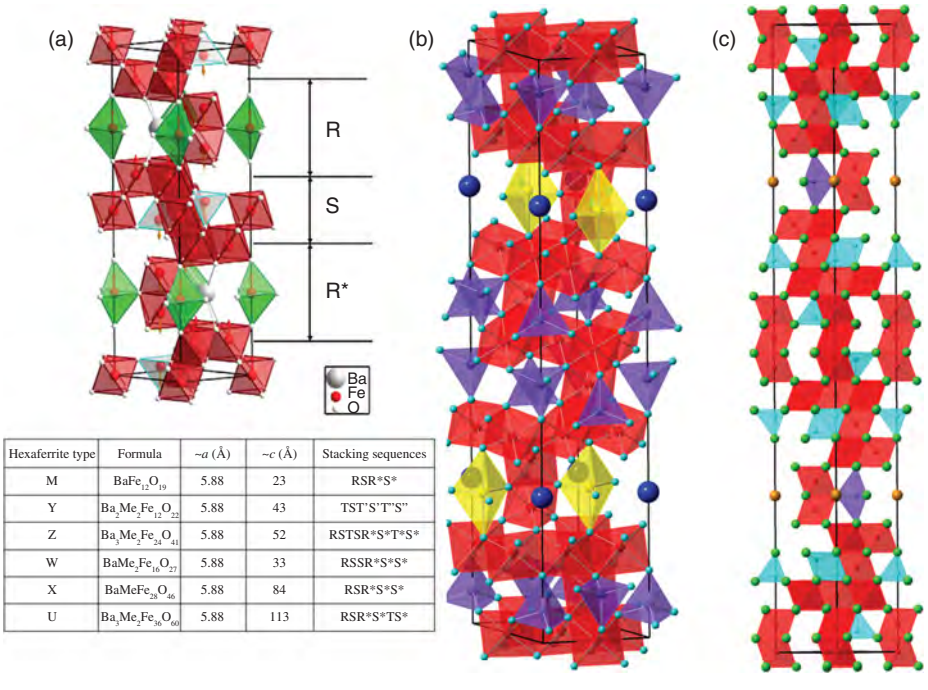

Hexaferrite type	Formula	~*a* (Å)	~*c* (Å)	Stacking sequences
M	$BaFe_{12}O_{19}$	5.88	23	RSR*S*
Y	$Ba_2Me_2Fe_{12}O_{22}$	5.88	43	TST'S'T"S"
Z	$Ba_3Me_2Fe_{24}O_{41}$	5.88	52	RSTSR*S*T*S*
W	$BaMe_2Fe_{16}O_{27}$	5.88	33	RSSR*S*S*
X	$BaMeFe_{28}O_{46}$	5.88	84	RSR*S*S*
U	$Ba_3Me_2Fe_{36}O_{60}$	5.88	113	RSR*S*TS*

Figure 14.2 *Schematic representation of hexaferrite structures of (a) M-type, (b) Y-type, and (c) Z-type variants. Table 1 presents structures and lattice constants for the hexaferrite structures including M, Y, Z, W, X, and U-type ferrites as the inset to this figure.*

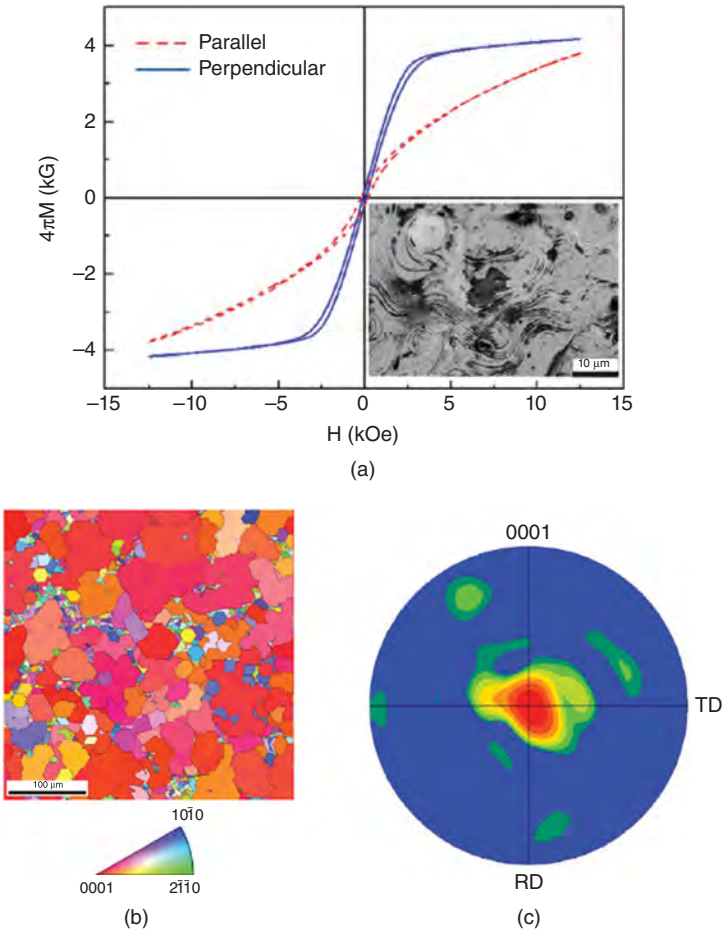

Figure 14.6 *(a) Magnetic hysteresis loops and SEM image of the surface morphology for the BaM compact sintered at 1350 °C for 10 hours by the topochemical growth process. Perpendicular and parallel refer to the orientation of the applied magnetic field with respect to the sample surface. (b) Orientation map along the [0001] direction measured by EBSD for the BaM ferrite sintered by the topochemical growth process. The color code for the crystallographic orientations is given in the stereographic triangle below the map. (c) Pole figure along the [0001] direction for the BaM ferrite sintered by the topochemical growth process. Source: Adapted from Y. Chen* et al. *2007 [24].*

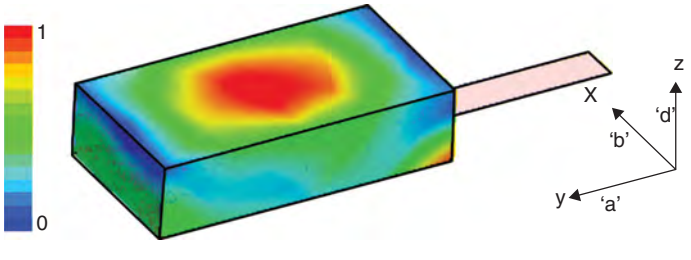

Figure 16.9 *Simulated H field distribution within the DR at f = 3.202 GHz. Source: Adapted from Mridula 2005 [51].*

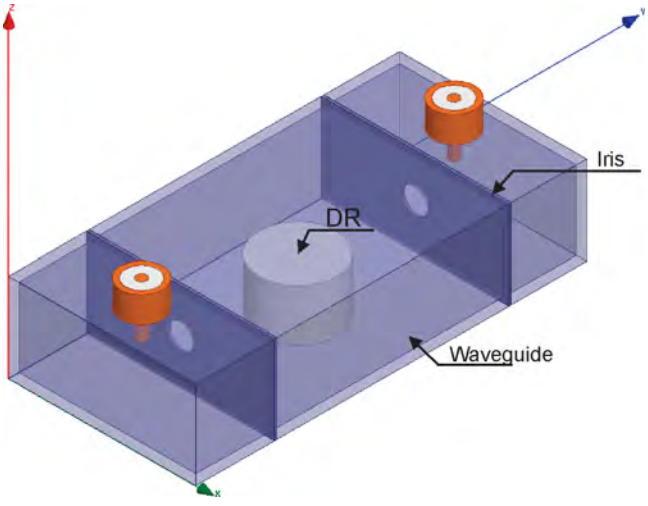

Figure 16.19 *Configuration of a typical dielectric resonator filter.*

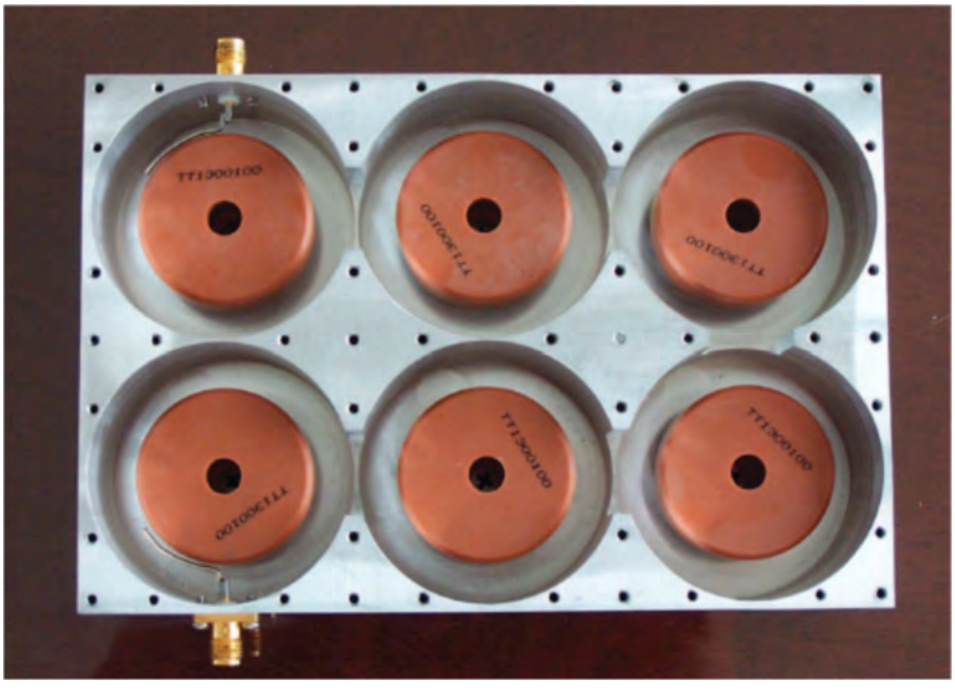

Figure 16.20 *A filter configuration realized using dielectric resonators. Source: Mansour 2009 [76]. Reproduced with permission of IEEE.*

WILEY END USER LICENSE AGREEMENT

Go to www.wiley.com/go/eula to access Wiley’s ebook EULA.